ECSSMET
Braunschweig Germany 2026



Book of Paper

DLR at a glance

DLR is the Federal Republic of Germany's research centre for aeronautics and space. We conduct research and development activities in the fields of aeronautics, space, energy, transport, security and digitalisation. The German Space Agency at DLR plans and imple-ments the national space programme on behalf of the federal government. Two DLR project management agencies oversee funding programmes and support knowledge transfer.

Climate, mobility and technology are changing globally. DLR uses the expertise of its 55 re-search institutes and facilities to develop solutions to these challenges. Our 10,000 emplo-yees share a mission – to explore Earth and space and develop technologies for a sustainable future. In doing so, DLR contributes to strengthening Germany's position as a prime location for research and industry.

Imprint

ECSSMET 2026 – Book of Papers
European Conference on Spacecraft Structures, Materials and Environmental Testing
21–25 September 2026 · Braunschweig, Germany

Publisher:
Deutsches Zentrum für Luft- und Raumfahrt e. V. (DLR) | German Aerospace Center (DLR)
Institute of Lightweight Systems

Published: 2026

DOI: 10.57965/y8xk-fy02

Organised by ESA, DLR and CNES

© 2026 DLR

Address:
Lilienthalplatz 7, 38118 Braunschweig
Phone + 49 531 2952301
E-Mail ECSSMET@dlr.de

DLR.de

Images DLR (CC BY-NC-ND 3.0),
unless otherwise stated.

Supported by:

Federal Ministry
for Economic Affairs
and Climate Action

on the basis of a decision
by the German Bundestag

DLR **Deutsches Zentrum für Luft- und Raumfahrt**
German Aerospace Center

Topics at a Glance

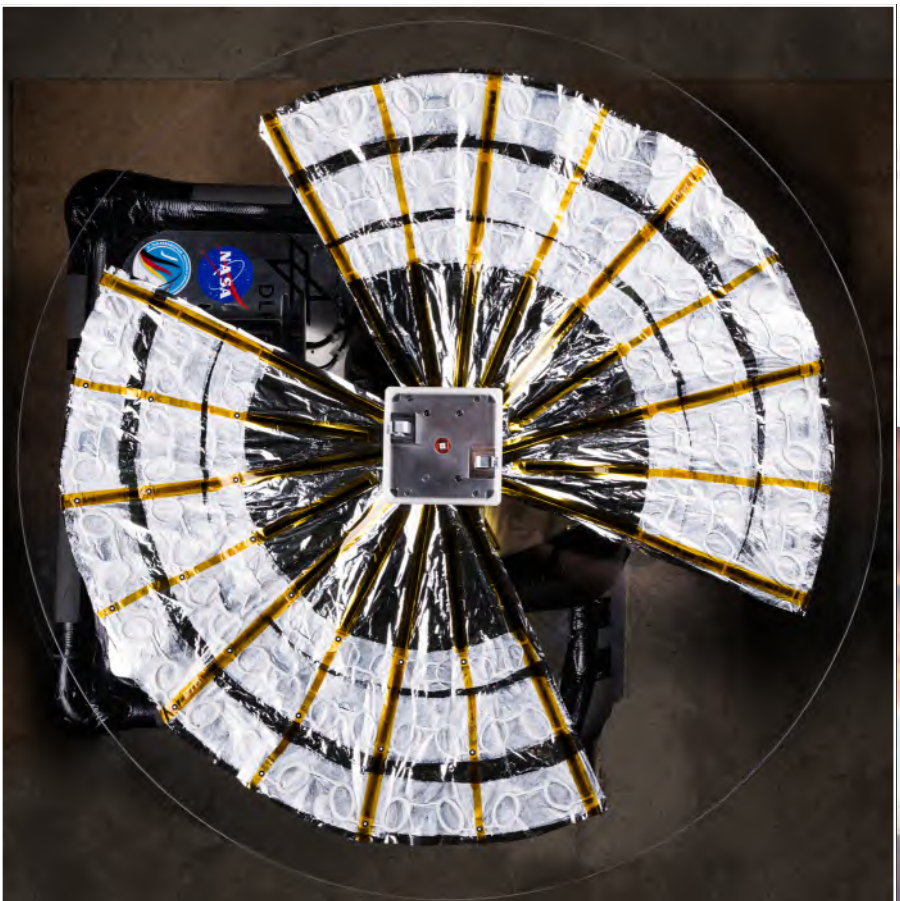
The ECSSMET 2026 programme reflects the broad range of challenges involved in designing, manufacturing and verifying spacecraft structures. From mechanical architecture and structural design to materials, manufacturing and environmental testing, the sessions bring together established engineering approaches with emerging technologies and new application fields.

A particular focus is placed on the development and qualification of lightweight and composite structures, advanced materials and additive manufacturing. Contributions explore topics ranging from CFRP and thermoplastic structures to high-entropy alloys, ceramic components and novel manufacturing processes. Digital engineering is also gaining importance, with approaches such as digital twins, data-based modelling and machine learning opening up new possibilities for design and analysis.

The programme further covers the dynamic behaviour of spacecraft and launch vehicles, including vibration, shock, acoustic and coupled-load analysis, as well as the correlation of simulations with experimental results. Environmental testing and innovative measurement and instrumentation methods provide the link between numerical prediction and real-world performance.

Another important strand is the development of deployable and multifunctional structures, thermal-mechanical design and verification, and structural concepts for reusable and future missions. Sustainability is increasingly becoming part of structural engineering, with contributions addressing demisability, atmospheric impact, eco-design and the use of sustainable materials.

Together, these topics provide a view of a field that is evolving rapidly – from established spacecraft engineering practices to technologies and methodologies shaping the next generation of space structures.



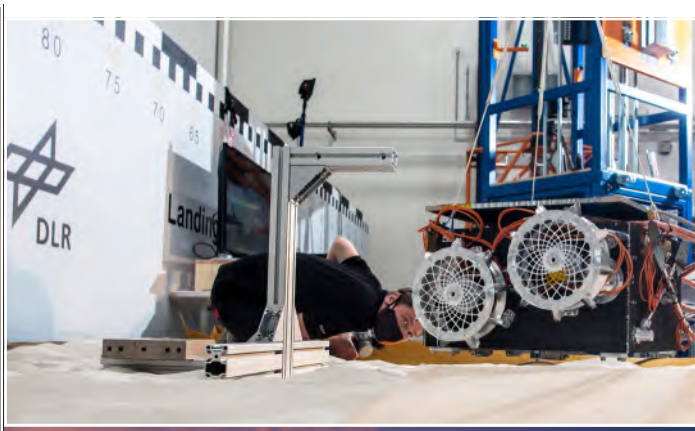




Table of Contents

Acoustic testing 4
Additive manufacturing 37
Buckling 106
Composite Design 135
Cryogenic 217
Demise 231
Deployable structures 260
Design and verification 342
DFAT 421
Dynamic 499
In-flight experiments 511
Material 549
Material imperfections 564
Material properties 595
Mechanism Testing 645

Micro vibration 713
Production 755
Shaker Test Prediction & Testing 777
Shock testing 813
Static load test & Test data evaluation 863
Structural analysis & simulation 881
Structural dynamics 922
Structure design 980
Structure engineering 1058
Structure optimization 1096
Sustainable Spacecraft Structures 1115
Test Prediction & Testing 1147
Thermal testing 1160
Thermoelastic 1200
Vibration testing 1238

ECSSMET
Braunschweig Germany 2026

Acoustic testing

TOWARDS A TRUE DIGITAL TWIN: VALIDATION OF A HIGH-FIDELITY NUMERICAL MODEL OF A DIRECT FIELD ACOUSTIC TEST

D. von Werne [(1)], A. Garcia de Miguel [(2)], A. Carella [(3)], A. Omalley[(3)]

[(1)] Siemens Industry Software NV, Interleuvenlaan 68, 3001 Leuven, Belgium, Email: dirk.vonwerne@siemens.com

[(2)] Siemens Industry Software SL, Av. Ronda Europa 5, 28760 Tres Cantos, Spain, Email: alberto.garcia_de_miguel@siemens.com

[(3)] MSI DFAT Services, , 4900 Wetheredsville Rd, Baltimore, 21207, USA Email: a.carrella@msidfat.com

KEYWORDS

Direct Field Acoustic Testing, Digital Twin, Pretest, Acoustic Simulation, Finite Element Method

ABSTRACT

This work presents use cases of pretest analysis of Direct Field Acoustic Testing/Noise (DFAT/DFAN). A Finite Element (FE) solver is used to simulate the acoustic field generated by a system of loudspeakers set up in a 6x6 configuration. To validate the proposed simulation framework, a dedicated experimental test campaign was conducted using a representative DFAN facility. Measured transfer functions, were systematically compared against model predictions. Good agreement between simulated and measured data confirmed the predictive capability of the model. The validated tool provides test engineers with a practical means to optimise DFAN system design parameters prior to test execution, ultimately improving acoustic field uniformity and control robustness for future spacecraft qualification campaigns.

1. INTRODUCTION

Direct Field Acoustic Testing/Noise (DFAT/DFAN) has emerged as a widely adopted method for performing environmental acoustic qualification of space hardware, offering significant advantages in cost, schedule, and risk management over traditional reverberant chamber testing [1]. In this approach, an electro-acoustic system comprising arrays of amplifiers and loudspeakers surrounds the test article, generating the required acoustic environments through direct sound radiation. Advanced Multiple-Input Multiple-Output (MIMO) control strategies are employed to achieve the spatially diffuse sound fields mandated by launcher authorities [2],[3].

There are two use-cases for creating a Digital Twin of a DFAN facility: First, predicting the performance of the electro-acoustic system – or else said, can we meet the reference profile with a given setup? Second, to look at a full pressure field – in addition to the 20-30 microphones we use in the test.

An add-on tool to the Simcenter 3D acoustics software was developed to facilitate the DFAN pretest simulation in acoustic Finite Element (FE) environment [4]. It automatically guides less experienced users through the various steps of most use cases, while allowing expert users to alter modelling and simulation steps as needed.

The workflow includes modelling of the speaker geometry, automatic placement of the speakers in stacks, import of the test structure geometric and/or structural FE representation, assigning speaker transfer functions of velocity over input voltage, assigning drives and solving the acoustic transfer functions to target microphones. Then, these transfer functions are coupled to a virtual MIMO controller working the same way as in test. The virtual pretest levels the responses to the targeted level and allows to select the most suitable control microphones. Moreover, the sound field can be visualised using microphone meshes.

2. SPEAKER CHARACTERISATION

The original development of the Pretest simulation tool [4] focused on representing the speaker diaphragm by a spring-mass damper system based on Thiele-Small Parameters [5]. High-performance Speaker systems frequently used in DFAN setups do not have their diaphragms exposed to the exterior but include a complex interior geometry to maximize the output of sound power evenly distributed over the frequency range. Therefore, the radiation of the speaker in the presented use cases was modelled based on scans of pressure and velocity using a PU probe. measurements. In a semi-anechoic environment, the front surface of the speaker is divided into small patches and each of these is scanned with a PU probe.

The velocity is processed as transfer function over input voltage. These are visualised by third octave band. Transfer functions are averaged over larger patches which in turn are used to define velocity and impedance boundary conditions in the FE model.

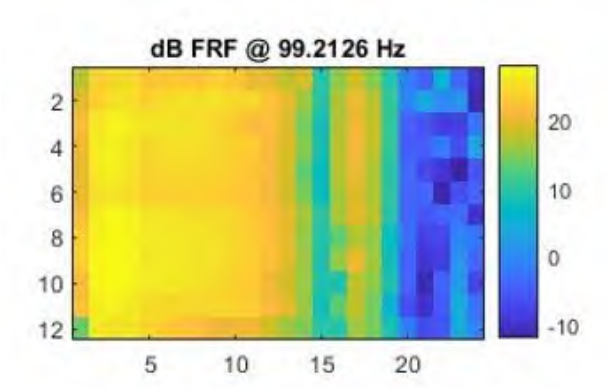


Figure 1: Post-processed velocity scan of MP-21 speaker

Within the same test campaign, also the response on a microphone array is measured on the reflecting ground. It has been demonstrated that the simulation replicates the directivity of the speaker with good accuracy.

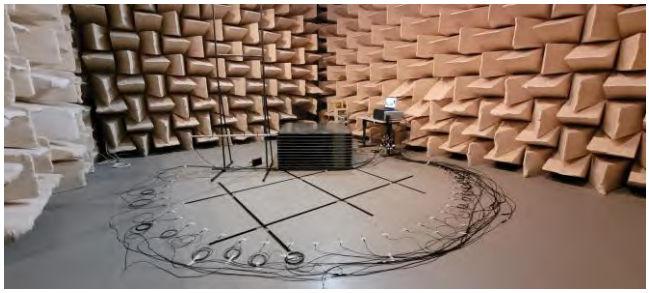


Figure 2: Validation measurement of MP-21 speaker: Sound field directivity

Pressure and velocity data from the probe is further process to generate the surface impedance to be used as a boundary condition in acoustic simulation.

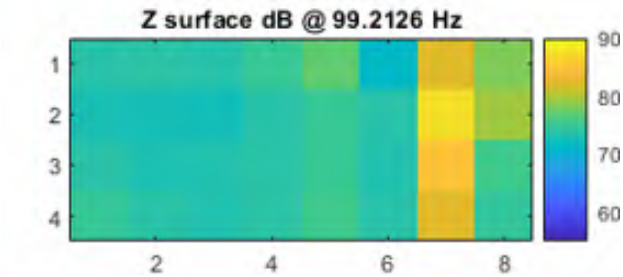


Figure 3: Processed surface impedance on MP-21 speaker

Replicating the test setup in acoustic FE environment, the directivity of the speaker could be predicted with good accuracy, see *Figure 4*.

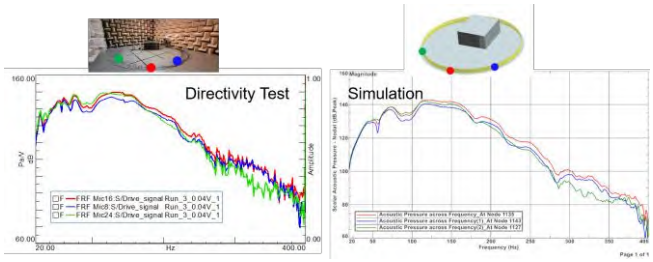


Figure 4: MP-21 speaker directivity from Test (left) and simulation (right)

The verified speaker models are available for future pretest activities of the same speaker type.

3. EMPTY TEST SETUP

As most applications of the pretest process concern confidential test objects, validation testing of a full speaker array has been performed on an empty setup.

Six MP21 woofers in double stacks and six single stacks of MP-150 mid/high frequency speakers are arranged at a radius of 10 ft. There are six drives with their own input voltage, controlled by a MIMO algorithm. Each drive is connected to one stack of each speaker type.

In the present work, the acoustic domain is modelled via an adaptive high-order finite element method (FEMAO) [6]. This solver, available in Simcenter 3D, reduces drastically the computational cost of the acoustic problem by automatically adjusting the polynomial order of the finite elements to the frequency requirements: The electro-dynamic actuators are modelled as rigid radiating surfaces with a prescribed acoustic normal velocity. Another important feature of the modelling approach is the application of free-field boundary conditions, which are imposed using the Automatically Matched Layer (AML) technology [7]. This simulation object, which may be defined on any convex shaped surface, efficiently absorbs outgoing acoustic waves regardless of their frequency and angle of incidence.

Using the validated speaker models from the previous step, the setup is modelled using the automatic DFAN tool.

It contains test microphone positions as well as a cylindrical and plane microphone mesh for visualisation of sound pressure distribution.

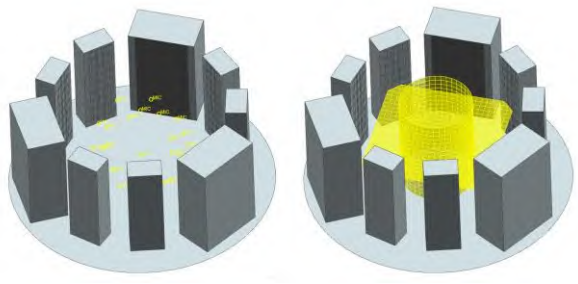


Figure 5: Model of empty test setup with test microphone positions (left) and microphone mesh for visualisation (right)

The transfer function from input voltage to microphone pressure has been validated against test data, as shown in *Figure 7*. In most frequency bands, good accuracy is obtained. In some lower frequency bands below 200 Hz, the difference between the two spectra is greater. Partly, this can be explained by the influence of the testing hall and its resonances, which are not included in the generated DFAN model.
Moreover, it was noted that different test runs yielded more variation in the results in this range than in others.

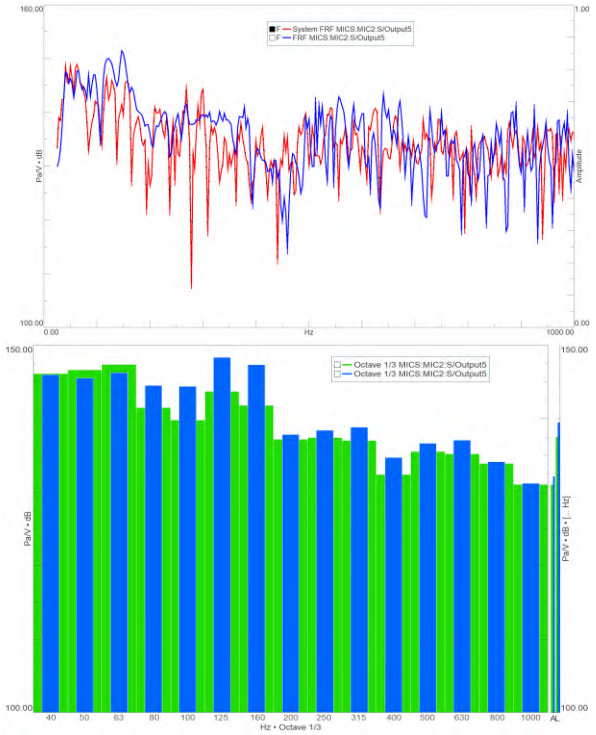


Figure 6: Example of pressure over voltage transfer function correlation, drive 5 to microphone 2. Top: Narrowband function, test: red, simulation: blue. Bottom: 3rd octave spectra test: green, simulation blue.

In the pretest analysis, the optimum set of control microphones is identified using predictions of the system responses achieved by the MIMO controller. The individual sound pressure levels by octave band are close to the target and to each other.

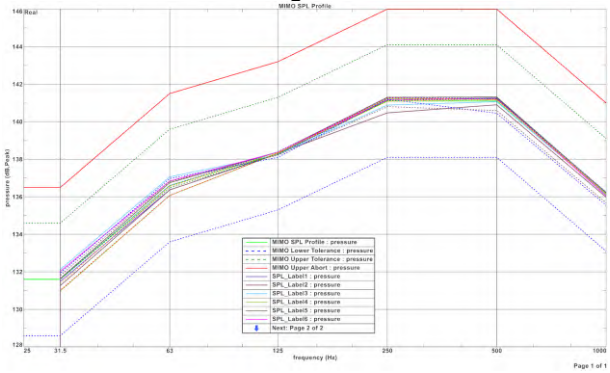


Figure 7: Predicted sound pressure levels in control microphones together with upper and lower tolerance bounds. Solid red line is abort pressure

The spatial distribution of sound pressures is relatively uniform in the central area of the setup. The test microphones – cubic blocks in *Figure 8* – have very similar pressure.

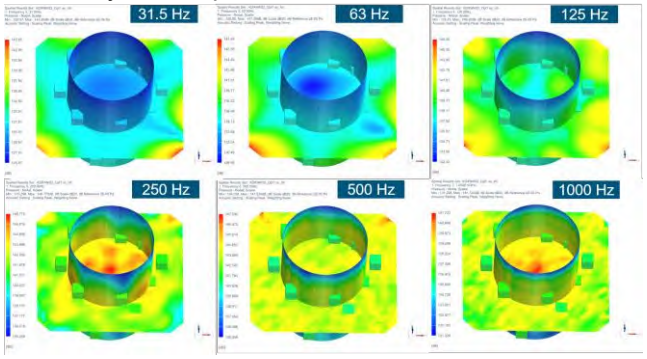


Figure 8: Predicted sound pressure levels in testing space and test microphones by octave band

4. SETUP WITH TEST OBJECT

A similar speaker setup of MP-21 and MS-25 speakers has been modelled to demonstrate the use of the tool in a typical pretest situation. Like in the empty case, velocity transfer functions from test have been assigned to patches of the speaker front faces and the speaker stacks connected virtually to drives.

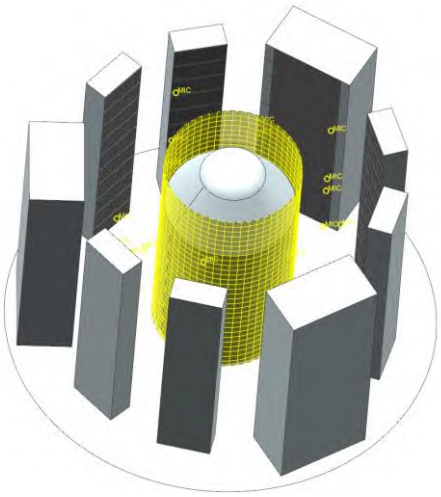


Figure 9: Model of test setup with spacecraft structure in the centre, candidate microphone points and a cylindrical visualisation mesh around the test object

For each patch on the faces, an individual transfer function is calculated using the acoustic FEM solver. As can be seen in *Figure 10*, the sound field from one single patch at a specific frequency shows a wave pattern similar to what typically results from a single point source.

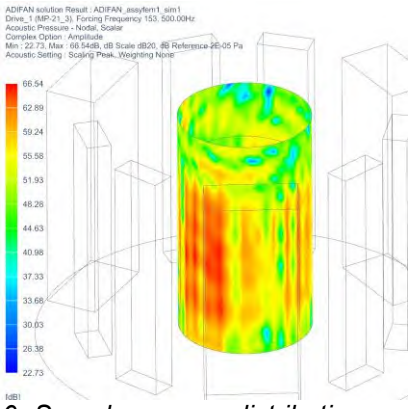


Figure 10: Sound pressure distribution around test object for discrete frequency 500 Hz and excitation from single patch on MS-21 woofer.

In a second step, the individual transfer functions are driven by the MIMO controller to generate the acoustic response in test condition. A randomly chosen combination of 12 control microphones results in most sound pressures being close to the target, whereas two of the microphone spectra fall out of the tolerance envelope.

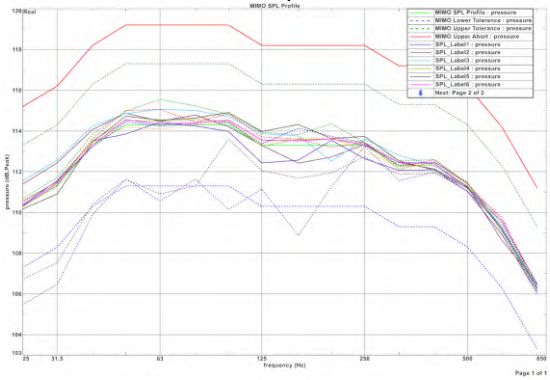


Figure 11: Control microphone response by 3rd octave band for randomly chosen set of 12 microphones.

Running the optimisation algorithm results in a better choice of control microphones, where all 3rd octave sound pressures are well within the tolerance band that was defined at the start of the simulation.

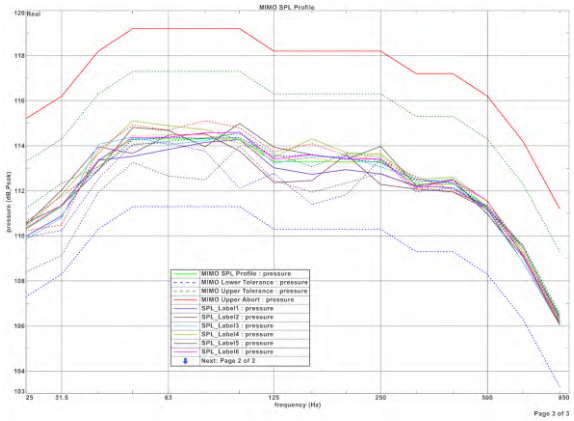


Figure 12: Control microphone response by 3rd octave band for optimised set of 12 microphones.

The pressure distribution around the test object is rather uniform with some interference in vertical direction at higher frequencies. The sound pressure in the top region of the microphone mesh is much lower for two reasons:
First, this region is at similar height as the top of the speaker arrays, so that a boundary effect occurs. Second, these microphones are farther away from the test structure that has a conical shape here. Therefore, the field pressure is not as much amplified by the reflection on the surface of the test object.

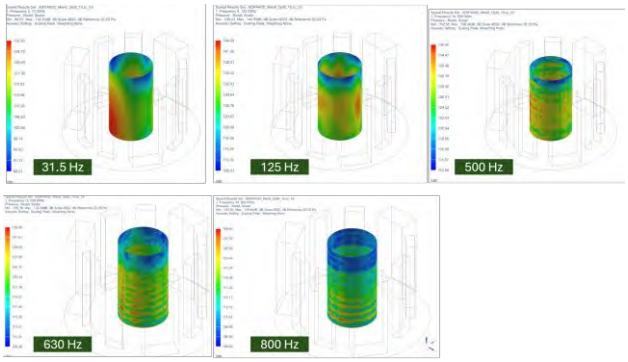


Figure 13: Sound pressure distribution around test object by 3rd octave band, controlled by optimised set of control microphones

5. OUTLOOK

The DFAN Pretest tool is now available for a commercially distributed and broadly used speaker system. After the validation and first applications, it can be fully used for pretest purposes. This can include prediction of vibration response and investigation of the room effect, like already presented in [4]. This is done to reduce the observed error when the room effects count.
Beside de-risking of test campaigns, also the layout of new test facilities can be supported.

6. CONCLUSION

The use of acoustic Finite Element simulation as pretest tool for Direct Field Acoustic Noise Testing has been demonstrated. Measured velocity fields at front faces of speakers have been implemented in the model. Validation with measured transfer functions shows good agreement. The use of the tool for the selection of control microphones has been demonstrated.

7. REFERENCES

1. NASA-HDBK-7010 (2016), Direct Field Acoustic Testing

2. P. Larkin (2014) "Developments in Direct-Field Acoustic Testing," in *Proc 28th Aerospace Testing Seminar*.

3. Alvarez Blanco, M., Janssens, K. and Bianciardi, F. (2016) "Experimental verification of projection algorithms and optimization routines for acoustic

field uniformity enhancement in MIMO direct field acoustic control," in *ISMA2016*.

4. Garcia de Miguel et al. (2021), Numerical Pre-test Analysis for Multi-channel Control Strategies in Environmental Acoustic Tests, *ECSSMET 2021*

5. Beranek, L. L. and Mellow, T. J. (2012) Acoustics: Sound Fields and Transducers, *Oxford: Academic Press*.

6. Bériot, H., Prinn, A. and Gabard, G. (2016) "Efficient implementation of high-order finite elements for Helmholtz problems," *International Journal for Numerical Methods in Engineering,* vol. 106, no. 3, pp. 213-240.

7. Bériot, H. and Modave (2020) “An automatic perfectly matched layer for acoustic finite element simulations in convex domains of general shape” *International Journal of Numerical Methods in Engineering*, p.1-24.

HIGH-PRECISION MICROPHONE LOCALISATION FOR DFAN TESTING THROUGH A HIGH-ACCURACY TDOA ALGORITHM

Vincenzo Di Pietro [(1)], Gawra Franceschini [(1)], Francesco Litardi [(1)], Fabio Di Perna [(1)], Piersante Micciché [(1)], Pietro Nali [(1)]

[(1)] Thales Alenia Space Italia, Via Saccomuro, 24 - 00131 Roma, Italy, Emails:

vincenzo.dipietro@thalesaleniaspace.com; gawra.franceschini@thalesaleniaspace.com; francesco.litardi@thalesaleniaspace.com; fabio.diperna@thalesaleniaspace.com; piersante.micciche@thalesaleniaspace.com; pietro.nali@thalesaleniaspace.com

KEYWORDS

DFAN testing, synchronous acoustic ranging, TDOA algorithm, microphone localisation, acoustic environmental testing, spacecraft qualification, trilateration.

ABSTRACT

Accurate control-microphone coordinates are required in Direct Field Acoustic Noise (DFAN) testing for repeatability, traceable reporting, and Sinc Indicator Function (SIF) assessment of acoustic-field uniformity. This paper presents a localisation framework combining trilateration with electrical-reference-to-microphone delay estimation from logarithmic chirps. Sub-sample interpolation refines the correlation peak, while robust estimation limits the influence of inconsistent ranges. Following a preliminary laboratory trial, the method was deployed in an operational DFAN configuration using the existing speaker stacks. Speaker Equivalent Point Sources (EPS) were first identified by inverse localisation using microphones with known coordinates; the resulting source coordinates were then used to reconstruct 28 microphone positions. Comparison with Laser Radar coordinates yielded a mean three-dimensional discrepancy of 3.77 cm; 26 of 28 discrepancies were at or below 8 cm. These results support the feasibility of automated coordinate reconstruction within the calibrated DFAN configuration.

1. INTRODUCTION

During vibro-acoustic qualification, aerospace structures are subjected to extreme sound pressure levels (SPL) to simulate launch or operational conditions. Direct Field Acoustic Noise (DFAN) testing has become a standard alternative to traditional reverberant chambers for satellite qualification [1]. However, as noted in the NASA-HDBK-7010 handbook [2], it is of paramount importance to "make accurate measurements of the speaker and microphone locations" to guarantee the scientific and industrial validity of the test.

Precise control microphone localisation serves three fundamental purposes within the aerospace industry:

1. **Test repeatability:** Supporting consistent spatial reconstruction of the acoustic setup across testing campaigns and dry runs.
2. **Formal reporting:** Providing traceable, high-fidelity geometric data required for qualification certificates and mission assurance documentation.
3. **Field uniformity verification:** Enabling the robust calculation of sound field diffusivity through the Sinc Indicator Function (SIF) method [3], which maps the spatial cross-correlation of the pressure field against an ideal diffuse model.

Despite these strict requirements, standard industry practices still rely heavily on manual coordinate entries using tape measures or laser distance meters. This manual process is not only time-consuming but also introduces an additional positioning uncertainty due to human error, parallax effects, and the difficulty of precisely identifying the acoustic centres of complex transducers.

To overcome these limitations, this work presents the development, scaling, and operational deployment of an automated, high-resolution microphone localisation framework. While preliminary laboratory investigations verified the core algorithm using a small array of 8 dedicated acoustic anchors and 4 microphones, this paper focuses on scaling the method to an industrial DFAN configuration, where 28 control microphones are localised simultaneously.

The framework uses the high-power speaker stacks as localisation sources, avoiding a separate acoustic source array. Surveyed coordinates are still required for initial calibration and Equivalent Point Source (EPS) identification. Subsequent localisation runs use the calibrated sources to reconstruct microphone coordinates. The industrial

comparison with Laser Radar coordinates yielded a mean 3D discrepancy of 3.77 cm, with sub-centimetre discrepancies at selected positions.

2. EXPERIMENTAL CONFIGURATION

2.1. Hardware and instrumentation

Delay estimation depends on the signal-to-noise ratio (SNR), channel synchronisation and stability of the electro-acoustic chain. The hardware was evaluated in two experimental configurations:

1. **Laboratory-scale setup:** A Siemens SCADAS-Lab mainframe acquired signals from four GRAS 40BD ¼-inch prepolarised pressure microphones [4]. Eight acoustic anchors were arranged at staggered heights. Anchor and microphone coordinates were surveyed with a tape measure to provide a preliminary reference for algorithm development and evaluation.
2. **Industrial DFAN setup:** The reduced-scale operational configuration comprises 10 vertical speaker columns around the test volume: five subwoofer columns and five TOP columns, each containing three enclosures (Fig. 1). The TOP cabinets emitted the high-frequency localisation chirps (15 independent anchors). The receiver array comprised 28 control microphones. Laser Radar measurements of microphone positions and speaker cabinet faces provided the geometric reference for calibration and comparison with reconstructed coordinates.

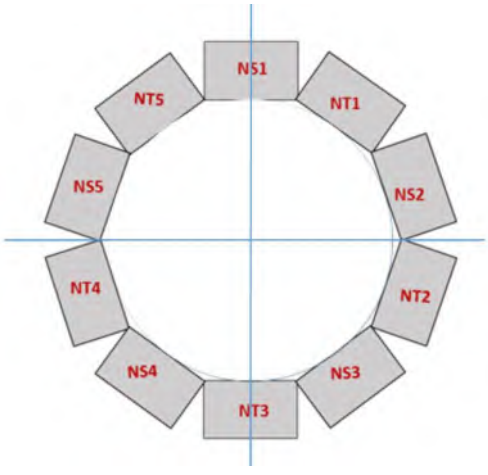


Figure 1: Top view of the reduced-scale DFAN setup. NT1–NT5 denote TOP columns; NS1–NS5 denote subwoofer columns.

2.2. Physical wiring and calibration layout

A dual-branch acquisition layout records an electrical reference and the microphone responses on a common acquisition clock.

As illustrated in Fig. 2, the analogue chirp signal $x(t)$ is split at the output of the digital-to-analogue converter (DAC) by an electrical Y-splitter:

- **Branch A (electrical reference):** The signal is routed directly to SCADAS input CH1, which records the electrical timing reference for each emission.
- **Branch B (acoustic path):** The signal drives the power amplifier and active speaker. Microphone responses are acquired on CH2 to CH$(M+1)$, where M is the number of microphones.

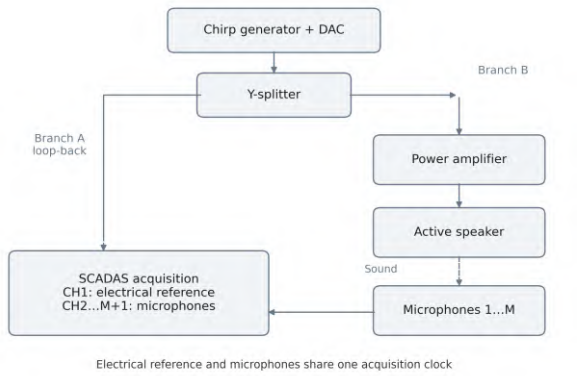


Figure 2: Electrical reference and acoustic acquisition paths. The DAC precedes the splitter; the power amplifier lies between the splitter and speaker.

Timing offsets upstream of the splitter are common to both paths and are rejected by the differential measurement [5]. The measured delay nevertheless retains the amplifier, speaker and receiver-chain delays, including any differential channel delay. These contributions require calibration; synchronous recording alone does not isolate the acoustic propagation time.

The preliminary calibration uses the surveyed distance $D_{\mathrm{cal},i}$ between the selected reference point on speaker i and a calibration microphone. The resulting effective timing bias depends on this geometric convention and on the electro-acoustic chain. Section 3.4 defines its subtraction before the EPS coordinates are used for localisation.

3. METHODOLOGY AND SIGNAL PROCESSING

3.1. Synchronous delay measurement and acoustic ranging

Each microphone recording is compared with the electrical reference from the same source emission. The observable is an electrical-to-acoustic delay. After bias correction it provides a source-to-microphone range, rather than the range difference used in conventional microphone-pair time-difference-of-arrival (TDOA) localisation [6]. Let i index the source and j the microphone. With both streams recorded on a common clock, the raw delay is:

$$\tau_{\mathrm{raw},ij} = t_{\mathrm{rec},ij} - t_{\mathrm{ref},i} \tag{1}$$

Here $t_{\mathrm{ref},i}$ is the electrical reference time and $t_{\mathrm{rec},ij}$ the corresponding microphone arrival time, both in seconds. Subtracting the effective source bias $\tau_{\mathrm{bias},i}$ gives the acoustic time of flight Δt_{ij} and range d_{ij}:

$$d_{ij} = c\,\Delta t_{ij} = c\left(\tau_{\mathrm{raw},ij} - \tau_{\mathrm{bias},i}\right) \tag{2}$$

The speed of sound c is in metres per second and d_{ij} in metres. This model assumes a stable calibrated chain and negligible or corrected receiver-channel delay differences. Temperature-dependent calibration and conversion are detailed in Section 3.4.

3.2. Linearised trilateration and radical planes

For microphone j, let $\mathbf{m}_j = [x_j, y_j, z_j]^{\mathsf{T}}$ be its unknown position and $\mathbf{S}_i = [x_i, y_i, z_i]^{\mathsf{T}}$ the position of source i. All coordinates and ranges are in metres in a common Cartesian frame. With N available sources, the range constraints are:

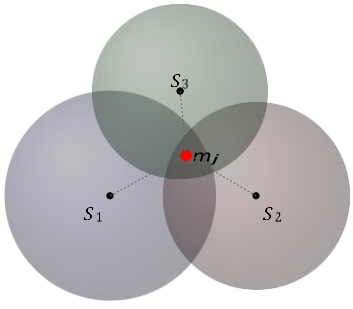


Figure 3: Spherical range constraints. Three sources are shown schematically; a unique unconstrained 3D solution requires additional geometric information.

$$\| \mathbf{m}_j - \mathbf{S}_i \|_2^2 = d_{ij}^2, \quad i = 1, \ldots, N \tag{3}$$

Subtracting the Nth sphere equation from each of the first $N-1$ equations eliminates the quadratic position terms and produces radical planes [7]. The resulting linear system is:

$$\mathbf{A}\mathbf{m}_j = \mathbf{b} \tag{4}$$

The Euclidean norm is denoted by $\|\cdot\|_2$ and transpose by T. For $i = 1, \ldots, N-1$, the rows of $\mathbf{A} \in \mathbb{R}^{(N-1)\times 3}$ and entries of $\mathbf{b} \in \mathbb{R}^{N-1}$ are:

$$\mathbf{A}_{i,:} = 2(\mathbf{S}_i - \mathbf{S}_N)^{\mathsf{T}} \tag{5}$$

$$b_i = \left(d_{Nj}^2 - d_{ij}^2\right) + \left(\| \mathbf{S}_i \|_2^2 - \| \mathbf{S}_N \|_2^2\right) \tag{6}$$

If $N \geq 4$ and $\mathrm{rank}(\mathbf{A}) = 3$, the least-squares estimate minimising $\| \mathbf{A}\mathbf{m}_j - \mathbf{b} \|_2^2$ is:

$$\hat{\mathbf{m}}_j = (\mathbf{A}^{\mathsf{T}}\mathbf{A})^{-1}\mathbf{A}^{\mathsf{T}}\mathbf{b} = \mathbf{A}^{+}\mathbf{b} \tag{7}$$

The symbol $\mathbf{A}^{+}$ denotes the Moore–Penrose pseudoinverse. This algebraic estimate minimises the linear-system residual, not directly the nonlinear range residual; the industrial robust refinement is described in Section 4.

3.3. Signal processing and sub-sample refinement

To quantify the acoustic time-of-flight (TOA), the excitation framework employs logarithmic chirp signals spanning from 2 kHz to 18 kHz with a burst duration of T = 100 ms. Acoustic sources are triggered sequentially via time-division multiplexing (TDM), emitting N = 5 consecutive bursts averaged in the time domain to maximize the signal-to-noise ratio. All channels are digitized at an industrial sampling rate of f_s = 51.2 kHz.

The raw microphone recordings and electrical reference signals are pre-filtered using a fourth-order Butterworth band-pass filter ($2\text{--}}18\text{ kHz}$) applied via zero-phase forward-backward filtering to prevent group delay distortion [8]. The coarse delay is found by correlating the electrical reference $x(t)$ with each microphone signal $y(t)$ from the same emission:

$$R_{xy}(\tau) = \int_{-\infty}^{\infty} x\,(t)y(t+\tau)\,\mathrm{d}t \tag{8}$$

Here t and τ are time and lag in seconds. A delayed microphone signal gives a positive lag with this convention. Correlation aligns the received chirp with the reference [9,10]; the peak includes chain delay as well as acoustic travel time. In sampled data, let $\hat{k}$ denote the discrete correlation at integer lag k samples and k_0 the selected peak of its

magnitude. Define $a_- = |R[k_0 - 1]|$, $a_0 = |R[k_0]|$ and $a_+ = |R[k_0 + 1]|$. Parabolic interpolation [11] yields:

$$\hat{k} = k_0 + \frac{a_- - a_+}{2(a_- - 2a_0 + a_+)}, \qquad \tau_{\text{raw}} = \frac{\hat{k}}{f_s} \tag{9}$$

The refined lag $\hat{k} = k_{\text{peak}} + \delta k$ is in samples; division by the sampling frequency f_s in samples per second gives t_{raw} in seconds. The interpolation requires an interior, non-flat peak and does not itself distinguish a direct arrival from a strong reflection.

The procedure is repeated for every source–microphone pair. Sub-sample interpolation reduces sampling quantisation; calibration then converts the raw delays into the ranges used by the localisation solver.

3.4. Electro-acoustic distance conversion and thermal compensation

Conversion to distance must separate the repeatable electro-acoustic timing bias from the temperature-dependent speed of sound.

For source i, let $\tau_{\text{raw,cal},i}$ be the raw calibration delay and $D_{\text{cal},i}$ the surveyed calibration distance. The effective bias is:

$$\tau_{\text{bias},i} = \tau_{\text{raw,cal},i} - \frac{D_{\text{cal},i}}{c_{\text{cal}}} \tag{10}$$

The calibration speed $c_{\text{cal}} = c(T_{\text{cal}})$ must correspond to the calibration temperature T_{cal}. Since the reference is taken after the DAC, its common upstream delay is already rejected. The bias represents the remaining chain delay under the chosen geometric reference convention.

For a later measurement of microphone j, the bias-corrected acoustic time of flight is:

$$\Delta t_{ij} = \tau_{\text{raw},ij} - \tau_{\text{bias},i} \tag{11}$$

The range uses the speed $c_{\text{meas}} = c(T_{\text{meas}})$ at the measurement temperature T_{meas}:

$$d_{ij} = c_{\text{meas}}\, \Delta t_{ij} \tag{12}$$

For temperature T expressed as a numerical value in degrees Celsius, the adopted dry-air approximation gives $c(T)$ in metres per second:

$$c(T) = 331.3\sqrt{1 + \frac{T}{273.15}} \tag{13}$$

Thus calibration and measurement may use different sound speeds. Each requires a representative ambient temperature; a single-temperature model neglects spatial temperature gradients and humidity effects. The effective timing bias is transferable only while the chain and source configuration remain stable However, since both the laboratory-scale and operational-scale measurements were conducted in a temperature-controlled environment (approximately 20 °C), the constant speed of sound at 20 °C was adopted.Robust localisation and experimental results

4. ROBUST LOCALISATION AND EXPERIMENTAL RESULTS

4.1. Multi-threshold random sample consensus outlier rejection

Wall, equipment and speaker-array reflections can produce secondary correlation peaks and inconsistent ranges in the industrial enclosure. The robust estimator reduces their influence but does not independently prove that every retained arrival is a direct path.

The industrial estimator applies Random Sample Consensus (RANSAC) with progressively relaxed range-residual tolerances:

$$\Theta = \{0.12,\ 0.25,\ 0.45\}\ \text{m}$$

These empirical thresholds accommodate increasing levels of range inconsistency caused by multipath.

Up to $K = 120$ random subsets are tested per threshold. Under the usual independent-trial approximation, with inlier fraction $\eta = 0.50$ and subset size $s = 4$, the probability of at least one all-inlier subset is $p = 1 - (1 - \eta^s)^K \approx 0.9996$. This is conditional on the assumed inlier fraction and non-degenerate geometry, rather than a guarantee for every dataset.

For each trial q, four anchors provide a candidate position $\mathbf{x}_q = [x_q, y_q, z_q]^{\mathsf{T}}$ using Sequential Quadratic Programming (SQP), within the test-volume bounds $-3 \le x_q, y_q \le 3$ m and $0.1 \le z_q \le 2.5$ m. The signed range residual for anchor i is:

$$e_i(\mathbf{x}_q) = \| \mathbf{S}_i - \mathbf{x}_q \|_2 - d_i \tag{14}$$

Here $d_i = d_{ij}$ for the microphone currently being solved; index j is suppressed in Section 4. The

range is calculated from the calibrated acoustic delay. Its calibration and the EPS anchor coordinates remain dependent on the initial metrology.

An anchor is an inlier when $\left|e_i(\mathbf{x}_q)\right| < \varepsilon$, where $\varepsilon \in \Theta$ is the current tolerance. Let $\mathcal{I}_q$ be the inlier-index set and $C_q = \left|\mathcal{I}_q\right|$ its cardinality. The tolerances are tested from 0.12 m to 0.45 m.Within each tolerance layer, the largest consensus size is:

$$C_{\max} = \max_q C_q \tag{15}$$

Among trials tied at $C_{\max}$, select $q^\star$ by the smallest sum of squared inlier residuals:

$$q^\star = \underset{q:C_q=C_{\max}}{\operatorname{argmin}} \sum_{i\in\mathcal{I}_q} e_i\left(\mathbf{x}_q\right)^2 \tag{16}$$

For the industrial configuration, the target is $C_{\max} \geq 12$ inlier anchors. This promotes redundancy but does not by itself ensure favourable source geometry. The target cannot be applied unchanged to the eight-anchor laboratory configuration.

If a layer does not reach 12 inliers, the tolerance is relaxed to the next value in Θ. If no layer reaches the target, the largest available consensus is retained with a lower-confidence flag. The final inlier set $\mathcal{I}$ is then fixed for refinement; rejected measurements receive no weight.

4.2. Iterative M-estimation via robust weighting

The final position is refined over eight iteratively reweighted least-squares (IRLS) iterations. This downweights residual outliers remaining in the RANSAC inlier set.

At iteration $\ell = 1, \ldots, 8$, the positive, dimensionless weight of inlier i is updated from the previous position:

$$w_i^{(\ell)} = \psi\left(\frac{\left|\left\|\boldsymbol{s}_i - \boldsymbol{x}^{(\ell-1)}\right\|_2 - d_i\right|}{\delta}\right) \tag{17}$$

where $\psi(\cdot)$ denotes the robust weighting function (e.g., Huber or Tukey bisquare [12]) and δ = 0.015 m is the residual scale parameter. With the RANSAC candidate as $\mathbf{x}^{(0)}$, the next estimate minimises the weighted sum of squared range residuals:

$$\mathbf{x}^{(\ell)} = \underset{\mathbf{x}\in\Omega}{\operatorname{argmin}} \sum_{i\in\mathcal{I}} w_i^{(\ell)} \left(\| \mathbf{S}_i - \mathbf{x} \|_2 - d_i\right)^2 \tag{18}$$

The admissible region Ω is the test volume defined in Section 4.1. SQP solves this constrained nonlinear objective. The final position is $\mathbf{x}_{\text{opt}} = \mathbf{x}^{(8)}$.

4.3. Geometric quality assessment

A weighted geometry indicator is evaluated at the final position. Relabel the $n = |\mathcal{I}|$ retained anchors locally as $i = 1, \ldots, n$. Let $r_i = \| \mathbf{x}_{\text{opt}} - \mathbf{S}_i \|_2$; the ith row of $\mathbf{G} \in \mathbb{R}^{n\times 3}$ is:

$$\mathbf{G}_{i,:} = \frac{\left(\mathbf{x}_{\text{opt}} - \mathbf{S}_i\right)^{\mathsf{T}}}{r_i} \tag{19}$$

Using the final robust weights, $\mathbf{W} = \operatorname{diag}\left(w_1^{(8)}, \ldots, w_n^{(8)}\right)$, the reported Geometric Dilution of Precision (GDOP) indicator is:

$$\text{GDOP} = \sqrt{\operatorname{tr}\left[\left(\mathbf{G}^{\mathsf{T}}\mathbf{W}\mathbf{G} + \lambda\mathbf{I}_3\right)^{-1}\right]} \tag{20}$$

Here $\lambda = 10^{-6}$ is dimensionless, $\mathbf{I}_3$ is the 3×3 identity matrix, and tr denotes the trace. This regularised, residual-weighted indicator is dimensionless; it is not a direct position-error estimate. Regularisation stabilises inversion but does not restore missing geometric information.

Internal range consistency is measured by $E_{\text{RMS}} = \sqrt{n^{-1}\sum_{i\in\mathcal{I}} e_i\left(\mathbf{x}_{\text{opt}}\right)^2}$. This quantity is distinct from the external coordinate discrepancy E_{TOT} reported against Laser Radar in Tab. 3. The internal review thresholds are GDOP > 4.0 or $E_{\text{RMS}} > 8$ cm. External coordinate discrepancies in Tab. 3 separately quantify agreement with Laser Radar.

4.4. Preliminary laboratory results

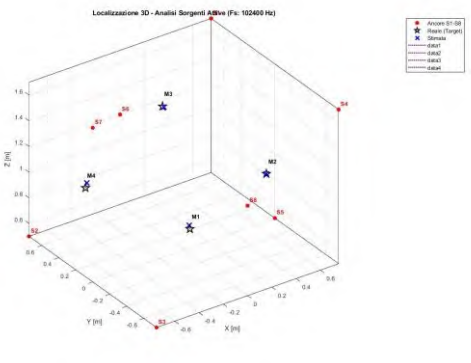


Figure 4: Laboratory source and microphone positions at $f_s = 102.4$ kHz. Surveyed and estimated microphone positions are compared.

Tabs. 1 and 2 summarise the preliminary laboratory comparison. Coordinates are rounded to two decimal places; error metrics are listed separately.

Table 1: Laboratory comparison. Coordinates are in metres and error magnitudes in centimetres.

ID	Real Z [m]	Est. Z [m]	Err Z [cm]	Err XY [cm]	Err Tot [cm]
1	1.00	1.00	0.27	4.38	4.39
2	1.15	1.16	1.49	2.35	2.78
3	1.50	1.50	0.29	1.78	1.80
4	0.90	0.91	1.14	4.60	4.74

Table 2: Mean laboratory error magnitudes.

Avg. Err Z [cm]	Avg. Err XY [cm]	Avg. Err Tot [cm]
0.80	3.28	3.43

The mean 3D discrepancy was 3.43 cm. The mean absolute Z discrepancy was 0.80 cm, versus a mean planar discrepancy of 3.28 cm. This is consistent with useful vertical constraints from the staggered anchors, but does not establish a causal advantage without a comparison layout. The tape-measure reference uncertainty limits the interpretation of absolute localisation accuracy.

4.5. Industrial DFAN deployment

Following preliminary validation, the framework was scaled up to an operational DFAN spacecraft testing enclosure. Ground-truth coordinates for all receivers and speaker cabinet faces were established using an industrial Laser Radar metrology system.

The industrial localisation was executed via a two-stage strategy:

1. **Inverse method (EPS characterisation):** A subset of primary control microphones with Laser Radar-verified coordinates was used as anchors to back-calculate the acoustic centres of the multi-driver speaker stacks, modelling them as Equivalent Point Sources (EPS).
2. **Direct localisation:** The identified EPS coordinates served as virtual acoustic anchors to localise the array of 28 control microphones distributed throughout the reverberant chamber.

Tab. 3 compares reconstructed positions with Laser Radar. X_{meas}, Y_{meas} and Z_{meas} denote the coordinates measured via TDOA algorithm . The axis errors are signed coordinate differences; the 3D discrepancy is:

$$E_{\mathrm{TOT}} = \sqrt{\mathrm{ErrX}^2 + \mathrm{ErrY}^2 + \mathrm{ErrZ}^2} \qquad (21)$$

Table 3: Industrial comparison with Laser Radar for 28 microphone entries. Coordinates are in metres; signed axis errors and 3D discrepancies are in centimetres. Status labels are as reported.

ID	Name	Xmeas [m]	Ymeas [m]	Zmeas [m]	ErrX [cm]	ErrY [cm]	ErrZ [cm]	ETOT [cm]	GDOP	Status
1	MC	0.0142	-0.0034	1.1232	0.00	0.00	0.00	0.00	1.35	OK
2	MN1_1	-0.2948	0.8130	0.6098	0.83	-0.94	-2.88	3.15	3.44	OK
3	MN1_2	-0.3019	0.8125	1.0148	1.95	-1.63	-6.14	6.65	3.21	OK
4	MN1_3	-0.3056	0.8122	1.7344	2.70	-1.84	9.00	9.58	2.58	CHECK
5	MN2_1	0.4088	0.8787	0.6173	-2.99	-0.12	-1.16	3.21	2.42	OK
6	MN2_2	0.4361	0.8672	1.0642	-1.75	-1.01	-1.00	2.25	2.75	OK
7	MN2_3	0.4155	0.8340	1.6904	-5.23	-3.92	5.38	8.47	1.50	CHECK
8	MN3_1	0.6413	0.4374	0.6907	-3.08	-0.23	5.15	6.01	2.46	OK
9	MN3_2	0.6945	0.4194	1.1160	0.81	-1.63	1.57	2.40	2.50	OK
10	MN3_3	0.7012	0.4168	1.6444	-2.28	-0.69	-0.61	2.46	3.01	OK
11	MN4_1	1.0267	0.0308	0.6303	-3.10	-2.28	1.44	4.11	2.34	OK
12	MN4_2	1.0439	0.0422	1.1134	0.52	0.75	4.10	4.20	3.65	OK
13	MN4_3	0.9950	0.1007	1.6758	-3.50	2.39	4.04	5.85	1.80	OK
14	MN5_1	0.6006	-0.0632	0.6295	-2.14	-2.02	-0.01	2.95	2.03	OK
15	MN5_2	0.5903	-0.0064	1.1324	0.53	0.03	-0.81	0.97	1.94	OK
16	MN6_1	0.5301	-0.7195	0.5786	-1.44	-0.88	-2.13	2.72	2.77	OK
17	MN6_2	0.5413	-0.7364	1.1445	1.45	-1.77	6.09	6.51	3.63	OK
18	MN6_3	0.5308	-0.7219	1.6316	-0.04	0.23	0.67	0.71	2.47	OK
19	MN7_1	-0.1000	-0.5717	0.5614	-1.76	1.01	-6.08	6.41	2.07	OK
20	MN7_2	-0.1303	-0.5576	1.1470	-0.53	1.93	4.78	5.18	2.22	OK
21	MN7_3	-0.0994	-0.5892	1.6459	0.37	0.13	3.94	3.96	1.75	OK
22	MN8_1	-0.3623	-0.7664	0.6340	1.54	1.79	3.12	3.91	2.63	OK
23	MN8_2	-0.3915	-0.7753	1.0694	-0.85	0.56	1.00	1.43	3.52	OK
24	MN9_1	-0.8013	-0.0566	0.6348	-1.17	0.88	2.10	2.56	2.85	OK
25	MN9_2	-0.7536	-0.0855	1.1081	-0.78	0.51	1.69	1.93	2.53	OK
26	MN10_1	-0.8799	0.3686	0.6309	-1.36	-2.19	1.28	2.87	1.81	OK
27	MN10_2	-0.8834	0.4013	1.0690	-1.29	1.71	-1.33	2.52	2.85	OK
28	MN10_3	-0.8804	0.3685	1.6357	-0.51	-1.10	2.19	2.51	2.77	OK

Table 4: Industrial summary across all 28 entries, including MC.

Metric	Value
Total Microphones Evaluated	28
Mean Absolute X Error ($\|Err_X\|$)	1.59 cm
Mean Absolute Y Error ($\|Err_Y\|$)	1.22 cm
Mean Absolute Z Error ($\|Err_Z\|$)	2.85 cm
Mean Planar Error ($\|Err_{XY}\|$)	2.10 cm
Mean 3D Total Error ($\bar{E}_{TOT}$)	**3.77 cm**
Median 3D Total Error	**3.05 cm**
Mean GDOP	2.53
3D discrepancy at or below 8 cm	92.9% (26/28)

4.6. Industrial performance analysis and error discussion

The industrial dataset provides a comparison within the calibrated DFAN configuration. Optical metrology was used for calibration and EPS identification; subsequent acoustic localisation used those identified source coordinates.

Key observations from the industrial dataset include:

1. **External coordinate agreement:** The mean 3D discrepancy was 3.77 cm and the median 3.05 cm. Twenty-six of 28 entries (92.9%) were at or below 8 cm. This count describes agreement with the surveyed coordinates and is distinct from an independently verified pass rate for the internal RMS criterion.
2. **Axis-specific discrepancies:** The mean absolute Z discrepancy was 2.85 cm, compared with 1.59 cm in X and 1.22 cm in Y; the mean planar discrepancy was 2.10 cm. The TOP cabinets are described as containing four vertically stacked compression drivers. Their extended radiating aperture may limit a single-EPS model in the vertical direction. The present data do not isolate that contribution from timing, geometry and calibration errors.
3. **Larger discrepancies:** MN1_3 and MN2_3 have external 3D discrepancies of 9.58 cm and 8.47 cm, respectively, and are reported as CHECK. Both lie above 1.69 m. Possible contributing factors include:
   - **Vertical source coverage:** The open-top source arrangement may give weaker vertical constraints at some locations. However, the two flagged entries have GDOP values of 2.58 and 1.50, so the reported geometry indicator alone does not explain their discrepancies.
   - **Speaker directivity:** Off-axis high-frequency radiation may reduce direct-arrival SNR and broaden or distort the correlation peak. Directivity and correlation data are needed to quantify this effect.
4. **Geometry indicator:** Mean GDOP was 2.53; all tabulated values were below the stated 4.0 review threshold. This describes the local weighted geometry, rather than an independent guarantee of position accuracy.

5. CONCLUSIONS

This paper presented a synchronous acoustic-ranging framework for microphone localisation in DFAN testing. The procedure combines an electrical timing reference, sub-sample correlation refinement, bias correction and temperature-dependent conversion to distance.

Following a preliminary laboratory trial, the method was applied to 28 industrial microphone entries. Existing TOP speaker cabinets were characterised as EPS anchors using surveyed microphone coordinates, then used for acoustic coordinate reconstruction. This reduces the need for additional localisation hardware during subsequent runs while retaining an initial metrology requirement.

The comparison with Laser Radar coordinates gave the following results:

- Mean and median 3D discrepancies were 3.77 cm and 3.05 cm; 26 of 28 entries (92.9%) were at or below 8 cm.
- The industrial solver combined multi-threshold RANSAC with robustly weighted nonlinear refinement. The mean weighted GDOP indicator was 2.53.
- The mean absolute vertical discrepancy was 2.85 cm. Extended source radiation and vertical coverage are possible contributors, requiring further investigation.

The results support further development for test-setup documentation and field-uniformity assessment. Independent validation with

microphones withheld from EPS calibration, quantified reference uncertainty and repeatability trials is needed to establish transferable accuracy. Future work will also examine temperature gradients and multi-driver source models.

6. REFERENCES

[1] Larkin, P. A. 2014. Developments in Direct-Field Acoustic Testing. *Sound & Vibration* 48:6-10.

[2] NASA-HDBK-7010. 2016. *Direct Field Acoustic Testing (DFAT)*. Washington, DC: National Aeronautics and Space Administration. Revalidated 9 January 2026 without changes.

[3] Carrella, A. and W. Mayne. 2023. Insight into the Sound Field During a Direct Field Acoustic Test (DFAT). *INTER-NOISE and NOISE-CON Congress and Conference Proceedings* 265(6):1383-1391. doi:10.3397/IN_2022_0188.

[4] GRAS Sound & Vibration. n.d. *GRAS 40BD 1/4" Prepolarized Pressure Microphone*. Product data sheet, https://www.grasacoustics.com/products/product-pdf/159-40bd (accessed 3 September 2026).

[5] Flammini, A. and P. Ferrari. 2010. Clock Synchronization of Distributed, Real-Time, Industrial Data Acquisition Systems. In M. Vadursi (ed.), *Data Acquisition*. IntechOpen. doi:10.5772/10458.

[6] Chan, Y. T. and K. C. Ho. 1994. A simple and efficient estimator for hyperbolic location. *IEEE Transactions on Signal Processing* 42:1905-1915. doi:10.1109/78.301830

[7] Manolakis, D. E. 1996. Efficient solution and performance analysis of 3-D position estimation by trilateration. *IEEE Transactions on Aerospace and Electronic Systems* 32:1239-1248. doi:10.1109/7.543845

[8] Stein, J. Y. 2000. *Digital Signal Processing: A Computer Science Perspective*. New York, NY: John Wiley & Sons. doi:10.1002/047120059X.

[9] Müller, S. and P. Massarani. 2001. Transfer-Function Measurement with Sweeps. *Journal of the Audio Engineering Society* 49:443-471.

[10] Stan, G-B., J-J. Embrechts, and D. Archambeau. 2002. Comparison of different impulse response measurement techniques. *Journal of the Audio Engineering Society* 50:249-262.

[11] Jacovitti, G. and G. Scarano. 1993. Discrete-Time Techniques for Time Delay Estimation. *IEEE Transactions on Signal Processing* 41:525-533. doi:10.1109/78.193198

[12] Huber, P. J. 1964. Robust Estimation of a Location Parameter. The Annals of Mathematical Statistics 35(1):73–101. doi:10.1214/aoms/1177703732.

INTEGRATING DFAN AND VIBRATION TESTING IN A SHARED FACILITY: ENGINEERING SOLUTIONS FOR RAL SPACE'S NEW ENVIRONMENTAL TEST CENTER

Cassandra Dutt [(1)]
Charly Knight, Ian Horsfall [(2)]
[(1)] *Acoustic Research Systems (ARS), 113 E. German St, Shepherdstown, WV 25443 Email: c.dutt@acouticrs.com*
[(2)] *RAL Space, STFC Rutherford Appleton Laboratory, Harwell Campus, Didcot, United Kingdom, Email: charly.knight@stfc.ac.uk, ian.horsfall@stfc.ac.uk*

ABSTRACT

RAL Space operates several major spacecraft environmental test facilities in Europe and recently expanded this infrastructure with the National Satellite Test Facility (NSTF). The NSTF is a large-scale test center, designed to bring a comprehensive suite of environmental test methods under one roof, including vibration and Direct Field Acoustic (DFAN) test methods within a shared floor space. Co-location offers considerable programmatic and logistical advantages, including elimination of inter-facility hardware transfers and the ability to schedule a battery of qualification tests within a single site visit.

Early in the design and procurement process, ARS and RAL identified that co-locating DFAN and vibration testing services in a fixed floor print of the Dynamics Lab presented several logistical challenges. The fixed vibration test interfaces which are flush with the floor are considered non-load bearing and could not accept the ground-supported loads of the DFAN acoustic system. Reconciling the completing structural and operational demands was paramount of the overall functionality of the multi-purpose testing space.

This paper documents the engineering assessment undertaken to resolve the conflict, from problem definition through concept selection and validation. A bespoke fiberglass reinforced plastic (FRP) platform system was ultimately selected to redistribute the weight of the DFAN system while preserving full reconfigurability of the floor space.

The paper concludes with a review of the commissioning for the integrated space which used a structural test model (STM) to demonstrate that the Dynamics Lab could be reconfigured between vibration and DFAN testing in an efficient manner. Selected results from commissioning tests are provided. This case study offers a practical reference for other facilities pursuing similar multi-modal test integration.

INTRODUCTION

Spacecraft environmental test facilities are increasingly being designed as multi-modal spaces; single rooms or buildings capable of hosting several distinct qualification test regimes rather than one dedicated capability per facility or space. Co-location of testing capabilities eliminates inter-facility hardware transfers, compresses schedule, and reduces the capital and footprint required to offer a full qualification campaign under one roof. The success of this approach depends on the thoughtfulness of the design and the flexibility of the final space, since requirements for different test methods are not always aligned.

In 2015, the UK Space Agency commissioned a gap study to review UK based aerospace support facilities [1]. The study concluded that the UK lacked a single facility of sufficient scale and comprehensiveness to test large, complex payloads. UK based programs that required full-scale environmental qualification often transported hardware and teams to mainland Europe, incurring significant logistical and programmatic cost.

RAL Space operates several major spacecraft environmental test facilities in the UK, with testing heritage across a wide spectrum of environmental test capabilities. In response to this study, RAL Space submitted a business case for the development of a large scale, environmental testing laboratory. The proposal was approved in June 2017 with an allocation of £99 million [2], later growing to a total investment of over £100 million as the project scope and construction timeline evolved [10]. The result of the investment was the National Satellite Test Facility (NSTF).

The NSTF is a large-scale environmental test center designed to consolidate a suite of environmental test methods under one roof. Thermal vacuum, vibration, acoustic, electromagnetic compatibility and antenna measurement, and mass properties testing capabilities are co-located in clean room conditions and sized to support spacecraft weighing up to 7 tonnes. Though originally planned to open in spring of 2020, construction progressed through a series of disruptions, including changes in government funding mechanisms and the COVID-19 pandemic, before reaching full customer readiness in early 2026.

Central to the NSTF design is shared infrastructure across test capabilities, rather than provisioning for each capability independently. Infrastructure for things like cleanrooms, cranes, chilled water distribution, reference earthing, and environmental monitoring are shared across test areas, following a precedent RAL Space had already established in its earlier R100 facility, operational since 2015 [3]. Sharing infrastructure this way reduces capital cost and facility footprint, echoing the same efficiencies that motivated the construction of a multi-modal testing facility.

This paper examines the NSTF design philosophy and implementation through a review of the multi-used Dynamics Lab, a single isolated space intended to host vibration, shock, and acoustic testing. Reconciling the spatial and operational requirements of vibration testing and acoustic testing within a shared room presented engineering challenges that, if left unaddressed, would have prevented the space from functioning as designed.

NSTF DYNAMICS LAB

The layout and test systems described below are directly relevant to the vibration and acoustic integration challenge addressed later in this paper.

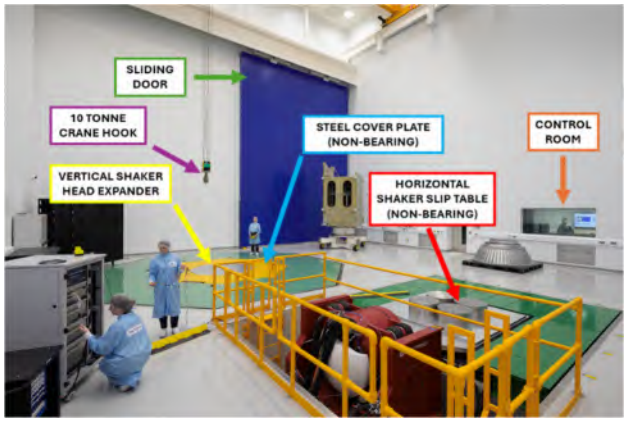


Figure 1 - Annotated Photograph of NSTF Dynamics Lab (courtesy of RAL Space)

The Dynamics (Vibration) Lab at the NSTF occupies a 16 m x 16 m x 16 m test room with an adjacent, acoustically isolated control room. The room and adjacent spaces are ISO class 8 cleanrooms, maintained at 20 °C. A large, sliding door on one wall provides equipment and spacecraft access.

An overhead crane rated for 10 tonnes provides coverage over the center portion of the floor print, with limited extents nearest the test area door. Fig. 2 shows a plan view of the lab with the crane coverage indicated with a hatch.

A unique, site-specific design requirement necessitated the recessing of shaker elements. The NSTF sits close to Diamond Light Source, the UK's national synchrotron, whose beam positions monitors that are sensitive enough to register ground vibration from seismic events on the other side of the globe [4]. Therefore, both shaker systems are mounted on recessed, 200 tonne seismic blocks that are raised on airbags during testing, fully isolating vibration tests from the surrounding environment.

The lab floor is a concrete slab on grade, load-rated to receive spacecraft, ground support equipment, and test hardware directly. Two recessed interfaces are built into the slab to service the shaker systems; an octagonal head expander for vertical testing and a rectangular slip table for horizontal testing, each set flush to the surrounding floor as shown in Fig. 1. Custom steel cover plates, green around the slip table and yellow around the head expander, are installed over the recesses allowing personnel and equipment to be moved across the room safely. The yellow cover plates surrounding the head expander are rated for foot traffic and light-weight ground support equipment only. The slip table at the horizontal shaker is also considered non-bearing floor area.

The lab can be configured to perform mass properties, vibration and shock deployment, and DFAN testing. Mass properties testing capabilities have been excluded for brevity.

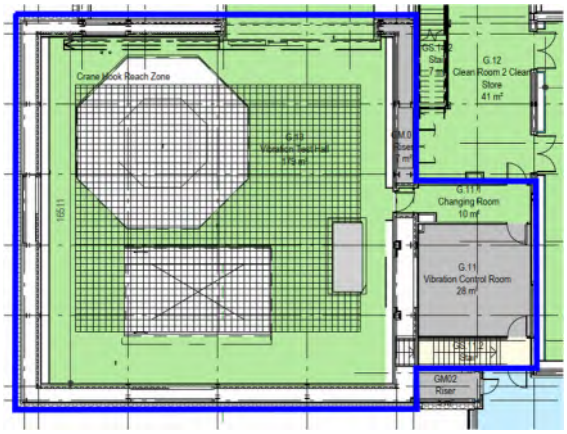


Figure 2 - Plan View of NSTF Dynamics Lab with Crane Coverage in Hatch

Vibration and Shock Deployment Testing

The vibration test system consists of a pair of Data Physics electro dynamic shakers, a guided head expander and slip table(s) supported by controllers and data acquisition systems. Each shaker can produce up to 222kN of thrust between 5-2000 Hz.

The facility can be arranged into three potential test

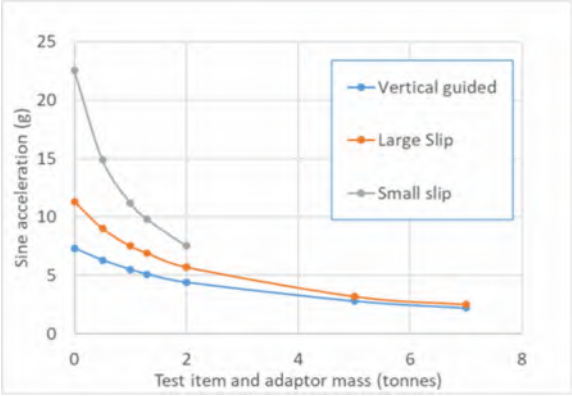


Figure 3 - NSTF Shaker Sine Capabilities g Level as Function of Test Item Mass & Test Configuration

configurations: 1) Vertical test in the guided head expander; 2) Horizontal test on the large slip table; 3) Horizontal test on the small slip table. The acceleration

limits in each configuration are a function of the moving mass of the shaker and/or slip tables/head expander with typical estimated performance shown in Fig. 3.

The shaker system is controlled using a 70 channel Data Physics 912 unit and SignalCalc software, supporting active control signals as well as acceleration, force, and moment limiting. This is supported by an independent 512 channel data acquisition system with a 100 kHz sample rate. The same data acquisition system is used across environmental test as DAQ racks can be moved with the spacecraft around the facility, allowing for a smoother transition between test types.

Direct Field Acoustic (DFAN) Testing

DFAN is an advantageous solution for integrating acoustic testing capabilities in a multi-purpose room, precisely because it is flexible, portable, and modular. The methodology has been used heavily in the United States since the late 1990s as it is a cost-effective solution for acoustic testing that can be performed in most facilities [5]. This removes the risk of transporting the test article to a suitable acoustic chamber. DFAN systems are designed to be deployed in various configurations and heights to provide adequate acoustic coverage of the test article. The methodology and test validity has been discussed thoroughly in industry publication and will not be expanded upon here.

The ARS Neutron acoustic testing solution was chosen in 2023 as the DFAN test solution through a competitive bidding process. The Neutron is a proprietary, full range (20 Hz to 10 kHz) acoustic device designed specifically for DFAN testing. It is manufactured by Acoustic Research Systems in conjunction with UK based EM Acoustics.

A system of forty-eight (48) Neutron devices, with associated amplifiers and cabling, was procured. The Neutron system was sized to accommodate a medium test-article envelope of up to 2.6 m x 2.6 m x 5.5 m in total height with the capability to expand the system for a large test-article envelope of up to 5 m in diameter and a maximum of 10.5 m in height. Both sizes were required to be capable of reproducing qualification-level acoustic environments spanning an envelope of launcher manuals requirements, as shown in Fig. 4. Additionally., the original tender also included an acoustic specification, in octave from 31.5 Hz to 8000 Hz, that required that the system be capable of achieving an OASPL of 147.3 dB

When not in use, the Neutron system can be broken down into modules that are stowed outside of the Dynamics Lab, freeing the room for other types of testing. The system was specified to be capable of full reconfiguration within 48 hours, a requirement set specifically to preserve the lab's ability to turn around between test regimes without extended downtime.

ENGINEERING CHALLENGE

Early in the design and procurement process, ARS and RAL identified that co-locating DFAN and vibration testing services in a fixed floor print presented several logistical challenges. Overcoming these challenges was paramount to the overall functionality of the multi-purpose testing space.

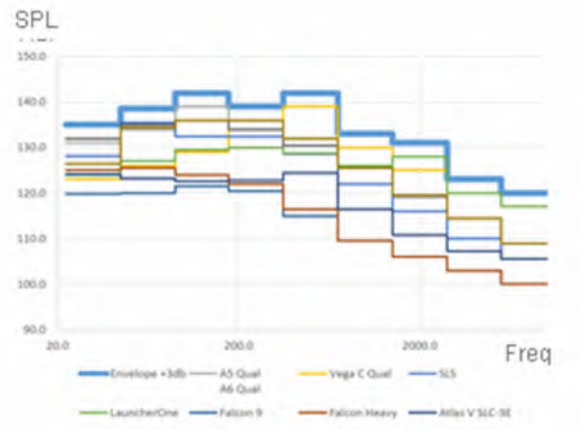


Figure 4 – DFAN Acoustic Spectrum Requirement

ARS provided a standard system outer diameter of 10.4 m, as shown in Fig. 5, with the ability to expand to an outer diameter of 11m. On paper, the 16 m x 16 m footprint of the room should have been of adequate size to support the extents of the largest proposed DFAN setup. However, two specific characteristics of the room, contrasted with the structural requirements of the Neutron, prevented the system from being assembled as required.

The Neutron is a ground supported structure, meaning the full weight of each stack must be carried by the floor structure beneath it. The bearing surface under the substantial footprint of each Neutron stack must be consistent, with adequate load capacity and levelness. As discussed above, the cover plates in the areas of floor around vertical and horizontal shakers do not have the capacity to support the weight of the Neutron acoustic devices and are therefore considered to be non-load bearing.

Neutrons are stacked and positioned within the room using the overhead crane. Stacks must be positioned so that the center of gravity of each stack falls within the crane extents. The crane coverage, as illustrated by the red line in Fig. 5, limits how far toward the room's perimeter any given stack can be placed. Combined with the non-bearing floor areas identified above, this reduced the number of positions in the room where a Neutron stack could be assembled without conflicting with either constraint.

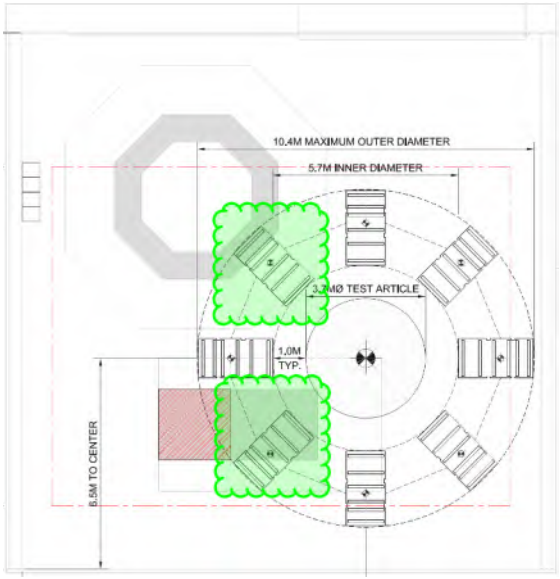


Figure 5 – Preliminary Plan Showing Configuration of Standard DFAN System Size in Dynamics Lab

Regardless of the system orientation, two (2) stacks of Neutrons must fall over designated non-bearing floor areas. A structural solution would be required to safely support the Neutron stacks without damaging existing, fixed infrastructure.

It should be noted that the architectural design of the NSTF was completed years before DFAN was considered as a testing capability. Therefore, the room was not sized with the capability in mind.

Engineering Design Methodology

Given the constraints identified above, ARS and RAL determined at the outset that a temporary structural solution, rather than a permanent modification to the room, was the only acceptable solution. A temporary structure could be installed only when needed and removed afterward, preserving the Dynamic Lab's flexibility to support other test regimes.

ARS and RAL performed an engineering assessment to determine how best to supplement the lab to accommodate larger acoustic tests. The assessment proceeded through a structured sequence: problem definition, development of design criteria, schematic design, concept selection, structural analysis and validation, and finalization of the selected technical solution. The highest priority when assessing potential solutions was maintaining the flexible nature of DFAN testing without hindering the vibration capabilities in the shared space.

Problem Definition

ARS went through an early drafting exercise to define the scope of the structure needed. This exercise included producing system layouts at a variety of inner diameters and configuring them within an as-built model of the lab. The lab model included overall room geometry, extents of the overhead crane, and exact placement of the head expander, slip plates, and other floor obstructions. Through careful and coordinated rotation and placement of the medium and large systems, the extent of the temporary structures required was determined.

The acoustic devices and associated kitting have significant weight that must be distributed out to the robust concrete slab on grade. To maintain the 48-hour reconfiguration requirement, it was determined that a portable, temporary structural solution was needed to maintain system flexibility.

Design Requirements & Evaluation Criteria

It was determined that the temporary structural solution had to meet the following requirements:

1. The temporary platform had to span the non-bearing areas of the floor, distributing the load of the acoustic devices out to the slab on grade.
2. The platform had to support a distributed load of 19.2 kN/m².
3. Deflection of the platform under the maximum applied load had to be less than 3.2 mm
4. The structural depth had to be minimized to reduce vertical offset between adjacent speaker stacks.
5. The structure had to be easy to assemble, place, and store, with minimal setup time.

This evaluation criteria, along with structural design standards were formalized in a Basis of Design document that was reviewed and approved by both RAL and ARS prior to schematic design.

Schematic Design & Concept Selection

Two primary structural solutions were explored as a part of the schematic design exercise.

Structural Steel Plinths

RAL contracted a fabricator to develop designs for bespoke structural steel frames or "plinths" for internal review. This concept used open rectangular hollow section (RHS) base frames in S355J mild steel to support each speaker stack as shown schematically in Fig. 6. Three distinct designs were developed: two separate frames to span over the horizontal and vertical shakers and a standard frame to elevate all other Neutron stacks to keep the bottom of stack elevations consistent.

While structurally straightforward, the steel concept was not carried forward for several reasons that emerged during the design review:

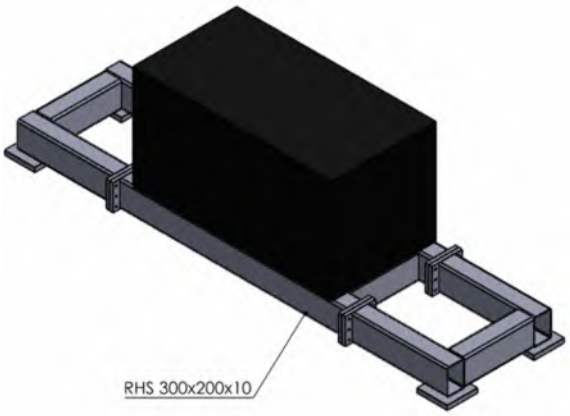


Figure 6 - Schematic Isometric of Steel Plinth at Slip Table

1. Excessive weight: The steel base frames alone added an estimated 4,215 kg of structure and would have required a dedicated transport and lifting solution for deployment.
2. Depth of structure: The RHS base frame depth added significant vertical offset between adjacent speaker stacks, which would compromise the design of the proposed lateral bracing elements between speaker stacks. To accommodate this, frames would be required under all stacks which added more equipment to the overall setup.
3. Limited flexibility: The steel frames were designed around fixed positions matched to a specific speaker layout, which offered less adaptability to the range of DFAN configurations the test facility needed to support. Fixed-position frames would have defeated the room's core purpose as a reconfigurable, multi-modal test space.

Taken together, the design issues associated with the steel concept made it a poor fit for governing design requirements. The limited flexibility presented by the steel frames led to the development of a second schematic structural solution. It was determined that if a solid platform could be provided, all configurations could be supported with the same structural solution.

FRP Temporary Platform System

ARS began exploring the design of a low-profile platform, like a temporary stage deck used in live entertainment events. Standard stage deck structures are composed of aluminium truss exterior members topped with a thin solid bearing surface and cannot support the weight of the Neutron devices regardless of span.

Fiberglass reinforced plastic (FRP) was selected as a candidate material for construction of a low-profile support platform. FRP is a structural composite in which continuous glass fibers reinforce a cured thermoset polymer resin. The glass fibers, which make up roughly 70% of the material's weight, provide tensile strength and stiffness, while the surrounding resin transfers load between fibers and protects them from environmental exposure [6]. This combination gives FRP a high strength-to-weight ratio relative to traditional structural materials like steel and concrete. FRP structures are also non-conductive, impact-resistant, and low-maintenance, reducing life-cycle cost.

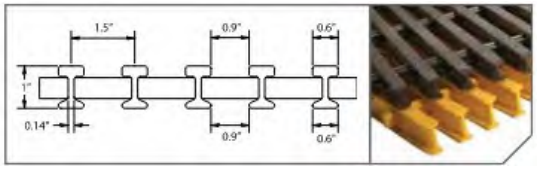


Figure 7 - Example of FRP Pultruded Grating (courtesy of Fibergrate Composite Structures)

Pultruded FRP grating was proposed as this was a high-capacity panel application, like those subject to vehicular loading. In the pultrusion process, continuous glass fiber reinforcement is pulled through a resin bath and heated die to form FRP profiles with controlled, consistent geometry. Grating panels are assembled from pultruded bearing bars, which carry the primary load, and cross-rods, which stabilize the panel and maintain consistent member spacing, as shown in Fig. 7. As a result, pultruded grating is designed to span in one direction [7].

BESPOKE FRP PLATFORM SOLUTION

Platform Construction

Covered pultruded FRP grating, manufactured by U.S.-based Fibergrate Composite Structures, was ultimately selected as the structural solution for the bearing platforms. A solid FRP plate was adhered to the top of high-capacity HI3730 grating [8], for a total material thickness of 85.7 mm. Four solid, full-length FRP runners of 50.8 mm depth were installed on the underside of the grating. The runners were aligned so that the grating spanned one-way over the non-bearing floor surfaces, distributing the load to areas of the floor capable of receiving the weight. Platform 1 is a three-span structure that is supported by the vertical head expander on one side and the concrete floor slab on the other. It is broken up into two (2) sections and has a maximum unsupported span of 1753 mm. Platform 2 is also a three-span structure that is supported entirely by the steel cover plate assembly around the horizontal shaker slip table. It is broken up into three (3) sections and has a maximum unsupported span of 2363 mm.

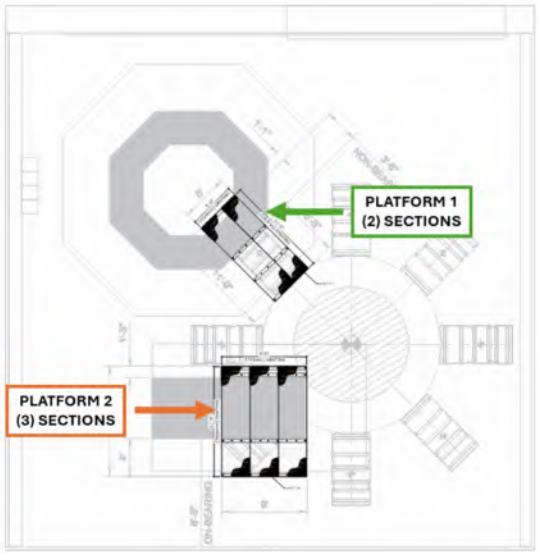


Figure 8 - Plan View of FRP Platform Locations

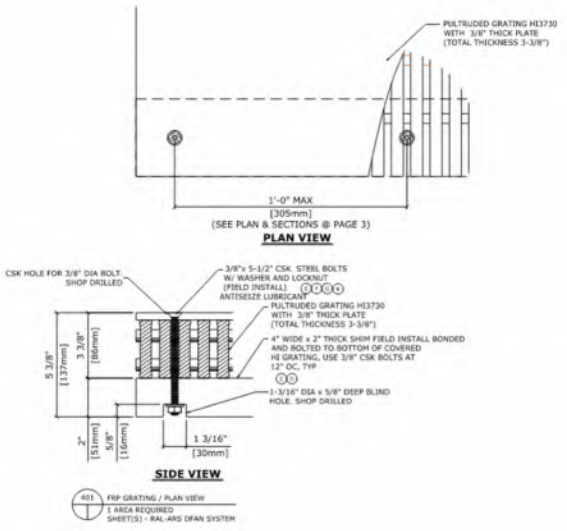


Figure 9 - Part Plan and Detail of FRP Platform Construction

The construction methodology is consistent across both platforms.

The final platform structures are rated for a live load of 19.2 kN/m², equivalent to the weight of seven Neutrons, while meeting the project's deflection criteria. The total depth of structure, 136.5 mm, is minimal enough that no redesign of the proprietary lateral bracing structure was required. To reduce component weight and simplify storage, the platform sections were broken into segments approximately 914–991 mm wide, with each section weighing between 338 kg and 345 kg. Each platform section was designed with four corner locations where an eyebolt and lifting shackle can be installed for lifting and placement.

Platform Analysis & Validation

Structural adequacy of the FRP platform was verified through two independent analyses. Analyses were performed in accordance with the load and resistance factor design (LRFD) recommendations made for FRP structures in the ASCE/SEI 74-23 design standard [9], evaluating the platforms against the applicable strength and serviceability limit states.

Fibergrate performed an independent hand calculation of the grating system, treating the platforms as multi-span structures under a uniform area load. The calculations consider a dead load (platform weight) of 1.1 kN/m², in addition to the live load of 19.2 kN/m². Deflection was calculated using standard static beam formulas for multi-span members, based on the average effective flexural stiffness (EI) of the grating panel derived from coupon testing of the pultruded material. The platform live load capacity was based on Fibergrate's published data for the HI3730 grating profile. The governing case for deflection under uniform load was found to be at the midspan of Platform 2 with a maximum predicted displacement of 5 mm, or L/476.

In parallel, ARS developed a finite element model of both platforms in RISA 3D to perform stress and strength checks as well as to calculate predicted deflection under a range of loading conditions. Because placement of the Neutron on the platform can vary, the analysis was performed for several representative loading conditions. Varying stack position within the model, rather than assuming a single uniformly distributed load, allowed the governing case for each span to be identified and checked against the design requirements. The model was built using Fibergrate's published section properties as well material coupon test results for the pultruded laminate. Grating was modelled as an equivalent orthotropic plate with properties matched to the manufacturer data. The governing deflection was also identified at the midspan of Platform 2 with a maximum predicted displacement of 3.9 mm, or L/606.

The hand calculation produced more conservative results, consistent with its simplified treatment of the platform as a uniformly loaded multi-span beam, whereas the FEA captures the actual distribution of the Neutron stack weight across the platform, allowing for a more refined prediction of deflection. Both governing predicted deflections exceed the initial design specification by between 0.7 mm and 1.8 mm however they meet the applicable strength requirements. ARS evaluated the additional deflection against the Neutron stack stability envelope and found that the additional deflection had no negative impact on the lateral stability of the structure.

Comparing the two approaches provided confidence that the platforms would perform to specification across the range of possible DFAN configurations, and both analyses showed good agreement that the structure would meet strength and serviceability requirements. On this basis, RAL did not require the platform structures to be proof tested prior to installation.

Platform Installation

The FRP structures were manufactured in the United States and shipped directly to RAL fully assembled. Upon receipt, the five (5) individual platform sections were unpacked and inspected. The visual inspection focused on material consistency, platform camber, and fastener installation. Visual inspection flagged one item for remediation. Bolts between the pultruded grating and the bearing strips were too long which prevented the platform from sitting flush with the floor. A representative of RAL cut the fasteners down and reinstalled rectifying the non-conformance.

The locations and extents of each platform were marked on the floor using known landmarks within the room. One by one, eyebolts and shackles were installed in the four (4) corner receivers on each platform, as shown in Fig. 10. Four slings were used to lift each platform, align it with its intended position, and lower it into place. Once placed, the lifting gear was removed and transferred to the next platform. This process took approximately ten (10) minutes per platform.

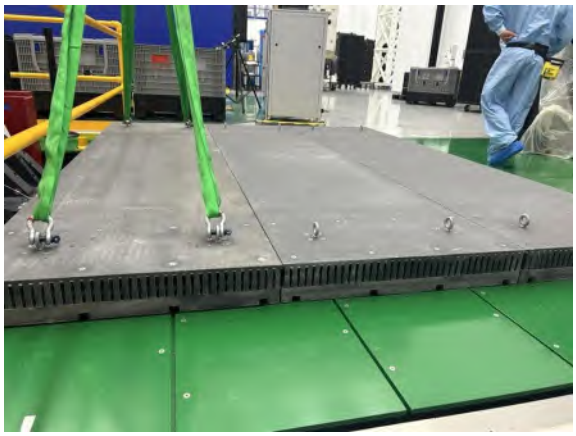


Figure 10 - Installation of Platform 2

Platform installation proceeded as planned with no major issues noted in the fabrication, geometry or placement methodology.

Once installed, a forty-eight (48) Neutron DFAN system, comprised of eight (8) stacks of six (6) devices was erected. Platforms were loaded as intended with no issue. While dial gauges were not installed to monitor deflection, no deflection of the long spans of the platform was noted visually when loaded.

The FRP platforms integrated smoothly with the balance of the Neutron system, adding little time or effort to the setup.



Figure 11 - Neutron Stack on Platform 1 at Head Expander

NSTF DYNAMICS LAB COMMISSIONING RESULTS

To commission the NSTF Dynamics lab each of the facilities were used to run tests using a Structural Tests Model (STM) lent to RAL by Surrey Satellite Technology Ltd (SSTL), which was nicknamed ORINOCO. These tests were designed to verify the technical performance of the different test facilities as well as the validation of test facility procedures. This was especially true moving between vibration testing and acoustic testing as the test hall needed to be reconfigured smoothly and efficiently. Reconfiguring the hall between tests, which included installation of floor platforms, setup of acoustic test system, as well as lifting of the spacecraft from shaker surface to acoustic trolley was performed in under a week.

Vibration Testing

ORINOCO first underwent vibration testing on the slip table (Fig. 13) and then head expander (Fig. 15).

Tab. 1 gives the applied vibration profiles, although notching was applied at key locations to both test the capabilities of the system and protect parts of the STM.

Table 1: Vibration Test Equalisation Sine Profile

Axis	Frequency Range Hz	Unnotched Levels g
Lateral	5-100	0.4
Axial	5-110	0.6

Results of the vibration test campaign confirmed that the shaker systems achieved the target control profiles. No anomalies were noted in the control signals shown in Fig. 12 and Fig. 14, and the system was cleared to proceed to acoustic testing.

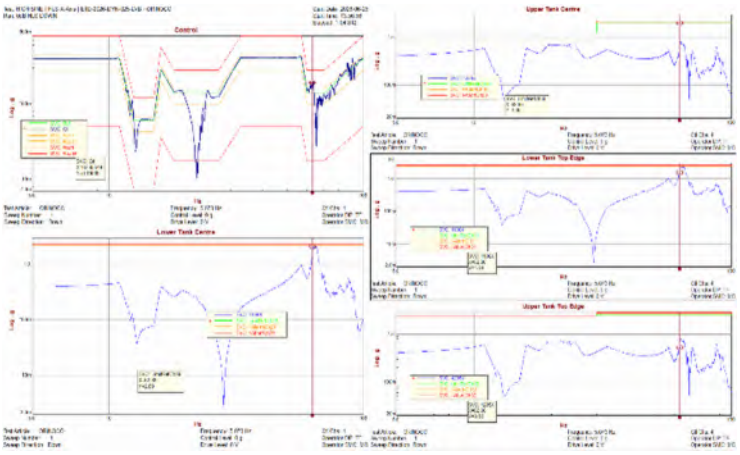


Figure 12 - Control Signals of Lateral Vibration Testing of ORINOCO



Figure 13 - ORINOCO on Slip Table ahead of Lateral Vibration Testing

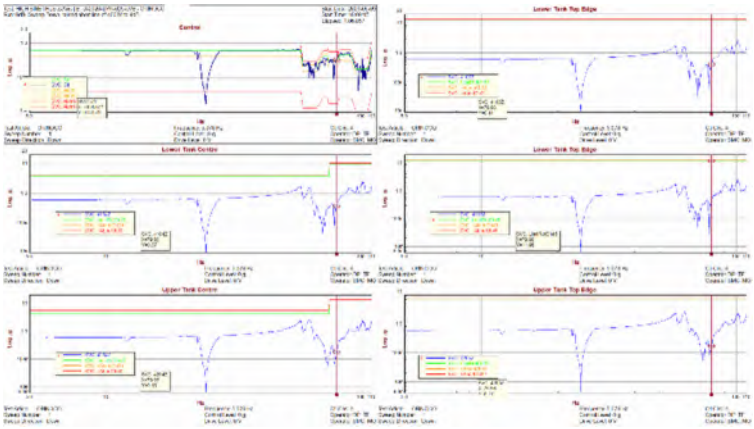


Figure 14 - Control Signals of Axial Vibration Testing of ORINOCO

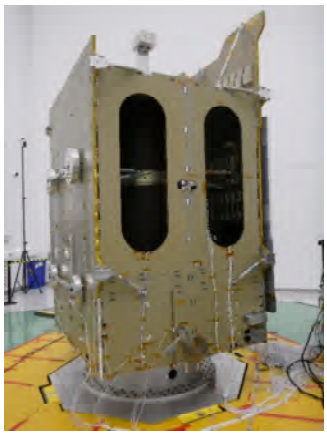


Figure 15 - ORINOCO on Head Expander ahead of Axial Vibration Testing

DFAN Testing

Once the vibration testing was completed the test hall was reconfigured to acoustic testing. This involved using the crane to remove ORINOCO from the head expander, place it on the acoustic trolley, and removing it from the hall. Once cleared, the team set out Platforms 1 and 2, built up eight (8) stacks of Neutron speakers, and placed them in the configuration shown in Fig. 5. Amplifiers were moved in, speakers were cabled, and control and monitor microphones were set out. Finally, ORINOCO was brought back into the centre of speakers, as shown in Fig. 16. The setup of the DFAN system and testing was done in just under a week by the NSTF team.

The Neutron stacks were arranged in a circle with an inner diameter of 5.7 m. The overall stack height was 6.7 m. Control and monitor microphones were supported using floor stands positioned in the space between the Neutrons and ORINOCO.

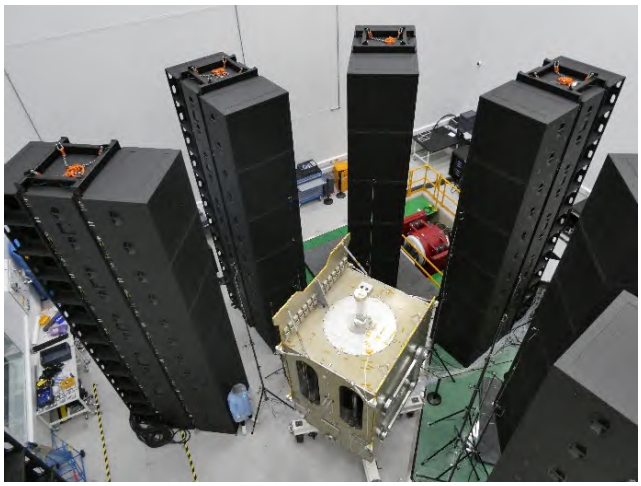


Figure 16 - Aerial View of ORINOCO Acoustic Testing Showing Platform 2 at Slip Table

For system commissioning, ORINOCO was subjected to acoustic loads as given in Tab. 2.

Table 2: ORINOCO Acoustic Test Profile in Octave

Centre Band (Hz)	Test Level (0dB)
31.5	125.4
63	127.7
125	129.1
250	128.2
500	123.1
1000	117.4
2000	113.8
4000	110.8
8000	107.8
OASPL	133.8

The average control and monitor microphone levels for the 0 dB run are shown in Fig. 17.

Results of the DFAN commissioning campaign confirmed that the Neutron achieved the target acoustic test profiles. System setup was achieved within the 48-hour reconfiguration tender requirement

RECOMMENDATIONS FOR FUTURE MULTI-MODALITY TESTING SPACES

The experience of integrating DFAN testing into the NSTF Dynamics Lab offers several lessons applicable to other facilities pursuing similar multi-modal test integration.

1. Where possible, consider all planned testing capabilities during the initial building design phases. When a facility's long-term roadmap includes capabilities that have not yet been defined in detail, reserving floor area, load paths, or crane coverage against a reasonable worst-case footprint can reduce complexity of later integration.
2. Evaluate fixed test-system interfaces, like slip tables, head expanders, and reaction masses, as permanent constraints on all capabilities sharing the space. Facilities planning multi-modal spaces should evaluate each fixed interface against the load, access, and clearance requirements of every test regime intended to share the room.
3. Favor temporary, removable structural solutions over permanent modifications when reconciling conflicting requirements. DFAN itself was an appropriate choice for acoustic test methodology because it is portable, allowing the lab to support other test regimes when not in use. This same concept extends to the FRP platform system which resolves the floor load conflict while preserving the flexibility of the space.

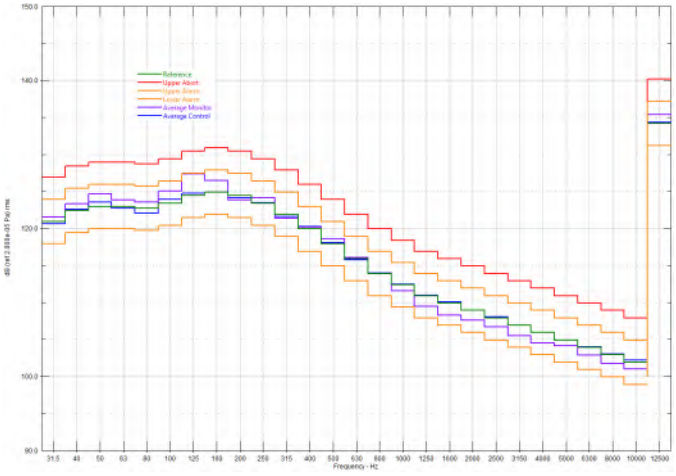


Figure 17 - Average Control and Monitor Microphone Levels Achieved Alongside Reference Lines

4. A structured engineering assessment can resolve conflicts a facility was not originally designed to accommodate. A structured review led to selection and validation of a solution that met all governing requirements without detrimentally impacting the functionality of the room or test system. Facilities facing a similar conflict between existing infrastructure and new capabilities should not view the conflict as disqualifying; assessment and solution implementation, as demonstrated here, can reconcile unintended conflicts between test system requirements.

CONCLUSION

This paper documented the engineering processes undertaken to integrate DFAN testing into the NSTF Dynamics Lab, a space designed and built prior to the acquisition of the Neutron system. The vibration test system's fixed, non-load bearing floor interfaces and the limited overhead crane coverage presented a structural and logistical conflict that, left unresolved, would have prevented the room from supporting DFAN testing at the scale required.

A structured engineering assessment, from problem definition through concept selection and validation selected a bespoke FRP platform system as the solution best suited to the competing system requirements. The platforms redistributed the load of the Neutron acoustic system away from the non-bearing floor areas and onto the surrounding slab, while remaining lightweight, modular, and fully removeable between test campaigns. Two independent analyses confirmed that the platform met the applicable strength requirements. While the selected structure is anticipated to deflect more than the original, conservative requirement, the additional deflection was not shown to affect the stability of the supported equipment.

Commissioning of the integrated Dynamics Lab, using the ORINOCO structural test model, demonstrated that the lab could be reconfigured between vibration and acoustic testing within the required timeframe, and that both test regimes could be performed to specification within a shared space.

The success of this integration shows that independent and conflicting design requirements can be reconciled without compromising either capability. Facilities facing similar challenges can look to this project for a practical reference on how to approach unique engineering challenges.

The authors would like to thank the RAL Space Environmental Test Division, Fibergrate Composite Structures, and Acoustic Research Systems teams for their support throughout the project.

All photographs are courtesy of STFC Ral Space.

REFERENCES

[1] UK Space Agency and Rutherford Appleton Laboratory, "UK Space Facilities Review," UK Space Agency, Swindon, UK, 2017.

[2] R. Elliott, "Removing Innovation Barriers through Open Access Test Facilities: Insights into Whole System and Subsystem Testing, Measurement and Calibration Infrastructure at the New National Satellite Test Centre," International Astronautical Congress, Bremen, Germany, 2018.

[3] Science and Technology Facilities Council, "Launch of Major Space Facilities," STFC RAL Space, Didcot, UK, 2015.

[4] Diamond Light Source, "Kamchatka Quake Reaches Diamond," Diamond Light Source, Didcot, UK, 2025.

[5] National Aeronautics and Space Administration, NASA-HDBK-7010 Direct Field Acoustic Testing, Pasadena, CA: Jet Propulsion Laboratory, 2015.

[6] Fibergrate Composite Structures Inc., "High Performance Composite Solutions: Fiberglass Structural Systems," Fibergrate Composite Structures Inc., Dallas, TX, n.d.

[7] American Composites Manufacturers Association, Fiberglass Grating Manufacturers Council, ANSI/ACMA/FGMC FG01-17-2019 FRP Composites Grating Manual for Pultruded and Molded Grating and Stair Treads, 2nd ed., Arlington, VA: American Composites Manufacturers Association, 2019.

[8] Fibergrate Composite Structures Inc., High Load Capacity Grating Details – HI37 Series, Dallas, TX: Fibergrate Composite Structures Inc., n.d.

[9] American Society of Civil Engineers, ASCE/SEI 74-23 Load and Resistance Factor Design (LRFD) for Pultruded Fiber Reinforced Polymer (FRP) Structures, Reston, VA: American Society of Civil Engineers, 2023.

[10] Science and Technology Facilities Council, "Lift off for UK's National Satellite Test Facility," STFC RAL Space, Didcot, UK, 2023.

CASE STUDY OF A LARGE SCALE DFAN TEST: PART TWO

Dann Hayes, Geoff Eckert, Kaileah Blazek-Freeman, Mitch Skinner

Acoustic Research Systems, Shepherdstown, WV, USA
Lockheed Martin, Kennedy Space Center, FL, USA

KEYWORDS

Direct Field Acoustic Noise (DFAN), large-scale acoustic testing, vertical control zones, discrete response limiting, spacecraft testing

ABSTRACT

Part One of this case study, presented at ECSSMET 2024, provided a holistic review of a Direct Field Acoustic Noise (DFAN) test campaign utilizing 48 full-range electrodynamic acoustic devices deployed to test a payload approximately 5 meters in height [1]. That work covered pre-test system design, structural stability analysis, installation procedures, safety considerations, and acoustic field qualification results, including a detailed comparison of bare chamber and spacecraft test runs. The conclusion of Part One identified the 48-device campaign as a critical stepping stone toward a significantly larger 90-device deployment to support taller payloads. This paper delivers on that objective by presenting a detailed case study of a test campaign that utilized 90 NEUTRON devices, nearly doubling the system size and introducing new technical and logistical challenges that required the development of novel approaches to system deployment, acoustic field control, and test article protection.

This campaign encompassed the acoustic testing of two test articles that were arranged in a stacked configuration. This required a 90 NEUTRON system deployed in 9 stacks of 10 NEUTRONs tall. A key technical contribution of this campaign was the development and deployment of multiple discrete vertical control zones. Additionally, discrete response limiting was introduced, enabling frequency-selective attenuation of specific 1/3-octave bands where structural response limits were approached, rather than applying broadband level reductions. This allowed the test to maintain full specification levels across most of the frequency range while protecting from over testing.

This test campaign required the introduction of a mobile crane as a critical operational asset for system assembly and reconfiguration. This, along with other challenges, necessitated developing detailed Concept of Operations (ConOps) for maintaining safety and schedule compliance. The paper presents the planning methodology and procedural documentation developed to support these operations.

This paper presents acoustic field measurements and key metrics. Comparisons are drawn between the 48-device and 90-device configurations to assess the scalability of acoustic field quality, operational efficiency, and system performance. Lessons learned are discussed, including recommendations for mobile crane integration, vertical zone implementation, and discrete response limiting, with the objective of supporting the continued development of industry best practices for large-scale DFAN testing.

1. INTRODUCTION

Part one of this case study presented an overview of a DFAN test campaign utilizing 48 ARS NEUTRON acoustic devices in an 8-stack by 6-tall arrangement. That paper covered the pre-test engineering including structural stability analysis, system installation and operation and test results. The payload tested was approximately 5 meters tall. The conclusion of part one noted that the 48-device test campaign was a stepping-stone towards the deployment of a 90-device configuration to support the testing of payloads approaching 10 meters in height.

This continuation references that forward-looking statement by presenting a detailed case study of a test campaign that utilized 90 NEUTRON acoustic devices. This campaign represents a substantial scaling of DFAN methodology, nearly doubling the number of acoustic devices and introducing new technical and logistical challenges.

The campaign, conducted at Lockheed Martin facilities in support of the Orion Multi-Purpose Crew Vehicle (MPCV) program, involved testing of an integrated Crew-Service Module (CSM) test article, comprised of the Environmental Test Article Crew Module (ETA CM) and the European Service Module Structural Test Article (ESTA). These tests required the development and deployment of dual-zone and triple-zone vertical configurations to address the differing acoustic requirements at various vertical positions along the test articles. This test was conducted at NASA's Kennedy Space Center (KSC).

Beyond the acoustic field performance data, this paper places an emphasis on the logistical and operational challenges that accompany large-scale DFAN deployments. Topics include the use of a

mobile crane for system assembly and disassembly, the development of ConOps for managing 90 NEUTRONs in a space constrained facility, and the implementation of novel acoustic control techniques including multiple discrete vertical zones each with discrete response limiting.

2. SCALING FROM 48 TO 90 DEVICES

2.1 System Configuration Overview

The transition from a 48-device configuration (8 columns of 6 devices) to a 90-device configuration (9 columns of 10 devices) required the scaling of multiple facets of the ARS system. The 10-tall NEUTRON configuration was designed to maintain adequate field uniformity and acoustic performance over the entire height of an article approaching 10-meters tall.

The increase from six to ten NEUTRON devices per stack introduced new structural stability considerations. The taller columns required updated structural analyses following the internal reference standards developed and discussed in Part One [1,2], with particular attention to the behavior of partially assembled configurations during the NEUTRON system build process.

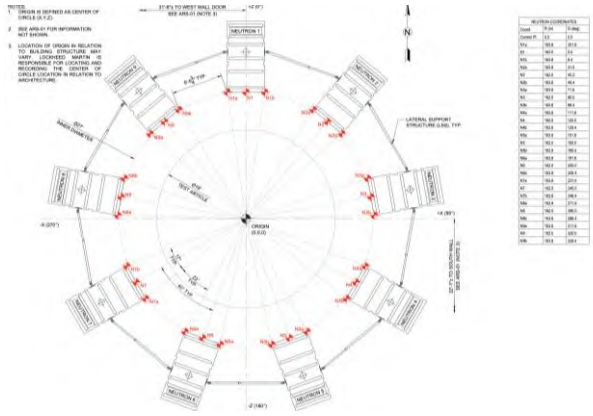


Figure 1: Overhead View of a 9-Stack NEUTRON System

2.2 Power and Signal Distribution

Scaling to 90 NEUTRONs required expanding both the power and signal distribution architecture that was discussed in Part One. Previously, ARS was able to assign 2 NEUTRONs to each drive which resulted in a total of 24 drives needed, with 24 corresponding control microphones. If this scaled linearly to the 90 NEUTRON configuration, it would have indicated use of 45 control microphones. For efficiency, the drive configuration was adjusted to use 4 drives per stack, leading to 36 drives and 36 control microphones overall. These drives are distributed to the NEUTRONs via the Dante Audio-Over-IP protocol. The increased drive count required additional audio processors that serve as the signal A-D and Dante distribution hub. The CORERACK amplifier rack count increased from 8 to 15, and the system power requirements were scaled to ensure an adequate mains power supply from the portable generator.

A 500 kVA generator was used for the 48 NEUTRON campaign, while a 1500 kVA generator was used for the larger 90 NEUTRON campaign. Using prior test data to compare the proposed test configuration and profile levels, the test team estimates the maximum OASPL that can be achieved given the maximum allowable output by the amplifier limiters. It can be assumed that the amplifier is pulling its maximum peak power of 15 kVA at this point, though in practice it will be somewhat less depending on the profile. This number can then be scaled down to the actual OASPL of the test given that every 3 dB reduction is half the power. This gives us the expected peak power draw for each amplifier for the overall test level. Multiplying that by the number of amplifiers in the system will give you the peak power draw seen by the generator. A 2:1 conservatism factor is also typically used to account for any discrepancies in the generator performance. For this test configuration and acoustic spectrum, ARS would typically use around a 1000 kVA generator. Generator availability issues necessitated using the larger unit. Generator availability can be challenging in warmer climates during summer months, especially during hurricane season. No adverse issues were noted from using the larger generator.

The combined DFAN control and data acquisition system (DAS) architecture validated during the 48-device campaign [3,4] was scaled to accommodate the increased channel count that included additional inputs and outputs.

The fiber optic transport link between the test circle and a remote control area was maintained. A dedicated DAS rack was assembled and positioned near the speaker circle during testing. This rack handled instrumentation input from the test article, parallel or tee'd outputs to an external DAS, digitization and distribution of the drive signals via Dante, and discrete ground connections for instrumentation.

3. LOCKHEED MARTIN TEST CAMPAIGN

3.1 Test Article Description

The Lockheed Martin test campaign encompassed two distinct test articles that were combined to create a flight representative test article. The Environmental Test Article Crew Module (ETA CM) is the former Artemis I Crew Module built by Lockheed Martin, which was re-purposed post-flight as a test article for an abort-level campaign. The European Service Module Structural Test Article (ESTA) is a structural representation of the Orion European Service Module (ESM), developed by the European Space Agency (ESA) and Airbus for structural qualification of the ESM [5]. The ESTA includes a model of the Crew Module Adapter

(CMA), built by Lockheed Martin, that joins the CM and ESM. These modules were stacked to create a high-fidelity test article of the combined Crew-Service Module (CSM). This test campaign was conducted from November 10, 2025, to November 22, 2025. The test was completed 2 days ahead of schedule after all test objectives were successfully completed.



Figure 2: Orion CSM DFAN Testing at LASF

3.2 Mobile Crane Operations and Logistical Challenges

One of the most significant logistical challenges encountered during the Lockheed Martin campaign was the management of 90 acoustic devices within the physical constraints of the test facility. With 10 NEUTRONs per stack and 9 stacks surrounding the test article, the process of constructing, opening and restoring the DFAN configuration for test article installation required careful choreography.

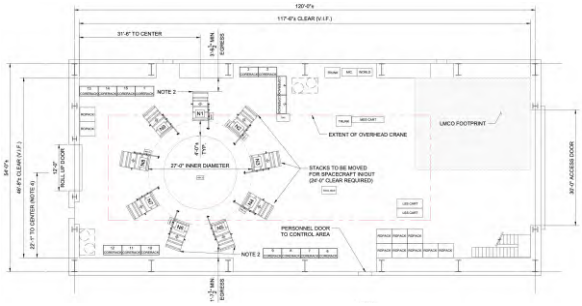


Figure 3: Overhead View of Speaker Circle Layout in the LASF

The main hurdle was the physical size of the specified test facility, the Launch Abort System Facility (LASF) at KSC. The diameter of the CSM test article and ground support equipment (GSE) was 19 ft, which necessitated an inner speaker circle diameter of 27 ft. The overhead crane at the LASF has a crane envelope width of just over 27 ft, leaving the rigging points of 3 NEUTRON stacks outside the crane footprint. If the diameter of the speaker circle was reduced to fit all speaker stack rigging points within the overhead crane envelope, the overall test performance would have been detrimentally impacted. ARS has developed best practices to keep the NEUTRON devices a minimum distance from the test article. Reducing the distance can affect the uniformity of the acoustic field and cause personnel and GSE access issues around the annulus of the speaker circle. Previous Orion testing was conducted using a full diameter speaker circle, so it was desired to have identical test configurations between the tests. Therefore, a different solution was pursued. An appropriately sized mobile crane for a 10-tall NEUTRON stack, weighing approximately 17,000 lbs, was introduced to handle the rigging and placement of the 3 NEUTRON stacks outside of the facility crane footprint. This applied to stacks N1, N5, and N6 depicted in Figure 3. The mobile crane became a critical path asset for the test campaign; its scheduling, positioning and operational constraints required integration into the overall ConOps.

Key considerations for mobile crane operations included: crane access pathways within the facility, floor loading limitations, minimum and maximum reach requirements for accessing the 3 NEUTRON stacks, coordination with the overhead bridge crane used for movement of the other 6 stacks, and development of a detailed schedule to accommodate mobile crane vendor availability.

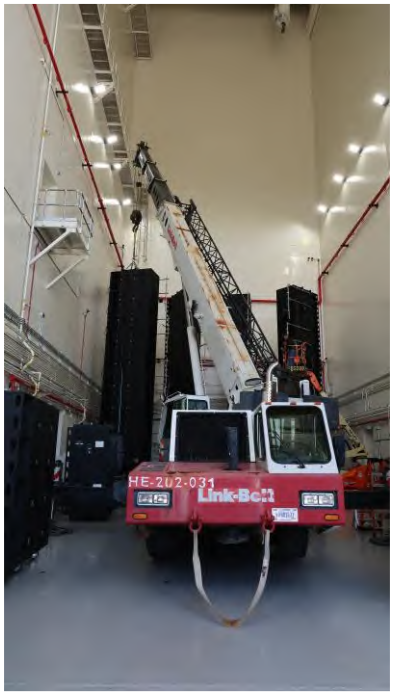


Figure 4: Mobile Crane Operations During Testing

At 10 NEUTRON units tall, the speaker stacks are in an unstable configuration until 4 stacks are supported in series by the Lateral Support System (LSS). Therefore, temporary ballasting was required during assembly of the speaker circle. A single standing stack utilized a ballast block support on either side of the stack. The ballast block could be removed once the LSS was connected to an adjacent speaker stack. Careful ConOps planning was performed to strategically erect NEUTRON

stacks, optimize ballast block usage, and minimize path interference for other assets, such as the mobile crane and personnel lifts. An example of a typical drawing for ballast deployment is depicted by Figure 5.

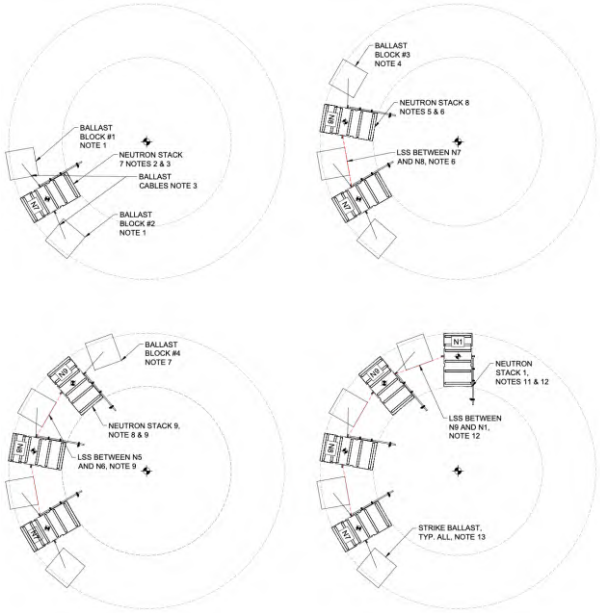


Figure 5: Ballast Block Deployment ConOps

An external generator was utilized for this test campaign. It was positioned on a concrete apron adjacent to the LASF, with the power feeder cabling run through building penetrations to the ARS CORERACK location. A power quality meter (PQM) was utilized on the generator to verify performance.

There were also other facility constraints to consider during the test operations. The LASF primarily supports activities for the Orion program that include the Launch Abort System (LAS) and working with vehicles fueled with hypergolics. Operating those systems require specialized fire detection hardware that could be sensitive to acoustic excitement. Due to the proximity of the LASF fire deluge system, the system was deactivated for the duration of the campaign by isolating the valves. The facility Infrared (IR) cameras were inspected for damage before and after the test. The overhead crane console was removed from the high bay for all test runs, since replacement parts for that console no longer exist. This required reinstallation of the console for any crane operations during the campaign. Lastly, a couple of crack gages were installed to monitor potential propagation of previous drywall damage in the high bay during acoustic test runs.

3.3 Multiple Discrete Vertical Zones

A significant technical advancement demonstrated during the Lockheed Martin campaign was the implementation of multiple discrete vertical zones within the DFAN system. In conventional DFAN testing, all acoustic devices in the system are controlled to achieve a single target spectrum across the entire acoustic field. Traditionally, the Orion Crew and Service modules have been DFAN tested independently before integrating the modules into the CSM configuration. Each module has its own acoustic spectrum that results from its position within the SLS rocket and its own acoustic cavities resulting from fairings and spacecraft architecture. The Service Module (SM) receives more low frequency excitation, while the Crew Module (CM) receives more high frequency noise. Testing the two modules simultaneously in the combined CSM configuration requires the application of at least 2 distinct vertical zones. For the primary campaign configuration, the top 4 devices in the NEUTRON stack were dedicated to the CM zone of the CSM, while the bottom 6 NEUTRONs targeted the SM zone.

Attached to the upper portion of the SM is the Crew Module Adapter (CMA). During launch, the CM is covered by the Launch Abort System (LAS) and its associated fairings and the ESM is enclosed by the Spacecraft Adapter Jettisonable (SAJ) fairings that jettison on orbit. The outer walls of the CMA are the only area of the Orion modules that are directly exposed to liftoff acoustics. As such, the expected flight environment on the CMA is higher than the bulk of the SM, which is covered by the SAJ fairings.

For this campaign, dual zone test runs were the emphasis. This is the most likely configuration to be used for a test on CSM flight hardware. Additionally, both single zone and triple zone configurations were explored. The single zone configuration involved leaving the bottom 6 NEUTRONs in the stack muted while only exercising the top 4. This is intended to simulate a CM only test but in the CSM configuration. Results for the single zone test are depicted by Figure 6.

The microphone configuration included 4 discrete rings of monitor microphones around the test article at varying heights. For all configurations, the monitor microphone averages were compared to the control mic averages for the given ring.

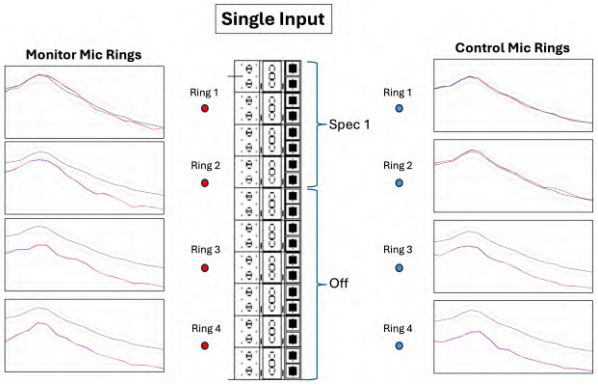


Figure 6: Schematic and Performance of Single-Zone Modified Vertical Configuration

Most of the test runs were conducted on the dual zone configuration. In this configuration, the top 4 speakers in the stack were dedicated to the CM spectrum and the bottom 6 speakers were dedicated to the SM spectrum. The influence of the zones on one another can be seen in Figure 7. Ring 2 was assigned the CM spectrum while the adjacent ring 3 was assigned the SM spectrum. Monitor microphone ring 2 shows somewhat elevated high frequency energy which more closely matches the SM spectrum. Even though the monitor microphones show the mixing of drive signals, the control microphones were responding nominally.

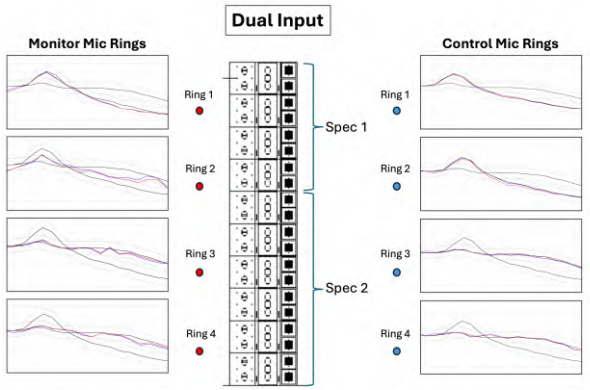


Figure 7: Schematic and Performance of Dual-Zone Vertical Configuration

A triple zone configuration was also demonstrated that added a discrete zone for the CMA. This allows the CMA to be driven harder than the remainder of the SM, with results depicted by Figure 8. As mentioned previously, the CMA is the only region of the Orion modules exposed directly to ascent acoustics, due to the lack of encompassing fairings.

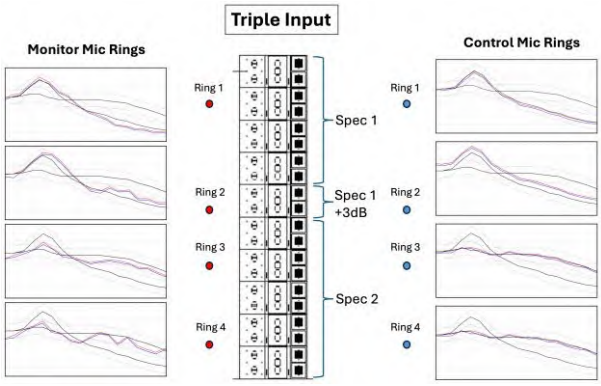


Figure 8: Schematic and Performance of Triple-Zone Vertical Configuration

The implementation of discrete vertical zones required modifications to the control system architecture. Each zone utilized its own set of control microphones positioned at the appropriate vertical height, and the 1/3-octave band Multiple Single Input, Single Output (SISO) controller was configured to manage each zone as an independent control. The uncorrelated drive signals within each zone ensured that spatial uniformity and sound pressure levels (SPL) were maintained within each controlled region.

Controllability between zones is highly dependent on the distance between microphones and the gradient of energy that exists between each zone. This can be characterized by measuring the response from all zones while activating only one at a time. For instance, in a two-zone system, if an output of 120 dB OASPL is driven into Zone 1, and the control microphone(s) for Zone 2 reads 114 dB OASPL, the difference between Zone 1 and 2 cannot exceed 6 dB OASPL. This example is a generalization, as the variation between 1/1 and 1/3 octave bands will depend on propagation of wavelengths, but studying the effects at higher resolutions can help predict the results with more detail.

3.4 Discrete Response Limiting

The traditional Orion module-level DFAN tests use a different configuration from that of flight. It also uses a test specific input acoustic spectrum that is not the same as the flight environment. Fairings add acoustic attenuation to the CM and SM during flight and add acoustic cavities. During DFAN testing, the vehicle fairings are not installed on the vehicle, so certain components respond higher (or differently) in the test environment than they would in flight. During the Structural Test Article (STA) program on Orion [5], an acoustic response limiting strategy was implemented to limit the response of specified components. This is achieved by specifying a do-not-exceed profile on a given sensor (i.e. accelerometer) [6]. By limiting components with less margin in the testing configuration, this enables other components to respond to a higher level. The goal is to reach the desired response (acceptance, qualification, etc.) on as much of the vehicle as possible without exceedances. This method of response limiting is preferred over input spectrum notching which causes a global reduction.

Before validating the discrete response limiting on the CSM test article, a test fixture comprised of 3 aluminum honeycomb panels mounted at different vertical levels on a support truss was used. One panel was located at the height of the CM, one at the height of the CMA, and one lower in the SM region. The 3 panels were instrumented with triaxial accelerometers. This fixture verified that discrete response limiting was effective on an easy-to-model analog. This also provided the opportunity to “tune” the notching capabilities of the response limits. Overly aggressive response limiting can cause test aborts or very reduced overall sound pressure levels.

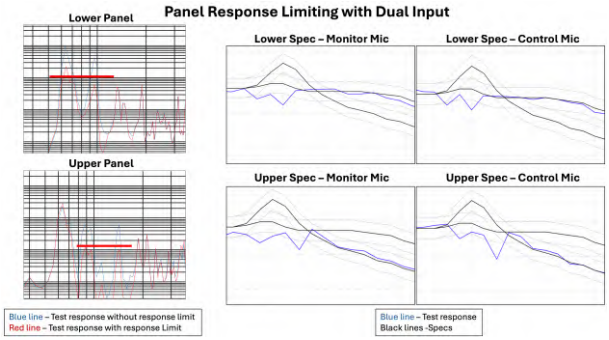


Figure 9: Orion CSM Pathfinder Demo Panel Response Limiting Results

During CSM DFAN pathfinder testing, components on both the CM and SM utilized response limiting. With separate acoustic input spectra applied to each module, discrete response limits were applied to each spectrum. This novel technique ensured vehicle protection and allowed for precise removal of energy. Limiting was seen on accelerometers on one side of the test article while the other side of the vehicle was minimally affected.

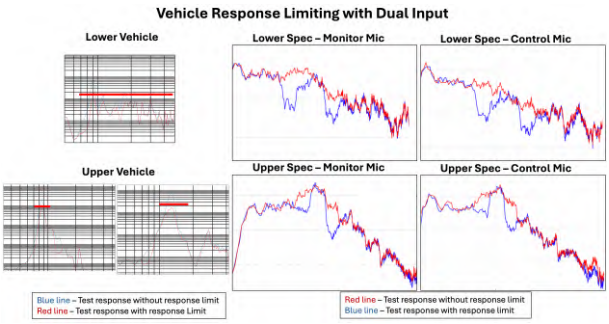


Figure 10: Orion CSM Pathfinder Demo Vehicle Response Limiting Results

4. COMPARISON AND DISCUSSION

4.1 Logistical Considerations at KSC

A previous DFAN capability demonstration was conducted for the Orion program at KSC's Space Systems Processing Facility (SSPF). This capability test featured the same 90-device NEUTRON configuration (9 columns of 10 devices). The logistical considerations for the original demonstration were distinct from the pathfinder campaign at the LASF that is the subject of this paper. The Orion pathfinder test campaign occurred at the LASF, which is a controlled facility only occupied by the Orion program. In contrast, the SSPF has many tenants that are all working on their own critical operations. The SSPF also directly supports missions to the ISS with extensive laboratory space and workstations. Time critical laboratory operations and the associated delays must be considered during initial scheduling. Even though the LASF and SSPF are only a ½ mile apart, different challenges were the main driver of ConOps changes.

For the original demonstration, a facility impact assessment followed the methodology described in Part One [1,8], utilizing inverse-square calculations and material Sound Transmission Class (STC) ratings to predict acoustic levels at key locations throughout the SSPF high bay and adjacent offices and laboratories. Given the proximity of other active spacecraft processing operations at KSC, these predictions were critical for establishing safe operating procedures and ensuring minimal disruption to neighboring programs.

Facility impact assessments for the testing at LASF focused on the impact to building systems such as fire detectors and operator safety. The Orion program was able to schedule and minimize parallel operations occurring inside the LASF which streamlined the testing schedule.

Similar power architectures can be utilized between test campaigns with some logistical differences. The external generator is placed outside of the test space and then has electrical feeder cable run into the test area to connect to the ARS system. Given that SSPF is an active secure integration facility, easily accessible external locations to place the generator were limited. The generator was set on an external ramp that leads to the airlock roll up door. This area is fenced and only accessible by badged NASA personnel. Access to the generator for operations and refuelling was limited as a result. Additionally, KSC rules forbade the operation of the generator outside during lightning warnings at KSC. Lightning is very common at KSC during certain times of the year. Strategies were implemented to negate the impact of generator access for all phases of the test campaign.

Generator operation at the LASF is more straightforward as the generator does not have to be placed in a secure area. In both cases, the generator was tied into an external ground connection on the testing buildings.

4.2 Scaling Effects on Acoustic Field Quality

A key question addressed by this campaign is whether the acoustic field quality demonstrated with 48 devices can be maintained when scaling to 90 devices. The results from this campaign indicate that the acoustic field characteristics – uniformity and diffusivity – are preserved at the larger scale [7].

4.3 Operational Efficiency at Scale

Despite the near-doubling of the device count, the operational procedures developed for the 48-device campaign scaled effectively to the 90-device configuration. The use of the ARS Microphone Support System (MSS) for pre-mounting instrumentation continued to reduce in-circle work time and trip hazards. The MSS allows microphone position to be fixed in 3D space relative to the

NEUTRON stack that it is mounted to. Each NEUTRON stack is then placed at a known position relative to a pre-determined location, typically the center of the speaker circle. This technique allows for the microphone-to-article relationship to be defined prior to test set up, rather than measuring in-situ for each microphone. It overcomes the hurdle of being able to accurately measure the location of a microphone in 3D space due to access limitations while the test article is located within the speaker circle. Custom laser cut jigs were also introduced to assist laying out the projection of the MSS from the front of a NEUTRON.

The primary area where operational complexity increased was in configuration changes requiring the mobile crane. These operations required more detailed planning, additional safety oversight, and tighter coordination between the DFAN team, facility operators, and mobile crane operators. The development of comprehensive lift procedures with clear signoff requirements was essential for maintaining safety and schedule compliance.

4.4 Key Metrics Summary

Parameter	48 Devices (Part One)	90 Devices (Orion)
Configuration	8 by 6	9 by 10
Drive Channels	24	36
Vertical Zones	Single	Dual / Triple
Response Limiting	Not Used	Yes, Discrete
Mobile Crane Required	No	Yes
Test Level Achieved	~141 dB OASPL	147 dB OASPL

5. LESSONS LEARNED

The execution of a 90-device DFAN campaign produced a few lessons learned that are relevant to the broader industry as DFAN testing continues to scale in size and complexity.

First, the importance of comprehensive ConOps cannot be overstated. A major example of this is the incorporation of a mobile crane in the testing flow. When device configurations grow beyond what can be handled within the footprint of the facility overhead crane, the mobile crane becomes a critical path resource. Early coordination with crane service providers, detailed pre-planning of access routes and lift sequences, and integration of crane operations into the test procedure documents are essential for maintaining schedule and safety.

Second, the development of multiple discrete vertical zones demonstrated that the DFAN methodology can be extended beyond uniform-field testing to provide spatially tailored acoustic environments. This capability opens new possibilities for testing tall, multi-element spacecraft assemblies where different sections may have different acoustic qualification requirements.

Third, discrete response limiting proved to be a valuable tool for protecting sensitive hardware while maximizing the qualification value of the test. By targeting level reductions to specific frequency bands rather than applying broadband reductions, the test team was able to maintain specification levels across a greater percentage of the frequency range (and test article).

Fourth, the successful deployment of the 90-device system at a facility that on paper was not ideal to use for a system of this size reinforces the portable and adaptable nature of the DFAN methodology. The facility impact assessment and acoustic propagation prediction techniques described in Part One [1,8] continue to provide reliable guidance for new deployment locations.

6. CONCLUSION AND FORWARD WORK

This paper has presented a detailed case study of a large-scale DFAN test campaign utilizing 90 ARS NEUTRON acoustic devices. The campaign conducted at NASA's Kennedy Space Center for the Lockheed Martin Orion program demonstrated that the methodology can be effectively scaled while maintaining acoustic field quality and operational safety and efficiency standards.

The introduction of multiple discrete vertical zones and discrete response limiting per zone represents a meaningful technical advancement in DFAN testing. These tools enable new testing configurations that could potentially reduce cost and schedule, while allowing for a test configuration that is more representative of the flight configuration.

The logistical and operational challenges encountered during this campaign reinforced the need for extensive pre-test planning and ConOps development. As tests grow, these operational considerations will become increasingly important to the overall outcome of the test.

Forward work includes the refinement of vertical zone control and discrete response limiting to support more complex multi module articles. The authors also plan to continue publishing operational and technical data from future campaigns to support the development of industry best practices for large-scale DFAN testing.

ACKNOWLEDGMENTS

The authors would like to express their gratitude to the engineering and operational teams at Lockheed Martin for their collaboration and support during this test campaign.

REFERENCES

1. E. Friedlander, G. Eckert and D. Schick, “Case Study of a Large Scale DFAN Test: Part One,” in European Conference on Spacecraft Structures, Materials and Environmental Testing, Noordwijk, 2024.
2. Acoustic Research Systems, "Structural Design Criteria," Shepherdstown, 2024.
3. E. Friedlander, E. Kinsella, D. Schick and T. Hoffmann, “Verifying a Novel Approach to Acoustic Testing: Acoustic Devices & Control Systems,” in 32nd ATS, Virtual, 2022.
4. P. Shorter, E. Friedlander, D. Schick and T. Hoffman, "Validation of Novel Direct Field Acoustic Test Workflow by Simulation and Measurement," in 17th ECSSMET, Toulouse, 2023.
5. M. McNelis, W. Hughes, J. Larko, S. Bittinger et al., "Examination of the Structural Response of the Orion European Service Module to Reverberant and Direct Field Acoustic Testing," in 23rd ICSV, London, 2017.
6. D. Schick, D. Hayes, R. Mangelschots and S. M. Schwarzendahl, "Case Study of an Octave Band Control Method for Structural Response Notching," in European Conference on Spacecraft Structures, Materials and Environmental Testing, Noordwijk, 2024.
7. E. Friedlander, E. Kinsella, D. Schick and T. Hoffman, "Qualification of DFAN Field & Improved Acoustic Control Methods," in 32nd ATS Conference, Los Angeles, 2023.
8. C. Dutt, "Structural and Practical Implications of Direct Field Acoustic Testing on Host Facilities: A Comprehensive Overview," in ECSSMET, Noordwijk, 2024.

ECSSMET
Braunschweig Germany 2026

Additive manufacturing

MULTIFUNCTIONAL BATTERY PACKAGING FOR SPACE SYSTEMS ENABLED BY METAL ADDITIVE MANUFACTURING: DESIGN AND VALIDATION OF THE BATMAM 96-CELL DEMONSTRATOR

H. Saudan [(1)], D. Novo [(1)], E. Onillon [(1)], V. Giuliani [(2)], A. Iglesias [(2)], M. Garcia [(2)], F. Rottmeier [(2)]

[(1)] CSEM, Rue de l'Observatoire 58, 2002 Neuchâtel, Switzerland, Email: herve.saudan@csem.ch
[(2)] Almatech, Quartier de l'innovation, 1015 Ecublens, Switzerland, Email: fabrice.rottmeier@almatech.ch

KEYWORDS

Additive manufacturing, electrically functional structures, embedded conductors, multifunctional battery packaging, LPBF, spacecraft energy systems

ABSTRACT

Embedding electrical functions within metallic additively manufactured structures offers a promising pathway toward enhanced functional integration in spacecraft equipment. However, most reported demonstrations remain limited to the incorporation of commercial off-the-shelf components, such as wires, connectors, and sensors, rather than the true integration of these functionalities directly into the structural design.

This paper presents the BatmAM project, which extends CSEM's electrical functionalization approach [16] to a representative spacecraft battery-pack demonstrator. The proposed design combines structural support, embedded electrical distribution, cell interfaces, heat-dissipation paths and assembly features within a reduced number of additively manufactured components.

In close collaboration with Almatech, a 96-cell (8S12P) demonstrator was designed, manufactured and assembled using a process combining LPBF, epoxy insulation casting and machining. The resulting architecture distributes structural and electrical functions between a multifunctional frame, covers and compliant contact interfaces, while remaining compatible with commercial lithium-ion cells and conventional verification approaches.

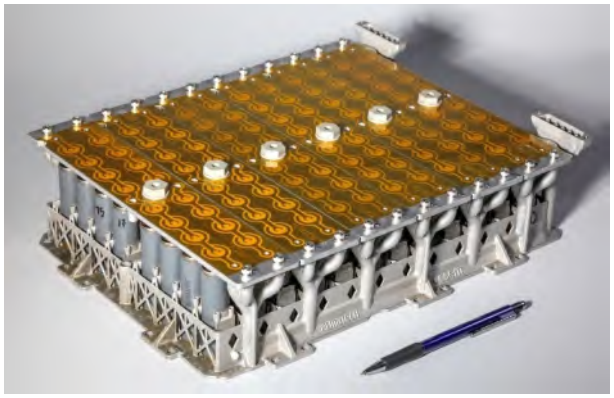


Figure 1: Final prototype of the battery pack

The demonstrator was subjected to electrical characterisation, vibration, shock and thermal-vacuum testing representative of space applications. The results confirmed that electrically functional metallic structures can be implemented at subsystem level while maintaining structural integrity and electrical continuity under representative environmental conditions. The approach also reduced packaging mass and manufacturing lead time compared with conventional battery-packaging solutions.

Beyond the battery application, the work contributes to the maturation of electrically functional additively manufactured structures. The packaging architecture reached TRL 5 and MRL 6, while the complete battery subsystem stands at TRL 4, confirming both the maturity of the demonstrated packaging concept and the remaining work required for full subsystem qualification.

1. INTRODUCTION

Electrical energy storage systems are critical elements of modern spacecraft, directly influencing mission lifetime, operational flexibility and overall system reliability [1,2]. While significant progress has been achieved at cell level, battery packaging architectures still rely largely on conventional mechanical integration approaches involving dedicated support structures, busbars and thermal interfaces [2,3].

While these solutions benefit from extensive flight heritage, they generally result in high part counts, significant assembly effort, and limited flexibility when adapting designs to mission-specific requirements. Future battery packs will require solutions that are simultaneously optimized, highly customized, and cost-effective. Achieving these objectives remains challenging with conventional manufacturing approaches, which constrain the achievable level of functional integration and limit opportunities for architectural simplification.

This work investigates Design for Additive Manufacturing (DfAM) as an enabling approach for enhanced system-level integration. Its potential is assessed through the development of a battery-

pack demonstrator within the BatmAM project, where structural support, electrical interconnections, and assembly interfaces are consolidated into a single additively manufactured platform. The objective is not to introduce a new electrochemical storage technology, but rather to demonstrate how electrically functional metallic structures can increase integration levels and contribute to the simplification of spacecraft equipment architectures.

2. STATE OF THE ART

2.1. Conventional Spacecraft Battery Packaging

Lithium-ion batteries have become the reference energy-storage technology for spacecraft due to their high specific energy, long cycle life and extensive operational heritage [2,8]. However, while cell technologies have evolved significantly, the packaging architectures surrounding them remain largely based on conventional mechanical and electrical integration principles [2,3].

A typical spacecraft battery is assembled from individual cells, integrated within a structural enclosure and interconnected through busbars, welded tabs, wire bonds or harness assemblies. Additional elements typically include fasteners, insulation materials, connectors, sensors, thermal-interface hardware and support structures. As a result, each engineering function is generally implemented through a dedicated set of components before being integrated into a complete battery assembly.

This design philosophy benefits from substantial flight heritage and mature qualification practices. However, the reliance on dedicated components and joining operations increases the number of parts, interfaces and manufacturing steps that must be designed, manufactured, procured, inspected and assembled. It also creates dependencies on external suppliers for COTS elements and reduces accessibility to individual cells and electrical interfaces when bonded or welded connections are used. Consequently, while conventional battery packaging remains robust and well understood, it still offers significant opportunities for architectural simplification and functional integration.

This motivates approaches that reconsider the battery package as an integrated engineering system rather than as a passive enclosure for electrochemical cells.

2.2. Additive Manufacturing for Electrically Functional Structures: Opportunities and Challenges

Over the last two decades, additive manufacturing has evolved from a prototyping technology into an established production method for aerospace and space applications [4,5]. LPBF is now routinely used to manufacture lightweight structural, thermal and fluidic hardware while enabling part consolidation and geometry optimisation through Design for Additive Manufacturing (DfAM) [5,8]. Beyond these established benefits, additive manufacturing also offers opportunities for integrating multiple engineering functions within a common architecture.

Several authors have explored the integration of electrical functions (*Figure 2*) into additively manufactured parts. Most early developments focused on structural electronics and relied on surface or near-surface integration of conductive tracks and electronic components on polymeric or dielectric substrates [9-13]. More recent work [14] extended these concepts towards multifunctional structures and metallic components through – among others – the integration of conductive pathways following CSEM's patented approach [16]. In parallel, additive approaches dedicated to spacecraft thermal-control hardware have demonstrated the direct printing of heating functions onto metallic tubing and other components [15].

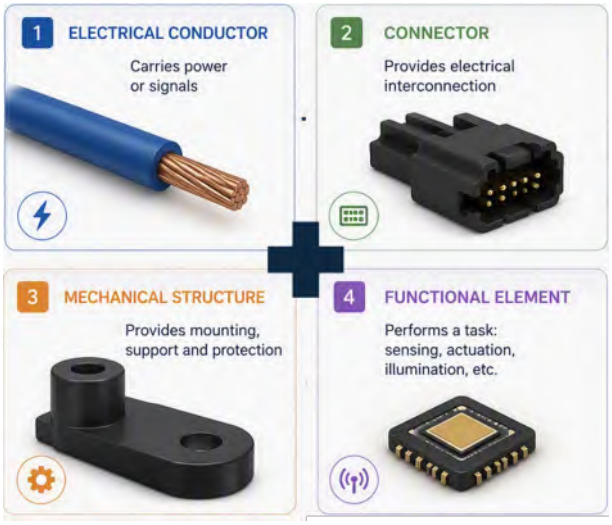


Figure 2: Key functional building blocks traditionally implemented as separate components and targeted for integration into a single structure.

These developments highlight the potential of additive manufacturing to reduce wiring complexity, interconnection hardware and assembly effort. However, implementing electrical functions within structural components remains challenging because conductive pathways, electrical insulation and load-bearing functions must coexist within the same architecture. Additional constraints arise from the manufacturing process itself, including feature resolution, material compatibility, dimensional tolerances, post-processing requirements and inspection capability. For metallic AM processes such as LPBF, these challenges are further compounded by support strategies, powder removal, surface roughness and machining requirements, all of which can directly influence electrical performance, insulation integrity, structural behaviour and overall manufacturability.

To address these limitations, CSEM developed the patented EP3740382 technology [16]. The concept, illustrated in Figure 3, relies on a manufacturing sequence in which an electrically conductive structure is produced by additive manufacturing with future electrical pathways temporarily connected to the surrounding material through sacrificial bridges or skins. Following the casting and solidification of the insulation material, these sacrificial elements are removed by conventional machining, thereby electrically isolating the conductive pathways from the surrounding metallic structure. When an epoxy resin is used as the insulation material, solidification is achieved through a polymerisation process.

This approach has already been demonstrated through applications such as an additively manufactured slip ring rotor [17] and a multifunctional pipe segment integrating built-in heating, sensing interfaces and connector [18] (see *Figure 4* & *Figure 5*).

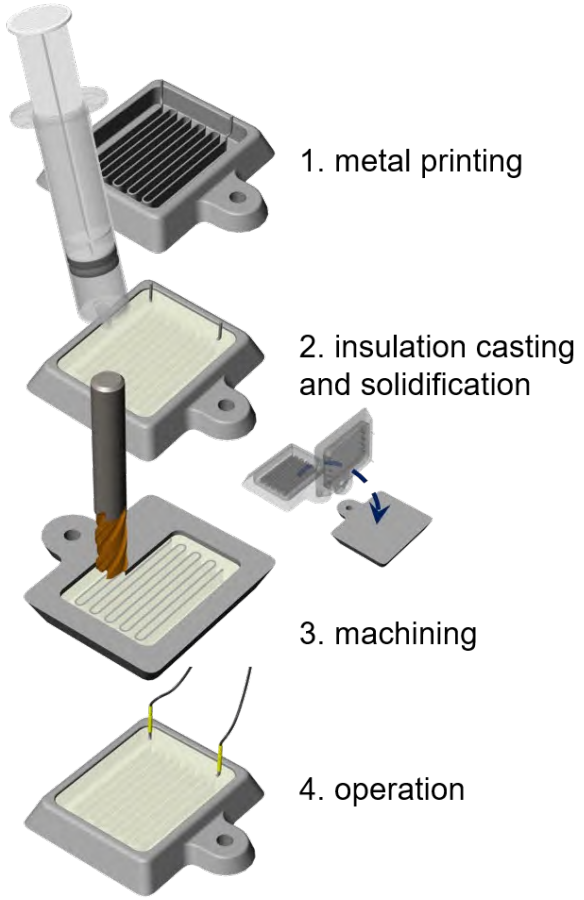


Figure 3: DfAM concept [16] for integrating electrically insulated conductive features within LPBF-manufactured metallic structures.

The BatmAM project extends this concept from component-level functionality to subsystem-level integration by investigating how electrically functional metallic structures can support structural functions and electrical distribution within a spacecraft battery pack.

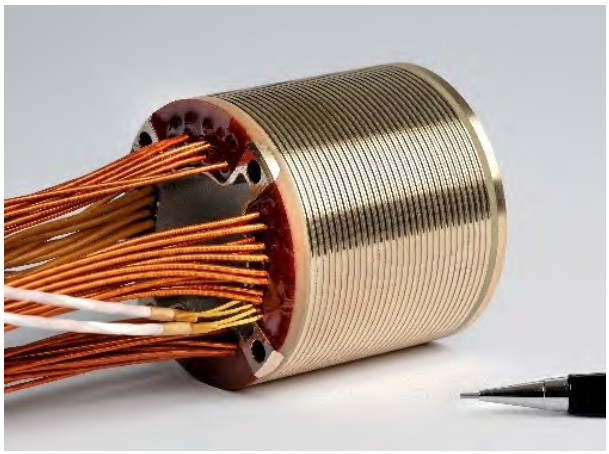


Figure 4: Slip ring rotor re-designed for AM [17]. For 30 tracks, the new design reduces the number of parts from > 60 to one single part.



Figure 5: Pipe segment with heater, temperature sensor and connector embedded in one part [18]. An animation of the manufacturing sequence is available here.

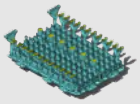
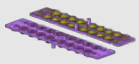
3. MULTIFUNCTIONAL DESIGN CONCEPT

In the BatmAM project, the objective was to simplify the pack architecture, reduce packaging mass and integration effort. The concept was therefore developed around a limited number of multifunctional structural elements designed to preserve compatibility with commercially available lithium-ion cells and established verification practices. This concept provides the basis for the function allocation described below and for the representative prototype presented in Section 4.

The proposed architecture applies the electrically functional LPBF approach introduced in Section 2.2 to battery packaging. Unlike conventional AM components, where electrical functions are typically provided by external wires, busbars or connectors, this approach allows conductive pathways to become part of the structural component itself. The same component can therefore contribute to mechanical support, electrical routing and thermal roles. This capability allows the battery package to be treated as an electrically functional mechanical component rather than as a passive enclosure

carrying separate wiring and busbar elements. The architecture was organised around a limited number of integrated elements, each carrying a defined subset of functions summarised in Table 1.

Table 1: Functional allocation overview

Function	Frame 	Covers 	Spring contacts 
Primary structure	X	X	
Mechanical interfaces to spacecraft	X		
Cell positioning	Radial	Axial	Axial compliance
Parallel electrical distribution	X		
Series electrical interconnection		X	
Cell-to-network electrical interface			X
Electrical connectors	X		
Tolerance and thermal-expansion accommodation	Cells - radial		Cells - axial
Thermal management	Cell heat dissipation path through the frame	Heaters glued on the covers	Thermal link between covers and cells

4. PROTOTYPE DETAIL DESIGN, MANUFACTURING AND ASSEMBLY

4.1. Design

The multifunctional architecture described in Section 3 was implemented through a representative 96-cell battery-pack prototype arranged in an 8S12P configuration (i.e. 12 parallel strings of 8 cells each). The multifunctional frame illustrated in *Figure 7* provides the primary load path while integrating the cell-positioning features. Each cell is held by a dedicated compliant bracket integrated into the frame. The geometry was defined to ensure controlled cell positioning, efficient load transfer and heat dissipation by conduction through the frame. Electrically conductive paths are embedded in the frame to implement the parallel cell interconnections (see *Figure 7* and *Figure 9*), while series interconnections were implemented within the covers (see *Figure 8* and *Figure 9*).

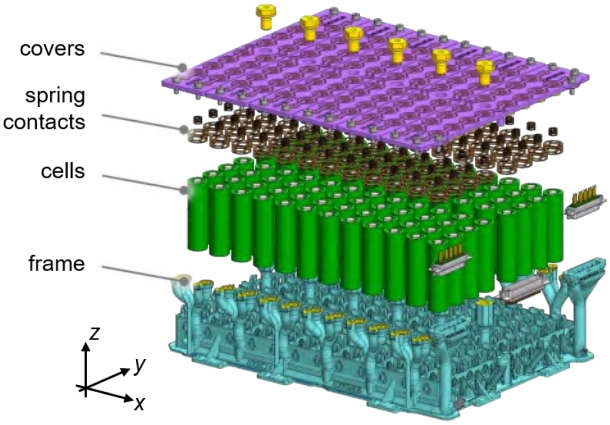


Figure 6: exploded CAD view of the battery pack

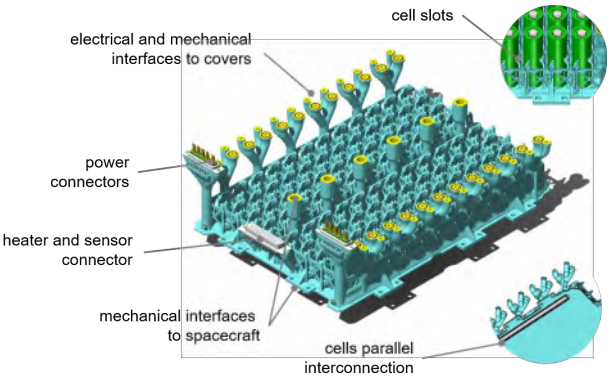


Figure 7: CAD view of the battery frame

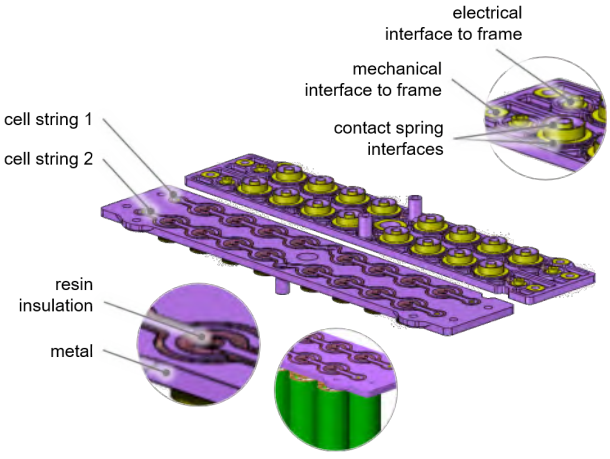


Figure 8: CAD view of the battery covers

Electrical contact between the cells and the integrated conductive network is achieved through compliant spring interfaces. These contacts accommodate dimensional tolerances and differential thermal expansion while avoiding welded or soldered joints at cell level.

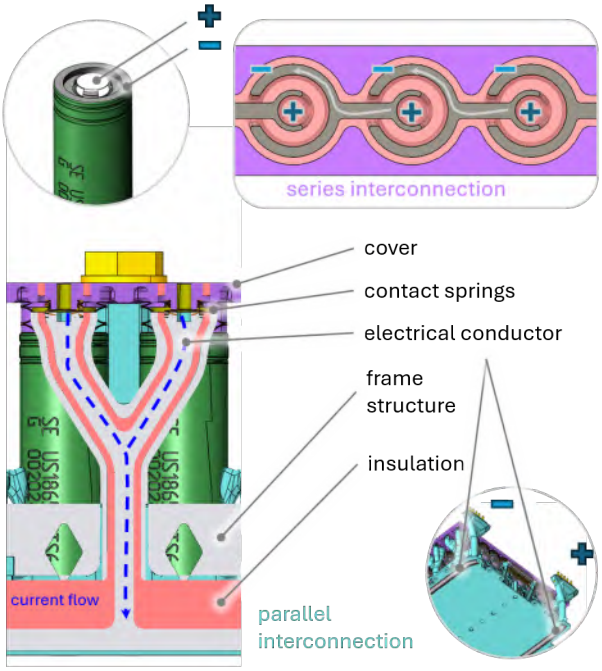


Figure 9: Electrical pathway implementation

The electrical interface to spacecraft uses male D-Sub connector geometries printed with the frame (*Figure 10*). During assembly, commercial female connectors are mounted on these printed interfaces and used as the nominal harness connection points (*Figure 6*). This avoids repeated mating/de-mating cycles directly on the printed connector features which, unlike the commercial female connectors, are not qualified COTS interfaces.

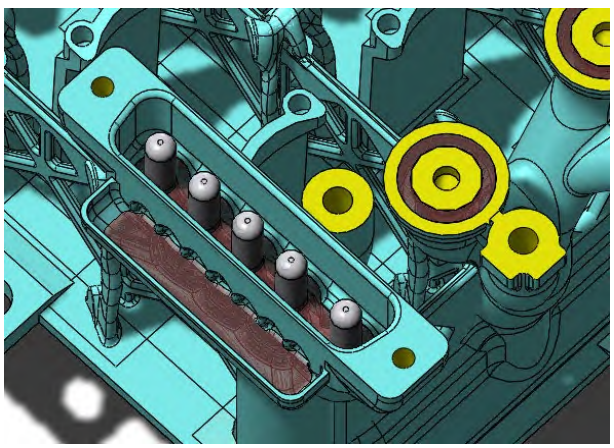


Figure 10: Detailed view of the male D-Sub connector

4.2. Design Benefits

By integrating electrical connections, connectors and routing features directly within the structural components, the proposed architecture significantly reduces the amount of dedicated wiring, interconnection hardware and assembly operations required to realise the battery pack. The architecture also enables a maintenance-oriented approach through mechanically clamped and demountable cells, making inspection, replacement and future servicing operations possible without modifying the overall packaging concept. In addition, the simplified architecture facilitates the development of representative multiphysics models by reducing the number of components and interfaces that need to be represented in the simulations.

From a manufacturing perspective, the combination of LPBF and electrically functional structures demonstrated an approximately 30% reduction in packaging mass, corresponding to about 15% reduction at complete battery-pack level. Manufacturing, assembly and cell-integration lead time were reduced from approximately 11 weeks to about 2 weeks. Finally, the architecture is inherently scalable and can be adapted to different electrical configurations and form factors while preserving the same integration principles.

Table 2: *comparison between conventional packaging and the BatmAM demonstrator.*

Aspect	Conventional battery packaging	BatmAM demonstrator
Electrical features	Assembled busbars, wires, connectors	Embedded conductive paths and connectors
Cell electrical interface	Welding or wire bonding	Compliant spring contacts
Cell mechanical interface	Individually glued in mechanical slots	Compliant radial and axial mounting.
Maintenance and repair	Challenging because of welded / bonded / glued components	Straightforward: remove the covers, replace cells, reinstall the covers
Packaging mass	Reference conventional packaging	~ 30% reduction at packaging level
Manufacturing and assembly time	~ 11 weeks	~ 2 weeks

4.3. Manufacturing

The frame and covers were produced by LPBF using AlSi10Mg alloy, followed by de-powdering and cleaning of internal features and cavities. An epoxy resin with space heritage was then cast and cured to provide electrical insulation between the conductive paths and the surrounding metallic structure. Final machining removed sacrificial material linking the electrical pathways to the structure and provided the dimensional accuracy required for the mechanical interfaces.

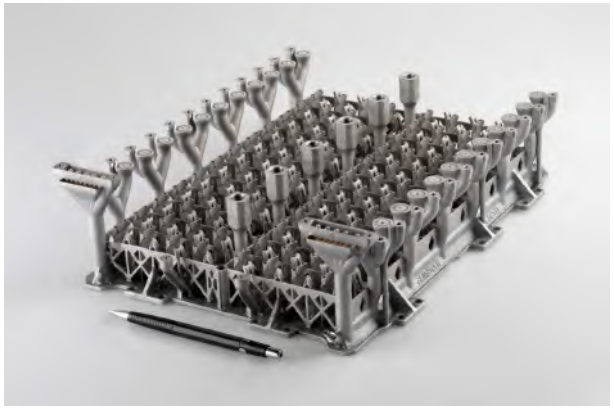


Figure 11: Battery pack frame ready for assembly



Figure 12: Battery pack cover ready for assembly

4.3 Assembly

The cells were inserted into their respective locations, as shown in *Figure 13*. The contact springs and covers were then installed to complete the mechanical closure and the electrical interconnections of the pack. External connectors, heaters and temperature sensors were subsequently integrated. The assembly sequence was concluded with electrical verification and functional checks before environmental testing.

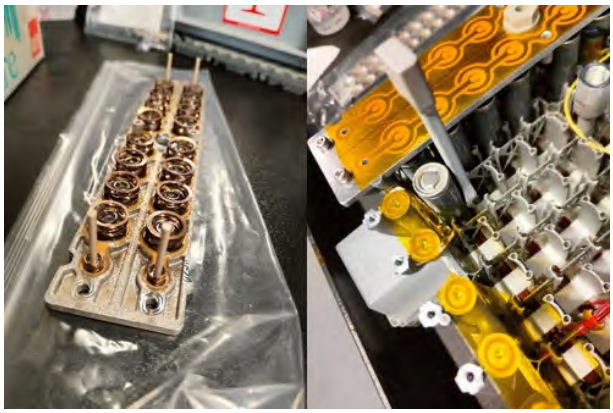
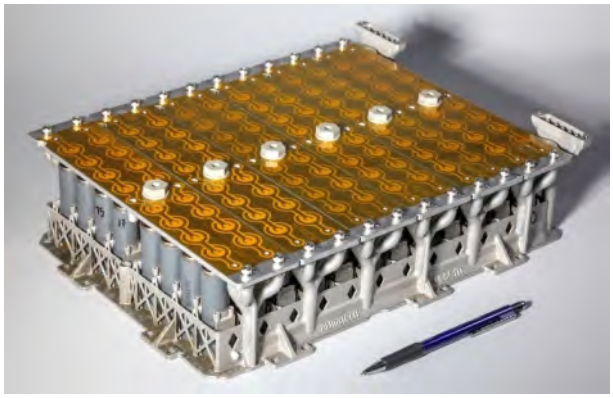


Figure 13: Left picture: cover with contact springs and fasteners. Right picture: integration of a cell. Click on this link to access a video showing the assembly sequence of the BatmAM prototype.



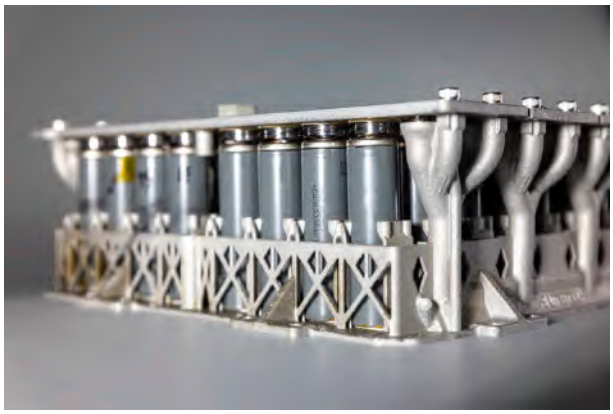


Figure 14: Final prototype ready for tests.

5. EXPERIMENTAL VALIDATION

The proposed multifunctional battery packaging architecture was validated through a comprehensive environmental and electrical verification campaign performed on two engineering model battery packs. The campaign included dimensional inspections, electrical characterisation, vibration, shock, thermal-vacuum testing and post-test electrical characterisation following an ECSS-inspired qualification philosophy. The qualification sequence is summarised in Tab. 3. It includes intermediate electrical health checks after each environmental phase, allowing potential degradation mechanisms to be isolated throughout the campaign.

Table 3: *Qualification campaign summary*

Test phase	Main activities	Objective
Initial conformity	Visual inspection, dimensions, insulation, continuity, heater verification	Manufacturing verification
Initial electrical characterisation	Cell voltages, Electro Impedance Spectroscopy (EIS)	Electrical reference
Mechanical qualification	Resonance search, sine vibration, random vibration, shock	Structural verification
Intermediate electrical characterisation	Voltage, EIS, capacity	Damage assessment
Thermal vacuum qualification	LEO cycles, GEO cycles, heater tests, thermal cycling	Thermal verification
Final electrical characterisation	Voltage, EIS, capacity	Performance verification
Final conformity	Visual inspection and functional checks	Final acceptance

5.1. Mechanical Qualification

Mechanical verification included resonance searches, sine vibration, random vibration and shock tests. Resonance searches performed before and after each test and visual inspections confirmed the absence of structural damage after vibration and shock testing.

[1] LEO & GEO electrical cycling tests were shortened due to cell imbalance in one string.

Table 4: *Mechanical qualification summary.*

Test	Qualification level	Result
Resonance search	Before/after each run	No significant modal shift
Sine vibration	Qualification level (25 g design case)	No amplification observed; first mode at 515 Hz
Random vibration	up to 17.39 g RMS equivalent qualification	Successful
Shock	Three shocks per axis (plateau at 2200 g)	Successful
Electrical health check	After each axis	No significant degradation

5.2. Thermal Vacuum Qualification

Thermal verification reproduced representative orbital environment including functional and non-functional operating conditions. During thermal testing, battery voltage, current, embedded temperature sensors and delivered capacity were continuously monitored.

Table 5: *Thermal-vacuum campaign summary*

Test	Description
Functional heater verification	Battery heaters operation
LEO cycling [1]	8 functional thermal cycles planned but only 4 performed (3 cold and 1 nominal)
GEO cycling [1]	3 functional thermal cycles planned but only 1 performed at nominal temperature
Thermal cycling	8 cycles between 0 °C and 30 °C
Continuous monitoring	Voltage, current, temperatures, capacity and energy

5.3. Electrical Performance

Electrical characterisation was performed before mechanical testing, after mechanical testing and after completion of the thermal-vacuum campaign.

Following mechanical qualification, electrical measurements showed negligible deviations from the reference values, with a battery capacity of approximately 35 Ah and an impedance of approximately 70 mΩ. These results confirm that

the multifunctional package maintained both structural integrity and electrical continuity during the mechanical test campaign.

After thermal-vacuum exposure, the estimated battery capacity decreased from the reference value of approximately 35 Ah to 27.3 Ah. Electrochemical impedance spectroscopy revealed an increase of approximately 35 mΩ in the real component of the pack impedance. Preliminary de-risking activities on cells from the same batch exposed to vacuum conditions support the hypothesis that the observed degradation originated from the commercial cells rather than from the multifunctional packaging architecture itself; the exact degradation mechanisms were not investigated in the project.

Table 6: *Electrical performance summary.*

Parameter	Result
Battery architecture	8S12P (96 × 18650 cells)
Measured capacity after TVAC	27.3 Ah
Reference capacity before TVAC	~35 Ah
Capacity degradation	Observed after thermal-vacuum exposure
Impedance evolution	~35 mΩ increase
Cell voltages after mechanical tests	No significant variation
Visual inspection	No structural damage

6. CONCLUSIONS

This paper presented the BatmAM multifunctional battery packaging architecture, a new approach to spacecraft battery integration that combines structural support, electrical interconnections and thermal management within a limited number of additively manufactured components. The proposed concept exploits commercially available cylindrical Li-ion cells and focuses on optimizing the surrounding packaging architecture through Design for Additive Manufacturing (DfAM) principles.
The proposed architecture demonstrates how additive manufacturing can be effectively leveraged to consolidate multiple subsystem functions into a lightweight, compact and highly integrated battery package. The multifunctional frame and covers simultaneously provide structural support, compliant cell retention, embedded electrical routing, and assembly interfaces while significantly reducing part count, mechanical interfaces and assembly complexity. Compared with conventional spacecraft battery designs, the new concept leads to approximately 30% reduction of the packaging mass and to a reduction of the manufacturing and assembly time from approximately 11 to approximately 2 weeks. The modular and parametric architecture also facilitates adaptation to different battery capacities, cell configurations and mission requirements, making it suitable for a wide range of future spacecraft platforms.

A comprehensive validation test campaign including mechanical, thermal-vacuum and electrical testing confirmed the feasibility and robustness of the proposed concept. Throughout the environmental qualification campaign, the multifunctional battery package successfully maintained its structural integrity, electrical continuity and thermal functionality under representative launch and space environmental conditions. Although electrical characterisation after thermal-vacuum testing revealed a reduction in battery capacity and an increase in internal impedance, the probable cause is a leakage of electrolyte at cell level. Indeed, the increase in impedance and loss of capacity were also observed in cells from the same batch that had been exposed to vacuum but had not undergone electrical cycling. The results therefore demonstrate that the proposed architecture effectively fulfils its intended structural, electrical and thermal functions while showing significant measurable impacts on mass reduction and production time reduction.

The manufacturing and successful environmental validation of the multifunctional battery packaging design in a representative environment advance supports the assessment of the packaging technology at TRL 5 and MRL 6. The complete battery subsystem is currently assessed at approximately TRL 4, as full system-level qualification, operational validation and long-duration performance assessment remain to be completed. This distinction appropriately reflects the maturity of the validated packaging technology relative to the overall battery subsystem and establishes a clear roadmap for its further development.

Future work will focus on advancing the complete battery subsystem toward higher technology readiness through optimisation and flight-representative qualification of the integrated thermal management strategy, extension to alternative cell formats and chemistries, and further exploitation of additive manufacturing (see *Figure 15*) to embed additional sensing and structural health-monitoring functions. The battery package design will also evolve to be compatible with state-of-the-art BMS (Battery Management System).

Beyond the BatmAM demonstrator, this work demonstrates how additive manufacturing can change the design philosophy of spacecraft energy systems by enabling true multifunctional integration

rather than simply replacing conventionally manufactured components. The methodology presented here is applicable to a broad range of spacecraft energy systems, including small satellites, telecommunication satellites, scientific missions and exploration platforms, particularly where reductions in mass, volume, interface count, and integration effort represent major system-level design drivers.

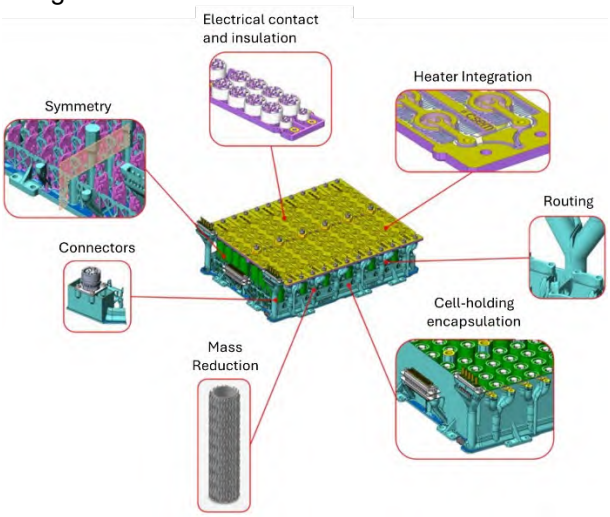


Figure 15: Design upgrades foreseen in future development steps

ACKNOWLEDGEMENTS

This work was performed within the BatmAM (Additive Manufacturing for Multifunctional Battery Packaging) project funded by the European Space Agency (ESA) under the ARTES, Contract No. 4000139904/22/NL/AF. The authors sincerely thank the ESA technical officers for their continuous technical support, constructive feedback and valuable guidance throughout the project.

REFERENCES

[1] J. R. Wertz, D. F. Everett and J. J. Puschell, Space Mission Engineering: The New SMAD. Hawthorne, CA, USA: Microcosm Press, 2011.

[2] P. Kurzweil and O. Dietlmeier, Electrical Energy Storage for Space Applications. Berlin, Germany: Springer, 2018.

[3] ECSS-E-ST-20C Rev.1, Electrical and Electronic Engineering, Noordwijk, The Netherlands, 2020.

[4] I. Gibson, D. Rosen and B. Stucker, Additive Manufacturing Technologies: 3D Printing, Rapid Prototyping and Direct Digital Manufacturing, 3rd ed. Cham: Springer, 2021.

[5] T. DebRoy, H. L. Wei, J. S. Zuback et al., "Additive manufacturing of metallic components: Process, structure and properties," Progress in Materials Science, vol. 92, pp. 112-224, 2018.

[6] D. W. Rosen, "Design for Additive Manufacturing: A Method to Explore Unexplored Regions of the Design Space," in Proceedings of the 18th Solid Freeform Fabrication Symposium, Austin, TX, USA, 2007, pp. 402-415.

[7] P. Vetter, P. Novák, M. R. Wagner et al., "Ageing mechanisms in lithium-ion batteries," Journal of Power Sources, vol. 147, no. 1-2, pp. 269-281, 2005.

[8] European Space Agency, Additive Manufacturing Harmonisation Roadmap, ESA/IPC/THAG(2026)6, Noordwijk, The Netherlands, 2026.

[9] M. Navarrete, F. Medina, E. MacDonald, R. Wicker, K. Church, M. Newton and B. Zufelt, "Integrated fabrication of a wireless sensor system using additive manufacturing and direct-write technologies," Solid Freeform Fabrication Symposium, Austin, TX, USA, 2007.

[10] S. Castillo, D. Muse, F. Medina, E. MacDonald and R. Wicker, "Electronics integration in conformal substrates fabricated with additive layer manufacturing," Solid Freeform Fabrication Symposium, Austin, TX, USA, 2009.

[11] J. Glasschroeder, E. Prager and M. F. Zaeh, "Powder-bed-based additive manufacturing of function-integrated parts," Rapid Prototyping Journal, vol. 21, no. 2, pp. 138-148, 2015.

[12] L. Li, A. Haghighi, Y. Yang and F. Liou, "Hybrid additive manufacturing of 3D electronic systems," Journal of Manufacturing Processes, vol. 23, pp. 110-121, 2016.

[13] D. Espalin, D. Muse, E. MacDonald and R. Wicker, "3D printing multifunctionality: structures with electronics," International Journal of Advanced Manufacturing Technology, vol. 72, pp. 963-978, 2014.

[14] J. Binder et al., "Additive manufacturing of electrically functional structures by embedding and contacting sensors in metallic components," Procedia CIRP, vol. 94, pp. 258-263, 2021.

[15] M. Aldorf, M. Greifzu, M. Berlin, J. Salmanow, J. vom Weg, A. Holz and L. Stepien, "Direct Printing of Heating Elements for Thermal Control Systems of Spacecraft," Proceedings of the 51st International Conference on Environmental Systems (ICES), 2022.

[16] H. Saudan and L. Kiener, "Method for manufacturing electrically functional metallic components by additive manufacturing," European Patent EP3740382B1, Nov. 2023.

[17] L. Kiener, H. Saudan, D. Novo, G. Bernard and M. Miler, "Slipring made by additive manufacturing: from redesign to validation test results," in Proc. ESMATS 2023, 2023.

[18] H. Saudan, L. Kiener, L. Salamin, J. Rouvinet, D. Novo, N. Blondiaux, M. Crenna, S. Khan, C. Marro, F. Montredon, P. Houy, C. Manoli, P. Petagna, A. Renecorail and S. Eyrignoux, "3D printed pipe segments with built-in heating and temperature sensing capabilities," in Proc. ECSSMET 2024, 2024.

Continuous (recycled) fiber-filaments printed in large-scale additive manufacturing

Jan-Uwe R. Schmidt [1], Souvik Chakraborty[1], Jens Jähnicke [2], Harsh Pawar [1], Steffen Opitz[1], Hans Peter Monner [1]

1 German Aerospace Center (DLR), Institute of Lightweight Systems, 38108 Braunschweig, Germany
2 Siemens AG, DI MC AMF, Clemens-Winkler-Straße 3, 09116 Chemnitz

jan-uwe.schmidt@dlr.de

KEYWORDS

Large-Scale Additive Manufacturing, Continuous Fibre Reinforcement, Recycled Carbon Fibre, High-Performance Thermoplastics, Path Planning, Aerospace Structures

ABSTRACT

Large-scale additive manufacturing (LSAM) of continuous fibre-reinforced thermoplastics offers significant potential for lightweight aerospace structures but remains limited by sustainable feedstock availability and restricted deposition strategies.

This work presents an integrated manufacturing approach combining the development of continuous 12K carbon fibre filaments manufactured from both virgin carbon fibres and recycled fibres originating from industrial production waste with advanced deposition strategies for uninterrupted structural additive manufacturing. High-performance thermoplastic matrices, including polyphenylene sulfide (PPS) and polyaryletherketone (PAEK), were processed using a co-extrusion process to produce continuous fibre filaments suitable for LSAM. Their processability, microstructure, and mechanical performance were evaluated to assess the suitability of recycled fibres for structural applications.

In addition, localized trajectory adaptations for continuous fibre crossings and support-free three-dimensional deposition strategies were developed and experimentally validated using representative demonstrator structures.

The results demonstrate that recycled continuous fibre feedstocks can be successfully combined with advanced toolpath strategies, preserving continuous load paths while extending the geometric design space of large-scale additive manufacturing.

The presented approach provides a promising pathway towards sustainable, load-path-oriented composite structures for future aerospace and space applications.

1. INTRODUCTION

The increasing demand for lightweight, resource-efficient and mission-adapted structures continues to drive the development of advanced manufacturing technologies for aerospace and space applications. Besides achieving high specific mechanical properties, future manufacturing processes must enable rapid design adaptation, efficient material utilisation and economically viable production of highly individualised structural components. Large-scale additive manufacturing (LSAM) has therefore emerged as a promising technology, combining the geometric freedom of additive manufacturing with the processing of engineering thermoplastics and fibre-reinforced composite materials. Compared with conventional manufacturing technologies, LSAM enables the direct fabrication of large and highly customised structures while significantly reducing tooling effort and material waste [1].

Among the various reinforcement concepts, continuous carbon fibres offer the greatest potential for enhancing the mechanical performance of additively manufactured thermoplastic structures. In contrast to short-fibre reinforced polymers, continuous fibres provide uninterrupted load paths that enable efficient stress transfer along the fibre direction, resulting in substantially increased stiffness, strength and damage tolerance. Consequently, continuous fibre reinforced additive manufacturing has attracted considerable attention for structural aerospace applications, where lightweight design and load-path-oriented reinforcement concepts are of central importance [2-4].

Despite these advantages, current continuous fibre additive manufacturing technologies still exhibit several fundamental limitations. Most existing systems remain restricted to planar layer-by-layer deposition, limiting the fabrication of spatial reinforcement architectures that efficiently follow three-dimensional load paths. Furthermore, intersecting toolpaths generally require interruption of the continuous reinforcement, introducing discontinuities that reduce structural efficiency. In addition, support-free deposition of spatial reinforcement structures remains a major

technological challenge [3,4].
Besides these process-related limitations, sustainability has become an equally important challenge for future composite manufacturing. Carbon fibre production is associated with high energy consumption and considerable material losses during industrial processing. Continuous fibre production waste is frequently discarded because local defects prevent its use in conventional high-performance laminate manufacturing, although a large proportion of the intrinsic mechanical properties of the fibres remains unaffected. Preserving these continuous fibres for structural applications therefore represents an attractive opportunity to improve resource efficiency while simultaneously reducing the environmental footprint of composite manufacturing [5].
Previous work at the German Aerospace Center (DLR) established a co-extrusion process for manufacturing continuous fibre thermoplastic filaments from both virgin and recycled 12K carbon fibre tows. These investigations demonstrated the feasibility of producing printable continuous fibre filaments based on high-performance thermoplastics and provided the technological foundation for recycled continuous fibre feedstocks in large-scale additive manufacturing [6,7]. Building upon these developments, further advances are required to fully exploit the structural potential of continuous fibre LSAM. In particular, reliable processing of recycled feedstocks, uninterrupted fibre deposition across intersecting toolpaths and support-free three-dimensional deposition remain key challenges for manufacturing highly load-adapted composite structures.
To address these challenges, this work presents an integrated manufacturing framework combining sustainable feedstock development with advanced deposition strategies for continuous fibre large-scale additive manufacturing. Continuous fibre filaments manufactured from virgin and recycled carbon fibre tows are comparatively evaluated regarding processability, microstructure and structural performance. Building upon these feedstocks, localized toolpath adaptations enabling uninterrupted fibre crossings and support-free spatial deposition strategies are developed and experimentally validated using representative demonstrator structures. The overall workflow of the presented research is illustrated in Figure 1. It highlights the two main contributions of this work: (i) the development of sustainable continuous fibre filaments from recycled carbon fibre production waste and (ii) the development of advanced deposition strategies for uninterrupted, load-path-oriented large-scale additive manufacturing. By combining these complementary developments within a single manufacturing framework, the presented approach extends both the material basis and the geometric design space of continuous fibre large-scale additive manufacturing for future aerospace and space structures.

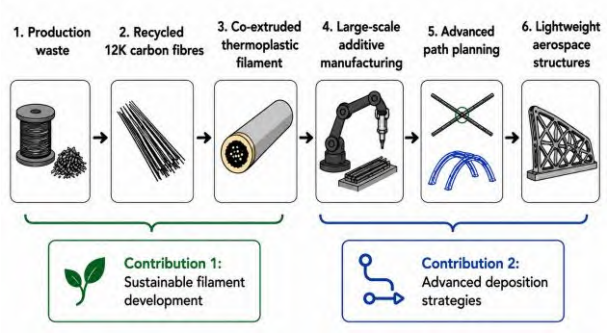


Figure 1: Overview of the presented workflow illustrating the two main contributions of this work: (1) the development of sustainable continuous fibre filaments from recycled carbon fibre production waste and (2) advanced deposition strategies for uninterrupted large-scale additive manufacturing of lightweight aerospace structures.

2. MATERIALS AND EXPERIMENTAL METHODS

This chapter describes the materials, filament manufacturing process, large-scale additive manufacturing system, and experimental procedures employed throughout this study. The experimental programme comprised the development and characterization of continuous fibre thermoplastic filaments manufactured from both virgin and recycled carbon fibres, followed by the experimental validation of advanced deposition strategies for uninterrupted continuous fibre placement and support-free three-dimensional printing. The overall methodology is structured to evaluate both the suitability of recycled continuous fibre feedstocks for structural large-scale additive manufacturing and the feasibility of the proposed process innovations.

2.1 Raw Materials

Two continuous carbon fibre reinforcement systems were investigated: a commercial 12K virgin carbon fibre tow and a recycled 12K carbon fibre tow recovered from industrial production waste. In contrast to conventional recycling approaches based on discontinuous fibres, the original continuous fibre architecture was preserved, enabling the recycled material to be processed directly as continuous reinforcement for extrusion-based additive manufacturing.
Three continuous fibre reinforced filament systems were investigated throughout this study. Two filament systems were manufactured at DLR using the ENDLOS-Effekt co-extrusion process and polyphenylene sulfide (PPS) as matrix material, reinforced with either virgin or recycled continuous carbon fibres. In addition to the in-house manufactured filament, a commercially available continuous carbon fibre reinforced polyaryletherketone (PAEK) filament was included

in the printing experiments as a reference material. All three filament systems were processed using the same large-scale additive manufacturing platform to evaluate the developed deposition strategies under comparable processing conditions. An overview of the investigated material systems is provided in Table 1.

Table 1: used material systems

Mat.-Sys-	Reinforc.	Matrix	Application
Dev. filament	Virgin continuous carbon fibre (12K)-AS7	PPS	Filament character. and printing
Dev. filament	Recycled continuous carbon fibre (12K)-T700	PPS	Filament character. and printing
Com. filament	Continuous carbon fibre	PAEK	Printing experiments

2.2 Continuous Fibre Filament Manufacturing

Continuous fibre reinforced thermoplastic filaments were manufactured using the DLR ENDLOS-Effekt co-extrusion process, which was developed for the continuous production of structural composite filaments for large-scale additive manufacturing [6,7]. The process integrates continuous fibre impregnation, filament consolidation, dimensional calibration and spool winding within a single continuous manufacturing route, resulting in printable composite feedstocks with homogeneous fibre distribution and stable filament geometry.

A major challenge in manufacturing continuous fibre thermoplastic filaments is the impregnation of densely packed carbon fibre bundles with highly viscous engineering thermoplastics. Since only a limited residence time is available within the processing zone, sufficient matrix infiltration must be achieved while maintaining continuous fibre alignment and a constant filament geometry. The resulting impregnation quality directly influences filament handling, extrusion stability and the mechanical performance of the printed components [7].

During manufacturing, the continuous carbon fibre tow is guided through the co-extrusion die, where the molten thermoplastic matrix is introduced under controlled thermal conditions. Ultrasonic excitation is applied within the impregnation zone to improve matrix infiltration and enhance process stability during continuous production [7]. After impregnation, the composite strand passes through a consolidation and cooling section before being calibrated to the target filament diameter and wound onto spools for subsequent additive manufacturing experiments. A schematic illustration of the manufacturing process is shown in Figure 2.

Both virgin and recycled 12K carbon fibre tows were processed using the same manufacturing route. Although the recycled fibres exhibited minor local variations resulting from their previous industrial processing history, only small adjustments to the fibre guidance were required. No modifications of the underlying co-extrusion concept were necessary, demonstrating the compatibility of recycled continuous carbon fibre production waste with the established filament manufacturing process.

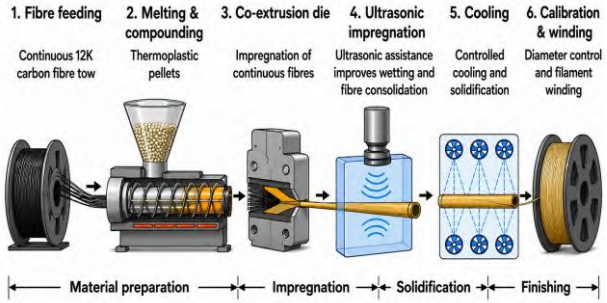


Figure 2: Schematic illustration of the DLR co-extrusion process for manufacturing continuous fibre thermoplastic filaments.

2.3 Large-Scale Additive Manufacturing System

Printing experiments were performed using a custom-developed large-scale additive manufacturing (LSAM) platform equipped with a high-temperature extrusion unit specifically designed for processing continuous fibre reinforced thermoplastic filaments. The system comprises a six-axis industrial robot, a heated extrusion unit and a temperature-controlled build platform to ensure reliable processing of high-performance thermoplastic materials.

The print head was developed to process continuous fibre reinforced filaments while maintaining homogeneous heating of the thermoplastic matrix and minimizing mechanical loading of the continuous fibre bundle during feeding. Stable processing requires a balanced interaction between material feed, extrusion rate and machine motion, as variations in fibre tension directly affect strand geometry, deposition accuracy and fibre alignment.

All printing experiments were performed using the same manufacturing platform. Process parameters, including nozzle temperature, printing speed and layer height, were adapted to the respective filament system and experimental objective. The investigated parameter ranges are summarized in Table 2. The parameter ranges cover all experimental investigations presented in this work and were adapted to the respective material system and demonstrator geometry.

Figure 3 shows the robotic LSAM platform used for the experimental investigations, while Figure 4 illustrates the custom-developed continuous fibre print head during the processing of continuous fibre reinforced thermoplastic filaments.



Figure 3. Experimental setup consisting of the robotic LSAM system

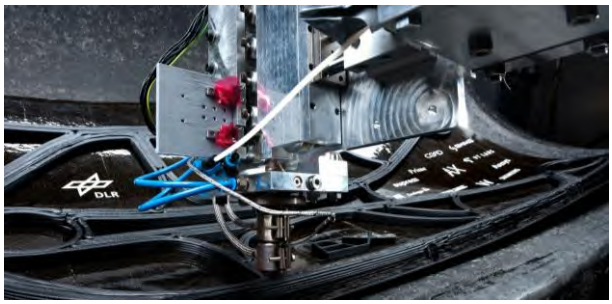


Figure 4. The custom-developed continuous fiber print head printing continuous CF/PAEK filament

Table 2: Parametersetup

Parameter	Value
Fibre	Virgin CF/ recycled CF
Matrix	PPS /PAEK
Filament diameter	1.2 mm
Nozzle diameter	1.3 mm
Nozzle temperature	350°C-490°C
Printing speed	30 – 3000 mm/min
Layer height	0.5 mm
Notch height	0.25 mm
Inclination angle	30° -90°

2.4 Experimental Methods

The experimental programme comprised both feedstock characterization and process validation experiments. Initially, the developed continuous fibre filaments were characterized with respect to their manufacturing quality, microstructure and mechanical performance. Optical microscopy was employed to evaluate fibre distribution and impregnation quality. Mechanical characterization was performed by tensile testing using a test procedure adapted from ASTM D638 [8]. A minimum of five specimens was tested for each material condition to compare the mechanical performance of filaments manufactured from virgin and recycled continuous carbon fibres.
Subsequently, the developed deposition strategies were investigated using representative demonstrator geometries addressing three key challenges of continuous fibre large-scale additive manufacturing. First, continuous fibre crossings were analysed to evaluate localized toolpath modifications designed to reduce material accumulation while preserving uninterrupted fibre continuity. Second, infrared thermography was employed to identify suitable thermal process windows for support-free deposition. Finally, progressively more complex demonstrator structures, including standing triangles, pyramid geometries and spatial lattice structures, were manufactured to validate uninterrupted free-space deposition under representative processing conditions.
The overall experimental workflow is illustrated in Figure 5.

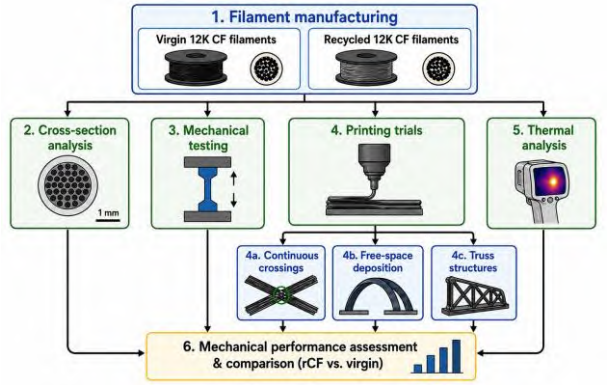


Figure 5: Overview of the experimental methodology employed for filament characterization and continuous fibre deposition investigations.

3. DEVELOPMENT AND CHARACTERIZATION OF CONTINUOUS FIBRE FILAMENTS

The successful implementation of continuous fibre reinforced large-scale additive manufacturing depends fundamentally on the quality of the employed feedstock material. Besides providing high mechanical performance, continuous fibre reinforced filaments must exhibit homogeneous fibre impregnation, stable geometry and reliable feeding behaviour during extrusion. Consequently, the development of robust filament feedstocks represents a prerequisite for the advanced deposition strategies presented in the following sections.
To evaluate the suitability of recycled continuous carbon fibres for structural additive manufacturing, continuous fibre reinforced PPS filaments were manufactured. The resulting filaments were subsequently characterized with respect to their manufacturing quality, microstructure and mechanical performance.

3.1 Filament Manufacturing

Continuous fibre reinforced thermoplastic filaments were successfully manufactured from both virgin and recycled 12K carbon fibre tows using the DLR ENDLOS-Effekt co-extrusion process described in

previous work [6,7]. Stable processing conditions were achieved throughout the manufacturing campaign, enabling continuous filament production without significant interruptions, fibre breakage or filament collapse. The manufactured filaments exhibited sufficient flexibility for spool winding while maintaining the stiffness required for reliable feeding during large-scale additive manufacturing.
Although the same manufacturing principle was applied to both fibre systems, slight differences in handling behaviour were observed. Owing to their previous industrial processing history, the recycled fibre bundles exhibited locally varying bundle morphologies, requiring minor adjustments to the fibre guiding system during manufacturing. These adaptations neither affected process stability nor required modifications to the underlying co-extrusion concept. As a result, both virgin and recycled continuous carbon fibre tows were successfully processed into continuous fibre reinforced thermoplastic filaments using the same manufacturing route, demonstrating the robustness and transferability of the developed process.
Representative cross-sections of the manufactured filaments are shown in Figure 6. Both filament systems exhibited continuous fibre bundles embedded within the thermoplastic matrix, confirming successful impregnation and providing the basis for the subsequent microstructural and mechanical characterization.

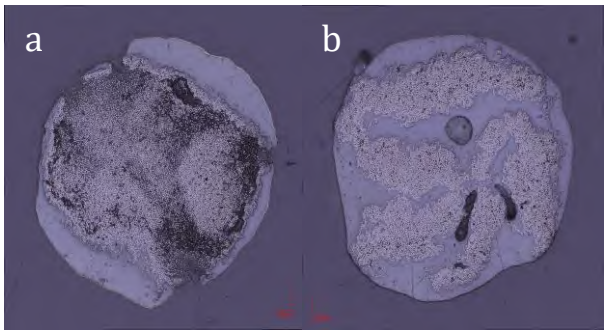


Figure 6: Cross-sectional optical micrographs of continuous fibre reinforced PPS filaments manufactured from (a) virgin and (b) recycled 12K carbon fibre tows. Both filament systems exhibit continuous fibre bundles embedded within the thermoplastic matrix. The recycled fibre filament shows locally increased variations in bundle morphology and matrix distribution resulting from the previous industrial processing history of the reinforcement.

3.2 Filament Microstructure

Representative polished cross-sections of the manufactured continuous fibre reinforced PPS filaments were analysed by optical microscopy to evaluate fibre distribution and impregnation quality.
Both filament systems exhibited continuous fibre bundles fully embedded within the thermoplastic matrix, confirming successful impregnation during the co-extrusion process [6,7]. The virgin fibre filaments displayed a comparatively homogeneous fibre distribution across the cross-section. In contrast, the recycled fibre filaments exhibited slightly larger local variations in bundle morphology and matrix distribution, which are attributed to the previous industrial processing history of the recovered carbon fibres.
Despite these local differences, no pronounced impregnation defects, extensive void formation or discontinuities of the continuous fibre reinforcement were observed. The matrix provided continuous encapsulation of the fibre bundles, indicating a sufficiently high impregnation quality for subsequent additive manufacturing.
Overall, the microstructural analysis demonstrates that the developed co-extrusion process is capable of producing structurally sound continuous fibre reinforced filaments from both virgin and recycled carbon fibre feedstocks. While the recycled material exhibits greater local variability, its overall microstructural quality is comparable to that of the virgin reference material and is suitable for the subsequent mechanical characterization and printing experiments.

3.3 Mechanical Performance

The mechanical performance of the developed continuous fibre reinforced PPS filaments was evaluated by tensile testing using specimens manufactured from both virgin and recycled continuous carbon fibre feedstocks. The corresponding results are presented in Figure 7.

Both filament systems exhibited high load-bearing capacities, confirming the successful manufacture of mechanically robust continuous fibre reinforced filaments. Under the investigated processing conditions, the recycled continuous fibre filaments achieved an average failure load of approximately 1.4 kN, compared with approximately 0.93 kN for the virgin reference material, corresponding to an increase of approximately 50%. Although both material systems exhibited a certain scatter in the measured values, the recycled filament consistently demonstrated excellent mechanical performance.

The unexpectedly high load-bearing capacity of the recycled filament indicates that continuous carbon fibres recovered from industrial production waste can be processed into structurally efficient thermoplastic composite filaments without compromising their mechanical performance. Combined with the stable manufacturing behaviour and homogeneous impregnation observed in the previous sections, these findings demonstrate that recycled continuous carbon fibre feedstocks represent a technically viable and resource-efficient alternative to virgin reinforcement for extrusion based large-scale additive manufacturing [5].

The recycled T700 production waste retained an excellent load-bearing capacity comparable to, and under the investigated conditions exceeding, that of

the virgin AS7 reference. These results indicate that the previous industrial processing history does not preclude the structural use of recycled continuous carbon fibres. A direct comparison using identical fibre grades will be the subject of future work.

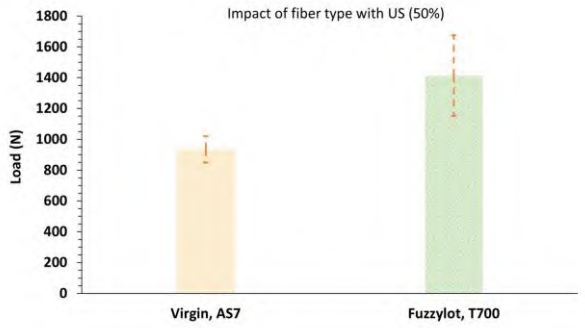


FIGURE 7: Average failure load of continuous fibre reinforced PPS filaments manufactured from virgin (AS7) and recycled (T700) 12K carbon fibre tows. The results represent the average of a minimum of five specimens per material condition tested using a tensile procedure adapted from ASTM D638 [8]. Error bars indicate the minimum and maximum measured values.

3.4 Discussion

The presented investigations demonstrate that continuous carbon fibre coming from production waste can be successfully transformed into continuous fibre reinforced thermoplastic filaments suitable for structural large-scale additive manufacturing. In contrast to conventional carbon fibre recycling approaches, which typically produce discontinuous or short fibre reinforcement with reduced structural efficiency [5], the developed manufacturing route preserves the original continuous fibre architecture and thus maintains uninterrupted load paths within the final composite.

The microstructural characterization confirmed that both virgin and recycled filament systems exhibited homogeneous impregnation without critical defects, despite the slightly greater local variability observed for the recycled reinforcement. Furthermore, the mechanical investigations demonstrated that the recycled filament system achieved a load-bearing capacity comparable to, and under the investigated conditions exceeding, that of the virgin reference material. These findings indicate that the previous industrial processing history of the recycled fibres does not preclude their use in structurally demanding additive manufacturing applications.

Overall, the combination of stable filament production, homogeneous microstructure and excellent mechanical performance demonstrates that recycled continuous carbon fibres represent a technically viable and resource-efficient feedstock for extrusion-based large-scale additive manufacturing. These results establish the material foundation for the advanced deposition strategies presented in the following section, where uninterrupted fibre crossings and support-free three-dimensional printing are investigated.

4. ADVANCED CONTINUOUS FIBRE DEPOSITION STRATEGIES

Having demonstrated the successful manufacturing and characterization of continuous fibre reinforced thermoplastic filaments from both virgin and recycled carbon fibre feedstocks, the next step is to evaluate their applicability in large-scale additive manufacturing. This section presents the development and experimental validation of advanced deposition strategies addressing two key challenges of continuous fibre printing: the realization of uninterrupted fibre crossings and the support-free deposition of three-dimensional continuous fibre reinforced structures.

4.1 Motivation

Continuous fibre reinforced thermoplastic composites are well established for the manufacture of lightweight structures using Automated Tape Placement (ATP) and Automated Fibre Placement (AFP). These technologies enable the efficient production of planar and moderately curved laminate structures with excellent mechanical performance. In contrast, comparatively little research has addressed the additive manufacturing of spatial continuous fibre reinforced structures, although such approaches offer considerable potential for realizing lightweight load-bearing components with increased geometric freedom [3,4].

Unlike conventional laminate manufacturing, extrusion-based large-scale additive manufacturing enables reinforcement paths to follow complex three-dimensional load paths rather than being restricted to stacked planar layers. This capability is particularly attractive for truss- and lattice-like structures, where continuous fibre reinforcement can efficiently carry tensile loads while maintaining a low structural weight. Consequently, support-free deposition of continuous fibre reinforced thermoplastics offers the potential to manufacture highly material-efficient lightweight structures without the need for sacrificial support material or subsequent post-processing.

Despite this potential, two major technological challenges currently limit the wider application of continuous fibre large-scale additive manufacturing. First, intersecting deposition paths typically require interruption of the continuous reinforcement or lead to localized material accumulation at crossing points. Second, successful support-free deposition requires the extruded filament to achieve sufficient mechanical stability immediately after extrusion, making the thermal behaviour of the thermoplastic matrix a critical process parameter.

The following investigations therefore focus on the development of localized toolpath strategies for

uninterrupted continuous fibre crossings and on the experimental validation of support-free three-dimensional deposition concepts for continuous fibre reinforced large-scale additive manufacturing.

4.2 Challenges of Continuous Fibre Crossings

Intersections between continuous fibre reinforcement paths represent one of the principal challenges in continuous fibre large-scale additive manufacturing. When two continuous fibre strands intersect, material is deposited twice within the same local region, resulting in increased bead height and a locally modified cross-sectional geometry. Conventional approaches typically avoid this problem by interrupting the continuous reinforcement prior to the intersection, thereby simplifying the deposition process at the expense of structural fibre continuity.
To overcome this limitation, a dedicated crossing strategy was developed that enables uninterrupted continuous fibre intersections. Instead of cutting the reinforcement, localized modifications of the deposition path are introduced to compensate for the additional deposited material while maintaining continuous fibre paths through the intersection.
A representative polished cross-section of an unoptimized fibre crossing is shown in Figure 8. The micrograph reveals pronounced local bead accumulation caused by the superposition of two deposited strands. This results in an increased bead height, localized porosity and insufficient consolidation beneath the upper strand. Such geometric irregularities impair the deposition of subsequent layers and may reduce the dimensional accuracy and structural quality of printed components [9].

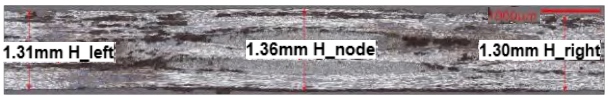


Figure 8: Cross-sectional micrograph of a baseline continuous fibre intersection without local toolpath optimization. Double deposition within the crossing region results in localized bead accumulation, increased bead height, localized porosity and insufficient consolidation beneath the upper continuous fibre strand [9].

Based on these observations, several localized notch geometries were investigated to compensate for the excess material deposited within the crossing region. The objective was to minimize local bead accumulation while preserving uninterrupted fibre continuity and ensuring stable deposition conditions. The resulting optimized crossing concept forms the basis for the deposition strategies presented in the following sections.

4.3 Continuous Fibre Crossing Strategy

Rather than interrupting the reinforcement at each intersection, a continuous crossing strategy was developed to preserve uninterrupted fibre paths throughout the printed structure. The proposed approach combines synchronized extrusion control with localized nozzle trajectory modifications, enabling intersecting continuous fibre strands while minimizing material accumulation at the node.
Based on the microstructural observations presented in section 4.2, the intersection defect was identified as a consequence of localized volumetric overload caused by the superposition of two deposited strands. To compensate for this effect, a tunnel-shaped notch is introduced into the lower strand by applying a localized vertical nozzle offset immediately before the intersection [9]. This additional volume accommodates the intersecting strand and promotes improved consolidation without requiring interruption of the continuous reinforcement. The localized notch inevitably introduces a minor geometric deviation at the crossing. However, the resulting increase in contact area between the intersecting strands improves consolidation and contributes to a stronger node connection, representing a favourable trade-off between geometric accuracy and structural integrity.
The developed crossing concept is illustrated in Figure 9. After generating the notch, the intersecting strand is deposited into the prepared cavity before the nozzle returns to the nominal deposition height. Consequently, uninterrupted continuous fibre reinforcement is maintained throughout the complete toolpath while reducing the local increase in bead height.

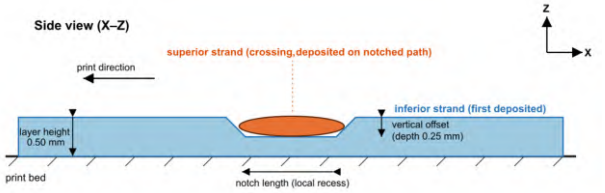


Figure 9: *Schematic illustration of the Notch Method for continuous fiber crossings.*

Several notch geometries were evaluated experimentally to identify a suitable balance between bead height reduction and consolidation quality. Particular attention was paid to preserving continuous fibre integrity while avoiding excessive local compression, which may promote fibre waviness, porosity or insufficient matrix consolidation. In contrast to conventional fibre interruption approaches, the proposed strategy relies exclusively on software-based toolpath adaptation and can therefore be implemented on existing robotic additive manufacturing systems without additional hardware modifications [9].

4.4 Thermal Behaviour During Free-Space Deposition

Following the analysis of continuous fibre crossings, the thermal conditions during deposition were

investigated to evaluate the feasibility of support-free continuous fibre printing. In contrast to conventional layer-based additive manufacturing, unsupported deposition requires the extruded filament to maintain its geometry immediately after leaving the nozzle. Since the continuous carbon fibres themselves provide only limited bending stiffness during deposition, the temporary structural stability is governed primarily by the cooling and solidification of the surrounding thermoplastic matrix. Consequently, the thermal behaviour of the deposited filament defines the process window for successful free-space manufacturing.

Infrared thermography was employed to characterize the temperature distribution of the extruded filament directly below the nozzle under representative processing conditions. A representative thermographic image is shown in Figure 10. The measurements revealed a pronounced temperature gradient, with the highest temperatures occurring immediately at the nozzle exit, followed by rapid cooling during deposition. Infrared thermography was therefore used to quantify the maximum unsupported deposition length prior to sufficient matrix solidification, which was approximately 8 mm during continuous printing and 6 mm under stationary conditions. The transition from non-self-supporting to self-supporting behaviour is gradual and therefore represents a transition zone rather than a discrete location.

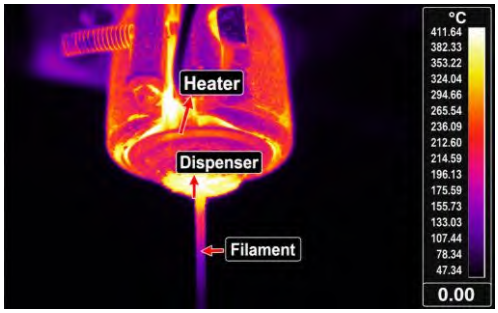


Figure 10: Infrared thermographic image of the continuous fibre deposition process showing the temperature distribution of the extruded filament directly below the nozzle under representative processing conditions.

The thermographic analysis demonstrates that the extruded filament remains highly deformable directly beneath the nozzle before progressively solidifying as its temperature decreases. Consequently, only a limited region adjacent to the nozzle lacks sufficient mechanical stability, whereas the deposited filament rapidly develops the stiffness required to maintain unsupported geometries. The identified cooling behaviour therefore defines the effective processing window for free-space deposition and determines the achievable combination of nozzle temperature, deposition speed and unsupported span length.

These observations provide the thermal foundation for the support-free deposition strategies presented in the following sections. By identifying the process window in which sufficient bonding and rapid solidification occur simultaneously, the subsequent manufacturing experiments could be performed with stable unsupported deposition while preserving continuous fibre reinforcement

4.5 Development of Support-Free Continuous Fibre Structures

Following the identification of a suitable thermal process window, the next objective was to investigate whether continuous fibre reinforced thermoplastic filaments could be deposited without sacrificial support structures. Rather than directly manufacturing complex lattice geometries, the experimental investigations followed an iterative development strategy in which the geometric complexity was progressively increased while continuously evaluating the resulting process limitations.

The initial experiments focused on the deposition of individual unsupported members in order to evaluate whether the extruded filament could maintain its geometry solely through the cooling and solidification of the thermoplastic matrix. These preliminary investigations confirmed the feasibility of unsupported deposition and provided important insight into the influence of thermal behaviour, deposition sequence and nozzle motion on the stability of the printed strand. Based on these findings, progressively more complex demonstrators comprising vertical members, inclined struts and node connections were manufactured using uninterrupted continuous fibre paths.



Figure 11. Standing triangular demonstrators manufactured without sacrificial support material. The structures served as the first benchmark for evaluating unsupported continuous fibre deposition under increasing geometric complexity.

The standing triangular demonstrators shown in Figure 11 represent the first stable support-free structures manufactured with the developed process. Their successful fabrication confirmed that continuous fibre reinforced thermoplastic filaments can be deposited without sacrificial support material while preserving uninterrupted fibre reinforcement. At the same time, the experiments revealed important process limitations. Stable manufacturing proved to be highly dependent on the selected thermal process parameters, while the continuously changing stiffness of the growing structure made the deposition sequence an essential process parameter alongside nozzle temperature and

printing speed.

Building upon these results, the developed manufacturing strategy was transferred to pyramid-shaped demonstrators introducing multiple unsupported inclined members and node intersections within a single continuous fibre path. Compared with the triangular benchmark, these geometries represent a substantially more demanding validation of the developed deposition strategy.

The successful manufacture of the pyramid structures confirmed that the identified thermal process window and optimized deposition sequence can be transferred to increasingly complex three-dimensional reinforcement architectures. Nevertheless, the larger geometries also revealed additional process limitations. Geometric deviations occurred primarily at the transitions between inclined and vertical members, where the deposited filament occasionally deflected before sufficient solidification of the thermoplastic matrix had occurred. These observations demonstrate that manufacturing stability is governed not only by thermal process control but also by nozzle accessibility, deposition sequence and the continuously increasing stiffness of the evolving structure.

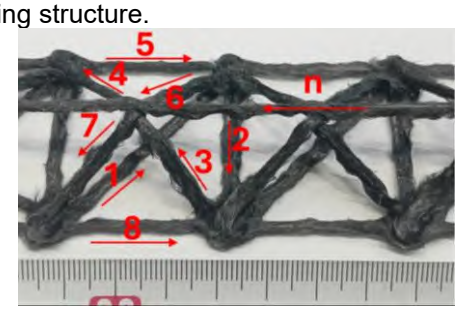


Figure 12. Evolution of the support-free deposition strategy from standing triangular demonstrators to pyramid-shaped lattice structures. The refined deposition sequence significantly improved geometric accuracy, process stability and manufacturing reproducibility.

Through iterative refinement of the deposition strategy, including optimized deposition sequencing and improved stabilization of unsupported members, the geometric accuracy and manufacturing reproducibility were significantly improved. The resulting evolution from simple unsupported members to standing triangles and finally pyramid structures is illustrated in Figure 12, demonstrating that support-free continuous fibre deposition can be systematically extended towards increasingly complex spatial reinforcement architectures. The pyramid-shaped demonstrators were selected because they combine unsupported inclined members (e.g. 3, 4, 6 and 7), vertical struts (e.g. 5, 8 and *n*), multiple node intersections (e.g. between members 3–4 and 6–7), and changes in deposition direction (e.g. member 6) within a single uninterrupted continuous fibre path, thereby representing a demanding validation geometry.

4.6 Overall Process Evaluation

The successful implementation of continuous fibre large-scale additive manufacturing relies not only on advanced deposition strategies but also on the availability of robust and reproducible feedstock materials. While the previous sections demonstrated the feasibility of uninterrupted fibre crossings and support-free three-dimensional deposition, these process developments fundamentally depend on the consistent manufacturing quality of the continuous fibre reinforced thermoplastic filaments.

Figure 13 summarizes the influence of the developed co-extrusion process on the mechanical performance of the manufactured filaments over the investigated processing conditions. In contrast to the material comparison presented in Figure 7, which evaluates representative filament systems processed under their respective optimized manufacturing conditions, Figure 13 isolates the influence of filament production speed by comparing specimens manufactured under identical process conditions (0% ultrasonic assistance and an impregnation pressure of 10 bar). The results demonstrate stable failure loads for both virgin and recycled continuous carbon fibre feedstocks, indicating that the manufacturing process provides a high degree of reproducibility despite variations in production speed. The absence of a significant reduction in mechanical performance confirms that the impregnation quality and fibre integrity are maintained throughout the investigated processing window.

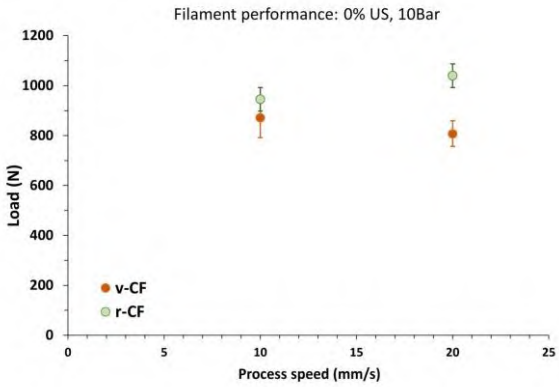


Figure 13. Influence of filament production speed on the failure load of continuous fibre reinforced thermoplastic filaments manufactured from virgin and recycled carbon fibre tows under identical processing conditions (0% ultrasonic assistance, 10 bar impregnation pressure).

These observations are particularly relevant for large-scale additive manufacturing, where continuous production of several hundred metres of reinforced filament is required for manufacturing structural components. The demonstrated process

stability therefore represents an essential prerequisite for reliable robotic deposition and validates the developed co-extrusion approach as a suitable manufacturing route for continuous fibre reinforced thermoplastic feedstocks.

The combination of stable filament manufacturing and the mechanical performance presented in section 3 establishes the material foundation for the deposition strategies introduced in the previous sections. Together, these results demonstrate that recycled continuous carbon fibres can be processed into structurally efficient feedstocks suitable for large-scale additive manufacturing without compromising manufacturing robustness.

4.7 Validation of the Continuous Fibre Crossing Strategy

Following the successful validation of the developed filament manufacturing process, the effectiveness of the tunnel-notch crossing strategy was assessed by comparing optimized intersections with the baseline deposition approach. The objective was to evaluate whether localized toolpath adaptation could improve the geometric quality of fibre crossings while maintaining uninterrupted reinforcement throughout the deposited structure.
Representative crossing geometries are presented in Figure 14. Compared with the unmodified deposition strategy, the optimized tunnel-notch approach significantly reduces local bead accumulation at the intersection. The additional cavity created within the lower strand accommodates the intersecting filament, resulting in a more uniform bead profile and improved consolidation of the crossing region. Consequently, the local increase in layer height is substantially reduced, facilitating the deposition of subsequent layers and improving the dimensional consistency of the printed structure. In the optimized configuration, the relative height increase at the intersection was reduced from 4.41 % (for the unmodified reference) to 0.73 % [9].
Beyond the geometric improvements, the developed strategy preserves continuous fibre reinforcement across the complete intersection without requiring fibre interruption or additional joining operations. This represents a key advantage over conventional continuous fibre deposition approaches, where reinforcement paths are frequently terminated prior to intersecting toolpaths to avoid local material accumulation.

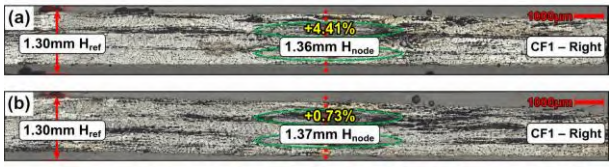


Figure 14. Microscopic comparison of continuous fibre intersections. (a) Conventional crossing showing localized material accumulation and increased bead height. (b) Optimized intersection manufactured using the Notch Method. The localized trajectory modification reduces bead accumulation while maintaining uninterrupted continuous fiber reinforcement and improving the geometric accuracy of subsequent deposition paths. (Orthogonal fiber strands are highlighted by green circles.)

The presented results demonstrate that localized software-based toolpath adaptation provides an effective solution for one of the principal geometric limitations of continuous fibre large-scale additive manufacturing. The developed strategy can be implemented without modifications to the deposition hardware and therefore offers a practical route towards manufacturing increasingly complex continuous fibre reinforced structures.

4.8 Scalable Support-Free Manufacturing of Three-Dimensional Structures

Having validated both the developed filament system and the optimized continuous fibre crossing strategy, the final stage of the experimental programme investigated the scalability of the manufacturing concept towards increasingly complex three-dimensional reinforcement structures. The objective was to assess whether the developed deposition strategies remain applicable as structural complexity and the number of unsupported members increase.

The representative demonstrators shown in Figure 15 illustrate the progression from simple unsupported geometries to increasingly sophisticated spatial reinforcement architectures manufactured along a single uninterrupted continuous fibre path. The successful fabrication of these demonstrators confirms that the developed process is not limited to isolated proof-of-concept specimens but can be extended to structures incorporating multiple inclined members, repeated node intersections, and complex three-dimensional load paths.

Stable support-free deposition was achieved only within a limited processing window. Insufficient thermal input (below 420 °C) resulted in inadequate interlayer bonding, whereas excessive thermal input (approximately 490 °C) at low printing speeds (<100 mm min^{-1}) delayed matrix solidification and promoted geometric deformation. As printing speed increased, higher nozzle temperatures were required to ensure complete filament heating. Printing speeds exceeding 1000 mm min^{-1} were only achievable at nozzle temperatures of approximately 490 °C, whereas lower speeds (<100 mm min^{-1}) could be processed below 450 °C provided that no fibre intersections were present. Conversely, excessively low nozzle temperatures resulting in poorly consolidated bead surfaces with locally exposed fibres. At fibre crossing locations,

substantially lower deposition speeds (<30 mm min^{-1}) were necessary to achieve reliable bonding while preventing fibre damage. Furthermore, unsupported node connections required an absolute positioning accuracy better than 0.1 mm to ensure reproducible node formation.

Manufacturing stability was governed by the interaction between thermal management, deposition sequence, print head accessibility, and the continuously evolving stiffness of the growing structure. During the initial deposition stages, unsupported members were susceptible to gravitational deflection before sufficient matrix solidification had occurred. As the structure developed, however, the increasing global stiffness progressively stabilised subsequent deposition, improving dimensional accuracy. The largest geometric deviations, reaching up to 2 mm, occurred at transitions between inclined and vertical members, where elevated temperatures and insufficient structural stiffness temporarily reduced positional stability.

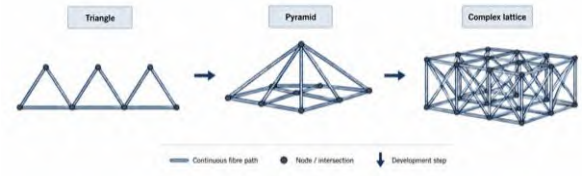


Figure 15. Progressive development of support-free continuous fibre demonstrator structures from standing triangles to pyramid geometries and complex lattice architectures.

Based on these observations, the toolpaths were iteratively refined by adapting the deposition sequence to the structural growth of the component. Previously deposited members were intentionally utilized as intermediate supports to increase the stiffness of the evolving structure, while unsupported deposition lengths were reduced to approximately 70 mm, which proved sufficient to ensure stable unsupported deposition under the investigated process conditions, resulting in significantly improved process stability and geometric accuracy.

The experimental validation demonstrates that the combination of optimized filament quality, localized fibre crossing strategies, and controlled thermal processing enables the reliable manufacture of complex continuous fibre reinforced structures without sacrificial support material. These results considerably expand the geometric design space of continuous fibre large-scale additive manufacturing and provide the technological foundation for future lightweight structural applications requiring continuous reinforcement along three-dimensional load paths.

4.9 Integrated Manufacturing Concept

The investigations presented in this chapter demonstrate that the successful realization of continuous fibre reinforced large-scale additive manufacturing requires the simultaneous optimization of both the feedstock material and the deposition process. Neither high-quality continuous fibre reinforced filaments nor advanced deposition strategies alone are sufficient to manufacture complex structural components. Instead, reliable processing is achieved through the interaction of reproducible filament manufacturing, controlled thermal management and dedicated toolpath planning.
The developed co-extrusion process enables the production of continuous fibre reinforced thermoplastic filaments from both virgin and recycled carbon fibre feedstocks with stable processing behavior and high mechanical performance. Building upon this material basis, the notch strategy overcomes one of the principal limitations of continuous fibre additive manufacturing by allowing uninterrupted fibre crossings while reducing local bead accumulation and improving geometric consistency. Furthermore, the experimental validation of support-free deposition demonstrates that increasingly complex three-dimensional reinforcement architectures can be manufactured without sacrificial support structures while maintaining continuous fibre paths throughout the complete component.
large-scale additive manufacturing technologies.

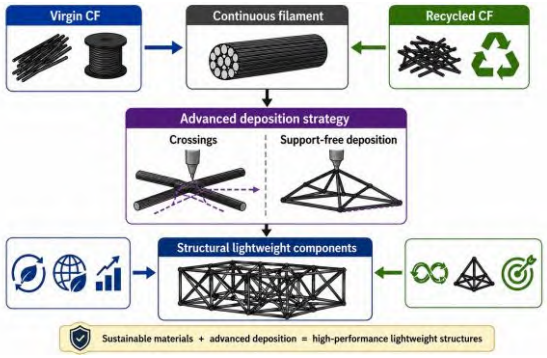


Figure 16. Integrated manufacturing concept combining continuous fibre filament production, optimized robotic deposition strategies and support-free manufacturing of three-dimensional continuous fibre reinforced structures.

The integrated manufacturing concept is summarized in Figure 16, illustrating the relationship between material development, filament production and robotic deposition. The presented process chain establishes a continuous workflow from recycled carbon fibre feedstocks to complex three-dimensional continuous fibre reinforced structures, demonstrating the feasibility of combining sustainable materials with advanced Overall, the presented approach significantly extends the manufacturing capabilities of

continuous fibre large-scale additive manufacturing by combining sustainable feedstock materials with software-based process innovations. The developed process chain provides a scalable foundation for the production of lightweight structural components with uninterrupted reinforcement and offers considerable potential for future aerospace and space applications, where both structural efficiency and resource sustainability are becoming increasingly important design requirements.

5 CONCLUSION AND OUTLOOK

This work presented an integrated approach for sustainable continuous fibre large-scale additive manufacturing by combining recycled continuous fibre reinforced filaments with novel deposition strategies for uninterrupted fibre paths and support-free three-dimensional printing. The proposed process chain demonstrates that sustainable feedstock materials can be successfully processed while simultaneously expanding the geometric capabilities of extrusion-based continuous fibre additive manufacturing.
Mechanical characterization showed that recycled continuous fibre reinforced PPS filaments exhibit a substantially higher failure load than virgin filaments, confirming their suitability as structural feedstock for large-scale additive manufacturing. In parallel, the developed continuous fibre crossing strategy successfully eliminated fibre interruptions at intersecting toolpaths without requiring additional hardware modifications. This software-based solution enables continuous reinforcement across complex deposition paths while preserving process efficiency.

To further extend the manufacturing capabilities, the thermal behaviour of the deposited filament was experimentally investigated to identify the process window required for support-free deposition. Based on these investigations, stable unsupported continuous fibre structures were successfully manufactured, progressing from simple unsupported members to increasingly complex three-dimensional lattice demonstrators. The experiments demonstrate that the rapid solidification of the thermoplastic matrix provides sufficient temporary structural stability to enable free-space deposition without sacrificial support structures. At the same time, the investigations revealed that process stability is governed by the interaction of thermal conditions, deposition sequence, nozzle accessibility and the continuously evolving stiffness of the growing structure.
Overall, the presented manufacturing concept combines sustainable material utilization, uninterrupted continuous fibre reinforcement and support-free spatial deposition within a unified process chain. The proposed approach therefore represents an important step towards the production of lightweight, resource-efficient composite structures with significantly increased design freedom for future aerospace and space applications.
Future work will focus on improving the robustness and industrial applicability of the process. In particular, optimized nozzle concepts are required to enable higher deposition speeds while maintaining adequate thermal control of the continuous fibre filament. Furthermore, strengthening fibre intersections, improving the dimensional reproducibility of unsupported structures and developing automated topology-optimized toolpath generation will further enhance process reliability and enable the efficient manufacture of increasingly complex lightweight structures. Additionally, future work should investigate improved nozzle concepts to reduce the limitations imposed by the thermal inertia of the print head and the limited heat transfer to the continuous fiber filament.

REFERENCES

[1] Duty, C.E., et al. Structure and Mechanical Behavior of Big Area Additive Manufacturing (BAAM) Materials. Additive Manufacturing, 18, 200–208 (2017).
[2] Ning, F., Cong, W., Qiu, J., Wei, J., Wang, S. Additive Manufacturing of Carbon Fiber Reinforced Thermoplastic Composites Using Fused Deposition Modeling. Composites Part B: Engineering, 80, 369–378 (2015).
[3] Matsuzaki, R., et al. Three-Dimensional Printing of Continuous-Fiber Composites by In-Nozzle Impregnation. Scientific Reports, 6, 23058 (2016).
[4] Dickson, A.N., Barry, J.N., McDonnell, K.A., Dowling, D.P. Fabrication of Continuous Carbon, Glass and Kevlar Fibre Reinforced Polymer Composites Using Additive Manufacturing. Additive Manufacturing, 16, 146–152 (2017).
[5] Oliveux, G., Dandy, L.O., Leeke, G.A. Current Status of Recycling of Fibre Reinforced Polymers: Review of Technologies, Reuse and Resulting Properties. Progress in Materials Science, 72, 61–99 (2015).
[6] Kroos, K., Diniz, S., Bachmann, J., Chakraborty, S., Kühnast, F., Schmidt, J.-U.R., Opitz, S. Filaments for Additive Manufacturing Reinforced with Carbon Fibers from Waste Stream. Proceedings of ECCM21, Nantes, France (2024).
[7] Schmidt, J.-U.R. Untersuchung der Voidsubtypen in endlosfaserverstärkten 3D-Druckfilamenten. Doctoral Dissertation, Otto-von-Guericke-Universität Magdeburg, Germany (2026) – to be published.
[8] ASTM International. ASTM D638. Standard Test Method for Tensile Properties of Plastics.
[9] Pawar, H. Optimization of Intersection Printing in Continuous Fiber-Reinforced Additive Manufacturing Using Robotic Printing. Master's Thesis, PFH Private University of Applied Sciences Göttingen, Göttingen, Germany, 2026.

MODELLING AND EXPERIMENTAL VALIDATION OF A LASER POWDER BED FUSION-MANUFACTURED ALUMINIUM LATTICE SANDWICH PANEL

Ph. Guy [1,2], G. Pommatau [3], F. Sgro [1,4], L. Gharbi [3], F. Montredon [3], S. Eyrignoux [5], M. Goudal [5]

[1] Icam, 75 av. de Grande-Bretagne, 31300 Toulouse, France, philippe.guy@icam.fr
[2] Université de Toulouse ; Institut Clément Ader, UMR CNRS 5312, INSA/UPS/ISAE/Mines Albi, 3 rue Caroline Aigle, 31400 Toulouse, France
[3] Thales Alenia Space, 5 allée des Gabians, 06156 Cannes La Bocca Cedex, France, gilles.pommatau@thalesaleniaspace.com, luna.gharbi@thalesaleniaspace.com, florence.montredon@thalesaleniaspace.com
[4] University of Modena and Reggio Emilia, Modena, Italy, francesco.sgro@2026.icam.fr
[5] LISI Aerospace Additive Manufacturing, 2 route Robert Algayon, 33640 Ayguemorte-les-Graves, France, sebastien.eyrignoux@lisi-group.com, marjorie.goudal@lisi-group.com

KEYWORDS

Metal Additive Manufacturing (MAM), Lattice Sandwich Structures, Laser Powder Bed Fusion (L-PBF), Mechanical Performance, Finite Element Analysis (FEA), Experimental Tests

ABSTRACT

This work investigates the predictive capability of two modelling strategies for an AlSi7Mg0.6 sandwich panel with a micro-lattice core, manufactured via L-PBF and used as a stiffener in a satellite platform. Using additive manufacturing to produce this stiffening panel resulted in a mass saving higher than 20%, compared to that of integrally machined aluminium stiffeners. Low-level swept-sine vibration tests were performed to identify the first six natural frequencies, providing a benchmark for validating an equivalent homogenised model (EHM) and a detailed full solid three-dimensional model (FS3D). The FS3D model reproduced the experimental modal response with good accuracy, with errors generally below 8% and an almost exact prediction of the fourth mode (0.1%), whereas the EHM systematically overestimated the natural frequencies by 22% to 85%, revealing an overly stiff representation of the lattice core. Despite this lower accuracy, the EHM preserved the global modal behaviour while reducing the computational cost dramatically, requiring 44 times fewer degrees of freedom and 339 times less CPU time than the FS3D model. The comparison also shows the influence of manufacturing-induced geometric deviations and defects on the dynamic response of as-built structures. Finally, the study proposes a model improvement strategy combining X-ray computed tomography-based geometry reconstruction and modal correlation to recalibrate homogenised models, enabling improved predictive capability while maintaining computational efficiency for industrial-scale structural analyses.

1. CONTEXT

Extensive research has long been conducted on lattice structures, especially aluminium lattices made via Laser Powder Bed Fusion (L-PBF), covering design, modelling, manufacturing, testing, and validation [1-3].

From an industrial point of view, substantial mass saving and cost gain for recurring parts have been identified a long time ago. The savings in cost and time-to-delivery lead time compared to bonded-core aluminium sandwich structures are easy to understand, given the economic advantages offered by bonding processes, particularly in terms of surface treatment, manufacturing lead times and inspection of several materials. Anyway, the current inability of L-PBF technology to produce large-scale structures (of around 1 m) drastically limits the range of applications of industrial interest.

In the frame of a telecom satellite project, an improved structural design imposed the implementation of six stiffeners between two large aluminium sandwich panels, as shown in Fig. 1.

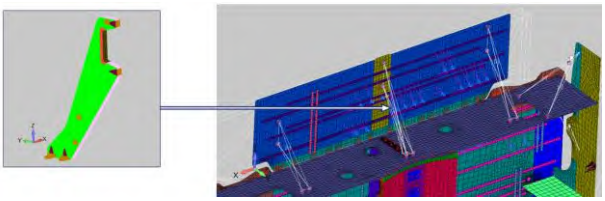


Figure 1: View of the location of three of the six stiffeners

The advantage of this application case was that the dimensions were compatible with existing L-PBF machines, making it possible to manufacture several parts in a single batch. In addition, the elementary bricks developed and tested in previous studies (up to TRL 6), such as interface designs and lattice pattern ideas, are proving useful for the design of this type of component.

This qualification process will enable the L-PBF lattice sandwich structure to be rapidly brought up to TRL 9. Given that these parts mainly require stiffness and strength at the interfaces, the qualification plan must be based on good correlations with the results of modal and static FE analyses. This article focuses on the dynamic vibration testing of the stiffener, and more specifically on its modal behaviour, albeit in a non-representative configuration. A forthcoming article will address the analyses and static tests in the representative configuration.

Another key industrial challenge is the inability to handle the extremely large number of finite elements needed to model each small lattice strut (a few millimetres thick) in large-scale satellite structures.

This paper furthers previous work led or followed by Thales Alenia Space (TAS-F) on lattice structures [4-7] in which several cellular solids were investigated in terms of thermal and mechanical performances, design, fabrication and experimental tests.

2. DESCRIPTION OF THE SPECIMEN

2.1. Geometrical Description

The specimen illustrated in Fig. 2 is a sandwich panel with overall dimensions of approximately 500 × 120 × 20 mm³ (length × width × thickness), consisting of two outer skins and a lattice core in between, featuring zones locally reinforced with solid material, *i.e.* the load introduction areas and fastening inserts.

The skins have a nominal thickness of 0.3 mm in standard areas and 0.6 mm in reinforced areas.



Figure 2: Photograph of the specimen

The specific geometry of the lattice unit cells is proprietary to Thales Alenia Space France (TAS-F) and will not be described for reasons of confidentiality. Nevertheless, the design of the unit cells was constrained by standard L-PBF manufacturability rules, including minimum strut diameter, overhang angles, and residual powder drainage requirements. What can be disclosed is the mass saving, higher than 20%, compared to that of integrally machined aluminium stiffeners.

2.2. Design, Manufacturing and Post-Treatment

The complex geometry of the panel reflects a Design for Additive Manufacturing (DfAM)-driven compromise between build orientation, self-supporting requirements, and process-specific tolerances inherent to L-PBF process. The fabrication of such a large and relatively thin aluminium panel is challenging because of the potential for thermal distortions, residual stress generation, and local deviations from the nominal CAD geometry. Consequently, the manufacturing strategy was defined to ensure both the manufacturability of the lattice core and the dimensional stability of the skins and mounting features.

The specimen was printed by LISI Aerospace Additive Manufacturing (LAAM), one of the major partners of TAS-F in Metallic Additive Manufacturing (MAM). The part was produced from AlSi7Mg0.6 aluminium alloy powder using a COLIBRIUM (Concept Laser) X-Line 2000R system, which has a large build volume of 400 × 800 × 500 mm³. This machine is qualified by TAS-F for the production of AlSi7Mg0.6 flight hardware.

The specimen was manufactured with the skins oriented vertically and parallel to the build direction. This orientation was selected to accommodate the overall dimensions of the panel and to ensure the manufacturability of the lattice core. A powder layer thickness of 50 µm was used, with a new powder layer being deposited before each laser-scanning operation.

After completion of the build, the specimen underwent a post-fabrication heat treatment for 6 h at 170°C in an air atmosphere while remaining attached to the build plate. The part was subsequently removed from the base plate using wire electrical discharge machining. The inserts and mounting lugs were then finish-machined by surface milling to obtain the required interface geometry and dimensional accuracy.

2.3. Geometry Control

Particular attention was paid to the dimensional control of the skins, lattice struts, inserts, and mounting lugs, as these features directly influence the mass, stiffness, and dynamic response of the panel. The inspection strategy therefore combined a visual examination, local dimensional measurements, and metrological X-ray computed tomography. These investigations were used to identify deviations from the nominal CAD geometry and to provide representative geometrical data for the subsequent finite element analyses.

A metrological micro X-ray computed tomography (µCT) scan was carried out by ELEMCA at CNES. The observations indicated higher skin-thickness values and provided additional information on the morphology of the lattice struts. 88% of the deviations fall between 0.3 and 0.5 mm, with an average of 0.39 mm (Fig. 3).

The µCT results were therefore used to characterise the as-built geometry more accurately than was possible from local manual measurements alone.

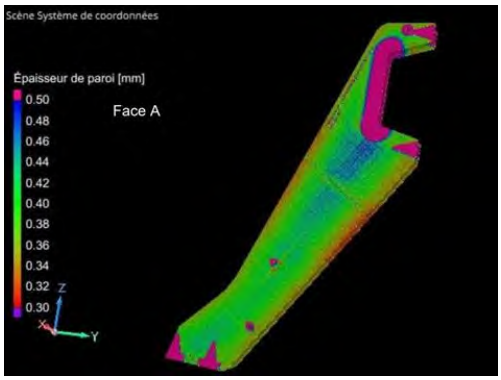


Figure 3: 3D visualisation of the measured thicknesses

3. VIBRATION TESTS

3.1. Test Setup

Dynamic tests were performed by the Mechanical Testing Lab of Icam in Toulouse (F) using a LDS V650 electrodynamic shaker. The specimen was mounted on the shaker via 4 CHc M6 screws. A low-level swept-sine test (0.1 'g', 2 oct / min) was carried out in order to obtain natural frequencies and damping. The frequency range of interest was from 10 Hz up to 1000 Hz.

Swept-sine excitation is applied along the vertical axis (X-axis) (Fig. 4).



Figure 4: Sine test shaker setup

Acceleration was measured using single-axis accelerometers along the X, Y, and Z axes (Fig. 5).

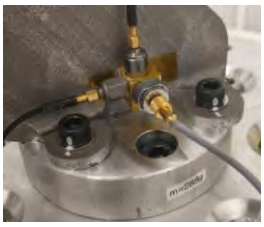


Figure 5: Photograph of 3 single-axis accelerometers

Data acquisition and post-processing were performed using BK Connect software.

3.2. Results

As the specimen was excited in the plane parallel to the skins, *i.e.* the XY plane, determining the natural frequencies of the out-of-plane modes is not easy. The excitation force has a very low modal participation factor for out-of-plane bending modes, resulting in weak resonance amplitudes that are either buried in noise or masked by in-plane modes (see Fig. 6). However, given that the test specimen is not symmetrical wrt the XY plane and that real structures are never perfectly decoupled, the modes remain detectable under such testing conditions.

To facilitate analysis, the test was repeated several times with the positions of certain accelerometers modified. Furthermore, to confirm the results, a rapid impact test (tap test) was also performed in the Z and Y directions. The interpretation of the measurements was also facilitated by the results of FE analyses (section 4).

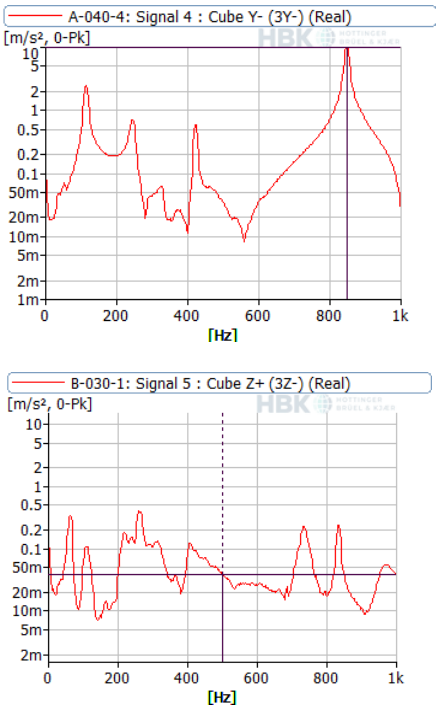


Figure 6: FFT measured for an accelerometer oriented along the Y-axis in-plane (top) and for an accelerometer oriented along the Z-axis out-of-plane (bottom)

Although the in-plane swept-sine excitation limited the excitation and identification of out-of-plane modes, the combination of repeated measurements, complementary tap tests, and FE analysis provided sufficient confidence to identify the first six natural modes within the investigated frequency range (10–1000 Hz), as presented in Tab. 1.

Table 1: Results of the sine vibration test

Mode	*Freq. [Hz]*	*Mode description*
1	63. (±8%)	1st out-of-plane bending mode
2	109. (±4%)	1st in-plane bending mode
3	244. (±3%)	1st torsion mode
4	422. (±0%)	2nd torsion mode
5	732. (±3%)	2nd out-of-plane bending mode
6	837. (±1%)	2nd in-plane bending mode

4. NUMERICAL ANALYSES

4.1. Finite Element Analyses (FEA)

The FEA objective is to assess the modal behaviour of the panel for the load case that have been experimentally tested (section 3). All the simulations were carried out using Msc.Nastran software v2024.1 in the linear elastic domain.

Two FE modelling approaches are proposed:

1. The use of an equivalent 3D-anisotropic metal foam with homogenised mechanical properties allowing the actual lattice core to be replaced by an equivalent material. This alternative is naturally the one privileged by industrial companies due to its low computational cost and the relative simplicity of mesh generation.

2. All geometric and property details of the structure are modelled with a full solid 3D mesh. This approach is technically difficult and time-consuming due to the huge amount of degrees of freedom (DOF) it generates. The main interest of this model for the present study lies in the possibility of comparing its results with those of the homogenised model.

These two approaches are fundamentally different. The choice depends on the design stage, the quantities of interest, and the required level of accuracy. It is obvious that a properly calibrated homogenised model is well-suited to large industrial components and enables good prediction of global behaviour, such as overall stiffness, global deformation, or natural frequencies. The full solid 3D model is useful for evaluating local behaviours, such as local stresses, stress concentrations, and the bending and/or torsion of the struts. It will be very useful for the subsequent work sizing the panel for static conditions and for conducting a future static test.

Initially, all input data were set to the nominal values of the CAD design, *i.e.* the geometrical dimensions correspond to a perfect defect-free structure. In a second step, once the specimen had been manufactured, the equivalent homogenized model was updated based on measured values (average skin thicknesses and mass).

As previously indicated, the panel is made of an AlSi7Mg0.6 aluminium alloy, the properties of which are as follows: E_s = 65 GPa for Young's modulus, ν_s = 0.3 for Poisson's ratio, and ρ_s = 2 675 kg/m^3 for density.

4.1.1. Equivalent Homogenised Model (EHM)

The mesh (Fig. 7) of the equivalent homogenised model EHM consists of three connected parts: (1) the solid zones (inserts and fixing areas), (2) the skins, and (3) the lattice core, modelled with an equivalent anisotropic continuum. Given the highly complex geometry of the inserts (Fig. 8), the entire mesh was generated using 10-node parabolic tetrahedral elements (CTETRA10).

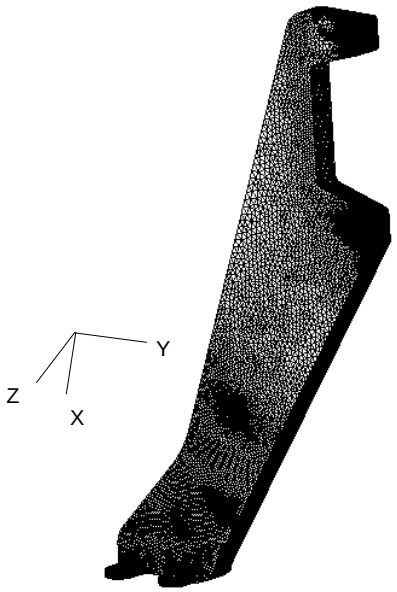


Figure 7: View of the mesh for the entire structure

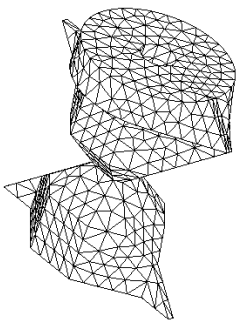


Figure 8: View of the mesh of an insert

The upper and lower skins are modelled using 6-node triangular 2D shell elements (CTRIA6) to ensure proper connection with the tetrahedral elements (CTETRA10) (Fig. 8).

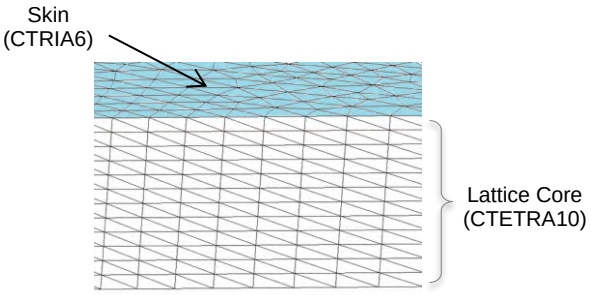


Figure 9: View of the skin and core mesh

The lattice core is represented as a homogenised 3D material possessing equivalent anisotropic elastic properties. This implies a predetermination by FE analysis of the stiffness matrix (Eq. 1) representative of the lattice pattern.

$$\underset{\sim}{\sigma} = \underline{\underline{C}}\,\underset{\sim}{\varepsilon} \qquad (1)$$

This was performed using the multi-scale material modelling platform Digimat developed by Hexagon and led to the stiffness matrix depicted in Fig.6 where: $G_{11} = G_{22} = 2580$ MPa, $G_{12} = 849$ MPa, $G_{13} = G_{23} = 142$ MPa, $G_{33} = 183$ MPa, $G_{44} = 969$ MPa, and $G_{55} = G_{66} = 138$ MPa (see the MAT9 Nastran matrix in Fig. 10).

$$\begin{pmatrix} \sigma_x \\ \sigma_y \\ \sigma_z \\ \tau_{xy} \\ \tau_{yz} \\ \tau_{zx} \end{pmatrix} = \begin{bmatrix} G_{11} & G_{12} & G_{13} & 0 & 0 & 0 \\ & G_{22} & G_{23} & 0 & 0 & 0 \\ & & G_{33} & 0 & 0 & 0 \\ & & & G_{44} & 0 & 0 \\ & sym. & & & G_{55} & 0 \\ & & & & & G_{66} \end{bmatrix} \begin{pmatrix} \varepsilon_x \\ \varepsilon_y \\ \varepsilon_z \\ \gamma_{xy} \\ \gamma_{yz} \\ \gamma_{zx} \end{pmatrix}$$

Figure 10: Stiffness matrix of the elastic anisotropic material equivalent to the lattice core

Boundary conditions applied to the model: the structure is fixed at the base at the four mounting holes (M6 screws) (Fig. 11).

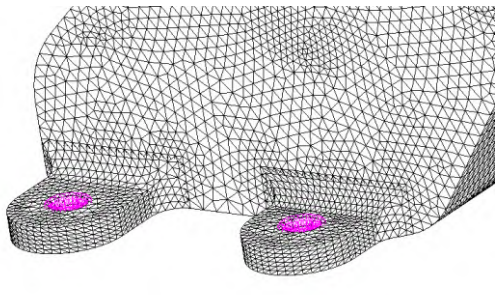


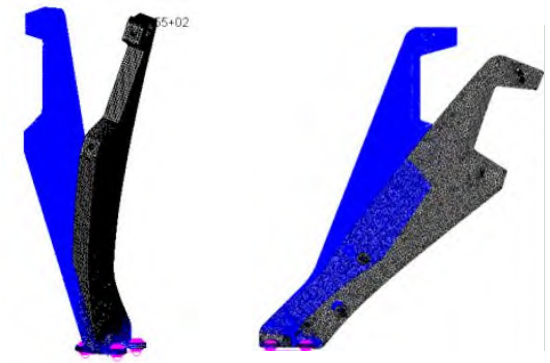
Figure 11: Boundary conditions: fixed at the 4 mounting holes (via RBE2 elements)

The results of the modal analysis are presented in Tab. 2 in terms of the first six natural frequencies and the corresponding effective masses. The mode shapes are shown and described in Fig. 12.

Table 2: FE Modal analysis results (EHM model)

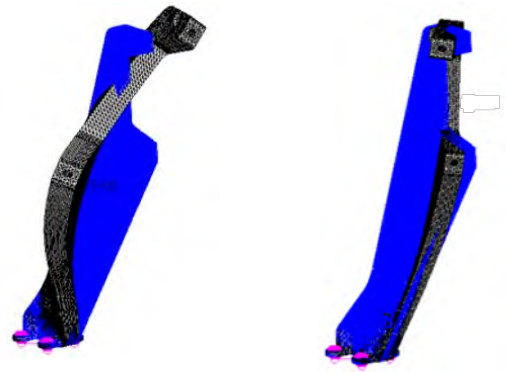
Mode	*Freq. [Hz]*	*Effective masses [kg]*		
		X	*Y*	*Z*
1	77.0	-	-	0.091
2	201.2	0.020	0.074	-
3	358.2	-	-	0.014
4	514.0	-	-	-
5	916.9	-	-	0.012
6	1078.4	-	0.015	-

FE model mass = 0.203 kg



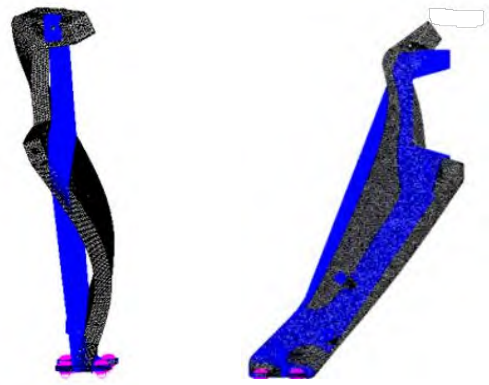
Mode 1: 77.0 Hz
1st out-of-plane
bending mode

Mode 2: 201.2 Hz
1st in-plane
bending mode



Mode 3: 358.2 Hz
1st torsion mode

Mode 4: 514.0 Hz
2nd torsion mode



Mode 5: 916.9 Hz
2nd out-of-plane
bending mode + torsion
of the upper part

Mode 6: 1078.4 Hz
2nd in-plane
bending mode

Figure 12: First six modal shapes (EHM Model)

4.1.2. Full Solid 3D Model (FS3D)

One of the principal challenges encountered during the generation of this FE model was the quality of the imported CAD geometry. The original geometry, provided as a STEP file, contained topological inconsistencies, such as disconnected or poorly connected surfaces, small gaps, and overlapping faces. These defects prevented the automatic generation of a conforming volumetric mesh and resulted in meshing failures. This is a common issue when importing lattice geometries from CAD software. The STEP file was imported into Abaqus/CAE v2020 software and automatically repaired. Next, the Tetra10 mesh was generated using Abaqus and converted to Nastran format in order to utilize its effective mass calculation capability and enable a comparison with the homogenised model. Due primarily to limitations in available computing resources and time, it was not possible to vary the mesh density across different zones of the specimen. The mesh was created by selecting a specific element size, and Abaqus/CAE generated the mesh automatically. Fig. 13 shows a view of the mesh generated in this way. A finer mesh was not possible.

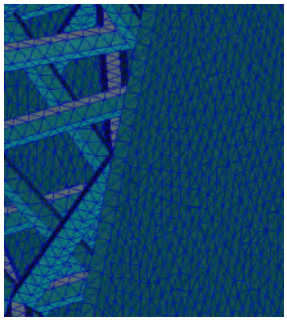


Figure 13: Zoomed-in view of the mesh of the full solid 3D model

The results of the modal analysis are presented in Tab. 3 in terms of the first six natural frequencies and the corresponding effective masses. The mode shapes remain identical to those of the homogenised model EHM (see in Fig. 11).

Table 3: FE modal analysis results (FS3D Model)

Mode	Freq. [Hz]	Effective masses [kg] X	Y	Z
1	67.2	-	-	0.085
2	146.9	0.019	0.068	-
3	299.4	-	-	0.013
4	422.0	-	-	-
5	751.2	-	-	0.013
6	807.2	-	0.014	-

FE model mass = 0.194 kg

4.1.3. Comparison of the EHM and FS3D models

The frequency results of the EHM and FS3D models are summarized in Tab. 4.

Table 4: Comparison of natural frequencies for the EHM and FS3D FE models

Mode	FS3D [Hz]	EHM [Hz]	Relative Error wrt FS3D model
1	67.2	77.0	+14,6%
2	146.9	201.2	+37,0%
3	299.4	358.2	+19,6%
4	422.0	514.0	+21,8%
5	751.2	916.9	+22,1%
6	807.2	1078.4	+33,6%

The homogenized model systematically shows higher natural frequencies than the detailed full-solid model. The overestimation ranges from approximately 15% to 37%, indicating that the equivalent model is globally stiffer than the full 3D solid model. It is noteworthy that the effective modal masses are similar for both models (Tab. 3 and Tab. 4). The FEM masses are also very close, 0.203 kg for the EHM model, and 0.194 kg for the FS3D model. The difference is approximately +4.6%, which is relatively small and cannot explain the differences in natural frequencies. These results suggest that the homogenized anisotropic material cannot fully capture all deformation mechanisms present in the actual lattice structure. In the full solid 3D model, the lattice struts deform through a combination of axial stretching, bending, torsion and local joint compliance, unlike in the homogenised model. The close agreement in effective modal masses indicates that the homogenisation preserves the global mode shapes and energy distribution, confirming that the equivalent model captures the overall dynamic behaviour of the sandwich panel even though its dynamic stiffness is somewhat overestimated.

The FS3D model has 163,340,700 DOFs, making it 44.4 times larger than the EHM model at 3,675,438 DOFs. Both models were solved on an Intel Xeon Gold 6246R processor with 32 physical cores (64 threads) and 512 GB of RAM. In terms of total CPU time, the FS3D model required 624,560 CPU seconds (approximately 173.5 hours), which is 339 times more CPU processing resources than the EHM model, which required 1,842 seconds (approximately 30.7 minutes). Unsurprisingly, the ratio of computation times is enormous, not to mention the pre- and post-processing times, which are also huge.

The objective of the full solid 3D model was to identify and quantify the differences compared to the equivalent homogenised model. The homogenised model clearly remains the preferred and appropriate tool for industrial structural sizing, enabling rapid assessment of large-scale spacecraft components. The full solid model is useful during research phases for understanding the mechanical behaviour of new lattice architectures, calibrating the homogenisation method, and investigating local phenomena.

5. RESULTS AND DISCUSSION

5.1. Comparison of experimental and numerical responses

The comparison of natural frequencies between the measurements and the numerical results from the two models, EHM and FS3D, is presented in Tab.5.

Table 5: Comparison between the measured and FEM natural frequencies

Mode	*Meas. [Hz]*	*FS3D [Hz]*	*Relative Error*	*EHM [Hz]*	*Relative Error*
1	63.	67.2	+7.5%	77.0	+23.2%
2	109.	146.9	+35.1%	201.2	+85.2%
3	244.	299.4	+22.6%	358.2	+46.6%
4	422.	422.0	+0.1%	514.0	+21.9%
5	732.	751.2	+2.6%	916.9	+25.2%
6	837.	807.2	-3.5%	1078.4	+28.9%

The L-PBF manufacturing process introduces inherent imperfections, such as deviations in strut diameter and cross-sectional shape, geometric distortions, internal porosity, and localised defects at the lattice junctions. These imperfections reduce the effective stiffness of the lattice sandwich structure. Consequently, and as observed, the as-built specimen exhibits natural frequencies lower than those predicted by finite element models based on the nominal CAD geometry, assuming a geometrically perfect, defect-free lattice structure.

The FS3D model reproduces the experimental dynamic behaviour with significantly greater accuracy than the homogenised model. Except for the second and third modes - respectively the first in-plane bending mode and the first torsion mode - the prediction error remains below 8%, with excellent prediction of the fourth mode (+0.1%). In contrast, the EHM model systematically overestimates all frequencies by approximately 22% to 85%, indicating that the equivalent model is significantly stiffer than the real structure.

As previously identified in Tab.1, 2, and 3, the first and fifth modes correspond to the first out-of-plane bending modes, the second and sixth modes represent the first in-plane bending modes, whereas the third and fourth modes are associated with the first torsional modes.

The FS3D model accurately reproduces out-of-plane bending behaviour. The first bending mode is predicted with an error of 7.5%, while the fifth mode differs from the experimental measurement by just 2.6%. This model captures the global flexural stiffness of the sandwich structure in the transverse direction. In contrast, the homogenised model overestimates out-of-plane bending frequencies by approximately 23% to 25%, suggesting that the equivalent material properties provide an overly stiff representation of the lattice core.

A different trend is observed for in-plane bending modes. The first in-plane mode (mode 2) shows the largest discrepancy for both numerical models, with errors of 35.1% for the FS3D model and 85.2% for the homogenised EHM model, whereas the second in-plane mode (mode 6) is accurately predicted by the FS3D model (−3.5%) but remains significantly overestimated by the homogenised model (+28.9%). This poorer correlation is difficult to interpret without an in-depth study of the overall in-plane stiffness, which could involve modelling the interaction between the lattice structure struts, the skins, and the solid regions.

The torsional response is reproduced more or less satisfactorily by the FS3D model. The second torsion mode (mode 4) is almost perfectly predicted, with an error of only 0.1%, while the first torsional mode (mode 3) shows a moderate overestimation of 22.6%. Conversely, the homogenised model overestimates both torsional frequencies by 21.9% and 46.6%, indicating that the homogenisation procedure does not fully capture the torsional compliance resulting from local deformation of the lattice members and their junctions.

5.2. Future Investigation for FE Model Improvement

The first and most important step in improving the predictive capability of FE models would be to account for the actual as-built geometry, rather than the nominal geometry derived from CAD. FE models should be updated by reconstructing them from the geometry obtained via X-ray computed tomography (work to be carried out).

A second important step for improving the FE models will be to incorporate material properties identified from dedicated test coupons manufactured in the same L-PBF build as the lattice sandwich panel. To this end, the TAS-F Mechanical Lab has already conducted tensile tests on printed coupons, together with edgewise and flatwise compression tests on specimens representative of the lattice sandwich panel. Although the results of these tests have not yet been analysed, they will provide valuable experimental data for calibrating the material properties of the numerical models.

The full 3D solid model (FS3D) shows much better agreement with experimental natural frequencies than the equivalent homogenised model (EHM), but it cannot be used in an industrial design phase. However, it can serve as a high-fidelity reference for recalibrating the homogenised model. Since the equivalent model must reproduce dynamic behaviour, the recalibration process would be guided by modal correlation. Starting from the equivalent elastic properties obtained via homogenisation, the stiffness parameters of the anisotropic material would be iteratively updated to

minimize discrepancies in natural frequencies and mode shapes. The objective would be to maximize the Modal Assurance Criterion (MAC) while minimizing the relative frequency difference.

6. CONCLUDING REMARKS AND OUTLOOK

This work presented the modelling and experimental validation of a Laser Powder Bed Fusion (L-PBF) manufactured aluminium lattice sandwich panel representative of lightweight space structures. Low-level swept-sine vibration tests enabled the identification of the first six natural modes of the structure, providing a reliable experimental basis for assessing the predictive capability of two finite element modelling strategies: an equivalent homogenised model (EHM) and a detailed full solid three-dimensional model (FS3D).

The comparison demonstrated that the FS3D model reproduces the measured dynamic behaviour with significantly greater accuracy than the homogenised model. The detailed representation of the lattice members captures local deformation mechanisms that cannot be fully represented by an equivalent anisotropic continuum. Conversely, although the EHM systematically overestimates the natural frequencies, it preserves the global modal behaviour while drastically reducing the computational cost, making it the most appropriate solution for the design of industrial structures and large-scale spacecraft analyses.

The comparison with the experimental results also highlights the importance of considering the as-built characteristics of L-PBF structures. Manufacturing-induced deviations from the nominal CAD geometry, including increased skin thickness, geometric imperfections and material defects, reduce the effective stiffness of the structure and therefore have a significant influence on its dynamic response.

Future work will therefore focus on improving the correlation between numerical predictions and experimental measurements. The first priority will be to reconstruct the FE models directly from X-ray computed tomography data. In parallel, the FS3D model will be used as a high-fidelity reference for recalibrating the homogenised model through modal correlation techniques. Such a methodology preserves the computational efficiency of the equivalent model while improving its predictive capability. Beyond the present modal analysis, the validated modelling framework will be extended to static and buckling analyses.

7. ACKNOWLEDGEMENTS

The authors wish to acknowledge and convey their appreciation to those individuals, Erasmus+ students, and corporations, in particular Thales Alenia Space - France (TAS-F) in Cannes, and LISI Aerospace Additive Manufacturing (LAAM) for the manufacturing of the test specimen. We also thank ELEMCA for carrying out the X-ray micro-computed tomography of the sample.

8. ABBREVIATIONS AND ACRONYMS

AM:	Additive Manufacturing
CAD:	Computer-Aided Design
CNES:	Centre National d'Études Spatiales
CPU:	Central Processing Unit
CT:	Computed Tomography
DfAM:	Design for Additive Manufacturing
DOF:	Degrees of Freedom
EHM:	Equivalent Homogenised Model
FE:	Finite Element
FEA:	Finite Element Analysis
FEM:	Finite Element Model
FFT:	Fast Fourier Transform
FS3D:	Full Solid 3D Model
GB:	Gigabyte
LAAM:	LISI Aerospace Additive Manufacturing
L-PBF:	Laser Powder Bed Fusion
MAC:	Modal Assurance Criterion
RAM:	Random Access Memory
TAS-F:	Thales Alenia Space France
TRL:	Technology Readiness Level
i.e.	*id est*
µCT:	micro-Computed Tomography
wrt:	with respect to
E_s:	Young's modulus of the solid material
ν_s:	Poisson's ratio of the solid material
ρ_s:	Density of the solid material

9. REFERENCES

1. Nickels, L. (2015). AM and Aerospace: an ideal combination, *Metal Powder Report*, Vol. 70 (6) 300e303, DOI: 10.1016/j.mprp.2015.06.005.
2. M. Bici et *al*. (2018). Development of a multifunctional panel for aerospace use through SLM Additive Manufacturing, *Procedia CIRP* 67 (1) 215e220.
3. Maconachie, T. et *al.* (2019). SLM lattice structures: Properties, performance, applications and challenges, *Materials & Design*, Volume 183, 108137.
4. Pommatau, G. et *al.* (2018). Issues for Design, Modelling and Laser Beam Manufacturing of Structures Including Aluminium Lattices. *Proceedings of 15th European Conference on Spacecraft Structures, Materials and Environmental Testing, Ecssmet 2018,* Esa-Estec, Noordwijk, The Netherlands.
5. Guy, Ph. et al. (2021), Modelling and Test Correlation of Space Structures Including Aluminium Micro-Lattices Manufactured by Additive powder Bed Laser Beam Melting, *Proceedings of 15th European Conference on Spacecraft Structures, Materials and Environmental Testing, Ecssmet 2021*, DLR, Braunschweig, Germany.
6. Guy, Ph. et al. (2023), Investigations into the mechanical properties of TA6V Dode-Thin lattice sandwich beams fabricated by powder bed laser

beam melting process, *CEAS Space Journal*, https://doi.org/10.1007/s12567-024-00543-1.
7. Pommatau, G. et al. (2024), Methodology for sizing lattice core of additive manufacturing metallic sandwich large structures, *Proceedings of 18th European Conference on Spacecraft Structures, Materials and Environmental Testing, Ecssmet 2024*, Esa-Estec, Noordwijk, The Netherlands.

Application of thermoplastic composite technology for satellites manufacturing

Piotr Kowalczyk[(1)], Ewa Kaczorowska-Łukasik[(1)], Wojciech Krauze[(1)], Radosław Szumowski[(1)], Artur Słodziński[(1)], Maciej Giżyński[(1)], Bartosz Taras[(2)], Paweł Maliński[(2)], Ugo Lafont[(3)]

[(1)] Łukasiewicz Research Network - Institute of Aviation, al. Krakowska 110/114, 02-256 Warsaw, Poland, Email: sekretariat@ilot.lukasiewicz.gov.pl
[(2)] Creotech Instruments S.A. ul. Jana Pawła II 66, 05-500 Piaseczno, Poland, Email: kontakt@creotech.pl
[(3)] European Space Agency (ESA), Keplerlaan 1, Postbus 299, 2200 AG Noordwijk, The Netherlands,

KEYWORDS

thermoplastic composites, automated fiber placement, press thermoforming, resistance welding, satellite

ABSTRACT

Within the ESA ARTES program, the Łukasiewicz – Institute of Aviation (Ł-ILOT) and Creotech Instruments (CTI) used weldable, high performance thermoplastic composite for fast fabrication of Engineering Model (EM) of a telecommunication satellite. The aim of the project was to build an EM of telecommunication satellite made entirely of thermoplastics materials with use of methods and technologies suitable for automation for future medium/large scale production. The Engineering Model (EM) passed required TVAC (Thermal-Vacuum) and vibration tests and have proven validity of used technologies reaching TRL 5.

1. INTRODUCTION

The small-satellite market is driven by trends such as miniaturization of payloads, deployment of large constellations and demand for faster time-to-orbit. At the same time, developers face challenges: tight mass/volume budgets, thermal and radiation management.
Therefore market is looking for new methods of fabrication of satellite structures, which will increase production speed and lower the costs. One of commonly used approach is to use 3D printing. This method however is limited to not very large geometries and material is used without additional reinforcements like e.g. carbon fibers [1][2]. The reasonable approach seems to be use of fiber composites with thermoplastic matrices. The thermoplastic composites utilizes remelting of thermoplastic matrix for impregnation or fibers, thermoforming in shapes and joining by welding. All of those processes are fast and do not require chemical reactions at any stages. The technologies used for thermoplastic composites are commonly Automated Fiber Placement (AFP) and press consolidation [3][4][5]. Those are fast technologies realized in highly automated processes. Those materials can be also joined by welding. Welding is also fast process of joining using fusion bonding of melted matrix [6][7].
One of the solutions for faster stiffeners fabrication is application of rib grids, which were tested in cylindrical satellite structures fabricated by winding [8][9]. This approach can be applied to thermoplastic composites with use of automated tape lay-up.
Therefore, to achieve rapid and scalable manufacturing the following approach was taken to:

- use thermoplastic composite technologies with potential for automation,
- simplify the design geometry (solid laminates with rib grids stiffeners),
- reduce number of parts and joining steps,
- use minimal amount of tooling,
- fabricate as many features as possible, such as walls, joining interfaces and stiffeners in one process.

In the task, full development of fabrication and joining technologies was carried out, with validation at the specimens level and up to full structure of Engineering Model. The research included development of in situ AFP fabrication using tapes, press thermoforming using fabric, characterization of materials, design of the platform, fabrication of parts, development of inserting technology, development of resistance welding, fabrication of tooling for machining and joining, joining of the structure (welding and screws), integration with instruments.

2. MATERIALS AND METHODS

2.1. Material

Material selected for the satellite structure is carbon fiber composite with semicrystalline Low Melt Polyaryletherketone (LM-PAEK) as matrix. The material has high service temperature up to 250 °C in short term, with processing temperatures around 340 °C [10]. In comparison, polyether ether ketone

(PEEK) has processing temperatures of 385 °C [11]. The lower processing temperature was one of the main factors of material selection. Material was used in two forms: UD tapes Victrex AE250 for AFP application and fabric Toray TC 1225 5HS for press thermoforming. The material was tested for outgassing compliance, with Total Mass Loss = 0,04% and Collected Volatile Condensable Material = 0.03%.
In resistance welding processes the Victrex LM-PAEK APTIV AE™ 250 foils were used.

2.2. Design

The aim of the EM of satellite was to be suitable for automated fabrication allowing for production in series with relatively short lead times. Those assumptions are reflected in EM design. The design was aiming to simplify the geometry, reduce number of parts and joining processes. Therefore the joining interfaces were designed to be fabricated in one process with satellite walls. Similarly simple solution for stiffeners in form of rib grids was introduced.
The joining interfaces in form of 45° degrees flanges allow to join walls without additional joining element like L-shape, and reduces joining processes from two to one.
The rib grid solution replaces solution in form of e.g. L-shapes or hat-shapes, which will be probably lighter solution but in would add parts and joining interfaces.

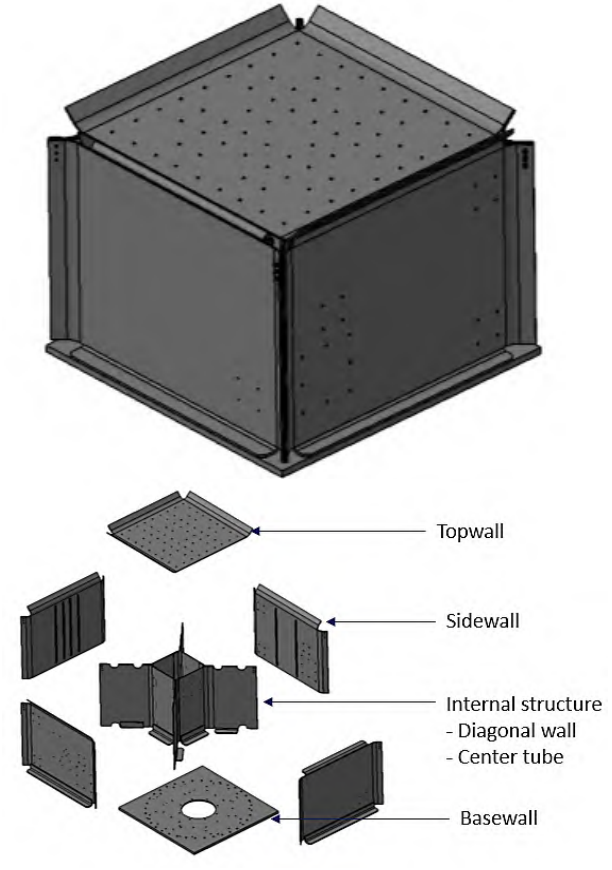


Figure 1: Composite structure exploded view

The design of the structure aimed to enable various manufacturing methods with either a press or AFP. The side walls, top wall and internal walls of structure were made on one tool. The base wall was made separately as a flat panel. The number of parts and joining steps were reduced by fabrication of walls, joining interfaces and rib grid stiffeners in one process.
The minimum external wall thickness of the spacecraft is set at 3,5 mm to ensure adequate radiation protection for the internal electronic units [12]. This decision is based on the assumption of utilizing Commercial-Off-the-Shelf (COTS) electronics, which are not inherently radiation-hardened. A density of 1.52 g/cm3 was used for the wall thickness calculations, representing the least dense composite material under consideration for the project.

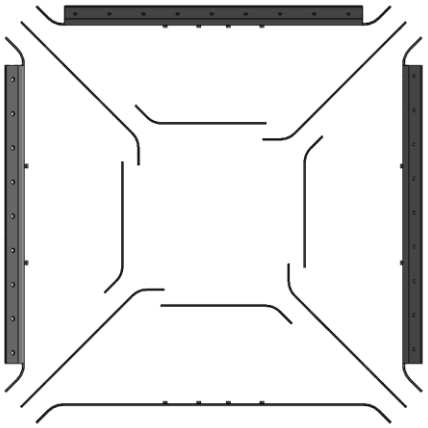


Figure 2: Exploded view of interal structure showing the strategy of joining (welidng)

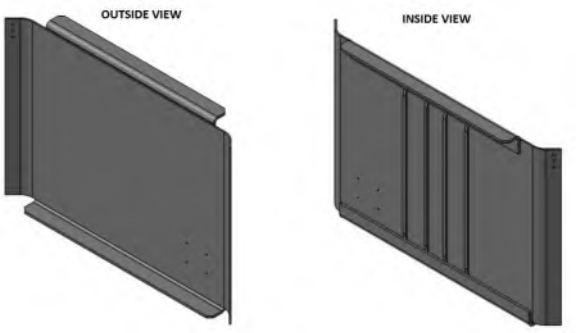


Figure 3: Sidewall design with joining interfaces and rib grid stiffeners

2.3. AFP

The Automated Fiber Placement is a technology where fabrication is performed by programmed robotic arm. It requires dedicated and process specific tooling, which often requires heating.
The technology can produce flat panels, curved shapes, grid stiffeners, which makes it highly versatile and can produce components with additional features like stiffeners.
The AFP can fabricate panels or elements directly on site without further processing,

which is called in situ process. This process was used for fabrication of side walls and base wall of the EM. The panels for side walls, top walls and for internal structure were fabricated with joining interfaces in forms of 45° flanges. In the same process the grid stiffeners were manufactured directly on the panels.

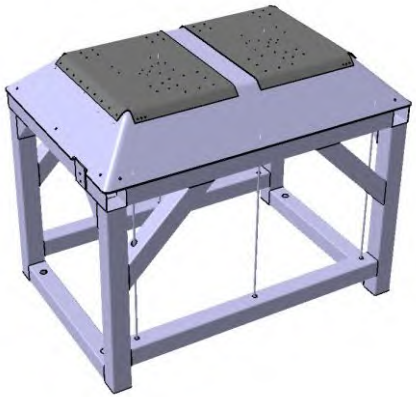


Figure 4: AFP tool design for fabrication of satellite walls

All above mentioned operations reduce number of fabrication steps, tools and machines and contribute to reduction of fabrication time. The fabrication time can be also shortened if multiple elements are joined and manufactured as a one piece to be cut and trimmed after layup.

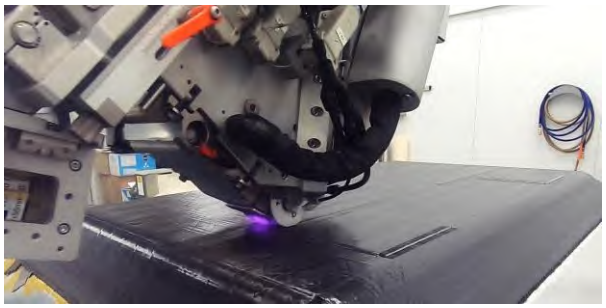


Figure 5: AFP sidewalls manufacturing

Actual layup time of 600x600mm 25 ply panel takes about 60 minutes. Straight section of 5 mm high rib is manufactured in minutes. Production rate expressed in kilograms of structure manufactured per hour is case specific.

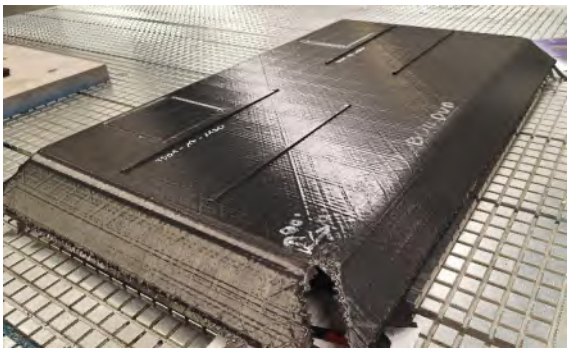


Figure 6: Two sidewalls with 45° joining flanges and rib grid stiffeners fabricated in one process ready for trimming.

2.4. Press thermoforming

Press is automated process which requires specially prepared moulds for fabrication of shapes. The thermoforming of profiles like L-shapes, trapezoid-shapes etc is highly efficient and fast - 20 min or less for one shape.

The procedure for thermoforming structures using thermoplastic composites consists of two elementary technological processes:

- Consolidation of prefabricated flat composite panels.
- Shaping (thermoforming) of previously consolidated flat composite panels into the desired part.

The press technology has high versatility in use of raw material in form of semipreg, prepreg or consolidated panel used for thermoforming. The higher level of raw material (e.g. panel) the smaller number of fabrication processes (e.g. only thermoforming), but higher cost of material.

The thermoforming process is usually combined of four steps: heating panel by Infrared (IR) heaters, fast transport in press, shaping using moulds and demoulding of shaped element (Figure 7).

Press is potentially more efficient for fabrication of simple, less complex shapes. Additionally, those parts can be produced even faster, when number of elements (panels, shapes) can be done in one process.

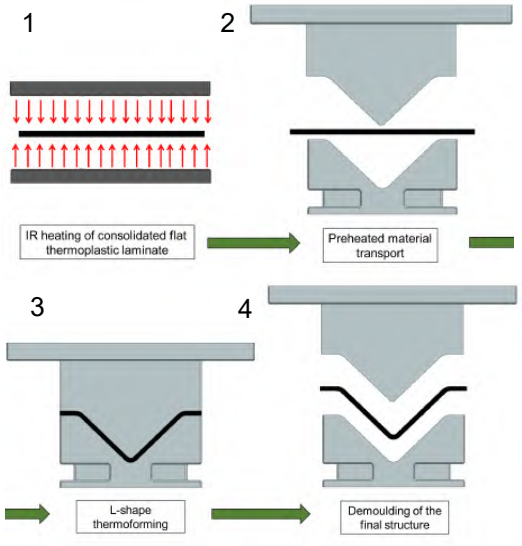


Figure 7: Thermoforming process workflow: 1 - IR heating of consolidated laminate, 2 – material transport, 3 – thermoforming, 4 - demoulding

The press consolidation of semipregs into panels takes up to 2 hours. Multiple panels (depends on thickness) can be consolidated in one process. The consolidated panels can be thermoformed in desired shape in 20 minutes, which is highly effective. Prior to that process the sheets for thermoforming should be cut from panels into desired shapes. Thermoforming can be performed also on AFP sheets. Process time is similar.



Figure 8: Moulds for thermoforming

The process parameters used were validated through quality control by non-destructive testing and through characterization of the material's mechanical properties.

The design of the satellite allows for versatility of the fabrication. The walls can be manufactured using press technology where panels with 45° flanges using thermoforming in fast processes. Grid stiffeners can be added after thermoforming or joined with panel during thermoforming.

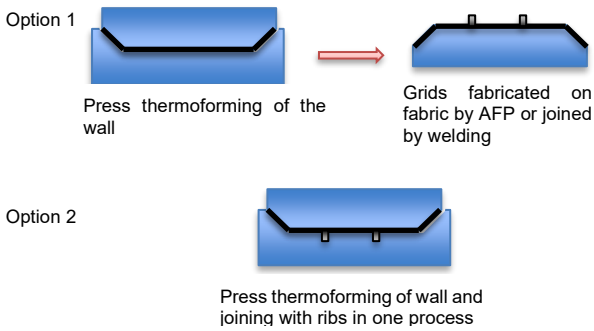


Figure 9: Alternative methods of walls fabrication using press

2.5. Joining

Resistance welding is the process where resistive heating element (metallic mesh or carbon fibres) is placed between joined thermoplastic surfaces. When electrical current passing through the metallic element, it heats up according to the Joule's law. The temperature rises at the interface, causing the polymer around the implant to melt and form a weld under pressure.

Resistance welding is a separate process which is done outside press or AFP. The process itself takes less than 10 minutes. Additional operations are preparation of welding element and electrical isolators, assembly of weld, applying pressure, placing electrical connectors. All of this steps can be accelerated by using highly automated welding rigs specific to certain application.

Unlike ultrasonic welding, the resistance welding is not limited by laminate thickness and is therefore suitable for the 3.5 mm thick walls of the satellite structure. Ultrasonic and conduction welding were excluded due to technological limitations, such as incomplete fusion, poor energy transfer, and limited process control in thicker laminates.

The drawback of resistance welding is current leakage phenomenon. During process the current can flow from heating element to conductive carbon fibres in welded materials. It causes local overheating and burning of the welded parts. Therefore the isolating material is placed between welded part and heating element. The most popular solution is glass fabric impregnated by polymer similar to matrices of a welded parts. It adds additional layer and mass to a weld, but prevents catastrophic current leakage.

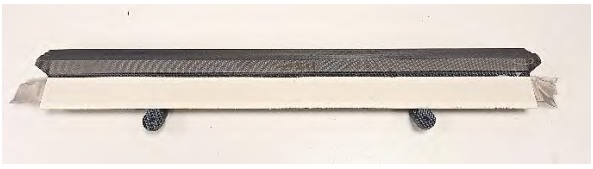


Figure 10: Thermoformed L-shape prepared for resistance welding with heating mesh and isolating layer

The solution with glass fabric was implemented in welds of the satellite EM. The welds were tested in

static lap-shear standard tests including elevated and lowered temperatures.

The welding was used on all vertical joints of the EM. Also all L-shapes were welded to vertical walls of the EM. In total 32 weld were performed. Welds have passed the vibration tests of the whole structure of the Engineering Model.

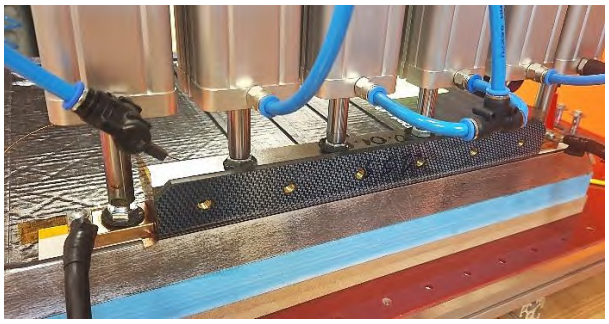


Figure 11: L-shape welding to side wall of EM.

Resistance welding has high potential for automation, and is suitable for production of joints in series. Resistance welding has limitation in case of complexity, where curved welds can pose problems and might require special design of heating element.

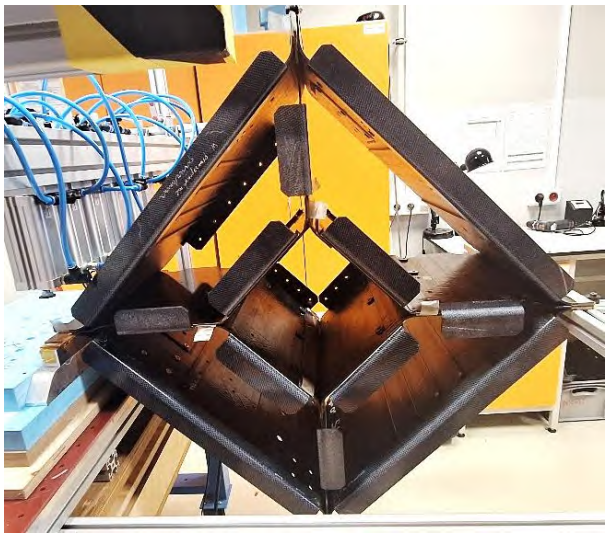


Figure 12: Welding of final joints of the EM of a satellite. All joint in the figure were made using resistance welding.

For detachable joints the metallic inserts technology was chosen. The heated inserts were pushed in the composite material with holes. The technology is fast and effective. The processes takes up to one minute per insert.



Figure 13: Fully inserted basewall

The inserts were also used in all fixing points for electronic instruments. Most inserts where put in basewall of the EM of telecommunication satellite. There were in total 254 inserts, 178 in basewall and 76 in walls.

2.6. Integration

Prior to integration of structure with instruments preliminary assembly was performed for confirmation of proper positioning of all parts. In this form structure was transported to Creotech Instruments for full integration.

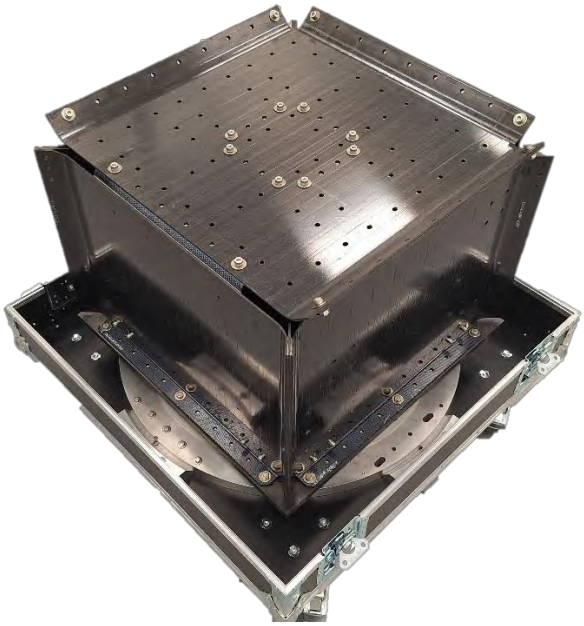


Figure 14: Composite structure of the Engineering Model in transport case prepared for instruments integration.

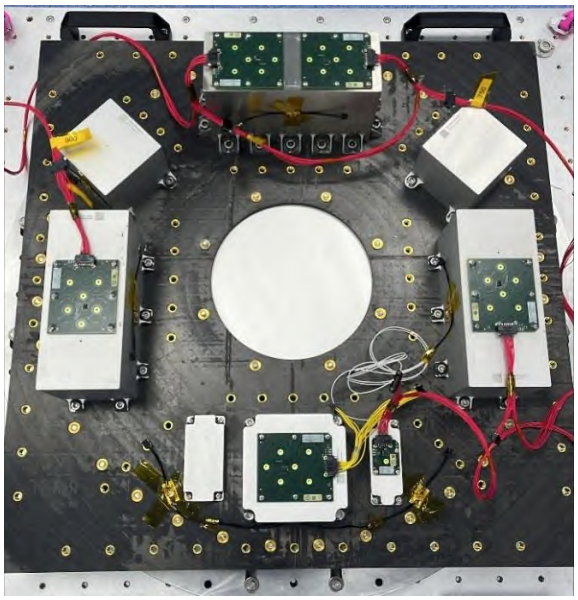


Figure 15: Basewall during integration, photo courtesy of Creotech Instruments

In the structure vertical walls were already joined (welded) which significantly reduced integration time – in the understanding of the last step of integration of the spacecraft with equipment. Thermoplastic structure allowed for distinction between integration of mechanical parts into bigger modules and much quicker integration with other components.

Practical experience shows that integrating the complete Structural Thermal Model (STM) model (including payload) took only ~2 weeks, which is lower than for traditional aluminum structures.

Such performance is rarely achievable with traditional aluminum structures, where panel mating requires more alignment and additional brackets and supporters are required.

Fully developed thermoplastic structures therefore may appear particularly beneficial for small satellite manufacturers facing rapid production cycles. Similar for projects which, by their very nature, require urgent and rapid integration.

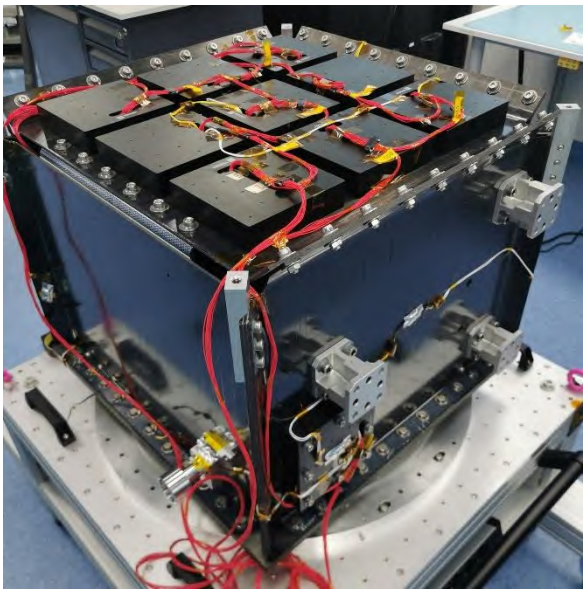


Figure 16: Fully integrated Engineering Model prepared for testing, photo courtesy of Creotech Instruments

2.7. Benefits

The full thermoplastic engineering model of a telecommunication satellite, measuring 655×655×506 mm with instrumentation was built.

In the project the strengths of thermoplastic composite technology was explored for application in satellite structures. The Engineering Model was designed to test wide scope of solutions utilized for those materials: AFP fabrication, press thermoforming, welding and inserting used on high performance thermoplastic composite. Some of the benefits of this approach are listed below.

1. Use of high performance resins with stability in temperatures temperature above 150 deg. C and thermal survivability above 200 deg. C, with high chemical and UV radiation resistance.
2. Materials have unlimited shelf life and do not require special infrastructure like freezers.
3. Utilization of in situ (on site) AFP fabrication, which do not require additional steps like post-consolidation in press or autoclave, which results in reduction of fabrication steps.
4. Utilization of simple rib grids, which can be fabricated with the panel in one process.
5. Utilization of press thermoforming, which is possibly the fastest method of composite material shaping. Technology was used for L-shapes for structural walls joining. Method highly suitable for medium/large scale production.
6. Utilization of welding technology. This is the fast technology of joining, where process takes less than 10 minutes and the weld does not require foreign materials like adhesives, which makes homogenous joint and ensures the same thermal properties of joint and joined parts.

7. Utilization of inserting technology for thermoplastic materials. Inserting methods for those materials use heated inserts which is fast and efficient.

All mentioned technologies are suitable for automation and application in medium/large scale production.

Unused material or production waste can be recycled or reused for other elements like secondary structures or used in out of space applications.

3. SUMMARY

The paper summarizes the overall approach to manufacture the EM of a telecommunication satellite.

The suggested approach was tailored to meet main requirement, which is increasing the fabrication rate due to:

- design simplification,
- reduction of fabrication steps and using fast fabrication methods distinctive to thermoplastic materials like:
    - AFP in situ fabrication,
    - press thermoforming,
    - welding,
    - inserting using heat.

The proposed solution supports fabrication optimization approach:

- one AFP tool for multiple elements fabrication: side walls, top wall and internal structure walls,
- one set of tooling for L-shape thermoforming,
- fabrication of walls with joining interfaces (45 degrees flanges), resulting in reduction of joining steps,
- fast joining methods like inserts and welding – methods with fast processes and suitable for automation.

The thermoplastic composites technology enable high-speed, repeatable production while maintaining structural integrity and performance. This approach marks a significant step toward redefining how future satellite platforms can be built – in a faster and more efficient way with scalability to medium/large scale production.

4. REFERENCES

1. Rinaldi, M., Cecchini, F., Pigliaru, L., Ghidini, T., Lumaca, F. & Nanni, F. (2021). Additive Manufacturing of Polyether Ether Ketone (PEEK) for Space Applications: A Nanosat Polymeric Structure. *Polymers* 13(1).
2. Aguilar, D., Christensen, S. & Fox, E.J. (2015). 3-D Printed Ultem 9085 Testing and Analysis. NASA Technical Reports Server (NTRS), National Aeronautics and Space Administration, Ames Research Center, Moffett Field, CA, USA.
3. Boon, Y.D., Joshi, S.C. & Bhudolia, S.K. (2021). Review: Filament Winding and Automated Fiber Placement with In Situ Consolidation for Fiber Reinforced Thermoplastic Polymer Composites. *Polymers* 13(12).
4. Engelhardt, S., Ehard, S., Wolf, T., Oelhafen, J., Kollmannsberger, A. & Drechsler, K. (2019). In Situ Joining of Unidirectional Tapes on Long Fiber Reinforced Thermoplastic Structures by Thermoplastic Automated Fiber Placement for Scientific Sounding Rocket Applications. *Procedia CIRP* 85, 189-194.
5. Miller, S.G., Heimann, P.J., Miller, A.J., Scheiman, D.A. & McCorkle, L.S. (2023). Manufacturing and Mechanical Testing of TC1225/LM-PAEK and TC1200/PEEK Thermoplastic Composite Panels (NASA/TM-20220015690). National Aeronautics and Space Administration, Glenn Research Center.
6. Seneviratne, W. & Tomblin, J. (2026). Certification of Thermoplastic Welding for Aircraft. *SAMPE Journal* 62, 12-24.
7. Kowalczyk, P., Sienicki, J. & Galińska, A. (2025). The Mechanical Performance of Resistance Welded Thermoplastic Composite Double Overlap Joint Tested Under Static and Fatigue Loading. *Fatigue Fract. Eng. Mater. Struct*. 48, 1236-1247.
8. Giusto, G. et al. (2021). Composite Grid Structure Technology for Space Applications. Mater. Today Proc. 34, 332-340.
9. Smeets, B., Telford, R., Murray, B., Matthews, K., & Pavlov, L. (2021). Development of a satellite central cylinder using uninterrupted pre-preg fibre-placed lattice structures. *Proceedings of ECSSMET 2021*.
10. Toray Advanced Composites. Toray Cetex TC1225. Available at: https://www.toraytac.com/product-explorer/products/gXuK/Toray-Cetex-TC1225
11. Toray Advanced Composites. Toray Cetex TC1200. Available at: https://www.toraytac.com/product-explorer/products/ovl4/Toray-Cetex-TC1200
12. Naito, M. et al. (2021). Applicability of Composite Materials for Space Radiation Shielding of Spacecraft. *Life Sci. Space Res.* 31, 71-79.

Acknowledgment

This work was founded by European Space Agency (ESA) and delivered under contract no. 4000141621/23/NL/FGL.

3D PRINTED SISIC FREE-FORM OPTIC MIRROR FOR S2NG

Dr.-Ing. Stephan Rapp [(1)], Thomas Sedlmaier [(1)], Matthias Meschenmoser [(1)], Dr. Sebastian Fray [(1)], Markus Erhard [(1)], Etienne Renotte [(2)], Fabrice Wolfs [(2)], Alexis Feutry [(2)], Philippe Klinkenberg [(2)], Dustin Kersberg [(3)], Dr. Clara Minas-Payamyar [(3)], Dr. Katrin Hirselandt [(3)], Dr. René Berlich [(4)], Roman Windpassinger [(4)]

[(1)] OHB System AG, Manfred-Fuchs-Straße 1, 82234 Weßling (Germany)
Email: stephan.rapp@ohb.de
[(2)] AMOS, Rue des Chasseurs Ardennais 2, 4031 Liège (Belgium), Email: etienne.renotte@amos.be
[(3)] Schunk Technical Ceramics GmbH, Hanns-Martin-Schleyer-Str. 5, 47877 Willich (Germany),
Email: dustin.kersberg@schunk-group.com
[(4)] ESA-ESTEC, Keplerlaan 1, 2200 AG Noordwijk (The Netherlands), Email: rene.berlich@esa.int

KEYWORDS

3D printing, additive manufacturing, SiSiC, IntrinSiC®, reaction bonded SiC, RBSiC, ultra-stability, lightweight mirror, free-form optics, telescopes, space application

ABSTRACT

The very stringent performance requirements for the telescope of the Copernicus Sentinel 2 next generation mission, require mirror surfaces with a strong freeform shape and materials with outstanding thermo-mechanical properties.
To mature the required technology, a consortium consisting of OHB System AG, AMOS and Schunk Technical Ceramics GmbH, developed and manufactured a corresponding mirror demonstrator in the frame of an ESA technology development program (TDE).
The 3D printed, reaction bonded SiC from Schunk (IntrinSiC®) provided unique design freedom to optimize for the demanding surface form error requirements of the mirror when loaded with gravity or thermal load cases. Modelling and optimization processes have been developed to find a compliant design.
AMOS developed corresponding metrology concepts, manufacturing jigs, tools and process steps to finally polish this high-performance mirror with large free-form characteristics to a surface form error of < 16 nm rms.

1. INTRODUCTION

The optical telescope of the satellites for the Copernicus Sentinel 2 next generation mission (S2 NG) needs to achieve within a small volume and a low mass a very large field of view by still providing a high ground resolution and opto-mechanical and thermo-elastic stability.
For that reason, mirror surfaces with a strong freeform shape have to be applied, and innovative materials with outstanding thermo-mechanical properties will need to be used.
In the frame of an ESA technology development program, called “Design and Breadboarding of a Wide Field-Of-View Telescope for the next generation Copernicus Sentinel-2” (ESA Contract No. 4000138864/22/NL/AR), the manufacturing process required to produce such kind of free-form mirrors was developed and demonstrated with the design and production of a flight representative free-form optic (FFO) mirror demonstrator (Figure 1).



Figure 1 3D printed, IntrinSiC® (RBSiC), free-form optic mirror demonstrator

The industrial consortium consisted of OHB System AG, as the prime contractor, AMOS and Schunk Technical Ceramics GmbH.

2. REQUIREMENTS

Based on the S2NG phase 0 study, ESA has derived a high-level set of requirements for one single mirror. These requirements are defined, to represent the critical technical challenges associated with the overall S2NG telescope optical system. OHB has derived additional requirements to guarantee a mirror design, suitable for the S2NG mission. The requirements listed in the following are not the complete set, but a relevant selection giving the impression of the challenges.

2.1. Optical and Performance requirements

The mirror overall size shall be 800 mm x 280 mm with a corner radius of 100 mm and an optical clear aperture clearance of 10 mm. The specified, complex free-form is defined by an extended polynomial expression [1], with a global sagita (SAG) of ~40 mm and a delta SAG of ~2 mm (see Figure 2 and Figure 3).

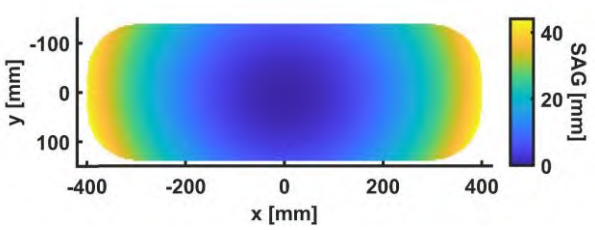


Figure 2 SAG of free-form mirror

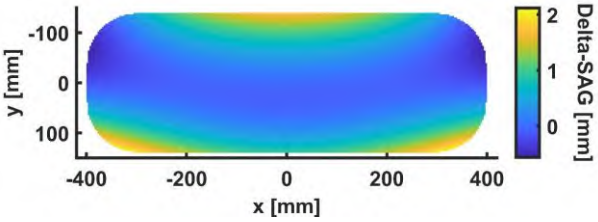


Figure 3 Delta-SAG of free-form mirror

The surface form error (SFE) shall be < 25 nm rms, while the SFE on any disk of 200 mm shall be < 10 nm RMS.
The gravity induced SFE shall be < 10 nm rms for in-plane (IP) loading and < 40 nm rms for out-of-plane (OOP) loading. The temperature induced SFE shall be < 3 nm rms for an operational temperature range of 20°C ± 5K.

2.2. Mechanical and structural requirements

The mass of the mirror shall be < 7 kg, its 1st Eigenfrequency > 500 Hz (without the iso-static mounting) and it shall sustain a quasi-static load of 37 g.
As from the beginning, 7 kg was assessed as too demanding within this project and the focus was on the free-form manufacturing and stability requirements, the goal was set to a mass of 8 kg.

3. INTRINSIC® – 3D PRINTED SIC FOR SPACE

For the realization of the mirror demonstrator the 3D printed, reaction bonded silicon carbide (RBSiC), IntrinSiC®, from the company Schunk Technical Ceramics GmbH, further on called Schunk, was utilized.

3.1. Manufacturing process

The manufacturing process for the RBSiC from Schunk consists of the following 4 major steps:

- Raw material provision and mixture
- Shaping the green body
- Pyrolysis
- Siliconizing

This process is depicted in Figure 4.
SiC powder is mixed with an organic binder and shaped. This shaping process can be done in different ways, e.g. isostatic pressing, slip casting or extrusion. The shaping method, which was utilized for this project was the 3D printing process (Figure 5).

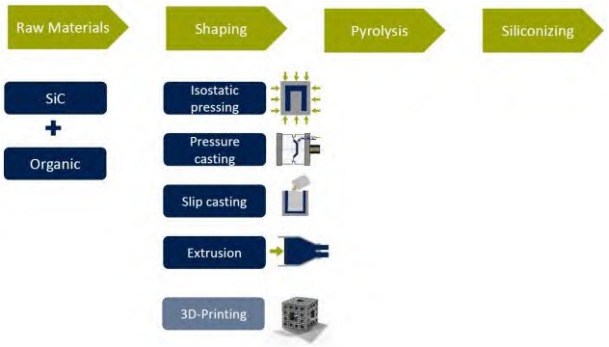


Figure 4 Schunks RBSiC manufacturing process

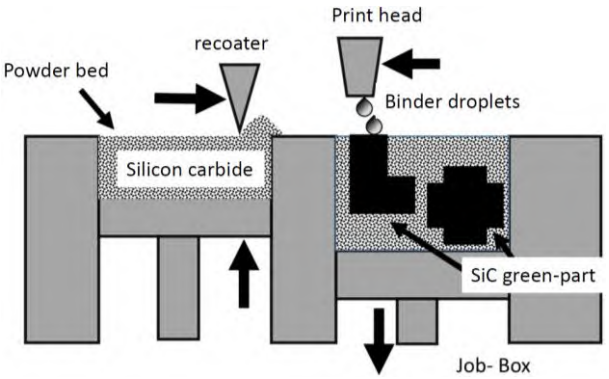


Figure 5 3D printing process of IntrinSiC®

The green body is shaped in a binder jetting process. Silicon carbide is placed in a powder bed with a recoater and a print head is applying binder droplets, binding the powder at the locations, you later on want to have the part material. After the binder has been applied, the powder bed is lowered and the recoater applies the next layer of silicon carbide powder.
The steps after the shaping are the same for all shaping methods. In a high temperature pyrolysis step, the organic material out of the green body is removed and porous carbon is remaining between the primary SiC powder grains (Figure 6).

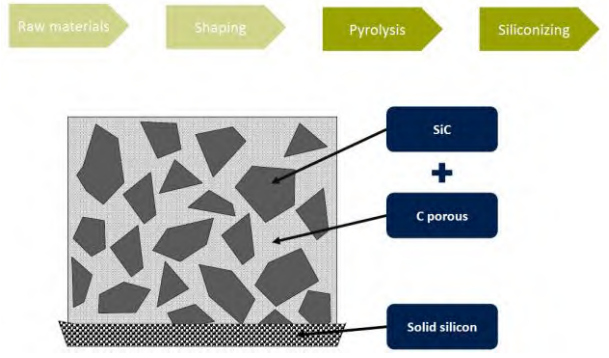


Figure 6 Pyrolysis step

In the final step, liquid silicone is infiltrating the porous carbon forming secondary silicon carbide. The final part thus is consisting of primary silicon carbide, secondary silicon carbide and a silicon phase (Figure 7).

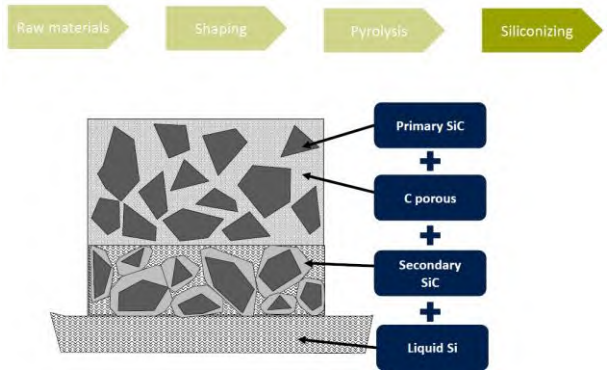


Figure 7 Siliconizing step

3.2. Material Properties

The resulting material properties can be found in [2] and some of them are listed and discussed within this section.
The chemical composition is 86% (mass) of SiC and 14% (mass) of silicon. The achieved density is 3,05 [g/cm³] with 0% of open porosity.
The properties most relevant for high performance optical space components are the specific stiffness and the thermal stability. The first is very relevant to reduce the effect of gravity release in orbit. As optical payloads are assembled and aligned on ground under 1 [g] environment, they experience a -1 [g] load case in space, which deforms them. To minimize this effect, optical payloads need to be designed very stiff with respect to gravity load cases. The thermal stability can be described by the ratio of thermal conductivity and coefficient of thermal expansion (CTE). The higher the conductivity, the smaller the thermal gradients in the parts, causing potentially undesired deformations. For the CTE it is vice versa. The smaller the CTE the smaller undesired deformations in space due to the thermal environment.
These two indicators are illustrated in Figure 8.
It can be seen, that SiC is very advantageous with respect to these properties compared to other materials.

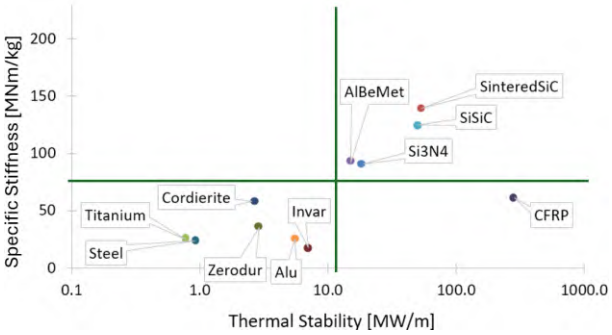


Figure 8 Specific stiffness and thermal stability

For IntrinSiC®, the Young's modulus is 380 [GPa]. Together with the moderate density, this leads to a very high specific stiffness of around 125 [MNm/kg]. The thermal conductivity at 20°C is 200 [W/mK] and the coefficient of thermal expansion at 20°C is 2.2 [1e-6/K]. This leads to a thermal stability of 90 [MW/m], which is a very competitive value.
According to the datasheet, the 4 point bending strength is 210 MPa and the Weibull Modul is 13. While the bending strength is rather low compared to other technical ceramics available, the Weibull modulus is rather high. As the allowable is calculated through a Weibull statistic, this results in acceptable values for designing space optical instruments. This is even more true as the designs for space instruments are typically driven by stiffness and not strength and the 3D printing capability allows to add material were necessary and develop a design suitable for brittle materials (round edges, smooth transitions, etc.).

4. DESIGN AND ANALYSIS

Within this chapter the mechanical design of the free-form optic mirror is introduced, and the analysis methodologies are described how this design and its performance was achieved.

4.1. Design

For this free-form optic mirror the design freedom offered by the 3D printing technology was strongly utilized, which resulted not only in a free form optic but also in a lightweighted, bionic design of the back structure. A very noticeable feature is the tapered backside (Figure 9), which results in a stiffness distribution that is beneficial for the gravity induced deformations.



Figure 9 Tapered mirror backside

The back face is partially closed, increasing the overall stiffness of the mirror. Shear walls inside the mirror are lightweighted by large pockets. Reinforcing ribs and radii are foreseen inside where necessary (Figure 10). These design features were only possible with the 3D printing technology.

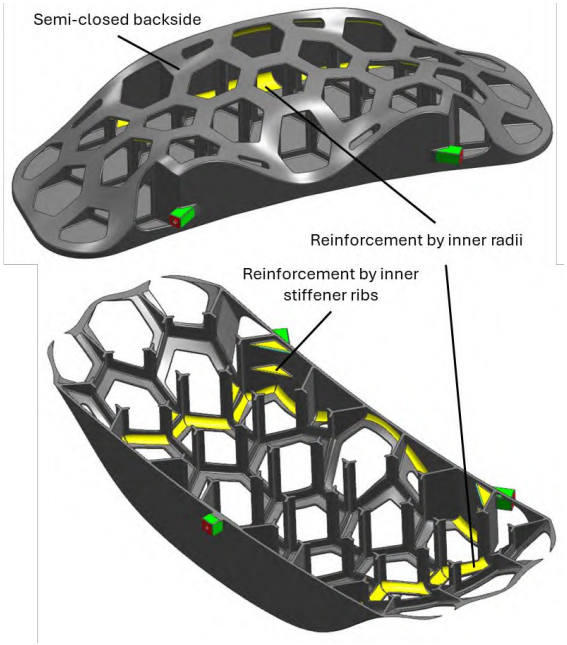


Figure 10 Design features, possible utilizing 3D printing

4.2. Optimization

The driving structural requirement for this mirror was the surface form error, induced by the gravity release. An optimization process was setup to come up with a compliant design for the demanding requirements. As the 3D printing technology allows a huge design freedom, optimization techniques can deploy their whole potential, what was fully utilized here. Before the optimization algorithm was applied, some manual steps were done to define design variables and fix some of the design features, such as Bipod location. For the final optimization step, an optimization finite element model (FEM) was setup in Altair Hypermesh 2022, providing a design space for the optimization algorithm in Optistruct (Figure 11). The mass of the full design space as shown in Figure 11 is 13 kg, exceeding the requirement by far.

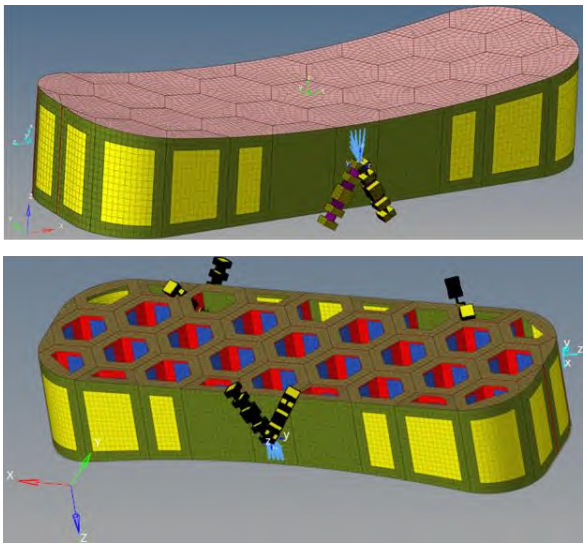


Figure 11 Optimization finite element model

Besides the free size optimization of wall thickness, 38 design variables have been defined, which the optimizer could vary. For example, the shapes of the tapered back structure. Figure 12 shows how the optimization algorithm can modify the shape of the back structure - a) only locally, b) the complete back face.

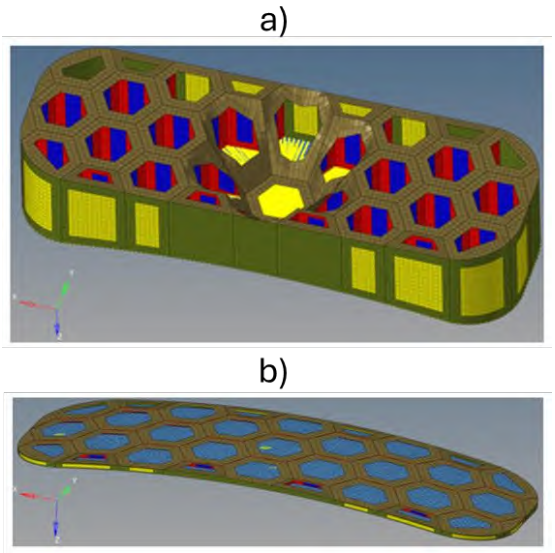


Figure 12 Examples of shape variation

The applied objective function was the surface form error under 1 [g] in x-direction, assuming that the instrument alignment will happen in this orientation. Additionally, constraints were applied, e.g. for mass. This optimization setup can be summarized as follows:

Design variables:
- back face shapes
- other geometrical features
- free size (thickness) of each element

Objective function:
- Minimize SFE RMS under 1 [g] X

Constraints:
- Mirror mass < 8 kg
- Others

The result of this optimization can be seen in Figure 13. The tapered back side is clearly visible. Higher stiffening ribs are necessary close to the bipod interfaces to increase the stiffness. No ribs are required at the mirror edges. The colour code indicates on top the element thickness. Blue is smaller thickness, red is higher thickness. It can be seen that the thickness was increased by the optimizer close to the surface and the back face at the bipod locations and along the ribs along the y-axis.

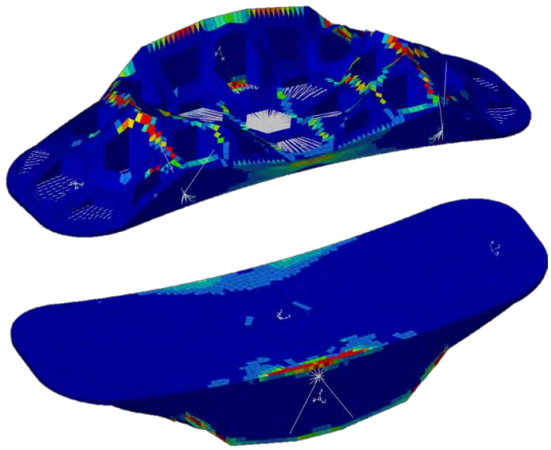


Figure 13 Optimization result

A varying thickness from element to element imposes a large challenge to the implementation from FE software into a CAD design.
Thus, the free-size optimization results cannot be used directly. However, they are implemented into the model by an engineering interpretation. Stiffening radii have been implemented at the locations where the free sizing optimization has added thickness. In a last optimization step, the free sizing has been replaced by additional design variables (e.g. wall thickness of specific surfaces) and different variants of rib lightweighting have been considered.
The final result of the optimization is summarized in Table 1.

Table 1 Optimization results

Objective/Constraint	Requirement	Result
RMS SFE 1g X [nm]	<10	3.34
RMS SFE 1g Y [nm]	<10	7.79
RMS SFE 1 g Z [nm]	<40	39.94
Mass w/o Bipods [kg]	<8	8

4.3. Analysis

As described already before, the optimization output cannot directly be transferred to a manufacturable design and some manual engineering work and design needs to be done leading to the final design. As this design is deviating in the details from the optimization result and the properties are very sensitive, a re-analysis step is added with the final design to confirm compliance. The final finite element model used for is analysis is shown in Figure 14.

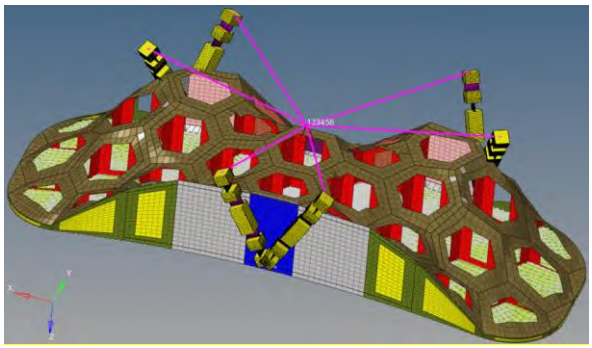


Figure 14 Final finite element model

4.3.1. Stiffness, stress and mass

The modal analysis shows that for the mirror assembly, including the bipods, the first two Eigenfrequencies are 285 Hz and 293 Hz. The mirror body alone without the bipods has an Eigenfrequency of 1038 Hz in a hard mounted configuration, which is well above the required 500 Hz.
Applying quasi-static loads (QSL) of 37 [g] in all three directions leads to stresses as summarized in Table 2. For the mirror principle stresses P1 are evaluated, for the bipods v. Mises stresses. All of these values lead to positive margins of safety.

Table 2 Stress results (QSL)

Load case	Max mirror stress [MPa]	Max bipod stress [MPa]
QSL 37 g X	20.66	195.41
QSL 37 g Y	43.80	166.92
QSL 37 g Z	12.29	83.30

Dynamic loads haven't been analysed as no requirements have been defined. Sine vibration would be covered by QSL as also the first natural frequency is well above the sine range. For random a primary notch would be applied, limiting the interface to the QSL. With these assumptions it is assessed that the mechanical integrity is covered with the QSL load case.
Interface tolerance load cases as well as thermal non-operational load cases have been analysed, leading to comfortable margins of safety for the bipods and the mirror.
A mass of 8 kg results in an area weight of approximately 35 kg/m², which is a competitive value for strongly rectangular mirrors.

4.3.2. Operational performance

To evaluate the operational performance, the surface form error (SFE) under the defined load cases is assessed as the sag deformation after subtraction of the mean displacements and rotations of the mirror surface (best fit plane). For sag deformations with large spherical content (e.g. uniform thermal expansion), a best-fit-sphere is subtracted. The root mean square (rms) of the SFE is computed and compared to the requirement.
The mean displacements and rotations resulting

from the gravity load cases are summarized in Table 3.

Table 3 Mean Displacements/Rotations under 1 g

Load case	Displacement [µm]	Rotation [µrad]
1g X	2.7	0.07
1g Y	3.1	0.2
1g Z	0.6	1.3
Requirement	<10	<5

The resulting SFE rms under the gravity load cases are summarized in Table 4.

Table 4 SFE RMS under 1 g

Load case	Requirement [nm]	SFE RMS [nm]
1g X	<10	3.16
1g Y	<10	7.19
1g Z	<40	37.75

Slight differences of these SFE rms values can be observed compared to the optimization results (Table 1). This can be explained by the manual adjustment of the design and the re-analysis. An exemplary plot for the SFE under gravity is shown in Figure 15.

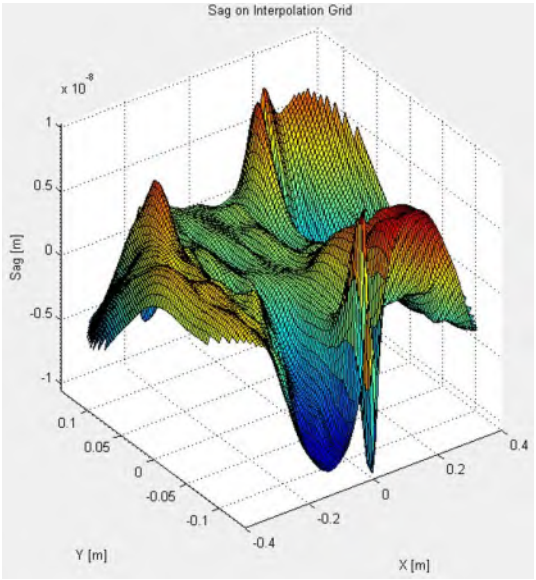


Figure 15 SFE plot for 1 g (X)

For a uniform temperature load of 5K, the SFE rms results in 2.2 nm, which is compliant wrt the required 3 nm. A corresponding SFE plot is depicted in Figure 16.

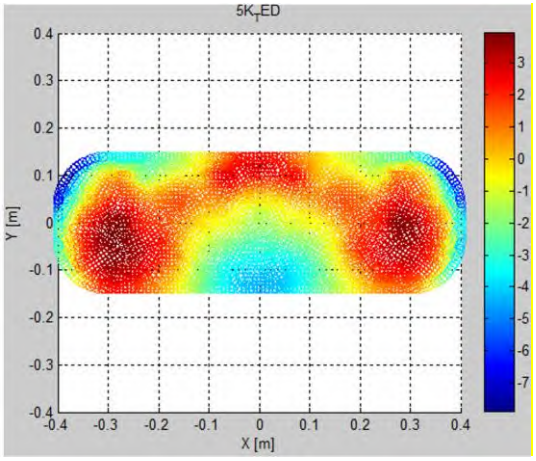


Figure 16 SFE irregularities wrt free-form for 5 K uniform temperature load

5. DEMONSTRATOR MANUFACTURING

The overall manufacturing process consists of the IntrinSiC® manufacturing steps as described in section 3.1, grinding of the functional surfaces, a cladding process to apply a polishable layer and the optical polishing, which itself might consist of several sub-steps.

5.1. Blank manufacturing

Schunk has 3D printing capacity of up to 1.8 m x 1.0 m x 0.7 m. The print job, independent of part size and complexity, is taking 1 day maximum. The printing is followed by some accompanying steps like de-sanding. The resulting green body has not yet its final mechanical strength and needs to be handled with care. The FFO mirror in its green state is shown in Figure 17.



Figure 17 3D printed FFO mirror in its green state

After the shaping by 3D printing, the pyrolysis and infiltration steps follow, before a grinding step finalizes the blank production. Figure 18 shows the FFO after finalization of the grinding, still on the grinding machine.

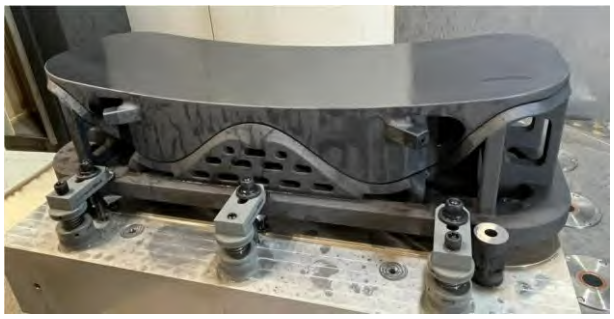


Figure 18 FFO during the grinding step

5.2. Cladding

The two-phase microstructure of reaction-bonded IntrinSiC®, which includes a softer silicon phase, makes it difficult to polish the material to the optical quality required for high-performance missions. Because of this, a layer of highly pure SiC is applied in a chemical vapor deposition (CVD) process by Schunk Carbon Technology. This CVD SiC technology is marketed by Schunk under the name P60 [3].

CVD SiC is a well known coating applied on SiC substrates for several ESA missions, such as Euclid, Gaia and Herschel [4], [5], [6], [7]. To not mix up with a potential final optical coating, this layer is called cladding throughout this paper.

A typical, initial cladding layer for a complex surface to be polished has a thickness of 600 µm. With this thickness, there is typically enough material to machine in, to achieve the final required surface shape. To avoid a 600 µm cladding layer all around the part, which would add a significant amount of mass, a masking can be foreseen to apply the cladding only on the functional surfaces and protect the others. This masked cladding step however is challenging and within this project a problem occurred for the first mirror blank during cladding and it needed to be scrapped. Thanks to a proper attrition concept, the impact on schedule was limited, but as the mass was not the focus within this project, the second mirror was cladded without a masking, successfully. This additional cladding mass led to a final mass of the mirror of 8.85 kg (instead of the 8 kg by design).

Within an OHB internal, parallel activity, the masked cladding could be demonstrated successfully with a 300 mm curved mirror demonstrator (Figure 19).

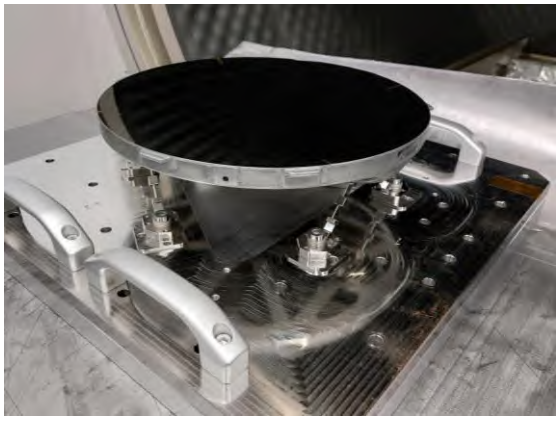


Figure 19 300 mm mirror demonstrator (OHB internal activity)

5.3. Polishing

After the cladding step, different machining steps towards the final mirror surface follow. The necessary steps also depend on the grinding quality before the cladding and can consist of another grinding step, a lapping step, a polishing step and for the final figuring an ion beam figuring step.

Besides the manufacturing tools themselves, the metrology is crucial to manufacture surfaces in the required quality (surface roughness < 1 nm rms; surface form deviation < 25 nm rms). For this reason, different measurement systems are utilized. A coordinate measurement machine (CMM) and laser trackers to align the mirror and a computer generated hologram (CGH) to measure the actual mirror shape (see Figure 20).



Figure 20 FFO in a measurement setup together with the CGH

In the case of the FFO, AMOS started with a lapping step after reception of the cladded mirror blank. AMOS designed a special mounting jig for the lapping operation. The blank mounted in this jig can be seen in Figure 21.



Figure 21 FFO mirror mounted on the lapping jig

Figure 22 shows the FFO mirror during lapping operation. The surface form error after lapping was 1-2 µm rms. Due to the anomaly during the cladding step, the surface form error before lapping was larger than expected and the remaining cladding thickness after lapping was not sufficient to fulfil the surface form error requirement for the full clear aperture, especially along the rim. To reduce the risk of machining through the cladding layer, it was decided, together with the customer, to reduce the relevant clear aperture by 10 mm around the rim. With this new goal, the next polishing steps were tackled.



Figure 22 FFO during lapping operation.

After lapping, a polishing (or classical figuring) step followed, ending up with a surface form error of 35 nm rms with a micro-roughness of 0,8 nm rms. The polishing sequence was finalized with an ion beam figuring step, bringing down the SFE to 16 nm rms. Figure 23 shows the FFO mirror during the ion beam figuring. Figure 24 shows the final surface form error map of the FFO mirror.

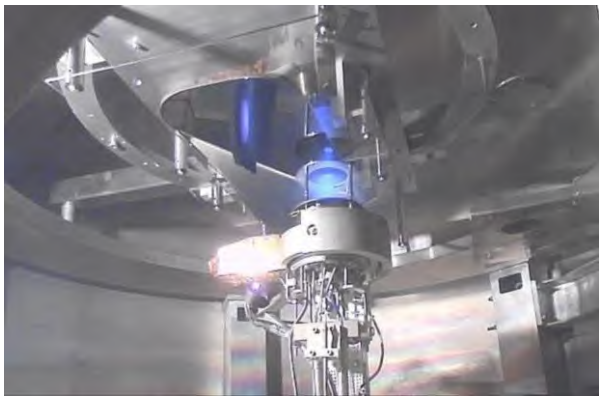


Figure 23 FFO in the ion beam figuring step

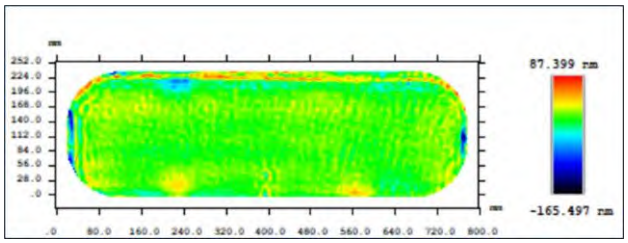


Figure 24 Final surface form error

6. Conclusion

The final state of the mirror demonstrator is shown in Figure 1. It can be concluded that this demanding free-form optic mirror could be designed to compliance wrt the demanding requirements wrt quasi static loads, mass and especially surface form error requirements wrt gravitational and thermal loads. This was possible by developing and applying analyses and optimization methods to derive a compliant mirror shape and utilizing the 3D printing capabilities.
The mass requirement of 8 kg could not be realized with the demonstrator as the required masking for the cladding could not be implemented.
Lapping and polishing were very demanding steps, especially due to the blank with a larger surface form error after cladding than expected. The resulting limited remaining cladding layer resulted in a non-compliance with respect to the original requirement of the clear aperture size. This needed to be reduced by 10 mm around the rim. Within this new relevant clear aperture however, polishing results were compliant and a surface form error of < 16 nm rms and a micro-roughness of 0.8 nm rms could be achieved.

7. References

1.ESA ESTEC, Invitation to Tender for Design and Breadboarding of a wide field of-view telescope for the next generation Copernicus Sentinel-2 – Expro Plus, Ref. ESA AO/1-11263/22/NL/AR
2.Schunk Technical Ceramics GmbH, IntrinSiC® Material datasheet, www.schunk-carbontechnology.com
3.Schunk Carbon Technology GmbH, https://www.schunk-group.com/technical-ceramics/en/materials/silicon-carbide
4. Breysse, J., Castel, D., Bougoin, M. (2012). All-SiC telescope technology at EADS Astrium, SPIE Proceedings Vol. 10564 (ICSO 2012)
5. Coe, G., Behar-Lafenetre, S., Cornillon, L., Rancurel, M., Denaux, D., Ballhause, D., Lucarelli, S. (2013), ESA Initiatives to Improve Mechanical Design & Verification Methods for Ceramic Structures, SPIE Proceedings Vol. 8837
6. Bougoin, M., Lavenac, J., Gerbert-Gaillard, A., Pierot, D. (2016), The SiC primary mirror of the EUCLID telescope, SPIE Proceedings Vol. 10562
7. Bougoin, M., Mallet, F., Lavenac, J., Gerbert-Gaillard, A. (2018), Full-SiC EUCLID's very large telescope, SPIE Proceedings Vol. 11180

3D printed SiSiC for space applications

Michael Bösl [(1)], Dr.-Ing. Stephan Rapp [(1)], Fulvio De Bonis [(1)], Thomas Sedlmaier [(1)], Dustin Kersberg [(2)], Dr. Clara Minas-Payamyar [(2)], Dr. Katrin Hirselandt [(2)]

[(1)] OHB System AG, Manfred-Fuchs-Straße 1, 82234 Weßling (Germany),
Email: michael.boesl@ohb.de
[(2)] Schunk Technical Ceramics GmbH, Hanns-Martin-Schleyer-Str. 5, 47877 Willich,
Email: dustin.kersberg@schunk-group.com

KEYWORDS

3D printing, additive manufacturing, IntrinSiC®, Reaction Bonded SiC, RBSiC, SiSiC, ultra-stability, lightweight mirror, ceramic optical system

ABSTRACT

Ceramic materials offer outstanding specific stiffness and thermo-elastic stability, making them attractive for next-generation high-performance optical space systems. To utilise these advantages, OHB and Schunk Technical Ceramics have established a comprehensive development roadmap based on 3D printed reaction-bonded silicon carbide like IntrinSiC®.

The roadmap covers material characterization, manufacturing process optimization, design methodologies, and analysis approaches tailored to the requirements of brittle ceramic structures. Advanced design workflows, including topology and parameter optimization, have been applied to fully utilize the freedom offered by additive manufacturing.

Development activities progressed from a representative ceramic optical bench and small-scale mirror demonstrators to lightweight mirrors up to 1.55m diameter, including free-form and aspherical optics. Structural qualification culminated in successful vibration and shock testing of a 1.55m SiC mirror assembly.

The latest milestone is a Ceramic Optical System integrating multiple ceramic mirrors, a mirror bracket, and an optical bench, aiming to demonstrate system-level assembly, environmental qualification, and thermo-elastic stability verification for future optical space missions.

1. INTRODUCTION

Over the past decades, OHB has established a strong heritage in the development of high-performance optical payloads for Earth observation applications, including optical subsystems and payload developments for missions such as EnMAP, MTG, Euclid, FLEX, FORUM, and other advanced European space programs.
As mission requirements continue to evolve toward larger apertures, higher spatial resolution, improved radiometric performance, and increased measurement stability, conventional material solutions increasingly become a limiting factor. In response, OHB identified all-ceramic optical systems, particularly based on silicon carbide (SiC), as a key enabling technology for future high-performance optical satellites. The primary drivers are the exceptionally high specific stiffness of SiC, which minimizes gravity-release effects while enabling lightweight large-aperture mirrors, its superior thermal stability resulting from high thermal conductivity and low coefficient of thermal expansion, and eliminating hygroscopic materials such as CFRP, thereby avoiding moisture-release induced dimensional changes and alignment drifts in orbit. In addition, the possibility of manufacturing mirrors and structural elements from the same material simplifies the realization of highly stable all-ceramic optical assemblies.
Consequently, OHB established a dedicated ceramic optical systems roadmap in 2020 and has since continuously invested in an extensive research and development programme aimed at mastering the complete lifecycle of ceramic space optics, including the realization of large SiC mirrors and structures, complex optical components, ultra-stable optical systems, and the corresponding system-level design, integration, and verification capabilities through full-scale hardware demonstrators and representative environmental testing.

2. INTRINSIC® – 3D PRINTED SIC FOR SPACE

For the realization of the demonstrators presented in this work, OHB partnered with Schunk Technical Ceramics GmbH, who are providing the 3D-printed reaction-bonded silicon carbide (RBSiC) material IntrinSiC® [1]. Schunk was chosen following a comprehensive assessment of available suppliers and manufacturing technologies, considering material performance, industrial maturity, production capacity, quality processes, and long-term supply-chain reliability. Emphasis was also placed on establishing a robust European capability for large optical ceramic components.

IntrinSiC® is manufactured using an additive binder jetting manufacturing process combined with proven RBSiC infiltration technology. The process enables the production of lightweight, highly

integrated, and geometrically complex structures that would be difficult or impossible to realize using conventional manufacturing methods. Furthermore, Schunk provides access to an industrialized production environment with established quality assurance processes and serial-production experience from high-precision semiconductor and industrial applications.

From an optical payload perspective, RBSiC offers an attractive combination of high specific stiffness, low coefficient of thermal expansion, and high thermal conductivity, as illustrated in Figure 1. Additionally, RBSiC has the advantage of near-zero shrinkage in the infiltration process.

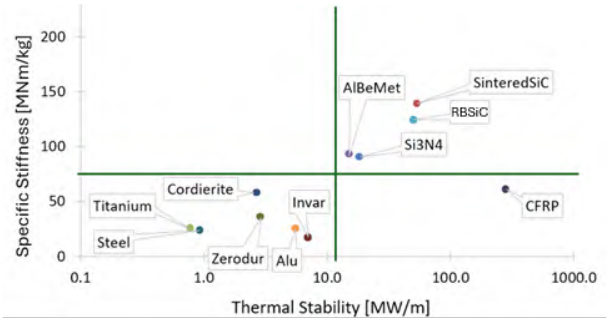


Figure 1 Specific stiffness and thermal stability

Beyond the technical benefits, the collaboration with Schunk provides an independent European supply chain from powder to finished product for advanced ceramic hardware.

3. CERAMIC ROADMAP DEVELOPMENT

The collaborative development between Schunk and OHB was kicked off with the development of a full-scale ceramic optical bench (COB) which was derived from representative requirements for optical systems of its size (Figure 2). The resulting topology optimized optical bench features a semi-closed design, incorporates through-holes and bonded inserts. The resulting design features a mass of 22.8 kg for the SiC part alone and a total mass of 88.4 kg when equipped with bipods, inserts, and four mass dummies representing subsystems mounted on the SiC structure. The first mode of the assembly is at 145 Hz.



Figure 2 ceramic optical bench after insert bonding

The assembly was successfully tested under sine and random vibration loads based on a QSL of 15 g in-plane and 25 g out-of-plane (Figure 3).

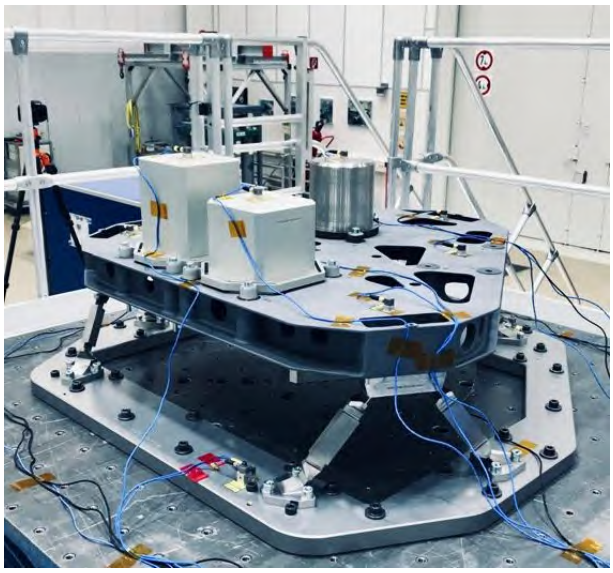


Figure 3 ceramic optical bench during vibration testing

Following the successful development, production, integration and testing of the Ceramic Optical Bench, a strategy was developed to mature the technology by upscaling demonstrator size and complexity of mirrors, mirror assemblies, structures and a full Ceramic Optical System (COS). The roadmap for the development of mirrors and mirror assemblies is shown in Figure 4.
Special emphasize was placed on the development of a green body joining technique, in which the additively manufactured green part is joined from individually printed sections before undergoing the infiltration process, resulting in a monolithic RBSiC part. Additionally, due to limitations of SiSiC / RBSiC with regard to the polishing of optical surfaces (see ch. 5.2), a cladding process was applied by Schunk Carbon Technologies GmbH in order to obtain a pure p60 SiC CVD layer suitable for optical polishing.

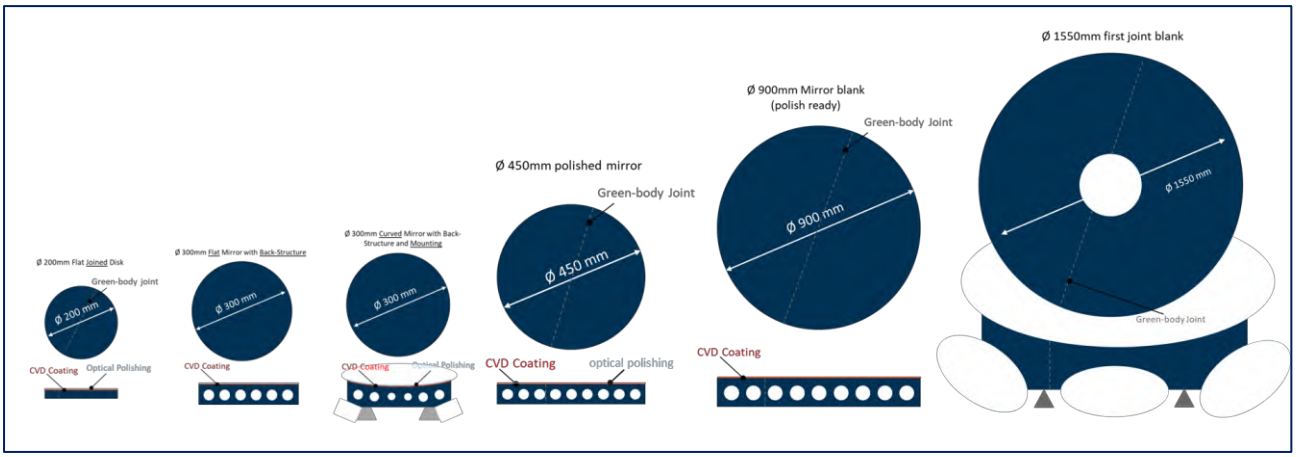


Figure 4 upscaling demonstrator size and complexity of mirror (assemblies)

The first optical component was a pair of Ø200 mm flat discs (Figure 5), one of which was produced with the green body joining technique. Both discs have been cladded with p60 SiC [2] and polished to an RMSt (total deviation) specified as better than 25 nm. These discs underwent unregular interferometric measurements to demonstrate stability following long-term storage, thermal vacuum cycling and damp heat testing.



Figure 5 Ø200 mm flat disc, SiC cladded and polished

The second mirror was a Ø300 mm flat mirror blank, the first mirror blank with a back structure (Figure 6).



Figure 6 Ø300 mm flat mirror blank in green state

The following step was a Ø300 curved mirror with a semi-closed back structure and a bipod bonding interface which is decoupled from the optical face of the mirror in order to avoid effects from curing shrinkage or moisture desorption effects of the adhesive (Figure 7). This mirror benefits from the design freedom possible when using the IntrinSiC® additive manufacturing process and has a competitive mass per optical area of 26.7 kg/m². This mirror blank underwent CVD SiC coating and was subsequently polished to an RMS < λ/4. After integration of INVAR bipods, the mirror assembly has a mass of 2.55 kg and a first eigenmode of 643 Hz. It was environmentally tested under thermal vacuum bake-out and cycling, sine and random vibration to 45g out-of-plane and 30g in-plane (Figure 8) and subjected to thermo-elastic deformation (TED) testing in OHB System AG's optical laboratory. These tests have been accompanied by interferometric SFE measurements before and after bipod bonding and after each environmental test (Figure 9). These measurements showed no deterioration of the optical properties of the mirror. The TED test demonstrated the high thermal stability through quick distribution of disturbances and fast return to initial SFE after application of temperature plateaus or gradients. [1)]



Figure 7 Ø300 mm curved mirror after firing

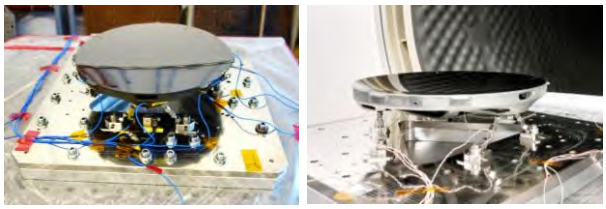


Figure 8 Ø300 mm curved mirror during vibration (left) and before TVAC testing (right)

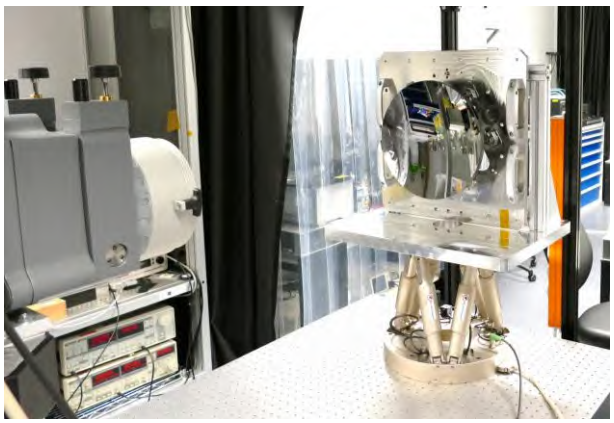


Figure 9 Ø300 mm curved mirror during SFE measurement

The next iteration in size is a Ø450 mm flat mirror which was RSiC coated and polished to specification (Figure 10). The mirror has a mass of 3.7 kg and a mass per optical area of 23.3 kg/m² and was produced with a largely closed back structure. The mirror has been produced from two parts and joined in the green state. The joining is not detectable on the optical surface after polishing.

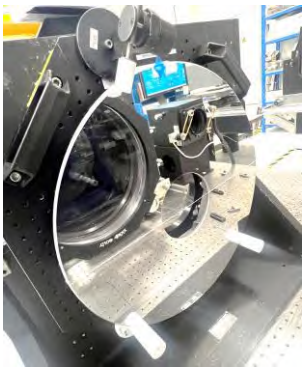


Figure 10 Ø450 mm flat mirror after polishing

Three Ø 900mm mirror blanks with a semi-closed back structure and an area mass of 22.8 kg /m² have been produced (Figure 11). These mirror blanks have been printed in three sections and joined in the green state. Fine grinding of the large curved optical face of the mirror has been applied in order to achieve a precise surface form already before cladding and polishing in order to minimize polishing times, which often drive the schedule for large mirrors. For this mirror, a thin p60 SiC CVD cladding layer was first applied to the full mirror blank and an additional layer for optical polishing applied to the optical surface only.
This mirror type has been used for the development of CT scanning know-how and for demonstrating the capability to perform proof testing on ceramic structures, see ch. 5.4.



Figure 11 Ø900 mm curved mirror blank after firing and grinding of interfaces

The largest element in the development is a Ø1550 mm curved mirror blank produced from three segments and joined in the green state. This IntrinSiC® mirror blank has been integrated with titanium isostatic mounts, which are thermally and mechanically decoupled from the ceramic structure (Figure 12Figure 12). The assembly possesses a first eigenfrequency of 144 Hz despite its large aperture, and a surface mass of only ~25.8 kg/m².
This mirror assembly has been vibration tested under sine and random loads at 15 g in-plane and out-of-plane (Figure 13) and shock tested to a representative level of 200 g SRS. [1)]



Figure 12 Ø1550 mm curved mirror blank after bipod integration

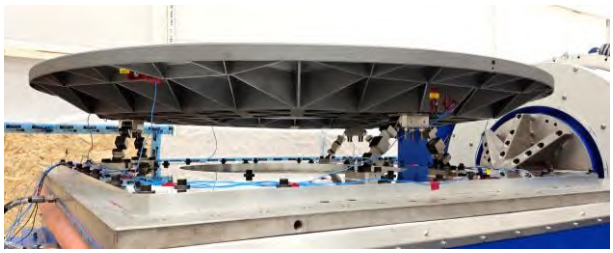


Figure 13 Ø1550 mm curved mirror assembly during vibration testing

4. CERAMIC OPTICAL SYSTEM [1)]

Moving from component to system level, an optical system was envisioned to demonstrate the potential of ultra-stability of full ceramic optical systems (Figure 14). The previously existing Ceramic Optical Bench and Ø300 mm curved mirror assembly serve as the basis for the optical system. As a second mirror with power, a convex folding mirror with integrated suspension and high slopes of ~50mrad (SICFoM, Figure 15) has been defined to meet the optical requirements in the limited envelope of the pre-existing Ceramic Optical Bench. Additionally, a bionic bracket made out of IntrinSiC® was developed to hold the Ø300 mm spherical mirror. The system is completed by a flat reference mirror made from IntrinSiC® which will be used as an absolute reference for positioning of the interferometer for repeated WFE measurements.

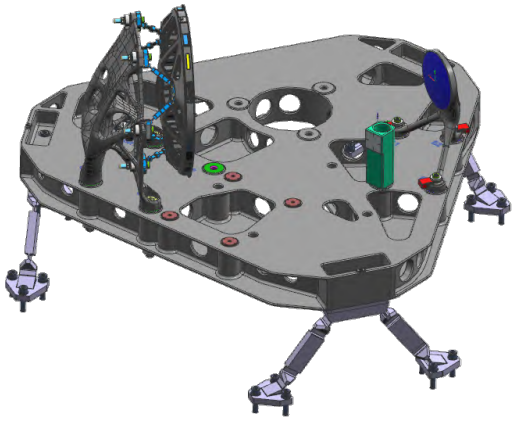


Figure 14 Sketch of the Ceramic Optical System

The design of this system was driven by the goal to achieve maximum optical stability through environmental testing. For this purpose, it is beneficial to reduce the number of non-ceramic parts and the number of interfaces. These requirements, along with the pre-defined interface points on the Ceramic Optical Bench, led to a demanding mechanical design and manufacturing of both the SICFoM and the bionic bracket for the Ø300 mm mirror. The high stiffness of the ceramic parts offers little compliance to interface tolerances, thus, tight tolerancing was defined for and achieved by Schunk, with a common zone better than 10 µm on both SICFoM and the corresponding interfaces on the Ceramic Optical Bench. The SICFoM was cladded all around with a layer of 600 µm before polishing to RMSi < λ/10. Polishing and optical measurement of this complex part required special care and tooling in order to accommodate the integrated design.



Figure 15 SICFoM after polishing

A different approach was taken for the bionic mounting bracket (Figure 16) of the Ø300 mm curved mirror. The topology optimized shape of the bracket and the pre-defined interface positions on the Ceramic Optical Bench drove the decision for a design allowing in-situ tolerance compensation during final integration on the Optical Bench, thereby compensating any tolerancing issues. The bracket weighs 2.5 kg and fully utilizes the capabilities of the ceramic 3D printing process.



Figure 16 Bionic mounting bracket for the Ø300 mm curved mirror

Finally, the reference mirror is the first IntrinSiC® part with p60 CVD SiC cladding which has been delivered by Schunk in the polished state, further strengthening the supply chain for optical space-grade mirrors. The mirror with a mass of 393 grams has been polished to RMSi < λ/10 with a 40/20 Scratch/Dig roughness on a clear aperture of 28mmx28mm (Figure 17). It features a hard-mounted SiC-SiC interface to the optical bench.



Figure 17 reference mirror and SICFoM test-fitted on the Ceramic Optical Bench

All parts of the Ceramic Optical System have been produced successfully and received by OHB System AG. The Ceramic Optical System is, as of summer 2026, in the integration and alignment phase. Once completed, a series of environmental and optical stability tests is planned:

- Repeated optical WFE measurements
- Bake-out and thermal vacuum cycling
- Vibration: sine and random
  15g in-plane, 25g out-of-plane
- Thermo-elastic testing

The goal of this testing is to demonstrate optical stability through-out representative environmental loads, to demonstrate different ceramic joining techniques and material combinations, and to correlate the analytical models used throughout the system design and analysis. Figure 18 shows a real-world mock-up of the COS.

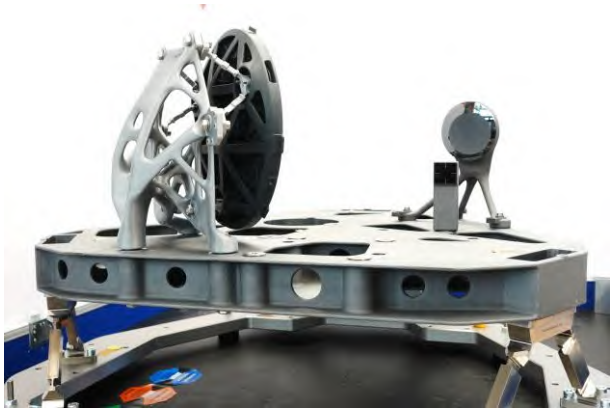


Figure 18 Mock-Up of Ceramic Optical System with as-built SICFoM and reference mirror; plastic mounting bracket and Ø300 mm curved mirror

5. MATERIAL QUALIFICATION AND CERAMIC PROCESS DEVELOPMENT

The ceramic roadmap is supported by a wide variety of material and process characterization methods. These include mechanical and optical properties testing, process optimization for the additive manufacturing, infiltration, machining, cladding and polishing processes. The following subchapters are providing a non-exhaustive selection of testing performed to support the ceramics development, gain a better understanding of material and processes characteristics, validating simulation models and building confidence in the applied technologies.

One area of development was the green body joining technology, in which sections of a larger part are joined in the green state and upon infiltration form a single, monolithic part. A focus of these activities was to demonstrate that the green body joint does not diminish the mechanical properties of the joined part as well as not impacting the optical properties of polished (mirror) parts.

5.1. Mechanical properties

For mechanical strength, bending samples (Figure 19) have been prepared and tested as-fired and grinded, with and without green body joint, and with and without CVD coating in a 4-point-bending (20/40) test according to DIN EN 843-1. A selection of samples underwent humidity and thermal cycling testing, which did not have a significant effect on the material properties, neither did the green body joint. Strength, elastic modulus and Weibull characteristics have been obtained for a statistical evaluation of the material parameters as used by OHB System AG for the development of their ceramic structures.



Figure 19 selection of tested 4-point-bending samples

5.2. Cladding and polishing

Since RBSiC possesses a soft silicon phase, directly polishing the ceramic material for high performance applications is not possible. To compensate for this, a pure SiC CVD cladding is applied by Schunk Carbon Technologies GmbH. This cladding has been qualified according to ECSS-Q-ST-70-17. The initial cladding samples underwent visual inspection, adhesion, cleanability, abrasion, Humidity, TVAC and SEM testing.

Polishability has been proven on full-scale demonstrators, accompanying polishing samples,

as well as dedicated polishing and long-term stability samples. For this purpose, two 200mm flat discs, one with a green body joint and one without, have been polished, subjected to thermal cycling, damp heat exposure, and extended storage duration with repeated WFE measurements in a controlled environment in order to demonstrate their long-term stability (Figure 20). Neither the coating nor the underlying green body joint of one of the discs showed a deterioration of the material or optical properties, supporting the feasibility of producing large space mirrors with the green body joining technology.

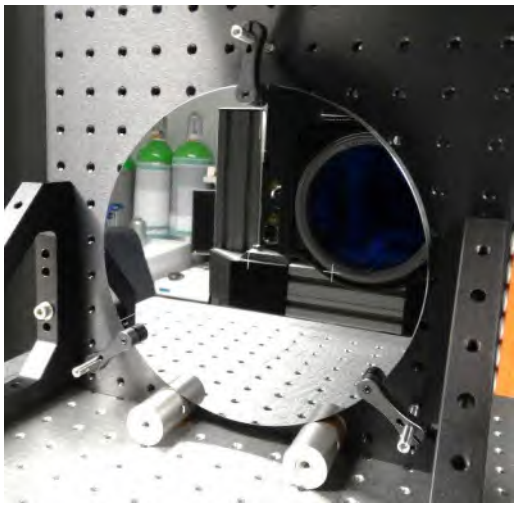


Figure 20 Ø200 mm flat disc, SiC cladded and polished, during SFE measurement

5.3. Joining and Interface Technologies

Interface and joining technology is of special interest for ceramic applications. In order to maximize the benefit of the high thermal stability of IntrinSiC® material, combinations with material of different CTE or thermal conductance shall be avoided. At the same time, (micro-) slippage effects on grinded interfaces, creeping or moisture desorption of adhesives shall be avoided.
To tackle these issues, several test campaigns on sample, part and system level have been conducted.
Pressure tests (Figure 21) have been conducted using typical material combinations like SiC-Aluminium, SiC-SiC, and SiC-Invar-SiC. The scope of the tests was to determinate the maximum compressive strength and, if applicable, the type of fracture failure of different bolted SiC sample assemblies. It has been shown that none of the SiC samples failed under the bearing stress generated by a bolt and corresponding washer even when exceeding the yield strength of the bolt.

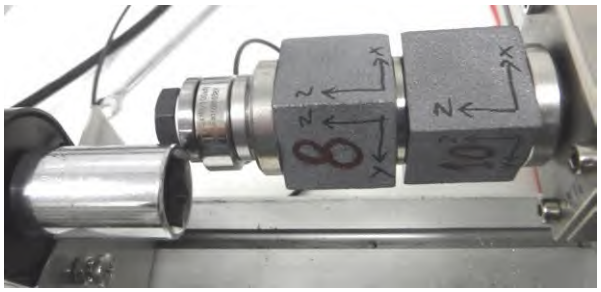


Figure 21 Exemplary bolt pressure test setup (SiC-Invar-SiC)

Standard equipment parts (tie-bases, thermistor dummies) have been bonded to rough as-fired surfaces using different types of typically used adhesives (Figure 22). Half of the bonded standard parts have been subjected to thermal vacuum cycling and damp heat. All artificially aged and reference samples withstood the forces specified in the “Pass” criterion under tensile testing (horizontal and vertical).

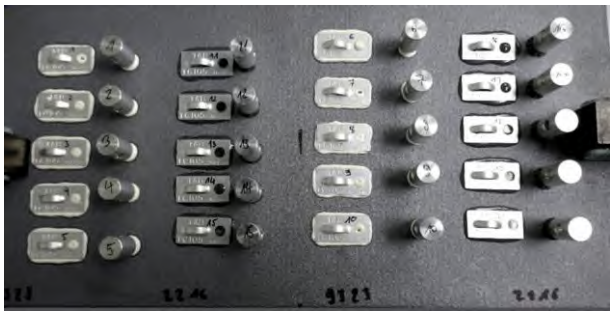


Figure 22 standard part samples after adhesive bonding

Shear and Tensile testing has been performed on adhesively bonded samples (Figure 23) with material combinations Ti6Al4V/CarSIK®-NT, Invar36/CarSIK®-NT, CarSIK®-NT/CarSIK®-NT and OHB standard structural adhesive EC9323-2 B/A. CarSIK®-NT is an isostatically pressed reaction-bonded SiC from Schunk with similar chemical composition as IntrinSiC®. From an adhesive bonding perspective, grinded bonding surfaces made from CarSIK®-NT are adequately comparable to bonding surfaces from grinded IntrinSiC®. All samples underwent a combination of bake-out, thermal vacuum cycling and damp heat.
Additionally, push-out tests have been performed on Invar36/CarSIK®-NT coupons with inserts bonded into a grinded through-hole, as it is typically used to provide threaded inserts in ceramic components (Figure 24).
A- and B-values have been determined from statistical evaluation of the test data and the resulting adhesive strength values have been flown into the development of ceramic parts and systems. The failure mode of all tested samples has been a combination of adhesive and cohesive failure in the adhesive.

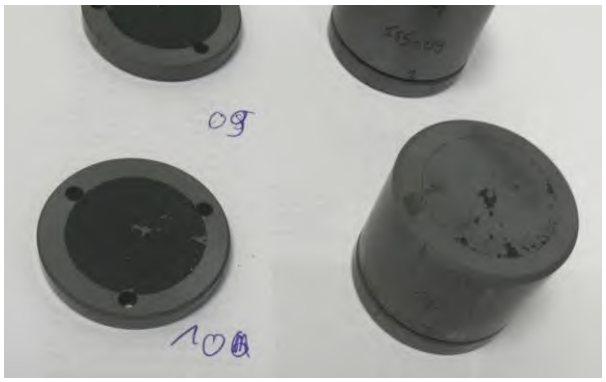


Figure 23 bonding sample after successful testing under shear loading



Figure 24 insert bonding sample after successful push-out testing

5.4. Non-destructive and proof testing

Proof testing has been identified as the most reliable verification technique, since screening of full parts (large samples) for small defects (relevant critical crack size) is challenging. A proof test setup has been developed exemplarily for the 900mm joined mirror (Figure 25), which allows applying static loads on-ground in a lab setting which generate stresses in the bulk material of comparable magnitude, location and shape of the stress field as in the relevant dynamic stress event, including margins. [3]
A benefit of the proof testing approach is the ability to apply relevant test loads and detect potential flaws in the material before integration of structural mounts (thus, the ability to perform vibration testing) and before entering a long and expensive polishing campaign, which is often the schedule driver for large space mirrors.

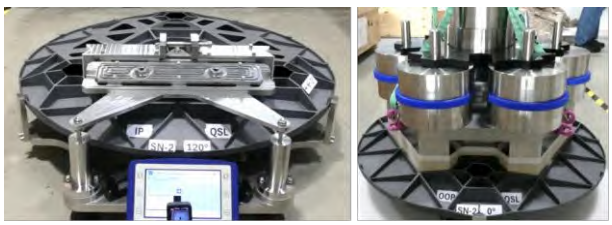


Figure 25 900mm demonstrator - IP (left) and OOP (right) proof test

CT scanning has been performed in critical areas before and after proof testing with support from Comet Technologies Germany GmbH. The non-destructive investigation using CT scanning showed no signs of deterioration from the proof test.

5.5. Supporting process and technology developments

Further investigations have been performed to cover Weibull statistics, CTE characterization, microstructure samples, fracture toughness, hardness, (fine) grinding of large free-form surface, cleaning processes on rough as-fired surfaces for optical-grade clean room conditions and bonding of heaters to as-fired surfaces of different roughness.
All derived values have been implemented in the design and analysis of ceramic parts and systems and successfully proven in environmental testing under representative loads on the respective specimen.

6. OUTLOOK AND CONCLUSION

Over the past five years, OHB System AG and Schunk Ingenieurkeramik GmbH have systematically matured ceramic optical technologies for space utilization from material characterization and process development to large-scale hardware demonstrators and a complete optical system. The performed activities demonstrate the feasibility of additively manufactured RBSiC structures and optics, including large mirror assemblies up to 1.55 m diameter, advanced optical components, and a ceramic optical system of representative size which will be tested under relevant environmental conditions.

The results confirm the suitability of the chosen processes and designs for future high-performance optical payloads requiring large apertures, low mass, and outstanding thermo-mechanical stability. In parallel, a strong industrial partnership with Schunk has established a scalable European capability covering the complete value chain from raw material production, additive manufacturing, cladding and polishing to optical system integration and verification.

The achieved technology maturity provides a solid basis for the application of ceramic optical systems in future Earth observation, science, and security missions, supporting the realization of increasingly large, lightweight, and ultra-stable spaceborne optical instruments.

7. ACKNOWLEDGEMENT

[1)] Schunk Technical Ceramics GmbH and OHB System AG received a partial funding from the German Aerospace Center for the collaborative development of the ceramic optical system, integration and testing of the 300mm curved mirror, and the integration and testing of the 1550mm mirror activities through the project "KeOpS - Keramische Optische Systeme - Teilvorhaben:

System Design, Analyse und Verifikation"; Förderkennzeichen: 50RK2403A

SiC parts have been produced by Schunk Ingenieurkeramik GmbH. Coating and Cladding activities have been performed by Schunk Carbon Technology GmbH. Polishing has been performed by AMOS s.a., Carl Zeiss Jena GmbH, Schunk Ingenieurkeramik GmbH. RSiC coating and polishing was performed by Safran Reosc.

Testing of demonstrators has been performed in-house at OHB System AG, Industrieanlagen-Betriebsgesellschaft mbH and ZARM Technik AG. CT scanning was performed by Comet Technologies Germany GmbH.

8. REFERENCES

1. Schunk Technical Ceramics GmbH, IntrinSiC® Material datasheet, www.schunk-carbontechnology.com
2.Schunk Carbon Technology GmbH, Grade P 60 SiC coating Data Sheet, https://www.schunk-group.com/carbon-technology/de
3. Coe, G., Behar-Lafenetre, S., Cornillon, L., Rncurel, M., Denaux, D., Ballhause, D., Lucrarelli, S. (2013), ESA Initiatives to Improve Mechanical Design & Verification Methods for Ceramic Structures, SPIE Proceedings Vol. 8837

With funding from the:

Federal Ministry of Research, Technology and Space

Application of a Methodology for Void Structure Control in Continuous Fiber Additive Manufacturing for Space Structures

Jan-Uwe R. Schmidt [1], Hans Peter Monner [1]
[1] *German Aerospace Center (DLR), Institute of Lightweight Systems, 38108 Braunschweig, Germany*

jan-uwe.schmidt@dlr.de

KEYWORDS

Continuous Fiber Additive Manufacturing; Void Structure Analysis; Process–Structure Relationship; Process Qualification; Thermoplastic Composites; Space Structures; Analytical Modelling

ABSTRACT

Continuous fiber-reinforced additive manufacturing (CF-AM) offers considerable potential for lightweight space structures by enabling high material efficiency, geometric flexibility, and functional integration. However, manufacturing-induced voids remain a critical challenge, as they directly influence structural performance and complicate process qualification. This paper presents the application of a methodology for the systematic characterization and prediction of void structures in continuous fiber-reinforced thermoplastic filaments. The methodology combines void subtype classification, image-based characterization, statistical regression, and physics-based analytical modelling to establish transferable process–structure relationships. Experimental investigations were conducted under controlled variations of key impregnation parameters to generate characteristic void morphologies. Regression analysis, together with physically based descriptors such as the modified capillary number and normalized impregnation depth, was used to identify the governing mechanisms of void formation and validate the predictive capability of the proposed framework. The results demonstrate that the methodology provides a defect-oriented assessment beyond conventional void content analysis, enabling a deeper understanding of process-dependent defect evolution. By linking manufacturing conditions to void subtype formation, the proposed approach supports qualification-oriented process development and contributes to the reliable implementation of continuous fiber-reinforced additive manufacturing for future space structures.

1. INTRODUCTION

Continuous fiber-reinforced additive manufacturing (CF-AM) has emerged as a promising manufacturing approach for lightweight composite structures requiring high specific stiffness, functional integration, and geometric design freedom [1-7]. Compared with conventional laminate manufacturing, CF-AM enables the near-net-shape fabrication of complex geometries while reducing material waste and manufacturing effort [5,6]. These capabilities make the technology particularly attractive for future space structures, where stringent mass limitations, structural reliability, and qualification-oriented manufacturing are key design requirements.

Despite these advantages, the qualification of continuous fiber-reinforced additively manufactured components remains a major challenge [8-10]. Unlike conventional composite manufacturing, CF-AM combines filament production, impregnation, consolidation, and deposition into a highly coupled process chain. As a result, manufacturing-induced defects may accumulate throughout the process and significantly influence the final material quality and structural performance.

Among these defects, voids represent one of the most critical quality characteristics [1,3,7]. Numerous studies have demonstrated their detrimental influence on interlaminar strength, fatigue resistance, thermal conductivity, and long-term durability [1-4]. For space applications, these effects become even more significant due to demanding environmental conditions such as thermal cycling, vacuum exposure, radiation, and extended mission lifetimes. Consequently, qualification strategies require a comprehensive understanding of defect formation mechanisms rather than relying solely on global quality indicators.

Most existing studies evaluate manufacturing quality using the overall void content as the primary quality metric [1-5,7]. Although this parameter provides a general assessment of material quality, it neglects differences in void morphology, spatial distribution, and formation mechanisms. Consequently, similar global void fractions may result from fundamentally different manufacturing conditions and therefore cannot adequately explain variations in structural performance or identify the governing process parameters responsible for defect formation.

To overcome these limitations, a methodology for the differentiated characterization and analytical

description of void structures has been developed. The methodology combines systematic void subtype classification, image-based characterization, statistical regression, and physics-based analytical modelling to establish direct process–structure relationships and enable a mechanistic interpretation of void formation.
This paper presents the application of the proposed methodology to continuous fiber-reinforced thermoplastic filament systems with particular emphasis on its relevance for qualification-oriented manufacturing of space composite structures. Rather than introducing another defect characterization technique, the work demonstrates how defect-specific analysis can be used to identify governing process parameters, validate analytical models, and support reliable manufacturing and future qualification strategies for continuous fiber-reinforced additive manufacturing.

2. METHODOLOGY

2.1 Concept of the Methodology

Conventional quality assessment of continuous fiber-reinforced thermoplastic composites is predominantly based on the determination of the global void content. Although this parameter provides a quantitative measure of manufacturing quality, it does not differentiate between void morphologies, spatial distributions, or formation mechanisms. Consequently, comparable global void fractions may result from fundamentally different manufacturing conditions and cannot adequately describe the resulting material quality.
To address this limitation, a methodology for defect-oriented void characterization is proposed. Instead of treating voids as a homogeneous defect population, individual voids are classified according to their geometry, location within the composite architecture, and presumed formation mechanism. This differentiation enables defect-specific evaluation and establishes direct relationships between manufacturing conditions and characteristic void populations.
The methodology comprises four consecutive stages. First, representative filament cross-sections are prepared using standardized metallographic procedures. Subsequently, high-resolution optical microscopy and automated image processing are employed to detect and segment individual voids [11]. The segmented defects are then assigned to predefined void subtypes before subtype-specific statistical evaluation is performed. Finally, the experimental results are combined with regression analysis and physics-based analytical modelling to identify the governing mechanisms of void formation and establish transferable process–structure relationships.
In contrast to conventional empirical process optimization, the proposed methodology links experimental observations with physically interpretable descriptors. This enables a generalized assessment of impregnation quality that is largely independent of a specific machine configuration and therefore transferable to different material systems and manufacturing platforms.

2.2 Experimental Application

The proposed methodology was applied to continuous fiber-reinforced thermoplastic filaments manufactured under controlled laboratory conditions using the experimental setup shown in Figure 1. The manufacturing system enables controlled variation of the principal impregnation parameters while ensuring reproducible processing conditions throughout the experimental campaign.

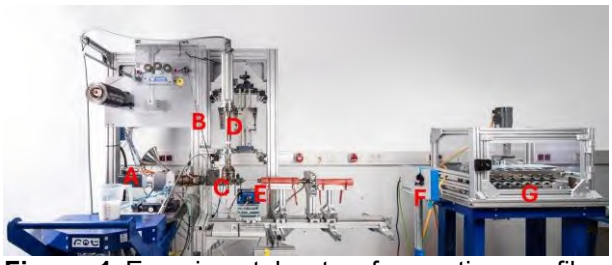


Figure 1 Experimental setup for continuous fiber filament manufacturing: (A) extruder, (B) fiber feed, (C) co-extrusion die, (D) ultrasonic transducer, (E) nozzle module, (F) inline measurement, (G) haul-off.

The experimental programme was designed to generate reproducible variations in impregnation quality while maintaining all remaining boundary conditions constant. Using the manufacturing system shown in Figure 1, processing temperature, consolidation pressure, fiber transport velocity, and ultrasonic excitation were systematically varied to investigate their influence on resin impregnation and void formation. The selected parameter combinations ensured stable manufacturing while generating representative void structures for subsequent analysis.
Following filament production, representative specimens were embedded, polished, and prepared for optical microscopy using a standardized preparation procedure.
The acquired micrographs formed the basis for the subsequent image analysis and void subtype classification. Each detected void was assigned to a predefined subtype prior to statistical evaluation, providing the experimental dataset required for the regression analyses and the validation of the analytical framework presented in the following sections.

3. APPLICATION OF THE METHODOLOGY

3.1 Void Subtype Identification

The application of the proposed methodology begins with the identification and classification of void structures generated during continuous fiber filament manufacturing. In contrast to conventional quality assessment based solely on the global void

fraction, the presented approach differentiates individual void populations according to their morphology, spatial location, and underlying formation mechanisms. This defect-oriented perspective enables a substantially more detailed interpretation of the manufacturing process and establishes the foundation for subsequent analytical evaluation.

Representative filament cross-sections were prepared following standardized preparation procedures and analysed using high-resolution optical microscopy. Automated image processing was subsequently employed to segment fibers, matrix, and void regions before individual defects were assigned to predefined void subtypes according to their geometric characteristics and position within the composite architecture, as illustrated in Figure 2. The classification procedure ensures objective and reproducible identification of defect populations while minimizing operator-dependent influences.

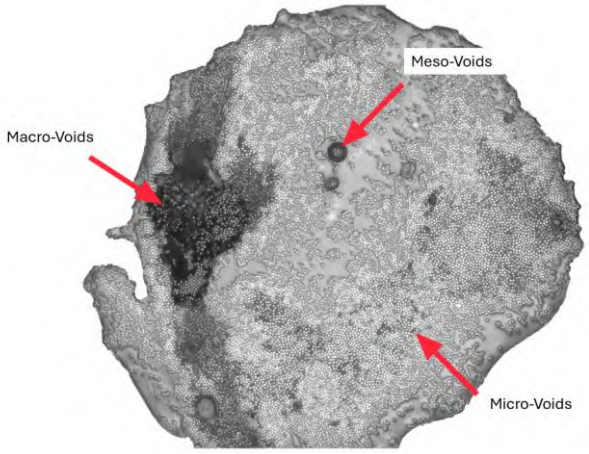


Figure 2 Classification of characteristic void subtypes.

The resulting subtype distributions reveal that comparable global void fractions may originate from fundamentally different manufacturing conditions. While the total void content provides a general indication of material quality, it does not distinguish between voids caused by insufficient fiber impregnation, incomplete consolidation, or local resin flow instabilities. Consequently, identical global quality indicators may represent considerably different defect mechanisms and therefore different implications for structural performance.

Representative examples of filament cross-sections with different impregnation qualities are shown in Figure 3. While homogeneous fiber distribution results in only small isolated voids, insufficient impregnation leads to non-uniform fiber distribution and the formation of pronounced dry regions within the fiber bundle.

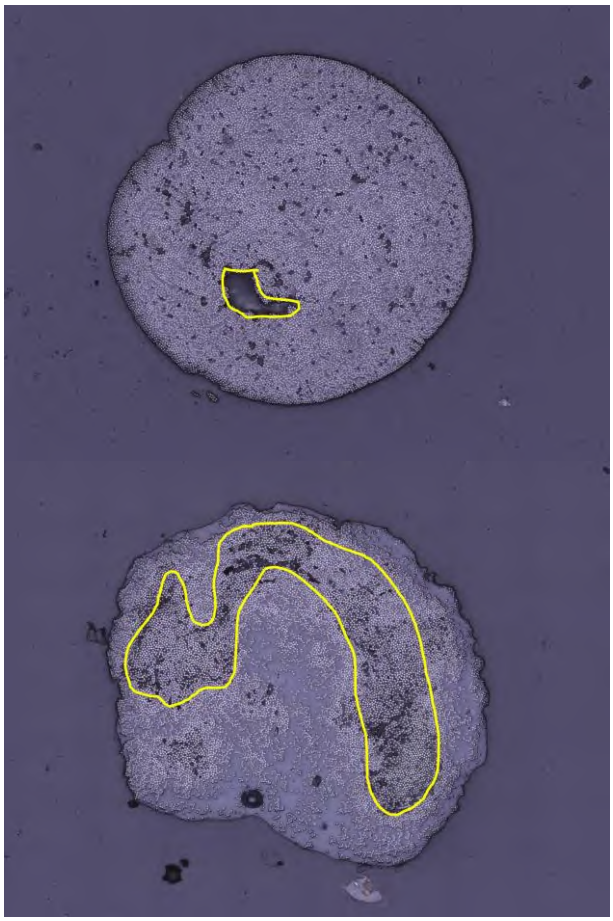


Figure 3 Representative filament cross-sections showing homogeneous (top) and insufficient (bottom) impregnation.

The proposed classification preserves this defect-specific information and enables a mechanistic interpretation of void formation. Instead of reducing manufacturing quality to a single scalar quantity, the defect population is transformed into a multidimensional dataset that forms the basis for statistical evaluation, analytical modelling, and process-specific interpretation.

3.2 Quantitative Image Analysis

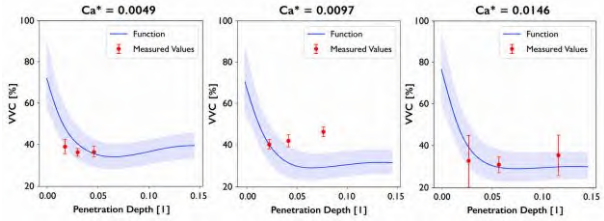
Following classification, each void subtype was quantitatively characterised using automated image analysis. Besides the number of voids, additional geometric descriptors including equivalent diameter, projected area, aspect ratio, and spatial distribution were determined for every manufacturing condition. This comprehensive characterization provides substantially more information than conventional void content measurements and enables a detailed comparison between different processing conditions.

To ensure statistical robustness, multiple cross-sections were evaluated for every experimental configuration, resulting in datasets comprising several thousand individual void objects. Rather than averaging all defects into a single quality parameter, subtype-specific distributions were analysed independently. This approach enables characteristic process signatures to be identified

and significantly improves the sensitivity of the evaluation.
The quantitative analysis demonstrates that manufacturing parameters affect individual void populations differently. Whereas certain parameter variations primarily influence intra-bundle impregnation defects, others predominantly affect voids located at the fiber–matrix interface or within matrix-rich regions. These observations indicate that void formation is governed by multiple interacting physical mechanisms rather than a single dominant process.
The resulting datasets provide the experimental basis for establishing statistically robust process–structure relationships. In the next step, subtype-specific regression analyses are performed to quantify the influence of individual manufacturing parameters on the observed void populations.

3.3 Statistical Correlation of Process Parameters

The quantified void subtype distributions were subsequently correlated with the investigated manufacturing parameters to identify the dominant mechanisms governing void formation. Rather than establishing empirical relationships for the overall void content, regression analyses were performed separately for each void subtype [12]. This defect-specific evaluation enables individual process influences to be distinguished and significantly improves the interpretability of the resulting models.
The statistical analysis revealed that the investigated process parameters exhibit markedly different sensitivities depending on the respective void subtype. Consolidation pressure predominantly influences inter-fiber impregnation by enhancing polymer infiltration into the fiber bundle, resulting in a significant reduction of impregnation-related voids. In contrast, processing temperature primarily affects resin viscosity and flow behaviour, thereby influencing matrix-associated defects generated during consolidation. Fiber transport velocity controls the available impregnation time and consequently governs the development of characteristic void morphologies throughout the manufacturing process. Representative regression models are shown in Figure 4.



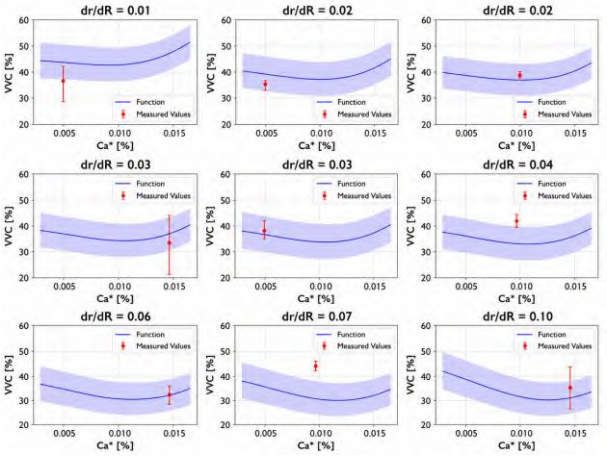


Figure 4 Regression models for predicting characteristic void subtype distributions.

The independent evaluation of individual void populations demonstrates that void formation cannot be attributed to a single governing process parameter. Instead, the observed defect structures result from the interaction of multiple transport, wetting, and consolidation mechanisms acting simultaneously during filament production. This observation explains why manufacturing conditions producing comparable global void fractions may nevertheless exhibit substantially different defect morphologies and, consequently, different structural properties.
Compared with conventional quality assessment based solely on the overall void content, the subtype-specific regression approach considerably increases the sensitivity of process evaluation. Parameter interactions that remain concealed within global quality indicators become directly identifiable when analysed on the level of individual defect populations. The statistical framework therefore enables process signatures to be extracted from the experimental data and provides a quantitative basis for interpreting defect evolution.
Beyond the statistical significance of individual parameter correlations, the regression models provide the experimental foundation for the analytical framework introduced in the following section. While regression analysis identifies which manufacturing parameters govern individual void populations, it does not explain why these relationships exist. Addressing this limitation requires a physics-based description of the impregnation process, allowing the experimentally observed correlations to be interpreted in terms of the governing flow and wetting mechanisms.

3.4 Analytical Prediction of Void Formation

Although the regression models presented in the previous section provide accurate predictions within the investigated process window, their applicability remains limited to the experimentally observed parameter space. To extend the methodology beyond empirical correlations, a physics-based analytical framework was developed that describes

the governing mechanisms of resin impregnation and void formation.
The analytical approach is based on the interaction between viscous resin flow, capillary forces, impregnation time, and the permeability of the continuous fiber bundle [13-15]. Instead of interpreting manufacturing behaviour solely through machine-specific parameters such as processing temperature, consolidation pressure, or fiber transport velocity, these influences are transformed into physically meaningful descriptors that characterize the impregnation process independently of a particular manufacturing system. The relationship between statistical regression and the analytical framework is illustrated in Figure 5. While regression analysis identifies statistically significant process influences, the analytical model provides a physics-based interpretation of the governing impregnation mechanisms and enables the prediction of void subtype formation beyond the investigated experimental conditions.

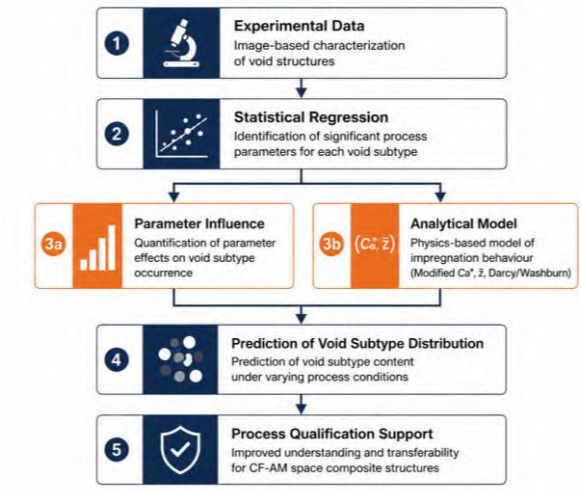


Figure 5 Combined statistical and analytical framework for void prediction.

A central element of the analytical framework is the modified capillary number, which represents the balance between viscous flow and capillary forces during resin infiltration [13-15]. Together with the normalized impregnation depth, describing the penetration of the polymer melt into the fiber bundle, these dimensionless parameters provide a unified representation of the governing impregnation mechanisms [13-15]. Consequently, manufacturing conditions that differ in machine settings or material combinations can be evaluated within the same physical framework.
The calculated analytical descriptors were correlated with the experimentally determined void subtype distributions. The results demonstrate that process conditions exhibiting comparable analytical characteristics also generate similar defect populations, despite differences in the individual manufacturing parameters. Compared with purely empirical regression models, the analytical framework therefore provides a substantially improved physical interpretation of the observed defect evolution.
The transformation from machine-specific process parameters to dimensionless physical descriptors represents one of the principal contributions of the proposed methodology. Rather than describing manufacturing behaviour exclusively through experimental observations, the approach establishes a mechanistic relationship between impregnation physics and defect formation. This significantly improves the transferability of manufacturing knowledge across different equipment configurations, material systems, and processing conditions.
By combining statistical regression with analytical modelling, the methodology links experimental observations with the underlying physical mechanisms governing void formation. While regression analysis identifies which process parameters influence individual void populations, the analytical framework explains why these relationships occur. The resulting combination provides a predictive basis for process optimisation and qualification-oriented manufacturing of continuous fiber-reinforced thermoplastic composites.

3.5 Validation of the Methodology

The predictive capability of the proposed methodology was evaluated by comparing analytically derived process descriptors with experimentally determined void subtype distributions obtained under different manufacturing conditions and material configurations. Rather than validating individual regression models alone, the objective was to assess whether the combined statistical and analytical framework consistently captures the governing mechanisms of void formation.
For each experimental configuration, the analytical descriptors were calculated from the measured manufacturing parameters and compared with the corresponding void subtype distributions obtained from microscopic image analysis. The comparison between measured and regression-predicted total void contents for the PPS/AS7 material system is presented in Figure 6. Overall, a good agreement between predicted and experimentally observed defect characteristics was achieved, demonstrating that the proposed framework adequately represents the dominant impregnation mechanisms responsible for void evolution.

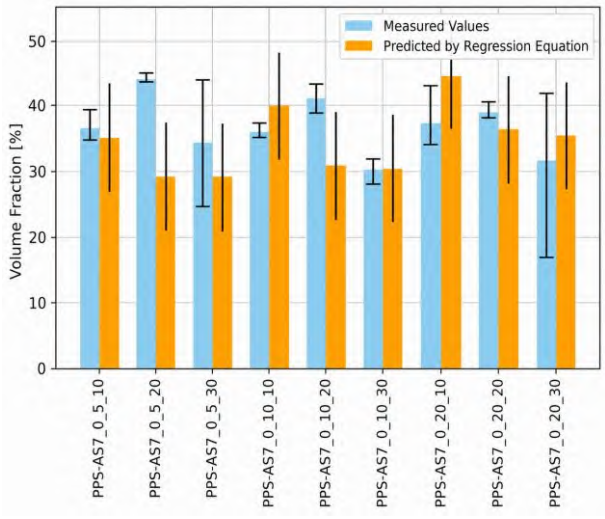


Figure 6 Comparison of measured and regression-predicted total void content (VVC) for PPS/AS7 filaments under different processing conditions. Error bars represent the experimental standard deviation (measured values) and the regression model uncertainty (RMSE) (predicted values). Sample names follow the format: polymer–fibre–ultrasonic influence – fibre velocity (mm s^{-1}) – impregnation pressure (bar).

4. APPLICATION OF THE METHODOLOGY TO SPACE STRUCTURES

4.1 Relevance of Void Characterization for Space Structures

Continuous fiber-reinforced thermoplastic composites are increasingly being considered for lightweight structural components in satellites, launch vehicles, and spaceborne support structures due to their high specific stiffness, corrosion resistance, and potential for functional integration [8-10]. In combination with additive manufacturing, these materials offer new design opportunities by enabling near-net-shape fabrication of highly integrated components while reducing manufacturing waste and assembly effort.

Despite these advantages, qualification remains one of the principal barriers to the adoption of continuous fiber-reinforced additive manufacturing for space applications [8-10]. Unlike conventionally manufactured composite laminates, the mechanical performance of additively manufactured structures is strongly influenced by process-dependent microstructural features generated throughout the manufacturing chain. Consequently, reproducible manufacturing quality is a prerequisite for reliable structural performance.

Among the various manufacturing-induced defects, voids represent one of the most critical microstructural features because they influence not only static strength but also fatigue behaviour, thermal conductivity, damage tolerance, and long-term durability [1-4]. Under representative space environmental conditions—including thermal cycling, vacuum exposure, and extended mission durations—localized defects may act as initiation sites for progressive degradation and premature structural failure [8-10].

Conventional qualification strategies therefore require more than the determination of the global void fraction. A detailed understanding of defect morphology, spatial distribution, and formation mechanisms is required to evaluate the relationship between manufacturing conditions and structural reliability. The methodology presented in this work addresses this requirement by linking characteristic void populations directly to the governing impregnation mechanisms and associated manufacturing parameters.

Rather than serving exclusively as a post-process inspection method, the proposed framework enables defect-informed process evaluation and supports qualification-oriented manufacturing by providing a physically interpretable description of defect formation. Figure 7 summarizes how the methodology links manufacturing parameters with defect evolution, local material properties, structural performance, and ultimately process qualification.

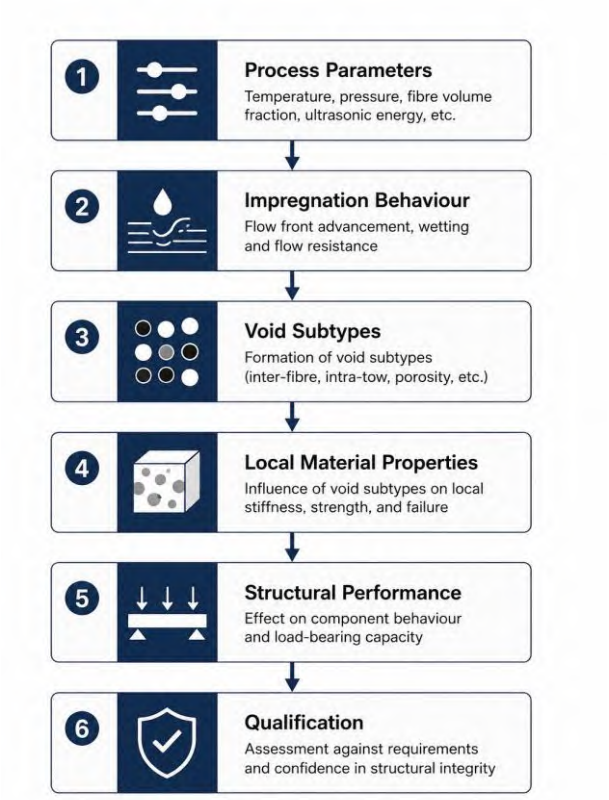


Figure 7 Process–structure–qualification framework of the proposed methodology.

4.2 Contribution to Process Qualification

The principal contribution of the proposed methodology lies in its ability to transform experimentally observed defect populations into transferable manufacturing knowledge. Instead of evaluating composite quality only after production, the methodology establishes quantitative relationships between manufacturing parameters,

impregnation behaviour, and resulting void subtype distributions. This enables process conditions to be assessed according to their expected influence on structural quality before extensive experimental validation is performed.

Within qualification campaigns, this information facilitates the identification of stable manufacturing windows by distinguishing parameter variations that primarily generate non-critical defect populations from those promoting structurally relevant void mechanisms. Consequently, process optimisation can focus on the physical origin of manufacturing defects rather than on global quality indicators alone.

An additional advantage is the use of dimensionless analytical descriptors describing the governing impregnation mechanisms independently of a particular manufacturing platform. Since these descriptors retain their physical interpretation across different equipment configurations and material systems, manufacturing knowledge generated during process development can be transferred more efficiently to future production environments.

Although application-specific validation remains necessary for each qualified component, the presented methodology significantly reduces the experimental effort required during process optimisation. The framework therefore represents a valuable tool for qualification-oriented manufacturing development, where reproducibility, traceability, and process understanding are essential requirements.

4.3 Transferability to Future Space Manufacturing

Although the methodology has been developed using continuous fiber-reinforced thermoplastic filament manufacturing, its underlying concept is not restricted to the investigated process. Because the analytical framework is derived from fundamental impregnation mechanisms and validated through statistically robust defect characterization, the methodology can be transferred to other continuous fiber manufacturing technologies with only minor adaptations.

Potential application fields include automated fiber placement with in-situ consolidation, robotic continuous fiber deposition, hybrid additive manufacturing processes [5-7], and future in-space manufacturing concepts, where process robustness and resource efficiency are expected to become key enabling technologies [8-10].

Beyond the investigated manufacturing process, the proposed methodology establishes a general framework for linking manufacturing conditions with microstructural defect evolution and resulting material quality. This systematic process–structure description provides a suitable basis for future digital qualification workflows combining experimental characterization, analytical modelling, numerical simulation, and process monitoring. The envisioned development pathway of the methodology towards predictive and qualification-oriented manufacturing is illustrated in Figure 8.

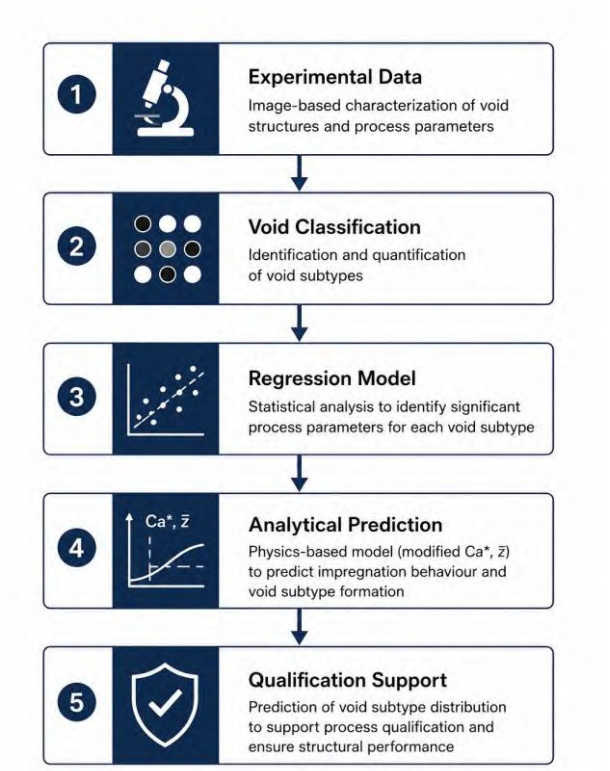


Figure 8 Roadmap towards predictive and qualification-oriented manufacturing of continuous fiber-reinforced composite structures.

Future developments should therefore focus on integrating the methodology with non-destructive evaluation techniques, in-situ monitoring systems, and digital twin concepts. Combined with representative environmental testing under space conditions, these extensions have the potential to establish qualification-oriented manufacturing strategies for continuous fiber-reinforced composite structures used in future space missions.

5. DISCUSSION

The results presented in this work demonstrate that a defect-oriented evaluation of void structures provides substantially more information than conventional quality assessment based solely on the global void fraction [5,6]. By differentiating individual void subtypes and relating them to their governing formation mechanisms, the proposed framework enables manufacturing quality to be interpreted on the basis of process physics rather than empirical quality indicators. This represents a fundamental shift from retrospective defect assessment towards process-oriented quality evaluation.

A key outcome of the investigation is that manufacturing conditions exhibiting comparable global void fractions may generate fundamentally different defect populations. Consequently, identical

global quality indicators cannot be assumed to represent equivalent structural behaviour. The presented methodology addresses this limitation by preserving defect-specific information throughout the evaluation process and establishing direct process–structure relationships between manufacturing conditions and characteristic void morphologies.

Another important contribution is the integration of experimental characterization with statistical evaluation and physics-based analytical modelling. Whereas regression analysis identifies statistically significant relationships between manufacturing parameters and void subtype distributions, the analytical framework provides a mechanistic explanation of the governing impregnation processes. The combination of both approaches extends the applicability of the methodology beyond empirical parameter optimisation and establishes a transferable framework that is largely independent of a specific manufacturing platform.

From a manufacturing perspective, this considerably improves process development by enabling manufacturing knowledge to be transferred between different equipment configurations, material systems, and processing conditions. Instead of generating isolated empirical datasets for individual manufacturing setups, the proposed framework provides generalized process descriptors that retain their physical interpretation across different applications.

For qualification-oriented manufacturing of space structures, this capability is particularly relevant. Future qualification concepts require not only reproducible manufacturing quality but also traceable relationships between manufacturing conditions, defect evolution, and structural performance [8-10]. By combining systematic defect characterization with analytical process modelling, the proposed methodology contributes to the development of physically interpretable qualification strategies for continuous fiber-reinforced additive manufacturing.

Nevertheless, several limitations should be considered. The present investigation is based on laboratory-scale continuous fiber-reinforced thermoplastic filament manufacturing and therefore represents a controlled manufacturing environment. Although the analytical concepts are transferable, additional validation is required for complete additively manufactured components, alternative impregnation technologies, and different thermoplastic material systems. Furthermore, the methodology currently relies on post-process characterization and therefore does not yet provide real-time assessment of manufacturing quality.

The future development of the proposed methodology is summarized in Figure 9. Building upon the experimental and analytical framework presented in this work, future developments aim to integrate inline monitoring, digital twins, and predictive qualification concepts into a unified process qualification strategy.

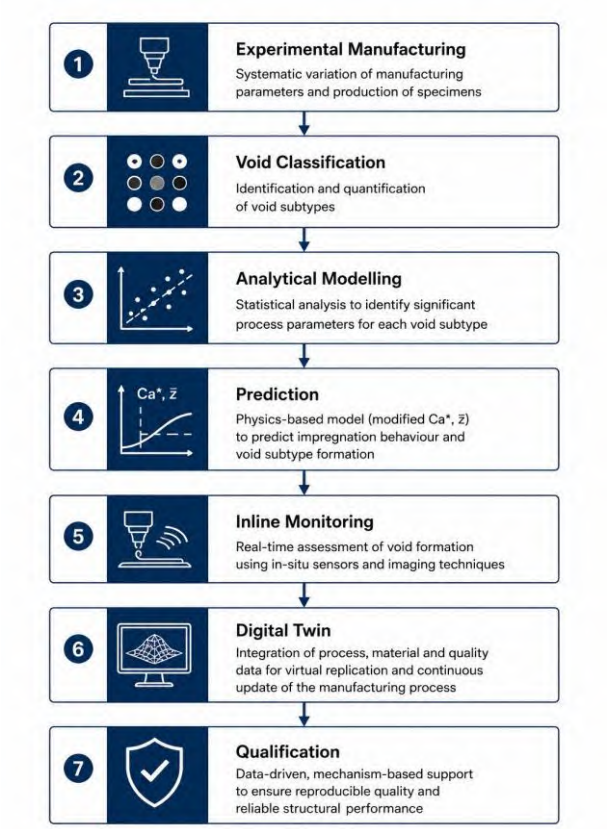


Figure 9 Future development roadmap of the proposed methodology towards predictive process qualification and digital manufacturing of continuous fiber-reinforced composite structures

Future research should therefore focus on extending the proposed framework towards in-situ process monitoring and digital qualification concepts. The integration of optical inspection systems, X-ray computed tomography, machine learning-assisted defect recognition, and process simulations has the potential to establish predictive quality assessment during manufacturing. Combined with digital twin approaches and representative environmental testing, these developments could significantly improve qualification methodologies for continuous fiber-reinforced composite structures used in future space missions.

6. CONCLUSIONS

This paper presented the application of a methodology for the differentiated characterization, analysis, and prediction of void structures in continuous fiber-reinforced thermoplastic composite filaments. By combining systematic void subtype classification with automated image analysis, statistical regression, and physics-based analytical modelling, the proposed framework establishes transferable process–structure relationships that extend beyond conventional void content evaluation.

The results demonstrate that defect-specific characterization provides significantly greater insight into manufacturing quality than global void fraction alone. Individual void subtypes were shown to respond differently to variations in processing conditions, allowing the governing impregnation mechanisms to be identified and interpreted within a unified analytical framework. The combination of statistical evaluation and physically based process descriptors therefore enables both quantitative prediction and mechanistic understanding of void formation.

From a manufacturing perspective, the proposed methodology transforms experimental observations into transferable process knowledge. The use of dimensionless analytical descriptors enables manufacturing behaviour to be compared across different material systems and equipment configurations, reducing the dependence on machine-specific empirical optimisation and supporting more efficient process development.

For qualification-oriented manufacturing of future space structures, the presented framework provides a structured approach for linking manufacturing parameters, defect evolution, and resulting material quality. Although further validation on complete components and under representative space environmental conditions is required, the methodology establishes an important foundation for predictive process qualification of continuous fiber-reinforced additive manufacturing.

Future work will focus on extending the framework towards complete additively manufactured structures, integrating non-destructive inspection techniques and inline process monitoring, and coupling the methodology with digital twins and qualification workflows. These developments have the potential to enable data-driven, physics-based qualification strategies for next-generation lightweight composite structures in space applications.

5. REFERENCES

[1] F. Ning, W. Cong, J. Qiu, J. Wei, and S. Wang, “Additive manufacturing of carbon fiber reinforced thermoplastic composites using fused deposition modeling,” *Composites Part B: Engineering*, vol. 80, pp. 369–378, 2015.

[2] X. Tian, T. Liu, C. Yang, Q. Wang, and D. Li, “Interface and performance of 3D printed continuous carbon fiber reinforced PLA composites,” *Composites Part A: Applied Science and Manufacturing*, vol. 88, pp. 198–205, 2016.

[3] R. Matsuzaki *et al*., “Three-dimensional printing of continuous-fiber composites by in-nozzle impregnation,” *Scientific Reports*, vol. 6, Art. 23058, 2016.

[4] A. N. Dickson, J. N. Barry, K. A. McDonnell, and D. P. Dowling, “Fabrication of continuous carbon, glass and Kevlar fibre reinforced polymer composites using additive manufacturing,” *Additive Manufacturing*, vol. 16, pp. 146–152, 2017.

[5] N. van de Werken *et al*., “Additive manufacturing of continuous fiber reinforced polymers: State of the art and future perspectives,” *Additive Manufacturing*, vol. 31, 2020.

[6] C. Thomas and A. H. Sakhaei, “Additive Manufacturing of Continuous Fibre Reinforced Composites: Process, Characterisation, Modelling, and Sustainability,” *Advanced Engineering Materials*, 2026.

[7] X. He *et al*., “3D printing of continuous fiber-reinforced thermoset composites,” *Additive Manufacturing*, vol. 40, 2021.

[8] European Cooperation for Space Standardization (ECSS), ECSS-E-ST-32 – Structural General Requirements.

[9] European Cooperation for Space Standardization (ECSS), ECSS-Q-ST-70 – Materials, Mechanical Parts and Processes.

[10] National Aeronautics and Space Administration (NASA), *NASA-HDBK-6016 – Materials and Processes*

[11] N. Otsu, “A threshold selection method from gray-level histograms,” *IEEE Transactions on Systems, Man and Cybernetics*, vol. 9, no. 1, pp. 62–66, 1979.

[12] D. C. Montgomery, *Design and Analysis of Experiments*, 9th ed. Wiley, 2017.

[13] H. Darcy, *Les Fontaines Publiques de la Ville de Dijon*. Paris, France, 1856.

[14] E. W. Washburn, “The dynamics of capillary flow,” *Physical Review*, vol. 17, no. 3, pp. 273–283, 1921.

[15] B. R. Gebart, “Permeability of unidirectional reinforcements for RTM simulations,” *Journal of Composite Materials*, vol. 26, pp. 1100–1133, 1992.

AM COMPLIANT MECHANISMS: WARPAGE COMPENSATION TO IMPROVE GUIDING PERFORMANCES

L. Kiener [(1)], H. Saudan [(1)], L. Salamin [(1)], G. Lang [(1)], J.-L. Helfer [(1)], S. Poly [(2)], A. Redwood [(3)], A. Hawkins [(3)], L. Oliveira [(3)]

[(1)] CSEM, Rue de l'Observatoire 58, 2002 Neuchâtel, Switzerland, Email: lionel.kiener@csem.ch
[(2)] Cadence Design Systems, 18 Rue Grange Dame Rose, 78140 Vélizy-Villacoublay, Email: spoly@cadence.com
[(3)] Additive Industries, Achtseweg Zuid 155, NL 5651 GW Eindhoven, The Netherlands, Email: l.oliveira@additiveindustries.com

KEYWORDS

compliant mechanisms, flexure blades, additive manufacturing (LPBF), warpage compensation

ABSTRACT

Metallic Additive Manufacturing (AM) has opened new possibilities for compliant mechanisms by enabling compact monolithic architectures combining rigid and flexible regions [1], [2]. Over the last decade, several mechanisms developed at CSEM demonstrated the benefits of Laser Powder Bed Fusion (LPBF) for space applications, including reduced lead time, functional integration and highly optimized compliant structures [3], [4], [5] & [6]. Nevertheless, the dimensional accuracy achieved by LPBF remains a significant limitation for high-precision compliant systems. In particular, thin flexure blades are highly sensitive to residual stresses generated during the build process and subsequent thermal treatments, leading to distortions that directly affect guiding performances, stiffness and fatigue life. Previous developments revealed global distortions of 0.3 to 0.9 mm on rigid structures and up to 2 mm on flexure elements.

This paper presents an investigation of distortion prediction and compensation methods applied to a Compliant Roto-Translation Mechanism (CRTM). A workflow based on Simufact Additive process simulation is evaluated for the prediction of warpage, generation of compensated geometries and optimization of support strategies. The limitations of conventional pre-distortion methods for flexure-dominated structures are analysed. A hybrid methodology combining process simulation, stabilization concepts and scan-based mesh morphing is introduced. Initial validation using high-resolution 3D scanning shows a substantial improvement in dimensional conformity. The proposed methodology represents a promising route toward achieving the dimensional accuracy required for future space-grade compliant mechanisms.

1. CONTEXT

Compliant mechanisms have become attractive solutions for space and harsh environment applications requiring tribology-free motion, high positioning accuracy and long lifetime. By relying on elastic deformation instead of conventional joints, they eliminate friction, backlash, lubrication and wear. However, their complex architectures traditionally require lengthy machining and assembly operations.

Recent developments in metallic additive manufacturing have significantly modified this paradigm [1] & [2]. Four major projects conducted by CSEM validated the capability of producing compliant mechanisms by LPBF:

- Interlocked Lattice Flexure Pivot (ILFP) [3]
- PULSAR compliant tripod [4]
- Compliant Rotation Reduction Mechanism (CRRM) [5]
- Compliant Roto-Translation Mech. (CRTM) [6]

These projects demonstrated the feasibility of manufacturing monolithic compliant systems integrating dozens of flexures and optimized structures within a reduced volume.

1.1. Remaining challenge: warpage

Despite these progresses, the dominant limitation for monolithic compliant mechanisms remains dimensional accuracy. Warpage originating from thermal gradients during LPBF and from subsequent thermal treatments affects all investigated materials, including 316L, 17-4PH, Invar 36 and Ti6Al4V. Distortions ranging from several hundred micrometres to nearly two millimetres (due to buckling) were measured on operational prototypes. The quality of flexure blades is critical to the guiding performance of compliant mechanisms. These elements require tight geometric tolerances, particularly for thin and slender structures, while also demanding minimal internal defects and high surface quality.

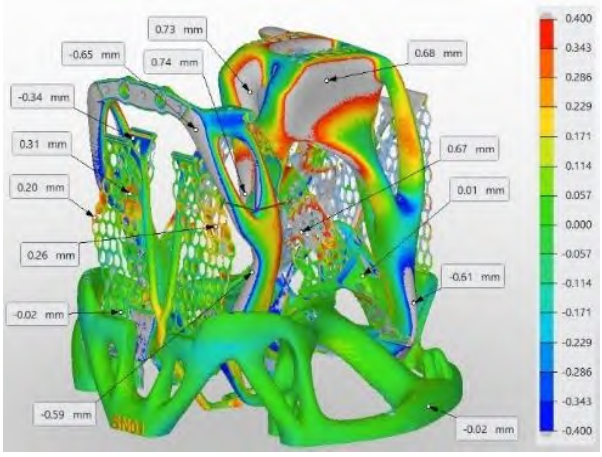


Figure 1. Distortions of CRTM printed in Ti6Al4V without compensation strategy compared to 3D CAD model, scale in mm

1.2. Objective

The objective of this work is to evaluate whether LPBF process simulation based on inherent strain method can be effectively used to predict and compensate distortions in compliant mechanisms and thereby improve the final guiding performances.

2. CRTM DEMONSTRATOR

The study is a follow-up activity with the reuse of the CRTM design developed during the ESA activity "Advanced Manufacturing Technologies for Compliant Mechanisms" ref. 4000122793/17/NL/PS The Compliant Roto-Translation Mechanism converts a rotational input of ±15° into a linear displacement of ±5 mm through a monolithic compliant architecture. It combines an interlocked cross pivot, a screw-based transformation stage and a compliant linear table.
The CRTM represents a particularly demanding test case because it includes multiple thin flexures (8 in total) with high aspect ratios, low bending stiffness and different printing orientations. Earlier prototypes produced in both 17-4PH and Ti6Al4V exhibited significant distortions affecting guiding performances.



Figure 2: Compliant Roto-Translation Mechanism

3. PROCESS SIMULATION METHODOLOGY

3.1. Simufact Additive Workflow

To anticipate manufacturing distortions, simulations were conducted using Cadence Simufact Additive.
The nominal workflow includes:

1. CAD preparation and build orientation selection.
2. Support generation.
3. Layer-wise process simulation.
4. Residual stress estimation.
5. Distortion prediction.
6. Automatic geometry compensation.
7. Iterative refinement.

This methodology – from point 1 to 6 is widely used for rigid LPBF components and aims at achieving first-time-right manufacturing by introducing a compensated CAD geometry before production. The new tool developed in Simufact Additive includes the seventh step with an iterative compensation based on the results of the first print 3D laser or Computed Tomography (CT) scan.
Note that CSEM proposes to choose the printing orientation during the design phase and not after, to fully benefit from the complex shapes possible with AM while considering at best the associated limitations.

3.2. Initial Simulation Results

A first simulation campaign was performed using automated support structures.
The simulations correctly predicted the overall distortion trends observed experimentally. However, significant discrepancies remained in thin flexure regions where nonlinear deformations dominated the behaviour.

4. LIMITATIONS OF CONVENTIONAL PRE-DISTORTION

4.1. Buckling Behaviour of Flexure Blades

Further analysis showed that the dominant distortion mechanism for flexures was not simple thermal shrinkage but rather buckling induced by warpage of the rigid structures linking the blades.
The inability of the iterative distortion optimization to converge provided the first indication of this phenomenon. Flexures behaved similarly to slender columns subjected to axial compression. When the build height exceeded a critical value, large out-of-plane deformations were developed.

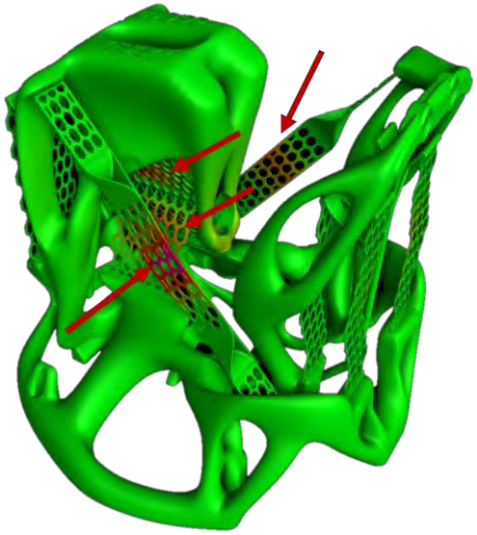


Figure 3: Identified buckling areas by Simufact Additive

These distortions cannot be addressed by conventional geometric compensation alone because the deformed shape depends on structural stability during fabrication.

4.2. Critical Regions

The process simulations identified several regions particularly sensitive to buckling. In conformity with the first results observed in the former project, these locations corresponded to long unsupported flexures and cross-blade structures. Numerical results highlighted that pre-distortion compensation became ineffective whenever the simulated build process entered an unstable regime.

5. IMPROVED COMPENSATION STRATEGY

5.1. Minimum Viable Supports

A first approach involved redefining the support strategy. Instead of maximizing support contact, the objective was to create a "minimum viable support" concept ensuring process stability while limiting post-processing effort and preserving fragile flexures. An additional advantage of this strategy is to ease and lower the support removal effort near delicate structures.
Further support refinement coupled with simulation iterations demonstrated a significant reduction of flexure distortions and enabled successful convergence of the compensation workflow for geometries previously considered impossible to compensate.

6. HYBRID SIMULATION AND METROLOGY APPROACH

Although process simulation captured the dominant deformation modes, discrepancies remained between simulations and measured geometries.

6.1. Limitations of Raw Scan Feedback

Direct use of 3D optical or X-ray CT scan data as a compensation reference is problematic because scans include:

- Surface roughness artefacts
- Residual support marks
- Measurement uncertainty
- Missing scan data
- Local manufacturing defects

These features do not represent systematic distortions and should not be compensated.

6.2. Mesh Morphing Methodology

A hybrid workflow was therefore introduced in Simufact Additive software. Instead of using scan data as the new reference geometry, the measured data is used as a target for mesh morphing applied to the nominal CAD model. This preserves the original design intent while capturing systematic distortion trends.
This methodology is inspired by workflows traditionally used in injection moulding and computed tomography analysis.

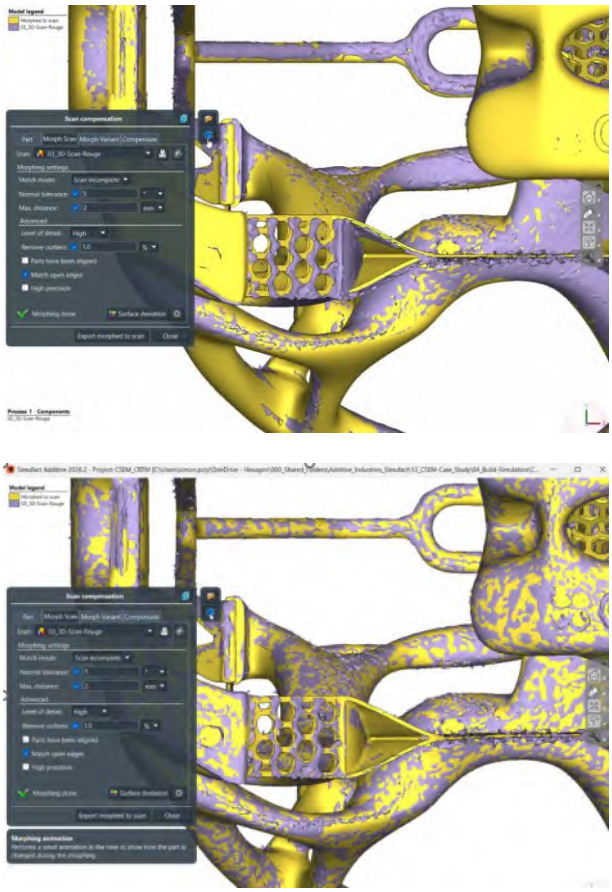


Figure 4: Example of mesh morphing in Simufact Additive, initial (top) and after morphing (bottom)

7. EXPERIMENTAL VALIDATION

7.1. First Compensated Build

Two compensated CRTM demonstrators were produced and inspected using high-resolution optical scanning.
The first build demonstrated encouraging agreement with the target geometry. Approximately 90% of the measured surface profile was located within ±0.2 mm of the reference geometry, including flexible blades.

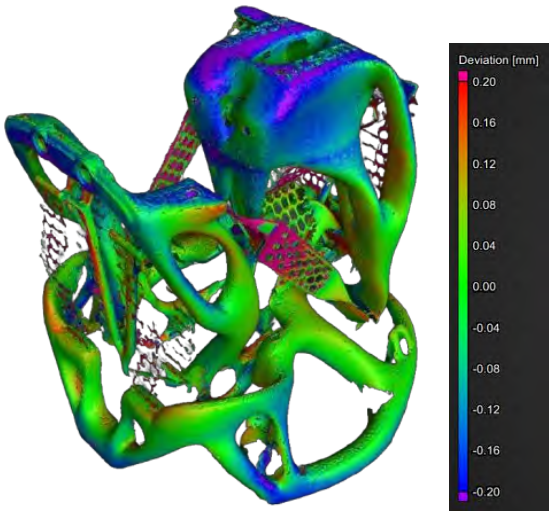


Figure 5: 3D scan of the first build job compared to CAD model

7.2. Geometrical Improvements

Results obtained during the iterative compensation process showed continuous improvement as shown in Table 1. These results demonstrate the capability of combining simulation and metrology to significantly improve dimensional conformity for complex compliant structures.

Table 1: Results with different strategies

Configuration	Surface within ±0.2 mm
Nominal geometry	39% (measured)
Simulation compensation	90% (measured)
Simulation + scan morphing	100% (prediction)

7.3. Impact on Guiding Performances

At the time of writing, correlation between geometrical improvements and guiding performances is ongoing. Future work will determine how the reduction of flexure distortions translates into improvements in parasitic displacement, stiffness prediction and lifetime performance. This evaluation is particularly important since previous projects demonstrated a strong relationship between warpage and guiding inaccuracy.

8. LESSONS LEARNED

Several key conclusions can already be drawn:

- Guiding compliant mechanisms are more sensitive to distortions than conventional rigid structures.
- Buckling induced by residual stresses is a critical distortion comportment for thin flexures.
- Conventional pre-distortion techniques alone are insufficient, especially for compliant geometries.
- Support strategy plays a critical role in distortion control.
- Combining process simulation and scan-based morphing substantially improves compensation performance.

These observations confirm the conclusions previously reached during the CRRM and CRTM projects while providing practical solutions for future developments.

9. CONCLUSIONS

This work investigated distortion prediction and compensation methods for LPBF compliant mechanisms using the CRTM demonstrator as a representative case.
Initial results confirm that Simufact Additive successfully predicts the major distortion modes affecting compliant mechanisms. However, conventional compensation approaches become ineffective when flexure blades enter residual-stress-driven buckling regimes. To address this limitation, dedicated stabilization concepts and a hybrid simulation-metrology methodology were developed.
Experimental validation demonstrated a substantial improvement in dimensional conformity, increasing the proportion of surfaces located within ±0.2 mm of the nominal geometry from 39% to full coverage after iterative compensation. These results represent a significant step towards achieving the dimensional accuracy required for future high-precision space compliant mechanisms.

Future work will focus on validating the methodology through guiding performance measurements, fatigue testing and extension to additional compliant mechanism architectures.

10. REFERENCES

1. E. G. Merriam, J. E. Jones, S. P. Magleby, and L. L. Howell, “Monolithic 2 DOF fully compliant space pointing mechanism,” Mech. Sci., vol. 4, no. 2, Art. no. 2, Dec. 2013, doi: 10.5194/ms-4-381-2013.
2. Ercolini, E., Calignano, F., Galati, M., Viccica, M., Iuliano, L., 2021. Redesigning a flexural joint for metal-based additive manufacturing. Procedia CIRP 100, 469–475. https://doi.org/10.1016/j.procir.2021.05.106.

3. Lang, G., Kiener, L., Lautenbacher, M. *et al.* Design for additive manufacturing of cryogenic flexible pivot enabling on-demand customization, and reducing failure risks. *CEAS Space J* (2026). https://doi.org/10.1007/s12567-026-00748-6.
4. Cosandier, F., Rouvinet, J., Ummel, A. et al. Development of an AM flexure-based tripod mechanism for the fine positioning of segmented telescope mirror tiles. Proc. ESMATS 2021.
5. Kiener, L., Saudan, H., Cosandier, F. et al. Compliant mechanism based on additive manufacturing. CEAS Space J 15, 37–53 (2023)
6. Kiener, L., Salamin, L., Saudan, H., et al. Compliant mechanisms made by additive manufacturing: the good, the bad and the lessons learned. Proc. ESMATS 2025.

ECSSMET
Braunschweig Germany 2026

Buckling

POST-BUCKLING ANALYSIS AND SIZING OF A SPACE STRUCTURE: APPLICATION TO INTER-TANKS SKIRT

J. Marchesini[(1)], Q. Jacob[(2)], G. Ibrahim[(2)], N. Rannou[(1)]

[(1)] INTES FRANCE, 1 rue de Clairefontaine, 78120 Rambouillet, France, Email: jacques.marchesini@intes.fr
[(2)] LATITUDE, 23 rue de Rosa Luxemburg, 51100 Reims, France, Email: quentin.jacob@latitude.eu

KEYWORDS

Post-Buckling, Sizing, Stability, Launcher Structures, FEA, Simulation, numerical Methods.

ABSTRACT

Large space structures, such as inter-tank skirts in launchers, face critical challenges under complex loading conditions (compression, bending, thermal stresses). Buckling, a primary failure mode, can cause sudden loss of load-carrying capacity, threatening mission success. Traditional design methods often rely on conservative safety margins, leading to over-designed, heavier structures that penalize performance.
To address this, stiffening solutions (ribs, stringers, ring stiffeners) are commonly used to enhance stiffness and delay buckling. However, structures can still retain load-bearing capacity in **the post-buckling regime**, though their behaviour becomes highly nonlinear and sensitive to imperfections. Quantifying this residual strength is essential for accurate structural assessment and mass optimization.

This study proposes a **numerical approach** combining nonlinear static analyses (large displacements, geometric nonlinearities) and incremental buckling analyses to identify critical modes and stiffness degradation, aiming to develop **robust design guidelines** for optimized sizing while ensuring aerospace compliance.

1. CONTEXT

Large space structures, such as the **Inter-Tank Skirt (ITS)**, play a pivotal role in launchers by providing structural continuity between propellant tanks. These components are subjected to complex loading conditions, including compressive, bending, and thermal stresses, which introduce significant **risks of buckling** like a critical failure mode that can lead to sudden loss of load-carrying capacity.

Traditional design philosophies often adopt conservative safety margins to mitigate buckling risks, but this approach frequently results in over-designed structures, penalizing overall system performance due to excess mass and increased costs.

A key question arises: **Can local buckling effects be tolerated in the design?**

Addressing this requires a deep understanding of post-buckling behaviour [1], where structures may retain load-bearing capacity despite initial instability. This regime is characterized by highly nonlinear responses, influenced by factors such as geometric imperfections, material nonlinearities, and boundary conditions.
By quantifying the residual stiffness and load redistribution in this phase via FEA simulations using PERMAS solver [2], engineers can unlock opportunities for mass optimization without compromising structural integrity.
The ITS serves as a prime example of this challenge: it must balance structural reliability with mass and cost constraints, all while adhering to stringent aerospace standards. This study **proposes an FEA-based methodology** to develop robust design guidelines that enable engineers to tolerate controlled buckling where safe, thereby achieving performance-driven sizing for space applications.

1.1. Role or the ITS Skirt

The Inter-Tank Skirt (ITS) serves as a **structural backbone** (Fig. 1) within launchers, fulfilling both mechanical and functional roles. Primarily, it ensures the connection of propellant tanks, guaranteeing structural continuity and load transfer between the upper and lower stages. Beyond its load-bearing function, the ITS provides a mechanical interface for integrating various fluidic and electrical equipment, enabling seamless system integration.

Additionally, the ITS **hosts critical systems**, such as avionics, sensors, and local control units, which are essential for mission operations. Its design also facilitates the routing of harnesses, utilities, and fluidic lines through dedicated trapdoors, optimizing space utilization while maintaining accessibility for maintenance and assembly. This multifunctional role underscores the ITS's importance not only as a structural element but also as a hub for equipment integration in launcher architectures.



Figure 1: Inter-Tank Skirt (ITS)

1.2. Applied Loads

The Inter-Tank Skirt (ITS) is subjected to a complex loading environment during all mission phases. General loads include compressive forces and bending moments transmitted by the upper structure, primarily induced by thrust and aerodynamic pressures during ascent. Additionally, the ITS experiences a global inertia load, a compressive effect generated by the launcher's acceleration, which further increases the axial stress distribution.

At the local scale, the ITS hosts critical equipment (e.g., avionics, sensors, and control units) that introduces Quasi-Static Loads (QSL**)**, adding localized stress concentrations to the global load scenario.

From a boundary condition perspective, the lower interface of the ITS is fully clamped, ensuring rigid fixation to the lower stage. Furthermore, structural interactions with surrounding connected components contribute additional stiffness, influencing the overall mechanical behaviour of the skirt.

This combination of global, inertial, and local loads, along with the constraints and interactions, defines the **critical loading conditions** that must be accounted for in the structural design and analysis of the ITS, as summarized in Fig. 2.

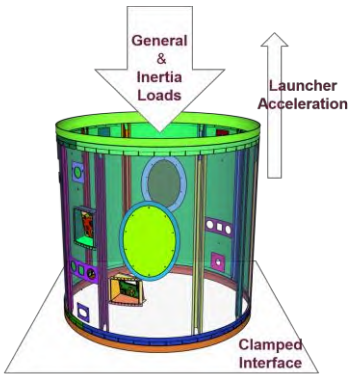


Figure 2: Applied Loads

1.3. Modelling Aspects & Simulation Environment

The Finite Element (FE) model of the ITS was developed using the NX environment, combining CAD modelling, mesh generation, and model completion. The main cylindrical parts, panels, and ribs were modelled using shell elements to efficiently capture bending and membrane behaviours, while flange parts were represented with solid elements to accurately simulate their 3D stress distribution. Local equipment, such as avionics and sensors, was modelled as lumped masses connected to the structure via beam and spring elements, ensuring a balanced trade-off between computational efficiency and accuracy.

To address mesh incompatibilities between different parts, Multi-Point Constraints (MPCs) were employed. Specifically, surface to surface connections *($SURFACE/$MPC ISURFACE – BSURF / BGSET)* were used to handle non-matching meshes. For equipment connections, rigid connectors *($MPC RIGID - RBE2)* and load distributor connectors *($MPC WLSCON - RBE3)* were applied respectively, to ensure robust load transfer while maintaining numerical stability.

Finally, for the simulation tasks, the completed FE model was directly read into the PERMAS solver via the Nastran Door interface [3], enabling seamless integration of the pre-processed model into the simulation environment. This workflow ensures consistency between pre-processing and solving phases, facilitating both accurate and computationally efficient structural analyses. The FE model is shown in Fig. 3.

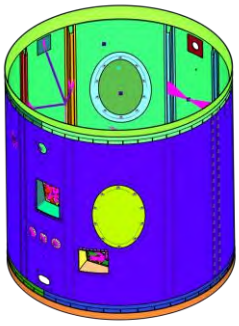


Figure 3: F.E. Model

2. MECHANICAL STRENGTH

A **linear static analysis** was conducted to evaluate the structural performance of the ITS under the applied loads. The results, as illustrated in Fig. 4, reveal that the mechanical strength of the structure is largely respected, with **no failure observed** under static loads. This confirms the design's adequacy for the expected operational conditions.

However, the analysis highlights the presence of localized stress concentrations, or hot spots, marked in Fig. 4 with von Mises stresses. These exhibit critical stress levels exceeding 85% of the material's yield strength (Re), particularly in geometrically discontinuous regions, such as small-

radius fillets (corner windows) or areas with MPC-based mesh connections, where mesh discretization could be refined.

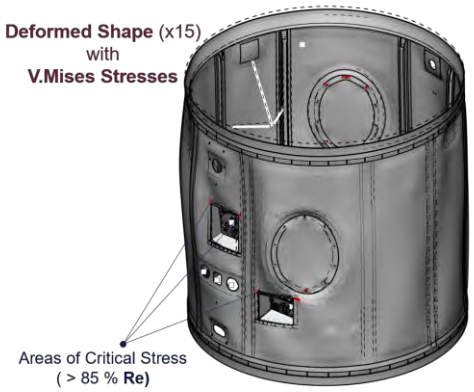


Figure 4: Results from Linear Static Analysis

This observation raises a **key question**: *Even if the mechanical strength is fully satisfied, what is the buckling behaviour of the structure under these conditions?* While the ITS demonstrates sufficient static strength, verification of its stability under compressive and bending loads is necessary. The presence of localized stress concentrations may influence the critical load factors, potentially reducing the buckling margin.

This motivates the need for **buckling analyses** to fully assess the structural robustness and ensure safety margins are maintained.

3. LINEAR BUCKLING

To assess the stability of the ITS under the previously identified loading conditions, a Linear Buckling Analysis (LBA) was performed using the PERMAS solver. This analysis follows a two-step approach, as described below.

3.1. Governing Equations

The LBA is based on the eigenvalue problem derived from the tangential stiffness matrix of the structure. The process involves:

1rst step: Linear Static Analysis (Pre-stress state)

A preliminary linear static analysis is conducted to determine the internal stress state σ_0 under the applied loads, using the elastic stiffness matrix $\boldsymbol{K}_e$:

$$\boldsymbol{K_e} u = F \qquad (1)$$

where u is the nodal displacement vector and F is the external load vector. The internal stress state σ_0 is then used to construct the geometric stiffness matrix $\boldsymbol{K_g}(\sigma_0)$.

2nd step: Eigenvalue Analysis of the Tangential Stiffness Matrix

The eigenvalue problem is formulated as:

$$\boldsymbol{K_t} X = \left[\boldsymbol{K_e} + s\boldsymbol{K_g}(\sigma_0)\right] X = 0 \quad \text{with} \quad X \neq 0 \qquad (2)$$

where $\boldsymbol{K_t}$ is the tangential stiffness matrix, s represents the scaling load factors, and X corresponds to the buckling shapes (eigenmodes). The critical load factors s are derived from the eigenvalues, while the buckling modes X provide insight into the deformation patterns at instability.

3.2. Interpretation of Scaling Load Factors

The scaling load factors s provide insight into the stability of the structure:

- If $s > 1$: The structure is **stable** under the applied load, with no buckling effect.
- If $s = 1$: The structure is at a **critical state** (neutral equilibrium), corresponding to a potential **bifurcation point**. At this point, the structure may:
  - → Collapse,
  - → Undergo bifurcation (e.g., transition to a new equilibrium configuration),
  - → Or remain stable depending on higher-order effects or imperfections.
- If $s < 1$: The structure is **unstable** and has undergone deformation due to buckling, which can manifest as:
  - → **Local buckling** (e.g., in individual components like plates or stiffeners),
  - → **Global buckling** (e.g., Euler buckling of columns or lateral-torsional buckling of beams).

3.3. Stability Check Assumptions

The LBA was performed under the following assumptions:

→ Material behaviour: Linear elastic.
→ Geometry: Perfect (no imperfections).
→ Displacements: Small (linearized theory).
→ Initial state: Pre-stressed.

These assumptions provide a **conservative baseline** for assessing the structure's stability, though they may not fully capture the effects of geometric imperfections or nonlinear material behaviour.

3.4. Results from Linear Buckling Analysis

The LBA results reveal critical load factors s for the ITS, as illustrated in Fig. 5. The first four buckling modes and their corresponding load factors are summarized as follows:

Table 1: Critical Load Factors

Mode	Critical Load Factor s	Description
1	0.71	Local buckling near manhole with 'front' door access
2	0.75	Local buckling in panel regions
3	0.76	Local buckling near manhole with 'rear' door access
4	0.81	Local buckling in stiffener regions

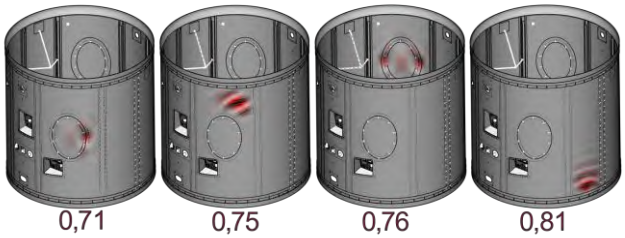


Figure 5: Results from Linear Buckling Analysis

Key observations:

→ The first load factors are below 1, indicating potential instabilities before reaching the nominal load.
→ The critical area is concentrated around the manhole with door access, where geometric discontinuities and stress concentrations are most significant.
→ Mesh discretization and MPC-based mesh connections are critical for the accuracy of the results, as they influence the localisation of buckling modes.

While the mechanical strength is largely respected under static loads, the buckling behaviour is present but does not lead to immediate collapse. This raises two key questions:

→ Is the observed buckling a **local or global effect**?
→ What is the **post-buckling behaviour** of the structure?

4. NON-LINEAR BUCKLING

The need for a non-linear buckling analysis arises from two key observations from the LBA:

→ Buckling occurs before nominal loads are reached,
→ Uncertainties remain regarding the nature of buckling (local vs. global effects) and the post-buckling behaviour of the structure, particularly its ability to retain load-carrying capacity after instability.

However, LBA assumes a linear material behaviour, which may not fully capture the structure's post-buckling response or its load-carrying capacity after instability.

To address these limitations, a post-buckling simulation based on a non-linear static analysis was performed using the PERMAS solver, following the methodology outlined below. This approach allows for:

→ **Assessment of residual strength** after buckling onset.
→ **Understanding of failure progression** and the structure's ability to redistribute loads.

4.1. Methodology: Non-Linear Static Analysis

The non-linear analysis was performed using an incremental loading process with the following key features:

4.1.1. Incremental Loading Process

The analysis accounts for:

→ **Large displacement effects:** Geometric non-linearity is captured through the geometrical stiffness matrix $\boldsymbol{K}_g$.
→ **Arc-length method**: This numerical technique overcomes singular points (e.g., limit points) to capture post-buckling states and track the structure's equilibrium path.
→ **Support for singular/negative diagonal terms**: Enables the simulation of snap-back effects, where the structure experiences sudden reductions in load-carrying capacity, as illustrated in Fig. 6.
→ **Co-rotational theory**: Ensures accurate geometric non-linearity by updating the coordinate system with the structure's deformation.

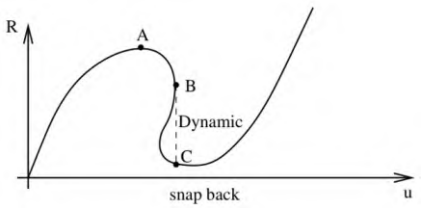


Figure 6: Snap-back Effect

4.1.2. Buckling Analysis at Each Equilibrium State

At each step of the incremental loading process, the tangent stiffness matrix $\boldsymbol{K}_t$ is updated and decomposed into:

→ **Material stiffness** K_m: Accounts for material non-linearity (e.g., plasticity).
→ **Geometrical stiffness** K_g: Accounts for geometric non-linearity (e.g., large displacements).

The eigenvalue analysis of the updated tangential stiffness matrix is performed at each step. This analysis also includes **tracking** of:

→ **Critical buckling modes**: To identify which modes are activated during loading.
→ **Evolution of load factors**: To monitor how the structure's stability changes as the load increases.

4.2. Results from Non-Linear Buckling Analysis

4.2.1. Resultant Load Diagram

The Resultant Load Diagram (Fig. 7) illustrates the load-displacement relationship of the ITS under incremental loading, with key observations:

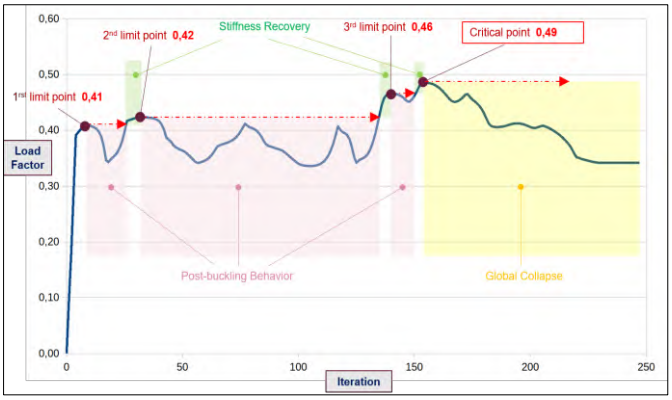


Figure 7: Resultant Load Diagram

Limit Points:

→ 1st limit point (0.41): Marks the onset of initial buckling.
→ 2nd limit point (0.42): Indicates the activation of a local buckling effect.
→ 3rd limit point (0.46): Indicates the activation of local buckling effect.
→ Critical point (0.49): Represents the ultimate load-carrying capacity of the structure before global collapse.

Post-Buckling Behaviour:

The structure exhibits stiffness recovery between limit points, where it temporarily regains stability before undergoing further buckling. This phenomenon is characteristic of non-linear post-buckling behaviour, where the structure can continue to carry load despite local instabilities.

4.2.2. Deformed Shape at Limit Points

Figure 8 illustrates the deformed shape of the ITS at each limit point, as well as at the last converged equilibrium state.



Figure 8: Def. Shapes (x15) with Displ. Length

4.2.3. Tracking Buckling Modes

The first three involved buckling modes (Mode-1, Mode-2, and Mode-3) are tracked throughout the loading process, as shown in Fig. 9.

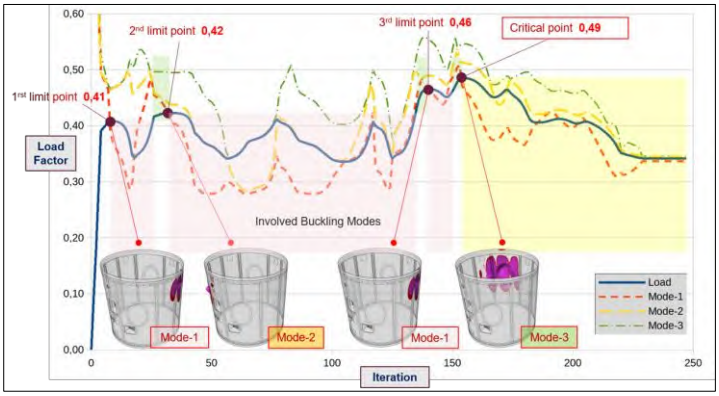


Figure 9: Evolution of Buckling Load Factors with the Load Diagram

For each limit point, the involved buckling mode is clearly identified, as its load factor evolution intersects the load diagram. This intersection explains the local failure mechanism at each stage. This approach demonstrates that the involved buckling modes differ significantly from those predicted by the Linear Buckling Analysis (LBA). Furthermore, the associated load factors are substantially lower than those obtained from the linear approach.

At the critical point, the involved buckling mode (buckling near the manhole with the 'rear' door access) triggers a global collapse effect.

At the last converged state, at least the first three buckling modes are involved (aggregation) in the global collapse mechanism.

4.2.4.: Last Converged State

The last converged state of the ITS, shown in Fig. 10, reveals the deformed shape, with displacement magnitudes and the active buckling modes. In Fig. 11, areas of critical stress (exceeding the material's yield strength R_e) highlighted in the von Mises stress distribution.

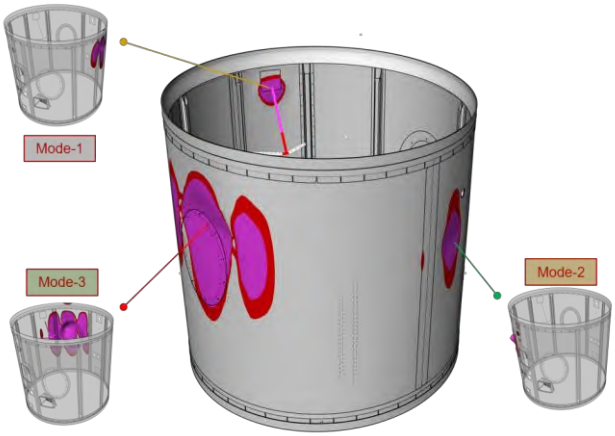


Figure 10: Deformed Shape (x1) with Displ. Length and Active Buckling Modes

The study of the deformed shape shows the participation of the "active" buckling modes:

→ Mode-3: Buckling near the (rear) manhole.
→ Mode-1: Local buckling in panel regions.
→ Mode-2: Local buckling of the cylindrical structure.

The global collapse behaviour is therefore interpreted as the combination of these three active buckling modes.

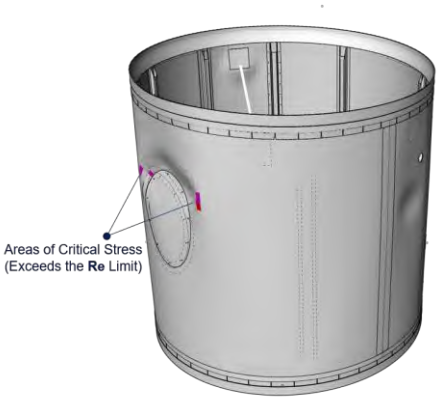


Figure 11: Deformed Shape (x1) with Von-Mises Stresses

Critical stresses, localized in small hot spot areas, imply that the onset of global collapse takes place within the elastic domain, characterizing this as an elastic stability problem.

4.2.5. Upper Interface Behaviour

The focus on the center point of the upper interface of the ITS provides useful insights into its behaviour, exhibiting complex interactions between translation and rotation (Fig. 12).

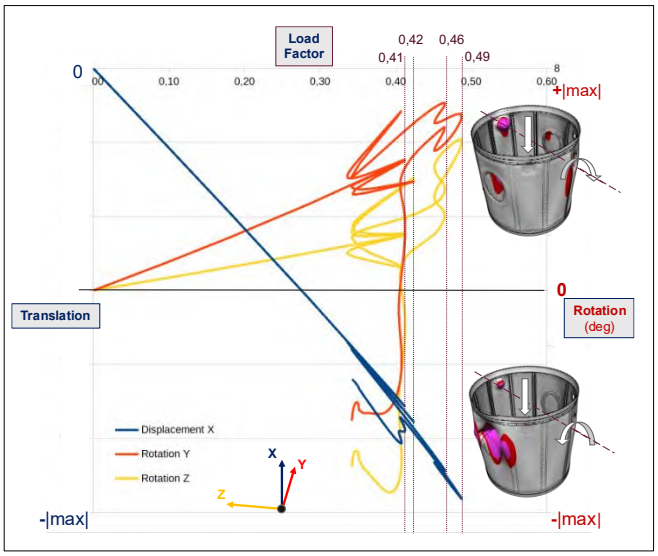


Figure 12: Load-Displacement Curves – Center of Upper Interface

The load-displacement curves at the center point reveal the following:

→ A regular shortening effect, accompanied by several snap-back effects, until the critical load (0.46) is reached, at which point the global collapse begins with the loss of rigidity.
→ A positive rotation in the Y and Z directions occurs alongside the shortening effect until the critical load (0.46). Beyond this point, a complete switch to large negative rotation initiates, marking the onset of the global collapse effect (similar to a tipping/overturning behaviour).

4.3. Conclusion on Non-Linear Buckling Results

The Non-Linear Buckling Analysis (NLBA) of the ITS has provided critical insights into its structural behaviour under realistic loading conditions. The key findings can be summarized as follows:

→ **Lower Critical Limit Load**: The NLBA reveals a critical limit load of 0.49, significantly lower than the 0.71 predicted by the linear analysis.
→ **New Critical Buckling Modes**: The non-linear approach identifies different dominant buckling modes compared to the LBA. These modes arise from the interaction between local instabilities and the global structural response,

providing a more accurate representation of the ITS's behaviour.

→ **Global Failure Initiation**: The onset of global failure is driven by a combination of local critical buckling modes, rather than isolated instabilities. This highlights the importance of considering mode interactions in structural design.

→ **Material Behaviour**: The material remains elastic throughout the analysis, with no significant plastic deformation observed at the applied load levels. This confirms that the buckling behaviour is primarily governed by geometric non-linearities.

→ **Mechanism Clarity**: The NLBA provides a clear explanation of the underlying failure path, revealing how the structure transitions from local buckling to global collapse.

However, the accuracy of these results remains highly sensitive to mesh discretization and MPC-based mesh connections. These factors influence the localization of stress concentrations and the activation of buckling modes, emphasizing the need for careful modelling in critical regions.

5. CONCLUSION & PERSPECTIVES

The analyses conducted in this study, Linear Buckling Analysis (LBA) and Non-Linear Buckling Analysis (NLBA), have provided a comprehensive understanding of the ITS's structural behaviour under nominal loads. The following key findings emerge:

→ **Buckling as a Critical Design Case**: Buckling is confirmed as a critical design consideration for large space structures, where local instabilities can lead to global collapse if not properly accounted for.

→ **Preliminary benchmark** conducted in this study yields **valuable insights** into the structure's post-buckling behaviour and stiffness performance reserves.

The use of PERMAS solver for non-linear analysis has demonstrated its comprehensive tools for efficient post-buckling analysis, including:

→ **Tracking critical buckling modes** during load increments.

→ **Providing clear mechanisms** to explain critical load paths.

The insights gained from this study enable the following practical outcomes:

→ **Targeted Design Modifications**: The results allow for targeted design modifications to overcome critical load limits without compromising mass performance. For example, reinforcing local areas to improve buckling resistance.

→ **Evaluation of Post-Buckling Behaviour**: The study facilitates the evaluation of post-buckling behaviour and stiffness performance reserves, ensuring that the structure can tolerate controlled buckling while maintaining overall stability.

→ **Design Guidelines**: The findings motivate the development of design guidelines that account for:

- Controlled buckling in non-critical regions.
- Post-buckling capacity to ensure safety margins.
- Stress concentrations to mitigate the effects of geometric singularities.

6. REFERENCES

1. Ledentu, H. & Sanchez, J.M. (2014) DCNS Cherbourg, France. Nonlinear Buckling and Design of Hull Structures. In Proc. 12th. *PERMAS User's Conference*, Stuttgart, Germany, 7-9 May 2014, INTES Publication No. 823.

2. *PERMAS User's Reference Manual*, INTES Publication No. 450, Stuttgart, Germany, 2026.

3. *Nastran-Door User's Manual*, INTES Publication No. 650, Stuttgart, Germany, 2026.

NON-LINEAR BUCKLING ANALYSIS OF THE INTER-TANK STRUCTURE FOR THE CALLISTO REUSABLE ROCKET DEMONSTRATOR: STRUCTURAL STABILITY ASSESSMENT OF THE LOX/LH2 INTERFACE

Alessandro Vescovini[(1)], Felipe Franzoni[(2)], Kevin Bergmann[(3)]

[(1)] Institute of Lightweight Systems, Structural Mechanics Department, German Aerospace Center (DLR), Lilienthal Platz 7, 38108 Braunschweig, Germany, Email: alessandro.vescovini@dlr.de
[(2)] Institute of Lightweight Systems, Structural Mechanics Department, German Aerospace Center (DLR), Lilienthal Platz 7, 38108 Braunschweig, Germany, Email: felipe.franzoni @dlr.de
[(3)] Institute of Space Systems, Space Launcher Systems Analysis, German Aerospace Center (DLR), Robert Hooke-Str. 7, 28359 Bremen, Germany, Email: kevin.bergmann@dlr.de

KEYWORDS

Inter-Tank Structure, Buckling, Non-Linear Analysis

ABSTACT

The CALLISTO project, a trilateral initiative between DLR, CNES, and JAXA, aims to develop a reusable vertical take-off and landing rocket demonstrator. This paper presents a structural stability assessment of the Inter-Tank Structure (ITS) connecting the LOX and LH2 tanks. Using a finite element model of the thin-walled barrel reinforced by hat stiffeners and incorporating equipment platforms and windows, the structure is evaluated under four operational flight load cases. The methodology combines linear perturbation buckling, and non-linear buckling analyses to account for geometric nonlinearities and imperfection sensitivities. By analysing force-displacement curves, critical load factors, safety margins, and stress locations were identified. This study validates the CALLISTO design, contributing to the maturation of European reusable launch vehicle technologies and providing a foundation for subsequent qualification testing campaigns.

ACRONYMS

ITS **–** Inter Tank Structure
LOX – Liquid Oxygen
LH2 – Liquid Hydrogen

1. INTRODUCTION

The development of cost-effective and operationally flexible launch systems has become a strategic priority, driving renewed industry focus on reusability technologies. Within this landscape, the CALLISTO project stands as a pivotal trilateral initiative between the German Aerospace Centre (DLR), the French National Centre for Space Studies (CNES), and the Japanese Aerospace Exploration Agency (JAXA). The program aims to develop and fly a reusable vertical take-off and vertical landing (VTVL) rocket demonstrator that validates critical technologies, refines technical assumptions, and demonstrates return-to-launch-site manoeuvres at a fraction of the cost of an operational vehicle [1]. By demonstrating (i) the capability to recover a vehicle with toss-back trajectory, (ii) Maintenance, Repair, and Overhaul (MRO) procedures to make the vehicle ready for the next fly with minimum turnaround and refurbishment effort, and (iii) to fly with the same reused vehicle, with a capability of several flights [2] [3] [4].

A load-critical element of this architecture is the Inter-Tank Structure (ITS), which mechanically connects the liquid oxygen (LOX) and liquid hydrogen (LH2) propellant tanks. To meet mass budgets, the ITS utilizes a thin-walled barrel design reinforced with hat stiffeners, cut-outs, and equipment platforms. While this lightweight configuration maximizes performance, it inherently increases susceptibility to buckling and geometric instabilities under complex operational loads [5]. During ascent, powered tilt-over manoeuvres, and propulsive landing phases, the structure experiences severe compressive stresses, bending moments, and thermal gradients that can trigger premature failure if not rigorously analysed. Consequently, advanced structural stability assessments are essential to ensure that reusable airframe components safely withstand repeated flight cycles without compromising vehicle structural integrity.

Historically, the design of such structures relied on conservative empirical knockdown factors (KDFs) derived from limited test data. Recently, analysis-based approaches were incorporated into the 2020 revision of NASA SP-8007, allowing less conservative, structure-specific knockdown factors to be determined [6] [7].

Research has demonstrated that initial geometric imperfections, thickness variations, and loading non-uniformities can drastically reduce buckling loads compared to idealized theoretical predictions. Techniques such as the single perturbation load approach and reduced energy methods have been developed to simulate worst-case geometric disturbances, enabling more accurate stability predictions without excessive conservatism [8]. Furthermore, probabilistic frameworks combined with deterministic non-linear analyses provide

robust tools for quantifying uncertainties in material properties, boundary conditions, and load introduction [9]. These modern methodologies underscore the necessity of moving beyond classical linear buckling estimates and explicitly incorporating imperfection sensitivity into the structural validation process.
This paper presents a comprehensive non-linear buckling analysis of the CALLISTO ITS to assess its mechanical stability and structural integrity under four representative operational flight conditions. By considering linear perturbation eigenvalue analyses and geometrically non-linear finite element simulations, the study evaluates load-carrying capacity, identifies critical imperfections, and establishes safety margins against instability. The methodology focuses on analysing force-displacement responses to verify that buckling instability is prevented well beyond nominal flight loads. Ultimately, this structural validation supports subsequent qualification testing campaigns and contributes to the broader maturation of reusable launch vehicle technologies.

2. STRUCTURAL DESCRIPTION AND MODELING

2.1. Geometry and Architecture

The ITS structure connects the LOX and LH2 tanks of the CALLISTO rocket. As shown in Figure 1, the structure consists of a thin-walled barrel reinforced by hat stiffeners and features two cut-outs that provide access to internal structure and equipment installation platforms.

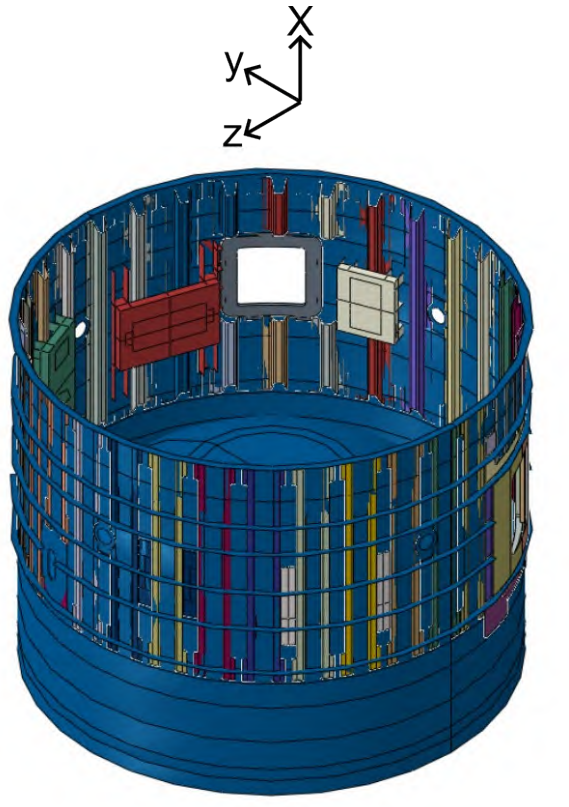


Figure 1: Overview of CALLISTO ITS structure.

The barrel has a nominal thickness of 1 mm, with thicker sections near its upper and lower ends.
The ITS contains 35 omega stringers, most of which span the full length of the barrel. Shorter stringers are used around the cut-outs and platforms. The stringers have a nominal thickness of 1 mm.
The modelled barrel is 875.8 mm long and has an inner diameter of 1100.9 mm, measured at the upper end below the LOX tank flange. The model includes the LH2 dome, connected to the rest of the barrel. The ITS model includes five platforms, two cut-out frames and three frames. Figure 2 defines the location of the equipment installation platforms for the application of the local loads.

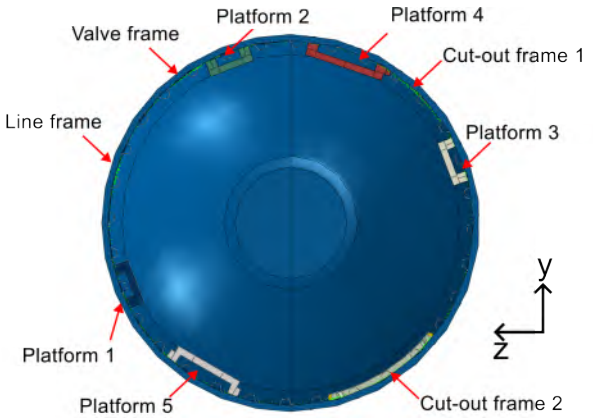


Figure 2: Identification of the system platforms of CALLISTO ITS structure.

The ITS model accounts for other components, such as cable ducts and lines. Although their connections are not explicitly modelled, their effect is represented by locally increasing the thickness.

2.2. Finite Element (FE) Model

The model is created in Abaqus and meshed with 4-node quadrilateral shell elements with reduced integration. The approximate mesh size applied to the barrel is 5 mm, based on the preliminary linear perturbation analysis, a compromise in terms of computational cost and experience. The platforms, stringers and other non-critical parts for the buckling analysis have larger mesh-size (10 mm ca.).
The fasteners are modelled using the Abaqus mesh-independent, point-based fastener formulation. Rigid beam MPCs connect the fastening points on the joined surfaces, while distributing couplings attach these points to the surrounding shell nodes. Distributing couplings (RB3) are also used to apply the local loads from the equipment installation platforms shown in Figure 2. An example of a platform (Fluid Retainer Valve Platform) is presented in Figure 3, highlighting its connectivity.

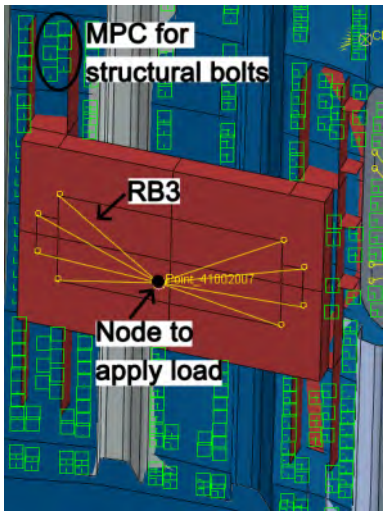


Figure 3: Example of platform connectivity.

The sections of the rocket surrounding the ITS, i.e., LOX and LH2 tanks, are represented in the analysis by super-elements with equivalent stiffness. The LH2 and LOX tank super-elements are defined using 173 and 115 retained nodes, respectively. For the LH2 tank super-element, 172 nodes are distributed around the circumference at the lower end of the ITS, while one node is located at the bottom of the launcher demonstrator, where the boundary conditions are applied. The nodes of the super-elements are connected to the ITS with rigid kinematic coupling (RB2). The modelling strategy for the rocket and the connection of the nodes of the super-elements to the ITS are shown in Figure 4.
The materials are considered in this analysis are reported in Table 1.

Table 1: Material properties. [10]

	Al 2000 series	Al 7000 series
Density [kg/mm^3]	2.851e-6	2.810e-6
E [MPa]	72395	71016
v [-]	0.33	0.33
σ_u [MPa]	420	482
Use	Dome assembly, ITS hull, ITS flange	Platforms, Stiffeners, Frames

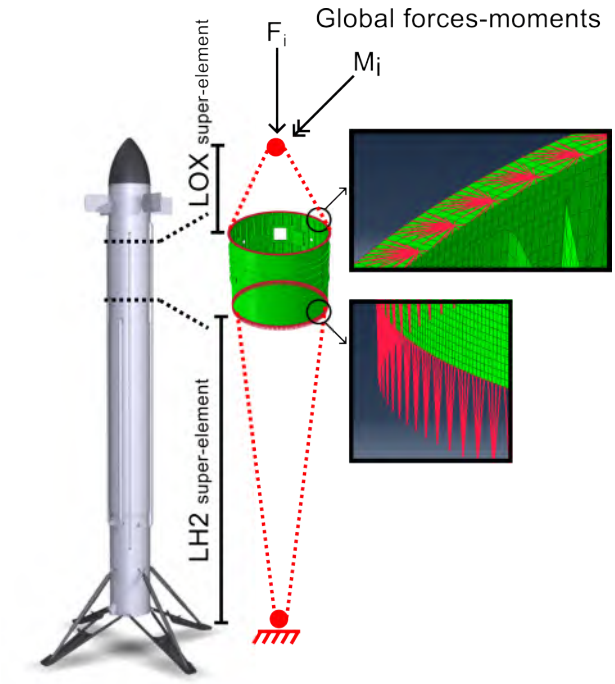


Figure 4: LOX and LH2 super-elements connection to the ITS.

2.3. Boundary Conditions and Load Cases

The boundary condition constraining the model is applied at the bottom-node of the LH2 tank super-element, corresponding to the bottom of the rocket. At this node all degrees of freedom are constrained (Ui = URi = 0, see Figure 4).
In this analysis of the ITS structure, four load-cases are considered. These load cases are defined taking into account all possible global and local loads that the ITS may be subjected to. With respect to buckling, this includes global compression, bending and torsion loads, all of which are applied to the LOX-tank super element. Additionally, an internal negative pressure is considered, together with local force loads introduced via the equipment platforms as well as resulting from the attachment of fluid lines and cable ducts. For the four load-cases regarded in this paper, these loads were combined in a way that maximized compressive principal stress ($\sigma_{I,min}$) inside the ITS.
For each load-case, global force and moments (as in Figure 4) are computed with the LOX tank super-element and applied to its nodes. The loads are then transmitted to the ITS flange according to the connectivity shown in Figure 4.
The concentrated load for each platform and frame is applied with distributed coupling, e.g., see Figure 3. In addition, loads are applied to cable ducts and lines; these loads are applied to the centre of mass of the surface corresponding to the components, then distributing the load on the surface with RB3s.
Table 2 summarizes the loads and moments that are applied in the model. The global forces and moments are reported as function of the components of LC1. The ITS pressure and the LH2 tank pressure is the same for all load-cases. For the

sake of conciseness, platforms loads, frames loads, duct loads and lines loads are reported as generic F_x, F_y and F_z components; a separate set of forces is applied to each of the ITS equipment mentioned.

Table 2: Schematic summary of forces and moments applied in the model

Loads	LC1	LC2	LC3	LC4
Platforms loads		$F_{x,a}$, $F_{y,a}$, $F_{z,a}$		
Frames loads		$F_{x,b}$, $F_{y,b}$, $F_{z,b}$		
Ducts loads		$F_{x,c}$, $F_{y,c}$, $F_{z,c}$		
Lines loads		$F_{y,d}$, $F_{z,d}$		
ITS pressure	$-P_1$	$-P_1$	$-P_1$	$-P_1$
LH2 tank pressure	P2	P2	P2	P2
Global force*	$-F_x$	$-F_x$	$-F_x$	$-F_x$
Global moment*	M_x	M_x	$-M_x$	$-M_x$
Global moment*	M_y	3.52 M_y	-6.06 M_y	-1.36 M_y
Global moment*	M_z	-0.83 M_z	-0.03 M_z	0.99M_z

*Forces and Moments reported as function of F_x and M_i of LC1

2.4. Analysis Approach

The following analyses are presented in this work:

- Linear Perturbation Buckling Analysis,
- Non-linear Buckling Analysis.

2.4.1. Buckling linear perturbation analysis

Buckling linear perturbation analyses are performed with the same boundary condition and loads outlined in Section 2.3. The outcome of the analyses is a scalar factor associated with a deformed shape. A general eigenvalue buckling analysis can provide useful estimates of collapse mode shapes, and the resulting scale factor can be interpreted as a scale factor for the critical buckling load, i.e., provide an initial buckling margin of safety. A total of 30 modes are extracted. Selected modes are then combined and introduced as geometric imperfections in the ITS model. The mode combinations used for each imperfection and load case are presented in Section 2.4.2.

In addition to the linear buckling analysis, a frequency analysis is performed to obtained alternative imperfection shapes. Unlike the localized buckling modes, the selected vibration modes produce imperfection patterns that extend over the entire structure. As these modes are used only as inputs for the nonlinear analysis, the frequency analysis results are not presented separately.

2.4.2. Non-linear buckling analysis

A series of non-linear analyses is carried out for each load-case. First, the non-linear analysis is performed for each load-case, then a combination of imperfections is applied to perturbate the geometry. Four combinations of imperfections are considered for each load-case, in particular, three combinations are the results of the buckling modes predicted by the buckling linear perturbation analysis, and the fourth combination results from the vibration modes. A progressively larger scale factor is applied to the linear combination of the modes. The deformed geometry resulting from the buckling linear perturbation analysis is very localized and usually characterized by buckling half-waves between or underneath stringers, while vibration modes affect the whole geometry and perturbate the whole model. It is worth underlining that the perturbation affects only the geometry and does not carry residual stress.

The scale factor applied to the imperfections multiplies the deformed geometry obtained by the linear perturbation and frequency analyses. For example, the displacement resulting from the buckling linear perturbation analyses is always ranging from 0 to 1, and since the scale factors range from 0.1 to 2, the largest offset from the original geometry for each buckling shape corresponding to an eigenvalue will vary from 0.1 to 2 mm. The scale factor is applied to each imperfection mode, which are linearly combined and applied to the geometry before the analysis starts. Since the displacement resulting from the frequency analyses is not normalized and larger than that from the buckling linear perturbation analyses, the same imperfections scale factors multiplied by a 0.1 factor are considered.

The non-linear analyses are performed by applying a progressively increasing scale factor to all the loads included in the analysis, ranging 0-400 %, in order to capture the instability onset, as well as to consider any change in the global structural behaviour and stress state. A scale factor of 100 % corresponds to the nominal load-cases provided. By applying a progressively increasing scale factor, it is possible to determine margins of safety, by looking at the force (i.e., load scale factor) vs displacement curves, establishing the onset of non-linear behaviour and instability.

The ID of each analysis is presented as follows in this work:

- The ID starts with the load-case considered, i.e., LC1, LC2, LC3 and LC4.
- The type of analysis, i.e., "b" and "nl", for the buckling linear perturbation analysis and non-linear analysis, respectively.

- For the analyses with imperfections, "1", "2", "3" and "4" are used to indicate the imperfection case.
- For the analyses with imperfections, “01”, "05", "10" and "20" are used to indicate the imperfection scale factor of 0.1, 0.5, 1 and 2 for the analyses considering buckling modes and 0.01, 0.05, 0.1 and 0.2 for the analyses considering vibration modes, respectively.

The ID looks like: LC"i" _ "type of analysis" _ "imperfection case" "imperfection scale factor".
In Figure 5 the list of non-linear analyses and the imperfection applied is summarized.

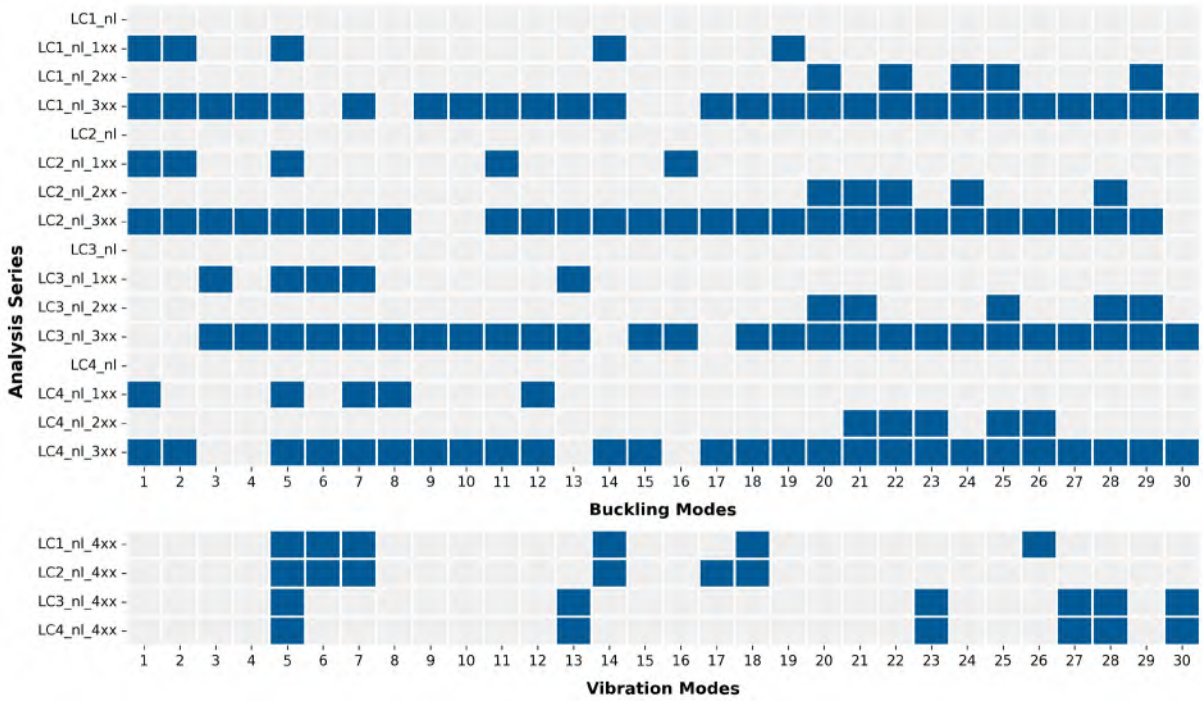


Figure 5: Summary of imperfection cases combination for non-linear analyses.

3. RESULTS AND DISCUSSION

3.1. Buckling Linear Perturbation Analyses

The results from the linear perturbation analysis performed to obtain the buckling eigenvalues are reported in Table 3 and Table 4.

Table 3: Eigenvalues resulting from the linear perturbation analysis – Part 1

Eigenvalue N.	LC1	LC2	LC3	LC4
1	2.40	2.54	-	2.50
2	2.66	2.59	-	2.79
3	2.69	2.70	3.12	-
4	2.94	2.75	3.23	-
5	3.06	2.81	3.32	3.12
6	-	2.82	3.35	3.21
7	3.12	2.85	3.39	3.25
8	-	2.91	3.4	3.28
9	3.35	-	3.42	3.33
10	3.35	-	3.46	3.35
11	3.37	3.05	3.48	3.39
12	3.45	3.12	3.49	3.40
13	3.48	3.13	3.51	-
14	3.52	3.18	-	3.42
15	-	3.20	3.52	3.48

Table 4: Eigenvalues resulting from the linear perturbation analysis – Part 2

Eigenvalue N.	LC1	LC2	LC3	LC4
16	-	3.20	3.53	-
17	3.60	3.22	-	3.50
18	3.63	3.23	3.55	3.52
19	3.66	3.27	3.56	3.55
20	3.67	3.33	3.58	3.55
21	3.67	3.34	3.59	3.61
22	3.70	3.34	3.60	3.62
23	3.71	3.36	3.62	3.62
24	3.72	3.40	3.65	3.65
25	3.77	3.42	3.66	3.68
26	3.79	3.51	3.67	3.73
27	3.79	3.51	3.70	3.73
28	3.81	3.53	3.72	3.74
29	3.84	3.55	3.74	3.75
30	3.87	-	3.76	3.76

The deformed shape of selected modes resulting from the buckling linear perturbation analysis for the Load-Case 1 are reported in Figure 6. The linear perturbation analyses provide the eigenvalues for each of the eigenmode. The resulting parameters can be considered a margin of safety, i.e., the factor that should multiply all the loads to obtain a certain buckling shape. A minimum value of 2.4 or higher

results from the four load-cases, indicating relatively large buckling margins of safety for the load-cases considered in this work. All the modes predicted by this analysis are local modes, so no global buckling was ever captured by the analysis. These local modes tend to occur between or underneath the stringers. When a dash line ("-") is reported in the Table 3, that indicates that the analysis predicts a negative eigenvalue, so a negative scale factor that does not make sense for this analysis.

Finally, the deformed shape of selected modes from the frequency analysis are reported in Figure 7 to highlight the difference in the imperfections and perturbed geometry resulting from the two different strategies.

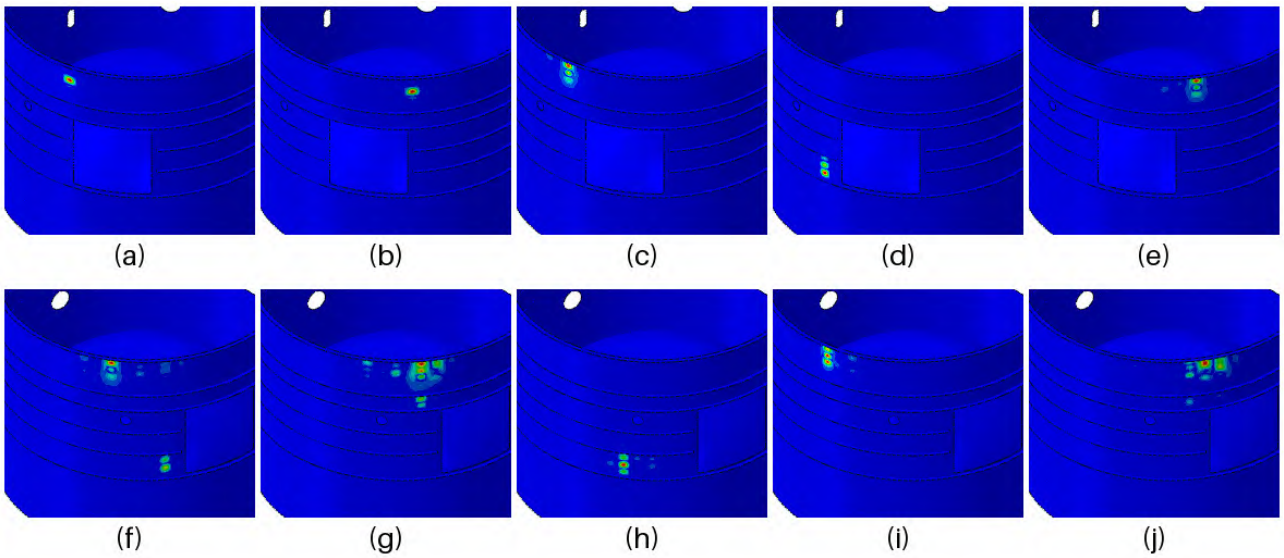


Figure 6: Perturbed geometry of modes 1 (a), 2 (b), 5 (c), 14 (d), 19 (e), 20 (f), 22 (g), 24 (h), 25 (i), and 29 (j) from buckling linear perturbation analysis for LC1

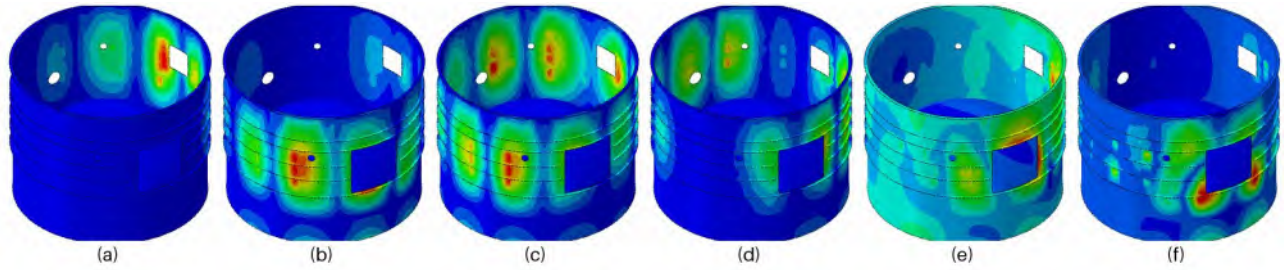


Figure 7: Perturbed geometry of modes 5 (a), 6 (b), 7 (c), 14 (d), 18 (e), 26 (f) from frequency linear perturbation analysis for LC1

3.2. Non-Linear Buckling Analyses

It is a standard approach when non-linear buckling analyses or tests are performed, to consider the bifurcation point in the force-displacement curve as the onset of instability for a structure. In an ideal shell subjected to longitudinal compression, one can consider the centre of mass of the top and bottom sections to calculate the longitudinal displacement; however, in this work the measurements for the displacement of the centre of mass resulted very small (~1e-1 mm). The reason is that for the load-cases provided, a significant bending was applied to the ITS, resulting in unequal end-shortening around the barrel. In addition, the results showed rigid motion of the rocket, since it was constrained at the bottom of the lower super-element and the force resulting from the bending moments were applied at the top. In Figure 8 the longitudinal displacements along four axes around the barrel are reported, function of the load scale factor (reported as [%] of the load-case). The 0° is considered the radial position of the point in the barrel where the highest stress is found in the analysis; the other three plots then show the displacement for axis aligned along the longitudinal direction of the barrel at radial positions of 90°, 180° and 270°. From the plots it is clear that the end-shortening is greater in one radial position, rather than the other. For this reason, the next plots, addressing the buckling onset and the effect of imperfections, are only reported for the 0° radial position, i.e., θ_i radial position where the element with the highest stress is found in each analysis.

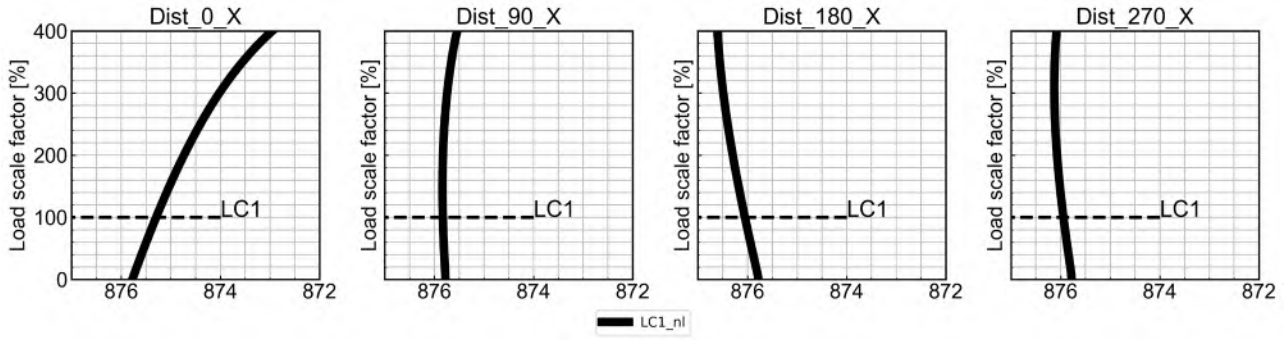
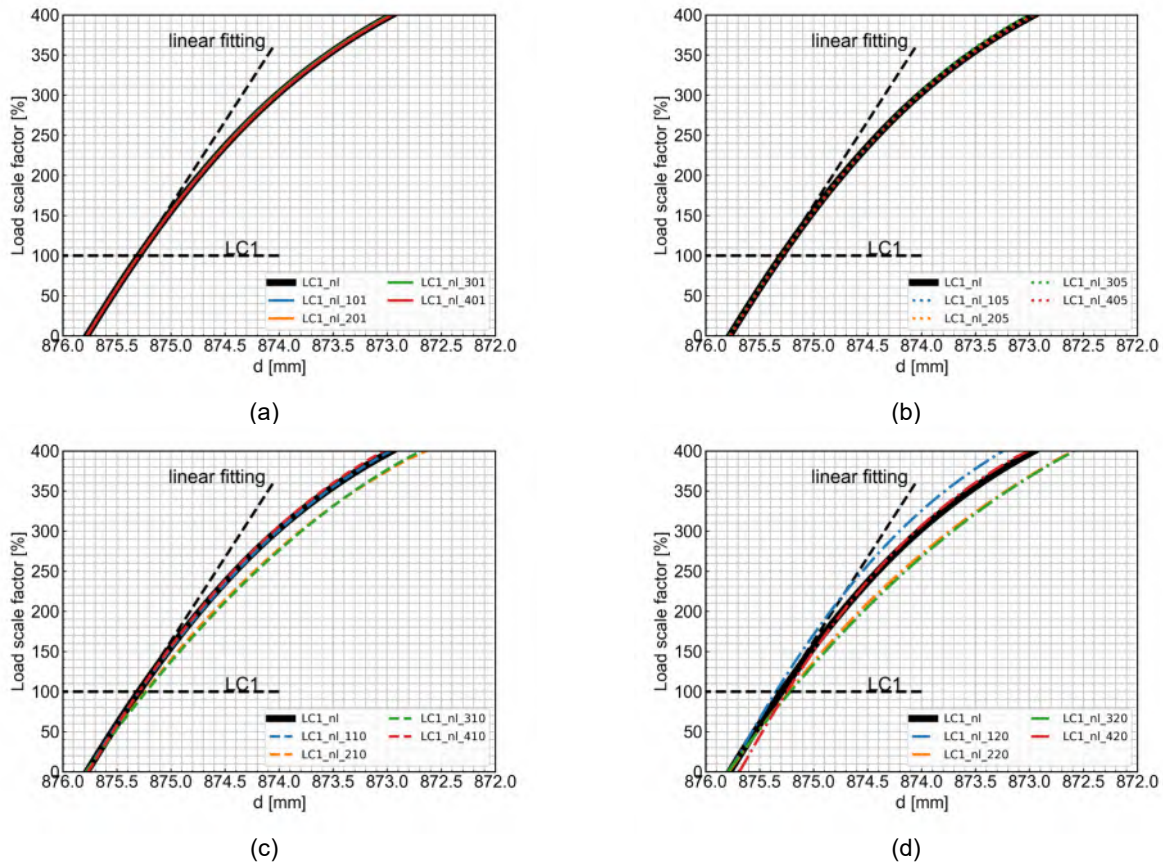


Figure 8: Longitudinal displacement along four axes around the barrel, i.e., (a) 0°, (b) 90°, (c) 180° and 270°, when 0° corresponds to the radial position where the highest stress is found

In Figure 9, Figure 10, Figure 11, and Figure 12 the plots are presented, showing the load scale factor as function of the longitudinal displacement measured along the axis passing on the barrel through the 0° radial position. The straight dashed line obtained from linearly fit the curves without imperfections (i.e., LC1_nl, LC2_nl, LC3_nl and LC4_nl) in the 0-100 % load range, is shown to visually highlight when the structure diverges from the linear behaviour. The results are summarized in Table 5, where the load scale factor corresponding to a 10% difference between the curve and the linear fit, and the percentage difference at 160 % of the load-case are reported for all the load-cases. For the sake of conciseness, for each load-case and imperfections scale factor, the average value and the standard deviation is reported. These two values are meant to give an estimation of the buckling safety factor.



(a) (b)

(c) (d)

Figure 9: LC1 - Load scale factor as function of longitudinal displacement for analyses with imperfection equals to (a) 0.1, (b) 0.5, (c) 1 and (d) 2.

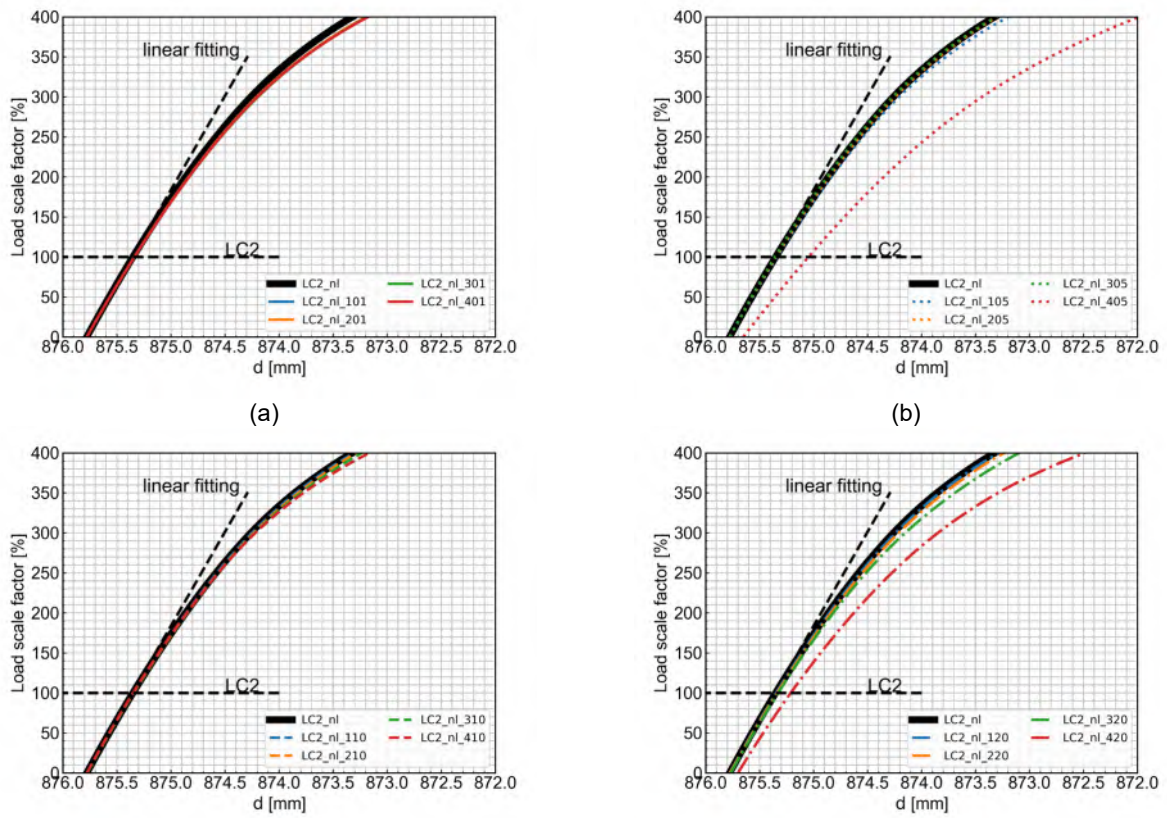


Figure 10: LC2 - Load scale factor as function of longitudinal displacement for analyses with imperfection equals to (a) 0.1, (b) 0.5, (c) 1 and (d) 2.

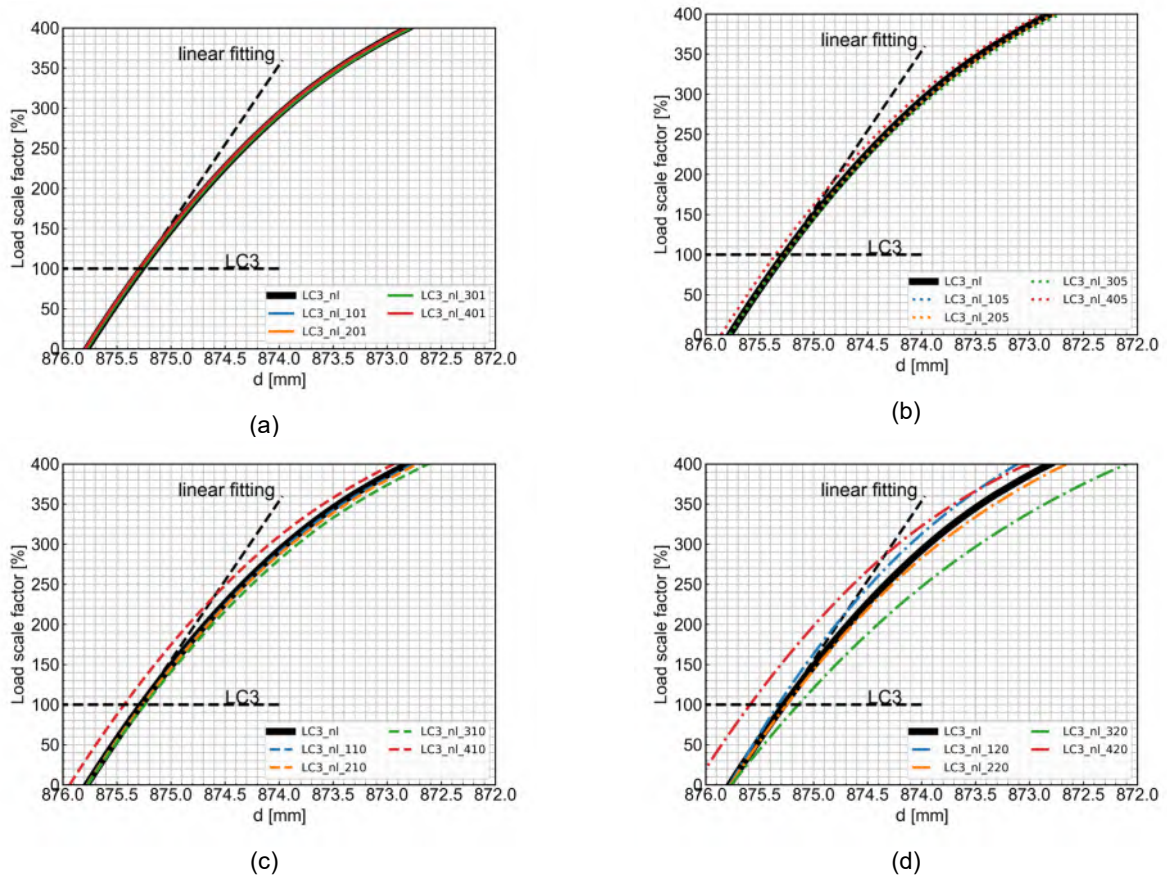


Figure 11: LC3 - Load scale factor as function of longitudinal displacement for analyses with imperfection equals to (a) 0.1, (b) 0.5, (c) 1 and (d) 2.

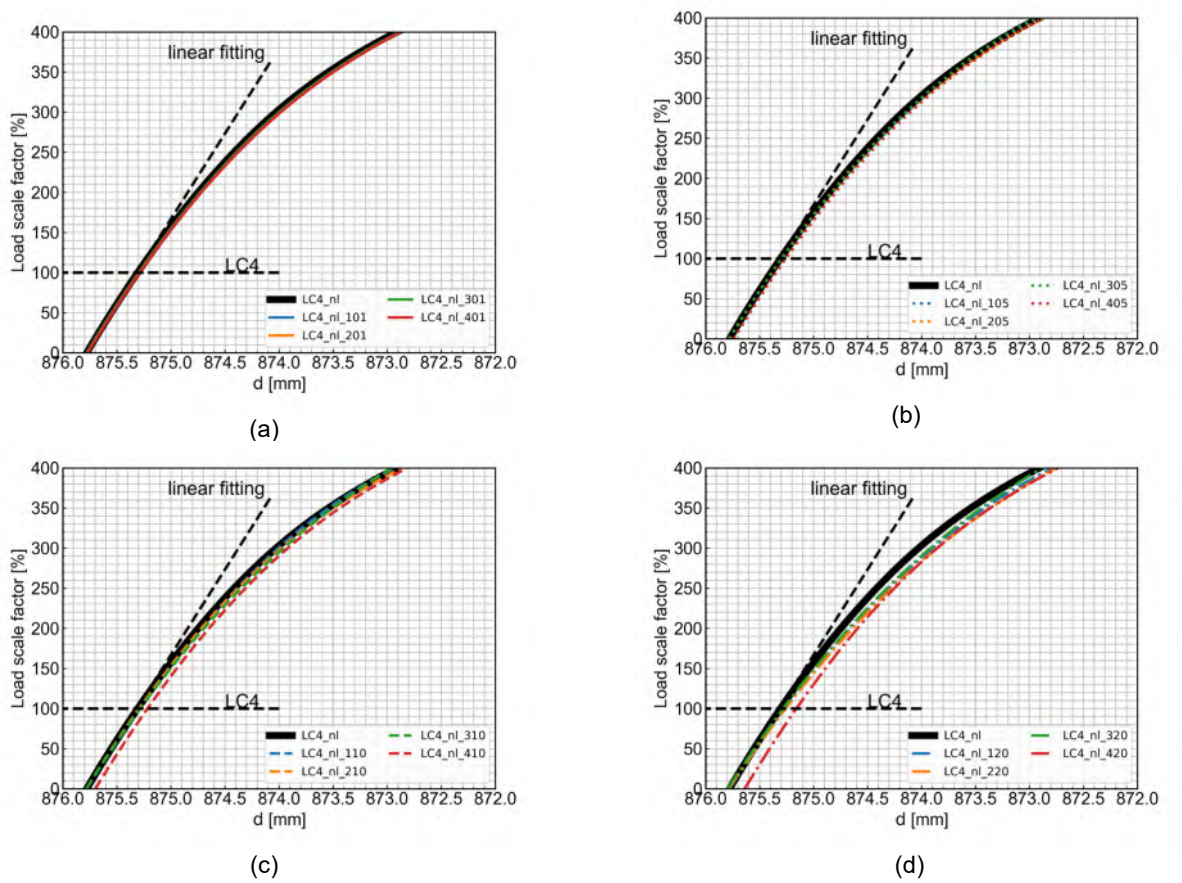


Figure 12: LC4 - Load scale factor as function of longitudinal displacement for analyses with imperfection equals to (a) 0.1, (b) 0.5, (c) 1 and (d) 2.

Table 5: Summary of load scale factors corresponding to 10% difference from linear fit and deviation at 160% of load-cases.

Analysis ID	Load Scale Factor ($\Delta L / L_{fit} > 0.10$)	STD Load Scale Factors	Deviation at 160% Load	STD Deviation at 160% Load
LC1_nl	220%		5.1%	
LC1_nl_x01	221%	1.73%	5.1%	0.04%
LC1_nl_x05	223%	3.32%	5.1%	0.11%
LC1_nl_x10	222%	3.46%	5.1%	0.11%
LC1_nl_x20	218%	4.47%	5.4%	0.18%
LC2_nl	236%		4.6%	
LC2_nl_x01	236%	0.00%	4.6%	0.04%
LC2_nl_x05	232%	4.00%	4.8%	0.15%
LC2_nl_x10	231%	5.20%	4.9%	0.21%
LC2_nl_x20	225%	13.08%	5.1%	0.57%
LC3_nl	216%		5.6%	
LC3_nl_x01	216%	0.00%	5.6%	0.00%
LC3_nl_x05	215%	1.73%	5.7%	0.05%
LC3_nl_x10	215%	1.73%	5.7%	0.04%
LC3_nl_x20	210%	3.46%	5.9%	0.17%
LC4_nl	208%		5.9%	
LC4_nl_x01	212%	0.00%	5.8%	0.00%
LC4_nl_x05	211%	1.73%	5.8%	0.08%
LC4_nl_x10	212%	0.00%	5.8%	0.07%
LC4_nl_x20	213%	1.73%	5.7%	0.12%

By looking at the "load" vs shortening curves, for all load-cases, the benchmark analyses (with no imperfection "_nl") begin showing non-linear behaviour between 150%-200%. As expected, this value is smaller than that predicted by the linear perturbation analyses, but still well above the 100% threshold.

Table 5 reports the load scale factor at which the

load-displacement response deviates by 10% from a linear best-fit, defining the onset of significant structural nonlinearity. For all load cases, this threshold exceeds 200%, indicating that the response remains approximately linear well beyond the reference load. This is further confirmed by the deviations at 160% of the applied load (a safety factor of 1.6), which remain below 10%, validating linear approximations within this critical range. Additionally, higher imperfection scale factors correspond to lower load scale factors, consistent with expectations for larger geometric perturbations. Finally, as expected from non-linear analysis, all reported load scale factors remain below those predicted by linear perturbation buckling analyses.

In Figure 13 the location of the elements with the highest stress is highlighted, and Table 6 summarises the results from the non-linear analyses without imperfections, reporting the highest Von Mises stress from the four load-cases, as well as the margin of safety, evaluated as the ration between the maximum stress and the material ultimate strength.

The results for the stress are presented showing the highest stress at the integration point across the thickness of the shell, and no nodal interpolation (averaging) is applied, effectively showing the worst-case scenario and conservative results. The stress contours are reasonable, and the highest stress is always below the ultimate strength of the Aluminium 2000 series. For the load-cases 2 and 3, the highest stress is located under the rails where a platform is connected, while for the LC1 it is around the frame duct plate and for the LC4 it is under the top flange, above a cable duct. When imperfections are applied, the stress tends to increase or even move to a different position with the larger imperfection scale factors applied. If the location of the highest stress changes, the new location is always in a point of the structure where the imperfections were applied. In some analyses and location, the stress reaches very high values (above plasticization stress), however these analyses are almost always associated with " load " vs shortening that differ from the benchmark curve; hence it can be concluded that these analyses are not reliable for stress analysis because the imperfection are too large.

Table 6: Maximum Mises stress summary

	LC1_nl	LC2_nl	LC3_nl	LC4_nl
Max Mises Stress [MPa]	288.3	279.4	277.3	339.9
Margin of safety [-]	0.69	0.66	0.66	0.81

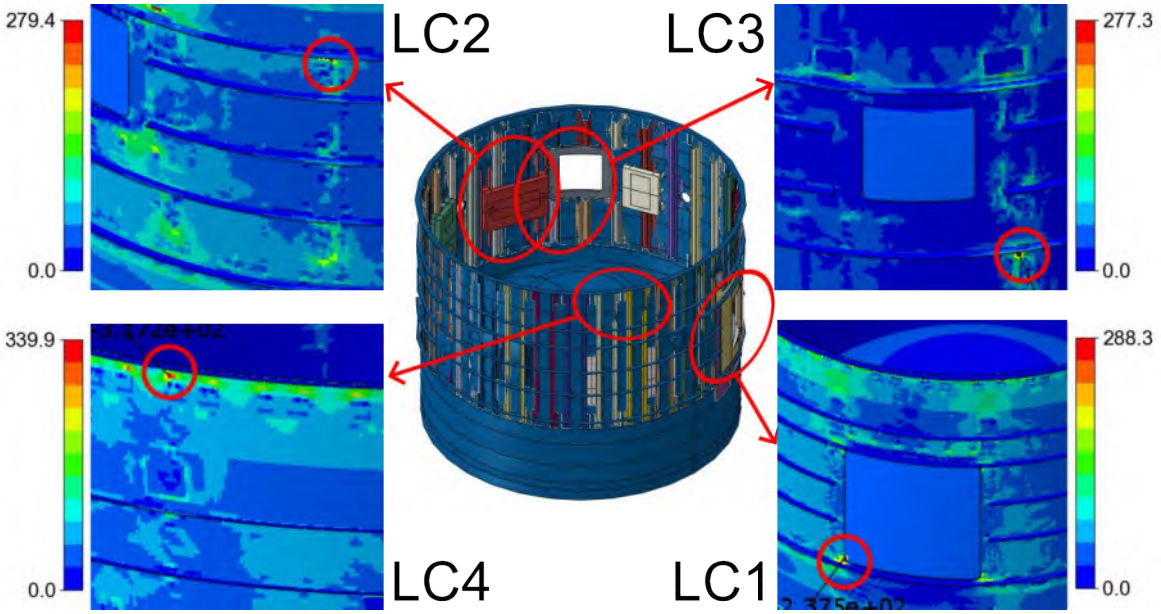


Figure 13: Summary of areas of elements with highest stress for each load-case.

The analysis carried out with imperfection from the vibration modes and scale factor equal to 0.2 ("_420"), differs too much from the benchmark curve, already from the beginning of the simulation, and is not considered reliable; indicating that the scale factor is too large and deforms the whole structure. A similar conclusion can be drawn from analyses with imperfections from the buckling linear perturbation analyses: it often appears that with scale factor equal to 2 that the curve starts from the same point at the beginning of the analysis, because the buckling imperfections are very localized; but then they diverge significantly from the benchmark curve. This is especially true for the combination of imperfection 3 (for all load-cases), this combination of imperfection is likely excessive for the structure and the applied imperfections are too large. The imperfection combination 3 for lower scale factors is comparable to the benchmark curve and deemed acceptable.

4. CONCLUSIONS

In this work the non-linear buckling analyses of the ITS structure of the CALLISTO project are presented; according to the load-cases provided and accounting for geometrical imperfection to investigate possible structure instability.
The objective of the analyses is to validate the design of the rocket, by verifying that instability is prevented given the load-cases, and the goal was achieved by applying a progressively increasing load until a non-linear behaviour of the structure was detected. For all load cases, the predicted buckling load was well above the corresponding reference load, and the structural response remained approximately linear, with no indication of buckling or instability up to a load factor of about 1.6. This relatively high buckling load factors indicate that other failure modes may become critical before buckling. It is also important to remark that all the load-cases had a large bending moment applied to the top of the rocket, resulting in a rigid motion of the rocket; as well as the ITS showing both end-shortening and tension around the structure.
Overall, this structural validation supports the CALLISTO architecture's readiness for subsequent qualification testing and contributes to the broader maturation of reusable vertical take-off and landing technologies.

5. ACKNOWLEDGMENT

This work has been performed in the frame of a project funded by the German Federal Ministry of Research, Technology and Space.

6. REFERENCES

[1] E. Dumont, T. Ecker, C. Chavagnac, L. Witte, J. Windelberg, J. Klevanski and S. Giagkozoglou, “CALLISTO - Reusable VTVL launcher first stage demonstrator,” in *Space Spropulsion Conference 2018*, Sevilla, Spanien, 2018.

[2] P. Tatiossian, J. Desmariaux and M. Garcia, “CALLISTO PROJECT - REUSABLE FIRST STAGE ROCKET,” in *7TH EUROPEAN CONFERENCE FOR AERONAUTICS AND SPACE SCIENCES (EUCASS)*, Milan, Italy, 2017.

[3] E. DUMONT, et al., “CALLISTO: Reusable rocket stage demonstrator: getting ready for implementation,” *Journal of Evolving Space Activities,* vol. 2, p. 201, 2024.

[4] E. Dumont, et al., “CALLISTO Reusable rocket stage demonstrator: consolidating the design,” in *2024 IEEE Aerospace Conference*, 2024.

[5] S. Giagkozoglou Vincenzino, W. Rotärmel, I. Petkov, H. Elsäßer, E. Dumont, L. Witte and S. Schröder, “Reusable Structures for CALLISTO,” in *8th European Conference for Aeronautics and Space Sciences (EUCASS)*, Madrid, Spanien, 2019.

[6] V. Weingarten, P. Seide and J. Peterson, “Nasa SP-8007 – buckling of thin-walled circular cylinders NASA space vehicle design criteria – structures,” 1965 [revised in 2020 by Hilburger MW].

[7] M. W. Hilburger, “On the Development of Shell Buckling Knockdown Factors for Stiffened Metallic Launch Vehicle Cylinders,” in *AIAA/ASCE/AHS/ASC Structures, Structural Dynamics,*, Kissimmee, Fl., 2018.

[8] S. G. Castro, R. Zimmermann, M. A. Arbelo, R. Khakimova, M. W. Hilburger and R. Degenhardt, “Geometric imperfections and lower-bound methods used to calculate knock-down factors for axially compressed composite cylindrical shells,” *Thin-Walled Structures,* vol. 74, pp. 118-132, 2014.

[9] R. Degenhardt, A. Kling, A. Bethge, J. Orf, L. Kärger, R. Zimmermann, K. Rohwer and A. Calvi, “Investigations on imperfection sensitivity and deduction of improved knock-down factors for unstiffened CFRP cylindrical shells,,” *Composite Structures,,* vol. 92, no. 8, pp. 1939-1946, 2010.

[10] U. States, Metallic materials properties development and standardization (MMPDS): MMPDS-07, April 2012, U. States, Ed., Federal Aviation Administration, 2012.

PROGRESS IN NON-DESTRUCTIVE BUCKLING PREDICTION OF REAL-SCALE THIN-WALLED STRUCTURES BY VIBRATION

Validation of the vibration-correlation technique on an Ariane 6 tank section subjected to bending-compression load cases

Theodor Dan Baciu[(1)], Richard Degenhardt[(1,2)], Felipe Franzoni[(2)], Adrian Gliszczynski[(1,3)]

[(1)] University PFH, Engineering Campus Stade, Airbusstr. 6, Stade, Germany, t.baciu@pfh.de
[(2)] DLR, Institute of Lightweight Systems, Lilienthalplatz 7, 38108 Braunschweig, Germany, Richard.Degenhardt@dlr.de, Felipe.Franzoni@dlr.de
[(3)] Lodz University of Technology, Stefanowskiego 1/15, 90-924, Lodz, adrian.gliszczynski@p.lodz.pl

KEYWORDS

Real-scale launcher structures, vibrations, buckling

ABSTRACT

Buckling is one of the primary design criteria in aerospace structures and is particularly critical for cylindrical launcher structures. Although significant progress has been made throughout the years in understanding the buckling behaviour of cylindrical shells, especially through finite element methods, reliably predicting buckling loads during design and validating them experimentally without damaging costly test specimens remains challenging. This is mainly due to the high imperfection sensitivity and unstable post-buckling behaviour of cylindrical shells under axial compression. To address these challenges and meet the demand for safe, lightweight space structures, non-destructive methods for predicting in-situ buckling loads have gained increasing interest. One such method is the Vibration Correlation Technique (VCT), which exploits the relationship between eigenfrequency and applied load. While VCT has shown promising numerical and experimental results for small-scale cylinders, its industrial adoption requires validation on full-scale structures. This paper presents the results of an experimental validation campaign on a full-scale structure.

1. INTRODUCTION

Buckling is a critical design consideration for lightweight thin-walled structures, particularly in aerospace applications where high structural efficiency is required. Cylindrical shells are widely employed in launch vehicles, spacecraft, aircraft, storage tanks, pipelines, and other engineering structures because of their favourable stiffness-to-mass ratio. However, their high sensitivity to geometric imperfections, material and manufacturing variability, and boundary conditions makes their buckling behaviour difficult to predict reliably. This uncertainty is particularly relevant for aerospace structures, where an over-conservative buckling design can result in significant mass penalties, while overprediction of the buckling load can compromise structural safety.

The design of aerospace cylindrical shells is still largely based on the NASA SP-8007 guidelines [1], first published in 1965 and revised in 2020, which provide knock-down factors as a function of the cylinder radius-to-thickness ratio. However, advances in manufacturing, particularly the widespread use of composite materials, have rendered these factors increasingly over-conservative. Finite element methods now enable highly accurate structural analyses, provided that the numerical models capture the structural details, experimental boundary conditions, and relevant imperfections, especially geometric deviations.

Nevertheless, particularly in the aerospace sector, experimental validation remains an indispensable component of the structural qualification process, both for validating numerical predictions and for establishing the actual load-carrying capability of a structure. Conventional buckling tests, however, typically require loading the structure until instability occurs, which can lead to plastic deformations or the complete failure of the test article [2]. This is particularly undesirable for expensive, large-scale structures such as launcher tanks and spacecraft primary structures, where manufacturing and testing costs are substantial, and therefore the possibility of reusing the test article is highly appealing.

These challenges, together with the growing interest in reusable launcher structures, have increased the appeal of non-destructive methods for estimating buckling loads. Among them, the Vibration Correlation Technique (VCT) predicts the buckling load by extrapolating the relationship between vibration frequencies and applied load [3]. By measuring the natural frequencies at several load levels and correlating their evolution with the applied load, the critical buckling load can be estimated without requiring the structure to be driven to failure. This makes VCT particularly

attractive for imperfection-sensitive structures, for which conventional buckling tests can be difficult to repeat, and numerical predictions may be affected significantly by uncertainties in the geometry, load and boundary conditions.

The potential application of VCT extends beyond aerospace structures. Any lightweight or thin-walled cylindrical structure for which buckling represents a relevant failure mode may benefit from a non-destructive buckling assessment. Potential applications include launch-vehicle and spacecraft structures, aircraft fuselage components, pressure vessels and storage tanks, marine structures, pipelines, and other cylindrical shells used in the energy and process industries. In these applications, VCT could provide an additional means of experimentally assessing structural margins while reducing the need for destructive qualification tests. The method's ability to operate on the actual test article also offers the potential to capture the combined effects of manufacturing imperfections, assembly conditions, material variability, and realistic boundary conditions that are difficult to reproduce completely in numerical models.

Despite these advantages, the industrial application of VCT remains challenging. The relationship between vibration characteristics and buckling load is influenced by geometric imperfections, loading and boundary conditions, mode interaction, measurement uncertainties, and the choice of vibration modes used for the correlation. Furthermore, most experimental validation of the technique has historically focused on small-scale cylindrical shells, while its applicability to large-scale industrial structures remains comparatively less established. Demonstrating reliable performance under realistic boundary and loading conditions is therefore an important step towards its wider adoption.

This paper summarises recent developments toward the industrial implementation of VCT and presents its application to a full-scale structural test. The VCT methodology is first introduced, followed by a preliminary numerical analysis used to define the measurement parameters and estimate the expected robustness of the method. Finally, the results of applying VCT to a real-scale test article, representative of a tank section of Ariane 6 lower liquid propulsion module, subjected to two combined bending-compression load cases are shown and discussed.

2. VIBRATION-CORRELATION TECHNIQUE

To the authors' best knowledge, the relationship between structural vibration and buckling load was first observed by Sommerfeld in 1910 [4], who showed that the vibration frequency of a clamped column decreases with increasing compressive load and tends to zero as the buckling load is approached. By the 1950s, this relationship had been analytically validated for beams, plates, and cylinders in the following form [5]:

$$f^2 + p = 1 \tag{1}$$

where f is the ratio between the frequency under load F and the unloaded frequency F_0, and p is the ratio between the applied load P and the critical buckling load P_{cr}. This led to the first theoretical VCT procedure, in which vibration frequencies measured at different load levels are used to establish a linear relationship between f^2 and p, allowing the buckling load to be estimated by extrapolation to the zero-frequency condition. In practice, however, the buckling load was usually directly extrapolated from an F^2 vs P chart, given that the frequency approached 0 Hz at buckling.

Experimentally, VCT requires a means of exciting the structure, typically a mechanical shaker, modal hammer or loudspeaker, and a means of measuring its response, usually accelerometers or laser vibrometers. Measurements are performed at constant load, and vibration modes must be tracked between successive load levels to ensure consistent frequency evolution. The Modal Assurance Criterion (MAC) is commonly used to correlate vibration modes between measurements.

An important mention here is that Eq. 1 is analytically valid only under several assumptions, namely simply supported boundary conditions, pure axial compression, coincident vibration and buckling modes, and geometrically perfect structures. Nevertheless, for imperfection-insensitive structures, like beams, the deviation from linearity is insignificant and the robustness of the method is thus conserved.

On the other hand, for imperfection-sensitive structures, the relationship between f^2 and p becomes increasingly nonlinear as the load increases and f^2 no longer reaches zero at buckling. Therefore, throughout the years, several VCT approaches have been proposed to account for this nonlinear behaviour [3,6,7]. Among them, the formulation introduced by Arbelo in 2014 [3] has become the most widely adopted one. In this approach, an imperfection reduction factor ξ^2 is determined as the minimum of the quadratic curve fitted to the $(1-p)^2$ versus $1-f^2$ characteristic chart. Then, the buckling load is estimated as:

$$P_{VCT} = P_{CR}(1 - \xi) \tag{3}$$

where ξ^2 needs to be larger than 0 for a valid prediction. Unlike the initial linear formulation, this approach assumes that the vibration frequency reaches a minimum, rather than zero, at buckling, thus complying with experimental observations and making it suitable for imperfection-sensitive structures. A schematic of the procedure is shown in Fig. 1.

Then, in 2019, Franzoni showed that rewriting Eq. 1 as a function of the load and frequency parameters proposed by Arbelo leads to the following relation [7]:

$$(1-p)^2 = [1-(1-f^2)]^2 \qquad (2)$$

showing thus analytically the quadratic dependence between $(1\text{-}p)^2$ and $1\text{-}f^2$.

Another difference of this approach with respect to the previous linear one is that an a priori estimate of the critical buckling load P_{cr} is required, and hence this approach is no longer purely experimental. This value may be obtained analytically, semi-analytically, or numerically, with the highest accuracy generally achieved using an idealised perfect structure [8].

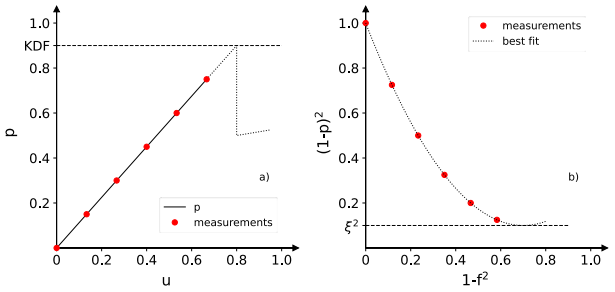


Figure 1: Generic load-shortening curve for cylinders under axial compression and load levels at which vibration measurements are taken a); Generic determination of the minimum value ξ^2 of the quadratic curve fitted between the points of the $(1-p)^2$ vs $(1-f^2)$ VCT characteristic chart b)

In practice, Arbelo's method displayed a low sensitivity to numerous aspects related to the article tested and the experimental environment, as reliable buckling load predictions were obtained in more than 48 experimental tests, using 28 different small-scale cylinders [9]. Within these experimental tests, the method proved equally reliable for isotropic or anisotropic materials, like steel or aluminium, and glass or carbon fibre reinforced plastics, respectively. Likewise, the VCT predictions were equally reliable for monocoque or reinforced cylinders. Furthermore, given the relatively large number of cylinders and testing environments, the low sensitivity of the method towards geometric, boundary and loading imperfections was also implicitly shown.

The aforementioned aspects are also in agreement with the observation drawn from multiple numerical investigations, where the influence of boundary conditions [10], loading [11] and geometric imperfections [12, 13] is easier to isolate and assess.

Besides cylindrical shells, the applicability of VCT to other types of structures was also investigated numerically. In [14], the authors evaluated the applicability of VCT to double-curved shells and showed that its robustness is comparable to that achieved for cylindrical shells. Similarly, in [15], the applicability of VCT to truncated cones was numerically assessed. The authors found that, while the method appeared more sensitive to geometric imperfections and to the maximum load ratio taken into account, VCT was nevertheless able to provide reliable buckling load estimations.

Given that, in practice, the load cases under which cylindrical shells within the industry are tested often contain additional loads besides compression, the feasibility of the method for combined load cases was also investigated. The compression-internal pressure was the first of these to be investigated in [15], numerically and experimentally, for a stiffened steel cylinder with pressure levels up to 0.03 bar. The authors reported that VCT provided accurate buckling load estimations for all the pressure levels tested, in both their numerical and experimental investigations.

Other combined load cases, in which additional bending, shear and torsion loads were applied besides compression, were also numerically assessed in [8]. In this investigation, the authors introduced the aforementioned additional loads either individually or all together, and compression was applied either sequentially or simultaneously with these additional loads. The outcome of this numerical investigation was that VCT provided reliable estimations of the compressive load at which the cylinders buckled, provided that the magnitude of the additional load was low enough, this magnitude being load-case dependent. Furthermore, for a simultaneous load introduction, a higher sensitivity of the predictions with respect to the maximum load level taken into account was observed and the magnitude of the additional loads applied beyond which VCT ceased to provide reliable estimations was also lower than when compression was introduced sequentially. Lastly, whether the additional load should be taken into account when determining the reference P_{cr} needed for the buckling load estimation also varied between the load cases. In this regard, for bending-compression, the P_{cr} in which the bending load was taken into account provided the best results, while for shear-compression the value obtained for the pure compression load case provided the best predictions. On the other hand, for the torsion-compression load case, as well as for the case in which bending, shear and torsion were applied alongside compression, the type of P_{cr} providing the best estimation depended on the cylinder, as well as on whether compression was applied sequentially or simultaneously alongside the additional loads.

3. TEST ARTICLE AND SETUP

The test article was a cylindrical barrel section representative of the Ariane 6 lower liquid hydrogen propulsion module, with a diameter of ~5.4 m, a height of ~3.1 m, and a wall thickness of 2.55 mm. A schematic of the barrel in the context of Ariane 6's lower liquid propulsion module is shown in Fig. 2.

The barrel structure was manufactured by MT Aerospace AG and comprised shaping 4 aluminium panels through a shot peening process up to the desired curvature and then welding them together using the TIG procedure. The material properties of the aluminium used are listed in Table 1.

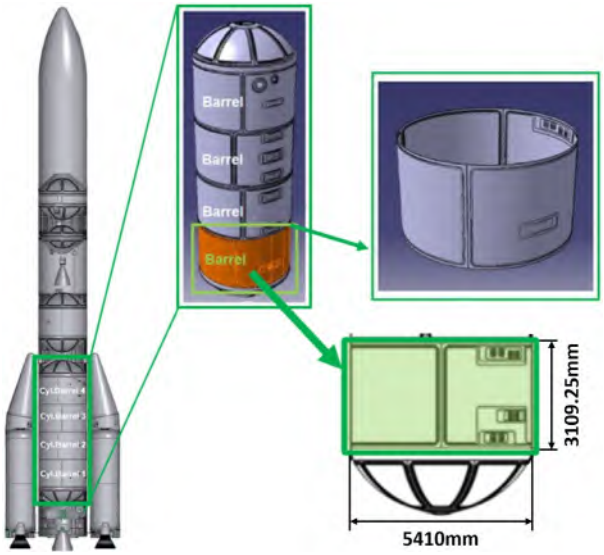


Figure 2: Barrel tank section in the context of Ariane 6's lower liquid propulsion module

Table 1: Aluminium alloy material properties

E [GPa]	ν_{12}	ρ [g/cm^3]
70	0.33	2.823

The barrel test was commissioned to IMA Dresden, who provided all the prerequisites for the buckling test under the supervision of MT Aerospace AG. The load was introduced by 4 hydraulic actuators distributed equally across the barrel's circumference and connected to the upper and lower loading surfaces of the test rig. The boundary conditions provided were simply supported via contact, with additional inner radial support. A schematic of the panel designation, actuator position, barrel in the test rig and boundary conditions is shown in Fig. 3.

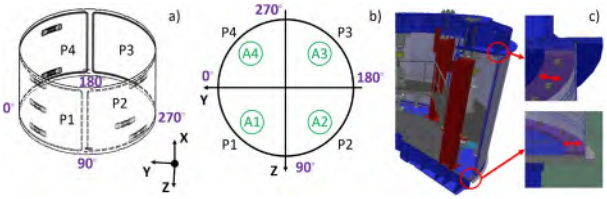


Figure 3: Panel labels a); Actuator layout b); Test rig and boundary conditions schematic c)

Two load cases were tested, defined to promote buckling initiation on specific areas of interest. The first load case was defined such that buckling would initiate on the bay of panel P2, this aspect being promoted by the higher load applied by actuator 2 with respect to the adjacent ones. Conversely, the second load case was defined to favour buckling initiation near the weld seam between panels P2 and P3, by having the same load magnitude applied by actuators 2 and 3. The load ratios applied during the two load cases tested are shown in Tab. 2. In the load application procedure, actuator 2 was considered the main one and applied a displacement-based load. Then, the loads of the secondary ones were defined based on the reaction force measured at actuator 2, such that the load ratios shown in Tab. 2 were applied. Furthermore, the influence of loading imperfections was mitigated by filling the gaps between the barrel edges and the load introduction surfaces with aluminium shims.

Table 2: Actuator load ratios for the tested load cases

Actuator	1	**2 (primary)**	3	4
Load case 1	0.898	1	0.898	0
Load case 2	0	1	1	0

The VCT measurement setup was composed of a loudspeaker placed at a 1-2 cm distance from the barrel to excite the structure and a Polytec PSV400 2D laser vibrometer to measure its vibration response. The former can be seen in Fig. 4, showing the top view of the barrel and test rig.
The load levels at which the vibration measurements were taken were based on the numerical estimates provided by MT Aerospace, given the higher level of detail of their numerical models, which included the measured shape imperfection as well. Given the limitations regarding the testing time, the vibration response was measured at 9 load levels for the first load case. The number of measurements was chosen based on the investigation shown in [10], where 9 measurements were found to be a minimum sufficient to significantly alleviate the influence of measurement deviations. Then, since the testing time for the first load case was longer than expected, the number of measurements was further reduced to 8 for the second load case. Additionally, the number of points in the grid measured was also reduced from 10x8 in the first load case to 7x9 for the second load case.

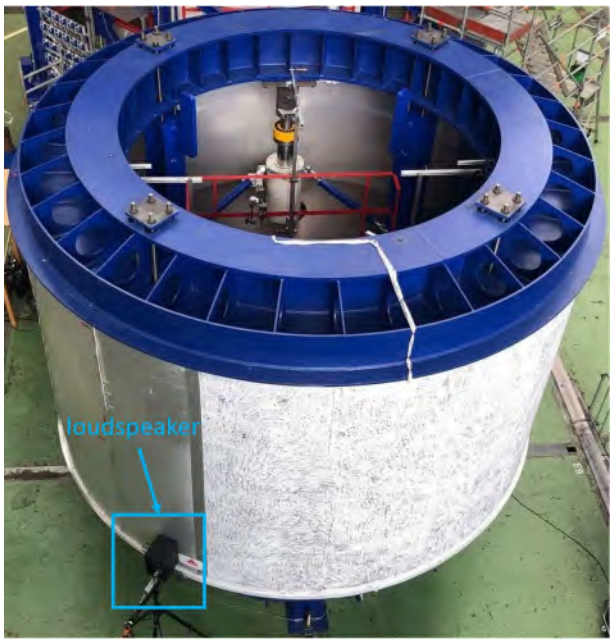


Figure 4: Top view of the barrel and test rig

Furthermore, given the novelty of applying VCT to a real-scale structure and even more notably, the

importance of the qualification test, precautionary measures were taken to minimise the risk of buckling occurring during the vibration measurements performed under constant load. These implied applying pre-loads before the last 3 vibration measurements at a magnitude significantly exceeding the load level of the subsequent vibration measurements. A more comprehensive description of the test article and experimental setup can be found in [16].

4. FINITE ELEMENT MODEL AND ANALYSIS

The finite element model used in this investigation was built in Abaqus, based on the original one in Nastran provided by MT Aerospace AG. In the original Nastran model, the barrel was meshed with 4-node CQUAD4 quadrilateral and 3-node CTRIA3 triangular shell elements, the Abaqus equivalent being the S4R and S3 shell elements, respectively. To introduce the loads and constrain the model, reference points were defined at the ends of the actuators and at the bottom of the test rig. The reference point at the bottom of the test rig was kinematically coupled with the nodes at the interface between the bottom loading plate and the test rig supporting legs and a clamped boundary condition was specified at this node. Similarly, the reference points at the ends of the actuators were coupled with the nodes at the interfaces between the actuator ends and the top and bottom loading plates. Then, the connection between the barrel and the loading surfaces of the top and bottom of the test rig was established via a tie constraint, given that under load the barrel edges would closely follow the displacements of the loading surfaces of the test rig. Lastly, the load was introduced by prescribing forces at top reference points, while the in-plane translations were constrained. The reference points used and regions with which they were coupled are shown in Fig. 5 a) and b), while the FE model in which the tie constraint is highlighted in red is shown in Fig. 5 c).

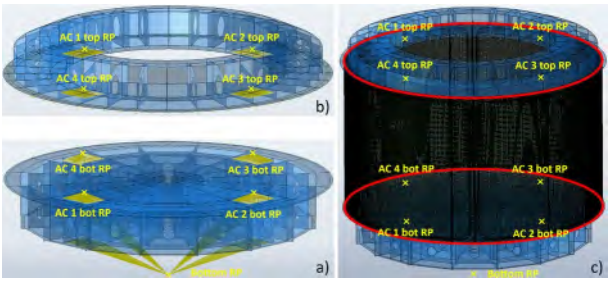


Figure 5: Couplings at the bottom of the test rig a); couplings at the top of the test rig b); FE model with tie constraint between the barrel edges and the load introduction surfaces of the test rig highlighted c)

5. NUMERICAL ANALYSIS

Considering that VCT estimates the knock-down factor as 1- ξ, buckling analyses were run using the Lanczos solver to obtain the P_{cr} values for the two load cases tested. Given that the shape imperfection measurement was not available, a buckling analysis was also run for the pure compression load case to extract the eigenmodes used in the non-linear analyses to introduce shape imperfections. A total of three buckling modes were chosen to disturb the mesh on the panel P2, including the welding seam between P2 and P3 panels. The magnitude with which these were applied was such that the maximum deviation from the original shape was 50% with respect to the barrel's wall thickness of 2.55 mm. These buckling modes are shown in Fig. 6.

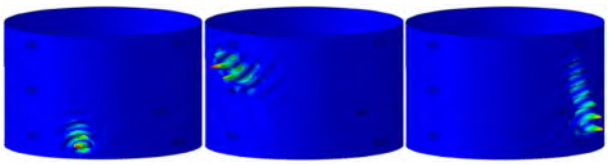


Figure 6: Buckling modes used in the non-linear analyses

The non-linear analyses were run using the Newton-Raphson solver, with the primary scope of performing numerical VCT. This involved running vibration analyses, using the Lanczos solver, at load levels in steps of 5% with respect to the non-linear buckling loads of the two load cases (20 load levels).

Besides providing an initial estimation of the expected robustness of VCT for the two load cases tested, these analyses also provided valuable initial estimates used to set up the measurement parameters. Namely, the starting point of the frequency measurement window was based on the vibration frequency of the first mode in an unloaded state, which had a value around 24Hz. Next, the initial measurement resolution was defined based on the lowest frequency change of the vibration modes between the first two load steps, this value being around 0.125Hz.

The relative errors of the numerical VCT predictions with respect to the non-linear buckling loads for the two load cases are shown in Fig. 7, as a function of the maximum load ratio used.

As shown in Fig. 7, for the first load case, the prediction accuracy was within 20% for the majority of the first 10 vibration modes for a load ratio of at least 75% and within 10% for a maximum load ratio of at least 85%. Conversely, for the second load case, the same was valid only for load ratios of at least 85% and 95%, respectively.

In addition, the sensitivity of the VCT prediction with respect to the maximum load ratio used was significantly larger for the second load case. For the first load case, once the evolution of the VCT predictions with respect to the maximum load ratio used became quasi-linear and ascending, the errors ranged from -30% to +8%. On the other hand, for the second load case, these ranged from -60% to -1%, showing thus a much greater sensitivity of the VCT predictions with respect to the maximum load level used. This was attributed to the higher bending component for the load case, this increase in the prediction sensitivity with increasing the bending

load being also found in [9].

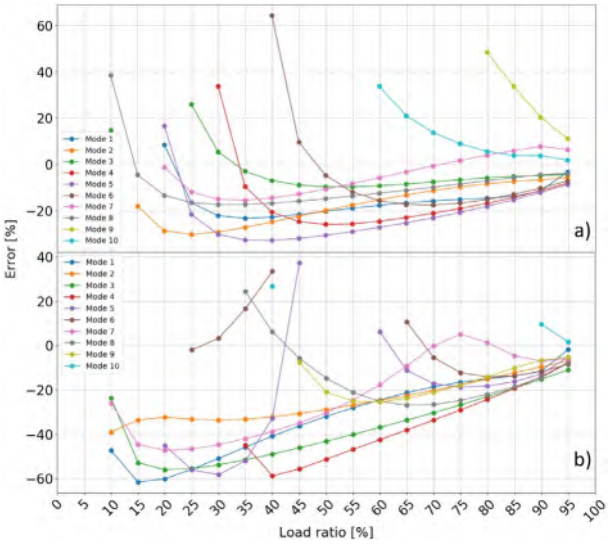


Figure 7: Numerical VCT predictions with respect to the non-linear buckling loads for load case 1 a); and load case 2 b)

6. EXPERIMENTAL RESULTS

6.1. Load case 1

Fig. 8 shows the load versus time curve for the first load case, in which the former is normalised with respect to the buckling load. As can be seen in this figure, the first measurement was taken at a relatively low load level, considered sufficient to provide consistent boundary conditions with the subsequent measurements. Furthermore, the pre-load approach for this load case was to increase the load to a level significantly above the levels of the last three vibration measurements. However, during this single, high pre-load, local bending occurred and remained present even when the load was decreased for the next vibration measurement.

This local bending also brought a change in the vibration response, meaning that most of the vibration modes identified up to the 6th load step could not be identified in the subsequent measurements. This change is best seen on the frequency response chart shown in Fig. 9, where it can also be noticed that the measurement at the lowest load level was omitted, as this load level proved to be insufficient to provide consistent boundary conditions with the subsequent ones.

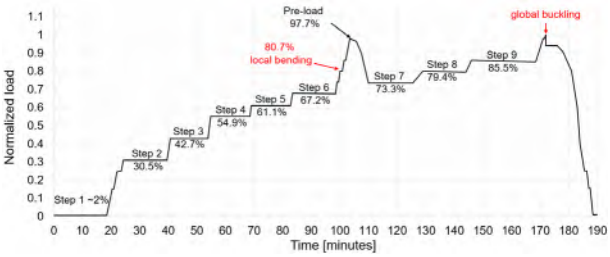


Figure 8: Load case 1 load-time history

When following the peaks within the 29-30Hz window, depicting the vibration mode frequencies, it can be seen that the vibration mode vanished completely beyond the 6th load step/vibration measurement. Conversely, when looking at the peaks within a 32.5-33.5Hz window, it can be seen that those corresponding to the last three measurements have the same frequency.

Another important aspect that can be seen in Fig. 9 is that peaks at 25Hz were recorded regardless of the load level tested. These were considered to be caused by interference from other functioning electronic equipment in the facility, especially since the frequency of 25Hz is half of that of the power supply and that at these frequencies no vibration modes were identified. A somewhat similar case can be seen around a frequency of 24Hz, for which no actual vibration modes were identified either. However, while these peaks might also be caused by some interference, this effect was not seen across all the measurements, as no such peak occurred during the third measurement.

Furthermore, it is also noticeable that some of the peaks were not that well defined. This implied that the 0.125Hz measurement resolution was not sufficient to accurately determine the vibration mode frequencies of all the modes identified.

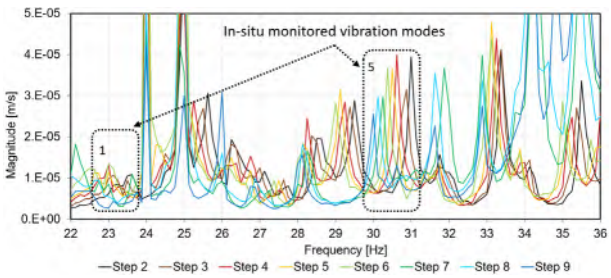


Figure 9: Vibration response chart for load case 1

Although the majority of the vibration modes could not be found after the frequency response change induced by the local bending occurring during the pre-load, there were still some vibration modes consistently found across the load levels measured and which showed the expected frequency decrease. Namely, the vibration modes labelled 1 and 5 showed in Fig. 10, with the latter also being considered the most reliable one during the test.

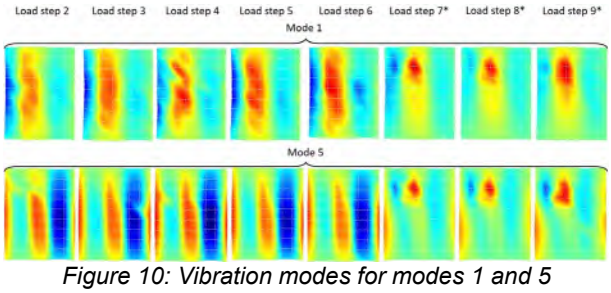


Figure 10: Vibration modes for modes 1 and 5

The relative errors of the VCT buckling prediction using the aforementioned vibration modes are shown in Fig. 11. Here, it is important to mention that the predictions were performed in-situ and provided before the buckling load was reached.

Nevertheless, to emphasise the accuracy of the method, the relative error of these predictions with respect to the experimental buckling load, instead of the actual buckling load prediction, is shown.
As considered during the test, indeed the best accuracy was obtained using mode 5, with a relative error around -6%. Moreover, the prediction using mode 1, although with a poorer accuracy around -20%, for a maximum load ratio of 85%, was still around the expected accuracy based on the preliminary numerical analysis.

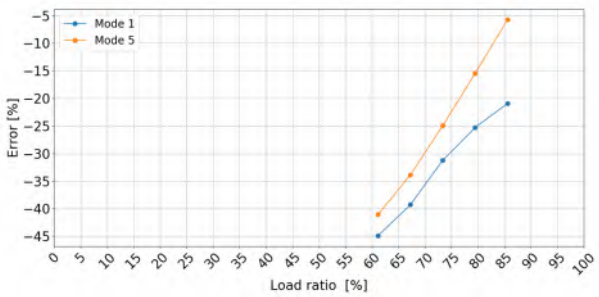


Figure 11: Relative error of the VCT predictions for vibration modes for Mode 1 and 5

On the other hand, the sensitivity of the experimental VCT prediction to the maximum load level used was significantly more pronounced than the one observed in the numerical results. This aspect can be clearly seen by comparing the relative errors from Fig.11 to those in Fig. 7a), where, for a load ratio around 60%, the experimental predictions were in a -45% to -41% window, while the numerical ones were in a -28% to -5% window.
Under the time constraints during the test to provide reliable in-situ predictions, focus was given to the first few occurring vibration modes, out of which modes 1 and 5 were identified as the most promising ones. However, the number of vibration modes within the 20-60Hz measurement window was significantly larger, and VCT predictions were performed using all the vibration modes identified in a post-test analysis. Nevertheless, the best predictions remained the ones performed in-situ.

6.2. Load case 2

Fig 12. shows the normalised load versus time curve for the second load case. Given the experience from the first test, several modifications were implemented for the second one. Firstly, the number of measurements during the test was reduced from 9 to 8, primarily due to time constraints. This implied dropping the measurement at a load ratio around 2%, particularly since for the first load case the vibration response at this load level was not consistent with those for the subsequent load levels. However, during the buckling test after the first vibration measurement was performed, it was found that some of the vibration modes identified in the pre-test calibration measurement remained. Therefore, the calibration measurement is also shown in Fig. 12, despite the fact that the test had only 8 planned vibration measurements for the purpose of VCT.
Secondly, measurement resolution was refined to 0.1 Hz, given that the 0.125Hz one used in the first test was not sufficient to accurately determine the frequencies for all the vibration modes identified.
Thirdly, the measurement window was increased from 20-60Hz for the first load case, to 20-100Hz for the second load case, to investigate the feasibility of the predictions using higher-order vibration modes.

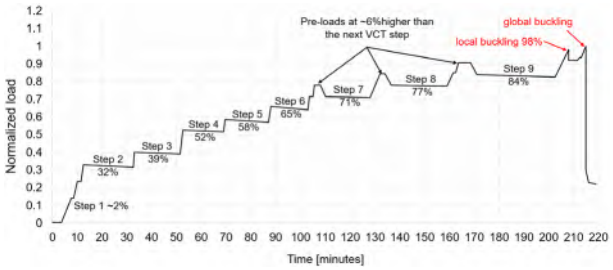


Figure 12: Load case 2 load-time history

Lastly, the risk of losing vibration modes due to local effects at high load levels was reduced by implementing a different pre-loading procedure. Instead of applying a single pre-load covering the load levels of the last three vibration measurements, a smaller pre-load was applied before each of the last three measurements.
During the test, similarly to the first load case, the vibration modes considered the most likely to provide the best predictions were identified. These can be seen in the vibration response chart shown in Fig. 13, while their shapes are shown in Fig. 14.
Also similarly to the first load case, a change in the vibration response occurred during the test of the second load case, here between the last two vibration measurements. This change can be easily observed when looking at the peaks in the 34-35Hz window from Fig. 13, where the peak in dark blue, corresponding to the last measurement, sits further than even the black one corresponding to the second measurement, thus describing a vibration mode frequency increase, instead of the expected decrease.

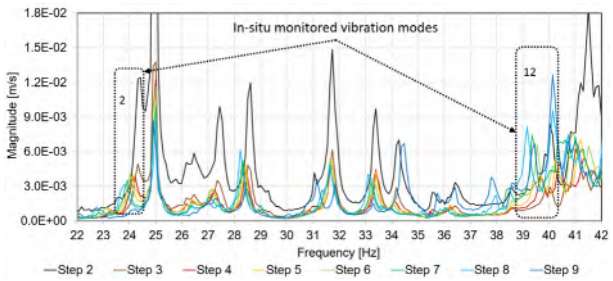


Figure 13: Vibration response chart for load case 2

Furthermore, while based solely on the frequency response chart it might seem that the change consisted primarily in a mere frequency shift of the vibration modes' frequencies, the visual inspection of the vibration modes revealed that the modes

found in the last measurement, although with frequencies close to the previously identified modes, had entirely different shapes. This implied that, unlike for the first load case, for the second load case none of the previously monitored vibration modes could be found after the change in the vibration response occurred. Hence, the maximum load ratio for the second load case that could be taken into account for VCT was 77%, as the measurement at 84% could not be used.

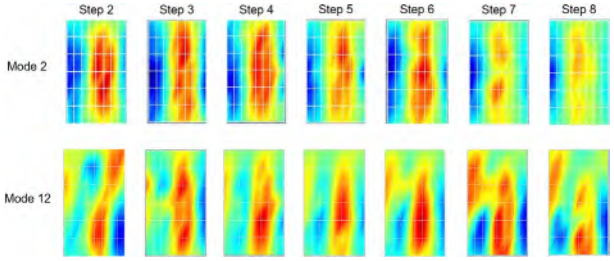


Figure 14: Vibration modes 2 and 12

Another aspect that can be noticed from Fig. 13 is that the definition of the peaks is still not ideal. Nevertheless, the improvement when compared to those in Fig. 9 for the first load case is clearly noticeable. Moreover, choosing an even finer resolution posed the risk of exceeding the time allocated for the test, especially since the testing time for the second load case already took longer than the first one, despite the fewer planned vibration measurements.

When comparing this figure with its counterpart Fig. 9 for the first load case, it can be seen that the constant signal at 25Hz was still present in each measurement. Similarly, there were no distinct vibration modes at this frequency, thus further supporting the assumption that it was caused by interference with the other functioning electronic equipment. In contrast, for the second load case, the peak at 24Hz seen for the first load case was no longer found.

Another similarity with the first load case is that, for the modes considered during the test to provide the best predictions, the measurement at a 2% load ratio could not be used.

The relative errors of the in-situ experimental buckling load predictions for the second load case are shown in Fig. 15. When comparing this figure with its corresponding Fig. 11 for the first load case, it can be noticed that the accuracy of VCT for this load case was poorer. For the second load case, the best prediction had a relative error around -15% and was obtained using mode 2, while the prediction based on mode 12 had an error around -24%. Although the accuracy of the VCT prediction for the second load case was lower than for the first one, for a maximum load ratio of 77%, these predictions were well within the estimated range based on the numerical analysis as well.

The lower VCT accuracy for the second load case was attributed firstly to the lower maximum load ratio that could be used for the VCT predictions (77% instead of 86%) and secondly, to the larger bending component compared to the one for the first load case.

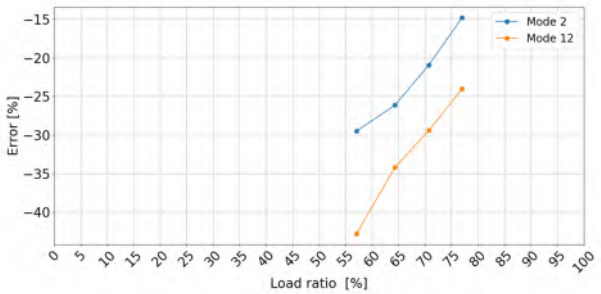


Figure 15: Relative error of the VCT predictions for vibration modes for Mode 2 and 12

A post-test investigation in which VCT predictions were performed for all the modes identified was also performed for the second load case. Although the number of vibration modes was significantly higher than for the first load case, due to the wider frequency range measured, there was only one potential mode providing a prediction better than the ones provided in situ, with a relative error of -1%. However, a vibration mode shape could not be found for all the peaks attributed to this mode in the visual inspection of the mode shapes. Therefore, the degree of confidence in the VCT prediction based on this potential mode is significantly lower than in the in-situ ones.

7. DISCUSSION

Given the novelty of applying VCT for both a real-scale structure and load cases presuming significant bending components, plus the designation of the test article itself, there are several aspects regarding the test and its limitations that need further discussion and contextualisation.

As already suggested throughout the paper, the learning curve was steep and there are multiple aspects that can be better optimised for future tests. As previously mentioned, the structure tested was a tank section representative of the Ariane 6 lower liquid hydrogen tank manufactured by MT Aerospace AG. For such a test article at the forefront of engineering innovation and efficiency, a full disclosure of its details to a third party is generally avoided. In this case, there was no information regarding the geometric imperfections.

For the sole purpose of assessing the feasibility of VCT for such load cases and scale, retaining this information for these particular tests had only a marginal impact, since the critical buckling loads provided were based on their high-fidelity models. However, having the shape and thickness imperfections implemented in the FE models used in the preliminary numerical VCT assessment could have improved the correlation between the numerical and experimental results in the context of VCT.

Arguably the most restraining factor during this

testing campaign was related to the limited testing time. For the first load case, the number of planned measurements was 9, which in an ideal scenario should be sufficient to significantly alleviate the influence of measurement deviations [9]. However, the load level of the first measurement was not sufficient to provide consistent boundary conditions. Therefore, the vibration response was different from that in the subsequent measurements, and this measurement could not be used for the purpose of VCT. Furthermore, the local bending that occurred during the pre-load and remained there for the last 3 measurements changed the vibration response. This implied that, for the majority of the vibration modes, there were only 5/9 measurements that could be used to perform VCT. At that point, had more time been available, the load could be dropped until the local bending disappeared, or the entire test could have been repeated without applying the pre-load, as it was already verified that the structure does not buckle globally at the load level of the last planned vibration measurement.

The measurement resolution chosen for the first test of 0.125Hz, although initially thought conservative, proved insufficient to accurately determine the frequencies of all vibration modes identified. For such small changes in the vibration mode frequencies as observed in this test, these inaccuracies may have had a significant influence even for the predictions based on the modes found across 8 load levels, let alone for those based on modes found only across 5. However, using a finer resolution would have increased the measurement time, given that the points in the grid measured would have likely needed an increased number of repeated measurements for an even finer measurement resolution.

The relatively long testing time for the first load case led to a further reduction in the number of vibration measurements performed during the test, from 9 for the first load case to 8 for the second one. As a compromise for this reduction and based on the experience gained during the first test, the measurement resolution was refined to 0.1Hz, the number of points in the grid measured was reduced, and the pre-loading procedure was changed. In hindsight, the latter modification proved to be an inspired one, given that a change in the frequency response was observed between the last two vibration measurements. Hence, using the same pre-load procedure as for the first load case would have probably rendered the two vibration measurements before this change occurred unusable for the purpose of VCT as well.

Given the change in the vibration response between the last two measurements for the second load case, the maximum load ratio that could be used was 77%, instead of 84%. Unlike for the first load case, the source and load level at which this change occurred could not be determined, especially without access to displacement and strain measurements, due to confidentiality reasons.

Nevertheless, a plausible estimate of the interval in which the best VCT prediction error could have been found can be made. Considering that generally the evolution of the predictions tends to become quasi-linear upon exceeding a certain load ratio threshold, the predictions based on modes 2 and 12 can be extrapolated to match the maximum load ratio measured of 84%. When doing so, an error around -9% is obtained for mode 2 and a -18% one for mode 12. Hence, had a vibration measurement been performed just before the change in the frequency response occurred, the relative error of VCT prediction for mode 2 would have likely been between -15% and -9% and for mode 12 between -24% and -18%.

8. CONCLUSIONS

In this paper, to the authors' best knowledge, the results of the first application of VCT for buckling load prediction for a real-scale structure, subjected to load cases with significant bending components, are shown.

The preliminary numerical analyses proved fairly reliable in preparing the measurement setup and parameters, even without the possibility to include the influence of measured imperfections in the FE model. For both load cases tested, the frequency at which the first vibration mode would appear was well predicted, given that in the vibration measurements the first vibration mode occurred in a 23-24 Hz frequency window, while in the numerical model it appeared at 24Hz. Furthermore, the accuracy of the method was within the expected range for the highest load levels available for both load cases as well. On the other hand, the sensitivity of the predictions with respect to the maximum load level used was only well predicted for the second load case, while for the first load case this sensitivity was significantly underestimated. Lastly, the numerical estimation of the vibration mode frequencies drop as the load increases was only fair, since the measurement resolution required to accurately determine the vibration frequencies of all the modes during the test was higher than the numerical estimate.

The best in-situ buckling load predictions for the first load case had an error around -6%, obtained for a maximum load ratio of 86%, while for the second load case the best in-situ prediction had an error around -15%, at a load ratio of 77%. However, the lower accuracy for the second load case is attributed primarily to the lower maximum load ratio available and secondly to the larger bending magnitude.

Overall, VCT was able to provide reliable in-situ buckling load predictions for the load cases tested. This achievement is particularly encouraging for the adoption of the method in further experimental campaigns, as its application not only proved successful for real-scale structures with complex loading and boundary conditions, but also under bending-compression load cases. Furthermore,

even without the possibility to include measured imperfections in the FE model used in the preliminary numerical analysis, a fairly good correlation between the numerical and experimental VCT results was achieved. Moreover, relevant aspects like the frequency at which the first vibration mode would occur and the required measurement resolution were also relatively well predicted. Lastly, vibration modes providing better predictions than the in-situ ones were not identified in the post-test investigation.

In light of the aforementioned considerations, VCT proved to be a reliable non-destructive method to predict the buckling load of cylindrical shells of sizes and testing scenarios relevant within the aerospace field.

9. ACKNOWLEDGEMENTS

The research leading to these results received funding from the European Community's Ninth Framework Programme under the ERDF priority (European Regional Development Fund), under grant agreement ZW6–87006427 (SIWIRA).

10. REFERENCES

1. Hilburger M.V. Buckling of Thin Walled Circular Cylinders, NASA/SP-8007-2020/REV 2, https://ntrs.nasa.gov/citations/20205011530

2. Castro S.G.P, Zimmermann R, Arbelo M.A, Khakimova R, Hilburger M.W, Degenhardt R. Geometric imperfections and lower-bound methods used to calculate knock-down factors for axially compressed composite cylindrical shells, *Thin-Walled Structures*, 74 (2014) 118-132, https://doi.org/10.1016/j.tws.2013.08.011

3. Arbelo M.A, de Almeida S.F.M, Donadon M, Rett S.R, Degenhardt R, Castro S.G.P, Kalnins K, Ozoliņš O. Vibration correlation technique for the estimation of real boundary conditions and buckling load of unstiffened plates and cylindrical shells, *Thin-Walled Structures*, 79 (2014) 119-128, https://doi.org/10.1016/j.tws.2014.02.006

4. Somerfeld A. Eine einfache Vorrichtung zur Veranschaulichung des Knick-ungsvorganges, *Z Ver Dtsch Ing*, 49 (1905) 1320–1323

5. Lurie H. Lateral vibrations as related to structural stability, *ASME Journal of Applied Mechanics*,19 (1952) 195–204, https://doi.org/10.1115/1.4010446

6. Souza M.A, Fok W.C, Walker A.C. Review of Experimental Techniques for Thin-walled Structures Liable to Buckling: Neutral and Unstable Buckling, *Experimental Techniques*, 7 Issue 9 (1983) 21-25, https://doi.org/10.1111/j.1747-1567.1983.tb01811.x

7. Franzoni F, Degenhardt R, Albus J, Arbelo M.A. Vibration correlation technique for predicting the buckling load of imperfection-sensitive isotropic cylindrical shells: An analytical and numerical verification, *Thin-Walled Structures*, 140 (2019) 236–247, https://doi.org/10.1016/j.tws.2019.03.041

8. Baciu T.D, Franzoni F, Degenhardt R, Gliszczynski A, Bisagni C. Vibration-correlation technique for predicting the compressive buckling load of cylindrical shells under combined loading. Thin-Walled Structures, Volume 216 Part B, 113576 (2025), 10.1016/j.tws.2025.113576

9. Baciu T.D, Degenhardt R, Franzoni F, Gliszczynski A, Arbelo M.A, Castro S.G.P, Kalnins K, Sensitivity analysis for buckling characterisation using the vibration correlation technique, *Thin-Walled Structures,* 183 110329 (2023), http://dx.doi.org/10.1016/j.tws.2022.110329

10. Gliszczynski A, Effect of boundary conditions and analytical bifurcation load on VCT-based buckling load predictions for CFRP cylindrical shells, *Composites Part B*, 312 113317 (2026), https://doi.org/10.1016/j.compositesb.2025.113317

11. Baciu T.D, Franzoni F, Degenhardt R, Gliszczynski A, Bisagni C, Shape and loading imperfection sensitivity of the vibration-correlation technique for buckling analysis of cylindrical shells, *Engineering Structures*., 304 117605 (2024), https://doi.org/10.1016/j.engstruct.2024.117605

12. Gliszczynski A, Franzoni F, Degenhardt R, Baciu T.D, Evaluation of the stability and load-carrying capacity of double-curved unstiffened shells under compression through analysis of different initial imperfection sources, *Aerospace Science and Technology*, 168 Part B 110907 (2026), https://doi.org/10.1016/j.ast.2025.110907

13. Gliszczynski A, Franzoni F, Degenhardt R, Baciu T.D, VCT-based buckling load prediction in unstiffened CFRP cylinders: Assessment of predictive robustness under varied imperfection maps and modifications to the Arbelo characteristic chart, Composites Part B: Engineering, 331 113201 (2026), https://doi.org/10.1016/j.compositesb.2025.113201

14. Gliszczynski A, Franzoni F, Baciu T.D, Degenhardt R, Predictive capabilities of Vibration-Correlation Technique applied to axially compressed CFRP truncated cones, *Composites Part B: Engineering*, 240 109984 (2022), https://doi.org/10.1016/j.compositesb.2022.109984

15. Franzoni F, Odermann F, Wilckens D, Skuķis E, Kalniņš K, Arbelo M.A, Degenhardt R, Assessing the axial buckling load of a pressurized orthotropic cylindrical shell through vibration correlation technique, *Thin-Walled Structures*, 137 (2019), 10.1016/j.tws.2019.01.009

16. Franzoni F, Baciu T.D, Degenhardt R, Gliszczyński A, Stromer K, Hornschuh J, Kalnins K, Skukis E, Albus J, Reliable buckling load prediction for Ariane 6 test article: Experimental validation of the vibration correlation technique, *Aerospace Science and Technology*, 178 113063 (2026), https://doi.org/10.1016/j.ast.2026.113063

ECSSMET
Braunschweig Germany 2026

Composite Design

DEVELOPMENT, CHARACTERIZATION AND FULL-SCALE VALIDATION OF INTEGRATED CFRP RING JOINTS FOR LAUNCHER PAYLOAD ADAPTERS

Araceli Cuesta López [(1)], Joaquín Martin Llorente [(2)]

[(1)] Airbus Defence & Space, C/Aviocar 2, Getafe Madrid (Spain), Email: Araceli.cuesta@airbus.com
[(2)] Airbus Defence & Space, C/Aviocar 2, Getafe Madrid (Spain), Email: Joaquin.martin@airbus.com

KEYWORDS

Composites, CFRP (Composite Fiber Reinforced Polymer), Launchers, Payload Adapter

ABSTRACT

This paper presents the development, characterization, and full-scale testing of a novel concept of primary structural joints on payload adaptors for launch vehicles. The proposed design replaces the conventional metallic ring-based riveted interfaces between composite shells with an integrated CFRP ring, providing enough local thickness to accommodate bolted joint connections and thereby reducing the number of discrete joints in the load path.

The interest in this type of joint is mainly due to its potential for mass reduction and simplified assembly, as it eliminates an integration step and the associated metallic ring. This approach enables a more efficient load transfer while maintaining, or potentially improving, the overall structural stiffness.

However, the sizing of such CFRP integrated ring cannot be based solely on analytical methods, as the governing failure modes are not straightforward. Consequently, a greater initial effort is required to ensure that the laminate definition, manufacturing process, and final geometry are compatible with the expected load levels. A dedicated test campaign with representative specimens is therefore necessary to validate the design and achieve proper characterization of the joint behaviour.

The concept is presented, highlighting the distinctive features and differences between several flight structures that use CFRP rings, including materials and manufacturing processes. Then, the characterization process is described, considering the set-up definition. The characterization process is based on applying the main critical external loads of the joints generating two different load cases, traction and moments loads. Once the load levels that the CFRP ring can withstand are known, capacity curves are derived and used as the basis for the evaluation of the joint margins under flight load conditions.

Once the previously defined approach is established, a challenging application case is presented in which two different CFRP integrated rings were implemented as internal interfaces for the same payload adapter, considering that the load levels in internal interfaces are higher than those typically found in launcher interfaces, where this kind of concepts were previously used. In this configuration, the joint design posed challenges for pure traction characterization, as the offset with respect to the structural axis introduced a local bending moment. A comprehensive instrumentation strategy was therefore required to enable validation of the structural behaviour and capacity by using a strain-based approach.

The development test campaign of representative specimens is presented, including the attempts to achieve correlation, as well as the use of the acquired data to support the real-time monitoring and assessment of the full-scale qualification test, ultimately resulting in a successful qualification campaign of a flight model.

1. INTRODUCTION

Structural joints in primary structures of launch vehicles play a critical role in load transfer between the payload and the launch interface, as well as in the overall stiffness and mass efficiency. In certain missions, particularly those involving multiple payload configurations, the mass of payload adapters becomes a critical parameter, as it directly impacts the payload capacity of the launcher. As a result, adapter mass is often strongly constrained, and solutions that enable mass optimization while maintaining structural performance are of significant interest from a programmatic and commercial perspective. Conventional solutions typically rely on metallic rings mechanically fastened to composite shells, introducing additional interfaces and integration steps.

Airbus Defence and Space in Madrid (ADSM) has been developing CFRP integrated ring concepts since 2003 using different technologies and design approaches. These developments have resulted in a broad portfolio of flight-qualified structures incorporating various integrated ring configurations, which have been successfully implemented in multiple missions.

Fig. 1 shows the SSO-A mission stack that successfully launched 64 customer spacecraft into orbit onboard a Falcon 9 launch vehicle on 3 December 2018. In that flight, the ADSM CFRP HUB payload adapter was part of the stack, Fig. 2, whose both upper and lower interface are manufactured with the CFRP interface ring solution.

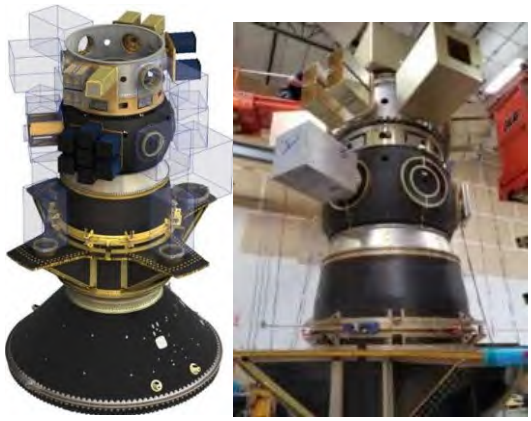


Figure 1: SSO-A mission. Multiple payload adapter stack [1].

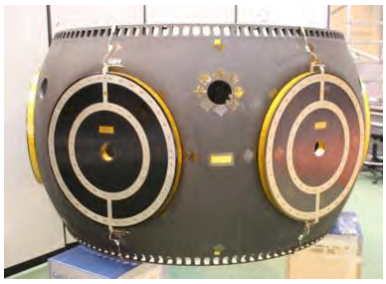


Figure 2: HUB – ADSM multiple payload adaptor.

This work builds upon the previously developed CFRP integrated ring concepts and their characterization methodologies. In Section 2, an overview of different CFRP integrated ring solutions, including the geometrical concepts, materials, and validated manufacturing processes is discussed. Additionally, the characterization methodology is presented to have a better understanding of how these joints behave and what their main failure modes are.

Then, Section 3 is focused on the solution implemented in a multiple-payload adapter (called MAS-H) with internal highly loaded CFRP interfaces. In this case, the presence of an offset between the bolt interface and the structural neutral axis introduces additional complexity, requiring an adaptation of the standard characterization approach for this particular application.

The evolution of the characterization methodology is described, including the use of strain-based measurements and enhanced instrumentation strategies to obtain representative structural data. This approach supports the correlation between specimen-level testing and full-scale behaviour, finally reported in Section 4, enabling the qualification of the flight structure under representative loading conditions.

Lastly, Section 5 outlines the conclusions of the new methodology and addresses the unresolved open points to guide future work.

2. STATE OF THE ART AND DESIGN CONCEPT

Traditional joint configurations are based on metallic rings riveted to CFRP shells, providing a mechanical interface for bolted connections to adjacent structures. This approach results in multiple discrete joints within the load path. Fig. 3 shows an example of a payload adaptor with metallic SC IF (Spacecraft Interface) and LV IF (Launch Vehicle Interface) riveted to the CFRP shell.

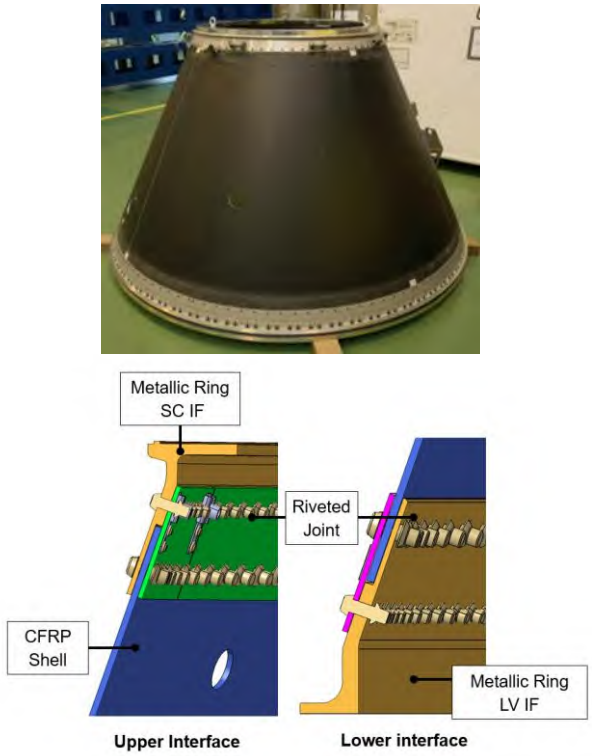


Figure 3: Payload Adaptor with traditional riveted joints between CFRP shells and metallic rings.

Integrated composite rings were first introduced in the 1194H payload adapter for Ariane 5 to reduce the mass and cost associated with metallic interface rings, Fig. 4. The concept aimed to compensate for the manufacturing and integration complexity of metallic rings (forged block production, machining, drilling, and fastening) by integrating the interface functionality directly into the composite structure.

In this approach, the composite shell is locally thickened at its edges and subsequently machined

to meet interface requirements, including flange definition and hole drilling, Fig. 4. This results in a more integrated structural solution with a reduced number of parts and interfaces

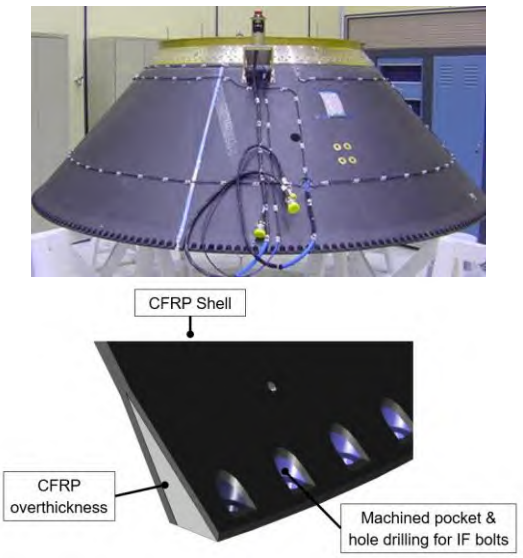


Figure 4: 1194H payload adapter for Ariane 5. Lower interface with CFRP integrated rings.

The replacement of forged aluminium rings with integrated CFRP rings provides several advantages:

- Mass reduction (up to approximately 9% at system level and up to 20% at joint level).
- Assembly time reduction (typically between 30% and 40%).
- Elimination of dedicated assembly tooling.
- Reduction in the number of parts within the manufacturing flow.

Two different concepts are proposed for the integrated rings: Recessed Ring and Castellated Ring.



Figure 5: 3936 ESC cone of Ariane 5 [2].

The **Recessed Ring** configuration was first implemented in the lower interface of the 1194H payload adapter for Ariane 5, Fig. 4. Since then, it has been applied in multiple flight structures, including payload adapter systems (PAS), as in the 3936 ESC cone of Ariane 5 ECA, Fig. 5. The structural capability of this configuration has been established through component-level testing, where combined loading conditions involving bending moments and longitudinal forces were applied to derive interaction relationships used for margin assessment. More details about the strength characterization will be discussed in Section 3.1.

In contrast, the **Castellated Ring** concept was initially investigated at component level and then implemented with the HUB in a flight hardware, Fig. 2. This configuration was assessed for both launch vehicle inter-stage structures and spacecraft structures, covering different thickness ranges and material. For launcher applications, the ring was integrated into a monolithic shell of approximately 8 mm thickness using high-strength carbon fiber, whereas for spacecraft structures, a thinner configuration of approximately 2 mm was evaluated using a high-modulus carbon fiber, Fig. 6

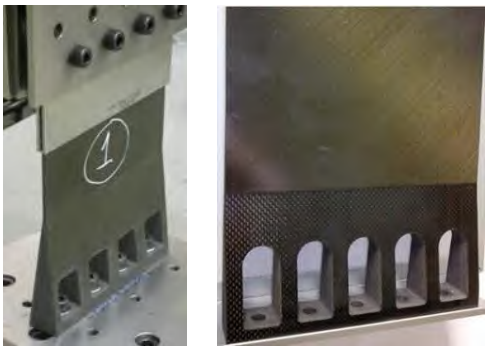


Figure 6: Castellated ring. Composite Design for Spacecraft Structures (left). Composite Design for Launch Vehicles (right).

To date, the Castellated Ring solution is widely used in multiple-launch dispensers with different carbon fiber materials (e.g., high-modulus and high-strength), whose geometry is close to a cylinder instead of a cone. Some examples are the HUB dispenser, Fig. 2, Skyfall multi-payload adaptor and Clessidra dispenser, Fig. 7.

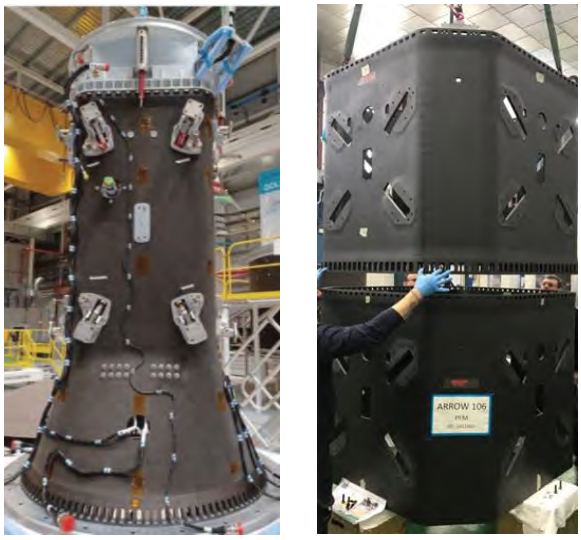


Figure 7: Multi-payload adaptor with Castellated ring. Clessidra Dispenser (left) and Skyfall Dispenser (right).

To address manufacturing cost and performance requirements, co-bonding technologies have been widely adopted. These allow integration of different composite subcomponents while improving structural continuity and reducing assembly complexity.

Two main manufacturing approaches have been developed for CFRP integrated rings:

Local Thickness Increase by Fiber Placement (FP)
The integrated ring is achieved through local thickening of the laminate using Automated Fiber Placement, Fig. 8. This approach allows direct integration of the joint region within the primary structure. Design validation is performed through dedicated testing.

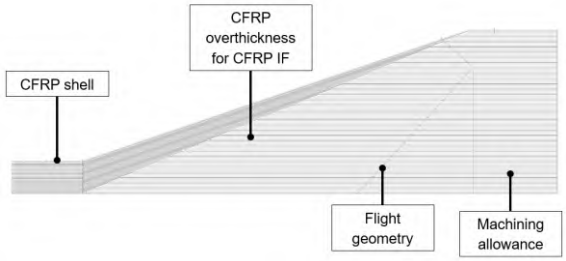


Figure 8: Local thickness increase by Fiber Placement

RTM-Manufactured Sectors with Co-Bonding
An alternative solution consists of manufacturing CFRP sectors (wedges) using Resin Transfer Molding (RTM), which are subsequently co-bonded to the main structure, Fig. 9. These wedges typically have lengths on the order of 800 mm and are manufactured using dry fiber and RTM-compatible resins. Co-bonding is performed using structural adhesives.

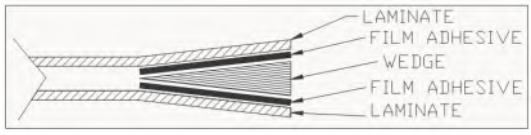


Figure 9: RTM-Manufactured Sectors with co-Bonding

Different laminate architectures (or lay-up and ply orientations) can be defined depending on the selected manufacturing approach, particularly for fiber placement-based solutions. Several lay-up examples of different implemented solutions are shown in Fig. 10. The definition of ply orientations, stacking sequences, and local reinforcements in the joint region is critical to ensure adequate load transfer and failure resistance.

Both approaches have been successfully validated through testing. For instance, the Cone 3936 adapter incorporating RTM wedges demonstrated equivalent structural performance to fiber placement-based integrated rings. Additionally, RTM-based solutions have shown robustness with respect to manufacturing tolerances, with no significant impact on structural performance due to positioning deviations during assembly.

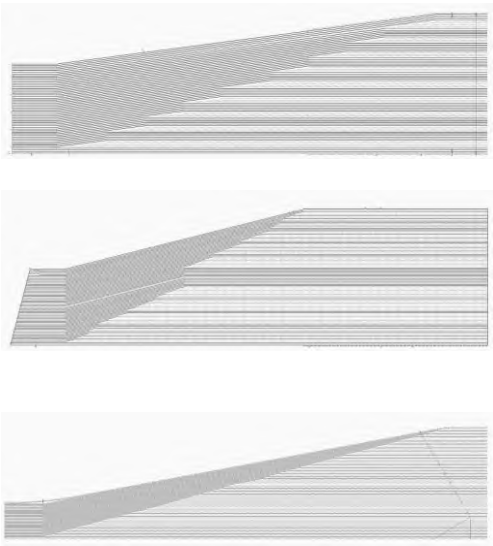


Figure 10: Laminate architectures by Fiber Placement

However, some manufacturing challenges remain. CFRP block-based solutions may require intermediate machining steps due to the lack of net-shape capability in prepreg processes. In contrast, RTM-based approaches rely strongly on dimensional accuracy to ensure proper co-bonding performance and overall structural integrity.

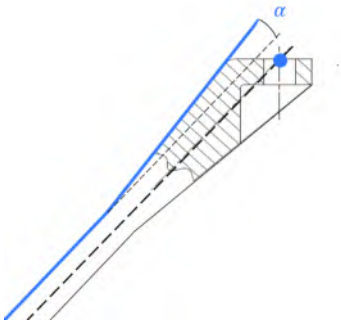


Figure 11: Local laminate geometry for bolted interfaces. Neutral line aligned with bolt IF

Additionally, from a manufacturing perspective, integrated CFRP ring solutions have historically been designed such that the neutral axis of the structure overlaps with the bolt interface. This requirement has led to the development of dedicated tooling with tailored geometries, including local thickness variations and angular features to accommodate fibre placement and ensure proper load alignment. In Fig. 11 the tooling surface is marked in blue, with a local change in the angle of

the cone. However, such tooling solutions are often associated with long lead times and require a high level of design maturity, which may not be compatible with project constraints.

2.1. Characterization Methodology

The sizing of CFRP integrated ring joints must consider the following design principle:

- No sliding at 1.1 x Limit Load
- No rupture at 1.25 x Limit Load (ultimate).

For in-plane loading, shear-out is typically the governing failure mode, defining the minimum edge distance and influencing the local joint geometry.

Given the complexity of the stress state and the limitations of purely analytical approaches, an empirical line load-based sizing methodology is adopted. This approach compares the acting loads—expressed as line force and line moment at a given circumferential position of the ring—with allowable values derived from experimental characterization. The relevant load components are the longitudinal line force and the circumferential moment, assumed to capture the dominant behaviour of the joint, see Fig. 12.

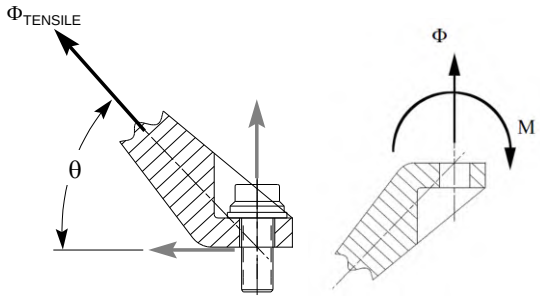


Figure 12: Local Loads for sizing CFRP integrated rings

A failure envelope is defined to represent the interaction between both load components. The allowable tensile line force decreases with increasing applied line moment, based on test results, and is represented by a bilinear relationship. In contrast, the allowable compressive line force is considered independent of the applied moment up to a limiting value, see Fig. 13.

The typical characterization is restricted to a representative quadrant of the load interaction domain, consistent with the expected loading conditions and sign convention adopted for the joint. This simplification assumes that the structural capability is governed by the interaction between axial force and circumferential moment, which is later supported through experimental validation. An example is shown in Fig. 14.

To characterize the joint behaviour and define the failure envelope, three types of tests are required: pure tension, pure moment, and combined loading.

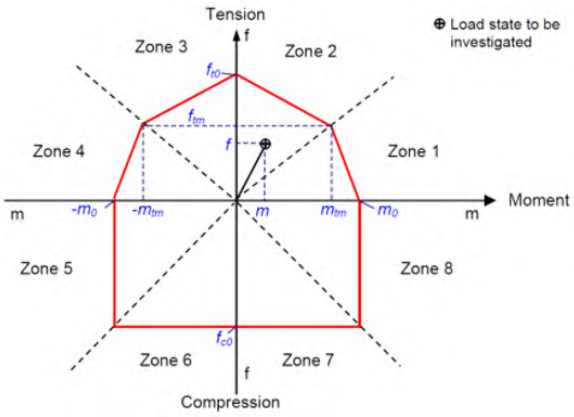


Figure 13: Failure envelope

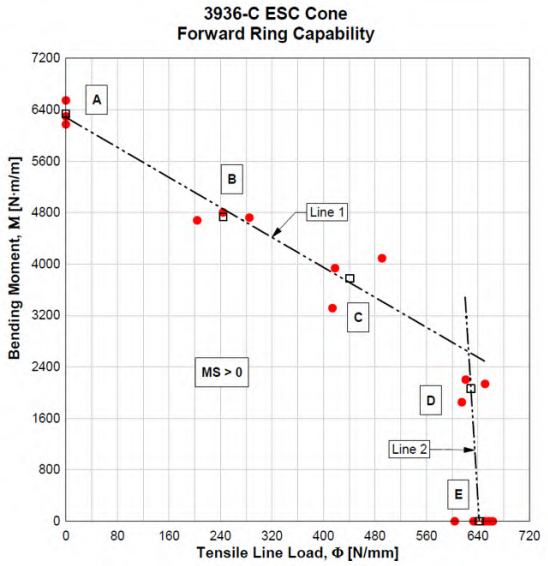


Figure 14: Failure envelope deduced from a specimen test campaign for 3936-C ESC Cone.

The characterization is performed using a dedicated set of specimens. Although the actual geometry of the ring is curved, specimens are typically manufactured as flat panels for practicality, provided that the same CFRP material and manufacturing process are used, Fig. 15. Comparative assessments between hand lay-up and automated fiber placement have shown no significant impact on the structural response for equivalent configurations. To ensure representativeness, all specimens must be extracted from the same panel and properly identified and inspected prior to testing.

The test configuration depends on the available facilities but generally aims to maximize setup commonality. Pure tension and pure moment tests are typically performed using the same fixture, with specimen orientation adjusted to apply the corresponding load condition, see Fig. 16.

Combined loading tests require a symmetric setup in which the bending moment is introduced through an offset or lateral load applied at the interface. These tests are inherently more complex and require iterative calibration and repeated executions to achieve the desired loading condition corresponding to specific points of the interaction curve.

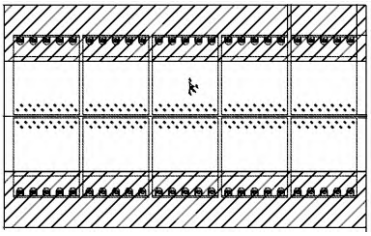


Figure 15: Typical drawing for manufacturing flat test pieces.

In standard practice, specimens are typically not instrumented, as the characterization is based on ultimate load capacity. The identification of failure is therefore derived from the load–displacement response recorded by the test machine, with limited insight into the local structural behaviour.

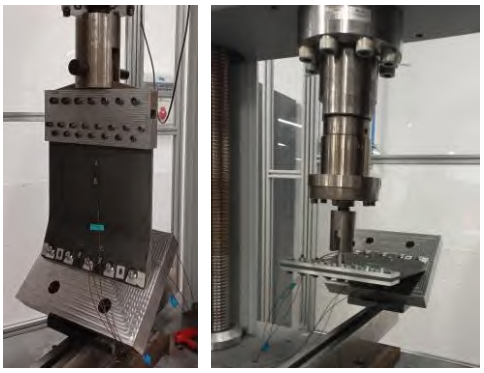


Figure 16: Test configuration for pure traction (left) and pure moment (right).

However, the present work highlights the potential advantages of incorporating strain gauge instrumentation, enabling a more detailed understanding of the load transfer mechanisms, local strain distributions, and progressive damage evolution within the joint.

A key limitation of the current methodology is the absence of reliable analytical or finite element models capable of accurately reproducing the observed failure modes. These joints exhibit highly non-linear behaviour driven by material characteristics and complex stress concentrations (pressure contact), particularly in regions with significant ply drop-offs over short distances. As a result, experimental characterization remains essential for defining allowable values and supporting design.

Experimental results enable the construction of representative failure envelopes, which form the basis for the empirical sizing methodology and subsequent structural assessment.

3. APPLICATION CASE: INTERNAL INTERFACES OF A PAYLOAD ADAPTER

The integrated CFRP ring concepts presented to date have been primarily applied to external interfaces of payload adapters. In such configurations, the load path is typically driven by the transfer of loads from an upper interface (payload) to a lower interface (launcher interface), resulting in conical or cylindrical structures that ensure an efficient distribution of axial and bending loads.

The case study addressed in this work departs from this conventional approach. It corresponds to a payload dispenser designed to accommodate two large spacecraft in side-by-side arrangement.

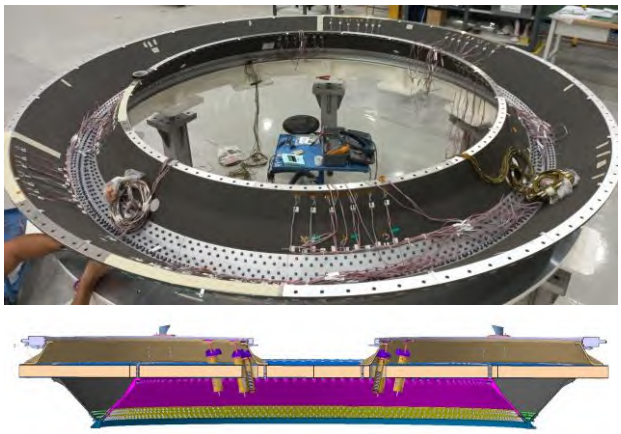


Figure 17: MASH dispenser. Inner and outer cone arrangement.

The configuration consists of two conical structures: an Outer inverted Cone, where the larger interface is located at the top, and an Inner Cone with a standard orientation, where the larger interface is located at the bottom, see Fig. 17. Both structures are connected through a common sandwich platform, which provides the support plane for both spacecraft, see Fig. 18. In this structure, the CFRP rings are in contact with the platform, namely the interfaces of the Inner and Outer cones with the platform.

This architecture introduces a significant deviation from traditional load paths, as the interfaces of interest are internal to the structure and are subjected to higher load levels than those typically encountered in external launcher interfaces. Additionally, the load introduction is more complex due to the geometric configuration and the interaction between both cones.

As mentioned in Section 2, structures with integrated rings have been designed such that the

neutral axis of the structure overlaps with the bolt interface. This requires developing a dedicated tooling associated with long lead times.



Figure 18: MASH dispenser with 2 Spacecraft in side-by-side arrangement.

In this case, an alternative approach was explored to increase design flexibility and reduce development time. The concept is based on the use of smooth tooling geometries, allowing the structure to be manufactured without complex local features. As a result, the integrated ring interface is no longer aligned with the structural neutral axis, introducing an offset that generates local bending loads at the joint level, see Fig. 19.

This design choice enables the reuse of existing tooling by adapting the structural geometry to mission-specific requirements, for instance by trimming the cone height to match the target interface diameters.

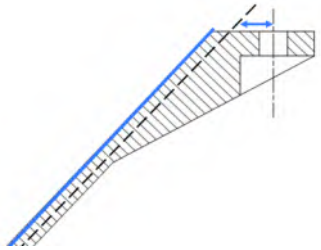


Figure 19: Local laminate geometry for bolted interfaces. Offset between neutral line and bolt IF.

While this approach provides clear advantages in terms of manufacturability and lead time, it also introduces additional challenges in terms of structural characterization and validation, particularly due to the combined loading state induced at the joint.

3.1. Strain – Based Characterization

To characterize the joint behaviour, a test campaign based on the traditional approach was defined, including the following load cases: Tension (T1) and Positive Moment (M1). The objective was to identify the governing failure modes and assess the interaction between axial force and bending moment, see Fig. 20. Additionally, a Negative Moment (M2) and Compression case (C1) were performed to verify that they are not the ones that size these joints. A total of 12 pieces were tested, 5 for T1 test, 5 for M1 test, and only 1 for C1 and M2.

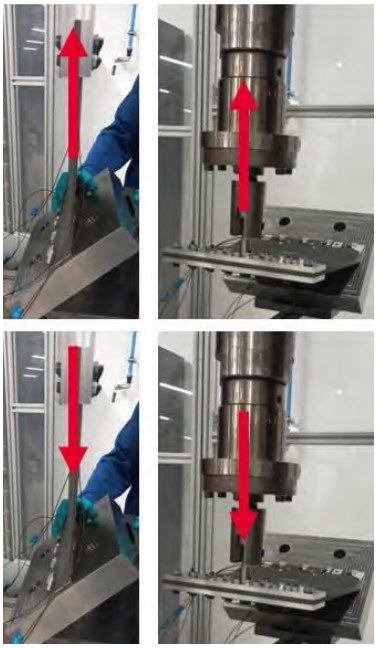


Figure 20: Load Cases for joint characterization. Top Left: Tension (T1); Top Right: Positive Moment (M1); Bottom Left: Compression (C1); Bottom Right: Negative Moment (M2)



Figure 21: Failure mode of the joint. Top Left: Tension (T1); Top Right: Positive Moment (M1); Bottom: Negative Moment (M2).

The experimental results showed that, due to the presence of the offset, the failure mode observed under pure tension (T1) was equivalent to that obtained under one of the bending configurations

(M1), as it can be seen in Fig. 21. This confirms that the induced moment associated with the offset dominates the local stress state, even under nominally axial loading. The failure mode seems to be associated with the local compression that appears close to the bolt interface, for both T1 and M1 loading.

In contrast, the failure mode associated with the opposite bending configuration (M2) occurred in a different region of the specimen and was identified as non-critical for the actual flight configuration), see Fig. 21.

A complementary compression test was also performed to verify the relevance of this load case. The results confirmed that compression is not a driving failure mode for these CFRP joints, with a demonstrated capacity exceeding the required flight levels by a factor of approximately three (the limit of the test facility was achieved before the failure of the joint. As a consequence, the failure mode could not be observed).

A simplified linear finite element model was used to extract the axial force and bending moment at the joint to support the interpretation of the test results. When represented in the classical force–moment interaction diagram, the available test data primarily covered the moment-driven region of the envelope, Fig. 22. While this was enough to cover the load conditions of the Outer Cone, it was identified that, for the Inner Cone—characterized by lower bending and higher axial load—a significant portion of the interaction domain remained uncharacterized.

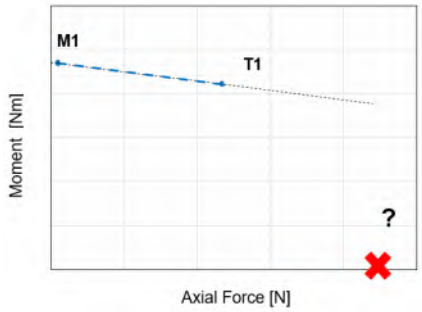


Figure 22: Failure envelope.

It should be noted that, in typical development campaigns, the most critical configuration is selected for testing. In this case, the Outer Cone was initially considered under the assumption that it would envelope the behaviour of both configurations. However, the test results highlighted the importance of local behaviour and strain distribution, which cannot be fully captured through global load metrics alone.

Furthermore, it is important to consider that flat specimens provide a conservative representation of the structural behaviour, as cylindrical or closed structures distribute circumferential moments more uniformly. This, combined with the incomplete definition of the interaction envelope, motivated the adoption of a different approach.



Figure 23: Test Specimen instrumentation on internal and external face on the test piece.

Specimens were instrumented to gain insight into the load distribution and local behaviour, as Fig. 23 shows. Strain gauges were placed at mid-height to monitor global load introduction, as well as on the castellated regions on both internal and external faces, from middle width to the edge, to ensure that failure was not driven by edge effects or non-uniform loading.

The measurements revealed a significant asymmetry in the strain distribution under tensile loading (T1), where the external face experienced compressive strains approximately 80% higher than the tensile strains measured on the internal face. This behaviour is a direct consequence of the offset in the joint. A similar strain distribution was observed in M1 tests, with comparable strain levels at failure on both faces, further supporting the equivalence between T1 and M1 loading conditions. In Fig. 24, the average levels of T1 and M1 are the same.

In contrast, Compression tests (C1) exhibited compressive strains on the internal face approximately 30% higher than the tensile strains measured on the external face. Local compression appeared in the internal face, which is the non-machined face. When comparing the local compression capacity of the internal face in T1 and C1 loading state (Average Min. of C1 vs. Average Min. of T1), the lectures during C1 test are double the ones during the T1. Note that the C1 test could not reach failure, which means that locally the non-machined face can support a higher local compression.

Based on the observed failure modes and strain measurements, a local strain-based failure criterion was defined using the experimental data. This criterion was then applied to the flight hardware by instrumenting the most loaded areas, Fig. 25, of these joints of the structure with strain gauges, enabling in-situ monitoring of the structural response during qualification testing.

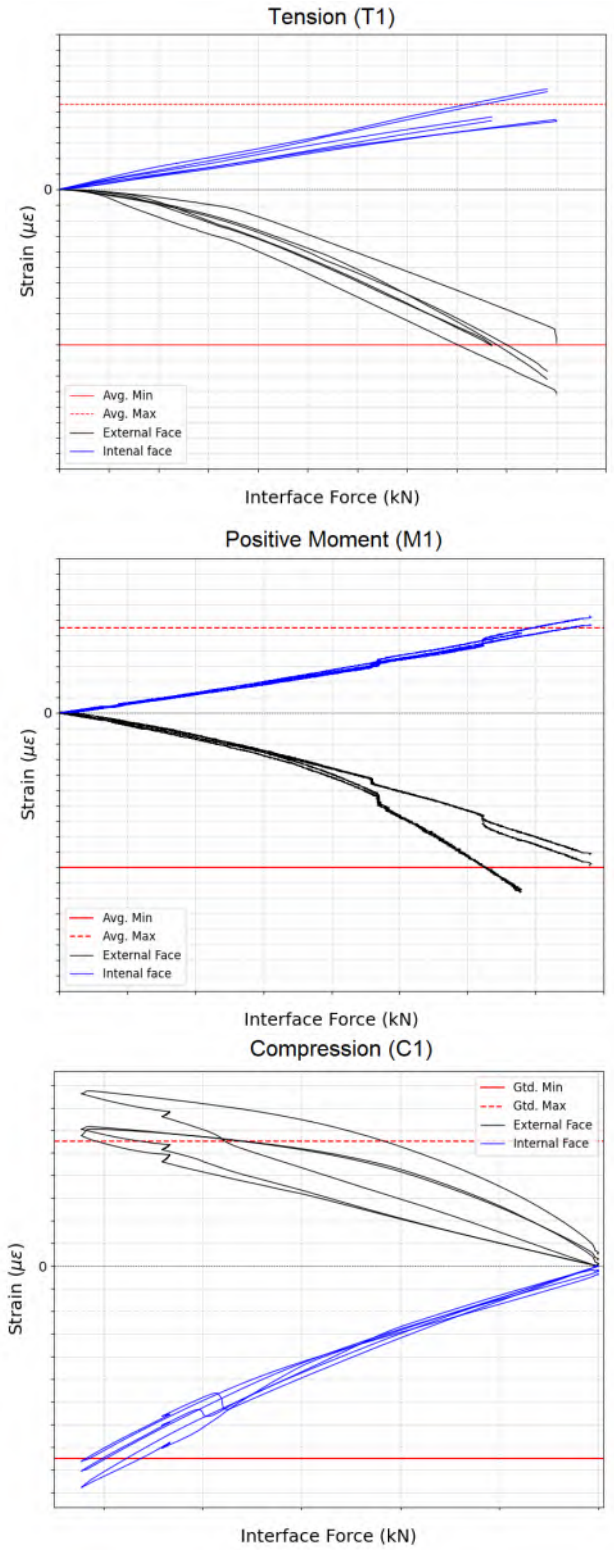


Figure 24: Local measurements during T1, M1 and C1 tests.

As no dedicated specimens were available for the Inner Cone, the same strain-based criterion was applied according to its expected (and then verified) behaviour, considering that the failure is triggered by local compression during the tensile loading state caused by the induced moment, Fig. 26.

This approach enabled the completion of the characterization despite the limitations in test coverage, providing a consistent and conservative basis for the subsequent full-scale qualification.

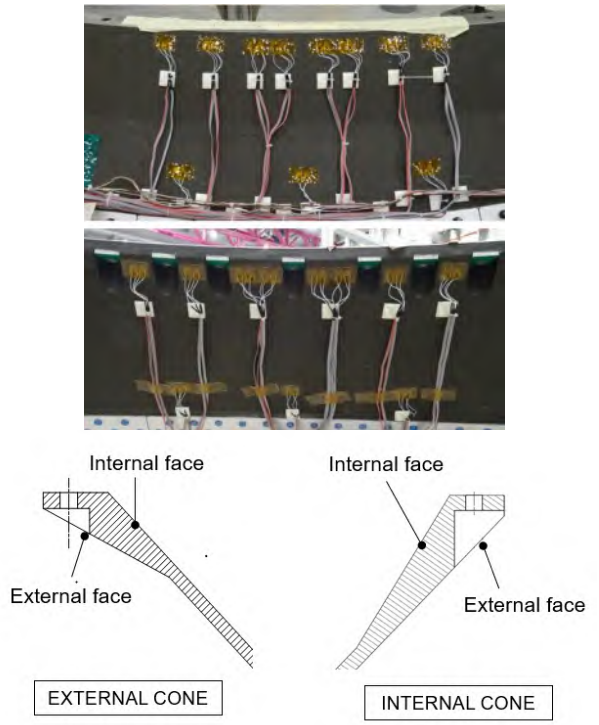


Figure 25: Proto-Flight Model (PFM) strain-gauges instrumentation at the internal and external face of both cones.

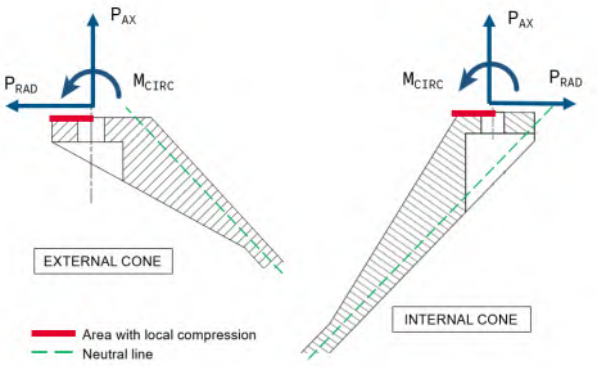


Figure 26: Comparison between Inner and Outer Cone behaviour.

4. PROTOFLIGHT MODEL QUALIFICATION RESULTS

The Qualification Test Campaign is composed of a stiffness test and a strength test. The objective of the stiffness test is to provide data for FEM (Finite Element Model) correlation to ensure the integrity of the structure during the strength tests, while the objective of the strength test is to demonstrate the load capability of the structure when subjected to critical loads (qualification loads).

A successful qualification campaign requires a detailed understanding of the expected structural

behaviour. To this end, predictions are generated using the same finite element model employed for the structural sizing, adapted to represent the test setup and associated boundary conditions, as shown in Fig. 27. The model is used to define expected global and local responses, as well as to support the placement and interpretation of instrumentation.

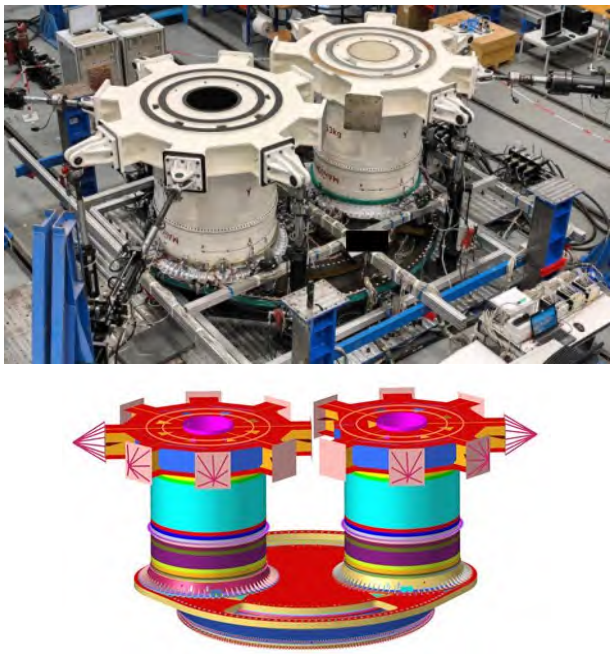


Figure 27: MASH qualification test set-up (top) and Finite Element Model (FEM) for test predictions (bottom)

The instrumentation strategy includes displacement transducers to validate the global stiffness of the structure, and strain gauges to assess load distribution across structural components. These measurements enable verification that the load paths are correctly represented and that no localised overloading occurs beyond the predicted levels.

Traditionally, structural margins were derived from the classical force–moment interaction curves, and instrumentation was typically placed slightly away from the joint, in regions where the mathematical model could provide reliable strain predictions.

In the present case, the methodology was extended by directly instrumenting the integrated ring interfaces, as Fig. 25. The strain measurements obtained during the Qualification Test were compared against the allowable limits derived from the specimen characterization campaign. This approach enabled a direct verification of the joint behaviour at full scale, using experimentally-based strain thresholds as a reference.

By combining model predictions for the global behaviour with experimentally derived local criteria for the joint, it was possible to achieve a more comprehensive validation of the structure.

4.1. Stiffness Correlation

The Stiffness Qualification Test aimed to verify the global structural behaviour of the flight model through correlation between predicted and measured displacements. The test campaign comprised six load cases:

- A1: Pure axial tension.
- A2: Pure compression.
- L1: lateral load in +X.
- L2: lateral load in +Y.
- B1: Moment about +X.
- B2: moment about +Y.

These load cases enabled the derivation of the global stiffness matrix of the structure.

For all cases, the acceptance criterion of a maximum 10% deviation between predicted and measured displacements was fulfilled. Additionally, it was consistently observed that the predicted displacements were higher than those measured during the test. Fig. 28 shows the comparison between the predicted values and the actual readings during the stiffness test; each point represents different displacements captors used during the test. The results indicate that the flight structure exhibited a stiffer global response than anticipated by the model, and therefore the stiffness requirement was successfully validated with a conservative margin.

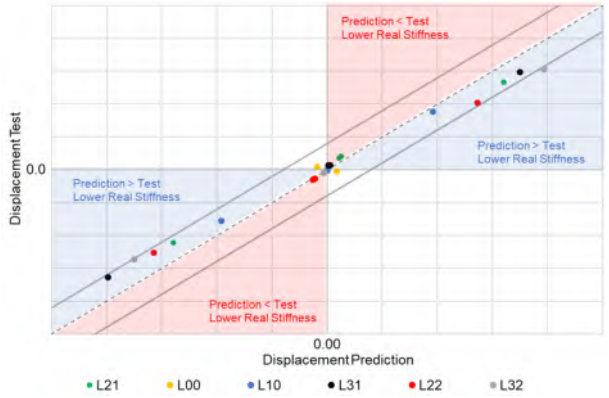


Figure 28: Predicted displacements vs. Actual displacement captor's readings.

Strain gauge measurements were also used to support the validation of the numerical model, particularly in terms of load introduction and load path distribution. For the CFRP integrated ring interfaces, the lateral +X and +Y load cases (L1 and L2) were identified as the most representative within the stiffness campaign, as they induced significant tensile loading in the cones.

The comparison between test measurements and specimen characterization data showed a good agreement for the Outer Cone, where strain levels

were consistent with those obtained during the development test campaign, see Fig. 29. In the case of the Inner Cone, the measured strain levels remained within a lower range, which is consistent with the reduced bending moment at the interface and the relatively low load levels associated with the stiffness test cases.

These results provided confidence in both the global structural model and the local behaviour of the integrated ring interfaces, supporting the transition to the resistance qualification phase.

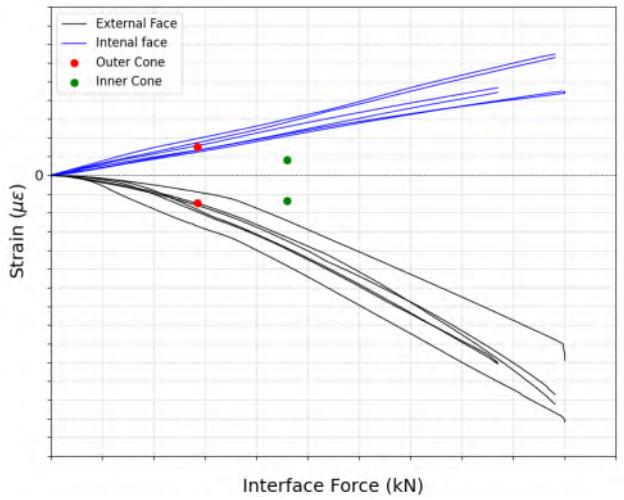


Figure 29: Maximum measured micro-strains during stiffness test campaign for Inner and Outer Cone.

4.2. Strength qualification

The Strength Qualification Test comprised five load cases representative of the critical conditions of the structure:

- S1: corresponding to the critical load case for the platform (non-critical for the cones).
- E1 and E2, representing maximum tension and compression, respectively, in the Outer Cone.
- I1 and I2, corresponding to maximum tension and compression, respectively, in the Inner Cone.

The S1 load case was used as an initial reference to extrapolate the load levels at the CFRP integrated ring interfaces and to confirm that enough margin existed for the subsequent critical cases. Following this verification, the four cone-driven load cases were executed, with the tensile cases (E1 and I1) identified as the most critical for the integrated joints.

For the Outer Cone, it was observed that, as the applied load increased, the local strain response progressively deviated from the trend obtained in the flat specimen characterization tests, increasing with a lower slope, as Fig. 30 shows. This behaviour is consistent with the expected differences between how circumferential moment is reacted in a closed geometry and in a flat specimen. As a result, qualification levels could be reached by maintaining enough margin with the defined guaranteed limits (green lines).

In the case of the Inner Cone, the strain evolution on both faces of the joint showed an asymmetric behaviour due to the local offset of the interface. This offset induces a moment in the opposite direction to that of the Outer Cone, resulting in very low strain levels on the external face (which has local compression), while the internal face (located at the bolted interface) carries the majority of the tensile load. The Maximum Compression load case of the Outer Cone (E2) was used to extrapolate the expected values for the Maximum Tension load case of the Inner Cone (I1), which was the most critical one since no data was available. The strain-gauges readings of the Inner Cone in comparison with the Outer Cone test pieces result are shown in Fig. 31.

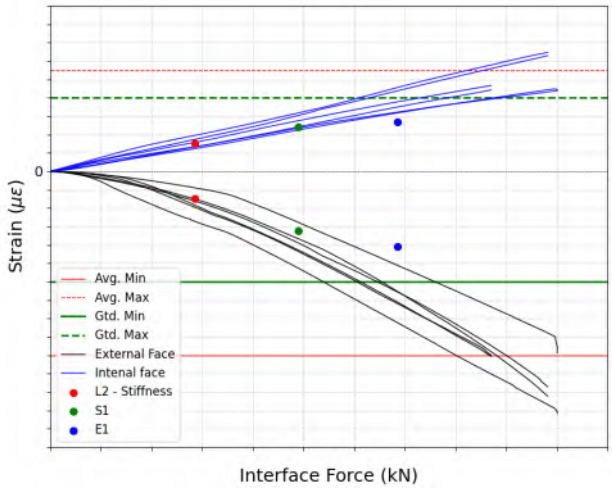


Figure 30: Maximum measured micro-strains during the strength test campaign for Outer Cone.

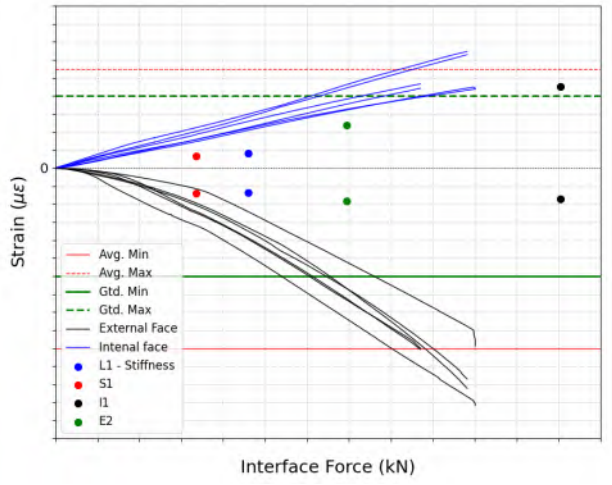


Figure 31: Maximum measured micro-strains during the strength test campaign for Inner Cone.

Although the maximum measurements at the

internal face were higher than the original threshold, note that this is the non-machined face in the Inner Cone configuration, as Fig. 25 shows. As a result, the deviation was accepted during the test due to the lack of risk, allowing the complete qualification of the flight model.

The successful completion of the Strength Qualification Test validates the proposed methodology, combining empirical characterization, strain-based criteria, and full-scale instrumentation to ensure the structural integrity of CFRP integrated ring interfaces under complex loading conditions.

5. CONCLUSIONS AND LESSONS LEARNED

This work has presented the evolution of CFRP integrated ring concepts from conventional external interfaces towards more complex internal interface applications. An empirical characterization methodology based on line loads and interaction envelopes has been reviewed and extended to account for configurations where axial and bending effects are inherently coupled due to geometric offsets.

A representative case study involving a dual-cone payload dispenser has been investigated, highlighting the impact of joint offset, manufacturing constraints, and assembly requirements on the local structural behaviour. The limitations of traditional approaches based solely on global load metrics for all applications have been addressed through the introduction of a strain-based characterization methodology, supported by dedicated specimen testing and local instrumentation.

The proposed approach has been successfully applied during the full-scale qualification of a flight model. Stiffness test results demonstrated good correlation with predictions, and strength test results confirmed that the integrated ring interfaces met the required performance with sufficient margin.

The direct monitoring of the joints provided valuable insight into their behaviour under representative loading conditions, enabling validation beyond conventional methods.

5.1. FUTURE WORK AND OPEN POINTS

Future developments should focus on extending the characterization database to cover a wider range of configurations and loading conditions, including the systematic testing of all relevant geometrical variants to reduce reliance on envelope assumptions. Although not critical in the present case, incomplete coverage could lead to unaccounted risks in other designs.

Additionally, further work is recommended to refine strain-based criteria and improve their integration into design and verification processes. The methodology presented offers clear advantages in terms of flexibility, reduced development time, and applicability to future structures with increased geometric and functional complexity.

6. REFERENCES

1. Roberts, J. & Hadaller, A. (2019). Behind the US's Largest Rideshare Launch: Spaceflight's SSO-A. In *Proc. 33rd Annual AIAA/USU Conference on Small Satellites*, Logan, UT, USA.
2. Moreland, D.W. (2009). Chapter 17 - Mechanical Systems Safety. In *Safety Design for Space Systems* (Eds. G.E. Musgrave, A.M. Larsen, & T. Sgobba), pp. 549-606.
3. Martin, J. (2001) Development of a Fully Integrated Structure. In Proc. 3rd. European Conference 'Structures and Technologies - Challenges for Future Launchers', Strasbourg, France.

DEVELOPMENT OF AN AFP MANUFACTURED CFRP LAUNCHER INTERFACE FRAME FOR ESA'S HARMONY MISSION SATELLITES

Andreas Uhl[(1)], Elias Hoffmann[(1)], Theresa Schneider[(1)], Thomas Zenker[(1)], Anna-Katharina Weiß[(1)], Marina Wolff [(1)], Luca Marinangeli [(2)]

[(1)] MT Aerospace AG, Franz-Josef-Strauß-Straße 5, 86153 Augsburg, Germany
Email: andreas.uhl@mt-aerospace.de, elias.hoffmann@mt-aerospace.de, theresa.schneider@mt-aerospace.de, thomas.zenker@mt-aerospace.de, anna-katharina.weiss@mt-aerospace.de, marina.wolff@mt-aerospace.de
[(2)] OHB Systems AG, Universitätsallee 27-29, 28359, Bremen, Germany
Email: luca.marinangeli@ohb.de

KEYWORDS

CFRP, satellite structures, AFP, launcher interface frame

ABSTRACT

Over the past several years, MT Aerospace AG has significantly advanced its expertise in Automated Fiber Placement (AFP), expanding the variety of composite structures and tanks that can be manufactured using this technology. As both technological capabilities and associated design knowledge have matured, the range of potential design solutions has increased, enabling components to be more precisely tailored to their specific requirements.
In addition to next-generation launcher applications, MT Aerospace has successfully applied AFP to satellite structures. One of the focused parts is the Launcher Interface Frame (LIF) for ESA's HARMONY mission, in which a CFRP frame represents the main interface towards the launcher through a dual launch adapter.

1. INTRODUCTION

The AFP technology opens up exciting new possibilities for designing satellite structures, delivering clear benefits over conventional metallic approaches-such as an improved stiffness-to-mass ratio and superior thermo-elastic performance. At the same time, it challenges the limitations of traditional co-bonded sandwich components by enabling complex, customised geometries that precisely meet mission requirements. This shift mitigates the dependency on manual layup techniques, thereby improving manufacturing repeatability and overall structural performance. Currently, MT Aerospace and OHB are developing a CFRP launcher interface frame (LIF) representing the core structure and main interface towards the launcher for the OHB Systems AG satellites of ESA's HARMONY mission, see Fig. 1.

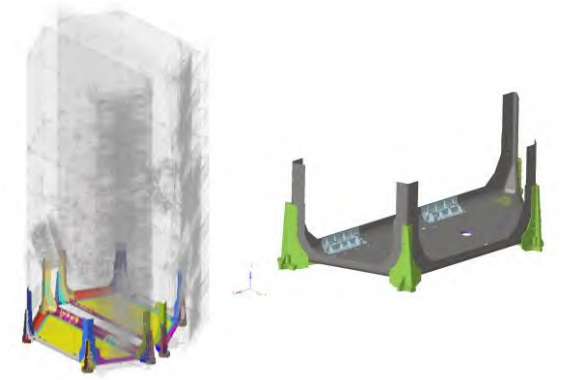


Figure 1: FE model of AFP manufactured CFRP frame with sandwich bottom part: integrated in spacecraft (left) and LIF w/o other parts (right)

Due to the high flexibility of the AFP process, the spectrum of design options for enhancing the performance extends from local reinforcements of the laminate or local adjustments of fiber orientations to the combination with stiffeners, and even to the integration of core materials to form sandwich structures. The latter approach is being implemented to the base plate of the depicted frame, demonstrating how advanced manufacturing can directly translate into performance gains and greater design freedom.
Notably, while the benefits are evident, the AFP process must be pushed to its limits for this structure. Especially the development of proper tow paths around the corners is challenging in terms of the material, the machine and the corresponding manufacturing engineering process. To fully leverage the advantages offered by complex design solutions, an integrated approach is essential - ensuring that critical manufacturing details, such as local fibre orientations, are consistently embedded in the sizing and validation process.
In 2025, MT Aerospace successfully designed and fabricated a structural model (SM) for qualification testing of the launcher interface frame, see Fig. 2 and Fig. 3.



Figure 2: AFP layup of the outer facesheet



Figure 3: AFP layup of the demolded raw part

The test sequence is currently conducted jointly with OHB in July/August 2026. The test setup includes not only the launcher interface frame itself but also one-third of the satellite structure, see Fig. 4. Static stiffness and strength tests are performed at MT Aerospace's facilities. The CFRP launcher interface frame, including metallic brackets, has been supplied by MT Aerospace, while OHB has provided the connected CFRP panels with integrated inserts (see Fig. 5). The test simulates both global satellite loads and localized high magnitude loads from a propellant tank. Given the tight project timeline, the Prototype Flight Model (PFM) is manufactured in parallel.

This paper presents the design, justification, manufacturing, and qualification process of the CFRP launcher interface frame - the primary interface between the OHB satellites of the HARMONY mission and the launcher.
Some content of this document has been published in [1] before.

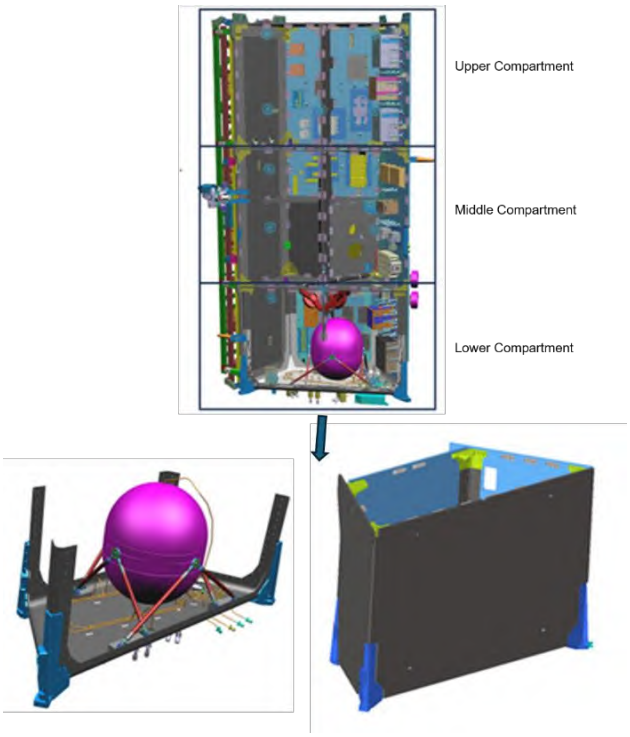


Figure 4: Harmony SM overview [1]

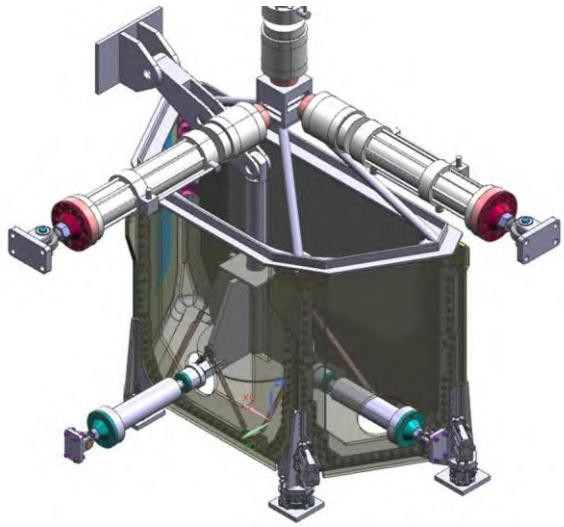


Figure 5: Structural Model of Harmony Spacecraft in Test Configuration

2. DESIGN AND JUSTIFICATION OF LIF

The MT Aerospace portion of the Harmony satellite structure is the LIF, which represents the primary interface to the launcher via a dual launch adapter. Beside the CFRP frame, the LIF includes also the HDRM (hold down release mechanism) and tank brackets including joints (see Fig. 6).

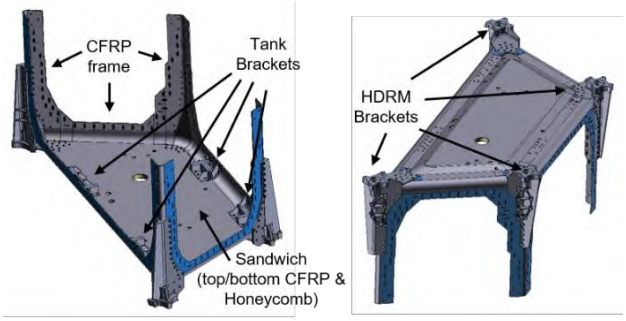


Figure 6: Top and bottom view of the design of the Harmony Launcher Interface Frame (LIF) with all components MT-A is responsible

The requirements for the LIF, which is a critical element of the Harmony spacecraft, must be coupled inherent with the spacecraft structure. Initial FE investigations demonstrated that the stiffness of the LIF can only be accurately analysed if the boundary conditions are modelled realistically. Furthermore, it was determined that the natural frequency requirement is the primary driver of mass. Consequently, the decision was made to perform the optimization using the full spacecraft (satellite) model (see Fig.7 left). Strength justifications were ultimately conducted on basis of the spacecraft model. At dedicated intervals, the current LIF design was regularly analysed within the SM (structural model) test configuration (see Fig. 7 right). To ensure representativity of the full spacecraft, the same structural interfaces, materials and components which will be used for the spacecraft are also used in the SM.

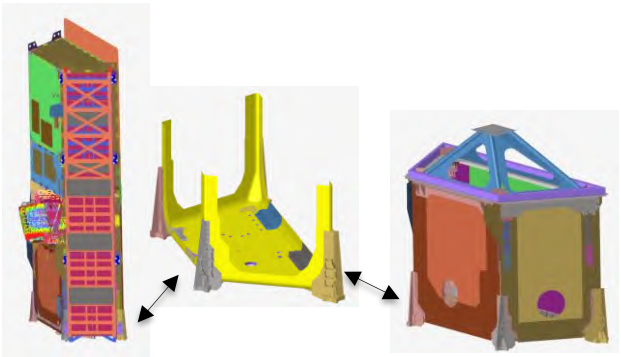


Figure 7: Spacecraft FE model for stiffness and strength evaluations (left), SM test configuration model (right) and all LIF components MT-A is responsible for (middle)

The most demanding aspect of the LIF is the development and production of its CFRP components. They constitute the structural core of the LIF (see Fig. 6.). The design of the LIF must facilitate interfaces for four HDRM brackets, four side sandwich panels, and the propellant tank support assembly. To manage the load transmission requirements of the additional interfaces on the ground of the LIF, a sandwich configuration was integrated into the bottom section of the CFRP component.

The geometry of the LIF's box-like configuration was heavily driven by the manufacturability requirements of the AFP process, especially at the challenging HDRM bracket corner interfaces. A key objective was to maximize ply continuity across structural transitions to achieve a high-performance laminate. Additionally, maintaining precise fiber orientations through these continuous plies was critical for ensuring optimal stiffness and strength. Through detailed engineering and tailored layup adaptations, a robust solution was implemented that meets all structural and manufacturing requirements, delivering a high-performance and manufacturable design.

During the design and justification process, FE analyses are performed. As previously stated, the LIF design is primarily stiffness-driven and is therefore optimized according to natural frequency requirements.

The CFRP frame (see Fig. 6) is modelled using shell elements (CQUAD4 and CTRIA3). The sandwich core, including the primary cut-outs, is discretized using solid elements (CHEXA8) with an orthotropic material definition. The tank and HDRM brackets are modelled using a hybrid approach consisting of solid and shell elements (CTRETRA10 and CTRIA6 on the outer surface). Within the MT-A scope, three specific joints are present: the connection from the CFRP frame to the HDRM brackets, the connection from the tank brackets to the CFRP frame, and the connection from the CFRP frame to the side panels; these joints are modelled using RBE2 and CBUSH elements.

For the CFRP parts the ply orientations are derived from AFP manufacturing data. To accurately predict the structural behavior of the complex CFRP component during stiffness and strength justifications, precise representation of the laminate layup within the finite element (FE) model is imperative. This requirement is intensified by the significant local variations in fiber orientation throughout the LIF geometry, particularly in high-load regions. To fully exploit the design's performance potential, an integrated methodology is employed, incorporating manufacturing-derived insights - such as precise local fiber orientations - directly into the sizing and verification workflow. This integration is achieved by systematically mapping the fiber orientations obtained from manufacturing simulations onto the FE mesh on an element-by-element basis.

Fig. 8 illustrates an example ply within the LIF corner region, showing how the simulated fiber layout is transferred to the finite element mesh.

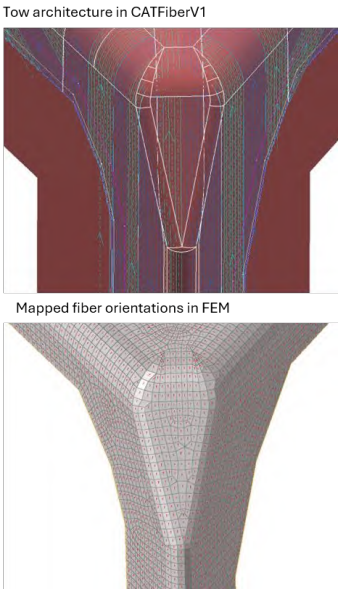


Figure 8: Tow architecture in CATFiberV1 (upper) and extracted fiber orientation mapped to FE (lower) [1]

Strength and local sandwich stability margins determined from customer-provided load cases:

- global quasi-static loads
- tank quasi-static loads
- local antenna load cases acting simultaneously on two HDRM brackets on the SAR (synthetic aperture radar) antenna interface

Given the absence of CFRP inter-fiber failure and metallic component yielding (specifically regarding the HDRM and tank brackets), as well as the occurrence of only small deformations, a linear strength analysis approach utilizing the Nastran SOL 101 solver (version 2022.4 64-Bit) is considered appropriate.
Overall, the design process and the co-engineering between OHB as prime and MT-A as supplier has resulted in a lightweight yet robust design that fully meets the requirements
At dedicated time points, the structural model (SM) was derived from the spacecraft model. The SM represents the lower compartment of the spacecraft (see Fig 9). The FE model of the SM test configuration comprises

- the Launcher Interface Frame (LIF)
- four PRM (payload release mechanism) brackets
- four sandwich panels
- the propellant-tank supporting structure incl. tank dummy
- Adjacent structure:
  - Load introduction frame
  - Load cells

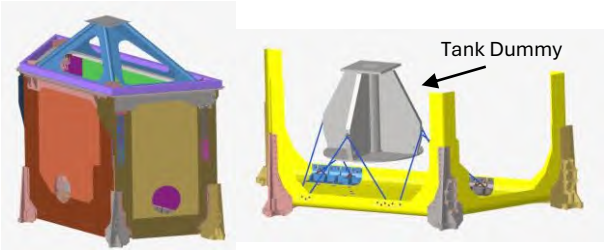


Figure 9: SM test configuration FE-model (left) and FE-model of LIF incl. tank dummy (right)

The SM test load cases are derived from the load cases investigated with the spacecraft model which are delivered to OHB. As a result of this, OHB as prime selected seven total test load cases for strength justification of the LIF: five based on Global Quasi-Static Loads (GQSL) and two based on Quasi-Static Tank Loads (Tank-QSL), selected from previous investigations.

3. MANUFACTURING PROCESS

The detailed manufacturing process is already published in [1]. Here a short overview is given.
The transformation of a composite design into a tow-discrete fiber architecture, tailored to manufacturing constraints, is a critical step in AFP engineering, providing the basis for robot trajectory generation and NC-code production. The process is implemented via the Coriolis CATFiberV1 R2024 software plug-in for CATIA V5. The main difficulty in complex AFP geometries is managing fiber steering to comply with requirements for angular deviation, ply coverage, and curvature. To optimize laminate quality for the SM, a detailed MBB-level study was conducted to facilitate local adjustments to the fiber architecture. Figure 10 depicts this optimization in a corner area; specifically, the wrinkles identified in the MBB (highlighted in red due to low steering radii) were successfully eliminated in the SM via targeted local optimizations.

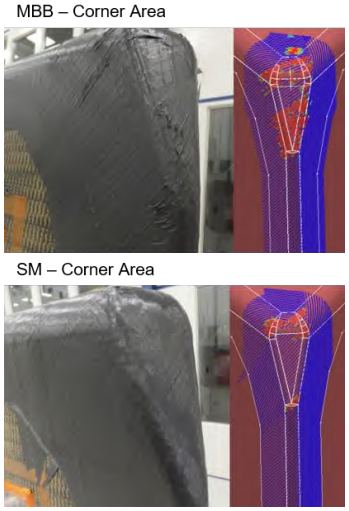


Figure 10: Optimization of the tow architecture: fiber steering analysis and corresponding layup result for MBB (upper) and SM (lower) in a corner area [1]

A linear compensation strategy was implemented to address spring-in and warpage effects during the transition from MBB to SM. By utilizing geometrical data derived from the MBB, the layup and curing tooling surfaces were remilled to ensure compliance with demanding geometrical tolerances. Manufacturing of the raw parts was conducted at MT Aerospace in Augsburg, Germany, where a Coriolis C1 8 x ¼" robot-based AFP system was used for the CFRP layup process, as illustrated in Fig. 11.

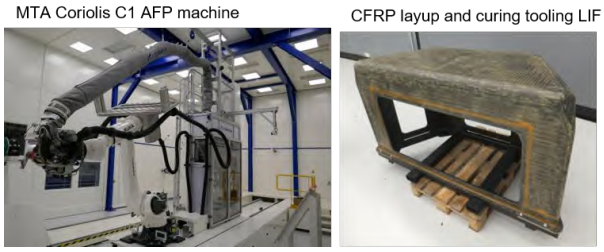


Figure 11: AFP machine and CFRP layup and curing tooling LIF [1]

The layup sequence for the LIF raw part is illustrated in Fig. 12. Following tooling preparation, the tool is mounted onto the vertical positioner system within the AFP workcell and calibrated. The process commences with the layup of the inner facesheet (IFS) CFRP laminate. Given the implementation of a one-shot curing process, the honeycomb core is integrated directly onto the uncured IFS. This is followed by the application of the outer facesheet (OFS). As a final lamination step, sacrificial GFRP patches are applied to the external interface areas.

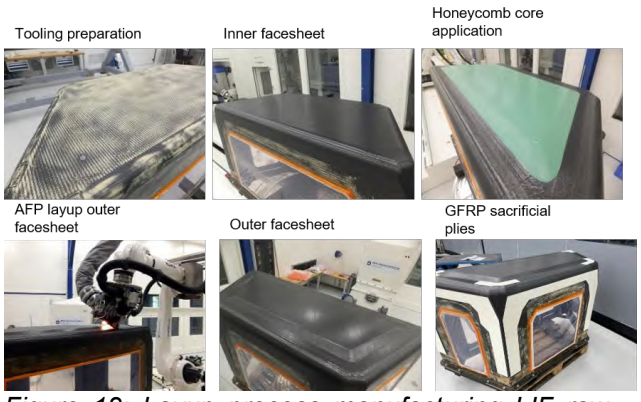


Figure 12: Layup process manufacturing LIF raw part [1]

After finishing the layup process, the frame is cured in an autoclave process (Fig. 13).



Figure 13: Curing process manufacturing LIF raw part [1]

Geometrical measurement of MBB and SM frame raw parts are performed. Measured deviations from the CAD model are shown in Fig. 14 via color-coded maps of the front view and pillar XpXn cross-sections.

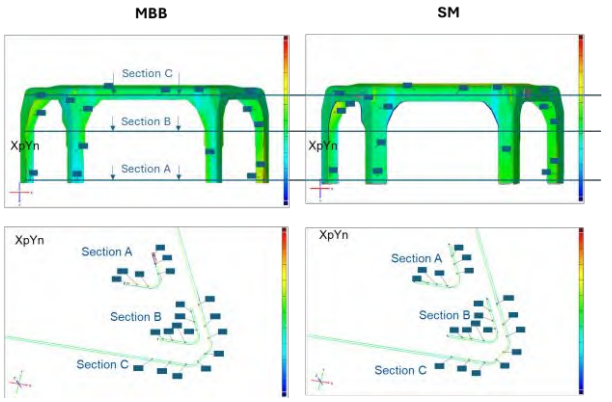


Figure 14: Results geometrical measurement MBB and SM - front view & sections XpXn pillar [1]

The MBB (Fig. 14 left) displays significant post-curing warpage, particularly in the pillars, where deviations intensify toward the tips (Sections A–C). The SM results (Fig. 14 right) confirm the success of the tooling compensation methodology, as evidenced by reduced overall deviations and the removal of torsional deformation.
Laminate quality was verified using squirter ultrasonic inspection for sandwich areas and manual impulse-echo for monolithic CFRP. MBB sections were further investigated macroscopically (Fig. 15) and via microscopy.



Figure 15: Section LIF MBB [1]

Following part release, the LIF is machined and assembled through milling and riveting, then integrated into the test rig via a test adapter for component testing.

4. QUALIFICATION PROCESS

To qualify the SM, a structural test is performed. The test was designed to support the qualification of the primary structure and its critical interfaces with major appendages, specifically the propellant tank, regarding the combined ground and flight acceleration envelopes, including associated local and global resonance effects. Compliance with strength and stiffness requirements shall be verified through the measurement of strains and displacements under representative static loads. Furthermore, the test shall demonstrate that the structure exhibits linear behavior within the elastic

range. Finally, the test data shall validate the mechanical analyses by correlating the stiffness and stress distribution of the finite element models with the measured values.
Prior to the test, a predictive analysis of the SM was conducted using the same mathematical model employed for the SM LIF justification. Generally, the prediction indicated low deformations and strains across all test and unit load cases, with a maximum overall deformation of approximately 2.6 mm (at the load introduction point of the loading frame) and approximately 1.2 mm in the area of the LIF components (upper end of the CFRP pillars). The highest CFRP strain among the selected sensors was predicted at approximately 260 µε, occurring perpendicular to the fiber direction on the inner side of pillar XNYP. These low values confirm that the structure is stiffness driven.
Following a successful Test Readiness Review (TRR) in July 2026, the test is conducted at the MT Aerospace testing facilities in Augsburg in July/August 2026. The test specimen, including the test setup, is shown in Fig. 16 and consists of:

- Launcher Interface Frame (LIF)
- Four sandwich panels
- Propellant-tank supporting structure
- Four Payload Release Module (PRM) Brackets
- Four PRMs
- Tertiary structures connecting panels and LIF

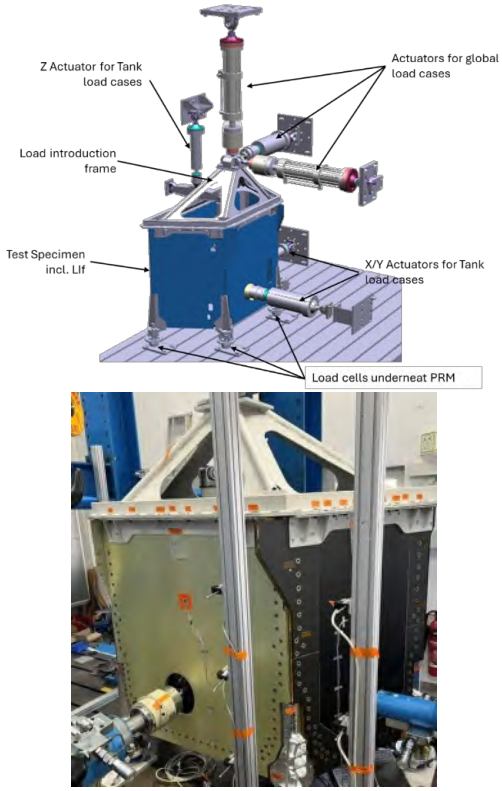


Figure 16: *CAD Model of SM test setup (upper) and side view of SM incl. load introduction frame (lower)*

The experimental setup incorporates three distinct types of sensors to facilitate data acquisition. First, load cells are utilized to measure and record loads and moments. Second, uni-directional and multi-directional strain gauges are integrated onto the LIF CFRP structure and its associated panels to monitor strains. Finally, displacement sensors are employed to track movement. These sensors are decoupled from the test specimen through a specialized supporting rig constructed from aluminum profiles.
As previously stated, OHB provided five test load cases based on global quasi-static loads and two test load cases based on quasi-static tank loads, selected from previous investigations. The derived forces are applied to the LIF structure via specific actuators. The following load levels and holding times are defined for the testing sequence:

- 40% Qualification Load, with a 30-second hold
- Deloading
- 80% Qualification Load, with a 30-second hold
- Deloading
- 100% Qualification Load, with a 60-second hold
- Deloading

In addition to the qualification load cases, unidirectional load cases will be applied following the QSL and Tank QSL load cases, to facilitate model correlation. These unidirectional load cases consist of a load application amounting to 90% of the full load in the respective directions.
Currently the qualification tests are performed at MT-A. All displacement and strain sensors are fully operational, providing data suitable for initial correlation studies. Fig 17 illustrates a strain sensor positioned on the inner surface of the SM bottom section, located within the LIF CFRP sandwich structure.

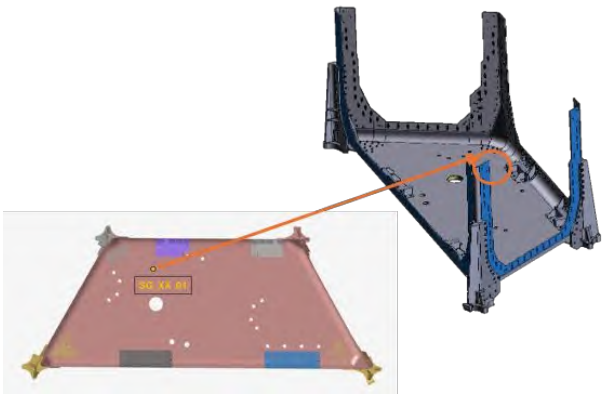


Figure 17: *Strain gauge on the inner side of the SM bottom on the LIF CFRP of the sandwich*

First evaluation of this strain sensor at the Tank QSL load case shows good agreements to the FE analysis, see Fig. 18.

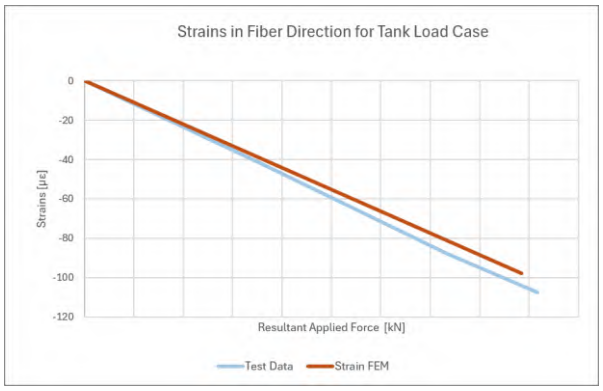


Figure 18: *Strain in Fiber Direction Test vs. FE results - Tank QSL load case*

5. CONCLUSION

The development and validation of the Launcher Interface Frame (LIF) for ESA's HARMONY mission demonstrates a significant advancement in utilizing Automated Fibre Placement (AFP) for primary satellite structures. The LIF requirements are coupled inherent with the spacecraft structure. By basing optimization and strength justification on the full spacecraft model, the design process ensured high structural fidelity and reliable validation of the LIF within the integrated spacecraft context. The justification performance is maximized by integrating manufacturing-derived fiber orientations into the sizing and verification workflow. The iterative manufacture transition from a Manufacturing Breadboard (MBB) to the Structural Model (SM) established a robust feedback loop. MBB-level studies identified critical warpage and spring-in effects, which were successfully mitigated through measurement-based tooling compensation and tow-architecture optimization.

SM structural testing for strength and stiffness verification is currently in progress. These tests serve also as basis for validation of the mechanical analysis.

The present development stage establishes a solid foundation for the ongoing advancement of AFP technology within the domain of primary satellite structures.

6. REFERENCES

1. Thomas Zenker, Andreas Uhl, Nicola Riva, Luca Marinangeli, Celalettin Yumus (2026). *Automated Fiber Placement Based Manufacturing of a Satellite Lanuncher Interface Frame.* 7th International Symposium on Automated Composite Manufacturing, Delft, the Netherlands.

Certain information contained in this paper may be subject to export control restrictions under Regulation (EU) 2021/821 (EU Dual-Use Regulation), including Items 9E001 and/or 9E002. Any use, disclosure, transfer, or export of such information must be conducted in accordance with all applicable legal and regulatory requirements.

BLACK ENGINE TECHNOLOGY - DESIGN OF A STRUCTURAL HEALTH MONITORING SYSTEM FOR A CFRP LOAD JACKET

Dominik Becker [(1)], Florian Mattburger [(2)], Markus Selzer [(3)]

[(1)] Aalen University of Applied Sciences, Institute for Sustainable Polymers and Composites iSPC, Beethovenstraße 1, 73430 Aalen, Germany, Email: dominik.becker@hs-aalen.de

[(2)] Aalen University of Applied Sciences, Institute for Sustainable Polymers and Composites iSPC, Beethovenstraße 1, 73430 Aalen, Germany

[(3)] German Aerospace Center, Institute of structures and design, Germany

KEYWORDS

Sensors, carbon fiber reinforced polymers, health monitoring composites

ABSTRACT

Structural Health Monitoring (SHM) of fiber-reinforced composite structures is becoming increasingly important, as carbon fiber reinforced polymers (CFRP) exhibit complex damage mechanisms that often develop beneath the visible surface. Typical damage modes such as matrix cracking, fiber–matrix debonding, delamination, and fiber fracture can gradually degrade structural integrity and are difficult to detect reliably. Embedded sensor systems therefore offer a promising approach for continuous monitoring of the material state.

In the present project, an integrated SHM system is developed for a CFRP rocket thrust chamber support jacket. The focus is on the selection and evaluation of suitable sensor technologies, including fiber-optic, acoustic, and piezoelectric sensors, for monitoring parameters such as strain, temperature, and damage-related events. A key challenge is the integration of sensors into the laminate without significantly affecting its mechanical properties. Therefore, sensor integration is investigated using both hand-laminated specimens and an automated filament winding process.

In parallel, a simulation-based model is developed to investigate the interaction between embedded sensors and the laminate structure.

The model focuses on the main model setup, sub-models, input parameters, and boundary conditions, enabling the prediction of sensor-induced effects on the mechanical behavior. The study presents the design and validation approach of the SHM concept and provides an outlook on the planned correlation of sensor data with mechanical material properties using quasi-static and cyclic testing.

1. STRUCUTRAL HEALTH MONITORING

Structural Health Monitoring refers to the repeated or continuous collection and evaluation of structural condition parameters using permanently or repeatedly installed sensors. The goal is not just to detect a deviation, but depending on the system also to locate, quantify, and assess it. An SHM chain includes the sensor or actuator, signal processing, data acquisition and transmission, data processing, and condition-related interpretation.

The suitability of a method depends on the diagnostic task. Local sensors can offer high sensitivity in their immediate area, while surface or distributed methods can cover a larger structural region. Additionally, long-term stability, calibratable, environmental influences, wiring, data volume, and the impact of sensor integration on the structure need to be considered. integration on the structure need to be considered.

Components show various, often interconnected damage mechanisms due to their heterogeneous and layered structure. The main types of damage include intralaminar matrix cracks, fiber-matrix debonding, and fiber breaks, as well as interlaminar delaminations. Their occurrence and development are influenced by factors such as the type of load, layer structure, manufacturing deviations, and environmental conditions [1–3].

Matrix cracks and interface failures can affect the local load transfer between fiber and matrix, which in turn can promote further damage mechanisms. Especially under impact loads, matrix cracks often appear together with delamination, fiber breaks, and local indentations. Delaminations weaken the interlaminar load paths and can thereby reduce the component's stiffness, stability, and load-bearing capacity [1, 4].

Fiber breaks, on the other hand, interrupt the load-bearing fibers and can especially cause significant changes in the electrical properties of electrically conductive CFRP structures [5].

Under cyclic loading, existing cracks and delaminations can grow and new damage can occur. Additionally, drilled holes and other geometric discontinuities can act as starting points for damage. Temperature and humidity effects can influence both the polymer matrix and fiber-matrix interfaces as well as the electrical measurement properties [2, 5, 6].

The complex interaction of these mechanisms makes it difficult to clearly assign measured signals to specific types of damage and highlights the importance of suitable, particularly non-destructive, monitoring methods for CFRP components.

1.1. Damage Mechanism in CFK Structures

Components show various, often interconnected damage mechanisms due to their heterogeneous and layered structure. The main types of damage include intralaminar matrix cracks, fiber-matrix debonding, and fiber breaks, as well as interlaminar delaminations. Their occurrence and development are influenced by factors such as the type of load, layer structure, manufacturing deviations, and environmental conditions [1–3].

Matrix cracks and interface failures can affect the local load transfer between fiber and matrix, which in turn can promote further damage mechanisms. Especially under impact loads, matrix cracks often appear together with delamination, fiber breaks, and local indentations. Delaminations weaken the interlaminar load paths and can thereby reduce the component's stiffness, stability, and load-bearing capacity [1, 4].

Fiber breaks, on the other hand, interrupt the load-bearing fibers and can especially cause significant changes in the electrical properties of electrically conductive CFRP structures [5].

Under cyclic loading, existing cracks and delaminations can grow and new damage can occur. Additionally, drilled holes and other geometric discontinuities can act as starting points for damage. Temperature and humidity effects can influence both the polymer matrix and fiber-matrix interfaces as well as the electrical measurement properties [2, 5, 6].

The complex interaction of these mechanisms makes it difficult to clearly assign measured signals to specific types of damage and highlights the importance of suitable, particularly non-destructive, monitoring methods for CFRP components.

1.2. Sensor technologies (embedded sensor systems)

For structural health monitoring (SHM), different sensor principles are used, which vary in terms of what they measure, their detection range, and the effort required to integrate them.

Piezoelectric sensors allow active monitoring by exciting and detecting guided waves and are particularly suitable for detecting local changes in stiffness. Fiber optic sensors, especially fiber Bragg gratings (FBGs), detect strain and temperature influences through spectral wavelength changes and are noted for their small size, light weight, and resistance to electromagnetic interference. Acoustic emission allows for passive monitoring by capturing elastic waves that occur during damage development and evaluating them based on their characteristic features. However, clearly assigning them to specific damage mechanisms is challenging due to overlapping signal characteristics [3].

In contrast, piezoresistive and self-sensing systems use changes in the electrical conductivity of the composite material caused by strain or damage. For CFRP, the intrinsically conductive carbon fiber network can be used for this purpose, which can sometimes eliminate the need for additional sensors [7, 8].

For electrical measurement methods, factors like electrode contact, temperature, humidity, measurement noise, and drift are particularly important. While single measurements mainly provide overall information about the area between the electrodes, using multiple electrodes and different current paths allows for spatial damage localization. A more advanced approach is Electrical Impedance Tomography (EIT), where spatial conductivity distribution—or changes in it—is reconstructed from electrical boundary measurements using a forward and inverse model [9–12].

1.3. Electrical Impedance Tomography (EIT)

Electrical health monitoring of CFRP initially evolved from global resistance measurements to spatially resolved techniques. Early studies demonstrated that strain, fiber breakage, and delamination cause measurable changes in electrical resistance or potential, with results heavily dependent on electrode arrangement, measurement configuration, and the anisotropic conductivity of the CFRP [5, 7]. Utilizing multiple electrodes and various measurement paths can improve damage localization; however, unambiguously correlating electrical changes with specific damage types and geometries remains challenging [5, 8]. The introduction of Electrical Impedance Tomography (EIT) expanded electrical health monitoring to include model-based spatial reconstruction. Research on CFRP indicates that EIT is fundamentally suitable for localizing impact damage and delamination and offers the potential for structural integration by leveraging the intrinsically conductive carbon fiber network [13]. However, the reconstructed conductivity distribution does not represent a direct geometric image of the actual damage. Reconstruction quality is significantly influenced by anisotropic material behavior, the forward model, electrode contact, the reference state, and the chosen measurement pattern [13]. Consequently, current research increasingly focuses on optimizing measurement configurations and improving damage characterization. Studies show that the number and selection of electrode combinations, as well as the current injection pattern, significantly affect localization, resolution, and artifacts [11, 13, 14]. While reducing the number of measurement channels is feasible in principle, such reductions must be tailored to the specific component geometry, layup, and underlying forward model [14]. Overall, the research focus is thus shifting from the mere detection of electrical changes toward the model-based localization and characterization of damage. Reliable application to CFRP requires, in particular, suitable material modeling, reproducible electrode contacts, and measurement and reconstruction procedures tailored to the specific component and type of damage. Electrode Contacting and Three-Dimensional EIT Electrode contacting is a critical factor in the EIT measurement chain, as electrode material, contact area, ply layup, and manufacturing conditions can influence the measured electrical resistance [10]. Embedded electrodes enable permanent, low-profile contact but require investigation into their long-term mechanical and electrical stability within the specific laminate layup. Furthermore, reliable EIT application necessitates considering not only the reconstruction process itself but also measurement noise, drift, accuracy, and the reproducibility of the entire measurement chain [9] . Conventional EIT systems with a single electrode plane provide spatially distributed sensitivity, from which primarily two-dimensional reconstructions are derived. Consequently, the position of damage located outside the plane of interest may be misinterpreted. Multiple electrode planes theoretically enable three-dimensional reconstruction, thereby improving the ability to determine damage location across the component thickness [12, 15]. However, for thin CFRP laminates, depth resolution poses a particular challenge due to the limited component thickness and pronounced electrical anisotropy. Reliable 3D reconstruction therefore requires appropriate consideration of geometry, electrode contact, conductivity, and the electrical coupling between individual plies.

Electrical Impedance Tomography (EIT) enables the reconstruction of a spatial conductivity distribution from electrical boundary measurements. To do this, defined currents are injected into the component via electrodes, and the resulting potentials are measured. By varying the pairs of injection and measurement electrodes, a measurement vector is generated, from which the conductivity distribution—or changes therein—is determined using a forward model and an inverse method [11].

Under quasi-stationary conditions and in the absence of internal current sources, the electric potential u in the domain Ω is given by.

$$\nabla \cdot (\sigma \nabla u) = 0 \; in \; \Omega \quad (1)$$

The current density is given by j = −σ∇u. Geometry, conductivity, electrode areas, contact impedances, and applied currents constitute the inputs to the forward problem. For complex geometries, the domain is typically discretized using the finite element method.

The forward problem describes the distribution of the electric potential within the component based on geometry, material conductivity, electrodes, and contact conditions. For complex component geometries, the finite element method is typically used for this purpose. The inverse problem, on the other hand, is ill-posed, since even small measurement or model deviations can lead to significant changes in the reconstructed conductivity distribution. In differential EIT, therefore, the current measurement state is compared with a reference state, and the change in conductivity is reconstructed [11].

The inverse problem consists of inferring the internal conductivity from boundary measurements. It is nonlinear and ill-posed: small deviations in measurements or models can cause large changes in the reconstructed distribution. In difference EIT, measurements of a state are compared with a reference. For small changes, the relationship can be linearized around a reference state:

$$\Delta v \approx J \, \Delta \sigma \quad (2)$$

where Δv denotes the voltage difference vector, Δσ the discretized conductivity change, and J the sensitivity or Jacobian matrix.

A regularized linear solution can generally be formulated as

$$\hat{\Delta\sigma} = (JTWJ + \lambda R)^{-1} JTW\Delta v \quad (3)$$

W weights the measurement data, R describes the regularization, and λ controls the trade-off between data fitting and stability.

The specific meaning of these quantities depends on the reconstruction method employed.

Regularization methods are used to stabilize the reconstruction. Among other things, Gauss–Newton methods enable the reconstruction of the change in conductivity, while the NOSER method stabilizes the solution to the inverse problem. The quality of the reconstruction can be assessed using various criteria such as position [11].

2. EXPERIMENTAL VALIDATION ON PLANAR SURFACES

For the experimental investigations, CFRP specimens are manufactured using the hand lay-up process. Unidirectional carbon fiber fabric serves as the reinforcement, combined with a three-component epoxy resin system consisting of resin, hardener, and accelerator. Thin copper foils are integrated into the laminates as electrodes to establish electrical contact. The manufacturing process is carried out under vacuum and comprises material preparation, a defined ply layup, and subsequent curing (Figure 1).

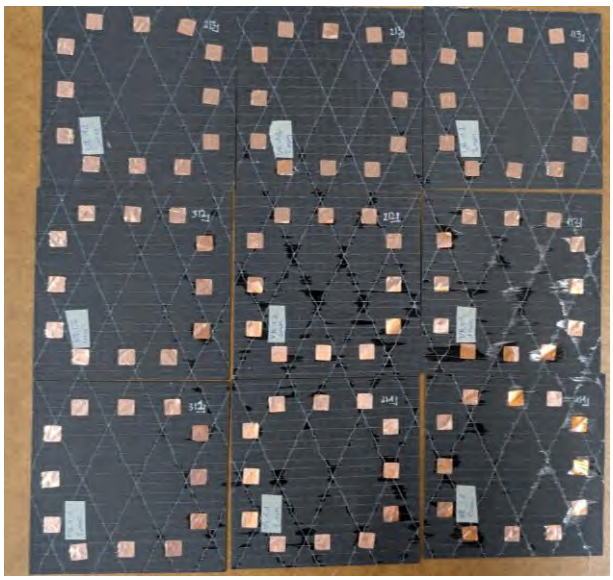


Figure 1: Testspecimen

The investigations are organized into three test series as stated in Figure 2. The first series employs four-ply CFRP specimens featuring a single electrode layer to investigate drilling-induced defects. The second series involves the fabrication of eight-ply specimens with electrode layers integrated on both sides and embedded Kapton inserts to simulate interlaminar defects. These specimens are subsequently used for EIT measurements in the third test series, which examines both the detection of the simulated defects and the influence of different measurement patterns.

VR1 Laminat-aufbau	VR2.1 Laminat-aufbau	VR2.2 Laminat-aufbau	VR2.3 Laminat-aufbau
	Vakuumfolie	Vakuumfolie	Vakuumfolie
	Saugvlies	Saugvlies	Saugvlies
	Abreißgewebe	Abreißgewebe	Abreißgewebe
	Elektroden	Elektroden	Elektroden
Vakuumfolie	UD-Gelege 0°	UD-Gelege 0°	UD-Gelege 0°
Saugvlies	UD-Gelege 90°	UD-Gelege 90°	UD-Gelege 90°
Abreißgewebe	UD-Gelege 90°	UD-Gelege 90°	UD-Gelege 90°
UD-Gelege 90°	UD-Gelege 0°	UD-Gelege 0°	UD-Gelege 0°
UD-Gelege 90°	UD-Gelege 0°	UD-Gelege 0°	Kapton-Tape
UD-Gelege 90°	UD-Gelege 90°	UD-Gelege 90°	UD-Gelege 0°
UD-Gelege 0°	UD-Gelege 90°	UD-Gelege 90°	UD-Gelege 90°
Elektroden	UD-Gelege 0°	Kapton-Tape	UD-Gelege 90°
Abreißgewebe	Elektroden	UD-Gelege 0°	UD-Gelege 0°
Glasplatte	Abreißgewebe	Elektroden	Elektroden
	Glasplatte	Abreißgewebe	Abreißgewebe
		Glasplatte	Glasplatte

Figure 2: Schematic representation of the different laminate layups

Three test series (VR1–VR3) are defined for the experimental investigation, differing in terms of laminate layup, electrode arrangement, and the method of defect introduction. In VR1, four-ply CFRP specimens featuring a single electrode layer are used to investigate drilling-induced defects. For VR2, eight-ply specimens are fabricated with electrode layers integrated on both sides. Kapton inserts are embedded at various ply positions to simulate defined interlaminar defects. The specimens produced in VR2 are subsequently used for EIT testing in VR3, where both the detectability of the simulated defects and the influence of different measurement patterns are analyzed.

Specimen fabrication thus differs between VR1 and VR2. While VR1 employs a uniform four-ply laminate layup, three variants are realized within a single laminate panel for VR2. Variant VR2.1 serves as a defect-free reference state. In VR2.2, a Kapton insert is positioned between the first and second plies, whereas in VR2.3, the insert is placed between the fourth and fifth plies. This variation in insert positioning creates defects at different depths within the laminate, enabling an investigation into the influence of defect location on EIT reconstruction.

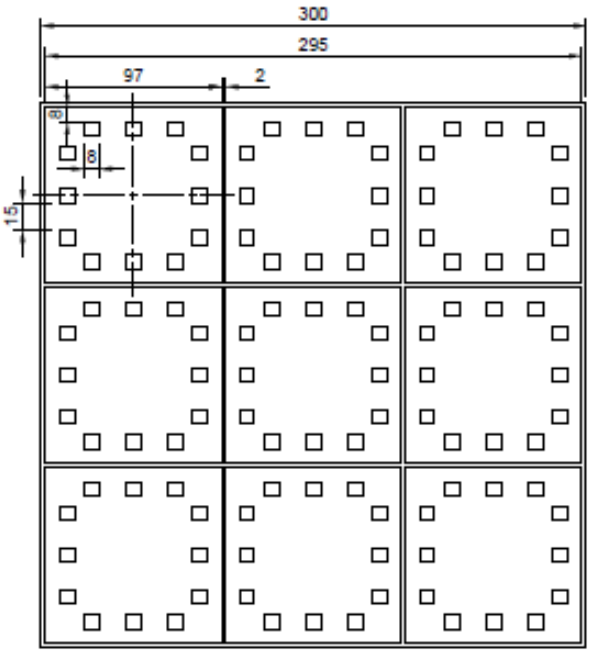


Figure 3: Plate geometry & electrode arrangement

Figure 3 shows that for each test specimen, up to twelve adjacent electrode pairs on side A were evaluated; non-conductive pairs were excluded from the statistics. n denotes the number of soldered test specimens with both pre- and post-test measurements. The relative change for each specimen is defined as $(R_{med,post} - R_{med,pre})/R_{med,pre}$.

Table 1: Resistances of adjacent electrode pairs (Side A) before and after soldering, summarized by laminate board. Shown are the median of the specimen medians, their range, and the median relative change of the median per specimen.

		R_{med} vor in Ω		R_{med} nach in Ω		
Laminatplatte	n	Median	Spannweite	Median	Spannweite	ΔR_{med} median
VR1 P1	9	5,50	2,75–18,80	20,85	6,20–69,70	+233 %
VR1 P2	6	3,55	2,25–12,50	11,78	5,25–31,50	+143 %
VR1 P3	7	4,45	2,10–17,25	23,65	4,15–56,55	+136 %
VR1 P4	7	7,70	3,45–17,95	34,85	9,60–67,20	+178 %
VR3 P1	3	4,30	4,00–4,75	5,10	5,05–7,60	+28 %
VR3 P2	6	7,92	3,60–14,65	11,55	5,35–26,65	+62 %

3. RESULTS

The test series VR1 investigates the influence of bore diameter (VR1.1), bore position (VR1.2), and electrode connection (VR1.3 and VR1.4) on EIT reconstruction. The reconstruction results are evaluated based on the reconstructed center of gravity (CoG), the positional error (PE), and the reconstruction energy (E).

For visualization purposes, a representative individual case is presented for each test condition. This selection is based on the mean positional error across the two reference states used. The statistical analysis of the entire test groups is performed using the parameters listed in Table 1.

Table 2: VR1: Reconstruction metrics from the primary analysis. Shown are the group median of the position error (PE) with its range, and the group median of the reconstruction energy (E) for each reference type.

			virtuelle Referenz		simulierte Referenz	
Bedingung	Serie	n	PE in mm	E in $(S/m)^2$	PE in mm	E in $(S/m)^2$
Ø 1 mm, zentrisch	VR1.1	3	6,9 (6,4–15,7)	29,4	7,2 (5,8–9,4)	15,0
Ø 2 mm, zentrisch	VR1.1	3	23,2 (14,5–25,1)	28,6	16,1 (3,2–19,2)	66,9
Ø 4 mm, zentrisch	VR1.1	3	13,4 (7,6–33,3)	23,9	5,8 (4,1–10,8)	61,0
Ø 4 mm, 10 mm versetzt	VR1.2	3	21,8 (19,7–23,7)	49,7	26,4 (18,6–35,5)	44,8
Ø 4 mm, 20 mm versetzt	VR1.2	3	36,6 (21,3–41,1)	41,4	22,4 (16,4–40,7)	157,2
Ø 4 mm, schlechte Anbindung	VR1.3	2	14,0 (3,3–24,7)	120,0	8,8 (8,6–9,1)	147,7
Ø 4 mm, repariert	VR1.4	2	17,1 (9,4–24,9)	61,7	10,6 (9,1–12,1)	143,3

3.1. Influence of the bore diameter

Table 2 shows the conductivity changes reconstructed via EIT for borehole diameters of 4, 2, and 1 mm, using both a virtual and a simulated reference. For all defect sizes investigated, the reconstructed centroid is located in the vicinity of the centrally placed borehole. However, the positional error shows no clear correlation with the borehole diameter. Similarly, no systematic trend is discernible regarding the reconstruction energy. Thus, the increase in reconstruction energy with increasing defect size—as predicted by the simulation—is not confirmed by the experimental results.

3.2. Influence of the delamination location in the laminate

In test series VR3, the interlaminar defects simulated using Kapton inserts are reconstructed using measurements from intact reference specimens. For each damaged specimen, the Top-only-Star and Top-Skip35 (TS35) measurement patterns are compared with respect to their suitability for damage detection and localization. The primary analysis includes three specimens with the defect located between plies 1 and 2 (Delam12) and two specimens with the defect located between plies 4 and 5 (Delam45). For statistical evaluation, the reconstruction results of each damaged specimen are first aggregated across the corresponding compatible reference specimens using the median. The resulting performance metrics are summarized in Table 3.

Table 3: VR3: Reconstruction of primary analysis metrics (group medians based on sample medians; positional error additionally includes range).

Lagenposition	Muster	n	PE in mm	E in $(S/m)^2$
Lage 1–2 (Delam12)	Star	3	11,5 (8,9–25,4)	25,3
Lage 1–2 (Delam12)	TS35	3	7,3 (3,1–12,4)	16,4
Lage 4–5 (Delam45)	Star	2	10,2 (2,7–17,7)	331,1
Lage 4–5 (Delam45)	TS35	2	8,1 (4,2–12,0)	161,2

Figure 4 show, for both ply positions, the released specimen exhibiting the lowest combined localization error obtained using the Star and TS35 measurement patterns against the same reference. The black rectangle indicates the nominal position of the Kapton insert, measuring 30 mm × 15 mm and located at the center of the plate.

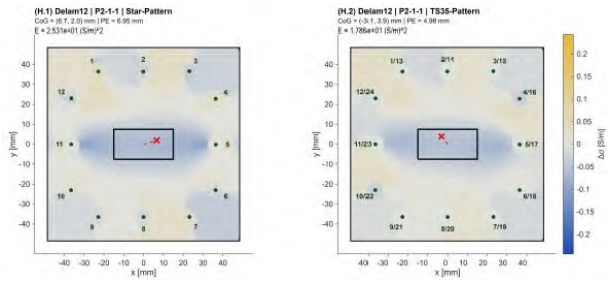


Figure 4: Reconstruction results VR3, Kapton insert between layer 1–2, sample P2-1-1 (left: Top-only Star, right: Top-Skip35)

In both cases, a continuous zone of reduced effective conductivity is reconstructed in the region of the Kapton insert, elongated along its longitudinal axis. The reconstructed centers of gravity are located within or directly adjacent to the nominal insert region. For the ply position between plies 1 and 2, the group median position errors are 11.5 mm for the Star pattern and 7.3 mm for the TS35 pattern. For the ply position between plies 4 and 5, the corresponding values are 10.2 mm and 8.1 mm, respectively.

Considerable variation between specimens is observed. Within the Delam12 group, for example, the position error obtained with the Star pattern ranges from 8.9 mm to 25.4 mm. Given the limited sample sizes (n = 3 and n = 2), no systematic difference in localization performance between the two ply positions can be established. Furthermore, the present analysis does not allow a reliable assessment of the reconstructed depth position of the inserts, as the reported metrics describe the in-plane localization and no systematic validation of depth resolution was performed on the experimental data.

3.3. Experimental validation on curved surfaces

Two concepts were investigated for the surface integration of the sensors during filament winding. In both concepts, the specimens were wound onto a 50 mm diameter PVA core, which can be removed after curing (see cross-section in Figure 5b).

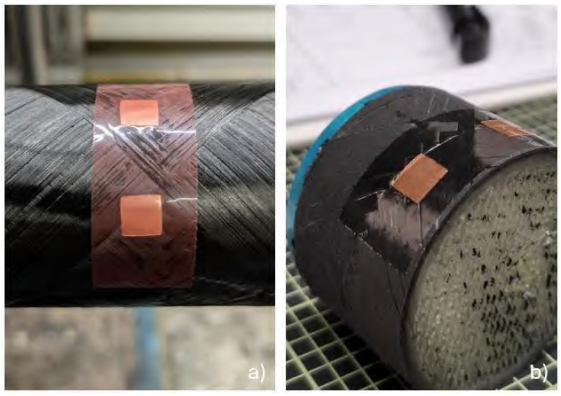


Figure 5: Recording of the wrapped test specimens a) uncured with red release film b) after curing and removing the film

Fine, high-modulus carbon fibers were used, with each roving consisting of 6000 filaments. A low-temperature-curing epoxy resin was used as the matrix material, with a glass transition temperature of approximately 100 °C.

In concept a), a release agent was applied to the upper sensor surface. The sensors were then aligned and wrapped with tensioning tape to ensure their positioning during the winding process. In concept b), the sensors were left untreated, while their upper surfaces were covered with a release film (red area in Figure 5a) and subsequently wrapped with tensioning tape. One specimen was manufactured according to each concept.

3.3.1. Electrical measurement

The electrical connection between the sensors and the surrounding carbon structure was evaluated by measuring the electrical resistance between the midpoints of the two sensors. The measured resistance was classified as good for values of 1–2 Ω, moderate for 10–30 Ω, and poor for 50–60.

3.3.2. Results

For concept a), the release agent applied to the sensor surfaces also spread to the underside of the sensors and consequently impaired their physical bonding to the carbon surface. In contrast, the electrical connection achieved with concept b) was measured at 1.6 Ω and was therefore classified as good according to the defined criteria.

To protect the sensors during removal of the PVA core, the sensor surfaces were covered with

polyester-film adhesive tape. After removal of the core, the adhesive tape was removed and the specimen was subsequently tempered. The electrical resistance measured after these processing steps remained low at 1.7–1.8 Ω, indicating a good and stable electrical connection.

Optical inspection at increased magnification showed a slight ingress of resin onto the upper sensor surface along the sensor edges. This resin accumulation forms a visible edge seal and provides additional mechanical protection against local delamination or lifting of the sensor edges (see Figure 6).

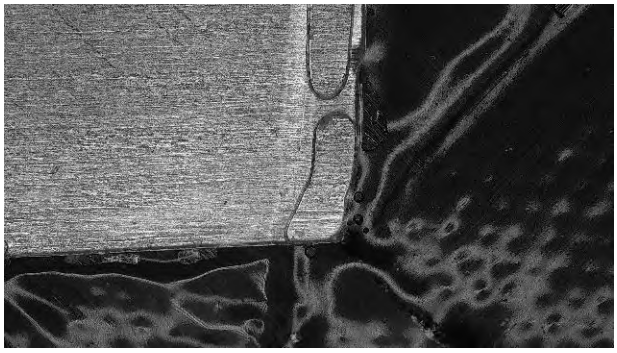


Figure 6: Enlarged image of the transition: sensor to component

4. SIMULATION

The simulation model offers significant advantages for optimizing the structural shell by enabling the simulation of laminate behavior under real-world conditions prior to manufacturing. In Ansys ACP, the simulation model is constructed using the base model of the structural shell, derived from the existing pipe model. This model is progressively refined to incorporate specific requirements and insights. A key aspect previously unaddressed is the assessment of the laminate's leak-tightness. To this end, small-scale samples are modeled and analyzed for micro-cracking and delamination under cryogenic loading. These simulation results must subsequently be correlated with actual damage patterns and experimental permeability data—ideally including cyclic loading—to evaluate damage progression. The structural shell is then simulated over multiple cryogenic cycles, allowing for an estimation of service life and leak-tightness. Additionally, an internal pipe coating can be simulated to reduce thermal gradients within the laminate.

A further step involves stress analysis of the pipe following manufacture. This entails analyzing the residual stresses generated by temperature differentials during the curing process. Simultaneously, winding tension plays a role and is integrated into the model to more accurately represent the stress distribution. Beyond residual stresses, the behavior of the interface between layers must be considered; this can be addressed by inserting an additional layer with specific material properties or, if applicable, an adhesive layer. The layup and individual layer properties must be modeled to reflect the specific manufacturing process in order to achieve realistic results. The manufacturing process itself must be taken into account, as tapering effects can impact structural integrity. A sandwich laminate structure could also be an option to provide additional stability. Realistic boundary conditions must be established for the interface region, particularly given the difficulty of predicting interface behavior under varying loads. Ansys now offers capabilities for simulating threaded connections within laminates, which can be integrated into the analysis. This process accounts for the effects of the thrust chamber, and transient thermal loads must be modeled precisely to ensure accurate results.

Additionally, the modeling approach is being expanded to include embedded sensors, the impact of which on structural strength must be factored into the simulation. Submodeling may prove beneficial for detailed analyses of specific areas—such as cryogenic tightness, interface behavior, and embedded sensors. This method employs a coarse, global model for rapid computation while utilizing detailed submodels at critical locations that adopt the boundary conditions from the larger model.

4.1. Workflow

Figure 7 illustrates the simulation workflow implemented in ANSYS Workbench. The workflow consists of several interconnected analysis systems that transfer the defined geometry and engineering data through material definition, composite layup modeling, and structural analysis. The composite laminates are defined using ACP (Pre), where the

laminate geometry, material properties, fiber orientations, and ply configuration are specified. The resulting composite model is subsequently transferred to the Mechanical environment, where the boundary conditions and loading are defined and the structural response is calculated using a Static Structural analysis. This sequential workflow enables the consistent transfer of the composite laminate definition into the structural analysis and provides the basis for evaluating the mechanical behavior of the investigated component under the specified loading conditions.

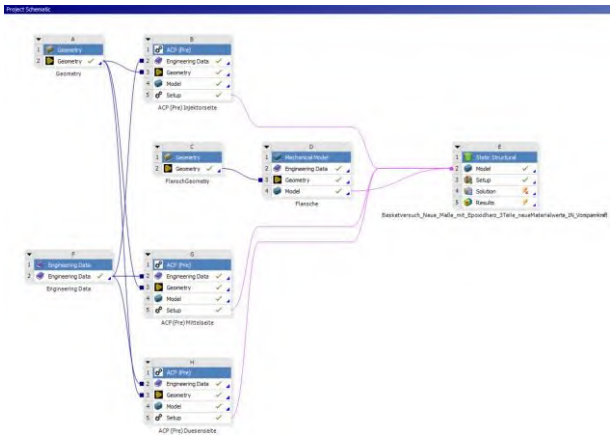


Figure 7: Figure X: Simulation workflow implemented in ANSYS Workbench

Figure 7 presents the finite element model of a slender structural assembly analyzed using a static structural simulation. The model consists of a long, approximately beam-like structural member connected to end components. The analysis setup is shown together with the applied boundary conditions and bolt-pretension loads.

The model tree on the left-hand side indicates that the simulation contains a static structural analysis with several load and constraint definitions. In particular, a fixed support, multiple prescribed displacement constraints, and bolt-pretension loads are included. The legend in the graphics window identifies the individual boundary conditions by color:

Fixed Support (blue): A fixed support is applied at one of the structural interfaces. This constraint suppresses the relevant translational and/or rotational degrees of freedom and provides the reference condition required for the static structural analysis.

Displacement 2 and Displacement 3 (yellow/green): Prescribed displacement boundary conditions are defined at selected locations of the structure. These constraints control the motion of the corresponding regions and can be used to represent mechanical guidance, support conditions, or imposed deformation.

Bolt Pretension (red): The red symbols indicate bolt-pretension loading. The model contains pretensioned bolted connections at the structural interfaces. The pretension is introduced into the bolts before the subsequent structural loading is evaluated, allowing the influence of the initial bolt preload on the mechanical response of the assembly to be considered.

Bolt Pretension: M20a / M20: The notation visible in the simulation tree indicates a pretensioned M20 bolted connection or a corresponding bolt-pretension definition. This suggests that the bolted interfaces are explicitly represented in the numerical model rather than being treated solely as simplified fixed connections.

The central graphical view shows the complete structural assembly in an isometric representation. The long central member extends between two end regions, where the connection and support components are located. The colored symbols overlaid on the geometry do not represent stress or deformation contours; rather, they visualize the locations and types of applied boundary conditions and loads.

The coordinate triad in the upper-left portion of the graphics window defines the global orientation of the model. The scale bar at the bottom indicates the approximate geometric extent of the structure, with the displayed range reaching approximately 500 mm. The model therefore represents a component with a characteristic length on the order of several hundred millimeters.

Importantly, the figure represents the simulation setup rather than a simulation result. No von Mises stress, strain, or displacement contour is displayed in the current view. Instead, the figure documents how the structural model is mechanically

constrained and how the pretensioned bolted connections are defined. These boundary conditions determine the load path and the resulting deformation and stress state calculated by the subsequent finite element analysis.

Figure 8 illustrates the finite element model and boundary conditions used for the static structural analysis of the pretensioned assembly. The model consists of a slender structural member with bolted connections at both ends. A fixed support, prescribed displacement constraints, and bolt-pretension loads are applied to reproduce the mechanical constraints and preload conditions of the investigated structure. The colored symbols identify the respective boundary conditions, while the model tree summarizes the corresponding analysis definitions. The figure shows the numerical model setup and does not represent a stress or deformation result.



Figure 8: Finite Element Model and Boundary Conditions of the Pretensioned Structural Assembly

The composite structure was modelled in ANSYS ACP (Pre) using a multi-material laminate layup. The laminate consists of carbon-fibre-reinforced epoxy plies combined with SAN foam core layers. Both unidirectional (UD) and woven carbon-fibre fabrics are considered, with material data defined according to their respective areal weights and fibre architectures.

The layup includes biaxial and triaxial carbon/epoxy fabric layers, as indicated in the ACP model, together with foam layers providing the required sandwich-core thickness. The individual plies are assigned within the ACP stacking sequence, allowing the local laminate thickness and fibre orientation to be explicitly defined. According to the displayed model, the resulting laminate thickness varies between approximately 19.98 and 20.94 mm over the analysed component (Figure 9).

This modelling approach enables the anisotropic mechanical behaviour of the composite to be captured while accounting for the influence of the individual fibre orientations, material properties, and sandwich-core configuration on the structural response.

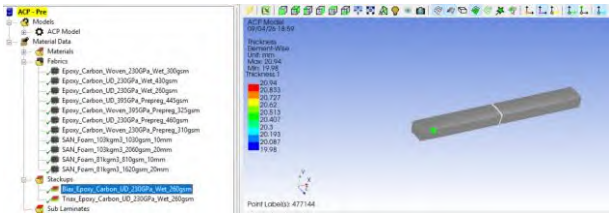


Figure 9: Laminate layup and through-thickness distribution of the composite structure in ANSYS ACP (Pre)

5. DISCUSSION AND OUTLOOK

The experimental investigations demonstrate the feasibility of EIT for detecting and localizing artificially introduced defects in CFRP laminates. The reconstructed conductivity changes were generally located close to the actual defect positions. However, no clear correlation between borehole diameter and reconstruction energy or positional error was observed. The results further show that the measurement pattern influences the localization accuracy, with the TS35 pattern providing lower median positional errors than the Star pattern for the investigated delamination positions. Due to the limited number of specimens, these findings should be considered indicative rather than statistically conclusive.

The experiments also demonstrate the importance of reliable electrode integration. The second integration concept achieved a stable electrical resistance of 1.6–1.8 Ω after manufacturing and thermal treatment, providing a suitable basis for further development of the embedded EIT system. The measured electrical contact behavior should be considered in future numerical models, as electrode

contact and material anisotropy can significantly influence the reconstructed conductivity distribution.

These experimental findings provide the basis for extending the numerical model. In addition to the mechanical behavior of the CFRP load jacket, the model should incorporate the anisotropic electrical properties of the laminate, electrode geometry, and contact conditions. Local submodels can be used to investigate the influence of embedded sensors on the mechanical behavior and to simulate defects at different positions within the laminate.

In a subsequent step, the numerical EIT model will be correlated with the experimental measurements. Different electrode configurations, defect sizes, and defect positions can then be systematically investigated. The validated model can subsequently be transferred from planar specimens to the curved CFRP load jacket and combined with the structural simulation.

For the final application, the model will be extended to thermo-mechanical and cyclic cryogenic loading. The aim is to investigate the relationship between damage development, changes in electrical conductivity, and structural integrity. This combined experimental and numerical approach provides the basis for a component-specific SHM system capable of relating measured electrical changes to damage evolution in the CFRP load jacket.

6. REFERENCES

[1] A. Wronkowicz-Katunin, A. Katunin, and K. Dragan, “Reconstruction of Barely Visible Impact Damage in Composite Structures Based on Non-Destructive Evaluation Results,” *Sensors (Basel, Switzerland)*, vol. 19, no. 21, 2019, doi: 10.3390/s19214629.

[2] T. Feng *et al.,* “Environmental Aging Mechanisms and Their Impact on the Mechanical Performance of Fiber-Reinforced Polymer Composites: A Comprehensive Review,” *Coatings*, vol. 16, no. 6, p. 742, 2026, doi: 10.3390/coatings16060742.

[3] M. Saeedifar and D. Zarouchas, “Damage characterization of laminated composites using acoustic emission: A review,” *Composites Part B: Engineering*, vol. 195, p. 108039, 2020, doi: 10.1016/j.compositesb.2020.108039.

[4] T. Huang and M. Bobyr, “A Review of Delamination Damage of Composite Materials,” *J. Compos. Sci.*, vol. 7, no. 11, p. 468, 2023, doi: 10.3390/jcs7110468.

[5] Q. Zhao *et al.,* “Review on the Electrical Resistance/Conductivity of Carbon Fiber Reinforced Polymer,” *Applied Sciences*, vol. 9, no. 11, p. 2390, 2019, doi: 10.3390/app9112390.

[6] L. Heinzlmeier, S. Sieberer, T. Wolfsgruber, C. Kralovec, and M. Schagerl, “Damage Propagation and Residual Strength of Simple Block-Loaded CFRP Plates with Circular Holes under Tension–Tension Fatigue Conditions,” *J. Compos. Sci.*, vol. 7, no. 9, p. 379, 2023, doi: 10.3390/jcs7090379.

[7] A. TODOROKI, M. UEDA, and Y. HIRANO, “Strain and Damage Monitoring of CFRP Laminates by Means of Electrical Resistance Measurement,” *JMMP*, vol. 1, no. 8, pp. 947–974, 2007, doi: 10.1299/jmmp.1.947.

[8] Y. Tao *et al.,* “A comprehensive review on fiber-based self-sensing polymer composites for in situ structural health monitoring,” *Adv Compos Hybrid Mater*, vol. 8, no. 5, 2025, doi: 10.1007/s42114-025-01413-y.

[9] M. Yasin, S. Böhm, P. O. Gaggero, and A. Adler, “Evaluation of EIT system performance,” *Physiological measurement*, vol. 32, no. 7, pp. 851–865, 2011, doi: 10.1088/0967-3334/32/7/S09.

[10] S. A. Malik, M. Jalalvand, M. D. Wadge, J. D. Acosta, and R. M. Felfel, “Robust Electrical Contact with Low Interface Resistance Using Embedded Co-cured Electrodes in Carbon Fibre Composites,” *Appl Compos Mater*, vol. 32, no. 6, pp. 2625–2652, 2025, doi: 10.1007/s10443-025-10345-1.

[11] M. Cheney, D. Isaacson, and J. C. Newell, “Electrical Impedance Tomography,” *SIAM Rev.*, vol. 41, no. 1, pp. 85–101, 1999, doi: 10.1137/S0036144598333613.

[12] B. Grychtol, B. Müller, and A. Adler, “3D EIT image reconstruction with GREIT,” *Physiological measurement*, vol. 37, no. 6, pp. 785–800, 2016, doi: 10.1088/0967-3334/37/6/785.

[13] S. Nonn, M. Schagerl, Y. Zhao, S. Gschossmann, and C. Kralovec, “Application of electrical impedance tomography to an anisotropic carbon fiber-reinforced polymer composite laminate for damage localization,” *Composites Science and Technology*, vol. 160, pp. 231–236, 2018, doi: 10.1016/j.compscitech.2018.03.031.

[14] L. W. Escalona-Galvis, P. Diaz-Montiel, and S. Venkataraman, “Optimum Electrode Configurations for Two-Probe, Four-Probe and Multi-Probe Schemes in Electrical Resistance Tomography for Delamination Identification in Carbon Fiber Reinforced Composites,” *J. Compos. Sci.*, vol. 2, no. 2, p. 29, 2018, doi: 10.3390/jcs2020029.

[15] J. Wagenaar and A. Adler, “Electrical impedance tomography in 3D using two electrode planes: characterization and evaluation,” *Physiological measurement*, vol. 37, no. 6, pp. 922–937, 2016, doi: 10.1088/0967-3334/37/6/922.

PHYSICS-INFORMED MACHINE LEARNING FOR THERMOPLASTIC INDUCTION HEATING OF CFRP STRUCTURES IN SPACE APPLICATIONS

Mattia Mazzeschi (1), Adrian Pedrosa Valbuena (2), Ruben Perez Torices (3), Esteban Cañibano Alvarez (4)

(1) *Fundación Cidaut, Pl. Vicente Aleixandre Campos, 2, 47151 Boecillo, Spain, Email: matmaz@cidaut.es*
(2) *Fundación Cidaut, Pl. Vicente Aleixandre Campos, 2, 47151 Boecillo, Spain, Email: adrped@cidaut.es*
(3) *Fundación Cidaut, Pl. Vicente Aleixandre Campos, 2, 47151 Boecillo, Spain, Email: rubper@cidaut.es*
(4) *Fundación Cidaut, Pl. Vicente Aleixandre Campos, 2, 47151 Boecillo, Spain, Email: estcan@cidaut.es*

KEYWORDS

Thermoplastic composites; induction heating; physics-informed machine learning; surrogate modelling; space manufacturing.

ABSTRACT

Thermoplastic carbon-fibre-reinforced polymers are attractive for future spacecraft structures because they combine low mass with weldability and the potential for automated or in-space assembly. Induction heating is particularly promising, but its repeatability is limited by the coupled electromagnetic and thermal response of anisotropic laminates. This work develops a physics-informed machine-learning framework that combines experiments, an electrothermal finite-element model, and low-cost neural-network surrogates. Four predictive routes are assessed: a semi-empirical first-order model, a fully data-driven model, a surrogate of the finite-element solution, and a hybrid residual model that corrects the physics-based prediction using experimental data. The hybrid formulation reduces the final-test RMSE from 43.3 °C for the FEM surrogate to 10.8 °C while retaining a physically meaningful baseline. The resulting model is used to construct power-time process maps and identify underheated, weldable, and thermally critical regions for different laminate thicknesses.

1. INTRODUCTION

Thermoplastic composite structures are increasingly considered for lightweight aerospace and space applications because they offer high specific properties together with short processing cycles, damage tolerance and, importantly, the possibility of fusion joining [1]. Welding avoids drilled holes, fasteners and long adhesive-curing operations and can therefore simplify assembly while reducing added mass. Among the available techniques, induction welding is attractive because energy is delivered without direct contact, heating can be rapid, and the process can be integrated with automated manufacturing equipment [2].

These characteristics are also relevant to future in-space manufacturing and assembly. Large structures may benefit from modular architectures in which thermoplastic subcomponents are joined after launch or repaired locally. In such scenarios the joining process must be energy-efficient, compact and robust, while the thermal history must remain within a narrow window: insufficient heating prevents adequate polymer interdiffusion, whereas excessive temperature can produce matrix degradation, distortion or damage to neighbouring components.

Achieving repeatable thermal histories remains a major challenge in the induction heating of carbon-fibre-reinforced polymers (CFRPs). Even under nominally identical process conditions, variations in the laminate can modify the electrical pathways through which induced currents circulate and, consequently, the resulting heat generation. In particular, differences in consolidation and interlaminar microstructure alter fibre-to-fibre contacts and through-thickness electrical conduction, producing markedly different induction-heating patterns [3]. Electrical conductivity itself is anisotropic and inherently variable, and uncertainty in its magnitude propagates directly into variability of the predicted temperature field [4]. This material-induced variability is compounded by the strong sensitivity of inductive heating to process parameters: heating rates depend on frequency, generator power, coil geometry and, particularly, coil-to-part coupling distance [5]. Consequently, relatively small material or process variations can produce appreciable differences in the thermal response, making robust prediction and repeatable temperature control difficult.

High-fidelity finite-element (FEM) models provide physical insight and spatial temperature fields, but calibration is demanding and repeated simulations are too expensive for rapid process exploration or control. Recent studies have explored neural networks and surrogate models to accelerate temperature prediction in induction-heating

processes, reducing the computational cost of repeated multiphysics simulations [6]–[8]. However, a key challenge remains to retain the physical information provided by FEM models while correcting their discrepancy from experimental CFRP heating behaviour. The objective of this work is therefore to develop a fast, experimentally corrected physics-informed framework for CFRP induction heating. The study: (i) compares semi-empirical, fully data-driven and physics-based predictive approaches; (ii) combines a FEM surrogate with data-driven residual correction; and (iii) exploits the resulting hybrid model to investigate power–time process windows relevant to thermoplastic welding.

2. EXPERIMENTAL AND PHYSICAL FRAMEWORK

2.1. Experimental Setup and Test Matrix

The experimental set-up consists of an induction welding head positioned close to a flat CFRP coupon (Fig.1). Temperature is monitored using thermocouples on the laminate, an infrared camera and pyrometers. The combination of contact and non-contact measurements provides both local time histories and information on the spatial thermal field. The coil is water cooled and mounted in a repeatable fixture relative to the panel.

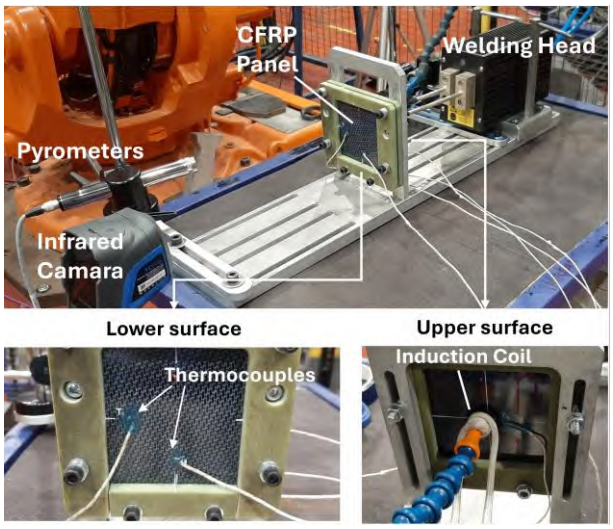


Figure 1 Induction-heating experimental setup and temperature instrumentation.

Three nominal laminate thicknesses were investigated: 0.62, 1.24 and 2.48 mm. Applied power was varied between 10 and 60% of the maximum available power (12 kW) according to the experimental matrix reported in Tab.1. Cases used for model development were separated from an independent test subset.

Table 1: Summary of the experimental design.

Case_ID	Thickness [mm]	Power [%]	Subset
EXP 1	0,62	10	Development
EXP 2		15	
EXP 3		20	
EXP 4		25	
EXP 5		30	
EXP 6		40	
EXP 7	1,24	10	Test
EXP 8		15	
EXP 9		20	
EXP 10		30	
EXP 11	2,48	10	Development
EXP 12		15	
EXP 13		20	
EXP 14		40	
EXP 15		60	

Data were partitioned on a case-wise basis, so that all time samples belonging to the same experimental heating history were assigned to the same dataset. This prevents information leakage between training and testing and provides a more representative assessment of the model performance on unseen experimental cases.

2.2. Physical Background

Induction heating of CFRP results from the coupling between the electromagnetic and thermal fields. The alternating current supplied to the induction coil generates a time-varying magnetic field, which induces electric fields and current densities within the electrically conductive carbon-fibre network. Under the quasi-static electromagnetic approximation, the local current density is related to the electric field through the electrical conductivity tensor,

$$J = \sigma E \qquad (1)$$

where J is the induced current density, E is the electric field, and σ is the electrical conductivity tensor of the laminate. CFRP exhibits strongly anisotropic electrical conductivity, with conductivity along the carbon fibres being several orders of magnitude greater than that in the transverse and through-thickness directions. Consequently, the induced current paths and the associated heat generation depend on the laminate architecture, ply orientation, coil geometry, and relative coil–laminate position.

The electromagnetic energy dissipated within the laminate is converted into heat by Joule losses. The corresponding volumetric heat source is

$$Q_{em} = J \cdot E \qquad (2)$$

For the non-ferromagnetic CFRP considered here, Joule dissipation associated with the induced currents represents the relevant electromagnetic heating mechanism. The resulting heat-source field is generally non-uniform and inherits the spatial characteristics of the electromagnetic coupling.
The subsequent temperature evolution is governed by transient heat conduction,

$$\rho c_p \frac{\partial T}{\partial t} = \nabla \cdot (k \nabla T) + Q_{em} \qquad (3)$$

where ρ is the laminate density, c_p is the specific heat capacity, and k is the thermal-conductivity tensor. As for the electrical properties, the thermal response of CFRP is anisotropic, with heat transport depending on the fibre directions and stacking sequence. Heat is simultaneously transferred within the laminate and dissipated to the surroundings. At the external boundaries, the main thermal losses can be represented by convection and radiation as

$$q_{conv} = h(T - T_0),\ q_{rad} = \varepsilon \sigma_{SB}(T^4 - T_0^4) \qquad (4)$$

where h is the convective heat-transfer coefficient, T_0 is the ambient temperature, ε is the surface emissivity, and σ_{SB} is the Stefan–Boltzmann constant. The measured thermal response therefore results from the balance between electromagnetic power deposition, thermal energy storage, anisotropic heat diffusion, and heat exchange with the environment.
For reduced-order modelling, this distributed thermal problem can be **approximated by a lumped energy balance** when the response at a given location is represented by a single dominant thermal timescale. For constant heating conditions, the balance may be expressed as

$$C_{th} \frac{dT}{dt} = \dot{Q}_{in} - G_{th}(T - T_0) \qquad (5)$$

where C_{th} is an effective thermal capacitance, G_{th} is an effective thermal conductance accounting for heat removal from the considered thermal domain, and $\dot{Q}_{in}$in represents the effective absorbed heating power. Assuming these effective quantities remain approximately constant during heating, integration gives the first-order response

$$T(t) = T_0 + (T_{steady} - T_0)\left(1 - e^{-t/\tau}\right) \qquad (6)$$

with

$$T_{steady} = T_0 + \frac{\dot{Q}_{in}}{G_{th}}, \qquad \tau = \frac{C_{th}}{G_{th}} \qquad (7)$$

Here, T_{steady} represents the asymptotic temperature associated with the balance between absorbed power and thermal losses, and τ is the effective thermal time constant governing the rate at which this condition is approached.
This reduced representation does not resolve the spatially distributed electromagnetic and thermal fields described by Eqs. 1-4. Instead, T_{steady} and τ condense their combined effect into two effective response parameters. This distinction provides the physical basis for the two modelling strategies investigated in this work: the **semi-empirical first-order model**, which predicts these reduced thermal parameters from the operating conditions, and the higher-fidelity data-driven and physics-guided models, which directly represent the transient temperature response without imposing a first-order temporal evolution.

3. PREDICTIVE MODELLING METHODOLOGY

Four AI-based predictive models were developed to reproduce the transient thermal response of CFRP laminates under induction heating, using experimental measurements, physics-based FEM simulations, or a combination of both.
Fig. 2 summarizes the overall modelling strategy. Experimental temperature histories are used to develop the semi-empirical and fully data-driven models, whereas numerical temperature histories generated by the electrothermal FEM are used to train the FEM surrogate. Experimental and physics-based information are finally combined in the hybrid model through a learned residual correction.

3.1. Experimental-Based Thermal Models

The first two models rely exclusively on experimental data. The **semi-empirical first-order model** uses the reduced thermal formulation introduced in Section 2.2. A feed-forward neural network predicts T_{steady} and $ln(\tau)$ from the applied power P, laminate thickness d, and thermocouple coordinates (x_{TC}, y_{TC}, z_{TC}). The predicted parameters are then used in Eq. 6 to reconstruct the complete temperature history.
The **fully data-driven model** removes the first-order assumption and directly predicts $T(t)$ from the same process and spatial variables, with heating time t included as an additional input. This formulation can therefore learn the transient response without imposing a predefined temporal

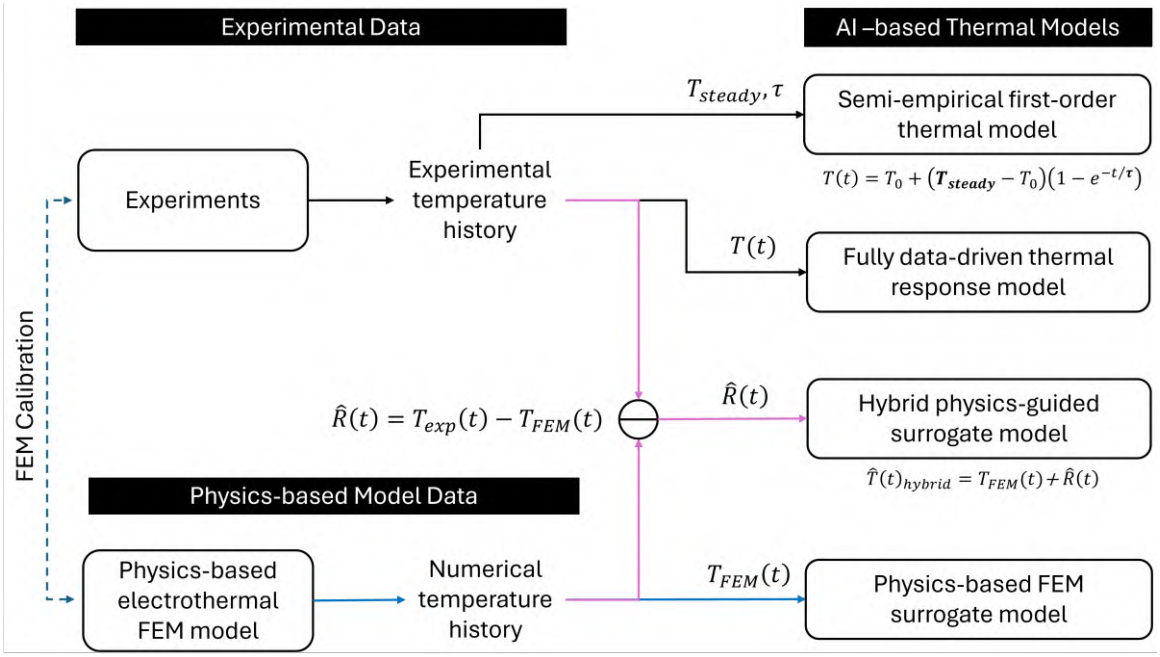


Figure 2 Predictive modelling framework combining experimental data, physics-based FEM simulations, and AI-based thermal models.

evolution. The architectures of both models are shown in Fig. 3 (a,b).

3.2. FEM Surrogate and Hybrid Physics-Guided Model

A coupled electrothermal model was implemented in COMSOL® Multiphysics to reproduce the induction-heating process. The computational domain includes the CFRP laminate, induction coil, and surrounding air, as shown in Fig. 4. Electromagnetic power deposition is coupled with transient anisotropic heat transfer, and the model is calibrated against the experimental temperature histories. The numerical temperature histories were subsequently used to train the **physics-based FEM surrogate model** shown in Fig. 3(c), which predicts the temperature increment ΔT_{FEM} from P , d , thermocouple coordinates, and time. This provides a computationally inexpensive approximation of the FEM response.

Finally, the **hybrid physics-guided model** learns the discrepancy between experimental and FEM temperatures using the network architecture shown in Fig. 3(d). The correction is learned from the residual between the experimental and numerical temperatures

$$\hat{R}(t) = T_{exp}(t) - T_{FEM}(t) \qquad (8)$$

thereby retaining the physics-based description of the process while compensating for systematic discrepancies between the numerical model and the experiments.

The corrected temperature prediction is

$$\hat{T}_{hybrid}(t) = T_{FEM}(t) + \hat{R}(t) \qquad (9)$$

All four neural models use three fully connected hidden layers with 32 neurons per layer. Inputs and outputs are standardised using training-set statistics, and independent test cases are excluded from model training.

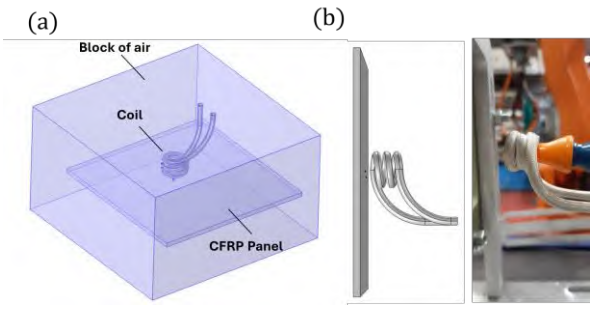


Figure 3 (a) Electrothermal FEM domain, (b) coil geometry and experimental coil.

3.3. Evaluation Metrics

Prediction performance is quantified by root-mean-square error (RMSE), mean absolute error (MAE) and mean bias. Metrics are calculated over the final-test temperature samples. Parity plots and residual-versus-temperature plots are used to identify systematic trends that a single scalar metric can hide.

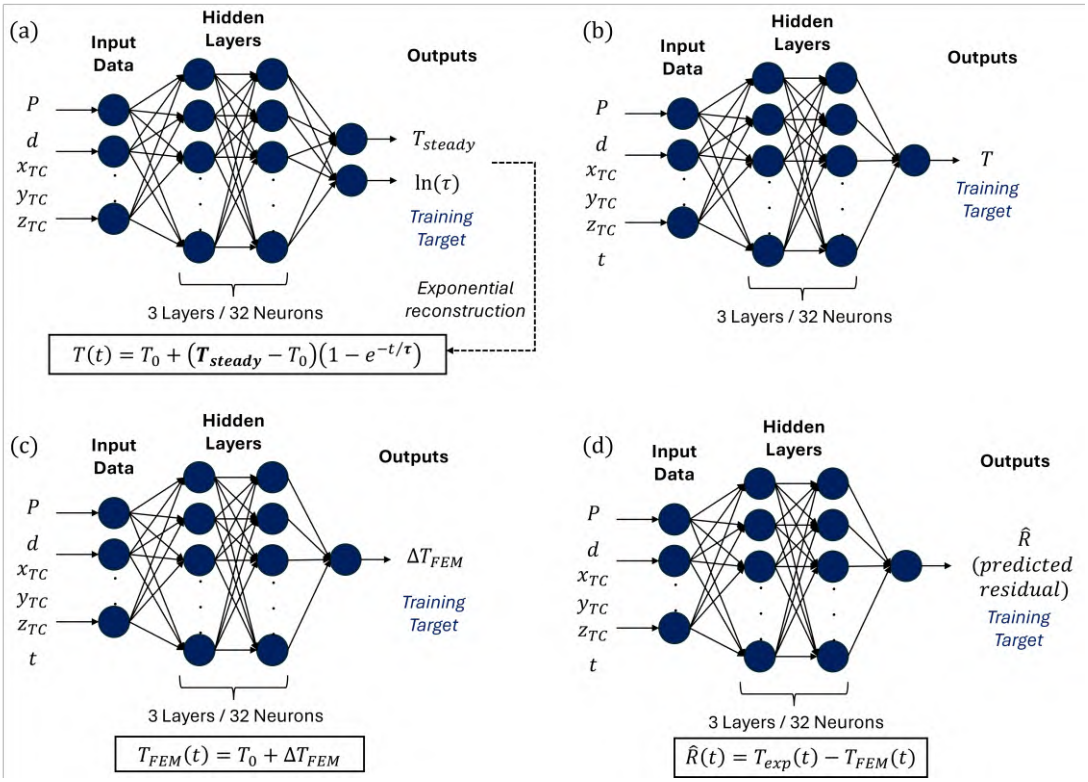


Figure 4 Neural-network architectures of the four predictive models: (a) semi-empirical first-order model, (b) fully data-driven temperature model; (c) physics-based FEM surrogate and (d) hybrid residual model.

4. RESULTS AND DISCUSSION

4.1. Physical Interpretability of the Semi-Empirical Model

The predicted first-order parameters show clear trends with laminate thickness and applied power (Fig. 5). As thickness increases, T_{steady} rises progressively from approximately 100 to 200 °C, reflecting the combined effects of electromagnetic power deposition, heat diffusion and thermal losses. In contrast, τ remains nearly constant at about 30 s for thicknesses up to 1.2-1.4 mm and increases thereafter. This behaviour suggests that, for thinner laminates, changes in thermal storage and heat transfer partially compensate each other, whereas at larger thicknesses the increased effective thermal inertia becomes more influential. Applied power has a stronger effect on T_{steady}, which increases from approximately 125 to 260 °C, while τ varies only moderately and approaches a plateau at high power. This different sensitivity is consistent with the physical meaning of the two parameters: T_{steady} is primarily associated with the balance between deposited energy and thermal losses, and is therefore strongly affected by the heating input, whereas τ represents the effective timescale resulting from the combined thermal storage and heat-transfer mechanisms.

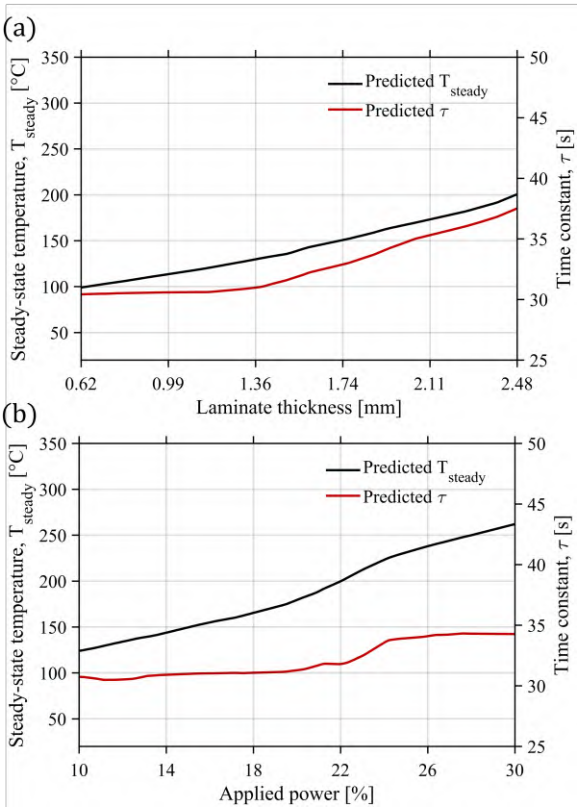


Figure 5 Predicted steady-state temperature and time constant versus (a) laminate thickness and (b) applied power.

Overall, the different responses of T_{steady} and τ demonstrate the value of the semi-empirical formulation not only for temperature prediction, but also as a compact representation of how the heating dynamics vary across the investigated process conditions.

4.2. Experimental Data-Driven Prediction

Representative test histories in Fig. 6 show that both experimental-data models reproduce the initial heating rate and the overall temperature evolution, although their performance differs as the heating conditions become more demanding.

At 10% of maximum power (Fig. 6(a)), both approaches provide a reasonable approximation of the measured response. At 20% and 30% (Fig. 6(b,c)), the fully data-driven model follows the experimental curves more closely, particularly during the transition from the rapid heating stage to the slower temperature evolution at longer times. The first-order model can instead underpredict or overpredict the final temperature when the measured response departs from a single exponential behaviour. This difference originates from the formulation of the two approaches. The semi-empirical model compresses each heating history into only two predicted quantities, T_{steady} and τ, and reconstructs the response using the first-order expression. This provides physical interpretability but constrains the shape of the predicted curve. Conversely, the fully data-driven model directly learns the relationship between process conditions, spatial position, heating time and temperature, allowing it to reproduce changes in the transient response without imposing a predefined temporal evolution. This flexibility becomes particularly beneficial when the heating rate changes during the experiment or when a clear steady state is not reached.

The improved interpolation capability is also reflected in the global final-test results reported in Tab. 2. The fully data-driven model reduces the RMSE from 20.0 to 15.3 °C and the MAE from 16.2 to 12.6 °C compared with the semi-empirical formulation. Both models show a negative mean bias, although its magnitude is slightly reduced from −6.2 to −5.1 °C, indicating an overall tendency to underpredict the measured temperatures.

Table 2: Final-test accuracy of the experimental-data models.

Model	RMSE [°C]	MAE [°C]	Bias [°C]
Semi-empirical first-order	20.0	16.2	-6.2
Fully data-driven	15.3	12.6	-5.1

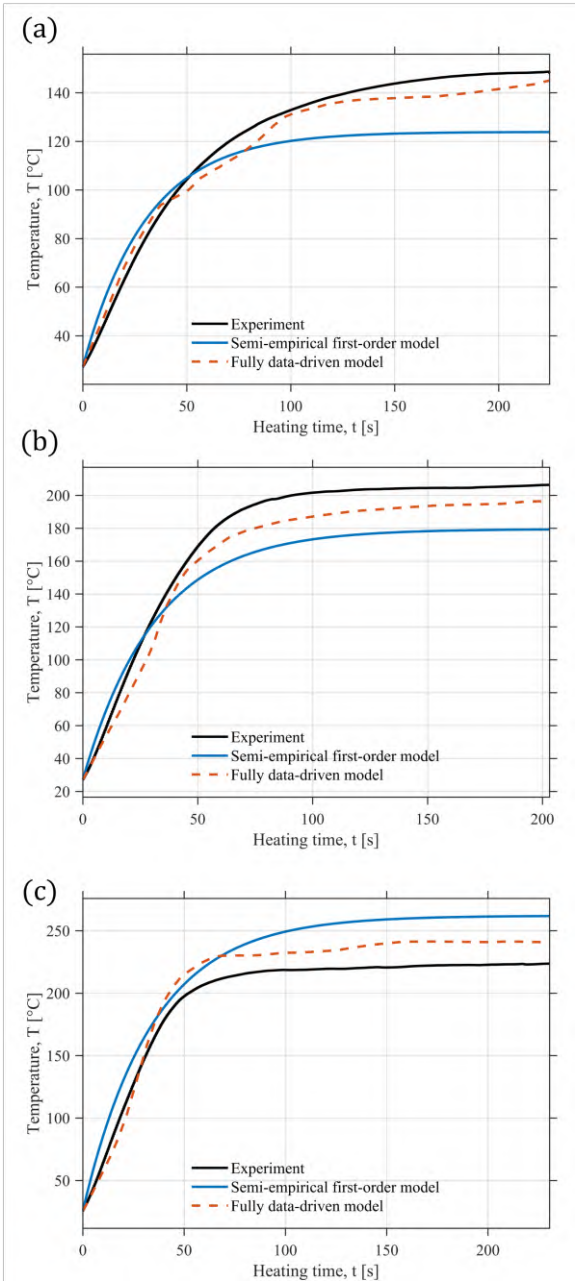


Figure 6 Representative experimental histories and predictions at (a) 10, (b) 20 and (c) 30% power for the 1.24 mm laminate.

The parity plot in Fig. 7(a) shows good overall agreement around the ideal-prediction line at low and intermediate temperatures, while the dispersion increases towards the upper part of the temperature range. The residual distributions in Fig. 7(b) show that prediction errors are not uniformly scattered around zero but follow distinct trends associated with individual heating histories. This indicates that some features of the transient response are not fully captured by the models. The larger residual spread at high temperatures further suggests reduced predictive accuracy under the more demanding

heating conditions. Nevertheless, the lower global errors reported in Tab. 2 demonstrate that the fully data-driven model provides the more accurate interpolation of the experimental thermal response, while the semi-empirical formulation retains the advantage of a compact and physically interpretable representation.

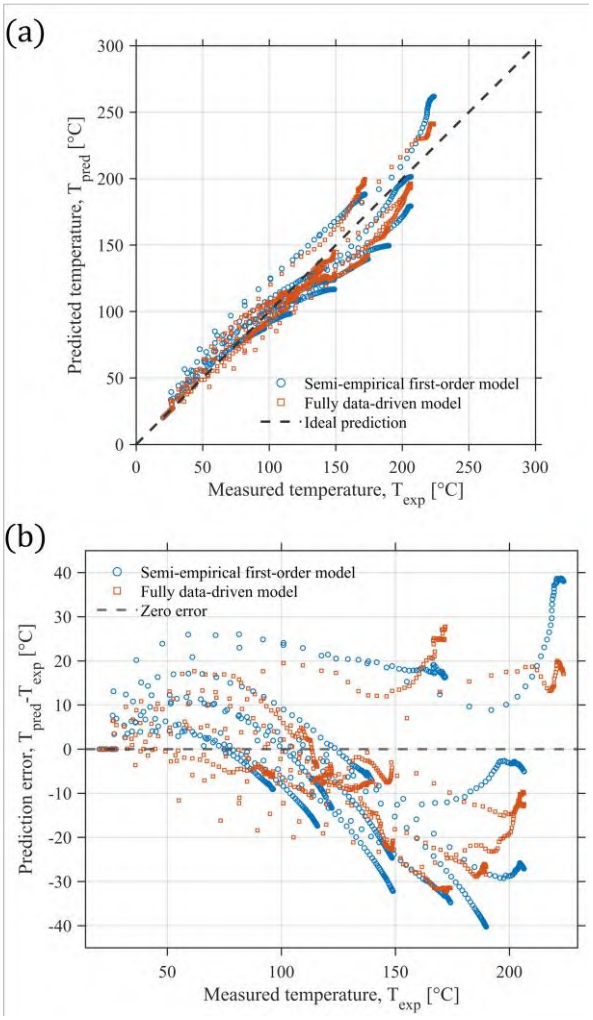


Figure 7 Parity and residual comparison of the semi-empirical and fully data-driven models.

4.3. Physics-Based FEM and Surrogate

The electrothermal FEM provides information that cannot be obtained from the limited number of experimental sensors. In addition to the local temperature histories, it resolves the complete temperature field and therefore allows hot-spot location, thermal gradients and spatial heat redistribution to be investigated. A representative field is shown in Fig. 8, where the highest temperatures are concentrated beneath the induction coil and the non-uniform distribution reflects the coupled electromagnetic and anisotropic thermal response of the CFRP laminate. This physical detail comes at the cost of a challenging calibration and validation process. Induction heating of CFRP involves strongly coupled electromagnetic and thermal phenomena, while several material properties are anisotropic, temperature dependent and affected by the laminate architecture. The numerical model necessarily introduces equivalent properties and simplified descriptions of heat losses and material behaviour. Moreover, uncertainties in electromagnetic coupling, through-thickness properties and experimental boundary conditions cannot be fully identified from a limited number of temperature measurements.

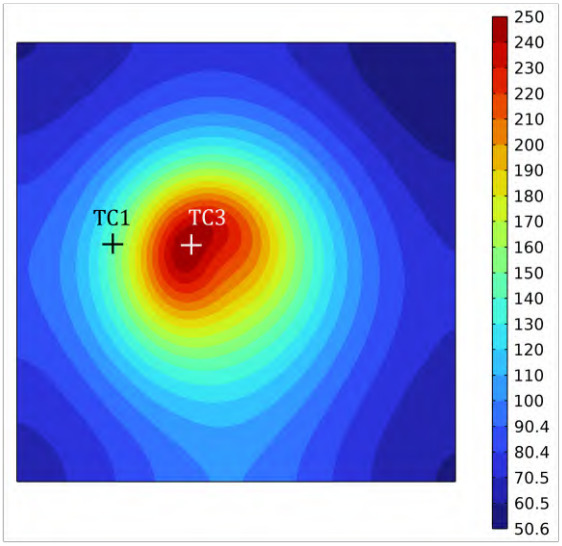


Figure 8 Representative FEM temperature field on the lower laminate surface, opposite to the induction coil. The markers indicate the locations of two of the four thermocouples used for experimental temperature measurements (TC1 and TC3).

These limitations are reflected in the comparison with the experiments. As reported in Tab. 3, the FEM RMSE increases from 36.6 °C for the 0.62 mm laminate to 44.2 °C for the 2.48 mm laminate, while the bias changes from −13.1 to 2.2 °C. The thickness dependence of the discrepancy indicates that a single calibrated parameter set does not fully capture the evolution of the coupled thermal response across the investigated design space. This represents an important limitation for direct predictive use of the FEM, despite the much richer physical information that it provides.

A second limitation is computational cost. Repeated transient multiphysics simulations become impractical when a large number of process conditions, spatial locations or heating times must be evaluated. The FEM surrogate addresses this

limitation by learning the numerical response and providing rapid access to selected FEM information without repeating the complete electrothermal solution.

Table 3: Experimental validation error of the calibrated electrothermal FEM as a function of laminate thickness.

Thickness [mm]	RMSE [°C]	MAE [°C]	Bias [°C]
0.62	36.6	33.9	-13.1
1.24	39.8	37.4	-1.5
2.48	44.2	39.8	2.2

The results in Fig. 9 demonstrate that this approximation introduces only a very small additional error.

The surrogate predictions closely follow the numerical FEM data over the complete temperature range, with RMSE = 2.44 °C, MAE = 1.73 °C and R2=0.999. The residuals remain predominantly concentrated around zero, with larger deviations limited to specific regions of the numerical dataset.

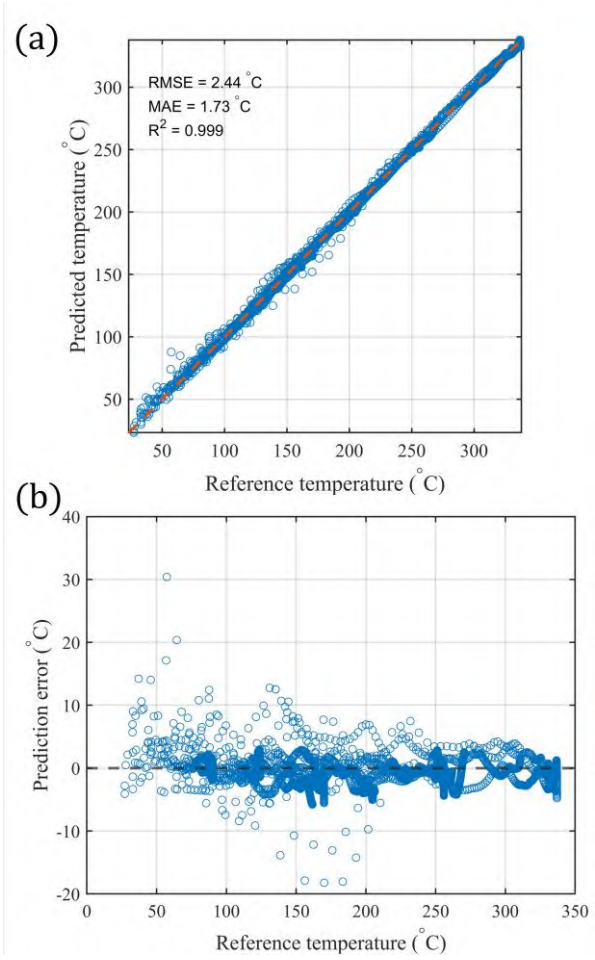


Figure 9 FEM-surrogate performance against numerical FEM data: (a) parity plot and (b) prediction residuals.

The surrogate therefore reproduces and interpolates the FEM response with high accuracy while substantially reducing the computational effort required for inference. Even though the surrogate does not correct the physical-model discrepancy identified in Table 3, it provides a computationally efficient representation of the calibrated FEM.

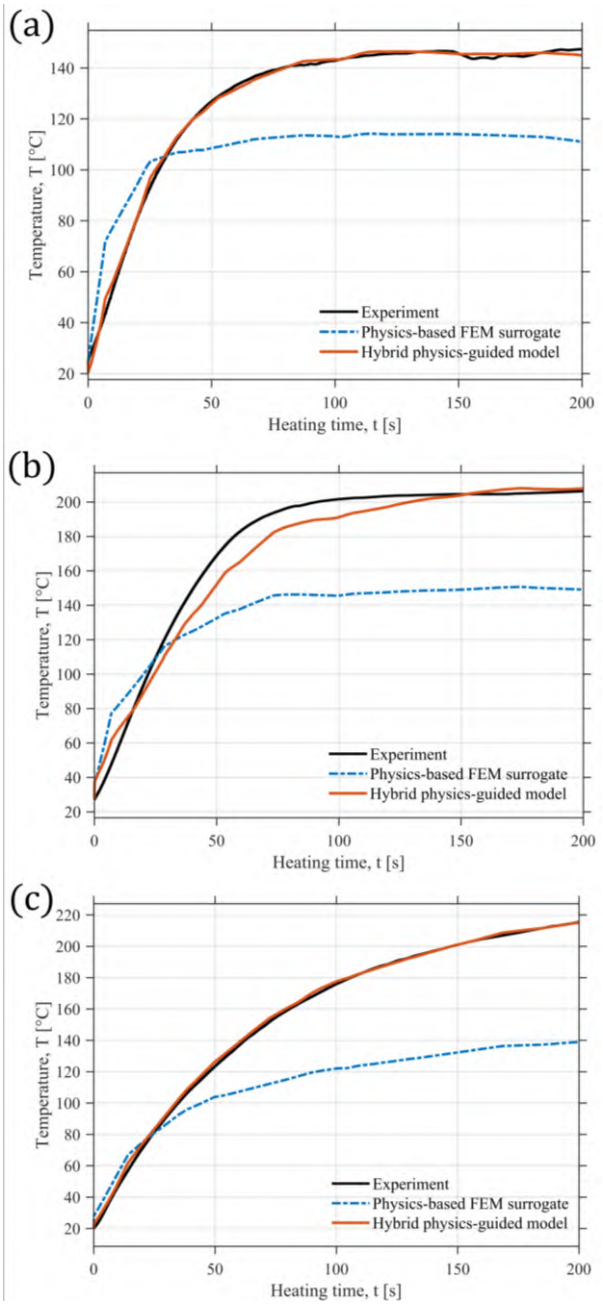


Figure 10 Representative experimental, FEM-surrogate and hybrid temperature histories. (a) 0.62, (b) 1.24, (c) 2.48 mm thickness.

This distinction motivates the hybrid strategy presented in the following section, where

experimental information is used to correct the systematic FEM-to-experiment residual.

4.4. Hybrid Physics-Guided Residual Correction

The hybrid approach addresses the main limitation identified for the physics-based model by learning the systematic discrepancy between FEM and experimental temperatures rather than replacing the physical prediction.

The FEM surrogate provides the baseline thermal response, while the residual network estimates the correction required to recover the measured behaviour.

This formulation combines the physical information embedded in the electrothermal model with the ability of experimental data to account for effects that are difficult to represent through a single set of calibrated material and boundary-condition parameters.

The representative histories in Fig. 10 clearly illustrate this behaviour. The FEM surrogate generally reproduces the overall heating trend but can substantially underestimate the temperature level, with the discrepancy depending on the investigated condition. After residual correction, the hybrid prediction follows both the transient heating rate and the final temperature much more closely. This is particularly evident in cases where the FEM captures the shape of the thermal response but incorrectly estimates the effective electromagnetic-to-thermal coupling. The correction is therefore not simply an adjustment of the final temperature, but acts over the complete transient response.

The improvement is confirmed quantitatively by the independent final-test results in Tab. 4. The RMSE decreases from 43.3 °C for the FEM surrogate to 10.8 °C for the hybrid model, corresponding to a reduction of approximately 75%. The MAE similarly decreases from 36.0 to 8.2 °C, while the mean bias is reduced from 4.2 to 1.5 °C. These results show that a large fraction of the FEM-to-experiment discrepancy is sufficiently systematic to be learned from the available experimental data.

Table 4: Final-test performance of the physics-based FEM surrogate before and after residual correction.

Model	RMSE [°C]	MAE [°C]	Bias [°C]
Physics-based FEM surrogate	43.3	36.0	4.2
Hybrid FEM + residual	10.8	8.2	1.5

The parity and residual distributions in Fig. 11 further confirm the improvement achieved by the hybrid model. The predictions closely follow the ideal parity line over most of the investigated temperature range, showing strong agreement with the experimental measurements. Consistently, the residuals are predominantly concentrated around zero and are substantially reduced compared with the uncorrected FEM surrogate. Some larger deviations remain at the highest temperatures, where prediction is more challenging. Overall, the results demonstrate that the learned residual effectively corrects the systematic FEM-to-experiment discrepancy and provides reliable temperature predictions across the investigated domain, including independent test cases never seen during model training. From a practical perspective, the hybrid architecture provides an important compromise between computational efficiency, physical information and predictive accuracy. Once the FEM surrogate and residual network have been trained, temperature predictions can be obtained without performing additional transient multiphysics simulations or repeatedly recalibrating the complete FEM for each operating condition.

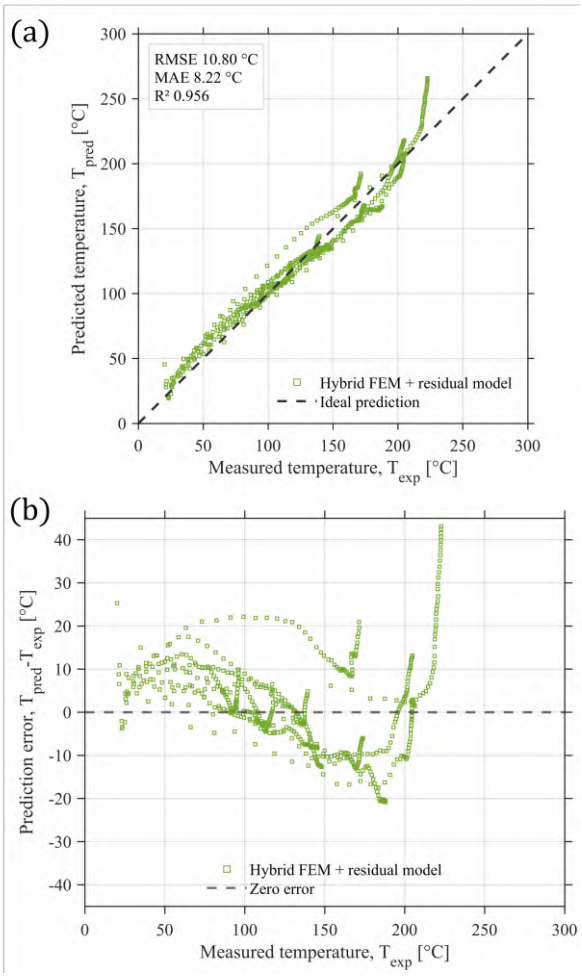


Figure 11 Final-test performance of the hybrid physics-guided model: (a) parity plot and (b) prediction residuals as a function of measured temperature.

The surrogate retains access to the physics-based baseline, while the residual model compensates for systematic model-form and calibration errors using experimental evidence. The resulting framework is therefore particularly attractive for rapid process exploration and prediction over the calibrated operating domain, where repeated high-fidelity FEM simulations would otherwise impose substantial computational time and resources.

4.5. Physics-Informed Process Window

The low inference cost of the hybrid framework enables dense exploration of the power–time design space beyond individual temperature histories.

Fig.12 maps the predicted temperature at a specific laminate location, corresponding to TC3, for the three investigated thicknesses. The 180 and 250 °C contours are adopted as lower and upper thermal criteria, respectively, defining a candidate processing window for thermoplastic joining. These limits provide preliminary thermal criteria, while the actual weld-quality boundaries may also depend on polymer grade, consolidation pressure, dwell time and joint configuration.

The maps can be directly used to identify the power–time combinations required to reach a target temperature. Considering 180 °C as the minimum criterion, for example, a minimum power level is required for each thickness: below approximately 25% for the 0.62 mm laminate and 17% for the 1.24 mm laminate, the predicted steady-state temperature remains below 180 °C and the target cannot be reached regardless of heating time. Above these thresholds, increasing power progressively reduces the heating time required to reach 180 °C, as illustrated by the corresponding contour. At longer heating times, the contour tends to flatten because the temperature approaches its steady-state value: the generated heat is increasingly balanced by conduction away from the heated region and heat losses to the surroundings, so extending the heating time produces progressively smaller temperature increases.

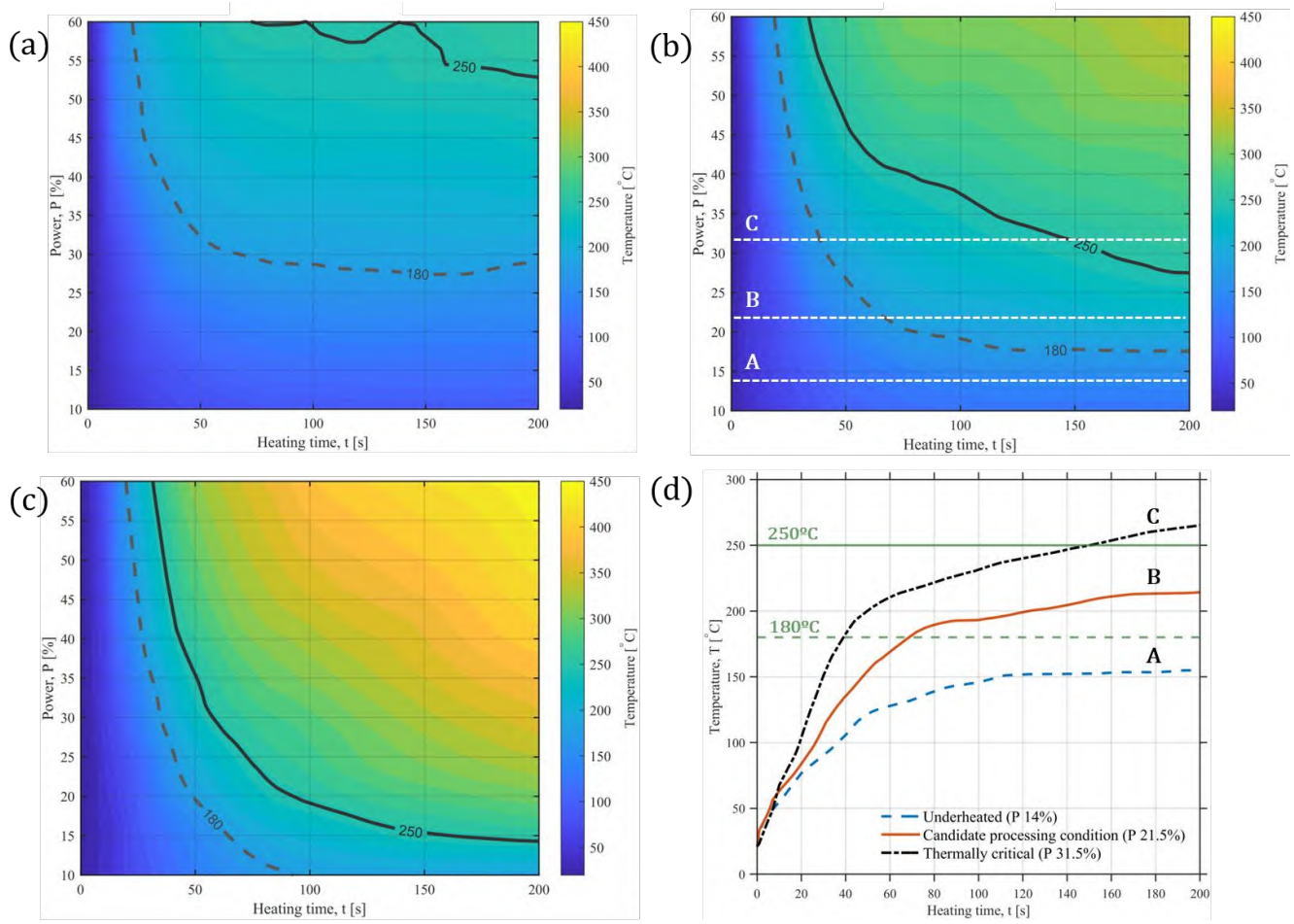


Figure 12 Hybrid-model power–time process maps for laminate thicknesses of (a) 0.62 mm, (b) 1.24 mm and (c) 2.48 mm, with 180 and 250 °C thermal criteria; (d) representative heating histories for underheated (A), candidate processing-window (B) and thermally critical (C) conditions.

Table 5: Computational requirements for power–time process-map generation using the electrothermal FEM and hybrid surrogate.

Approach	No. of considered temperature curves	Computational time	Computational resources	Relative cost
FEM	302	~ 54.6 h*	14 CPU cores	1×
Hybrid surrogate	302	54 s	1 CPU	~3640 × faster

*FEM computational time was extrapolated from 40 transient simulations requiring around 7 h and 12 min in total

Fig. 12(d) illustrates this interpretation for the 1.24 mm laminate, where condition A remains below the lower thermal criterion, condition B reaches the candidate processing range, and condition C exceeds the upper temperature limit.

Laminate thickness markedly shifts these thermal boundaries. For the 0.62 mm laminate, the 180 °C criterion requires comparatively high power and the 250 °C contour is largely outside the investigated domain, whereas increasing thickness shifts both contours towards lower power and shorter heating times.

A particularly important consequence is the strong dependence of the thermal processing window on laminate thickness. Increasing thickness reduces the power and heating time required to reach the minimum temperature criterion, but also shortens the margin before the upper thermal limit is exceeded. For the 1.24 mm laminate, the region between 180 and 250 °C covers a relatively broad range of power–time combinations, whereas for the 2.48 mm laminate the 250 °C contour shifts markedly towards lower powers and shorter times, resulting in a narrower operating window. This behaviour arises from the thickness-dependent electromagnetic–thermal response: changes in conductive volume and induced-current paths affect electromagnetic power deposition, while thermal storage and heat diffusion also vary with thickness. Under the investigated conditions, the resulting balance produces a faster temperature rise at larger thicknesses, making the process increasingly sensitive to the selected power–time combination and reducing the operating margin before potentially damaging temperatures are reached.

The value of these process maps therefore lies not only in identifying thickness-dependent operating limits, but also in the possibility of exploring them at low computational cost. As summarised in Tab. 5, generating an equivalent power–time map directly with the electrothermal FEM would require repeated transient multiphysics simulations and substantial computational resources.

Once trained, the hybrid surrogate evaluates the same design space with a much lower inference time, enabling dense screening of operating conditions while retaining the physics-based FEM response corrected against experimental measurements. This capability is particularly relevant for induction joining in space manufacturing, where robust parameter selection and process repeatability are critical and opportunities for rework may be limited. With further validation and the inclusion of weld-quality indicators, the approach could support rapid process optimisation and ultimately model-assisted closed-loop control.

5. CONCLUSIONS

A physics-informed machine-learning approach was developed for induction heating of thermoplastic CFRP laminates by combining experimental data, electrothermal FEM modelling and neural-network surrogates. While the semi-empirical and fully data-driven models provide complementary descriptions of the experimental thermal response, their accuracy is inherently constrained by the availability and coverage of experimental training data. The proposed hybrid approach complements this information with a physics-based FEM prediction and learns its systematic discrepancy from experimental data. This residual correction reduces the final-test RMSE from 43.3 °C to 10.8 °C and the MAE from 36.0 °C to 8.2 °C on independent cases not used during training.

The low inference cost of the hybrid surrogate enables dense exploration of the power–time design space, revealing a strong thickness dependence of the candidate thermal processing window and a reduced operating margin at larger thicknesses. The approach therefore provides a computationally efficient tool for process investigation and parameter selection while retaining a physics-based description of the thermal response. The present maps are limited to temperature-based criteria within the investigated experimental domain and coil configuration. Future work will extend the process domain, establish a direct link between thermal predictions and weld quality, and investigate model-assisted closed-loop control.

6. ACKNOWLEDGMENT

The authors would like to acknowledge the financial support provided by the Instituto para la

Competitividad Empresarial de Castilla y León (ICECYL), the Junta de Castilla y León, and the European Union through the European Regional Development Fund (ERDF) (Project No. CCTT6/23/VA/0016).

7. REFERENCES

1. Krueger, R., Bergan, A. (2004). Advances in Thermoplastic Composites Over Three Decades-A Literature Review. *NASA Technical Memorandum* (May), Available online: https://ntrs.nasa.gov/citations/20240005376

2. Liu, J., Quan, D., Scarselli, G., Alderliesten, R., Wang, H., Zhao, G. (2025) Developments and future prospects of welding technology for carbon fiber thermoplastic composites. *Compos. Part B Eng.* 297, 112314.

3. Kidangan, R. T., Unnikrishnakurup, S., Krishnamurthy, C. V., Balasubramaniam, K. (2022) The influence of interlaminar microstructure on the induction heating patterns of CFRP laminates. *Mater. Today Commun.* 33, 104338.

4. Schuttert, W. J., Abdul Rasheed, M. I., Rosić, B. (2024) Modeling variability of the electrical conductivity tensor for the induction welding of composites. *Proc. Appl. Math. Mech.* 24(3), e202400058.

5. Becker, S., Mitschang, P. (2022) Process Improvement of Continuous Induction Welding of Carbon Fiber-Reinforced Polymer Composites. *J. Mater. Eng. Perform.*, 31(9) 7049–7060.

6. Asadzadeh, M. Z., Raninger, P., Prevedel, P., Ecker, W., Mücke, M. (2021) Hybrid modeling of induction hardening processes," *Appl. Eng. Sci.* 5, 100030.

7. Di Barba, P. Dughiero, F., Forzan, M., Lowther, D. A., Marconi, A. Mognaschi, Maria E., Sykulski, J. K. (2023) Neural metamodels and transfer learning for induction heating processes (TEAM 36 problem). *Int. J. Appl. Electromagn. Mech.* 73(4), 389–398.

8. Shi, M., Zhang, Y., Chen, G., Huang, W., He, S. (2026) Physics-constrained surrogate modelling of hotspot-resolved thermochemical response in continuous-wave laser heating of carbon-fiber-reinforced polymer. *Comput. Mater. Sci.* (272), 114831.

DEVELOPMENT OF COMPOSITE SANDWICH INTERTANK AND INTERSTAGE STRUCTURES

H. Lang[(1)], J. Seip[(1)], A. Weiß[(1)], T. Wiedemann[(1)], M. Wolff[(1)]

[(1)] MT Aerospace AG, Franz-Josef-Strauß-Straße 5, 86153 Augsburg, Germany
Email: holger.lang@mt-aerospace.de, jonas.seip@mt-aerospace.de, anna-katharina.weiss@mt-aerospace.de, tim.wiedemann@mt-aerospace.de, marina.wolff@mt-aerospace.de

KEYWORDS

CFRP, Sandwich, Intertank Structure, Interstage Structure

ABSTRACT

Within the FLPP COSTELAS and A6 CIP C-ITS (Composite ULPM Inter Tank Structure) projects, MT Aerospace AG in Augsburg has been developing a composite inter tank structure (ITS) for the ARIANE 6 upper stage (d ≈ 5.4 m) using sandwich-technologies.

The development included the manufacturing of a full-scale demonstrator and various test components to show the design's potential for a full product development within the launch vehicle program.

In this paper, an overview of the projects COSTELAS and A6 C-ITS will be given. Special focus will be set on the complete full-scale manufacturing demonstrator and the test breadboards TBB1 and TBB2. The design of the C-ITS is developed to fulfil the same requirements and exhibits the same interfaces as the metallic ITS so that a 1:1 swap from the metallic to the composite ITS would be possible. The design follows a segmented approach of eight sandwich panels, which are manufactured in a one-shot curing process. The strength of the design is evaluated and justified by finite element analyses in ABAQUS.

To verify the structural performance of the design as well as the implementation approach, several components of critical design elements have been manufactured, tested and correlated to the analyses.

1. INTRODUCTION

The competitive landscape of the launch vehicle market requires efforts concerning improved performance through mass and cost reduction. In this context, the replacement of conventional metallic structures by advanced composite materials offers a viable path towards these objectives. Composite materials, particularly carbon fibre-reinforced polymers (CFRP), provide high specific stiffness and strength, enabling lighter robust structural designs. When combined with automated manufacturing processes, such as automated fibre placement (AFP), they support scalable production while reducing cycle times and material waste.

MT Aerospace AG in Augsburg has been developing a composite upper liquid propulsion module (ULPM) inter tank structure (C-ITS) with sandwich technology based on requirements of the ARIANE 6 launch vehicle. Fig. 1 shows the ARIANE 6 with its metallic ULPM inter tank structure to be replaced by the composite structure.

The decision for a general sandwich design has been taken after a trade-off between the sandwich and the technology of lattice structures [1]. It was driven by a balance of stiffness-to-mass ratio, manufacturability, integration compatibility and cost. A general sandwich design offers superior out-of-plane rigidity and consistent load distribution, which aligns with the requirements for inter tank stability under launch loads and thermal gradients. The current design demonstrates compliance with key structural and interface requirements.

The initiative evolved under ESA's **F**uture **L**aunchers **P**reparatory **P**rogramme (FLPP), beginning with the PACE (**P**reparatory **A**ctivities for **C**FRP Sandwich T**e**chnologies) and COSTELAS (**C**ost **O**ptimised **S**andwich **Te**chnology for **La**rge-Scale **S**tructures) projects in 2021. These projects focused on demonstrating the feasibility of composite sandwich panels, including material characterisation, process development for cost-efficient manufacturing of large CFRP sandwich structures and full-scale test breadboard validation.

The C-ITS project, which ran under the A6 Competitiveness Improvement Programme (CIP), project aimed to mature the design to a tailored pMG5 (product Maturity Gate 5) status, which supports future integration into product development.

To validate the design and manufacturing strategy, a full-scale demonstrator (DM0, see Fig. 20) was manufactured following multiple test elements and test breadboards (TBB1 and TBB2).

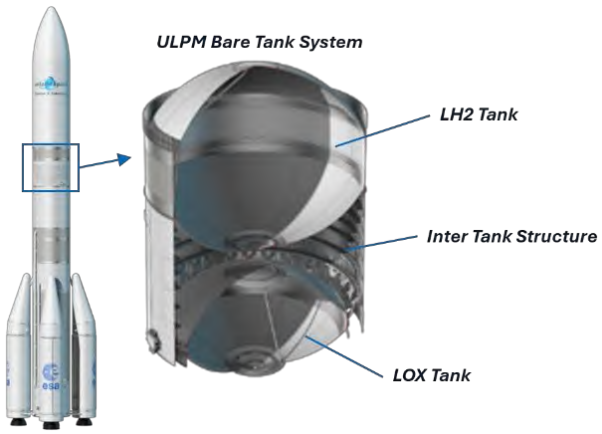


Fig. 1: ARIANE 6 Launcher ULPM Bare Tank System [©ESA]

2. INTER TANK STRUCUTRE

The ARIANE 6 has two metallic inter tank structures, one for the lower liquid propulsion module (LLPM) and one for the upper liquid propulsion module (ULPM), see Fig. 2. They serve as the primary structural interface between the liquid hydrogen (LH2) tank and the liquid oxygen (LOx) tank, while accommodating equipment access and tank connections.

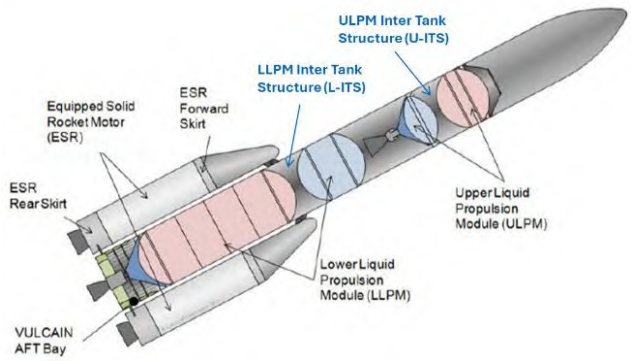


Fig. 2: Schematic View of ARIANE 6 Launcher [©ESA]

Within the launcher architecture, the upper stage plays a critical role in determining payload performance. Unlike the main stage, where mass savings yield a payload increase ratio of approximately 1:0.3, every kilogram saved in the upper stage directly translates to a 1:1 payload gain. This makes structural optimization at this level particularly important and is the reason why the upper stage inter tank structure has been chosen. The C-ITS design is fully aligned with the baseline of the existing metallic A6 U-ITS in terms of geometrical bounds, local and global loads as well as mechanical interfaces.

3. DEVELOPMENT AND VERIFICATION APPROACH

To improve the technology (TRL) and manufacturing readiness level (MRL) and achieve a tailored pMG5 status maturity level, coupon samples, test elements and breadboards were designed, manufactured and tested while ensuring that all design decisions are backed by analytical validation, experimental evidence, and manufacturability assessments. Additionally, a full-scale manufacturing demonstrator has been produced featuring the principle design of the reference architecture. This approach follows a hierarchical progression from material-level characterization to full-scale structural demonstration, with each stage feeding into the next to reduce uncertainty and build-up confidence in the final reference architecture, see Fig. 3.

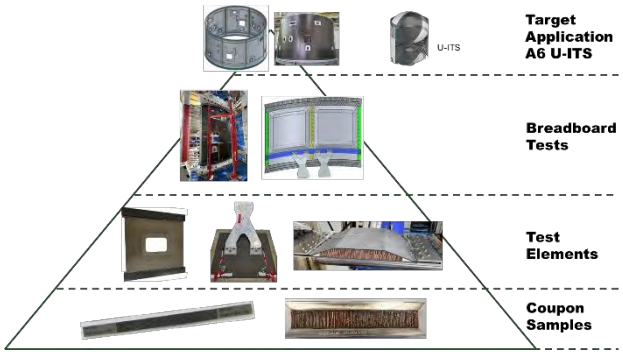


Fig. 3: Development and Verification Approach

The reference architecture is the basis of this development logic. It represents the intended full-scale target application design, a 1:1 scale composite inter-tank structure for the ARIANE 6 upper stage. The reference architecture provides the basis, from which the smaller scale elements are derived. On the lowest level are the coupon tests, which are used for material characterisation, providing the input for the analyses. Test elements are used for testing of singular effects and critical regions under representative loading conditions. Breadboard tests provide the experimental verification of the target application. The demonstrator verifies the manufacturing and assembly capabilities of the full structure. Each level serves a distinct purpose: material property acquisition, functional validation of key design features, verification of manufacturing processes and system-level demonstration while enabling iterative refinement of both physical and numerical models.

3.1. C-ITS Reference Architecture

The key requirements of the C-ITS reference architecture, which is the full-scale target application design as shown in Fig. 4, include the ability to transfer high flux loads in compression and

tension, connections to the adjacent structures like the metallic LOx and LH2 tank as well as the composite interface structure (IFS) which connects main and upper stage of the launcher. Furthermore, compliance with local interfaces and their loads for equipment and access, ability to withstand high thermal gradients as well as providing considerable mass and cost savings compared to the metallic U-ITS while using a highly automated manufacturing process with AFP are main goals of the project. Functional integration is achieved through monolithic regions at cut-outs and interfaces, which simplify mounting and preserve structural integrity. The design leverages existing metallic interface geometries to ensure compatibility without requiring major rework of adjacent sub-systems. The C-ITS reference architecture is arranged as a segmented structure composed of eight composite sandwich panels, replicating the segmentation and interface layout of the existing metallic inter tank structure.

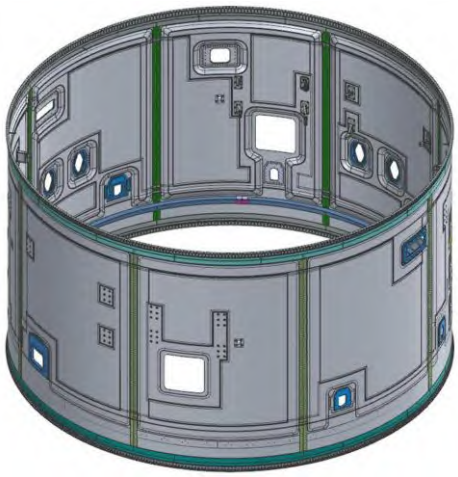


Fig. 4: C-ITS Reference Architecture

Riveted joints using composite splice sheets connect adjacent panels and metallic interface rings are retained for integration with metallic adjacent structures. The panels utilize a sandwich design with honeycomb cores, optimized into far- and near-field zoning: high core density and thicker face sheets are implemented in regions of high mechanical demand (e.g. interfaces and load transfer zones), while lower core density and thinner face sheets are used in less critical areas to achieve mass savings (see Fig. 5). Monolithic zones are incorporated at all interface locations to enable robust mechanical fastening to metallic components, ensuring structural continuity and ease of integration.

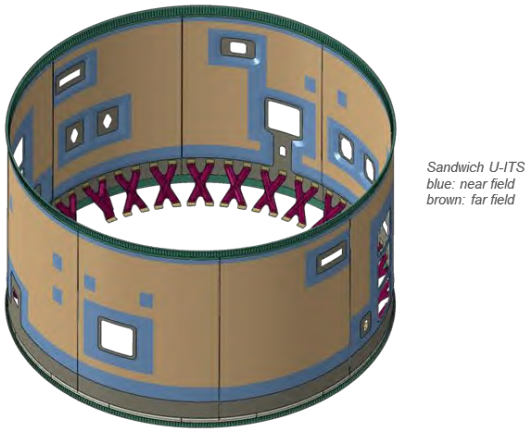


Fig. 5: C-ITS Far- and Near-Field distribution

Structural performance is assessed through a multi-scale non-linear finite element analysis (FEA) approach using ABAQUS. A global FE model (GFEM, see Fig. 6), implemented with solid and shell elements, captures the overall deformation and load distribution. Adjacent structures like the LOx tank and IFS are included in the model to generated representative boundary conditions.

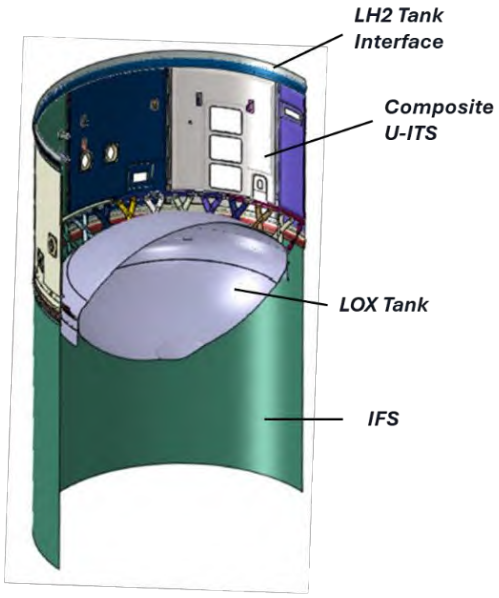


Fig. 6: Global FE Model (GFEM) for C-ITS

Local detailed FE models (DFEMs) are employed at critical zones such as the main and LOx tank attachment structure (LTAS) interfaces to resolve high-stress gradients and joint behaviour, see Fig. 7. The nodal displacements of the GFEM are used as boundary conditions to drive the DFEMs as sub-models. Mechanical loads from relevant flight phases are combined with thermal fields from transient analyses for the structural assessment.

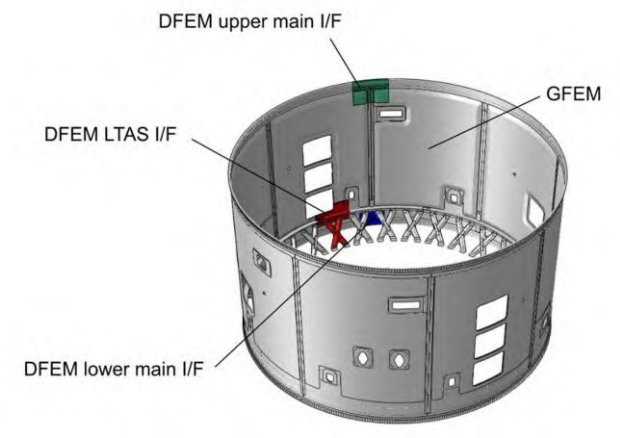


Fig. 7: Overview of FE Models for C-ITS Reference Architecture without LOX Tank and IFS

The reference architecture provides the basis from which the smaller scale elements are derived. The data obtained from the various tests are utilized to validate and calibrate the analysis approach.

3.2. Coupon Tests

Following the initial optimization loops of the reference architecture, the material selection has been finalized. Based on these results, coupon samples (see Fig. 8) are utilized to characterize the general mechanical behavior of the selected materials under varying environmental conditions. These tests are conducted using the same manufacturing processes as the higher level elements and the reference architecture, ensuring that the material data reflect the structural performance in the application. The primary objective is to determine key mechanical properties such as strength and modulus as well as thermal expansion coefficients for all material directions across different environmental conditions.



Fig. 8: Honeycomb core coupon samples

Furthermore, statistical design allowables are derived to account for material variability and enable robust design margins in subsequent FE modelling and structural justifications.

3.3. Test Elements

Following material characterisation, test elements are derived to validate specific technology elements under representative loading conditions. These elements are not full-scale components but rather derived from the design of the reference architecture to isolate and assess singular structural features that are critical for the integrity of the reference architecture. The primary purpose of the test elements is twofold: first, to calibrate and verify finite element (FE) models against experimental data and second, to demonstrate the feasibility of individual design solutions prior to integration. All test elements are evaluated at room temperature under controlled loading conditions to eliminate thermal complexities during initial validation. Load paths are designed to mimic those expected in the reference architecture, allowing for direct correlation between simulation and test results. The resulting data are used to refine analysis aspects, such as failure modes or rivet loads, as these are treated with conservative analytical approaches.

3.3.1. Cut-outs

Cut-outs are necessary for integrating local equipment, sensors, access points, and internal hardware within the inter tank structure. These features introduce significant stress concentrations and local load redistribution, making them high-risk areas for structural integrity. In the C-ITS reference architecture, cut-outs are designed as monolithic sections for an easier integration (via riveting) of metallic components like interface plates. The test element includes a representative cut-out geometry concerning size and shape, see Fig. 9. It is subjected to compression loading representing the axial flux loads acting in the reference architecture.



Fig. 9: Cut-out test element

The test is conducted until failure, with displacement transducers, strain gauges and digital image correlation (DIC) used to monitor deformation fields and identify the onset of failure up to final fibre failure propagating from the monolithic cut-out area. The failure load and mode are compared against predictions from FE models. A close correlation between measured and predicted results (see Fig. 10) confirms the fidelity of the modelling approach.

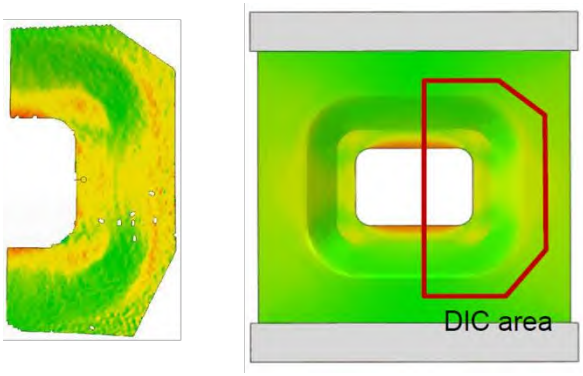


Fig. 10: Major strain from DIC (left) and FEA (right)

3.3.2. LTAS Interface

The **L**Ox **T**ank **A**ttachment **S**tructure (LTAS) interface is a critical connection point that transfers out-of-plane loads from the LOx tank and the Vinci engine into the C-ITS. The corresponding test element evaluated the mechanical behaviour of the LTAS interface in a monolithic composite design. It features a metallic attachment structure with a bolted connection joint, see Fig. 11.



Fig. 11: LTAS interface test element

The test assessed failure load and failure mode under quasi-static out-of-plane tension loading. Digital image correlation (DIC) and strain gauges provided detailed deformation and strain data across the interface. The relating finite element model was able to capture the characteristics of the test sample during the test. The reached load level confirmed the feasibility of the interface concept for the reference architecture.

3.3.3. Main Interface

The main interfaces at the upper and lower ends of the C-ITS connect the composite panels to metallic rings, which in turn link to the metallic LH2 tank as well as the composite interface structure (IFS). The test element, in this case for the upper main interface, depicts the full configuration, including the core ramp from sandwich to monolithic and the riveted joint between composite panel and metal ring, see Fig. 12. Testing under tensile loading conditions is used to verify the interface design and analysis approach.

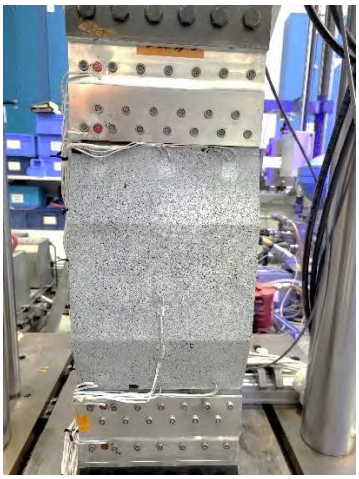


Fig. 12: Main interface test element

Failure initiation for the test element occurred in the form of delamination at the tip of the sandwich ramp. This could be replicated in FEA via VCCT analysis. The whole ramp configuration including the riveted joint was able to transfer loads higher than the required load level j>1.25, which validates the interface design for the reference architecture.

3.4. Breadboards

With the foundational elements validated, the next phase involved breadboard testing, which serves as a bridge between component-level validation and sub-system-level demonstration. Two primary breadboards are defined: Test breadboard 1 (TBB1) and test breadboard 2 (TBB2). The first one is focussing on the test of a single panel out of the C-ITS and the second one on the test of the panel joint configuration.

3.4.1. TBB1 – Full-Scale Panel Test

TBB1 is a 1:1 scale panel representative of the reference architecture, produced using the same materials, manufacturing and assembly processes. It incorporates key features like cut-outs, interface rings and reinforcement zones, see Fig. 13. Struts at the lateral interface were introduced to mimic boundary conditions equivalent to those in a complete U-ITS with all panels.
The test objective is to experimentally demonstrate the structural definition, manufacturing quality, numerical model fidelity and cost realism. The test was carried out in collaboration with Applus+ IMA Dresden. The panel is subjected to representative global compression loads derived from the reference architecture, where the load level has

been adjusted to match the most critical failure mode and load identified in the reference architecture.

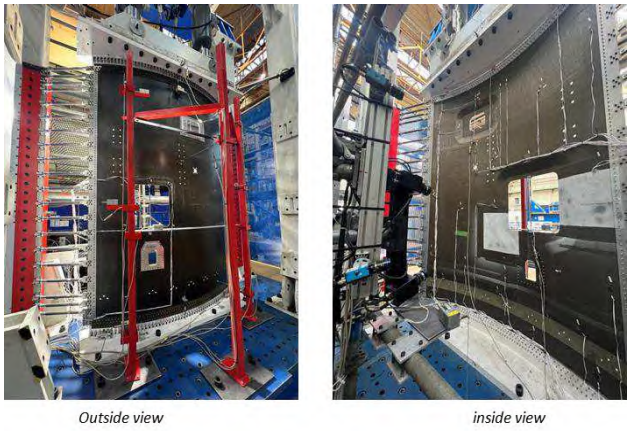


Fig. 13: TBB1 breadboard test set-up

FE analyses are employed to predict the test behaviour and to evaluate the experimental results, particularly with respect to deformation characteristics and failure mechanisms. Failure initiation occurred at the large cut-out following a significant out-of-plane deformation at the lateral edge. The final failure of the panel occurred significantly above the required load level relating the reference architecture (j>1.25). Consequently, the required load level with the required safety margins were reached before failure. The failure could be replicated in the FEA by a dynamic implicit analysis, see Fig. 14. Furthermore, the deformation behaviour observed during the test monitored via strain gauges, displacement transducers, and digital image correlation (DIC) was generally well reproduced in the numerical simulations. The successful test confirms that the technology works as intended in a relevant environment, proving structural integrity of the design under primary loading. It also demonstrates that manufacturing processes are mature enough to produce high-quality, repeatable components.

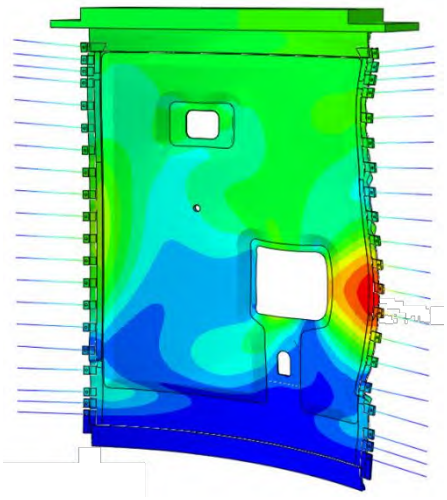


Fig. 14: TBB1 global FE deformation at failure load (scale x10)

3.4.2. TBB2 – Panel-to-Panel Interface Test

TBB2 focuses on the panel-to-panel joint, which is a challenging interface in the segmented C-ITS (see Fig. 15). This joint is realized by a riveted splice joint and an additional reinforcing composite L-frame. The test reproduces the combined axial (compression) and out-of-plane loading in this area representing loading conditions seen in the reference architecture in flight load cases.

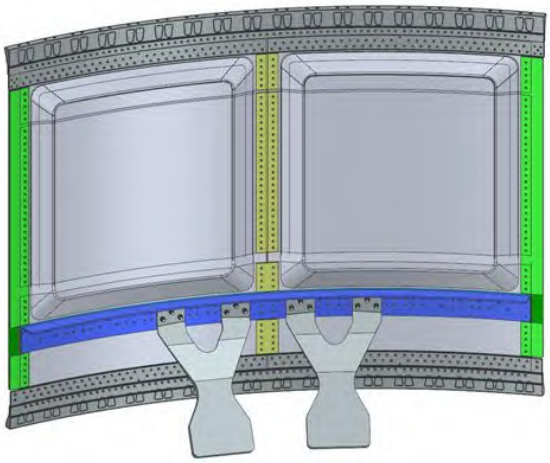


Fig. 15: TBB2 breadboard design

The breadboard consists of two adjacent panels joined by splice sheets with rivets installed using a production tooling. A simplified, in the interface area representative, LTAS structure is used to introduce out-of-plane loads during the test. This out-of-plane load is generating local loads in circumferential direction in the panel joint. Strain gauges, displacement sensors, and DIC were used to capture deformation fields across the TBB2 with focus on the joint region. The test was performed at an external site - Applus+ IMA in Dresden. A suitable test bench (see Fig. 16) has been defined in a co-engineering phase with the external partner. The necessary boundary conditions, test machine

interface, test bed interface and lateral interface (segment joint) to compensate for the missing circumferential stiffness were defined in close cooperation.

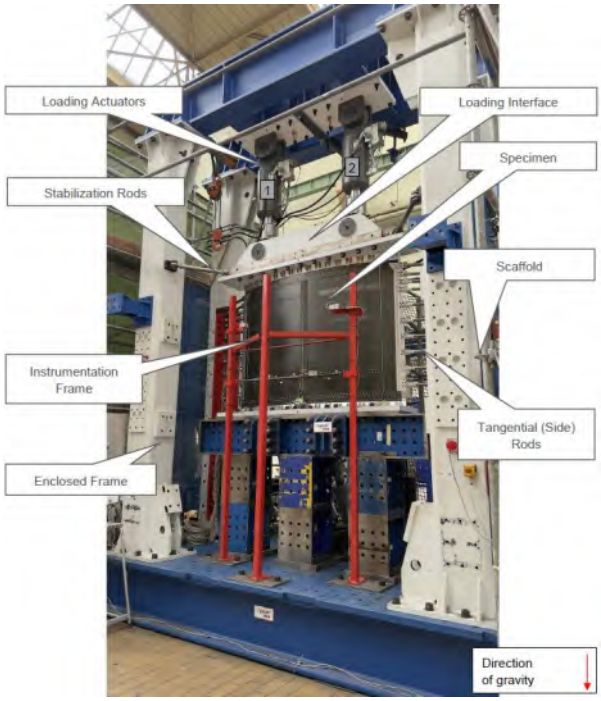


Fig. 16: TBB2 breadboard test set-up

FE analyses are performed in conjunction with the test to further increase the accuracy of numerical modelling techniques of joint behavior and validate the design of the segmented C-ITS. Not only the TBB2 bread board but also a wide area of the test rig, especially the lower part, is implemented in the FE analyses. This leads to a more realistic adjacent stiffness. For the out-of-plane load introduction, a representative approach by including the actuator itself in form of a connector element of ABAQUS type axial is considered. The out-of-plane load is applied via a connector force (see Fig. 17).

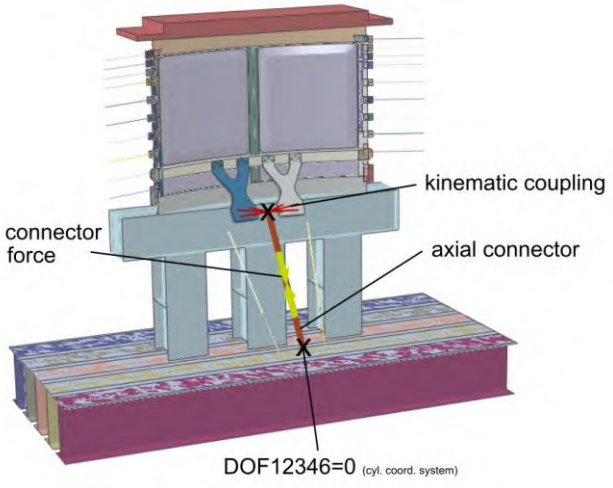


Fig. 17: FE Model of TBB2 breadboard test

The C-ITS TBB2 has been tested under global compression and local out-of-plane tension load. The failure has been determined at a load level of j=1.50 (F=660 kN) due to local fiber failure in the area of the out-of-plane load introduction. The failure followed a preceding deformation of the TBB2, which has been marked by high non-linearities resulting from the out-of-plane loading. The FEA could reproduce the general characteristics observed in the test. A good correlation of the deformations could be achieved. Only in areas with small deformations, higher relative deviations between test and FEA occur. Also, the failure mode and load (fiber failure at out-of-plane load introduction) correlates to the test very good (see Fig. 18).

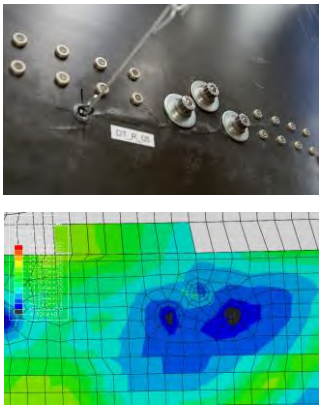


Fig. 18: Comparison of the failure mode in test and FEA

The analyses show that the implementation method of such structures in FE is very suitable for further investigations.

3.5. Full-scale demonstrator model

The focus of this development logic is the final full-scale C-ITS target application design. Gained knowledge from the tests on different levels are introduced and taken over in the design of the C-ITS target application. In addition, the analysis methods were refined according to the derived results especially during the evaluations of the various test results. Based on the final design, the Demonstrator Model 0 (DM0, see Fig. 20) has been built. DM0, which has a diameter of roughly 5.4 m and a height of about 3 m, is a full-scale prototype that incorporates all relevant design features of the reference architecture: eight panels, cut-outs, interfaces, splice sheets, and joint details.
DM0 serves to validate manufacturing capabilities, process repeatability, and assembly fidelity, demonstrating end-to-end production readiness.
Manufacturing is driven by full automation in CFRP part layup via automated fibre placement (AFP, see Fig. 19), enabling high repeatability and reduced

manufacturing costs. Digital integration links design, analysis, and manufacturing workflows, ensuring consistency and traceability. Each sandwich structure is cured in a single cycle, minimizing production steps and enhancing process efficiency. This approach aligns with planned industrial production setups for serial production.



Fig. 19: AFP Manufacturing of a panel

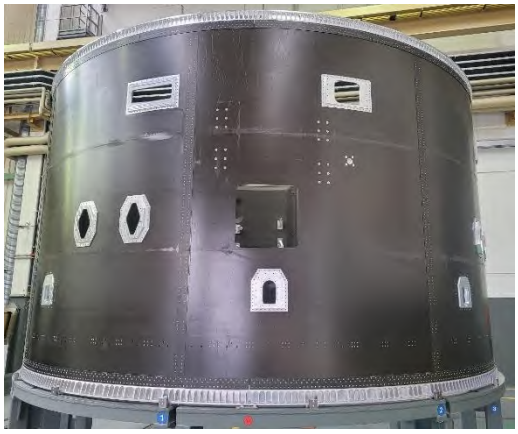


Fig. 20: Assembled C-ITS demonstrator DM0

3.6. Conclusion

The described development approach ensures that by the time the maturation toward flight qualification is reached, all key risks have been mitigated through incremental validation, resulting in a design with high technical confidence.

4. FURTHER DEVELOPMENT

The project ARESCA (Advanced Resistance WElding for ThermoSet Carbon Assembly), set up as in the framework of FLPP, continues the development of a high-performance future composite launcher upper stage structure. Within this project, the riveted joints between the structural panels as well as between the L-frame and the panels shall be replaced by welded joints, providing mass savings as well as a reduction in manufacturing and rivet costs. This includes the development of a robust welding process for thermoset CFRP structures, to be scaled from coupon level to part level and to be tested (DM1) in comparison to a riveted structure. The demonstrator model to be tested is a replica of TBB2 from the C-ITS project, in which the rivets in the panel joint region and at the attachment of the stiffener frame are replaced by resistance welding (see Fig. 21).

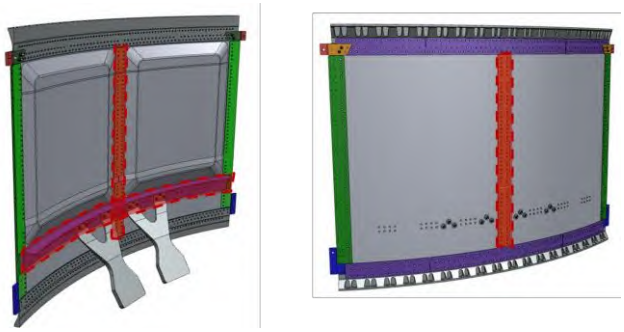


Fig. 21: DM1 sketch, red dotted: welded interface

The testing for the DM1 is currently planned in the first months of 2027.

5. CONCLUSION AND OUTLOOK

The development of the composite upper stage inter tank structure (C-ITS) successfully demonstrates the feasibility of replacing the conventional metallic design with a full-scale composite sandwich architecture. Based on the COSTELAS technology foundation, C-ITS achieved a tailored pMG5 level, confirming readiness for advancement towards flight application. Key performance targets, particularly in mass reduction of about 200 kg and manufacturing cost efficiency, are proven through detailed design, analysis, and demonstrator validation. Since mass savings in the upper stage directly increase payload capability, the associated economic benefit, expressed in terms of launch cost per kilogram, enables the development costs to be amortized after only a limited number of launches. The 1:1 scale DM0 technology demonstrator, produced with segmented composite panels and integrated metallic interface plates and rings, has proven the manufacturability of the complete structure from panel to assembly, including critical features such as cut-outs and interface joints. The testing of TBB1 and TBB2 proved the overall stability of the panels and the riveted joints between two CFRP panels under representative loading conditions. Finite element (FE) modelling approaches have been continuously validated through correlation with test data from test elements and breadboard assessments.
Looking forward, the development is continued by replacing riveted joints by welds to improve mass saving and reduce costs.

The current development status establishes a solid foundation for a continuous improvement of the ARIANE 6. The C-ITS program marks a key step towards lightweight, high-performance composite

sandwich structures in future launch vehicle systems.

6. ACKNOWLEDGEMENTS

MT Aerospace would like to thank our customers, main suppliers and partners. The technology maturation and development of a composite inter tank structure is only possible due to the German funding of the DLR Agency via ESA's Future Launchers Preparatory Programme (FLPP) and A6 Competitiveness Improvement Programme (CIP). Without our project partner, ArianeGroup Germany, and their input, the project C-ITS wouldn't be possible.
Furthermore, we thank all our partners, especially Applus+ IMA Dresden and Euro-Composites S.A. for the good collaboration.

7. REFERENCES

[1] Wolff, M; Dr. Lang, H; Wiedemann, T.; Malcherzyk, M. (2023). *Maturation of promising CFRP-lattice and sandwich technologies for representative future launcher interstage and intertank structures*, ICCM23.

Certain information contained in this paper may be subject to export control restrictions under Regulation (EU) 2021/821 (EU Dual-Use Regulation), including Items 9E001 and/or 9E002. Any use, disclosure, transfer, or export of such information must be conducted in accordance with all applicable legal and regulatory requirements.

DESIGN, ANALYSIS, AND TESTING OF GRID-STIFFENED COMPOSITE MULTI-PAYLOAD ADAPTERS AS AN ALTERNATIVE TO METALLIC ESPAS

Carlo Alberto Socci[(1)], Brendan Murray[(2)], Valerio Cardini[(3)], Robert Telford[(2)], Athanasios Gkekas[(1)], Kelly Matthews[(2)]

[(1)] ATG Europe, Huygensstraat 34, 2201 DK Noordwijk, the Netherlands, Email: carlo.socci@atg-europe.com

[(2)] ATG Europe, Office 11 and 12, Level One, Unit 8, Galway Technology Park, Parkmore, Galway, Ireland,

[(2)] ATG Europe, Via Ludovisi 16, 00187 Roma RM, Italy

KEYWORDS

ESPA, rideshare, lattice, grid-stiffened, composite, multi-payload adapter.

ABSTRACT

Three lattice composite multi-payload adapter (lattice CMPA) configurations were developed, analysed, and assessed against equivalent metallic ESPA ring designs using standard launcher static and vibration environments, as well as payload capacities of 7711 kg for the primary payload and 450 kg/700 kg for each secondary payload. Predicted mass savings ranged from 21% to 41%. A breadboard test campaign on a near 1:1 scale was also undertaken, focusing on the secondary payload port region, including its interface with the grid-stiffened structure. Testing was successful, showing good correlation with predictions, and de-risked future full-scale demonstrator design, manufacturing and qualification, which are currently underway as part of a follow-on project.

1. INTRODUCTION

Small satellites and lighter payloads (<500 kg) are traditionally deployed using metallic multi-payload adapters (MPAs), such as EELV Secondary Payload Adaptor (ESPA) rings, which provide a universal interface for multiple payloads on a single launch, increasing payload mass utilisation and reducing deployment costs.

Historically, MPAs have been metallic structures machined directly from single billets of 7000-series aluminium, an expensive and time-consuming process with high levels of material wastage, which also results in heavier components. These ESPA adaptors are available in a variety of sizes and configurations, while still adhering to standard interface dimensions to facilitate their use on multiple launchers. However, these metallic structures are still heavy in comparison to composite structures, so potential savings in the cost/kg of payload as well as mission extension options would offer significant benefits if efficient composite alternatives can be found. ATG Europe has therefore designed and analysed replacement lattice CMPAs as a solution to this problem.

Lattice structures consist of a repeating grid pattern of intersecting stiffeners or ribs creating a mass optimised structural design. Composite lattice designs can provide potential mass savings of up to 30-50% in comparison to traditional designs (sandwich, monolithic, etc), making them incredibly attractive for structural applications in large scale space components. ATG Europe has developed [1-7] and patented [8] a cost-efficient manufacturing methodology for continuous pre-preg fibre placed grid-stiffened and lattice structures that allows for the manufacturing of high quality, complex, integrated grid-stiffened composite products in a true one-shot process. Two examples of ATG's lattice structures are shown in Fig. 1.



Figure 1: Example of ATG's lattice structures, specifically an interstage for RFA ONE (top) and a central tube demonstrator (bottom).

The project presented in this paper aimed to assess ATG's lattice CMPA designs versus the current standard metallic ESPA designs to evaluate viability of these structures as a replacement component. Compared to a traditional ESPA ring, a CFRP lattice CMPA would provide the following major benefits:

- Significant mass-savings and associated launch cost reductions and/or mission extension options.
- Increased production sustainability through significant reduction in material wastage and optimized manufacturing process.
- Increased flexibility in the production process through accommodation of change in size and/or location of payload ports during the design and manufacturing phase.

2. PROJECT OUTLINE AND GOALS

To assess the feasibility of lattice CMPAs as an alternative to traditional ESPA rings, the following technical objectives were defined. This paper covers each objective in its own respective section.

- Consolidation of requirements for ESPA rings.
- Design and iterative analysis of lattice CMPAs as a replacement to ESPA ring variants.
- Mass comparison against existing metallic ESPA counterpart.
- Manufacture and testing of lattice CMPA breadboard samples to de-risk and validate the port region design, analysis, and manufacturing.

3. EXISTING ESPA RINGS AND THEIR REQUIREMENTS

3.1. Existing ESPA ring configurations

An ESPA consists of a cylindrical ring structure with two standardised Launch Vehicle Adapter (LVA) interfaces at the forward and aft of the structure, as well as a number of payload ports (4-12 depending on port sizes) located around the circumference of the ESPA ring. The LVA interfaces, which allow for the integration of the ESPA between the launch vehicle and the primary payload, consist of a standard EELV 1575 mm diameter bolt circle with 120 equally spaced holes.

The port interfaces allow for the attachment of secondary payloads to the ESPA and consist of a number of different designs. The most common ports designs are the standard 15" and 24" designs, which follow a similar pattern to the LVA ring where an equally spaced bolt pattern of 24 and 36 holes, for the 15" and 24" ports respectively, are used to attach payloads to the ESPA port structures. Additional ports sizes exist, but are less common.

While the LVA interfaces and port structures are the common features of ESPAs, there are multiple configurations for their designs which are identified with a part number defined as:

ESPA N-D-H

N = Number of circular ports, between 4-12
D = Port diameter in inches, usually 15" or 24"
H = Ring height in inches, usually 24" or 42"

The most common ESPA designs which act as a "baseline" are listed in Tab. 1.

Table 1: Baseline ESPA configurations [9]

Name	N	D	H	Payload Capacity (kg) *		ESPA Mass (kg)
				Second. Port	Primary	
ESPA Heavy	6	15	24	450	7711	133
Grande Heavy	4	24	42	700	7711	211
ESPA Stretched	4	24	60	700	7711	286

** Port payload capacities assume payload centre of gravity at 508 mm from port interface and use of load factors derived from the ESPA MAC [9]*

3.2. Existing ESPA ring requirements

The main technical requirements for the ESPA/CMPA design centre around its major functions and the loads it must support during all launch activities. Given the large number of requirements, this paper focuses on those that are key design drivers. ESPAs are currently only rated for flight on the Delta IV, Atlas V, and Falcon launch vehicles (based on historical design definitions for the ESPA load envelopes) and this project aimed to produce a 1:1 comparison between lattice CMPAs and existing ESPA ring qualification campaigns. The static load environment is presented in Tab. 2., while Payload masses and their offset distances are listed in Tab. 3. Both the primary and secondary payload factors have been derived from the ESPA ring user manual [9] and qualification campaigns [10].

Table 2: Static load factors (limit level) for primary and secondary payloads on ESPA rings [9, 10]

Load Case	Primary		Secondary			
			15" & 450 kg		24" & 700 kg	
Set	**Radial**	**Axial**	**Radial**	**Axial**	**Radial**	**Axial**
LS1	0.5g	-6.5g	5.6g	-6.5g	4.6g	-6.5g
LS2	2.0g	-3.5g	5.6g	-6.5g	4.6g	-6.5g

Table 3: Payload masses and offset distances [9]

Payload Location	Mass (kg)	Offset Distance (m)	Offset Location
Primary	7711	3.05	LVA Interface
Secondary 15" Port	450	0.508	Port Interface
Secondary 24" Port	700	0.508	Port Interface

Modal frequency requirements and sinusoidal vibration limits have been assessed against Falcon 9 requirements [11] where axial and lateral frequency limits of 25 Hz and 10 Hz respectively have been defined, while the sine vibration design limits are showcased in Tab. 4. Additional requirements for Random Vibration, Acoustic response and Shock are defined in [11], but are not reported here since they were not used for the preliminary design activities reported in this paper.

Table 4: Falcon 9 sinusoidal vibration environment (limit level) [11]

Axial		Lateral	
Freq. (Hz)	**Acceler. (g)**	**Freq. (Hz)**	**Acceler. (g)**
5	0.5	5	0.5
20	0.8	85	0.5
35	0.8	100	0.6
35	0.6		
75	0.6		
85	0.9		
100	0.9		

4. DESIGN OF ATG'S LATTICE COMPOSITE MULTI-PAYLOAD ADAPTER (CMPA)

4.1. ATG lattice background

The lattice grid is comprised of unidirectional composite pre-preg tows which are arranged in a repeating, overlapping pattern. Due to the use of uninterrupted tows (which do not feature fibre cuts along their length), this architecture manifests in the creation of strong, stiff, and ultra-lightweight structures. The sections of unidirectional tows (with no overlaps) are referred to as ribs, while the overlapping sections are referred to as nodes.



Figure 2: several types of attachment patches on ATG's lattice central tube demonstrator (see Fig. 1)

To accommodate global load introduction, the lattice grid transitions into a monolithic composite laminate. This section can then be used to interface to other structures (e.g. by attaching an interface ring). The means of local load introduction is through interface patches, shown in Fig. 2. The patches are areas of a filled in lattice cell, using regularly laminated pre-preg layers which are interwoven with the rib plies. These patches allow for attaching payloads and assemblies. Patches can also be implemented to provide localized reinforcement when needed, allowing for design changes late into the design and manufacturing process, with minimal localized changes to tooling.

4.2. Lattice CMPA designs

Since the purpose of this project was to provide a direct lattice alternative to existing ESPA rings, specific ESPA designs and configurations had to be selected in order to carry out a 1:1 comparison Considering the wide range of ESPA ring designs and configurations, it was decided to focus on the most common designs that would also cover a wide envelope of secondary payloads (see Tab. 1). The corresponding lattice CMPA designs were therefore named CMPA 6-15-24, CMPA 4-24-42 and CMPA 4-24-60. All three designs share the same basic architecture (shown in Fig. 3 for lattice CMPA 4-24-42):

- Carbon fibre composite main body, using ATG's proprietary lattice technology in a grid-stiffened configuration (i.e. a skin is present).
- Metallic ports to attach secondary payloads.
- Cutouts are surrounded by attachment patches (to fasten the ports) and reinforcement patches.
- Metallic rings for primary interfaces (fastened to monolithic end-laminates).

ATG's lattice grid does not possess a set of fixed design parameters. As a result, the grid geometry, size and configuration can be optimized for each specific application. Some of the design parameters optimized across each of the three lattice CMPA designs include: number of ribs, angle of ribs, height and width of ribs, height and thickness of the monolithic end-laminates, skin layup and thickness, patch layup and thickness. The optimization loops were carried out across several iterations of the analyses covered in Section 4.3.

The 15-inch and 24-inch metallic ports, as well as the primary interface rings are bespoke designs engineered by ATG specifically for the lattice CMPA. Both port designs can be seen in Fig. 3, Fig. 7 and Fig. 8. The ports are fastened to the lattice CMPA by means of Hi-Lite fasteners. Fig. 8 (right) also shows the grid design of lattice CMPA 6-15-24, which is also representative of lattice CMPA 4-24-42 and 4-24-60.

As shown in Fig. 3, Fig. 7 and Fig. 8, the cutouts were designed with a hexagonal shape and are delimited by the ribs, thus preserving the integrity of adjacent cells.



Figure 3: Example of lattice CMPA design, specifically CMPA 4-24-42, featuring four 24-inch ports, and 42 inches tall in total.

4.3. Lattice CMPA analyses and performance

Finite Element (FE) models were used to iteratively design the three lattice CMPAs introduced in Section 4.2. The models used linear plate elements for the structure along with mass elements (CONM2) for the payload masses. Primary and secondary payloads were connected via rigid RBE2 elements to each model, with the physical port structures and primary interface rings included through bolted connections within the models. An example of such an FE model is shown in Fig. 4. The following analyses were run for each lattice CMPA design: linear quasi static (QSL), modal, linear buckling, and sine vibration. The results of each analysis are summarized in the subsections below.

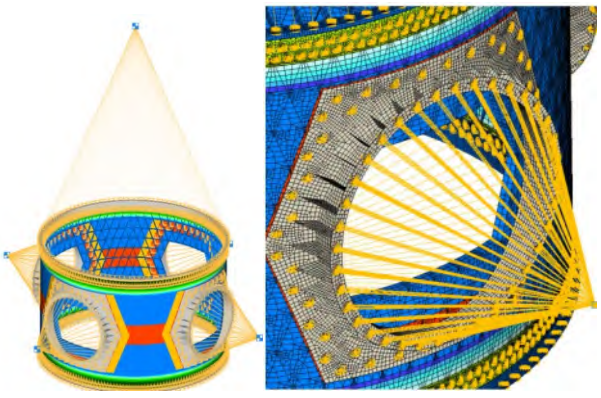


Figure 4: example of FE model setup for the lattice CMPA 4-24-42 (left: overview, right: detail)

4.3.1. Quasi Static Load (QSL) FE Results

The CMPA designs show positive strength margins across the majority of the structure. A few small areas of localized negative margins were also predicted, induced by modelling discontinuities and numerical peaks. The bolted interface points are an example of such numerical discontinuity, where infinitely rigid CBUSH and RBE2 spiders represent the bolted connections, thus introducing notable conservativism in the stresses seen immediately around the bolt.

An example of QSL results is provided in Fig. 5, for the lattice CMPA 4-24-42. Numerical values have been removed from the colour bar to preserve the confidentiality of the (preliminary) design's performance. Negative margins (in black) are only present in a handful of small areas, all confined to the few expected instances of numerical artifacts (such as the one mentioned above). The most "widespread" highly loaded areas (in yellow) still provide a comfortable margin of safety.

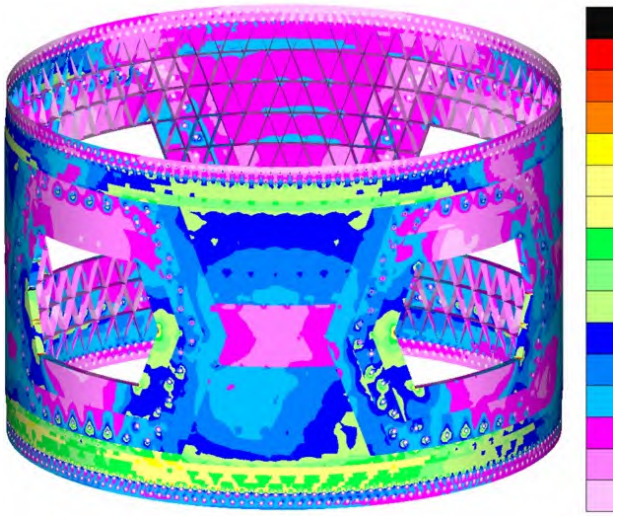


Figure 5: Enveloped laminate Failure Indices (FI) for all QSL load cases of the lattice CMPA 4-24-42. Colour-bar values intentionally omitted.

4.3.2. Modal and linear buckling FE Results

Tab. 5 summarizes the performance of all three lattice CMPA designs under modal and linear buckling FE analyses. The requirements are met with an ample margin of safety.

Table 5: Summary of lattice CMPA performance under modal and linear buckling FE analyses.

Lattice CMPA	First Lateral Mode (Hz)	First Axial Mode (Hz)	First Buckling Eigenvalue (-)
6-15-24	≥ 15	≥ 34	> 4
4-24-42	≥ 15	≥ 34	> 4
4-24-60	≥ 15	≥ 34	> 4
Min. Allowable	10	25	2

4.3.3. Sine Vibration FE results

Across all sine vibration analyses, primary notching was performed to ensure that dynamic loads did not exceed QSL levels. The overall output of sine analyses is similar to the QSL results (Section

4.3.1), presenting positive strength margins across the majority of the structure, accompanied however by a wider variety of small areas of localized negative margins. These include, for example, some bolted connection points, a few small regions in hoop ribs at the equator, and a few of the stiffness transitions areas (e.g. adjacent reinforcement patches of different thickness). Fig. 6 provides a representative example of a sine vibration FE output, showing levels similar to those seen in QSL, albeit with a few more regions of slightly higher negative margins.

Sine vibration analyses in the follow-on phase of this project (Section 6.2) have already indicated that the application of secondary notching (keeping the secondary payloads within QSL levels) results in positive margins of safety in the aforementioned regions, therefore bringing sine vibration failure indices in line with QSL performance (Section 4.3.1). As a last precaution, if during detailed design analyses any regions were to present negative margins of safety, reinforcement patches could be added within the interested cells to increase the strength and stiffness of the affected area.

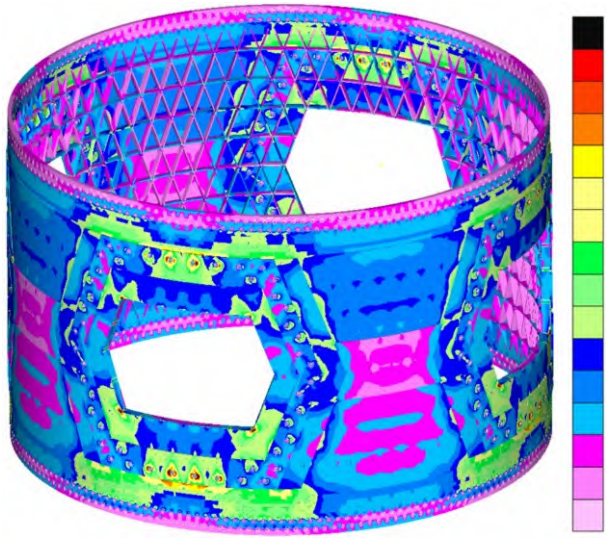


Figure 6: Laminate Failure Indices (FI) for axial sine excitation of the lattice CMPA 4-24-42. Colour-bar values intentionally omitted

4.4. Mass performance comparison

Tab. 5 provides a mass overview for the three lattice CMPA designs, including a comparison against their ESPA counterparts. A mass maturity margin (MMM) of 20% is included in the CMPA mass values. Lattice CMPAs present substantial mass savings of 6-29% with MMM, and 22-41% reductions without the MMM.

It should be noted that metallic components (secondary ports and primary interface rings) still represent a considerable fraction of the total mass of the lattice CMPA designs. This is particularly true for shorter designs (such as the 6-15-24), where the secondary payload ports extend over a large portion of the design. The follow-on project (Section 6.2) has already identified potential for additional mass savings in the metallic interfaces thanks to additional design iteration loops. Potential for further mass savings has also been identified in the CFRP components. Therefore, it is reasonable to expect the final mass savings for the lattice CMPA to be in line with the "savings without 20% MMM" from Tab. 5. This would yield savings of 20% to 40% compared to the corresponding ESPA designs.

Table 6: Mass savings overview for ESPA and CMPA designs in kg. A 20% mass maturity margin (MMM) is included for CMPA only.

Mass (kg)	6-15-24		4-24-42		4-24-60	
	ESPA	CMPA	ESPA	CMPA	ESPA	CMPA
Metallic	133	61	211	73	286	70
CFRP	-	63	-	96	-	132
Total	**133**	**125**	**211**	**169**	**286**	**202**
Savings with 20% MMM	**-**	**6%**	**-**	**20%**	**-**	**29%**
Savings without 20% MMM	**-**	**22%**	**-**	**33%**	**-**	**41%**

5. BREADBOARD SAMPLE DESIGN, MANUFACTURING AND TESTING

The integration of secondary payload metallic ports onto ATG's grid stiffened structures represented the most critical aspect of lattice CMPA design that ATG wished to de-risk and validate within this project. To this end, a static breadboard test was performed on a flat grid stiffened panel with a metallic port integrated to it, with both the panel and port bearing the same design parameters used in the CMPA designs presented in this paper (specifically the lattice CMPA 6-15-24).

The breadboard tests therefore served to de-risk and validate the designs, analysis, manufacture and integration of the port region, with each of these aspects being discussed in its respective Section below.

5.1. Breadboard sample design

The test breadboard (TBB) sample design is shown schematically in Fig. 7. The TBB sample features a flat CFRP grid stiffened panel, encased along its boundaries in a potting compound (for fixation with the test frame). A flat, 15-inch metallic port is fastened to the panel by means of Hi-Lite fasteners.

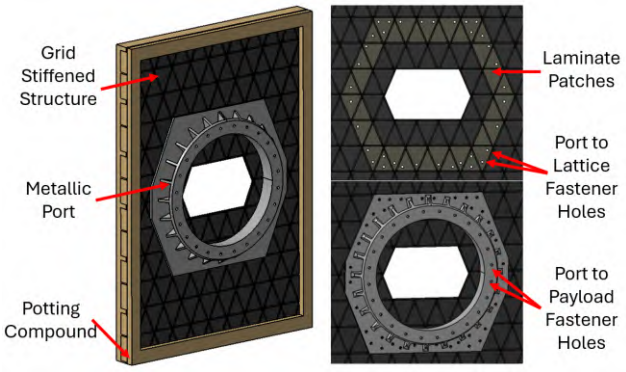


Figure 7: Test breadboard (TBB) sample design.

Some concessions had to be made when translating the "full" lattice CMPA 6-15-24 design into a simplified flat TBB sample. The grid-stiffened panel presents the same grid parameters (rib size, angle and spacing) as the lattice CMPA design, but its skin and patches are thinner with a balanced/symmetric layup (to limit warpage), while the patch layout has also been simplified by removing adjacent reinforcement patches. The port uses the exact same design ATG developed for the lattice CMPA 6-15-24.
It follows that the test sample cannot explicitly achieve the same performance as a 1:1 CMPA design, but this does not hinder the de-risking and validation goals discussed at the beginning of Section 5.

5.2. Breadboard sample manufacturing

Two TBB samples were manufactured, one of which is shown in Fig. 8. The metallic port was manufactured by machining an aluminium billet. Panel manufacturing and port integration activities were carried out at Eligio Re Fraschini (in Legnano, Italy), with the support of ATG personnel.

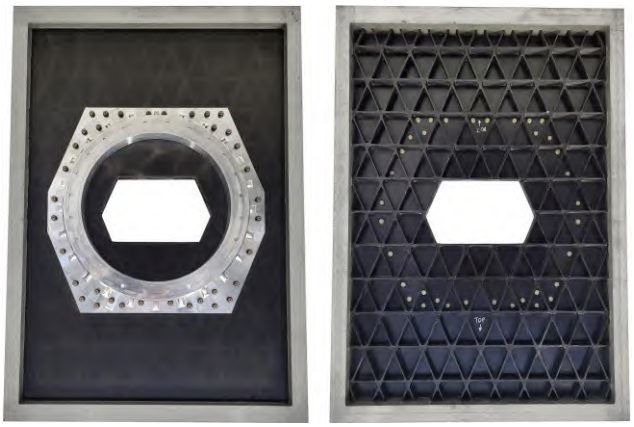


Figure 8: Front (port) and back (grid) views of TBB sample nr1.

As a result of the successful manufacturing of both TBB samples, the following items were de-risked and validated:

- Cutout manufacturing and integration.
- Port manufacturing and integration, including the performance assessment of multiple fasteners within a single patch, and fasteners in close proximity to ribs.
- Manufacturing of equivalent lattice design parameters (rib height, cell size, etc.).

5.3. Breadboard sample testing

5.3.1. Test plan

The test load environment consisted of a single shear load, aligned with the axial direction of the TBB sample and applied at a distance of 0.508 meters from the payload port (see Tab. 3).

The test sequence accounted for three cycles at low load levels to assess repeatability and ensure sample embedding. These were to be followed by ramps and holds at increasingly higher load levels, until total sample failure is achieved.

The applied load and displacement were controlled by manually increasing (or decreasing) the hydraulic pressure in the actuator. The hydraulic system setup ensured that the actuator could only move at a maximum speed of 0.125 mm/s, thus ensuring that no sudden load changes could be imparted by the system.

The load cell, potentiometer and strain gauges were to record data over the entirety of the test including during integration of the test panel within the test setup, to capture any assembly strains. The tests were carried out at DTM Technologies in Modena (Italy)

5.3.2. Test setup

The overall test setup is shown in Fig. 9. The test load was introduced through contraction of the actuator, which is supported by the actuator support and load head. Both pieces of bespoke MGSE were made of S355 steel and were sufficiently stiff to ensure that their own deformations were negligible compared to test displacements. The head fixture was designed to ensure even load introduction into the port, at a distance of 0.508 meters from the port.

The sample was held in place by the sample fixation frame, which provided sliding contact (normal to load direction) at the front and back of the panel, and reaction contact (aligned with load direction) at the top and bottom. The fixation frame interfaced exclusively with the panel's potting, without touching the rest of the sample. The fixation frame rested on spacer disks which ensured planarity of the sample.

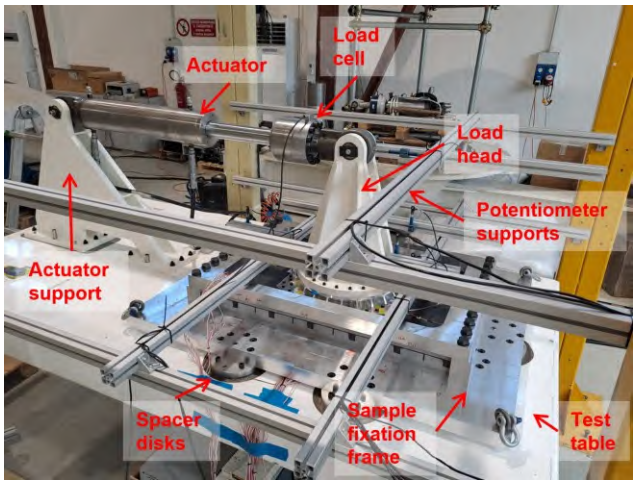


Figure 9: Breadboard test setup

The load was recorded by means of a load cell sitting between the actuator and load head. Strains were measured through 48 strain gauges per sample, of which 42 were placed on the panel, with 34 on the ribs (which carry the majority of the load), and 8 on the laminate patches and skin. The focus was placed on areas that would experience high loads, high deformations, and around the cutout. The remaining 6 strain gauges were placed on the metallic port. Displacements were measured through 8 linear potentiometers. Out of the 8 potentiometers, 3 were placed on the skin (port-side) of the panel, at locations expected to experience higher deformations; 2 were positioned at the load application point to track displacement along the loading direction, and to verify that the load remained centred. Finally, 1 potentiometer tracked displacement at the base of the load head, and 2 were positioned on the fixation frame to ensure deformations would be negligible.

5.3.3. Test results

The actuator displacement and normalized load are plotted against test time in Fig. 10 for both TBB samples. The applied load has been normalized against the failure load observed in FE analyses of the TBB sample. In comparing the two sets of results, it should be noted that the "shift" in x-axis values between the two is caused by the test execution times differing between samples. The following can be observed:

- The embedding cycles were successful, with excellent repeatability of loads and displacements across both samples.
- Repeatability of loads and displacement, and the associated "sample stiffness", remained excellent at higher load cycles, both within a same sample as the load increased, and across both samples for the same load values.
- Failure of samples 1 and 2 was sudden and occurred at 113% and 105% of the FE failure load (respectively).

The above observations demonstrate that the samples behaved linearly until failure, with both samples also exhibiting the same stiffness and very similar failure loads. As explained below, both samples also presented the same failure mode. The repeatability and consistency across both samples proves that that the de-risking and validation of manufacturing and integration activities (see end of Section 5.2) was successfully demonstrated by this test campaign.

Sample failure occurred as a rib delamination affecting the half of the panel on which the metallic port exerted a pulling force.

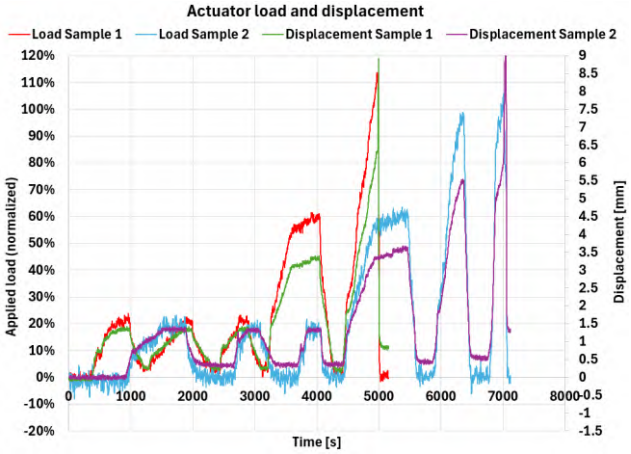


Figure 10: Actuator displacement and applied load (normalized against FE failure load), plotted against time, for TBB samples 1 and 2.

5.3.4. Test FE model and correlation

The detailed FE model of the TBB test includes both the test sample and test setup. The composite grid stiffened panel was modelled using a structured mesh consisting of PCOMPS elements. Other components were modelled with PSOLID definitions.

The metallic port is fastened to the panel by means of RBE2 spiders. Each fastener hole has two spiders: one connected to the port, and one connected to the panel. The independent nodes of the two spiders then interface into a coincident zero length CBUSH at the midpoint of the fastener. The same RBE2 spider configuration is used for the fasteners securing the port to the load head.

Components of the test setup in direct contact with the sample (sample fixation frame, load head) were modelled with solid elements, while shell elements were used for the test table and the actuator support. Linear contact was used between the potting and fixation frame to provide realistic boundary conditions to the sample. Linear contact was also set up between the panel's skin and port to ensure proper load distribution in regions where the shear load on the load head caused the port to "push" against the panel's skin.

Strain correlation of the FE model against test data

yielded good results. All trends observed in the strain data were captured by the predictions, with the FE remaining slightly conservative in critical (highly loaded) areas. After removal of obvious outliers, all strain gauge readings were within the expected range based on FE correlation results. Correlation of displacement data was also excellent, with no outliers among the 8 potentiometers, and with the recorded values being again within the expected range based on FE correlation.

As illustrated in Section 5.3.3, failure of both samples occurred in the form of a delamination within the ribs in the "top half" of the panel (being "pulled" by the port).

Due to the nature and location of the failure, it is hypothesized that the delamination originated within a rib in close proximity to one of the fasteners being loaded under tension by the port. This is in line with the FE predictions, which present failure index hotspots in the two regions highlighted in Fig. 11 (top), specifically in proximity to the fasteners (see example in Fig. 11 bottom). Actual FE results are not shown to preserve the confidentiality of the FE methods and practices ATG developed to model lattice structures. Normalized against the test failure loads of samples 1 and 2 respectively, these failure indices yield failure loads of 89% and 96% for one hotspot, and 111% and 120% for the other hotspot. Designating the most critical hotspot as the failure predictor, the failure mode observed during the test is correctly predicted by the FE model while still being slightly conservative, thus demonstrating that ATG's FE methodology has been successfully validated through this test and can be relied upon for further design of the secondary payload port region. Strain data recorded during the test seems to support the failure hypothesis presented above, since at the exact moment of failure initiation for sample 2, a small spike in strain readings was recorded in one of the regions shown in Fig. 11 (sample 1 strain recordings did not present the same spike).

To evenly distribute out of plane loads from the fasteners into the surrounding ribs, an optimal design should guarantee a minimum rib-fastener distance, dependent on fastener load. As mentioned in Section 5.2, ATG wished to further explore the performance envelope for this design by integrating multiple fasteners within a single patch and positioning some of them in close proximity to the ribs (see Fig. 11). To this end, this test has provided valuable data, asserting the importance of fastener-rib distance while also validating the accuracy of ATG's FE models, which were capable of accounting for this effect, and correctly predict the failure mode, load and location.

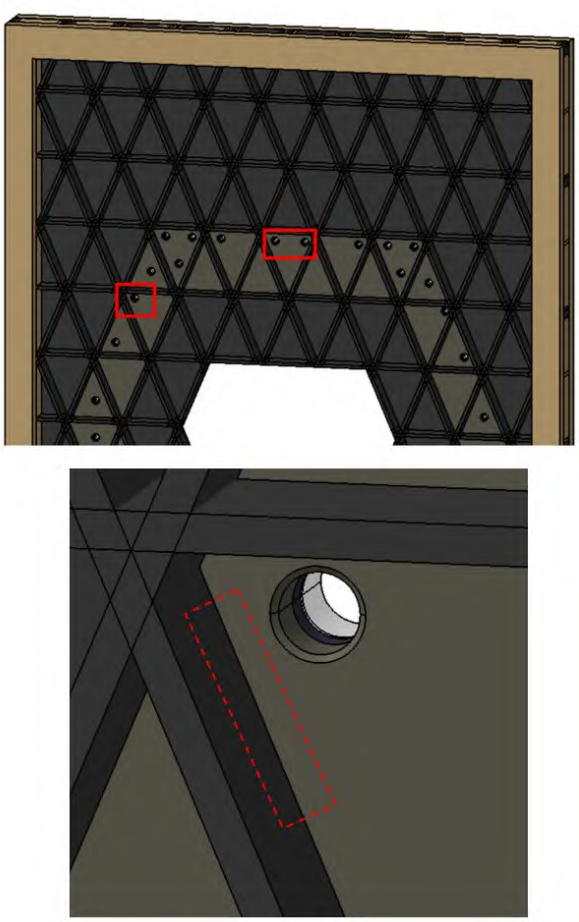


Figure 11: TOP, suspected locations of failure initiation. BOTTOM, closeup of region adjacent to fastener hole, where FE analyses predict failure index peaks (dashed rectangle).

6. CONCLUSIONS AND FOLLOW-ON PROJECT

6.1. Conclusions

ATG designed three lattice CMPAs as a direct alternative to existing ESPA ring designs. Analysis of each lattice CMPA covered QSL, primary modal frequencies, buckling, and dynamic responses based on defined levels from Falcon 9 launch vehicles [11] and previous metallic ESPA tests and defined performances [9, 10].
Overall, the lattice CMPA designs are deemed to be compliant with requirements with limited alterations and mass penalties moving forward. This is a positive result and, combined with the mass comparisons in Section 4.4, shows that the lattice CMPA designs offer significant mass savings across all designs analysed (6-29% with mass maturity margin, 22-41% without, where potential for further mass savings has already been identified in a follow-on project).

The TBB samples have successfully de-risked and validated the port-to-lattice interface, having successfully carried out its design, analysis, manufacturing, assembly and testing. The port-

lattice interface represents the most critical region of the lattice CMPA design. Manufacturing and assembly of the lattice CMPA TBB sample with the metallic port included the addition of a cutout structure for access, as well as all integration steps necessary for the port assembly procedure. These steps have directly informed future manufacturing studies and have shown successful production methods for all components.

Testing of the TBB samples showed repeatable linear behaviour for all load, displacement, and strain measurements, with all sensors falling within the expected range based on FE correlation results. Failure correlation showed accurate and conservative assessments of the predicted failure location and loads, with significant lessons learned for the lattice CMPA designs based on these findings.

Overall, the lattice CMPA designs and analyses have shown compliance with ESPA requirements and prescribed load environments while offering reduced mass, meaning these structures offer strategic improvements over their metallic ESPA counterparts for lightweighting of structures, allowing for additional payload and enhanced mission operation capabilities. The design and manufacture of the lattice samples and ports, machining of the cutouts, and assembly of the entire structure, have significantly de-risked future operations for lattice CMPA components. The lessons learned from design and test outcomes will contribute to future programs, showcasing the impact of this program and enhanced knowledge gained from its undertaking.

6.2. Follow-on project

A follow-on project is already underway. The most promising lattice CMPA design will be selected (among the three presented in this paper). The selected design will undergo detailed analysis and iteration loops, followed by manufacturing of a full-scale qualification model, which will then undergo qualification testing.

7. ACKNOWLEDGEMENTS

The authors would like to acknowledge the funding and support provided by the European Space Agency (ESA) and the Italian Space Agency (ASI) under the Future Launchers Preparatory programme (FLPP), without whom this project would not have been possible. They would also like to thank the manufacturing team at Eligio Re Fraschini in Legnano, the testing team at DTM Technologies in Modena, as well as the ESA Technical Officer for this project, Bernard Decotignie and his colleagues. This highly collaborative project would not have succeeded without the effort and dedication of all involved.

8. REFERENCES

1. Smeets, B.J.R., Fagan, E.M., Matthews, K., Telford, R., Murray, B.R., Pavlov, P., Weafer, B., Mieir, P., Goggins, J (2021). Structural testing of a shear web attachment point on a composite lattice cylinder for aerospace applications. *Compos. B. Eng.* (212) 108691.
2. Pavlov, L., Te Kloeze, I., Smeets, B.J.R., Simionian, S.M. (2016). Development of mass and cost-efficient grid-stiffened and lattice structures for space applications. *14th Eur. Conf. Spacecr. Struct. Mater. Environ. Test.* Toulouse, France. 1149–1151.
3. Smeets, B.J.R., Pavlov, L., Kassapoglou, C. (2016). Development and testing of equipment attachment zones for lattice and grid-stiffened composite structures. *14th Eur. Conf. Spacecr. Struct. Mater. Environ. Test.*, Toulouse, France.
4. Pavlov L., Smeets B., Simonian S. M. (2016). Optimization of a Composite Lattice Satellite Central Cylinder Structure Using an Efficient Semi-automated Approach, *AIAA 2016-1497*, DOI: 10.2514/6.2016-1497.
5. Maes, V.K., Pavlov, L., Simonian, S.M. (2019). An efficient semi-automated optimisation approach for (grid-stiffened) composite structures: Application to Ariane 6 Interstage. *Compos Struct.* (209) 1042–1049.
6. Smeets, B.J.R., Telford, R., Murray, B.R., Matthews, K., Pavlov, L. (2021). Development of a satellite central cylinder using uninterrupted pre-preg fibre-placed lattice structures. *ECSSMET 2021*, Bremen, Germany.
7. Murray, B.R., Matthews, K., Telford, R. (2023). Testing interfaces of lattice spacecraft structures. *ECSSMET 2023*, Toulouse, France.
8. Pavlov, L., Te Kloeze, I., Smeets, B.J.R., Simonian, S.M. (2017). WO2017099585A1: Composite Grid Structure Patent.
9. Moog Inc., *ESPA User Guide*, 2024, https://www.moog.com/products/spacecraft-payload-interfaces/espa.html
10. Maly, J.R., Sanford, G.E., Williams, A., Roybal, F.A., Hultberg, R. (2018). ESPA Grande Qualification. *32nd Annual AIAA/USU Conference on Small Satellites,* Logan, Utah.
11. SpaceX, *Falcon User's Guide*, Version 7, 2021.

FEASIBILITY STUDY OF MULTIFUNCTIONAL SANDWICH PANELS FOR SPACE RADIATION SHIELDING

Tetiana Pittsyk (1), Hendrik Traub (1), Oliver Völkerink (1)

(1) Technische Universität Braunschweig, Institute of Mechanics and Adaptronics, Langer Kamp 6, Brunswick, 38106, Lower Saxony, Germany,
Email: t.pittsyk@tu-braunschweig.de, h.traub@tu-braunschweig.de, oliver.voelkerink@tu-braunschweig.de

KEYWORDS

Space radiation, shielding, composite material, structure, spacecraft

ABSTRACT

Commercial off-the-shelf electronics deliver the performance and low cost that space missions rely on, but they are the most vulnerable to space radiation. Passive structural shielding is a complementary protection, yet the materials that shield best are not structural. This feasibility study investigates whether the core volume of a carbon fibre reinforced polymer sandwich panel can be converted into a shielding element using hydrogen-rich, space-relevant materials. Two concepts were manufactured and tested in four-point bending: an aluminium honeycomb filled with polyamide 11 inserts, and a layered core of polyetherimide plates and epoxy-impregnated aramid. The layered concept responds 40 to 43 % stiffer in bending than the honeycomb reference with identical face sheets, while the areal density rises from 0.48 to 1.56 g/cm^2. The layered core combines shielding function with enhanced mechanical performance and remains transferable to established manufacturing routes.

1. INTRODUCTION

Spacecraft increasingly rely on commercial off-the-shelf (COTS) electronics, which offer state-of-the-art performance at competitive cost and short procurement times, but are the least resistant design class against space radiation [1,2]. In orbit, electronics are exposed to trapped particles, solar particle events (SPE), and galactic cosmic rays (GCR) [3], which degrade components through the total ionising dose (TID) and displacement damage and disturb their function through single-event effects (SEE) [4,5]. Radiation hardening addresses these mechanisms at the device level, but drives up cost and design complexity and leads to technologies that perform worse than state-of-the-art commercial devices [5]. Software-based measures can correct or bypass soft SEE during operation [4,6], whereas passive shielding reduces part of the incoming radiation load and thereby lowers the probability of radiation-induced failure. Passive shielding therefore remains a relevant complementary strategy for missions using COTS electronics.

From a shielding standpoint, the incident particles divide into three groups with opposing material requirements: high-energy protons, heavy ions, and fast neutrons are moderated most effectively by nuclei of low atomic mass [7]; thermal neutrons are attenuated by capture in elements with a high thermal neutron capture cross section, such as boron [8]; and electrons and photons call for elements of high atomic number [8]. No single material can therefore shield all groups effectively at once. This work focuses on the first group, which contains the high-energy particles that are the most difficult to shield and against which hydrogen-rich materials are the most effective: a low mean atomic mass increases the fragmentation probability per unit mass [7], and hydrogen moderates fast neutrons most efficiently [9]. Hydrogen-rich polymers such as polyethylene consequently outperform aluminium per unit areal density and produce fewer secondary particles [10–12], while carbon fibre reinforced polymer (CFRP) lies between the two [13,14]. The most effective shields, however, are not structural materials, and dedicated shielding mass competes directly with payload capacity. This conflict motivates structural concepts in which the load-bearing structure itself contributes to shielding.

Sandwich panels with CFRP face sheets and an aluminium honeycomb core are an established structural solution on satellites, such as Olympus or space probe Rosetta [15]. Their core occupies a substantial volume that is conventionally filled by a honeycomb of negligible areal density and shielding contribution. Replacing or augmenting this core volume with hydrogen-rich constituents could add a shielding function within the existing structural envelope. On small platforms, where the mass budget is strictly capped, such multifunctionality is particularly attractive: a 1U CubeSat, for example, is limited to 2 kg [16], its electronics are typically COTS, and the enclosing solar panels are conventionally printed circuit boards [17–19]. No studies were found in which they are executed as sandwich panels. Whether a core modification preserves acceptable mechanical performance is, however, an open question, since the core governs the transverse shear behaviour and the separation of the face sheets [20].

This work presents a feasibility study on whether the

core volume of a structural sandwich panel can be converted into a shielding element without compromising its load-bearing function. Two integration routes are investigated: filling the unused volume of a honeycomb core with a hydrogen-rich and structurally weak filler; and replacing the core entirely with a stack of load-bearing layers that are more hydrogen-rich than carbon. Both concepts were manufactured using established composite processing routes and evaluated in four-point bending against a conventional sandwich baseline, with the flexural stiffness *D* as the main comparison criterion. The following sections derive the material selection and specimen design from these two routes, describe the manufacturing and testing, and discuss the mechanical cost at which the shielding function is gained.

2. MATERIALS AND METHODS

2.1. Sandwich concepts

All configurations share the same sandwich architecture: two CFRP face sheets of 1 mm enclosing a core volume of 10 mm. The reference sandwich represents the established spacecraft solution and combines face sheets made of eight plies of IM7/8552 prepreg in a symmetric cross-ply layup $[0,90,0,90]_s$ with an aluminium honeycomb core of type PAMG-XR1-8.1-1/8-20-P-5056, bonded with Redux 312 adhesive film. In this configuration, only the face sheets, with an areal density of about 0.3 g/cm^2, contribute to shielding (Fig. 1a).

The two concepts modify the core volume while keeping the face-sheet thickness unchanged. They are intended for the established prepreg route. For the feasibility question of this study, however, the qualified aerospace prepreg is required only for the reference, representing the established solution, not for the concept specimens themselves. Their face sheets were therefore laid up from four layers of 3K carbon 2x2 twill fabric at 200 g/m^2 and infused with epoxy, reaching approximately the same 1 mm thickness as the prepreg baseline and an equally balanced [0,90] fibre architecture. The concept face sheets thus reproduce the geometry of the reference, while the manufacturing route differs.

The infusion system used, R&G epoxy resin L with hardener GL2, is not space-qualified. Its strength values are comparable to those of the space-qualified infusion system Araldite LY 556 with Aradur 906, which is sufficient to address the feasibility question in this study. Since the L/GL2 resin tolerates only 85 °C, the concept specimens were bonded at room temperature with a two-component adhesive instead of the adhesive film. However, the material selection for the concepts follows the requirements of the intended prepreg route.

The material selection of both concepts rests on two atomic parameters introduced in the shielding literature [7]: the ratio *Z/A* of mean atomic number to mean atomic mass, proportional to the mass stopping power for charged particles, and $A^{-1/3}$, proportional to the fragmentation cross section per unit mass. Tab. 1 compares the candidate materials against polyethylene, consistently the most effective of the considered materials, and carbon, the stiffest constituent. Since *Z/A* varies only weakly across these materials, their shielding differences are governed by the fragmentation parameter, and thus by their hydrogen content. All selected materials lie between the two bounds: they shield less than polyethylene but more than the carbon fibres of the face sheets.

Table 1: Shielding parameters of the candidate materials: density, hydrogen mass fraction, mass stopping power parameter Z/A and fragmentation parameter $A^{-1/3}$ (larger is more effective), computed as atom-fraction weighted means from standard atomic weights

Material	ρ (g/cm^3)	H (wt %)	Z/A	$A^{-1/3}$
HDPE (CH_2)	0.95	14.4	0.570	0.598
PA 11 ($C_{11}H_{21}NO$)	1.04	11.55	0.556	0.570
Epoxy (C_2OH_3)	1.10	7.0	0.534	0.518
para-Aramid ($C_{14}H_{10}N_2O_2$)	1.44	4.2	0.520	0.490
PEEK ($C_{19}H_{12}O_3$)	1.30	4.2	0.520	0.490
PEI ($C_{37}H_{24}O_6N_2$)	1.27	4.1	0.520	0.489
Carbon (C)	1.8	0	0.500	0.437

The first concept fills the honeycomb cells (Fig. 1d) with a relatively hydrogen-rich body, which can preserve its geometric shape at the curing temperatures required by the adhesive film, so that the surrounding sandwich carries the load and the filler is exempt from structural requirements. PA 11, or Nylon 11, was selected as the filler material: with a hydrogen content of 11.55 wt% it approaches polyethylene in fragmentation effectiveness (Tab. 1), but unlike polyethylene it remains form-stable up to 150 °C [21] and therefore can withstand the 120 °C curing step of the aerospace Redux 312 adhesive film, which keeps the concept transferable to the prepreg route. The baseline core provides cells too small (3.18 mm) to be filled efficiently, so a different core was required. It was selected for shielding rather than for mechanics: the lightest available aerospace honeycomb, PAMG-XR1-1.0-3/8-07-P-5056, maximises filler volume through its larger 9.53 mm cells and minimises the aluminium in the shielding path, and, with it, the secondary radiation, through its thinner walls (Fig. 1c,d). The mechanical contribution of the core was deliberately set aside at this stage. The consequences of this

choice are quantified later in Section 3.
The second concept replaces the honeycomb entirely with a layered stack of two load-bearing constituents, epoxy-impregnated aramid fabric and polyetherimide (PEI) plates, both more efficient at shielding against the chosen particle group than carbon (Tab. 1). Aramid 2x2 twill fabric at 170 g/m^2, impregnated with epoxy, retains 80 to 90 % of the shielding efficiency of polyethylene against heavy ions [22] and is established in space applications as debris protection, as in the Columbus shield [23]. In laminate form aramid can also carry load. PEI, an amorphous thermoplastic with a glass transition temperature of 217 °C [24], shields comparably to aramid, since both materials nearly coincide in their fragmentation parameter (Tab. 1). Its selection over the equally shielding polyether ether ketone (PEEK) rests on three properties: it bonds exceptionally well to epoxy systems, forming a gradient interphase during co-curing above 120 °C [25]; its ductility as a thermoplastic, with failure strains exceeding those of epoxy laminates by more than an order of magnitude, mitigates the brittleness of a thick epoxy stack; and its temperature tolerance permits co-curing with aerospace prepregs in the autoclave, which makes the concept adaptable to the established prepreg route. The stack is symmetric and reaches the 10 mm thickness of the replaced core. Two variants with identical PEI content were built: three PEI plates of 2 mm (Layered 3x2) and two plates of 3 mm (Layered 2x3), with 16 aramid layers filling the remaining thickness (Fig. 1e,f).
The face sheets of the concepts and of the reference thus differ in their manufacturing route. Comparing a concept directly against the reference would therefore vary two parameters at once: the core and the face-sheet manufacturing route. Two bridge panels resolve this. Bridge 1 combines the infused face sheets with the baseline 8.1 pcf core and serves as the reference for the layered concept with aramid and PEI, while Bridge 2 combines the infused face sheets with the unfilled 1.0 pcf core, separating the effect of the core exchange from that of the filling. Every comparison in Section 3 is thus made between panels that differ in exactly one parameter. Tab. 2 summarises all six configurations, and Fig. 1 shows their cross-sections.

Table 2: Specimen series with face-sheet route, core configuration and areal density

Series	Face sheets	Core volume	Areal density [g/cm^2]
Baseline	prepreg	8.1 pcf	0.48
Bridge 1	infused	8.1 pcf	0.48
Bridge 2	infused	1.0 pcf	0.40
Filled honeycomb	infused	1.0 pcf + PA 11 inserts	1.16
Layered 3x2	infused	3 PEI plates + aramid	1.59
Layered 2x3	infused	2 PEI plates + aramid	1.56

2.2. Manufacturing

The baseline was produced in two stages. The prepreg face sheets were cured in the autoclave at 180 °C and 7 bar, then ground on the core-facing surfaces and bonded to the honeycomb with Redux 312 film at 120 °C and 2 bar. The concept face sheets were infused and post-cured at up to 70 °C. All concept and bridge sandwiches were then bonded at room temperature with the two-component adhesive Loctite EA 9466 (Section 2.1). For the filled honeycomb, hexagonal inserts, 9 mm across and 8.5 mm high, were laser-sintered from PA 11 powder and placed into the cells before bonding (Fig. 1d).
The filled-honeycomb concept is intended for the prepreg route, in which the assembled sandwich is bonded with the film adhesive under autoclave pressure (Section 2.1). To verify this step, prepreg face sheets were additionally bonded to the 1.0 pcf core with the Redux 312 film. This attempt failed: the core collapsed under the 2 bar consolidation pressure, so the prepreg route is not processable with this core. The consequences are taken up in Section 3.

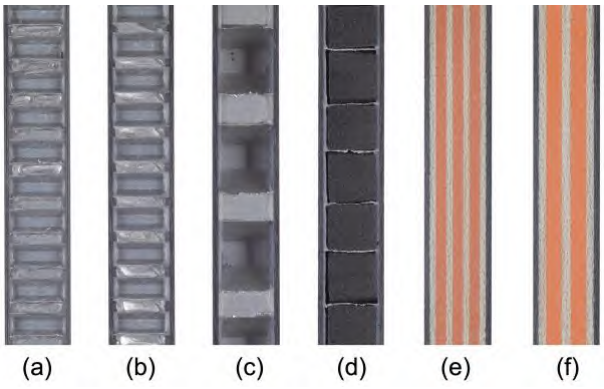


Figure 1: Cross-sections of the manufactured specimen series: (a) Baseline sandwich; (b) Bridge 1; (c) Bridge 2; (d) Filled honeycomb with PA 11 (Nylon) inserts; (e) Layered 3x2; (f) Layered 2x3.

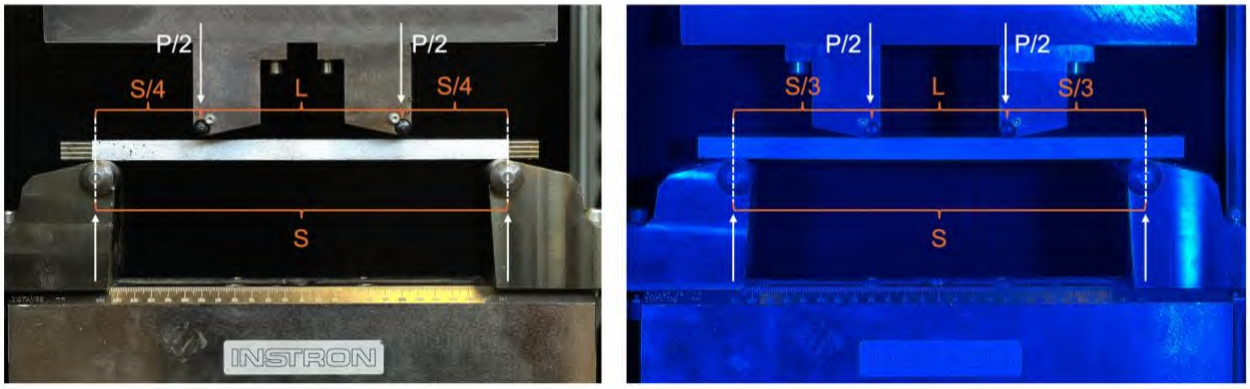


Figure 2: Loading configurations according to ASTM D7250, method 10.2.5: quarter-span (left, L=S/2) and third-span (right, L=S/3). The photo on the right is illuminated by the ARAMIS measurement system.

For the layered concept, the PEI plates were first fused from 0.5 mm PEI-SF Dexnyl© foils (Bieglo GmbH) in a heated press to the required thicknesses. The complete stack, consisting of carbon face-sheet layers, aramid layers and PEI plates, was then infused in a single shot (Fig. 1e,f). Because the PEI plates are impermeable, a linear inlet was used, with flow media wrapped down the sides of the preform so that the resin reaches every aramid layer in-plane. In a prepreg-based version of the concept, where the plies arrive pre-impregnated, this measure would not be necessary.

2.3. Four-point bending tests and data reduction

The mechanical cost of the core modifications was quantified in four-point bending following the standard ASTM D7250 [26], which separates the mid-span deflection of a sandwich beam into a bending and a shear contribution,

$$\Delta = \frac{P\,(2S^3 - 3SL^2 + L^3)}{96\,D} + \frac{P\,(S - L)}{4\,U} \qquad (1)$$

where P is the total force, S is the support span and L is the load span. The flexural stiffness D (the sandwich counterpart of the beam bending stiffness EI) and the transverse shear rigidity U are the two unknowns; from U, the core shear modulus G_c follows. Since the face-sheet modulus of the wet-laid laminates is a process outcome rather than a datasheet value, both unknowns must be determined by testing each specimen in two loading configurations with different L/S ratios and solving the two instances of Eq. 1 simultaneously.

All specimens measure 290x30 mm. The support span of 240 mm is the largest the specimen length permits and simultaneously the smallest that keeps simple beam theory valid ($S/d > 20$ at a panel thickness of 12 mm). Both loading configurations are therefore bound to the same support span and differ only in the load span: 120 mm ($L = S/2$) and 80 mm ($L = S/3$), as shown in Fig. 2. The consequences of this geometric constraint for the shear extraction are shown in Section 3. Tests were run on an Instron 5584 machine at 1 mm/min, within the elastic range, since both configurations must be applied to the same specimen. The mid-span deflection was measured directly on the specimen by digital image correlation (ARAMIS), so that machine compliance does not enter Eq. 1 . For evaluation, the toe region of each record was removed by linear extrapolation to zero force, and D, U and G_c were computed at ten evenly spaced force levels per specimen and averaged, with five to six specimens per series.

3. RESULTS AND DISCUSSION

3.1. Force-deflection response and flexural stiffness

All series respond linearly over the evaluated range. Fig. 3 compares the Baseline with Bridge 1, which share the 8.1 pcf core and differ only in the face-sheet route: the prepreg face sheets respond 55 to 60 % stiffer than the infused ones (751 against 469 N/mm in the quarter-span configuration, Tab. 3) and reproduce within about 1 % against 2 to 3 % for the infused series. This difference quantifies the price of the substitute face-sheet route and defines Bridge 1 as the reference level for the concepts.

Fig. 4 shows the central result. Both layered variants respond 40 to 43 % stiffer than Bridge 1 in both loading configurations: replacing the honeycomb with the PEI/aramid stack increases bending stiffness rather than degrading it. This gain answers whether the shielding layers themselves carry load: a stiffness above the honeycomb reference is only possible if the interfaces between the PEI plates and the aramid laminate transfer shear, so the layered core participates in the load transfer rather than being carried by the face sheets. The two variants respond almost identically (the Layered 3x2 variant about 2 to 3 % stiffer), so the distribution of the PEI through the thickness has only a minor influence, consistent with the identical PEI content of both variants. The Layered 2x3 variant is the most reproducible series of the study, with a scatter below 1 %.

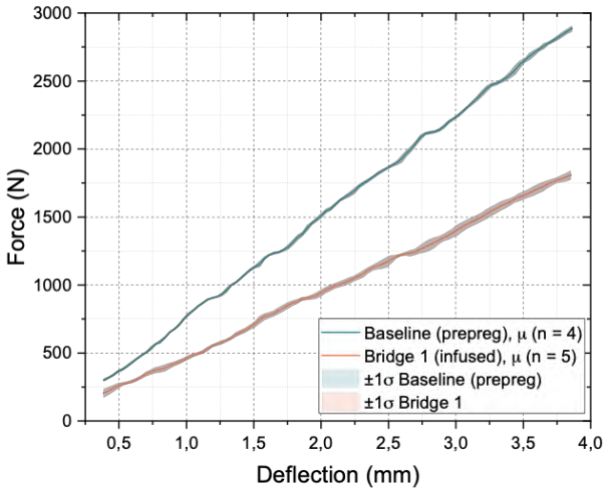


Figure 3: Force-deflection response of the Baseline and Bridge 1 sandwiches in the quarter-span configuration (mean and standard deviation across each series, toe-compensated).

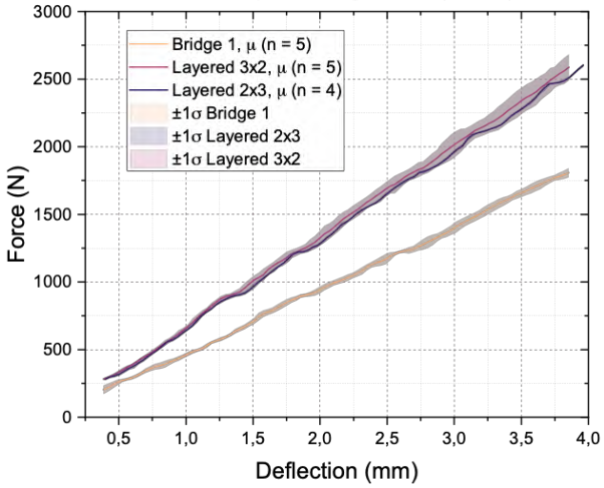


Figure 4: Force-deflection response of the Bridge 1 sandwich and Layered concepts in the quarter-span configuration (representation as in Fig. 3).

Fig. 5 completes the isolation chain for the filled honeycomb. The core exchange dominates: at a given deflection, Bridge 2 carries only about one-quarter of the force of Bridge 1. The PA 11 inserts partially restore this loss: the filled honeycomb carries about 63 % more force than the unfilled Bridge 2 (199 against 122 N/mm). The loss is therefore caused by the core exchange itself, the price of the larger cells and thinner walls selected in Section 2.1, not by the inserts. The soft-core records scatter more than those of the stiff-core series because the fluctuations in the machine load signal, present in all series, become visible against the low forces these specimens carry. The low-density core is, in addition, sensitive to local compressive damage, and both loading configurations are run consecutively on the same specimen. For these two series, the first run therefore provides the only measurement that is certain to represent the unloaded state, and the quarter-span configuration, tested first, is used for the comparison.

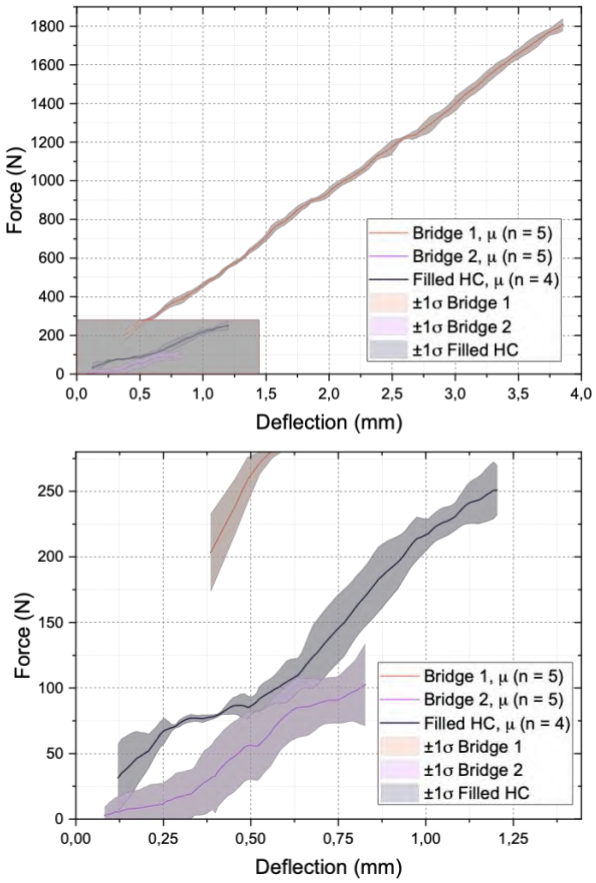


Figure 5: Force-deflection response of the Bridge 1 and Bridge 2 sandwiches and the Filled honeycomb concept in the quarter-span configuration (representation as in Fig. 3).

Table 3: Mean slopes k of the force-deflection records per loading configuration and flexural stiffness D (mean, CV) of the valid specimens. For the soft-core series, only quarter-span configuration is reported

Series	n	*k* quarter (CV) [N/mm]([%])	*k* third (CV) [N/mm]([%])	D (CV) [×10^8 N mm^2]([%])
Baseline	4	751 (0.6)	599 (0.7)	1.79 (24.2)
Bridge 1	5	469 (1.4)	385 (2.3)	0.99 (13.4)
Bridge 2	5	122 (25)	–	–
Filled honeycomb	4	199 (11)	–	–
Layered 3x2	5	672 (2.9)	550 (2.3)	1.19 (18.7)
Layered 2x3	4	656 (0.4)	533 (0.6)	1.13 (3.3)

Tab. 3 summarises the evaluation. The flexural stiffness D confirms the ranking of the slopes for the four stiff-core series. The coefficients of variation of D exceed the scatter of the underlying curves because the data reduction is divided by a term that is only about 0.07 for the present span combination, so a deviation of 1 % in the deflection ratio changes D by about 15 %. The ranking of the series remains unchanged. Only the absolute values carry this amplified uncertainty. With four valid specimens for the Baseline and the Layered 2x3 variant, one below the five recommended by the practice, the absolute values are indicative rather than qualification data.

3.2. Transverse shear extraction

The transverse shear rigidity U, and with it the core shear modulus G_c, could not be reliably determined for any series. The cause is geometric. The specimen length limits the support span to 240 mm, which is simultaneously the minimum span for beam theory, so both loading configurations are bound to the same support span and their shear-to-bending ratios differ by only about 7 %, against a factor of about 16 between the standard configurations the practice recommends. For pure bending, Eq. 1 gives a deflection ratio of exactly 368/297 for this span combination, and the U equation divides by the distance of the measured ratio from this value. The expected shear contribution of the stiff cores raises the ratio by less than about 1 %, while the measurement scatter reaches 1 to 3 %: the equation system becomes nearly singular, and the sign of the extracted U is decided by scatter rather than by the material. The response of all series is thus bending-dominated at the spans accessible to this specimen geometry, which defines a lower bound on U rather than a value: U is at least large enough that its deflection contribution stays below the measurement resolution, so the shear contribution can be neglected for stiffness predictions at comparable spans. A dedicated shear test according to ASTM C273 [27] is the appropriate method for the layered concept, and the only way to obtain G_c for a core that is itself a laminate.

3.3. Trade-off and application perspective

The layered concept does what it was designed to do, using materials and processes available today. Its price is the areal density, which rises from 0.48 g/cm^2 for the baseline sandwich to 1.56 g/cm^2 for the Layered 2x3 variant. This mass, however, is not spent on a single function: it carries a load, attenuates the first particle group, and consists of a material established for space debris protection. Of the two variants, the Layered 2x3 configuration carries forward: it contains fewer bonded interfaces, is the most reproducible series, and is slightly lighter than Layered 3x2. For the intended prepreg route, the stiffness values measured here are a lower estimate, since the prepreg face sheets respond 55 to 60 % stiffer than the infused ones (Fig. 3). The bonding pf the PEI plates may improve as well: gradient interphase between PEI and epoxy [25] forms only during co-curing above 120 °C, which the room-temperature route of this study does not reach.

The filled honeycomb is rejected, for a processing rather than a material reason. The concept was designed for the prepreg route, and the core selected in Section 2.1, with large cells for the filler volume and thin walls for less aluminium in the shielding path, collapsed under the consolidation pressure of the film adhesive (Section 2.2). Between the two tested cores, cell size and wall thickness trade the filler volume against the pressure the core can carry, so a compromise grade, with thicker walls, somewhat smaller cells, or both, might survive the autoclave cycle. The stiffness contribution of the inserts, about 63 % over the unfilled core, suggests that such a configuration could reach a sufficient mechanical performance. The filling effort, however, remains for every core: the cells have to be filled one by one, about 95 cells for a 100 x 100 mm panel and a multiple of that for larger panels, which is difficult to automate reliably at present. The layered concept, in contrast, is compatible with existing prepreg and autoclave infrastructure.

The shielding itself remains to be quantified. The fragmentation parameter of Tab. 1 is a proxy: it contains no information about the energy spectrum, the secondary particles, or the angular distribution of the incident flux. The areal densities reached here, about 1.5 g/cm^2, are one order of magnitude below the 5 to 23 g/cm^2 of the accelerator studies reviewed in the introduction, so an effect on the accumulated dose from trapped particles can be expected, whereas heavy GCR ions are only partly fragmented. Whether the secondary particles increase or decrease the single-event rate requires a radiation transport simulation, which is the necessary next step. For mass-capped platforms, the concept meets a hard boundary: at 1.56 g/cm^2, all six faces of a 1U CubeSat would amount to about 1.0 kg of its 2 kg budget, against about 0.31 kg for the baseline sandwich, so the concept is more attractive for larger satellites, where added mass can be traded for mission reliability.

4. CONCLUSIONS

This work examined whether the core volume of a structural sandwich panel can be converted into a shielding element against protons, heavy ions, and fast neutrons without compromising its load-bearing function. Two concepts, both realised with space-relevant materials and established composite processes, were manufactured and tested in four-point bending against a prepreg baseline and against bridge panels that isolate the effect of the face-sheet route. The layered concept, in which PEI plates and epoxy-impregnated aramid layers replace the honeycomb core, proves feasible. It

responds 40 to 43 % stiffer in bending than the honeycomb reference with the same face sheets, so the shielding layers themselves carry the load. Its price is the areal density, which rises from 0.48 g/cm^2 for the baseline sandwich to 1.56 g/cm^2 for the selected variant with two 3 mm PEI plates, the most reproducible series of this study. This mass serves several functions at once: it carries a load, attenuates the targeted particle group, and consists of a material established for debris protection. The temperature tolerance of PEI permits co-curing with aerospace prepregs, which makes the concept compatible with existing prepreg and autoclave infrastructure.

The filled-honeycomb concept, in which laser-sintered PA 11 inserts fill the cells of a lightweight aluminium core, is not pursued further. The inserts work as intended: they partially restore the stiffness lost by the core exchange, and the material withstands the bonding temperature of the prepreg route. The concept nevertheless fails at the process. The thin-walled core selected for shielding collapsed under the consolidation pressure of the film adhesive, and while a compromise core grade could resolve this, the filling of the cells one by one remains for every core and is difficult to automate for panel quantities.

The transverse shear properties could not be extracted for any series, since the specimen geometry forces both loading configurations onto the same support span, and the shear signal stays below the measurement scatter. A dedicated shear test according to ASTM C273 is the appropriate method for the layered concept. What this study demonstrates is therefore the feasibility, not shielding performance: more effective shielding materials can be integrated into a structural panel without loss of bending stiffness, using materials and processes available today, while the shielding gain itself remains to be quantified by radiation transport simulation.

ACKNOWLEDGEMENTS

During the preparation of this work, the author used Claude (Anthropic) to assist with structuring and language editing. The author reviewed and edited all content and takes full responsibility for the content of this publication.

REFERENCES

[1] Sinclair, D. & Dyer, J. (2013). Radiation Effects and COTS Parts in SmallSats. *27th Annu. AIAAUSU Conf. Small Satell.*

[2] Todd, B. & Uznanski, S. (2016). Radiation Risks and Mitigation in Electronic Systems.

[3] Durante, M. & Cucinotta, F.A. (2011). Physical basis of radiation protection in space travel. *Rev. Mod. Phys.* 83(4), 1245–1281.

[4] Baumann, R. & Kruckmeyer, K. (2020). Radiation Handbook for Electronics.

[5] Aguiar, Y.Q.D., Wrobel, F., Autran, J.-L. & García Alía, R. (2025). *Single-Event Effects, from Space to Accelerator Environments: Analysis, Prediction and Hardening by Design*, Springer International Publishing, Cham.

[6] Selčan, D., Kirbiš, G. & Kramberger, I. (2017). Nanosatellites in LEO and beyond: Advanced Radiation protection techniques for COTS-based spacecraft. *Acta Astronaut.* 131, 131–144.

[7] O'Connor, A., Park, C., Baciak, J.E. & Manuel, M.V. (2024). Mitigating space radiation using magnesium(-lithium) and boron carbide composites. *Acta Astronaut.* 216, 37–43.

[8] Turner, J.E. (2010). *Atoms, radiation, and radiation protection*, 3., completely revised and enl. ed., 2. repr, Wiley-VCH, Weinheim.

[9] Horst, F., Boscolo, D., Durante, M., Luoni, F., Schuy, C. & Weber, U. (2022). Thick shielding against galactic cosmic radiation: A Monte Carlo study with focus on the role of secondary neutrons. *Life Sci. Space Res.* 33, 58–68.

[10] Cohen, M.M. (2004). Carbon Radiation Shielding for the Habot Mobile Lunar Base. In , pp. 2004-01–2323.

[11] Guetersloh, S., Zeitlin, C., Heilbronn, L., Miller, J., Komiyama, T., Fukumura, A., Iwata, Y., Murakami, T. & Bhattacharya, M. (2006). Polyethylene as a radiation shielding standard in simulated cosmic-ray environments. *Nucl. Instrum. Methods Phys. Res. Sect. B Beam Interact. Mater. At.* 252(2), 319–332.

[12] Zeitlin, C., Guetersloh, S.B., Heilbronn, L.H. & Miller, J. (2006). Measurements of materials shielding properties with 1GeV/nuc 56Fe. *Nucl. Instrum. Methods Phys. Res. Sect. B Beam Interact. Mater. At.* 252(2), 308–318.

[13] Naito, M., Kitamura, H., Koike, M., Kusano, H., Kusumoto, T., Uchihori, Y., Endo, T., Hagiwara, Y., Kiyono, N., Kodama, H., Matsuo, S., Mikoshiba, R., Takami, Y., Yamanaka, M., Akiyama, H., Nishimura, W. & Kodaira, S. (2021). Applicability of composite materials for space radiation shielding of spacecraft. *Life Sci. Space Res.* 31, 71–79.

[14] Naito, M., Kodaira, S., Ogawara, R., Tobita, K., Someya, Y., Kusumoto, T., Kusano, H., Kitamura, H., Koike, M., Uchihori, Y., Yamanaka, M., Mikoshiba, R., Endo, T., Kiyono, N., Hagiwara, Y., Kodama, H., Matsuo, S., Takami, Y., Sato, T. & Orimo, S. (2020). Investigation of shielding material properties for effective space radiation protection. *Life Sci. Space Res.* 26, 69–76.

[15] ECSS-E-HB-32-20 (2011). *Structural materials handbook*.

[16] Johnstone, A. (2022). *CubeSat Design Specification*, Cal Poly – San Luis Obispo, CA.

[17] Asundi, S., Mahin, M., Nagabhushan, V., Lin, T.Y. & Fitz-Coy, N. (2010). Composite and PCB Based Implementations of a Solar Panel

Design for SwampSat.
[18] Bhattarai, S., Go, J.-S., Kim, H. & Oh, H.-U. (2021). Development of a Novel Deployable Solar Panel and Mechanism for 6U CubeSat of STEP Cube Lab-II. *Aerospace* 8(3), 64.
[19] Park, Y.-K., Kim, G.-N. & Park, S.-Y. (2021). Novel Structure and Thermal Design and Analysis for CubeSats in Formation Flying. *Aerospace* 8(6), 150.
[20] Zenkert, D. (1995). *An Introduction to Sandwich Structures*, Advisory Services.
[21] Reichelt Chemietechnik GmbH+Co. (2026). Polyamid 11.
[22] Lobascio, C., Briccarello, M., Destefanis, R., Faraud, M., Gialanella, G., Grossi, G., Guarnieri, V., Manti, L., Pugliese, M., Rusek, A., Scampoli, P. & Durante, M. (2008). Accelerator-based tests of radiation shielding properties of materials used in human space infrastructures. *Health Phys.* 94(3), 242–247.
[23] Destefanis, R., Amerio, E., Briccarello, M., Belluco, M., Faraud, M., Tracino, E. & Lobascio, C. (n.d.). Space environment characterisation of Kevlar®: good for bullets, debris and radiation too.
[24] Fink, J.K. (2008). Poly(imide)s. In *High Perform. Polym.*, pp. 475–519.
[25] Teuwen, J.J.E., Asquier, J., Inderkum, P., Masania, K., Brauner, C., Villegas, I.F. & Dransfeld, C. (2018). Gradient interphases between high-Tg epoxy and polyetherimide for advanced joining processes.
[26] ASTM D7250/D7250M − 20 (2020). Practice for Determining Sandwich Beam Flexural and Shear Stiffness.
[27] ASTM C273 - 00 (2000). Test Method for Shear Properties of Sandwich Core Materials.

AUTOMATED STRUCTURAL ANALYSIS AND DATA-DRIVEN MODELLING OF A LARGE DEPLOYABLE REFLECTOR ANTENNA

R. Grammatico[(1),*], P. Di Re[(3)], M. Lapi[(2)], W. Lacarbonara[(1)]

[(1)] Sapienza University of Rome, Dept. of Structural and Geotechnical Engineering, Via Eudossiana 18, 00184 Rome, Italy

[(2)] Thales Alenia Space Italia, Via Saccomuro 24, 00131, Rome, Italy

[(3)] University of Genoa, Dept. of Civil, Chemical and Environment Engineering, via Montallegro 1, 16145, Genoa, Italy

[*] Email: riccardo.grammatico@uniroma1.it

Keywords

large reflector antenna, prestressed cable net, OpenSees, modal identification, operational deflection shapes, pre-stress transitions, thermal sensitivity, surrogate modelling

Abstract

Large Deployable Reflector (LDR) antennas maintain their reflecting surface through the pretension of lightweight cable networks, so the operational configuration is the equilibrium of a tension-stiffened geometrically nonlinear system. Thermal excursions and manoeuvre-induced transients perturb the initial equilibrium: heating reduces cable tension and can cause surface drift and beam depointing, while dynamic loads may temporarily cause members to become slack and impose a recovery time before the design configuration is regained. This work presents a Python-controlled OpenSees workflow for the dynamic assessment of a prescribed LDR design. A new cable finite element is implemented to represent the main thermo-mechanical effects governing tensioned cable networks, including pretension, thermal variation, tension-only behaviour, geometric stiffness and distributed dynamic effects. The formulation is verified through analytical benchmarks and numerical comparisons with commercial finite element software. The pipeline is then used to investigate sensitivity to thermal and dynamic operating conditions, identifying modal changes, loss of tension and operational response shapes. As a proof of concept, a compact feed-forward neural-network classifier trained on the resulting database reproduces the dynamic loss of tension at reduced inference cost, providing a basis for data-driven screening of operating conditions.

1 INTRODUCTION

Large Deployable Reflector (LDR) antennas are used in space applications requiring high-gain, large-aperture radiating systems under severe mass and stowage constraints (Fig. 1). In mesh-reflector architectures, such as AstroMesh-like and tensegrity-based concepts, the reflecting surface is a prestressed assembly of a deployable structure, front and rear cable nets, tensioning ties and a metallic reflective mesh [1,2]. The target paraboloid is therefore an equilibrium configuration whose stiffness and shape accuracy depend primarily on the pretension field. The static design of deployable mesh reflectors is generally addressed through form-finding procedures. The Force Density Method remains a classical tool because it rewrites cable-network equilibrium in terms of force-to-length ratios [3]. Related approaches include dynamic relaxation and other network-based form-finding strategies [4,5], while reflector-specific procedures account for topology, surface accuracy, mesh properties, supporting-truss compliance and shape adjustment [6,7,8,9]. Manufacturing-oriented studies

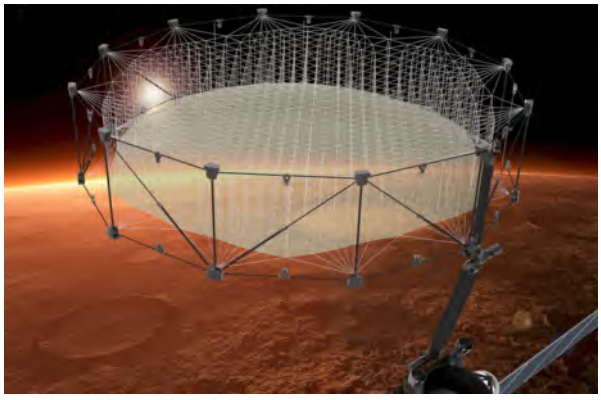


Figure 1: Thales Alenia Space LDR antenna architecture. The reflecting surface is supported by a lightweight prestressed cable-net and mesh assembly.

recover the zero-stress configuration used to define rest lengths, cutting patterns and assembly tolerances [10], and robust-design studies show how manufacturing deviations propagate into surface errors [11]. These contributions provide the static and geometric basis for LDR design.

Cable mechanics provides the reference scale for the dynamic assessment of prestressed cable nets. Taut-string theory gives the dependence of transverse frequencies on axial tension, while sag-extensibility models describe the effects of sag, axial compliance and boundary conditions [12,13]. Thermoelastic extensions show how temperature modifies stress and natural frequencies, providing benchmarks for thermally stressed cables [14]. These models identify the mechanisms that the finite element formulation must reproduce: tension-dependent transverse stiffness, thermal detensioning, local cable-span dynamics and slack to taut transitions.

Operational assessment adds system-level requirements. In orbit, thermal gradients and transient disturbances associated with attitude manoeuvres, deployment events and platform vibrations modify the pretension field and may detension members. Slack locally removes stiffness, alters the modal spectrum, degrades the reflecting surface shape and increases the time needed to recover the operational configuration. Previous reflector studies have addressed form-finding and modal analysis through dedicated dynamic models [15], and recent work has shown that internal cable-member displacements can affect vibration predictions in large reflector networks [16]. Scaling analyses further confirm that mesh-reflector dynamics are tied to geometry, mass distribution and structural layout [17].

Numerical simulation is essential, but the modelling environment must support repeated and reproducible analyses. General-purpose finite element frameworks provide truss, link or cable elements for prestressed structures, and commercial solvers offer cable formulations suitable for numerical comparison [18,19,20]. However, reflector studies often rely on models tailored to one architecture or analysis objective [15,16]. Such models are effective for isolated calculations, but less suited to thermal and load campaigns where the same structure must be generated, solved and post-processed many times while tracking slack, modal changes and operational indicators.

A further difficulty is modal interpretation. Prestressed cable nets contain a few global network modes and many closely spaced local cable modes. Eigenvalue analysis orders all modes by frequency, but does not indicate which modes are excited by a given operational load or which subset is suitable for coupled spacecraft descriptions [21]. Operational deflection shapes (ODSs) extracted from transient frequency-response data describe the actual response pattern, including phase. Their comparison with eigenvectors through the Modal Assurance Criterion (MAC) distinguishes dynamically relevant network modes from local cable-dominated modes [22].

Beyond a single validated model, dense thermal and dynamic campaigns are computationally expensive, which motivates data-driven surrogates that map operating parameters directly to operational indicators such as the onset of dynamic slack. Machine-learning models have recently been applied to deployable reflector antennas and cable-net structures, for example to predict and adjust the reflecting-surface accuracy of cable-net and mesh reflectors [23,24] and to forecast the dynamic behaviour of deployable space mechanisms by combining physics-based and data-driven models [25]. Compact neural networks can therefore provide fast approximations that are retained alongside the high-fidelity model for verification near the operational limits.

This work addresses these issues through an automated OpenSees-based framework for a prescribed prestressed LDR design. A new cable finite element is implemented directly in the solver to represent, at element level, pretension, thermal effects, tension-only response, geometric stiffness, mass modelling and distributed cable dynamics. The formulation is verified through analytical benchmarks and numerical comparisons, and the workflow is used to assess the dynamic sensitivity of the design to thermal and transient operating conditions.

2 CABLE ELEMENT FORMULATION

2.1 Modelling requirements

The cable-net model can be built through different levels of description, depending on which physical effects are represented directly at element level. The starting point is a more conventional approach adopting corotational truss with initial stress, which provides a useful OpenSees baseline for a prestressed configuration but does not treat temperature and slack as native cable-state variables. A two-node prestressed cable element adds assigned pretension, runtime thermoelasticity, tension-only response, geometric stiffness and cable mass within the element formulation. The modal cable element further enriches this description by adding internal transverse coordinates, so that local cable-span dynamics is represented without subdividing each cable into several physical elements. Tab. 1 summarises the modelling routes considered in this work, distinguishing what was already available, what was added, and how each model is used in the validation path. The assigned pretension is denoted by P_0, the cable area by A, Young's modulus by E, the density by ρ, and the thermal-expansion coef-

ficient by α. The uniform temperature change is $\Delta T = T - T_{\text{ref}}$, where T_{ref} is the reference temperature of the prestressed state. The number of internal transverse modes retained per local direction is denoted by N. The objective of the proposed formulation is therefore to combine assigned pretension, runtime thermoelasticity, unilateral tension-only response, smooth slack-to-taut transition, geometric stiffness and distributed dynamic mass in one tangent-consistent finite element.

2.2 Two-node thermo-mechanical kinematics

The reference end positions are $\boldsymbol{X}_1$ and $\boldsymbol{X}_2$, while $\boldsymbol{x}_1$ and $\boldsymbol{x}_2$ are the current positions (Fig. 2). The nodal displacements are $\boldsymbol{u}_i = \boldsymbol{x}_i - \boldsymbol{X}_i$, with $i = 1, 2$. The reference and current chord lengths, L_0 and L_n respectively, and the chord direction unit vector $\boldsymbol{n}$ are

$$L_0 = \|\boldsymbol{X}_2 - \boldsymbol{X}_1\|, \quad L_n = \|\boldsymbol{x}_2 - \boldsymbol{x}_1\|, \quad \boldsymbol{n} = \frac{\boldsymbol{x}_2 - \boldsymbol{x}_1}{L_n}. \tag{1}$$

Pretension is assigned as initial strain $\varepsilon_0 = P_0/(EA)$. The mechanical strain used by the two-node element is

Table 1: Cable descriptions considered in the formulation and validation. The table separates the modelling route, the capability available within one cable member, and the role assigned to each model in the paper.

Description	Element-level capability	Role in this work
Corotational truss with initial stress	Initial axial stress imposed through the material state. Temperature is not a native runtime cable parameter and slack is handled indirectly.	Legacy OpenSees baseline for the prestressed configuration at $\Delta T = 0$. Used to check the consistency of the initial modal response.
Two-node prestressed cable	Assigned pretension P_0, temperature update ΔT, tension-only response, geometric stiffness and cable mass are element quantities.	Intermediate formulation used to isolate the effect of native pretension, runtime thermoelasticity and smooth slack treatment.
Modal cable element	Same thermo-mechanical state as the two-node cable, plus internal amplitudes a_k and b_k describing transverse span motion.	Main formulation used in the cable-net campaigns to include local cable dynamics without refining each member.
CABLE280 reference	Independent commercial cable formulation evaluated through the adopted ANSYS linear-perturbation setup.	External numerical reference for modal frequencies, mode-shape correlation and interpretation of residual modelling differences.

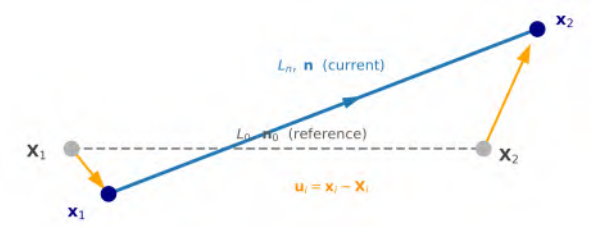


Figure 2: Two-node corotational cable kinematics. Reference and current chord lengths and directions define the geometric stretch used together with assigned pretension and runtime thermal strain.

$$\varepsilon_{\text{m}} = \frac{L_n - L_0}{L_0} + \varepsilon_0 - \alpha \Delta T. \tag{2}$$

In the taut branch the axial force is $P = EA\varepsilon_{\text{m}}$. The linearised tangent contains an axial contribution and the geometric stiffness associated with the current tension is

$$\boldsymbol{K}_{\text{T}} = \boldsymbol{K}_{\text{A}} + \boldsymbol{K}_{\text{G}}, \qquad \boldsymbol{K}_{\text{G}} \propto \frac{P}{L_n}\left(\boldsymbol{I} - \boldsymbol{n} \otimes \boldsymbol{n}\right). \tag{3}$$

The geometric term is the source of lateral stiffness in a pretensioned cable and vanishes when the member detensions. If $L_n = L_0$, the temperature increment that balances the assigned pretension is

$$\Delta T_{\text{crit}} = \frac{\varepsilon_0}{\alpha} = \frac{P_0}{EA\alpha}. \tag{4}$$

2.3 Internal modal enrichment and slack law

The two-node formulation does not represent transverse motion between fixed end nodes. Let $s \in [0, L_0]$ be the material coordinate along the reference chord and let $\boldsymbol{e}_2, \boldsymbol{e}_3$ be the two local transverse directions of the corotational frame. The enriched element approximates the current centreline as

$$\boldsymbol{p}(s) = \boldsymbol{x}_1 + \frac{s}{L_0}(\boldsymbol{x}_2 - \boldsymbol{x}_1) + w_2(s)\boldsymbol{e}_2 + w_3(s)\boldsymbol{e}_3, \tag{5}$$

with

$$w_2(s) = \sum_{k=1}^{N} a_k \sin\frac{k\pi s}{L_0}, \qquad w_3(s) = \sum_{k=1}^{N} b_k \sin\frac{k\pi s}{L_0}. \tag{6}$$

The amplitudes a_k and b_k are internal generalised coordinates associated with the two transverse polarisations (Fig. 3). The sine basis vanishes at the end nodes, so that physical connectivity remains two-node. The generalised state is $\boldsymbol{q} = [\boldsymbol{x}_1^{\mathsf{T}}, \boldsymbol{x}_2^{\mathsf{T}}, \boldsymbol{a}^{\mathsf{T}}, \boldsymbol{b}^{\mathsf{T}}]^{\mathsf{T}}$, with $\boldsymbol{a} = (a_1, \ldots, a_N)$ and $\boldsymbol{b} = (b_1, \ldots, b_N)$. The internal variables add the uniform stretching generated by transverse motion,

$$\varepsilon(\boldsymbol{q}) = \frac{L_n - L_0}{L_0} + \varepsilon_0 - \alpha\Delta T + \frac{\pi^2}{4L_0^2}\sum_{k=1}^{N} k^2(a_k^2 + b_k^2). \tag{7}$$

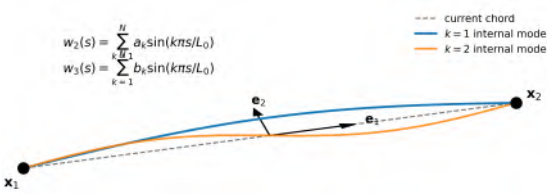


Figure 3: Internal modal enrichment of the cable span. The physical end nodes define the moving chord, while the internal modal amplitudes represent distributed cable motion in the two transverse polarisations.

A smooth unilateral law is used to avoid compression and tangent discontinuities at zero tension, i.e.

$$P(\varepsilon) = \frac{EA}{\beta} \log\left[1 + \exp(\beta\varepsilon)\right], \qquad \frac{\mathrm{d}P}{\mathrm{d}\varepsilon} = EA\, S(\beta\varepsilon), \tag{8}$$

where β is the softplus sharpness and $S(z) = 1/(1 + e^{-z})$ is the logistic function. In the taut regime Eq. 8 tends to the linear elastic law. In slack it keeps the axial force non-negative and preserves a continuous tangent.

2.4 OpenSees implementation

The formulation is implemented in the OpenSees source code as a native finite element. A new C++ element class was added through corresponding header and source files, registered in the element API and exposed to Tcl input files. The implementation is developed in a mixed C++, Tcl and Python workflow: the compiled solver evaluates the element residual, tangent stiffness, mass matrix and response queries, while Python generates the parametric Tcl decks used for the LDR campaigns. The user-level command is

```
element ModalCable3D eleTag iNode jNode A P0
  -modes N -E E -rho rho -alpha alpha
  -Tref Tref -beta beta [-etaSlack eta]
  [-lumped] [-condensed]
```

Here ρ is the material density and N is the number of modes per transverse direction. Setting $N = 0$ recovers the two-node prestressed cable. The optional flags `-etaSlack`, `-lumped` and `-condensed` set, respectively, the smoothing parameter of the unilateral law, a lumped instead of consistent mass matrix, and the static condensation of the internal amplitudes; they are kept at their default settings in the present campaigns. Preliminary checks verified parsing, pretension initialisation, temperature updates, tangent-force consistency, mass assembly and response extraction.

3 VALIDATION STRATEGY AND COMPARISONS

The validation path combines analytical checks, application-scale case studies and external numerical comparisons. The isolated cable span checks elementary cable physics. The complete cable net checks whether the same modelling ingredients remain relevant at reflector scale. The external comparisons separate the benefit over a conventional OpenSees truss baseline from consistency with a commercial cable-element model.

3.1 Isolated-cable comparison

A straight taut cable is analysed using five approaches: the analytical string solution; `ModalCable3D`, `PrestressedCable`, and `corotTruss` with initial stress in OpenSees, and `CABLE280` in ANSYS software. The cable properties were $L_0 = 0.28$ m, $P_0 = 12.6$ N, $A = 5.026548 \times 10^{-7}$ m^2, $E = 72$ GPa, and $\rho = 2200$ kg m^{-3}. Both ends are fixed, gravity and thermal loading are neglected, and consistent mass is used in all numerical models.

The analytical transverse frequencies are

$$f_n = \frac{n}{2L_0}\sqrt{\frac{P_0}{\rho A}}, \qquad n = 1, 2, \ldots \tag{9}$$

A single `ModalCable3D` element with three internal modes per transverse polarisation reproduces the first three analytical frequencies to machine precision. Its internal sine basis represents the distributed cable modes without intermediate physical nodes.

The `PrestressedCable` and `corotTruss` models are discretised with $N = 2, 4, 8, 16, 32,$ and 64 straight elements. Pretension is assigned directly in `PrestressedCable` and through `InitStressMaterial`, with $\sigma_0 = P_0/A$, in `corotTruss`. The two formulations produce identical frequencies at every mesh level, confirming their equivalence in the straight, isothermal, fully taut limit.

Tab. 2 reports the first three transverse frequencies and the corresponding relative errors with respect to the analytical solution. At a fixed discretisation, the error of the straight two-node elements grows with the order of the mode. With 16 elements, the maximum error over the first three modes is 1.451%; with 64 elements, it decreases to 0.090%. `CABLE280` reaches a maximum error of 0.008% with 16 elements, whereas `ModalCable3D` reproduces the same spectrum with one physical element.

All finite-element approaches provide mode shapes. `PrestressedCable` and `corotTruss` return eigen-

Table 2: First three transverse frequencies and relative errors for the representative taut cable.

Approach	Discretisation	f_1	f_2	f_3	e_1	e_2	e_3
		[Hz]			[%]		
Analytical string	continuum	190.6123	381.2246	571.8370	-	-	-
`ModalCable3D`	1 element, 3 modes	190.6123	381.2246	571.8370	0.0000	0.0000	0.0000
`PrestressedCable`	64 elements	190.6315	381.3778	572.3538	0.0100	0.0402	0.0904
`corotTruss`	64 elements	190.6315	381.3778	572.3538	0.0100	0.0402	0.0904
ANSYS `CABLE280`	16 elements	190.6134	381.2327	571.8827	0.0006	0.0021	0.0080

vectors at the physical mesh nodes, with the span-wise field reconstructed by interpolation. `CABLE280` uses quadratic interpolation, while `ModalCable3D` directly returns the amplitudes of the internal sinusoidal modes.

3.2 Complete cable-net application and numerical validation

The second case study applies the formulation to the complete prestressed cable net (Fig. 4), where global nodal motion and local cable-span dynamics coexist within the same frequency range. The model therefore provides a representative benchmark for both the conventional two-node formulation and the enriched modal cable element.

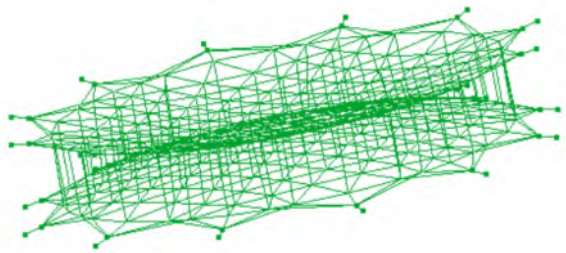


Figure 4: Reference NET-only model used in the modal and transient campaigns, including the prestressed front net, anchor nodes and internal cable coordinates of the enriched formulation.

Three complementary comparisons are performed at the reference thermal state, $\Delta T = 0$, and are summarised in Tab. 3. First, the two-node prestressed cable element is compared with the conventional OpenSees model based on corotational trusses and an initial-stress material. The close modal agreement confirms that both formulations reproduce the same prestressed equilibrium. In the conventional model, however, pretension is embedded in the material state, whereas the native cable element directly updates temperature and axial force during the thermoelastic campaign.

The effect of the internal cable coordinates is then assessed on the NET-only model. Their activation reduces the first twenty frequencies by an almost uniform 9.3%, showing that span-wise inertia and deformation remain relevant at network scale. The enriched model also separates a limited number of global net modes from dense clusters dominated by local cable motion.

Table 3: Numerical comparisons for the complete cable-net application at $\Delta T = 0$.

Comparison	Numerical evidence	Main conclusion
Corotational truss with initial stress versus two-node prestressed cable, ring plus net	Maximum relative frequency difference of 1.3% over the first six modes; 3.4% RMS over the first 35 modes.	Both formulations reproduce the same reference prestressed state; the native element additionally permits runtime thermoelastic updates.
Two-node versus enriched modal cable, NET-only	Almost uniform 9.3% reduction over the first twenty frequencies.	Local span-wise deformation and inertia remain relevant in the complete-network response.
Enriched modal cable versus CABLE280, NET-only	MAC $= 0.9992$ and 0.9993 for modes 1 and 2; ANSYS frequencies approximately 4.4% higher, comprising 1.59% from mass modelling, 2.74% from realised pretension and about 0.07% residual.	The mode shapes coincide and the frequency difference is attributable to modelling assumptions rather than solver disagreement.

Finally, the enriched OpenSees model is compared with an independent ANSYS model using CABLE280 elements and linear-perturbation modal analysis about the prestressed state. The first two mode shapes give MAC values of 0.9992 and 0.9993. The approximately 4.4% higher ANSYS frequencies are explained by the different mass formulation and by the realised front-net pretension. Once these effects are accounted for, the residual discrepancy is approximately 0.07%.

4 AUTOMATED ANALYSIS PIPELINE

The analyses are managed through a Python-controlled OpenSees pipeline. For each parameter combination, Python generates the Tcl model and the required analysis block, launches the locally compiled OpenSees interpreter, and parses the re-

sulting outputs. Input parameters, execution time, timeout status and convergence flags are stored for every run, while the physical quantities recorded depend on the specific campaign.

Three complementary campaigns are considered. The modal thermal campaign, denoted phase M, evaluates 56 temperature offsets between $-180\,^{\circ}$C and $+45\,^{\circ}$C. At each temperature, the prestressed net is re-equilibrated and the static slack count, minimum and maximum cable tensions, and first twenty eigenfrequencies are extracted.

The transient slack-threshold campaign, denoted phase T, samples the $(\Delta T, F_0)$ plane. After thermal re-equilibration, a half-sine impulse with peak amplitude F_0 and duration $T_P = 8$ ms is applied. The stored outputs include the static and transient convergence states, the possible failure step, the initial slack count and the maximum number $N_{\text{slack,max}}$ of simultaneously slack cables. Since the modal state is established before the impulse, the corresponding eigenfrequencies are taken from phase M rather than recomputed for each value of F_0.

A third high-resolution transient campaign, denoted phase H, is performed only at selected operating conditions. A 25 s observation window gives the frequency resolution $\Delta f = 0.04$ Hz. The input force and selected nodal displacement histories are recorded, from which fast Fourier transform (FFT) spectra are computed. Operational deflection shapes and MAC values are evaluated only for the selected all-node datasets. Transient analyses use the average-acceleration Newmark method with $\gamma = 0.5$ and $\beta_N = 0.25$, where γ weights the acceleration contribution in the velocity update and β_N its contribution in the displacement update. This choice was retained after preliminary Hilber–Hughes–Taylor (HHT) analyses showed greater sensitivity near simultaneous taut–slack transitions. Campaign points are executed sequentially because the analyses are memory-bound and unsuccessful runs must be retained in the response map. Non-converged or timed-out cases are stored with their numerical status and are not automatically interpreted as physical slack states. The resulting structured database supports modal interpretation, operational-limit identification and surrogate modelling.

5 MODAL AND OPERATIONAL IDENTIFICATION OF THE CABLE NET

5.1 NET-only model and thermally evolving prestress

The application study focuses on the overall prestressed cable net. The model contains 955 cable members and 302 physical nodes, of which 24 are fixed at the interface with the perimeter structure. Cable properties are uniform: Young's modulus $E = 72$ GPa, area $A = 5.0265 \times 10^{-7}$ m^2, density $\rho = 2200$ kg m^{-3}, and thermal expansion coefficient $\alpha = 10^{-5}\,^{\circ}$C^{-1}. The form-found cable tensions range from approximately 1 N to almost 200 N. This spread of more than two orders of magnitude leads to a global dynamic behaviour not governed only by an average prestress level: the least tensioned members determine the first local cable frequencies and control the approach to slack. The temperature offsets considered below are applied uniformly with respect to the reference temperature. For each thermal state, the net is first re-equilibrated and the tangent stiffness is then evaluated about the resulting prestressed configuration. The corresponding eigenvalue problem therefore provides a linearised modal description of a thermally updated equilibrium state.

5.2 Thermal modal map and slack-sensitive spectrum

The first campaign sweeps 56 uniform temperature offsets and extracts twenty eigenvalues at each re-equilibrated state. In the fully taut regime, the first global frequency decreases monotonically as thermal expansion reduces the cable pretension. Over the investigated interval, the first global frequency decreases from approximately 58 Hz in the cold state to approximately 25 Hz near the warm edge of the taut domain. Fig. 5(a) shows that this evolution remains smooth only while every cable carries a positive tensile force. The transition is abrupt: when the first members detension, near-zero local mechanisms enter the lower part of the spectrum and the lowest computed eigenfrequency collapses. Consequently, the first frequency ceases to be a meaningful indicator of the global network stiffness as soon as the first slack member appears. The minimum cable tension in Fig. 5(b) is a more reliable precursor because it identifies the member that first approaches the unilateral boundary.

Slack is also load-dependent. A second campaign maps the $(\Delta T, F_0)$ plane by applying half-sine impulses and monitoring the maximum number of simultaneously slack cables during each transient. The admissible impulse decreases as the network warms: a disturbance that leaves the cold network fully taut may cause several members to unload when applied close to the warm thermal margin. The thermal state therefore controls not only the linearised modal frequencies but also the available manoeuvre margin.

The modal map and the slack count must conse-

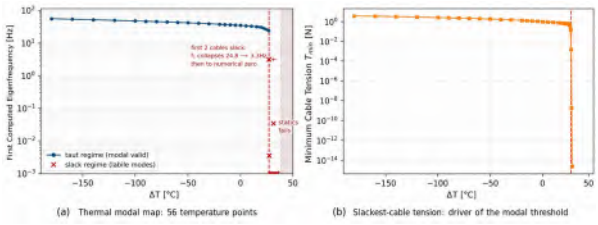


Figure 5: Thermal evolution of the cable-net modal response versus temperature offset. (a) Thermal modal map, showing modal softening along the taut branch and the collapse at cable detensioning. (b) Minimum cable tension, the indicator of the approaching slack transition.

quently be interpreted together. Frequency softening describes the evolution of the tangent dynamics while the net remains taut, whereas the slack count identifies the onset of a different response regime in which the set of active tensile members may change during the motion. Beyond this boundary, a single frequency extracted from the initial tangent system is insufficient to characterise the complete transient response.

5.3 Network modes, cable modes and the slackest-cable threshold

The eigenvectors split into two physically different populations. Global network modes involve appreciable motion of the physical nodes, while the cable spans translate approximately with their end chords. Local cable modes instead leave the physical nodes almost stationary and are dominated by the internal transverse deformation of one or more spans. The resulting spectrum is therefore not a sequence of global reflector modes, but a combination of a small number of network modes and a dense forest of local cable modes. The lower boundary of this forest can be estimated directly from taut-string theory. The first transverse frequency associated with cable e is

$$f_{\mathrm{c},e} = \frac{1}{2L_{0,e}}\sqrt{\frac{P_e}{\rho A}}, \tag{10}$$

and the lowest local-cable frequency in the complete net is therefore

$$f_{\mathrm{c,min}} = \min_{e}\left[\frac{1}{2L_{0,e}}\sqrt{\frac{P_e}{\rho A}}\right], \tag{11}$$

where $L_{0,e}$ and P_e are the reference length and current tension of element e. Since the minimum is generally attained by one of the least tensioned members, Eq. 11 provides a direct connection between the local tension state and the architecture of the global spectrum.

Below $f_{\mathrm{c,min}}$, there is not a first cable that interacts with a network mode, which can therefore remain spectrally isolated. Above this threshold, network modes enter the dense cable-mode population and may hybridise with local span vibrations.

As shown in Fig. 6, the prediction agrees closely with the observed onset of the cable-mode clusters. The predicted and computed thresholds are, respectively, 77.83 and 77.70 Hz in the cold state (Fig. 6(a)), 39.06 and 39.03 Hz at the reference temperature (Fig. 6(b)), and 25.35 and 25.34 Hz close to the warm margin (Fig. 6(c)). The corresponding errors remain below 0.2%. At the same time, the number of spectrally separable network modes decreases from three in the cold state to two at the reference temperature and finally to zero near the warm limit.

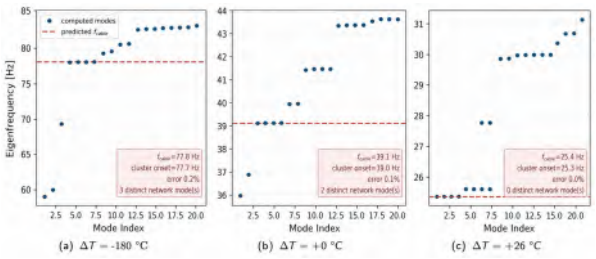


Figure 6: Computed spectra compared with the threshold set by the slackest cable. (a) Cold, $\Delta T = -180\,^{\circ}$C, with three isolated network modes; (b) reference, $\Delta T = 0\,^{\circ}$C, with two; (c) warm, $\Delta T = +26\,^{\circ}$C, with none.

Eq. 11 should be interpreted as a conservative spectral threshold rather than as proof that every mode above it is strongly hybridised. It indicates where interaction with cable modes becomes possible. Whether a particular global mode remains dynamically identifiable must subsequently be assessed from its nodal participation and from the operational response.

5.4 Effective-mass classification

To distinguish global network modes from local cable modes, the first forty eigenvectors of the NET-only model are classified through their effective mass at the reference thermal state, $\Delta T = 0$, after equilibration of the prescribed prestress. For mode i and rigid-body direction d,

$$M_{i,d}^{\mathrm{eff}} = \frac{\left(\boldsymbol{\phi}_i^{\mathsf{T}}\boldsymbol{M}\boldsymbol{r}_d\right)^2}{\boldsymbol{\phi}_i^{\mathsf{T}}\boldsymbol{M}\boldsymbol{\phi}_i}, \tag{12}$$

where $\boldsymbol{\phi}_i$ is the eigenvector, $\boldsymbol{M}$ is the mass matrix and $\boldsymbol{r}_d$ is the dragging vector associated with one of the three global translations or three global rotations. The reported percentages are normalised with

respect to the corresponding total mass or rotational inertia.

As shown in Fig. 7(a), only modes 1 and 2, at approximately 35.71 and 36.64 Hz, exceed the adopted 10% significance threshold. Their translational participation remains below 0.5%, whereas the rotational participation reaches approximately 70.5% about the x-axis for mode 1 and 82.0% about the y-axis for mode 2. Fig. 7(b) shows that the remaining thirty-eight modes have maximum participation below approximately 0.51%, consistently with their classification as local cable modes.

The antisymmetric deformation of modes 1 and 2 produces limited net translation but significant rotational participation. Since the present model contains only the cable net, these values do not represent interface loads transmitted to the spacecraft; they indicate only that these two modes have the greatest potential to couple with rotational motion of the supporting structure.

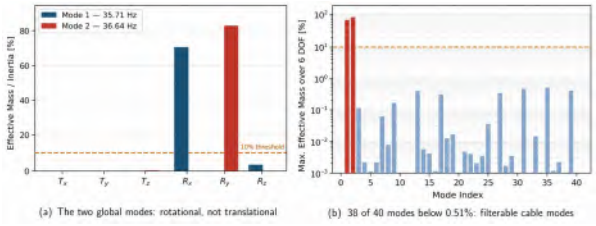


Figure 7: Effective-mass classification of the first forty modes of the NET-only model at $\Delta T = 0$. (a) Modes 1 and 2 across the six rigid-body directions, dominated by rotation. (b) Maximum participation of all forty modes, with only modes 1 and 2 above the significance threshold.

5.5 Transient spectra and operational-shape extraction

Modal analysis identifies the possible vibration patterns of the tangent system, but it does not determine which of them are actually reached by a prescribed disturbance. This distinction becomes essential when many of the lowest-frequency eigenvectors are internal cable modes with negligible displacement at the physical nodes.

A half-sine impulse is applied at one node in the direction normal to the net. Its time history is

$$F(t) = \begin{cases} F_0 \sin\left(\dfrac{\pi t}{T_P}\right), & 0 \le t \le T_P, \\ 0, & t > T_P, \end{cases} \qquad T_P = 8\,\text{ms}. \tag{13}$$

For the all-node identification runs, the response is computed for 5 s with a time step of 10^{-4} s. The

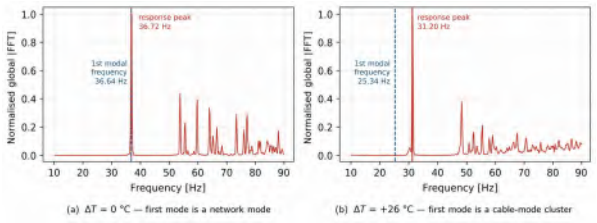


Figure 8: Global FFTs of the all-node impulse responses. (a) Reference, $\Delta T = 0\,^\circ$C, where the dominant peak is a global network mode. (b) Warm, $\Delta T = +26\,^\circ$C, where the dominant peak lies above the cable-mode cluster.

displacement histories of all 302 physical nodes are recorded and subsequently decimated to a sampling frequency of 2 kHz. The reference-state analysis uses $F_0 = 20$ N, whereas the warm-state analysis uses $F_0 = 10$ N to reduce the probability of inducing slack–taut commutations in a configuration already close to detensioning.

For displacement channel j, the discrete Fourier transform is denoted by

$$\widehat{u}_j(f_k) = \sum_{n=0}^{N-1} u_j(t_n) \exp\left(-\mathrm{i}2\pi f_k t_n\right). \tag{14}$$

At a selected response frequency $f^\star$, the complex operational deflection shape is assembled directly from the channel amplitudes and phases,

$$\phi_{\mathrm{ODS}}(f^\star) = \left[\widehat{u}_1(f^\star) \quad \widehat{u}_2(f^\star) \quad \cdots \quad \widehat{u}_{n_{\mathrm{ch}}}(f^\star)\right]^{\mathsf{T}}. \tag{15}$$

The correspondence between the operational shape and eigenmode i is evaluated through the complex modal assurance criterion,

$$\mathrm{MAC}_i(f^\star) = \frac{\left|\phi_{\mathrm{ODS}}^{\mathsf{H}}(f^\star)\phi_i\right|^2}{\left[\phi_{\mathrm{ODS}}^{\mathsf{H}}(f^\star)\phi_{\mathrm{ODS}}(f^\star)\right]\left[\phi_i^{\mathsf{H}}\phi_i\right]}, \tag{16}$$

where the superscript $(\cdot)^{\mathsf{H}}$ denotes the Hermitian transpose. A value close to unity indicates that the measured operational response is approximately proportional to one eigenvector and can therefore be interpreted through a single-mode linear description.

Fig. 8(a) and (b) compare the normalised global spectra obtained at the reference temperature and close to the warm slack margin, respectively. The two spectra illustrate why the lowest eigenfrequency and the dominant operational frequency are not necessarily the same quantity.

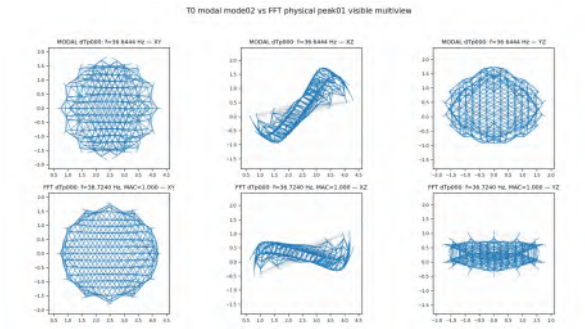


Figure 9: Operational-shape identification at the reference thermal state. The isolated FFT peak at 36.72 Hz produces an ODS that coincides with eigenmode 2 at 36.644 Hz, with complex MAC equal to 0.99997.

5.6 Reference thermal state

At the reference temperature, Fig. 8(a) shows an isolated response peak at 36.72 Hz, approximately 10–17 dB above the surrounding spectral content. The corresponding ODS has a MAC of 0.99997 with eigenmode 2 at 36.644 Hz. The internal-to-nodal motion ratio, defined as the ratio between the Euclidean norm of the internal modal amplitudes and that of the physical nodal displacements of the mode, is approximately 0.16, confirming that the responding shape is a global network mode rather than a local cable mode.

The operational and modal shapes are compared in Fig. 9. Their near-perfect agreement confirms that the response is dominated by one isolated mode and that a linear, time-invariant modal interpretation is accurate at this frequency.

The complex phase also provides information that is absent from a plot of displacement magnitude alone. At the response peak, 168 physical nodes move in one direction while 134 move in antiphase. The transition between the two groups identifies the nodal lines directly from the simulated transient response, rather than imposing them from the eigenvector.

5.7 Operational response near the warm slack margin

Near the warm margin, the modal spectrum changes qualitatively. The first eigenfrequencies form a dense cluster close to 25.34 Hz. These modes have internal-to-nodal motion ratios of approximately 8 and are therefore dominated by transverse cable-span motion. Since a nodal force performs work through physical-node displacement, it cannot efficiently excite modes whose end nodes remain nearly stationary.

Accordingly, Fig. 8(b) does not show its dominant response at the first eigenfrequency. The main operational peak occurs at 31.2 Hz, approximately 5.9 Hz above the lower cable-mode cluster. The ODS extracted at this frequency has a MAC of 0.9999 with mode 20 at approximately 31.16 Hz and negligible correlation with the modes of the 25.34 Hz cluster.

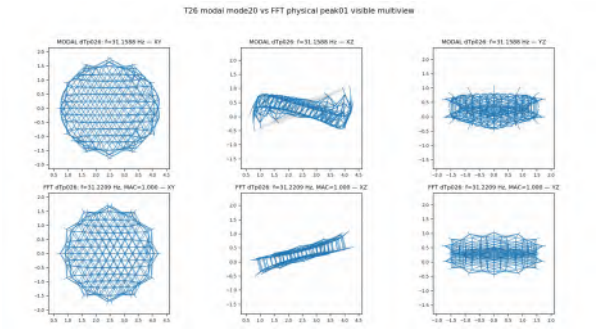


Figure 10: Operational-shape identification near the warm slack margin. The lowest eigenmodes are dominated by internal cable motion, whereas the ODS at the dominant nodal-response peak identifies mode 20 at approximately 31.16 Hz with MAC equal to 0.9999.

Table 4: Operational identification from the all-node transient response.

Thermal state	Spectral response	ODS–mode correspondence
Reference state	Isolated peak at 36.72 Hz	Mode 2 at 36.644 Hz, with MAC $= 0.99997$. The nodal impulse excites a clean global network mode.
Warm margin	Cable-mode cluster near 25.34 Hz; dominant nodal peak at 31.2 Hz	Mode 20 at 31.16 Hz, with MAC $= 0.9999$. The lowest modes are local cable modes, whereas the ODS identifies the higher mode reached by the nodal load.

Fig. 10 confirms that the nodal impulse selects a higher-frequency mode that retains appreciable motion of the physical network. The result demonstrates that frequency ordering alone is insufficient: the first eigenmode is not necessarily the first mode observable or excitable through the spacecraft–net interface.

Tab. 4 summarises the operational identification at the two thermal states.

5.8 Validity of the linear modal interpretation near slack

The eigenvalue analyses are linearisations about thermally re-equilibrated configurations, whereas the transient simulations retain the tension-only

constitutive response and can therefore capture changes in the set of taut members. An FFT–ODS interpretation remains valid only while the motion stays close to one equilibrium state and the response near the selected frequency is dominated by a single eigenvector.

At the reference temperature, the isolated spectral peak and the nearly unit MAC confirm this condition. Near the warm margin, however, the cable-mode forest enters the frequency range of the global modes, the lowest eigenvalues become increasingly dominated by local cable motion, and small changes in temperature or displacement may produce taut–slack commutations and a time-dependent tangent stiffness.

The 5.9 Hz difference between the first eigenfrequency and the dominant warm-state response peak should therefore not be interpreted as a nonlinear resonance shift. In the analysed case, it is primarily an observability effect: the lowest modes are dominated by internal cable motion and are weakly excited by the nodal impulse, whereas mode 20 has sufficient nodal participation. Its MAC of 0.9999 shows that the response at 31.2 Hz is still well represented by a single eigenvector.

The slackest-cable threshold in Eq. 11 and the operational MAC provide complementary information. The former indicates where interaction with local cable modes becomes possible, whereas the latter verifies whether the observed response remains effectively separable. A decreasing MAC, broadband or harmonic content, force-dependent peak shifts, or an increasing slack count would instead indicate departure from the linear time-invariant regime. The combined FFT–ODS–MAC procedure therefore identifies the dynamically active mode rather than simply selecting the lowest eigenvalue, which near the slack boundary may correspond to a local cable mode with negligible nodal observability.

6 SURROGATE MODELLING FOR FAST EVALUATION

The structured database generated by the automated OpenSees campaigns was used to train a compact feed-forward neural-network (FFNN) classifier [25] for the rapid identification of dynamic slack onset,

$$\widehat{p}_{\text{slack}} = \mathcal{N}_{\text{s}}\left(\widetilde{\Delta T}, \widetilde{F}_0\right), \qquad s = \mathbb{I}\left(N_{\text{slack,max}} > 0\right), \tag{17}$$

where $\mathcal{N}_{\text{s}}$ denotes the trained classifier and $\widetilde{\Delta T}$ and $\widetilde{F}_0$ are the standardised temperature offset and impulse amplitude. The binary target is $s = 1$ when at least one cable becomes slack during the transient and $s = 0$ otherwise, with $N_{\text{slack,max}}$ denoting the maximum number of simultaneously slack cables. The sigmoid output $\widehat{p}_{\text{slack}} \in [0, 1]$ is used as a continuous classification score: values close to zero and one indicate conditions classified as no-slack and slack, respectively, whereas the $\widehat{p}_{\text{slack}} = 0.5$ contour defines the estimated decision boundary.

Only simulations for which both the static and transient analyses completed were assigned a physical label. This retained 154 of the 345 phase-T cases, comprising 127 no-slack and 27 slack samples. Static failures and timed-out analyses were retained in the campaign database but excluded from supervised training.

Each classifier contains two hidden layers with 16 neurons and hyperbolic-tangent activations, followed by a sigmoid output. The networks were trained using the limited-memory BFGS algorithm and balanced sample weights. To reduce sensitivity to the random initialisation, 20 classifiers with the same architecture were trained independently and their sigmoid outputs were averaged to obtain the final prediction shown in Fig. 11.

Validation was performed by leaving one complete temperature level out of the training set at each iteration. The resulting out-of-fold predictions achieved a balanced accuracy of 0.900, an F_1 score of 0.863, and an area under the receiver-operating-characteristic curve of 0.951. A further numerical challenge was performed on 25 longer phase-H transients whose exact $(\Delta T, F_0)$ pairs were not included in the training set, giving an accuracy and an F_1 score of 0.960.

The classifier does not remove the cost of generating the original high-fidelity database. Its purpose is to convert the completed simulations into a continuous approximation of the operational taut–slack boundary, allowing interpolation between the sampled conditions and identifying regions in which additional OpenSees analyses are required.

The computational advantage was assessed using the hardware and numerical settings adopted for the present campaigns. Under these conditions, a completed OpenSees transient required a median wall time of approximately 133 s, whereas batched evaluation of the 20-network ensemble required approximately 10 μs per state. These values are specific to the adopted model, solver settings and computational platform, and exclude model-loading and file-management overhead. They nevertheless show the substantial reduction in evaluation cost obtained once the classifier has been trained. Predictions close to the $\widehat{p}_{\text{slack}} = 0.5$ boundary, within sparsely

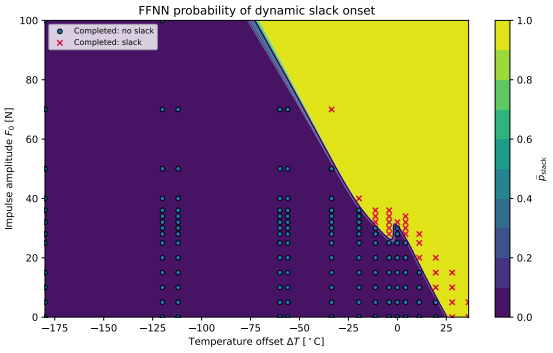


Figure 11: Ensemble-averaged FFNN classification score in the temperature–impulse plane. Symbols denote completed OpenSees simulations, while the $\widehat{p}_{\text{slack}} = 0.5$ contour approximates the predicted taut–slack boundary.

sampled regions, or outside the training domain are returned to the high-fidelity OpenSees model for verification.

7 CONCLUSIONS

This work presented an automated OpenSees-based framework for the dynamic analysis of pre-stressed cable-net reflector antennas. The proposed workflow combines automated model generation with a newly developed cable finite element that directly incorporates pretension, thermoelastic effects, tension-only behaviour, smooth slack–taut transition, geometric stiffness and distributed cable dynamics within a single formulation. The proposed element was successfully validated against analytical cable solutions and commercial finite element models, demonstrating excellent agreement while enabling thermo-mechanical analyses that are difficult to perform with conventional formulations. The enriched element also captures internal cable-span dynamics without requiring mesh refinement, providing an efficient representation of large reflector cable networks. The automated thermal and transient analyses reveal several important physical findings. The key outcomes can be summarized as follows:

- increasing temperature progressively reduces cable pretension, softens the global structural response and eventually causes local cable detensioning;
- transient dynamic loads can also induce slack, with the allowable disturbance level decreasing significantly as the structure approaches its thermal limit;
- the modal spectrum consists of only a few global reflector modes embedded within a dense population of local cable modes, making modal identification based solely on eigenvalue ordering unreliable;
- combining effective modal mass, operational deflection shapes (ODS) and MAC provides a robust procedure for identifying the dynamically relevant modes under operational loading.

Finally, the large database generated through the automated simulations enables efficient data-driven modelling. A compact feed-forward neural network accurately predicts the onset of dynamic slack, providing a computationally inexpensive surrogate for rapid operational screening while preserving the high-fidelity finite element model for verification near critical operating conditions. Future work will extend the methodology to the complete reflector assembly, including the supporting ring and interface dynamics, with the long-term objective of supporting digital-twin applications for large deployable space reflectors.

REFERENCES

[1] Thomson, M.W. (1999). The AstroMesh deployable reflector. In *Proc. IEEE Antennas and Propagation Society International Symposium*, Orlando, FL, USA, Vol. 3, 1516-1519.

[2] Tibert, A.G. & Pellegrino, S. (2002). Deployable tensegrity reflectors for small satellites. *J. Spacecraft Rockets* 39(5), 701-709.

[3] Schek, H.-J. (1974). The force density method for form finding and computation of general networks. *Comput. Methods Appl. Mech. Eng.* 3(1), 115-134.

[4] Veenendaal, D. & Block, P. (2012). An overview and comparison of structural form finding methods for general networks. *Int. J. Solids Struct.* 49(26), 3741-3753.

[5] Barnes, M.R. (1999). Form finding and analysis of tension structures by dynamic relaxation. *Int. J. Space Struct.* 14(2), 89-104.

[6] Li, T., Jiang, J., Deng, H., Lin, Z. & Wang, Z. (2013). Form-finding methods for deployable mesh reflector antennas. *Chin. J. Aeronaut.* 26(5), 1276-1282.

[7] Morterolle, S., Maurin, B., Quirant, J. & Dupuy, C. (2012). Numerical form-finding of geotensoid tension truss for mesh reflector. *Acta Astronaut.* 76, 154-163.

[8] Zhang, Y.Q., Zhang, H., Yang, D.W., Qin, Q.Y. & Zhu, R.S. (2019). Form-finding design of cable-mesh deployable reflector antennas considering wire mesh properties. *AIAA J.* 57(11), 5027-5041.

[9] Du, J., Zong, Y. & Bao, H. (2013). Shape adjustment of cable mesh antennas using sequential quadratic programming. *Aerosp. Sci. Technol.* 30(1), 26-32.

[10] Argentesi, F., Pasquali, M., Atek, S., Gaudenzi, P., Lapi, M., Lanuti, M., Colella, A., Scarozza, D.,

Palomba, L. & Adamo, F. (2026). Geometrically nonlinear model of cable net and mesh for the manufacturing of large deployable mesh reflectors. *Aerosp. Sci. Technol.* 178, 113185.

[11] Labella, G., Sicolo, E., Tampelloni, A., Argentesi, F., Atek, S., Pasquali, M. & Gaudenzi, P. (2026). Optimizing the design of large deployable mesh reflectors in presence of manufacturing defects. *CEAS Space J.*

[12] Irvine, H.M. (1981). *Cable Structures*. MIT Press, Cambridge, MA, USA.

[13] Ernst, H.J. (1965). Der E-Modul von Seilen unter Beruecksichtigung des Durchhanges. *Der Bauingenieur* 40(2), 52-55.

[14] Treyssede, F. (2009). Free linear vibrations of cables under thermal stress. *J. Sound Vib.* 327(1-2), 1-8.

[15] Li, P., Liu, C., Tian, Q., Hu, H. & Song, Y. (2016). Dynamics of a deployable mesh reflector of satellite antenna: form-finding and modal analysis. *J. Comput. Nonlinear Dyn.* 11(4), 041017.

[16] Tan, N., Zhang, J., Kazoleas, C., Zhu, W., Zhou, K. & Yuan, S. (2026). Dynamic modeling and vibrations of large deployable mesh reflectors. *Appl. Math. Model.* 150, 116329.

[17] Suh, J.-E., Dassanayake, S.P., Thomson, M.W. & Pellegrino, S. (2024). Scaling laws for deployable mesh reflector antennas. *AIAA J.* 62(10), 3948-3959.

[18] McKenna, F., Fenves, G.L. & Scott, M.H. (2000). *Open System for Earthquake Engineering Simulation*. University of California, Berkeley, CA, USA.

[19] Zhu, M., McKenna, F. & Scott, M.H. (2018). OpenSeesPy: Python library for the OpenSees finite element framework. *SoftwareX* 7, 6-11.

[20] Ansys, Inc. (2026). *Mechanical APDL Element Reference, Release 2026 R1*. Ansys, Inc., Canonsburg, PA, USA.

[21] Craig, R.R. Jr. & Bampton, M.C.C. (1968). Coupling of substructures for dynamic analyses. *AIAA J.* 6(7), 1313-1319.

[22] Allemang, R.J. (2003). The modal assurance criterion - twenty years of use and abuse. *Sound Vib.* 37(8), 14-23.

[23] Tang, Y.Q., Li, T.J., Liu, Y. & Wang, Z.W. (2019). Minimization of cable-net reflector shape error by machine learning. *J. Spacecraft Rockets* 56(6), 1757-1764.

[24] Ren, Z., Du, J., Bao, H., Ge, D. & Wang, F. (2023). Shape adjustment for uncertain mesh reflectors using machine learning. *Int. J. Mech. Sci.* 244, 108082.

[25] Tao, Y., Guo, Q., Zhou, J. et al. (2026). Dynamic parameters prediction of the spatial deployable mechanism: a hybrid approach combining physics-based and data-driven models. *Acta Mech. Sin.* 42(5), 524814.

ECSSMET
Braunschweig Germany 2026

Cryogenic

Structural supports for optical systems in cryogenic environments

M. SANSA BERNAT [(1)], C. MAURIS-DEMOURIOUX [(1)], S. ORSINGHER [(1)], T. GILET[(2)]

[(1)] MECANO ID, 9 rue Paul Charrier - 31100 Toulouse - FRANCE, +33 534 608 400,
m.sansa-bernat@mecano-id.fr , c.mauris-demourioux@mecano-id.fr , s.orsingher@mecano-id.fr
[(2)] CNES, 18 avenue Edouard Belin – 31400 Toulouse – FRANCE, +33 561 273 131
Thomas.Gilet@cnes.fr

KEYWORDS

cryogenic structures, optical supports, CFRP, bonded joints, titanium, thermal decoupling, micro-struts

ABSTRACT

Scientific optical payloads for space observation missions operate at extremely low temperatures, typically below 4K and in some cases down to the millikelvin range. Under such conditions, structural supports must fulfil two conflicting requirements: they must provide high mechanical stiffness and dimensional stability while minimizing conductive heat transfer between stages. This makes the design of compact cryogenic supports particularly challenging.

This paper presents the development of compact hybrid supports based on carbon-fibre-reinforced polymer (CFRP) tubes bonded to metallic end-fittings for cryogenic optical systems. A literature review first confirmed the relevance of CFRP for such applications due to its favourable stiffness-to-thermal-conductivity ratio, low thermal expansion in the fibre direction, and strong potential for thermally efficient structural design. Particular attention was paid to the behaviour of bonded multi-material interfaces at low temperature, since thermoelastic compatibility between CFRP, adhesive and metal end-fittings is a key driver for structural integrity.

A material trade-off was then conducted for the development of very small CFRP tubes. Among the candidate prepreg systems, a high-modulus carbon/epoxy prepreg compatible with out-of-autoclave consolidation was selected as the best compromise between process feasibility, low areal weight, high stiffness and expected low thermal conductivity. The selected material was subsequently characterized on flat samples. The experimental results showed high and consistent mechanical performance with limited scatter, together with a porosity level <1%.

In parallel, a preliminary numerical mechanical analysis and a bonded CFRP/metal micro-struts were carried out on representative cryostrut configurations. The numerical work confirmed the structural relevance of the concept while identifying thermoelastic loading as the main design driver. The experimental results further showed that the CFRP/titanium configuration provided the most favourable overall mechanical behaviour under cryogenic conditions. More generally, the bonded concept remained mechanically robust after cryogenic exposure, with performance levels improving relative to ambient-temperature reference tests.

The combined material, numerical and experimental results support the relevance of bonded CFRP/titanium hybrid supports for compact cryogenic optical structures. Thermal conductivity and outgassing characterization of the selected CFRP material are still ongoing and will complete the validation of the concept for future space applications.

1. INTRODUCTION

Future scientific space missions increasingly rely on optical instruments operating at cryogenic temperatures in order to improve detector sensitivity, reduce thermal noise and preserve dimensional stability. In many architectures, optical subsystems are distributed over several thermal stages, ranging from a few kelvin down to sub-kelvin domain. The structural parts connecting these stages must therefore provide both mechanical continuity and thermal isolation.

This dual requirement is especially demanding for compact structural elements integrated within optical payloads. On the one hand, these supports must withstand launch loads and maintain alignment accuracy during operation. On the other hand, they must limit the conductive heat transfer between thermal stages. The trade-off becomes even more challenging when the available volume is limited and the support geometry must remain very small.

Cryogenic optical systems therefore impose a strong coupling between thermal, mechanical and manufacturing constraints. The support architecture cannot be defined from stiffness considerations alone. It must also account for cooldown-induced deformations, thermal mismatch between materials, manufacturability of parts, interface robustness, and compatibility with space environmental constraints. In practice, these constraints often lead to the development of hybrid structural concepts rather than monolithic metallic designs.

Carbon-fibre-reinforced polymer (CFRP) materials are attractive candidates for such applications because they combine high specific stiffness with low thermal conductivity, especially at low temperature. However, when a structural support includes metallic interfaces, the design challenge extends beyond the CFRP tube itself to the behaviour of the bonded multi-material assembly. The thermal expansion mismatch between the composite, the adhesive and the metallic end-fittings may generate significant thermoelastic stresses during cooldown and thermal cycling.

The present work addresses the development of compact hybrid micro-struts composed of CFRP tubes and metallic end-fittings for cryogenic optical systems. These developments are carried out with ATHENA X-IFU as the targeted application, providing a representative framework for the definition and assessment of compact cryogenic support structures. The approach combines literature review, material trade-off, flat-coupon mechanical characterization, numerical structural analysis and bonded assembly testing under cryogenic-relevant conditions. The objective is not only to identify suitable material system, but also to build a coherent design for compact cryogenic supports compatible with future optical payload architectures.

2. FUNCTIONAL REQUIREMENTS AND DESIGN DRIVERS

The targeted application concerns compact structural supports for optical instruments operating below 4K, with some potential use cases extending down to the sub-kelvin range. In such systems, the support elements are required to ensure a stable mechanical link between stages while avoiding excessive thermal conduction from warmer interfaces to colder functional equipment.
The primary functions of these supports are:

- to ensure the mechanical support of the optical stages (high stiffness and strength),
- to provide thermal decoupling between colder and warmer parts of the structure,
- to maintain dimensional stability over severe thermal excursions.

These functions are directly driven by the operating environment. In orbit, the structure is expected to remain stable under cryogenic conditions for long durations. Before operational use, it must also withstand integration constraints, thermal variations and launch-related mechanical loading. Because the same component must respond to all these situations, its design becomes a multi-criteria optimization problem.

The geometry is constrained by the architecture of the instrument. The study focuses on CFRP tubes with small dimensions:

- inner diameter < 10mm
- thickness <1mm
- length around 200mm

Such small geometries are representative of compact cryogenic structural parts intended for highly integrated optical systems. They are attractive from a thermal standpoint because they reduce conductive paths, but they are also more demanding in terms of manufacturing and local interface design.

In addition to the mechanical and thermal requirements, the selected material system must be compatible with space environmental constraints, including vacuum operation, radiation exposure, low porosity and outgassing compliance. For bonded solutions, special attention must also be paid to the durability of the interface and to the behaviour of the adhesive during thermal cycling and cooldown.

3. DESIGN BASIS AND STATE-OF-THE-ART REVIEW

A literature review was first performed to identify the most relevant material families for cryogenic support structures. This review showed that thermal conductivity is a critical driver for the design of supports connecting cryogenic stages. In the cryogenic temperature range relevant to optical payloads, composite materials offer a better stiffness-to-thermal-conductivity ratio than conventional metals.

Aluminium was rapidly excluded as a candidate material for the structural tube itself because of its excessive thermal conductivity at very low temperatures. Titanium remains attractive for interface parts thanks to its lower thermal conductivity and relatively moderate thermal expansion. CFRP was identified as the most promising candidate for the tube because of its very low thermal conductivity at low temperature, its high longitudinal stiffness, and its near-zero coefficient of thermal expansion along the fibre direction [1,4,6,7]. Contrary to popular belief, GFRP is more thermally conductive than CFRP at temperatures below 15K.

The literature also highlighted the importance of fibre orientation and constituent compatibility [1,2]. In composite materials, thermal and mechanical behaviours are highly anisotropic, and the axial direction of a unidirectional carbon reinforcement is particularly favourable when high stiffness and low thermal expansion are required. This makes high-modulus CFRP especially attractive for small structural components for a cryogenic cooling system.

However, the structure under study cannot be reduced to the composite tube alone. The interface with metallic end-fittings is a critical feature of the design. Bonded joints are attractive because they enable compact integration, optimize mass and avoid local mechanical weakening associated with

drilling or bolted joints on very small tubular geometries. At the same time, bonded interfaces remain sensitive to thermal mismatch and adhesive behaviour at low temperature [8].

The review of low-temperature bonded assemblies suggested that properly selected epoxy adhesives may retain satisfactory mechanical behaviour under cryogenic exposure, although stiffness increases and brittleness may become more pronounced [8,11]. In addition, the thermo-mechanical compatibility between CFRP/titanium appears more favourable than between CFRP/aluminium [9,10].

4. MATERIAL SELECTION STRATEGY FOR CFRP MICRO-TUBES

4.1. Process constraints

For small tubular geometries, manufacturing constraints strongly influence the feasible material and process solutions. Standard liquid moulding routes were considered unsuitable because of the difficulty of setting up consumables and ensuring satisfactory impregnation and compaction in such small diameters.
As a result, prepreg technology was selected as the most realistic route. This choice focuses primarily on simplifying the process by manually draping plies around a mandrel using the roll-wrapping technique. This approach ensures optimal compaction, thereby guaranteeing excellent structural integrity and material health of the tubes.

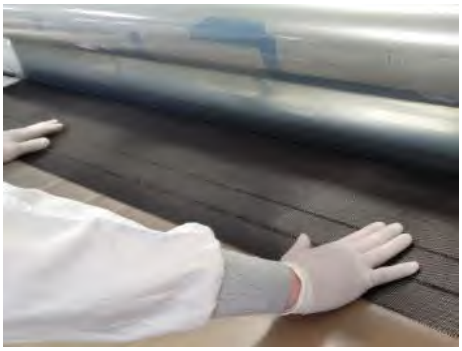


Figure 1: Manual roll-wrapping process

4.2. Trade-off criteria

The targeted prepreg had to satisfy the following criteria:

- high-modulus unidirectional carbon fibres,
- epoxy resin compatible with space applications and high-temperature capability,
- out-of-autoclave consolidation,
- low areal weight,
- compatibility with manual lay-up.

A trade-off was conducted between several candidate prepreg systems. The ranking considered process feasibility, areal weight, technical performance, expected cryogenic thermal behaviour, space qualification potential and recurring cost. This step was essential because material selection could not be driven by stiffness alone. For such compact geometries, processability and robustness of fabrication are equally critical.



Figure 2: Micro-tube CAD design

4.3. Outcome of the trade-off

Among the candidate materials, a high-modulus carbon/epoxy prepreg was selected as the best overall compromise. It combines high stiffness, low areal weight, processability for very small tubular geometries and compatibility with out-of-autoclave consolidation. This material was therefore retained for subsequent characterization.

The outcome of this trade-off illustrates a key point of cryogenic structural development: the best theoretical material is not always the best engineering solution. For very small supports, the selected system must not only deliver good thermomechanical properties but must also be manufacturable with repeatable quality and sufficiently low defect levels.

5. MECHANICAL CHRACTERIZATION OF THE SELECTED CFRP MATERIAL

5.1. Experimental approach

The selected prepreg was characterized using flat laminates in order to obtain representative input data for future structural modelling. Unidirectional and angle-ply laminates were manufactured to investigate the main mechanical properties relevant to the design of small cryogenic supports. The test campaign included:

- micrographic analysis for porosity assessment,
- interlaminar shear testing,
- three-point bending,
- tensile testing in the fibre direction,
- in-plane shear characterization from angle-ply tensile specimens.

This strategy was chosen because flat-coupon characterization provides a robust first database for material selection and early design calculations. Even though the final product is a tube, coupon-level tests remain highly valuable to compare process outcomes, confirm the quality level of the selected material system and provide the first set of engineering properties.

5.2. Experimental results

The mechanical characterization demonstrated a high level of performance together with limited scatter. The unidirectional laminate exhibited:

- a very high longitudinal tensile strength,
- a high tensile modulus and flexural properties,
- and a strong interlaminar shear response for this class of material.

The angle-ply laminate provided in-plane shear properties in line with expectations for a high-modulus carbon/epoxy system. Porosity remained below 1% after process adjustment, which is compliant with the targeted requirement. More generally, the results showed good repeatability, with low dispersion across the different test campaigns. This point is particularly important because the mechanical efficiency of compact cryogenic supports depends strongly on process quality and on the stability of the manufactured microstructure.

5.3. Discussion

These results are consistent with the expected behaviour of a high-modulus carbon/epoxy system. They confirm that the selected prepreg is suitable for small structural supports requiring high axial stiffness and limited material variability. The low porosity levels are also a positive indicator for both structural performance and future environmental compatibility.

From a design perspective, the coupon results support the use of a highly oriented CFRP architecture for the main load-carrying direction. They also provide a basis for estimating the expected behaviour of the tube under axial loading and for feeding the first numerical models of the cryostrut concept.

At this stage, thermal conductivity and outgassing measurements are still in progress and are required to complete the full validation of the material for cryogenic space applications. Nevertheless, the mechanical characterization already confirms that the selected material system is a credible candidate for the targeted application.

6. NUMERICAL MECHANICAL ANALYSIS

In addition to material-level characterization, a preliminary numerical mechanical analysis was performed on a representative cryostrut configuration developed for a cryogenic optical application. The analysed configuration was based on CFRP struts bonded to metallic end-fittings, and the model was used to assess global stiffness, quasi-static behaviour, thermoelastic response and dynamic performance.

The objective of this numerical work was twofold. First, it aimed at verifying whether the proposed structural concept could achieve the required stiffness and general mechanical integrity at assembly level. Second, it aimed at identifying the most critical areas of the design before detailed hardware maturation, especially with respect to cooldown-induced stresses at bonded interfaces.

The numerical assessment showed that the overall stiffness of the structure is compatible with the design intent. The quasi-static behaviour was found to be globally satisfactory, although local stress concentrations were identified in the end-fitting area, indicating that local geometric refinements are required. These results are typical of compact hybrid assemblies, in which the global architecture may be mechanically efficient while still requiring local design optimization near interfaces and geometric transitions.

The thermoelastic load cases appeared to be the most critical, with the highest stress levels located in the bonded regions and in the CFRP close to the glued interfaces. This result is particularly important because it confirms that the main design challenge is not the global load-carrying capability of the concept, but rather the local behaviour of the multi-material interface during cooldown. In this respect, the analysis supports the use of titanium end-fittings rather than aluminium in order to reduce thermo-mechanical mismatch effects.

The modal analysis also confirmed a high level of structural stiffness, with the first global modes located in a frequency range consistent with a mechanically efficient support architecture for compact cryogenic systems. The model therefore supports the overall relevance of the concept not only from a static point of view, but also from a dynamic one.

More generally, the numerical model proved useful for identifying the most critical design areas and for guiding local design improvements, including end-fitting geometry and bonded interface definition. At this stage, the results should nevertheless be regarded as preliminary design guidance, since some cryogenic material properties and interface allowables still require further correlation with dedicated test data. This point is especially relevant for glued interfaces, for which material data at very low temperature often remain limited.

7. BONDED HYBRID MICRO-STRUTS

7.1. Test purpose and justification

In parallel with the coupon-level material characterization, the project investigated bonded hybrid supports composed of CFRP tubes and metallic end-fittings. The objective was to assess the influence of the metallic interface material and thermal exposure on the mechanical performance of the bonded assembly. Two metallic end-fitting materials were considered:

- aluminium,
- titanium.

An aerospace-grade structural adhesive was used for the tested assemblies.



Figure 3: Micro-strut prototype

The choice to compare two metallic partners was motivated by both thermal and mechanical considerations. From a thermal standpoint, titanium is more attractive than aluminium for cryogenic interfaces. From a mechanical standpoint, the question was whether this advantage could be maintained once the full bonded assembly was tested after thermal exposure.

7.2. Results after thermal cycling

A first tensile test series was carried out on bonded micro-struts at room temperature before and after thermal cycling from 300 to 83K. Cycling is not conducted at lower temperature because below 83 K, molecular motion freezes and thermoelastic stresses become negligible. The most significant stresses occur between 300 K and 83 K. Both configurations remained mechanically satisfactory after exposure. However, the CFRP/titanium pairing systematically provided higher bond performance than CFRP/aluminium.

In addition, the bonded assemblies showed an increase in strength after thermal cycling relative to the ambient-temperature reference condition. This trend is consistent with the known evolution of epoxy-based bonded systems at lower temperature, where increased stiffness may contribute to a higher apparent resistance, provided that no premature damage is induced at the interface.

7.3. Results after cooldown to cryogenic temperature

Additional tensile tests were then performed at room temperature after cooldown to 4K on the same bonded concept. The results confirmed the robustness of the bonded architecture and again showed that the CFRP/titanium configuration outperformed the CFRP/aluminium alternative.

The bond stress levels remained in a range consistent with structural use for compact cryogenic assemblies, and the observed scatter was low.

7.4. Discussion

The results indicate that cryogenic exposure does not degrade the bonded concept. On the contrary, an increase in bond strength was observed after thermal cycling and after cooldown to cryogenic temperature. This behaviour is consistent with the known stiffening of epoxy adhesives at low temperature.

Beyond purely mechanical results, titanium is also advantageous thermo-mechanically. The literature review indicates that CFRP and titanium exhibit better compatibility in thermal expansion than CFRP and aluminium, which likely contributes to a reduction in thermoelastic stresses within the bonded interface during cooldown. The combined experimental and bibliographic evidence therefore supports the selection of titanium as the preferred end-fitting material for cryogenic bonded supports.

These results are also coherent with the numerical findings. The latter highlighted thermoelastic loading as the critical case and suggested that interface behaviour would govern design maturity. The experiments confirm that the choice of the metallic partner is indeed decisive and that the CFRP/Ti configuration offers the most favourable balance for further development.



Figure 4: Tensile test setup for the bonded CFRP/metal micro-strut

8. DISCUSSION

The results presented in this work highlight the importance of approaching cryogenic support development as a coupled material-process-interface problem. The final performance of the concept does not depend on a single parameter, but on the consistency of the overall design strategy.

First, the material trade-off and coupon characterization confirm that high-modulus CFRP is well suited for compact cryogenic supports. Its high axial stiffness and favourable expected thermal behaviour make it a strong candidate for low-conductivity structural members. However, the study also shows that process feasibility must be considered at the same level as material performance, especially when the target geometry

is very small.

Second, the numerical mechanical analysis shows that the global structural concept is mechanically relevant, but also that thermoelastic effects remain the main challenge. This point is essential for cryogenic optical structures: the structure may appear satisfactory under conventional mechanical loading while still being driven by local interface behaviour during cooldown. In this context, early numerical analyses are valuable not only to size the structure, but also to orient the choice of materials and local design features.

Third, the bonded assembly tests provide a direct experimental validation of the interface strategy. They demonstrate that the concept is robust under cryogenic exposure and that titanium offers a clear advantage over aluminium for the metallic end-fittings. This advantage is not limited to thermal conductivity considerations; it also improves the overall thermo-mechanical compatibility of the bonded assembly.

Taken together, these three levels of investigation — material, numerical and experimental — define a coherent pathway for the development of compact cryogenic supports. They also show that the proposed concept is already supported by converging evidence, even though some validation tasks remain ongoing.

The main remaining steps concern thermal conductivity quantification and outgassing characterization of the selected CFRP material. These activities are necessary to complete the qualification logic for future space applications. In parallel, additional refinement of the end-fitting geometry and further correlation between analysis and testing will strengthen the maturity of the concept.

9. CONCLUSION

This work presents the development of compact structural supports for cryogenic optical systems based on bonded CFRP/metal hybrid micro-struts. The design challenge arises from the need to simultaneously achieve high stiffness, low thermal conductivity, dimensional stability and robust multi-material interfaces under severe thermal excursions.

A literature review first confirmed the relevance of CFRP for cryogenic support structures and identified titanium as a particularly suitable interface material. A dedicated material trade-off then led to the selection of a high-modulus carbon/epoxy prepreg for the manufacture of small CFRP tubes. Mechanical characterization of this material demonstrated high performance, low scatter and acceptable porosity levels.

In parallel, a preliminary numerical mechanical analysis highlighted the structural relevance of the concept and identified thermoelastic loading as the most critical design case. Experimental testing of bonded hybrid assemblies then showed that the CFRP/Ti configuration consistently outperformed the CFRP/Al alternative and remained mechanically robust after cryogenic exposure.

Overall, the combined material, numerical and experimental results confirm that bonded CFRP/titanium hybrid supports constitute a promising solution for structural applications in cryogenic optical payloads. The ongoing thermal conductivity and outgassing characterization will complete the validation of the selected material system and support future qualification of the concept for space applications.

10. PERSPECTIVES

Beyond the present material, numerical and bonded-interface investigations, the next steps of the development will focus on the maturation of the cryostrut concept at product level. This includes consolidating the tube manufacturing process, refining the end-fitting design and bonded interface geometry, and correlating the numerical models with dedicated experimental results. Early work on the manufacture of small CFRP tubes has already been initiated, as this aspect is considered a key factor for compact cryogenic architectures.



Figure 5: Prototype of a small CFRP tube (inner diameter <5mm)

Further work will also address the assessment of the assembled cryostrut after thermal exposure and extend the analysis to thermo-mechanical performance. The project aims to develop and validate a compact support solution combining structural efficiency, thermal decoupling and compatibility with cryogenic optical payload requirements. This development is conducted with the support of CNES as part of an R&T initiative, aiming for TRL 5 by mid-2027.

11. ACKNOWLEDGEMENTS

MECANO ID would like to thank CNES for supporting this development and the teams involved in material characterization whose contributions supported the maturation of the cryostrut concept.

12. REFERENCES

1. D.J. Radcliffe, H.M. Rosenberg, The thermal conductivity of glass-fibre and carbon-fibre/epoxy composites from 2 to 80K (1982), *CRYOGENICS.*
2. G. Hartwig, Low-temperature properties of epoxy resins and composites (1984), *CRYOGENICS.*
3. E.D. Marquardt, J.P. Le, R. Radebaugh, Cryogenic Material Properties Database (2000)
4. Z. Sapi and R. Butler, Properties of cryogenic and

low temperature composite materials – a review (2019), *CRYOGENICS.*
5. R. P. Reed and M. Golda, Cryogenic properties of unidirectional composites (1994). *CRYOGENICS*
6. L. Risegari, M. Barucci, L. Lolli, G. Ventura, Low temperature thermal conductivity of Ti6Al4V (2008). *J Low Temp Phys*.
7. P. E. Bradley, R. Radebaugh, Properties of selected materials at cryogenic temperature.
8. S.-G. K., M.-G. K., and C.-G. K., Evaluation of cryogenic performance of adhesives using composite-aluminum double-lap joints (2005).
9. M. Reytier, F. Kircher, and B. Levesy, Characterization of titanium alloys for cryogenic applications.
10. F. Rondeaux, Ph. Bredy, and J.-M. Rey, Thermal conductivity measurements of epoxy systems at low temperatures (2002). *Advances in Cryogenic Engineering: Proceedings of the International Cryogenic Materials Conference.*
11. A. Yoshimura, T. Takaki, Fracture toughness of CFRP adhesive bonded joints at cryogenic temperature (2014), *Journal of Adhesion Science and Technology.*

HEALABLE COMPOSITE STRUCTURES FOR TANK APPLICATIONS AND BEYOND

C. Scazzoli[(1)], R. Trigueira[(1)], A. Cohades[(1)], B. Gresle[(1)], G. Luyckx[(2)], S. Unterhofer[(3)], V. Pejchal[(3)], M. Sanchez[(1)]

[(1)] CompPair Technologies SA, EPFL Innovation Park, Building C, CH-1015 Lausanne, Switzerland, contact@comppair.ch
[(2)] Com&Sens BV, Begoniastraat 17 PB 5, B-9810 Eke, Belgium
[(3)] CSEM, Rue Jaquet-Droz 1, 2000 Neuchâtel, Switzerland

KEYWORDS

Cryogenic tanks, composites, microcracking, healable, structural health monitoring.

ABSTRACT

Traditional thermoset composites are widely used in structural applications, including aerospace pressurized and cryogenic tanks, but their inherent brittleness makes them vulnerable to microcracking and damage. CompPair addresses these limitations with HealTech™ products, allowing to build composites that rapidly heal cracks and delamination through localized heating between 100°C and 150°C. CompPair has developed slit-tapes specifically designed for cryogenic tanks. These materials offer high resistance to microcracking and can heal damage caused by thermal cycling, supporting the development of lightweight Type V tanks as an alternative to metallic solutions. CompPair and its partners have also integrated autonomous sensing and heating technologies, allowing composite structures to detect and heal damage without external intervention. This paper highlights the mechanical performance, healing efficiency, and space-environment compatibility of these materials, as well as real-time damage monitoring and autonomous repair capabilities. Developed within ESA programs, these innovations also have promising applications in aeronautics and sustainable mobility.

1. INTRODUCTION

A cost-effective and high-performance space transportation ecosystem for the 2025-2050 horizon is expected to rely on reusable launchers, high-orbit parking strategies, and a “hub-and-spoke” in-space logistics network supporting constellation deployment, exploration missions, orbital servicing, and propellant depots. In this context, lightweight and durable materials are essential. Fibre Reinforced Polymers (FRPs), particularly epoxy-based composites, are widely used in space structures and ideally in particular in cryogenic propellant tanks because of their excellent stiffness-to-weight ratio, high glass transition temperature, and chemical resistance.

In the specific case of cryogenic tanks, despite these advantages, conventional thermoset composites remain vulnerable to manufacturing defects, such as gaps, overlaps, voids, and excess fibre buildup (the typical defects generated by winding and automatic fibre placement) [1], [2], [3], [4], as well as in-service damage caused by thermal cycling, cryogenic conditions, and impacts [5]. Matrix microcracking and delamination can compromise structural integrity and create leakage paths for cryogenic propellants, limiting the adoption of liner-less Type V tanks, which otherwise offer significant weight savings compared to metallic or lined alternatives [3], [5].

To address these challenges, CompPair has developed healable composite technologies capable of repairing microcracks and delamination through controlled heating (100 °C – 150 °C) [6][7], restoring structural performance without additional repair materials. Additionally, this process can be repeated multiple times.
Within the frame of ESA OSIP, CompPair specifically developed slit tapes for cryogenic tanks applications (HealTech™ CS03 slit tapes). Within the scope of a FLPP FIRST! initiative CompPair teamed up with Com&Sens and CSEM to achieve autonomous damage sensing and healing in HealTech™ composites structures by embedding optical fibres sensors [8] and metallic heaters in its composite structures. These innovations are key enablers for sustainable space transportation, in-orbit servicing, and long-duration orbital infrastructure.

2. MATERIALS AND METHODS

2.1. Materials

Two different types of thermoset based healable pre-impregnated textiles (prepregs) from CompPair Technologies were used: HealTech™ CS03 AS7 unidirectional prepregs with a fibre areal weight of 200 g/m^2 and HealTech™ CS01 T700S unidirectional prepregs with a fibre areal weight of 200 g/m^2. AS7 fibres are manufactured by Hexcel, while T700S fibres by Toray.

2.2. Tensile tests

Tensile tests were performed on HealTech™ CS03 AS7 unidirectional laminates in the longitudinal

direction according to standard ISO 527-5 at room temperature. 5 samples per test condition were tested.

2.3. Outgassing

Outgassing tests were performed on HealTech™ CS03 AS7 unidirectional laminates according to standard ECSS-Q-ST-70-02 by Deutsches Zentrum für Luft- und Raumfahrt e.V. (DLR).

2.4. Healing

Quantitative healing tests were performed on HealTech™ CS03 carbon twill laminates with a $[(\pm 45)]_9$ layup. Samples 135x20 mm^2 were mounted on the unsupported impact setup visible in Figure 2 and impacted 18 times with a 10J energy. A part of the samples was healed for 20 minutes at 150 °C. Virgin, damaged and healed samples have been tested in 3-point bending based on ASTM D790 to assess the flexural modulus. Healing efficiency was computed in terms of recovery of flexural modulus:

$$Healing\ efficiency = \frac{E_{healed}}{E_{virgin}}$$

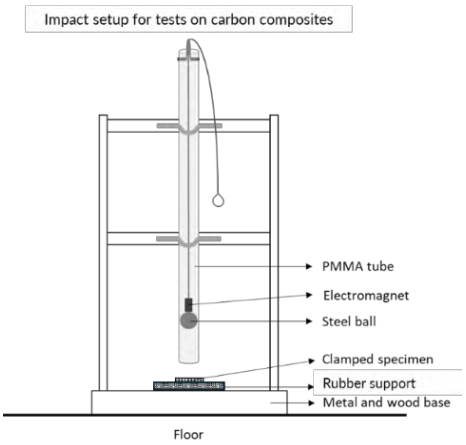


Figure 1: A schematic of the impact setup.

2.5. Cryogenic micro-cracking

3 samples 50x50 mm^2 were obtained cutting HealTech™ CS03 carbon twill laminates with a $[(+-45)/(0/90)]_{4s}$ layup. They were immerged in liquid nitrogen for 2 min and 30 seconds and put on aluminium plates to heat back up at room temperature as fast as possible (between 12 and 17 minutes were necessary). This procedure was repeated 10 times to simulate the typical thermal shock a cryogenic vessel could experience (the thermal history experienced by the samples is visible in
Figure , the thermocouple was placed on the surface of samples which was always in contact either with air or with liquid nitrogen). Optical microscopy (OM) observations were carried out on the 3 samples before and after thermal shock cycling. This enabled to assess the material resistance to microcracking induced by this cycling.

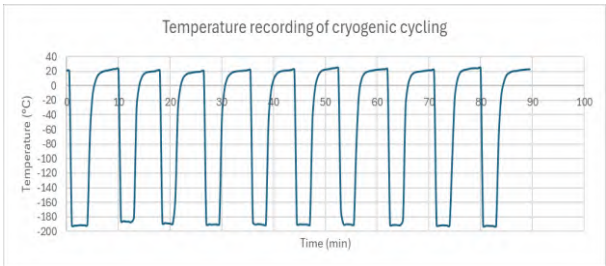


Figure 2: the thermal history experienced by HealTech™ CS03 carbon laminates.

2.6. Breadboard integrating optical fibres and metallic heaters

In order to assess the achievable performances in terms of autonomous damage sensing and healing a flat laminate made of HealTech™ CS01 carbon prepregs was manufactured. The fibres were T700 unidirectional fibres, with an areal weight of 200 g/m^2. The plies were 32 in total. Optical fibres were integrated between ply 27 and 28 and between ply 29 and 30. 3D printed aluminium grids were embedded in between 2 mat glass veils with an areal weight of 30 g/m^2 in the middle of the laminate. Figure 3 depicts the geometry of the laminate as well as the geometry and position of optical fibres and metallic grids in the laminate.

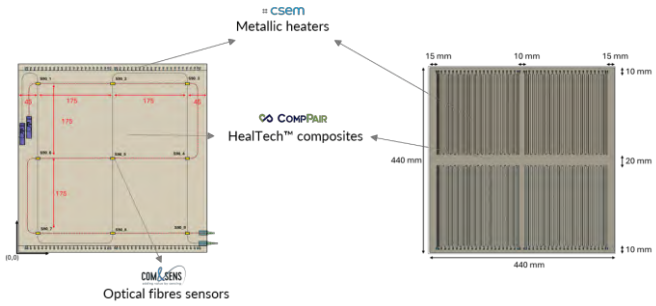


Figure 1: A schematic depicting the geometry of the laminate integrating autonomous damage sensing and healing. The geometry and position of optical fibres and metallic heaters is detailed.

2.7. Breadboard impact test

A Rosand impact tower equipped with a cylindrical impact head with diameter 40 mm and weighing 5,79 kg was used to impact the breadboard integrating autonomous damage sensing and healing in 3 selected locations, depicted in red in Figure 2. The impact test was monitored using optical fibres.

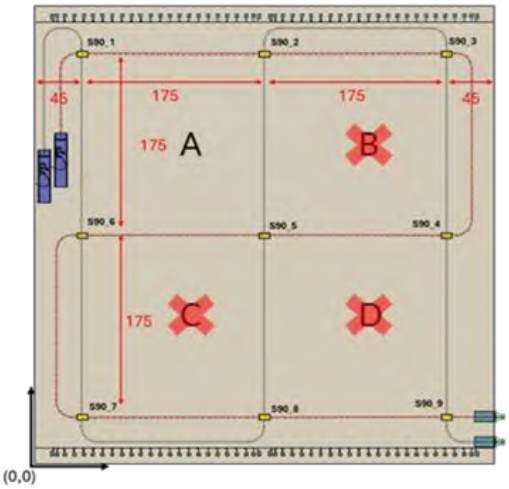


Figure 2: A schematic of the impact locations of the breadboard, highlighted as red crosses.

2.8. Breadboard healing test

In order to perform the autonomous healing, 2 power supplies were connected to the integrated aluminium grids. The power supplies were connected so to each cover a 6 pins distance between the 2 clamps. The current and the voltage were then gradually increased until reaching a 100 °C < T < 140 °C in the whole heated area and then a 15 min timer was started keeping the temperature constant.
This step was also monitored using optical fibres.

2.9. Breadboard quantitative healing test

Samples were made of sixteen layers of HealTech™ CS01 unidirectional T700 prepregs, arranged in a ±45° stacking sequence. The integrated damage sensing and healing systems were integrated in the laminates. A 3D-printed aluminium grid was embedded at the mid-plane, with wires oriented along the 0° direction, serving as the electrical heating element. Glass fibre veils (30 gsm, mat) were placed immediately above and below the grid to ensure electrical insulation and reduce the risk of short circuits. Optical fibres were inserted one ply below the top surface and aligned with the 0° direction. These fibres are non-functional in the present test but included to replicate the full configuration of the final smart composite system. Mechanical testing was performed on a Shimadzu AGS-X 10 kN Universal Testing Machine (UTM). Five-point bending was used, with a load span of 30 mm and a total support span of 60 mm. Support and loading pins were 6 mm in diameter, and the crosshead speed was 1 mm/min. Five samples were tested without any induced damage or healing to establish baseline performance. Seven samples were tested after a single 5 J impact to induce matrix damage. Impact was performed using the setup shown in Figure . Eight samples were tested after a single 5 J impact followed by the healing procedure (20 minutes at 150 °C)

3. RESULTS AND DISCUSSION

3.1. HealTech™ CS03 slit tapes characterization

The longitudinal tensile strength and modulus of HealTech™ CS03 laminates are shown in Figure as compared to standard composite benchmarks [9]. This highlights that HealTech™ CS03 has competitive mechanical performances.

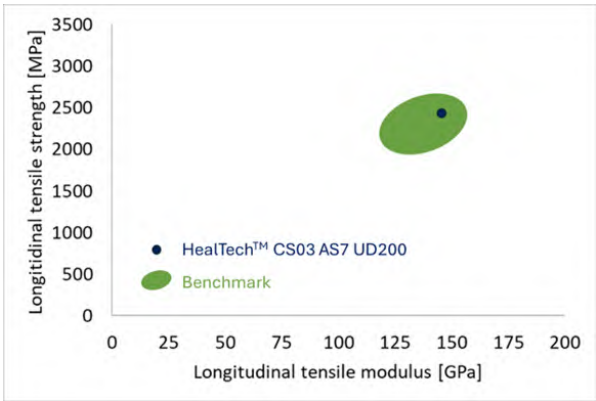


Figure 5: the longitudinal tensile modulus and strength of HealTech™ CS03 laminates as compared to standard composite benchmarks [9].

Outgassing tests on HealTech™ CS03 laminates were performed by DLR according to ECSS-Q-ST-70-02. The total mass loss (TML), the recovered mass loss (RML) and the collected volatile condensable materials (CVCM) (Figure) resulted well below the limits set by the standard, confirming HealTech™ CS03 compatibility with space conditions.

Material	TML [%]	RML [%]	CVCM [%]
HealTech™ CS03 AS7 UD 200 g/m²	0,37	0,18	0,01
ECSS requirements	< 1,00	< 1,00	< 0,10

Figure 6: TML, RML and CVCM for HealTech™ CS03 laminates as compared to the requirements set in the ECSS standards.

A quantitative healing test was performed on carbon twill laminates according to the procedure described in the section 2.4. The damage procedure (18 impacts at 10J) generated a 20.5% loss in flexural modulus (Figure), and a healing efficiency of 92% was achieved heating the samples for 20 minutes at 150°C. This proved the healing capabilities of the developed product, HealTech™ CS03.

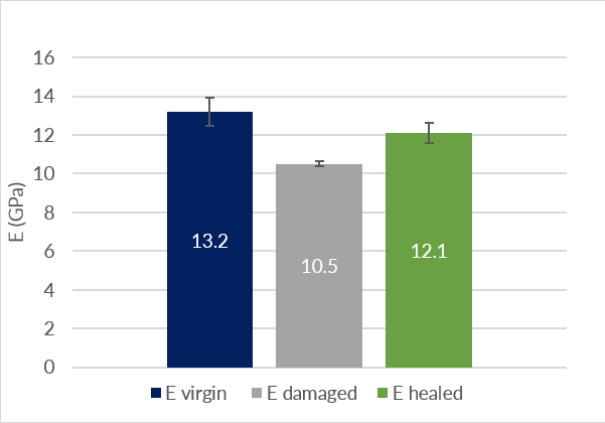


Figure 7: The flexural modulus of virgin, damaged and healed HealTech™ CS03 carbon composite samples.

Figure shows optical microscopy (OM) observations with different magnifications of the cross section of HealTech™ CS03 carbon laminates as produced and after thermal shock cycling between -196 °C and room temperature. No sign of microcracking is visible in any of the samples. This highlights CS03 has a superior cryogenic microcracking resistance, making it a good candidate to be integrated in a cryogenic propellant tank.

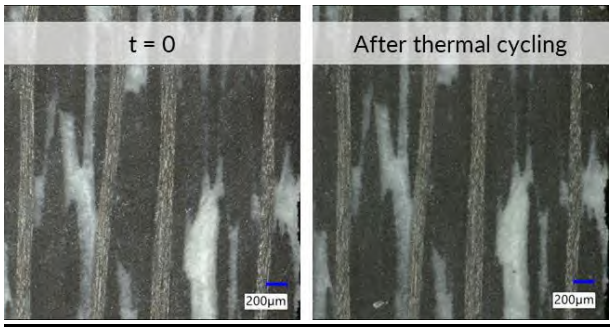


Figure 8: OM observation of the cross section of HealTech™ CS03 carbon laminates as produced and after thermal shock cycling between -196 °C and room temperature.

These tests confirmed the potential of HealTech™ CS03 slit tapes to build cryogenic propellant tanks. Consequently, following the OSIP project that allowed to develop such product, a subsequent activity started within the frame of a FLPP FIRST! initiative, in order to increase the maturity of CS03 for cryogenic tanks applications. This project is currently ongoing in collaboration with Invent GmbH. One of the main results that could be achieved so far is the successful manufacturing of tank shaped structure via slit tape winding. Figure 3 shows the intermediate steps followed to manufacture the part. These tests allowed to proof the compatibility of CS03 slit tapes with the typical processes used to manufacture tanks, like winding, and confirmed the capability to manufacture complex shape parts with a geometry representative of the final application targeted.

3.2. Autonomous damage sensing and healing

The breadboard integrating optical fibres and aluminium heaters was successfully impacted in the 3 targeted locations shown in Figure 2 with a 3.5 J energy without registering any malfunction in the impact machine. The system preventing double rebound of the impact head worked correctly.
For each impact position, the raw data signal collected using the optical fibres and the connected interrogator were used to calculate the impact location considering the 4 sensors with the fastest time of flight. This method allowed to locate the impact location with a maximum error of 40 mm. Figure 4 shows the actual location of the impact damage, as an example for impact location D, as compared to the location computed with the optical fibres sensors.

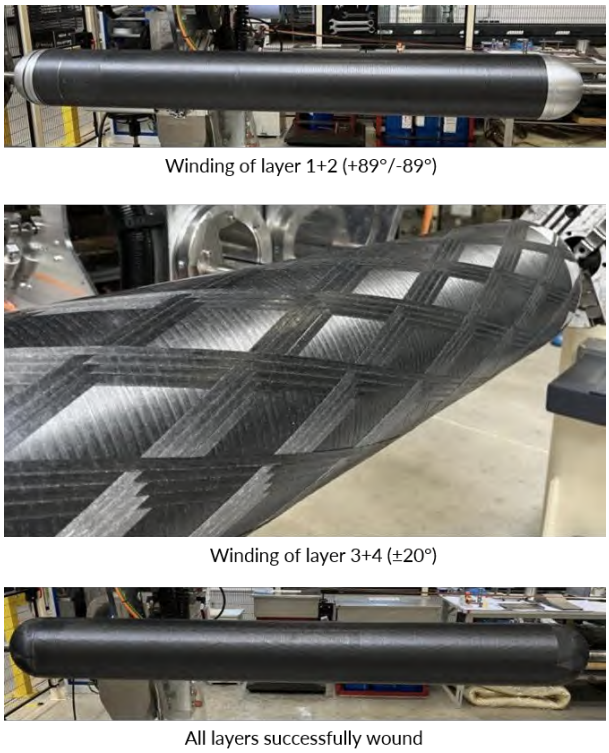


Figure 3: The winding steps to manufacture a tank shaped demonstrator with HealTech™ CS03 slit tapes.

After impacting the breadboard and locating the generated damage, the breadboard was healed via the integrated heating system consisting of aluminium grids. Having 4 independent grids covering the full surface of the breadboard and having several locations to which it was possible to apply current allowed to activate the heating only in the needed area, where damage was located. Figure 5 shows the typical temperature distribution over the breadboard surface that could be obtained. It highlights that temperature was homogeneous over the area heated by joule effect and that the temperature was in the range needed to achieve efficient healing, i.e. between 100 °C and 140 °C.

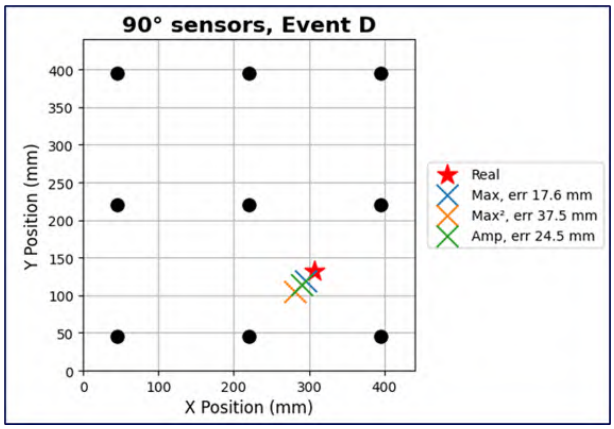


Figure 4: the red star indicates the actual location of the impact in zone D of the breadboard. The other crosses indicate the location computed using the signal from the 4 sensors with the fastest time of flight. Different colours indicate different computation methods.

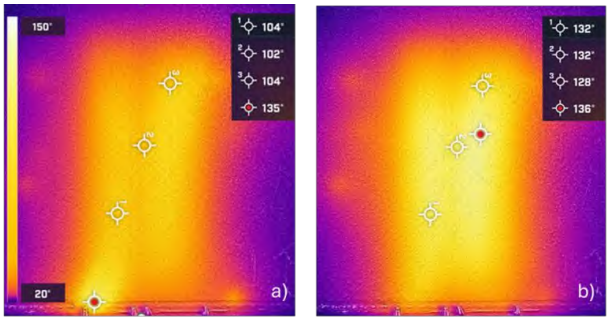


Figure 5: thermal camera images of the surface of the breadboard showing a mapping of the temperature that was achieved connecting the aluminium grids to the power supplies.

The healing capabilities of HealTech™ composites integrating autonomous damage sensing and healing systems were quantitatively assessed via mechanical testing on smaller samples that could be subjected to 5-point bending flexural tests with the methodology described in section 2.9.

To evaluate the performance of the different sample types, the maximum surface stress was considered. According to beam theory, on the surface at midspan the sample experiences the highest tensile or compressive stress during bending. Using the maximum force recorded by the testing machine, the corresponding maximum bending moment experienced by the specimen can be calculated using the following equation:

$$M_{max} = \frac{3}{32} P_{max} L$$

And subsequently, the max compressive and/or tensile stress at the external layers can be calculated as:

$$\sigma_{max} = \frac{9}{8} \frac{PL}{wt^2}$$

5 samples were tested in a virgin state (“virgin”), 7 after impacting once with 5J of energy (“impacted”), and 8 after impacting once with 5J of energy and healing via the integrated metallic grids (“healed”).

The results of the average maximum stress for each sample type are summarized in the graph in Figure 6. The damage procedure induced a 17.7% loss of mechanical performances and the healing procedure with the integrated autonomous damage healing system allowed to achieve a 92% healing efficiency.

An interesting observation during testing was that delamination in the virgin samples did not occur at the mid-plane, in correspondence with the aluminium grids, where the theoretical shear stress is expected to be highest, but rather between the mid-plane and the outer plies (see Figure 7). This suggests that the presence of the aluminium grids and glass veils enhances the samples’ ability to withstand higher levels of interlaminar shear stress.

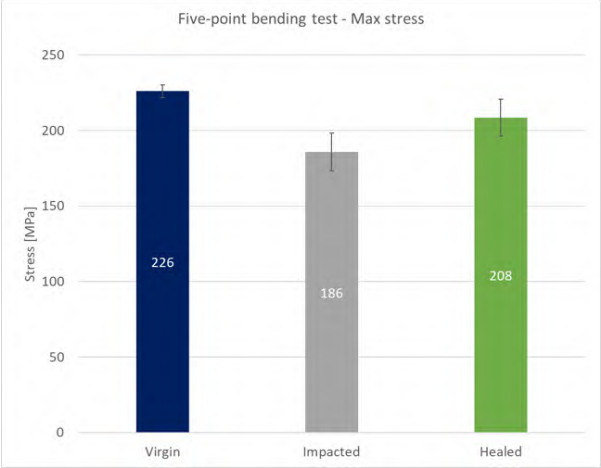


Figure 6: the average maximum stress of virgin, damaged and healed samples integrating optical fibres and metallic grids.



Figure 7: The typical failure mode observed in virgin samples.

4. CONCLUSION

The results demonstrate that HealTech™ CS03 is a promising multifunctional composite material for space and cryogenic applications. The developed slit tapes exhibited mechanical properties comparable to conventional high-performance composites, while meeting ECSS outgassing requirements and showing excellent resistance to cryogenic thermal shock, with no evidence of microcracking after cycling between room

temperature and liquid-nitrogen temperatures.
The self-healing capability of the material was successfully validated, achieving 92% recovery of the initial mechanical performance after impact-induced damage.
The successful manufacture of tank-shaped demonstrators by slit-tape winding confirmed the compatibility of HealTech™ CS03 with industrial processing routes and its suitability for complex aerospace structures.

The integration of optical fibre sensors and embedded metallic heating grids in HealTech™ CS01 composites enabled autonomous damage detection, localization, and localized repair. Impact events were identified with a maximum error of 40 mm, while the integrated heating system provided homogeneous temperatures within the optimal healing range, resulting in a healing efficiency of 92%.

Overall, the combination of structural performance, cryogenic durability, damage sensing, and efficient self-healing highlights the strong potential of HealTech™ materials for next-generation cryogenic propellant tanks and other resilient space structures.

5. REFERENCES

[1] V. V. Vasiliev and E. V. Morozov, “Composite Pressure Vessels,” *Adv. Mech. Compos. Mater. Struct.*, pp. 787–821, 2018.

[2] M. Leavitt and K. M. Nelson, “Development of Advanced Manufacturing Technologies for Low Cost Project Period,” 2014.

[3] A. Air, M. Shamsuddoha, and B. Gangadhara Prusty, “A review of Type V composite pressure vessels and automated fibre placement based manufacturing,” *Compos. Part B Eng.*, vol. 253, no. January, 2023.

[4] E. Oromiehie, U. Garbe, and B. Gangadhara Prusty, “Porosity analysis of carbon fibre-reinforced polymer laminates manufactured using automated fibre placement,” *J. Compos. Mater.*, vol. 54, no. 9, pp. 1217–1231, 2020.

[5] D. Grogan, “Damage and permeability in linerless composite cryogenic tanks.”

[6] C. Scazzoli, R. Trigueira, A. Cohades, and V. Michaud, “A Novel Method to Quantify Self-Healing Capabilities of Fiber-Reinforced Polymers,” *Front. Mater.*, vol. 9, no. July, pp. 1–10, 2022.

[7] https://www.comppair.ch/

[8] T. Juwet, G. Luyckx, A. Lamberti, F. Creemers, E. Voet, and J. Missinne, “Monitoring of Composite Structures for Re-Usable Space Applications Using FBGs: The Influence of Low Earth Orbit Conditions,” *Sensors*, vol. 24, no. 1, 2024.

[9] A. Nema, C. B. Mallineni, P. K. Penumakala, R. Adusumalli, and K. Tejasvi, “Influence of Temperature on Tensile Properties of Unidirectional Carbon-Epoxy Composites,” *Polym. Compos.*, vol. 47, no. 5, pp. 4699–4709, 2026.

6. ACKNOWLEDGEMENTS

The authors would like to express their sincere gratitude to Ugo Lafont and Bernard Decotignie, the ESA Technical Officers, for their valuable guidance, continuous support, and constructive contributions throughout the ESA projects within which the work presented in this paper was carried out. The authors also wish to acknowledge the European Space Agency (ESA) for its support, trust, and commitment.

ECSSMET
Braunschweig Germany 2026

Demise

DEVELOPMENT OF DEMISABLE STRUCTURAL JOINTS

Marcel Övermöhle [(1)], Martin Sauerbrey [(1)], Bradley Lockett [(2)], Britta Ganzer [(2)], Tobas Lips [(3)], Thorn Schleutker [(4)], Volker Liedtke [(5)], James Beck [(6)]

[(1)] INVENT GmbH, Christian-Pommer-Str. 47, 38112 Braunschweig, Germany, marcel.oevermoehle@invent-gmbh.de
[(2)] OHB System AG, Universitätsallee 27-29, 28359 Bremen, bradley.lockett@ohb.de
[(3)] HTG - Hyperschall Technologie Göttingen GmbH, Am Handweisergraben 13, 37120 Bovenden, Germany, t.lips@htg-gmbh.com
[(4)] Deutsches Zentrum für Luft- und Raumfahrt e.V. (DLR), Linder Hoehe, 51147 Cologne, Germany, thorn.schleutker@dlr.de
[(5)] Aerospace & Advanced Composites GmbH, Viktor-Kaplan-Straße 2, 2700 Wiener Neustadt, Austria, volker.liedtke@aac-research.at
[(6)] Belstead Research, 66 Top Common, Warfield, Bracknell, United Kingdom, james.beck@belstead.com

KEYWORDS

Design for Demise, Structural Joints, Space Debris, Clean Space

ABSTRACT

As part of the Design-for-Demise (D4D) effort of the Zero Debris approach, one area of research and development focuses on the primary structural joints of satellites to improve the break-up behaviour during re-entry. With an early opening of the structure, a better demise of critical components is expected.
This paper presents the demisable joint developments within the ESA-funded D4D SAFER project. Several technologies and joint designs are presented, as well as their current testing and results. With the focus being on the demise performance, extensive testing has been performed as part of a first test campaign in the re-entry chamber of AAC and the L2K plasma wind tunnel facility of the DLR. The results and findings, as well as the conclusions and the next phases of the development, are being presented.

1. STUDY GOAL AND USE-CASE

The number of satellites in Low-Earth-Orbit (LEO) are growing each year, especially due to telecommunication constellations such as Starlink, OneWeb or Iridium. To ensure that orbits remain usable in the long term, satellites must be removed from orbit at the end of their service life, for example by an uncontrolled re-entry due to natural orbit decay. However, as this approach does not allow for control over where the satellite re-enters the Earth's atmosphere, it must be ensured that the satellite burns up completely upon re-entry to prevent the risk of falling debris on the ground. Large and heavy components, such as reaction wheels or fuel tanks, often survive re-entry, thereby creating an on-ground causality risk.
One approach to solving this problem and thereby reducing the risk is to open the outer satellite structure early during re-entry. This allows more heat to reach the critical internal components at an earlier stage, giving them more time to burn up completely. In previous studies [1], the connecting elements of the primary structure were identified as a promising solution. The aim of the ESA study, part of their Design for Demise (D4D) effort, described in this paper is therefore to develop demisable primary structural joints for use in LEO telecommunications satellite up to a Technology-Readiness-Level (TRL) of 4.
To investigate the potential effect of demisable joints on re-entry using simulations, a representative model of a telecommunications satellite was required. This involved conducting an analysis of the designs of current and planned constellations, with the aim of creating a representative model based on the results. The CAD model of this satellite, nicknamed FrankensteinSat, is shown in Fig. 1. It includes all major components of a typical telecom satellite, especially critical components such as the reaction wheels, main payload, and a large tank. The total mass of this satellite is roughly 860 kg, with a dry mass of 700 kg. The primary structure consists of aluminium panels joined by aluminium brackets.

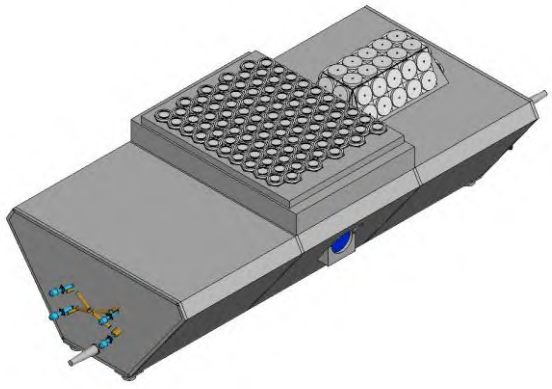


Figure 1: CAD model of FrankensteinSat

This model was used for re-entry simulation to access the demisability of a conventional design

without any demisable technology to get a baseline for later comparison. The simulations were performed by HTG using SCARAB. In total, 15 simulations were done. All simulations started at the initial orbital state (at about 125 km above the equator, inclination 68.4 degrees), but with different initial attitudes. In all simulations, the batteries, main payload, reaction wheels, and the tank survived the re-entry and therefore contributed to a causality risk area. In addition, the temperature profile at two critical joints was examined during re-entry, one at the outer edge of the satellite structure (pos. 1 in Fig. 2), the other in the shielded centre of the structure (pos. 2).

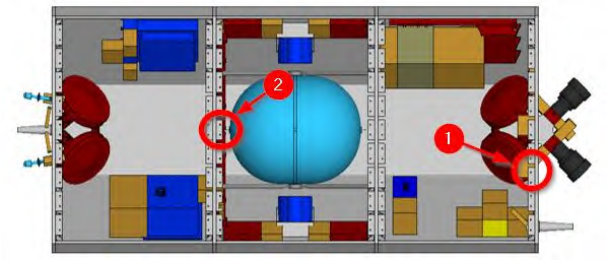


Figure 2: Inside of FrankensteinSat with marked joint positions

Assuming an arbitrary failure temperature of this joint of 450 K, this temperature is reached at the outer edge in an altitude range of 82-110 km. The centre joint reached this temperature at a much lower altitude range of 70-82 km, meaning the structure would only have opened fully at this altitude. This demonstrates the need for demisable joints that allow the structure to be separated at comparatively low temperatures.

2. DEVELOPMENT APPROACH

The development of the joints is taking place in six phases as part of the project. During the first phase, the use case described above was developed, re-entry simulations were carried out to establish the baseline, and the requirements and constraints were defined. In the second phase, feasible joints were then designed based on the requirements provided, and a test plan and sample geometry were prepared. The third phase involves the first test campaign. The aim here was to examine the concepts and understand how they performed, with a particular focus on any potential shortcomings. With the lessons learned, the designs of the joints will be reiterated in phase four, in which the project is currently at the time of writing this paper. The optimisations and improvements will then be verified in a second test campaign in phase five. In phase six, development within the scope of the project will be completed, and outstanding issues for further development and testing will be defined within a roadmap.

3. OVERVIEW OF DEMISABLE JOINT TECHNOLOGIES

The study focused on passive technologies that are activated by the rising temperature during re-entry. There are several options available for implementation. Technologies that can be used for separation at temperatures around 150 °C were of particular interest. Either the technology can be integrated directly into the sandwich panel – for example, in the form of a demisable insert – or the aluminium bracket can be replaced with a demisable version.
Three technologies, which could replace joints, and five support technologies, which could additionally be integrated into demisable joints, were investigated. Those are:

- Demisable Inserts for sandwich panels with a low melting point solder material
- Demisable Anchor Nuts with a low melting point solder material, to be used in combination with standard brackets
- CFRP cleats with a demisable resin system
- Adhesives, which separate at defined temperature

Based on these concepts, multiple joint design variants were created. The demisable insert consists of two aluminium parts, which are interlocked with a third part made from a low-melting point solder. The target separation temperature is between 130 °C and 150 °C. Two variants were designed. The first one is a replacement for conventional face-to-face inserts (also known as spool inserts), which are to be used with cleats to form a panel-to-pan
el joints. When reaching the triggering temperature, the inner part of the insert, connected to the cleat, can separate from the outer part, which remains in the panel. A similar approach is used for the second variant, an edge insert, which are integrated at the corner of the panel. Two edge inserts are directly connected and therefore form the joint without the need of extra hardware like cleats. Both variants are shown in Fig. 3.

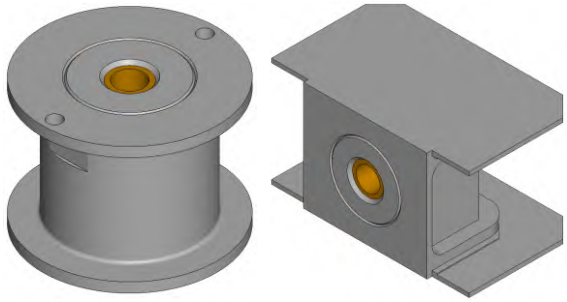


Figure 3: Demisable Inserts - Face-to-Face insert (left) and Edge Insert (right)

The design principle of the demisable insert is also used for the demisable anchor nut. The major difference is the location of the separation mechanism. While the inserts are integrated into the

sandwich panel and therefore need to be selected early in the design and manufacturing process of the satellite structure, the demisable anchor nut is attached to a cleat. This means that, even at a relatively late stage in the design process, a panel-to-panel connection can be changed from a standard design to a demisable design without making any major alterations to the surrounding structure.
The CFRP cleat offers a similar advantage, albeit based on a different operating principle. Tests have shown that standard aerospace epoxy and cyanate ester resins, such as Araldite LY 556 or EX-1515, decompose only with difficulty under re-entry conditions, meaning that CFRP structures are relatively robust. However, there are certain resin systems which have performed significantly better in material tests and have allowed the structure to disintegrate. This observation is now to be examined at component level. Additionally, an extra sample was produced in which 1% aluminium-magnesium particles were mixed into the matrix. This is based on the findings found in [2], which have shown that the additional particles are thought to promote heat transfer in the thickness direction of the laminate and thus accelerate its disintegration. The anchor nut and the CFRP cleat are shown in Fig. 4.

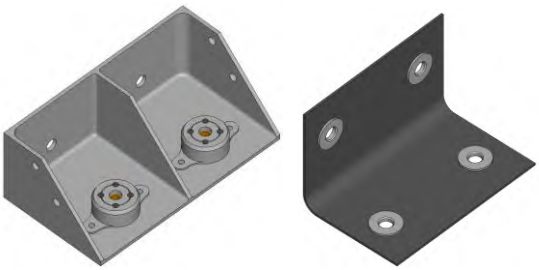


Figure 4: Demisable Anchor Nuts attached to an aluminium cleat (left) and CFRP cleat with demisable matrix (right)

The last joint concept based on adhesives, which separate at a temperature of around 150 °C. To incorporate this technology, the cleat was split into two parts – a base plate and a bracket – and joined together using an epoxy structural adhesive. A total of three different design variants were developed. The basis was a two-part CFRP cleat, which, like the previous cleats, is fitted in the conventional location on the inside of the panel-to-panel joint. In order to investigate the influence of the material on this concept, aluminium was used for the second variant. The position remained unchanged. In the third variant, the position of the CFRP cleat was moved to the outer side of the joint. As a result, the component is directly exposed to heat during the test and degradation occurs sooner. Two of the cleats are shown in Fig. 5.

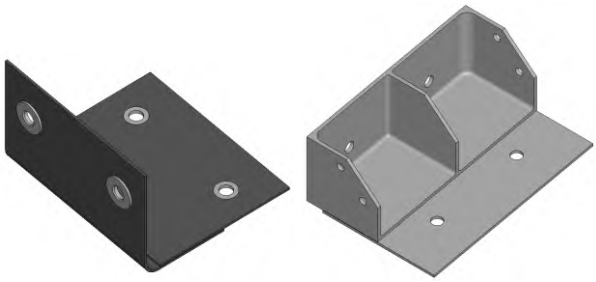


Figure 5: Two-part, bonded cleats made from CFRP (left) and aluminium (right)

4. TESTING

Preliminary testing of the demisable joints was performed at INVENT for mechanical properties as well as at DLR and AAC for demise testing.

4.1. Mechanical Properties

The mechanical investigations were mainly limited to the most significant characteristics, as the focus is on the demise behaviour. Nevertheless, a small number of tests were carried out.
As the material used for the Demisable Inserts had not previously been used in load-bearing structures, several tensile tests were carried out, both at the material level for characterisation and at the component level to verify the design.
The load-bearing capacity of the demisable insert was investigated on the basis of the face-to-face design. Typically, for the test, an insert is fitted into a small section of sandwich panel, which is then mounted in a tensile testing machine. The test setup and procedure are described in [3]. However, in such cases, the panel usually fails significantly before the insert does. For a panel and insert such as those used in the case study mentioned, the failure load would be around 3200 N.
The panel was therefore replaced with a solid piece of aluminium to ensure that any failure occurred in the insert during the test, thereby enabling the maximum load-bearing capacity to be determined. The graph of the tensile test is shown in the Fig. 6. As it was not possible to fit a displacement transducer directly to the insert, the diagram shows only the movement of the crossbeam and, consequently, the deformation of all components in the load path. The insert did not fail during the test; instead, a constant, almost linear displacement was measured until the test machine's maximum load of 20 kN was reached. After the test, the insert was inspected and a permanent displacement of 0.35 mm between the inner and outer component was detected.
The tensile test successfully demonstrated the design's load-bearing capacity at 21 °C, which significantly exceeds that of the surrounding sandwich structure. This allows conventional inserts to be replaced with the demisable variant without the need for structural modifications.

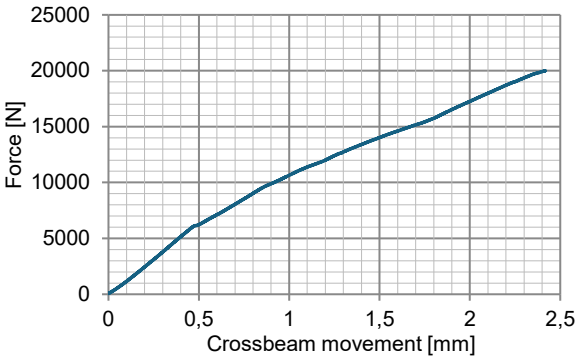


Figure 6: Force/displacement diagram of the out-of-plane tensile test on the demisable face-to-face insert at 21 °C

The second type of mechanical testing concerned the adhesive technology used for the cleats. In this case, single-lap shear samples were used to investigate the mechanical properties at room temperature and following thermal stress. The data was used to design the bonded seams and to determine the operating temperature for this technology.

4.2. Demise Testing

In total, 20 samples were manufactured for testing, with 12 samples for the re-entry chamber (RC) and 8 samples for the plasma wind tunnel (PWT).

4.2.1. Sample Designs

The basic design of all demise samples is always the same. It consists of two sandwich plates connected to one another via the demisable joint. The upper plate is fixed statically in the test setup, whilst the lower plate can detach itself downwards when the joint is triggered, either under its own weight or under additional loads, depending on the test setup. The configuration of the sandwich panels, shown in Tab. 1, corresponded to the design typically used for the outer structure of satellites, such as closure panels.

Table 1: Sandwich Panel Configurations

	Aluminium	**CFRP**
Total Thickness	20 mm	
Facesheet Material	EN AW-2024	EX-1515 / M55J
Facesheet Thickness	0,5 mm	0,3 mm (4 plies)
Honeycomb Material	EN AW-5056	
Honeycomb Density	50 kg/m³	32 kg/m³
Adhesive Film	HexBond 312UL	
Panel Size for RC	200 mm x 200 mm	
Panel Size for PWT	200 mm x 100 mm	

The samples were mounted in the test setup with the corner of the panel-to-panel joint facing in the direction of the heat flux and the panels oriented at a 45° angle to the direction of flow. The temperature distribution during testing on the demisable joint as well as the panels are recorded using multiple thermocouples on the surface as well as integrated into the sample. At least one video camera was used during testing to capture the separation behaviour of the joint. A representative CAD model of the sample (in this case for RC testing) is shown in Fig. 7.

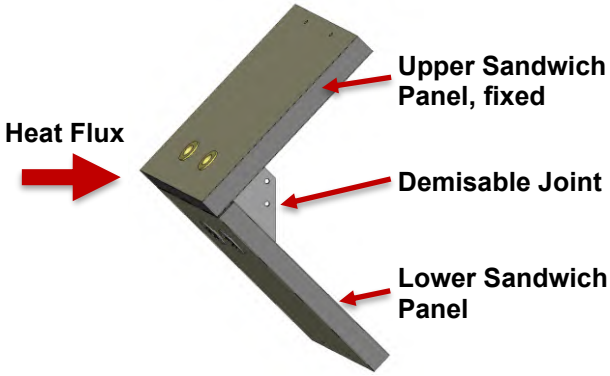


Figure 7: CAD model of demise sample

4.2.2. Re-entry Chamber Testing

The testing was performed in AAC's re-entry chamber (RC). It is a multi-purpose thermal vacuum chamber specifically designed for testing materials and small components under re-entry relevant heat fluxes. The samples are heated using radiation heaters, so heat fluxes up to ~100 kW/m² can be tested. For this test, a gradually increasing heat flux, representing a re-entry trajectory, is used. The heat flux values were determined in the previous D4DBB project using a re-entry simulation; see [1]. The parameters are shown in Tab. 2. The chamber with a mounted sample is shown in Fig. 8.
Using an adjustable pulley system and weights, which attached to the outer edge of the lower panel, the load on the demisable joint was varied during testing.

Table 2: Trajectory Heat Flux

Time [s]	**Heat Flux [kW/m²]**
0	3.2
285	3.2
465	5.0
765	20.0
965	50.0

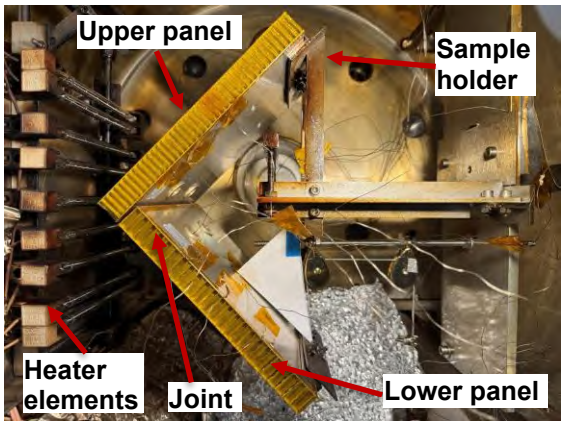


Figure 8: Sample mounted in RC

4.2.3. Plasma Wind Tunnel Testing

The testing was conducted by the DLR in the L2K facility. The test parameters were selected so that tests could be carried out at the lowest possible heat fluxes, whilst at the same time ensuring stable flow conditions around the specimen. These conditions were achieved with a heat flux of 50 kW/m².
A mounting setup similar to the re-entry chamber was used, although with a reduced sample size, since the original panel length of 200 mm resulted in unstable flow conditions. Therefore, the length was reduced to 100 mm. A mounted sample is shown in Fig. 9.

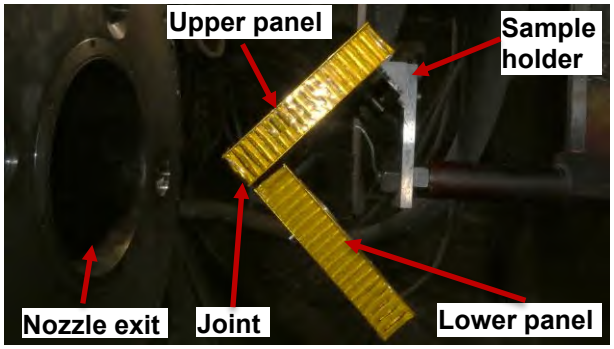


Figure 9: Sample mounted in PWT

4.2.4. Results

The test results depended heavily on the concepts being tested, but were consistent between RC and PWT. Concepts that showed separation in the RC exhibited similar behaviour in the PWT. Similarly, concepts that did not show separation did so in all tests.
In particular, the 'Demisable Insert' concept proved problematic in terms of separation during the trials. A root cause analysis was carried out through repeated tests in the RC using various loads. This identified a specific design feature as the cause, which can lead to the insert becoming jammed under certain loads. This behaviour was subsequently also observed in simplified tests. As the anchor nuts and insert designs were based on a very similar design principle, they also suffered from jamming during the tests.

At the same time, however, the triggering could be reliably demonstrated in all tests. Thermocouples were embedded in the solder material of the two inserts, so that the point at which the phase transition from solid to liquid occurred was clearly visible in the measurement data. This can be seen in the diagram in Fig. 10 from around the 10 min point onwards.

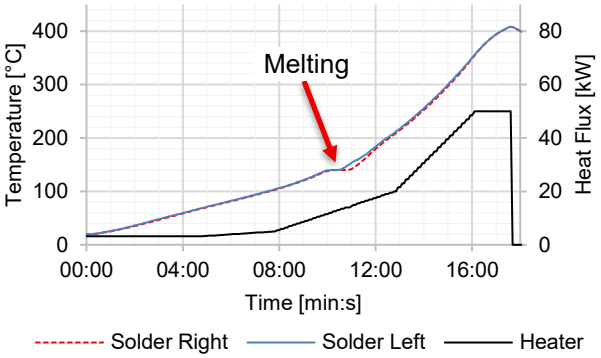


Figure 10: Temperature data of the demisable insert sample in the RC

The concept of the detachable CFRP cleat did not prove successful in the tests. In the re-entry chamber, the cleat material did not reach the temperature required to cause decomposition of the matrix material. One issue encountered was that, at a certain point during the test, the temperature of all the other materials in the sample such as the adhesive in the sandwich panel had risen to such an extent that they began to off-gas heavily and emit smoke. This smoke filled the test chamber, which not only caused the radiation intensity on the sample to decrease significantly, but also posed the risk of combustion residues settling on the sensitive heating elements and damaging them. The test therefore had to be terminated at this time.
In the PWT, this was not an issue, so the sample could be tested until it had completely disintegrated. Here, however, it became apparent that, although the matrix system softened and the cleat deformed, it retained its structural integrity overall. Ultimately, therefore, the sandwich panels collapsed before the cleat did, meaning that the joint did not lead to premature separation. The remnants of the sample after the test in the plasma wind tunnel are shown in Fig. 11. The total test duration was 2:40 min and was stopped after the upper sandwich panel disintegrated and the whole sample detached from the sample holder.

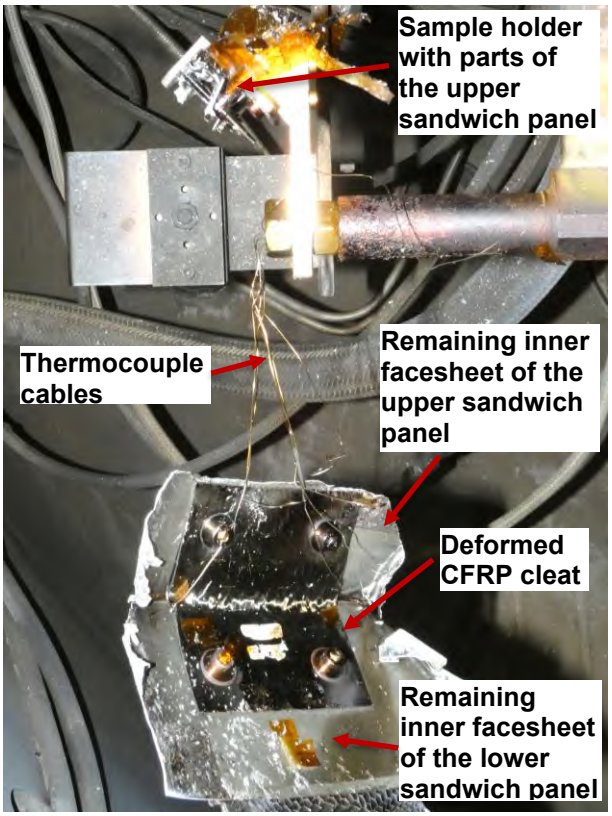


Figure 11: Remnants of the Demisable CFRP Cleat sample

The samples with a two-part, bonded cleat showed in general a similar behaviour. The joint separated in the bond line well before any significant damage occurred to the surrounding structure, such as the panels. A sample after the test in the PWT is shown in Fig. 12, which separated in 12 s.

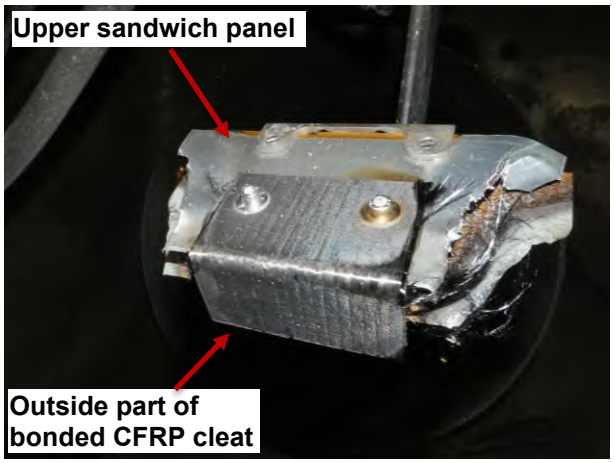


Figure 12: Sample after test with adhesive technology integrated in a two-part CFRP cleat, which separated during the test

The outlier was the test of the bonded CFRP cleat on the inside position in the PWT in which no clear separation was observed. Instead, the lower panel deformed and likely became stuck on the sample holder and therefore did not detach. In post-test investigation a clear debonding of the bond line was found, indicating the adhesive triggered. Nevertheless, it was not possible to determine a definite time to separation.

The difference between the samples lay in the time taken for separation, which depended not only on the specific joint design but also on the test. The samples in which the joint was positioned on the outside generally fragmented more quickly than those in which the joint was on the inside. In addition, the test sample in which aluminium was used for the cleat material instead of CFRP fractured even sooner.

The times required until the joint separates, or – in the case of inserts – until the solder melts, at which point separation would have been possible, are listed in Tab. 3 for the RC and in Tab. 4 for the PWT. The times between the two test set-ups naturally differ due to the different heat fluxes. In the RC test, the radiant heat is gradually increased over several minutes – the full power of 50 kW/m² is only applied after 965 s – whilst the PWT heats the sample immediately at full power. Another difference between the tests is the aerodynamic forces in the PWT, which enable material to be ablated. The difference is also clear from the condition of the sandwich panels after the testing. Whilst the samples in the RC clearly show the effects of the heat – the panels are all slightly deformed and warped following the tests – their fundamental structural integrity remains intact, even after tests lasting 20 minutes. On the other hand, samples in the PWT are usually destroyed after just a few minutes. The facesheets melt and the honeycomb disintegrates, causing the sandwich panels to lose their structural integrity and fall out of the sample holder. This effect is therefore also reflected in the times taken for separation.

Table 3: Results of the RC testing

Sample	Time [s]	Note
Demisable Insert in aluminium panel	590	Only melting of solder
Bonded 2-part CFRP cleat, inside location	751	Full separation
Bonded 2-part CFRP cleat, outside location	626	
Bonded 2-part alu cleat, inside location	596	
Demisable Anchor Nuts	726	Only melting of solder
CFRP cleat with demisable matrix	n/a	No separation
CFRP cleat with demisable matrix and added AlMg particles	n/a	

One anomaly was observed during the tests at the PWT, which affected all samples. The tests revealed that the width of the samples was slightly greater than the homogenous plasma flow core, which resulted in deflection of the flow and instable

flow conditions, shown in Fig. 13 on the left. This resulted in excessive heating by the shear layer at the outer edges of the panels. As a result, within a few seconds of the test beginning, the edges of the sample had melted away, shown in Fig. 14. This meant that the sample now fitted back into the homogeneous flow core and the flow stabilised, shown in Fig. 13 on the right, so the problem effectively resolved itself and the tests could continue.



Figure 13: Deflected flow at the beginning of test at 6 s (left), and stabilised flow at 36 s (right)



Figure 14: Areas of increasing heating on sample and subsequent "cutting" to size

Table 4: Results of the PWT testing

Sample	Time [s]	Note
Demisable Insert in aluminium panel	~55	Only melting of solder
Bonded 2-part CFRP cleat, inside location	n/a	No definite measurement possible
Bonded 2-part CFRP cleat, outside location	12	Full separation
Demisable Insert in CFRP panel	~50	Only melting of solder
CFRP cleat with demisable matrix	n/a	No separation
Demisable Edge Insert	~30	Only melting of solder
Demisable Anchor Nuts	~65	

5. CONCLUSION & OUTLOOK

The re-entry simulations of the FrankensteinSat case study, carried out at the start of the project, demonstrated, firstly, the need for 'design-for-demise' and, secondly, the requirement for the joints to begin to separate as early as possible at low temperatures in order to be effective. As part of the first series of tests, initial mechanical and demise properties were characterised, providing a good understanding of the design's behaviour. Whilst some designs and technologies, such as bonded cleats, have already demonstrated their potential and met the requirements, tests on other technologies, such as inserts and anchor nuts, have revealed design flaws. Only those designs that relied solely on a change of material to a demisable matrix system failed to achieve any observable improvement in the test and will therefore not be considered further in the next phase of the project.
Revising the designs will be the primary task for further development in the next phase of the project. For the inserts, the design issue of jamming must be resolved, whilst at the same time maintaining mechanical performance as far as possible. For the bonded cleats, reliability is to be optimised, and future development will also place greater emphasis on mechanical properties. The design is therefore optimised for stiffness using simulations and verified through testing on samples. These design changes will then be verified as part of the second test campaign, which will again take place in the RC of AAC and PWT of the DLR.
As primary joints, the designs developed must, of course, also meet all other requirements apart from those relating to improved demise, in particular the loads that occur when the satellite is launched into space. Further qualification work is therefore required in this area. These tests include, amongst other things, vibration tests, thermal cycling, shock loading and, where new materials are used, qualification on material level like outgassing.

6. REFERENCES

1. Mark Fittock (2019). D4D Breadboarding Final Report, D4DBB-OHB-FR-001, OHB System AG, Bremen, Germany.
2. Alexandre Achille Looten (2024). Design for demise applied to spacecraft structural panels and experiments for ClearSpace One platform, EPFL, Lausanne, Switzerland.
3. European Cooperation for Space Standardization (2011). Insert Design Handbook, ECSS-E-HB-32-22A, ESA Requirements & Standards Division, European Space Agency, Noordwijk, The Netherlands.

7. ACKNOWLEDGEMENTS

A major part of the work presented here has been carried out within the ESA funded ARTES Advanced Technology study "D4D SAFER" (Structures with Advanced Demisability Function During Earth Re-entry).

OPTIMIZATION OF A REPRESENTATIVE LEO SATELLITE SYSTEM ARCHITECTURE FOR DEMISE

Federico Marrucci[(1)], Alexander Ring [(1)], Isil Sakraker Ozmen[(1)], Tobias Lips[(2)], Patrik Kärräng[(2)], Ines Uriol Balbin[(3)]

[(1)] Deutsches Zentrum für Luft- und Raumfahrt e.V. (DLR), Pfaffenwaldring 38-40, 70569 Stuttgart, Germany, federico.marrucci@dlr.de; alexander.ring@dlr.de; isil.sakraker@dlr.de
[(2)] HTG-Hyperschall Technologie Göttingen GmbH, Am Handweisergraben 13, 37120 Bovenden, Germany, t.lips@htg-gmbh.com; p.kaerraeng@htg-gmbh.com
[(3)] Delft University of Technology, Postbus 5 2600 AA Delft, the Netherlands, I.UriolBalbin@tudelft.nl

KEYWORDS

Design for Demise (D4D), Re-entry technology, Uncontrolled re-entry, SCARAB, Casualty risk, Satellite structures

ABSTRACT

The rapid growth of low Earth orbit activity has increased the importance of end-of-life disposal and the safety implications of uncontrolled atmospheric re-entry. This work develops a methodology for progressively evaluating a representative LEO mid-mass satellite architecture for improved demise. A traceable baseline is used to define a bounded design space in which Design-for-Demise measures and architecture choices are translated into explicit variables. These are evaluated through a SCARAB simulation campaign, first individually and then in selected combinations to assess interactions. Total debris casualty area is used as the main comparison metric, supported by surviving mass and subsystem contributions. The single-variable results show reductions in total debris casualty area of up to 38.0%, while some modifications reduce surviving mass but increase casualty area. Subsystem-level results also show that architecture changes can affect components other than those directly modified, and the preliminary interaction analysis shows that the response to a design change can vary when combined with other architecture modifications. The aim is to provide a structured and traceable methodology for identifying architecture changes that improve demisability and for assessing how their effects change when combined.

1. INTRODUCTION

The increase in the number of objects in Low Earth Orbit (LEO) has increased the attention given to end-of-life disposal [1]. For spacecraft undergoing uncontrolled re-entry, safety requirements are commonly expressed in terms of human casualty risk from surviving debris. Both ESA and NASA adopt a maximum human casualty risk of 10^{-4} per re-entry event [2] [3]. Reducing this risk requires limiting the number and casualty area of fragments surviving to ground impact [4]. Design-for-Demise (D4D) is a method to address this by designing the spacecraft around these requirements, for example by promoting earlier break-up or reducing subsystem survivability during re-entry [5].

D4D is often associated with individual components or technologies, but their effect also depends on the surrounding architecture. Due to shielding and exposure timing, specific D4D technologies can have indirect effects on subsystems they are not directly targeting [6]. As a consequence, the effect of a D4D measure cannot always be inferred from the modified component alone.

Existing work provides D4D concepts at the component or system level and detailed re-entry analyses, but implementing these measures within a complete spacecraft creates a large and coupled architecture design problem. Many possible technologies can be used to improve demisability, with interactions and indirect effects on other subsystems. The effect of combining different measures therefore cannot necessarily be inferred from their isolated performance. The resulting architecture design problem is explored progressively, with the design space reduced through successive evaluation of individual measures and their interactions. Individual measures are first evaluated independently, and the resulting changes in DCA and surviving components are then used to select combinations for the assessment of interactions.

This paper presents a structured methodology for representing and progressively evaluating D4D measures through a bounded variable table. To test this methodology, a representative LEO satellite is used as a baseline, and candidate D4D technologies are converted into explicit variables describing component modelling, accommodation, shielding, and structural openings. The methodology is tested through a SCARAB simulation campaign, with debris casualty area (DCA) used as the main comparison metric. Total DCA, surviving mass, and their distribution among subsystems are used to identify the effects of

individual technologies and to guide subsequent simulation iterations.

2. ARCHITECTURE DESIGN-SPACE METHODOLOGY

2.1. Representative Baseline

To apply the proposed methodology, a baseline satellite architecture is required. To avoid arbitrary geometry and keep the architecture physically plausible, an existing satellite architecture is used as a starting reference. A communication-platform architecture is selected because communication satellites account for more than 80% of recent LEO payload launch traffic, making them particularly representative of current LEO activity [1]. Where public information is insufficient, representative subsystem references and modelling assumptions are used to complete the architecture.

Iridium NEXT and the ELiTeBUS 1000 documentation are used as the main spacecraft and platform references. The latter provides the broad platform configuration and subsystem list [7], while the first provides information on the communication payload and antenna functions [8]. More information is taken from public references to define individual subsystems. Where the required geometry, material, or accommodation information is not available, modelling assumptions are introduced. The resulting baseline therefore combines platform information, subsystem references, and assumptions to provide a physically realistic and representative starting architecture for the simulation campaign.

2.2. Design-variable Table

After running the re-entry simulation of the baseline model, the main demise-critical subsystems and surviving components can be identified. These results are then used to select relevant D4D measures and possible architecture changes for the components of interest, which are translated into explicit design variables. For the representative baseline used in this study, the critical components identified are the propellant tank, reaction wheels, magnetorquers, and the Solar Array Drive Mechanisms (SADM) so dedicated variables are defined for their design and accommodation. Additional variables are used to represent architecture changes that can influence shielding, exposure, and structural break-up.

For the present study, the design space is bounded to the variables implemented in the simulation campaign and those required for the selected interaction cases. Each variable defines a baseline condition and one or more implemented variants that can be represented directly in the re-entry model. The resulting design variables are summarized in Tab. 1.

The variable identifiers are retained from the broader design space to maintain consistency with the simulation campaign. Missing identifiers correspond to variables that are not included in the analysis presented here.

Table 1: Architecture design variables

ID	Design variable	Baseline state	Implemented variants	Intended effect
V1	Tank material and construction	Titanium tank	**B:** Aluminium tank; **C:** Al/carbon-fibre-reinforced polymer overwrapped tank	Reduce the heat required for tank demise and modify its break-up behaviour
V2	Reaction wheel accommodation	Two reaction wheels mounted on each side of the platform	**B:** Alternative accommodation with separated reaction wheel pairs	Modify shielding and exposure timing
V3	Reaction-wheel construction	Baseline Al housing with steel internal components	**B:** Aluminium flywheel; **C:** early-release baseline construction; **D:** Al flywheel and early-release	Reduce the survivability of dense components and promote earlier separation
V5	Magnetorquer construction	Steel core, full housing and baseline support configuration	**B:** Hiperco core; **C:** segmented core; **D:** exposed core; **E:** demisable fastener	Reduce survival of the dense core and increase its thermal exposure
V9	Local panel opening	No local openings	**B:** Local break-out patches placed near selected critical subsystems	Increase local exposure with minimal intervention
V10	Demisable panel joints	Baseline structural panel connections	**B: T**op-panel release; **C:** front/back-panel release; **D:** side-panel release	Promote earlier structural opening and exposure of internal subsystems
V12	Solar Array Drive Mechanism release interface	Baseline SADM connections	**B:** Demisable interface between the SADM and its support	Promote early separation of the SADM and solar array assemblies

2.3. Design-space Reduction and Interaction Logic

The design variables reported in Tab. 1 can be combined into a large number of possible spacecraft configurations. Testing every possible combination would require an equally large number of re-entry simulations. The design space is therefore explored progressively, starting from isolated variable changes before introducing selected combinations.

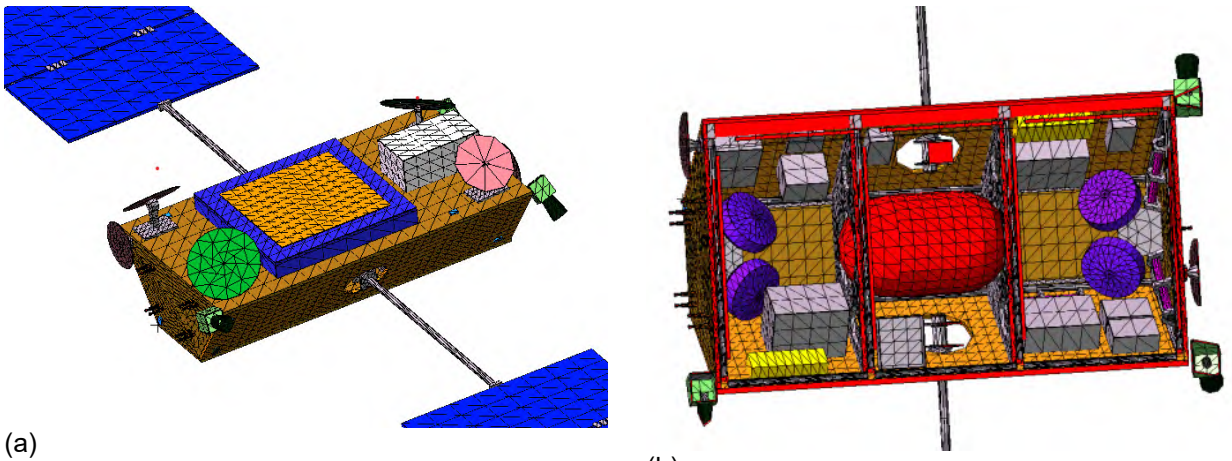
The first stage consists of a single-variable campaign. In each case, one design variable is modified with respect to the baseline while the remaining architecture and simulation conditions are kept unchanged. The resulting changes are used to identify the effect of each variable when applied independently and the subsystems that remain critical after the modification.

The single-variable results are then used to guide the selection of subsequent interaction cases. Particular attention is given to variables whose effect may depend on shielding, exposure timing, or structural break-up. A D4D modification applied to an internal component, for example, may have a limited effect if the component remains shielded until late in the re-entry, while its effect may change when combined with an architecture modification that promotes earlier exposure [6]. The interaction cases are therefore selected based on the remaining critical subsystems and the expected physical interaction between the corresponding design variables, rather than by testing all possible combinations.

3. RE-ENTRY MODEL AND SIMULATION SETUP

3.1. Re-entry Model

The destructive re-entry simulations are carried out in SCARAB, where the spacecraft model is constructed from simple primitive shapes such as boxes, cylinders and spheres. The geometry is simplified while preserving properties relevant to demise, including component envelope, mass, relevant material properties, accommodation, shielding relationships, and hard-to-demise internal hardware. Smaller details that are not relevant to break-up or exposure are omitted. Changes to the reference model are then made according to the D4D measure under investigation, while all other model features are kept unchanged, to create the modified geometric model. The resulting baseline model is shown in Fig. 1, including the external configuration and the internal subsystem accommodation.



(a) (b)

Figure 1: Representative SCARAB baseline model: (a) external spacecraft configuration; (b) internal subsystem accommodation.

In addition to the reference baseline (BL), a second baseline configuration (BL2) is defined with a more detailed battery representation. In BL, each battery module is represented as a single uniform component. In BL2, the same battery inventory is instead resolved into the module housing and its internal cells as separate modelled components. This changes the way the battery can heat, fragment, and contribute surviving objects during re-entry, while the remaining spacecraft architecture is kept unchanged. BL2 is therefore used as an alternative reference configuration for part of the simulation campaign.

3.2. Simulation Setup and Evaluation Metrics

All baseline and variant simulations use the same initial state, environmental models, and numerical settings, so that differences between cases can be attributed to the implemented architecture changes. The initial conditions are summarized in Tab. 2.

Table 2: Common initial conditions used for all simulations

Semi-major axis	6510 km
Eccentricity	0.001
Inclination	84.5°
RAAN, argument of perigee, and true anomaly	0°
Geodetic Altitude	125.35 km
Velocity	7.8 km/s

The primary evaluation metric is the total DCA, with the change relative to the baseline used to compare the individual variants. Additional outputs, including surviving mass, number of surviving fragments, and DCA and surviving mass by subsystem, are used to support the interpretation of the results.

Since the DCA calculation depends on the representation of the surviving fragments, a specific post-processing treatment is applied to the small electronic units modelled within the L-band antenna and hosted payload. These units are represented with explicit internal cards, consistent with the electronics-box approach described in the DIVE guidelines [9]. However, details such as their mass, dimensions, and internal card layout are not available from public information, and the resulting representation can therefore vary significantly depending on the assumptions adopted. More recent ESA SARA guidance instead recommends representing small and medium electronic components as an aluminium housing containing a generic electronics material, while explicit GFRP cards are reserved for large components as an exception [10]. To approximate this coarser representation, surviving cards belonging to the same small electronic unit are grouped in post-processing for the DCA calculation. Their masses are summed, while the group DCA is taken as the maximum DCA of its constituent cards. This aggregation rule is an assumption introduced in the present study and is not prescribed by the SARA guidance.

Casualty risk is retained as the wider compliance context but is not used as the architecture-comparison metric, since it additionally depends on the population distribution associated with the re-entry case.

3.3. DCA Interaction Metric

For the selected combination cases, the interaction between two design changes is evaluated relative to a common background configuration. The DCA of the common background is denoted by D_0, while D_A, D_B, and D_{AB} denote the DCA obtained after applying change A, change B, and both changes together, respectively. The effect of a change is measured as the difference between the DCA with and without that change:

$$\Delta D_A = D_A - D_0;\ \Delta D_B = D_B - D_0 \quad (1)$$

The interaction term between two changes is then calculated as

$$\Delta D_{int} = \Delta D_{B|A} - \Delta D_B \quad (2a)$$

$$\Delta D_{int} = D_{AB} - D_A - D_B + D_0 \quad (2b)$$

where the interaction is defined as the difference between the effect of B when A is present, and the effect of B on the background. An interaction term equal to zero therefore indicates that the effect of B is unchanged by the presence of A.

A value of $\Delta D_{int} = 0$ indicates an additive response, which means that the changes do not interact. Negative values ($\Delta D_{int} < 0$) indicate a favourable interaction, for which the combined DCA is lower than expected from the isolated effects. Positive values ($\Delta D_{int} > 0$) indicate an interaction that is less favourable than the additive expectation.

The sign of the interaction alone, however, does not indicate whether the combined configuration is beneficial compared with the individual changes. For this reason, the combined DCA is also compared with the best individual case. Three responses are distinguished:

$$D_{AB} < D_A + D_B - D_0 \quad (3a)$$

Indicates a favourable interaction, for which the combined DCA is lower than the additive expectation;

$$D_A + D_B - D_0 \leq D_{AB} < \min(D_A, D_B) \quad (3b)$$

indicates that the combination improves upon the best individual change, but the DCA is higher than or equal to the additive expectation; and

$$D_{AB} \geq \min(D_A, D_B) \quad (3c)$$

indicates that the combination does not improve upon the best individual change.

The resulting interaction is dependent on the background used for the comparison. The same pair of changes can therefore be evaluated around either BL or BL2, provided that the same background is used for all four cases. For example, for an interaction evaluated around BL2, the comparison is made between BL2, BL2+A, BL2+B, and BL2+A+B.The interaction obtained for the same pair A and B can therefore change when evaluated around a different background.

The resulting interaction is dependent on the background used for the comparison. The same pair of changes can therefore be evaluated around either BL or BL2, provided that the same background is used for all four cases. For example, for an interaction evaluated around BL2, the comparison is made between BL2, BL2+A, BL2+B, and BL2+A+B. The interaction obtained for the same pair A and B can therefore change when evaluated around a different background.

4. RESULTS

4.1. Baseline

The baseline simulation establishes the reference case for the subsequent architecture variants and allows the critical surviving components to be identified. The baseline results are also used to refine the design-variable table presented in Section 2.2 towards the components that remain relevant after re-entry.

The baseline model has a starting mass of 634.13 kg, of which 134.12 kg survives to ground impact, corresponding to 21.15% of the initial mass. The baseline total DCA is 14.00 m². The surviving mass and DCA are not distributed uniformly across the spacecraft, with the main contributions associated with the propellant tank, reaction wheels, magnetorquer, SADM and the payload and electronic assemblies. The subsystem-specific baseline results are summarized in Tab. 3.

The surviving components are consistent with those expected from the initial design-space definition. The propellant tank survives as a single large fragment, while the reaction wheels retain 37.74 kg across six surviving fragments. The SADM and solar arrays, and the magnetorquer, also remain present at ground impact. The L-band antenna and hosted payload contain surviving internal electronic units, resulting in DCA contributions of 2.07 m² and 0.68 m², respectively.

Table 3: Baseline surviving fragment results by subsystem

Subsystem	Surv. mass [kg]	Surv. fragments	DCA [m²]
Antennas	44.79	2	2.07
Hosted Payload	7.69	1	0.68
Reaction wheels	37.74	6	3.29
Electronic boxes	19.20	6	3.45
Propellant tank	17.57	1	1.63
SADM + solar arrays	4.52	4	1.79
Magnetorquers	1.75	1	0.5
Multiple	0.87	1	0.59

The breakup sequence shows that these internal assemblies remain shielded until comparatively late in the re-entry. This behaviour is supported by the subsequent architecture variants. The baseline therefore identifies both the main demise-critical components and a strong dependence of the surviving-fragment burden on the exposure timing of the internal electronics.

4.2. Single-variable Results

The single-variable cases are first compared through the percentage change in total DCA relative to the baseline, as shown in Fig. 2. The greatest reduction is produced by the top-panel release (V10B), with a decrease of 38.0%. The side-panel release (V10D) reduces the total DCA by 20.9%, followed by the aluminium tank (V1B), with a reduction of 15.6%. Smaller reductions are obtained with V2B, V3B and the magnetorquer variants V5C–V5E. Several variants instead increase the total DCA, with the largest increases obtained for the aluminium flywheel with early release (V3D), the Al/CFRP overwrapped tank (V1C), and the front/back-panel release (V10C), with increases of 17.3%, 15.6%, and 8.4%, respectively.

The absolute DCA and its distribution among the spacecraft subsystems are shown in Fig. 3.

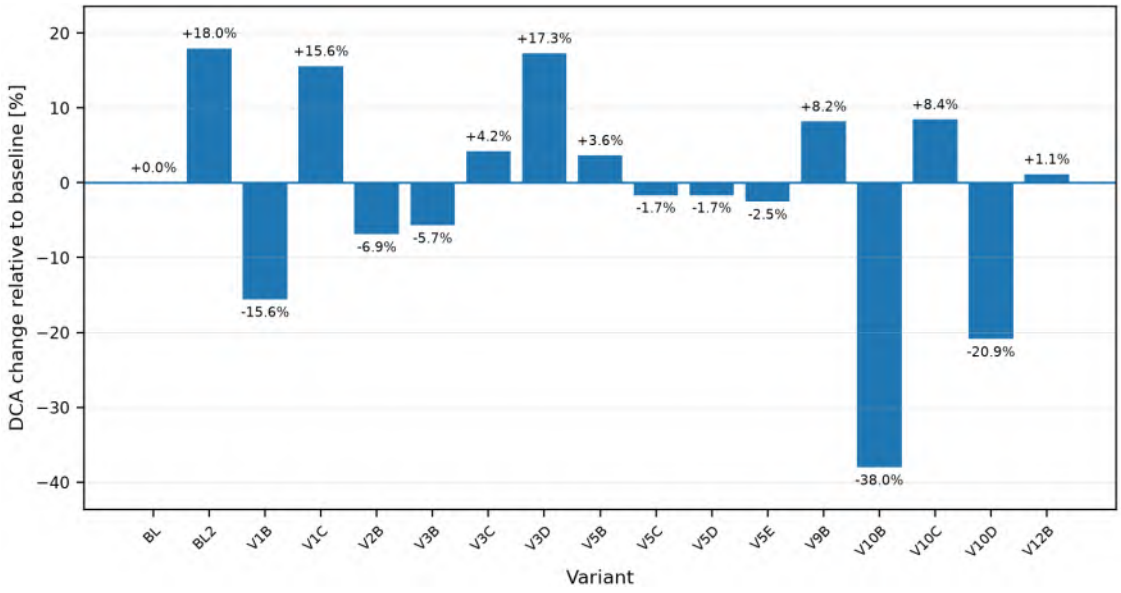


Figure 2: Percentage change in total debris casualty area relative to the baseline for the single-variable cases.

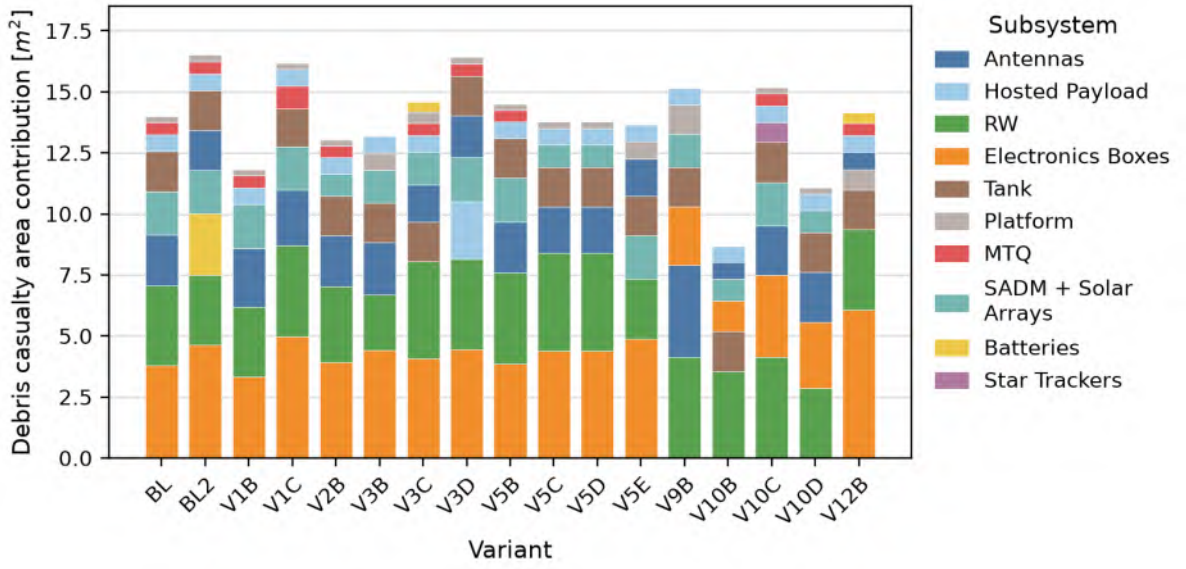


Figure 3: Total debris casualty area for the baseline and single-variable cases.

The change in each subsystem contribution relative to the baseline is shown in Fig. 4. For the top-panel release, the largest reductions come from the electronic boxes and antennas, whose DCA contributions decrease by 2.5 m² and 1.4 m², respectively. The SADM and solar-array contribution is reduced by 0.9 m² and the magnetorquer no longer survives, while the tank remains unchanged and the reaction-wheel contribution increases slightly. The reduction is therefore mainly associated with the earlier exposure of the internal electronics and antenna assemblies. The local break-out patches (V9B) instead reduce the electronic-box, magnetorquer, and SADM contributions, but these reductions are outweighed by increases in the antennas, reaction wheels, and platform, resulting in an overall DCA increase of 8.2%. The side-panel release produces a more distributed reduction, mainly through the electronic boxes, SADM and solar arrays, magnetorquer, and reaction wheels. The propellant tank remains unaffected in both panel-release cases.

The aluminium tank (V1B) instead produces a more direct response, with its reduction in total DCA resulting primarily from the complete demise of the tank. This result should be treated with caution when assessing the realistic behaviour of the variant. The aluminium tank completely demises in the present model, whereas Grassi et al. found that an aluminium-lithium tank fragmented into several surviving pieces and increased the casualty area in their re-entry analysis [6].

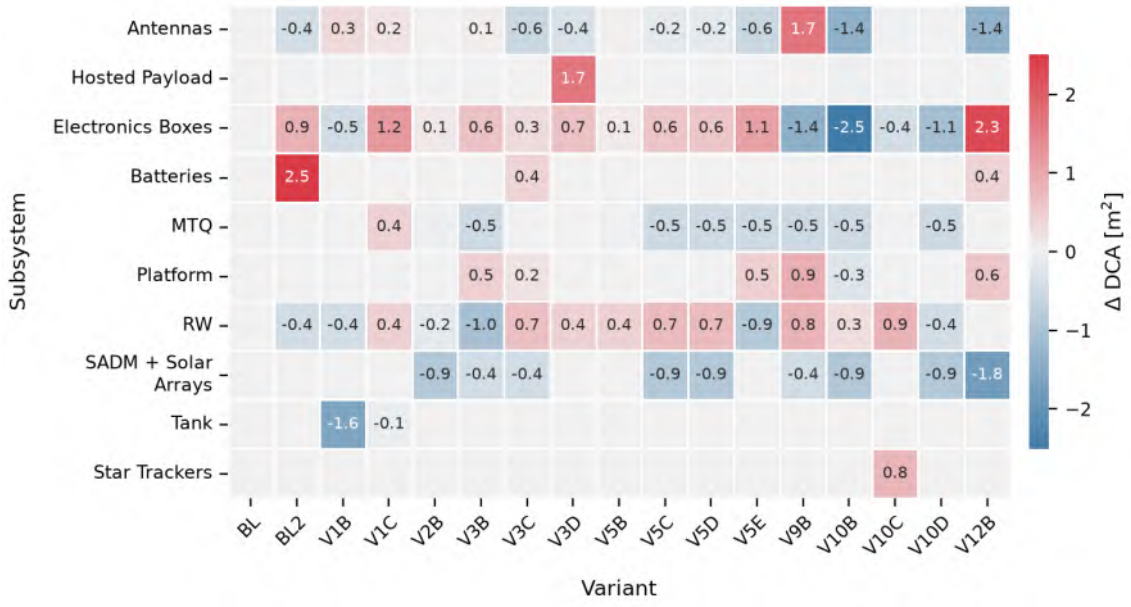


Figure 4: Change in debris casualty area by subsystem relative to the baseline for the single-variable cases.

The subsystem results also show cases where the change in total DCA is not driven primarily by the component being modified. The alternative reaction-wheel accommodation (V2B) reduces the total DCA by 6.9%, while the reaction-wheel contribution decreases by only 0.2 m². Most of the reduction instead comes from the SADM and solar arrays, whose contribution decreases by 0.9 m². Conversely, the aluminium flywheel with early release (V3D) increases the total DCA by 17.3%, while the reaction-wheel contribution increases by only 0.4 m². The hosted-payload and electronic-box contributions increase by 1.7 m² and 0.7 m², respectively. A substantial part of the overall response therefore occurs outside the subsystem directly modified.

Surviving mass provides an additional comparison, as shown in Fig. 5. The top-panel release again gives the largest reduction, decreasing the surviving mass from 134.12 kg to 60.26 kg. However, surviving mass and DCA do not always follow the same trend. The front/back-panel release (V10C) and the aluminium flywheel with early release (V3D) reduce the surviving mass to 121.73 kg and 104.99 kg, respectively, while increasing total DCA by 8.4% and 17.3%. Reducing the amount of surviving material therefore does not necessarily reduce the casualty area, since the number, size, and distribution of the surviving fragments also change.

These results show why total DCA needs to be considered together with subsystem contributions and surviving mass. Some modifications mainly affect the component they target, while others produce larger changes elsewhere in the spacecraft or alter the surviving-fragment population in ways that are not reflected by surviving mass alone. Surviving-mass reduction can nevertheless help identify design changes that improve the demise of specific subsystems, particularly when a clear reduction is observed in their surviving mass. The single-variable results are therefore used to identify the remaining critical components and select the interactions investigated in the following section.

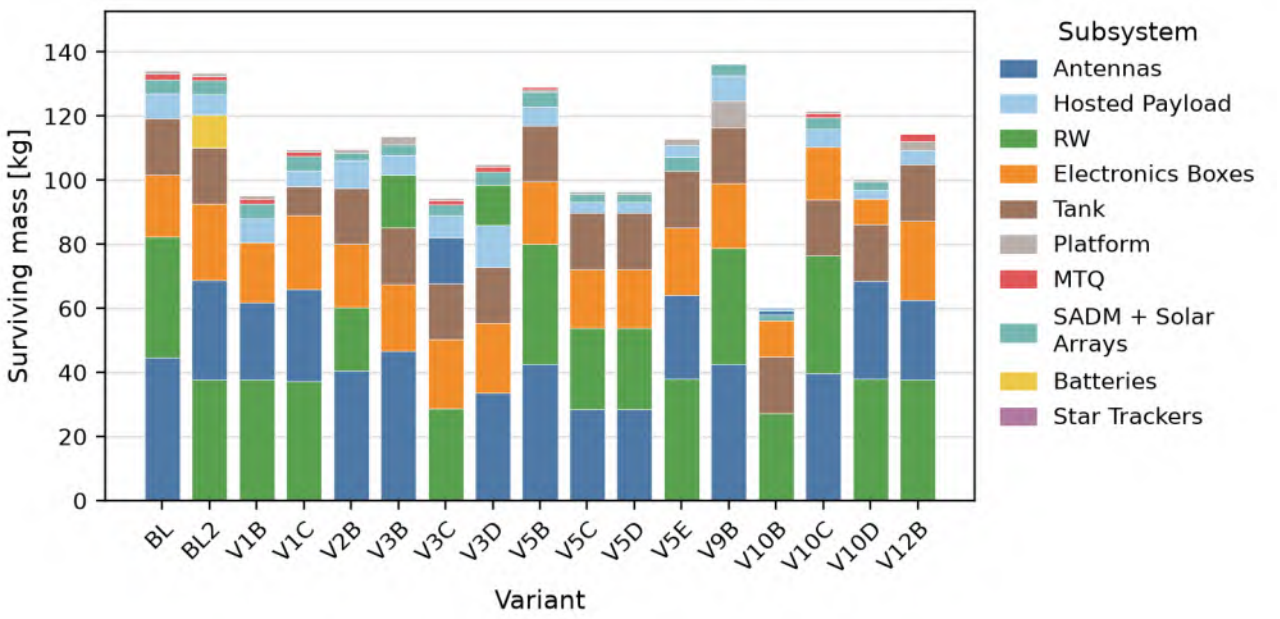


Figure 5: Absolute surviving mass by subsystem.

4.3. Preliminary Combination Results

The wider optimization campaign is still ongoing. Rather than drawing conclusions from an incomplete interaction matrix, one completed interaction is considered here to demonstrate the analysis method and examine the resulting subsystem behaviour. The interaction between the top-panel release (V10B) and the aluminium reaction-wheel flywheel (V3B) is evaluated around BL2. This pair combines a change to the spacecraft opening and exposure sequence with a modification to a critical internal component. The four configurations required for the interaction analysis are summarized in Tab. 4.

Table 4: DCA and surviving mass for the V10B–V3B interaction cases around BL2

Configuration	Total DCA [m²]	ΔDCA	Surviving mass [kg]
BL2	16.51	-	133.34
BL2 + V10B	8.43	-49.0%	74.73
BL2 + V3B	14.93	-9.6%	117.30
BL2+V10B+V3B	7.18	-56.5%	52.30

V10B produces the dominant isolated effect, reducing DCA by 8.09 m², while V3B reduces it by 1.58 m². When V3B is added to a configuration already containing V10B, the DCA decreases from 8.43 m² to 7.18 m², corresponding to an effect of −1.24 m². The interaction term is therefore:

$$\Delta D_{int} = (-1.24) - (-1.58) = 0.34 m^2 \qquad (4)$$

This case falls within the response defined by Eq. 4b: the interaction is less favourable than additive, while the combined configuration still achieves a lower DCA than either individual change.

The subsystem contributions show that the mechanism also changes between the isolated and combined cases. When V3B is applied independently to BL2, the reaction-wheel DCA decreases by only 0.35 m², while the largest reduction occurs in the electronic boxes, at 1.48 m². The platform contribution simultaneously increases by 0.37 m². When V3B is instead added with V10B already present, the reaction-wheel contribution decreases by 0.77 m², while the antenna and magnetorquer contributions decrease by 0.53 m² and 0.49 m², respectively. The electronic-box contribution, however, increases by 0.54 m². The effect of V3B is therefore smaller in total DCA when V10B is present, despite producing a larger reduction in the subsystem it directly modifies.

This case shows why the mechanism behind the interaction cannot be interpreted from total DCA alone. A change in the surrounding architecture can alter both the magnitude and the subsystem distribution of the response to a component-level modification.

The present case is one selected pair from a broader interaction campaign that is still in progress. The interaction values currently available for the BL2 background are assembled in Fig. 6. As the campaign is completed, separate interaction matrices will be constructed for BL and BL2 and interpreted together with the corresponding subsystem DCA and surviving-mass changes. A positive interaction indicates that the combined effect is less favourable than an additive response, but does not necessarily mean that the combined configuration performs worse than the individual modifications. Cases where the combined configuration does not outperform the best

individual modification are therefore outlined in black.

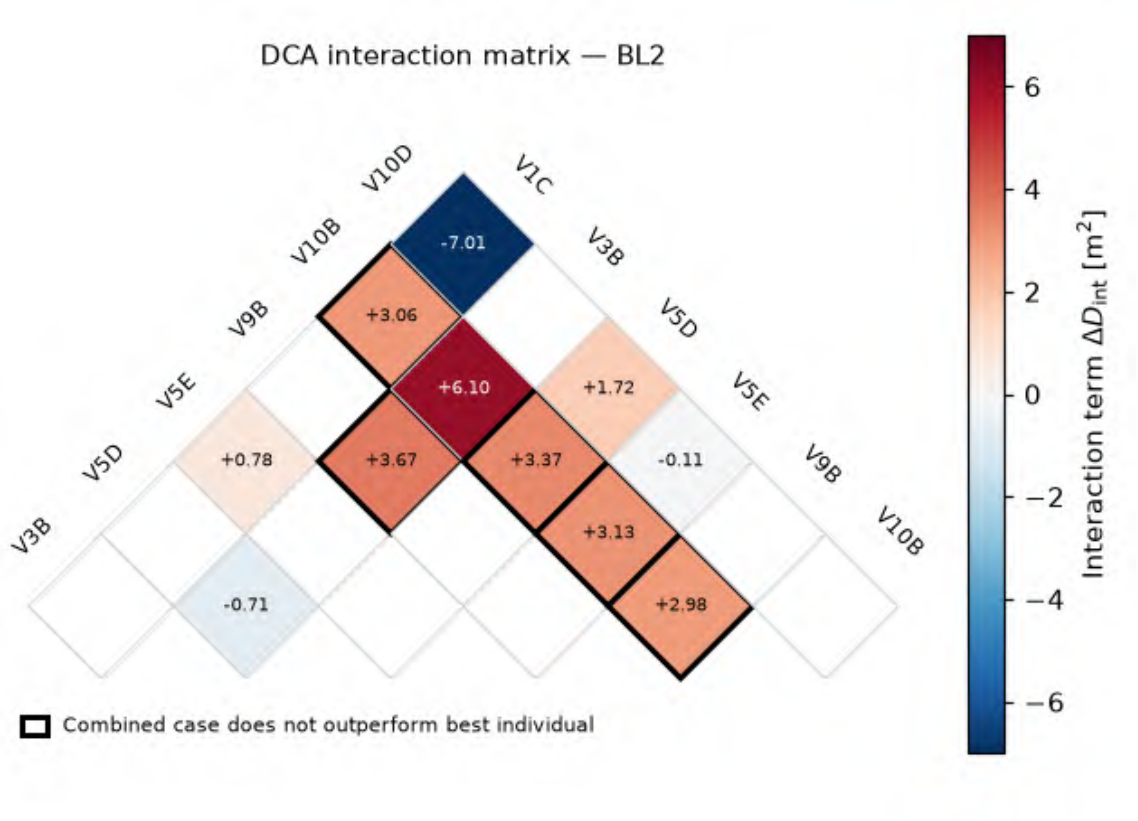


Figure 6: Preliminary normalized DCA interaction matrix for the BL2 background.

5. DISCUSSION

The single-variable results show that the effect of a D4D measure is not limited to the subsystem directly modified. Changes in shielding, exposure and break-up sequence can also affect other parts of the spacecraft. This is most evident for the panel-release cases: the top- and side-panel releases reduce DCA, while the front/back-panel release increases it despite reducing the surviving mass. The effectiveness of an early-release concept therefore depends on where the release occurs and which components are subsequently exposed or released. More generally, reducing surviving mass does not necessarily reduce DCA, since the resulting number, size and distribution of surviving fragments can also change.

The selected interaction between the top-panel release and the aluminium reaction-wheel flywheel shows that the effect of a design change can depend on the surrounding architecture. Although the interaction in total DCA is small, the subsystem response of the reaction-wheel modification changes when the top-panel release is already present. The preliminary interaction matrix in Fig. 6 also shows that the magnitude and direction of the interactions vary between different variable pairs. Interaction effects therefore need to be considered together with both the resulting combined DCA and the corresponding subsystem response, rather than being interpreted from the interaction term alone. Evaluating D4D measures as architecture variables rather than as isolated component modifications is supported by this.

The results also highlight the importance of the adopted modelling representation. For components whose detailed internal architecture is not publicly available, different assumptions can change the resulting surviving-fragment population and therefore the calculated DCA. This is particularly relevant for the small electronic units considered in this study, for which a specific aggregation treatment is applied in post-processing. The absolute DCA values should therefore be interpreted together with the assumptions used to represent these components.

More generally, destructive re-entry predictions are subject to modelling uncertainty. SCARAB has been validated against in-flight measurements, re-entry observations and wind-tunnel experiments, and has been compared with other international re-entry prediction tools [11]. The present study therefore focuses primarily on relative differences between

consistently modelled configurations rather than exact predictions of absolute DCA.

6. CONCLUSION

This work develops a progressive method for evaluating D4D measures as spacecraft architecture variables using destructive re-entry simulations. The investigated combinations already achieve substantial reductions in total DCA, with the lowest value obtained so far by combining the aluminium reaction-wheel flywheel (V3B), local break-out patches (V9B), and top-panel release (V10B) around the BL2 configuration. This combination reduces the DCA from 16.51 m² to 6.943 m², corresponding to a reduction of 57.9%. The results show that modifications can affect subsystems other than the one directly targeted and that lower surviving mass or earlier release does not necessarily result in lower DCA.

A normalized interaction metric is also introduced to quantify how the effect of one D4D measure changes when combined with another relative to a common background configuration. The interaction results show that these combined responses can differ in both magnitude and subsystem distribution from the corresponding isolated effects.

The interaction campaign will be continued around both baseline configurations, with the completed pairwise interactions used to select further multi-variant configurations and progressively reduce the design space towards architecture optimization.

BIBLIOGRAPHY

[1] EuropeanSpace Agency, “ESA Annual Space Environment Report,” 2024.

[2] ESA Space Debris Mitigation Working Group, “Re-entry Safety Requirements, ESSB-ST-U-004, Issue 1,” 2017.

[3] National Aeronautics and Space Administration, “Process for Limiting Orbital Debris,” 2021.

[4] P. Kärräng, T. Lips and T. Soares, “Demisability of Critical Spacecraft Components During Atmospheric Re-entry,” *Journal of Space Safety Engineering,* vol. 6, no. 3, pp. 181-187, 2019.

[5] L. Suriani, A. Caiazzo, B. Ganzer, T. Lips, P. Laurenti, B. Lockett, T. Schleutker, T. Soares and J. Beck, “Re-entry Safety: Analysis and Plasma Wind Tunnel Testing of Spacecraft Design Solutions to Reduce On-ground Casualty Risk,” *Journal of Space Safety Engineering,* vol. 11, no. 1, pp. 52-66, 2024.

[6] L. Grassi, S. Bianchi, R. Destefanis, R. Kanzler, P. Bassaler and S. Heinrich, “Design for Demise Techniques for Medium/Large LEO Satellite Re-entry,” in *7th European Conference on Space Debris*, Darmstadt, Germany, 2017.

[7] Thales Alenia Space, “ELiTeBUS 1000,” 2021.

[8] Iridium Communications, “Iridium NEXT Engineering Statement,” 2013.

[9] European Space Agency, “DIVE: Guidelines for Analysing and Testing the Demise of Man Made Space Objects During Re-entry,” 2020.

[10] European Space Agency, Space Debris Mitigation Team, “SARA Modelling and Materials: New Guidelines,” 2026.

In-Orbit Demonstration Mission Concept of Bio-Based Materials for Spacecraft Applications

Pedro Oura (1,2), Max Preis (2), Isil Sakraker Özmen (2), Ines Uriol Balbin (1)
(1) Delft University of Technology, Delft, The Netherlands, Email: info@tudelft.nl
(2) German Aerospace Center (DLR), Stuttgart, Germany, Email: contact-dlr@dlr.de

KEYWORDS
Bio-based materials; wood materials; CubeSat; spacecraft structures; in-orbit demonstrator; sustainability.

ABSTRACT
This work develops a 3U CubeSat concept to obtain in-orbit data on bio-based materials. The mission uses the International Space Station (ISS) orbit and exposes twelve samples for 8 to 12 months. The selected payload uses four internal cameras with 30 mm deployable mirrors at a 40° angle and forty-eight thermocouples. Structural analyses based on the NanoRacks CubeSat Deployer (NRCSD) loads show stress results below the material strengths in all evaluated cases, with a first natural frequency of 888.74 Hz. Thermal analyses show material-dependent sample temperatures; balsa reaches -60 to 18°C in the longest-eclipse mixed-material case, while degraded optical properties increase internal temperatures by about 3 to 4°C and exposed-wood temperatures by about 8 to 30°C. An engineering model confirms that the selected mirror geometry images the full sample height.

1. INTRODUCTION

The increasing number of spacecraft in low Earth orbit (LEO) and the associated growth in re-entry mass have increased interest in the environmental impact of space activities [1]. Spacecraft structures primarily use aluminium alloys, titanium alloys, and carbon-fibre reinforced polymers because of their structural performance and flight heritage [2]. At the same time, supply and sustainability concerns are increasing for several raw materials used by European industry [3].

Wood and other bio-based materials are being investigated for selected spacecraft applications. Their advantages include low density, low thermal conductivity, renewable origin, and improved demisability, but their behaviour in space is still poorly characterised [4]. A recent ISS exposure experiment tested three hardwood species for about ten months. The specimens were installed on a different port after an accident at the originally planned port, which placed them opposite to the intended flight direction and reduced the atomic-oxygen (AO) exposure. Visible surface and colour changes were still observed [5].

The German Aerospace Center (DLR) Institute of Structures and Design has been investigating wood and other bio-based materials for spacecraft structures within the DLR Bio Strux project [6,7]. Previous work assessed the structural and space environment feasibility of wooden satellite concepts [8], followed by life cycle assessment and plasma wind tunnel demisability testing of wood-aluminium laminated panels [9]. The mission proposed here extends this work by evaluating how these materials could be monitored directly in orbit.

For this purpose, a 3U CubeSat in-orbit demonstrator is developed. The experiment focuses on visible surface degradation, thermal cycling, dimensional changes, ultraviolet (UV) and atomic oxygen (AO) exposure, and moisture loss in vacuum. The work covers the mission and payload definition, CubeSat system design, structural and thermal analyses, and an engineering model of the camera and mirror system.

2. EXPERIMENT DEFINITION

2.1. Mission Definition

The main objectives are to monitor surface changes, including erosion, cracking, and colour changes, relate these effects to UV and AO exposure, evaluate thermo-mechanical behaviour during thermal cycling, assess shrinkage caused by moisture loss in vacuum, and assess surface charging effects.

The mission requirements are divided into orbit, environment, performance and design. The orbit parameters are summarised in Tab. 1. The nominal mission duration is 10 months, within an acceptable range of 8 to 12 months. The ISS wood experiment measured visible surface changes after a similar exposure time [5]. The actual orbital lifetime remains uncertain because it is mainly influenced by atmospheric drag, which varies with solar activity [10].

Table 1: Baseline mission orbit and deployment parameters.

Parameter	Selected value
Orbit type	Circular, ISS-like
Deployment	Release from ISS
Altitude	420 km
Inclination	51.6°
Period	88 min
Maximum eclipse	35.5 min

The orbit is kept in LEO because AO is one of the main degradation mechanisms of interest. ISS deployment provides the selected altitude and inclination and allows comparison with the previous ISS exposure experiment. The CubeSat is transported to the ISS as pressurised cargo and deployed through the NanoRacks CubeSat Deployer (NRCSD), which is used as the baseline 3U dispenser [11,12].

The mission scenario is divided into six phases, including the pre-launch phase. Phase 0 covers sample preparation, bake-out, and integration into the NRCSD. Phase 1 covers cargo launch to the ISS, ISS handling, and deployment. Phase 2 is the early-orbit phase, where survival, first contact, and solar-panel deployment are checked. Phase 3 is commissioning, including subsystem checks and mirror deployment. Phase 4 is nominal operation and lasts about nine months. Images and sensor data are stored and downlinked during this phase. Phase 5 starts after the exposure campaign, when payload operations stop, final data are downlinked, and the spacecraft is passivated before natural orbital decay.

2.2. Material Selection

A material trade-off was used to select representative bio-based candidates. Two candidate groups were created based on their intended use. Load-bearing candidates were evaluated mainly on mass, stiffness, strength, and dimensional stability. The second group included candidates for other applications, such as thermal insulation or energy absorption, and was evaluated on mass, thermal performance, dielectric performance, energy absorption, and dimensional stability. Space compliance, availability, and sustainability were considered for both groups [4,13-15]. The candidates and selected materials are summarised in Tab. 2.

Table 2: Material trade-off summary.

Group	Candidates	Selected
1: load-bearing	Scots pine; Norway spruce; Douglas-fir; European larch; European beech; oak; birch; flax; hemp	Scots pine; birch
2: other uses	Radiata pine; balsa; poplar; black alder	Balsa; poplar

Scots pine performed well because of its low density, availability, and sustainability, whereas birch was stronger in stiffness and strength. In Group 2, balsa stood out for its very low density and thermal conductivity and high specific energy absorption, while poplar performed well in dielectric behaviour, dimensional stability, availability, and sustainability. These four materials obtained the highest overall scores and were selected for the later design and analysis phases.

2.3. Sensor Selection

The payload must capture the main material responses to the space environment. Vacuum can remove absorbed water and other volatiles, causing shrinkage; thermal cycling produces temperature gradients and dimensional changes; UV and vacuum-UV radiation can degrade the surface; AO can oxidise and erode organic materials; and charging is relevant because wood is electrically insulating [4,16,17].

The subject trade is summarised in Tab. 3. The subjects were ranked using relevance to material behaviour, measurability, integration complexity, data usefulness, power and data demand, and risk. Relevance to material behaviour received the highest weight.

Table 3: Sensor subject trade outcome.

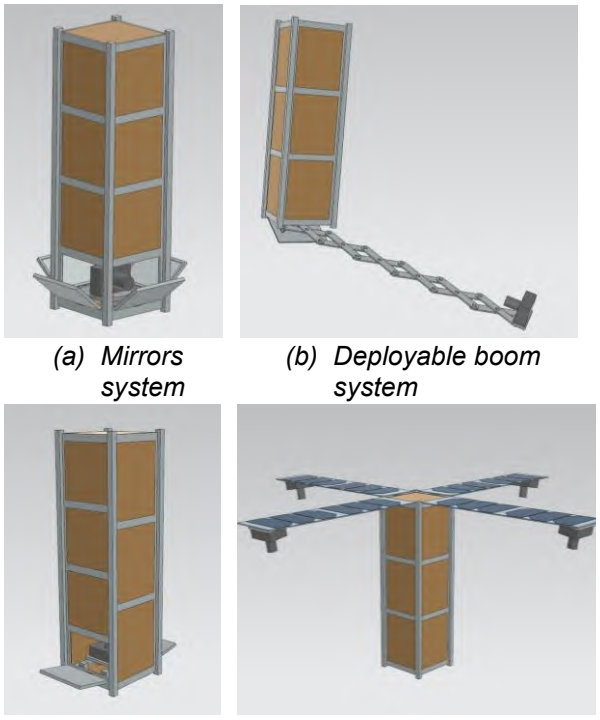
Subject	Measurement location
Temperature	Samples, frame and electronics
Strain	Samples and frame
Acceleration	Near CubeSat center-of-gravity (CG)
Visual degradation (images, colour metrics)	External sample surface
Radiation exposure (ionising, UV and AO)	External samples
Pressure	CubeSat cavity
Radio-frequency (RF) and magnetic transparency	Internal antenna and magnetometer
Spacecraft charging	External samples to spacecraft ground

Temperature, strain, visual inspection, UV and AO exposure were classified as primary subjects.

In this work, only the camera and temperature measurement systems are developed in detail. A Raspberry Pi Camera Module V2 was selected, with the Raspberry Pi 4 Model B and the Arducam B012001 as the board and multi-camera adapter, respectively. Four images per day, one from each lateral side, are used as the reference imaging rate. Type-T thermocouples were selected for the expected temperature range, with MCC 134 boards used for data acquisition. Strain gauges remain relevant for a future flight model, but vacuum testing is needed first to determine the required measurement range.

2.3.1. Camera Mechanism

Four camera concepts were investigated, as shown in Fig. 1: an internal camera with mirrors (a), a deployable boom (b), a rail-mounted camera (c), and cameras on deployable solar panels (d). The mirrors concept was divided into three variants: one with adjustable mirrors with one rotating camera, one with deployable mirrors with one rotating camera, and one with deployable mirrors with four fixed cameras. The boom concept is similar to the WISA WoodSat camera configuration [18]. The solar-panel concept was inspired by the Orion camera system, which uses cameras on the solar arrays for external inspection [19,20].



(a) Mirrors system *(b) Deployable boom system*

(c) Rails system *(d) Solar-panel system*

Figure 1: Camera-mechanism concepts.

The mirror system candidate was selected, specifically the concept with four cameras and deployable mirrors. Out of its variants, it is the simplest because the cameras remain fixed and no stepper motor for camera rotation is required.

A MATLAB geometric model was then used to define the mirror length and deployment angle. The model represents the camera, the mirror, and the upper and lower limits of the exposed sample section. For each tested geometry, the real camera position was reflected across the mirror plane to create an equivalent virtual camera. Rays were then drawn from the upper and lower limits of the samples towards this virtual camera. It was then calculated where both rays crossed the mirror surface. A configuration is feasible when both intersection points fall within the mirror boundaries, meaning that light from both the top and bottom of the sample section reaches the camera through the mirror. The geometry used for this calculation is shown in Fig. 2.

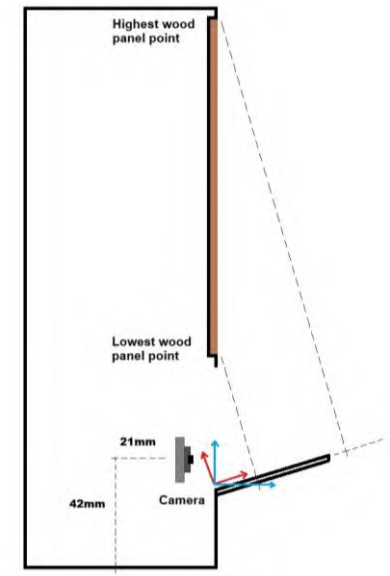


Figure 2: Geometric model of the mirror concept.

The feasible mirror length and deployment angle combinations are shown in Fig. 3. Below approximately 30°, no tested mirror length captures both sample limits. A 20° feasible deployment range was used as the design target. A 30 mm mirror provides a feasible range from 33.59° to 53.85°, and 40° was selected for the final design.

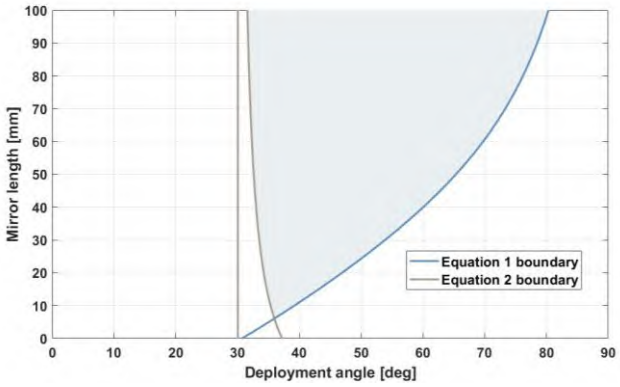


Figure 3: Feasible mirror geometries.

3. ENGINEERING MODEL

A physical engineering model was built to check the selected mirror and camera geometry. The imaging system uses the Raspberry Pi components previously discussed. The mirror supports, camera mounts, and sample interfaces were printed in polylactic acid (PLA) using a Bambu Lab H2D printer. Reflective aluminium foil was applied to the

mirror surfaces. The complete model is shown in Fig. 4.



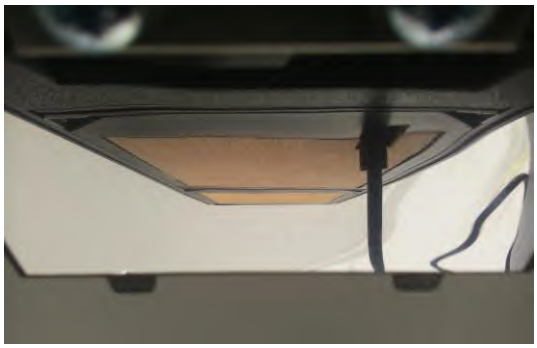
(a) Side view



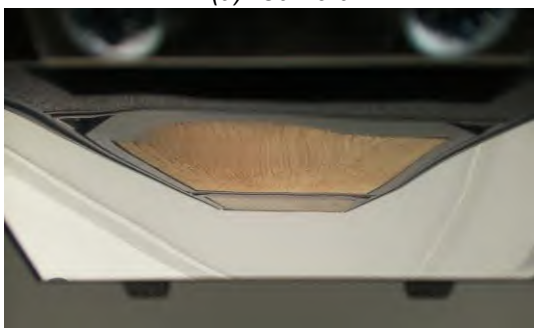
(b) Front view

Figure 4: Physical engineering model.

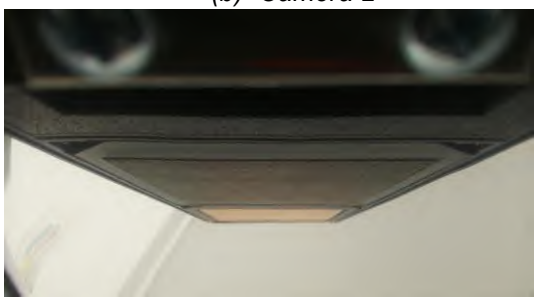
The four cameras were operated sequentially. The images in Fig. 5 confirm that a 30 mm mirror at 40° allows the complete height of the material samples to be imaged. The regions farther from the mirror occupy fewer pixels and contain less detail. Local distortion is also visible because the aluminium foil follows the roughness of the 3D-printed surface.



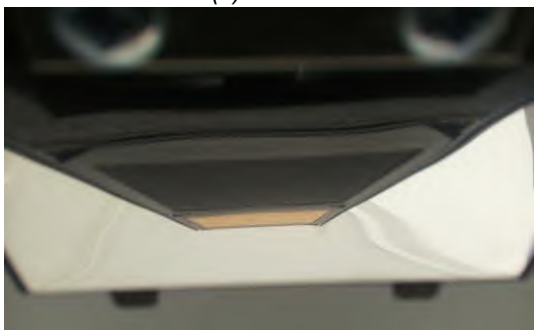
(a) Camera 1



(b) Camera 2



(c) Camera 3



(d) Camera 4

Figure 5: Engineering-model images obtained from the four cameras.

4. CUBESAT SYSTEM DESIGN

The imaging architecture tested in the engineering model is also used for the CubeSat design. Regarding the amount of data produced, 1.7 MB per image and four images per day give 6.8 MB/day. The temperature system uses four thermocouples per sample, sampled once per minute. Thus, the temperature data produced is 0.55 MB/day.

For the attitude determination and control system (ADCS), passive magnetic stabilisation is selected. Four permanent magnets create a fixed magnetic dipole that tends to align the CubeSat with the local geomagnetic field, while four hysteresis strips dissipate rotational energy. The layout follows the AstroBio 3U CubeSat reference [21]. A MATLAB script was used to visualise the CubeSat orientations throughout one orbit, with its Z-axis aligned with the magnetic field, as shown in Fig. 6.

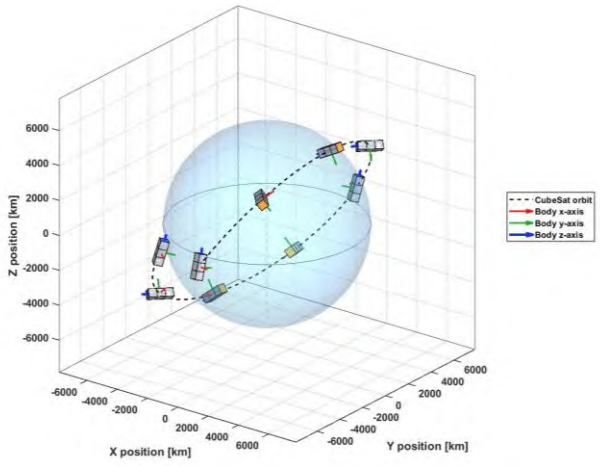


Figure 6: Visualisation of CubeSat attitude behaviour.

The Structure and Mechanisms System (SMS) uses separate aluminium 6061-T6 corner rails and removable sample panels. The design was inspired by available 3U CubeSat structures from 2NDSpace, NPC Spacemind, ISISpace, AAC Clyde Space, Serenum Space, and EnduroSat, together with university reference designs. The mirrors and solar panels use the EXA Hinge Nano+ and Hold-Down and Release Mechanism (HDRM) Nano as reference deployment hardware. Silicon carbide is used as the reference mirror substrate.

The Electrical Power System (EPS) uses four laterally deployable AAC Clyde Space PHOTON-SIDE solar panels, a GomSpace NanoPower P60 Power Conditioning and Distribution Unit (PCDU), and a NanoPower BPX 100 Wh battery. The Communication System (CS) uses a GomSpace NanoCom AX100 ultra-high-frequency transceiver and an ISISpace deployable very-high/ultra-high-frequency antenna. The Command and Data Handling System (C&DHS) uses an AAC Clyde Space Q7S as the main on-board computer (OBC), with separate Raspberry Pi, thermocouple acquisition, and deployables control boards for payload functions, together with an inertial measurement unit (IMU).

The preliminary mass distribution is given in Tab. 4. For the margins, 5% is used on commercial-off-the-shelf (COTS) components and 10% on components that need to be manufactured. The operating temperature limits used for thermal verification are listed in Tab. 5, while the main power consumption values used in the design are given in Tab. 6.

Table 4: Preliminary mass distribution.

System	Component	Qty.	Mass (g)
SMS	Primary structure	–	393.3
SMS	Secondary structure	–	419.8
SMS	Hinge	8	4.9
SMS	HDRM	8	1.0
ADCS	Neodymium magnet	4	2.6
ADCS	Hysteresis strip	4	1.7
EPS	Battery	1	500
EPS	PCDU	1	191
EPS	Solar panel	4	135
CS	Transceiver	1	24.5
CS	Antenna	1	90
C&DHS	Main OBC	1	32
C&DHS	Camera control board	1	66
C&DHS	Thermocouple control board	5	50
C&DHS	IMU	1	33
C&DHS	Deployables control board	1	29.6
Payload	Camera	4	3
Payload	Camera adapter	1	50
Total mass (kg)			2.696
Total mass with margins (kg)			2.872

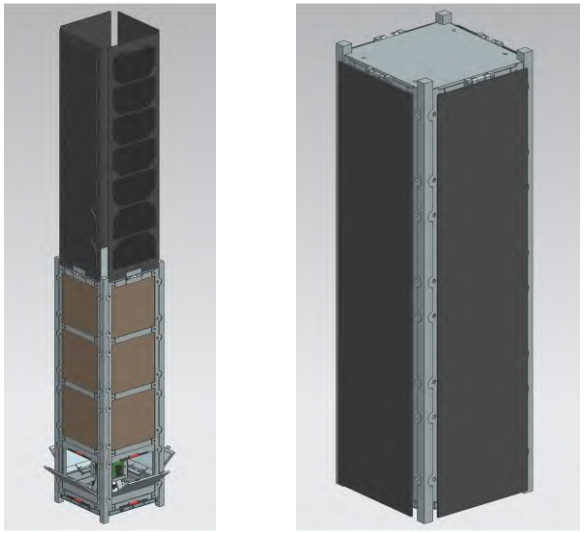
Table 5: Component operating temperature requirements.

Component	Operating temperature (°C)
Hinge	-100 to +150
HDRM	-270 to +1750
Battery	-20 to +60 charge / 0 to +45 discharge
PCDU	-35 to +85
Solar panel	-40 to +80
Transceiver	-30 to +85
Antenna	-20/-5 to +60
Main OBC	-40 to +85
Camera control board	0 to +50
Thermocouple board	0 to +55
IMU	-40 to +85
Deployables board	-100 to +150
Camera	-20 to +60
Camera adapter	Not specified
Thermocouple	-75 to +260

Table 6: Main component power consumption.

Component	Qty.	Nominal power (W)
Battery	1	0.23
PCDU	1	0.60
Transceiver	1	0.1815 receive / 2.64 transmit
Antenna	1	0.04 - 0.06 operation / 2 deployment
Main OBC	1	1.0
Camera control board	1	2.7 idle / 5.1 moderate
Thermocouple board	5	0.083 each
IMU	1	0.05
Deployables board	1	0.5
Camera	4	0.66 - 0.825 each
Camera adapter	1	Not specified
Thermocouple	48	≈0

The internal components were arranged to balance the CubeSat and keep the wiring simple. From top to bottom, the main stack contains the battery, PCDU, transceiver, main OBC and IMU, thermocouple boards, camera adapter, camera control board, passive ADCS strips, cameras, mirror assembly, ADCS magnets, deployables control board, and antenna. The battery is placed near the top to balance the payload mass at the lower end, while the IMU is kept near the spacecraft centre and away from the permanent magnets. The final deployed and stowed layouts are shown in Fig. 7. The final internal stack is shown in Fig. 8.



(a) Deployed *(b) Stowed*

Figure 7: Final CubeSat assembly.

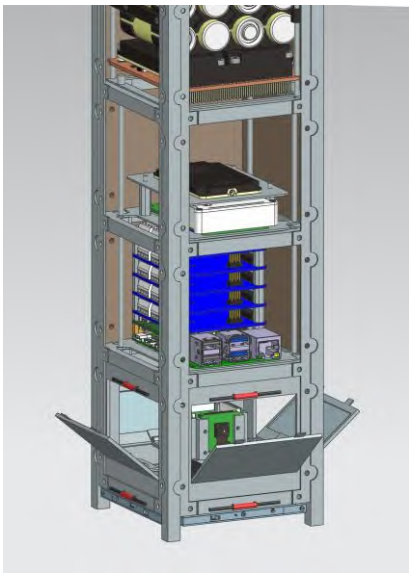


Figure 8: Final CubeSat internal stack.

5. SIMULATION CAMPAIGN

5.1. Structural Simulations

The structural model is based on the stowed assembly. The rails, braces, plates, samples, mirrors, mirror supports, hinges, and HDRMs are maintained, while electronic subsystems are replaced by point masses. The 4 mm wood panel samples are shell elements defined as orthotropic Scots pine, with the longitudinal grain direction aligned with the CubeSat Z-axis. The simplified finite-element model is shown in Fig. 9.

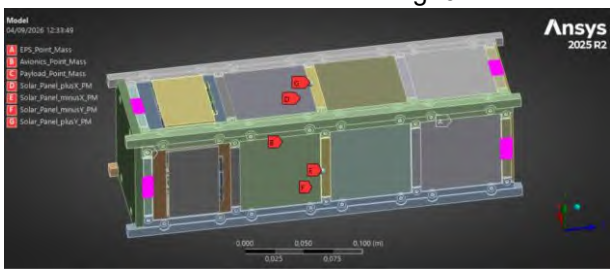


Figure 9: Simplified structural model.

Bolted interfaces are represented by bonded annular washer regions with frictional contact on the remaining overlap. Adhesive interfaces are bonded, free contact surfaces are frictionless, and interfaces that must remain closed use no-separation contact. The EPS, avionics, payload, and solar-panel groups are represented by point masses at their respective centres of mass. The rail faces parallel to the XZ plane are constrained in X, the faces parallel to the YZ plane in Y, and the four lower rail ends in Z.

The structural cases follow the NRCSD launch requirements [12]. The most critical quasi-static load case applies +7 g in X and -1.8 g in Z together with angular accelerations of +13.5 rad/s² about X, Y, and Z. An integrated rail load case applies 1200

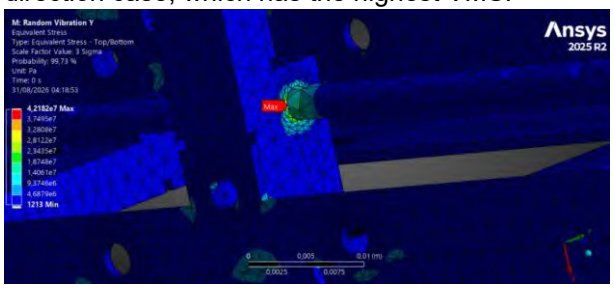
N compression across the rail ends. Modal analysis is followed by random-vibration analyses in X, Y, and Z using the 20 to 2000 Hz soft-stow profile at 5.76 g root-mean-square. The monitored outputs are total deformation, metallic von Mises stress, and longitudinal, radial, and longitudinal-radial (LR) shear stresses in the wood.

Metallic von Mises stress (VMS) is compared with the corresponding yield strength. For Scots pine, the values used for direct comparison are 102.0 MPa longitudinal tensile strength, 50.0 MPa longitudinal compressive strength, 3.0 MPa radial tensile strength, 4.7 MPa radial compressive strength and 9.2 MPa LR shear strength [13,22,23]. The main results are summarised in Tab. 7.

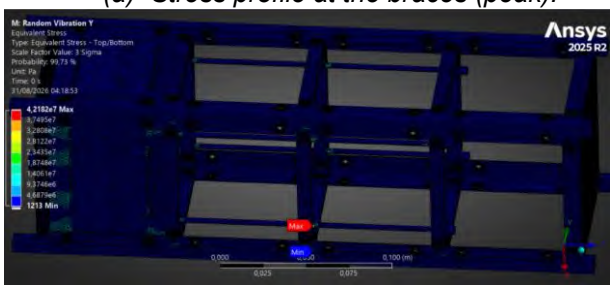
Table 7: Structural simulation results.

Case	Max. def. (mm)	Max. VMS (MPa)	Max. stress L / R / LR (MPa)
Quasi-static load	0.008	5.6	0.108 / 0.026 / 0.031
1200 N rail load	0.031	26.3	0.855 / 0.335 / 0.225
Random vibration X	0.037	37.8	1.211 / 0.292 / 0.316
Random vibration Y	0.037	42.2	1.220 / 0.378 / 0.283
Random vibration Z	0.040	33.5	2.884 / 0.468 / 0.428

All reported stresses remain below the material strengths. The Y-direction random-vibration case gives the highest metallic stress, while the Z-direction case gives the highest wood longitudinal and LR shear stresses. The first natural frequency is 888.7 Hz. Fig. 10 shows the random vibration Y-direction case, which has the highest VMS.



(a) Stress profile at the braces (peak).



(b) Stress profile in the entire CubeSat.

Figure 10: Random vibration Y-direction case, von Mises stress distribution.

5.2. Thermal Simulations

The thermal model is developed in ESATAN-TMS. The 4 mm wood panels use an isotropic conductivity equal to the longitudinal wood value. This represents heat transfer along the vertical grain direction but overestimates radial, tangential, and through-thickness conduction. Thin structural parts are represented by shell elements, hinges are replaced by conductive interfaces, and two lumped nodes represent the payload and internal bus. The simplified thermal model is shown in Fig. 11.

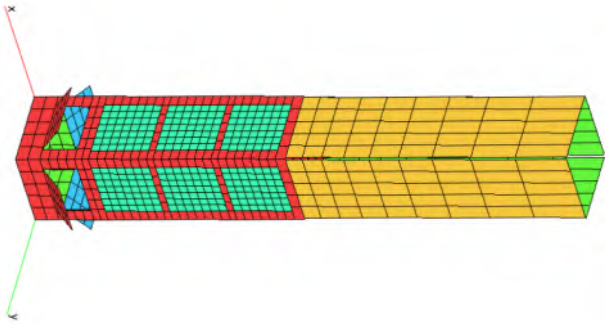


Figure 11: Simplified ESATAN model.

The beginning-of-life (BOL) wood surface uses a solar absorptivity of 0.49 and an emissivity of 0.91. For the end-of-life (EOL) sensitivity case, wood absorptivity is increased to 0.64. No measured EOL optical properties are available for the selected wood species over an 8 to 12 month LEO mission, so the +0.15 change is used as a conservative estimate based on spacecraft contamination data [24]. Smaller changes are applied to the white coating, mirror, and solar cells. White paint is retained on the aluminium surfaces because of its low solar absorptivity and high infrared emissivity [25,26].

The wood-aluminium interface was also evaluated. Removing the conductive interface increases the hot and cold extremes of the wood samples and makes the payload and internal-bus nodes about 2 to 4°C warmer than in the conductive cases. In contrast, changing the contact conductance from 328.95 to 740.1 W/(m²K) produces almost identical profiles.

The nominal operations case uses 0.885 W at the payload node and 10.035 W at the internal bus. The transient model is run for five orbits. Radiative cases use the 420 km, 51.6° ISS-like orbit and evaluate no-eclipse and longest-eclipse conditions. Fixed-face, 2.5°/s first-day rotation and 0.25°/s nominal rotation cases were defined.

A black-versus-white coating comparison was first used to select the aluminium surface finish. With white paint, the no-eclipse payload remains at about 12 to 14°C and the internal bus at 2 to 5°C; under the longest eclipse, they reach about -2 to 2°C and

-22 to -8°C, respectively. White paint is therefore chosen and used for the remaining analyses.

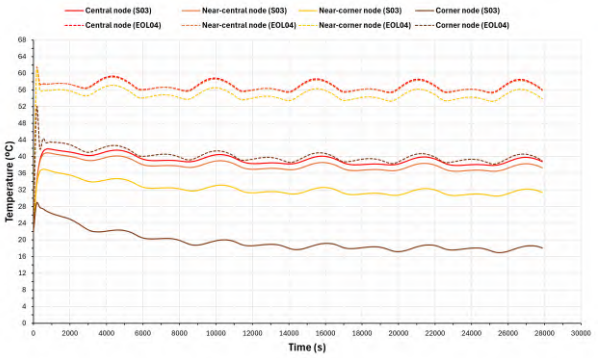
The main BOL/EOL comparisons are grouped in Fig. 12. Across the evaluated eclipse and pointing cases, the EOL payload and internal-bus temperatures are about 3 to 4°C higher than the corresponding BOL values. The exposed wood shows larger differences of about 8 to 30°C, depending on face and orbital condition. This temperature change is large enough to be measured by the selected thermocouples. Visible wood darkening after about ten months of ISS exposure has already been reported, although that experiment did not measure the corresponding change in solar absorptivity [5].

The 0.25°/s mixed-material configuration is the main nominal material comparison. The temperature ranges are summarised in Tab. 8, and the corresponding Poplar, Scots pine and Balsa profiles are grouped in Fig. 13 and Fig. 14. Balsa has the largest temperature extremes because it has the lowest thermal conductivity and density of the four materials. The corner node has a narrower range than the interior nodes because it is more strongly coupled to the aluminium frame.

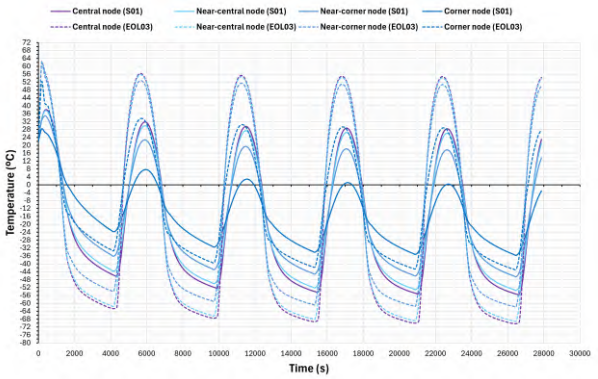
Table 8: Mixed-material sample temperature ranges under nominal 0.25°/s rotation.

Material	No eclipse (°C)	Longest eclipse (°C)
Poplar	-12 to 30	-44 to 6
Balsa	-32 to 44	-60 to 18
Scots pine	-14 to 28	-44 to 16
Birch	-12 to 24	-42 to 8

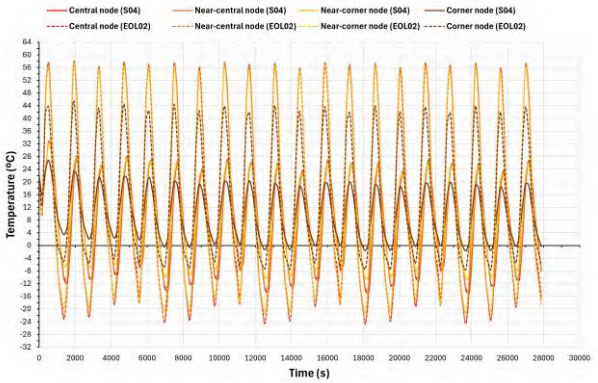
For the mixed-material no-eclipse case, the payload remains at about 16 to 18°C and the internal bus at 8 to 10°C. Under the longest eclipse, the payload reaches about -2 to 4°C, and the internal bus reaches -21 to -8°C.



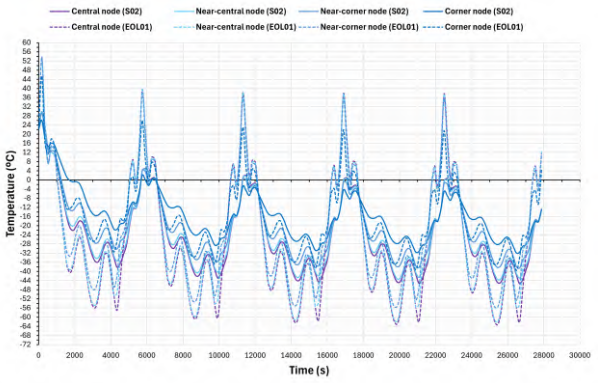
(a) No eclipse with fixed-face case



(b) Longest eclipse with fixed-face case

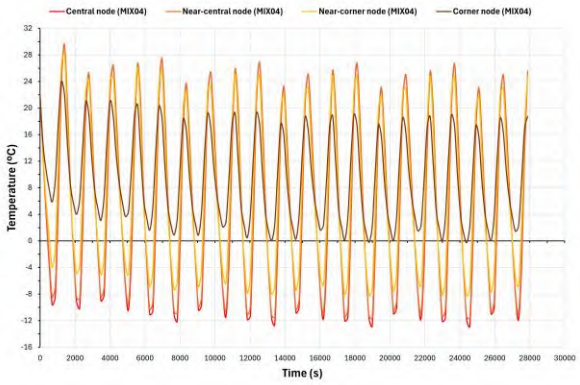


(c) No eclipse with 0.25°/s rotation

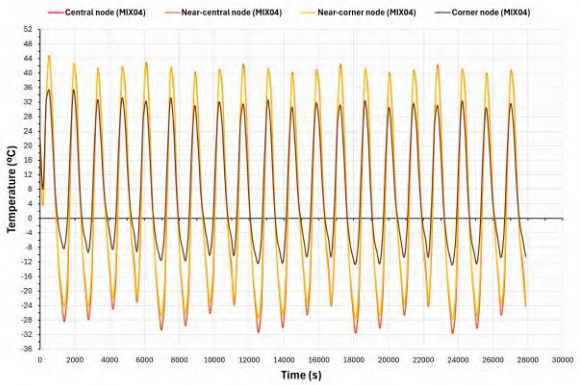


(d) Longest eclipse with 0.25°/s rotation

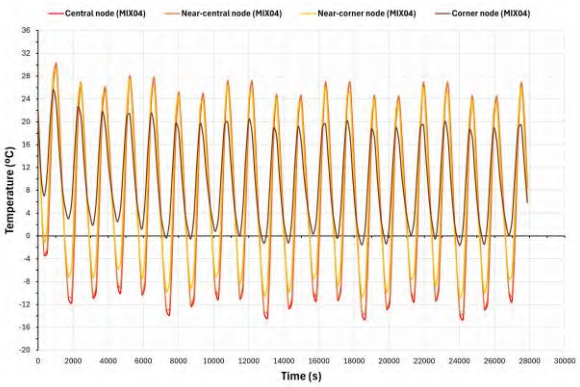
Figure 12: BOL vs. EOL temperature comparisons (face with highest exposure).



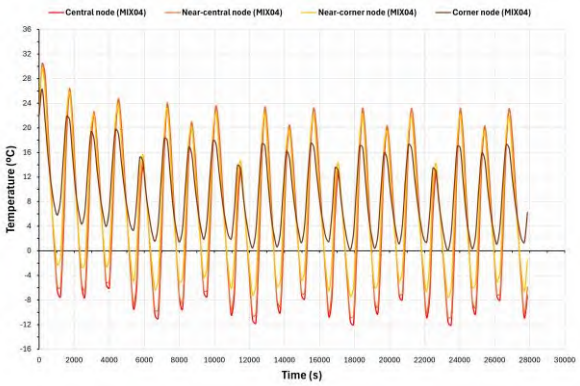
(a) Poplar



(b) Balsa

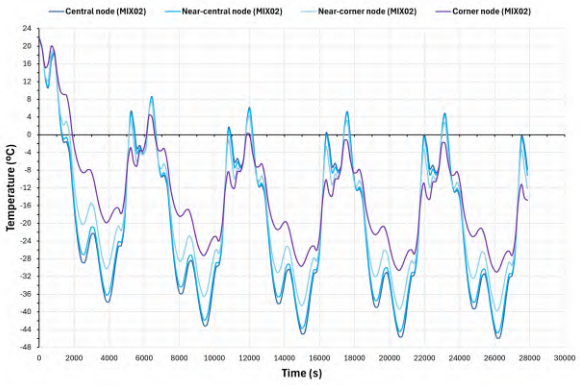


(c) Scots pine

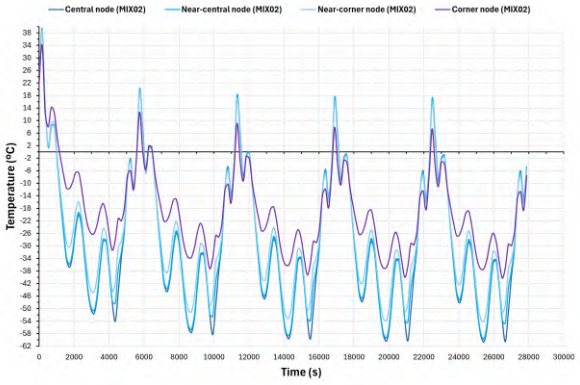


(d) Birch

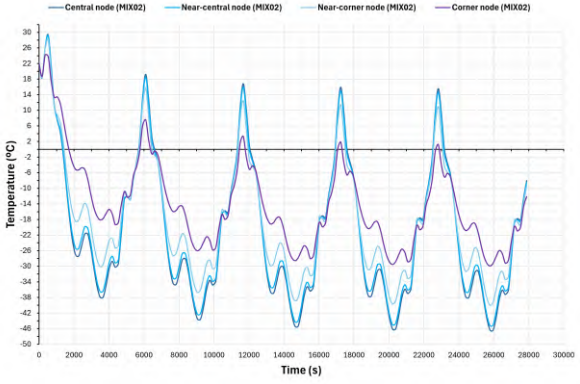
Figure 13: Mixed-material temperature profiles at 0.25°/s and no eclipse.



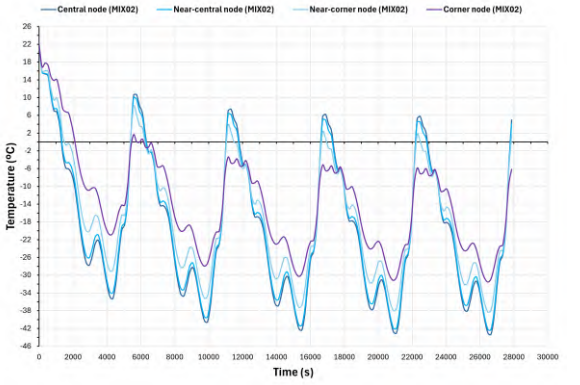
(a) Poplar



(b) Balsa



(c) Scots pine



(d) Birch

Figure 14: Mixed-material temperature profiles at 0.25°/s and longest eclipse.

6. CONCLUSIONS

This work defines a 3U CubeSat concept that can extend DLR bio-based material development from ground-based characterisation toward in-orbit testing. The mission uses an ISS-like orbit and an 8 to 12 month exposure period, with Scots pine, birch, balsa, and poplar as the main wood candidates. The selected payload focuses on two main measurements: visual monitoring and temperature. The four-camera deployable mirror concept provides full four-side coverage while keeping the cameras inside the CubeSat. The geometric study selected a 30 mm mirror and 40° deployment angle, and the engineering model confirmed that this geometry captures the complete sample height. The structural analyses remain below the material strengths used for the evaluated NRCSD load cases, with a first natural frequency of 888.7 Hz. The thermal analyses define the expected operating ranges and show clear material-dependent behaviour. Balsa gives the widest nominal temperature range, while the EOL sensitivity cases increase internal temperatures by about 3 to 4°C and exposed-wood temperatures by about 8 to 30°C.

The concept therefore provides a practical way to collect temperature and image data that can be compared with ground tests and thermal predictions during a long-duration LEO exposure. This is directly relevant to the Bio Strux objective of developing bio-based materials for satellite structures.

Future work should extend the numerical verification with thermo-elastic and solar-panel deployment analyses. A representative test campaign should then cover thermal cycling, outgassing, atomic oxygen, radiation, vibration, electrical behaviour, mechanical properties and deployment mechanisms. These tests can be used to qualify the final sensor attachments and mechanisms before moving from the current concept toward a flight demonstrator.

REFERENCES

1. European Space Agency. ESA Space Environment Report 2025. ESA Space Debris Office, 2025. Available online

2. National Aeronautics and Space Administration. State-of-the-Art of Small Spacecraft Technology, Chapter 6: Structures, Materials, and Mechanisms, 2026. Available online

3. European Parliament and Council. Regulation (EU) 2024/1252 establishing a framework for a secure and sustainable supply of critical raw materials, 2024. Available online

4. Guenther, R., Tajmar, M. & Bach, C. (2024). Wood and Wood-Based Materials in Space Applications - A Literature Review of Use Cases, Challenges and Potential. *Aerospace* 11(11), 910. Available online

5. Murata, K., Nakamura, M., Kariya, K. et al. (2024). Space exposure test of hardwood specimens in the International Space Station. *Journal of Wood Science* 70, 49. Available online

6. German Aerospace Center (DLR). Structures for Satellites and Exploration. Available online

7. German Aerospace Center (DLR). Big future for small satellites. *DLRmagazine* 178, 2025. Available online

8. Dauphin, T. (2024). Feasibility Analysis on the Use of Wood-Based Structures in Satellites. MSc thesis, University of Stuttgart. Available online

9. Sakraker-Özmen, I., Dauphin, T., Wolfgramm, L., et al. (2025). Feasibility Analysis, LCA and Demisability Tests of Wood-composites as Demisable and Eco-friendly Satellite Structures. Proc. 9th European Conference on Space Debris, Bonn, Germany. Available online

10. Russell, A., Peticolas, L., Lugaz, N. & Mehta, S. (2026). Lifetime modeling of one-unit to three-unit CubeSats. *Advances in Space Research* 77(4), 4885-4900. Available online

11. National Aeronautics and Space Administration. State-of-the-Art of Small Spacecraft Technology, Chapter 10: Integration, Launch, and Deployment, 2026. Available online

12. NanoRacks. NanoRacks CubeSat Deployer Interface Definition Document, NR-NRCSD-S0003 (2018). Available online

13. Castanié, B. et al. (2024). Wood and plywood as eco-materials for sustainable mobility: A review. *Composite Structures* 329, 117790. Available online

14. Thünen Institute. Results of the 2022 National Forest Inventory, 2024. Available online

15. European Space Agency. Natural fibres threaded into satellites for safer missions, 2020. Available online

16. National Aeronautics and Space Administration. NASA-HDBK-6024, Spacecraft Polymers Atomic Oxygen Durability Handbook, Change 2, 2022. Available online

17. National Aeronautics and Space Administration. NASA-STD-4005A, Low Earth Orbit Spacecraft Charging Design Standard, Change 1, 2021. Available online

18. WISA WoodSat. WISA WoodSat. Available online

19. Redwire. Redwire Successfully Delivers First Set of Orion Camera System to Lockheed Martin for Future NASA Artemis Missions, 2022. Available online

20. European Space Agency. Artemis II: solar wings, Orion blog, 2025. Available online

21. Carletta, S. et al. (2022). Characterization and Testing of the Passive Magnetic Attitude Control System for the 3U AstroBio CubeSat. *Aerospace* 9(11), 723. Available online
22. Norwegian Institute of Bioeconomy Research. Pine, 2024. Available online
23. Akter, S.T., Olsson, A. & Bader, T.K. (2025). Stiffness and Strength of Scots Pine Wood Under Compression Perpendicular to the Grain and Rolling Shear Loading. *Applied Sciences* 15(19), 10775. Available online
24. Pippin, G. & Finckenor, M.M. (2009). Contamination Examples and Lessons from Low Earth Orbit Experiments and Operational Hardware. Available online
25. National Aeronautics and Space Administration. State-of-the-Art of Small Spacecraft Technology, Chapter 7: Thermal Control, 2026. Available online
26. European Cooperation for Space Standardization. ECSS-E-HB-31-01 Part 6A, Thermal Design Handbook - Part 6: Thermal Control Surfaces, 2011. Available online

ECSSMET
Braunschweig Germany 2026

Deployable structures

Low-Cycle Fatigue Behaviour of a Deployable CFRP Lenticular Mast System for Small Satellite Applications

Mikhail Maximchuk [(1)], Martin E. Zander [(2)], Martin Hillebrandt [(2)], Marco Straubel [(2)]

[(1)] Ronda Ferrer de Canet 7, 08360 Canet de Mar, Spain, Email: mikemaximchuk@gmail.com
[(2)] Deutsches Zentrum für Luft- und Raumfahrt (DLR), Institute of Lightweight Systems, Lilienthalplatz 7, 38108 Braunschweig, Germany, Email: martin.zander@dlr.de

KEYWORDS

deployable composite boom, DCB, fatigue of composites, carbon fibre reinforced polymer

ABSTRACT

Deployable composite booms are seeing increasing interest as solar array wings, antenna supports, and drag sail structures on small satellites, where mass and stowage volume are at a premium. SpaceMast, a motorised collapsible tubular mast developed at DLR's Institute of Lightweight Systems, achieves this through a coilable CFRP lenticular cross-section that can be repeatedly deployed and retracted. Repeated coiling induces large strains and, as observed in demonstration models, can lead to premature fatigue failure after relatively few cycles, raising concerns for missions requiring reliable, repeated actuation.

This paper investigates the underlying fatigue damage mechanisms through coupon-level and full-scale deployment testing. The results point to a dominant failure mode: transverse cracking on the compression side, driven by localised strain concentrations from compressive buckling during coiling, and accelerated by manufacturing imperfections, friction, and boom tension. These findings inform recommendations for coupon test design and highlight the value of full-scale deployment testing for reliable fatigue characterisation.

1. INTRODUCTION

Deployment mechanisms are widely used in spacecraft design to fold oversized components for launch and unfold them once in orbit, from the deployable antennae and solar array wings of large missions such as ESA's Jupiter Icy Moons Explorer [1] to the smaller instruments, antennae, and drag sails used on individual CubeSats and constellations. The growing use of deployable structures on small satellites has created demand for reliable, affordable deployment mechanisms.

Within research done by NASA, its Deployable Composite Boom (DCB) project began with the Storable Tubular Extendible Member (STEM), a slit-overlapped circular tube developed for the antenna of Canada's Alouette 1 satellite, which flattens and coils onto a reel much like a self-straightening steel measuring tape [2, 3]. Later designs, such as the Triangular Rollable and Collapsible (TRAC) boom, adopted open Λ-, N-, or M-shaped cross-sections built from bonded circular arcs [4]. Both the STEM and TRAC families share open cross-sections, which suffer from low torsional stiffness. DLR addressed this with a closed lenticular cross-section, the Collapsible Tubular Mast (CTM) [5], which is the design underlying the SpaceMast project. The adoption of fibre-reinforced polymer composites, and CFRP in particular, in place of metals has since become the dominant trend in deployable boom design, owing to their favourable stiffness-to-weight ratio, low coefficient of thermal expansion, and the tailorability of ply sequence and orientation to further limit thermal distortion in orbit [6, 7]. Deployable boom research has grown rapidly in recent years, but has concentrated on mechanical behaviour such as buckling, vibration, creep, and thermal distortion for a small number of established cross-sections [6]; to the authors' knowledge, no fatigue characterisation of deployable booms has previously been published, likely reflecting the low cycle counts typical of space operations.

SpaceMast booms, a spin-off project and technology plattform of DLR's Institute of Lightweight Systems, are manufactured from a single ply of plain-weave CFRP, reducing mass relative to metallic alternatives while allowing tailoring of the laminate for thermoelastic stability. Motorised actuation gives these booms the ability to be deployed and stowed repeatedly and in a controlled manner, simplifying functional testing and enabling operational concepts such as retracting the boom in orbit to reduce the spacecraft's angular mass moment of inertia. However, the high strains induced in the boom during coiling mean that repeated deployment and stowage cycles can lead to fatigue damage of the CFRP material, and failures have already been observed in SpaceMast demonstration units after a comparatively small number of deployment cycles.

Due to the absence of prior fatigue research on deployable composite booms, expectations for their low-cycle fatigue (LCF) behaviour must be drawn from the broader composites' literature. LCF of composites, defined as cyclic loading at a peak stress high relative to the material's static failure stress and limited to fewer than approximately 10^4 cycles, produces a markedly steeper stress-life relationship than high-cycle fatigue, reflected in a bilinear or knee-shaped S-N curve with the transition typically located between 10^3 and 10^4 cycles [8]. Harik and Bogetti attribute much of this steepened degradation to non-cyclic damage accumulated within roughly the first 20 cycles, arising not from progressive crack growth but from pre-existing manufacturing and material imperfections (weak fibre-matrix interfaces, micro-voids, fibre waviness, and thermally induced micro-cracking) at which local fibre stresses exceed their strength once load approaches the failure stress [9]. Woven single-ply CFRP shells further complicate this picture: because the fibre tows in a plain-weave laminate behave as individual beams bending about their own neutral axes rather than as a homogeneous plate, surface strain measured on such shells underestimates true fibre strain, allowing single-ply woven flexures to sustain considerably higher bending strains than standard tension or compression coupon failure strains would suggest [10]. The compressive response of thin CFRP shells is additionally nonlinear, governed by fibre misalignment and matrix shear rather than simple elastic buckling, with very thin shells (below roughly 350 μm) tending to fail by tensile fibre fracture and thicker shells transitioning toward compressive micro-buckling and discrete damage events such as fibre blistering [11].

Buckling behaviour is of particular relevance to SpaceMast, since the boom must repeatedly coil onto a spool. DLR's own finite-element modelling of coiled lenticular boom sections shows that local buckles form on the compression side during coiling, each acting as a localised strain concentration and creating gaps between adjacent layers of the reeled boom [12]. Separately, DLR's assessment of the boom's manufacturing quality identified waviness in the flanges connecting the two halves of the lenticular cross-section, an imperfection expected to further lower the critical buckling load [13]. Taken together, this prior work motivates buckling-induced strain concentration, amplified by manufacturing imperfections, as a plausible driver of fatigue damage in the coiled boom - but because no fatigue testing of a lenticular cross-section composite boom has previously been performed, whether this mechanism actually governs failure under repeated cyclic deployment, and how it compares with material-level fatigue behaviour, remained unknown prior to this work.

This paper reports the results of an experimental campaign combining coupon-level material characterisation with full-scale cyclic deployment testing of the SpaceMast boom and derives design and testing recommendations from a comparison of the two datasets. Section 2 describes the two testing methodologies; Section 3 presents the results; Section 4 discusses the failure mechanism and the discrepancy between coupon and full-scale behaviour; and Section 5 concludes with recommendations for future work.

2. METHODOLOGY

2.1. Coupon Testing

Flat coupons of the single-ply plain-weave CFRP material were subjected to pure bending on a custom column-bending jig, adapted from the counter-weight balanced column bending fixture developed by Fernandez and Murphey [14] and later adopted by Meyer et al. [15] for compliant-mechanism flexure testing. As in the original design, the jig converts a vertical displacement applied by the testing machine into pure bending at the clamped coupon ends, while a load cell measures reaction force and a Digital Image Correlation (DIC) system captures surface strain and jig rotation.



Figure 1: Column-bending coupon testing jig used in this study, adapted from Fernandez and Murphey's design [14].

Because CAD files for the original jig in [14] are not publicly available, the jig used in this study was redesigned from scratch and manufactured by Fused Deposition Modelling (FDM) and by Stereolithography (SLA) 3D printing, following the same general fabrication approach as the original. Said jig can be seen in Figure 1. The initial coupon size matched that used by Fernandez and Murphey [14] (1.5 in × 2 in, giving a bendable length of 10 mm between clamps), but trial tests showed that this geometry could not reach the curvature needed to fracture the coupons even at the jig's maximum rotation - consistent with the original jig having been used to characterise large-deformation bending response rather than to deform specimens to failure. The bendable coupon length was therefore reduced to 3 mm, based on a breaking curvature estimated from a simple platen test. This shorter length caused the clamps to interfere with one another at large bend angles, requiring the clamp geometry to be modified by thinning the lower clamp profile to eliminate the interference. Static tests were performed to characterise the force-displacement and strain-rotation response up to failure; fatigue tests cyclically loaded coupons to 95%, 90%, and 80% of the static failure load to characterise stiffness degradation and crack initiation under repeated bending.

2.2. Deployment Testing

Full-scale cyclic deployment testing was performed using the SpaceMast mechanism itself, consisting of an enclosed spool driven by a motor that reels and unwinds the boom, deployed vertically to represent realistic operating conditions.

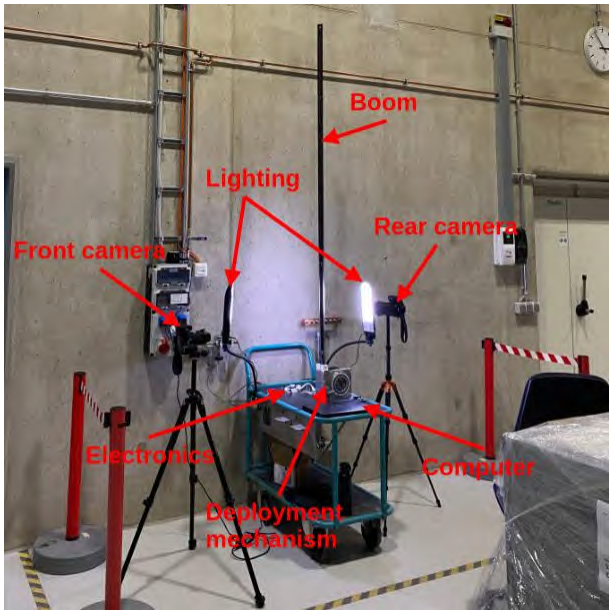


Figure 2: Full-scale deployment testing setup, showing the SpaceMast mechanism mounted for vertical cyclic deployment.

Since the mechanism did not natively support automatic direction switching, physical end-stops were added: a tab on the boom tip actuates a switch at full retraction, and a string-actuated switch triggers at full extension, avoiding the drift that a timer-based switching scheme would introduce over many cycles. Because the region of the boom most likely to fail - inside the coiled spool - is enclosed by an opaque casing, DIC and strain gauges could not be used to monitor strain directly. Instrumentation was therefore limited to two cameras recording both faces of the deployed boom to visually track the appearance of damage, and continuous logging of motor current, voltage, and state by the mechanism's Arduino controller, providing an indirect measure of mechanical resistance and cycle count. The boom was manually inspected for new damage at fixed cycle intervals throughout each test.

Three booms were tested under these conditions. Boom 1 served as the baseline test. Boom 2

experienced an unplanned failure of the retraction end-stop partway through testing, which allowed the boom to over-retract; the resulting tension, transmitted through the electronic harness and the coiled boom onto the spool, produced a substantial increase in compressive tensioning of the coil. Boom 3 was manufactured using a modified process resulting in a rougher inner surface compared with the smoother, matte surface of Booms 1 and 2. Because tensioning of the coiled boom against itself is controlled by the mechanism's disk brake and, in Boom 2's case, was further altered by the end-stop failure, the three tests together provide a basis for comparing damage accumulation and current draw across different tensioning conditions.

3. RESULTS

3.1. Coupon Testing

As shown in Fugure 3, static bending tests showed the compressive softening effect, with compressive surface strain reaching approximately 5-6% at failure, notably higher than the roughly 3% failure strain on the tension side. Additionally, the bending modulus could be computed using a kinematic model of the jig. This had an initial rise to 15 GPa before decreasing steadily with increasing deflection - well below the 48 GPa axial elastic modulus obtained from tensile coupon testing.

Fatigue coupon tests at 95%, 90%, and 80% of the static failure load produced unexpectedly long lives: most coupons did not reach complete fracture even after several thousand cycles, with only two of the eighteen tested specimens failing at all, - one after 439 cycles and another after 141 cycles. Partial edge damage was observed in many coupons but could not be reliably related to applied load level, and was attributed largely to non-uniform clamping rather than representative material fatigue behaviour.

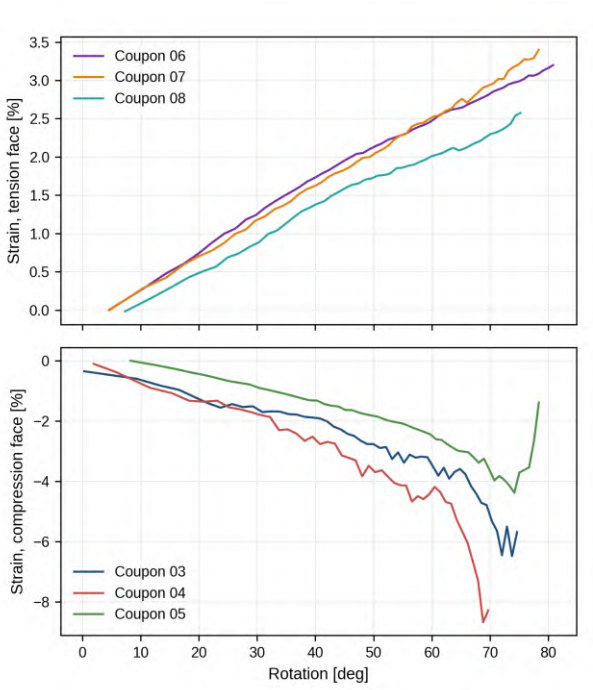


Figure 3: Coupon-level strain-rotation response in pure bending, showing tension-face strain (top) and compression-face strain (bottom) for three coupons per condition, used to characterise material behaviour.

3.2. Deployment Testing

All three booms failed exclusively by transverse fracture on the compression side of the boom, typically at the boundary between transverse strands where longitudinal strands cross over. The number of cycles to first observable damage differed sharply across the three tests and was closely tied to boom tensioning.

Figure 4 shows the motor current trends for the three tested booms, separated by deployment and retraction modes. Damage count was tracked only for the booms 2 and 3, with data shown in Figure 5. Boom 1 accumulated resistance gradually, with increasing motor current draw over roughly twelve hours of testing (approximately 90 cycles) before the test was terminated by repeated over-current stops. Boom 2, following the end-stop failure and associated over-tensioning at cycle 40, showed an abrupt surge of new damage: thirteen new transverse fractures were counted immediately after the failure, followed by eighteen more over the next ten cycles, after which no further damage appeared up to cycle 80 - indicating a finite, geometry-limited number of damage sites that saturates once populated. Boom 3, tensioned nominally throughout, began accumulating damage from the first ten cycles, peaked at twenty cycles, and ceased entirely by sixty cycles, over a test extended to 100 cycles. An example of the damage is shown in

Figure 6, where a transverse crack is underlined with a white marker.

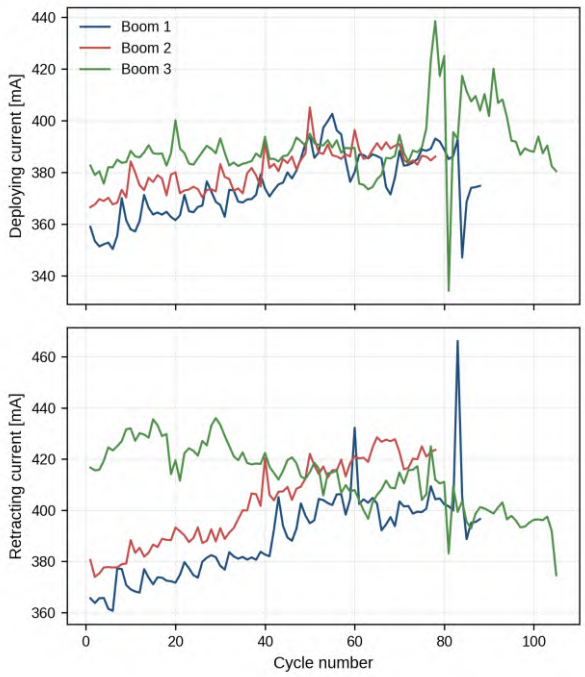


Figure 4: Mean deployment and retraction motor current per cycle for Booms 1-3, showing the differing friction trends associated with manufacturing surface finish and mechanical resistance.

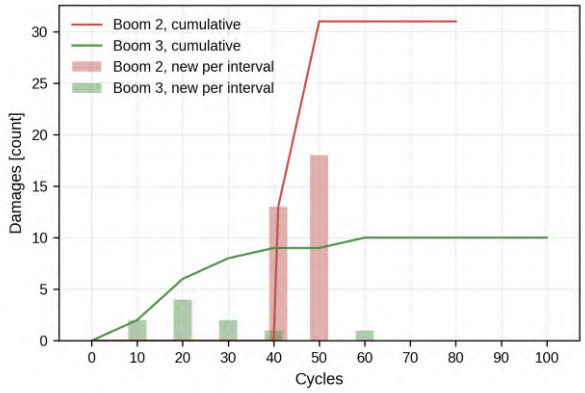


Figure 5: Damage accumulation per cycle interval for Booms 2-3, showing the saturating damage count and the effect of the Boom 2 tensioning event.

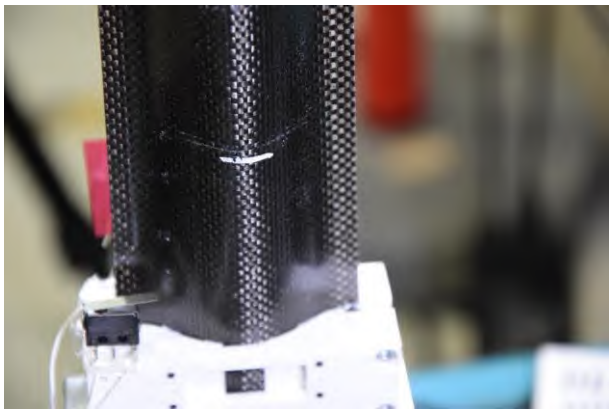


Figure 6: Representative transverse fracture damage observed on the compression side of the boom after cyclic deployment testing.

Motor current trends also diverged between booms. Booms 1 and 2 showed a general increase in both deployment and retraction current over the course of testing, consistent with growing mechanical resistance from crack accumulation, loose manufacturing residue collecting at the mechanism hub, and gearbox wear (confirmed by powder accumulation observed inside the gearbox at the end of testing). Boom 3, by contrast, showed a decreasing retraction current trend, attributed to its rougher as-manufactured inner surface being progressively abraded smooth by repeated cycling - an effect that outweighed any resistance increase from crack accumulation over the tested range.

4. DISCUSSION

The deployment tests point to a single, geometry-governed failure mechanism: fatigue damage on the SpaceMast boom occurs as transverse fractures on the compression side, at locations that plausibly coincide with the local buckles that form when the lenticular cross-section is coiled onto the spool. The saturation of new damage after a fixed number of sites are populated, most clearly seen in Boom 2, where damage stopped appearing entirely once thirty-one fractures had accumulated across two 10-cycle intervals, supports the interpretation that the number and spacing of buckle-induced high-strain sites is fixed by boom geometry rather than by continued cycling.

Boom tensioning, controlled by the disk brake that prevents the coiled boom from unrolling under its own elasticity, is the dominant driver of damage rate and extent. The unplanned over-tensioning of Boom 2 produced immediate, extensive damage that would otherwise have accumulated far more gradually, directly demonstrating that the compressive pressure the coiled layers exert on one another, rather than cycle count alone, governs how quickly the fixed set of damage sites is populated. This is consistent with the eventual cessation of new damage in all three tests: once tensioning-driven local strain has activated every available site,

further cycling under the same tensioning condition produces no additional first-time damage, though it may still contribute to wear-related effects such as the rising motor current in Booms 1 and 2.

The manufacturing-related divergence in motor current trend between Boom 3 and the first two booms further indicates that surface finish and residual manufacturing debris measurably affect mechanical resistance independent of fatigue damage, and should be controlled for in future comparative testing.

A central finding of this study is the substantial discrepancy between coupon-level and full-scale fatigue behaviour. Coupon specimens subjected to pure bending survived, in most cases, several thousand cycles, whereas the full-scale boom showed extensive damage within roughly fifty cycles, - two to three orders of magnitude sooner. This discrepancy is attributed to the loading condition applied at coupon level: pure bending does not reproduce the complex, biaxial strain state generated by local buckling and by the compressive pressure the coiled boom exerts on itself inside the mechanism. Because the exact strain state at the buckle, and specifically whether cracking initiates at the buckle peak or valley, remains unknown, and finite-element simulations do not yet account for coil-on-spool pressure, coupon-level pure-bending tests cannot presently be used to predict the fatigue life of the SpaceMast boom or, by extension, similar DCB designs. Full-scale or representative-loading testing is therefore necessary until a coupon-level loading condition that reproduces the governing strain state can be identified.

5. CONCLUSION & RECOMMENDATIONS

This study investigated the low-cycle fatigue behaviour of the SpaceMast deployable composite boom through coupon-level pure-bending tests and full-scale cyclic deployment tests of three boom units. The results show that fatigue failure in the full-scale boom occurs exclusively as transverse fracture on the compression side, at a fixed number of locations plausibly linked to coiling-induced local buckling, and that the rate and extent of damage accumulation are strongly governed by the tensioning applied by the deployment mechanism's disk brake. Coupon-level pure-bending tests, by contrast, do not reproduce this failure mode or timescale and cannot presently be used to predict full-scale fatigue life, indicating that the strain state driving failure is dominated by buckling and coil-on-coil pressure rather than simple bending.

Two categories of recommendations follow from these findings.

Design recommendations for the SpaceMast mechanism and similar DCB deployment systems: (i) disk brake pressure should be reduced to the minimum level needed to retain the boom in its stowed state, since excess tensioning directly accelerates damage formation; and (ii) end-stops should be permanently integrated into the mechanism, both for improved fatigue performance predictability and because timer-based direction switching is prone to drift and consequent mechanical damage over extended cyclic operation.

Research-methodology recommendations for future fatigue characterisation of DCBs: (i) full-scale or otherwise representative-loading deployment testing should be prioritised over coupon-level pure-bending characterisation as the primary means of establishing fatigue life, since it requires no assumptions about the governing loading condition and is comparatively inexpensive to perform; and (ii) if coupon-level testing is retained for material property characterisation, the clamping method should be revised, for example by bonding coupons to expendable end blocks rather than relying on thin, deformable clamp lips, and DIC strain measurement accuracy improved through reduced lens aperture, before coupon data is used to inform fatigue predictions.

6. ACKNOWLEDGEMENTS

The authors thank the colleagues at DLR's Institute of Lightweight Systems who supported the testing campaign, and the thesis committee at Delft University of Technology for their guidance throughout this research.
This research was funded by the German Aerospace Center (DLR) through the Executive Board department “Innovation, Transfer and Research Infrastructure” and by the German Federal Ministry for Economic Affairs and Energy (BMWE) through the EXIST Transfer of Research programme.

7. REFERENCES

1. European Space Agency (2014). *JUICE (JUpiter ICy moons Explorer): Exploring the Emergence of Habitable Worlds around Gas Giants – Definition Study Report*. ESA, Noordwijk, The Netherlands.
2. Rimrott, F.P.J. & Fritzsche, G. (2000). Fundamentals of STEM Mechanics. In: Gladwell, G.M.L., Pellegrino, S. & Guest, S.D. (Eds.), *IUTAM-IASS Symposium on Deployable Structures: Theory and Applications*, Vol. 80, Springer Netherlands, Dordrecht, pp. 321–333.
3. Fortier, R. (2022). Alouette, gentille alouette, Alouette, je te lancerai; Or, How the Cold War propelled Canada into space via the Alouette satellite, part 1. *Ingenium – Canada's Museums of Science and Innovation*.
4. Murphey, T.W. & Banik, J. (2011). *Triangular Rollable and Collapsible Boom*. US Patent 7,895,795 B1, United States of America as represented by the Secretary of the Air Force,

Washington, DC.
5. Herbeck, L., Eiden, M., Leipold, M., Sickinger, C. & Unckenbold, W. (2000). Development and Test of Deployable Ultra-Lightweight CFRP-Booms for a Solar Sail. In *Proc. European Conference on Spacecraft Structures, Materials and Mechanical Testing*, European Space Agency, Noordwijk, The Netherlands.
6. Liu, T.-W., Bai, J.-B., Fantuzzi, N. & Zhang, X. (2024). Thin-walled deployable composite structures: A review. *Prog. Aerosp. Sci.* 146, 100985.
7. Straubel, M., Block, J., Sinapius, M. & Hühne, C. (2011). Deployable Composite Booms for Various Gossamer Space Structures. *52nd AIAA/ASME/ASCE/AHS/ASC Structures, Structural Dynamics and Materials Conference*, American Institute of Aeronautics and Astronautics, Denver, Colorado.
8. Harik, V.M. (2002). Low-cycle fatigue of unidirectional composites: Bi-linear S-N curves. *Int. J. Fatigue* 24(2-4), 455–462.
9. Harik, V.M. & Bogetti, T.A. (2003). Low Cycle Fatigue of Composite Laminates: A Damage-mode-sensitive Model. *J. Compos. Mater.* 37(7), 597–610.
10. Yee, J. & Pellegrino, S. (2005). Folding of woven composite structures. *Compos. Part A Appl. Sci. Manuf.* 36(2), 273–278.
11. Schlothauer, A., Pappas, G.A. & Ermanni, P. (2020). Material response and failure of highly deformable carbon fiber composite shells. *Compos. Sci. Technol.* 199, 108378.
12. Meyer, S. & Hillebrandt, M. (2018). Preliminary Study of the Local Buckling Behavior of DLR's CFRP Booms Induced by the Stowing Process. *Proceedings of the European Conference on Spacecraft Structures, Materials and Environmental Testing (ECSSMET)*, Noordwijk, The Netherlands.
13. Zander, M.E. (2020). *Robustness Assessment of Deployable Gossamer Structural Space Systems*. Doctoral Dissertation, Carolo-Wilhelmina Technical University, Braunschweig.
14. Fernandez, J.M. & Murphey, T.W. (2018). A Simple Test Method for Large Deformation Bending of Thin High Strain Composite Flexures. *2018 AIAA Spacecraft Structures Conference*, American Institute of Aeronautics and Astronautics, Kissimmee, Florida.
15. Meyer, P., Finder, J. & Hühne, C. (2023). Test Methods for the Mechanical Characterization of Flexure Hinges. *Exp. Mech.* 63(7), 1203–1222.

Application of Metamaterials for Vibration Attenuation in Space Structures: A Case Study on a Simplified Large Deployable Reflector Ring

Gregorio Giannini[(1)], Vittoria Malaman[(1)], Emanuele Riva[(1)], Marco Lapi[(2)], Mario Lanuti[(2)], Francesco Braghin[(1)]

[(1)] Department of Mechanical Engineering, Politecnico di Milano, Via privata Giuseppe La Masa 1, Milano, 20156, Italy, Email: gregorio.giannini@polimi.it
[(2)] Thales Alenia Space Italia, Via Saccomuro 24, Roma, 00131, Italy, Email: Marco.Lapi@thalesaleniaspace.com

KEYWORDS

mechanical metamaterials; locally resonant structures; vibration attenuation; deployable space structures; bandgaps; large deployable reflectors.

ABSTRACT

This paper investigates vibration attenuation for in-plane vibrations of the annular support ring (Secondary Holddown and Release Mechanism - SHRM) of the Large Deployable Reflector (LDR) developed by Thales Alenia Space. The paper combines dispersion and frequency response analyses to characterize the generation of a bandgap, i.e. a frequency region where waves are attenuated. The role of curvature is critically discussed, and the limitation of linear metamaterials is highlighted. This work sheds light on the dynamics of curved metastructures in the context of vibration attenuation.

1. INTRODUCTION

The continuous demand for increased payload capacity and reduced launch costs is driving the development of increasingly lightweight spacecraft structures. This trend is particularly evident for large deployable components, such as reflector antennas, solar arrays and instrument-supporting panels, whose dimensions must be maximized while satisfying stringent mass and stowed-volume requirements. However, the reduction of structural mass and stiffness generally results in low natural frequencies and increased sensitivity to dynamic loading. During launch, spacecraft are exposed to a combination of broadband acoustic excitation, random and sinusoidal vibrations and transient mechanical loads, which may induce significant dynamic amplification and represent a critical design condition for large deployable reflectors [1] as well as other space systems and sub-systems.

Traditional vibration-mitigation strategies are commonly based on structural stiffening, additional damping treatments or tuned vibration absorbers. Although effective, these solutions may introduce a considerable mass penalty or require substantial modifications to the primary structure. These drawbacks are especially relevant in space applications, where the available mass budget is limited and any added component must comply with demanding integration and qualification requirements. Consequently, major research effort has recently been devoted to lightweight periodic devices for passive vibration attenuation.

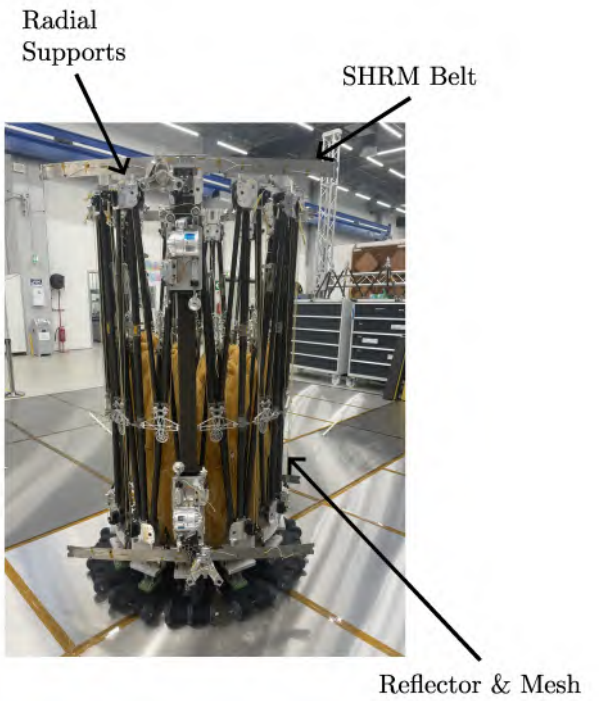


Figure 1: Image of the LDR in the stowed configuration, with the SHRM belts yet to be closed on the radial supports.

Phononic crystals and mechanical metamaterials provide a promising framework for controlling elastic-wave propagation [2]. This new family of materials allows to inhibit wave propagation within selected frequency intervals, generally referred to as bandgaps. In classical phononic crystals, bandgaps are predominantly generated by Bragg scattering mechanism and therefore occur when the structural pe-

riodicity is comparable with the wavelength. This condition generally requires large unit cells when low-frequency vibrations are targeted, limiting the applicability of Bragg-based solutions to compact aerospace structures.

Locally resonant metamaterials overcome this limitation by embedding resonant substructures whose characteristic dimensions are substantially smaller than the wavelength. The interaction between the host structure and the local resonators generates an effective dynamic inertia and can produce attenuation bands in the vicinity of the resonator natural frequency. This mechanism has been investigated extensively for rods, beams and plates, demonstrating that periodically distributed resonators can suppress flexural and longitudinal wave propagation and reduce the vibration response of finite structures [3, 4]. Furthermore, the resonance suppression observed in the finite metastructure is related to the dispersion diagram of the corresponding infinite medium [5, 6].

Despite these advantages, low-frequency locally resonant metamaterials remain subject to important practical limitations. For a prescribed tuning frequency, the attainable bandgap width is strongly influenced by the ratio between the resonator mass and the mass of the host structure [5]. Therefore, obtaining a broad attenuation region at very low frequencies may require large additional masses, which is undesirable for spacecraft applications.

Electromechanical resonators exploiting piezoelectric patches, and hybrid mechanical–electromechanical concepts have been proposed to increase tunability and broaden the attenuation bandwidth without relying exclusively on added mechanical mass [7]. Recent investigations have also demonstrated the potential of vibroacoustic metamaterials for representative launcher and satellite components, highlighting their compatibility with lightweight structural design [8, 9].

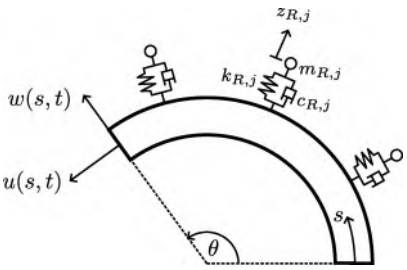
Nevertheless, most analytical studies of locally resonant metastructures focus on straight beams, rods, or flat plates [10–12]. Application of these concepts to curved members is nontrivial because curvature couples deformation mechanisms that are uncoupled in the corresponding straight geometry. Previous studies have addressed locally resonant curved panels and actively controlled curved beams and rings [13, 14]. However, the role of wave polarization in passive locally resonant closed rings, and its relation to the attenuation achieved in the corresponding finite structure, remains insufficiently understood. For the in-plane motion of an annular beam, radial bending and circumferential extension are intrinsically coupled, and the polarization of the propagating branches varies with frequency. Consequently, resonators acting only in the radial direction may attenuate bending-dominated waves while leaving a circumferentially polarized propagation channel unaffected.

This work investigates locally resonant vibration attenuation in the annular support ring of the large deployable reflector reported in Fig. 1. The figure shows the reflector in the stowed configuration and the Secondary Holddown and Release Mechanism (SHRM) in the open configuration. The radial supports hosting the SHRM before deployment of the Large Deployable Reflector (LDR) are also visible. The ring is modeled as an extensible curved beam, and two resonator layouts are compared under the same total added-mass constraint: a radial-only configuration and a configuration containing both radial and circumferential resonators. A complex-wavenumber analysis of the homogenized periodic medium is used to identify propagating and evanescent branches and to compute their polarization. The response of the corresponding finite ring is then evaluated using an assumed-modes formulation and validated against finite-element simulations. The results are compared with those of an equivalent straight beam to isolate the effects of curvature-induced coupling and stiffness. Finally, a realizable flexural resonator is implemented in a detailed finite-element model. The study therefore links dispersion, wave polarization, and finite-structure attenuation, while assessing the extent to which locally resonant concepts developed for straight members retain their effectiveness in annular structures.

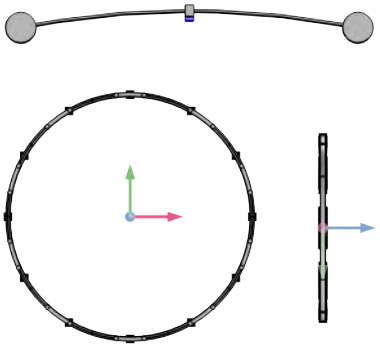
1.1. Analytical model of the system

The analysis starts with the analytical model of the system, limited to in-plane vibrations, thereby including radial and tangential vibrations of the ring, as shown in Fig. 2a. Wave propagation and in-plane vibrations of thin ring are well documented subjects [15–17], hence the governing equations can be easily written (Eq. 1). Here $w = w(s,t)$ and $u = u(s,t)$ denote the radial and circumferential displacements, respectively, as functions of the position along the arclength and of time. $(\cdot)^{(i)}$ indicates the *i–th* derivative with respect to s, while $\dot{(\cdot)}$ indicates derivative with respect to time.

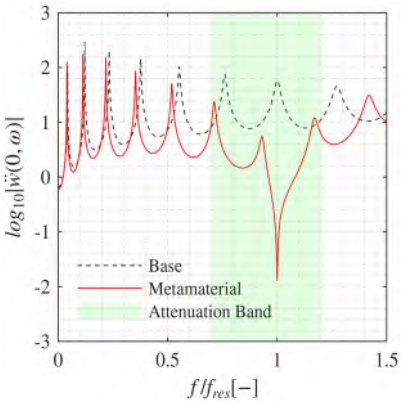
$$\begin{cases} \dfrac{EI}{R}\left(u^{(3)} - Rw^{(4)}\right) - \dfrac{EA}{R}\left(\dfrac{w}{R} + u^{(1)}\right) = \rho A\ddot{w} & \text{(1a)} \\ \dfrac{EI}{R}\left(\dfrac{u^{(2)}}{R} - w^{(3)}\right) + \dfrac{EA}{R}\left(w^{(1)} + Ru^{(2)}\right) = \rho A\ddot{u} & \text{(1b)} \end{cases}$$



(a) Schematic of the extensible thin-ring model with periodically distributed local resonators. The radial and circumferential displacements of the ring are denoted by $w(s,t)$ and $u(s,t)$, respectively, while $z_{R,j}$ represents the relative displacement of the j-th radial resonator located at $s = s_j$.



(b) Final design of the single resonator (top), front view of the metamaterial ring (bottom left) side view of the metamaterial ring (bottom right).



(c) Comparison between the frequency response function of a base structure (black dashed line), and the one of a metastructure (red solid line). The attenuation band is highlighted in green. Results are reported in terms of normalized frequency f/f_{res}.

Figure 2: Overview of the analysis and design workflow for metamaterials in annular structures:

The curved beam has radius $R = 0.3761$ m, height $h = 12$ mm, depth $b = 20$ mm, elastic modulus $E = 70$ GPa and density $\rho = 2700\,\mathrm{kg/m^3}$. Being the section of the beam rectangular, the value of the area moment of inertia can be computed as $I = bh^3/12$. The correspondence between the mode shapes of the analytical model and those of the SHRM was assessed through the modal assurance criterion applied to the mode shapes obtained from the finite element models of the systems; however, a detailed analysis is beyond the scope of the present work.

Since the aim of the current study is to assess the influence of discrete resonators, their contribution can be added to Eq. 1, yielding Eq. 2.

$$\begin{cases} \frac{EI}{R}\left(u^{(3)} - Rw^{(4)}\right) - \frac{EA}{R}\left(\frac{w}{R} + u^{(1)}\right) + \\ \quad + \sum_j k_{Rj} z_{Rj} \delta(s - s_j) = \rho A \ddot{w} \end{cases} \tag{2a}$$

$$\begin{cases} \frac{EI}{R}\left(\frac{u^{(2)}}{R} - w^{(3)}\right) + \frac{EA}{R}\left(w^{(1)} + Ru^{(2)}\right) + \\ \quad + \sum_j k_{Aj} z_{Aj} \delta(s - s_j) = \rho A \ddot{u} \end{cases} \tag{2b}$$

$$m_{Rj}\ddot{z}_{Rj} + k_{Rj} z_{Rj} + m_{Rj}\ddot{w}(s_j, t) = 0 \tag{2c}$$

$$m_{Aj}\ddot{z}_{Aj} + k_{Aj} z_{Aj} + m_{Aj}\ddot{u}(s_j, t) = 0 \tag{2d}$$

In Eq. 2, the subscripts R and A refer respectively to radial and axial resonators, the symbol z describes the relative displacement of resonators, δ is Dirac delta function, and s_j is the arclength coordinate of the $j-th$ attachment. Moreover, damping is neglected for dispersion analysis, while a lightly damped structure is considered in the analysis of the finite system (Sec. 3).

The governing equations are solved to study the underlying dynamics. In the present work, two cases will be studied: a first case in which the resonators are purely radial, and a second case in which resonators can act both in radial and circumferential (also referred to as axial) direction.

2. INFINITE STRUCTURE

2.1.Dispersion relation computation

The dispersion relation can be computed starting from a unit cell by imposing a wave solution and assuming long-wavelength conditions. A comparison of the two cases with the equivalent beam-like case is provided. Note that the study has been conducted at constant added mass ratio $\mu = 0.1$ and at constant unit cell length $a_{UC} = \frac{2\pi R}{N_{res}}$, where $N_{res} = 20$.

Starting from Eq. 2, the governing equations for the unit cell can be found considering a single radial resonator, while the stiffness is considered distributed into the entire domain, since the wavelength is larger than spatial periodicity. This yields Eq. 3 if the first case is considered.

$$\begin{cases} \frac{EI}{R}\left(u^{(3)} - Rw^{(4)}\right) - \frac{EA}{R}\left(\frac{w}{R} + u^{(1)}\right) + & \text{(3a)} \\ + \frac{k_R}{a_{UC}} z_R = \rho A \ddot{w} & \\ \frac{EI}{R}\left(\frac{u^{(2)}}{R} - w^{(3)}\right) + \frac{EA}{R}\left(w^{(1)} + Ru^{(2)}\right) = & \text{(3b)} \\ = \rho A \ddot{u} & \\ m_R \ddot{z}_R + k_R z_R + m_R \ddot{w}(s_R, t) = 0 & \text{(3c)} \end{cases}$$

The *ansatz* is reported in Eq. 4, and can be substituted into Eq. 3, yielding Eq. 5.

$$\begin{aligned} w(s,t) &= \hat{w}_0 e^{i(\kappa s - \omega t)}, \\ u(s,t) &= \hat{u}_0 e^{i(\kappa s - \omega t)}, \\ z_R(t) &= \hat{z}_0 e^{-i\omega t} \end{aligned} \tag{4}$$

$$\begin{cases} \frac{EI}{R}\left(-i\kappa^3 \hat{u}_0 - R\kappa^4 \hat{w}_0\right) - \frac{EA}{R}\left(\frac{\hat{w}_0}{R} + i\kappa \hat{u}_0\right) + & \text{(5a)} \\ + \frac{k_R}{a_{UC}} \hat{z}_0 + \omega^2 \rho A \hat{w}_0 = 0 & \\ \frac{EI}{R}\left(-\frac{\kappa^2}{R} \hat{u}_0 + i\kappa^3 \hat{w}_0\right) + & \text{(5b)} \\ + \frac{EA}{R}\left(i\kappa \hat{w}_0 - R\kappa^2 \hat{u}_0\right) + \omega^2 \rho A \hat{u}_0 = 0 & \\ -m_R \omega^2 \hat{z}_0 + k_R \hat{z}_0 - \omega^2 m_R \hat{w}_0 = 0 & \text{(5c)} \end{cases}$$

Notice that Eq. 5 can be written as the polynomial eigenvalue problem in Eq. 6 by defining the matrix $\mathbf{P}(\kappa, \omega) = \mathbf{A_0}(\omega) + \kappa \mathbf{A_1} + \kappa^2 \mathbf{A_2} + \kappa^3 \mathbf{A_3} + \kappa^4 \mathbf{A_4}$.

$$\mathbf{P}(\kappa, \omega)\nu = \mathbf{0}, \text{ where } \nu = [\hat{w}_0, \hat{u}_0, \hat{z}_0]^T \tag{6}$$

By prescribing the frequency ω the polynomial eigenvalue problem can be solved for the eigenvalues κ and eigenvectors ν. This is referred to as inverse problem and yields complex eigenvalues $\kappa(\omega)$.

Solutions characterized by $\Im[\kappa] = 0$ are propagating modes, whereas branches with $\Im[\kappa] \neq 0$ are representative of spatially attenuated waves. Generally, an attenuating solution may have both nonzero real and imaginary part.

Conversely, the direct dispersion problem is solved by prescribing a real wavenumber κ and solving for the corresponding frequencies ω and eigenvectors. This formulation provides a more immediate representation of the dispersion branches and facilitates the identification of complete bandgaps. When no complete band gap is present, the eigenvectors can be used to identify frequency intervals in which radial or circumferential waves are selectively suppressed.

The relative amplitude of each eigenvector can be used to infer the polarization of the corresponding branch. For the *j–th* eigenvector, the radial displacement polarization factor can be computed as:

$$p_{radial} = \frac{|\hat{w}_{0j}|^2}{|\hat{w}_{0j}|^2 + |\hat{u}_{0j}|^2} \tag{7}$$

A polarization factor equal to 1 is representative of a radially dominated motion, while a polarization factor close to 0 means that axial motion is predominant.

2.2.Results

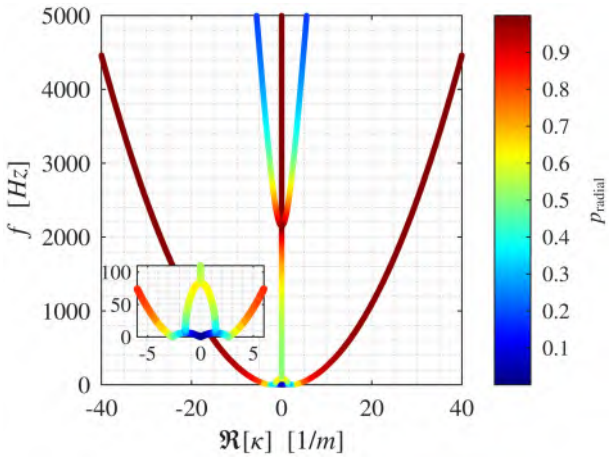
The dispersion relation of the bare ring is shown in Fig. 3. Each forward-propagating wave with positive wavenumber ($+\kappa$) is paired with a backward-propagating wave with opposite wavenumber ($-\kappa$). Depending on the frequency, either one or two pairs of propagating waves exist.

Consistently with [17], three frequency regions can be identified. For our choice of parameters, below approximately 7 Hz, the propagating waves exhibit a predominantly axial polarization. Between 7 Hz and 2150 Hz, only the flexural branch supports propagation, whereas the axial-dominated solutions are evanescent. Above 2150 Hz, an additional pair of axial-dominated propagating waves appears.

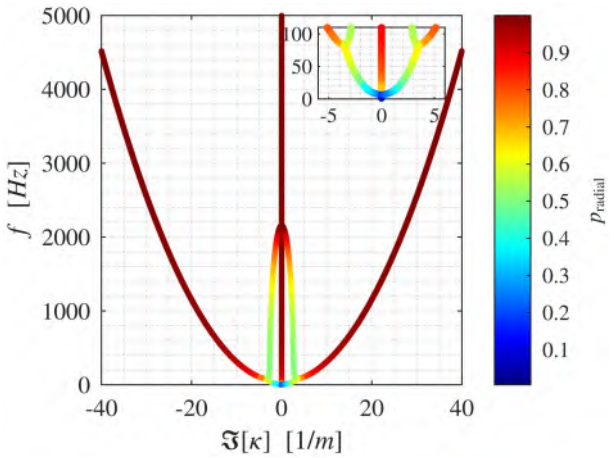
This frequency-dependent polarization is a consequence of the coupling between axial and radial motion introduced by the curvature of the ring.

By targeting bending-dominated branches, resonators can be employed to alter the dispersion diagram, creating a frequency range in which the corresponding wave becomes evanescent. In terms of the polynomial eigenvalue problem in Eq. 6, a bandgap is identified as a frequency interval in which no purely real wavenumber solutions exist for the bending-dominated branches.

Fig. 4 shows a comparison of the computed dispersion relations for the equivalent straight beam and the two cases. Notice that only the propagating branches, i.e. those with $\Im[\kappa] = 0$ have been reported for the sake of clarity. Fig. 4 shows that no bandgap is created in the first case. However, a frequency range in which only axial waves can propagate exists. We observe that: below the resonator tuning frequency, the relation is mostly unaffected by the resonators; at the target frequency, a propagative axial branch is found, while the branch supporting bending displacement becomes complex (i.e. both $\Re[\kappa] \neq 0$ and $\Im[\kappa] \neq 0$) as shown in Fig. 5; at higher frequency, the propagative axial branch supports flexural waves. On the other hand, the second case shows the nucleation of a bandgap, where



(a) Real part.



(b) Imaginary part.

Figure 3: Complex dispersion relation of the bare ring represented in the $(\Re[\kappa], \Im[\kappa], f)$ space. The color scale indicates the radial polarization factor p_{radial}.

wave propagation is prohibited for both polarizations, as shown in the rightmost column of Fig. 4.

The bandwidth of the spectral gap is also a key performance metric, and can be directly evaluated from the dispersion relation. The resulting bandgap widths are summarized in Tab. 1. Since the first case does not exhibit a well-defined bandgap, its upper bound was defined as the frequency at which the bending and axial components contribute equally to the wave polarization, corresponding to ($p_{radial} = 0.5$). Above this threshold, the branches become predominantly bending-dominated.

Finally, the relative bandwidth can be computed as $\delta f = \Delta f / f_{res}$. Its value is constant and related to the added mass ratio μ. For the straight beam computation of the aforementioned indicator yields $\delta_f = 0.05$, consistently with [5], where $\delta f = \sqrt{1+\mu} - 1 = 0.0488$. On the other hand, for the ring structure,

Table 1: Summary of bandgap widths Δf for the equivalent beam and the two cases. In parentheses the natural frequency f_n, which is also the resonator tuning frequency f_{res} is reported for each mode.

Mode	Beam	Case 1	Case 2
–	Δf (f_n) [Hz]	Δf (f_n) [Hz]	Δf (f_n) [Hz]
4	14.6 (279)	12.2 (467)	11.6 (467)
3	7.6 (150.1)	8.4 (289)	7.7 (289)
2	3.0 (60.8)	3.9 (150.5)	3.8 (150.5)
1	0.6 (11.3)	1.4 (53.2)	1.3 (53.2)

$\delta_f \approx 0.025$, suggesting that bandgaps span a much lower frequency range in the curved case. Another consequence of δf being constant is the fact that, for a given mass ratio, targeting lower frequencies leads to lower absolute bandgap width, confirmed by Tab. 1.

To check whether the bandgap leads to any major improvement in vibration attenuation of the structure, the finite structure has been analyzed as detailed in Sec. 3.

3. FINITE STRUCTURE

To investigate the effect of resonators on the finite structure, the Frequency Response Function (FRF) is computed with two different methods: Assumed Modes Method (AMM), and Finite Element Method (FEM). The former is discussed in detail within Sec. 3.1, while the latter has been implemented in COMSOL Multiphysics, where resonators are modeled as lumped mechanical systems, while the ring is modeled as a linear elastic aluminum solid.

The ring is forced by a radial point force on one side, and the response is measured in terms of acceleration of the opposite side ($\ddot{w}(0,\omega)$).

3.1.FRF via assumed modes method

In the AMM, radial and tangential displacements are written as a sum of comparison functions:

$$\begin{aligned} w(s,t) &= \sum_{m=-M}^{M} \eta_m(t)\phi_m(s), \\ u(s,t) &= \sum_{m=-M}^{M} \xi_m(t)\phi_m(s) \end{aligned} \tag{8}$$

The functions $\phi_m(s), m = -M, ..., M$ must be compliant with boundary conditions. These, in case of a free closed ring, require 2π-periodic displacements in θ (Eq. 9), allowing to choose the exponential functions reported in Eq. 10.

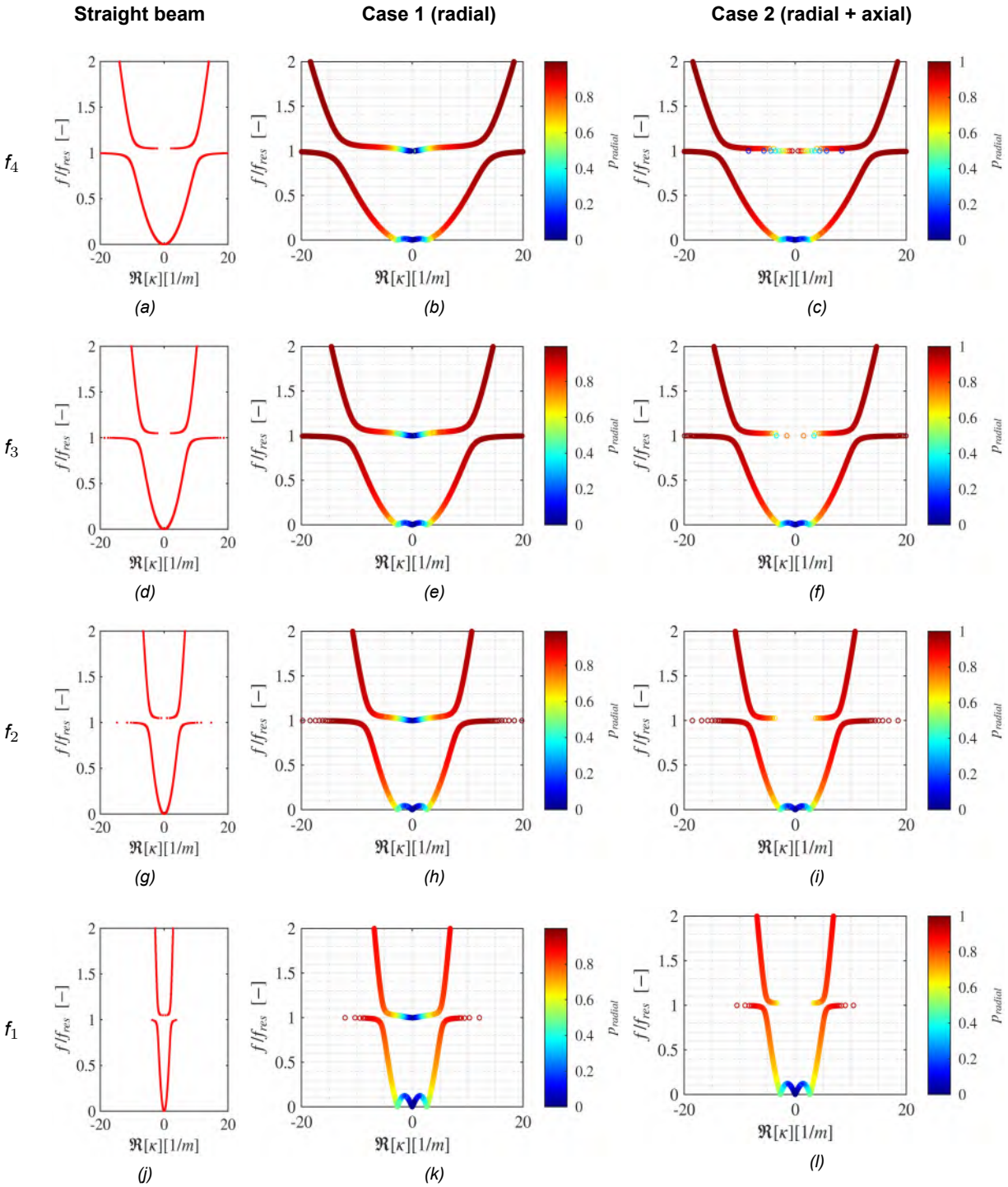
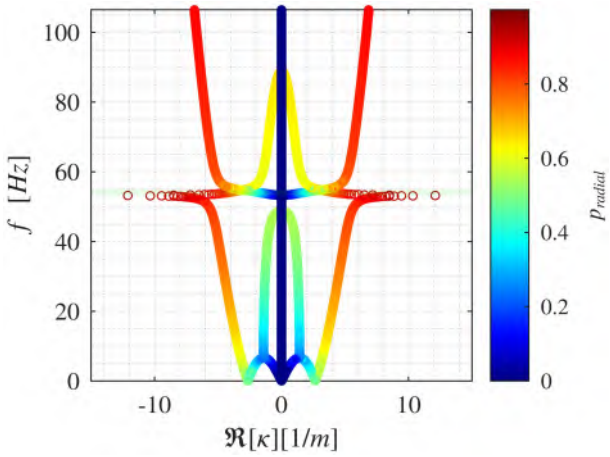
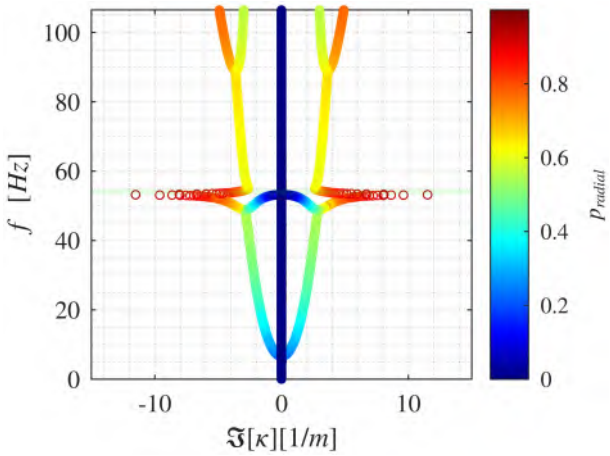


Figure 4: Comparison of the real-wavenumber dispersion diagrams for the equivalent straight beam and the two cases. From top to bottom, the rows correspond to resonator tuning at f_4, f_3, f_2, and f_1. For the ring configurations, the color scale indicates the radial polarization factor p_{radial}.



(a) Real part.



(b) Imaginary part.

Figure 5: Complex dispersion relation of the first case in the $(\Re[\kappa], \Im[\kappa], f)$ space. The color scale indicates the radial polarization factor p_{radial}. The green shaded area indicates the attenuation zone.

$$\begin{aligned} w(s,t) &= w(s+2\pi R,t), \\ u(s,t) &= u(s+2\pi R,t) \end{aligned} \tag{9}$$

$$\phi_m(s) = \frac{e^{i(sm/R)}}{\sqrt{2\pi R}}, m = -M, ..., M \tag{10}$$

The expansions in Eq. 8 are substituted into the governing equations before multiplying by the complex conjugate mode shape ϕ_r^*. Integrating along the entire domain, and exploiting orthogonality of the exponential functions, yields the coupled system in Eq. 11.

$$\begin{cases} \frac{EI}{R}\left(-i\frac{r^3}{R^3}\xi_r - \frac{r^4}{R^3}\eta_r\right) - \frac{EA}{R}\left(\frac{\eta_r}{R} + i\frac{r}{R}\xi_r\right) + \\ -\sum_{j=1}^{N_{res}} m_j \ddot{z}_j \phi_r^*(s_j) + \\ -\sum_{j=1}^{N_{res}} m_j \sum_{m=-M}^{M} \phi_m(s_j)\phi_r^*(s_j)\ddot{\eta}_m + q_r = \rho A \ddot{\eta}_r \end{cases} \tag{11a}$$

$$\begin{cases} \frac{EI}{R}\left(-\frac{r^2}{R^3}\xi_r + i\frac{r^3}{R^3}\eta_r\right) + \\ + \frac{EA}{R}\left(i\frac{r}{R}\eta_r - \frac{r^2}{R}\xi_r\right) = \rho A \ddot{\xi}_r \end{cases} \tag{11b}$$

$$\begin{cases} m_j \ddot{z}_j + k_j z_j + \\ + m_j \sum_{m=-M}^{M} \phi_m(s_j)\ddot{\eta}_m = 0, j = 1, \ldots, N_{\text{res}} \end{cases} \tag{11c}$$

In Eq. 11, q_r is the modal forcing term, that for a point force of amplitude F_0 applied at location s_{force} can be computed as $q_r = F_0\phi_r^*(s_{force})$.

Writing Eq. 11 for each mode $r = -M, ..., M$, and accommodating the coefficients in $\mathbf{x} = [\eta_{-M}, ..., \eta_M, \xi_{-M}, ..., \xi_M, z_1, ..., z_{N_{res}}]^T$, yields:

$$\mathbf{M}\ddot{\mathbf{x}} + \mathbf{C}\dot{\mathbf{x}} + \mathbf{K}\mathbf{x} = \mathbf{F} \tag{12}$$

Where the damping matrix **C** includes two different contributions: structural damping of the host structure and lumped damping of the resonators. Structural dissipation is represented through a Rayleigh damping model,

$$\mathbf{C}_s = \alpha\mathbf{M}_s + \beta\mathbf{K}_s,$$

with $\alpha = 1.1\,\text{s}^{-1}$ and $\beta = 2.8 \times 10^{-6}$s. These coefficients were selected to provide a low damping, representative of the actual structure in the frequency range of interest. Resonator damping is instead modeled by a discrete viscous element acting on the relative motion between the resonator and the ring. This representation is consistent with the localized nature of the resonator dissipation and allows its contribution to be introduced independently of structural damping.

Notice that, in the absence of resonators, the structural stiffness matrix K_s is block diagonal, with each block coupling the modes η_r, ξ_r.

Eq. 12 can be solved in the frequency domain for the response of the entire structure.

3.2.Results

Fig. 6 shows a comparison of the FRFs for the different cases, plotted as a function of the normalized

frequency f/f_{res}, where f_{res} is the resonator tuning frequency, selected as one of the eigenfrequencies of the ring. The first conclusion that can be highlighted is that, in both cases, resonators are able to suppress the target resonance peak, creating an attenuation band. The width of the attenuation band decreases for lower target modes, consistently with Sec. 2.2. Moreover, two additional peaks appear before and after the bandgap, although with smaller amplitude than the case without resonators. In the distribution of the modes outside the bandgaps also lies the main difference between the cases, since performance in terms of vibration isolation is only mildly improved by axial resonators. Moreover, the bandgap in the case of the beam is sharper, with well defined start and end frequency. The same does not happen in the case of the ring, due to the coupling between the axial and radial degrees of freedom.

Fig. 7a shows the spatial distribution of the ring acceleration as function of frequency for $N_{res} = 20$. Within the bandgap, the response is strongly attenuated over the entire structure, indicating that the periodically distributed resonators inhibit wave propagation throughout the ring. By contrast, when a single resonator (i.e. a tuned mass damper) is employed, the reduction in dynamic response is primarily localized in the vicinity of the attachment point, located at $\theta = 0$ in Fig. 7b. This comparison highlights a key advantage of periodically distributed resonators: rather than providing only local vibration mitigation, they enable attenuation of the response in the entire structure.

Finally, Fig. 8 shows, for three different modes, the radial acceleration response as a function of the excitation frequency for different values of the number of resonators N_{res} and of the total added-mass ratio μ. For $N_{res} < 5$, the frequency response remains strongly dependent on the number of attachments, irrespectively of the targeted mode. In this regime, the resonators are too sparsely distributed for the finite ring to reproduce the dynamics predicted by the periodic model. Conversely, for $N_{res} > 5$, the response becomes insensitive to increase in the number of resonators, indicating the establishment of an attenuation region consistent with bandgap behavior.

The added-mass ratio mainly influences the width of the attenuation region. Increasing μ strengthens the interaction between the host structure and the local resonators, resulting in a larger separation between resonances and, consequently, a broader bandgap width.

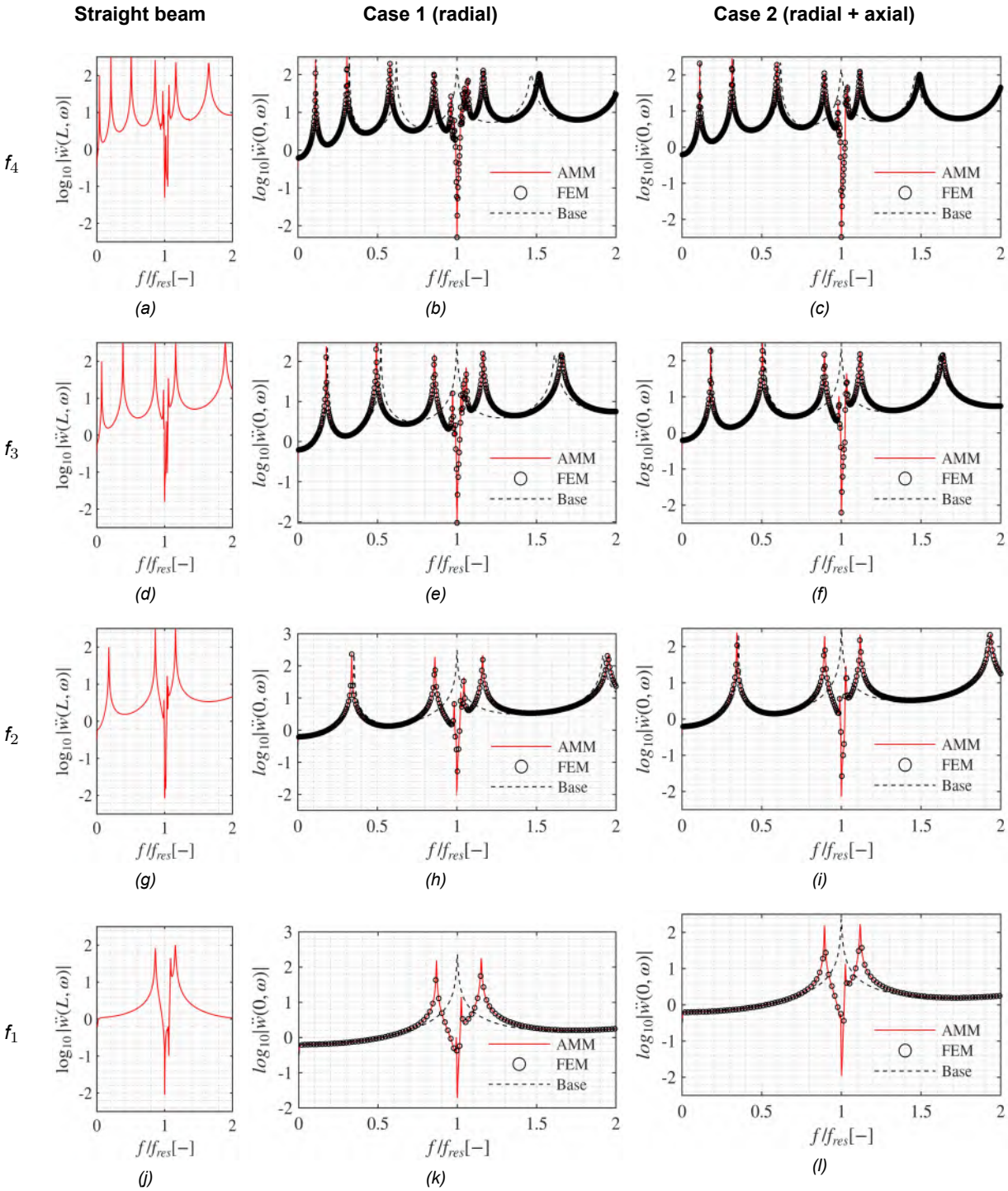
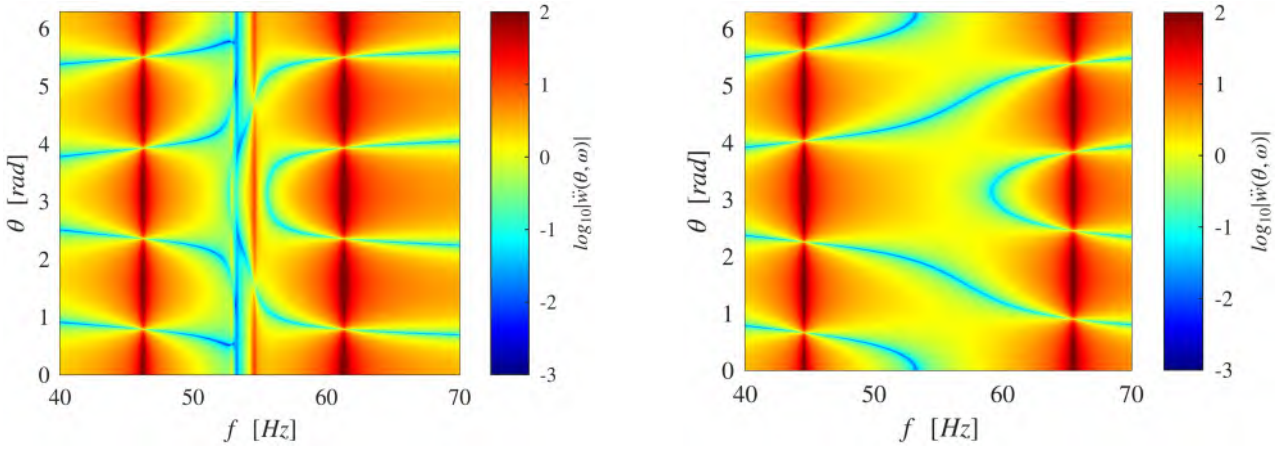


Figure 6: Point-to-point radial acceleration frequency-response functions for the equivalent straight beam and the two ring configurations. From top to bottom, the rows correspond to tuning at f_4, f_3, f_2, and f_1. Solid red lines denote the assumed-modes results, open circles denote the finite-element results, and dashed black lines represent the corresponding bare structures. Frequencies are normalized by the resonator tuning frequency f_{res}.



(a) Metastructure with $N_{res} = 20$.

(b) Structure with tuned mass damper.

Figure 7: Frequency-space maps of radial acceleration amplitude along the ring for the first case with target frequency ω_1:

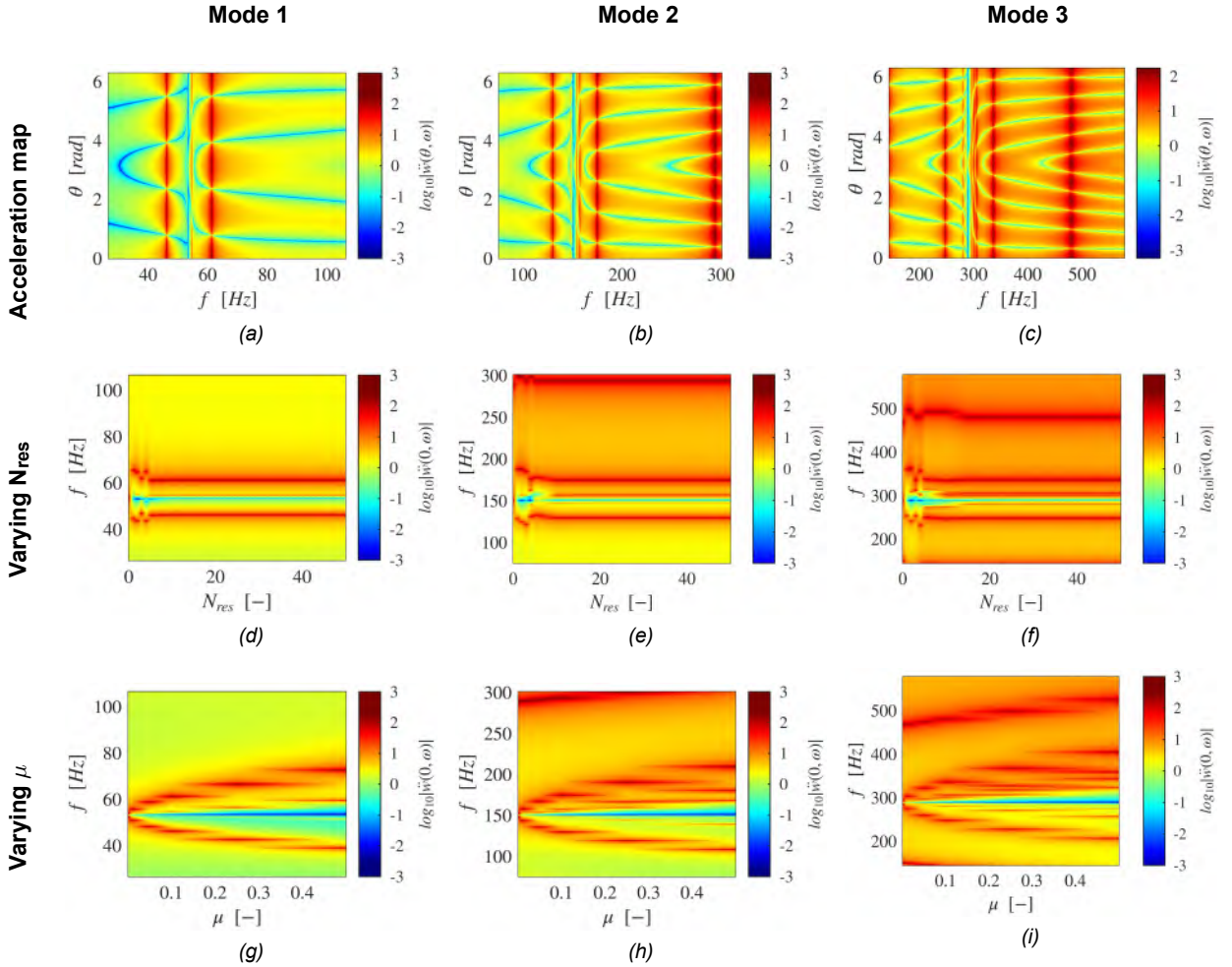


Figure 8: Comparison of the frequency–space response maps (top row), the effect of varying the number of resonators N_{res} (middle row), and the effect of varying the total added-mass ratio μ (bottom row) for the first three target modes.

4. NUMERICAL VALIDATION WITH COMSOL

In order to validate the proposed framework, design of the resonators is carried out using a more realistic model. The ring is equipped with 20 radial resonators, for a total added mass ratio $\mu = 0.1$. The resonators are realized exploiting the bending stiffness of a slender beam, which hosts a total resonating mass of $m_{res} = 0.0076\,\text{kg}$, made in aluminum. Fig. 2b shows the final design of the single resonator. Notice that the beam has been slightly curved to follow the ring geometry, and that the resonating mass has been divided at the extremes of the beam. The structural parameters of the beam, made of the same material as the ring have been tuned to ensure that the first natural frequency is located at $f_{res} = 53.2\,\text{Hz}$, yielding: length $L_{beam} = 73.2\,\text{mm}$, thickness $t_{beam} = 1\,\text{mm}$, width $b_{beam} = 5\,\text{mm}$.

The final design consists of 20 such resonators, 10 for each side of the ring, connected through a rigid element, as shown in Fig. 2b.

Results in terms of frequency response, reported in Fig. 9 show that acceleration amplitude is reduced by up to two orders of magnitude at the measurement point, confirming the effectiveness of the metamaterial in reducing vibration amplitude in a narrow frequency range. Moreover, we find good agreement between the theoretical framework and the final design. Small differences are attributed to the deviation from the ideal conditions assumed for the theoretical approach, mainly: the resonating mass being not perfectly lumped to the attachment, hence the displacement not perfectly radial; damping, which is assumed lumped in the theoretical model while it is distributed in the numerical one.

5. CONCLUSION

This work investigates the use of locally resonant metamaterials for the attenuation of in-plane vibrations in the annular support ring of a large deployable reflector. An extensible curved-beam model is developed to account for the coupling between radial bending and circumferential extension. Complex-wavenumber dispersion analysis, an assumed-modes formulation, and finite-element simulations are combined to relate wave propagation in the associated periodic medium to the forced response of the finite ring.

The radial-only resonator layout produces a bending-polarized partial bandgap: the bending-dominated solutions become evanescent near the tuning frequency, while a circumferentially polarized branch remains propagative. Introducing resonators in both the radial and circumferential directions affects polarization and opens a complete bandgap. However, comparison with the equivalent straight beam shows that curvature substantially modifies both the dispersion characteristics and the finite-structure response. In particular, the relative attenuation bandwidth decreases from approximately 0.05 for the straight beam to approximately 0.025 for the ring, and the boundaries of the attenuation region become less distinct. This reduction in performance is attributed to curvature-induced coupling between radial and circumferential motion and to the higher effective stiffness of the annular configuration.

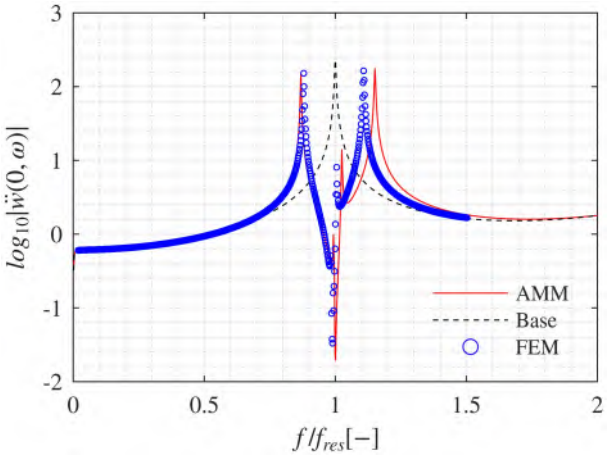


Figure 9: Validation of the designed resonator configuration through the radial acceleration frequency-response function. The response of the bare ring (black dashed line) is compared with the idealized assumed-modes model (red solid line) and with the detailed finite-element model containing the flexural resonators (blue circles).

The assumed-modes and finite-element results are in good agreement. In all the investigated configurations, the distributed resonators suppress the targeted structural resonance and split it into two resonances bounding an attenuation region. The absolute width of this region decreases when lower-frequency modes are targeted. Moreover, although the radial-circumferential configuration generates a complete bandgap in the periodic model, it produces only a moderate improvement in the point-to-point frequency response relative to the radial-only configuration. For the considered configuration, the spatial response map also shows that periodically distributed resonators provide a more uniform attenuation around the ring if compared with a tuned mass damper.

Finally, a realizable flexural resonator is implemented in finite-element model. The configuration containing 20 resonators, with an added-mass ratio $\mu = 0.1$ and a tuning frequency of $53.2\,\text{Hz}$, reduces the acceleration response by up to two orders of

magnitude. These results demonstrate the potential of locally resonant concepts for annular space structures, while also showing that designs for straight members cannot be directly transferred to curved elements. Further improvements will address the use of more exotic dynamical mechanisms with the aim of improving the low-frequency performance of the curved metastructure.

REFERENCES

[1] A. Yarza, O. Castro, J. Santiago-Prowald, and J. L. Pardo. Reflector vibroacoustic response to launch acoustic excitation. In *Proceedings of the Fourth European Conference on Antennas and Propagation*, pages 1–4, 2010.

[2] Mahmoud I. Hussein, Michael J. Leamy, and Massimo Ruzzene. Dynamics of Phononic Materials and Structures: Historical Origins, Recent Progress, and Future Outlook. *Applied Mechanics Reviews*, 66(4):040802, July 2014.

[3] Yong Xiao, Jihong Wen, Dianlong Yu, and Xisen Wen. Flexural wave propagation in beams with periodically attached vibration absorbers: Band-gap behavior and band formation mechanisms. *Journal of Sound and Vibration*, 332(4):867–893, February 2013.

[4] Yong Xiao, Jihong Wen, and Xisen Wen. Broadband locally resonant beams containing multiple periodic arrays of attached resonators. *Physics Letters A*, 376(16):1384–1390, March 2012.

[5] Christopher Sugino, Stephen Leadenham, Massimo Ruzzene, and Alper Erturk. On the mechanism of bandgap formation in locally resonant finite elastic metamaterials. *Journal of Applied Physics*, 120(13):134501, October 2016.

[6] C. Sugino, Y. Xia, S. Leadenham, M. Ruzzene, and A. Erturk. A general theory for bandgap estimation in locally resonant metastructures. *Journal of Sound and Vibration*, 406:104–123, October 2017.

[7] C. Sugino, M. Ruzzene, and A. Erturk. Merging mechanical and electromechanical bandgaps in locally resonant metamaterials and metastructures. *Journal of the Mechanics and Physics of Solids*, 116:323–333, July 2018.

[8] Daria Manushyna, Moritz Hülsebrock, Alexander Kuisl, Alessio De Vivo, Pierrick Heloret, Heiko Atzrodt, and Stephan Rapp. Application of vibroacoustic metamaterials for structural vibration reduction in space structures. *Mechanics Research Communications*, 129:104090, May 2023.

[9] Madeline P. Lowry, Carson L. Willey, Vincent W. Chen, Mostafa Nouh, and Abigail T. Juhl. Passive low-frequency vibration mitigation in large space structures. *MRS Communications*, 14(5):1007–1014, September 2024.

[10] Zhenyu Wang, Pei Zhang, and Yongqiang Zhang. Locally Resonant Band Gaps in Flexural Vibrations of a Timoshenko Beam with Periodically Attached Multioscillators. *Mathematical Problems in Engineering*, 2013:1–10, 2013.

[11] Dianlong Yu, Yaozong Liu, Gang Wang, Honggang Zhao, and Jing Qiu. Flexural vibration band gaps in Timoshenko beams with locally resonant structures. *Journal of Applied Physics*, 100(12):124901, December 2006.

[12] Peng Guo, Qizheng Zhou, Jun Yang, Xinyi He, and Ziyin Luo. The Low-Frequency Vibration Control Mechanism of a Finite Locally Resonant Beam with Elastic Supports. *Journal of Vibration Engineering & Technologies*, 12(3):3919–3930, March 2024.

[13] A. Nateghi, L. Van Belle, C. Claeys, E. Deckers, B. Pluymers, and W. Desmet. Wave propagation in locally resonant cylindrically curved metamaterial panels. *International Journal of Mechanical Sciences*, 127:73–90, July 2017.

[14] Jie Xu, Youqi Zhang, Mehrdad Negahban, Weihan Wang, and Zheng Li. Piezoelectric metamaterial curved beams with feedback control for manipulating bandgaps. *International Journal of Mechanical Sciences*, 311:111175, February 2026.

[15] Singiresu S. Rao. *Vibration of continuous systems*. Wiley, Hoboken, N.J, 2007.

[16] Isaac Elishakoff. *Mechanical vibration: where do we stand?* Number no. 488 in Courses and lectures. Springer, Wien, 2007.

[17] S.-K. Lee, B.R. Mace, and M.J. Brennan. Wave propagation, reflection and transmission in curved beams. *Journal of Sound and Vibration*, 306(3-5):636–656, October 2007.

DEPLOYMENT DEMOSTRATOR FOR STACKED TRIBAND ANTENNA FOR PNT

Guillermo GONZÁLEZ[(1)], Pepe NIETO[(1)], Diego CHICO[(1)], Mara ESCARTÍ([1)], Rubén CABALLERO[(2)], Benedikt BYRNE[(3)], Ewelina RYSZAWA[(3)]

[(1)] COMET Aerospace SL, Ronda Auguste y Louis Lumière 23, Nave 7, 46980, Paterna, Valencia, Spain
Email: guillermo.gonzalez@comet-aerospace.com, pepe.nieto@comet-aerospace.com, mara.escarti@comet-aerospace.com

[(2)] EOSOL Engineering Consulting SL, Camino de Labiano 45, 31192, Mutilva, Navarra, Spain
Email: ruben.caballero@eosolgroup.com

[(3)] ESA-ESTEC, Noordwijk, The Netherlands

KEYWORDS

Deployable antennas, coilable boom, triband, TRL4.

ABSTRACT

Future satellite missions increasingly demand compact, lightweight, and high-performance antennas capable of covering multiple frequency bands for Positioning-Navigation-Timing (PNT) applications. Traditional antenna systems are limited by rigid structures and size constraints, which can impair deployment feasibility and RF performance in small satellite platforms.

In this context, the research for versatile solutions with high compaction ratios becomes particularly interesting, being the structure explored in this paper especially attractive, as it studies the possibility of housing three antennas for three different bands in a single deployable structure.

1. INTRODUCTION

This project, developed within the framework of the ESA Contract Nº 4000143515/23/NL/AS, [DD-STRA], focuses on the design, analysis, and validation of a stacked tri-band deployable antenna operating in the UHF, L, and S bands, optimized for use in low Earth orbit (LEO) missions. The solution is based on a single-body deployable coilable boom structure that integrates all three bands in a stacked configuration, enabling compact stowage and robust deployment. This structure is composed of four flexible longerons and 20 custom-designed mounts manufactured of space validated plastic, providing both mechanical strength and guidance for the helical antenna elements.

The antenna mechanism deployment is passive, and it is controlled by a motorized system that ensures non-violent and controlled deployment. The deployment mechanism includes a non-pyrotechnic Hold Down and Release Actuator (HDRA) that triggers the self-deployment of the boom using the elastic energy stored in the longerons. The mechanism design eliminates the need for post-deployment locking systems due to the inherent stiffness and cable tension of the deployed structure. Each antenna band is supported by its own coaxial cable feed and PCB.
A comprehensive RF simulation was performed using FEKO software, incorporating detailed geometry, coaxial feeds, and platform effects. The results show compliance with most RF specifications, including gain patterns, return loss, and axial ratio. The antenna achieves a deployed length of 3.25 m and a mass of 4.3 kg, fitting within the LEO mission requirements.

The Manufacturing, Assembly, Integration, and Testing (MAIT) plan includes procurement, mechanical assembly, and RF integration steps, along with a detailed test campaign covering frictional deployment, S-parameters, radiation pattern verification, and mechanical qualification. The finalization of these activities will allow a TRL4 maturity achievement and demonstrate the feasibility of the concept as a modular, efficient, and space-compatible multi-band antenna system.

The project represents a major step forward in deployable antenna technology for small satellites and is the result of a successful collaboration between industry, academia, and the European Space Agency.

2. DESIGN AND ANALYSIS

Mechanical Design

The designed solution consists of a single deployable structure capable of compacting and positioning three antennas of UHF-, L- and S-bands. The deployable structure is based on a coilable boom architecture which can transition from a stowed state, forming the longerons a low-pitch helix, to a deployed state where they are completely straight, providing stiffness and stability to the structure.

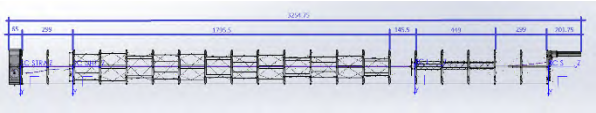


Fig. 1. Deployed STRA.

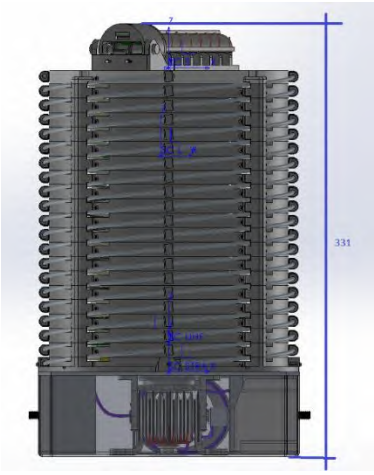


Fig. 2. Stowed STRA.

From the mechanical structure point of view, it consists of four GFRP (Glass Fiber Reinforced Plastic) longerons which are responsible for the passive motorisation of the antenna due to their ability to store elastic strain potential energy in the stowed state, and 20 Ultem mounts that spaced at a length that ensures geometric compatibility between the stowed and deployed states.

The structure is braced by a set of p-aramid tensors with a triple purpose (see Fig. 3).

- Red: deployment control tensors which prevent violent deployment of the structure.
- Green: counter-tensors which stiffen and latch the antenna in the final stage of deployment.
- Yellow: fixed tensors which form St. Andrew's crosses together with the counter-tensors, to brace the structure.

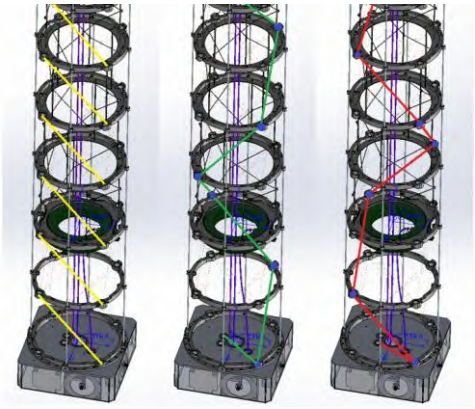


Fig. 3. Antenna control and bracing tensors

The structure remains stowed thanks to the action of an HDRA (Hold Down and Release Actuator). This device has a dual function: on the one hand, it is responsible for releasing the antenna, allowing it to deploy passively; on the other hand, it has the mission of compressing the structure with enough force to ensure that its stiffness in the stowed situation is adequate and to prevent loss of contact (and subsequent bumping) between any of its parts during launch. To withstand this preload, the upper antenna mount (top disc) is made of fibreglass and it is connected by a hollow titanium rod to the HDRA screw, housed in the metal box under the structure.

The deployment control system is driven by a stepper motor. When the HDRA releases the antenna, it tends to deploy explosively, but its movement is controlled by the speed imposed by the motor.

Finally, detailed described the supporting structure, the location of the three antennas on it is shown in Fig. 4.

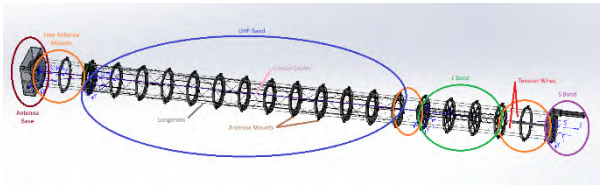


Fig. 4. STRA parts.

The UHF band antenna consists of four wires forming a conical helix with a base diameter of 162 mm, a top diameter of 120 mm, a pitch of 450 mm, and a total height of 1795.5 m. It is housed within 13 of the first mounts, which are connected between them with four non-structural p-aramid threads holding the wires in the approximated helix shape.
The L-band antenna is housed in a similar way to the previous one, consisting of four wires forming a straight helix with 50 mm diameter, 145 mm pitch and a total height of 452 mm. This antenna is comprised in the space between four mounts, after the UHF-band antenna.

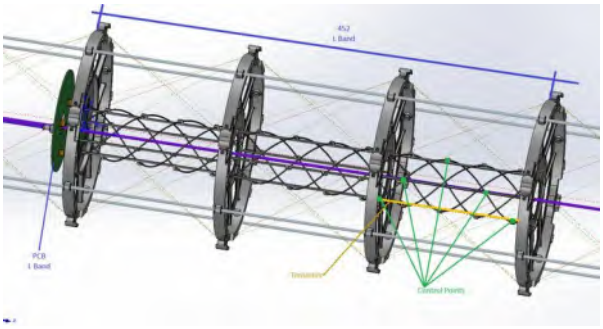


Fig. 5. L-band antenna housing.

The S-band antenna is too small to maintain the deployable concept of the previous two. Therefore, this antenna, consisting of four helical wires with 25 mm diameter, 70 mm pitch and a total height of 140 mm; is embedded in a plastic structure connected to the top disc by means of a hinge and a spring that brings it into position during the deployment manoeuvre.

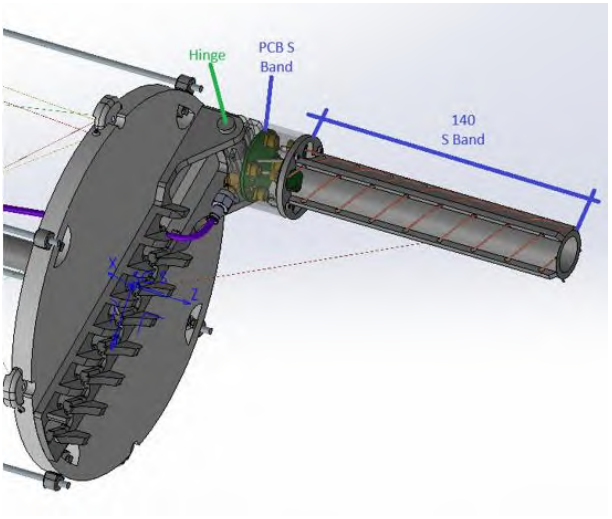


Fig. 6. S-band antenna housing.

Mechanical analysis

Two FEM (Finite Element Model) are built to analyse two different scenarios: stowed structure (preload case and launch load case analyses) and deployed structure (flight case analyses).

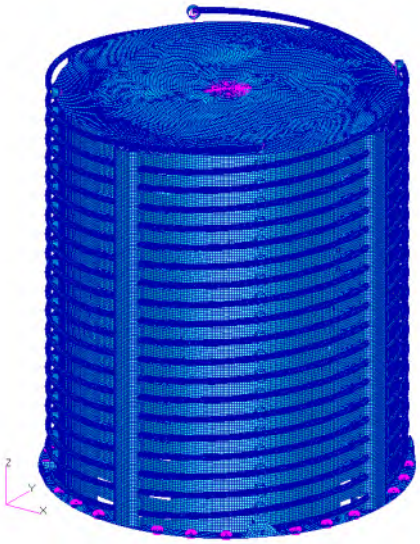


Fig. 7. STRA stowed FEM.

Preload analysis

Employing the stowed FEM, the HDRA is sized on the premise that the compression exerted by the device is enough to prevent separation and bumping of any part of the antenna during launching. To do this, axial (V) and shear (S) forces are recovered at all interfaces of the stowed structure in all launch load cases. The preload required at each interface, knowing the insertion angle of the tongue and groove joint that allows the mounts to fit together when stowed (θ), is calculated as shown below.

$$Preload_{Min} = (V + S \cdot \tan(\theta)) \cdot SF \qquad (1)$$

The effective load distribution of the HDRA preload between the interfaces is calculated using a unit case which, combined with the above information, defines that the minimum device preload required is 14366 N.

Known this value, it is introduced in the stowed model to verify that the structure can withstand it, obtaining the maximum Von Mises stress and the minimum MoS (Margin of Safety) in each part.

Table 1: Preload analysis strength results

	σ_{VM} (MPa)	MoS
Ultem (mounts)	42.66	0.68
GFRP (longeron)	34.06	>5.00
Prepreg glass fabric (top disc)	308.01	0.43

Launch loads analyses

Natural frequencies of the stowed FEM are analysed to better understand its dynamic behaviour under launch loads. The structure has been designed with the aim of achieving a 1st natural frequency greater than 100 Hz (outside the sine specification). As a result, the 1st mode of the structure is at 130.34 Hz.

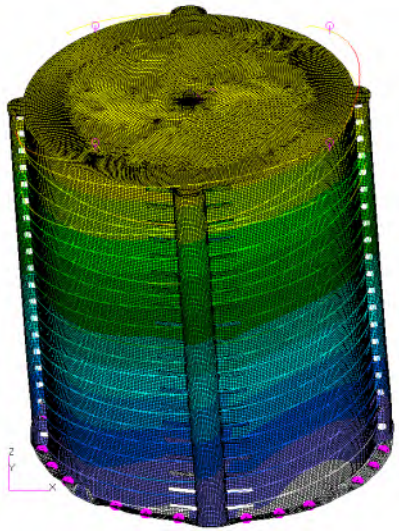


Fig. 8. Stowed FEM 1st vibration mode.

The stowed FEM is analysed under each of the launch loads (Quasi-Static, Sine, Random and Shock), combining the obtained stress results with those from the preload analysis, resulting in the Table 2. It is verified that the random load case is the most critical.

Table 2: Launch load analyses MoS results

	Ultem MoS	GFRP MoS	Prepreg MoS
Pr. + QS	0.28	>5.00	0.41
Pr. + Sine	0.34	>5.00	0.43
Pr. + Random	0.02	>5.00	0.43
Pr. + Shock	0.25	3.96	0.31

Analyses in flight situation

The deployed FEM is built from the previous one, expanding its mounts and adding the tensors that brace the structure.

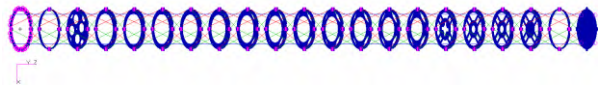


Fig. 9. STRA deployed FEM.

In this situation, only the stiffness and thermoelastic stability of the structure are analysed. The modal analysis shows vibration modes very similar to those of a cantilever beam, being the 1st frequency of 1.76 Hz; while the thermoelastic analysis concludes that both the geometric distortion of the antenna and the stresses derived from the temperature are negligible.

RF Design

The presented triband antenna is basically comprised of three quad-helix antennas, one per frequency band, placed along a deployable boom. Each antenna generates a circularly polarized isoflux pattern that maximizes the uniform power distribution for a global coverage.
Each of the antennas is fed by its own feeding network which is placed just under each one of the helixes. The signal distribution until each feeding network is done through coaxial cables located in the middle of the antenna. The long cables that are required to reach the feeding points of L band and the S band antennas lead to high insertion losses. Fortunately, the application link budget has a large margin, and they can be tolerated.
Many key aspects have been considered in the design, such as the adequate materials selection, the custom shaped feeding networks and the optimized placement of each helix inside the boom.

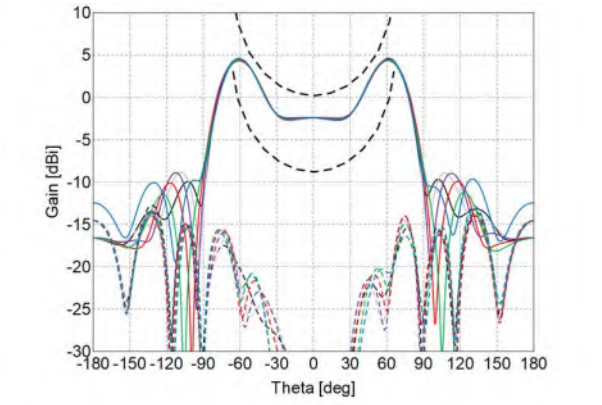


Fig. 10. UHF band isoflux radiation pattern

RF Analysis

The antenna has been modelled in FEKO software for its RF simulation. The electrical model simplification has been key to improve the simulation speed and reduce the required computational resources while maintaining high precision results. This simplification allows the simulation of the antenna including the boom, the support structure, the satellite platform, the feeding network and the cables. This complete electrical model ensures precise RF simulation results.
The copolar and crosspolar radiation patterns (See *Fig. 10* UHF radiation pattern as example), the gain, the axial ratio, the return loss, the phase centre variation, the phase centre stability, the group delay and some more parameters have been simulated and calculated.
The following *Table 3* summarizes some of the most important electrical parameters that define the antenna:

Table 3. Electrical performance summary

Parameter	Value
Frequency band	UHF band, L band and S band
Pattern shape	Isoflux
Polarization	Right-handed circular
Field of view	132º
Bandwidth	50 MHz per frequency band
Return loss	> 10 dB

3. CRITICAL BREADBOARD MANUFACTURING AND TESTING

Mechanical CBB

A mechanical critical breadboard of the structure with dummy electrical parts is manufactured and assembled to verify its mechanical performance and serve as a derisking model.

As the objective is the functional check of the structure, materials used have representative characteristics for this purpose, but they do not necessarily have to be the final ones. Furthermore, different manufacturing and assembly procedures are evaluated to select the best method for building the future final breadboard.



Fig. 11. STRA deployed CBB.

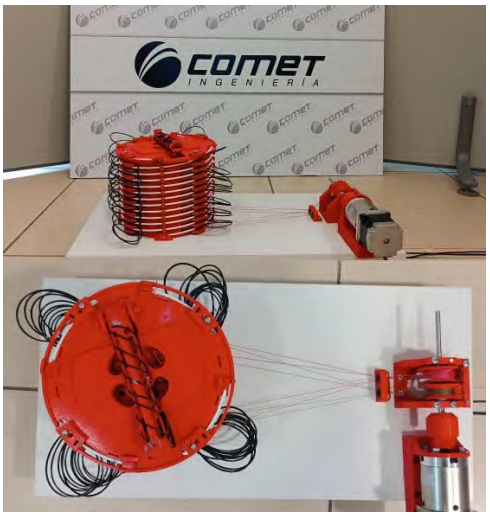


Fig. 12. STRA stowed CBB.

Having finalised the CBB manufacturing, 30 folding and deployment cycles are performed to assess the robustness of the solution. This process starts with the CBB in its stowed state when the stepper motor begins to rotate at a controlled speed, allowing longerons to gradually release elastic potential energy and transition to their nominal position. When the longerons have exhausted their energy, the structure is almost fully deployed, so the last step consists of reversing the rotation direction of the motor to pulling the corresponding tensors (green in Fig. 3) and latching the antenna.

The following lessons are extracted from these experiences:

- The kinematic operation of the structure is correct, and it is able to stow and deploy passively without becoming stuck. There are certain points with slight geometric incompatibilities (Fig. 13) at intermediate stages of the manoeuvre which are corrected in the final model.

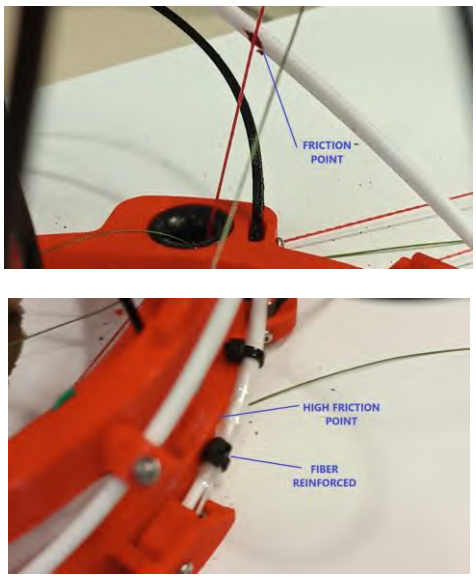


Fig. 13. CBB Collision points.

- The manufacturing methods and 3D printing orientations are correct and suitable for the intended purpose of the structure. No strength issues have been detected in the functional operation, and manufacturing procedures, such as the embedding of the low-friction washers through which the tensors run, have been validated.
- The use of TPU material for the fixed tensors (yellow in Fig. 3) is discarded. The decision to use this material was based on the idea of having threads with adaptive flexibility, all manufactured to the same length using 3D printing; however, it has been concluded that its advantages do not justify its disadvantages and, for the BB, rigid tensors manufactured using a tool will be considered.
- There is enough stowed volume to accommodate the radiating wires that comprise antennas.

RF CBB

In parallel, in the frame of this project, electrical models and feeding networks CBBs are also manufactured and tested.

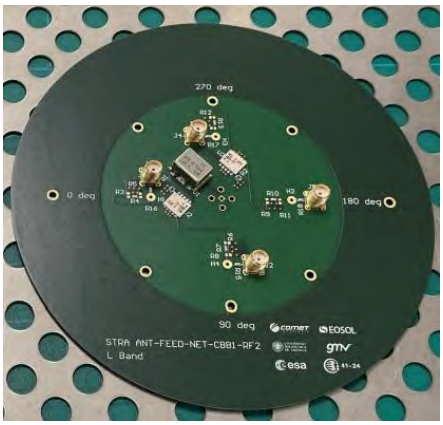


Fig. 14. Manufactured PCB of the CBB L-Band antenna.

There are key parameters that must be verified to validate the design and the manufactured antenna. The isoflux copolar and crosspolar radiation pattern in amplitude and phase, the gain and the return loss are the most important parameters that will be measured over the frequency bands. Many other important parameters such as the phase center related parameters will be calculated from the mentioned ones and compared with simulations.
The antenna will be tested in an anechoic chamber that is able to measure it with a reasonable accuracy even at the UHF frequency band, allowing the validation of the antenna.

4. BREADBOARD MANUFACTURING

After the reduced-scale CBB, a BB of nominal dimensions is manufactured and assembled. The BB measures 200 mm in diameter, 266 mm in height when stowed and 3190 mm when deployed.



Fig. 15. STRA deployed and stowed BB.

The BB manufacture is aligned with the objectives of a TRL 4 project; consequently, the materials of the structure are mechanically representative (and in many cases, conservative), but not necessarily qualified for spatial applications. This includes, for example, the use of UHMWPE tensors, or PLA for the 3D printed parts. Furthermore, the HDRA is omitted as no vibration test campaign is planned, and the motor and electrical components are not space-qualified.



Fig. 16. UHF wire positioning tensors (left top), base (left bottom), L wire positioning tensors (right).

The process is handmade and it begins with the purchase of the raw materials and the manufacturing of the components that comprise the deployable structure (longerons, mounts and tensors). All of these are assembled onto a metal base, which supports the deployable mechanism and houses the harnesses that feed the PCBs.

The wires of the three antennas are measured and installed. Each one is attached to the structure using a slightly different method. The UHF band antenna is supported at its intersections with the mounts, forming a “helix” of straight segments between the mounts and the only support point between each pair of them. The L-band antenna uses a similar system, but due to its smaller size, there are four fixing points between each pair of mounts, which confers its radiating wires a more helical shape. Finally, the S-band antenna is not deployable due to its dimensions, so it is embedded into a plastic fixture that folds 90º and deploys by means of a torsion spring.

The PCBs and their corresponding harnesses, which are housed in the base and deploy at the same time as the structure, are installed and, at this point, the BB is fully assembled and operational.

Before to the test campaign, preliminary deployments are performed to check the BB mechanism works properly.

It is verified that the BB has enough motorisation to deploy against gravity force, without the need for equipment which compensate for this. However, in the stages of the manoeuvre prior to final tensioning (when the longerons are not vertical yet) the flexural stiffness of the assembly is significantly low. Therefore, to prevent buckling due to the gravity action, the deployment takes place inside a methacrylate tube (Fig. 15 right) which acts as an MGSE.

5. MECHANICAL TEST PROCEDURES

Mechanical and radio-electrical tests are performed on both the BB and some of its components. Specifically, on the mechanical side, motorisation and deployment tests are conducted on the complete BB. On the RF side, S-parameters of the complete antenna, the feeding networks, their harness and the SMA connectors are measured; and radiation pattern and gain tests of the complete BB are obtained. In addition, dimensional and mass inspections are also done.

This paper focuses on the mechanical aspects of the project, so procedures of mechanical tests are described in detail below.

Motorisation test

The motorisation test aims to obtain an initial estimation of the axial force exerted by the structure at each moment of the deployment manoeuvre, to assess its motorisation margin.

It is identified that the motorisation force comes from the stored elastic energy of the longerons, while the resistive forces arise from friction at the joints of the structure, friction of the tensors, the resistance exerted by the radiating wires that comprise the antennas, and the resistance of the harness that supplies the PCBs. The deployment mechanism introduces no resistance, as the brake consists of a stepper motor, which is an active element.

Due to the nature of the structure, it is extremely speculative to establish a formulation for estimating the friction of each element at each moment of the manoeuvre. The structure deploys sequentially, with each segment being in a different position to the rest, and the overall configuration being unique at every instant. For this, the experimental approach has been adopted.

Grouping, in one side, as the internal friction of the antenna (R_{Fric}) the resistance originated in joints, tensors and radiating wires; and in the other, the resistance of the harness (R_{Harn}), it is agreed that the motorisation margin of the structure for each deployment % can be expressed as follows.

$$MM(\%) = \frac{F_{Mot}(\%)}{R_{Fric}(\%) + R_{Harn}(\%)} \qquad (2)$$

By analysing the nature of each term in the above expression and assuming that the internal frictions are symmetrical (same magnitude and opposite direction when folding and deploying), the following diagram of forces depending on the movement direction is obtained.

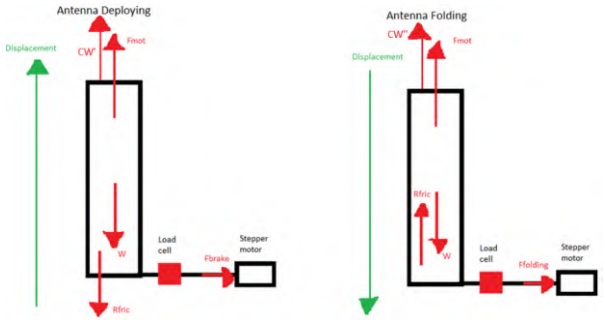


Fig. 17. Force diagram of the BB in deployment and folding.

Where F_{mot} is the motorisation force of the structure, W is the weight of the BB, R_{fric} represents the internal friction, F_{brake}/$F_{folding}$ are the forces reaching the stepper motor and read by the load cell, and CW'/CW'' are the forces exerted by the counterweight (a different value when folding and deploying). It is decided to use a counterweight to prevent the structure from buckling due to the force of gravity instead of the MGSE, so as not to introduce noise into the measurement caused by friction between the BB and the MGSE.

To determine F_{mot}, R_{fric} and R_{Harn}, it is decided to measure the axial force of the BB in three scenarios.

a) Deployment force test without harness.
b) Folding force test without harness.
c) Deployment force test with harness.

In each of which, the load cell measurement can be expressed as a combination of the terms above.

$$F_{a)}(\%) = F_{mot}(\%) - W(\%) - R_{Fric}(\%) + CW' \qquad (3)$$

$$F_{b)}(\%) = F_{mot}(\%) - W(\%) + R_{Fric}(\%) + CW'' \qquad (4)$$

$$F_{c)}(\%) = F_{a)}(\%) - R_{Harn}(\%) \qquad (5)$$

And combining these three measurements it is possible to obtain the variables involved in the calculation of the motorisation margin.

$$R_{Fric}(\%) = \frac{F_{b)}(\%) - F_{a)}(\%) - (CW'' - CW')}{2} \qquad (6)$$

$$R_{Harn}(\%) = F_{a)}(\%) - F_{c)}(\%) \qquad (7)$$

Deployment test

The deployment test aims to demonstrate that the structure is robust enough to withstand 30 deployment manoeuvres without compromising the antenna performance. Along these deployments, the repeatability of the manoeuvre and the deviations and distortions of the structure that could affect the antennas are assessed.
The possible distortions that the structure allows without any of its components evident breaking are as follows.

- Deformation of the structure due to global bending or torsion, resulting in the three antennas being displaced from their nominal position.
- Local diameter reduction of the UHF and L-band antennas due to loss of tension in the positioning threads (Fig. 18 left)
- Random local distortion of the radiating wires of the UHF and L-band antennas between control points (particularly in the UHF-band antenna).

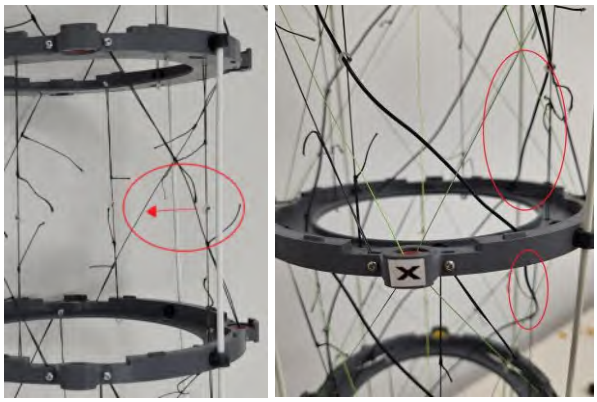


Fig. 18. Unrestricted movement direction of the control points (left), radiant wires with random local distortions (right).

A different measurement strategy will be followed for each of the possible distortions.
To determine the global deformation of the structure, which is expected to be minimal, the position and angle of the top disc is measured by a laser every 15 deployments, extrapolating this measurement linearly to the rest of the length.
To determine the reduction in the diameter of the antennas due to a loss of tension in the threads, the distance between each pair of opposing washers is measured every 15 deployments.
To determine the effect of random local distortions, different models of the UHF and L-band antennas with curvatures of the order of those seen in the BB are randomly generated, and their RF parameters are obtained.

Finally, after the completion of the test campaign, a wear study is performed to identify which areas of the BB suffer more.

6. MECHANICAL TEST RESULTS

Motorisation test results

The axial force exerted by the BB is measured three times for each of the three scenarios described and the mean value is calculated. The graphs obtained from the raw deploying and folding measurements appear as follows.

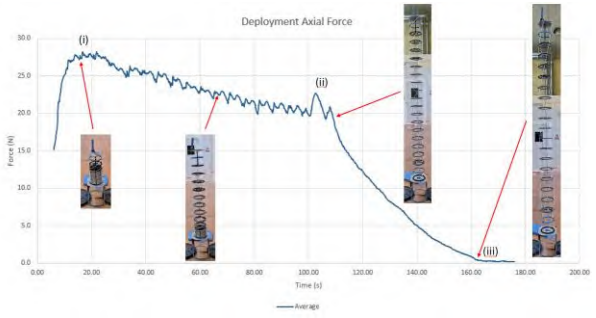


Fig. 19. BB deploying axial force graph shape and phases.

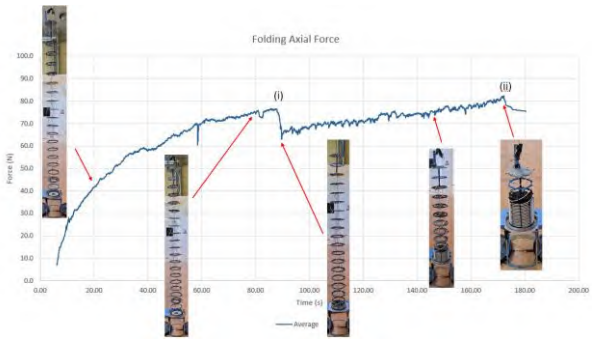


Fig. 20. BB folding axial force graph shape and phases.

Next, the BB mass and the contribution of the counterweight are compensated analytically and by means of auxiliary tests, so that the results represent only the motorisation minus the internal friction and harness resistances. The blue curve corresponds to scenario a), the orange one to b) and the grey one to c).

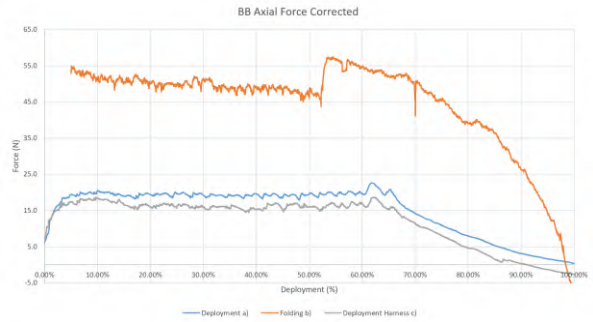


Fig. 21. BB axial force corrected in scenarios a), b) and c).

Operating with the system of equations formed by (3), (6) and (7), the terms F_{mot}, R_{fric} and R_{harn} are obtained. These are calculated along the uniform section of the graph (approximately between 3% and 65% of the deployment). This is because in the final phase of deployment the axial force of the BB tends towards 0; however, the counter-tensioning system starts to operate, providing the extra energy necessary to complete the manoeuvre.

$$\boldsymbol{F_{mot} \in [32.2;\ 36.8]\ N}$$
$$\boldsymbol{R_{fric} \in [12.8;\ 17.7]\ N}$$
$$\boldsymbol{R_{harn} \in [0.9;\ 5.0]\ N}$$

To calculate the motorisation margin, the most appropriate safety factors specified in [1] are applied.

$$MM(\%) = \frac{F_{Mot}(\%)}{2R_{Fric}(\%) + 3R_{Harn}(\%)} \qquad (8)$$

Resulting in an MM in the uniform section of:

$$\boldsymbol{MM \in [0.77;\ 1.02]}$$

In accordance with the ECSS recommendation, the motorisation margin obtained is low, as the standard recommends a margin of 2 once safety factors have

been applied. However, it should not be forgotten that the BB's manufacturing methods are in line with the scope and budget of a TRL4 project; consequently, the surface quality of parts with relative motion between them has significant margin for improvement, so R_{fric} may be reduced. Furthermore, it has been found that the measurement setup introduces some additional friction, which adds a degree of conservatism to the results.

Deployment test results

At the time of the elaboration of this paper, 20 of the 30 planned deployments of the BB campaign have been done; consequently, some results are preliminary, but certain conclusions can already be extracted.

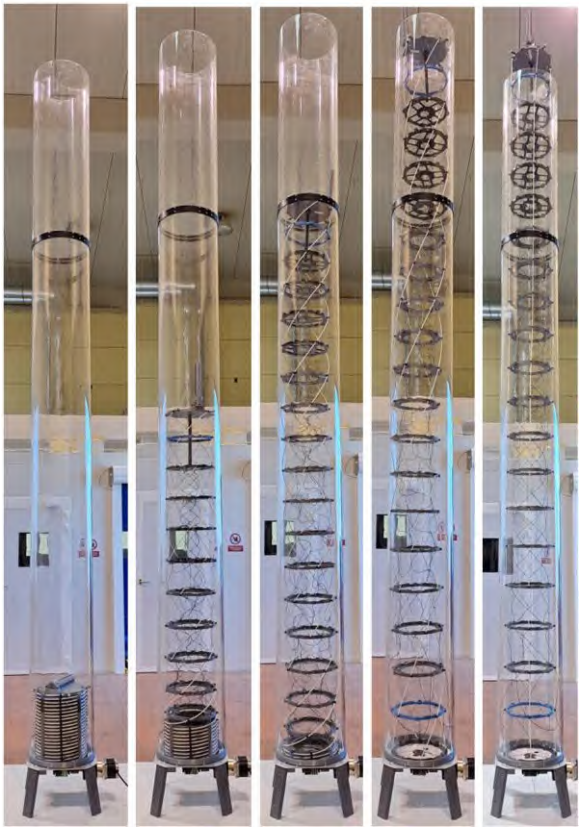


Fig. 22. BB deployment sequence.

First, there is no apparent loss of motorization in the structure due to a possible gradual deterioration. Furthermore, the final position reached by the BB can be forced to be always the same (with a margin of error of a few millimetres), as this is controlled by the tensioning system.

The global deviation of the BB has been measured after manufacture and after 15 deployments. The structure exhibits an approximate deflection of 20 mm and torsion of 16° at its free end, with similar results for both measurements done. The immediate conclusion is that the deviations are caused by manufacturing inaccuracies and tolerances in the model, rather than deterioration by operation. The residual torsion appears to be of some significance, but it has been verified that it has no appreciable impact on the performance of the antennas. The reason for this distortion is that the tensioning by the stepper motor takes place at the base, reducing the latching torque as the height increases due to friction.

Local diameter reduction has increased by around 3 – 4 mm comparing measurements at the start and halfway of the campaign on the UHF band antenna. This distortion is negligible in the L-band antenna. The test campaign needs to continue to determine if this phenomenon worsens with the remaining manoeuvres, or if it has already reached its limit. The impact of this distortion at RF level has not yet been assessed.

The RF impact of random local distortions in radiating wires has not yet been assessed.

7. CONCLUSIONS AND FURTHER STEPS

Conclusions extracted at this stage of the project are listed below:

- An antenna solution has been proposed to satisfy the need identified in the project framework.
- Satisfactory compliance with mechanical and electrical requirements has been verified by analysis.
- It has been confirmed that the solution proposed is feasible and that its deployable structure is functional
- The in-house manufacturing processes for building this type of helical structures have been validated and refined.
- The BB is perfectly capable of deploying against gravity, but the calculated motorisation margin is lower than ECSS recommendation. However, it is considered that there is margin for improvement by removing conservatism.
- It has been verified that the deployment system is robust enough to ensure that the global position of the structure remains unchanged despite the number deployments.
- There are indicators that the reduction in the diameter of the UHF-band antenna local distortions is affected by the number of deployments, but their impact at RF level has not yet been assessed.
- At this stage of the project, it is considered that a robust BB resulting from a design that fulfils the requirements has been achieved; with some areas to improve but leaving a positive impression.

Further steps to mature the technology presented up to TRL4 within the framework of this project are:

- Complete the deployment test campaign and ensure the repeatability and robustness of the structure can be deployment.
- Measure the BB in an anechoic chamber and correlate the results to validate its RF performance.
- Quantify the positional deviations of the radiating elements to assess their impact at RF level is acceptable.

After achieving a design that fulfils the requirements at TRL4 level, the next steps would be:

- Eliminate the conservatism observed regarding motorisation test and study the MM in greater detail.
- Consider flight-grade materials in the manufacturing so that the structure can be tested in representative mechanical environments and under TVAC conditions.
- To frame the antenna within a project involving flight projections that provides more mature requirements and a framework for the development of the solution.

8. ACKNOWLEDGEMENTS

Authors acknowledge the support of the European Space Agency under contract Deployment Demonstrator of Stacked Tri-Band Antenna for Positioning-Navigation-Timming Use Cases on Small Satellites (DD-STRA).

9. REFERENCES

[1] ECSS-E-ST-33-01C Rev 2. *"Mechanisms"*.

EXPERIMENTAL AND ANALYTICAL STUDY ON CFRP BISTABLE BOOM CONSIDERING TIME- AND TEMPERATURE-DEPENDENCE

Yuta Sunaga [(1)], Sho Kajihara [(2)], Tomohiro Yokozeki [(3)], Akihito Watanabe [(4)]

[(1)] Department of Aeronautics and Astronautics, The University of Tokyo, 7-3-1 Hongo, Bunkyo-ku, Tokyo, Japan, Email: sunaga-yuta856@g.ecc.u-tokyo.ac.jp
[(2)] Department of Mechanical Engineering, Meiji University, 1-1-1 Higashi-Mita, Tama-ku, Kawasaki-shi, Kanagawa, Japan, Email: kajihara@meiji.co.jp
[(3)] Department of Aeronautics and Astronautics, The University of Tokyo, 7-3-1 Hongo, Bunkyo-ku, Tokyo, Japan, Email: yokozeki@aastr.t.u-tokyo.ac.jp
[(4)] Sakase Adtech Co., Ltd., 14-10 Shimoyasuda, Maruoka, Sakai-shi, Fukui, Japan, Email: a-watanabe@sakase.co.jp

KEYWORDS

Composite material, Deployable structure, Bistable, Viscoelasticity, Temperature-dependence

ABSTRACT

A thin-walled semi-cylindrical boom made of Carbon Fiber Reinforced Plastic (CFRP) with appropriate fiber orientation angles and their stacking sequence has two stable shapes. This CFRP bistable boom is expected to be applied to deployable structures on spacecraft. From the design perspective, this boom requires evaluation of the effects of long-term storage and high-temperature environments due to its flexibility and the presence of resin in CFRP. In this study, the test on bistable booms was conducted to examine the influence of storage temperature and duration on the re-deployed boom shape. Also, the analytical method corresponding to the test conditions was proposed to evaluate the test data.



Figure 1: CFRP Bistable Boom
(Upper: deployed configuration, lower: coiled configuration)

1. INTRODUCTION

Carbon Fiber Reinforced Plastic (CFRP) is increasingly being adopted in the aerospace sector because of its high specific strength and stiffness, as well as the ability to design the mechanical properties by choosing fiber directions and their stacking. Especially, a properly designed CFRP open-section semi-cylindrical boom keeps the shape in both deployed and coiled configuration as shown in Fig. 1. This CFRP bistable boom is expected to be used as deployable components on spacecraft because of its lightweight and the easiness of storage and deployment. For example, in Japanese space projects, the use of CFRP bistable booms is being considered for the storable support columns of solar array paddles on a crewed pressurized rover on the moon [1]. Also, the boom considered here is made of woven CFRP, which leads to less twisting deformation in the coiled configuration than the boom made of unidirectional (UD) laminate [2].

Deployable structures on spacecraft are exposed to the long-term storage until their deployment and to the harsh temperature environment in space. From the point of material properties, it is essential to consider time- and temperature-dependent properties called thermoviscoelasticity and the effect of it on the structural behavior. Deployable structures are subjected to deformation during the storage period, and the resulting stress relaxation causes the shape change in both coiled and re-deployed configuration. Regarding the temperature dependence of viscoelastic properties, time-temperature superposition (TTS) principle was widely used and the accelerated testing of booms based on this principle is considered.

Previous studies focused on the resin thermoviscoelasticity and calculated the relaxation properties of woven CFRP by finite element analysis [3]. They dealt with the difficulty to experimentally obtain all the viscoelastic properties for the structural analysis by using numerical method. However, discrepancy between the experimental and numerical values was observed, and the long-term properties were not fully

evaluated. Other studies investigated the shape change of booms with deformation history experimentally and numerically considering the base material thermoviscoelasticity [4,5]. Test conditions for storage time and temperature were insufficient for actual spacecraft applications and accelerated testing.

This study aims to examine the effect of storage time and temperature conditions on shape changes of CFRP bistable booms through boom tests and analyses. In the boom tests, the booms were stored under multiple storage and temperature conditions, and the time-dependent changes in their coiled and re-deployed configurations were measured. In particular, the master curve for storage time and re-deployed shape were created by shifting the test data based on TTS principle. Besides, approximation methods and numerical analyses were conducted under conditions corresponding to the test.

2. BASE MATERIAL CHARACTERIZATION

2.1. Constitutive Equations

A bistable boom in the deployed configuration and the boom coordinate system is shown in Fig. 2. The *x*-axis is defined as the longitudinal direction and the *y*-axis as the circumferential direction of the cross-section. Due to the anisotropy of the boom base material, the constitutive equations are expressed using the stiffness matrices in this coordinate system.

The constitutive equations combine classical lamination theory and linear viscoelasticity and are shown in Eq. 1.

$$\begin{Bmatrix} \boldsymbol{N}(t) \\ \boldsymbol{M}(t) \end{Bmatrix} = \begin{bmatrix} \boldsymbol{A}(t) & \boldsymbol{B}(t) \\ \boldsymbol{B}(t) & \boldsymbol{D}(t) \end{bmatrix} \begin{Bmatrix} \boldsymbol{\varepsilon}(0) \\ \boldsymbol{\kappa}(0) \end{Bmatrix} + \int_0^t \begin{bmatrix} \boldsymbol{A}(t-s) & \boldsymbol{B}(t-s) \\ \boldsymbol{B}(t-s) & \boldsymbol{D}(t-s) \end{bmatrix} \begin{Bmatrix} \dot{\boldsymbol{\varepsilon}}(s) \\ \dot{\boldsymbol{\kappa}}(s) \end{Bmatrix} ds \quad (1)$$

where: {***N***(*t*)} and {***M***(*t*)} are resultant force and moment, {***ε***(*t*)} and {***κ***(*t*)} are middle surface in-plane strain and curvature, and [***A***(*t*)], [***B***(*t*)] and [***D***(*t*)] are the relaxation stiffness matrices.

Previous studies [6] revealed the coupling matrix [***B***(*t*)] and 16 and 26 components of matrices affect the torsion deformation in the coiled configuration. Thus, the woven textile CFRP that can be regarded to have macroscopically four-fold rotational symmetry is used with a fiber orientation angle of ±45°. Then, relaxation stiffness matrices are expressed as Eq. 2.

$$[\boldsymbol{A}(t)] = \begin{bmatrix} A_{11}(t) & A_{12}(t) & 0 \\ & A_{11}(t) & 0 \\ \text{sym.} & & A_{66}(t) \end{bmatrix}$$
$$[\boldsymbol{B}(t)] = [\boldsymbol{O}] \quad (2)$$
$$[\boldsymbol{D}(t)] = \begin{bmatrix} D_{11}(t) & D_{12}(t) & 0 \\ & D_{11}(t) & 0 \\ \text{sym.} & & D_{66}(t) \end{bmatrix}$$

Note that each component is expressed as a linear combination of a constant term and exponential functions with relaxation time τ_k as shown in Eq. 3.

$$A_{ij}(t) = A_{ij,0} + \sum_{k=1}^{n} A_{ij,k} e^{-t/\tau_k}$$
$$D_{ij}(t) = D_{ij,0} + \sum_{k=1}^{n} D_{ij,k} e^{-t/\tau_k} \quad (3)$$

2.2. Time-Temperature Superposition Principle

The temperature dependence of viscoelasticity is described by an empirical law known as the time-temperature superposition (TTS) principle [7]. TTS allows stress relaxation at any given temperature to be represented by shifting that at a reference temperature along the time axis as shown in Fig. 3.

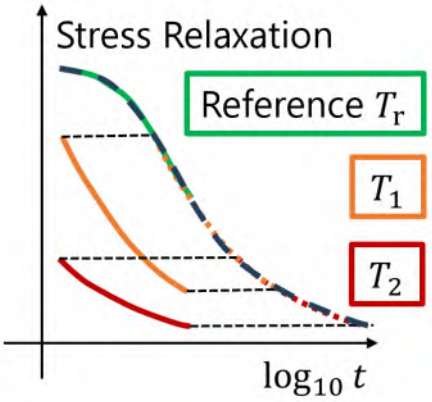


Figure 3: Schematic Diagram of TTS

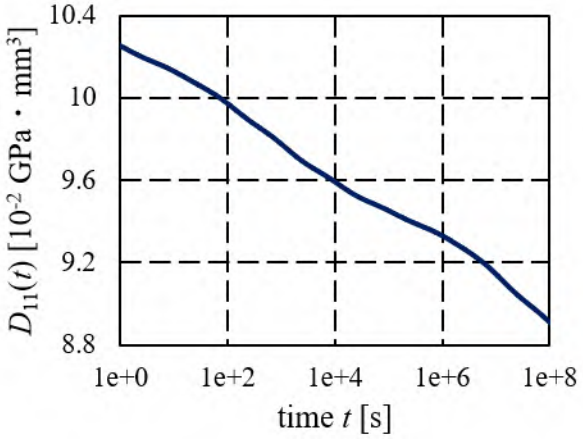


Figure 4: Relaxation Out-of-Plane Stiffness of the Base Material 2-ply 2/2 Twill CFRP

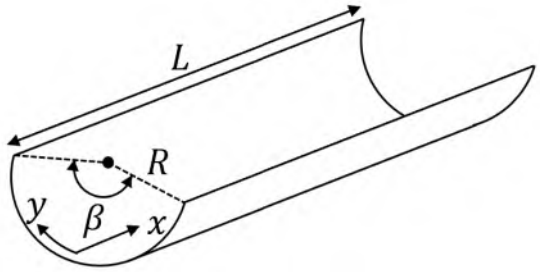


Figure 2: Bistable Boom in the Deployed Configuration and the Coordinate System

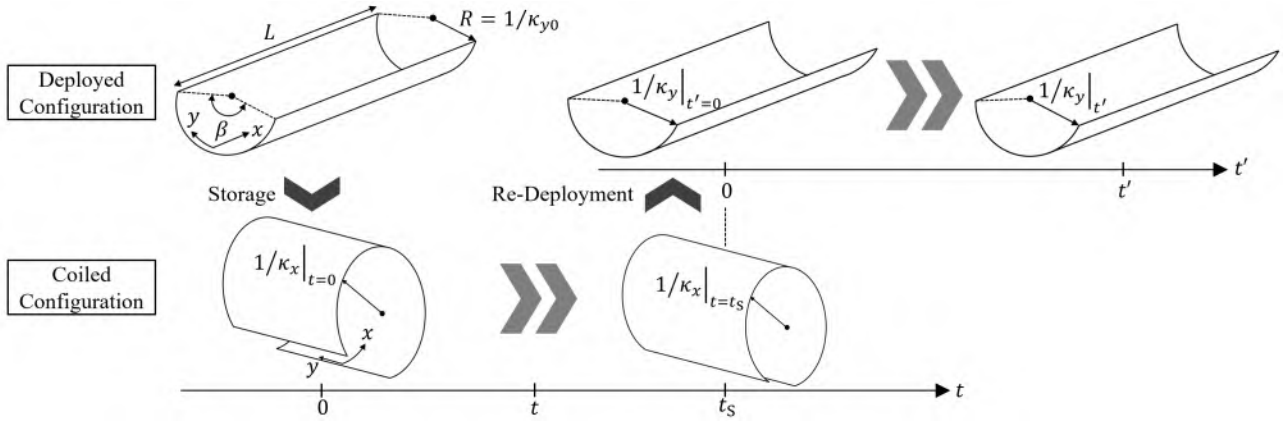


Figure 5: Overview of Boom Deformation

Using the TTS-based time shift factor a(T), the time increment *dt* at temperature *T* is converted to the time increment *dξ* at the reference temperature according to Eq. 4.

$$d\xi = \frac{dt}{a(T)} \tag{4}$$

2.3. Base Material Properties

In this paper, the base material is 2-ply CFRP 2/2 twill weave textile composite. The properties required for the boom shape prediction described later are the relaxation out-of-plane stiffness $D_{11}(t)$ and $D_{12}(t)$. As for $D_{11}(t)$, parameters estimated from DMA test results [8] are used, and the relationship between time and relaxation stiffness is shown in Fig. 4. Note that the relaxation stiffness is expressed with the fiber orientation angle of ±45°, which is the same as bistable booms. Regarding $D_{12}(t)$, the limited temperature dependence was revealed [2], so it is assumed to be expressed by Eq. 5.

$$D_{12}(t) = 0.71 \times D_{11}(0) \tag{5}$$

3. APROXIMATE SOLUTION

3.1. Boom Deformation Flow

This study deals with the boom shape change resulting from the long-term storage and re-deployment, which accounts for the deformation history anticipated for flexible deployable structures on spacecraft. The schematic diagram of the boom deformation is shown in Fig. 5. First, the boom without any deformation history is instantaneously coiled. Next, it keeps its coiled configuration for the given storage duration t_S. During this period, no external force acts on it, and its shape changes over time. Then, it is instantaneously re-deployed, and the boom shape changes over time. As shown in Fig. 5, *t'* represents the elapsed time since the re-deployment.

3.2. Boom Deformation Flow

Previous studies [9,10] derived the analytical method to calculate the coiled shape change based on the principle of minimum potential energy. However, this approach does not cover the re-deployed shape prediction because of the difficulty to analytically jump between the two stable configurations. In this study, the principle of virtual work was adopted to calculate both coiled and re-deployed shape. No external force condition and the integral through the thickness direction yield the following Eq. 6, which is the formulation of the principle.

$$\iint_A \left(N_x\delta\varepsilon_{x0} + N_y\delta\varepsilon_{y0} + N_{xy}\delta\gamma_{xy0} + M_x\delta\kappa_x + M_y\delta\kappa_y + M_{xy}\delta\kappa_{xy}\right)dxdy = 0 \tag{6}$$

To solve boom stable shape change over time using Eq. 6, boom shape approximation is considered. Here, the curvature distribution is assumed to be uniform and the curvature changes during the storage duration and after the re-deployment are expressed in Eqs. 7-8.

Storage duration ($0 \leqq t \leqq t_S$)

$$\begin{cases} \kappa_x(t) = C_0 - \sum_{i=1}^{n} C_i\left(e^{-t/\tau_i} - 1\right) \\ \kappa_y(t) = 0 \\ \kappa_{xy}(t) = 0 \end{cases} \tag{7}$$

After re-deployment ($0 \leqq t'$)

$$\begin{cases} \kappa_x(t') = 0 \\ \kappa_y(t') = C_0' - \sum_{i=1}^{n} C_i'\left(e^{-t'/\tau_i} - 1\right) \\ \kappa_{xy}(t') = 0 \end{cases} \tag{8}$$

Resultant moment components at each time can be calculated using Eqs. 1-3 and Eqs. 7-8. Substituting them into Eq. 6 yields equations to be solved. In this study, the conditions under which the equation holds immediately after the deformation and after the relaxation time τ_k has passed are calculated. This allows the constants C_i and C_i' in Eqs. 7-8 to be determined via a system of n+1 linear equations.

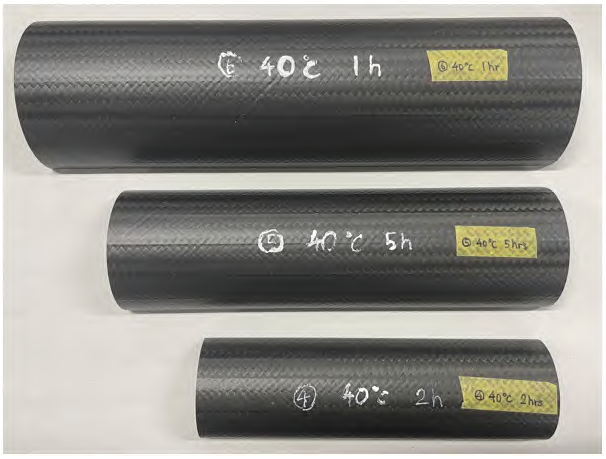


Figure 6: Boom Specimens in the Deployed Shape

Table 1: Boom Specimen Dimensions

Specimen	Radius R [mm]	Length L [mm]
A	20	140
B	25	175
C	30	210

4. BOOM TEST

Tests on bistable booms made of 2-ply 2/2 twill CFRP (See Fig. 6) were conducted to obtain the coiled and re-deployed boom shape data. Among the dimensions determining the initial boom shape shown in Fig. 2, the subtended angle β is 180° in common, while the others are listed in Tab. 1. Tests were performed under multiple conditions of storge time t_S and storage temperature T to evaluate the effects of thermoviscoelasticity. Storage time t_S was set to 10, 20 and 40 minutes, 1, 2 and 5 hours, and 1, 4 and 14 days. Storage temperatures were set to 25 (room temperature), 40, 60, 80 and 100℃. Note that boom specimens were exposed to the room temperature environment except for the storage duration.

Measurement items are the boom cross-section shape before the storage and immediately after the re-deployment. Considering the flexibility of the boom, the boom shape was determined using the cross-section image and the processing software GIMP.

5. RESULTS AND DISCUSSION

5.1. Uniformity of the Cross Section Curvature

In deriving the approximate solution, it was assumed that the curvature distribution of the boom is uniform for both stable configurations. Fig. 7 and Fig. 8 are the cross-section images of coiled and re-deployed boom respectively with the yellow circular arc. As shown in Fig. 7, the most area of the coiled boom almost follows the circular arc, but deviations from it are observed around both ends. This is due to the free-edge effect resulting from the boundary conditions that external forces are zero. Fig.8 shows that the free-edge effect is limited and that the re-deployed boom cross-section can be regarded as

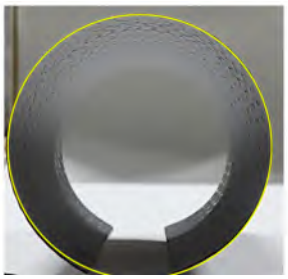


Figure 7: Coiled Boom Cross-Section and Circular Arc Approximation



Figure 8: Re-Deployed Boom Cross-Section and Circular Arc Approximation

the circular arc. Based on this observation, the test data are examined by the cross-section curvature in the following sections.

5.2. Re-Deployed Boom Shape

Fig. 9 shows the relationship between storage time and the cross-section shape immediately after re-deployment. The horizontal axis represents the storage time t_S, and the vertical axis represents the curvature of re-deployed boom cross section (See Fig. 8) κ_y. To compare the re-deployed boom shape recovery of different boom size, the curvature κ_y is normalized by its initial one $1/R$ (See Fig. 2). The test results are presented as a scatter plot, with the prediction results from the approximate solution indicated by dashed and dash-dotted lines. Considering the time lag between re-deployment and shape measurement, prediction results are shown as curves indicating the shape at 1 minute and 10 minutes after re-deployment for each storage time.

Test data indicate the decrease in the cross-section curvature in accordance with rise in storage time and temperature. Also, more than half of the test data at the room temperature condition fall within the predicted range of boom shapes from the approximate solution. However, the discrepancy between test results and the predicted range increases under long-term storage conditions. The reason for this is supposed to be the test method to obtain the relaxation out-of-plane stiffness. The DMA test [8] was conducted with a specimen that is neither sufficiently large relative to the woven CFRP unit cell nor slender. Bending tests with larger specimens are expected to improve the prediction accuracy of relaxation stiffness and boom shape.

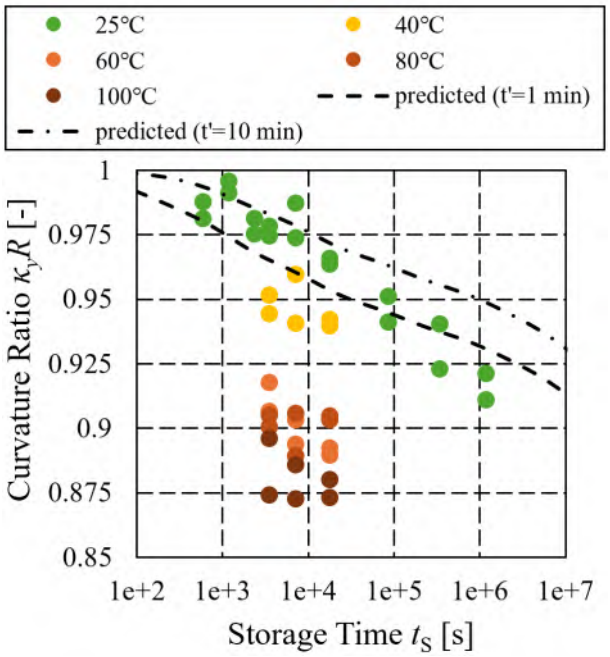


Figure 10: Test and Predicted Results of the Re-Deployed Bistable Boom Shape

5.3. TTS of Boom Test Results

From the practical aspect, the boom shape prediction at the full-scale level is expected using a master curve generated from test data under multiple temperature conditions, which is based on the TTS principle. The master curve of the re-deployed boom shape based on the boom test results and the time shift factors determined from the DMA test [8] is shown in Fig. 10. The equivalent storage time at the reference temperature 25℃ is obtained from dividing the actual storage time by the time shift factor at the storage temperature. There is some variability in the test data, but their distribution allows for fitting with a single curve. This result suggests the validity of acerated testing for bistable booms using the time shift factor of the base material. This master curve can be modified by adding the storage time and temperature conditions so that the shifted data partially overlap.

6. CONCLUSIONS

In this paper, the analytical prediction and sub-scale test were conducted based on the deformation history anticipated for CFRP bistable booms on spacecraft. Test results for room temperature storage conditions were consistent with the analysis. Besides, it was implied that the acceleration under high temperature storage conditions can be characterized by the thermoviscoelastic properties of the boom base material.

REFERENCES

1. Kajihara, S. et al. (2025). Deformation and Buckling Analysis of CFRP Bistable Deployable Boom for Application to Solar Array Paddle Support Members on Lunar Pressurized Rover. 76th IAC, Sydney, Australia.
2. Fujioka, E., Yokozeki, T., Watanabe, A. & Aoki, T. (2019). Analysis on temperature-dependent deployment behavior of bi-stable composite rods. *Adv. Compos. Mater.* 28(3), 245-257.
3. Kwok, K. & Pellegrino, S. (2017). Micromechanics Models for Viscoelastic Plain-Weave Composite Tape Springs. *AIAA J.* 55(1), 309-321.
4. Loulou, Z. & Yokozeki, T. (2020). Evolution Prediction of Bistable Tape Springs' Deployed Shape While Undergoing Stowage at High Temperature. *Trans. JSASS Aerospace Tech. Japan* 18(6), 404-411.
5. Shen, Z., Liu, C. & Li, H. (2020), Viscoelastic analysis of bistable composite shells via absolute nodal coordinate formulation. *Compos. Struct.* 248, 112537.
6. Galletly, D. A. & Guest, S. D. (2004). Bistable composite slit tubes. I. A beam model. *Int. J. Solids Struct.* 41, 4517-4533.
7. Brinson, H. F. & Brinson, L. C. (2008). Polymer Engineering Science and Viscoelasticity: An Introduction, *Springer*, New York, US.
8. Sunaga, Y., Kajihara, S., Yokozeki, T. & Watanabe A. (2026). Thermoviscoelastic Multi-Scale Analysis on Woven CFRP Bistable Semi-Cylindrical Booms. ASC 41st Annual Technical Conference, Madison, Wisconsin, US.
9. Zhang, Z., Li, Y., Wu, H., Chen, D., Yang, J., Wu, H. & Jiang, S. (2018). Viscoelastic bistable behaviour of antisymmetric laminated composite shells with time-temperature dependent properties. *Thin-Walled Struct.* 122, 403-415.
10. Guo, N., Wang, H., Luo, Y., Wang, S., Li, D. & Xu, X. (2024). Viscoelastic modeling and creep behavior analysis of composite bistable column-shell structures based on model validation technology. *Thin-Walled Struct.* 204, 112290.

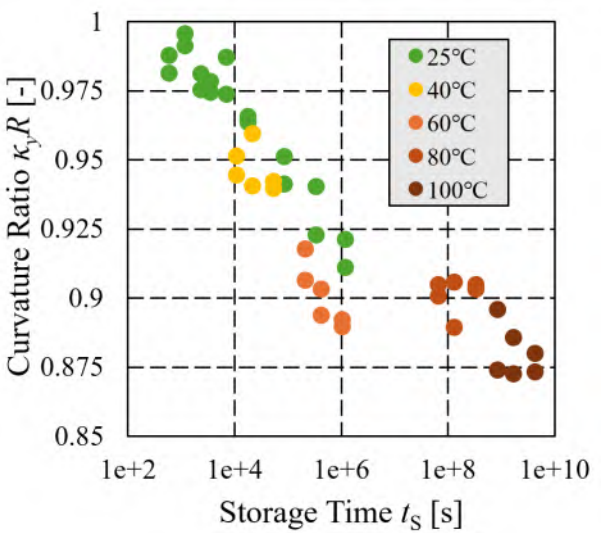


Figure 9: Boom Re-Deployed Shape Master Curve Based on the Base Material Time Shift Factors

DEPLOYMENT DEMOSTRATOR FOR STACKED TRIBAND ANTENNA FOR PNT

Guillermo GONZÁLEZ[(1)], Pepe NIETO[(1)], Diego CHICO[(1)], Mara ESCARTÍ([1)], Rubén CABALLERO[(2)], Benedikt BYRNE[(3)], Ewelina RYSZAWA[(3)]

[(1)] COMET Aerospace SL, Ronda Auguste y Louis Lumière 23, Nave 7, 46980, Paterna, Valencia, Spain
Email: guillermo.gonzalez@comet-aerospace.com, pepe.nieto@comet-aerospace.com, mara.escarti@comet-aerospace.com

[(2)] EOSOL Engineering Consulting SL, Camino de Labiano 45, 31192, Mutilva, Navarra, Spain
Email: ruben.caballero@eosolgroup.com

[(3)] ESA-ESTEC, Noordwijk, The Netherlands

KEYWORDS

Deployable antennas, coilable boom, triband, TRL4.

ABSTRACT

Future satellite missions increasingly demand compact, lightweight, and high-performance antennas capable of covering multiple frequency bands for Positioning-Navigation-Timing (PNT) applications. Traditional antenna systems are limited by rigid structures and size constraints, which can impair deployment feasibility and RF performance in small satellite platforms.

In this context, the research for versatile solutions with high compaction ratios becomes particularly interesting, being the structure explored in this paper especially attractive, as it studies the possibility of housing three antennas for three different bands in a single deployable structure.

1. INTRODUCTION

This project, developed within the framework of the ESA Contract Nº 4000143515/23/NL/AS, [DD-STRA], focuses on the design, analysis, and validation of a stacked tri-band deployable antenna operating in the UHF, L, and S bands, optimized for use in low Earth orbit (LEO) missions. The solution is based on a single-body deployable coilable boom structure that integrates all three bands in a stacked configuration, enabling compact stowage and robust deployment. This structure is composed of four flexible longerons and 20 custom-designed mounts manufactured of space validated plastic, providing both mechanical strength and guidance for the helical antenna elements.

The antenna mechanism deployment is passive, and it is controlled by a motorized system that ensures non-violent and controlled deployment. The deployment mechanism includes a non-pyrotechnic Hold Down and Release Actuator (HDRA) that triggers the self-deployment of the boom using the elastic energy stored in the longerons. The mechanism design eliminates the need for post-deployment locking systems due to the inherent stiffness and cable tension of the deployed structure. Each antenna band is supported by its own coaxial cable feed and PCB.
A comprehensive RF simulation was performed using FEKO software, incorporating detailed geometry, coaxial feeds, and platform effects. The results show compliance with most RF specifications, including gain patterns, return loss, and axial ratio. The antenna achieves a deployed length of 3.25 m and a mass of 4.3 kg, fitting within the LEO mission requirements.

The Manufacturing, Assembly, Integration, and Testing (MAIT) plan includes procurement, mechanical assembly, and RF integration steps, along with a detailed test campaign covering frictional deployment, S-parameters, radiation pattern verification, and mechanical qualification. The finalization of these activities will allow a TRL4 maturity achievement and demonstrate the feasibility of the concept as a modular, efficient, and space-compatible multi-band antenna system.

The project represents a major step forward in deployable antenna technology for small satellites and is the result of a successful collaboration between industry, academia, and the European Space Agency.

2. DESIGN AND ANALYSIS

Mechanical Design

The designed solution consists of a single deployable structure capable of compacting and positioning three antennas of UHF-, L- and S-bands. The deployable structure is based on a coilable boom architecture which can transition from a stowed state, forming the longerons a low-pitch helix, to a deployed state where they are completely straight, providing stiffness and stability to the structure.

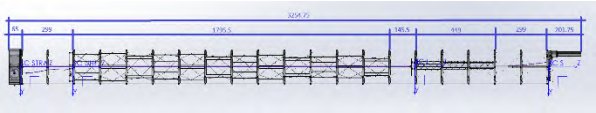


Fig. 1. Deployed STRA.

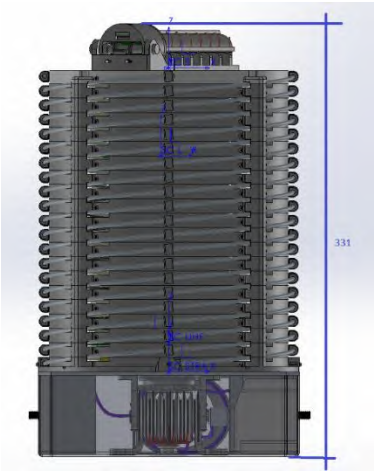


Fig. 2. Stowed STRA.

From the mechanical structure point of view, it consists of four GFRP (Glass Fiber Reinforced Plastic) longerons which are responsible for the passive motorisation of the antenna due to their ability to store elastic strain potential energy in the stowed state, and 20 Ultem mounts that spaced at a length that ensures geometric compatibility between the stowed and deployed states.

The structure is braced by a set of p-aramid tensors with a triple purpose (see Fig. 3).

- Red: deployment control tensors which prevent violent deployment of the structure.
- Green: counter-tensors which stiffen and latch the antenna in the final stage of deployment.
- Yellow: fixed tensors which form St. Andrew's crosses together with the counter-tensors, to brace the structure.

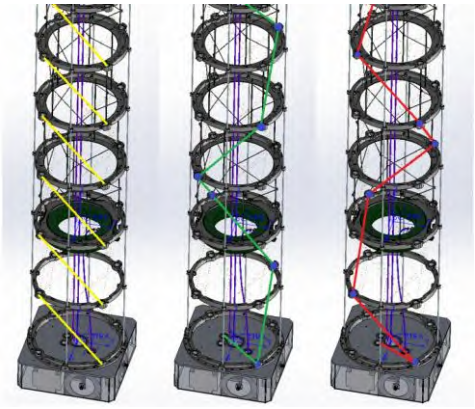


Fig. 3. Antenna control and bracing tensors

The structure remains stowed thanks to the action of an HDRA (Hold Down and Release Actuator). This device has a dual function: on the one hand, it is responsible for releasing the antenna, allowing it to deploy passively; on the other hand, it has the mission of compressing the structure with enough force to ensure that its stiffness in the stowed situation is adequate and to prevent loss of contact (and subsequent bumping) between any of its parts during launch. To withstand this preload, the upper antenna mount (top disc) is made of fibreglass and it is connected by a hollow titanium rod to the HDRA screw, housed in the metal box under the structure.

The deployment control system is driven by a stepper motor. When the HDRA releases the antenna, it tends to deploy explosively, but its movement is controlled by the speed imposed by the motor.

Finally, detailed described the supporting structure, the location of the three antennas on it is shown in Fig. 4.

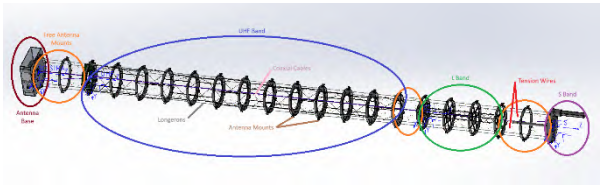


Fig. 4. STRA parts.

The UHF band antenna consists of four wires forming a conical helix with a base diameter of 162 mm, a top diameter of 120 mm, a pitch of 450 mm, and a total height of 1795.5 m. It is housed within 13 of the first mounts, which are connected between them with four non-structural p-aramid threads holding the wires in the approximated helix shape.
The L-band antenna is housed in a similar way to the previous one, consisting of four wires forming a straight helix with 50 mm diameter, 145 mm pitch and a total height of 452 mm. This antenna is comprised in the space between four mounts, after the UHF-band antenna.

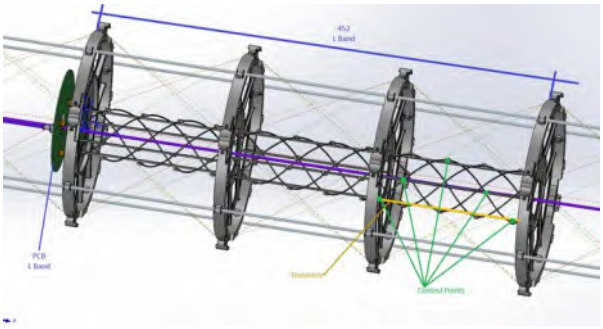


Fig. 5. L-band antenna housing.

The S-band antenna is too small to maintain the deployable concept of the previous two. Therefore, this antenna, consisting of four helical wires with 25 mm diameter, 70 mm pitch and a total height of 140 mm; is embedded in a plastic structure connected to the top disc by means of a hinge and a spring that brings it into position during the deployment manoeuvre.

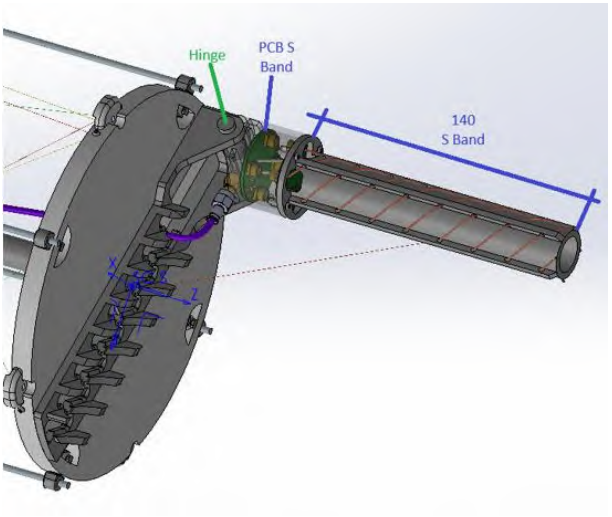


Fig. 6. S-band antenna housing.

Mechanical analysis

Two FEM (Finite Element Model) are built to analyse two different scenarios: stowed structure (preload case and launch load case analyses) and deployed structure (flight case analyses).

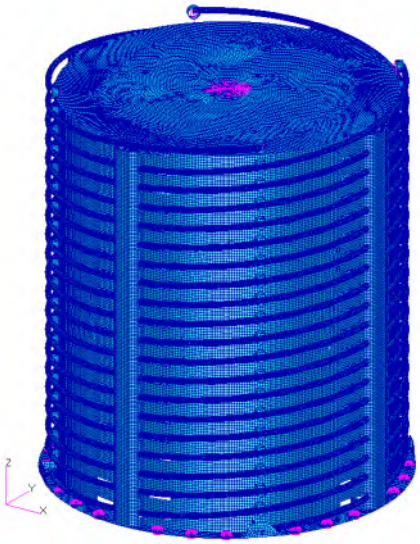


Fig. 7. STRA stowed FEM.

Preload analysis

Employing the stowed FEM, the HDRA is sized on the premise that the compression exerted by the device is enough to prevent separation and bumping of any part of the antenna during launching. To do this, axial (V) and shear (S) forces are recovered at all interfaces of the stowed structure in all launch load cases. The preload required at each interface, knowing the insertion angle of the tongue and groove joint that allows the mounts to fit together when stowed (θ), is calculated as shown below.

$$Preload_{Min} = (V + S \cdot \tan(\theta)) \cdot SF \qquad (1)$$

The effective load distribution of the HDRA preload between the interfaces is calculated using a unit case which, combined with the above information, defines that the minimum device preload required is 14366 N.

Known this value, it is introduced in the stowed model to verify that the structure can withstand it, obtaining the maximum Von Mises stress and the minimum MoS (Margin of Safety) in each part.

Table 1: Preload analysis strength results

	σ_{VM} (MPa)	MoS
Ultem (mounts)	42.66	0.68
GFRP (longeron)	34.06	>5.00
Prepreg glass fabric (top disc)	308.01	0.43

Launch loads analyses

Natural frequencies of the stowed FEM are analysed to better understand its dynamic behaviour under launch loads. The structure has been designed with the aim of achieving a 1st natural frequency greater than 100 Hz (outside the sine specification). As a result, the 1st mode of the structure is at 130.34 Hz.

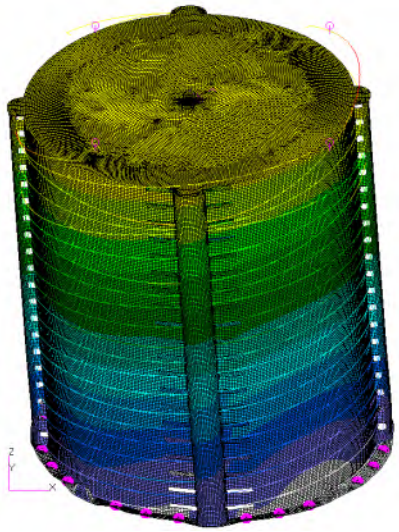


Fig. 8. Stowed FEM 1st vibration mode.

The stowed FEM is analysed under each of the launch loads (Quasi-Static, Sine, Random and Shock), combining the obtained stress results with those from the preload analysis, resulting in the Table 2. It is verified that the random load case is the most critical.

Table 2: Launch load analyses MoS results

	Ultem MoS	GFRP MoS	Prepreg MoS
Pr. + QS	0.28	>5.00	0.41
Pr. + Sine	0.34	>5.00	0.43
Pr. + Random	0.02	>5.00	0.43
Pr. + Shock	0.25	3.96	0.31

Analyses in flight situation

The deployed FEM is built from the previous one, expanding its mounts and adding the tensors that brace the structure.

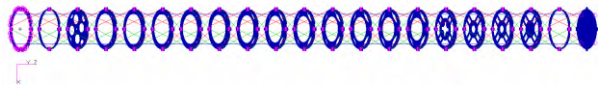


Fig. 9. STRA deployed FEM.

In this situation, only the stiffness and thermoelastic stability of the structure are analysed. The modal analysis shows vibration modes very similar to those of a cantilever beam, being the 1st frequency of 1.76 Hz; while the thermoelastic analysis concludes that both the geometric distortion of the antenna and the stresses derived from the temperature are negligible.

RF Design

The presented triband antenna is basically comprised of three quad-helix antennas, one per frequency band, placed along a deployable boom. Each antenna generates a circularly polarized isoflux pattern that maximizes the uniform power distribution for a global coverage.
Each of the antennas is fed by its own feeding network which is placed just under each one of the helixes. The signal distribution until each feeding network is done through coaxial cables located in the middle of the antenna. The long cables that are required to reach the feeding points of L band and the S band antennas lead to high insertion losses. Fortunately, the application link budget has a large margin, and they can be tolerated.
Many key aspects have been considered in the design, such as the adequate materials selection, the custom shaped feeding networks and the optimized placement of each helix inside the boom.

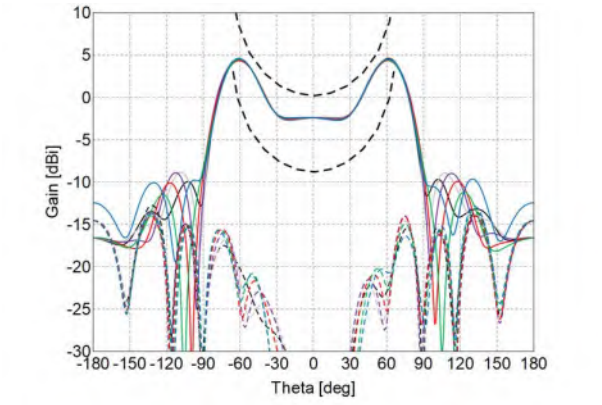


Fig. 10. UHF band isoflux radiation pattern

RF Analysis

The antenna has been modelled in FEKO software for its RF simulation. The electrical model simplification has been key to improve the simulation speed and reduce the required computational resources while maintaining high precision results. This simplification allows the simulation of the antenna including the boom, the support structure, the satellite platform, the feeding network and the cables. This complete electrical model ensures precise RF simulation results.
The copolar and crosspolar radiation patterns (See *Fig. 10* UHF radiation pattern as example), the gain, the axial ratio, the return loss, the phase centre variation, the phase centre stability, the group delay and some more parameters have been simulated and calculated.
The following *Table 3* summarizes some of the most important electrical parameters that define the antenna:

Table 3. Electrical performance summary

Parameter	Value
Frequency band	UHF band, L band and S band
Pattern shape	Isoflux
Polarization	Right-handed circular
Field of view	132º
Bandwidth	50 MHz per frequency band
Return loss	> 10 dB

3. CRITICAL BREADBOARD MANUFACTURING AND TESTING

Mechanical CBB

A mechanical critical breadboard of the structure with dummy electrical parts is manufactured and assembled to verify its mechanical performance and serve as a derisking model.

As the objective is the functional check of the structure, materials used have representative characteristics for this purpose, but they do not necessarily have to be the final ones. Furthermore, different manufacturing and assembly procedures are evaluated to select the best method for building the future final breadboard.



Fig. 11. STRA deployed CBB.

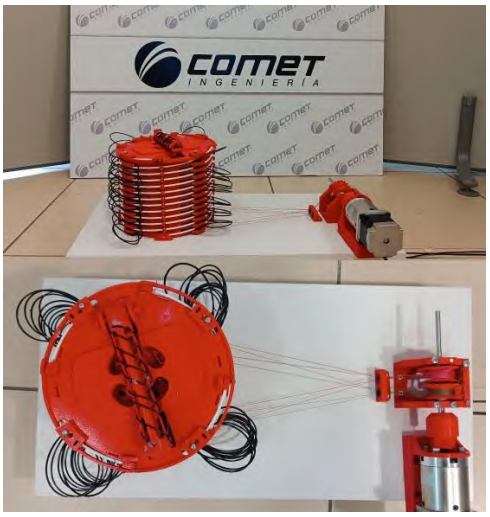


Fig. 12. STRA stowed CBB.

Having finalised the CBB manufacturing, 30 folding and deployment cycles are performed to assess the robustness of the solution. This process starts with the CBB in its stowed state when the stepper motor begins to rotate at a controlled speed, allowing longerons to gradually release elastic potential energy and transition to their nominal position. When the longerons have exhausted their energy, the structure is almost fully deployed, so the last step consists of reversing the rotation direction of the motor to pulling the corresponding tensors (green in Fig. 3) and latching the antenna.

The following lessons are extracted from these experiences:

- The kinematic operation of the structure is correct, and it is able to stow and deploy passively without becoming stuck. There are certain points with slight geometric incompatibilities (Fig. 13) at intermediate stages of the manoeuvre which are corrected in the final model.

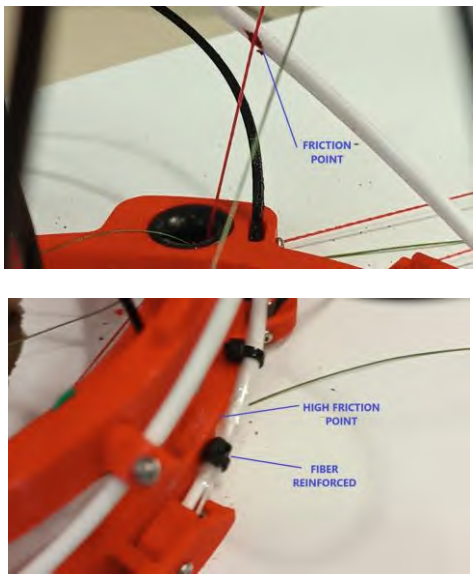


Fig. 13. CBB Collision points.

- The manufacturing methods and 3D printing orientations are correct and suitable for the intended purpose of the structure. No strength issues have been detected in the functional operation, and manufacturing procedures, such as the embedding of the low-friction washers through which the tensors run, have been validated.
- The use of TPU material for the fixed tensors (yellow in Fig. 3) is discarded. The decision to use this material was based on the idea of having threads with adaptive flexibility, all manufactured to the same length using 3D printing; however, it has been concluded that its advantages do not justify its disadvantages and, for the BB, rigid tensors manufactured using a tool will be considered.
- There is enough stowed volume to accommodate the radiating wires that comprise antennas.

RF CBB

In parallel, in the frame of this project, electrical models and feeding networks CBBs are also manufactured and tested.

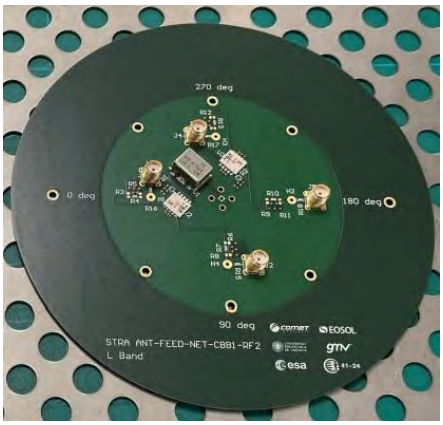


Fig. 14. Manufactured PCB of the CBB L-Band antenna.

There are key parameters that must be verified to validate the design and the manufactured antenna. The isoflux copolar and crosspolar radiation pattern in amplitude and phase, the gain and the return loss are the most important parameters that will be measured over the frequency bands. Many other important parameters such as the phase center related parameters will be calculated from the mentioned ones and compared with simulations.
The antenna will be tested in an anechoic chamber that is able to measure it with a reasonable accuracy even at the UHF frequency band, allowing the validation of the antenna.

4. BREADBOARD MANUFACTURING

After the reduced-scale CBB, a BB of nominal dimensions is manufactured and assembled. The BB measures 200 mm in diameter, 266 mm in height when stowed and 3190 mm when deployed.



Fig. 15. STRA deployed and stowed BB.

The BB manufacture is aligned with the objectives of a TRL 4 project; consequently, the materials of the structure are mechanically representative (and in many cases, conservative), but not necessarily qualified for spatial applications. This includes, for example, the use of UHMWPE tensors, or PLA for the 3D printed parts. Furthermore, the HDRA is omitted as no vibration test campaign is planned, and the motor and electrical components are not space-qualified.



Fig. 16. UHF wire positioning tensors (left top), base (left bottom), L wire positioning tensors (right).

The process is handmade and it begins with the purchase of the raw materials and the manufacturing of the components that comprise the deployable structure (longerons, mounts and tensors). All of these are assembled onto a metal base, which supports the deployable mechanism and houses the harnesses that feed the PCBs.

The wires of the three antennas are measured and installed. Each one is attached to the structure using a slightly different method. The UHF band antenna is supported at its intersections with the mounts, forming a “helix” of straight segments between the mounts and the only support point between each pair of them. The L-band antenna uses a similar system, but due to its smaller size, there are four fixing points between each pair of mounts, which confers its radiating wires a more helical shape. Finally, the S-band antenna is not deployable due to its dimensions, so it is embedded into a plastic fixture that folds 90º and deploys by means of a torsion spring.

The PCBs and their corresponding harnesses, which are housed in the base and deploy at the same time as the structure, are installed and, at this point, the BB is fully assembled and operational.

Before to the test campaign, preliminary deployments are performed to check the BB mechanism works properly.

It is verified that the BB has enough motorisation to deploy against gravity force, without the need for equipment which compensate for this. However, in the stages of the manoeuvre prior to final tensioning (when the longerons are not vertical yet) the flexural stiffness of the assembly is significantly low. Therefore, to prevent buckling due to the gravity action, the deployment takes place inside a methacrylate tube (Fig. 15 right) which acts as an MGSE.

5. MECHANICAL TEST PROCEDURES

Mechanical and radio-electrical tests are performed on both the BB and some of its components. Specifically, on the mechanical side, motorisation and deployment tests are conducted on the complete BB. On the RF side, S-parameters of the complete antenna, the feeding networks, their harness and the SMA connectors are measured; and radiation pattern and gain tests of the complete BB are obtained. In addition, dimensional and mass inspections are also done.

This paper focuses on the mechanical aspects of the project, so procedures of mechanical tests are described in detail below.

Motorisation test

The motorisation test aims to obtain an initial estimation of the axial force exerted by the structure at each moment of the deployment manoeuvre, to assess its motorisation margin.

It is identified that the motorisation force comes from the stored elastic energy of the longerons, while the resistive forces arise from friction at the joints of the structure, friction of the tensors, the resistance exerted by the radiating wires that comprise the antennas, and the resistance of the harness that supplies the PCBs. The deployment mechanism introduces no resistance, as the brake consists of a stepper motor, which is an active element.

Due to the nature of the structure, it is extremely speculative to establish a formulation for estimating the friction of each element at each moment of the manoeuvre. The structure deploys sequentially, with each segment being in a different position to the rest, and the overall configuration being unique at every instant. For this, the experimental approach has been adopted.

Grouping, in one side, as the internal friction of the antenna (R_{Fric}) the resistance originated in joints, tensors and radiating wires; and in the other, the resistance of the harness (R_{Harn}), it is agreed that the motorisation margin of the structure for each deployment % can be expressed as follows.

$$MM(\%) = \frac{F_{Mot}(\%)}{R_{Fric}(\%) + R_{Harn}(\%)} \qquad (2)$$

By analysing the nature of each term in the above expression and assuming that the internal frictions are symmetrical (same magnitude and opposite direction when folding and deploying), the following diagram of forces depending on the movement direction is obtained.

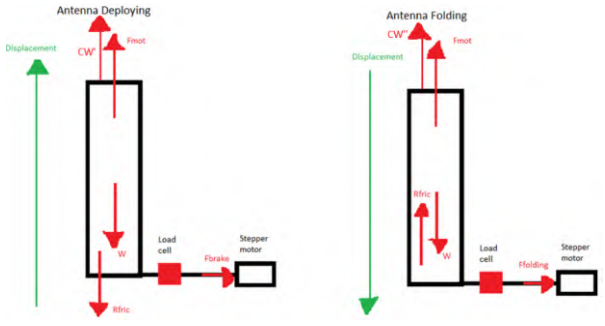


Fig. 17. Force diagram of the BB in deployment and folding.

Where F_{mot} is the motorisation force of the structure, W is the weight of the BB, R_{fric} represents the internal friction, F_{brake}/$F_{folding}$ are the forces reaching the stepper motor and read by the load cell, and CW'/CW'' are the forces exerted by the counterweight (a different value when folding and deploying). It is decided to use a counterweight to prevent the structure from buckling due to the force of gravity instead of the MGSE, so as not to introduce noise into the measurement caused by friction between the BB and the MGSE.

To determine F_{mot}, R_{fric} and R_{Harn}, it is decided to measure the axial force of the BB in three scenarios.

a) Deployment force test without harness.
b) Folding force test without harness.
c) Deployment force test with harness.

In each of which, the load cell measurement can be expressed as a combination of the terms above.

$$F_{a)}(\%) = F_{mot}(\%) - W(\%) - R_{Fric}(\%) + CW' \qquad (3)$$

$$F_{b)}(\%) = F_{mot}(\%) - W(\%) + R_{Fric}(\%) + CW'' \qquad (4)$$

$$F_{c)}(\%) = F_{a)}(\%) - R_{Harn}(\%) \qquad (5)$$

And combining these three measurements it is possible to obtain the variables involved in the calculation of the motorisation margin.

$$R_{Fric}(\%) = \frac{F_{b)}(\%) - F_{a)}(\%) - (CW'' - CW')}{2} \qquad (6)$$

$$R_{Harn}(\%) = F_{a)}(\%) - F_{c)}(\%) \qquad (7)$$

Deployment test

The deployment test aims to demonstrate that the structure is robust enough to withstand 30 deployment manoeuvres without compromising the antenna performance. Along these deployments, the repeatability of the manoeuvre and the deviations and distortions of the structure that could affect the antennas are assessed.
The possible distortions that the structure allows without any of its components evident breaking are as follows.

- Deformation of the structure due to global bending or torsion, resulting in the three antennas being displaced from their nominal position.
- Local diameter reduction of the UHF and L-band antennas due to loss of tension in the positioning threads (Fig. 18 left)
- Random local distortion of the radiating wires of the UHF and L-band antennas between control points (particularly in the UHF-band antenna).

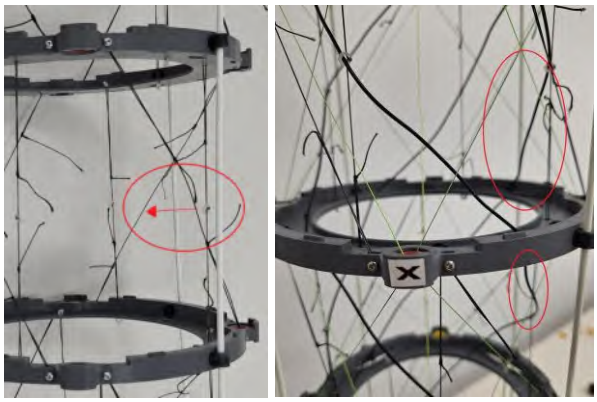


Fig. 18. Unrestricted movement direction of the control points (left), radiant wires with random local distortions (right).

A different measurement strategy will be followed for each of the possible distortions.
To determine the global deformation of the structure, which is expected to be minimal, the position and angle of the top disc is measured by a laser every 15 deployments, extrapolating this measurement linearly to the rest of the length.
To determine the reduction in the diameter of the antennas due to a loss of tension in the threads, the distance between each pair of opposing washers is measured every 15 deployments.
To determine the effect of random local distortions, different models of the UHF and L-band antennas with curvatures of the order of those seen in the BB are randomly generated, and their RF parameters are obtained.

Finally, after the completion of the test campaign, a wear study is performed to identify which areas of the BB suffer more.

6. MECHANICAL TEST RESULTS

Motorisation test results

The axial force exerted by the BB is measured three times for each of the three scenarios described and the mean value is calculated. The graphs obtained from the raw deploying and folding measurements appear as follows.

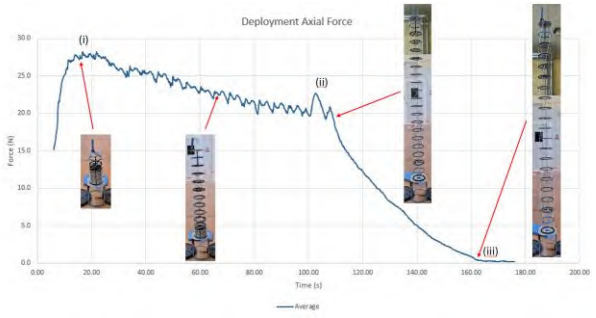


Fig. 19. BB deploying axial force graph shape and phases.

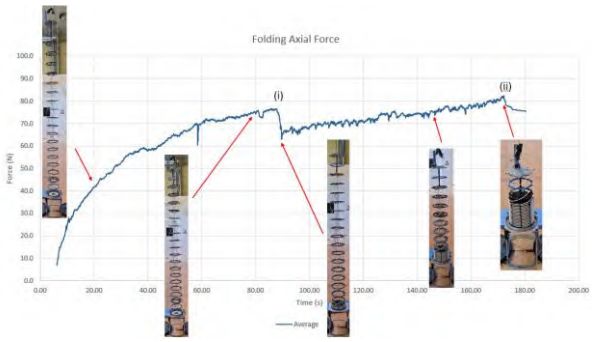


Fig. 20. BB folding axial force graph shape and phases.

Next, the BB mass and the contribution of the counterweight are compensated analytically and by means of auxiliary tests, so that the results represent only the motorisation minus the internal friction and harness resistances. The blue curve corresponds to scenario a), the orange one to b) and the grey one to c).

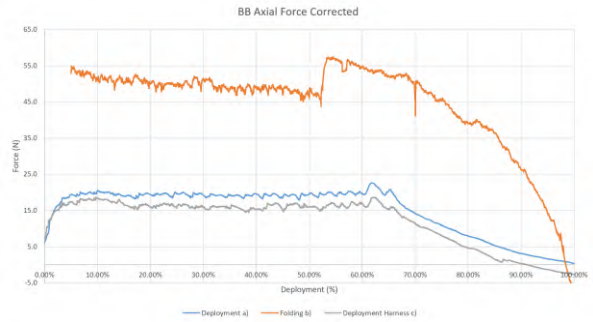


Fig. 21. BB axial force corrected in scenarios a), b) and c).

Operating with the system of equations formed by (3), (6) and (7), the terms F_{mot}, R_{fric} and R_{harn} are obtained. These are calculated along the uniform section of the graph (approximately between 3% and 65% of the deployment). This is because in the final phase of deployment the axial force of the BB tends towards 0; however, the counter-tensioning system starts to operate, providing the extra energy necessary to complete the manoeuvre.

$$\boldsymbol{F_{mot} \in [32.2;\ 36.8]\ N}$$
$$\boldsymbol{R_{fric} \in [12.8;\ 17.7]\ N}$$
$$\boldsymbol{R_{harn} \in [0.9;\ 5.0]\ N}$$

To calculate the motorisation margin, the most appropriate safety factors specified in [1] are applied.

$$MM(\%) = \frac{F_{Mot}(\%)}{2R_{Fric}(\%) + 3R_{Harn}(\%)} \qquad (8)$$

Resulting in an MM in the uniform section of:

$$\boldsymbol{MM \in [0.77;\ 1.02]}$$

In accordance with the ECSS recommendation, the motorisation margin obtained is low, as the standard recommends a margin of 2 once safety factors have

been applied. However, it should not be forgotten that the BB's manufacturing methods are in line with the scope and budget of a TRL4 project; consequently, the surface quality of parts with relative motion between them has significant margin for improvement, so R_{fric} may be reduced. Furthermore, it has been found that the measurement setup introduces some additional friction, which adds a degree of conservatism to the results.

Deployment test results

At the time of the elaboration of this paper, 20 of the 30 planned deployments of the BB campaign have been done; consequently, some results are preliminary, but certain conclusions can already be extracted.

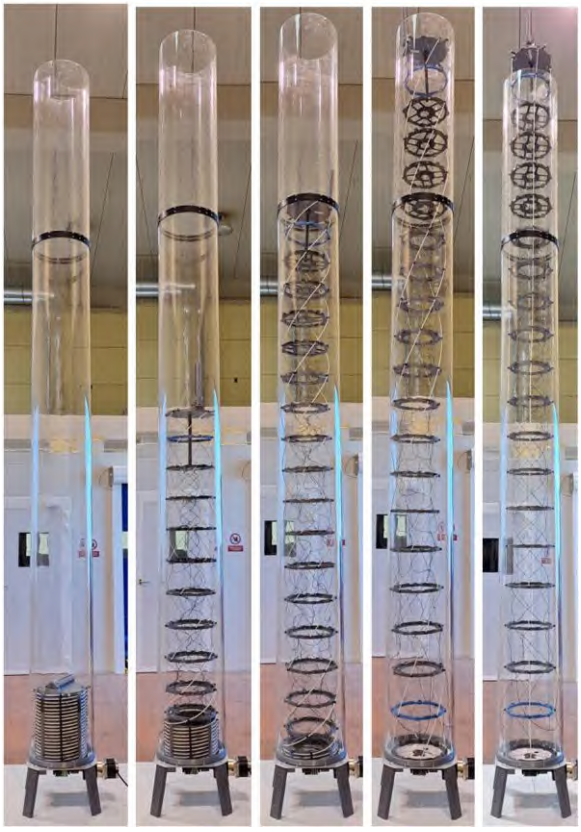


Fig. 22. BB deployment sequence.

First, there is no apparent loss of motorization in the structure due to a possible gradual deterioration. Furthermore, the final position reached by the BB can be forced to be always the same (with a margin of error of a few millimetres), as this is controlled by the tensioning system.

The global deviation of the BB has been measured after manufacture and after 15 deployments. The structure exhibits an approximate deflection of 20 mm and torsion of 16° at its free end, with similar results for both measurements done. The immediate conclusion is that the deviations are caused by manufacturing inaccuracies and tolerances in the model, rather than deterioration by operation. The residual torsion appears to be of some significance, but it has been verified that it has no appreciable impact on the performance of the antennas. The reason for this distortion is that the tensioning by the stepper motor takes place at the base, reducing the latching torque as the height increases due to friction.

Local diameter reduction has increased by around 3 – 4 mm comparing measurements at the start and halfway of the campaign on the UHF band antenna. This distortion is negligible in the L-band antenna. The test campaign needs to continue to determine if this phenomenon worsens with the remaining manoeuvres, or if it has already reached its limit. The impact of this distortion at RF level has not yet been assessed.

The RF impact of random local distortions in radiating wires has not yet been assessed.

7. CONCLUSIONS AND FURTHER STEPS

Conclusions extracted at this stage of the project are listed below:

- An antenna solution has been proposed to satisfy the need identified in the project framework.
- Satisfactory compliance with mechanical and electrical requirements has been verified by analysis.
- It has been confirmed that the solution proposed is feasible and that its deployable structure is functional
- The in-house manufacturing processes for building this type of helical structures have been validated and refined.
- The BB is perfectly capable of deploying against gravity, but the calculated motorisation margin is lower than ECSS recommendation. However, it is considered that there is margin for improvement by removing conservatism.
- It has been verified that the deployment system is robust enough to ensure that the global position of the structure remains unchanged despite the number deployments.
- There are indicators that the reduction in the diameter of the UHF-band antenna local distortions is affected by the number of deployments, but their impact at RF level has not yet been assessed.
- At this stage of the project, it is considered that a robust BB resulting from a design that fulfils the requirements has been achieved; with some areas to improve but leaving a positive impression.

Further steps to mature the technology presented up to TRL4 within the framework of this project are:

- Complete the deployment test campaign and ensure the repeatability and robustness of the structure can be deployment.
- Measure the BB in an anechoic chamber and correlate the results to validate its RF performance.
- Quantify the positional deviations of the radiating elements to assess their impact at RF level is acceptable.

After achieving a design that fulfils the requirements at TRL4 level, the next steps would be:

- Eliminate the conservatism observed regarding motorisation test and study the MM in greater detail.
- Consider flight-grade materials in the manufacturing so that the structure can be tested in representative mechanical environments and under TVAC conditions.
- To frame the antenna within a project involving flight projections that provides more mature requirements and a framework for the development of the solution.

8. ACKNOWLEDGEMENTS

Authors acknowledge the support of the European Space Agency under contract Deployment Demonstrator of Stacked Tri-Band Antenna for Positioning-Navigation-Timming Use Cases on Small Satellites (DD-STRA).

9. REFERENCES

[1] ECSS-E-ST-33-01C Rev 2. *"Mechanisms"*.

A MANUFACTURING-ORIENTED GEOMETRICALLY NONLINEAR PROCEDURE FOR IDENTIFYING THE OPTIMAL ZERO-STRESS CONFIGURATION OF CABLE NETS AND MESHES IN LARGE DEPLOYABLE REFLECTORS

Fabio Argentesi [*(1)], Michele Pasquali [(1)], Sofiane Atek [(1)], Paolo Gaudenzi [(1)], Marco Lapi [(2)], Mario Lanuti [(2)], Antimo Colella [(2)], Davide Scarozza [(2)], Luca Palomba [(2)], Federico Adamo [(2)]

[(1)] Department of Mechanical and Aerospace Engineering, Sapienza University of Rome, Via Eudossiana 18, Rome, 00184, Italy

[(2)] Thales Alenia Space, Via Saccomuro 21-24, Rome, 00131, Italy

[*] Email: fabio.argentesi@uniroma1.it

KEYWORDS

Large Deployable Reflector Design, Nonlinear Finite Element Analysis, Nonlinear Cable-Mesh Structures, Zero-Stress Configuration, Orthotropic Membrane Modelling, Mesh Reflectors Manufacturing.

ABSTRACT

The manufacturing of Large Deployable Mesh Reflectors (LDRs) requires the zero-stress geometry of the cable-mesh assembly, which form finding procedures do not deliver directly. This work presents a geometrically nonlinear, incremental-iterative finite element procedure recovering the unstressed configurations of the front net, rear net and reflective mesh, starting from the deployed prestressed state obtained through an extended Force Density Method. A total Lagrangian description is adopted to release the pretension by progressive load reduction; at each increment the strain and stress states are consistently updated, while rigid body modes are removed via spectral decomposition of the singular tangent stiffness matrix. Cable slackening, reactivation and mesh orthotropy are consistently handled. For a 12.25 m case study, the recovered cable rest lengths match the analytical prediction within 0.01%, and the strongly nonlinear stiffening response observed during unloading confirms the relevance of geometric nonlinearity for an accurate determination of the unstressed state.

1. INTRODUCTION

Modern satellite communication, Earth observation and science missions demand antennas with ever larger apertures and tighter surface accuracy, while keeping mass and stowed volume to a minimum. Large Deployable Reflectors (LDRs) address these competing requirements and have become a cornerstone of next-generation spaceborne antenna systems [1,2]. Among them, mesh reflectors stand out for their lightness, compactness when stowed and scalability [3]. The state-of-the-art architecture in deployable reflector antennas is the the one introduced with AstroMesh [4,5]: a deployable ring truss is coupled with two cable networks, front and rear nets, connected by a system of tensioning ties, while a reflective metallic mesh, beneath the front net, realizes the effective reflecting surface. The same architecture underlies the LDR design developed by Thales Alenia Space Italia (TAS-I), taken as reference in this work (Fig. 1).

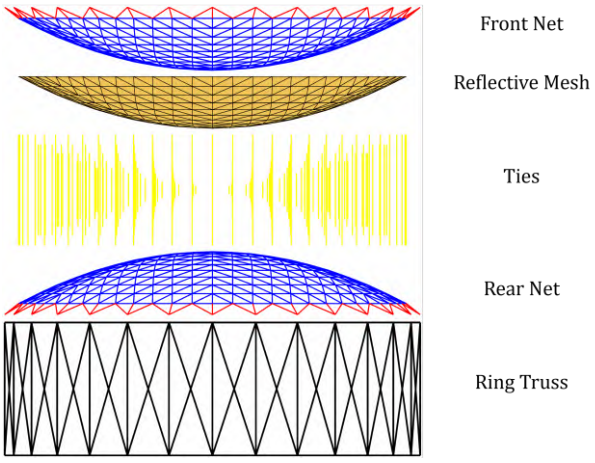


Figure 1: Exploded view of the TAS-I mesh reflector architecture considered in this work..

Cable-mesh structures are tensile structures: their members possess negligible compression and bending stiffness, so their shape is kinematically indeterminate and strongly affected by the member stress levels. Thus, the form-finding process, i.e. the identification of the ideal prestress and the corresponding deployed shape [6], is governed by strong geometric and physical nonlinearities [7,8, 9,10] and is highly sensitive to the zero-stress configuration of the constituent elements [11,12]. The form-finding problem has been extensively investigated [13,14]: Schek introduced the Force Density Method (FDM) [15] as a tool for the linearization of the nonlinear equilibrium equations through the prescription of force-to-length ratios; later developments include the Dynamic Relaxation

Method [16], the Updated Reference Strategy [17], the Natural Force Density Method [18] and the Surface Stress Density Method [19]. Tang et al. [20,21] decompose the membrane stresses into axial and transverse force densities, representing the mesh equilibrium within a nonlinear solution scheme, while Zhang et al. [22] include the compliance of the supporting truss in the cable-network solution.

The equilibrium configuration delivered by most form-finding approaches is not directly related to the unstressed state, which is essential for manufacturing, since cutting patterns, cable rest lengths and assembly tolerances are all defined on the zero-stress geometry. Zero-stress determination for membranes and cable structures has been studied mainly in the civil and architectural literature. Chen et al. [23] propose a least squares treatment of compatibility to handle indeterminacy, releasing selected boundary constraints under minimum-constraint principles, so that the recovered zero-stress state depends on the release scheme. Fan et al. [24] address symmetric cable-strut systems via a Newton iteration method progressively reducing the forces in active members identified by an importance index, while Zhang et al. [25] unify zero-stress form-finding, construction sequencing and prestress force-finding within a single Newton-Raphson loop. Being tailored to civil construction, such techniques translate poorly to spaceborne mesh reflectors, which combine multiple cable nets, a fine reflective mesh and a compliant ring truss; their high static indeterminacy also rules out strategies based on activating individual members or driving selected boundaries.

The present work addresses the recovery of the zero-stress configuration of the cable nets and reflective mesh of a mesh reflector. The deployed, pre-stressed state used as input is obtained through an extended FDM tailored to cable-mesh reflectors [26]. From this balanced reference, a geometrically nonlinear incremental-iterative finite element (FE) procedure gradually reduces the prestress, driving the nodal residual forces to zero. Whenever an element reaches its stress-free length, it is excluded from the equilibrium (and re-admitted if tensioned again), while rigid-body motions are filtered at every step through a modal decomposition of the tangent stiffness matrix. Rather than activating members one by one or replaying a construction sequence, the procedure operates at the structural level, minimizing the nodal residual over each unloaded substructure.

This paper is organized as follows. Section 2 summarizes the equilibrium of the cable-mesh assembly with flexible ring truss, which defines the input of the FE procedure. Section 3 details the geometrically nonlinear FE formulation for the cable and membrane elements and the unstressing algorithm. Section 4 reports the results for the selected case study, and Section 5 draws the conclusions.

2. EQUILIBRIUM OF THE CABLE-MESH ASSEMBLY

This section recalls the equilibrium relations that define the reference (deployed) configuration feeding the FE unstressing procedure. The full derivation of the extended FDM and of the associated multi-objective optimization is given in [26].

2.1. Equilibrium of the cable net

The reflector surface is obtained by cutting a parent paraboloid with an offset cylinder, see Fig. 2. Their intersection curve, called rim, marks the outermost circumferential section of the reflector and is attached to the ring truss through the links, as shown in Fig. 3.

For a cable net made of n_c cables connected by n nodes, the connectivity matrix $\mathbf{C} \in \mathbb{R}^{n_c \times n}$ expresses its topology: the k-th row, associated with a cable joining nodes i and j, has entries +1 and −1 in columns i and j and zero elsewhere [15]. Here, a single quasi-geodesic connection pattern [27] is adopted for both the front and the rear net. Denoting by $\mathbf{q}_c \in \mathbb{R}^{n_c}$ the force density vector of the cables and by $\mathbf{Q}_c \in \mathbb{R}^{n_c \times n_c}$ its corresponding diagonal matrix, the equilibrium equations read

$$\mathbf{I}_3 \otimes (\mathbf{C}^{\mathrm{T}}\mathbf{Q}_c\mathbf{C})\mathbf{r} = \mathbf{f}_c \qquad (1)$$

where $\mathbf{r} = [\mathbf{x}^{\mathrm{T}}, \mathbf{y}^{\mathrm{T}}, \mathbf{z}^{\mathrm{T}}]^{\mathrm{T}} \in \mathbb{R}^{3n}$ collects the nodal coordinates in the global Cartesian frame $(\mathrm{x}, \mathrm{y}, \mathrm{z})$, $\mathbf{f}_c \in \mathbb{R}^{3n}$ is the vector of the external forces acting on the nodes, $\mathbf{I}$ is the identity matrix (with the subscript indicating its dimension) and $\otimes$ denotes the Kronecker product.

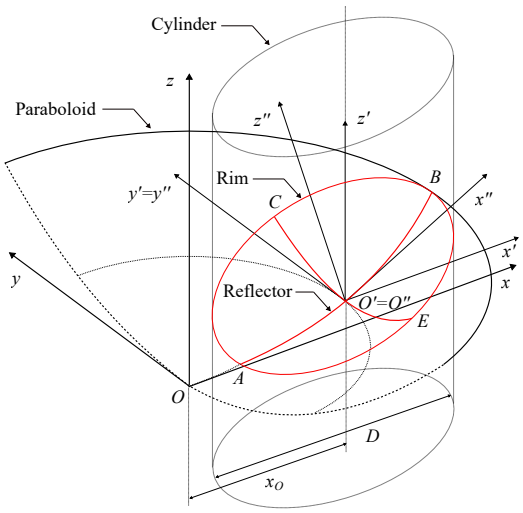


Figure 2: Construction of the offset parabolic surface: a parent paraboloid is intersected with a cylinder of diameter D at an offset distance x_O from the origin of the global reference frame O, yielding the ideal parabolic surface of the reflector [26].

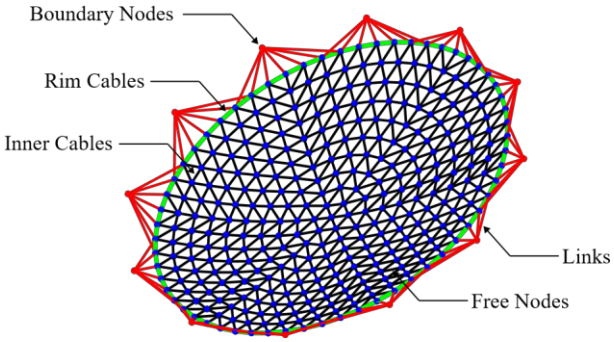


Figure 3: Example of front net topology: free (blue) and boundary (red) nodes; internal cables in black, rim cables in green, links (connecting the net to the ring truss) in red [26].

2.2. Equilibrium of the reflective mesh

Unlike cables, membrane elements work in a plane-stress regime. Their stress state can be described through equivalent axial and transverse forces acting at the element edges, $\mathbf{f}_\mathbf{i}^\tau$ and $\mathbf{f}_\mathbf{i}^\mathbf{n}$ respectively (see Fig. 4). These components are obtained by projecting the equivalent edge tension, and the corresponding force densities can be computed as [21]

$$\mathrm{q}_{\mathrm{m_i}} = \frac{\mathbf{f}_\mathbf{i}^\tau}{|\mathbf{l}_\mathbf{i}|^2} = \frac{1}{2} t_o \mathbf{T}_{\mathbf{q}_\mathbf{i}} \overline{\boldsymbol{\sigma}}, \quad \mathrm{p}_{\mathrm{m_i}} = \frac{\mathbf{f}_\mathbf{i}^\mathbf{n}}{|\mathbf{l}_\mathbf{i}|^2} = t_o \mathbf{T}_{\mathbf{p}_\mathbf{i}} \overline{\boldsymbol{\sigma}} \qquad (2)$$

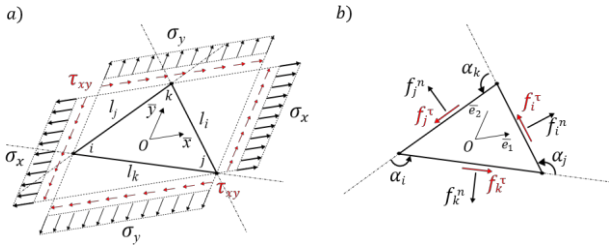


Figure 4: Schematic representation of the a) nominal and b) equivalent tensions in a triangular membrane element [26].

where $\mathbf{l}_\mathrm{i}$ and $\overline{\boldsymbol{\sigma}}$ denote the triangle edge vectors and the Cauchy stress components (in Voigt notation) in the local element frame, and t_o is the membrane thickness. Introducing the shorthand $s_i = sin\,\theta_i = \frac{y_k - y_j}{|l_i|}$, and $c_i = cos\,\theta_i = \frac{x_k - x_j}{|l_i|}$

$$\mathbf{T}_{\mathbf{q}_\mathbf{i}} = \begin{bmatrix} s_i c_i & -s_i c_i & s_i^2 - c_i^2 \\ s_j c_j & -s_j c_j & s_j^2 - c_j^2 \\ s_k c_k & -s_k c_k & s_k^2 - c_k^2 \end{bmatrix} \qquad (3)$$

$$\mathbf{T}_{\mathbf{p}_\mathbf{i}} = \begin{bmatrix} s_i^2 & c_i^2 & -2 s_i c_i \\ s_j^2 & c_j^2 & -2 s_j c_j \\ s_k^2 & c_k^2 & -2 s_k c_k \end{bmatrix} \qquad (4)$$

The choice of the local reference frame is arbitrary. In this work, the origin of each mesh element's local frame is located at the centre of the facet plane; denoting by $\bar{\mathbf{z}}$ the element unit normal vector, directed toward the concavity of the paraboloid, the in-plane axes are defined as $\bar{\mathbf{x}} = (\bar{\mathbf{z}} \times \mathbf{y})/||\bar{\mathbf{z}} \times \mathbf{y}||$ and $\bar{\mathbf{y}} = (\bar{\mathbf{z}} \times \bar{\mathbf{x}})/||\bar{\mathbf{z}} \times \bar{\mathbf{x}}||$ completing a right-handed Cartesian frame.

Similarly to the cable-net case, for a mesh made of n_m triangular elements the topology is described by the matrices $\mathbf{G}, \mathbf{B} \in \mathbb{R}^{3n_m \times n}$: for the generic element m_s connecting the nodes i, j, k sorted counterclockwise ($i \to j \to k$). The rows $3(m_s - 1) + 1, \ldots, 3m_s$ of $\mathbf{G}$ contain the $(+1, -1)$ pairs associated with the ordered edges $(i,j), (j,k)$ and (k,i), while the corresponding rows of $\mathbf{B}$ contain $+1$ in the columns of both nodes of each edge. The mesh equilibrium equations in the edge axial direction then read

$$\mathbf{I}_3 \otimes (\mathbf{B}^\mathrm{T} \mathbf{Q}_\mathrm{m} \mathbf{G}) \mathbf{r} = \mathbf{f}_{\mathrm{m}\tau} \qquad (5)$$

where $\mathbf{Q}_\mathrm{m} \in \mathbb{R}^{3n_m \times n_m}$ collects the membrane axial force densities on its diagonal and $\mathbf{f}_{\mathrm{m}\tau}$ is the vector of the external loads acting along the edge axial direction. The transverse counterpart reads

$$\mathbf{I}_3 \otimes \left(\frac{1}{2} \mathbf{B}^\mathrm{T} \mathbf{P}_\mathrm{m} \boldsymbol{\Gamma}_\mathrm{m} \mathbf{G}\right) \mathbf{r} = \mathbf{f}_{\mathrm{mn}} \qquad (6)$$

where $\mathbf{P}_\mathrm{m} \in \mathbb{R}^{3n_m \times 3n_m}$ is the diagonal matrix of the transverse force densities, $\mathbf{f}_{\mathrm{mn}}$ represents the external loads along the edge transverse direction and $\boldsymbol{\Gamma}_\mathrm{m}$ is the $3n_m \times 3n_m$ block matrix composed of the 3×3 matrices $\boldsymbol{\Gamma}_\mathrm{m}^\mathrm{i}$ relating the transverse force densities to the global frame:

$$\boldsymbol{\Gamma}_\mathrm{m}^\mathrm{i} = \begin{bmatrix} \frac{\cos\alpha_k}{\sin\alpha_k} & -\frac{d_{ij}}{\sin\alpha_k} & 0 \\ 0 & \frac{\cos\alpha_i}{\sin\alpha_i} & -\frac{d_{jk}}{\sin\alpha_i} \\ -\frac{d_{ki}}{\sin\alpha_j} & 0 & \frac{\cos\alpha_j}{\sin\alpha_j} \end{bmatrix} \qquad (7)$$

where for the i-th facet, $\alpha_i, \alpha_j, \alpha_k$ denote the internal angles and d_{ij}, d_{jk}, d_{ki} the edge lengths.

2.3. Ring-truss flexibility and coupled assembly

The cable-net nodes can be partitioned into n_f free and n_g boundary nodes, so that $\mathbf{r} = [\mathbf{r}_\mathbf{f}^\mathrm{T}, \mathbf{r}_\mathbf{g}^\mathrm{T}]^\mathrm{T}$. Denoting by $\mathbf{K}_\mathbf{g} \in \mathbb{R}^{3n_g \times 3n_g}$ the ring-truss stiffness matrix, the ring-truss equilibrium reads

$$\mathbf{K}_\mathbf{g}(\mathbf{r}_\mathbf{g} - \mathbf{r}_\mathbf{g}^\mathbf{0}) = \mathbf{f}_\mathbf{g} \qquad (8)$$

with $\mathbf{r}_\mathbf{g}^\mathbf{0}$ the unstressed boundary-node coordinates. Here, $\mathbf{K}_\mathbf{g}$ is treated as a user-supplied input, obtainable through condensation methods, as done in [28], or via finite element software. Coupling the three sets of equilibrium equations, cable net, mesh and ring truss, through the action-reaction forces exchanged at the interface, and recalling that the

mesh extends only up to the last internal ring, the overall equilibrium of the assembly can be rewritten as:

$$\begin{aligned}\mathbf{I_3}\otimes\left(\mathbf{C}_\mathrm{f}^\mathrm{T}\mathbf{Q}_\mathrm{c}\mathbf{C}_\mathrm{f}+\mathbf{B}_\mathrm{f}^\mathrm{T}\mathbf{Q}_\mathrm{m}\mathbf{G}_\mathrm{f}+\frac{1}{2}\mathbf{B}_\mathrm{f}^\mathrm{T}\mathbf{P}_\mathrm{m}\boldsymbol{\Gamma}_\mathrm{m}\mathbf{G}_\mathrm{f}\right)\mathbf{r}_\mathrm{f}\\ +\mathbf{I_3}\otimes\left(\mathbf{C}_\mathrm{f}^\mathrm{T}\mathbf{Q}_\mathrm{c}\mathbf{C}_\mathrm{g}\right)\mathbf{r}_\mathrm{g}=0\\ \mathbf{I_3}\otimes\left(\mathbf{C}_\mathrm{g}^\mathrm{T}\mathbf{Q}_\mathrm{c}\mathbf{C}_\mathrm{f}\right)\mathbf{r}_\mathrm{f}+\mathbf{I_3}\otimes\left(\mathbf{C}_\mathrm{g}^\mathrm{T}\mathbf{Q}_\mathrm{c}\mathbf{C}_\mathrm{g}\right)\mathbf{r}_\mathrm{g}\\ +\mathbf{K}_\mathrm{g}\left(\mathbf{r}_\mathrm{g}-\mathbf{r}_\mathrm{g}^0\right)=0\end{aligned}\qquad(9)$$

where $\mathbf{C_f}\in\mathbb{R}^{n_c\times n_f}$ and $\mathbf{C_g}\in\mathbb{R}^{n_c\times n_g}$ denote the free- and boundary-node partitions of the cable-net connectivity matrix, and $\mathbf{G_f}$, $\mathbf{B_f}\in\mathbb{R}^{3n_m\times n_f}$ are the analogous partitions for the mesh. Solving Eq. 9 yields the deployed configuration and the prestress field used as the reference state in the following sections. In addition, several strategies for node placing and gradient-based multi-objective optimization can be considered while solving Eq. 9 to obtain a constrained deployed configuration [26].

3. GEOMETRICALLY NONLINEAR FE FORMULATION

The unstressed geometry is retrieved by progressively reducing the forces that the ring truss, as sized in the design stage, applies to the cable-mesh assembly in the deployed state. Two features specific to this class of structures deserve attention before detailing the procedure.

3.1. General assumptions and methodology

Both the mesh and the cable net lack bending and compressive stiffness, thus, infinitely many spatial configurations share the same (null) stress state, differing by zero-strain motions. For manufacturing it is enough to determine one sufficiently regular representative of this family, which legitimizes simplifying assumptions on the path itself: the tensioning forces of net and mesh are taken as fixed in direction and decreasing in magnitude, so that the residual forces are minimized with respect to a known term. Under this assumption the coupling forces arising between mesh and net during unloading can be neglected, and the two subsystems can be unloaded independently. A full Newton-Raphson scheme [29,30] is therefore adopted, linearly reducing the magnitude of the tensioning forces while keeping their direction constant; for each load decrement, an iterative procedure minimizes the balance residual forces until convergence.

A final consideration concerns matrix inversion. Once net and mesh are separated from the ring truss, their tangent stiffness matrices become singular. Rigid-body content is therefore removed at every iteration through a spectral decomposition [29,31]. Let $\boldsymbol{\Phi}\in\mathbb{R}^{k\times k}$ and $\boldsymbol{\Lambda}\in\mathbb{R}^{k\times k}$ denote the orthonormal eigenvectors ($\boldsymbol{\Phi}^\mathrm{T}\boldsymbol{\Phi}=\mathbf{I}$) and the diagonal eigenvalue matrix of $\mathbf{K}\in\mathbb{R}^{\mathrm{k}\times\mathrm{k}}$. The nodal displacements are mapped to modal coordinates $\mathbf{p}=\boldsymbol{\Phi}\,\hat{\mathbf{p}}$ and only the $k-m$ modes with non-zero eigenvalue are in the reduced basis $\boldsymbol{\Phi}_\mathrm{r}\in\mathbb{R}^{k\times(k-m)}$, free of rigid-body modes. In this reduced space, $\boldsymbol{\Lambda}_\mathrm{r}$ denotes the diagonal stiffness and $\hat{\mathbf{f}}_\mathbf{r}$, $\hat{\mathbf{p}}_\mathbf{r}$ the reduced force and displacement vectors. Thus, the (invertible) reduced system reads

$$\hat{\mathbf{p}}_\mathrm{r}=\boldsymbol{\Lambda}_\mathrm{r}^{-1}\,\hat{\mathbf{f}}_\mathrm{r}\qquad(10)$$

and the displacement field is finally reconstructed as $\mathbf{p}=\boldsymbol{\Phi}_\mathrm{r}\,\hat{\mathbf{p}}_\mathrm{r}$.

3.2. Kinematics of the cable net

Following Fig. 5, in the global frame, let the reference position, the displacement and the current position of the nodes be denoted, respectively, by

$$\mathbf{r}^\mathrm{T}=[\mathrm{x},\mathrm{y},\mathrm{z}],\quad \mathbf{p}^\mathrm{T}=[\mathrm{u},\mathrm{v},\mathrm{w}],\quad \mathbf{h}=\mathbf{r}+\mathbf{p}\qquad(11)$$

where u, v and w are the displacement components along the global x, y and z directions. For a generic cable element connecting nodes i and j, the nodal coordinate and displacement vectors read $\mathbf{r}_\mathrm{e}^\mathrm{T}=[x_i,\ x_j, y_i, y_j,\ z_i,\ z_j]$ and $\mathbf{p}_\mathrm{e}^\mathrm{T}=[u_i,\ u_j,\ v_i,\ v_j,\ w_i,\ w_j]$, henceforth denoted by $\mathbf{r}$ and $\mathbf{p}$ dropping the $[\cdot]_e$ subscript for clarity. From these, the support entities $\mathbf{r}_\delta^\mathrm{T}=[x_{ji},\ y_{ji},\ z_{ji}]$ and $\boldsymbol{p}_\boldsymbol{\delta}^T=[u_{ji},\ v_{ji}, w_{ji}]$ are defined, with $x_{ji}=x_j-x_i$ and analogous expressions for the remaining components. The reference and actual squared lengths of the element are $\mathrm{l}_0^2=4\alpha_0^2=\mathbf{r}_\delta^\mathrm{T}\mathbf{r}_\delta$, and $\mathrm{l}^2=(\mathbf{r}_\boldsymbol{\delta}+\mathbf{p}_\boldsymbol{\delta})^\mathrm{T}(\mathbf{r}_\boldsymbol{\delta}+\mathbf{p}_\boldsymbol{\delta})$ so that the Green Lagrange expression of the element strain reads [32]

$$\varepsilon=\frac{1}{\mathrm{l}_0^2}\left(\mathbf{r}_\delta^\mathrm{T}\mathbf{p}_\delta+\frac{1}{2}\mathbf{p}_\delta^\mathrm{T}\mathbf{p}_\delta\right)=\mathbf{b}_1^\mathrm{T}\mathbf{p}+\frac{1}{2\alpha_0^2}\mathbf{p}^\mathrm{T}\mathbf{A}\mathbf{p}\qquad(12)$$

where the following supporting variables were used:

$$\mathbf{b}_1^\mathrm{T}(\mathbf{r})=\frac{1}{4\alpha_0^2}\left[-\mathrm{x}_{\mathrm{ji}},\ \mathrm{x}_{\mathrm{ji}},\ -\mathrm{y}_{\mathrm{ji}},\ \mathrm{y}_{\mathrm{ji}},\ -\mathrm{z}_{\mathrm{ji}},\ \mathrm{z}_{\mathrm{ji}}\right]\qquad(13)$$

$$\mathbf{A}=\frac{1}{4}\begin{bmatrix}1&-1&0&0&0&0\\-1&1&0&0&0&0\\0&0&1&-1&0&0\\0&0&-1&1&0&0\\0&0&0&0&1&-1\\0&0&0&0&-1&1\end{bmatrix}\qquad(14)$$

An increment (or, as here, a decrement) of the external load produces an element displacement variation: $\Delta\mathbf{p}^\mathrm{T}=[\Delta u_i,\ \Delta u_j,\ \Delta v_i,\ \Delta v_j,\ \Delta w_i,\ \Delta w_j]$. The corresponding strain variation is

$$\Delta\varepsilon=(\mathbf{b}_1+\mathbf{b}_2)^\mathrm{T}\boldsymbol{\Delta}\mathbf{p}+\frac{1}{2\alpha_0^2}\boldsymbol{\Delta}\mathbf{p}^\mathrm{T}\mathbf{A}\boldsymbol{\Delta}\mathbf{p}\simeq\mathbf{b}^\mathrm{T}\boldsymbol{\Delta}\mathbf{p}\qquad(15)$$

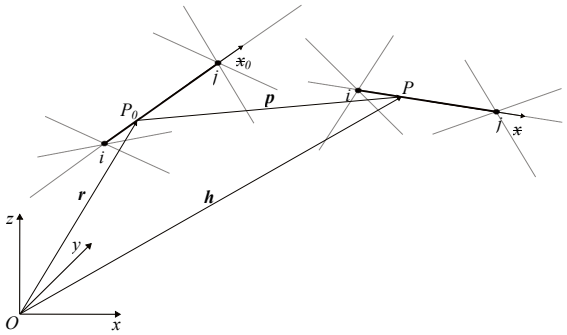


Figure 5: Reference and current configuration of a cable-net element [26].

where

$$\mathbf{b}_2^{\mathrm{I}}(\mathbf{p}) = \frac{1}{4\alpha_0^2}\left[-u_{ji},\, u_{ji},\, -v_{ji},\, v_{ji},\, -w_{ji},\, w_{ji}\right] \qquad (16)$$

so that $\mathbf{b} = \mathbf{b}_1 + \mathbf{b}_2$. For small displacements, the quadratic term in Eq. 15 can be neglected. With linearly elastic, isotropic cables of Young's modulus E, the Second Piola-Kirchhoff stress increment is $\Delta\sigma = \mathrm{E}\,\Delta\varepsilon$. Following the standard full Newton-Raphson scheme [29], after each load update the displacement corrections $\mathrm{d}\mathbf{p}$ are iterated to reduce the balance residual, with the associated strain and stress corrections $\mathrm{d}\varepsilon \simeq \mathbf{b}^{\mathrm{T}}\mathrm{d}\mathbf{p}$ and $\mathrm{d}\sigma = \mathrm{E}\,\mathrm{d}\varepsilon$.

3.3. Tangent stiffness matrix of the cable net

The principle of virtual work for the cable element, written in terms of the internal force vector $\mathbf{f}$ and of virtual displacement $\delta\mathbf{p}$ reads

$$\begin{aligned}\sum_{\mathrm{e}} \delta\,\mathbf{p}^{\mathrm{T}}\mathbf{f} &= \sum_{\mathrm{e}} \int_{\mathrm{V_0}} \sigma\,\delta\varepsilon \mathrm{dV} \\ &\simeq \sum_{\mathrm{e}} \delta\,\mathbf{p}^{\mathrm{T}} \int_{\mathrm{V_0}} \sigma\,\mathbf{b}\mathrm{dV}\end{aligned} \qquad (17)$$

where $\sum_{\mathrm{e}}$ denotes summation over elements. Since Eq. 17 must hold for any $\delta\mathbf{p}$

$$\begin{aligned}\mathbf{f} &= \int_{\mathrm{V_0}} \sigma\,\mathbf{b}\mathrm{dV} = 2\alpha_0 \mathrm{A}_0 \sigma(\mathbf{b}_1(\mathbf{r}) + \mathbf{b}_2(\mathbf{p})) \\ &= \mathbf{f}_1(\mathbf{r}) + \mathbf{f}_2(\mathbf{p})\end{aligned} \qquad (18)$$

with A_0 the cable cross-section area. Introducing the out-of-balance element force vector $\mathbf{g} = \mathbf{f} - \mathbf{f}_{\mathrm{c}}$, with $\mathbf{f}_{\mathrm{c}}$ the element external forces (assumed constant), the tangent stiffness matrix is defined as [32]

$$\mathbf{K_t}(\mathbf{r},\mathbf{p}) = \frac{\partial \mathbf{g}}{\partial \mathbf{p}} = \frac{\partial \mathbf{f}}{\partial \mathbf{p}} = 2\alpha_0 \mathrm{A}_0 \left(\mathbf{b}\frac{\partial \sigma}{\partial \mathbf{p}} + \frac{\partial \mathbf{b}}{\partial \mathbf{p}}\sigma\right) \qquad (19)$$

Since $\partial\sigma/\partial\mathbf{p} = \mathrm{E}\,\partial\varepsilon/\partial\mathbf{p} = \mathrm{E}\,\mathbf{b}^{\mathrm{T}}$, the first term of Eq. 19 becomes $2E\alpha_0 A_0 \mathbf{b}\mathbf{b}^{\mathrm{T}} = \mathbf{K_{t1}} + \mathbf{K_{t2}}$, where

$$\mathbf{K_{t1}}(\mathbf{r}) = 2\mathrm{E}\mathrm{A}_0\alpha_0 \mathbf{b_1}\mathbf{b_1}^{\mathrm{T}} \qquad (20)$$

$$\begin{aligned}&\mathbf{K_{t2}}(\mathbf{r},\mathbf{p}) \\ &= 2\mathrm{E}\mathrm{A}_0\alpha_0\left(\mathbf{b_1}\mathbf{b_2}^{\mathrm{T}} + \mathbf{b_2}\mathbf{b_1}^{\mathrm{T}} + \mathbf{b_2}\mathbf{b_2}^{\mathrm{T}}\right)\end{aligned} \qquad (21)$$

while the second term, exploiting the fact that only $\mathbf{b}_2$ depends on $\mathbf{p}$ and that $\mathbf{A}$ is as in Eq. 14, yields the geometric (stress) contribution

$$\mathbf{K_{t\sigma}}(\mathbf{r},\mathbf{p}) = 2\alpha_0 \mathrm{A}_0 \frac{\partial \mathbf{b_2}}{\partial \mathbf{p}}\sigma = \frac{2\mathrm{A}_0\sigma}{\alpha_0}\mathbf{A} \qquad (22)$$

The contribution $\mathbf{K_{t1}}(\mathbf{r})$ is the linear stiffness involving only the initial geometry of the net and is therefore unchanged throughout the unloading. Summing the terms, the element tangent stiffness matrix is

$$\mathbf{K_t} = \mathbf{K_{t1}} + \mathbf{K_{t2}} + \mathbf{K_{t\sigma}} \qquad (23)$$

3.4. Kinematics of the mesh

Consider now a triangular element with vertices i, j and k, whose global positions and displacements are collected in $\mathbf{r}^{\mathrm{T}} = [x_i, x_j, x_k, y_i, y_j, y_k, z_i, z_j, z_k]$ and $\mathbf{p}^{\mathrm{T}} = [u_i, u_j, u_k, v_i, v_j, v_k, w_i, w_j, w_k]$ (Fig. 6).
Adopting an isoparametric formulation in the local element frame $(\bar{x}, \bar{y})$, the position and displacement fields are interpolated as $\bar{x} = [\bar{x}_i, \bar{x}_j, \bar{x}_k]\boldsymbol{\chi}^{\mathrm{T}}$, $\bar{y} = [\bar{y}_i, \bar{y}_j, \bar{y}_k]\boldsymbol{\chi}^{\mathrm{T}}$, $\bar{u} = [\bar{u}_i, \bar{u}_j, \bar{u}_k]\boldsymbol{\chi}^{\mathrm{T}}$ and $\bar{v} = [\bar{v}_i, \bar{v}_j, \bar{v}_k]\boldsymbol{\chi}^{\mathrm{T}}$ $\bar{w} = [\bar{w}_i, \bar{w}_j, \bar{w}_k]\boldsymbol{\chi}^{\mathrm{T}}$, where $\boldsymbol{\chi} = [\xi, \eta, 1 - \xi - \eta]^{\mathrm{T}}$ is the shape-function vector, defined as the ratios between the areas of the three sub-regions identified by the element vertices and its centre and the total element area. The Jacobian matrix of the element in the local frame is

$$\bar{\mathbf{J}} = \begin{bmatrix} \frac{\partial \bar{x}}{\partial \xi} & \frac{\partial \bar{y}}{\partial \xi} \\ \frac{\partial \bar{x}}{\partial \eta} & \frac{\partial \bar{y}}{\partial \eta} \end{bmatrix} = \begin{bmatrix} (\overline{x_i} - \overline{x_k}) & (\overline{y_i} - \overline{y_k}) \\ (\overline{x_j} - \overline{x_k}) & (\overline{y_j} - \overline{y_k}) \end{bmatrix} \qquad (24)$$

The displacement derivative vector $\mathbf{d}$, collecting the six in-plane gradients $u_x, u_y, v_x, v_y, w_x, w_y$ (where $(\cdot)_x$ denotes $\partial(\cdot)/\partial x$), is obtained as,

$$\mathbf{d} = \mathbf{G}\mathbf{p} \qquad (25)$$

with $\mathbf{G}$ the block diagonal operator built from

$$\mathbf{G}_{\mathrm{b}} = \begin{bmatrix} \bar{\mathbf{J}}_{1,1}^{-1}\boldsymbol{\chi}_{\xi}^{\mathrm{T}} + \bar{\mathbf{J}}_{1,2}^{-1}\boldsymbol{\chi}_{\eta}^{\mathrm{T}} \\ \bar{\mathbf{J}}_{2,1}^{-1}\boldsymbol{\chi}_{\xi}^{\mathrm{T}} + \bar{\mathbf{J}}_{2,2}^{-1}\boldsymbol{\chi}_{\eta}^{\mathrm{T}} \end{bmatrix} \qquad (26)$$

with $\boldsymbol{\chi}_{\xi} = [1, 0, -1]^{\mathrm{T}}$ and $\boldsymbol{\chi}_{\eta} = [0, 1, -1]^{\mathrm{T}}$ the shape-function derivatives. The Green-Lagrange nonlinear deformations, expressed in engineering form via Voigt notation, read [32]

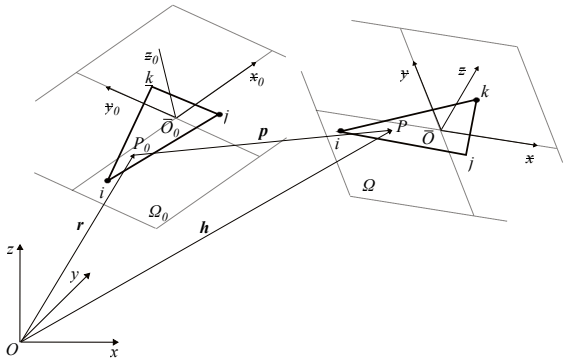


Figure 6: Reference and current configuration of a triangular mesh element [26].

$$\bar{\boldsymbol{\varepsilon}} = \begin{bmatrix} \bar{\varepsilon}_{xx} \\ \bar{\varepsilon}_{yy} \\ \bar{\gamma}_{xy} \end{bmatrix} = \left[\mathbf{H} + \frac{1}{2}\bar{\mathbf{A}}\right]\bar{\mathbf{d}} = \bar{\boldsymbol{\varepsilon}}_1 + \bar{\boldsymbol{\varepsilon}}_2 \qquad (27)$$

where the constant Boolean-like matrix $\mathbf{H}$ extracts the linear part,

$$\mathbf{H} = \begin{bmatrix} 1 & 0 & 0 & 0 & 0 & 0 \\ 0 & 0 & 0 & 1 & 0 & 0 \\ 0 & 1 & 1 & 0 & 0 & 0 \end{bmatrix} \qquad (28)$$

and the displacement-dependent matrix collects the quadratic terms,

$$\bar{\mathbf{A}}(\bar{\mathbf{d}}) = \begin{bmatrix} \frac{\partial \bar{u}}{\partial \bar{x}} & 0 & \frac{\partial \bar{v}}{\partial \bar{x}} & 0 & \frac{\partial \bar{w}}{\partial \bar{x}} & 0 \\ 0 & \frac{\partial \bar{u}}{\partial \bar{y}} & 0 & \frac{\partial \bar{v}}{\partial \bar{y}} & 0 & \frac{\partial \bar{w}}{\partial \bar{y}} \\ \frac{\partial \bar{u}}{\partial \bar{y}} & \frac{\partial \bar{u}}{\partial \bar{x}} & \frac{\partial \bar{v}}{\partial \bar{y}} & \frac{\partial \bar{v}}{\partial \bar{x}} & \frac{\partial \bar{w}}{\partial \bar{y}} & \frac{\partial \bar{w}}{\partial \bar{x}} \end{bmatrix} \qquad (29)$$

The corresponding element local stress is $\bar{\sigma} = [\bar{\sigma}_{xx}, \bar{\sigma}_{yy}, \bar{\sigma}_{xy}] = \bar{\mathbf{Q}}\bar{\boldsymbol{\varepsilon}}$, where $\bar{\mathbf{Q}}$ is the membrane local stiffness matrix. $\bar{\mathbf{Q}}$ accounts for the deposition angle θ of the reflective mesh: a counterclockwise rotation about the local normal describing how far the element axes deviate from the material isotropy axes (Fig. 7). For an orthotropic membrane with isotropy axes L (longitudinal) and T (transverse), the stiffness matrix in the LT frame is, with $\Delta = 1 - \nu_{LT}\,\nu_{TL}$,

$$\boldsymbol{C}^{(LT)} = \frac{1}{\Delta}\begin{bmatrix} E_L & \nu_{TL}E_L & 0 \\ \nu_{LT}E_T & E_T & 0 \\ 0 & 0 & G_{LT}\kappa \end{bmatrix} \qquad (30)$$

Introducing the Reuter matrix, $\mathbf{R}$, and the in-plane rotation matrix $\mathbf{T}(\theta)$ relating the true and engineering strains as

$$\mathbf{R} = \mathrm{diag}(1, 1, 2) \qquad (31)$$

$$\mathbf{T}(\theta) = \begin{bmatrix} c^2 & s^2 & 2sc \\ s^2 & c^2 & -2sc \\ -sc & sc & c^2 - s^2 \end{bmatrix} \qquad (32)$$

with $s = sin\ \theta$ and $c = cos\ \theta$, the local stresses read

$$\bar{\boldsymbol{\sigma}} = \mathbf{T}_\sigma \mathbf{C}^{\mathrm{LT}} \mathbf{T}_\varepsilon \bar{\boldsymbol{\varepsilon}},\ \mathbf{T}_\sigma = \mathbf{T}^{-1}, \mathbf{T}_\varepsilon = \mathbf{R}\mathbf{T}\mathbf{R}^{-1} \qquad (33)$$

so that $\bar{\mathbf{Q}} = \mathbf{T}_\sigma \mathbf{C}^{(\mathrm{LT})} \mathbf{T}_\varepsilon$.

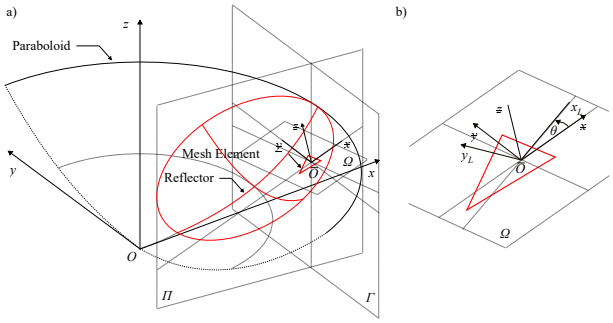


Figure 7: Local frame $\bar{x}$, $\bar{y}$ and the isotropy frame x_L, y_L, the latter rotated counterclockwise by an angle θ: a) overall and b) close-up view [26].

3.5. Tangent stiffness matrix of the mesh

Similarly, the tangent stiffness matrix for the mesh case can be evaluated from the virtual work principle. For a single element,

$$\bar{\mathbf{f}}^{\mathrm{T}} \delta\bar{\mathbf{p}} = \int_{\mathrm{V_o}} \bar{\boldsymbol{\sigma}}^{\mathrm{T}}\, \delta\bar{\boldsymbol{\varepsilon}} \mathrm{dV} \simeq \int_{\mathrm{V_o}} \bar{\boldsymbol{\sigma}}^{\mathrm{T}}\, \bar{\mathbf{B}}\, \delta\bar{\mathbf{p}} \mathrm{dV} \qquad (34)$$

where $\mathbf{f}$ denotes the element internal force vector and

$$\bar{\mathbf{B}} = \bar{\mathbf{B}}_1 + \bar{\mathbf{B}}_2 = \mathbf{H}\bar{\mathbf{G}} + \bar{\mathbf{A}}\,\bar{\mathbf{G}} \qquad (35)$$

so that the internal forces read

$$\bar{\mathbf{f}} = \int_{\mathrm{V}} \bar{\mathbf{B}}^{\mathrm{T}} \bar{\boldsymbol{\sigma}}\, \mathrm{dV} \qquad (36)$$

Introducing the out-of-balance element force vector $\mathbf{g} = \mathbf{f} - \mathbf{f}_{\mathrm{m}}$, the local tangent stiffness matrix is

$$\bar{\mathbf{K}}_{\mathrm{t_m}} = \frac{\partial \bar{\mathbf{g}}}{\partial \bar{\mathbf{p}}} = \int_{\mathrm{V_o}} \frac{\partial \bar{\mathbf{B}}^{\mathrm{T}}}{\partial \bar{\mathbf{p}}} \bar{\boldsymbol{\sigma}}\, \mathrm{dV} + \int_{\mathrm{V_o}} \bar{\mathbf{B}}^{\mathrm{T}} \frac{\partial \bar{\boldsymbol{\sigma}}}{\partial \bar{\mathbf{p}}} \mathrm{dV} \qquad (37)$$

The first term on the right-hand side is the geometric contribution, representing the internal stress effect:

$$\bar{\mathbf{K}}_{\mathrm{t}\sigma_{\mathrm{m}}} = \left(\bar{\mathbf{G}}^{\mathrm{T}} \bar{\boldsymbol{\Sigma}}\, \bar{\mathbf{G}}\right) \mathrm{t_o S_o} \qquad (38)$$

with $\boldsymbol{\Sigma}$ the 6×6 block diagonal matrix built from the 2×2 blocks of the local stress components, and S_o and t_o the element reference surface and thickness, respectively. The second term, using $\mathrm{d}\bar{\boldsymbol{\sigma}} = \bar{\mathbf{Q}}\bar{\mathbf{B}}\, \mathrm{d}\mathbf{p}$, provides the material contributions $\bar{\mathbf{K}}_{\mathbf{t1_m}}$ and $\bar{\mathbf{K}}_{\mathbf{t2_m}}$. Integrating over the reference configuration of the element,

$$\overline{\mathbf{K}}_{\mathrm{t1_m}} = \left(\overline{\mathbf{B}}^{\mathrm{T}}\overline{\mathbf{Q}}\,\overline{\mathbf{B}}_1\right)\mathrm{t_o S_o}$$
$$\overline{\mathbf{K}}_{\mathrm{t2_m}} = \left(\overline{\mathbf{B}}^{\mathrm{T}}\overline{\mathbf{Q}}\,\overline{\mathbf{B}}_2\right)\mathrm{t_o S_o} \qquad (39)$$

The global tangent stiffness matrix is assembled from the individual contributions expressed in the global frame,

$$\mathbf{K_{t_m}} = (\mathbf{R}_{\mathrm{G}}^{\mathrm{L}})^{-1}\,(\overline{\mathbf{K}}_{\mathbf{t1_m}} + \overline{\mathbf{K}}_{\mathbf{t2_m}} + \overline{\mathbf{K}}_{\mathbf{t\sigma_m}})\mathbf{R}_{\mathrm{G}}^{\mathrm{L}} \qquad (40)$$

with $\mathbf{R}_{\mathrm{G}}^{\mathrm{L}}$ the 9×9 rotation matrix mapping global into local components.

3.6. Evaluation of the zero-stress state

The zero-stress state of net and mesh is computed with the incremental-iterative Newton-Raphson algorithm sketched in Fig. 8, taking the optimized equilibrium configuration as the starting point. At each increment the load is lowered by a fixed amount and the displacement field is obtained from the current tangent stiffness, purged of rigid-body modes, as in Eq. 10. Strains and stresses are then updated with the expressions of Sections 3.2 and 3.4 and the unstrained elements are removed from the equilibrium or restored if re-tensioned later. The force densities are recomputed in the current configuration and, whenever the residual exceeds the tolerance, the Newton corrector loop is entered. In the present formulation, strains and stresses in the reference configuration are expressed in terms of the Green-Lagrange tensor $\mathbf{E}$ and of the Second Piola-Kirchhoff tensor $\boldsymbol{\sigma}$. The equilibrium, instead, must be evaluated in the current configuration of the system, implying that the force densities entering the equilibrium equations must be mapped from the reference stress state through the Cauchy stresses $\boldsymbol{\tau}$,

$$\boldsymbol{\tau} = \frac{1}{\mathrm{J}}\,\boldsymbol{F}\,\boldsymbol{\sigma}\,\boldsymbol{F}^{\mathrm{T}}, \qquad \mathrm{J} = \det(\boldsymbol{F}) \qquad (41)$$

with $\mathbf{F}$ the deformation gradient. Because each element frame is body-fixed, the rotation embedded in $\boldsymbol{F}$ is the identity, and $\boldsymbol{F}$ reduces to

$$\boldsymbol{F} = (2\mathbf{E} + \mathbf{I})^{1/2} \qquad (42)$$

4. RESULTS AND DISCUSSION

The case study reproduces the architecture of the TAS-I reflector,, shown in Fig. 9. Its main geometric parameters are taken from the literature as a representative benchmark for this class of antennas:$D = 12.25\,m$ and $\mathcal{F}/D = 0.45$ [33], $\mathcal{F}$ being the focal length. The number of triangular elements is determined by the number of circumferential subdivisions (rings) and zones (sectors), N and M respectively, set to satisfy the minimum requirements imposed by the target operating frequency of 4 GHz [27,34]:

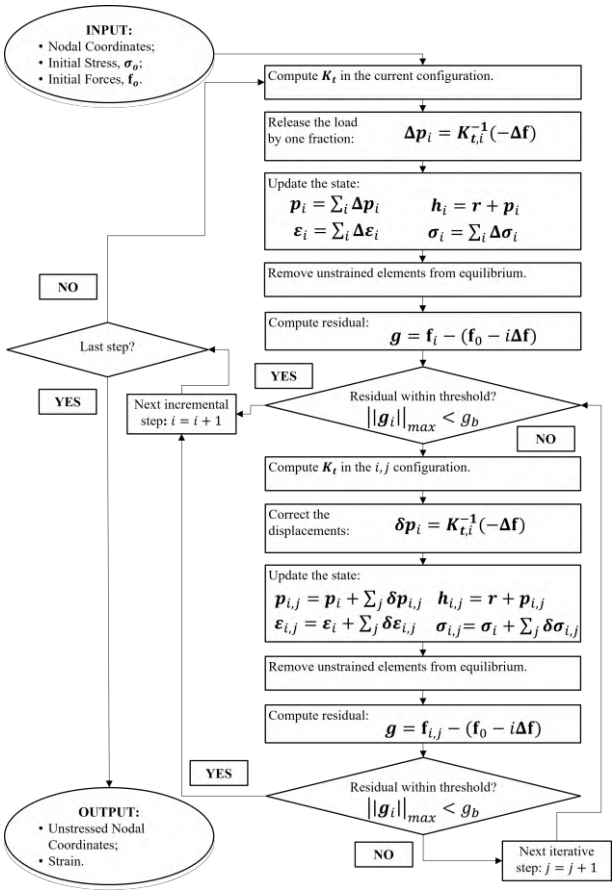


Figure 8: Flow chart of the nonlinear FE unstressing algorithm for cable net and mesh [26].

$$N = max(2, \lceil D/(2L_{max,0})\rceil)$$
$$M = max(3, \lceil (\pi D)/(NL_{max,0})\rceil) \qquad (43)$$

where $L_{max,0} = \eta\sqrt{\lambda\mathcal{F}/\psi}$ is the maximum cable length and λ the wavelength. The parameters ψ and η are set to 50 and 7.872 respectively, ensuring the gain loss of the faceted surface is below 0.3 dB [27]. Material parameters are taken from the literature: Kevlar for the cables [35], and an orthotropic fabric for the mesh [36]. Due to the orthotropic mesh properties, different tensile loads are prescribed in the longitudinal and transverse material directions [37], N_L and N_T respectively, within the $5 - 20\,N/m$ range typical of mesh reflectors [4]. The detailed design of the ring truss falls outside the scope of this study: $\mathbf{K_g}$ is entered as a diagonal matrix, letting the boundary nodes act independently; in general, the reduced $3n_g \times 3n_g$ matrix could be obtained via static condensation of a full ring-truss FE model. Tab. 1 collects the geometric and constitutive parameters of the form-finding and unstressing procedures, and Tab. 2 maps node and cable IDs to the portions of the cable net, to help the reading of the figures. The reference (deployed) configuration is the optimized output of the form-finding stage, for which a final nodal RMS of $2.58 \times 10 - 4\ \mu m$ with respect to the ideal paraboloid is achieved.

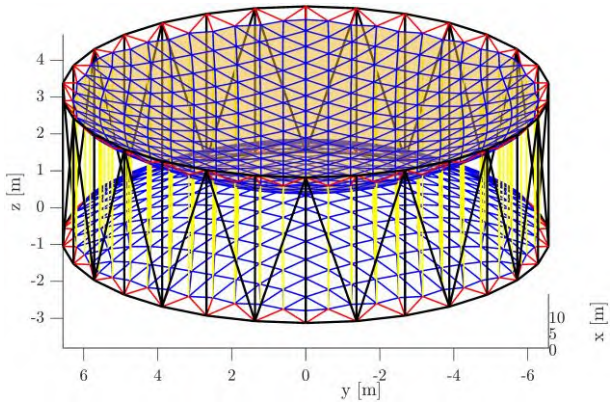


Figure 9: Balanced configuration of the reflector considered in the case study.

Table 1: Geometric and material parameters of the form-finding and unstressing procedures for the cable net and mesh.

Geometry	
Aperture diameter, D [m]	12.25
Focal length, $\mathcal{F}$ [m]	5.52
Clearance [m]	3.06
Ring-truss diameter [m]	13.2
Number of boundary nodes, n_b	60
Number of rings / sectors	10 / 6
Form-finding	
Inner-cable force density [N/m]	50
Link force density [N/m]	175
Local boundary node stiffness (x,y,z) [N/m]	[9.2, 5.3, 5]×10^5
Mesh thickness, t_o [mm]	0.822
Mesh deposition angle, θ [°]	0
Mesh preload (longitudinal), N_L [N/m]	10
Mesh preload (transverse), N_T [N/m]	5
Finite element method	
Cables Young's modulus, E [GPa]	20
Mesh longitudinal modulus, E_L [kPa]	50
Mesh transverse modulus, E_T [kPa]	104
Mesh shear modulus, G_{LT} [kPa]	350
Shear Poisson ratio, ν_{TL}	0.588
Number of unloading steps, n_{steps}	100
Maximum residual force, max(|$\boldsymbol{g}$|) [N]	0.001

Table 2: Node and cable ID intervals identifying the portions of the cable net.

Node type	**ID range**
Front net inner (free) nodes	1–331
Rear net inner (free) nodes	332–662
Front net boundary nodes	663–692
Rear net boundary nodes	693–722
Cable type	**ID range**
Front net inner cables	1–930
Rear net inner cables	931–1860
Ties	1861–2191
Front net links	2192–2281
Rear net links	2282–2371

4.1. Zero-stress configurations

With the optimized form-finding completed, the tensioning forces are gradually released through the nonlinear FE procedure to obtain the undeformed geometries of net and mesh. Figs. 10 and 11 show the zero-stress states identified for the cable nets and the mesh, respectively, overlapped with the corresponding tensioned configurations.

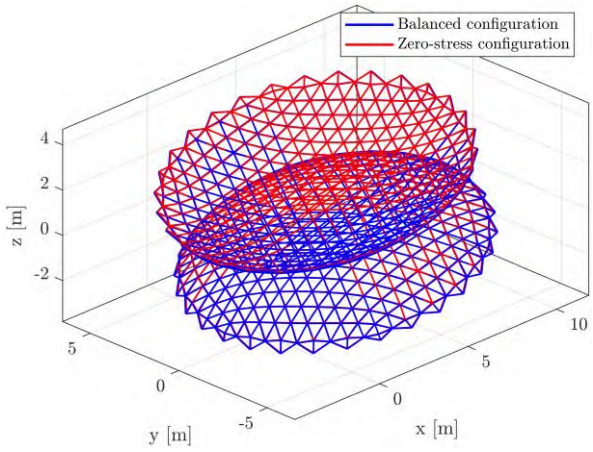


Figure 10: 3D view of the zero-stress configuration (red) overlapped with the tensioned configuration (blue) of the front and rear nets.

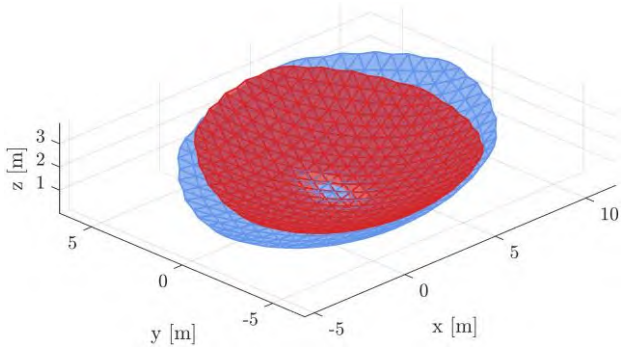


Figure 11: Undeformed mesh (red) superimposed on its tensioned configuration (light blue).

4.2. Validation against analytical predictions

As a first check, the unstressed cable lengths from the FE procedure are set against the Hooke's-law estimate. Fig. 12a and Fig. 12b show the absolute and relative difference between the two predictions, respectively, with an average relative difference below 0.01%, validating the method for the cable network.

The mesh strains obtained from the present Newton-Raphson procedure are shown in Fig. 13a. These values can also be compared with analytical predictions: each triangular facet is tensioned with the same values of N_L and N_T, assuming constant

thickness t_o and deposition angle $\theta = 0°$; in these conditions, Hooke's law $\bar{\boldsymbol{\varepsilon}} = \bar{\mathbf{Q}}^{-1}\,\bar{\boldsymbol{\sigma}}$ yields, substituting the input values of Tab. 1,

$$\bar{\boldsymbol{\varepsilon}} = \begin{bmatrix} 0.2089 \\ -0.0103 \\ 0 \end{bmatrix} \qquad (44)$$

These values match the numerical results of Fig. 13a. The values shown here can be compared with the local strain estimates obtained for $\theta \in [0, 90°]$ in Fig. 13b. The strain field can be better visualized in quasi-polar coordinates, as done in Fig. 14, where the radial, tangential and shear strain components over the mesh surface are reported for $\theta = 0°$.

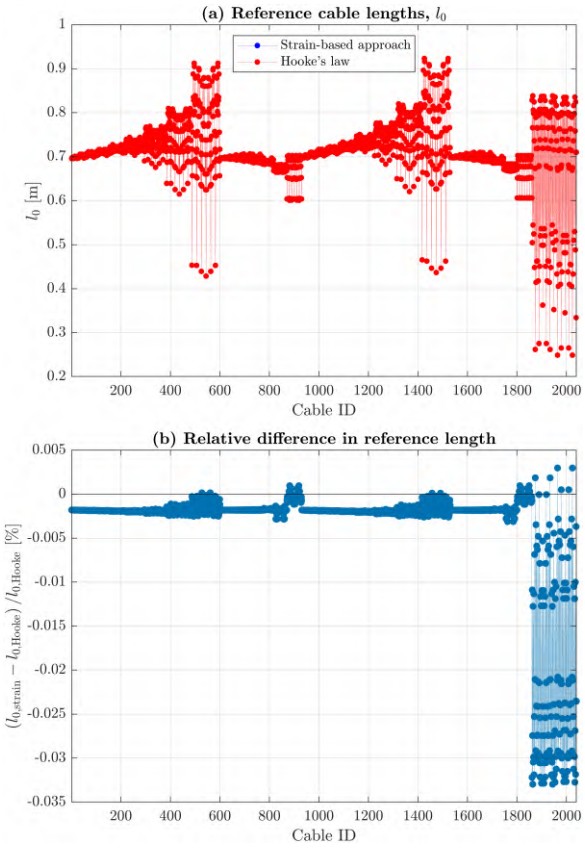


Figure 12: (a) Unstrained cable-length estimates from FE (blue) and the direct Hooke's law (red) predictions, (b) relative difference between the two predictions.

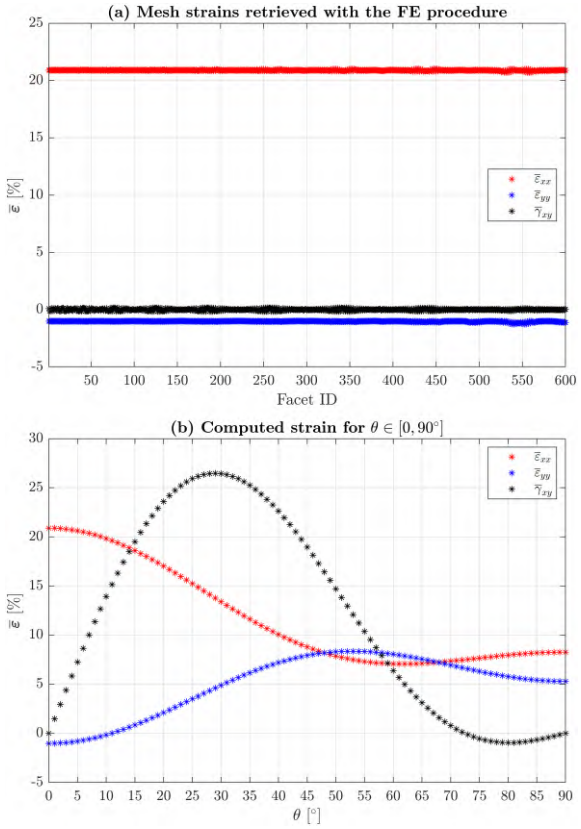


Figure 13: Mesh strain components evaluated with (a) null and (b) varying deposition angle θ.

4.3. Role of geometric nonlinearity

The role of geometric nonlinearity emerges clearly from the unloading path itself. In Fig. 15a and Fig. 15b the mean radius at the rim nodes is tracked against the mean tensioning force applied there, for both net and mesh, and compared with the linear estimate obtained by freezing the tangent stiffness at the reference configuration, $\mathbf{K}_\mathbf{t}^{(1)}$. Fig. 15c and Fig. 15d repeat the comparison for the depth, i.e. the maximum vertical distance from the boundary-node or rim-node plane, respectively. Both structures stiffen noticeably along the path: as unloading proceeds their geometric stiffness drops, and equal force reductions produce progressively larger displacements. Against this, the linear extrapolation accumulates substantial error, evidence that neglecting geometric nonlinearity would impact negatively on the computed zero-stress geometries and, through them, the deployed shape and the RF performance of the reflector.

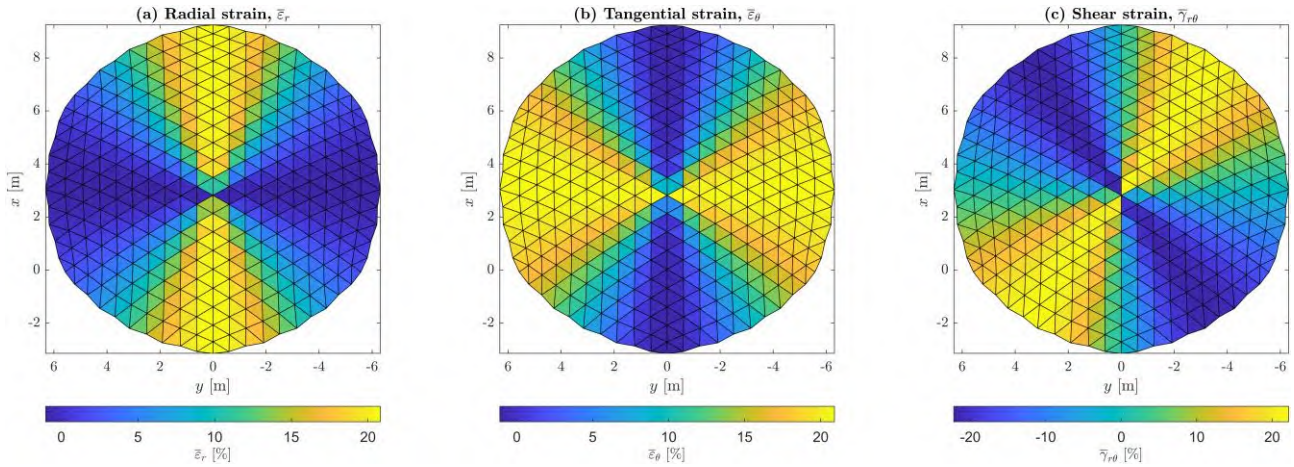


Figure 14: Facets' strain in quasi-polar coordinates for $\theta = 0°$: (a) radial component, (b) tangential component, (c) shear component.

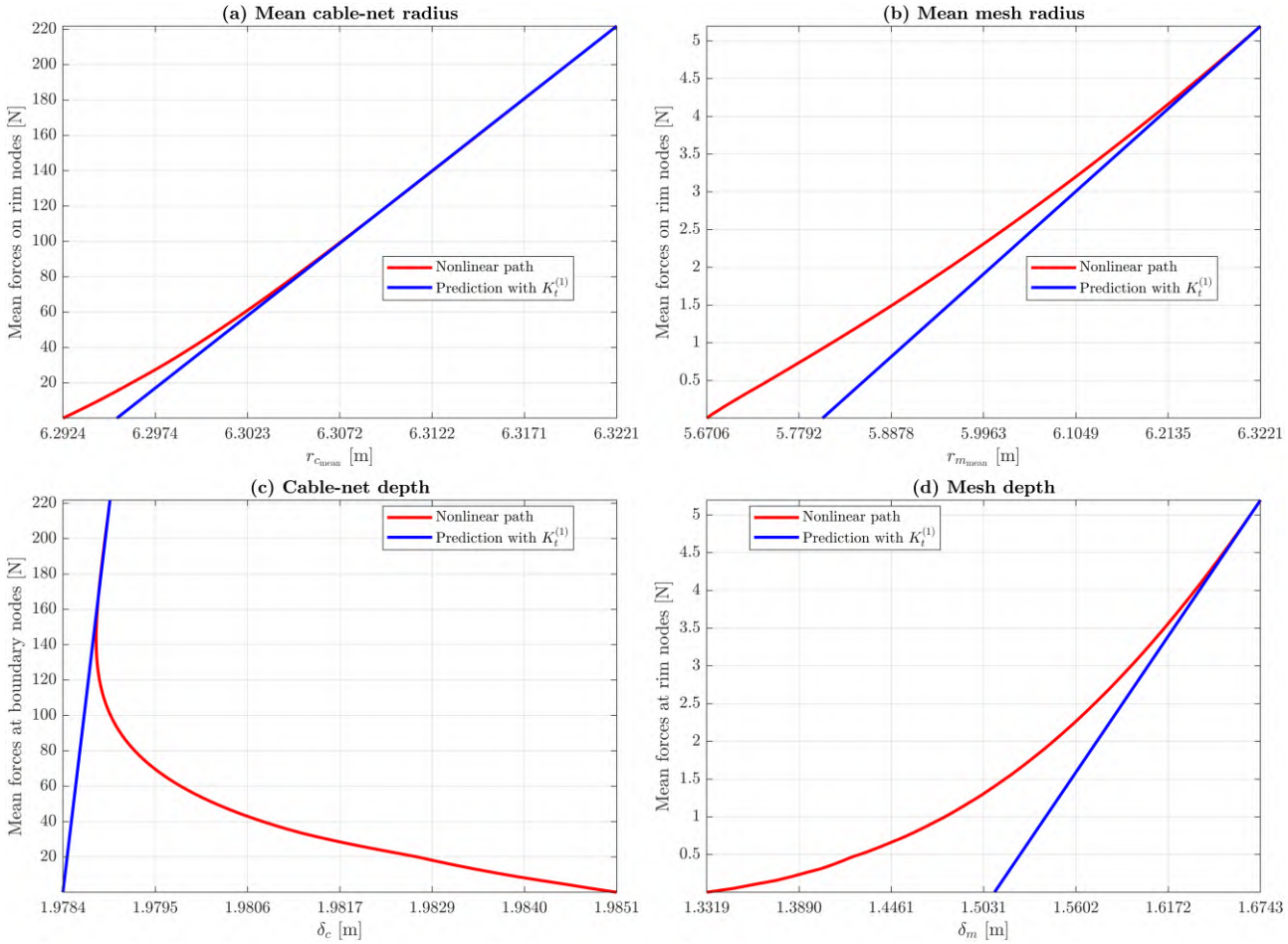


Figure 15: Front net and mesh unloading paths, compared with the linear predictions: mean rim radius for the (a) cable net and (b) mesh, and depth for the (c) cable net and (d) mesh.

5. CONCLUSIONS

A geometrically nonlinear, incremental-iterative finite element procedure has been presented to recover the zero-stress configurations of the cable nets and reflective mesh of a large deployable mesh reflector, starting from the deployed prestressed state provided by an extended Force Density Method [26]. The prestress is released by progressive load reduction within a total Lagrangian description, with consistent updating of the strain and stress states, treatment of cable slackening and reactivation, and orthotropic modelling of the mesh, including its deposition angle; numerical stability is ensured by filtering rigid-body modes through spectral decomposition of the singular tangent stiffness matrix.

For the 12.25 m case study considered, the

recovered cable rest lengths match the analytical Hooke's law prediction within 0.01%, and the mesh strain field reproduces the analytical orthotropic solution. The strongly nonlinear stiffening observed during unloading, in contrast with the linear prediction, demonstrates that geometric nonlinearity must be retained to obtain manufacturing-grade unstressed geometries: cutting patterns, cable rest lengths and assembly tolerances derived from a linearized model would introduce errors that directly propagate to the deployed shape and, ultimately, to the RF performance of the reflector.

Scalability guided the design of the proposed framework: rings, sectors, boundary nodes and aperture can each be varied on their own, so the design space can be swept systematically; and since the ring truss is decoupled from the net-mesh subsystems, one cable-mesh layout can serve supporting structures of different geometry.

Next steps include bringing the ring truss inside the nonlinear unloading model and enriching the cable and mesh constitutive laws with the material nonlinearities of lightweight space-grade components, towards realistic simulations of the complete deployment and tensioning sequence.

6. REFERENCES

1. Scialino, L., Ihle, A., Migliorelli, M., Gatti, N., Datashvili, L., van 't Klooster, C.G.M. & Santiago-Prowald, J. (2013). Large deployable reflectors for telecom and earth observation applications. *CEAS Space J*. 5, 125–146.

2. Datashvili, L., Maghaldadze, N., Baier, H., Friemel, M., da Rocha-Schmidt, L. & Luo, T. (2017). Enabling technologies and architectures at LSS GmbH for European large deployable and reconfigurable reflector antennas. In *Deutscher Luft- und Raumfahrtkongress*, Garching/Munich, Germany.

3. Cappellin, C., Lasson, J., Jorgensen, R., Datashvili, L., Pauw, J., Maghaldadze, N., Migliorelli, M. & Angevain, J.-C. (2016). Large mesh reflectors with improved pattern performances. In *37th ESA Antenna Workshop*, Noordwijk, The Netherlands.

4. Tibert, G. (2002). *Deployable Tensegrity Structures for Space Applications*. Ph.D. thesis, KTH, Stockholm.

5. Thomson, M. (1999). The AstroMesh deployable reflector. In *IEEE Antennas and Propagation Society International Symposium*, 1516–1519.

6. Veenendaal, D. & Block, P. (2012). An overview and comparison of structural form finding methods for general networks. *Int. J. Solids Struct*. 49 (26), 3741 – 3753.

7. Pasquali, M. & Lacarbonara, W. (2011). A geometrically exact formulation for thin multi-layered laminated composite plates: theory and experiment. *Compos. Struct.* 93(7), 1649–1663.

8. Pasquali, M. & Gaudenzi, P. (2012). A nonlinear formulation of piezoelectric plates. *J. Intell. Mater. Syst. Struct.*, 23 (15), 1713-1723.

9. Pasquali, M. & Gaudenzi, P. (2016). A nonlinear piezoelectric shell model: theoretical and numerical considerations. *J. Intell. Mater. Syst. Struct.*, 27 (6), 724-742.

10. Sufian, F.M. & Templeman, A.B. (1993). Analysis and design of cable net structures through optimization techniques. In *Computer Aided Optimum Design of Structures III*, WIT Trans. Built Environ., Vol. 2, 491 – 508.

11. Du, J., Wang, C., Bao, H. & Wang, L. (2017). Robust shape adjustment with finite element model updating for mesh reflectors. *AIAA J.* 55(4), 1450–1459.

12. Labella, G., Sicolo, E., Tampelloni, A., Argentesi, F., Atek, S., Pasquali, M. & Gaudenzi, P. (2026). Optimizing the design of large deployable mesh reflectors in presence of manufacturing defects. *CEAS Space J*.

13. Basso, P. & Del Grosso, A. (2011). Form-finding methods for structural frameworks: a review. In 35th *Annual Symposium of IABSE/52nd Annual Symposium of IASS*, London, United Kingdom.

14. Tibert, G. & Pellegrino, S. (2003). Review of form-finding methods for tensegrity structures. *Int. J. Space Struct.* 18(4), 209–223.

15. Schek, H.-J. (1974). The force density method for form finding and computation of general networks. *Comput. Methods Appl. Mech. Eng.* 3(1), 115–134.

16. Barnes, M.R. (1999). Form finding and analysis of tension structures by dynamic relaxation. *Int. J. Space Struct.* 14(2), 89–104.

17. Bletzinger, K.-U. & Ramm, E. (1999). A general finite element approach to the form finding of tensile structures by the updated reference strategy. *Int. J. Space Struct.* 14(2), 131–145.

18. Pauletti, R.M.O. & Pimenta, P.M. (2008). The natural force density method for the shape finding of taut structures. *Comput. Methods Appl. Mech. Eng.* 197(49-50), 4419–4428.

19. Maurin, B. & Motro, R. (1998). The surface stress density method as a form-finding tool for tensile membranes. *Eng. Struct.* 20(8), 712–719.

20. Tang, Y. & Li, T. (2017). Equivalent-force density method as a shape-finding tool for cable-membrane structures. *Eng. Struct.* 151, 11–19.

21. Tang, Y., Li, T., Ma, X. & Hao, L. (2017). Extended nonlinear force density method for form-finding of cable-membrane structures. *J. Aerosp. Eng.* 30(3), 04016101.

22. Zhang, S., Zhang, S., Zhang, Y. & Ye, J. (2021). Force density sensitivity form-finding design method for cable-mesh reflector antennas considering interactive effects between cable network and supporting truss. *Eng. Struct.* 244, 112722.

23. Chen, W.-J., Zhou, J.-Y. & Zhao, J.-Z. (2014). Computational methods for the zero-stress state and the pre-stress state of tensile cable-net structures. *J. Zhejiang Univ. Sci. A* 15(10), 813–828.
24. Fan, L., Sun, Y., Fan, W., Chen, Y. & Feng, J. (2020). Determination of active members and zero-stress states for symmetric prestressed cable-strut structures. *Acta Mech.* 231(9), 3607–3620.
25. Zhang, N., Luo, B., Liu, H. & Zhang, M. (2022). Prestress self-equilibrium force-finding method for cable-supported grid structures considering zero-stress state form-finding and the construction process. *Buildings* 12(6), 749.
26. Argentesi, F., Pasquali, M., Atek, S., Gaudenzi, P., Lapi, M., Lanuti, M., Colella, A., Scarozza, D., Palomba, L. & Adamo, F. (2026). Geometrically nonlinear model of cable net and mesh for the manufacturing of large deployable mesh reflectors. *Aerosp. Sci. Technol*. 178, Part D, 113185.
27. Yuan, P., He, B., Zhang, L., Nie, R. & Ma, X. (2021). Pretension modeling and form-finding for cable-network antennas with varying topologies and parameters. *Aerosp. Sci. Technol.* 112, 106631.
28. Nie, R., He, B., Hodges, D.H. & Ma, X. (2019). Integrated form finding method for mesh reflector antennas considering the flexible truss and hinges. *Aerosp. Sci. Technol.* 84, 926–937.
29. Bathe, K.-J. (2006). *Finite Element Procedures*. Prentice Hall.
30. Bonet, J. & Wood, R.D. (1997). *Nonlinear Continuum Mechanics for Finite Element Analysis*. Cambridge University Press, Cambridge, UK.
31. Golub, G.H. & Van Loan, C.F. (2013). *Matrix Computations*. JHU Press, Baltimore, MD.
32. Crisfield, M.A. (1991). *Non-linear Finite Element Analysis of Solids and Structures. Volume 1: Essentials*. John Wiley & Sons, Chichester, UK.
33. Liu, W., Li, D. & Jiang, J. (2014). General mesh configuration design approach for large cable-network antenna reflectors. *J. Struct. Eng.* 140(2), 04013051.
34. Agrawal, P., Anderson, M. & Card, M. (1981). Preliminary design of large reflectors with flat facets. *IEEE Trans. Antennas Propag.* 29(4), 688–694.
35. He, B., Dong, X., Nie, R., Fan, Y. & Wang, G. (2026). Methodology for cable network design and error analysis with high engineering consistency. *Aerosp. Sci. Technol.* 168, 110781.
36. Zhang, Y., Zhang, H., Yang, D., Qin, Q. & Zhu, R. (2019). Form-finding design of cable-mesh deployable reflector antennas considering wire mesh properties. *AIAA J.* 57(11), 5027–5041.
37. Bassily, S.F. & Uribe, J. (1999). Mesh tensioning, retention and management systems for large deployable reflectors. U.S. Patent No. 5,969,695.

KINEMATICS-DRIVEN DEPLOYMENT ANALYSIS OF AN INFLATABLE LUNAR HABITAT WITH NONLINEAR MEMBRANE RESPONSE

Alfonso Caiazzo[1,*], Sergio De Rosa[2], Giuseppe Petrone[3]

(1) Department of Industrial Engineering, University of Naples Federico II, Via Claudio 21, 80125 Naples, Italy, alfonso.caiazzo@unina.it

(2) Department of Industrial Engineering, University of Naples Federico II, Via Claudio 21, 80125 Naples, Italy, sergio.derosa@unina.it

(3) Department of Industrial Engineering, University of Naples Federico II, Via Claudio 21, 80125 Naples, Italy, giuseppe.petrone@unina.it

(*) Corresponding author

Keywords: Inflatable lunar habitat, Deployable structures, Multibody dynamics, Nonlinear membrane, Kevlar membrane

Abstract

Inflatable lunar habitats offer launch-volume efficiency but couple mechanism dynamics to a highly compliant restraint layer. This paper isolates deployability from subsequent pressurization and links three models: a FEMAP finite-element model of the complete habitat for static material screening; an MSC Adams multibody model of a three-ring, two-stage module for joint forces, work and power; and a geometrically and materially nonlinear LS-DYNA model of the dry Kevlar K300T2 restraint layer. Linear, half-cosine and quintic minimum-jerk laws are assessed for synchronized and staged motion under equal-global-time and equal-local-stroke-time criteria. At equal local time, staging reduces peak mean absolute force by $22.6 - 30.6\%$, cumulative mechanical work by $30.4 - 33.3\%$, and peak power by $59 - 63\%$. For the minimum-jerk case, the selected deployability-affected membrane area falls from 14.86% to 9.53% of nominal lateral area. Staging is therefore beneficial only when allowed a longer global maneuver, showing that motion smoothness, timing and membrane response must be co-designed.

1 INTRODUCTION

Expandable softgoods habitats can provide a larger habitable volume per launch volume than an equivalent rigid shell, but their structural function is distributed among a multilayer structure composed of a bladder, restraint, thermal and protective layers. TransHab and later NASA developments established the feasibility of large layered inflatables and the need for full-scale structural testing [1,2,3]. Certification studies further show that human-rated softgoods require a building-block approach, statistically supported knock-down factors and explicit treatment of material variability [4]. These issues become more severe for surface-based habitats because deployment must also interact with the ground, mechanisms and lunar gravity. Recent reviews classify lunar and Martian habitat concepts by architecture, material and construction strategy and identify deployable/inflatable solutions as mass-efficient but validation-intensive [1]. A related safety study emphasizes the risk of assigning packing, deployment and pressure retention to an insufficiently separated structural function [5]. The present work therefore treats deployment before inflation: only the structural restraint layer and the frame-guide mechanism are retained in the dynamic models. Pressure qualification, gas-barrier performance and the complete multilayer stack are outside the current study. The geometry originates from the authors' conceptual pressurized lunar habitat, for which a cylindrical configuration was selected after geometric, static, thermal and habitability trade-offs [6]. The contribution is a kinematics-driven, multi-model assessment that connects: (i) full-structure static screening, (ii) actuator demand from a multibody representation and (iii) nonlinear dry-fabric deformation under the same prescribed motions. Thin membranes may develop localized slack and wrinkles through geometric instability, making a large-deformation finite-element treatment essential [9,10]. Table 1 positions the analysis relative to the literature base.

Table 1: Literature basis and resulting modelling decisions.

Source	Established point	Decision in this work
Kennedy [2]	TransHab architecture and structural tests	Retain a layered-habitat context
Valle et al. [3]	Softgoods design, analysis and test hierarchy	Separate structural restraint from other layers
Jones [4]	Certification depends on tests, variability and factors	Treat the model as pre-qualification
Siviero et al. [5]	Safety-critical functions and material risks	Decouple deployment from inflation

Source	Established point	Decision in this work
Caiazzo et al. [1,6]	Environmental review and cylindrical baseline	Adopt the previously screened habitat
Wong; Vatankhahghadim [9,10]	Wrinkling and support-motion coupling	Use geometrically nonlinear shell analysis

2 HABITAT CONCEPT AND MODEL CHAIN

2.1 Static structural screening in FEMAP

The reference habitat consists of a cylindrical softgoods shell with a hemispherical endcap, eight internal rectangular rings, and a carbon-fibre floor with its support structure. The complete FEMAP model was subjected to a 1 atm pressure load. Five dry woven restraint candidates (see Tab. 2) from the project material catalogue have been compared using consistent geometry, boundary conditions and shell representation. The catalogue thickness, rather than a fitted laminate thickness, was used for this screening; the fibres are non-impregnated dry fabrics and are not treated as a resin-matrix composite.

$$\sigma_\theta = \frac{pR}{t},\ \sigma_x = \frac{pR}{2t} \tag{1}$$

For a cylindrical membrane, Eq. 1 provides the hoop and axial sizing references. Introducing safety factor SF and a restraint efficiency η = 0.80 gives the minimum thickness in Eq. 2. For Kevlar K300T2, $SF = 4$ gives $0.28\,mm$, below the $0.42\,mm$ catalogue thickness used in the finite-element comparison. This calculation is a screening check; discontinuities at rings and endcaps are resolved by the FEMAP model rather than by membrane theory.

$$t_{req} = SF \cdot \frac{pR}{\eta\,\sigma_u} \tag{2}$$

Table 2: Dry-fabric catalogue data used in the static screen.

Material	Mass/area (g/m²)	σ_u (MPa)	E (GPa)	t (mm)
Kevlar K300T2	300	2930	102.0	0.42
Vectran V200T2	200	3200	100.0	0.21
Zylon Z300T2	300	5800	270.0	0.42
CF50/Vectran50	200	3716	151.8	0.21
CF61/Aramid39	210	3850	179.0	0.25

Table 3: FEMAP response under 1 atm pressure differential.

Material	ucyl (mm)	uend (mm)	σcyl (MPa)	σend (MPa)
Kevlar K300T2	2.164	0.864	180	101
Vectran V200T2	11.02	3.95	679	385
Zylon Z300T2	2.00	0.73	341	92
CF50/Vectran 50	7.09	2.60	682	385
CF61/Aramid 39	5.06	1.86	571	323

According to Tab.3, Zylon gives the smallest displacement but the project trade also weights stress distribution, durability, availability and technology maturity. Kevlar K300T2 was consequently retained as the engineering compromise: its full-structure cylinder displacement is $2.164\,mm$ and its average cylinder stress is $180\,MPa$.

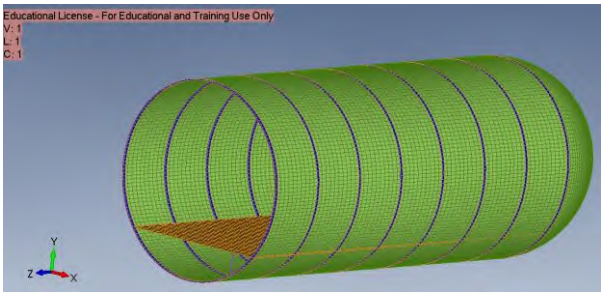


Figure 1: FEMAP finite-element model of the complete cylindrical habitat used for static screening.

2.2 Deployment module and information transfer

The modularity of the deployable structure has a radius of $R = 1600$ mm and total undeployed length of $L = 2000\,mm$. Three rigid frames are initially located at $0, 1000$ and $2000\,mm$, so each undeployed inter-ring span is $L_{span} = 1000\,mm$. The two telescopic deployable mechanism have a stroke of $\Delta = 500\,mm$. The modularity preserves the frame spacing and fabric span relevant to deployment while excluding the floor, secondary softgoods and pressure. Lunar gravity is included in the multibody model. Table 4 summarizes the analysis chain. FEMAP selects geometry and dry restraint material; MATLAB generates consistent kinematics; the same kinematic family is prescribed in MSC Adams and LS-DYNA. Adams's actuator forces are evaluated rather than imposed back into LS-DYNA.

Table 4: Purpose and information flow of the three numerical models.

Model	Representation	Inputs	Outputs
FEMAP FE	Complete habitat	1 atm; material candidates	Static stress, displacement, selection
MSC Adams MBD	3 rings; 2 prismatic stages	Lunar gravity; prescribed q(t)	Joint force, work, power
LS-DYNA FE	Dry Kevlar cylindrical span	Large motion; nonlinear table	u, strain, energy, affected area

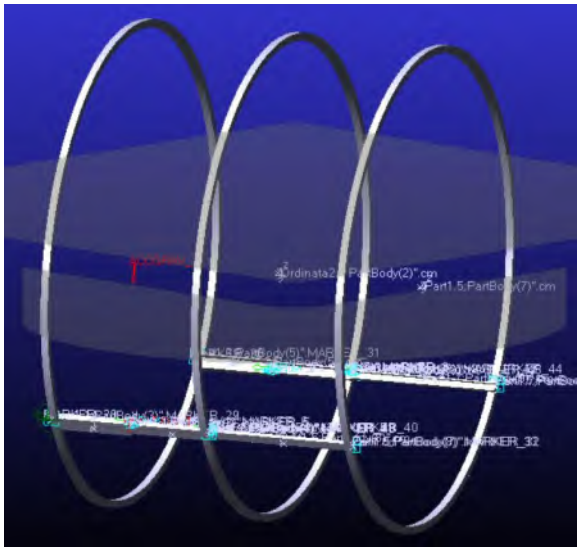


Figure 2: MSC Adams habitat's modularity with three frames and the telescopic guide system.

3 PRESCRIBED DEPLOYMENT KINEMATICS

3.1 Motion laws

For each stage, normalized time is $s = \tau/T_{loc}$ on $0 \le s \le 1$ and closure is $q = \Delta f(s)$. Three laws are screened: linear, half-cosine and quintic minimum jerk (QMJ). The QMJ polynomial is the standard zero-velocity, zero-acceleration endpoint trajectory [8].

$$f_{lin}(s) = s \tag{3}$$

$$f_{cos}(s) = \frac{[1-\cos(\pi s)]}{2} \tag{4}$$

$$f_{QMJ}(s) = 10s^3 - 15s^4 + 6s^5 \tag{5}$$

$$q = \Delta f, \quad \dot{q} = (\Delta/T_{loc})f', \quad \ddot{q} = (\Delta/T_{loc}{}^2)f'' \tag{6}$$

For the linear law, the in-stroke velocity is constant but jumps instantaneously between zero and Δ/T_{loc} at the stroke boundaries. In an ideal analytical description, this velocity discontinuity produces impulsive endpoint acceleration; therefore, the linear law is retained only as a baseline. The half-cosine law has zero endpoint velocity, providing a continuous transition in position and velocity. However, its acceleration is finite and non-zero at both endpoints, so the trajectory is not acceleration-continuous when connected to a stationary phase. The QMJ law has both zero velocity and zero acceleration at the stroke boundaries. It therefore provides a C^2-continuous transition between motion and hold phases, avoiding artificial velocity or acceleration discontinuities in the flexible-structure analysis.

Table 5: Kinematic-law properties for a single 500-mm stroke.

Law	Endpoint velocity	Endpoint acceleration	Implication
Linear	jump	impulsive	Baseline only
Half-cosine	zero	non-zero	Smooth velocity
QMJ	zero	zero	C² transition

3.2 Strategies and timing criteria

Synchronized motion commands both stages simultaneously. Staged motion commands stage 1 inserts a stabilization pause of $0.10T_{loc}$ and then commands stage 2; opening reverses the order. The monitored absolute positions are $x_2 = x_{2,0} - d_2$ and $x_3 = x_{3,0} - d_1 - d_2$, with $x_{2,0} = 1000\,mm$ and $x_{3,0} = 2000\,mm$. Hence the distal ring accumulates both closures. The equal-global-time criteria, named *criterion A* imposes equal global closure/opening time; staged local strokes must therefore be faster. The equal-local-stroke-time criteria, named *criterion B* imposes equal local stroke time; staged motion then takes longer globally. A reference velocity of $10\,mm/s$ has been chosen as the upper limit; a consequent reference time of $240\,s$ has been used. Table 6 gives the resulting cycle durations.

Table 6: Timing definition for the 200-s reference analysis.

Crit.	Strategy	T_{loc} (s)	Pause (s)	Closure (s)	Cycle (s)
A	Staged	114.29	11.429	240	600
A	Sync.	240	0	240	600
B	Staged	240	24	504	1128
B	Sync.	240	0	240	600

Table 7: Peak local velocities and finite accelerations.

Case	Linear v (mm/s)	Cosine v (mm/s)	QMJ v (mm/s)	QMJ a (mm/s²)
A-staged	4.375	6.872	8.203	0.2210
A-sync.	2.083	3.272	3.906	0.0501
B-staged	2.083	3.272	3.906	0.0501
B-sync.	2.083	3.272	3.906	0.0501

Table 7 reports actuator-level quantities. During synchronized deployment, the distal-frame velocity and finite acceleration are twice the corresponding local actuator values because the distal position depends simultaneously on $d_1$and d_2. During staged deployment, only one actuator moves at a time, and the distal-frame kinematic quantities therefore coincide with the active local actuator values. The highest prescribed local actuator velocity is $8.2031\ mm/s$ for the staged QMJ case under Criterion A, which remains below the selected reference limit of $10\ mm/s$.

4 MULTIBODY ACTUATOR-DEMAND ANALYSIS

4.1 MSC Adams model and metrics

The three frames are modelled as rigid bodies connected by two actuated translational joints, representing the two telescopic deployment stages. The first joint controls the motion of the intermediate frame, whereas the second joint contributes to the motion of the distal frame. Since the distal frame is affected by both telescopic stages, its absolute displacement includes the contributions of both joint motions. The axial forces calculated at the two translational joints are used to evaluate the actuator demand. At each time step, the absolute joint forces are averaged and the maximum value reached during the complete simulation is defined as the peak mean absolute force. The mechanical power associated with joint j is calculated as:

$$P_j(t) = \mid F_j(t) \cdot \dot{q}_j(t) \mid \qquad (7)$$

where $F_j(t)$ is the axial joint force and $\dot{q}_j(t)$ is the corresponding actuator velocity. The total mechanical power is obtained by summing the contributions of the two joints. Its maximum value defines the peak total power, whereas the cumulative mechanical work corresponds to the area under the total power-time curve. Stage 2 consistently requires a higher force because it moves a larger equivalent mass and carries the contribution associated with the distal frame.

4.2 Force, work and power results

Tables 8 to10 report the Criterion-B values at the precision available from the MSC Adams postprocessing. The reductions are calculated relative to the synchronized case of the same law. Criterion A is intentionally not mixed into these tables because its global time budget is different at the actuator level.

Table 8: Peak mean absolute force at equal local stroke time (Criterion B).

Law	Sync. (N)	Staged (N)	Reduction
Linear	≈ 31	≈ 24	22.6%
Half-cosine	≈ 44	≈ 31	29.5%
QMJ	≈ 49	≈ 34	30.6%

Table 9: Cumulative mechanical work at equal local stroke time (Criterion B).

Law	Sync. (J)	Staged (J)	Reduction
Linear	≈ 56	≈ 39	30.4%
Half-cosine	≈ 65	≈ 44	32.3%
QMJ	≈ 72	≈ 48	33.3%

Table 10: Peak total mechanical power at equal local stroke time (Criterion B).

Law	Sync. (W)	Staged (W)	Reduction
Linear	≈ 0.117	≈ 0.048	59.0%
Half-cosine	≈ 0.260	≈ 0.101	61.2%
QMJ	≈ 0.350	≈ 0.131	62.6%

At equal local time, staging reduces all the three actuation metrics. The power reduction is the largest $(59 - 63\%)$ because simultaneous motion superposes the power demand of both stages. Within either strategy, QMJ has the largest peak power for the selected duration. Thus, an endpoint-smooth trajectory protects the flexible model from kinematic discontinuities but is not automatically the lowest-power command.

5 NONLINEAR MEMBRANE ANALYSIS IN LS-DYNA

5.1 Dry-fabric model and convergence

The LS-DYNA model uses (i) dry Kevlar K300T2 for the cylindrical fabric segment and (ii) frame-driven boundary motion. Large deformation is enabled and the woven restraint response is introduced through a tabulated nonlinear orthotropic law. Independent tests on Kevlar 49 fabric show nonlinear, direction-dependent tension, strain-dependent transverse contraction and nonlinear in-plane shear [7], supporting a tabulated fabric representation rather than a single isotropic

modulus. The stress-strain curve for the fabric material has been added in the solve. Maximum transverse displacement $u_\perp$ is used as a global convergence indicator for the mesh sensitivity analysis. For time sample k and a small denominator regularization δ, the relative difference between two meshes i and j is $\frac{100|u_{\perp i}-u_{\perp j}|}{max(|u_{\perp j}|,\delta)}$. Table 11 shows the mean and maximum error of the mesh sensitivity analysis.

Table 11: Mesh-convergence statistics for maximum transverse displacement.

Mesh pair	Elems. i	Elems. j	Mean error	Max. error
1 → 2	127500	255000	6.4%	15.9%
2 → 3	255000	582500	0.8%	5.5%

5.2 Closure ratio and membrane-response metric

The imposed closure is normalized by the undeployed inter-ring span, $r = \Delta/L_{span}$. Here $\Delta = 500\,mm$ and $L_{span} = 1000\,mm$ at the beginning of the maneuver. Across the screened configurations, maximum transverse deflection rises rapidly at low r and then approaches a lower-sensitivity regime. This trend is represented phenomenologically by Eq. 8; in order to interpret the response.

$$w(r) = w_\infty[1 - exp(-kr)] \quad (8)$$

The final configurations are additionally compared through an affected-area indicator. In LS-PrePost, elements satisfying the same transverse-displacement selection operation are activated and their current surface area A_{aff} is measured. With the nominal cylinder lateral area $A_0 = 2\pi RL = 20.106\,m^2$, the percentage is

$$\eta_{aff} = 100\,A_{aff}/A_0 \quad (9)$$

This definition quantifies the selected affected surface, not wrinkle wavelength or amplitude, and remains dependent on the displacement threshold. It is therefore reported as a comparative indicator using an identical selection for the synchronized and staged cases.

Table 12: Final affected area for QMJ deployment under Criterion B.

Strategy	A_{aff} (m²)	η_{aff}	Change vs sync.
Sync.	2.98724	14.857%	Baseline
Staged	1.91557	9.527%	−35.87%

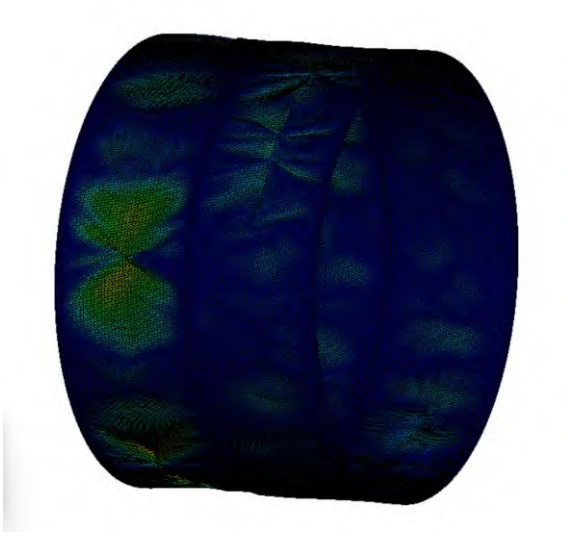


Figure 3: Final QMJ synchronized configuration under Criterion B; contours display transverse YZ displacement ($u_\perp$).

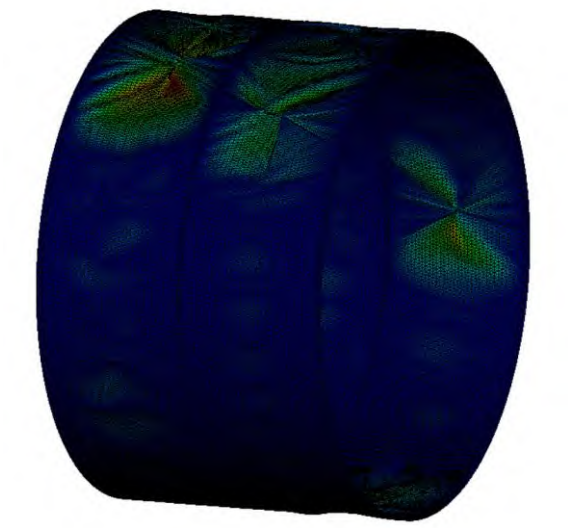


Figure 4: Final QMJ staged configuration under Criterion B; contours display transverse YZ displacement ($u_\perp$).

Sequential QMJ motion reduces the selected affected area from $2.987\,m^2$ to $1.916\,m^2$, i.e. the 35.87% in relation to the synchronized deployment. The result is consistent with reduced simultaneous forcing and with the staged redistribution of slack; it does not by itself establish a reduction in local peak strain.

6 DISCUSSION AND CONCLUSION

The combined FEMAP/MSC Adams/LS-DYNA methodology separates three complementary aspects of the habitat design. FEMAP establishes the full-structure static baseline and supports the

selection of dry woven Kevlar K300T2. MSC Adams evaluates the forces, work and power required by the telescopic deployable mechanism while LS-DYNA captures the geometric and material nonlinearities of the unpressurized fabric during deployment. The results show that the advantage of staged deployment depends on the adopted timing criterion. Under Criterion B, where both strategies have the same local stroke time, staging reduces peak mean absolute force from 22.6% to 30.6%, cumulative mechanical work from 30.4% to 33.3% and peak power from 59% to 63%. For the QMJ law, the affected membrane area also decreases from 14.857% to 9.527% of the nominal lateral area. However, the staged close-hold-open cycle increases from $600\,s$ to $1128\,s$. Under Criterion A, the same global duration requires the staged local stroke to be completed in $114.29\,s$, increasing its kinematic severity. QMJ remains the preferred law for nonlinear membrane analysis because its velocity and acceleration vanish at the motion boundaries, although it does not provide the lowest peak power at fixed duration. Future work will focus on manufacturing a scaled prototype of the aforementioned habitat's modularity. The prototype will be used to reproduce the staged and synchronized deployment sequences and experimentally measure joint forces, ring motion and fabric deformation. These tests will validate the interaction between prescribed kinematics and nonlinear structural dynamics before extending the analysis to the complete pressurized habitat.

REFERENCES

1. Caiazzo, A., Casaburo, A., Petrone, G., De Rosa, S. & Franco, F. (2026). Structures for extraterrestrial habitat: A review. *Acta Astronautica* 238, 471–493. https://doi.org/10.1016/j.actaastro.2025.10.029
2. Kennedy, K.J. (2000). Inflatable Habitats Technology Development. In *Mars Greenhouses: Concepts and Challenges*, NASA/TM-2000-208577, pp. 64–76.
3. Valle, G.D., Litteken, D.A. & Jones, T.C. (2019). Review of Habitable Softgoods Inflatable Design, Analysis, Testing, and Potential Space Applications. *AIAA SciTech 2019 Forum*, AIAA 2019-1018. https://doi.org/10.2514/6.2019-1018
4. Jones, T.C. (2018). Structural Certification of Human-Rated Inflatable Space Structures. *2018 IEEE Aerospace Conference*, pp. 1–13. https://doi.org/10.1109/AERO.2018.8396616
5. Siviero, A., Delpiano, D., Castagneri, D., Amoikon, S., Demaria, L. & Davies, R. (2024). Structural Design and Safety Critical Conditions Analysis on Composite and Modern Materials Applied in Construction of Inflatable Modules for Lunar and Martian Bases. *75th International Astronautical Congress*, IAC-24, D3,2A,4, x88273, pp. 73–86. https://doi.org/10.52202/078374-0009
6. Caiazzo, A., Petrone, G., Casaburo, A., De Rosa, S. & Franco, F. (2026). Conceptual Structural Design of a Pressurized Inflatable and Deployable Habitat Optimized for Lunar Surface Missions. *Materials Research Proceedings* 69, 1278–1282. https://doi.org/10.21741/9781644904251-221
7. Zhu, D., Mobasher, B. & Rajan, S.D. (2011). Characterization of Mechanical Behavior of Kevlar 49 Fabrics. In T. Proulx (Ed.), *Experimental and Applied Mechanics*, Vol. 6, pp. 377–384. Springer. https://doi.org/10.1007/978-1-4614-0222-0_46
8. Flash, T. & Hogan, N. (1985). The coordination of arm movements: An experimentally confirmed mathematical model. *The Journal of Neuroscience* 5(7), 1688–1703. https://doi.org/10.1523/JNEUROSCI.05-07-01688.1985
9. Wong, Y.W. & Pellegrino, S. (2006). Wrinkled membranes. Part III: Numerical simulations. *Journal of Mechanics of Materials and Structures* 1(1), 63–95. https://doi.org/10.2140/jomms.2006.1.63
10. Vatankhahghadim, B. & Damaren, C.J. (2021). Nonlinear deployment dynamics and wrinkling of a membrane attached to two axially moving beams. *Journal of Spacecraft and Rockets* 58(6), 1714–1732. https://doi.org/10.2514/1.A34962
11. Miyazaki, Y. (2006). Wrinkle/slack model and finite element dynamics of membrane. *International Journal for Numerical Methods in Engineering* 66(7), 1179–1209. https://doi.org/10.1002/nme.1588

STRUCTURAL DESIGN TRADE-OFFS FOR A DEPLOYABLE ROLLABLE SOLAR ARRAY

Martin Hillebrandt [(1)], Marco Straubel [(1)], Martin E. Zander[(1)], Christian Hühne[(1)]

[(1)] *Lightweight Design Department, DLR Institute of Lightweight Systems, Braunschweig, GERMANY*

KEYWORDS

Solar Array, Deployable Structure, Deployable Boom, CTM, Flexible Blanket Solar Array

ABSTRACT

A design trade study on a deployable solar array is presented. The array consists of a rollable boom and a flexible, rollable blanket, allowing even large arrays to be stowed in a compact volume. Based on a functional demonstrator that has been tested during a parabolic flight campaign, the flight model is currently being designed. However, major design decisions regarding configuration and architecture still need to be finalized. Therefore, a design tool is developed that allows detailed trade studies to assess the performance impact of specific design decisions in terms of power per mass and power per volume.

The tool employs an analytical approximation of the stiffness and stability of the boom based on non-linear FEA results. To assess volume, mass, and mass distribution, appropriate scaling laws are formulated for each component. The trade study is performed over a power range of 0.5 kW to 20 kW per wing and investigates, among other aspects, the deployment configuration, number of booms, and type of photovoltaic technology.

Analysis of the trade study results shows that, in the low-power region, the lower limits in the component scaling laws have a strong impact on array performance. In the high-power region, mass-related performance remains at a high level. However, maintaining high volume-related performance at high power levels is found to be challenging. Increasing the number of booms and carefully defining stability requirements are found to be effective means of improving this performance metric.

1. INTRODUCTION & PREVIOUS WORK

DLR has developed a deployable solar array [1] based on its rollable boom technology (see Figure 1) which originates from previous solar sail developments. The array is a so called flexible blanket solar array (see Figure 2) which uses a flexible sheet as the carrier of the photovoltaic (PV) cells. As boom and blanket are both rollable, even large arrays can be stowed within a compact form for space transport thus enabling high-power applications even with strong payload volume limitations.



Figure 1: DLR's rollable boom technology.

The main components of the solar array are the boom, the boom deployment mechanism, a spreader bar at the tip, the flexible blanket and a roller core. The roller-core allows stowage of the blanket. The deployment mechanism of the boom also drives the entire array deployment. A special feature is that it is also retractable to its stowed form wherefore frequent deployment-retraction-cycles are enabled.



Figure 2: Single and double wing array configuration with one central boom.

The solar array is a modular design that allows several variants that differ in configuration and architecture. From the same deployment mechanism and roller-core either one or two wings can be unfolded. Also, the number of booms can be altered and deployment can be conducted from the root and the tip.

A functional demonstrator of the solar array has been built and tested on ground as well as in zero-g during a parabolic flight campaign [2] (see Figure 3). During the test, repeated extension and retraction cycles of a double-wing configuration were demonstrated and no functional or behavioural anomalies were observed.

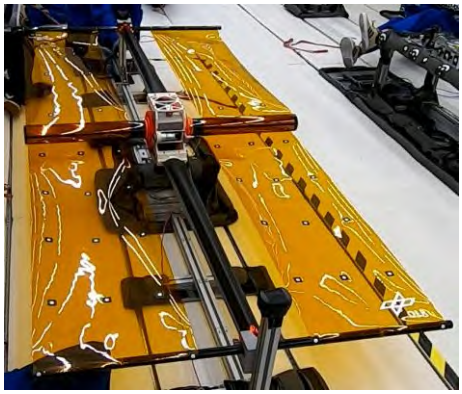


Figure 3: Double wing solar array demonstrator during a parabolic flight campaign.

2. MOTIVATION & AIM

The next step in the development of the solar array is the design of the flight hardware (see Figure 4). Its baseline design features a single mast with two blankets to its sides that are deployed from the root. Thereby, heavy parts such as the roller-core remain close to the spacecraft interface and the single boom and deployment mechanism reduces complexity.



Figure 4: CAD-images of the current baseline solar array design.

Although a baseline design is selected, major design decisions like the array configuration and architecture are not yet finalized as their impact on the array performance are not well understood. For this purpose, a design tool is established that allows quantification of specific design decisions in terms of the two main performance metrics of a solar array which are power per mass (in W/kg) and power per stowed volume (in W/m³).

3. SOLAR ARRAY DESIGN TOOL

The design tool was developed for use in the preliminary design phase. Consequently, the level of detail is limited to a practical level, in which only those components are considered in the underlying model that are significant in terms of volume, mass, and mass distribution. These components are the boom as the main load carrying structure, the blanket, spreader bar, roller-core, deployment mechanism and the spacecraft interface.

3.1. Solar Array Model

The underlying solar array model of the design tool consist of a structural model of the boom as well as mass and volume models of the main components. The array is sized to comply with two design constraints which are the deployed fundamental frequency f_{req} of the array and the resistance against a lateral acceleration load a_{req} given by equations (1) and (2):

$$f_0 > f_{req} \quad (1)$$

$$a_{crit} > a_{req} \quad (2)$$

The constraint functions impose certain loads on the boom. To comply with the fundamental frequency requirement the flexible blanket needs to be set under tension which induces a compression load P in the boom. The lateral acceleration induces lateral loads in the boom. If the boom mass is small in comparison to the other components, the lateral acceleration results mainly in a lateral tip load Q.

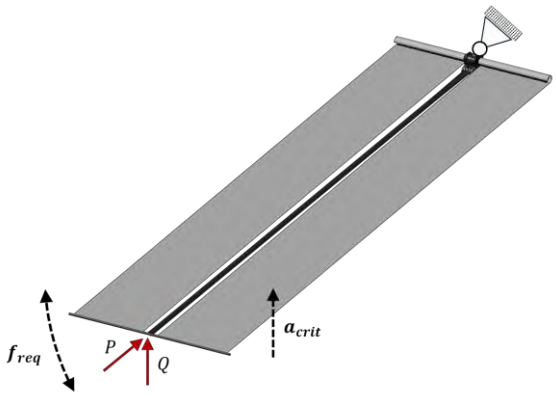


Figure 5: Solar array design requirements and corresponding boom laoding for a root deployment configuration.

The loads P and Q resulting from the dynamic requirements f_{req} and a_{req} depend on the component masses and the mass distribution throughout the array. However, these in turn depend on the boom sizing results, wherefore sizing of the array is done numerically.

3.2. Boom Stability Approximation

The boom is the main load carrying component in the deployed state and is sized according to the applied load set (P,Q). To simplify the sizing process the boom is approximated as a thin-walled tube of radius R and wall thickness t (see Figure 6).

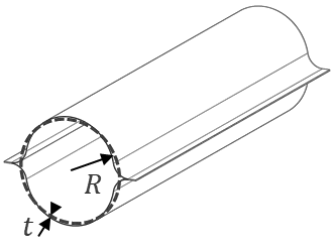


Figure 6: Approximation of the boom cross-section.

For a thin-walled ($t \ll R$), slender ($R \ll L$) tube subjected to compression and lateral force bending the failure mechanisms to be considered are global column and local shell buckling as well as cross-sectional collapse. An approximation of the boom stability behaviour is required for the design tool. The approximation is done on the basis of finite element analysis (FEA) results. It is found that within the considered slenderness and wall-thickness ratios the main failure mechanisms to be considered are global column buckling and cross-sectional collapse. Hence, the approximation needs to consider the interaction of both depending on the applied load set (P,Q).

3.2.1. Cross-Sectional Collapse

Cross-sectional collapse of a slender cylinder under pure bending is described by Brazier [3]. The longitudinal stresses from the bending load result in a lateral component due to the curvature of the beam. This lateral component causes the cross-section to ovalize. Brazier gives an expression for the critical moment of an isotropic cylinder:

$$M_{Brazier} = \frac{2\sqrt{2}}{9} \frac{ERt^2}{\sqrt{1-\nu^2}} \qquad (3)$$

Although the type of loading and the boundary conditions differ, the failure mechanism also occurs for the cantilever beam under combined axial and lateral tip load (see Figure 7).



Figure 7: Deformed boom in a cantilever cofiguration wih axial and lateral tip lad and deformed cross-section.

The maximum ovalization occurs in some distance to the clamped root where deformation of the cross-section is restricted. The location remains constant with increasing load and bending deformation (see Figure 8 and Figure 9) but is sensitive towards the beam slenderness ratio L/R.

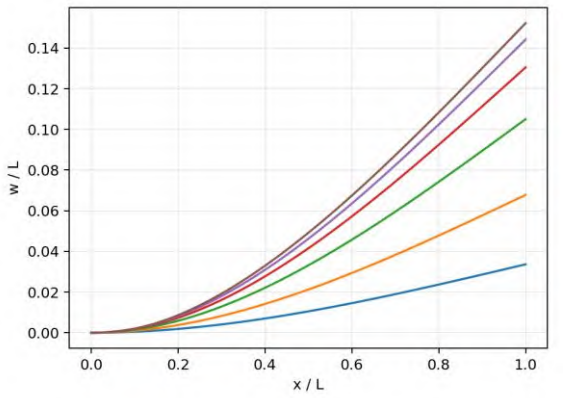


Figure 8: Displacement curves of the boom with increasing load.

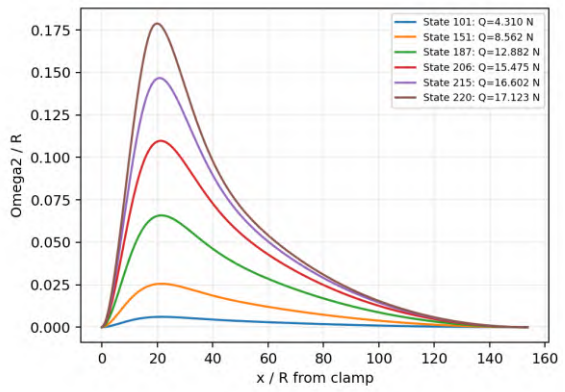


Figure 9: Ovalization profile over the boom length with increasing load.

However, in how far cross-sectional collapse or column buckling is the main failure mechanism depends on the ratio of compression P and lateral force bending Q.

3.2.2. P-Q-Interaction

A non-dimensional expression for the interaction of P and Q is established through approximation of FEA results. The non-dimensional form is achieved through formulation using the load ratios p and q:

$$p = \frac{P}{P_0} \qquad (4)$$

$$q = \frac{Q}{Q_0} \qquad (5)$$

Thereby, P_0 and Q_0 are the critical compression and lateral forces. The resulting interaction curve (see Figure 10) is derived for a slenderness ratio L/R of 154 and is approximated through the following bi-power-law:

$$p^{\alpha} + q^{\beta} = 1 \qquad (6)$$

The exponents are determined to $\alpha = 1.224$ and $\beta = 0.675$.

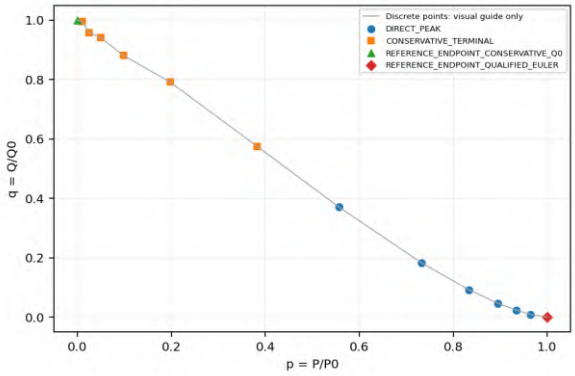


Figure 10: p-q-interaction curve based on FEA results.

The critical compression force P_0 is well described through Euler's expression for global column buckling:

$$P_0 = \frac{\pi^2 EI}{(2L)^2} \tag{7}$$

For calculation of the critical lateral force Q_0, it is found that the corresponding moment acting in the region with maximum ovalization is well described by Brazier's expression. However, as this maximum occurs in some distance to the clamping and this distance is sensitive towards the beam slenderness ratio L/R, a correction factor is introduced to enable the calculation of Q_0 based on Brazier's formula:

$$Q_0 = \frac{M_{Brazier}}{L}\left(1 + \frac{A_Q}{\frac{L}{R} + B_Q}\right) \tag{8}$$

The constants are determined to $A_Q = 25.495$ and $B_Q = 9.222$. Sensitivities are checked regarding influence of the slenderness ratio L/R and the wall thickness ratio t/R within certain intervals:

$$0.005 \leq \frac{t}{R} \leq 0.010 \tag{9}$$

$$51 \leq \frac{L}{R} \leq 307 \tag{10}$$

It is found that within these limits the interaction curve scales well with the boundaries P_0 and Q_0.

3.3. Component Scaling Laws

Scaling laws are formulated for the mass and volume of the array components. While the dimensions necessary to calculate the volume can mostly be derived based on the array size and the boom scaling result, this is not the case for the component masses. The latter is also relevant for accurate calculation of the boom loading as the component masses and the mass distribution throughout the array is required. The mass of a component m_j is derived using a power law based on a measured or calculated reference design:

$$m_j = \max\left(m_0, m_{ref}\prod_{i=1}^{n}\left(\left(\frac{X_i}{X_{i,ref}}\right)^{\alpha_i}\right)\right) \tag{11}$$

Thereby, m_0 is the lower scaling limit of the component, m_{ref} is the measured or calculated reference mass, the term $X_i/X_{i,ref}$ is the scaling term and the exponent α_i gives the scaling behaviour of X_i.
For the boom scaling is done through sizing regarding the applied loading. However, there are certain constraints which limit the design space. As the mast is stowed through elastic deformation the strain shall not exceed the region of elasticity during flattening and reeling. This is considered through a strain limit ε_{max}:

$$\varepsilon \leq \varepsilon_{max} \tag{12}$$

A lower scaling limit t_{min} is also set for the wall-thickness of the boom as availability and handling of very thin materials is limited:

$$t \geq t_{min} \tag{13}$$

A constraint similar to the strain limit is set to the wall-thickness ratio t/R of the boom. For small ratios local shell buckling becomes dominant which is not covered by the chosen boom stability approximation. For high ratios the strain during flattening becomes dominant, which would severely limit the available strain for reeling:

$$\left(\frac{t}{R}\right)_{min} \leq \frac{t}{R} \leq \left(\frac{t}{R}\right)_{max} \tag{14}$$

3.4. Design Tool Work Flow

The work flow of the design tool (see Figure 11) starts with reading the list of requirements and the study definition. This information is used to generate the initial mass and load values for the numerical sizing process. The results are the boom dimensions and a set of component mass and volume properties which in turn are used for the performance calculation of the overall array. Output is a list with all case results of the study definition.

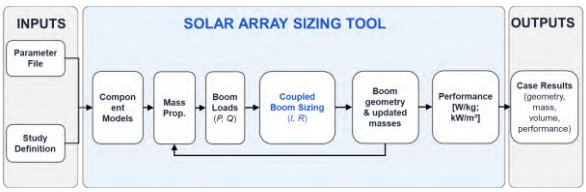


Figure 11: Design tool flow chart.

4. DESIGN TRADE STUDY

For the trade study several case studies have been defined. Within this paper the major design decisions in the early design process are addressed

as well as some sensitivities towards the design requirements. Addressed are the selection of the solar cell technology, the number of booms, the deployment configuration and the impact of the lateral acceleration requirement. For the discussion the solar array performance values in terms of power per mass in W/kg and power per volume in W/m³ is used. For calculation of the array mass the sum of all component masses is used. For calculation of the stowed array volume an envelope is defined. The width of the envelope corresponds to the array width, while the depth and height are determined by the largest dimensions of the components along those specific axes. In most cases, these dimensions correspond to those of the boom deployment mechanism. This approach of using an enclosing envelope for volume calculation ensures that the volume specifications are meaningful to engineers and mission planners.

4.1. Baseline Solar Array Performance

The results of the trade study are presented in reference to a baseline design. This baseline design is characterized as follows:

- PV-technology: Low cost, flexible Si-cells with 20% efficiency,
- Array architecture: Single, centrally aligned boom with two adjacent blankets,
- Deployment configuration: Root deployment,
- Design requirements:
    - Fundamental frequency $f_{req} = 0.1\text{Hz}$,
    - Lateral acceleration $a_{req} = 0.05\text{g}$.

The study is conducted over a power range per wing of 0.5kW to 20kW. The resulting mass specific performance of the baseline design (see Figure 12) shows a steep increase in the low power region with a pronounced peak of 285W/kg at 1.6kW. Hereafter the performance decreases but remains well above 200W/kg. The initial steep increase is a result of the lower scaling limits defined in the scaling laws. In this power region the minimum dimensions and mass properties are reached. The decline in the higher power region is a result of the increasing structural effort to support the large blanket.

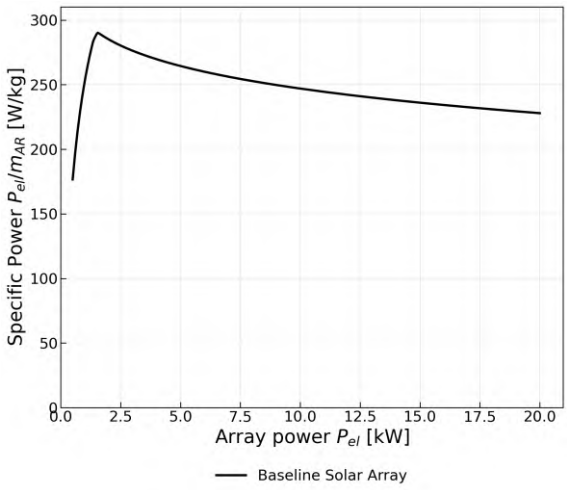


Figure 12: Mass specific performance of the baseline solar array plotted over array power.

The volume specific performance (see Figure 13) shows the same trend but even more pronounced. Initially a steep increase is observed with a peak at 44kW/m³ at 2.1kW. Afterwards the performance drops significantly with power to 13kW/m³ at 20kW. The initial increase is again a result of the lower, dimensional scaling limits. The decline in performance in the higher power region is primarily a result of the stowed boom dimensions and subsequently those of the boom deployment mechanism. The stowed array volume is driven by the largest component and regarding depth and height this component is the deployment mechanism. When the outer coiling diameter of the stowed boom increases, this also drives the deployment mechanism dimensions and thus stowed array volume.

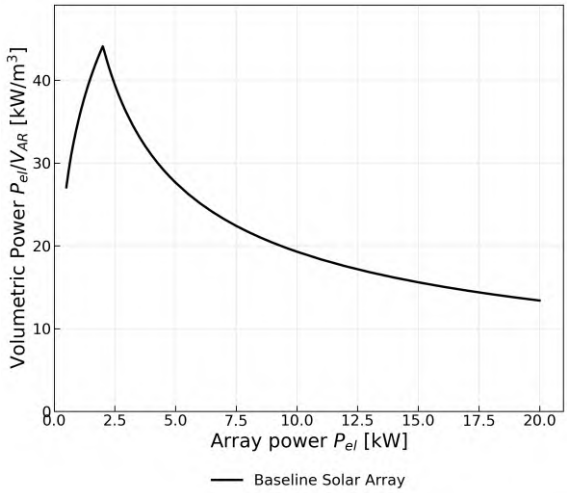


Figure 13: Volume specific performance of the baseline solar array plotted over array power.

In the following all trade study results are normalized by the according performance values of the baseline design and thereby given in non-dimensional form.

4.2. Solar Cell Technology

The solar cell technology is the driver for the blanket mass, minimum blanket reeling diameter and required array surface. In the trade study three types of solar cell technologies are compared:

- Flexible Si-cells with 20% efficiency, 150mm reeling diameter and 0.5kg/m² areal blanket mass,
- Rigid 3J-cells with 30% efficiency, 200mm reeling diameter and 1kg/m² areal blanket mass,
- Flexible Perowskit cells with 20% efficiency, 80mm reeling diameter and 0.2kg/m² areal blanket mass.

For Perowskit cells an optimistic assumption on performances available in the near future based on current data generated under laboratory conditions are considered.

The mass specific performance (see Figure 14) shows for state-of-the-art triple junction cells a decrease by 20% to 25% in comparison to the baseline design over the main part of the power interval. The higher performance reduces the required blanket surface area but the higher blanket mass is not sufficiently compensated.
The mass specific performance of the lightweight Perowskit blanket shows a strong increase in the small power region with a peak at almost 75% near 3kW. Hereafter, the gain in performance decreases slightly but still possesses a value of 59% at 20kW wing power. This strong increase in performance is the result of the lightweight blanket which in turn allows for a smaller boom and thereby less structural mass despite the larger surface area of the array. Hence, in terms of mass specific power a lightweight blanket promises significant gains in performance even when this comes with lower cell efficiency.

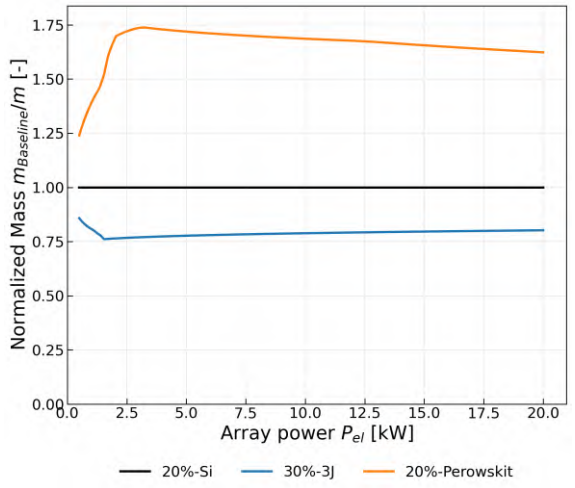


Figure 14: Mass specific performance for various cell technologies plotted over array power.

Looking at the volume specific performance (see Figure 15) the 3J-cells lead to a drop in performance by around 30% in the lower power region but to an increase of nearly 10% in the higher power region above 3kW. The initial decrease is caused by the in terms of stowage volume more severe lower scaling limits, particularly the higher initial reeling radius. However, above 3kW this restriction no longer applies and the increase in cell efficiency and thus reduced blanket surface area pays off.
The curve for the Perwoskit cell technology shows below 3kW a steep negative slope in the low power region with performances well above the baseline. This is again an interaction effect of the lower dimensional scaling limits, mainly the minimum reeling diameter. In the high-power region Perwoskit offers an increase in performance by 22% which is almost constant over the entire power range. This increase is a result of the low reeling diameter and also the low blanket thickness which adds less volume than the other two technologies.

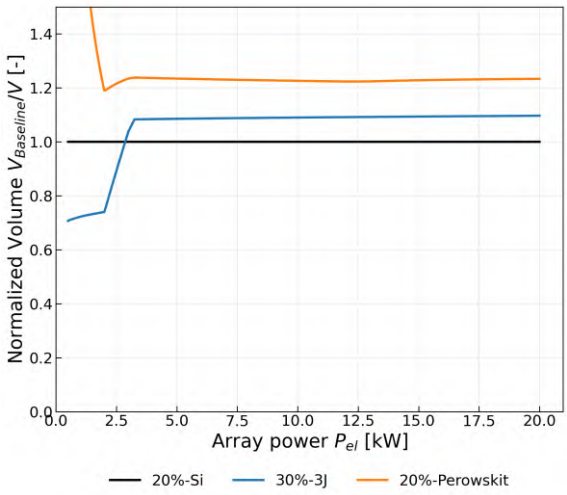


Figure 15: Volume specific performance for various cell technologies plotted over array power.

4.3. Number of Booms

The modular design of the array allows variation of the number of booms. However, adding one or more booms also adds complexity, increase in costs and differences in blanket segmentation. In the following the impacts of using 1, 2 and 3 booms on the array performance are studied.

The influence on the mass performance (see Figure 16) shows the same characteristic for 2 and 3 booms in comparison to the baseline with just a single boom. In the low power region below 3kW the added mass from the second and third boom and boom deployment mechanism significantly reduce performance. This results particularly from the lower mass scaling limits. However, above 3kW a moderate loss of 6 % to 8% for the 2-boom-architecture and of 8% to 12% for the 3-boom-architecture is visible.

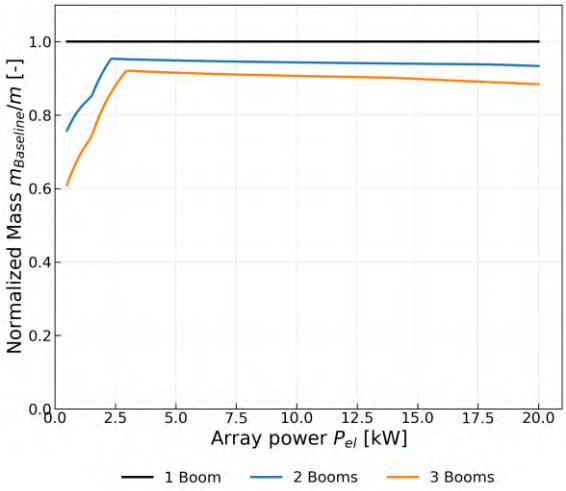


Figure 16: Mass specific performance for various numbers of booms plotted over array power.

The decrease in mass specific performance may be overcompensated through the gains in volume specific performance (see Figure 17). Below 2kW of array power slightly lower values are reached. Above a strong increase is observed culminating in an increase of 45% in case of the 2-boom-architecture and even 78% in case of the 3-boom-architecture. While again the smaller power region is dominated by the lower scaling limits of the boom and boom deployment mechanism, the reduction in individual boom loading pays off for higher power demands. As the load per boom is halved or even reduced to a third, smaller masts with lower wall-thickness can be used. These booms can be reeled more compactly which in turn reduces the depth and height of the array's stowage envelope and thus the overall stowed volume.

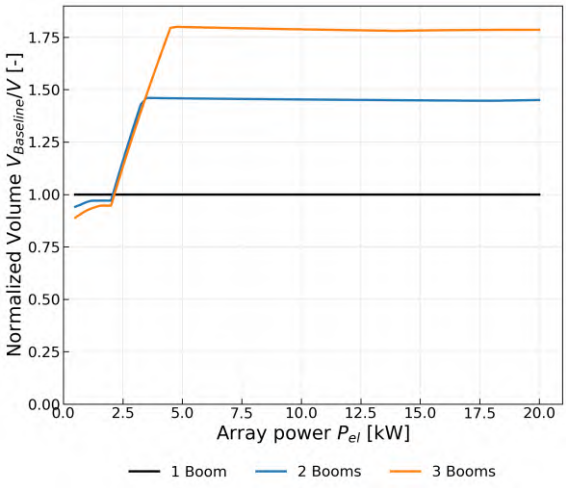


Figure 17: Volume specific performance for various numbers of booms plotted over array power.

Hence, increasing the number of booms adds mass, complexity and costs but is a very efficient measure to increase volume specific performance.

4.4. Deployment Configuration

Another major design decision is the deployment configuration whether a root or tip deployment shall be used. In the first case heavy components such as blanket roller core and deployment mechanism remain close to the spacecraft interface and do not contribute to the boom loading. On the other hand, in case of a tip deployment harnessing becomes less complex as getting power off the blanket is simplified as a continuous harness with rigid interface can be used.

The influence on the mass specific performance (see Figure 18) is significant. While the baseline design uses a root deployment the added mass at the boom tip when using a tip deployment becomes increasingly significant with higher power. While in the small power region a loss in performance of 15% to 20% is observed, this increases to more than 30% at 20kW of wing power.

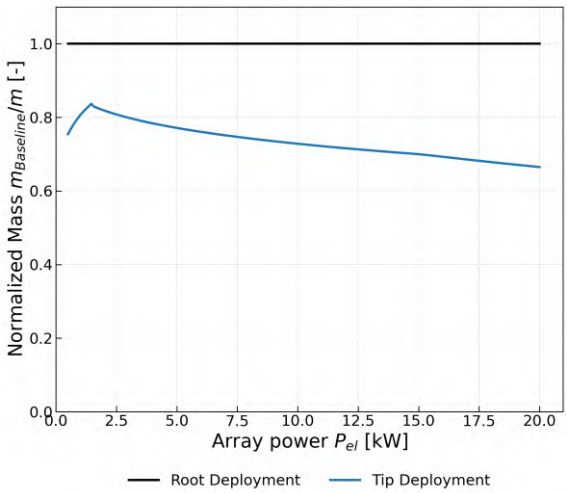


Figure 18: Mass specific performance for root and tip deployment plotted over array power.

The same behaviour is visible for the volume specific performance (see Figure 19). While in the small power region the losses are with 5% to 10% less pronounced, the loss at 20kW of wing power reaches again more than 30%.

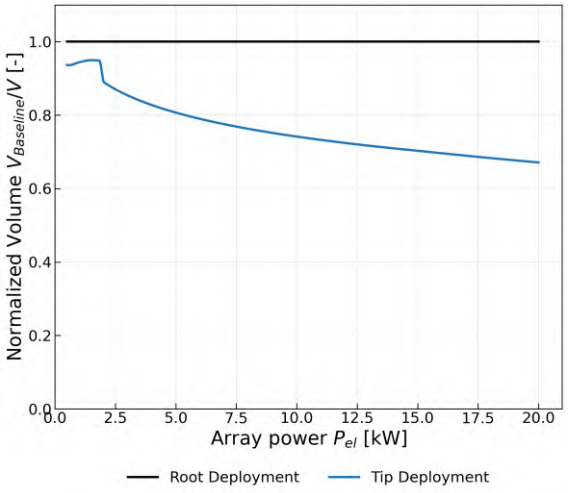


Figure 19: Volume specific performance for root and tip deployment plotted over array power.

Hence, the deployment configuration is a fundamental design decision. While for smaller arrays a tip deployment may be reasonable as the harness design and thereby array complexity and costs are reduced, for larger arrays a root deployment is advised.

4.5. Lateral Acceleration

Requirements are in general resulting from mission constraints. However, in some cases there is some influence on the requirement definition itself by tuning the mission design accordingly or introducing less demanding safety margins. In this case the sensitivity regarding lateral loads resulting from accelerations such as orbit correction or attitude control manoeuvres is studied. This is of particular interest for the presented solar array design as it features the ability to fully retract the array. Thereby, high load events can be avoided thus significantly reducing the constraints in the structural performance.

The baseline design considers a lateral acceleration of 0.05g. This is compared with acceleration requirements of 0.1g and 0.025g. In terms of array mass increasing the lateral acceleration requirement the array structure has to comply with leads to a loss in mass specific performance by 11% to 15% (see Figure 20). Lowering this requirement to 0.025g leads to a moderate increase in performance by 9% at around 3kW dropping to 7% at 20kW per wing.

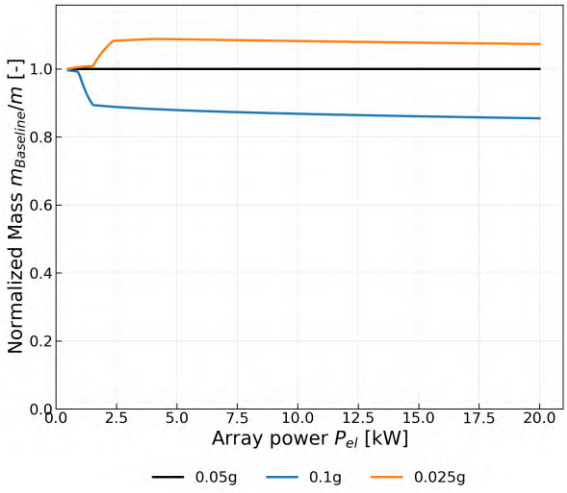


Figure 20: Mass specific performance for various lateral acceleration requirements plotted over array power.

Looking at the volume specific performance (see Figure 21) a significantly larger impact is observed. Increasing the acceleration loading to 0.1g, this causes a drop in performance by 36% to 38%. Lowering the same to 0.025g boosts volume specific performance by 55% at 3kW to 62% at 20kW of power per wing.

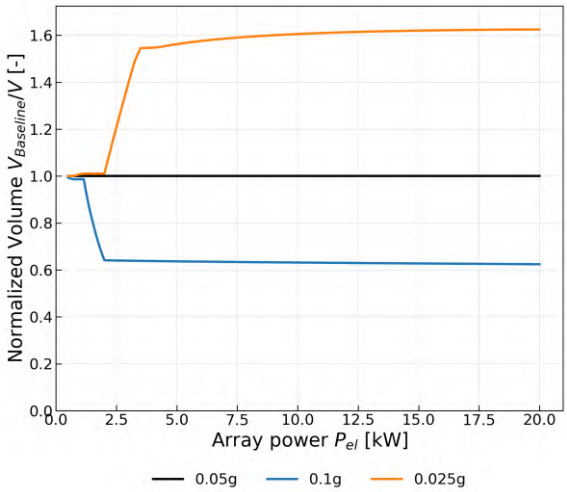


Figure 21: Volume specific performance for various lateral acceleration requirements plotted over array power.

Hence, carefully choosing the lateral acceleration requirement pays off especially in terms of volume specific power. Selecting an according mission design and less demanding margin policy are key factors to reduce array volume. In this regard, making use of the retraction capability of the presented array can generate significant volume savings.

5. CONCLUSION & OUTLOOK

A design tool to quantify the impact of the major design decision in the early design process of a

rollable solar array is developed. Based on this tool, a trade study regarding some of these decisions is conducted.
A major finding is that achieving high volume specific performance at power levels above 5kW per wing is a challenging design task that requires careful selection of array architecture, deployment configuration and mission driven design requirements. Especially, reducing the individual lateral boom load is an effective measure. This can be done either through increasing the number of booms, selecting a more favourable mass distribution through choosing a root deployment configuration or reducing the requirement regarding the lateral acceleration. The latter can effectively be addressed by making use of the retraction capability of the presented array design.
Major design drivers for the mass specific power are the photovoltaic technology and the deployment configuration. Selecting a PV-blanket with low areal mass is advantageous even when lower cell efficiency needs to be compensated through an increase in blanket surface area. Furthermore, it is found that the concentration of heavy components close to the spacecraft interface is beneficial. Therefore, a root deployment configuration is advised to minimize overall array mass particularly when aiming for high power levels per wing.

The presented results are based on the very first iteration of the solar array design tool. The trade study shows significant sensitivities in the small power region towards the component scaling limits. The same is true for the exponents in the scaling terms for the higher power region. Hence, further refinement of the scaling laws based on actual measurements on hardware or CAD-models is necessary to tune their accuracy.
Another update is necessary for the boom stability approximation. In this first design tool iteration, the p-q-interaction curve does not consider a follower force for the boom compression load. In a flexible blanket solar array, the compression load is always pointing in the direction of the boom root. This has a strong impact on the booms load carrying capability in compression which is not yet reflected in the tool and the results.

6. REFERENCES

1. Hillebrandt, M. & Straubel, M. & Zander, M. E. & Hühne, C. (2023). "*A Novel Rollable, Deployable and Retractable Solar Array Structure*", 17th European Conference on Spacecraft Structures Materials and Environmental Testing, 2023-03-28 - 2023-03-30, Toulouse, France.
2. Hillebrandt, M. & Meyer, S. & Stegmaier, M. &Straubel, M. & Zander, M. E. und Hühne, C. (2023). „*Zero-G Deployment Testing of a New Rollable and Retractable Solar Array*", 2023 AIAA Science and Technology Forum and Exposition (AIAA SciTech Forum), 2023-01-23 - 2023-01-27, Gaylord National Harbor, National Harbor, USA.
3. Brazier, L. G. (1927). "*On the Flexure of Thin Cylindrical Shells and Other "Thin" Sections*", Proceedings of the Royal Society of London. Series A, 1927-09-01, London, United Kingdom.

NANOMAGSAT: AN ULTRACOMPACT DEPLOYABLE BOOM FOR SMALLSAT AND CUBESAT MISSIONS

Jorge PINAZO [(1)] , Víctor LÓPEZ [(1)] , Juan FAYOS [(1)] , Pepe NIETO [(1)] , Marina MERCHÁN [(2)]

[(1)] COMET Aerospace, Ronda Auguste y Louis Lumiere, 23, Paterna, Spain, Email: jorge.pinazo@cometaerospace.com

[(2)] Open Cosmos Ltd, Unit 8, BEP0 Building, Thomson Ave, Didcot, OX11 0GD (United Kingdom), Email: Marina Merchán Bravo <marina.merchan@open cosmos.com>

KEYWORDS
Boom, Deployable, NanoMagSat, NMS, nonmagnetic, modular

ABSTRACT

NanoMagSat is an ESA mission of the Scout program implemented with a constellation of three 16U nanosatellite, leveraging on the heritage of the ESA Swarm mission, aimed at monitoring the Earth's magnetic field and ionospheric environment on low Earth orbit.

A 3meter deployable nonmagnetic boom is used to keep the magnetometers away from any magnetic interference coming from the satellite platform, once in orbit.

The boom has recently reached TRL6 and this paper presents the results of the Qualification Test Campaign recently completed, which included vibration, shock and functional tests.

The qualification of the Speed Control Device (SCD), a critical component which allows controlling the deployment speed of the boom, is also described within this paper.

1. MISSION

The NanoMagSat (NMS) mission consists of a constellation of three geomagnetic observation satellites, aimed at monitoring the Earth's magnetic field and ionospheric environment on low Earth orbit in an innovative way to guarantee a coverage of all local times within an unprecedented timeframe.

One of the satellites is in a polar orbit and the rest have the same inclination with a Right Ascension of the Ascending Node (RAAN) of 90 degrees.

Each satellite contains the following instruments to monitor Earth's magnetic field and ionosphere:

- Miniaturised Absolut Magnetometer (MAM) with two startrackers (STR) at the tip of the boom.
- High Frequency Magnetometer (HFM) located at the middle of the boom.
- A Langmuir mNLP probe to measure electron density.
- Dual frequency GNNSS receiver.



Figure 1: NanoMagSat inorbit simulated view

Currently the project is undergoing an implementation phase to qualify a first model in 2026 and manufacture a total of 3 flight models to be launched from 2027 onwards.

The project is led by Open Cosmos Ltd. and CEA-Leti, with the scientific contribution of IPGP.

2. BOOM DESIGN

The complete boom assembly (Figure 2 & Figure 3) consists of the boom itself and the optical bench at the top, which includes the STR support. Payloads include the MAM, the HFM and two STR.

Metallic harness containers are also necessary to stow the different harness in stowed configuration.

A Speed Control Device (SCD) is located at the bottom of the boom assembly to control de boom deployment speed.

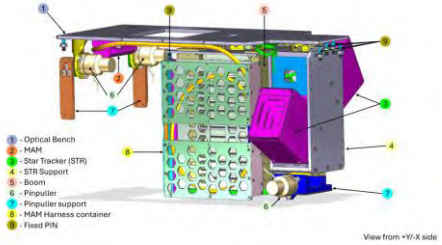


Figure 2: Boom assy. in stowed config. (view A)

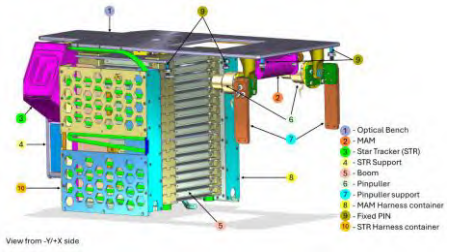


Figure 3: Boom assy. in stowed config. (view B)

In stowed configuration (Figure 4), the complete boom assembly fits within the 16U platform. A set of pinpullers are used to maintain the stowed position before deployment. The total height of the assembly in stowed configuration including the optical bench is 255 mm.



Figure 4: Stowed configuration

When deployed (Figure 5), the total height including the optical bench is 3017 mm, with the MAM located 2904 mm away from the platform reference system, which is the main objective of the boom, to separate as much as possible the MAM from any magnetic source coming from the satellite platform. Thus, a compaction ratio of 12 is accomplished.

The margin of motorization achieved is 2.2, obtained following ECSS standards and based on the measurements obtained during several deployment tests performed.

The following table includes the mass of the main boom assembly components:

Table 1: Mass breakdown

Component	Mass (kg)
Boom	3.26
Optical Bench	1.33
SCD (including HFM harness container)	0.68
MAM and STR harness containers	0.78
Interfaces	0.69
Harnesses	0.77

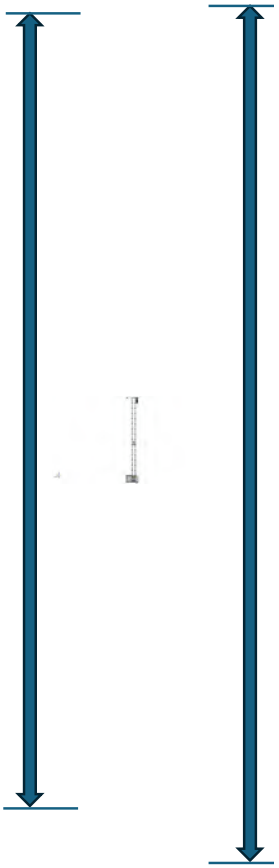


Figure 5: Deployed configuration

The boom consists of different modules joined through mechanical joints including torsion springs, which produce the boom deployment in a passive way. The final height of the deployed boom might then be easily adaptable to other mission requirements and applications.

The main parts of the boom: longerons and platforms are made of CFRP and the brackets and axis connecting the different elements are made of aluminium and titanium.

One of the most challenging mission requirements to accomplish is the thermoelastic stability of the optical bench. The relative position between MAM and STR accommodated at the optical bench has to be totally controlled and stable along the different orbit phases. To accomplish with this critical requirement, thermal stable materials are used as much as possible and the connection between the boom, optical bench and STR support has been

defined by means of elastic connections, to decouple as much as possible the thermoelastic deformations of the connected parts. Thermal and thermoelastic analyses have been performed to simulate the inorbit real behaviour and guarantee the fulfilment of the requirement.

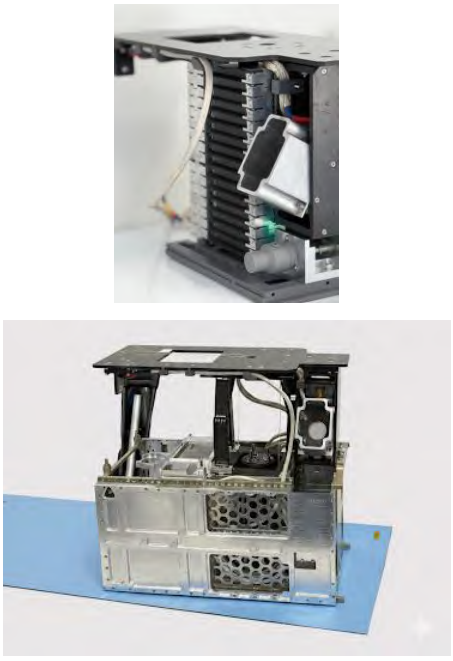


Figure 6: Boom assembly images

3. BOOM TEST CAMPAIGNS

Different test campaigns have been already performed through the different project phases since 2023.

- October 2023: when some resistance tests from loads envelope for quasistatic, sine, random vibration and shock were performed at room temperature. No damage was observedand all subsequent deployments were successful.
- March 2024: deployment tests after implementing some improvements on harness stowage, with successful results.
- October 2024: successful deployment tests including flight interfaces through pinpullers and the SCD.

3.1. Modal Test

As part of a previous consolidation phase, a modal test was performed on the boom Engineering Model in deployed configuration.

The boom was clamped at its base and the test was performed using the impact hammer method, with an accelerometer located at the upper module.

A first frequency of 1.03 Hz was obtained.

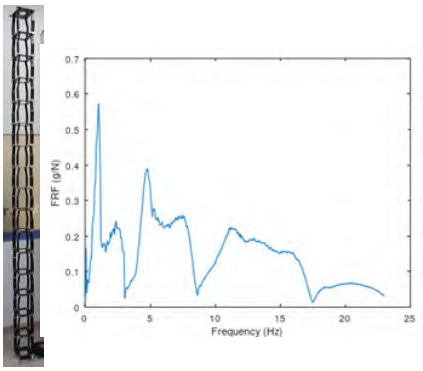


Figure 7: Boom modal test results

3.2. Qualification Test Campaign

As part of the qualification test campaign performed during 2026, a set of vibration and shock tests was performed. The boom assembly was tested within a NanoMagSat satellite platform, together with other satellite components.

3.2.1. Vibration Test

The satellite was housed inside an Exolaunch Exopod Nova test pod, fixed to an electromechanical shaker table and vibrated according to test specification.

A set of triaxial accelerometers were installed at different positions on the platform and boom assembly (see Figure 8).

Random vibration tests were performed in the three axis X, Y and Z independently in the range 52000 Hz.

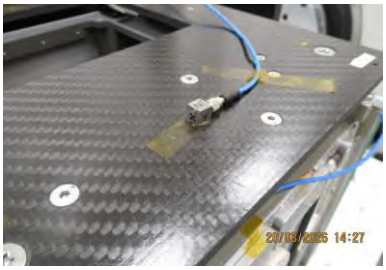


Figure 8: Accelerometers installation

Sine resonance search at 0.25 g were performed before and after each axis test and between each test level.

Random vibration test levels and durations were defined taking into account the envelope of the preselected launchers (potential candidates for NMS mission).

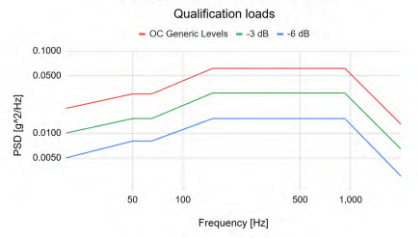


Figure 9: Random vibration levels

The test success criteria defined for the boom assembly was to achieve a complete boom deployment after vibration tests in all directions. This was successfully accomplished in March 2026, so the boom assembly was considered qualified and the TRL6 achieved.



Figure 10: Successful deployment after vibration test

3.2.2.Shock Test

Shock tests were performed at Surrey Space Centre facilities in Guildford, UK.



Figure 11: Shock test

Shock test levels applied are shown below, defined from the envelope of the preselected launchers (potential candidates for NMS mission).

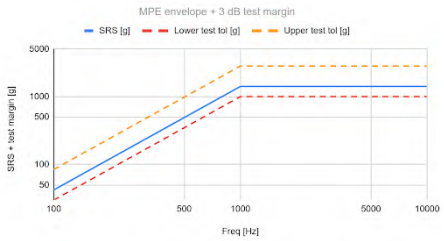


Figure 12: Shock levels

The test success criteria defined for the boom assembly was to achieve a complete boom deployment after shock tests. This was successfully accomplished in May 2026, so the boom assembly was considered qualified.

4. SCD QUALIFICATION TEST CAMPAIGN

The deployment of the boom depends on the elastic energy stored by the torsion springs installed along the boom articulations (passive deployment). Therefore, to prevent a sudden deployment a device to control and reduce the speed to the allowable value is necessary. This function is performed by the Speed Control Device (SCD), designed and developed specifically for this mission.



Figure 13: SCD and deployment test jig

The SCD operation is based on a control cable wound inside the SCD and connected to the boom, that is released with a constant and controlled speed.

A dedicated Qualification Test Campaign was recently performed on the SCD alone, in July 2026.

The test campaign consisted of a set of functional tests at room and cold temperature, vibration tests at qualification load levels, thermal cycling, bakeout and functional tests in TVAC conditions.

- Room temperature: 24ºC
- Cold temperature: 5ºC
- Thermal cycling from 6 ºC to 47.5ºC
- Bakeout at 60ºC and 10^4 torr.
- TVAC: 0°C, 24°C, 47.5°C and 10^4 torr.

The deployment speed can be adapted to the mission requirements. For this mission, the following values were obtained: 42 mm/s at ambient conditions.

30 mm/s at 0ºC and vacuum conditions.

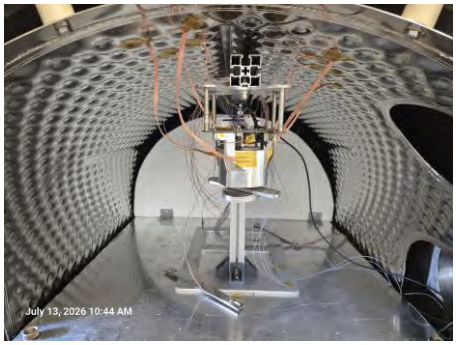


Figure 14: Installation of the SCD in TVAC

The functional test and the test success criteria is based on the control cable unwinding successfully, with constant and controlled speed.

All tests were completed successfully.

The SCD demonstrated good performance under lowtemperature and vacuum conditions, even up to 0ºC, despite the device was originally designed for a lower limit of 5ºC. No significant impact on performance was observed due to the vacuum environment, with results remaining comparable to those obtained under ambient conditions.

5. CONCLUSIONS

The design of the ultracompact deployable boom has been presented. The modular design allows to adapt the height of the boom to different missions and requirements with a very high compaction ratio of 12. The boom is nonmagnetic and the optical bench highly stable to thermoelastic deformations, as required for this specific mission.

Currently the boom assembly has successfully passed a Qualification Test Campaign, achieving a TRL6 and therefore, ready for integration into flight models, to be launched from 2027 onwards.

The critical device SCD to control the deployment speed has been also qualified for the mission.

6. ACKNOWLEDMENTS

The authors acknowledge the support of the European Space Agency (ESA) under the SCOUT program and members of the Consortium working on the NanoMagSat mission.

DEVELOPMENT OF THE BISTABLE ASYMMETRIC COLLAPSIBLE MASTS FOR ROLL-OUT MECHANISM

Jun-Yong Kim [(1)], Jun-Hyeong Choi [(2)], Jin-Ho Roh [(3)]

Department of Aeronautical and Astronautical Engineering, Korea Aerospace University, Gyeonggi-do, 10540, Republic of Korea

[(1)]Email: junyongkim@kau.kr [(2)]Email: chlwnsgud120@kau.kr [(3)] Email: jinhoroh@kau.ac.kr

KEYWORDS

Roll-out Mechanism, Bistability, Asymmetric cross-section

ABSTRACT

Passive roll-out deployment requires collapsible tubular masts (CTMs) that remain stable in both deployed and coiled configurations. This study develops an asymmetric collapsible tubular mast (ACTM) to improve bistability and stowage compactness. The effects of the inner-shell radius on the bistability parameter and predicted coiled diameter are evaluated analytically. Relative to a symmetric CTM, the selected asymmetric configuration is predicted to exhibit a higher bistability parameter and a smaller coiled diameter. A fabricated ACTM maintains both stable configurations without an additional locking device. Its free-deployment behavior is investigated through numerical simulations and experiments and compared with that of the symmetric CTM. Finally, a guided roll-out mechanism incorporating a spindle guide and an outlet roller is developed to regulate boom release and prevent premature unwinding. These results demonstrate the feasibility of the ACTM and guided mechanism for compact, passive roll-out deployment.

1. INTRODUCTION

Collapsible Tubular Masts (CTMs) are attractive for deployable space structures because they provide high stiffness in the deployed configuration while allowing compact coiled stowage. For passive roll-out applications, bistable CTMs are particularly advantageous because both the deployed and coiled configurations correspond to stable equilibrium states. If bistability is not achieved, additional components are required to maintain the stowed configuration and to enable deployment, which results in an increase in the overall system mass. Bistable behavior can be achieved by tailoring the laminate stacking sequence, constituent materials, and cross-sectional geometry. Bistable CTMs require less energy to maintain the stowed state and show more predictable self-deployment compared to monostable designs [1].

Guest and Pellegrino [2] proposed a two-parameter strain-energy formulation for predicting bistability in composite cylindrical shells. Lee and Fernandez [3] extended this framework to two-shelled deployable booms and demonstrated that variations in laminate stiffness and shell geometry, including asymmetric configurations, can induce bistability and alter the stable coiled diameter [1]. In practical systems such as the NEA Scout solar-sail deployer, long booms are stored in multiple wraps [4]. To account for the resulting variation in coiled radius along the boom length, Liu et al. [5] incorporated Archimedean spiral geometry into the analytical formulation. Other studies have investigated the mechanical characteristics, flattening, buckling, folding, and deployment-related instability of composite CTMs [6–12]. Collectively, these studies establish the analytical basis for predicting bistability and identify cross-sectional geometry as an important design variable.

This study develops a bistable Asymmetric Collapsible Tubular Mast (ACTM) for passive roll-out deployment. The effects of the inner shell radius on the bistability parameter and predicted coiled diameter are evaluated analytically. The free-deployment behavior of the developed ACTM is then investigated through numerical simulations and experiments and compared with that of a symmetric CTM to determine the effect of ACTM on blossoming behavior. Finally, a guided roll-out mechanism incorporating a spindle guide and an outlet roller is developed to control the release of the coiled boom.

2. BISTABLE ASSESSMENT OF CTM

2.1. Geometry design

In the coiled configuration, the shell closer to the spindle is designated as the inner shell, whereas the shell farther from the spindle is designated as the outer shell. The subscripts (i) and (o) therefore refer to the inner and outer shells, respectively. Each shell consists of a central arc segment, denoted by subscript 1, and an edge arc segment, denoted by subscript 2. Accordingly, (r_{o1}) and (α_{o1}) represent the radius and subtended angle of the outer-shell central segment, while (r_{o2}) and (α_{o2}) represent those of the outer-shell edge segment. The corresponding geometric parameters of the inner shell are denoted by (r_{i1}), (α_{i1}), (r_{i2}), and (α_{i2}), as shown in Fig. 1. The outer-shell geometry of the ACTM and the web width (w) are defined as summarized in Tab. 1.

When the ACTM is fully flattened, each shell

forms a planar strip. The flattened lengths of the inner and outer shells are given by Eq. 1.

$$h_{i,o} = 2\left(L_{i,o1} + L_{i,o2} + w\right) \tag{1}$$

The arc lengths of the central and edge segments are defined by Eq. 2 and Eq. 3, respectively.

$$L_{i,o1} = r_{i,o1}\alpha_{i,o1} \tag{2}$$

$$L_{i,o2} = r_{i,o2}\alpha_{i,o2} \tag{3}$$

Geometric compatibility between the inner and outer shells must be maintained in both the deployed and flattened configurations. First, the flattened lengths of the two shells must be equal to prevent in-plane incompatibility during flattening and coiling. This requirement gives the compatibility condition in Eq. 4.

$$2\left(r_{o1}\alpha_o + r_{o2}\alpha_o + w\right) = 2\left(r_{i1}\alpha_i + r_{i2}\alpha_i + w\right) \tag{4}$$

Second, the edges of the inner and outer shells forming the longitudinal webs must coincide in the deployed configuration to preserve continuity of the closed cross-section. This condition is expressed by Eq. 5.

$$r_{o1}\sin\left(\alpha_o\right) + r_{o2}\sin\left(\alpha_o\right) = r_{i1}\sin\left(\alpha_i\right) + r_{i2}\sin\left(\alpha_i\right) \tag{5}$$

From Eq. 4, the relationship between the subtended angles of the inner and outer shells is expressed by Eq. 6.

$$\alpha_o = \frac{r_{o1} + r_{o2}}{r_{i1} + r_{i2}}\alpha_i \tag{6}$$

Substituting Eq. 6 into Eq. 5 gives Eq. 7.

$$\left(r_{o1} + r_{o2}\right)\sin\left(\frac{r_{i1} + r_{i2}}{r_{o1} + r_{o2}}\alpha_i\right) = \left(r_{i1} + r_{i2}\right)\sin\left(\alpha_i\right) \tag{7}$$

Eq. 7 is satisfied when the sums of the curvature radii of the inner and outer shells are equal, resulting in the geometric compatibility condition given by Eq. 8.

$$r_{i1} + r_{i2} = r_{o1} + r_{o2} \tag{8}$$

Based on the geometric compatibility condition in Eq. 8, the inner-shell edge radius (r_{i2}) is varied while satisfying ($r_{i1} + r_{i2} = 20mm$ to introduce cross-sectional asymmetry. The bistability criterion (S) is used to determine whether the coiled configuration constitutes a stable second equilibrium state, with a positive value indicating bistability. The predicted coiled diameter ($\emptyset$) represents the diameter of the second stable configuration. As summarized in Tab. 2, the symmetric CTM has a bistability criterion (S) of 0.68 and a predicted coiled diameter of $40.43\ mm$. The corresponding ACTM results are summarized in Tab. 3. Case 1, Cases 2 and 3 satisfy the condition. Case 3 is selected because it has the largest bistability criterion while maintaining a smaller predicted coiled diameter than the symmetric CTM. The radii of the inner segments are selected such that their sum is $20\ mm$. The outer-segment parameters are set to the values listed in Tab. 1, and the width of the web connecting the upper and lower shells is fixed at $3\ mm$.

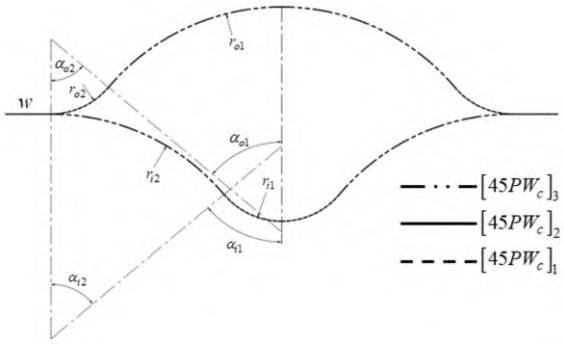


Figure 1: Coordinate geometry of the ACTM

Table 1: Geometric parameters of the outer segments

$r_{o1}\ [mm]$	$r_{o2}\ [mm]$	$\alpha\ [°]$	$w\ [mm]$
15	5	50	3

r_{o1}, r_{o2}: Radii of the outer shell
α: Subtended angle
w: Width of the web

To introduce geometric asymmetry, the radii of the outer and inner shells are intentionally defined to be different. Various geometric cases are investigated, as summarized in Tab. 3, to evaluate whether the bistable condition of the collapsible boom structure can be satisfied. When the inner-shell edge radius, fabrication becomes impractical because of the insufficient space available for web bonding. Therefore, larger values are not considered in this study.

Table 2: Bistability parameters of the symmetric CTM

S	$\emptyset\ [mm]$
0.68	40.43

S: Bistability criterion
$\emptyset$: Predicted coiled diameter

Table 3: Design cases and bistability parameters of the ACTM

Design case	$r_{i2}\ [mm]$	S	$\emptyset\ [mm]$
Case 1	6	0.74	39.79
Case 2	11	1.17	37.52
Case 3	15	1.79	36.61

r_{i1}, r_{i2}: Radii of the inner shell
S: Bistability criterion
$\emptyset$: Predicted coiled diameter

2.2. Laminate design

The ACTM is fabricated from T300/E7 plain-weave prepreg. The corresponding mechanical properties, adopted from [13], are summarized in Tab. 4. After determining the cross-sectional geometry of the ACTM, the laminate stacking sequences are designed to achieve the required bistable behavior.

Table 4: Mechanical properties of T300/E7

Properties	Value
Density $[kg/m^3]$	1760
Longitudinal Young's Modulus $[GPa]$	69
Transverse Young's Modulus $[GPa]$	69
Poisson's ratio	0.15
In-plane Shear Modulus $[GPa]$	3.3
Thickness $[mm]$	0.12

Different laminate stacking sequences are assigned to individual segments of the ACTM to tailor the bending-stiffness distribution and induce bistable behavior. Specifically, the laminate configuration $[45PW_c]_3$ is applied to segments that bend in the equal-sense bending relative to the initial transverse curvature. In contrast, segments experiencing bending in the opposite-sense bending are designed with reduced bending stiffness through ply drop implementation, resulting in the laminate configuration $[45PW_c]$ in those regions. This segment-wise stiffness tailoring enables controlled redistribution of bending rigidity between the shell segments, which plays a critical role in achieving bistable behavior in the collapsible boom with asymmetric cross-section. The web region connecting the two composite shells is formed by co-bonding the shells along the longitudinal web interface using the epoxy resin pre-impregnated in the prepreg, resulting in an effective laminate configuration of $[45PW_c]_2$. This co-bonded interface provides structural continuity between the inner and outer shells while maintaining sufficient compliance in the web region.

Based on the material properties of each ply and the corresponding stacking sequences, the equivalent laminate properties are evaluated using the Classical Lamination Theory (CLT). Furthermore, due to the symmetric laminate arrangement between the inner and outer shells, corresponding segments share identical stiffness characteristics. Based on these assumptions, the equivalent ABD matrices for the arc segments (segments 1 and 2) of the inner shell and the web region are computed.

2.3 Experimental validation of bistability

The bistable behavior of the ACTM is confirmed. Both the deployed and coiled configurations remain stable without external force. The diameter of the coiled configuration is measured using a vernier caliper and found to be $50.49\ mm$, which is larger than the predicted value of $36.61\ mm$. The experimentally measured coiled diameter is therefore approximately $37.9\ \%$ greater than the analytical prediction. This difference is mainly attributed to manufacturing effects such as thickness variation of the laminate, increased local stiffness in the web region, geometric deviation during the molding process, residual stress generated during curing, and spring-back after demolding. Because the analytical model assumes an ideal geometry, a uniform laminate thickness, and perfect bonding, these fabrication-induced effects can result in a larger stable coiled diameter than predicted.

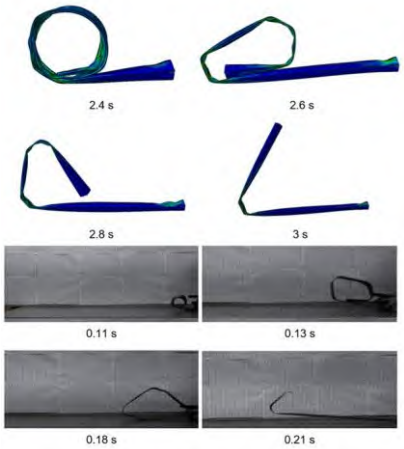
Although bistability provides two stable equilibrium states, it does not necessarily ensure stable deployment behavior. In practical deployment processes, dynamic instabilities such as blossoming may occur due to the rapid release of strain energy. Consequently, evaluation of deployment performance requires consideration of both static and dynamic stability. To investigate the effect of cross-sectional asymmetry on deployment behavior, a symmetric CTM is designed as a baseline configuration. The symmetric boom is constructed using identical upper and lower shell geometries, while the proposed boom employs an asymmetric cross-section obtained by introducing different radii in the inner and outer shell segments. Comparative free deployment analyses and experiments are conducted for asymmetric and symmetric configurations.

2.4 Free deployment experiments

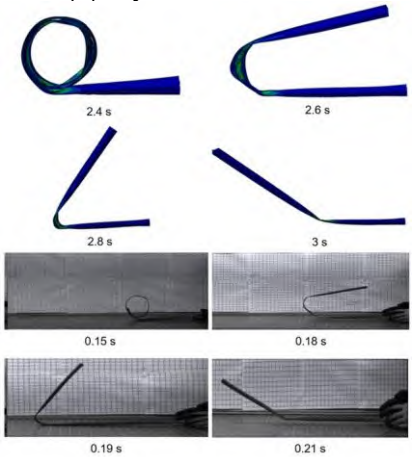
To evaluate and validate the dynamic free-deployment behavior of the proposed structure, both experimental tests and numerical simulations using ABAQUS/Explicit are conducted, and the

resulting deployment sequences are compared (Fig. 2). The boom length used in the simulation is 600 mm, consisting of 5,474 nodes and 5,120 S4R shell elements. The simulation is carried out in four sequential stages: flattening, coiling, holding, and deployment.

A comparative analysis of the deployment sequences reveals a clear distinction in structural stability between the two configurations. For the symmetric configuration, both experimental observations and numerical results demonstrate that the coiled region rapidly expands after deployment initiation, leading to significant blossoming and loss of the initial coiled geometry. In contrast, the asymmetric configuration maintains its stable coiled geometry and releases the stored strain energy in a more controlled manner. These consistent qualitative trends indicate that the proposed asymmetric configuration reduces dynamic blossoming and provides a more controlled deployment response under the tested conditions.



(a) Symmetric cross-section



(b) Asymmetric cross-section

Figure 2: Free deployment analysis and experiments

2.5 Controlled deployment of asymmetric boom

To evaluate the controlled deployment behavior of the asymmetric boom, a deployment mechanism is fabricated, as shown in Fig. 3. The mechanism is configured to reproduce the boundary conditions employed in the numerical simulations and to enable controlled release of the boom from the coiled configuration.



Figure 3: Deployment device for the collapsible boom

An actuator briefly rotates the spindle to initiate the release of the coiled boom. After the initial release, no additional motor input is applied, and the boom deploys passively using the elastic strain energy stored during coiling. A guide installed around the spindle constrains the coiled boom and suppresses premature unwinding of the inner wraps. In addition, a roller positioned at the outlet flattens and guides the boom as it leaves the spindle. The guide and roller therefore control the release path during deployment without maintaining the static coiled equilibrium.

3 CONCLUSIONS

A bistable ACTM and a guided roll-out mechanism are developed for small-satellite deployment applications. Bistability is achieved by adjusting the inner-shell geometry and locally tailoring the laminate stacking sequences. The fabricated T300/E7 plain-weave prepreg ACTM maintains stable deployed and coiled configurations without an external locking device. Free-deployment simulations and experiments show that the ACTM maintains a more stable coiled shape and exhibits less pronounced blossoming than the symmetric CTM under the tested conditions. The guided roll-out mechanism incorporates a spindle guide and an outlet roller. The guide restricts premature unwinding of the inner wraps, whereas the roller controls the boom exit path. The results demonstrate the feasibility of integrating the

developed bistable ACTM with the guided roll-out mechanism for small-satellite applications.

ACKNOWLEDGEMENT

This research was supported by the National Research Foundation of Korea (NRF) grant funded by the Korean government (Ministry of Education, Science and Technology) in 2025 (Grant No. 2120251815513), through the “BK21 Four Program for Institute for Sustainable VLEO Space Service Development.”

This research was conducted with the support of the Korea Institute for Advancement of Technology funded by the government (Ministry of Trade, Industry and Resources) in 2026 (Project No. RS-2022-KI002569, Specialized Workforce Development Program for an expert-to-be building up in the Urban Air Mobility).

4 REFERENCES

1. Lee, A.J. & Fernandez, J.M. (2019). Inducing Bistability in Collapsible Tubular Mast Booms with Thin-Ply Composite Shells. *Composite Structures 225*, *111166*.
2. Guest, S.D. & Pellegrino, S. (2006). Analytical Models for Bistable Cylindrical Shells. *Proceedings of the Royal Society A 462(2067), 839-854.*
3. Lee, A.J. & Fernandez, J.M. (2018). Mechanics of Bistable Two-Shelled Composite Booms. In Proc. 2018 AIAA Spacecraft Structures Conference, AIAA 2018-0938.
4. Sobey, A.R. & Lockett, T.R. (2016). Design and Development of NEA Scout Solar Sail Deployer Mechanism. In Proc. 43rd Aerospace Mechanisms Symposium, NASA/CP-2016-219090, San Jose, CA, USA, pp315-328.
5. Liu, T.W., Bai, J.B., Wang, Z.Z. & Fantuzzi, N. (2023). Determining Folded Stable State of Bistable Deployable Composite Boom: An Improved Two-Parameter Analytical Model. *Acta Astronautica 213, 507-515.*
6. Liu, T.W., Bai, J.B. & Fantuzzi, N. (2024). Analytical Model for Predicting Folding Stable State of Bistable Deployable Composite Boom. *Chinese Journal of Aeronautics 37(8)*, *460-469*.
7. Hu, Y., Chen, W., Li, R. & Fang, G. (2016). Mechanical Characteristics of Deployable Composite Thin-Walled Lenticular Tubes. *Composite Structures 153, 601-613.*
8. Hu, Y., Chen, W., Gao, J., Hu, J., Fang, G. & Peng, F. (2017). A Study of Flattening Process of Deployable Composite Thin-Walled Lenticular Tubes under Compression and Tension. *Composite Structures 168, 164-177.*
9. Liu, Z., Li, Q., Bian, W., Lan, X., Liu, Y. & Leng, J. (2019). Preliminary Test and Analysis of an Ultralight Lenticular Tube Based on Shape Memory Polymer Composites. *Composite Structures 223, 110936*.
10. Jia, Q., An, N., Ma, X. & Zhou, J. (2021). Exploring the Design Space for Nonlinear Buckling of Composite Thin-Walled Lenticular Tubes under Pure Bending. *International Journal of Mechanical Sciences 207, 106661*.
11. Wang, S., Sun, L., Shi, C. & Wang, B. (2023). Blossoming Failure Analysis of a Composite Collapsible Tubular Mast (CTM) Boom. In Proc. AIAA SCITECH 2023 Forum, AIAA 2023-1508.
12. Lee, A.J., Fernandez, J.M. & Daye, J.G. (2024). Bistable Deployable Composite Booms with Parabolic Cross Sections. *Journal of Spacecraft and Rockets 61(3), 757-772.*
13. Park, J.H., Kim, Y.B., Jung, G.S. & Lim, J.H. (2025). A Theoretical, Experimental and Numerical Investigation on the Dynamic Deployment Stability of Bistable Composite Tape Springs. *Composite Structures 372, 119546.*

ECSSMET
Braunschweig Germany 2026

Design and Verification

VERIFICATION OF THE TANGO INSTRUMENT THERMAL-MECHANICAL DESIGN THROUGH ANALYSIS AND TESTS

Jan de Vreugd [(1)], Bas Ouwerkerk [(1)], James Day [(1)], Rik Jansen [(1)], Eleonie van Schreven[(1)], Nurcan Alpay Koc[(1)], Martin Lemmen[(1)], Bryan de Goeij[(1)], Nikolaos Sarantinos [(2)], Daniel Farinha [(2)], Christiaan Hobijn [(3)], Zeger de Groot [(3)], Anne André [(3)].

(1) TNO, P.O. box 155, 2600 AD Delft, The Netherlands, Email: jan.devreugd@tno.nl
(2) ATG, Noordwijk, The Netherlands, Email: nikolaos.sarantinos@atg-europe.com
(3) ISISPace, Delft, The Netherlands, Email: c.hobijn@isispace.nl

KEYWORDS

TANGO Scout mission, Earth observation, greenhouse gas/air quality monitoring, imaging spectrometer, damped struts, telescope stability, shock, random vibration, thermal-elasticity, STOP, CMM.

ABSTRACT

The Twin ANthropogenic Greenhouse Gas Observers (TANGO) mission is a small satellite mission under the ESA Scout Programme tapping into NewSpace to quickly deliver affordable and innovative science, as part of ESA's FutureEO Programme, within a budget of 35M€ and a schedule of three years from mission kick-off to launch. It was kicked off in June 2025 and is planned to be launched in the middle of 2028, ready for operational service to start in Q4 2028.
TANGO aims to measure CO_2, CH_4 and NO_2 emissions at the level of individual facilities using two agile CubeSat platforms flying in close formation. Each 16U satellite carries a compact imaging spectrometer, with TANGO Carbon operating in the SWIR1 band for CO_2 and CH_4, and TANGO Nitro targeting NO_2 in the visible spectral range. To achieve the required optical performance within an 8U instrument envelope, both payloads employ freeform mirror optics, resulting in stringent mechanical and thermo-elastic stability requirements.

This paper discusses the mechanical and thermal design of the TANGO Nitro and Carbon instruments. Results of vibration testing on a Structural Thermal Mechanical (STM) representative model are discussed as well as stability measurements that were executed to assess the robustness of the instruments against severe vibration and shock loads.

1. INTRODUCTION

Accurate identification and quantification of anthropogenic greenhouse-gas emissions are important for understanding emission sources and supporting effective mitigation measures. The Twin ANthropogenic Greenhouse Gas Observers (TANGO) mission addresses this need by targeting carbon dioxide (CO_2), methane (CH_4), and nitrogen dioxide (NO_2) emissions at the scale of individual industrial facilities. The mission uses two agile CubeSats flying in close formation. One satellite carries the TANGO Carbon imaging spectrometer, operating in the short-wave infrared spectral range to measure CO_2 and CH_4, while the second carries the TANGO Nitro instrument, operating in the visible spectral range to measure NO_2. The combined observations provide complementary information for detecting emission plumes and attributing them to individual sources.
Both instruments build on the Spectrolite instrument family and on technologies developed for earlier Earth-observation instruments, including freeform mirrors, monolithic aluminium housings, opto-mechanical mounts, and damped struts. The instruments comprise a telescope and a spectrometer integrated into a stiff, box-shaped aluminium housing.

The mechanical coupling between the compact instrument, the CubeSat platform, and the launch deployer is complex design challenge. The instrument is suspended from the platform by six titanium struts incorporating passive damping. These struts must simultaneously provide sufficient launch stiffness, reduce the dynamic response transmitted to sensitive optical components, and provide conductive thermal isolation. Because the instrument represents a relatively large and stiff part of the satellite, its dynamic behaviour cannot be assessed reliably as an isolated, rigidly constrained subsystem. Verification therefore requires coupled structural modelling of the deployer, satellite platform, and instrument, complemented by testing at representative integration levels.

The thermal-mechanical development of the TANGO instruments follows an iterative Structural-

Thermal-Optical Performance (STOP) approach. Mechanical and thermal load cases are applied to finite-element and thermal models to calculate rigid-body motions and surface deformations of the optical components. These deformations are transferred to the optical model to determine their effect on instrument performance.

A dedicated Structural Thermal Model, subsequently upgraded to the STM configuration, supports the verification of the analysis and the representativeness of the instrument design. The STM includes a mechanically and thermally representative instrument housing, struts, optical-component dummies, mounts, interfaces, heaters, temperature sensors, and accelerometers. It has been integrated with the satellite structural model including satellite deployer and subjected to sine-burst (QSL), sine-vibration, random-vibration, shock, and thermal tests. The measurements are used to correlate the structural and thermal models, assess the damping behaviour of the struts, and derive local loads for critical equipment interfaces. Coordinate Measuring Machine (CMM) measurements performed before and after environmental testing provide an independent assessment of the positional stability of the installed optical elements relative to the instrument mechanical reference frame.

This paper describes the thermal-mechanical design and verification of the TANGO instruments. It first presents the principal mechanical and thermal design choices, including the aluminium housing, opto-mechanical mounts, damped struts, and active thermal-control concept. It then discusses the coupled structural analyses and the STOP methodology used to evaluate optical performance under mechanical and thermal loading. Finally, results from STM vibration, shock, thermal, and dimensional-stability measurements are presented and compared with the numerical predictions. Together, these activities demonstrate the followed combined analysis-and-test approach to verify the maturity of the TANGO instruments designs and their compliance to mechanical, thermal and stability requirements.

2. MECHANICAL DESIGN TANGO INSTRUMENT

Most of the design choices are based on TNO's heritage from the TANGO predecessor Spectrolite and other optical instruments like TROPOMI, Sentinel 5 (UV1 spectrometer and TSBOA telescopes).

The TANGO Nitro and Carbon instruments share an identical telescope design. Their spectrometers, however, differ slightly in layout and are equipped with different cameras. The tested STM model is a representative combination of both instruments: Carbon housing lay-out with a dummy Nitro camera attached to an adapter (see Figure 2-1 and Figure 2-2).

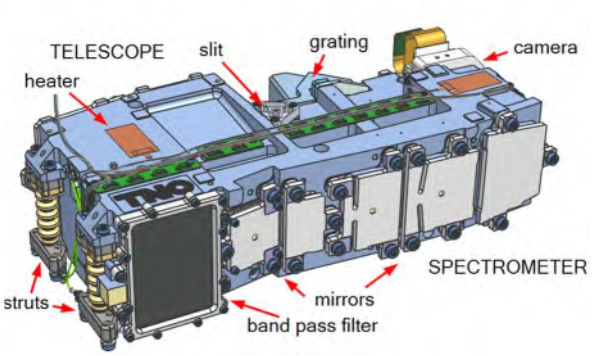


Figure 2-1 TANGO Carbon Instrument PDR design

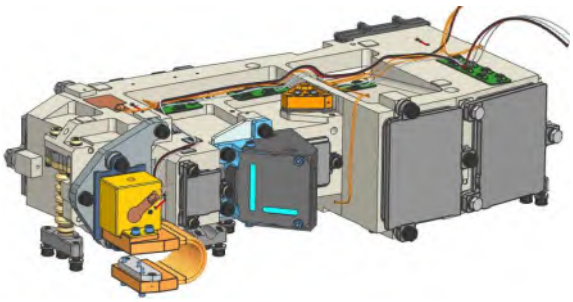


Figure 2-2 TANGO STM model (seen from the spectrometer side)

The housing is a box-shaped hollow structure with high stiffness and dimensional stability made from standard Aluminium (6082 T651). The Instrument contains two compartments: the Telescope and the Spectrometer. The milled internal chambers follow the optical light path with margin through the instrument. A stress-relief heat treatment is applied to minimize residual stresses.

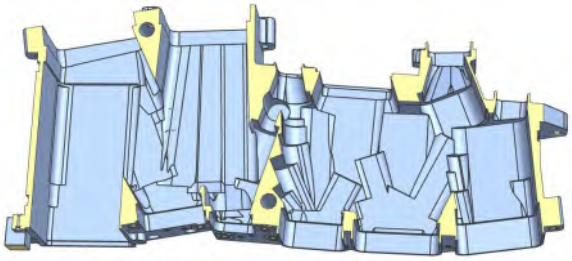


Figure 2-3 milled-out Instrument Housing (cross section)

The instrument is isostatically suspended by 6 orthogonal oriented damper struts. The damper struts, developed by TNO for the CubeCAT satellite 3], support the instrument and dampen the external vibration to the instrument.
The TNO Damper Strut contains an outer structure (the flexure) and an inner structure (the damper), both made by additive manufacturing from Laserform Ti Gr23 (A). The damper structure contains a dedicated rubber layer (SCVBR60)

which bears the shear loads. The rubber material is provided by the Dutch company ERIKS and is designed for applications where high precision and extreme cleanliness are demanded. The damper strut is 3D-printed, injection moulded, post milled and assembled with precise fittings and screws.
The axial stiffness of the flexure is carefully tuned by design and analyses to balance the stiffness ratio between the damper and the flexure. From numerical simulations the damping ratios of the rigid body modes of the TANGO instrument are predicted to be at least 7%.

The struts also provide a good thermal isolation: Analysis shows that the conduction of an individual strut is 1W/128K = 0.0078W/K. A cross-section CAD render of one of the damper struts is provided in Figure 2-4. The orange-coloured component represents the rubber material.

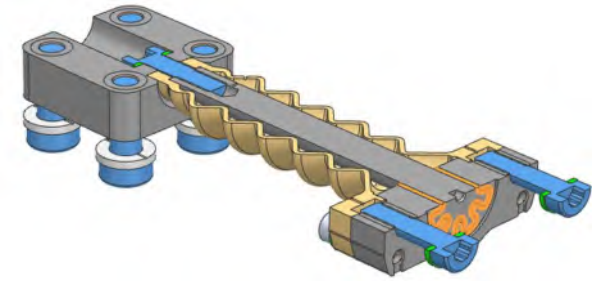


Figure 2-4 Damper struts

The instrument optical elements are bolted onto the housing on accurate pads with shims in between. The lateral position can be tuned +/- 0,5 mm by means of gauge blocks and reference features on the housing. Its position is fixated by the pre-loaded bolts.

The mirror consists of three segments: a body with the mirror surface at the front, a plate with mounting and aligning features at the back and a pedestal in between. It is able to handle structural and integration loads with little effect on the mirror surface shape. The enlarged plate at the back reduces the opening between the mirror and the housing, blocking external light. The mirror material is the same as for the housing.
The mirrors for this STM are coated with Surtec 650 and have no optical quality.

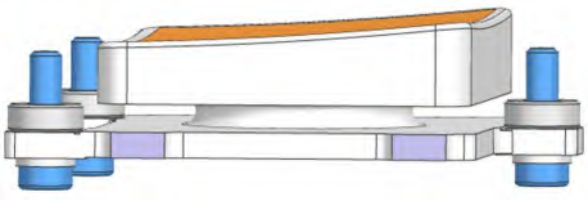


Figure 2-5 mushroom shaped telescope mirror

The grating is isostatically fixed via three flexures and glue spots to overcome the thermal expansion difference between the Fused Silica grating and the aluminium bracket.

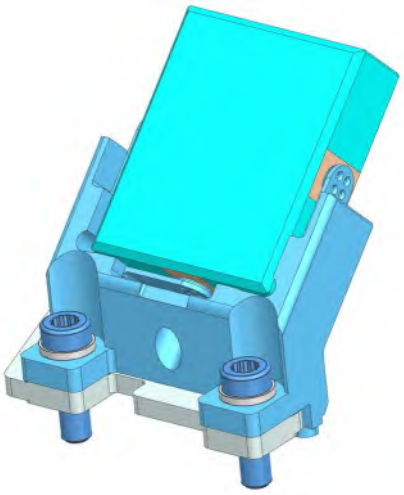


Figure 2-6 grating mount assembly of the TANGO Carbon Instrument

A coated Silica Bandpass / optical Filter is attached at the entrance of the Instrument. The filter is clamped within two frames with rubber in between. An accurate compression is set with use of shim rings.

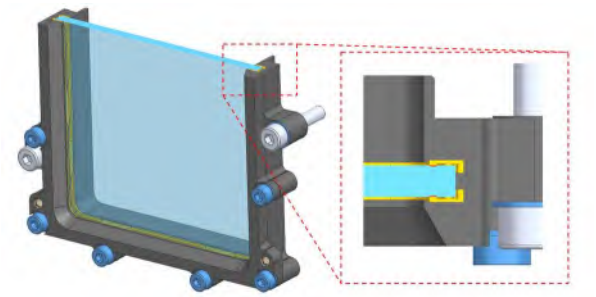


Figure 2-7 Band Pass Filter assembly (cross section)

A slit assembly is placed in between the Telescope and the Spectrometer compartment and functions as a field stop. The preliminary design consists of an etched silicon wafer containing the slit, mounted on an Invar carrier. The detailed design and manufacturing of the slit assembly are subcontracted to Fraunhofer IOF. For the STM vibration campaign, a representative dummy slit assembly was used. The measured responses were subsequently used to derive the vibration design loads for the slit assembly analyses.

A dummy camera assembly is attached to the housing that is structurally and thermally representative of the Nitro camera. An adapter was used to match the mechanical interfaces. A Camera back-end electronic box is attached behind the camera to the satellite frame.

3. THERMAL DESIGN

The both TANGO instruments operate in a thermally unstable environment. The effects of the orbit and the operation of surrounding platform electronics cause fluctuating thermal loads to the instrument. To mitigate these fluctuations, the instrument is thermally isolated from its environment. Conductive isolation is realized through the damped struts, Radiative isolation is achieved through a Surtec-650 coating, providing an effective emissivity of 0.12.
The heaters are distributed symmetrically along the instrument housing as shown in Figure 2-1.
The temperature of the instrument is controlled at the Thermal Reference Point, located at the geometrical center of the instrument housing.
Both TANGO instrument are equipped with a nominal and redundant heater circuit to maintain the instrument housing at a controlled temperature between 21 °C and 24 °C. The heating system consists of a series-connected heater chain comprising four Kapton heater pads manufactured by Zoppas Industries. Each heater pad has a nominal electrical resistance of 7.0 Ω and a surface area of 50 × 25 mm. To ensure redundancy, each heater pad incorporates two electrically independent heater elements within a single pad, see Figure 3-1.
the minimal and maximum power dissipation are respectively 4.8W and 5.5W. The heaters of the circuit are positioned such that the thermal gradient along the instrument housing is minimized. The heaters will be covered with aluminium adhesive foil to ensure a low emissivity of the instrument housing.

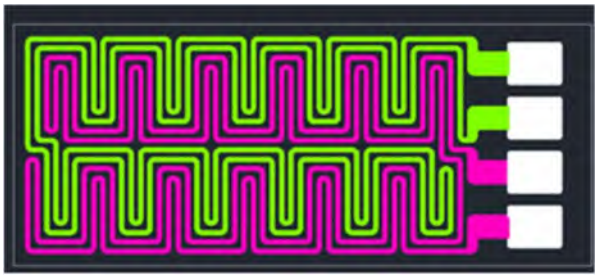


Figure 3-1 Schematic overview of the single layer heater with double circuit.

The Thermal Reference Point is the location at which the temperature of the instrument housing is monitored and controlled using a thermistor of type 15K4D489. The instrument housing is equipped with a main and redundant thermistor at the TRP location. Both heater strings and the thermistors are wired to a single connector on the housing of the instrument, for interfacing with the control electronics of the platform.

4. MECHANICAL ANALYSIS

The instrument was modelled and analysed in NASTRAN, in a combined FEM with the deployer and CubeSat platform. A deployer-platform-instrument combined analysis was favoured over an instrument analysis in isolation because of the strong coupling between all three elements. This strong coupling is due to the high relative stiffness and size of the instrument relative to the platform, and to the extended contact interface between deployer and platform over the entire length of the platform. Because of these reasons, standalone instrument and platform analyses with hard mounted conditions, even with impedance correction using interface forces (notching), proved to yield unrealistic results both for load derivation and strength margins. The coupled load analysis would achieve to capture more realistically the dynamic amplification, modal coupling, and local interface load redistribution.

After the model checks, the combined model was analysed for QSL, Sine and Random for Qualification Loads levels, which were derived as an envelope of VEGA, F9, and ISAR.

Since the mission's launcher has not yet been decided, the loads used consist of an envelope of the loads featured in the launcher manuals of all candidate launchers. Additionally, since the orientation of the deployer mounting on the launcher main interface is different for some of the candidate launchers, two configurations were analysed for the deployer boundary conditions: side-mounted and back-mounted.

Primary notching using the Peak RMS method was performed only for the random vibration load case, using the SPCF data extracted from the analysis.

In Figure 4-1 the combined model and instrument FEMs are shown.

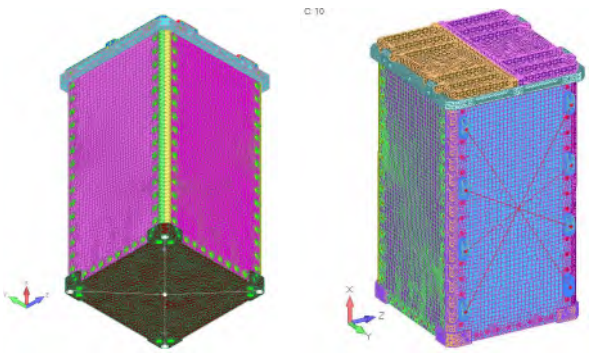


Figure 4-1 Boundary conditions for a) side mounted and b) back-mounted configuration.

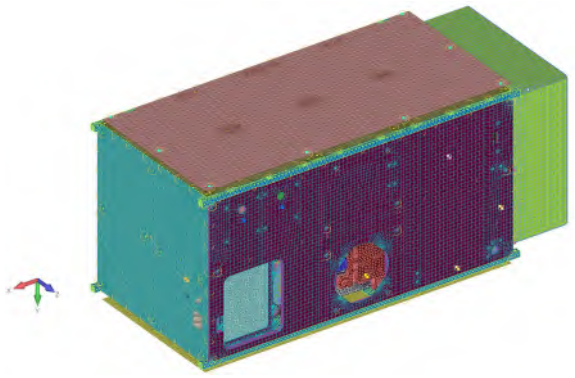


Figure 4-2 FE Mesh of the S/C Platform

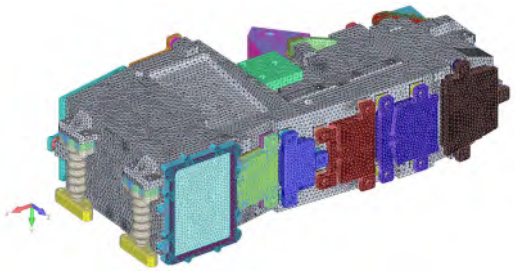


Figure 4-3 FE Mesh of the STM optical instrument

The instrument was modelled using primarily quadratic solid elements. For the damper struts the rubber material was modelled explicitly, while all fastener joints were modelled using RBE2+spring elements.

The modal analysis results show the first eigenfrequency to be at 146 Hz and 149 Hz, for the side-mounted & back-mounted configurations respectively, satisfying the first eigenfrequency requirement of 115 Hz. The eigenmode is shown in Figure 4-4. As shown, the instrument is rocking within the S/C, while being attached to a structural frame.

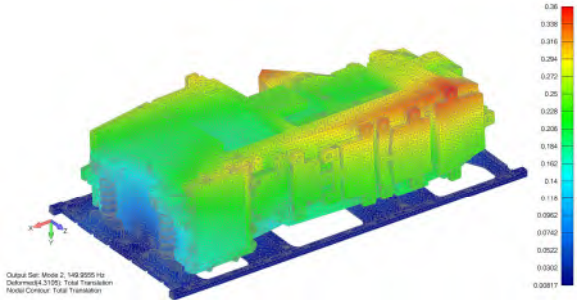


Figure 4-4 1st Global Eigenmode of the STM instrument side-mounted (146 Hz)

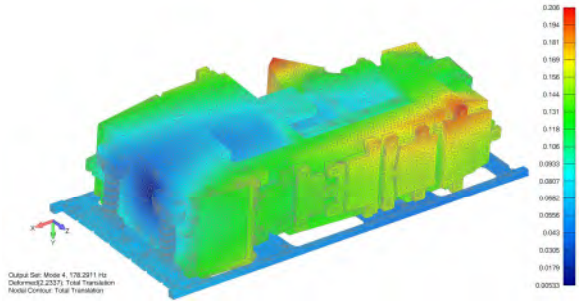


Figure 4-5 2nd Global Eigenmode of the STM instrument side-mounted (178 Hz)

All analyses (QSL, Sine & Random) were performed, and all margins of safety (MoS) for part stresses in the instrument were shown to be positive.
Moreover, bolt analysis was performed following ECSS standards, also showed positive MoS for most joints. In some fastener group cases where negative MoS were present, they were accepted as they had negative MoS for flange bearing in the range of -0.06 to 0, as they should be covered by the additional margin taken from the Kp, Km, and other fastener safety factors.

5. VIBRATION TESTING

The vibration test was performed on the TANGO STM which included the platform STM, the deployer STM and the STM instrument at ETS (Noordwijk, The Netherlands).

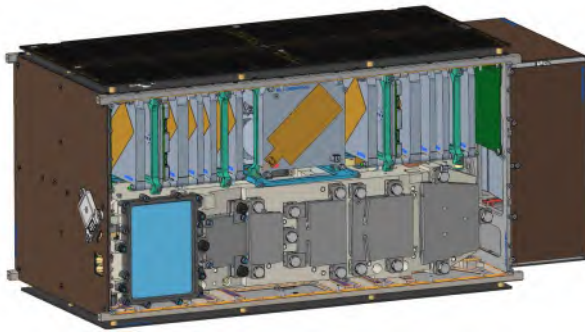


Figure 5-1 CAD render of the TANGO STM platform.

The TANGO STM was mounted in the deployer in both side-mounted (see Figure 5-2) and back-mounted configurations to cover all possible launch configurations. The loads associated with these launch configurations were a combination of VEGA, F9, and ISAR launchers. In this way, the instrument was subjected to all relevant flight conditions, with particular attention paid to the vibration levels experienced by the camera, slit assembly, and grating mount. The results show a clear damping effect provided by the struts, indicating that they performed as intended and thus the instrument passed all vibration tests.



Figure 5-2 The STM TANGO satellite including the deployer mounted on the vibration table (side mounted configuration)

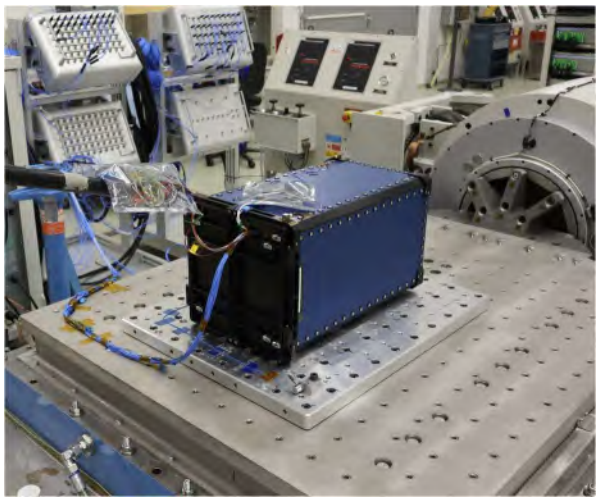


Figure 5-3 The STM TANGO satellite including the deployer mounted on the vibration slip table (side mounted configuration)

5.1. Sine-burst (QSL), Sine and Random vibration test

The sine-burst (QSL), sine and random vibration tests were carried out in the 80kN shaker. For all tests, acceptance level loads were used and are shown in Table 5-1 for side-mounted, and for back-mounted in
Table 5-2. No notching was performed.

Table 5-1 QSL, Sine & Random Acceptance loads side-mounted configuration

QSL - All directions			RND - All directions	
Accel [g]	15		f [Hz]	PSD [g^2/Hz]
			20	0.0071
Sine - All directions			50	0.0071
f [Hz]	Accel [g]		100	0.0142
5	2		200	0.0355
110	2		500	0.0355
110	1		1000	0.0142
125	1		2000	0.0071
			GRMS	**5.89**

Table 5-2 QSL, Sine & Random Acceptance loads back-mounted configuration

QSL - All directions			RND - All directions	
Accel [g]	18.7		f [Hz]	PSD [g^2/Hz]
			20	0.01
Sine - All directions			50	0.01
f [Hz]	Accel [g]		100	0.015
5	2		200	0.0355
110	2		300	0.0355
110	1		500	0.0355
125	1		700	0.03
			800	0.03
			925	0.03
			1000	0.0284
			2000	0.0071
			GRMS	**6.63**

Both test campaigns were successfully completed without any major anomalies. Post-processing of the test data after the test showed that there was a good match between the predicted and measured accelerometer responses, even before any changes were performed as part of the model correlation. The comparison between the predicted and measured transfer functions is shown in Figure 5-4 for the sensors that see the highest amplification for the main modes in each direction. This comparison is only shown for the side mounted configuration, but very similar plots were obtained for the back-mounted configuration.

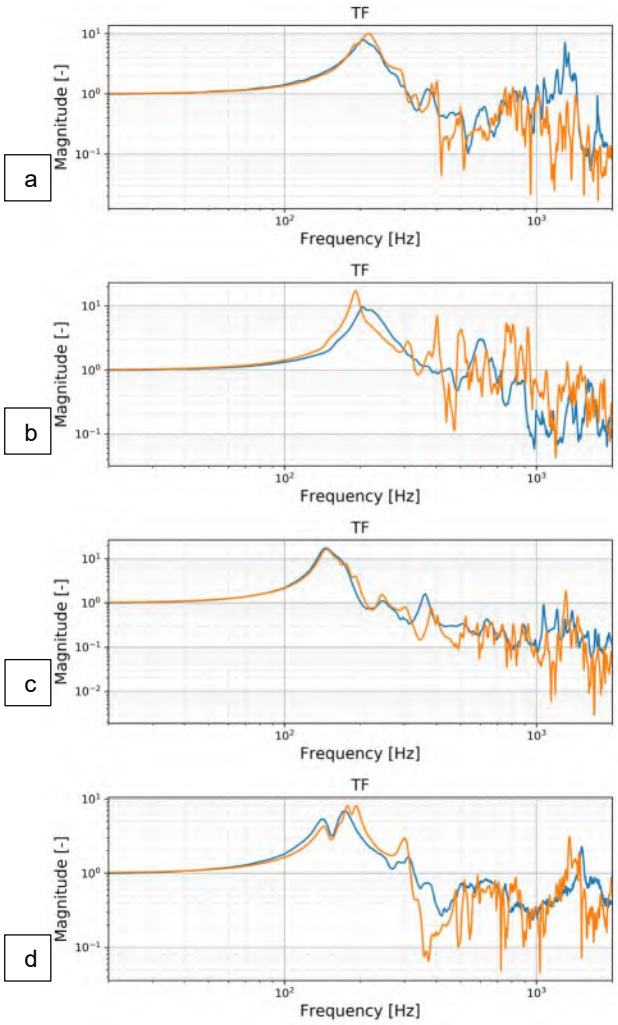


Figure 5-4 Derived transfer functions, comparing uncorrelated FEM (orange) and test data (blue), for the highest amplification sensor location. a) X-axis, b) Y-axis, and c), d) Z-axis

5.2. Shock testing

The shock analysis indicated negative margins of safety with respect to structural integrity and stability for a significant number of optical components mounted on the instrument housing of both TANGO instruments. It is however possible that the SRS shock analysis method overestimates the reaction forces and stresses as pointed by some researchers [5]. Therefore, shock testing is needed to qualify the TANGO satellite and the instrument for shock loads. An STM of the satellite, deployer and instrument is used for shock testing. The STM instrument is provided with shock sensors to monitor the shock response of the interface of a number of components mounted on the instrument. Figure 5-5 provides the location of the shock sensors on the instrument housing. Note that the sensors are mounted on the instrument housing close the optical components of interest. The sensor labelling is provided in Table 5-3. Note that tri-axial shock monitor sensors are used.

Table 5-3 shock sensors on the STM instrument

Sensor ID	Locations
SKCS-04	I/F Camera Mount
SCKS-05	I/F Grating Mount
SCKS-06	I/F Slit Mount

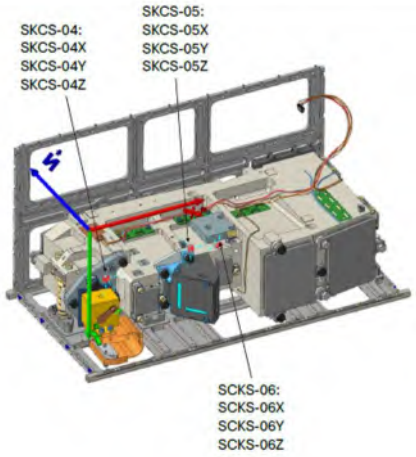


Figure 5-5 shock sensors mounted on the TANGO STM instrument.

The shock tests are executed at ETS in Noordwijk. A photo of the shock test setup is provided in Figure 5-6. Shock tests are done in side-mounted configuration and in back-mounted configuration. The applicable qualification shock loads are provided in Table 5-4 and Table 5-5.

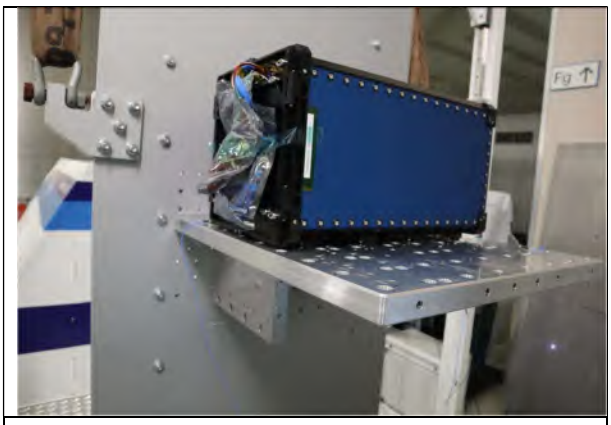


Figure 5-6 STM satellite and deployer mounted on the shock bench at ETS Noordwijk.

Table 5-4 Shock loads side mounted configuration

Y-direction			X- and Z-direction	
f [Hz]	SRS [g]		f [Hz]	SRS [g]
100	28.2		100	35.3
800	1551		800	1057.5
1600	2538		1600	2115
10000	2538		10000	2115

Table 5-5 Shock loads back mounted configuration

X-direction			Y- and Z-direction	
f [Hz]	SRS [g]		f [Hz]	SRS [g]
100	42.3		100	42.3
800	1551		800	1106.1
1000	1797		1000	1410
1600	2538		1600	2115
10000	2538		10000	2115

Tuning of the shock setup was done with a dummy deployer construction.

Visual inspection of the of the STM before and after shock tests did not show any signs of damage of the mechanical construction.
The responses at the shock sensors were used to derive qualification shock loads for the camera DCU and DPU, the nitro grating mount and the slit mount. Shock spectra are derived by enveloping the responses of the shocks applied in the different directions. As an example, the derived shock loads for the slit mount (based on shock sensor 6) are provided in Table 5-6. Note that the derived shock loads are lower than the applied shock loads, most likely due to the attenuation effect of the damped struts on which the instrument STM is mounted. Similar levels were also derived for the camera DPU and the grating mount.

Table 5-6 Derived qualification shock loads for the slit mount.

X-direction			Y-direction			Z-direction	
f [Hz]	SRS[g]		f [Hz]	SRS[g]		f [Hz]	SRS[g]
100	60		100	80		100	100
240	40		200	200		1200	440
830	2200		1400	600		3000	700
2000	2000		4500	700		10000	700
10000	900		10000	700			

6. CMM MEASUREMENTS

CMM measurements are performed before and after the vibration test of the STM. Comparing these two measurements enables the stability of the installed optical elements to be assessed. The Zeiss Prismo Ultra CMM is used which is a high-accuracy, bridge-type Coordinate Measuring Machine (CMM), designed for extreme precision metrology. The CMM is provided with advanced air bearings, high resolution Zerodur scales, and high scanning speeds for demanding industrial and scientific use. The length measurement error E0 = 0.5+L/500 µm, the repeatability is 0.4 µm. The CMM is installed in a temperature-controlled cleanroom at TNO to ensure measurement stability and accuracy.
The positions of several components are determined with respect to a global reference frame defined on the instrument housing. This global reference frame is established using six reference surfaces located on the housing. These six surfaces define three reference planes, whose intersections determine the origin of the Mechanical Reference Frame (MRF). Figure 6-2 shows the MRF and the six reference surfaces, highlighted in red.

The locations and orientations of the following components are assessed with the CMM: The Camera mount, Dummy Camera, Grating, Grating Mount, Slit mount, TM2 mirror, TM2 Stop aperture, TM3 mirror. The positions of the components are defined with respect to the mechanical reference frame on the STM instrument housing.



Figure 6-1 Zeiss CMM measurement setup to measure the stability of the STM instrument.

The translational and angular movements of the dummy optical components mounted on the STM instrument housing after vibration and thermal testing are presented in Table 6-1 and
Table 6-2. All the movements are calculated with respect to the mechanical coordinate frame which is shown in Figure 6-2.

Table 6-1 Derived translational movements of the STM components after Random Vibration and Shock testing.

Component:	ux [µm]	uy [µm]	uz [µm]
Camera Mount	0.5	-0.4	2.3
Dummy Camera	12.2	-3.3	-1.2
Grating Mount	-0.4	0.2	1.2
EM Grating	-0.7	1.2	1.0
Slit assembly	-1.7	1.1	1.1
TM2 mirror	-0.6	-1.7	1.6
TM2 stop	-1.8	-0.1	0.4
TM3 mirror	0.8	-0.2	2.4

Table 6-2 Derived angular movements of the STM components after Random Vibration and Shock testing.

component	Rx [µrad]	Ry [µrad]	Rz [µrad]
Camera Mount	-0.2	29.3	16.4
Dummy Camera	-28	-36.6	-303.1
Grating Mount	6.2	-5.4	5.4
EM Grating	45.1	-0.7	-6.8
Slit assembly	4.1	14.2	16.3
TM2 mirror	25.6	-3.9	3.6
TM2 stop	13.7	-30.0	-3.2
TM3 mirror	-4.9	16.7	30.7

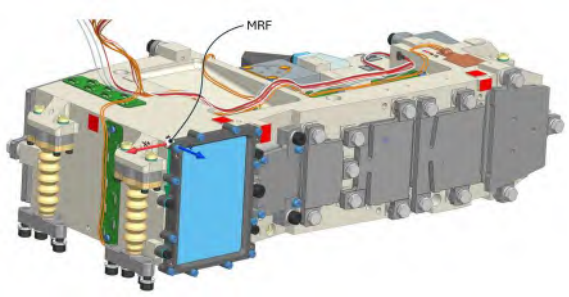


Figure 6-2 Definition of the main reference system on the STM instrument housing.

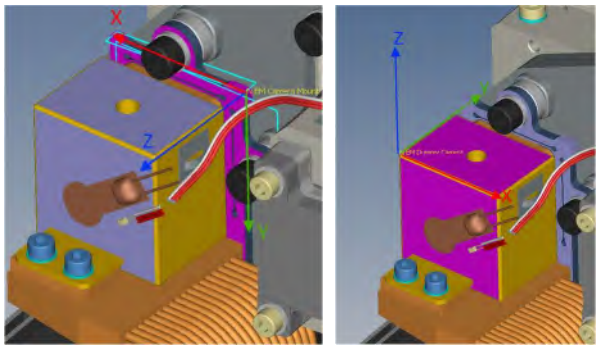


Figure 6-3 Local coordinates of the camera mount and the dummy camera.

7. STOP ANALYSIS

Structural Thermal Optical Performance (STOP) analysis is done to assess the impact of mechanical and thermal loads to the optical performance of the TANGO instruments.
The following load cases are considered:

- Gravity release
- Fluctuations in ambient temperature
- Manufacturing and integration loads
- I/F loads
- Thermal mechanical loads

The thermal-mechanical deformed state of all optical components is assessed for all load cases. Next, the Zemax STAR module is used to import the point clouds of the deformed optical surfaces. Finally, these deformed surfaces are used to analyse the performance degradation of the instrument, see Figure 7-1 with the nominal and (exaggerated) deformed state of the TM1 mirror during thermal load.

The STOP process was used iteratively in the instrument design process to improve the thermal mechanical design and control. Instrument requirements that were most sensitive to the STOP load cases were (amongst others): the stability of the spectral response function and energy distribution function, the co-registration and the pointing stability. The largest change that had to be made was to add an active thermal control of the instrument housing. With the current design, the impact of the thermal-mechanical loads on the performance budgets is acceptable and in most cases no longer driving.

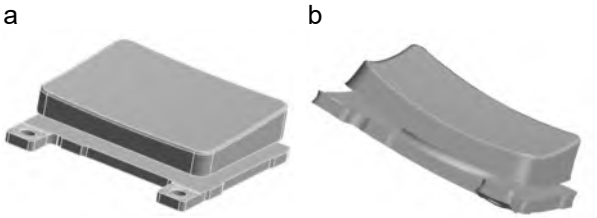


Figure 7-1 TM1 mirror in nominal (a) and deformed configuration due to a thermal load (b)

8. CONCLUSIONS AND FUTURE WORK

The thermal-mechanical design of the TANGO Carbon and Nitro instruments has been verified through a combination of numerical analyses and representative environmental testing. The instrument architecture combines a stiff aluminium housing, thermally isolating damped struts, active thermal control, and compact freeform optics to meet the challenging stability requirements imposed by the ESA Scout mission concept.

A coupled deployer-platform-instrument finite element model was developed to accurately capture the dynamic interactions between the spacecraft and payload. The analyses demonstrated compliance with the stiffness and structural integrity requirements, with the first eigenfrequency above 145 Hz and positive margins of safety for all critical instrument components. Environmental vibration testing of the STM confirmed the predicted dynamic behaviour and demonstrated the effectiveness of the damped struts in reducing the transmission of launch loads to sensitive optical hardware.

Shock testing was performed to derive realistic qualification loads for critical instrument subsystems, including the camera, grating mount, and slit assembly. The measured responses showed substantial attenuation relative to the applied shock environment, validating the use of the damped suspension concept. In addition, high-precision CMM measurements before and after vibration and shock testing showed that the mounted optical components remained stable within a few micrometres and tens of microradians, demonstrating the robustness of the mechanical design.

The developed STOP methodology links thermal and mechanical loads directly to optical performance and has been used throughout the design process as both an optimisation and verification tool. Combined with the successful environmental test campaign, the results provide confidence that the TANGO instruments can maintain the required optical stability during launch and in orbit.

Future work will focus on completing the correlation of the thermal and structural models, extending the STOP analyses with flight-model configurations, and verifying optical performance at instrument and satellite level during the upcoming qualification and flight campaigns.

9. ACKNOWLEDGEMENT

This work was performed in the scope of the Scout Programme of European Space Agency (ESA). The authors gratefully acknowledge ESA's support for this activity.

10. REFERENCES

1. Brenny, B., Day, J., et al (2022), Development of Spectrometers for the TANGO Greenhouse Gas Monitoring Missions, Proc. SPIE 12777, *International Conference on Space Optics*.
2. Day, J., Brenny, B., de Goeij, B., Ouwerkerk, B., et al (2023). Development of the TANGO carbon instrument for greenhouse gas detection. Proc. SPIE 12735, *Remote Sensing Technologies and Applications in Urban Environments VIII.*
3. Witvoet, G., de Bruijn, D., et al (2025), First-light results of the in-orbit demonstration of a CubeSat-compatible optical communication terminal. *Proc. SPIE 13699, International Conference on Space Optics, ICSO 2024*.
4. De Vreugd, J., Jansen, R., et al (2023), Verification of the Sentinel-5 UV1 spectrometer mechanical design through analysis and tests. *Proceedings ECSSMET 2023*.
5. Development of an Efficient Analysis Method for Prediction and Structural Dimensioning of Space Structures Subjected to Shock Loading. Nadeem Siam, Master thesis, Luleå University of Technology, 2010

IN-FLIGHT CALIBRATION OF OPTICS FOR OCEAN COLOUR MISSION: QUALIFICATION OF A STEPPER MOTOR-HARMONIC DRIVE BASED MECHANISM WITHOUT HDRM

Gonzalo Ezequiel Pereyra [(1)], Leonardo Gabriel Andreassi [(1)]

[(1)] INVAP, 8400, San Carlos de Bariloche, Argentina, Email: gpereyra@invap.com.ar

KEYWORDS

Qualification, Protoflight Model (PFM), Calibration, Mechanism, Vibration, Stepper motor, INVAP, Torsion.

ABSTRACT

Ocean Colour Mission Satellite developed and manufactured by INVAP, performs In-Flight calibrations of the main optical instruments by using a Stepper motor - harmonic drive actuator that rotates a disc into different positions to expose specific surfaces in front of the electro-optical modules. These mechanisms are called Calibrators and the main distinctive feature is the lack of any type of Hold Down and Release Mechanism (HDRM) to keep both disc and motor in position during launch phase.
This paper describes the qualification campaign of Calibrators, including:

- Breadboard model to evaluate and validate the position sensing system, torque Ratio and Back Electromotive Force (EMF) measurements, and to conduct a lifetest of the entire mechanism and its associated control electronics.
- An innovative vibration test developed to assess the torsional behavior of the mechanism under dynamic angular accelerations induced to actuator flange.
- Final PFM qualification environmental campaign where several functional and performance test were conducted.

1. MISSION OVERVIEW

Ocean colour Satellite low and medium resolution data are used to study the ocean´s biosphere.
The main instruments on-board are:

- Visible – Near Infrared (VIS-NIR) Camera, multispectral 11 bands camera.
- Near Infrared – Short Wave Infrared (NIR-SWIR) Camera, multispectral 6 bands.

2. CALIBRATOR KEY REQUIREMENTS

There are two calibrators mounted on the Satellite, each one in front of each main instrument.

Both Calibrators share the same requirements, and they were therefore developed following the same design philosophy.

2.1. High level requirements

The key requirements that guided the calibrator conceptual and basic design are:

- They shall allow the following 4 functions:
  - Allow free instruments field of view (FOV).
  - Allow to shut the instruments exposition to the light.
  - Allow the exposure of two quasi-lambertian surfaces to sunlight and instruments.
- Design shall allow lambertian surfaces to be replaced at any time during Assembly. Integration and Test (AIT) process.
- Design has to be based in a rotary disc that expose all the required surfaces in front of the instrument´s optics, as seen in Figure 1.

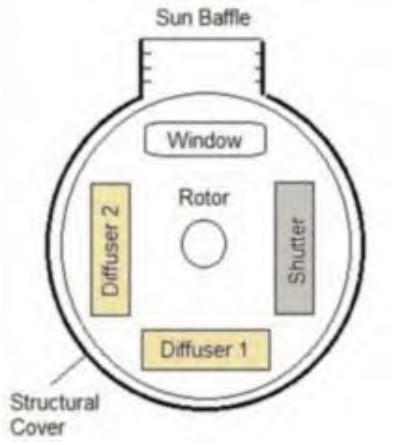


Figure 1: Calibrator Conceptual Design Scheme.

2.2. Performance requirements

Based on the high level requirements, there are key performance requirements that shall be accomplished:

- The disc positioning shall have an accuracy of +/- 0.25°.
- The actuator torque ratio shall be greater than 3 for both calibrators.
- The Calibrator actuator shall be capable to operate a number of cycles that doubles the

ones expected for AIT and in flight operations.

2.3. Environmental requirements

Considering the expected in-flight environments, the following requirements are derived:

- The calibrator´s operating temperature range shall be -20°C to 50°C. For non-operating conditions, this range shall be extended by ±10°C.
- Calibrators shall withstand sine loads of 12g peak in the out-of-plane (OP) condition and 10g peak in the in-plane (IP) condition. Random loads requirements shall be 14.1 gRMS OP and 10.3 gRMS IP.

3. CALIBRATOR DESIGN DESCRIPTION

3.1. Design overview

Calibrator design is presented in Figure 2. The disc contemplates four positions to achieve the main functions, Free FOV, Shutter and two diffusers (quasi-lambertian surfaces). Disc rotation is made by a stepper motor - harmonic drive mechanism that allows calibrators to have zero backlash and to reach each position with the required accuracy.
There are three structural components called front, ring and rear cover. The covers are attached to a main support that interfaces with the spacecraft. Disc is located inside the covers. Ring cover is where position sensing system is located.
There are two apertures in calibrators, each one followed by baffles that limit light entrance to the optical system while improving stray light performance, one points at nadir for science image acquiring (noted as Science Baffle in Figure 2), and the other, called solar baffle, is intended to capture sunlight to perform in-flight solar calibration.

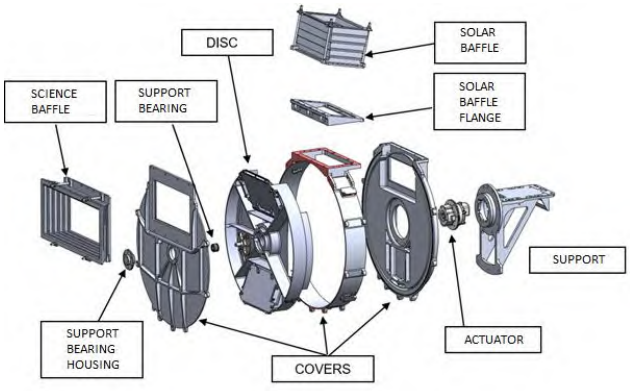


Figure 2: Calibrator Design.

3.2. Subassemblies: Drive Mechanism

In order to accomplish mission requirements regarding performance on accuracy of the disc positioning, torque ratio and the necessity to use a heritage proven component, a commercial off-the-shelf rotary actuator was selected. The main features of the actuator are:

- Actuator type: Stepper motor – Harmonic Drive mechanism set.
- Zero backlash.
- Output step angle: 0.0375°.
- Output torque: 3.6 Nm.
- Unpowered Holding Torque (UHT): 3.51 Nm.

Corresponding to its reduced disc dimensions and mass, the NS Calibrator has a cantilevered configuration with the disc attached only to the actuator. Opposed to that, the VN disc incorporates a spherical bushing on its front side, allowing to withstand bending and radial loads during launch, see Figure 3.

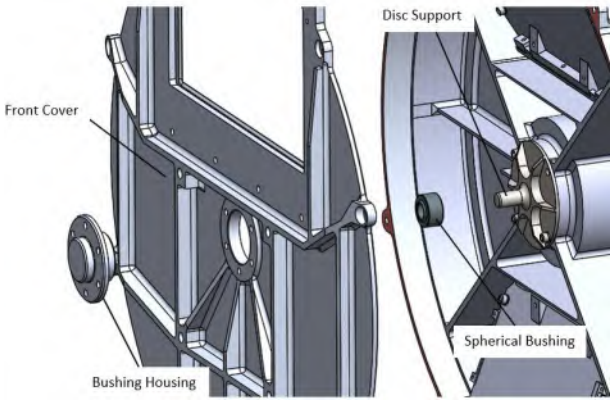


Figure 3: VN Disc support configuration.

In order to minimize the friction added in VN configuration by the spherical bearing, a self-lubricated polytetrafluoroethylene (PTFE) liner bearing was selected.
Given the lack of any Hold Down and Release Mechanism (HDRM), and that there is no extra mechanism implemented for managing the launch loads, the torsional induced loads and their transfer to the disc must be supported by the actuator itself.

3.3. Subassemblies: Position Sensing System

The position sensing system is composed by eight position sensors or switches placed on the ring cover, two for each disc position (nominal and redundant). On the perimeter of the disc, there is a tab that obtrudes the sensors when it reach a certain position.
There are two types of position sensor, optic and Hall Effect. Hall Effect sensors were selected given their heritage in previous projects, however, when it comes to calibration positions (exposure of the diffusers to the instrument´s optics), optical sensors were preferred given their better accuracy and the criticality of the position accuracy for diffuser mode. Hall Effect sensors were selected for the FOV and shutter positions, and Optic Sensors for the two diffuser positions. The tab development regarding its material, surface finishing and final dimensions is explained in section 5.1.1 and 5.1.2.

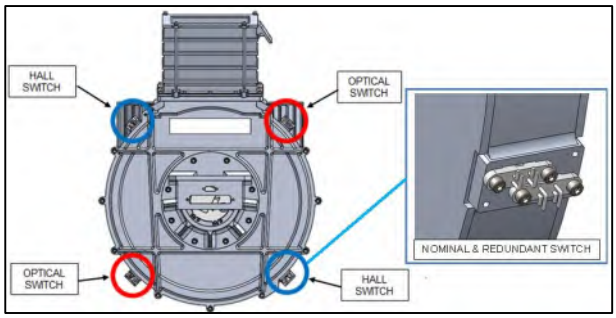


Figure 4: Disc Position Sensor Arrangement.

3.4. Subassemblies: Structure

Calibrator's structure is composed by three covers on the front, back and perimeter of the disc, and the rear cover is attached to a main support that interfaces with the Spacecraft structure.
As mentioned before, there are also two baffled apertures that allows the light entrance coming from earth surface for image acquisition and from the sun for solar calibration. The baffles also limit the stray light that enters the optical systems, improving their performance. In line with that, calibrator structure is completely black painted on its interior for optical proposes and on its exterior for improved thermal performance as there is no active thermal control on this equipment.
One major feature regarding calibrator structure is the fixing mechanism for the diffusers (quasi-lambertian surfaces) on the disc. Those are made of a material, similar to PTFE that has a greater thermal expansion coefficient than the aluminium used on the support. The fixing shall not induce high mounting pressures on the diffusers to keep their optimal optical properties and their physical integrity. To overcome this and allow the Diffuser to expand and contract within the entire required thermal range, flexure brackets were designed, allowing Diffusers to expand and contract within its resistance limits while keeping it in place during launch phase.

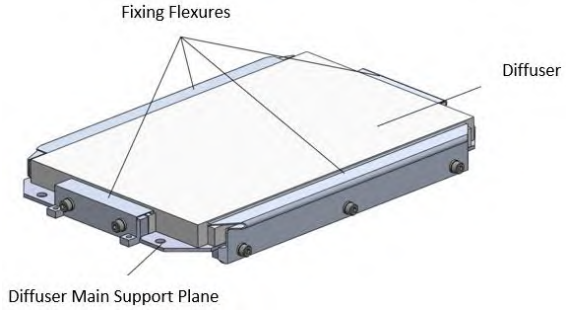


Figure 5: Diffuser Support.

4. TEST SEQUENCE

The test sequence was designed for the evaluation and validation of each subsystem critical aspects before their implementation in proto-flight model (PFM). In order to achieve that, a breadboard model was developed for the earlier stages of the design.
Test sequence is presented in the figure below:

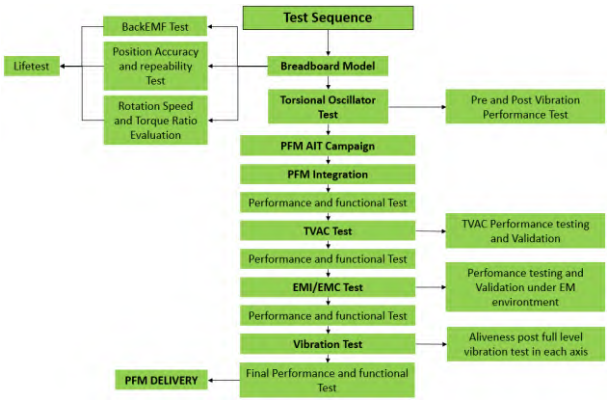


Figure 6: Test Sequence.

4.1. Contamination Control Plan

Because the calibrators are placed right in front of the optics of the main instruments of the mission, strict contamination control had to be taken into account during all PFM AIT stages, including the use of covers on both baffles, only dismounted for thermal-vacuum (TVAC) and electromagnetic interference / compatibility (EMI/EMC) campaigns. For vibration testing, lummaloy covers were used in order to keep the contamination budget as lower as possible and not to add considerable mass to the device under test (DUT). Furthermore, diffuser is made of a highly hydrophobic material which easily absorbs contaminants and is almost impossible to clean back to its previous state, therefore diffuser dummies were integrated into PFM for all the AIT campaign, flight diffusers will be integrated on calibrators for the spacecraft delivery to launch site.

5. TEST DESCRIPTION AND RESULTS

5.1. Breadboard Model

5.1.1. Development model for Position Sensing System

The first test aimed to define tab minimum thickness in order to accomplish the 0.25° accuracy requirement coming from clock-wise and counter clock-wise direction.
The setup indicated in Figure 7 was implemented.
Several engineering tabs from calibrated gauges were manufactured, then, each one was placed on a linear translation table actuated by a micrometre, over that, an optical switch was placed.

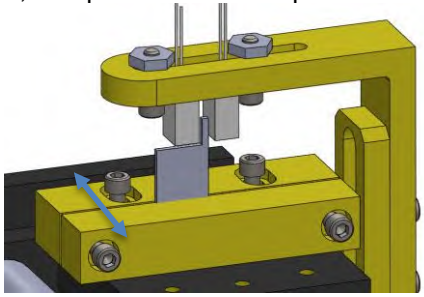


Figure 7: Setup for determining optimal tab thickness.

The tab was then slowly moved inside the sensor gap, and the switch response was measured. Several switch activation cycles were executed, from left to right and vice versa, starting from a 0.3 mm thickness tab and increasing it by 0.1 mm increments. The minimum tab thickness required to activate the switch in all cases was 0.5mm.

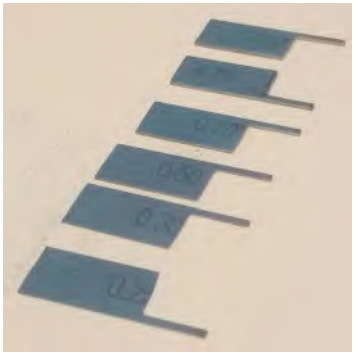


Figure 8: Engineering tabs.

This test concluded with the determination of minimum tab penetration into the optical switch gap. The same testing procedure was executed, moving manually the tab up and down, measuring and registering tab penetration. The minimum tab penetration required to activate the switch in all cases was 2.8 mm.

5.1.2. Breadboard model for evaluation and validation of the Sensing System

Once the main dimensions of calibrators were determined by design, a new breadboard model was developed. This included an engineering model (EM) actuator with the same features and performance of Flight Models (FM) also incorporating Hall Effect and optical sensors.

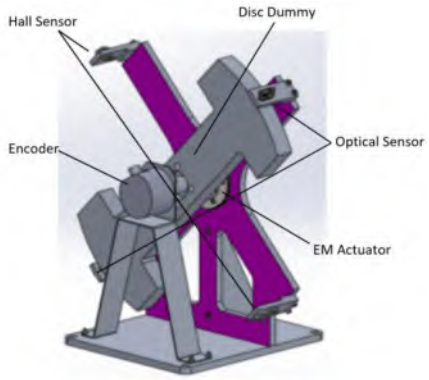


Figure 9: Final Breadboard model.

The electronic drive of the mechanism sends a signal to the stepper motor after checking if any sensor is activated in order to achieve that the tab detection is completely independent from the rotational speed.
For the first test, the penetration of the tab was determined to be 3 mm for ease of manufacturing and the material used was AISI 304 Stainless Steel.

At the very beginning of the test, it was noticed that the tab only activated the optical switch, and was not detected by the Hall Effect Switch. For further tests, SAE 1008 steel was selected due to its higher magnetic permeability. In order to avoid oxidation during on-ground storage and manipulation, a low phosphorus niquel plated surface finish had to be developed at INVAP´s surface treatment facility, keeping also in mind that this surface treatment does not affect the magnetic behaviour of the tab. Furthermore, it was noticed that for Hall Effect switches, besides section and penetration of the tab, the mass of the tab teeth had also influence in the detection.
With this first test, the optimal tab dimension that activated all types of switches was defined, being substantially different that the one determined for the optical switches in the previous test. This implied that the position accuracy requirement for reaching the sensor in clockwise (CW) and Counter-Clockwise (CCW) positions could not be met. In order to accomplish the requirement, it was required to add a certain quantity of steps after the tab was detected by the switch.
Depending on the direction of the rotation, the tab reaches the switch for the left or the right, giving two positions for the same sensor.

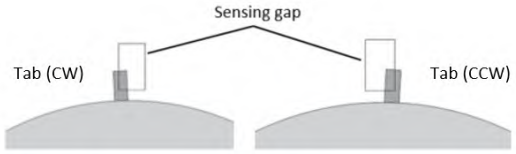


Figure 10: Differences in sensing position CW and CCW.

However this steps quantity will be then defined in PFM during integration, the strategy was tested on breadboard model in order to verify that the same number of steps are required when approximating the tab CW or CCW. This is, commanding a “Go To” CW the desired switch, then commanding a fixed number of steps (200) in CW direction and finally, command a “Go To” command to the same sensor but in CCW direction relieving in real time by the actuator telemetry the number of steps that it takes to reach the sensor in this last command (calling it B), then, the quantity of steps to be added to reach the theoretical central position in the sensor gap is:

$$Steps\ to\ be\ added = \frac{200 - B}{2} \qquad (1)$$

During the test it was verified that the steps to be added did not depend on the direction of the tab approximation to the switch (CW or CCW).
With all the data acquired during testing, the position accuracy requirement was considered fulfilled, and allowed the manufacturing of the PFM tab.

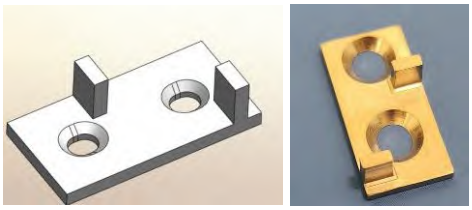


Figure 11: Final Tab design and PFM Tab.

5.1.3. Rotation Speed and Preliminary Torque Ratio Evaluation

The following step in breadboard model testing was to define the optimal rotation speed and a torque ratio evaluation.

The electronic drive of the actuator gave the possibility to tune the output rotational speed of the mechanism from 0.5 to 2.5 revolutions per minute (RPM). It also allowed to adjust the power current for the actuator (with a fixed voltage, given by the Spacecraft power bus). The nominal current was 360 mA.

The dummy disc integrated in breadboard model has the same rotational inertia that PFM VN calibrator disc, so it is representative of the worst condition for the actuator, given NS has lower inertia because of its smaller size.

Torque ratio evaluation was carried out at room temperature. The motor current power was decreased from the nominal until the disc did not indicate any movement when a command was sent, in this case, step loosing was not a problem because the disc only had to travel between two positions, no matter how many steps it took to do it in that condition. The current shall be one third of the nominal power current, taking into account that the actuator was tested in the current range where torque is directly proportional to power current. The result of this test finally indicated that the minimum actuation current was from 100 mA to 105 mA which accomplish the requirement. Torque ratio will also be measured during PFM TVAC test in order to verify the requirement in vacuum environment.

In parallel to that test, different rotation speeds were tested, founding that 1 RPM was the optimal speed. Above that value, the minimum actuation current starts to get higher, particularly at the beginning of the rotation (the electronic ground support equipment –EGSE- electronic drive is not able to control acceleration ramp), speed below that value presented vibrations on the entire mechanism and were therefore discarded.

5.1.4. Back EMF and Unpowered Holding Torque measurements

It was required by the Power team to measure the Back EMF that produces the actuator when the disc is turning by hand while actuator is connected to its EGSE turned off. Given that the mechanism is clearly reversible and there is no HDRM for the launch phase, verification was required to ensure that the voltage generated by the motor remained within the allowable limits of the electronics upstream the Motor Actuation Module. Figure 12 shows the back EMF measurement on the oscilloscope.

Finally, a static unpowered holding torque measurement was done. The measurement consisted in attaching a torque-meter wrench to the disc to measure the minimum toque value that initiates the rotation. Minimum measured values were between 3.2 and 3.3 Nm. Those holding torque values are important for considering the torsional load management as explained in section 5.2. For the measurements, the motor was connected to the EGSE (turned off) replicating the flight configuration. The motor behaviour changes depending if it is connected or not to its EGSE, when connected, every step of the motor induces a resistance torque to the wrench and when disconnected, once the UHT is reached, the rotor turns much easily, without the same resistance between motor steps.

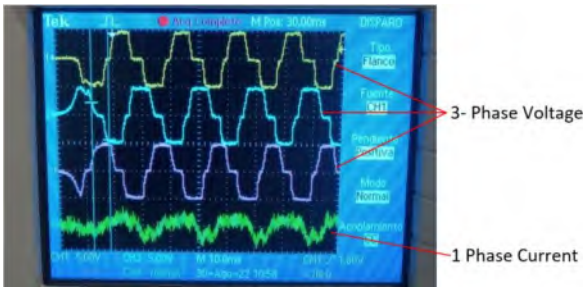


Figure 12: Back EMF measurement.

5.1.5. Lifetest

Finally, breadboard model was used to carry out a lifetest of the entire mechanism and its associated electronic drive EGSE.

This lifetest was executed in clean room ISO 8, it could not be done in thermal vacuum environment because of programmatic conflicts with other spacecraft (SC) subsystems that required the INVAP´s Thermal Vacuum facility at the same time that the test was being executed.

The breadboard cycling quantity was calculated based in the standard GEVS gsfc-std-7000B [1], considering the number of operating cycles expected for the mechanism in orbit and during functional testing.

For this test, breadboard included the spherical bushing of the VN configuration, to make the test the most representative possible for that stage of the project.

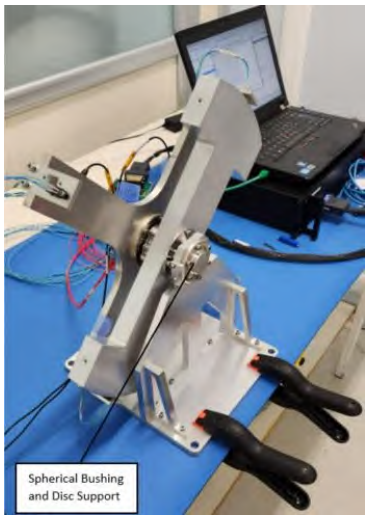


Figure 13: Breadboard lifetest configuration.

Control software was modified for autonomous operation of the breadboard requiring only personal supervision during the test. The cycles applied were divided with five stops in between, being programed stops for measuring a series of variables that allowed to evaluate the evolution of the mechanism during the test. In the Table 1 the test schedule is shown, each actuator drive indicate that the disc goes from one point to another in one movement sequence following a flight representative behaviour:

Table 1: Lifetest sequence.

Applicable Test	**Actuator drives**				
	Start	1600	3200	4800	6360
A1	R	R	R	R	R
A2	R	MIEM			R
B	R	R	R	R	R
C	R	MIEM			R
D1	R	MIEM			R
D2	R		R		R
E	R		R		R
G	R	R	R	R	R
I	R	MIEM			R

Being:

A1: Root Mean Square (RMS) current in each phase and RMS voltage between every phase.

A2: RMS current in one selected phase and RMS voltage between two selected phases.

B: Electrical resistance between every phase.

C: Step signal sent to the actuator by the electronic in every movement, automated acquire.

D1: Steps between fixed physical positions, for step loss evaluation.

D2: Accuracy and repeatability on positioning, evaluated with graphic scale.

E: Actuator vibration measurement with accelerometer.

G: Minimum actuation current, plus oscilloscope capture of current per phase and voltage between phases characteristic curves.

I: Actuator temperature acquisition.

And:

R: Required.

MIEM: Measure In Every Movement.

The Success criteria was:

- To complete all the proposed cycles.
- The variation of the minimum current shall remain below 30% of the value measured at the beginning of the test.
- The variation of the RMS current shall remain below 20% of the value measured at the beginning of the test.
- The variation of the resistance between phases shall remain below 20% of the values measured at the beginning of the test.
- The variation of steps executed between same positions shall no change more than 10%.
- Position accuracy shall be within limits (±0.25°) by the end of the test.

During the test, the software that controlled the automated actuation of the mechanism presented two failures, mainly due to the delay in the transfer rate of the data from the oscilloscope to the PC that stores it, however, the personal supervision implemented during lifetest execution allowed to take actions over the software almost immediately, reducing test delays and also preventing test data loses.

Post processing the data obtained from test, it was found that all the success criteria were accomplished, proving that the mechanism could execute al the cycles without failures.

Some of the data acquired and post processed is presented hereby, note that one calibration cycle indicated in the graphics is equivalent to 4 movements:

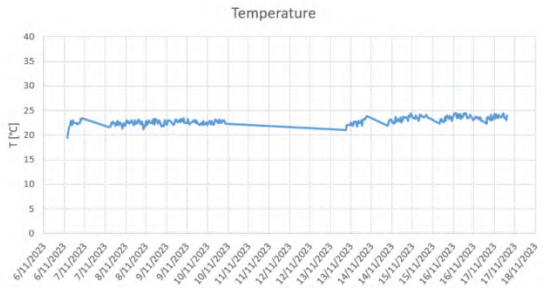


Figure 14: Temperature Acquisition (note that the test stopped in the middle because of non-availability of personal supervision).

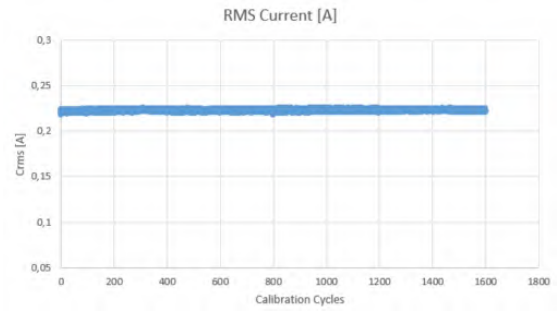


Figure 15: one phase RMS Current Acquisition.

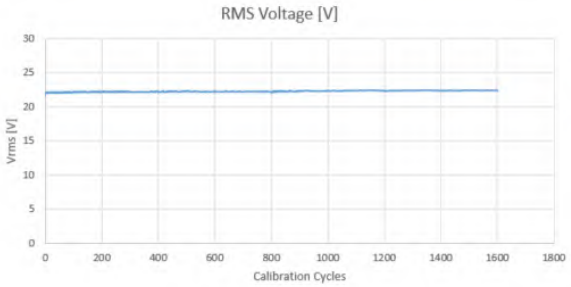


Figure 16: RMS Voltage between two phases Acquisition.

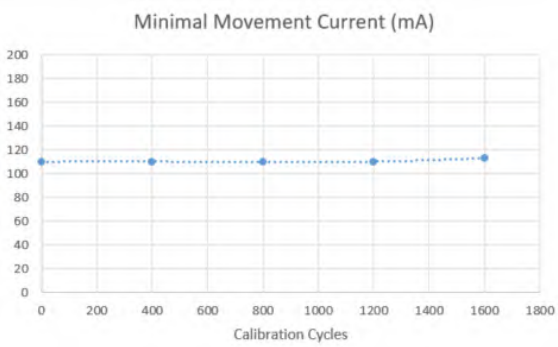


Figure 17: Minimum actuation current measurment.

- No changes in the step number were registered in any movement between same two positions.
- The main vibration modes invariable by the end of the test, verifying that no damage to the internal actuator mechanism was registered.

After visual inspection of the components that were subjected to friction (disc support and spherical bushing) no appreciable changes were noted respect to the pre-test visual inspection, together with the almost invariant minimum actuation current, verifying that the friction wear did not produce appreciable effects in the mechanism.

5.2. Dynamic Angular Oscillator Vibration Test

Because of the lack of HDRM keep the disc in position during launch phase, a test was developed to assess the behaviour of the actuator mechanisms when subjected to torsional loads.

Because of a natural mode of the spacecraft structure where both calibrators are mounted, an angular acceleration is induced on the actuator flange. This natural SC mode could couple with the natural frequency of the actuator-disc torsional mode given that the frequencies are similar (around 69 Hz), particularly for NS calibrator.

At early stages of the design, it was supposed that once the torsional loads reached the UHT, the mechanism would slip between actuator steps, without compromising either the motor or the harmonic reducer. To verify this hypothesis, a novel angular oscillator test was developed. This oscillator consist in a pedestal where the EM actuator is mounted. Dummy disc is attached to the actuator. This dummy disc had the same inertia and mass than PFM NS calibrator disc. This pedestal was designed to replicate the behaviour of the SC structure regarding de angular acceleration induced on the actuator flange.



Figure 18: FEM Model and test Setup for Dynamic Oscillator.

Instrumentation for the test was developed considering the variables that determine the theoretical torque calculation for the actuator. Instrumentation consisted of one control accelerometer on the test adapter for shaker control, one accelerometer in the front face of the disc, two accelerometers on the actuator flange and four accelerometers placed tangentially on the back of the disc.

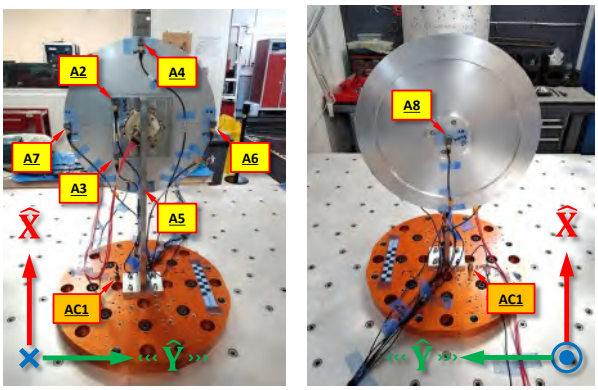


Figure 19: DUT instrumentation and test axis.

The methodology for the torque calculation [2] assumed that the disc behave as a rigid body and it is perfectly balanced. Given that, the equation that represents the torque estimation for the rotor axis is

given by:

$$M_P = I_P \ddot{\theta}_P \qquad (2)$$

$$\ddot{\theta}_P = \frac{\ddot{X}_B - \ddot{X}_A}{2s} \qquad (3)$$

Considering:

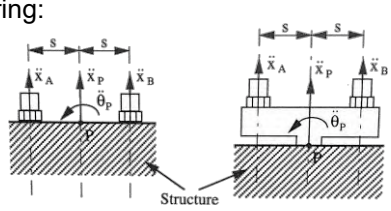


Figure 20: Torque calculation hypotesis.

Inertia of the disc was obtained from the finite elements model (FEM), and the accelerations were extracted from the data acquired during the test, decoupling acceleration in the flange zone versus those acquired from tangential disc accelerometers.

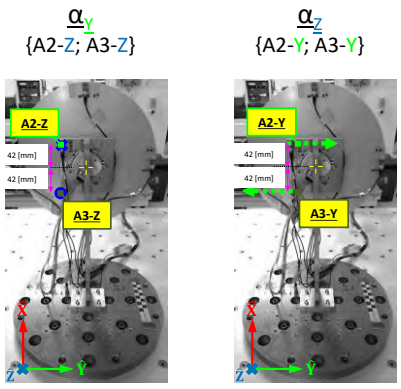


Figure 21: Angular acceleration on motor flange estimation.

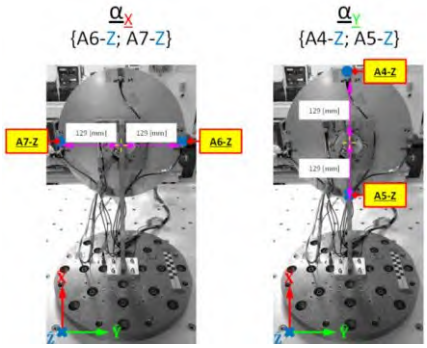


Figure 22: Angular acceleration on disc estimation (X,Y).

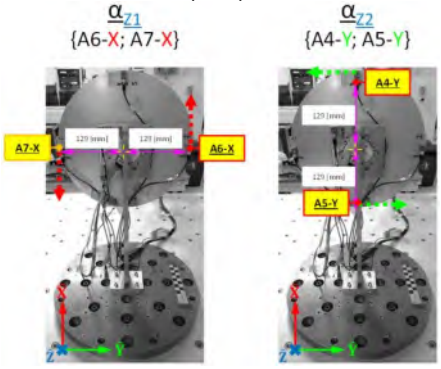


Figure 23: Angular acceleration on disc estimation (Z).

This metodology was useful for determining the test level based on the UHT previoulsy measured.

An oscilloscope was also used for monitoring the tension between phases during the vibration test, in case that the motor behaves as a generator, as predicted.

The first low level vibration test was aimed to give feedback to adjust the FEM model, however, as the test levels were increased, many non-linearities were detected, difficulting test vibration level estimation, so test levels were increased in small steps.

Due to this non-linearities, the UHT of the actuator was not reached for the imposed levels during the test as it was expected, as seen in Figure 24:

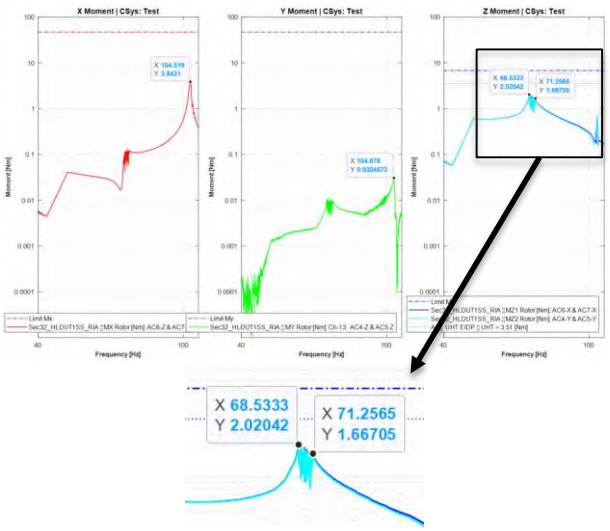


Figure 24: Torque for UHT level test, note that the torque is below UHT (3.2 Nm).

Until this test, the hypothesis considered that the torque would not increase up more than the UHT value seemed to be valid as the vibration amplification stopped at resonance frequency, but in the following tests at higher levels, something different was observed, furthermore, the acceleration and the moments registered in the disc did not increase linearly with the test level. Also, the frequency range in where the resonance of the mechanism is observable started to get wider as test level went up. After several tests, the final one is shown in Figure 25.

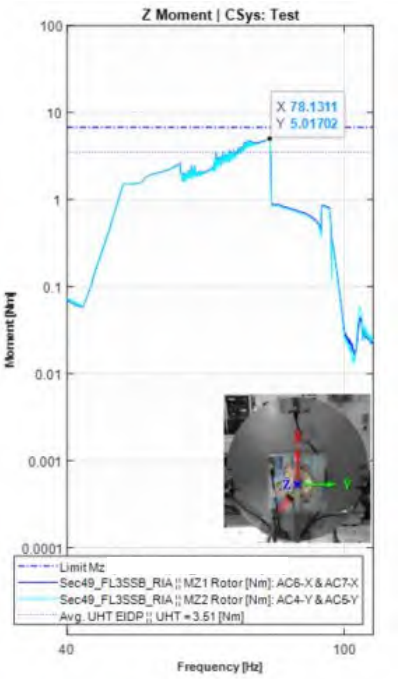


Figure 25: Torque, final dynamic oscillator test.

In the previous figure, is shown that the resonance continued amplifing even once the UHT was reached, which was opposed to the intial hyposthesis.
It was resolved to abort the test in order to protect the EM actutator and use the data already obtained to drive PFM dynamic test control. Figure 26 shown a maximum amplitude for tension between phases while the actuator behaves as a generator, which may constraint the PFM testing.
After each vibration test, an aliveness of the actuator was executed, checking that the minimum actuation current remains the same. Visual, audible and resistance between motor phases inspections were also carried out.

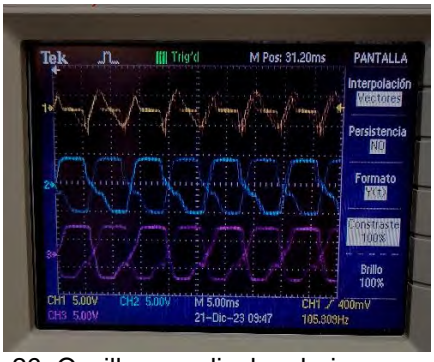


Figure 26: Oscillosope display during resonance. Tension between phases. Last test.

5.3. PFM Environmental Qualification Campaign

With all the data acquired during previous tests, PFM calibrators were manufactured, integrated and prepared for their environmental qualification campaign.

5.3.1. EMI / EMC

It was not expected to have any issues during electromagnetic interference/compatibility test. Data acquired during breadboard tests guided the pass / no pass criteria for the calibrator´s performance expected during EMI/EMC test.
RF Emissions generated by the actuator and position sensors power supply and operation were measured. All emissions were within the requirements.
No susceptibility to EM environment was shown during the test. Optical and Hall Effect switches kept performing as expected for Tab detection, there was not any fake telemetry status detected when disc reached any position. Actuator did not lose steps between two same positions.
Setup for EMI/EMC test is shown in Figure 27.



Figure 27: PFM VN Calibrator during EMI/EMC test.

5.3.2. TVAC

For thermal vacuum test, special functional and performance tests were developed, as for EM life test, taking special care in controlling the actuator temperature in order to avoid overheating during consecutive testing.
The functional test consisted in:

- Tab detection: Prove that all the position sensors detect the tab for the whole operation temperature range, given that there are tight manufacturing and assembly tolerances and the thermal distortions of materials could influence the sensors performance.
- Step loss and position repeatability: Check that the steps sent by the electronic drive between all fixed sensor position remained the same during two complete turns of the disc for every temperature tested and the summation after the complete turn is 9600 steps. Given the 0.25° requirement, the allowable difference between turns is 6 actuator steps.
- Minimum actuation current, torque ratio shall continue to be 3 or more, so, for each temperature, when limiting power motor current, this could not fall below 120mA.

This had two implications, on one hand, motor windings resistance goes up with temperature, while friction goes down. When temperature goes down, resistance also does and friction goes up.

- Then, electric variables characterization were carried out. Those variables were tension/voltage and resistance between phases, and phase current. However there is no requirement for this variable, they allow us to monitor the operational integrity of the actuator along the test and to detect any potential problem.

Test temperature profile is shown in Table 2.

Table 2: TVAC test temperatures.

	Tmin Qual [°C]	Tmax Qual [°C]	Cold Start up [°C]
Operative	-30	60	-30
Non Operative	-40	70	

There were 4 operative hot plateaus (HP), 4 operative cold plateaus (CP), 1 Non operative hot plateaus (Nop HP) where no test were executed and 1 non operative cold plateaus (Nop CP) where tab detection was tested and verified.

Before TVAC closing, all the test were executed at room temperature, after TVAC opening, the same test were executed in order to verify that calibrator performance remained invariable after thermal cycling.

Test were satisfactory, some remarks are:

- The steps executed between positions vary with temperature as expected, because of thermal expansion/contraction of materials, but for the same plateau, it was verified that no difference was perceived after two complete turns of the disc. Only in one single test Hall Effect sensor varied 1 step between turns which is, however, within requirement.
- The electronic drive GSE showed that in cold plateaus with nominal current (360mA), given the decrease in motor windings resistance, the voltage powered to the actuator had to be controlled in order to maintain the imposed current limit, as seen in oscilloscope display in Figure 28. The electronic drive is the same that the one that will be used in flight and it's expected to happen also in orbit.

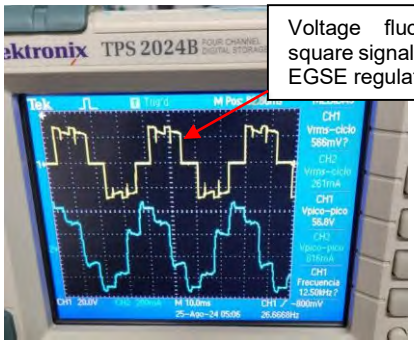


Figure 28: Oscilloscope display during CP.

- During one HP, temperature in the actuator varied significally enough to stop the test for a few minutes in order to allow the heat to escape from the motor. It was not considered as an issue because the actuator´s contact area is enough to dissipate heat trough calibrator´s structure and in-flight operations consist in a reduced number of sequences per orbit that the ones executed during TVAC testing and characterization.
- In CP, minimum actuation current reached 140 mA, which overpass the torque ratio requirement.
  This non-compliance was analyzed together with the thermal control team, who indicated that thermal analysis for in-orbit temperature profiles showed that neither NS nor VN calibrators temperatures fall below 0°C. Given that information, the test result was accepted.
- Elastic brackets that hold diffusers in place were visually inspected with satisfactory results. Optical tests were carried out at system level, showing that no performance degradation on diffusers was detected.

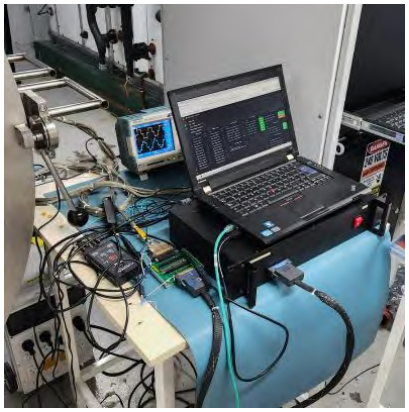


Figure 29: Test setup at INVAP´s TVAC facility.

5.3.3. Vibration Test

Dynamic test target was to manage the torsional loads on the actuator. Because of the configuration of the test, in where calibrators were hard mounted to a rigid test adapter, it was not foreseen that the adapter modes induce torsional loads in motor flange. The only expected torsional excitation of the

motor was because of minimal misbalances on the discs.
Torsional loads on actuator were controlled in real time while the test was executed by the use of an oscilloscope. The actuator was connected to its EGSE and the EGSE was turned off, same as for the UHT measurement. As explained before, the actuator behaviour under torsional loads changed when the UHT test was carried out with actuator connected or disconnected.
One of the test no-abort criteria was not to exceed the back EMF signal amplitude measured during Angular Oscillator testing. If that happened during PFM vibration test, it would be immediately aborted and vibration levels recalculated prior to continue shaker campaign. Oscilloscope display was however recorded during all the PFM testing.
Test setup and configuration is hereby presented.

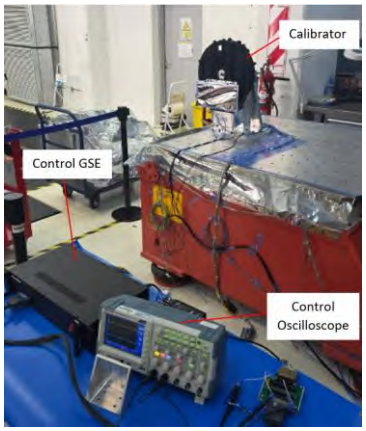
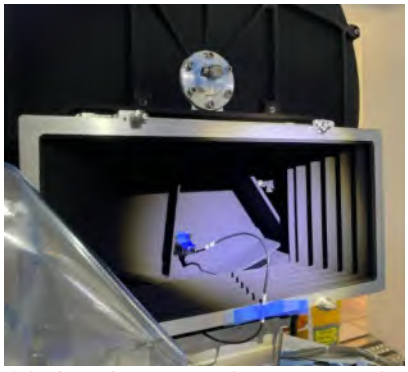


Figure 30: Test setup at INVAP´s Shaker facility.

During sine sweep test, when actuator first frequency mode was reached, the oscilloscope showed signals of the motor actuating as a generator. However, the levels remained sufficiently low to ensure that the dynamic Oscillator test levels would not be exceeded during any test. During random test, this behaviour was less noticeable.
Furthermore, for VN configuration, calibrator dimensions allowed to instrument a unique accelerometer on calibrator disc, the information acquired with this accelerometer will be especially important for system level dynamic test.


Figure 31: Accelerometer instrumented on disc.
As mentioned before, aliveness test was carried out between each axis testing. This test allowed to verify the functional integrity of calibrator at every step of dynamic testing and included:

-Actuator driving and tab detection in every position.

-Vibration Acquisition by an accelerometer instrument on motor flange during motor actuation, similar to the life test.

- Minimum actuation current test
- Resistance between phases.

The extensive characterization made on Breadboard model of all variables that indicated calibrator performance, as well as the functional and performance testing made during the rest of AIT campaign, allowed to evaluate and assure that the performance of calibrators remained the same during each step of vibration testing, giving confidence along the test and providing more variables to evaluate than only low level sine sweep signatures.
As an example of the previously explained, when testing VN calibrator, low level sine sweep signatures showed a sway in one natural calibrator frequency mode greater then the internal pass / no pass criteria. This sway was not a systematical frquency mode drop, instead of that, it fluctuated around within a frequency range around the mode frequency.
All functional test were executed for calibrator performance evaluation with no diference with previous environmental testing stages. Given that the frequency sway gone up and below one value, this did not necessary represent a structural damage as one might have thought with a systematical mode frequency drop.
After further analyses, it was noticed that the axial play between the spherical bushing and its housing, caused the bushing to move and re-allocate its position after each vibration test. This was the cause of the frequency mode oscillation, and was determined as a non-critical phenomenon.
Dynamic test concluded satifactory, as all the variables evaluated during functional and aliveness tests remained invariable, if compared to the test executed in the rest of environmental campaign and no structural damage was registered. Furthermore, observing the flexures that fixes diffusers to calibrators disc, allowed to confirm that the adopted solution was correct since no visually appreciable diffuser movements were observed. Adittionaly, an optical test was carried out together with the electro-optical components after mating, showing that the position of the diffuser remained without changes as designed.

6. CONCLUSIONS AND LESSONS LEARNED

Calibrators for the main instruments of ocean colour mission were successfully designed, manufactured, tested and qualified, getting its PFM delivered for integration on spacecraft.
All the data acquired and registered during the test campaign will now be available for performance evaluation during system level testing as well as in-

orbit performance, since the obtained telemetry will be compared with the obtained ground test data.
Design was optically validated in post environmental testing together with the electro-optics components in flight configuration at optic laboratory at INVAP facility.
The lessons learned from the qualification campaign are:

- Testing and validation of the data obtained at every stage of components development, is a key factor for the success of the subsequent testing, allowing to evaluate the performance at any stage of the qualification campaign. Letting to predict what to expect and even to drive PFM or system level testing control and functionality monitoring.
- Testing as early as possible every subsystem involved allowed several design feedbacks that improved and optimized system performance.
- Consider that many of the testing can be done in parallel to the different equipment subsystems development in order to avoid programmatic issues. On the other hand, this testing philosophy allowed to detect deficiencies in the design or its implementation that can be discovered as early as the test is carried out, if it is not done this way, programmatic issues will come from rework of pieces, re-manufacturing or even re-testing.
- The variables to be controlled or measured during testing have to be always carefully selected. Incorrect selection of these variables can lead to re-testing, under-testing or wrong interpretation of test results
- Data given by providers of COTS or customized equipment should be always tested in house when the concerns comes about some critical aspect of the component, as seen for the value of UHT of calibrator actuators.



Figure 32. Calibrators Being Mounted on SC at INVAP Facility.

7. REFERENCES

1. General Environmental Verification Standard (GEVS) for GSFC Flight Programs and Projects. GSFC-STD-7000B.
2. Nuno Manuel Mendes Maia, Júlio Martins Montalvão e Silva. Theoretical and Experimental Modal Analysis. 1997.

PRELIMINARY DESIGN STUDY FOR THIN-LAYERED THERMAL PROTECTION SYSTEMS FOR FUTURE, REUSABLE SPACECRAFT STRUCTURES EXPOSED TO MODERATE HEAT LOADS

Max Beitinger [(1)], Silas Eichel [(1)], Felix Krziwanie [(1)]

[(1)] German Aerospace Center (DLR), Institute of Structures and Design, Pfaffenwaldring 38-40, 70569 Stuttgart, Germany, Email: Max.Beitinger@dlr.de, Silas.Eichel@dlr.de, Felix.Krziwanie@dlr.de

KEYWORDS

Thermal Protection System (TPS), Reusability, Launcher, Material Testing, Database

ABSTRACT

To reduce launch costs for space projects, research and development efforts are increasingly focusing on reusable rocket first stages. For applications subjected to moderate thermal loads (<1000 °C), ceramic solutions as Thermal Protection Systems (TPS) are often complex, expensive, and oversized; Ablators as alternative are not fully reusable.
The goal of the hereafter presented work is to bridge this technological gap by developing concepts for a passive, reusable, thin-layered thermal protection system designed for use on reusable first-stage rockets and intended to offer economic benefits through reusability.
To achieve this, a database was created that contains relevant material properties and enables the comparison of material candidates that are potentially suitable for the application.
Then, supported by thermal-transient numerical optimization analyses, concepts for future, passive and thin-layered TPS are developed and compared. The investigated materials and concepts are finally tested within a burner-testbench setup to prove their feasibility.

1. INTRODUCTION

Since the German Federal Ministry for Economic Affairs and Energy identified "New Space" ten years ago as a major economic opportunity for the German economy [1], projects aiming at the development of Vertical Take-off Vertical Landing (VTVL) launch vehicles were commenced:
With Themis, ESA aims to develop a flagship European demonstrator for low-cost rocket recovery and reuse [2].
And with CALLISTO (Cooperative Action Leading to Launcher Innovation in Stage Toss-back Operations) the German Aerospace Center (Deutsches Zentrum für Luft- und Raumfahrt e.V., DLR) is partner of a project that aims to develop and operate a technology demonstrator for a reusable rocket first stage capable of VTVL [3].
As many structures of these spacecrafts are exposed to moderate thermal loads, a state-of-the-art solution is to use thin layers of ablative materials as TPS.
Phenolic cork ablators, for example, are an often-used solution. While they offer certain advantages, these ablative material systems are generally not reusable.
Ablators pyrolyze during heating, absorbing energy, with the decomposition gases additionally cooling the boundary layer. While this works for very high heat fluxes, due to the caused recession of the

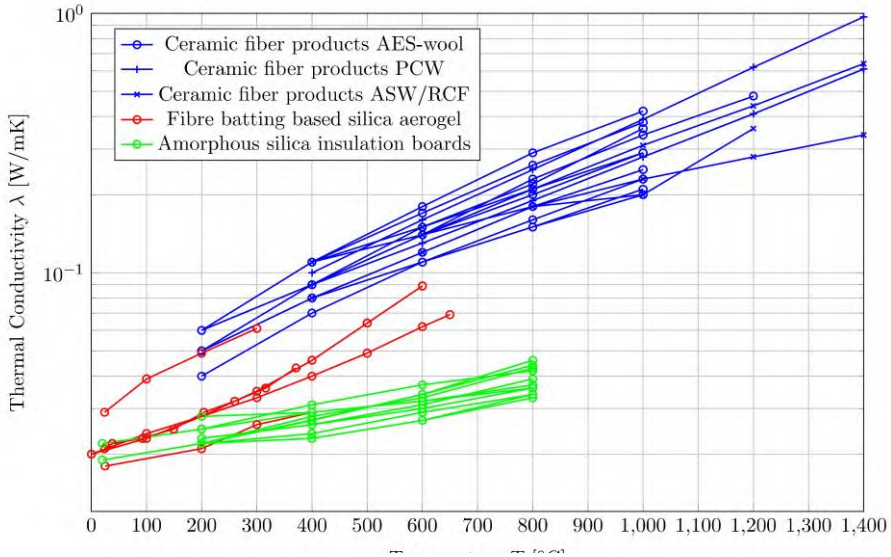


Figure 1: Collection of potentially interesting, commercially available, high temperature resistant insulation materials.

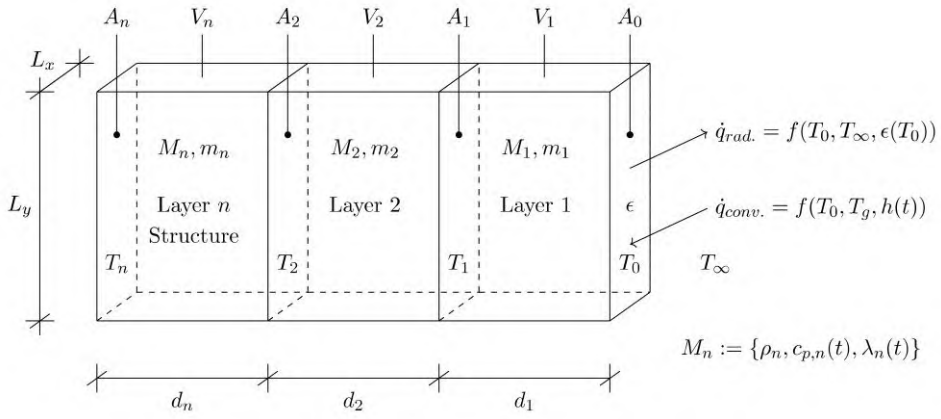


Figure 2: Nomenclature used for simulation and optimization of multi-layer TPS-solution.

materials surface, ablators are mostly single use materials and can only be refurbished to a limited extent [4].

Therefore, alternatives for a passive TPS were explored. First, material research and collection of material candidates for the application were performed. This was then followed by a thermal transient calculation and optimization of different materials and material layers to test their thermal performance regarding different use-case specific load cases. Subsequently, concepts for designing a TPS out of the thermally suitable material combinations are developed. This was concluded by experimental tests in the burner testbench to test the insulation materials for their thermal performance and the concepts for their feasibility.

2. MATERIAL CANDIDATE COLLECTION

To investigate the possibilities of designing a passive TPS solution, material research was conducted. Therefore, the relevant requirements regarding material characteristics, such as e.g thermal conductivity, were identified. Then, a database was created that contains relevant material properties and enables the comparison of material candidates that are potentially suitable for the application. Here, particular focus was placed on commercially available high temperature resistant insulation materials. The results of this research are shown in Fig. 1 for thermal conductivities of said materials. An emphasis was placed on ceramic fibre products, aerogel composite materials and microporous insulations.

Regarding ceramic fibre products, Alkaline Earth Silicate (AES) products were chosen for investigation. This is because of their possible application within the desired temperature range and fewer health concerns compared to the alternatives (Poly-crystalline-wool (PCW) or Aluminium Silicate Wool (ASW) / Refractory Ceramic Fibers (RCF)) [5].

Silica Aerogel Composite Materials and Microporous insulations were investigated alternatives due to even lower thermal conductivities of the materials, while being in a comparable weight range. The type of Silica Aerogel investigated has a temperature limit of 650°C for long term exposure. Aerogels of higher temperature capabilities are currently in research [6].

In addition to the collected data regarding high temperature resistant insulation materials, possible material candidates for coatings, adhesives and structural connections were collected.

3. NUMERICAL SIMULATION AND OPTIMIZATION

A parametric study was conducted to compare the previously identified material candidates for the intended application and to identify optimal combinations and layer arrangements for the thermal loading regarding the use case on a VTVL Reusable Launch Vehicle (RLV). Thermal transient FE-simulations were performed using ANSYS simulation software and OptiSLang optimization extensions.

3.1. Methodology

The Methodology for the numerical calculations is explained in the following.

3.1.1.Load Cases

Two load cases were used in the simulations.

These two specified load cases were defined as generic loads applicable for typical VTVL RLV TPS in the scope of this work and were defined as requirement. They are derived from internal data and various sources and do not represent a specific, real-world mission. Both load cases represent the dimensioning load case of the mission scenario for a VTVL rocket stage. The retro-boost maneuver is leading to the highest thermal loads during the mission. As these loads are additionally strongly dependent on the parameters of the flown trajectory and especially the angle of attack in which the rocket stage descents through its exhaust plume, the two different load cases are used for comparison reasons, addressing diverse scenarios. Both load

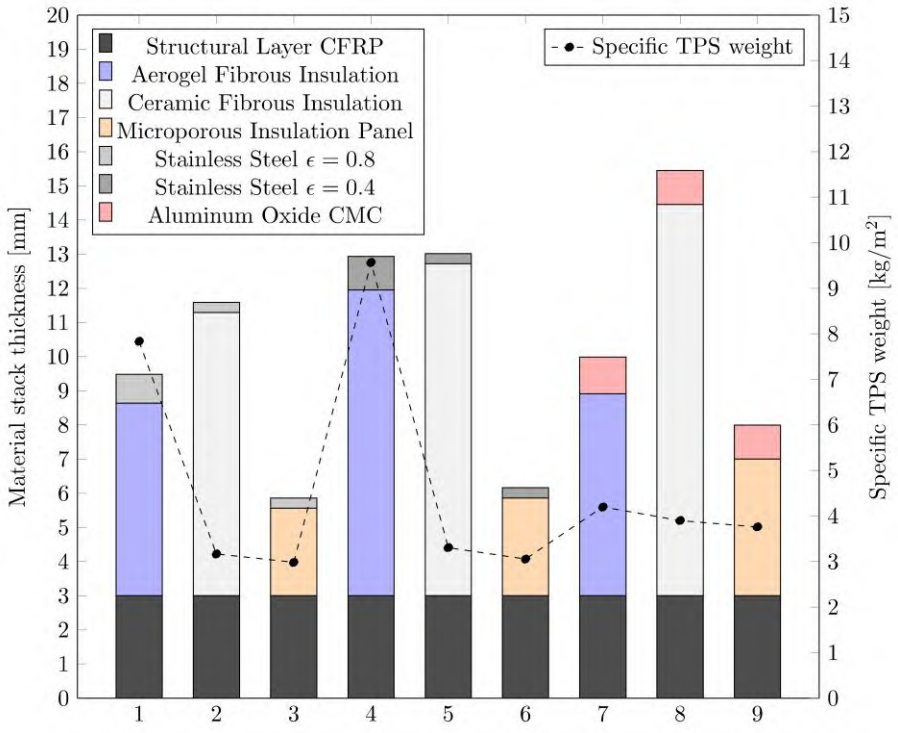


Figure 3: Results of three-layer simulations and optimizations regarding the needed TPS insulation to protect a 3 mm thick CFRP structure in a VTVL scenario.

cases shall represent the thermal loads on the aft bay of the rocket stage, with calculations beginning at the moment of engine ignition for the retro-boost maneuver. The rocket then is not only subjected to thermal loads for approx. 30s - 60s, depending on the load case, due to the surrounding rocket engine exhaust flow, but also to additional heating after touchdown. This is due to remaining on the landing platform, which has been significantly heated by the exhaust plume.

To reconstruct these load cases, the time-dependent heat flux is given dependent on the temperature of the outer structure wall for both load cases.

For practical implementation reasons, those values are converted into a convective boundary condition for the simulations.

3.1.2. Simulation Model

Those load cases are then used in a parameterized, extendable simulation model. It uses adaptive optimization algorithms to adjust the layer thicknesses of the individual materials within specified limits, based on the generic load cases. This allows to determine the optimal solution in terms of the thermal protection systems weight per unit area for various materials and their combinations. Simultaneously, the employed optimization method ensures that the thermal load on the substructure component remains within specified limits.

The nomenclature used for this model is shown in Fig. 2.

3.1.3. Optimization

Optimizations were performed to adapt the layer thicknesses of the investigated materials to optimize them towards minimal weight for the subjected loads. These optimizations were performed for multiple material combinations, and for up to four material layers.

The optimizations were performed using ANSYS Version 2025 R2, and OptiSLang extensions. ANSYS One Click Optimization (OCO) was used, generally using at least 100 Design Point (DP) iterations as limitation for the number of individual optimization simulations. Convergence of the optimization was considered reached, when the maximum temperature of the substructure is not exceeding the defined limit of 100°C with a maximally allowable deviation of 1%.

ANSYS OCO uses adaptive Algorithms to avoid local minima, arbitrary changes, and the overhead that comes with a manual selection of the optimization procedure [7].

4. OPTIMIZATION RESULTS

The results of the optimizations show, that the aforementioned insulation materials are well suitable for light-weight and thin TPS solutions.

For two-layer simulations and both load cases examined, necessary material thicknesses for insulation of CFRP or Aluminium substructures would stay below 10 mm and insulation weights below 1 kg/m^2. The results for some of the performed two-layer calculations are shown in Fig.5

The main disadvantage, later confirmed by experimental testing, is seen in the poor mechanical

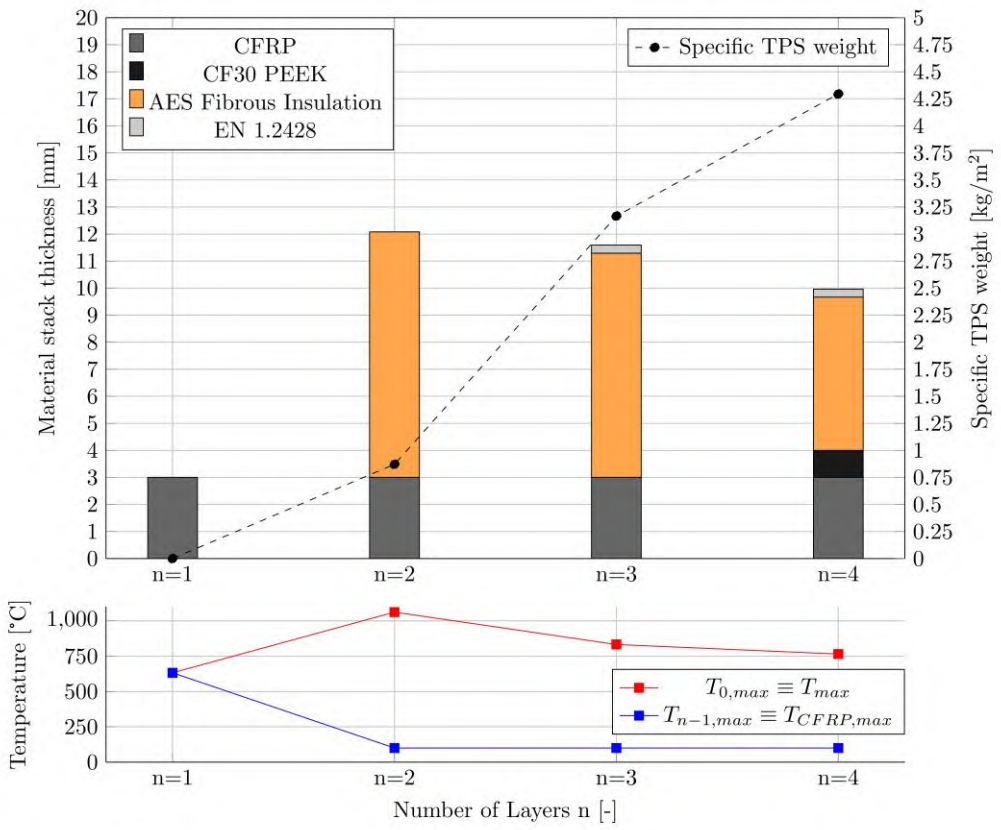


Figure 4: Results of one-layer to four-layer simulations and optimizations regarding the needed TPS insulation to protect a 3mm thick CFRP structure in a VTVL scenario.

characteristics of all the insulation options. To investigate possible mitigation strategies, the effects of additional material layers were implemented into the simulations, leading to three- and four-layered simulations. They are particularly covering the underlying insulations with top-layers of different materials, enhancing the mechanical strength of the TPS.

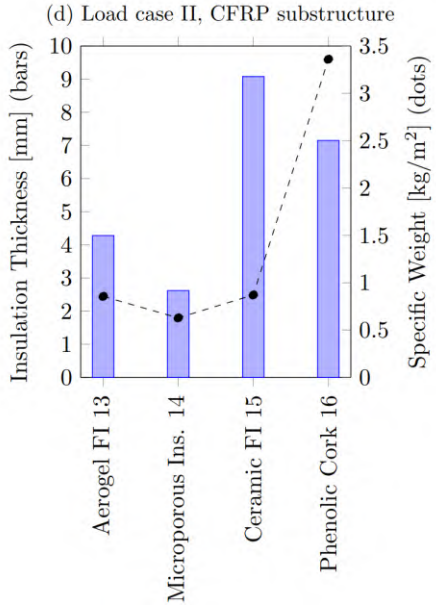


Figure 5: Results of two-layer simulations and optimizations regarding the needed TPS insulation to protect a 3mm thick CFRP structure in a VTVL scenario.

The three-layer simulation results show, that covering the insulations with thin layers of austenitic high temperature resistant steel would provide weight benefits compared to expensive CMC covering, especially considering the constraints regarding possible material thicknesses.

The results of these calculations are summarized in Fig. 3. A three-layer solution would result in a TPS of 3 - 4 kg/m² weight. A high temperature resistant stainless-steel alloy in combination with a microporous material is the theoretically calculated best combination in terms of thickness and weight.
The four-layer simulation results showed that adding a connection layer between structure and material could make the needed material stack for thermal protection even thinner, but would result in an additional weight disadvantage. The results of these calculations are shown in Fig. 4.

5. CONCEPT CREATION

Based on the results of the conducted material research, the results of the simulations and considering also historic and state-of-the-art TPS designs, different concepts for passive & reusable TPS were developed.
As a result of chapter 4, high temperature resistant insulation materials with low mechanical stability were identified as promising materials to build a lightweight, thin-layered TPS, using the described FE-calculations and optimizations. The developed

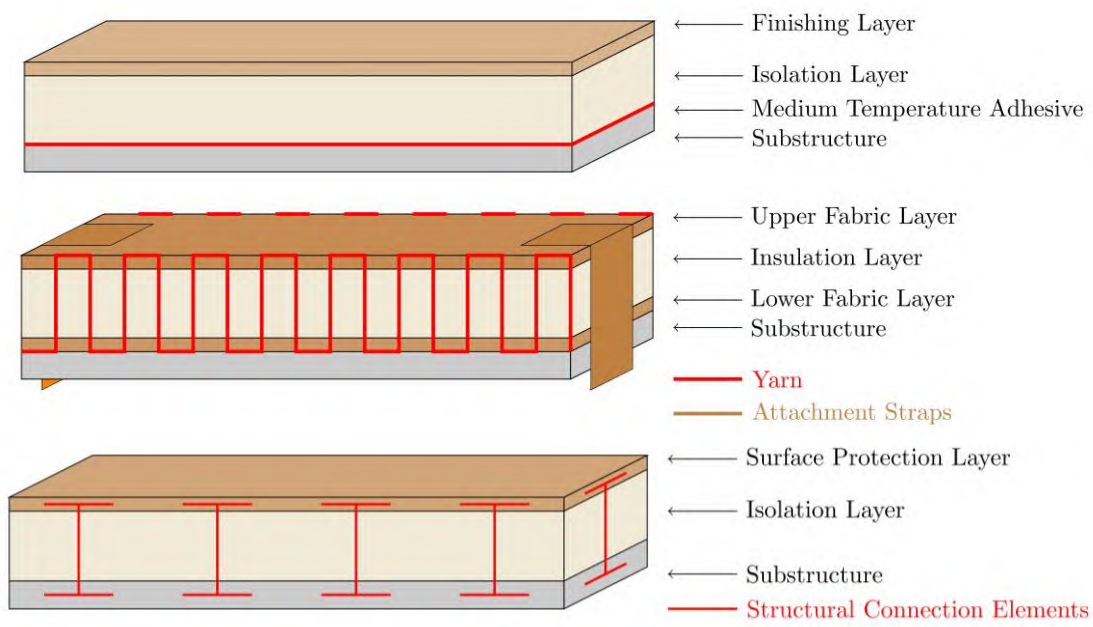


Figure 6: Schematics of concepts for thin-layered passive TPS solutions.

concepts address how these materials could be attached to the substructure, resulting in a TPS with the lowest weight, while providing the necessary thermal protection, as well as providing the required structural rigidity to withstand the environment of high-velocity atmospheric flight. For each concept, matching materials out of the material database compiled were assigned for each needed component. A schematic overview of the three developed concepts can be seen in Fig. 6. and are briefly described in the following.

Concept I is based on the idea of gluing an insulative material directly to the structure and improving the surface quality with an additional coating to rigidize it and enhance thermal properties, forming a very lightweight TPS solution.

Concept II uses methods of packaging and attaching insulative materials to the structure using textile technology, namely high temperature resistant ceramic fabrics and yarns.

Concept III can be understood as a tiled TPS solution. Here, the functions of heat absorption and re-radiation are separated from the insulative function of the intermediate material, and the surface-exposed tile is mechanically attached to the substructure.

Those three concepts were systematically compared using a procedure based on a VDI guideline on design engineering methodics: Engineering design at optimum cost [8], in which evaluation criteria are defined, weighted using a decision matrix and then used to evaluate the developed concepts using a Weighted Sum Model (WSM) calculation. This evaluation showed best results for Concept I (63%) and Concept III (67%), compared to Concept II (42%), which is why they were selected for further investigation and experimental testing regarding feasibility.

6. EXPERIMENTAL TESTING

Based on the calculated material thicknesses in chapter 4 and the concepts evaluated in chapter 5, a simplified test series was conducted. Samples of the promising material combinations were built, glueing the insulation materials to GFRP and CFRP plates with high temperature resistant epoxy-based glue. Temperature measurements were conducted using thermocouples and LabVIEW software to allow for the analysis of temperature profiles in between insulation and substructure (sublayer thermocouple) and on the outer surface (surface thermocouple).

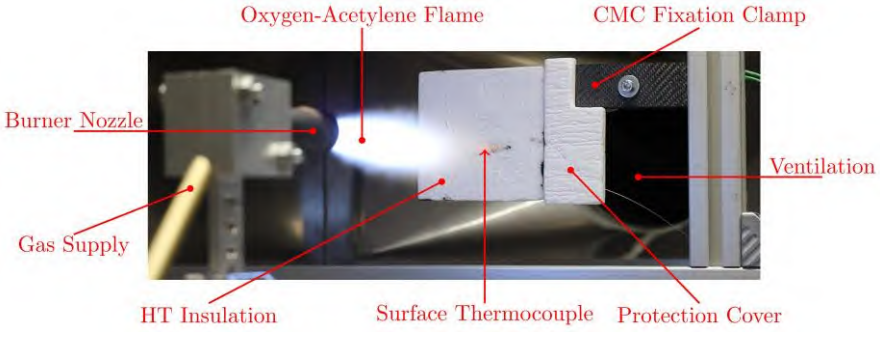


Figure 7: Torch testbench experimental setup with calibration sample.

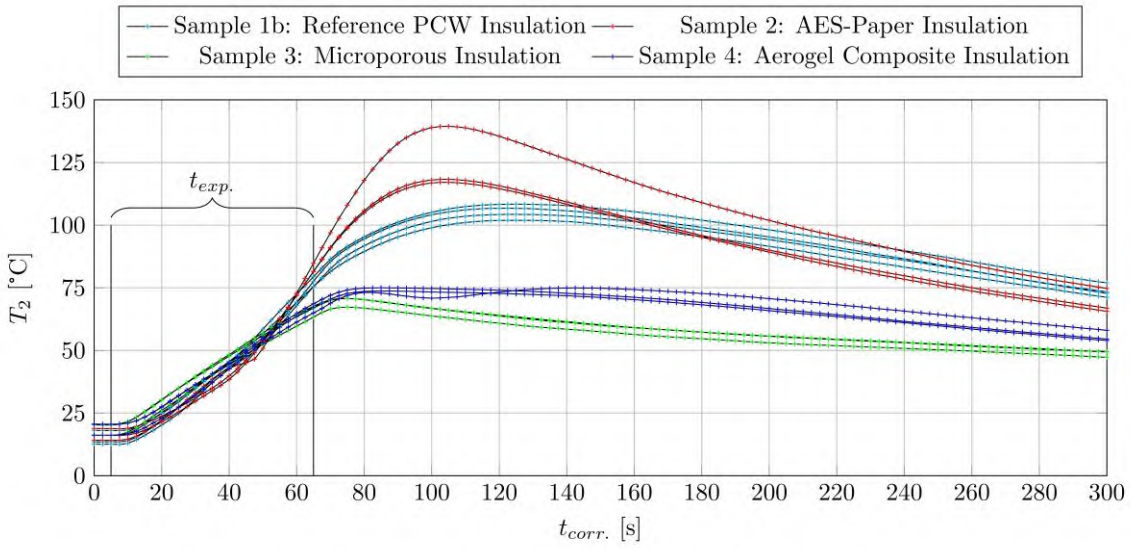


Figure 8: Temperature measurements on the sublayer thermocouple at the structure for an equal exposure time and distance to the torch flame for the different insulation materials.

These samples were then exposed to thermal loads in the torch-testbench of the DLR Institute of Structures and Design in Stuttgart. To allow for a qualitative comparison of the thermal insulation performance, the thermal load and insulation thickness used for testing were kept constant for all samples and test runs. All insulations were therefore tested with a thickness of 10mm.

6.1. Tested Samples and Materials

A picture of the experimental setup can be seen in Fig. 7, showing the calibration sample during test. Tab. 1 lists all the tested samples and which insulation and top-layer materials they are made of.

Table 1: Material Combination of Samples tested.

	Insulation	Top-Layer
1a	PCW-Wool	None
1b	PCW-Wool	None
2	AES Wool Paper	None
3	Microporous Insulation	None
4	Aerogel Composite	None
5	AES Wool Paper	Ceramic Coating
6	Microporous Insulation	Ceramic Coating
7	Aerogel Composite	Ceramic Coating
8	AES Wool Paper	EN 1.4841 0.3mm
9	Microporous Insulation	EN 1.4841 0.3mm
10	Aerogel Composite	EN 1.4841 0.3mm

6.2. Test Results

The results for the different tested insulation materials and used concepts are described in the following. The temperature measurements of the sublayer thermocouple for Samples 1b to 4 are shown in Fig. 8.

6.2.1. Insulation Materials

The results show that aerogel composite materials and microporous insulations outperform the commonly used ceramic fibrous insulation materials, regarding their thermal insulative performance, comparing material samples of the same thickness of 10 mm. Especially the aerogel composite material, weighing 1,92 kg/m^2, additionally showed good material handling, while being lightweight and comparatively cheap. The microporous material had best insulative properties of the materials tested, but serious disadvantages regarding handling and the weight of 3,68 kg/m^2. An AES-Wool material tested, weighing 2.11 kg/m^2, insulated far less effective than expected. It was intended to be a cheaper, less health hazardous, ceramic fibre insulative option, compared to commonly used PCW ceramic fibre products. This result was likely caused in part by the material's higher gas permeability, but can also be seen with the covered material. The adhesive connection resisted the thermal loads for the insulative materials tested. For microporous insulation, some problems with glue adhesion occurred.

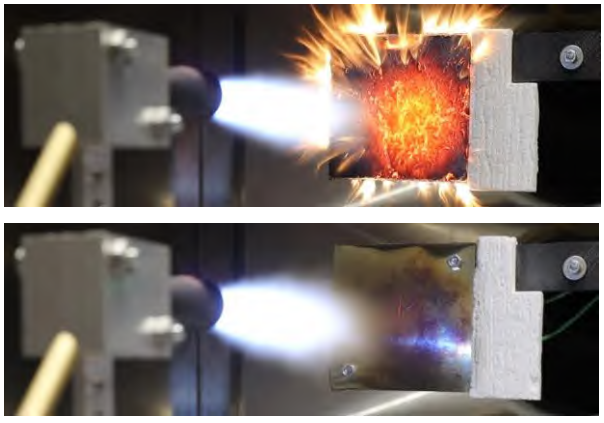


Figure 9: Reaction of two tested surface cover options for insulation materials: High temperature resistant ceramic paint coating (Top) proved to be unsuitable due to ignition under load and high temperature resistant austenitic steel.

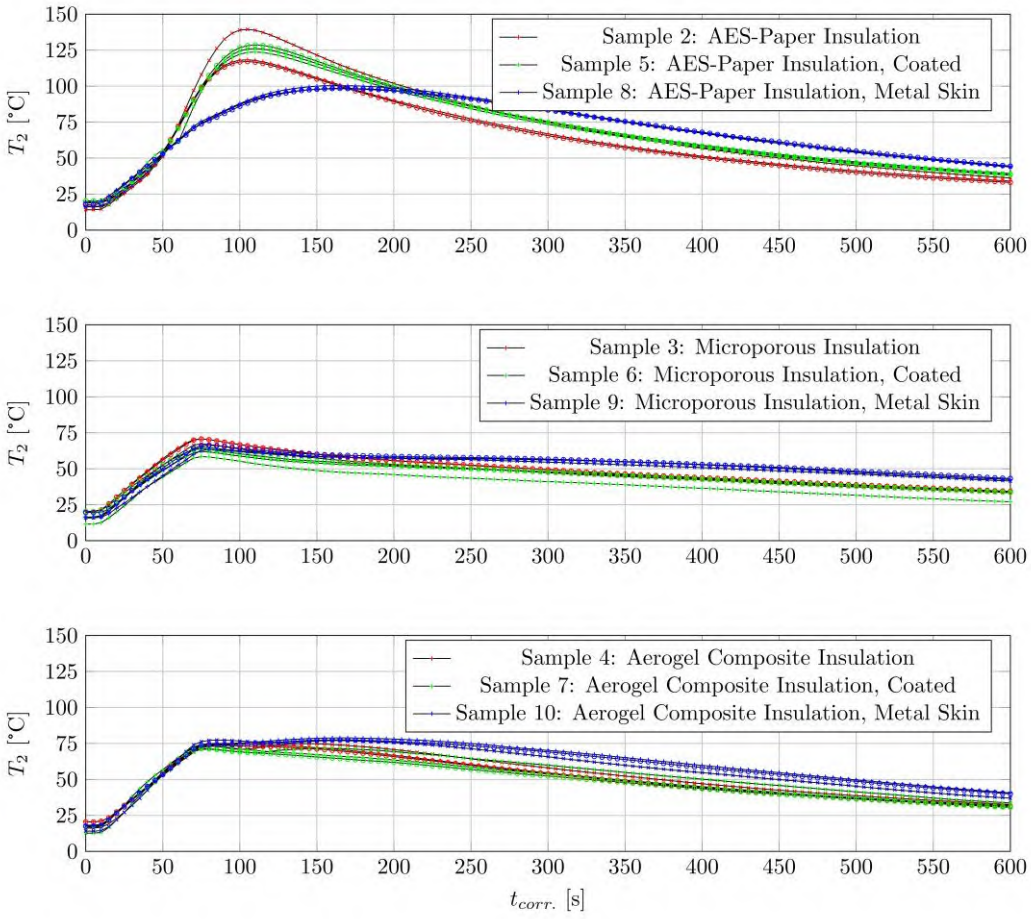


Figure 8: Comparison of the effect of adding two different surface protections to the insulation materials: high temperature resistant ceramic paint coating and a cover out of high temperature resistant austenitic steel alloy.

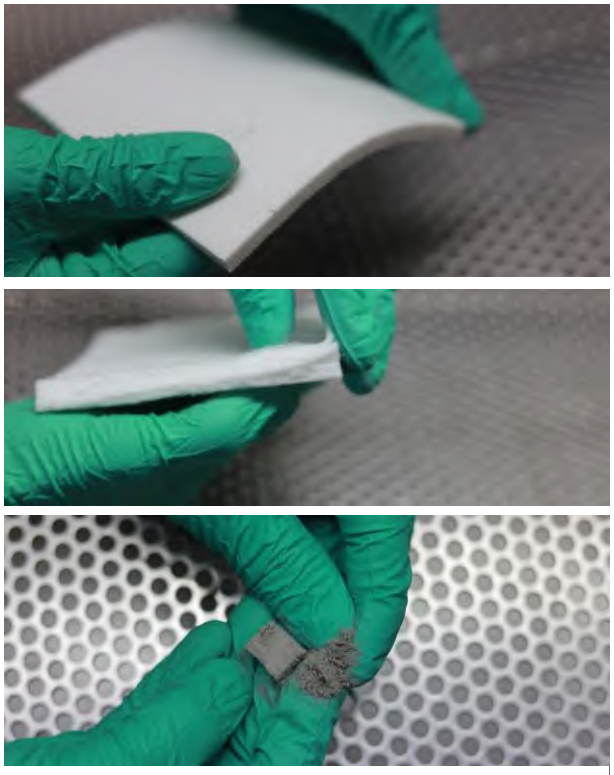


Figure 9: AES-wool paper, aerogel composite material and microporous insulation

6.2.2. Top-Layer Materials

The experiments were not only designed to test for the insulative components suitability, but also to comparatively test the developed concepts.
Therefore, the three insulation materials were also tested covered with (i) a high temperature resistant ceramic black paint coating and (ii) a high temperature resistant austenitic steel (EN 1.4841 / X15CrNiSi25-21). The resulting measurements of the sublayer thermocouple are shown in Fig. 10. The reactions of the tested surface cover materials to the torch flame exposure are shown in Fig. 9.

As expected, the test results show, that the impact from covering the insulation surface with the ceramic coating is negligible. One of the coating options tested ignited under torch flame exposure, despite the coating being rated for higher temperatures than exposed to. The selected coating therefore proved to be unsuitable. A surface rigidizing effect was achieved, but surface quality was less smooth than expected. As this solution was shown to be far lighter than the steel covered option it is nonetheless considered a favourable option in principle. Other surface reinforcing coatings are proposed for further investigation, e.g.

borosilicate glass coating, special ceramic fibre rigidizers or thermal sputtering. Benefits are then expected to be mainly the mechanical reinforcement and a negligible effect on thermal performance for the intended use case.
The steel covered version showed very good resistance to the thermal loads, while increasing cooldown times of the samples after torch flame exposure. For realization of a comparable TPS, the design of a thin mechanical connection to the substructure is seen as the main challenge for further development. The design needs to accommodate the thermal expansion cycles of the top-layer material, while being of low thermal conductivity.

6.2.3.Material Handling

In addition to the results regarding the thermal insulation of the different insulations and cover materials tested, valuable experience regarding handling and assembly of the investigated materials was gained. Fig. 11 illustrates specific behaviour of the tested AES wool product, aerogel composite and microporous insulation.
Especially microporous insulation materials could only be used in an enclosed fabric wrap or under a metal covered protection, as they are very brittle and dusty with low mechanical stability. They are nonetheless the best insulative material available and tested for higher temperature applications.

6.3. Outlook

A general focus as basis for further development needs to be laid on acquiring reliable properties for selected materials, which can then be better used for simulations regarding specific projects. Values provided by manufacturers' Technical Data Sheets (TDS) were partially unreliable for the application. Further, systematic material testing would have to be done to qualify the used materials for use on spacecraft structures. For insulative materials, this particularly includes their behavior under vacuum conditions and their resistance to a larger number of thermal cycles. In addition, determination of thermal conductivity and heat capacity across the operating temperature range is required.
A specific focus for further research is set on (i) finding better suitable protective surface rigidizers for the application, based on concept I, and (ii) constructing a suitable structural connection for a stainless steel-covered metallic TPS, based on concept III. Furthermore, using the tested aerogel composite material as insulative layer in combination with the tested austenitic steel is suggested. With the proposal of these two TPS concepts, a basis is placed to develop a more detailed design for a specific mission of future RLVs.

7. SUMMARY

The work presented in this paper investigated lightweight, thin layered TPS for spacecraft structures exposed to moderate heat loads.
Initial ideas to protect temperature sensitive spacecraft structures have been gathered, based on available materials and their limitations. They were formulated into concepts based on FE simulations performed and were subsequently tested for feasibility. As a result, promising approaches for future TPS exposed to moderate heat loads evolved.
Especially a tested Silica Aerogel composite proved to be a promising insulation choice for future use in an application as insulator in a TPS exposed to moderate heat loads. Despite the nominal degradation of the material above 650°C no degradation of insulative performance was measured in multiple test runs. As a surface protective measure, a tested high temperature resistant ceramic paint coating did not resist the exposed loads. Covering the surface with high temperature resistant austenitic steel resulted in very good results.

8. REFERENCES

1. Bundesministerium für Wirtschaft und Energie: NewSpace - Geschäftsmodelle an der Schnittstelle von Raumfahrt und digitaler Wirtschaft. 2016. url: https://www.bundeswirtschaftsministerium. de / Redaktion / DE / Downloads / B / bmwi - new - space - geschaeftsmodelle - an - der - schnittstelle-von-raumfahrt-und-digitaler-wirtschaft-kurzfassung.html.

2. European Space Agency: Themis. 2026. url: https://www.esa.int/Enabling_Support/ Space_Transportation/Themis.

3. German Aerospace Center: CALLISTO: Launcher Innovation for Vertical Landing. 2026. url: https://www.dlr.de/en/research-and-transfer/projects-and-missions/callisto.

4. Bouslog, S.: Thermal Protection Systems: State of the Industry. Houston, TX, 2023. url: https://ntrs.nasa.gov/api/citations/20230015883/downloads/TPS-StateofIndSAMPE-Final2.pdf.

5. European Ceramic Fibre Industry Association. 2026. url: https://www.ecfia.eu /materials/

6. NASA: Ceramic Aerogels for Space High Temperature Applications. 2023. url: https://ntrs.nasa.gov/citations/20230003647.

7. ANSYS, Inc.: optiSLang Documentation Set. 2026. url: https://ansyshelp.ansys.com/ public/account/secured?returnurl=/Views/Secured/ corp/v252/en/opti_multi_ disc/opti_multi_disc_intro.html.

8. Verein Deutscher Ingenieure: Technisch-wirtschaftliche Bewertung: VDI 2225 Blatt 3. Berlin, 1998.

DYNAMIC TEST MODEL CORRELATION AND LOAD ASSESSMENTS FOR THE ROSE-L SPACECRAFT: LESSONS LEARNED FROM SINE AND ACOUSTIC QUALIFICATION

Daniele Cardinali (1), Alexander Ihle (2), Gabriele Muto (1), Pietro Nali (1), Rocco Raffaele Trento (1), Amedeo Giancarlo Tenore (1)

(1) Thales Alenia Space Italia, 00131 Rome, Italy, Email: daniele.cardinali@thalesaleniaspace.com
(2) European Space Agency, 2200 AG Noordwijk, The Netherlands, Email: alexander.Ihle@esa.int

KEYWORDS

Spacecraft, mechanical test, correlation

ABSTRACT

This paper presents the dynamic test correlation strategy developed for the European Union's and European Space Agency - ESA's Copernicus Radar Observing System for Europe at L-band (ROSE-L) spacecraft during sine and acoustic qualification. The campaign addressed prediction and interpretation of structural responses during sine vibration testing of CFRP–aluminium spacecraft structures intended for refurbishment after qualification.

The ROSE-L platform consists of two cylindrical sections connected to a base cone, interfacing with a 1194 mm Launch Vehicle Adapter and optimized for the Vega-C fairing envelope, while remaining compatible with Ariane 6 launch environments. Testing was performed on the Structural Model, representative of flight mass properties, materials, and geometry, and planned for refurbishment into Flight Model 2.

During sine testing, the first longitudinal mode was measured at a higher frequency than predicted by the initial finite element model, requiring dedicated model correlation. Frequency correlation was achieved through refinement of interface stiffness modelling, while amplitude correlation relied on calibration of amplification factors using accelerometers employed for notch control.

The novelty lies in a correlation strategy for CFRP–aluminium spacecraft structures qualified with refurbishable models, balancing correlation accuracy with conservative load prediction. The correlated model reproduced measured responses and enabled interface load verification.

Acoustic qualification was performed using the DFAN system, with exceedances evaluated through Extreme Response Spectrum severity assessment. The proposed methodology provides practical guidance for dynamic test correlation and interface load assessment in spacecraft qualification campaigns.

1. INTRODUCTION

The mechanical test campaign conducted on the spacecraft (S/C) structural model was aimed at qualifying the structure against launcher-induced mechanical environments. In this context, it is standard practice to subject the structure to limit loads, which may result in localized structural damage or failure.

Within the framework of the Rose-L program, the structural model is planned to be refurbished following qualification activities and subsequently converted into Flight Model 2 (FM2). Accordingly, the structural model hardware is fully representative of the flight configuration. In particular, the primary, secondary, and tertiary structures accurately replicate the mass and stiffness properties of the flight hardware, together with the main dummy appendages and representative dummy units (Fig. 1,.2).

Under these conditions, the loads induced by the sine vibration environment on the structural components—specifically the tertiary structures supporting the payload—must be evaluated through a correlated spacecraft finite element (FE) model.

This paper presents the model correlation methodologies adopted to achieve the target correlation criteria, including the matching of the principal lateral and longitudinal natural frequencies, accelerometer response amplitudes employed for notching control, damping characteristics, and overall mass properties. Furthermore, the procedures implemented for the assessment of the primary internal mechanical interface loads and their verification against structural requirements are described.

In addition, the random vibration environment generated by acoustic excitation was assessed with respect to the qualification levels of all onboard equipment.

The paper also addresses the severity assessment of the random vibration transmitted by the platform to the onboard units. In this context, the already consolidated Extreme Response Spectrum (ERS) methodology is introduced and discussed. Nevertheless, the ERS application for random vibration severity is a novelty for the Rose-L programme.

2. REFERENCE FRAME AND HARDWARE DESCRIPTION

The Rose-L S/C has an innovative configuration, born with the aim to fit inside the Vega-C launcher's fairing and to be compatible with the mechanical environment of both Vega-C and Ariane-6 launchers.
The platform is embraced by the SAR Antenna in L-Band and is composed by the primary, secondary and tertiary structure. The primary structure is composed by two internal cylinders supported by the base cone, all made by CFRP.
The secondary structure, is composed by several sandwich panels made of aluminium honeycomb core and both aluminium and CFRP skins. The panels are identified as shear, horizontal, top, bottom, lateral and radiator panels, and have the purpose to sustain all the units and all the mechanical supports (brackets), as well as to transmit the loads to the primary structure.
The tertiary structure is composed by all the brackets. The several brackets have the purpose to connect the panels of secondary structure with the primary structure, as well as to sustain the external units and appendages (figure 1).

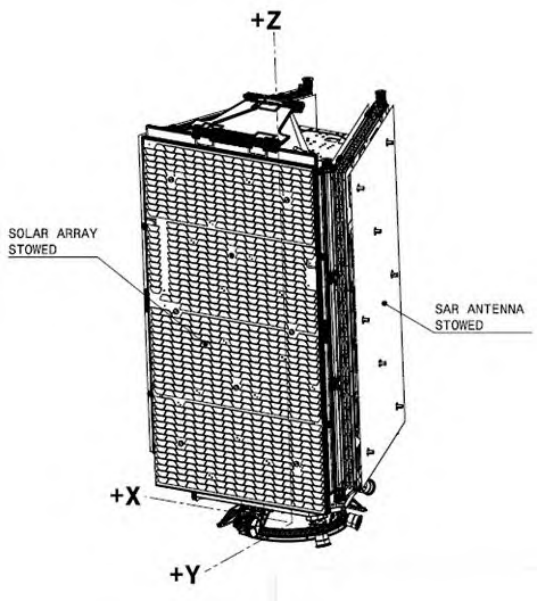


Figure 1: Rose-L Spacecraft stowed configuration and satellite mechanical reference frame description

This paper proposes highlights the load evaluation of the brackets of both SAR antenna and Solar array (Payload Brackets), which loads evaluation has a crucial role in the verification of the structural wellness of the S/C mechanical design.
The S/C reference frame is a Cartesian reference frame, positioned at the geometrical centre of the LVA ring, with the Z axis parallel with the S/C longitudinal direction, the X axis is parallel to the velocity direction and the Y axis defined as the consequence of the two other axis (Fig. 1).

The payload bracket local reference frame is a Cartesian reference frame with the Z axis parallel with the S/C longitudinal direction, the X axis oriented in the out of plane direction of the mechanical interface towards the payload and the Y axis is defined as a consequence of the other axis. (Fig. 2)

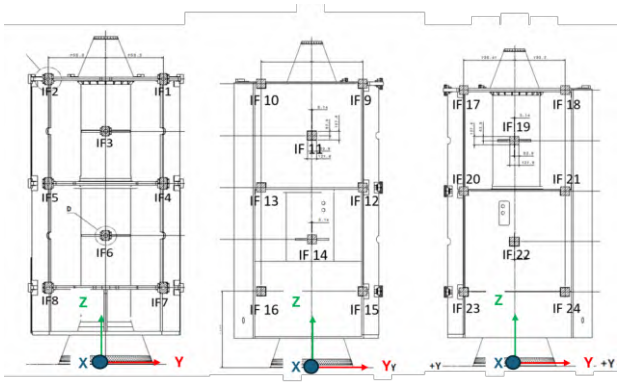


Figure 2: Payload interfaces local reference frame

3. SINE TEST FINDINGS AND FINITE ELEMENT MODEL CORRELATION

3.1. Findings and finite element model correlation

The correlation acceptance criteria applied for the correlation of the model Structural Model (SM) are resumed in the following table.

Table 1: Finite Element Model correlation acceptance criteria.

Parameter	Acceptance criteria (delta between test and model)
Main mode frequency	<5%
Amplitude	<10%

During the Structural Model (SM) sine vibration test campaign [1], a discrepancy was observed between the predicted and measured main longitudinal natural frequencies, exceeding the acceptance criterion of 5% (Table 2)

Table 2: Comparison between predicted and observed S/C main longitudinal frequency

Sine Z	Predicted	Observed	Frequency %Delta
Long. Freq.	47.1Hz	51.86Hz	-9.17

The comparison between model prediction and real main frequency is reported as a percentage delta, computed as follows:

$$Frequency\ \%Delta = \frac{f_{model} - f_{Observed}}{f_{Observed}} \quad (1)$$

Where:
$f_{Observed}$ is the main frequency in a specific direction.
f_{model} is the main frequency predicted in the same specific direction.

In this context, the primary objective of the model correlation activity was to improve the agreement with the experimentally observed S/C main longitudinal frequency without modifying the material properties of the model.
The correlation issue was addressed through a more realistic modelling of the primary mechanical junctions connecting the shear panels to the internal cylinders, top and bottom decks, and external panels. In the actual hardware configuration, these junctions exhibit distributed contact interfaces (Fig. 3)

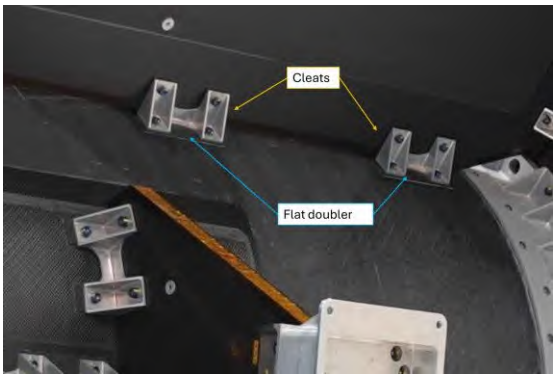


Figure 3: Detail from real hardware of Cleats-Cylinder mechanical junction.

Whereas the original FE model represented the connection through a single-node linkage between adjacent elements (Fig. 4)

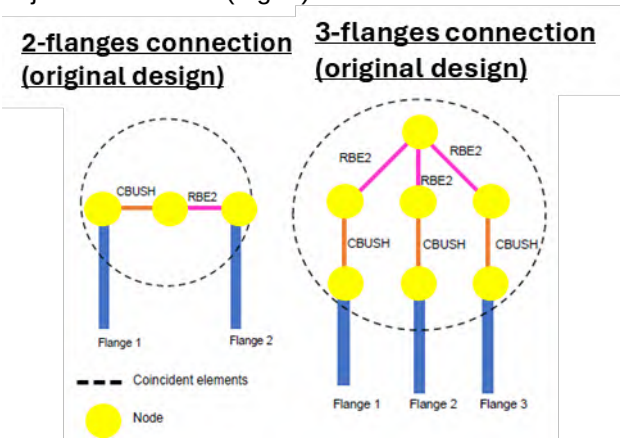


Figure 4: Original model of Flanges connections

Although such an approach could have some inner conservatism from a structural strength verification standpoint, as it tends to simulate localized load concentrations, it does not accurately reproduce the actual stiffness characteristics of the junctions.

Consequently, the rigid elements (RBE2) connecting the mechanical junctions to the primary structure were updated as reported in (Fig. 5).

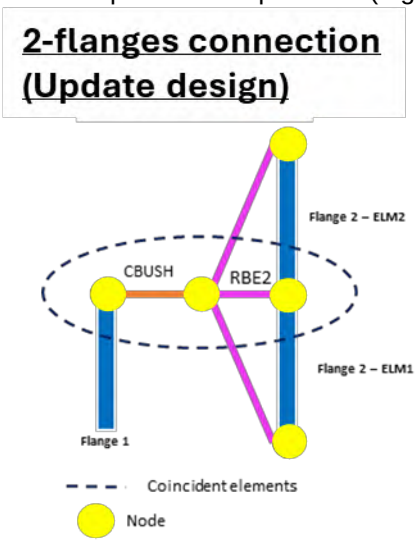


Figure 5: Modified model of flanges connection

in order to provide a more representative distribution of the interface stiffness and increase the local structural rigidity.
Following the implementation of these modifications, the predicted main longitudinal natural frequency achieved compliance with the acceptance criterion (Table 2).

Table 2: Comparison on main longitudinal frequency between S/C correlated model and SM test results.

Sine Z	Predicted	Observed	Frequency %Delta
Long. Freq.	49.36Hz	51.86Hz	-4.8

Additional correlation activities were performed on the response amplitudes measured by the primary accelerometers. In particular, the structural model exhibited damping characteristics different from those initially predicted by the analytical model.
Therefore, the correlation of the acceleration response amplitudes was achieved through the tuning of the damping matrices along all three axes and across the entire frequency range considered in the analysis. In the following is reported the three-step strategy applied, on each axis, for the amplitude correlation:

Step 1) For each axis, the frequency spectrum is divided into three sub-ranges, defining the corresponding frequency bands: Low, Medium, and High.

Step 2) Within each frequency band, the accelerometer that was active in the notching control is selected as the reference for the amplitude correlation.

Step 3) For each frequency band, the damping parameter is adjusted to match the amplitude response of the selected reference accelerometer.

The amplitude correlation is quantified by using the following equation:

$$Amplitude\ \%Delta = \frac{A_{model} - A_{Observed}}{A_{Observed}} \quad (2)$$

Where:
$A_{Observed}$: is the peak amplitude of the transfer function of the selected accelerometer, in the selected frequency range.
A_{model}: is the predicted peak amplitude of the transfer function of the node correspondent to the selected accelerometer, in the selected frequency range.

3.2. Rose-L structural model correlation results

The verification by test of the launcher main frequency requirement is fundamental for the success of a S/C design [9,10]. Therefore, the correlated model must be representative of the main modes.

This paragraph aims to show the results of the FE model correlation performed in the frame of Rose-L mission, providing the evidence of the representativeness of the real main S/C modes.

The accelerometer (A1302XYZ) used for the main modes of the satellite is placed on the top panel of the structure. The tables 3 and 4 show the results of model correlation on the three axes, highlighting both frequency and amplitude correlation.

Table 3: Model correlation results - Main frequency comparison

Frequency	Target	Correlation result	Frequency %Delta
Sine X	14.67Hz	15.07HZ	+2.7
Sine Y	15.04Hz	15.71Hz	+4.5
Sine Z	51.86Hz	49.36Hz	-4.8

Table 4: Model correlation results - Amplitude comparison

	Frequency range (Hz)	Sensor ID	Test Max Amplitude	Model Max Amplitude	Amplitude %Delta
SINE X	1 – 35	A1302X	28.3	28.6	1.0%
	35 – 90	A1004X	6.59	6.64	0.8%
	90 – 140	A7033Y	75.7	74.1	-2.1%
SINE Y	1 – 35	A1302Y	26.1	26.1	0.0%
	35 – 60	A1002Y	4.54	4.73	4.2%
	60 – 90	A7012Z	29.96	30.82	3.2%
	90 – 140	A7033Y	11.6	11.8	1.7%
SINE Z	1 - 60	A1302Z	20.8	20.3	-2.4%
	60 - 90	A7012Z	20.5	19.68	-4.0%
	90 - 140	A1203Y	3.12	3.07	-1.6%

In the following (Fig. 6, 7, 8) is shown the comparison between the transfer function of the response of the accelerometer A1302XYZ and the transfer function of the correspondent node on the correlated model, in both in-plane (X,Y) and out of plane (Z) directions.

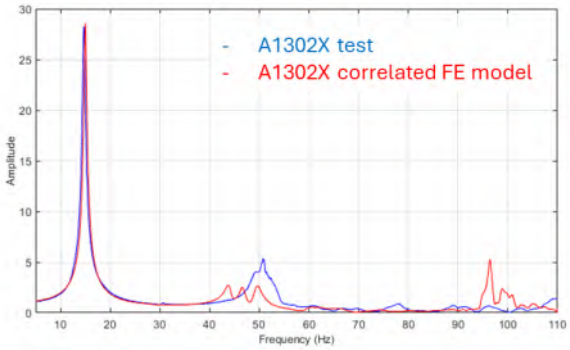


Figure 6: Sine X - test vs correlated FEM - transfer function comparison

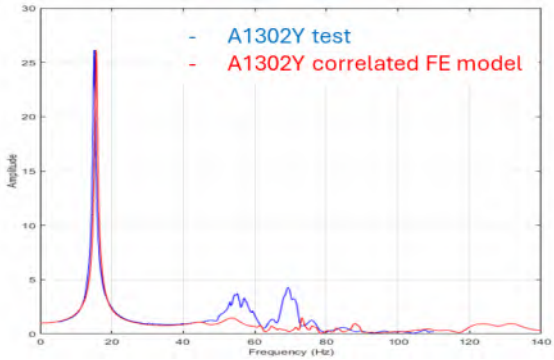


Figure 7: Sine Y - test vs correlated FEM - transfer function comparison

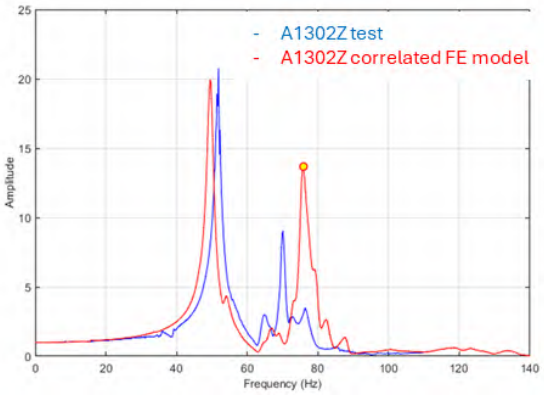


Figure 8: Sine Z - test vs correlated FEM - transfer function comparison

The model correlation results show in the in-plane directions almost a perfect agreement between the first mode of FE model and the test both in frequency and amplitude.
Instead, as already mentioned in the paragraph 3, shows a minor discrepancy between the first mode of FE model and the test both in frequency and amplitude. Nevertheless, both the differences are inside the acceptance criteria. In addition, the main longitudinal mode of the FE model is lower than the once of shown by the test. Therefore, since the main

frequency predicted from the correlated model is well above the launcher main longitudinal frequency requirement, the result is considered acceptable.

4. PAYLOAD BRACKETS LOADS EVALUATION

4.1. Correction Factor

The payload bracket loads evaluation is based on the following strategy.
The acceleration results acquired on the payload brackets during the SM sine test have been compared with the acceleration predicted on the correspondent node of S/C correlated model
From the acceleration comparison, the corrective factor (CF) between test data and model results has been defined as in equation (3)

$$CFi = A_m i / A_t i \qquad (3)$$

$A_m i$ = maximum acceleration level in the whole frequency range computed with the correlated FE model, in the node coincident with the accelerometer i.
$A_t i$ = maximum acceleration level in the whole frequency range observed during sine test in the accelerometer i.

The Corrective factors computed on all Payload brackets accelerometers have been computed for every direction of local reference frame, for all the positions (described in paragraph 2) on all the three-excitation axis.
The Payload brackets load computed from the correlated FE model are then corrected by using the following rationale:

Force Evaluation→

If the CF is >1 → No correction is applied since the model results are on the conservative side.
If the CF is <1 → The correction is applied with the following formula:

$$Fnew_i = Fmodel_i / CF_i \qquad (4)$$

$Fnew_i$ → Corrected force value in the direction i.
$Fmodel_i$ → Force value predicted by the correlated FE model in the direction I, without any correction applied. The formula is applied on each force direction. [2]

Moment Evaluation→

Since no rotation measurement are available, the moment correction was done with the following criteria:

$$Mnew_i = Mmodel_i / MinCF \qquad (5)$$

Where:

$Mnew_i$ → Corrected moment value.
$Mmodel_i$ → Predicted moment value, without any correction applied.
$MinCF$ → The minimum CF computed on the three directions of each sensor. [2]

Even if, in principle, the CF is not derived from the interface rotation responses, the proposed approach is deemed to be the best compromise. Indeed, it adds some conservativism on the interface moment evaluation on the payload bracket. It is important to mention that CF application for the moment evaluation is an engineering choice, driven by the instrumentation availability and facility limitation in channels acquirement. It is not intended to be a generic physical relation.

In addition, the above load correlation strategy is enforced by the good linear behaviour observed on the S/C. Indeed, from the low level to the qualification run the response of the accelerometers increased accordingly with the excitation levels. Therefore, the load computation by means of accelerometer responses is deemed reliable.

5. VIBRO ACOUSTIC TEST

The vibro-acoustic test was performed with the DFAN technology (Fig. 9), with the aim to predict the random environment transferred to the platform unit on the proto flight model (PFM), in order to evaluate the compatibility with the item's random qualification levels.

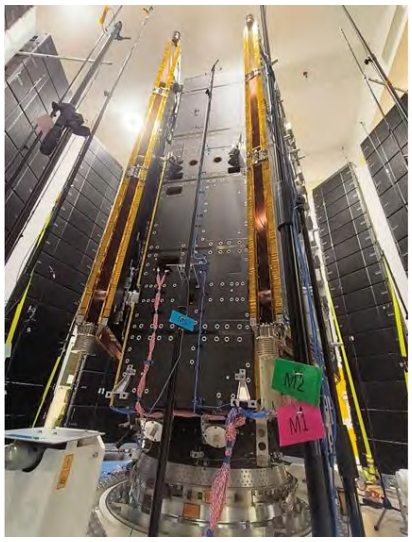


Figure 9: SM Vibro-acoustic test configuration

The post processing of vibro-acoustic test data concerns in comparing the measured acceleration PSDs with the PSDs of the random qualification profiles of the units.
It may happen that some spikes on the tests surpass the unit qualification. The evaluation of the spikes is done through the ERS (Extreme Response Spectrum).

5.1. Extreme response spectrum (ERS)

The Extreme Response Spectrum (or Maximum Response Spectrum, MRS) of a random acceleration $\ddot{x}(t)$ is defined as a curve that gives the value of the largest peak Z_{sup} of the response of a single-degree-of-freedom linear Mass-Spring-Damper system to the given vibration for a given damping factor ξ, accordingly to its natural frequency f_0.
The ERS can be computed both from time random signal and PSD signal.
This paper highlights the methodology of ERS computation directly from the PSD [4].

Under the assumption that the random vibration $\ddot{x}(t)$ is Gaussian and of zero mean, it is possible to compute the mean number per second n_a^+ of crossing a given level 'a' with positive slope:

$$n_a^+ = n_0^+ e^{-\frac{a^2}{2z_{rms}^2}} \qquad (6)$$

Where:

a: target level
n_a^+: mean number per second of positive crossing of the target value a.
n_0^+: number of positive crossings of the 0 value.
z_{rms}: root mean square of relative displacement of the Mass Spring Damper system.

The (5) can be written, over a time duration T, as follows:

$$N_a^+ = n_0^+ T e^{-\frac{a^2}{2z_{rms}^2}} \qquad (7)$$

Where:

N_a^+: is the mean number per second of positive crossing of the target value a, over duration T.

The largest level a during the time T is the one which is exceeded only one time. That lead to the following equation:

$$N_a^+ = 1 = n_0^+ T e^{-\frac{a^2}{2z_{rms}^2}} \qquad (8)$$

That allows to compute the maximum level a:

$$a = z_{rms}\sqrt{2\ln(n_0^+ T)} \qquad (9)$$

The ERS amplitude can be than computed by multiplying the maximum level a by ω^2, in order to covert displacement to acceleration.
In addition, under the engineering assumption of a one degree of freedom (DoF) system, responding at its main frequency f_0, the value n_0^+ can be substituted by f_0. Therefore, the ERS final equation can be plotted as (10), for a selected value of the amplification factor Q.

$$ERS = (2\pi f_0)^2 z_{rms}\sqrt{2\ln(f_0 T)} \qquad (10)$$

5.2. ERS Approximate expressions

This paragraph aims to share some simplified approaches to determine the ERS of the random vibration [4]. Nevertheless, those are not applied for Rose-L mission.
Considering a Single DoF linear system submitted to white noise with main frequency f_0 and amplification factor Q, the ERS can be approximated by means of the Miles equation, under the assumption of low damping a:
The simplified ERS expression at each point of the PSD (G_i) becomes:

$$R_i = k\sqrt{\frac{2}{\pi} f_{0_i} Q G_i} \qquad (11)$$

Where:
R_i = Simplified ERS expression of point i.
k = a constant value imposed to the computation.

Sometimes the k is considered = 3, in relation with the 3σ Gaussian probability approach.
K. Foster chooses k = 2.2 for the study of fatigue failure [5]. Sometimes, the value of k is even considered = 1

Even if the simplified approach is valid for a white noise excitation, it remains usable under the following conditions:
-The PSD experiences little variations between half-power points
-The natural frequency of the one DoF. system is inside the frequency boundaries of the PSD.

The error of this formulation is significant at PSD edges and in the frequency ranges where it presents great variations

5.2.1. Validity of the approximation

This paragraph reports an example that shows the precision of the ERS calculation methods.
Indeed, as reported in reference [4], the computation of the ERS of a PSD with the simplified expression (11), considering K=1 and K=3, leads to a not excellent approximation in the PSD frequency range and to a poor approximation at frequencies above the frequency domain of the PSD.
Instead, the computation of the ERS with the expression (10) leads to a spectrum larger than three times the rms value, even for small values of duration T.

This example highlights that the ERS computation

by using the rms values (Miles relation) could lead to a not sufficient approximation in the severity evaluation of a PSD.

5.3. Rose-L vibro-acoustic test post processing

This paragraph aims to show some examples on the random environment severity evaluation by means of ERS.

Indeed, in the frame of the post-processing activity of ROSE-L SM vibro-acoustic test, some dummy equipment shown higher amplification with respect to the qualification level. That means that the probability to see a seminal behavior in the frame of PFM/FM2 testing activities is not negligible.

In figure, is reported the random vibration (APSD/ERS) measured at the base of the dummy unit (A1402Z), compared with the random qualification profile (APSD and ERS).

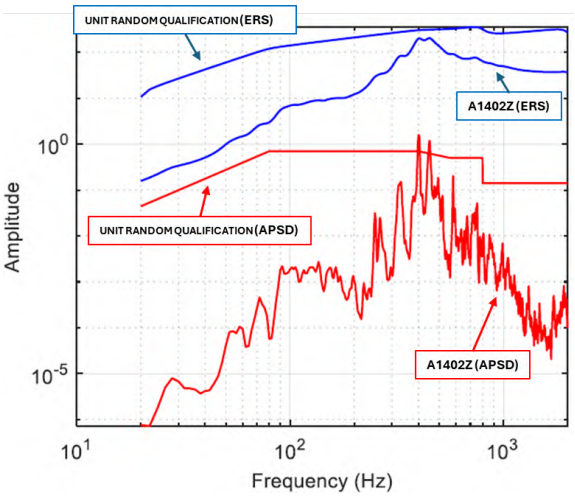


Figure 10: A1402Z - APSD and ERS - test responses vs unit random qualification

The red curves represent the comparison in terms of APSD. Instead, the blue curves represent the same comparison in terms of ERS.
Conventionally, the ERS is computed considering Q=10. Instead, the T parameter used for the qualification profile is dependent on the test duration.
Since the qualification test duration is 120 seconds [8], the duration considered for the ERS calculation is 120 seconds.
The ERS computation of both random profiles, shown that, even if the A1402Z response (APSD) surpass the qualification profile (two spikes are above the qualification profiles), the severity of the random environment induced at the base of the unit is below with respect to the environment seen by the unit during the qualification campaign.

The example shows how, the ERS is a helpful methodology to verify the compatibility of the random vibration induced by the S/C to the units against the unit qualification status.

6. CONCLUSIONS

This paper is an overview of the S/C testing, model correlation and post-processing activities.

It reports a description of the ROSE-L mission platform and design. Also, it emphasizes the methodologies applied for FE model correlation, sine test load (force and moment) computation and random environment severity evaluation, providing some detailed examples related to the mission.

In particular, the paper highlights some lesson learned, which are hereto summarized:

- Model main frequency correlation: It shows a fast methodology to improve the connection element model.
- Model amplitude correlation: It shows how the damping matrix can be modified for tuning the model responses with the real ones.
- Payload interface loads evaluation: Is shows the methodology of interface load evaluation by means of correlated model, developed in the frame Rose-L program.
- The evaluation of the severity of random vibration environment by means of ERS (Extreme Response Spectrum)

7. ACKNOWLEDGEMENTS

This work has been developed within the framework of the European Union and the European Space Agency (ESA) Copernicus programme, in the context of the ROSE-L (Radar Observing System for Europe at L-band) mission.

8. REFERENCES

1. ECSS (2013). Spacecraft Mechanical Loads Analysis Handbook, ECSS-E-HB-32-26A, ESAESTEC, February.
2. D. Cardinali (2025). ROSE-L SM Sine Test Evaluation Report, Thales Alenia Space technical report ROSE-RP-TAI-SC-0013.
3. D. Cardinali (2025). ROSE-L SM Acoustic Test Evaluation Report, Thales Alenia Space technical report ROSE-RP-TAI-SC-0014.
4. C. Lalanne (2014). Mechanical Vibration and Shock Analysis Volume 5.
5. K. FOSTER (1982), Response spectrum analysis for random vibration, Proceedings IES, Designing Electronic Equipment for Random Vibration Environments, 25–6 March 1982.
6. B. BOISSIN, A. GIRARD, J.F. IMBERT (1961), Methodology of uniaxial transient vibration test for satellites, Recent Advances in Space Structure Design–Verification Techniques, ESA–SP 1036, 35–63, October 1961.

7. A.E. HATHEWAY, C. MONTANO (1982). Analysis and test of ceramic substrates for packaging of leadless chip carriers, Proceedings IES, 49–51.
8. ECSS (2022). Space engineering testing, ECSS-E-ST-10-03C Rev.1, ESAESTEC, May.
9. Arianespace (2018). VEGA C user's manual Issue 0 revision 0, May.
9. Arianespace (2021). ARIANE 6 user's manual Issue 2 revision 0, February.

QUALIFICATION OF OXFORD SPACE SYSTEMS LARGE DEPLOYABLE OFFSET REFLECTOR

Ciarán McHale [(1)(2)], Muhammad Anees [(1)(3)], Nick Long [(1)(4)], Peter Ashworth [(1)(5)], Mario Corso [(1)(6)]

[(1)] Oxford Space Systems Ltd, Zephyr Building, Harwell Space Cluster, Harwell, OX11 0RL, United Kingdom
[(2)] Email: Ciarán.McHale@oxford.space
[(3)] Email: Muhammad.Anees@oxford.space
[(4)] Email: Nick.Long@oxford.space
[(5)] Email: Peter.Ashworth@oxford.space
[(6)] Email: Mario.Corso@oxford.space

KEYWORDS

Deployable Reflector Antenna, SAR (Synthetic Aperture Radar), mechanical qualification, deployable mechanisms, redundancy verification, surface accuracy

ABSTRACT

Oxford Space Systems has qualified a large deployable offset reflector antenna accommodated on a 300 kg-class spacecraft platform for a C-Band SAR application. Building on prior Engineering Model design and correlation activities, this paper presents the qualification-level mechanical verification campaign of critical subassemblies and the full stowed antenna. The campaign covers functional and environmental qualification of the Hold Down and Release Mechanism (HDRM) arms, strap band release mechanism, hinge and deployable arm, and the Reflector Deployment Structure (RDS), including a single-failed-actuator case to demonstrate deployment redundancy. A motorisation margin of 3 was demonstrated across all required thermal conditions for all mechanisms, and deployed surface accuracy remained within the RF loss budget throughout the campaign, with RMS deviation from the ideal paraboloid of 1.91 mm pre-test, degrading to 2.42 mm after twelve cumulative stow/deploy cycles, vibration, thermal cycling, and five months of stowage. Manufacturing and design lessons captured during the campaign including preload control methods and bond-preparation verification are discussed. The results demonstrate qualification of the mechanisms and structural architecture for flight, with the qualification methodology and lessons learnt directly applicable to future small-sat class deployable antennas for SAR and other applications.

1. INTRODUCTION

Spaceborne SAR deployments have grown exponentially over the past two decades, from 16 satellites launched between 1978 and 2006 to 109 satellites from 2022 alone, bringing the total to 200 SAR satellites in orbit by mid-2025 [1]. This growth has been driven primarily by the proliferation of small and micro-satellite platforms on rideshare launches [1]. Average spacecraft mass across the commercial sector has fallen sharply, from 3281 kg in 2003 to 248 kg in 2022, as launch costs declined and smallsat share of commercial launches rose to over 95% [2]. Within SAR specifically, average satellite mass has followed the same trajectory, contracting significantly over the past twenty years as microsatellite buses replace traditional large legacy platforms [1]. This trend is forecast to continue, with approximately 16,900 small satellites under 500 kg projected for launch between 2026 and 2035, representing roughly a third of all satellites launched globally in that period [3]. A key technology enabler for small-sat SAR is a large deployable reflector. For the deployable reflector design stowed volume, deployment reliability, deployed surface accuracy, and structural mass efficiency must be reconciled without compromising RF performance.

In line with these trends, Oxford Space Systems has qualified a large deployable offset reflector antenna for the Space Norway MicroSAR mission, accommodated on a 300 kg-class SSTL satellite platform. The antenna's design was first presented at the Engineering Model level, covering the Reflector Deployment Structure, hinge, HDRM, and cable-network architecture, along with early static and modal FEA results [4]. Subsequent work reported further Engineering Model structural testing in stowed and deployed configurations, test-analysis correlation, and lessons learnt [5]. The present paper builds on this development history, presenting the qualification-level verification of mechanical performance in both stowed and deployed configurations.

2. ANTENNA ARCHITECTURE

The architecture of the OSS offset reflector antenna is briefly described here. The reflective surface consists of a foldable Carbon Fibre Reinforced Surface (CFRS) which is held in place through a pretensioned cable network. This cable network is supported by a deployable Carbon Fibre Reinforced Polymer (CFRP) ring truss structure called the

Reflector Deployment Structure (RDS). The RDS is attached to a deployable arm and a hinge which is used to actuate the RDS to the right location and orientation once deployed in orbit. In the stowed configuration the RDS is supported by two retractable arms which constitute a Hold Down and Release Mechanism (HDRM). The two arms are connected through a CFRP shield, also referred to as “beetle wings”. A further strap band restrains the RDS in stowed configuration to avoid blooming of the RDS structure when partially deployed from the HDRM. Once the strap band is released through a pin puller mechanism, motors drive the RDS into the fully deployed offset reflector configuration. Deployed and stowed configurations are shown in Fig. 1 and Fig. 2 respectively.

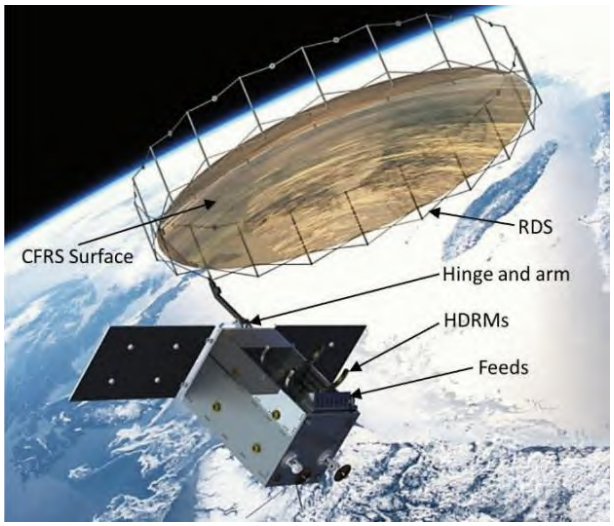


Figure 1 Offset Reflector Antenna in full deployed configuration. Credit: SSTL/Space Norway [4]

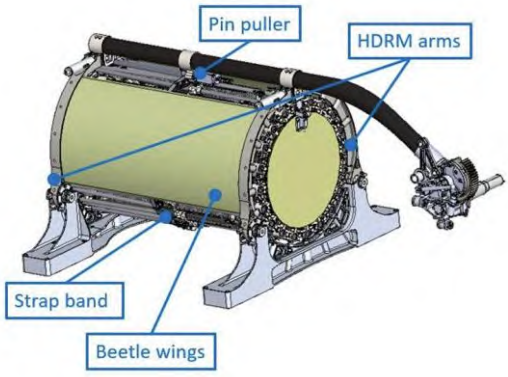


Figure 2 Offset reflector antenna in stowed configuration for launch.

Due to the large size and flexibility of the complete antenna, the qualification approach was to break down the antenna into its constituent subassemblies for functional and environmental testing, then combine them together for stowed vibration, shock and thermal cycling of the complete antenna while integrated into a Structural Qualification Model (SQM) spacecraft. After stowed testing the antenna was removed from the S/C SQM then broken down again for functional testing of the subassemblies post vibration and thermal cycling. This paper therefore discusses qualification testing of the different subassemblies that constitute the antenna: the RDS, the HDRM arms, the strap band deployment mechanism, and the deployable arm and hinge mechanism. The paper then goes on to describe the stowed antenna qualification vibration testing at S/C level. This paper discusses key mechanical qualification tests performed and is not exhaustive of the full qualification campaign of the antenna. Fig. 3 shows the overview of the testing sequence described in this paper. Note that, for brevity, results from all test instances of a given subsystem have been combined within each section, for example hinge testing performed pre-vibration, post-vibration, and post-thermal-cycling has been reported together rather than as separate sub-sections.

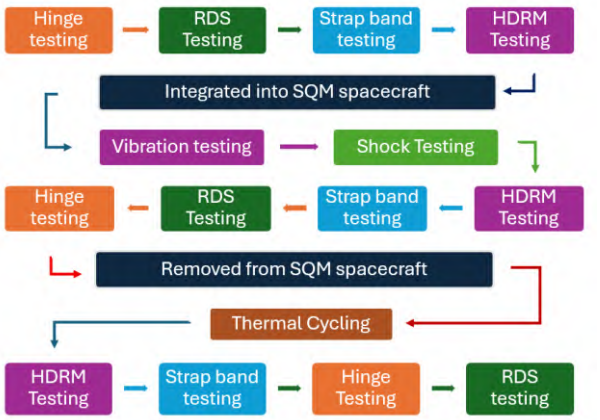


Figure 3 Qualification test campaign procedure as discussed in the paper.

3. HINGE TESTING

The objectives of this subassembly test campaign were to verify the motor performance during ambient, Worst Hot (WH) and Worst Cold (WC) temperatures pre and post Environmental Verification Testing (EVT). To demonstrate a motorisation margin of 3, hinge deployment tests were performed at 1/3 of the nominal current limit including WH and WC conditions.

The hinge test setup inside the climatic chamber is shown in Fig. 4. The assembly was orientated so that the hinge could fully rotate about the RDS support arm without obstruction. The hinge motor was connected to a power supply with set voltage and current limits of maximum current and 1/3rd of the max current. The power supply was set to record the current and voltage of actuation. A camera was setup to record the actuation of the hinge and thermocouples were attached to the hinge to monitor the temperature of the different elements of the hinge.



Figure 4 The hinge test setup inside climatic chamber

The graph in Fig. 5 shows the voltage and current variation at 1/3rd of the current limit at WH temperatures. The current initially peaks at the beginning and then reduces for the rest of the actuation, before reaching the current limit as it latches at the end of travel. The current in the middle of actuation was slightly lower than in the ambient test. Similarly tests at ambient and WC conditions showed nominal deployment and current withdrawal. The hinge motor successfully actuated to the latching point in all of the test conditions, with both the full and 1/3 current limits. The desired temperature was reached in all tests within a margin of +4°C/-0°C in the hot tests and +0°C/-4°C in cold tests. In the WC condition test at -20°C, the hinge actuated slowly with the reduced current limit, but it still latched within 540s, which is the requirement of maximum time allowable for hinge deployment. The hinge had no issues actuating in the other tests. This demonstrates that the hinge has a Margin of Safety (MoS) of at least 3 as torque margin. No degradation to the hinge assembly was observed during the testing.

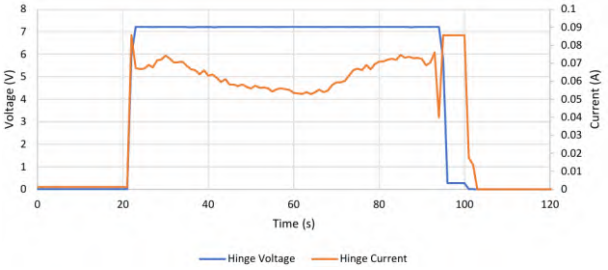


Figure 5 Functionality Test at WH temperature with 1/3 Current Limit

Hinge sub-assembly tests were repeated after the system-level vibration, shock and thermal cycling by detaching it from the RDS, and no degradation in the performance was observed. An additional initial motion functional check was carried out post vibration and thermal testing whilst the full stowed Qualified Model (QM) antenna was still integrated to the S/C. This also rehearsed planned flight model testing. The weight of the RDS and deployment arm was offloaded to minimise gravity effects. The antenna and Ground Support Equipment (GSE) were then mounted on horizontal test GSE, and the HDRM arms were manually opened. The overhead crane was positioned directly above the far end of the deployment arm. One end of the bungee cords was hooked into the overhead crane, and the other end was connected to the load cell using the lifting eye bolts. Proper offload was applied to the other end of the bungee cord after removing the slack in the bungee cord. The load cell was zeroed before applying the offload, then an offload of 9kg was applied to the end of the arm. The offload reduced as the arm deployed. Due to these limitations in the offloading setup, the motor was run only for a few seconds rather than through a full deployment; this was considered acceptable because the initial motion was identified as the most critical phase. Voltage limit of 7.21V with a current limit of 260mA was set up for the hinge motor. The resulting current profile was compared with the hinge-only run and remained within the defined limits and the current limit was not reached during the test. Fig. 6 shows the test setup used for the initial-motion hinge test along with RDS with the gravity-offset setup.

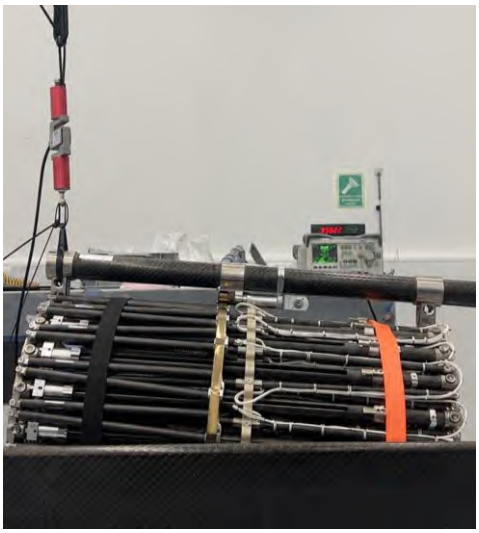


Figure 6 Test setup of hinge deployment with RDS under gravity offloading whilst integrated to the SQM S/C

4. STRAP BAND AND HDRM TESTING

This section describes the testing that was performed to qualify the functional and environmental aspects of the HDRM arms and strap band, critical for the release of the antenna prior to deployment in orbit. Reliable and repeatable pretensioning of the HDRM is key to achieve the required hold down forces and stiffness to survive the launch environment. To perform the pretensioning of the HDRM, the RDS is mounted into the HDRM assembly. Special care is needed to ensure that the cup and cones of the RDS and hinged arms are seated correctly. Two ratchet straps are used to assist in compressing the hinged arms around the RDS. Once the two hinged arms were lined up, the release bolt (release nut mechanism) was inserted into the HDRM. To

achieve the desired control and accuracy on the preload, bolt stretch measurements are used. The bolt stretch target was calculated from the structural FE model to be 0.2mm. The bolt stretch target was found to be hard to achieve in practice, however in the end the desired bolt stretch was achieved with a total tolerance of 0.02mm. The bolt stretch method for measuring preload was selected because of the perceived higher preload control accuracy, however during assembly the difficulties in measuring stretch ended up negating any benefits anticipated. Lesson learnt: Alternative preload measurement methods should be traded considering downstream implementation and trialled & reported on during earlier engineering development model phases to conclude on the most suitable preload measurement approach prior to qualification models.

After the hinged arms were preloaded, the strap band was attached to the RDS. Equivalent strain required to obtain desired preload was 530 με which was derived from previous EM phase testing. A strain gauge was attached to each of the strap bands while they were loosely attached to the RDS. The strain gauge was zeroed while the band was loose so that the change in strain when tightening the band can be measured during the test.

During the test, desired preload in the strap band could not be achieved. Only approximately 300με was achieved instead of 530με, equating to a tension of 113N. The difference was due to the test setup. In EM test campaign the preloading was done without the HDRM arms, while in QM testing the HDRM arms were assisting to compress the blooming force and hence resulted in lesser strains achieved. The preload was accepted as full stowage of the antenna was achieved and later no issues during the vibration test or deployment were observed. Lesson learnt: Consistent measuring method should be used during different stages of testing. The test plans for the Flight Model (FM) were updated for preload measurement after placing the RDS in the HDRM arms and preload applied to them.

After preloading the hinged arms and strap band, their functionality was tested. The test assembly was mounted in vertical position to eliminate any gravity related effects on the HDRM arms as shown in Fig. 7.

A high-speed camera was used to capture the retraction of the release bolt. HDRM arms were successfully deployed. Following successful HDRM arm deployment, the hinge motor was powered briefly to confirm the RDS was fully clear of the HDRM assembly. Full RDS deployment was not performed at this stage, as the antenna cannot be fully deployed under gravity in this configuration. Full RDS deployment was carried out later, following separation from the HDRMs, and is discussed in the subsequent RDS testing section. Fig. 8 shows the voltage and current drawn by the hinge motor. In this vertical test setup, the motor initially does not require much torque to move the RDS, however as it actuates further, more torque is required, increasing the required current. After a few seconds the motor was turned off as the RDS was free of the HDRM assembly

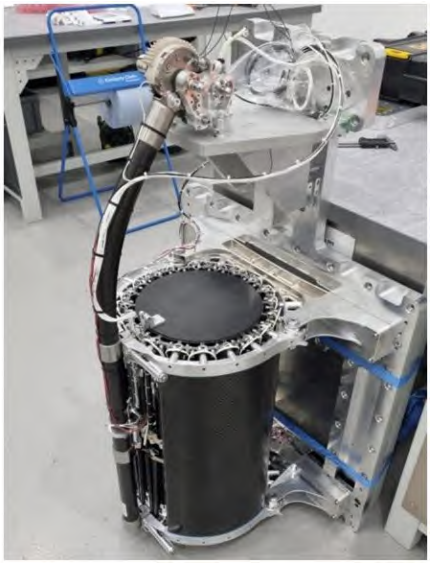


Figure 7 Vertical Test Setup for HDRM Arms Deployment

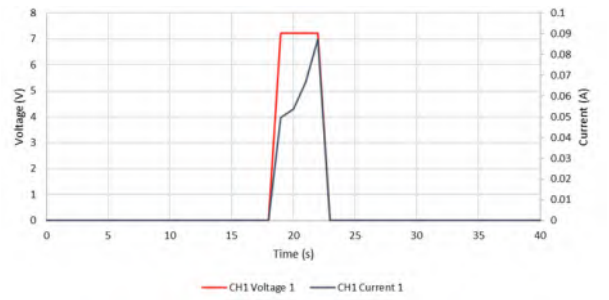


Figure 8 Hinge Motor Current and Voltage

After HDRM Arm and hinge tests, the antenna was set up for the strap band HDRM deployment test. Two pull straps were loosely wrapped around the RDS to prevent it from deploying fully, while not affecting the deployment of the Strap Band HDRM. Bubble wrap was attached to the inside of the HDRM Arms to protect them from the deploying strap band. This is not an issue in flight as the strap band is not normally fired until the RDS Support Arm is fully actuated. Again, high speed camera was used to capture movement of the pin-puller. The strap band deployed successfully when the actuator was supplied with the required voltage and current. Deployment occurred too quickly for the power supplies to record instantaneous current. Lesson learnt: Use data acquisition with sufficient sampling rate to capture current during rapid deployments in future testing.

Strap band deployment was also carried out at WC. Measured strap tension was 334 με above the nominal 530 με, attributed to strap-band shrinkage at low temperature. Deployment was successful, confirming release capability at strains well above nominal. Deployment in WH condition was not performed. In WH the strap band expands and results in reducing tension below nominal. Since deployment at the higher WC tension was already demonstrated, and release becomes easier as tension decreases, WH is inherently bounded by the WC case and does not require separate verification.

After firing the HDRM actuators, the test article is inspected to check the successful deployment, i.e. there are no loose or missing parts, no damage to test article, no marks on actuator rods etc. The inspection showed that even with the bubble wrap, the strap band HDRM deployment caused minor damage to the inside of the beetle wings, again not an issue for flight due to deployed configuration of the arm. This resulted in action to cover shields with higher energy absorbing material for any future deployment testing.

5. VIBRATION AND SHOCK TESTING

The objective of this test is to qualify the full antenna assembly under vibration at the levels as per the specifications defined by spacecraft provider for the SQM sine, random vibration and shock loading. The success criteria for the test is that there is less than 10% in frequency shift, and less than 20% amplitude shift for modes with an effective mass greater than 10% during the vibration testing and the antenna maintains its structural integrity after the test and deploys successfully. High-level sine, quasi-static and random level testing were performed, and low-level resonance search was performed before and after each test to check the antenna's integrity. Six accelerometers were attached to the antenna as shown in Fig. 9. Three accelerometers were attached to the active members, one was on the hinge housing, one on the deployment arm and one on the HDRM arm. The accelerometer on the antenna interface was positioned between the two HDRM base brackets. Fig. 10 shows the complete antenna mounted into spacecraft for vibration testing.

Fig. 11 and Fig. 12 shows the Low-Level Resonance Search (LLRS) response, at the key sensor locations pre and post the entire vibration test campaigns. The response is along the X-axis which is the worst axis in terms of loading at the antenna. From the comparison it can be observed that there has been no major shift in peak and amplitude throughout the high-level sine, quasi-static and random vibration levels. Responses in the other axes similarly remained within the defined success criteria. No further correlation was done at QM level as the FE model had been correlated at the EM stage.

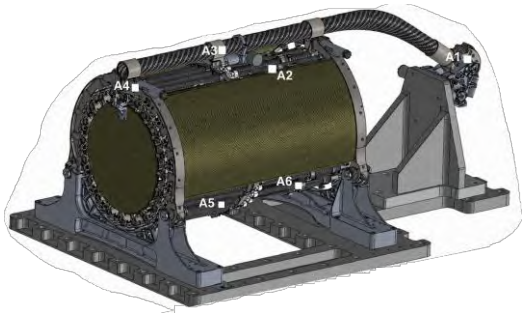


Figure 9 Accelerometer locations in stowed configuration during vibration testing

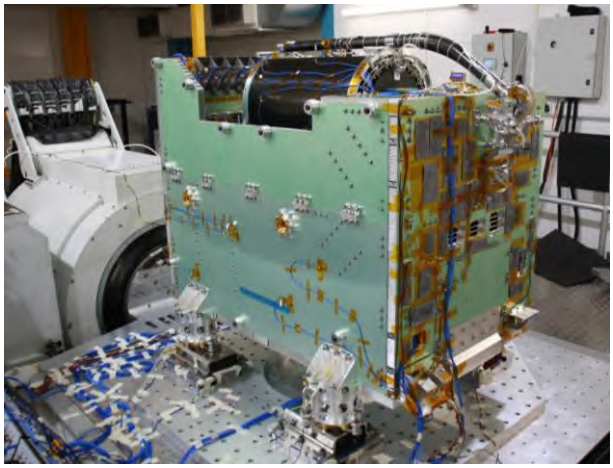


Figure 10 complete antenna mounted into spacecraft for vibration testing.

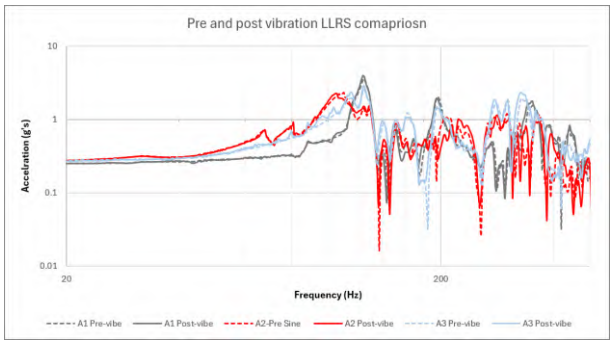


Figure 11 Pre and post LLRS comparison on accelerometers # 1, 2 and 3

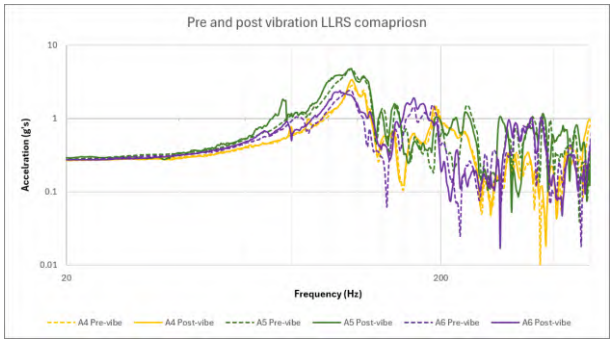


Figure 12 Pre and post LLRS comparison on accelerometers # 4, 5 and 6

After the vibration testing, antenna was subjected to deployment shock loading coming from the spacecraft solar panels and separation system. The antenna survived the shock loading with no degrading effects on the subsequent deployments.

The HDRM release of the arms and the strap band test was also performed after the vibration and shock testing, Energy absorbing foam was used on the inside of the HDRM shields, to prevent possible damage from the Strap Band HDRM firing as per the lesson learnt from the previous deployment in similar configuration. All the post-test releases and deployments were successful.

6. THERMAL CYCLING

Thermal cycling was carried out in stowed configuration in climatic chamber after attaching to a fixture. At this point, the HDRM actuators had already been fired. Therefore, dummy actuators were used to simulate the HDRMs. Prior to the closing of the HDRM arms, the release bolt stretch was measured. The HDRMs were preloaded by stretching the release bolts by 0.2mm. Five thermocouples were be placed on the antenna to monitor the temperature during the test. One on the hinge, one on the active members, one on the deployment arm, one on the top of the far HDRM arm and one at the base of the far HDRM arm. Fig. 13 shows the antenna when placed inside the climatic chamber and Fig. 14 shows the temperatures limits achieved by all the sensors during hot and cold cycles.

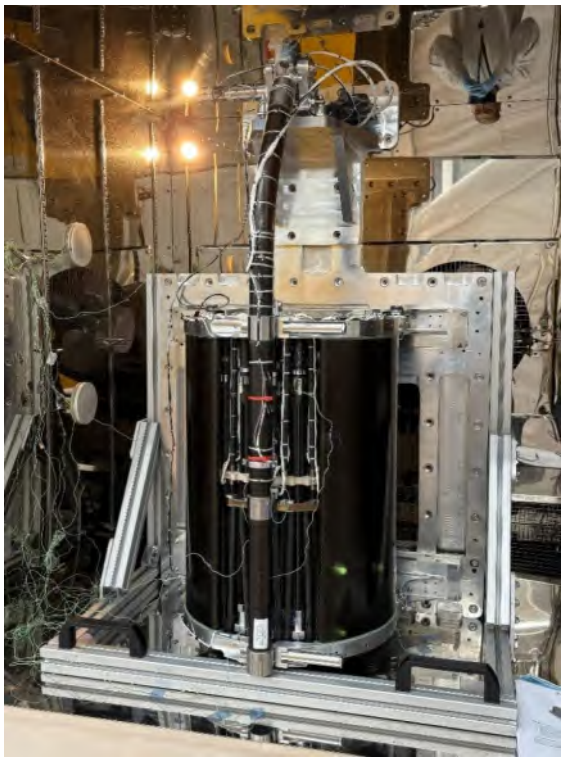


Figure 13 QM Antenna inside of Climatic Chamber

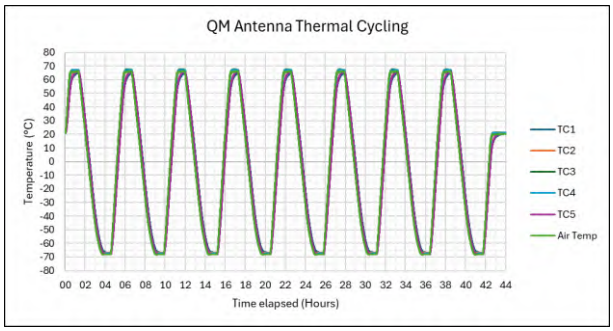


Figure 14 Thermocouple Data for QM Thermal Cycling

7. REFLECTOR DEPLOYMENT STRUCTURE (RDS) TESTING

The objectives of this subsystem test campaign were to verify that

- The RDS can be deployed in ambient, hot and cold conditions.
- Verify that the RDS can be deployed with one failing actuator.
- The manufacturing accuracy respects the surface accuracy budget.
- Verify that after subjecting to mechanical and thermal environmental loading and consecutive deployments in temperature the deformation of the reflector surface is still within specification.

This test campaign was performed with the QM Reflector Dish Test Article as shown in Fig. 15. The subsystem is intended to be representative in fit, form and function of the FM build, including the harness which will be routed and dressed as for flight.

Ambient deployment was carried out to characterise the subassembly before testing it at the extreme operating conditions and to check the motorisation margin. Test Success Criteria was that each active member needs to travel until it latches without interruptions or failure and with all the v-folds latching. Also to demonstrate the MoS of 3 as motorisation margin, the same condition needs to be verified when the current limit is set 1/3rd of full current limit.



Figure 15 QM Reflector Dish Ambient Deployment Setup

This test was conducted twice in each of ambient, hot and cold conditions, once with the full current limit and once at 1/3rd of the current limit. Hot and cold deployment tests were carried out in a large climatic chamber to achieve the full deployed configuration. The first active member was fixed to the GSE and rest were allowed to move freely on the floor by use ball bearing attachments. Four thermocouples were installed at different locations to ensure that desired temperature is achieved consistently across the antenna. The required temperature was achieved on all thermocouples in WC and WH cases as shown in Fig. 16 and Fig. 17 respectively. Fig. 18 shows the test setup for RDS deployment inside the climatic chamber prior to and post deployment.

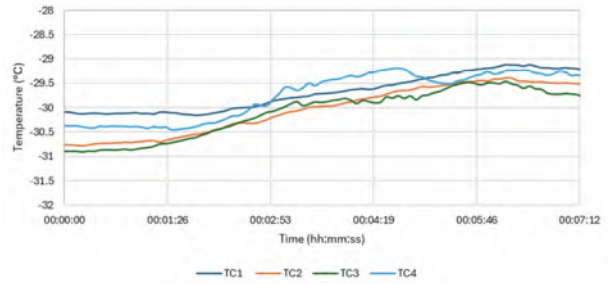


Figure 16 Thermocouple temperatures for cold deployment

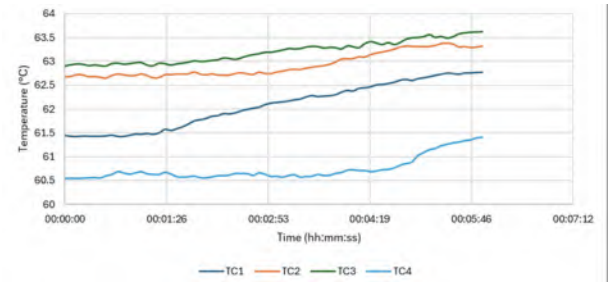


Figure 17 Thermocouple temperatures in hot deployment

All these tests were successful, and all the motors latched into place at the end of deployment and all V-folds deployed, tensioning the cable network and membrane surface. The deployment at WC conditions at 1/3rd of the current limit was slower as compared to other temperatures as the maximum current limit was hit, however still all the test objectives were met.

An RDS Deployment test with one non-operating actuator was carried out to ensure the built-in redundancy of the Reflector Dish subsystem, by having one of the 20 motors non-operating. The reflector dish assembly is designed to continue in deployment in the event of one failed motor. Test success criteria was that each powered active member needs to latch correctly at the end of travel and the “failed” active member stops within 10mm of the latching point. To replicate the failure mechanism, one of the actuators was not powered.

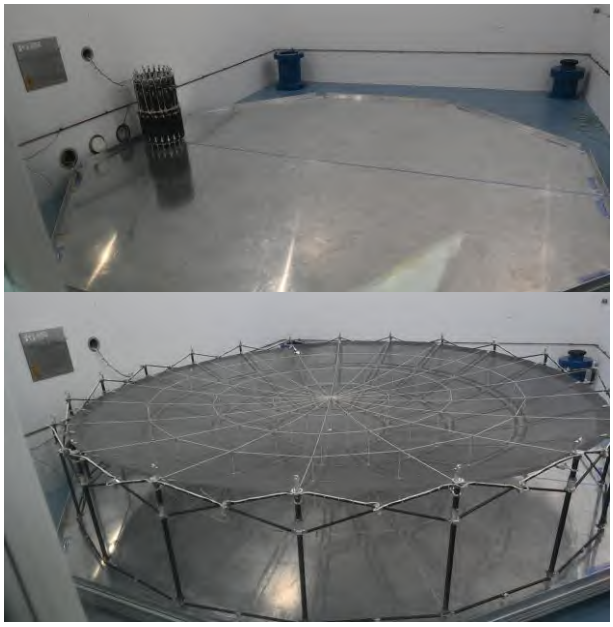


Figure 18 Test setup of RDS deployment inside climatic chamber pre and post deployment

The test was successful and the ‘failed actuator’ was found to be within 9mm of its latched position. One observation was that the motors close to the ‘failed’ actuator drew more than nominal current at ambient conditions as more torque was required to deploy the reflector, however this current was still within the 1/3rd of the maximum current limit, hence demonstrating sufficient margin and redundancy in the design.

To measure the manufacturing accuracy of the as-built reflector, laser scanning was done to characterise the reflective surface accuracy and provide justification for the surface accuracy assessment and loss budget. The reflector dish was deployed inside of the Gravity Offset jig and hung on springs. The setup is shown in Fig. 19.

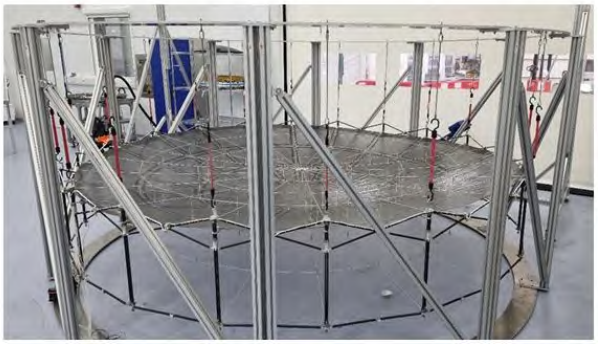


Figure 19 Reflective Dish Surface in deployed configuration in gravity offset jig.

A laser tracker (AT960) was used for measuring the surface accuracy of the reflective membrane, with either a medium range or a long-range scanner head. The long-range scanner can quickly measure the surface of the reflective membrane, which was

useful when making tension adjustments in the cable network, however it has some losses in accuracy and detail. The medium-range scanner is much more accurate and has an accuracy of 0.001mm, however scanning takes much longer, and the scanner needs to be much closer to the surface which makes it tedious due to the presence of the cable network. This was used to get the final scan of the reflective membrane surface. Great care was taken not to touch the GSE or the reflector dish during the scans as this would create a shift in the scan clouds. Fig. 20 shows the reflective surface of the antenna using the medium-range scanner after no further adjustments. The overall Root Mean Square (RMS) deviation of the measured surface as compared to ideal paraboloid surface was found to be 1.91mm.

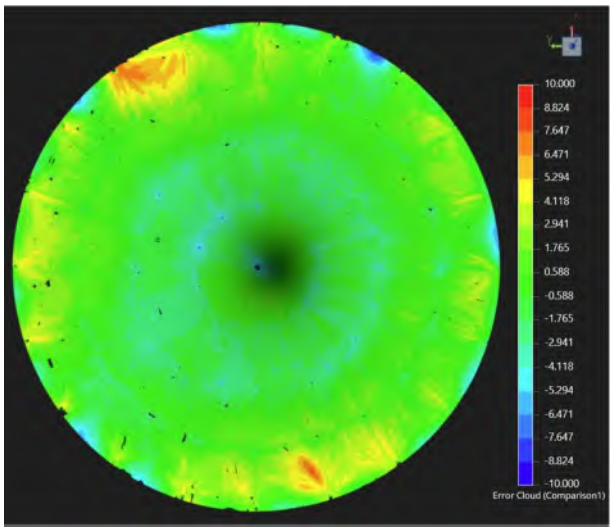


Figure 20 Pre-Test Medium Range Scan (RMS = 1.91 mm)

During one stowage cycle of the antenna, it was discovered that one of V-fold bonds had failed and one CFRP tube was cracked. Upon investigation, it was found that the CFRP tubes were not being abraded properly prior to bonding with end attachments. Then in one of the V-fold deployments, the bond failed and the tube was damaged. To prevent this issue from occurring again, the manufacturing and assembly procedures were updated to include proper abrasion and surface roughness checks of a sample of the tubes to ensure the abrading step is done properly.

During the thermal deployment testing, it was discovered that the staking had failed on the membrane connector shaft, allowing it to rotate, distorting the shape of the reflector. The staking was on a single M2 bolt on the connector shaft, which did not have enough preload to resist the forces of the manual stow of the antenna. The connector shaft was redesigned to have a key in the design to prevent rotation, rather than relying just on the bolt preload. Future recommendation: do not solely rely on bolt preload to prevent rotation when using only a single bolt.

The post EVT test campaign scan showed some degradation and the RMS increased from 1.91 to 2.42mm. This degradation captured the effect from 12 stowed and deployed cycles, including 4 deployments in each of ambient, hot and cold conditions. The antenna had also been subjected to vibration and thermal cycling in stowed configuration, and a total stowed storage time of 5 months. This value was consistent with the allowable surface accuracy error requirements as per the RF loss budget for C-Band SAR operation.

8. CONCLUSION

The successful qualification campaign for the OSS offset reflector has been presented covering the approach and highlights of critical subsystem level tests and full stowed antenna level testing, including lessons learned.

Hinge and deployable arm motorisation margin was demonstrated across all thermal conditions, with successful latching in all cases. HDRM and strap band testing was successful with preload control issues accepted based on successful stowage and no downstream issues.

Full stowed antenna Vibration and thermal cycling testing showed no significant frequency or amplitude shift pre- to post-test, confirming structural integrity, with successful releases and deployments post EVT.

Full RDS deployment succeeded across all thermal conditions, and single-failed-actuator testing confirmed built-in redundancy. Surface accuracy remained within the RF loss budget throughout the campaign, despite some degradation following repeated stow/deploy cycling, thermal cycling and extended stowage.

The campaign demonstrates qualification of the mechanisms and structural architecture for flight, with methodology and lessons learnt applicable to future small-sat class deployable SAR antennas.

9. REFERENCES

1. D'Errico, M. (2025). Evolution of Spaceborne SAR Missions in Earth Orbit. *Remote Sens.* 17(22), 3773.
2. Marcucci, E., Gatta, V., Ciucci, C. & Cucina, D. (2026). When Launch Costs Fall, Do Satellites Shrink and Constellations Grow? The Role of SpaceX in the SmallSat Revolution. *Acta Astronaut.*
3. Novaspace (2026). Prospects for the Small Satellite Market, 11th ed., Novaspace, Paris, France.
4. Skrzyńska, A., Corso, M., McGlashan, N., Brear, S., Hamer, S. & Fraux, V. (2023). Mechanical

Design and Technology Demonstration of an Offset Reflector Antenna. In Proc. *20th European Space Mechanisms and Tribology Symposium (ESMATS 2023),* ESMATS, Toulouse, France.
5. Anees, M., McHale, C., Corso, M., Ashworth, P. & Hamer, S. (2024). Development of a Large Deployable Offset Antenna Through Mechanical Analysis, Testing and Correlation. In Proc. *European Conference on Spacecraft Structures, Materials and Environmental Testing (ECSSMET 2024),* ESA/ESTEC, Noordwijk, The Netherlands.

STRUCTURAL ARCHITECTURE AND MECHANICAL DESIGN OPTIMIZATION OF THE HAWK PLUS MODULAR PLATFORM

Corinna Cerini [(1)], Marco Giolo [(1)], Domenico Prestanicola [(1)], Mattia Benericetti [(1)]

[(1)] Argotec, Via Luigi Borgo 8, 10099 San Mauro Torinese, Turin (Italy)
E-mail: corinna.cerini@argotecgroup.com

KEYWORDS

Small Satellite; Platform Standardization; Design for manufacturing; High-cadence production; Modularity; Industrialization

ABSTRACT

The increasing demand for small satellite constellations is driving a shift from mission-specific structural designs toward standardized, production-oriented platforms. This paper presents the mechanical architecture of HAWK PLUS, a multi-mission microsatellite platform developed by Argotec to combine modularity, structural efficiency, and industrial scalability.
The platform adopts a bay-level modular architecture in which the primary structure is subdivided into self-contained functional modules connected through standardized mechanical interfaces. Particular focus is placed on the design of the inter-bay interfaces, developed to preserve load path continuity and alignment accuracy while enabling assembly-based production. The paper discusses the structural trade-off between monolithic and modular concepts, highlighting the application of Design for Manufacturing and Assembly (DFMA) principles to reduce part count and simplify production.
The manufacturing and verification strategy of the Structural Thermal Model (STM) is also presented, including impact and environmental testing used to validate the structural concept at both platform and payload-interface level. Finally, the paper discusses the management of mission-specific structural deltas within a standardized platform core.

1. INTRODUCTION

1.1. Background and Motivation

The classical spacecraft development lifecycle, as defined by the NASA Systems Engineering Handbook [1] and ECSS standards [2], follows a sequential process of requirements definition, design, manufacturing, integration, verification, and operation. While this approach ensures high reliability and mission-specific adaptability, it is poorly suited to the emerging New Space paradigm, where commercial constellations require shorter development cycles, recurring production, and reduced Non-Recurring Engineering (NRE).

These constraints are driving a shift toward standardized and production-oriented platform architectures. In this context, modularity has emerged as a key enabler for scalability and recurring manufacturing, while introducing challenges related to structural efficiency, load path continuity, and interface complexity.
Within this framework, HAWK PLUS platform builds on Argotec's heritage in small satellite missions [3,4,5] progressively evolving from mission-specific spacecraft designs toward a standardized modular platform architecture. Applications range from optical and Synthetic Aperture Radar (SAR) Earth Observation (EO) to 5G satcom, space-based Intelligence, Surveillance, and Reconnaissance (ISR), distributed edge computing, and CubeSat dispenser missions. The platform, with a launch wet mass in the 100–200 kg range (including payload), is designed for series production at Argotec's SpacePark facility, where streamlined manufacturing and assembly processes embody the industrialization model required to meet the demands of next-generation satellite production [6].

1.2. Structural Modularity Challenges

The adoption of a bay-level modular architecture requires the primary structure to satisfy two contrasting objectives. On one hand, the structure must provide the stiffness, strength, and dimensional stability required to withstand launch environments. On the other, it must allow independent manufacturing, integration, and replacement of functional modules without compromising the structural integrity of the spacecraft.

Achieving this balance presents major engineering challenges, particularly in mitigating structural mass penalties and preventing a proliferation of Part Numbers (PNs). Standardized modular joints naturally introduce local mass overhead compared to tailored, monolithic structures; furthermore, maintaining platform flexibility without over-complicating the supply chain requires an aggressive strategy of component commonality.

These objectives are reconciled through the definition of standardized mechanical interfaces that ensure repeatable assembly, controlled load transfer, and accurate positioning of adjacent

modules. The interface design thus becomes the cornerstone of the structural architecture—directly influencing global dynamic behavior, manufacturing repeatability, and the ability to accommodate mission-specific configurations while preserving an optimized, low-complexity platform core.

1.3. Scope of the Paper

This paper presents the structural architecture and mechanical design approach adopted for HAWK PLUS platform, with particular focus on the trade-off between structural performance, modularity, and manufacturability.
The paper first describes the deck-and-bay structural architecture and the mechanical interface philosophy adopted to enable standardized and repeatable configurations. The manufacturing and verification approach is then presented through the Structural Thermal Model (STM) test campaign, including modal, vibration, and thermal testing.
The paper also discusses how manufacturing and verification feedback was incorporated into the structural design, leading to targeted design optimizations. Finally, the approach adopted to manage mission-specific structural modifications is presented, highlighting how configuration-specific requirements are progressively incorporated into a common and evolving platform baseline.

2. MECHANICAL ARCHITECTURE OF HAWK PLUS

2.1. Design Drivers and Structural Requirements

The mechanical design of HAWK PLUS has been developed to support high-cadence, cost-effective microsatellite production while preserving structural performances, mission adaptability and minimizing non-recurring engineering. Key structural drivers include:

- **Standardization** end-to-end: establish common mechanical, electrical, and data interfaces, with selected components and controlled Bill of Materials (BOM), to reduce variants, simplify integration, and accelerate configuration qualification.
- **Modularity** and **functional segregation**: implement function-specific modules that are pre-integrable and testable in isolation, enabling a plug-and-play architecture and parallel Assembly, Integration and Verification (AIV) workflows to increase throughput and compress the integration critical path, while maintaining deterministic structural interfaces between functional modules.
- **Scalability** and **Multi-Mission Compatibility**: Define a flexible baseline architecture designed to easily adapt to diverse operational scenarios, accommodating a wide spectrum of payload configurations and ensuring broad compatibility across multiple launch vehicles.
- **In-House Manufacturing Optimization:** Design and optimize structural components specifically tailored for Argotec's internal manufacturing capabilities and equipment, ensuring direct control over fabrication quality, reducing lead times, and maximizing production efficiency.
- **DFMA** and PNs reduction: minimize part diversity and geometry complexity to support repeatable assembly processes, lower production risk, and stabilize cycle times across series builds.
- Design for **testability**: architect modules and interfaces that are observable and verifiable during the platform AIV process.
- **Model-driven verification**: maintain a coherent set of physical and software models to validate the platform early, reduce the risk of interfaces and environments, and validate the flow AIV.

These requirements define the basis for a modular structural concept in which performance and industrialization constraints are treated as coupled design drivers.

2.2. Deck-and-Bay Structural Architecture

The HAWK PLUS platform adopts a deck-and-bay structural architecture in which the spacecraft primary structure is functionally partitioned into three decks: payload, avionics, and propulsion. Each deck represents a distinct structural partition with dedicated load paths and interfaces, enabling independent integration and testing prior to system-level assembly. This architecture is a direct consequence of the platform's DFM-oriented design. Each deck can be manufactured, assembled, and verified independently before final spacecraft integration, enabling parallel production and AIV activities.

- **Payload Deck**: The platform provides standardized mechanical, electrical, and data interfaces for a wide range of payloads. The top payload envelope supports dimensions up to 540 × 540 × 300 mm, referenced to the baseline Falcon 9 launch vehicle with a RPUG half-plate configuration. Payloads up to 340 × 340 × 360 mm can be accommodated within the internal Core envelope, depending on the Propulsion System (PS) tank configuration. For instruments mounted on the top plate, the baseline payload mass is up to 30 kg; however, both higher masses and expanded envelope dimensions for top-plate payloads can be evaluated on a case-by-case basis.
- **Avionic Deck**: Accommodates the core satellite bus functions. This architecture

enables scalability in both functionality and performance while preserving a common mechanical framework.

- **Propulsion Deck**: Accommodates the propulsion subsystem and the primary attitude actuators while providing the mechanical interface with the LV through the standard 15-inch separation ring. Different propulsion configurations can be integrated without modifying the structural architecture of the upper decks.

The HAWK PLUS architecture therefore combines two levels of modularity: **deck-level functional partitioning** and **bay-level subsystem modularity**. The former enables independent integration of major spacecraft functions, while the latter provides configuration flexibility within a common structural framework.
From a structural perspective, the deck architecture ensures that the primary launch loads are transferred through well-defined and repeatable load paths while preserving the modularity required for independent manufacturing and integration.

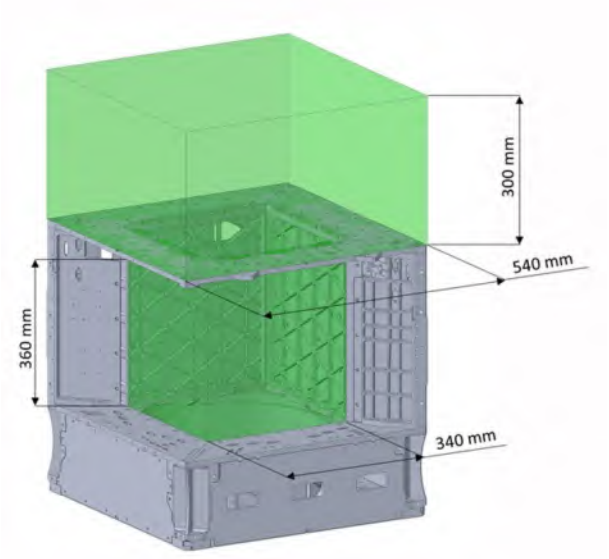


Figure 2-1 Mission-specific available envelope

Mission diversity in terms of payload characteristics, pointing requirements, communication capability, and available power is accommodated through a modular bay architecture within the Avionic Deck. Each bay constitutes a self-contained structural module with standardized mechanical, electrical, and data interfaces, allowing independent manufacturing, assembly, inspection, and acceptance testing prior to deck integration. The common interface philosophy enables different subsystem configurations to be accommodated without modifications to the surrounding structure.

- **Avionics Bay**: Accommodates the OBC and telecom suite.
- **AOCS Bay**: Accommodates the ADCS electronics, GNSS receiver and star trackers.
- **EPS Bay**: Accommodates the electrical power subsystem through three standardized configurations based on mission power requirements. Scalability is achieved using Argotec ZEUS PCDUs and ELEKTRA battery modules while preserving identical external mechanical interfaces.

Across all bays, standardized bracketry, connector layouts, and predefined routing paths ensure repeatable assembly, simplified visual inspection, and consistent integration procedures. The connector arrangement maintains accessibility throughout the assembly process, enabling bay-level acceptance testing prior to deck integration while preserving access for subsequent system-level verification.

2.3. Structural Load Paths and Interface Philosophy

The HAWK PLUS structural architecture is based on a decentralized primary load path strategy that eliminates the need for a traditional load-bearing central thrust tube. Instead, each bay operates as an autonomous, self-supporting structural module, with the spacecraft's primary structural loop and global stiffness closed directly through standardized deck-to-deck and inter-bay interfaces.

This approach provides a clear, predictable load distribution from the launch vehicle adapter straight to the payload interface. By maintaining a modular primary load path without a central core, the mechanical loads transmitted to the payload can be uniquely characterized and evaluated. This enables rapid structural and mission assessments to efficiently verify compatibility across a wide range of payload configurations and mission profiles, while preserving full manufacturing and integration independence for each individual bay.

3. STM MANUFACTURING AND VERIFICATION

3.1. Verification Approach

To support recurring production across multiple missions, the verification strategy is designed to be applicable at platform level rather than mission-specific. Structural load paths, thermal behaviour, electrical/data interfaces, and flight software are validated early using representative models that replicate flight ICDs and environmental envelopes. This approach enables reuse of analyses, test procedures, and acceptance criteria across builds, limiting mission-specific effort to well-defined configuration deltas.
To operationalize this methodology, the verification plan is based on three complementary models:

- a STM, correlated with the finite element model, used to anchor mechanical and

thermal predictions and to define representative environmental test conditions;
- a 3D-printed harness mock-up used to validate routing paths, cable lengths, bend radii, connector accessibility, and geometric fit against the CAD definition prior to hardware integration;
- a system RackSat reproducing the platform electrical and data architecture and integrating the relevant avionics and flight software, providing a representative environment for end-to-end functional and interface validation, early system bring-up, and regression testing prior to spacecraft integration.

3.2. STM Configuration

The STM reproduces the flight-representative primary and secondary structure of the HAWK PLUS platform. The avionic units are replaced by dedicated mass dummies designed to replicate the mass properties, center of gravity, envelope, and mechanical interfaces of the corresponding flight hardware.

In detail:

- Mass dummies represent all platform subsystems, including a modular propulsion dummy to cover different configuration scenarios and a modular payload dummy designed to reproduce representative payload mass properties and mechanical interfaces. The payload dummy enables the assessment of the structural dynamic response under different payload mass configurations while covering the relevant payload envelopes.
- The primary and secondary structural assemblies are identical to those of the Flight Model, including materials, manufacturing processes, fastening philosophy, and secondary retention methods.
- All load-carrying interfaces between decks, bays, payload, and the launcher adapter are fully representative of the flight configuration, ensuring representative load transfer and boundary conditions during the test campaign.
- The STM configuration was defined to support representative combinations of platform subsystems and payloads. Dedicated modular dummies can be adapted to reproduce the relevant mass properties and mechanical interfaces of different PS and PL configuration.

The resulting STM, as assembled prior to the test campaign, is shown in Figure 3-1.

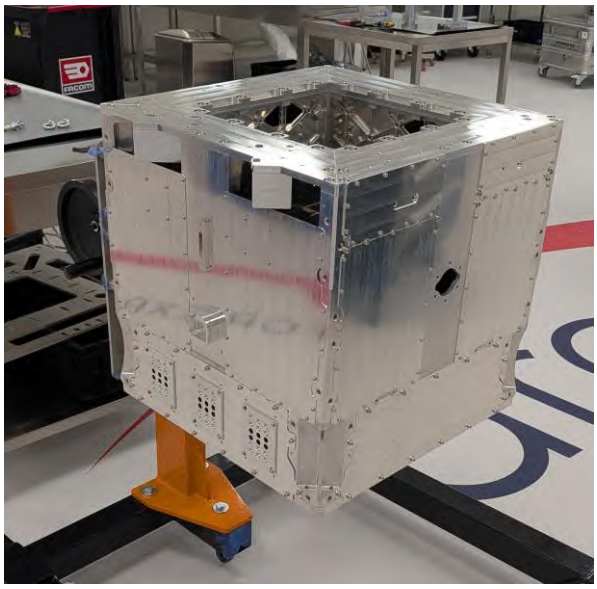


Figure 3-1: STM assembled in the cleanroom at Argotec's SpacePark facility.

3.3. STM Testing

The STM test campaign was structured to characterize and verify the mechanical and thermal behavior of the platform while simultaneously supporting model correlation activities. The comprehensive test flow encompassed physical property measurements, impact testing for Experimental Modal Analysis (EMA), vibration testing, and Thermal VACuum (TVAC) testing. The whole test campaign was performed at the Argotec facility.

The impact testing was performed to identify the structural modal parameters and provide experimental data for correlation of the Finite Element (FE) model. The test campaign also provided transfer functions and Shock Response Spectra (SRS) between the separation system interface and selected locations on the Item Under Test (IUT), considering both free-free and fixed boundary conditions.

Vibration testing was performed an IMV 65 kN electrodynamic shaker. The campaign included Random Vibration, Sine Load, and Static Load tests performed at the qualification levels specified by the Falcon 9 RPUG [7], which serves as the baseline for the platform requirements.

Resonance surveys were performed before and after each test to monitor changes in the dynamic behaviour and verify the predefined acceptance criteria. The experimental setup comprised 19 triaxial accelerometers for structural response measurements and 2 monoaxial accelerometers for vibration control (Figure 3-2).



Figure 3-2: HAWK PLUS STM mounted for vibration testing in the SpacePark cleanroom facility at Argotec.

The STM subsequently underwent a TVAC test campaign to support correlation of the Thermal Mathematical Model (TMM). Aluminum dummy masses coupled with resistors were used to reproduce representative subsystem dissipations, while 51 type T thermocouples were placed in key locations of the platform to monitor temperature variations, as shown in Figure 3-3. Both cold- and hot- case conditions were tested by varying the power dissipated by the dummy resistors.

The resulting test data provide a reference for structural and thermal model correlation and support the assessment of the platform across the defined configuration space. This approach reflects the broader industrialization strategy adopted for HAWK PLUS, in which both the product and its verification process are conceived to support recurring missions while limiting configuration-specific activities.

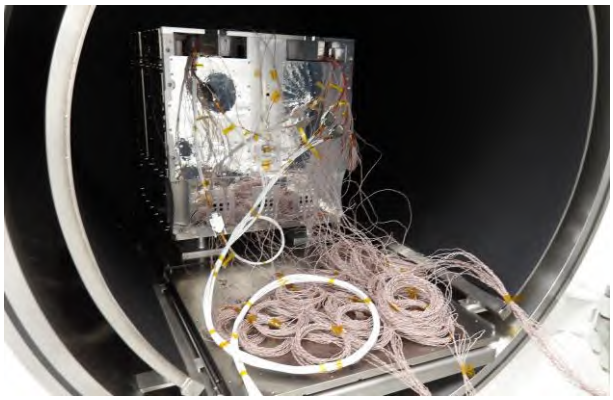


Figure 3-3: HAWK PLUS STM equipped for TVAC testing in the SpacePark cleanroom facility at Argotec.

3.4. Structural Design Optimization

The manufacturing and verification campaign performed on the STM generated valuable feedback extending beyond the structural verification. The practical experience gained during machining, assembly, and testing enabled the identification of design improvements aimed at increasing manufacturability, simplifying integration, and improving the structural performance of the platform. These modifications were implemented in the flight configuration, demonstrating the iterative design-to-manufacturing approach adopted during the industrialization of HAWK PLUS.

Optimization activities were carried out across several primary and secondary structural elements to streamline manufacturing processes while enhancing structural stiffness. Among these improvements, the most notable modification was applied to the Propulsion Deck central core. The initial cylindrical geometry was redesigned using the SOL 200 topology optimization of Simcenter Nastran, resulting in an octagonal cross-section that better distributes structural material along the principal load paths. Besides increasing the overall stiffness of the structure, the new geometry improves the accommodation of propulsion components and other internal equipment by creating additional usable volume and more regular installation surfaces. Furthermore, it significantly simplifies machining operations, shortening lead times and ensuring tighter manufacturing tolerances.

Another notable modification targeted the secondary structure supporting the solar array attachment interfaces. Measurements collected during the STM vibration campaign highlighted local dynamic amplification in this region. Consequently, the geometry was locally reinforced and redesigned, resulting in a 16% reduction in the measured grms level at the relevant interface.

Beyond component-level structural enhancements, the STM campaign proved essential for testing and refining the assembly procedures. Hands-on experience during the integration phase allowed the team to optimize AIV workflows, eliminate assembly

bottlenecks, and collect empirical timing and handling data. These preliminary operational insights provided the necessary foundation to size and structure an efficient, high-throughput industrial production line for series manufacturing.

These optimizations illustrate the iterative development process adopted for HAWK PLUS, where manufacturing experience and verification results are continuously fed back into the design. Rather than qualifying a single spacecraft configuration, the STM campaign was used to mature the baseline platform, improving both its structural robustness and its suitability for repeatable industrial production.

4. MANAGEMENT OF CONTROLLED STRUCTURAL DELTAS

4.1. Baseline Evolution

The industrialization of a multi-mission platform does not imply the complete elimination of mission-specific structural modifications. Rather, the objective is to progressively reduce their extent by distinguishing between recurring requirements that can be incorporated into the platform baseline and changes that are inherently driven by a specific mission configuration.

The first HAWK PLUS implementations provided practical feedback on this distinction. Requirements emerging from customer missions, manufacturing activities, and verification campaigns highlighted structural features and interfaces that could be improved or made more versatile. When a modification was identified as beneficial across multiple configurations, it was incorporated into the baseline design. Conversely, changes directly driven by a specific payload, propulsion configuration, or mission environment were retained as configuration-specific deltas.

To ensure long-term platform stability, the mechanical design is architected so that mission-driven variations remain strictly localized. Structural interfaces and load paths are decoupled in a way that prevents design changes from propagating to adjacent assemblies or core platform components. Modifications are thus confined exclusively to designated, adaptable structural elements without impacting the qualified core platform.

The objective is therefore not to freeze the platform design, but to progressively mature it while preserving the standardized interfaces, load paths, and manufacturing processes that define the common architecture.

4.2. Lessons Learned

The STM manufacturing and test campaign provided direct feedback on both structural performance and manufacturability. This feedback resulted:

1. **Modularity Must Be Interface-Centric:** True modularity extends beyond merely dividing a structure into discrete bays. The mechanical interfaces themselves become the primary drivers of structural performance, controlling overall dynamic behavior, load distribution, and platform stiffness.
2. **Verification Results Drive Baseline Maturation:** Empirical feedback gathered during environmental testing and AIV must be systematically fed back into the core design, ensuring that baseline qualifications continuously evolve to reflect real-world testing insights.
3. **Structural Optimization Must Account for Production:** An analytically optimal structure is not necessarily the best solution for series production. Optimization must strike a trade-off between structural performance and Design for Manufacture and Assembly (DFMA) to safeguard throughput, lead times, and repeatability.
4. **Standardization Should Enable Controlled Variation:** The goal of platform industrialization is not to eliminate mission-specific adaptations entirely, but to confine and control them. By localizing variations to dedicated structural elements, custom mission requirements can be accommodated without invalidating the qualified core architecture.

5. CONCLUSIONS

This paper presented the structural architecture and mechanical design approach adopted for the HAWK PLUS modular platform, focusing on the integration of structural performance, modularity, manufacturability, and recurring production requirements. The deck-and-bay architecture provides standardized interfaces and continuous load paths while enabling independent manufacturing and integration of structural modules.

The STM manufacturing and verification campaign provided experimental data for structural and thermal model correlation and generated practical feedback on both manufacturability and structural dynamic behaviour. This feedback was incorporated into the platform design through targeted structural optimizations, demonstrating the iterative interaction between design, manufacturing, and verification.

The HAWK PLUS development demonstrates that platform standardization does not require the complete elimination of mission-specific modifications, but rather their controlled management within an evolving common baseline. This approach supports a more scalable and repeatable development and production model for multi-mission small satellites.

6. REFERENCES

1. Hirshorn, S.R., Voss, L.D. & Bromley, L.K. (2017).

System Engineering Handbook. NASA/SP-2016-6105 Rev 2, NASA, Washington DC.
2. European Cooperation for Space Standardization. (2009). ECSS-M-ST-10C Rev 1, *Space Project Management – Project and Implementation.* ESA.
3. Simonetti, S. (2020). Argomoon: Italian cubesat technology to record the maiden flight of sls towards the moon. In *Annual Small Satellite Conference,* 2024.
4. Bonariol, T (2025). Agile deployment and automation of Argotec flight operations segment for Iride cubesat constellation. In *SPACEOPS 2025*.
5. Giolo, M., Saita, G., La Bella, E., Pasini, G., Pedrazzini, C., Cerini, C., Di Matteo, M. and Fazzoletto, E. (2025). Hawk Plus: a standardized and scalable platform for industrialized small satellite production. In *76th International Astronautical Congress,* 2025.
6. Space X. *Falcon user's guide*. Space Exploration Technologies Corp, 8th edition, March 2025.

OPTIMISED GAS EXPANSION TUBE FOR FRANGIBLE JOINT APPLICATIONS: DESIGN AND VERIFICATION APPROACH

M. Conrad [(1)], T. Kühni [(1)], F. Marques Novo [(2)], M. Cattepoel [(2)], G. Molinari [(2)], E. Odinolfi [(2)], A. Sánchez Cebrián [(2)]

[(1)] Saab Bofors Dynamics Switzerland Ltd, Allmendstrasse 74, CH - 3600 Thun, Switzerland
Email: markus.conrad@saabgroup.com
[(2)] Beyond Gravity Schweiz AG, The Circle 23, 8058 Zürich Flughafen, Switzerland

KEYWORDS

gas expansion tube; detonative loading; Euler–Lagrange simulation; shock response; frangible joint, payload fairing separation

ABSTRACT

This paper presents the design and verification of an optimised pyrotechnic Gas Expansion Tube (GET) for integration into a Frangible Joint (FJ) system used for horizontal separation of Payload Fairings (PLF). An advanced simulation framework was developed to model the detonative loads, the consequent expansion of the explosive tube assembly and the controlled severance of the associated structural profile assembly.
A coupled Euler-Lagrange finite element approach was used to simulate the detonation-driven gas expansion and the structural deformation of the GET together with the coupled FJ profile assembly. Explosive loading was represented using the Jones-Wilkins-Lee (JWL) equation of state to simulate the detonation-driven gas expansion. A hierarchy of finite element models was developed to investigate the coupled physical mechanisms at different levels of geometric detail and computational effort.
The numerical models were iteratively refined using experimental data from development and qualification test campaigns, including sub-length, intermediate-length, and full-length separation tests. The resulting GET design provides the required separation performance while maintaining structural integrity over the qualification envelope and enabling improved control of the transmitted shock level.

1. INTRODUCTION

The horizontal separation of large PLF is a mission-critical event requiring a highly reliable separation system with predictable fracture behaviour and a controlled shock environment. In the FJ system considered in this study, separation is initiated by a pyrotechnic GET, which converts the energy released by the explosive charge into a controlled mechanical load acting on the structural profile. The design of the GET is therefore a key factor governing the functional performance of the separation system.
A major challenge in the development of such pyrotechnic separation systems is the simultaneous fulfilment of functional and structural integrity requirements over the complete thermo-mechanical qualification envelope. The GET must withstand the high transient pressure generated by the detonative event while expanding sufficiently to provide the energy required for reliable severance of the FJ assembly.
At the same time, the expansion process must be carefully controlled to prevent tube rupture and unwanted secondary fractures in the surrounding structural components. These requirements must be fulfilled over a wide range of operating conditions while accounting for temperature variations, manufacturing tolerances, and the inherent statistical scatter associated with energetic materials. For the FJ system investigated in this programme, the qualification temperature range extends from −43 °C to +125 °C.
In practice, this means that the same design must reliably sever the FJ under the least favorable explosive underload condition (80 % of the nominal charge) while simultaneously preventing rupture of the GET under the most severe overload condition (120 % of the nominal charge). Such margin conditions give rise to conflicting design requirements. At low temperatures and reduced explosive loading, the FJ must still sever completely and reliably. Conversely, at elevated temperatures and increased explosive loading, the GET must maintain its structural integrity and hermetic tightness while ensuring the absence of secondary fractures within the profile assembly.
An overview of the overall development, verification, and qualification programme of the final frangible joint separation system solution is presented in the companion paper by F. Marques Novo et al. [1]. The present work focuses specifically on the physical mechanisms governing the initial GET design, its expansion and the resulting severance process, together with the characterisation of the shock generated by the separation event.
Experimental investigations were performed throughout the programme to characterise the behaviour of the separation system and to measure the shock transmitted to representative adjacent structures. In parallel, advanced finite-element models based on an Euler-Lagrange coupling approach

were developed to simulate the detonation process, the expansion of the GET, the severance of the FJ, and the resulting structural response. The explosive loading is represented using the JWL equation of state, enabling the transient interaction between the detonation products and the deforming structural components to be captured.
Emphasis is placed on the correlation and validation of the numerical models against the initial set of experimental data, the influence of test-specific boundary conditions, and the use of model scaling to enable efficient parametric investigations. While experimental testing is essential for demonstrating functionality and validating the simulation methodology, the inherent scatter of shock measurements can make it difficult to isolate the influence of individual design parameters. Numerical simulation therefore provides an important complementary tool for understanding the governing physical mechanisms and systematically assessing design modifications.
The objective of this work is to demonstrate how the combination of early development testing and advanced Euler-Lagrange simulation can be used to characterise, optimise and verify the performance of a pyrotechnic GET-based separation system, with particular emphasis on the expansion and severance mechanisms and the transmitted shock environment.

2. DEVELOPMENT APPROACH

2.1. Development Tests

Initial development tests were performed to investigate the structural response of the GET under extreme detonative loading conditions and to identify the associated failure modes and structural limits.



Figure 1: Failure of a GET specimen under extreme overload conditions in an unconstrained region

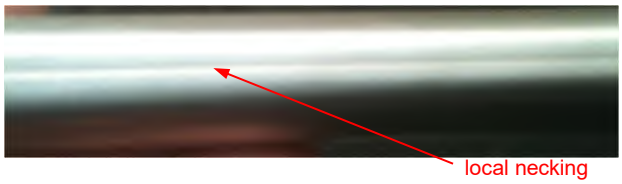


Figure 2: Local necking observed along GET length after expansion under overload conditions

The centre of Figure 1 shows a section of a ruptured tube specimen observed during an early detonative test performed under deliberately extreme explosive overload conditions. The test combined an increased explosive charge with a large unsupported region of the tube. To the left of the specimen, part of an L-shaped angle profile is visible. The profile incorporates a closely fitting passage that provides support to the tube and locally constrains its expansion. The explosive initiation point was located on the left-hand side, and the detonation wave propagated towards the right. Under these extreme conditions, the tube specimen ruptured in the unsupported region following the passage of the detonation wave. As illustrated in Figure 1, the failure occurred along the direction of detonation propagation.
Prior to detonation, the GET has an oblong cross-section. During the detonation event, the gaseous reaction products generated by the explosive cause the tube to expand, resulting in an approximately circular cross-section. As shown in Figure 2, the expanded tube exhibits pronounced local necking along its length, creating a preferential failure path. In tests performed with such deliberately excessive explosive loading, the resulting internal pressure exceeded the structural capacity of the unconstrained tube section. Consequently, the GET ruptured along the preferential failure path formed by the local necking. This failure mode was consistently observed in tests, in which the explosive loading exceeded the allowable range.

2.2. Design Optimisation

Representative sub-length specimens were conditioned to the required functional temperature extremes prior to separation testing, either by heating them in an oven or by cooling them in a refrigerator. In selected tests, the acceleration of the clevis profile was measured and in most tests the separation process was recorded using a high-speed video camera.
The following design parameters were investigated:

- Explosive loading of the detonation cord, expressed as the amount of High-Explosive (HE) contained within the GET;
- Design and material of the inserts used to position the detonation cord within the GET;
- Thickness of the separation plane in the FJ structural assembly;
- Distance between consecutive pins and collars.

Based on these parametric studies, the combination of detonation-cord loading and frangible-joint notch thickness was optimised to achieve consistently the required explosive loading margins under both underload and overload charge conditions across the complete temperature range. The selected design provides adequate design margins against both insufficient severance capability and loss of tube structural integrity along the complete temperature and explosive loading envelope. Its influence on the transmitted shock environment was subsequently investigated through dedicated output shock testing and numerical simulation.

2.3. Output Shock Characterisation

Following the initial design activities, a dedicated output shock characterisation test campaign was conducted to establish the shock environment generated by the initial GET and FJ configurations. This campaign provided the initial experimental data used

for correlation of the numerical models and for subsequent investigation of design modifications.
Figure 3 shows the test setup used for the initial characterisation and measurement of the structural shock generated during actuation of the initial FJ system configuration. The setup is representative of the flight configuration but installed in an inverted orientation. The aluminium plate with dimensions of 1 m × 2 m, represents a surrogate for the Launch Vehicle (LV) structure. Shock sensors A_0, A_1, A_2, A_3, and A_7 measure the transverse (out-of-plane) acceleration, while sensor A_{10} records the accelerations in all three spatial directions.

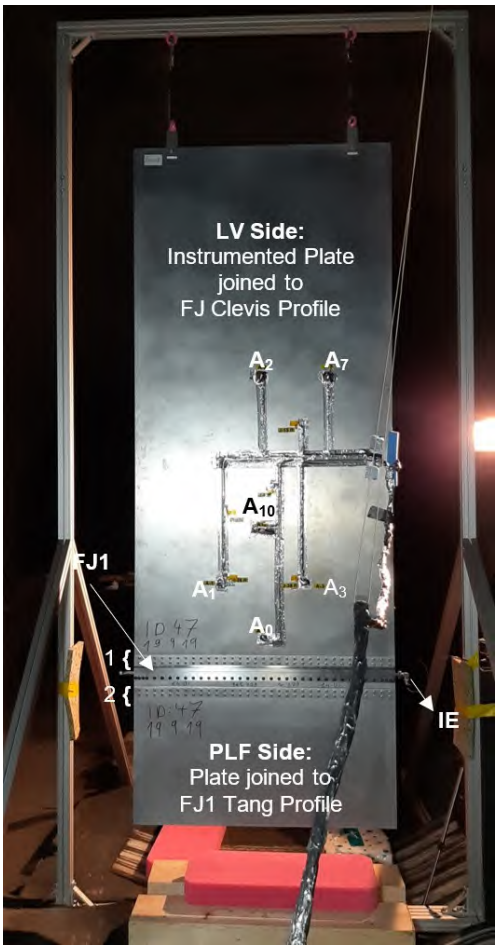


Figure 3: Output shock panel test setup of initial FJ design

The FJ is integrated into the clevis profile (CP), with the GET clamped inside the profile. The detonation cord is initiated at the Ignition End (IE), causing the FJ assembly to sever progressively from right to left. The plate representing the LV shell is attached to the CP using a splice plate and a series of screws, as shown in Figure 3 (item 1). A second plate, representing the PLF, is attached to the FJ tang profile (TP) using a similar connection. Details of this interface are shown in Figure 4 (item 2). A small gap is maintained between the TP and the PLF-representative plate. This feature ensures that the shock wave reflected from the bottom edge of the plate does not return to the FJ before completion of the severance process.

Figure 4 shows the deformation of the CP of the initial FJ design following the separation process. The TP is connected to the CP by means of a press fit pin-and-collar assembly (item 4). On the right-hand side, the plate representing the PLF side is visible. It is attached to the CP using a splice plate, screws, and nuts (item 2).

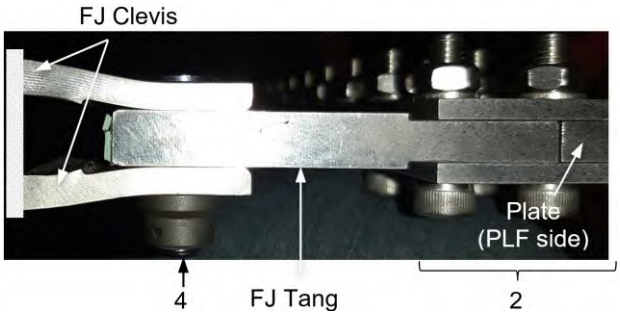


Figure 4: Deformation of FJ Clevis (initial design)

The corresponding Shock Response Spectra (SRS) measured during the initial development campaign are shown in Figure 5. The SRS curves were calculated from the measured acceleration time histories using the methodology described by Irvine [2].

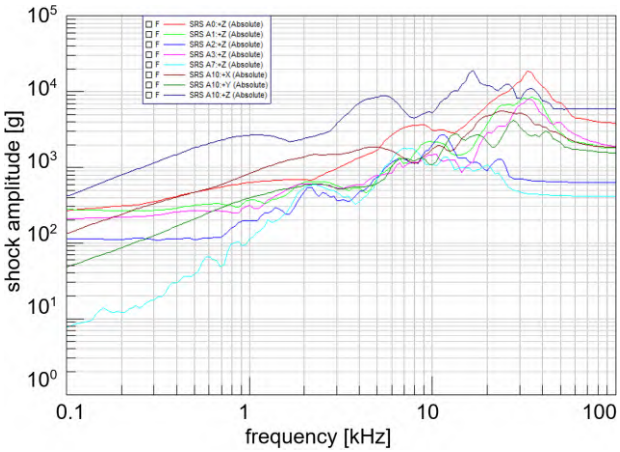


Figure 5: Measured SRS for initial FJ design

3. NUMERICAL MODELLING APPROACH

3.1. Numerical Models

Three finite-element models with different levels of geometric detail and computational size were developed to investigate both the structural response and the shock transmission of the initial FJ design, while enabling efficient evaluation of GET structural integrity and FJ severance behaviour.
The GET system following to Figure *6* was modelled using a coupled Eulerian-Lagrangian finite element formulation. The tube (item T) was discretised using Lagrangian hexahedral elements, whereas the detonation cord and the centring holders (item H) were represented as material volumes within a structured Eulerian mesh. This formulation enables the interaction between the rapidly expanding detonation products and the deforming tube to be captured without explicitly prescribing the tube expansion. The high-

explosive (item HE) charge is located at the centre of the model and is surrounded by the cable sheath (item C), together forming the detonation cord. The influence of the holder configuration on the dynamic expansion of the GET and the subsequent severance behaviour was investigated as part of the numerical study.

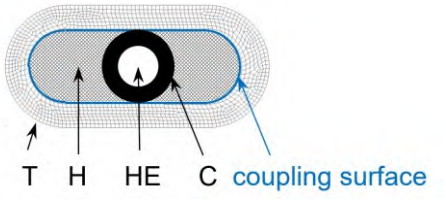


Figure 6: Eulerian-Lagrangian coupling used for the GET model

The full-scale model, corresponding to the experimental configuration shown in Figure 3, is presented in Figure 7. The dark-grey regions represent the attached plates and are modelled using shell elements, while the light-grey regions correspond to the FJ separation system. Details of the separation system are shown in Figure 8 and Figure 9.

Acceleration time histories were extracted at nodal locations corresponding to the positions of shock sensors A_0, A_1, A_3, and A_{10}, as well as at additional locations in the vicinity of the frangible joint. In addition, stress time histories were extracted from selected solid elements located within the FJ notch to assess the local structural response during severance.

The full-scale model was computationally demanding because of the large structural dimensions and the fine spatial and temporal resolution required to capture the relevant high-frequency shock response. The full-scale model contained 3'225'235 Eulerian multi-material elements, 807'796 first-order Lagrangian solid elements and 31'920 quadrilateral shell elements. The total simulated time was 20 ms, with output data recorded at intervals of 1 µs. This temporal resolution was required to evaluate the SRS over the specified frequency range, from 0.1 kHz to 100 kHz. A complete simulation required approximately three months of computational time. To reduce the computational effort, an intermediate-scale model exploiting geometric symmetry was developed. The model retained the relevant structural details of the full-scale configuration while reducing its length from 1.0 m to 0.5 m. For configurations with initiation from both ends of the detonation cord, as in the nominal flight configuration, the two detonation fronts meet at the symmetry plane. This allows the reduced model to reproduce the relevant structural response while substantially reducing the computational cost.

For the extensive parametric studies, a further sub-length model was developed. This model represents the narrow strip between the two red dash-dotted lines indicated in the full-scale model of Figure 8. Its length was reduced to half the distance between two adjacent pin-and-collar connections. Owing to its significantly lower computational effort, this model was used for most of the design investigations, with a typical computation time of approximately 30 hours per simulation.

Table 1: Three-scale FE modelling approach

Model	Length	Computational Effort
full-scale	1.0 m	~3 months
intermediate-scale	0.5 m	~6 weeks
sub-length	half pin/collar pitch	~30 h

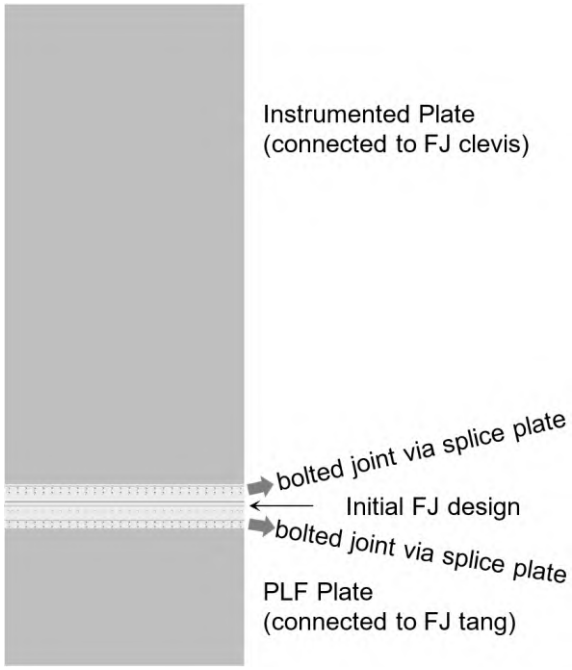


Figure 7: Complete Finite Element model of the test setup

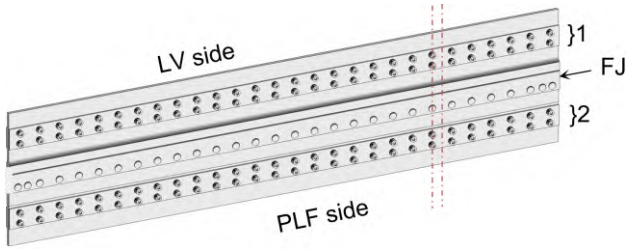


Figure 8: Full-scale model of the profiles with initial FJ and splice plate connections; 1 m length

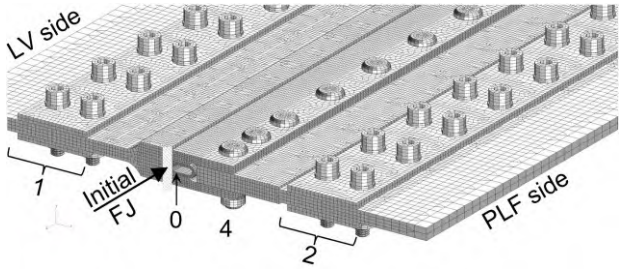


Figure 9: Detail of the Full-Scale FE-Model

The different design configurations and parameter variations introduced in section 2.2 were analysed using the sub-length model, as illustrated through Figure 10 to Figure 13.

Figure 10 shows the connection between the representative LV shell and the initial CP definition using a splice plate, screws, and nuts (item 1). A gap is present between the LV shell and the CP, as shown in greater detail in Figure 11. This configuration corresponds to the experimental setup shown in Figure 3. In selected simulations, this gap was intentionally closed, as illustrated in Figure 12. Furthermore, the splice, screws, and nuts were either included or omitted in the model to investigate the influence of their additional mass on the dynamic response. The initial GET (item 0) is clamped within the CP, which is connected to the TP by a pin-and-collar assembly (item 4). Due to limitations of the finite-element software, the preload introduced by the pin-and-collar connections, as well as that generated by the screws and nuts could not be explicitly represented. Consequently, all such connections were modelled without initial pre-stress.

The initial FJ configuration incorporates the original separation-plane design. The notch shape and thickness were varied as part of the parametric study to investigate their influence on the severance behaviour and the resulting structural response. The results were subsequently used to support the transition towards the final optimised design.

The most significant difference between the investigated configurations is illustrated by the two separation-system concepts shown in Figure 10. The upper configuration represents the reference design, whereas the lower configuration incorporates a shock-attenuation feature in the CP. The slits reduce the axial stiffness of the CP and consequently modify the propagation of stress waves through the structure, with a portion of the shock energy shifted towards lower frequencies. The slits introduced into the clevis profile reduce its axial stiffness. As a result, a reduction of the high-frequency shock response is expected. This attenuation concept was patented by John A. Graham [3] and has been used in here for investigation purposes only. Such shock-attenuation features can also be implemented in the TP.

The complete set of design parameters and combinations is summarised in Figure 13. Items 1 and 2 represent the interfaces between the separation system and the representative LV and PLF shell structures, respectively. The corresponding gaps G_1 and G_2 were modelled either in their nominal open configuration or as closed interfaces. For the closed-interface configurations, the corresponding splice plates, screws, and nuts were either included or omitted to assess the influence of their additional mass on the structural response. The shock-attenuation features (items 10 and 20) were compared with equivalent solid profiles without slits.

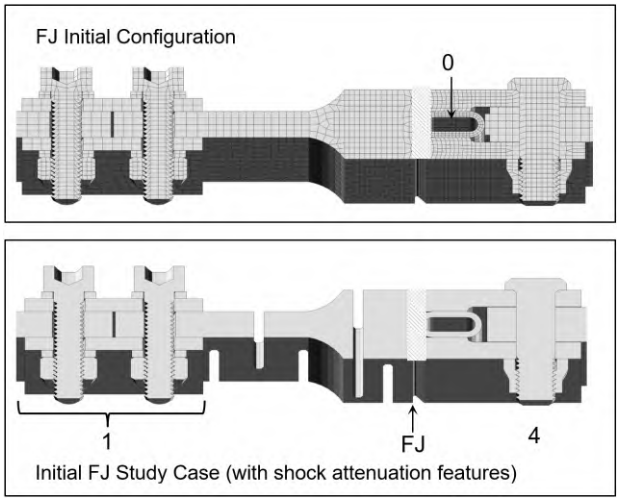


Figure 10: Initial FJ configurations investigated in the numerical study

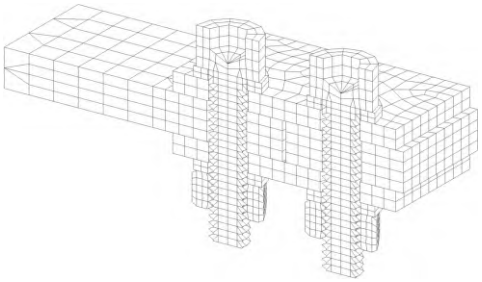


Figure 11: Detail of the splice connection between the plate and the clevis profile (CP)

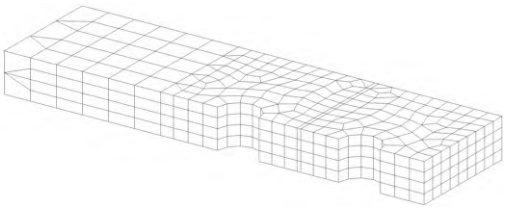


Figure 12: Model variant with plate and clevis profile (CP) represented as a single component

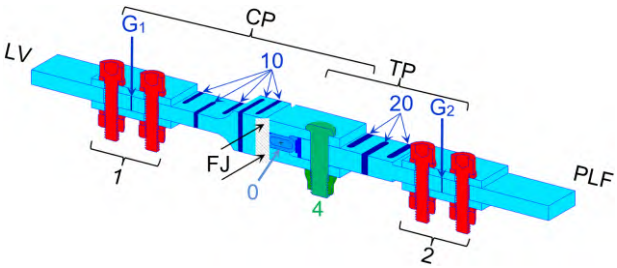


Figure 13: Generic numerical model of GET embedded in the profiles with initial FJ configuration and connections to adjacent plates by means of splices

3.2. Material Models

In this study, special emphasis was placed on the characterisation of the GET tube and structural profiles, as their material behaviour directly influences both the structural integrity of the GET and the severance response of the FJ. Material properties inevitably exhibit manufacturing and batch-to-batch

variations and therefore cannot be represented by a single unique set of parameters. For metallic materials, quantities such as yield strength, ultimate strength, and elongation at break are usually provided as ranges with specified tolerances. Nevertheless, numerical simulations require a well-defined reference material model. Such a reference model enables a consistent assessment of the influence of individual design parameters and facilitates the identification of comparatively small design effects. The material characterisation presented in this section begins with the metal used for the GET tube. The constitutive models adopted for the tang and clevis profiles were developed in an analogous manner. All remaining metallic components, such as screws, nuts, pins, and collars, were represented as purely elastic materials. The final part of this section addresses the modelling of the energetic material and its detonation products.

The Johnson-Cook constitutive model Eq. (1) was used to describe the behaviour of the metallic components.

$$\sigma_y = \left(A + B \cdot \varepsilon_p^n\right) \cdot \left(1 + C \cdot ln\left(\frac{\dot{\varepsilon}}{\dot{\varepsilon}_0}\right)\right) \qquad (1)$$

A, B, C are material parameters

Yield stress σ_y is a function of plastic strain ε_p, strain rate $\dot{\varepsilon}$ with respect to reference strain rate $\dot{\varepsilon}_0$

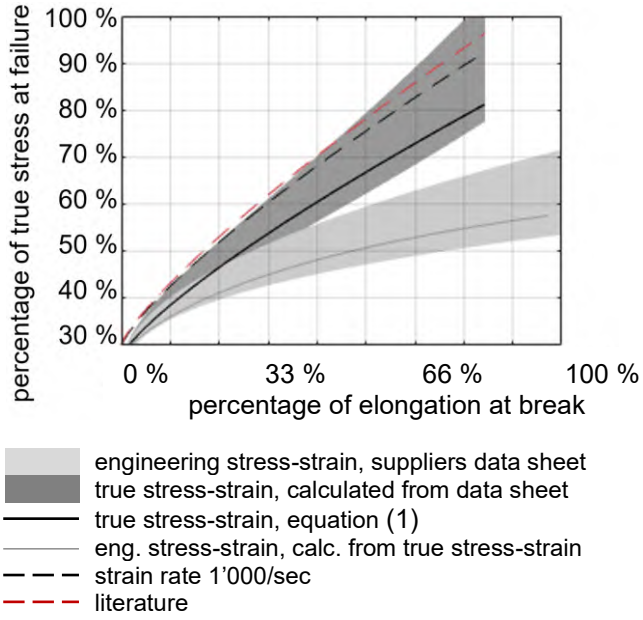


Figure 14: Yield stresses of GET tube

Material parameter ranges derived from the respective supplier specifications were considered to assess the sensitivity of the structural response to material variability. The resulting envelopes are shown as light-grey shaded areas in Figure 14. As the supplier data were provided in terms of engineering stress and engineering strain, the data were converted into true stress and true strain before implementation in the numerical model. The dark-grey shaded areas represent the scatter bands obtained from the corresponding uniaxial tensile tests. For the material parameters used in our simulations, the predicted elastic-plastic response remains within the ranges of the suppliers' specifications. The solid black curves show the true stress-strain response under quasi-static loading conditions. The black dashed curve illustrates the predicted behaviour at elevated strain rates according to the Johnson-Cook model. In addition, Figure 14 includes a red dashed curve taken from peer-reviewed scientific literature including studies of material behaviour at high strain rates and under severe deformation. These data were used to assess whether the selected reference model adequately represents the dynamic response of the material over the range of loading conditions relevant to the present study.

The JWL equation of state, given by Eq. (2), was used to describe the pressure-volume behaviour of the detonation products. The JWL formulation is widely used for numerical modelling of high-explosive detonation products, with material parameters available for a broad range of energetic materials [4-6].

$$p = A \cdot \left(1 - \frac{\omega \cdot \rho}{\rho_0 \cdot R_1}\right) \cdot e^{-R_1 \frac{\rho_0}{\rho}} + B \cdot \left(1 - \frac{\omega \cdot \rho}{\rho_0 \cdot R_2}\right) \cdot e^{-R_2 \frac{\rho_0}{\rho}} + \omega \cdot \rho \cdot e \qquad (2)$$

A, B, R_1, R_2, and ω are material parameters

Pressure p is a function of the volumetric expansion ρ_0/ρ and internal specific energy e.

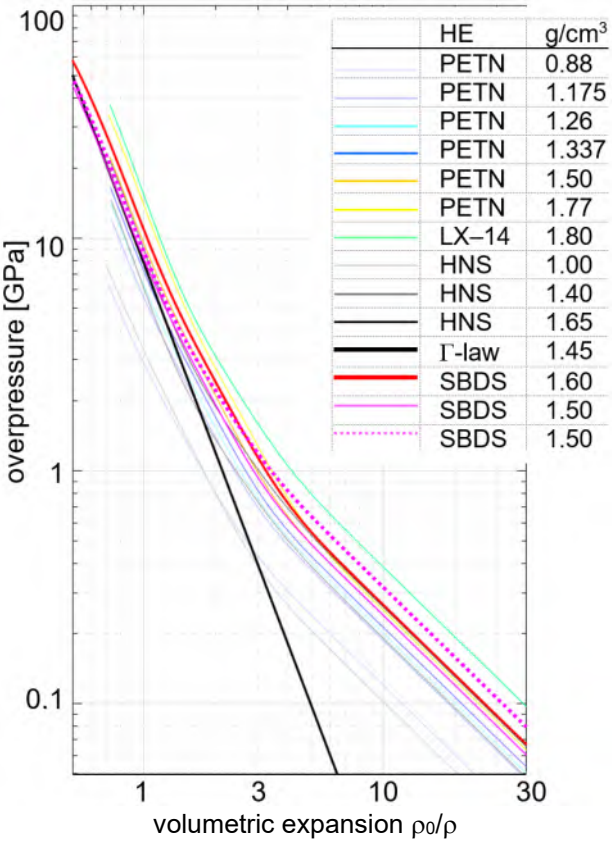


Figure 15: Overpressure versus volumetric expansion of different high explosives

Figure 15 shows the pressure-volume relationships of the detonation products for various explosives. Materials with different densities, such as PETN and HNS, were considered and compared with LX-14, a high-performance explosive commonly used in shaped-charge applications.
Based on these reference data, a set of JWL parameters was derived to represent the low-density HE charge, which are labelled as SBDS in Figure 15. For the simulations presented in this work, the material properties corresponding to the solid pink curve, representing HE with a density of 1.50 g/cm³, were adopted. The two SBDS curves with a density of 1.50 g/cm³ differ primarily at expansion ratios greater than approximately two. Beyond this point, the dotted pink curve predicts higher pressures than the solid pink curve. Consequently, higher pressures are sustained in the fully expanded GET, resulting in an increased deformation of the CP (see Figure 4).
It is interesting to note that an increase in the deformation of the frangible joint does not necessarily imply a corresponding increase in the shock transmitted through the clevis profile to the LV shell. Once the frangible joint has fractured and the separation process has been completed, the mechanical load path between the two structures is significantly reduced. Therefore, pressure differences occurring during the later stages of tube expansion may contribute to additional deformation of the joint while having only a limited influence on the shock transmitted to the LV shell.

4. NUMERICAL RESULTS

4.1. Tube Deformation

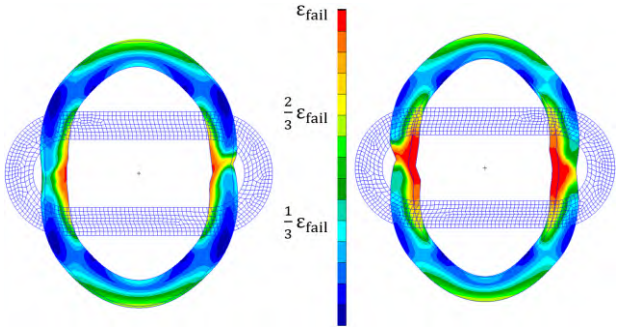


Figure 16: Initial GET: effective plastic strain (w.r.t. elongation at break ε_{fail}) at nominal (left) and overload (right)

Figure 16 shows the cross-section of the GET obtained from the numerical simulation. In this specific case, the tube was not confined by the surrounding structure. The results should therefore be compared with the experimental observations presented in Figure 2. For clarity, only the tube, modelled using Lagrangian hexahedral elements, is shown. The blue mesh represents the original geometry of the GET before the detonation front passed the cross-sectional plane. The coloured contour plot shows the effective plastic strain, normalised with respect to the material elongation at break, at the instant of maximum tube expansion. The simulation on the left corresponds to the nominal explosive loading, whereas the simulation on the right represents an overloaded condition.
The numerical results show good agreement with the experimental observations shown in Figure 2. In particular, the characteristic localised necking observed experimentally is reproduced by the simulation. Under the increased explosive loading, the strain concentration becomes significantly more pronounced along the necking region, reaching the material failure criterion and resulting in local rupture of the tube. These results demonstrate the capability of the Eulerian-Lagrangian model to reproduce the characteristic deformation and failure mechanism of the GET under unconstrained conditions. Moreover, they also illustrate the optimised structural margin of the unconfined tube under increased explosive loading, providing a useful reference for the subsequent analyses of the constrained GET configuration.

4.2. Profile Deformation

Figure 17 compares the profile deformation predicted by the simulation of the initial design configuration with the permanent plastic deformation observed in the initial development tests, as previously presented in Figure 4. The simulation result is shown in the foreground in the upper image, while the tested specimen is shown in the foreground in the lower image.

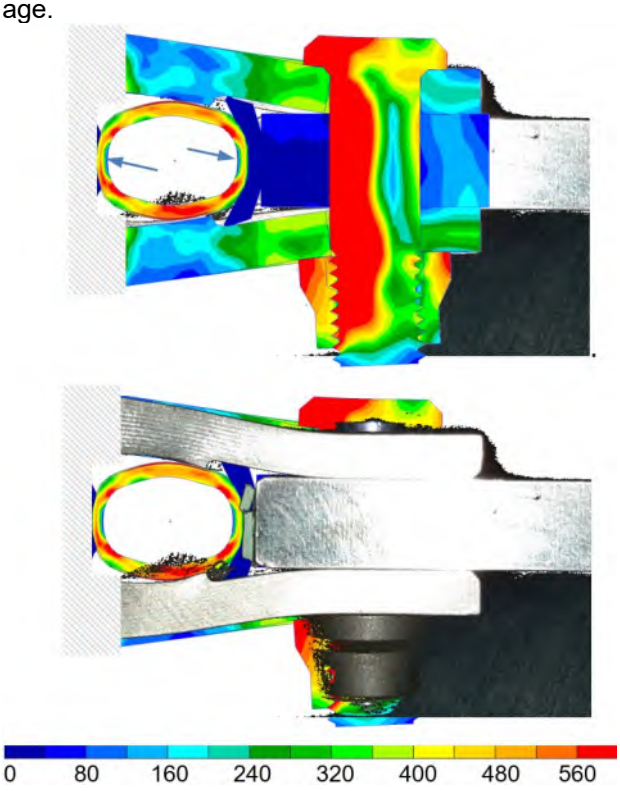


Figure 17: Equivalent stress in N/mm² and deformation of the simulation vs. test results (Figure 4)

Overall, the predicted deformation pattern is in good agreement with the experimental observations. However, the simulation results correspond to the instant of maximum displacement, and do not account for

the subsequent elastic recovery of the actual specimen.
High stresses are predicted in the pin-and-collar connections, which are subjected to a combination of tensile and bending loads. Comparable stress levels are also observed in the GET. However, the stresses on the inner side of the tube appear to vanish locally, as indicated by the arrows in the upper image of Figure 17. This behaviour is a consequence of the implemented material's failure criterion. Once the equivalent plastic strain exceeds the prescribed elongation at break, the material strength is locally reduced to zero, thereby representing the onset of material failure. Although local failure initiation is predicted at the inner surface of the tube, the damage does not propagate through the wall thickness. Consequently, the tube remains intact, which is consistent with the experimental observations. The simulation therefore reproduces both the observed deformation pattern and the absence of a complete tube rupture.

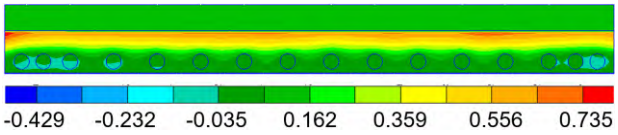


Figure 18: Intermediate-scale model, transverse displacement field in mm

Figure 18 shows the transverse displacement field of the FJ clevis profile. The model used for this analysis has a length of 0.5 m. In contrast to the intermediate-scale model described before, no symmetry boundary condition was applied. Instead, both side edges were modelled as free boundaries. Consequently, the model exhibits a dynamic behaviour similar to that of the full-scale model with a length of 1 m, while requiring only approximately half the computational effort.
The primary objective of this specific analysis was to compare the predicted transverse deformation with the permanent deformation observed in the test specimens. Between adjacent pins, the simulation predicts a slightly increased transverse displacement. Under favourable lighting conditions, a similar phenomenon can also be observed visually on the tested hardware, where the resulting deformation appears as subtle reflections on the slightly polished metallic surface. The presence of such wave-shaped deformation pattern suggests that the regions between neighbouring fasteners could be further adapted to improve the robustness of the separation system. In particular, the spacing and arrangement of the screws may offer opportunities for locally tailoring the structural compliance of the overall system assembly.
As in the simulations presented in Figure 21, the detonation front propagates from the right-hand side towards the left-hand side of the model. The transverse displacement at the left end is slightly larger than at the initiation end. This behaviour can be explained by the treatment of the free surfaces within the Eulerian domain. At the end of the GET, the approaching detonation products are reflected, resulting in a local increase in pressure. A similar effect was observed during the experimental tests. In the actual separation system, the GET must remain tight to prevent the release of hot gaseous detonation products that could potentially endanger the payload. Consequently, the detonation-induced pressure wave is reflected at the closed end of the tube, leading to locally elevated pressure levels and increased structural deformation in this region.

4.3. Shock Wave Propagation

The simulation results are first examined in terms of stress-wave propagation through the separation system and into the surrounding structure. Figure 19 to Figure 21 show selected stages of the wave propagation, with associated contour plots of the effective stress. The colour scales differ between the images because the stress levels within the separation-system components are approximately two orders of magnitude higher than those transmitted to the representative PLF and LV shell plates. Individual scales were therefore adopted to make the relevant stress patterns visible in each part of the structure.
The corresponding SRS curves are presented subsequently in section 4.4.

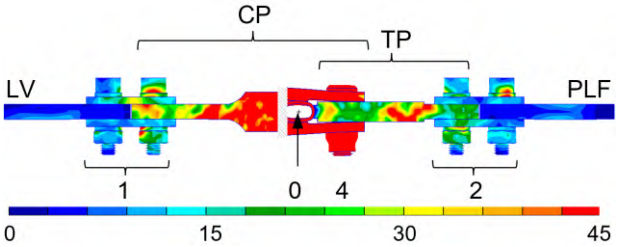


Figure 19: Effective stress in N/mm² after 135 µs

For orientation, the item numbers and nomenclature used in Figure 19 are identical to those introduced in Figure 4, Figure 9, and Figure 13.
As expected, the highest stress levels occur within the separation system at the centre of Figure 19, whereas significantly lower stresses are observed in the plates representing the LV shell and the PLF. The stress distribution clearly reveals the bending-dominated character of the transverse wave component. In particular, the highest stresses in the cross-section of the plate representing the PLF occur near the outer surfaces of the plate, while the stresses close to the mid-plane remain comparatively low.
The observed stress distribution is also governed by the way the plates are connected to the separation system. In particular, the gaps between the front edges of the plates and the profiles, which are connected by means of splices, screws, and nuts (items 1 and 2), interrupt the direct transmission of membrane waves across the interface. Consequently, the direct transmission of axial membrane forces is reduced. The resulting impedance discontinuity promotes a conversion of wave modes and attenuates the longitudinal shock component transmitted into

the adjacent shell structures.
The FJ opens progressively in a zipper-like manner, with the detonation front acting as a moving driver that advances progressively the severance along the joint. The highest local stress levels occur in the pin-and-collar connections, whose structural strength is considerably higher than that of the surrounding profiles, as also indicated by the results presented in Figure *20*. The detonation front requires approximately 135 µs to travel from one end of the FJ specimen to the other. The resulting severance process therefore occurs within a very short time interval compared to the overall simulation duration.

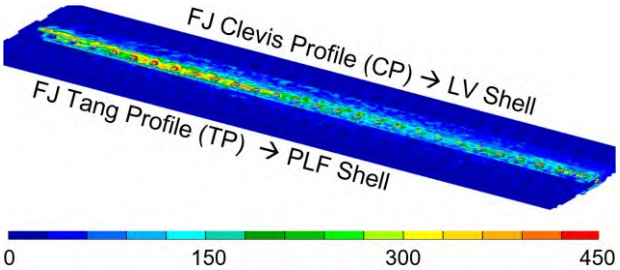


Figure 20: Effective stress in N/mm² after 135 µs

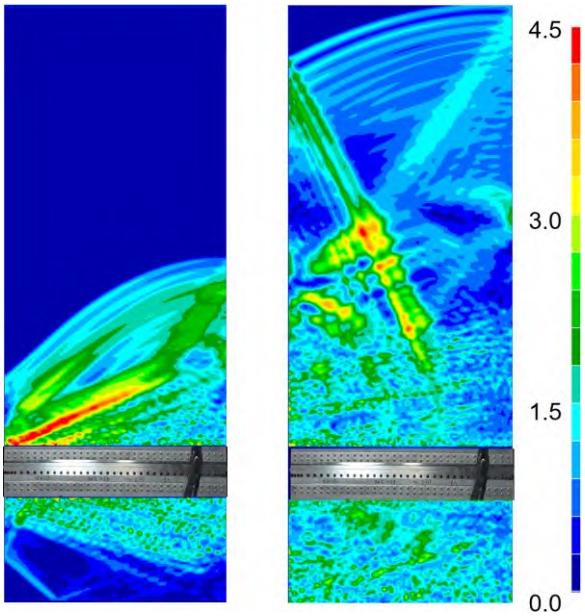


Figure 21: Effective stress in N/mm² after 260 µs (left) and 480 µs (right)

Figure 21 illustrates the subsequent propagation of stress waves within the plate representing the LV shell. For clarity, stress contours are not shown for the profiles. Instead, a detail of the profiles taken from Figure 3 is superimposed at the corresponding locations to facilitate the interpretation of the wave field.
Near the wave front, the stress pattern resembles water waves propagating and reflecting at structural boundaries. At larger distances behind the wave front, however, the wave field becomes increasingly complex owing to the superposition of incident and reflected waves. This behaviour can be observed in Figure 21 at 480 µs, where the stress distribution above and below the profiles already exhibits a highly irregular pattern. As the wave propagates further through the structure, repeated reflections and mode conversions lead to a progressive loss of coherence of the wave field. After approximately 20 ms, the deterministic wave propagation has largely evolved into a broadband structural vibration with an essentially stochastic character. Based on this observation, it is expected that the SRS obtained from the sub-length model will not differ significantly from that of the full-scale model, despite the substantially different boundary conditions at the side edges of the plates. Since the shock energy has undergone multiple reflections and redistributions before the SRS is evaluated, the local response is governed more by the overall statistical characteristics of the vibration field than by the exact geometry of the remote boundaries.

4.4. Shock Response Spectra

Owing to the large number of investigated design variants during the initial development phase, it is neither practical nor necessary to present the SRS results for every configuration in this paper. Before discussing individual design variants, it is necessary to assess the influence of model scaling and test-specific boundary conditions on the predicted shock response of the initial design definition of the FJ system. This comparison also provides insight into the extent, to which subtle design effects can be distinguished from the variability inherently present in experimental shock measurements.
The figures in the remaining part of this paper (Figure 22 to Figure 29) are organised as follows: The plots on the left-hand side show the transverse out-of-plane shock amplitudes, i.e. in the radial direction of the LV, whereas the plots on the right-hand side show the longitudinal shock amplitudes in the axial direction of the LV. The coloured curves correspond to the numerical simulations, while the grey curves represent the experimental results obtained from the test series described in Figure 5. The lowest grey band represents the range bounded by the minimum and maximum SRS values measured by sensors A_1 and A_3. Since these sensors are located at comparable distances from the separation system, this band provides an indication of the repeatability of the shock measurements. The shock levels measured by sensor A_0 are generally higher, which is expected because this sensor is located closer to the profile. Sensors A_0, A_1, and A_3 measure only the transverse acceleration. Their SRS results are nevertheless included in all plots to facilitate the comparison between transverse and longitudinal shock amplitudes. Sensor A_{10} is capable of measuring acceleration in all three spatial directions. Its transverse shock response is shown in the plots on the left-hand side. Surprisingly, these measurements exhibit the highest shock amplitudes, although sensor A_{10} is located furthest away from the separation system. This behaviour might be related to the mounting

configuration of this specific sensor, which was attached to the plate by means of an L-shaped adapter. Consequently, the measured amplitudes may be influenced by local structural dynamics of the sensor mounting arrangement rather than by the shock environment itself, as demonstrated in the final characterisation tests presented in [1]. For this reason, the corresponding transverse shock levels should be interpreted with caution. The longitudinal shock response measured by sensor A_{10} is shown as the dark-grey curve in the plots on the right-hand side.
In summary, the transverse shock measurements obtained from sensors A_0, A_1, and A_3 exhibit the expected behaviour. In particular, the comparison between sensors A_1 and A_3 provides a useful indication of the measurement variability and repeatability expected in pyroshock testing.

4.4.1. Influence of Model Scaling

Excellent agreement between experiment and simulation is observed for the transverse shock response of the full-scale model in the frequency range between approximately 2 kHz and 10 kHz (Figure 22, sensor A_0). Within this frequency range, the corresponding shock amplitudes predicted by the sub-length model are noticeably lower (Figure 23). One possible explanation is related to the boundary conditions. In the sub-length model, the edges of the narrow strip are constrained by symmetry conditions. In contrast, the corresponding location in the full-scale model is situated at a considerable distance from the free side edges of the plate. Consequently, the structural response is less affected by the artificial confinement introduced in the sub-length model, leading to lower transverse shock amplitudes. A similar discrepancy is not observed for the longitudinal shock response. Figure 25 and Figure 26 show a good agreement between the full-scale and sub-length models over a wide frequency range. Furthermore, the transverse shock amplitudes predicted by the full-scale and sub-length models show excellent agreement for frequencies below approximately 1 kHz. In contrast, and as already mentioned above, the longitudinal shock amplitudes of the sub-length model are slightly reduced in the frequency range between 1 kHz and 10 kHz.
Overall, the results indicate that the sub-length model tends to underestimate the shock response owing to the symmetry constraints applied at the lateral boundaries. These constraints increase the effective stiffness of the structure and therefore reduce the predicted shock amplitudes. Consequently, absolute shock levels obtained from the full-scale and sub-length models should not be compared directly. Instead, each model scale should be regarded as a separate analysis environment. The purpose of the sub-length model is not to reproduce the exact shock amplitudes of the full-scale configuration, but to efficiently evaluate the relative influence of design modifications under consistent boundary conditions.

4.4.2. Influence of Test-Specific Boundary Conditions

In the experimental setup, the plates are connected to the profiles by means of splices, screws, and nuts, as illustrated in Figure 11. A gap is usually present between the front edge of the plate and the corresponding edge of the profile. To assess the influence of this feature, additional simulations were performed with the gap closed. The corresponding SRS results are shown in Figure 24 and Figure 27. Additional simulations were carried out without the splices, screws, and nuts. In these configurations, the plates and profiles were merged into a single continuous part. By comparing both configurations, the effect of the additional mass can be isolated. In general, the resulting shock levels are higher than those obtained for the reference configuration with the gap present. For the transverse shock response, this increase is most pronounced at frequencies above approximately 10 kHz. However, a large part of this increase can be attributed to the omission of the additional mass represented by the splices, screws, and nuts. The direct influence of the gap itself becomes noticeable only at frequencies above approximately 20 kHz to 30 kHz. The effect of the gap is considerably more pronounced for the longitudinal shock response. At frequencies above approximately 10 kHz, closing the gap leads to shock amplitudes that are up to an order of magnitude higher than those predicted for the reference configuration. At lower frequencies, the differences are of the same order as those observed between the transverse shock measurements of sensors A_0 and A_1/A_3.
In summary, the test setup incorporating the gap provides representative measurements of the transverse shock response. The influence of the gap remains smaller than the scatter observed between repeated experiments and is therefore of limited practical significance for the evaluation of transverse shock levels. In contrast, the experimental data do not allow a reliable validation of the longitudinal shock predictions, despite the significant influence of the gap observed in the numerical simulations.

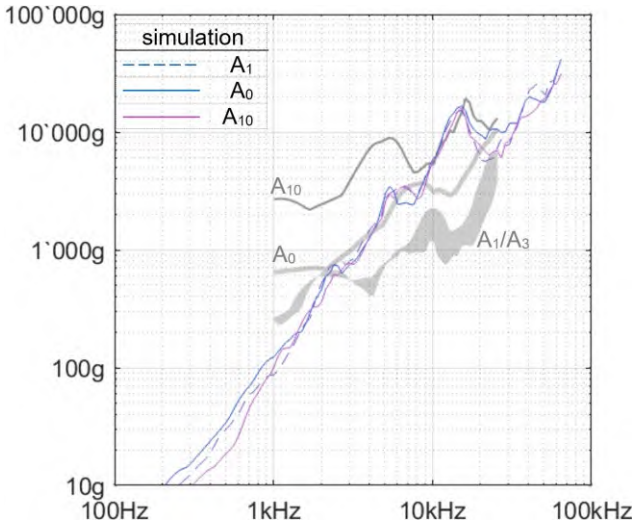


Figure 22: Full-scale model, transverse shock

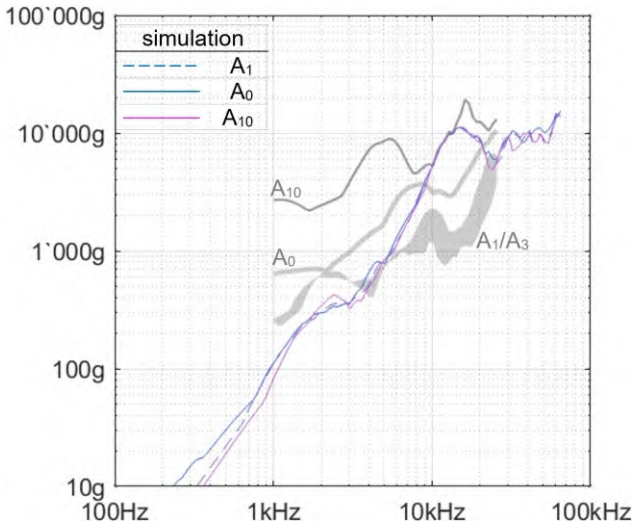


Figure 23: Sub-length model, transverse shock

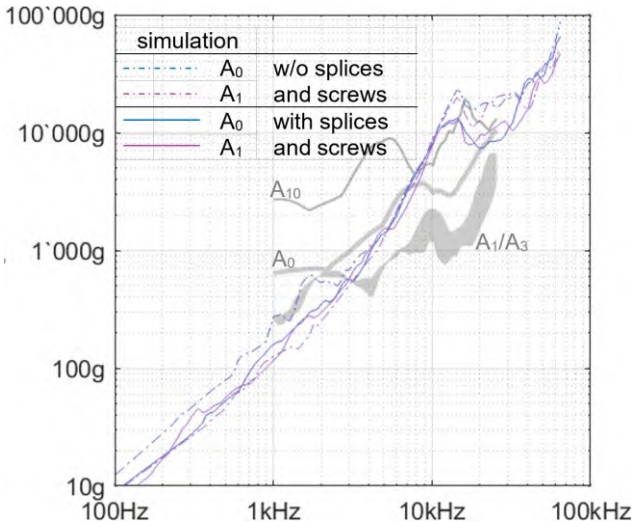


Figure 24: Sub-length model, transverse shock, profile and plate represented as one part without gap

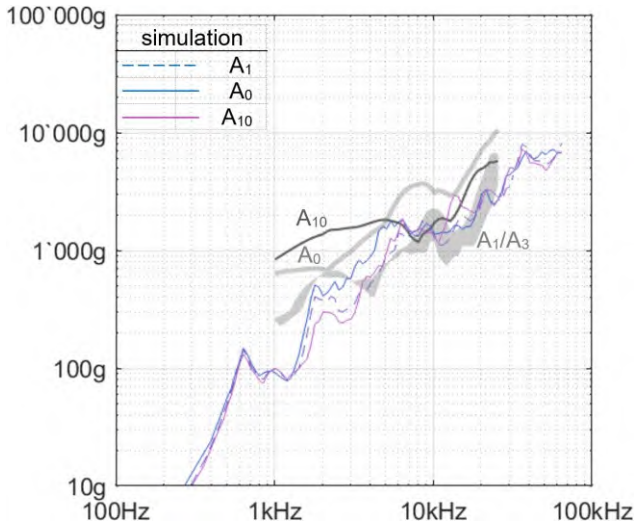


Figure 25: Full-scale model, longitudinal shock

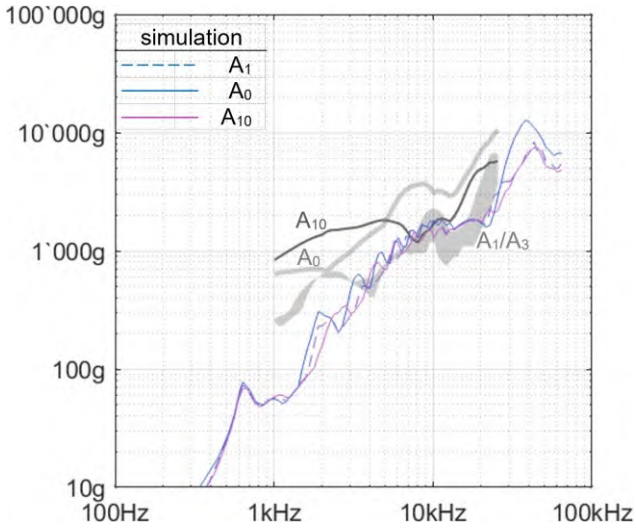


Figure 26: Sub-length model, longitudinal shock

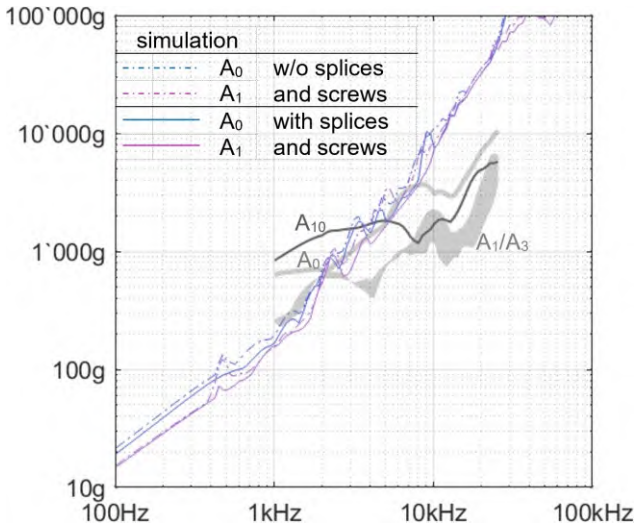


Figure 27: Sub-length model, longitudinal shock, profile and plate are one part without gap

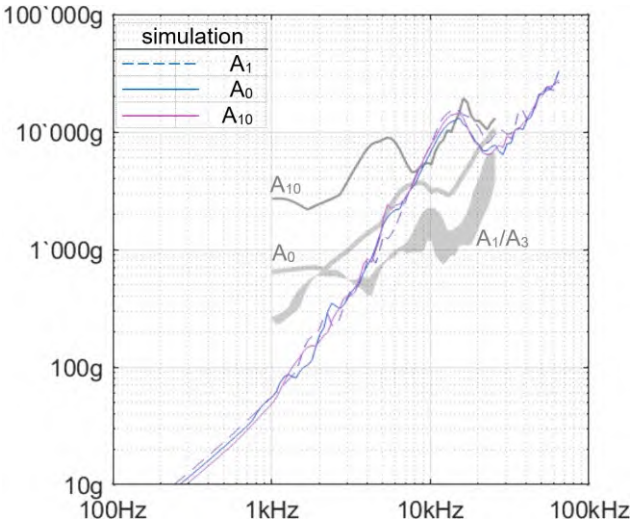


Figure 28: Full-scale model, transverse shock, clevis profile with shock-attenuation feature

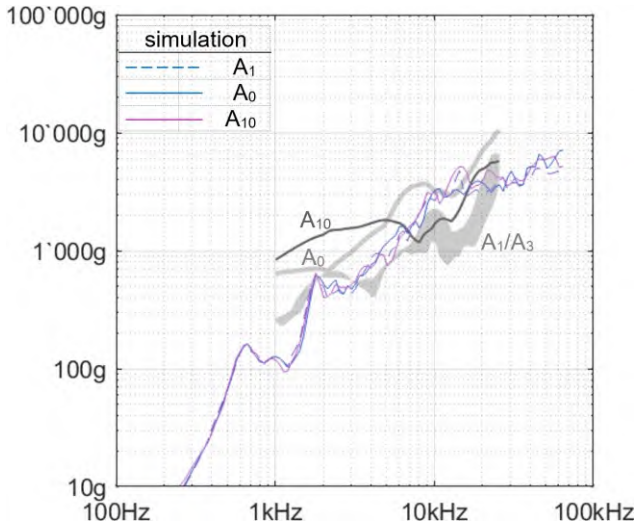


Figure 29: Full-scale model, longitudinal shock, clevis profile with shock-attenuation feature

4.4.3. Influence of Shock-Attenuation Feature

Finally, the influence of the shock-attenuation concept proposed by John A. Graham [3], introduced in Figure 10, was investigated. The results obtained with the full-scale model are shown in Figure 28 and Figure 29 and should be compared with the corresponding reference results presented in Figure 22 and Figure 25, respectively. The numerical model represents the actual experimental configuration, including the small gap between the edges of the profiles and the plates. As expected, no significant reduction of the longitudinal shock response is observed. The reason is that the gap itself already provides a very effective attenuation mechanism for longitudinal wave propagation. Fortunately, the connection by means of splices, screws, and nuts does not substantially interrupt the transmission of transverse shock waves. Consequently, the influence of the patented feature remains clearly visible in the transverse response. The results demonstrate that the shock-attenuation concept efficiently reduces the transverse shock levels at frequencies below approximately 4 kHz to 5 kHz. These findings confirm that the patented feature can also effectively mitigate low-frequency transverse shock loads.

5. CONCLUSION

The present study investigated the behaviour of a pyrotechnic separation system consisting of a GET and a FJ assembly by means of experimental testing and numerical simulation. The experimental campaign demonstrated reliable operation of the separation system over a wide range of operating conditions and provided the basis for validating the finite-element models. Good correlation was obtained for both the deformation behaviour of the separation system and the predicted shock response in the most relevant frequency ranges.

Moreover, dedicated simulations of the initial output shock test setup revealed that the gap between the FJ profile assembly and the attached test plates acts as an efficient attenuator of longitudinal shock waves, while having only a limited influence on the transverse response. The latter effect remains within the experimental scatter and therefore does not compromise the suitability of the test setup for the evaluation of transverse shock levels.

Although shock measurements proved essential for validating the numerical approach, the observed scatter between repeated experiments was found to be larger than the influence of various secondary design parameters. Consequently, subtle design effects can only be assessed reliably by means of validated numerical simulations. The combination of testing and simulation therefore represents the most effective approach for the development and optimisation of robust pyrotechnic separation systems operating under severe environmental and performance constraints.

6. REFERENCES

1. F. Marques Novo, N. Madenas, M. Cattepoel, G. Molinari, E. Odinolfi, A. Sánchez Cebrián, Frangible Joint 1: Overview of Design, Validation and Qualification Test Programme, ECSSMET Conference 2026

2. T. Irvine, An Introduction to the Shock Response Spectrum, Revision S, 2012

3. J. A. Graham, Separation System with Shock Attenuation, Patent US 2013/0136525 A1

4. E. L. Lee, H. C. Hornig, J. W. Kury, Adiabatic Expansion of High Explosives Detonation Products, Lawrence National Laboratory, 1968

5. E. Lee, M. Finger, W. Collins, JWL Equation of State Coefficients for High Explosives, Lawrence Livermore Laboratory, 1973

6. E. Anderson, “Explosives” in “Tactical Missile Warheads”, ed. J. Carleone, Progress in Astronautics and Aeronautics, Volume 155, 1993

CFRP SANDWICH INSERTS: DESIGN, TEST & VERIFICATION METHODS

Nicholas Olesen [(1)], Nikolay Asmolovskiy [(1)]

[(1)] Space Structures GmbH, Fanny-Zobel-Str. 11, 12435 Berlin, Germany, office@spacestructures.de
This activity was performed under ESA project 4000141370/23/NL/GLC, with industrial partners Optimal Structural Solutions Lda (OPT) and Adamant Composites Ltd (ADM)

KEYWORDS

Sandwich Panels, CFRP, Inserts, Testing, FEA

ABSTRACT

Sandwich panels are used extensively in spacecraft structures, with CFRP facesheets becoming ever more prevalent. Current design guidelines in the ECSS insert design handbook focus predominantly on metallic facesheets, with some gaps in the guidelines for CFRP facesheets or notes that CFRP skins require further investigation or extensive testing. This often leads to cost and schedule impacts, or limits designs to existing heritage.
With the aim of eventually reducing the cost and effort of extensive qualification testing, work was performed to advance the understanding of insert design and performance in CFRP facesheet sandwich panels, including finite element (FE) modelling, testing, and correlation activities. The resulting design and analysis guidelines are proposed for an update of the ECSS insert handbook.

1. INTRODUCTION

Design methods for CFRP panels and inserts are currently based on the ECSS insert design handbook (ECSS-E-HB-32-22A), design rules or heritage.
When using CFRP panels, extensive time and resources are spent in order to ascertain the validity of the design (extensive test and qualification activities); alternatively, design solutions may be constrained by existing (company) heritage in order to avoid long and costly qualification campaigns. Significant conservatism (safety factors) is also usually applied to alleviate any residual risks.
The current ECSS insert design handbook focuses primarily on inserts potted in sandwich panels with metallic facesheets, with some gaps in the guidelines for CFRP facesheets. Often the ECSS HB notes that failure modes associated with CFRP skins are too complex and require further investigation. Alternatively, the ECSS handbook recommends performing extensive insert specimen testing in order to quantify insert load capability. This inevitably leads to an extensive test campaign, which is costly and time-consuming.
The work performed focused on the in-plane load capability of inserts, since this is primarily driven by the facesheet properties. Out-of-plane load capability is also considered, but is secondary to the main objectives, which are to:

- Derive updated design and analysis methods for CFRP skin sandwich inserts to reduce the test effort currently required for all ESA missions
- Produce high fidelity finite element models of inserts for typical configurations in order to predict failure
- Test the modelled configurations to confirm the predictions
- Raise technology readiness level from TRL4 to TRL6

Both undisturbed inserts as well as inserts with edge and proximity effects have been considered.

2. BACKGROUND

CFRP sandwich panels are commonly composed of CFRP facesheets with a metallic honeycomb core and spool type inserts potted in a cold bonding process. Alternative materials, configurations and manufacturing methods are feasible, however are not considered common in the industry.
Facesheets are predominantly quasi-isotropic (QI) layups, with different numbers of plies to achieve the necessary skin thickness and mechanical properties.
The core is commonly a honeycomb core made of Al 5056 alloy with varying foil thickness and cell size. Typical core densities range from 50 kg/m^3 (3/16” cell size) to 130 kg/m^3 (1/8” cell size).
Inserts are usually Al 7075 alloy with SurTec 650 coating, potted in a cold-bonding process using an adhesive such as Stycast 1090.

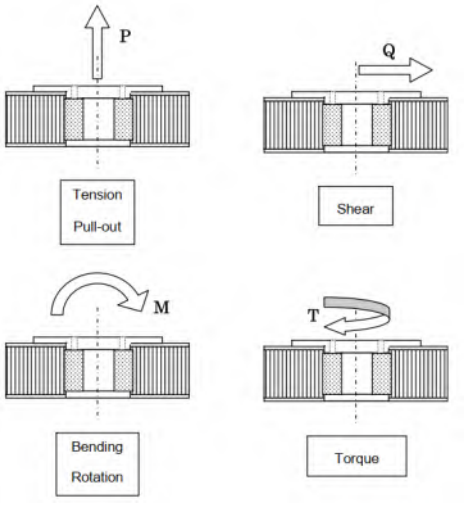


Figure 1: Typical Insert Loading Modes [1]

Reference [1] is the primary source for analytical

insert sizing methods, considering facesheet, core, and potting adhesive failure modes. Figure 1 shows the possible insert loading modes, however it is considered best practice to react torsion and bending loads via groups of inserts. Pull-out and shear loads are therefore the dominant loading modes.

There are however limitations and gaps in the analytical methods for CFRP facesheet sandwich panels. In order to explore these limitations, a test and analysis plan was derived based on typical sandwich panel and insert configurations with existing flight heritage. The plan consists of:

- Elementary material property testing of the panel laminates, to derive mechanical properties for analysis
- Pin-hole bearing tests and FE model correlation, in order to understand the bearing strength of the laminates
- Insert breadboard tests and FE model correlation, including insert design variations

3. TESTING

Testing was performed on the elementary CFRP material properties, on pinhole bearing test samples, and on insert samples with varying configurations.

For this activity a common sandwich panel configuration was selected for consistency, based on configurations from company heritage:

- EX-1515 AFC49 M55JB 6K 50B 80g 33% 0.6m CQP47 prepreg
- HexBond 312L, 150 g/m2 film adhesive
- Phosphoric Acid Anodized Al 5056 honeycomb core, perforated, with two cell sizes (3/16" – 50 kg/m^3, and 1/8" – 130 kg/m^3)

Two independent manufacturers (OPT and ADM) of sandwich panels were used to source the raw laminate and panel samples, with a single batch of M55J/EX-1515 prepreg procured to ensure consistency in raw materials. The manufacturer cure cycles deviated, mainly due to different heating ramp rates and use of their own consumables, resulting in some differences in mechanical properties. Three companies subsequently performed potting of inserts, all of the same design and supplier, with different insert types. Variations due to manufacturing differences are thus included in the study.

3.1. Elementary Material Properties

As a quality check of the cured laminates, the following tests are performed on uni-directional (UD) and QI (24 ply symmetric [45°/-45°]) laminates:

- Tg (ASTM D7028)
- Fibre Volume Content (FVC) and Void Content (VC) (EN 2564)

The following material tests were performed in order to characterize the CFRP material, to obtain properties which can be processed and used in the FE model (FEM) setup:

- Tensile modulus and strength (ASTM D3039) on 0° and 90° UD laminates
- Compressive modulus/strength (ASTM D3410) on 0° and 90° UD laminates
- ILSS (ASTM D2344) on UD laminates
- In-plane shear strength (ASTM D3518) on symmetric 24 ply [45°/-45°] laminate

Both panel manufacturers have performed these characterization tests independently, and the corresponding material properties are used for FE models representing the relevant test samples. It is important to note that this study is dedicated to the modelling and correlation of the insert test specimen results; average material property data is hence used for correlating against average insert test results. The material characterization test data are summarized in Table 1.

Table 1: CFRP Characterization Test Results

Property	OPT	ADM
0-deg Tens. Strength [MPa]	2243.5[1]	1356.3[2]
0-deg Tens. Modulus [GPa]	341.0[1]	306.9[2]
90-deg Tens. Strength [MPa]	20.5	20.7
90-deg Tens. Modulus [GPa]	5.7	5.4
0-deg Comp. Strength [MPa]	740.0	380.0
0-deg Comp. Modulus [GPa]	275.8	248.8
ILSS [MPa]	57.6	61.6
IPS Strength [MPa]	67.8	55.4
IPS Modulus [GPa]	4.1	4.1

[1] *No post-curing cycle*
[2] *With post-curing cycle*

The FVC for all insert and pin-hole plate test specimens was measured to be within the range 58-62%, hence 60% is a reasonable average value. The UD test laminates used to determine the 0-degree moduli and strength values have larger variation in FVC measurement, therefore these values have all been normalized to 60% FVC.

In addition, the 0- and 90-degree tensile and compressive moduli have been averaged to derive E_1 and E_2 moduli values for the purposes of the FE modelling. The resulting material properties used in the FE models is summarized in Table 2.

Table 2: Summary of FEM Material Data

Property	OPT	ADM
E_1 [GPa]	296[1]	281[2]
E_2 [GPa]	6.1	5.8
G_{12} [GPa]	4.1	4.1
Xt [MPa]	1994[1]	1284[2]
Xc [MPa]	774	380
Yt [MPa]	20	21
Yc [MPa]	125	142
S [MPa]	68	55

[1] *No post-curing cycle*
[2] *With post-curing cycle*

3.2. Pin-Hole Bearing Tests

Both double shear and single lap shear pin-hole bearing tests were performed, in order to determine the bearing failure stress of laminates with different thicknesses and pin-hole diameters. The laminate is representative of the insert breadboard definition, with M55J/EX-1515 prepreg in a QI layup with either

8-plies ([0°/45°/-45°/90°]s) or 16-plies (2x [0°/45°/-45°/90°]s). The configurations tested are summarized in Table 3. The test setups are shown in Figure 2.

Table 3: Pin-Hole Bearing Test Configurations

Config.	Hole Diam. [mm]	Edge Dist. [mm]	Laminate (No. of Plies)
1	14	14	8
2	14	21	8
3	14	28	8
4	14	21	16

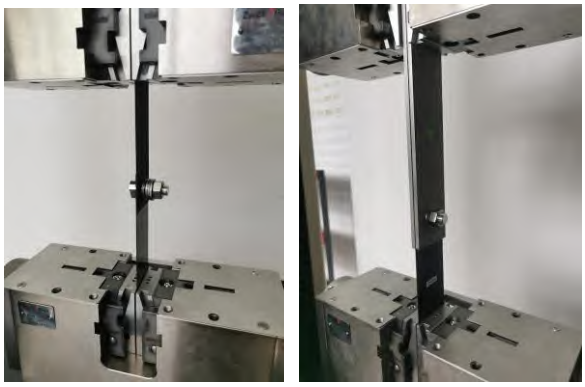


Figure 2: Pin-Hole Bearing Test Setups (Left Side Single Shear; Right Side Double Shear)

Results of the single shear tests are summarized in Table 4, while those of the double shear tests are summarized in Table 5. All samples failed in bearing failure. In single shear, five specimens per configuration and manufacturer were tested, while in double shear three specimens per configuration and manufacturer were tested. Bearing stress at failure was determined and averaged. The coefficient of variance (CoV) is in the range 5-15%.

Table 4: Single Lap Shear Test Results

Config.	Manuf.	Avg. Bearing Stress (Failure) [MPa]	CoV (%)
4	OPT	191	8
4	ADM	150	11

Table 5: Double Lap Shear Test Results

Config.	Manuf.	Avg. Bearing Stress (Failure) [MPa]	CoV (%)
4	OPT	284	7
4	ADM	248	4
3	OPT	190	15
3	ADM	177	5
2	OPT	217	8
2	ADM	179	7
1	OPT	200	8
1	ADM	194	5

The OPT average stress at failure is generally higher than that of the ADM samples, consistent with the findings from the material characterization tests, due to small differences in actual cure cycle.
The results from the double shear test with thicker laminate tests (config 4) show higher bearing strength than the thinner laminates. Also of note is that no significant edge effect observed.
Figure 3 shows an example of the ductile bearing failure mode observed in the pin-hole bearing test samples.



Figure 3: Double Shear Ductile Bearing Failure

3.3. Insert Breadboard Tests

Insert specimen tests were performed following the testing guidelines laid out in [1] (100mm x 100mm sample size, with test jigs as recommended in section 29 of [1]). Figure 4 shows the insert test setup used for shear and pull-out tests. A total of 254 breadboard specimens have been tested, broken down into study groups with varying parameters as summarized below. Typically, five samples per configuration were tested.

Laminates:
- M55J/EX1515, QI layup
- Variations:
  - Baseline: 8 plies [0°/45°/-45°/90°/90°/-45°/45°/0°]
  - Thin skin: 4 plies [0°/45°/-45°/90°] → very sensitive to imperfections!
  - Thick skin: 16 plies [0°/45°/-45°/90°/90°/-45°/45°/0°] + [0°/45°/-45°/90°/90°/-45°/45°/0°]

Core:
- Al alloy 5056, honeycomb core, perforated
- Preferred product: CR III – 5056 series
- Core height: 20mm
- Variations:
  - Baseline core: 3/16-5056-0.001P (50 kg/m^3)
  - Heavy core: 1/8-5056-0.002P (130 kg/m^3)

Potting:
- Loctite Stycast 1090 with Catalyst 9

Insert:
- Material: Al alloy 7075, SurTec 650
- Insert flange: 14mm
- Variations:
  - Baseline: blind with a collar
  - Through insert with a collar
  - Blind flush

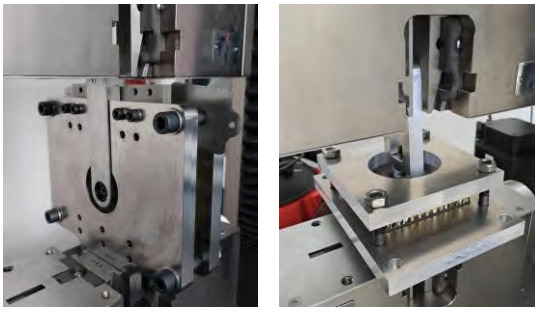


Figure 4: Insert Test Setup (Shear and Pull-Out)

A small number of 2-insert breadboards were tested

in shear using the setup shown in Figure 5. This approach avoids loading of the insert breadboard at the jig contact edge, which can result in crushing of the CFRP facesheet, which is visible in the load-displacement curve. The 2-insert specimen load-displacement plots show a clearer linear relationship up to a clear failure peak load. Figure 6 compares the load-displacement plot for a single insert specimen (right side) versus that of a two-insert specimen (left side); the insert configurations in the two plots were otherwise the same.



Figure 5: Two-Insert Shear Test Setup

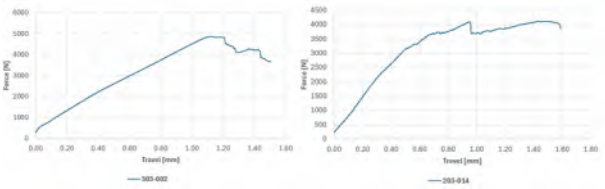


Figure 6: Load-Displacement Curve for 2-Insert Specimen (Left) vs. 1-Insert Specimen (Right)

The insert breadboards were tested to failure, with some tests stopped immediately after the first indication of failure was observed in the load-displacement plot. Figure 7 shows the typical pull-out failure mode (core shear), while Figure 8 shows the typical in-plane failure mode (ductile bearing failure).



Figure 7: Typical Core Shear Failure Mode

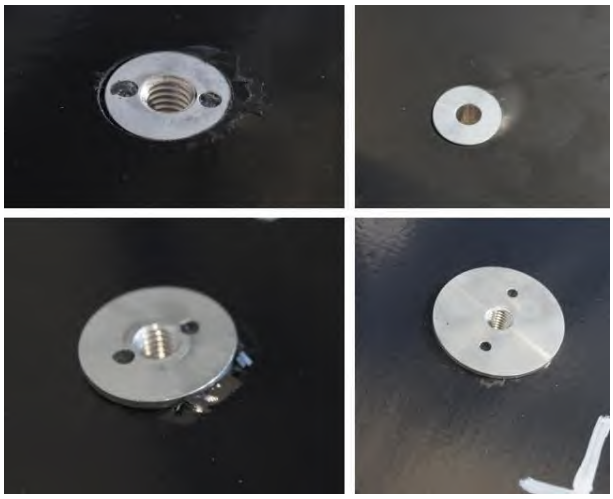


Figure 8: Typical Ductile Bearing Failure Mode

A number of samples were subsequently cut through the cross-section in order to observe the failure modes. Examples are shown in Figure 9 (core shear failure), Figure 10 (facesheet bearing failure) and Figure 11 (potting adhesive failure).

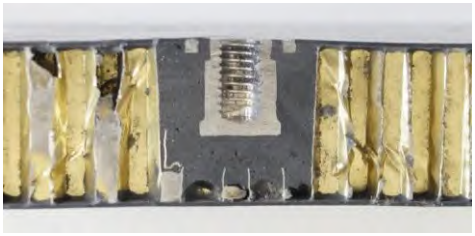


Figure 9: Core Shear Failure Mode

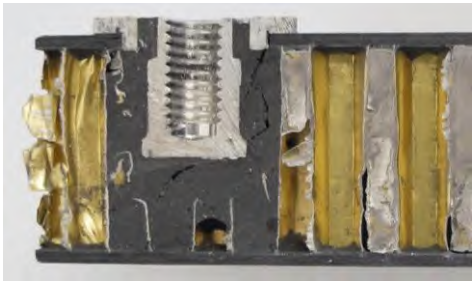


Figure 10: Facesheet Bearing Failure Mode

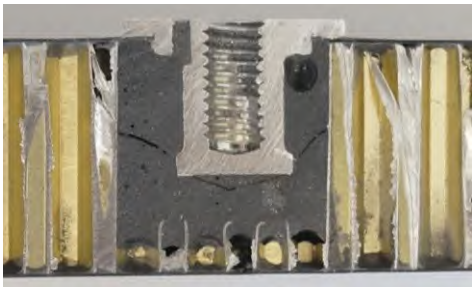


Figure 11: Potting Adhesive Failure Mode

The failure load of each insert has been identified, and the failure loads plotted per insert configuration. These are shown in Figure 12 (shear) and Figure 13 (pull-out). The CoV in both shear and pull-out tests was in the range of 1-7%.

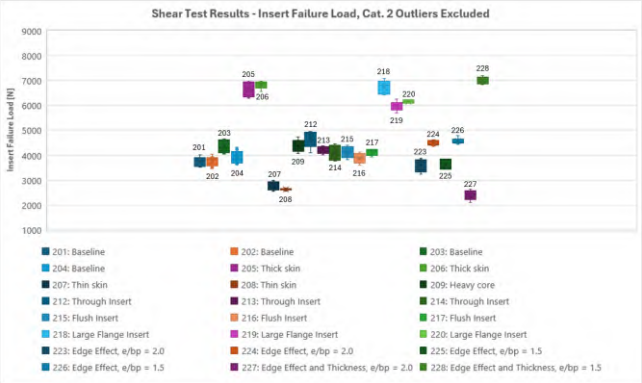


Figure 12: Insert Shear Test Failure Loads

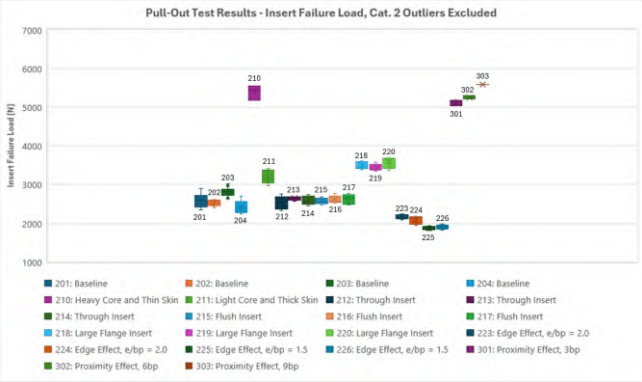


Figure 13: Insert Pull-Out Test Failure Loads

4. FE MODELLING

For the FE modelling phase of this activity, Nastran SOL101 has been used as the solver, i.e. a linear elastic modelling approach, with the use of existing laminate failure theories to predict laminate failure. This approach is pragmatic and available to most of the industry. While progressive failure modelling and advanced models such as LaRC05 are available, they are not commonly used in industry. The selected approach therefore explores the standard available methods before moving into more advanced modelling and post-processing techniques.

4.1. Pinhole Bearing FEM

The double shear tests have been modelled with laminates represented by solid elements using PCOMPS card property with MAT11 material card to define the CFRP material properties. The pin is also modelled with solid elements (PSOLID with MAT1 card), with sliding contact between the pin and laminate via a BCTSET card. This modelling is selected in order to capture the bearing contact between parts. The smallest element size (around the pin-hole location) is comparable to the laminate thickness. A 1kN unit load is applied to the pin in the shear direction, and the model is constrained at the opposite laminate edge via SPC. An additional out-of-plane SPC is applied to the pin, to ensure pure shear is applied.

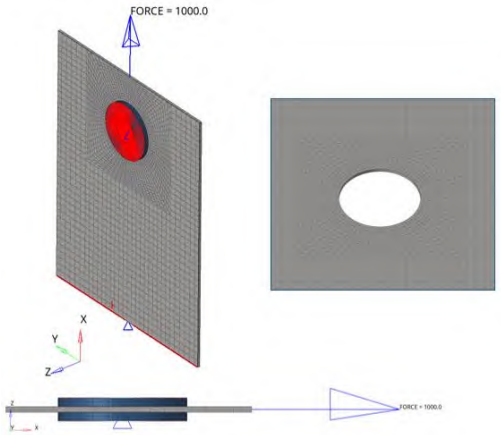


Figure 14: Double Shear Pin-Hole Bearing FEM

The single shear FEM is similar to the double shear FEM, but with additional contacts to represent the more complex interaction between components. Sliding contact is defined between the laminates, at the laminate to pin contacts, and between the pin flange and the laminates. One laminate is constrained via SPC, while the other has the 1kN unit load applied at the opposite end.

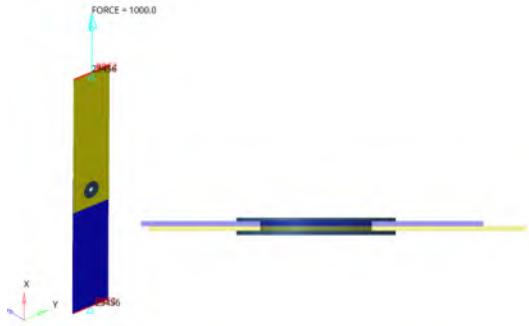


Figure 15: Single Shear Pin-Hole Bearing FEM

4.2. Insert Breadboard FEM

Baseline insert breadboard FEM are generated using solid elements for all components except the bolt, which is represented by an RBE2 element. Figure 16 shows a typical FEM from the study. A single FE model is used for both in-plane and out-of-plane loading scenarios. A unit load is applied to the bolt RBE2 central node. Sliding contact is defined via BCTSET card between the insert flange (where present) and the facesheet with a 0.2 friction coefficient; details are shown in Figure 17.

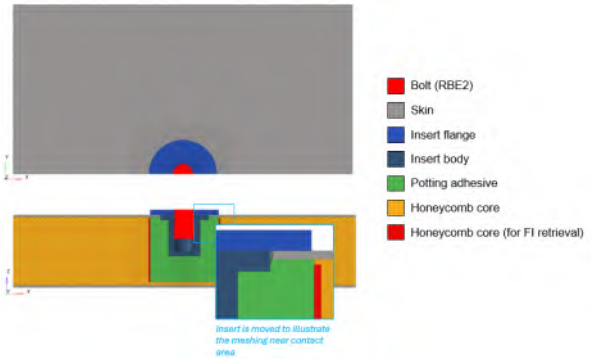


Figure 16: Insert Specimen FEM Overview

Solid elements representing the facesheets are defined via a MAT11 card using the elementary material characterization test data and a PCOMPS card to define the CFRP layup.
The honeycomb solid elements are defined via a MAT9 card (solid element anisotropic property). The MAT9 card parameters are computed based on the honeycomb datasheet homogenised properties with the following assumptions:

- Low stiffness in in-plane directions: $E_X = E_Y \approx 0$
- $E_Z = E_C$ – compression modulus of the core material (stabilized)
- $G_{XZ} = G_L$ – shear modulus in L-direction
- $G_{YZ} = G_W$ = shear modulus in W-direction
- $\mu_{XZ} = \mu_{YZ} \approx 0$

The potting adhesive is modelled via isotropic material (PSOLID with MAT1 cards). For simpler evaluation of the core strength during post-processing, one layer of elements representing the core, adjacent to the potting compound, is highlighted by a dedicated property.
Contact between the potting, insert body and flange, and the core is realized via merged nodes shared between different components. The adhesive layer between skin and core is ignored as it does not contribute to the failure mode (assuming proper bonding between skin and core).

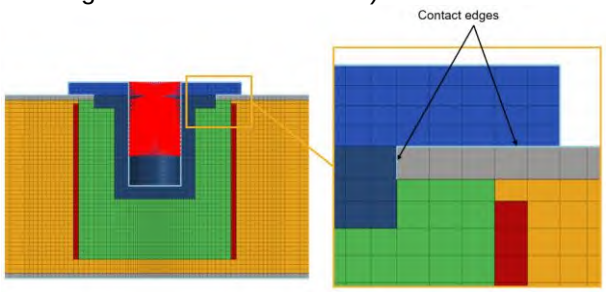


Figure 17: Insert FEM – Insert to Skin Contact

From this baseline FEM, the FEM of other tested configurations is quickly produced by minor modifications:

- Skin thickness:
  - Translation of upper/lower surfaces of skins and insert
  - Update of the PCOMPS card by adding or removing plies
- Potting radius: change in element assignment between core and potting, using concentric rows of elements
- Core density: change in MAT9 card values
- Insert type:
  - Change in insert geometry requires mesh update
  - Change in potting radius

Some of the FEM design variants are shown in Figure 18.

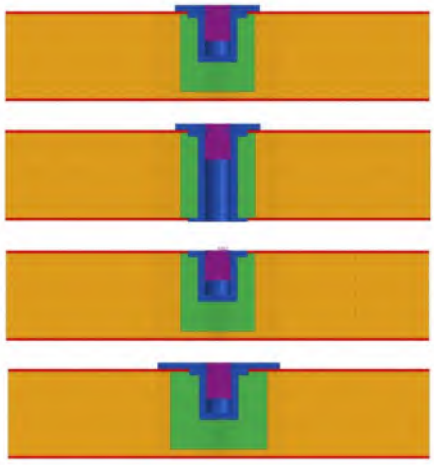


Figure 18: Insert FEM – Design Variants

The FEM are loaded and constrained as follows (Figure 19 shows the shear load FEM boundary conditions):

- DOF 345 on the outer surface nodes of the top skin, except for a 50mm diameter zone around the insert consistent with the test jig contact
- 500N load applied either in-plane or out-of-plane to the central independent node of the bolt RBE2 element
- DOF 246 on the XZ symmetry plane nodes
- In-plane loading:
  - DOF 23456 on the bolt RBE2 independent node
  - DOF 14 on the +X side of the specimen upper skin, over the distance of the contact with the test jig
- Out-of-plane loading:
  - DOF 12456 on the bolt RBE2 independent node

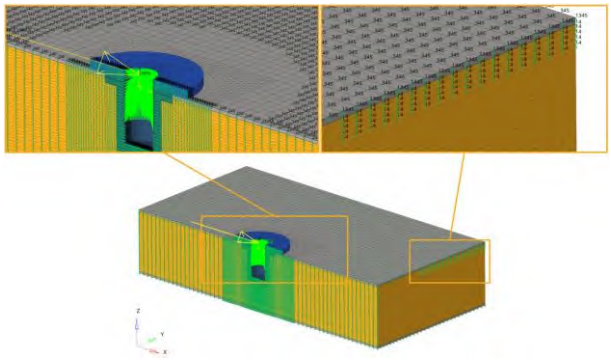


Figure 19: Insert In-Plane FEM Boundary Conditions

5. POST-PROCESSING & CORRELATION

5.1. Laminate Failure Models

The following failure models have been considered: Hill; Tsai-Hill; Hoffman; Hashin.
All of these failure models work via the calculation of a failure index (FI), where a FI > 1 indicates onset of failure. The FI is calculated for each ply in every laminate element of the FE models, based on the

elemental stress data. The FI for each element is thus the maximum FI among the plies in the element – this is the first-ply failure assumption.
Calculation of the failure indices has been performed externally to the FEM, using a python script with the following approach:

1. Apply a 1kN load in the FEM and obtain elemental stress data (output in HDF format)
2. Compute the maximum FI throughout each ply for each laminate element (first-ply failure assumption)
3. Determine the critical load leading to FI = 1.0

5.1.1.Generic Hill

The following formulation of Hill's failure criterion has been used and is implemented directly in NX Nastran and in Digimat:

$$FI = \frac{\sigma_1^2}{X^2} + \frac{\sigma_2^2}{Y^2} + \frac{\sigma_3^2}{Z^2} - \left(\frac{1}{X^2} + \frac{1}{Y^2} - \frac{1}{Z^2}\right)\sigma_1\sigma_2 - \left(-\frac{1}{X^2} + \frac{1}{Y^2} + \frac{1}{Z^2}\right)\sigma_2\sigma_3 - \left(\frac{1}{X^2} - \frac{1}{Y^2} + \frac{1}{Z^2}\right)\sigma_1\sigma_3 + \frac{\sigma_{12}^2}{S_{12}^2} + \frac{\sigma_{13}^2}{S_{13}^2} + \frac{\sigma_{23}^2}{S_{23}^2} \quad (1)$$

Where:

$\sigma_1, \sigma_2, \sigma_3$ are the element stresses in the 1-, 2- and 3-directions
X, Y, Z are the allowable stresses in the 1-, 2- and 3-directions
S_{12} is the allowable in-plane shear strength
S_{13} and S_{23} are the allowable shear strengths in the 13- and 23-directions

The sign of the directional stress components $\sigma_1, \sigma_2, \sigma_3$ is used to determine the appropriate allowable (tensile or compressive) in X, Y, Z. Strength properties in the 2- and 3-directions are assumed to be the same.
Although this is an anisotropic plasticity yield criterion that may not be applicable for CFRP, it is included in the study since it is implemented directly in commercial software.
The critical load F_{crit} leading to FI = 1.0 is then a simple quadratic function of the load applied in the FEM and the FI:

$$F_{crit} = {F_{app}}\Big/{\sqrt{FI}} \quad (2)$$

5.1.2.Tsai-Hill

The Tsai-Hill failure criterion is a failure specific adaptation of Hill's criterion for composite materials formulated for plane stress assumption. Since the FE models use 3D elements to represent the laminate (in order to achieve more accurate contact modelling between the insert and laminate), the following 3D formulation of the Tsai-Hill criterion has been used, as implemented in RADIOSS. Note that there are several different extension forms available in literature.

$$FI = \frac{\sigma_1^2}{X^2} - \frac{\sigma_1\sigma_2}{X^2} - \frac{\sigma_1\sigma_3}{X^2} + \frac{\sigma_2^2}{Y^2} + \frac{\sigma_3^2}{Z^2} + \frac{\sigma_{12}^2}{S_{12}^2} + \frac{\sigma_{31}^2}{S_{12}^2} \quad (3)$$

Similar to the Hill criterion, the sign of the directional stress components $\sigma_1, \sigma_2, \sigma_3$ is used to determine the appropriate allowable (tensile or compressive) in X, Y, Z. Strength properties in the 2- and 3-directions are assumed to be the same. The critical load leading to FI = 1.0 is determined using the quadratic function defined in Eq. (2).

5.1.3.Hoffman

The Hoffman criterion is originally expressed in 2D, however due to the use of 3D elements in the FEM for the laminates, the 3D formulation as implemented in RADIOSS has been used. Note that there are several different 3D extension forms available in literature.

$$FI = \left(\frac{1}{X_t} - \frac{1}{X_c}\right)\sigma_{11} + \left(\frac{1}{Y_t} - \frac{1}{Y_c}\right)\sigma_{22} + \left(\frac{1}{Z_t} - \frac{1}{Z_c}\right)\sigma_{33} + \frac{\sigma_{11}^2}{X_tX_c} + \frac{\sigma_{22}^2}{Y_tY_c} + \frac{\sigma_{33}^2}{Z_tZ_c} - \frac{\sigma_{11}\sigma_{22}}{X_tX_c} - \frac{\sigma_{11}\sigma_{33}}{X_tX_c} + \frac{\sigma_{12}^2}{S_{12}^2} + \frac{\sigma_{13}^2}{S_{12}^2} \quad (4)$$

The strength properties in the 2- and 3-directions are assumed to be the same. The FI is a complex function of the load (second order polynomial), hence the critical load is found via root-finding algorithms. A python post-processing script using Brent's method in the scalar root finding function of the SciPy library has been used.

5.1.4.Hashin

The Hashin criterion is a partial interaction model that distinguishes between different failure modes.
For the tensile/shear fibre mode ($\sigma_{11} > 0$):

$$FI = \frac{\sigma_{11}^2}{X_t^2} + \frac{\sigma_{12}^2 + \sigma_{13}^2}{S^2} \quad (5)$$

For the compressive fibre mode ($\sigma_{11} < 0$):

$$FI = \frac{\sigma_{11}^2}{X_c^2} \quad (6)$$

For the tensile matrix mode ($\sigma_{22} + \sigma_{33} > 0$):

$$FI = \frac{(\sigma_{22} + \sigma_{33})^2}{Y_t^2} + \frac{\sigma_{12}^2 + \sigma_{13}^2}{S^2} + \frac{\sigma_{23}^2 + \sigma_{22}\sigma_{33}}{S^2} \quad (7)$$

For the compressive matrix mode ($\sigma_{22} + \sigma_{33} < 0$):

$$FI = \frac{(\sigma_{22}+\sigma_{33})^2}{4S^2} + \frac{\sigma_{12}^2+\sigma_{13}^2}{S^2} + \frac{\sigma_{23}^2+\sigma_{22}\sigma_{33}}{S^2} + \left[\left(\frac{Y_c}{2S}\right)^2 - 1\right]\frac{\sigma_{22}+\sigma_{33}}{Y_c} \quad (8)$$

Due to the different formulations for each failure mode, comparison of the failure indices is not a reliable means of determining first failure mode. Instead, the critical load to reach FI = 1.0 is calculated for each failure mode, and the minimum critical load is taken for each element.

The critical failure loads for the tensile fiber failure, compressive fiber failure and tensile matrix failure are calculated following the quadratic function in Eq. (2). Since the compressive matrix failure is a second order polynomial, the critical load is found via root-finding algorithms. Consistent with Hoffman model implementation, a python post-processing script using Brent's method in the scalar root finding function of the SciPy library has been used.

5.2. FEM Checks & Mesh Sensitivity Study

Plausibility checks have been performed on the pin-hole bearing test FEMs. Deformation and contact force vector plots indicate realistic distributions. An example for the double shear test FEM is shown in Figure 20.

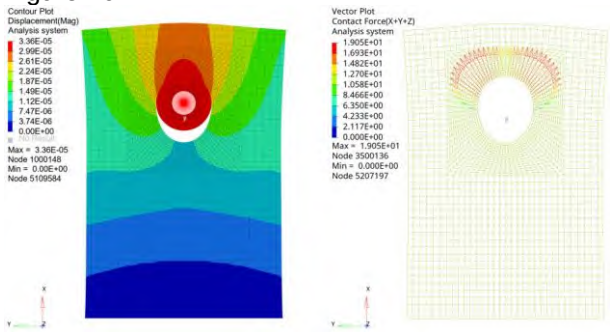


Figure 20: Double Shear FEM Plausibility Checks

A mesh sensitivity study was also performed. The convergence study used PSOLID and MAT1 cards for simplification. As the mesh is refined, the von Mises stress peak increases, whereas the overall stress distribution remains the same. This is primarily due to the nature of the contact problem, where stress levels are highly dependent on the discretization and contact model parameters.

Solid elements modelling was selected for this study to enable surface-to-surface contact definition at the bearing surface of the laminate. For PCOMPS modelling, a single element in the thickness is considered sufficient, and element size is recommended to be comparable with the plate thickness. For the results correlation, it is thus necessary to fix the mesh and contact parameters for consistency. Note that further mesh refinement than shown resulted in irregularities in the stress levels near the contact region, likely caused by the contact algorithm implementation.

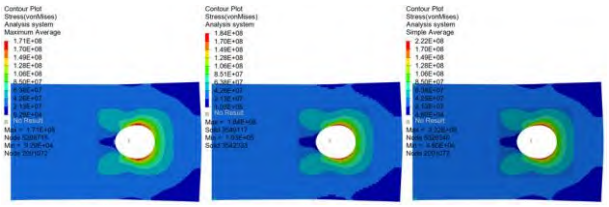


Figure 21: Double Shear FEM Mesh Study

5.3. Post-Processing Methods

The post-processing method is determined by the component and failure mechanisms. The insert and potting adhesive stresses are compared against the datasheet yield strength allowable values. For the skin and core components, a FI is calculated; a FI of 1 or greater indicates failure of that component.

5.3.1. Insert and Potting Adhesive

Failure of the insert is determined by comparison of the peak insert von Mises stress from the FEM versus the yield strength in Table 6. Similarly, failure of the potting adhesive – a brittle material – is determined by comparison of the maximum principal stress from the FEM versus the yield strength in Table 6. Failure is considered to occur when the stress exceeds the specified allowable yield strength. Potting strength is computed based on minimum and maximum principal stresses (P1 and P3) and corresponding compression and tensile allowables.

Table 6: Insert and Potting Adhesive Allowables

Component	Yield Strength [MPa]	Ref.
Insert	393	[2]
Potting Adhesive	20.7 (tension) -82.7 (compression)	[3]

5.3.2. Laminates

The laminates are post-processed using the described failure models, considering the maximum FI in each ply (first ply failure assumption).

5.3.3. Core

For the honeycomb core, a FI, FI_{core}, is calculated based on the shear stress components τ_{xz} and τ_{yz} from the FEM compared to the allowable shear stress (τ_L or τ_W) in the respective plane:

$$FI_{core} = \sqrt{\left(\frac{\tau_{XZ}}{\tau_L}\right)^2 + \left(\frac{\tau_{YZ}}{\tau_W}\right)^2} \quad (9)$$

Table 7: Honeycomb Core Shear Strength Allowables (MPa, Typical)

Core Designation	L-Dir.	W-Dir.
ECM 4.8-50 5056 PAA-CP	1.862	1.069
ECM 3.2-130 5056 PAA-CP	6.619	3.964

All of the honeycomb core failures observed in the test specimens were shear failures of the cell walls immediately adjacent to the potting adhesive. This

is consistent with the typical honeycomb core pull-out failure mode predicted by [1].

A common approach is to determine the insert pull-out load capability based on the maximum FI of the core elements near the potting. However, the ECSS equations are based on the total applied pull-out load, therefore it is more representative to assess the average core strength capability rather than using the peak element FI from the FEM. The core post-processing has therefore calculated the critical force based on minimum, maximum, and average FI in the first row of concentric elements adjacent to the potting adhesive component.

The honeycomb core component defined in the FEM is used to define the single row of concentric elements directly adjacent to the potting adhesive component; this allows for easier retrieval of the FI and automation of the post-processing. Note that the uppermost (and lowermost, in the case of a through insert) row of elements has been excluded from this component.

The critical load is calculated from the FI (minimum, maximum or average) obtained from the FEM according to Eq. (10).

$$P_{failure} = P_{app} * \frac{1}{FI_{core}} \qquad (10)$$

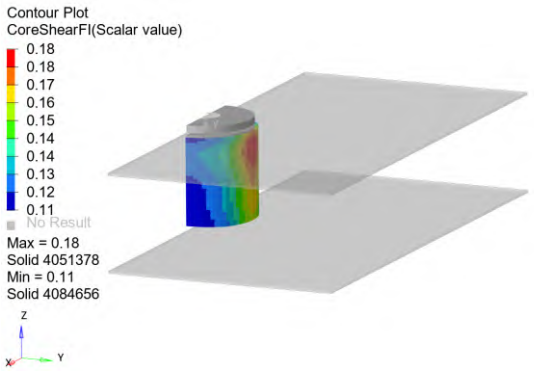


Figure 22: Core FI Example

5.4. Correlation

5.4.1. Pin-Hole Bearing Tests

The FEM of the baseline (configuration 2) pin-hole bearing tests were initially run and processed using the material characterization test allowables and the laminate failure models. Comparison of the FI plots (Figure 23) shows that the Hill failure model results in a significantly lower failure load prediction, together with an unusual stress distribution. The Tsai-Hill and Hashin models show consistent distributions with similar failure load predictions, with the Hoffman model marginally more conservative. Of these three models, the Hashin model is the simplest in terms of correlation, since the failure is driven by the fibre compressive failure, which is governed by a single parameter, X_c. Correlation of the FEM has therefore been performed by scaling X_c in order to achieve a FEM critical load prediction approximately equal to the average value from the tests. This was done for both double shear and single lap shear tests independently. The correlated double shear FI plots are shown in Figure 24. The resulting correlated X_c values are shown in Table 8 and correlated average bearing stresses for the double shear tests shown in Table 9.

Table 8: Correlated Xc [MPa] (Pin-Hole Bearing Tests)

Test Type	Manuf.	Mat. Test X_c	Scale Factor	Correlated X_c
Double Shear	OPT	774	0.90	697
	ADM	380	1.52	576
Single Shear	OPT	774	1.17	906
	ADM	380	1.90	722

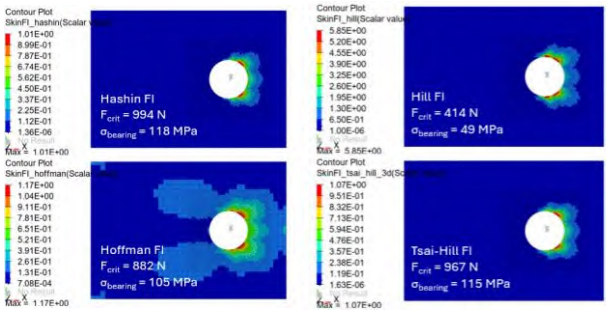


Figure 23: Double Shear Bearing Test FEM FI, Uncorrelated

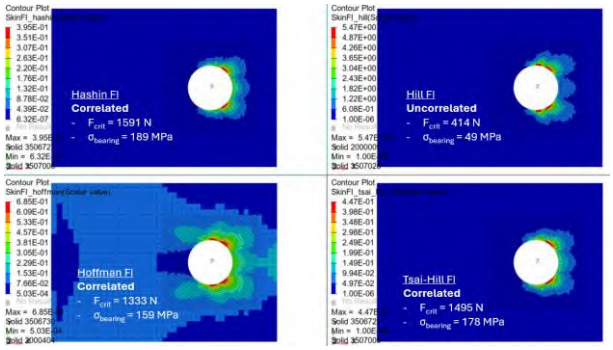


Figure 24: Double Shear Bearing Test FEM FI, Correlated

Table 9: Double Shear Bearing Test Correlated Results

Config.	Test / Failure Model	Avg. Bearing Stress [MPa] OPT	ADM
4	Test	284	248
	Hoffman	176	162
	Tsai-Hill	200	180
	Hashin	219	192
3	Test	190	177
	Hoffman	188	172
	Tsai-Hill	214	191
	Hashin	231	203
2	Test	217	179
	Hoffman	173	159
	Tsai-Hill	199	178
	Hashin	217	189
1	Test	200	194
	Hoffman	140	130
	Tsai-Hill	164	148
	Hashin	185	162

5.4.2. Insert Breadboard Tests

Correlation of the insert breadboard FEM to the shear test results was performed using the same approach as for the pin-hole bearing test FEM correlation, using the Hashin failure model and scaling the X_c parameter only. The baseline configuration (8-ply laminate, 50 kg/m^3 core, blind insert) from each manufacturer was used. The scaled X_c values are shown in Table 10. Figure 25 shows an example of the FI plots (uncorrelated and correlated) for the Hashin, Tsai-Hill and Hoffman failure models.

Table 10: Correlated Xc [MPa] (Insert Tests)

Manuf.	Mat. Test X_c	Scale Factor	Correlated X_c
OPT	774	1.27	983
ADM	380	2.15	817

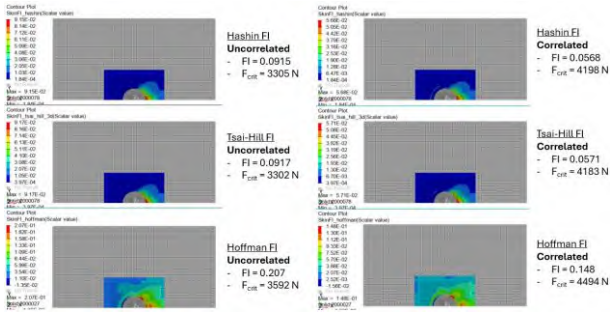


Figure 25: Insert FEM Correlation (OPT)

6. ANALYSIS RESULTS AND COMPARISON TO TEST AND ECSS GUIDELINES

The correlated Xc values were used to post-process all insert FEM. In addition, failure modes for the core, insert and potting adhesive are post-processed.

The FEM correctly predicted the failure mode observed in the tests in all cases. In shear, the critical failure mode is bearing failure of the skin; in pull-out, the failure mode is shear of the core with the exception of one configuration where the potting adhesive fails.

Figure 26 (shear) and Figure 27 (pull-out) compare the FEM predictions against both the ECSS predictions and the test results for each study group. It is worth noting that the ECSS predictions use the facesheet yield strength in the calculations. For the purposes of the comparison below, the baseline configurations (groups 201 to 204 in the plots) have been used to correlate an effective yield strength value for the CFRP facesheets for use in the calculations. In practice, sizing analysis is typically performed based on an initial, conservative, strength estimate. The actual performance of the facesheets, and hence insert strength, would normally only be evaluated by test specimens later in the development.

In pull-out, the FEM is able to predict core shear failure more accurately than the more conservative ECSS predictions.

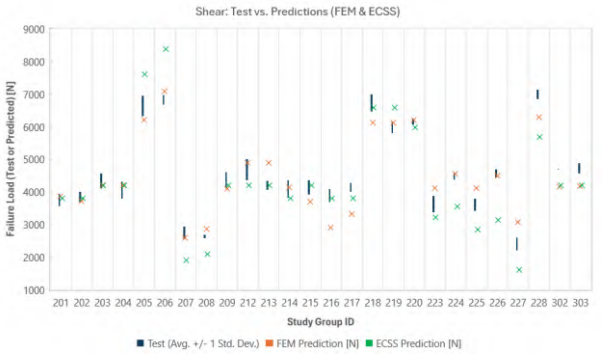


Figure 26: Shear Test Predictions vs Test

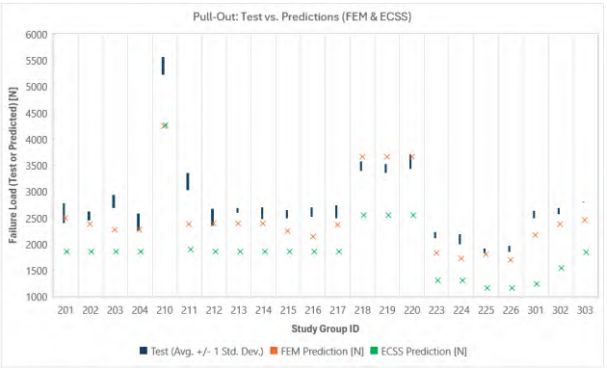


Figure 27: Pull-Out Predictions vs Test

6.1. Potting Adhesive Failure

The core is the failing component in all configurations tested in pull-out, with the exception of one study group where failure is observed in the potting adhesive at the base of the blind insert. The same failure is predicted by the FEM and is also consistent with the ECSS prediction. Figure 28 shows the stress contour plot from the FEM adjacent to the cross-section view of the failed test specimen, with a crack propagating from the insert base corners to the outer edge of the potting adhesive.

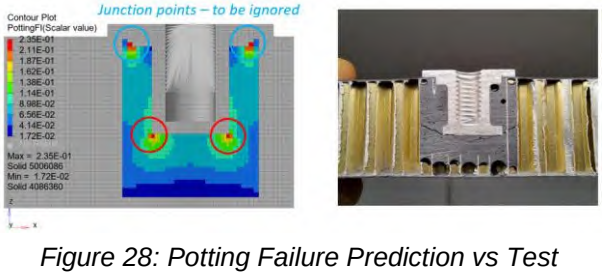


Figure 28: Potting Failure Prediction vs Test

6.2. Core Post-Processing

The core has been post-processed using the minimum, maximum and average FI from each FEM. The closest match between FEM predictions and test result was obtained using:

- Minimum core FI for configurations where a symmetric core stress distribution is expected, with no geometric disturbances
- Average core FI for configurations where edge proximity introduces a geometric disturbance

leading to asymmetry in the stress distribution
- Maximum core FI for configurations with insert proximity effects

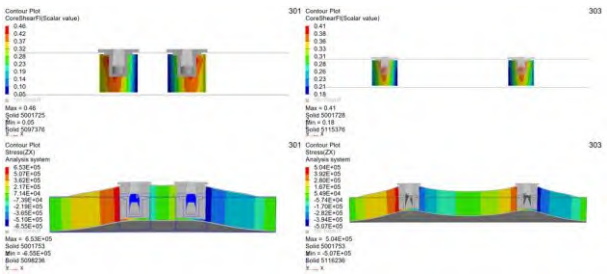


Figure 29: Core FI Distribution Asymmetry

6.3. Edge Effects

An insert potted close to a panel edge has reduced load capability in both in-plane and out-of-plane directions. The out-of-plane knockdown factor (KDF) of an insert's load-carrying capability is defined in [1] by Eq. (11), considered applicable for metallic and CFRP sandwich panels.

$$\eta_{EN} = 0.55\sqrt{\frac{e}{b_p}} - 0.05\,{}^{e}/_{b_p} \quad \text{for } e \leq 5b_p \qquad (11)$$

In the in-plane loading scenario, [1] recommends performing tests to obtain reliable data for edge coefficients in CFRP skin panels.
From the test failure loads, FEM failure load predictions, and ECSS failure load predictions, KDFs have been calculated for the edge effect study groups. These are shown in Figure 30 (pull-out) and Figure 31 (shear).
In pull-out, the KDF trend is consistent between all approaches; ECSS calculations are the most conservative, the test results the least, and the FEM providing a middle-ground between the ECSS and test values.
In shear, no discernible edge effect is noticeable from the test data; this is also predicted by the FEM for the Hashin and Tsai-Hill failure models. The Hoffman model predicts a KDF trend similar to the ECSS KDF trend.

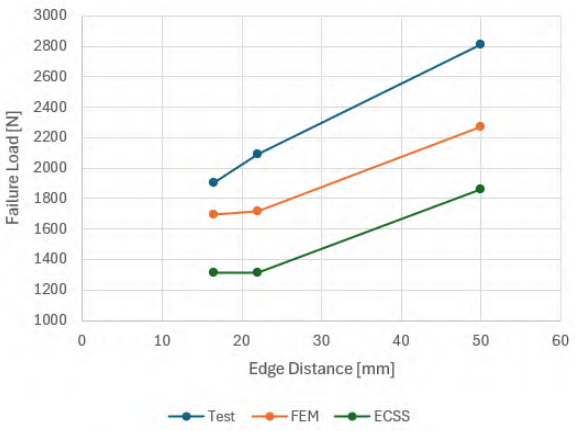


Figure 30: Edge Effect – Pull-Out

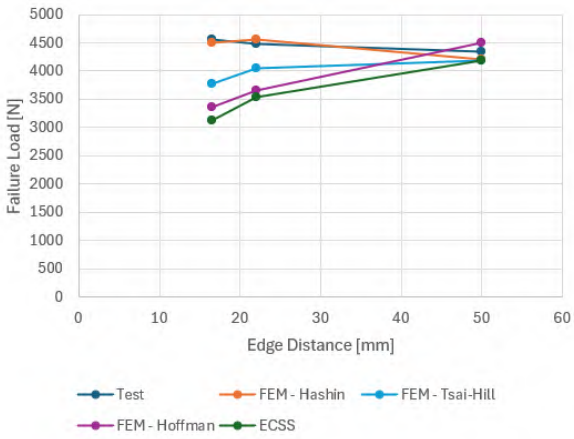


Figure 31: Edge Effect – Shear

6.4. Insert Proximity

Inserts potted in the vicinity of another insert experience a reduction in load capability in both in-plane and out-of-plane directions. In the scenario of two inserts loaded in the same out-of-plane direction – as is the case in the current study – the insert's pull-out load-carrying capacity is reduced by an interference coefficient. When the two insert potting radii are the same, the KDF equation is given in Eq. (12).

$$\eta_{IS} = \frac{1}{2}\left(1 + \frac{a}{5b_{p1}}\frac{1}{2}\right) \quad \text{for } a \leq 5(b_{p1}+b_{p2}) \qquad (12)$$

In the in-plane direction, [1] recommends performing tests to obtain reliable data in CFRP sandwich panels. In this study, insufficient two-insert specimen in-plane test data is available to draw any conclusions.
In pull-out, test failure loads, FEM failure load predictions, and ECSS failure load predictions are compared in Figure 32. The maximum core FI has been used to post-process the FEMs, due to the asymmetry in honeycomb core stress resulting from the insert proximity. A small influence of the proximity effect is visible in the test and FEM data; the KDF from both data sets is very comparable. The ECSS KDF is more conservative, however shows a similar trend.

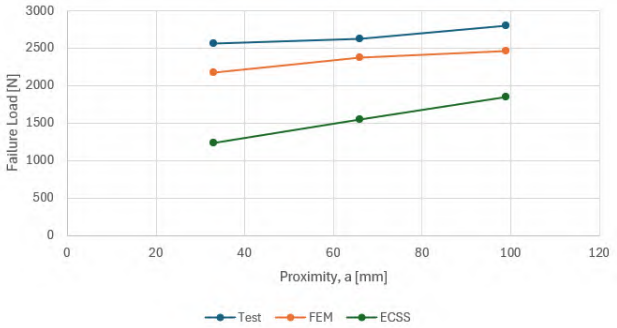


Figure 32: Proximity Effect – Pull-Out

7. APPROACHES TO MATERIAL TESTING & CORRELATION

As demonstrated in this study, for in-plane strength the fibre compression is the primary failure mode. The laminate fibre compressive strength X_c can hence be considered as the main correlation parameter for the laminate in-plane strength, when the model discretization and contact parameters are fixed. Three methods of determining X_c are identified:

- Material tests (UD compression test)
- Pin-hole bearing tests (with subsequent FE analysis and correlation of X_c to the test results)
- Insert shear tests (with subsequent FE analysis and correlation of X_c to the test results)

The X_c values obtained from these three approaches are summarized in Table 11, for both laminate manufacturers.

Table 11: Summary of X_c Values [MPa]

Manuf.	Mat. Test	Pin-Hole Bearing		Insert Test
		Double Shear	Single Shear	
OPT	774	697	906	983
ADM	380	576	722	817

The UD compression tests displayed high sensitivity, resulting in significant scatter in the obtained values. The tests may be sensitive to the test setup. Data obtained this way may therefore be unreliable; however, comparison with the correlated values shows that it is generally a conservative approach to determining X_c.

The pin-hole bearing test offers a method of determining X_c with a similar level of testing effort compared to the UD compression tests, but with results that tend to be less conservative compared to the UD compression tests, and with variation of approximately 10%. The single-shear test method results in less conservative X_c values compared to the double-shear test and is recommended over the double-shear test method, which may be influenced by the constraint of the laminate bulging in the failure zone. Some additional effort is required to setup representative FE models and correlate the analysis results to the test values compared to the material characterization test approach.

The insert tests provided the least conservative X_c values, with the smallest variation (ca. 5%). This approach therefore introduces the least amount of conservatism, however the effort to manufacture the test specimens and correlate the results is also the highest of all methods.

The selection of a test approach must take into account the usual project considerations:

- Budget and timeline
- Tools and capability within the organization to perform the analysis and correlation activities
- Desired – or acceptable – level of conservatism in the results

Note that regardless of the material testing method selected, a sufficient number of test specimens should be planned to ensure repeatability of the result, and to allow for A/B-basis value determination without a significant penalty due to a small sample size. As a minimum, 10 test samples are recommended to avoid a significant statistical penalty.

8. CONCLUSIONS

This investigation has shown that standard modelling techniques with commercial solvers are sufficient to model CFRP bearing failure and insert capability, with good correlation to both test data and ECSS predictions demonstrated.

The Hashin, Tsai-Hill and Hoffman failure models all provide similar critical load predictions for the CFRP skins and can be used interchangeably depending on the solver features or data availability.

For the studied laminates, the fibre compressive strength X_c is demonstrated to play the dominant role in the bearing and insert capability; correlation of this parameter alone is sufficient to obtain accurate insert load capability predictions.

X_c can be determined via different test methods: material characterization tests, pin-hole bearing tests, or insert specimen tests. The lower-level tests are found to provide more conservative estimates of X_c.

The analysis approach described can allow for a reduced quantity of physical tests, but does not entirely replace testing.

In shear, the edge effect data from test and the Hashin and Tsai-Hill models suggest only a minor influence. However, the Hoffman model and ECSS predictions are similar and suggest a KDF is applicable. Further data and study are necessary. In pull-out, the ECSS KDF predictions are more conservative than the FEM predictions and the test results, but all show a similar trend.

In pull-out, the ECSS KDF for two-insert proximity is shown to be conservative, and the FEM is able to provide accurate prediction of a realistic KDF.

The analysis has shown that the use of a MAT9 card to represent the core via 3D elements is viable, enabling prediction of both shear and pull-out capabilities of an insert. The core FI distribution symmetry adjacent to the potting can be used to determine which failure index approach is most suitable for a particular configuration. The minimum FI is applicable for undisturbed inserts; the average FI for asymmetry due to edge proximity; and the maximum FI for asymmetry due to insert proximity.

9. REFERENCES

1. ECSS-E-HB-32-22A (20 March 2011). Space Engineering – Insert Design Handbook.
2. MMPDS 14 (1 July 2019) – Metallic Materials Properties Development and Standardization
3. TDS Loctite Stycast 1090 Cat 9 (April 2020) – Loctite Stycast 1090 Cat 9 Technical Datasheet

ECSSMET
Braunschweig Germany 2026

DFAT

SATELLITE MODAL SURVEY TESTING WITH A DFAN SETUP: COMPARING ACOUSTIC AND SHAKER EXCITATION

Bart Peeters [(1)], Kevin Napolitano [(2)], Edward Heyd [(3)], Dale Schick [(3)], Umberto Musella [(1)], Chrisopher Sensor [(4)]

[(1)] Siemens Industry Software NV, Leuven, Belgium, Email: bart.peeters@siemens.com
[(2)] ATA Engineering, Inc., San Diego, CA, USA
[(3)] Acoustic Research Systems, Inc., Shepherdstown, WV, USA
[(4)] Siemens Industry Software Inc, Plano, TX, USA

KEYWORDS

Environmental testing, acoustic testing, modal survey testing, experimental modal analysis

ABSTRACT

Direct Field Acoustic Noise (DFAN) testing of satellites is a proven alternative for reverberant room acoustic testing and, in certain cases, even random vibration testing. The objective of this paper is to propose a method that allows to use a DFAN setup also successfully for modal survey testing of a spacecraft, further increasing the efficiency of the testing program. Another important advantage of adopting acoustic excitation, compared to impact or shaker excitation, is that mechanical contacts with the satellite are avoided.

This paper presents the results of a large test campaign on the Structural Test Article of the Emirates Mission to the Asteroid Belt spacecraft which was tested at the Laboratory for Atmospheric and Space Physics at the University of Colorado (CU LASP). Eigenfrequencies, damping ratios, and mode shapes of the satellite have been identified from a DFAN test setup and compared with results from modal shaker excitation.

1. INTRODUCTION

There is increasing interest in the aerospace community to reduce testing cost, risk, and schedule impacts by combining as many structure-related tests as practicable into a single test setup [1,2]. One potential opportunity is to perform a modal survey test while a test article is configured for a Direct Field Acoustic Noise (DFAN) qualification test, and to verify this approach a modal survey test of the Emirates Mission to the Asteroid Belt Structural Test Article (EMA-STA) was performed using acoustic, impact, and shaker excitation.

There have been earlier successful demonstrations of applying (operational) modal analysis to data from a preliminary acoustic (system identification) test or to the acoustic qualification test data itself [3-6]. The specific objectives of the EMA-STA tests are to verify the feasibility of using acoustic excitation well below 20 Hz, to explore and compare some specific excitation signals, to compare different data processing and modal analysis strategies, and to further develop the fixed-base correction method combining acoustic excitation with additional structural excitation at the interface of the satellite. This last topic is discussed in a separate paper [7].

Uncorrelated multiple-input broadband random acoustic excitation will be compared to multiple-input random shaker excitation. Operational Modal Analysis (OMA) using satellite structural responses only will be compared to Experimental Modal Analysis using Frequency Response Functions (FRFs).

The measurement campaign and this paper have been the result of a collaborative effort from Acoustic Research Systems (ARS), ATA Engineering, and Siemens Digital Industries Software, bringing together competences on DFAN testing, acoustic devices, aerospace & defense advanced engineering, data acquisition, (MIMO) control and experimental & operational modal analysis.

This paper will discuss modal survey testing using Neutrons as acoustic excitation devices, describe the EMA-STA test setup, discuss excitation signals and measurement functions required for modal analysis. EMA and OMA results will be discussed, and modal shaker results will be compared to acoustic excitation results. Finally, the conclusions will be presented.

2. MODAL SURVEY TESTING USING ACOUSTIC EXCITATION

There has been a surge in research efforts that verify that DFAN sources can be used to excite test articles well enough to conduct modal surveys [3-8]. Experimental Modal Analysis (EMA) can be performed when FRFs are available, i.e. next to the structural responses, also signals representative for the acoustic sources need to be available. Alternatively, Operational Modal Analysis (OMA) can be applied as long as the magnitude and pattern

of the acoustic pressure varies slowly as a function of frequency such that the main assumption associated with OMA – that the input power spectra are constant as a function of frequency – is broadly true over reasonable frequency ranges.

A typical acoustic qualification test setup used by Acoustic Research Systems is shown in Figure 1. In this configuration six stacks of three ARS Neutron acoustic devices are placed around the test article. Typically, a controller that acts upon multiple field microphone signals generates incoherent broadband acoustic noise to approximate a diffuse acoustic field, which excites the article. The controller adjusts the generated drive signals such as to reproduce the target acoustic spectrum, typically expressed in full or 1/3rd octave bands.

DFAN systems consist of multiple stacked acoustic devices surrounding the test article to produce the high-intensity output required by launch vehicle acoustic qualification testing. At the same time, it is important to avoid the creation of interference patterns, non-characteristic of diffuse acoustic fields, which can over/under excite test articles.

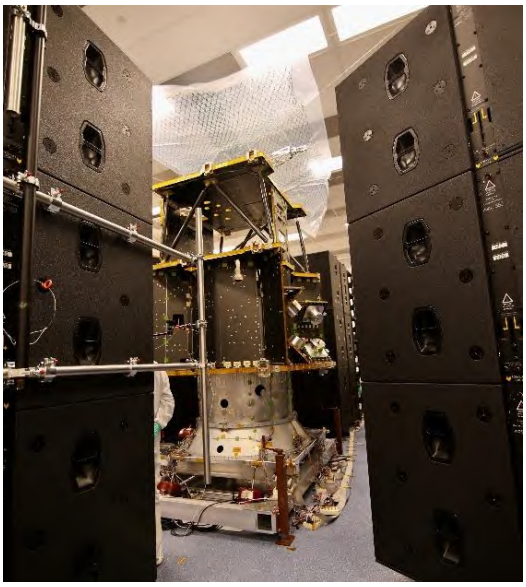


Figure 1: Acoustic qualification test setup showing ARS Neutron system in 6x3 testing configuration surrounding EMA-STA

The Neutron was designed with the highest possible initial efficiency across the frequency ranges most prominent in most launch vehicle payload fairings. Particularly in the low frequencies, the unique driver-loading mechanism in the Neutron produces equal pressure both behind and in front of the transducer. This mechanism somewhat unexpectedly allows the device to actively extend excitation into infrasonic frequencies without over excursion of the transducers.

This sort of excitation scheme is perfectly aligned with a typical multi-input/multi-output modal survey test where independent random excitation is applied to each conventional modal shaker. While many acoustic sources would be damaged if excited at low frequencies, the ARS Neutrons are designed to be robust and self-limiting. At lower frequencies when acoustic inputs are less efficient, acoustic input can be concentrated in the frequency domain to allow the acceleration response to rise above the sensor noise floor. One such excitation is a multi-sine excitation pioneered by ATA [9].

Interesting to note is that all typical shaker excitation signal can also be used to drive ARS Neutron acoustic devices: random, burst random, pseudo-random, pink noise, sine dwell, sine sweep. The Neutron has demonstrated the capability to provide effective modal excitation at frequencies above 2 Hz. Furthermore, all Neutrons utilize a common subwoofer design spanning frequencies from below 2 Hz to 400 Hz, thereby covering the complete frequency range of interest for most aerospace modal test applications.

3. TEST SET-UP

The EMA-STA is shown in Figure 1. It is connected to a reinforced isolated plate (“base plate” and “stiffening beams” in Figure 2) through a payload adapter. The isolated plate is connected to a transportation cart through four wire rope isolators. The isolated plate was reinforced to help increase its out of plane stiffness. The wire rope isolators keep higher frequency shock type loads from passing into the test article. The cart itself rests directly on the ground. The ARS Neutrons were configured in a 6x3 configuration. For this test, each stack of three Neutrons used the same input voltage for a total of 6 sets of independent acoustic sources.

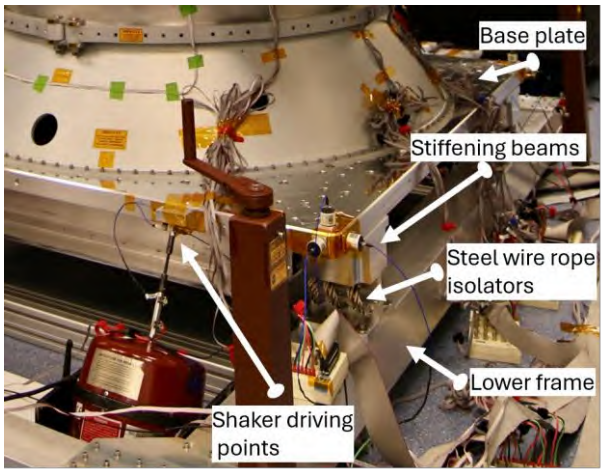


Figure 2: EMA-STA boundary condition

A total of 147 100 mV/g modal accelerometers were mounted to the test article. Twelve 1000 mV/g seismic accelerometers were mounted to the isolated plate at four corners in order to measure the rigid body motion of the plate and the primary out of plane twist mode (Figure 3). An example of a

microphone to monitor acoustic input sound pressure levels is shown in Figure 3.

Seven modal shakers were mounted at the base in a configuration to excite the six rigid body modes and the primary vertical twist mode of the isolated plate. The shaker configuration was selected for applying the fixed-base correction method [7] but in this paper the shaker data will be used to compare more classical shaker modal results with acoustic excitation modal results. A schematic of the accelerometer and shaker locations is shown in Figure 4.

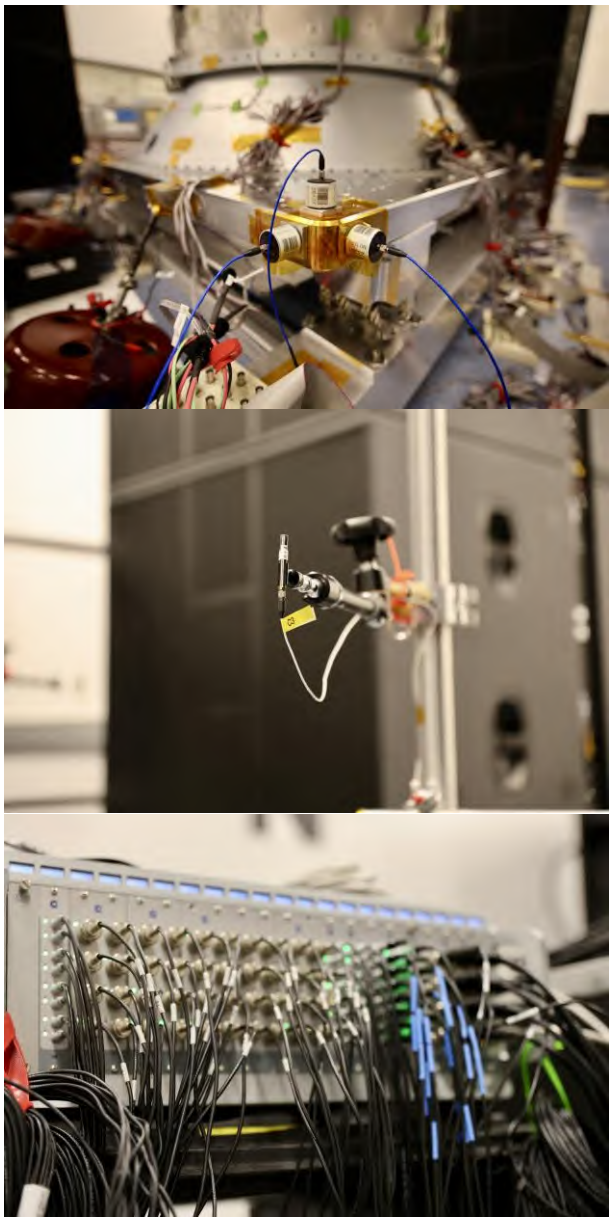


Figure 3: (Top) Modal shaker and seismic accelerometer installation; (Middle) Control microphone; (Bottom) Simcenter SCADAS

Data was collected using Siemens Simcenter Testlab software and two SCADAS Lab frames daisy-chained together with a fiber optic connection for a total of 224 channels (Figure 3). This test recorded a total of 188 channels including all accelerometers, load cells, microphones, and input voltages. Data was sampled at 6.4 kHz. Voltage signals to both the modal shakers and the Neutrons were provided by the SCADAS drive (DAC) channels. The SCADAS system provided two types of excitation signals to the shakers and acoustic sources: broadband random generated internally and digitally generated multi-sine sweep excitation provided by ATA and replayed using the “arbitrary source” capability of the SCADAS. While open-loop excitation was used for the modal survey test data presented in this paper, Testlab is also capable of MIMO control for DFAN qualification testing [10].

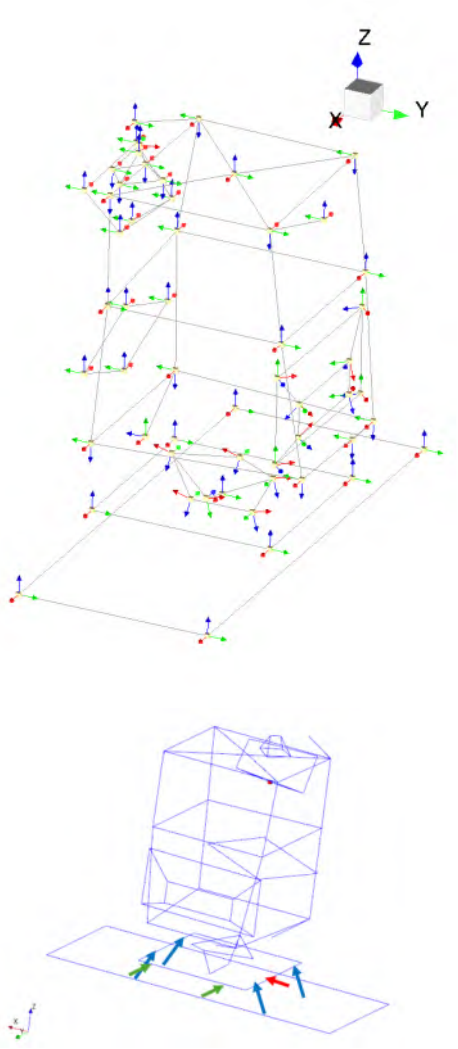


Figure 4: (Top) Accelerometer locations; (Bottom) Modal shaker excitation locations

4. EXCITATION SIGNALS AND MEASUREMENT FUNCTIONS

The 7 shakers at the base have been driven by uncorrelated white noise signals [V], which means that the 7x7 power spectrum matrix of the drives is a diagonal matrix. With shaker testing, a stinger is used to transfer a point force into the structure. This force can be measured by a force sensor that is placed between the stinger and the structure

(Figure 2). FRFs [g/N] can be computed relating structural acceleration responses [g] to the forces [N]. Classical EMA can be applied to these FRFs to identify the modes of the satellite.

The acoustic devices have been driven by 6 uncorrelated signals of the following type:

- White noise (2-200 Hz): this is a standard excitation signal that is also used in shaker testing to excite the frequency range of interest in a modal test.
- Pink noise (20-2000 Hz): this is a typical acoustic signal and is somewhat representative of the excitation during a typical DFAN test.
- Multiple parallel sine sweeps (1-25 Hz): this is a special excitation signal developed by ATA [9] where as many sine sweep signals as independent excitation devices (in this case 6) are used. Each sweep starts at a different frequency, but each sweep covers the entire frequency of interest. Idea is to focus more energy in the lowest frequency range, where acoustic devices are typically less efficient, and still obtain structural responses well above the noise floor.

Figure 5 compares the power spectral densities [V^2/Hz] of these drive signals sent to the 6 independent acoustic devices. As will be demonstrated, high-quality results have been obtained by using the standard white noise excitation signals and the data obtained using other excitation signals will not be further discussed.

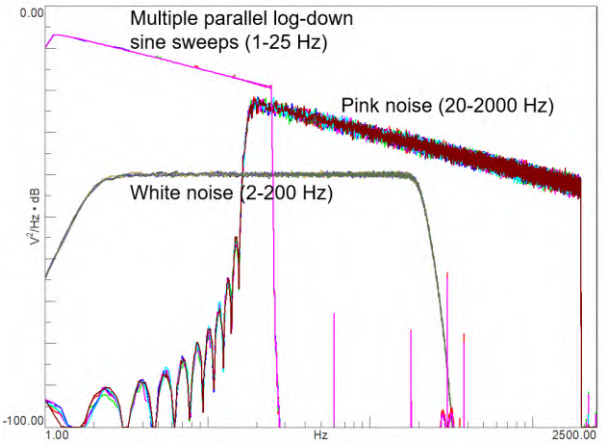


Figure 5: Power Spectral Densities of the drive signals sent to the 6 independent acoustic devices: comparing white noise, pink noise, and multiple parallel sine sweeps

When using acoustic devices as excitation, it is more challenging to quantify the forces acting on the structure. To still be able to calculate FRFs, surrogate signals can be used:

- Drives [V], although not directly representative for the actual "acoustic force"; resulting FRFs will have [g/V] as unit.
- Microphones [Pa] in front of acoustic devices; resulting FRFs will have [g/Pa] as unit.

Figure 6 (Top) shows the power spectra [V^2] of the drives and (Bottom) the drive to microphone FRFs [Pa/V]. The curves represent direct FRFs, i.e. between the microphone in front of a source and the drive sent to that source. The matrix insert shows the full 6x6 FRF matrix, indicating that the diagonal elements are the most important ones.

Although flat drives have been used, it is obvious that the acoustic pressure decreases at the lower end of the spectrum. Nevertheless, the low-frequency modes were still very well excited (lowest mode is around 7 Hz) – see further.

Both [g/V] and [g/Pa] FRFs could be used for EMA, but as an alternative, it is also possible to consider an OMA approach, where no FRFs are needed; response power and cross spectra [g^2] are used instead. EMA and OMA will be discussed in next section.

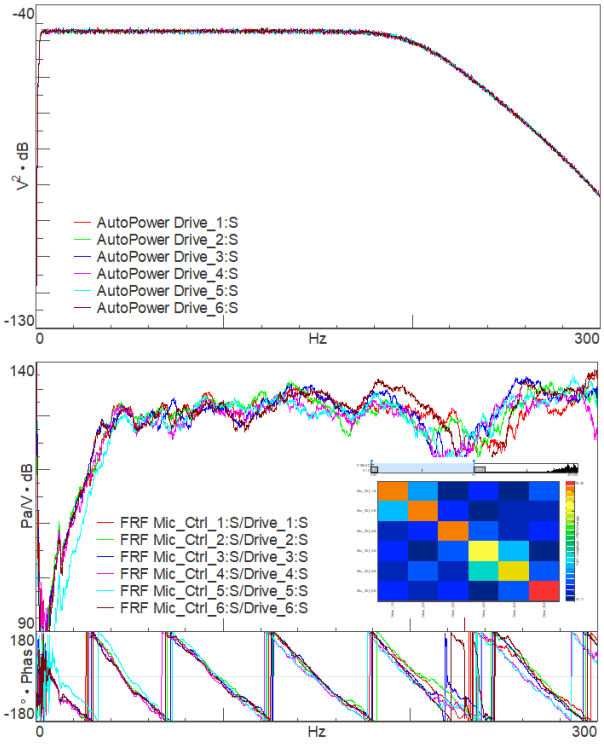


Figure 6: (Top) Power spectra of the white noise drives; (Bottom) FRFs from drives to microphones

When comparing shaker excitation FRFs [g/N] with acoustic excitation FRFs [g/V] (Figure 7), it can be observed that the acoustic FRFs have significantly lower magnitudes at the lower frequencies. Nevertheless, both types of FRFs show an identical "modal content" (same resonance frequencies are apparent in both). Owing to the high quality of the entire measurement chain, the lower frequency modes clearly exceed the noise floor for the acoustic FRFs as well.

It is also interesting to look at the phase behaviour of some measurement functions that can be processed from the shaker and acoustic excitation:

- Shaker FRFs [g/N] show the typical “modal” phase behaviour when crossing through resonances (Figure 8).
- Acoustic FRFs [g/V] show a superimposed linear phase which is caused by the time delay in the acoustic excitation path (Figure 9). Such phase behaviour is typically not accounted for in the (modal) models that are used in the curve-fitting process.
- Acoustic excitation cross spectra between structural responses [g^2] do not suffer from the time delay in the acoustic path. Again, a “modal” phase behaviour is observed (Figure 10).

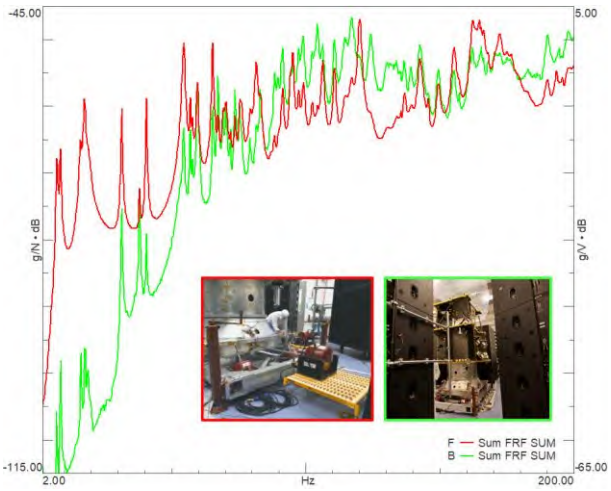


Figure 7: Sum of FRFs: comparing white noise shaker excitation (red) with white noise acoustic excitation (green)

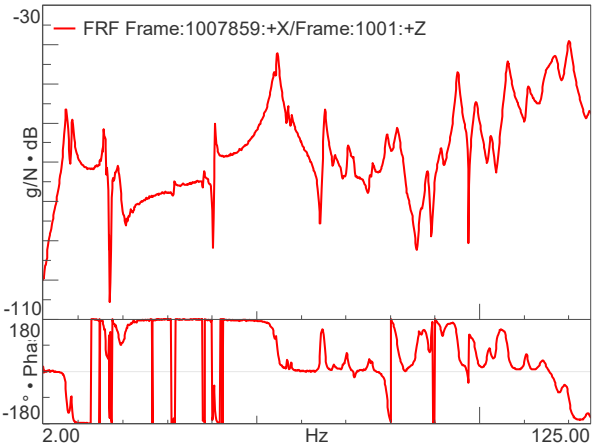


Figure 8: White noise shaker FRF [g/N] with typical “modal” phase behaviour

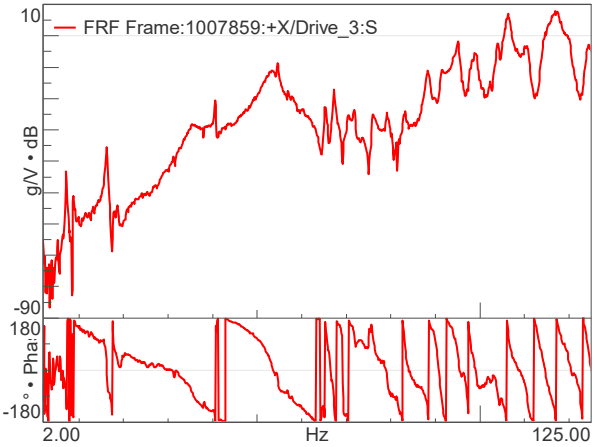


Figure 9: White noise acoustic excitation FRF [g/V] shows additional time delay (linear phase)

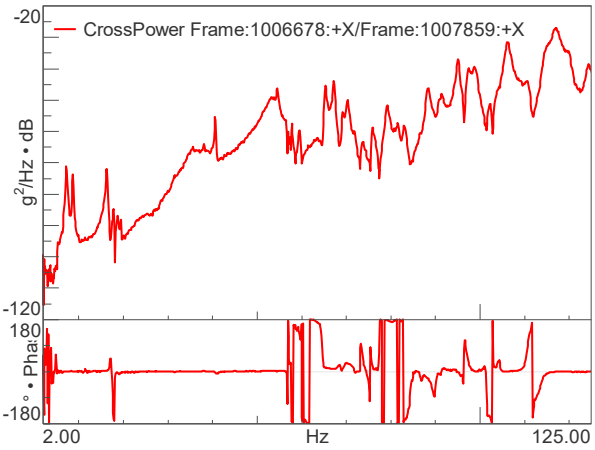


Figure 10: White noise acoustic excitation cross spectrum [g^2] without time delay

5. EMA AND/OR OMA

Next step is to estimate the modal parameters from the measurement functions calculated as explained in previous section. Experimental Modal Analysis is the process of estimating structural modes (eigenfrequencies, damping ratios, and mode shapes) based on vibration measurements in either controlled experimental or operational conditions, respectively. This happens by so-called curve-fitting techniques where a modal model is fitted to the measurement data.

When trying to estimate the modal parameters from sometimes noisy data, it is generally a good idea to over-specify the model order considerably, i.e. to try to fit high-order models that contain much more modes than present in the data. Afterwards the true physical modes are separated from the spurious numerical ones by interpreting a so-called stabilization diagram (Figure 11 – Figure 13). The poles corresponding to a certain model order are compared to the poles of a one-order-lower model. If their differences are within pre-set limits, the pole is labelled as a stable one. The spurious numerical poles will not stabilize very well during this process

and can be sorted out of the modal parameter data set more easily.

Nevertheless, the interpretation of stabilization diagrams may be intimidating for the non-expert and the selection of the “right” poles can be a time-consuming and error-prone process. Therefore, the automation of pole selection in modal analysis is important to accurately process complex datasets without user-dependent interaction and with repeatability. Such automated modal analysis method was recently proposed in [11]: a Hybrid AI method was developed using a Machine Learning (ML) density-based clustering technique, combined with domain knowledge of modal parameter selection.

Polymax [12] as implemented in Simcenter Testlab was selected as the EMA method and applied to both shaker [g/N] and acoustic FRF [g/V] data (Figure 8, Figure 9). The Polymax stabilization diagrams can be found in Figure 11 and Figure 12. The Operational Modal Analysis (OMA) variant of Polymax [13] will be used to estimate the modes from the acoustic excitation cross spectrum data. A detailed discussion on data pre-processing for Operational Modal Analysis can be found in [13] and references therein.

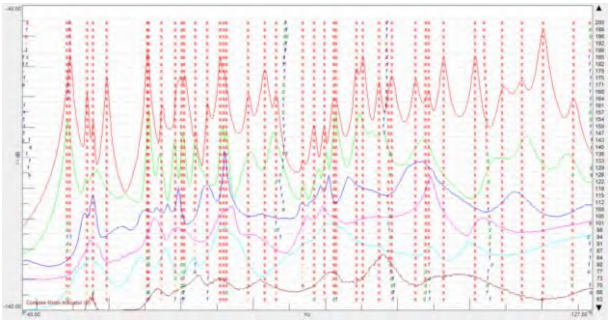


Figure 11: EMA applied to shaker FRFs [g/N] – stabilization diagram

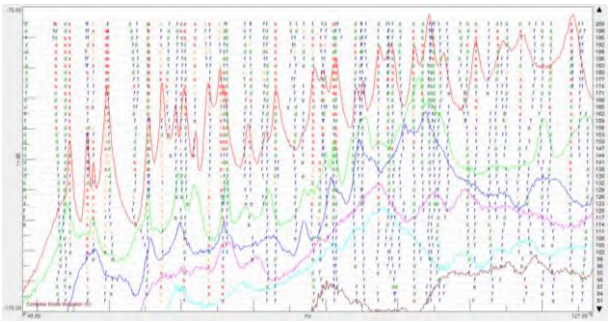


Figure 12: EMA applied to acoustic excitation FRFs [g/V] – stabilization diagram

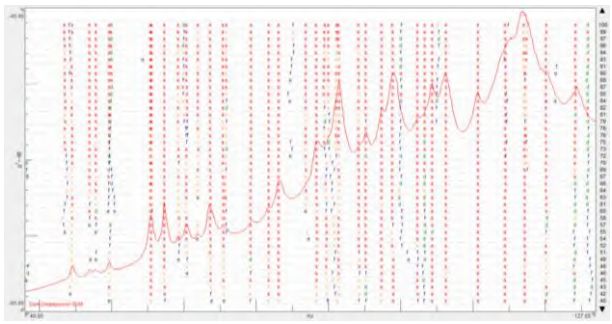


Figure 13: OMA applied to acoustic excitation cross spectra [g^2] – stabilization diagram

Following observations can be made from the stabilization diagrams:

- Polymax applied to clean (high-coherence) shaker FRFs [g/N] results in very clear stabilization diagram (Figure 11).
- Polymax applied to acoustic excitation FRFs [g/V] results in a stabilization diagram from which it is more challenging to select the poles (Figure 12). These FRFs are somewhat noisier (lower coherence) and show a linear phase behaviour (Figure 9) which is not fully compatible with the modal model that is used for the curve-fitting.
- OMA Polymax applied to acoustic excitation cross spectra [g^2] again results in a very clear stabilization diagram from which the pole selection is straightforward (Figure 13).

As one of the objectives of this work is to verify the feasibility of using acoustic excitation well below 20 Hz, OMA was also applied in the lower frequency range (2 - 25 Hz) of the white noise acoustic excitation data. The stabilization diagram in Figure 14 indicates that the lower modes could be easily found. The comparison between the measured and synthesized cross spectra (Figure 15) confirms the high quality of the OMA results in the lower frequency range.

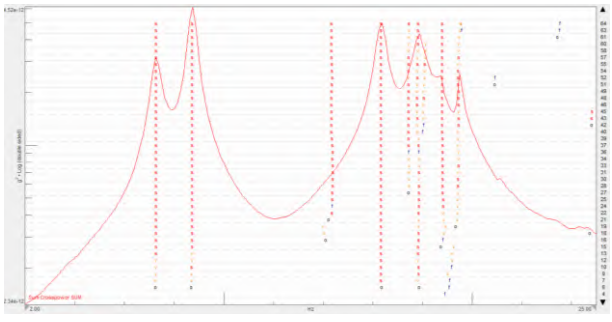


Figure 14: OMA applied to acoustic excitation cross spectra [g^2] in the lower frequency range (2-25 Hz) – stabilization diagram

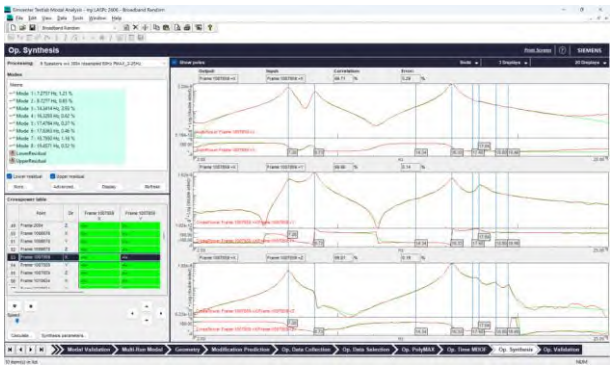


Figure 15: Comparison between measured and synthesized cross spectra (2-25 Hz)

Some acoustic excitation OMA modes are shown in Figure 16 (lower-frequency rigid body modes) and Figure 17 (some examples of flexible deformation modes).

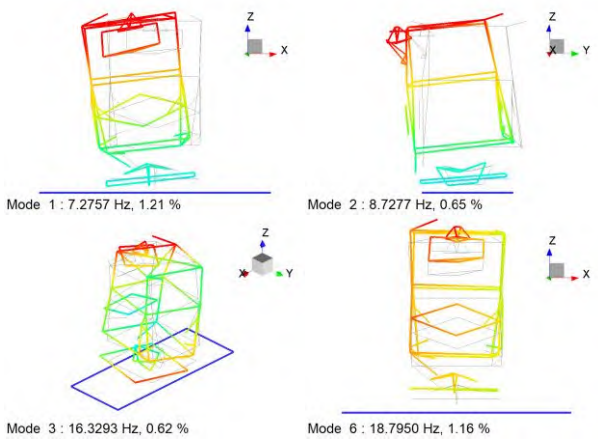


Figure 16: Rigid body modes

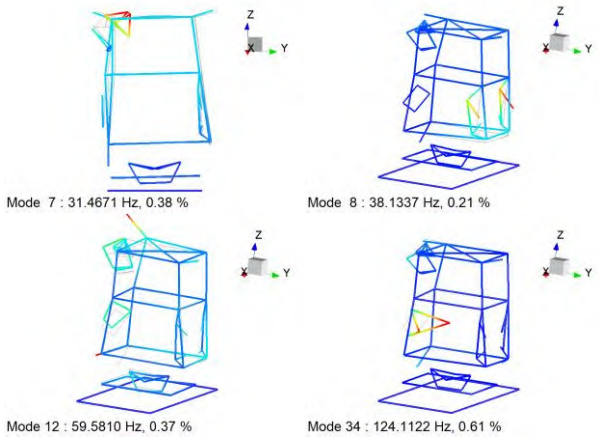


Figure 17: Examples of flexible modes

It is interesting to compare the modes obtained by applying EMA to the shaker FRFs with the modes obtained by applying OMA to the acoustic excitation cross spectra:

- Figure 18 shows the relative frequency difference [%] and the ratio between the shaker and acoustic damping ratios [-]. The first six (rigid body) modes show the largest discrepancies. In general, the frequencies and damping ratios agree very well.
- Figure 19 shows the MAC values between the shaker and acoustic excitation modes. Again, they agree very well.

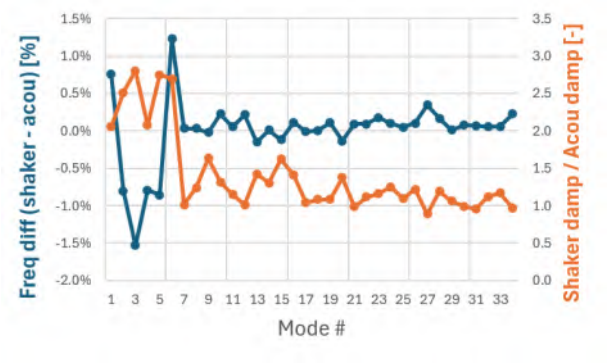


Figure 18: Frequency and damping ratio comparison between shaker EMA and acoustic excitation OMA results (34 modes in range 2-127 Hz)

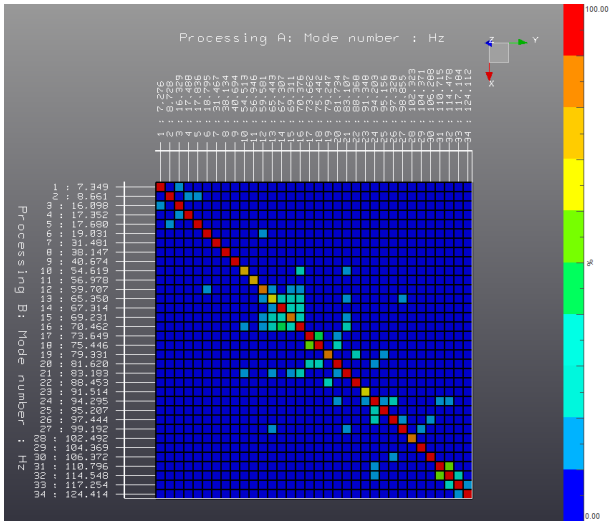


Figure 19: Mode shape comparison (MAC) between shaker EMA and acoustic excitation OMA results (34 modes in range 2-127 Hz)

6. CONCLUSIONS

- Acoustic excitation using Neutrons in a typical DFAN setup can successfully support satellite modal survey testing, extending the value of an existing acoustic qualification setup without requiring mechanical contact with the specimen.
- Despite acoustic devices being traditionally less efficient at low frequencies, white noise acoustic excitation (2–200 Hz) produced structural responses well above the noise floor, allowing reliable identification of modes down to the 2–25 Hz range.
- Both Experimental Modal Analysis (using acoustic FRFs [g/V]) and Operational Modal Analysis (using response cross spectra [g^2]) are viable for acoustic excitation data. However,

OMA on cross spectra produced noticeably cleaner stabilization diagrams than EMA on acoustic FRFs, most probably because the FRFs have a superimposed linear phase (time delay) from the acoustic excitation path that is not well captured by standard modal curve-fitting models. Cross spectra are not affected by this delay and retain the expected “modal” phase behavior.

- Modes identified via OMA on acoustic excitation cross spectra closely match those from EMA on shaker FRFs across 34 modes spanning 2–127 Hz, in terms of both frequency/damping (ratios/differences) and mode shapes (high MAC values). The largest discrepancies occur for the first six rigid body modes.
- The results validate combining DFAN qualification testing with modal survey testing in a single setup, reducing test program cost, schedule, and handling risk.

7. REFERENCES

1. Cross, K., Melendez, G., Arnold, F., Brenner, K., Throneberry, G. & Soine, D. (2025). Combining Pyroshock with MIMO Vibration. In Proc. 34th Aerospace Testing Seminar, Los Angeles, CA, USA.

2. Throneberry, G., Melendez, G. & Cross, K. (2025). Developments on Combined Thermal-Vibration MIMO Testing. In Proc. 34th Aerospace Testing Seminar, Los Angeles, CA, USA.

3. Peeters, B., Alvarez Blanco, M., Musella, U., Waimer, S., Di Lorenzo, E. & Carrella, A. (2017). Identifying the Structural Behaviour of a Specimen During Spacecraft Acoustic Testing by Operational Modal Analysis. In Proceedings of the 7th Int. Operational Modal Analysis Conf., Ingolstadt, Germany.

4. Peeters, B., Garica de Miguel, A., Musella, U. & Ngan, I. (2025). Operational Modal Analysis of Satellites using Direct-Field Acoustic Test Data. In Proc. 43rd Int. Modal Analysis Conf., Orlando, FL, USA.

5. Napolitano, K., Yang, M., Friedlander, E. & Schick, D. (2025). Mode Shape Extraction Using Direct Field Acoustic Noise Test Data. In Proc. 43rd Int. Modal Analysis Conf., Orlando, FL, USA.

6. Napolitano, K., Yang, M., Schick, D., Hayes, D. & Kimpton, D. (2025). Experimental Modal Analysis Using Acoustic Excitation. In Proc. Spacecraft and Launch Vehicles Dynamic Environments Workshop, El Segundo, CA, USA.

7. Napolitano, K., Heyd, E., Schick, D., Peeters, B., Musella, U. & Sensor, C. (2026). Application of the fixed base correction method to direct field acoustic noise test data on the Emirates Mission to the Asteroid Belt structural test article. In Proc. ISMA 2026, Int. Conf. on Noise and Vibration Engineering, Leuven, Belgium.

8. Napolitano, K. & Schick, D. (2026). Modal Survey Test of Emirates Mission to the Asteroid Belt (EMA) Structural Test Article Using Direct Field Acoustic Noise as the Excitation Source. In Proc. Spacecraft and Launch Vehicle Dynamic Environments Workshop, El Segundo, CA, USA.

9. Hoople, G. & Napolitano, K. (2010). Implementation of Multi-Sine Sweep Excitation on a Large-Scale Aircraft. In Proc. 28th Int. Modal Analysis Conf., Jacksonville, FL, USA.

10. Fabries, C., Pechevis, M., Guillaume, P., Garcia de Miguel, A. & Musella, U. (2024). Direct Field Acoustic Noise Test Power versus Control Strategy. In Proc. 18th European Conf. on Spacecraft Structures, Materials and Environmental Testing, Noordwijk, The Netherlands.

11. Tavares, A., Di Lorenzo, E., Cornelis, B., Manzato, S., Peeters, B., Desmet, W. & Gryllias, K. (2025). Automated experimental modal analysis with density-based clustering: A benchmark validation through jury testing. Mech. Syst. Signal Proc. 232, DOI: 10.1016/j.ymssp.2025.112714.

12. Peeters, B., Van der Auweraer, H., Guillaume, P. & Leuridan, J. (2004). The Polymax frequency-domain method: a new standard for modal parameter estimation? Shock and Vibration 11, 395-409.

13. Peeters, B., Van der Auweraer, H., Vanhollebeke, F. & Guillaume, P. (2007). Operational modal analysis for estimating the dynamic properties of a stadium structure during a football game. Shock and Vibration 14(4), 283-303.

On the effect of a panel inclination during a Direct Field Acoustic Test

G. Diodati [(1)], A. Carrella [(2)], C. Carandente Tartaglia [(1)], V. Quaranta [(1)], A. Sorrentino [(1)]
[(1)] CIRA Italian Aerospace Research Centre, Capua 81043, Italy, g.diodati@cira.it
[(2)] MSIDFAT Services LLC, Baltimore, MD 21207, USA, a.carrella@msidfat.com

ABSTRACT

Diffuse Field Acoustic Noise (DFAN) testing is widely employed for the environmental qualification of spacecraft structures and equipment, where a sufficiently diffuse and spatially uniform acoustic field is required to provide representative excitation conditions. The size and geometry of the test article may, however, be constrained by the physical dimensions and acoustic characteristics of the DFAN facility. For large planar structures, an inclined test configuration may provide an alternative approach for increasing the effective dimensions of the structure that can be accommodated within the facility.

This study investigates the feasibility of using panel inclination in DFAN testing and assesses its effects on both the acoustic excitation and the structural dynamic response. A steel panel was considered as a representative planar structure and tested at different inclination angles under diffuse acoustic excitation. Particular attention was given to the spatial uniformity of the acoustic field over the frequency range of interest and to the possible changes in the structural response associated with panel orientation.

A finite element model was developed to evaluate the effect of gravity-induced static deformation on the natural frequencies and mode shapes of the panel for different inclination angles. The numerical predictions were validated through experimental modal analysis using impact hammer testing. Subsequently, a series of DFAN tests was performed with the panel at different orientations. Acoustic field measurements and structural response measurements were compared to assess the uniformity of the excitation and to quantify the variations in the panel response associated with inclination.

The results provide an assessment of the extent to which panel orientation affects both the acoustic excitation and the structural dynamic response. In particular, the study evaluates whether an inclined configuration can provide sufficiently representative acoustic excitation while maintaining structural behaviour suitable for qualification testing. The findings contribute to the assessment of inclined DFAN configurations as a potential approach for testing large planar spacecraft structures and provide practical guidance for their application and interpretation in environmental qualification campaigns.

1. INTRODUCTION

Diffuse Field Acoustic Noise (DFAN) testing is widely employed for the environmental qualification of spacecraft structures and equipment to reproduce the severe acoustic loads experienced during launch. The acoustic environment represents one of the principal dynamic environments considered during spacecraft qualification, and aerospace standards and launcher documentation define the requirements and procedures used to reproduce these conditions in laboratory testing [2,9,10]. Measurements performed during actual launch events have also demonstrated the complex spatial characteristics of the acoustic environment experienced by spacecraft during lift-off [15].

Traditionally, high-intensity acoustic qualification has been performed in reverberant acoustic test facilities, where multiple reflections within the chamber are used to generate an approximately diffuse sound field. A diffuse field provides acoustic energy arriving from multiple directions and is therefore intended to expose the test article to a broad range of excitation conditions. The spatial uniformity and diffuseness of reverberant acoustic fields have consequently been the subject of extensive investigation [1,12,13]. In particular, diffuseness and spatial coherence are key parameters for assessing the extent to which a measured acoustic field approximates an ideal diffuse-field condition [12,13]. These characteristics are particularly relevant when evaluating whether an acoustic test environment provides a representative and sufficiently uniform excitation of the test article [1].

An alternative approach is Direct Field Acoustic Noise (DFAN) testing, in which arrays of high-power loudspeakers are used to generate the acoustic excitation directly around the test article. DFAN offers several practical advantages over conventional reverberant acoustic testing, including reduced facility requirements, increased flexibility in test configuration, and enhanced control of the acoustic excitation [2,3]. The approach has been progressively developed and applied to spacecraft and subsystem qualification, with experimental and numerical studies demonstrating its feasibility and comparing its performance with conventional reverberant-field testing [3,14,16–19]. In particular, comparisons between direct-field and reverberant-field excitation have shown that the structural response of a test article can depend not only on the overall acoustic spectrum but also on the spatial characteristics of the incident acoustic field [3,5,14].

The achievement of a sufficiently uniform and diffuse acoustic environment therefore remains an important consideration in DFAN testing. Investigations of direct-field acoustic testing have demonstrated that the generated acoustic field can contain spatial variations and non-diffuse components depending on the arrangement of the loudspeakers, the control strategy, and the test configuration [5]. The acoustic environment generated by a DFAN system is consequently not determined solely by the prescribed overall sound pressure level. The number and position of acoustic sources, the location of control microphones, and the interaction between the acoustic field and the test article can all influence the

resulting spatial distribution of acoustic energy [3,5].

The development of Multiple-Input Multiple-Output (MIMO) control strategies has provided additional possibilities for controlling the acoustic environment generated by loudspeaker arrays. MIMO approaches allow multiple acoustic sources to be controlled simultaneously and can be used to achieve the desired acoustic spectrum at several measurement locations [4,6]. Pre-test numerical analysis can support the design of these control strategies, while experimental investigations have demonstrated the implementation and validation of acoustic devices and control systems for direct-field testing [7]. These developments have contributed to the increasing application of DFAN as an alternative to conventional reverberant acoustic qualification. Nevertheless, the characterization of the resulting acoustic field remains important, particularly when changes in the geometry or orientation of the test article may alter the spatial distribution of the acoustic excitation.

A relevant practical limitation of acoustic qualification facilities is the size of the test article that can be accommodated within the effective acoustic test volume. This limitation is particularly relevant for large planar spacecraft structures, such as solar panels, whose dimensions may exceed the nominal dimensions of the available DFAN configuration. Increasing the available test volume or modifying the facility itself may not always be technically or economically feasible. An alternative approach is to modify the orientation of the test article. In particular, an inclined configuration may allow a planar structure to make more effective use of the available test volume, potentially enabling the testing of structures whose characteristic dimensions exceed the corresponding nominal facility dimensions.

The use of an inclined configuration, however, introduces several aspects that must be experimentally assessed before it can be considered a viable approach for acoustic qualification. Changing the orientation of the test article modifies the direction of gravity relative to the structure and may therefore alter its static deformation and stress state. For a flexible structure, these changes can affect its dynamic characteristics through geometric stiffness effects, resulting in variations of natural frequencies and mode shapes. Although such effects are expected to be limited for relatively stiff metallic panels, they may become relevant when interpreting differences in structural response between different orientations.

At the same time, changing the orientation of the test article may modify the acoustic environment generated by a multi-speaker DFAN system. The specimen can interact with the incident acoustic waves through reflection and scattering, potentially affecting the local distribution of acoustic energy and the degree of spatial uniformity of the field. This effect is particularly relevant in DFAN facilities, where the acoustic environment is generated directly by discrete loudspeaker sources rather than primarily through the reverberation of a test chamber [3,5,16–18]. Consequently, any variation in the measured structural response between different orientations may result from changes in the structural dynamic properties, changes in the acoustic excitation, or a combination of both.

The objective of this work is therefore to experimentally and numerically investigate the feasibility of using inclined configurations to extend the applicability of DFAN testing to large planar spacecraft structures. A steel panel is considered as a representative structural element, and different inclination angles are investigated. The study is divided into two complementary investigations.

The first investigation addresses the structural effects associated with the change in orientation. A finite element model of the steel panel is developed to evaluate the influence of gravity loading on its static deformation and modal characteristics for different inclination angles. The numerical predictions are validated through experimental modal analysis using impact hammer testing. This analysis provides a quantitative assessment of the extent to which the structural dynamic behaviour changes as a function of panel inclination.

The second investigation addresses the acoustic aspects of the proposed configuration. The same panel is tested in the CIRA MSI-DFAT facility equipped with multiple loudspeaker columns at different inclination angles. Acoustic measurements are performed to characterize the spatial distribution and diffuseness of the acoustic field over the frequency range of interest. At the same time, the structural response of the panel is measured and compared between the different configurations. Particular attention is given to determining whether the inclined configurations maintain a sufficiently representative acoustic excitation and whether the corresponding changes in structural response can be attributed to the orientation of the panel rather than to significant modifications of the acoustic field.

The combination of finite element modelling, experimental modal analysis, acoustic field characterization, and DFAN testing provides a comprehensive assessment of the effects associated with panel inclination. The results are used to determine whether an inclined configuration can provide a sufficiently representative and spatially uniform acoustic excitation while potentially allowing planar structures with dimensions exceeding the nominal dimensions of the DFAN test volume to be accommodated. The study therefore provides a basis for evaluating inclined DFAN configurations as a potential approach for the environmental qualification of large spacecraft structures, including solar panels, and for defining practical criteria for their implementation in acoustic qualification campaigns.

2. TEST ARTICLE DESCRIPTION

The test article consists of a rectangular steel panel with overall dimensions of 2.0 m × 0.76 m. The structure comprises a flat central plate with a uniform thickness of about 1.7 mm, enclosed by a continuous peripheral flange. The flange has a thickness of 3.4 mm, approximately twice that of the central panel, and extends

15 mm out of the plane of the plate along the entire perimeter. This integral edge reinforcement increases the stiffness of the panel boundaries, enhancing the overall bending rigidity and reducing edge deformations while introducing only a limited increase in structural mass. The transition between the central plate and the peripheral flange is continuous, resulting in a monolithic configuration without cut-outs, discrete stiffeners, or other geometric discontinuities.



Figure 1: Test article investigated in this study: the rectangular steel panel with a reinforced peripheral flange installed in the Direct Field Acoustic Noise (DFAN) facility.

Owing to its simple geometry and well-defined structural layout, the panel exhibits dynamic characteristics representative of a broad class of thin-walled reinforced structures. The combination of a compliant central plate and a stiffened perimeter makes the structure particularly suitable for investigating the influence of gravity-induced orientation changes on the modal characteristics, as well as for assessing the consistency of the structural response under diffuse acoustic excitation in a Direct Field Acoustic Noise (DFAN) environment.

3. EXPERIMENTAL MODAL ANALYSIS

Prior to the acoustic testing campaign, an experimental modal analysis was performed to characterize the baseline dynamic behaviour of the panel. The identified natural frequencies and mode shapes were subsequently used as a reference for the numerical model correlation and for evaluating possible orientation-dependent variations.

3.1 Experimental Setup

The experimental modal analysis was conducted using the impact hammer method. Data acquisition and post-processing were performed with an LMS SCADAS SCM2E05 acquisition system. The structure was excited using a PCB Piezotronics 086C03 instrumented impact hammer, which was sequentially applied at all measurement locations according to a roving-hammer strategy. The structural response was measured by means of two PCB Piezotronics 356A16 triaxial ICP accelerometers, permanently mounted at grid locations P4 and P15 throughout each measurement. The use of two fixed reference sensors improved the observability of the global modes and increased the reliability of the modal parameter estimation. The acquisition system, hammer and accelerometer used for the impact testing are shown in Fig. 2

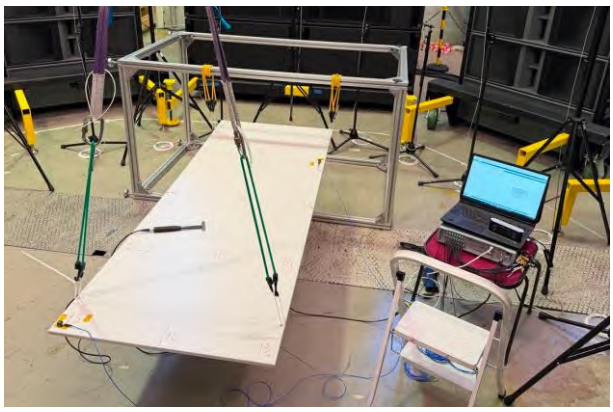


Figure 2: Experimental setup adopted for the impact modal testing, showing the suspended panel, the instrumented impact hammer, the two triaxial reference accelerometers, the LMS SCADAS SCM2E05 data acquisition system, and the Simcenter Testlab 2406 software used for data acquisition and modal analysis.

The measurement geometry consisted of a 3 × 5 grid of evenly distributed excitation points covering the panel surface. Frequency response functions (FRFs) were acquired by impacting each grid location while simultaneously recording the responses from the two reference accelerometers.
The complete experimental procedure was repeated for seven panel inclination angles (0°, 15°, 30°, 45°, 60°, 75°, and 90°) to investigate the influence of orientation on the dynamic characteristics of the structure.

3.2 Modal Identification Results

The experimentally measured frequency response functions (FRFs) were processed using the PolyMAX frequency-domain modal parameter estimation algorithm implemented in Simcenter Testlab 2406. PolyMAX was selected owing to its robustness in identifying closely spaced modes and its capability to provide stable estimates of the modal parameters from multiple FRFs.
Modal identification was performed over the frequency range 1–72 Hz, adopting a model order of 56. The stabilization diagram obtained from the identified poles was used to distinguish physical modes from numerical poles, allowing the extraction of the natural frequencies, damping ratios, and associated mode shapes. To ensure a consistent comparison between the different panel configurations, identical identification parameters were employed for all datasets, thereby minimizing the influence of the processing procedure on the identified modal characteristics. This approach enabled the observed variations in the modal parameters to be attributed solely to changes in the structural behaviour

associated with the panel orientation. An example of the stabilization diagram obtained for the 0° inclination configuration during the PolyMAX modal identification process is reported in Fig. 3. The stable poles selected for the extraction of the modal parameters are highlighted

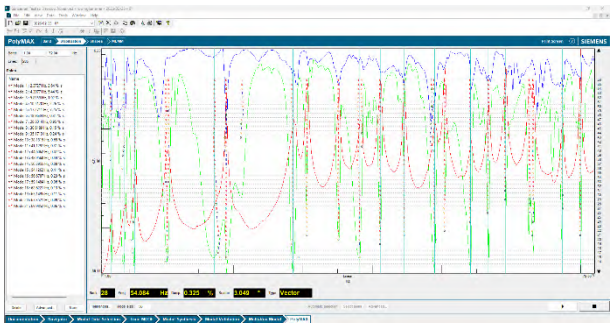


Figure 3: Representative PolyMAX stabilization diagram for the 0° inclination configuration, showing the identified poles and the stable poles used for modal parameter estimation.

The identification procedure was repeated for each of the seven panel inclination angles (0°, 15°, 30°, 45°, 60°, 75°, and 90°). Particular attention was paid to maintaining a consistent mode numbering throughout the analysis by comparing the spatial distribution of the identified mode shapes across all configurations. This ensured an unambiguous tracking of the modal evolution with increasing inclination and facilitated the subsequent comparison with the numerical predictions.

The resulting experimental modal model constitutes the reference dataset for the subsequent finite element model correlation and for assessing the influence of panel orientation on the structural dynamic behaviour. The identified natural frequencies and damping ratios are summarized in Tab. 1 and 2, while the evolution and correspondence of the identified modes with the inclination angle are reported in the modal tracking map shown in Fig. 4. Modal tracking results show an overall decrease in natural frequencies with increasing inclination angle, due to the reduction of the gravity component perpendicular to the panel surface. The frequency shift is mode-dependent, as it is influenced by the modal deformation pattern. The variation becomes more pronounced above approximately 60° inclination, as the panel approaches the vertical configuration.

Table 1: Identified natural frequencies for the different panel inclination angles

FREQUENCY [Hz]							
Mode	**0_deg**	**15_deg**	**30_deg**	**45_deg**	**60_deg**	**75_deg**	**90_deg**
1	4.31	5.81	3.86	3.50	3.23	3.21	5.35
2	5.84	10.40	5.67	5.61	5.63	4.89	7.71
3	10.52	17.54	10.02	9.18	8.66	7.76	14.47
4	17.27	18.97	17.24	9.83	9.28	8.53	15.03
5	18.96	28.58	19.02	17.07	16.41	16.76	17.96
6	28.60	30.46	28.49	18.81	18.57	18.05	23.29
7	30.62	34.98	30.12	28.59	27.56	23.79	26.24
8	35.17	37.97	34.51	29.24	28.59	27.60	26.96
9	38.18	41.03	37.20	33.63	31.32	28.54	34.11
10	41.13	44.55	40.72	35.78	33.62	30.39	35.46
11	44.61	48.76	44.36	40.21	39.39	37.37	38.62
12	48.96	49.97	48.05	44.00	42.53	38.79	41.13
13	50.40	53.93	48.65	45.72	43.27	41.72	42.81
14	54.13	56.45	53.05	47.37	45.84	43.99	47.50
15	56.68	58.94	55.87	51.38	48.72	45.18	49.97
16	59.15	62.33	58.20	55.16	54.30	51.67	51.78
17	62.62	62.77	61.02	56.79	56.62	53.28	56.89
18	63.15	67.27	62.07	58.92	59.75	54.20	60.10
19	67.35	69.82	67.02	61.06	66.20	58.07	62.80
20	69.99		69.30	66.69	66.67	64.14	66.30
21				68.29	70.20	65.27	70.80
22				71.98		68.00	71.91

Table 2: Identified damping ratios for the different panel inclination angles

DAMPING [%]							
Mode	**0_deg**	**15_deg**	**30_deg**	**45_deg**	**60_deg**	**75_deg**	**90_deg**
1	5.44%	1.71%	5.81%	0.57%	0.74%	0.95%	1.26%
2	1.92%	1.88%	2.09%	1.58%	2.49%	3.62%	2.51%
3	2.26%	6.95%	3.17%	2.88%	3.32%	0.69%	0.17%
4	7.25%	0.31%	5.31%	2.04%	2.29%	3.34%	0.19%
5	0.31%	0.96%	0.39%	4.77%	3.32%	2.51%	0.58%
6	0.95%	0.23%	0.80%	0.88%	0.47%	0.72%	0.42%
7	0.15%	0.27%	0.36%	0.55%	0.46%	0.94%	0.20%
8	0.24%	0.76%	0.26%	0.24%	0.39%	0.23%	0.82%
9	0.65%	0.31%	0.69%	0.57%	0.22%	0.54%	0.34%
10	0.31%	0.09%	0.29%	0.75%	0.43%	0.19%	0.48%
11	0.07%	0.45%	0.07%	0.37%	0.43%	0.65%	0.03%
12	0.44%	0.11%	0.45%	0.20%	0.11%	0.26%	0.57%
13	0.08%	0.42%	0.18%	0.08%	0.19%	0.18%	0.14%
14	0.41%	0.20%	0.34%	0.32%	0.19%	0.62%	0.35%
15	0.23%	0.07%	0.18%	0.27%	0.33%	0.17%	0.13%
16	0.06%	0.12%	0.05%	0.26%	0.18%	0.09%	0.44%
17	0.13%	0.15%	0.11%	0.07%	0.13%	0.19%	0.31%
18	0.11%	0.08%	0.16%	0.11%	0.15%	0.16%	0.19%
19	0.09%	0.07%	0.05%	0.18%	0.09%	0.12%	0.34%
20	0.06%		0.08%	0.07%	0.10%	0.23%	0.90%
21				0.09%	0.16%	0.19%	0.12%
22				0.11%		0.10%	0.16%

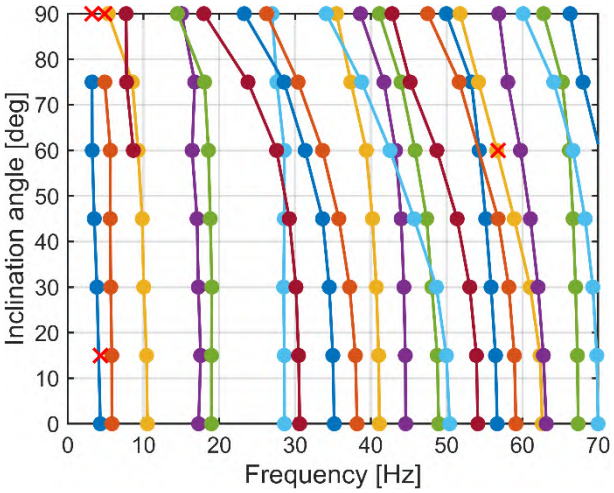
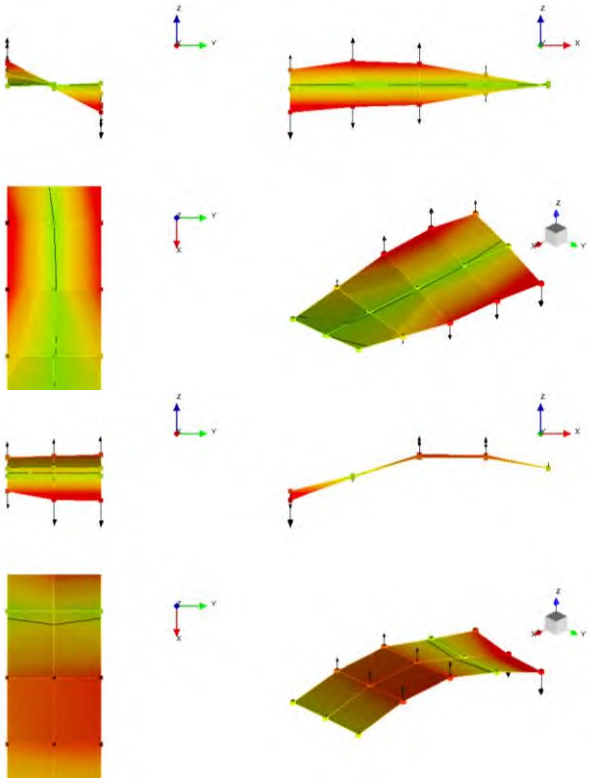


Figure 4: Experimental modal tracking map highlighting the correspondence and frequency evolution of the identified structural modes over the full range of panel inclination angles.

As a representative example, selected mode shapes measured for the panel at 0° inclination are reported in Fig. 5.



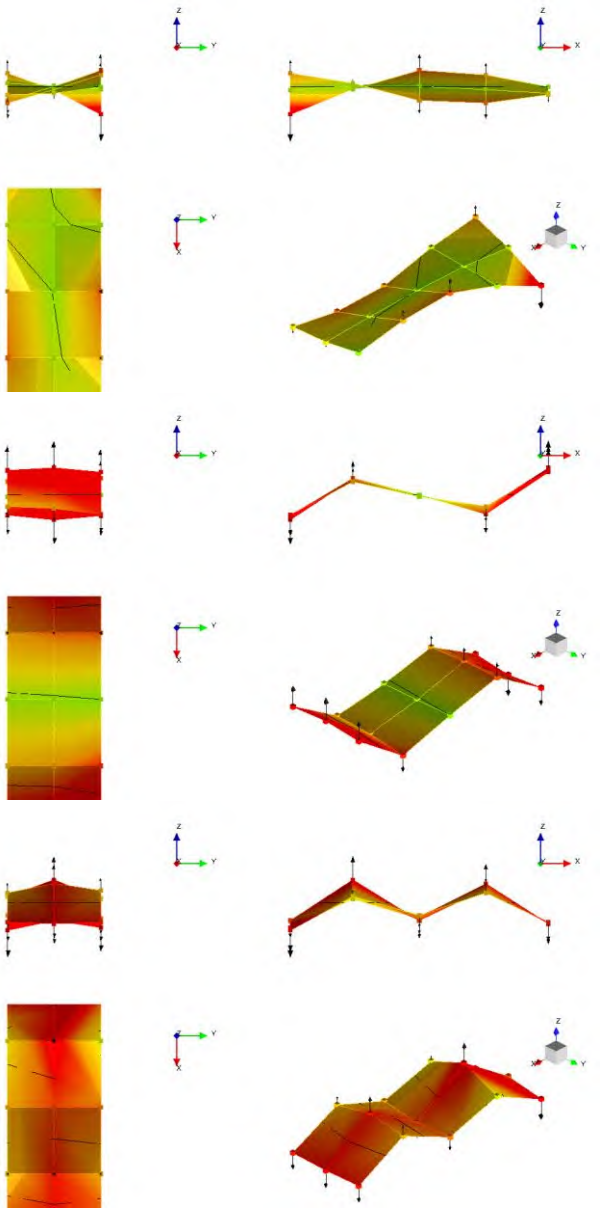


Figure 5: Representative experimental mode shapes of the panel at 0° inclination obtained from the PolyMAX modal identification. The QUAD visualization from Simcenter Testlab reports the identified modes in descending order from top to bottom, corresponding to natural frequencies of 4.31, 5.84, 10.52, 18.96, and 30.62 Hz.

4. FEM MODEL AND CORRELATION

The finite element model of the panel was developed using Simcenter Nastran. The structure was discretized using 15,992 nodes and 15,734 four-node shell elements (CQUAD4). Two shell property regions were defined to reproduce the different thicknesses of the structure: the central plate was modelled with a thickness of 1.7 mm, while the peripheral flange was represented with a thickness of 3.4 mm. The material was assumed to be isotropic steel, with a Young's modulus of 210 GPa, Poisson's ratio of 0.3, and density of 7850 kg/m³. The modal analysis was performed using the SOL

SEMODES solution sequence, with the extraction of the first 200 elastic modes through the EIGRL eigenvalue solver. The model was generated in FEMAP and subsequently solved using MSC-Nastran solver.
The initial finite element model was updated through an in-house model updating procedure to reduce the discrepancy between the numerical predictions and the experimental modal results. The procedure considered the variation of key parameters affecting the dynamic response, namely material density, elastic stiffness, and panel thickness. A Design of Experiments (DOE) methodology was first employed to construct a surrogate model relating the selected parameters to the predicted modal frequencies. The surrogate model was then coupled with an optimization algorithm to identify the parameter combination minimizing the frequency error between the experimental and numerical modes. The resulting updated FEM provided an improved correlation with the experimentally identified modal behaviour.

Table 3: Updated finite element model parameters obtained through the model updating procedure and adopted for the subsequent numerical analyses

Density [Kg/m^3]	7796
Young Modulus [Pa]	2.13E+11
Panel Thickness [mm]	1.6755
Flange Thickness [mm]	3.3352

The updated finite element model was then used to perform a modal analysis up to approximately 700 Hz. The identified natural frequencies were analysed to determine the frequency range in which the modal density progressively approaches a nearly constant value. This analysis allowed the identification of the transition between the low-frequency regime, where the structural response is governed by distinct and identifiable modes, and the higher-frequency regime, where the response becomes increasingly characterized by overlapping modal contributions under diffuse acoustic excitation. The transition was identified at approximately 90 Hz, beyond which the modal density remains nearly constant with an average value of 0.283 modes/Hz, as shown in Fig. 6

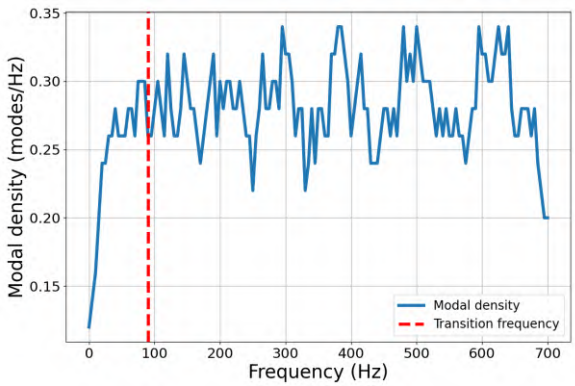


Figure 6: Modal density of the updated finite element model as a function of frequency, highlighting the transition to the nearly constant modal density region

The first two elastic mode shapes obtained from the updated finite element model are presented in Fig. 7 as a representative illustration of the finite element mesh and the numerical modal characteristics of the panel

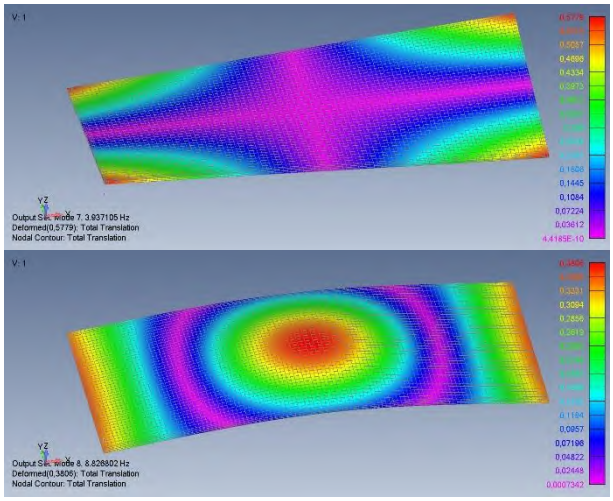


Figure 7: First and second elastic mode shapes of the updated finite element model at 3.94 Hz and 8.83 Hz, respectively.

5. DFAN TESTING AND ORIENTATION EFFECTS

Acoustic testing is a key milestone of any space-hardware mechanical qualification campaign, alongside vibration, shock, and thermal-vacuum testing. Traditionally carried out in reverberant chambers, acoustic qualification has increasingly moved toward Direct Field Acoustic Testing (DFAT) — also referred to in the literature as Direct Field Acoustic Noise (DFAN) testing — which reproduces the reverberant acoustic field using an array of loudspeakers driven by a centralized Multi-Input-Multi-Output (MIMO) closed-loop controller: most generally 16 to 32 microphones are placed randomly to cover the entire test volume. Configurations vary based on the size of test article so that every test is compliant with industry standards in terms of prescribed distance between loudspeakers and article. By removing the need for a dedicated chamber, DFAT offers substantial advantages in cost, portability, and test-schedule flexibility, and has been used to qualify flight hardware including the Orion crew module, the Nancy Grace Roman Space Telescope OTA, and the Proba-V satellite. The method is referenced in NASA HDBK-7010, and standardization work is currently ongoing under ESA/ECSS.
A specific application of DFAT concerns the acoustic qualification of solar arrays, whose large dimensions may impose geometrical constraints on the test configuration. In such cases, the test article may need to be inclined with respect to the nominal orientation in order to fit within the available test volume while satisfying the required distances from the acoustic sources. Although DFAT is intended to reproduce a diffuse acoustic field, the field generated by a finite loudspeaker array is not perfectly diffuse and may exhibit spatial variations in acoustic pressure level and direction of incidence. Consequently,

the orientation of an extended test article may affect the acoustic loading acting on its surfaces and, ultimately, its structural response. This aspect is particularly relevant for large and lightweight structures such as solar arrays, for which the acoustic loading may be sensitive to variations in the local incident sound field. The influence of the test article inclination on the acoustic response therefore represents a relevant aspect to be assessed when defining and interpreting DFAT configurations. In particular, the extent to which variations in the inclination angle modify the acoustic excitation and the resulting structural response remains to be quantified.

To investigate the influence of test article inclination on the acoustic excitation and structural response under DFAT conditions, an experimental campaign was conducted at the CIRA acoustic testing facility using the test article described in the previous sections. The campaign was specifically designed to assess the variation of the test conditions and of the resulting structural response as a function of the test article orientation. The experimental setup, the selected inclination angles, and the adopted test procedure are presented in the following sections. First, the CIRA DFAT facility and its main characteristics are described. The experimental campaign is then presented, including the test configurations, instrumentation, and measurement approach adopted for the different test article orientations. Finally, the experimental results are analysed and discussed, with the aim of assessing the extent to which the inclination of the test article affects the acoustic excitation and the corresponding structural response.

5.1 CIRA DFAN Facility

The experimental campaign was conducted at the CIRA Space Qualification Center using the Direct Field Acoustic Noise (DFAN) system developed by MSI-DFAT within the framework of the ASI-funded PNRR Space Factory 4.0 program. The facility is based on a mobile Direct Field Acoustic Testing (DFAT) system designed to reproduce the high-intensity acoustic environment experienced during launch without requiring a reverberant chamber.

The Noise Generation System (NGS) consists of high-power loudspeakers arranged in a circular configuration around the test article. The system combines 30 MP-21 low-frequency subwoofers, covering the frequency range from approximately 20 to 300 Hz, with 48 MP-150 three-way loudspeakers for the mid- and high-frequency range. The loudspeakers are driven by dedicated high-power amplifiers and are distributed around the test article to generate an acoustic field representative of the reverberant conditions required for qualification testing. The system is designed to operate over a broad frequency range, approximately from 25 Hz to 10 kHz, and to generate sound pressure levels suitable for high-intensity aerospace qualification tests.

The acoustic field is controlled through a Multiple-Input Multiple-Output (MIMO) closed-loop Noise Control System (NCS), implemented using Siemens Simcenter TestLab. Up to 24 control microphones are available for the MIMO control, with a minimum of 16 microphones required for the standard configuration. The microphones are distributed around the test article and provide the feedback signals used to control the individual loudspeaker drives. In addition to matching the target acoustic spectrum within prescribed tolerances, the control system monitors the coherence and phase relationships between microphone pairs. This allows the generated field to be optimized not only in terms of overall sound pressure level but also with respect to its spatial characteristics, thereby providing an acoustic environment that approximates a diffuse field.

The NCS is based on SCADAS hardware, providing up to 50 input channels and 16 output channels, and allows additional monitoring channels to be integrated into the test configuration. Accelerometers can also be included to monitor the structural response of the test article and, when required, to implement response limiting. The combination of the MIMO control strategy and the circular loudspeaker arrangement enables the acoustic excitation to be adapted to different test articles and configurations while maintaining a controlled and repeatable acoustic environment.

5.2 Experimental Test Campaign

The experimental campaign was performed on the test article described in the previous sections to investigate the influence of its inclination on the acoustic excitation and structural response during DFAT. Seven different test article orientations were considered, corresponding to inclination angles of 0°, 15°, 30°, 45°, 60°, 75°, and 90° with respect to the reference configuration. The same acoustic test configuration, control strategy, target spectrum, and test procedure were maintained for all orientations, with the inclination angle representing the main parameter varied throughout the campaign. This approach allowed the effect of test article orientation on the acoustic loading and resulting structural response to be assessed independently of changes in the test configuration.

The DFAT test was controlled using a MIMO random control strategy implemented in Siemens Simcenter TestLab. A total of 16 microphones were used as control microphones for the MIMO control loop. The microphones were distributed around the test article to provide feedback on the acoustic field and to enable the controller to reproduce the prescribed target spectrum. The microphones were PCB Piezotronics 378C10 ICP microphones, with nominal sensitivities close to 1 mV/Pa.

The structural response of the test article was monitored using nine accelerometers arranged in a 3 × 3 regular grid on the plate under investigation. The instrumented plate has dimensions of approximately 0.76 × 2.0 m, with the accelerometers distributed over its surface to provide spatially distributed measurements of the vibration response. The accelerometers had a nominal sensitivity of 5 mV/g. The microphone and accelerometer configurations were kept unchanged throughout the

different test conditions to ensure consistency in the comparison of the results.
The target acoustic spectrum imposed on the MIMO controller corresponded to a nominal OASPL of 130 dB. The target spectrum covered the frequency range from 15.63 Hz to 2 kHz and was defined with a frequency resolution of 3.125 Hz. The target levels, together with the prescribed lower and upper tolerances and abort limits, are reported in Tab. 4. The target spectrum was controlled within lower and upper tolerances of ±3 dB, while an abort limit of +6 dB was applied to prevent excessive acoustic excitation. The frequency resolution adopted for the control was 3.125 Hz, with 120 degrees of freedom (DOF) specified for the MIMO control configuration.

Table 4: Target acoustic spectrum and control limits used for the MIMO control

Freq. [Hz]	Target level [dB]	Lower tolerance [dB]	Upper tolerance [dB]	Abort limit [dB]
16	86.13	3	3	6
31.5	90.02	3	3	6
63	120.02	3	3	6
125	121.72	3	3	6
250	124.52	3	3	6
500	124.52	3	3	6
1000	119.52	3	3	6
2000	115.52	3	3	6
4000	112.52	3	3	6
8000	109.52	3	3	6

The acoustic test was conducted through a controlled level ramp-up procedure. Starting from a level 9 dB below the target spectrum, the acoustic excitation was increased in 3 dB steps until the full target level was reached. Once the nominal test level was achieved, the spectrum was maintained for approximately 120 s. This procedure was applied consistently to all seven test article orientations.
The test sequence consisted of three main phases: system identification, system verification, and the final MIMO random control test. During system identification, the dynamic relationship between the loudspeaker drive signals and the acoustic responses measured by the control microphones was characterized. The subsequent system verification phase was used to verify the identified model and the capability of the system to reproduce the prescribed acoustic field. Following successful verification, the MIMO random control test was performed.
During the final test, the six independent drive signals generated by the MIMO controller were distributed among the acoustic sources according to the DFAN configuration. Three signals were used to drive the MP-21 low-frequency loudspeaker stacks, while the remaining three signals controlled the MP-150 mid- and high-frequency loudspeaker stacks. The resulting acoustic excitation was therefore generated through six independently controlled drive channels, while the microphone array provided the feedback required to maintain the target acoustic spectrum and its spatial characteristics.
Fig. 8 shows the test article installed in the DFAN facility at three representative inclination angles, corresponding, from top to bottom, to 0°, 30°, and 60°. The panel is suspended using the elastic suspension system adopted for the test campaign, with the nine accelerometers arranged in a 3 × 3 grid on its upper surface. A spirit level was used during the setup procedure to accurately define and verify the inclination angle and was removed before the acoustic test. The DFAN loudspeaker stacks surrounding the test article can be observed in the background.



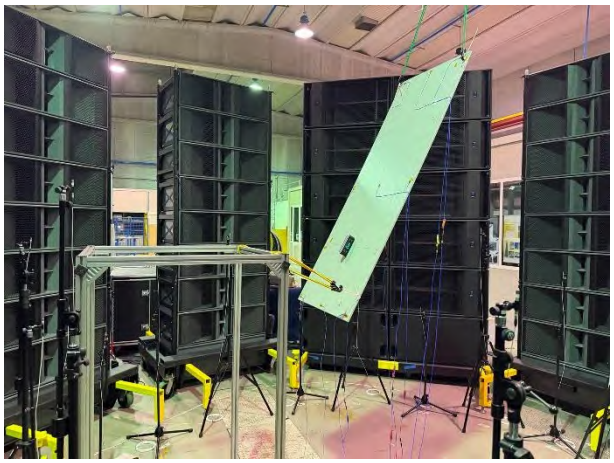


Figure 8: Test article configuration at different inclination angles: 0°, 30°, and 60° from top to bottom.

Fig. 9 presents the acoustic pressure measurements recorded by the 20 microphones during the MIMO control phase, including the 16 control microphones and four additional measurement microphones. The measurements are reported in octave bands, with the individual microphone responses shown in light grey and their arithmetic mean shown in black. The target acoustic spectrum imposed by the MIMO controller is shown in green, together with the lower and upper control limits in violet and the abort limit in red. The comparison between the measured responses and the target spectrum shows that the acoustic field generated during the test is maintained within the prescribed control limits over the considered frequency range, confirming the capability of the MIMO system to reproduce the required acoustic excitation.

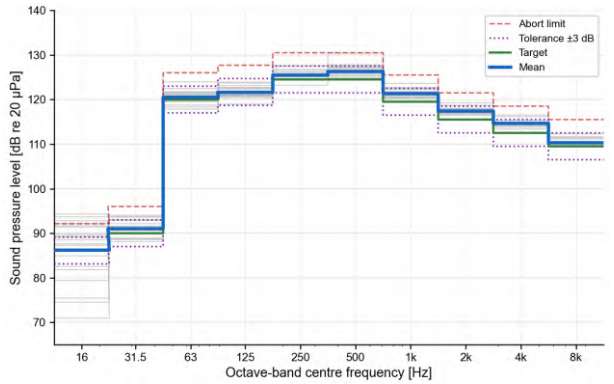


Figure 9: Acoustic pressure levels measured by the 20 microphones during MIMO control (panel inclination: 0°), together with the mean spectrum, target spectrum, ±3 dB control limits, and upper +6 dB abort limit.

5.3 Results and Discussion

To investigate the influence of test article inclination on the acoustic–structural coupling, the Vibro-Acoustic Gain (VAG) was evaluated in one-third-octave frequency bands. The VAG was calculated as the ratio of the mean structural acceleration response to the mean acoustic pressure acting on the test article. The mean acoustic pressure was obtained from the 16 control microphones and four additional measurement microphones, whereas the mean structural acceleration was calculated from the nine accelerometers distributed over the test panel. By expressing the structural response relative to the acoustic excitation level, the VAG provides a normalized indicator of the acoustic-to-structural response transfer, thereby facilitating comparison between test configurations with different acoustic field levels. The VAG obtained for the seven investigated inclination angles is reported in Fig. 10.

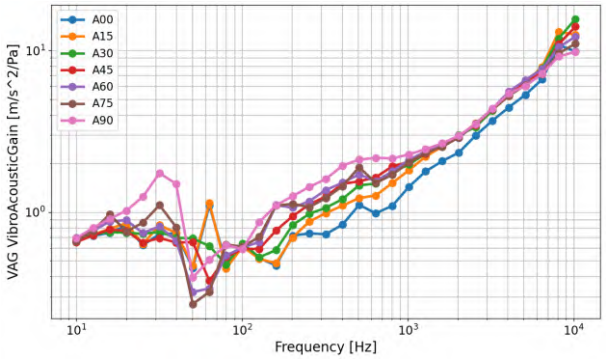


Figure 10: Vibro-Acoustic Gain (VAG) as a function of frequency for the seven investigated test article inclination angles, evaluated in one-third-octave frequency bands.

The results show a clear frequency-dependent influence of the test article inclination. Up to approximately 90 Hz, the structural response is strongly governed by the modal characteristics of the panel. In this frequency range, the relatively low modal density allows individual structural modes to dominate the response, resulting in significant differences between the investigated orientations. The change in inclination modifies the coupling between the incident acoustic field and the structural modes, leading to substantial variations in the VAG.

Between approximately 100 Hz and 1 kHz, the influence of the inclination remains evident, although the response is no longer dominated by a limited number of clearly distinguishable modes. The increasing modal density leads to a more distributed structural response, while the orientation of the panel continues to affect the efficiency of the acoustic–structural coupling. Within this frequency range, several intermediate orientations, particularly those between approximately 45° and 75°, exhibit very similar VAGs over extended frequency ranges. This behaviour is of particular interest for the practical definition of DFAT configurations, as it suggests that a relatively broad range of intermediate orientations can produce comparable structural responses.

Above approximately 1 kHz, the differences associated with the inclination angle progressively decrease, and the responses corresponding to most orientations tend to converge. This indicates that the structural response becomes less sensitive to the orientation of the test article at higher frequencies. An exception is observed for the 0° configuration, which exhibits a distinct response compared with the other orientations. This behaviour is

attributed to the influence of gravity on the structural configuration, which can modify the static state of the panel and consequently affect its dynamic response.

The limiting configurations at 0° and 90° also provide useful reference conditions for interpreting the overall trend. The large difference between these orientations, particularly at low frequencies, confirms that the inclination angle affects the efficiency with which the acoustic field excites the structure. At intermediate angles, the response progressively approaches a region in which several configurations exhibit comparable behaviour. In particular, the similarity observed between approximately 45° and 75° is relevant to the practical use of inclined configurations when the dimensions of the test article impose geometrical constraints on the DFAT setup.

The results therefore indicate that the effect of test article inclination is primarily concentrated in the low- and mid-frequency ranges. Below approximately 90 Hz, the response is strongly associated with the modal behaviour of the structure, while between approximately 100 Hz and 1 kHz the inclination continues to influence the Vibro-Acoustic Gain (VAG) despite the higher modal density. Above approximately 1 kHz, the effect of inclination becomes comparatively small, apart from the specific behaviour observed for the 0° configuration. Importantly, the analysis of the acceleration-to-pressure ratio indicates that the differences between orientations are not primarily associated with variations in the applied acoustic field, but rather with the different transfer of acoustic energy to the structure as a function of its orientation.

From a practical perspective, these findings support the use of intermediate inclination angles when the geometry of a large test article prevents testing in the nominal orientation. For example, an inclination of 45° may provide a suitable compromise between the available test volume and the resulting structural response, while the results show that orientations in the approximate range of 45°–75° can produce similar responses over a significant frequency range. However, the present analysis does not, by itself, establish that an inclined configuration is equivalent to the reference 0° configuration from a qualification standpoint. In particular, the use of averaged acceleration levels may mask local increases in vibration response, since an increase at one accelerometer can be compensated by a reduction at another location.

Therefore, a final assessment of the potential over-test or under-test associated with an inclined configuration requires a more localized comparison. The acceleration response at each measurement point should be compared, frequency band by frequency band, with the corresponding response obtained in the reference 0° configuration. Such a sensor-by-sensor analysis would allow local increases and reductions in structural response to be identified and would provide a more robust basis for determining whether an inclination such as 45° can be adopted for qualification testing without introducing unacceptable over-test or under-test conditions.

CONCLUSIONS

This work investigated the influence of test article inclination on the structural response of a large flexible panel subjected to Direct Field Acoustic Noise (DFAN) excitation. The study was conceived to assess whether inclined configurations can be used as a practical approach to accommodate large planar structures within the available test volume of a DFAN facility, while maintaining representative acoustic excitation conditions. The investigation combined experimental modal characterization, finite element model updating, and an experimental acoustic campaign performed at the CIRA Space Qualification Center.

The panel was first characterized through impact hammer testing, and the experimentally identified modal parameters were used to update the finite element model. The updated model was subsequently used to investigate the modal behaviour of the panel up to approximately 700 Hz for the different inclination conditions. The analysis identified a transition at approximately 90 Hz between a low-frequency regime dominated by distinct structural modes and a higher-frequency regime characterized by increasing modal density. Above this transition, the modal density approached an approximately constant value of 0.283 modes/Hz, corresponding to approximately one mode every 3.5 Hz.

The DFAN campaign was performed at seven inclination angles, from 0° to 90° in 15° increments, while maintaining the same acoustic control configuration. The prescribed acoustic target spectrum was successfully reproduced for the investigated configurations, and the structural response was monitored using nine accelerometers distributed over the test panel. The Vibro-Acoustic Gain (VAG), defined as the ratio between the mean structural acceleration and the mean acoustic pressure, was used as a normalized indicator to investigate the influence of panel inclination while mitigating the effect of variations in the overall applied acoustic pressure level.

The experimental results show that panel inclination has a significant influence on the frequency-dependent acoustic-to-structural transfer, particularly below approximately 1 kHz. The strongest variations were observed in the low-frequency modal regime below approximately 90 Hz, where the response is dominated by individual structural modes and is therefore highly sensitive to changes in structural configuration. Between approximately 100 Hz and 1 kHz, the influence of inclination remains evident, although the increasing modal density progressively reduces the sensitivity to individual modal variations. Above approximately 1 kHz, the VAG responses associated with most orientations tend to converge, indicating a progressively lower sensitivity of the global acoustic-to-structural response to panel inclination. Intermediate orientations, particularly between 45° and 75°, exhibited similar VAG trends over extended frequency ranges.

The numerical and experimental modal results provide a

quantitative assessment of the structural changes associated with different orientations, while the DFAN measurements demonstrate that these changes, together with possible variations in the acoustic excitation, can affect the measured structural response. The results therefore indicate that an inclined configuration cannot in general be assumed to be equivalent to the reference 0° configuration solely on the basis of the applied overall acoustic spectrum. Both the frequency-dependent structural response and the spatial characteristics of the acoustic excitation must be considered when defining and interpreting DFAN configurations for large planar structures.

From a practical perspective, the results support the feasibility of using inclined configurations as a potential approach for accommodating planar structures whose dimensions may exceed the nominal dimensions of the DFAN test volume. In particular, the intermediate orientations investigated in this study, including the 45° configuration, showed promising behaviour over significant portions of the frequency range and may provide a practical compromise between geometrical accommodation and structural response. However, the present results do not by themselves establish the equivalence of an inclined configuration with the reference configuration for qualification purposes.

In particular, the spatially averaged VAG is not sufficient to demonstrate that an inclined configuration provides an equivalent qualification environment. A sensor-by-sensor comparison with the 0° reference configuration, performed over appropriate frequency bands, is required to identify local increases or reductions in structural response and to assess potential over-test or under-test conditions. Such an analysis should be complemented by an assessment of the spatial characteristics of the acoustic field for each orientation, in order to distinguish variations associated with the structural dynamics from those arising from changes in the acoustic excitation.

Overall, the study demonstrates that panel inclination is a promising approach for extending the practical applicability of DFAN testing to large planar spacecraft structures, including solar panels, potentially allowing structures whose dimensions exceed the nominal geometrical envelope of the test facility to be accommodated. The results provide an experimental basis for the development of acceptance criteria for inclined DFAN configurations. Future work will focus on establishing quantitative limits for structural response variation, including sensor-level over-test and under-test criteria, and on correlating these limits with the spatial characteristics of the acoustic field. This will support the definition of a robust methodology for selecting and qualifying inclined configurations for the environmental testing of large spacecraft structures.

REFERENCES

1. *Reverberation Room and Spatial Uniformity,* R Ramakrishnan, A Grewal, Canadian Acoustics/ Acoustique Canadienne Vol. 36 No. 3 (2008) – 28
2. NASA Handbook 7010
3. *Direct Field Acoustic Testing Comparison to Reverberant Chamber Testing on Orion's EFT-1 CM*, Mitch Skinner John Neuman, 30th Aerospace Testing Seminar, March 2017
4. *New Method to Determine Optimized Reference SDM for MIMO Random or Acoustic Testing*, M. Underwood, 90th Shock and Vibration Symposium, November 2019, Atlanta, GA
5. *Comparisons of the Structural Response of a Test Article Excited by DFAT™ Diffuse and Non-Diffuse Acoustic Fields*, M. Underwood, 91st Shock and Vibration Symposium September 19 - 23 2021, Orlando FL
6. *Pre-test analysis for the design of MIMO control strategies on DFAX*, M. Alvarez Blanco, A. Carrella, K. Janssens, B. Peeters, ECSSMET 2018, Noordwijk, The Netherland
7. *Verifying a Novel Approach to Acoustic testing: acoustic Devices & Control System*, D Shick, T Hoffmann, E Friedlander, E Kinsella, 32nd Aerospace Testing Seminar, LA 5-7 Oct 2021
8. IEC 801-23-31, https://www.electropedia.org/iev/iev.nsf/display?openform&ievref=801-23-31
9. *ARIANE 6 USER'S MANUAL,* ISSUE 2 REVISION 0, FEBRUARY 2021
10. NASA NASA-HDBK-7005 "DYNAMIC ENVIRONMENTAL CRITERIA", 2001
11. *Study of Diffusseness in a Launch Vehicle Fairing*, Yang M., Spacecraft and Launch Vehicle Dynamic (SCLV) Environments Workshop, June 4-6, 2019, Los Angeles
12. *Zhang, S.; Lee, J. Diffuseness Quantification in a Reverberation Chamber and Its Variation with Fine-Resolution Measurements. Buildings, 2021-11,519. https://doi.org/10.3390/buildings11110519*
13. *The coherence of reverberant sound fields,* Jacobsen F. and Roisin T., J. Acoust. Soc. Am. 108 (1), July 2000, 204-210
14. *Acoustic test effective methods and recommendations to excite structural vibration modes equivalent to those during launch: Reverberant Field vs. Direct Field*, Q. Shi, H. Akagi. 30th ATS, 2017, Los Angeles
15. *Observations of the sound field during Lift-off of the Cassini spacecraft*, B Gardner, SCLV Dynamics Environment Workshop, 2000, LA
16. *Direct Field Testing Simulation for Subystem Acoustic Qualification,* C Fabries, B Brevart, S Clamagirand, ECSSMET 2016, Noordwijk, The Netherlands
17. *Direct Field Acoustic Testing in Space Industry Facility,* C. Fabries, B. Brevart, N. Saggini, A. Ciriello, ECSSMET 2018, Noordwijk, The Netherland

18. *Experimental Validation of Direct Field Acoustic Testing*, C Fabries, B Brevart, A Carrella, M Alvarez, D DalFitto, S Scharfenberg, ECSSMET 2016, Noordwijk, The Netherlands
19. *Direct Acoustic Test of Quikscat Spacecraft*, D. Anthony, T. Scharton, A. Leccese, 1999 World Aviation Conference, October 19-21, 1999, San Francisco, CA

A MULTI-SISO ONE-THIRD-OCTAVE CONTROL ARCHITECTURE FOR DIRECT FIELD ACOUSTIC NOISE TESTING

Dr.-Ing. Sebastian M. Schwarzendahl (1), Dale Schick (2), Geoff Eckert (2), Ed Kinsella (3)

(1) m+p international, Hannover, Germany
(2) Acoustic Research Systems, Shepherdstown, WV, USA
(3) EM Acoustics, Dunsfold Park, UK

KEYWORDS

direct field acoustic noise testing, DFAN, acoustic control, one-third-octave control, M-SISO, diffuse acoustic field

ABSTRACT

This paper presents a Multi-SISO (M-SISO) one-third-octave acoustic control architecture for direct field acoustic noise (DFAN) testing. The method uses multiple broadband random drives, each assigned to a control microphone and a one-third-octave feedback loop, rather than a narrowband phase-targeted multivariable controller. The objective is to regulate the broadband spectrum while allowing the global field to result from the statistical superposition of uncorrelated sources. The paper focuses on the control philosophy, loop structure, signal processing, representative test configuration, and field-quality observations. Data from a 32-device DFAN system with separate control and monitor microphone positions show close agreement between the two microphone groups and consistent exposure over time. The results demonstrate the practical viability of M-SISO control for DFAN applications in which a spatially uniform, low-coherence acoustic field is an appropriate test objective. The work does not provide a direct performance comparison with narrowband MIMO control and does not claim that low coherence alone constitutes a complete diffuse-field qualification.

1. INTRODUCTION

Acoustic qualification testing for spacecraft and other launch-borne hardware seeks to reproduce the broadband sound-pressure environment inside a launch-vehicle fairing [1]. Reverberant chambers remain an established reference technology, while direct field acoustic noise (DFAN) systems offer a portable alternative that can be deployed without a dedicated reverberation facility [2]. DFAN systems have commonly used narrowband multivariable control, selected microphone locations, and partially coherent source arrangements. These methods can be effective, but phase-sensitive summation and standing-wave effects may influence the spatial field and the structural response of a device under test [3,4].

The present paper examines a different control philosophy: a Multi-SISO one-third-octave architecture in which many locally controlled loops regulate filtered sound-pressure levels while the global field is formed by the superposition of uncorrelated broadband sources. The target is a stable and repeatable broadband test environment rather than a prescribed narrowband pressure pattern. The paper therefore concentrates on the architecture and on field-quality observations. Detailed structural-response comparisons are outside its scope.

2. BACKGROUND AND CONTROL PHILOSOPHY

2.1 Diffuse-field objective

For the purposes of this paper, field uniformity and field diffusivity are treated as related but distinct properties. Uniformity describes the spatial variation of sound-pressure level over the test region. Diffusivity describes the statistical and directional character of the acoustic field. Low spatial coherence is consistent with reduced dominance of persistent coherent wavefronts, but it is not, by itself, a complete measure of diffusivity. In a direct field system, these properties must be influenced through source arrangement, source independence, and controller behavior because they are not generated by the long reverberation time of a chamber.

2.2 Architectural rationale

If the acoustic devices provide sufficient broadband output, the system need not rely primarily on coherent summation between separate low- and high-frequency source groups to reach the required level. Each device, or small group of devices, can instead be assigned an independent broadband drive and a dedicated feedback loop. The controller regulates one-third-octave sound-pressure levels and does not prescribe phase relationships between source groups. This paper treats that choice as an architecture decision rather than as a tuning variation. Previous work has demonstrated octave-band DFAN control and purpose-built broadband acoustic devices [6,7].

3. M-SISO ARCHITECTURE

3.1 Loop structure

In the M-SISO architecture, each loop contains an independent broadband random source, an acoustic device or device group, a logically assigned control microphone, and a band-domain feedback controller. The control microphone is dedicated to that loop in the controller configuration, although its measured pressure contains

contributions from all acoustic sources in the field. The microphone signal is analyzed in one-third-octave bands and compared with the target spectrum. The resulting band-level error is used to adjust the drive amplitude of the associated source. Additional source groups are accommodated by repeating the same loop structure. Figure 1 illustrates an example in which the acoustic devices are divided into independently controlled groups around the test article.

The loops are locally controlled rather than acoustically isolated. They interact through the common sound field, and practical operation therefore includes an inter-loop gain-stabilization mechanism that prevents individual source groups from moving toward extreme operating points in response to local deviations. The present paper describes the function of this mechanism but does not disclose implementation-specific controller gains or update equations. Consequently, the work should be read as an architecture and experimental-observation paper rather than as a complete reproducible controller specification.

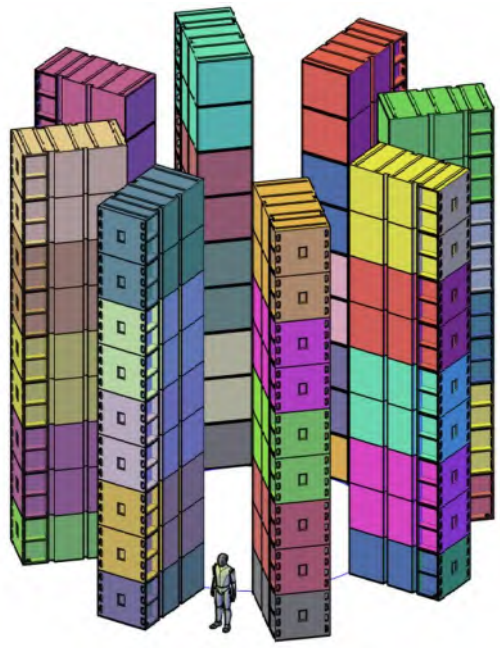


Figure 1: Example arrangement of independently controlled acoustic device groups in an M-SISO system.

3.2 Signal processing and control law

The controller operates in the one-third-octave domain using filter banks compliant with ANSI S1.11 [5]. The controlled quantity is the filtered one-third-octave sound-pressure level at each assigned control microphone. Band levels are updated at a fixed control interval and compared with the target spectrum. This processing avoids the need to use FFT-based cross-power and phase-correlation terms in the acoustic control law. It also permits short update intervals without requiring long narrowband averaging windows. No prescribed phase alignment is maintained between source groups, and no narrowband interference pattern is intentionally synthesized at selected microphones. The actual reaction time, loop gains, saturation logic, and convergence behavior are implementation-dependent and are not quantified in the present data set.

3.3 Interface to protection and notching

The absence of narrowband acoustic control does not preclude narrowband structural protection. High-resolution acceleration monitoring may be operated in parallel with the octave-band acoustic controller. In that arrangement, the M-SISO loops generate the acoustic field, while warning, abort, or notching actions are derived from a separate structural-monitoring path. Structural notching performance was not evaluated in the data presented here and is included only to define the interface between acoustic control and test-article protection.

4. EXPERIMENTAL SETUP

The representative setup used 32 acoustic devices arranged as eight stacks of four around the device under test. The acoustic control system provided 32 source outputs and 60 microphone inputs. A total of 51 microphones was used: 32 microphones positioned in front of the acoustic devices served as control microphones, and 19 additional microphones served as independent monitors. Of the monitor microphones, 12 were placed at positions representative of conventional narrowband control layouts and seven were placed outside the principal target region. The distinction between control and monitor positions allows the field to be assessed both where the controller directly measures it and at locations that do not contribute to the feedback law. The physical 32-device installation is shown in Fig. 2.



Figure 2: Representative 32-device DFAN system used for architecture validation.

The system was exercised with launch-derived target spectra up to approximately 145 dB overall sound-pressure level and exposure durations of one or two minutes. Three source-patching configurations were used in the broader test

programme: 32, 16, and 8 independent drives. The 32-drive arrangement assigned one drive to each acoustic device. The lower-drive-count configurations grouped devices and therefore introduced increasing source coherence. Figure 3 shows the 8x4 arrangement together with the approximate control and monitor microphone locations. The present paper uses these configurations only to illustrate field consistency and temporal behaviour; their structural-response consequences are outside the present scope.

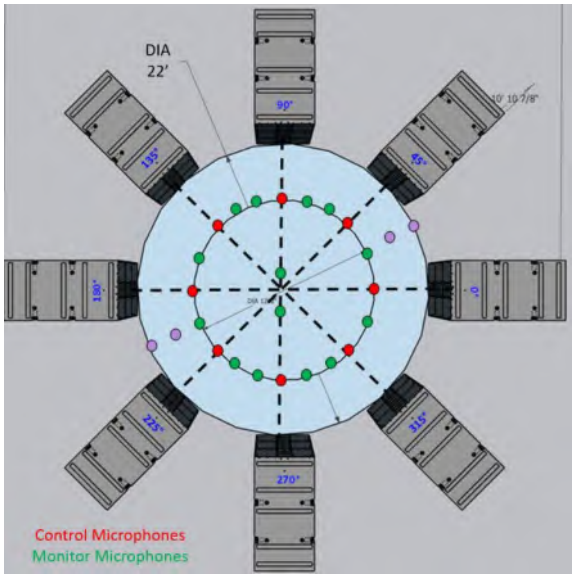


Figure 3: Representative 8x4 DFAN configuration with control and monitor microphone locations.

5. RESULTS

5.1 Control and monitor response

The first result of interest is the relationship between the control microphones and the independent monitor microphones. During representative 32-drive M-SISO operation, both microphone groups followed the target spectrum closely in the one-third-octave presentation. In several frequency regions, the monitor traces grouped as tightly as, or more tightly than, the control traces. This control-to-monitor agreement is illustrated in Fig. 4. Because the monitor microphones were not part of the feedback loops, this observation indicates that acceptable spectral agreement was not confined to the directly controlled locations.

The corresponding power spectral density representations show a similar relationship between the controlled and monitored positions. These narrowband plots are used as an independent description of the generated field; they are not the basis of the octave-band control law. The current data support a qualitative conclusion of broad field agreement. A formal statistical acceptance criterion, including spatial standard deviation or maximum deviation from the target, was not applied in this paper and remains a subject for further work.

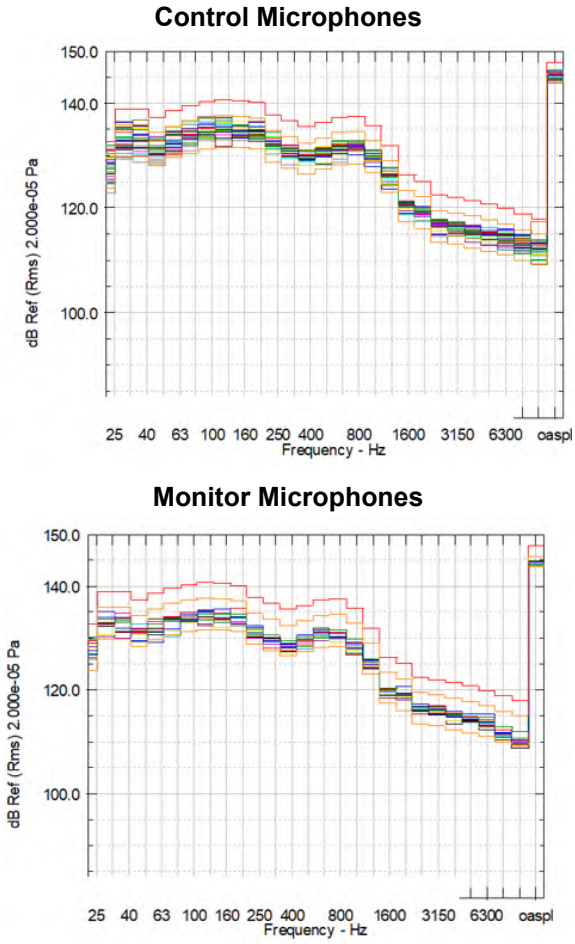


Figure 4: Representative control and monitor microphone agreement during 32-drive M-SISO operation.

5.2 Field diffusivity and coherence

A second observation concerns spatial coherence. Because the source signals are intentionally uncorrelated, coherence between spatially separated microphones remains comparatively low over most of the measured frequency range. This behaviour is consistent with reduced dominance of persistent coherent wavefronts. It does not, on its own, prove that the field is ideally diffuse, because coherence also depends on microphone separation, estimator settings, signal-to-noise ratio, and the selected reference channel.

The coherence plots in Fig. 5 are therefore used as a diagnostic indicator rather than as a complete field-qualification metric. They complement the comparison of control and monitor spectra by showing that acceptable spectral agreement is obtained without intentionally maintaining narrowband phase relationships between source groups. A future qualification method should combine coherence with spatial level variation, control-to-monitor agreement, and temporal stability.

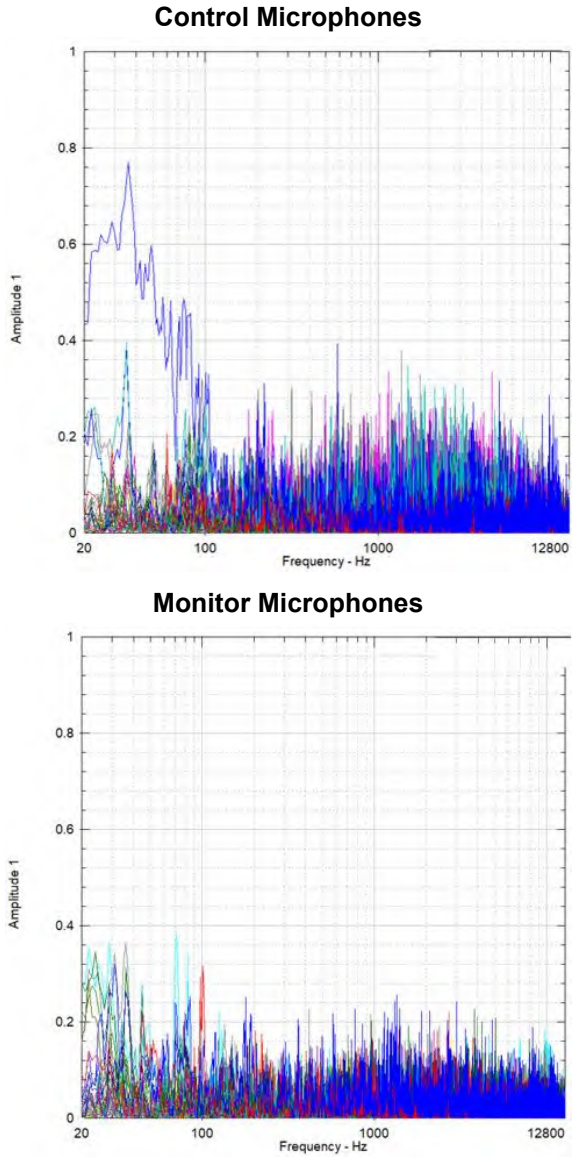


Figure 5: Representative control and monitor coherence plots for M-SISO operation.

5.3 Controller stability and temporal consistency

Temporal consistency was evaluated using short-duration linear averages calculated at five-second intervals over the exposure time. The rolling-average results for the different drive configurations are shown in Fig. 6 and show no obvious drift or loss of target tracking during the displayed runs. The 16-drive case contains more averaging intervals because that exposure lasted 120 seconds. These plots demonstrate stable operation for the tested cases, but they do not constitute a dynamic step-response or disturbance-rejection measurement. No quantitative rise time, settling time, or overshoot is claimed.

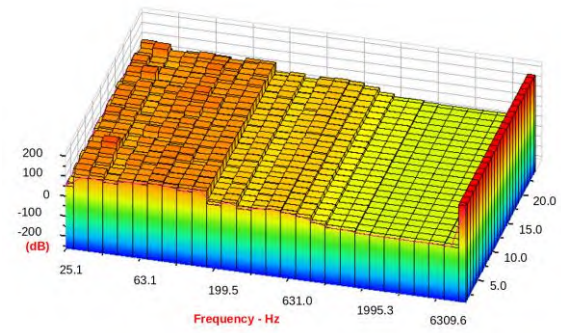


Figure 6: Representative rolling averages showing stable M-SISO behavior for multiple drive configurations.

6. DISCUSSION

The main distinction of the proposed method is architectural. Traditional narrowband MIMO DFAN control attempts to manage a coupled, phase-sensitive multivariable problem. The M-SISO approach instead decomposes the system into many independent broadband energy-control loops and accepts that the global field should be evaluated statistically rather than as a deterministic narrowband construct. That shift offers several practical advantages: simpler system implementation, straightforward scaling, fast loop updates, and reduced dependence on exact source, microphone, and DUT placement.

These benefits do not imply that M-SISO is a universal replacement for every acoustic control problem. The method is best suited to applications in which a diffuse acoustic field is an appropriate objective and where broadband qualification levels are more important than fine-grained line-by-line phase shaping. It also assumes acoustic hardware capable of producing the required levels without excessive reliance on coherent summation. Where structural protection is critical, a separate monitoring and notching path remains advisable. Within those bounds, however, the results support M-SISO as a robust and practical DFAN architecture.

An additional advantage is communicability. Because the architecture is conceptually simple, it is easier to explain, validate, and maintain than a highly coupled controller whose behaviour depends on multiple hidden interactions between loops. This has practical value for test preparation, review with customers, and troubleshooting during a campaign. A system that is easier to reason about is often also easier to trust in operation.

From a test-campaign perspective, the decentralized structure also simplifies commissioning. Each loop can be verified locally, source by source, without first solving a high-dimensional coupled control problem. This makes it easier to identify problematic channels, microphone issues, amplifier limitations, or local acoustic anomalies during setup. In a practical program, that reduction in diagnostic effort can translate directly

into shorter preparation time and more confidence before the first full-level run.

The architecture also scales cleanly. Adding devices does not fundamentally change the controller philosophy; it increases the number of repeated control elements. That characteristic is attractive for large or reconfigurable DFAN systems in which the physical arrangement may change from campaign to campaign. It also supports a more modular software and hardware implementation, which is useful for maintenance, future feature development, and transparent communication of system behavior to review boards and customers.

At the same time, the architecture has clear boundary conditions. It depends on acoustic devices that can produce the necessary broadband output without excessive reliance on coherent summation, and it does not eliminate the need for structural monitoring when the DUT is sensitive to narrowband resonance effects. These are not weaknesses of the concept so much as design assumptions that should be stated explicitly. Future work can therefore focus on quantifying the boundaries of applicability rather than on re-establishing the basic viability of the control approach.

This risk is not merely theoretical. A related large-scale test of a representative satellite mass model found that column-coherent drive—equivalent to a single drive per stack, as used in traditional line-array DFAN systems—produced 11% higher overall structural acceleration than a fully incoherent M-SISO configuration, concentrated below 200 Hz [8]. At a 148 Hz solar-array mode, the column-coherent drive left the solar array almost unexcited while the main structure responded strongly, an outcome inconsistent with impact-modal predictions; the fully incoherent drive excited both consistently and in agreement with the modal survey (Fig. 7). Avoiding this kind of unpredictable, geometry-dependent blind spot is one of the motivating principles behind the M-SISO architecture's preference for independent, uncorrelated sources over coherent summation.

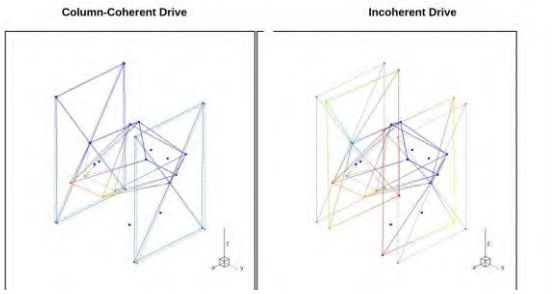


Figure 7: 148 Hz solar-array mode excited by column-coherent drive (left) vs. fully incoherent drive (right). Reproduced from [8].

The reverse outcome is equally plausible. Because coherent summation creates spatially fixed interference patterns rather than a statistically uniform field, a structural mode could just as easily coincide with a pressure anti-node and be overexcited, rather than left dormant, depending on how the mode's spatial distribution (its joint acceptance) aligns with the interference pattern. In either direction, the excitation a given mode receives becomes a matter of geometric coincidence rather than a predictable, bounded quantity, further favoring a statistically diffuse field over deterministic coherent summation whenever the DUT's response is not fully characterized in advance.

7. CONCLUSIONS

A Multi-SISO one-third-octave control architecture provides a credible and technically coherent alternative to narrowband phase-targeted DFAN control. By pairing independent broadband sources with dedicated control microphones and one-third-octave feedback loops, the method generates the acoustic field through statistical superposition rather than deliberate phase enforcement. Representative system data show good agreement between control and monitor locations together with stable exposure over time. These characteristics make the architecture well suited to direct field acoustic noise testing when the target is a practical, repeatable, and sufficiently diffuse acoustic environment.

The next step for this line of work is targeted consolidation. Because the core architecture has now been framed clearly, follow-on studies can evaluate one additional dimension at a time without broadening the paper again. Suitable next studies include loop-dynamics characterization, microphone-placement sensitivity, scalability with larger numbers of channels, and field-qualification procedures that combine monitor positions, coherence measures, and rolling averages into a compact acceptance framework.

That staged validation path is one of the strengths of the architecture-based presentation. It allows the M-SISO concept to be assessed first on its own terms and then extended systematically. In that sense, the present paper is intended not only as a report of a controller implementation, but also as a foundation for a family of focused DFAN papers that address performance, robustness, and qualification methodology in a structured way.

REFERENCES

[1] W. O. Hughes and A. M. McNelis, "Investigation of Acoustic Fields for the Cassini Spacecraft: Reverberant Versus Launch Environments," 5th Aerocoustics Conference and Exhibit, 1999.

[2] P. Larkin, "Developments in Direct-Field," Sound and Vibration, Nov. 2014.

[3] A. R. Kolaini, B. Doty and Z. Chang, "Impact of Acoustic Standing Waves on Structural Responses: Reverberant Acoustic," Jet Propulsion Laboratory, California Institute of Technology, 2012.

[4] R. Roe, NASA-HDBK-7010, NASA, 2016.

[5] American National Standard, ANSI S1.11 Specification for Octave-band and Fractional-Octave-Band Analog and Digital Filters, Acoustical Society of America, 2004.

[6] E. Friedlander, D. Schick and T. Hoffman, “Qualification of DFAN Field & Acoustic Control Methods,” 31st Space Simulation Conference, 2022.
[7] D. Schick, E. Friedlander, T. Hoffman and E. Kinsella, “Verifying a Novel Approach to Acoustic Testing: Acoustic Devices & Control Systems,” 32nd Aerospace Testing Seminar, 2021.
[8] D. Schick, G. Eckert, E. Kinsella, S. M. Schwarzendahl and C. Eike, “Examining a Multi SISO Acoustic Control Method and Structural Response,” AIAA SciTech Forum, 2026.

Evaluating the effect of stacked structures on their vibroacoustic response during acoustic testing using Direct Field Acoustic Testing (DFAT®)

Alexander D. O'Malley [(1)] , Arloe W. Mayne III[(1)] , Alex Carrella[(1)]

[(1)] MSI-DFAT, 4900 Wetheredsville Road, Baltimore, MD, 21207, USA,
a.omalley@msidfat.com , w.mayne@msidfat.com, a.carrella@msidfat.com

Keywords

Direct field acoustic test (DFAT), stacked spacecraft, constellation satellites, structural response, finite element analysis (FEA), experimental modal analysis (EMA), Vibroacoustic gain

Abstract

Direct Field Acoustic Testing (DFAT®) is widely used to reproduce launch acoustic environments for spacecraft qualification. With the increasing demand for high-volume spacecraft production, particularly for constellations, testing throughput has become an important consideration. Rather than running N acoustic tests on N articles, one could envision performing a single acoustic test on N articles stacked together, saving the time and cost of N-1 tests, which may be substantial. However, both launch authorities and OEMs raise a key question: Would the vibroacoustic excitation experienced by a single unit remain representative when multiple units are stacked? In addition, spacecraft are often integrated and launched in a stacked configuration within a rocket fairing, where adjacent units are mechanically connected to one another, which alters the acoustic loading and structural response. This physical coupling increases the effective mass that each spacecraft's structure must support, shifting its dynamic response to lower frequencies relative to a single, isolated unit.

This study investigates the feasibility of simultaneously testing multiple spacecraft in a stacked configuration during DFAT while maintaining a representative acoustic and structural environment for each unit. Three identical panels, used as simple spacecraft models, were tested first singularly and then in stacked configurations of two and three units. Experimental modal analysis (EMA) and vibroacoustic (DFAT) testing were performed for each case and the results were compared.

1. Introduction

The purpose of these tests is to characterize the acoustic and structural dynamics of an individual constellation satellite simulator during DFAT, and to observe how those dynamics change when multiple simulators are stacked and tested simultaneously. This study does not aim to determine whether stacked acoustic qualification is feasible: that determination belongs to spacecraft analysts, qualification authorities, and launch providers, and can only be established through testing of representative flight hardware with mission-specific analysis. Instead, the goal is to document the general trends that emerge when multiple spacecraft simulators are stacked and tested together, informing future qualification decisions.

A MATLAB finite element analysis (FEA) of the constellation satellite simulator was performed to characterize its structural dynamics; damping was excluded from this model. The FEA results directly informed the panel separation distance used in testing, as detailed in Section 2.

A circular array of loudspeakers surrounded the test article, with an annulus of control microphones feeding a MIMO controller to produce a spatially uniform, quasi-diffuse acoustic field. Monitor microphones tracked the local field around the panel of interest, which carried 20 accelerometers to measure structural response. Experimental modal analysis identified natural frequencies and mode shapes for the single panel and three panel configurations, tracking how structural dynamics changed as panels were added to the stack.

2. Test Configuration

The tests were conducted using a 6×6 DFAT speaker stack configuration: a speaker circle with a height of 3.66m (12ft) and an inner test radius of 3.66m (12ft) surrounding the test article, with six low-frequency stacks (one MP-40 speaker below four MP-21 low-frequency speakers) and six mid/high-frequency stacks (six MP-150 speakers each). Sixteen control microphones were deployed in an annulus around the test article, numbered 1-16 clockwise beginning at 0°, as seen in *Fig. 1.*

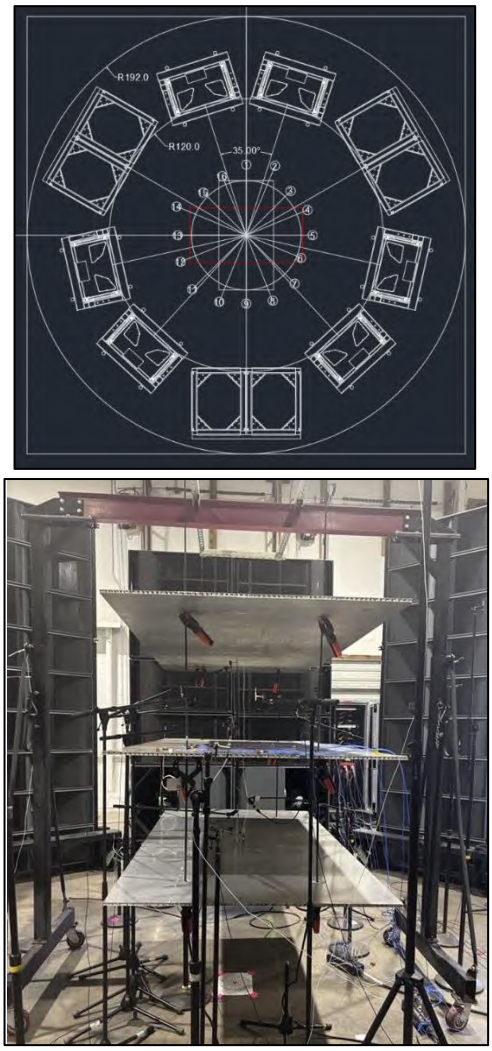


Figure 1: CAD top-down view of the speakers, test article, and control microphones (top) and panel stack suspended from the gantry suspension fixture inside the DFAT speaker circle (bottom).

The SpaceX Falcon 9 acoustic spectrum was selected as the basis for the test profile because the Falcon 9 family currently performs more orbital launches per year than any other launch vehicle, making its environment broadly applicable to the spacecraft community [1]. The spectrum was extended down to the 1/3-octave band centered at 16 Hz, see Fig. 2, since the pre-test FEA placed the panel's fundamental bending mode near 15 Hz. A Siemens SCADAS MIMO controller generated correlated drive signals to maintain the target quasi-diffuse environment. Although the specification was defined in 1/3-octave bands, control was performed in narrowband 3.125-Hz bands.

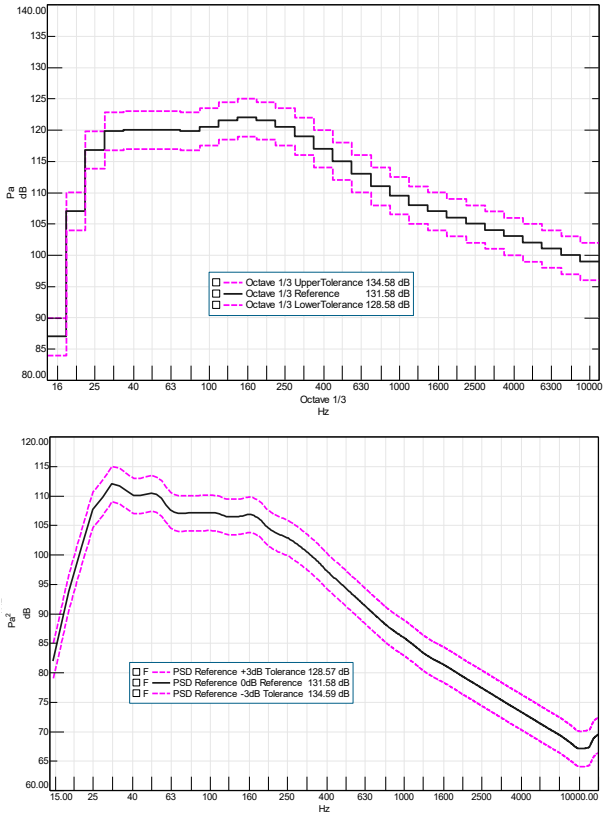


Figure 2: Modified Falcon 9 reference spectrum in 1/3-octave bands (top) and narrowband (bottom).

The test article (TA) was a 1.27cm thick (0.5in), 1.21m (4ft) × 2.43m (8ft) aluminum honeycomb panel. A simple panel geometry was chosen because the study targets dynamic trends associated with stacked testing in general, not a specific spacecraft program, and its simplicity makes the acoustic and structural behavior easier to interpret. This panel had also been studied by Underwood and Lamparelli [2], allowing reuse of established instrumentation and methodology, though direct comparison with their findings is not possible due to differences in boundary conditions and panel orientation relative to the incident field.

In Fig. 1, a gantry fixture suspended the panels in air: bungee cords passed through holes drilled in each panel, with the panels resting on clamps attached to the cords. This suspension was assumed to approximate a free-free boundary condition with minimal constraint from the support structure.

Each panel was tested individually, then in stacked configurations of two and three panels on the same bungee system. In all configurations, only one panel, referred to as the test panel, was instrumented with accelerometers, as seen in Fig. 3; the remaining panel(s) are referred to as auxiliary panels. Monitor microphones 17–24 maintained a fixed geometry relative to the test panel throughout testing. For the single and two panel configurations, the test panel sat 0.91m (36in) above the ground; for the three panel configuration, it occupied the middle position and was raised, together with all monitor microphones, by 0.59m (23.5 in) to a final height of 1.51m (59.5in).

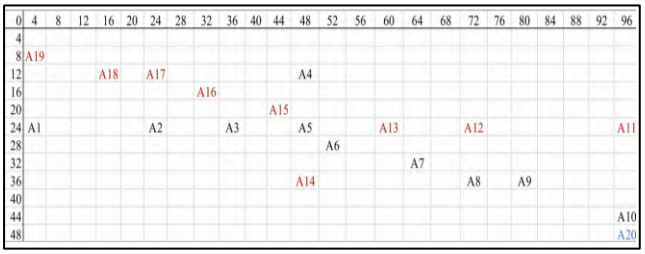


Figure 3: Accelerometer (A1–A20) layout on the test panel.

Panel Separation Distance

The separation distance between panels was selected on acoustic grounds: to generate a standing wave between adjacent panels at a targeted low-frequency panel mode, since low-frequency excitation carries most of the acoustic energy at launch and drives much of the vibroacoustic loading on spacecraft structures. Normalizing separation by panel thickness was rejected because the panel's aspect ratio is unrealistic relative to flight hardware, and representative spacing information from operational constellation stacks were not available.

The FEA, using free-free boundary conditions and simplifying the honeycomb plate to an isotropic plate of equivalent stiffness and mass, was studied using Irvine's honeycomb plate techniques [3]. The 285-Hz mode was chosen as the basis for plate separation for three reasons: it lies in the lower-frequency regime where acoustic energy is concentrated; it corresponds to an even panel mode, simplifying interpretation; and its half wavelength gives a separation of 0.601m (23.68in), reasonably representative of spacing between neighboring spacecraft in a stacked launch configuration. Assuming a one-dimensional standing wave in the vertical direction and considering only the first acoustic mode of the cavity between panels [4], the 3D standing wave equation

$$p_{lmn} = A_{lmn}\cos(k_{xl}x)\cos(k_{ym}y)\cos(k_{zn}z)\,e^{j\omega_{lmn}t} \quad (1)$$

reduces, for a one-dimensional standing wave in the vertical z-direction with n = 1, i.e. mode (0,0,1), to

$$p_{0,0,1} = A_{0,0,1}\cos(k_{z1}z)\,e^{j\omega_{0,0,1}t} \quad (2)$$

so that a standing wave is created when

$$\omega_{0,0,1} = \frac{c\pi}{L_z} \rightarrow f_{0,0,1} = \frac{c}{2L_z} \rightarrow L_z = \frac{c}{2f_{0,0,1}} \quad (3)$$

Substituting the 285-Hz target and a speed of sound of 343m/s (1125ft/s) results in

$$L_z = 0.601m\ (23.68in) \quad (4).$$

Due to fixture and hardware limitations, the realized spacing was adjusted to 0.600m (23.625in). The derivation assumes rigid, stationary panel surfaces. The selected spacing was expected to reduce the response of the targeted even mode through interaction between the standing wave and the panel's transverse motion; this hypothesis is evaluated by comparing the single-panel and stacked configurations. The targeted mode is shown in Fig. 4.

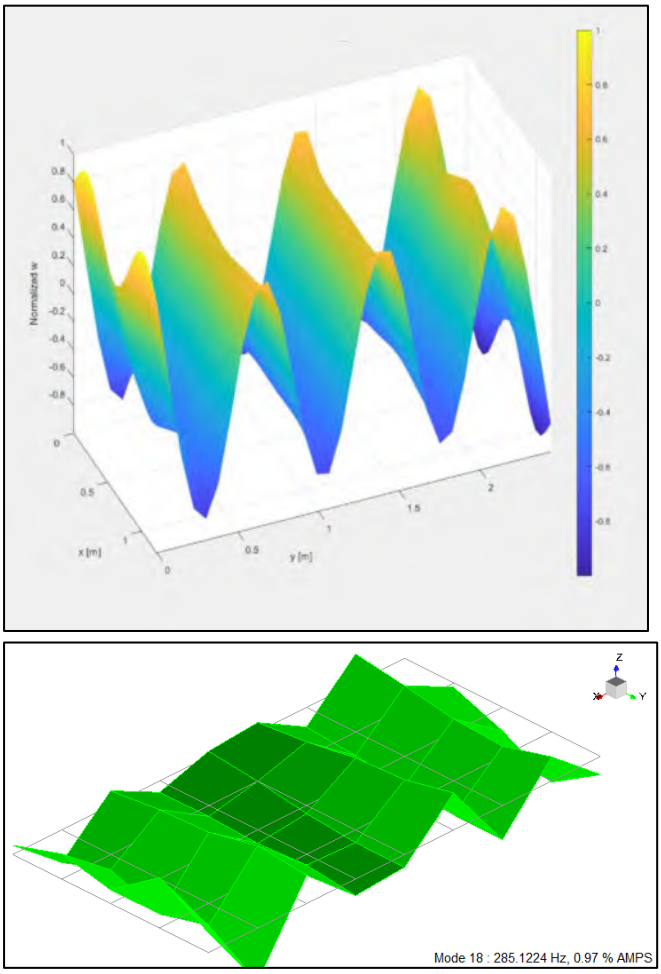


Figure 4: Honeycomb FEA prediction at 285Hz (top) and the even panel mode near 285Hz (bottom) from the EMA.

3. Results

In the microphone PSD plots that follow, control microphones are blue, monitor microphones orange, the control average green, the reference spectrum black, and the ±3 dB tolerance bands pink. In all other graphs, the green, red, and blue curves display the results from the single panel, two panel, and three panel tests, respectively.

The microphone PSDs for all three configurations, Figs. 5-6, together with the Sinc Indicator Function (SIF) results, Fig. 6, (bottom), which is a proxy measure for the diffuseness of the acoustic field [5], show that the input acoustic fields were nearly identical in SPL uniformity and diffuseness. Variations at the monitor microphones or accelerometers can therefore be attributed to the stacked configuration rather than the input field, and the analysis below compares the single panel response with the two and three panel responses.

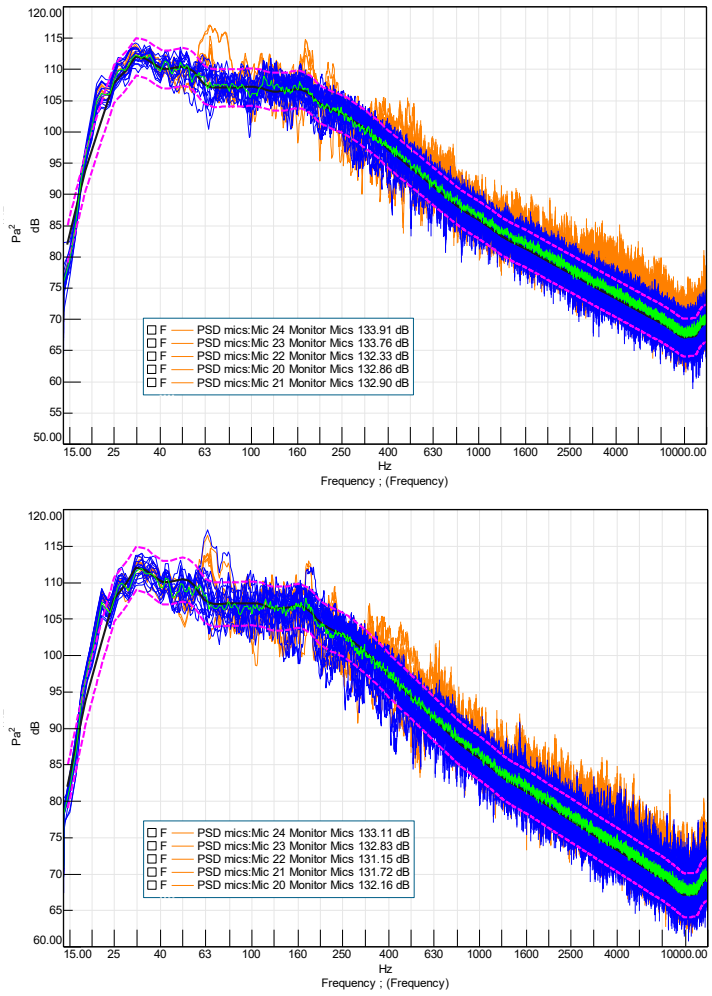


Fig. 5: Control and monitor microphone narrowband PSDs: single-panel (top) and two-panel (bottom) configurations.

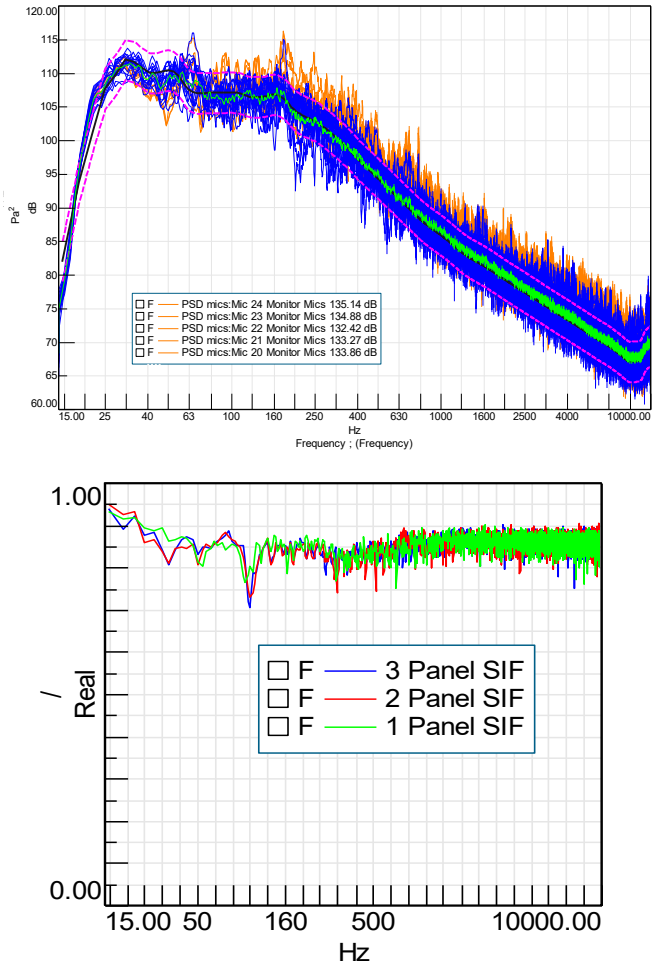


Fig. 6: Three-panel microphone PSDs (top) and Sinc Indictor Function of the control field for the three configurations (bottom).

Average monitor microphone levels exceeded control levels in all configurations, as expected: the panel acts as an acoustically rigid surface, reflecting incident energy and raising local SPL. The excess in average monitor OASPL grew from about 1 dB (single panel) to 1.25 dB (two panels) and 2 dB (three panels), attributable to the proximity of reflective surfaces: in the two-panel test the panel sat 0.91m (36in) above the ground and 0.59m (23.625in) below the auxiliary panel, while in the three-panel test it sat 0.59m (23.625in) from reflective panels both above and below.

While several individual frequencies exceeded the +3 dB tolerance band, monitor OASPL stayed within test tolerances for all configurations. The largest amplifications occurred near 64, 175, 678, and 779 Hz, peaking 6-8 dB above reference. The 64-Hz amplification was most pronounced in the single- and two-panel tests, while the others peaked in the three-panel test. These amplifications are not consistently tied to panel count; rather, they are governed by the geometric arrangement of panels and acoustic field.

The test panel's acceleration response generally tracked the monitor microphone PSDs, with dominant peaks at frequencies of elevated local SPL (Fig. 7), though not perfectly: some frequencies with elevated monitor levels produced little structural response, possibly because the associated modes have odd shapes or limited net pressure loading (speculative, pending further analysis). Notably, the single-panel configuration consistently showed the highest acceleration response, with the two and three panel configurations lower and similar in magnitude, consistent with the standing wave between panels reducing transverse panel motion near the targeted frequencies. Several peaks also shifted modestly in frequency between configurations, suggesting added structural coupling from the supports and neighboring panels.

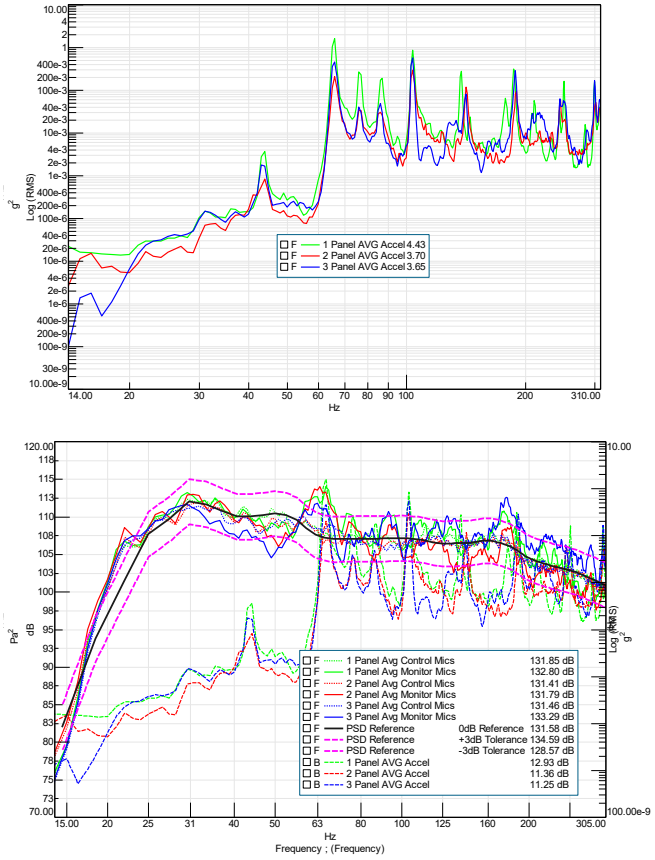


Fig. 7: Single-panel microphone PSDs overlaid with the average panel acceleration response.

Vibroacoustic gain (acceleration response normalized by acoustic input) was calculated as a direct measure of acoustic-structural coupling efficiency (Fig. 8). Distinct gain peaks began near the fundamental bending mode at approximately 15 Hz and continued through the upper test frequency range; above roughly 1000 Hz, individual modal peaks became difficult to distinguish from broadband response and noise. The single-panel configuration showed the highest overall gain, followed by the three-panel and then the two-panel configuration, an ordering that was somewhat unexpected: a monotonic decrease with panel count might have been anticipated if the panels simply constrained transverse motion. Instead, the interaction between panel spacing, local acoustic field formation, and structural coupling appears configuration-dependent rather than a simple function of panel count. This also underscores that structural response cannot be inferred from local acoustic pressure or acceleration alone: gain captures how effectively acoustic energy transfers into structural motion.

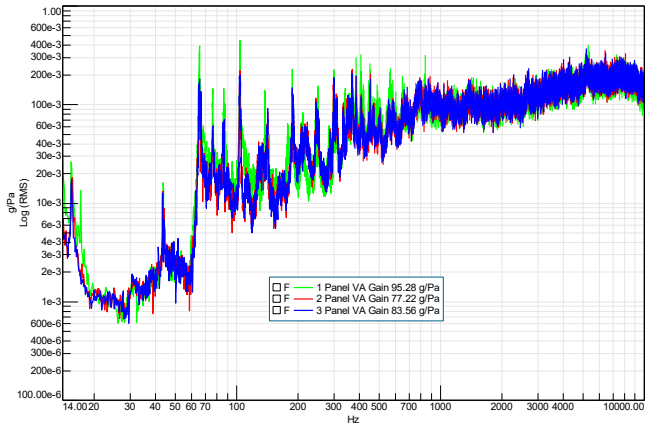


Fig. 8: Vibroacoustic gain of the test panel for the three configurations.

The behavior near the targeted 285-Hz standing wave is of particular interest (Fig. 9). The acceleration PSD shows a pronounced, well-defined single-panel response near 285 Hz; the three-panel peak is broader, less pronounced, and more heavily damped; and the two-panel response is almost entirely absent, making the mode effectively unobservable. Vibroacoustic gain tells a different story: well-defined peaks remain near 285 Hz for all three configurations, with the single panel still highest, so the mode was not eliminated by stacking; rather, the efficiency with which the field excited it changed substantially. The monitor PSDs complicate the picture further: the three-panel test had the highest local pressure near 285 Hz while the single- and two-panel environments were nearly identical, yet their structural responses differed dramatically. Local SPL alone is therefore insufficient to explain the response; acoustic loading distribution, mode shape, and structural coupling all play significant roles.

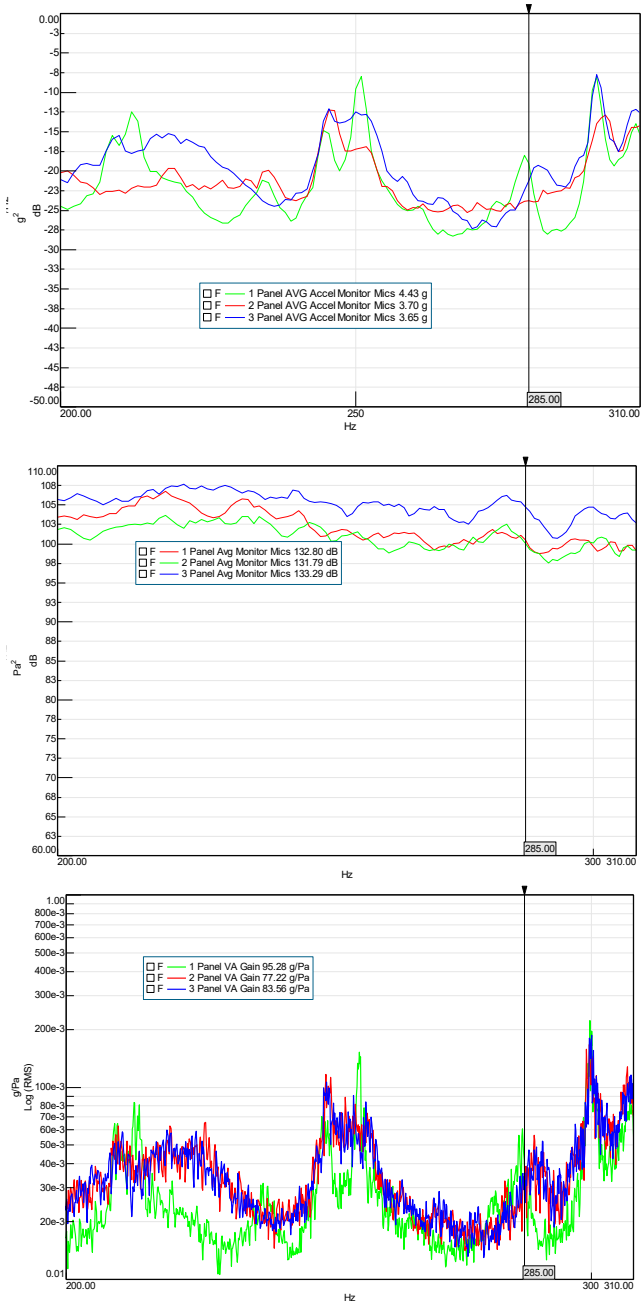


Fig. 9: Detail near 285 Hz: average acceleration response (top), monitor microphone PSDs (middle), and vibroacoustic gain (bottom).

The EMA results showed strong correlation between the single-panel and three-panel configurations, per the MAC comparison in Fig. 10 and the frequencies in Tab. 1. High diagonal MAC values indicate that the test panel's dominant mode shapes remained largely consistent after adding auxiliary panels, while several modes shifted modestly in frequency: the auxiliary panels altered effective dynamic properties while preserving deformation patterns. The mechanisms behind these shifts cannot be determined definitively from the present data, particularly since the boundary conditions were designed to minimize structural coupling. One exception: a single-panel mode at 216.9 Hz was not identified in the three-panel EMA, and the 293.7-Hz single-panel mode shifted down to 285.1 Hz in the three-panel configuration, landing on the intentionally selected standing-wave frequency. This may indicate interaction between the inter-panel acoustic cavity and the structure, though additional analysis would be needed to establish causality.

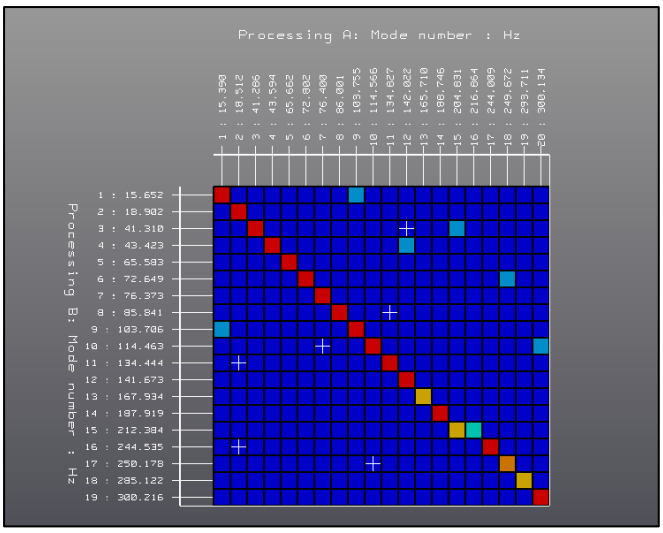


Fig. 10: MAC comparison of the single-panel and three-panel EMA mode shapes.

Table 1: Natural frequencies identified by EMA in the single-panel and three-panel configurations.

1 Panel		3 Panel	
Mode	**Frequency (Hz)**	**Mode**	**Frequency (Hz)**
1	15.3901	1	15.6516
2	18.5122	2	18.9024
3	41.2862	3	41.3105
4	43.5936	4	43.4233
5	65.6618	5	65.5829
6	72.8025	6	72.6492
7	76.4003	7	76.3725
8	86.0009	8	85.8413
9	103.7547	9	103.7062
10	114.5657	10	114.4627
11	134.8274	11	134.4442
12	142.0216	12	141.6727
13	165.7096	13	167.9336
14	188.7462	14	187.9193
15	204.8308	15	212.3839
16	216.8643	16	NA
17	244.0087	17	244.5352
18	249.6718	18	250.1778
19	293.711	19	285.1224
20	300.134	20	300.2163

4. Analysis and Conclusions

This study asks a practical question: When spacecraft are stacked and tested together, does the vibroacoustic environment each unit experiences stay representative? The goal was not to establish blanket feasibility of stacked DFAT qualification, but to document the general trends that emerge when spacecraft are tested in a stacked configuration.

Control microphone and SIF measurements confirmed the input field was highly repeatable across configurations, so observed changes in monitor levels, acceleration, and vibroacoustic gain are attributable to the neighboring panels, not the DFAT control field.

Neighboring panels alter the local acoustic environment through reflections and cavity effects, but these effects are strongly frequency dependent with no simple relationship to panel count. Structural response likewise can not be predicted from sound pressure levels alone: loading distribution, mode shapes, and acoustic-structural coupling all matter. This was clearest at the standing-wave frequency the test was deliberately tuned to target, where the single-panel configuration responded strongly, the two-panel configuration nearly suppressed the mode, and the three-panel configuration fell in between, suggesting standing-wave/structural-dynamics interaction can meaningfully affect stacked spacecraft behavior. EMA results reinforce this: mode shapes stayed largely consistent despite

frequency shifts, so stacking alters modal excitation and acoustic coupling more than the spacecraft's underlying structure.

If adopted, stacked acoustic testing would function as a workmanship test and should be run at the OEM facility, so a failing unit can be reworked without shipping delays. The mock-up support structure should also match the dynamics of the actual flight stacking structure, since a mismatch would undermine test fidelity. Stacked testing may also be more flight-accurate than testing units individually, since stacked spacecraft do not fly as isolated bodies, and the added mass introduces low-frequency content closer to actual flight dynamics.

Frequency-specific sensitivities from standing waves can be response-limited with narrowband control, which notches a single structural or room mode without affecting the rest of the band, unlike 1/3-octave control, which would notch the whole band. Since test requirements are typically written in 1/3-octave terms, a configuration can pass tolerance while still carrying a meaningful narrowband variation, so a detailed vibroacoustic FEA is needed to judge whether that variation matters.

Overall, stacked DFAT testing is highly configuration dependent and cannot be evaluated by spacecraft count alone. RMS acceleration response decreased with stacking, but this should be verified with mode-specific FEA rather than taken at face value. No disqualifying behavior was observed, and the concept warrants further study with representative hardware and mission-specific analysis. If validated, stacked DFAT testing could meaningfully cut schedule and cost for high-volume constellation production, saving N-1 acoustic tests per stack.

Acknowledgements

The author sincerely thanks Wes Mayne III for his general consultation throughout this work.

References

1. Falcon User's Guide, Version 8, SpaceX, March 2025.
2. Underwood, M. A., and Lamparelli, M. D., “A New Method Using Pseudovelocity-Based Fatigue Analysis to Determine the Effectiveness of Acoustic Fields Used for Acoustic Testing,” MSI-DFAT/Tu'tuli Enterprises and Spectral Dynamics.
3. T. Irvine, *Natural Frequencies of a Honeycomb Sandwich Plate*, Revision F, Vibrationdata, Aug. 25, 2008. [Online]. Available: https://www.vibrationdata.com
4. Kinsler, L. E., Frey, A. R., Coppens, A. B., and Sanders, J. V., Fundamentals of Acoustics, 4th ed., John Wiley & Sons, New York, 2000, Ch. 9.
5. Carrella, A., “Acoustic Testing: Investigating the Sinc Indicator Function (SIF) as a Metric for the Diffuseness of the Acoustic Field,” 34th Aerospace Testing Seminar (ATS), Los Angeles, CA, USA, Mar. 31–Apr. 4, 2025.

About the Authors

Alexander “Xander” O’Malley earned his B.S. in Mechanical Engineering from The Johns Hopkins University in 2025. He continues his studies at JHU and is pursuing his M.S. in Mechanical Engineering while working full-time. At MSIDFAT, he is a vibroacoustic test engineer and is actively supporting client programs for testing, data analysis, and special R&D projects.

Arloe “Wes” Mayne, III, has worked with test facility development and testing for almost 40 years, including many aerospace acoustic test facilities around the world. Wes currently provides project management and vibroacoustic support for DFAT tests, including the largest DFAT tests that have been done anywhere to-date. He is also engaged in general customer interface, project development, DFAT system R&D, and vibroacoustic modeling. Customers can call Wes about any aspect of vibroacoustic testing and DFAT.

DEVELOPMENTS IN DIFFUSE SOUND FIELD MODELLING AND ITS APPLICATION TO DIRECT FIELD ACOUSTIC NOISE (DFAN) TEST PERFORMANCE QUANTIFICATION: METRICS AND CASE STUDIES

Jonathan A. Hargreaves [(1)], Charly Knight [(2)], Ian Horsfall [(3)]

[(1)] Acoustic Research Centre, Newton Building, University of Salford, Salford, M5 4WT, UK,
Email: j.a.hargreaves@salford.ac.uk
[(2,3)] RAL Space, STFC Rutherford Appleton Laboratory Harwell Campus, Didcot, OX11 0QX, UK,
Email: charly.knight@stfc.ac.uk, ian.horsfall@stfc.ac.uk

KEYWORDS

Environmental Testing, Direct Field Acoustic Noise (DFAN) Testing, Structural Dynamics.

ABSTRACT

In Direct Field Acoustic Noise (DFAN) testing, large arrays of high-powered loudspeakers are used to produce a high intensity acoustic environment for payload qualification and/or pre-flight assurance-testing purposes. Over the past two-decades, this has become an increasingly popular alternative to equivalent tests performed in Reverberant Acoustic Test Facilities (RATFs). Nonetheless, there remains a need to qualify the similarity of the sound fields produced by these two types of tests to ensure equivalence of the two approaches and de-risk the transfer between one testing technology and the other. There is, therefore, a continued demand for evidence that the sound field produced by a DFAN system is – or can be – equivalent to that produced by a RATF. By design, both produce sound fields that are inherently random, so what is required to compare them is metrics that capture & quantify the key characteristics of these random sound fields.

This paper will report some recent developments in the modelling of diffuse sound fields, as both types of test aim to achieve, including in metrics that aim to quantify how 'diffuse' a produced sound field is. The effectiveness of these approaches will be illustrated through two case studies – one at smaller scale and lower SPL and a second at full scale and full test SPL – via which recommendations for best practice going forwards will be suggested.

1. INTRODUCTION AND MOTIVATION

The space-launch industry has an established need for acoustic environmental testing. This aims to replicate, in a precisely controlled way, the structural response that would occur during launch due to its extreme acoustic environment [1]. Such testing is used to qualify new payload designs and for pre-flight assurance testing purposes.

Traditionally, such acoustic tests have been performed in Reverberant Acoustic Test Facilities (RATFs), but these have disadvantages including high construction and operation costs, and the logistical challenge of moving the payload to the test facility, which can be costly and/or risky when large payloads and/or distances are involved.

Since the mid-1990s, Direct Field Acoustic Noise (DFAN) testing – also known as Direct Field Acoustic Testing (DFAT®) – has existed as an alternative. In this technology, large arrays of high-powered loudspeakers are used to produce the necessary acoustic environment. The scope of what sound field DFAN testing systems could render is broad, enabled by the powerful control systems they use [2,3], but demand from the space launch industry has, to date, been for them to replicate the sound field produced by RATFs, since this derisks the transfer from one test technology to the other.

Since RFAT is an accepted test method within the space industry, and tests are likely to continue in parallel with DFAN systems, it is highly desirable to show equivalence. As both test methods are designed to produce diffuse random sound fields, what is required are metrics that can fully characterise these acoustic environments.

1.1. The UK National Satellite Test Facility

The UK National Satellite Test Facility (NTSF) at RAL Space in Harwell, Oxfordshire, opened in May 2024. DFAN was selected as the Acoustic testing technology for this facility, allowing acoustic and vibration testing to share clean room space. This leads the Dynamics Group to have an interest in developing and utilising appropriate sound field metrics, with the purpose of both demonstrating that



Figure 1: The UK National Satellite Test Facility Left: Exterior view. Right: Elevated view of a mid-sized DFAN test in the clean room.

theirs is a well-proven test system capable of providing an acoustic environment equivalent to a RATF test, and for quality assurance of individual tests. Moreover, being part of the UK STFC, RAL Space's mission includes furthering fundamental knowledge, motivating collaboration on research studies such as the ongoing one reported herein.

1.2. Outline of this paper

The remainder of this paper is organised as follows:

- Section 2 gives an overview of diffuse field theory and metrics, including recent developments.
- Section 3 then reports some work that was done in 2024 on the design of linear microphone arrays for quantification of sound field 'diffuseness', including some updated perspectives.
- Section 4 reports full-scale tests where the array from 3 was used, including some unintended properties of it that have recently been identified.
- Section 5 relates this to DFAN 'drive matrices', leveraging findings from a scale-model 'mini-DFAN' test conducted at the University of Salford.
- Finally, section 6 draws conclusions and reflects on areas where further research is needed.

2. DIFFUSE FIELD THEORY AND METRICS

A diffuse field is a theoretical sound field commonly defined as being one in which sound energy arrives from all directions with equal probability [4]. Further requiring that the waves arriving from differing directions are incoherent leads to several well-known properties, such as the coherence between pressure signals at a pair of spaced microphones and homogeneity of Sound Pressure Level (SPL), given sufficient time-averaging.

Before getting into diffuse field metrics, however, it is worth noting that the commonplace starting assumption of RATFs – that they produce a diffuse field – is not strictly true, since they largely contain the same sound recirculating. With sufficient scattering objects and distance from boundaries, the sound field is chaotic and isotropic enough to be effectively diffuse above a specified frequency, but even then, deviations from diffuse can be detected if long time-averaging is done in specific ways [5]. Thus, when discussing the metrics used later in this report, it should be born in mind that many are capable of showing up flaws in RATF too [6].

The other 'elephant in the room' is that it highly unlikely that the sound field inside a rocket fairing is diffuse; limited data is available on this but that which is shows different characteristics [7]. Indeed, a fairing is a relative tight-fitting air volume where the acoustic energy source is incoherent vibration of its external boundary (due to chaotic aerodynamic loading), a scenario that a DFAN system would arguably be better able to simulate than a RATF.

Nonetheless, a diffuse field remains a useful target for environmental acoustic testing because panel structures are usually most susceptible to acoustic excitation from specific angles, and a diffuse field includes all of them. It is also the testing requirement specified in launch manuals, so from a pragmatic perspective is what DFAN systems must achieve.

2.1. Diffuse field metrics prevalent in DFAN

An established method for assessing how close a sound field produced by a DFAN system is to diffuse is to compare measurements of coherence between spaced pairs of microphones to the theoretical trend that would occur if the sound field truly was diffuse. This approach has been in use for around 14 years, with one of the first appearances being [8] in 2012. Notably, it is extremely versatile; since no special arrangement of microphones is in principle required, existing monitor and control microphone signals can be analysed in this way.

The coherence $\gamma(f)$ between a pair of microphones is the ratio of the cross Power Spectral Density (PSD) between the signals they capture, normalised by the square root of the product of their auto PSDs. These PSDs are dependent on frequency f, hence coherence γ also is. In a diffuse field it is well know that this – like the signals' covariance [5,10] – follows a $\mathrm{sinc}(kr)$ trend. Here r is the separation distance between the microphones in meters and $k = 2\pi f / c_0$ is the acoustic wavenumber, where c_0 is the speed of sound in meters per second.

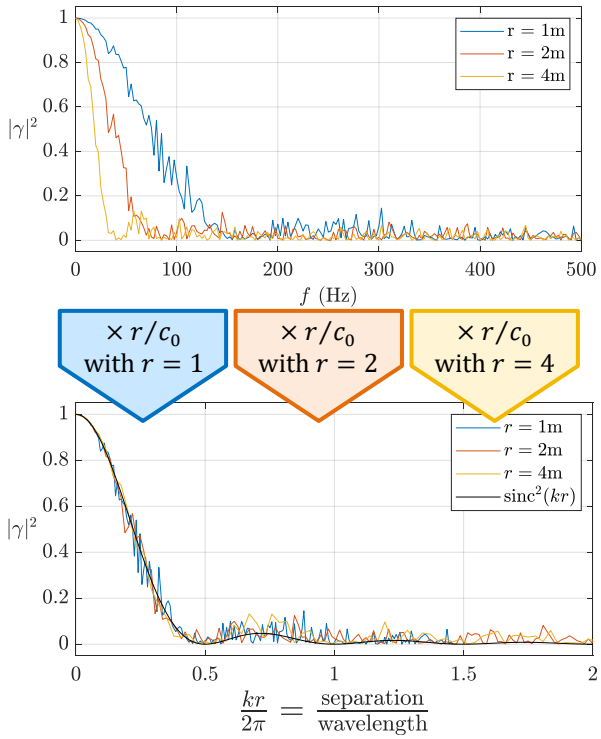


Figure 2: Coherence for three microphone pair spacings in a simulated diffuse field. Top: versus frequency. Bottom: versus separation / wavelength, with the theoretical trend overlaid.

In practice, it is more common for the Magnitude Squared Coherence (MSC) $|\gamma|^2$ to be plotted, which follows a $\mathrm{sinc}^2(kr)$ trend due to the squaring.

Simulated diffuse field microphone MSC data is plotted in Fig. 2 for three example microphone spacings. Each line contains a natural randomness because a diffuse field is a random field, and here – as is representative of measurement – it has been observed for a finite period of time (64 FFT blocks).

The main thing to note is that in the top plot, where MSC is plotted against frequency, the lines do not lie on top of one another due to the differing spacing. In the bottom plot, however, plotting the same data w.r.t. kr has compensated for the differing spacing such that the lines do align both with each other and the theoretical trend line (black). This is the benefit of kr plots when viewing coherence data.

Some practitioners have anecdotally voiced some hesitation about the use of kr as the abscissa axis, since the physical meaning of it is far less immediate than frequency f. But here, normalisation by 2π (as plotted) is helpful since it can be readily shown that $kr/2\pi = r/\lambda$, the ratio of separation to wavelength, which has an immediate physical meaning.

Another barrier perceived by some is the scaling of MSC data w.r.t. frequency $|\gamma(f)|^2$ by $2\pi r/c_0$ in its abcissa to give $|\gamma(kr)|^2$ (or by r/c_0 for the plotted normalized version), because r is another array of data (of size $N_{\mathrm{mics}} \times N_{\mathrm{mics}}$). This is somewhat tedious in a spreadsheet, but in a scripted array language* such as Matlab™ or NumPy it is trivial.

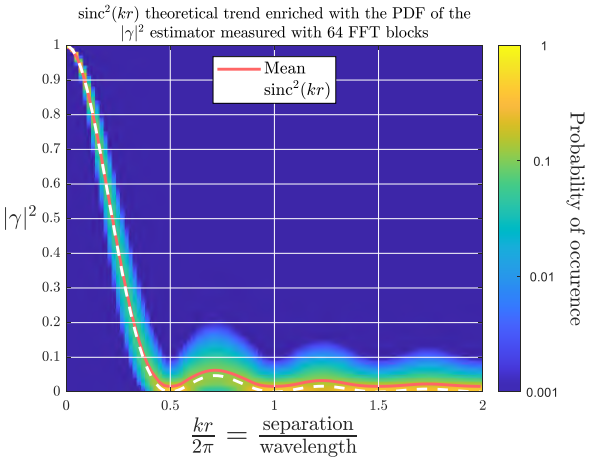


Figure 3: Theoretical $sinc^2(kr)$ trend (white dashed line) enriched with the PDF of $|\gamma|^2$ (colourmap) when 64 FFT blocks are used in its calculation. Mean of the distribution is in red.

In terms of a quantitative metric, Carrella and Mayne proposed the "Sinc Indicator Function (SIF)" in 2022 [10]. This computes the magnitude of the difference between $|\gamma(f)|^2$ measurements and the theoretical trend $\mathrm{sinc}^2(2\pi fr/c_0)$, then averages this over microphone pairings to produce a single figure of merit. The purpose of this is well-meaning and the scale and notion of averaging over microphone pairs – being joint spatial samples of the coherence statistics – are well-founded, but concerns have been anecdotally raised over the heteroscedastic properties of the MSC, on which it is based.

The Probability Density Function (PDF) of the MSC, as explored in [6], captures the root of this concern. Since that paper, the lead author of this manuscript has found a new use for this PDF, in 'enriching' theoretical results computed based on 'Expected' values (what would be seen if observing forever) to capture the distribution of values likely to be measured in a finite time. Fig. 3 shows a simple example of this – enriching the $\mathrm{sinc}^2(kr)$ trend – but the same approach can also be applied to more sophisticated Finite Element or Boundary Element Method based models, which – being based on the Expected values of the Cross-Spectral Density Matrices (SDMs) [11,12], normally fail to capture the variance due to finite-time measurement windows.

The heteroscedastic properties of the MSC are clearly visible in Fig. 3. When the theoretical line (dashed white) is close to 1, the variance (vertically as plotted here) of the PDF tends to zero. But when the theoretical line tends to zero, the variance is significant and – potentially more problematic for the SIF – has a biased mean (red versus white lines).

A solution to this bias comes in the form of complex coherence, which has recently been championed by Allen and co-workers at NASA [13], and for which the theoretical curve $(\mathrm{sinc}(kr))$ is known and the mean is unbalanced. This paper presents results as both magnitude-squared and complex coherence for comparison, additionally using histogram plots in the style of Fig. 3 to show the proportion of mic pairs achieving a given value more clearly than line plots do. Moreover, as a thought experiment, the SIF is computed on this complex data† for comparison too.

A correction for the vanishing variance of measured coherence as true coherence approaches unity is discussed in Section 5 of [6]. A slight modification of this appears applicable to complex coherence too, potentially leading to almost uniform variance and a quasi-Gaussian PDF over the full range, but further research on this is required; it is not presented here.

* There are strong benefits to choosing such languages over spreadsheets in terms of reproducibility and quality assurance too, since they lead to processes that are more easily audited and less prone to human error.

† To be precise, it is computed on the signed magnitude-squared real part of coherence; it was found that the imaginary part added relatively little information, and squaring was necessary to achieve the same scale

2.2. Other Diffuse Field Metrics

Outside the DFAN community, the spaced-mic coherence trend above is known [5] but not widely utilised. Instead, a metric involving the ratio of the magnitude of the real part of acoustic intensity to the acoustic potential energy (a scaling of magnitude-squared pressure) attracts attention; see, e.g., the two recent review articles by Zotter et al [14,15]. Another metric is isotropy, as developed by Nolan and co-workers to study room acoustic RATF; see section 2.3.3.2 of [1] for an overview of this and refs. Zotter notes that isotropy is a stricter measure than the intensity measure since the former compares energy levels arriving from all directions, while the latter only requires opposite pairs to be equal.

A potential concern for the DFAN community raised by [14] is that it concludes that the intensity metric and homogeneity of SPL can only be achieved by a loudspeaker array concurrently in 3D if the array is spherical. This is in opposition to standard DFAN practice where, for practical reasons, arrays are cylindrical. But an important caveat is that the analysis in [14] only considers direct sound from theoretical source layers, and scattering from the DUT and array hardware is ignored. Such scattering has the potential to increase diffusivity beyond the predictions in [14] and is even done deliberately in some cases (e.g. in EP4260039A4). However, more research is required to validate this hypothesis.

As is unsurprising given the spherical homogeneity of directional energy comprising a diffuse field, metrics have also been suggested that leverage spherical harmonics decomposition in various ways. These assume use of a spherical microphone array. Perhaps the most sophisticated of these is the COMEDIE metric of Epain and Jin [16], which is defined based on covariance but could be adapted to coherence. Use of spherical harmonics also overcomes some limitations of the more widespread 'sum of plane waves' model, on which Tanaka and Otani [17,18] have made recent useful fundamental contributions. This gets to the nub of the problem of many of the metrics above: they are designed so they return 1 for a perfectly diffuse field and 0 for a plane wave, but their behaviour between these limits is not well understood because there is no universally accepted way to synthesise a sound field that is diffuse to some arbitrary percentage. In the view of the leading author, more research is required to bottom this issue out before any metrics can have their properties fully understood.

2.3. Other considerations

Another consideration is that no measurements to quantify sound field quality should be taken too close to the loudspeaker or DUT, since these respectively have evanescent nearfield properties and cause scattering that disrupts the sound field's statistical properties [19]. However, putting a limit on exactly where this effect becomes insignificant is difficult since it depends on the size of objects and the mic spacing compared to wavelength, and the object's boundary properties (surface impedance, often likely to be non-locally reacting) and the analysis frequency bandwidth (e.g. 3Hz PSD or fractional octave bands). Measuring 1 meter from a boundary is standard in outdoor environmental acoustics and can be shown to be sufficient for spacing more than half a wavelength if the analysis is done in full octave bands (narrower bandwidth analysis requires a greater distance to stabilise). But these results are based on reflections from an infinite rigid plane (such as a chamber floor) and more relaxed constraints are likely to be sufficient for DFAN tests due to scattering and diffraction.

3. MICROPHONE ARRAY DESIGN FOR SPACED COHERENCE MEASUREMENT

While a benefit of spaced microphone coherence measures is that they can be applied to arbitrarily placed microphones, this section explores if array designs can be conceived that optimise the quality and discriminating power of the analysis. Moreover, if the microphones are attached to an array structure then their relative positions are fixed, meaning that the data processing can be repeatedly run for different placements easily (to use control & monitor mics, position data must be measured).

There is precedent for using fixed spacing mic arrays for DFAN sound field quantification. Kolaini and co-workers used a planar array of microphones [8], though the focus there was mainly on checking for arena modes. Arrays with four microphones in a cartesian configuration – one in a corner and three offset in perpendicular directions by an identical distance – have also been shared in personal communications with the leading author.

The motivation behind the design report here was the observation (inspired by conversations with Dr. Marcos Underwood at ECSSMET2024) that the comparison of MSC to $\mathrm{sinc}^2(kr)$ is most informative in the range $1/8 \leq kr/2\pi \leq 3/8$. Referring again to Fig. 3, it can be seen that: i) the variance is very small for $kr/2\pi < 1/8$, with almost all coherence data likely to lie very close to unity; ii) the variance is very wide and the mean value biased for $kr/2\pi > 3/8$, leading to wide, skewed confidence intervals that make drawing conclusions difficult. Since $1/8 \leq kr/2\pi \leq 3/8$ spans less than 2 octaves for a single mic separation value r, it is clear that multiple mic spacings would be required to ensure that some coherence data always lies in this optimal kr region.

This suggests microphone arrays designed to give a wide distribution of differing spacings. A caveat to this objective is that using complex coherence now makes the data with $kr/2\pi > 3/8$ more useful, but the design approach is reported here, nonetheless.

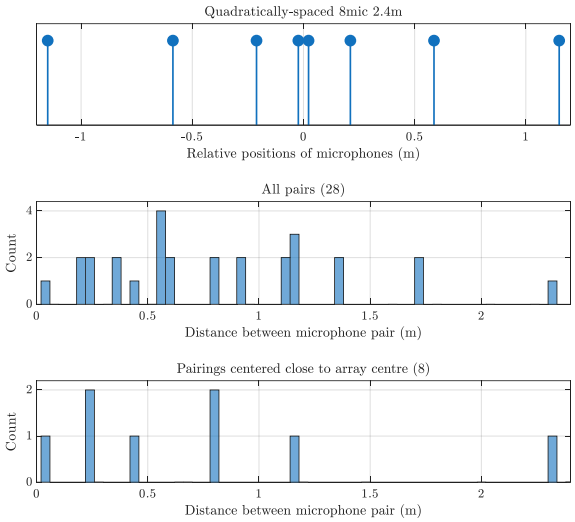


Figure 4: Mic placements (top) and spacing histograms (middle and bottom) for the manufactured quadratically-positioned array.

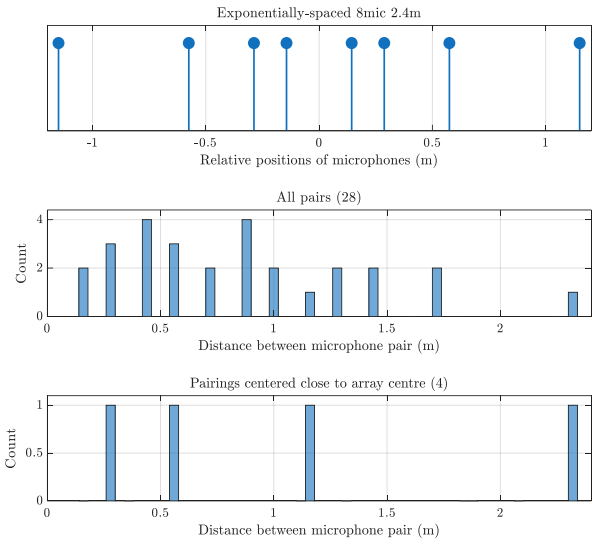


Figure 5: Mic placements (top) and spacing histograms (middle and bottom) for an array with exponential spacings.

For practical reasons a linear array was considered. This only has the capability to measure sound field statistics in a single direction, but it was felt to be a suitable test of the design principles, and full 3D characterisation could be achieved either by manufacturing multiple arrays to form a 2D or 3D cross, or by reorienting the array and repeating.

The array was made quite long – the maximum mic spacing was 2.3m – to ensure that the 25Hz third-octave band, as is typically the lowest frequency band in a DFAN SPL specification, could produce coherence data with $kr/2\pi \geq 1/8$. A quadratic positioning rule was followed, leading to the nearest mic pair being only 4.6cm apart, which satisfies $kr/2\pi \leq 3/8$ up to 2.8kHz. The positions can be seen in the top subplot of Fig. 4. Clearly this is a large array, but the aim was to devise a highly discriminating device with a wide bandwidth.

At the time, the quadratic rule was selected by considering the spacing statistics of all mic pairs (Fig. 4, middle subplot), but it was later realised that this led to a significant number of pairs having their centre away from the array centre. To address this the selection of pairs used was revised, leading to 8 pairings being analysed (Fig. 4, bottom subplot).

An intuitive way of visualising the contribution of these different microphone spacings is to consider a certain analysis bandwidth and display where the differently spaced pairs contribute data on a kr plot. This is shown for a full octave band in Fig. 7. The $\mathrm{sinc}^2(kr)$ trend is overlaid in black and the range $1/8 \leq kr/2\pi \leq 3/8$ is highlighted in yellow. The top and middle plots both pertain to the quadratically spaced array in Fig. 4 that was constructed; the top plot shows the 80Hz octave band and the middle shows the 250Hz octave band, illustrating how these contribution areas shift with frequency.

It is clear from this, however, that even with the reduced set of pairings used, there is often a lot of overlap, and there is also a gap present (which would close with a wider analysis bandwidth, but if analysing in octave bands then is present). Noting that an octave is a doubling in frequency, it makes sense to also space microphones according to an exponential rule, where each mic spacing is a doubling of the preceding one. This design is shown in Fig. 5, in which the doubling of spacing trend is visible in the bottom subplot; only symmetrical mic pairings centred on the array centred are utilised. The bottom panel of Fig. 7 shows how this makes the kr ranges each pairing contributes data for line up optimally on the kr plot, with the upper corner of each pair meeting the lower corner of the next. This array design has not been tested but is the logical next generation if linear arrays tests are continued.

The next section reports data gathered with the quadratically spaced design in Fig. 4.

4. FULL SCALE TEST RESULTS AT THE UK NATIONAL SATELLITE TEST FACILITY

This section reports tests conducted at the UK NSTF during two campaigns; one in April 2025 and the other in August 2026. Both used the microphone array shown in Fig. 6, which was constructed following the specification in Fig. 4. Note that a ball joint is present at top of the stand to allow changes in orientation around a common centre position.

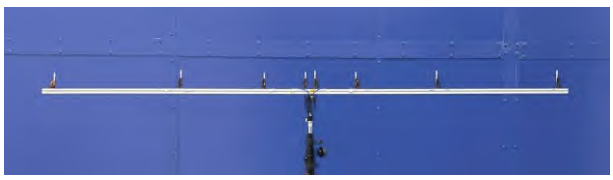


Figure 6: Photograph of the quadratically spaced mic array constructed at the NSTF

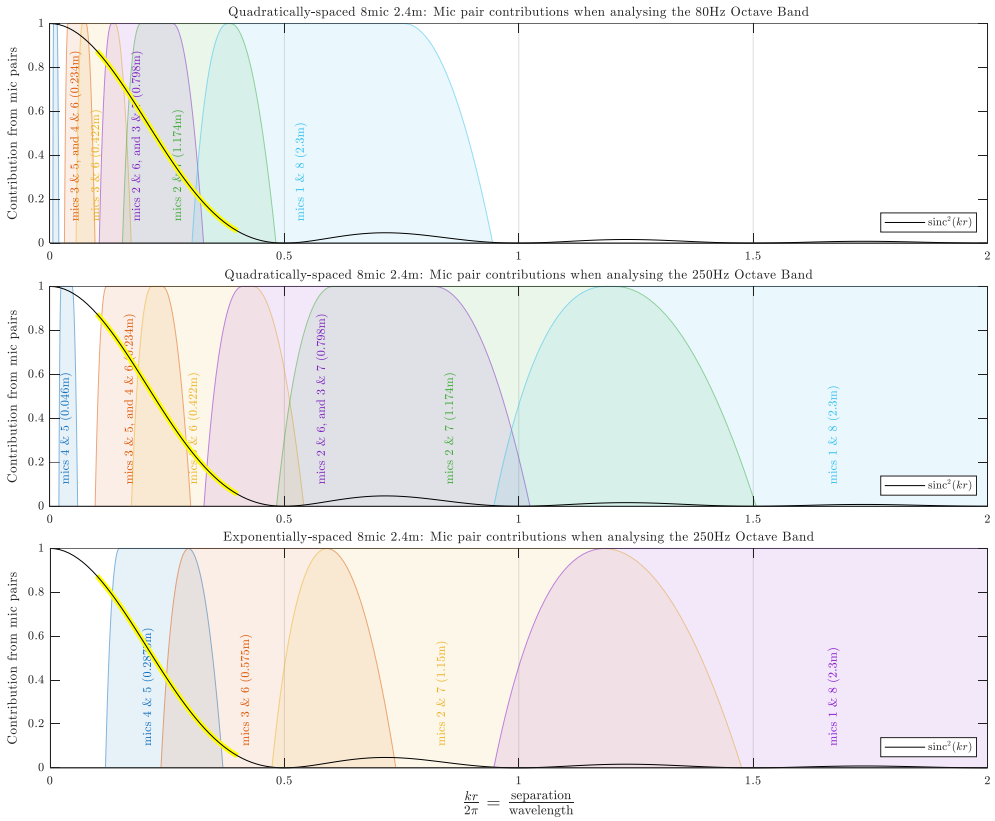


Figure 7: Contribution from different mic pairs displayed graphically on a kr plot, illustrating where they contribute data for the specified Octave Band (OB). Top: Quadratically spaced for 80Hz OB; Middle: Quadratically spaced for 250Hz OB; Bottom: Exponentially spaced for 250Hz OB.

The microphones were ¼" PCB Piezotronics model 378A12 (max SPL = 194dB), held in custom 3D printed holders on 2cm square linear extrusion. These were connected to a National Instruments NI-9231 8-channel input module in a cDAQ9181 caddy, which communicated via ethernet directly with the data acquisition toolbox in Matlab, allowing direct and immediate analysis of the captured data.

Both tests used an ARS Neutron system with six stacks, driven by an m+p control system. The stacks were raised 20cm off the floor on wheel boards and the arena diameter was 3.3m in both tests.

Mic array data was processed identically in both these tests and the Salford tests that follow in Section 5, except that data was captured for 50 seconds in these tests and only 30 seconds in the Salford ones. The sampling rate of the NI module was 51.2kHz. PSDs were computed by Welch's method, with an FFT length of 2^{14} samples, 50% overlap and a Hanning window; these settings give a frequency resolution of 3.125 Hz, as is often used for DFAN test control and analysis. For 50 seconds duration this leads to averaging of 311 FFT blocks. Third-octave filtering to compute SPLs was done using the octaveFilterBank object from the Matlab Audio Toolbox, with its filter order set to 6. With this setting, these filters satisfy BS EN 61260-1:2014.

To compute the histogram plots that mimic the PDF in Fig. 3, bins stepped by 0.01 and 0.02 were used for the ordinate coherence and abcissa $kr/2\pi$ axes respectively. To avoid the measure being biased by

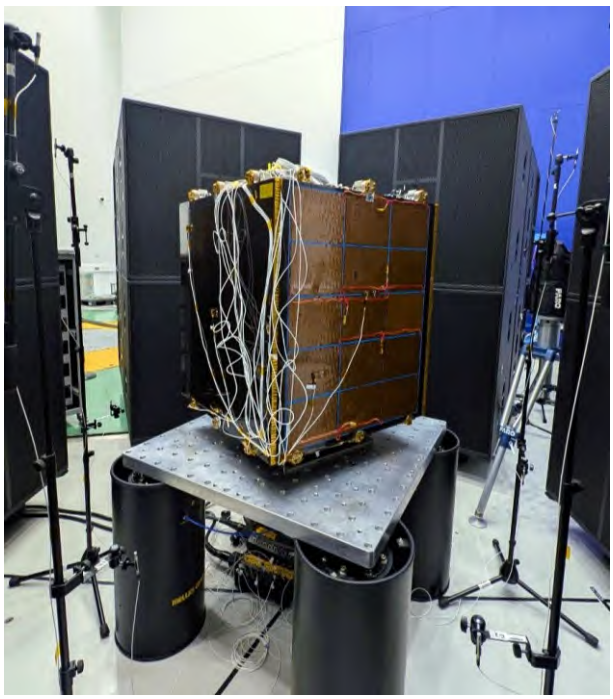


Figure 8: Photograph of the PROBA-V STM in the DFAN test area at the NSTF, mounted on a structural isolation table.

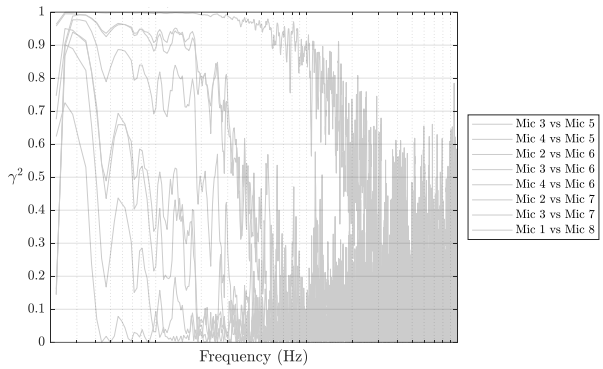


Figure 9: MSC between selected microphone pairs for the PROBA-V test as lines versus frequency

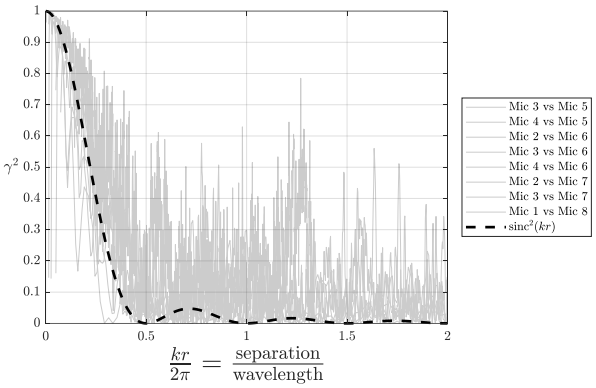


Figure 10: MSC between selected microphone pairs for the PROBA-V test as lines versus kr

the differing number of FFT lines in each kr bin, which is affected by spacing r, the histogram was first computed for each microphone separately, then combined. These were also weighted by 6th-order high & low pass filters at the limits of the frequency analysis range (25Hz – 10kHz). Bin counts were normalised per kr bin, yielding a probability distribution over each vertical stripe. The mean was then computed as the first moment of this. The same processing was applied to magnitude-square and complex coherence, but with differing ranges.

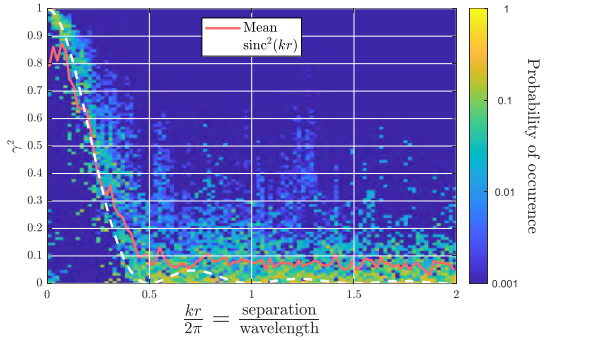


Figure 11: MSC between selected microphone pairs for the PROBA-V test as a histogram vs. kr

4.1. Proba V Test April 2025

This test campaign used the Structural and Thermal Model (STM) of the PROBA-V satellite as the DUT, as has been used in several comparative studies, e.g. [21, 22]. This is shown in Fig. 8. The Neutron loudspeakers were stacked two high, which – with the 20cm spacing off the floor – meant the top of the stacks were 2.4m from the floor (each Neutron is 1.1m high and 1.2m wide). The mic array could not be positioned in the middle of the test arena due to the presence of the DUT (a limitation due to its length). In the data presented here it was above the DUT and slightly tilted, meaning mic 1 was slightly higher than 2.4m. Other positions and orientations were also tested.

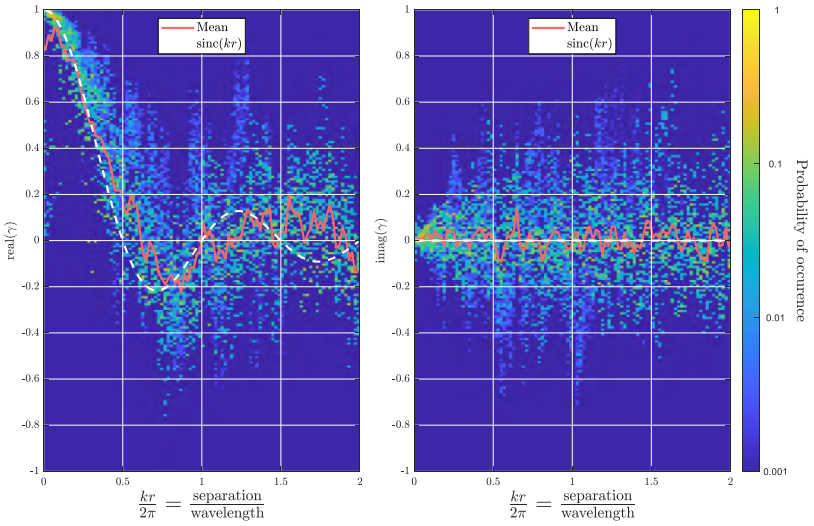


Figure 12: Complex coherence between selected microphone pairs for the PROBA-V test as histograms vs. kr.

Figures 9-12 all show the same coherence data. Fig. 9 shows it as MSC lines versus frequency, mainly to illustrate the point from Fig. 2; that plotting it this way does not allow trends to be seen. Fig. 10 shows the same lines but versus $kr/2\pi$; trends can now be seen but one can only estimate visually, and very crudely in a way dependent on plot line thickness, the density of data at different ordinal MSC values.

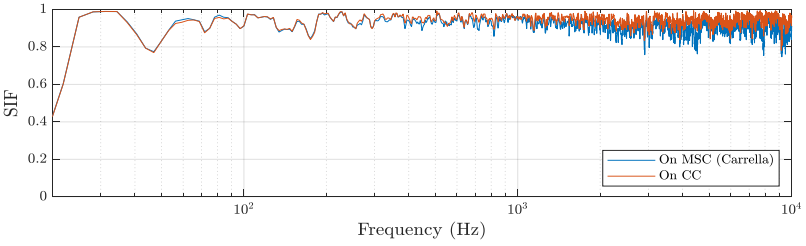


Figure 13: The Sinc Indicator Function (SIF), on MSC as per [10] (blue line) and adapted to complex coherence (orange).

Fig. 11 addresses this issue by plotting the same data as a histogram. Now the portion of data close (or not so close) to the theoretical trend line can be clearly read from the plot. Note that data in this plot appears rather scattered; increasing FFT resolution to narrower than 3Hz improves and smoothes this. The mean line is also shown in pink, which is – as expected – biased above the most commonly occurring data due to the highly skew distribution.

Fig. 12 shows the same data as histograms of the real and imaginary parts of complex coherence. The real part is seen to roughly follow the theoretical $\mathrm{sinc}(kr)$ trend, while the imaginary data clusters around zero because the theoretical trend is purely real. Now, because of the reasonably symmetrical distribution, the pink mean line follows the most commonly occurring data.

Fig. 13 shows the SIF, both the definition in [10] and an adaption of this (see footnote on page 3) for complex coherence. Both metrics behave very similarly, but the adapted version based on complex coherence is able to get slightly closer to unity at high frequencies because it is not deflected from this by the skew distribution of the MSC estimator.

In summary, it can be seen that:

- The properties of the sound field produced by the DFAN system for this test were appropriate.
- Plotting coherence data gathered form multiple mic pairs as a histogram aids interpretability.
- Working with complex coherence eliminates the bias in the mean that occurs due to skew when data is predominantly incoherent ($|\gamma| \to 0$).

4.2. Further Testing August 2026

Further testing of the linear array was conducted in August 2026, still with the mic spacing in Fig. 4. This was undertaken with an empty arena, the rationale being that it is more appropriate to assess the sound field the system produces against the diffuse field theoretical target when a DUT is not present, since the sound field statistics around the DUT would not match free-field theory even if the incident sound field were perfectly diffuse, because it's scattering would perturb them*. The test was otherwise like that in the previous section, except that: i) a higher and different SPL target spectra was used, and ii) the stacks were of three Neutrons, rising 3.5m tall.

Numerous tests were conducted varying the drive pattern to be all independent, all the same, or group by stack or ring / tier. These are not included here, however, since they show trends similar to those in section 5.1 but less clearly.

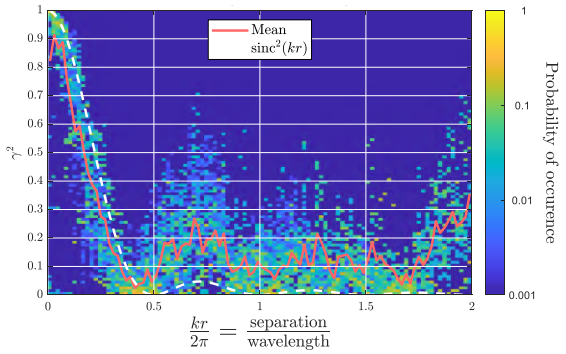


Figure 14: MSC histogram for an empty arena with array level & aligned to two loudspeaker centres.

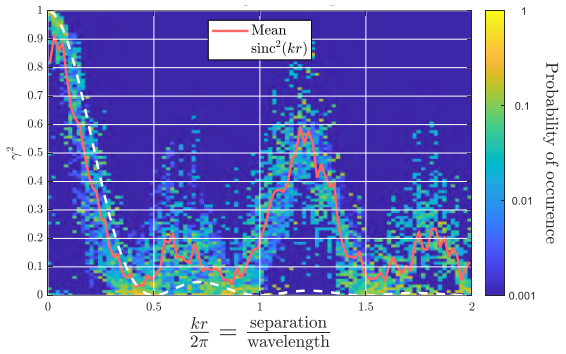


Figure 15: As Fig. 14, but with array rotated 30° horizontally to be aligned with a pair of gaps.

What is worthy of mention is the result in Figs. 14 & 15 that appears to show an issue with the use of the linear array. This is visible with all loudspeakers driven independently – so maximally diffuse – and depended on array orientation. In Fig. 14, when the array was aligned with a pair of speakers, the MSC trend looks mainly as expected. But in Fig. 15, when it is rotated 30° to align with a gap, a significant anomaly occurs at $kr/2\pi \approx 1.2$. Note that it is not a mode. Mics with different spacings see it at different frequencies; it is a sound field correlation property. While the physical meaning of this anomaly is yet to be fully explained, it is clear that it is due to the symmetry of the test arena – this hypothesis was validated by performing Boundary Element Method simulations, which showed the same trend.

This result does not mean that DFAN system and arena symmetry is undesirable; diffuse fields are symmetrical and [14] showed that this means loudspeaker systems should be symmetrical too.

What it shows is that a linear array has no ability to discriminate across its width, and instead achieves a sort of 'super-resolution' in the direction it is oriented, which highlights some sound field properties to a disproportionate extent. This may be

* On this, we note that no simple model currently exists for how the presence of a DUT changes a diffuse field. Such a model would be valuable both to corroborate or deny this assumption, and to inform more realistic sound field targets when a large DUT means a test arena has a high fill factor.

useful in some cases, where the desire is to closely scrutinise certain directional behaviour (examples follow in the next section), but it suggests that a long linear array such as this is not ideal for providing a general sense of sound field diffuseness. Thus, it is not ideal for generic DFAN quality assurance.

It also casts questions over empty area testing, though with a less directionally biased mic array this practice should still be informative in relevant cases.

5. 'MINIDFAN' SCALE MODEL TEST RESULTS AT THE UNIVERSITY OF SALFORD

These tests were conducted in April 2025, two weeks before those reported in Section 4.1. The system, which is shown in fig. 16, comprised 16 loudspeaker 'stacks', each 1.18m high, around a 1.8m diameter test arena. Each stack contained 8 KEF Ci100QR coaxial loudspeakers, each with their own internal chamber, driven by Cloud CX-A850 amplifiers and RME audio interfaces. A unique feature of the setup was that all 128 loudspeakers could be fed audio independently from Matlab via MADI, hence the drive matrices – the effect of which was the main research question – could be changed in software on the fly. Eleven drive patterns were tested; the four reported here plus seven orthogonal Fourier-Legendre patterns. Note that there was no controller in use; the system ran open-loop.

A linear array was also used to gather data here, comprising 12 GRAS model 40PQ ¼" mics. The spacing of these was fixed at 5cm due to mounting hardware restrictions, so 55cm was the maximum spacing. Signals were fed into three 4-channel NI-9234 input modules in a cDAQ-9174 frame, which fed audio data directly into Matlab via USB. In addition, a 48 mic spherical array from a gfai Acoustic Camera system was used to capture data; this was exported to .wav and imported into Matlab for processing. This was done primarily to measure isotropy, but here coherence data from it is reported instead. A Microflown Scan & Paint 3D Acoustic Intensity Mapping system was also used, and a structural response simulator, but page limits prevent reporting on that.

5.1. Linear Array Measurements

Selected results from the linear array are shown in fig. 19. Here the array's ability to interrogate the directional sound field properties is exploited to show the different effects that drive patterns have vertically and horizontally. Note that the plots here use an earlier version of the histogram analysis than the other plots in this paper, causing them to show slightly different scatter. Unfortunately, the raw data was corrupted so these cannot be updated with the latest version of that analysis.

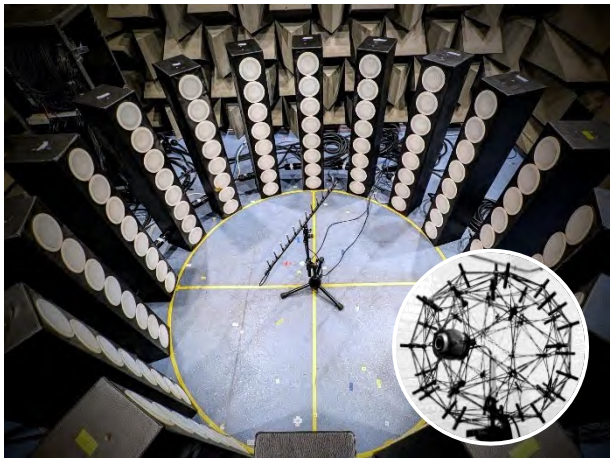


Figure 16: 'MiniDFAN' scale model test setup at the University of Salford. Photo shows linear mic array in horizontal central position. Circular inset shows the 48 mic spherical array also used.

The results clearly show that 'all independent' drive is most diffuse whereas using a single drive produces a field that is not diffuse at all. Additionally, it can be seen that correlating drives by stack or ring greatly reduces diffuseness in the corresponding direction. This suggests that if one groups drives too systematically then this will likely affect the structural response of the DUT. For example,

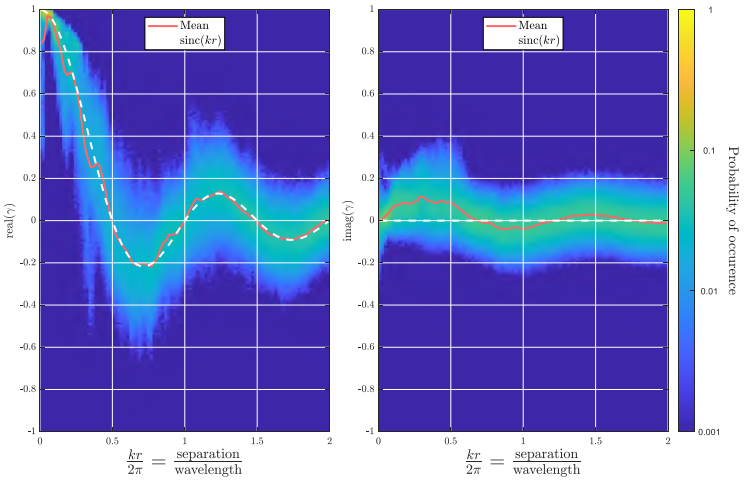


Figure 17: Complex coherence for the 'MiniDFAN' with LS driven independently, measured with the spherical array.

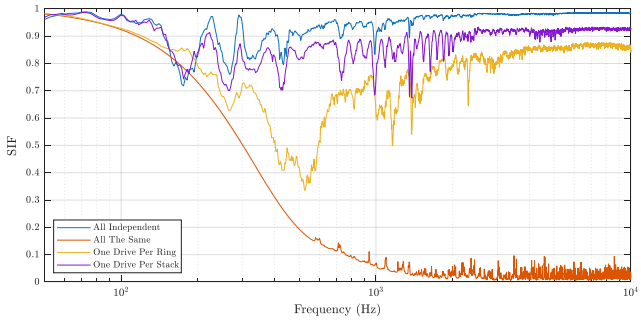


Figure 18: SIF versus frequency for the 'MiniDFAN' measured with the spherical array, comparing drive types.

grouping loudspeakers by stack is likely to greatly change the excitation on the top face of the DUT.

5.2. Spherical Array Measurements

Fig. 17 shows complex coherence results from the mic pairs from the spherical array. Its 48 mics yield 1128 unique pairings, with their separations differing in length and orientation. This provides excellent averaging over angle especially, leading to a distribution of data whose mean almost exactly tracks the $\mathrm{sinc}(kr)$ trend in its real part.

This suggests that spherically symmetric arrays may be a good choice for DFAN quality assurance.

Fig. 18 shows the MSC SIF [10] calculated from the spherical array data for the four drive patterns. At low frequencies all lines tend towards unity; this is because the array – which is 40cm diameter – is too small to discriminate effectively and all signals are coherent in all cases. But at higher frequencies it discriminates between the drives, albeit with all taking quite high values that don't entirely reflect the extent of differences seen with the linear mic array.

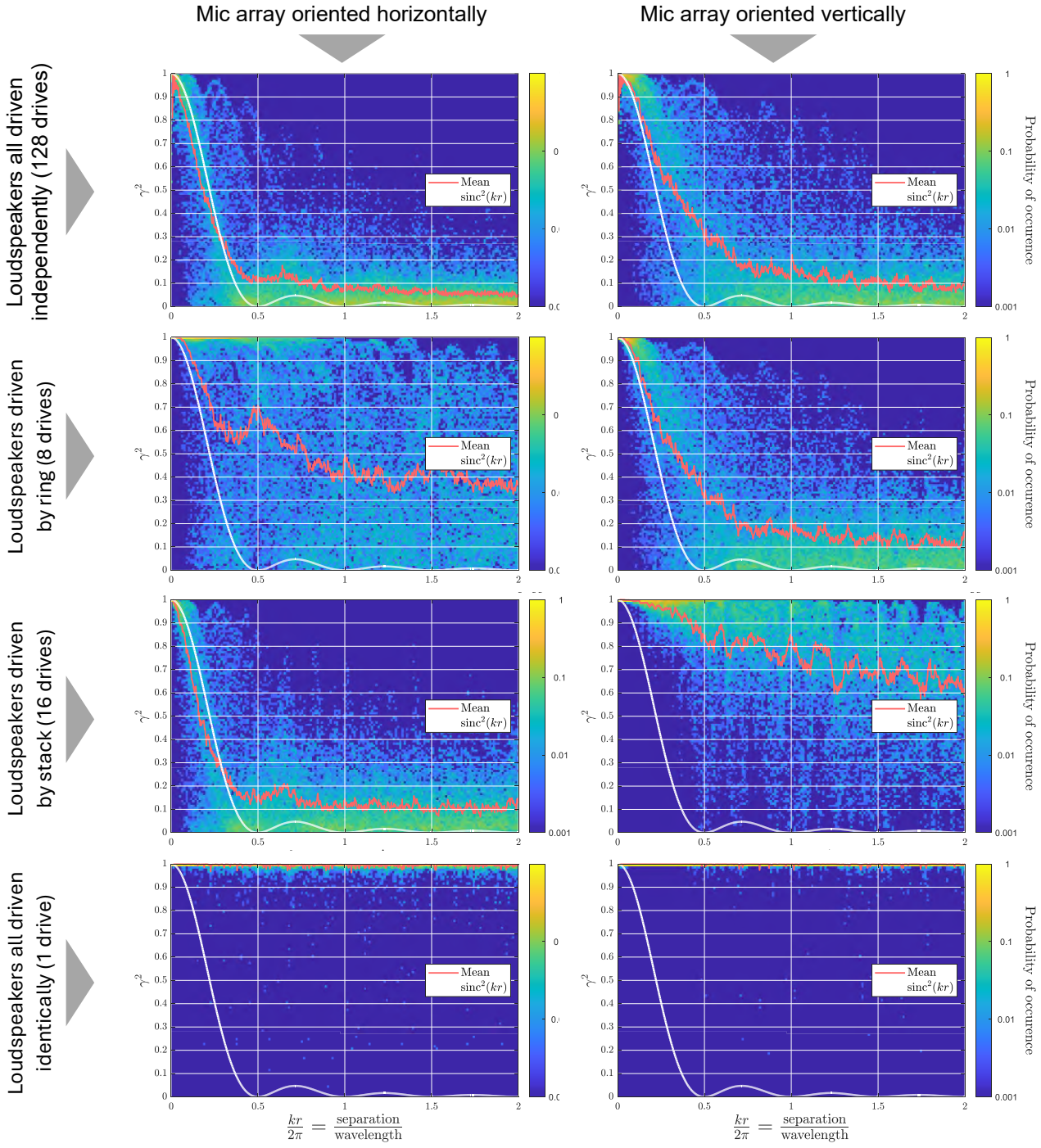


Figure 19: MSC histograms for the MiniDFAN with four differing drive patterns, as measured by the linear array in horizontal and vertical configurations. Individual subplots show combinations as labelled.

5.3. Outlook for scale model testing

More data exists from these scale model tests, and from other diffuse field comparison tests conducted in Sept 2022, which are currently being collated and prepared for journal publication. This is intended to also include isotropy measures, scanned intensity maps and metrics, structural response comparisons and corroborating simulations.

Nonetheless, the limited amount of data presented here already shows that a good deal can be learnt about sound field fundamentals while testing at smaller scale, notably in which the reduced size, weight and SPL expedite laboratory practices.

6. CONCLUSIONS AND FURTHER WORK

Coherence between spaced microphone pairs is an established and practical means of quantifying how similar a DFAN sound field is to a diffuse field. This paper has suggested improvements to how that data might be processed and displayed, notably using complex coherence – or its signed real part at least – and histograms instead of line plots to show results aggregated from many microphone pairs.

A new paradigm for designing microphone arrays tailored to this metric has also been presented. This was demonstrated with a linear array, which was successful but proved to be more useful as a diagnostic tool for querying directional properties of sound fields in great detail, than it was for general sound field diffuseness quantification. For DFAN sound field quality assurance it is suggested that a smaller spherical 3D array might be more suitable.

The linear array did, however, prove useful in demonstrating the significant changes that drive patterns have on the sound field produced by a DFAN system. The conclusion is that the drive 'matrix' – being the mapping from M controller outputs to N loudspeakers, where $N > M$ typically, should always be detailed in DFAN test reports.

6.1. Areas requiring further research

This work, and the review of recent literature it contains, shows that more fundamental research is needed if the properties of the various diffuse field metrics that exist are to be fully understood.

Firstly, a means of synthesising a field with a given % 'diffuseness' is required in order for terms such as 'diffuseness' or 'diffusivity' to move from being qualitative descriptors to quantitative metrics. As noted in [18], summation of plane waves is not the ideal model for this, and variable partial coherence between energy from different directions also needs to be captured in the model somehow.

On coherence, progress has been made on better understanding its properties in [6], but similar needs to be done for complex coherence, as is presented herein and in [13]. Such understanding will allow more informed design of metrics that avoid issues caused by its heteroscedastic estimator properties.

Specific to DFAN applications, better understanding is required of the effect of DUT scattering on diffuse field metrics and targets, and of how this and loudspeaker proximity cause local changes that mean control and monitor microphones should be positioned a certain distance away into the cavity. These effects depend on obstacle geometry and acoustic properties, so would need to be quantified by a parametric sweep of representative geometrics, ideally including or informed by nearfield loudspeaker radiation and impedance data.

Extension of the array design paradigm herein to 3D arrays would also be desirable, ideally with analysis tools informed by the improved models of partially diffuse fields discussed above. Arrays with spherical symmetry seem desirable, which for low/moderate microphone counts can be based on Platonic solids.

7. ACKNOWLEDGEMENTS & IP

The authors acknowledge the contribution of Finn Alderson, a student studying at the University of Salford, who helped conduct the measurements at Salford that are reported in section 5.

The initial linear microphone array design in section 3 was funded by RAL Space in 2024, so its IP is co-created by RAL Space and the University of Salford. The measurements undertaken at the National Satellite Test Facility (reported in Section 4) are the IP of RAL Space. All other material is the IP of the leading author and the University of Salford; RAL Space has kindly funded dissemination of this work at ECSSMET 2026, but the research itself was undertaken without external funding.

The gfai 'Sphere 48' Acoustic Camera system used in section 5 is property of the (now defunct) STFC Equipment Loan Pool that was funded by EPSRC.

8. CREDIT AUTHOR STATEMENT

All: Conceptualisation, organisation of resources, manuscript editing and review, and administration.

CK: Methodology, investigation, data curation.

JH: All of the above plus formal analysis, software development and original draft writing.

IH: Supervision and funding acquisition.

9. REFERENCES

1. Hargreaves, J. A. (2022), Literature review of Direct Field Acoustic Noise (DFAN) testing. *U. Salford rep.* https://doi.org/10.17866/h20g-8587
2. Underwood, M. A. (2023) “A New Method Using Pseudo-Velocity-Based Stress Analyses to Evaluate Effectiveness of Acoustic Fields Used for Acoustic Testing”, *Proc. Aerop. Test. Sem.*
3. Underwood, M. A. (2022) “New Method Determines Optimized Reference SDM for MIMO Testing,” *J. IEST* 65 (1): 21–50.
4. Jacobsen, F. (1979). *The Diffuse Sound Field*. *Report No. 27, Acoust. Lab.*, Tech. U. Denmark. ISSN 0105-3027.
5. Jacobsen, F. and Roisin, T. (2000) “The coherence of reverberant sound fields,” *J. Acoust. Soc. Am.* 108 (1): 214-210.
6. Underwood, M. A. and Hargreaves, J. A. (2024). Confidence Limits for Coherence – Toward a Better Understanding of its use as a Diffuse Field Metric for Quantifying the Quality of Direct Field Acoustic Noise (DFAN) Testing Systems. *Proc. ECSSMET*
7. Gardner, B. (2000). Observations of the Sound Field During Liftoff of the Cassini Spacecraft. *Proc. SLVDE Wksp.*
8. Maahs, G. (2012). DFAT Development and Flight Testing of Radiation Belt Storm Probe (RBSP) Satellites, in: *Proc. Aerosp. Test. Sem.*
9. Cook, R.K. et al (1955). Measurement of Correlation Coefficients in Reverberant Sound Fields. *J. Acoust. Soc. Am.* 27: 1072–1077
10. Carrella, A. and Mayne, W. 3rd (2022) "Insight into the Sound Field During a Direct Field Acoustic Test", in: *Proc. Internoise*
11. Gardner, B. *et al* (2017). Investigating DFAT Diffusivity Using Wavenumber- Frequency Analysis with BEM. *Proc. SLVDE Wksp.*
12. Rouse, J. W. (2017). A boundary element based method for accurate prediction of the surface pressure cross-spectral density matrix. *Proc. 173rd Meet. Acoust. Soc. Am.*
13. Allen, A. R. *et al* (2026). Assessing Sound Field Diffuseness in Direct Field Acoustic Test Using Fractional Octave Band Coherence. *AIAA SciTech F*. https://doi.org/10.2514/6.2026-0417
14. Zotter, F. *et al* (2024). Diffuse sound field synthesis: Ideal source layers. *Acta Acustica*, *8*, 34. https://doi.org/10.1051/aacus/2024023
15. Zotter, F. *et al* (2025). Diffuse sound field synthesis: Towards practical source layouts. *Acta Acustica*, *9*, 33. https://doi.org/10.1051/aacus/2025018
16. Epain, N., & Jin, C. T. (2016). Spherical Harmonic Signal Covariance and Sound Field Diffuseness. *IEEE/ACM Trans. Audio, Speech, Lang. Proc. 24* (10), 1796–1807. https://doi.org/10.1109/TASLP.2016.2585862
17. Tanaka, T., & Otani, M. (2023). An isotropic sound field model composed of a finite number of plane waves. *Acoust. Sci. Tech.* 44(4), E2277. https://doi.org/10.1250/ast.44.317
18. Tanaka, T., & Otani, M. (2024). Directionally characterized pseudo-perfect diffuseness: A detailed comparison of its theoretical formulations. *Acoust. Sci. Tech.* 45(5), e24.16. https://doi.org/10.1250/ast.e24.16
19. Waterhouse, R. V. (1955). Interference Patterns in Reverberant Sound Fields. *J. Acoust. Soc. Am.* 27 (2): 247–258.
20. Kolaini, A.R. *et al* (2012). Impact of Acoustic Standing Waves on Structural Responses: Reverberant Acoustic Testing (RAT) vs. Direct Field Acoustic Testing (DFAT), in: *Proc. 28th Testing Aerosp. Test. Sem.*
21. Garcia de Miguel, A. et *al* (2024). Analysis of the vibro-acoustic interaction in direct field acoustic noise tests via optical measurement techniques. *Proc. ECSSMET.*
22. Peeters, B. *et al* (2024). Using direct-field acoustic test data for Operational Modal Analysis of the PROBA-V satellite. *Proc. ECSSMET.*

The Importance of the Degree of Diffuseness of the Achieved Acoustic Field on the Vibroacoustic Response of a Test Article from Direct Field Acoustic Testing

Marcos A. Underwood, PhD[(1)], Arloe W. Mayne III[(2)] and Alexis Castel, PhD[(3)]

[(1)]MSI-DFAT through Tu'tuli Enterprises, 33741 S. Highway 1, Gualala, CA 95445, USA, M.Underwood@msidfat.com
[(2)]MSI-DFAT, 4900 Wetheredsville Road, Baltimore, MD, 21207, USA, W.Mayne@msidfat.com
[(3)]*Keysight Technologies, 28350 Cabot Dr., Suite 100, Novi, MI, 48377, USA, alexis.castel@keysight.com*

KEYWORDS

Direct Field Acoustic Test, Vibroacoustic Response, Vibroacoustic Gain (VAG), MIMO Acoustic Control, Acoustic Field, Near-Diffuse, Non-Diffuse, and Modal Analysis

ABSTRACT

This paper is based on the methodology of a recent paper presented at the 2026 AIAA SciTech Forum [1] but instead is used to simulate representative test results presented by the paper (and its references) published in the 2023 Volume 66: Issue 1 of the IEST Journal [2]. That paper contains a study of the vibroacoustic response of an aluminum honeycombed 2.44m x 1.22m (8'x4') test-panel that results from using advanced MIMO acoustic control of Direct Field Acoustic (DFA) tests [3] to create multiple types of acoustic fields consisting of a near-diffuse and four other non-diffuse fields with various panel orientations, for a total of 30 tests, where all DFA tests were specified to have the same OASPL and 1/3-Octave spectrum test reference [2].

Each discussed test uses the same 24 randomly arranged approximate circle of control microphones that are in turn surrounded by an approximately concentric outer circle of 8x8 MSI DFAT loudspeaker stacks that contain the described test article at their mutual center. The test panel's experimental modal analysis (EMA) results were used as the basis to determine how well each of the five types of acoustic fields, described in [2], excited the EMA identified modes of the test panel.

The vibroacoustic test results from three of the five described DFA tests [2] were selected for this paper, where each test creates a different acoustic field that will be discussed first. This will be followed by a discussion of the vibroacoustic response simulation from the same DFA test's acoustic fields exciting the test panel, which are compared to the described test results and to the EMA and FEM based modal analysis, by its ability to create and analyze the various fields and associated panel vibroacoustic responses using numerical simulation [1]. These two sets of discussions in the paper are jointly designed to demonstrate the importance of conducting DFA testing using a near-diffuse acoustic field.

1. INTRODUCTION

1.1 Overall Testing Goals of Selected DFA tests

The purpose of previous testing [2,4-5] was to further justify the advantages and need to have a Near-Diffuse [3] acoustic field that can fully excite the structural modes of a test article. The tests were designed to compare the vibroacoustic response of a test article (TA) under test using MSI-DFAT 8x8 loudspeaker stacks, shown in Fig. 1, where the TA is shown by Figs. 1 and 2, is a 2.44m x 1.22m (8'x4') rectangular test-panel (panel) that is instrumented with 20 accelerometers. Figs. 1 and 2 illustrate the location of the 20 accelerometers that were used and Fig. 2 (bottom) shows their coordinates relative to the Panel in inches (2.54 cm/inch).

The analyses in [2,4] used PSDs with Δf = 0.1563 Hz for Experimental Modal Analysis (EMA) and Δf = 0.1953 for their other analyses of the panel to better distinguish between closely spaced panel modes. This paper will instead use a unified Δf = 0.78125 for all PSD analyses and simulations performed to simplify the following presentations, for which the frequency range used in this paper, in the interest of shortening the simulation time, will be either 20 or 30 Hz to 200 Hz, instead of the 20 Hz to 10 kHz or 40 Hz to 300 Hz used by [2,4], for microphone (mics) and accelerometer (accels) data analyses.

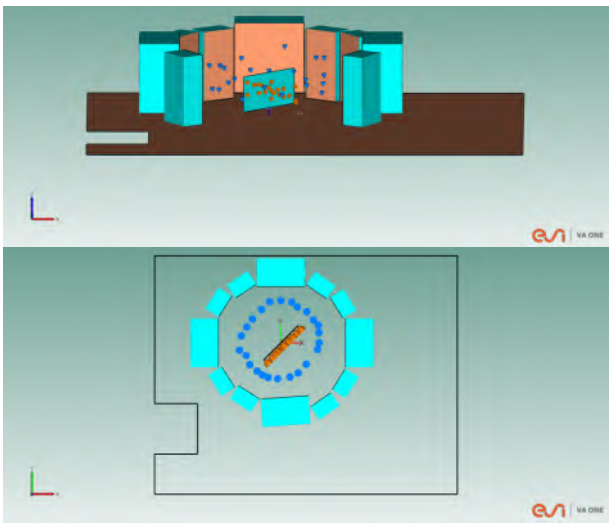


Figure 1: (top) elevation & (bottom) plan views of 8x8 Stack configuration with 8 or 1 independent drives; 24 control Mics; 8'x4' Test Panel & Accels

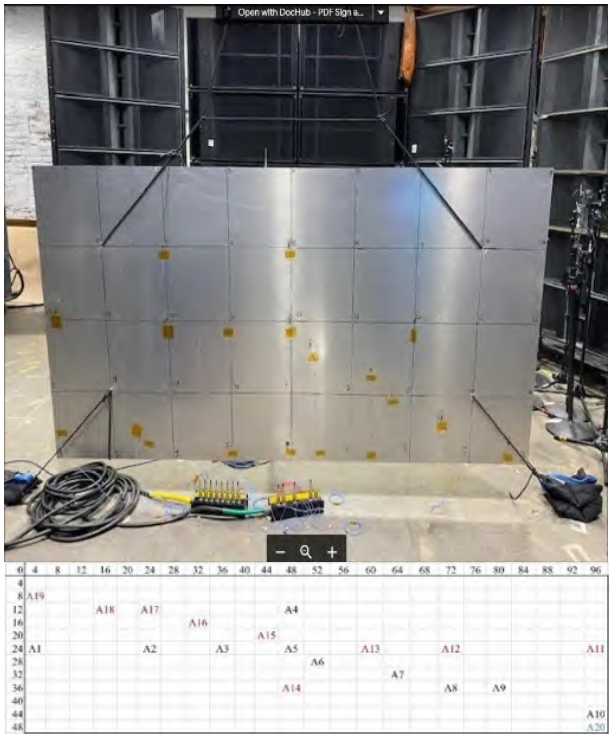


Figure 2: (top) 2.44m x 1.22m (8'x4') Test Panel; and (bottom) Coordinates of Panel Accelerometers

The test panel and accelerometers shown in Figs. 1 and 2 are at the center of the microphone circle in its 45° orientation, which is the only test panel configuration discussed in this paper. The panel, on the other hand, was tested in [2,4] using three rotational configurations, 0°, 30°, and 45° with respect to the speaker and microphone circle.

1.2 Importance of Nearly Diffuse Acoustic Fields

It is generally recognized [2-5] that only a nearly diffuse acoustic field will properly excite all the modes of the structure under test and that an acoustic field with measured coherence between microphones throughout the acoustic field differing "significantly" from a theoretical sinc^2 function is not nearly diffuse, and in general, not capable of similarly exciting all its structural modes [2-5].

Similarly, it is also known that if an acoustic field is excited with uncorrelated drive signals for the loudspeakers, the response of a test article and control microphones may not be consistent with the response from a diffuse acoustic field due to the underlying acoustic modes that may be excited by uncorrelated drives without MIMO control [2-5].

The test campaign in [2,4-5] was designed to demonstrate that only a Near-Diffuse acoustic field created using modern optimal adaptive MIMO methods to control the test-facility's acoustic modes [3] can properly excite the test panel in general, for which the use of non-diffuse acoustic fields may not provide, by employing a more comprehensive suite of tests as used for the testing described by [2].

1.3 Test Configuration Used for this Paper

The testing in [2,4] used two configurations of MSI-DFAT's loudspeaker 8x8 stacks with five acoustic fields, whereas this paper uses only one form that is based on 8 full stacks of MP21's for the lowest frequencies and 8 of MP150's for the mid and high frequencies and three fields. Stacks are driven by the control system using either 8 independent drives for two tests using MIMO to create Near-Diffuse and Directed-Coherent acoustic fields and one test with 1 drive using MISO control [2,4], to excite the panel in the 45° configuration as illustrated by Fig. 1.

The Panel is instrumented with 20 Accelerometers. Their locations are illustrated by Fig. 2 using the colors black, red, and blue. Accelerometers A1-A10, in black, were used for the first testing [5] and A11-A19 in red were added for the newer test campaigns [2,4]. Accelerometer A20 in blue was used for operational modal analysis (OMA), as a test performance metric [2,4], which is not used here.

Three types of acoustic tests are described and simulated that were performed to excite the test panel using three types of acoustic fields: 1) Near-Diffuse to approximate a theoretically diffuse field with zero mean random phase between control-microphones, as described in [2-5], using multiple-input-multiple-output (MIMO) control [3]; 2) to approximate a Directed-Coherence Field using a "push-pull" configuration with MIMO control [2-5]; and 3) to drive all the loudspeaker stacks with a single drive, which is controlled with multiple-input-single-output (MISO) control, where MISO uses the average of the 24 control microphones for control, whereas MIMO controls each of the amplitudes of the 24 control microphones as well as the relative coherence and phase between all microphones, i.e., by controlling the microphone's spectral density matrix (SDM) by finding the proper drive's SDM [3].

1.4 Experimental Modal Analysis Results

Before testing, an experimental modal analysis (EMA) was performed on the panel to determine its structural modes between 10 Hz and 300 Hz. Table 1 contains the obtained EMA results [2,4].

Table 1: 22 EMA Panel Modes

Mode	Natural Frequency (Hz)	Damping Ratio (Hz)	Damping Ratio (%)	Damped Resonant Frequency (Hz)	Observed Resonant Frequency (Hz)	Observation Discrepancy (%)
1	15.71	0.14	0.86	15.71	15.6	-0.70
2	18.9	0.72	3.83	18.89	18.8	-0.46
3	41.7	0.34	0.8	41.7	41.8	0.24
4	43.37	0.13	0.31	43.37	43.38	0.02
5	65.19	0.25	0.38	65.19	65.04	-0.23
6	72.37	0.28	0.38	72.37	72.3	-0.10
7	75.92	0.26	0.34	75.92	75.98	0.08
8	86.19	0.22	0.25	86.19	86	-0.22
9	103.5	0.16	0.16	103.5	103.3	-0.19
10	114.35	0.4	0.35	114.35	114.1	-0.22
11	137.51	0.26	0.19	137.51	137.5	-0.01
12	144.45	0.23	0.16	144.45	144.3	-0.10
13	166.07	0.33	0.2	166.07	166	-0.04
14	179.08	0.48	0.27	179.08	178.7	-0.21
15	187.03	0.53	0.28	187.03	186.92	-0.06
16	188.34	0.34	0.18	188.34	188.5	0.08
17	208.52	0.29	0.14	208.52	208.4	-0.06
18	210.7	0.32	0.15	210.7	210.2	-0.24
19	234.81	0.49	0.21	234.81	234.4	-0.17
20	243.56	0.37	0.15	243.56	243.2	-0.15
21	249.77	0.56	0.23	249.77	249.8	0.01
22	285.08	0.57	0.2	285.08	285.2	0.04

- The 22 Mode's f_n and ζ_n were used to determine the Damped Resonant Frequencies.
- A Roving Hammer Technique and Star Modal [2] provided the 45-Point EMA, where only Modes 3 to 22 are used.

1.5 DFA Test's Reference Amplitude Spectra

The references are shown in Fig. 3 that follows.

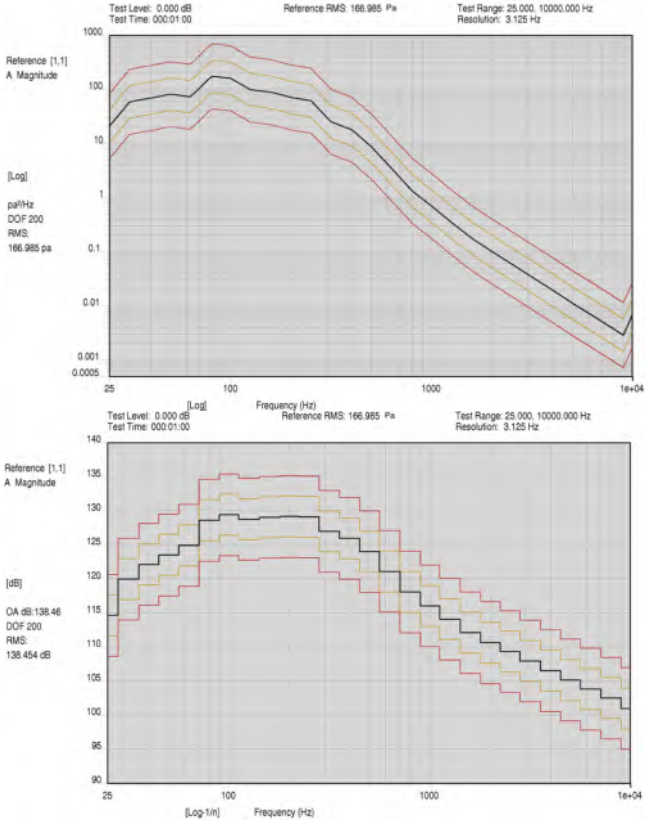


Figure 3: (top) Reference PSD and (bottom) 1/3 OB Spectrum Used for 24 Control Microphones for DFA Tests

2. TEST RESULTS

2.1 Comparison of the Acoustic Fields Used

The measured acoustic characteristics of the three fields used to excite the test panel under the described conditions, and their summary response results are discussed, which [2-6] cover in detail.

The degree of diffuseness of the fields will be assessed by examining typical plots of coherence compared to the sinc^2 function vs. Kr, which adjusts coherence for differing delays between microphone pairs, and the variations of the 1/3 OB SPL Spectra of all 24 control microphones between each other to assess the uniformity of the three acoustic fields.

These comparisons also assess how well the 3 tests agree in acoustic levels and spectra and how well the measured coherence approximates that of an ideal diffuse field and how uniform the field is, where both are required for a field to be Near-Diffuse [2,4].

2.2 Near-Diffuse Field

Fig. 4 contains the plot of the 24 1/3 Octave SPL spectra for each of the 24 Control Microphones, from 25 Hz to 200 Hz, on its top, where the alarm tolerances are +/- 3dB and the abort tolerance are +/- 6dB. Notice how uniform the spread between the spectra of control microphones is in the Fig. 4 (top) plot, i.e., mostly within the +/- 3dB tolerance, except at 25 Hz.

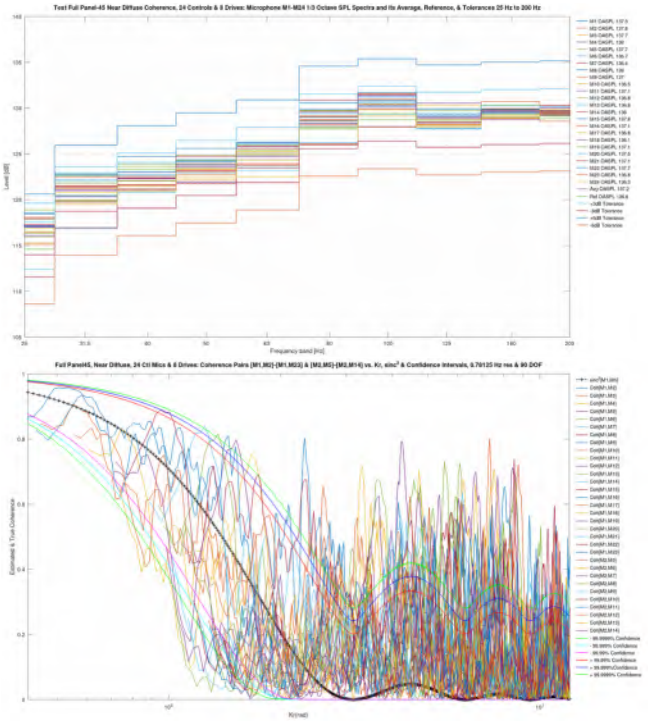


Figure 4: (top) 1/3 Octave SPL Spectra of the 24 Control Mics & (bottom) Relative Coherence vs. Kr

The plot of Fig. 4 (bottom) is of 32 typical coherence spectra between control microphones 1 and 2 to 23 and between microphones 2 to 14, which uses Kr (in radians of the sinc^2 function shown), as further discussed in subsection 3.1 and [6], as the x-axis, which compensates for the differing delays between them [6], which allows all the coherences plotted to be compared to a single sinc^2 function [6], which represents the plot of the ideal coherence for diffuse fields [6]. This plot shows how close to an ideal diffuse field the Near-Diffuse acoustic field is, which is validated by the fact that most of coherence spectra in the first lobe of the sinc^2 are within the +99.9999% confidence intervals of coherence [6], in spite of the fact the coherence spectra were measured with a low 90 DOF and FFT Δf=0.78125 Hz, which allows the high coherence spikes we see just above Kr=2, which didn't occur when at least 200 DOF and Δf=3.125 Hz were used [2,4].

This indicates that the Near-Diffuse field coherence spectra estimate approximates the ideal coherence well. Additionally, the Optimal Adaptive MIMO Control [3] that is used reduces the coherence between the displayed microphone pairs below the -99.9999% confidence intervals of the ideal sinc^2 coherence curve, where the plot on the bottom of Fig. 4 demonstrates this less than theoretical effect.

2.3 Non-Diffuse Directed-Coherence Field

The 24-control microphone 1/3 Octave SPL spectra and Coherence vs. Kr results in Figs. 5 (top and bottom) match what is expected from a Directed-Coherence acoustic field [2,4-5]. It is further shown that this field does not excite all expected test panel resonances properly in what follows and in [2,4-5]. This is a result of the response enhancement-

cancellation effects discussed for this field in [2,4-5], upon which subsection 2.4 will further elaborate.

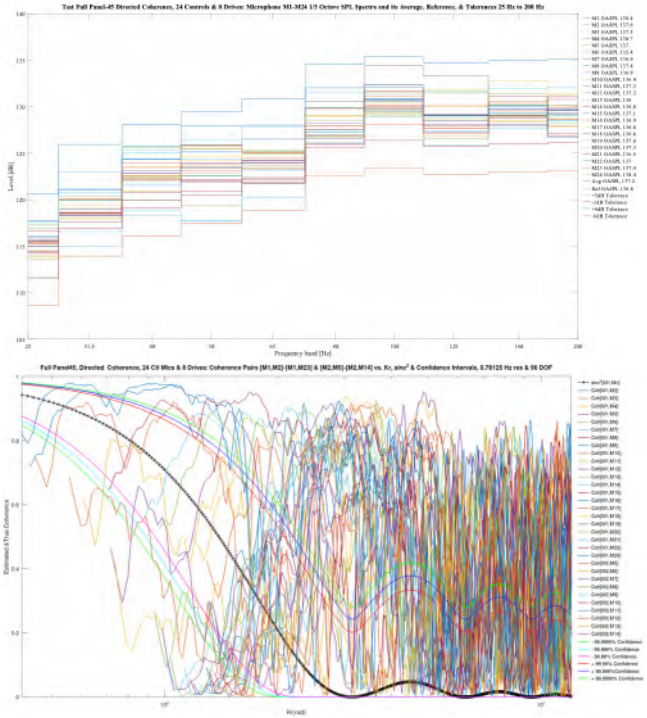


Figure 5: 1/3 Octave SPL Spectra of the 24 Control Mics & (bottom) Relative Coherence vs. Kr

Note that the uniformity in Fig. 5 (top) is not as good as what we see in Fig. 4 (top) for the Near-Diffuse field. Also, Fig. 5 (bottom) is quite different than what we see in Fig. 4 (bottom). Thus, the Directed-Coherence field is not Near-Diffuse. This is by design since its MIMO control is programmed with judicious choices for the setting of the off-diagonal coherence and phase terms [5] in its reference SDM [3] to have a higher coherence as the plot in Fig. 5 (bottom) shows, but by having its SDM set to create a push-pull sound pressure condition by the setting the phases between the front to 0° and front and rear microphones to 180°, i.e., as the front of panel loudspeaker's sound pressure waves push, the rear of panel loudspeaker's sound pressures pull the panel, effectively in theory doubling the pressure force on the panel, which becomes apparent above 137 Hz and continuing above 200 Hz as discussed in [2, 4-5]. This will be discussed further in the following subsection 2.5 describing the panel's vibroacoustic responses to the 3 acoustic fields.

2.4 Non-Diffuse MISO Field

As compared to the Directed-Coherence test, the Fig. 6 (top) 24-control microphone 1/3 Octave SPL spectra are much less uniform and the (bottom) Coherence vs. Kr results are mostly 1, which demonstrate the MISO created acoustic field [2,4-5] is not diffuse, where [2,4-5] demonstrate in detail that as a result this field performs the poorest, by not being able to excite all expected test panel resonances properly, which will be briefly discussed in following section.

The poor performance largely results from the in-phase, shown in [2,4-5], high coherence sound pressure waves being measured by the control microphones response shown in Fig. 6 (top and bottom) causing more significant enhancement-cancellation effects due to their interaction with plate mode's relative phase that is explained for this field in [2,4-5]. This field simply cannot match what is expected from an acoustic field that was created using MIMO, which instead uses a multiple-input-single-output (MISO) control, which has no ability to control the relative phase and coherence between sound waves coming from the speaker stacks, which are driven by a single drive. The result is that this field provides the poorest proper excitation of the expected test panel modes by the 3 discussed fields, as will be discussed later and as described in detail in [2,4-5].

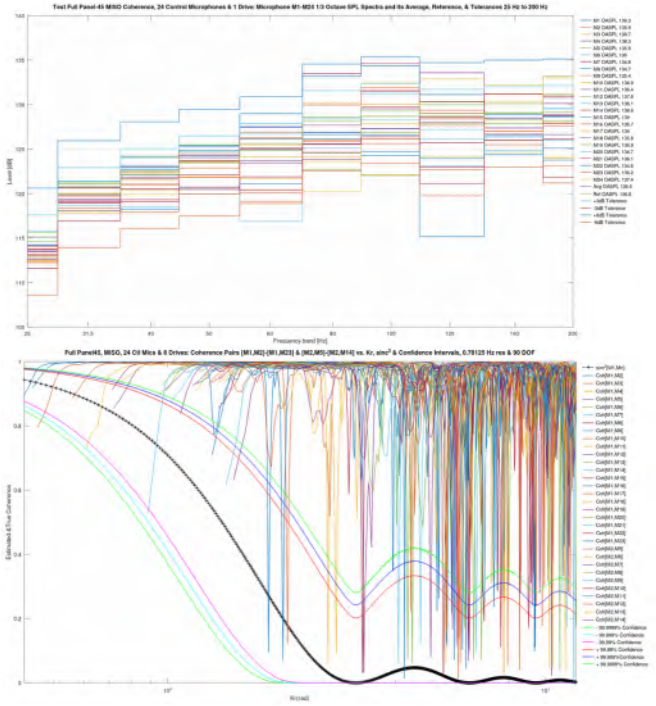


Figure 6: (top) 1/3 Octave SPL Spectra of the 24 Control Mics & (bottom) Relative Coherence vs. Kr

2.5 The 3 Field's Panel Response Comparison

Comparison is not detailed, since [2,4] has details. The following Fig. 7 provides a simpler comparison.

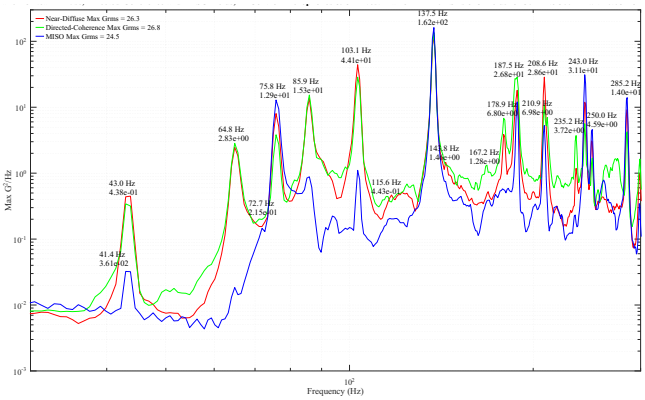


Figure 7: Comparison of the Maxima of the PSDs from the 20 Accels A1-A20 from each of 3 Fields

Note that Fig. 7 displays the comparison of the

three fields to 300 Hz, to be more consistent with [2,4] and because that is needed by section 3. Consequently, Fig. 7 also better demonstrates the differences between the 3 Acoustic Fields.

The MISO Field (in blue) is shown by Fig. 7 to have the lowest maximum response in general, except for also creating the highest responses for the 75.8 Hz, 137.5 Hz, 243 Hz, 250 Hz, and 285.2 Hz panel modes, which are examples of response enhancement [2,4-5]. In contrast, MISO excites the rest of the panel's modes the least, with the 43 Hz, 64.8 Hz, 85.9 Hz, 103.1 Hz, 167.2 Hz, 178.9 Hz and 235.2 Hz modes barely responding, which are examples of response cancellation [2,4], where both results are inconsistent modal responses not directly linked to the spectral and OASPL specified for the acoustic test, which are not present in the responses due to the Near-Diffuse Field. This behavior is most likely caused by the high coherence and in-phase behavior [2,4-5] demonstrated by the response of the control microphones, which characterizes the acoustic field that excites the panel modes.

Fig. 7 also indicates that the Directed-Coherence Field (in green) performs better in this regard than MISO due to the higher sound pressure force exerted by this field on the panel at the same OASPL as that of MISO and the Near-Diffuse Fields, where its responses exceed those due to the Near-Diffuse field for the 64.8 Hz, 85.9 Hz, 167.2 Hz, 178.9 Hz, 187.5 Hz, and 235.2 Hz modes, but interestingly not so for the 75.8 Hz, 103.1 Hz, 208.6 Hz, 243 Hz, 250 Hz, and 285.2 Hz modes, where they are at lower g^2/Hz level than what the Near-Diffuse field achieves, as Fig. 7 demonstrates, even though there is a doubling of sound pressures acting on the panel due to its push-pull excitation, where this lack of consistency is not present with the Near-Diffuse Field.

Also note in Fig. 7 that for the modal responses above 137.5 Hz, the Directed-Coherence Field has a consistent response growth trend, where the modal responses rise to higher levels, as the modal frequencies increase to 187.5 Hz with significant drop in g^2/Hz level of the following 208.6 Hz mode, where thereafter that trend changes into a more hit and miss pattern as far the modal responses go. Also note the response levels between the modes is highest for the Directed-Coherence field, as displayed in Fig. 7, which starts at 37 Hz persisting throughout the 37 Hz to 300 Hz range, but increasing significantly above the 137.5 Hz mode to 300 Hz. This set of phenomena appears to be caused by the enhancement-cancellation effects discussed earlier for the Directed-Coherence and MISO cases, but which also appear more consistently in the modes after the 137.5 Hz mode, which is also where the differences between the Near-Diffuse and Direct-Coherent fields become more apparent. This phenomenon, which Fig. 7 demonstrates, is explained more fully in the following subsection 3.4 of the following section in conjunction with Fig. 22.

Other significant differences between the vibracoustic response of the panel's mode between the Near Diffuse and the other two fields are discussed in more detail, along with 2 other non-diffuse fields that were used for DFA testing, in [2,4-5]. These demonstrate that the Near Diffuse field is more effective in exciting the panel's modes in a consistent manner, by using various performance comparison metrics using pseudo-velocity (PV) based Partial Damage time-domain [2]; PV VAG and PSD frequency domain [4]; and Acceleration PSD comparison [5] methods.

As seen, Fig. 7 is also useful to compare the 3 maximum acceleration PSDs obtained from each of the 20 PSD panel accelerometers from each of the 3 fields and annotates the overall maximum g^2/Hz level and frequency for each of the 20 modes. The comparison also supports the view that the Near-Diffuse field excites the panel modes more consistently than the other fields [2,4-5], since the Near-Diffuse field does not, like the Directed-Coherent field, switch from being the highest performer at 64.8 Hz to the lowest performer at 75.8 Hz and again above the 137.5 Hz mode to the 187.5 Hz mode being the highest performer and then low again at the 208.6 Hz mode and then again the lowest for the 243 Hz, 250 Hz and 285.2 Hz modes. This behavior is consistent with response enhancement-cancellation we see to a greater extent for MISO. In [2,4-5] similar behavior for the other non-diffuse fields that were tested was demonstrated.

2.6 Conclusions about the DFA testing results

- This section presented the control microphone 1/3 OB spectra and a typical set of coherence vs Kr spectra of the Near-Diffuse, Directed-Coherence, and MISO Fields using the same OASPL and spectrum from Testing in 2021.
- It also presented the comparison of the vibroacoustic response that resulted from exciting the panel with those Acoustic Fields. The comparison and the references cited demonstrated the coherence settings for the 3 tests, which differed as explained in the paper, created significant response level differences that showed that the Near-Diffuse field is more effective in exciting the panel's modes in a consistent manner than the other two fields.
- The 2021 test data provided an opportunity to test digital vibroacoustic simulation systems, since we had both the vibroacoustic acceleration response SDMs and Acoustic Field excitation sound pressure level SDMs. These are imported into the VA One simulator to compare its simulated panel vibroacoustic response PSDs and other analyses with the test results. These will be discussed in the following section 3 on simulation.

3. COMPARISON OF NUMERICAL SIMULATION AND MEASURED RESULTS

The DFAT panel test was modelled using the VA One vibroacoustic simulation software, and the results of the simulation were compared to the measured data for the same three cases: Near-Diffuse, Directed-Coherence, and MISO. Fig. 8 shows the complete model. The aluminum honeycomb test panel was modelled as a finite element structure and the speakers and test volume were modelled with the Boundary Element Method (BEM) technique. The frequency domain was limited to 200 Hz with a constant analysis bandwidth of 0.78125 Hz in order to capture the low-frequency structural modes while keeping the run time of the BEM solution reasonable. The results are however constrained by the 200 Hz upper limit, and should be viewed with that constraint in mind.

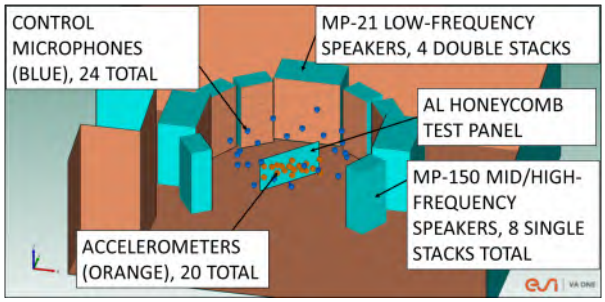


Figure 8: Complete VA One Model

The measured data below about 30 Hz, where the microphone signals had rolled off significantly, appeared unreliable due to instrumentation noise at low SNR and possible ambient sound and vibration. For this paper, we have presented SPL data above 20 Hz and acceleration data above 30 Hz to avoid confusion from the unreliable low-frequency measurements.

There were 24 control microphones distributed around the test panel and 20 accelerometers attached to the panel. The room in which the tests were performed was included in the model.

For each of the three simulation cases, the Spectral Density Matrix (SDM) that was measured during the actual test was imported into VA One and applied to the 24 control microphones. VA One solved for the speaker output that matched the SDM at those 24 microphones, and then solved the coupled vibroacoustic problem to get the structural response of the test panel. The comparisons shown here are between the measured and simulation SPLs and acceleration PSDs.

An Experimental Modal Analysis (EMA) was performed on the test panel in 2021, and the mode frequencies and shapes from the current FE model of the panel were checked against the EMA results (Tab. 1). Below 200 Hz, all 16 panel modes were in agreement, but there was a reversal of the order of modes 15 (187.0 Hz) and 16 (188.3 Hz), which were the two highest frequency modes. That reversal was ignored for this paper.

3.1. Near-Diffuse Field Case

The simulation of the Near-Diffuse Field case produced microphone and accelerometer responses that were very similar to the measured test data.

Virtually all DFAT tests and tests in Reverberant Acoustic Test Facilities (RATFs) are either explicitly or implicitly required to approximate a diffuse field. For aerospace vibroacoustic tests, the primary exception to this historically has been progressive wave testing with a Progressive Wave Tube. There has also been interest in fields with other spatially varied characteristics, but the primary field of interest is an approximately diffuse field. An ideal diffuse field is spatially homogeneous, and at any frequency, provides a uniform intensity in all directions. The coherence between a pair of microphones in an ideal diffuse field will have a $\text{sinc}^2(kr)$ shape [6] and the phase will be 0 or pi, where k = wavenumber and r = microphone separation distance. Actual test fields can only approximate an ideal diffuse field. The Near-Diffuse Field case was such an approximation. Graphs of measured coherence vs. kr for the three cases are shown in Fig. 4, 5, and 6. In Fig. 4 for the Near-Diffuse case, the measured coherence is shown for a number of microphone pairs, and generally follows the $\text{sinc}^2(kr)$ function.

The Near-Diffuse test used MIMO (Multiple-Input Multiple-Output) control [3], where the 24 control microphones were the multiple inputs to the controller, and the outputs were 8 drive signals that were mixed and used to drive the speaker stacks. Each double stack of low-frequency MP-21 speakers was driven by the same signal over its height, and each single stack of mid/high-frequency MP-150 speakers was driven by the same signal over its height. The Near-Diffuse simulation used the same MIMO control configuration of 24 control microphones and 16 speaker stacks as the actual tests, but the specific generation and mixing of the drive signal between the controller and the speakers was not modelled. Rather, for the simulation, VA One matched the SDM at the 24 control microphones by adjusting the speaker stack outputs.

The measured SDM for the Near-Diffuse case was imported into VA One and the model was solved to match the SDM at the 24 control microphones. Fig. 9 shows the SPL reference spectrum, the measured average spectrum for the 24 control microphones, and the average spectrum from the VA One simulation. All three spectra are essentially identical. There is a small hump in the measured and VA One spectra at 90 Hz.

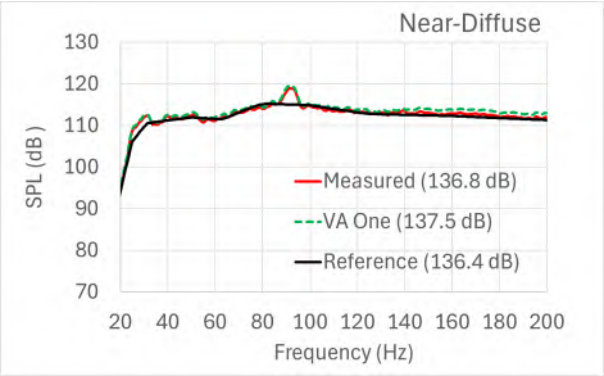


Figure 9: SPL Spectra for Near-Diffuse Case

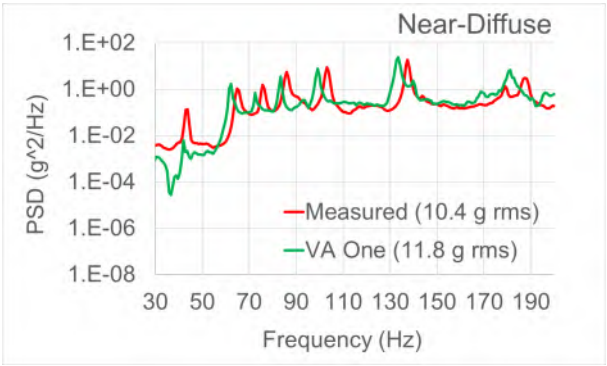


Figure 10: PSDs for Near-Diffuse Case

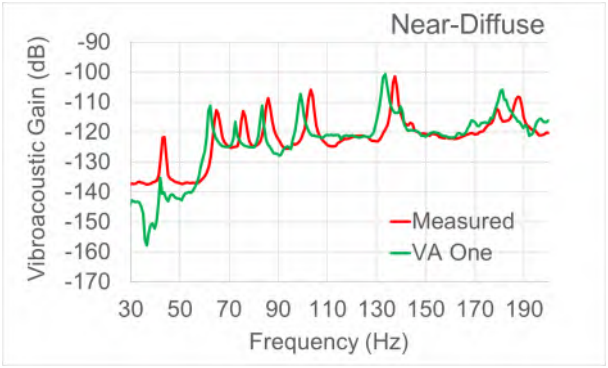


Figure 11: Vibroacoustic Gain for Near-Diffuse Case

Fig. 10 shows the measured average PSD for the 20 accelerometers and the average PSD from the VA One simulation. The two spectra are very similar. Above 50 Hz, the amplitudes of the modal responses are similar. The frequencies of the modes from the simulation are slightly lower than the measured frequencies, but the modes from the simulation still correspond well to the measured data.

Fig. 11 shows the Vibroacoustic Gain (VAG) calculated from both the measured data and the VA One simulation. The VAG is defined here as the acceleration level in dB ref. 1 g minus the SPL in dB ref. 20 microPa, and its purpose is to normalize only the acceleration response with respect to SPL. The VAG does not normalize the response with respect to coherence and phase, so differences in VAG can be attributed to joint acceptance. The measured and simulation values of VAG in Fig. 11 are very similar. The measured VAG is higher than the simulation values below about 40 Hz, and this could be due to instrumentation noise or ambient sound and vibration. Unfortunately, we did not make measurements of the ambient environment for comparison.

3.2. Directed-Coherence Case

The simulation of the Directed-Coherence case produced microphone and accelerometer responses that were very similar to the measured test data and also very similar to the Near-Diffuse case.

The intent of the Directed-Coherence case was to produce a field that had different coherence and phase on each side of the test panel, but the same SPL spectrum as the other two cases. That illustrates the effect of coherence and phase on the panel response independent of SPL. The coherence and phase were defined for the Directed-Coherence case to produce a sort of push-pull effect on the panel. Fig. 5 shows the measured coherence vs. kr for the Directed-Coherence case, which differs significantly from the coherence of the Near-Diffuse case (Fig. 4).

Fig. 12 shows that the average control microphone SPL spectra for the measured and simulation Directed-Coherence cases were essentially identical and very similar to the reference spectrum. The slight hump at 90 Hz is still evident, as for the Near-Diffuse case. So, the change in cases was not the SPL but rather coherence and phase, as intended.

Fig. 13 shows the measured, average PSD for the 20 accelerometers and the average PSD from the VA One simulation. The two spectra are very similar, and both are similar to the PSDs for the Near-Diffuse case (Fig. 10).

Fig. 14 shows the VAG calculated from both the measured data and the VA One simulation. As with the PSDs, the two VAG spectra are very similar, and both are similar to the VAG curves for the Near-Diffuse case (Fig. 11). The measured VAG is higher than the simulation values below about 40 Hz, similar to the other two cases.

The overall, average acceleration for the 20 accelerometers increased for both the measured data and the simulation (Fig. 10 and 13), by 1.1 g rms for the measured data and 1.8 g rms for the simulation, but the responses for the Directed-Coherence and Near-Diffuse cases show that the two fields had a very similar effect on the test article. This was not true for the MISO case, which had the most different field and will be discussed next.

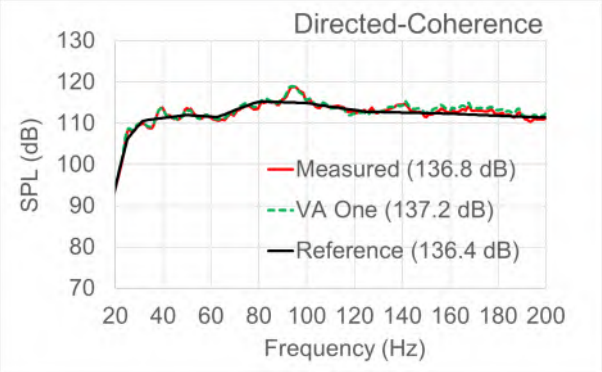


Figure 12: SPL Spectra for Directed-Coherence Case

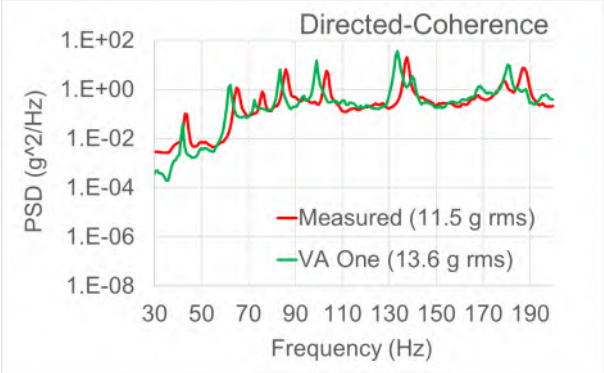


Figure 13: PSDs for Directed-Coherence Case

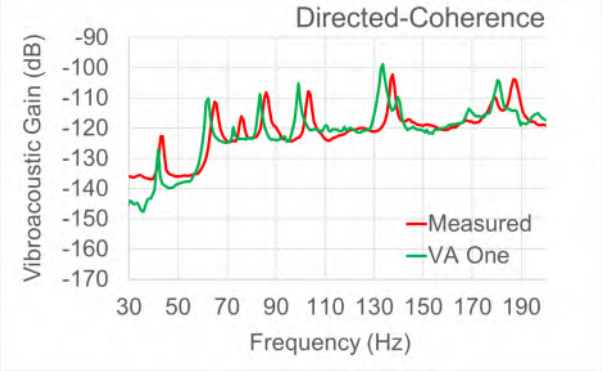


Figure 14: Vibroacoustic Gain for Directed-Coherence Case

3.3. MISO Case

The simulation of the MISO case produced microphone and accelerometer responses that were similar to the measured data, but that differed significantly in some respects. The MISO field was the most different of the three cases and the most atypical for aerospace vibroacoustic testing, so it was expected that the MISO case would exhibit significant differences.

The MISO test used Multiple-Input Single-Output control. The multiple inputs were the 24 control microphones. Their signals were averaged and input to the controller. The controller produced a single drive signal output that was band-passed and used to drive all speakers within a given frequency band. This is the way early DFAT tests were controlled before the transition to the higher-fidelity MIMO rectangular control that was used for the Near-Diffuse and Directed-Coherence cases. The simulation of the MISO case was similar to the simulation of the MIMO cases in that VA One matched the SDM at the 24 control microphones by adjusting the speaker stack outputs.

The drawback to a MISO field for testing is that its symmetry produces large spatial variations in SPL (even if they aren't reflected in the average) and a much less diffuse test field. This was the motivation for transitioning to MIMO control during the early development of DFAT.

Fig. 15 shows that the measured, average SPL spectrum for the MISO case was similar to the reference spectrum. The average spectrum from the simulation was also similar to the reference and measured spectra, but had lower SPLs in the range of 80-120 Hz, and a significant local minimum at 113 Hz. The MISO spectrum did not show the small hump at 90 Hz that was in the Near-Diffuse and Directed-Coherence spectra. As for the Directed-Coherence case, the intent for the MISO case was to maintain the SPL spectrum while changing only the phase and coherence of the field. Fig. 6 shows the measured coherence vs. kr for the MISO case, and in comparison to Fig. 4 and 5, can be seen to differ significantly from the coherence of the other two cases. The differences in the MISO SPL spectra are normalized away by the VAG.

Fig. 16 shows the measured, average PSD for the 20 accelerometers and the average PSD from the VA One simulation. The two spectra differ significantly. Above 60 Hz, the measured curve is lower than the simulation curve, and the actual test essentially did not excite the modes at 62 Hz and 99 Hz (frequencies per the VA One results), which were excited in the simulation. Below 60 Hz, the measured response is significantly higher than the simulation response. This difference is also evident for the other two cases, and again may have been due to instrumentation noise or ambient sound and vibration.

Fig. 17 shows the VAG calculated from both the measured data and the VA One simulation. The VAG spectra exhibit the same differences as the corresponding PSDs. The measured VAG is higher than the simulation values below 60 Hz, similar to the other two cases.

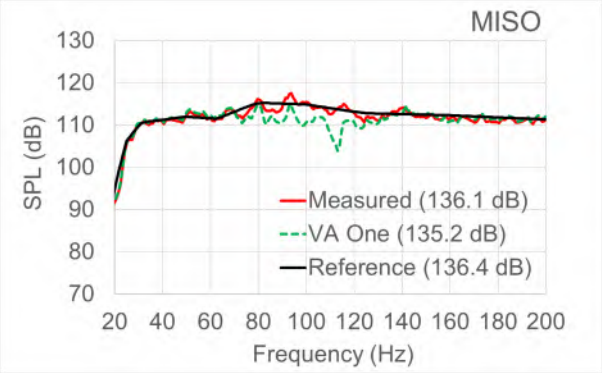


Figure 15: SPL Spectra for MISO Case

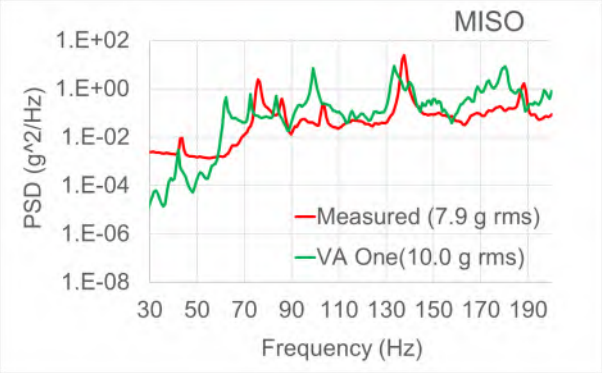


Figure 16: PSDs for MISO Case

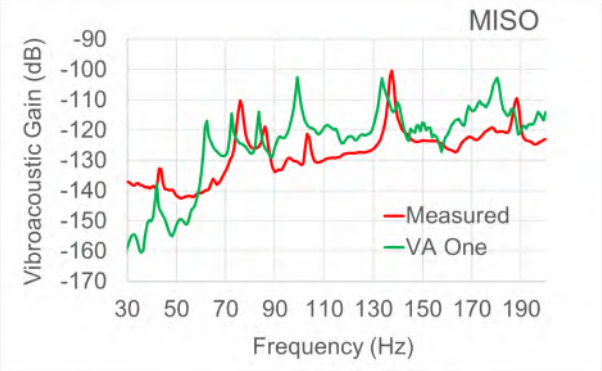


Figure 17: Vibroacoustic Gain for MISO Case

The measured responses for the MISO case were quite different than for the Near-Diffuse and Directed-Coherence cases, as was expected (Fig. 18 and 20). However, the simulation responses for the MISO case were different than the measured responses, which was unexpected (Fig. 16 and 17).

In particular, the simulation did excite the modes at 62 Hz and 99 Hz but the measured field did not. The differences in the measured and simulation SPL spectra shown in Fig. 15 don't really explain this. The model may not have been configured right for the MISO case, or perhaps the 24 control microphones were insufficient to capture some important aspect of the field. The agreement between the measured and simulation data was good for the Near-Diffuse and Directed-Coherence cases, which implies that the fidelity of the basic model is good. We have not drawn any specific conclusion about the differences.

3.4. Comparison of PSDs and Vibroacoustic Gain

Fig. 18 shows the measured acceleration PSDs for the three cases. The curves for the Near-Diffuse and Directed-Coherence cases are essentially identical. There are some differences, but they are small. This similarity was somewhat unexpected, but was repeated in the simulation PSDs shown in Fig. 19. The similarity is probably due to limiting the analysis domain to 200 Hz coupled with the size of the test article, and that the SDMs for the Near-Diffuse and Directed-Coherence cases, while quite different as shown in Fig. 4 and 5, weren't different enough to cause significantly different responses below 200 Hz. The response of a structure to a field is not only a function of the field characteristics (SPL, coherence, and phase), but also a function of the ratio of the size of the structure to the wavelength of the acoustic excitation. Reference 7 by Sutherland has an excellent discussion of this in Chapter 8. Fig. 22 is an example for a baffled, simply-supported beam, and was taken from that reference. Note that at low L/λ, the values of joint acceptance are about the same for both a diffuse field and a progressive wave for a given value of L/λ (particularly for the odd modes). However, these are distinctly different fields. In contrast, at high values of L/λ, the joint acceptances for the diffuse and progressive-wave fields differ significantly. In Fig. 22, λ is equal to the actual acoustic wavelength for a diffuse field, and equal to the trace wavelength across the length of the beam for a progressive wave. Fig. 22 is for a beam, and so is only an example, and does not apply directly to the test panel, except with regard to the overall concept.

If we had extended the domain to a higher frequency, then the acceleration responses for the Near-Diffuse and Directed-Coherence cases would have shown more differences [2,4]. In Fig. 7, the maxima of the PSDs are plotted for those cases, and more significant differences between them are evident at 150-300 Hz.

The measured PSD for the MISO case in Fig. 18 is different than the other two cases, as expected, since the field control and SDM were much different (Fig. 6). Again, the measured MISO field did not excite the mode at 62 Hz and poorly excited other modes. However, for the simulation PSDs in Fig. 19, the curves for all three cases are similar, and excite all the modes to similar levels. This includes the simulation MISO PSD curve, which makes it different than the measured MISO PSD curve.

Fig. 20 and 21 show the vibroacoustic gain for the measured and simulation data respectively. The

relationships between the curves are similar to Fig. 18 and 19.

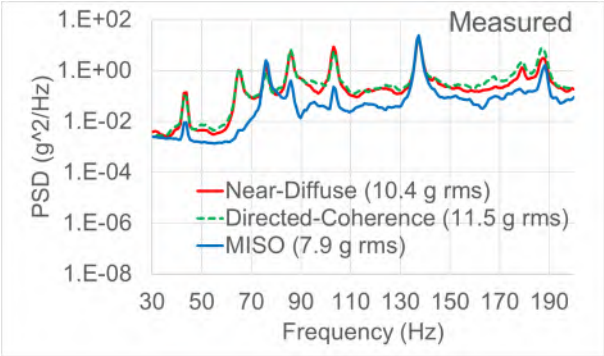


Figure 18: Measured PSDs for all 3 Cases

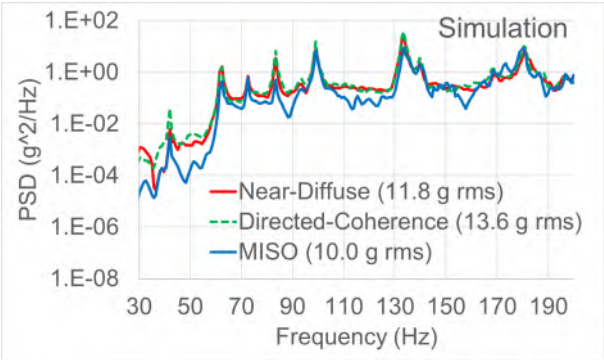


Figure 19: Simulation PSDs for all 3 Cases

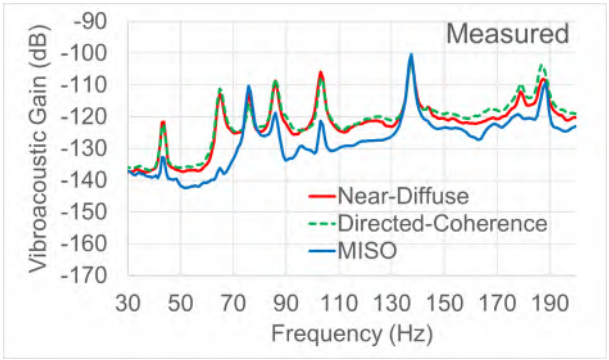


Figure 20: Measured VAG for all 3 Cases

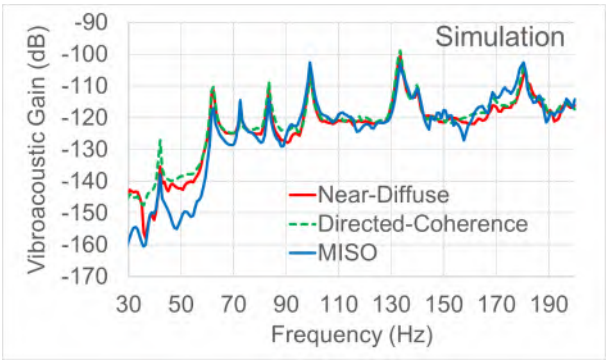


Figure 21: Simulation VAG for all 3 Cases

3.5. Conclusions about Measured vs. Simulation Data

Some conclusions concerning the comparison of the measured and simulation data are listed here.

- The VA One simulations provided results that were good approximations of the measured results. The authors always learn things about the tests from the simulations, and this project was no different.
- The Near-Diffuse and Directed-Coherence responses were quite similar, and this was probably due partly to the frequency domain being limited to 200 Hz, coupled with the panel dimensions. It would not be correct to conclude that all fields excite the test article similarly, and the MISO case shows clearly that this isn't true. Extending the analysis and simulation beyond 200 Hz would show more differences between the Near-Diffuse and Directed-Coherence cases.
- We recommend that ambient sound and vibration be measured and taken into consideration for these types of investigations. Ambient sound at very low frequencies is not audible, so it has to be measured. Also, the simulation assumes a noise floor of zero, which won't be true in practice.
- The measured response for the MISO case was different than for the other two cases even though the measured, average SPL spectra for all three cases were very similar and also similar to the reference spectrum. This reinforces the idea that the test article can show different responses depending on the spatial correlation of the field, even if the SPL spectra are the same. It is not theoretically sufficient to specify only an average SPL spectrum for a test.
- The difference between the measured and simulation responses for the MISO case could indicate that the model was not configured right for the MISO case or that the spatial resolution of the microphones was insufficient, but the specific cause wasn't investigated and warrants further analysis.

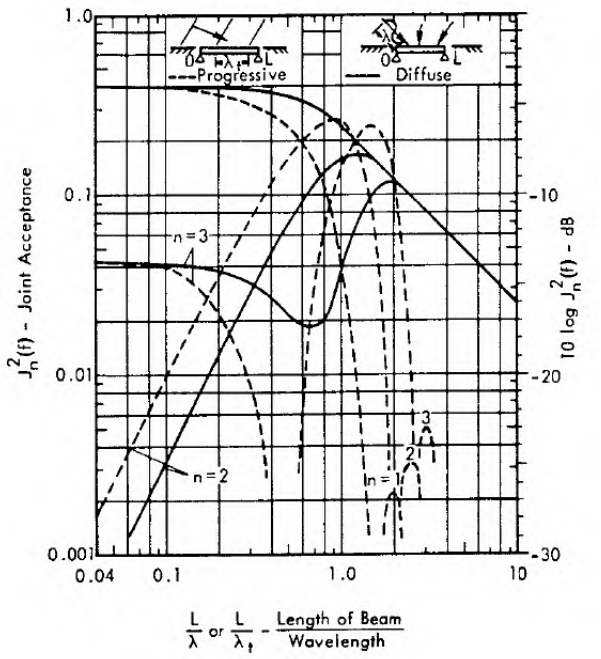


Figure 22: Joint Acceptance of Beam in Diffuse and Progressive-Wave Fields [7]

4. REFERENCES

1. Underwood, M. A., Mayne, A. W. III, Hadjit, R, and Castel, A., "The Importance of Microphone Placement with Respect to the Test Article for Direct Field Acoustic (DFA) Testing – A Case Study," American Institute of Aeronautics and Astronautics SciTech Forum Proceedings, January 2026.

2. Underwood, M. A. and Lamparelli, M. D., "A New Method Using Pseudovelocity-Based Fatigue Analysis to Determine the Effectiveness of Acoustic Fields Used for Acoustic Testing," *IEST Journal, Volume 66: Issue 1*, December 2023, DOI: 10.17764/1557-2196-66.1.1.

3. Underwood, Marcos A., "New Method Determines Optimized Reference SDM for MIMO Testing," *IEST Journal, Volume 65: Issue 1*, Dec. 2022, DOI: 10.17764/1557-2196-65.1.21

4. Underwood, Marcos A., "A New Method Using Pseudo-Velocity-Based Stress Analyses to Evaluate Effectiveness of Acoustic Fields Used for Acoustic Testing. 33rd Aerospace Testing Seminar, May 15-18, 2023, Los Angeles, CA.

5. Underwood, Marcos A., Comparisons of the Structural Response of a Test Article Excited by DFAT Diffuse and Non-Diffuse Acoustic Fields. 91st Shock and Vibration Symposium, September 19-23, 2021, Orlando, FL.

6. Underwood, Marcos A., and Hargreaves, Jonathan A., "Confidence Limits for Coherence – Toward a Better Understanding of its Use as a Diffuse Field Metric for Quantifying the Quality of Direct Field Acoustic Noise (DFAN) Testing Systems," *Proceedings of the 18th European Conference on Spacecraft Structures Materials and Environmental Testing,* Noordwijk, The Netherlands, Sept. 2024.

7. Sutherland, L.C. (1968), Sonic and Vibration Environments for Ground Facilities – A Design Manual, Wyle Laboratories Research Staff Report Number WR 68-2, 8-19.

THE INVAP METHODOLOGY FOR HIGH-FIDELITY VIBRO-ACOUSTIC CORRELATION OF A STOWED SOLAR ARRAY VIA DFAT

Soledad Fioroni [(1)], Nicolás Acuña [(1)]

[(1)] INVAP S.A.U., Cmte. Luis Piedrabuena 4950, S.C. de Bariloche - Argentina, Email: sfioroni@invap.com.ar

KEYWORDS

Vibro-Acoustic, DFAT, Solar Array, Correlation, INVAP

ABSTRACT

The structural qualification of solar arrays requires high confidence in numerical predictions under launch environments due to complex fluid-structure interactions in stowed configurations. This paper presents an integrated methodology developed and validated at INVAP's facilities to close the gap between structural modeling and environmental testing.

A detailed finite element model of a carbon fiber/Honeycomb solar array was developed using a two-way vibro-acoustic coupling formulation to account for entrained air mass and radiation damping. Validation involved a sine sweep test to correlate structural modes via modal projection, followed by Direct Field Acoustic Testing (DFAT) simulated as a diffuse acoustic field.

Results show an exceptional match in Power Spectral Density (PSD) levels across the 20-2000 Hz band. This study validates the diffuse field assumption for DFAT and demonstrates how two-way coupling establishes a highly predictive digital twin for spacecraft qualification.

1. INTRODUCTION

Structural qualification during the launch phase represents a critical risk-reduction milestone in spacecraft mission design. Due to high surface-area-to-mass ratios, lightweight appendages like stowed solar arrays (SAs) are particularly vulnerable to high-intensity acoustic excitation and the resulting fluid-structure interactions. While these environments are traditionally simulated in Reverberant Acoustic Test Facilities (RATF) to achieve a uniform sound field, the aerospace industry has increasingly adopted Direct Field Acoustic Testing (DFAT) – or Direct Field Acoustic Noise (DFAN) – as a flexible, cost-effective alternative ([1]). By deploying high-power loudspeaker arrays directly around the flight hardware within a standard test bay, DFAT bypasses the logistical transportation risks and massive infrastructure costs associated with fixed acoustic chambers, ensuring the direct sound field heavily dominates over room reflections ([2]).

A comprehensive literature review compiled by [3] establishes the engineering maturity and remaining challenges inherent to contemporary DFAN frameworks. Modern DFAT methodologies, operating under institutional guidelines like [4] and [5], utilize Multi-Input Multi-Output (MIMO) control strategies to translate narrow or third-octave test specifications into wideband drive commands. However, achieving precise spatial field diffusivity and managing low-frequency modal coupling remain persistent technical difficulties. Because the enclosing loudspeaker stacks physically form an open-topped cylindrical cavity around the test article, they introduce distinct acoustic cavity modes ([2]). In the absence of significant damping, these modes generate severe peaks and nulls in the sound pressure level (SPL) spectrum, leading to spatial non-uniformity and temporal ringing [2]. Reference [3] highlights historical validation campaigns, including the Orion European Service Module, where structural components like the SA wing exhibited severe coupling with acoustic cavity environments and local boundary effects, risking localized over-testing or under-testing.

Addressing these phenomena requires robust numerical predictive tools. The Salford review specifically identifies the Finite Element Method (FEM) and the Boundary Element Method (BEM) as the primary standard industrial approaches for low-frequency vibro-acoustic simulation, alongside advanced cross-spectral density control schemes designed to overcome theoretical diffuse field limitations ([3], [6]).

Despite these advancements in numerical modeling, standard industrial workflows frequently oversimplify fluid-structure coupling by treating the acoustic field as purely uncoupled or ignoring the boundary layer constraints between closely packed structures. This frequently results in either overly conservative design margins or non-conservative physical predictions.

This study addresses these limitations through an integrated numerical and experimental framework developed and executed within INVAP's specialized simulation and testing facilities. By implementing a high-fidelity, two-way coupled vibro-acoustic formulation in NX Siemens software (version 2312), the proposed methodology explicitly accounts for the entrained air mass, radiation damping, and acoustic cavity resonance trapped within stowed panel configurations. This predictive model is sequentially validated against a low-frequency modal sine sweep campaign and a full-scale DFAT

qualification run. The results demonstrate how a predictive "digital twin" can accurately capture complex structural-acoustic responses under high-intensity, diffuse acoustic field assumptions, offering a verifiable path toward reducing safety factors on advanced flight hardware.

The remainder of this paper is organized as follows. Section 2 details the mathematical and numerical formulation of the fully coupled fluid-structure model. Section 3 focuses on the low-frequency mechanical qualification, describing the shaker slip table sine sweep configuration, the structural model tuning, and the custom spatial visualization tool used to track mode shapes. It also analyzes the amplitude-dependent mechanism damping extracted from the final high-level test runs. Section 4 covers the high-frequency acoustic qualification, establishing the analytical frequency limits of the simulation before detailing the physical DFAT setup, its compliance with [4] instrumentation guidelines, and the final g_{RMS} response correlation results. Finally, Section 5 presents the conclusions of this study and outlines directions for future work.

2. NUMERICAL FORMULATION AND BASELINE MODEL

This finite element modeling section can be broken down into different subsections. First, a description of the structural model of the solar array (SA) is addressed. Then, the fluid setup for the vibro-acoustic analysis is discussed, and last but not least, the general assumptions made regarding dynamic settings of the solutions are detailed.

2.1. The Structural Setup

The properties and element types used to model the main components of the SA are summarized in Tab. 1, including the carbon fiber reinforced polymer (CFRP) and aluminum honeycomb sandwich panels, the Restrain Release (RR) towers, the yoke and the hinges. The composite facings are modeled as orthotropic laminates using shell elements, while the aluminum honeycomb core is represented via equivalent core properties to capture out-of-plane shear flexibility. The resulting FE model consists of ~248k elements and ~372k nodes, and is depicted in Fig. 1.

Table 1: Properties and Element type of the main components of the SA

Component	Property	Element Type
Sandwich Structure	2D Laminate Shell	CQUADR
RR towers	Shell	CQUADR
Yoke	Solid/Beam	CTETRA10/Beam
Hinges	Rigid/Spring	RBE2/CBUSH

To represent the launch configuration, the RR towers and the yoke are rigidly constrained (all six degrees of freedom fixed) at their respective base interface to the satellite structure, establishing a fixed-base boundary condition. Furthermore, the mass of the solar cells, wiring harness, and surface components is accounted for by applying a uniformly distributed non-structural mass (NSM) across the facesheet elements, ensuring the model's total mass and center of gravity match the physical properties of the hardware.

A preliminary normal modes analysis (NX Nastran SOL 103) was conducted to extract the baseline structural natural frequencies and effective modal mass in the stowed configuration. Tab. 2 compiles the dominant normal modes that capture more than 5% of the effective modal mass up to 150 Hz. Notably, only three modes fall strictly within the operational sine sweep range (5-100 Hz). However, the first fundamental in-plane mode along the X-direction lies immediately adjacent to the upper frequency boundary, indicating a high probability of structural excitation during physical testing.

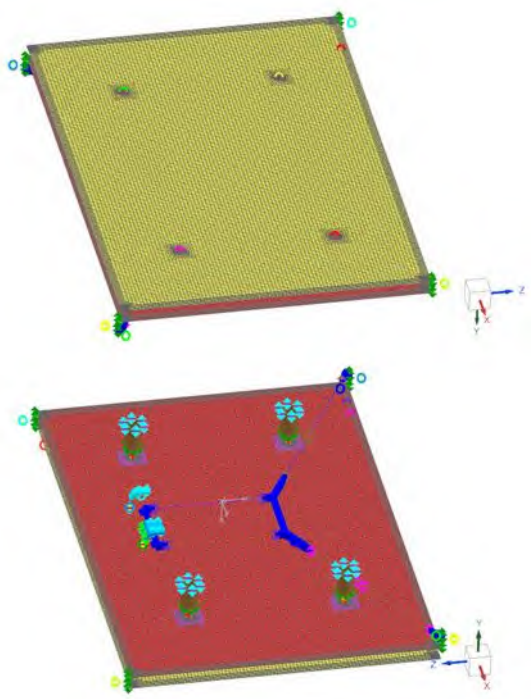


Figure 1: Solar Array's FE model – The Structural Mesh

Table 2: Modes with >5% of associated effective modal mass

#Mode	Frequency	% TX	% TY	% TZ
***7**	75.06	0	10	0.07
***9**	76.58	0	9.95	0.79
***10**	85.32	0	6.73	0.31
***13**	105.1	7.01	0.02	0
***17**	120.3	0	19.93	0.06
***19**	145.8	0.01	0.01	56.32
***20**	147.6	1.09	0.04	8.93
***21**	149.5	0.28	0.01	13.39

2.2. The Fluid Setup

To capture the complex fluid-structure interactions (FSI) driving the SA's vibro-acoustic response, a dedicated acoustic fluid domain was modeled surrounding the stowed panels. The acoustic

environment is simulated as a high-intensity diffuse sound field, reflecting the operational assumptions of the full-scale qualification test. Rather than using multiple nested fluid volumes, a continuous, single acoustic FE mesh was generated. This fluid domain encapsulated the highly confined air cavities trapped between the stowed composite facesheets and extends outward to an external radiation boundary.

To prevent artificial acoustic reflections from the truncation boundary of the FE air volume back to the structure, an Automatically Matched Layer (AML) boundary condition was applied to the outer faces of the fluid domain. The AML formulation dynamically simulates an acoustic free field, allowing radiated acoustic energy to pass through the boundary without reflection, while explicitly capturing the entrained air mass effects and radiation damping within the narrow inter-panel gaps. The fluid elements are populated using standard ambient properties for air, with a nominal density of $\rho_0 = 1.21\ kg/m^3$ and a speed of sound $c_0 = 343\ m/s$.

During the physical qualification campaign, the SA is mounted vertically within the cylindrical loudspeaker array using specialized Mechanical Ground Support Equipment (MGSE) designed and manufactured at INVAP's facilities, replicating its flight-stowed orientation in the satellite structure. To mirror this experimental architecture, the MGSE geometry and its structural interface stiffness were explicitly incorporated into the simulation boundary conditions. Due to its reticulated, frame-like architecture, the MGSE is efficiently discretized using one-dimensional beam elements, which accurately capture the global bending and torsional stiffness of the fixture without introducing unnecessary computational overhead. Concurrently, the MGSE adapter plate – which interfaces directly with the SA and represents the localized stiffness of the satellite body – is modeled using two-dimensional shell elements due to its high surface-area-to-thickness ratio. Fig. 2 depicts the fully integrated FE mesh of the SA mounted onto the hybrid beam-and-shell representation of the MGSE.

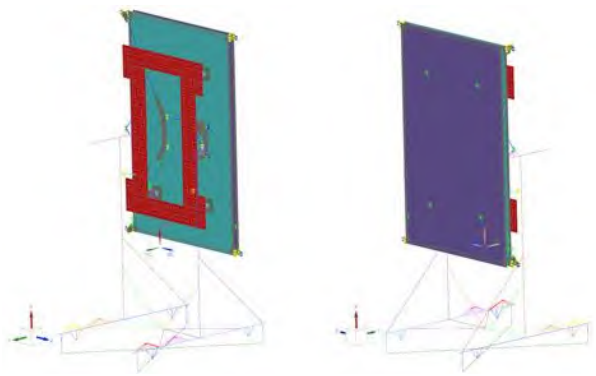


Figure 2: FE model of the SA mounted on the MGSE

The FSI across the wet faces of the composite panels is enforced via a fully coupled, two-way surface-to-surface acoustic coupling card. As illustrated in Fig. 3, the acoustic solid fluid mesh tightly envelopes all structural components characterized by a high surface-area-to-thickness ratio, including both the laminate facesheets and the MGSE adapter plate. Under this bi-directional formulation, the micro-vibrations of the structural panel facesheets generate localized acoustic back-pressure within the fluid mesh, while the pressure waves from the diffuse acoustic field simultaneously act as a surface force driving structural excitation. This localized coupling logic is critical for accurately capturing the radiation damping and entrained air mass effects inside the narrow stowed cavities, which directly govern the low-frequency modal responses of the array during the test.

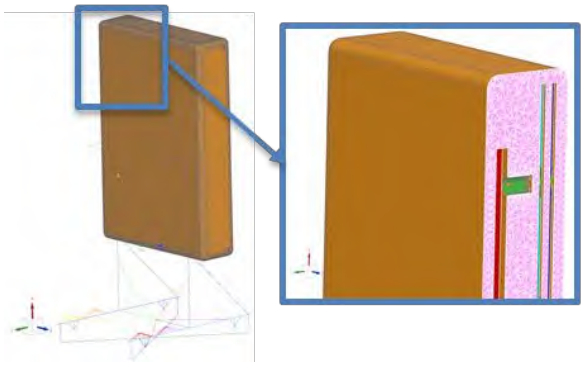


Figure 3: Detail on the acoustic fluid mesh

2.2.1. Coupled Governing Equations

The bi-directional FSI is mathematically discretized at the wetted boundary interfaces. Following the definitive unsymmetrical finite element formulation utilized by NX Nastran, the coupled system of equations governing the combined structural-acoustic domain is expressed in block matrix form as:

$$\begin{bmatrix} M_s & 0 \\ -A^T & M_f \end{bmatrix} \begin{Bmatrix} \ddot{u} \\ \ddot{p} \end{Bmatrix} + \begin{bmatrix} B_s & 0 \\ 0 & B_f \end{bmatrix} \begin{Bmatrix} \dot{u} \\ \dot{p} \end{Bmatrix} + \begin{bmatrix} K_s & A \\ 0 & K_f \end{bmatrix} \begin{Bmatrix} u \\ p \end{Bmatrix} = \begin{Bmatrix} P_s \\ P_f \end{Bmatrix} \quad (1)$$

Where:

- Subscripts s and f represent the structural and fluid partitions of the system, respectively.
- $\{u\}$ is the structural nodal displacement vector, and $\{p\}$ is the fluid nodal acoustic pressure vector.
- $[M_s], [B_s]$, and $[K_s]$ are the structural mass, damping, and stiffness matrices.
- $[M_f], [B_f]$, and $[K_f]$ represent the acoustic fluid compressibility, boundary impedance damping, and mobility stiffness matrices, respectively.
- $\{P_s\}$ and $\{P_f\}$ denote the external structural load and fluid acoustic source vectors, respectively.
- $[A]$ is the fluid-structure coupling (area)

matrix mapping the shared degrees of freedom across the wetted interface.

A key practical advantage of this solver architecture is that the structural and fluid mesh topologies are permitted to be completely non-conformal at the interface. The coupling matrix, $[A]$, is automatically computed via surface-to-surface projection algorithm (governed by the ACMODL bulk data entry). This computes a conservative spatial interpolation that bridges the dissimilar nodal boundaries. Consequently, the cross-coupling term $[A]\{p\}$ projects the fluid pressure fields into localized equivalent face forces on the structural elements, while the structural acceleration coupling term $-[A]^T\{\ddot{u}\}$ enforces complete kinematic continuity by driving pressure fluctuations back into the acoustic mesh domain.

This fully coupled matrix block is solved simultaneously across the frequency range of interest when executing a strong two-way coupling. However, within the modal frequency response framework of NX Nastran (e.g. SOL 111), the solver handles this computation via a multi-stage workflow: the uncoupled normal modes of the structure and the fluid domain are initially extracted separately and sequentially, after which they are projected into modal coordinates to assemble and solve the coupled matrix system. This approach drastically optimizes solver times while capturing true two-way entrained air mass variations and radiation damping effects.

2.3. Dynamic Settings and Solution Assumptions

To validate the analytical predictions against experimental data, two distinct numerical solution paths were configured within the NX Siemens architecture: a low-frequency structural modal response analysis for the sine sweep campaign, and a broadband coupled modal frequency response analysis for the acoustic field simulation.

2.3.1. Structural Sine Sweep Configuration

The structural sine sweep analysis is implemented using an NX Nastran SOL 103 normal modes solution, with the dynamic output subsequently evaluated via the Response Dynamics module to simulate multi-directional base excitation. The frequency sweep is evaluated from 5 Hz up to an upper limit of 250 Hz; extending the solution range well beyond the nominal test band ensures that out-of-band high-frequency modal contributions and residual vectors are fully captured.

The frequency resolution is defined using a hybrid discretization approach: a baseline linear step size of 1 Hz is maintained, supplemented by localized modal clustering (Cluster 2 configuration) that injects 10 additional frequency points between adjacent natural frequencies to precisely resolve sharp resonant peaks. Energy dissipation across the assembly is modeled using a uniform critical damping ratio of $\zeta = 1\%$ across all structural modes.

2.3.2. Vibro-Acoustic Analysis Configuration

The broadband diffuse acoustic simulation is executed via the NX Nastran SOL 111 Modal Frequency Response solver, coupling the structural panel modes with the fluid cavity modes. The operational frequency range spans a broad spectrum from 20 Hz to 2000 Hz. To match standard acoustic data reduction formats while optimizing computational efficiency, the solution frequency steps are discretized using a 1/12-octave band fractional distribution, resulting in a true analytical frequency sweep ranging from 19.4 Hz to 2050 Hz. Consistent with the structural validation path, a critical damping ratio of $\zeta = 1\%$ is applied to the modal basis.

The high-intensity diffuse sound field environment is numerically simulated by applying a Distributed Acoustic Plane Wave load card across the outer boundaries of the fluid domain. This boundary condition models a superposition of randomly oriented, spatially uncorrelated plane waves that uniformly envelop the vertically mounted assembly, as displayed in Fig. 4. This loading strategy ensured an omnidirectional acoustic energy distribution that accurately replicates the diffuse field characteristics generated within the loudspeaker array during physical qualification.

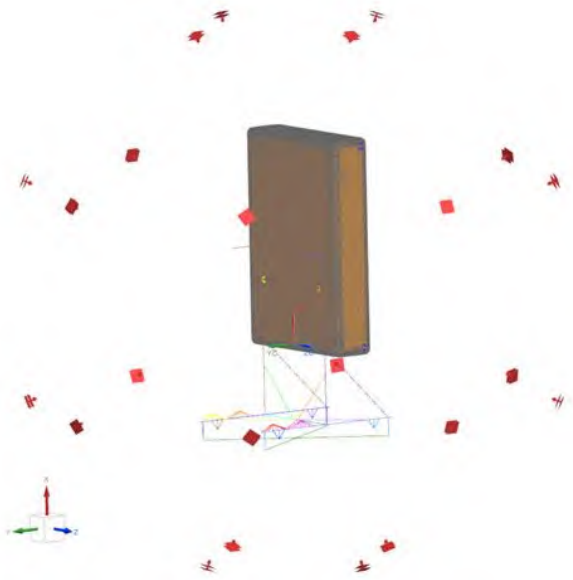


Figure 4: Distributed Acoustic Plane Wave load

3. LOW FREQUENCY QUALIFICATION: THE SINE SWEEP CAMPAIGN

3.1. Experimental Configuration

The physical sine sweep qualification campaign was conducted to verify the structural integrity of the stowed SA and ensure compliance with launcher launch environment requirements. Unlike the vertical layout planned for the acoustic campaign, the SA was mounted directly to the shaker table utilizing only the specialized MGSE adapter plate. This adapter plate was secured flat against the

shaker's slip table for horizontal axes and onto the head expander for vertical testing, bypassing the reticulated frame to establish a direct, rigid interface with the moving armature, as depicted in Figs. 5 and 6.

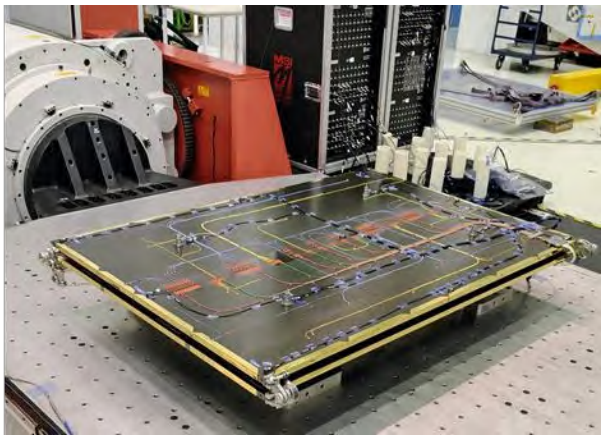


Figure 5: SA mounted onto the shaker's slip table for in-plane Z-direction Sine Sweep Test

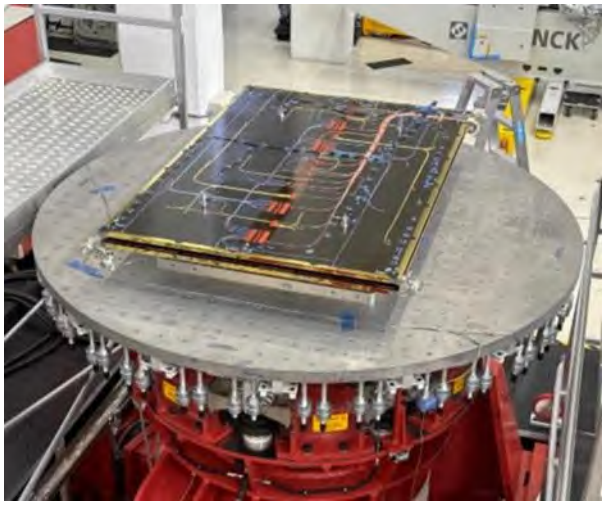


Figure 6: SA mounted onto the head expander for out-of-plane Y-direction Sine Sweep Test

Base-excitation testing was executed sequentially across the three orthogonal axes following a strategic order: first along the in-plane Z-direction, followed by the in-plane X-direction, and concluding with the out-of-plane vertical Y-direction. The horizontal Z-direction was intentionally selected as the initial testing axis because it represents the least responsive axis of the stowed assembly. Starting with this axis allowed the team to isolate and extract a cleaner, less coupled set of initial normal modes, baseline transfer functions, and signature markers before moving to the more highly coupled axes.

To monitor localized dynamic responses, the hardware was instrumented with a dedicated array of triaxial accelerometer affixed to the composite facesheets, the RR towers, and the yoke interfaces. Prior to exposing the flight hardware to full qualification-level loads, a low-level signature sweep (0.1g, 5-250 Hz) was executed at the start of each axis run to experimentally extract the baseline natural frequencies and transfer functions of the undegraded assembly.

Rather than subjecting the flight-critical hardware directly to full qualification-level loads, the excitation profile was increased incrementally through a series of intermediate scaled testing levels. This progressive step-up approach provides two vital technical advantages. First, evaluating intermediate-level telemetry allows the engineering team to closely monitor response trends and proactively characterize structural non-linearities or amplitude-dependent damping behaviors that are fundamentally absent or un-excited during the baseline 0.1g signature sweep. Second, tracking the response scaling across these intermediate stages enables highly accurate, empirical predictions for force-limiting, critical location "notching", and shaker abort thresholds. This ensures that as the input spectrum safely approaches full qualification intensity, the hardware is tightly protected against inadvertent over-testing or destructive resonance peaks.

Crucially, low-level signature sweeps were repeated between each consecutive intermediate and high-level run. These intermediate checks allowed for an immediate, direct comparison of the transfer functions against the baseline signature. A primary criterion for verifying structural health was ensuring that no significant frequency shifts occurred in the peak responses at the main resonant frequencies. Any unexpected downward shift in frequency would serve as an immediate indicator of structural degradation, limit exceedance, or joint slippage, signaling that the test must be halted to prevent hardware damage.

3.2. Model Correlation and Tuning Methodology

To provide an accurate structural baseline for subsequent broadband vibro-acoustic simulations, a systematic model tuning workflow was carried out sequentially based on the initial testing phases. Discrepancies between the initial finite element predictions and the physical test signatures were addressed by focusing on parameters with inherent manufacturing or assembly tolerances.

1. **Mass Profile Refinement**: Prior to the dynamic vibration runs, a physical mass properties test was executed to determine the precise total weight and center of gravity (CoG) of the hardware assembly. The non-structural mass (NSM) distributed across the composite facesheet elements was adjusted to match these measured physical properties, correcting minor mathematical discrepancies in the cable harnesses and adhesive layers.
2. **Pre-load Interface Stiffness Tuning**: Following the completion of the first dynamic run (Z-direction), the experimental transfer functions revealed a slight frequency shift in the primary modes associated with the RR mechanism. To resolve this, the stiffness

values of the CBUSH spring elements located at the top of the RR towers (see Fig. 7) – which model the high-tensile pre-loaded RR bolts – were fine-tuned. Adjusting these localized axial and shear stiffness values successfully captured the true contact compliance and tension state of the flight-release hardware.

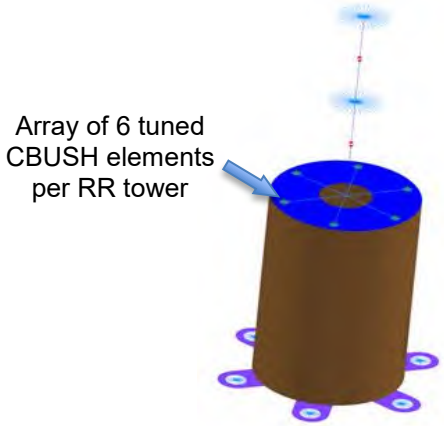


Figure 7: CBUSH elements with tuned stiffness

While these targeted physical updates significantly improved the overall model representation, the highly coupled and dense nature of the spectrum meant that a perfect ±0.5% frequency deviation criteria (see [7]) could not be strictly met for every single secondary or higher-order mode across the wide 5-250 Hz sweep.

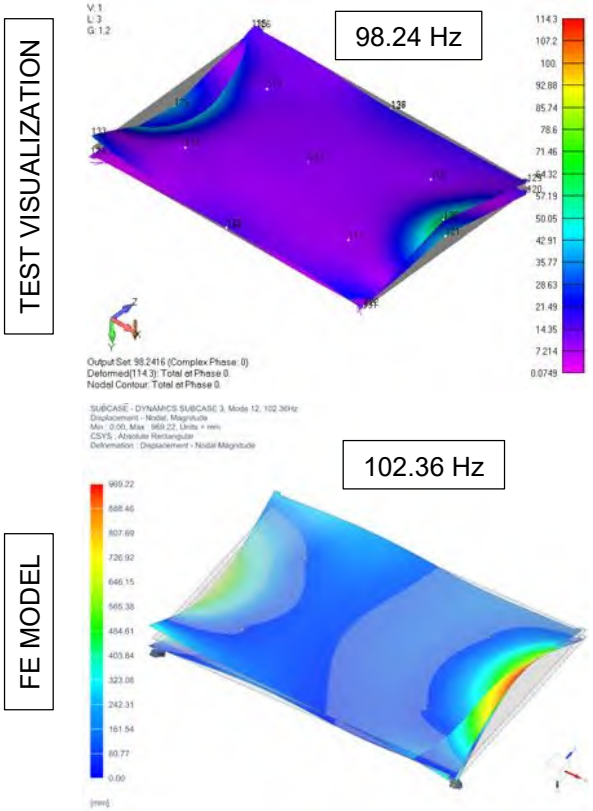


Figure 8: Example of mode shape comparison between FE model and Test visualization – First fundamental mode for Sine Sweep in X direction

To overcome this limitation and ensure complete confidence in the model's predictive capabilities, an advanced, custom mathematical visualization technique was developed. This method directly projected the discrete physical accelerometer frequency response functions (FRFs) captured during the test onto the model's analytical modal eigenvectors. By transforming the experimental response vectors into the analytical mode space, the team achieved a direct spatial comparison of the mode shapes despite the discrepancies in absolute resonant frequencies. As an example, Fig. 8 illustrates a side-by-side comparison of the first fundamental mode shape captured during the X-direction sine sweep, showing excellent correlation between the FE model's prediction and the test visualization. Notably, even when minor frequency shifts occurred, this spatial tracking technique allowed the primary modes to be confidently identified and tracked throughout the remainder of the testing campaign.

This spatial correlation approach definitely proved that the physical modes were structurally tracking the analytical ones. Armed with this rigorous spatial verification, the team was confident that the response limits set to protect the flight hardware were mathematically sound. This allowed the qualification campaign to safely proceed to the high-level sine sweep tests with full validation authority, bypassing the rigid frequency deviation constraint.

3.3. Post-Test Damping Characterization

Because structural damping in complex space mechanisms is inherently amplitude-dependent, a definitive evaluation of energy dissipation could not be established using only the low level 0.1g signature sweep. Instead, the real damping ratios were characterized via post-processing the transmissibility curves obtained directly from the high level qualification runs using the half-power bandwidth method.

Due to high modal density and closely spaced, coupled responses in certain accelerometer channels, clean isolated peaks were not universally present, preventing a global automated extraction. However, localized evaluations revealed significant amplitude–dependent energy dissipation near key deployment mechanisms – such as the hinges and synchronism cables – where local modal damping values reached up to 2.5% around 46 Hz (Fig. 9). In contrast, the clean sandwich panel structure consistently exhibited damping values around or below 1% (see Figs. 10 through 12).

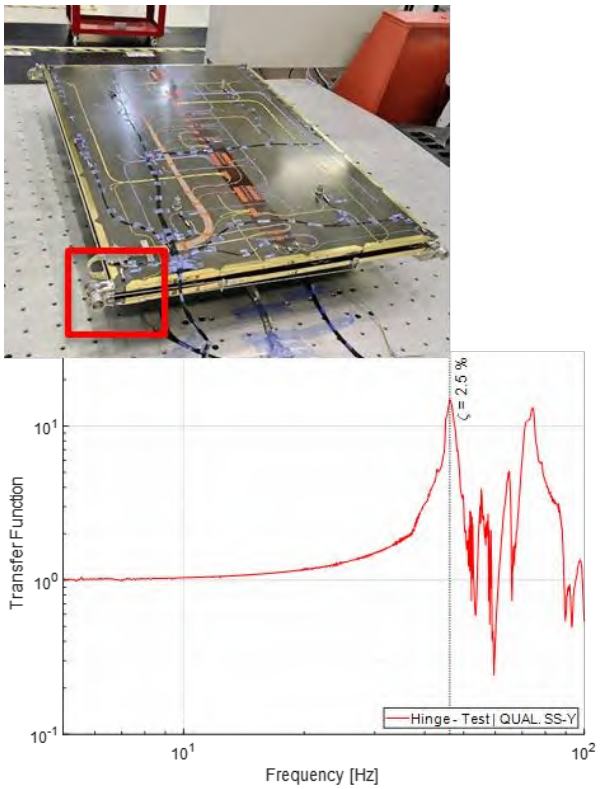


Figure 9: Local Damping @ Hinge | Sine Sweep Y-Direction Qual-level transmissibility

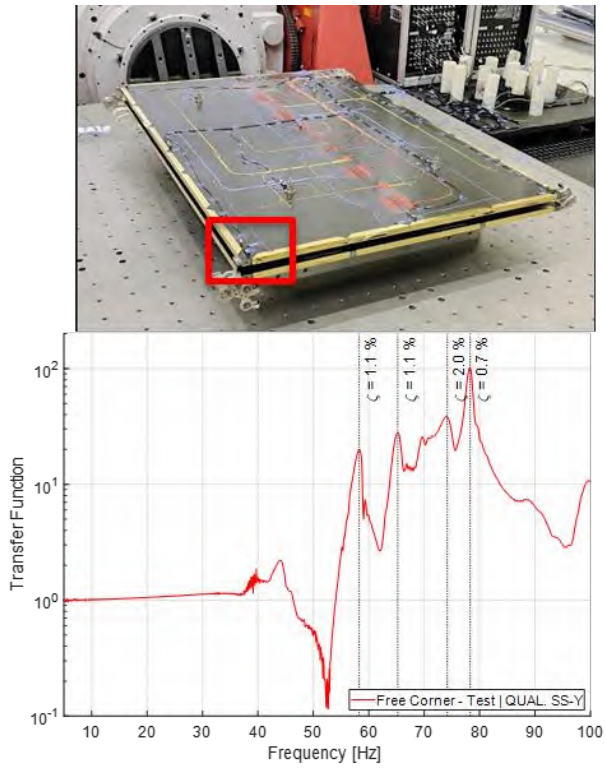


Figure 10: Local Damping @ Free Corner | Sine Sweep Y-Direction Qual-level transmissibility

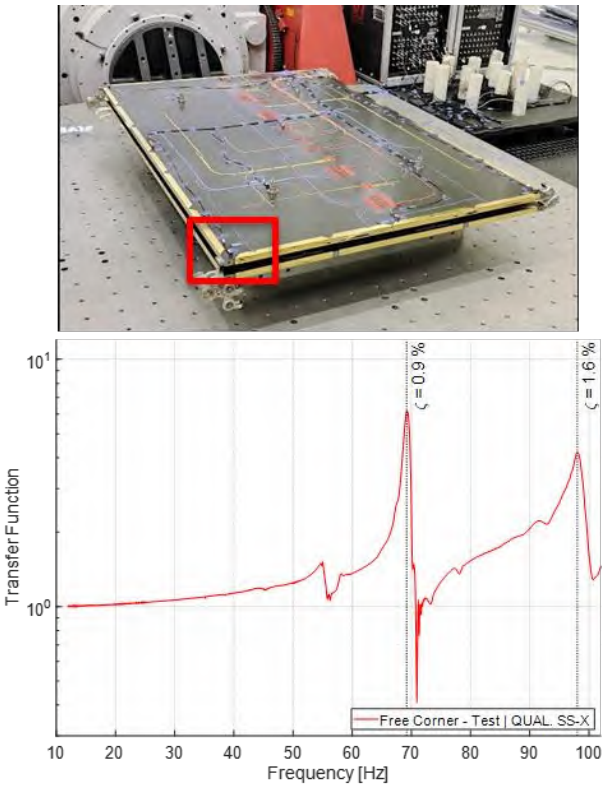


Figure 11: Local Damping @ Free Corner | Sine Sweep X-Direction Qual-level transmissibility

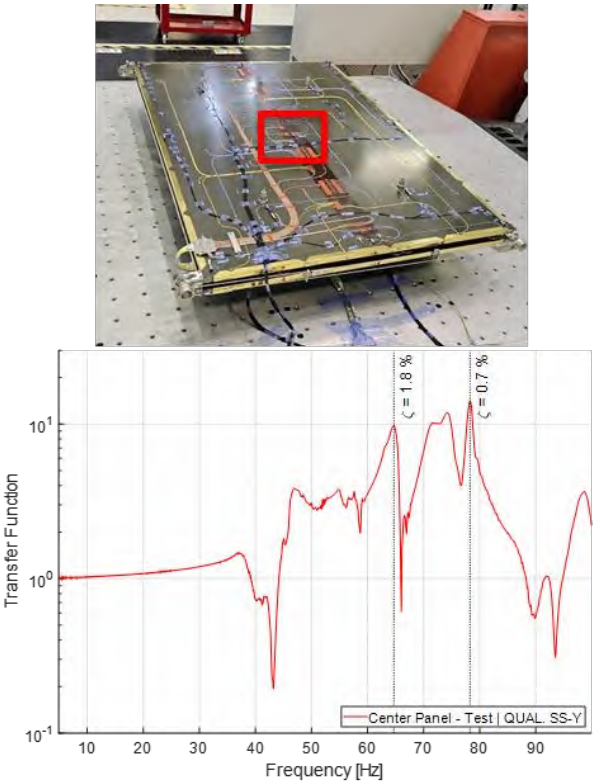


Figure 12: Local Damping @ Center Panel | Sine Sweep Y-Direction Qual-level transmissibility

A post-test cost-efficiency and safety analysis confirmed that implementing a spatially varying, non-uniform damping matrix was computationally expensive and unnecessary for global predictions. Retaining a uniform critical damping value of $\zeta = 1\%$ across the entire frequency spectrum was justified as a safe engineering approach, establishing a reliable, conservative upper bound for the responses at critical mechanism locations.

4. HIGH FREQUENCY QUALIFICATION: THE DFAT CAMPAIGN

4.1. Analytical Scope and Model Limitations

Prior to evaluating the experimental correlation, two fundamental modeling assumptions must be established regarding the scope and kinematic boundaries of the vibro-acoustic simulation.

First, a deliberate constraint was placed on the analytical bandwidth of the fully coupled FE model, capping the simulation spectrum strictly at 2000 Hz despite the physical DFAT campaign capturing telemetry up to 10000 Hz. This truncation is dictated by the fundamental physics of numerical discretization and modal density in deterministic methods. As the excitation frequency exceeds 2000 Hz, the acoustic wavelengths in air contract significantly, requiring an exponentially higher mesh refinement to prevent numerical dispersion errors.

Furthermore, in this high-frequency regime, the modal density of both the thin composite panels and the internal air cavities increases dramatically, making deterministic, phase-retaining predictions (like SOL 111) highly sensitive to microscopic manufacturing variations and physically non-representative. Truncating the numerical model at 2000 Hz captures the entirety of the macroscopic, high-energy global interactions while keeping computational solve times efficient.

Second, because the sandwich panels are mathematically idealized using 2D shell elements, the model lacks a physical thickness profile or cross-sectional surface area along its edges. Consequently, the solver's surface-to-surface projection algorithm cannot apply acoustic pressure forces in the in-plane directions (X and Z). In a pure acoustic simulation, this representation would typically result in a significant under-prediction of in-plane responses.

Thankfully, the low-frequency sine sweep campaign definitely demonstrated that the structural assembly's primary response axis is overwhelmingly dominated by the out-of-plane Y-direction, regardless of the input excitation axis. Because the physical cross-coupling drives almost all critical acoustic energy into out-of-plane panel bending, the 2D shell modeling limitation has a negligible impact on the global accuracy of the qualification predictions.

4.2. Acoustic Test Configuration

To evaluate the structural resistance of the stowed SA against the extreme broadband acoustic loads encountered during the launch phase, a Direct Field Acoustic Testing (DFAT) qualification campaign was performed. Unlike the horizontal slip-table configuration used in the low-frequency sine campaign, the SA was tested in its true vertical, flight-stowed orientation. The assembly was integrated onto the full, specialized MGSE – incorporating both the interface adapter plate and the primary reticulated frame structure – and positioned centrally within a high-power cylindrical loudspeaker array (see Fig. 13).



Figure 13: Vibro-Acoustic Test Setup

Fundamentally, a circular array of acoustic drivers generates a direct acoustic field. However, to closely simulate the diffuse, reverberant sound field characteristic of a launch vehicle fairing, the system was optimized to achieve maximum spatial diffusion and field uniformity around the specimen. The excitation spectrum covered a broadband frequency range running up to 10000 Hz, matching the launcher's most probable environment (MPE) specifications. The testing campaign followed a highly controlled, incremental acoustic loading sequence: beginning with a very low-level acoustic signature run, progressing to a low-level acoustic signature, followed by the flight level and culminating with the qualification level (0 dB). For both the flight and qualification runs, the scaling was applied progressively. This step-up sequence was vital to closely monitor and control microphone convergence – ensuring the closed loop controller established a stable, uniform target Power Spectral Density (PSD) spectrum before exposing the flight hardware to maximum acoustic power.

To monitor and regulate this environment in real time, a specialized control ring comprising 12 independent control microphones was deployed. These microphones were distributed on the ground at varying heights around the perimeter of the SA.

To mitigate localized near-field acoustic anomalies, boundary absorption errors, and speaker acoustic-center reflections, the positioning of the instrumentation strictly adhered to the standardized spatial clearance boundaries recommended in [4]. Specifically, the microphones were placed with a minimum clearance threshold of 0.6 m away from the responsive surfaces of the solar array, and no closer than 0.9 m from the face of the loudspeaker drivers. The drive signals to the acoustic drivers were dynamically regulated via a closed-loop controller utilizing the narrow-band average of this 12-microphone cluster.

4.3. Vibro-Acoustic Response Evaluation & Correlation Results

The predictive accuracy of the fully coupled fluid-structure FE model (SOL 111) was validated by comparing the analytical acceleration PSD responses directly against the experimental accelerometer telemetry. The spatial distribution of these physical accelerometers across the solar structure is illustrated in Fig. 14.

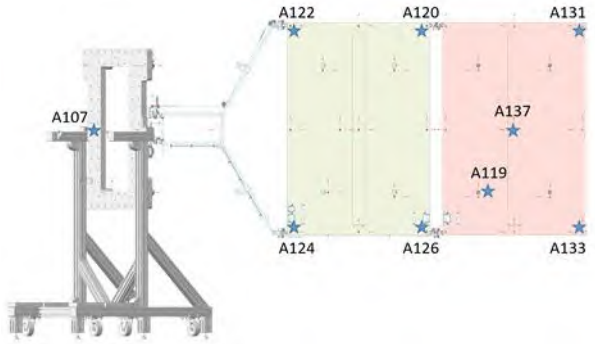


Figure 14: Spatial distribution of accelerometers

Table 3: Structural Acceleration g_{RMS} Correlation (FE model vs. Experimental Test)

Accel ID	Location	FEM	Test	% Error	Test - Capped	% Error - Capped
A107X	Adapter Plate	0,5603	0,7217	28,81%	0,5825	3,96%
A107Y		2,7289	3,8769	42,07%	3,6049	32,10%
A107Z		0,5169	1,5029	190,75%	1,3177	154,92%
A119X	RR Bolt - Outer Panel	3,9123	5,0468	29,00%	3,9739	1,57%
A119Y		5,7639	8,5473	48,29%	5,9514	3,25%
A119Z		3,2579	4,919	50,99%	3,7295	14,48%
A131X	Free Corner	7,752	10,3841	33,95%	9,7639	25,95%
A131Y		19,5326	19,7767	1,25%	19,511	0,11%
A131Z		8,5224	11,6849	37,11%	10,926	28,20%
A126X	Hinge (Sync. Cables)	8,7611	8,9782	2,48%	8,3712	4,45%
A126Y		22,8548	16,5679	27,51%	14,185	37,94%
A126Z		7,7082	10,0651	30,58%	7,9317	2,90%
A137X	Center Outer Panel	3,4215	6,3621	85,94%	5,4043	57,95%
A137Y		25,8886	33,3349	28,76%	32,293	24,74%
A137Z		3,7038	6,7951	83,46%	5,5678	50,33%
A122X	Hinge - Panel&Yoke	7,0207	7,1581	1,96%	6,7987	3,16%
A122Y		18,8102	19,2701	2,44%	19,155	1,84%
A122Z		8,7508	8,3747	4,30%	7,3438	16,08%
A124X	Hinge - Panel&Yoke (Sync. Cables)	6,9497	6,6784	3,90%	6,3817	8,17%
A124Y		19,4256	15,4833	20,29%	14,335	26,21%
A124Z		7,9518	7,6395	3,93%	7,3438	7,65%
A133X	Free Corner (Sync. Cables)	7,6067	10,9964	44,56%	10,568	38,93%
A133Y		21,05	16,9805	19,33%	15,924	24,35%
A133Z		8,357	10,1134	21,02%	9,4412	12,97%
A120X	Hinge	8,396	9,8585	17,42%	9,2587	10,28%
A120Y		20,3083	19,4906	4,03%	19,051	6,19%
A120Z		7,5379	10,8224	43,57%	9,5938	27,27%

The evaluation utilizes overall root-mean-square acceleration (g_{RMS}) values, assessing both the full physical test spectrum and the strictly capped analytical bandwidth (20-2000 Hz) across all three orthogonal directions. Tab. 3 outlines the complete correlation dataset. Notably, highlighting green indicates a highly successful structural correlation within standard engineering limits.

4.3.1. Direct Load Path & Out-of-Plane Validation

Analysis of the complete dataset strongly validates the mathematical foundations and boundary conditions established in the modeling phase. Specifically, the model exhibits high predictive capability along the primary structural load path of the assembly.

As shown in the layout in Fig. 14, accelerometer A119 is physically positioned on the outer sandwich facesheet in the immediate vicinity of a RR bolt, representing the direct load path from the satellite interface adapter plate into the SA's structural panels. In this highly critical region, once high-frequency noise is capped to the model's analytical limit, the correlation is exceptionally tight: 1.57% error in X and 3.25% error in Y. This provides strong empirical validation of the localized joint stiffness tuning detailed in Section 3.2.

Furthermore, the primary out-of-plane response (Y-axis) shows excellent global correlation in standard structural zones. The unconstrained free corner (A131Y) tracks with a near-perfect 0.11% capped error, while the structural panel-to-yoke hinge (A122Y) matches within 1.84%. These results demonstrate that the numerical formulation captures the global bending modes of the panels with high fidelity.

4.3.2. Physics-Based Analysis of Divergence Trends

Where the numerical and experimental results diverge, the variations can be attributed to three well-defined physical behaviors:

- **Z-Axis Cylindrical Boundary Variations**: The Z-axis corresponds to the vertical, axial axis of the cylindrical loudspeaker array. In a physical DFAT setup, the cylinder's open top and bottom boundaries naturally prevent the acoustic field from achieving perfect, uniform spatial diffusivity along the axial direction. This boundary leakage introduces real-world axial pressure variations that an idealized, perfectly diffuse-field model cannot reproduce, explaining the higher Z-axis correlation discrepancies (such as A107Z and A137Z), even though the absolute response magnitudes remain relatively low compared to the dominant bending axis.
- **In-Plane Shell Truncation**: Because the sandwich panels are modeled using 2D shell elements, the FE model lacks the true physical cross-sectional edge area required to capture in-plane (X and Z axis) shear and compression

wave pressures. However, because the structural assembly's response is overwhelmingly dominated by out-of-plane bending (with Y-axis acceleration magnitudes reaching up to 300% higher than the orthogonal in-plane axes), these in-plane deviations have no detrimental impact on the global structural verification.

- **Localized Cable Energy Dissipation**: The FE model systematically over-predicts out-of-plane (Y) responses in zones with synchronization cables (e.g., A124Y at 26.21% and A126Y at 37.94%). Under intense acoustic excitation, the synchronization cables act as localized, highly non-linear damping mechanisms through friction and cable-guide sliding. Because the simulation employs a globally uniform, conservative 1% damping ratio, it safely over-predicts these localized peak responses, maintaining a reliable safety envelope for the flight hardware.

4.3.3. Spectral Density Alignment and Modal Trends

While integrated g_{RMS} scalar values in Tab. 3 provide a useful macroscopic validation metric, evaluating spectral distribution across the frequency domain is vital to proving the model's physical fidelity. To this end, Figs. 15 and 16 compare the analytical and experimental acceleration PSD curves for two distinct structural zones representing the extreme bounds of the correlation envelope.

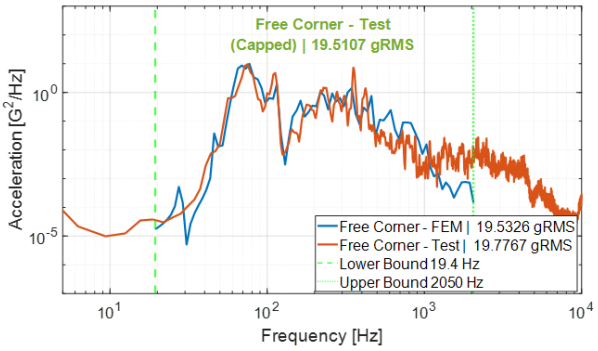


Figure 15: Acceleration PSD comparison at the Free Corner – A131Y

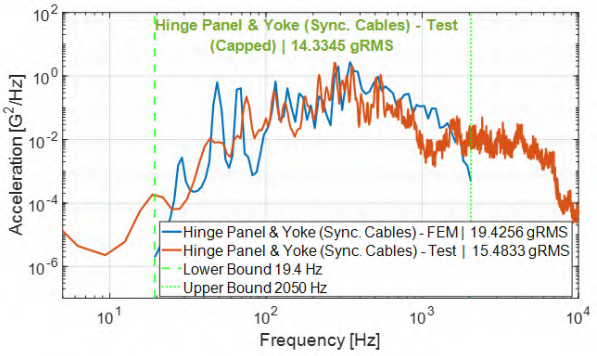


Figure 16: Acceleration PSD comparison at the Hinge with Sync. Cables – A124Y

Fig. 15 illustrates the out-of-plane (Y-direction) response at the unconstrained free corner (A131Y). The spectral alignment is exceptionally tight, with the primary global structural mode near 75 Hz matching perfectly in both frequency and peak amplitude. Throughout the mid-frequency band up to the 2000 Hz analytical threshold, the FE model faithfully tracks the physical modal density, validating the distribution mass and stiffness. The plot also visually justifies the high-frequency capping strategy: beyond the vertical green boundary marker (2050 Hz), the physical hardware's response is dominated by high-frequency, low-energy residual modes that do not significantly contribute to the global g_{RMS} area.

Fig. 16 displays the PSD comparison at the panel-to-yoke hinge near the synchronization cables (A124Y). Despite the 26.21% numerical over-prediction in total g_{RMS}, the structural tendencies of the curves are remarkably similar. The FE model accurately captures the distribution of resonances and anti-resonances across the entire three-decade logarithmic scale. However, the visual comparison reveals that the analytical resonant peaks (blue curve) are systematically narrower and taller than the corresponding experimental peaks (orange curve). This behaviour provides direct, visual proof of the local damping mismatch theorized in Section 4.3.2. Because the global model utilizes a conservative 1% damping ratio, it under-predicts the localized dissipative effects of the synchronization cables, resulting in higher simulated peaks while still preserving the correct physical modal behaviour of the assembly.

5. CONCLUSIONS AND FUTURE WORK

5.1. Summary of Achievements

This paper presented a comprehensive, sequentially validated structural and vibro-acoustic qualification framework for a flight stowed solar array assembly. By bridging the gap between deterministic FE analysis and experimental boundary realities, the study demonstrated a highly reliable methodology for protecting flight hardware under severe launcher environments.

The primary contributions drawn from this engineering campaign include:

- **Advanced Spatial Correlation**: The development of a custom visualization technique – which directly projected experimental frequency response functions onto analytical modal eigenvectors – successfully bypassed the rigid limitations of traditional absolute frequency deviation metrics. This spatial mapping proved that physical mode shapes closely tracked the analytical predictions, providing the mathematical justification needed to safely execute high-level sweeps with total confidence in the hardware's safety margins.
- **Effective Data-Driven Assumptions**: Post-

test characterization using the half-power bandwidth method on high-level transmissibilities isolated localized, amplitude-dependent mechanism damping reaching up to 2.5% near the hinges and synchronism cables. Applying a conservative, uniform 1% critical damping value across the global model proved to be a highly efficient, computationally cost-effective engineering approach, yielding excellent predictive accuracy while maintaining safe, conservative upper-bound envelopes in highly damped mechanism zones.

- **High-Fidelity Multi-Axis Validation**: The fully coupled fluid-structure model utilizing a non-conformal fluid mesh achieved exceptional alignment with physical Direct Field Acoustic Testing (DFAT) telemetry across multiple monitoring zones. Within the modeled 20-2000 Hz bandwidth, the primary out-of-plane response (Y-axis) at the free corner of the panel correlated with a near-perfect 0.11% error. Furthermore, the model exhibited high predictive capability along the direct structural load path near the RR interfaces, capturing the experimental response within 1.57% in the X-axis and 3.25% in the Y-axis.
- **Characterization of Boundary and Kinematic Mismatches**: Expanding the dataset to all three orthogonal axes successfully isolated and justified localized modeling discrepancies. The higher errors observed along the in-plane axes (X and Z) were physically matched to the 2D shell element modeling assumptions, while the localized over-predictions near the hinges (up to 37.94%) were directly mapped to energy dissipation from the physical synchronization cables. Additionally, the Z-axis correlation trends highlighted the real-world pressure variations introduced by the open boundaries of the cylindrical loudspeaker array, which are omitted by idealized diffuse-field assumptions.

5.2. Future Work

While the deterministic FE approach proved highly accurate for the low-to-mid frequency regimes, extensions of this work will focus on addressing the high-frequency boundaries beyond 2000 Hz. Future research will explore the integration of Statistical Energy Analysis (SEA) or hybrid FE-SEA methods to capture the high-density, localized acoustic response spectrum up to 10000 Hz without inducing expensive computational costs. Additionally, further investigations will be directed toward explicitly modeling non-conformal, amplitude dependent mechanism damping and localized non-linear boundary conditions directly within the frequency domain to adaptively update joint properties as acoustic loading levels increase.

6. REFERENCES

1. Larkin, P., & Goldstein, B. (2008). Direct Field Acoustic Testing. *In 25th space simulation conference*.
2. Hargreaves, J. A. (2022b). Analysis and Control of Acoustic Modes in Cylindrical Cavities with application to Direct Field Acoustic Noise (DFAN) Testing. *Proceedings of the International Congress on Acoustics (ICA)*.
3. Hargreaves, J.A. (2022a). Literature Review of Direct Field Acoustic Noise (DFAN) Testing. *Acoustics Research Centre, University of Salford, UK*.
4. NASA-HDBK-7010. Acoustic Space Payload Identification and Response Estimation (ASPIRE). National Aeronautics and Space Administration.
5. NASA-STD-7001B. Payload Vibroacoustic Test Standard. National Aeronautics and Space Administration.
6. Underwood, M. A. (2019). New Method to Determine Optimized Reference SDM for MIMO Random or Acoustic Testing, *in: Proc. 90th Shock Vib. Symp, Atlanta, 2019*.
7. ECSS-E-ST-32-11C. Modal Survey Assessment. European Cooperation for Space Standarization, 2008.

VIRTUAL SHAKER TESTING FOR TEST DE-RISKING: NOTCH PREDICTIONS ON A FULL-SCALE SPACECRAFT SETUP

Umberto Musella [(1)], Mattia Dal Borgo [(1)], Roland Pastorino [(1)], Silvia Vettori [(1)], Emilio Di Lorenzo [(1)], Bart Peeters [(1)], Vincenzo Di Pietro[(2)], Gawra Franceschini[(2)], Piersante Micciché[(2)]

[(1)] Siemens Digital Industries Software N.V., Interleuvenlaan 68, 3001 Leuven, Belgium, emails: umberto.musella@siemens.com, mattia.dal_borgo@siemens.com, roland.pastorino@siemens.com, emilio.dilorenzo@siemens.com, silvia.vettori@siemens.com, bart.peeters@siemens.com

[(2)] Thales Alenia Space Italia SPA, via Tiburtina 1210, 00131 Rome, Italy. Email: vincenzo.dipietro@thalesaleniaspace.com, gawra.franceschini@thalesaleniaspace.com, piersante.micciche@thalesaleniaspace.com

KEYWORDS

Spacecraft Testing, Vibration Control, Environmental Testing, Virtual Shaker Testing.

ABSTRACT

Vibration control tests are used to verify that a spacecraft and its sub-systems can withstand the specified launch vibration environment. Because these campaigns are executed under severe schedule constraints and involve high-value hardware, early, reliable and risk-free predictions of test responses are essential. A Digital Twin of the complete test set-up (spacecraft, shaker, and controller) can be used to replicate the physical campaign in a virtual environment for test de-risking. This approach - known in the dynamic environmental testing community as Virtual Shaker Testing (VST) - is particularly important when transient phenomena should be captured. One typical example is a sine control of a full spacecraft, where accurate simulation of primary and secondary notch behavior can support both notch definition and the optimal tuning of the controller parameters.

This paper proposes a new VST workflow that completely changes the traditional paradigm of Virtual Shaker Testing. Rather than building a simulation of the test, we propose a workflow that allows to test a simulation.

Test engineers first identify an onsite, executable Digital Twin (xDT) of the excited system and then use this stable model to generate high-fidelity VST predictions. The methodology is demonstrated on a full-scale industrial case study, where the proposed framework accurately predicts notch levels during a sine test of a spacecraft-representative mass model.

Finally, preliminary results indicates that the approach can be coupled with Frequency Based Substructuring to predict key test outcomes much earlier in the spacecraft development cycle.

1. INTRODUCTION AND OBJECTIVES

Environmental testing in spacecraft (S/C) engineering is critical to demonstrate and verify the global integrity of the designed structure, to screen the flight hardware for workmanship errors, and to validate mathematical models. In particular, vibration control (VibCo) testing is a mandatory part in the S/C development process to qualify the mechanical designed structure for launch as defined in several handbooks and standards by the National Aeronautics Space Agency (NASA) [1] and European Space Agency (ESA) [2].

During VibCo tests, dynamic coupling between the test specimen, the vibration testing facility, and the vibration controller can critically affect test outcomes [3,4], particularly in the presence of transient phenomena. The shaker (including amplifier), the Device Under Test (DUT), and any additional equipment such as fixtures and force measurement devices (FMDs) cannot be treated as independent systems; instead, the coupled dynamic ensemble must be accurately represented. To better assess control deviations and beating effects at structural resonances [5-8], Virtual Shaker Testing (VST) approaches have been developed to numerically simulate the entire closed-loop test environment [8-10].

Previous VST implementations have relied on detailed finite element models [7-8] or experimental data-driven approaches [9-12]. However, these often require deep simulation and testing expertise, which can generate challenges in translating information from one domain to the other. Moreover, they also require extensive data sharing among manufacturers, which can pose confidentiality challenges and impede industrial application. Despite its clear advantages, the widespread implementation of VST is often hindered by high computational costs and the lack of transparent, accessible mathematical models shared between spacecraft manufacturers and testing facilities.

2. REAL-TIME VIRTUAL SHAKER TESTING

To address these challenges and bridge the gap between test engineers and simulation specialists, this work presents a real-time VST framework where the physical twin (amplifier + shaker + DUT) is replaced by an executable digital twin (xDT) [13-

14], as illustrated in Figure 1.

There are three main actors in a real-time VST setup:

1. A vibration controller (e.g. Siemens Simcenter SCADAS and Testlab) for spacecraft qualification testing. This shall be the same system used during the physical shaker tests.
2. A real-time platform (e.g. Simcenter Testlab RT) connected to analogue input-output (I/O) modules via EtherCAT, where the virtual replica of the system can run in real-time.
3. A discrete state-space model of the coupled shaker-DUT system, exported as a Functional Mock-up Unit (FMU), capable of running in real-time with the required numerical stability.

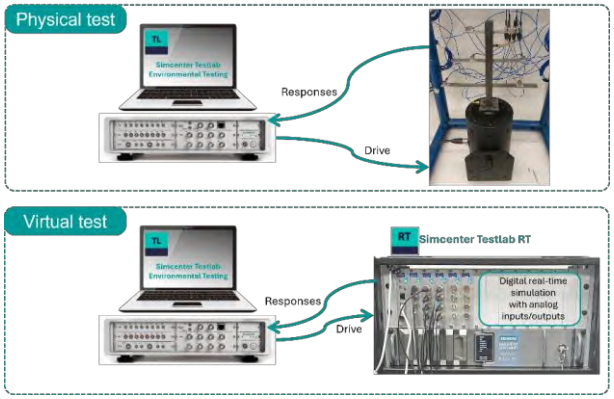


Figure 1 - Physical shaker test and real time Virtual Shaker Test

In the proposed approach, the vibration controller interfaces with the digital twin running on a real-time platform instead of the physical shaker facility and sensors. The output signal from the controller, which would normally drive the shaker amplifier, is then connected to the analogue input of the real-time platform. Similarly, the simulated sensor responses are fed back from the analogue output to the SCADAS input channels, in the same way a physical sensor is connected during the physical test. This approach enables the controller to drive a virtual replica of the test in real-time, accurately predicting transient responses and enabling optimization of control parameters.

There are two primary use-cases for the VST:

1. *Onsite derisking:* using stable experimental data driven model derived from System Identification to tune the controller settings and predict notches, including potential overshoots. This use-case requires the physical system in its final test configuration.
2. *Offsite derisking and test-informed design*: using hybrid or fully virtual multi-physics models to address test performances of a system early in the development cycle. The goal is still to allow test-engineers to run their vibration controller as they would do with the physical system.

This approach has been introduced and validated by Siemens and Thales Alenia Space Italy (TAS-I). Preliminary results were presented in previous works on small scale models the onsite derisking use-case, e.g. [15] and [16].

The idea of this paper is to demonstrate that the real-time VST can be used to predict sine control test results with a full-scale system. The data for the validation were provided by TAS-I.

3. REAL TIME VIRTUAL SHAKER TESTING PREDICTION FOR ONSITE DERISKING

The main goal of this work is to predict control, notch and measure responses of a sine control run performed on the LDS V994 shaker of TAS-I (Rome Tiburtina).

The different steps for the real time VST are reported in Figure 2 for the onsite derisking use-case.

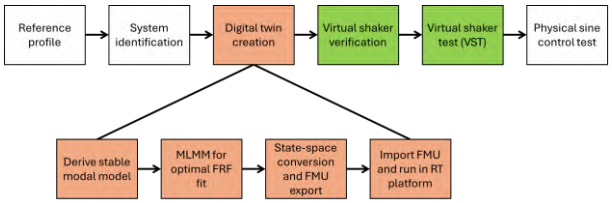


Figure 2 - Schematic of a sine control test workflow including the VST steps in orange and green.

TAS-I provided several runs performed for the characterization and the acceptance of their facility in longitudinal test configuration with a slip table. The runs and the System Identification data are here adopted to validate the onsite derisking use-case for the real-time VST.

In this exercise, the physical sine control tests were performed before the real-time VST predictions. This of course does not hinder the validation of the approach since the sine control settings could also be loaded to define the VST setup from the physical setup.

3.1. Physical Test setup

The physical test setup is shown in Figure 3. Figure 4 (top view) provides a visual representation of the location of the 4 pilots (P1, P2, P3 and P4). The excitation axis is the longitudinal axis X.



Figure 3 – LDS V994 shaker at Thales Alenia Space in Rome (via Tiburtina) and test setup adopted for the validation.

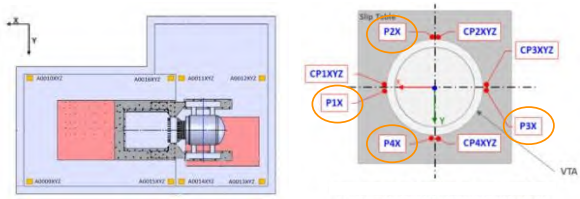


Figure 4 – Top view of the test setup. Slip table instrumented with 4 pilots (circled in orange).

The Device Under Test (DUT) is shown in Figure 3 and illustrated in Figure 5. It is an assembly of a conical structure and a cylindrical mass designed to replicate the mass and the modal properties of Sentinel-type spacecrafts.
The total mass of the device is 2390 Kg and its CoG is located at approximately 1.615 m from its base. The structure is axial-symmetric and attached to the shaker via a payload adapter.

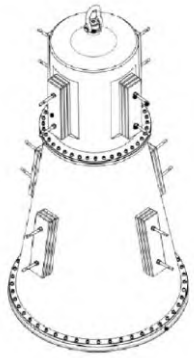


Figure 5 - Conical structure and a cylindrical mass designed to replicate the mass and the modal properties of Sentinel type spacecrafts.

The DUT was also instrumented with different accelerometers. The 4 locations illustrated in Figure 6 were identified as of interest by the experts of TAS-I. The sensors A10, A11 and A12 were connected on the cone in proximity of the attachment flanges. The sensor A14 is located on top of the cylindrical mass.

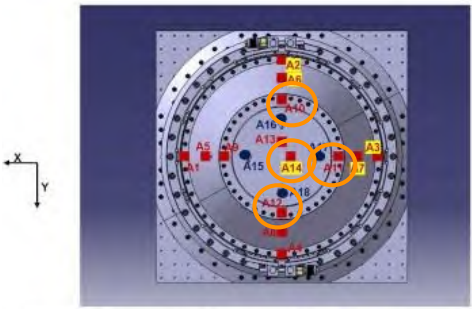


Figure 6 – instrumentation of the DUT (the sensors used for the validation are circled in orange).

As mentioned, different tests were recorded during the characterization, and the acceptance of the facility. Some of these runs were also replicated virtually. We will focus on a complete case of a longitudinal run with an activated notch to show the capability of the VST to also predict notch overshoots. The Sine Control setup for this run is illustrated in Figure 7. The main settings are also reported here below for completeness

- Sweep Mode: logarithmic
- Sweep Rate: 4 Oct/min
- Compression Factor = 4
- Control estimator: harmonic
- Control strategy: maximum

A flat 1.8 g notch profile was applied to the response channel A14:+X. The definition of the limit followed the application of an acceleration method that translates the interfaces force and moment to accelerations of the DUT. The notch profile is reported in Figure 8.

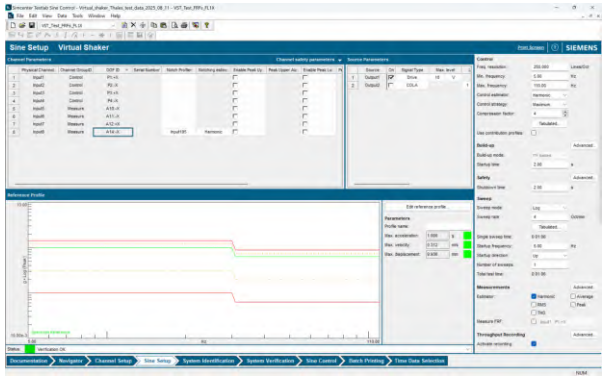


Figure 7 – Sine control setup

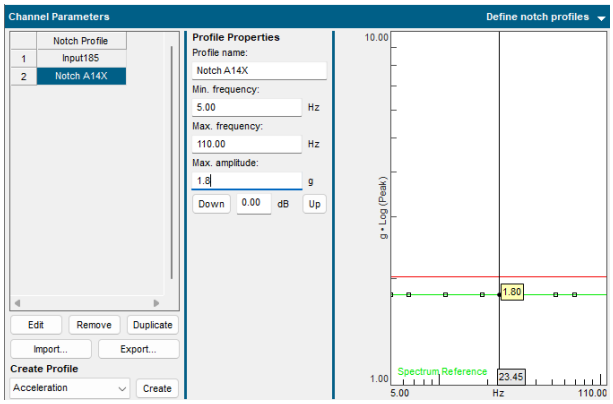


Figure 8 - Notch Profile applied on A14:+X

3.2. Virtual Shaker Test setup

Figure 9 shows the real-time VST system at the TAS-I facility in Rome Tiburtina.

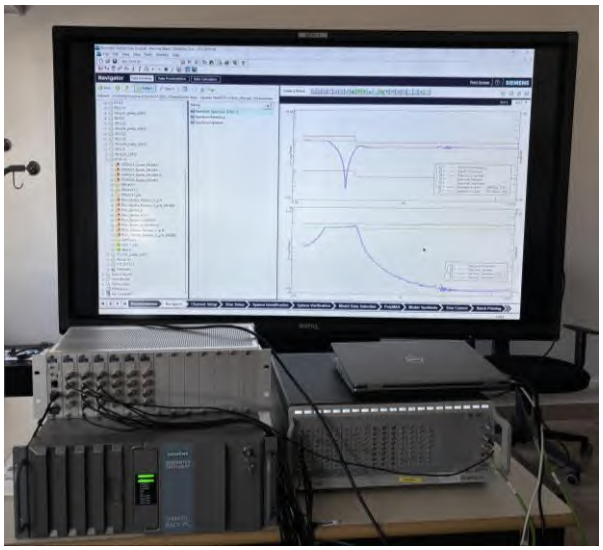


Figure 9 - Virtual Shaker Test setup in Thales Alenia Space Italy (Rome, via Tiburtina).

In this configuration, the vibration controller (Simcenter SCADAS and Testlab) is connected to the analog inputs and outputs slave devices that are connected via EtherCAT to the Simcenter Testlab RT Simatic IPC master device. Simcenter Testlab RT will execute a real time model derived from the physical test setup. When starting a test from Simcenter Testlab, the inputs and outputs of this model will be the drive voltage and the responses coming-from/going-to the Simcenter SCADAS.

3.3. Derivation of the executable digital twin

The main difference between the onsite and the offsite derisking use-cases is the origin of the model that is executed in real-time.

For the onsite derisking use-case, System FRFs obtained from a low-level System Identification runs (SI) can be used to derive the executable digital twin of the entire system under test as a state space model.

The algorithm developed in [9] and [10] can be used to derive a stable model directly from the System FRFs measured during System Identification.

- The Polymax algorithm is executed on the System FRF to synthetize a modal model. This step guarantees a stable system.
- The modal model obtained by Polymax is then modified into a maximum likelihood modal model (MLMM) [17]. This step is critical, because it optimizes the match between the System FRFs and the FRFs synthetized from the modal model and preserves its stability.
- The synthesized optimal stable model can then be converted to a discrete-time state-space model with a specified sampling frequency.

Figure 10 shows the results of applying this approach to the recorded SI data.

The results of the modal synthesis (green) and the derived state-space model (in blue) are shown in Figure 10 for the pilots, but comparable results can be obtained for the measure.

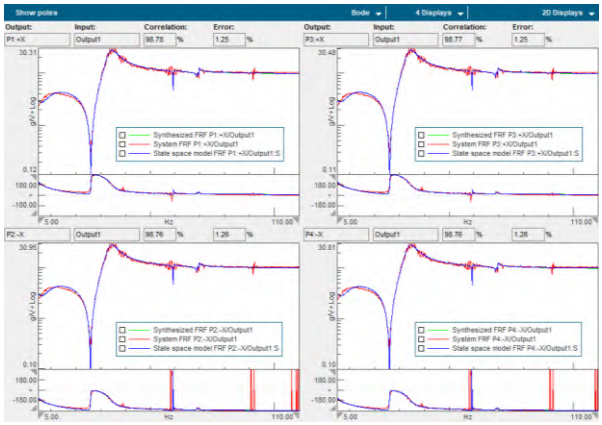


Figure 10 – State Space model (in blue) obtained from synthetized FRFs (green) fitting a stable modal model. In red measured FRF.

The state space model can then be exported as an fmu, uploaded in Simcenter Testlab RT (Figure 11) and executed in real time in the Siemens Simatic

IPC.

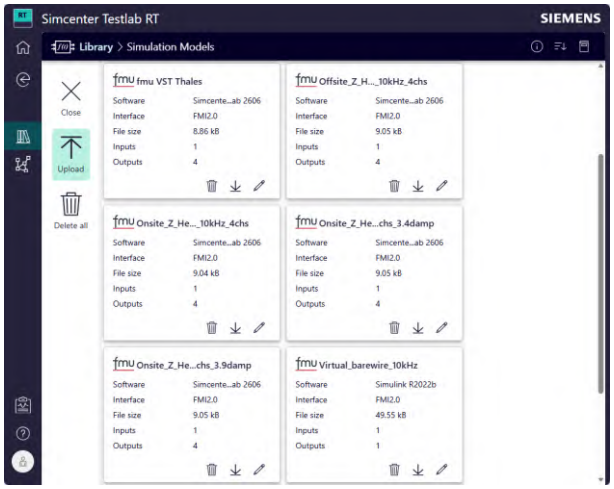


Figure 11 – the state space model can be uploaded and executed in real time in Simcenter Testlab RT

The setup can now be used to run tests virtually, optimize control settings and evaluate the effects on the test results, without exciting the spacecraft and adopting the same control hardware and software that are used during the physical tests.

3.4. Test Results

To validate the workflow, the settings of the virtual test described were loaded directly from the physical Sine Control run (see section 2.1). It is worth remembering that this is the inverse of what would be done during real test preparation, because the physical runs were chronologically executed earlier.

As a verification step of the VST setup, it is preferable to run a system identification on the virtual system. This is done to check that the test engineer has correctly defined the real-time settings, uploaded the right model and/or correctly mapped the sensors in the channel setup of the virtual test. These checks can be done by comparing the virtual System FRF from SI to the physical one. Figures 12 and 13 show the comparison between the System Identification results of the physical (magenta) and the virtual (blue) test. The figures show that the System FRF are matching accurately over the entire frequency range for the pilot and the measure channels.

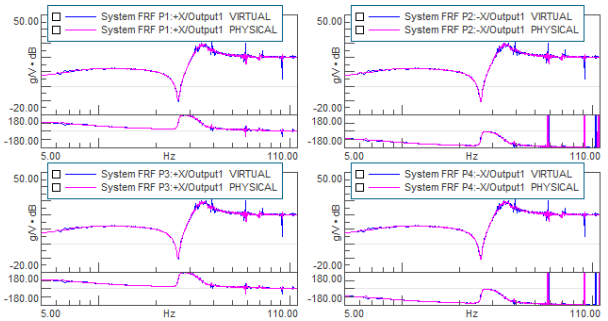


Figure 12 – Pilots system FRFs. Comparison between the SI on the physical (magenta) and virtual (blue) model.

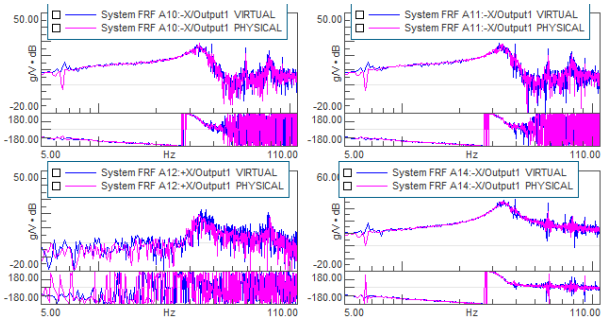


Figure 13 - Measure channels system FRFs. Comparison between the SI on the physical (magenta) and virtual (blue) model.

The comparison of the virtual (blue curves) versus the physical (magenta curves) sine control tests are finally shown in Figure 14, 15, 16 and 17. The results show that the VST can accurately predict the behavior of the physical test within the entire frequency range of interest. Transient phenomena that are characteristic of sine control runs, and that also depend on the control settings, are also well captured by the VST. Figure 17 shows for example how the proposed approach can capture notch overshoots. If needed, this overshoot could be mitigated with a local modification of the compression factor or ultimately a local negotiation on the sweep rate. Experimenting such changes would traditionally require at least a low-level sine test. The spacecraft will be subjected to the sine excitation, and the operators will be left with the uncertainty of what will happen at full level when sweeping through a local or global resonance and triggering a notch. The proposed VST approach provides the extra possibility of experimenting on a simulation model considering the transient nature of the test and the sensitivity to the control parameters.

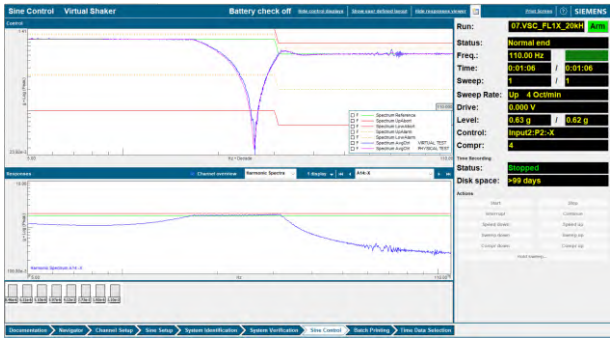


Figure 14 – VST online results. Physical Average control harmonic spectrum overlayed in the control display in magenta.

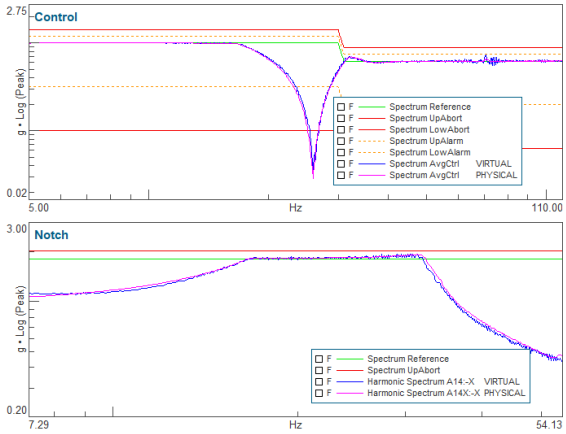


Figure 15 – Top: Average control harmonic spectrum. Bottom: harmonic spectrum of the notch channel A14:+X. VST results in blue, physical test results in magenta.

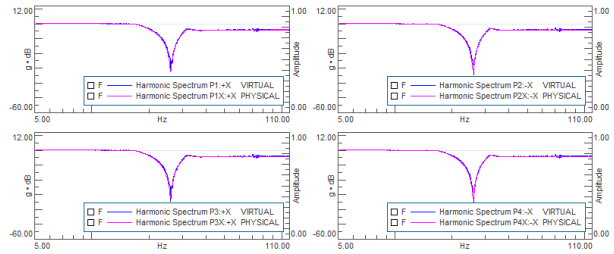


Figure 16 - Harmonic spectra of the individual pilots. VST results in blue, physical test results in magenta.

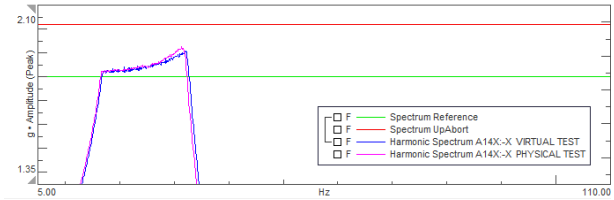


Figure 17 – Detail of a notch response overshoot (channel A14:+X).

4. HYBRID COUPLING FOR THE OFFSITE DE-RISKING USE-CASE

The present work focuses on a validation of the onsite derisking use-case. Validation of the off-site de-risking with the described full-scale setup is unfortunately still ongoing at the time of this publication.

Also in this case, the approach that is being developed tries to take a significant step forward compared with traditional methods. The idea is to perform off-site derisking adopting the real-time VST in combination with hybrid models, as shown in Figure 18**Error! Reference source not found.**.

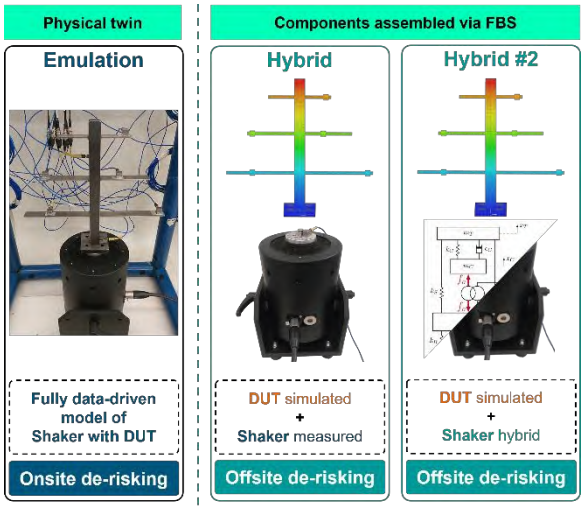


Figure 18 - Build a digital twin starting from a physical twin or a hybrid assembly of components.

Instead of requiring the physical assembly for system identification, the method developed combines:

- Experimental characterization of the shaker facility using multi-axis FRF measurements and Virtual Point Transformation (VPT) to extract complete 6-DoF dynamics.
- Numerical models of the head expander and DUT from Finite Element Analysis (FEA).
- Frequency-Based Substructuring (FBS) to couple these models in the frequency domain [18].

This approach offers several critical advantages:

- early-stage test predictions: virtual tests can be performed before the physical DUT is available, enabling test-informed design decisions during the spacecraft development process.
- Intellectual property preservation: only interface FRFs need to be shared between manufacturers and test facilities, not complete FE models, addressing confidentiality concerns.
- Ease of use and accessibility: the FBS-based workflow enables rapid assembly of FRFs from various sources without requiring deep expertise in both simulation and testing domains.
- Multi-DoF accuracy: the systematic application of VPT captures 6-DoF dynamics including rocking modes, essential for off-

centered or asymmetric spacecraft configurations that are common in practice.

The proposed method and the results on the small-scale setup shown in Figure 18 were recently published in [19] and are hereby reported for completeness.

The virtual tests for offsite derisking were performed on a hybrid system: experimentally measured shaker (force rating: 300 N) coupled with an FE model of a head expander and a DUT (a resonating structure with high COG).

Figure 19 presents the comparison of three scenarios for a centered DUT mounting.

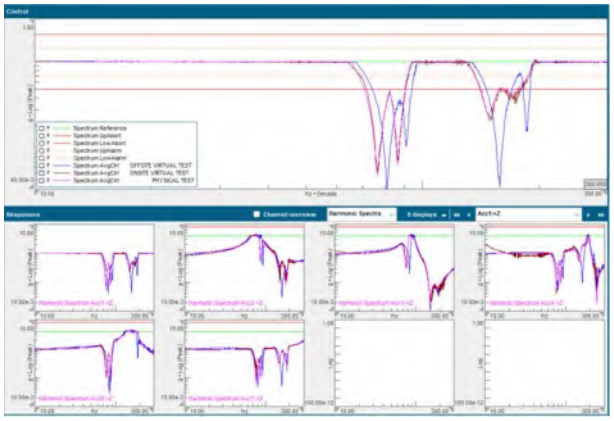


Figure 19 - Comparison of the Average control harmonic spectrum (top) and of notch channels (bottom). Offsite derisking (blue), onsite derisking (brown), and physical test (magenta).

The blue curve represents the harmonic spectrum of the control accelerometer (and the notching channels in the lower part of the picture) during the offsite de-risking virtual shaker test, performed with the hybrid coupled system. The brown curve, instead, shows the response of the virtual shaker test during the onsite derisking, hence using a fully experimental system identification of the physical twin to derive the FMU. The physical test is shown with the magenta curve, which confirms an excellent agreement when compared with the VST. The minor discrepancies are observed mainly for the offsite de-risking virtual test. Those can be attributed to the assumptions and approximations made in the FEM modelling of the DUT. As an example, the modal damping has been set to 1.5% for all modes, which is clearly not the case as the notch visible in Figure 19 shows that a higher damping is present. It is important to highlight that this exercise has been done without model updating of the FEM of the DUT in order to preserve the same scenario that test engineers will be confronted with in case of off-site de-risking, i.e. prediction potentially performed before the DUT is even built.

Figure 20 compares the harmonic spectrum of the control accelerometer for the virtual and the physical tests with an off-centered DUT configuration.

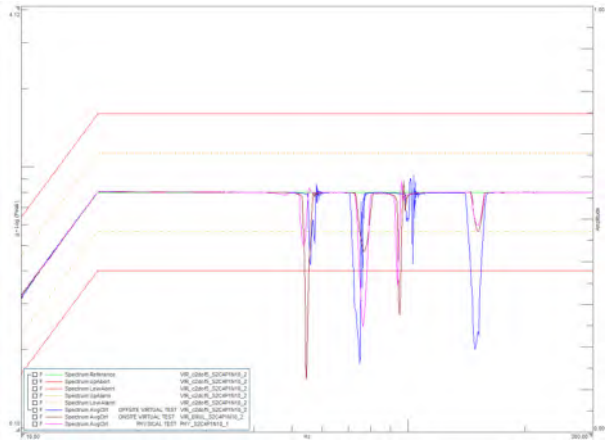


Figure 20 - Comparison of harmonic spectrum of control accelerometer. Offsite derisking (blue), onsite derisking (brown), and physical test (magenta) for the 3 scenarios with the off-centred DUT.

The blue curve represents the offsite VST, the brown curve shows the onsite VST and lastly the magenta curve reports the result of the physical test. This represents a more challenging test case where significant rocking modes are excited, and the cross-axis coupling is pronounced. The results demonstrate that the hybrid FBS approach successfully predicts the primary features of the dynamic behavior of the system even though some notches have significant discrepancy in terms of amplitude with respect to the onsite virtual shaker test and the physical test. Nevertheless, this approach allows to investigate such a complex scenario in advance of the physical test execution and can then be fine-tuned by running an onsite virtual shaker test prior to the physical test.

5. CONCLUSIONS

This work demonstrates on a full-scale system the application of a new real-time Virtual Shaker Testing workflow for onsite derisking. The physical system is replaced by an executable digital twin driven by the same vibration control hardware and software used during the physical test campaign. For the onsite de-risking case, a stable state-space model is derived from low-level System Identification FRFs.
Virtual sine-control runs accurately matched the physical tests in the control bandwidth in terms of average control, response at the individual pilots and notch behavior, including transient overshoots.

These results confirm that the proposed workflow can support test engineers in tuning the vibration controller and assessment the response at the notch channels before exposing a spacecraft to a sine excitation, particularly at full level.

Preliminary offsite de-risking results obtained on a small-scale system and based on hybrid coupling and Frequency Based Substructuring (FBS) indicate that early test predictions (before the complete physical system is available) are possible and can be accurate, considering the limited fidelity of early models. The proposed methodology for off-site derisking presents also several practical advantages derived from the fact that it combines via FBS an experimental characterization of the shaker facility using multi-axis FRF measurements and numerical models of the head expander and the DUT.

6. FUTURE WORK

It is the intention of the authors to apply the methodology described in [19] and section 4 to the full-scale setup described in section 3.

7. ACKNOWLEDGMENT

The authors would like to acknowledge the Agenzia Spaziale Italiana (ASI) for supporting this project as part of the Space Smart Factory initiative.

8. REFERENCES

1. NASA (2014). *Spacecraft Dynamic Environments Testing*. NASA-HDBK-7008, Office of the NASA Chief Engineer, NASA Technical Standards Program, National Aeronautics and Space Administration.
2. ECSS, *Space Engineering, Spacecraft Mechanical Loads Analysis Handbook*, ECSS-E-HB-32-26A, //ecss.nl/hbs/published-hbs-on-line/active-engineering-handbooks/, European Cooperation for Space Standardization (February 2013), Noordwijk, The Netherlands.
3. Appolloni, M. & Cozzani, A. (2007). Virtual testing simulation tool for the new quad head expander electrodynamic shaker. In *Proceedings of the 6th International Symposium on Environmental Testing for Space Programmes*, ESA-ESTEC, Noordwijk, The Netherlands.
4. Appolloni, M., Dacal, R. B., Cozzani, A., Knockaert, R. & Thoen, B. (2015). Multi-degree-of-freedom vibration platform with MIMO controller for future spacecraft testing: an application case for virtual shaker testing. In *Proceedings of the 29th Aerospace Testing Seminar*, Los Angeles, USA.
5. Bettacchioli, A. (2014). Simulation of satellite vibration test. In *Proceedings of the 13th European Conference on Spacecraft Structure, Materials and Environmental Testing*, Brunswick, Germany.
6. Bettacchioli, A. & Nali, P. (2015). Common issues in S/C sine vibration testing and a methodology to predict the sine test responses from very low-level run. In *Proceedings of the 29th Aerospace Testing Seminar*, Los Angeles, USA.
7. Nali, P. & Bettacchioli, A. (2014). Beating phenomena in spacecraft sine tests and an attempt to include the sine sweep rate effect in the test-prediction. In *Proceedings of the 13th European Conference on Spacecraft Structure, Materials and Environmental Testing*, Brunswick, Germany.
8. Nali, P., Augello, G., Bettacchioli, A., Landi, G. & Gnoffo, M. (2016). A virtual shaker testing experience: modeling, computational methodology and preliminary results. In *Proceedings of* the 14th European Conference on Spacecraft Structures, Materials and Environmental Testing, Toulouse, France.
9. Waimer, S., Manzato, S., Peeters, B., Carrella, A., Wagner, M. & Guillaume, P. (2018). Virtual Shaker Testing approach based on experimental data. In *Proceedings of the 31st Aerospace Testing Seminar*, Los Angeles, USA.
10. Waimer, S. (2018). *Advanced Environmental Dynamic Testing for Space Applications using Virtual and Physical Laboratories*. PhD thesis, Vrije Universiteit Brussel, Brussels, Belgium.
11. Remedia, M., Aglietti, G. S. & Kiley, A. (2015). Vibration testing: post-test correlation approach based on virtual testing. *In Proceedings of the 29th Aerospace Testing Seminar*, Los Angeles, USA.
12. Remedia, M., Aglietti, G. S., Appolloni, M., Cozzani, A. & Kiley, A. (2017). An enhanced methodology for spacecraft correlation activity using virtual testing tools. *Journal of Sound and Vibration*, 409, 180–200.
13. dos Santos, F. L. M., Pastorino, R., Peeters, B., Faria, C., Desmet, W., Góes, L. C. S. & Van Der Auweraer, H. (2016). Model based system testing: bringing testing and simulation close together. *In Structural Health Monitoring, Damage Detection & Mechatronics*, Volume 7: Proceedings of the 34th IMAC, A Conference and Exposition on Structural Dynamics 2016, pp. 91–97. Springer International Publishing.
14. Thielemans, L., Sputh, B. H. C., Pastorino, R., Desmet, W. & Swevers, J. (2024). Industrial application of residual power method as co-simulation performance indicator for e-motor hybrid-physical-virtual test setup. In *Proceedings of ISMA 2024*, Leuven, Belgium.
15. Dal Borgo, M., Musella, U., Thielemans, L.,

Vettori, S., Garcia de Miguel, A., Pastorino, R., Di Lorenzo, E. & Peeters, B. (2024). Real-time virtual shaker testing using an executable digital twin. In *Proc. ISMA 2024 – International Conference on Noise and Vibration Engineering*, pp. 684–693, Leuven, Belgium.

16. Dal Borgo, M., Musella, U., Thielemans, L., Vettori, S., Garcia de Miguel, A., Pastorino, R., Di Lorenzo, E. & Peeters, B. (2025). Virtual shaker testing: a real-time framework for predicting spacecraft vibration tests. In *Proc. 10th CEAS Aerospace Europe Conference and 28th AIDAA International Congress*, Turin, Italy.
17. El-Kafafy, M., Peeters, B., Geluk, T. & Guillaume, P. (2019). The MLMM modal parameter estimation method: a new feature to maximize modal model robustness. *Mechanical Systems and Signal Processing*, 120, 465–485.
18. Manzato, S., Risaliti, E., Napoli, C., Tamarozzi, T. & Peeters, B. (2015). A review of frequency-based substructuring methods and their applicability to engineering structures. In *Proc. Int. Conf. Structural Engineering Dynamics (ICEDyn)*, Lagos, Portugal.
19. Dal Borgo, M., Musella, U., Bentivoglio, F., Garcia de Miguel, A., Pastorino, R., Di Lorenzo, E. & Peeters, B. (2026). Real-time virtual shaker testing using hybrid coupling for shaker, head expander and device under test. To be included in the *Proceedings of the International Conference on Noise and Vibration Engineering*, Leuven, Belgium.

ECSSMET
Braunschweig Germany 2026

Dynamic

FLOW INDUCED VIBRATIONS IN FLEXIBLE LINES – PHENOMENON AND METHODS TO ASSESS ASSOCIATED RISKS

Michal Vorel [(1)], Giampiero Pampolini [(2)], Robert Meitzner [(3)]

[(1)] ArianeGroup GmbH, 28361 Bremen, Germany, Email: michal.vorel@ariane.group
[(2)] ArianeGroup SAS, 27207 Vernon Cedex, France
[(3)] ArianeGroup GmbH, 28361 Bremen, Germany

KEYWORDS

Flow induced vibrations, flexible line hoses.

ABSTRACT

This paper presents the phenomenon of flow induced vibrations in flexible hoses. The hitorical origins and the risks of the resulting mechanical behaviour are explained. The phenomenon is described using basic mathematical relations for the various mechanical modes. The overall engineering approach is based on the state-of-the-art literature. Coming out of A5 experience the phenomenon of FIV was considered in Ariane 6 development since the very beginning. The particular application to the development in Ariane 6 launcher is presented using both analysis and test, as well as a dedicated toolset developed for this purpose.

1. INTRODUCTION

Flow induced vibrations (FIV) is a phenomenon that occurs due to a turbulent flow interacting with a structural part. In an unsuitable case FIV can generate a strong mechanical response in the structural part that finally can lead to its disintegration. In broader terms, FIV can be understood as a subset of various flow-structure phenomena.

In the context of launchers the FIV is of a particular concern in the design of flexible lines (hoses) and compensators made of convoluted bellows. Under unsuitable conditions, the fluid conveyed by those parts excites the bellow convolutions. By their dynamic response, the convolutions in turn reinforce the vibrations fluctuations in the fluid itself.

In certain operational ranges of the fluid flow, this interaction can generate unsustainable stress amplitudes in the convolutions, resulting in failure by high cycle fatigue and consequently a leak or burst.

In space history the FIV phenomenon was the cause for the failure of Saturn V spark igniter of the J2-S engine [1,2].



Figure 1: FIV induced failure of a flexible [2].



Figure 2: Failure of the J2-S engine due to FIV anomaly in a flexible [2].

As of today, the design methods to assess the risk of FIV and the critical conditions are well established in [3,4]. Due to the high complexity of the phenomenon the design methods have their natural uncertainties and limits. In such cases, additional verification by a realistic test is essential.

In the current paper, the verification of FIV was performed in the frame of A6 hot firing tests with specific measurements. The verification by test concentrated in particular on flexible hoses, which were considered at risk of unacceptable FIV. A dedicated passenger test was performed in the hot firing test campaings in order to assess the response for few critical flexible hoses. Finally, the stress amplitudes in the convolutions were determined. A positive assessment for all flexible hoses could be achieved.

Among the known analytical challenges, the damping factor in the transfer function between the measurement sensors and the displacement at the convolutions plays a major role. While measurements for some specific test configurations are available, the information in the literature is scarce, cf. [5,6,7], often supported by NASA.

2. MODELIZATION

In this section the concept of the modelization of the FIV is outlined. For detailed description the reader should refer to state-of-the-art literature in [3,4].

Flow induced vibrations (FIV) occur due to a turbulent flow interacting with a structural part. For a convolution the vibration generates due to periodic vortex formation and shedding. This causes a periodic pressure difference, which is exerted on the convolutions, Figure 1.

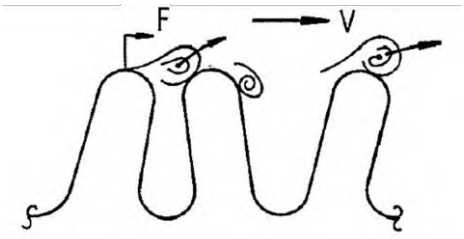


Figure 3: Generation of excitation force F on the convolution, due to flow of velocity V and the resulting vortex shedding, picture adapted from [3].

The main characteristic parameter is the dynamic pressure, defined as:

$$p_{dyn} = \frac{1}{2}\rho_f V^2 \qquad (1)$$

where ρ_f is the fluid density at a given temperature and V is fluid flow velocity. The excitation force on the convolution can be determined as:

$$F = C_x A_p p_{dyn} \qquad (2)$$

Where C_x is a product of characteristic coefficients, and A_p is the convolute height area (pressure excitable area). The total cofficient Cx largely depends on the the local geometry of the convolution and its response to the vortex sheding. That coefficient is determined experimentally.

This excitation force is resisted by the convolution, for which the displacement is:

$$x = C_m Q \frac{F}{k_A} \qquad (3)$$

where k_A is the spring rate, C_m is a vibration mode coefficient, and Q is the dynamic amplification factor. The vibration mode factor C_m describes the participation of the convolutions to the longitudinal vibration of the hose. The dynamic amplification factor Q depends on the type of the hose and the conveying fluid. This factor is derived from large experimental knowledge and it strongly influences the analytical predictions.

Finally, the maximum stress in the convolution can be determined as:

$$Stress = \left(C^*, p_{dyn}, SSR, V, geometry\right) \qquad (4)$$

where C^* is a specific coefficient, SSR is a specific spring rate based on ka, and V is flow velocity.

Beyond the state-of-the-art method, AG has historically developed an in-house relation for the determination of the stress amplitude. That model is based on the same concept of dynamic pressure and convolution stiffness, and it has a slightly different geometry definition. The resulting stress is similar to the state-of-the-art model.

Depending on the operational regime (mass flow and temperature) the convolutions may respond in three modes:

- In-phase longitudinal mode, where all convolutions vibrate in the same direction.
- Out-of-phase longitudinal mode, where convolutions vibrate in opposite direction to each other.
- Bending mode, where the walls of the convolute develop a higher order local response.

The mechanical natural frequencies of the convolutions are different for the three modes. The natural frequency can be expressed as:

$$f_m = \frac{1}{2\pi}\sqrt{\frac{2k_A}{m_m + m_{fl}}} \qquad (5)$$

where m_m is the mass of the metal and m_{fl} is the mass of the fluid active in the convolution in the studied mode.

The natural frequency and the velocity are related via the Strouhal number defined as:

$$St = \frac{fd}{V} \qquad (6)$$

or

$$f = \frac{St\,V}{d} \qquad (7)$$

where d is a characteristic (normalized) dimension of the hose. The critical Strouhal number were intensively investigated by NASA in the 1960's [4]. Depending on the definition of the characteristic dimension, and for the first mode, the St values are ca. between 0.2 and 0.5.

The last FIV excitation to be considered is the acoustic interaction, for which the first acoustic mode frequency is:

$$f = \frac{FNCO \cdot C_{\Phi}}{2\pi r_i} \qquad (8)$$

Where *FNCO* is a non-dimensional acoustic mode coefficient, C_{Φ} is the speed of sound in the fluid, and r_i is the internal diameter of the hose.

It is important to note that the mechanical modes may overlap in the operational regime, and that the acoustic excitation can occur together with a mechanical excitation.

The detailed formulaic description as well as application examples can be found in [3,4].

3. VERIFICATION APPROACH

In the chapter above the various elements to the modelization have been presented. The actual verificaiton approach and criterion will be described herewith.

The main uncertainty in the modelization is the Strouhal number, which is experimentally based, and depends mainly on the particular convolution geometry.

Therefore, the risk of excitation needs to be investigated with an uncertainty factor applied to that number. An uncertainty of +/-50% is applied on the Strouhal number. The risk of excitation is investigated over the whole uncertainty field, and not only at the two extremes.

Hence, the excitation frequency is determined based on Eq.7 for a range of Strouhal numbers.

The mechanical frequency for each mode is compared to the excitation frequency. Due to various uncertainties a safety factor is required: the mechanical frequency shall be below the excitation frequency by factor 2, which means:

$$f_m < 0.5f \qquad (9)$$

If this requirement is violated, a matching of the frequencies and self-induced excitation is assumed. In that case the assessment of the stress amplitude is mandatory. Due to further uncertainties a safety factor of 2.5 is applied. In case that acoustic mode occurs simultaneously, another safety factor of 1.5 is applied on top, Eq. 10.

The resulting stress shall be lower than the safety reduced fatigue limit of the convolution material, and its welds, at the operational temperature.

$$Stress < \frac{1}{2.5\ (\cdot\ 1.5)} \cdot fatigue\ limit \qquad (10)$$

4. ACTIVITIES PERFORMED ON ARIANE 6

The above described analytical approach developed by NASA is based on numerous test evidence. As described, many uncertainties need to be considered, which requires the implementaiton of significant safety factors.

However, over the history of various space projects, including the Ariane launchers, this approach proved to be viable and useful for the verification of the flexible hoses without extensive tests.

During the Ariane 5 development and operational accompaniment various tests of flexible hoses were performed, where the validity of the state-of-the-art approach was confirmed. Therefore, for the development of A6 the criticality of the flexibles was assessed first with the same approach, i.a. using an analytical framework.

Prior to the physical design definition the basic operational regime was defined including the temperature and mass flow ranges. Also, the various fluid end consumers were initially only linearly added.

Based on those inputs the particular geometry of the suitable flexible hoses was selected, and the risk of FIV was analytically assessed in full detail.

An efficient analysis was possible thanks to a dedicated toolset developed for this purpose. The main feature of it is the capability to assess the FIV iteratively over a range of the various input parameters, and not only at their extremes. Beyond the temperature and mass flow, the various parameters include the Strouhal number, dynamic amplification factor, as well as geometry parameters.

This process was repeated in several loops up to MG11 (launcher QR), along with the increasing precision of the predicted operational ranges as well as procured hardware properties.

As mentioned in Section 2 the dynamic amplification factor is one of the most influencing factors. Therefore, and beyond the literature data, additional effort was invested in this point.

A passenger test was organized on the hot firing test model of the ULPM stage (Upper Liquid Propulsion Module) for selected flexible hoses, to measure local vibration responses during the engine firing and other events in the propulsive system.

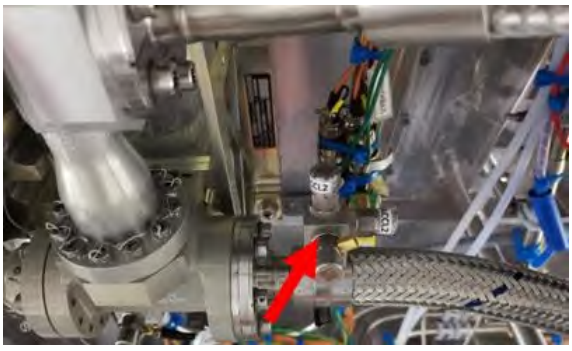


Figure 4: Example of dedicated vibration sensors on a flexible.

Beyond the usual tasks in performance of such test, one of the major challenges was to guarantee a high data acquisition rate. This is necessary as frequencies of the flexibles in order of magnitude of 10kHz are not unusual.

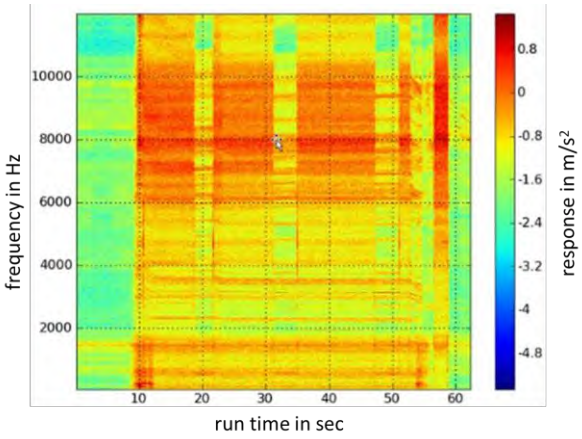


Figure 5: Example of evaluation of a test with a flexible. The response is spread over a range of frequencies, with high intensity at approx. 8kHz.

Concerning the signal post-processing, the determination of modal damping properties from measured operational vibration responses is a non-standard task. As a part of the toolset a software package was developed to extract modal damping properties from measured operational vibration responses.

In the second step, the determined excitation was post-processed to reconstruct the (maximum) amplitude in strains. With this information, the maximum stress was caclulated, both with a dedicated FEM model and with the state-of-the-art analytical solutions.

The results out of this approach and the predictions based on NASA related work [3,4,5] were in fairly good agreement, considering the large uncertainties in the assumptions.

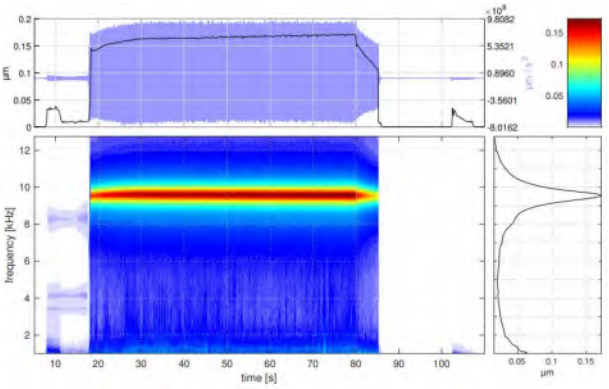


Figure 6: Example of the post-processing for the convolution amplitude. The maximum response at approx. 10kHz is well visible.

In result, it was possible to verify that none of the A6 flexible hoses coincided with the critical FIV frequencies. However, in the final design configuration the safety factor was slightly violated for few hoses, i.e. $f_m \prec 0.5f$. Using the toolset the maximum stress amplitudes were always evaluated and available for comparison to the material fatigue limit.

Due to the various uncertainties the good practice at AG is to keep the analytical stress amplitude at very low level, typically much below 10MPa. Only in cases for which test evidence is established, higher values are accepted, up to a few dozens of MPa.

This was the case for few impacted flexibles, for which investigations by test were additionally performed in the stage hot firing test, described above.

5. CONCLUSION

With A5 heritage and A6 development AG has gained deep industrial knowledge of the FIV phenomenon in flexible hoses. A comprehensive toolset was developed in orded to assess the phenomenon quickly and to avoid the risk of FIV since the beginning.

For future designs the following recommendations can be formulated:

- Risk of FIV should be avoided in the early design stages.
- The preliminary inputs should be defined with possibly large reserves, as the operational range of the propulsion subsystem is bound for modifications along the development.
- In engineering terms, it is sufficient to dimension the flexible hoses by the state-of-the-art analytical approach.
- Fatigue regime should be avoided completely. Normally, this is possible at no added mass/cost by selecting an appropriate design.

- For potentially critical flexibles a test evidence is recommended at propulsion subassembly level (test as you fly).
- Sophisticated diagnostics is necessary to evaluate the test and the risk of FIV in detail.

For future activities the characterization of local damping in the convolutions would help for deeper modelling of the dynamic behaviour.

As of writing this article, Ariane 6 has a record of eight successful operational flights since its maiden qualification flight. Fully nominal operation of the flexible hoses has been observed.

6. REFERENCES

1. J-2 Rocket Engine Augmented Spark Igniter http://heroicrelics.org/info/j-2/augmented-spark-igniter.html, retreived 24 July 2026.
2. J 2 Engine Semi-Annual Film Report - August 1968, https://youtu.be/ZUPTgpBhhBI, retreived 24 July 2026
3. MSFC-DWG-20M02540 Rev.E1: Assessment of flexible lines for flow induced vibrations.
4. NAS8-21133: Flow-Induced Vibrations of Bellows With Internal Cryogenic Fluid Flows, NASA Interim Technical Report, 1970.
5. Higgins, Stephen L.: Methods for predicting flow-induced vibrations in bellows expansion joints. Thesis, University of Georgia, 2017.
6. Tran, Patrick K. et al : Numerical Investigation of the Flow Structure of Cryogenic Hydrogen in Corrugated Metal Flexhoses Due to Fluid–Structure Interactions. J. Eng. Gas Turbines Power. Feb 2025, 147(2).
7. Watanabe, M., Oyama, M.: Vortex-induced vibrations and lock-in phenomenon of bellows structure subjected to fluid flow. WIT Transactions on The Built Environment, Vol 84, 2005.

Compliance Of Spacecraft Units to Random Vibration Environment: Assessment Methodology and Practical Applications

Enrico Spigarolo[(1)], Nikolay Asmolovskiy [(2)]

[(1)] Space Structures GmbH, Fanny-Zobel-Str. 11, 12435 Berlin, Germany, Email: spigarolo@spacestrcutres.de
[(2)] Space Structures GmbH, Fanny-Zobel-Str. 11, 12435 Berlin, Germany, Email: asmolovskiy@spacestrcutres.de

KEYWORDS

e.g. Random Vibration, Finite Element Analysis, Random Response Spectrum

ABSTRACT

The verification of spacecraft units against launch and specifications environments is typically performed using a coupled load finite element analysis in which payloads and secondary units are assembled with the structure models by employing Craig-Bampton reduced order models. Tight schedules and the growing availability of off-the-shelf components results in situations that these models are often not available. In these cases, it is common to model the payloads with a simplified approach consisting of a lumped mass and rigid connections. This simplification makes the assessment of the random vibration response of the units more challenging.
This paper proposes a practical methodology based on the Random Response Spectrum (RRS) which allows for a simple assessment of the compliance of units when limited information is available. The proposed workflow is demonstrated through a simple example that highlights the strengths and the limitation of the simplified approach.

1. BACKGROUND

In the context of structural design and verification of a spacecraft, one of the many requirements that needs to be satisfied is the compliance of subsystems to the different load environments experienced during the mission. This includes, to name a few, quasi-static, vibrational and thermo-elastic loads. The nature of space missions is such that subsystems and payloads are typically designed as stand-alone units and follow a parallel product cycle to the spacecraft's one. As a result, they can be designed and qualified separately. The requirement of compliance is then translated into assuring that the loads experienced during the mission (or the tests) are compliant with the qualification loads of the units. This paper focuses on the evaluation of the response of units due to random vibration loads and the comparison against the tested qualification specifications.

The most common way of performing this assessment is by implementation of a Finite Element Model (FEM), comprising the primary structure (e.g. the spacecraft) and all the secondary structures and payloads attached to it. In the ideal case, a representative FEM of the different modules is available, and the structural performance can simply be assessed by the coupled analysis.

However, despite the continuous increase in computational capabilities, the implementation of fully representative FEM is complicated by the overall size of the models and the complexity of the configuration control. Furthermore, detailed models are sometimes subjected to intellectual property restriction.

The widely accepted way around this is to make use of Craig-Bampton reduced models [1]: the reduced models maintain the dynamic behaviour while significantly reducing the computational time. During the reduction process key elements such as nodal accelerations and elemental forces can be preserved so that they can be monitored during the coupled load analysis. In this way, it is possible to assess directly whether units' responses are compliant with their qualification loads. For instance, one can directly compare peak interface force with the design limit load of the component.

However, reduced models may not always be available. Common reasons are project scheduling constraints, development limitations and the increasing availability of off-the-shelf components for which FEM do not exist. The result is that a dynamically representative model cannot be used and a much simpler modelling approach needs to be adopted: a common approach is to use a rigid element connecting the interfaces between unit and spacecraft and a lumped mass positioned in the unit's centre of gravity. This simplified modelling can be effectively used to assess the compliance of static loads resulting from the coupled analysis with the quasi-static loads the units have been qualified (or sized) to.
The absence of any dynamic information on the units' side, however, complicates the comparison between the dynamic responses between simulations and qualification.

2. ASSESSMENT WITH SIMPLIFIED MODELS

Assuming that modal information (such as main frequencies) are known and that the qualification specifications are available, a first simplified approach would be to extract the RMS interface force or the equivalent interface acceleration from the FE random vibrations analysis and compare it with the Power Spectral Density (PSD) applied during the qualification testing.

Lacking a better option, the simplified rigid element-lumped mass model can still be used to compare the random response from the analysis to the qualification loads.

This approach in practice consists in comparing the input load from qualification (the PSD) with the interface acceleration response from the random vibration analysis as shown in Figure 2-1. As such, exceedances of the response with respect to the qualification input could be interpreted as not-compliance whereas a response fully enveloped by the PSD indicates compliance. A rule that is commonly adopted in the presence of exceedances is the peak clipping, which consists in ignoring sharp peaks, or peaks with a relatively small bandwidth, if they exceed by a maximum of 3dB the input profile.

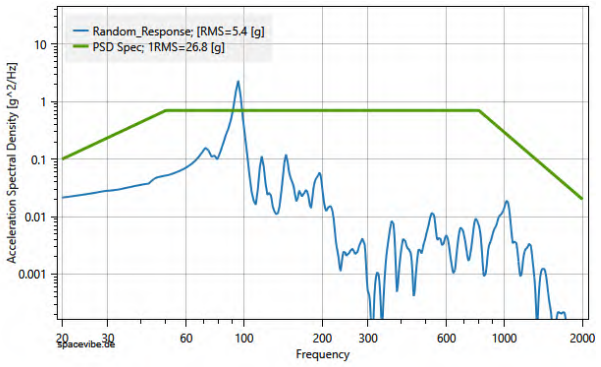


Figure 2-1:Interface Acceleration Response vs Qualification PSD of an antenna

By not considering the modal content of the unit, this approach treats PSD exceedances purely based on their amplitude. By doing so, exceedances occurring in frequency ranges far from the main modes of a unit (where the dynamic amplification occurs) are mistakenly interpreted as non-compliance, leading to excessive redesign or requalification.

A more appropriate evaluation of the response can be done by means of the Random Response Spectrum (RRS).

2.1. Random Response Spectrum Section

The Random Response Spectrum (RRS), also known as Vibration Response Spectrum (VRS) allows to consider the modes of the units when comparing the PSD with the random vibration response.

The RRS can be interpreted as the response of an array of independent single-degree-of-freedom (SDOF) oscillators with same damping assuming different natural frequency. The RRS function gives the RMS response of each oscillator to a fixed input [2].
The RRS function is a generalisation of the Miles Equation:

$$\ddot{x}_{GRMS}(f_N,\xi)=\sqrt{\sum_{i=1}^{N}\frac{1+(2\xi\rho_i)^2}{(1-\rho_i^2)^2+(2\xi\rho_i)^2}\hat{Y}_{ASPD}(f_i)\Delta f_i} \quad (1)$$

Where:

ξ	critical damping
f_i	assumed frequency
$\hat{Y}_{ASPD}$	base input acceleration PSD
ρ_i	f_i/f_N

And x is the solution of the SDOF problem with base excitation y, stiffness k and damping c. Figure 2-2 shows how the response PSD is translated into a curve for which each point is the total gRMS seen by the simplified SDOF model at an assumed natural frequency (f_N).

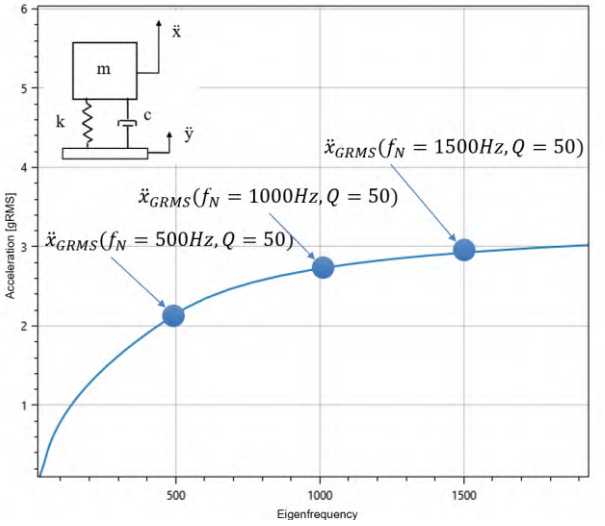


Figure 2-2: Random Response Spectrum (RRS) Plot

The VRS is extensively described in [2], where it is also demonstrated how the Shock Response Spectrum can be efficiently adapted to the random vibration environment: the RRS is used to compare different random vibration specification and to identify critical frequency ranges based on the available response. At the same time, it is shown how the RRS can be useful for test data assessment, derivation and revision of test specifications.

The RRS method is also described in [3] where it is highlighted how the method can provide a rational

approach to derive test specifications from measured data and to assess the random response of a unit based on acoustic test measurements.

Indeed, Eq. 1 can be applied to the RMS acceleration response of a unit obtained from the random vibration analysis: the output, combined with the info about the unit's modes and qualification loads, offers a practical tool to evaluate the response's compliance.

In simple words, the RRS function returns the equivalent interface force (expressed in net-g) that a unit would experience assuming that the full unit mass is excited at a certain frequency with specified Q. The equivalent interface force is a key parameter used for units sizing and strictly relevant to assess the structural integrity.

The critical difference between the response of the simplified lumped model with the reduced model is that for the latter the force spectral density at the interface can be integrated (giving the cumulative RMS) capturing all modal content and accounting for the difference in interface stiffness. This provides a significantly more representative interface force estimate.

In practice, the assessment consists in a comparison of the RRS of the specification PSD (from the qualification test) and the RRS of a unit's random response. In the next section, a workflow is proposed to efficiently interpret the results.

2.2. Suggested Workflow

The first step is to compare the interface acceleration response against the Qualification Loads PSD: if the first is enveloped by the second, the response can be considered as compliant.

If the response exceeds the PSD, the RRS function can be applied to the Qualification Loads PSD and the interface acceleration response obtained from the random vibration analysis. The comparison of the resulting curves, combined with minimal qualification data, provides a practical tool to assess the compliance of a unit. In particular, four main scenarios can be identified:

No Exceedances
The RRS of the Qualification Loads PSD completely envelopes the RRS of the random response. In other words, there are no exceedances (Figure 2-3a). In this case, the qualification loads cover the response of the unit independently of the unit's modes and the unit can be considered compliant.

Exceedances
The RRS of the random response exceeds the RRS of the Qualification PSD. Three sub-scenarios can be identified:

1) **Exceedances below the unit's main modes:** exceedances occur at frequencies sufficiently lower than the unit's primary modes (Figure 2-3b). In this case, the unit's dynamic is not excited, and it is possible to assume that the response is quasi-static. A practical rule is to consider a $\sqrt{2}$ factor between exceedance and main mode.
2) **Exceedance at (or near) the main modes:** the exceedances coincide with the primary modes (Figure 2-3c) meaning that the total Qualification Loads do not cover the predicted response. Actions such as design changes or unit's requalification shall be considered.
3) **Exceedances above the unit's main modes:** In this situation (Figure 2-3d) the interpretation of the results becomes less trivial and the assessments needs to account for data such as secondary modes or, if available, the qualification test results.

In the first case, the simplified approach can be expanded to assess the unit's compliance: since the exceedances are below the unit's primary modes, the response can be approximated as quasi-static. Therefore, the total gRMS calculated from the random response can be compared against the larger between: (i) quasi-static qualification loads and (ii) the gRMS of the qualification PSD below the unit's primary mode. If the response's gRMS is lower, the unit can be considered compliant.

The workflow is simplified in Figure 2-4.

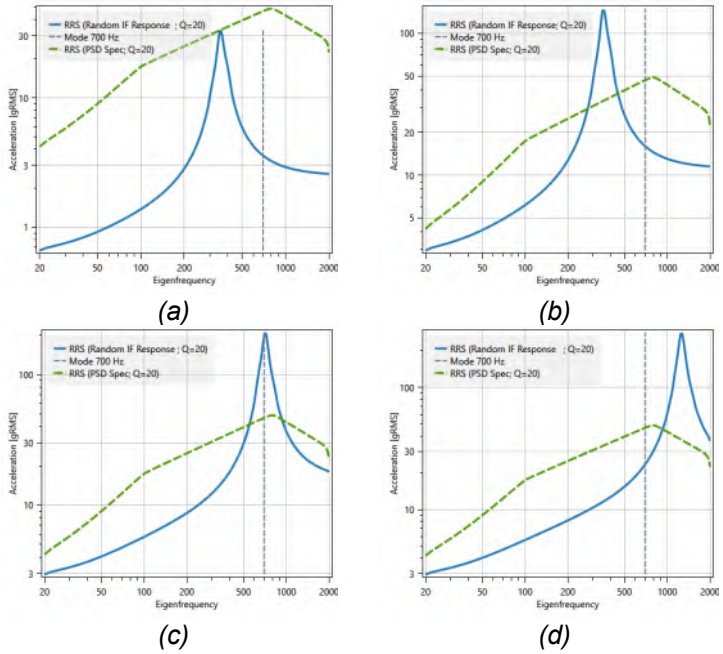


Figure 2-3: Subcases

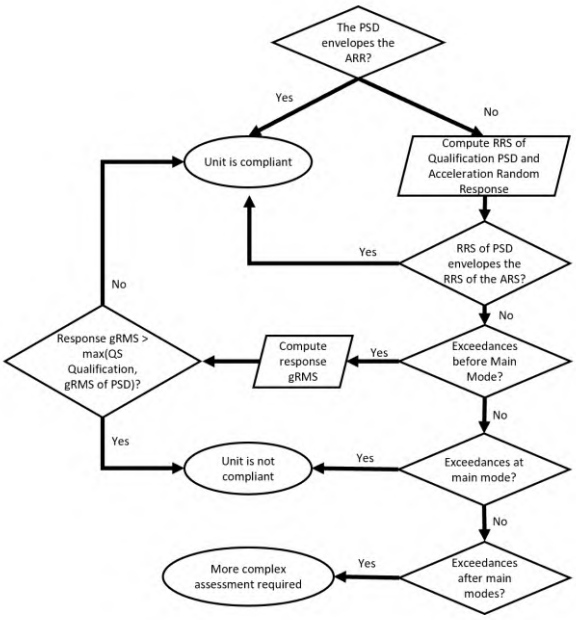


Figure 2-4: Simplified Workflow Chart

2.3. Practical Example

In this section, the approach is put to practice. In the example, an electronic box is mounted on the side of a spacecraft as shown in Figure 2-5.

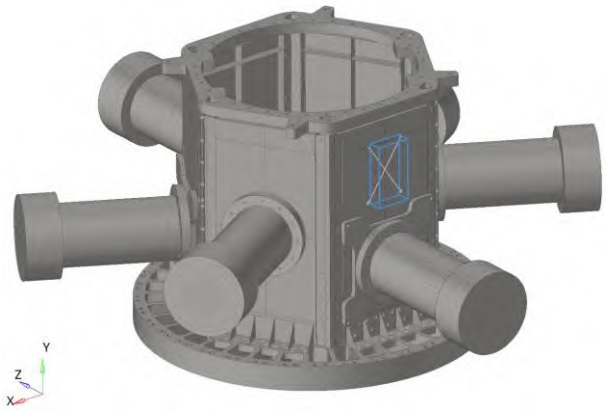


Figure 2-5: Example Structure FEM

The e-box's mechanical characteristics are listed in Table 2-1, while its primary modes are summarised in Table 2-2.

Table 2-1: E-Box Properties

Mechanical Properties		
Mass	2.3 kg	
Centre of Gravity	[0.0; 0.0; 0.016] m	
#Interfaces	4	
Qualification		
Quasi-static Loads	20g	
	Frequency [Hz]	PSD [g^2/Hz]
Random Loads	20	0.0584
	50	0.5
	400	0.5
	2000	0.0584

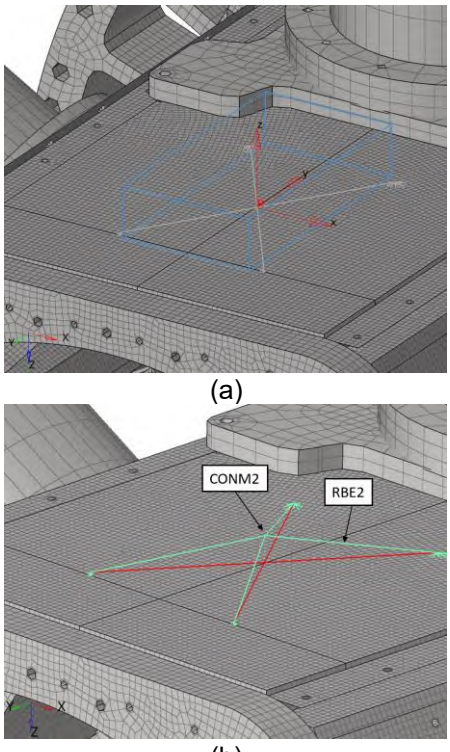
Table 2-2: E-Box Main Modes

Mode #	Frequency [Hz]	Mass fraction X	Y	Z
1	730.04	0.06%	0.07%	21.91%
2	954.77	0.25%	0.00%	32.50%
3	1040.25	0.00%	0.01%	0.01%
4	1448.14	6.91%	0.05%	3.27%
5	1472.78	7.67%	0.13%	3.76%
6	1575.97	34.65%	24.86%	0.20%
7	1591.74	19.07%	49.66%	0.12%
8	1696.40	0.60%	15.28%	0.22%
9	1829.13	0.01%	0.67%	1.13%
10	1859.41	6.40%	0.00%	1.15%

Two modelling approaches are followed:

- Model 1: the unit is attached to the platform as a reduced model (Figure 2-6a)
- Model 2: the unit is modelled as an RBE2 element connecting a CONM2 element positioned at the unit's Centre of Gravity (Figure 2-6b)

In both models, an RBE3 element has been defined at the unit's interface to retrieve the average interface acceleration. The element is expressed in the unit's coordinate system.



(a)

(b)

Figure 2-6: E-box's modelling

The random vibration analysis is performed with NX Nastran applying the Random Vibration Environment specified in [4] (shown in Table 2-3) at the fixed base of the structure with the box mounted on it. For the sake of this example, the analysis is performed in the Z (lateral) axis only.

Table 2-3: Random PSD Input

Frequency [Hz]	PSD [g²/Hz]
20	0.01
50	0.015
700	0.015
800	0.03
925	0.03
2000	0.00644
Total gRMS	**5.57**

The response of both models is plotted in Figure 2-7 against the PSD from the unit's qualification loads (Table 2-1), while the RRS is plotted in Figure 2-8.

When considering the simplified model, the interpretation of the exceedances in Figure 2-7 is not trivial as the peaks would indicate that the response is non-compliant even when applying the 3dB clipping method.

When switching to the RRS domain (Figure 2-8), the picture is cleared: all the exceedances (140 Hz, 250 Hz, 434 Hz and 508 Hz) happen in a dynamic range that is sufficiently far from the unit's own dynamics: following the approach described in §2.1, the maximum acceptable exceeding peak is at 730/√2=516Hz. It can also be appreciated how the RRS of the response after this threshold is below the RRS of the PSD, meaning that the loads induced by the primary structure are enveloped by the qualified random loads.

The response can be then assumed to be quasi-static, and the total gRMS seen due to the random loads (13 gRMS, see Figure 2-7) are compared with the quasi-static loads reached in the qualification tests: according to the qualification data shown in Table 2-1, the unit has been tested to 20g, which corresponds to 6.7g when considering 3σ values, or 15.2 gRMS when computing the gRMS up to 508Hz using the PSD specs. The response is considered compliant.

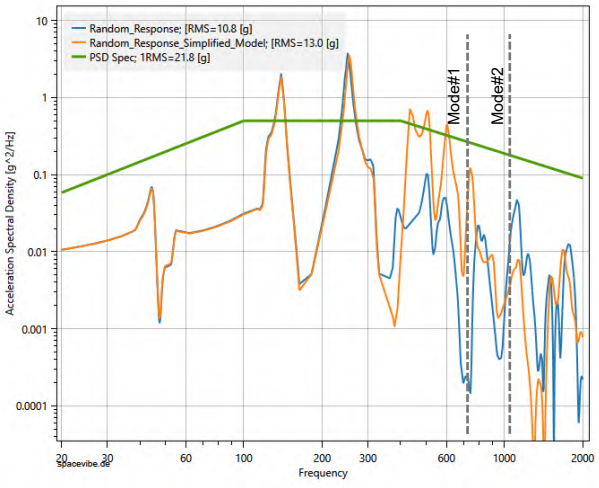


Figure 2-7: Acceleration Response and Qualification PSD

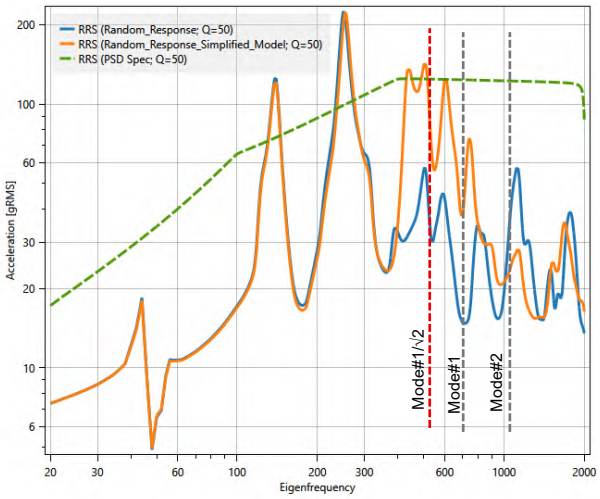


Figure 2-8: RRS of Acceleration Response and Qualification PSD

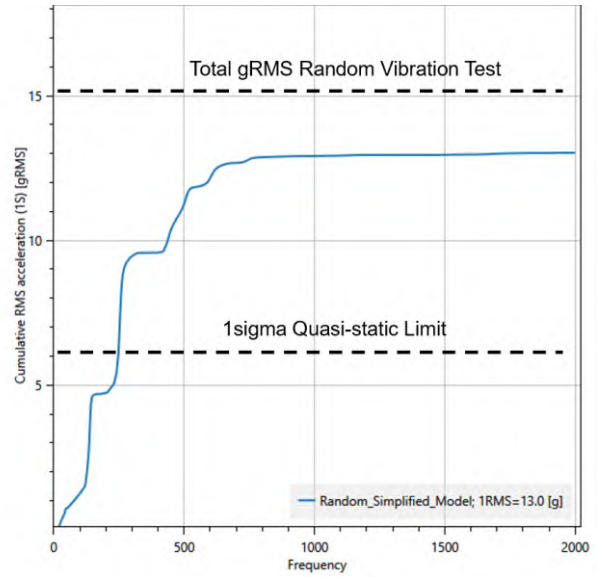


Figure 2-9: Cumulative gRMS of the simplified model

The response of the reduced model confirms what observed for the simplified model: the two main peaks at 125 Hz and 254 Hz are related to the main structure local modes and the e-box's own dynamic is not excited. Hence, the random vibration qualification covers the dynamic response and the compliance can be assessed on a quasi-static basis.

2.4. Method Limitations

The example highlights how the RRS approach is effective in assessing the random vibration response in absence of a detailed reduced model: with a limited amount of information (mass, unit's COG and qualification data) the RRS domain allows for a quick evaluation of whether the response excites the unit's dynamic and if the qualification loads envelope it.

The proposed methodology is based on several assumptions that shall be considered when performing the assessment. In the first place, the rigid element/lumped mass modelling by definition has no own dynamic and an infinitely rigid interface: this results in the peaks seen in Figure 2-8 at 434 Hz and 508 Hz. The peaks are absent from the response of the reduced model which is not infinitely rigid.

At the same time, the RRS itself comes with its own limitation:

- Eq. 1 is also dependent on the damping factor which significantly affects the RRS curve and therefore the assessment.
- As also highlighted already in [2], the method is valid as long as the modes are not coupled.
- Following Eq. 1, in the RRS domain each peak (or each point) represents the total gRMS of a SDOF model with one single mode i.e. the method assumes that the whole modal mass goes in one single mode, neglecting that this is not a realistic case.

Keeping these limitations in mind, the approach can still be used to assess the compliance of units and it offers an alternative where more detailed information is lacking.

3. CONCLUSION

This paper has shown that the Random Response Spectrum is a useful tool that can be employed to assess the random response of spacecrafts' units when detailed information or reduced order models are not available.

The proposed workflow combines the response of a simplified lumped mass/rigid element model from the finite element analysis with basic information such as the primary modes of the units and its qualification loads. The comparison between response and qualification loads in the RRS domain allows to identify whether the units' dynamics are excited by the primary structure and whether the response can be approximated as quasi-static.

The methodology has been applied to the simple example of an electronic box mounted on the side wall of a spacecraft: the results shown that a simple comparison between response and qualification loads can be wrongly interpreted and that the RRS approach allowed to determine that the qualification environment actually covered the predicted response.

The proposed methodology is subject to limitations implicit to the simplified modelling of the units and with the hypothesis at the basis of the RRS method. Nevertheless, when taking into account these limitations the proposed methodology provides a simple and practical approach that can be streamlined to efficiently assess the compliance of the unit against random vibration loads using a limited set of inputs.

4. REFERENCES

1. Craig Jr, Roy R., and Mervyn CC Bampton. "Coupling of substructures for dynamic analyses." *AIAA journal* 6.7 (1968): 1313-1319.
2. Irvine, Tom. "An introduction to the vibration response spectrum." *Revision D, Vibrationdata* (2009).
3. ECSS Secretariat, ESA-ESTEC, "Spacecraft mechanical loads analysis handbook." *European Cooperation for Space Standardization* (2013).
4. Space Exploration Technologies Corp. (SpaceX). (2024). *Rideshare Payload User's Guide* (Ver. 10) [Manual].

ECSSMET
Braunschweig Germany 2026

In-flight experiments

Flight Correlation Status of ESA Coupled Loads Analysis Tool for Vega-C

S. Caeiro [(1)], S. Fransen [(1)], A. Yanez [(1)], F. Battie [(2)], S. Kiryenko [(1)]

[(1)] European Space Agency, ESTEC, Keplerlaan 1, Noordwijk, The Netherlands, sofia.caeiro@esa.int, sebastiaan.fransen@esa.int, alberto.yanez@esa.int, stefan.kiryenko@esa.int
[(2)] European Space Agency, ESRIN, Largo Galileo Galilei 1, Frascati, Italy, francois.battie@esa.int

ABSTRACT

This paper presents the on-going activities in maintaining the correlation of the launcher/spacecraft Coupled Loads Analysis (CLA) tool for Vega-C at the European Space Agency (ESA). A first paper on this topic was presented during ECSSMET 2024, where the Lares-2 flight measurements were compared to the ESA internal CLA tool predictions and used to adjust the forcing functions of the ignition and pressure oscillation load cases. This paper presents an overview of the correlation status based on Biomass flight measurements and will identify whether any additional tuning of the previously correlated CLA tool is required.

This case presents an added value for the correlation status check, as Biomass is a spacecraft of a different mass class and presents dynamic properties more typical of a single launch mass class, unlike the Lares-2 configuration, which is lighter and for which the main modes lie above the sine frequency range.

A brief summary of the CLA tool update in terms of methodologies and software tools is also provided. The CLA tool update has been taking place in parallel of the correlation activity and the benefits are presented in view of the Biomass flight exploitation. Two powerful capabilities that can be used together to deepen the understanding of the dynamic behaviour of the coupled launcher/spacecraft system are the modal gain tool and mode shape recovery. While the first is still under development, the usefulness is mentioned in view of this correlation exercise.

The interest of ESA missions with this launcher for medium mass class payloads is very high and early compatibility with its mechanical environment is of outmost importance. CLA is in turn a key element in spacecraft testing and qualification to support the assessment of this compatibility in the quasi-static and low-frequency range dynamic loads. The ESA internal CLA tool is used in support to ESA projects in early stages of development or after design changes. The tool complements but does not substitute the CLA of the launcher authority. It allows an agile assessment of structural loads and identification of potential criticalities in the design of the spacecraft when on-board the Vega-C launcher.

Keywords: Coupled Loads Analysis, Correlation, Forcing Function, Vega-C, Flight Measurements, Superelement Method

INTRODUCTION

The ESA CLA experience started in the 90s with the Space Shuttle and Ariane-5 launcher. The CLA tool relied on FABE (Fluid Analysis with Boundary Elements) [1] software to model Fluid-Structure Interaction (FSI) and used a combination of MSC Nastran and direct matrix abstraction programme (DMAP) for the reduction of the physical Finite Element (FE) models to Craig-Bampton (CB) models [2] and for the implementation of forcing functions, assembly of the different CB models, damping methods, and the solution of transient and frequency response analysis. From 2001 onwards, the CLA experience from Ariane-5 and the Space Shuttle programs was used to create a new CLA tool for the Vega launcher. The final CLA tool for Vega used MSC Nastran v2005.0 and all DMAPs were written to be compatible with this version. Starting in 2018, the tool was adapted to be used for Vega-C, keeping the same methodology and software. The goal of the ESA CLA tool is to support ESA projects in an agile risk assessment before a CLA with the launcher authority is possible, or to evaluate the impact of design changes in the spacecraft. Starting in 2024, the Vega-C CLA tool has undergone a major update in terms of the software used. The step to move from MSC Nastran 2005 in combination with extensive DMAP library to more recent versions of Nastran was taken, and today, the CLA tool is running in MSC Nastran 2023.1, with a very reduced need of DMAPs, making the updated CLA tool easily compatible with following versions of Nastran.

CLA TOOL UPDATE

After the CLA tool correlation based on VC01, Lares-2 flight, the ESA internal CLA tool was updated in terms of software. As described in the previous section, the CLA tool for Vega-C was developed based in MSC Nastran 2005 combined with an extensive DMAP library. The DMAPs were used to perform the launcher FEM reduction to Craig-Bampton models, including filtering of modes with effective masses below a pre-defined threshold, generation of equivalent damping matrices and running transient and frequency response analysis, extracting the generalized responses to then multiply by the payload or launcher OTMs.

With the CLA tool update, the library of DMAPs used is reduced to a minimum and only to perform specific operations. The current CLA tool after its update uses MSC Nastran 2023.1 and can be easily updated due to the minimal usage of DMAPs. The largest part of the previous DMAP library is replaced by Nastran standard Superelement method for Craig-Bampton model and OTM generation. Mode filtering based on modal effective mass and equivalent viscous damping matrix based on structural damping and modal damping is performed via dedicated python scripts. The extraction of the generalized responses is done by including the generalized response list as part of the OTMs.

With the Nastran Superelement method, mode shape visualization is straightforward with the inclusion of PLOTEL elements in the launcher and spacecraft reduced FEM.

FSI capabilities have been studied to evaluate if it is possible to implement for Vega-E, since the third stage will be a liquid propulsion stage. It has been concluded that Nastran Superelement method has the necessary capabilities to re-introduce FSI in the CLA tool [3].

The methodology followed in the CLA process remains the same: the CLA driver script in python is the same, with only a few adaptations, and the same MATLAB post-processing scripts to compute equivalent sine, QSL and min-max tables are used.

FEM MODELS

The launcher FEM used in the CLA tool have been provided by AVIO. The FEM models have been used without modification until the correlation exercise with VC01, Lares-2 flight.

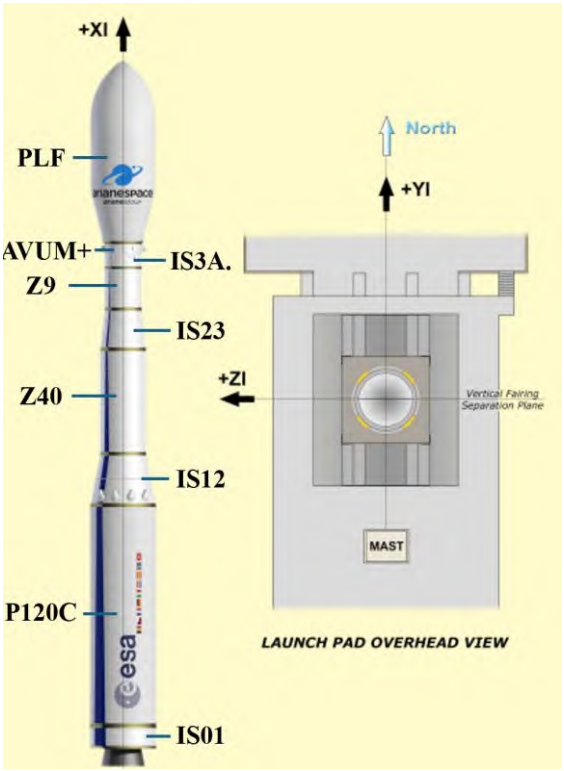


Figure 1: Vega-C Coordinate System [4] and its main components

After the correlation exercise, minor adaptations have been introduced in terms of introducing structural damping in the nozzle flexible joint of the Zefiro 9. In this paper, other launcher FEM adaptations are presented for the correlation to Biomass flight, VC04.

FORCING FUNCTIONS

The ESA internal CLA tool uses forcing functions that have been developed independently from AVIO.

For the Solid Rocket Motors (SRMs), P120C, Zefiro 40 and Zefiro 9 ignition cases are driven by the fast build-up of internal pressure in the propellant cavity and rupture of the nozzle membrane. The forcing functions were originally derived from CFD analyses and when static firing tests became available, these were also used to improve these forcing functions. Since Zefiro 9 was also used on Vega, for this case, the same forcing functions were kept for Vega-C. The ignition forcing functions are pressure and force time histories applied inside the propellant cavity, the igniter, the nozzle and the floaters (space between the domes and the propellant). For each SRM, the different internal pressure time histories are applied in different sections of the SRM.

Because the Zefiro 9 forcing functions remain the same as for Vega, but the Vega-C FEM is different, the only necessary adaptation was to update the mapping of the loads to the new Zefiro 9 FEM mesh. With the VC01 flight correlation, the forcing functions of the SRMs were updated. The effect of changing the different pressure time histories in the different sections was evaluated and it was seen that mainly the pressures in the floaters of the SRMs were affecting the acceleration outputs at the payload interface. For the particular case of the P120C ignition, also lateral forces were added to the nozzle, to be able to cover the lateral responses measured in flight at the payload interface.

On the other hand, the SRMs pressure oscillations (POs) result from the acoustic modes of the propellant combustion gases inside the propellant cavity which induce oscillations in the internal pressure, in the thrust, and excite the launcher longitudinal modes. The forcing functions are also pressure and force time histories applied in different sections of the SRMs and have been developed based on the SRMs static firing tests. Before the VC01 correlation the CLA tool included the PO of the P120C, 3 seconds after ignition and of the Zefiro 40, 15 seconds after ignition. The Zefiro 9 does not present significant pressure oscillation events. Despite the P120C and Zefiro 40 presenting more pressure oscillations, only the sizing ones for each SRM were initially considered in the CLA tool. After the VC01 correlation activity, an additional PO case was included for the P120C, around 31s after ignition. Although with lower amplitude than the PO 3 seconds after ignition, it was seen that it could happen simultaneously with the wind gust at Mach1 case.

Lastly, the CLA tool includes wind gust cases that occur at Mach1 and at Maximum Dynamic Pressure (MaxQ). These are cases which induce a worst case wind gust to maximize the bending moment at the spacecraft interface and take into account the aerodynamic instabilities at Mach1 and MaxQ. The forcing functions are based on CFD analyses performed at different Mach numbers and at different angles of attack and the two mentioned cases were selected as dimensioning. The lift and drag coefficients for these cases are considered and translated to forces applied on the external surfaces of the launcher.

LOAD CASES

As described in the previous section, there are several forcing functions applied on the launcher FEM which simulate the following load cases:

- P120C ignition
- P120C PO at 3 seconds
- Wind gust at Mach 1
- P120C PO at 31 seconds, added after Lares-2 correlation
- Combination of the two above as result of Lares-2 correlation
- Wind gust at MaxQ
- Zefiro 40 ignition
- Zefiro 40 PO at 15 seconds
- Zefiro 9 ignition

PO cases are treated by means of frequency response analysis while all the others cases are treated as transient analysis [5].

SUMMARY OF LARES-2 (VC01) CORRELATION

In 2024 the correlation of the ESA CLA tool predictions with Lares-2 flight, VC01, was presented. The objective of this correlation was to improve the prediction of the dynamic behaviour at the spacecraft interface, based on the equivalent sine (EQS). This was focused on ignition load cases and pressure oscillation load cases. Wind gust cases were not targeted as each flight will be subject to different weather conditions.

The correlation exercise was based on adjusting forcing functions of the different load cases rather than updating the launcher FEM provided by AVIO. For the Vega CLA tool correlation, it was performed differently going through three steps: SRM mass and static stiffness correlation, SRM SFT correlation, flight correlation. In the first step only the FEM was correlated, in the second step both FEM and forcing functions were correlated. In step 3 only the forcing functions were adjusted only by factoring and/or by introduction of additional forcing functions in specific frequency bands [6], [7]. The following methodology was followed for the ignition cases:

- Compute the EQS predicted by the ESA CLA at spacecraft interface.
- Compute the EQS based on the flight measurements in the same location.
- Compare the EQS and identify frequency ranges where the CLA is underpredicting or overpredicting the flight.

- Sensitivity analysis to identify which forcing functions are affecting the EQS in the target frequency (each load case has several forcing functions applied in different areas of the launcher).
- Apply a band-pass filter to the identified forcing functions and introduce this new forcing function, with an adequate scaling factor, as an additional forcing function.
- Only if needed, adjust damping parameters in specific areas of the launcher.

For the ignition cases, it was concluded that the forcing functions with the most impact on the correlation where the pressures applied in the floaters (area between domes and propellant grain). For P120C ignition particular case, lateral forces on the nozzle were added to cover other events such as possible blast waves and launch table detachment, which are not modelled as separate load cases. For the pressure oscillation cases, the correlation methodology is simpler:

- Compute the sine environment predicted by the ESA CLA at spacecraft interface.
- Compute the EQS based on the flight measurements in the same location.
- Compare the sine with the EQS and compare the frequency range where the pressure oscillation occurs and its amplitude.
- Adjust the frequency range and amplitude of the pressure oscillations to better predict the flight measurements, using pressure measurements when possible.

An important point to consider is that the Lares-2 payload is lightweight and does not present dynamics in the sine frequency range, acting as a rigid payload. For this reason, a correlation with a more typical single launch payload, with eigenfrequencies within the sine frequency range was required to verify the correlation status of the ESA CLA tool with this type of payload.

BIOMASS (VC04) CORRELATION OBJECTIVES

The Biomass flight correlation objectives are:

- Improve the CLA prediction of the dynamic behavior at the spacecraft interface, based on the EQS/sine, for SRMs ignition and pressure oscillation cases.
- Improve launcher FEM representativity of the 1st, 2nd bending and 1st longitudinal modes.
- Improve prediction of lateral QSL for wind gust cases.

While the first objective is the same objective taken for the Lares-2 correlation, two additional goals are targeted for this correlation exercise. For the second objective, there is the need to update the launcher FEM to achieve the intended correlation. This is a difference with respect to Lares-2 flight correlation, where the main correlation parameters were the different load cases forcing functions.

CORRELATION METHODOLOGY

The correlation methodology for Biomass flight is partially the same as for the Lares-2 flight. As discussed previously, it will go further and include the launcher FEM as a correlation parameter, instead of focusing only on forcing functions. For the forcing functions correlation, the same procedure as described for Lares-2 case is used.

For the launcher FEM correlation, the first step is to identify at which frequency the 1st and 2nd bending and 1st longitudinal modes are predicted to occur. For this, the mode shapes of the launcher including the Biomass payload are visualized to properly identify the modes.

The second step is to identify the same modes based on the flight measurements. Waterfall plots which show the measurements amplitude as function of time and frequency are generated for accelerometers located not only on the spacecraft interface but also along the launcher. Since these modes are global modes of the launcher, these should be identified in accelerometers along the launcher and not only on the spacecraft interface. This allows to exclude that the identified modes are local modes.

With the FEM predictions and flight measurements, it is possible to determine the error between the two. The last step is to identify which properties need to be tuned in the launcher FEM to change the frequency of the identified modes to match the flight measurements. For this, PRIMODAL software is used, in particular, the POST module. In this module, it is possible to perform a sensitivity analysis where the launcher FEM properties and materials can be varied and the change in each of the eigenfrequencies is estimated. This methodology requires the computation of the distribution of modal strain energy and modal kinetic energy on the launcher [8]. Therefore, only a few selected properties and materials are targeted as correlation parameters.

Based on the described procedure for forcing functions and FEM correlation, the actual steps taken for each family of load cases is described below.

SRM ignition:

- Original CLA comparison to VC04
- Forcing Functions (FFU) tuning
- Updated FFU CLA comparison to VC04
- FEM tuning
- Updated FFU+FEM CLA comparison to VC04
- Forcing Functions fine tuning
- Updated FFU+FEM+FFUv2 CLA comparison to VC04

Pressure Oscillations:

- Original CLA comparison to VC04
- Updated FEM CLA comparison to VC04
- Forcing Functions fine tuning
- Updated FEM+FFU CLA comparison to VC04

Wind Gusts:

- Original CLA comparison to VC04
- Updated FEM CLA comparison to VC04
- Forcing Functions fine tuning
- Updated FEM+FFU CLA comparison to VC04

The described process requires several iterations on each step and, furthermore, there is a dependency between the different tuning parameters. For example, tuning the launcher bending and longitudinal modes after tuning the forcing functions will affect the correlation achieved by tuning the forcing functions alone, making it necessary to have a second step of iterations to fine tune the forcing functions. This makes the correlation exercise very time consuming.

FEM CORRELATION

The waterfall plots show an example of the result in an accelerometer measuring in the lateral direction and in an accelerometer measuring in the longitudinal direction. It is worth noting that the same behaviour is seen in other accelerometers along the launcher, confirming that the identified modes are global modes.

While the bending modes are identified during Mach1 flight event, the longitudinal mode is identified during lift-off. As a confirmation that the identified modes are the global bending and longitudinal modes, the flight measurements were imported to PRIMODAL software, in particular, the TOMA module. In this module, an “experimental mesh” can be visualized. This is, the flight accelerometers represented in space and connected via artificial PLOTEL elements (elements used for visualization only), are displayed and the mode shapes based on the flight data can be visualized. These modes did resemble the targeted bending and longitudinal modes of the launcher, with the only drawback that the measurement locations are very limited. Still, a visual confirmation could be obtained. For the FEM bending and longitudinal modes identification, this is done visually by plotting the corresponding mode shapes.

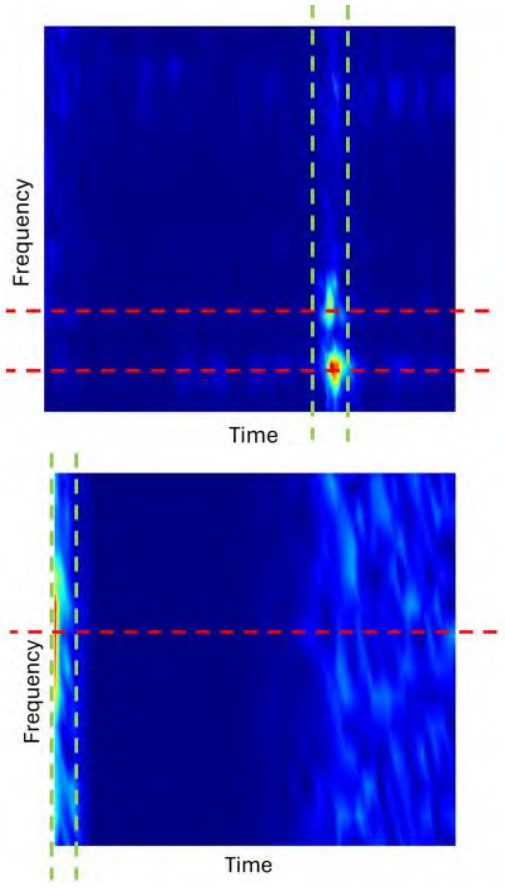


Figure 2: Waterfall plot of accelerometer measurements in lateral direction (top) and longitudinal direction (bottom) to identify launcher bending and longitudinal modes. Red lines identify the frequency, green lines the transonic and lift-off

After identifying which launcher FEM properties are driving the frequency of the identified modes, these properties were tuned in an iterative process until the FEM prediction is close enough to the flight measurement.

Table 1: Error in frequency prediction before and after correlation

Error in frequency	Initial	Correlated
1st bending mode	14.6%	0.2%
2nd bending mode	9.9%	1.0%
1st longitudinal mode	11.8%	0.6%

The achieved correlation is very satisfactory, as the launcher updated FEM is predicting the targeted bending and longitudinal modes with an error within 1%. However, to achieve this correlation, some material properties had to be changed quite significantly. Without more detailed FEM updating, for example, by remeshing areas of the FEM or updating the connections between different components of the launcher, the needed correlation requires significant FEM properties changes.

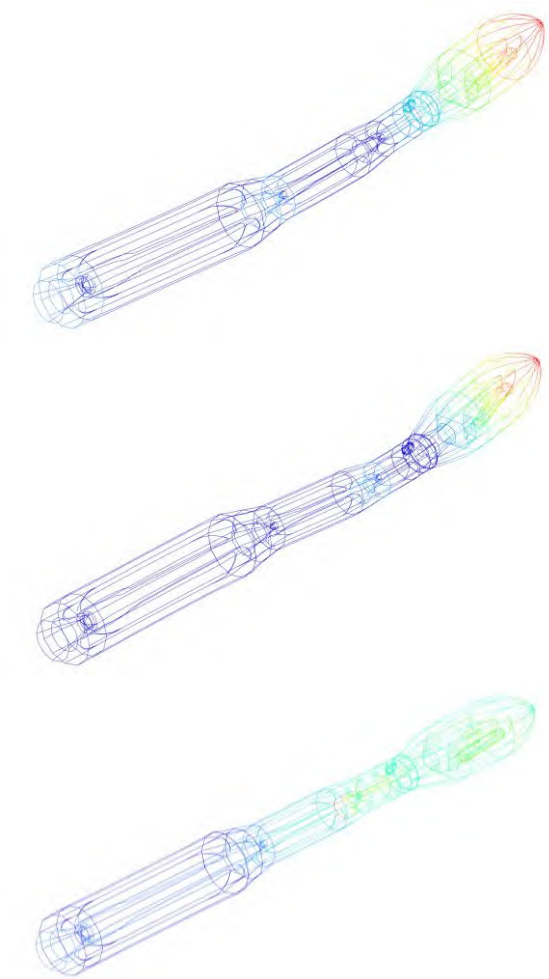


Figure 3: Mode shape of launcher first and second bending modes (top and middle) and first longitudinal mode (bottom)

FORCING FUNCTIONS CORRELATION

The steps taken to perform the forcing functions correlation will be described in this section.

P120C Ignition

1. Forcing Function tuning: Adjust amplitude of existing forcing functions (pressures) inside the P120C SRM. Adjust amplitude of lateral forces acting on the nozzle to cover blast wave and launch table detachment at lift-off. Remove frequency content from forcing functions to remove nonexistent peak at mid-frequency.
2. Effect of FEM correlation: the load case is ran with updated FFU and FEM.
3. FFU fine tuning: Adjust amplitude of lateral forces acting on the nozzle to cover blast wave and launch table detachment at lift-off.

The EQS based on flight measurements is shown in the plot in black and the EQS from the initial CLA is in green. The effects of applying point 1, 2 and 3 are represented by the curves in yellow, purple and red, respectively.

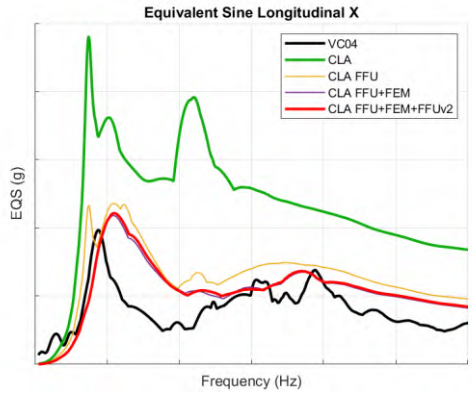


Figure 4: P120C ignition flight longitudinal X EQS comparison to CLA

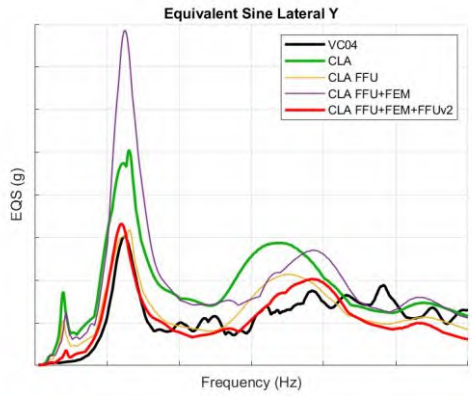


Figure 5: P120C ignition flight lateral Y EQS comparison to CLA

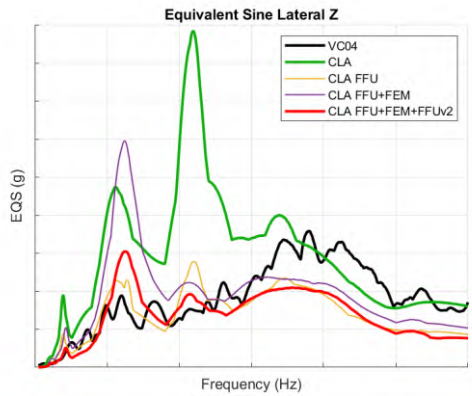


Figure 6: P120C ignition flight lateral Z EQS comparison to CLA

The following plot shows an example of the adjustment of the forcing function applied on the forward floaters of the P120C. The green function is subtracted from the black to obtain the red FFU.

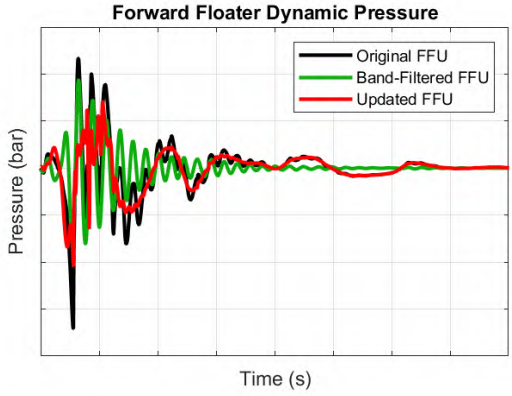


Figure 7: Pressure loads applied on the forward floater for P120C ignition case

Zefiro 9 Ignition

1. Forcing Function tuning: Adjust amplitude of existing forcing functions (pressures) inside the Z9 SRM. Remove frequency content from forcing functions to reduce 1st peak.
2. Effect of FEM correlation: the load case is ran with updated FFU and FEM.

For the Zefiro 9 ignition, the FFU fine tuning step was not required, as the updated FEM model did not affect significantly the spacecraft interface EQS. As a note, the lateral Y direction is overestimated while the lateral Z direction underestimated. The Z direction has lower amplitude (plots with different scales), so the correlation is acceptable. In the future, an attempt to tune the two lateral directions independently should be pursued, possibly based on the modal gain tool which still needs to be implemented in the updated CLA tool. The modal gain tool allows to select target responses per degree of freedom and identify which launcher and spacecraft coupled modes drive the selected responses.

The EQS based on flight measurements, EQS based on CLA before correlation, after FFU tuning and after FEM correlation are shown in the plots, in black, green, yellow, and red, respectively.

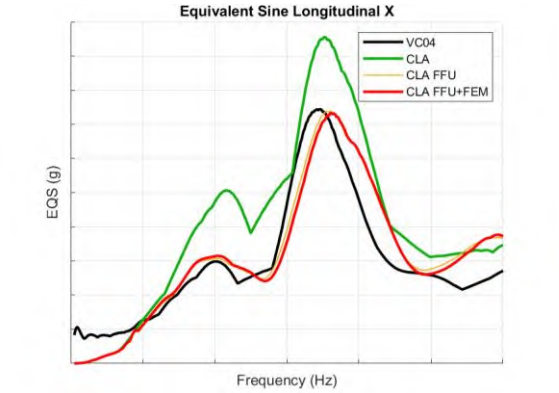


Figure 8: Zefiro 9 ignition flight longitudinal X EQS comparison to CLA

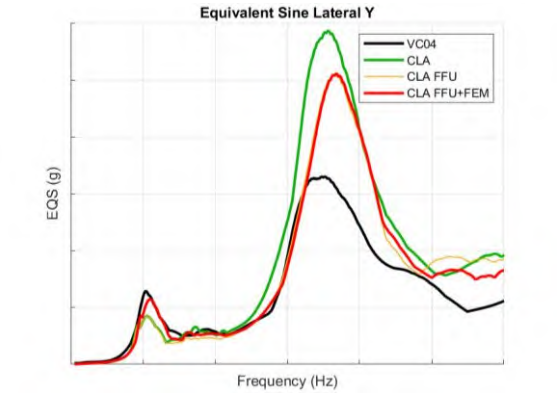


Figure 9: Zefiro 9 ignition flight lateral Y EQS comparison to CLA

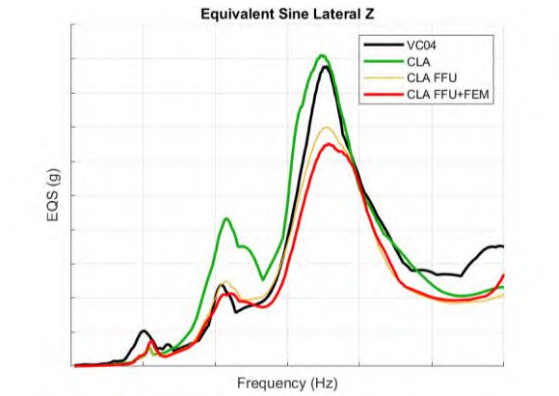


Figure 10: Zefiro 9 ignition flight lateral Z EQS comparison to CLA

The following plot shows an example of the adjustment of the forcing function applied on the forward floaters of the P120C.

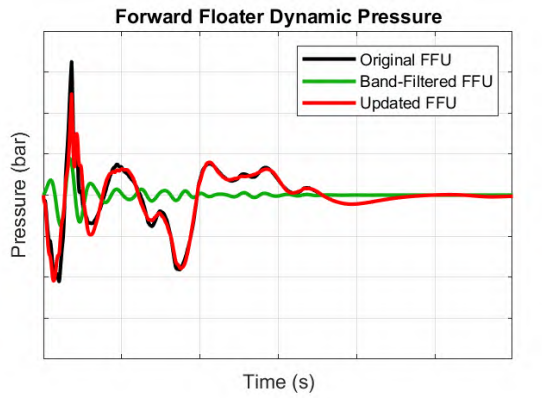


Figure 11: Pressure loads applied on the forward floater for Zefiro 9 ignition case

Zefiro 40 Ignition

The Zefiro 40 ignition flight event shows lower EQS amplitude, therefore, no dedicated correlation was envisaged. The flight measurements EQS, initial CLA EQS and CLA after FEM correlation EQS are shown in the following plots in black, green and red, respectively.

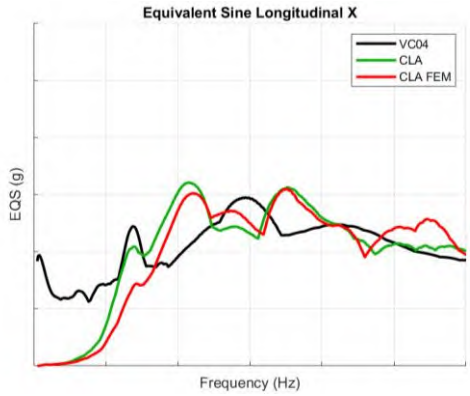


Figure 12: Zefiro 40 ignition flight longitudinal X EQS comparison to CLA

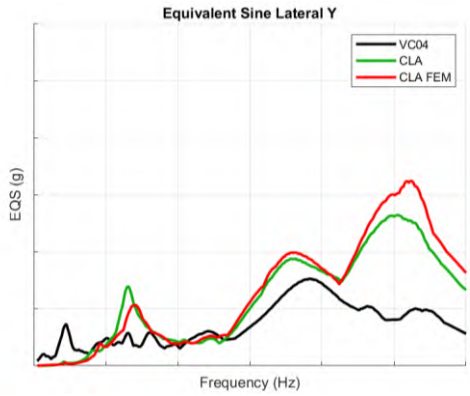


Figure 13: Zefiro 40 ignition flight lateral Y EQS comparison to CLA

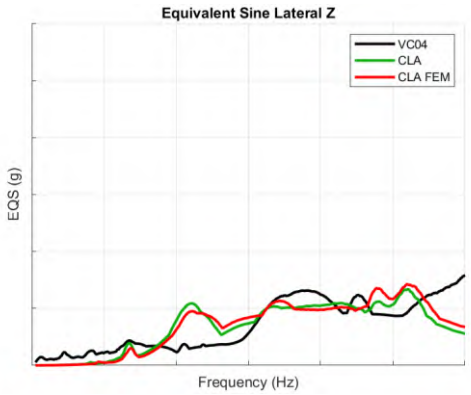


Figure 14: Zefiro 40 ignition flight lateral Z EQS comparison to CLA

P120C PO@3s and @31s

The pressure oscillation amplitude is slightly reduced for the occurrence at 3s, and for the occurrence at 31s the reduction is higher. The tuning of the amplitude is implemented with the delta-pressure measured in flight, but the acceleration at the payload interface is overestimated, as seen in the following plots. The frequency range of the forcing function is not changed, as it is according to flight.

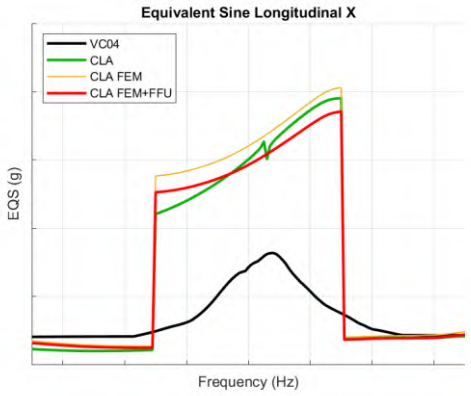


Figure 15: P120C PO@3s longitudinal X EQS / sine comparison to CLA

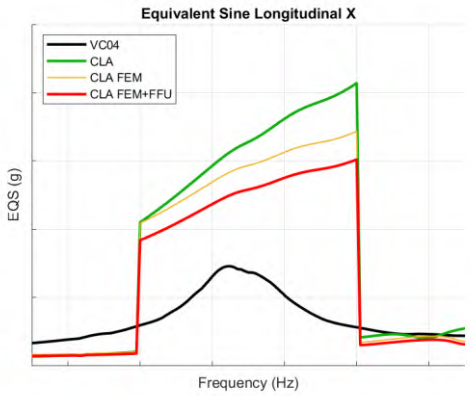


Figure 16: P120C PO@31s longitudinal X EQS / sine comparison to CLA

Zefiro 40 PO@15s

For the Zefiro 40 pressure oscillations, the frequency range of the excitation was changed. This is because the flight data shows several pressure oscillation events in time, with increasing frequency. This is shown in the waterfall plot below.

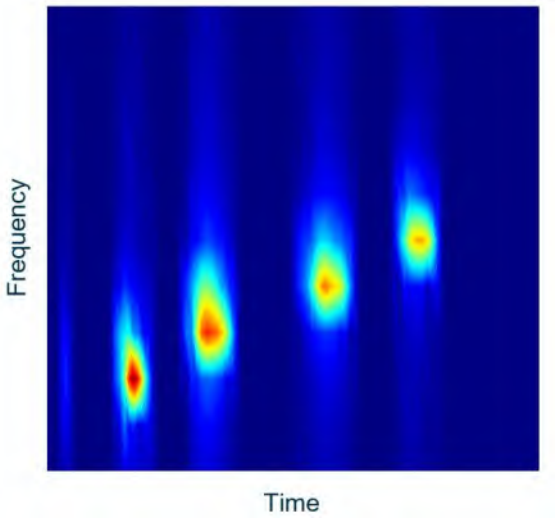


Figure 17: Waterfall plot of dynamic pressure measured inside the Zefiro 40 SRM, showing several pressure oscillation events with increasing amplitude.

To cover all the pressure oscillation events, it was decided to take the centre frequency of the excitation as the mid-frequency of all the events. This leads to a shift of the CLA curve to higher frequency, as shown in the following plot.

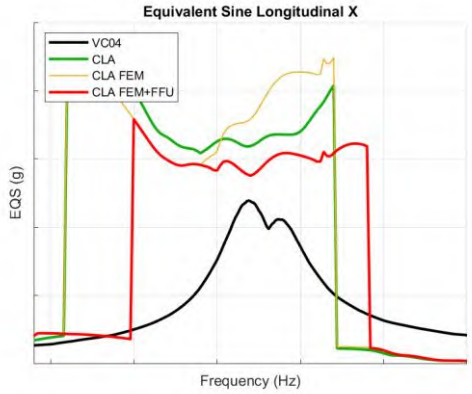


Figure 18: Zefiro 40 PO@15s longitudinal X EQS / sine comparison to CLA

Wind Gust @Mach=1 and @MaxQ

The initial CLA without correlation predicts the lateral QSL based on flight measurements. However, due to the launcher FEM correlation, the lateral QSL predicted is reduced and does not cover the flight measurements. The forcing functions for the wind gust cases are therefore increased by using a global scale factor of the forcing function, to recover the initial lateral QSL prediction. The equivalent sine for the wind gust cases is not targeted for the correlation goals because it is covered by other flight events.

OVERALL CORRELATION STATUS

The correlation status before Biomass flight correlation is shown in the following plots.

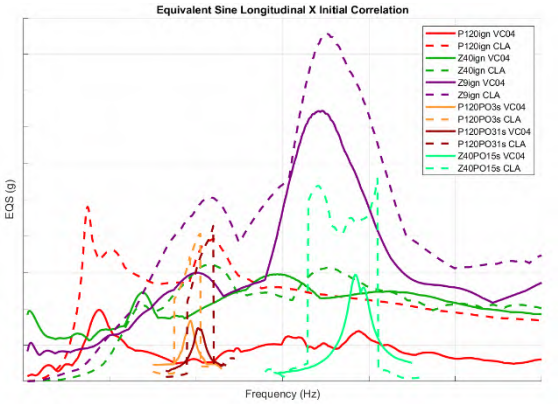


Figure 19: CLA (dashed line) vs Flight measurements (full line) EQS / sine in longitudinal X direction, before correlation

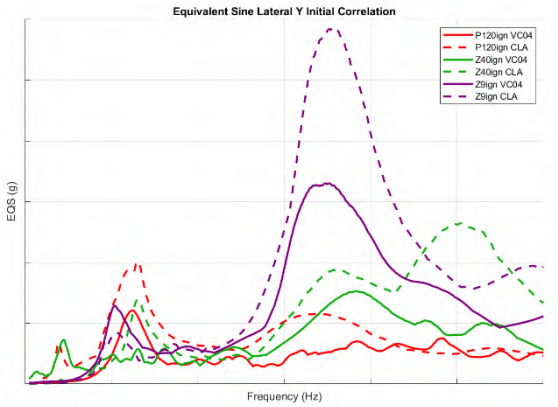


Figure 20: CLA (dashed line) vs Flight measurements (full line) EQS / sine in lateral Y direction, before correlation

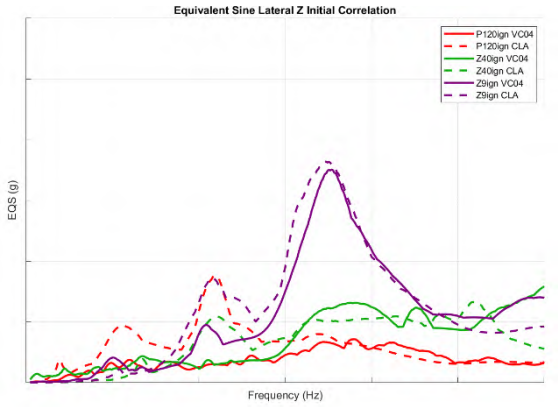


Figure 21: CLA (dashed line) vs Flight measurements (full line) EQS / sine in lateral Z direction, before correlation

The correlation status after Biomass flight correlation is shown in the following plots.

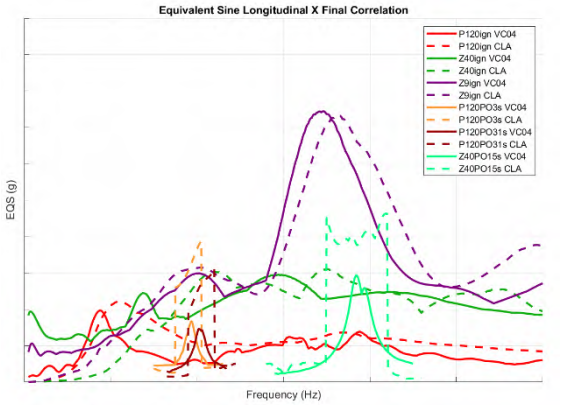


Figure 22: CLA (dashed line) vs Flight measurements (full line) EQS / sine in longitudinal X direction, after correlation

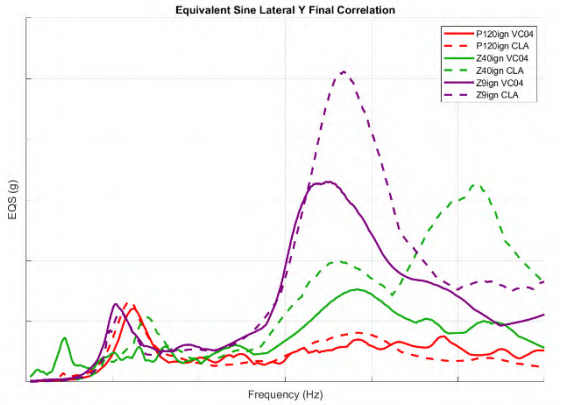


Figure 23: CLA (dashed line) vs Flight measurements (full line) EQS / sine in lateral Y direction, before correlation

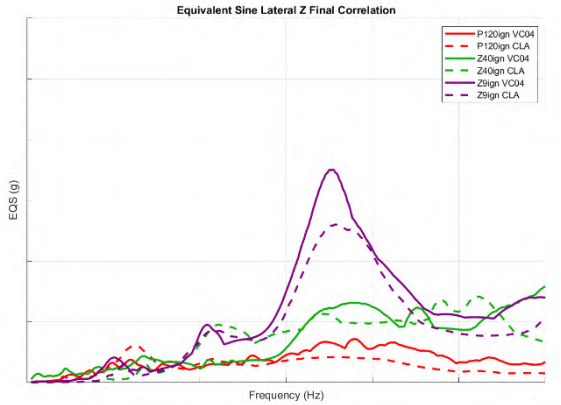


Figure 24: CLA (dashed line) vs Flight measurements (full line) EQS / sine in lateral Z direction, before correlation

The plots presented in this section show the different EQS comparing the initial CLA prediction to flight and the final CLA prediction to flight. It is seen that there are overall improvements.

For the longitudinal direction:

- For the low frequency environment, most of the overpredictions with respect to flight have been resolved by correlating the P120C ignition case (red plots).
- For the mid-frequency range, the overpredictions for the Zefiro 9 ignition have also been resolved (purple plots).
- The pressure oscillations are slightly less conservative (orange, bordeaux and light green plots) and the frequency range of the Zefiro 40 occurrences is better correlated to flight (light green plots).

For the lateral directions:

- For the low frequency environment, most of the overpredictions are resolved by P120C ignition case correlation (red plots).
- For the mid-frequency range, the overprediction for the Zefiro 9 ignition in Y direction is reduced but the Z direction is underpredicted (purple plots). This is acceptable because in typical CLA an uncertainty factor is applied to the dynamic part of the responses, while correlation CLA is performed with uncertainty factor set to 1. The underprediction is therefore resolved by the application of this factor.
- For higher frequency, the Zefiro 40 ignition in Y direction shows an overprediction with respect to flight, but the amplitude is overall low, so this is acceptable (green plots).

Besides the EQS correlation that was achieved, the first and second bending modes and first longitudinal mode of the launcher have been tuned from an error of 10-15% to an error up to 1%, and the lateral QSL during the wind gust at Mach=1 and MaxQ has been tuned after the FEM correlation to still cover the QSL based on flight measurements.

FUTURE STEPS

The correlation exercise should continue beyond the Lares-2 and Biomass flight to ensure that the ESA CLA tool is up to date and can predict as accurately as possible the QSL and low frequency environment for different spacecraft and launch configurations. For this reason, two future steps are identified for the short term:

1. Implementation of Modal Gain tool: the change from MSC Nastran 2005 + DMAPs to newer versions of Nastran is still on-going. The implementation of the Modal Gain tool will allow

the identification of the coupled launcher/spacecraft modes driving the target responses amplitude, per degree of freedom.

2. Expand CLA vs flight database: To ensure all flights are covered, the same exercise should be done for other flights, for example, Sentinel-1C single launch and FLEX + Sentinel-3C dual launch. This will allow to identify if specific spacecraft properties or launch configurations affect specific CLA results

CONCLUSION

The ESA CLA tool relies on FEM models provided by AVIO, while the forcing functions were developed internally and independently, based on the experience from past CLA tools for Ariane-5 and Vega. Because there are uncertainties in both the FEM models used and in the forcing functions, both were targeted as parameters for this correlation exercise, unlike for the Lares-2 correlation where the FEM remained mostly untouched. For the FEM correlation, PRIMODAL software was used to support the identification of the launcher FEM properties driving the target frequencies to correlate. For the forcing functions correlation, target frequencies are selected based on which frequencies of the EQS at the spacecraft interface are under or overpredicted. To be noted that only the dynamic part of the forcing functions is targeted, as the static part is related to launcher's thrust. An additional note is that the CLA performed for correlation purposes uses an uncertainty factor equal to 1 for the dynamic part of the responses, while CLA for ESA projects (not intended for correlation) includes a dynamic uncertainty factor. Therefore, any underprediction can still be covered in a typical CLA by using this uncertainty factor.

The three objectives for this correlation exercise were achieved:

1) EQS prediction at payload interface improved in most cases.
2) Launcher first and second bending modes and first longitudinal mode frequencies correlated to flight measurements.
3) Wind gust cases lateral QSL predicted by CLA cover the measured maximum lateral QS during flight.

This correlation activity emphasizes the improvement of the launcher FEM, unlike the past correlation exercise for Lares-2 which only targeted forcing functions as correlation parameters. This means that a representative behavior of Vega-C launcher is considered as important as capturing the correct responses at the payload interface.

The ESA internal CLA complements but does not substitute the Launcher CLA. It offers ESA projects an agile assessment of quasi-static and low frequency range loads. CLA is of outmost importance for the design process of spacecraft and can be used in early stages of projects for load derivation, or after design changes for de-risking purposes.

To ensure the CLA tool is able to predict flights loads as accurately as possible, it is of high priority to continue to compare CLA predictions to new flight measurements, to ensure that any variability is taken into account in the tool. This means that the correlation activities should be continued in the future for a proper maintenance of the tool. However, it is expected that after the extensive flight correlation campaign performed for Biomass, future flight correlations would not lead to significant changes in the currently derived forcing functions.

REFERENCES

[1] Kreis, A. (2000). FABE 2.6b User Documentation

[2] Craig, R.R., Bampton, M.C.C. (1968). Coupling of Substructures for Dynamic Analysis. In AIAA Journal, 6(7):1313-1319

[3] Maugis, N., Fransen, S. (2026). Dynamic Modelling of Fluid-Structure Interaction in Thin-Walled Liquid Propulsion Stages with the Real Coupled Modes Method. In Proceedings of the 19th European Conference on Spacecraft Structures Materials and Environmental Testing

[4] Vega-C User's Manual Issue 1 Revision 0

[5] Caeiro, S., et al (2024). Development and Correlation of a Coupled Loads Analysis Tool for Vega-C. In Proceedings of the 18th European Conference on Spacecraft Structures Materials and Environmental Testing

[6] Fransen, S, Fischer, H., Germès, S., et al. (2011), VEGA 3D-Evol4 Substructure Model Description and Correlation. In ESA internal report

[7] Fransen, S. (2012). VV01 Flight Correlation. In ESA internal report

[8] Roy N. (2024). PRIMODAL User's Manual Version 3

IN-ORBIT TEST OF A DLR CAMERA SPACEMAST SYSTEM

Marco STRAUBEL[(1)], **Martin F. HILLEBRANDT**[(1)], **Martin E. ZANDER**[(1)], **and Christian HÜHNE**[(1)]

[(1)]*Lightweight Design Department, DLR Institute of Lightweight Systems, Braunschweig, GERMANY*

KEYWORDS

In-orbit demonstration, SpaceMast, telemetry, deployable mast, imaging

ABSTRACT

The DLR Camera SpaceMast integrates a rollable composite mast, deployment module and instrument payload for in-orbit demonstration. This paper reports its first in-orbit deployment test over 8.6 h on 19 August 2026. Across six actuation phases, the mast reached a maximum extension of 1.72 m before final retraction to the fully stowed configuration. A premature deployed-limit signal, attributed to local narrowing of the trimmed mast flange, prevented the planned 2.5 m position but does not preclude further extension tests. Supply voltages remained within limits, and deployment currents of 213 to 290 mA were consistent with ground tests. Forty-eight images documented the deployed configurations. High-rate acceleration and angular-rate data from an IMU at the boom tip revealed responses near 1.0 and 1.85 Hz with preliminary equivalent damping ratios of 0.8% and 1.6% and initial displacement amplitudes of 0.57 and 0.072 mm. Acceleration–rate phase relationships support bending in different directions, while the single sensor location and short record limit modal assignment.

1. INTRODUCTION

The DLR Camera SpaceMast was developed to demonstrate a potential application of DLR's SpaceMast platform and to provide flight evidence in support of qualification of the underlying deployment system. Here, the deployment system comprises a rollable carbon-fibre-reinforced polymer (CFRP) mast of the coilable tubular mast (CTM) subtype and its deployment module.

A compact, low-mass instrument and camera box (ICB) was designed for the mast tip to limit the volume and complexity of the complete system and thereby reduce the cost of the in-orbit demonstration. The cameras serve as a representative instrument application and provide visual evidence of the deployed configuration.

The Camera SpaceMast was integrated into D-Orbit's ION orbital transfer vehicle (OTV) in autumn 2025 (see Fig. 1). It was launched in March 2026 aboard the SpaceX Transporter-16 rideshare mission from Vandenberg Space Force Base, California, USA.

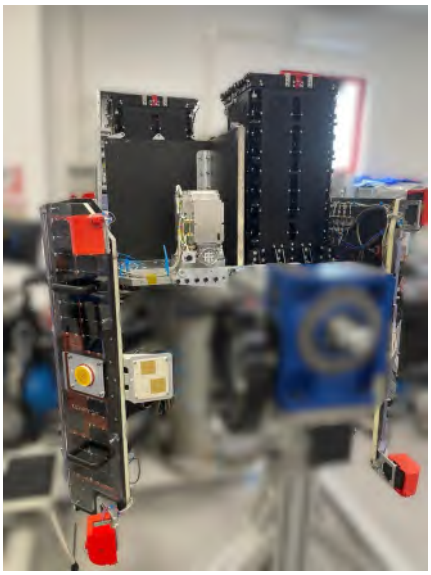


Figure 1: Camera SpaceMast integrated into D-Orbit's ION orbital transfer vehicle. (Source: D-Orbit)

The primary mission objective is to demonstrate mast deployment and retraction while recording supply voltages, motor currents, temperatures, encoder position, limit-switch states and high-rate inertial data to characterise system operation. Further planned tests include repeated deployment and retraction cycles and, towards the end of ION's operational lifetime, continuous cycling until motion is blocked. Camera imaging was a secondary objective, intended to illustrate a potential application of the mast rather than serve as a primary measure of mission success.

This paper describes the flight system, the six-orbit

test design and the results of the first in-orbit mast deployment test. The evaluation covers deployment and retraction performance, thermal and electrical behaviour, camera observations and the dynamic response recorded by the ICB IMU after the final deployment movement.

2. MECHANICAL CONFIGURATION

Fig. 2 provides an overview of the flight hardware and its camera locations. The system consists of a stationary main module mounted on the upper test platform of the host satellite and a deployable module, the ICB. A custom hold-down and release mechanism (HDRM) holds the ICB firmly against the main module. It is released by a release-nut actuator based on a shape memory alloy (SMA). A second HDRM uses a different mechanical design but the same type of actuator to secure the internal drive components of the main module. These two launch-lock mechanisms retain the system in its stowed configuration until initial operation in orbit. Once released, they require manual intervention to be reset.

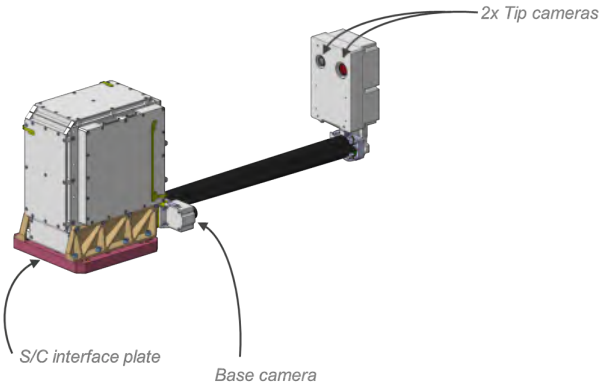


Figure 2: CAD overview of the Camera SpaceMast system.

The rollable mast provides a compact stowed configuration and separates the instrument payload from the stationary deployment module when extended. The deployment module winds and unwinds the mast through its electric drive and associated mechanisms. One encoder and four end switches provide information on mast travel, the fully deployed and stowed positions, and the states of the two launch-lock mechanisms. The architecture is intended to support instrument payloads; the cameras were selected for this demonstration because they provide a useful observation function with a comparatively low payload mass.

The smallest and lightest CTM variant currently available at DLR was selected because the expected mast loads were comparatively low. The deployed mast cross-section measures approximately 55 mm × 35 mm, while its flattened width is 67 mm. The shell consists of a single-layer plain-weave laminate with a thickness of approximately 0.15 mm. In the mast flanges, the laminate is doubled, resulting in a thickness of approximately 0.30 mm. The mass per unit length of this mast configuration is about 21 g/m.

The main module, excluding the ICB, has overall dimensions (length × height × width) of approximately 210 mm × 200 mm × 110 mm (without base camera). In the same axis order, the ICB dimensions are approximately 55 mm × 180 mm × 85 mm. The total mass of the integrated system is approximately 3.2 kg, of which about 400 g is attributable to the ICB.

The installed mast has a total length of 3.8 m. Because the fixed end attached to the coiling mandrel and the portion routed through the internal guide paths remain within the mechanism, the maximum usable deployment length is about 3.2 m.

The main module is a slightly modified version of a deployment module originally designed for a solar sail [1]. The original design had to accommodate a deployment unit for four 6 m booms within a 4U CubeSat envelope. Consequently, the module used here is larger than required for a single, comparatively short mast, and only a small fraction of the coiling mandrel's storage capacity is used. The existing design was nevertheless retained because reducing the module dimensions by a few centimetres did not justify the redesign effort.

3. AVIONICS, INSTRUMENTATION AND SPACECRAFT INTERFACE

3.1. Avionics and sensor instrumentation

The Camera SpaceMast has two avionics units, one located in the stationary main module and the other in the deployable ICB. Each unit incorporates a programmable microcontroller running a real-time operating system. The main avionics unit provides the interface to the on-board computer of the ION host vehicle.

The ICB avionics unit is connected to the main avionics unit through a custom-designed slip ring and a cable routed inside the mast. The cable is unwound and rewound together with the mast during deployment and retraction, respectively. All communication between the ICB avionics unit and the ION on-board computer is relayed through the main avionics unit, as the ICB has no direct connection to the host computer.

The main module has 20 digital temperature sensors. Some sensor integrated circuits (ICs) are soldered directly to the main avionics printed circuit board (PCB) near critical components, such as the

motor driver IC or voltage converters. Others are attached directly to the motor or to structural and mechanical components, such as outer panels or launch-lock actuators.

The main module also incorporates a rotary encoder that monitors the angular position of the mast deployment drive unit, end switches that confirm the fully stowed and fully deployed positions, and switches that indicate the states of the launch-lock mechanisms.

The ICB avionics unit is connected to a distributed sensor harness with five temperature sensors and a 4 W heater unit. In addition, two temperature sensors and a microelectromechanical systems (MEMS) inertial measurement unit (IMU) are mounted directly on the ICB avionics PCB; the IMU measures angular rates about and linear accelerations along all three axes.

The ICB microcontroller samples the six IMU channels at 20 Hz and writes the measurements continuously to a circular buffer. Each new sample is compared with configurable individual trigger thresholds for both acceleration and angular rate. When one threshold is exceeded in two consecutive samples, acquisition in the current buffer continues for 90% of its capacity before the buffer is closed. For a fully primed buffer, the resulting record contains approximately 1 s before and 9 s after the triggering event. Logging then continues in the next of eight buffers. Each buffer holds 200 measurement sets, corresponding to 10 s at the nominal sampling rate; the eight buffers therefore provide a total recording capacity of 80 s. The buffers are stored in the volatile memory of the ICB microcontroller and can be requested by the test script running on the ION onboard computer. This event-triggered approach provides high-rate monitoring throughout deployment, retraction and spacecraft attitude manoeuvres without requiring the complete data stream to be transferred continuously. It was intended to retain transient loads and oscillatory responses that could, if sufficiently excited and measured, support subsequent estimation of the deployed mast's dynamic properties.

Fig. 3 illustrates the rigid-flex PCB design used for the sensor harnesses. PCB traces route signals from sensors distributed across the structure to the avionics units, replacing individual cable connections. Flexible sections allow the harnesses to be folded around corners or wrapped around the cylindrical motor, while rigid sections support the sensors at their required locations and provide attachment points for bolting the harnesses to the structure.

In the main module, the harness also incorporates the end switches that terminate mast deployment and a dedicated connector to a separate rotary encoder PCB. In the ICB, the harness includes sensors

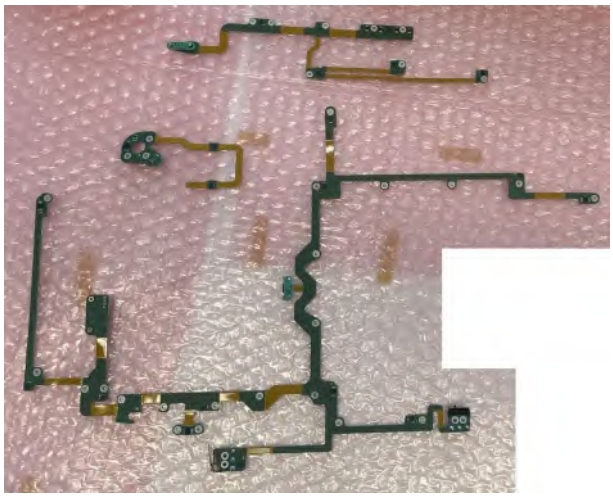


Figure 3: Rigid-flex PCB sensor harnesses: ICB temperature sensor and heater harness (top), motor and gearbox sensor harness (upper centre-left), and main module sensor harness (bottom).

for camera temperature monitoring and a custom-designed heater PCB section for heating one of the two cameras.

Fig. 4 shows the integrated flight model with its dark-green external rigid-flex PCB sensor harness visible.

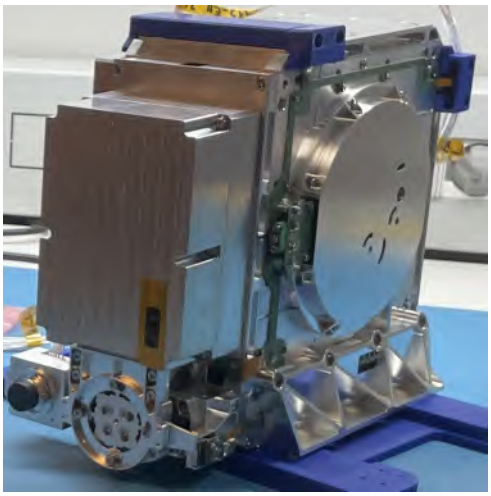


Figure 4: Integrated flight model with the external rigid-flex PCB sensor harness visible.

3.2. Camera system

The system carries three colour cameras based on two different models, designated Type A and Type B. Camera 1 (C1) is a Type A camera, whereas cameras 2 and 3 (C2 and C3) are Type B cameras. C1 and C2 are mounted in the ICB at the mast tip, while C3 is mounted on the deployment

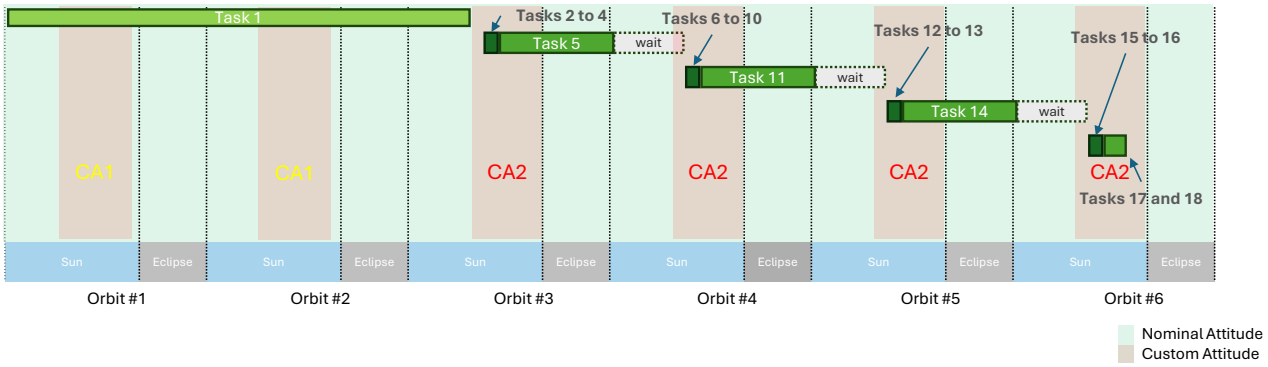


Figure 5: Planned in-orbit test sequence across six orbits, showing task and waiting periods, sunlit and eclipse phases, and nominal and custom spacecraft attitude windows.

module at the mast base and views along the mast towards the ICB. Both types support image resolutions of up to 5 megapixels and can output images in RAW and JPEG formats. Type A can acquire image sequences and store them in local memory for subsequent transfer one image at a time. Type B acquires single images, each of which must be transferred before the next image can be captured. Both camera types provide manual control of image-acquisition settings, including white balance, exposure and gain. Type B additionally supports automatic adjustment of these parameters. Manual control allows the acquisition settings to be tailored to specific structural details under the varying illumination conditions encountered in orbit. Automatic exposure and gain control may not make the features of interest sufficiently visible, in which case manual adjustment is needed.

3.3. Spacecraft interface and test control

The main avionics unit communicates with the ION host spacecraft through an RS-485 link, and the spacecraft supplies electrical power to the payload during payload operation. Test sequences are executed running scripting procedures on an ION onboard computer (OBC). The DLR operations team develops the control scripts on the ground and provides them to the spacecraft provider for upload to the OBC. The scripts can be replaced during the mission, so testing is not limited to the sequences defined before launch.

The scripts issue commands to the payload and collect the returned telemetry and images. A storage area on the OBC is available to retain these data for subsequent downlink to the ground. Image transfer from the payload to the host computer and downlink to the ground are thus separate operations.

The DLR Camera SpaceMast firmware provides an extensive set of low-level commands for individual operations, including actuation and requests for sensor readings. Each commanded motor movement can be terminated by four independently configured criteria: the relevant end switch, an adjustable motor-current threshold, an adjustable maximum actuation time, and a commanded encoder target. The host-side scripts combine these commands into complete test sequences, allowing the test logic to run on the OBC while keeping the payload firmware comparatively simple. The scripts can execute a predefined test plan and respond to detected conditions, for example by aborting a test if a critical condition is detected. Within the capabilities of the existing command set, new test sequences and diagnostic or mitigation procedures can therefore be implemented by replacing the scripts without modifying the payload firmware. This separation allows the test programme to be adapted to new objectives and to anomalies observed during the mission.

4. IN-ORBIT TEST DESIGN

4.1. Test objectives

The reported sequence was the first in-orbit deployment test, with further tests planned for October 2026. The primary objective of the in-orbit test was to demonstrate the deployment and retraction of the rollable mast while recording telemetry data to characterise the system's operational behaviour. The secondary objective was to acquire images of the deployed configuration to illustrate a potential application of the mast. The test was deliberately planned for conservative thermal and operational conditions rather than to explore the system's operating limits.

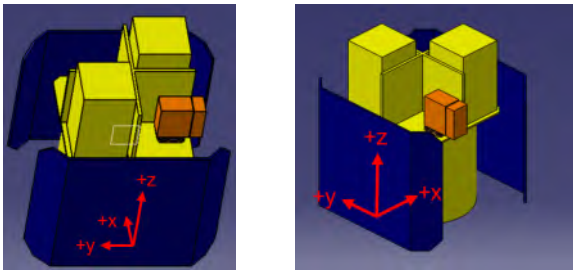
4.2. Test plan

Fig. 5 shows the planned task sequence in relation to the orbital illumination and spacecraft attitude windows; Tab. 1 defines the 18 numbered tasks and their nominal durations. The two custom spacecraft attitudes referenced in the plan are illustrated in Fig. 6a (CA1) and Fig. 6b (CA2). The plan

combined thermal conditioning, incremental deployment, a short retraction check, image acquisition and transfer to the ION OBC, followed by full retraction and payload power-down. Successful retraction from approximately 0.35 m to 0.30 m in Task 6 was a condition for continuing the test; failure to confirm retraction was an abort criterion. The lengths and durations in the table are planning values; the measured movement endpoints and durations are reported in Tab. 2.

4.3. Thermal conditioning and execution windows

The plan allocated approximately 3 h, or two heat-soak orbits, to initial warming with passive telemetry logging; the flight script included an additional 35 min before the first actuation. As shown in Fig. 5, approximately 25 min of each orbit were reserved for ION's nominal attitude to maintain the spacecraft power balance over the six-orbit sequence. In this attitude, the spacecraft $+X$ direction defined in Fig. 6 is pointed towards the Sun, allowing the primary solar array to generate electrical power and recharge the spacecraft batteries. The nominal-attitude intervals are intended to prevent the battery state of charge from falling to a critical level during the extended test. However, with $+X$ pointed towards the Sun, the solar array, CubeSat dispensers and an intervening transverse panel completely shield the Camera SpaceMast on the upper deck from direct sunlight. The deployment system therefore remained at temperatures between -30 °C and -25 °C during the many days of nominal-attitude operation preceding this test.



(a) Custom Attitude 1 (CA1) *(b) Custom Attitude 2 (CA2)*

Figure 6: Visualisations of the two custom spacecraft attitudes referenced in the test plan. The red triads indicate the positive axes of the spacecraft body-fixed coordinate system.

During the custom-attitude portions of the two initial heat-soak orbits, CA1 oriented the spacecraft to expose the deployment system to sunlight. Earlier tests had identified CA1 as the most effective heating attitude, with one to two orbits sufficient to raise the temperatures of the critical components above 0 °C. CA2 provided a compromise between maintaining system temperatures and obtaining suitable illumination for the ICB cameras while avoiding glare in C3.

Ground testing in a thermal-vacuum chamber had already demonstrated system operation from $-40\,^{\circ}$C to $+80\,^{\circ}$C. The initial warming was therefore an additional precaution for the first deployment test, not a prerequisite established by the ground tests. Deployment and retraction were likewise restricted to sunlit orbital intervals, although neither the mast nor the deployment mechanism requires sunlight to operate. The script scheduled six movements and seven image-acquisition sessions, with a time reserve before the end of each sunlit operating window; image transfers could continue beyond these windows.

4.4. Image-transfer time budget

The overall test duration was governed mainly by the two initial heat-soak orbits and the time required to transfer images to the ION OBC. Packet exchanges and acknowledgements on the payload-to-host link add overhead to these transfers. Rates between 0.5 kB/s and 0.8 kB/s are typical. At these rates, a 500 kB JPEG requires approximately 11 min to 17 min, respectively, which explains the extended image-transfer blocks in the plan. These rates describe image transfer to the host computer, not the subsequent downlink to the ground.

5. TEST RESULTS

5.1. Data sources and time alignment

The analysis uses two telemetry sources: payload housekeeping recorded by the test script running on the OBC, and S/C telemetry from the OBC, including orbit and attitude data. Additional sources comprise the flight-script debug log, 27 IMU-buffer files, and two OBC synchronisation records. Decoding produces 1,479 housekeeping records and 1,064 S/C records. The separate IMU files provide 5,172 measurement sets, including their calibration records.

The flight-script log provides explicit movement-completion times, durations and camera attempts. SpaceMast housekeeping is placed on the same elapsed test-time axis using the synchronisation records.

5.2. Boom extension measurement

During ground testing of the flight model, the fully deployed end switch was reached at 4,057 encoder ticks and a measured boom extension of 3,273 mm. This reference corresponds to 0.807 mm per encoder tick and defines the boom extension values

Table 1: Planned tasks corresponding to Fig. 5. Durations are nominal estimates; no duration was specified for payload power-down.

Task	Planned operation	Duration
1	Thermal soak over two orbits with passive telemetry logging.	3 h
2	Acquire initial low-quality reference images in the retracted configuration.	2 min
3	Deploy 0.35 m of mast.	30 s
4	Acquire images at this extension.	10 min
5	Transfer images to the ION OBC.	About 1 h
6	Retract to 0.30 m and verify successful retraction; abort if the check fails.	30 s
7	Deploy to 0.5 m.	1 min
8	Acquire images at this extension.	2 min
9	Deploy to 1.5 m.	3 min
10	Acquire images at this extension.	10 min
11	Transfer images to the ION OBC.	About 1 h
12	Continue deployment to 2.5 m.	3 min
13	Acquire images at this extension.	5 min
14	Transfer images to the ION OBC.	About 1 h
15	Fully retract the mast.	5 min
16	Acquire reference images of the stowed configuration.	2 min
17	Transfer images to the ION OBC.	About 10 min
18	Power down the payload.	—

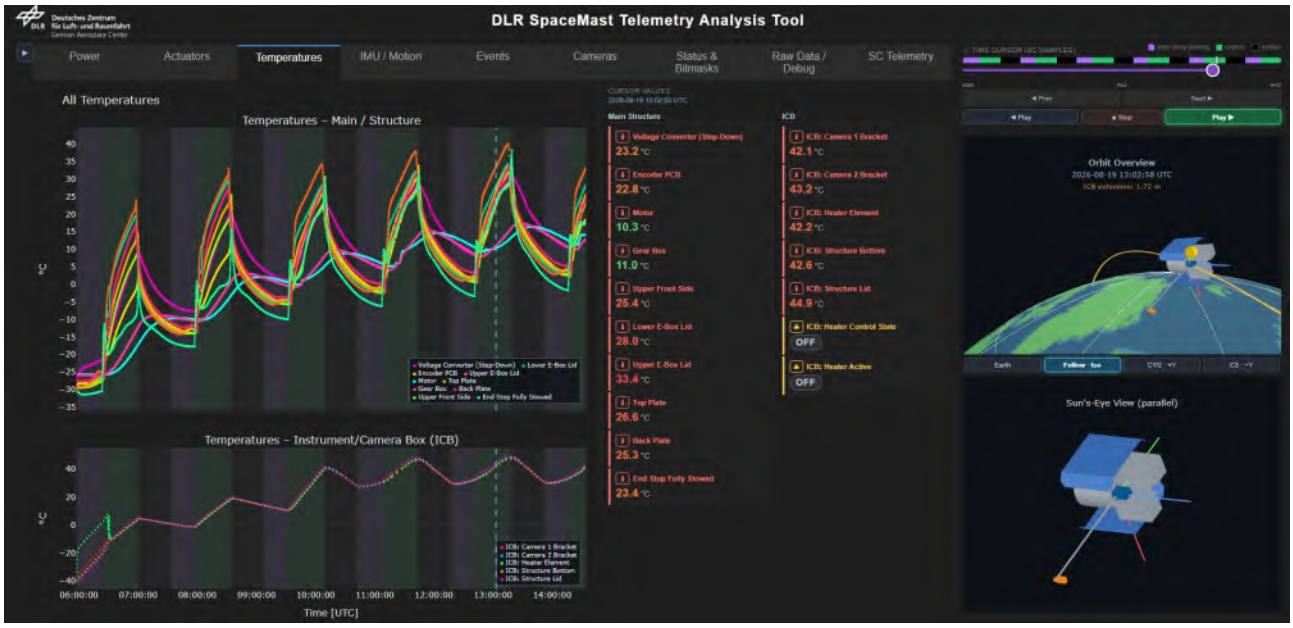


Figure 7: Custom Python-based analysis tool: temperature histories of the main module and ICB (left), numerical values at the selected time (centre), and synchronised orbit and Sun's-eye views (right). Green, purple and black bands indicate custom attitude, nominal attitude and eclipse, respectively.

reported here. The launch-lock mechanisms had already been released in a preceding in-orbit test, during which elastic preload caused a small outward movement of the ICB. The encoder was subsequently zeroed before the reported deployment test while the ICB was no longer fully stowed. Final retraction continued to the fully stowed end switch; the resulting value of -2 ticks therefore reflects the offset between the test-specific encoder zero and the fully stowed position rather than a physical negative extension.

5.3. Custom analysis software tool

A custom Python-based software tool was developed to combine and analyse the different datasets. Despite AI assistance, its development required approximately two weeks of active engineering work. Fig. 7 shows the temperature tab of the analysis tool. Temperature histories for the main module, labelled

Table 2: Movement results from log completion records. Length and mean velocity are calculated from the measured boom extension and movement duration.

Phase	Target [ticks]	Start → end [ticks]	End [mm]	Duration [s]	$\bar{v}$ [mm/s]	Outcome
DEPL1	434	$0 \rightarrow 434$	350	51.17	6.84	Target reached
RETR1	372	$434 \rightarrow 371$	299	7.80	-6.52	One tick below target
DEPL2	620	$371 \rightarrow 620$	500	30.67	6.55	Target reached
DEPL3	1859	$620 \rightarrow 1859$	1500	133.67	7.48	Target reached
DEPL4	3099	$1859 \rightarrow 2126$	1715	30.00	7.18	Premature limit signal
RETR2	Stowed	$2126 \rightarrow -2$	Stowed	168.10	-10.21	Stowed switch reached

“Main / Structure”, and the ICB occupy the left-hand side. The plots cover the complete test of approximately 8.6 h across six orbits.

The time cursor at the upper right allows the user to navigate the dataset and inspect the recorded temperatures together with the reconstructed spacecraft position and attitude at a selected time. A vertical dashed line marks this time in the temperature plots, while the central panel displays the corresponding numerical values. Both the plot backgrounds and the band above the time cursor distinguish custom-attitude intervals in green, nominal-attitude intervals in purple and eclipse intervals in black. This common colour scheme relates the temperature evolution to eclipse entry and exit, nominal-attitude periods for spacecraft battery charging, and custom-attitude periods used for payload heating and operations such as mast deployment.

Two synchronised 3D views on the right provide the spatial context for the selected time. The upper view shows the spacecraft’s position above the Earth, while the lower view presents the spacecraft and deployment system from the Sun’s perspective. The displayed boom extension is derived from the encoder value at the selected time. The latter is particularly useful for thermal interpretation because it allows the user to assess which parts of the deployment system face the Sun and which are geometrically shaded by surrounding spacecraft structures.

The other tabs allow the user to inspect the boom extension, power-related parameters, end-switch states, and IMU measurements in a similar manner.

5.4. Deployment and Retraction Performance

The script executed all six actuation phases and seven image-acquisition sessions and switched off the payload at an elapsed time of 08:36:51.

Tab. 2 separates completion of a movement command from achievement of its intended endpoint. DEPL1, DEPL2 and DEPL3 reached their encoder targets. RETR1 stopped one tick below its nominal value. DEPL4 ended at 2,126 ticks rather than 3,099 ticks, limiting the measured boom extension to 1.72 m. The subsequent RETR2 movement returned from this configuration to the stowed switch in approximately 168 s.

The four extension phases had mean speeds between 6.55 and 7.48 mm/s. DEPL4 lay within this range up to its stop. The final retraction was faster on average, at approximately 10.21 mm/s.

Fig. 8 relates boom extension and motor operation over the complete test. The upper image covers all six orbits, while the lower image resolves the fourth orbit with one retraction and several deployments up to 1.50 m. The displayed channels comprise boom extension, motor current, the temperatures of the motor-driver IC and motor housing, and the commanded motor states.

Most of the elapsed test time was spent in thermal conditioning, acquisition, transfer and waiting intervals, rather than moving the mast.

The premature termination of DEPL4 was not part of the planned sequence. Telemetry shows that the fully deployed end switch became active at a measured boom extension of 1.72 m, although the mechanism provides about 3.2 m of usable mast travel. The state of this switch is shown in the bottom subplot of the upper subfigure in Fig. 8. The payload avionics therefore terminated the deployment as designed and reported the end-switch condition to the test script running on the OBC.

The fully deployed end switch is implemented differently from the fully stowed switch because the mechanism provides no comparably accessible rigid component at the deployed endpoint. During deployment, a roller attached to the switch bears laterally against the narrow edge of the flattened mast flange. A notch in this edge at the intended fully deployed position allows the roller to enter the recess and actuate the switch.

Tests with an equivalent copy of the flight hardware showed that a sufficiently narrow local section of the mast can reproduce premature switch actuation. The current working hypothesis is that local width variation introduced when the laminated mast edges were trimmed caused the flight mast flange near the observed switch point to be narrow enough to mimic the intended notch. This hypothesis is further sup-

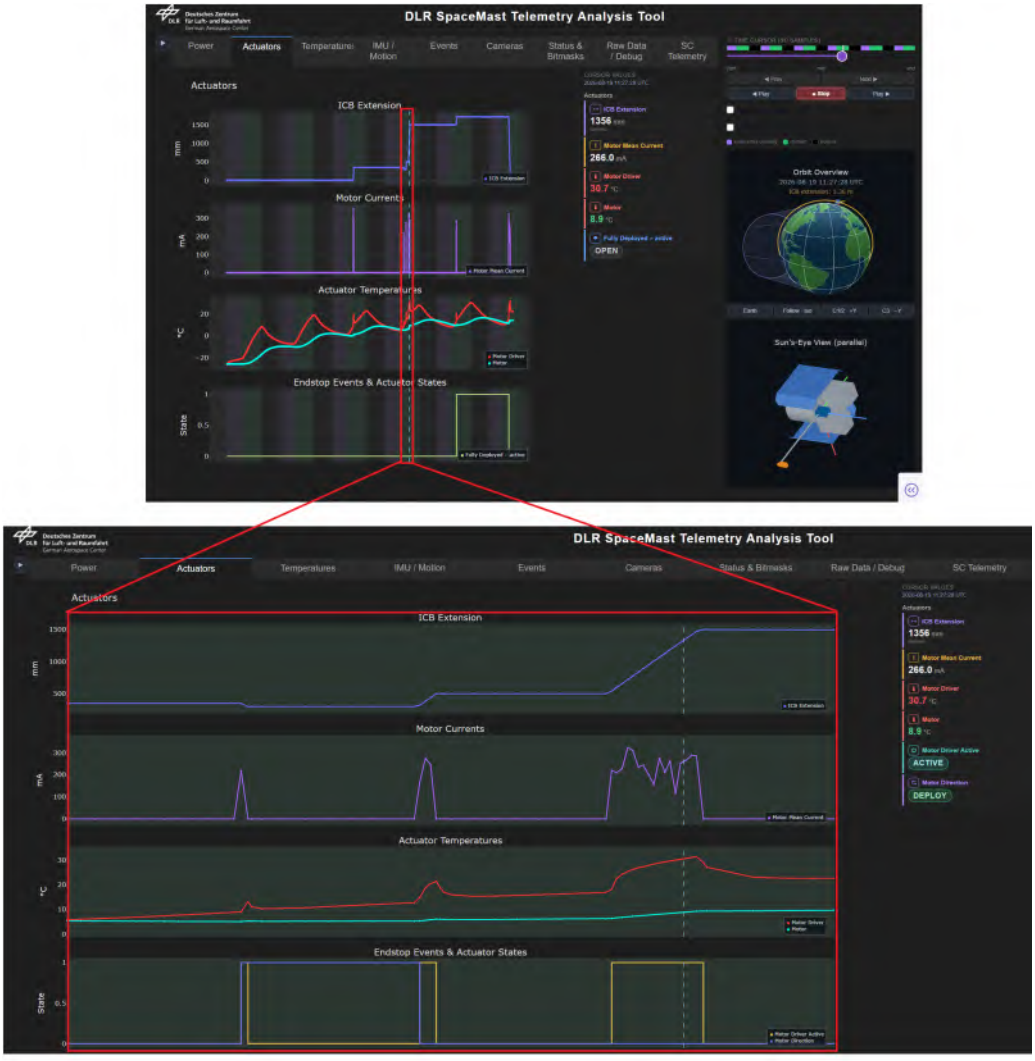


Figure 8: Actuator data across all six orbits (upper image) and a detailed view of the fourth orbit, including one retraction and several deployments up to 1.50 m (lower image).

ported by the fully deployed switch returning to its inactive state during retraction as the suspected locally narrowed section moved away from the roller. The signal therefore did not remain latched, and no persistent failure of the switch was observed after the mast had returned to its fully stowed configuration. The available evidence supports this mechanism as a plausible explanation, but the local width deviation has not been quantified or directly verified on the flight mast.

The event limited the achieved extension but did not prevent the autonomous sequence from continuing. After the payload firmware stopped the motor, the host-side script treated the deployment command as completed, proceeded with the planned camera sessions, and commanded full retraction during the following orbit. The mechanism subsequently returned to its fully stowed configuration.

5.5. Thermal Behaviour

At the beginning of the available housekeeping sequence, the C1 and C2 brackets were at -40.5 and $-40.8\,^{\circ}$C, respectively. The flight procedure permitted this initial cold condition and provided active heating with a configured minimum-temperature set point of $-10\,^{\circ}$C. With the 4 W heater operating, C1 exceeded its lower operating-temperature limit of $-30\,^{\circ}$C after approximately eight minutes and C2 after approximately fifteen minutes. Apart from the heater element, the ICB structure and camera brackets are made of aluminium; the resulting heat distribution kept the remaining ICB temperature measurements within a $7\,^{\circ}$C band.

Fig. 7 shows the active heating of the ICB as well as the passive warm-up and subsequent temperature evolution. The gearbox temperature was above the configured $-10\,^{\circ}$C movement threshold at every ac-

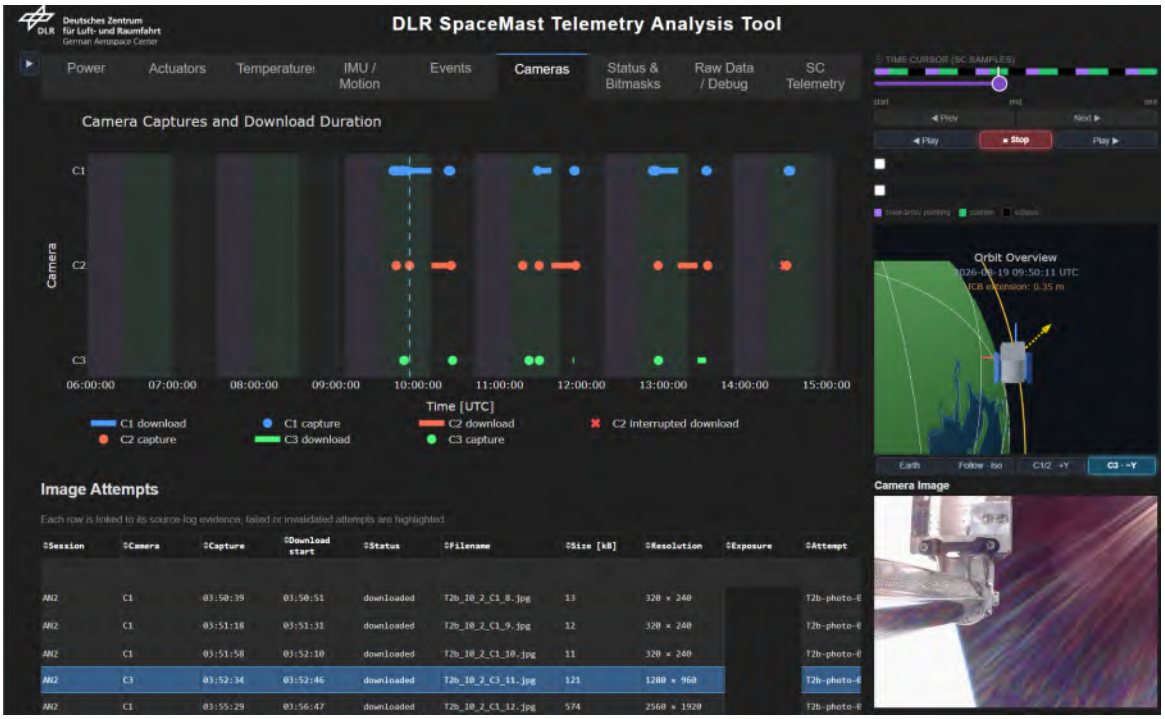


Figure 9: Camera tab of the custom analysis tool, combining capture and transfer events for all three cameras with the associated log records, spacecraft geometry and selected on-board image.

tuation. The long initial soak therefore separated the cold start from the first commanded movement. No post-initialisation overtemperature shutdown was reported in the flight log.

The C1 bracket reached 47.8 °C over the full test, while the PCB channel below the voltage converter reached 55.6 °C. These maxima occurred at different locations and should not be combined into a temperature cycle for a single component. The highest C1-bracket value was approximately 32 °C below the configured 80 °C emergency threshold. This comparison describes margin to that script threshold only.

The test script also included a staged response for an ICB overtemperature condition. At the first protection stage, it would have switched off the cameras to reduce heat dissipation from electrical loads within the ICB. If the temperature had continued to increase, the main avionics would have disconnected power from the ICB avionics and re-enabled it only periodically, at intervals of several minutes, to obtain updated temperature records. This contingency was not invoked during the reported test.

5.6. Electrical Behaviour

All monitored supply voltages remained within their defined operating thresholds throughout the sampled housekeeping data. The external input voltage of the main avionics ranged from approximately 15.63 to 15.97 V, while the 15-V input measured in the ICB ranged from approximately 15.31 to 15.82 V. The locally generated 3.3-V rails remained between approximately 3.323 and 3.332 V in the main avionics and between 3.288 and 3.304 V in the ICB. No relevant voltage excursion or unexpectedly high current was observed in the recorded data. No persistent sensor failure occurred, and all 27 temperature channels provided valid measurements during the test.

Fig. 8 relates the actuator currents and temperatures to the changes in boom extension. In the lower panel, every commanded change in extension coincides with motor-current activity. The phase-averaged filtered motor currents for the four deployment movements ranged from 213 to 290 mA and therefore indicate comparatively low motor loading. For comparison, the motor can sustain currents of approximately 0.8 to 1.0 A for extended operation under substantially greater mechanical load. Ground tests of the integrated deployment system produced maximum motor currents of approximately 400 mA. The phase-averaged flight values are therefore consistent with the ground-test current range and provide no indication of increased mechanical loading or degraded drive performance in orbit.

The temperature response in the same panel follows the actuator activity. Both the motor and the motor-driver IC on the main avionics PCB warm slightly

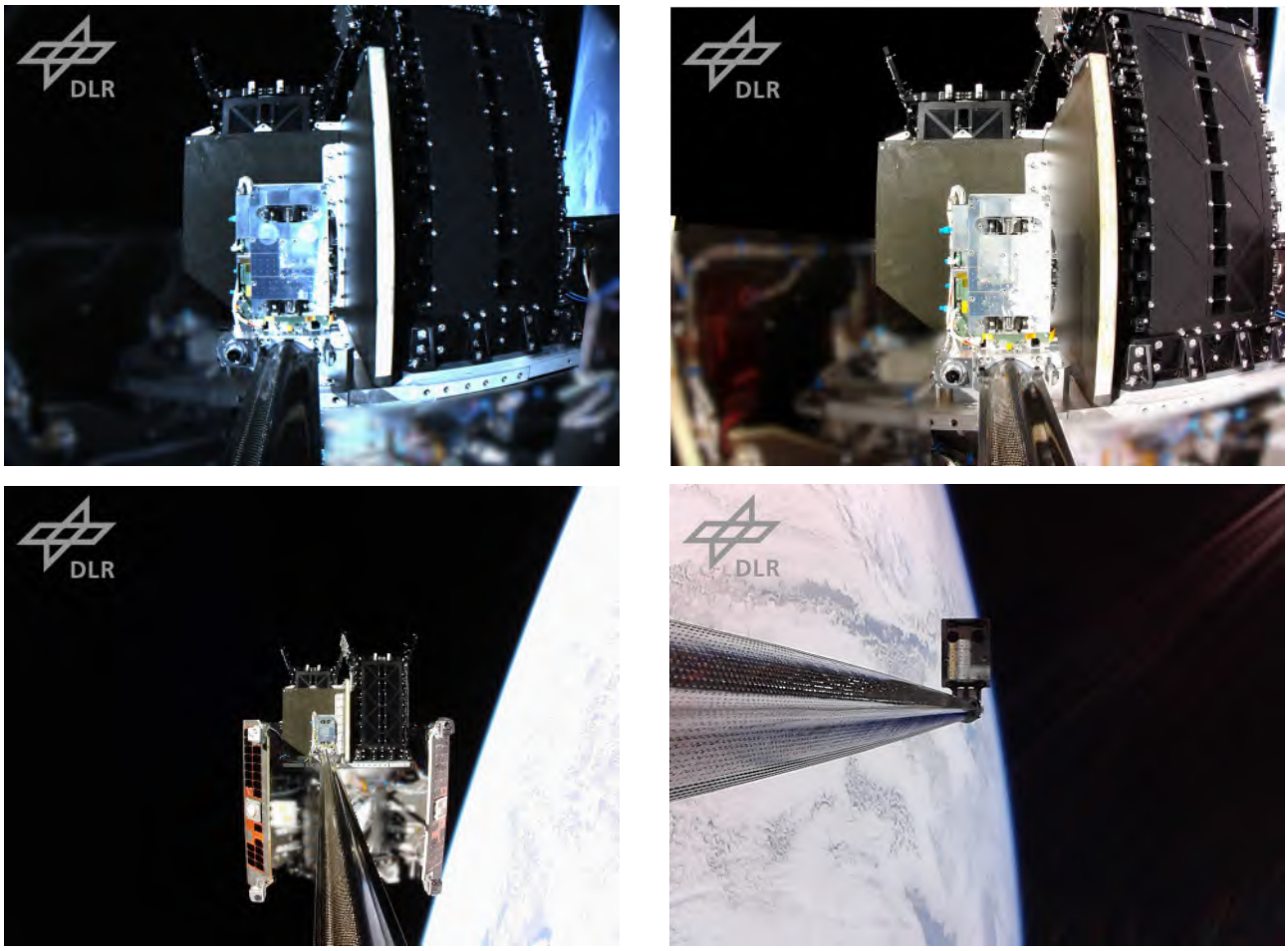


Figure 10: On-board views during sunlit acquisition phases. Top left: C1 at a boom extension of 0.35 m. Top right: C2 at 0.35 m. Bottom left: C2 at 1.72 m. Bottom right: C3 looking along the mast towards the ICB at 1.72 m. The C1 frame and both C2 frames were recorded at the full 5-megapixel resolution; the C3 frame is a 640×480 *pixel test image.*

during operation, with the clearest increase occurring during the longer deployment to a boom extension of 1.50 m. The motor-driver temperature during this interval shows an approximately first-order rise towards an apparent asymptote rather than an uncontrolled increase. Although the finite actuation interval does not establish a steady-state temperature or thermal time constant, the recorded response provides no indication of thermal overload under the executed duty cycle.

6. CAMERA OBSERVATIONS

6.1. Image acquisition

The parsed log records the transfer of 48 unique image files: 34 from C1, nine from C2 and five from C3. Fig. 9 shows the corresponding camera tab of the analysis tool, which combines capture and transfer events with the associated log records, spacecraft attitude, and a selected on-board image.

Fig. 10 compares the C1 and C2 views at a boom extension of 0.35 m with the C2 and opposing C3 views at 1.72 m. In the C1 and C2 images at 0.35 m, the deployment module occupies a substantial part of the image. At 1.72 m, a larger portion of the host is visible in the C2 image and its apparent size is reduced. This is consistent with the increased camera separation. The C3 image shows the mast extending towards the ICB, including the two camera apertures.

6.2. Image quality and camera settings

Of the four frames in Fig. 10, the C1 frame and both C2 frames were acquired at the full 5-megapixel resolution. The C3 frame was acquired at 640×480 pixels as a low-resolution test image. Despite its lower resolution, it provides a clear view along the mast towards the ICB and is therefore included in the figure.

Selected regions in the four presentation images

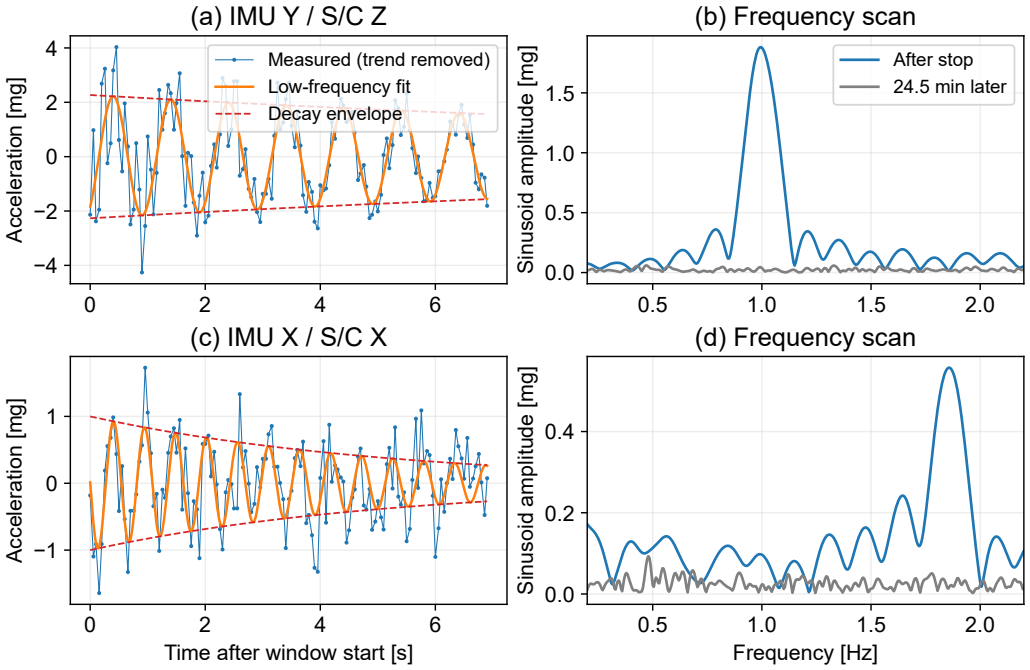


Figure 11: ICB acceleration after deployment to 1.72 m. Left: trend-corrected measurements, fitted low-frequency components and decay envelopes. Right: constant-amplitude sinusoid scans immediately after stopping and 24.5 min later. Time zero is 06:54:48.011 elapsed test time.

were lightly blurred at the request of the host-satellite operator to limit the visibility of spacecraft details. The images should therefore be treated as presentation copies rather than unmodified downlinked files. The processing does not obscure the SpaceMast features discussed here.

The Type B images from C2 and C3 provide a useful exposure balance under the strong scene contrast. Illuminated spacecraft and mast features remain visible, while space and deeply shaded regions are rendered nearly black. The settings used for Type B were therefore suitable for documenting the deployed configuration.

A test series with manually selected exposure settings was acquired with the Type A camera C1. The reviewed images indicate that the selected exposure times were still slightly too short to provide the desired detail in darker regions. Longer exposure times are planned for subsequent tests and are expected to improve the usable image detail to a level comparable with the Type B results.

7. DYNAMIC RESPONSE OF THE DEPLOYED MAST

7.1. Recorded response and frequency content

When the final deployment movement stopped at a boom extension of 1.72 m, the motion of the ICB did not cease immediately. The ICB IMU recorded a decaying oscillatory response even though no dedicated excitation device was available. The movement of the mast–ICB assembly and its subsequent stop are therefore the likely excitation sources.

The analysed interval starts at elapsed test time 06:54:48.011, about one second after the logged movement completion, and contains 139 samples over 6.9 s at a nominal sampling rate of 20 Hz.

Fig. 11 shows distinct oscillatory components near 1.0 and 1.85 Hz. The lower-frequency response appears most clearly in acceleration along IMU Y and angular rate about IMU X; the higher-frequency response appears in acceleration along IMU X and angular rate about IMU Z. The spacecraft body-frame convention is shown in Fig. 6. For the installed sensor, IMU X, Y and Z correspond to spacecraft X, Z and negative Y, respectively. A least-squares frequency scan fitted a sinusoid, offset and linear trend directly to the native samples without band-pass filtering. Both peaks remained when the start of the analysis window was varied, and an additional Fourier-transform check confirmed their locations. A second acquisition 24.5 min later at the same extension contained substantially smaller amplitudes at both frequencies, linking the initial response to the preceding deployment movement.

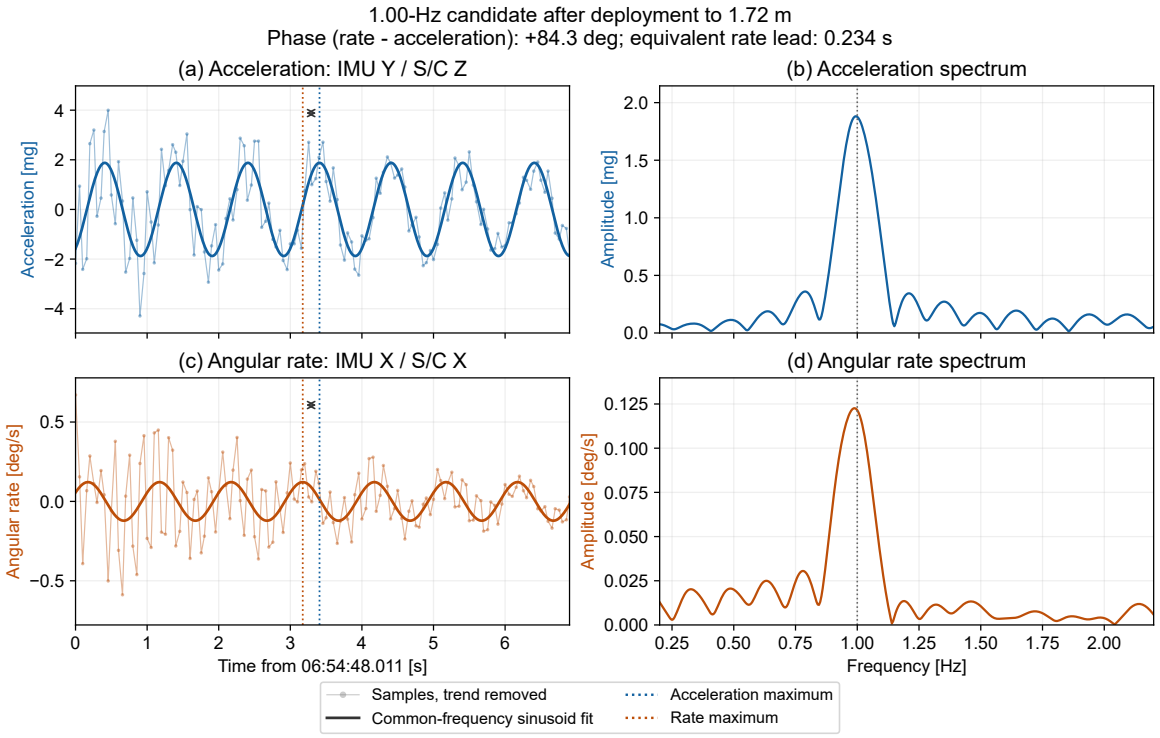


Figure 12: Acceleration and angular rate associated with the 1.0-Hz response. Upper row: IMU Y acceleration; lower row: IMU X angular rate. Left: trend-corrected samples and constant-amplitude sinusoid fits with freely determined phases. Dotted lines mark corresponding fitted maxima. Right: amplitude spectra from sinusoidal least-squares scans.

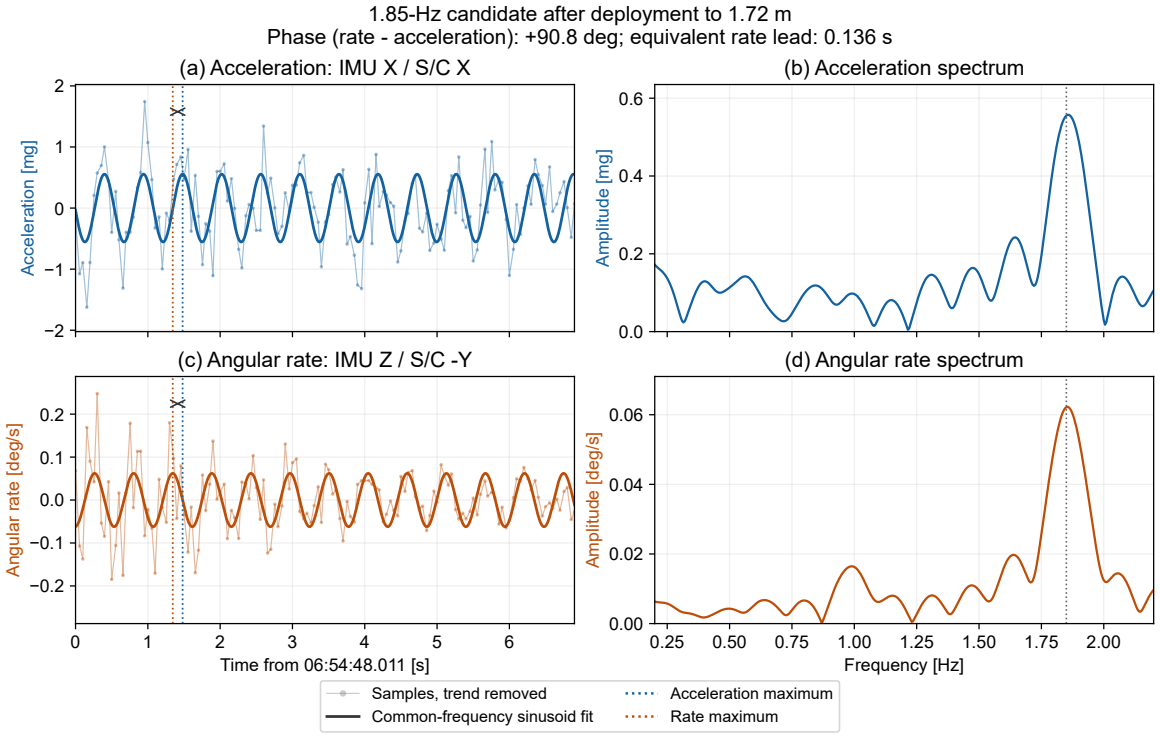


Figure 13: Acceleration and angular rate associated with the 1.85-Hz response, using the same window and display conventions as Fig. 12. Upper row: IMU X acceleration; lower row: IMU Z angular rate, corresponding to rotation about the negative spacecraft Y-axis.

7.2. Phase relationship and mode interpretation

Figs. 12 and 13 compare the associated acceleration and angular-rate channels separately for each frequency component. The time histories use identical time axes, and the spectra show matching dominant peaks within each pair. For each comparison, both channels were fitted at the same frequency, while their phases were determined independently without shifting either signal. In the native IMU coordinates, angular rate leads acceleration by 84.3 degrees at 1.0 Hz and by 90.8 degrees at 1.85 Hz. Including the previously fitted decay and higher-frequency terms gives similar phase differences of 83.3 and 92.1 degrees, respectively.

These near-quarter-period phase differences are consistent with bending motion involving both translation and rotation of the ICB. For a single bending mode, local displacement and slope depend on the same modal coordinate; acceleration contains its second time derivative, whereas angular rate contains its first. An approximately harmonic response therefore gives a phase difference near 90 degrees, with the sign depending on the coordinate directions and local mode shape. This relationship supports the bending interpretation but does not identify the mode order.

The non-circular CTM cross-section gives the mast different bending stiffnesses in its two transverse directions. The two measured frequencies and their different dominant acceleration components are therefore compatible with bending responses in these directions. This difference in bending stiffness provides a physical basis for interpreting the 1.0- and 1.85-Hz components as the lowest bending modes of the mast–ICB assembly in the two respective directions, including the compliance of the root interface.

The present measurement cannot confirm this mode assignment because all six IMU channels originate from a single sensor location and do not describe the spatial mode shapes. A higher bending mode could produce the same local phase relationship, while a lower mode could have remained weakly excited or unresolved in the short record. Ground modal tests with spatially distributed measurements and a model including ICB mass, inertia and root compliance are required to establish the mode order. Longer in-orbit recordings at several boom extensions would then show whether the measured frequencies vary as expected for the proposed modes.

7.3. Damping estimates

The decay visible in Fig. 11 was quantified by fitting an exponentially damped sinusoid together with an offset and linear trend:

$$a(t) = c_0 + c_1 t + A_0 e^{-\sigma t} \cos(2\pi f_d t + \phi). \quad (1)$$

Here, f_d is the damped frequency and σ is the amplitude decay rate. Acceleration amplitudes in mg denote thousandths of standard gravity. Additional fits included a second oscillatory term near 5.3 or 6.9 Hz to account for higher-frequency content visible in the raw signals. Allowing either positive or negative decay rates avoided imposing decay on the data. For an equivalent viscously damped mode, the damping ratio is $\zeta = \sigma / \sqrt{(2\pi f_d)^2 + \sigma^2}$.

The reference-window fits yielded approximate damping ratios of 0.8% and 1.6% for the 1.0- and 1.85-Hz components, respectively (Tab. 3). Separate acceleration and angular-rate fits gave similar values within this window. The corresponding amplitude time constants were about 20 and 5.3 s, showing that the 1.0-Hz response persisted longer.

Table 3: Estimated dynamic-response parameters at 1.72 m. Amplitudes refer to the beginning and end of the 6.9-s reference window.

Parameter	1.0 Hz	1.85 Hz
Equivalent damping ratio	0.8%	1.6%
Amplitude time constant [s]	20	5.3
Initial acceleration amplitude [mg]	2.27	1.00
Initial displacement amplitude [mm]	0.57	0.072
Final displacement amplitude [mm]	0.39	0.020

The damping values are preliminary because the record contains only about seven cycles of the lower-frequency response and less than one of its estimated decay time constants. Across five window starts, three fit models and the associated acceleration and rate channels, the estimates varied from 0.3 to 1.9% at 1.0 Hz and from 1.0 to 2.4% at 1.85 Hz. These ranges describe sensitivity to the selected window and model rather than statistical confidence intervals. The 1.85-Hz angular-rate result was more stable and remained between 1.4 and 1.7%.

7.4. Oscillation amplitudes and interpretation

Analytical double integration of the fitted acceleration components gives the displacement histories in Fig. 14. For the damped sinusoid, the displacement envelope is

$$X(t) = \frac{A_0 e^{-\sigma t}}{(2\pi f_d)^2 + \sigma^2}. \quad (2)$$

Acceleration was converted to SI units before integration; offset, trend and unknown integration constants were excluded. This yields the oscillatory displacement without accumulating drift from direct integration of the full measured signal.

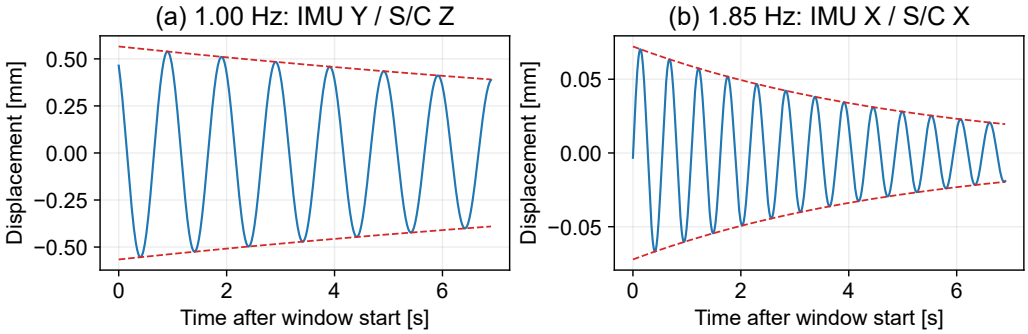


Figure 14: Estimated displacement components at the ICB IMU from analytical double integration of the acceleration fits. Dashed curves show the amplitude envelopes. Time zero is the same as in Fig. 11.

At the beginning of the reference window, the estimated one-sided amplitudes were 0.57 mm along spacecraft Z and 0.072 mm along spacecraft X. They decreased to 0.39 and 0.020 mm, respectively, over the following 6.9 s. These values describe the selected components at the IMU location, rather than the total motion or the maximum excursion during motor stopping. Their interpretation as mast-tip displacement relative to the deployment module assumes negligible base motion; rotation of the ICB also contributes to translation at an offset sensor location.

Although small, these amplitudes provide quantitative evidence of a sub-millimetre dynamic response following deployment and allow first estimates of its damping. The spacecraft telemetry, sampled at roughly 30-s intervals, cannot independently resolve these oscillations. Longer post-stop recordings are needed to improve the damping estimates, check the influence of sensor filtering and aliasing, and support the mode assignment described above.

8. FURTHER IN-ORBIT TESTS

8.1. Dynamic testing

The post-deployment response in Sec. 7 shows that stopping an ordinary mast movement can provide sufficient excitation for an initial in-orbit structural characterisation. A separate release impulse is therefore not essential for the next measurement. Instead, the flight script should reserve IMU-buffer capacity for the stopping event and retain a longer continuous record afterwards. The longer record is particularly important for the slowly decaying 1.0-Hz component and for comparing the response at different boom extensions.

8.2. Further mast deployment

The premature deployed-limit signal does not establish a physical travel limit at 1.72 m and does not preclude subsequent tests at greater extensions. For a subsequent deployment, a low-level command can instruct the payload avionics to ignore the deployed-limit input over a predefined encoder interval around the suspected false-trigger region. The commanded encoder target, motor-current threshold and maximum actuation time remain available as independent termination criteria while the switch input is masked. The masking interval should include suitable margin because the repeatability and exact encoder position of a future false trigger have not yet been established. The consistent deployment velocity and the motor currents within the ground-test range provide reference values for monitoring this movement. Additional deployments across a wider motor-temperature range could further establish a temperature-dependent current envelope for plausibility monitoring.

8.3. Camera operation

The image results show that the cameras can serve as engineering instrumentation when illumination, viewing geometry and acquisition settings are selected for the structural feature of interest. The differences between the two camera types also show that successful image transfer alone is not a sufficient criterion for a useful observation. Future scripts should therefore treat image acquisition, exposure settings and illumination as one operational task. Thermal conditioning must be considered at the same time because extended acquisition and transfer sessions influence the ICB temperature.

9. CONCLUSIONS

The primary objective of the reported in-orbit test was met: the integrated Camera SpaceMast completed controlled intermediate deployments, a short reverse movement and final retraction to the stowed end switch. The maximum boom extension was 1.72 m. The final planned extension to 2.5 m was not achieved because a premature deployed-limit signal terminated further deployment. The premature signal is attributed to a locally narrowed section of

the trimmed mast flange. This explanation is supported by tests on equivalent hardware and by the switch returning to its inactive state during retraction. This event does not impose an operational extension limit at 1.72 m because future commands can mask the switch input over the affected range while retaining the encoder target, motor-current threshold and maximum actuation time as independent termination criteria.

All monitored supply voltages remained within their defined operating thresholds, all 27 temperature channels returned valid measurements, and no persistent sensor failure occurred. The phase-averaged deployment currents of 213 to 290 mA remained within the ground-test range and provided no indication of increased mechanical loading in orbit. Thermal conditioning separated the initially cold ICB from the first actuation, and the configured overtemperature contingency was not invoked.

The autonomous sequence returned 48 unique image files, and the sunlit views provide independent visual evidence of the deployed configurations. The Type B cameras produced a useful exposure balance under the high scene contrast. For the Type A camera, the test series showed that longer manually selected exposure times are required to improve detail in darker regions.

High-rate IMU measurements revealed oscillatory responses near 1.0 and 1.85 Hz following the final deployment movement. The paired acceleration and angular-rate signals exhibit phase differences close to a quarter period, consistent with bending motion. The direction-dependent bending stiffness of the mast makes it plausible that these responses are the lowest bending modes in the two transverse directions, although the single sensor location cannot establish their mode order. Preliminary equivalent damping ratios are 0.8% and 1.6%, with estimated initial displacement amplitudes at the ICB sensor of 0.57 and 0.072 mm in the analysed post-stop window. Despite the short record, the event-triggered instrumentation captured sufficient information for an initial dynamic characterisation in orbit.

The test thus provides the operational reference data needed for further deployments beyond 1.72 m and shows that ordinary mast actuation can also excite a measurable structural response. The next tests should combine greater boom extensions with longer post-stop IMU records and camera settings selected for the expected illumination and structural detail. These measurements are required to improve the damping estimates and establish the modal assignments; full-travel performance and formal system qualification also remain to be demonstrated.

ACKNOWLEDGMENTS

The Camera SpaceMast and the reported in-orbit demonstration build on many years of development and contributions from numerous colleagues at DLR. The project benefited in particular from the longstanding technical and administrative support of Prof. Christian Hühne, Head of the Lightweight Design Department; Olaf Mierheim, Manager of the Space Business Area at the DLR Institute of Lightweight Systems; Prof. Martin Wiedemann, long-serving former Director of the Institute; and Prof. Michael Sinapius, former Deputy Director of the Institute. Their sustained support helped establish the technical and organisational basis for this work. The authors also thank Dr. Andree Altmikus, who succeeded Prof. Wiedemann as Director of the Institute in May 2026, for his support of the continuing in-orbit activities.

The in-orbit demonstration was funded by the German Aerospace Center (DLR) through the Executive Board department “Innovation, Transfer and Research Infrastructure”, under the responsibility of Executive Board Member Prof. Karsten Lemmer. The technical development was carried out within a spin-off project supported by the German Federal Ministry for Economic Affairs and Energy (BMWE) through the EXIST Transfer of Research programme.

DECLARATION OF AI USE

Generative AI tools were used to assist with text drafting and revision, and the development of scripts for telemetry analysis and data visualisation. The authors reviewed and revised the resulting text, checked the analysis procedures and results against the underlying test data, and take responsibility for the final content.

REFERENCES

[1] Marco Straubel, Constantin Bauda, Martin Hillebrandt, Laury Pouillet, Antoine Sauvage, Clara Sautereau, Andrew Nutter, and Martin E. Zander. Ground deployment testing of 4x4m solar sail demonstrator. In *ECSSMET 2024 – European Conference on Spacecraft Structures, Materials and Environmental Testing*, Noordwijk, The Netherlands, September 2024. URL `https://elib.dlr.de/209908/`.

Tightly coiled boom deployment dynamics

Annalisa Tresoldi[(1)$_a$], Jason Shore[(1)$_b$], Alfonso Pagani[(2)] and Guglielmo S. Aglietti[(1)$_c$]

[(1)] *Te Pūnaha Ātea - Space Institute, University of Auckland, Auckland, 1010, New Zealand*
[(1)$_a$] Corresponding author: annalisa.tresoldi@auckland.ac.nz,[(1)$_b$] jason.shore@auckland.ac.nz,
[(1)$_c$] g.aglietti@auckland.ac.nz
[(2)] *MUL2 Lab, Department of Mechanical and Aerospace Engineering, Politecnico di Torino, alfonso.pagani@polito.it*

KEYWORDS
Boom dynamics, passive deployment, deployable boom

ABSTRACT
The Tape Spring Unwrapping Nanosatellite Arm (TUNA) is a passive mechanism for deploying small payloads on CubeSats. Housed within a launch pod's "Tuna-Can" kick-off spring volume, TUNA unwraps from a stationary drum—unlike most linearly-extending booms—driven by the tape spring's strain energy. Knowledge of the deployment dynamics is critical for spacecraft control and structural integrity. This paper extends a literature model of a passively unwrapping tape spring with a tip mass, using a single-DoF Lagrangian formulation. Experiments agree well with predicted speed and geometry. Adding $0.87\,\mathrm{g}$ of tip mass reduces predicted maximum speed from 13.9 to $10.5\,\mathrm{m/s}$, matching the measured $\approx 10.2\,\mathrm{m/s}$, and correctly predicts failure to fully deploy in laboratory conditions. With added mass representing a camera payload, the model performs well; removing gravity and drag shows on-orbit deployment differs markedly from laboratory conditions: $\approx 9\,\mathrm{m/s}$ on orbit and $\approx 2\,\mathrm{m/s}$ in the laboratory.

1. INTRODUCTION

Tape springs, deployable booms, and STEMs have become effective solutions for space applications, particularly for small satellite platforms, where they enable the compact stowage and reliable deployment of payloads, such as solar sails, antennas, solar arrays, and sensing instruments [1, 2]. Their main advantage is their ability to undergo large elastic deformations during packaging while recovering a stiff, naturally curved configuration upon deployment. This behaviour enables them to provide structural support and tension to the deployed payload while minimising system mass, stowed volume, and overall mission cost. Typically, the deployment process of STEM and tape springs consists of a "tip-out" release mechanism where a single or a system of booms [3, 4] uncoil from a central hub or spool around which they have been coiled or co-coiled for stowage. In this configuration, the boom root's edge is constrained flat or partially flat [5] to the drum while the tip is maintained at its natural curvature and extends outwards during deployment, as illustrated in Fig. 1 (a).

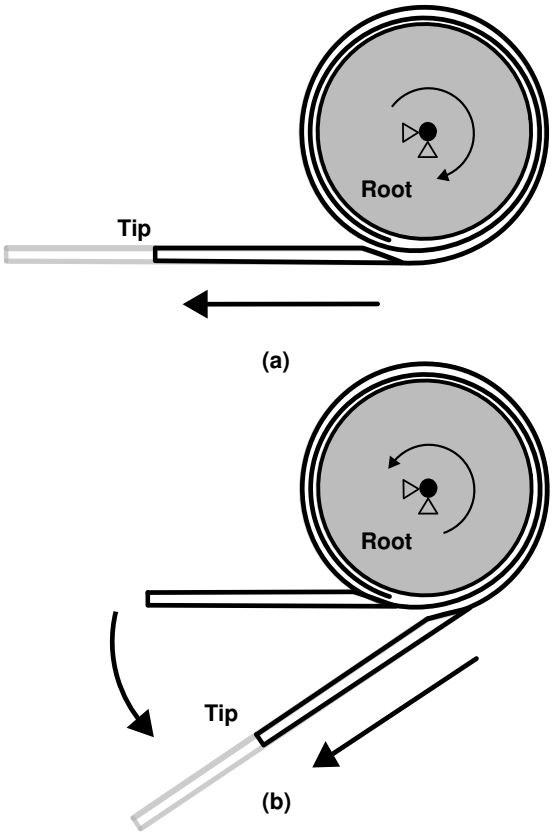


Figure 1: (a) Linear tip-out deployment configuration. (b) Rotating tip-out deployment configuration.

The boom tip-out deployment has been used to support membrane structures [6] and deorbiting mechanisms, such as the deployable gossamer sail [5] developed under the ESA ARTES 5.1 programme, and the dragsail payload designed to fit the "Tuna-Can" volume of a CubeSat and launched as part of the TPA-1 mis-

sion [7]. These systems consist of four tape springs deploying from a central spool and pulling from the tip four quadrants of sails (or membranes) into their deployed configuration. Other examples of linear deployment were used to support deploying antennas [4, 8], solar arrays [9, 10] and imaging systems, such as the inspection boom system developed for the same mission in [7].

Based on the deployer configuration and deployment actuation method, another adopted approach is the "rotating tip-out" mechanism. Unlike linear deployment, this configuration couples the outward boom extension with a rotating motion, as illustrated in Fig. 1(b). These systems are typically passive (i.e. no motorisation or rotating parts), therefore deemed simpler, and have a higher stowage efficiency when compared to active systems. Because the deployment only relies on the elastic stored energy for actuation, the free deployment dynamics are effected by stowage time and temperature, which are critical aspects to successful deployment [11]. Other key design parameters for this type of system are the maximum angular deployment velocity and momentum generated during deployment [12]. Excessively high deployment velocities can induce undesired dynamic disturbances that affect the spacecraft Attitude Determination and Control System (ADCS) [13], while also generating shock loads that may damage both the boom and satellite. An example of rotating tip-out deployment is presented in [12], where a system of two antenna tape springs are mounted and wrapped around a central disk and deploy freely. To evaluate the velocity requirements, angular rates and deployment time for their subsystem's design, they adopted the analytical model on deployment dynamics of tape springs developed by Seffen and Pellegrino [14]. In [14], the authors demonstrate how stored elastic energy drives self-deployment in a purely conservative two-dimensional problem resolved with a Lagrange approach. In their study, they provide a closed-form solution for the case of a tape spring deploying from a fixed spool in a gravity-free vacuum environment. Moreover, the coiling radius is assumed to be equal to the natural radius to favour the tape's natural bending without requiring external forces to maintain the equilibrium state [15]. Starting from [14], a similar approach is developed in [16] to describe the dynamics of multiple tape springs that are uncoiled from a fixed central hub. In this case, the coil thickness is accounted for and the longitudinal section of the coiled part is approximated with an Archimedean spiral.

This paper presents a novel deployable boom that is stowed for launch inside the volume of the deployer's kick-out spring, which is informally known as the "Tuna-Can" volume. The boom extends using the passively driven rotating tip-out deployment method to keep the mechanism design as simple as possible. The development model is illustrated through deployment frames in Fig. 2. Presented first are the details of the mechanism, which is aptly named TUNA – Tape spring Unwrapping Nanosatellite Arm. TUNA is reasonably agnostic to the type of payload that it can support, within the mass and volume limits, but the baseline payload in this paper is a Commercial Off The Shelf (COTS) camera. The payload at the tip will affect the deployment during ground testing and in a micro-gravity environment. To consider the tip mass the Lagrangian model presented in [14] is extended and the new governing equation of motion is presented. The analytical model is used to predict the deployment path and speed of the boom, which are then compared to experimental measurements made on boom samples using a motion capture facility.

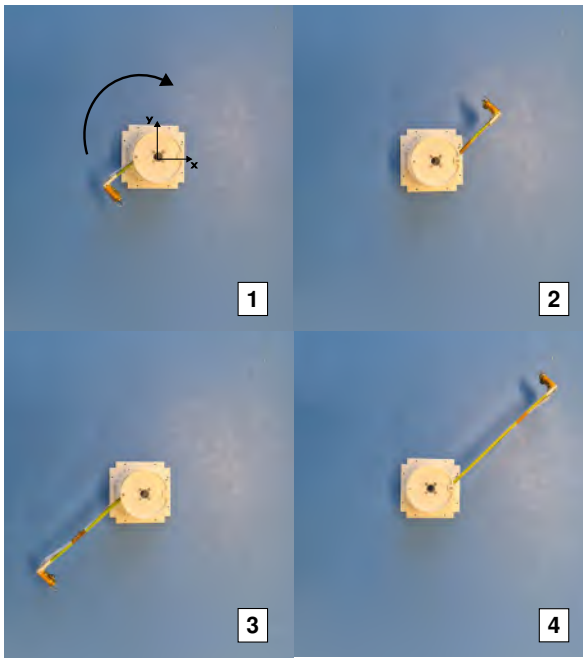


Figure 2: Rotating boom deploying by unwrapping around the central hub.

2. TUNA DESIGN

TUNA is a deployable boom that can extend small payloads from the body of a CubeSat. TUNA has been designed to be accommodated inside the deployment spring of most commercial CubeSat launch pods on the market (ISIS, EXOpod, Maxwell, UARX and NANOrasks). The payload baselined in this paper is a single Raspberry Pi camera, which is mounted to the end of the boom via an interface bracket. The camera would serve to monitor the visible external facets of the spacecraft, as well as providing promotional photographs. With some minor modifications to the bracket and boom material TUNA could also deploy scientific equipment such as magnetometers. A dimensioned CAD model of TUNA is shown in Fig. 3 in both the stowed and

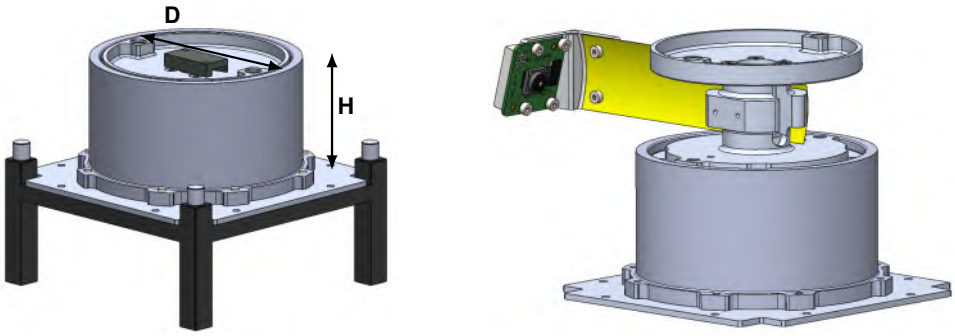


Figure 3: Left, stowed TUNA, which measures 39 mm from the interface of a CubeSat's deployer plate (H), and has an outer diameter (D) of 79 mm. Right, TUNA deployed with a RaspberryPi camera at the tip.

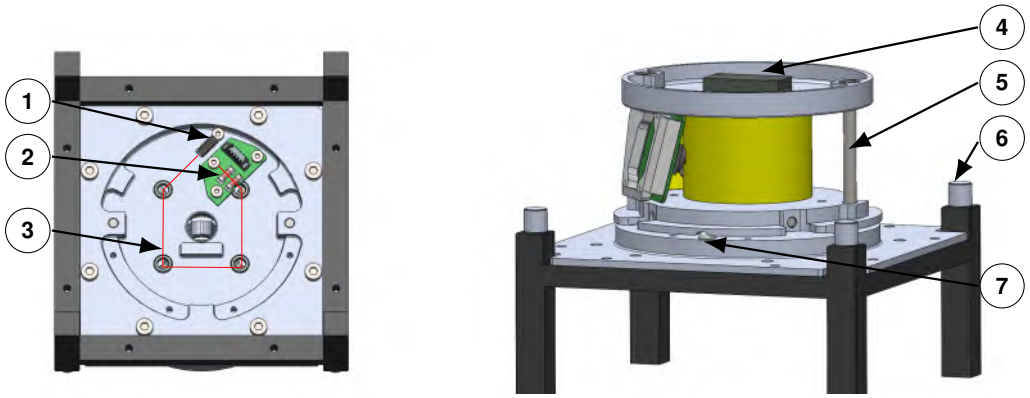


Figure 4: Left, inside face of TUNA showing the burnwire path (3), which is routed from a tensioning spring (1) and terminated shortly after running over two resistors (2). Right, TUNA with the housing hidden to reveal the inside. One of the alignment ball-vee couple is highlighted (7). Sun sensor (4), Linear guide deployment (5) and spacecraft kill switch (6).

deployed configurations. Taking inspiration from the NANOSail unit, a dragsail on TPA-1, TUNA deploys in two stages. First, the sprung assembly is deployed in a jack-in-the-box style by a single compression spring. This step is required to push the rotating boom away from the CubeSat structure's feet and, critically, the kill-switches that open to turn the satellite on. In the second stage of the deployment the boom with the tip-mounted camera unwraps itself from a stationary central hub using the strain energy stored in the boom. At this stage of development, the boom is spring steel, cut from the traditional carpenter's tape measure, but future iterations will explore low-friction coatings and Beryllium Copper for magnetically sensitive tip payloads.

Starting from the fixed baseplate, this structure acts as the entire Z facet with a hole pattern to match whichever CubeSat structure is being baselined: in this case it is a 3U structure from NanoAvionics. The fixed baseplate supports the boom housing, linear deployment spring, deployment guide pins and the Hold-Down Release Mechanism (HDRM) board. The concept for the HDRM is the same of the NANOSail from TPA-1, Dyneema string is run between the sprung assembly and the fixed baseplate through a series of grooved pins and rings, as shown in Fig. 4. Owing to the string's path there is a mechanical advantage of eight. The Dyneema is run over a set of resistors mounted to the board that, when powered, heats up and melts the Dyneema. The HDRM board is internally facing and can therefore be reset by flipping the unit over. The burnwire board is interfaced to the spacecraft via a 5-pin vertical Picoblade connector. The sprung assembly is seated and aligned on the baseplate using a Maxwell clamp configuration (three balls and three vees), one of which is visible in Fig. 4. The sprung assembly consists of just two parts, the body and the lid. The boom is mounted to the body and is wrapped around the central hub. The ribbon cable harness that provides power and data connectivity to the payload is cocoiled with the boom and is constrained to it at intervals along the length of the boom. At the root, there is a cutout in the structure to allow the ribbon cable to pass through and out to the internal spacecraft. To enable the initial vertical deployment of the sprung assembly, the harness is coiled inside the central hub with overlapping layers so that when the assembly is deployed the harness will elongate. Included in both the

body and lid of the sprung assembly there are a total of four bushings. These bushings slide over two fixed stainless-steel pins that are bonded into the baseplate, shown in Fig. 4. The bushing and pin combination prevent the sprung assembly from tilting or laterally moving during deployment. A secondary function of the pins is to keep the payload on the tip of the boom from moving and pressing against the inside of the housing before it is pushed clear. A polycarbonate baffle-like structure is proposed to be bonded to the camera to prevent the lens directly impacting the coiled boom. The lid of the sprung assembly is recessed to accommodate a sunsensor on this facet of the Spacecraft, as shown in Fig. 3. The wiring for the sensor is passed down the same through hole as the ribbon cable harness used by the camera payload. A development model, utilising a combination of 3D printed and metallic parts, is shown in Fig. 5 along with still frames taken of TUNA during its deployment (Fig. 2).

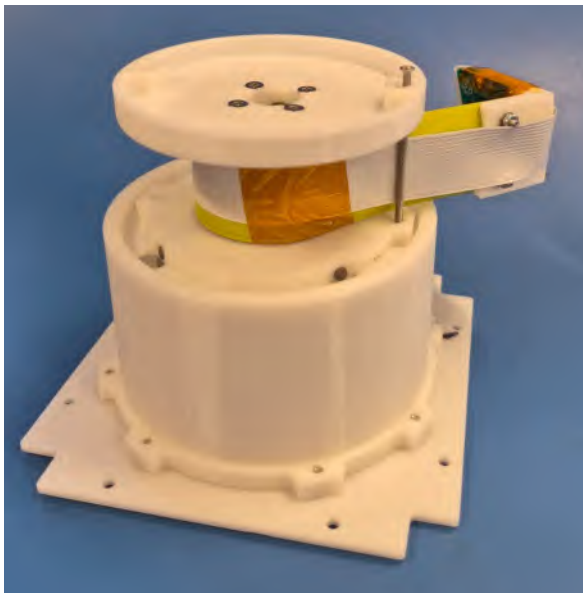


Figure 5: Development model with Raspberry Pi camera and harness.

The total mass of the system, including the wall of the Z facet, is $260\,\mathrm{g}$, with structural analysis and mass optimisation to follow. The mass of the proposed payload is $13\,\mathrm{g}$ and the current allowable tip payload volume is 25 x 13 x 31 mm. While not presented in detail here, this design does allow for a second co-coiled boom and payload to be deployed using the second stainless steel pin to restrain the bracket, as shown in Fig. 6.

3. DEPLOYMENT TESTING SETUP

Deployment testing was conducted to track the motion of the boom tip throughout the deployment process and to characterise the overall deployment dynamics. The experiments provided measurements of the

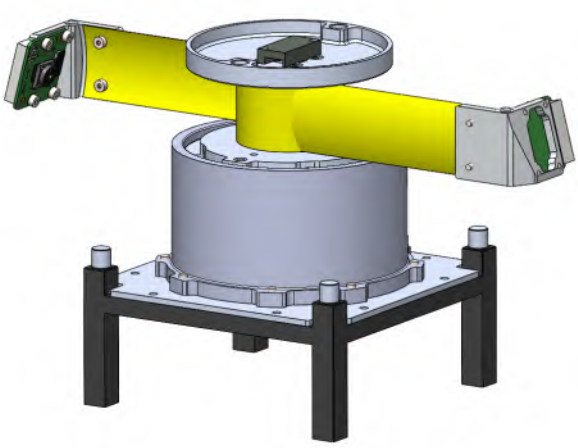


Figure 6: Dual boom TUNA configuration to deploy a second inspection camera.

boom's speed and path in a gravity environment, enabling the evaluation of its repeatability and the comparison with analytical predictions. The boom used for testing was an isotropic COTS steel tape measure with length $L = 0.65\,\mathrm{m}$, width $b = 25\,\mathrm{mm}$ and natural radius $R = 17.8\,\mathrm{mm}$. The material properties are $E = 210\,\mathrm{GPa}$, $\nu = 0.3$, $G_{12} = 80.8\,\mathrm{GPa}$, thickness $h = 0.1\,\mathrm{mm}$ and density $\rho = 7800\,\mathrm{kg\,m^{-3}}$. Fig. 7 shows the testing setup for the stowed and deployed configurations. For stowage, one boom's edge was flattened and screwed to a deployment drum (Fig. 7 (6)) of radius $r = 17.5\,\mathrm{mm}$, while the other edge was left in its stress-free state and coiled around the drum to leave a deployed distance of $42\,\mathrm{mm}$ from the drum's tangent point. Due to the shallow geometry, the ploy region between the flat and curved sections was considered negligible and was therefore omitted from the analytical model. Two retro-reflective markers were used to create a local dynamic object and track the relative displacement during deployment, as illustrated in Fig. 8. One marker was placed at the tip (Marker 1), the other at the centre of the drum (Marker 2) to provide a fixed reference point for calculating the relative displacement, as shown in Fig. 7. The retro-reflective part of the Marker 1 offset from the boom edge by $5\,\mathrm{mm}$ in the y-direction, and the weight of the marker was $0.87\,\mathrm{g}$. Once the boom was released, the tip displacement was recorded and tracked by 12 infrared cameras that were positioned around the testing room. The software used for object tracking was Vicon Nexus Tracker. Displacement and velocity data were collected with a sampling frequency of $320\,\mathrm{Hz}$. The cameras were calibrated to a maximum error of $\pm 0.6\,\mathrm{mm}$, which yields an error of $\pm 0.91 \times 10^{-3}\,\mathrm{ms^{-1}}$ when considering error propagation in the calculation of the speed within the software. Deployment tests were performed on the boom in two configurations: with only the retro-reflective marker attached at the tip, and with an addi-

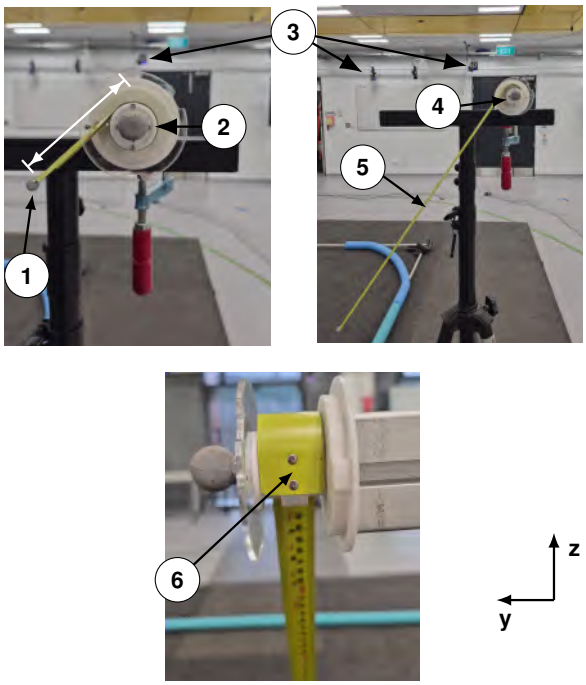


Figure 7: Experiment setup: Marker 1 (1), Marker 2 (2), motion cameras (3), fixed drum (4), Boom (5) and boom constraint at the root (6).

tional tip mass representing the sensor, resulting in a total tip mass of $13\,\mathrm{g}$. From the experimental observations, the tip marker changed its position relative to the centre of the drum as a result of the boom's radial extension and angular rotation during deployment. This kinematic behaviour was consistent and repeatable across the test series, providing the basis for the formulation of the analytical model.

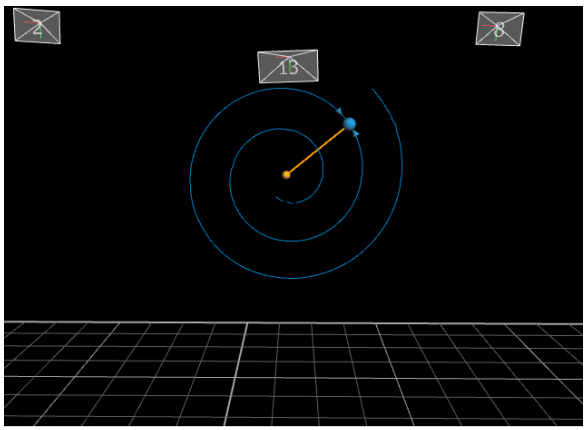


Figure 8: Local dynamic object defined by the two markers by the Vicon Nexus tracking tool. The central marker is orange and the tip is blue. The blue spiral line is the tip's displacement path.

4. ANALYTICAL MODEL

The analytical model presented in this paper is based on the tape spring deployment model developed by Seffen and Pellegrino [14], which provides the foundation for describing the deployment dynamics of TUNA. In [14], the deployment configuration consists of a coiled tape spring that uncoils and tangentially extends driven by a rotating spool. Such motion is fully described by two degrees of freedom: the angle subtended by the coiled tape spring and the spool rotation. In this study, the spool is fixed from the start, and the motion is initiated by the release of the coil's stored energy. This reduces the system to 1 Degree of Freedom (DoF) where the only time-dependent variable is $\theta(t)$, which is the angle subtended by the coil. In fact, during the deployment, as the boom extends, the coil rotates to allow for the extension, varying the arc length and, therefore, θ. As in [14], the coiling radius is constant $r = R$, therefore the coil expansion is not investigated in this model. A schematic illustration of the 1 DoF boom dynamics is shown in Fig. 9.

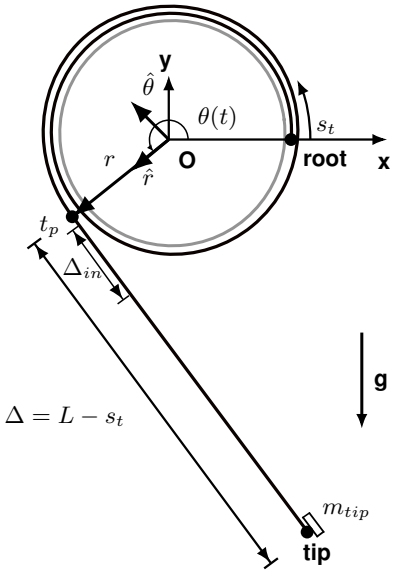


Figure 9: Rotating deploying boom model.

To account for the sensor mass placed at the tip, the total kinetic and gravitational potential energy of the system as calculated in [14] are modified to construct the lagrangian of the system, $\mathcal{L} = T - V$, to resolve the equation of motion:

$$T = \frac{1}{2}\int_0^{\Delta} \rho_m \mathbf{v}^2 \, d\Delta + \frac{1}{2} m_{tip} \mathbf{v}^2 = \frac{1}{2}\rho_m \left(\dot{\theta}^2 \frac{(L - r\theta)^3}{3} \right) + \frac{1}{2} m_{tip} \dot{\theta}^2 (L - r\theta)^2 \tag{1}$$

$$
\begin{aligned}
&V = \frac{1}{2} bD \int_0^{s_t} \left(\frac{1}{r^2} - \frac{2\nu}{rR} + \frac{1}{R^2} \right) ds + \\
&\int_0^{s_t} \rho_m g \left(r \sin(\theta) \right) ds + \\
&\int_0^{\Delta} \rho_m g \left(r \sin(\theta) + \Delta \cos(\theta) \right) d\Delta + \\
&m_{tip} g \big(r \sin(\theta) + (L - r\theta) \cos(\theta) \big) = \\
&br\theta \left(\frac{D(1-\nu)}{R^2} \right) + \rho_m g r^2 \left(1 - \cos(\theta) \right) + \\
&\rho_m g \left(r(L - r\theta) \sin(\theta) + \frac{(L - r\theta)^2}{2} \cos(\theta) \right) + \\
&m_{tip} g \big(r \sin(\theta) + (L - r\theta) \cos(\theta) \big)
\end{aligned}
\tag{2}
$$

Where $\Delta = s - r\theta$ is the deployed length, and s is the curvilinear coordinate of a generic material point along the boom length $s \in [0, L]$. As in [14], the interface between the coil and the extended region is defined by a transition point, t_p, which corresponds to the instantaneous position of θ. This point represents a moving boundary condition that evolves over time to ensure that the geometric constraint in Eq. (3) is continuously satisfied.

$$
s_t = r\theta \tag{3}
$$

Where s_t is the instantaneous arc of a circle for a given position of the moving boundary. The other parameters in Eqs. (1) and (2) are ρ_m, the linear density of the boom, g, gravity and m_{tip} the mass of the sensor; L, b and D are the boom's length, arc width and flexural rigidity, respectively. The zero potential gravity plane is co-linear with the x axis. From the kinematics in [14], the velocity $\mathbf{v}$ is:

$$
\mathbf{v} = \left(-(s - s_t)\dot{\theta} \right) \hat{\mathbf{r}} \tag{4}
$$

The motion starts from an initial configuration where the boom is partially coiled at an initial $\theta_{in}(t) > 2\pi$ around the fixed drum and partially deployed at an initial length Δ_{in}. In this configuration, the centre of the drum is the origin of the system of reference O, and the increment of the radius given by overlapping layers is neglected, as assumed in [17] for coiled thin shells. For the initial state of non-conservative generalised forces Q_i = 0, (i.e. no external forces), the equation of motion in Eq. (5) is resolved by numerical integration using the MATLAB ode15s algorithm.

$$
\begin{aligned}
&\ddot{\theta} \left(\rho_m \frac{(L - r\theta)^3}{3} + m_{tip}(L - r\theta)^2 \right) \\
&- \frac{1}{2} r\dot{\theta}^2 (L - r\theta) \left(\rho_m (L - r\theta) + 2m_{tip} \right) \\
&+ brD \left(\frac{1 - \nu}{R^2} \right) \\
&- \frac{1}{2} (L - r\theta) g \sin(\theta) \left(\rho_m (L - r\theta) + 2m_{tip} \right) = 0
\end{aligned}
\tag{5}
$$

Following the approach in [14], in a second instance, dissipative effects are introduced into the model to account for primary external forces acting on the system. The non-conservative generalised force Q_i associated with air drag is derived by applying the principle of virtual work. It is assumed that air drag is generating resistance along the normal direction on the extending convex boom surface, therefore $\mathbf{v}$ in Eq. (4) is the velocity vector used to calculate the air drag force.

5. RESULTS AND DISCUSSION

This section compares the analytical predictions of the deployment path, speed and deployed length with the experiments results. Deployment tests were conducted both without the sensor mass and with the sensor mass attached at the boom tip. In both configurations, the retro-reflective marker remained attached to the tip throughout the tests to enable the motion tracking and data acquisition. To validate the proposed analytical model against the solution presented by [14], Eq. (5) was solved for the case of $g \neq 0$ and $Q_i \neq 0$ (i.e. accounting for gravitational effects and air drag), first neglecting any additional tip mass (i.e. $m_{tip} = 0$), consistent with the assumptions adopted in their work. Secondly, to account for the presence of the retro-reflective marker alone, Eq. (5) was solved with a tip mass of m_{tip} = $0.87\,\mathrm{g}$. Comparison with the experimental results shows that including the marker mass in the equation of motion significantly improves the prediction of the deployment speed. As shown in Fig. 10, the inertia of the mass at the tip slightly increases the deployment time and effectively reduces the initial peak deployment speed from $13.9\,\mathrm{m/s}$ to $10.5\,\mathrm{m/s}$. This change enhances the accuracy of the model prediction, so that it is in strong agreement with the measured peak speed of $10.2\,\mathrm{m/s}$. In this configuration, the boom does not reach full deployment. Instead, at $t \approx 2.5\,\mathrm{s}$, it reaches its maximum deployed length before reversing its motion and oscillating as the remaining kinetic energy is dissipated. This behaviour is accurately captured by the analytical model and it can be clearly seen in Fig. 11, which shows the development of the normalised deployed length λ over time, as in [14]. Again, it can be seen that at $t \approx 2.5\,\mathrm{s}$ λ is at a maximum but never reaches 1, indicating that full deployment is not achieved. Instead at this time, the boom tip reverses

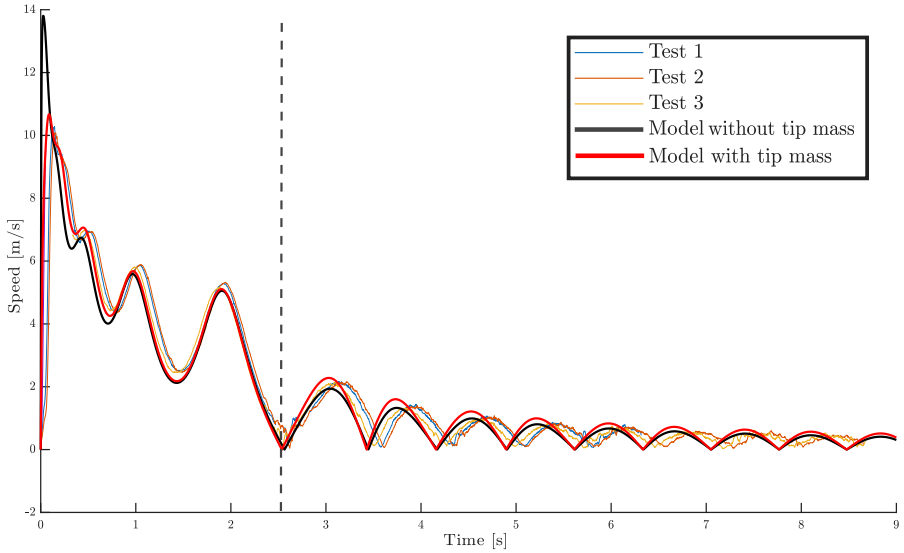


Figure 10: Speed comparison between tests results and the analytical predictions (Eq. (5)*) with no mass at the tip (black curve) and with the marker mass at the tip (red curve). The black dashed line at $t \approx 2.5$ s highlights the deployment time at the maximum deployed length achieved.*

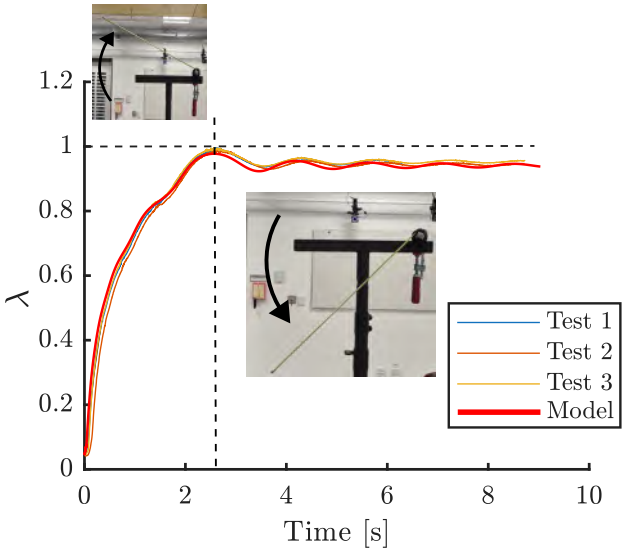


Figure 11: Normalised deployed length comparison between tests results and the analytical prediction for the configuration with the marker mass at the tip. The black dashed line at $t \approx 2.5$ s highlights the deployment time at the maximum deployed length achieved.

direction and oscillates until the system reaches its final equilibrium configuration.

Later, the second series of tests was conducted on the boom with the sensor mass at the tip (13 grams) to simulate the actual configuration of the device. Note that at this time, the distributed harness mass is neglected. As expected, the increased inertia at the tip reduces the deployment speed while increasing the overall deployment time. In contrast to the previous configuration, the deployment is completed and the boom reaches full deployment at $t \approx 2.9$ s, driven by the increased gravitational work acting on the tip mass, as shown in Fig. 12. This behaviour is again illustrated in Fig. 13, where λ reaches 1 at its maximum point, indicating complete deployment. Furthermore, the approximated spiral path as captured from the Vicon Nexus motion tracking system (Fig. 8) is accurately predicted by the analytical model, as shown in Fig. 14.

From these figures, it can be seen that the model predicts the boom deployment dynamics accurately and correlates well with the experimental data during the initial stage of deployment. However, the model breaks down at deployment completion ($t \approx 2.9$ s), hence when the entire boom has transitioned from the coiled to the straight configuration. Specifically, the model stops when the remaining coiled arc length reaches zero and the boom is fully straight, therefore neglecting the structural behaviour occurring beyond this point. In contrast, the experimental tests showed that, after full deployment, the boom buckled in the opposite direction to the motion and twisted out of plane before dissipating the remaining kinetic energy through damped oscillations. This post-deployment behaviour is evident in Fig. 13 and Fig. 14. In Fig. 13, λ decreases after the dashed black line, indicating that the boom is no longer fully straight and buckling is occurring. Similarly, in Fig. 14, the experimental curves develop chaotically at the end of the spiral-like path, reflecting structural unstable behaviour. Furthermore, buckling is associated with the peak in deployment speed observed at $t \approx 4.5$ s in Fig. 12, after which oscillations develop. Such phenomenon was consistently observed during tests as a consequence of the

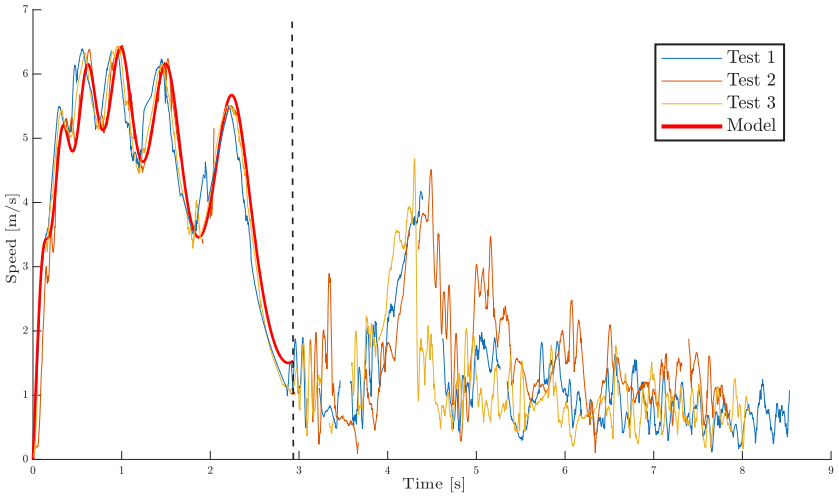


Figure 12: Speed comparison between tests results and the analytical prediction for the configuration with the marker mass and the sensor mass at the tip. The black dashed line at $t \approx 2.9\,\mathrm{s}$ highlights the deployment time at the maximum deployed length achieved.

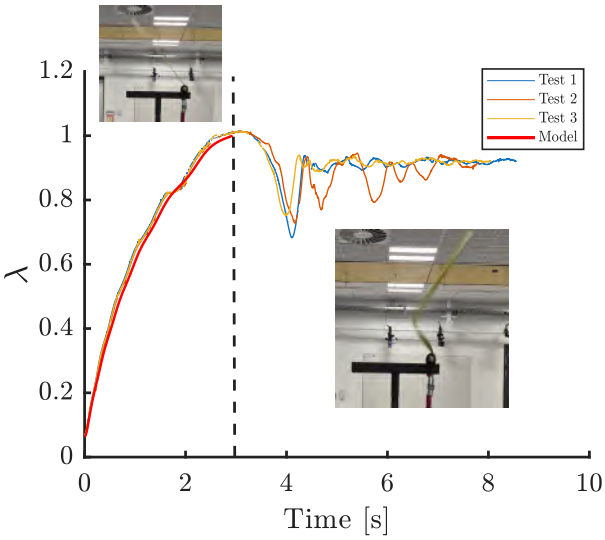


Figure 13: Normalised deployed length comparison between tests results and the analytical prediction for the configuration with the marker mass and the sensor mass at the tip. The black dashed line at $t \approx 2.9\,\mathrm{s}$ highlights the deployment time at the maximum deployed length achieved.

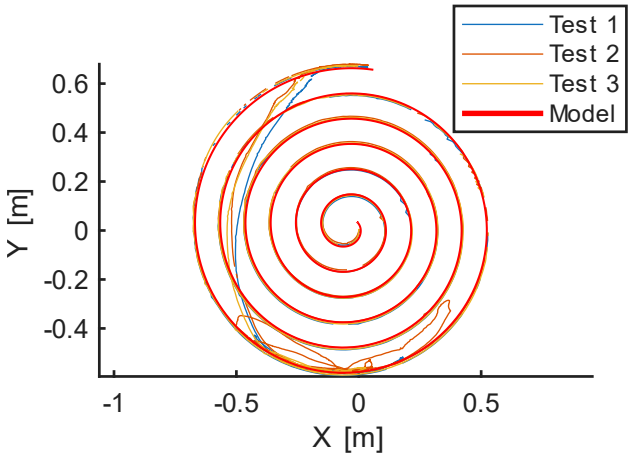


Figure 14: Spiral-like deployment path comparison between tests results and the analytical prediction for the configuration with the marker mass and the sensor mass at the tip.

boom's root boundary condition and the effect of gravity, whereas it is not captured by the analytical model due to its initial assumptions and end condition. As shown in Fig. 7, the boom root's condition constraints the boom edge in place, generating a reaction force and moment opposite to the motion's direction once the boom reaches full extension. This reaction, assisted by gravity, causes the boom to buckle and twist out of plane. Although gravity is included in the analytical model and the root boundary condition is correctly enforced through the kinematic constraint $(x_{root}, y_{root}) = (r, 0)$ throughout the simulation, the model cannot reproduce this behaviour because of its simplified representation. In fact, the deployed boom is modelled as a rigid rod extending tangentially from the coil, thereby excluding any structural deformations along its length, such as torsion, bending, and any out of plane effects. In addition, the model capabilities are limited to describe the deployment process up to the instant at which the boom is fully deployed (i.e. when no coiled part remains). Consequently, it cannot capture buckling and dissipation of the residual kinetic energy, unless a reaction moment prediction is considered and the model is extended to post-deployment dynamics. Buckling was observed consist-

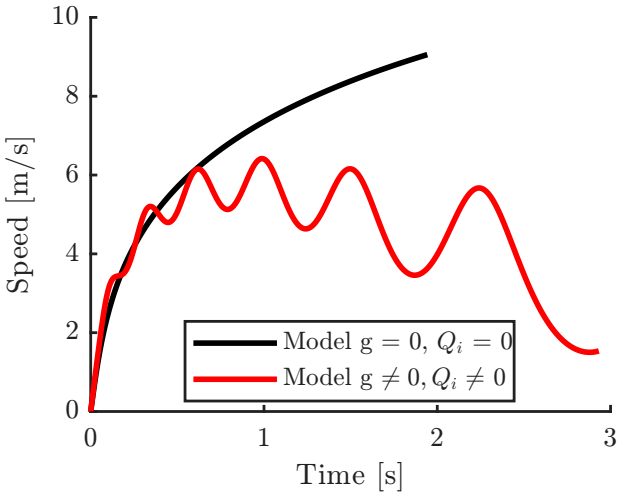


Figure 15: Comparison between the analytical predictions of the speed for the configuration with the marker mass and the sensor mass at the tip for the case of $g \neq 0, Q_i \neq 0$ (red curve) and $g = 0, Q_i = 0$ (black curve).

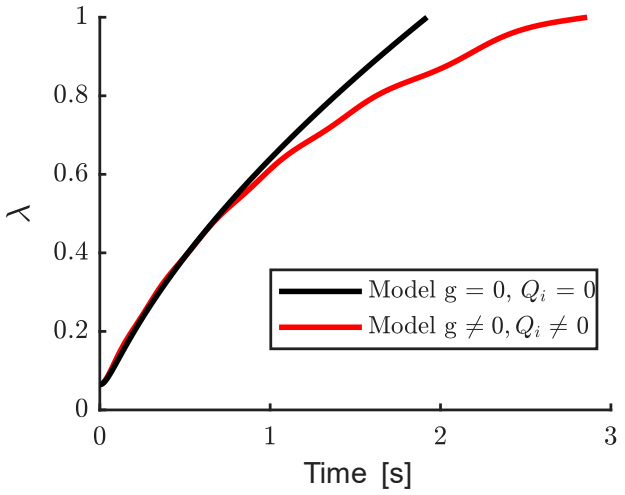


Figure 16: Comparison between the analytical predictions of the deployed length λ for the configuration with the marker mass and the sensor mass at the tip for the case of $g \neq 0, Q_i \neq 0$ (red curve) and $g = 0, Q_i = 0$ (black curve).

ently across all experimental test series, showing the repeatability of the phenomenon and confirming that it is a characteristic feature of the physical system under on-ground conditions. In general, the presence of gravity and air drag are responsible of the low-frequency undulating and damped behaviour observed in the deployment speed curves (Fig. 10 and Fig. 12), significantly influencing the boom deployment dynamics, as previously reported for thin-shell structures [17].

To highlight these effects, Fig. 15 presents the analytical predictions of the deployment speed obtained by solving Eq. (5) for $g = 0$ and $Q_i = 0$ against the solutions presented above. This configuration represents on-orbit conditions, where the effects of gravity and air drag are neglected. It can be seen that, in the absence of gravity, the deployment speed curve increases faster exhibiting a monotonic profile, without the oscillations observed during on-ground conditions, until approximately $9\,\mathrm{m/s}$. Compared with the ground-test configuration, the maximum deployment speed on-orbit increases by approximately $7\,\mathrm{m/s}$, while the deployment time is reduced by about $1\,\mathrm{s}$. The increased rapidity of deployment can also be seen in Fig. 16. These results show that gravity and air drag play a significant role in slowing the deployment and introducing oscillatory behaviour into the system, consistent with previous findings reported in [14, 17]. Consequently, the proposed model enables the prediction of successful deployment of the TUNA system under on-ground conditions and with an increased speed and reduced time under on-orbit conditions. Nevertheless, a complete prediction of the deployment dynamics would require the analytical model to be extended beyond full deployment so that the post-deployment response, including any structural instabilities, can also be captured.

6. CONCLUSION AND FUTURE WORK

This paper has presented a new deployable boom mechanism, TUNA, for CubeSats. TUNA occupies the "Tuna-can" volume of launch pod deployers and, therefore, does not encrouch into the inside volume of the spacecraft. In this first iteration of the design, TUNA deploys in two stages: an initial vertical popup to clear the CubeSat's structure and turn on switches, followed by an unwrapping of the tape springs. The primary features of the design have been described, which include the HDRM approach, harness management and overall geometry. To address the critical question of the deployment dynamics of such a mechanism, an analytical model is presented that uses a single DoF to describe the deploying system. Novel to the model is the added consideration of a tip mass i.e. a small payload mounted at the tip of the boom. Considering a mass at the tip of the boom in the equation of motion is shown to be vital to accurately capture the initial speed of the deployment. With just $0.87\,\mathrm{g}$ added, which is the mass of a small tracking retroreflective marker, the predicted speed drops from $13.9\,\mathrm{m/s}$ to $10.5\,\mathrm{m/s}$, which is in excellent agreement with the value obtained from experiment, $10.2\,\mathrm{m/s}$. Having validated the analytical model, more mass was added to the tip to represent a RaspberryPi camera and a supporting bracket. The deployment test was repeated and again the analytical model captured the speed and deployment path of the boom with excellent accuracy. The analytical model was then used to predict the on orbit deployment of TUNA to com-

pare it with the ground environment, i.e. with gravity and air drag. The final deployed speed is shown to be much higher, $9\,\mathrm{m/s}$ against $2\,\mathrm{m/s}$, without the presence of these forces. In future work, the model is to be extended to iterate the design of TUNA by deriving the final reaction moment of deployment. This moment can then be used to make an assessment of the tape spring's likelihood of buckling at the end of deployment. Work will also continue to raise the TRL of TUNA through further design, analysis and testing.

References

[1] J. M. Fernandez. Advanced deployable shell-based composite booms for small satellite structural applications including solar sails. In *International Symposium on Solar Sailing*, 2017. URL https://ntrs.nasa.gov/api/citations/20170001569/downloads/20170001569.pdf.

[2] W. Belvin, M. Straubel, J. Fernandez, M. Zander, and M. Hillebrandt. Advanced deployable structural systems for small satellites. In *NATO Specialists' Meeting AVT-257-RSM-041 "Best Practices for Risk Reduction for Overall Space Systems" organised by the Applied Vehicle Technology Panel*, 2016.

[3] J. M. Fernandez, L. Visagie, M. Schenk, O. R. Stohlman, G. S. Aglietti, V. J. Lappas, and S. Erb. Design and development of a gossamer sail system for deorbiting in low earth orbit. *Acta Astronautica*, 103:204–225, 2014. ISSN 0094-5765. doi: https://doi.org/10.1016/j.actaastro.2014.06.018.

[4] T. Murphey, S. Jeon, A. Biskner, and G. Sanford. Deployable booms and antennas using bi-stable tape-springs. In *Proceedings of the Small Satellite Conference, Mission Enabling Technologies 1, SSC10-X-6*, 2010. URL https://digitalcommons.usu.edu/smallsat/2010/all2010/58/.

[5] J. M. Fernandez, M. Schenk, G. Prassinos, V. Lappas, and S. Erb. Deployment mechanisms of a gossamer satellite deorbiter. In *15th European Space Mechanisms and Tribology Symposium*, 2013.

[6] N. Okuizumi, N. Katsumata, M. C. Natori, and H. Yamakawa. Stepwise deployment of membrane space structures with rolled-up booms: Experiments and simulations. In *Spacecraft Structures Conference*, 2014. doi: https://doi.org/10.2514/6.2014-1039.

[7] B. Taylor, V. Lewis, J. Shore, M. Seth, A. Tresoldi, M. Longato, G. Aglietti, and C. Jackson. Te Pūnaha Ātea-1 (TPA-1): A Capability Development and Validation Mission from New Zealand. In *Proceedings of the Small Satellite Conference, Next on the Pad – Research & Academia, SSC24-WIV-03*, 2024. URL https://digitalcommons.usu.edu/smallsat/2024/WE-S4-2024/.

[8] J. Costantine, Y. Tawk, C. G. Christodoulou, J. Banik, and S. Lane. Cubesat deployable antenna using bistable composite tape-springs. *IEEE Antennas and Wireless Propagation Letters*, 11:285–288, 2012. doi: https://doi.org/10.1109/LAWP.2012.2189544.

[9] D. Turse, L. Adams, K. A. Medina, K. Steele, and T. Stern. Design, analysis and testing of a composite beam roll-out array (COBRA) for small satellites. In *AIAA 2019-2024*, 2019. doi: https://doi.org/10.2514/6.2019-2024.

[10] B. Hoang, S. White, B. Spence, and S. Kiefer. Commercialization of deployable space systems' roll-out solar array (ROSA) technology for space systems loral (SSL) solar arrays. In *2016 IEEE Aerospace Conference*, pages 1–12, 2016. doi: https://doi.org/10.1109/AERO.2016.7500723.

[11] J. Deng, N. An, Q. Jia, and X. Ma. Deployment analysis of composite thin-walled lenticular tubes with effect of storage time and temperature. *Chinese Journal of Aeronautics*, 37(1):162–172, 2024. ISSN 1000-9361. doi: https://doi.org/10.1016/j.cja.2023.05.011.

[12] A. R. Ranade and S. S. Kulkarni. Modeling Deployment of Tape Spring Antennas and Its Effects on CubeSat Dynamics. In R. S. Priyadarsini and T. Sundararajan, editors, *Advances in Small Satellite Technologies*, pages 163–173, Singapore, 2023. Springer Nature Singapore. ISBN 978-981-19-7474-8. doi: https://doi.org/10.1007/978-981-19-7474-8_15.

[13] M. M. Longato, T. Hughes, V. Yotov, and G. S. Aglietti. Microvibration simulation of reaction wheel ball bearings. *Journal of Sound and Vibration*, 567:117909, 2023. ISSN 0022-460X. doi: https://doi.org/10.1016/j.jsv.2023.117909.

[14] K. A. Seffen and S. Pellegrino. Deployment dynamics of tape springs. *Proceedings of the Royal Society Lond. A*, 455:1003–1048, 1999. doi: https://doi.org/10.1098/rspa.1999.0347.

[15] C. Calladine. *Theory of Shell Structures*. Cambridge University Press, 1983. doi: https://doi:10.1017/CBO9780511624278.

[16] F. Liu, M. Wu, P. Xiang, and J. Kim. Dynamic analysis of the uncoiling process of multiple tape springs. *Thin-Walled Structures*, 211:113079, 2025. ISSN 0263-8231. doi: https://doi.org/10.1016/j.tws.2025.113079.

[17] A. Tresoldi, J. Shore, A. Pagani, and G. Aglietti. Deployment dynamics of a high strain deployable rolled-up composite SAR antenna. *International Journal of Solids and Structures*, 310:113208, 2025. ISSN 0020-7683. doi: https://doi.org/10.1016/j.ijsolstr.2024.113208.

ECSSMET
Braunschweig Germany 2026

Material

AMOCSIS: DEVELOPMENT OF A CUTTING PROCESS FOR CFRP TUBES IN AUTOMATED IN-ORBIT MANUFACTURING

David Schäfer [(1)]

[(1)] *Institute of Lightweight Systems, German Aerospace Center, Germany, Email: https://www.dlr.de/en/sy*

KEYWORDS

On-Orbit Manufacturing, CFRP, Composite Processing, Cutting Process, Tube Manufacturing, Process Development, In-Space Assembly

ABSTRACT

The Automated Manufacturing of Composite Structures in Space (AMoCSiS) approach, developed by the German Aerospace Center (DLR), enables the in-situ fabrication of lightweight truss structures using carbon fiber-reinforced plastic (CFRP) tubes combined with additively manufactured thermoplastic nodes. This concept addresses the demand for large, scalable, and structurally efficient space systems by overcoming limitations imposed by launch vehicle constraints and enabling the realization of extended structures directly in orbit.

Within the AMoCSiS process chain, CFRP tubes represent the primary load-bearing elements and are manufactured in a continuous process. Following fabrication, a precise and reliable cutting process is required to produce elements with defined lengths and high-quality end geometries. The positioning and strategy of the cutting unit, either integrated into the manufacturing process or applied as a downstream step are considered. Key aspects include achieving accurate tube lengths, maintaining cut quality, and enabling defined cutting patterns within a constrained installation space, while ensuring reliability and controlled debris generation under space-relevant conditions.

This paper focuses on the development of a cutting process for CFRP tubes meeting the requirements of automated in-orbit manufacturing. Key process requirements are derived, including high geometric precision, reproducibility, and low process-induced damage under space-relevant constraints. In contrast to terrestrial manufacturing, additional challenges arise from the need for robust, low-maintenance processes with limited tool intervention and controlled debris generation.

Different cutting approaches are assessed with respect to their suitability for processing CFRP materials under these conditions. Attention is also given to typical damage mechanisms such as fiber pull-out, delamination, and thermal degradation, as well as tool wear and process stability. Based on this analysis, a dedicated cutting strategy is developed and evaluated.

The process development is intended for application under space conditions; however, initial cutting tests are conducted under atmospheric conditions to establish a baseline for process performance.

The presented work contributes to the advancement of manufacturing technologies for in-space assembly by addressing a key process step within the AMoCSiS concept. The results support the development of reliable and high-quality tube processing methods, enabling the realization of structurally efficient truss systems for future space applications.

1. INTRODUCTION

Large space structures are required for a variety of applications, including communication systems, Earth observation, scientific instruments, and future space infrastructure. Conventionally, such structures are manufactured on ground and launched either in their final configuration or as deployable systems. Consequently, their design is strongly influenced by the available launch mass and volume. In-space manufacturing provides an alternative approach by producing structural elements after launch, thereby reducing the direct dependence of the final structure size on the available launch volume.

The Automated Manufacturing of Composite Structures in Space (AMoCSiS) project of the German Aerospace Center (DLR) investigates the automated in-space manufacturing and assembly of lightweight truss structures. The concept combines carbon fiber-reinforced plastic (CFRP) tubes as primary load-bearing elements with additively manufactured thermoplastic nodes. Both components are produced from compactly stored feedstock and subsequently assembled into truss structures using robotic systems.

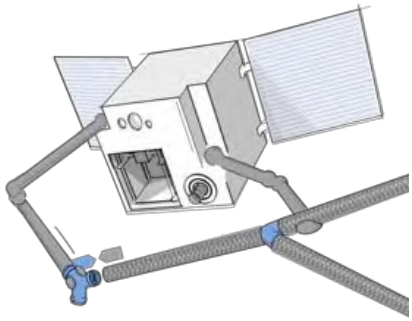


Figure 1: Concept drawing of an AMoCSiS production unit

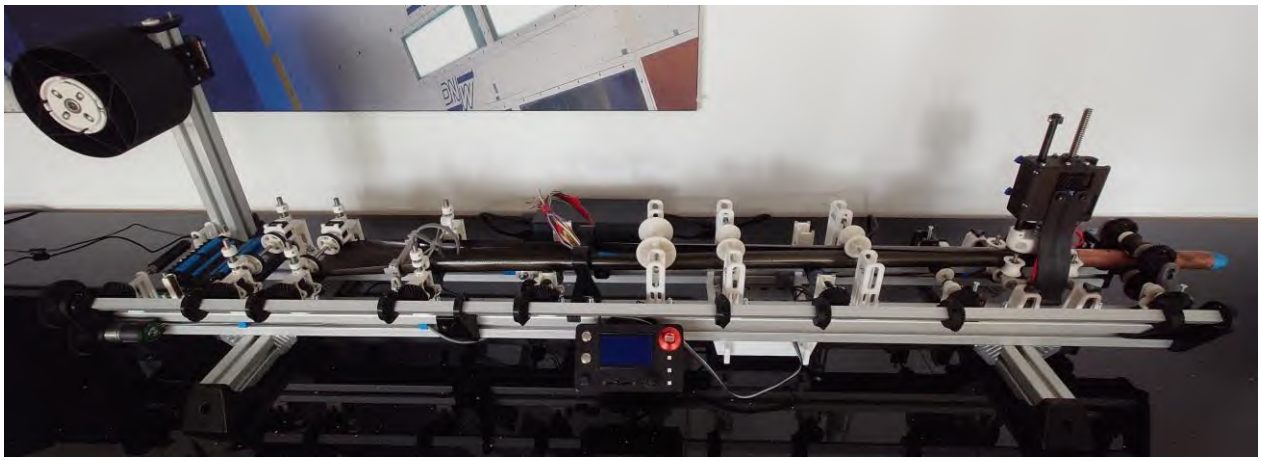


Figure 2: CFRP Tube Manufacturing Demonstrator

1.1. AMoCSiS Concept

The AMoCSiS concept enables truss structures to be manufactured and assembled according to application-specific requirements rather than being limited to a predefined structural configuration. The combination of continuously manufactured CFRP tubes and geometrically adaptable nodes allows the dimensions and topology of the resulting structure to be defined according to its intended on-orbit application.

A key characteristic of this approach is that the resulting structure can primarily be designed for its operational requirements rather than for launch and deployment. Furthermore, the final structural configuration does not necessarily have to be fully defined when the AMoCSiS manufacturing system is launched. The design of structures to be manufactured later can therefore continue or be adapted while the manufacturing system is already deployed in orbit.

The development of the AMoCSiS tube-to-node connection is complemented by activities within LISA-C, an ESA Open Space Innovation Platform (OSIP) project conducted in cooperation with Munich University of Applied Sciences and Dcubed. The project investigates the additive manufacturing of node elements using photopolymer-based processes. Within this context, a tube-to-node connection mechanism was developed that requires a specific geometry at the tube end. The resulting cutting pattern provides a representative geometry for the cutting-process development presented in this work.

1.2. CFRP Tube Manufacturing

The CFRP tubes are produced from a flat, cured CFRP strip that can be stored densely on a spool. During manufacturing, the material is continuously unwound and elastically formed into a tubular cross-section. The overlapping edges are subsequently joined using a thermoplastic joining process, resulting in a continuous CFRP tube. Once the required structural element has been produced, the tube has to be separated from the continuous material feed.

1.3. Motivation and Scope of the Cutting Process

The cutting operation therefore represents an interface between continuous tube production and the manufacturing of individual structural elements. Besides defining the final tube length, the cutting process may be required to produce geometries associated with the subsequent tube-to-node connection. This introduces requirements beyond simple material separation and motivates the investigation of a flexible and automated cutting process.

An initial mechanical cutting concept was developed for the AMoCSiS tube manufacturing process. With the further development of the manufacturing system and the tube-to-node interface, the requirements imposed on the cutting operation have evolved. This work therefore reassesses the initial cutting approach and investigates laser cutting as an alternative process. The laser-based process is experimentally characterized with respect to material separation, process parameters, representative cutting geometries, and particle generation. In addition, resulting challenges for the integration of the cutting process into the continuous AMoCSiS tube manufacturing system and its further development toward space-relevant operation are discussed.

2. CUTTING PROCESS REQUIREMENTS

The cutting process forms the interface between continuous CFRP tube manufacturing and the provision of individual structural elements for assembly. Its requirements are therefore determined by both the tube manufacturing process and the intended tube-to-node connection. In addition to reliable separation of the CFRP tube, the

process must provide the required geometry with sufficient accuracy and without unacceptable damage to the surrounding laminate. For a future integration into an in-space manufacturing system, additional constraints regarding installation volume, process reliability, tool intervention, thermal effects, and debris generation have to be considered.

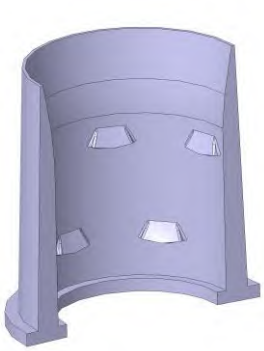


Figure 3: Detail of the tube-to-node interface illustrating the locking features relevant to the required tube-end geometry

2.1. Tube-to-Node Interface and Cutting Geometry

The cutting geometry is derived from the requirements of the tube-to-node interface. Besides separating individual structural elements from the continuously manufactured CFRP tube, the cutting process has to generate defined features at the tube end that enable the subsequent connection to the node. Consequently, the cutting task extends beyond a simple transverse separation of the tube.

The investigated tube-to-node connection requires a specific contour with locking features along the tube circumference, as illustrated in Figure 3. When the tube geometry is unwrapped, these features result in a complex two-dimensional cutting trajectory. Since the CFRP material passes through the manufacturing process in a flat state before being formed into the tube, the required contour can potentially be introduced at this stage. This avoids the need to execute the cutting trajectory on the three-dimensional tube surface.

The detailed design and structural assessment of the tube-to-node connection are outside the scope of this work. Instead, the resulting contour is used as a representative cutting geometry for the development and experimental evaluation of the cutting process. The process must therefore provide sufficient geometric accuracy while retaining the flexibility to accommodate different tube lengths and interface geometries.

2.2. Manufacturing Requirements

In addition to the required geometry, the cutting process has to fulfill the following manufacturing requirements:

- **Reliable material separation:** Complete separation of fibers and matrix along the intended cutting path.
- **Cut quality:** Limitation of delamination, fiber pull-out, fraying, and other process-induced defects.
- **Reproducibility:** Consistent cutting results under comparable process conditions.
- **Process stability:** Reliable execution of the complete cutting operation without process interruption.
- **Low mechanical interaction:** Limitation of loads and deformation introduced into the CFRP material and manufacturing system.
- **Automation capability:** Execution of the cutting process without manual intervention.

CFRP presents particular challenges for cutting due to its heterogeneous material structure and the abrasive nature of the carbon fibers. Depending on the cutting principle, damage may result from mechanical interaction or thermal energy input [1]. Consequently, the selected process must provide sufficient cut quality while remaining compatible with automated tube production.

2.3. System and Space-Related Requirements

For integration into the AMoCSiS manufacturing system, additional requirements arise from the intended application:

- **Low installation volume and mass:** Compact integration into the existing manufacturing system.
- **Limited power demand:** Compatibility with the available system resources.
- **Low maintenance requirements:** Minimization of tool replacement and other manual intervention.
- **Controlled thermal impact:** Limitation of thermal loads on the material and surrounding hardware.
- **Controlled debris generation:** Limitation of particles and residues affecting the material, equipment, or surrounding environment.
- **Vacuum compatibility:** Potential for operation under space-relevant environmental conditions.
- **Continuous-process integration:** Compatibility with the continuous transport of the CFRP material.

These requirements represent boundary conditions for the selection and integration of the cutting process rather than independent performance metrics. In particular, cutting-related particles and residues have to be controlled to limit contamination

of the material, surrounding hardware, and spacecraft environment. Furthermore, the continuous material transport has to be considered when generating the required cutting trajectory.

3. CUTTING PROCESS SELECTION

Based on the requirements identified in Section 2, different approaches for implementing the cutting operation were considered. An initial mechanical cutting concept had already been developed for the AMoCSiS tube manufacturing system. With the evolving requirements regarding cutting geometry, automation, and system integration, this concept was reassessed and alternative cutting principles were investigated.

3.1. Initial Mechanical Cutting Concept

The initial AMoCSiS cutting concept was based on mechanical separation of the CFRP material in its flat state before tube forming. A blade was guided along a mechanically defined cutting path, while the cutting platform was designed to move with the continuously transported material. This enabled the cutting operation to be integrated without interrupting the material feed. Figure 4 shows the developed mechanical cutting unit.

The concept provides a comparatively simple cutting principle with low power demand and limited thermal interaction with the CFRP. However, the direct mechanical contact introduces tool wear and loads into the material. In addition, the cutting geometry is defined by the mechanical guide, requiring hardware modifications when different tube-end geometries are introduced. The increasing demand for geometric flexibility therefore motivated the investigation of alternative cutting principles.

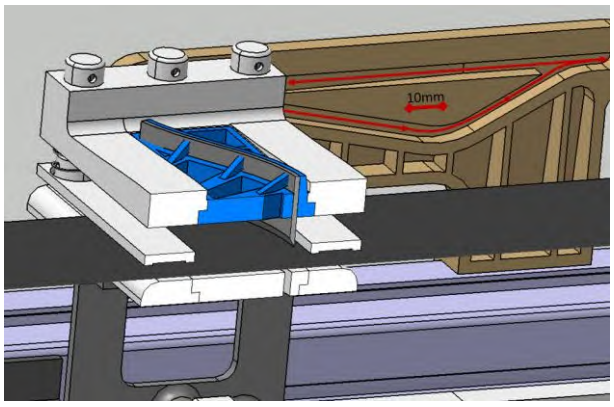


Figure 4: First automated CFRP-Cutting Approach

3.2. Alternate Cutting Technology

Based on the requirements identified in Section 2, laser cutting was considered as an alternative to the initial mechanical cutting concept. Contactless material removal eliminates direct cutting forces and mechanical tool wear, while programmable beam motion enables different cutting trajectories without geometry-specific cutting guides. These characteristics are particularly relevant for the variable tube-end geometries considered within AMoCSiS.

At the same time, laser cutting introduces different process-related challenges. The interaction of the laser radiation with the heterogeneous CFRP material can result in thermal effects, matrix degradation, and process-related residues [1,2]. The suitability of a laser-based process therefore depends not only on achieving complete material separation, but also on the selected laser source, process parameters, and its integration into the manufacturing system.

3.3. Comparative Assessment

The considered cutting approaches were qualitatively assessed against the requirements of the AMoCSiS manufacturing system. Since the objective was to select a technology for further experimental development rather than to provide a general comparison of CFRP cutting processes, the assessment focuses on criteria relevant to the intended application and system integration. The ratings represent a qualitative system-level assessment based on the requirements identified in Section 2 and on characteristics of mechanical and laser-based CFRP processing reported in literature [1,2,4].

Table 1 summarizes the resulting assessment. In addition to cutting-path flexibility and mechanical interaction, system-related aspects such as installation volume, system complexity, power demand, and thermal interaction were considered. Compatibility with transparent optical barriers was included as an additional criterion, since optical separation between the laser source and the cutting region may provide an option for future system integration. This criterion depends on the selected wavelength and window material and does not imply that an optical window is required by the current AMoCSiS architecture.

Table 1: Qualitative assessment of cutting technologies for the AMoCSiS application

Criterion	***Mech***	***CO_2***	***IR***	***UV***	***450 nm***
Contactless proc.	−−	++	++	++	++
Cutting-path flex.	−	++	++	++	++
Compact integr.	+	−	0	−	++
Complexity	++	−	0	−	+
Power demand	++	−	0	−	+
Thermal interaction	++	−−	−	+	0
Transparent-barrier compatibility	n/a	−	+	0/−	++

The comparison illustrates the different trade-offs associated with the investigated cutting principles. Mechanical cutting provides a comparatively simple and energy-efficient solution with limited thermal interaction, but requires direct contact with the CFRP and provides limited flexibility when the cutting geometry is defined by mechanical guides. Laser-based processes eliminate direct mechanical interaction and enable programmable cutting trajectories, but introduce thermal effects and additional requirements regarding the laser source and optical system [1,2,4].

Based on this qualitative assessment, a blue diode laser with a wavelength of approximately 450 nm was selected for further experimental investigation. The approach combines contactless processing and programmable cutting trajectories with the potential for compact system integration. The visible wavelength also provides compatibility with commonly available transparent optical materials, which was considered beneficial for investigating potential optical separation between the laser source and the cutting region.

The selection represents an application-specific choice for the further development of the AMoCSiS cutting process and does not imply a general superiority of blue diode lasers for CFRP processing. The achievable cutting performance, thermal effects, and process-related contamination are therefore investigated experimentally in Section 4.

4. EXPERIMENTAL LASER CUTTING INVESTIGATION

Following the selection of laser cutting, experimental investigations were conducted to characterize the cutting behavior of the CFRP material and to establish suitable process parameters for the further development of the AMoCSiS cutting system. The investigations focused on material separation, the influence of commanded laser power and feed rate, the transferability of the resulting parameters to a representative cutting geometry, and process-related particle generation. In addition, the feasibility of introducing the laser radiation through a transparent optical barrier was investigated.

All experiments presented in this work were conducted under atmospheric conditions and therefore represent an initial baseline for further development toward operation under space-relevant conditions.

4.1. Experimental Setup and Methodology

The cutting experiments were performed using a blue diode laser with a nominal wavelength of 450 nm and an optical output power of approximately 20 W. For the initial investigation, the laser was integrated into a modified Cartesian 3D-printer system, providing controlled relative motion between the laser and the CFRP specimen. The investigated material consisted of a 0.3 mm thick single-layer CFRP with a 0°/90° woven-fabric architecture, corresponding to the material used for the AMoCSiS tube manufacturing process.

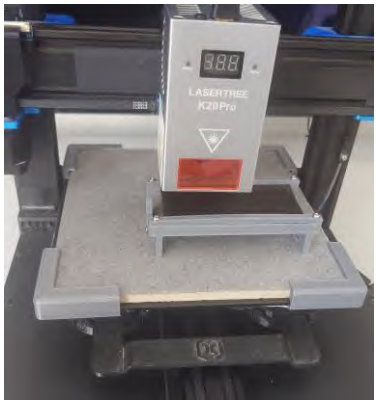


Figure 5 Experimental setup for CFRP cutting using the 450 nm diode laser.

The experimental investigation was conducted in successive steps. Initially, straight reference cuts were performed at different commanded laser powers and feed rates to identify parameter combinations providing complete material separation. Based on these results, additional experiments at increased feed rates were conducted to investigate the transition between complete separation and incomplete removal of the CFRP constituents. Single- and multi-pass strategies were subsequently compared to evaluate whether increased feed rates could be combined with repeated laser exposure.

The resulting specimens were visually inspected with particular attention to complete fibre separation, matrix removal, soot deposition, and visible alteration of the material surrounding the cutting path. The investigation was intended to establish an initial process window and identify relevant process trends rather than to perform a comprehensive optimization of the laser parameters.

4.2. Cutting Performance and Process Parameters

The cutting performance was investigated in several successive test series, with the observations from each series defining the parameter range and objectives of the subsequent experiments. The first series comprised 25 straight single-pass cuts combining five commanded laser-power levels between 60% and 100% PWM with feed rates between 2 and 10 mm/s. The resulting cutting performance is summarized in Figure 6.

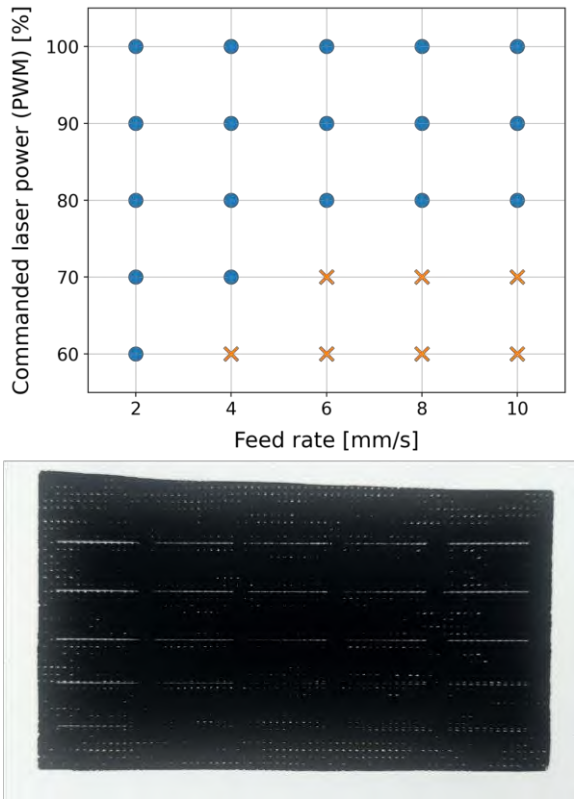


Figure 6: Results of the initial cutting investigation as a function of commanded laser power and feed rate

At 60% PWM, complete material separation was achieved only at 2 mm/s. Increasing the commanded laser power progressively extended the range of feed rates resulting in complete separation. At 70% PWM, complete cuts were obtained at 2 and 4 mm/s, while at 80% PWM and above, complete separation was achieved for all investigated feed rates up to 10 mm/s. These results demonstrated the expected dependence of cutting performance on commanded laser power and feed rate and motivated a second test series focusing on increased feed rates.

The second series comprised 15 straight single-pass cuts at commanded laser powers of 80%, 90%, and 100% PWM, with feed rates extending up to 40 mm/s. The investigated parameter combinations and resulting material separation are shown in Figure 7. Complete separation was achieved only for the 80% PWM, 10 mm/s reference condition. At the higher feed rates, the cuts remained incomplete. In several cases, substantial matrix removal was observed while carbon fibres remained across the cutting path. This observation indicates that visible matrix removal alone is not sufficient to assess successful separation of the CFRP material.

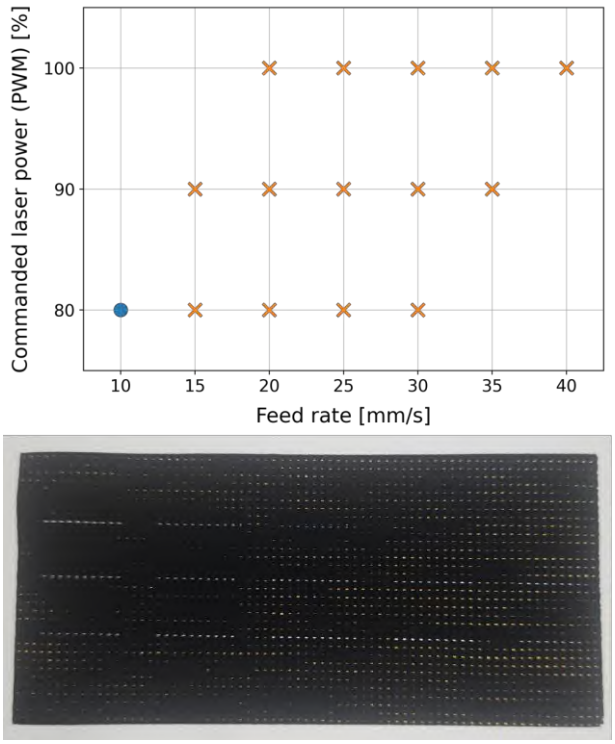


Figure 7: Results of the increased-feed-rate cutting investigation

In addition to the separation behavior, visible burning and soot formation were observed during laser processing. Dark deposits developed on and around the processed region, with their extent depending on the applied process parameters. These observations are particularly relevant with respect to the intended in-space application. The experiments were conducted under atmospheric conditions, where the presence of oxygen affects thermal decomposition and oxidation of the CFRP constituents. Consequently, the observed burning and soot formation represent characteristics of the investigated atmospheric process and cannot be transferred directly to processing under vacuum conditions [3].

From a system-integration perspective, reliable separation in a single pass is preferable where feasible. A single-pass process reduces the number of required trajectory executions and avoids the need to reproduce the same cutting path during a subsequent pass. This becomes particularly relevant for complex cutting geometries and for integration into the continuously operating AMoCSiS tube manufacturing process. However, the results of the first two test series indicated that the achievable feed rate for reliable single-pass separation is limited with the investigated laser system.

As a subsequent experimental step, the possibility of performing the cutting operation through a quartz-glass window was investigated in a separate series of nine cuts. Since these experiments address the potential integration of a transparent optical barrier

rather than the fundamental cutting parameters, their results are discussed separately in Section 4.5. Following these experiments, the laser optics were cleaned and additional direct-cutting reference tests were conducted without the quartz-glass window.

At 100% PWM, complete separation was achieved at 10 mm/s using a single pass, whereas single-pass cuts at 15 and 20 mm/s remained incomplete. For the investigated setup and material, the transition from complete to incomplete single-pass separation at maximum commanded laser power therefore occurred between 10 and 15 mm/s. To investigate whether increased feed rates could be combined with repeated exposure, additional straight cuts were performed using two consecutive passes. Complete separation was achieved at both 20 and 25 mm/s at 100% PWM using two passes.

Among the investigated straight reference cuts, the 25 mm/s two-pass configuration showed the least visible alteration of the matrix surrounding the cutting path while still achieving complete material separation. The results therefore indicate a trade-off between feed rate, number of passes, and the resulting material condition. Although a single-pass process remains preferable with respect to trajectory execution and process integration, a multi-pass strategy allows higher feed rates per pass and can provide complete separation while limiting the visible material alteration associated with slower processing. The 25 mm/s two-pass configuration was therefore selected as the starting point for the representative cutting geometry investigated in Section 4.3.

4.3. Representative Cutting Geometry

Following the straight-cut investigations, the selected process parameters were transferred to a representative cutting geometry derived from the AMoCSiS tube-to-node interface described in Section 2.1. The contour was implemented as a programmable two-dimensional cutting trajectory and processed on the flat CFRP material.
Based on the results of Section 4.2, an initial test was performed at 100% PWM and a feed rate of 25 mm/s using two passes. Although these parameters had provided complete separation for straight reference cuts, complete fibre separation was not achieved along the entire representative geometry. In particular, sections involving changes in cutting direction and closely spaced features showed remaining fibres and locally varying material removal.
The result demonstrates that process parameters established using straight reference cuts cannot be transferred directly to more complex cutting trajectories. Changes in direction, local trajectory geometry, and repeated exposure of adjacent regions alter the interaction between the laser and the material. Consequently, the representative geometry requires trajectory-specific process development rather than the application of a single parameter set derived from straight cuts.
Nevertheless, the experiment demonstrated that the required AMoCSiS contour can be implemented directly as a programmable laser trajectory without geometry-specific mechanical tooling. This geometric flexibility represents a principal advantage of the laser-based approach, while reliable material separation along the complete contour remains subject to further process development.
The complete two-pass trajectory required approximately 49 s of processing time.

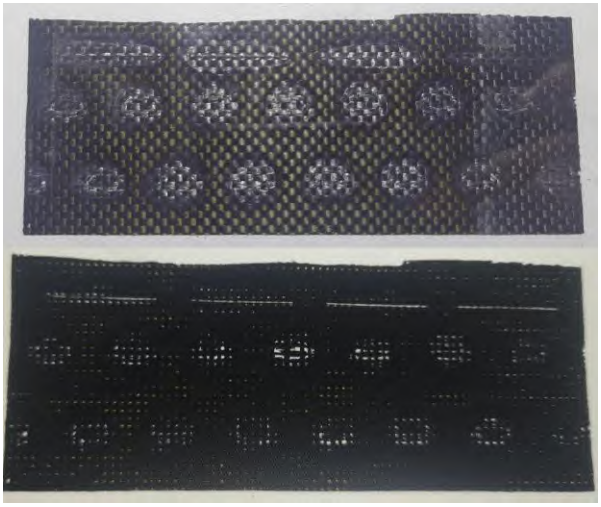


Figure 8: Representative AMoCSiS cutting geometry processed at 100% PWM and 25 mm/s using two passes. Complete fibre separation was not achieved along the entire contour.

4.4. Particle Measurement during Laser Cutting

The visible soot formation observed during the cutting experiments motivated an additional investigation of airborne particle generation. A Sensirion SPS30 particulate-matter sensor was positioned in the vicinity of the cutting region and used to record particle mass and number concentrations during laser processing under atmospheric conditions. The measurement was intended to provide a qualitative indication of process-related particle generation rather than a quantitative characterization of the emitted particle mass.
Figure 9 shows a representative measurement sequence. A pronounced increase in both particle mass concentration and particle number concentration was observed during the cutting sequence, followed by a gradual decrease toward the initial concentration level. The measurement therefore demonstrates a pronounced increase in airborne particle concentration associated with the laser-cutting sequence.

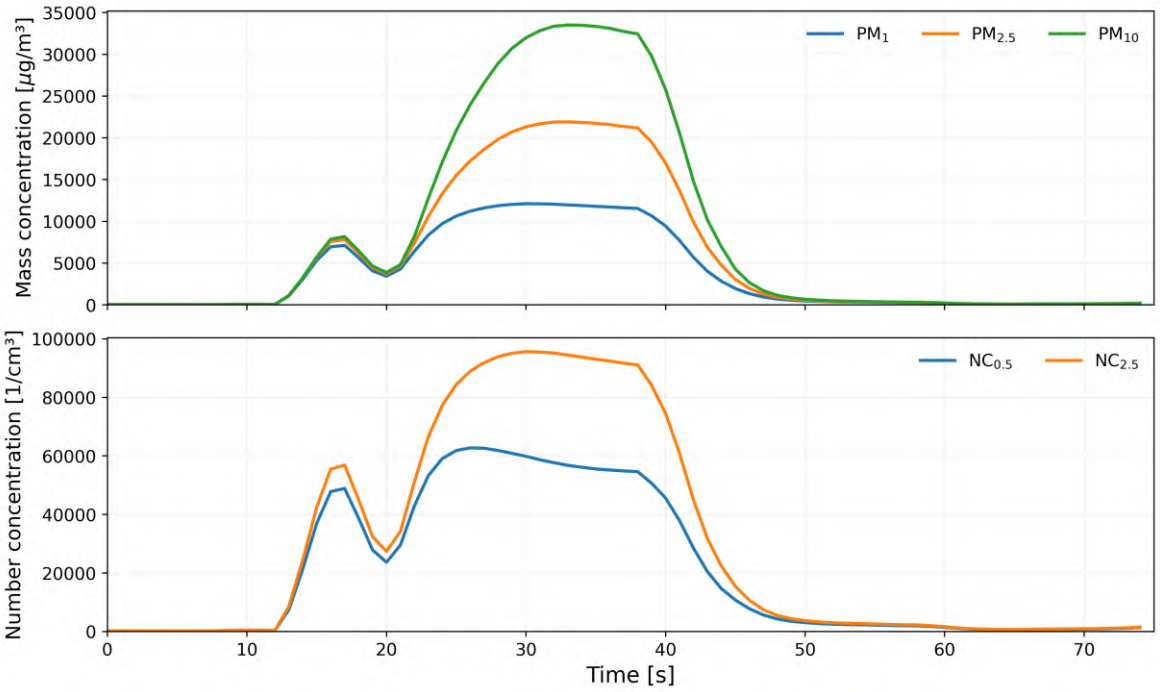


Figure 9: Representative SPS30 measurement during laser cutting, showing particle mass and number concentrations

Individual cutting events cannot be assigned unambiguously to individual concentration peaks. Successive cuts were performed with comparatively short intervals, and the measured concentration had not returned to its initial level before subsequent cutting events. The measurements are therefore

interpreted qualitatively and no particle concentration is attributed to a specific set of cutting parameters.

The results support the consideration of process-related contamination as a relevant aspect of system integration. However, the measurements were performed in an oxygen-containing atmospheric environment and include particle transport through the surrounding air. Both particle formation and transport are expected to differ under vacuum conditions. Consequently, the measurements provide an atmospheric baseline and cannot be directly transferred to the intended space environment.

4.5. Quartz-Glass Investigation

As part of the investigation of potential system-integration concepts, the feasibility of transmitting the 450 nm laser radiation through a transparent barrier was examined using a quartz-glass plate. The experiment was intended as an initial feasibility investigation rather than a characterization of the optical properties of the glass.

As a reference, the laser was first operated through the quartz glass without a CFRP specimen. No visible modification of the glass was observed. Subsequently, nine CFRP cutting tests were performed through the quartz glass at 100% commanded laser power. The feed rate was varied from 11 to 19 mm/s in increments of 1 mm/s, with a dwell time of 60 s between successive cuts. The resulting glass surface and the spatially corresponding cutting parameters are shown in Figure 10.

During the test series, soot and process residues accumulated on the glass surface facing the CFRP specimen. Visible marks were also observed at the locations corresponding to several cutting paths. The appearance and intensity of these marks varied along the parameter series. However, no quantitative characterization of the surface modification was performed. Complete separation of the CFRP was not achieved for any of the investigated parameter combinations.

Since the experiment does not independently quantify optical transmission, surface contamination, thermal loading, or changes in beam propagation, the origin of the observed marks and their influence on cutting performance cannot be conclusively determined. Nevertheless, the results indicate that interaction between the cutting process and a nearby optical barrier has to be considered when evaluating such an integration concept.

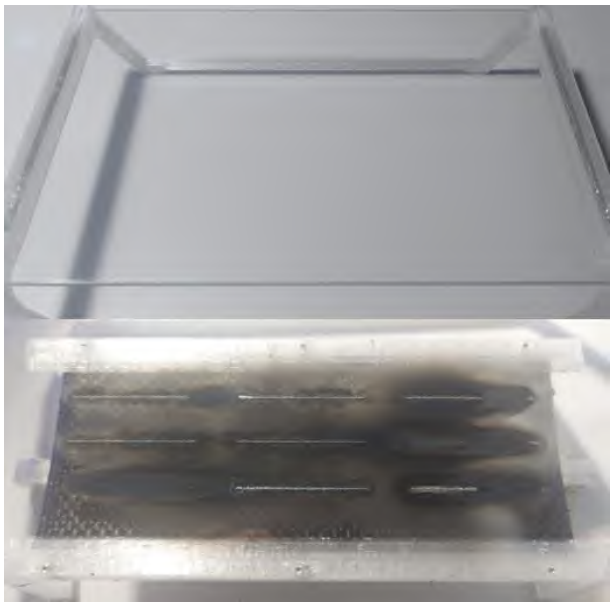


Figure 10: Quartz-glass investigation: (a) reference exposure without CFRP specimen and (b) glass surface after CFRP cutting experiments, showing process-related deposits and visible surface modification.

5. SYSTEM INTEGRATION AND PROCESS CONSIDERATIONS

The experimental investigations demonstrate the feasibility of laser-based separation of the investigated CFRP material, while also identifying several aspects that have to be addressed for integration into the AMoCSiS manufacturing system. In addition to the cutting performance itself, the cutting unit has to be integrated into the existing hardware, synchronized with the continuous material transport, and operated while limiting process-related contamination. Processing time, power demand, reliability, and the requirements associated with a future space application further influence the system design.

5.1. AMoCSiS compatible Cutting Station

To investigate the integration of the laser-cutting process into continuous tube manufacturing, a dedicated test station was developed. The station represents the continuous transport of the flat CFRP material by means of a movable platform driven by a stepper motor and timing belt. This allows the material-feed motion to be reproduced independently of the cutting motion and provides a platform for the further development of synchronized cutting strategies.

An initial version of the test station provided one-axis laser motion transverse to the material-transport direction. This configuration enabled straight cuts across the moving material, but did not provide sufficient relative motion to generate arbitrary two-dimensional cutting trajectories during continuous transport.

Based on these limitations, the test station was further developed by introducing a second laser-motion axis parallel to the material-transport direction. The current configuration therefore combines continuous material-feed motion with two-axis laser positioning. By superimposing the longitudinal and transverse laser motion on the material transport, more complex cutting trajectories can be generated relative to the moving CFRP material. Figure 11 shows the initial and current configurations of the integration test station.

Processing time represents an additional consideration for continuous operation. The representative two-pass cutting trajectory investigated in Section 4.3 required approximately 49 s to execute. Although this value does not represent an optimized cycle time, it illustrates that cutting duration, available motion range, and material-feed velocity have to be considered jointly when defining the synchronized cutting strategy.

The test station is intended as an integration-development platform rather than a representation of the final AMoCSiS cutting hardware. Further development has to consider positioning accuracy, synchronization, processing time, installation volume, power demand, and the mechanical integration of the cutting unit into the existing tube-manufacturing system.

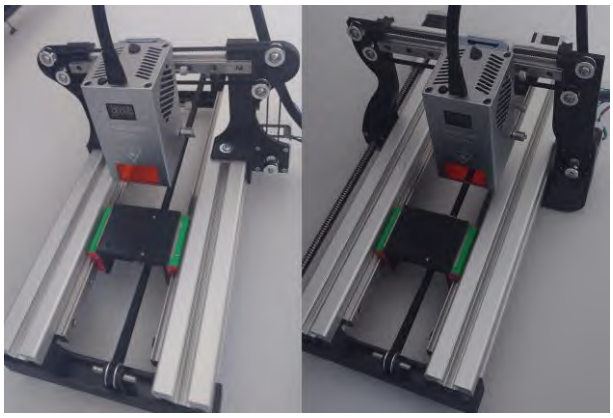


Figure 11: Development of the integration test station: (a) initial configuration with transverse laser motion and movable material platform; (b) current configuration providing two-axis laser motion for the generation of complex cutting trajectories during continuous material transport.

5.2. Contamination and Space-Related Considerations

The experimental investigations identified process-related contamination as an additional challenge for system integration. Visible soot and residues were deposited on the CFRP material and surrounding surfaces, while the SPS30 measurements showed an increase in airborne particle concentration associated with the cutting sequence. For an integrated AMoCSiS cutting process, such residues have to be considered with respect to both the manufactured structure and the surrounding

equipment.
The quartz-glass experiments further showed that surfaces positioned close to the cutting region may be affected by process-related deposits. Although the use of an optical window is not currently defined as part of the AMoCSiS system architecture, the observations illustrate the importance of considering the propagation and deposition of cutting residues when developing potential contamination-control concepts.

The present experiments were conducted under atmospheric conditions and therefore cannot directly represent the behavior expected during in-space operation. Changes in oxidation and thermal interaction under vacuum may alter the cutting process and the resulting contamination behaviour [3]. Experimental characterization under space-relevant conditions is therefore required before suitable contamination-control measures can be defined.

In addition, the integrated cutting system has to satisfy the general requirements of a space-based manufacturing system. These include limited mass, installation volume, and power demand as well as reliable operation with minimal maintenance or intervention. The hardware developed in this work therefore represents a platform for process and integration development rather than a space-qualified cutting system.

6. DISCUSSION AND FURTHER DEVELOPMENT

The investigations presented in this work demonstrate the general feasibility of laser-based processing for the CFRP material used within AMoCSiS, while also identifying limitations that remain to be addressed before integration into an operational in-space manufacturing system. The results should therefore be interpreted as an intermediate stage in the development of the cutting process rather than as a finalized cutting solution.

6.1. Demonstrated Capabilities and Limitations

The experiments demonstrated complete separation of the investigated 0.3 mm CFRP material using the 450 nm diode laser. Straight cuts with a length of 105 mm were successfully produced at feed rates of up to 25 mm/s using two passes. In addition, the experiments showed that the laser can selectively remove substantial amounts of matrix material without necessarily separating the carbon fibres. This behaviour may provide additional processing possibilities, but also demonstrates that visible material removal alone is not a sufficient criterion for successful cutting.

The investigated process parameters showed a clear relationship between cutting performance and the resulting material condition. Lower feed rates provided sufficient interaction for reliable separation but were associated with more pronounced visible alteration of the surrounding matrix. Higher feed rates reduced the interaction time per pass, while repeated passes enabled complete separation at increased feed rates. The results therefore indicate a trade-off between cutting speed, number of passes, complete fibre separation, and visible material alteration.

However, the transfer of parameters from straight reference cuts to the representative AMoCSiS cutting geometry was not directly successful. The 25 mm/s two-pass parameter set provided complete separation for straight cuts but left fibres unseparated along parts of the complex trajectory. Reliable processing of the required tube-end geometry therefore requires further trajectory-specific parameter development.

Process-related contamination represents an additional limitation. Soot formation, airborne particle concentration, and deposits on nearby surfaces were observed under atmospheric conditions. Their behaviour under vacuum remains unknown, preventing direct extrapolation of the present contamination results to an in-space process.

6.2. Further Development

Further development should initially focus on establishing reliable process parameters for the representative cutting geometry. This includes the investigation of trajectory-dependent feed rates, single- and multi-pass strategies, and the influence of local changes in cutting direction. Higher optical power may provide an additional means of increasing cutting speed while maintaining reliable fibre separation. Alternative laser technologies and wavelengths should also remain subject to investigation, particularly where they offer advantages regarding energy efficiency, thermal interaction, or system integration.

The current integration test station provides a basis for developing synchronized cutting during continuous material transport. Future work should address coordinated control of material feed and two-axis laser motion, positioning accuracy, available travel range, and the relation between cutting duration and production speed. These investigations are required to transfer the demonstrated stationary cutting process to continuous AMoCSiS operation.
Environmental testing represents another essential development step. Laser-material interaction, contamination behavior, and thermal transport have to be characterized under vacuum and, subsequently, under representative space conditions. Based on these results, suitable measures for contamination control and protection

of surrounding hardware can be developed. The quartz-glass experiments presented in this work provide an initial investigation of optical separation but do not establish the use of a window as the preferred system architecture.
Finally, the cutting unit itself has to evolve from the present experimental hardware toward a space-suitable subsystem. This includes reduction of mass, volume, and power demand as well as assessment of reliability, lifetime, maintenance requirements, thermal management, and compatibility with the overall AMoCSiS system.

7. CONCLUSION AND OUTLOOK

This work investigated laser cutting as a flexible alternative to mechanical separation within the continuous CFRP tube manufacturing process of AMoCSiS. Using a 450 nm diode laser, complete separation of the investigated 0.3 mm CFRP material was demonstrated, including straight cuts at feed rates of up to 25 mm/s using two passes. The experiments further showed the influence of process parameters on material separation and visible material alteration, while the representative cutting geometry demonstrated that parameters obtained from straight cuts cannot be transferred directly to more complex trajectories.

The developed integration test station provides a basis for transferring the process to continuous material transport. At the same time, observed particle and soot generation, trajectory-dependent cutting performance, and the atmospheric test conditions identify relevant areas for further development. Future work will therefore focus on process optimization, synchronized continuous cutting, contamination behaviour under vacuum, and the development of space-suitable cutting hardware.

8. REFERENCES

1. Herzog, D., Jäschke, P., Meier, O. & Haferkamp, H. (2008). Investigations on the thermal effect caused by laser cutting with respect to static strength of CFRP. *International Journal of Machine Tools and Manufacture,* 48(12-13), 1464-1473.
2. Riveiro, A. et al. (2012). Experimental study on the CO2 laser cutting of carbon fiber reinforced plastic composite. *Composites Part A: Applied Science and Manufacturing,* 43(8), 1400-1409.
3. Tao, N. et al. (2021). Temperature-dependent material removal during pulsed laser processing of CFRP composites. *Optics & Laser Technology* 144, 107445.
4. Jiao, J. et al. (2023). A Review of Research Progress on Machining Carbon Fiber-Reinforced Composites with Lasers. *Micromachines,* 14(1), 24.

Stress rupture prevention of composite high-pressure vessels

Herbert Haller [(1)]

[(1)] *INTALES GmbH, 6161 Natters, Austria, Email:haller@intales.com*

KEYWORDS

COPV, pressure vessel, CFRP, stress rupture.

ABSTRACT

Stress Rupture is a time dependent failure mode occurring in composite overwrapped pressure vessels (COPV) used in long missions under constant high pressure. In order to illuminate this phenomenon a numerical study in conjunction with a test campaign has been performed. Based on literature and knowing from experience that the time dependent effects are mainly driven by the resin of the overwrap, the numerical model was built in order to consider matrix creep. Thus, in a first test series the creep behaviour of the matrix was identified. In a second test campaign the short-term behaviour of the COPV was tested by burst tests. The layup and the burst pressure level were determined by numerical sizing and predictions. For these burst tests strain gauges have been applied at certain locations identified by the prediction in order to validate the numerical model.

1. GENERAL

The project objective is to develop a method that might afterwards be usable in industry projects for sizing of COPVs against stress rupture. Therefore, a phenomenological approach was used, i.e. use a global, macroscopic modelling approach with which the stress rupture phenomenon can be predicted.

Based on experience and findings in literature, it was decided to define resin creep as the only time-dependent property of the COPV model ([3], [4], [5]). Therefore, a viscoelastic constitutive law would be defined for the resin material, based on material tests on resin coupons. Attempts would be made to make numerical predictions of the long-term behaviour of COPVs using only such a simple approach.

2. NUMERICAL MODEL

Several numerical models were created to analyse the COPV and the stress rupture phenomenon, using the FEM-software ABAQUS.

To be able to properly consider resin creeping, the carbon fibre and matrix had to be separated.

Therefore, a DFEM 3D rebar-solid model was created. Here, the resin was modelled using continuum elements. The carbon fibres were modelled using a 1D rebar definition. These rebar elements were then embedded into the resin elements. This definition allowed for a proper interaction between fibres and resin where loads were transmitted between the two similar as in a CFRP compound.

The following constitutive laws for the vessel have been considered:

- Aluminium Liner: elastoplastic plastic damage
- Resin: elastic creep
- CFRP fibre: linear elastic damage ([7], [9])
- The analyses have been performed under consideration of geometric nonlinearity (large deflections).

The input parameters for the materials are stemming from a sample test campaign performed by PEAK Technology.

3. SENSITIVITY STUDY

A sensitivity analysis (SA) was performed using the DFEM 3D rebar solid model. Monte Carlo Simulation was used as the basis for this SA ([8]).

The method described by [6] is extended focussing on the state variable stress and strain.

Sampling was performed using the Latin Hypercube Sampling (LHS) approach in combination with a correlation control, to obtain samples with a low correlation between the separate variables. Several different correlation coefficients were used to detect possible correlations between input and output variables, both unranked and ranked. Lastly, confidence intervals were determined using Bootstrap samples, created by re-sampling existing samples. These new samples gave the spread of the correlation coefficients from which a confidence interval could be determined.

The considered input parameters were:

- creep behaviour of the matrix
- fibre undulation
- fibre pre-stress
- fibre damage
- geometrical imperfections, e.g. stemming from manufacturing:
- physical imperfections:

The considered output parameters were:

- Fibre stress
- Resin (creep) strains

An example of SA results can be seen in Figure 1, showing the partial correlation coefficients (PCC) Bootstrap confidence intervals

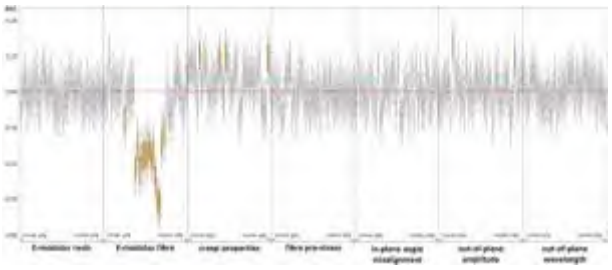


Figure 1: PCC Bootstrap confidence intervals from SA using DFEM 3D solid-rebar model

4. FULL SCALE TETS AND NUMERICAL PREDICITIONS

4.1. Short term burst tests

All short-term burst tests were executed in accordance with ISO 111119-3.

The first COPV tested burst at 593.65 bar. The predicted burst pressure deviated by less than 1% (considering the mean CFRP strength of 3046 MPa). Also, the predicted strains matched the strain measurements relatively accurately. Both the near linear trend in the cylinder and the nonlinear trends over the domes were captured well by the FEM model. The COPV burst in the cylinder, which was also as predicted.

An example of a burst COPV can be seen in Figure 2. It can clearly be seen that the damage occurred only in the cylinder of the COPV.



Figure 2: COPV after burst

4.2. Long-term stress rupture tests

Long-term stress rupture tests on full-scale COPVs were performed to investigate the stress rupture failure phenomenon. The main plan was to perform these tests according to the Mair method ([1], [10]), where the pressure would be increased from a certain starting pressure at a very low constant pressurisation rate up to burst.

To achieve this, a specialised testing set-up had to be created. For this, several objectives were defined:

- Up to five COPVs should be able to be tested in parallel
- The effect of one COPV burst on the others should be negligible
- The pressure should be controllable to a very high degree of accuracy, to allow for very low pressurisation rates
- Monitoring of the strain gauges should be possible over a long period of time without leading to data storage problems

An example of pressure curves during a certain long-term test with five COPVs can be seen in Figure 3.

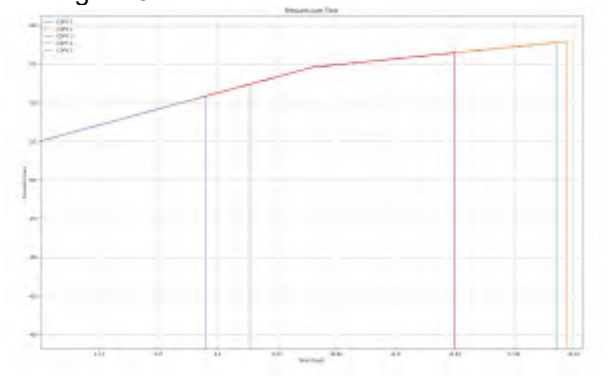


Figure 3: Example pressure curves during a long term stress rupture test.

The strain measurements over time during the long-term phase of the test can be seen in Figure 4.

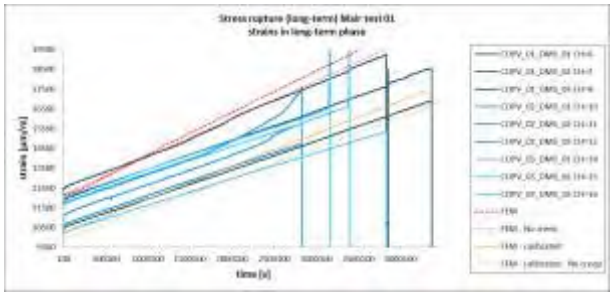


Figure 4: Stress rupture (long term) test 02 – strain comparison in cylindrical region.

The numerical predictions matched the measurements very well, indicating that using resin creep as the only time dependent phenomenon in the analysis could give very accurate predictions of the actual long-term behaviour of a COPV.

Even though the strain predictions match are relatively accurate, predicting the actual time to failure or burst pressure was more challenging. The strains increased by about 3% over 40 days due to creeping of the matrix along. This change is small compared to the scatter of the material properties themselves, which have a variation coefficient of ±7.5%. Therefore, failure of the COPVs is in the end more driven by the material scatter than by the long-term strain increase.

The probability distributions of the resulting strains and burst pressures are plotted in Figure 5. The distributions can be fitted very well using a Weibull distribution (see also [2]), similar to the coupon test results.

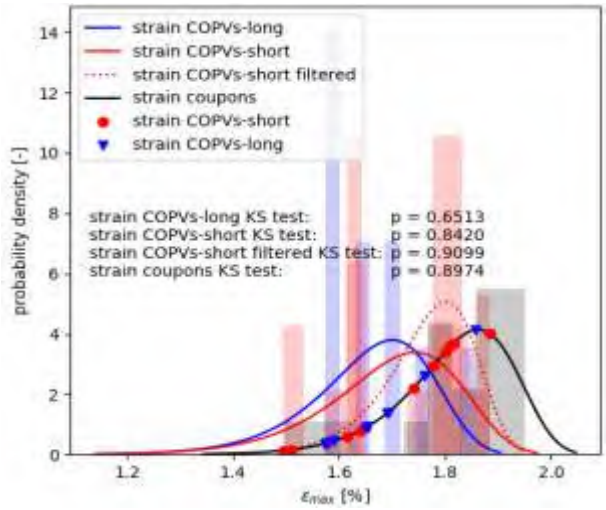


Figure 5: Probability distribution of maximum strain from coupon tests, short term burst tests and long term stress rupture tests.

5. EVALUATION OF RESULTS AND DEFINITION OF SAFETY CONCEPT

Based on all tests performed, it was concluded that the detected stress rupture phenomenon in the investigated COPVs had only a minimal effect on the final failure of the tanks. The main driver was the short-term creep occurring during the first few days of the long-term tests. Increasing the laminate thickness would increase the amount of resin creep and, therefore, the dominance of stress rupture failure.

5.1. Effect of overwrap on stress rupture failure

The numerical models with a viscoelastic law for the resin were proven to make accurate predictions of the fibre strains, both in the short-term and long-term, with a deviation of about 5-10%. Therefore, these models were used in a study of the influence of the overwrap on the stress rupture phenomenon. Several overwrap designs were investigated. The designs and inner pressures were always chosen such that the stresses and strains in the critical ply were similar between all analyses.

The following range of COPV sizes, layups and inner pressures were investigated:

- COPV radius: 43.5 mm to 174.0 mm
- Layup thickness: 2.0 mm to 8.0 mm
- Inner pressures: 400 bar to 1500 bar
- Layup: hoop layer dominated to helix layer dominated

It was determined that two main stress components are driving for the creep phenomenon:

- σ_{rr} and $\sigma_{\theta\theta}$

In principle, it can also be stated that thin layups exhibit lower creep phenomenon than thick ones. Thus, the thicker the layup, the more driving the stress rupture phenomenon is for the sizing of the COPV.

5.2. Testing

A Mair test could be performed to capture the effect that short-term creep has on the burst pressure. This test could be performed in addition to a short-term burst test, where the pressure is rapidly increased up to burst, but also instead of a standard burst test.

5.3. Safety factor

The fibre strength measured using coupon tests as well as short-term full-scale tests can both be fitted well using a Weibull distribution

Thus, choosing a certain failure probability, a safety factor for a certain safety index can be derived from probability analysis under additional consideration of significant parameters of the structure

Even though using an A-basis allowable in combination with a burst factor, which provides a certain margin of safety, in the end, long-term stress rupture failure is a failure mode that must always be considered during the sizing of a COPV. Depending on the exact requirements, e.g. size, MEOP and service lifetime, stress rupture failure could be a driving failure mode or not. Uncertainties in terms of long-term effects, like ageing, should also be taken into account during this evaluation.

6. REFERENCES

1. Mair G.. (2019). Safety Assessment of Composite Cylinders for Gas Storage by Statistical Models.
2. L. Grimes-Ledesma, P.L.N. Murphy (2005), *DOT-VNTSC-FAA-05-01-Operational Guidelines for Spaceflight Pressure Vessels*.
3. S.L. Phoenix, P.L.N. Murthy (2007) Pros's and Cons of Proof Testing Carbon Composite Overwrapped Pressure Vessels: A Comparison of two Mathematical Models.
4. A. Thionet, A.R. Bunsell., H.Y. Chou (2016). Intrinsic Mechanisms Limiting the Use of Carbon Fibre Composite Pressure Vessels.
5. S. Blassiau, A. Tionnet, A.R. Bunsell (2007). Micromechanics of Load Transfer in a unidirectional carbon fibre reinforced epoxy composite due to fibre failures. Part 1, 2, and 3.
6. J.R. Reeder (2012). Composite Stress Rupture: A New Reliability Model Based on Strength Decay.
7. J.L. Chaboche (1988). A non-linear continuous fatigue damage model.
8. J. King (2007). Stochastic Simulation Methods in Sensitivity Analysis.
9. C. Bucher (2009). Computational Analysis of Randomness in Structural Mechanics.
10. R.L. Saulsberry et al (2010). Composite overwrapped pressure vessels (COPV) stress rupture testing.

7. ACKNOWLEDGEMENT

This project was funded by the EUROPEAN SPACE AGENCY.

The hardware and performance of the tests have been performed by PEAK-Technology.

ECSSMET
Braunschweig Germany 2026

Material imperfections

Influence of Deterministic & Probabilistic Verification Methods on Failure Probability & Margin of Safety for Ceramic Space Structures

Jonas Kollmeier [(1)], Tanguy Vitrou [(1)], Dr.-Ing. Stephan Rapp [(1)], Dustin Kersberg [(2)], Dr. Clara Minas-Payamyar [(2)], Dr. Katrin Hirselandt [(2)]

[(1)] OHB System AG, Manfred-Fuchs-Straße 1, 82234 Weßling (Germany), Email: jonas.kollmeier@ohb.de
[(2)] Schunk Technical Ceramics GmbH, Hanns-Martin-Schleyer-Str. 5, 47877 Willich (Germany), Email: dustin.kersberg@schunk-group.com

KEYWORDS

Ceramic, SiSiC, IntrinSiC®, Reaction Bonded SiC, Deterministic, Probabilistic, Verification, Size Effect, FEM, Weibull Distribution

ABSTRACT

High-performance ceramics, such as silicon carbide (SiC), offer outstanding advantages in terms of specific stiffness and thermo-elastic stability. However, their strength is fundamentally limited by the weakest-link effect. Due to the statistical nature of failure stress, a 2-parameter Weibull distribution is typically established based on reference sample testing. For conservative design, a 95% confidence interval at 4σ (Gaussian normal distribution), which implies a failure probability of 63 in $1{,}000{,}000$ parts, is applied.

Because test samples represent only a fraction of the final part volume, Size Effects must be considered, especially in highly loaded slender structures along primary load paths, which introduce increasing uncertainty with larger part volumes. To overcome the (non-conservative) over-prediction of the margin of safety (MoS) inherent in deterministic analyses, a probabilistic approach was adopted. This method accounts not only for peak stresses but also for the volume of material under stress in relation to the tested sample.

A workflow was developed to evaluate stresses and volumes for each individual mesh element, enabling the assessment of Size Effects. The probability of failure and the effective MoS_P at 4σ for the entire component can be determined and compared to classical deterministic MoS_D. From this, a Size Effect factor (SF) for deterministic analysis was derived with multiple load cases, geometries, manufacturing and mesh configurations.

While the deterministic analysis shows large areas under high stress with very smooth transition zones, the probabilistic approach exhibits that only a small number of highly stressed elements significantly contribute to the overall probability of failure.

Mesh convergence studies indicate that the probabilistic approach requires finer meshes than the deterministic approach to achieve mesh independence. Thus, at this stage, absolute failure probabilities are not assessed; so the focus of this paper is on relative variations across various parameters.

1. FUNDAMENTALS & WEIBULL STATISTICS

Ceramics are known for their brittle behaviour, i.e., no yield occurs before failure compared to ductile materials like metals. This phenomenon is due to the missing relaxation at local stress tips. Based on that, failure is mainly governed by the largest critical flaw within the stressed volume. The size, location, orientation and shape of those flaws is constantly varying throughout the part, so that no deterministic value can be derived for ceramics. (see Fig. 1)

A statistical 2-parameter Weibull method is therefore employed, by conducting several 4-point-bending-tests on a reference sample with given constant stressed volume $V_0 = 7.74mm^3$. Different manufacturing states are covered in separate test batches. The results are described by σ_0 (failure stress at 31.7% failure) and m_0 (Weibull Modulus) under a 95% confidence interval. The higher the failure stress and the less scattered the values are, the higher σ_0 and m_0 will be and vice-versa. [1]

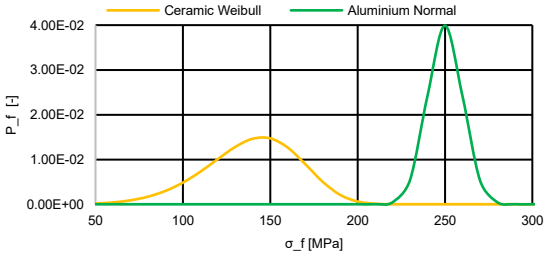


Figure 1: Failure Strength Distribution for Materials

Most space applications require a probability of failure of 4σ, which is equal to $P_{allow} = 6.3e^{-5}$ in allowable failure probability. This reduces the allowable stress drastically. Tab. 1 shows the two main manufacturing states with their m_0, σ_0 and σ_{allow} maximum absolute principal stress allowable at 4σ. [2]

Table 1: Stress Allowable for Manufacturing

Manufacturing	m_0	σ_0 (1σ)	σ_{allow} (4σ)
As-Fired	13.6	$152\ MPa$	$74\ MPa$
Machined	11.8	$209\ MPa$	$92\ MPa$

2. SIZE EFFECT & PARAMETRIC STUDY

The σ_{allow}-values would only be applicable to geometries and parts having a similar effective volume V_{eff} like the sample V_0 ($V_{eff} \sim V_0$). The higher the stressed volume in the real part gets, the more uncertainties due to the weakest link theory must be accounted for. This phenomenon is called Size Effect and can be covered within the subsequent approaches. [3] It shall be noted that apart from Size Effect, no additional safety factors will be applied.

2.1. Deterministic Approach

Within the classical deterministic approach this uncertainty in the Margin of Safety (MoS_D) is only accounted by adding a Size Effect factor (SF) to the maximum stress hotspot σ_{max}. [4, 5]

$$MoS_D = \left(\frac{\sigma_{allow}}{\sigma_{max} \cdot SF}\right) - 1 \qquad (1)$$

This factor is commonly just estimated by selecting a certain stress threshold and comparing the volumes of the sample to the part. This process cannot be easily automated and is not repeatable.

2.2. Probabilistic Approach

In the unconventional probabilistic approach this SF factor does not need to be applied, since it is already inherent in the probability of failure of the part $P_{f,part}$ by accounting for stress and its distribution. [4, 5]

$$P_{f,elem} = 1 - \exp\left(-\frac{V_{elem}}{V_0} \cdot \left(\frac{\sigma_{elem}}{\sigma_0}\right)^{m_0}\right) \qquad (2)$$

$$P_{f,part} = 1 - \prod_{i=1}^{N}\left(1 - P_{f,elem,i}\right) \qquad (3)$$

$$P_{f,part} = 1 - \exp\left(-\sum_{i=1}^{N} \frac{V_{elem,i}}{V_0} \cdot \left(\frac{\sigma_{elem,i}}{\sigma_0}\right)^{m_0}\right) \qquad (4)$$

$$MoS_P = \left(\frac{ln(1-P_{allow})}{ln(1-P_{f,part})}\right)^{1/m_0} - 1 \qquad (5)$$

Instead of taking any arbitrary volume as a reference, it will be calculated for each single finite element V_{elem} with its respective stress σ_{elem}. To establish an effective workflow the extraction of both values is embedded into the post-processor as well as the manufacturing state of certain properties. By substituting $P_{f,elem}$ of (2) in (3), the mathematical simplification (4) can be set up. In this case HyperMesh's Matrix Browser was chosen with a suitable tcl-macro automated process. By selecting the regions and load cases of interest, a contour plot of $P_{f,elem}$ is shown and by using (4) and (5), $P_{f,part}$ and the probabilistic Margin MoS_P can be extracted.

2.3. SF-Derivation & Study Setup

Since a useful and practical procedure has been set up with the probabilistic approach, an analytical derivation of SF on the deterministic side can be done by equating both MoS_D and MoS_P values and solving for SF. Since both methods need to have the same MoS outputs, one can define [4, 5]:

$$MoS_D = MoS_P \qquad (6)$$

$$SF = \frac{\sigma_{allow}}{\sigma_{max}} \cdot \left(\frac{\ln\left(1-P_{f,part}\right)}{ln(1-P_{allow})}\right)^{1/m_0} \qquad (7)$$

All values of this equation are known or can be calculated under the given load case with the established workflow.
Subsequently, a parametric study of different load cases, geometries, manufacturing states and mesh configurations will be conducted to rate the effect on SF. So, non-influential and worst-case combinations can be easily extracted. To exclude the effect of the varying peak maximum absolute principal stress σ_{max} on SF, while changing the parameters, the input load will be set/tuned to a constant value of $\sigma_{max} = 45\ MPa$ for the highest stressed element.

3. RESULTS

The results shall present the relative influence of certain parameters on the SF factor. Please note, that the absolute $P_{f,part}$ or SF values have not been part of this study. As baseline a QSL load case on a $\emptyset\ 900\ mm$ mirror (internal technology development) has been chosen with an as-fired manufacturing state, modelled with a 2D PSHELL mesh at constant $5\ mm$ mesh size. This configuration is marked **bold** in all tables. Bipods and other interfaces have not been considered in this study, but its boundary conditions are represented by SPC conditions.

3.1. Load Case (LC)

The observed load cases were Quasi-Static Loading (QSL), Random (RAN), Thermoelastic Distortion (TED) and Interface Tolerance (IF-TOL). In the subsequent plots (see Fig. 2 - Fig. 5), the stress outcomes σ_{elem} are represented on the left side, while the contours for $P_{f,elem}$ are shown on the right-hand side. All plots have the same relative scaling, i.e., same colours represent same σ_{elem} or $P_{f,elem}$. The plots show that only red-coloured stress regions are accounted for the $P_{f,elem}$ plot and thus, increase SF. Even though green-coloured stress regions make up the largest area, they will not be represented in the right plot.

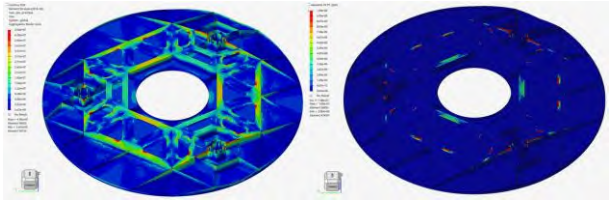


Figure 2: QSL with σ_{elem} (left) and $P_{f,elem}$ (right)

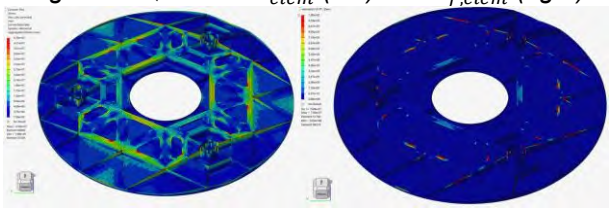


Figure 3: RAN with σ_{elem} (left) and $P_{f,elem}$ (right)

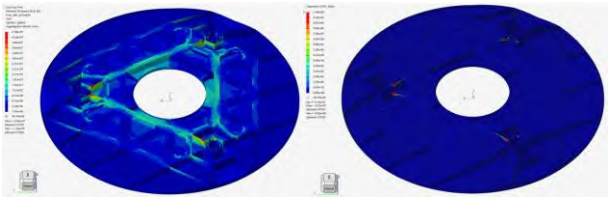


Figure 4: TED with σ_{elem} (left) and $P_{f,elem}$ (right)

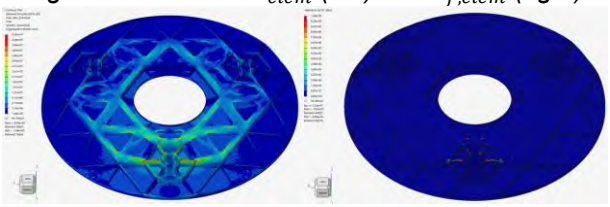


Figure 5: IF-TOL with σ_{elem} (left) and $P_{f,elem}$ (right)

Table 2: SF-Sensitivity for Load Cases

Load Case (LC)	SF
QSL (OOP)	**1.57**
RAN (OOP)	1.55
RAN (IP)	1.41
QSL (IP)	1.40
TED	1.38
IF-TOL	1.31

Looking at the upcoming SF factors (see Tab. 2) one can identify the link between the $P_{f,elem}$-plot, $P_{f,part}$, MoS_P and SF. The more high stress regions are shown in the right plots, the higher $P_{f,part}$ and SF get. I.e., QSL is the most critical load case whereas IF-TOL is less critical since it affects only a smaller portion of area. Also, a directional dependency can be observed with out-of-plane (OOP) loadings having higher impact on SF than in-plane (IP).

3.2. Geometry Type (GT)

Apart from circular mirrors in different sizes and diameters (see Fig. 6), also rectangular ones with free-form-optics (FFO) shape as well as two optical benches, named Ceramic-Optical-Bench (COB) and Sentinel-2 Next-Generation Optical-Bench (S2NG-OB) (see Fig. 7), have been investigated.

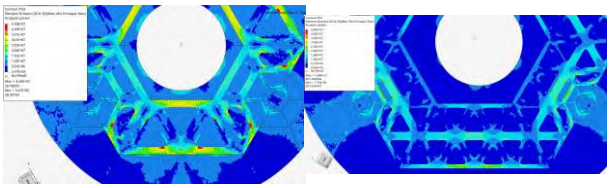


Figure 6: Circular Mirror with Ø $900\ mm$ (left) and Ø $1550\ mm$ (right) with σ_{elem}

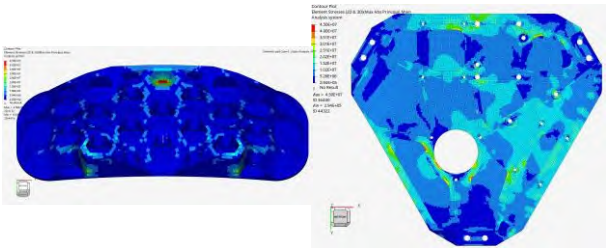


Figure 7: FFO (left) and COB (right) with σ_{elem}

Table 3: SF-Sensitivity for Geometry Types

Geometry Type (GT)	SF
Circular Mirror (small)	**1.57**
Circular Mirror (medium)	1.45
Circular Mirror (large)	1.43
FFO	1.42
COB	1.37
S2NG-OB	1.12

The first counterintuitive observation from these results is that a smaller mirror has a higher SF under the same load and boundary conditions. It should be explained that between a small and a large circular mirror not only size changes, but also the shape and geometry of the structure. Each mirror must meet different requirements. The larger the mirror, the higher the stiffness requirements for optical performance; thus, a large mirror tends to warp less and is subjected to less stress.
Additionally, due to the constant mesh size defined for this study larger mirrors tend to have more precise representation of certain features. This leads to a better stress resolution and less tendency towards potential stress singularities in corners compared to smaller mirrors.
All non-circular-symmetric geometries are having three different SF values (instead of only OOP & IP) in each loading direction. Only the worst-case directions are shown in Tab. 3.

3.3. Manufacturing State (MS)

In this section the effect of the manufacturing state on SF has been studied. Three different versions have been analysed: the entire mirror to be machined, a combined realistic approach, where only optical and mechanical interfaces are mechanically ground and a completely unprocessed mirror with only as-fired surfaces.

Table 4: SF-Sensitivity for Manufacturing States

Manufacturing State (MS)	SF
Machined	1.71
Combined	1.57
As-Fired	**1.57**

By switching from an as-fired to a combined manufacturing approach the SF remains unchanged due to the machined areas/volumes being quite small and not under high stress. Whereas having an all-machined approach leads to an increase in SF, even though having higher σ_0 and σ_{allow} values. The main cause of that increase is the Weibull-Modulus m_0 being lower (more scattered) (see Tab. 4).

3.4. Mesh Dimension (MD)

The effect of the mesh dimension has also been studied. The baseline 2D PSHELL mesh already shows a decent SF. When switching to a 3D PSOLID model not only the final SF value but also the entire stress pattern is looking differently (see Fig. 8 & Fig. 9).

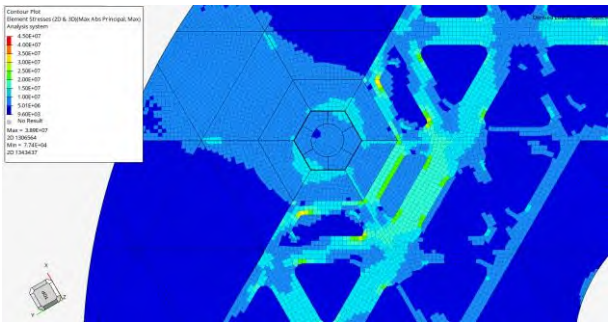


Figure 8: 2D (PSHELL) Mesh with σ_{elem}

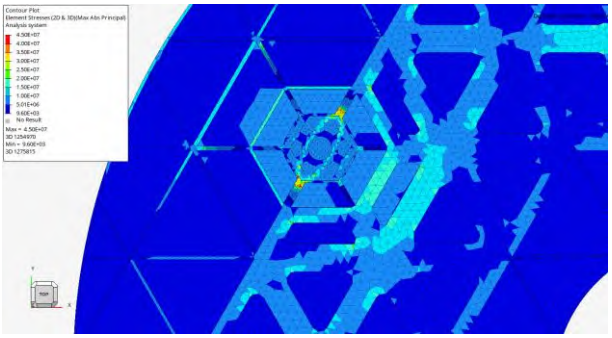


Figure 9: 3D (PSOLID) Mesh with σ_{elem}

Table 5: SF-Sensitivity for Mesh Dimensions

Mesh Dimension (MD)	SF
2D (PSHELL)	**1.57**
3D (PSOLID)	1.03

In general, a 3D (PSOLID) model is expected to represent the real geometry more accurately than a 2D (PSHELL) model and therefore provides a more detailed description of the stress field. Therefore, σ_{max} predicted by a 3D model is often higher even with the same defined mesh. In addition, shell elements tend to deform more than solid elements under bending loads, which may affect the global stiffness of the structure (see Tab. 5).
From a probabilistic perspective, the 2D (PSHELL) model appears to be more conservative, as it leads to a higher $P_{f,part}$ and stronger SF. This result is reassuring because, in the development logic of early phases one usually starts with a 2D (PSHELL) model, which shall have higher conservatism.

4. BOUNDARIES & LIMITATIONS

During the parametric studies several boundaries and limitations could be observed:

1. Currently only relative and no absolute $P_{f,part}$, MoS_P and SF values have been derived.
2. Mesh size, which defines V_{elem} has huge impact.
3. Local Stress hotspots, which artificially increase σ_{max} have a huge impact.

To address all three points, multiple convergence studies on the stress peak σ_{max} and $P_{f,part}$ have been conducted depending on the element size V_{elem}. Here, a simplified 2D model has been chosen, which was subjected to gravity bending loading.

Shown in the plots below (see Fig. 10 & Fig. 11) is the inverse of the mesh size $1/V_{elem}$, meaning the size decreases or the number of total elements increases to the right along the x-axis.

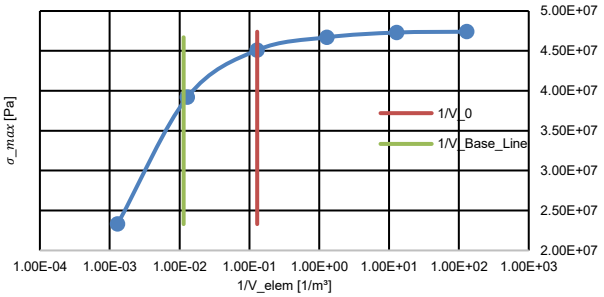


Figure 10: Convergence of σ_{max} depending V_{elem}

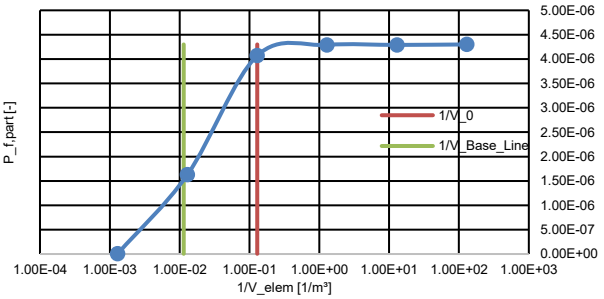


Figure 11: Convergence of $P_{f,part}$ depending V_{elem}

Interestingly, both criteria reach their convergence, when $V_{elem} = V_0$. Additionally, the peak stress σ_{max} has a flatter/less steep convergence compared to the $P_{f,part}$ one. Comparing the outputs at baseline volume V_{base} to the sample volume V_0, the peak stress σ_{max} has already converged by 87% of the final value, while for $P_{f,part}$ only 40% have been reached. The rationale behind is the $m_0 > 1$ in the exponent of the stress fraction in (2). These phenomena indicate that the chosen mesh volume is quite critical to not underestimate the output. Therefore, following criterion is introduced, which sets the mesh size equal to the sample volume:

$$V_{elem} = V_0 \tag{8}$$

The $P_{f,part}$-equation of (2) can now be simplified such that the output is independent from volumes:

$$P_{f,part} = 1 - \exp\left(-\sum_{i=1}^{N}\left(\frac{\sigma_{elem,i}}{\sigma_0}\right)^{m_0}\right) \tag{9}$$

This fixed mesh size can cause computational issues with large components. Since the larger the parts get, the more elements are required. This could be solved either by only local mesh refinement where high stressed areas are expected over a certain stress threshold. To generally decrease the impact of SF from the test sample to the final part a larger sample geometry with higher V_0 could be defined. This of course would lead to higher cost due to remanufacturing the larger samples and complete rerunning of the 4-point-bending-tests.

5. SUMMARY & CONCLUSION

Subsequent key takeaways could be made:

1. *The Size Effect cannot be ignored when designing large ceramic structures:*

   The results demonstrate that the Weibull Size Effect cannot be neglected, as it systematically increases the failure risk compared to a purely deterministic approach. The Size Effect factor is therefore always greater than one. In this study, a value of $SF = 1.57$ was found to conservatively cover all investigated cases. Using such a factor is highly practical, as it allows engineers to remain within a standard deterministic design framework while implicitly accounting for the statistical nature of brittle failure and the influence of stressed volume.

2. *Material statistical characterization is as important as structural design:*

   The influence of the manufacturing state and the number of tested samples proved to be critical. Increasing the dataset significantly modifies the Weibull parameters and can lead to large variations in predicted failure probability, even for identical stress levels. Reliable probabilistic design therefore requires sufficiently large and representative test batches and experimental datasets.

3. *A conservative early design starts with 2D PSHELL models:*

   The comparison between 2D and 3D models showed that PSHELL elements tend to predict higher probabilities of failure. While 3D models provide higher local stress values, PSHELL models lead to a broader stress distribution and therefore amplify the Size Effect. This makes them particularly suitable for conservative assessments during early design.

4. *The load that spreads the stress the most and affects the highest volume is the load that breaks the part:*

   The probabilistic analysis identified the quasi-static load case (QSL) as the most critical, followed by random vibration, thermal loads, and finally interface tolerance loads. For circular mirrors and similar structures, out-of-plane loading conditions are the dominant contributors to failure. This ranking is consistent with both the numerical results and industrial experience and should guide the prioritization of load cases during design.

5. *Requirements can compensate for Size Effect:*

   The study showed that larger structures do not necessarily exhibit higher $P_{f,part}$. Differences in geometry, stiffness distribution, and structural optimisation can significantly alter stress fields and therefore the failure probability. In this paper, the largest variations in SF were observed for different geometry types. Consequently, if a new design does not belong to the investigated configurations, a dedicated probabilistic analysis should be performed to evaluate its failure probability and to recompute an appropriate SF using the methodology developed in this paper.

6. *Probabilistic late-stage analysis should guide deterministic early-stage design:*

   Both approaches offer a fast, efficient and reliable estimation of the final MoS by considering realistic assumptions for the Size Effect SF. For first stage design and optimisation of a newly developed component the classical deterministic approach is the better choice, because it provides a more conservative contemplation by using an SF high enough covering all possible load cases right up front. The probabilistic approach on the other hand is less conservative, but closer to reality and shall be used for final design verification, which is load-case-dependent. By extracting the SF from the probabilistic analysis of the finalised part, the initial SF assumptions during the deterministic approach can be correlated. This flow-back loop of SF allows for continuous improvement of early estimation by e.g. setting up databases and rules for combining different LS, GT, MS with MD.

6. REFERENCES

[1] Nemeth, N.N., Powers, L.M., Janosik, L.A. & Gyekenyesi, J.P. (2013). CARES/LIFE Ceramics Analysis and Reliability Evaluation of Structures Life Prediction Program. NASA.

[2] Danzer, R., Lube, T., Supancic, P. & Damani, R. (2008). Fracture of Ceramics. In Advanced Engineering Materials, Vol. 10, No. 4. Wiley-VCH.

[3] K. Takeo, Y. Aok, T. Osada, W. Nakao and S. Ozaki, “Finite Element Analysis of the Size Effect on Ceramic Strength,” *MDPI Materials,* 2019

[4] Béhar-Lafenetre, S., Denaux, D. & Lucarelli, S. (2014). Mechanical Design and Verification of Ceramic Structures. ESA.

[5] Munz, D. & Fett, T. (2001). Ceramics, Mechanical Properties, Failure Behaviour, Materials Selection. Springer-Verlag, Berlin-Heidelberg.

PROBABILISTIC ASSESSMENT OF SPACE COMPONENTS MANUFACTURED BY L-PBF

Lorenzo Rusnati [(1)], Guglielmo Landi [(2,3)], Mauro Ravaioli [(2)], Gilles Pommatau [(4)], Stefano Beretta [(1,5)]

[(1)] Politecnico di Milano, Department of Mechanical Engineering, via La Masa 1, 20156 Milano, Italy, Email: lorenzo.rusnati@polimi.it, stefano.beretta@polimi.it

[(2)] LEONARDO S.p.a. Space Business Unit, Via delle Officine Galileo, 1, Campi Bisenzio, FI, Italy, 50013, Email: guglielmo.landi@leonardo.com, mauro.ravaioli@leonardo.com

[(3)] International PhD Programme, UNESCO Chair "Environment, Resources and Sustainable Development", 80143 Naples, Italy

[(4)] THALES ALENIA SPACE FRANCE 5 allée des Gabians, BP 99 – 06156 Cannes La Bocca Cedex, France, Email: gilles.pommatau@thalesaleniaspace.com

[(5)] Auburn University, National Center for Additive Manufacturing Excellence (NCAME), Auburn, Al 36849, USA

KEYWORDS

additive manufacturing; fatigue assessment; probabilistic fracture mechanics

ABSTRACT

Laser powder bed fusion enables the production of complex components for space applications, but manufacturing defects and surface roughness harm their expected fatigue strength. Their effect must therefore be addressed within fracture-control assessments, which commonly rely on crack growth calculations and conservative assumptions on the initial defect size. Probabilistic approaches offer an alternative by combining the statistical distributions of defects, material properties and local stress fields to estimate component reliability.

This work investigates the fatigue behaviour of Ti-6Al-4V and Scalmalloy aerospace brackets manufactured with and without deliberately introduced sub-surface defects and tested under vibration loading. Defect populations derived from material characterization campaigns on specimens were employed by ProFACE software to obtain fatigue life estimates that were compared with the experimental fatigue results.

1. INTRODUCTION

Among the additive manufacturing (AM) processes, laser powder bed fusion (PBF-LB) is distinguished for its great versatility and net-shape possibilities. In recent years, metal components for aerospace applications have been manufactured by PBF-LB [1], supporting the wide expansion of the technology. The application of the PBF-LB process is hindered by the formation of anomalies, generated by localized sub-optimal manufacturing parameters. These anomalies present notable differences in formation cause, morphology and density; nonetheless, these flaws must be assessed to demonstrate an acceptable fatigue strength in light of the parts' qualification [2].

Fracture mechanics theory is the typical approach that is adopted for evaluating the structural integrity of components in relation to the presence of defects. Flaws are in fact treated as short cracks and assessed using the concept of stress intensity factor, linked to the Murakami size parameter $\sqrt{\text{area}}$ [3], i.e. the square root of the defect area projected on the plane on which the stress is applied. Fracture control standards of relevant space agencies [4], [5] prescribe the assessment of structural, fatigue critical components by crack propagation calculations adopting, for instance, NASGRO software [6]. Under a deterministic perspective, these standards require the verification of parts with the application of a service life factor of 4; the initial defect size is either observed by non-destructive evaluations or bounded through the detection capability.

As an alternative to a deterministic assessment approach, NASA-STD-5019 proposes the use of a probabilistic assessment route [5], in which all the acting quantities are stochastic variables and their combination shall derive a probability of failure of the component. As per NASA-HDBK-5026 [7], this approach is "potentially significantly less conservative than a deterministic approach but is still technically rigorous". It is for this purpose that ProFACE software was developed, a finite element (FE) post-processor for the probabilistic assessment of AM components [8]. The software calculates the probability of failure of a part adopting the weakest-link theory among the sub-volumes of a FE analysis, from which the applied stress and the volume of each element is extracted. ProFACE adopts the statistics of extremes to determine the likelihood of occurrence of a defect within each sub-volume and derives the reliability of the element by comparing it to the probabilistic critical defect size. Moreover, the software is capable of handling complex geometries and of evaluating the effect of volumetric defects and surface features on the total reliability.

The present work focuses on the manufacturing of two sets of aerospace components by PBF-LB and their subsequent fatigue testing. The adopted

components are an isostatic mounting device (IMD) bracket, manufactured in Ti-6Al-4V, and an antenna deployment and pointing mechanism (ADPM) bracket in Scalmalloy. The IMD, which is a proprietary technology of Leonardo S.p.A., is used to sustain the optical heads of space-borne payloads by providing structural stiffness while ensuring an efficient thermal decoupling between the optical assembly and the surrounding spacecraft structure. The ADPM, instead, is a system for the deployment of antennas and for the adjustment of the reflector during mission.

2. EXPERIMENTAL CAMPAIGN

2.1. Manufacturing of components

The Ti-6Al-4V brackets, displayed in Figure 1, were manufactured with a Renishaw AM500Q PBF-LB system, equipped with four 500 W ytterbium laser. The parts were manufactured in Ar environment and with a Ti alloy baseplate heated to 170 °C. After the completion of the single job, the printed items underwent a stress relieving thermal treatment at 650 °C for 2 hours, followed by furnace cooling. The build job contained a total of 5 IMD brackets; a set of 3 of these parts were manufactured with a deliberately induced sub-surface anomaly located in the region of the component which would see the highest stress state during the fatigue test campaign; the artificial defect was obtained by seeding a spherical void with 0.45 mm radius.

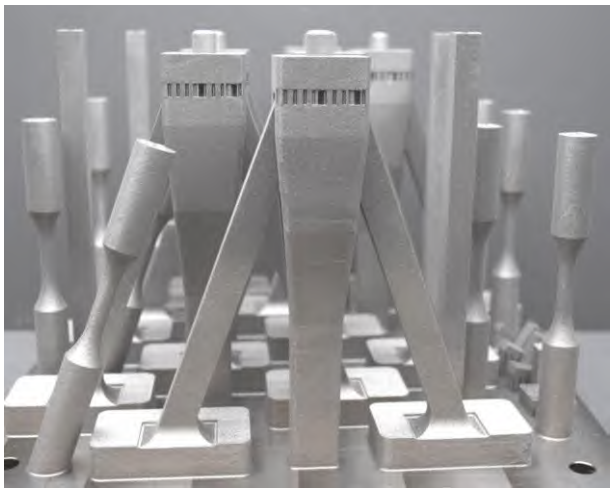


Figure 1: Manufacturing of Ti-6Al-4V components.

Scalmalloy components, shown in Figure 2, were manufactured using the SLM 280 HL Twin system, featuring two yttrium fibre laser sources with a power of 400 W each. Before their removal from the build platform, the parts were subjected to a thermal treatment at 325 °C for 4 hours. Prior to the machining of the interface surfaces, the components were sand-blasted using corundum and a pressure of 6 bar. Two jobs were required to manufacture 4 ADPM brackets; similarly to the IMD brackets, half of the samples were manufactured with an artificial defect located beneath the surface in the part's most stressed area. Out of the four samples, a component experienced manufacturing defect and therefore was not considered in the campaign.

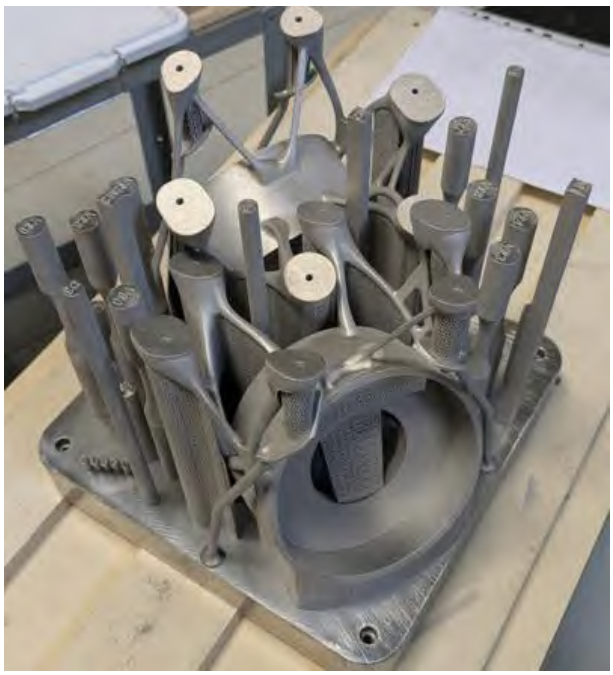


Figure 2: Manufacturing of Scalmalloy components.

2.2. Materials characterization

Both alloys were fully characterized in previous works by part of the authors [9], [10]. Static, fatigue and crack propagation properties were determined on standard samples in accordance with the current ASTM and ISO standards [11], [12], [13], [14].
As regards static tensile properties, Ti-6Al-4V exhibited an ultimate tensile strength of 1187 MPa, a slightly lower yield strength equal to 1146 MPa and an elongation to failure of approximately 12 %. Fatigue crack growth tests were conducted on single edge-notched bending specimens preceded by compression pre-cracking; the experiments were carried out at stress ratios ranging from R = 0.7 to R = -2; the results were fitted by the NASGRO crack propagation equations. Eventually, in compliance with ECSS-Q-ST-70-80C requirements for the additive manufacturing verification plan (AMVP), 24 fatigue specimens were manufactured across two distinct build jobs, inspected by X-ray micro-computed tomography (CT) with a voxel size of 16 µm and tested at load ratio R = -1 on a MTS servo-hydraulic system. The specimens were manufactured in two batches, the first having the axis aligned to the build direction and the second with a 70° inclination with respect to the build plate. After fatigue failure, all fracture surfaces were inspected by scanning electron microscopy to determine the defect at the failure origin. These results were post-processed according to the statistics of extremes to fit a largest extreme value distribution function modelling the size of the surface critical anomalies. Also the porosity

analyses conducted on the micro-CT scans were processed with the extreme values statistics to fit a negative exponential function that would model the size of the largest internal anomalies. Such results are illustrated in Figure 3.
A similar approach was adopted for Scalmalloy. Static, fatigue and crack growth rate tests were performed on dedicated build jobs according to the logic of the AMVP. The material showed high values of tensile properties, such as an UTS of 535 MPa, a YS equal to 518 MPa and an average elongation to fracture of 11.7 %. From the point of view of the crack growth curves, the same experimental campaign was conducted on this alloy, fitting the NASGRO propagation equations. The 24 fatigue specimens were manufactured with similarities with the components: to correctly capture the fatigue behaviour of the part's hotspot, the specimens were manufactured with an inclination of 55 °C between the samples' axes and the horizontal direction and were sand-blasted. 20 µm voxel size micro-CT scans were performed on all the samples, to fit the defects' $\sqrt{area}$ parameter with a LEVD function. SEM imaging of the fracture surfaces were used to determine the distribution of the size of surface defects' population. Moreover, to better characterize the population of defects occurring in the components, within the brackets' build jobs a total of 16 fatigue specimens were added, with a vertical axis and sand-blasted surfaces. These samples were inspected through micro-CT and tested at load ratio R = -1 (with resulting S-N curve illustrated in Figure 4a), followed by SEM observation of fracture surfaces. Their respective results are reported in Figure 4.

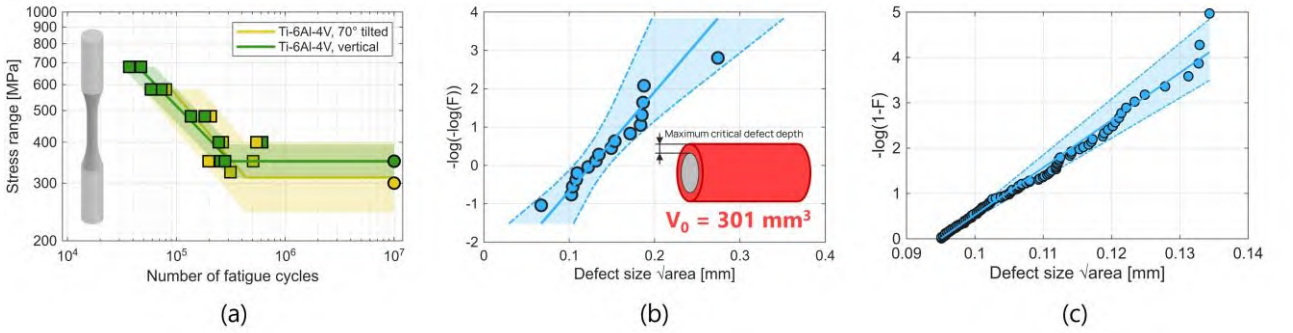


Figure 3: Experimental results on Ti-6Al-4V fatigue specimens: (a) S-N curves; (b) distribution of surface anomalies' size from fractography; (c) distribution of internal defects' size from micro-CT scans.

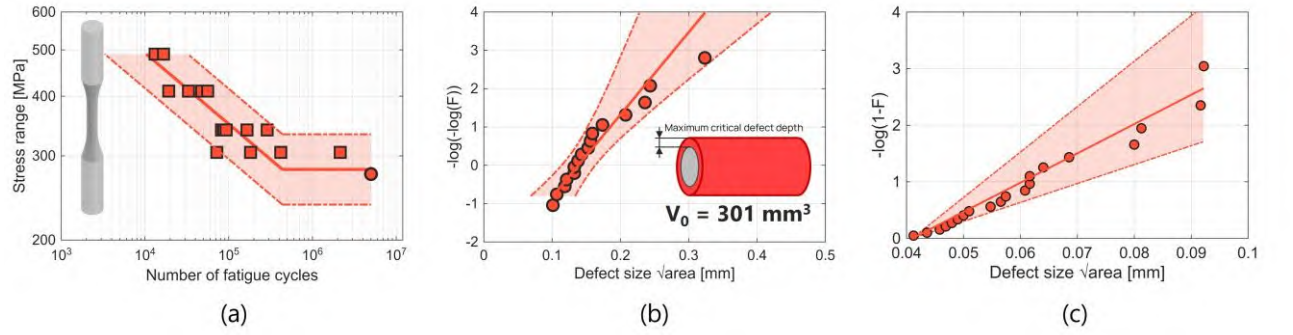


Figure 4: Experimental results on Scalmalloy fatigue specimens: (a) S-N curve; (b) distribution of surface anomalies' size from fractography; (c) distribution of internal defects' size from micro-CT scan.

2.3. Testing of components

For both materials, all components were tested in high cycle fatigue regime on shakers through a constant-frequency, constant-amplitude, sine load acting on a single direction. The goal was to create a dynamic stress not changing in time until the fatigue failure. In this sense, the two parts were tested with two set-ups aiming at representing the items' operative conditions. All tests were monitored through piezoelectric tri-axial accelerometers and, for Ti-6Al-4V parts only, strain gauges mounted at mid-height not to be affected by strong stress gradients.

As regards Ti-6Al-4V components, the test parameters were designed to achieve an applied stress range of 360 MPa in the most stressed region of the part (depicted as region "B" in Figure 5), with region "A" reporting a stress range of 336 MPa. To do so, a sine acceleration of 20.5 g in amplitude at a frequency of 115 Hz (73 % of the frequency associated with the first mode of vibration, as illustrated in Figure 6) was applied.
As for the ADPM brackets manufactured in Scalmalloy, instead, the applied stress range was 355 MPa in the region of the artificial defect and 343 MPa in the cusp located above the artificial defect

(see Figure 7). This was achieved through a 46 g 0-p acceleration vibration at 120 Hz (60% of the first resonance frequency). This condition was applied to two specimens, with the remaining one tested with a 10 % reduction in acceleration amplitude.

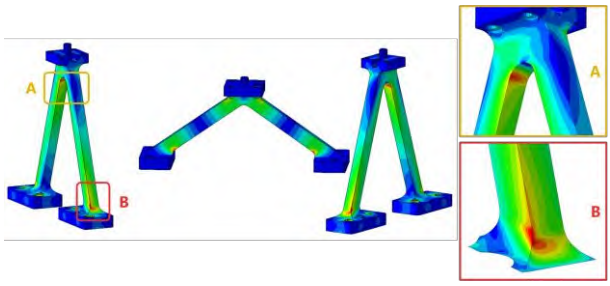


Figure 5: FE analysis of the IMD.

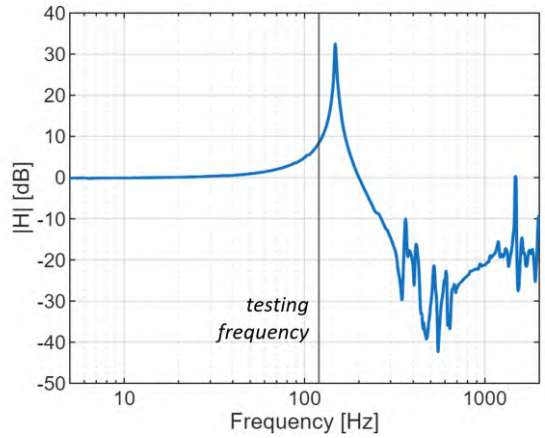


Figure 6: Resonance search on a Ti-6Al-4V component, with indication of the frequency of the fatigue test.

3. RESULTS

The test outcomes, which are reported in Table 1, show that all items were tested until fatigue failure in high cycle regime. The test campaigns on both materials produced results pertaining to different stress levels: in Ti-6Al-4V, this was obtained from experiencing failure in two distinct locations, featuring a different applied stress range; in Scalmalloy, it was due to the dual acceleration amplitude values.

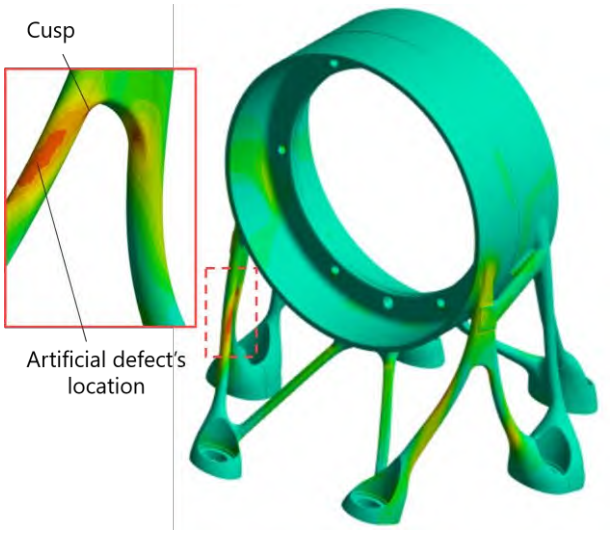


Figure 7: FE analysis of the ADPM bracket.

3.1. Experimental results on Ti-6Al-4V parts

On a total of three Ti-6Al-4V components featuring a deliberately induced defect, two parts experienced a failure-initiating crack nucleated from such defect. In fact, as reported in Table 1, specimens 85-BPSD-3 and 86-BPSD-3 contained an artificial defect and ruptured in region “B”. On the contrary, 86-BPSD-2 shared the same failure location of the items manufactured without artificial flaws in region “A”.
After the completion of the tests, all fracture surfaces were observed through SEM and the defects at the origin of failure were located and sized. The observations revealed the following information:

- Artificial defects could be systematically achieved, with $\sqrt{\text{area}}$ values of 432 µm and 436 µm for the two components failed in region “B” (see Figure 8);

Table 1: Experimental results of the test campaigns on components.

Alloy	Specimen ID	Artificial defect	Experimental life	Failure location	Applied stress range [MPa]
Ti-6Al-4V	85-BPSD-3	YES	395,000 cycles	Region “B” – artificial defect	360
	86-BPSD-3	YES	414,000 cycles	Region “B” – artificial defect	360
	86-BPSD-2	YES	351,000 cycles	Region “A” – natural defect	336
	85-BPND-1	NO	386,000 cycles	Region “A” – natural defect	336
	85-BPND-3	NO	320,000 cycles	Region “A” – natural defect	336
Scalmalloy	SN1	NO	66,960 cycles	Cusp – natural defect	343
	SN2	NO	136,404 cycles	Cusp – natural defect	309
	SN3	YES	44,400 cycles	Cusp – natural defect	343

- All the other samples revealed a roughness-induced defect as the failure initiating anomaly, with an equivalent crack size computed as the maximum valley depth times $\sqrt{10}$ being comparable to the deliberately induced flaws (as illustrated in Figure 9).

Following the execution of the fatigue tests, a component’s leg was used for surface roughness measurements in the down-facing areas (i.e., the inner part of the leg and the upper cusp region, close to region “A”). The measurements were done by focal variation microscopy using Alicona system. These measurements were analysed through the

extreme values statistics to fit two distinct LEVD for the inner leg and the cusp.

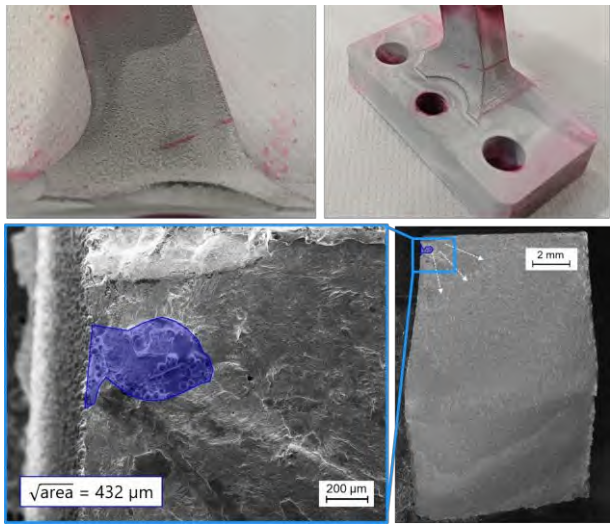


Figure 8: Example of failure of a Ti-6Al-4V part from an artificial defect.

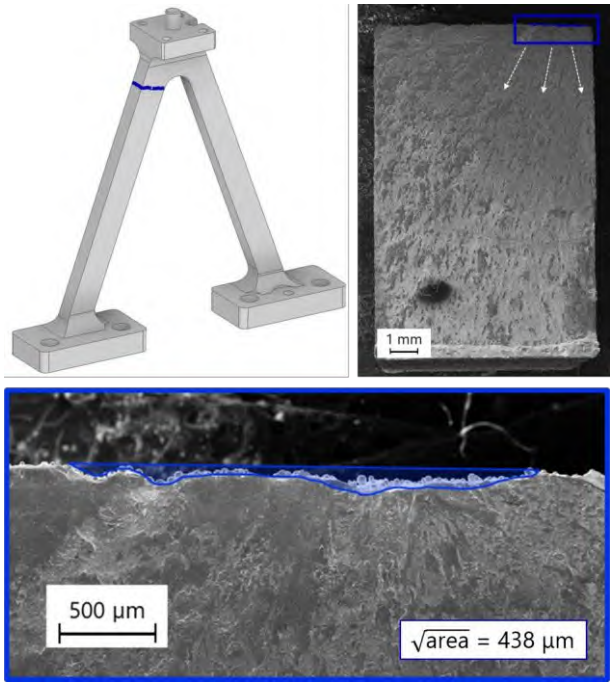


Figure 9: Example of failure of a Ti-6Al-4V components from a surface feature.

3.2. Experimental results on Scalmalloy parts

In contrast to Ti-6Al-4V items, Scalmalloy parts never failed from artificial defects. In components with no deliberately induced defects as well as in those with artificial flaws, the rupture occurred in the cusp region, despite the slightly lower stress state. This could be ascribed to the different outcome of the sand-blasting operation in an area characterized by a pronounced curvature.

SEM imaging of the fracture surfaces revealed the critical defects: in two cases, the parts failed because of a surface flaw ascribed to the roughness of the part (Figure 10); in other two occurrences, instead, the critical anomaly was a sub-surface volumetric defect (Figure 11).

4. DISCUSSION

A probabilistic assessment of such components, and therefore the life estimates and comparison with experimental results, can be performed exploiting the large database of the AMVP campaigns on specimens. With this intent, both components are analysed employing the distributions of defects' populations that were observed on standard specimens, coupled with the applied stress state determined by FE analyses.

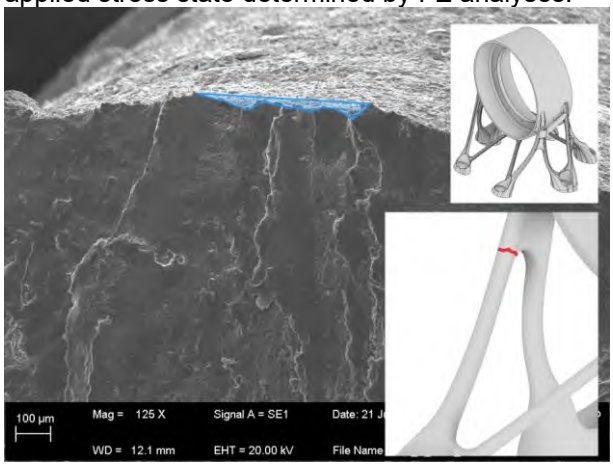


Figure 10: Surface anomaly observed in Scalmalloy parts.

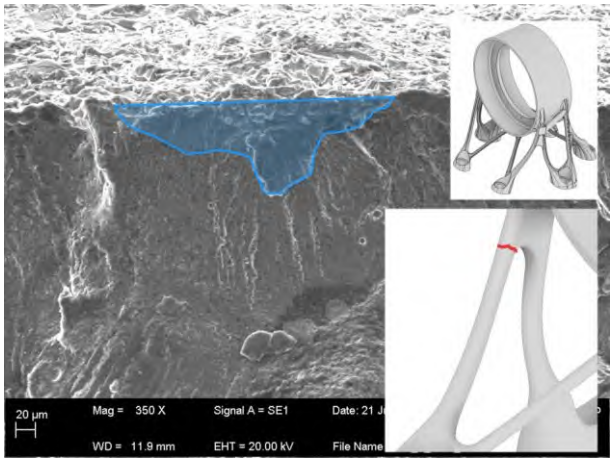


Figure 11: Sub-surface volumetric critical defect observed in Scalmalloy parts.

4.1. Probabilistic assessment of Ti-6Al-4V components

Since the components labelled 85-BPSD-3 and 86-BPSD-3 failed in correspondence of the artificial defect, which must be treated as an outlier of the distribution function, the assessment of these parts must follow a deterministic path, impeding any probabilistic attempt at estimating the components' reliability. On the contrary, the other fatigue failures may be discussed in probabilistic terms from specimens data.

ProFACE software was used for a zone-based assessment of the components through the definition of multiple surface defects' distributions

over the part. In detail, the distribution of roughness obtained on the cusp region was adopted for the same zone (yellow area in Figure 12); the population of down-facing surface defects was associated with the inner surfaces of the legs (red area in Figure 12) and the surface defects from SEM imaging of specimens was linked to every other surface. ProFACE software computed the global reliability of the parts according to this description of defects' populations, and Figure 13 shows the results of the calculations: the solid line, representing the failure probability value of 50%, correctly predicts the experimental failures from roughness-induced cracks.
In Figure 13, moreover, the dashed black line shows the predicted S-N curve obtained by numerically integrating the NASGRO propagation equation, determining the cycles to failure associated with an initial crack with the same size of the artificial flaws. This prediction well captures the two experimental results from components with deliberately induced defects.

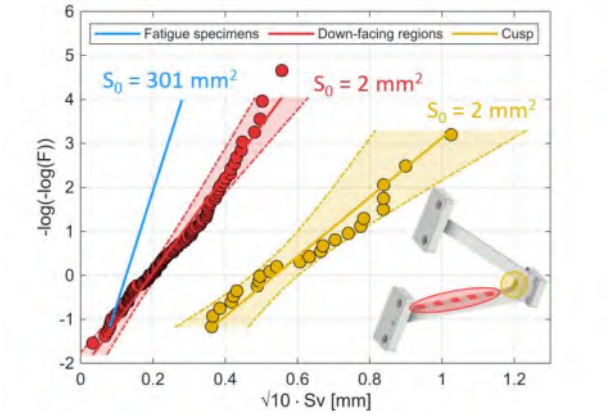


Figure 12: Distribution of equivalent surface flaws: from fatigue specimens (blue line) and from roughness measurements on components (red and yellow lines).

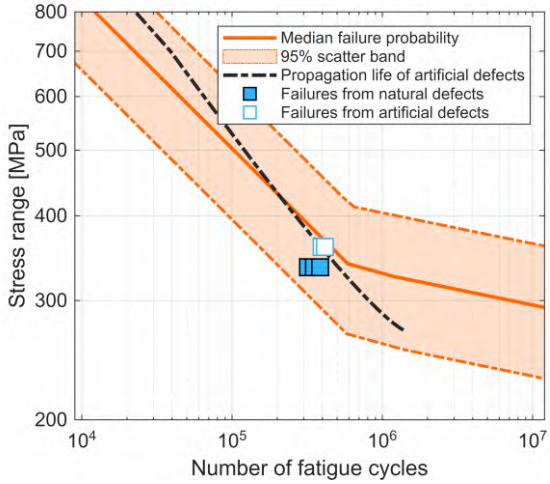


Figure 13: Probabilistic life estimates of Ti-6Al-4V components and S-N curve prediction for artificial defects.

4.2. Probabilistic assessment of Scalmalloy components

A similar workflow was adopted for the evaluation of the prospective life associated with Scalmalloy parts. With this perspective, ProFACE software was employed exploiting the information derived from fatigue specimens, reported in Figure 4. The analysis assumes the absence of residual stressed despite the sand-blasting post-processing: this hypothesis is justified by the strong curvature of the failure location, which hinders the outcome of the sand-blasting operation; this assumption shall also maintain a conservative approach for the analysis of sections which may not have developed the expected compressive residual stress state.

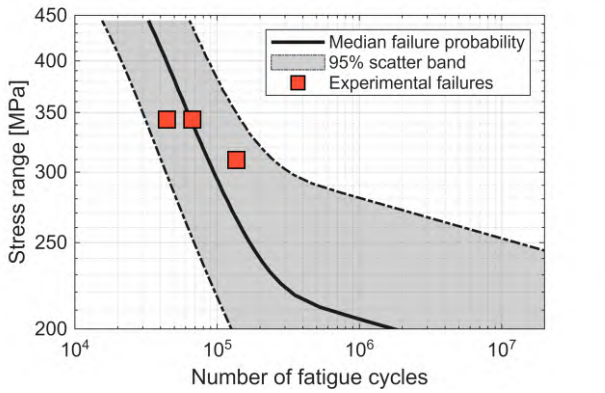


Figure 14: Life estimates of Scalmalloy components through ProFACE software.

As illustrated in Figure 14, the prediction well captures the fatigue failures of three components out of four, with the exception of a component which showed manufacturing defects.

5. CONCLUSIONS

Fatigue tests on Ti-6Al-4V and Scalmalloy components manufactured by laser powder bed fusion showed the competition between artificial sub-surface anomalies and surface-related features.
For Ti-6Al-4V, defect distributions obtained only from standard specimens did not adequately represent the component behaviour: a zone-based assessment incorporating local surface conditions correctly captured the experimental failures through ProFACE software. For Scalmalloy, the probabilistic model predicted three of the four fatigue lives, while one component showed an unexpectedly short life.
Overall, probabilistic fracture-mechanics methods can support the assessment of PBF-LB space components, provided that defect populations, local geometry, surface condition and post-processing effects are properly represented.

6. ACKNOWLEDGEMENTS

The activities were supported by the European Space Agency under AO/1-11042/22/NL/AR grant agreement (coordinator: Politecnico di Milano (IT); partners: Leonardo S.p.A. (IT), Thales Alenia Space

(FR), The Manufacturing Technology Centre (UK), BEAMIT (IT)).

7. REFERENCES

[1] B. Blakey-Milner *et al.*, “Metal additive manufacturing in aerospace: A review,” *Mater. Des.*, vol. 209, p. 110008, Nov. 2021, doi: 10.1016/J.MATDES.2021.110008.

[2] M. Seifi *et al.*, “Progress Towards Metal Additive Manufacturing Standardization to Support Qualification and Certification,” *JOM*, vol. 69, no. 3, pp. 439–455, Mar. 2017, doi: 10.1007/s11837-017-2265-2.

[3] Y. Murakami, *Metal Fatigue: Effects of Small Defects and Nonmetallic Inclusions*. Elsevier, 2002.

[4] ECSS, “ECSS-E-ST-32-01C Rev.1 - Fracture Control,” 2009.

[5] NASA-STD-5019A, “Fracture Control Requirements for Spaceflight Hardware,” 2024.

[6] South West Research Institute, “NASGRO Reference Manual Version 10.0,” 2023.

[7] NASA-HDBK-5026, “Guidance on Strength, Fatigue, and Fracture Control Requirements for Additively Manufactured Spaceflight Hardware,” 2024.

[8] L. Rusnati, G. Minerva, L. Patriarca, S. Miccoli, and S. Beretta, “Comparison of methods for the determination of fatigue critical flaw size and implementation for probabilistic fatigue assessment,” *Int. J. Fatigue*, vol. 203, p. 109252, Feb. 2026, doi: 10.1016/J.IJFATIGUE.2025.109252.

[9] T. Risposi, L. Rusnati, L. Patriarca, A. Hardaker, D. Luczyniec, and S. Beretta, “Fatigue of Ti6Al4V manufactured by PBF-LB: A comparison of failure mechanisms between net-shape and electro-chemically milled surface conditions,” *Eng. Fail. Anal.*, vol. 172, p. 109403, May 2025, doi: 10.1016/J.ENGFAILANAL.2025.109403.

[10] D. Perghem, L. Rusnati, L. Patriarca, F. Uriati, and S. Beretta, “Comparison of Fatigue Life and Strength Models for Defective Materials: Application to Scalmalloy in Different Surface Conditions,” *Fatigue Fract. Eng. Mater. Struct.*, vol. 48, no. 7, pp. 3185–3205, Jul. 2025, doi: 10.1111/FFE.14638.

[11] ASTM E8-24, “Standard Test Methods for Tension Testing of Metallic Materials,” 2015, *ASTM International, West Conshohocken, PA*.

[12] ASTM E466-21, “Standard Practice for Conducting Force Controlled Constant Amplitude Axial Fatigue Tests of Metallic Materials,” 2015, *ASTM International, West Conshohocken, PA*.

[13] BS ISO 12107:2003, “Metallic materials — Fatigue testing — Statistical planning and analysis of data,” 2003, *ISO*.

[14] ASTM E647-24, “Standard Test Method for Measurement of Fatigue Crack Growth Rates,” 2024, *ASTM International, West Conshohocken, PA*.

PROBABILISTIC FATIGUE DESIGN OF ADDITIVELY MANUFACTURED STRUCTURES USING CUMULATIVE PROBABILITIES OF CRITICAL DEFECTS

A. Mösenbacher[1], J. Sturm[2]

(1) IABG mbH, Einsteinstraße 20, 85521 Ottobrunn, Germany, Email: moesenbacher@iabg.de
(2) IABG mbH, Einsteinstraße 20, 85521 Ottobrunn, Germany, Email: sturmj@iabg.de

KEYWORDS

Structural Reliability, Defect-Based Design, Probabilistic Fatigue Assessment

ABSTRACT

Lightweight space structures require fatigue design methods that adequately account for internal manufacturing-related imperfections. To use the full potential of the material not every defect with a specific size is equally critical. This paper presents a deterministic probabilistic framework coupling finite-element stress fields, element volumes, quality-class-specific defect distributions and fracture-mechanics-based fatigue relationships. For each finite element, the method determines the defect size that would become critical for the required life, evaluates the probability of exceeding this size within the element volume, and multiplies the resulting element survival probabilities to obtain component reliability. The approach is extended to automatically assign local minimum material-quality classes. Experimental Ti-6Al-4V data from three additive-manufacturing quality classes demonstrate the required characterisation by tensile testing, S-N testing, fractography and Kitagawa-Takahashi-El Haddad evaluation. A numerical bending example illustrates reliability-driven quality allocation and its potential to translate structural margins into local non-destructive-testing requirements and rejection-rate targets for space hardware.

1. INTRODUCTION

The demand for lightweight and simultaneously highly reliable structures is a persistent driver in space systems engineering. Structural mass directly affects launch performance and system-level margins, while the consequences of fatigue failure can be serious. Design methods therefore have to use the full material capability without hiding relevant damage mechanisms behind global safety factors or overly conservative defect assumptions.
This balance becomes particularly challenging when fatigue cracks initiate in the material interior. Defect-driven internal initiation is promoted by high-strength materials, high-cycle fatigue loading, large highly stressed material volumes and surface treatments that suppress surface initiation. Under these conditions, the structural response is not governed by the mere presence of imperfections. It is governed by the joint probability that a sufficiently critical defect is present at a sufficiently highly stressed location and that the local material resistance is exceeded. Treating a single maximum defect size as a representative for an entire component can therefore eliminate much of the available lightweight potential.

Additive manufacturing (AM) makes this issue especially relevant. Process-related lack-of-fusion defects, pores and other internal imperfections form populations whose size and frequency depend on process quality or location on the platform. At the same time, AM provides unusual freedom to tailor process parameters, local build conditions and quality-assurance strategies. Material quality can consequently be treated as an engineering variable rather than as a single immutable property. This creates the possibility of manufacturing a component 'as good as necessary': high quality where structural reliability demands it and less quality where local stresses and volumes permit it.

Conventional stress-based fatigue life design remains indispensable, but a purely surface-based crack-initiation view does not explicitly represent the spatial interaction between defect populations and local stress fields. Fracture-mechanics-based safe-life approaches address defects directly, whereas probabilistic formulations are required when the occurrence of the critical defect itself is uncertain. In the European space framework, ECSS-E-ST-32-01C Rev. 2 defines fracture-control requirements and links safe-life verification to non-destructive testing (NDT) capability [1]. The method proposed here is intended to complement, not replace, such a fracture-control programme by providing a quantitative connection between local allowable defect size, defect occurrence probability, fatigue resistance and inspection capability.

This paper first compares three approaches for the fatigue assessment of internally defected components: Monte-Carlo defect sampling, an effective-volume approach with stress-integral, and the proposed Cumulative Probabilities of Critical Defects (CPoCD) method. The experimental characterisation required by the CPoCD framework is then illustrated using additively manufactured Ti-

6Al-4V specimens representing three quality classes. Finally, a simplified bending example demonstrates automatic quality-class assignment and discusses how the resulting local defect limits can support space-structure design and quality assurance.

2. SELECTED APPROACHES FOR STRENGTH ASSESSMENT OF COMPONENTS WITH INTERNAL IMPERFECTIONS

A defect-based probabilistic assessment has to connect four quantities: the local stress state, the material volume exposed to that stress, the statistical distribution of imperfections within a defined reference volume, and the fatigue strength associated with a defect of a given size or criticality. Fig. 1 illustrates this chain. A finite-element (FE) analysis provides the stress distribution and the volume represented by each element (1). The respective stressed element volume defines, in relation to a defect size distribution determined from a reference volume, the probability (2) corresponding to an expected defect size (3) within that element volume. A fracture-mechanics model (e.g. Kitagawa-Takahashi-El Haddad) translates the defect size into an endurable fatigue strength. Comparing this strength value with the local stress closes the assessment loop.

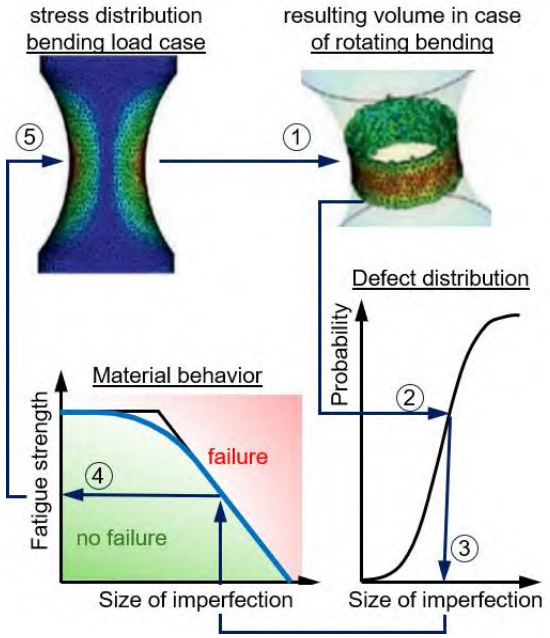


Figure 1: Conceptual correlation of local stress and volume, expected defect size and defect-dependent fatigue strength.

2.1. Monte-Carlo simulation

In a Monte-Carlo simulation, defects are sampled from statistical distributions and spatially inserted into the FE mesh. Depending on the available material and process information, the sampled features may include defect density, size, shape, orientation and location (cf. Fig. 2). The simulated population is then evaluated with the local FE stress state and a defect-sensitive fatigue approach or fracture-mechanics model. Repeating the random experiment provides an empirical distribution of the structural response and allows the desired probability of failure to be estimated. A related approach has been applied to gear-flank fracture assessment [2].

The main advantage is unrestricted modelling flexibility. Correlations between several defect features and complex spatial material variations can, in principle, be represented explicitly. The disadvantage is a high computational effort: rare target probabilities require large numbers of samples, and convergence has to be demonstrated. In addition, each simulation run remains dependent on the random realization. Mesh changes or different random-number sequences can lead to different local critical defects even when the statistical input is unchanged. These properties make the method powerful for detailed investigations but less attractive for fast iterative design loops or automated local quality allocation.

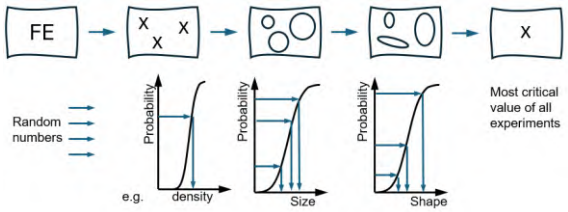


Figure 2: Schematic Monte-Carlo workflow in which randomized defect density, size and shape are sampled and the most critical realization is retained.

2.2. Effective volume with stress integral

A computationally efficient alternative is to reduce the non-uniform stress field into an effective volume. The procedure as demonstrated in detail by Rödling et al. [3] weights each differential material volume by its stress relative to the maximum component stress. In the notation of the working model, the effective volume is

$$V_e = \int_V \left(\frac{\sigma_{xyz}}{\sigma_{max}}\right)^{\frac{1}{m}} dV \qquad (1)$$

where V is the component volume considered, σ_{xyz} is a representative local stress measure, σ_{max} is the maximum stress and m is the exponent given by defect distribution (cf. Fig. 3) which is controlling the stress weighting. Furthermore, this effective volume is used to determine the probability of occurrence (P_A) representing a defect size relevant to the component's design (cf. Eq. 2). This design-relevant defect size is derived from the distribution of the most critical defects investigated with reference volume V_0 which is representative for the material quality, as shown in Fig. 3. It thus incorporates information regarding material quality (accounting

for the defect distribution) as well as the stress distribution within the component, based on the effective volume. The parameter n_B in Eq. 2 defines the batch size of the components in that no failure should occur.

$$P_A = \frac{1}{1 + \frac{V_0}{n_B \cdot V_e}} \quad (2)$$

Once a design-relevant defect size a has been selected, the corresponding fatigue strength amplitude σ_a can be obtained from a fracture-mechanics model (Eq. 3). The formulation used in this study is aligned to Kitagawa-Takahashi-El Haddad corresponding to

$$\sigma_a = Y \frac{\Delta K_{th}/2}{\sqrt{\pi(a + a^*)}} \quad (3)$$

with Y denoting the geometry-related factor, ΔK_{th} the relevant threshold parameter and a^* the intrinsic defect-size as a model parameter. The effective-volume approach is deterministic, fast and robust. Its principal limitation is the reduction of the full stress field into one volume and one maximum-stress value. Consequently, the formulation is best suited to proportional loading and homogeneous material quality. Local quality changes or strongly non-proportional loading reduce its direct applicability.

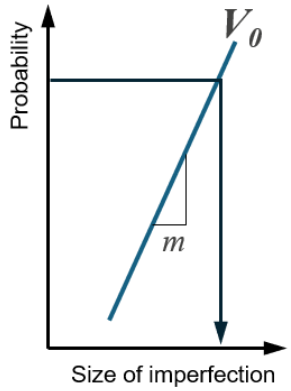


Figure 3: Illustration of a defect distribution of most critical defects referred to a reference volume V_0 and characterized by slope m with transformed axes

2.3. Cumulative Probabilities of Critical Defects

The approach of Cumulative Probabilities of Critical Defects (CPoCD) uses the same physical relations but reverses the assessment question. Instead of asking which defect from the distribution is expected to occur in an effective component volume, it asks how large a defect may be at each FE location before the local fatigue strength requirement is violated. That critical defect size is then evaluated against the defect distribution associated with the actual element volume and local quality class. Each element therefore receives its own survival probability, and the component survival probability results from cumulative multiplication over all elements, as applied for gear boxes in [4].

The basic implementation consists of five steps. First, a conventional fatigue life calculation is performed with either the best available quality class, or a defect-free reference curve (S-N reference with a fatigue strength $\sigma_{a,ref}$, cf. Eq. 4 and Fig. 4). If the required probability of survival is not satisfied even for this reference state, the geometry or load path must be redesigned before a defect-probability calculation is meaningful. Second, for every element the critical fatigue strength $\sigma_{a,crit}$ of a local S-N curve is derived from the reference damage d_{ref} in relation to a selected critical one d_{crit}, using the slope k as illustrated in Fig. 4 and formulated in

$$\sigma_{a,crit} = \sigma_{a,ref} \left(\frac{d_{ref}}{d_{crit}}\right)^{1/k}. \quad (4)$$

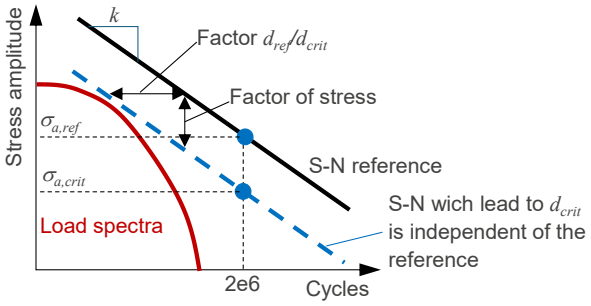


Figure 4: Derivation of a local S-N curve critical for the load case, based on a reference damage value obtained from a reference S-N curve.

Third, the critical fatigue strength is mapped to a critical defect size using the Kitagawa-Takahashi-El Haddad relationship for the material as illustrated in Fig. 5 left.

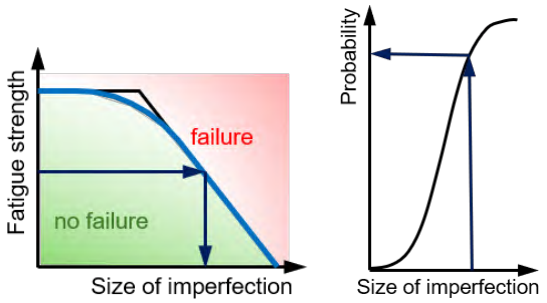


Figure 5: Derivation of the critical defect size based on a minimum required fatigue strength $\sigma_{a,crit}$ (left) and of the probability of occurrence of a defect larger than the critical size (right).

Fourth, the quality-class-specific defect distribution and the element volume are used to calculate the probability that a defect does not exceed the critical size in that element as illustrated in Fig. 5 right. This value corresponds to the element survival probability $P_{s,i}$. Finally, the component survival probability is

$$\prod_{Elements} P_{s,i}. \quad (5)$$

2.4. Automated assignment of quality classes

The element-wise formulation of the CPoCD-approach enables an inverse use of the reliability model. Instead of merely assessing a predefined material quality, the minimum required quality to meet the final target value of probability of survival, can be assigned automatically. In this case for every FE element, the survival probability is first calculated for all available quality classes, for example high (QC1), medium (QC2) and low (QC3).

The resulting element probabilities are sorted by criticality as illustrated in Tab. 1. A cumulative probability trend is then generated for each quality class (as also illustrated in Fig. 6 for QC1-3) by successively multiplying the sorted element probabilities. In the notation used for the demonstration, the running trend is

$$\prod_{i=600}^{i} P_{s,i} \tag{6}$$

starting from the element with the highest survival probability.

Table 1: Exemple calculation of the probability trend based on the individual probabilities Ps,i by multiplying the individual rows, starting from the bottom (600) at the highest survival probability, analogous to Eq. 6.

i	$2a_{crit}$	$P_{s,i}$	trend
1	0.038	0.9496	0.87
…	…	…	…
6	0.04	0.9880	0.97
…	…	…	…
300	1.28	0.9999	0.99
…	…	…	…
600	Inf	1.0	1.0

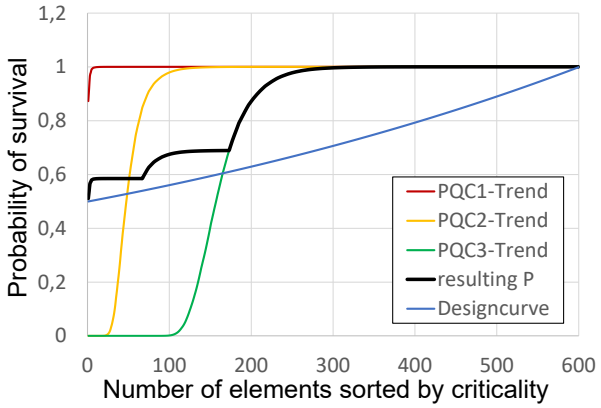


Figure 6: Illustration of the probability trends for the various quality classes, showing their development during multiplicative accumulation from the element with the highest survival probability (i=600) to the one with the lowest (i=1) (red, yellow, green), along with the design curve (blue), derived from the calculated mean individual probability, required to achieve the target survival probability, and the automated assignment of quality classes (black).

A design curve represents the trend resulting with an average probability which is required to reach the specified component survival target for the number of elements considered. Comparing the quality-class trends with this design curve permits a first automated class assignment. A final recalculation is recommended after assignment, and becomes mandatory when the S-N curves of the quality classes have different slopes or different knee-points. This second loop ensures that the change of local S-N characteristics is reflected consistently in the damage calculation.
The main characteristics of the three approaches are summarized in Tab. 2.

Table 2: Qualitative comparison of the three strength assessment approaches discussed in this paper.

Criterion	Monte-Carlo simulation	Effective volume with stress integral	CPoCD
Flexibility / adaptability	Very high. Multiple defect features, local properties and complex load scenarios can be sampled. Automated local quality optimization is possible only with substantial iterative effort.	Limited to formulations that can be represented by an effective volume; most suitable for proportional loading and homogeneous material quality.	High. Local load scenarios, element volumes and spatially varying quality classes can be considered; automated quality class assignment is quick and easy to implement.
Complexity / effort	High computational effort, especially for low target failure probabilities and convergence verification.	Very low computational effort and very fast after FE results and distribution parameters are available.	Low computational effort; and simple set of formulas comparable to effective volume.
Accuracy / robustness	Potentially very detailed, but numerical estimates depend on random sampling and the number of realizations.	Deterministic and reproducible within the assumptions of the effective volume model.	Highly robust and reproducible due to deterministic relationships.

3. MATERIAL CHARACTERISATION FOR DIFFERENT QUALITY CLASSES

3.1. Specimen manufacture and test concept

The experimental data used for this method development originates from additively manufactured Ti-6Al-4V specimens investigated at the IABG fatigue laboratory [5]. Three different batches were selected to represent high, medium and low internal quality. The specimens were manufactured by laser beam melting with the specimen longitudinal axis oriented in build direction *Z*. After the build process, all specimens were stress-relief heat treated, machined to the final geometry shown in Fig. 7 and polished in the gauge section. As-built surfaces were deliberately excluded because the objective was to isolate the influence of process-related internal imperfections. Hot-isostatic pressing was likewise omitted in order not to remove or significantly modify the defect populations to be characterized.

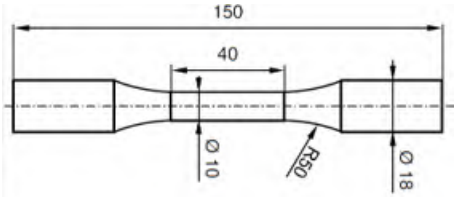


Figure 7: Dimensions of the specimen geometry used for material characterisation.

3.2. Quasi-static behaviour

Six tensile tests per quality class were performed according to DIN EN ISO 6892-1, method B [6]. The stresses in Fig. 8 are normalised by the mean ultimate tensile strength of the high-quality batch. The 18 stress-strain curves are nearly coincident and show a ductile response without a pronounced quality-class dependence. Within the investigated parameter range, the quality class had no practically visible influence on the quasi-static strength response. This observation is important for the subsequent fatigue assessment: a quality class that appears equivalent in a tensile test can still produce substantially different high-cycle-fatigue behaviour.

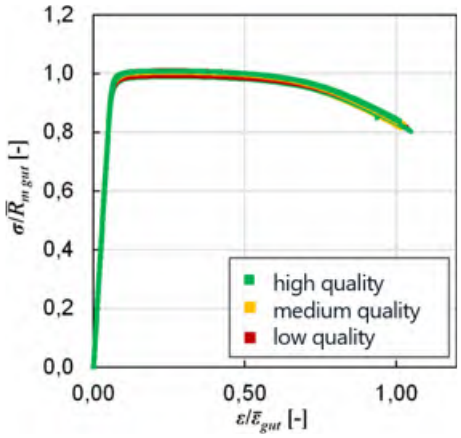


Figure 8: Normalised stress-strain curves for six tensile tests per quality class.

3.3. Fatigue strength and observed quality effect

Fatigue tests were conducted on a resonance test system at a stress ratio R = -1 in the test sequence corresponding to Fig. 9 right and the final results in Fig. 9 left. The high-quality batch was characterized using a combination of staircase and boundary methods following Klubberg and Beiss [7], with evaluation according to DIN 50100 [8] and the staircase procedure described by Hück [9]. The first nine tests established the staircase sequence. Additional tests were used to validate the highest level in the stair to estimate long-life strengths for different failure probabilities with higher accuracy. The resulting mean long-life strength of QC1 was approximately 33% of the mean ultimate tensile strength of that batch; the values associated with nominal 10% and 90% failure probabilities were approximately 28% and 37%, respectively. The finite-life regime was evaluated using the horizon method of DIN 50100.

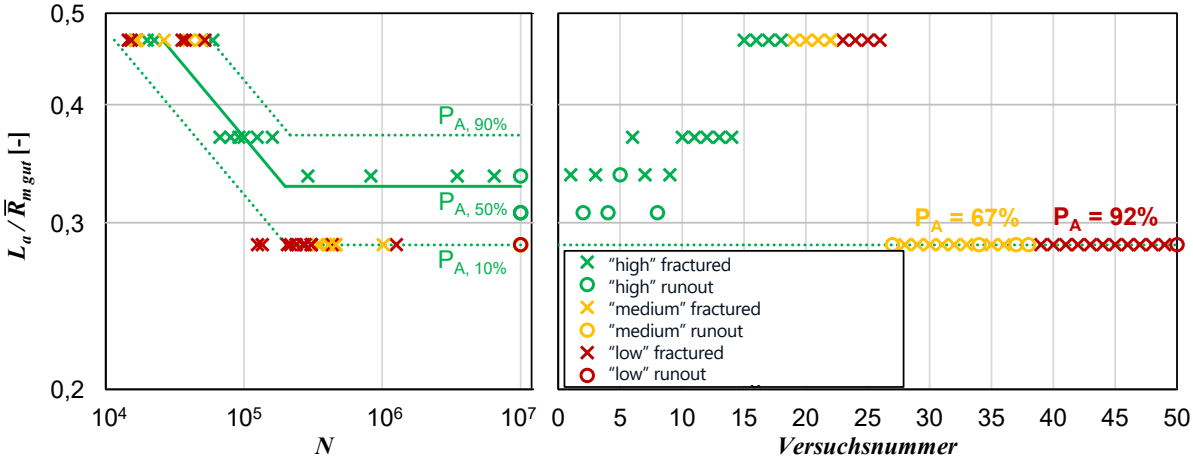


Figure 9: Results of performed fatigue tests (left) and test sequence of the individual samples (right)

The medium- and low-quality batches were then tested relative to the QC1 S-N curve. At the highest finite-life level, the results of both lower-quality classes remained inside the QC1 scatter band, indicating no pronounced quality effect at comparatively low cycle counts. The difference became distinct in the long-life regime. At a load level corresponding to a nominal QC1 failure probability of 10%, 8 of 12 medium-quality specimens fractured and 11 of 12 low-quality specimens fractured. These observed fractions correspond to approximately 67% and 92%, probability of failure. Several QC3 specimens also failed at unexpectedly low cycle counts. The test series therefore demonstrates a strong interaction between different quality classes with different internal imperfection population and high-cycle-fatigue behaviour, despite the essentially identical quasi-static behaviour.

3.4. Derivation of a Kitagawa-Takahashi-El Haddad relationship

For the present method screening and derivation of the Kitagawa-Takahashi-El Haddad relationship, the fatigue results were transformed to a reference cycle number of 2 Mio cycles. Each finite-life result, investigated also with fractography, was shifted along the mean S-N slope of all quality classes, as illustrated in Fig. 10, resulting in new, transformed fatigue-strength values for this number of cycles. This approach enables a comparison of fatigue strength values based on a uniform expected number of load cycles. Consequently, any resulting difference in strength arises from varying defect characteristics within the specimen. It is noted, that shifting to 2 Mio cycles is a conservative approach with respect to the distinct knee point of the best quality class.

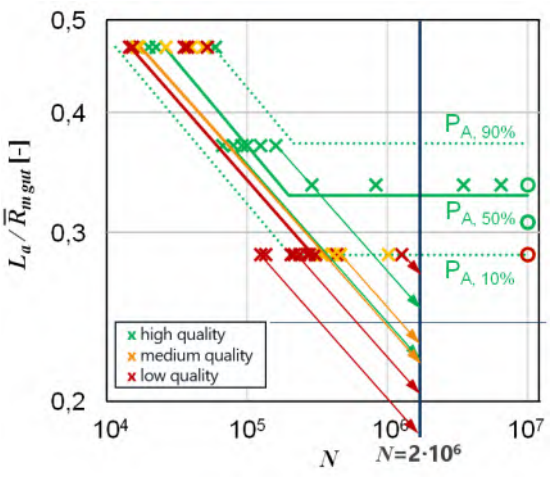


Figure 10: Schematic transformation of fatigue test results to the reference cycle number of 2 Mio cycles using the mean S-N slope.

The crack-initiating defects of all shifted test data were subsequently identified by SEM fractography. An equivalent defect dimension *2a*, corresponding to the diameter of a circle with the same projected area as the investigated defect, was derived for each crack-initiating imperfection. Using these defect dimensions and the transformed fatigue-strength values, the Kitagawa-Takahashi-El Haddad diagram shown in Fig. 11 was constructed.

Within the present screening dataset, the results from all three quality classes follow a common defect-size-dependent trend. The experimentally observed differences in long-life fatigue strength can therefore be interpreted primarily as differences in the distributions of crack-initiating defects rather than as different intrinsic defect sensitivity of the matrix material. Additional investigations reported in [5] indicate that including defect shape can further improve the correlation.

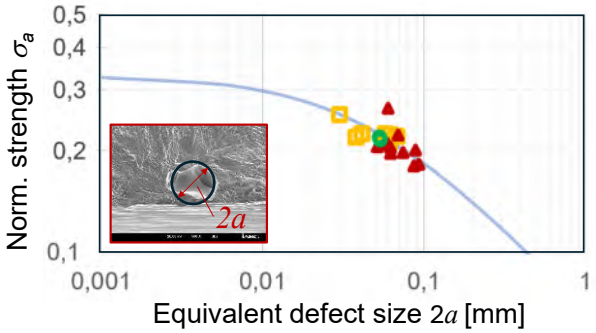


Figure 11: Kitagawa-Takahashi-El Haddad Diagram derived from corrected fatigue strength values and SEM-investigated crack-initiating defect sizes.

The diagram in Fig. 11 is used only for method development and screening. The number of tests conducted is insufficient to establish a valid design value for development. Product development would require a broader campaign covering relevant process parameters, build positions, load states and statistical scatter.

3.5. Correlation with computed tomography for quality assurance

Fractographic analysis identifies the imperfection from which fatigue cracking actually initiated and therefore provides the most direct basis for deriving a distribution of fatigue-critical defects. For production quality assurance, however, a non-destructive testing (NDT) method is required. Computed tomography (CT) enables volumetric defects to be detected and characterized within a defined inspection volume. To assess whether CT can provide a representative estimate of fatigue-relevant defect populations, CT-derived defect distributions were compared with fracture-initiating defects identified by scanning electron microscopy (SEM).

For the CT evaluation, defects were characterized by their projected area in the axial direction. A

defined section of the specimen gauge volume was scanned and subdivided into smaller control volumes, from each of which the largest detected defect was extracted (Fig. 12). Fig. 13 compares the resulting extreme-value distributions with the distribution of fracture-initiating defects obtained from the fatigue tests. Defect sizes were normalised by the median of the fractographically determined initiating defects associated with the reference volume V_0.

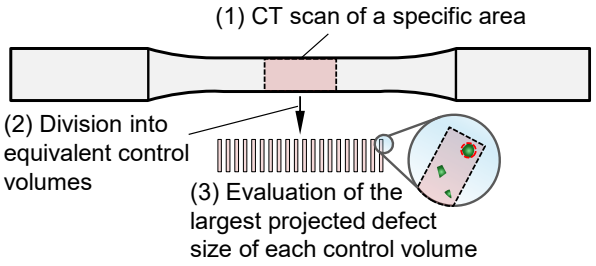


Figure 12: Derivation of an extreme-value defect distribution from CT data using subdivided control volumes

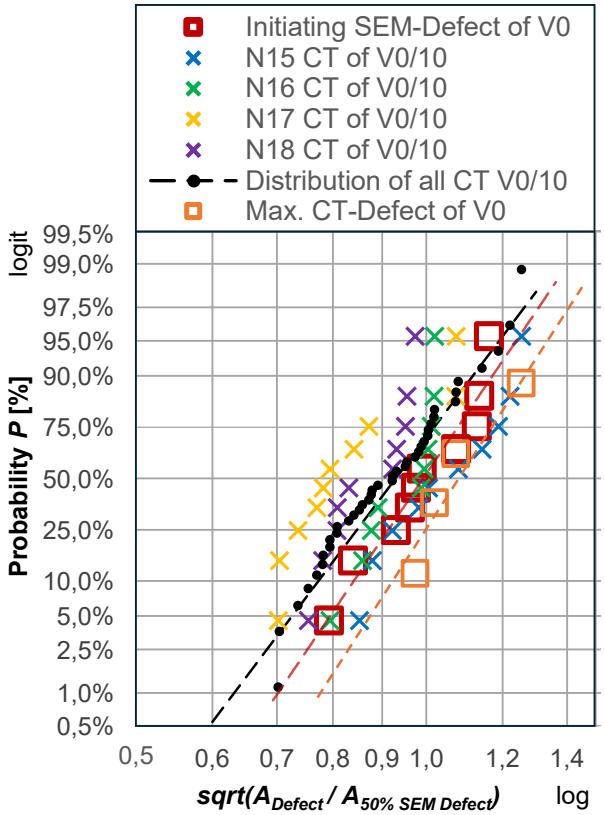


Figure 13: Comparison of defect-size distributions obtained from CT examinations and fracture-initiating defects identified by SEM after fatigue testing

For specimens N15 to N18, evaluation of the smaller control volumes $V_0/10$ resulted in normalised median values of approximately 0.78 to 1.0. Combining all subdivided control volumes resulted in a median of approximately 0.91 relative to the fractographic reference value, consistent with the smaller underlying volume. In contrast, evaluating the largest CT-detected defects within a volume comparable to V_0, based on the scanned volumes of four specimens, resulted in slightly larger and therefore conservative defect sizes compared with SEM. Despite the limited number of data points and associated scatter, the slopes of the CT- and fractography-based distributions were comparable.

The results indicate that CT can provide an estimate of fatigue-relevant defect distributions within a defined material volume. This opens the possibility of using CT for production quality assurance, rapid screening of manufacturing quality and derivation of defect-distribution parameters for probabilistic component design. The present investigation represents an initial screening only; no calibrated quantitative transfer function between CT and fractography is claimed. For industrial application, this relationship must be established for the specific manufacturing process, component geometry, CT inspection parameters and detectability limits before CT-derived distributions are used as quantitative input for structural assessment.

4. EXEMPLARY APPLICATION AND POTENTIAL FOR SPACE ENGINEERING

4.1. Simplified bending example

A simplified beam under fully reversed bending is used to demonstrate the inverse quality-allocation capability. The FE model contains a stress gradient comparable to a cantilever-bending situation (cf. Fig. 14). The FE simulation provides for each element, the local stress amplitude and the element volume, the initial fatigue post-processing provides the reference damage value d_{ref} for each element. The demonstration uses deliberately simplified dummy parameters so that the assignment logic can be shown independently of a proprietary design case. The values listed in Tab. 3 are therefore not design allowables.

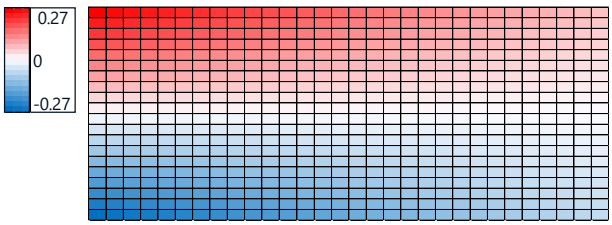


Figure 14: Stress distribution of the simplified beam under bending load

The calculation follows the sequence described in Section 2.3. For each element, the reference fatigue damage is converted into a critical S-N curve using Eq. 4. The corresponding critical defect dimension is obtained from the Kitagawa relationship, and the probability that a defect is less or equal to the critical size within the element volume is evaluated for

QC1, QC2 and QC3. After sorting the element survival probabilities, the cumulative trends are compared with the design curve. The resulting automated assignment is shown in Fig. 15.

As expected, high quality is concentrated where the stress makes large defects most critical, while lower quality material is permitted over large portions of the less critical region. The probability trends which lead to this classification are shown in Fig. 6.

Table 3: Dummy input parameters used for the simplified bending demonstration.

Component target			
Desired probability of failure	50%		
Number of cycles	1 000 000		
Critical damage d_{crit}	1.0		
Material parameters	**QC1 to QC3**		
Reference volume V_0	3 141.6		
Normalised S-N fatigue strength	0.33		
S-N knee point	2 000 000		
S-N slope k	7.0		
Threshold value	5.8		
Geometry factor	0.64		
Example defect distributions	**QC1**	**QC2**	**QC3**
Median defect size 2a50%	0.05	0.20	0.60
Logit distribution parameter Td	1.5	2.0	2.5

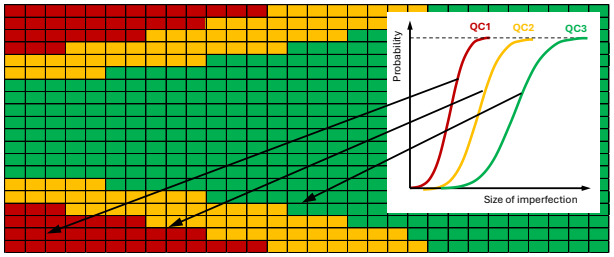


Figure 15: Automated allocation of three quality classes for the simplified bending example

4.2. Design and quality-assurance outputs

The most relevant output is not the colour-coded quality map itself but the local critical defect size behind every element. Material quality and NDT capability thereby become explicit design parameters. The method can be used in both forward and inverse directions: a specified quality class yields a component survival probability, whereas a specified reliability target yields the minimum local quality required to meet it. This supports several practical design decisions.

- Local NDT requirements can be derived from the maximum allowable defect size of each FE region instead of applying one global detection limit to the entire component.
- Different AM process-quality levels can be allocated to different regions when the manufacturing process can realize such spatial differentiation, enabling an 'as good as necessary' strategy.
- Different build-platform positions or locally varying process conditions can be represented as different quality classes if their defect distributions have been characterized.
- Geometry-dependent NDT limitations can be fed back into design. If a thicker region requires a larger CT voxel size and thus a poorer detection threshold, the method makes the resulting structural penalty visible during the design phase.
- For a planned e.g. 100% NDT inspection, the combination of the defect distribution and acceptance threshold can be used to estimate an expected reject fraction. This enables economic manufacturing consequences to be considered together with structural reliability rather than after the design is frozen.

4.3. Relation to ECSS fracture control

For space hardware, the CPoCD outputs are particularly relevant to the interface between structural analysis and fracture-control/NDT planning. Its potential contribution is to invert the usual inspection-design interaction. Rather than beginning with one assumed detection limit for an entire component, the structural calculation supplies the maximum defect size that is locally tolerable for the required fatigue reliability. This locally allowable size can then be compared with the qualified NDT capability. Where the available inspection is insufficient, the designer can improve geometry, reduce local stress, request a better process quality or specify an enhanced inspection. Where the available inspection is substantially better than necessary, the analysis identifies potential over-specification. For low-risk fracture planning, the same transparency can support selection of critical zones and inspection strategy, but final compliance remains subject to the complete ECSS requirements and customer approval.

5. CONCLUSIONS

Defects do not automatically imply component failure. For internally initiated fatigue, structural reliability is governed by the probability that a sufficiently large defect occurs at a critical location and exceeds the local defect-dependent fatigue strength. Consequently, probabilistic defect-based approaches are particularly relevant for high-strength materials, high-cycle fatigue applications and large highly stressed material volumes.

Three approaches for considering internal imperfections were discussed with respect to flexibility, computational effort and robustness. Monte-Carlo simulation offers high flexibility but requires considerable computational effort, whereas effective-volume concepts provide efficient and deterministic assessments but are restricted in their applicability. The proposed Cumulative Probabilities of Critical Defects (CPoCD) approach combines local FE-based fatigue assessment with deterministic probability calculations and is therefore efficient, reproducible and applicable to spatially varying material qualities and complex loading conditions.

The experimental investigations on additively manufactured Ti-6Al-4V showed essentially no influence of the investigated quality classes on quasi-static strength, but pronounced differences in high-cycle fatigue behaviour. Fractographic investigations identified internal imperfections as crack-initiation sites. The results could be represented by a largely quality-independent Kitagawa-Takahashi-El Haddad relationship. This indicates that the observed differences in fatigue performance are predominantly governed by the different defect distributions associated with the manufacturing quality. Further investigations indicate that additional defect characteristics, such as shape, can improve this correlation.

A key capability of CPoCD is the automated determination of locally required material quality. By deriving an individual critical defect size and corresponding survival probability for each FE element, the method directly links structural stress values, defect statistics and material quality. Material quality and NDT capability can therefore become explicit design parameters. For space applications, this provides the potential to derive locally tailored quality and inspection requirements according to the actual structural criticality of individual regions rather than applying one global defect limit to the entire component. In this way, the approach can support reliability-driven lightweight design, targeted NDT strategies and an “as good as necessary” manufacturing philosophy, while providing a quantitative interface between structural assessment, manufacturing quality and quality assurance.

The approach is not limited to additive manufacturing and can generally be applied wherever statistically describable imperfections are relevant to structural integrity. Further work should focus on well-validated material properties, quantitative CT-to-fractography correlations with extended criticality assessments for imperfections, validated NDT probability-of-detection characteristics and experimental validation on components.

6. REFERENCES

1. European Cooperation for Space Standardization (2021). ECSS-E-ST-32-01C Rev. 2: Space engineering - Fracture control, 30 July 2021.
2. Meis, J.A. (2017). Flank fracture assessment under consideration of material quality. In Proc. VDI International Conference on Gears, Garching, Germany.
3. Rödling, S., Fröschl, J., Hück, M. & Decker, M. (2011). Einfluss nichtmetallischer Einschlüsse auf zulässige HCF-Bemessungskennwerte. Materials Testing 53(7-8), 455-462. https://doi.org/10.3139/120.110250.
4. Weber, R. (2015). Auslegungskonzept gegen Volumenversagen bei einsatzgehärteten Stirnrädern. Forschungsbericht aus dem Institut für Werkstofftechnik - Metallische Werkstoffe der Universität Kassel, Band 20, Kassel, Germany.
5. Slaby, S.A., Eiber, M., Mösenbacher, A. & Näke, T. (2020). Einfluss von Poren auf statische- und schwingende Festigkeit von additiv gefertigtem Titan. In Proc. 5. Tagung des DVM-Arbeitskreises Additiv gefertigte Bauteile und Strukturen, November 2020.
6. DIN Deutsches Institut für Normung e. V. (2017). DIN EN ISO 6892-1: Metallic materials - Tensile testing - Part 1: Method of test at room temperature, Berlin, Germany.
7. Klubberg, F. & Beiss, P. (1995). Modifizierte Prüf- und Auswertemethodik im Übergangsgebiet zur Dauerschwingfestigkeit. VDI-Bericht 1151: Effizienzsteigerung durch innovative Werkstofftechnik, 777-780.
8. DIN Deutsches Institut für Normung e. V. (2016). DIN 50100: Load controlled fatigue testing - Execution and evaluation of cyclic tests at constant load amplitudes on metallic specimens and components, Berlin, Germany.
9. Hück, M. (1983). Ein verbessertes Verfahren für die Auswertung von Treppenstufenversuchen. Zeitschrift für Werkstofftechnik 14, 406-417.

INFLUENCE OF LASER POWDER BED FUSION (LPBF) PROCESSING PARAMETERS (CONTOUR SCAN) ON MICROSTRUCTURAL PROPERTIES AND RESULTING CRACK INITIATION BEHAVIOR UNDER CYCLIC LOADING FOR ALSI7MG0.6 MATERIAL

Vala, Paresh [1,2], Guth, Stefan [2], Amkreutz, Marc [3], Veller, Sebastian [4], Buchenau, Theresa [5]

[1,3,4,5] Fraunhofer Institute for Manufacturing Technology and Advanced Materials (IFAM), Wiener Str. 12, 28359 Bremen, Germany, E-mail: paresh.vala@ifam.fraunhofer.de [1], marc.amkreutz@ifam.fraunhofer.de[3], sebastian.veller@ifam.fraunhofer.de[4], theresa.buchenau@ifam.fraunhofer.de[6]

[2] Karlsruher Institut für Technologie (KIT): Institut für Angewandte Materialien - Werkstoffkunde (IAM-WK), Campus Süd, Engelbert-Arnold-Straße 4, 76131 Karlsruhe, Germany, E-Mail: stefan.guth@kit.edu[2]

KEYWORDS

Laser Powder Bed Fusion (LPBF); AlSi7Mg0.6; contour scan strategy; near-surface integrity; fatigue crack initiation; residual stress; spacecraft structures; fatigue; melt pool microstructure.

ABSTRACT

Laser Powder Bed Fusion (LPBF) of AlSi7Mg0.6 alloys constitutes a promising pathway toward lightweight solutions, particularly for high-performance spacecraft structures. However, the fatigue behaviour of as-built, complex-structured components are predominantly governed by surface and near-surface integrity, which is dictated by the contour scan strategy. Preliminary investigations on AlSi7Mg0.6 demonstrated that contour scan speed and pre-sintering can modulate the fatigue endurance limit by nearly a factor of 1.5 at equivalent density and strength; however, the governing microstructural mechanisms remain insufficiently characterised. This lack of understanding represents a critical knowledge gap for the qualification of LPBF components in aerospace and defence applications.

This study presents a systematic experimental investigation correlating different contour scan speed and the influence of pre-sintering with near-surface integrity, fatigue performance, and crack initiation in LPBF AlSi7Mg0.6. Existing datasets are re-evaluated to identify critical parameters and failure locations. Specimens undergo metallographic and X-ray diffraction characterisation, followed by axial fatigue testing, fractography, and nano-hardness profiling, establishing a mechanistic link between contour scan parameters and crack initiation behaviour.

1 INTRODUCTION

The demand for lightweight metallic components with complex internal geometries and high structural efficiency continues to grow in aerospace, automotive, and defence engineering [1, 2, 3]. Aluminium alloys are central to this trend owing to their high specific strength, corrosion resistance, and established processing heritage. Among these, AlSi7Mg0.6, represents this combination of properties, with good hardening capability, and has been widely deployed in investment casting for structural components such as housings and load-bearing frames [4, 5, 6]. These traditional routes, however, reach fundamental limitations for small-batch, geometrically complex components due to high tooling costs and shrinkage-induced porosity [1,3, 7].

Laser Powder Bed Fusion (LPBF) addresses these limitations by enabling near-net-shape production directly from sliced CAD geometry, offering integral manufacturing and topology-optimised designs inaccessible to conventional forming [1, 2, 8]. For AlSi7Mg0.6, LPBF further provides a microstructural advantage with rapid solidification rates of 10^3-10^6 K/s imposing a fine cellular substructure and supersaturated α-Al matrix, yielding as-built tensile strength exceeding that of conventionally cast and heat-treated material [4, 5, 9].

Nevertheless, reliable structural application of LPBF AlSi7Mg0.6 remains limited by insufficiently resolved process-property relationships [10, 11]. Unlike widely studied alloys such as AlSi10Mg or Ti-6Al-4V, the influence of LPBF process parameters on this alloy's microstructure and defect state has been characterised only to a limited extent [12, 13]. Fatigue under cyclic loading is the primary design-limiting failure mode for such structures [7, 11, 14]. In LPBF parts, however, fatigue performance is governed less by bulk properties than by the as-built surface state, which is itself dictated by the contour scan strategy applied along each layer's geometric boundary. While bulk parameters consolidate the internal volume, the contour scan determines thermal history, surface morphology, and defect population in the near-surface zone, the region most critical under fatigue loading [10, 15]. Associated defects, such as partially melted particles, LoF defects, surface valleys, and subsurface pores, are often undetectable by optical profilometry and can directly influence crack initiation [10, 16, 17].

Prior work has shown that varying contour scan speed alone, while holding bulk parameters, density (>99 %), and tensile strength constant, shifts the high-cycle fatigue endurance limit at 10^6 cycles from 45 MPa to 84 MPa, a near two-fold change attributable exclusively to the near-surface condition. The optimised as-built LPBF specimens, tested directly in the as-fabricated state without any post-processing such as heat treatment or surface finishing, even exceed the fatigue strength of investment-cast AlSi7Mg0.6 specimens that underwent T6 heat treatment by approximately 15 % [10]. Despite this macroscopic evidence, the underlying microstructural mechanisms remain insufficiently resolved. Specifically: (i) near-surface microstructural evolution (grain morphology, Si network continuity, melt pool boundaries) as a function of contour scan speed and pre-sintering has not been systematically characterised for AlSi7Mg0.6 [5, 18]; (ii) defect geometry and distribution at the contour and transition zone have not been quantified by cross-sectional metallography as a function of contour parameters [15, 17]; (iii) the near-surface residual stress state has not been independently measured by XRD alongside surface texture and microstructure in a unified framework [19]; (iv) the mechanistic basis for roughness-dependent crack initiation behaviour has not been established at the microstructural scale [10, 20].

Accordingly, this study systematically evaluates the role of LPBF contour scan parameters in controlling fatigue crack initiation behaviour, surface topography, residual stress, and near-surface microstructure in as-built AlSi7Mg0.6, establishing a mechanism-based process-microstructure-fatigue framework. The experimental programme comprises: (i) pre-testing analysis of existing surface and fatigue data to identify critical descriptors and reference crack initiation locations; (ii) metallography of as-built specimens to characterise melt pool geometry, near-surface grain structure, and transition defects; (iii) SEM analysis of contour and transition microstructure; (iv) axial tension-tension fatigue testing (stress controlled) per ASTM E466; (v) post-fracture metallography of crack propagation paths; (vi) SEM-EDX fractography of crack initiation behaviour; (vii) XRD residual stress measurement ($\sin^2\psi$ methodology) at the contour surface and 30 µm depth; and (viii) AFM based nano-hardness mapping (QNM) resolving hardness gradients across the contour as well as the transition zone.

2 MATERIALS AND EXPERIMENTAL DETAIL

2.1 Sample Manufacturing:

All specimens were produced at Fraunhofer IFAM Bremen using fixed bulk LPBF parameters, with systematic variation confined to the contour scan strategy. The testing plan follows a pre-fatigue characterisation phase (surface topography, XRD residual stress, metallography, hardness, SEM-EDX) followed by fatigue testing and post-fatigue analysis, establishing a direct process-microstructure-fatigue property chain. Specimens were manufactured from gas-atomised produced AlSi7Mg0.6 powder (Table 1) on a Trumpf TruePrint 1000 LPBF system under Ar shielding (residual O_2 < 0.1 vol.%). Fatigue specimens conforming to ASTM E466-15 [22] were used for fatigue and other testing, with a 6 mm * 3 mm section, 40 mm gauge and 80 mm total length. All specimens were oriented at 45° to the re-coater and gas flow directions, following prior work.

Table 1: Chemical composition of AlSi7Mg0.6 feedstock powder (wt. %)

Material	Al	Si	Mg	Ti	Fe
AlSi7Mg0.6	93.13	6.15	0.60	0.09	0.05

The bulk scan strategy applied parallel hatch lines rotated 66° per layer with skywriting (Figure 1); bulk parameters (Table 2) were held constant, following a prior density-optimisation study. Contour scan speed was varied from 300-1800 mm/s, with/without a pre-sinter pass at 97.5 W (50 % of contour power), with seven parameter sets (Table 2). No post-processing was applied to any specimen.

Table 2: Bulk and Contour scan parameters

Layer thickness (µm)	Hatch distance (µm)	Scan speed (mm/s)	Laser power (W)	Pre-sinter (Y/N)	Set No.
30 (Bulk)	120	1000	166	No	-
30 (Contour)	120	300	195	Yes	A
		600		Yes	C
		600		No	D
		900		Yes	E
		1200		Yes	G
		1200		No	H
		1800		No	J

2.2 Material Characterisation Methods

A multi-technique characterisation campaign was conducted before and after fatigue testing to study the parameter effect on fatigue and crack behaviour. Surface texture analysis was quantified using a Keyence VR3100 (120×) per ISO 25178-2 (S_k, S_{pk}, S_{vk}) [21, 23]. Cross-sectional metallography on untested fatigue specimen across all seven contour conditions was prepared via wire cutting, mounting, polishing to 1 µm, and Keller's etching to expose melt pools, grains, and the Si network, examined by Zeiss Axio Vert.A1 (50–500×) and Keyence VHX-X1 DIC microscopy. An FEI Helios 600 Dual-Beam SEM provided SE/BSE imaging (at 125–2000×) with Oxford X-Max80 EDX mapping (Si, Mg, Al, O). Near-surface residual stress was measured on as build samples by laboratory XRD ($\sin^2\psi$-method, {422} α-Al reflection) on samples A,

E, G, H at the surface and 30 µm depth. XRD was performed on four of the seven contour scan conditions: A, E, and G, all pre-sintered, representing the minimum, middle, and maximum tested speeds; and H, without pre-sinter), which shares G's scan speed but omits pre-sintering, enabling a direct comparison of the pre-sinter effect. This selection captures the combined influence of scan speed and pre-sintering on residual stress. Localized hardness was assessed via AFM-based QNM nanoindentation (50 µN max load) across all conditions with 20-60 indents per region.

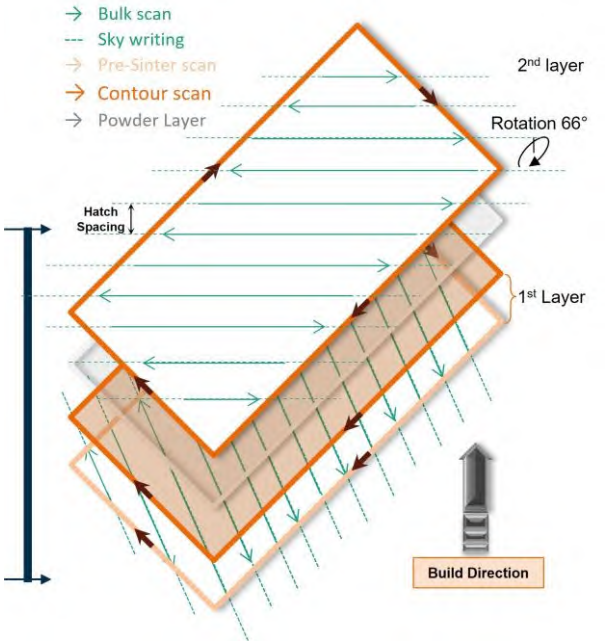


Figure 1: Schematic of the LPBF exposure strategy: bulk hatch direction rotated 66° per layer

Mechanical performance was evaluated through stress-controlled axial tension-tension fatigue testing (by Instron® 8874, at R = 0.1, f=20 Hz). At least two specimens per sample condition were tested at $0.5\times\sigma_{UTS}$, with one specimen retained per condition for fractography. Fractography (by Zeiss EVO MA10 SEM) of all failed specimens documented fracture surfaces and initiation sites.

3 RESULTS

3.1.1 Surface texture characterization

Areal surface texture was characterized on gauge surfaces of all sample conditions. Two parameters were used to describe the surfaces: Sa (arithmetic mean height), which represents the overall average roughness, and S_{vk} (reduced valley depth), which represents the depth of the deepest surface dales and is of particular interest as a potential fatigue-crack initiation site. Both parameters increased monotonically with contour scan speed from 300 to 1800 mm/s as shows in Diagram 1 and Figure 2.

Condition A (300 mm/s) showed the lowest texture values ($S_a \approx 3.5$ µm, $S_{vk} \approx 3.1$ µm), while condition J (1800 mm/s) having the highest across all parameters.

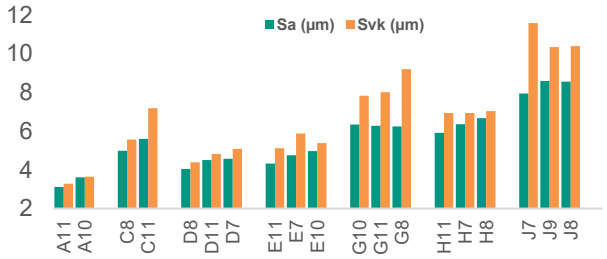


Diagram 1: Areal surface texture parameters for all investigated samples. S_a, S_{vk} (µm) evaluated using the applicable S- and L-filters

Comparing pre-sinter effects at same scan speeds: at 600 mm/s, conditions C and D showed comparable S_a and S_{vk} within scatter. At 1200 mm/s, condition G (with pre-sinter) exhibited S_{vk} = 8.75 µm and 7.60 µm for condition H (without pre-sinter), a 15.2 % difference, with condition H. Representative topography maps (Figure 2) illustrate these morphological trends.

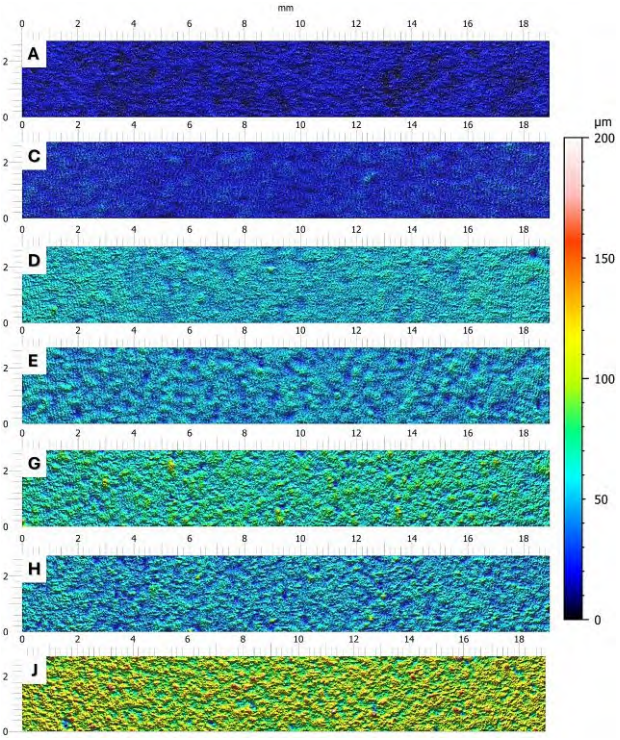


Figure 2: Areal surface topography maps for all investigated conditions, as-built samples.

3.1.2 Microstructural Investigation

Etched XZ-plane cross-sections (Figure 3) revealed a distinct near-surface contour-to-transition zone in all conditions, marked by a finer cellular substructure, reduced columnar grain aspect ratio, and altered Si network distribution relative to the bulk, indicating partial near-surface grain refinement. Condition A (300 mm/s) showed a uniform Si network and consistent layer widths, reflecting a unidirectional, solidification-oriented Si

network; this uniformity progressively broke down with increasing scan speed (E, J), producing a coarser Si network and Al grains near the fusion line/HAZ and finer structures toward the layer interior, with heterogeneity intensifying from A to J. At matched scan speeds, pre-sintering (C vs. D; G vs. H) did not refine grains but instead coarsened them within the HAZ, indicating that it promotes localized grain growth rather than complete refinement.

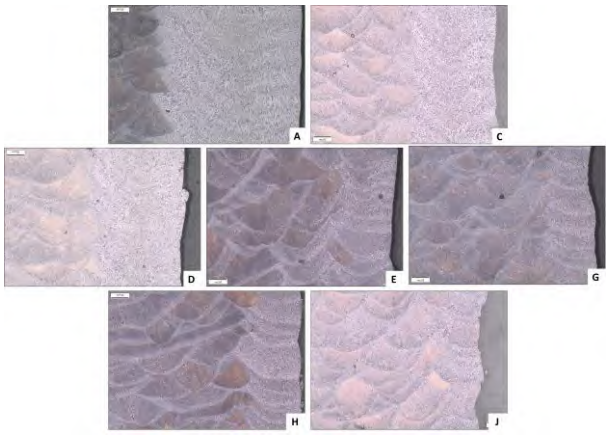


Figure 3: optical micrographs (200X, Keller-etched) of XZ-plane cross-sections for all investigated conditions, as-built LPBF AlSi7Mg0.6, showing melt pool geometry and near-surface transition zone

3.1.3 Fatigue Testing

Tests were conducted at R = 0.1, 20 Hz, room temperature, run out at 10^7 cycles, and a target load of $0.5\times\sigma_{UTS}$ (σ_{max} = 196 N/mm^2). Condition A (300 mm/s) exhibited the highest fatigue life and the narrowest scatter, indicating a consistent initiation mechanism. Fatigue life decreased progressively with increasing contour scan speed, from condition D to G and J. Condition H exhibited the widest scatter, compared to the narrower range for G.

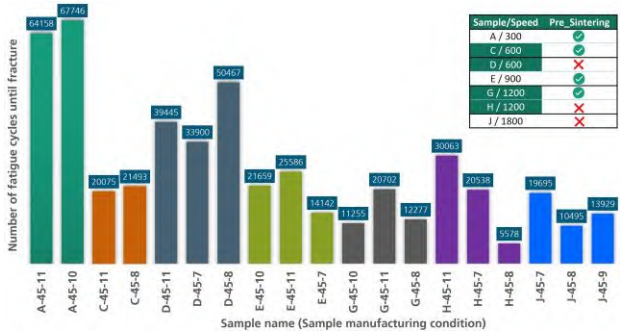


Figure 4: Fatigue life (N_f) of all investigated conditions, LPBF AlSi7Mg0.6 as-built; σ_{max} = 196 N/mm^2, R= 0.1, f = 20 Hz, load level= 0.5σ_{UTS}*

All results are shown in Figure 4. Post-fatigue sectioning of condition A revealed a crack that initiated with propagation perpendicular to the load direction, transitioning to 45° propagation in the bulk region, with multiple secondary crack initiation sites observed alongside the primary origin.

3.1.4 Residual Stress Measurement

XRD measurements (sin$^2\psi$-method, {422} α-Al reflection) on conditions A, E, G, and H (Figure 5) revealed tensile residual stress at all as-built contour surfaces, ranging from +82 MPa to +157 MPa. Condition A recorded the lowest mean RS surface stress (+109 MPa) and was the only condition showing a decreasing stress gradient with depth ($\Delta\boldsymbol{\sigma}_{RS}$ = −22 MPa at 30 µm). Conditions E, G, and H ($\Delta\boldsymbol{\sigma}_{RS}$ ≈ 124, 123, 142 MPa at surface, respectively) exhibited increasing stress with depth ($\Delta\boldsymbol{\sigma}_{RS}$ = +9, +21, +13 MPa, respectively). Among the 1200 mm/s conditions, G (with pre-sinter) showed a more increasing Residual stress rate than H (without pre-sinter), when moving from surface to depth. In addition to residual stress, the full width at half maximum (FWHM) of the diffraction peak was evaluated as a qualitative indicator of lattice microstrain and dislocation density, with broader peaks generally reflecting greater microstructural disorder near the surface. The FWHM of the {422} peak increased monotonically with scan speed, from ~0.485º (condition A) to ~0.710° (condition G) at the surface. All measured stresses remained below the nominal yield strength.

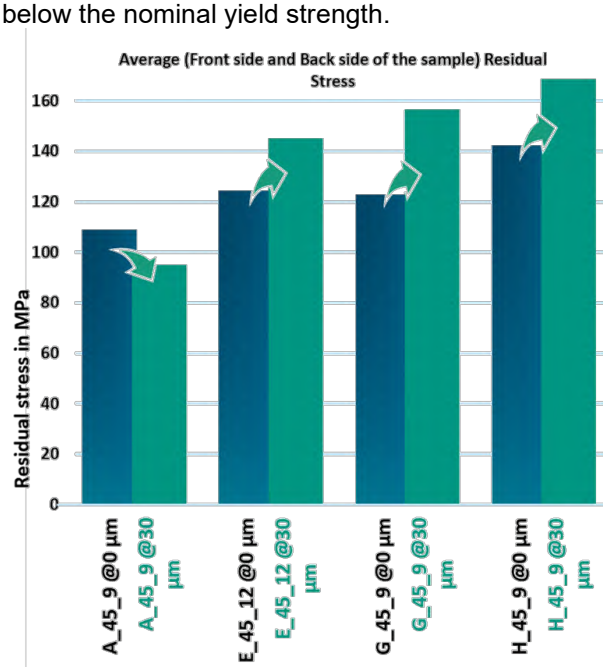


Figure 5: Graphical representation for residual stress measurement results for A, E, G, and H.

3.1.5 Nano-hardness

AFM-based QNM nanoindentation (Figure 6) measured hardness values between 1.13 and 2.30 GPa for conditions A, C, E, and G. The upper chart shows that hardness generally increases with scan speed from C to G. Condition A is an exception: it has the highest hardness even though it used the lowest scan speed. This is likely because condition A had a uniform Si network, while higher speeds caused coarser grains near the fusion line/HAZ

(3.1.2), which likely lowers hardness compared to A's more even structure. The lower chart compares samples with and without pre-sintering, tested at the same scan speed. Hardness is lower in the pre-sintered samples.

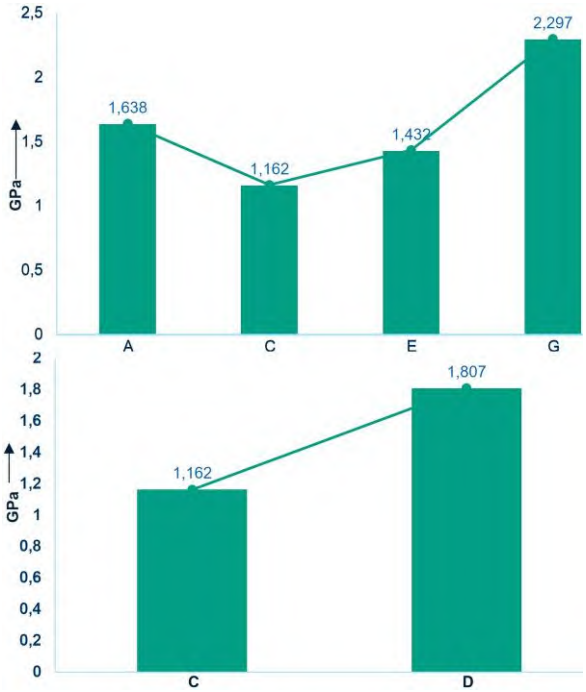


Figure 6: Charts shows Nano indentation results for samples (A, C, E, and G) in GPa.

3.1.6 SEM and EDX Analysis

SEM imaging confirmed the characteristic cellular-dendritic substructure across all conditions, with α-Al cells surrounded by a continuous Si-rich eutectic network. The width of the contour scan zone decreases with increasing scan speed, as shown in *Figure 7*. As EDX area mapping (*Figure 8* & *Figure 9*) showed uniform Al-Mg-Si distribution in condition A, consistent with lower scan speed with a coarser cellular substructure and Si agglomeration at cell boundaries, whereas condition G exhibited visibly smaller grains and distinct Si segregation in the heat-affected zone despite an overall finer microstructure. No qualitative bulk compositional differences were detected between conditions.

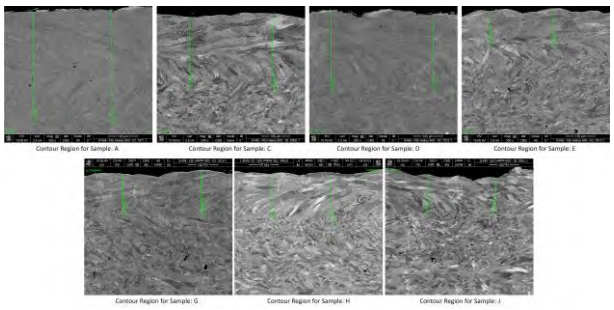


Figure 7: SEM micrographs of as-built surfaces for conditions A to J at 250X magnification.

EDX line scans across the near-surface region indicated increased Al, Si, and Mg weight fractions following the pre-sinter pass, suggesting pre-sinter-induced elemental redistribution near the contour surface.

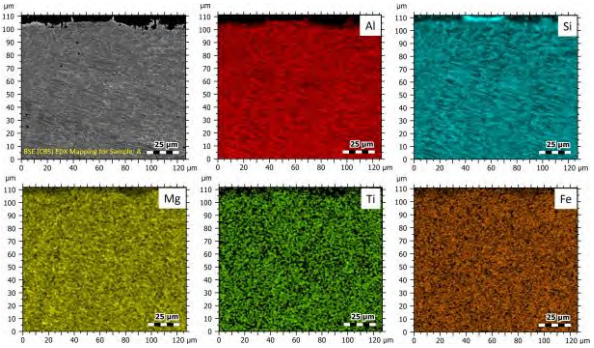


Figure 8: Representative EDX maps of Condition A (2113X).

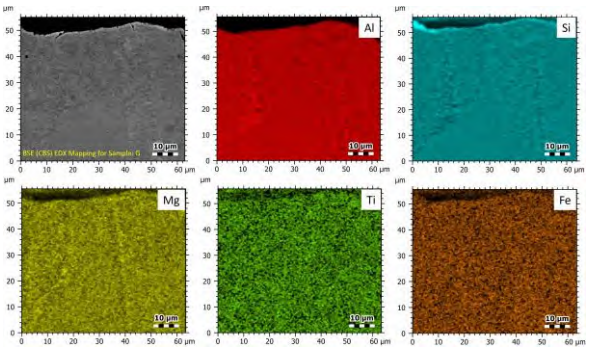


Figure 9: Representative EDX maps of condition G at 4225X.

3.1.7 Fractography

Condition H exhibited fatigue crack initiation at the contour surface, originating from multiple surface-connected pores, partially unfused powder particles, and surface valleys associated with the coarse as-built contour morphology, as illustrated in *Figure 10*. Distinct chevron marks were observed on the fracture surface, indicating the crack propagation path. Furthermore, small secondary microcracks were identified at location 3.

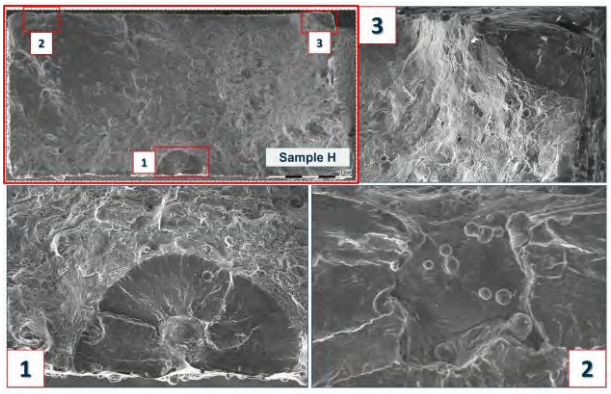


Figure 10: SEM fractography of Condition H and enlarged views of the probable crack initiation site.

Condition G (*Figure 11*) exhibited multiple crack initiation sites, both at the surface and within the bulk, similar to condition H. Unfused powder particles and deep surface valleys were clearly visible on the fracture surface, showing that surface irregularities contributed to initiation alongside internal sources, even with pre-sintering applied.

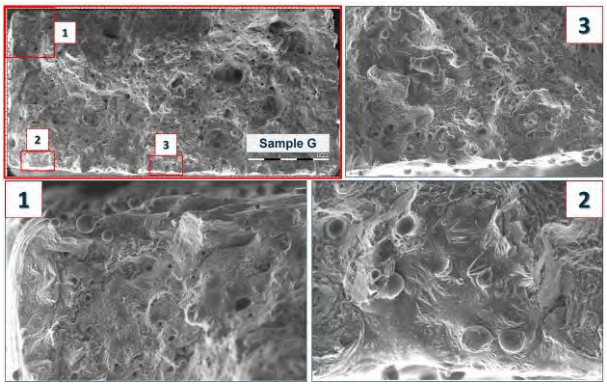


Figure 11: SEM fractography of Condition G and enlarged views of the probable crack initiation site.

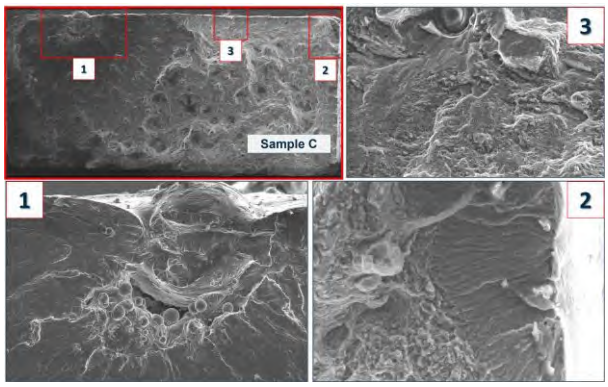


Figure 12: SEM fractography of Condition C and enlarged views of the probable crack initiation site.

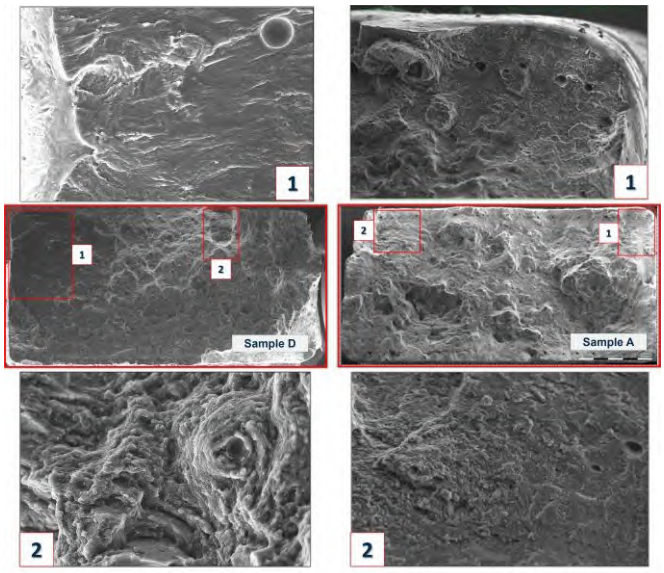


Figure 13: SEM fractography of sample C & A with enlarged views with probable crack initiation sites.

Condition C (*Figure 12*) exhibited fewer crack initiation sites than condition H, with the major defect located in the sub-surface transition zone, consisting of lack-of-fusion and porosity. Crack propagation showed distinct chevron marks, and the transition zone displayed incomplete fusion. The primary crack initiated from both surface and sub-surface regions, indicating that pre-sintering did not fully eliminate these initiation sources.

In condition D (*Figure 13*), fewer crack initiation sites were observed, with the major defect located at the surface. A large surface valley was identified as a contributing factor to crack initiation in this condition. In contrast, condition A (*Figure 13*) did not exhibit any major surface defects, unlike the other conditions examined. However, small centreline porosities were observed within the contour scan layer passes, representing a comparatively minor and localized initiation source.

4 DISCUSSION

4.1.1 Contour Scan Speed: Influencing Surface Texture Key Parameter

Surface texture parameters increased monotonically with contour scan speed (300–1800 mm/s), with S_{vk} rising from 3.1 µm (condition A) to 10.8 µm (condition J). S_{vk}, rather than Sa, is confirmed as the fatigue-relevant descriptor, consistent with Buchenau et al.'s exponential S_{vk}-N_f relationship for AlSi7Mg0.6 (R^2 = 0.872). The present work extends this relationship, broadening its validated range beyond the original 300-1200 mm/s window. This also corroborates Maleki et al.'s finding that S_{vk} correlates more strongly with crack initiation than S_a, and Yonehara et al.'s observation that valley-depth parameters track near-surface defect density in LPBF components.

4.1.2 Near-Surface Microstructure

A distinct transition zone was observed between the contour and bulk-hatch regions under all conditions, with its width generally decreasing as the scan speed increased. This agrees with the relationship reported by Buchenau et al. between laser dwell time and melt-pool penetration depth in AlSi7Mg0.6. At higher scan speeds, the shorter dwell time produces a shallower melt pool and a narrower heat-affected zone (HAZ). However, conditions C and D, as well as G and H, showed similar transition-zone widths despite differences in pre-sintering. This suggests that pre-sintering had no clear influence on the transition-zone width under the investigated conditions. The three-zone melt pool structure and the loss of Si-network continuity at higher speed are consistent with the standard LPBF Al–Si picture, in which cell size and Si continuity depend on local cooling rate.

4.1.3 Residual Stress: Contour scan dependence

The near-surface residual stress measured here is

tensile in all conditions. This supports the thermal gradient mechanism proposed by Mercelis and Kruth. The increase in residual stress with scan speed reflects the reduced time available for stress relaxation before solidification. This work identifies two distinct depth gradient regimes. Condition A shows a decreasing trend, with surface RS exceeding subsurface RS by 11 to 32 MPa, while conditions E, G, and H show an increasing trend, with subsurface RS exceeding surface RS by roughly 15 MPa. Mercelis and Kruth did not distinguish between these two regimes. The finding that condition H exhibits higher residual stress than condition G, yet does not show inferior fatigue life, may be explained by the different residual stress gradients from the surface to a depth of 30 µm. This observation also supports the argument of Maleki et al. that residual stress governs crack initiation when surface severity is comparable between conditions. Here, the S_{vk} gap between G and H is meaningful, at 8.75 versus 7.60 µm, so surface roughness remains the dominant factor, consistent with Maleki et al.'s findings.

4.1.4 SEM-EDX: Compositional and Microstructural Effects

SEM imaging reveals, The Si segregation observed near the HAZ in condition G, versus the homogeneous distribution in condition A, reflects faster solidification pushing solute toward the resolidified shell rather than allowing it to disperse, consistent with the cellular Al-Si microstructure reported for LPBF AlSi7Mg0.6 by Pereira et al. and Kluczynski et al. This segregation compounds the fatigue and surface texture trends already discussed. Condition G combines the residual stress, highest Svk, highest FWHM, and now the most severe Si segregation, giving cracks a combined geometric, microstrain, and compositional initiation path, while condition A's homogeneity aligns with its lowest values across all three and its longest fatigue life.

EDX line scans show elevated Al, Si, Mg, and O in pre-sintered conditions (C, G) versus D and H. This points to elemental redistribution during pre-sintering, and possibly Mg_2Si formation, along with higher oxygen content from the extra thermal cycle, though neither was confirmed microstructurally. The results suggest pre-sintering has an adverse effect on fatigue life at high scan speeds, but this remains an indirect, signal-based inference rather than a confirmed mechanism.

4.1.5 *Nanoindentation*: Contour and Transition Zone

Sample condition A shows the most homogeneous hardness profile (contour-to-transition differential <4%), limiting preferential strain accumulation and reinforcing its fatigue advantage. Condition G shows both peak contour hardness and maximum hardness scatter, reflecting a brittle, chemically heterogeneous near-surface state. Comparison with H (lower hardness, lower scatter, superior fatigue life) confirms that high contour hardness is not synonymous with improved fatigue resistance; rather, hardness magnitude, spatial scatter, and zone-to-zone gradient jointly indicate defect-controlled crack initiation susceptibility.

4.1.6 Fractographic *Synthesis*

Fractography confirms that condition A stands apart because it lacks the surface valleys, unfused particles, and pores seen elsewhere. Its only possible initiation source is minor centreline porosity within the contour layer, consistent with A's homogeneous Si distribution established earlier, meaning no compositional or mechanical weak point existed to compete with this minor porosity as a crack starter.

Conditions G and H, both run at 1200 mm/s, show cracks starting from multiple points at the surface and inside the bulk. Pre-sintering did not fix this in G, even with the extra heating step, and G still had its Si segregation and biggest hardness gradient from before, so pre-sintering seems to add problems rather than solve them here. H shows a similar spread of crack starting points, but without G's Si problem, suggesting cracks simply start wherever the surface is weakest rather than at one clear defect. Together, G and H support Buchenau et al.'s point that it is the near-surface condition, not the bulk material, that drives fatigue scatter at this speed

Conditions C and D, both at 600 mm/s, had fewer crack starting points, but different defect types. C, with pre-sintering, shows lack-of-fusion and porosity just below the surface, while D, without pre-sintering, shows a single large surface valley, a straightforward roughness issue. This suggests pre-sintering at this lower speed introduces its own subsurface defect rather than improving on the surface-roughness problem seen in D. This supports Cerri et al. and Buchenau et al.'s argument that fatigue behaviour in LPBF AlSi7Mg0.6 comes from a mix of surface, chemical, and mechanical factors together, not from any one measurement alone.

5 CONCLUDING REMARKS

This work establishes contour scan speed as the stronger influence compared with pre-sintering parameters on fatigue performance in LPBF AlSi7Mg0.6 within the investigated conditions, acting through coupled near-surface mechanisms rather than any single parameter. S_{vk}, not Sa, is the key surface descriptor, and residual stress becomes fatigue-limiting only when acting alongside compromised surface or compositional states, extending the Buchenau, Maleki, and Mercelis and Kruth frameworks to a broader speed range and identifying two distinct depth-wise stress regimes not previously separated.

Condition A represents the fatigue-optimal state: a homogeneous, low-stress, low-hardness-gradient microstructure with only minor centreline porosity as a possible crack source. Condition G represents the opposite extreme, where high scan speed compounds Si segregation, higher residual stress, elevated FWHM, and hardness heterogeneity into a brittle, multi-site failure mode that pre-sintering does not correct. The comparison between G and H further shows that surface roughness, not residual stress, remains the primary fatigue driver once compositional severity is comparable, while the C-D comparison shows pre-sintering's effect on defect type is speed-dependent, producing subsurface lack-of-fusion at lower speeds rather than the surface segregation seen at higher speeds. Pre-sintering did not improve fatigue performance at either scan speed or in some conditions introduced additional defects, suggesting it is not beneficial for fatigue-critical LPBF AlSi7Mg0.6.

Collectively, these findings confirm that fatigue life in as-built LPBF AlSi7Mg0.6 depends on the combined severity of surface roughness, residual stress, Si segregation, and hardness gradient at a given scan speed and pre-sinter condition, rather than on any one of these factors alone.

6 OUTLOOK

Two extensions follow directly from this work. First, the sub-critical porosity in condition A should be tested under higher stress amplitudes and multiaxial loading to confirm it remains non-critical outside the fatigue regime studied here. Second, S_{vk}'s relationship with fatigue life should be validated on a larger dataset before adoption as an acceptance criterion.

An oscillating contour scan pass is recommended as a priority direction for future optimisation. By distributing energy more evenly across the contour zone, it could reduce porosity and residual stress relative to the static approach in condition A, while improving surface uniformity and contour-to-bulk fusion, potentially extending fatigue life beyond what was achieved here.

7 ABBREVIATIONS AND ACRONYMS

AM: Additive Manufacturing
AFM: Atomic Force Microscopy
ASTM: American Society for Testing and Materials
BSE: Backscattered Electron
DED: Directed Energy Deposition
EDX: Energy-Dispersive X-ray Spectroscopy
FCG: Fatigue Crack Growth
FDM: Fused Deposition Modelling
FWHM: Full Width at Half Maximum
HAZ: Heat-Affected Zone
HCF: High-Cycle Fatigue
ISO: International Organization for Standardization
LoF: Lack of Fusion
LPBF: Laser Powder Bed Fusion
MP: Melt Pool
PBF-LB: Powder Bed Fusion – Laser Beam
QNM: Quantitative Nanomechanical Mapping
RS: Residual Stress
SE: Secondary Electron
SEM: Scanning Electron Microscopy
SLM: Selective Laser Melting
SLS: Selective Laser Sintering
TGM: Temperature Gradient Mechanism
UTS: Ultimate Tensile Strength
VED: Volumetric Energy Density
XRD: X-ray Diffraction.

8 ACKNOWLEDGMENT

This thesis was completed at Fraunhofer IFAM Bremen in cooperation with the wbk Institute, KIT, which provided academic supervision and the institutional framework for this work. I sincerely thank Fraunhofer IFAM Bremen for continuous support throughout this work.

I am also grateful to the Fatigue, SEM imaging and fractographic analysis team and the AFM group at Fraunhofer IFAM Bremen for their experimental support, and to the Institute for Applied Materials (IAM), KIT, for providing access to XRD measurement facilities and input on residual stress analysis. My thanks extend to the entire Fraunhofer IFAM Bremen team for their collegial support and research infrastructure.

9 REFERENCES

1. Gu, D., Meiners, W., Wissenbach, K., and Poprawe, R. (2012). Laser additive manufacturing of metallic components: materials, processes and mechanisms. *International Materials Reviews*, 57, 133–164.
2. Sing, S. and Yeong, W. (2020). Laser powder bed fusion for metal additive manufacturing: perspectives on recent developments. *Virtual and Physical Prototyping*, 15, 359–370.
3. Aboulkhair, N., Simonelli, M., Parry, L., Ashcroft, I., Tuck, C., and Hague, R. (2019). 3D printing of aluminium alloys: Additive manufacturing of aluminium alloys using selective laser melting. *Progress in Materials Science*, 106, 100578
4. Pereira, J., Gil, E., Solaberrieta, L., San Sebastián, M., Bilbao, Y., and Rodríguez, P. (2020). Comparison of AlSi7Mg0.6 alloy obtained by selective laser melting and investment casting processes: Microstructure and mechanical properties in as-built/as-cast and heat-treated conditions. *Materials Science and Engineering.*
5. Kluczyński, J., Dražan, T., Joska, Z., Łuszczek, J., Kosturek, R., and Jasik, K. (2024). Microstructural investigation of process parameters dedicated to laser powder bed fusion of AlSi7Mg0.6 alloy. *Materials (Basel,*

Switzerland), 17.
6. Chakraborti, N. and Lukas, H. (1992). Thermodynamic optimization of the Mg-Al-Si phase diagram. *Calphad*, 16, 79–86.
7. Romano, S., Brückner-Foit, A., Brandão, A., Gumpinger, J., Ghidini, T., and Beretta, S. (2018). Fatigue properties of AlSi10Mg obtained by additive manufacturing: Defect-based modelling and prediction of fatigue strength. *Engineering Fracture Mechanics*, 187, 165–189.
8. Yap, C., Chua, C., Dong, Z., Liu, Z., Zhang, D., Loh, L., and Sing, S. (2015). Review of selective laser melting: Materials and applications. *Applied Physics Reviews*
9. Huang, S., Guo, S., Zhou, B., Zhang, G., and Zhang, X. (2021). Microstructure and properties of AlSi7Mg alloy fabricated by selective laser melting. *China Foundry*, 18, 416–423.
10. Buchenau, T., Amkreutz, M., Bruening, H., and Mayer, B. (2023). Influence of contour scan variation on surface, bulk and mechanical properties of LPBF-processed AlSi7Mg0.6. *Materials (Basel, Switzerland)*, 16
11. Bonneric, M., Brugger, C., Tranchand, B., Castro Moreno, A., Lesseur, J., and Saintier, N. (2024). Defect sensitivity in L-PBF AlSi7Mg0.6 alloy subjected to fatigue load: Effect of load ratio and torsion loading. *International Journal of Fatigue*, 181, 108154.
12. Grande, A., Cacace, S., Demir, A., and Sala, G. (2019). Fracture and fatigue behaviour of AlSi7Mg0.6 produced by selective laser melting: effects of thermal-treatments. *Italian Association of Aeronautics and Astronautics*.
13. Bassoli, E., Denti, L., Comin, A., Sola, A., and Tognoli, E. (2018). Fatigue behavior of as-built L-PBF A357.0 parts. *Metals*, 8, 634.
14. Suresh, S. (1998). *Fatigue of Materials*.
15. Kleen, A., Glaubitz, E., and Gockel, J. (2024). The influence of contour offset in laser powder bed fusion on melt pool behaviors, surface roughness, and sub-surface porosity.
16. Nudelis, N. and Mayr, P. (2021). A novel classification method for pores in laser powder bed fusion. *Metals*, 11, 1912.
17. Hamidi Nasab, M., Giussani, A., Gastaldi, D., Tirelli, V., and Vedani, M. (2019). Effect of surface and subsurface defects on fatigue behavior of AlSi10Mg alloy processed by laser powder bed fusion (L-PBF). *Metals*, 9, 1063.
18. Buchenau, T. (2024). *Tailored Surface Texture Characterisation of Metal Additive Components for Aerospace Applications*. Doctoral dissertation, Universität Bremen, Germany.
19. Maleki, E., Bagherifard, S., and Guagliano, M. (2023). Correlation of residual stress, hardness and surface roughness with crack initiation and fatigue strength of surface treated additive manufactured AlSi10Mg: Experimental and machine learning approaches. *Journal of Materials Research and Technology*, 24, 3265–3283.
20. Cerri, E. and Ghio, E. (2023). Metallurgical analysis of laser powder bed-fused Al–Si–Mg alloys: Main causes of premature failure. *Materials Science and Engineering: A*, 881, 145402.
21. ISO 25178-2:2021. *Geometrical Product Specifications (GPS) – Surface Texture: Areal – Part 2: Terms, Definitions and Surface Texture Parameters*.
22. ASTM E466-15 (2015). *Standard Practice for Conducting Force Controlled Constant Amplitude Axial Fatigue Tests of Metallic Materials*.
23. Digital Surf (2023). *MountainsMap Surface Imaging and Analysis Software*, Version 9. Available at: https://www.digitalsurf.com.

ECSSMET
Braunschweig Germany 2026

Material properties

ASSESSMENT OF HIGH ENTROPY ALLOYS FOR SPACE APPLICATIONS

Carlos Belei [(1)], Zuzana Kovacova [(1)], Johannes Bieg [(2)], Erich Neubauer [(1)]

[(1)] RHP-Technology GmbH, Technologie- und Forschungszentrum, 2444 Seibersdorf, Austria
[(2)] European Space Research and Technology Centre (ESTEC), Keplerlaan 1, NL-2200 AG Noordwijk, The Netherlands

KEYWORDS

Hot Pressing; Powder Metallurgy; Additive Manufacturing; High-Entropy Alloys; Process Optimization; High-Temperature Applications; Oxidation Resistance; Wear Resistance.

ABSTRACT

This project investigated the processing–microstructure–property relationships of selected high-entropy alloys (HEAs) manufactured via hot pressing (powder metallurgy route) and additive manufacturing (liquid route). Three HEA compositions were selected based on a literature review and trade-off analysis, targeting high-temperature ($CrMo_{0.5}NbTa_{0.5}TiZr$ and AlCrMoNbTi, termed HEA-01 and HEA-02, respectively) and wear-related applications (AlCrNiFeTi, HEA-03). The selected alloys had their optimized, followed by systematic microstructural characterization and mechanical testing, culminating in the production and testing at relevant application conditions. The results revealed complex, multi-phase microstructures dominated by BCC matrices and extensive intermetallic precipitation, significantly deviating from the single- or dual-phase BCC structures commonly reported for arc-melted counterparts in literature. These microstructural features led to pronounced brittleness and limited ductility at room temperature across all investigated compositions and processing routes. Despite these limitations, selected alloys exhibited promising application-relevant properties. In particular, the refractory HEA-01 demonstrated high strength and acceptable oxidation resistance at temperatures up to 1000 °C, while HEA-03 showed favorable wear resistance associated with high hardness. Finally, based on these findings, the project identified realistic application windows, key process-induced constraints, and potential mitigation strategies, which provided a solid knowledge base and clear guidance for future HEA development and optimization.

1. INTRODUCTION

High-entropy alloys (HEAs) have emerged as a highly promising class of materials for demanding structural applications because of their potential for high strength, thermal stability, and wear resistance. Their broad compositional design space offers opportunities to tailor properties for specific service conditions, particularly at elevated temperatures and in harsh environments. However, the relationships between composition, processing, microstructure, and performance are still not fully understood, especially for HEAs produced by industrially relevant manufacturing routes.

As such, the objective of this work is to improve the understanding of HEAs and how their properties are influenced by processing conditions. In particular, the study focuses on three selected compositions: the refractory alloys $CrMo_{0.5}NbTa_{0.5}TiZr$ and AlCrMoNbTi, intended for high-temperature applications, and AlCrNiFeTi, selected for wear-related applications. By examining these alloys under different processing conditions, the work aims to identify promising material–process combinations and to better understand the microstructural features that govern their behavior.

To address this, the selected HEAs were processed by hot pressing (HP) and additive manufacturing via plasma metal deposition (PMD), with the manufacturing parameters and subsequent heat treatments systematically optimized. The resulting materials were characterized with respect to microstructure and application-relevant properties, with particular attention to high-temperature performance and wear resistance. This approach was used to link processing conditions to alloy response and to define realistic application windows for the investigated HEAs.

2. MATERIALS AND METHODS

2.1. Powder preparation

The HEA powders used in this study were prepared by two different routes, depending on the manufacturing process. For the PMD experiments, the alloys were produced by elemental blending of commercially available elemental powders with particle-size distributions in the 63-150 µm range. For the HP experiments, powders were prepared by mechanical alloying using steel jar and balls, with hexane used as a medium. After preparation, the powders were dried and stored under appropriate conditions prior to further processing.

2.2. Hot Pressing

Hot pressing was performed in graphite dies of 20 mm diameter under a constant pressure of 30 MPa, with heating and cooling rates fixed at 10 K/min. The

process was optimized in a one-factor-at-a-time manner by varying temperature first, then dwell time. To minimize reactions with the graphite tooling, the die surfaces were coated with boron nitride before consolidation.

2.3. Plasma Metal Deposition

Plasma Metal Deposition was carried out by depositing 50 mm-long seams with three layers under argon shielding, using constant plasma gas flow, powder-feeding gas flow, voltage, and interlayer cooling time. The main variables were plasma current, deposition speed, and printing strategy. All alloys were deposited on Ti Gr.1 substrates.

2.4. Characterization

Relevant information on characterization methods is disclosed in the relevant subchapters of Chapter 3.

3. RESULTS AND DISCUSSION

3.1. Hot Pressing experiments

In general, hot pressing of mechanically alloyed HEA powders produced dense material samples, but only within limited process windows. Lower temperatures led to poor densification and extensive unreacted particles, whereas higher temperatures promoted material loss due to the squeezing phenomenon.

3.1.1. HEA-01

Hot Pressed HEA-01 consisted of a BCC matrix interspersed with intermetallic phases that, in the etched OM images, appear as bands or wave-like distributions of particles throughout the microstructure (Figure 1). XRD analysis confirmed the presence of five distinct intermetallic phases (Figure 2), with the dominant one being a C14-type Laves phase, identified as Cr_2Nb. Laves phases of this type ($MgZn_2$ prototype) are characterized by a hexagonal structure, high hardness, and a tendency to form in Cr-rich, Nb-containing regions under elevated-temperature conditions. In terms of mechanical properties, this material exhibited an average hardness of 659 ± 8 HV10, with a K_{Ic} estimated at 3.19 ± 0.16 MPa.m$^{0.5}$, demonstrating a highly brittle behaviour that could be reasonably attributed to the presence of the aforementioned intermetallic phases.

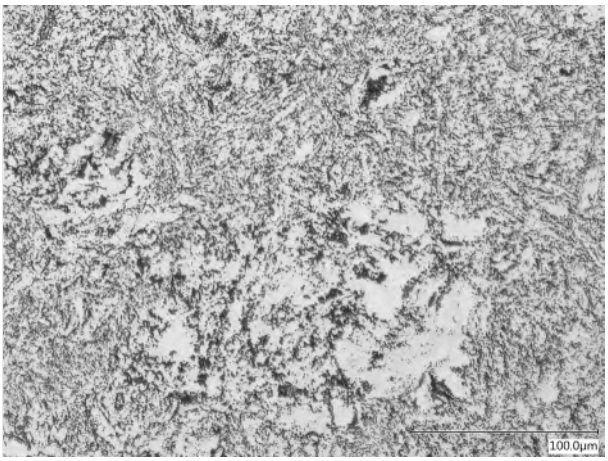


Figure 1: Mechanically alloyed HP HEA-01. Samples were etched prior to microscopy using a 5 % aqueous HBF_4solution for 60 s

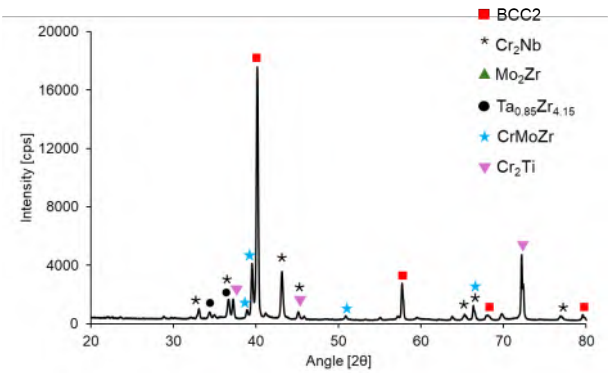


Figure 2: XRD analysis of mechanically alloyed HP HEA-01

3.1.2. HEA-02

Similar to HEA-01, microstructural analysis of hot-pressed HEA-02 revealed a complex structure, with a matrix containing intermetallic particles distributed in an inhomogeneous manner; notably, these phases tend to form around preexisting mechanically alloyed powder particles that remain after the process (Figure 3). XRD analysis identified a single dominant BCC phase in the matrix, accompanied by several intermetallic phases, primarily containing Cr and/or Ti. Among these, the main intermetallic phase was identified as $AlTi_2$, followed by Cr_2Nb (Figure 4).

Moreover, carbon was detected in at least two compounds (TiC_8 and C_2MoTi), indicating the presence of contamination in the mechanically alloyed powder in the as-received condition. In this case, it is assumed that incomplete solvent removal or the formation of carbon-containing byproducts during milling likely introduced carbon into the system.

Along these lines, additional contamination was observed in the form of iron oxide (FeO). Such contamination is commonly encountered in mechanically alloyed powders, given that the milling process is performed in steel jars using steel grinding media, which unavoidably introduce wear

debris and oxide fragments into the powder.

Similar to the previous HEA, this material was also considered highly hard and brittle, with average hardness and K_{Ic} estimated at 855 ± 19 HV10 and 2.37 ± 0.35 MPa.m$^{0.5}$, respectively.

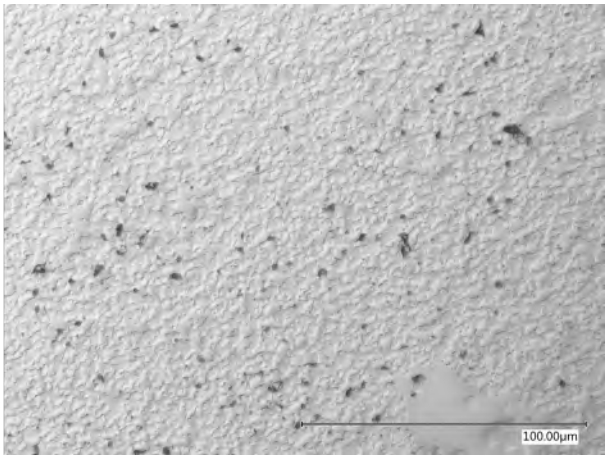


Figure 3: Mechanically alloyed HP HEA-02

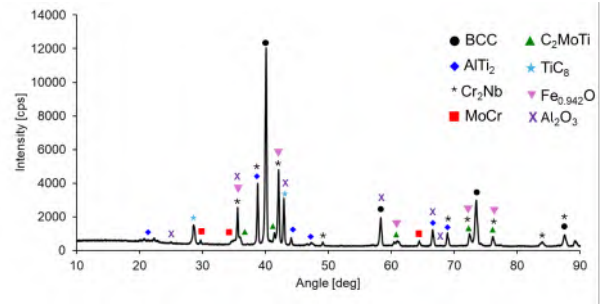


Figure 4: XRD analysis of mechanically alloyed HP HEA-02

3.1.3.HEA-03

Microstructural analysis on as-pressed HEA-03 revealed a three-phase microstructure consisting of a dual-phase matrix (observed as dark regions in the OM images, containing lighter patches) and finely dispersed intermetallic particles (<1 µm), which were predominantly located within the darker matrix regions, see Figure 5.

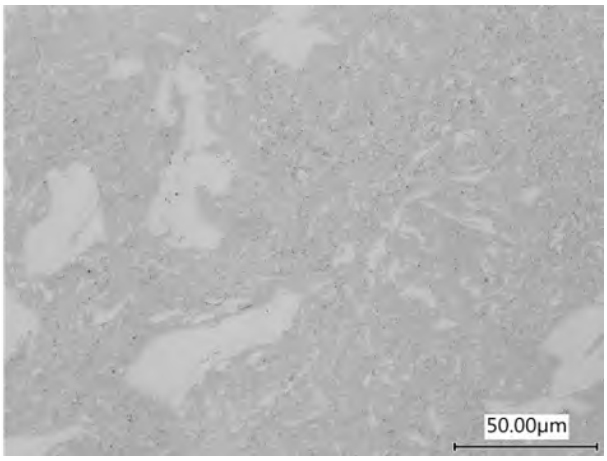


Figure 5: Mechanically alloyed HP HEA-03

XRD analysis (Figure 6) supported the observations from microscopy, revealing two BCC phases alongside at least three distinct intermetallic phases that could not be differentiated by OM. Most of these intermetallics correspond to aluminides, with the exception of FeO. The latter had also been observed in HEA-02 and, in this case, may originate either as a by-product of the mechanical alloying process (as previously discussed) or from oxidation associated with the Fe content inherently present in the alloy. Average hardness and K_{Ic} were estimated at 733 ± 7 HV10 and 2.09 ± 0.47 MPa.m$^{0.5}$, respectively, again demonstrating the characteristic profile of a very hard but brittle alloy that had been observed in the other hot-pressed HEA compositions.

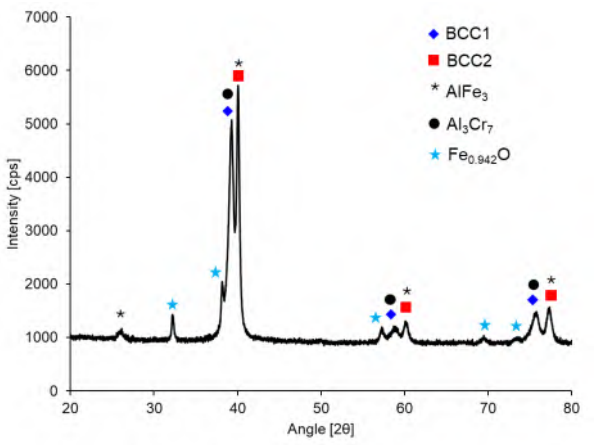


Figure 6: XRD analysis of mechanically alloyed HP HEA-03

3.2. Plasma Metal Deposition experiments

Generally, the PMD trials showed that printability depended strongly on alloy composition, powder flowability, and deposition energy, as follows.

3.2.1.HEA-01

HEA-01 exhibited sufficiently robust processability via PMD, with broad processing parameter

windows. Closer examination of the resulting cross section revealed that the absence of surface cracks extended throughout the bulk, as no cracks were identified internally (Figure 7). The sample could also be considered virtually pore-free. However, unmolten (or partially molten) particles were observed, particularly near the top of the deposition. The lower concentration of these residual particles at the bottom of the deposit may be attributed to an in-situ dissolution effect, as these regions are exposed to elevated temperatures for longer durations. In terms of hardness, the deposited HEA-01 ranged between 468 (close to substrate) and 582 HV5 (top regions).

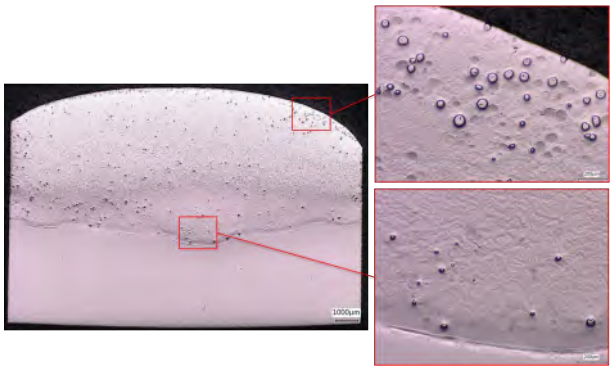


Figure 7: Overview of the microstructure observed on PMD using elemental mixed HEA-01

Closer inspection via EDX at the regions where püartially-reacted particles were present (Figure 8) showed dendrites enriched in Ti and particularly Mo, while Cr and Zr are largely rejected to the interdendritic space. Nb was found distributed equally between both the dendritic and interdendritic regions, whereas Ta is predominantly retained within the unreacted or partially reacted particles, although some of it can also be seen within the dendrites. The intermediate zone of the wall exhibits a mixture of these two microstructural features, i.e. Nb-Zr platelets embedded on a dendritic microstructure.

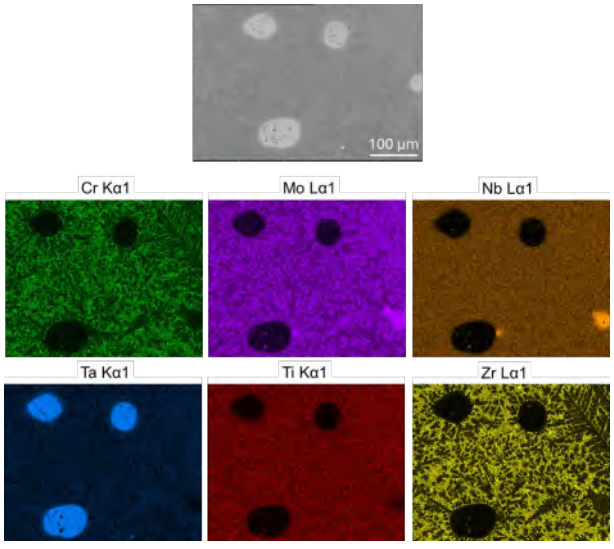


Figure 8: EDX analysis performed at the top of the PMD HEA-01 seam

Finally, another noteworthy factor that must be considered is the diffusion of substrate elements, in this case mainly Ti, into the deposited HEA. Figure 9 illustrates the extent of this effect. Within the first 600 µm above the substrate, the Ti signal (measured as counts per second of Ti Kα1 along an EDS line scan) was roughly twice as high as the baseline level. Beyond this region, the Ti concentration gradually decreased over the next 1400 µm before stabilizing at the nominal composition.

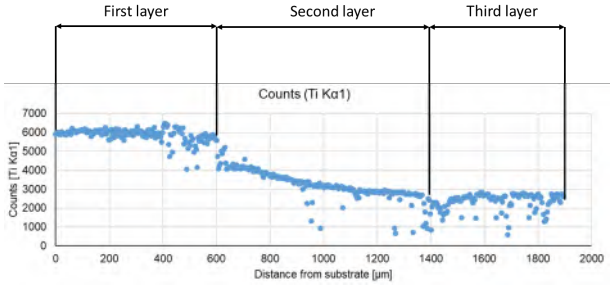


Figure 9: EDX line analysis for Ti on PMD HEA-01 seam deposited on a Ti Gr.1 substrate

3.2.2.HEA-02

Upon closer examination, two main features were identified on HEA-02 processed via PMD: the presence of unreacted or partially reacted particles, similar to those observed in HEA-01, and the occurrence of cracks that most likely formed during the cooling stage. There was also a clear transition between the first layer and the subsequent ones, which was not observed on HEA-01 (see Figure 10). Within the evaluated process parameters, the elemental-mixed, in-situ alloyed HEA-02 did not produce viable candidates for further analysis within this study.

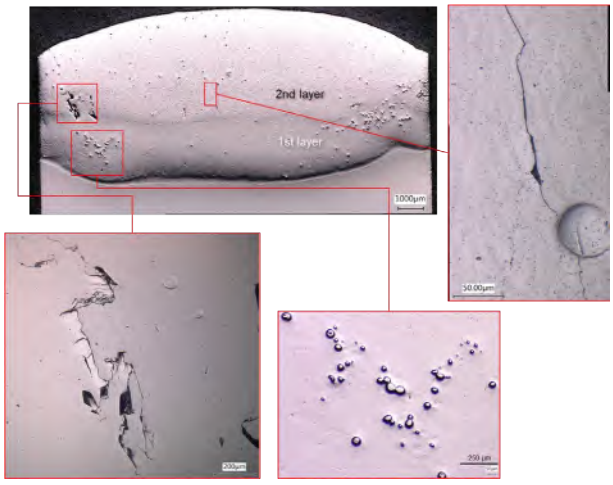


Figure 10: Overview of the microstructure observed on PMD using elemental mixed HEA-02

3.2.3. HEA-03

HEA-03 was by far the worst material in terms of processability via PMD. Cross-sectional analysis revealed an extensive network of cracks throughout the deposit (Figure 11), with some features resembling lack-of-fusion defects. These defects were unexpected given the high energy input employed during deposition. The presence of these voids indicates that, despite optimizing the parameters for higher heat input, the material remains highly susceptible to cracking, with hot cracking likely being the dominant mechanism. Similar to HEA-02, the additively manufactured HEA-03 was also deemed unsuitable in the present study due to its poor processability.

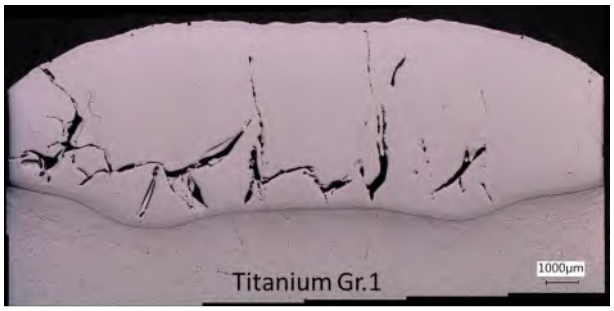


Figure 11: Overview of the microstructure observed on PMD using elemental mixed HEA-03

3.3. Characterization of best performing candidates

For application-related characterization, two candidates were selected based on their performance in terms of processability: $CrMo_{0.5}NbTa_{0.5}TiZr$ (HEA-01), processed via PMD, intended to be used in high-temperature applications, and AlCrFeNiTi (HEA-03), processed via HP, for wear applications.

3.3.1. $CrMo_{0.5}NbTa_{0.5}TiZr$ (HEA-01) for high-temperature applications

3.3.1.1. Tensile testing at Room Temperature

HEA-01 samples were extracted with geometry based on ASTM E8 (“Tension Test Specimens for Powder Metallurgy (P/M) Products”) and tested on a M500-100CT universal testing machine (Testometric, UK). Test parameters were selected in accordance with ASTM E8 for powder metallurgy products, with a test speed of 1.6 mm/min, corresponding to a strain rate of 0.00083 s^{-1}.
Tested samples included as-printed specimens as well as samples subjected to stress-relieving heat treatments (HT) at 700 °C and 1200 °C, both for 24 h. These HT were done directly on the dog bone samples after extraction from the 3D-printed wall. A total of five replicates per condition were tested. Representative pictures of the tested samples for each HT condition are shown in Figure 12. Test results are presented in Table 1.

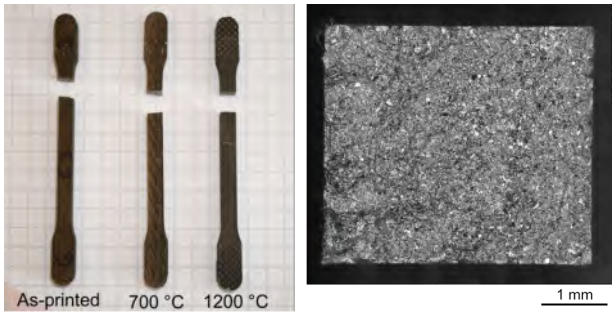


Figure 12: Right: representative samples of MPD HEA-01 after tensile test at room temperature, for different HT temperatures; Left: typical fracture surface

Table 1: Summary of results from tensile tests of PMD HEA-01 at RT for different heat treatment conditions

Condition	UTS [MPa]	A [%]
As-printed	230.8 ± 35.8	1.02 ± 0.24
700 °C // 24 h	265.6 ± 27.8	0.62 ± 0.09
1200 °C // 24 h	208.4 ± 24.0	0.18 ± 0.05

Overall, this material exhibits moderate mechanical strength under tensile, comparable to some aluminum alloys [1], mild steel or cast iron [2]. However, HEA-01 in most cases exhibits brittleness comparable to ceramics, rendering it unsuitable for most structural applications.
Based purely on average UTS values, HT at 700 °C for 24 h led to a noticeable improvement in mechanical performance. However, analysis of the variance revealed no statistically significant difference in UTS among the three sample conditions (at a significance level of $\alpha = 0.05$), with a P-Value of 0.1704 between groups (i.e. HT conditions).
On the other hand, the improvement in average elongation observed after HT at a higher temperature (1200 °C) could be considered statistically significant, with a P-Value of 2×10^{-4}, therefore much lower than α. Thus, these results indicate that while the 3D-printed HEA-01 does not show a significant improvement on UTS after heat treatment, treating it at high temperatures can lead to increase ductility, although still highly limited (i.e. in the range of 1%).

3.3.1.2. Compression testing at High Temperatures

Compression tests were performed on an MTS 810 servo-hydraulic testing machine (MTS, USA) equipped with a Mellen split oven and a high-temperature extensometer (Epsilon, USA). All tests were conducted at a constant actuator velocity of 0.54 mm/min (equivalent to a strain rate of 0.001 s^{-1}) and at temperatures of 800 °C and 1000 °C (three

samples each).
Compression testing of HEA-01 at high temperatures reveals a significant combination of strength and ductility. At 800 °C, the material exhibited a yield strength of approximately 600 MPa and a compressive failure stress more than 1100 MPa, with an associated Young's modulus of 82 GPa. When further tested at 1000 °C, the yield and failure stresses decrease to 302 MPa and 532 MPa, respectively, while the Young's modulus reduced to 30 GPa.
Despite this reduction in stiffness and strength, the material exhibited substantial plastic deformation capacity, with measured plastic strains of 54% at 800 °C and close to 70 % at 1000 °C. This can be visualized in Figure 13. These results suggest that the material undergoes extensive plastic accommodation under compressive loading even at elevated temperatures.

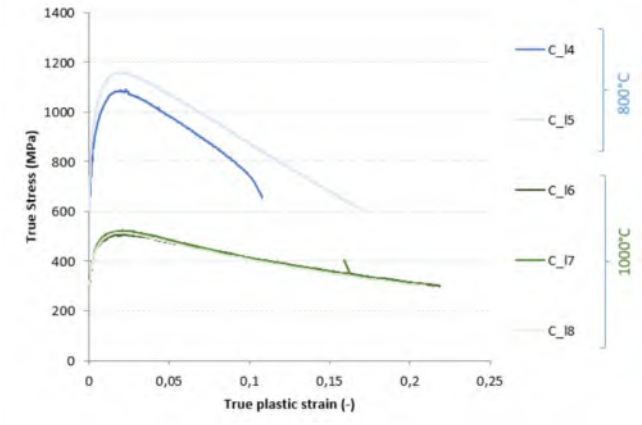


Figure 13: True Stress vs. true Strain curves obtained via compression test of PMD HEA-01 at different test temperatures

Overall, the combination of moderate high-temperature softening and retained ductility indicates that this material is capable of sustaining significant compressive loads while accommodating thermal and mechanical strains.

3.3.1.3. Dynamic oxidation testing using an oxyacetylene torch

The oxy-acetylene torch tests were conducted with an O_2:C_2H_2 ratio of 2.0, and a total gas flow rate of 4.5 L/min. Exposition time was limited to 60 s in open atmosphere, at temperatures of 1350 °C, 1500 °C, and 1650 °C, with the torch–sample distance adjusted dynamically to maintain a constant surface temperature. The material tested was HEA-01 (PMD), prepared as 20 mm × 2 mm discs with a P320 surface finish. An overview of the test setup is shown in Figure 14.

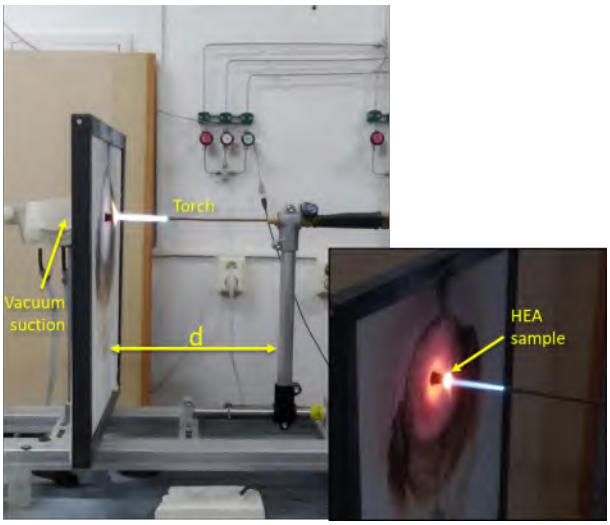


Figure 14: Test setup for dynamic oxidation tests. "d" denotes the distance between torch and HEA-01 sample

As a result of the test, an average mass gain was measured at 3.89 ± 0.74% for experiments performed at 1650 °C, with an average oxidation rate of 58.7 ± 11.1 mg/cm². During testing, the samples developed a brownish oxidation layer, see Figure 15. At this temperature, the material also appeared significantly softer, making it more susceptible to ablation under the torch exposure. Early signs of ablation were identified at 1500 °C, while no ablation was detected at 1350 °C.

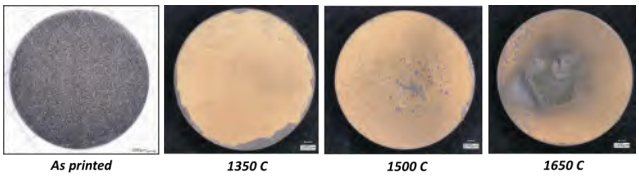


Figure 15: HEA-01 discs (Ø20 mm) subjected to dynamic oxidation tests at different temperatures

Microstructurally, HEA-01 developed an oxide layer of approximately 200 µm after 60 s exposure at 1350 °C (Figure 16). The bulk microstructure remained largely unchanged compared to the as-printed condition, consisting of two BCC phases, intermetallic particles, and unreacted Ta and Mo, as discussed earlier. The characteristics of the oxide layer became more pronounced in samples exposed to 1650 °C (Figure 17), where a significantly thicker layer of roughly 800 µm formed.

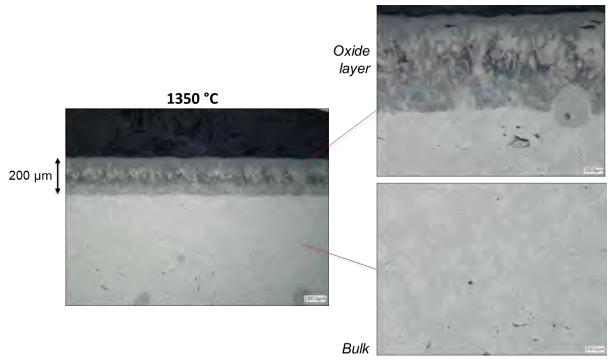


Figure 16: Microstructure of HEA-01 exposed to the oxyacetylene torch at 1350 °C for 60 s

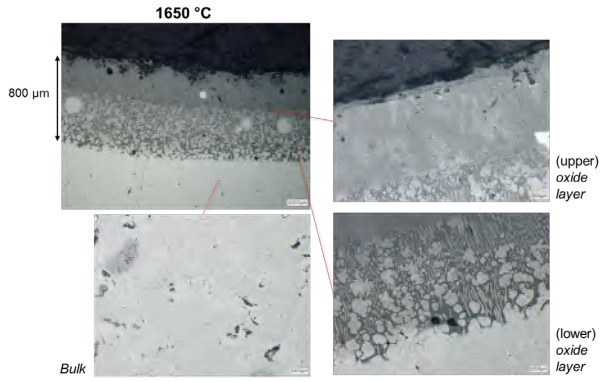


Figure 17: Microstructure of HEA-01 exposed to the oxyacetylene torch at 1650 °C for 60 s

This layer exhibited two distinct morphologies: a finer structure at the surface and a coarser structure at the base, the latter likely forming earlier and thus having more time to grow. Regarding the composition of the oxide layer, XRD analysis of a sample exposed to 1350 °C showed a pattern nearly identical to that observed in the oxide layers formed during static oxidation tests at comparable temperatures, see Figure 18. Note to readers: static oxidation tests were conducted prior to the oxyacetylene torch firing tests at comparable temperatures within the present project, although the corresponding results remain unpublished.

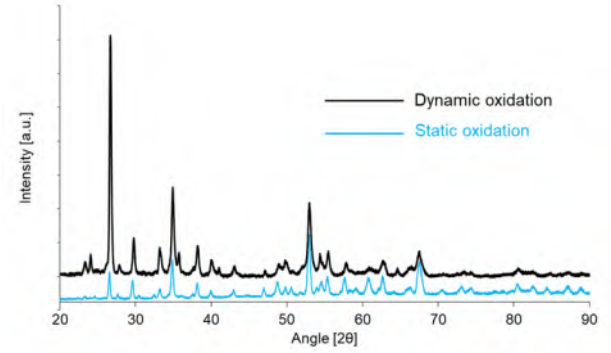


Figure 18: Comparative XRD analysis between oxides found on dynamic oxidation HEA-01 samples vs. static oxidation results (not published)

The XRD analysis indicated that the oxide scale consisted of a complex mixture of several oxide phases. Among these, Cr_2O_3, with its main reflections at 2θ ≈ 33°, 36°, and 54°, is the only phase expected to provide effective protection, owing to its relatively slow growth kinetics and ability to form a dense, adherent layer [3].

In contrast, oxides formed by the other major constituents, namely TiO_2, ZrO_2, Nb_2O_5, Ta_2O_5, and Mo-containing oxides, are generally non-protective. TiO_2 and ZrO_2 exhibit high Pilling–Bedworth ratios, favoring thick, crack-prone scales with significant volume expansion, leaving bulk material unprotected as oxidation progresses [4,5]. Nb_2O_5 and Ta_2O_5 exhibit even larger volume mismatches, making their oxide scales also highly prone to cracking and spallation, which in turn facilitates oxygen ingress into the underlying metal. Mo further worsens oxidation behavior: MoO_3 and related Mo-containing oxides volatilize at intermediate temperatures, leaving behind porous, non-adherent regions that accelerate further oxidation [6,7].

In such a scenario, these complex oxides rarely form continuous or protective layers [8]; instead, they develop locally, as different regions of the alloy oxidize according to their local composition. Their formation indicates that the alloy fails to establish a single dominant protective phase, decomposing instead into a chemically heterogeneous, mechanically fragile scale.

3.3.1.4. Thermal shock testing using a plasma torch

A custom thermal-shock setup was developed using a plasma torch as the heat source followed by direct water quenching. The plasma torch operated in open atmosphere with argon as both plasma and shielding gas, using a current of 300 A at a stand-off distance of 60 mm. Each specimen was exposed to the plasma for 3 minutes, reaching a target surface temperature of approximately 1200 °C, after which it was immediately quenched in water maintained at 25 °C, which can be approximated to a cooling rate in the range of 300-400 °C/s. This cycle was reproduced 0, 1, 2 and 4 times.

The tests were performed on HEA-01 (PMD) discs with a diameter of 20 mm, thickness of 2 mm, and a P320 surface finish. The primary outcomes assessed were the visual appearance of the surfaces after testing, including changes in coloration, surface degradation, and any formation of cracks, as well as microstructural features.

Visual inspection revealed no signs of cracks or other structural failures even after 4 times quenching. The samples exhibited mild oxidation, with the oxide layer appearing dark gray rather than the typical brownish hue as shown in previous chapters. Additionally, traces of unreacted particles (Ta and Mo) became even more evident on the surface.

A more detailed examination of the longitudinal section of the sample quenched 4 times confirms the initial observation: the material did not develop cracks under thermal shock (Figure 19). Microstructurally, the material resembles the as-printed state (compare it to Figure 7), with intermetallic phases distributed throughout the matrix. Overall, these observations indicate that the material exhibits good resistance to rapid thermal cycling.

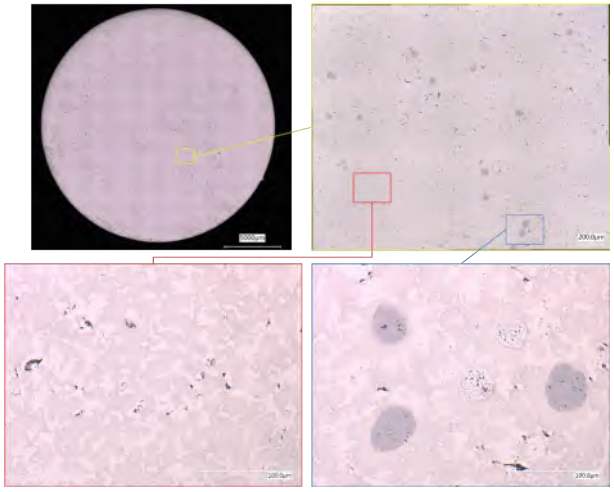


Figure 19: Microstructure of HEA-01 after 4 cycles of thermal shock from 1200 °C to 25 °C

3.3.2.AlCrFeNiTi (HEA-03) for wear applications

3.3.2.1. Tensile testing at Room Temperature

Testing of HP HEA-03 was performed with an identical test setup and sample geometries as described ion Chapter 3.3.1.1.

While tensile testing was indeed attempted on the these specimens, their extreme brittleness made the procedure largely unfeasible. In all nine trials, the samples fractured at the grips rather than within the gauge section, either partially during the clamping procedure (leading to artificially low failure loads) or entirely, preventing the test from being carried out at all.

This behavior is illustrated in Figure 20, where fracture surfaces were exclusively located in the clamping region instead of the intended gauge length. As a consequence, the measurements obtained cannot be considered representative of the intrinsic mechanical performance of the alloy.

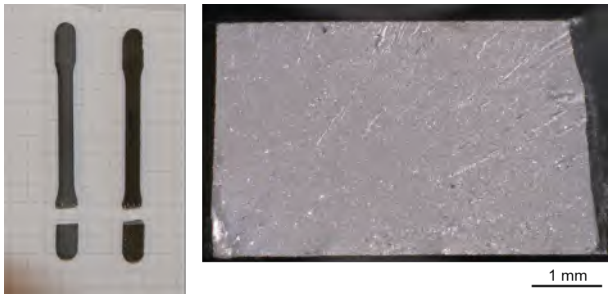


Figure 20: Right: representative samples of HP HEA-03 after tensile test at room temperature; Left: typical fracture surface

Among the few tests that did not fail catastrophically before loading, the maximum failure stress did not exceed 234 MPa, with the viable specimens exhibiting an average strength of 169 ± 39 MPa. The corresponding strain was essentially negligible in all cases, further confirming the highly brittle nature of the material. Taken together, these results demonstrate that conventional tensile testing is not suitable for this alloy in its current processed state, and that alternative mechanical-testing strategies or modified specimen geometries would be required to obtain meaningful tensile properties.

3.3.2.2. Pin-on-disc tests

The pin-on-disk tests were carried out in vacuum at RT. The normal load was applied using dead weights, and the resulting friction force was continuously measured. The friction coefficient, calculated as μ = FR/FN, was recorded as a function of the sliding distance, and the steady-state value was determined for each test. A track radius of 12 mm and a sliding speed of 0.1 m/s were used, with an intended total sliding distance of 1000 m, corresponding to approximately 13 300 revolutions. The counter body consisted of Al_2O_3 spheres with a radius of 3 mm, while the disk specimens were HEA-03 discs (30 mm in diameter and 2 mm thick), polished to P800 prior to testing. Three normal loads (5 N, 10 N, and 15 N) were applied to evaluate the load-dependent behavior of the material. After completion of each test, the wear track on the disk was analyzed using profilometry to assess the wear extent and characteristics.

Figure 21 shows a representative sample for each preset normal load, along with the evolution of the friction coefficient throughout the test. Only samples tested at a preset normal load of 5 N were viable, with the others exhibiting premature disc failure at very low revolution counts. On the fully tested samples at 5 N load, the friction coefficient μ was measured at 0.745.

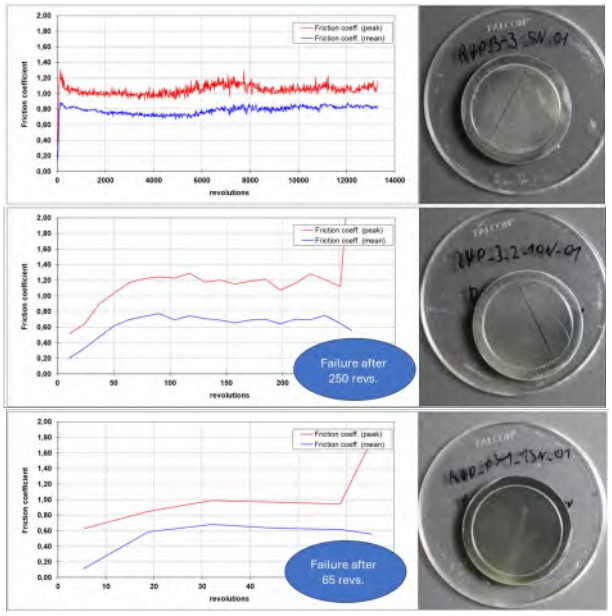


Figure 21: Evolution of friction coefficient in function of the number of revolutions during pin-on-disc tests at 5 N (top), 10 N (mid) and 15 N (bottom). Representative samples for each of these experiments are also presented

Moreover, Figure 22 shows a representative track profile from one of the 5 N samples, extracted from three different locations. The average track depth was 6.96 µm, and the average width was 0.58 mm.

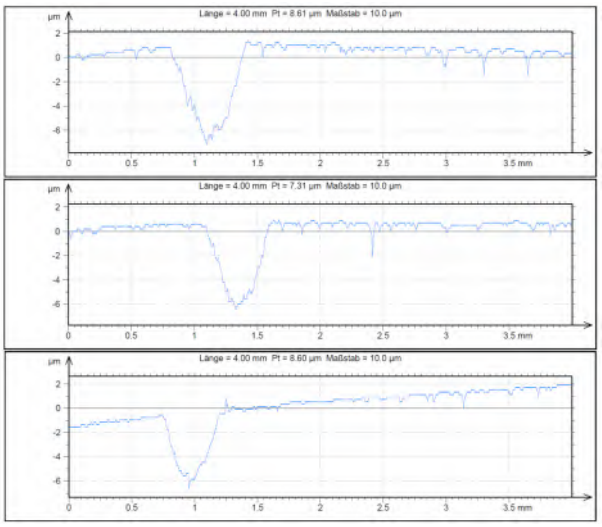


Figure 22: Representative profiles depicting worn track width and depth on a HEA-03 disc after pin-on-disc test, using an normal force of 5 N

The observed scar width (Figure 23) reflects a larger effective contact due to material transfer on the ball, along with some sideways movement of material during sliding, rather than just plastic deformation at the center of the contact. These observations indicate adhesive wear as the main mechanism, possibly in combination with mild abrasive wear during the running-in phase.

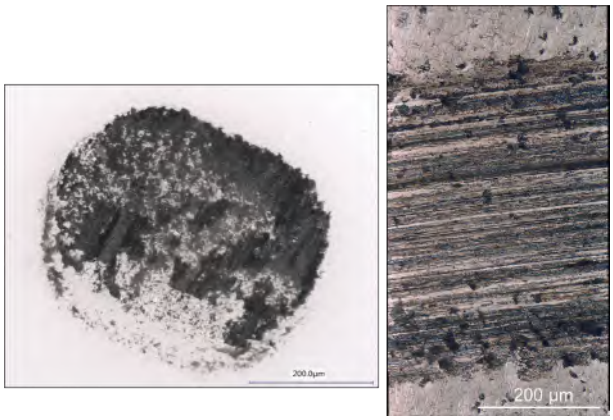


Figure 23: OM images of Al_2O_3 sphere (left) and HEA-03 disc at the track region (right) after 13300 revolutions of pin-on-disc test using a normal force of 5 N

For the only load level at which testing was feasible (5 N), the measured wear rate was in the order of 10^{-5} mm³/N·m. On its own, this indicates a satisfactory wear performance. However, this positive aspect is overshadowed by the pronounced brittleness of this alloy, as discussed earlier.
Consequently, HEA-03 has very limited potential as a bulk or load-bearing component in tribological applications, with its practical use being difficult to be justified in structural form. At most, the alloy might find relevance as a surface coating, where its high hardness and moderate wear resistance could protect more ductile and compatible substrates such as aluminum or steel, provided the coating process and adhesion can be managed effectively.

4. CONCLUSION

This study assessed three high-entropy alloy compositions ($CrMo_{0.5}NbTa_{0.5}TiZr$, AlCrMoNbTi and AlCrNiFeTi) processed by hot pressing and additive manufacturing (Plasma Metal Deposition), with the aim of identifying viable material–process combinations for high-temperature and wear-related space applications. Across both routes, manufacturability proved to be the main limiting factor. Hot pressing of mechanically alloyed powders enabled the production of dense and relatively homogeneous samples, although the resulting materials remained highly brittle due to the persistence of intermetallic phases. In PMD, HEA-01 was the only composition that could be processed successfully, while HEA-02 and HEA-03 were limited by cracking and poor printability.
Among the investigated materials, PMD-processed HEA-01 emerged as the most promising candidate for high-temperature applications, combining moderate tensile strength at room temperature with satisfactory compressive performance up to 1000 °C, together with moderate oxidation resistance and good thermal shock resistance. However, its extremely limited ductility remains a major drawback, restricting its use in most load-bearing applications.
HEA-03, processed by HP, showed high hardness

and moderate wear resistance, but its extreme brittleness severely restricted its use as a bulk structural material.
Overall, the results highlight that, for the selected HEAs, processability and microstructural stability are more critical than nominal composition alone, and that future development should focus on reducing intermetallic formation and improving alloy homogenization.

Acknowledgement
The activities hereby reported were carried out under a program funded by the European Space Agency (ESA). The views expressed in the present publication can in no way be taken to reflect the official opinion of the European Space Agency.

5. REFERENCES

1. Committee, A.H. *Properties and Selection: Nonferrous Alloys and Special-Purpose Materials*; ASM International, 1990; ISBN 978-1-62708-162-7.
2. Committee, A.H. *Properties and Selection: Irons, Steels, and High-Performance Alloys*; ASM International, 1990; ISBN 978-1-62708-161-0.
3. Veselkov, S.; Samoilova, O.; Shaburova, N.; Trofimov, E. High-Temperature Oxidation of High-Entropic Alloys: A Review. *Materials* **2021**, *14*, 2595, doi:10.3390/ma14102595.
4. Lim, H.P.; Liew Yun Hsien, Ir.Dr.W.; Melvin, G.J.H.; Jiang, Z. A Short Review on the Phase Structures, Oxidation Kinetics, and Mechanical Properties of Complex Ti-Al Alloys. *Materials* **2021**, *14*, 1677, doi:10.3390/ma14071677.
5. Xu, C.; Gao, W. Pilling-Bedworth Ratio for Oxidation of Alloys. *Mat Res Innovat* **2000**, *3*, 231–235, doi:10.1007/s100190050008.
6. Szoszkiewicz, R.; Rogala, M.; Dąbrowski, P. Surface-Bound and Volatile Mo Oxides Produced During Oxidation of Single MoS2 Crystals in Air and High Relative Humidity. *Materials (Basel)* **2020**, *13*, 3067, doi:10.3390/ma13143067.
7. Qin, L.; Pei, Y.; Li, S.; Zhao, X.; Gong, S.; Xu, H. Role of Volatilization of Molybdenum Oxides during the Cyclic Oxidation of High-Mo Containing Ni-Based Single Crystal Superalloys. *Corrosion Science* **2017**, *129*, 192–204, doi:10.1016/j.corsci.2017.08.025.
8. Birks, N.; Meier, G.; Pettit, F. Introduction to the High Temperature Oxidation of Metals, Second Edition. *Introduction to the High Temperature Oxidation of Metals, Second Edition* **2006**, 1–338, doi:10.1017/CBO9781139163903.

POLYIMIDE-BASED NANOCOMPOSITE COATINGS FOR QUARTZ COMPONENTS IN DEPLOYABLE SPACE ANTENNA STRUCTURES

Lorenzo Ferri [(1)], MariaGabriella Santonicola [(1)], Marco Lapi [(2)], Daniele Finocchi [(2)], Danilo Zola [(3)]

[(1)] Department of Chemical Engineering, Materials and Environment, Sapienza University of Rome, Via del Castro Laurenziano 7, 00161 Rome, Italy, Email: lorenzo.ferri@uniroma1.it, mariagabriella.santonicola@uniroma1.it

[(2)] Thales Alenia Space, Via Saccomuro 24, 00131 Rome, Italy, Email: marco.lapi@thalesaleniaspace.com, daniele.finocchi@thalesaleniaspace.com

[(3)] ENEA Centro Ricerche Casaccia, Via Anguillarese 301, 00123 Rome, Italy, Email: danilo.zola@enea.it

KEYWORDS

polyimide; nanocomposite coatings; few-layer graphene; few-layer hexagonal boron nitride; spin coating; quartz; space antennas

ABSTRACT

Large deployable reflector antennas require lightweight materials capable of withstanding ionizing radiation, repeated thermal cycling and mechanical loading without compromising radio-frequency performance. This work investigates commercial P84 polyimide supplied as a 25 wt% solution in N-methyl-2-pyrrolidone (NMP) and reinforced with few-layer graphene, few-layer hexagonal boron nitride and hybrid fillers up to 5 wt%. All formulations were deposited by spin coating on planar quartz substrates representative of antenna support-network components; selected films were subsequently detached to obtain free-standing specimens for tensile testing. The experimental study was contextualized using a previously developed SPENVIS/MULASSIS radiation-transport assessment for P84-based systems. Thermal, mechanical and surface characterization evaluated solvent removal, thermal stability, tensile behaviour, wettability, coating thickness and roughness. Filler incorporation generally increased stiffness while affecting surface morphology and strain at break. Pull-off tests before and after repeated thermal cycling assessed coating adhesion and interfacial stability on quartz substrates.

1. INTRODUCTION

Large deployable reflector (LDR) antennas rely on lightweight structural networks that can be compacted during launch and deployed in orbit while preserving the required geometrical accuracy [1, 2]. Within these architectures, quartz-based components may be employed as tensioning dielectric supports (net) located above the reflective mesh [3]. Materials used in these regions must combine low areal mass, dimensional stability and radio-frequency compatibility with resistance to ionizing radiation, vacuum, thermal cycling and mechanical loading [4]. Thin surface coatings are attractive because they can introduce protective and functional properties without substantially changing the geometry or mass of the underlying component. Aromatic polyimides are widely considered for demanding aerospace applications because their rigid molecular structure provides high thermal stability, mechanical integrity, dielectric performance and resistance to the harsh space environment [5-7]. Among commercially available systems, P84 is a soluble polyimide that can be processed from solution into micrometric films and coatings [8]. This processing flexibility is particularly relevant for quartz components with complex or slender geometries, where conventional bulk materials would introduce an unacceptable mass or dimensional penalty. The present experimental campaign was deliberately restricted to the commercial P84 system to establish a reproducible reference process. Transfer of P84 processing to green solvents such as dimethyl isosorbide (DMI) is being pursued as a subsequent development activity and is not included in the dataset reported here.

The functional response of the P84 matrix can be tailored through the incorporation of two-dimensional fillers. Few-layer graphene (FLG) is of interest for mechanical reinforcement and electrostatic-charge dissipation [9], whereas few-layer hexagonal boron nitride (FLh-BN) combines high intrinsic thermal conductivity with electrical insulation and dielectric stability [10]. Hybrid FLG/FLh-BN formulations may therefore provide a means of tuning electrical and thermal transport by combining the electrically conductive contribution of graphene with the electrically insulating behaviour of boron nitride [11]. More generally, the response of two-dimensional-filler/polymer nanocomposites depends strongly on filler loading, dispersion state, platelet organization and polymer–filler interfacial interactions. These parameters govern the resulting composite morphology and mechanical response and may promote filler agglomeration and defect formation at increasing loading [12]. In this study, P84-based films containing FLG, FLh-BN and hybrid fillers are investigated by combining numerical radiation screening with experimental thermal, spectroscopic, mechanical, surface and adhesion characterizations. The numerical analysis evaluates the total ionizing dose (TID) deposited behind idealized P84-based shields in

representative low Earth orbit (LEO), geostationary orbit (GEO) and Martian-orbit environments. Experimentally, the influence of filler type and loading on film formation, tensile response, wettability, coating thickness and roughness is examined. Thermogravimetric analysis is restricted to neat P84 and is used to assess the selected thermal-treatment cycle. Pull-off adhesion is compared before and after thermal cycling, while dedicated electromagnetic measurements remain necessary before any qualification claim can be made.

2. MATERIALS AND METHODS

2.1 Materials

A commercial P84 polyimide solution containing 25 wt% polymer in N-methyl-2-pyrrolidone (NMP) was supplied by Evonik Fibers GmbH and used as received. Few-layer graphene (FLG) and few-layer hexagonal boron nitride (FLh-BN), purchased from BeDimensional S.p.A., were used as nanofillers.

2.2 Film preparation

The P84 solution was used as received, without solvent exchange or further dilution. FLG and FLh-BN were incorporated individually at 1, 3 and 5 wt% relative to the polymer mass, while hybrid formulations were prepared at the same total filler loadings using an FLG:FLh-BN mass ratio of 1:1. The neat and nanofiller-containing formulations were subjected to magnetic stirring prior to deposition. Before coating deposition, the quartz substrates were subjected to ultraviolet-C (UVC) irradiation for substrate cleaning. All formulations were then deposited onto planar quartz substrates by spin-coating. The deposited coatings were subjected to a staged thermal treatment from 80 °C to 250 °C for 6 h. Selected films were then detached from the quartz substrates to obtain free-standing specimens, while the remaining coatings were retained on quartz for surface and adhesion characterizations.

2.3 Space-radiation simulations

A previously developed radiation-transport assessment was used to contextualize the experimental study [13]. The simulations considered representative low Earth orbit (LEO), geostationary orbit (GEO) and Martian-orbit environments. The LEO scenario corresponded to a 7-year mission at an altitude of 600 km and an orbital inclination of 97°, while the GEO scenario corresponded to a 15-year mission at 36,000 km and 0° inclination. The Martian scenario considered a 3-year mission in a 300 km orbit. Trapped-proton and trapped-electron spectra in the terrestrial orbits were described using the AP-8 and AE-8 models, respectively, whereas solar-proton fluences were estimated using ESP-PSYCHIC. Only the solar-proton contribution was considered for the Martian orbit. Particle transport and total ionizing dose behind idealized P84 and P84/filler shielding configurations were evaluated using the Multilayered Shielding Simulation Software Tool (MULASSIS), version 1.26, implemented within the Space Environment Information System (SPENVIS) and based on Geant4 [14, 15].

2.4 Thermal and spectroscopic characterization

Thermogravimetric analysis (TGA) was conducted exclusively on the neat P84 film after the staged thermal treatment using a Mettler Toledo TGA/DSC 3+ (Greifensee, Switzerland) [16]. Samples weighing 5–10 mg were heated from 25 to 800 °C at a constant heating rate of 10 °C/min under a nitrogen flow of 50 mL/min. The initial mass-loss region was examined to quantify residual volatile species and assess the effectiveness of the drying and thermal-treatment cycle, whereas the main degradation event was characterized from the onset temperature and the derivative thermogravimetric (DTGA) peak. The chemical structures of the neat and nanocomposite films were investigated using a Nicolet Summit Fourier-transform infrared (FTIR) spectrometer (Thermo Fisher Scientific, Waltham, MA, USA) in attenuated total reflectance (ATR) mode. Each spectrum was acquired by co-adding 64 scans at a spectral resolution of 4 cm^{-1} over the wavenumber range 4000-400 cm^{-1}. Spectral acquisition and analysis were performed using the OMNIC software (Thermo Fisher Scientific).

2.5 Tensile testing

Tensile tests were performed at room temperature using a Mark-10 F505-EM electromechanical test frame equipped with EasyMESUR software and an FS05-5 force sensor with a 25 N capacity and 0.01 N resolution (Mark-10 Corporation, Copiague, NY, USA). Rectangular free-standing specimens measuring 30 × 5 mm were tested at a crosshead speed of 10 mm/min using an initial grip separation of 13.5 mm and a minimum of three valid specimens per formulation. A small preload was applied only to remove slack before acquisition. Stress was calculated as the measured force divided by the initial cross-sectional area, determined from the specimen width and mean film thickness, while strain was calculated from the crosshead displacement relative to the initial grip separation. Ultimate tensile strength was taken as the maximum stress and elongation at break as the strain at failure. Owing to the restricted dimensions of the available films, the procedure was a miniaturized configuration adapted from ASTM D882 [17] and supported by tensile testing reported for free-standing polyimide films [18], rather than a fully standard-compliant ASTM D882 test.

2.6 Profilometry and wettability

Coating thickness and line-profile roughness were measured using a KLA Tencor P-17 contact stylus profilometer (KLA Corporation, Milpitas, CA, USA). Two-dimensional profiles were acquired with a diamond stylus having a 2.0 µm tip radius and an applied force of 0.50 mg. The scan length was 2000 µm, the scan speed was 20 µm/s and the sampling rate was 50 Hz, providing 5001 data points with an interval of approximately 0.400 µm; the 65 µm

vertical range was selected. For thickness measurements, the stylus crossed the step between an exposed quartz region and the adjacent coated surface and ten independent profiles were acquired for each sample. Coating thickness was calculated from the difference between the mean heights of the levelled substrate and coating plateaus. Surface roughness was evaluated from one 2000 µm line scan acquired entirely within the coated region, from which the arithmetic mean roughness (Ra) and root-mean-square roughness (Rq) were calculated. Surface wettability was evaluated using an OCA 15Pro optical analyser (DataPhysics Instruments, Filderstadt, Germany) by the static sessile-drop method. Droplets of 3 µL were deposited using ultrapure water (Milli-Q, 18.2 MΩcm) and diiodomethane as the probe liquids. Ten droplets were analysed at different positions on each film. Contact angles were determined by drop-shape analysis using the DataPhysics SCA 20 software module and the total surface free energy (SFE), together with its dispersive (γ^d) and polar (γ^p) components, was calculated according to the Owens–Wendt method [19].

2.7 Thermal cycling and pull-off adhesion

Adhesion to quartz was evaluated for coatings in the as-prepared condition and after 20 thermal cycles between −180 and +180 °C. Pull-off testing was performed using a PosiTest AT-M adhesion tester, following the general procedure described in ASTM D4541 [20]. Circular dollies with a diameter of 20 mm were bonded directly to the coated surface using Loctite 4471 adhesive and allowed to cure for 24 h under ambient conditions. Before testing, the coating was circumferentially scored around the dolly perimeter down to the quartz substrate to isolate the test area. During testing, the tensile load was applied perpendicular to the coated surface until detachment occurred. The instrument was configured according to the 20 mm dolly diameter and directly reported the pull-off strength. Owing to the limited availability of quartz substrates, only one specimen was tested for each formulation and condition. Following detachment, the dolly and substrate surfaces were visually examined to classify the failure mode as adhesive failure at the coating–quartz interface, cohesive failure within the coating or adhesive layer or mixed failure. Thermal cycling was conducted between −180 and +180 °C at a heating and cooling rate of 2 °C/min. The complete sequence of 20 cycles lasted approximately 120 h.

3. RESULTS AND DISCUSSION

3.1 P84-based nanocomposite coatings

All formulations yielded macroscopically continuous coatings after spin coating and thermal treatment, with no visible cracks or delamination. Representative coatings deposited on quartz substrates are shown in Fig. 1. Neat P84 exhibited the characteristic amber colour of the polyimide matrix, whereas the incorporation of FLG produced a pronounced darkening of the coating. The FLh-BN-containing coating retained a yellow–amber appearance, while the hybrid formulation exhibited an intermediate greyish-amber colour. These differences are primarily associated with the distinct optical characteristics of the nanofillers.

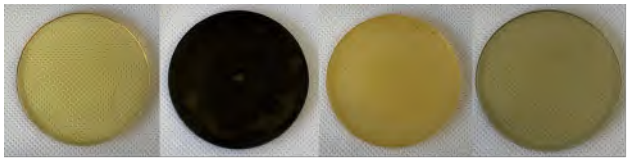


Figure 1: Representative neat and nanocomposite P84 coatings deposited on quartz substrates.

3.2 Total ionizing dose

The simulated total ionizing dose (TID) values for neat P84 and the 70:30 P84/filler configurations are summarized in Tab. 1 for representative LEO, GEO and Martian-orbit missions. The calculated dose was on the order of 10^5 rad in LEO, 10^7 rad in GEO and 10^4 rad in Mars orbit. The substantially higher GEO values reflect the longer mission duration and the trapped-electron environment, whereas only the solar-proton contribution was considered for Mars orbit.

Table 1: Simulated total ionizing dose for neat P84 and 70:30 P84/filler shielding models at an areal density of 0.003 g/cm^2.

Environment	Material	Total TID (rad)
LEO	P84	2.175×10^5
LEO	P84/FLG	2.160×10^5
LEO	P84/FLh-BN	2.173×10^5
GEO	P84	6.672×10^7
GEO	P84/FLG	6.652×10^7
GEO	P84/FLh-BN	6.670×10^7
Martian orbit	P84	1.452×10^4
Martian orbit	P84/FLG	1.454×10^4
Martian orbit	P84/FLh-BN	1.454×10^4

Only minor differences were observed among the investigated compositions. At constant areal density, the incorporation of FLG or FLh-BN changed the total TID by less than 1% relative to neat P84. The calculated dose levels remain below or within the broad radiation-tolerance interval of approximately 10^6–10^8 rad reported for polyimide materials in long-term CERN studies [21]. This comparison supports the selection of P84 as a candidate matrix for further investigation. The simulations therefore do not indicate a substantial ionizing-radiation shielding advantage from either filler; their incorporation is primarily motivated by the electrical, thermal, dielectric and mechanical functions introduced into the P84 matrix. Experimental irradiation remains necessary to

assess the retention of coating properties after exposure.

3.3 Thermal stability assessment and chemical structure

The thermogravimetric (TGA) and derivative thermogravimetric (DTGA) profiles of the neat P84/NMP film after the staged thermal treatment are shown in Fig. 2. A limited mass loss of approximately 0.98 wt% was detected prior to the main degradation stage and was assigned to the release of absorbed moisture and residual volatile species. The onset of the principal thermal-decomposition process occurred at approximately 505 °C, whereas the DTGA curve exhibited a maximum degradation rate at about 593 °C. The low mass loss observed below the degradation region indicates that the adopted drying and thermal-treatment protocol was effective in removing most of the volatile fraction. Since the analysis was performed only on neat P84, these results provide a reference for the thermal stability of the processed matrix and cannot be used to determine the effect of nanofiller incorporation on the degradation behaviour.

The FTIR spectra of neat P84 and the nanocomposite films exhibited the characteristic absorption bands of the aromatic polyimide matrix. The bands observed at approximately 1777 and 1717 cm^{-1} were assigned to the asymmetric and symmetric stretching vibrations of the imide C=O groups, respectively. The absorption near 1362 cm^{-1} was attributed to C–N stretching within the imide ring, whereas the band at approximately 721 cm^{-1} was associated with imide-ring deformation involving the C=O groups [22]. Aromatic C=C stretching was detected near 1508 cm^{-1}, while the band at approximately 2920 cm^{-1} was assigned to aliphatic C–H stretching [23]. The characteristic absorption bands of P84 were retained in all the investigated nanocomposite formulations, including FLG-, FLh-BN- and hybrid-filled films with filler loadings up to 5 wt%. No appreciable band shifts or additional absorption features were observed, indicating that filler incorporation did not produce detectable modifications of the polyimide chemical structure within the investigated concentration range. For graphical clarity, Fig. 2 reports only the spectra of neat P84 and the representative nanocomposite formulations containing 1 wt% filler. No distinct absorption bands attributable to residual NMP were detected within the sensitivity of the measurement. This observation is consistent with the limited volatile fraction determined by TGA, although trace amounts of solvent below the FTIR detection limit cannot be excluded.

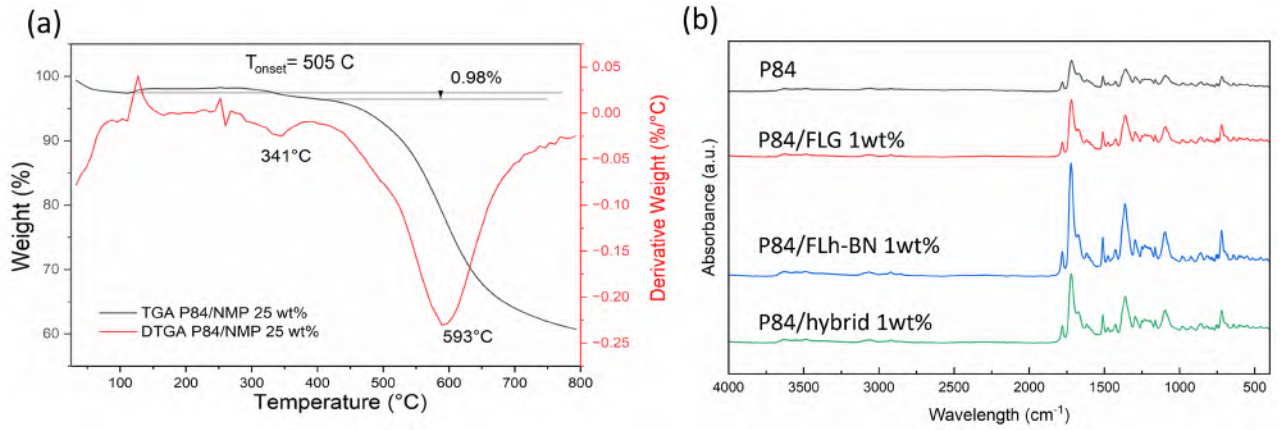


Figure 2: (a) TGA/DTGA profiles of neat P84 film after the staged thermal-treatment cycle and (b) FTIR spectra of neat P84 and 1 wt% nanocomposite films.

3.4 Tensile behaviour

The tensile properties of the free-standing films are summarized in Tab. 2 and Fig. 3. Neat P84 exhibited a Young's modulus of 1310 ± 200 MPa, an ultimate strength of 121.2 ± 3.2 MPa, and an elongation at break of 21.0 ± 3.2%. The introduction of the fillers generally increased stiffness but reduced deformation at failure, indicating that the nanofillers constrain polymer-chain mobility while simultaneously increasing sensitivity to defects and local stress concentrations [24]. The highest modulus values were obtained for P84/FLG 3 wt% and P84/hybrid 1 wt%, which reached 1988 ± 83 and 2000 ± 280 MPa, respectively. These values correspond to increases of approximately 52% and 53% relative to the neat film. The mechanical response was not monotonic with FLG concentration. Increasing the FLG content from 1 to 3 wt% produced a marked increase in modulus, whereas a further increase to 5 wt% reduced the modulus to 1374 ± 52 MPa. Ultimate strength simultaneously decreased from 100.9 ± 4.7 MPa at 3 wt% to 59.2 ± 5.9 MPa at 5 wt%, while elongation remained close to 9%, with values of 9.3 ± 1.5% and 9.0 ± 1.7%, respectively. This combination of reduced stiffness, strength and ductility suggests a reduced reinforcement efficiency at the highest FLG loading, potentially associated with agglomeration, local porosity or weaker polymer–filler interfaces. The roughness measured for the same formulation supports this interpretation, although microscopy is

required to identify the governing defect morphology. The FLh-BN series showed a more gradual stiffening response. The Young's modulus increased to 1750 ± 210 MPa at 3 wt% and remained comparable at 5 wt%, while strength decreased from 119.4 ± 6.6 MPa at 1 wt% to 108 ± 15 MPa at 5 wt%. The hybrid formulations combined relatively high stiffness with better strength retention than the 5 wt% FLG film. In particular, the hybrid films containing 1 and 3 wt% filler exhibited moduli of 2000 ± 280 and 1863 ± 30 MPa together with strengths of 100 ± 13 and 111.0 ± 11.9 MPa. These results identify low-to-intermediate filler contents as the most balanced formulations. More generally, they show that nominal filler loading alone does not determine performance; nanofiller dispersion, orientation and interfacial stress transfer control whether the increase in stiffness is obtained without a disproportionate loss of strength and ductility.

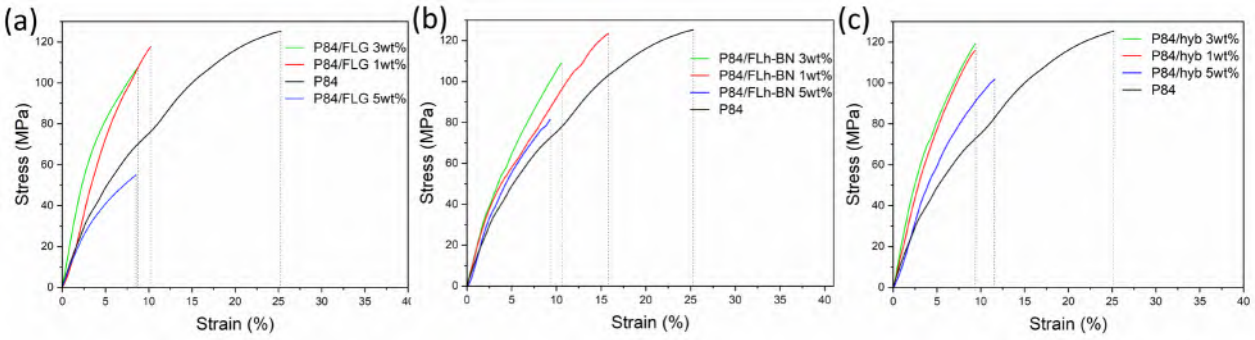


Figure 3: Representative stress–strain curves of neat P84 and nanocomposite films containing (a) FLG, (b) FLh-BN, and (c) hybrid FLG/FLh-BN fillers at different loadings.

Table 2: Tensile properties of P84-based nanocomposite films.

Material	Young's modulus (MPa)	Ultimate strength (MPa)	Elongation at break (%)
P84	1310 ± 200	121.2 ± 3.2	21.0 ± 3.2
P84/FLG 1 wt%	1380 ± 310	106.8 ± 8.1	12.9 ± 0.5
P84/FLG 3 wt%	1988 ± 83	100.9 ± 4.7	9.3 ± 1.5
P84/FLG 5 wt%	1374 ± 52	59.2 ± 5.9	9.0 ± 1.7
P84/FLh-BN 1 wt%	1508 ± 88	119.4 ± 6.6	18.6 ± 1.3
P84/FLh-BN 3 wt%	1750 ± 210	98.1 ± 8.3	11.2 ± 1.4
P84/FLh-BN 5 wt%	1720 ± 360	108 ± 15	16.6 ± 0.9
P84/hybrid 1 wt%	2000 ± 280	100 ± 13	8.3 ± 1.9
P84/hybrid 3 wt%	1863 ± 30	111.0 ± 11.9	12.1 ± 1.7
P84/hybrid 5 wt%	1810 ± 100	107.8 ± 5.3	12.4 ± 1.8

3.5 Thickness, roughness and dimensional comparison with RF wavelengths

Representative step-height and surface profiles used for thickness and roughness evaluation are shown in Fig. 4. The coating thicknesses measured from the step profiles are reported in Tab. 3. All formulations deposited using the same spin cycle produced mean values between 13.7 and 15.84 µm, indicating that the process maintained a relatively narrow thickness range despite variations in filler chemistry and loading. A tendency toward increasing thickness with filler loading was observed for several formulations at 3 and 5 wt%. In spin coating, the final thickness depends on factors including solids content, solution rheology and solvent evaporation. The observed increase may therefore result from reduced radial expulsion of the more concentrated suspensions during the spin-coating step. Neat P84 exhibited the smoothest surface, with Ra ≈ 1.6 nm and Rq ≈ 2.0 nm. Filler addition increased roughness in all series, although the magnitude and loading dependence varied markedly with filler type. FLG produced the clearest concentration-dependent change: Rq increased from 46.2 nm at 1 wt% to 149 nm at 3 wt% and 330 nm at 5 wt%. By contrast, the FLh-BN coatings remained within a narrower Rq range of 53.8–62.2 nm. The hybrid systems exhibited Rq values of 77.9 at 1 wt%, 157 nm at 3 wt% and 141 nm at 5 wt% showing a non-monotonic dependence on filler loading. At 1 and 3 wt%, their Rq values were slightly higher than those of the corresponding single-filler coatings, whereas at 5 wt% the hybrid coating exhibited an intermediate roughness between the FLh-BN and FLG systems. The lower roughness of the FLh-BN series may reflect a more favourable dispersion or platelet arrangement under the selected processing conditions, while the non-monotonic behaviour of the hybrid coatings suggests a combined influence of the two fillers on local organization and film levelling.

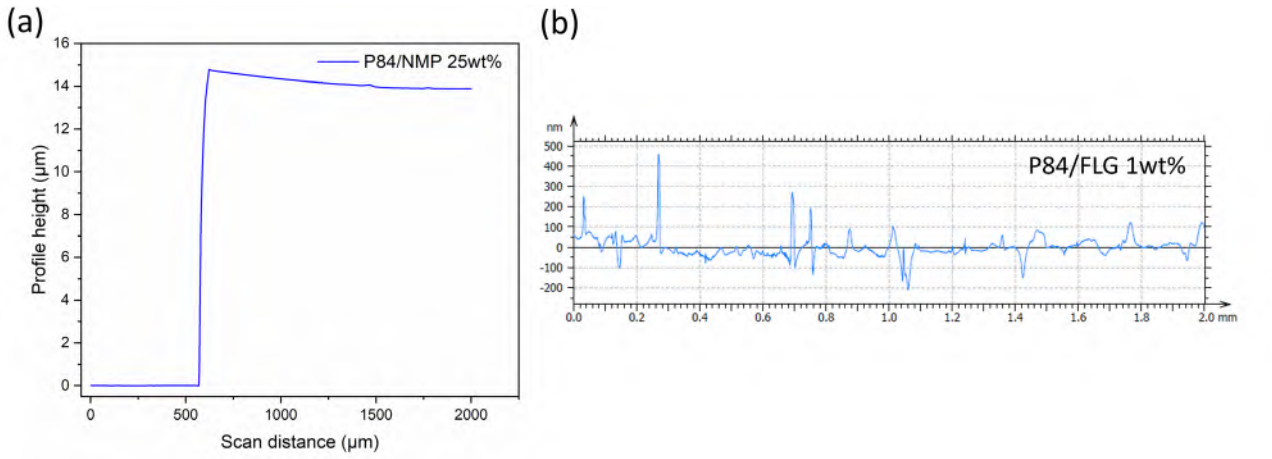


Figure 4: Representative profilometry profiles used for coating characterization: (a) step-height profile of neat P84 for thickness determination; (b) surface profile of the P84/FLG 1 wt% coating for roughness evaluation.

Table 3: Coating thickness and line-profile roughness parameters.

Material	Thickness (µm)	Ra (nm)	Rq (nm)
P84	13.967 ± 0.025	1.6	2.0
P84/FLG 1 wt%	13.93 ± 0.53	26.4	46.2
P84/FLG 3 wt%	14.87 ± 0.45	108.0	149.0
P84/FLG 5 wt%	15.64 ± 0.73	224.0	330.0
P84/FLh-BN 1 wt%	13.7 ± 0.70	37.2	53.8
P84/FLh-BN 3 wt%	15.31 ± 0.26	33.3	60.6
P84/FLh-BN 5 wt%	15.84 ± 0.26	41.6	62.2
P84/hybrid 1 wt%	14.77 ± 0.53	45.0	77.9
P84/hybrid 3 wt%	14.85 ± 0.48	81.7	157.0
P84/hybrid 5 wt%	15.45 ± 0.16	92.9	141.0

The coated quartz components considered in this study are not part of the LDR antenna reflective surface (mesh) but are located within the supporting antenna structure (net). As a preliminary dimensional assessment, the measured coating thickness and surface roughness were compared with the free-space wavelength at 40 GHz, corresponding to approximately 7.50 mm. The maximum measured coating thickness of 15.84 µm corresponds to approximately 2.11×10^{-3} λ, while the maximum Rq value of 330 nm corresponds to approximately 4.40×10^{-5} λ. Thus, even the highest measured roughness amplitude is more than four orders of magnitude smaller than the free-space wavelength at 40 GHz. From a purely geometrical perspective, this large dimensional separation suggests that roughness-induced scattering is expected to be negligible [25]. However, this comparison does not demonstrate the radio frequency (RF) compatibility of the coated components, which also depends on complex permittivity, dielectric losses, electrical conductivity, component geometry, polarization and position within the antenna structure. Direct electromagnetic measurements on coated quartz specimens are therefore required to assess their actual influence on antenna performance.

3.6 Surface wettability and surface free energy

Water contact angle (WCA) and surface free energy (SFE) results are summarized in Tab. 4. Neat P84 showed a WCA of 84.3 ± 2.0°, corresponding to moderate wettability. The FLG series exhibited the strongest compositional effect: the angle increased to 89.8 ± 2.0° at 1 wt% and 98.5 ± 1.9° at 3 wt%, indicating a progressively less wettable surface over this interval. The result for P84/FLG 5 wt% was not available at the time of preparation.

By contrast, the FLh-BN and hybrid coatings remained within a relatively narrow WCA interval of 83.1–86.3°, with no monotonic dependence on loading. Total SFE varied only from 33.8 to 37.2 mJ/m^2 and was dominated by the dispersive component. The polar component decreased markedly in P84/FLG 3 wt% to 0.5 ± 0.3 mJ/m^2, consistent with its higher WCA. The surface free energy of the P84-based films, ranging from 33.8 to 37.2 mJ/m², was lower than values reported for clean silica-based surfaces [26]. This surface-energy relationship is consistent with favourable interfacial contact between the polymeric phase and

the higher-energy quartz substrate and with the formation of continuous coatings.

Table 4: Water contact angle, total surface free energy and dispersive and polar components of the P84-based nanocomposite films.

Material	WCA (°)	SFE (mJ/m²)	γ^d (mJ/m²)	γ^p (mJ/m²)
P84	84.3 ± 2.0	35.3 ± 1.8	31.3 ± 2.2	4.0 ± 0.8
P84/FLG 1 wt%	89.8 ± 2.0	33.8 ± 2.2	31.8 ± 2.5	2.1 ± 0.4
P84/FLG 3 wt%	98.5 ± 1.9	34.7 ± 1.3	34.2 ± 1.5	0.5 ± 0.3
P84/FLG 5 wt%	—	—	—	—
P84/FLh-BN 1 wt%	85.5 ± 2.5	36.2 ± 1.1	33.2 ± 1.4	3.0 ± 0.8
P84/FLh-BN 3 wt%	86.3 ± 2.5	37.2 ± 1.5	33.9 ± 1.3	3.3 ± 0.9
P84/FLh-BN 5 wt%	83.8 ± 0.9	35.4 ± 1.8	30.9 ± 2.4	4.5 ± 0.7
P84/hybrid 1 wt%	83.1 ± 2.4	35.6 ± 1.4	31.0 ± 2.1	4.5 ± 1.1
P84/hybrid 3 wt%	83.4 ± 2.5	34.5 ± 0.6	29.8 ± 1.2	4.7 ± 1.0
P84/hybrid 5 wt%	85.2 ± 1.9	34.6 ± 2.0	30.8 ± 2.1	3.9 ± 0.4

3.7 Pull-off adhesion before and after thermal cycling

Pull-off strength values measured for the P84-based coatings before and after thermal cycling are reported in Tab. 5. A representative pull-off test performed on the P84/FLh-BN 1 wt% coating after 20 thermal cycles is shown in Fig. 5, including the specimen configuration before testing and the complementary dolly and quartz surfaces after detachment. In the as-prepared condition, the measured values ranged from 0.83 MPa for neat P84 to 3.15 MPa for P84/hybrid 1 wt%. Filler incorporation did not produce a monotonic variation in pull-off strength, suggesting that the measured response was influenced by both nanofiller type and loading. After 20 thermal cycles between −180 and +180 °C, the measured pull-off strengths ranged from 0.67 to 1.42 MPa. Within the single-filler series, the 1 wt% formulations showed values equal to or higher than those measured in the as-prepared condition: P84/FLG 1 wt% increased from 0.93 to 1.42 MPa, whereas P84/FLh-BN 1 wt% changed only slightly from 1.28 to 1.35 MPa. By contrast, the corresponding 3 wt% formulations decreased from 1.48 to 0.67 MPa for P84/FLG and from 1.84 to 1.06 MPa for P84/FLh-BN. P84/hybrid 1 wt% exhibited the highest as-prepared value but decreased from 3.15 to 1.33 MPa after thermal cycling, whereas P84/hybrid 3 wt% decreased from 0.88 to 0.77 MPa. These preliminary observations suggest a possible loading-dependent response within the single-filler formulations, with the 1 wt% coatings showing less pronounced changes in measured pull-off strength than the corresponding 3 wt% coatings. At higher filler loadings, increased stiffness, surface heterogeneity, agglomeration or local defects could promote stress concentration near the coating–quartz interface. However, pull-off measurements may also be affected by local specimen variability, adhesive-layer geometry, dolly alignment and scoring quality. Since only one valid measurement was available for each formulation and condition, the observed differences cannot be considered statistically significant and should be interpreted as preliminary trends. Macroscopic examination of the complementary fracture surfaces was consistent with complete adhesive failure at the coating–quartz interface for neat P84, P84/FLG 1 wt% and P84/hybrid 1 wt% in the as-prepared condition, as well as for all coatings tested after thermal cycling. The as-prepared P84/FLG 3 wt%, P84/FLh-BN 1 wt%, P84/FLh-BN 3 wt% and P84/hybrid 3 wt% specimens exhibited predominantly adhesive failure at the coating–quartz interface, with detachment occurring over most of the tested area; localized substrate failure was additionally observed for the P84/hybrid 3 wt% specimen. Minor localized deviations from complete interfacial detachment were observed in some specimens; therefore, these cases were conservatively classified as predominantly adhesive rather than fully adhesive. For comparison, pull-off strengths of 1.87–3.03 MPa have been reported in the literature for thin polyimide coatings tested according to ASTM D4541 [27]. Some of the as-prepared P84-based coatings investigated in the present work exhibited pull-off strengths within the same order of magnitude.

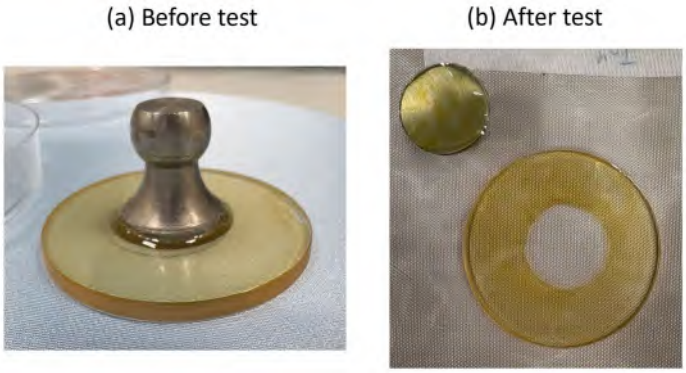


Figure 5: Representative pull-off test on the P84/FLh-BN 1 wt% coating after 20 thermal cycles: (a) dolly bonded to the coated quartz substrate before testing and (b) complementary dolly and quartz surfaces after detachment.

Table 5: Pull-off adhesion strength and failure mode before and after 20 thermal cycles.

Material	Adhesion strength 0 cycles (MPa)	Adhesion strength 20 cycles (MPa)	Failure mode 0 cycles	Failure mode 20 cycles
P84	0.83	1.02	Adhesive	Adhesive
P84/FLG 1 wt%	0.93	1.42	Adhesive	Adhesive
P84/FLG 3 wt%	1.48	0.67	Predominantly adhesive	Adhesive
P84/FLh-BN 1 wt%	1.28	1.35	Predominantly adhesive	Adhesive
P84/FLh-BN 3 wt%	1.84	1.06	Predominantly adhesive	Adhesive
P84/hybrid 1 wt%	3.15	1.33	Adhesive	Adhesive
P84/hybrid 3 wt%	0.88	0.77	Predominantly adhesive / local substrate failure	Adhesive

4. CONCLUSIONS

This work investigated P84-based nanocomposite coatings containing FLG, FLh-BN and hybrid FLG/FLh-BN fillers using numerical and experimental characterization. Spin coating followed by staged thermal treatment produced visually continuous coatings with thicknesses of approximately 13.7–15.8 µm. Filler incorporation generally increased stiffness and surface roughness, with the strongest roughness increase observed in coatings with high FLG loading. TGA of neat P84 indicated effective removal of most volatile species and a degradation onset near 505 °C. The simulated TID values provided a preliminary radiation-environment context but did not constitute material qualification. Preliminary pull-off measurements showed a formulation-dependent response to thermal cycling, with failure occurring predominantly at the coating–quartz interface. The maximum measured roughness remained several orders of magnitude below K/Ka-band wavelengths, although direct electromagnetic testing is still required. Future work will include additional adhesion replicates, microscopic fracture-surface analysis, and P84 processing in DMI as a lower-impact alternative to NMP.

5. ACKNOWLEDGEMENTS

L.F. is supported by a PNRR PhD scholarship (MUR. D.M. 630/2024) co-funded by Sapienza University of Rome and Thales Alenia Space Italia.

6. REFERENCES

1. Chahat, N., Hodges, R.E., Sauder, J., Thomson, M., Peral, E. & Rahmat-Samii, Y. (2016). CubeSat deployable Ka-band mesh reflector antenna development for earth science missions. *IEEE Transactions on Antennas and Propagation*. 64(6), 2083-2093.
2. Lee, T.-H., Ruddock, R. & Bailey, M.C. (1989). A surface distortion analysis applied to the hoop/column deployable mesh reflector antenna. *IEEE transactions on antennas and propagation*. 37(4), 452-458.
3. Ueda, M., Nunokawa, M. & Goto, K. (2018). Cyclic Tensile Loading Test for a Quartz Fiber Cable of a Deployable Antenna Reflector on Satellite. *Experimental Techniques*. 42(4), 421-428.
4. Hołyńska, M., Tighe, A. & Semprimoschnig, C. (2018). Coatings and thin films for spacecraft thermo-optical and related functional applications. *Advanced Materials Interfaces*. 5(11), 1701644.
5. Wu, Z., He, J., Yang, H. & Yang, S. (2022). Progress in aromatic polyimide films for electronic applications: Preparation, structure and properties.

Polymers. 14(6), 1269.
6. Barra, G., Guadagno, L., Raimondo, M., Santonicola, M.G., Toto, E. & Vecchio Ciprioti, S. (2023). A comprehensive review on the thermal stability assessment of polymers and composites for aeronautics and space applications. *Polymers*. 15(18), 3786.
7. Blondelli, F., Campanella, M., Toto, E., Laurenzi, S. & Santonicola, M.G. (2025). Electrically Conductive Polyimide/Graphene Nanocomposites for Advanced Space Applications. *Macromolecular Symposia*. 414(6), e70242.
8. *Polyimide P84® – High-performance coatings. Technical brochure. Schörfling am Attersee: Evonik Fibres GmbH.*
9. Sultana, S.N., Helal, E., Gutiérrez, G., David, E., Moghimian, N. & Demarquette, N.R. (2024). The influence of a commercial few-layer graphene on electrical conductivity, mechanical reinforcement and photodegradation resistance of polyolefin blends. *Crystals*. 14(8), 687.
10. Rasul, M.G., Kiziltas, A., Arfaei, B. & Shahbazian-Yassar, R. (2021). 2D boron nitride nanosheets for polymer composite materials. *npj 2D Materials and Applications*. 5(1), 56.
11. Lewis, J.S., Barani, Z., Magana, A.S., Kargar, F. & Balandin, A.A. (2019). Thermal and electrical conductivity control in hybrid composites with graphene and boron nitride fillers. *Materials Research Express*. 6(8), 085325.
12. Potts, J.R., Dreyer, D.R., Bielawski, C.W. & Ruoff, R.S. (2011). Graphene-based polymer nanocomposites. *Polymer*. 52(1), 5-25.
13. Ferri, L., Toto, E., Santonicola, M., Finocchi, D. & Lapi, M., *Modeling space environment effects on novel nanocomposite materials for satellites using ESA's SPENVIS*, in *PROCEEDINGS BOOK-EUCASS 2025*. 2025. p. 5286-5296.
14. Martinez, L.M. & Kingston, J. (2012). Space radiation analysis: Radiation effects and particle interaction outside the earth's magnetosphere using GRAS and GEANT4. *Acta Astronautica*. 72, 156-164.
15. Yoon, S., Shin, Y., Jeon, J., Seo, Y., Jeon, J., Woo, J. & Seon, J. (2014). Analysis of the charged particle radiation effect for a CubeSat transiting from Earth to Mars. *Current Applied Physics*. 14(4), 575-581.
16. Toto, E., Tortorici, D., Garofolo, R., Laurenzi, S. & Santonicola, M.G. (2026). Advancing Sustainable Composites: Processing and Properties of Bio-Based Epoxy Resin Reinforced With Flax Fibers. *Polymer Composites*. 47(13), 11640-11654.
17. ASTM International, "ASTM D882-18 (2018), Standard Test Method for Tensile Properties of Thin Plastic Sheeting, *Annual Book of ASTM Standards*, 08.01, Plastics (1), 1–12.
18. Zhang, H., Fujiki, K., Ido, K., Kusayanagi, N., Sakagami, D., Li, J. & Okamura, Y. (2020). Tensile testing of freestanding polymer thin films with non-standard geometries. *Polymer Testing*. 91, 106825.
19. Ciarleglio, G., Pagani, L., Toto, E., Laurenzi, S. & Santonicola, M.G. (2025). Electrospun PLA/nano-hydroxyapatite fiber coatings for improved corrosion protection of titanium implants. *Surfaces and Interfaces*. 107848.
20. ASTM International, ASTM D4541-22 (2022), Standard Test Method for Pull-Off Strength of Coatings Using Portable Adhesion Testers, Annual Book of ASTM Standards, 06.02, Paint—Products and Applications; Protective Coatings; Pipeline Coatings, 1–18.
21. Tavlet, M. (2003). Effects of ageing of electrical insulators after exposure for 11 years in the large electron–positron collider at CERN. *Nuclear Instruments and Methods in Physics Research Section B: Beam Interactions with Materials and Atoms*. 208, 476-479.
22. Qiao, X., Chung, T.-S. & Pramoda, K. (2005). Fabrication and characterization of BTDA-TDI/MDI (P84) co-polyimide membranes for the pervaporation dehydration of isopropanol. *Journal of Membrane Science*. 264(1-2), 176-189.
23. Fazlifard, S., Allahgholi, N., Mohammadi, T. & Bakhtiari, O. (2017). P84/ZIF-8 mixed matrix membranes for pervaporation dehydration of isopropanol. *Desalination and Water Treatment*. 77, 282-290.
24. Qian, Y., Wu, H., Yuan, D., Li, X., Yu, W. & Wang, C. (2015). In situ polymerization of polyimide-based nanocomposites via covalent incorporation of functionalized graphene nanosheets for enhancing mechanical, thermal, and electrical properties. *Journal of Applied Polymer Science*. 132(44).
25. Ruze, J. (1966). Antenna tolerance theory—A review. *Proceedings of the IEEE*. 54(4), 633-640.
26. Zgura, I., Moldovan, R., Negrila, C., Frunza, S., Cotorobai, V. & Frunza, L. (2013). Surface free energy of smooth and dehydroxylated fused quartz from contact angle measurements using some particular organics as probe liquids. *J. Optoelectron. Adv. Mater*. 15(7-8), 627-634.
27. Badaik, S., Nayak, S., Ambade, B. & Rout, T.K. (2026). High-performance polyimide coatings for mild steel: the impact of benzophenone, biphenyl, and bisphenol-a core structures. *RSC advances*. 16(4), 3244-3260.

NANOWELD® REINFORCED CFRP LAMINATES FOR SPACE APPLICATIONS: MECHANICAL PERFORMANCE AND DIFFUSION BARRIER EFFECTS WITH IMPLICATIONS FOR CRYOGENIC HELIUM PERMEABILITY

Savvas Assiotis [(1)], Andreas Stavrou [(1)], Carlos Basilio Mangas Calvo [(2)], Ruben Torres Narbona [(2)], Vassilios Drakonakis [(1)], Bernard Decotignie [(3)]

[(1)] AmaDema – Advanced Materials Design & Manufacturing Ltd, Agiou Demetriou 92, 1027 Nicosia, Cyprus, Email: s.assiotis@amdmcomposites.com
[(2)] Airbus Defence and Space SAU, [street, postcode, city], Spain, Email: carlos.mangas@airbus.com
[(3)] European Space Agency, ESTEC, Keplerlaan 1, 2201 AZ Noordwijk, The Netherlands, Email: bernard.decotignie@esa.int

ABSTRACT

Nanofibrous interleaving is a candidate route to improving the interlaminar and barrier performance of carbon fibre reinforced polymer (CFRP) structures for launcher applications. This paper reports the Testing Phase 1 (lamina level) campaign of the ESA FLPP-funded NanoLauncher activity, in which electrospun polyacrylonitrile (PAN)/carbon-nanotube veils were interleaved into HexTow® IM7/8552 laminates, via NanoWeld and compared with a baseline laminate on a B-basis design-allowable basis. The longitudinal tensile modulus allowable increases by 12.6 % as manufactured and by 20.7 % after thermal-vacuum conditioning; the transverse tensile allowables increase by 38.8 % in stiffness and 114.2 % in strength; the in-plane shear modulus allowable increases by 26.3 %; and the pre-cracked Mode II toughness allowable increases by 31.6 % and 47.1 % respectively. A systematic reduction in specimen-to-specimen scatter is identified as a principal contributor. Moisture content falls by 21.3 % with approximately 25 % slower desorption kinetics, while direct helium permeation testing shows no statistically significant change in intrinsic permeability.

KEYWORDS

CFRP; nanofibrous interlayers; electrospinning; design allowables; interlaminar toughness; moisture diffusion; helium permeability; thermal-vacuum cycling; launcher structures.

1. INTRODUCTION

1.1. Composite structures in launch vehicles

Carbon fibre reinforced polymer (CFRP) laminates are established in launcher primary structure because of their specific stiffness, specific strength and dimensional stability. Their attraction is strongest where mass is traded directly against payload: interstage and fairing structures, thrust frames, strut and truss members, and, increasingly, linerless cryogenic propellant tankage. The last of these is the most demanding, because the laminate must act simultaneously as a structural member and as a permeation barrier against liquid hydrogen, liquid oxygen or pressurant helium [1, 2].

The governing difficulty is not the intrinsic transport behaviour of the cured matrix. Diffusion of small gas molecules through a well-consolidated, void-free epoxy laminate is slow enough that the as-manufactured leak rate is generally acceptable. The difficulty is that the laminate does not stay in that condition. Two damage mechanisms dominate. The first is thermal: contraction mismatch between fibre and matrix, and between adjacent plies of differing orientation, generates residual stresses on cool-down to cryogenic temperature that are sufficient to initiate transverse matrix microcracks [3, 4]. The second is mechanical: low-velocity impact, whether from ground handling, debris during ascent, or micrometeoroid and orbital debris in service, produces matrix cracking and delamination that is frequently barely visible on the surface yet extends through a significant fraction of the thickness.

Both mechanisms converge on the same outcome. Once cracks in adjacent plies of different orientation intersect, a percolating network of leak paths is established and the measured permeability rises by orders of magnitude relative to the pristine state [5, 6]. Permeability of a cryotank laminate is therefore a damage-state property far more than it is a material constant, and any technology that raises the threshold for crack initiation and delamination growth acts directly on the quantity of interest.

1.2. Nanofibrous interleaving

Because the mechanism is crack-driven, the natural mitigation is to raise the resistance of the interlaminar region to crack initiation and growth. Toughened matrices and thermoplastic interleaves are the conventional routes; both are effective but both add resin-rich thickness, and therefore mass, and can depress compression-dominated properties.

Electrospun nanofibrous veils offer an alternative at a far lower areal weight penalty. A veil of sub-micron polymer fibres deposited between prepreg plies occupies the resin-rich interlaminar region, is impregnated during cure, and can act through several mechanisms in parallel: crack deflection at the nanofibre-matrix interfaces, nanofibre bridging behind the crack tip, and local matrix toughening

where the veil polymer is partially soluble in the matrix. Carbon nanotube additives raise interfacial shear strength and interlaminar properties when introduced either as a matrix dispersion or as a reinforcement at the ply interface [7, 8, 9, 10]. The same geometry that makes an interleaved veil effective against delamination is also, in principle, favourable against through-thickness transport: a dense, randomly oriented fibrous mat lying normal to the diffusion direction increases the tortuosity of the diffusion path.

1.3. The NanoLauncher activity

The NanoLauncher project is an ESA Future Launchers Preparatory Programme activity carried out by AmaDema (Cyprus) in collaboration with Airbus Defence and Space (Spain), addressing the insertion of the NanoWeld® nanofibrous interlayer technology into aerospace-grade CFRP for launcher structural application. NanoWeld® is an additive-doped, polymer-based electrospun veil interleaved between prepreg plies to form a fractal nanofibrous network within the interlayer, bridging consecutive laminae and generating additional load-transfer mechanisms between the fibrous reinforcement, the polymer matrix and the nano-scale additives.

This paper reports the Testing Phase 1 experimental evidence. Results are presented on a design-allowable basis throughout, because the quantity that governs whether a technology can be inserted into a qualified structure is not the batch mean but the value that survives statistical reduction. Two questions are addressed: whether interleaving imposes a structural penalty on the properties that size a compression-critical launcher component, and whether the barrier effect observed in moisture transport translates into a measurable reduction in helium permeability.

2. MATERIALS & EXPERIMENTAL METHODS

2.1. The NanoWeld® nanofibrous membrane

The interlayer is an electrospun polyacrylonitrile (PAN) nanofibrous membrane reinforced with multi-wall carbon nanotubes (MWCNT), produced by AmaDema on a dedicated electrospinning line. PAN was selected over polyvinylidene fluoride because it decomposes at approximately 300 °C and therefore retains its fibrous morphology through the 180 °C cure of the IM7/8552 system, whereas PVDF melts at 140–150 °C.

Two process parameters were optimised: areal weight and MWCNT loading. Dynamic mechanical analysis of PAN membranes at 2, 4 and 6 g/m² identified 2 g/m² as giving the highest storage modulus, and a tensile screening across MWCNT loadings from 0.25 to 2.0 wt% identified 0.5 wt% as the optimum: it gives the highest membrane stiffness of the series while retaining high toughness, the combination required to resist crack propagation without embrittling the interlayer. Properties of the selected formulation are given in Tab. 1, and the membrane morphology in Fig. 1.

Table 1: NanoWeld® membrane, selected formulation (7 wt% PAN, 0.5 wt% MWCNT).

Property	Value
Areal weight [g/m²]	2.57 ± 0.32
Mean fibre diameter [nm]	210 ± 23
Tensile strength [MPa]	24.56 ± 2.35
Young's modulus [MPa]	1826 ± 277
Toughness [MJ/m³]	2.14 ± 0.35
Air permeability [m³/min·m²]	1.49 ± 0.05

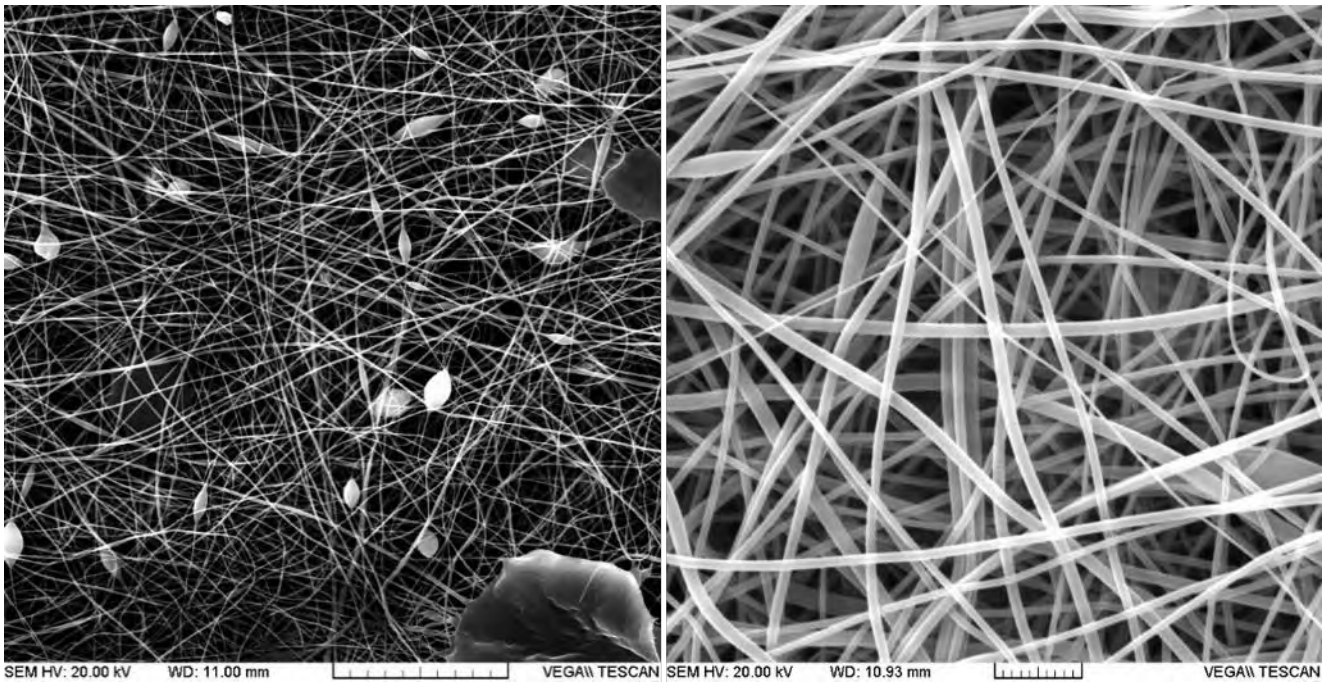


Figure 1: Scanning electron micrographs of the selected NanoWeld® membrane (7 wt% PAN, 0.5 wt% MWCNT). Scale bars 50 µm (left) and 1 µm (right).

2.2. Prepreg enhancement and panel manufacture

The baseline material is HexTow® IM7/8552 unidirectional (UD) prepreg at 268 g/m², an intermediate-modulus carbon fibre in a toughened epoxy matrix, selected because it is used for European launcher structure and because published property data exist against which the control laminate can be verified. Enhancement of an off-the-shelf prepreg was preferred to development of a new prepreg system so that the technology remains a drop-in modification.

The membrane is transferred onto the dry side of the prepreg by thermocompression on a roll-to-roll line, in which the assembly passes through an oven and then a pair of consolidation rollers. A two-level factorial study of temperature (90 and 105 °C), dwell (60 and 120 s) and roller force established 105 °C for 120 s as the consolidation window at which the nanofibres are completely wetted by the resin without degrading the membrane. The enhanced prepreg is subsequently handled, cut and laid up by conventional means and cured to the standard 180 °C autoclave cycle of the baseline system; no change to lay-up sequence, cure cycle or tooling is required. The resulting interleaving architecture is shown in Fig. 2.

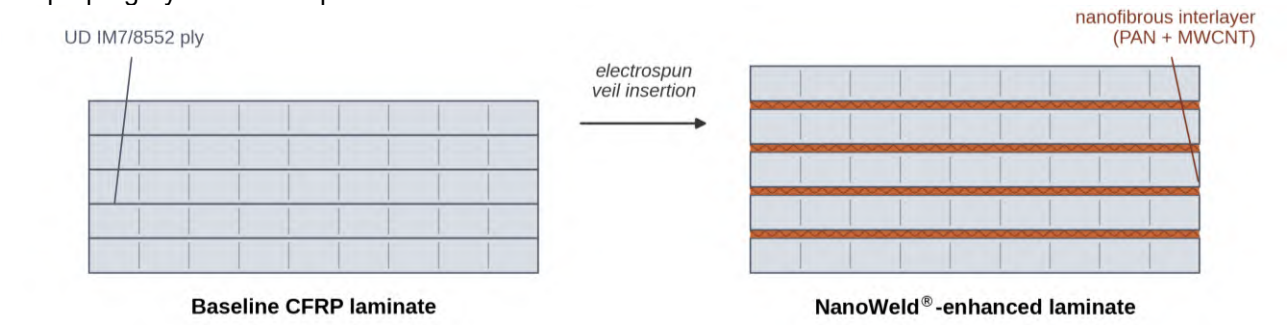


Figure 2: Interleaving architecture. The electrospun veil occupies the resin-rich interlaminar region between consecutive unidirectional plies.

2.3. Panels and quality control

Three material conditions were characterised. The Control condition (CF panels) is the unmodified IM7/8552 laminate; the NanoWeld® condition (NW panels) is the same laminate with the veil interleaved at every ply interface; and the NanoWeld®-TVAC condition is a NanoWeld® panel subjected to thermal-vacuum conditioning before mechanical testing. Eight-ply panels were manufactured for in-plane and short-beam testing and twelve-ply panels for fracture testing.

All eight panels were inspected ultrasonically by the reflector-plate technique to AITM 6-0011, and all returned 100% of the inspected area within the 0–6 dB attenuation band with no indication exceeding the 6×6 mm acceptance threshold. Cured ply thickness and fibre volume fraction derived from panel thickness and prepreg areal weight are given in Tab. 2; constituent analysis of the Control panel to ASTM D3171 returned a void content of 0.55 ± 0.30 % v/v. The interleaved panels are therefore of equivalent consolidation quality to the baseline, and at equal ply count they are no thicker, the 2 g/m² veil represents less than 1 % of the prepreg areal weight, so fibre volume fraction is not measurably diluted.

Table 2: Panel geometry and fibre volume fraction.

Panel	Plies	CPT [mm]	FVF [%]
CF001A (Control)	8	0.263	59.7
CF001B (Control)	8	0.266	59.2
NW003A	8	0.258	60.9
NW003B	8	0.261	60.3
NW006TVAC	8	0.261	60.3
CF002 (Control)	12	0.302	52.0
NW004	12	0.304	51.8
NW005TVAC	12	0.302	52.1

2.4. Test matrix

The mechanical and thermo-physical programme is summarised in Tab. 3. In-plane and short-beam testing was performed at Applus+ Laboratories, fracture and V-notch shear testing at Applus+ RESCOLL, thermal expansion at DatapointLabs and helium permeation at Aerospace and Advanced Composites GmbH.

Table 3: Experimental programme and applicable standards.

Test	Standard	Conditions
Tension, 0°/90°	ASTM D3039	CF, NW, NW-TVAC
Compression, 0°/90° (CLC)	ASTM D6641	CF, NW
Short-beam strength	ASTM D2344	CF, NW
V-notch shear, 0°/90°	ASTM D5379	CF, NW, NW-TVAC
Mode I toughness	ASTM D5528	CF, NW, NW-TVAC
Mode II toughness	ASTM D7905	CF, NW, NW-TVAC
Constituent content	ASTM D3171	CF
Thermal expansion	ASTM E831	CF, NW
Moisture, drying phase	ASTM D5229	CF, NW

Test	Standard	Conditions
Helium permeability	ASTM E493 / E498	CF, NW
Ultrasonic inspection	AITM 6-0011	all panels

2.5. Thermal-vacuum conditioning

Thermal-vacuum conditioning was applied to panels NW005TVAC and NW006TVAC prior to mechanical testing, in order to establish whether the interlayer survives the space environment without loss of the properties measured in the as-manufactured state. Conditioned panels were subsequently tested to the same standards and with the same specimen geometries as the unconditioned material, so that the comparison is direct. [Conditioning profile — temperature range, dwell, number of cycles and chamber pressure — to be inserted from the conditioning report.]

2.6. Moisture and helium permeation

Moisture behaviour was evaluated to ASTM D5229 in the drying configuration: six Control and six NanoWeld® coupons, conditioned at the same ambient state, were dried at 65 °C and weighed weekly over 2 540 h until the mass change between two successive readings fell below the stabilisation criterion of the standard. The total mass lost is the moisture held by the as-received laminate, and the shape of the curve gives the desorption kinetics.

Helium permeation was measured on four pristine coupons per condition. Each coupon was clamped between two flanges sealed with indium wire, both sides evacuated for one hour, and the feed side then pressurised to 9.5 bar with helium 4.6 while a mass-spectrometer leak detector recorded the downstream leak rate continuously for approximately 48 h at room temperature. A steel reference plate established a background of 1×10^{-10} mbar·l/s. Permeability K, diffusivity D and solubility S were obtained by least-squares fitting of the transient flux solution of Fick's second law to the recorded history, the three quantities being related by the solution-diffusion expression of Eq. 1:

$$K = D \cdot S \tag{1}$$

The decomposition of Eq. 1 is central to the interpretation of Section 4.3, because the interlayer is expected to act on D and on S in opposite senses.

2.7. Statistical basis of the comparison

Comparisons in this paper are made on B-basis design allowables rather than on batch means. A B-basis value is the property that at least 90 % of the material population is expected to equal or exceed, at 95 % confidence; it is the form in which material data enter structural substantiation for components whose failure is not single-point critical, and it is required by ECSS-E-ST-32-10C. Comparing allowables rather than means accounts for batch, processing and specimen variability, exposes process sensitivity, and answers the question a designer actually asks.

For a normally distributed population the allowable follows from the sample mean and standard deviation and a one-sided tolerance factor which depends only on sample size, Eq. 2:

$$B = \bar{x} - k^{b} \cdot s \tag{2}$$

with k^{b} = 3.708 for n = 6, 4.203 for n = 5 and 7.656 for n = 3, following CMH-17. An equal number of specimens is used for all three conditions within any one property, so that no comparison is biased by the tolerance factor itself; where a condition yielded more valid specimens than the others, the population was truncated to the common size. All allowables reported here were recomputed independently from the batch statistics as a verification step and reproduce the reduced values to within 0.1 %.

3. DESIGN ALLOWABLES

The complete reduced property set is given in Tab. 4 and the changes relative to Control in Fig. 3.

3.1. In-plane properties

The longitudinal tensile modulus allowable rises from 131.1 GPa to 147.6 GPa with interleaving, an increase of 12.6 %, and to 158.2 GPa after thermal-vacuum conditioning, an increase of 20.7 %. The underlying batch means are 156.6 ± 6.9, 166.0 ± 5.0 and 168.8 ± 2.8 GPa; a Welch test on the means gives p = 0.025 for the as-manufactured comparison and p = 0.006 for the conditioned one, so the stiffness increase is statistically supported and is not an artefact of the reduction. Longitudinal tensile strength is essentially unchanged, the allowable rising 3.5 %.

The transverse allowables show the largest gains of the campaign: 38.8 % in modulus and 114.2 % in strength. Both are matrix- and interface-dominated properties, which is where an interlaminar modification would be expected to act, and both are influenced by the scatter reduction discussed in Section 3.3.

Compressive properties move in the opposite direction. The longitudinal compressive modulus allowable falls 7.5 % and the corresponding strength 12.0 %, with the transverse values falling 8.0 % and 9.2 %. On batch means the compressive changes are much smaller, 139.6 to 137.5 GPa in modulus, a reduction of 1.5 %, and 1412 to 1372 MPa in strength, a reduction of 2.8 %, so the larger allowable reductions reflect increased scatter in the interleaved compression populations rather than a loss of mean capability. Compression is the one test group in which the interleaved material is the more variable of the two, and it is the group to address in process optimisation.

In-plane shear behaves like the tensile case: the 0° shear modulus allowable rises 26.3 % as manufactured and 38.5 % after conditioning, against batch means that are effectively constant at 8.94, 8.97 and 9.07 GPa. Shear strength allowables

fall by 11.3 % in the 0° orientation while rising 17.9 % in the 90° orientation after conditioning.

3.2. Interlaminar properties

Short-beam strength, the practical measure of interlaminar shear capability, improves by 2.7%. Under Mode II shear loading the pre-cracked toughness allowable, generally taken as the conservative and design-relevant measure, since it removes the influence of the artificial insert, rises from 465.9 J/m² to 612.9J/m², an increase of 31.6%, and to 685.4J/m² after thermal vacuum conditioning, an increase of 47.1%. On batch means the same comparisons give +10.6% and +29.9%, with p = 0.020 and p = 0.0005. This is the single most important interlaminar result for the target application, because delamination growth in a compression-loaded shell and crack propagation under thermal cycling are both shear-dominated.

The opening-mode response moves the other way: the Mode I allowables fall by 31.4 % non-pre-cracked and 38.9 % pre-cracked, and the non-pre-cracked Mode II allowable falls by 53.2 %. Two observations temper this. First, thermal-vacuum conditioning raises the as-manufactured Mode I mean by 17 % rather than degrading it, which is not the behaviour of an intrinsically weak interface. Second, the veil areal weight, nanofibre diameter and impregnation state were held at their first-iteration values throughout the campaign, and the opening-mode response of veil-toughened laminates is known to be strongly dependent on precisely these parameters. The deficit is therefore treated as a process-optimisation target: fractographic examination of the fracture surfaces and a parametric study of interlayer areal weight are the two actions defined to close it.

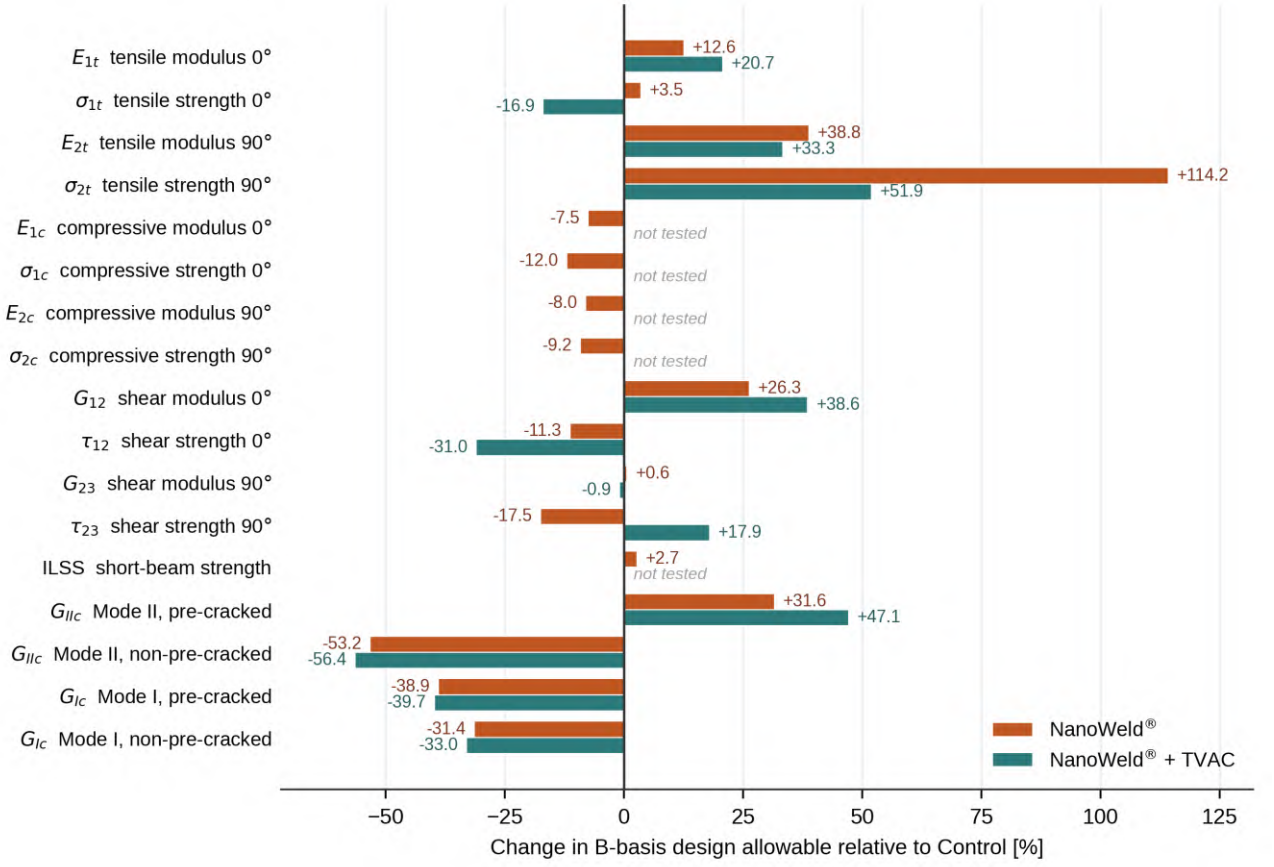


Figure 3: Change in B-basis design allowable relative to the Control laminate for the complete Testing Phase 1 property set.

3.3. The role of scatter

A design allowable is penalised by standard deviation, so a technology that makes a laminate more consistent raises the allowable even where the mean is unchanged. This is the dominant mechanism behind several of the gains in Fig. 3, and it is a real engineering benefit rather than a statistical artefact: reduced variability is exactly what permits a designer to work closer to the mean capability of the material.

Fig. 4 shows the coefficient of variation for each property. Interleaving reduces scatter in eight of the ten populations. The transverse tensile strength CoV falls from 15.0 % to 5.8 %, the transverse modulus CoV from 11.0 % to 5.9 %, the in-plane shear modulus CoV from 8.5 % to 3.8 %, and the pre-cracked Mode II CoV from 3.6 % to 1.8 %. Thermal-vacuum conditioning reduces scatter further in the stiffness-controlled properties, the longitudinal tensile modulus CoV reaching 1.7 %.

The exceptions are informative. Longitudinal compressive modulus becomes more variable, and

the conditioned longitudinal tensile strength CoV rises from 3.0 % to 9.0 %, which is why that one allowable falls by 16.9 % despite a mean 10.7 % above Control. Reducing the scatter of the conditioned material is as important to the design case as raising its mean.

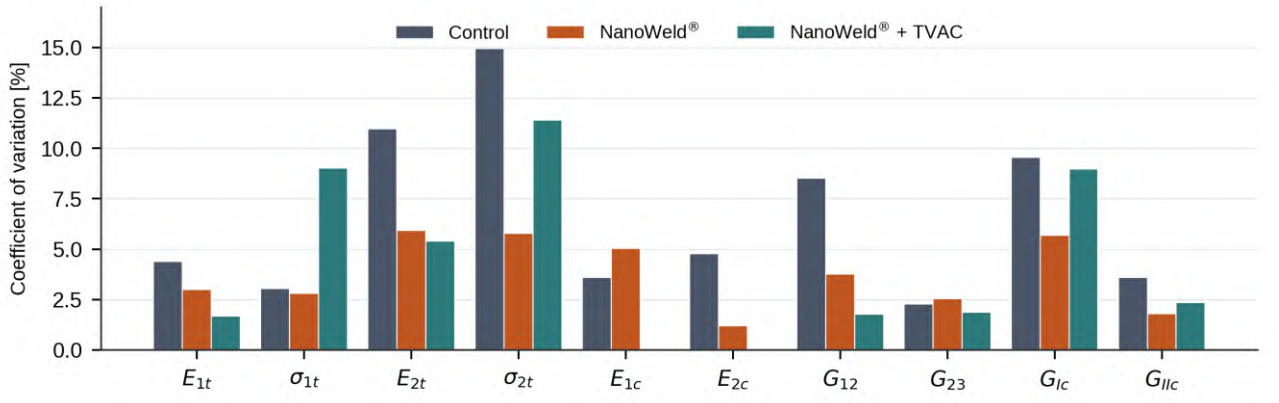


Figure 4: Coefficient of variation by property and material condition. Lower is better; scatter governs the design allowable.

3.4. Thermo-physical properties

Thermal expansion is of first-order importance for a cryogenic application, since the microcracking that drives permeability is itself generated by thermal mismatch. Over 23–120 °C the longitudinal coefficient is 0.27 ± 0.15 × 10^{-6}/°C for the Control and 1.03 ± 0.50 × 10^{-6}/°C for the NanoWeld® laminate, and the transverse coefficient is 32.2 ± 1.3 and 31.1 ± 0.7 × 10^{-6}/°C respectively. Both are equivalent within the uncertainty of the method, so the interlayer introduces no thermo-elastic penalty.

Table 4: Testing Phase 1 B-basis design allowables. Percentage columns are relative to Control. PC and NPC denote pre-cracked and non-pre-cracked.

Property	Symbol	Control	NanoWeld®	NW-TVAC	Δ NW [%]	Δ NW-TVAC [%]
Tensile modulus 0° [GPa]	E_{1t}	131.09	147.56	158.21	+12.6	+20.7
Tensile strength 0° [MPa]	σ_{1t}	1784.7	1847.6	1482.5	+3.5	−16.9
Tensile modulus 90° [GPa]	E_{2t}	8.38	11.64	11.18	+38.8	+33.4
Tensile strength 90° [MPa]	σ_{2t}	20.89	44.75	31.74	+114.2	+51.9
Compressive modulus 0° [GPa]	E_{1c}	120.90	111.85	–	−7.5	–
Compressive strength 0° [MPa]	σ_{1c}	1203.6	1058.7	–	−12.0	–
Compressive modulus 90° [GPa]	E_{2c}	9.33	8.58	–	−8.0	–
Compressive strength 90° [MPa]	σ_{2c}	225.46	204.78	–	−9.2	–
Shear modulus 0° [GPa]	G_{12}	6.11	7.72	8.47	+26.3	+38.5
Shear strength 0° [MPa]	τ_{12}	88.73	78.71	61.19	−11.3	−31.0
Shear modulus 90° [GPa]	G_{23}	7.15	7.19	7.08	+0.6	−0.9
Shear strength 90° [MPa]	τ_{23}	40.58	33.48	47.86	−17.5	+17.9
Short-beam strength [MPa] *	ILSS	112.51	115.54	–	+2.7	–
Mode II toughness, PC [J/m²]	G_{IIc}	465.9	612.9	685.4	+31.6	+47.1
Mode II toughness, NPC [J/m²]	G_{IIc}	1624.0	759.3	707.6	−53.2	−56.4
Mode I toughness, PC [J/m²]	G_{Ic}	202.59	123.75	122.13	−38.9	−39.7
Mode I toughness, NPC [J/m²]	G_{Ic}	243.99	167.34	163.48	−31.4	−33.0

*

4. ENVIRONMENTAL DURABILITY AND BARRIER BEHAVIOUR

4.1. Thermal-vacuum conditioning

Thermal-vacuum conditioning degraded none of the stiffness-controlled properties and improved most of them. The longitudinal and in-plane shear modulus allowables reached their highest values in the conditioned material, the pre-cracked Mode II allowable recorded the largest single improvement of the campaign at 47.1 %, and the Mode I mean recovered by 17 % relative to the unconditioned interleaved laminate. A plausible explanation is continued cure and interphase development between the veil polymer and the matrix during the thermal exposure; confirming this requires glass-transition and fractographic characterisation of the conditioned material.

The strength-controlled properties are more mixed, and the reason is scatter rather than mean capability, as set out in Section 3.3. The environmental robustness of the interlayer is therefore demonstrated at coupon level, with the qualification that the consistency of the conditioned material requires attention.

4.2. Moisture transport

Fig. 5 shows the drying curves. The NanoWeld® laminate had held 21.3 % less moisture than the Control at the end of the test, and the deficit

exceeds 25 % through the early part of the curve, peaking near 28 % at 650–1200 h. Both the equilibrium capacity and the transport rate are therefore reduced.

The mechanism is consistent with the geometry. A dense mat of randomly oriented sub-micron fibres lying in the plane of the laminate presents a high-tortuosity obstacle to transport normal to that plane, which is the direction of interest. The reduced capacity compounds the benefit, because absorbed water plasticises the matrix and expands its free volume, so a laminate that holds less water also retains a lower-diffusivity matrix state.

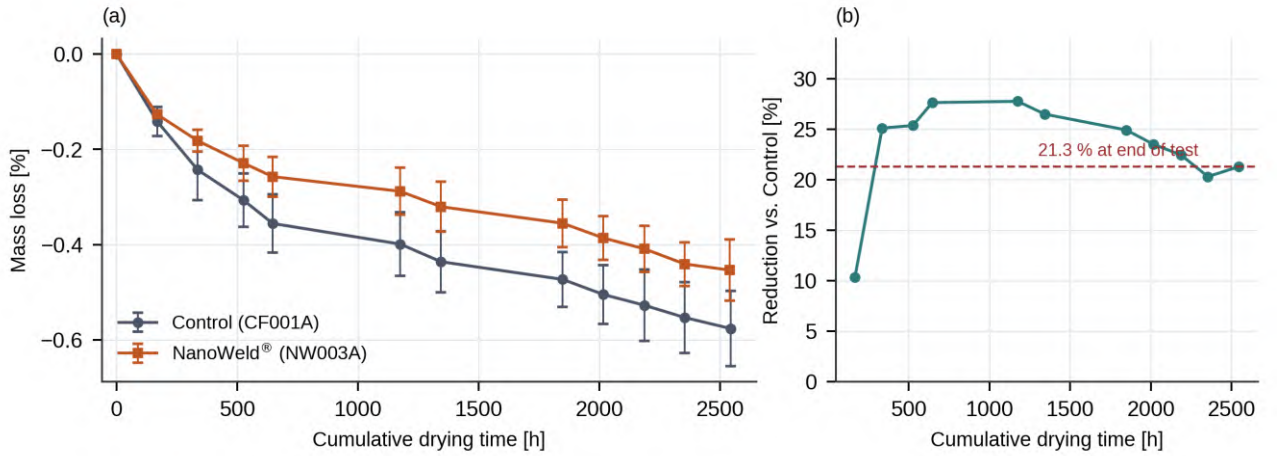


Figure 5: (a) Mass loss during drying at 65 °C to ASTM D5229, mean of six coupons per condition, error bars ± 1 SD. (b) Reduction in moisture content of the NanoWeld® laminate relative to Control.

4.3. Helium permeability of pristine laminates

The moisture result raised an obvious expectation: that helium permeability would fall correspondingly. Direct measurement does not support that expectation, and the reason it does not is itself informative.

Table 5: Helium permeation results, pristine coupons, n = 4 per condition, room temperature, 9.5 bar feed.

Parameter	Control	NanoWeld®	Δ
Leak rate [mbar·l/s]	6.33×10^{-7}	6.58×10^{-7}	+3.9 %
K [mol/(m·s·Pa)]	1.49×10^{-17}	1.58×10^{-17}	+6.0 %
D [m²/s]	1.45×10^{-11}	1.37×10^{-11}	−5.5 %
S [mol/(m³·Pa)]	1.03×10^{-6}	1.15×10^{-6}	+11.7 %

None of the differences in Tab. 5 is statistically significant. The relative standard deviations are 3.3% for the Control permeability and 5.6% for the NanoWeld® permeability, so the 6.0% mean separation is comparable to the within-group scatter and a two-sample test returns $p \approx 0.12$. The product of the fitted diffusivity and solubility reproduces the measured permeability to within rounding in both conditions, so Eq. 1 is satisfied and the fits are well behaved. Two of the interleaved coupons exhibited edge delamination introduced during specimen preparation; one required the delaminated region to be removed and sealed with indium before a working vacuum could be established, so the interleaved set carries slightly more preparation-related uncertainty than the Control. The defensible statement is that intrinsic helium permeability is indistinguishable between the two systems on pristine coupons.

4.4. Reconciling the moisture and helium results

The decomposition of Eq. 1 resolves the apparent contradiction. Diffusivity falls by 5.5 %, the direction that tortuosity theory predicts and which is qualitatively consistent with the moisture kinetics. Solubility rises by 11.7 %. The two effects act in opposition and approximately cancel, leaving net permeability marginally higher but statistically unchanged.

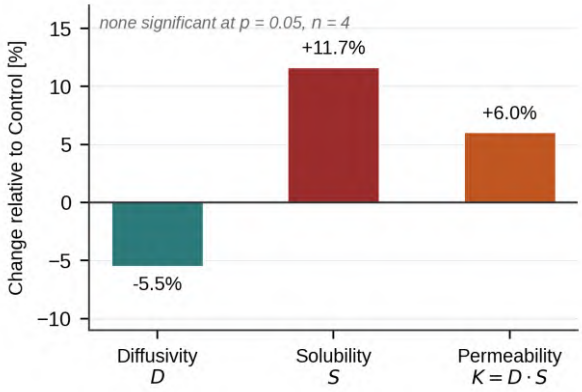


Figure 6: Decomposition of the helium permeability change into its diffusivity and solubility contributions.

The solubility increase is a capacity effect rather than a transport effect. Helium is small, inert and non-condensable, with a kinetic diameter of approximately 0.26 nm, and its uptake in a polymer is governed by available free volume rather than by chemical affinity. Interleaving adds thermoplastic-rich material at every ply interface, and that material dissolves more helium than the epoxy it replaces. Water behaves differently because its transport is dominated by hydrogen-bonding interactions with the matrix, which is why the moisture and helium results diverge.

This is a useful result rather than a discouraging one. It establishes that the stiffness, interlaminar and durability benefits of the interlayer are obtained without a barrier penalty on the as-manufactured laminate, and it identifies precisely where the barrier benefit must be sought: not in the intrinsic transport properties of the undamaged matrix, but in the damaged state.

5. IMPLICATIONS FOR CRYOGENIC PERMEABILITY

The evidence assembled here allows the cryogenic permeability question to be posed more precisely than at the outset. Permeability of a CFRP cryotank wall in service is controlled by matrix microcrack density, not by matrix diffusivity [5, 6]. Grenoble and Gates showed leak rate in IM7-based laminates to be a function of applied strain, crack density and temperature [11]; Yokozeki and co-workers quantified the step change in gas permeability that accompanies the formation of intersecting crack networks in adjacent plies [5]; and Timmerman and co-workers showed matrix toughening to reduce cryogenic microcracking propensity directly [3].

The chain of reasoning for an interleaved laminate is therefore: interlayer, suppressed or delayed crack initiation and delamination growth under thermal cycling and impact, reduced crack density, reduced permeability in the damaged state. The present campaign establishes the first and the last links but not the middle. The interlayer demonstrably raises resistance to shear-driven delamination growth, retains interlaminar shear capability, and does not raise intrinsic permeability. What has not yet been measured is the crack density and leak rate of an interleaved laminate after cryogenic thermal cycling or after a calibrated impact, and those are the measurements on which the barrier case stands or falls.

It is worth being explicit about why the moisture result cannot on its own substitute for that measurement. The moisture data demonstrate a real matrix-level tortuosity effect and are legitimate evidence that the interlayer alters through-thickness transport. But they characterise a mechanism that the helium data show to be second-order for a small inert gas, and they say nothing about the damage state. The moisture result is supporting evidence for a mechanism, not evidence for a permeability reduction.

6. CONCLUSIONS

A comparative campaign on NanoWeld®-interleaved and baseline IM7/8552 laminates, assessed on B-basis design allowables, supports the following conclusions.

Interleaving raises the stiffness allowables that size a stability-critical launcher component. The longitudinal tensile modulus allowable increases 12.6 % as manufactured and 20.7 % after thermal-vacuum conditioning, and the in-plane shear modulus allowable 26.3 % and 38.5 %. The underlying mean increases are statistically significant.

Matrix- and interface-dominated transverse properties improve most, by 38.8 % in stiffness and 114.2 % in strength, indicating improved fibre-matrix load transfer.

Compressive allowables fall by 7.5 % to 12.0 %, driven principally by increased scatter in the interleaved compression populations rather than by loss of mean capability, which changes by 1.5 % to 2.8 %.

The interlaminar fracture response is mode dependent. Pre-cracked Mode II toughness, the design-relevant measure for compression-driven and thermally driven delamination, improves by 31.6 % as manufactured and 47.1 % after conditioning, and short-beam strength by 2.7 %. Mode I allowables fall by 31 % to 39 %, a deficit attributed to interlayer areal weight and impregnation at the first manufacturing iteration and identified as a process-optimisation target.

A systematic reduction in specimen-to-specimen scatter, in eight of ten property populations, is a principal contributor to the allowable gains and is itself an engineering benefit.

Thermal-vacuum conditioning degraded no stiffness-controlled property and improved most of them, including the largest interlaminar gain of the campaign.

Moisture content falls by 21.3 %, with a deficit exceeding 25 % through the early part of the desorption curve, confirming a genuine matrix-level barrier effect attributable to increased tortuosity.

Direct helium permeation measurement on pristine coupons shows no statistically significant change in intrinsic permeability, diffusivity falling 5.5 % and solubility rising 11.7 % so that the two effects approximately cancel. The mechanical and durability benefits are therefore obtained without a barrier penalty, and the barrier case must be made in the damaged state rather than the pristine one.

7. FURTHER WORK

The decisive next step is a combined cryogenic thermal cycling and helium permeation campaign on both material conditions, in which crack density is characterised after a defined number of cycles and leak rate measured on the cycled coupons; a low-velocity impact and post-impact-permeation sequence would address the second damage mechanism identified in Section 1.1. In parallel, a parametric study of interlayer areal weight and impregnation, supported by fractographic examination of the Mode I fracture surfaces, is required to close the opening-mode deficit, and the scatter of the compression and conditioned-strength populations requires attention. Multidirectional laminate and component-level validation on the

demonstrator strut follow the Technology Readiness Review.

8. ACKNOWLEDGEMENTS

This work was carried out under ESA Contract 4000141307/23/NL/SC/rp within the Future Launchers Preparatory Programme. The authors acknowledge the contributions of Applus+ Laboratories, Applus+ RESCOLL, DatapointLabs and Aerospace and Advanced Composites GmbH to the experimental programme.

9. REFERENCES

1. Liu, N., Ma, B., Liu, F., Huang, W., Xu, B., Qu, L. & Yang, Y. (2021). Progress in research on composite cryogenic propellant tank for large aerospace vehicles. *Composites Part A* 143, 106297.
2. Flanagan, M., Grogan, D.M., Goggins, J., Appel, S., Doyle, K., Leen, S.B. & Ó Brádaigh, C.M. (2017). Permeability of carbon fibre PEEK composites for cryogenic storage tanks of future space launchers. *Composites Part A* 101, 173-184.
3. Timmerman, J.F., Tillman, M.S., Hayes, B.S. & Seferis, J.C. (2002). Matrix and fiber influences on the cryogenic microcracking of carbon fiber/epoxy composites. *Composites Part A* 33, 323-329.
4. Edwards, H., Galpin, D., Walls-Bruck, M., Dulieu-Barton, J. & Kim, B.C. (2023). Microcracking of CFRP composites during cryogenic thermal cycling. Industrial Doctorate Centre in Composites Manufacture, University of Bristol / National Composites Centre.
5. Yokozeki, T., Aoki, T. & Ishikawa, T. (2004). The effect of matrix cracks on gas permeability through CFRP laminates. *Advanced Composite Materials* 13(3-4), 227-236.
6. Zheng, H., Zeng, X., Zhang, J. & Sun, H. (2018). The application of carbon fiber composites in cryotank. In *Solidification*, IntechOpen, Ch. 6. DOI 10.5772/intechopen.73127.
7. Yokozeki, T., Iwahori, Y., Ishiwata, S. & Enomoto, K. (2007). Mechanical properties of CFRP laminates manufactured from unidirectional prepregs using CSCNT-dispersed epoxy. *Composites Part A* 38(10), 2121-2130.
8. Sager, R.J., Klein, P.J., Lagoudas, D.C., Zhang, Q., Liu, J. & Dai, L. (2009). Effect of carbon nanotubes on the interfacial shear strength of T650 carbon fiber in an epoxy matrix. *Composites Science and Technology* 69(7-8), 898-904.
9. Wicks, S.S., de Villoria, R.G. & Wardle, B.L. (2010). Interlaminar and intralaminar reinforcement of composite laminates with aligned carbon nanotubes. *Composites Science and Technology* 70(1), 20-28.
10. Qiu, J., Zhang, C., Wang, B. & Liang, R. (2007). Carbon nanotube integrated multifunctional multiscale composites. *Nanotechnology* 18(27), 275708.
11. Grenoble, R.W. & Gates, T.S. (2005). Hydrogen permeability of polymer matrix composites at cryogenic temperatures. In *Proc. 46th AIAA/ASME/ASCE/AHS/ASC Structures, Structural Dynamics and Materials Conference*, Austin, Texas, AIAA 2005-2086.
12. Manu, M., Reby Roy, K.E., Mubarak Ali, M. & Aravind, J. (2021). Review on development of effective carbon fiber based cryogenic storage tank materials for space applications. *IEEE Conference Proceedings*.
13. Lee, J.K., Song, S. & Kim, B. (2012). Functionalized graphene sheets-epoxy based nanocomposite for cryotank composite application. *Polymer Composites* 33(8), 1263-1273.
14. Borrego, L.P., Costa, J.D.M., Ferreira, J.A.M. & Silva, H. (2014). Fatigue behaviour of glass fibre reinforced epoxy composites enhanced with nanoparticles. *Composites Part B* 62, 65-72.
15. Dong, C., Li, K., Jiang, Y., Arola, D. & Zhang, D. (2018). Evaluation of thermal expansion coefficient of carbon fiber reinforced composites using electronic speckle interferometry. *Optics Express* 26(1), 531-543.
16. Parham, S., Kharazi, A., Bakhsheshi-Rad, H., Kharaziha, M., Ismail, A., Sharif, S., Razzaghi, M., RamaKrishna, S. & Berto, F. (2022). Antimicrobial synthetic and natural polymeric nanofibers as wound dressing: a review. *Advanced Engineering Materials* 24(6), 2101460.
17. Kang, Y.K., Park, C.H., Kim, J. & Kang, T.J. (2007). Application of electrospun polyurethane web to breathable water-proof fabrics. *Fibers and Polymers* 8(5), 564-570.
18. Schreuder-Gibson, H., Gibson, P., Senecal, K., Sennett, M. & Walker, J. (2002). Protective textile materials based on electrospun nanofibers. *Journal of Advanced Materials* 34(3), 44-55.
19. ECSS-E-ST-32-10C Rev.2 (2019). *Space engineering - Structural factors of safety for spaceflight hardware*. ECSS Secretariat, ESA-ESTEC, Noordwijk, The Netherlands.
20. Composite Materials Handbook CMH-17, Volume 1, Revision G (2012). *Polymer Matrix Composites: Guidelines for Characterization of Structural Materials*. SAE International.

A DAMAGE MECHANICS MODEL FOR FAILURE ASSESSMENT OF FILAMENT WOUND FRP MATERIALS ON [±α]-PLY LEVEL

Carla Beckmann [(1)], Sebastian Seidel [(2)], Jörg Hohe [(3)]

[(1)(2)(3)] *Fraunhofer-Institut für Werkstoffmechanik IWM, Wöhlerstr. 11, 79108 Freiburg, Germany, Email: joerg.hohe@iwm.fraunhofer.de*

KEYWORDS

CFRP, Pressure vessels, Filament winding, Material modelling, Damage mechanics

ABSTRACT

The present contribution is concerned with the development and implementation of a damage mechanics material model for filament wound CFRP pressure vessels. The model is formulated on the level of the integrated [±α]-plies developing due to the filament winding process. Adopting Puck's failure criterion for both the [+α]- and the [-α]-ranges, an integrated failure envelope is derived. Assuming the approach of a strain state point towards the failure envelope to drive the damage evolution, the failure model is transformed into a damage mechanics material model. The model is implemented as a user defined material model into a commercial finite element system.

1. INTRODUCTION

Filament wound carbon fibre reinforced plastics are common materials used in the design of pressure vessels for propellants and other gaseous substances in space missions. Their integrity assessment is usually based on the classical laminate assumption considering separate [+α]- and [-α]-plies for the different winding angles α through the pressure vessel shell. However, due to the filament winding process, integrated [±α]-plies develop, which cannot be rigorously separated into [+α]- and [-α]-constituents.

The present study is concerned with the development, formulation, and implementation of a continuum damage mechanics material model formulated on the level of the integrated [±α]-plies. Towards a damage tolerant design process, the model is formulated such that fibre failure and limited inter-fibre failure events not necessarily leading to catastrophic failure are treated in a separated manner. Considering a representative [±α]-section and starting from the classical Puck-Schürmann failure theory [1], [2] assumed for the individual [+α]- and [-α -filaments, integrated failure envelopes on the [±α]-ply level are derived. Towards a more efficient formulation of the damage model, a strain-space rather than a stress-space formulation is employed.

In a second step, the damage model is formulated by introduction of separate damage variables for each of the damage mechanisms. Assuming the approach of a strain state point (ε_{11}, ε_{22}, ε_{12}) towards the respective portion of the failure envelope being the damage driver and adopting the concept of microplasticity, damage evolution equations for the fibre and inter-fibre damage variables are obtained.

The model is implemented as a user defined material subroutine into a commercial finite element code. It is validated against an experimental data base of split disk experiments on filament wound CFRP materials with a variety of winding angles. Finally, the capabilities of the model are demonstrated in a case study on the burst of a filament wound CFRP hydrogen pressure vessel.

2. INTEGRATED FAILURE ENVELOPE

The damage model is defined and formulated on the level of the filament wound [±α]-plies, using the standard Cartesian coordinate system with x_1 being the projected winding axis, x_2 being the second in-plane axis of the pressure vessel shell, and x_3 being the shell normal direction. Local fibre oriented Cartesian systems are defined for both the [+α]- and the [-α]-ranges within the considered [±α]-ply, where the winding angle α is defined in the usual manner as the angle between the fibre orientation and the x_1-axis.

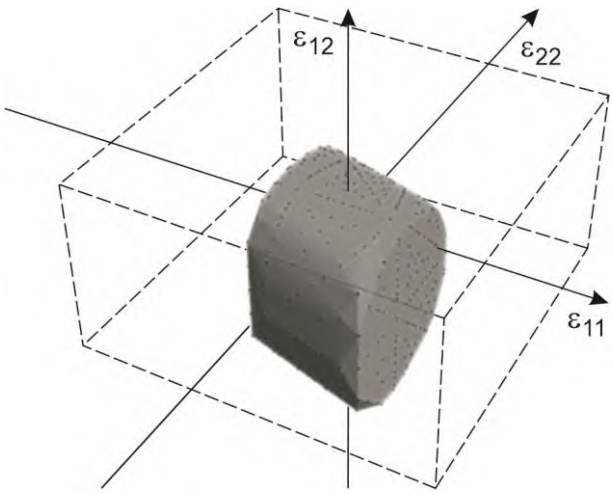


Figure 1: Integral failure envelope for α = 0°

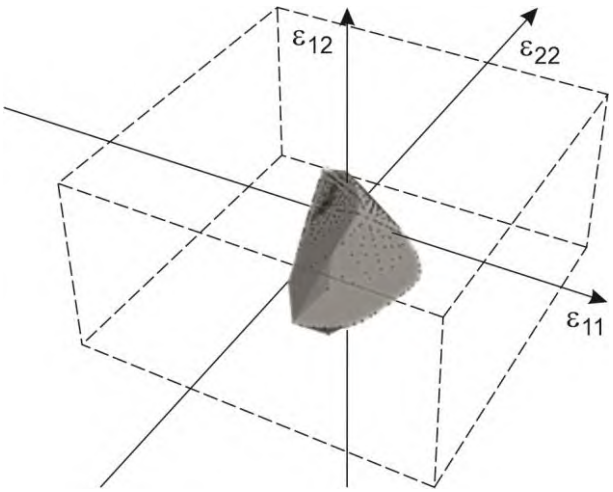


Figure 2: Integral failure envelope for α = 30°

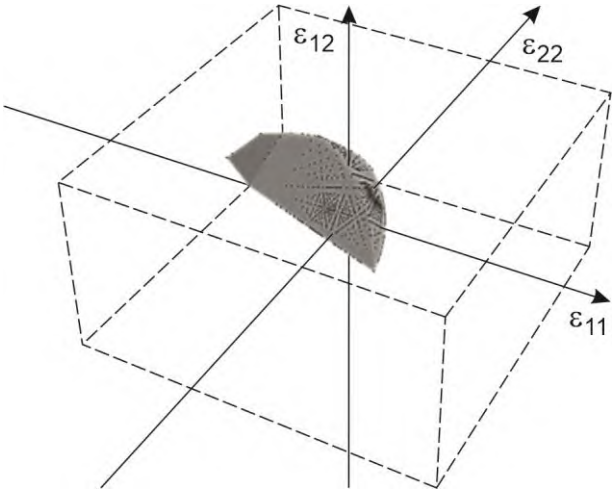


Figure 3: Integral failure envelope for α = 60°

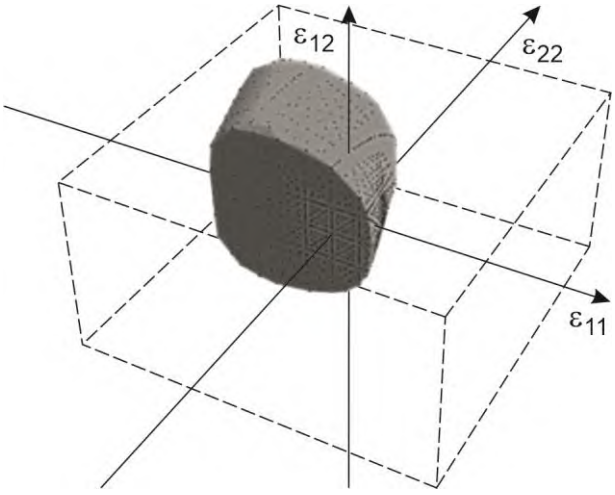


Figure 4: Integral failure envelope for α = 90°

For both the [+α]- and the [-α]-ranges, the classical Puck-Schürmann failure theory [1], [2] is adopted.To determine an integrated failure envelope on the [±α]-ply level, Puck's criterion is reformulated in strain space. Subsequently, the strains in the local fibre oriented coordinate system are expressed in terms of the global strains ε_{11}, ε_{22}, and ε_{12} using the standard formulae for tensor transformation. As a result, integrated strain-space failure envelopes in dependence on the winding angle α are obtained. As for the original Puck failure envelope, the integrated failure envelopes can be subdivided into sub failure envelopes for fibre and inter fibre failure. Examples for winding angles of α = 0°, 30°, 60°, and 90° are presented in Figs. 1 to 4.

3. DAMAGE MECHANICS MATERIAL MODEL

Based on the failure envelopes defined in Sec. 2, a damage mechanics material model is defined. Two separated damage variables D^{f} and D^{i} for fibre and inter fibre failure with

$$D^f, D^i \in [0,1] \qquad (1)$$

are defined where D = 0 denotes the undamaged initial state whereas D = 1 is the fully damaged state, i.e. is related to material failure.

Adopting Hooke's law as the base material constitutive equation, a brittle damage mechanics model is defined in the Kachanov-Lemaitre [3], [4] sense by redefining the elastic moduli on the level of the individual [+α]- and [-α]-ranges by

$$\begin{aligned} E_1 &\rightarrow \left(1 - D^{\mathrm{f}}\right) E_1 \\ E_2 &\rightarrow (1 - D^{\mathrm{i}}) E_2 \\ G_{12} &\rightarrow (1 - D^{\mathrm{i}}) G_{12} \end{aligned} \qquad (2)$$

in the respective local coordinate system. Again, the corresponding equations are transformed back into the global coordinate system using the rules of tensor transformation. Finally, the material model for the integrated [±α]-ply is obtained by superposition of the constitutive equations for the [+α]- and [-α]-ranges. Full details will be provided in an oncoming contribution [5].

4. DAMAGE EVOLUTION

For both damage variables, according to Eq. 1, appropriate damage variables are required. Similar as in the Maimí et al. model [6], [7], it is assumed that the approach of a state point (ε_{11}, ε_{22}, ε_{12}) towards the failure envelope

$$\Phi^f, \Phi^i = 1 \qquad (3)$$

in strain space acts damage driver. Assuming that the accumulation of microplastic work [8], [9] is the relevant micromechanical damage mechanism and estimating the microplastic work from the elastic solution by means of a Ramberg-Osgood law, results in a damage evolution equation of the form

$$\mathrm{d}D = \begin{cases} A\, \Phi^n\, \mathrm{d}\Phi & \text{for: } \mathrm{d}\Phi \geq 0 \\ 0 & \text{else} \end{cases} \qquad (4)$$

for both the fibre and the inter fibre damage variables. In Eq. 4, the parameters *A* and *n* are additional material parameters with different values for fibre and inter fibre damage.

Using explicit time integration, the material model is implemented as a user-defined material subroutine into a commercial Finite Element system. Full details on the mathematical formulation and the numerical implementation will be provided in an oncoming contribution [5].

5. VALIDATION

For validation, the material model defined and implemented in Secs. 2 to 4 is applied to an experimental data base on an epoxy based, filament wound CFRP material with different winding angles α. The material has been provided in form of filament wound tubes from which ring-shaped specimens were manufactured. The specimens were tested till failure in an instrumented split-disk test rig.

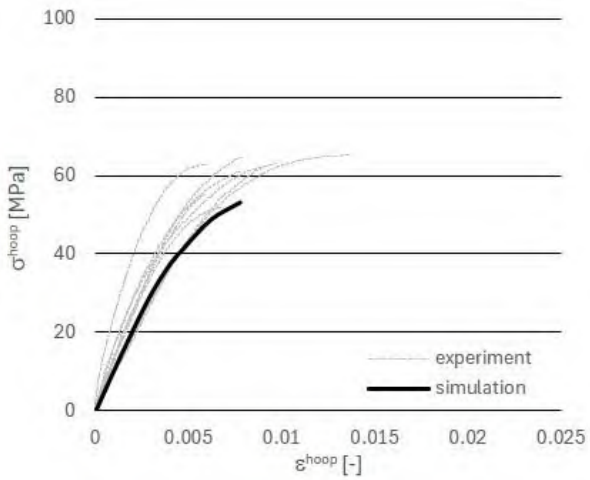


Figure 5: Validation for α = 30°

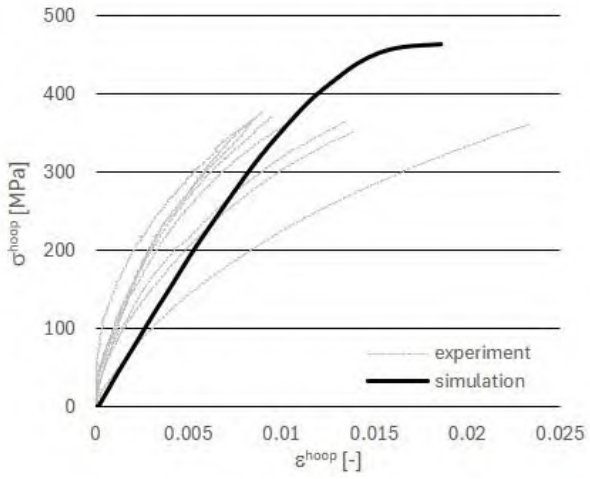


Figure 6: Validation for α = 60°

The results for winding angles of α = 30°, 60°, and approximately 89° are presented in Figs. 5, 6, and 7, respectively. For all winding angles α, the simulation by means of the proposed damage mechanics material model is found to provide a good approximation of the experimental observation, despite some scatter observed in the experimental data.

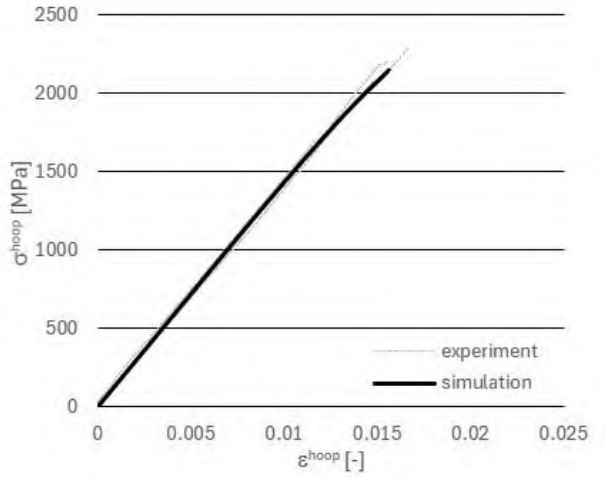


Figure 7: Validation for α = 89°

6. CASE STUDY

For demonstration, the proposed model with the material data determined in Sec. 5 is applied in a numerical case study of a burst experiment of a filament wound CFRP pressure vessel. The geometry and the distribution of both damage variables are presented in Fig. 8.

For the assumed design of the filament wound vessel shell, the fibre damage variable D^f is found to be larger than the inter fibre damage variable throughout the cylindrical section whereas inter fibre damage is the dominant mechanism in the dome sections. Final burst failure is predicted to e initiated in a fibre failure mode at a spot in the cylindrical shell as indicated in Fig. 8. Notice that following the development of localized fibre damage, even the amount of inter fibre damage at this spot is increased compared to the neighbouring sections of the pressure vessel shell. Hence, the proposed model is able to predict not only the development of the fibre and inter fibre damage modes but also the interaction of the two damage modes.

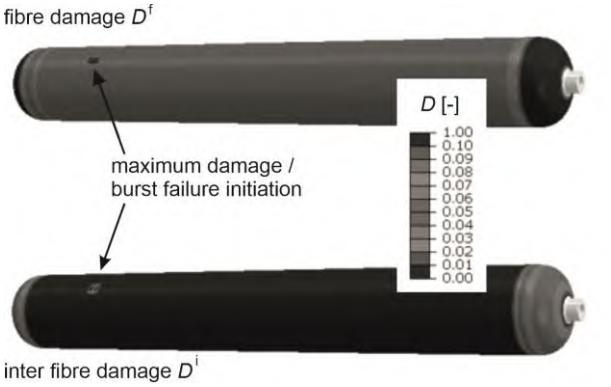


Figure 8: Case study

7. CONCLUSIONS

The present study is concerned with the development, formulation and finite element implementation of a continuum damage mechanics material model for filament wound CFRP materials. The model is based on Hooke's law together with an integrated failure envelope for the filament wound [±α]-plies, derived from a strain space formulation of Puck's criterion.

In an application to split disk experiments, the model is found to provide accurate predictions of both the stress-strain response and the failure initiation. Especially, the nonlinearity of the material response induced by damage evolution is predicted in the correct manner, despite the essentially linear formulation of the underlying base material model.

The numerical implementation using explicit time integration is found to be numerically rather efficient. Due to the strain space formulation, the numerical errors induced by the explicit time integration are rather limited since even in an implicit formulation no local iterative solution of non-linear equations would be required.

8. ACKNOWLEDGEMENTS

The present study has been funded by the German Federal Ministry of Science, Technology, and Space under Grant no. 19S22006L. The financial support is gratefully acknowledged.

The authors wish to express their thanks to their project partner Leibnitz-Institute for Composite Materials IVW for manufacturing the reference material for the experimental investigation.

9. REFERENCES

1. Puck, A. & Schürmann, H. (1998). Failure analysis of FRP laminates by means of physically based phenomenological models, *Composites Science and Technology* 58, 1045-1067.

2. Puck, A. & Schürmann, H. (2002). Failure analysis of FRP laminates by means of physically based phenomenological models, *Composites Science and Technology* 62, 1633-1662.

3. Kachanov, L.M. (1986). *Introduction to Continuum Damage Mechanics*, Martinus Nijhoff Publishers, Dordrecht.

4. Lemaitre, J. (1992). *A Course on Damage Mechanics*, Springer Verlag, Berlin.

5. Beckmann, C., Seidel, S., Hohe, J. (in preparation). *An integrated damage mechanics material model for filament wound fibre .reinforced materials.*

6. Maimí, P., Camanho, P.P., Mayugo, J.A., Dávila, C.G. (2007). A continuum damage model for composite laminates: Part I – Constitutive model, *Mechanics of Materials* 39, 897-908.

7. Maimí, P., Camanho, P.P., Mayugo, J.A., Dávila, C.G. (2007). A continuum damage model for composite laminates: Part II – Computational implementation and validation, *Mechanics of Materials* 39, 909-919.

8. Hohe, J., Gall, M., Fliegener, S., Abdul Hamid, Z.M.: (2020). A continuum damage mechanics model for fatigue and degradation of fiber reinforced materials, *Journal of Composite Materials* 54, 2837-2852.

9. Abdul Hamid, Z.M., Findeisen, C., Laveuve, D.M., Rohrmüller, B., Richter, H., De Monte, M., Spancken, D., Hohe, J. (2024) A continuum damage mechanics model for fatigue degradation and failure of short fiber reinforced composites, *Composites Science and Technology* 254, 110679.

Fatigue and Fracture Behaviour of Al2618-TiB_2 Metal Matrix Composite Produced by PBF-LB

Luca Mariotti [(1)], Giorgia Lupi [(1)], Stefano Beretta [(1,2)], Donato Girolamo [(3)], Riccardo Casati [(1)], Luca Patriarca [(1)]

[(1)] Department of Mechanical Engineering, Politecnico di Milano, Via G. La Masa 34, 20156 Milano, Italy, Email: luca.mariotti@polimi.it

[(2)] Auburn University, National Center for Additive Manufacturing Excellence (NCAME), 311 W. Magnolia Ave., Auburn, AL 36849, USA

[(3)] European Space Agency, Keplerlaan 1, 2201 AZ Noordwijk, The Netherlands

KEYWORDS

Metal matrix composites, additive manufacturing, LPBF, fracture toughness, fatigue crack growth, defects analysis, damage tolerance

ABSTRACT

Aluminium metal matrix composites produced by Powder bed fusion – laser based (PBF-LB) are attractive for stiffness-critical space structures, but their industrial employment requires reliable mechanical properties. This paper summarizes the characterization of Al2618 reinforced with 7.1 wt% TiB_2 produced by PBF-LB. Static properties were assessed and compared with literature data. Fatigue crack growth and high-cycle fatigue tests were performed to calibrate a Nasgro based fatigue model which well reproduced specimen lives when considering the residual stresses. It was successfully applied to a representative industrial demonstrator, supporting transferability of the specimens data to component assessment.

1. INTRODUCTION

Powder bed fusion – laser based (PBF-LB) is increasingly used for metallic components in the aerospace sector because it combines high geometric freedom with a level of process maturity high enough for producing industrial lightweight structural parts [1,2]. Current material development for additive manufacturing (AM) is moving beyond the direct transfer of conventional alloys and towards compositions designed to exploit the thermal conditions of the AM process. Aluminium-based metal matrix composites (MMCs), in which a metallic matrix is reinforced by ceramic particles, are particularly attractive when stiffness, dimensional stability and mass efficiency are primary design drivers [3,4].

A higher elastic modulus can reduce structural deformation, increase natural frequencies and improve payload stability without requiring a proportional increase in mass [5,6]. These benefits are relevant to optical benches, brackets and support structures for which stiffness and vibration control are often more restrictive than static strength. However, the structural use of PBF-LB MMCs requires more than a high tensile modulus. Fracture resistance, fatigue crack growth, manufacturing defects and residual stresses must be characterized in a consistent framework suitable for damage-tolerant assessment.

Many studies about AM aluminium MMCs focus on density, hardness or tensile strength, while fewer report the fracture and fatigue properties which are needed for structural component qualification. Ceramic particles may increase stiffness and strength, but can also restrict plastic flow, fracture locally or promote debonding at the particle-matrix interface. At the same time, process-induced surface and near-surface defects can dominate high-cycle fatigue and reducing the potential of the MMC [7].

The investigated material is an Al2618 alloy matrix reinforced with 7.1 wt% TiB_2 and produced by PBF-LB within the ENCOMPASS ESA founded project. Three works of the authors on powder development and production, microstructure analysis, heat treatment optimization, specimens manufacturing, test procedures and the complete material properties dataset have been previously published [8–10]. The present paper focuses on the static and fatigue characterization of the MMC at specimen level and on properties transferability form specimens to a representative space-structure demonstrator which was fatigue tested.

First, the paper presents the tensile properties and the temperature dependence of the elastic modulus. Second, fracture toughness and long-crack growth are used to fit the Nasgro fatigue model and to identify build-orientation and load-ratio effects. Third, fatigue life is interpreted through fractography analysis, X-ray computed tomography (CT) and residual stress (RS) measurements. Finally, the resulting dataset is combined and used to estimate the fatigue life of the MMC component using a damage-tolerance approach.

2. MATERIAL AND METHODS

2.1 Material and specimen production

The MMC investigated has an Al2618 alloy matrix and 7.1 wt% total amount of TiB_2 reinforcement particles. It was manufactured by PBF-LB and the feedstock combined in-situ (nano-metric) and ex-situ (micro-metric) TiB_2 particles; the complete powder production route and process optimization are reported in [8] and are not repeated here.

All specimens received a T5 heat treatment (HT) consisting of direct ageing at 180 °C for 2 h followed by air cooling. Tensile, fatigue crack growth (FCG) and axial fatigue specimens were produced in the vertical orientation, which

represented the conservative condition identified during preliminary screening as prescribed by the ECSS-Q-ST-70-80C [11]. Fracture toughness specimens were produced in horizontal (H), vertical (V) and diagonal (D) orientations. Axial fatigue specimens were tested in the net-shape condition after corundum sandblasting.

Cylindrical specimens with a 5 mm gauge diameter were adopted for tensile and axial fatigue tests. Single edge bending specimens were used for FCG characterization because the resonance flexural test configuration enabled efficient threshold testing over positive and negative load ratios. Compact tension (CT) specimens were selected for fracture toughness because their lateral surfaces remained accessible for DIC measurements. The CT specimen thicknesses were chosen to promote a dominant plane-strain condition at the central portion of the crack front.

Table 1: Mechanical test programme

Test	n	Orientation	Test condition
Tensile	14	V	RT tensile; E from −50 to 150 °C
Toughness	9	H, V, D	Pre-cracked CT specimens
FCG	7	V	R = -1, 0 and 0.7
Fatigue	28	V	Net-shape; sandblasted; R = -1

2.2 Mechanical and defect characterization

Tensile tests followed ASTM E8/E8M [12]. Elastic modulus was measured through repeated ten loading-unloading cycles between 10% and 40% of yield strength over the temperature range from −50 to 150 °C. Fracture toughness tests on compact-tension specimens followed ASTM E399 [13].

Long-crack growth rate was measured in accordance with ASTM E647 [14]. Compression pre-cracking procedures were used to obtain closure-free cracks from the notch of the SEB specimens. Threshold data were obtained at R = -1, 0 and 0.7 with compression pre-cracking load reduction tests, while data on the Paris region at R = 0 and 0.7 with compression pre-cracking constant amplitude tests.

Axial fatigue tests followed ASTM E466 [15] and they were performed at 50 Hz and R = -1, with a runout criterion of 10^7 cycles.

Fracture origins were subsequently examined by scanning electron microscopy. Defect size was expressed through the Murakami √area parameter [16]. In-depth RSs were measured using electrolytic material removal. Axial and circumferential directions were investigated by X-ray diffraction from the free surface to a depth of 400 µm in 50 µm steps. Surface measurements on additional specimens were used to verify that the near-surface values were repeatable

All fatigue specimens were inspected by X-ray CT before testing using a 10 µm voxel size. With the selected voxel size and segmentation procedure, the defect size corresponding to a 90% probability of detection was approximately 34 µm, below the smallest maxima used in the statistical analysis. The detected flaws were divided into core, sub-surface and outer populations to account for their different proximity to the free surface and their different relevance to fatigue initiation.

3. Results and discussion

3.1 Tensile response and elastic modulus

The tensile response is shown in Figure 1.a and it was repeatable with a yield stress of 345 ± 4 MPa and an ultimate tensile strength of 387 ± 34 MPa.

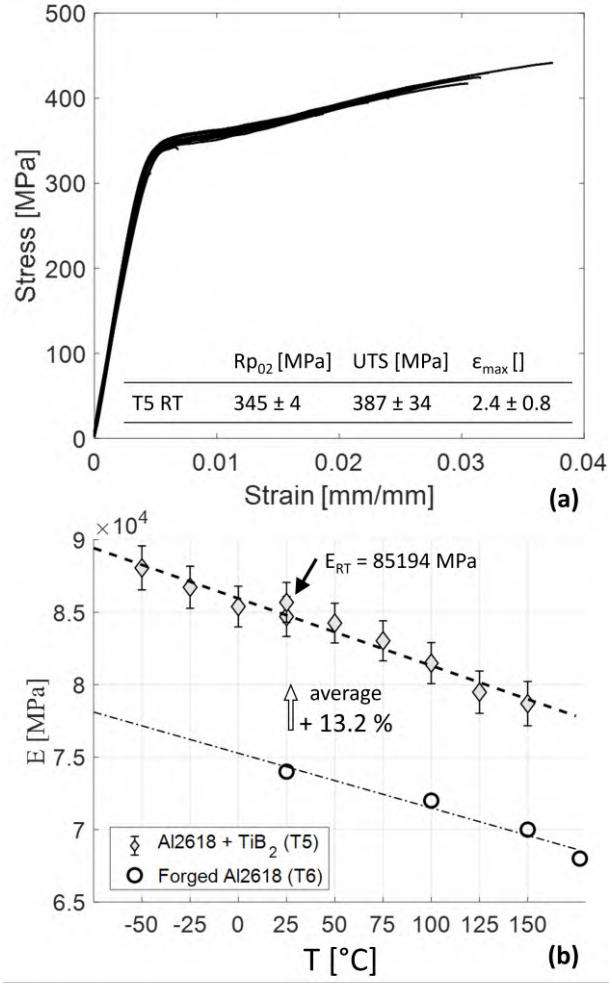


Figure 1: a) tensile results and material properties; b) elastic modulus dependence with temperature

The larger scatter in ultimate strength and elongation, 2.4 ± 0.8%, was associated with the presence of manufacturing defects that affected the final fracture stage.

At room temperature the elastic modulus was 85.2 GPa, corresponding to an increase of 13.2% over the unreinforced Al2618 reference, as shown in Figure 1.b [17]. The modulus changed almost linearly with temperature, from 88.1 GPa at −50 °C to 78.7 GPa at 150 °C. The retained stiffness at elevated temperature is relevant to thermo-mechanical design and to structures exposed to wide thermal excursions. The modulus increase is

a clear benefit of the TiB_2 reinforcement and positions the material between structural aluminium alloys and higher-stiffness lightweight alternatives.
The approximately linear trend also provides a practical input for thermo-mechanical finite-element analyses, where a temperature-dependent modulus can be introduced without requiring a complex formulation.

3.2 Fracture toughness

Fracture toughness showed a clear orientation dependence. The horizontal orientation provided the highest average value, 23.9 MPa√m, followed by the vertical orientation at 18.0 MPa√m and the diagonal orientation at 15.3 MPa√m. Despite the high ceramic fraction, the measured values remained competitive with PBF-LB aluminium alloys used for structural applications and were aligned with cast Al2618-based materials reported in the literature [8].
The DIC strain maps on the lateral surface of the specimen in correspondence of the crack tip and the post-test microstructural sections provided a physical interpretation of this anisotropy. In the V and D specimens, the crack preferentially follows melt-pool boundaries, which formed energetically favourable paths for crack growth. In the H orientation, the crack crossed the melt pool structure and a larger plastic region is developed before unstable propagation.
The results also show that the ceramic particles did not introduce a single dominant brittle fracture mechanism. Particle cracking, particle-matrix debonding and local ligament reduction remain possible sources of toughness loss, but the homogeneous reinforcement distribution and the absence of extensive particle clusters limited their macroscopic effect.

3.3 Static properties comparison

Fig. 2.b and 2.c compare the static properties obtained from tensile and fracture tests with literature data using $K_{IC}-E$ and $R_{p0.2}-E$ diagrams. Although the available literature data are limited, the comparison includes AM Al2618 + TiB_2, cast Al2618 + TiB_2, cast Al2618, AM AlSi10Mg and AM Scalmalloy® [8]. The investigated MMC shows a high elastic modulus, supporting its use in stiffness-critical applications while maintaining competitive fracture toughness and yield strength compared with alloys exhibiting higher strength but generally lower stiffness levels.

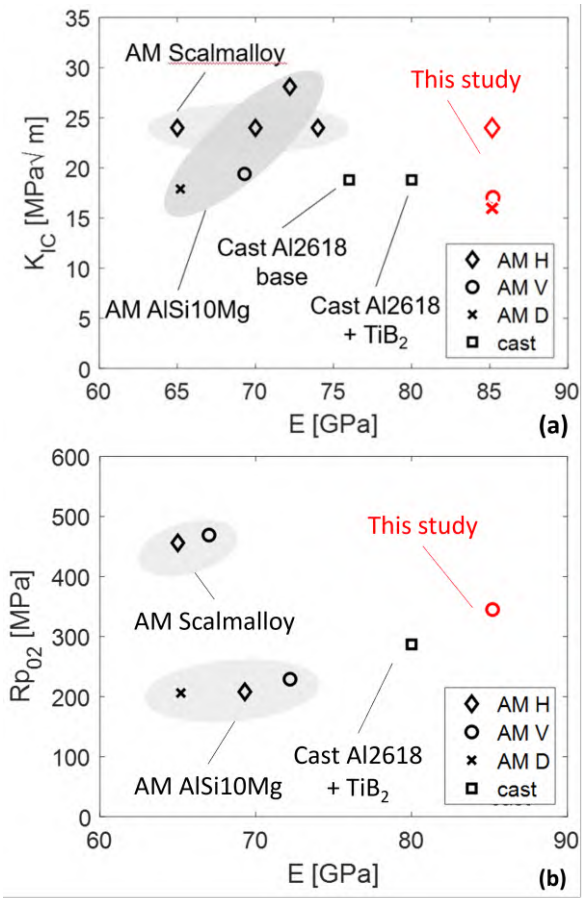


Figure 2: b) K_{IC} vs E map c) Rp_{02} vs E map [8]

3.4 Fatigue crack growth

The FCG results are shown in terms or crack growth rate vs applied *ΔK* in Figure 3 for the three investigated load ratios. The complete Paris curve was obtained only at *R = 0.7* (plotted in red). Data obtained for *R = 0* are in the threshold region and in upper part of the Paris region while data for *R = -1* are just in the threshold region (plotted respectively in green and blue). The $\Delta K_{th,LC}$ values of two repeated R = -1 tests gave values of 2.03 and 1.61 MPa √m; the values at R = 0 and 0.7 were 1.56 and 1.04 MPa √m, respectively. The effect of high tensile RS is clear from the data on the Paris region at R = 0 which are completely overlapped with the R = 0.7 curve and thus they indicate that the effective load ratio is increased by the tensile RS not fully relieved by the T5 HT. Therefore, a curve fitting option that allowed the crack opening function to be bypassed (α = 5.845, S_{max}/ S_{flow} = 1.0) was used as suggested in the Nasgro user manual [18].

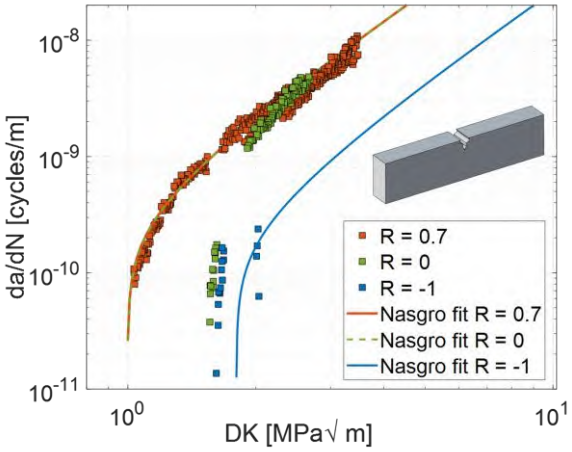


Figure 3: Crack growth rate results with Nasgro fitting

3.5 High cycle fatigue and defects analysis

The axial fatigue results are shown in the SN diagram in Figure 4.a in terms of stress range and number of cycles to failure.

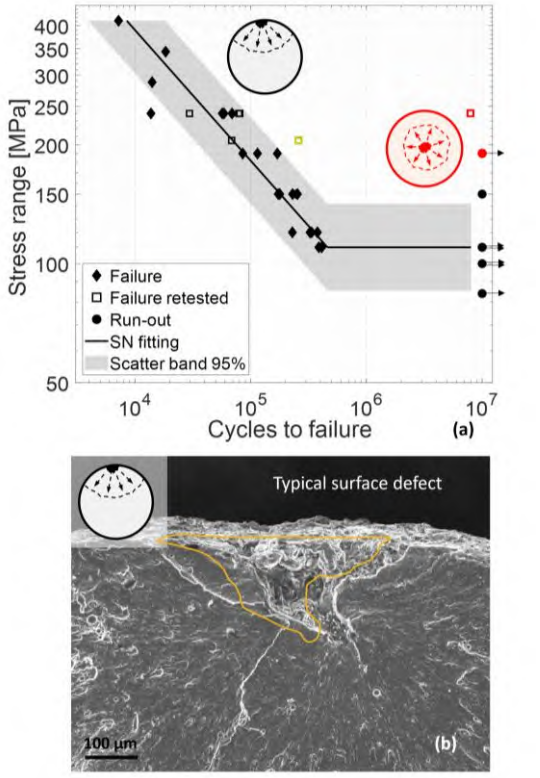


Figure 4: a) SN diagram expressed in stress range; b) SEM image of typical killer defect

The line representing the SN curve was obtained by fitting the finite life region of the experimental data with Eq. (**1**, in accordance with ASTM E739 [19]:

$$N = A \cdot S^{B} \qquad (1)$$

The estimated parameters are reported in Table 1 which also contains the experimental fatigue limit ($\Delta\sigma_w$) and the number of cycles to failure at the knee-point of the SN diagram (N_{lim}).

Table 1. Parameters of the SN fitting

$\log_{10}$ (A)	B	σ_{logN}	N_{lim} *[cycles]*	$\Delta\sigma_w$ *[MPa]*
11.835	-3.024	0.1692	459889	110

The 95% bilateral scatter band was calculated using σ_{logN} and it is reported in the SN.

Fractography analysis showed that almost all failures initiated from surface or near-surface defects similar to the one reported in Figure 4.b. A single specimen failed from a small internal defect (plotted in red) and it survived almost 8 × 10^6 cycles when retested at a stress range of 240 MPa. The killer-defect size is plotted in a Gumbel diagram in Figure 5.a and the average value resulted √area = 311 µm. The defects depth where also evaluated as shown in Figure 5.b and was plotted in the chart in Figure 5.c together with the measured RS.

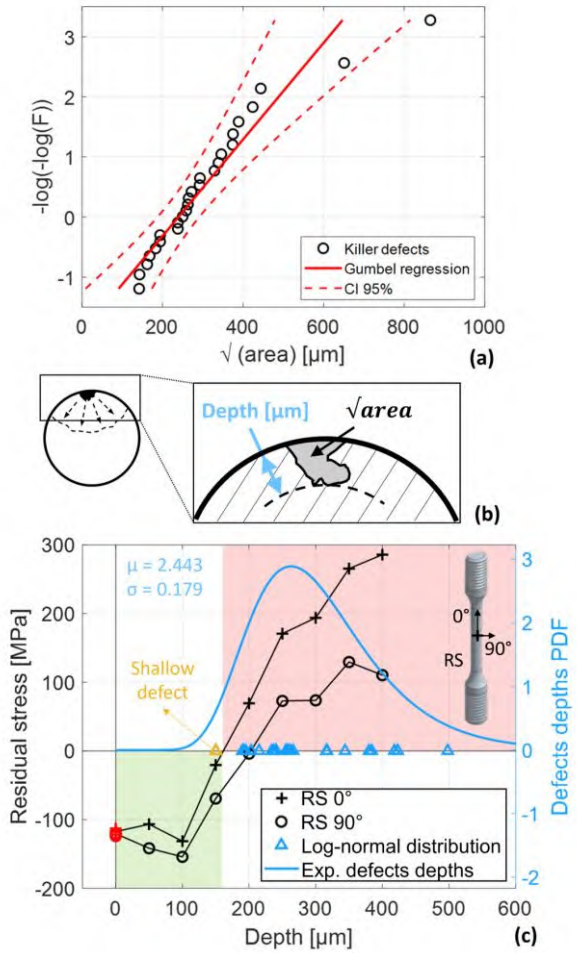


Figure 5: a) killer defects Gumbel plot; b) schema of the considered killer defect depth c) overlapping of the defects' depths with the measured RS

RS measurements revealed a compressive layer close to the sandblasted surface followed by high tensile stresses towards the specimen interior. The axial component of the RS, which acts directly on the fatigue crack, approached 300 MPa at a depth of 400 µm. The average maximum depth of the killer defects is 277 µm with almost all the defects tips embedded in the tensile RS region. Consequently, nominally fully reversed tests

experienced a much higher local effective load ratio with a detrimental effect on the fatigue life.
An SN prediction was done in Figure 6.a using the average size of the killer defects and considering or not the RS in the Nasgro SC35 crack model. The prediction is consistent with experimental data when RS are accounted in the Nasgro fatigue model. The same conclusion is shown for each fatigue specimen in a plot experimental vs predicted life in Figure 6.b where the prediction closely matches the experimental life considering the RS. These results confirm a successful calibration of the fatigue model on fatigue specimens.

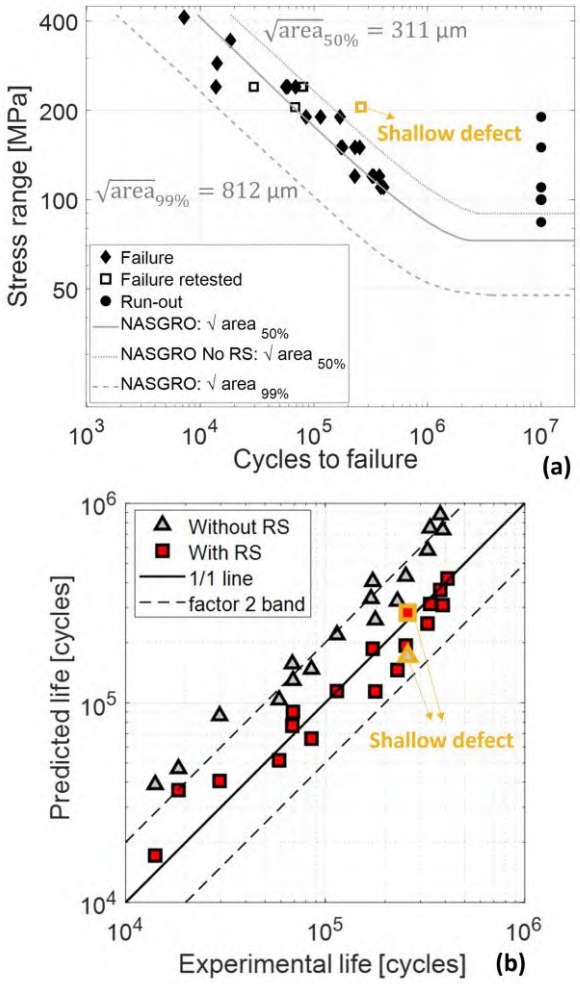


Figure 6: a) SN prediction with average size of killer defects; b) fatigue specimens experimental vs predicted life with and without RS

3.6 XCT defect populations

The pre-test XCT data were used to perform a porosity analysis for every fatigue specimen. The obtained defects were divided into core, sub-surface and outer depending on the positioning in the specimen volume and they were analysed through block-maxima sampling to obtain the maxima distribution [20,21]. The sampling volumes were selected separately, as shown in Figure 7.a, for core and subsurface regions, while for outer population was considered a sampling surface. The core and sub-surface populations were similar, with average maximum defect sizes of 164 and 140 µm, respectively. As can be appreciated in Figure 7.b, the outer population was distinctly larger, with an average of 389 µm, and closely matched the killer defects.
From the maxima defects distributions, it is clear how the killer defects belong to the outer distributions being completely different compared to volumetric core and sub-surface defects.
This correspondence indicates that the fatigue-controlling flaws belonged to a specific surface-connected population.

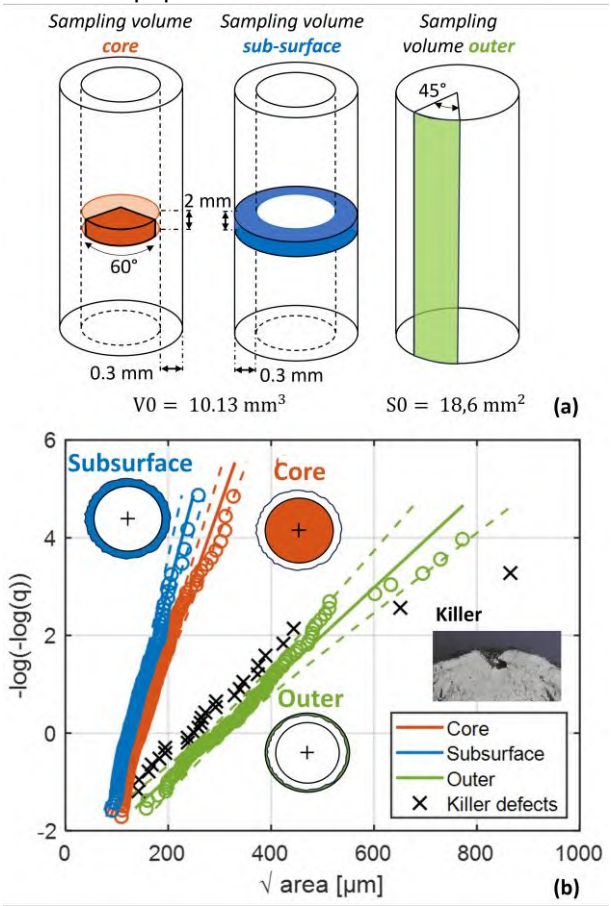


Figure 7: a) block maxima sampling schemas for core, sub-surface and outer defects; b) estimated maxima defects distributions for core, subsurface and outer compared to killer defects

Analysis of the slicing strategy suggested that the killer defects formed in the contour region. An overlapping between the start-end points of the two contour passages was found in the layer of many killer defects. This overlap could locally increase heat accumulation and disturb melting and solidification. The typical flaw dimensions were also consistent with the contour depth and one or two layers thicknesses. Although this mechanism requires dedicated process verification, it identifies the contour strategy as the main route for improving the fatigue performance of the present material.

Under the hypothesis of contour strategy optimization which can avoid the formation of such defects, the prospective fatigue curve obtained by considering the average core-defect size was obtained using the calibrated fatigue model. It approached the response of sandblasted PBF-LB AlSi10Mg, as shown in Figure 8, particularly in the short-life region where the higher static strength of the MMC becomes beneficial. The comparison separates the intrinsic potential of the material from the current surface-defect limitation.

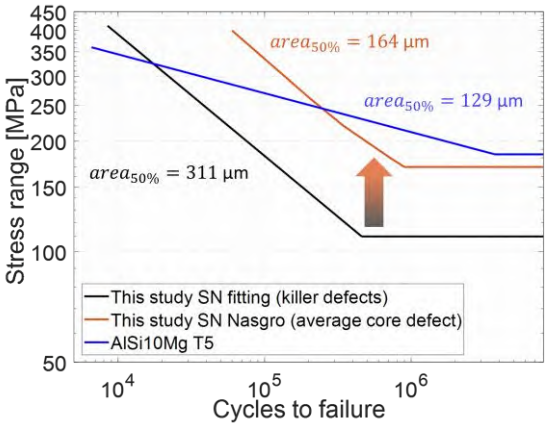


Figure 8: prospective SN diagram and comparison with AlSi10Mg T5 literature data [22]

4. Demonstrator manufacturing and testing

A PBF-LB bipod which is part of an assembly that support an opto-mechanical payload was manufactured successfully and it is shown in Figure 9.

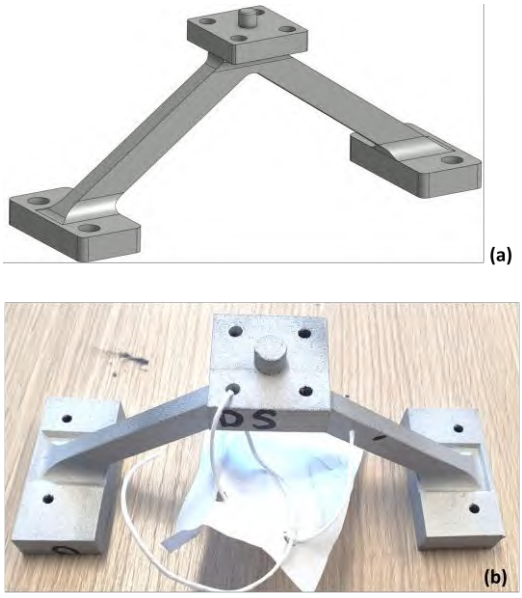


Figure 9: a) CAD model of the component; b) picture of the printed component

However, during post print inspections a manufacturing induced crack was found on the lateral side of the leg. A mono-axial fatigue test on an MTS load frame was designed and three monitoring techniques to track the damage evolution during the fatigue loading were employed. The stable crack growth evolution was successfully tracked independently by digital image correlation (DIC), direct current potential drop (DCPD) and strain gauges applied on both the legs. Applying load ratio R = 0.05 and maximum load Fmax = 2.5 kN, the crack propagated stably to final failure.

The three monitoring techniques provided mutually consistent evidence of damage evolution, although only the DIC crack-length history was used for the direct comparison with the propagation model.

Experimental failure occurred after 588618 cycles. The crack propagation based on the specimen-level Nasgro model was estimate and the crack tip evolution was compared with the experimental one measured by DIC. Under the hypothesis that the component has the same RS of the SEB specimens the yellow curve in Figure 10.a were used in the simulations and the predicted life of the component resulted 152527 cycles and the fatigue life is highly underestimated.

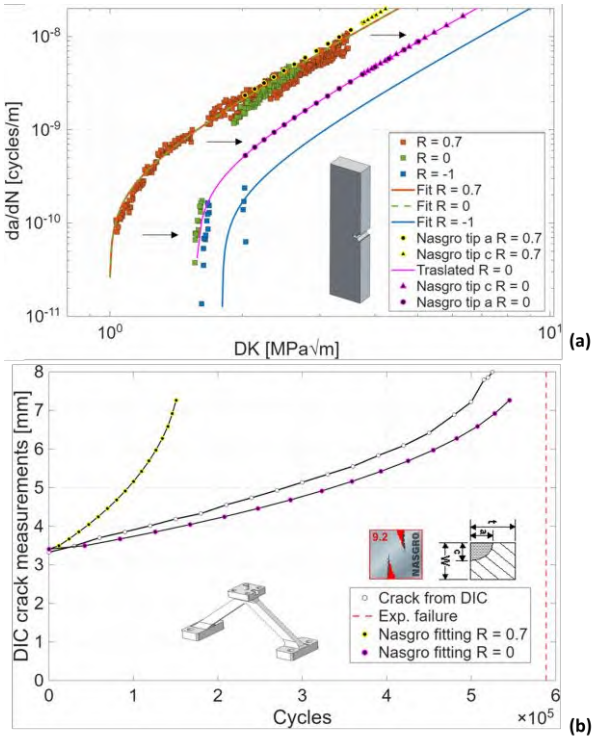


Figure 10: a) specimens crack propagation data used in the component fatigue prediction; b) Crack experimental vs estimated measurements using Nasgro model of specimens

If we assumed no RS present in the component the purple curve in Figure 10.a is used in the simulations and the predicted life becomes close to the experimental one with 556786 cycles, corresponding to a difference of 5.4%. This result supports the transferability of the measured material properties while confirming that residual stresses must be assessed for the actual component geometry, orientation and thermal history. Direct transfer of the high tensile residual-stress condition of the vertical SEB specimens to

the component produced a strongly conservative life prediction.

The same results can be seen in terms of crack tip evolution comparison between simulations and experimental in Figure 10.b. The purple curve highly close to the experimental points obtained by DIC on the surface of the bipod leg.

5. CONCLUSIONS

The mechanical characterization of PBF-LB Al2618 + 7.1 wt% TiB_2 establishes a coherent property set for stiffness-driven and damage-tolerant design. The principal conclusions are:

- The TiB_2 reinforcement increased the room-temperature elastic modulus to 85.2 GPa, 13.2% above the unreinforced reference, while the material retained a yield strength of 345 MPa.
- Fracture toughness remained competitive despite the high ceramic content. The values ranged from 15.3 to 23.9 MPa √m.
- The FCG response was successfully calibrated at R = -1, 0 and 0.7 using Nasgro propagation model. Tensile residual stresses caused the R = 0 Paris-regime data to approach the open-crack R = 0.7 response.
- Fatigue life of net-shape specimens was controlled by a surface-connected defect population with a mean √area of 311 µm. The location of each defect relative to the compressive and tensile residual-stress regions was essential to the observed life.
- XCT block-maxima analysis separated the critical outer-defect population from smaller core and sub-surface populations. Reducing contour-region defects offers the clearest path to achieving fatigue performance comparable with established PBF-LB aluminium alloys.
- A NASGRO model combining FCG data, defect geometry and residual stresses gave a component-level fatigue life prediction within 5.4% error, when the component residual-stress condition was treated independently.

Future work should prioritize contour-parameter refinement and heat treatments able to reduce tensile residual stresses while preserving the high stiffness and static strength of the reinforced alloy.

ACKNOWLEDGEMENTS

This study was performed within the ENCOMPASS project (Design of Enhanced Metal Matrix Composites for Additive Manufacturing of Space Structures), funded by the European Space Agency under Contract No. 4000139305/22/NL/AR.

REFERENCES

1. T. DebRoy, H.L. Wei, J.S. Zuback, Tukherjee, J.W. Elmer, J.O. Milewski, A.M. Beese, A. Wilson Heid, A. De, W. Zhang, Additive manufacturing of metallic components – Process, structure and properties, *Prog. Mater. Sci.* 92 (2018) 112–224. https://doi.org/10.1016/j.pmatsci.2017.10.001.

2. D. Herzog, V. Seyda, E. Wycisk, C. Emmelmann, *Additive manufacturing of metals*, Acta Mater. 117 (2016) 371–392. https://doi.org/10.1016/j.actamat.2016.07.019.

3. U. Essien, S. Vaudreuil, Issues in Metal Matrix Composites Fabricated by Laser Powder Bed Fusion Technique: A Review, *Adv. Eng. Mater*. 24(2022).https://doi.org/10.1002/adem.202200055.

4. P. Samal, P.R. Vundavilli, A. Meher, M.M Mahapatra, Recent progress in aluminum metal matrix composites: A review on processing, mechanical and wear properties, *J. Manuf. Process.* 59 (2020) 131–152. https://doi.org/10.1016/j.jmapro.2020.09.010.

5. S. Amirkhanlou, S. Ji, A review on high stiffness aluminum-based composites and bimetallics, *Critical Reviews in Solid State and Materials Sciences* 45 (2020) 1–21. https://doi.org/10.1080/10408436.2018.1485550.

6. J. Christudasjustus, T. Larimian, J. Esquivel, S. Gupta, A.A. Darwish, T. Borkar, R.K. Gupta, Aluminum alloys with high elastic modulus, *Mater. Lett.* 320 (2022) 132292. https://doi.org/10.1016/j.matlet.2022.132292.

7. A. Yadollahi, N. Shamsaei, Additive manufacturing of fatigue resistant materials: Challenges and opportunities, *Int. J. Fatigue* 98 (2017) 14–31. https://doi.org/10.1016/j.ijfatigue.2017.01.001.

8. L. Mariotti, G. Lupi, A. Pozzoli, S. Beretta, B. Madejski, D. Girolamo, R. Casati, L. Patriarca, Fatigue and fracture properties of Al2618 + TiB2 reinforced metal matrix composite produced by Laser-powder bed fusion, *Int. J. Fatigue* 208 (2026) 109566. https://doi.org/10.1016/j.ijfatigue.2026.109566.

9. G. Lupi, L. Mariotti, S. Lu, W. Xu, L. Patriarca, R. Casati, Unforeseen precipitation sequences in ex situ/in-situ TiB2-reinforced Al2618 Composites Manufactured by Laser-based powder bed fusion, *Materials Science and Engineering*: A 950 (2026) 149500. https://doi.org/10.1016/j.msea.2025.149500.

10. G. Lupi, L. Mariotti, A. Mistrini, J. Larsson, L. Patriarca, R. Casati, Microstructure and tensile properties of TIB2-reinforced Al-2618 thin walls produced by laser powder bed fusion, *Mater. Charact.* 228 (2025) 115372. https://doi.org/10.1016/j.matchar.2025.115372.

11. ECSS-Q-ST-70-80C(30July2021), (n.d.).

12. Metallic materials. Tensile testing. Method of test at room temperature, (2019). Internal pdf://3.175.119.126/2016-Metallic materials. Tensile testing. Meth.pdf.

13. E. Committee, others, E399--12e1 standard test method for linear-elastic plane-strain fracture toughness KIc of metallic materials, *West Conshohocken*, PA: ASTM International (2012).

14. American Society for Testing and Materials (ASTM), *ASTM E647-11*. Standard test method for measurement of fatigue crack growth rates, (2011).
15. *ASTM E466-21*, Practice for Conducting Force Controlled Constant Amplitude Axial Fatigue Tests of Metallic Materials, (2021). https://doi.org/10.1520/E0466-21.
16. Y. Murakami, Inclusion rating by statistics of extreme values and its application to fatigue strength prediction and quality control of materials, *J. Res. Natl. Inst. Stand. Technol.* 99 (1994) 345. https://doi.org/10.6028/jres.099.032.
17. John Gilbert Kaufman, Properties of aluminum alloys: Tensile, creep, and fatigue data at high and low temperatures, *ASM International*, 1999.
18. Nasgro Fracture Mechanics and Fatigue Crack Growth Analysis Software Reference Manual, Version 9.2, 2020. www.nasgro.swri.org.
19. A. International, E739-10 Standard Practice for Statistical Analysis of Linear or Linearized Stress Life (S-N) and Strain-Life (ε-N) Fatigue Data, (2015). https://doi.org/https://doi.org/10.1520/E073910R15
20. E.J. Gumbel, Statistics of Extremes, *Columbia University Press*, New York, 1957.
21. F. Steinhilber, J. Lachambre, D. Coeurjolly, J.Y. Buffiere, G. Martin, R. Dendievel, A methodology for the 3D characterization of surfaces using X-ray computed tomography: Application to additively manufactured parts, *Addit. Manuf.* 84 (2024) 104144. https://doi.org/10.1016/J.ADDMA.2024.104144.
22. F. Sausto, C. Tezzele, S. Beretta, Analysis of Fatigue Strength of L-PBF AlSi10Mg with Different Surface Post-Processes: Effect of Residual Stresses, *Metals* (Basel). 12 (2022) 898. https://doi.org/10.3390/met12060898.

HEALING MATERIALS FOR HARSH SPACE ENVIRONMENTS: INTRINSIC SELF-HEALING COPOLYIMIDES FOR LUNAR EXPLORATION

Francesca Blondelli[1], Guido Saccone[2], Nunzia Favaloro[2], Susanna Laurenzi[3], Bruno Delacourt[4], Maria Gabriella Santonicola[1]

[1]Department of Chemical Engineering Materials Environment, Sapienza University of Rome, Italy, Email: francesca.blondelli@uniroma1.it, mariagabriella.santonicola@uniroma.1.it
[2]Italian Aerospace Research Centre, Italy, Email: g.saccone@cira.it, n.favaloro@cira.it
[3]Sapienza Aerospace Structures Laboratory, Sapienza University of Rome, Italy, Email: susanna.laurenzi@uniroma1.it
[4]European Space Agency (ESA), European Space Research and Technology Centre (ESTEC), Noordwijk, The Netherlands, Email: bruno.delacourt@esa.int

KEYWORDS

Polyimide, Intrinsic Self-healing, Lunar dust, Moon environment

ABSTRACT

Future lunar exploration missions pose critical challenges for polymeric materials due to the severe degradation caused by adhesive and highly abrasive lunar regolith. Conventional fully aromatic polyimides (PIs), although widely used in space for their excellent thermo-mechanical stability, low outgassing, and chemical resistance, possess rigid backbones that prevent intrinsic self-healing and promote progressive surface degradation. In this work, semi-aromatic branched copolyimides (coPIs) with intrinsic self-healing ability are developed by tailoring the stoichiometric ratio between aromatic and aliphatic monomers. The aromatic fraction enhances thermo-mechanical stability, whereas the aliphatic fraction promotes chain mobility and self-healing through supramolecular interactions. The thermo-optical properties were investigated in terms of solar absorptance and emittance. The chemical structure was confirmed by Fourier transform infrared spectroscopy (FTIR), whereas thermal stability and self-healing performance were investigated by thermogravimetric analysis (TGA) and confocal microscopy, respectively. The self-healing capability of the membranes was also investigated after VUV irradiation and thermal cycling (20 cycles from -80 °C to 125 °C). The developed coPIs combine good thermal stability, and efficient thermally activated intrinsic self-healing, demonstrating their potential as multifunctional materials for long-duration lunar exploration missions.

1. INTRODUCTION

Polyimides (PIs) are a class of high-performance polymers widely used in aerospace applications due to their excellent thermal stability, mechanical strength, chemical resistance, low outgassing, and electrical insulation [1,2]. They are employed in satellites, multilayer insulation (MLI), flexible solar arrays, deployable structures, and other spacecraft components [2,3]. In recent years, PIs have attracted increasing interest for future lunar exploration missions. The harsh lunar environment poses significant challenges, particularly the severe abrasion caused by highly adhesive lunar regolith, which can progressively degrade exposed polymeric surfaces and compromise mission reliability [4]. Indeed, lunar dust represents one of the major challenges for future long-duration lunar missions. Unlike terrestrial dust, lunar particles are highly angular, abrasive, and electrostatically charged due to exposure to unfiltered UV radiation since the substantial absence of a gaseous atmosphere [5] on the Moon. These conditions promote strong adhesion to exposed surfaces, leading to progressive sticking, abrasion, and degradation of polymeric materials and thermal protection systems [6].

Self-healing polymers have emerged as a promising and reliable strategy to improve the durability and service life of aerospace materials [7,8] conceived for application on celestial bodies where the maintenance operations are extremely complex or almost not strictly feasible. Unlike extrinsic systems, which rely on encapsulated healing agents or hollow fibres, intrinsic self-healing is based on reversible molecular interactions and polymer chain mobility, without the need for encapsulated healing agents [9]. Self-healing can be classified as either autonomous or non-autonomous. In autonomous self-healing systems, the damage itself is the trigger for the healing process, without requiring external intervention. In contrast, non-autonomous self-healing systems require the application of an external stimulus, such as heat, pressure, light, or other environmental triggers, to activate the healing mechanism [9].

Conventional fully aromatic PIs possess rigid backbones with limited chain mobility, preventing intrinsic self-healing despite their outstanding thermo-mechanical properties [10]. This limitation is particularly relevant for space applications, where materials are subjected to intense radiation, potential micrometeoroid impacts and lunar dust abrasion.

However, one effective strategy to overcome this

constraint is the incorporation of flexible aliphatic segments into the aromatic polyimide backbone. Previous studies [11,12] demonstrated that long-chain aliphatic diamines, such as Priamine 1075, can promote intrinsic self-healing through supramolecular interactions, although often at the expense of thermal and mechanical performance. Therefore, achieving an optimal balance between chain mobility and structural rigidity remains a key challenge for space applications.

In this work, semi-aromatic branched copolyimides (coPIs) were designed by varying the stoichiometric ratio between aromatic and aliphatic monomers to tailor the balance between intrinsic self-healing and thermal stability. The fully aromatic polyimide (PI) was synthesized as a reference material for comparison with the semi-aromatic copolyimides.

The materials were characterized in terms of FTIR, TGA, thermo-optical properties and self-healing ability. The influence of molecular architecture on self-healing efficiency and thermal performance was systematically investigated to identify compositions suitable for long-duration lunar applications. The developed copolyimides combine intrinsic self-healing, excellent thermal stability, and favorable thermo-optical properties, making them promising candidates for advanced space applications such as MLI systems, lightweight spacecraft structures, lunar dust-resistant coatings, and robotic components operating in harsh extraterrestrial environments.

2. EXPERIMENTAL SECTION

2.1. Materials

2,2-bis(3,4-dicarboxyphenyl) hexafluoropropane dianhydride (6FDA, Alfa Aesar, Kandel, Germany); 2,2′-bis(trifluoromethyl)benzidine (TFMB, BLD Pharmatech Ltd, China); a fatty dimer diamine derived from vegetable oil (Priamine 1075; Croda Nederland B.V.) was kindly provided by CARGILL BIOINDUSTRIAL B.V. (The Netherlands). The diamine appears as a light yellow viscous liquid with melting point at −30 °C at 1.013 hPa, boiling point > 350 °C, density 0.9 g cm^{-3}, dynamic viscosity 316 mPa.s at 20 °C, molecular weights of 536.80 g mol-1, and 100% renewable carbon content; N,N-dimethylacetamide (DMAc, Sigma-Aldrich, Milan, Italy) with boiling point 164.5–166 °C at 1 atm, density 0.937 g mL-1 at 25 °C, and dynamic viscosity 0.92 mPa s at 25 °C; 2-Propanol (IPA, Sigma-Aldrich, Milan, Italy) with boiling point 82 °C at 1 atm, density 0.786 g mL^{-1} at 25 °C, and dynamic viscosity 2.2 mPa.s at 20 °C.

2.2. Copolyimides and Polyimide Development

The fully aromatic polyimide (PI) was synthesized by a conventional two-step polycondensation procedure [13]. Briefly, TFMB and 6FDA (1:1 molar ratio) were dissolved in a DMAc/IPA (1:1, v/v) solvent mixture and stirred for 24 h at room temperature under an argon atmosphere to obtain the poly(amic acid) (PAA). PAA solution was cast into 30 × 30 mm square molds and dried at 60 °C for 48 h. The resulting membranes were thermally imidized by sequential heating at 80 °C for 2 h, followed by 120, 150, 180, and 200 °C for 30 min each to remove residual solvent and complete the imidization process.

The semi-aromatic copolyimides (coPIs) were synthesized using mixtures of Priamine 1075 and TFMB at different molar ratios (0.7:0.3, 0.5:0.5, and 0.3:0.7), while maintaining a 1:1 overall diamines/6FDA stoichiometry. The resulting PAA membranes were thermally imidized using the same stepwise thermal treatment described for the fully aromatic PI. All polymerizations were carried out in DMAc/IPA (1:1, v/v) using a total monomer concentration of 15 wt% under argon for 24 h at room temperature.

2.3. Characterization Methods

The chemical structures of polyimides were characterized using a Nicolet Summit FTIR Spectrometer (Thermo Fisher Scientific, Waltham, MA, USA) with an attenuated total reflectance (ATR) accessory equipped with a diamond crystal. Each spectrum was acquired from 64 scans co-added at a spectral resolution of 4 cm^{-1}, in the wavenumbers range of 4000-400 cm^{-1}. An ATR correction was applied to the spectra to account for ATR-related intensity and band position distortions, followed by automated baseline correction.

The thermogravimetric analysis (TGA) of PIs was investigated using a TGA/DSC 3+ STARe System instrument (Mettler Toledo, Greifensee, Switzerland). Approximately 5-10 mg of each sample was placed in a 70 µL alumina crucible and analyzed over the temperature range of 25-700 °C at a heating rate of 10 °C min^{-1} under a nitrogen atmosphere. The first derivative of the TGA curves was calculated to obtain the derivative thermogravimetric (DTGA) curves. The DTGA curves were used to determine the onset temperature (T_{onset}) and the temperature corresponding to the maximum degradation rate (T_d) for each material. The curves are normalized by the sample weight.

The total reflectance of the samples was measured over the wavelength range 250-2500 nm using a Cary 5000 UV/Vis-NIR spectrophotometer (Agilent Technologies, USA) under ambient laboratory conditions (22 ± 3 °C, 55 ± 20 % RH), equipped with an external integrating sphere All measurements were performed at near-normal incidence. The reflectance measurements were referenced against the certified reflectance standard ISO-WS#1-Dif-10. The transmittance of the membranes was measured in the UV/VIS-NIR range (200-2500 nm) using an Agilent Cary 7000 spectrophotometer (Agilent Technologies, USA).

For the transparent semi-aromatic and fully aromatic PI samples, both the reflectance and the transmittance curves were considered to calculate

the solar absorptance (α). Solar absorptance (α) was calculated using an in-house Python script. The spectral transmittance and reflectance were weighted by the spectral solar irradiance, using the ASTM E490 solar spectral irradiance distribution [14].

The emittance was measured using the SOC ET-100 Emissometer (Surface Optics Corporation, USA) under ambient laboratory conditions (22 ± 3 °C, 55 ± 20 % RH). The ET-100 Emissometer conforms to ASTM E408. The ET 100 measures the integrated surface reflectance of a surface at two different angles of incidence (20° and 60°). The integrating sphere captures the reflected light from the target material, integrating reflections in all directions. Prior to the measurements, the ET-100 Emissometer was calibrated using certified reference standards with known emissivity values (NIST Traceable Gold Cal. Coupon 6501RG-03 at 20° and 60°).

A confocal laser microscope (Keyence VK-X1000 3D laser scanning microscope, Keyence Corporation, Osaka, Japan) equipped with a N Plan 20× /0.46 objective lens (Nikon Corporation, Tokyo, Japan) were used to quantify the self-healing of semi-aromatic coPIs and fully aromatic PI. A cut was first introduced on the surface of the material using a blade. The initial cut volume (V_i) was determined using the Multifile Analyzer software integrated with the confocal microscope. The volume of the cut was calculated as length × height × depth, based on measurements acquired from the confocal images. Subsequently, the sample was placed inside an MPS-PT (Micro Probe Station-Peltier type) chamber under reduced pressure (0.3 mbar). A thermal healing cycle was then applied by heating the specimen from 25 °C to 130 °C at a rate of 10 °C min^{-1}, followed by an isothermal hold of 30 min at the target temperature. Afterward, the sample was cooled to 10 °C and held at this temperature for 1 min. Following the thermal cycle, the damaged area was examined again to evaluate the healing efficiency and the evolution of the cut volume (V_f). The healing efficiency (SH_{eff}) was determined according to the equation [15]:

$$SH_{eff}\,(\%) = \left(1 - \frac{V_f}{V_i}\right) * 100 \qquad (1)$$

The self-healing ability of the materials was investigated under three different conditions: pristine, after vacuum ultraviolet (VUV) irradiation, and after thermal cycling.

Thermal cycling test was performed using a CTS climatic chamber (Clima Temperatur Systeme, CTS GmbH, Lotzenäcker 21 72379 Hechingen, Germany). The samples were thermally cycled between -80 and +125 °C, for a total of 20 cycles (RH 60%). The samples were cooled and heated at rates of about 5°C min^{-1} and held for 1 h on each temperature extreme of the cycle.

Semi-aromatic coPIs and aromatic PI were exposed to VUV radiation inside a high-vacuum chamber equipped with four VUV lamps operating between 100 and 200 nm. The VUV irradiance spectrum measured inside the facility was integrated over the relevant wavelength range and compared with the corresponding integrated solar irradiance. The ratio between the two integrated irradiances provided the acceleration factor, expressed in solar constants. An acceleration factor of 3.5 equivalent solar constants was obtained. The pressure was kept below 10^{-5} mbar. Three exposure conditions were considered for the test: 500 ESH, 840 ESH, and 1260 ESH.

3. RESULTS AND DISCUSSION

3.1. Copolyimides and Polyimide Development

A series of semi-aromatic copolyimides (coPIs) and a fully aromatic polyimide (PI) were synthesized in a mixture of conventional (DMAc) and non-toxic (IPA) solvents using the protocol described in section 2.2. The semi-aromatic copolyimides were prepared by reacting two diamines (Priamine 1075 and TFMB), at different stoichiometric ratios, with the same aromatic dianhydride (6FDA). The fully aromatic polyimide was synthesized from aromatic monomers (TFMB and 6FDA). All synthesized polyimides were subjected to a thermal curing treatment up to 200 °C to complete the imidization process and remove residual solvent. Tab. 1 lists the chemical compositions, stoichiometric ratios, and sample designations of the synthesized polyimides. coPI-07 contains the highest aliphatic content, whereas coPI-03 contains the lowest. In contrast, the fully aromatic PI does not contain any aliphatic segments.

Table 1: Polyimide chemical composition, stoichiometric ratio of monomers, and sample designations.

Polyimide chemical composition	Stoichiometric ratio	Name of the sample
TFMB:6FDA	1:1	PI
Priamine 1075: TFMB: 6FDA	0.3:0.7:1	coPI-03
Priamine 1075: TFMB: 6FDA	0.5:0.5:1	coPI-05
Priamine 1075: TFMB: 6FDA	0.7:0.3:1	coPI-07

3.2. FTIR Analysis

The chemical structures of the polyimides were investigated by FTIR spectroscopy and compared. The FTIR spectra of polyimides are shown in Fig. 1, where the characteristic absorption peaks of the imide bonds are observed. The analysis revealed distinct peaks at the following frequencies: 1777

cm^{-1}, corresponding to the asymmetric stretching vibrational modes of the C=O bond; 1717 cm^{-1}, corresponding to the symmetric stretching vibrational modes of the C=O bond; 1368 cm^{-1}, corresponding to the stretching vibrational modes of the C-N bond; 724 cm^{-1}, corresponding to the bending vibrational modes of the C=O bond [1,6]. The absence of the characteristic peaks at the frequencies of 3330, 1710, 1650, and 1550 cm^{-1}, associated with the absorption of COOH and NH_2, C=O(COOH), C=O(CONH), and C-NH in the PAA macromolecule, respectively, is an indication of the successful conversion and imidization of the PAA amide groups into imide groups (PI). The absorption bands at 2925 cm^{-1} and 2855 cm^{-1}, observed only in the semi-aromatic PI and coPIs, are assigned to the asymmetric and symmetric stretching vibrations of aliphatic C-H bonds associated with the dimer diamine (Priamine 1075) segment [16].

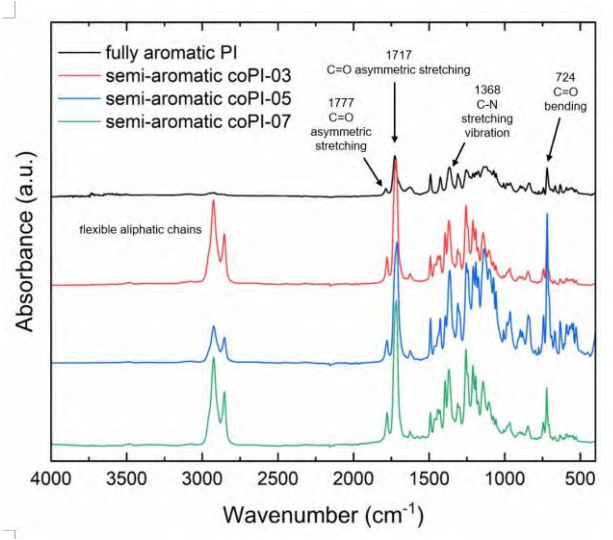


Figure 1: FTIR spectra of polyimide membranes in the range 4000-400 cm^{-1}. Data are offset for clarity.

3.3. Thermal Stability by TGA

Thermal stability is one of the most critical requirements for space polymeric materials. The thermal stability of the synthesized polyimides was investigated by TGA, which provides information on their degradation behaviour and thermal stability. The results are summarized in Tab. 2. The degradation behaviour was strongly influenced by the polymer composition. Fully aromatic PI exhibits a single-step degradation process, whereas coPI-03, coPI-05, and coPI-07 showed a two-step degradation profile. The first degradation stage, occurring at approximately 460-485 °C, is associated with the decomposition of the aliphatic segments introduced by Priamine 1075 [17], while the second stage above 550 °C corresponds to the degradation of the aromatic polyimide backbone and the formation of char [18]. As expected, the fully aromatic PI exhibited the highest thermal stability, with an onset degradation temperature (T_{onset}) of about 494 °C. Nevertheless, the semi-aromatic copolyimides also showed excellent thermal resistance, with T_{onset} values approximately 420 °C, confirming their suitability for applications requiring high thermal stability. The temperature corresponding to 5% weight loss ($T_{95\%}$) was used as an additional indicator of the thermal stability of the investigated polyimides. All semi-aromatic samples exhibited $T_{95\%}$ values above 420-430 °C (Tab.2), confirming their excellent resistance to thermal degradation and highlighting their aptness for applications involving prolonged exposure to elevated temperatures.

Table 2: Thermal stability parameters of the synthesized polyimides obtained from TGA analysis.

Polyimide	$T_{95\%}$ [°C]	T_{onset} [°C]	T_d [°C]	Weight Loss [%]
PI	510.66	493.89	597.99	78.56
coPI-03	431.16	419.75	463.00 & 592.20	78.28
coPI-05	421.33	421.56	460.99 & 593.35	87.80
coPI-07	424. 17	418.72	467.33 & 555.13	76.37

These results are particularly relevant for potential applications in the lunar environment, where materials are exposed to extreme thermal conditions due to the absence of a substantial gaseous atmosphere. During a lunar day, surface temperatures can reach approximately +130 °C depending on the exact location. The high thermal stability demonstrated by the synthesized semi-aromatic copolyimides, with T_{onset} values above 420 °C and excellent resistance to thermal degradation, provides a significant safety margin with respect to the maximum temperatures expected on the lunar surface.

3.4. Thermo-Optical Properties

The thermo-optical properties of the synthesized polyimides were investigated by measuring their solar absorptance (α) and infrared emittance (ε). The ratio between α and ε provides information about the radiative thermal balance of a spacecraft. A low α reduces the amount of incident solar energy absorbed by the surface, while a high ε promotes efficient radiative heat dissipation to the surrounding space. The ratio between α and ε value is one of the primary parameters used to characterize the thermo-optical properties of MLI. It is a high-performance thermal insulation system consisting of

multiple low-emissivity layers separated by spacers, designed to minimize heat transfer by thermal radiation. It is widely used as the outer thermal protection layer of spacecraft and satellites [19]. Lower α/ε values are generally preferred for external spacecraft applications, as they minimize solar heat absorption while maintaining a high capability to reject heat by infrared emission, thereby improving the thermal
performance of the insulation system.
Kapton® film with an aluminium backing, one of the most widely used outer-layer materials for spacecraft MLI blankets, typically exhibits a solar absorptance of 0.20–0.25 and an infrared emittance of approximately 0.25 for a thickness of 0.08 mil. The same material with a thickness of 5.00 mil exhibits a higher α (0.46) and an ε of 0.86 [20].
Teflon® FEP (fluorinated ethylene-propylene) is commonly used on exterior spacecraft surfaces in the low Earth orbit (LEO) environment for thermal control. Silverized or aluminized FEP (Ag-FEP and Al-FEP, respectively) is used for the outer layer of thermal control blankets because of the low solar absorptance (α = 0.08 and 0.13, respectively) and high thermal emittance (ε= 0.81 and 0.81 respectively) of these materials. These optical properties provide very low solar absorptance to thermal emittance ratios (α/ε 0.10 and 0.16, respectively) which are required for maintaining spacecraft temperatures in LEO [21].
In the present work, the investigated coPIs exhibited α/ε ratios ranging from 0.363 to 0.150 for a thickness of approximately 200 μm (Tab.3), suggesting that thermo-optical properties strongly depended on the aromatic/aliphatic ratio. Increasing the aromatic content progressively reduced the solar absorptance while maintaining a high infrared emittance, resulting in lower α/ε ratios.
CoPI-07, which has the highest aliphatic content, exhibited the highest solar absorptance (α) and the lowest infrared emittance (ε), whereas coPI-03, with the lowest aliphatic content, exhibited the lowest α and the highest ε. The results indicate that the investigated coPIs tend to absorb a limited amount of solar radiation, while efficiently emitting thermal radiation, resulting in favourable α/ε ratios for passive thermal control applications. The main advantage of the developed self-healing coPIs lies in their potential use as substrate materials for the outer layer of spacecraft MLI systems.

Table 3: The solar absorptance (α), the emittance (ε), and the ratio between them.

Polyimide	α	ε	α/ε
PI	0.143	0.955	0.150
coPI-03	0.173	0.953	0.182
coPI-05	0.241	0.953	0.253
coPI-07	0.336	0.926	0.363

The measured α/ε values are comparable to those reported for several polymeric materials employed in spacecraft thermal control systems. In particular, the thermo-optical performance of coPI-03 approaches that of fluoropolymer-based outer layers, while providing the additional functionality of intrinsic self-healing.

3.5. Self-Healing Ability

3.5.1. Self-Healing Ability of Pristine Materials

To evaluate the potential of the synthesized polyimides for future lunar applications, their intrinsic self-healing capability was investigated by comparing the initial and final cut volumes, as described by Eq. 1. The semi-aromatic coPIs exhibit an intrinsic, non-autonomous healing mechanism, in which damage recovery is activated by an external thermal stimulus (heating at 130 °C).
Fig. 2a shows a representative example of the self-healing behaviour of coPI-05 (0.5:0.5:1) at 130 °C. The cut is clearly visible in the image on the left, whereas after 30 min at 130 °C under 0.3 mbar, it is no longer detectable, indicating successful healing. In contrast, Fig. 2b shows a representative example of the self-healing behaviour of fully aromatic PI (1:1) at 130 °C. The cut is clearly visible in both the optical images also after 30 min at 130 °C under 0.3 mbar, suggesting a negligible self-healing capability.

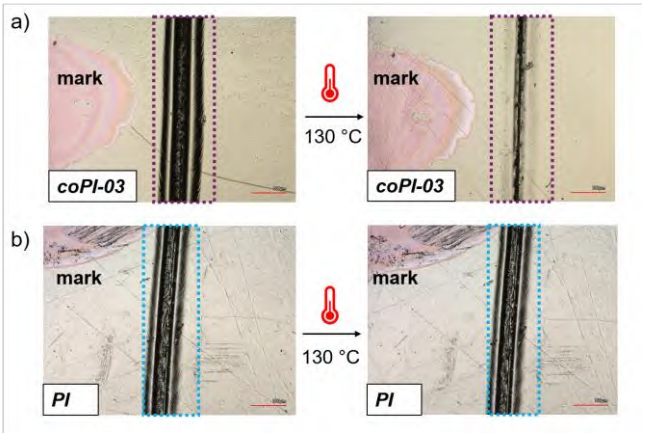


Figure 2: Confocal microscopy images of the damaged surfaces of a) coPI-05 and b) the fully aromatic PI before (left) and after (right) heating at 130 °C. The dashed rectangles highlight the damaged region. The pink mark was used as a positional reference to identify the same region of the sample before and after the healing treatment.

The corresponding 3D surface reconstructions obtained using the analysis software of Fig. 2a are shown in Fig.3 for the semi-aromatic coPI-05.

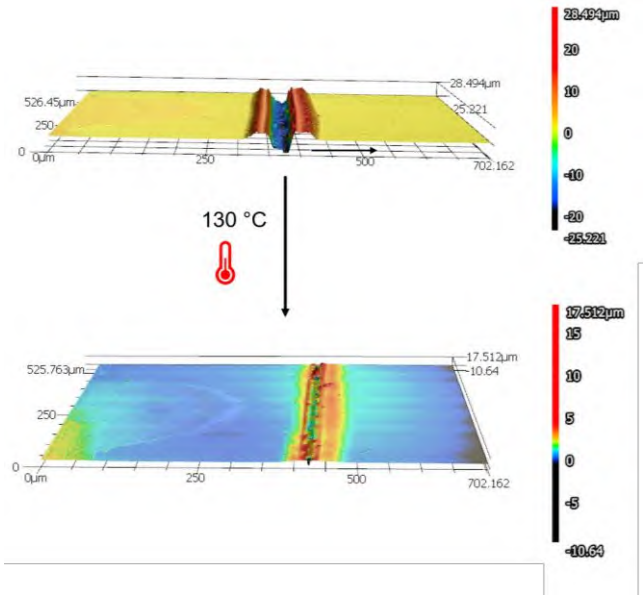


Figure 3: 3D surface reconstructions of the damaged coPI-05 surface before (top) and after (bottom) heating at 130 °C.

Fig. 4 presents the 3D surface topography of fully aromatic PI reconstructed from the data processed with the analysis software illustrated in Fig. 2b.

.

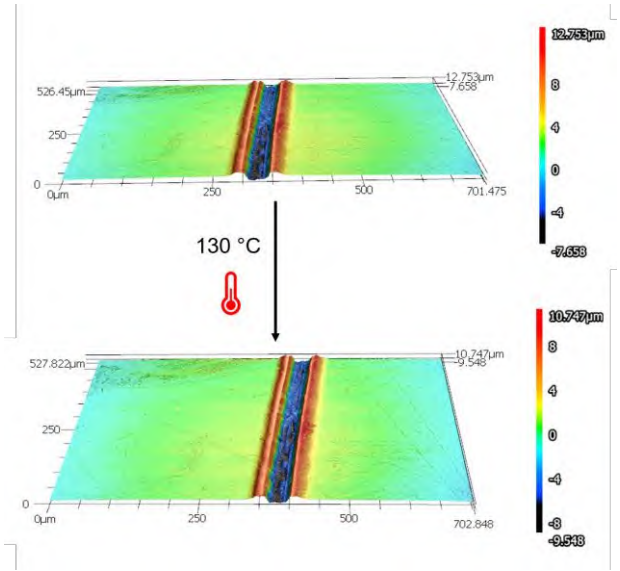


Figure 4: 3D surface reconstructions of the damaged PI surface before (top) and after (bottom) heating at 130 °C.

Tab. 4 reports the self-healing efficiency (SH_{eff}) for semi-aromatic coPIs, and fully aromatic PI evaluated at 130 °C and calculated by Eq.1. The fully aromatic PI shows no self-healing behaviour (SH_{eff} < 15%). This behaviour can be attributed to the presence of highly stable and rigid aromatic structures, which significantly restrict polymer chain mobility. As a result, the diffusion and rearrangement of polymer chains across the damaged interface are hindered, preventing the establishment of the intermolecular interactions required for effective healing. In contrast, the coPIs containing the aliphatic diamine exhibited high self-healing efficiencies, reaching values above 80%. This remarkable healing capability can be attributed to the increased chain mobility imparted by the flexible aliphatic segments, which facilitates the rearrangement of polymer chains after damage. Furthermore, the formation of secondary interactions and supramolecular forces between the branched polymer chains promotes cut closure and structural healing, thereby enhancing the self-healing process.

Table 4: Self-healing efficiency at 130 °C after 30 min at 0.3 mbar calculated by Eq.1.

Polyimide	SH_{eff} (%)
PI	14.20
coPI-03	78.90
coPI-05	99.05
coPI-07	100

These results demonstrate the ability of the investigated materials to recover from mechanical damage, highlighting their potential for applications where durability and long-term structural integrity are critical. Components operating in lunar environments are continuously exposed to lunar dust that can induce the formation of microcracks and surface defects over time. The ability to repair such damage could significantly extend the service life of structural and functional components, reduce maintenance operations, and improve mission reliability.

3.5.2. Self-Healing Ability After Thermal Cycling

The synthesized polyimides were subjected to repeated thermal cycles between -80 °C and +125 °C to investigate the effect of thermal cycling on their self-healing capability. This temperature range was selected to simulate representative conditions encountered in the lunar environment. The self-healing performance was subsequently assessed after thermal cycling. All materials retained their structural integrity without showing any visible deformation after the thermal cycling treatment, except for the copolyimide with the highest aliphatic content (coPI-07), which exhibited noticeable deformation.

Tab. 5 shows the self-healing efficiency (SH_{eff}) at 130 °C for 30 min at 0.3 mbar before and after 20 thermal cycles. All semi-aromatic coPIs exhibited high SH_{eff}. Also in this condition, the aromatic PI showed significantly lower healing efficiency. These

results indicate that the coPIs retain their self-healing ability also after thermal cycling.

Table 5: Comparison of the self-healing efficiency (SH_{eff}, %) of the investigated semi-aromatic coPIs and fully aromatic PI before and after 20 thermal cycles.

Polyimide	SH_{eff} (%) before thermal cycling	SH_{eff} (%) after thermal cycling
PI	14.20	19.89
coPI-03	78.90	82.50
coPI-05	99.05	98.96
coPI-07	100	93.45

3.5.3. Self-Healing Ability After VUV Exposure

The samples were subjected to three different exposures to VUV radiation (0 ESH, 500 ESH, 840 ESH, and 1260 ESH). The objective of this test is to evaluate the resistance and potential degradation of the developed materials under VUV radiation, simulating the harsh conditions encountered in the space environment. Fig. 5 shows the samples before and after 500 ESH VUV exposure. A mask was used during irradiation to preserve a non-exposed reference area on each sample, allowing a direct comparison between the irradiated and pristine regions. The VUV-exposed area does not exhibit any visible colour change compared to the masked region, indicating that the irradiation did not induce any surface modifications detectable to the naked eye.

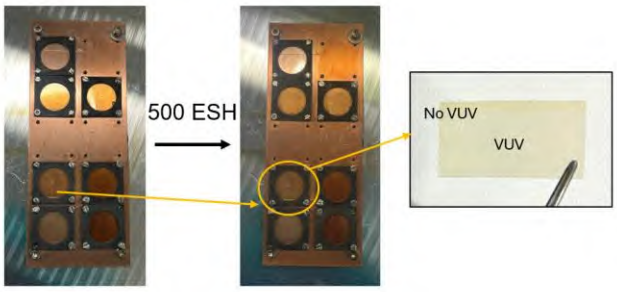


Figure 5: Photographs of the coPI-03 before and after exposure to 500 equivalent sun hours (ESH) of vacuum ultraviolet (VUV) irradiation. The magnified image highlights the boundary between the VUV-exposed and masked regions, showing no visible colour change after irradiation.

Tab. 6 summarizes the self-healing efficiency (SH_{eff}) of the investigated polyimides before and after VUV exposure. The semi-aromatic coPIs containing the highest amounts of aliphatic diamine (coPI-07 and coPI-05) retained their excellent healing capability, exhibiting high self-healing efficiencies even after 1260 ESH. This result indicates that the molecular interactions responsible for the healing process remain largely unaffected by VUV exposure.
In contrast, the semi-aromatic coPI-03 (0.3:0.7:1) showed a progressive reduction in self-healing efficiency with increasing irradiation dose, decreasing from approximately 78% before exposure, to about 60% after 1260 ESH. This behaviour suggests that prolonged VUV irradiation may partially affect the chain mobility and the reversible intermolecular interactions involved in the healing mechanism. Nevertheless, the material maintained a self-healing efficiency above 50% throughout the entire exposure range, demonstrating that a significant healing capability is preserved even after prolonged VUV irradiation.

Table 6: Self-healing efficiency (SH_{eff}, %) of the investigated semi-aromatic coPIs and fully aromatic PI as a function of VUV exposure (0, 500, 840, and 1260 ESH).

Polyimide	VUV Exposure (ESH)	SH_{eff} (%)
Fully aromatic PI	0	14.20
	500	12.60
	840	5.71
	1260	17.81
Semi-aromatic coPI-03	0	78.90
	500	64.92
	840	65.00
	1260	60.49
Semi-aromatic coPI-05	0	99.05
	500	99.01
	840	96.08
	1260	99.62
Semi-aromatic coPI-07	0	100
	500	98.66
	840	97.13
	1260	99.07

4. CONCLUSION

Semi-aromatic intrinsically self-healing copolyimides were successfully synthesized by tailoring the ratio between aromatic and aliphatic diamine monomers. The developed materials combine excellent thermal stability, good thermo-optical properties, and efficient thermally activated and inherent self-healing, while the fully aromatic polyimide was used as a reference to highlight the role of the flexible aliphatic segments on the healing mechanism. Although the incorporation of Priamine 1075 slightly reduced the thermal stability compared with the fully aromatic PI, all copolyimides exhibited degradation temperatures well above the maximum temperatures (T_{onset}~ 420 °C) expected in the lunar environment, demonstrating their suitability for space applications.
The semi-aromatic coPIs exhibited high self-healing efficiencies, reaching values close to 100% for the formulations containing the highest aliphatic

content, whereas the fully aromatic polyimide showed negligible auto-reparation because of its limited chain mobility. Moreover, the self-healing capability was largely preserved after thermal cycling between -80 °C and +125 °C and after prolonged VUV irradiation (500, 840 and 1260 ESH), demonstrating the robustness of the healing mechanism under representative space environmental conditions.

In addition, the investigated coPIs exhibited favourable thermo-optical properties, characterized by low solar absorptance and high infrared emittance, resulting in α/ε ratios suitable for passive thermal control applications.

Overall, these results demonstrate that introducing flexible aliphatic segments into the polyimide backbone provides an effective strategy to balance thermal stability and intrinsic self-healing. The developed copolyimides therefore represent promising multifunctional materials for future lunar exploration missions, particularly as substrate materials for MLI systems and protective coatings against lunar dust abrasion.

Acknowledgment

This work was conducted in collaboration with the European Space Research and Technology Centre (ESTEC) under ESA Cooperative Agreement No. 4000150081/25/NL/GLC. The authors would like to thank Dr. Adrian Tighe and the members of the Materials Physics and Chemistry Section for their support during the visiting period of F.B. at ESTEC. F.B. is financially supported by a PNRR PhD scholarship (MUR D.M. 117/2023) cofunded by Sapienza University of Rome and the Italian Aerospace Research Centre (CIRA).

5. REFERENCES

1. Blondelli, F.; Toto, E.; Botti, S.; Bonfigli, F.; Laurenzi, S.; Santonicola, M. G. Polyimide/graphene nanocomposites for space applications: Potential antibacterial coatings for human exploration missions. *Acta Astronaut*. 2026, 238, 957-965. https://doi.org/10.1016/j.actaastro.2025.09.074.

2. Prakash, P.; Weerasinghe, J.; Levchenko, I.; Prasad, K.; Alexander, K. Polyimide nanocomposites for next generation spacesuits. *Mater. Horiz.* 2025, 12 (11), 3633-3666. http://dx.doi.org/10.1039/D4MH01816H

3. Zhang, Y.; Dai, S.; Yin, Z.; Yan, W.; Li, Q.; Yuan, H.; Zhang, X.; Chen, L.; Luo, J.; Ouyang, X.; et al. Integration fabrication of polyimide composite films for aerospace applications. *SmartMat* 2024, 5 e1225. https://doi.org/10.1002/smm2.1225.

4. Afshar-Mohajer, N.; Wu, C.-Y.; Curtis, J. S.; Gaier, J. R. Review of dust transport and mitigation technologies in lunar and Martian atmospheres. *Adv. Space Res.* 2015, 56 (6), 1222-1241. https://doi.org/10.1016/j.asr.2015.06.007.

5. C.I. Calle, C.R. Buhler, M.R. Johansen, M.D. Hogue, S.J. Snyder, Active dust control and mitigation technology for lunar and Martian exploration, Acta Astronaut., 69 (2011) 1082-1088, https://doi.org/10.1016/j.actaastro.2011.06.010.

6. F. Blondelli, G. Saccone, E. Toto, N. Favaloro, M.G. Santonicola, Poly(Imide-Siloxane) Copolymer Materials for Lunar Dust Mitigation: Synthesis and Characterization of Surface Properties, Macromolecular Symposia, 414 (2025) e70246, https://doi.org/10.1002/masy.70246.

7. Kausar, A.; Ahmad, I.; Maaza, M.; Bocchetta, P. Self-Healing Nanocomposites—Advancements and Aerospace Applications. *J. Compos. Sci.* 2023, 7 (4), 148. https://doi.org/10.3390/jcs7040148.

8. Hager, M. D.; Greil, P.; Leyens, C.; van der Zwaag, S.; Schubert, U. S. Self-Healing Materials. *Adv. Mater.* 2010, 22 (47), 5424-5430. https://doi.org/10.1002/adma.201003036.

9. Bekas, D. G.; Tsirka, K.; Baltzis, D.; Paipetis, A. S. Self-healing materials: A review of advances in materials, evaluation, characterization and monitoring techniques. Compos. Part B Eng. 2016, 87, 92-119. https://doi.org/10.1016/j.compositesb.2015.09.057.

10. Kim, Y. N.; Jo, J. Y.; Park, J.; Lee, J.; Kim, J.; Jeon, D.-y.; Han, H.; Jung, Y. C. Challenge for Trade-Off Relationship between the Mechanical Property and Healing Efficiency of Self-Healable Polyimide. ACS Appl. Mater. Interfaces 2023, 15 (47), 54923-54932. https://doi.org/10.1021/acsami.3c12594.

11. Susa, A.; Bijleveld, J.; Hernandez Santana, M.; Garcia, S. J. Understanding the effect of the dianhydride structure on the properties of semiaromatic polyimides containing a biobased fatty diamine. *ACS Sustain. Chem. Eng.* 2018, 6 (1), 668-678. https://doi.org/10.1021/acssuschemeng.7b03026.

12. Susa, A.; Mordvinkin, A.; Saalwächter, K.; van der Zwaag, S.; Garcia, S. J. Identifying the Role of Primary and Secondary Interactions on the Mechanical Properties and Healing of Densely Branched Polyimides. *Macromol.* 2018, 51 (21), 8333-8345. https://doi.org/10.1021/acs.macromol.8b01396.

13. H. Inoue, Y. Sasaki, T. Ogawa, Comparison of one-pot and two-step polymerization of polyimide from BPDA/ODA, J. of Appl. Polym. Sci-, 60 (1996) 123-131, https://doi.org/10.1002/(SICI)1097-4628(19960404)60:1<123::AID-APP14>3.0.CO;2-9

14. ASTM E490-21, Standard Solar Constant and Zero Air Mass Solar Spectral Irradiance Tables; ASTM International: West Conshohocken, PA, 2021.

15. J. Dahlke, J. Kimmig, M. Abend, S. Zechel, J. Vitz, U.S. Schubert, M.D. Hager, Quantification of the scratch-healing efficiency for novel zwitterionic polymers, NPG Asia Mater., 12 (2020) 13, https://doi.org/10.1038/s41427-019-0190-2.

16. Błażek, K.; Kasprzyk, P.; Datta, J. Diamine derivatives of dimerized fatty acids and bio-based

polyether polyol as sustainable platforms for the synthesis of non-isocyanate polyurethanes. Polymer 2020, 205, 122768. https://doi.org/10.1016/j.polymer.2020.122768.
17. B. Pan, D. Tang, Synthesis and Properties of Fully Biobased Thermoplastic Elastomers from Priamine, ACS Macro Lett., 14 (2025) 1661-1667, https://doi.org/10.1021/acsmacrolett.5c00614.
18. L. Li, Y. Xu, J. Che, X. Su, C. Song, Preparation, characterization and degradation kinetics of transparent fluorinated polyimides with low dielectric constants and excellent hydrophobic properties, Polym. Bull., 75 (2018) 5777-5793, https://doi.org/10.1007/s00289-018-2352-8.
19. D. Singh, M.K. Singh, A. Chaubey, A.K. Ganguly, V. Singh, Thermal performance improvement of multilayer insulation technique, Heat and Mass Transfer, 59 (2023) 1365-1378, https://doi.org/10.1007/s00231-022-03330-y.
20. J.H. Henninger, Solar absorptance and thermal emittance of some common spacecraft thermal-control coatings, in, 1984.
21. K.K. de Groh, D.C. Smith, Investigation of Teflon FEP Embrittlement on Spacecraft in Low Earth Orbit, NASA Technical Memorandum 113153, NASA Lewis Research Center, Cleveland, OH, 1997.

ECSSMET
Braunschweig Germany 2026

Mechanism Testing

Development of a Cost-Efficient Fused Filament Fabrication-Printable Thermoplastic for Structural and Non-Structural Low Earth Orbit Applications

Lisa Wolf [1], Ugo Lafont [2], Holger Ruckdäschel [3], Philipp Häfner[4]

[1] University of Bayreuth, Universitätsstraße 30, 95447 Bayreuth, Germany, Email: l.wolf1@gmx.de
[2] European Space Agency, ESTEC Keplerlaan 1, PO Box 299, Netherlands Email: ugo.lafont@esa.int
[3] University of Bayreuth, Universitätsstraße 30, 95447 Bayreuth, Email: ruckdaeschel@uni-bayreuth.de
[4]Ansbach University of Applied Sciences, Residenzstraße 8, 91522 Ansbach, Email: philipp.haefner@hs-ansbach.de

KEYWORDS

UV, gamma irradiation, outgassing, thermoplastic, additive manufacturing, Fused Filament Fabrication (FFF)-printing, CubeSat, Shaker testing

ABSTRACT

Additive manufacturing is becoming increasingly important for the production of cost-effective, lightweight, and geometrically complex components for both structural and non-structural space applications. At present, however, most flight-qualified components are still manufactured from metallic materials because of their superior mechanical strength and stiffness. Nevertheless, thermoplastics processable by Fused Filament Fabrication (FFF) are attracting increasing interest in the space sector due to their lower manufacturing costs, broader accessibility, and inherent recyclability. Current research and industrial activities predominantly focus on FFF-printable high-performance materials such as polyether ether ketone (PEEK), polyether ketone ketone (PEKK), and polyetherimide (PEI). Although these polymers have demonstrated suitability for space applications, they are associated with high material costs and demanding processing requirements. Consequently, the development of low-cost, readily processable materials capable of withstanding the space environment represents a highly attractive alternative.

The objective of this work is to develop and evaluate a novel FFF-printable material that combines cost-efficiency, ease of processing on commercially available desktop printers, and resistance to the environmental conditions encountered in Low Earth Orbit (LEO). To assess its suitability for space applications, established environmental testing procedures and characterization methods were employed, including outgassing investigations as well as vacuum ultraviolet (VUV) and gamma irradiation exposure. The developed material was characterized before and after environmental exposure with respect to its mechanical performance, using tensile testing, and its thermo-optical properties. The obtained results provide insight into the material's potential for lightweight and cost-effective space applications.

1. INTRODUCTION

High performance thermoplastic material, such as PEEK, PEKK and PEI are increasingly applied for non-structural applications such as sensor boxes and mounts. Nowadays, they are able to compete with thermoset materials in non-structural applications. However, the usage of thermoplastics in structural applications is still limited to a few thermoplastics, due to the sparce knowledge of the material behaviour, such as outgassing, erosion, mechanical strength etc. under space conditions. So far, only selective smaller secondary structure applications were manufactured using thermoplastics, [1]. Processing was mainly performed by conventional, time consuming and expensive methods such as autoclave consolidation and/or milling compression-moulded semi-finished compounds [2], [3].

Additive manufactured thermoplastics for structural and non-structural parts is only recently emerging for spaceflight applications [4]. In this context, mainly Selective Laser Sintering (SLS) is used for smaller structural parts such as picosat launch systems from alba obital [5]. Fused Filament Fabrication (FFF) based methods are currently used for prototyping and in-situ space manufacturing of smaller tools for ISS, and not for structural applications in space [4], [6]. Here, only small parts, mainly based on PEEK compounds, are produced, due to ductility and toughness of PEEK. However, material costs, the printability and reproducibility limit applications [7].

These limitations highlight the need for cost-effective, readily printable, and reproducible FFF materials. Despite the increasing relevance of thermoplastics in space applications, reservations remain regarding the use of newly developed FFF-printed thermoplastics in structural and non-structural flight components, particularly with

respect to their reliability after exposure to the space environment.

Therefore, this study addresses the following research question: Can a cost-effective FFF-printable thermoplastic provide the environmental stability and reliability required for structural and non-structural applications in Low Earth Orbit (LEO)?

2. FFF-PRINTED PARTS FOR LOW EARTH ORBIT APPLICATIONS

2.1. Material development

For the material formulation, a literature review was conducted to identify the most relevant environmental factors in LEO and to select a suitable base polymer and potential fillers using a simple target weighting method that can withstand LEO conditions. The base polymer and the fillers were then compounded via a micro compounder (Xplore MC15) and then injection-moulded into tensile probes after ISO 527-1 1A (thickness 2 mm).

The following formulations were produced:

- Raw Polymer (Raw)
- Polymer + Filler 1 (F1)
- Polymer + Filler 2 (F2)
- Polymer + Filler 1 + Filler 2 (F1+F2)

To investigate if the material can reach a tensile strength of at least 50 MPa and to find the best formulation, the injection-moulded probes were tensile tested on a Zwick & Roell ProLine machine. The best mixture was then compounded on a twin-screw extruder, pelletized and finally extruded on a single screw extruder to obtain filaments. The raw material was also extruded to filaments. Both filaments were used to print tensile probes according to ISO 527-1 1A (2 mm thickness).

For printing the optimal printing parameters, i.e. nozzle temperature, bed temperature and printing speed, regarding warping, layer adhesion and dimensional stability were chosen via the Taguchi-Method. X-Y-Z Cubes were printed at different parameters and the dimension, warpage was measured via 3D-Scanning, the layer adhesion was tested by pressing the Cube with a defined force and a visual inspection of the breaking damage. Numbers from 1-10 (10 best result) were given to each parameter. Out of these parameter sets the best parameter were chosen.

The material was then prepared as described in Section 2.2.2 for further testing under LEO-relevant environmental conditions, as outlined in Section 2.2.

2.2. Material testing for LEO

2.2.1. Material testing standards

To evaluate the potential behavior of the material in the LEO environment, the following standards were applied:

- Outgassing after ECSS-Q-ST-70-02
- Thermal vacuum cycling (TVAC) after ECSS-Q-ST-70-04C15
- UV and particle testing after ECSS-Q-ST-70-06

In addition, the material was characterized before and after UV exposure, thermal-vacuum cycling (TVAC), and particle irradiation using the following methods:

- Thermo-optical properties after ECSS-Q-ST-70-09C 31.
- Tensile testing

The shaker test was performed according to the guidelines specified in the CubeSat Handbook provided by SpaceX. The test setup and applied vibration loads were selected to evaluate the structural integrity of the CubeSat assembly under representative launch-induced mechanical conditions.

2.2.2. FFF printing material qualification

Outgassing tests were conducted on both printed and injection-moulded materials in the unirradiated state, as described in Section 2.2.1.

The printed specimens described in Section 2.1 were subsequently subjected to tensile testing. Selected printed and injection-moulded specimens were gamma-irradiated using a Co-60 source at Helmholtz-Zentrum Berlin for 13 h and 54 min at a dose rate of 3.6 krad/h and at room temperature (24 °C ± 6 °C). This corresponds to Level F (50 krad/500 Gy) and to the standard dose-rate range according to Window 1 (3.6 to 36 krad/h, equivalent to 36 to 360 Gy/h) as specified in ESCC 22900.
The irradiated printed specimens were subsequently tensile tested using the ZwickRoell testing machine.

Some of the printed non-irradiated, printed γ-irradiated and injection-moulded non-irradiated and injection-moulded γ-irradiated tensile probes were then subjected to TVAC for 25 circles from -100 °C to +120 °C with (± 5 °C). The heating rate was 3 K per minute and a dwell time at 125 °C (± 2 °C) (baseplate temperature) for 30 minutes. The cooling rate was 3 K per minute with 110 °C (± 2 °C) and a dwell time of 35 minutes (baseplate temperature). The vacuum was in the range of 10^{-6} to 10^{-5} mbar.

Furthermore, samples of the following materials were subjected to VUV irradiation:

- printed F1+F2 γ-irradiated
- printed F1+F2 non irradiated
- injection-moulded F1+F2 y-irradiated

material were VUV irradiated in Vacuum at 10^{-6} mbar with 3,65 solar constants for 350 hours, resulting in 1260 equivalent sun hours (ESH) and with 3,65 solar constants for 137 hours resulting in 500 ESH.

Spectral reflectance (see figure 4) of the samples was measured with the help of Cary 5000 UV-Vis-NIR spectrometer over a wavelength range of 300 – 2500 nm.

2.3. Applications in LEO

Although a material can be developed and optimized based on LEO environmental requirements, its evaluation has limited relevance without a defined application scenario.

Therefore, the developed material was considered for use as a CubeSat frame structure in a Low Earth Orbit mission. Because the material is intended for structural applications, its mechanical integrity and resistance to launch-induced vibrations must also be validated. Accordingly, the CubeSat structure was subjected to shaker testing to assess its structural performance under representative launch conditions.

Shaker testing was performed in accordance with the SpaceX CubeSat Handbook, which specifies random vibration testing. Low-level sine sweeps were conducted before and after the vibration test as described in the handbook. In addition, the CubeSat frame was 3D scanned before and after the shaker test, and the resulting scans were compared to identify geometric deviations. The frame was also optically inspected and documented photographically.

3. RESULTS

Tensile Testing

The tensile strength of the best-performing filled formulation remained close to that of the neat polymer, despite the incorporation of fillers (Table 1), indicating effective filler-matrix adhesion. However, filler addition also increased the brittleness of the material. Formulations containing only F1 or F2 exhibited slightly lower performance than the combined F1+F2 formulation, suggesting improved compatibility or synergistic effects when both fillers were used. The neat polymer, the F1+F2 formulation, and the F2-containing formulation exceeded the required tensile strength of 50 MPa, whereas the F1-containing formulation remained below this threshold. After TVAC treatment, the injection-moulded materials generally exhibited increased brittleness compared with the untreated specimens, as reflected by reduced elongation at break. Compared with the unfilled material, the filled material showed a reduction in tensile strength after TVAC treatment. By contrast, TVAC treatment of the injection-moulded neat polymer led to increased stiffness, reflected by a higher Young's modulus, and, in the gamma-irradiated material, a slight increase in tensile strength. The underlying mechanisms require further investigation.

Table 1: Medium tensile test values of Injection Moulded Formulations and preparations

Material	Young's modulus [MPa]	Tensile strength [MPa]	Elongation at breake [%]
IM Raw	1220 (σ=288)	65,6 (σ=7,7)	8 (σ=0)
IM Raw TVAC	2546 (σ=34)	64 (σ=11,6)	4,7 (σ=1,2)
IM Raw y-TVAC	2444 (σ=77)	71,2 (σ=3,5)	4,6 (σ=1,2)
IM F1+F2	3310 (σ=657)	61,9 (σ=2,9)	6 (σ=0,5)
IM F1+F2 y-TVAC	2953 (σ=12)	51,2 (σ=3,7)	3 (σ=0,3)
IM F1	3330 (σ=727)	59 (σ=2,9)	6 (σ=0,5)
IM F2	2790 (σ=138)	42,6 (σ=6,8)	4 (σ=0,9)

As expected, the tensile strength of the FFF-printed specimens was reduced to less than half of the corresponding injection-moulded values. Compared with the printed neat polymer, the filled best-performing formulation showed improved printability and consequently higher tensile strength (Table 2), while also exhibiting slightly higher stiffness.

Gamma irradiation further reduced the tensile strength of the printed filled formulation to an average value of 22 MPa. However, the irradiated material displayed slightly higher flexibility than the non-irradiated filled material, similar to the behavior observed for the printed neat polymer.

After TVAC treatment, all printed materials showed increased brittleness, similar to the injection-moulded specimens, resulting in reduced elongation at break. An increase in Young's modulus was observed for the printed neat polymer, indicating material stiffening after TVAC exposure. The filled printed material exhibited a reduction in Young's modulus, consistent with the behavior observed for the injection-moulded filled material. However, when the filled material was first gamma-irradiated and subsequently subjected to TVAC, the reductions in stiffness, ductility, and tensile strength were less pronounced than in the non-irradiated TVAC-treated material. An increase in tensile

strength was observed for the gamma-irradiated and TVAC-treated material. The reduced tensile strength of the printed TVAC-treated material may also be related to printing variability, since these specimens were not manufactured in the same batch as the other printed specimens.

Table 2: Medium tensile test values of FFF-printed Formulations and preparations

Material	Young's modulus [MPa]	Tensile strength [MPa]	Elongation at breake [%]
Print Raw	925 (σ=84)	31,5 (σ=5,0)	6,3 (σ=2,0)
Print Raw γ-TVAC	1689 (σ=173)	26,4 (σ=2,6)	2,1 (σ=0,2)
Print F1+F2	4228 (σ=373)	37,2 (σ=7,4)	3,8 (σ=0,9)
Print F1+F2 γ	1332 (σ=128)	22,1 (σ=1,3)	5,6 (σ=1,6)
Print F1+F2 γ-TVAC	1633 (σ=306)	34,6 (σ=9,1)	3,4 (σ=0,3)
Print F1+F2 TVAC	1377 (σ=159)	25,3 (σ=4,3)	2,6 (σ=0,5)

The increase in Young's modulus while maintaining tensile strength observed for the unfilled TVAC-treated materials, irrespective of the manufacturing process, suggests physical ageing and/or post-crystallisation induced by the TVAC treatment. However, further investigations are required to confirm the underlying mechanisms.

A slight increase in tensile strength after γ-irradiation and TVAC was observed for the injection-moulded neat material and the printed filled material. This behaviour may indicate delayed crosslinking through recombination of residual radicals and/or thermally induced annealing or post-crystallisation, resulting in improved load transfer within the material. This interpretation is supported by the initial reduction in both tensile strength and Young's modulus observed for the printed filled material after γ-irradiation alone. Nevertheless, additional characterisation, such as differential scanning calorimetry (DSC) and dynamic mechanical analysis (DMA), is required to verify these assumptions.

In contrast, the Young's modulus of the filled materials generally decreased after TVAC treatment and γ-irradiation compared with the untreated reference. This indicates that any beneficial changes within the polymer matrix were insufficient to compensate for the reduced reinforcing efficiency of the fillers. A possible explanation is degradation of the filler–matrix interface during TVAC exposure, leading to impaired stress transfer between the matrix and the reinforcing particles. However, this hypothesis likewise requires further experimental validation

Outgassing

The outgassing test of the FFF-printed optimum F1+F2 formulation fulfilled the requirements specified in ECSS-Q-ST-70-02C. In contrast, the injection-moulded F1+F2 formulation slightly exceeded the specified limits (see Table 3).

Regarding the total mass loss (TML), the injection-moulded specimens exhibited lower values compared with the printed material. However, the recovered mass loss (RML) was higher for the injection-moulded samples. This behaviour indicates differences in moisture storage and desorption mechanisms between the two manufacturing approaches. Water within polymer-based materials can be present as molecularly dissolved moisture within the polymer matrix or accumulated within porous regions. The desorption kinetics are therefore influenced by diffusion pathways, material morphology, and the accessible surface area.

The higher porosity of the FFF-printed parts (see Figure 1) may result in increased moisture uptake due to additional storage sites, while simultaneously facilitating moisture release during the outgassing procedure through increased surface accessibility and shorter diffusion pathways. Consequently, a larger fraction of the absorbed moisture may be removed within the initial test period, resulting in a lower RML compared with the injection-moulded material. In contrast, the denser structure and the presence of an injection-moulding skin may limit moisture transport and slow down both desorption and subsequent moisture exchange with the environment.

Additional measurements of the injection-moulded material after 72 h under the controlled recovery conditions specified in ECSS-Q-ST-70-02C support this interpretation. Compared with the measurement directly after 24 h of vacuum exposure, the specimens exhibited a slight weight increase, indicating moisture reabsorption from the environment. The slower moisture uptake compared with the FFF-printed material may be attributed to the denser morphology and the presence of an injection-moulding skin, which reduce the accessible surface area and limit diffusion pathways.

For both manufacturing approaches, the collected volatile condensable material (CVCM) remained well below the ECSS-Q-ST-70-02C limit, indicating negligible condensation of volatile species (see Tables 3 and 4).

3Table : Outgassing Test Results injection-moulded F1+F2

		TML [%]	CVCM [%]	RML [%]
Injection Moulded Material		1.340	0.02	1.025
		1.487	0.02	1.117
		1.353	0.02	1.036
	Average	**1.39**	**0.02**	**1.06**
	SD	**0.08**	**0.00**	**0.05**
	Uncertainties k=2	0.06	0.05	0.06

4Table : Outgassing Test Results 3D-printed F1+F2

		TML [%]	CVCM [%]	RML [%]
3D Printed		2.086	0.00	0.731
		2.062	0.00	0.718
		2.100	0.03	0.746
	Average	**2.08**	**0.01**	**0.73**
	SD	**0.02**	**0.04**	**0.01**
	Uncertainties k=2	0.06	0.05	0.06

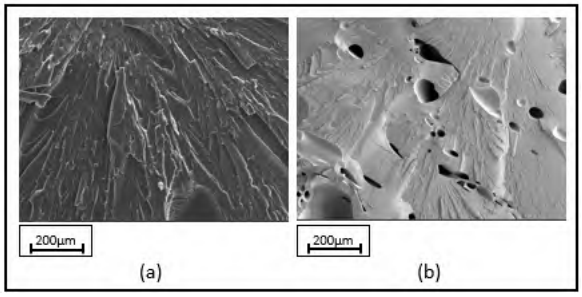


Figure 1: Structure Injection Moulded Material raw (a) and FFF-printed raw (b)

Furthermore, FTIR analysis of the collector plates after the outgassing tests (see Figures 2 and 3) revealed no significant traces of additional volatile compounds. This suggests that the majority of the released mass can be attributed to moisture rather than to low-molecular-weight degradation products or processing-related volatiles.

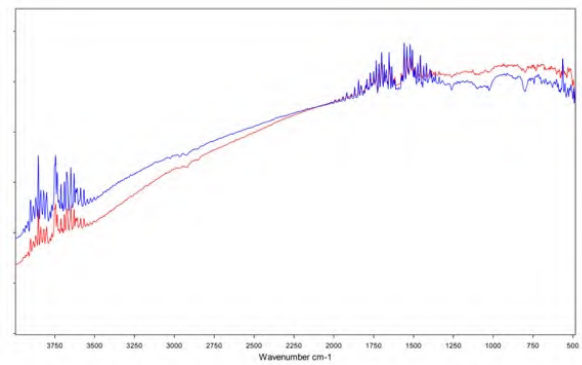


Figure 2: FTIR of the outgassed CVCM according to AD2 (based in RD2) Injection Moulded F1+F2

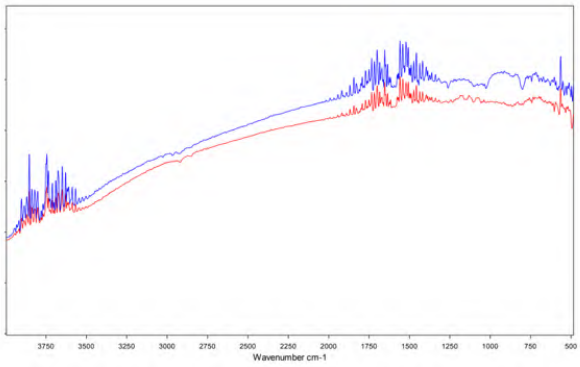


Figure 3: FTIR of the outgassed CVCM according to AD2 (based in RD2) 3D-Printed F1+F2

Thermo-Optical Properties

Irrespective of the manufacturing route, the neat polymer exhibited high solar absorptance values in the range of approximately α = 0.74-0.82, as well as high thermal emissivity values of ε = 0.91-0.93. Due to the opacity of the neat material, these values should be interpreted with caution. In contrast, injection-moulded and FFF-printed F1+F2 specimens exhibited favorable thermo-optical properties irrespective of gamma irradiation, with α = 0.26 for the printed specimens, both irradiated and non-irradiated, and α = 0.33 for the injection-moulded specimens. Thermal emissivity remained high, with ε = 0.89-0.91. The α / ε ratio of the F1+F2-filled materials was approximately 0.3-0.4, which is favorable for passive thermal-control applications. The best overall performance was observed for the non-irradiated printed F1+F2 specimens and the gamma-irradiated printed F1+F2 specimens, which combined low solar absorptance with high thermal emissivity. In addition, F1+F2-containing specimens showed increased reflectance in the near-infrared range (1.5-2.0 um), with values of approximately 0.44-0.47, whereas the neat pressed materials remained below 0.07 in the same spectral range. However, due to the opacity of the neat pressed material, these values are not fully conclusive. Reflectance in the thermal infrared range (5-21 um) remained relatively low for all samples. Gamma-irradiated specimens showed no significant changes compared with the non-irradiated material, indicating good environmental stability. Only negligible differences were observed. Furthermore, vertically and horizontally oriented printed F1+F2 specimens showed nearly identical optical properties, suggesting that the investigated printing orientation of 45° had no significant influence on the thermo-optical properties of the material system.

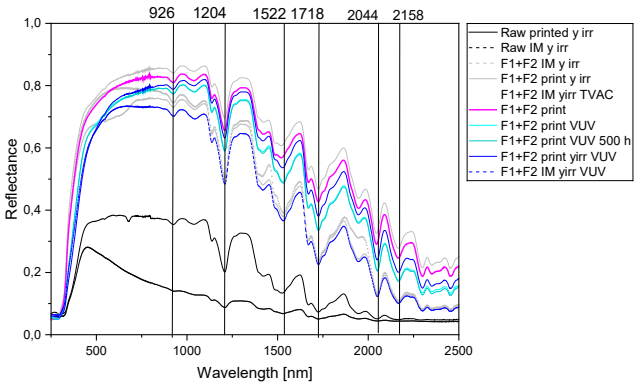


Figure 4: Spectral reflectance (300 - 2500 nm) of printed and injection-moulded, filled and unfilled, samples before and after space environmental exposure

The untreated neat material showed substantially lower reflectance than the filled materials, which can be attributed to its opacity. In contrast, all filled materials exhibited higher reflectance, particularly in the visible and near-infrared regions. This indicates that the addition of fillers may have a beneficial effect on the optical performance of the material.

Injection-moulded specimens exposed to TVAC, gamma irradiation, and VUV irradiation exhibited similar behavior in the wavelength range from 750 to 2500 nm, suggesting that these treatments had only a minor influence on reflectance. The injection-moulded specimens showed slightly lower reflectance than the printed specimens. Although this difference was small, it may be attributed to differences in surface morphology, leading to variations in light scattering.

The printed VUV-irradiated material exhibited similar reflectance curves irrespective of irradiation duration, indicating that prolonged VUV exposure did not substantially alter the material within the investigated parameter range. Gamma irradiation, with or without additional VUV exposure, tended to result in higher reflectance than VUV treatment alone or the untreated reference state. This suggests that gamma irradiation may induce slight surface or chemical modifications affecting optical response, whereas VUV irradiation may promote photo-induced degradation. The exact mechanisms remain unresolved and require further investigation.

Shaker Testing

The evaluation of the CubeSat structure before and after the shaker test was performed using visual inspection and 3D scanning to assess potential damage, deformation, or dimensional changes induced by the applied mechanical loads (see figure 5). No visible differences or signs of damage were observed after the vibration test. Furthermore, the positions and orientations of all screws within the CubeSat structure remained unchanged, as confirmed by the applied markings. The markings were still aligned after the test, indicating that no relative movement or loosening of the screw connections occurred. Additionally, the screws used for mounting the CubeSat structure within the shaker fixture showed no signs of rotation or loosening during the test.

The 3D scan comparison further confirmed the mechanical stability of the structure, with all measured dimensional deviations remaining within the defined tolerance range (green area) and below 0.1 mm. These results demonstrate that the applied vibration loads did not induce measurable deformation or compromise the structural integrity of the CubeSat assembly

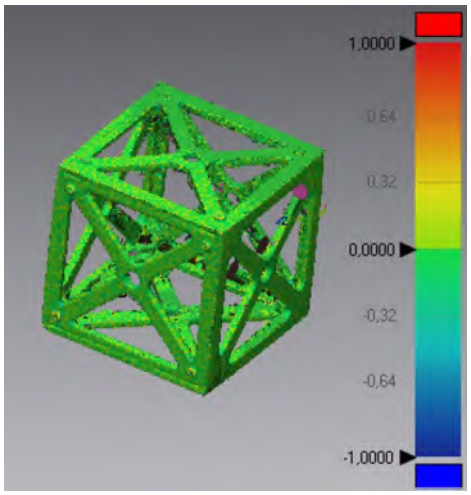


Figure 5: Dimensional deviation analysis of the CubeSat structure before and after the shaker test obtained by 3D scanning.

4. CONCLUSION

The developed material shows promising potential for use in small structural components. Tensile testing demonstrated that filler addition, gamma irradiation, TVAC treatment, and the manufacturing route significantly influence material flexibility and tensile strength. The combination of fillers F1+F2 suggests improved compatibility and resulted in enhanced tensile properties. The filled printed material also exhibited improved printability, which irradiation reduced the tensile strength of the printed specimens but also reduced brittleness. TVAC treatment generally increased brittleness irrespective of the manufacturing route. In the neat materials, Young's modulus increased after TVAC treatment, whereas filled materials showed a decrease, suggesting changes in filler-matrix adhesion and/or crystallinity. Indications of delayed crosslinking and/or crystallinity changes after TVAC exposure were observed, although further research is required to confirm these mechanisms. Overall, both gamma irradiation and TVAC treatment contributed to aging of the polymer.
The outgassing investigations demonstrated that the FFF-printed material fulfilled the ESA-

recommended requirements for space applications. The observed differences in moisture recovery behaviour depending on the manufacturing process highlight the importance of considering material morphology and moisture transport mechanisms in future outgassing evaluations.

Regarding the thermo-optical properties, the filled material exhibited promising characteristics independent of the manufacturing approach. The combination of low solar absorptance and high thermal emittance indicates a high potential for efficient thermal management by reducing solar heat input while promoting heat dissipation.

Comparable results were obtained by UV-Vis-NIR spectroscopy using the Cary 5000, where the filled specimens exhibited increased reflectance over the investigated wavelength range. This behaviour is beneficial for thermal control applications, as enhanced reflectance reduces the absorption of incident solar radiation and can therefore contribute to lower component temperatures.

Only negligible changes in reflectance were observed after TVAC exposure, indicating good environmental stability of the investigated materials under combined vacuum and thermal cycling conditions. In contrast, VUV irradiation resulted in a slight reduction in reflectance, suggesting photo-induced surface modifications or degradation processes. However, the limited difference between 500 ESH and 1260 ESH of VUV exposure indicates that the material retains its favourable reflective properties even after prolonged irradiation, demonstrating its potential for long-term application in space environments.

The comparison of the CubeSat structure before and after the shaker test using 3D scanning revealed no visible damage or measurable dimensional changes. This indicates that the mechanical loads applied during the vibration test did not negatively affect the structural integrity of the CubeSat structure.

Overall, the material shows promising potential for use in CubeSat structures or smaller components located in shielded environments. Nevertheless, VUV- and gamma-irradiation induced degradation should be considered when assessing the lifetime and application limits of the material.

5. REFERENCES

[1] U. Lafont, E. Laurent, E. Amorim, and C. Semprimoschnig, ‘Future of Thermoplastics in Space’. n.d.

[2] N. Shetty, S. M. Shahabaz, S. S. Sharma, and S. Divakara Shetty, ‘A review on finite element method for machining of composite materials’, *Composite Structures*, vol. 176, pp. 790–802, Sep. 2017, doi: 10.1016/j.compstruct.2017.06.012.

[3] E. T. M. Krämer, J. N. Swamy, T. J. Asijee, and S. Wijskamp, ‘Advances in out-of-autoclave consolidation of thermoplastic composites’, in *Int SAMPE Tech Conf*, Soc. for the Advancement of Material and Process Engineering, 2023. doi: 10.33599/nasampe/s.23.0320.

[4] S. K. Georgantzinos *et al.*, ‘A Comprehensive Review of Additive Manufacturing for Space Applications: Materials, Advances, Challenges, and Future Directions’, *Adv. Eng. Mater.*, vol. 27, no. 22, 2025, doi: 10.1002/adem.202501082.

[5] 3Druck.com, ‘Mit 3D-Druck hergestellte System zur Freisetzung von Mikrosatelliten’, 3Druck.com - The Independent AM Magazine. Accessed: May 11, 2026. [Online]. Available: https://3druck.com/case-studies/3d-druck-mikrosatelliten-21108391/

[6] D. Thomas, ‘Improving the Reliability of Satellite Components Using Finite Element Analysis and 3D Printing as a Vital Tool for Modern Space Missions’, *J Fail. Anal. and Preven.*, vol. 25, no. 2, pp. 552–554, Apr. 2025, doi: 10.1007/s11668-025-02145-3.

[7] A. El Magri, S. Vanaei, and S. Vaudreuil, ‘An overview on the influence of process parameters through the characteristic of 3D-printed PEEK and PEI parts’, *High Perform Polym*, vol. 33, no. 8, pp. 862–880, 2021, doi: 10.1177/09540083211009961.

MAIN FUNCTIONAL TESTS OF CALLISTO'S LANDING SYSTEM – TOUCHDOWN AND DEPLOYMENT

Anton Schneider[(1)], Jan Bertram[(1)], Felix Krziwanie[(2)], Waldemar Rotärmel[(2)]

Silvio Schröder[(1)], Torben Wippermann[(1)], Lars Witte[(1)]

[(1)] German Aerospace Center, Institute of Space Systems, Bremen, Germany,
Email: anton.schneider@dlr.de, jan.bertram@dlr.de, silvio.schroeder@dlr.de, torben.wippermann@dlr.de, lars.witte@dlr.de
[(2)] German Aerospace Center, Institute of Structures and Design, Stuttgart, Germany,
Email: felix.krziwanie@dlr.de, waldemar.rotaermel@dlr.de,

KEYWORDS

reusable launch vehicle, landing system, verification, touchdown, deployment, experimental investigation, test

ABSTRACT

Reusable launch vehicles will inevitably face the challenge of a safe touchdown, which is essential to fulfil the re-usability objectives. Before touching down, the deployment of landing legs within a harsh load environment needs to be mastered. The engine plume, the aerodynamics, and vehicle dynamics influence the deployment dynamics, while the induced torques and forces must be carried by the central core structure and compensated by the Guidance Navigation and Control system. Once the deployment is mastered, the landing system's main function is enabled, allowing a safe transition from flight to ground. At the arrival gate, which marks the handover from deployment to touchdown phase, the vehicle's attitude and dynamic state is afflicted with uncertainties. The landing system must handle the majority of these states and provide tip-over stability, sufficient ground clearance, load attenuation capability, and the energy absorption capability that is required to dissipate the residual kinetic energy of the vehicle at touchdown. Understanding the complex dynamics of a landing system therefore requires, beside numerical tools, tests on landing leg level.

Within the CALLISTO project, single leg touchdown and deployment tests were performed in the Landing and Mobility Test Facility (LAMA) located at the German Aerospace Center in Bremen. These tests experimentally investigated the deployment and touchdown performance of the development model of CALLISTO's Approach and Landing System (ALS), which is driven by a pneumatic deployment system. The deployment tests verified the functionality of the pneumatic deployment system and the entire functional chain starting from the reception of the deployment signal through to completion of the transient deployment phase. The energy absorption and the load carrying capability of CALLISTO's landing leg were assessed on the single leg drop test stand. The resulting test data were used for the validation process of the developed simulation tools, which were used for generating predictions and assess the deployment and touchdown dynamics at both the landing leg and vehicle level. This paper presents the conducted deployment and touchdown tests and how these tests incorporate into the landing system verification program.

1. INTRODUCTION & CALLISTO PROJECT

Currently, several launch vehicles are under development worldwide with the goal of cost reduction by re-usability. Examples of these launch systems include SpaceX's Starship (USA), Deep Blue Aerospaces Nebula-M Rocket (China), and MaiaSpace (France). All these launch systems share a common feature: they employ deployable landing legs, offering the advantage of a significantly reduced projected area when stowed compared to the deployed configuration. To capitalize on this benefit, the landing leg system requires a novel deployment mechanism that is relatively new to the space industry. While common deployment operations in space industry have been conducted in near-vacuum or low-density atmospheric conditions, the landing system of a reusable launch vehicle (RLV) must perform its deployment in a dense atmosphere, near sea level and subsequently pin-point land the vehicle on

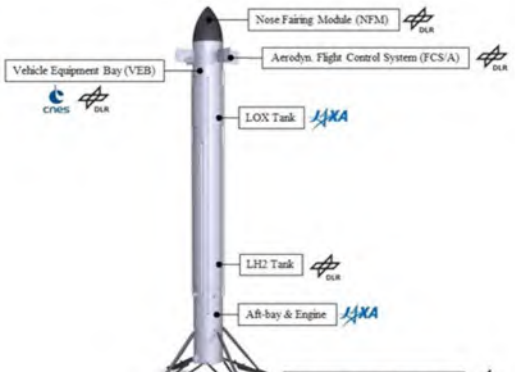


Figure 1: CALLISTO sub-scale booster demonstrator. Responsibility shares between partners

ground. This presents unique challenges compared to previous missions and operational environments. Subsequently, after the deployment, the vehicle needs to master the touchdown dynamics that are afflicted to vehicle state uncertainties.

To gain a better comprehension of the characteristics of RLVs regarding the required design and operations, and to mature the required key technologies, CNES of France, DLR of Germany, and JAXA of Japan have chosen to combine their expertise in the CALLISTO project (Cooperative Action Leading to Launcher Innovation in Stage Toss-back Operations). The trilateral partners aim to develop, build, and test a subscale reusable first stage demonstrator vehicle. Responsibility and tasks are distributed based on the expertise and knowhow of the partners. An overview of this sharing is illustrated in Figure 1 and well described in [1-4]. The Approach and Landing System (ALS) is under the responsibility of DLR. In addition to developing, building, and testing it, a major contribution is the simulation of the landing leg's dynamic behaviour.

The following section describes the ALS main structure and the deployment subsystem, followed by a description of the ALS main functions. The last section explains how physical tests and virtual simulations incorporate into the landing leg development program.

2. APPROACH AND LANDING SYSTEM

During ascent and descent, the landing legs are folded and secured against the vehicle. Just before touchdown, they are deployed via the pneumatic deployment subsystem. Once fully extended, two latching mechanisms located at the segment interfaces of the telescopic struts engage to prevent retraction under external loads. The legs remain locked in place until manual reset, after successful touchdown, by the ground operational staff. These two configurations are illustrated in Figure 2. Additionally, the legs are equipped with an ablative thermal protection system (TPS) to withstand the intense thermal conditions experienced during the final approach and landing phase.

2.1. Landing Leg Structure

The ALS consists of four deployable inverse tri-pod landing legs and a deployment subsystem. The primary and secondary strut are attached to the vehicle's aftbay and transmit flight, deployment, and touchdown loads. The telescopic primary strut consists of three cylindrical carbon fibre reinforced plastic (CFRP) segments that slide coaxially within one another, providing a compact stowed volume (expansion factor of 3). Two passive latching mechanisms lock the segment-to-segment degree of freedom in fully deployed state. The extension is initiated by the deployment subsystem. Once the primary strut is pressurized the pneumatic force drives the segments outwards.

The third segment is divided into two sub-parts that enclose a crushable energy absorption element. Upon touchdown, when the crush load is exceeded, the crushable element absorbs the residual kinetic energy of the vehicle by plastic deformation of the energy absorption element.

The aeroshell is formed by the secondary strut outer hull. Contact with the landing site is established via the rubberized footpad. Beside the main structural

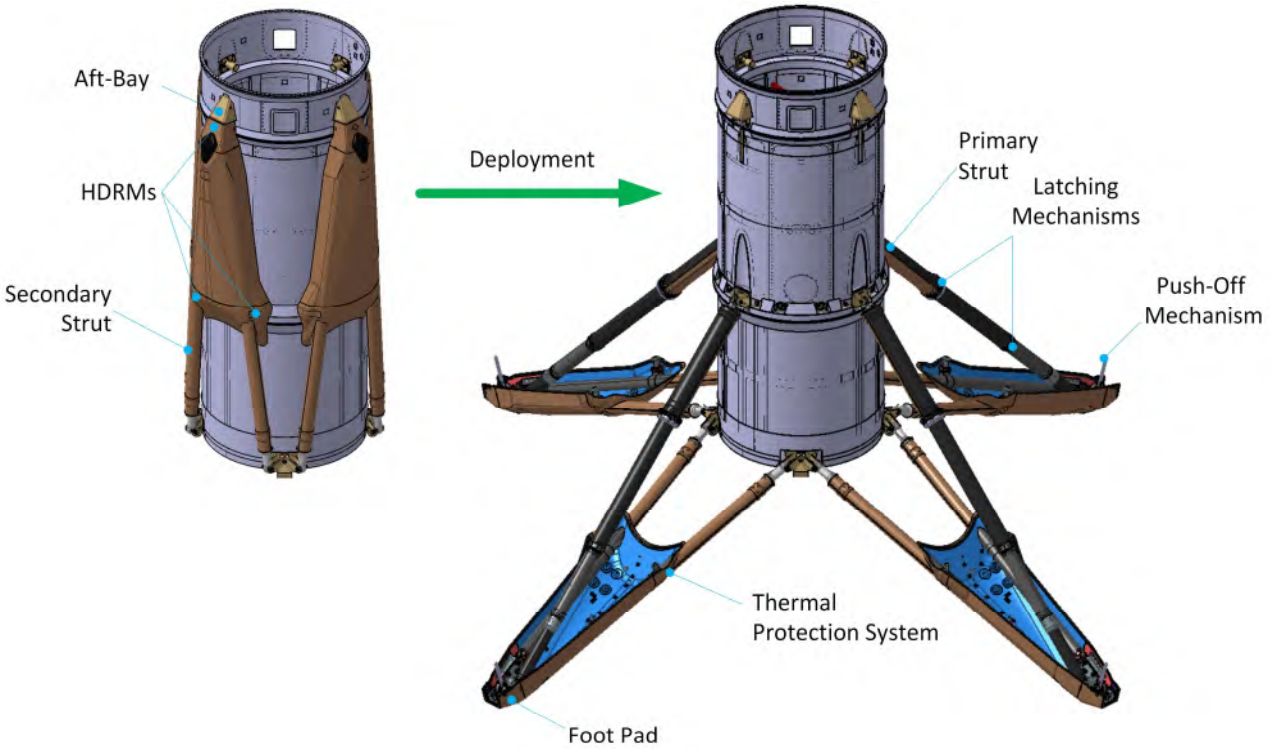


Figure 2: ALS subassemblies. Left figure shows the stowed and right the deployed state.

parts, the landing leg structure entails a thermal protection to protect the structure from heat loads generated throughout all flight and ground phases. CALLISTO's load carrying structure development has been studied in [9].



Figure 3: Falcon 9 asymmetric deployment dynamics. [adapted from Bob Montanaro (https://lunarcabin.com/) with permission]

2.2. Deployment Subsystem

The pneumatic deployment subsystem combines equipment and actuators for extending the landing-leg struts. It is composed of a high-pressure storage vessel, an isolation valve, a pressure-relief valve, a fill-and-drain valve, tubing, electromechanical release mechanisms, and the associated pneumatic telescopic strut actuators (primary strut). A deployment controller is integrated into the subsystem; it receives the deployment command from the launcher's onboard-computer (OBC), converts it into an opening signal for the isolation valve, fires the hold down release mechanisms (HDRM), and routes key instrumentation data, system pressure, HDRM status, and latch status, to the launcher's OBC [5]. These components are accommodated within CALLISTO's aftbay, as shown in Figure 4. This architecture was selected because it brings the following technical advantages:

- Limited mechanical and fluidic interface management – No fluidic interface to the rocket propulsion system for helium supply and the push-off is mounted directly on each leg, reducing the number of mechanical interfaces with the launcher.
- Pneumatically driven actuators provide the ability to modulate the generated pneumatic force, enabling adjustment of pneumatic force for a range of deployment conditions.
- Asynchronicity mitigation – By adjusting the actuator force, the relative timing of the landing legs can be limited.
- Reliance on COTS flight-heritage components – All major elements (valves, tubing, HDRMs) are commercially available, flight-tested parts, ensuring high reliability and simplifying procurement and qualification.
- Re-usable and field resettable deployment system, as no single use components are implemented. Reduces MRO duration and hence increases economic efficiency

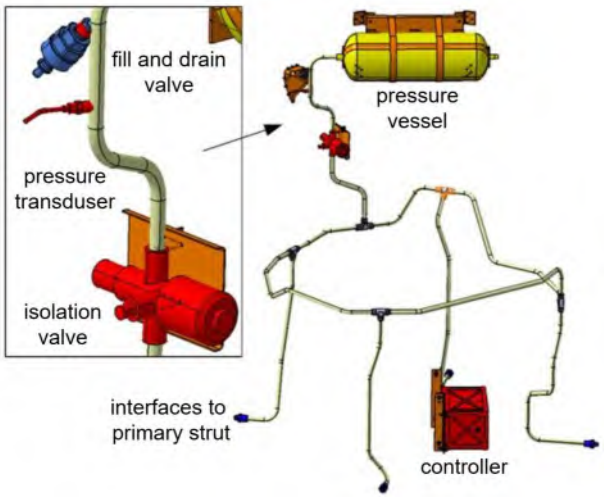


Figure 4: Aftbay internal components of the ALS deployment subsystem equipment.

3. LANDING GEAR MAIN FUNCTIONS

The ALS supports the vehicle in standing autonomously without the need for ground support equipment. Upon touchdown, the ALS landing gear fulfils the following primary functions: (1) absorbing the remaining kinetic energy, (2) ensuring both dynamic and static tip over stability, (3) maintaining ground clearance, and (4) attenuation of loads transferred to the vehicle's aftbay. In general, the ALS facilitates a safe transition from flight to ground state.

A necessary pre-condition for these functions is a successfully deployed landing system. To ensure this, the deployment subsystem needs to fulfil the following functions: (1) to keep the landing gear in stowed position until deployment initiation, (2) to maintain the landing gear in deployed position after deployment finalisation and during touchdown. (3) to provide sufficient amount of energy to deploy successfully and (4) to release the landing legs within a pre-defined time window.

The deployment and, in particular, the touchdown functions are vehicle level capabilities that require holistic analysis on vehicle level.

3.1. Deployment Challenges

The landing system of a RLV must withstand a harsh, highly unsteady load environment. The loads arise from the complex interaction of aerodynamics and engine plume with the leg structure, from a large spectrum of possible deployment conditions, and from the vehicle-induced accelerations that

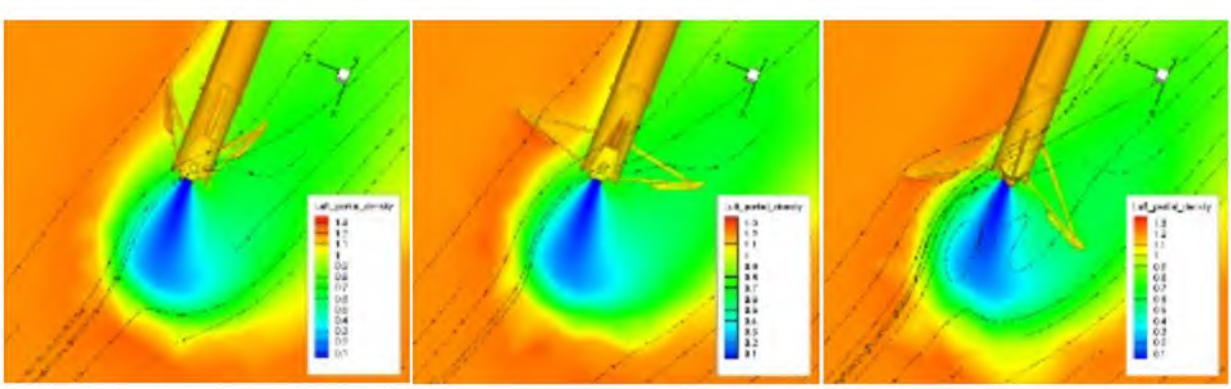


Figure 5: Flow field around ALS. One leg is oriented leeward and is therefore covered with plume, whereas the windward oriented leg faces the full dynamic pressure.

occur during the descent. Because the magnitude and orientation of these loads are tightly coupled to the chosen descent trajectory, the deployment dynamics are sensitive to approach trajectory-design decisions. Figure 5 illustrates the asymmetric flow field around CALLISTO's landing leg at different opening angles, which contributes to the non-linear load environment [7,8]. An example for an asymmetric landing leg deployment caused by the non-linear load environment has been observed during Falcon 9 landings. An example of the NROL-76 mission is shown in Figure 3.

This highly non-linear environment and the criticality of this function require high-fidelity numerical simulations, to predict the deployment dynamics and understand the influences. DYNOS (Deployment dYnamics OptimisatioN Simulation) has been developed within the course of the development of the ALS and used for the definition of specifications and for deployment dynamics studies. A block-diagram of this tools is shown in Figure 6.

The influences on CALLISTO's deployment dynamics have been studied in [6]. Here, it is shown that deployment dynamics are not only influenced by the product parameter (vessel, pressure, timings, friction, …) but mainly on vehicle dynamic states parameters such as:

- Non-gravitational acceleration – higher value, leg tends to open faster
- Angle of attack profile – AoA =/= 180 deg leads to asymmetric load environment, leeward oriented leg opens faster
- Approach velocity – defines the absolute value of the aerodynamic forces
- Angle of roll – Defines which legs are lee- or windward oriented.

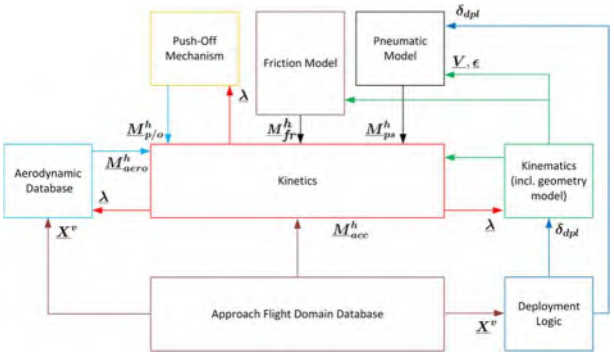


Figure 6: Block diagram of the DYNOS deployment dynamics simulator, with coloured blocks representing sub-models, and arrows indicating the data flow

3.2. Touchdown Challenges

The safe transition from flight to ground state is considered a primary prerequisite for fulfilling the objectives of an RLV. The touchdown, which follows the successful deployment and latching of the landing legs, is regarded as the culmination of this vehicle state transition.

The vehicle's touchdown dynamics are driven not only by the landing gear and engine characteristics but are also influenced by the vehicle's dynamic state at the handover from the approach phase to the landing phase. The initial vehicle dynamic states are defined by the trajectory design, whereby the translational and angular velocities, and consequently the kinetic energy to be absorbed by the landing gear, are prescribed. This dynamic state is affected by Guidance Navigation and Control (GNC) system dispersions, by which the number of possible dynamic states to be handled by the landing gear spans a broad parameter space. This dispersion is determined by the control capability of the GNC system.

Induced interface forces at touchdown are attenuated by the energy absorption system, whereby the residual kinetic energy is also absorbed through the plastic deformation of the honeycomb cartridge. The number of touchdown cases to be analysed is increased by product-related uncertainties, caused for instance by manufacturing imperfections or varying foot pad friction coefficients. Additionally, the touchdown dynamics are influenced in a non-linear manner by fluid-structure interactions, such as residual propellant sloshing [10,11], and the elastic properties of the central core.

The vehicle's touchdown dynamics are impacted by the combination of all the aforementioned performance drivers. The majority of possible touchdown conditions must be handled by the landing gear, wherein tip-over stability, ground clearance, load attenuation capability, and energy absorption capability must be ensured.

The touchdown dynamics are rendered a complex function by the sheer number of possible initial vehicle states at the handover from the approach phase to the landing phase, combined with

uncertainties related to the landing gear. Numerous possible touchdown conditions are generated by these factors collectively. Experimental coverage of all possible conditions at the vehicle level is cost-intensive. Therefore, high-fidelity numerical simulations are indispensable. Given the extensive number of variables and associated uncertainties, a statistical Monte Carlo simulation strategy was utilised to efficiently explore the large parameter space.

4. DEPLOYMENT TEST CAMPAIGN

The landing-leg deployment test campaign is organized around a set of objectives that verify functional performance, safety-critical features, and provide the data required to validate the deployment simulator:

- to verify the deployment function
  - to demonstrate the capability to transform pneumatic power into mechanical power
  - to verify the mechatronic functional chain
  - to check whether ALS can withstand induced latching loads
  - to maintain the deployed configuration
  - to check whether ALS can successfully latch within its application domain
- to characterise induced load level
  - HDRM release induced shock
  - latching shock
  - end stop induced forces
- to gather test data for deployment simulator validation

4.1. Test Stand & Instrumentation Concept

The testing of the leg's deployment functionality and its performance characterization are conducted in the Landing and Mobility Test Facility (LAMA, DLR Bremen) and utilising a dedicated deployment test rig. This test stand is depicted in Figure 7 and is configured to accommodate a single leg assembly, the pneumatic sub-assembly and the landing gear controller as well as laboratory instrumentation for the acquisition of test data. External forces are represented by a system of counterweights acting via cable pulleys on the respective leg assembly to represent external forces. This mass is defined as the net effect of non-gravitational forces and dynamic pressure. The counterweight system adds inertia to the tested landing leg, whereby the landing leg deployment dynamics are fundamentally altered compared to the flight dynamics. Different qualitative characteristics are exhibited by the counter-force compared to the expected net load of aerodynamic forces and non-gravitational acceleration.

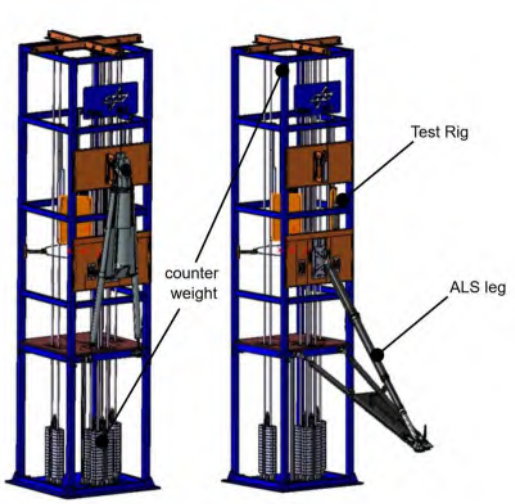


Figure 7: Deployment Test Stand. Left: Stowed leg. Right: Deployed leg. The ALS leg is connected via a rope with the counterweight.

4.2. Performed Deployment Tests

To verify the deployment function, multiple tests with increasing levels of integration were performed. Initially, the pneumatic flow parameters were characterised at different pressure rates. Additionally, the stiffness and damping characteristics of the structure were determined using strain gauges during a partial unfolding test with an initial secondary strut opening angle of approximately 100°.
The electromechanical functional check-out of the deployment system (excluding the primary strut and push-off) was performed to ensure correct timings of the deployment functional chain. As a secondary outcome, safety-related features, such as the pressure relief valve, were verified during the deployment test campaign.
Finally, the full deployment test campaign was performed under different test conditions. A cautious approach was applied, whereby the first deployment was performed at low speed and successively increased to high speed with varying test parameters up to a 130 kg counterweight and a vessel pressure ranging from 2 to 8.5 MPa. A summary of the total number of tests is presented in Table 1.
For each test, the latch state signals of both latching mechanisms were checked to verify the secure engagement of the primary strut. The induced shock levels were calculated and analysed.

The resulting leg deployment opening angle evolution in comparison with the simulated case with DYNOS is shown in Figure 8.

Table 1: List of performed tests within the scope of the deployment test campaign.

Test	Number of tests
Parameter characterisation tests	4 (2x structural,

	4 pneumatic)
Landing Gear Controller functional test	1
Safety valve functional test	1
Deployment tests	14
Total number of tests	21

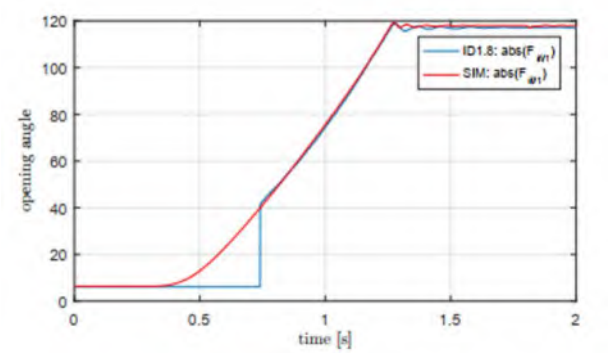


Figure 8: Opening angle vs. time. Blue line represents the measured opening angle, whereas the red line the simulated opening angle evolution.

5. TOUCHDOWN TEST CAMPAIGN

CALLISTO's goal is to perform multiple flights, beginning with low-energy (hover-like) test flights, followed by a cautious increase in flight velocity and altitude to high-energy demonstration flights. For each flight the nominal touchdown conditions differ and, additionally, the vehicle's dynamic state is subject to uncertainties. These project-driven constraints define the application domain of the ALS and hence influence the test definition.

The CALLISTO ALS development program involves single-leg drop tests at DLR's LAMA in Bremen, complemented by numerical touchdown simulations, with the following objectives:

- to characterise the dynamics of the landing-leg assembly
- to demonstrate the energy-absorption capability
- to demonstrate the load-attenuation capability
- to demonstrate the load carrying capability of a landing leg
- to generate test data for correlation of the LANDing SIMulation (LANDSIM) tool

Together, these objectives provide a comprehensive assessment of the landing leg's dynamic behaviour, energy dissipation, force attenuation, structural capacity, and simulation fidelity.

5.1. Test Stand & Instrumentation Concept

The LAMA comprises the single leg drop Test stand, which consists of a rail tower on which a sledge can slide. The device under test, in this case the ALS leg, is attached to the sledge. Depending on the required touchdown orientation, the sledge can incline the ALS leg in multiple directions (pitch & yaw). The energy at touchdown is adjusted by the initial height of the sledge and the total mass, which can be adjusted with weights. The landing site surface can be simulated with, e.g., a concrete slab. Figure 10 illustrates the single leg drop test stand with its subassemblies and the ALS landing leg.

For the characterisation of the interface load environment induced by touchdown dynamics, the interfaces between the ALS landing leg and the sledge were equipped with force sensors at the primary strut interface and acceleration sensors at the secondary strut interfaces.

The dynamic behaviour of the ALS landing leg is acquired with acceleration sensors at the footpad and HDRM interfaces. Furthermore, the sliding of segment 3b into 3a caused by the crushing of the energy absorption element is recorded with a laser sensor. The sledge is equipped with a laser sensor to capture the vertical movement and dynamics of the sledge/ALS landing leg assembly.



Figure 9: ALS deployment sequence of the ALS attached to the deployment test stand in the LAMA. The left image depicts the stowed configuration, with the sequence progressing to the right, showing the stages of deployment. (0°, 25°, 45°, 90°, ~ 110°) Please scan the QR-code for a full deployment video (link to youtube.com).

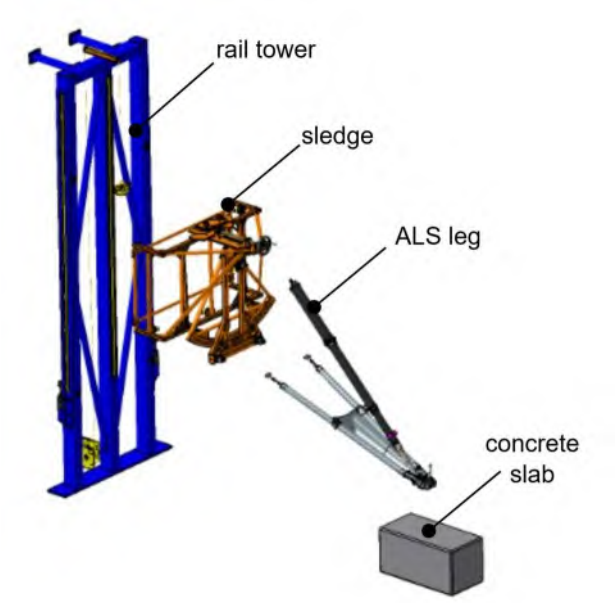


Figure 10: Explosion drawing of the Single Leg Drop Test Facility.

5.2. Performed Touchdown Tests

During the landing leg development process, two dedicated development test campaigns have been performed. Based on the test results, feedback has been systematically forwarded to the design iteration loop. The test campaigns incrementally increased the touchdown mass and velocity to evaluate performance under, in terms of load, progressively more demanding landing conditions. Throughout all tests, the mechanisms maintained fully engaged, ensuring the load path from footpad to the interfaces. In initial state the landing leg attached to the sledge is elevated to the desired height and released upon the reception of the release signal. The initial and final state are illustrated in Figure 11.

To capture the range of vehicle attitudes and leg attachment positions encountered during real landings, the legs were tested at various inclination angles. Additionally, different crush-force levels were applied to verify energy absorption capabilities across varying crush extents. Structural integrity was continuously monitored throughout the testing, while the function of the latching mechanisms was thoroughly checked to confirm reliable operation.

The results demonstrate that performance aligns with intended design objectives. As illustrated in Figure 12, a plateau of plastic absorption is observed following a rapid increase in primary strut load, with dynamic oscillation occurring until the system comes to rest. These findings confirm that the ALS landing leg can provide effective energy absorption capability without compromising structural integrity and that it successfully reduces induced forces transmitted to the vehicle.

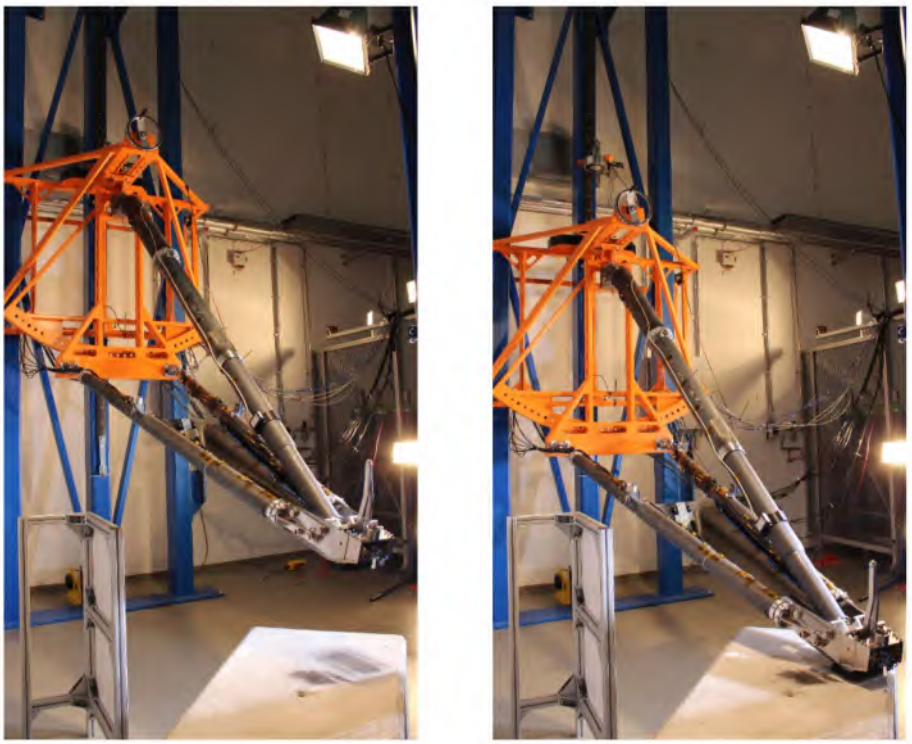


Figure 11: Left: Prior to touchdown. Right: After touchdown, leg in rest, honeycomb crushed

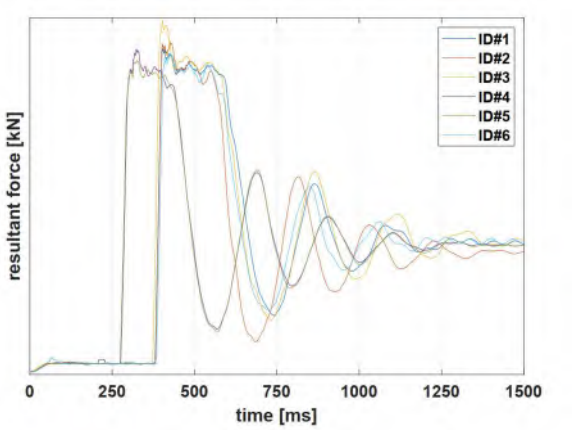


Figure 12: Primary Strut resultant force of performed drop tests. The time line starts with release of the sledge, followed by a free flight phase and rapid increase of the force, which marks the contact between foot pad and concrete slab. The plateau indicates the energy absorption. Please note the force values on the y axis have been omitted for confidentiality.

6. INCORPORATION OF LANDING GEAR MAIN FUNCTIONAL TESTS INTO CALLISTO'S LANDING SYSTEM DEVELOPMENT PROGRAM

The single leg functional tests described in the preceding sections cannot be utilised to verify the main landing gear functions, as it is not possible to reproduce the vehicle dynamics or the complex aerodynamic load environment on a test stand, due to highly non-linear external loads and vehicle dynamics.

A development process based on three pillars, as illustrated in Figure 13, was applied to the ALS development, comprising physical functional test campaigns conducted in the LAMA, numerical simulation tools, and the environmental context, which defines the initial vehicle dynamic state in addition to the external load conditions for the landing leg deployment.

The ALS is represented as both a physical development model for testing purposes and as a numerical model in this development process. The touchdown and deployment functions are simulated with the LANDSIM and DYNOS simulations tool. These tools are used to generate single leg deployment and touchdown test predictions. The subsequent single leg touchdown and deployment tests are performed in the LAMA. The generated test data is utilised for the validation of the numerical simulation tools. This loop involving the generation of test predictions and the feedforward of test data for the validation of simulation tools is iterative.

The vehicle level simulations are performed with the same numerical tools, however, the full landing system is incorporated. The external context is defined by the third pillar. This contains the vehicle's initial state at the beginning of the landing phase. Additionally, the broad approach flight domain is defined within this pillar as well. The numerical simulation results are post-processed and, in cases where landing gear functions are violated, the conclusions are fed back as engineering constraints. For instance, in the case of deployment dynamics, constraints are defined in terms of maximum allowable interface forces or induced disturbance torques and forces. A holistic analysis of the landing leg system is facilitated by this process.

7. SUMMARY

This paper discusses the challenges and testing of reusable launch vehicles, specifically focusing on CALLISTO's ALS. One of the primary challenges for RLVs is achieving a safe transition from flight to ground phases, which requires mastering the deployment of landing legs in a harsh load environment. The deployment of landing legs is sensitive to trajectory parameters such as non-gravitational acceleration, angle of attack, approach velocity, and angle of roll.

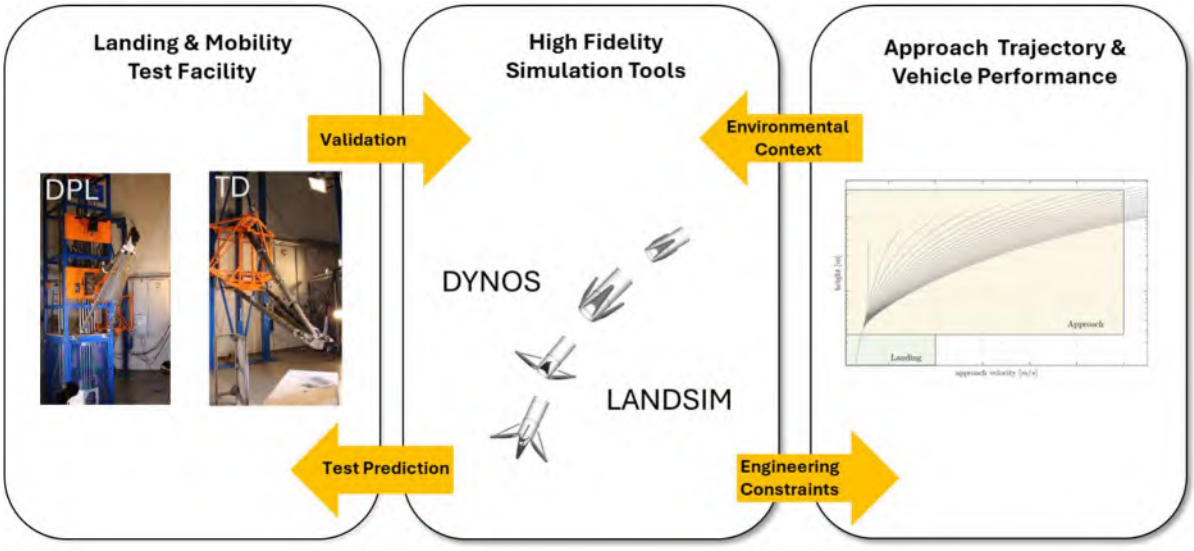


Figure 13: Three pillar development process of the CALLISTO Landing Gear.

The paper describes the ALS of CALLISTO, which includes a pneumatic deployment subsystem and deployable inverse tripod landing legs. The system is designed to absorb the residual kinetic energy of the vehicle during touchdown while maintaining stability and ground clearance.
The paper highlights the complexity of deployment and touchdown dynamics, which are influenced by aerodynamics, engine plume, trajectory design, and vehicle-induced accelerations. High-fidelity numerical simulations and Monte Carlo methods were employed to explore the large parameter space of possible touchdown conditions.
In conclusion, the CALLISTO project represents a significant step towards the development of reusable launch vehicles, with a strong emphasis on testing and simulation to ensure safe deployment and touchdown. The results of the tests demonstrate the effectiveness of the ALS in absorbing energy and reducing induced forces, validating the design and performance of the landing system.
The development process relies on three pillars: functional test campaigns, numerical simulation tools (LANDSIM and DYNOS), and the environmental context. The tests were conducted at DLR's Landing & Mobility Test Facility (LAMA) and included deployment tests and single leg drop tests. The results of these tests were used to validate the numerical simulation tools.
The functional test campaigns of CALLLISTO's landing system ALS were presented and how their results contribute to the overall landing system development strategy. The criticality of the deployment function was explained and rationales for the numerical deployment simulator given. The touchdown is one of the main functions of an RLV. The criticality and influences coming from GNC and trajectory design were shown.
In short, landing (deployment and touchdown) is a system level capability with unique load cases that require novel high-fidelity tools and novel development approaches to master a safe transition from flight to ground phases.

8. REFERENCES

[1] Dumont, E., Ishimoto, S., Tatiossian, P., Klevanski, J., Reimann, B., Ecker, T., Witte, L., Riehmer, J., Sagliano, M., Vincenzino, S.G., Petkov, I., Rotärmel, W., Schwarz, R., Seelbinder, D., Markgraf, M., Sommer, J., Pfau, D., Martens, H.: Callisto: a demonstrator for reusable launcher key technologies. Trans. JSASS Aerospace Tech. Japan 19(1), 106–115 (2021).

[2] Dumont, E., Ishimoto, S., Illig, M., Sagliano, M., Solari, M., Ecker, T., Martens, H., Krummen, S., Desmariaux, J., Saito, Y., Ertl, M., Klevanski, J., Reimann, B., Woicke, S., Schwarz, R., Seelbinder, D., Markgraf, M., Riehmer, J., Braun, B., Aicher, M.: Callisto: towards reusability of a rocket stage: current status. In: 33rd ISTS Conference (2022). https://elib.dlr.de/185543/

[3] Krummen, S., Briese, L.E., Dumont, E. et al. CALLISTO: on the design and development of a reusable first stage demonstrator. CEAS Space J (2026). https://doi.org/10.1007/s12567-026-00710-6

[4] Desmariaux, J., Cliquet-Moreno, E., Chavagnac, C., Dumont, E., Saito, Y.: Callisto: Its flight envelope and vehicle design. In: 8th European Conference for Aeronautics and Space Sciences (EUCASS), Madrid, Spain (2019). https://elib.dlr.de/133317/

[5] Schneider, A., Bertram, J., Schröder, S., Witte, L., Landing leg deployment dynamics simulation and excessive deployment test campaign of CALLISTO's Approach and Landing System. In: Proceedings of the International Astronautical Congress, IAC. Proceedings of the International Astronautical Congress, IAC, 2024, Milan, Italy, ISSN 0074-1795

[6] Schneider, A., Desmariaux, J., Klevanski, J. et al. Deployment dynamics analysis of CALLISTO's approach and landing system. CEAS Space J 15, 343–356 (2023). https://doi.org/10.1007/s12567-021-00411-2

[7] Ecker, T., Ertl, M., Klevanski, J. et al. Aerothermal characterization of the CALLISTO vehicle during descent. CEAS Space J (2024). https://doi.org/10.1007/s12567-024-00561-z

[8] Klevanski, J., Reimann, B., Krummen, S., Ertl, M., Ecker, T., Riehmer, J., Dumont, E., Progress in Aerodynamic Studies for CALLISTO - Reusable VTVL Launcher First Stage Demonstrator, 9TH EUROPEAN CONFERENCE FOR AEROSPACE SCIENCES (EUCASS), 2022, Lille, France

[9] Krziwanie, F., Rotärmel, W., Giagkozoglou Vicenzino S., Schneider, A., Development of the Landing Leg Structure for CALLISTO. JESA 2024 . https://doi.org/10.57350/jesa.168

[10] Krämer, C., Witte, L., Experimental investigations of fluid-to-vehicle interactions during a reusable launcher's touchdown impact, CEAS, 2024, https://doi.org/10.1007/s12567-025-00649-0

[11] Krämer, C., Witte, L., Experimental Investigation of Fluid Impact on Landing Behaviour of Vertically Landing Vehicles. 2025, Rom, Italy. doi: https://doi.org/10.13009/EUCASS2025-214

EXPERIMENTAL CHARACTERIZATION OF A DEPLOYABLE PIEZOELECTRIC POLYMER REFLECTOR DEMONSTRATOR FOR CUBESAT APPLICATIONS

Carl Johan G. Nielsen [(1)], Damien Robert [(2)], Julie Passion [(2)], Thomas Godfroid[(2)], Michel Géradin[(3)], Gonçalo Rodrigues[(4)] and André Preumont[(1)]

[(1)] Université Libre de Bruxelles, Brussels, Belgium Email : cjgn44@gmail.com, andre.preumont@ulb.be
[(2)] MateriaNova, Mons, Belgium, Email: thomas.godfroid@materianova.be
[(3)] University of Liège, Liège, Belgium. Email: mgeradin@gmail.com
[(4)]ESA/ESTEC, Netherlands, Email: goncalo.rodrigues@esa.int

KEYWORDS

deployable reflector, polymer mirror, piezoelectric actuation, PVDF-TrFE, CubeSat, SCOTS, deflectometry

ABSTRACT

This work presents the experimental characterization and predicted control performance of a deployable 16cm actively controlled multilayer petal polymer reflector developed within the Advanced Multilayer Adaptive Thin Shells (AMATS) project, supported by the ESA GSTP program. The reflector demonstrator, manufactured by MateriaNova (Mons, Belgium) and characterized at the Université Libre de Bruxelles (Brussels, Belgium).

The demonstrator is tested using a custom deflectometry setup, and measured influence functions are compared with finite element predictions, validating the simulation models. The validated influence function model is then used to estimate the wavefront correction achievable against representative aberration fields, including thermal distortion and residual viscoelastic deployment error. The measured deployment shape accuracy of the demonstrator is also reported.

1. INTRODUCTION

With conventional monolithic glass or ceramic space telescope mirrors, modern fabrication achieves impressive performance. However, with the desire for ever increasing capability in small satellite platforms for constellation, other architectures can be considered. Figure 1 shows the deployable rigid mirror petal of Utah State University [1], an attempt to fit more aperture into a small CubeSat. In our project, we wish to develop this idea further, with active control substituting a heavy rigid structure. The system overview is shown in Figure 2, where the piezoelectric multilayer structure achieves control by the actuation of symmetric PVDF-TrFE layers with aluminium electrodes. The symmetry is necessary due to the high thermal expansion of the piezoelectric material, which would otherwise deform the structure. Viscoelastic folding of the reflector is achieved with the petal geometry, as shown in Figure 3. In this short paper, we report a summary of experimental measurement of influence functions, numerical models, and we demonstrate that the residual aberration left after deployment can be adequately recovered using the active control.

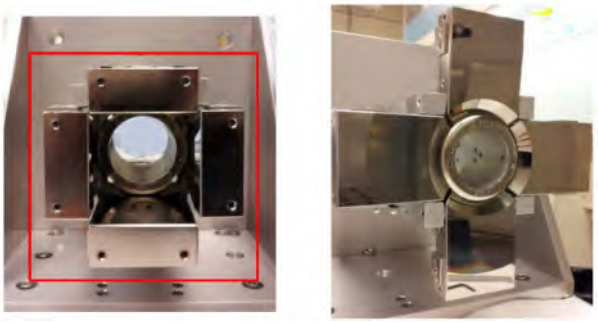


*Figure 1 Utah State University Deployable Petal Telescope **Left:** Stowed configuration. **Right**: Deployed configuration. The red square indicates 10x10 cm2*

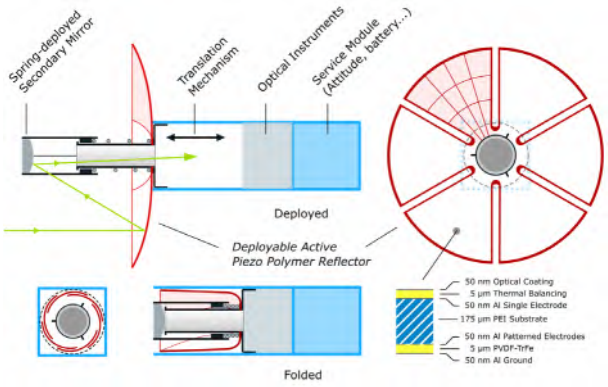


Figure 2 System overview of a CubeSat using an actively controlled deployable polymer thin shell.

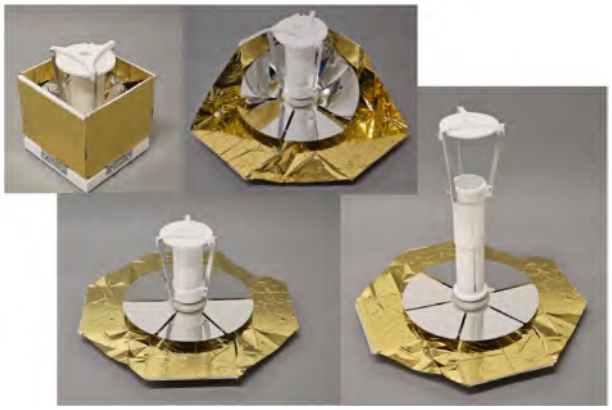


Figure 3 Deployment Concept Mockup for the

adaptive polymer reflector in a 1U volume.

2. METROLOGY

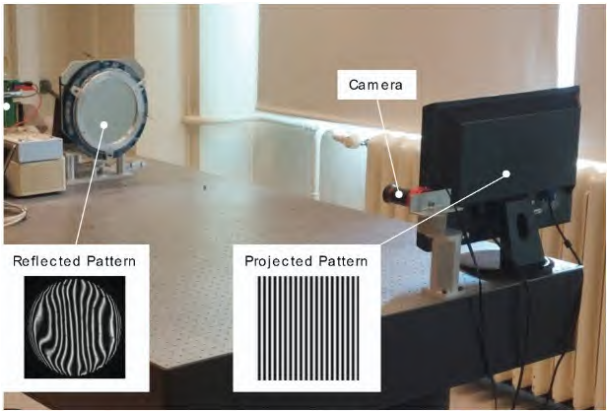


Figure 4 SCOTS metrology: Experimental configuration for measuring the surface figure of a spherical shell, showing screen, reflector, camera, and control electronics. The shape of the reflector is found from the distortion of the reflected pattern.

The metrology used in the paper is inspired by the SCOTS (software configurable optical testing setup) of University of Arizona [2]. An example of the measurement of a simple mirror is shown in Figure 4, where a projected pattern is reflected off of the test mirror and used to reconstruct the shape of the mirror. The metrology system has been commissioned over a long campaign, and a detailed explanation of the recovery method can be found in the thesis [3].

3. DEMONSTRATOR & ACTIVE CONTROL

3.1. Numerical simulation

Utilizing finite element modelling in the software SAMCEF based on extensive numerical work in the group [4]–[8], we may compute the actuator response for each individual actuator, and from it the combined control response to a representative aberration. The most critical disturbance is the changing temperature of the reflector in the space environment, modelled as a thermal gradient of 20K across the reflector.

Such an aberration and its resulting control is shown in Figure 5, based on the material properties and layer configuration of Table 1. The symmetry of the reflector ensures that the thermal aberration is manageable. After control with 36 electrodes, the aberration is reduced from 5.7 µm to 0.44 µm RMS.

Responses to a much wider range of aberrations can be found in the thesis [3].

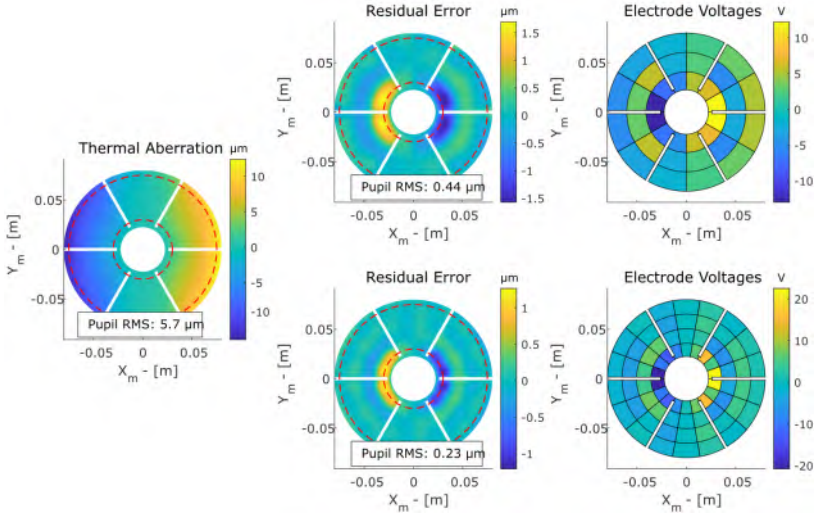


Figure 5 Control of a left-to-right thermal gradient of ±10 ◦K. The reflector is clamped on the inner circle. The RMS error in the pupil is reduced from 5.7 µm to 0.44 µm with 6 electrodes per petal, and it drops to 0.23 µm with 12 electrodes per petal

Table 1. Material and layer properties used in simulations.

Function	Material	Thickness	Stiffness (GPa)	Poisson's Ratio	CTE (10^{-6}/K)	d_{31} (10^{-6} µm/V)
Reflection	Al	50 nm	68	0.32	23	–
Balance	PVDF	5 µm	2.5	0.34	140	15
Electrode	Al	50 nm	68	0.32	23	–
Substrate	PEI	175 µm	2.9	0.38	56	–
Electrodes	Al	50 nm	68	0.32	23	–
Actuator	PVDF	5 µm	2.5	0.34	140	15
Ground	Al	50 nm	68	0.32	23	–

3.2. Demonstrator fabrication

Figure 6 shows the main features of the demonstrator in an exploded view. The reflector consists of 7 layers. The substrate is achieved by high temperature forming on a diamond turned precision mandrel. Both the reflector substrate and the plastic clamp are made of the same material (PEI Ultem 1000), to minimize the effect of thermal differential expansion on the surface figure. The thermal balance layer and the active control layer are made simultaneously by dipcoating of the piezoelectric material (PVDF-TrFE); they are polarized simultaneously to keep the symmetry. Electrode aluminium layers are achieved with sputtering, patterned using UV lithography.

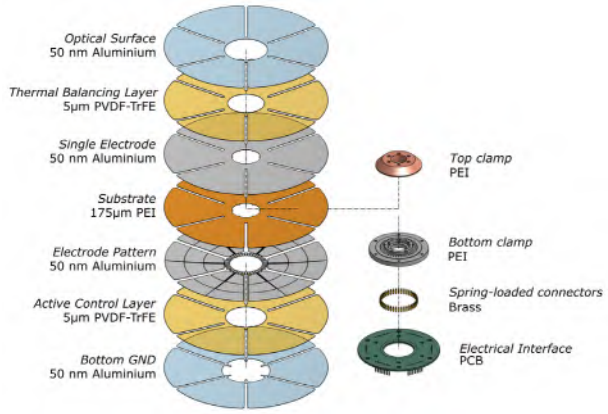


Figure 6 Exploded view of the piezoelectric reflector assembly and layers.

Photos of the produced reflector hardware are shown in Figure 7. All the electrodes (36 control electrodes plus ground) are connected to the PCB by POGO connectors. The mechanical clamp is machined to fit the radius of curvature of the reflector to minimize stresses. The figure also shows the detailed view of the electrode tracks and their connection points to the PCB. High voltages can be applied to the PCB in parallel using a 64 channel controller developed for the project.

The demonstrators shown were manufactured by MateriaNova, and the detailed description is given in [3].

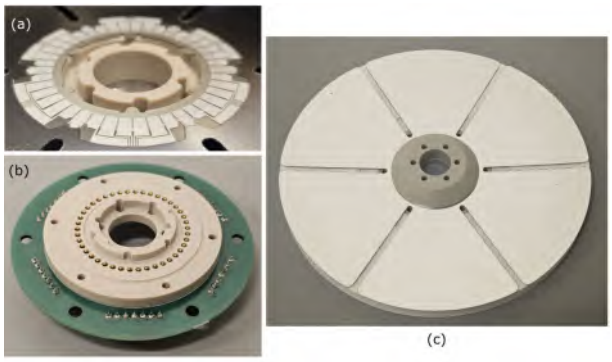


Figure 7 Demonstrator hardware. (a) Bottom view showing the electrode tracks created by lithography. (b) Electromechanical interface with clamping hardware and POGO connectors to connect the PCB to the reflector electrodes. (c) Assembled polymer reflector.

3.3. Experimentally measured control

Figure 8 compares the deformed shape of the reflector (measured with SCOTS, reflector name 99A) when 100 V is applied to the second electrode of the 6 petals, N ◦ [2,8,14,20,26,32] with numerical predictions. The top left and top right diagrams show the experimentally measured influence functions and the numerically predicted ones respectively. The bottom diagram shows the cross- sections of the deformed shape along a line at 15◦ in petal 1 and similarly rotated in the other petals. The numerical results are obtained using the nominal values d31 = 15 × 10−6 µm/V, PVDF-TrFE thickness t = 5µm, and radius of curvature RoC = 850mm. The piezoelectric coefficient d31 was measured by matching the voltage-driven frequency response function of a small cantilever plate sample to a finite element model. A significant scatter is observed in the cross section diagrams. The dip-coating process naturally leads to a variation in PVDF-TrFE layer thickness, estimated using capacitance measurement at t = [4.9, 5.1, 5.7, 6.1, 6.0, 5.5]µm for N ◦ [2,8,14,20,26,32]. Previous numerical studies using varying thickness of PVDF-TrFE show very little change in control stroke (because the actuator force is proportional to the product of the active material thickness and the electric field which, for a given voltage, is proportional to the inverse of the thickness). Therefore, the thickness gradient alone cannot explain the scatter observed in the experiments. Residual anisotropy in the reflector substrate, the mismatch of the radius of curvature between the reflector and clamp, and the possible variation in polarization, may affect the control response.

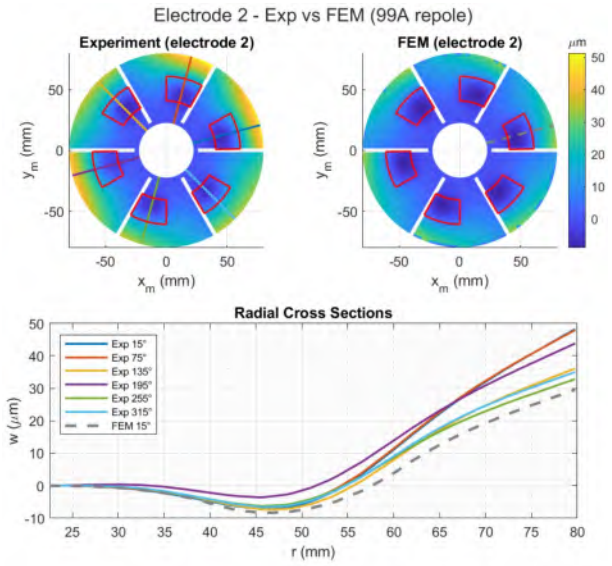


Figure 8 ***Top left****: Experimental deformed shape of the reflector when a voltage of 100V is applied to electrodes 2, 8, 14, 20, 26, and 32.* ***Top right****: Numerical finite element simulation of the reflector shape with the PVDF-TrFE thickness t = 5.0μm.* ***Bottom****: corresponding cross-sections of the deformed shape along a line at 15◦ in petal 1 and along similarly rotated lines in the other petals. The dashed line corresponds to the numerical simulation*

Using the measured influence functions in the control calculations, we may revisit the control of e.g. thermal aberrations. This is illustrated in Figure 9, where the RMS error is reduced from 5.7 μm to 0.48 μm for a ±10 K thermal gradient aberration using *measured* influence functions. The figure is to be compared to Fig. 5, where the residual error was instead 0.44 μm (simulated), demonstrating a close fit between numerically obtained results and those of the physical measurements. We note finally that where a measured influence function mainly differs in amplitude from the numerical prediction, the discrepancy is absorbed by the required electrode voltage rather than affecting the residual RMS error.

3.4. Manufacturing aberration

Although the control behaviour of reflector is behaving according to control predictions and with good performance, the main limitation of the project is currently the initial fabrication error arising from anisotropic properties of the thermoformed PEI film. The aberration of the full sample (99A) is illustrated in Figure 10 along with the resulting control. As can be seen, the needed electrode voltages to correct the manufacturing aberration are outside of the control envelope by a factor of more than three (the maximum voltage is around 300V before breakdown of the PVDF-TrFE layer begins)

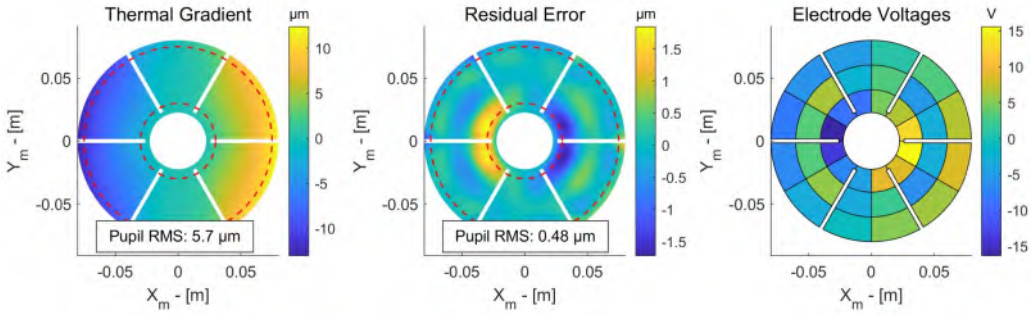


Figure 9 From left to right: ±10 K thermal gradient aberration, residual error after control using measured influence functions, and corresponding voltage map. The pupil is indicated by the dashed red circles. To be compared with Fig. 5 (top)

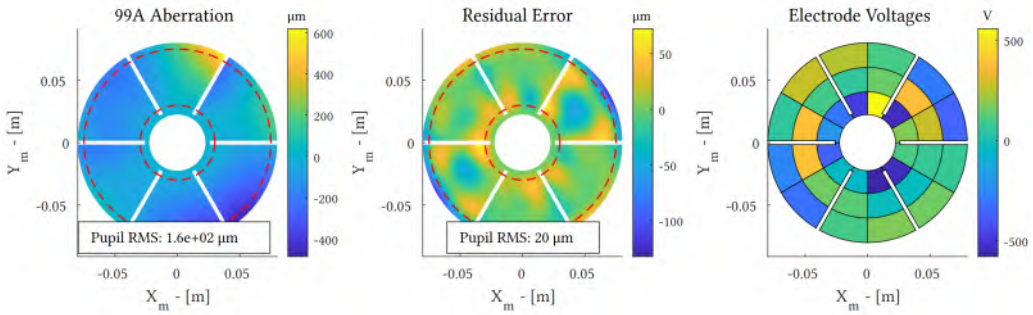


Figure 10 From left to right: Manufacturing aberration of Reflector 99A, residual error after control using measured influence functions, and corresponding voltage map. The pupil is indicated by the dashed red circles

4. VISCOELASTIC RESPONSE & CONTROL

Using the SCOTS deflectometry, a reflector with PEI substrate and Aluminium coating (no PVDF-TrFE) is clamped and the initial error is tracked over 24 hours with no disturbance, to ensure a stable reference. The reflector is subsequently stowed in a cylinder with Ø10cm diameter for 24 hours as illustrated in Figure 11, and finally deployed. The viscoelastic deployment behaviour of the reflector is illustrated in Figure 12

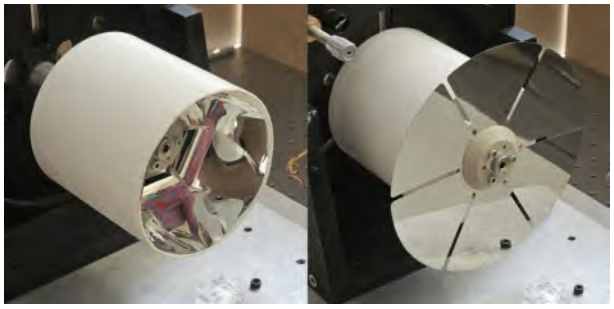


Figure 11 Left: Reflector stowed in a Ø10cm cylinder (launch configuration). Right: Reflector deployed after storage, with a slight aberration from viscoelasticity. To facilitate metrology, the cylinder is moved while the clamp and reflector remain stationary.

Using the measured influence functions found from reflector 99A, the control of the viscoelastic aberration can be investigated. 34 hours post deployment, the deployment error is still outside the bounds of control. However, after 58 hours, the control voltages are safely within the allowable range of the PVDF-TrFE layer, as shown in Figure 13. The residual error is within the control range of a possible downstream MEMS adaptive optics instrument. Material selection and improvement in geometry near the clamp could possibly reduce this further.

The results suggest that the viscoelastic residual aberration is not a main limitation of the project and could likely be controlled on-orbit within the error budget.

5. CONCLUSIONS

A successful hardware demonstration of the multilayer actively controlled polymer reflector has been presented. Comparison of experimental and simulated influence functions revealed good agreement, and simulated control *using measured influence functions* reduced a representative thermal aberration from 5.7 µm to 0.48 µm RMS.

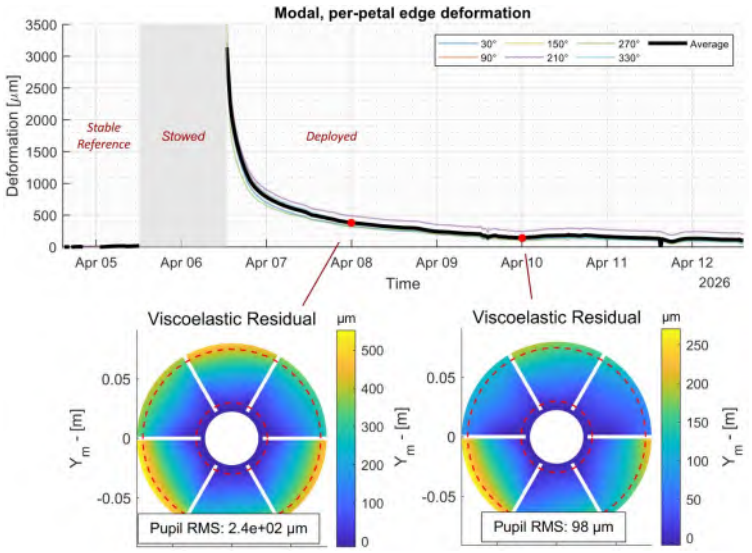


Figure 12 Top: The deployment aberration of the reflector after 24 hours in stowed configuration. Bottom: Residual viscoelastic aberration after 34 hours (left) and 58 hours (right).

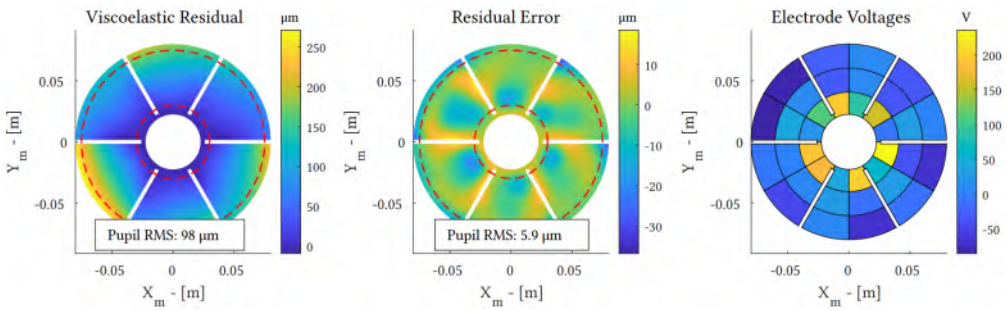


Figure 13 From left to right: Residual viscoelastic aberration after 58 hours, residual error after control using measured influence functions, and corresponding voltage map. Control voltages are within the control budget.

The viscoelastic deployment residual was found to be within the available control stroke after relaxation, leaving manufacturing-induced anisotropy of the PEI substrate as the main limitation of the demonstrator.

REFERENCES

[1] J. A. Champagne, S. M. Hansen, T. T. Newswander, and B. G. Crowther, “CubeSat Image Resolution Capabilities with Deployable Optics and Current Imaging Technology.”

[2] P. Su, R. E. Parks, L. Wang, R. P. Angel, and J. H. Burge, “Software configurable optical test system: a computerized reverse Hartmann test,” Applied Optics, vol. 49, no. 23, p. 4404, 2010.

[3] C. J. G. Nielsen, “Adaptive Petal Polymer Reflector for CubeSat Applications” Thesis, Université Libre de Bruxelles, Brussels, 2026.

[4] K. Wang, T. Godfroid, D. Robert, and A. Preumont, “Adaptive Shell Spherical Reflector Actuated with PVDF-TrFE Thin Film Strain Actuators,” Actuators, vol. 10, no. 1, p. 7, 2020.

[5] K. Wang, T. Godfroid, D. Robert, and A. Preumont, “Electrostrictive PVDF-TrFE Thin Film Actuators for the Control of Adaptive Thin Shell Reflectors,” Actuators, vol. 9, no. 3, p. 53, 2020.

[6] K. Wang, Y. Yu, and A. Preumont, “Wavefront Control Strategies for Large Active Thin Shell Primaries with Unimorph Actuators,” Actuators, vol. 12, no. 3, p. 100, 2023.

[7] K. Wang, “Piezoelectric Adaptive Mirrors for Ground-based and Space Telescopes,” PhD Thesis, Université Libre de Bruxelles, Brussels, 2019.

[8] V. Piefort, “Finite Element Modeling of Piezoelectric Active Structures,” PhD Thesis, Université Libre de Bruxelles, Brussels, 2001.

6. FUNDING

This research was carried out under the “Advanced Multilayer Adaptive Thin Shells (AMATS)” project, funded by the European Space Agency General Support Technology Programme (ESA GSTP) RFQ/3-17686/22/NL/RA/va

STUDIES ON PRELOAD RELEASE MECHANISMS FOR SHOCK REDUCTION

Kristian Schneider [(1)], Siebo Reershemius [(2)]

(1) German Aerospace Center (DLR), Institute of Space Systems, Mechanics and Thermal Systems, Robert-Hooke-Straße 7, 28359 Bremen, Germany, Kristian.schneider@dlr.de

(2) German Aerospace Center (DLR), Institute of Space Systems, Mechanics and Thermal Systems, Robert-Hooke-Straße 7, 28359 Bremen, Germany, Siebo.reershemius@dlr.de

KEYWORDS

Hold-down and release mechanism, shape memory alloy, low-shock

ABSTRACT

During ECSSMET 2024, the preload release device (PRD) for shock reduction was introduced [1]. The mechanism can slowly release the elastic energy stored in an assembly consisting of a preloaded hold-down pin (HD-pin) and structure. This allows a shock-free release of the deployable structure. Since the last ECSSMET two more concepts of the PRD were designed and preliminary tested. One uses shape memory bolts and the other one elaborates a force-gear to slowly decrease the preload.

This paper introduces these two new concepts and discusses the first test results. It concludes with a comparison of the concepts, and the most suitable one is selected.

1. INTRODUCTION

The initial concept of the preload release device (PRD) was introduced at ECSSMET 2024, detailing its primary motivations and fundamental functionality [1]. While the preliminary technology demonstration proved the feasibility of the system for its intended application, several critical drawbacks were identified, including poor scalability, high temperature dependency and a complex assembly process.

To mitigate these limitations, two advanced design concepts were developed and evaluated. This paper presents a comprehensive discussion and comparative analysis of these new designs. To quantify their performance, an extensive testing campaign was conducted, including ambient activations, vibration and pyroshock testing. Finally, this paper concludes with the selection and justification of the most suitable design.

2. MOTIVATION

The motivation of the development is to solve a reoccurring issue during development of space systems. Small stowing volume require to have deployable structures, which are preloaded to the main system in order to survive launch loads. But at activation this preload is causing shock, which might damage sensitive instruments. Another issue is the large uncertainty of shock propagation within space systems, which cannot be determined accurately using theoretical models. Therefore, tests with the real hardware need to be done in order to determine the shock level at sensitive instruments and the damping behaviour between the interfaces. Representative models are required for those tests. But those are only available at later stages of the project. Therefore, sensitive instruments are located apart from the shock source at the initial system configuration or they are equipped with shock damping features. This might limit the system performance.

The PRD is able to store or slowly dissipate large amounts of the elastic energy stored in the clamped components of a release system. This reduces the preload force before the actual release of the holding and separating mechanism so that the stored energy is not released abruptly. This minimises the shock load. Figure 1 shows the qualitative preload force curve. When the release system is activated, the preload force is reduced to almost zero. When the minimum is reached, the actual holding and separating mechanism is triggered and the holding bolt is released.

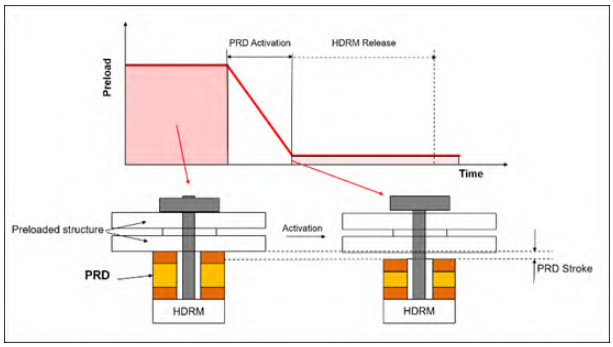


Figure 1: Characteristically activation of a preload release system (PRD)

3. STATE OF THE ART

There are several mechanisms that reduce the preload in order to reduce the shock loads. Some of these devices are presented and discussed in this brief review.

3.1. MASCOT Preload Release Device

The Mobile Asteroid Surface Scout (MASCOT) is a lander which landed on an Asteroid [2]. This lander was locked with a special preloaded separation system. The preload was approximately 2500 N. If the system had been released abruptly, the stored elastic energy would have been converted into kinetic energy. This would have greatly increased the speed of the lander. A preload release mechanism was used to reduce the preload before releasing the lander to prevent that increase of speed. The mechanism used a thermoplastic material which was heated during the preload release. In combination with the preload, the thermoplastic material began to creep. That creeping process led to a slow and smooth release of the preload and stored elastic energy. After that, a separation of the lander with a maximum preload of about 100 N was possible [2]. The Figure 2 shows the preload release device of the MASCOT lander.



Figure 2: MASCOT preload release device [2]

3.2. LSRU

The LSRU (High Load Low Shock Release Unit) is a mechanism which can be used for a preload of 30 kN [3]. Maximum shocks of 500 g's (SRS) are produced. The function of the mechanism is based on the conversion of the preload into a rotational movement. Therefore, the stored elastic energy could dissipate and a low shock release is possible. A non-self-locking screw is used for the conversion between the preload and the rotation. This means that the screw starts to rotate even at low forces and starts to move axially. The mass of the mechanism is 900 g. And the qualification temperature is between -95 °C and +120 °C [3]. The Figure 3 shows the High Load Low Shock Release Unit.

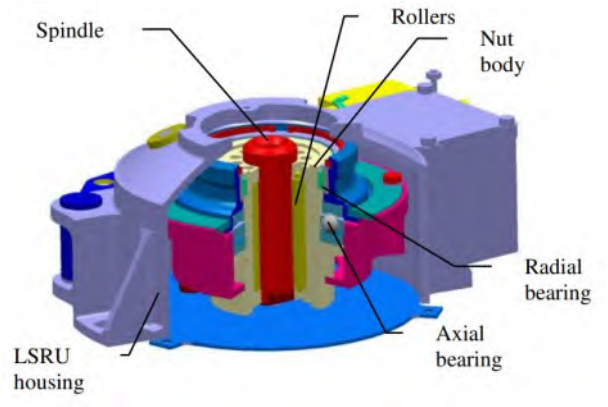


Figure 3: LRSU [3]

4. REQUIREMENTS

Table 1 summarizes the most important requirements of the PRD. A detailed discussion of these requirements was presented during ECSSMET 2024 [1].

Table 1: List of requirements

No.	Requirement	Verification
1	Minimum preload of 20 kN	Analysis and test
2	Mass < 500 g	Review of design
3	Resettable	Test
4	20 life cycles	Analysis and test

5. CONCEPTS

Three different concepts of the PRD were designed and preliminarily tested. This section will introduce these three concepts and describe the functional principles.

5.1. SMA-wire PRD

The first concept is a preliminary technology demonstrator to show the basic functionality of this approach. This concept could be described as a very stiff spring, which is able to provide a stroke between 1 and 2 mm. Figure 4 shows a simplified illustration of the functional principle. The PRD is combined with a commercial HDRM and is assembled into the load path of the HD-pin. When the PRD is activated, the PRD contracts and the elastic deformations of the pin and preloaded structure is removed. Therefore, a shock-free release is possible. Figure 5 shows the engineering model of the wire-based PRD. The mechanism consists of a mobile part and static frame. These parts are connected by superelastic and shape memory alloy wires. Both wire types are preloaded against each other resulting in a force equilibrium between the mobile and the static part.

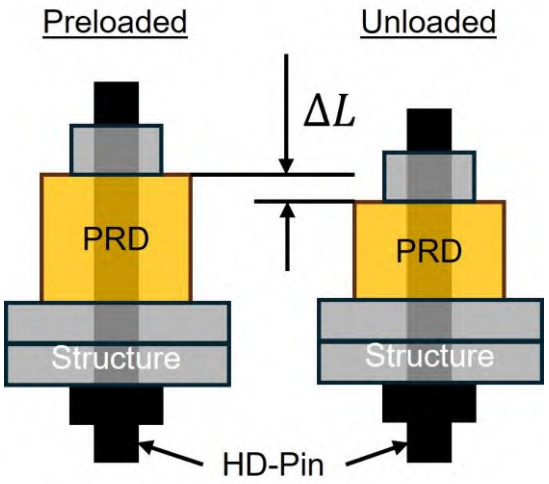


Figure 4: Functional principle of the wire-PRD

During installation and preloading of this system the superelastic wire is further tensioned until a preload of 10 kN is reached. The activation is achieved by applying a current to the SMA wires, which causes them to heat up and contract. That leads to a significant travel of the mobile part and further elongation of the superelastic wires. Hence the overall structure is unloaded and a shock free separation with an HDRM is possible.

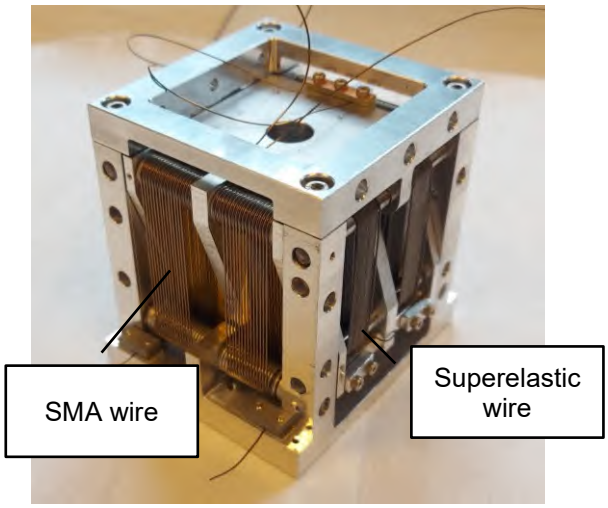


Figure 5: Wire-based preload release device

5.2. SMA-bolt PRD

The second concept is quite similar to the concept from section 5.1. This concept can be used for preloads up to 23 kN. The superelastic wires were replaced with a ring spring, and the SMA wires were replaced with SMA bolts, to achieved higher forces. Furthermore, a locking mechanism is implemented to release the HD-pin without a separate HDRM. The PRD can be seen in Figure 6.

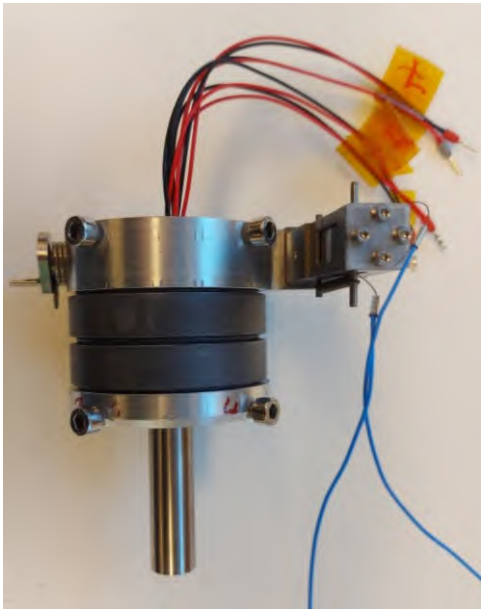


Figure 6: SMA-bolt-based preload release device

As schematically illustrated in Figure 7, a heating wire is wrapped around the SMA-bolts. This wire is used for heating the SMA-bolts above their austinite transformation temperature. A specially designed connection is implemented to get a prober connection between the SMA-bolt and the overall system.

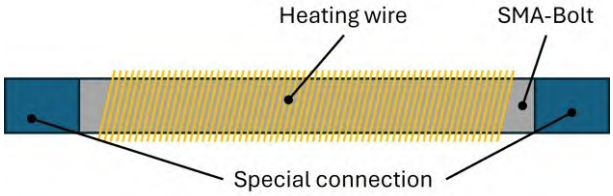


Figure 7: Schematic illustration of the SMA-bolt

5.3. Combined PRD

The third concept uses a completely different principle than the previous introduced variants. The concept is hereafter referred as “combined PRD” as it combines the preload release and the un-locking in one device. This is considered a significant advantage, as the electrical interfaces can remain the same.

The extension of the preloaded HD-pin is slowly reduced by a force-gearbox. Once this is finished, a second locking mechanism releases the bolt. Consequently, the mechanism provides an axial stroke that allows a preload release and an automatic un-locking of the HD-pin. A separate HDRM is not required.

Due to ongoing patenting process no further information can be shared.

The engineering model of the combined PRD can be seen in Figure 8. The locking mechanism of the gear is shown on the right side of the figure.



Figure 8: Engineering model of the combined PRD

5.4. Technical data

Table 2 summarizes the technical data of the three concepts introduced.

Table 2: Technical data of the PRD concepts

	Wire	Bolt	Combined
Mass (g)	446 g	699 g	313 g
Volume (mm^3)	82x70x82	Ø65x57	Ø52x45
Preload (kN)	10	23	35
Activation time(s)	≈ 10	≈ 40	<0.1
HD-Pin I/F	Extra HDRM	M10 Adapter	M10 Thread

6. PRELIMINARY TECHNOLOGY DEMONSTRATION

The described concepts of the PRD are used for a preliminary technology demonstration. The tests are used to characterize the behaviour and the performance to compare these different concepts.
The aim of the tests is to identify the most suitable PRD that meets the requirements and delivers the best performance.
The tests conducted included ambient activations, vibrations tests, pyroschock tests and shock measurements to characterize shock emissions.

6.1. SMA-Wire PRD

This section presents the technology testing campaign of the SMA-wire PRD to evaluate the functionality. First, an ambient activation was performed to characterize the preload release behaviour. Second, thermal cycling was conducted to characterize the temperature dependence of the preload.

6.1.1. Ambient activation

Figure 9 shows the test setup for the force measurement during the unloading process. The setup includes a bolt which is used to preload the mechanism. Furthermore, the mechanism is attached to an MGSE and a force gauge is added at the bottom of the test setup. This force gauge records the preload that acts on the bolt.

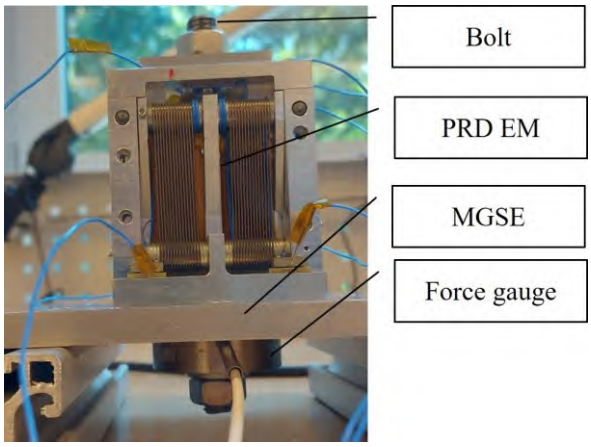


Figure 9: Test setup for preload release demonstration

To test the performance of the PRD the system was preloaded up to 10 kN by tightening the nut on top of the test setup. After preloading, the SMA- wires were powered by an external power supply. Figure 10 shows the preload during powering of the SMA-wires. It can be seen that the preload is nearly completely unloaded after 30 s. A residual force of about 0.16 kN still acts on the bolt. This corresponds to a force reduction of approximately 98%.

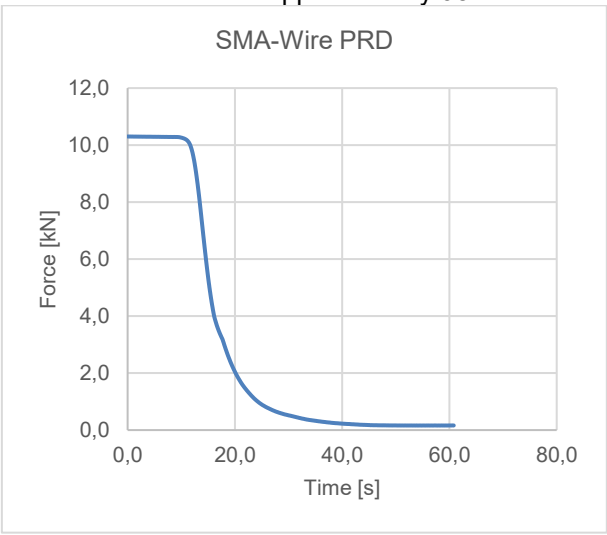


Figure 10: Unloading curve of the SMA-wire-based PRD

6.1.2. Thermal behaviour

Both the SMA-wire and the superelastic have a significant temperature dependence. A temperature increase and decrease can lead to an austinite or martensite transformation. This causes the material properties to change significantly. To characterize this behaviour the PRD was preloaded up to 10 kN. After that, the mechanism was cycled inside a climate chamber between 43°C and 0°C.

Figure 11 illustrates the results of the thermal cycling test. The preload correlates directly with the temperature changes, rising during heating phases and dropping during cooling phases. At the minimum temperature, the preload decreases by approximately 25%, reaching a low of 7.5 kN.

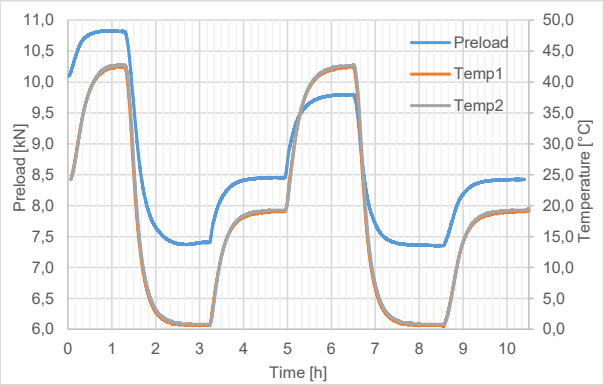


Figure 11: Preload during thermal cycling

6.2. SMA-Bolt PRD

This section presents the technology testing campaign of the SMA-bolt PRD to evaluate the functionality. First, an ambient activation was performed to characterize the preload release behaviour. Second, vibration testing was conducted to determine the mechanism's ability to withstand the mechanical loads that occur during the launch.

6.2.1. Ambient activation

The experimental setup utilized is identical to the one described in section 6.1. Therefore, no further description is provided.
The mechanism was preloaded up to 23 kN. After preloading the SMA-bolts were heated until they reached the transformation temperature. Figure 12 shows the unloading curve which was measured during the activation. It can be seen that the preload drops to nearly zero after about 50 s.

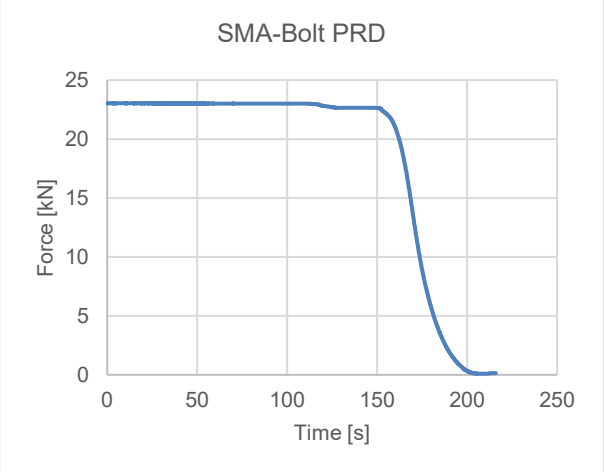


Figure 12: Unloading curve of the SMA-bolt-based PRD

6.2.2. Vibration test

The sinusoidal and random vibration tests were performed on the shaker at DLR in Bremen. These tests were conducted to determine whether the preload force decreases during vibration and whether subsequent activation remains possible. Table 3 shows the specifications for the vibration tests. The tests were performed in the out-of-plane axis. Figure 13 shows the test setup of the vibration test.

Table 3: Vibration Test Specification

Sinusoidal Vibration Specification				
Frequency Range [Hz]	5		20 – 130	
Acceleration Level [g]	2.3		20	
Sweep Rate	2 oct/min (one up-sweep)			
Random Vibration Specifications				
Frequency Range [Hz]	20	50	800	200
Acceleration Level [g^2/Hz]	0.0637	0.392	0.392	0.0637
Overall Level [g_{RMS}]	22.13			
Duration [s]	120			

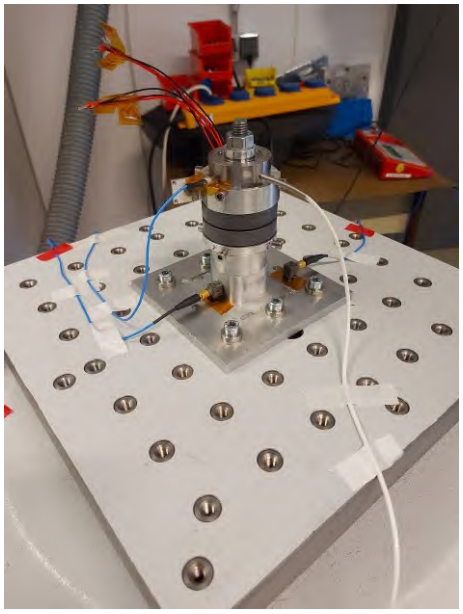


Figure 13: Vibration test of the SMA-bolt PRD

This test was successfully conducted, without a significant preload loss (<1%). After vibration the PRD was successfully activated.

6.3. Combined PRD

This section presents the technology testing campaign of the combined PRD to evaluate the functionality. First, an ambient activation was performed to characterize the release behaviour. Second, vibration testing and pyroshock testing was conducted to determine the mechanism's ability to withstand the mechanical loads that occur during

the launch. Furthermore, a shock characterization was performed to evaluate the shock emissions during activation.

6.3.1. Ambient activation

To evaluate the possible preload, an ambient activation of the new PRD was conducted. For measuring the preload, a force gauge was used. A threaded pin was screwed into the PRD and preloaded up to 35 kN. For activation, the PRD was powered with a 100 ms 4 A current pulse.
Figure 14 shows the measured force during the activation of the system. It can be seen, that the preload dropped to 0 N and the pin was released after the PRD was activated. Therefore, the functionality of the new design was proven. In summary, the PRD is able to release a structure preloaded with 35 kN using a 100 ms current pulse.

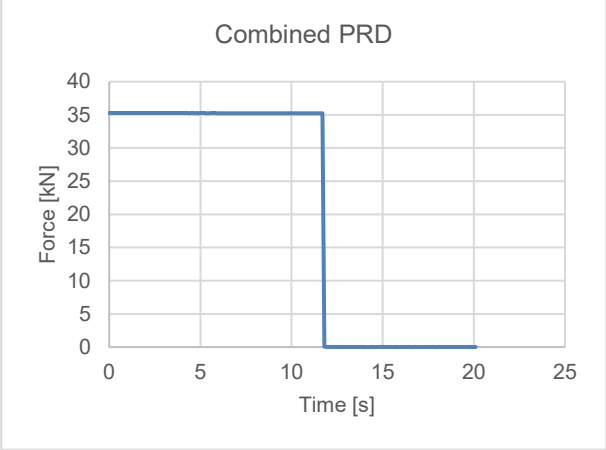


Figure 14: Ambient activation of the combined PRD

6.3.2. Vibration test

The sinusoidal and random vibration tests were performed on the shaker at DLR in Bremen. These tests were conducted to determine whether the preload force decreases during vibration and whether subsequent activation remains possible. The test specifications can be found in Table 3.

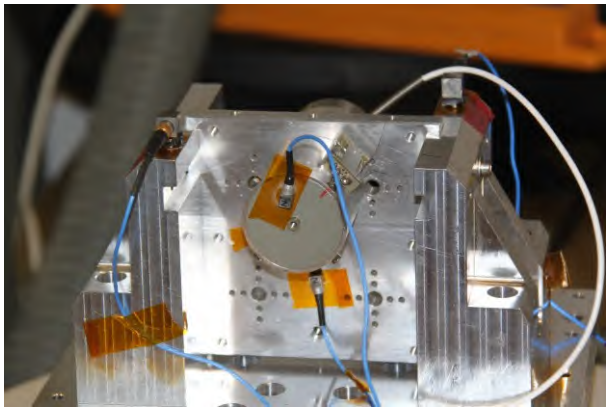


Figure 15: Vibration test of the combined PRD

This test was successfully conducted, without a significant preload loss (<<1%). After vibration the PRD was successfully activated.

6.3.3. Pyroshock test

For verifying the performance during shock loads, a preliminary pyroshock test was conducted. Table 4 summarizes the specification of the pyroshock test.

Table 4: Pyroshock test specification

Axis	Frequency	Level SRS
3 shock inputs in each axis X, Z	100 Hz 1000 Hz 10000 Hz	100 g 1500 g 1500 g

This test was successfully conducted without a significant preload loss (<<1%). After pyroshock test the PRD was successfully activated.

6.3.4. Shock measurement

The shock measurement was conducted in order to quantify the shock emissions during activation. The emitted shock at the point of activation is the most important indicator to evaluate the shock reduction of the newly developed combined PRD. The emitted shock was measured on a free-hanging ringing plate. The setup is shown in Figure 16. The plate is made of aluminium and measures 1 m x 1 m with a thickness of 5 mm. The PRD is mounted underneath the plate. The preload of 35 kN is measured with a force gauge. Three Triax accelerometers are located on top of the ringing plate for monitoring the shock loads. The distances of the accelerometers from the shock source are shown in Figure 16.

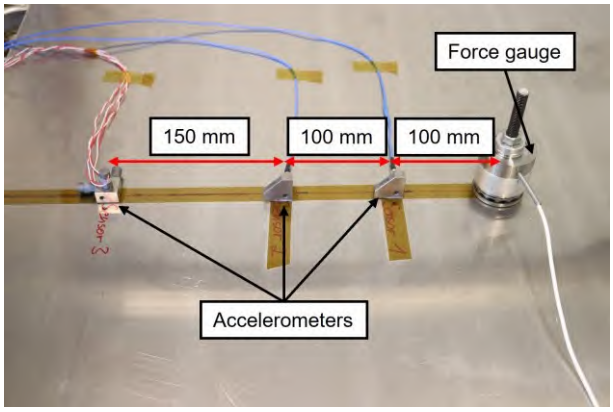


Figure 16: Shock characterization test setup

Figure 17 shows the shock measurement results for every axis at every sensor. It can be seen that all results are lower than 400 g.

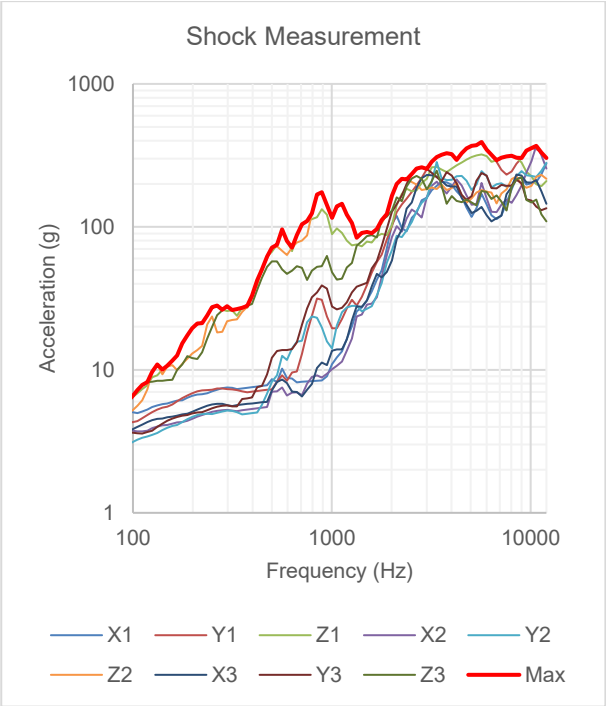


Figure 17: Shock characteristics of PRD with 35 kN

7. COMPARISON OF THE CONCEPTS

In this section, the concepts are compared with one another, and the most suitable one is selected at the end.

The wire- and bolt-PRD both are able to reduce the preload to nearly zero in several seconds. Therefore, the energy dissipation is quite slow and the occurred shock is just emitted by the HDRM or locking mechanism. A shock because of the stored elastic energy can be nearly completely avoided. But this advantage comes with some drawbacks. At first, the maximum preload is strongly limited. An increase from 10 kN to 23 kN results in a significant mass increase. Furthermore, both concepts need several seconds for heating. Therefore, the S/C must provide enough electrical energy for the activation.

One further drawback of the wire-PRD is the significant temperature dependence. The temperature sensitivity of the bolt-PRD is a little less because no superelastic material is used in combination with the SMA-actor elements.

The combined PRD demonstrates the lowest mass and volume among all tested design. Furthermore, this concept achieves the highest possible preload of about 35 kN. Consequently, the specific mass and the specific volume of the 35 kN and an 18 kN combined PRD are quite low compared with the other concepts (see Figure 18). The dynamic mechanical tests were successfully completed without any abnormalities and the emitted shock reaches only a maximum of 400 g above 1000 Hz. Besides, the reset can be done in a single step.

In conclusion, the combined PRD combines the advantages of the other concepts and even improves upon them. The discussed disadvantages are almost completely eliminated. Consequently, the combined PRD is selected for the qualification campaign.

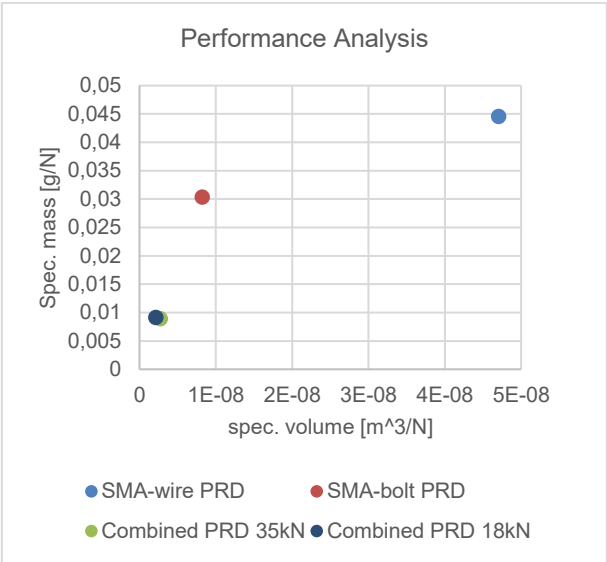


Figure 18: Performance analysis of the PRDs

8. CONCLUSION AND OUTLOOK

This paper presented three different concepts for a preload release device and the preliminary technology demonstration of these concepts. The combined PRD shows the best performance compared with the other PRDs. This mechanism combines a high preload of 35 kN with a short activation time of 100 ms and a low shock emission of 400 g. Furthermore, the system is on-site resettable with one single step. After that de-risking campaign, the qualification campaign of the 35 kN and an 18 kN PRD will start in September 2026.

9. REFERENCES

1. Schneider, K., Reershemius, S., Sasaki, K., Sproewitz, T.(2024). A Novel Preload Release Device for Shock Reduction. ECSSMET 2024
2. Grimm, C.D., Lange, C., Lange, M. et al. (2020). *The MASCOT separation mechanism*. CEAS Space J 12, 343–365 https://doi.org/10.1007/s12567-020-00302-y
3. Müller, Jens; Anderaus, Christian (2009): *High Load Low Shock Release Unit (30kN)*. Vienna: 13th European Space Mechanisms and Tribology Symposium – ESMATS. Available online at https://www.esmats.eu/esmatspapers/pastpapers/pdfs/2009/muller.pdf.

FRANGIBLE JOINT 1: OVERVIEW OF DESIGN, VERIFICATION AND QUALIFICATION TEST PROGRAMME

F. Marques Novo [(1)], M. Cattepoel, G. Molinari, E. Odinolfi, A. Sánchez Cebrián
[(1)] Beyond Gravity Schweiz AG, The Circle 23, 8058 Zürich Flughafen, Switzerland
Email: francisco.marquesnovo@beyondgravity.com

KEYWORDS
Frangible Joint; payload fairing separation; gas expansion tube; multi-physics finite element analysis; analysis–test correlation; output shock; qualification testing

ABSTRACT
Payload Fairing separation is a mission-critical event requiring exceptionally high reliability. Frangible joints enable rapid and clean separation through a controlled structural fracture. This paper presents the integrated design, verification, and qualification approach adopted for an optimized Frangible Joint system for horizontal fairing separation. The development combined high-fidelity analytical modelling with extensive experimental verification and qualification test campaigns. These activities demonstrated the required separation performance across operational extremes while accounting for inherent variability in the coupled energetic and structural subsystems and confirmed the optimized low-shock behaviour. Qualification included environmental life testing on sub-length samples followed by full-scale separation tests. The results demonstrate robust, repeatable, and end-to-end system performance while establishing a systematic engineering methodology for the development and qualification of advanced pyrotechnic separation systems.

1. INTRODUCTION

The separation of large Payload Fairings (PLFs) constitutes one of the most critical events of a launch mission, requiring high reliability and robust performance while minimizing dynamic disturbances transmitted to the payload and surrounding launch vehicle structures.
Frangible joints provide an attractive separation solution by enabling rapid release through a controlled and repeatable structural fracture, while avoiding the mass penalties, mechanical complexity, and integration constraints associated with conventional mechanical separation mechanisms.
Their lightweight architecture, structural efficiency, and predictable fracture behaviour make them particularly suitable for large launch vehicle applications under demanding environmental and operational conditions.
This paper presents the engineering methodology adopted for the design, development, verification, and qualification of Beyond Gravity's Frangible Joint 1 (FJ1), as illustrated in Figure 1. The methodology combines high-fidelity multi-physics simulation, progressive experimental verification, and staged qualification within a unified development framework. Particular emphasis is placed on the interaction between the pyrotechnic and structural subsystems and on the progressive reduction of engineering uncertainty achieved through continuous correlation between analytical predictions and experimental observations.

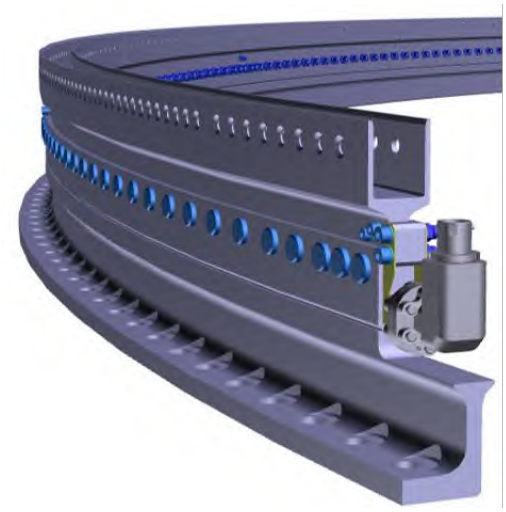


Figure 1: Frangible Joint 1 System

The development programme was structured as a sequence of complementary activities addressing the energetic, structural, dynamic, environmental, and system-level performance of the separation architecture. Explosive performance margin testing on representative sub-length specimens was used to establish robust severance capability across the operational envelope while accounting for intrinsic scatter across the various elements and parameters. Intermediate-length assemblies were subsequently employed for dedicated output shock characterization, providing experimental assessment of the dynamic response.
The qualification programme then combined structural load qualification, environmental life testing, and progressively representative full-scale separation demonstrations. The final tests were performed on structural assemblies replicating the cylindrical section of a 5.4 m diameter PLF, providing end-to-end verification of the separation system under representative boundary conditions.
Beyond demonstrating the performance of the FJ1

system, the programme established a validated analysis–test–correlation methodology capable of supporting design optimization, margin assessment, and prediction of system behaviour throughout the qualification envelope. The resulting integrated engineering approach provides a scalable basis for the development and qualification of future high-performance pyrotechnic separation systems for increasingly demanding launch vehicle applications.

2. FRANGIBLE JOINT SYSTEM

The FJ1 system was designed to operate within a thermo-mechanical qualification envelope representative of the most demanding large PLF applications. Its development was driven by stringent requirements for structural performance, separation reliability, environmental robustness, and operational safety, in compliance with the applicable international standards governing pyrotechnic separation systems, including [1], [2], [3], as well as relevant best-practice guidelines and methodologies [4], [5].

The structural and energetic subsystems were conceived as a unified assembly, enabling a combined optimization throughout the development process.

The architecture comprises a segmented structural profile assembly and a hermetically sealed Gas Expansion Tube (GET) assembly incorporating the linear explosive subsystem and the interfaces for the electro-pyrotechnic initiation devices. The resulting architecture provides the structural load path required throughout launch while enabling controlled structural severance upon pyrotechnic activation.

The principal elements of the optimized FJ1 system and the associated design, verification and qualification activities are further described in the following sections.

2.1. Segmented Profile Assembly

The structural profile assembly comprises interlocking tang and clevis elements, as per Figure 2, providing a robust primary load path throughout the launch mission. The configuration was optimized to achieve an effective balance between structural performance, manufacturability, integration requirements, and cost, while preserving the functional characteristics required for consistent and repeatable separation.

The resulting architecture combines high structural efficiency with predictable and repeatable separation behaviour, providing a robust structural solution tailored to the demanding requirements of large PLF applications.

The segmentation strategy and the intentional discontinuity of the tang and clevis structural members were developed through an extensive design optimization process to minimise local stiffness transitions and stress concentrations at the separation plane. Moreover, the segmented profile architecture enables a more controlled and repeatable fracture propagation through multiple interconnected structural sections, while making the overall architecture easily scalable to larger diameters.

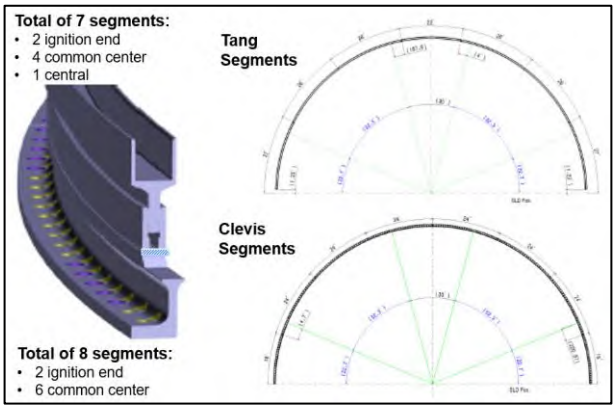


Figure 2: Segmented Profile Assembly – Main Elements

The radial interfaces between adjacent structural segments are interconnected using press-fit pins and collars, which constitute a key functional feature of the assembly. In addition to providing the preload and load-transfer capability required to withstand the combined launch loading, the radial fastening system ensures a highly clamped and stiff structural interface throughout the operational life of the vehicle. Maintaining controlled preload and interface stiffness is essential to achieve consistent fracture initiation and stable fracture front propagation during separation. Consequently, the fastening philosophy was treated as an integral element of the system design rather than a conventional structural joining method, balancing structural efficiency with the functional reliability requirements.

Finally, the assembly also defines internal and external structural interfaces, alignment features, and geometric tolerances required for the integration of the expansion tube assembly.

2.2. Gas Expansion Tube Assembly

An optimized GET assembly was designed, verified, and qualified as an integral element of the frangible joint system architecture.

The assembly comprises the expansion tube and associated ignition-end bodies, providing the mechanical and pyrotechnic interface with the initiation devices, as per Figure 3. Together, these elements ensure the reliable coupling between the electro-pyrotechnic initiation devices and the remainder of the explosive assembly.

The GET assembly represents the core functional subsystem of the architecture, providing the conversion of the detonation energy into the mechanical loading required to drive the expansion of the tube and the subsequent severance of the profile assembly. Its primary function is to distribute

the detonation energy uniformly along the full joint length while maintaining structural integrity under the associated transient pressure loading and dynamic boundary conditions.

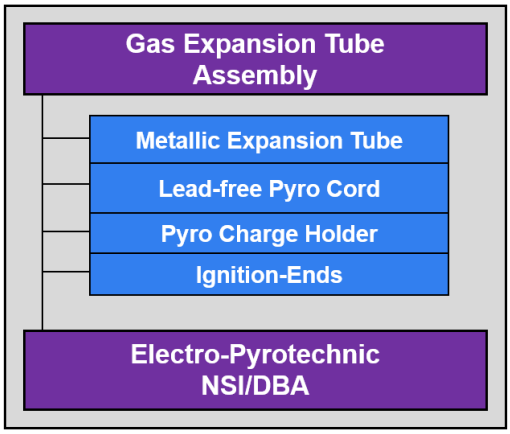


Figure 3: GET Pyrotechnic Assembly

The resulting balance between the required energetic output and structural containment is fundamental to achieving controlled and repeatable separation performance. Therefore, the tube material, manufacturing and geometry were optimized together with the explosive assembly to achieve the required balance.

The complex interaction between detonation loading, tube expansion, and surrounding structural response was a key driver for the development of the coupled Eulerian-Lagrangian Finite Element modelling approach briefly described in the next section and further discussed in the companion paper by M. Conrad et al. [6].

Moreover, the GET assembly was designed to preserve dimensional stability, hermetic sealing (prior to functioning), and leak-tightness (post functioning) throughout all phases of the product lifecycle, including manufacturing, storage, transportation, integration, and operational service.

2.3. Electro-Pyrotechnic Initiation Architecture

The electro-pyrotechnic initiation architecture provides the critical interface between the launch vehicle initiation system and the GET assembly. During the initial development programme, the architecture was based on a commercial NASA Standard Initiator (NSI) combined with a dedicated booster assembly integrated within the Ignition-End Body. This configuration ensured robust transfer of the initiation energy to the GET assembly, providing reliable ignition of the linear explosive transfer subsystem.

As the programme progressed, the initiation architecture was further developed into a modular family of configurations ensuring compatibility with a broader range of customer-specific flight initiation systems. In addition to the baseline initiation solution, the architecture was successfully adapted to accommodate alternative configurations, including a qualified Detonator Booster Assembly (DBA) solution as shown in Figure 4. This modular approach provides increased flexibility for integration with different launch vehicle platforms while preserving the functional performance and reliability of the system.



Figure 4: NASA Standard Initiator (left) & Detonation Booster Assembly, DBA (right)

The complete initiation architecture was verified and qualified through dedicated detonation transfer margin campaigns, explosive margin validation and qualification life tests, demonstrating reliable initiation performance under all operating conditions as well as under the applicable explosive margin and environmental conditions.

3. ANALYTICAL VERIFICATION APPROACH

A high-fidelity Finite Element (FE) modelling methodology was developed as a central element of the FJ1 programme. Rather than serving solely as a post-design verification tool, the simulation approach formed an integral part of an iterative engineering process, enabling continuous design refinement, structural margin and severance capability assessment, and correlation with experimental testing throughout the programme.

The separation event constitutes a highly transient multi-physics problem involving explosive detonation, confined gas expansion, strong fluid–structure coupling, extreme strain-rate plastic deformation, contact interactions, fracture initiation and propagation, all occurring within microseconds. Capturing these interacting phenomena with sufficient fidelity was essential to accurately predict the governing physical mechanisms, reduce dependence on experimental testing, and establish a predictive engineering capability. Conventional implicit structural analysis techniques were insufficient for this purpose. Therefore, a coupled Eulerian–Lagrangian formulation was implemented to model the interaction between the explosive assembly, the containment tube, and the surrounding structural assembly – as illustrated in Figure 5 – throughout the separation sequence.

The numerical framework employed Eulerian meshes to represent the explosive materials and the confined gaseous domain generated during detonation, while Lagrangian meshes were adopted for all structural components. This formulation enabled the simulation of the key physical phenomena governing the separation process and their interactions throughout the highly transient event. Particular attention was devoted to the detailed representation of the profile assembly,

including the separation plane and the radial press-fit pin-and-collar connections, whose stiffness and load-transfer characteristics influence the local structural response during separation.

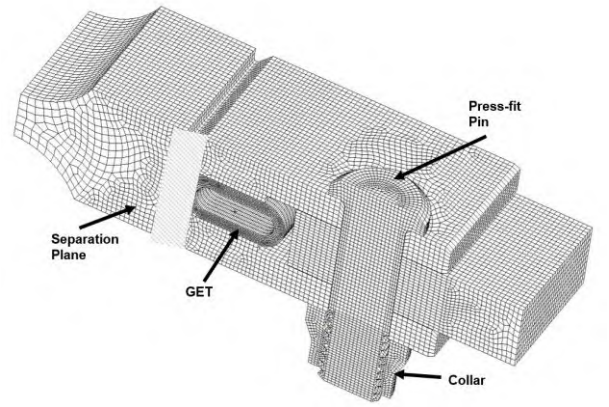


Figure 5: High-Fidelity Finite Element Models

Local mesh refinement was applied to the GET to accurately capture the large strain gradients, stress localization, contact interactions, and deformation mechanisms governing tube expansion. This level of refinement was essential to adequately represent the highly localized and transient structural response occurring during the separation event, as illustrated in Figure 6.
The FE methodology constituted a key engineering tool throughout the iterative design optimization process.

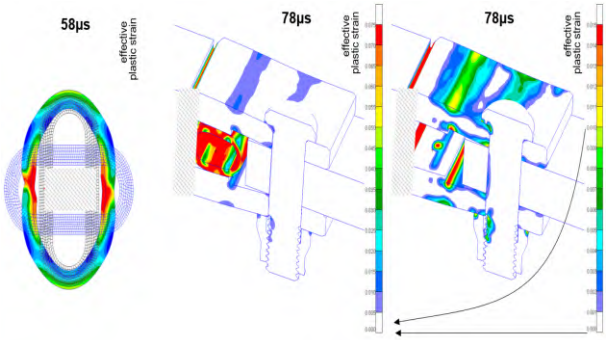


Figure 6: Modelling Explosive Margin Levels & Sensitivity Effects

Sensitivity analyses were performed to quantify the influence of the principal design parameters, including variations in tube material properties, wall thickness, and elongation at break using representative upper- and lower-bound material properties. These investigations provided valuable insight into the governing design sensitivities. The analytical methodology was progressively validated and refined.
Closed-loop analysis–test–correlation activities extended beyond verification of the global separation response and included comparison of GET expansion, structural deformation and output shock measurements. Iterative comparison between numerical predictions and experimental data enabled continuous refinement of the modelling assumptions and calibration of the numerical models, as illustrated in Figure 7.

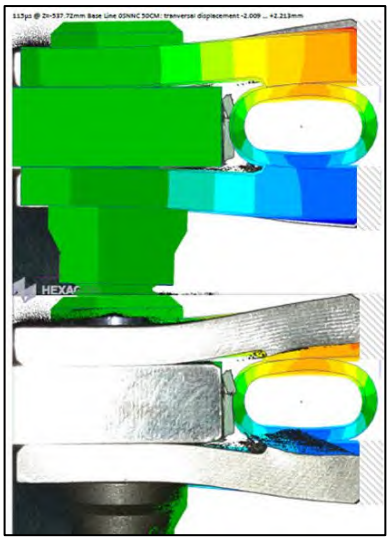


Figure 7: FEM Predictions (top) vs. Test Measurements (bottom)

Finally, dedicated shock prediction methodologies, were further employed as complementary analytical tools to characterize the shock wave propagation and to optimize the overall shock levels, as per [6].

4. EXPERIMENTAL VERIFICATION APPROACH

The development and qualification of the FJ1 system followed a structured and progressive experimental verification programme, in accordance with [1], [2] and [3].
The programme was organized into a sequence of complementary test campaigns, each addressing specific technical objectives while progressively maturing both the system design and the underlying analytical models. Consequently, each campaign contributed not only to verification of the associated test objectives, but also to the continuous refinement and maturation of the corresponding simulation models.
The verification activities were deliberately structured to progressively increase the complexity and representativeness of the test articles. Initial sub-length specimens were employed to investigate the behaviour of the system. Intermediate-scale assemblies were subsequently used to characterize the dynamic response and output shock behaviour under representative boundary conditions, while the final verification stage culminated in full-scale separation tests representative of the flight configuration.
The complete verification programme and its progressive test philosophy are summarized in Figure 8.
The hermetic sealing of the GET assembly prior to functioning and its post-functioning tightness were systematically verified throughout the development programme. The results of the various tests

confirmed the ability of the assembly to maintain the required leak-tightness before activation and to preserve the specified post-functioning integrity and tightness following the separation event.

Verification Activity	Representative Test Article	Primary Objective
Structural Profile Assembly Static Load Qual Test	Sub-length specimens	Qualification of structural profile assembly against quasi-static loads
Explosive Performance Margin Testing	Sub-length specimens	Validation of underload and overload explosive margins
Output Shock Characterization Testing	Intermediate-length with representative panel (1m × 2m)	Characterization and optimization of transmitted shock environment
Environmental Qual Life Testing	Sub-length qualification specimens	Demonstration of environmental robustness and functional reliability
Full-Scale Separation Qual Test	Representative PLF structural assembly	End-to-end verification of complete system performance

Figure 8: FJ1 Experimental Verification and Qualification Testing Programme

4.1. Explosive Performance Margin Validation

Comprehensive explosive performance margin testing was conducted on representative sub-length specimens to establish the robustness of the separation system across the complete operational temperature range.

The primary objective of these tests was to demonstrate adequate functional margins under underload and overload explosive margin conditions, as illustrated in Figure 9 and Figure 10, respectively.

The majority of specimens were initiated using single-sided ignition, representative of the baseline configuration. The influence of double-sided ignition was also specifically investigated, including under overload explosive margin conditions, to assess the robustness of the GET and the overall separation mechanism against variations in the initiation configuration.

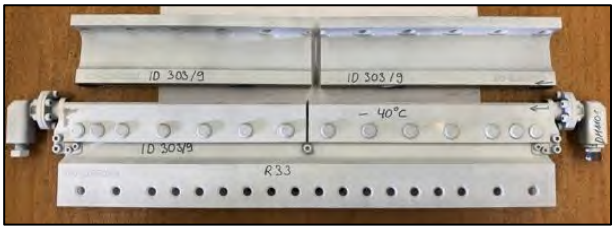


Figure 9: FJ1 Underload Explosive Margin Testing

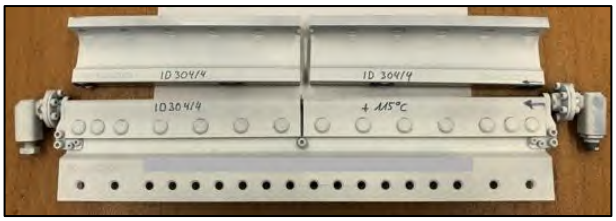


Figure 10: FJ1 Overload Explosive Margin Testing

4.2. Output Shock Characterization

Dedicated output shock characterization campaigns were conducted using intermediate-length frangible joint specimens. The primary objective was to experimentally verify the effectiveness of the optimized FJ1 architecture in minimizing transmitted pyrotechnic shock. Testing was performed using a representative 2 m panel configuration specifically designed to reproduce relevant boundary conditions and load-transfer paths, as illustrated in Figure 11, thereby enabling accurate characterization of the transient dynamic environment generated during separation and comparison with other frangible joint systems tested with equivalent setups.



Figure 11: FJ1 Output Shock Panel Testing

High-frequency instrumentation distributed throughout the test panels, as per Figure 12, enabled detailed characterization of both the spatial and temporal evolution of the shock environment generated during the separation event.

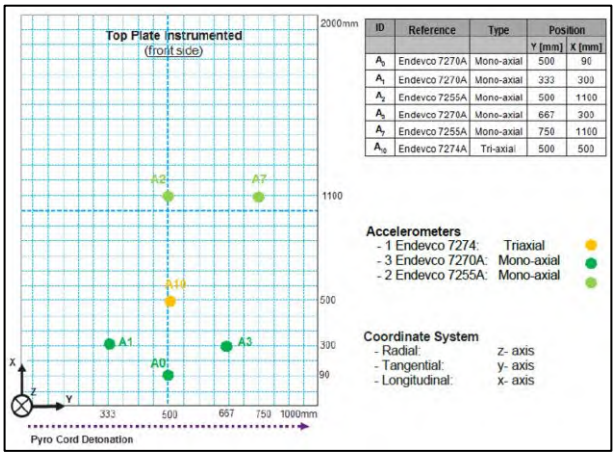


Figure 12: FJ1 Instrumented Plate

Across the various panel test campaigns, the measured Shock Response Spectra (SRS) consistently remained below 9000 g, 6000 g, and 4000 g within the 10 kHz frequency range, for the radial, axial, and tangential directions, as per Figure 13, respectively. Moreover, the results were further substantiated during the final full-scale qualification test, verifying that the optimized shock behaviour observed during intermediate-scale testing was sufficiently representative of the full-scale configuration.

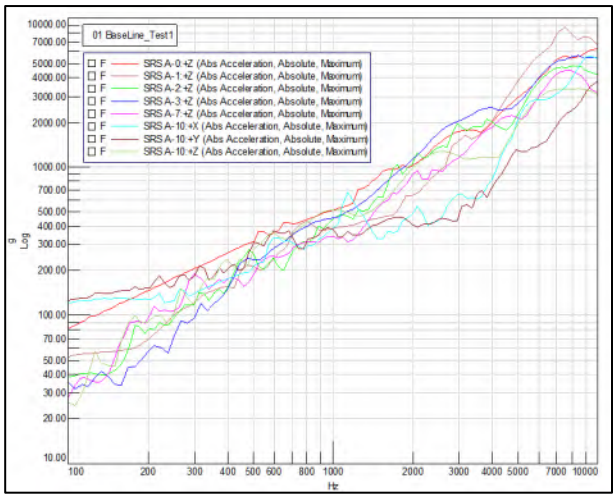


Figure 13: FJ1 Output Shock Source Levels

The resulting measurements enabled correlation with the analytical shock prediction methodologies described in [6], supporting further refinement of the numerical models and increasing confidence in their predictive capability. The close agreement between analytical predictions and experimental measurements demonstrated the capability of the modelling approach to reproduce the observed shock response, while confirming that the optimized interaction between the structural profile and the GET assembly contributes to minimizing the transmission of high-frequency shock into the surrounding structure.

Overall, the combined analytical and experimental investigations confirmed that the implemented design optimization strategy successfully minimized transmitted pyrotechnic shock while preserving robust separation performance and structural integrity. The resulting shock environment demonstrates the effectiveness of the integrated design philosophy underpinning the FJ1 system and establishes the architecture as a shock-optimized pyrotechnic separation solution for PLF applications. The measured reduction in transmitted shock is primarily attributed to the optimized interaction between the controlled expansion behaviour of the GET assembly and the tang-and-clevis profile architecture, with its optimized separation plane, which together minimize secondary structural impacts, limit high-frequency dynamic amplification, and promote a smooth and highly repeatable separation process.

Beyond supporting analytical model validation, the shock characterization programme generated the experimental database required for payload compatibility assessments and verification of the dynamic performance objectives established during system development.

5. QUALIFICATION TESTING APPROACH

Following completion of the development and verification activities described in the previous sections, the FJ1 system was subjected to a comprehensive qualification programme to demonstrate compliance with the applicable structural, functional, environmental, and system-level performance requirements.

The overall qualification campaign combined dedicated structural qualification testing, environmental life testing, and increasingly representative full-scale separation tests, thereby providing comprehensive verification of the complete separation system.

The programme was intentionally structured to progressively increase the representativeness and complexity of the test articles, beginning with structural qualification of the profile assembly, followed by environmental qualification of representative sub-length specimens, and culminating in full-scale system-level separation tests. Each successive qualification stage increased the technical maturity of the hardware and strengthened confidence in the overall system and analytical methodology, ultimately providing evidence of the readiness of the complete separation system for flight applications.

5.1. Static Load Qualification Testing

The profile assembly was subjected to a dedicated static load qualification test campaign to demonstrate its capability to withstand the structural load environment encountered throughout the launch mission, as illustrated in Figure 14. Qualification load cases were completed under both tensile and compressive loading, with the assembly maintaining full structural integrity and exhibiting no evidence of permanent deformation.

To further quantify the available structural margin, additional overload testing was performed beyond the required qualification levels. The assembly sustained tensile and compressive loads exceeding the qualification levels without rupture or detrimental structural effects. The ultimate structural capability was subsequently demonstrated through a tensile overload test in which the assembly was loaded to failure, with fracture occurring at the intended separation plane.

These results demonstrated that the profile assembly possesses adequate structural margins against the applicable mechanical loading envelope. The campaign also validated the load-transfer capability of the tang-and-clevis architecture, the effectiveness of the press-fit pin-

and-collar fastening system, and the overall structural efficiency of the optimized FJ1 design prior to pyrotechnic activation. Furthermore, the demonstrated structural stiffness and integrity of the assembly throughout the qualification load envelope confirmed that the conditions required for stable and repeatable fracture initiation during subsequent pyrotechnic separation were maintained.



Figure 14: FJ1 Static Load Qualification Testing

5.2. Environmental Life Qualification Testing

Environmental qualification was performed through extensive life testing of representative sub-length specimens, as illustrated in Figure 15, to demonstrate that the FJ1 system preserves its structural integrity, functional performance, and separation capability following exposure to the complete environmental qualification life sequence. The qualification tests included successive exposure to the applicable ageing, thermal, mechanical, and environmental conditions covering the complete product life cycle, including manufacturing, transportation, storage, launch preparation, and final operational service.

Following completion of the environmental test sequence, the specimens were functionally tested at the corresponding cold and hot qualification temperature extremes, respectively -43°C and +125°C.

The successful completion of the environmental qualification programme demonstrated that both the structural and energetic characteristics governing the separation mechanism remained stable throughout the qualification envelope. The campaign therefore confirmed that the system preserves its functional capability throughout its operational life while providing the robustness, durability, and long-term reliability required for demanding PLF applications.



Figure 15: FJ1 Environmental Qualification Life Testing

5.3. Full-Scale Separation Testing

The qualification programme culminated in a series of full-scale separation demonstrations, including both 180° and 360° configurations.

The initial system-level demonstrations were conducted using 180° assemblies, as per Figure 16, with the system activated through the nominal double-sided ignition configuration. These tests confirmed the scalability of the separation system and demonstrated the adequacy of the preceding sub- and intermediate-length testing approach for predicting and verifying full-scale system behaviour.

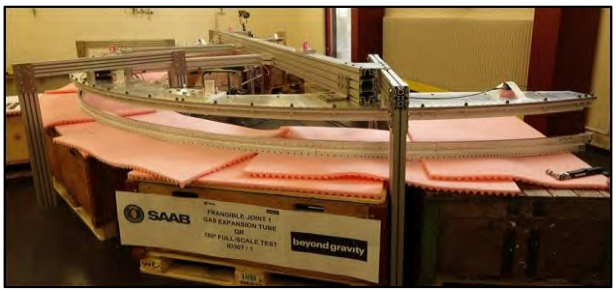


Figure 16: FJ1 Full-Scale 180° Sep Testing

The programme subsequently progressed to a complete 360° separation qualification test on a structural stack incorporating representative adjacent structures and mechanical interfaces, as illustrated in Figure 17. This final activity represented the highest level of system representativeness achieved during the programme, enabling end-to-end verification of the FJ1 architecture. The progression from 180° to 360° demonstrations provided incremental validation of the global separation behaviour while progressively increasing system complexity, structural representativeness, and interaction with adjacent structures.

The successful completion of the full-scale qualification campaign demonstrated reliable and uniform fracture propagation around the complete circumference, controlled structural separation, successful interaction with the surrounding PLF structure, and compatibility with the representative flight interfaces. The good agreement between the measured behaviour and the analytical predictions further demonstrated the maturity and predictive capability of the verification methodology.

Overall, the qualification programme demonstrated not only compliance of the final product with the applicable requirements, but also the maturity of the

development methodology supporting the complete programme.

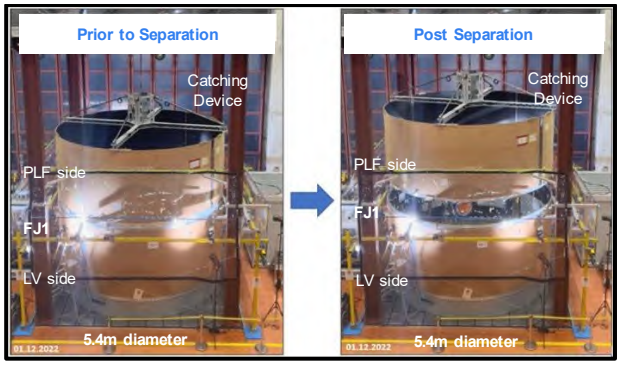


Figure 17: FJ1 Full-Scale 360° Sep Testing Including Representative Adjacent Structures

6. CONCLUSION

This paper has presented the integrated development, verification, and qualification approach adopted for the Frangible Joint 1 separation system.

The programme demonstrated the required structural, functional, environmental, and low-shock performance, leading to the qualification of the FJ1 system and its adoption as the baseline payload fairing separation solution for Beyond Gravity's large launch vehicle applications.

Beyond the FJ1 system itself, the programme established a validated engineering methodology based on the integration of high-fidelity multi-physics simulation, progressive experimental verification, and systematic analysis–test correlation.

This methodology provides a scalable basis for the development and qualification of future high-performance pyrotechnic separation systems, supporting increasingly demanding launch vehicle and payload requirements.

7. REFERENCES

1. NASA MSFC-SPEC-3635 (2018), Marshall Space Flight Center Standard for Pyrotechnic Systems
2. AIAA S-113A-2016 (2016), Criteria for Explosive Systems and Devices on Space and Launch Vehicles
3. MIL-HDBK-83578(1999), DoD Handbook: Criteria for Explosive Systems and Devices used on Space Vehicles
4. GTPS Severe Tests Statistical Method, Recommendation for designing and mastering reliable pyrotechnic devices, GTPS N°11F, October 2012
5. GTPS Statistical Method of PROBIT, Recommendation for designing and mastering reliable pyrotechnic devices, GTPS N°11 A, October 2014
6. Conrad, M., Kuhni, T., Marques Novo, F. (2026) Design and Verification of the Optimized Gas Expansion Tube for Frangible Joint Applications, ECSSMET Conference 2026

Separation Mechanisms and Ejection Kinematics Verification for Rosalind Franklin Mission

Idoia Bueno [(1)], Juan Arrue [(1)], TAS-I EXM RFM Team [(2)], ESA EXM RFM Team [(3)]

[(1)] SENER Aeroespacial y defensa, Avda. Zugazarte, 56 - 48930 Las Arenas - Spain,
Email: idoia.bueno@aeroespacial.sener , juan.arrue@aeroespacial.sener
[(2)] Thales Alenia Space (TAS)
[(3)] European Space Agency (ESA)

KEYWORDS

Separation Interface Testing, Hold-Down and Release Mechanism, High-Speed Image Analysis, Non-Explosive Actuator, Separation Dynamics.

ABSTRACT

This paper presents the verification approach for the separation mechanisms installed at the three critical interfaces of the ejectable module of ExoMars Rosalind Franklin Mission during the Entry, Descent and Landing sequence: Carrier Module to Entry, Descent and Landing Module (CM-EDLM), Backshell to Frontshield (FS-BS), and Backshell to Landing Platform (BS-LP). Each interface includes dedicated separation mechanisms that maintain structural and, where applicable, electrical continuity up to release, which is initiated by non-explosive actuators and driven by calibrated spring systems.

The objective is to check that the separation behaviour measured during the tests is representative of the expected behaviour in flight. The verification approach includes worst-case analyses, system-level Monte Carlo simulations and representative separation tests. High-speed image analysis is used to measure the ejection kinematics and to correlate the analytical models. The paper presents the main analysis and test results, the correlation process and the lessons learned.

1. INTRODUCTION

Separation mechanisms play a key role in spacecraft separation events, as their performance directly affects the relative motion between the separating bodies. For this reason, it is important to verify both the correct actuation of each mechanism and the behaviour of the complete interface. The mechanisms must release in a balanced way, with adequate simultaneity and without introducing undesired effects on the ejection kinematics.

In the ExoMars Rosalind Franklin Mission, SENER is responsible for the separation mechanisms of the three interfaces and although they are different, they all require a consistent methodology to define, analyse and validate the separation performance.

The verification is challenging because ground tests cannot fully reproduce the in-flight separation conditions. Gravity effects, test article mass properties, boundary conditions, external loads and test setup limitations must be considered, as they may affect the measured kinematic response. In addition, dispersions between mechanisms, such as spring force, friction, tolerances and release timing, can influence the final separation behaviour.

For this reason, the test setup definition is a key part of the verification activity. The test configuration must reproduce the relevant aspects of the flight case as far as practical, considering representative dummies, rigid support structures and interface boundary conditions. At the same time, the measurement and post-processing methodology must provide reliable kinematic data for comparison with the analytical predictions.

In this context, high-speed image analysis was selected as the main method to evaluate the separation motion. The recorded images are processed with a dedicated tool developed in-house for the project, allowing the main parameters to be extracted and used for model correlation.

2. SYSTEM OVERVIEW AND SEPARATION SEQUENCE

The separation system considered in this paper covers the three interfaces of the Entry, Descent and Landing sequence: CM-EDLM, FS-BS and BS-LP. These separation events occur at different stages of the sequence and allow the progressive release of the spacecraft elements required for the continuation of the descent phase.

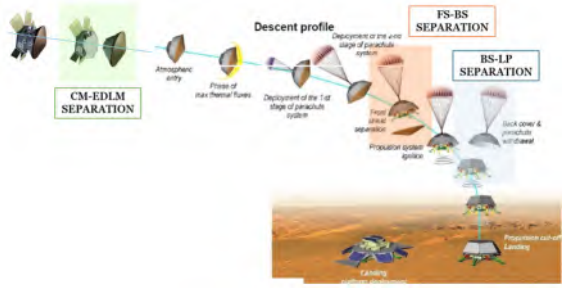


Figure 1: ExoMars Rosalind Franklin Mission Separation Sequence.

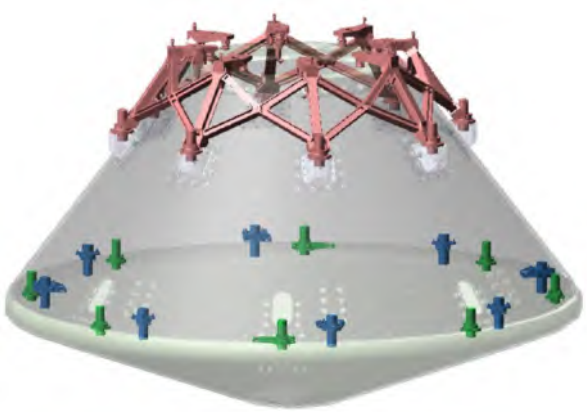


Figure 2: Location of the separation interfaces considered in the paper: CM-EDLM in red, FS-BS in green and BS-LP in blue.

Although the three interfaces are based on the same general separation philosophy, their configurations and boundary conditions are different. For this reason, the verification approach must keep a common logic while adapting the analyses and test setups to each specific case. The main elements of the separation systems and their implementation in each interface are described in the following section.

3. SEPARATION MECHANISM DESCRIPTION

The separation systems are based on Hold-Down and Release Mechanisms (HDRMs) distributed around each interface. During the previous mission phases, these mechanisms maintain the structural, and where applicable electrical, continuity between the two sides of the interface. When separation is required, they allow the interface to be released in a controlled way.

Figure 3 shows representative HDRM hardware used across the three separation interfaces, while Figure 4 presents the five HDRM configurations implemented in the system. The electrical connectors are not shown in these figures, although their functional contribution is considered in the analyses and tests. Table 1 summarises the HDRM types implemented in each interface and their main functional features.



Figure 3: Representative separation mechanism assemblies.

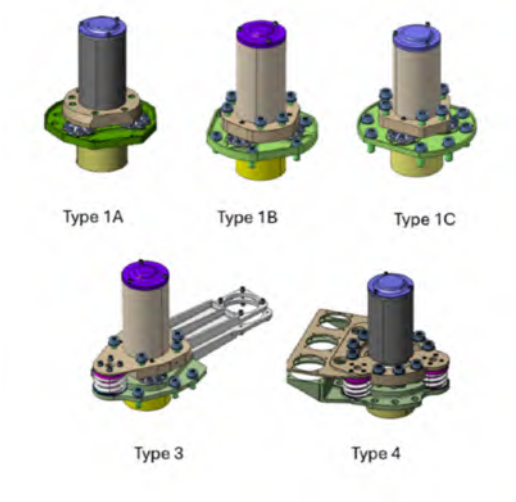


Figure 4: HDRM configurations: Type 1A for CM-EDLM, Type 1B and Type 3 for FS-BS, and Type 1C and Type 4 for BS-LP.

The CM-EDLM interface uses Type 1A mechanisms. These mechanisms provide the hold-down and release function between the separation adapter structure (see Figure 5) and the EDLM, but they do not include integrated separation springs or electrical connectors. In this interface, the separation adapter provides the structural transition between the Carrier Module and the EDLM. The ejection function is generated by dedicated pusher springs located on the Carrier Module side of the adapter. During separation, the adapter remains attached to the Carrier Module side through preloaded rods, while Type 1A release the EDLM from the adapter.



Figure 5: CM-EDLM separation adapter structure.

The FS-BS interface combines two HDRM configurations. Type 1B mechanisms provide the hold-down and release function only. Type 3 mechanisms provide the same hold-down and release function but also integrate one separation spring and one electrical connector. Therefore, the Type 3 mechanisms are the active mechanisms responsible for generating the ejection motion and enabling connector demating in this interface.

The BS-LP interface follows the same functional logic, but with a different mechanism configuration. Type 1C mechanisms provide the hold-down and release function only, while Type 4 mechanisms integrate three separation springs and three electrical connectors.

The release function is performed by non-explosive actuators. Until this point, the mechanisms keep the interface closed, withstand the applicable loads and contribute to the required interface stiffness.

A common feature of the HDRMs is the use of three spherical contact points arranged around the preloading rod. This configuration provides a stable preloaded contact at the interface and allows the mechanism to withstand axial and lateral loads, as well as bending and torque moments. As a result, the spherical contacts contribute to a well-defined mechanical interface before release and reduce the risk of mechanical blockage during separation.

In the CM-EDLM interface, apart from the Type 1A mechanisms and the separation adapter, the architecture includes the Connector Compliance Mechanism (CCM) and the Connector Protection Mechanism (CPM). The CCM provides compliance between the two separating bodies, allowing relative motion without imposing excessive loads on the connector. After separation, the CPM protects the exposed connector by covering it once the interface has been released.

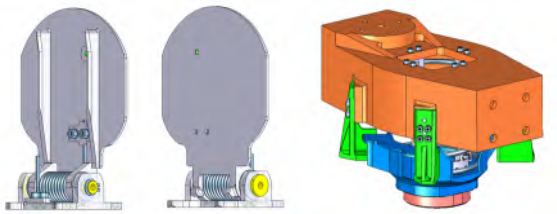


Figure 6: CM-EDLM connector devices: CPM on the left and CCM on the right.

Table 1: HDRM types and main features per separation interface.

Interface	**HDRM Type**	**Springs/Connectors**
CM-EDLM	Type 1A	No integrated springs or connectors
FS-BS	Type 1B	No integrated springs or connectors
FS-BS	Type 3	1 separation spring + 1 electrical connector
BS-LP	Type 1C	No integrated springs or connectors
BS-LP	Type 4	3 separation springs + 3 electrical connectors

4. REQUIREMENTS AND VERIFICATION LOGIC

The separation test campaign was defined to verify the functional performance of the separation system at complete assembly level and to support the correlation of the analytical model used to predict the flight separation behaviour. The campaign covered the three separation interfaces separately: FS-BS, BS-LP and CM-EDLM. Each interface was tested in a dedicated configuration, representative of its specific mechanical architecture.

The verification logic was based on demonstrating that each interface could be released in a controlled way and that the resulting separation dynamics were compatible with the applicable requirements. The main parameters used for this assessment were the axial relative velocity, the transverse velocity and the angular velocities induced during the release. These quantities are directly linked to the ability of the system to generate sufficient separation clearance while limiting lateral motion and rotational disturbances.

To support this verification, a combination of analytical predictions and representative separation tests was used. The definition of the test configurations and the corresponding experimental methodology are presented in the following sections.

5. ANALYTICAL METHODOLOGY

Several analyses of the separation event have been performed to support the design, verification, and validation of the mechanisms involved. These analyses were carried out throughout the

development process to evaluate the expected performance of the system and to ensure compliance with the design requirements.

A functional analysis was conducted during the design phase to obtain a theoretical understanding of the mechanisms' behaviour during separation. This analysis allowed the evaluation of the kinematic relationships between the different components and the design parameters selection, as well as an initial assessment of the expected separation sequence and overall system performance.

A structural analysis was performed using NX Nastran to determine the stiffness characteristics and natural frequencies of the mechanisms. The finite element model was used to assess the structural response of the system and to verify that the design meets the required mechanical performance and dynamic behaviour criteria.

A Monte Carlo analysis was carried out to study the separation process considering all possible combinations of the relevant variables and tolerances. This approach enabled the evaluation of the sensitivity of the system to parameter variations and provided valuable statistical information regarding the expected dispersion of the separation results and the probability of successful operation under different conditions.

In addition, several separation cases were simulated in ADAMS to validate the results obtained from the Monte Carlo analysis and to increase confidence in the calculations performed. These multibody dynamic simulations provided a detailed representation of the separation event, enabling verification of the predicted system behaviour and the identification of potential discrepancies.

This section focuses on the statistical simulations performed and on the validation of selected cases using ADAMS.

5.1. Monte Carlo Analysis

The Monte Carlo simulation was performed in Excel, considering 9,000 iterations.

The analysis involves simulating a large set of randomly generated separation cases and evaluating the results using statistical methods.

All parameters involved in the calculation have been treated statistically, applying uniform or Gaussian distributions according to each parameter type. For Gaussian variables, a normal distribution with a confidence level greater than 99.7% (±3 sigma) is assumed.

Some parameters are modelled using statistical distributions different from the standard normal distribution. One example is the connector separation force. At the unit level, the separation force of each connector is randomly sampled from a Gaussian distribution within a predefined range. Furthermore, at the assembly level, the maximum difference in separation force between connectors within the same arrangement is defined by a range that follows a uniform distribution. This methodology accounts for both individual connector variability and assembly-level dispersion effects.

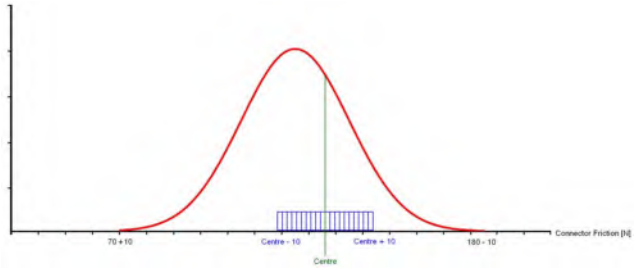


Figure 7: Combined Statistical Distributions for Umbilical Connectors.

For requirements verification, the analysis considers only the internal contributions of the system, such as separation springs and umbilical connectors. In contrast, flight-case simulations account for both internal and external effects, including parachute loads, aerodynamic drag, and bio-sealing forces. Throughout the analysis, separating bodies are modeled as rigid bodies.

The analysis focuses primarily on the calculation of axial, lateral, and angular velocities.

All results are reported at the instant at which contact between the separating bodies is lost. For all separation cases, this condition is reached upon release of the pushing device, which implies that the last separation spring has completed its design-defined stroke. At this stage, the umbilical connectors have already separated.

5.2. ADAMS Validation

Two cases were analyzed to validate the Monte Carlo methodology. The first corresponded to the nominal case, with no deviations applied to the input parameters. The second was a statistically assessed case in which a failure of one of the separation springs was assumed.

Both cases were evaluated considering only the internal contributions of the system, including separation springs, connectors, friction effects, and other internal mechanisms.

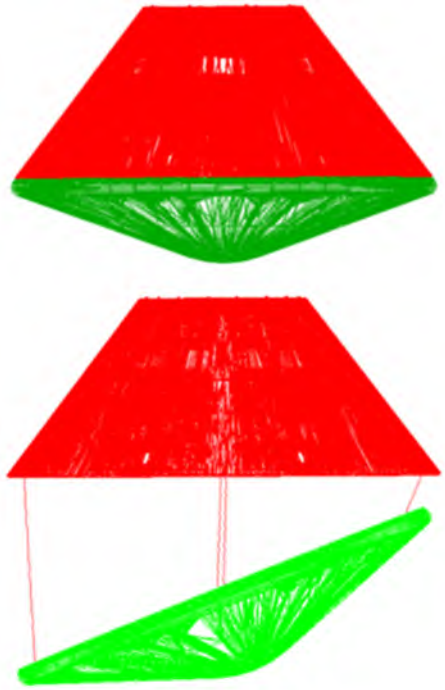


Figure 8: ADAMS Model, Spring Failure Case Sequence: FS-BS.

The validation of the Monte Carlo analysis against the multibody simulations conducted in ADAMS is based on the relative velocities between the two separating bodies, specifically the axial, transverse, and angular components. In accordance with the Excel-based analysis, these results are extracted at the instant of complete separation. This occurs when the last pusher spring reaches the end of its design-defined stroke, marking the loss of contact between the two bodies.

The satisfactory correlation observed between the Monte Carlo predictions and the ADAMS multibody simulation results provides validation of the proposed Monte Carlo methodology. This validation marks the completion of the theoretical analyses performed prior to the experimental test campaign.

6. EXPERIMENTAL VERIFICATION

The experimental campaign was designed to verify the separation performance of the three interfaces and to provide the data required for analytical model correlation. Apart from demonstrating the correct release of the mechanisms, the tests were intended to characterize the resulting kinematics and assess compliance with the applicable requirements.

A dedicated test article was developed for each interface, reproducing the functional elements governing the separation event. For the FS-BS and BS-LP interfaces, the configurations included Type 3 and Type 4 mechanisms, respectively. For the CM-EDLM interface, the setup incorporated the separation adapter structure, pusher springs, CCM, CPM and representative Type 1A mechanisms, capturing the main features driving the separation dynamics.

Particular attention was devoted to the test setup definition. Dedicated rigs were developed to reproduce the relevant interface architecture, mass properties and boundary conditions within the limitations of the ground environment. For the FS-BS and BS-LP interfaces, a large support gantry was used as the primary test structure. The bolt catcher side of the active mechanisms was attached to the fixed structure, while a representative octagonal dummy mass was connected to the NEA side and released during the test. The dummy mass was sized to reproduce the relevant inertial properties of the separating body. Protective mats were installed below the setup to safely absorb the impact after completion of the event.

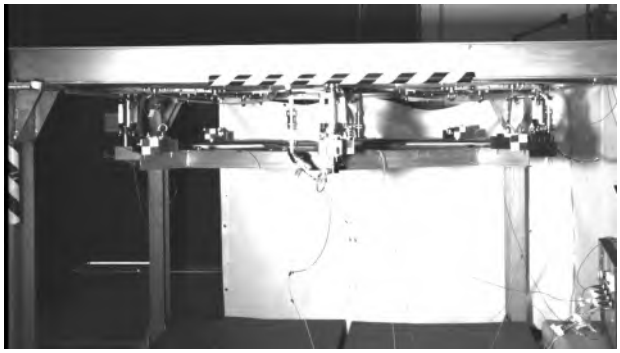


Figure 9: Representative FS-BS separation test setup.

For the CM-EDLM interface, a dedicated configuration was developed to reproduce the flight architecture. The adapter remained attached to the Carrier Module side of the setup, while a representative EDLM mass was connected to the mechanisms located at the lower interface. Dedicated support arms reproduced the interface with the pusher springs installed between the EDLM and the Adapter, allowing the separation event to be generated through the same functional chain as in flight.

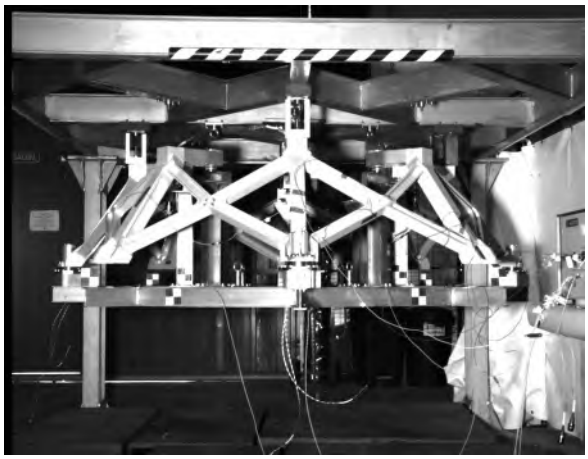


Figure 10: Representative CM-EDLM separation test setup.

The separation events were recorded using high-speed cameras. Visual targets attached to the test articles were tracked throughout the event, and the image sequences were processed using a dedicated software tool developed by SENER. Accurate measurements were achieved using stroboscopic lighting specifically selected for this application. The tracking software was tailored to the characteristics of the imaging system in order to ensure reliable and repeatable results.

In summary, the tracking methodology is based on contrast recognition and spatial proximity. In the first frame of each video sequence, the targets are manually identified and selected. These targets feature a predefined black-and-white pattern, which allows them to be reliably distinguished from the background. Provided that no significant shadows or abrupt lighting variations occur along the marker trajectory, the tracking process remains robust. Furthermore, the contrast characteristics used for marker identification are continuously updated each time the marker is detected, enabling the algorithm to accommodate gradual illumination changes, such as those resulting from non-uniform lighting conditions within the camera field of view.

In addition, taking advantage of the high frame rate of the camera, the search for a marker in each subsequent frame is restricted to a region surrounding its previously detected position. Since the displacement between consecutive frames is expected to be small, this proximity-based approach improves both tracking reliability and computational efficiency.

All contrast- and proximity-related parameters are user-configurable, allowing the algorithm to be adapted when variations in recording conditions are encountered.

Particular attention was paid to the optical characteristics of the measurement setup. To minimize lens-induced distortions, the camera was positioned as far as practicable from the test article while maximizing the optical zoom. Although this approach significantly reduces distortion effects, residual image distortion remains unavoidable. For those test configurations in which setup constraints prevented the optimal adjustment of the camera, markers occasionally traversed regions near the edge of the field of view, where lens distortion is more severe. In these cases, a dedicated distortion correction was applied as a function of the lens focal length and zoom configuration.

Furthermore, the conversion of image coordinates into physical coordinates requires precise knowledge of the marker geometry. As markers were distributed across two distinct planes within the separation assembly, separate pixel-to-distance calibration factors were determined for each plane. This calibration process is critical for obtaining accurate displacement measurements and, therefore, reliable velocity estimations.

After applying the corresponding corrections and calibrations, the methodology enabled the extraction of the axial, transverse, and angular velocity components of the separation event.

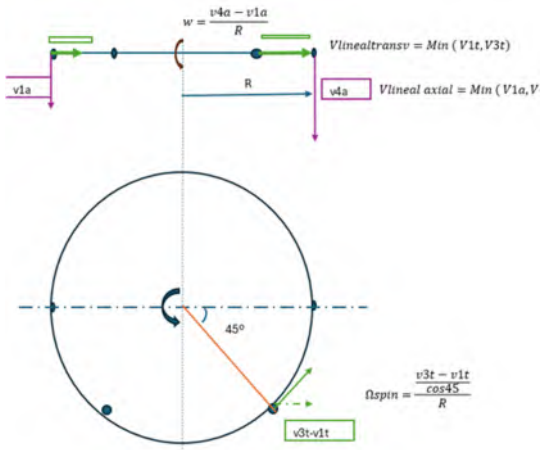


Figure 11: Analytical procedure for the determination of the spin velocity.

The performance of the tracking software was verified through comparison with data obtained from capacitive accelerometers mounted on the test article. The velocity histories derived from the video-based tracking system were compared with those obtained from the accelerometer measurements.

A satisfactory correlation was observed between the two independent measurement techniques, providing confidence in the accuracy and robustness of the tracking methodology. This verification demonstrated the suitability of the software for extracting the kinematic parameters required for the experimental assessment of the separation system.

7. TEST RESULTS AND MODEL CORRELATION

This section presents the results of the separation tests performed on the FS-BS, BS-LP, and CM-EDLM interfaces and compares them with the corresponding model predictions.

For the FS–BS configuration, the initial setup was found to be affected by the low stiffness of the mounting interface, resulting in non-representative behaviour. A revised configuration with increased interface stiffness, closer to the flight configuration, was therefore adopted.

Following the separation tests, raw data were collected from both the tracking system and the

accelerometers. To assess the consistency and reliability of the two measurement approaches, the resulting position, velocity, and acceleration profiles were compared.

As an example, Figure 12 and Figure 13 show the test velocity profiles obtained using the two measurement techniques. Agreement is observed between the results derived from the capacitive accelerometer data and those obtained from sticker-based tracking, demonstrating the consistency of both measurement approaches. The accelerometer-derived data have been appropriately scaled to account for the conversion from g units to SI units.

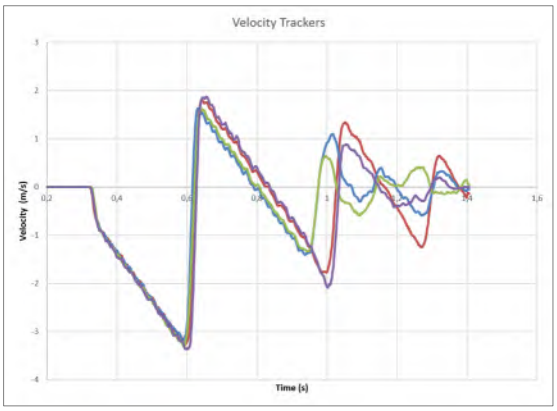


Figure 12: Time history of tracker velocities during the BS–LP separation test. Velocity vs Time.

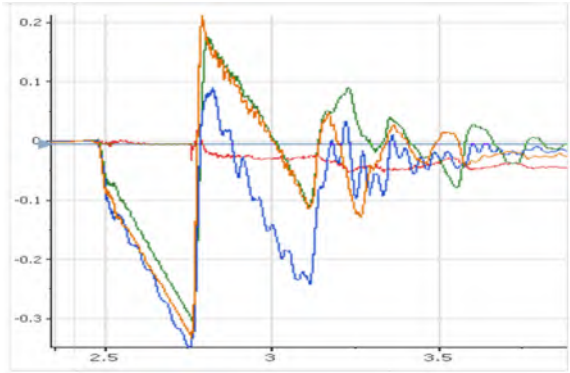


Figure 13: Accelerometer time histories recorded during the BS–LP separation test. Velocity vs Time.

Before the execution of the separation tests, pre-test analytical predictions were performed for each interface using the available characterized data, including spring properties, connector resistance and test article mass properties. These predictions provided the expected axial separation velocity for the planned test configurations and were used as a reference for the subsequent comparison with the experimental results.

Once the measurement methods were validated, the test results were correlated with the theoretical analysis. For this purpose, the effect of gravity was removed, and the mass properties were scaled to their flight-representative values. The correlated results were then assessed against the applicable requirements and compared with the pre-test analytical predictions.

The comparison between test results and pre-test analytical predictions was mainly focused on the axial separation velocity, as this parameter is primarily driven by the available spring energy, connector resistance and equivalent mass properties. The transverse and angular velocity components were not directly correlated with the nominal analytical predictions, since they are strongly influenced by small assembly misalignments, release-force dispersions, connector behaviour and local flexibility effects, which are not fully represented in the nominal analytical model. Therefore, these components were assessed against the applicable requirement limits.

The following tables summarize the correlated kinematic parameters used for requirement verification. The axial velocity is compared with the pre-test analytical prediction, while transverse and angular velocity components are assessed against the applicable requirement limits.

Table 2 presents the axial velocities obtained from the experimental tests and the theoretical analysis, together with the corresponding requirement applicable to each separation event.

Table 2: Axial velocity measurements, predictions, and requirements.

	Test Result (m/s)	**Analytical Prediction (m/s)**	**Requirement (m/s)**
FS-BS	0,155	0,49	>0,1
BS-LP	0,53	0,67	>0,4
CM-EDLM	0,78	0,73	0,6<v<0,8

The FS-BS measured axial velocity is significantly lower than the pre-test analytical prediction, although it remains compliant with the applicable requirement. This difference is associated with additional energy losses observed during the assembly-level test, mainly linked to the behaviour of the FS-BS mechanisms during connector demating. The corresponding design feedback is discussed in the following section.

Table presents the transverse velocities obtained from the experimental tests and the theoretical analysis, together with the corresponding requirement applicable to each separation event.

Table 3: Transverse velocity measurements and

requirements.

	Test Result (m/s)	Requirement (m/s)
FS-BS	0,00063	<0,01
BS-LP	0,0026	<0,01
CM-EDLM	0,0028	<0,01

Table presents the torsional speed (TorSp) (about the axial axis) and rotational speed (RotSp) (about the radial axis) velocities obtained from the experimental tests, together with the corresponding requirement applicable to each separation event.

Table 4: Angular velocity measurements and requirements.

	Test Result (TorSp) (deg/s)	Test Result (RotSp) (deg/s)	Requirement (deg/s)
FS-BS	0,00016	0,568	-
BS-LP	0,266	0,1	-
CM-EDLM	0,47	0,042	<1,5

With respect to angular velocities, another requirement was specified for the CM–EDLM separation event. A constraint is imposed between the torsional angular velocity about the vertical axis and the maximum angular velocity about the axis orthogonal to the torsion axis, such that:

$$\arctan\left(\frac{RotSp}{TorSp}\right) < 3 \qquad (1)$$

This criterion limits the misalignment of the resulting angular velocity vector with respect to the nominal torsional axis.

Table 5: Angular velocity vector misalignment and requirements.

	Test Result Atan(RotSp/TorSp)	Requirement Atan(RotSp/TorSp)
CM-EDLM	0,17	<3

The correlated test results satisfy the specified kinematic requirements for all three separation events. The comparison between the theoretical predictions and the measured axial separation velocity shows good agreement for the BS–LP and CM–EDLM cases. The lower velocity observed in the FS–BS case remains compliant and is further discussed in the following section as part of the design feedback derived from the test campaign.

8. KEY FINDINGS AND LESSONS LEARNED

The separation test campaign provided several findings that are relevant for the verification of spacecraft separation interfaces.

First, the campaign confirmed that assembly-level testing is essential to understand the real separation behaviour. Individual characterization of springs, connectors or release devices is necessary, but it does not fully reproduce the interaction between mechanisms, structural flexibility, connector demating and boundary conditions. This was especially evident during the FS-BS test campaign, where the behaviour of the interface was strongly influenced by the stiffness of the test setup and the local attachment conditions.

A key lesson learned was the importance of maintaining a sufficiently stiff and well-aligned test configuration. In the first FS-BS test, the local flexibility of the setup introduced additional rotation of the separating body. This rotation produced a non-axial connector demating motion, increasing the connector resistance and affecting both the axial velocity and the induced rotations. This showed that connector forces measured under controlled axial conditions may not be fully representative when moments or lateral displacements are introduced at assembly level. For this reason, the stiffness of the test setup should be assessed against the expected stiffness of the flight interface to ensure that the measured behaviour is representative.

The campaign also provided direct feedback to the mechanism design. The first FS-BS test highlighted that, in the Type 3 mechanisms, the offset between these elements can generate a bending moment during ejection. When combined with local flexibility, this effect may deform the mechanism, introduce connector misalignment and increase the force required for demating. Based on this observation, the mechanism design was modified to increase local stiffness and improve connector alignment during separation. This result illustrates the value of testing the complete interface, since this behaviour was not evident from the individual spring and connector characterizations.

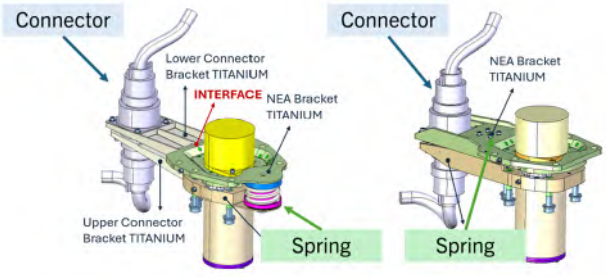


Figure 14: Type 3 design modification to improve connector alignment during demating.

Another important outcome was the validation of the high-speed image processing methodology. The

dedicated SENER tool provided the position and orientation of the separating body from visual targets, allowing the calculation of axial, transverse and angular velocities. The comparison with accelerometer-derived velocities gave additional confidence in the optical tracking results. At the same time, the accelerometer data showed the typical limitations of this measurement method, such as sensitivity to noise, zero shift and integration interval selection. The use of both techniques therefore proved useful to obtain robust kinematic data.

The campaign also showed that the quality of the high-speed images is a critical part of the measurement chain. Due to the high frame rate, short exposure times are required, making dedicated lighting necessary. Target contrast, target visibility, camera position and lens distortion have to be considered before the test, since they directly affect the reliability of the tracking process. The evaluation point must also be defined in advance; in this campaign, the end of the spring stroke was selected to extract the relevant kinematic parameters before rebounds, impacts or safety elements could affect the measured motion.

Overall, the main lesson learned is that a representative separation test depends on the complete verification chain: representative hardware, realistic boundary conditions, sufficient setup stiffness, reliable measurement techniques and a consistent method to correlate test results with the analytical flight predictions.

9. CONCLUSIONS

This paper has presented the verification approach followed for the three separation interfaces of the ExoMars Rosalind Franklin Mission: CM-EDLM, FS-BS and BS-LP. Although the three interfaces have different architectures and boundary conditions, a common methodology was established, combining analytical predictions, Monte Carlo simulations, multibody validation cases and dedicated assembly-level separation tests.

The analytical activities provided the basis to predict the expected separation behaviour and to assess the influence of parameter dispersions on the final kinematics. The Monte Carlo approach allowed a wide range of possible separation cases to be evaluated, including variations in spring performance, connector forces, friction, tolerances and release timing. This statistical approach complements the experimental campaign by covering conditions that cannot be fully reproduced in a limited number of ground tests.

The assembly-level tests provided representative information on the behaviour of the complete separation interfaces, including the interaction between release mechanisms, springs, connectors, structural flexibility and test boundary conditions. The use of high-speed image analysis and a dedicated SENER post-processing tool allowed the main linear and angular kinematic parameters to be extracted and used for correlation with the analytical predictions.

The comparison between analysis and test results showed that the analytical models are suitable to represent the main contributors to the separation performance when the actual test conditions and measured hardware parameters are introduced. The campaign also provided valuable feedback to the design, particularly through the behaviour observed during the FS-BS test campaign, which supported the modification of the FS-BS active mechanism to improve local stiffness and connector alignment during demating.

Overall, the work confirms the value of combining statistical analysis, representative assembly-level testing and dedicated kinematic measurements for the verification of spacecraft separation systems. The methodology and the image-processing tool developed for this project can also be adapted to other separation tests and interface architectures, providing a consistent link between analytical predictions, ground-test results and expected flight behaviour.

ExoMars Landing Leg Mechanism Qualification Testing

Kevin Picton[(1)], Aiala Artiagoitia[(1)], Yon E. Jauregui[(1)] , Andoni Ruiz[(1)], Rubén Ibarra[(1)],Juan Arrue[(1)], ADS [(2)], TAS-I [(3)] & ESA[(4)] RFM Teams

[(1)] SENER Aeroespacial y defensa, Avda. Zugazarte, 56 - 48930 Las Arenas - Spain, kevin.picton@aeroespacial.sener, aiala.artiagoitia@aeroespacial.sener, yon.jauregui@aeroespacial.sener, [(2)]Airbus Defence & Space UK (ADS), [(3)]Thales Alenia Space Italy (TAS), [(4)] European Space Agency (ESA)

KEYWORDS

Landing Legs Assembly, Touch Down Sensor, Qualification Testing, Impact Testing, Deployment Functional Testing

ABSTRACT

The Landing Leg Assembly (LLA) developed for the ExoMars Rosalind Franklin Mission is a critical subsystem whose successful qualification required a verification campaign extending beyond conventional environmental testing. Although the mechanism incorporates several novel architectural features, the main engineering challenge was not the hardware itself but the demonstration that deployment, touchdown detection and landing energy absorption would perform reliably under representative mission conditions.

This paper presents the verification philosophy adopted for the LLA together with the most representative environmental and functional qualification activities. Particular emphasis is placed on deployment verification (performed under thermal vacuum, Earth and Martian atmospheric conditions), qualification of the touchdown detection function, characterization of the landing impact energy absorption capability under representative pressure environments, and correlation between dedicated subsystem tests and system-level verification.

1. INTRODUCTION

The Rosalind Franklin Mission represents the continuation of the European ExoMars exploration programme, that aims to bring a Rover to the Martian surface. Within this programme, the Landing Leg Assembly (LLA) provides the mechanical interface between the landing platform and the Martian surface, ensuring touchdown stability while limiting the loads transmitted to the platform.

The LLA performs several mission-critical functions simultaneously: It must deploy reliably upon command after cruise and during descent achieving a repeatable landing configuration, detect the first contact with the Martian surface upon impact to command hold-down thrust shutdown and, finally, absorb touchdown energy ensuring landing stability under a wide variety of potential landing scenarios. The qualification of these functions required an extensive verification campaign combining environmental testing, dedicated functional tests and system-level demonstrations.



Figure 1. Qualification Model of the Landing Leg Assembly in stowed and deployed configurations

The objective of this paper is to describe the verification approach adopted during development and the challenges faced (design details where presented in [1]). Particular attention is devoted to the environmental representativity of the qualification campaign, the rationale behind dedicated verification activities and the main engineering lessons derived from testing. The paper therefore focuses on those aspects considered of greatest relevance for spacecraft structures, materials and environmental testing.

2. VERIFICATION CHALLENGES

From a verification perspective, the Landing Leg Assembly presented several challenges that could not be addressed through standard qualification testing alone.

The first challenge was deployment verification. Although the flight deployment takes place under low-pressure Martian conditions (after exposure to the space thermal-vacuum environment applicable during cruise phase), part of the qualification programme had to be performed under terrestrial conditions for practical reasons. Demonstrating that these tests remained representative of flight behaviour required dedicated investigations.

A second challenge was associated with the touchdown detection function. The touchdown sensor commands engine cut-off at system level, a

critical function, as early engine cut-off upon first landing impact is required for platform stability. The sensor must not activate during descent vibration and aerodynamic loading (potential catastrophic failure) while still detecting extremely low-energy contacts on soft terrain. Verifying this balance required a combination of vibration testing, dedicated drop tests and force correlation measurements.

Landing energy absorption characterization introduced an additional verification challenge. LLA crushable pistons are sensitive to the surrounding atmosphere because trapped air influences the crushing process at high deformation rates. Consequently, representative qualification required comparison of Earth-atmosphere and Mars-pressure drop tests to establish the validity of analytical predictions and the representativity of the system-level landing campaign. An extensive impact drop test campaign at single LLA leg level was conducted in order to verify the structural integrity and the adequacy of the energy absorption capability under a wide variety of extreme landing impact conditions.

Finally, the overall qualification programme had to be completed within an exceptionally demanding development schedule imposed by the mission launch opportunity. This combination of technical and programmatic constraints strongly influenced the verification philosophy adopted for the Landing Leg Assembly and motivated several dedicated environmental campaigns described in the following sections.

3. QUALIFICATION STRATEGY

The qualification programme was conceived to demonstrate the correct performance of the Landing Leg Assembly under representative environmental conditions while simultaneously providing confidence in the analytical predictions used throughout the development. Rather than considering qualification as a collection of independent environmental tests, the campaign was organised around the critical functions performed by the mechanism. Each activity was therefore associated with a specific verification objective and, where appropriate, with dedicated analytical correlation.

Four verification topics drove the complete qualification strategy. 1) Deployment reliability 2) Touchdown detection 3) Landing impact energy absorption capability. 4) Finally, complete system-level campaigns were used to demonstrate compatibility with the landing platform and to validate the behaviour of the integrated hardware. Tests at different levels were carried out to complete the LLA verification, with different dedicated models, summarized in the table below and explained in the following section.

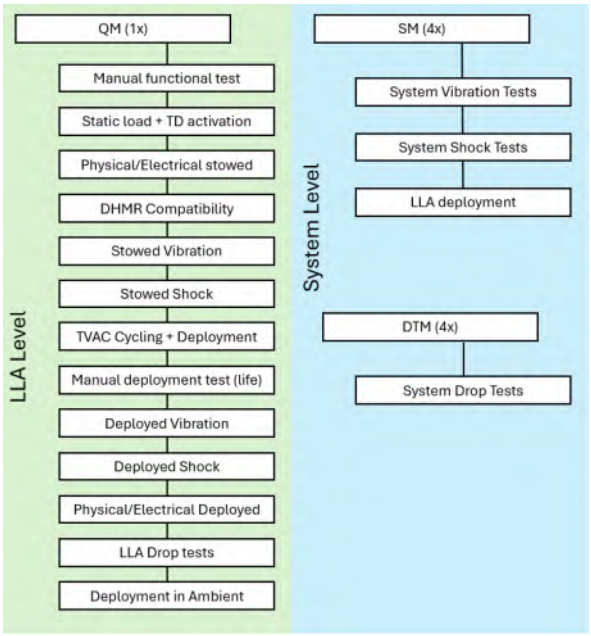


Figure 2. Overall qualification flow showing the relationship between subsystem qualification and system-level verification

3.1. Verification Philosophy

For verification purposes the following models were developed early in the project:

1. Structural Model (SM): Vibration and deployment at system level
2. Drop Test Model (DTM): Drop tests at system level with dummy platform
3. Qualification Model (QM): Tests at Landing Leg level

Due to the demanding project schedule all 3 models were manufactured simultaneously without any previous prototypes, being one of the main project risk and technical & programmatic challenge. In addition to this, the overall verification campaign (both at single LLA level and at upper system level, i.e. Landing Platform and complete Entry Descent and Landing Module (EDLM) level) included relevant tests that needed to be carried out under Earth atmospheric pressure for practical reasons.

An important consequence of this philosophy was that not every engineering question could be answered through a conventional qualification test and in time to mitigate the technical risks shared among models (QM, SM, DTM). In several cases, additional parallel dedicated investigations were required to determine whether a standard test environment remained representative of flight conditions. Consequently, qualification evidence resulted from the combination of analytical predictions, dedicated characterization tests and formal qualification activities rather than from the standard qualification flow alone.

Correlation with analytical models represented another essential element of the strategy. Test results were systematically compared with the expected mechanism behaviour to increase confidence in the predictive capability of the analytical models used during development. This approach proved particularly valuable when assessing deployment dynamics and crushable behaviour under different atmospheric conditions.

3.2. Qualification Campaign Overview

The qualification campaign included thermal-vacuum deployment, deployments under representative Martian pressure, deployments in Earth atmosphere, vibration testing in stowed and deployed configuration, dedicated touchdown sensor characterisation, subsystem drop tests for crushable verification and complete system-level qualification activities. Together these campaigns covered the principal functional and environmental requirements of the Landing Leg Assembly. Although each campaign addressed a different verification objective, all were connected through a common objective: demonstrating that the qualification evidence remained representative of the actual Martian mission environment. This consideration strongly influenced both the selection of the test sequence and the interpretation of the results obtained during qualification.

The following sections present the most representative qualification activities together with the principal engineering conclusions extracted from each campaign.

4. DEPLOYMENT VERIFICATION

Deployment verification represented one of the most demanding parts of the qualification campaign because deployment performance depended not only on the mechanism itself but also on the environmental conditions under which the verification activities were performed. The objective of the campaign was therefore twofold: to demonstrate reliable deployment under representative flight conditions and to establish the representativity of ground-based verification activities required during subsystem and system-level testing.

4.1. Qualification Deployment Test

The flight deployment occurs after prolonged exposure to the launch, cruise and Entry and Descent environments. Consequently, qualification required demonstrating successful deployment following thermal-vacuum exposure under representative low-temperature conditions. A dedicated TVAC campaign was therefore performed using the Qualification Model. The mechanism completed deployment successfully, providing confirmation that the selected deployment philosophy and motorization margins remained adequate under representative environmental conditions. The TVAC campaign provided valuable information regarding deployment dynamics. Accelerometers installed at the mechanism interfaces allowed deployment timing and shock levels to be characterised, providing an experimental reference for subsequent analytical correlation. The measured deployment sequence showed good agreement with the expected mechanism behaviour and confirmed that no abnormal dynamic events occurred during release, stage latching or end-of-stroke conditions.

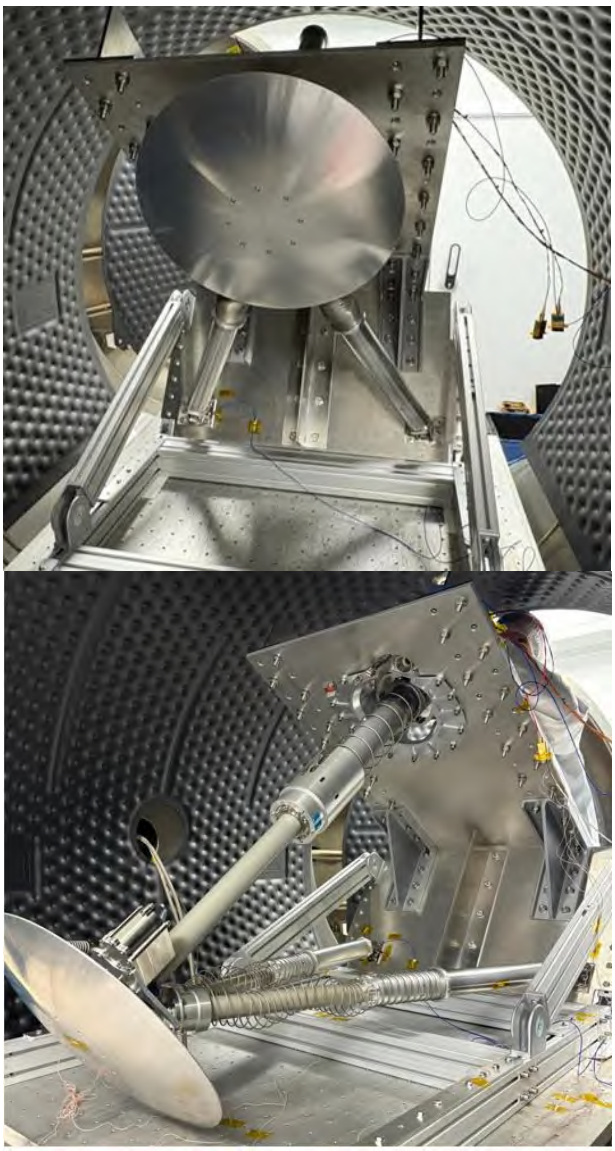


Figure 3. Thermal-Vacuum deployment before and after test (stowed vs deployed configurations)

4.2. Deployment Representativity under Earth atmospheric conditions

Following the successful TVAC qualification, additional deployment tests were performed under ambient laboratory conditions to characterise deployment dynamics using high-speed camera measurements and accelerometer instrumentation. Although complete deployment was achieved, the

measured deployment speed was significantly lower than expected and differed from both analytical predictions and TVAC observations. Since the same hardware had previously deployed successfully under representative environmental conditions, this discrepancy initiated a dedicated investigation into the representativity of the ambient test environment.

The investigation identified insufficient venting of enclosed internal volumes as the primary cause of the reduced deployment speed. During rapid extension of the telescopic stages, trapped air generated an additional damping effect that was not representative of either vacuum or Martian atmospheric conditions.

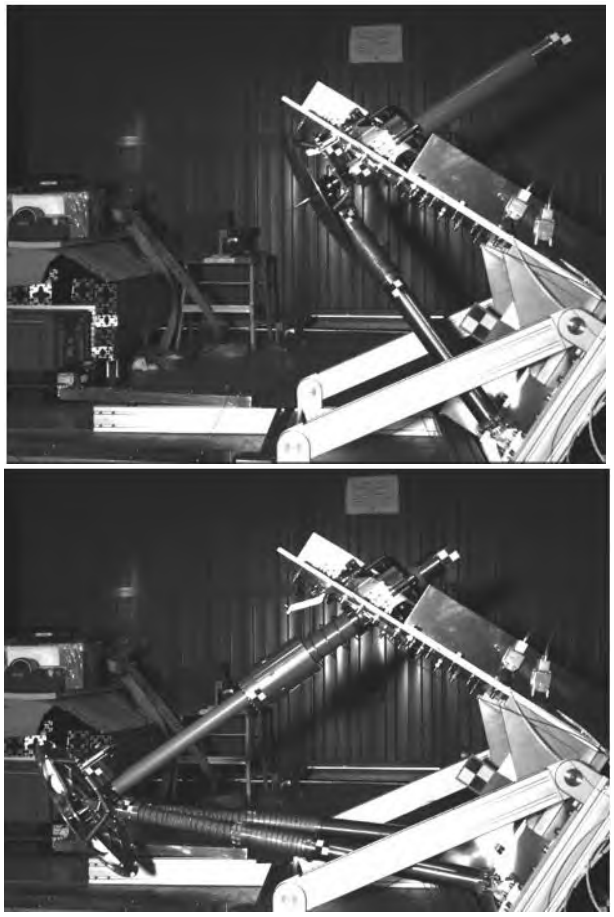


Figure 4. 1st deployment in ambient test: failed, no-latching achieved

Interestingly, the crushable pistons had already incorporated dedicated venting provisions because atmosphere-dependent crushing behaviour upon landing impact had been identified early in the project. However, equivalent venting requirements for deployment representativity had not initially been recognised because ambient deployment was not considered representative of the flight environment.

As direct consequence of this unexpected result, a dedicated set of additional tests was conducted to confirm the adequacy of the design and performance in flight representative environment, and to solve the issue of Earth-pressure deployments already foreseen at upper system-level testing campaigns.

4.3. Deployment Representativity under Mars atmospheric conditions

To verify this hypothesis, complementary deployment campaigns were carried out under representative 1) Martian pressure (~10 mBar) & 2) as well as under Earth atmosphere after introducing additional venting provisions on the deployment load path (only for testing purposes).

The resulting deployment times in both cases showed excellent agreement with analytical predictions and demonstrated that the observed discrepancy originated from the terrestrial test environment rather than from the deployment mechanism itself. Shock measurements and high-speed camera tracking confirmed that deployment dynamics remained consistent with the expected sequence under both representative conditions.



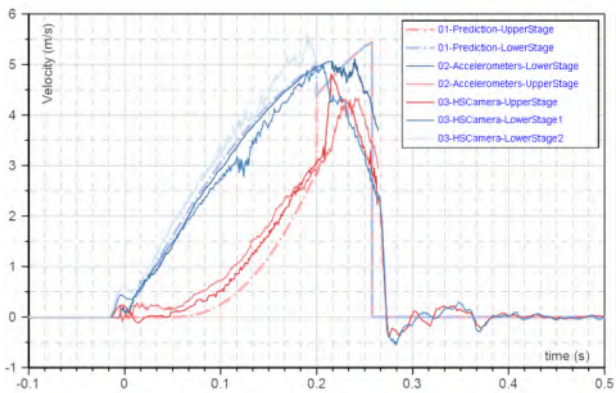


Figure 5. 2nd deployment test in ambient pressure: successful (latching achieved) - Comparison wrt. Analytical prediction

From a verification standpoint, the deployment campaign demonstrated that environmental representativity must be assessed not only for the operational mission environment but also for the qualification environments selected during development, including also the activities foreseen at upper system level. The venting provisions included in the test were also provided to the Customer chain for upper system-level testing purposes.

5. TOUCHDOWN SENSOR VERIFICATION

Among all functional elements of the Landing Leg Assembly, the touchdown detection system required the most extensive verification effort.

Unlike conventional deployable mechanisms, the touchdown sensor performs a critical mission-level function by initiating engine shut-down after first contact with the Martian surface. Consequently, verification was driven by the need to demonstrate immunity against false activations while maintaining sufficient sensitivity to detect low-energy touchdowns. The final architecture employed an adjustable preload concept acting on a triplet of micro-switches.

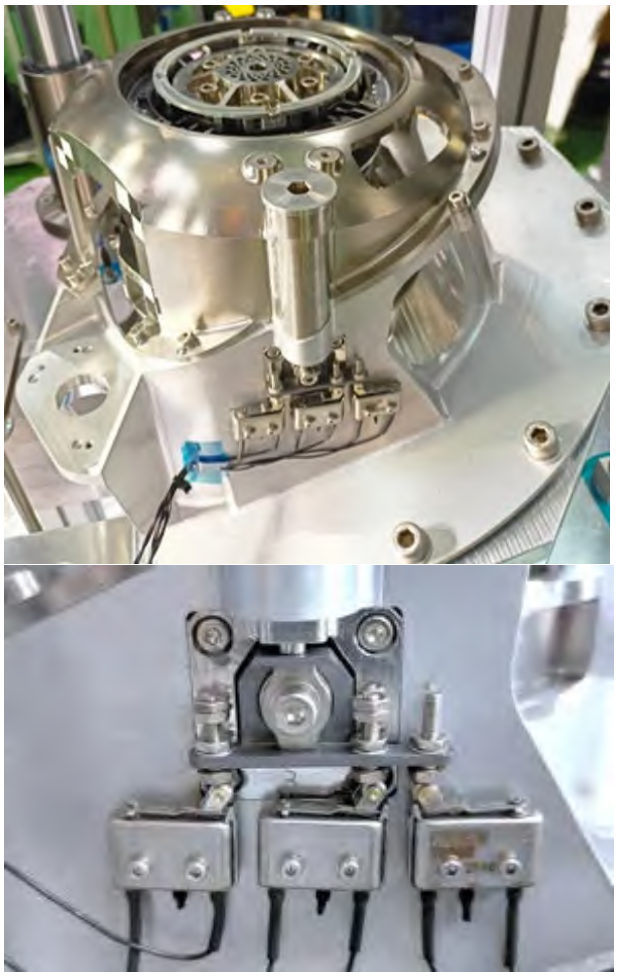


Figure 6. Touchdown sensor location within the LLA upper IF bracket and detail of its design

Qualification concentrated on demonstrating that the complete sensing function behaved correctly under representative operational conditions. Dedicated verification therefore combined vibration testing in LLA deployed configuration (for non-activation verification) plus subsystem drop tests and force correlation measurements (for positive touch-down activation verification). This combination allowed the activation threshold to be evaluated over the expected operational envelope while confirming adequate robustness against launch and descent environments.

Dedicated drop-tests provided a direct correlation between the load transmitted through the primary strut and the corresponding touchdown signal. Complementary vibration tests reproduced the dynamic environment expected during Entry, Descent and Landing, including representative descent loading conditions on the LLA. Together these activities demonstrated that the selected configuration simultaneously fulfilled the conflicting requirements of sensitivity and robustness.

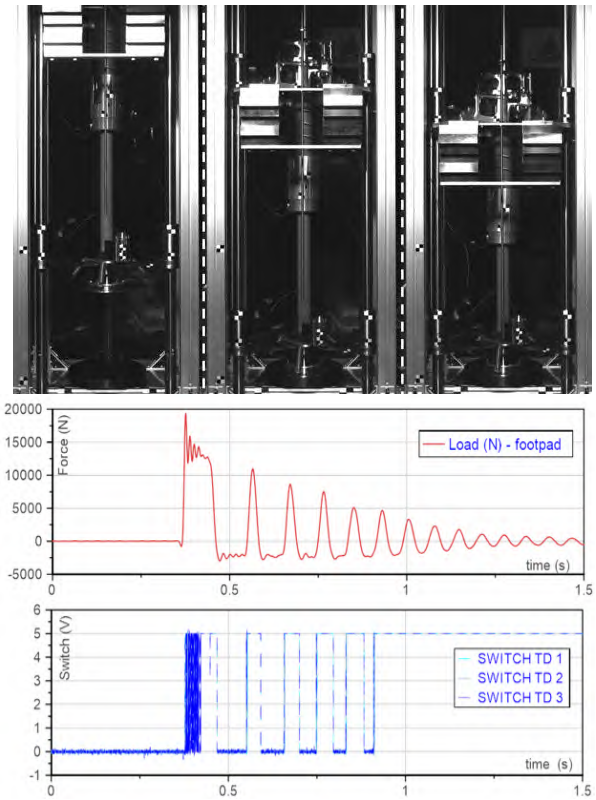


Figure 7. Touchdown sensor performance under impact testing (landing force vs microswitches signal)

6. LANDING IMPACT VERIFICATION

The landing energy absorption capability of the LLA relies on dedicated honeycomb crushable cartridges integrated within the structural load paths. Previous experience from planetary landing systems indicated that the crushing response of cellular materials enclosed within pistons may depend on the surrounding atmosphere due to

compression of trapped air during high-speed deformation. For this reason, verification of the compression pistons was considered a dedicated qualification topic rather than simply part of the final landing campaign.

6.1. Impact tests at main-strut level

A series of drop tests at main-strut subassembly level (one strut only, crushable cartridge inside) was therefore performed under both ambient laboratory conditions at Earth-pressure and representative Martian pressure. Identical impact configurations were used to isolate the effect of the surrounding atmosphere. In addition to crush stroke measurements, interface accelerations and transmitted forces were recorded to permit direct comparison with analytical predictions.

The results confirmed that atmospheric pressure influences the early stages of the crushing process, already known from past projects [2]. Under terrestrial conditions, trapped air inside the crushable piston produced a moderate increase in crushing force together with a corresponding reduction in total crush stroke. Under representative Martian pressure, the measured behaviour approached the analytical prediction more closely.

.

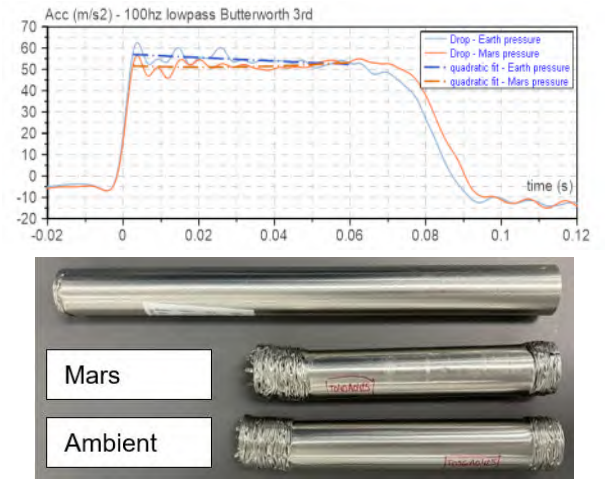


Figure 8. Comparison of crushable response under ambient and Martian pressure. Acceleration vs time & crushable response

The observed differences demonstrated the importance of understanding atmosphere-dependent mechanisms before interpreting subsystem or system-level test results.

6.2. Impact tests at LLA level

A drop test campaign at complete LLA level (single leg, Qualification Model) was carried out to verify the energy absorption capability as part of the Qualification flow. The drop test campaign included a variety of extreme landing cases, including maximum vertical and lateral speeds combined with worst-case terrain slopes in several orientations, as well as low-energy cases barely reaching the touch-down sensor activation threshold.

Tests provided confirmation of the adequacy of the landing architecture to absorb the impact energy, the correct functioning of the Touch-Down Sensor in all landing cases, and valuable information concerning the structural capability of the design.

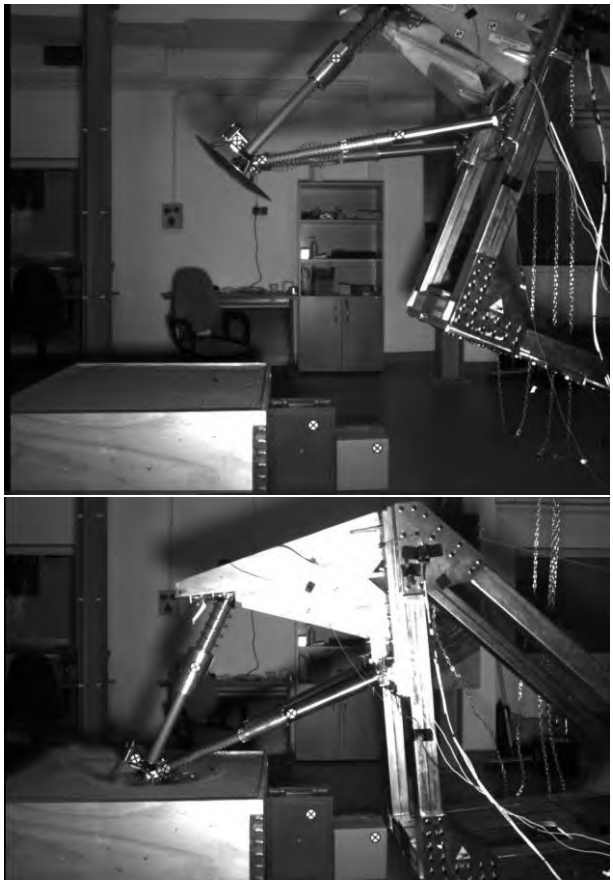


Figure 9. Qualification landing impact test on soft terrain (sand)

7. SYSTEM LEVEL TESTING

With deployment, touchdown detection and crushable behaviour individually characterised, the remaining objective of the qualification programme was to demonstrate the behaviour of the complete Landing Leg Assembly within the integrated landing platform. The following section therefore presents the principal system-level verification activities together with the engineering lessons extracted from the overall campaign.

Two complementary Qualification Model-like Landing Leg sets (4 legs each) were delivered to support higher system level campaigns: Dedicated Drop Test Models were employed to reproduce touchdown dynamics, while LLA Structural Models supported environmental campaigns at spacecraft level. Together these activities provided the final verification evidence that subsystem behaviour remained representative after integration.

From a verification perspective, system-level testing also represented an opportunity to assess exported loads, deployment shock and mechanical compatibility with neighbouring subsystems.

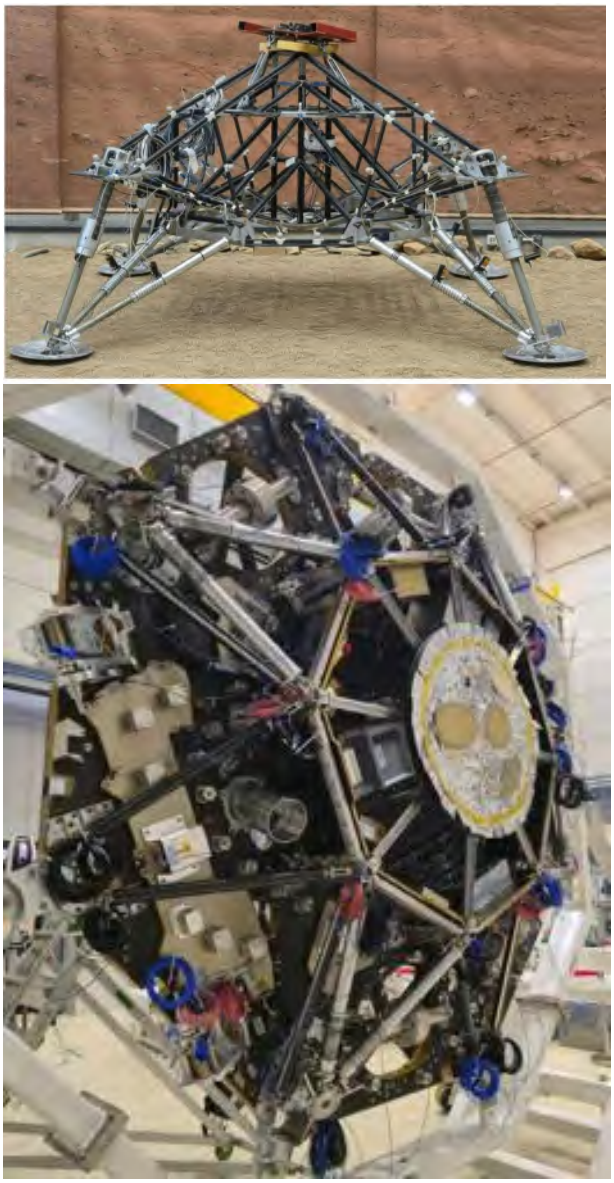


Figure 10. System level tests with Drop Test Models and Structural Models, (Courtesy of ADS)

8. CONCLUSIONS

The qualification programme of the ExoMars Rosalind Franklin Landing Leg Assembly demonstrated that verification of planetary landing mechanisms extends beyond the execution of standard environmental qualification campaigns.

Throughout the programme, representative verification required combining conventional environmental testing with dedicated functional investigations specifically conceived to characterise physical phenomena that could not be fully reproduced through standard qualification activities. Among the most significant outcomes was the demonstration that environmental representativity must be evaluated not only with respect to flight conditions but also with respect to the environments for ground verification. The deployment campaign clearly showed that terrestrial atmospheric effects influence functional behaviour despite being absent during the actual mission. Dedicated investigations under Martian pressure therefore proved essential to correctly interpret the qualification evidence.

Verification of the touchdown detection function also highlighted the importance of addressing system-level requirements from the earliest project phases. The most demanding engineering activity was not the implementation of the sensing hardware itself but the definition and verification of a touchdown event compatible with both mission safety and operational sensitivity. Close interaction between subsystem development and system engineering proved essential to achieve a robust qualification.

Characterisation of crushables confirmed that atmosphere-dependent behaviour should be understood before interpreting subsystem or integrated landing tests. Although Earth-based testing was suitable for qualification purposes, Martian-pressure testing significantly increased confidence in both the analytical models and the interpretation of system-level verification results.

Overall, the qualification philosophy adopted for the Landing Leg Assembly demonstrated that combining analytical correlation, dedicated characterisation activities and representative environmental testing provides a robust verification methodology for complex planetary landing mechanisms. The engineering experience obtained during this programme is considered directly applicable to future planetary exploration missions.

9. ACKNLOWDEGMENTS

The authors acknowledge the contribution of Airbus Defence and Space, Thales Alenia Space and the European Space Agency throughout the development and qualification of the ExoMars Rosalind Franklin Mission Landing Leg Assembly. The successful completion of the qualification campaign was the result of a close collaboration between all partners involved in the programme.

10. REFERENCES

[1] Picton, K. et al., ExoMars Landing Leg Mechanism Development and Qualification, Proceedings of the 48th Aerospace Mechanisms Symposium, NASA Marshall Space Flight Center, May 13-15, 2026

[2] Jauregui, Y.E. et al., 'A Statistical Approach to Touchdown Dynamics for ExoMars 2016', Proceedings of the 13th European Conference on Spacecraft Structures, Materials and Environmental Testing (SSMET), Braunschweig, Germany, 2014.

QUALIFICATION TESTING OF THE MMX PUSH-OFF MECHANISM

Sebastian Meyer [1], Michael Lange [2], Christian Hühne [3]

[1] DLR, Institute of Lightweight Systems – Composite Design, Lilienthalplatz 7, 38108 Braunschweig, Germany, Email: Sebastian.Meyer@dlr.de
[2] DLR, Institute of Lightweight Systems – Composite Design, Lilienthalplatz 7, 38108 Braunschweig, Germany, Email: M.Lange@dlr.de
[3] DLR, Institute of Lightweight Systems – Composite Design, Lilienthalplatz 7, 38108 Braunschweig, Germany, Email: Christian.Huehne@dlr.de

KEYWORDS

MMX, Push-Off Mechanism, Qualification Testing

ABSTRACT

The JAXA-led MMX mission will study Martian moons Phobos and Deimos. DLR's and CNES' contribution is the IDEFIX rover, which explores Phobos's surface. Separation from the spacecraft occurs at about 40 m altitude via the MECSS platform, utilizing a dedicated push-off mechanism (POM) that releases stored energy to propel the rover away. Since the POM's reliability is critical for mission success, this paper addresses its extensive qualification testing. After introducing the mechanism's design and functionality, the paper outlines the conducted performance, environmental and lifetime tests with the POM. Particularly challenging was the thermal vacuum test with actuations of the mechanism under extreme hot and cold conditions in order to determine and qualify the most critical operational case. The paper concludes by summarizing the comprehensive qualification campaign results, confirming the mechanism's readiness for flight.

1. INTRODUCTION

The origin and composition of the Martian moons Phobos and Deimos have not yet been fully established. Previous observations from Martian orbit, including those conducted by the European missions MARS EXPRESS, launched in 2003, and the EXOMARS TRACE GAS ORBITER (TGO), launched in 2016, have already provided extensive data and imagery of both moons. However, a successful landing on the surface of a Martian moon has not been achieved yet. With the MMX (Martian Moons eXploration) mission [1], the Japanese space agency JAXA aims to address these remaining gaps in knowledge. On 19th of October 2026, the MMX spacecraft is scheduled to start its journey to Martian system. After approximately one year, the spacecraft is expected to reach Martian system and begin investigating the two Martian moons from orbit.

The French space agency CNES (Centre National d'Études Spatiales) and the German Aerospace Center (DLR) developed the IDEFIX rover [2], which will explore the surface of Phobos for several weeks. For the first time, material from the surface of a Martian moon is intended to be returned to Earth by the MMX spacecraft.

The rover will be carried by the MMX spacecraft to approximately 40 m above the surface of Phobos and will subsequently be separated from the spacecraft by means of a separation mechanism, initiating the free-fall trajectory of IDEFIX towards the surface of Phobos. The interface between the spacecraft and the rover is referred to as the Mechanical and Electrical Chassis Support System (MECSS). In addition to four Hold-Down and Release Mechanisms (HDRMs), this interface structure incorporates an electrical connection and a dedicated push-off mechanism (POM), which is designed to push the rover away from the spacecraft once all four HDRMs have been activated (see Figure 1). Due to the extremely low

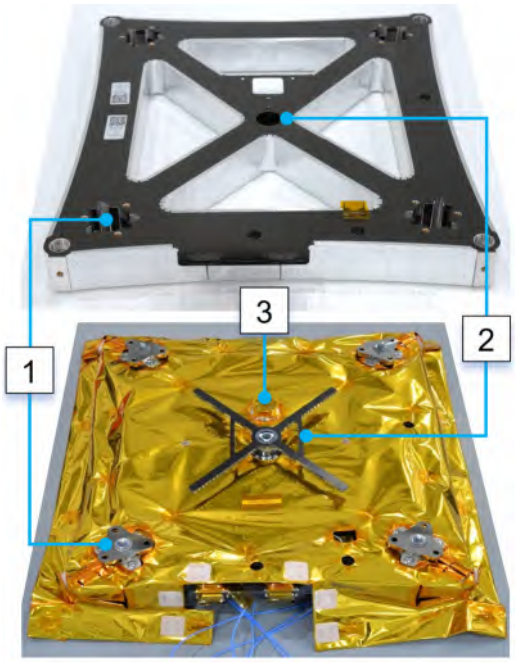


Figure 1: MECSS FM structure with separation mechanism: 1-Hold Down & Release Mechanism, 2-Push-Off Mechanism, 3-Electrical Connection

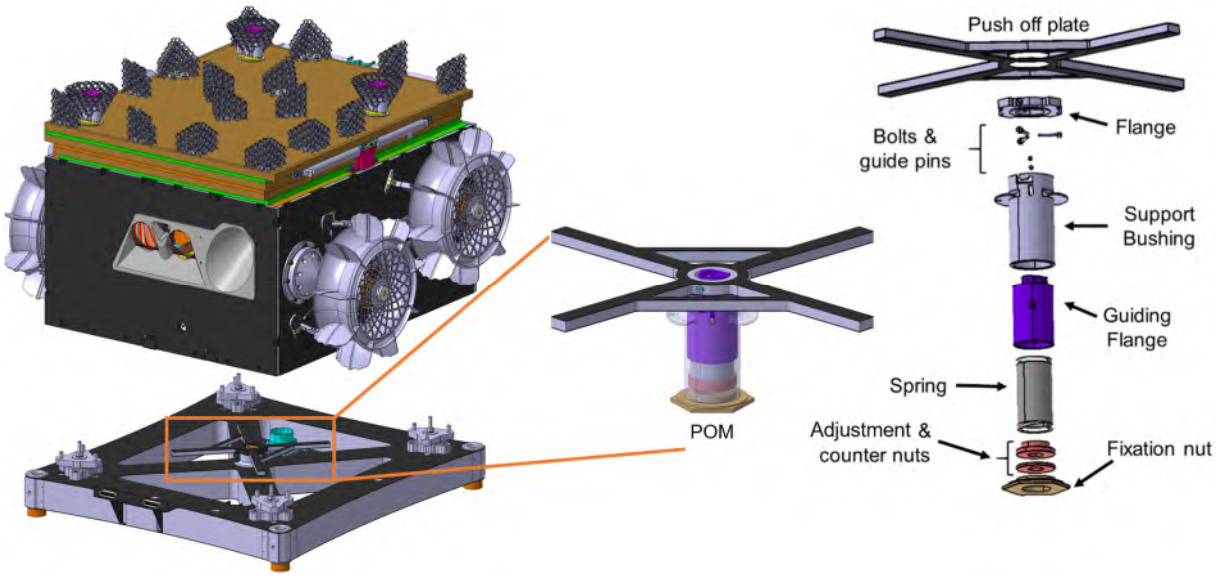


Figure 2: Location and design of the push-off mechanism

gravity at Phobos, approximately 1/1700 of the gravity on Earth, this mechanism is required to ensure a safe and well-defined separation.

The POM is a non-redundant mechanism and must operate reliably. It operates only once and remains on the spacecraft (together with the MECSS) after activation. Without this mechanism, a controlled and well-defined separation of the rover from the MECSS and MMX spacecraft cannot be ensured.

2. DESIGN OF THE PUSH-OFF MECHANISM

The design of the push-off mechanism is based on the version of the push-off mechanism, which was used in the MASCOT mission [3]. The POM is located in the centre of the MECSS (cf. Figure 2, left). The detailed design is shown in exploded view in the right picture of Figure 2. The mechanism is composed of two sub-assemblies: a push-off plate, which is in physical contact with the rover bottom plate for load transfer, and a bushing assembly for lateral guidance in the push-off direction. The push-off plate is designed as a CFRP sandwich with an aluminium honeycomb core, providing sufficient stiffness while maintaining low mass. The spring is selected in order to provide the necessary amount of motorization energy to push the MMX rover away from the mothership with a pre-set ejection speed. Changes in the rover mass can be considered by adjusting the preload of the spring via a fine-tuning screw.

The total motion of the mechanism is limited by a pin/slot arrangement, such that the spring operates within its nominal elongation range of 9.4 mm. The spring is located inside the inner cylinder (guiding flange), which slides inside the outer support bushing. The guiding flange is equipped with small pins, which interact with the slots in the outer support bushing.
The support bushing is made out of titanium with a polished surface. The inner guiding flange is made out of aluminium, which is entirely treated with SurTec 650. The guiding flange's cylindrical contact surface (towards the support bushing) is coated with a wear-resistant Eloxal-PTFE coating (Eloxal/ Anodizing + PTFE particles). This is the same combination as already used for the flight-proven MASCOT POM.

3. REQUIREMENTS

The gravity at Phobos is about 1/1700 of the gravity on earth, which is not strong enough to safely release the rover from the mothership. By using a dedicated POM, a safe release can be realized with a given ejection velocity and a pyramidal volume that the rover has not to leave [4].

- Ejection velocity in separation direction: $v_{ej} = 20 \pm 2 \frac{cm}{s}$
- Velocity perpendicular to the separation direction: $v = 0 \pm 2 \frac{cm}{s}$
- Angular velocity in all directions: $\omega = 0 \pm 10 \frac{^\circ}{s}$

4. TEST PLAN

The POM qualification model (QM) is built from components identical to those of the flight model (FM) in order to be representative with the qualification test campaign. The following tests were conducted with the POM QM:

Tests conducted on coupon level:

- Fretting (cold welding)
- Friction testing

Tests conducted on subsystem level:

- Extended temperature range test for rover post separation phase
- Performance characterization of the POM under lab conditions
- Performance characterization of POM at release thermal case (hot & cold)
- Ground & Flight life testing

Tests conducted on system level:

- Pendulum separation test with MECSS
- Qualification tests (Shaker + TVAC) with MECSS + Rover

For the POM FM only a performance characterization under lab conditions was conducted on subsystem level and before integration. On system level an acceptance test (shaker + TVAC) was performed.

This report addresses only subsystem level testing, especially performance characterization under lab conditions, hot/cold separation and life testing.

5. CONFIGURATION OF THE POM

The baseline pre-tension of the POM QM and FM are adjusted to reach an ejection velocity of $v = 21\ \frac{cm}{s}$ considering a rover mass of 24.85 kg. This setup considers a margin of 5% for the ejection velocity (nominal: $v = 20\ \frac{cm}{s}$), which is allocated for unknown influences and friction.

6. QUALIFICATION TESTING

Extensive qualification testing has been performed with the POM QM. This section addresses the performance and life tests done with the POM QM subsystem as well as the performance characterization under hot and cold thermal cases.

6.1. Performance Test

The performance characterization of the POM QM subsystem is done at room temperature under lab conditions. A quasi-static test is chosen using the force measurement device IMADA MX-2 with a 500 N load cell. The item under test is the POM QM without push-off plate.

Test objectives:

The objectives of this test are:

- Measure the ejection force generated by the POM at room temperature
- Calculation of the motorization energy for the push-off process
- Tracking of potential degradation

The ideal force-displacement curve is schematically shown in Figure 3. The motorization energy E_{mot} is the area under the force-displacement curve and can be calculated to

$$E_{mot} = \frac{F_{comp} + F_{depl}}{2} \Delta s\ ,$$

where F_{comp} and F_{depl} are the spring forces in fully compressed and fully deployed state. s_{comp} and s_{depl} are the respective displacements and Δs the elongation range of the POM of 9.4 mm.

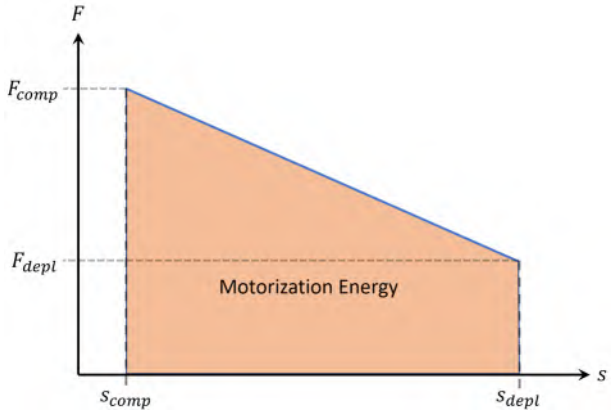


Figure 3: Schematic of motorization energy stored as potential energy in the POM spring

Test setup:

The test setup is shown in Figure 4. The POM is mounted in a special aluminium adapter (number 5 in Figure 4), which is representative in terms of support length and through hole diameter compared to the MECSS structure. The adapter holds the POM on the table of the force measurement device. Before the test, a special pressure stamp is adjusted in order to apply a defined axial force on the guiding flange.



Figure 4: Force measurement device with mounted test adapter and POM (1 – Force measurement device, 2 – pressure stamp, 3 – Guiding Flange, 4 – Support Bushing, 5 – Mounting Adapter)

Test conduction:

A very low speed of 10 mm/min is chosen for quasi static actuation of the spring. Then the resulting force-displacement values are measured during the compression and relaxation phase each. The test starts with the pressure stamp slightly above the guiding flange. By touching the top of the guiding flange, the trigger starts the measurement. First, the force-displacement values during the compression phase are measured. After the spring is fully compressed, the direction of the pressure stamp is changed and the deployment (ejection) phase is measured.

This measurement is repeated 10 times for the performance test.

Test results:

In Figure 5 the measured ejection forces are depicted over the guiding flange displacement from fully stowed (spring is compressed) to fully deployed (spring is relaxed) state. The orange and the blue graph indicate a corridor of ± 5% around the mean value of the ejection forces (reproducibility corridor). It can be seen that the ejection forces slightly oscillate around its mean value, especially at the first half of the guiding flange travel. In total, the ejection forces have a good reproducibility.

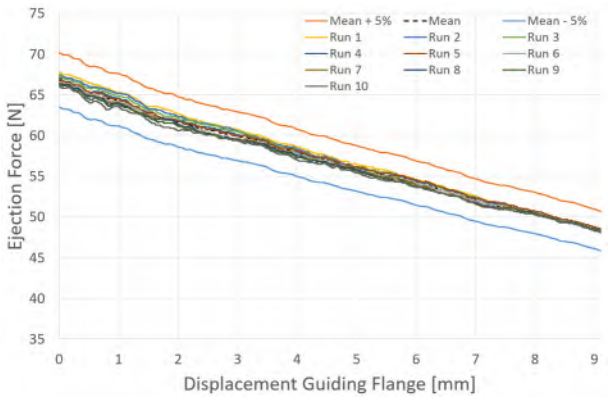


Figure 5: Ejection forces for test run 1-10 with mean values ±5% (orange, blue)

In Figure 6 the motorization energy from the first 10 test runs is presented. The energy generated from the POM is well within the upper and lower limit given by the requirement. The mean value is 0.5264 Nm, which theoretically gives an ejection velocity of 20.58 cm/s for an allocated rover mass of 24.85 kg.

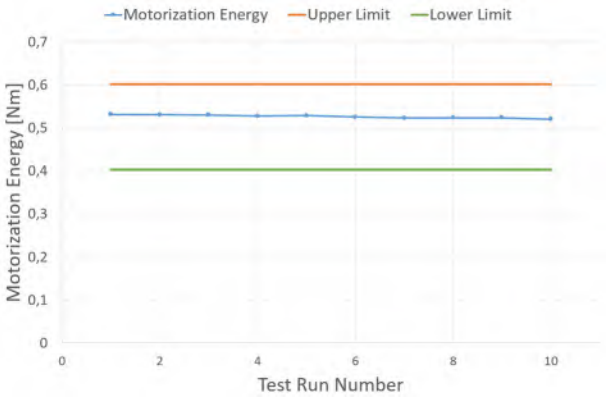


Figure 6: Motorization energy for test run 1-10

6.2. Life Test

The number of actuations for life testing is derived from the actuations of the POM FM using life testing factors from ECSS standard [5]. In Table 1 the actuation type of the POM FM, the number of cycles and the corresponding factor for life testing are listed. In total, the POM QM life testing consist of 64 (from POM FM perf. testing) + 10 (from 1 in orbit actuation) + 36 (from 9 actuations of the POM FM reserved for on ground operations) = 110 cycles.

Table 1: Life Test Actuations

POM FM actuation type	Number of cycles	Factor	Total
Performance Test	16	4	64
In Orbit	1	10	10
On Ground (for fit check, mating etc.)	9	4	36

After the ten cycles for performance testing with the POM QM, additional 100 cycles were performed to fulfil the number of cycles for life testing. In Figure 7 the measured ejection forces over guiding flange displacement are shown for test run 10 – 110. The ejection forces do not oscillate more than 5 % around its mean value between actuation 10 to 110. The related motorization energy is depicted in Figure 8. The motorization energy slightly decreases over the number of cycles, but it is well between the lower and upper limit.

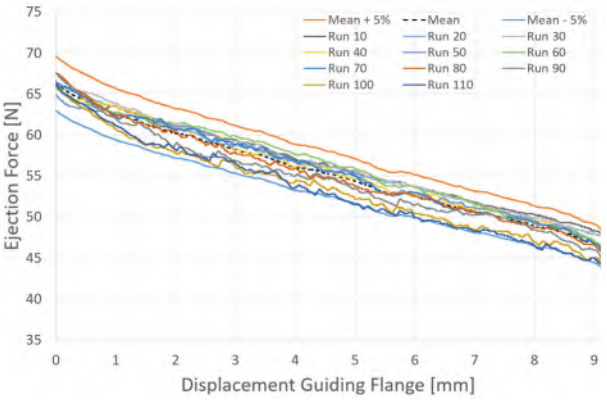


Figure 7: Ejection forces for test run 10-110 with mean values ±5% (orange, blue)

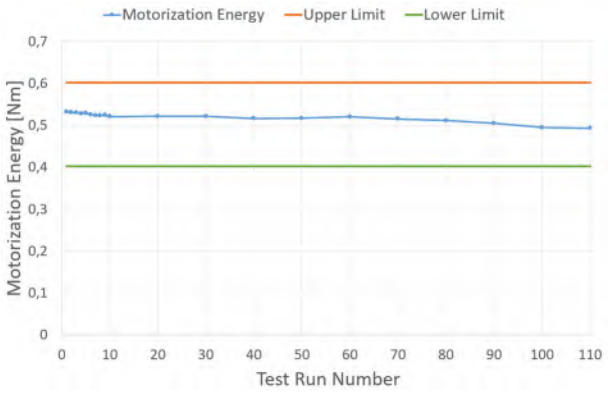


Figure 8: Motorization energy for test run 1-110

The motorization energy of the last test run (run #110) is 0.4929 Nm, which leads to a theoretical ejection velocity of 19.92 cm/s considering an allocated rover mass of 24.85 kg.

6.3. Hot/Cold separation test

A separation test at hot and cold condition is done with the POM QM mechanism after life-testing in order to determine the lower peak velocity.

Test objectives:

The objectives of the hot/cold separation test are:

- Measurement of acceleration of the dummy pendulum mass at -105°C and +45°C
- Calculation of peak velocity of the dummy mass via numerical integration

Test setup:

For the hot/cold separation test, the POM, without the push-off plate, is installed in a dedicated test rig inside the thermal vacuum chamber (see Figure 11). The POM is maintained in its launch configuration by means of a weight-compensated dummy mass and a 0.95 mm steel wire, which ensures the required pretension within the system (see Figure 9 and Figure 10). The permanent tension is applied by a loading mass (see Figure 9), thus pulling the dummy mass against the POM. Distance shims between the dummy mass and the POM support maintain a gap (see Figure 10), which leads to a spring compression representing the nominal case in stowed configuration. The loading mass is connected via the CREAM release mechanism ([6], [7]) to the steel wire. The separation process is initiated by actuating the CREAM mechanism, which releases the POM and consequently accelerates the dummy mass in the X-direction. The acceleration of the dummy mass is measured using an acceleration sensor, which is attached near the POM in the centre of the dummy mass. After the POM and the dummy mass have

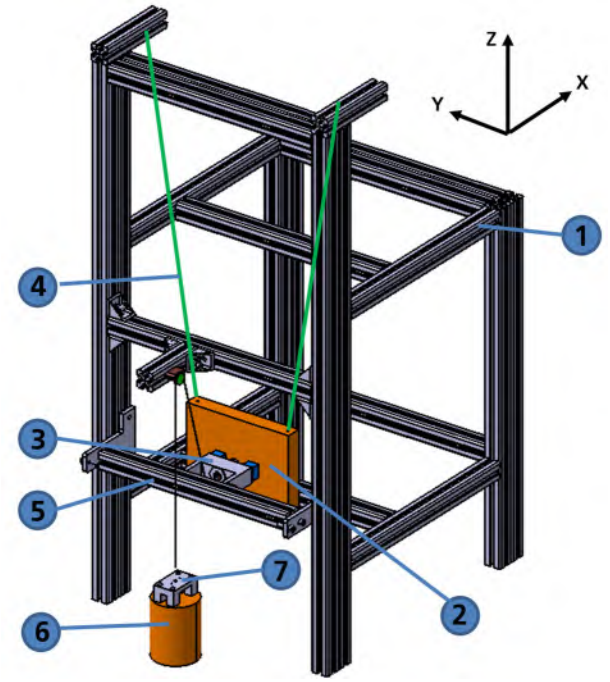


Figure 9: Test setup for hot-cold separation testing (1 – test rig, 2 – mass dummy with accelerometer, 3 – POM support and POM, 4 – dummy mass weight compensation, 5 – POM support bracket, 6 – loading mass, 7 – Interface bracket mass/steel wire with CREAM Release Mechanism)

separated, the POM rotates by approximately 90°.This configuration provides sufficient clearance for the dummy mass in the event that the catching mechanism, consisting of a magnet, fails and the dummy mass swings back towards the POM.

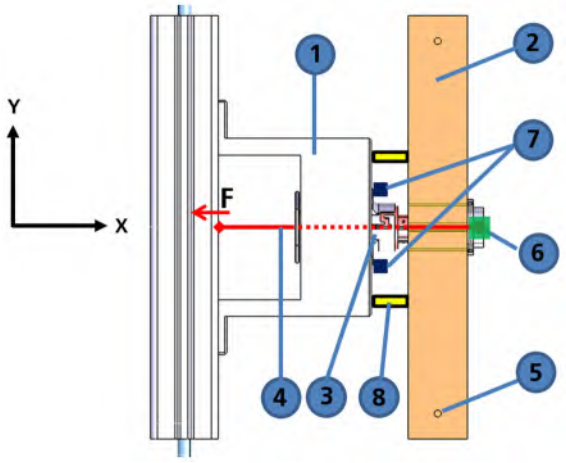


Figure 10: Detailed view - POM Support: (1 – POM support, 2 – mass dummy, 3 – POM, 4 – Steel wire, 5 – attachment point for dummy mass weight compensation, 6 – acceleration sensors, 7 – reference temperature sensor (one back-up), 8 – distance shim)

Test conduction:

First, the test principle is verified at room temperature outside the thermal vacuum chamber. Afterwards the test rig is placed inside the thermal vacuum chamber and the thermal cycling is started. For each test, a complete thermal cycle is done before setting the desired release temperature, i.e. +45°C and -105°C, respectively. This means for both cases:

- Hot case:
  RT → +75°C → -110°C → +45°C
- Cold Case:
  RT → +75°C → -110°C → -105°C

The temperature is measured with a reference temperature sensor at the POM support bushing (see Figure 10). After reaching the set release temperature and 30 min dwell time the separation is initiated.

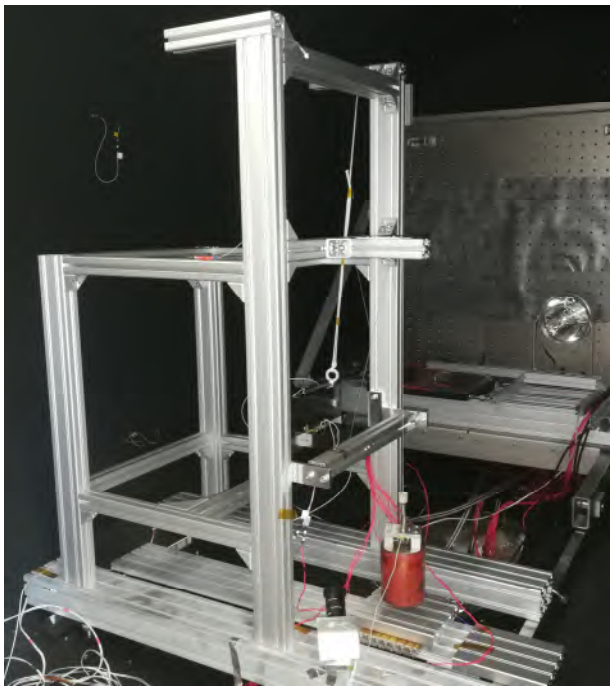


Figure 11: Test setup in thermal vacuum chamber

Test prediction and results:

The motorization energy of the POM QM after life testing was $E_{mot} = 0.4929\ \mathrm{Nm}$ (see section 6.2). In the ideal case the motorization energy of the POM will be completely transferred into kinetic energy of the pendulum mass. The resulting velocity of the pendulum mass is

$$v_p = \sqrt{\frac{2E_{mot}}{m_p}}\,.$$

The weight of the pendulum mass including all sensors, screws etc. is $m_p = 4.862\ kg$, which leads to a peak velocity of $v_{p,pred} = 0.4503\,\frac{m}{s}$.

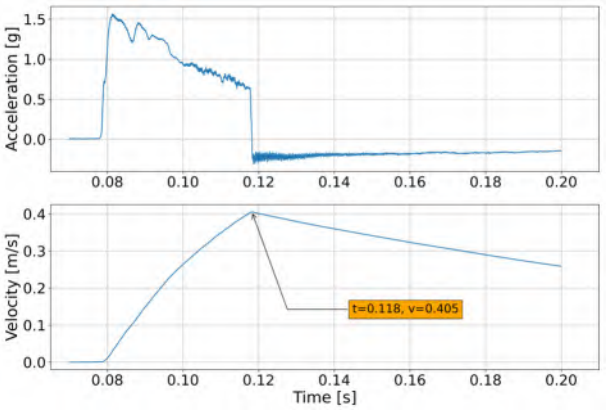


Figure 12: Pre-Test under ambient conditions: acceleration and velocity of the pendulum mass

A pre-test at ambient conditions is performed in order to verify the test setup including all mechanisms and the data acquisition unit. The measured acceleration signal is depicted in Figure 12 in the upper graph. The related velocity signal is derived by numerical integration and is shown in the lower graph in Figure 12. The peak velocity of the pendulum mass during the pre-test at ambient conditions is $v_p = 0.405\,\frac{m}{s}$, which is about 10 % lower than the predicted value. One possible explanation for this could be the non-ideal transfer of energy from the POM to the pendulum mass. Since the suspension strings have a finite length, a small fraction of the transferred energy may theoretically be converted into gravitational potential energy of the pendulum mass, rather than being converted entirely into kinetic energy.

In Figure 13 and Figure 14 the results from the hot and cold actuation are presented. The peak velocity during the cold separation is higher than the peak velocity during hot separation. The difference in the peak velocity between the hot and cold case is about 10%. In general, the hot separation delivers the lower separation peak velocity, which can be caused by the change of the gap size between the inner guiding flange and the outer support bushing of the POM.

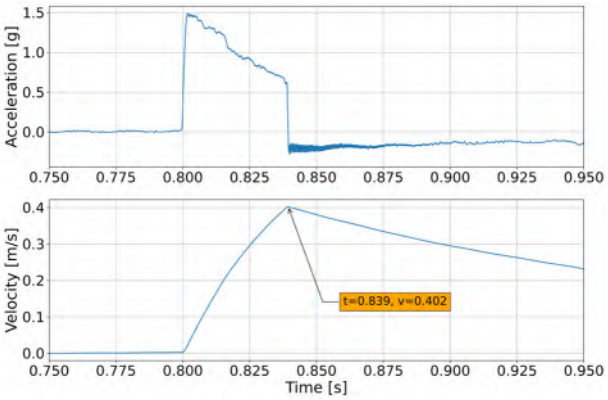


Figure 13: Hot actuation at +45°C: acceleration and related velocity signal of the pendulum mass

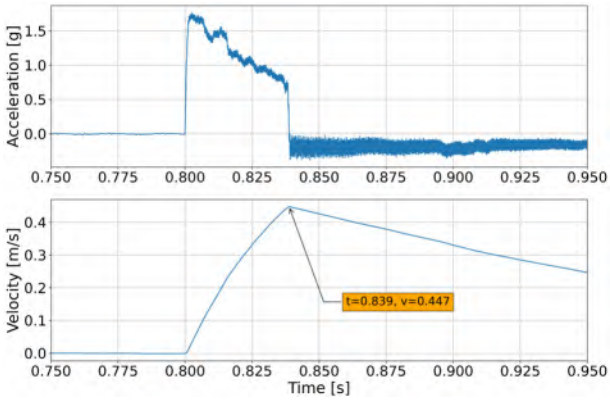
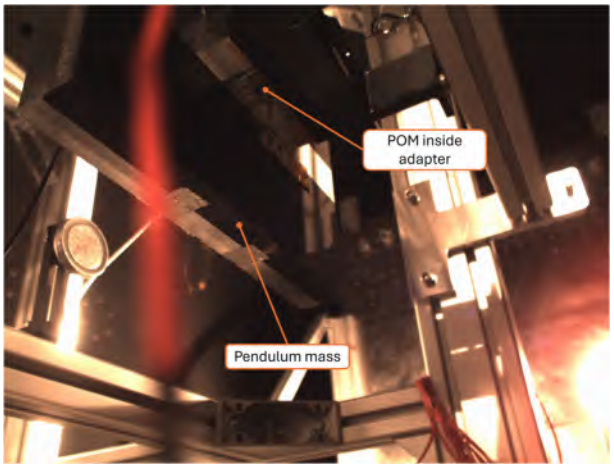
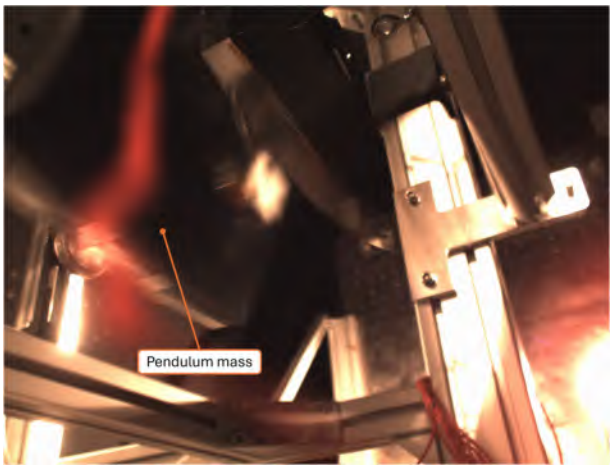


Figure 14: Cold actuation at -105°C: acceleration and related velocity signal of the pendulum mass

For the cold case the gap increases and for the hot case the gap decreases. This is due to the different CTE's of aluminium (inner part) and titanium (outer part), which can influence the frictional forces. A sequence of the hot separation filmed by a camera inside the thermal vacuum chamber is shown in Figure 15. The first picture shows the support structure of the POM close to the pendulum mass. In the second picture the system is shown during the activation. In the last picture, after the separation event, the pendulum mass is hold by the catching system and the support structure including the POM is turned by 90 degrees.





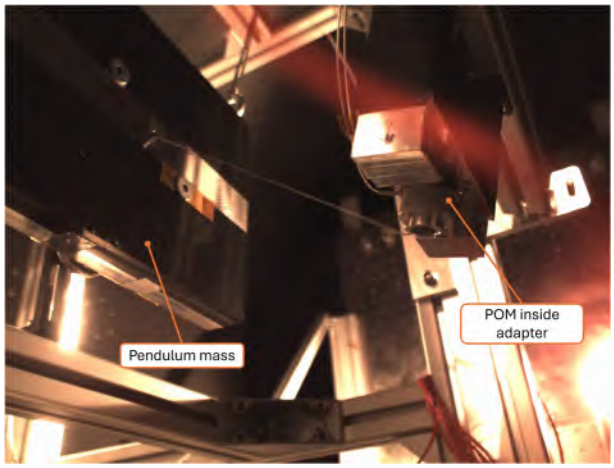


Figure 15: Short sequence of the hot actuation inside the thermal vacuum chamber

Overall, the following peak velocities are measured:

- $v_{p,RT} = 0.405 \frac{m}{s}$,
- $v_{p,hot} = 0.402 \frac{m}{s}$,
- $v_{p,cold} = 0.447 \frac{m}{s}$.

The maximum velocity at actuation under hot conditions is slightly lower than that observed at room temperature and approximately 10% lower than under cold conditions. Consequently, the hot case represents the more critical temperature condition with regard to separation.

7. CONCLUSION

This paper addresses the push-off mechanism of the MMX separation system. Starting with an overview of the mechanism's design and functionality, it then examines the performance and life tests, as well as a separation test under hot and cold conditions in the thermal vacuum chamber. These tests constituted a major part of the overall test programme for qualification of the POM.

It has been shown, that the performance of the POM decreases slightly over its lifetime, but remains well within the lower and upper performance limits. It also shows that the energy, that can be delivered by the POM, is temperature-dependent. The maximum velocity of a dummy pendulum mass was approximately 10% higher at −105°C than at +45°C, which is most likely due to a reduction in internal friction.

In conclusion, the POM mechanism is fully qualified and ready for launch on 19th of October 2026. The separation of the rover IDEFIX from the mothership is expected approximately one year later allowing IDEFIX to start the exploration of the surface of Phobos.

REFERENCES

[1] K. Kuramoto, Y. Kawakatsu, M. Fujimoto, A. Araya, M. A. Barucci, H. Genda and N. Hirata et al., “MMX mission overview,” in *44th COSPAR Scientific Assembly*, Athens, Greece, 2022.

[2] S. Ulamec, P. Michel, M. Grott, U. Böttger and S. Schröder et al., “Science objectives of the MMX rover,” *Acta Astronautica 210,* pp. 95-101, 2023.

[3] C. Grimm, C. Lange and M. Lange et al., "The MASCOT separation mechanism," *CEAS Space J 12,* pp. 343-365, 2020.

[4] A. Pignède, F. Buse, J. T. Grundmann, S. Reershemius, H. Patscheider, T. Wippermann, M. Lange, O. Mierheim and S. Meyer, “MMX rover MECSS - separation from the mothership: multibody simulation analysis of the ejection,” *Multibody System Dynamics,* no. 66, pp. 329-347, 2026.

[5] E. C. F. S. STANDARDIZATION, *ECSS-E-ST-33-01_0820317,* 2019.

[6] S. Reershemius, K. Sasaki and T. Spröwitz, “THE DEVELOPMENT OF A SELF-RESETABLE, LOW-SHOCK HOLD-DOWN AND RELEASE MECHANISM,” in *ECSSMET*, Toulouse, 2023.

[7] T. Spröwitz, S. Reershemius and K. Sasaki, “The Qualification of a Self-Resettable 4.5 kN Hold-Down and Release Mechanism,” *2025 IEEE Aerospace Conference,* pp. 1-7, 2025.

DESIGN, ANALYSIS AND EXPERIMENTAL VALIDATION OF A DEPLOYABLE ARCHITECTURE FOR VERY LARGE SOLAR ARRAYS

Marco Blanco (1), Cas De Groot (1), Alvaro Pipo (1), Paul Hodgetts (2)

(1) PROSIX Engineering, Calle Calzada Vieja de Ategorrieta, 157 - 1, San Sebastian, 20013, Gipuzkoa, Spain. Email: marco.blanco@prosix.es; cas.degroot@prosix.es; alvaro.pipo@prosix.es
(2) European Space Agency - ESTEC, Keplerlaan 1, 2201 AZ Noordwijk, Netherlands. Email: Paul.Hodgetts@ext.esa.int

KEYWORDS
Deployable structures, solar arrays, space mechanisms, breadboard testing, large deployable systems.

ABSTRACT
Future high-power missions and planetary surface infrastructure require solar arrays that can unfold from compact launch volumes into very large, stable power-generation surfaces. This paper presents the design, preliminary analysis and breadboard validation of the Very Large Solar Array (VLSA), an ESA activity developed by PROSIX around a deployable architecture of segmented elements. The full-scale concept targets an 18.8 m Martian configuration with 253 m2 deployed surface. Mechanical analysis focused on the structural modes in stowed and deployed configurations, while a 6 m-class demonstrator was built and tested to validate the deployment concept. The campaign demonstrated controlled mechanism interaction, membrane tensioning, latching behaviour and repeated full deployment, confirming the feasibility of the architecture at breadboard level and identifying the main drivers for the next full-scale design iteration.

1. INTRODUCTION

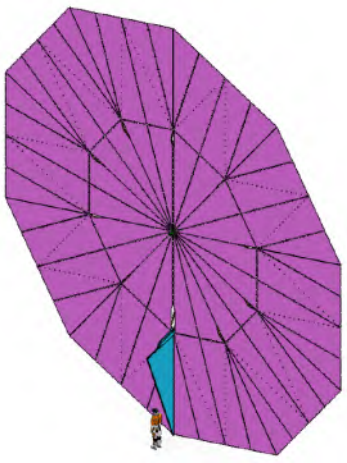
Large deployable solar-array systems are a direct answer to a simple mission-level challenge: future spacecraft and planetary surface infrastructure need more power, but launch vehicles impose strict limits on volume. The most valuable architectures are therefore those that package efficiently, deploy reliably and create a large, usable surface once in operation.

The Very Large Solar Array (VLSA) activity addresses this challenge through a compactly stowed architecture that transforms a rectangular launch stack into a large, supported polygonal surface. The work combines full-scale concept design, preliminary mechanical analysis and a physical 6 m-class demonstrator campaign. The central achievement of the breadboard phase is the experimental confirmation that the key deployment functions can work together as an integrated system, not only as isolated mechanisms.

2. DESIGN CONTEXT AND ARCHITECTURE

The VLSA concept is based on an ESA patent solar-array architecture conceived to deploy from a compact rectangular stowed block into a supported, pretensioned, surface with polygonal circumference. The architecture combines pressure plates, foldable carrier segments, articulated spoke assemblies, segmented ring structures and a deployment actuator. The pressure plates retain and protect the stack in the stowed state, while the ring and spoke mechanisms coordinate the transformation into the deployed configuration.

At full scale, the preliminary Martian configuration reaches a deployed diameter of 18.8 m and a deployed surface of 253 m2. The architecture is divided into spoke mechanisms, ring structures, a foldable solar-array membrane, pressure plates and a root-hinge interface. The solar array is arranged into ten foldable segments. Deployment occurs through a sequence of operations: root-hinge release, ring-structure deployment, outer-array deployment and inner-segment deployment.



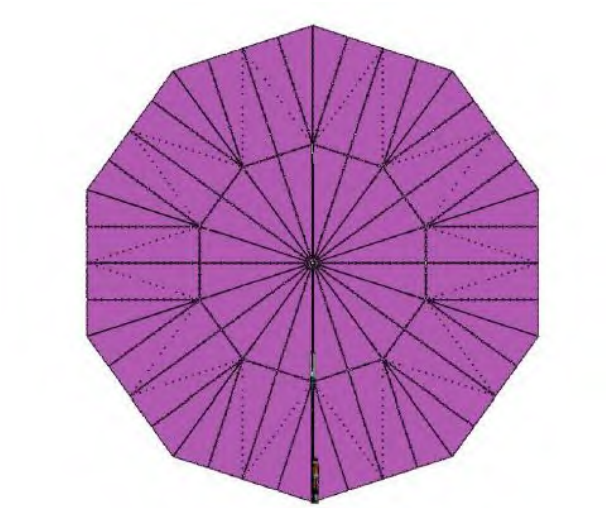


Figure 1: VLSA deployed configuration.

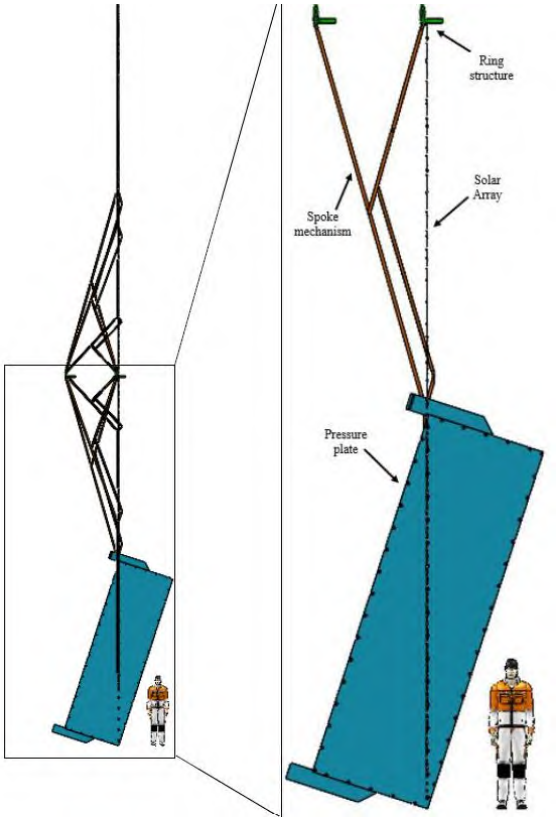


Figure 2: VLSA subsystem breakdown.

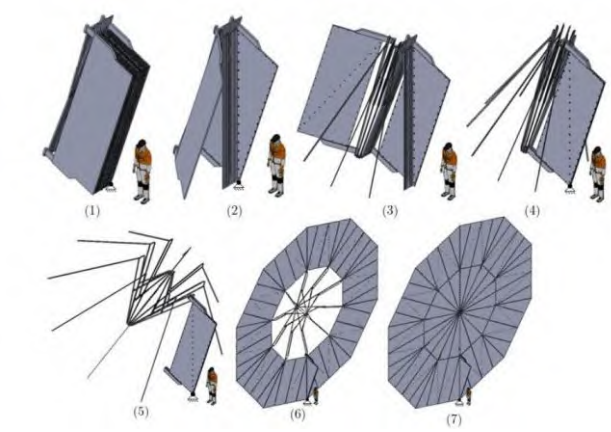


Figure 3: Four-phase deployment sequence.

3. FULL-SCALE DESIGN AND SYSTEM FIGURES

The preliminary design uses compact stowage as a central design driver. In stowed configuration, the full-scale VLSA is represented by a 5.13 m x 1.78 m x 0.65 m envelope with a total stowed volume of 5.94 m3. The mass estimate is based on subsystem volumes and assigned material densities, with a 20% system-level mass margin applied to the nominal dry mass. The nominal dry mass is 428 kg, increasing to 514 kg including margins.

The combined membrane and photovoltaic-cell subsystem is the dominant mass contributor, accounting for approximately 65% of the nominal mass. Under idealised AM0 beginning-of-life conditions, the system achieves a maximum theoretical output power of 79.7 kW. When combined with the 514 kg mass including margin, this corresponds to 155 W/kg, meeting the bound of the specified power-to-mass target. The stowed-volume figure remains a consolidation driver for subsequent design iterations.

Table 1: Summary of full-scale system figures

Figure	Value
Deployed diameter	18.8 m
Deployed surface	253 m2
Stowed envelope	5.13 m x 1.78 m x 0.65 m
Stowed volume	5.94 m3
Nominal dry mass	428.1 kg
Mass with 20% margin	513.7 kg
Maximum theoretical AM0 BOL power	79.7 kW
Power-to-mass ratio	155 W/kg

4. PRELIMINARY MECHANICAL ANALYSIS

Preliminary finite element analyses were performed for both stowed and deployed configurations. Solar panels and pressure plates were represented by plate elements, corrugations, spoke bars and ring elements by bar elements, and tension cords by rod elements. The analysis was used to identify the dominant first-modes behaviour of each configuration and to highlight the structural features that most strongly influence the next design iteration.

The stowed configuration is governed by compact stack stiffness and load introduction through the pressure plates. The deployed configuration is governed by a much larger structural span, low-frequency behaviour and the ability to maintain a supported surface under planetary gravity and wind loading. The first modes of each configuration provide a useful indicator of the main structural consolidation needs.

In the stowed configuration, the first modal frequency was 34.2 Hz. The corresponding mode is dominated by lateral sliding of panels within the compact stack, linked to spacer flexibility. This result indicates that spacer stiffness and stack constraint are key improvements for increasing robustness in the launch configuration.

In the deployed configuration, the first pre-stressed modal frequency was 0.117 Hz, close to the 0.1 Hz target. The first deployed mode reflects the large-span behaviour of the supported polygonal surface and confirms that the preliminary concept reaches the required low-frequency threshold, while root-spoke loading and root-attachment behaviour remain important consolidation drivers.

Table 2: Main mechanical analysis outcomes

Configuration	First mode result	Main design insight
Stowed configuration	f1 = 34.2 Hz	Dominated by lateral panel sliding; spacer stiffness and stack constraint are key consolidation needs.
Deployed configuration	f1 = 0.117 Hz	Large-span behaviour, root-spoke loading and root attachment remain design drivers.

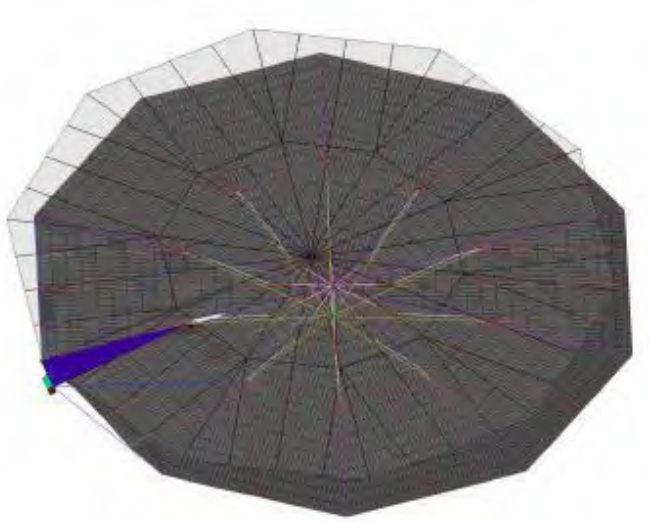


Figure 4: Deployed configuration, first mode shape at f1 = 0.117 Hz.

5. BREADBOARD DESIGN AND REPRESENTATIVENESS

A 6 m-class breadboard demonstrator was developed to validate the critical deployment mechanisms. The demonstrator is derived from the 18.8 m preliminary desig. Its role is to preserve the deployment architecture and geometry required to validate ring deployment, spoke deployment and inner membrane-section deployment within project constraints.

The breadboard retains the key kinematic features of the full-scale configuration. The spoke cross-sections are not geometrically scaled down; instead, profiles of similar size are retained because verifying stowage and deployment without volume conflicts is more relevant at this stage than reproducing full-scale stiffness. The root hinge is excluded because it depends strongly on the platform interface. Solar cells and photovoltaic harness are also excluded, with solar-cell mass represented by equivalent masses integrated into the membrane spokes.

The breadboard implements ring-to-pressure-plate hold-down and release functions, ring latching and pressure-plate latching using COTS items. This allows the test campaign to focus on mechanism interaction and gives the system a controlled and rapidly resettable configuration. The demonstrator contains two ring structures, nine regular spoke mechanisms and one base spoke, with a 25.5 m2 membrane surface, 68.2 kg mass and a 0.78 m3 stowed volume inside a 1.78 m x 0.67 m x 0.65 m bounding box.

Table 3: Full-Scale Design Vs Breadboard Representativeness

Feature	Full-scale	Breadboard
Deployed diameter	18.8 m	6 m
Objective	Planetary solar-generator architecture	Deployment-mechanism validation
Spoke cross sections	Full-scale design profiles	Representative profiles
Solar cells	Integrated PV assembly	Not included
PV mass	Real cells and harness	10 equivalent masses
Root hinge	Included in full system	Excluded
HDRM / latching	Space mechanism concepts	Electromagnet representation
Critical mechanisms	Ring, spokes, inner segments	Preserved

Table 4: Breadboard key parameters

Figure	Value
Deployed diameter	6 m
Membrane surface	25.5 m2
Spoke deployed radial length	2.9 m
A-B deployment stroke	~1 m
Demonstrator mass	68.2 kg
Stowed box	1.78 m x 0.67 m x 0.65 m
Stowed volume	0.78 m3
Equivalent masses	10 x 1.8 kg



Figure 5: Compact stowed configuration and partially deployed full-scale architecture.

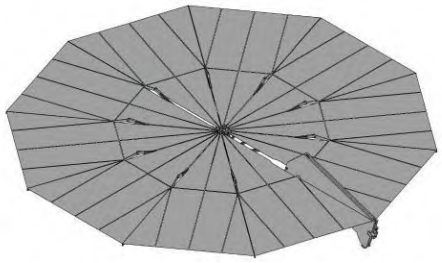


Figure 6: 6 m-class breadboard demonstrator illustrating the deployed architecture.

6. TEST SETUP AND PROCEDURE

Deployment testing was performed in a horizontal plane using a support suspended gantry. The support frame includes nine rails with rolling carriages. The VLSA demonstrator is suspended from the carriages by tension springs connected at hinge points, allowing the mechanism to define the position of the suspension points during deployment.

The gantry is not intended to provide full gravity compensation. Its purpose is to enable proof-of-concept validation of geometric compliance, manufacturing tolerances and deployment mechanisms. A vertical deployment would introduce additional mechanical loads and synchronisation risks that are outside the objective of the breadboard campaign.

The test campaign progresses from sub-mechanism checks to complete deployment. It covers ring-structure range of motion, spoke mechanism range of motion, base-spoke range of motion, ring-structure functionality, pressure-plate latching repeatability, actuator functional ranges, membrane tension, inner-segment deployment repeatability and complete deployment repeatability.

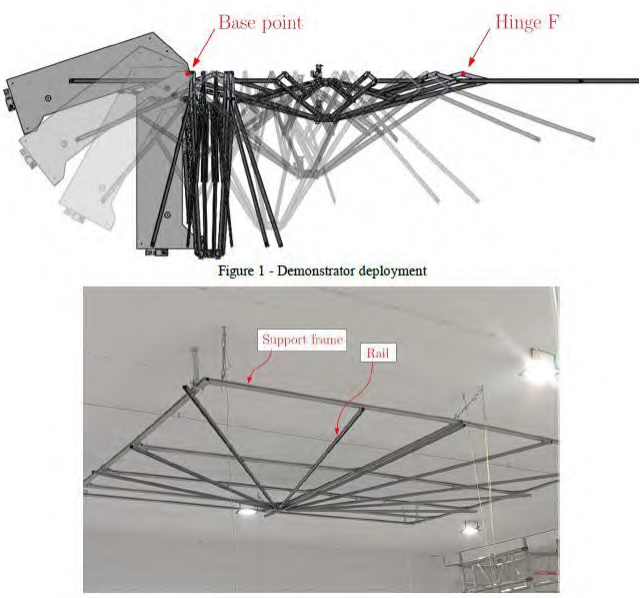


Figure 7: Horizontal deployment test setup with gantry, rails, carriages and suspension springs.

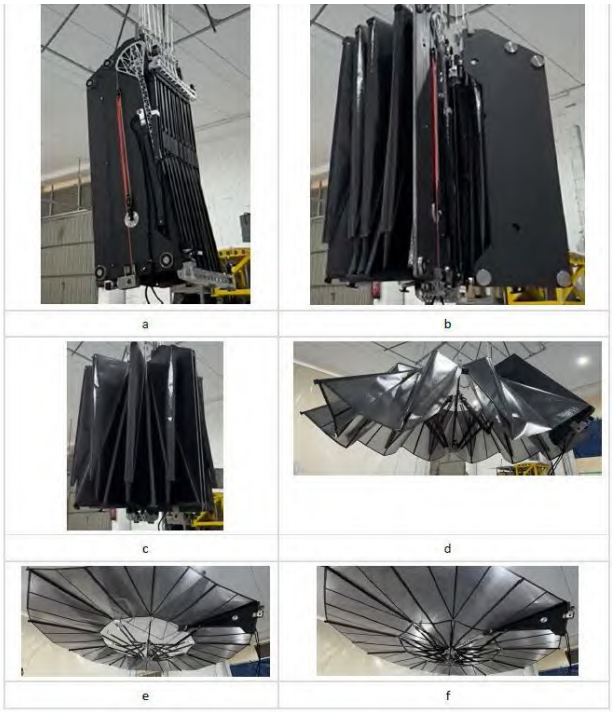


Figure 8: Full deployment sequence of the complete breadboard demonstrator.

7. EXPERIMENTAL RESULTS

The completed breadboard campaign validated the main deployment functions of the VLSA demonstrator as an integrated system. Mechanism mobility, ring deployment, pressure-plate latching, actuator sequencing, membrane tensioning, inner-segment deployment and full-system repeatability were all demonstrated successfully.

The demonstrator showed that a large, folded surface can be released, guided and progressively opened without loss of deployment control. Pressure-plate latching was repeatable when alignment was correct.

The actuator tests also clarified how deployment loads should be introduced. The base-spoke actuator is effective during the initial opening phase, whereas distributed actuation through the ring structures provides better geometric control for the remaining deployment. This is a significant result because it turns the breadboard into a practical tool for refining the deployment sequence, not only for proving that deployment is possible.

The final repeatability runs demonstrated the most visible achievement of the campaign: the complete 6 m-class demonstrator, including membrane and equivalent masses, deployed fully five times. The result confirms the feasibility of the selected architecture at breadboard level and provides a clear technical basis for the next design iteration.

8. CONSOLIDATED DESIGN DRIVERS

The breadboard campaign confirmed that the VLSA deployment principle is technically feasible and that the main remaining challenges are engineering refinements rather than fundamental architectural limitations. The first consolidation driver is pressure-plate latching robustness and the second driver is base-spoke stiffness. The base spoke is the entry point for future root-hinge integration and carries higher structural demand than regular spokes. The third driver is deployment tolerance control, including ring-link end-stop tolerances, pressure-plate alignment and actuator switching between base-spoke and ring-structure actuation. Addressing these points will improve repeatability and scalability while preserving the overall deployment concept validated by the demonstrator.

9. CONCLUSIONS

The VLSA activity has matured a compactly stowed deployable solar-array architecture for large-area power generation. The work demonstrates a practical route from patented deployment theoretical principle to full-scale preliminary design and then to physical breadboard validation. The resulting architecture transforms a compact rectangular stack into a large supported polygonal surface, addressing one of the central challenges of future high-power space systems: generating more

area and power from a constrained launch envelope.

Mechanical analysis confirmed the feasibility of the preliminary design at concept level. The 6 m-class breadboard demonstrator validated the key deployment mechanisms in an integrated campaign. The demonstrator achieved repeated full deployment, verified membrane tensioning and exposed the main design improvements required for scale-up. These results provide a concrete experimental basis for maturing the VLSA architecture towards a robust full-scale deployable solar-array system.

10. ACKNOWLEDGEMENTS

The authors acknowledge the support of the European Space Agency and the engineering team involved in the preliminary design, breadboard development, test planning and test execution.

11. REFERENCES

1. European Space Agency. Solar array for a spacecraft, patent document 84306PC01, ESA AO/1-12379/24/NL/MGu.
2. ECSS-E-ST-32-10C Rev.2 Corrigendum 1, Structural factors of safety for spaceflight hardware, 2019.
3. ECSS-E-ST-20-08C Rev.2, Photovoltaic assemblies and components, 20 Apr. 2023.

ECSSMET
Braunschweig Germany 2026

Micro vibration

Frequency Domain Methodology For Microvibration Analysis

Grégory Ladurée [(1)], Alexandru Vargalui [(2)]

[(1)] European Space Agency-ESTEC, Keplerlaan 1, Postbus 299, 2201 AZ, Noordwijk, Netherlands, Email: Gregory.Laduree@esa.int

[(2)] European Space Agency-ESTEC, Keplerlaan 1, Postbus 299, 2201 AZ, Noordwijk, Netherlands, Email: Alexandru.Vargalui@esa.int

KEYWORDS

Microvibrations, harmonic noise source, pointing

ABSTRACT

The trend in the on-going and future science and Earth observation missions definition is showing a clear increase of payloads and instruments performances, more stringent observational requirements, more demanding pointing stability for sensors with challenging environment (e.g. cryogenic, microphonics…). Microvibration environment has become in this context a driver for missions with demanding performance requirements. Prediction and management of microvibration impact on the instrument performance is therefore a key aspect intervening early in the overall project development. This environment is a typical multi-disciplinary problem, and it is usually best managed at system level where the coupling of multiple noise sources with their supporting structure propagating the noise and the payloads are modelled together in an end-to-end analysis.

The required microvibration performance is often expressed in terms of maximum allowed error of a defined metric associated to a given probability over observation windows or ensemble of observations during the mission. As such, it is intrinsically and most of the time best represented as a time domain error allocation requiring a system budget to be derived representing the probability distribution of the considered error. Time domain simulations provide good insight but are time consuming for large systems and only represent one realisation of the overall system, which may not be worst case. Frequency domain analysis is another popular approach because it normally allows to consider some of the main noise sources, which are generating harmonics, like reaction wheels (RW) or cryo-cooler (CCU). The challenge of a frequency domain approach is how to consider, at a given instant, the proper combination of all contributors, namely all the noise sources with broadband frequency content exciting several degrees of freedoms (DOFs), and to estimate the impact on the overall error metric. The summation rules usually applied are linear or quadratic summations of the various contributors. However, experience shows that they are sometimes failing in representing accurately the time domain error distribution. They are indeed relying on underlying assumptions on the resulting distribution of errors (typically Gaussian distribution is usually assumed), where in reality, the presence of harmonics excitation coupled with potential structure modes with low damping are generating different types of distributions (i.e. bimodal or sine distribution).

This paper presents a methodology for microvibration analysis of harmonic sources in the frequency domain considering an end-to-end process starting from the noise disturbance to the final performance metric budget derivation. The emphasis is put on deriving the resulting distribution of the error metric and then consider the exact probability requirement (i.e. quantile) defining the microvibration performance. The final uncertainty (and associated uncertainty factors) is then concentrated on the building blocks of the environment (harmonics amplitude, transfer functions of the system, variance of random noise) instead of the summation process of all these contributors.

1. NOTATIONS & ABBREVIATIONS

Acronym	Definition
AIT	Assembly Integration and Testing
APE	Absolute Pointing Error
CCU	Cryo-Cooler Unit
CDF	Cumulative Distribution Function
DOF/dof	Degree of Freedom
FFT	Fast Fourier Transform
FRF	Frequency Response Function
LoS	Line of Sight
MPC	Multi Point Constraint
MPE	Mean Pointing Error
PDE	Performance Drift Error
PDF	Probability Distribution Function
RPE	Relative Pointing Error
RPM	Rotations Per Minute
RSS	Root Sum Square
RW	Reaction Wheel
STFT	Short Time Fourier Transform
TED	Thermo-Elastic Deformation
TPA	Transfer Path Analysis

Symbol	Definition
ω	Frequency vector
Ω	RW speed or cooler H_0
r	Harmonic rank
s	Noise source interface node
i	Noise source interface or input dof (Tx, Ty, Tz, Mx, My, Mz)
o	Output dof

$H_i^r(\omega)$	Harmonic profile of rank *r* along *i* direction
$\mathrm{FRF}_{\mathrm{io}}(\omega)$	Frequency Response Function between input dof *i* and output dof *o*
$C_{so}^r(\omega)$	Contribution from noise source interface node *s* to output dof *o* including all input dofs
Km	Safety factor on harmonics amplitude
$budgetFreq_{so}(\omega)$	Frequency domain budget between noise source interface node *s* and output *o* function of ω
$\Gamma_{so}^r(\Omega)$	Contributions from input node s to output dof o projected onto the RW speed Ω
$budgetTime_{so}(\Omega)$	Time domain budget (function of speed or rate Ω) noise source interface node *s* and output *o*
$J_{so}(\Omega)$	Summation of all harmonics of a source s to output *o* function of Ω
$Q_o(\Omega)$	Summation of all sources s to output *o* function of Ω
$f_X(x)$	Probability distribution function of random variable X (PDF)
$F_X(x)$	Cumulative distribution function of random variable X (CDF)
$*$	Convolution operator
$\underline{F}(x)$	Plausibility function
$\overline{F}(x)$	Belief function
e_x, e_y	Line of Sight error around RX, RY
$\varepsilon(t)$	Gaussian noise
σ	Standard deviation of Gaussian noise (equal to RMS for centred noise)

2. INTRODUCTION

The main steps of harmonic sources microvibration analysis are summarized hereafter and described in more details in sections 3 to 6:

1. Extraction of harmonics profiles $H_i^r(\omega)$ from waterfall plots using Short-Time Fourier Transform (STFT) of the measured exported interface forces and moments (usually on a Kistler table) of the harmonic noise sources while operated. The number of harmonics per input dofs can vary. Phase between x and y directions of rotating forces may be included in the waterfall data. The harmonics of ranks r shall be regrouped or binned in order to identify common harmonics present on several dofs (e.g. harmonic of rank r_i identified on Tx, Ty, or Mx and My). This is for instance the case of Harmonic H_i^1 (i.e. $\propto$ wheel speed) identified on all dofs. It is preferable to measure these forces on a representative model (EM, PFM, FM).
2. Calculation or measurement of transfer functions $\mathrm{FRF}_{\mathrm{io}}$ (flexibilities or accelerances i.e. displacement or acceleration over force) between the noise source interface dofs *i* and the output nodes *o*. The input nodes dofs shall cover all forces and moments generated by the noise source, i.e. Tx, Ty, Tz, Mx, My and Mz at the interface node *s*. FRF can include magnitude and phase, though phase is not mandatory. If the harmonics profiles $H_i^r(\omega)$ are directly extracted from microvibration signature test of the clamped noise source (e.g. on Kistler table), then the system FEM shall include the noise source model (even simplified) representing the dynamic of the noise source, in particular the main modes (e.g. rocking, radial and axial modes of a RW or main structural modes of a cooler). The presence of the noise source model is necessary to account for the dynamic coupling between the noise source model and its support as shown in [1]. In those conditions, the measured blocked force extracted from the microvibration signature test can be directly used as excitation at the noise source interface of the coupled model. Some limitations apply when the noise source is rotating, i.e. rocking modes frequencies are frequency dependent. In such case, the coupled model usually corresponds to zero speed case. This is a limitation of the transfer calculation using only linear model of the noise and spacecraft structure. The maximum frequency ω_{max} of the calculated $\mathrm{FRF}_{\mathrm{io}}$ will limit the maximum frequency of the derived budgets.
3. Definition of a set of requirements applicable to output dofs *o* or a function of output dofs *o*. The most common function of output dofs is the modules of several dofs. Like rotations or displacements (e.g. $LoS = \sqrt{e_x^2 + e_y^2}$).
4. Combination of impacts of each harmonic calculated at the output o through transfer functions and derive time and frequency domain microvibration budgets (see [2]) to be compared with requirements. New summation rules are proposed in this method to derive more representative budgets: harmonics combination using convolution and uncertainty propagation.

The above four steps are detailed in the coming chapters and summarized in Figure 1.

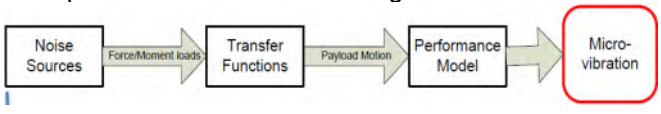
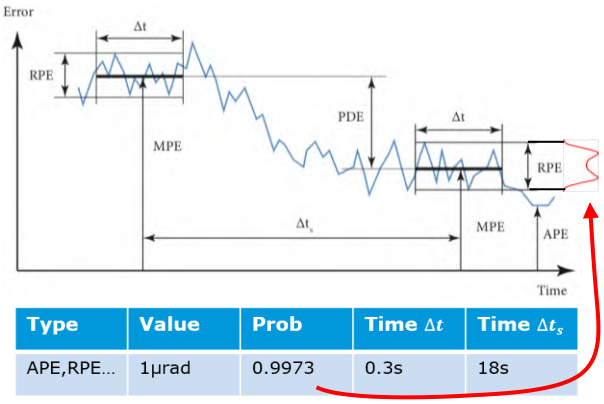


Figure 1: Overall microvibration analysis process for harmonic sources

3. MICROVIBRATION REQUIREMENTS

Microvibration requirements are usually defined from an allocation of pointing requirements or payload performance requirements. Microvibration is one contributor among others like TED, AIT deformation, Ground to Orbit deformation, Water desorption deformation… This allocation is normally associated to a probability, an observation window or period of time in between observations.
Examples of typical pointing requirement types are shown in Figure 2. A full list of pointing requirements is defined in [8].



Type	Value	Prob	Time Δt	Time Δt_s
APE,RPE…	1µrad	0.9973	0.3s	18s

Figure 2: Example of pointing requirements

Microvibration interface requirements for subsystems and equipment define frequency-dependent disturbance levels at interfaces between subsystems (e.g. at the interface between platform and instrument). From the allocation, various types of sub-requirements can be derived

- Noise source emissivity requirement
- Payload susceptibility requirement
- Transfer function limit profiles

Emissivity requirements specify the maximum allowed microvibration disturbance generated by a subsystem or equipment (and "emitted" towards the remaining part of the system).

Susceptibility requirements specify the level of "external" microvibration disturbance under which a subsystem or equipment is required to function while guaranteeing its performance.

Transfer function limit profiles define the maximum allowable frequency-dependent amplification between the source and receiver interfaces.

4. NOISE SOURCES

Harmonics noise sources produce disturbances that are characterised by some harmonic signals usually dominating the overall signal amplitude. The exported forces/moments can be expressed for each DOF *i* as

$$F_i(t) = \sum_{r=1}^{N} H_i^r(t) + \varepsilon_i(t) = \sum_{r=1}^{N} A_i^r \cos(r\omega t + \varphi_i^r) + \varepsilon_i(t) \quad (1)$$

with $\varepsilon_i(t)$ some Gaussian noise of 0 mean and variance σ_i^2 associated to DOF *i*, A_i^r and φ_i^r the amplitude and phase of the harmonic of rank *r*. A_i^r is usually not constant and may depend on some operational mode of the noise source (e.g. speed of the reaction wheel, fundamental frequency of cryo-cooler…). The phase φ_i^r is usually random and will be considered as such in the rest of the paper. The residual noise $\varepsilon_i(t)$ may result from the combination of all harmonics of ranks *r>N* and/or any other random process contained in the noise source.

These interface forces can be visualized using waterfall or FFT as shown in Figure *3* for a RW and Figure *4* for a cryo-cooler. The first step of the method consists in extracting the relevant harmonics ranks and amplitude vs frequency profiles from the waterfall or FFT such that the overall envelope of the interface force is well approximated by the retained *N* harmonics in the frequency range $[0, \omega_{max}]$ as shown in Figure 5 and Figure 6.

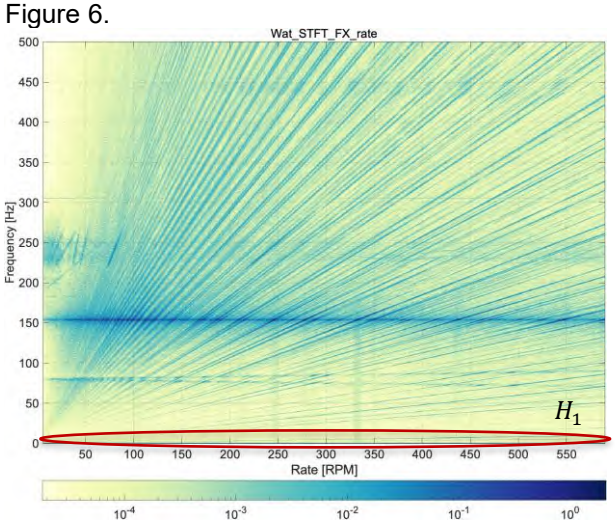


Figure 3: Example of RW waterfall plot

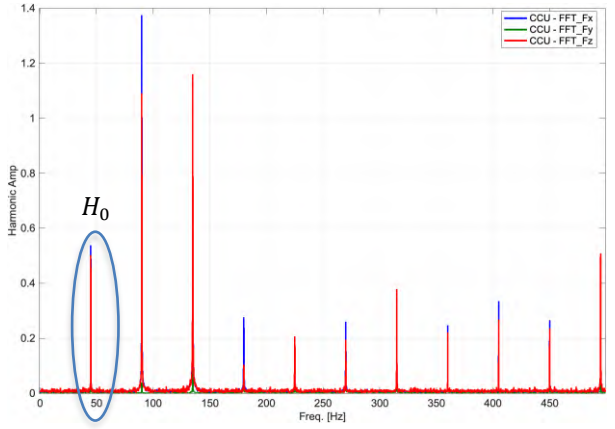


Figure 4: Example of cryo-cooler harmonics

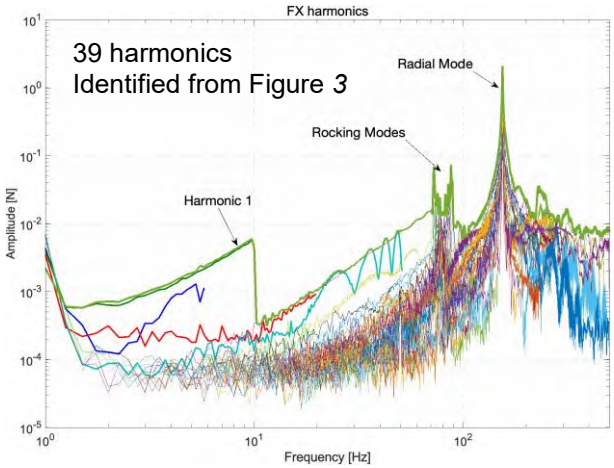


Figure 5: Extracted harmonics profiles for a RW – green curve is the waterfall envelope

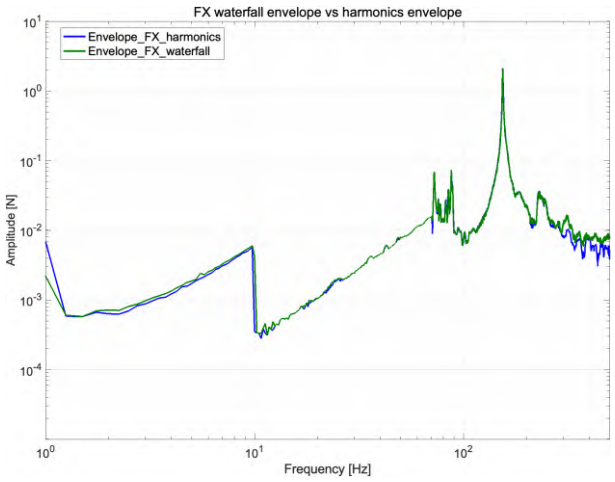


Figure 6: waterfall envelope vs extracted harmonics envelope

5. TRANSFER PATH ANALYSIS

Realistic system performance prediction can only be obtained by coupled analysis and/or test at system level. The presence in the spacecraft model of a dynamic representative model of the noise source is considered mandatory. Applying directly a measured force without source model or a simple lumped mass for the source leads to neglect some potential dynamic coupling between the noise source and its supporting structure. Transfer functions are usually dynamic flexibilities (Displacement/Force) or accelerances (Acceleration/Force). However, the physical origin of microvibration noise is typically internal to the source and usually not directly accessible to measurement. A blocked force approach, as described in [3] and illustrated in Figure 7 is proposed in this method. It consists in using directly the extracted harmonics profiles from Figure 5 to excite the interface DOFs of the noise source in the coupled model. A correlated noise source model is necessary, even though it can be simplified or condensed if a detailed model is not available. This transfer path method is valid if the internal source excitation is independent of the source mounting, which is a reasonable assumption for RW or coolers.

Output responses can be either physical (e.g. interface point of a receiver) or virtual nodes (e.g. LoS modelled through MPC relationships).

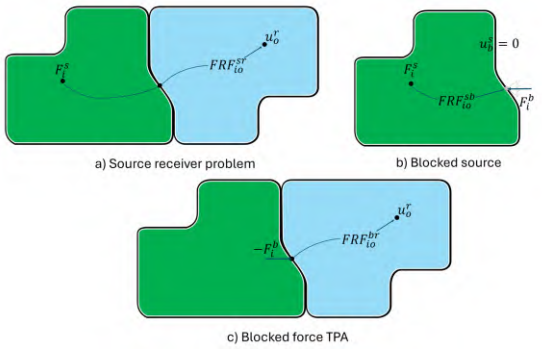


Figure 7: Blocked force approach principle from [3]

6. MICROVIBRATION BUDGET DERIVATION

Frequency and time domain budgets for a given harmonic source contain different information. Frequency budget represents the envelope in the frequency domain of all harmonics contribution produced by one or more noise sources when they are operated inside their respective specified range. Time budget represents a statistical envelope corresponding to a given probability in the time domain of all harmonics contribution produced by one or more noise sources when they are operated inside their respective specified range. The time domain budget is plotted against the noise source operation range (e.g. RW speed Ω or cryo-cooler fundamental frequency H_0). The time domain budget can be directly compared to the defined pointing requirement as it gives the overall error envelope of the output dof at the specified probability and considering the correct metric (e.g. RPE, MPE, PDE…).

When several harmonic noise sources are operated simultaneously, frequency and time domain budgets can be computed at the point of interest with the contribution of all selected noise sources.

The following Figure 8 and Figure 9 illustrate the two different budgets concepts for a RW and a cryo-cooler. They consist in some projection of harmonics contribution along frequency axis or the noise source operation range axis (e.g. RW speed Ω or cryo-cooler fundamental frequency H_0). The projection along the frequency axis is a classic one. The projection along the noise source speed or fundamental frequency axis aims at deriving a statistical envelope in the time domain of all simultaneously present harmonics at the receiver output nodes.

The frequency and time domain budgets illustrated below are described in detail in the following sections. They are derived by summation of contributions of

1. All six DOFs of noise source exported forces/moments
2. All harmonics of a given noise source
3. All sources acting simultaneously

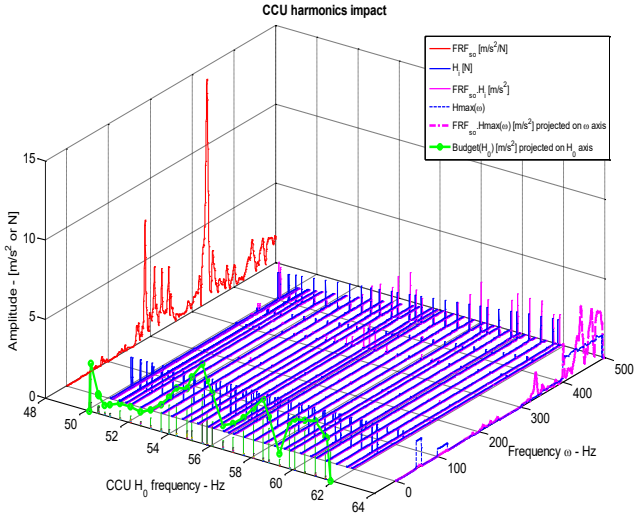


Figure 8: Cryo-cooler microvibration budget example

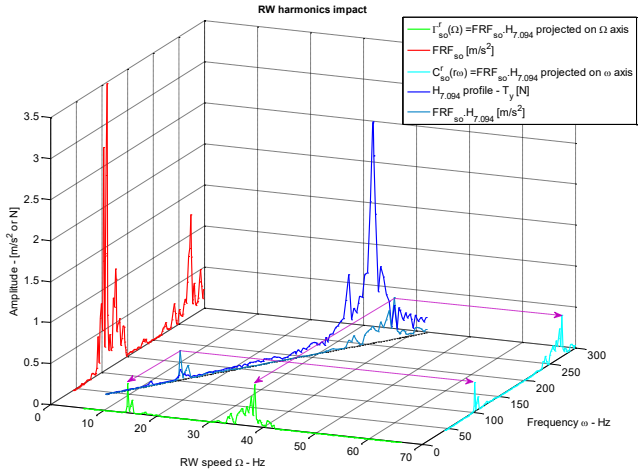


Figure 9: RW microvibration budget example

6.1. Degrees of Freedom Summation

Several options are possible to combine all dofs (i.e. Tx, Ty, Tz, Mx, My, Mz) contribution together. They differ by their degree of conservatism. Two alternative summations are proposed below, the first one being more conservative than the second. Other options also exist (module of the sum, sum of modules considering phase for rotating forces, convolution of DOFs as defined for the harmonics).

6.1.1. Sum of Modules

For each harmonic *r* and each input node, the contributions C_{so}^r from input node *s* to output dof *o* is defined as follow:

$$C_{so}^r(r\omega) = \sum_{i \in dof_s} |FRF_{io}(r\omega).H_i^r(r\omega)| \qquad (2)$$

with $dof_s \overset{\text{def}}{=} [Tx, Ty, Tz, Mx, My, Mz]_s$

6.1.2. RSS

For each harmonic *r* and each input node, the contributions C_{so}^r from input node *s* to output dof *o* is defined as follow:

$$C_{so}^r(r\omega) = \sqrt{\sum_{i \in dof_s} \left|FRF_{io}(r\omega).H_i^r(r\omega)\right|^2} \qquad (3)$$

6.2. Harmonics Summation

The next step consists in combining all harmonics *r* together to estimate the maximum output amplitude response for the selected source. It is expressed with respect to the speed rate Ω, which means that the contributions $C_{so}^r(r\omega)$ must be projected on the speed rate Ω vector. Numerically, the projection is realised by a simple linear interpolation onto the Ω vector. The contribution $\Gamma_{so}^r(\Omega)$ of a harmonic *r* between input node *s* and output dof *o* is defined by:

$$\Gamma_{so}^r(\Omega) = interpolate(r\omega, C_{so}^r(r\omega), r\Omega) \qquad (4)$$

Several methods can then be used to combine all harmonics contributions $\Gamma_{so}^r(\Omega)$ together. They are described hereafter.

6.2.1. Linear harmonics combination

The most conservative method is the linear sum of all harmonics contribution. An additional factor of safety Km can also be added to cover the uncertainty on the harmonics amplitude:

$$J_{so}(\Omega) = \sum_{r=1}^{nr} \Gamma_{so}^r(\Omega).Km \qquad (5)$$

6.2.2. RSS harmonics combination

The RSS method is the RSS sum of all harmonics contribution:

$$J_{so}(\Omega) = Km \sqrt{\sum_{r=1}^{nr} (\Gamma_{so}^r(\Omega))^2} \qquad (6)$$

Remark: RSS summation of harmonics should be used with care as it may not lead to conservative budget.

6.2.3. Harmonics combination by convolution

The main limitation of the previous summation methods is that they do not consider the probability *p* of the considered requirement. The linear sum is obviously a worst case while the RSS summation method is usually not conservative, in particular when the requirement probability is high, e.g. 3 sigma or 99.7%. The proposed method by convolution is answering this problem by computing the distribution of the resulting contributions of all harmonics at the output dof *s* and then deriving the proper quantile corresponding to the defined probability.

Each harmonic is considered as a random variable whose amplitude is known but angle $\theta_i = r\omega t + \varphi_i^r$ is considered random. All these harmonics are summing up at the output dof *o*. The method consists then in estimating statistically the distribution of the sum of independent random

variables. The resulting distribution is the convolution of the probability density functions (PDF) of each random variable. Indeed, if *X* and *Y* are independent random variables then, *Z=X+Y* is a random variable with the following PDF

$$f_Z(z) = (f_X * f_Y)(z)$$
$$f_Z(z) = \int_{-\infty}^{\infty} f_X(x)\, f_Y(z-x)dx \qquad (7)$$

with $*$ the convolution operator.
The probability density function of a sine signal of amplitude *A* is given by (see [4])

$$f_X(x) = \begin{cases} \frac{1}{\pi\sqrt{A^2 - x^2}} & for\ x \in [-A, A] \\ 0 & otherwise \end{cases} \qquad (8)$$

Here is an example of PDF of 2 sine signals of amplitude 2 and 1.2. The corresponding distribution of the sum is bimodal and is shown below in green

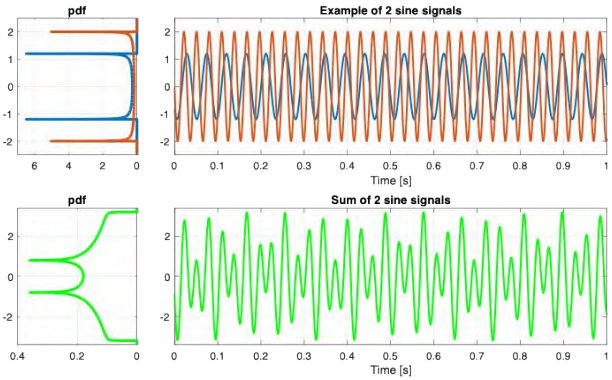


Figure 10: PDF of 2 sine signals of different amplitudes and frequencies and their sum

In the above example, frequency and phase are random.

When the number *n* of sine signals to be summed up is increasing, the central limit theorem shows that the resulting distribution is a Gaussian distribution $N(\mu, \sigma)$ with

$$\mu = \frac{1}{n}\sum_{i}^{n} \mu_i \ , \quad \sigma = \sqrt{\sum_{i}^{n} \sigma_i^2} \qquad (9)$$

Considering that $\sigma = A/\sqrt{2}$ for a sine signal of amplitude *A*, the resulting standard deviation can be expressed by

$$\sigma = \frac{1}{\sqrt{2}}\sqrt{\sum_{i}^{n} A_i^2} \qquad (10)$$

However, if one or several harmonics amplitude are largely dominating the others, the resulting distribution remains largely bimodal. An example summing 30 harmonics amplitudes with the first one dominating the others by a factor larger than 10 is shown in Table 1.

Table 1: Amplitudes of 30 harmonics

Amplitude		
10.000	0.4961	0.8265
0.9091	0.1110	0.2654
0.7846	0.0948	0.9892
0.1627	0.8669	0.2325
0.2807	0.9163	0.8963
0.3301	0.6761	0.6828
0.1218	0.3734	0.6273
0.0241	0.5601	0.7967
0.7097	0.4042	0.8455
0.1790	0.9161	0.7745

The resulting distribution of the sum is shown in Figure 11. It is clearly a bimodal distribution (far from Gaussian) reflecting the impact of the dominating harmonic amplitude on the sum. From this distribution of the sum, statistics can be derived (e.g. 1σ, 2σ, 3σ …).

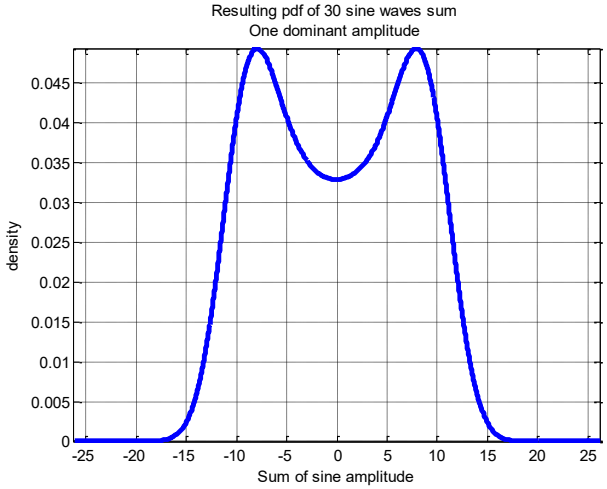


Figure 11: PDF of sum of 30 sine waves with one dominant amplitude

An empirical example is shown below with a signal generated by the sum of the above 30 harmonics whose amplitudes include an uncertainty factor as well of 20% (i.e. the amplitudes in Table 2 have been multiplied by a random factor uniformly distributed between 1 and 1.2). Frequencies and phases have been also randomized uniformly. The resulting signal and its empirical distribution is shown in Figure 12.

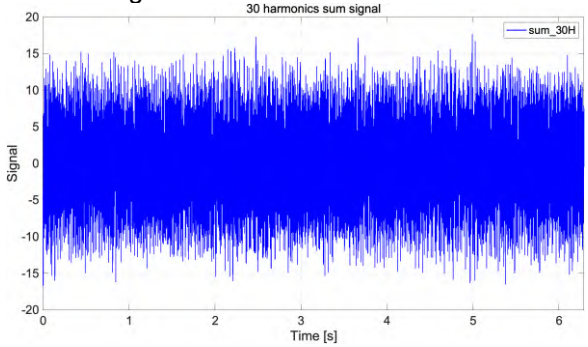


Figure 12: Example of sum of 30 harmonics

The corresponding empirical distribution is shown below. It confirms the analytical one in Figure 11. The uncertainty on the amplitude is also reflected in the slight difference of amplitude between the two modes of the distribution as shown in Figure 13.

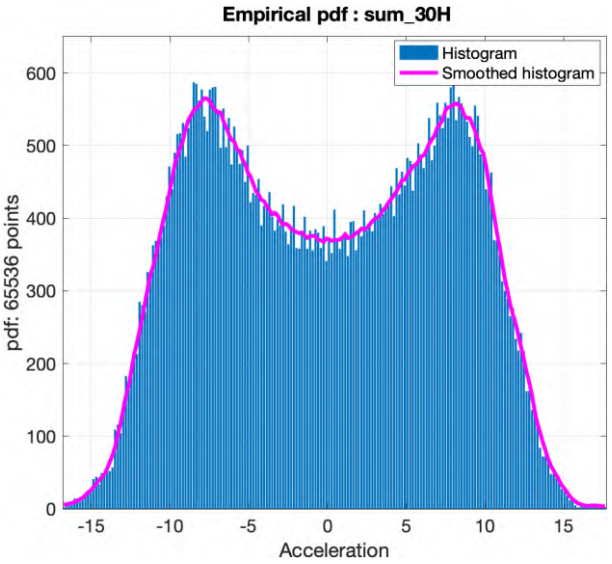


Figure 13: PDF of 30 harmonics summed

The above example of dominating harmonic amplitude is critical to the microvibration budget as it corresponds to the case where a given source harmonic is amplified by a low damped structural mode of the spacecraft which can lead to high microvibration levels at the receiver interface. In such case, considering (as often done) a standard Gaussian distribution for the sum of all harmonics may lead to wrong results.

The proposed convolution method is considering, at each source speed value Ω_j, that the contribution $\Gamma_{so}^r(\Omega_j)$ of Eq (4) for each harmonic *r* is distributed as a sine signal of amplitude $A_{so}^r(\Omega_j)$. Its phase is not known, hence $\Gamma_{so}^r(\Omega_j)$ can be considered as a random variable. The sum of all these independent random variables is also a random variable, called $\Sigma_{so,j}$.

$$\forall \Omega_j \quad \Sigma_{so,j} = \sum_{r=1}^{nr} \Gamma_{so}^r(\Omega_j) \tag{11}$$

Its resulting distribution is calculated by the convolution of the corresponding densities

$$\forall \Omega_j \quad f_{\Sigma_{so,j}}(x) = f_{\Gamma_{so,j}^{r1}}(x) * f_{\Gamma_{so,j}^{r2}}(x) * \ldots * f_{\Gamma_{so,j}^{rn}}(x) \tag{12}$$

with $f_{\Gamma_{so,j}^r}(x)$ the sine distribution of amplitude $A_{so}^r(\Omega_j)$ and $f_{\Sigma_{so,j}}(x)$ the resulting distribution of the sum of sine random variables. $f_{\Gamma_{so,j}^r}(x)$ is given by

$$\forall \Omega_j \quad f_{\Gamma_{so,j}^r}(x) = \begin{cases} \frac{1}{\pi\sqrt{A_{so}^r(\Omega_j)^2 - x^2}} & x \in \left[-A_{so}^r(\Omega_j), A_{so}^r(\Omega_j)\right] \\ 0 & otherwise \end{cases} \tag{13}$$

The calculation of the resulting density in Eq (12) allows to define the corresponding cumulative distribution function (CDF) at Ω_j defined by

$$F_{\Sigma_{so,j}}(x) = P\left(\Sigma_{so,j} \le x\right) = \int_{-\infty}^{x} f_{\Sigma_{so,j}}(u)du \tag{14}$$

Finally the inverse distribution function (or quantile function) $F_{\Sigma_{so,j}}^{-1}(p)$ is used to derive the value x such that $F_{\Sigma_{so,j}}(x) = p$ at Ω_j. The value p corresponds to the probability defined in the considered requirement (e.g. p = 0.9973). It must be noted that the time domain signal is generally centred around 0 and that the requirement applies to both positive and negative cycles, which translates in x value such that $F_{\Sigma_{so,j}}(x) = \frac{1+p}{2}$ (2-sided distribution). Two types of requirements can be considered: requirement specifying 0 to peak limit value (e.g. RPE) or peak-to-peak limit value (e.g. PDE). Finally the resulting harmonic summation J_{so} can then be expressed as

0 to peak value	Peak-to-peak value
$\forall \Omega_j \quad J_{so}(\Omega_j) = F_{\Sigma_{so,j}}^{-1}\left(\frac{1+p}{2}\right)$	$\forall \Omega_j \quad J_{so}(\Omega_j) = F_{\Sigma_{so,j}}^{-1}\left(\frac{1+p}{2}\right) + F_{\Sigma_{so,j}}^{-1}\left(\frac{1-p}{2}\right)$

(15)

The uncertainty on the harmonics profiles (through safety factor Km) is considered in the following section.

Imprecise probability propagation

In practice, the computation of Eq (12) using PDF with singular points (as in the case of sine distributions of amplitude *A*, the points *–A* and *+A* are singular) is numerically difficult around the tails. An alternative method is to use the notion of "uncertain numbers", allowing to define probability boxes (using Demspter–Shafer structures, see [5]). These structures allow using practical algorithms for computing bounds on the result of addition, subtraction, multiplication and division of random variables when only bounds on their input distributions are given. The algorithms employ upper and lower discretizations of the quantile function (i.e. the inverse of the distribution function) in a manner that rigorously contains all discretization error that arises from using a finite number of levels to represent a continuously changing function.

This method has the advantage of directly considering the uncertainty on the harmonics

amplitudes in the propagation of the probabilities. As suggested above, it is possible to consider a safety factor on top of each harmonic amplitude (factor Km above). Each harmonic is then a random variable with an amplitude in the interval $[A, \quad A.Km]$.
A probability-box or p-box is a mean to provide for a random variable *X* whose cumulative distribution *F* is unknown, a pair of functions called Plausibility $\overline{F}$ and Belief $\underline{F}$ allowing to bound the real distribution $F(x)$ such that

$$\underline{F}(x) \leq F(x) \leq \overline{F}(x) \tag{16}$$

The two above functions form a box or corridor in which the uncertain distribution is. $\underline{F}(x)$ and $\overline{F}(x)$ are used to find a given quantile corresponding to the probability p. Both functions provide then an interval $[\underline{q} \quad \overline{q}]$ for the requested requirement. The above imprecise probability propagation algorithm has been implemented through a dedicated Matlab toolbox [9].

The same 30 harmonics signal example is shown in Figure 14 (green curve) to illustrate the concept of Plausibility and Belief functions and corresponding quantiles ($p = 0.99$ in this case).

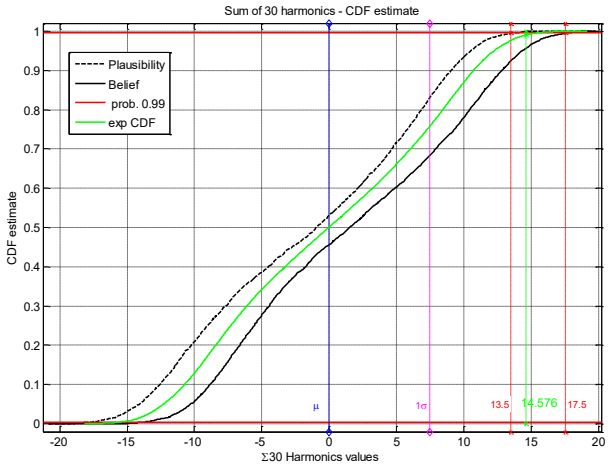


Figure 14: CDF estimate of 30 harmonics example signal

As shown on Figure 14, the 0.99 quantile of the empirical signal is equal to 14.6. It is correctly estimated by the Demspter-Shafer method leading to an interval [13.5 – 17.5]. As a comparison, the linear sum of all 30 harmonics is 25.85. This illustrates the conservatism of the linear summation technique when one harmonic amplitude is largely dominating the others. The delta is however reduced in case all harmonics have similar amplitudes. The convergence toward a normal distribution is then faster.

Direct CDF derivation
The probability distribution associated with the sum of several sine waves and Gaussian noise has been studied in a number of other fields and a closed-form solution has been derived and is recalled by Rice in [6]. Defining the sum signal by

$$y = \sum_{i=1}^{n} b_i \cos(\theta_i) + V \tag{17}$$

with V and θ_i independent random variables. The angles θ_i are supposed to be distributed uniformly over $[-\pi, \pi]$, and V is Gaussian variable with 0 mean and variance σ^2.

The CDF of *Y* is then given by Eq (18).

$$\begin{aligned} F(x) &= \Pr(Y \leq x) \\ &= \frac{1}{2} + \frac{1}{\pi} \int_0^{\infty} \prod_{i=1}^{n} J_0(b_i t)\, e^{-\sigma^2 t^2/2} \frac{\sin(xt)}{t} dt \end{aligned} \tag{18}$$

with J_0 Bessel function of the first kind of order 0.

As explained in [7], Formulas like Eq (18) may be difficult to evaluate by numerical integration. When the tails of the distribution are sought, many steps of numerical integration of the oscillatory integrand are needed to accurately determine its value and avoid round-off errors. Therefore, numerical integration in Eq (18) shall be used with care, in particular if no noise (i.e. $\sigma = 0$) is considered. The example of the sum of 30 harmonics evaluated with Eq (18) shows a very good agreement with the empirical CDF (called exp CDF in Figure 14).

6.3. Sources Summation

When operated simultaneously, different sources contributions must be combined to estimate the total budget. The first component to be summed up is the residual noise of each source σ_{so} if present.

6.3.1. Sources residual noise combination

The residual noise of each source *s* is considered independent (not correlated). The overall noise from all sources at output level o is therefore Gaussian (linear system) with an RMS value equal to

$$\sigma_o = \sqrt{\sum_s \sigma_{so}^2} \tag{19}$$

The corresponding noise is normally distributed with 0 mean and variance σ_o^2.

6.3.2. Linear sources summation

Linear summation is also possible if sources are highly correlated. For what concerns the noise term, it is considered conservatively at 3 sigma.

$$Q_o(\Omega) = \sum_{s=1}^{n_{source}} J_{so}(\Omega) + 3\sigma_o \tag{20}$$

6.3.3. RSS sources summation

RSS summation is often used because sources are

generally considered independent. It is important to remind that in Eq (21) shown below the $Q_o(\Omega)$ term corresponds however to a 1 sigma of the sum of contributors. Even if the harmonics are summed using convolution at 3 sigma, the following RSS summation of sources will not lead to a correct 3 sigma of the sum if some dominant harmonics are present since the overall sum distribution will not be Gaussian. The sources RSS combination is therefore to be used with care and in general not recommended if the probability of the requirement is not 1 sigma. It is better to use the sources combination by convolution described in the next section.

$$Q_o(\Omega) = \sqrt{\sum_{s=1}^{n_{source}} J_{so}^2(\Omega) + \sigma_o^2} \tag{21}$$

Taking again the example shown in Figure 10, it can be easily calculated that the RSS of the two sine signals is $\sqrt{2^2 + 1.2^2} = 2.33$, while the 3 sigma value of the combined signal is closer to the maximum value of 3.2.

6.3.4. Sources combination by convolution

The convolution method is considering, at each noise source speed value Ω_j, that the contribution $\Gamma_{so}^r(\Omega_j)$ for each harmonic *r* and of each source *s* is distributed as a sine signal of amplitude $\mathrm{A}_{so}^r(\Omega_j)$. As for the harmonics, the phase of $\Gamma_{so}^r(\Omega_j)$ is considered as a random variable. The sum of all these random variables is also a random variable, called $\Sigma_{s1\ldots spo,j}$. The noise term of Eq (19) can be added to this contribution. Its resulting distribution is

$$\begin{aligned} &f_{\Sigma_{s1\ldots spo,j}}(x) \\ &= f_{\Gamma_{s1o,j}^{r1}} * \ldots * f_{\Gamma_{s1o,j}^{rn}} * \ldots * f_{\Gamma_{spo,j}^{r1}} * \ldots \\ &* f_{\Gamma_{spo,j}^{rm}} * f_{\sigma_o} \end{aligned} \tag{22}$$

with $f_{\Gamma_{s1o,j}^{r1}}$ given by Eq (13) and f_{σ_o} the normal distribution centred around 0 with standard deviation σ_o given by

$$f_{\sigma_o}(x) = \frac{1}{\sqrt{2\pi\sigma_o^2}} e^{-\frac{x^2}{2\sigma_o^2}} \tag{23}$$

In Eq (22), the number of sine signals to be combined includes all harmonics of all sources *s*. After having computed the resulting CDF as per Eq (14), the inverse distribution function (or quantile function) $F^{-1}_{\Sigma_{s1\ldots spo,j}}(p)$ is used to derive the x value such that $F_{\Sigma_{s1\ldots spo,j}}(x) = p$ at each Ω_j. With similar considerations about the type of requirement, the final source summation is leading to Eq (24).

0 to peak value	Peak-to-peak value
$\forall\Omega_j \quad Q_o(\Omega_j)$ $= F^{-1}_{\Sigma_{s1\ldots spo,j}}\left(\frac{1+p}{2}\right)$	$\forall\Omega_j \quad Q_o(\Omega_j)$ $= F^{-1}_{\Sigma_{s1\ldots spo,j}}\left(\frac{1+p}{2}\right)$ $+ F^{-1}_{\Sigma_{s1\ldots spo,j}}\left(\frac{1-p}{2}\right)$

(24)

The convolution of Eq (22) being numerically sensitive with sine PDF, the same imprecise probability propagation method described earlier can be used.

Once all three steps (DOF, harmonics and sources combinations) have been performed, the frequency and time domain budgets can be estimated.

6.4. Frequency domain budget

The frequency budget from input node *s* to output dof *o* is defined as an envelope of C_{so}^r in the frequency domain:

$$budgetFreq_{so}(\omega) = \max_{r_{min} \le r \le r_{max}} C_{so}^r(r\omega) \tag{25}$$

This budget provides the maximum contribution of all harmonics at a given frequency ω.
A specific factor of safety Km can be added to account for the uncertainty on the harmonics amplitude extraction and/or the FRF or model accuracy.

6.5. Time domain budget

The time domain budget from several sources *s* to output dof *o* is defined as

$$budgetTime_{so}(\Omega) = Q_o(\Omega) \tag{26}$$

with $Q_o(\Omega)$ as per Eq (20) or (21) or (24) depending on the selected source summation rule.

7. EXAMPLE

An example of the application of the methodology is shown below, focusing specifically on the use of the convolution methodology which was used to combine the effects of the different DOFs, harmonics and sources.

An analysis was performed with the ESA internally developed tool COMBMV to compute the impact on the LoS of a payload considering 4 RWs operating at the same speed across the operation range 0 to 100 Hz (worst case).

The resulting LoS impact from the 4 RWs across the operational range is shown in Figure 15. Two peak representative of different distributions are selected to illustrate the results in the rest of the section. Please note that in the time domain budget plots below, the X axis shows the RW speed Ω in Hz and not the frequency content.

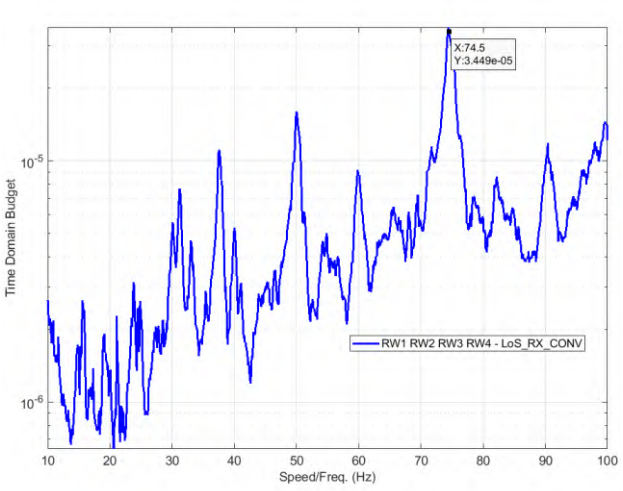


Figure 15: Example of RW time budget for LoS RX

The CDF estimate for the peak around 65.7 Hz is shown in Figure 16. The estimated distribution is closer to a Gaussian distribution shown in the plot as the blue curve.

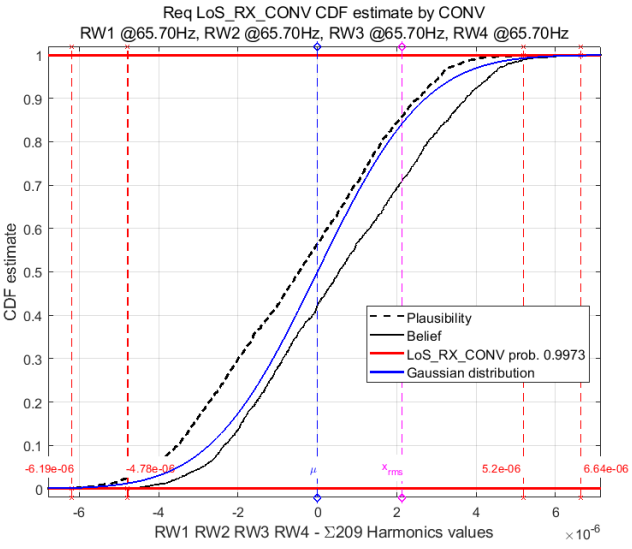


Figure 16: CDF estimate for peak at 65.8 Hz

For the peak around 74.4 Hz, the distribution is the one shown in Figure 17. For reference the theoretical Gaussian and bimodal distributions are shown as the blue and green curves respectively. It is easily observed that the estimated CDF is not Gaussian due to the dominant impact of one of the RW harmonics.

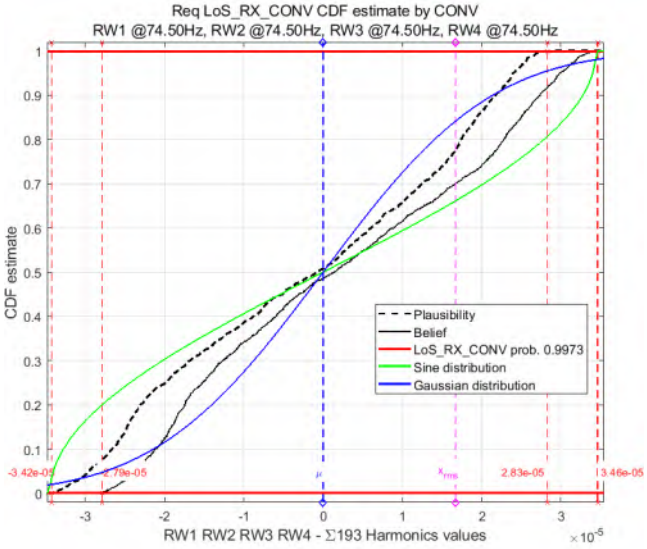


Figure 17: CDF estimate for peak at 74.5 Hz

The source of the investigated peak can be traced in this case to RW2. The computed budget from this RW is shown in Figure 18. The information provided for the datapoint also reveals that the peak is driven by harmonic 5.27 of this RW and the frequency content is 393.1 Hz.

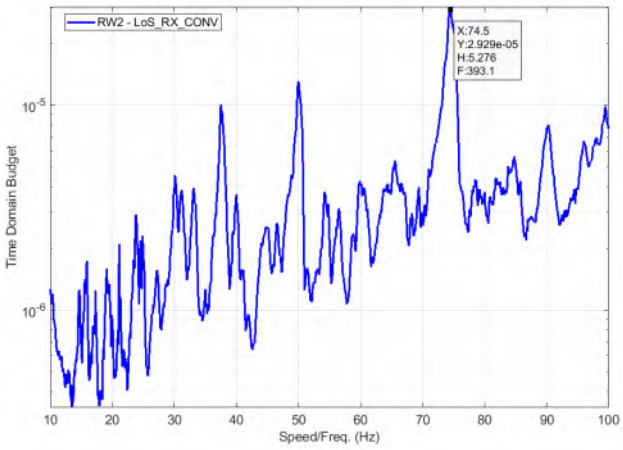


Figure 18: LoS impact from RW2

The peak can finally be traced to the harmonic 5.27 of the force in the Z component which is shown in Figure 19.

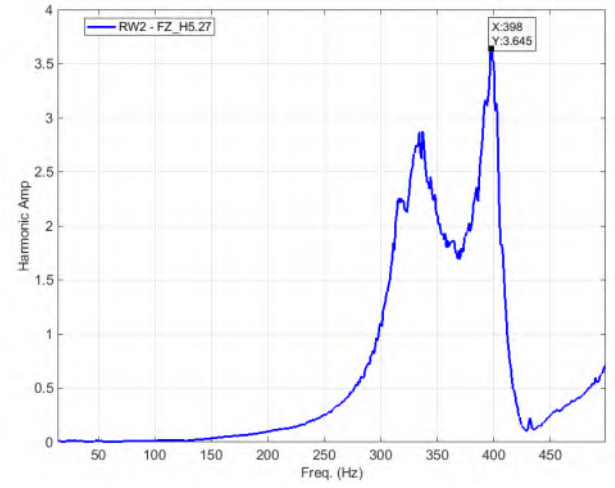


Figure 19: Plot of RW2 FZ Harmonic 5.27

Investigating the CDF estimate of RW2 at the speed of 74.4 Hz the distribution is strongly bimodal due to the dominant harmonic as shown in Figure 20.

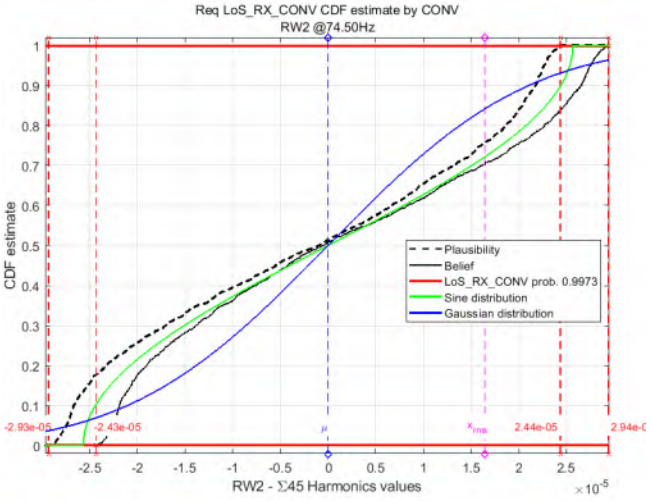


Figure 20: CDF estimate of RW2 impact at 74.5 Hz

Finally, a comparison between the budget computed with the convolution and RSS approaches respectively is shown in Figure 21.

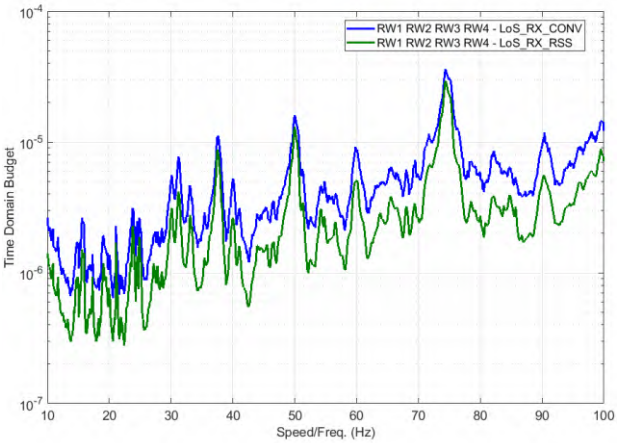


Figure 21: Comparison of budgets with CONV and RSS approaches

8. CONCLUSIONS

This paper has presented a frequency-domain methodology for spacecraft microvibration analysis, covering the complete process from harmonic disturbance characterization and transfer-path modelling to the derivation of system-level performance budgets. The method is specifically aimed at translating harmonic source disturbances into time-domain performance metrics that can be directly compared with probability-based microvibration requirements.

A key contribution of the methodology is the use of probability distributions and convolution-based summation to combine the effects of multiple DOFs, harmonics, and sources. Unlike conventional linear or RSS approaches, the proposed method explicitly accounts for the statistical nature of harmonic signals and enables the derivation of requirement-specific quantiles. Uncertainties can furthermore be propagated through the analysis using imprecise probability techniques, concentrating margins on the physical inputs rather than on the summation process itself.

The reaction wheel example demonstrates the practical application of the method and highlights its ability to identify both Gaussian-like and strongly non-Gaussian response distributions. The analysis also shows how critical contributions can be traced back to individual sources, harmonics, and force components, providing valuable insight for design optimization and requirement allocation.

Overall, the proposed methodology provides a more representative and traceable framework for microvibration budget derivation than conventional summation techniques, while remaining fully compatible with standard harmonic disturbance data and system frequency-response models. It therefore offers a practical approach for the prediction and management of microvibration performance in future spacecraft missions.

9. REFERENCES

[1] SSTL, Methodology for Analysis of Structure-Borne Microvibration, Final Presentation, TRP T719-083MC, ESA/ESTEC Contract No. 4000101914/10/NL/RA.

[2] Astrium, Methodology for Analysis of Structure-Borne Microvibration (METAMIC), Final Presentation, TRP T719-083MC, ESA/ESTEC Contract No. 4000101886/10/NL/RA.

[3] Haeussler, M., Kobus, D., and Rixen, D. J., “Combining Blocked Force Transfer Path Analysis and Dynamic Substructuring for Acoustic Design,” Proceedings of ICEDyn 2019, 2019.

[4] Boyle, F. A., et al., “Detecting Signal Structure from Randomly-Sampled Data,” IEEE/SP 14th Workshop on Statistical Signal Processing, 2007. DOI: 10.1109/SSP.2007.4301273.
[5] Ferson, S., Kreinovich, V., et al., Constructing Probability Boxes and Dempster-Shafer Structures, Sandia National Laboratories, Albuquerque, NM, USA, 2003.
[6] Rice S.O., "Probability Distributions for Noise Plus Several Sine Waves - The Problem of Computation," in IEEE Transactions on Communications, vol. 22, no. 6, pp. 851-853, June 1974, doi: 10.1109/TCOM.1974.1092281.
[7] Helstrom, C. W., “Computing the Distribution of Sums of Random Sine Waves and of Rayleigh-Distributed Random Variables by Saddle-Point Integration,” IEEE Transactions on Communications, Vol. 45, No. 11, pp. 1487-1494, 1997. DOI: 10.1109/26.649781.
[8] ESA, ESA Pointing Error Engineering (EPEE) Handbook, ESSB-HB-E-003, 2011.
[9] Limbourg, P., Imprecise Probability Propagation Toolbox, MATLAB Central File Exchange, 2020.

HYBRID MICROVIBRATION DAMPING PLATFORM WITH DATA-DRIVEN ROBUST ADAPTIVE DISTURBANCE REJECTION CONTROL

Elias Klauser[(1)] **and Alireza Karimi**[(2)]

[(1)] *CSEM SA, Rue Jaquet-Droz 1, CH-2002 Neuchâtel, Switzerland, elias.klauser@csem.ch*
[(2)] *Laboratoire d'Automatique, École Polytechnique Fédérale de Lausanne, CH-1015 Lausanne, Switzerland, alireza.karimi@epfl.ch*

KEYWORDS
Active Microvibration Damping Systems, Data-driven Control Design, Robust Adaptive Control

ABSTRACT

This paper presents the experimental validation of data-driven robust adaptive control methods on the hybrid microvibration damping platform MIVIDA. The proposed architecture combines online harmonic disturbance frequency estimation with LPV disturbance rejection control designed directly from experimentally identified frequency response functions. Robustness to mechanical parameter variations is ensured through an IQC-based formulation using elliptical uncertainty domains derived from experimental data. Experimental results demonstrate up to $19.74\,\mathrm{dB}$ performance improvement over classical disk-based uncertainty descriptions while preserving robust stability. Additional experiments with a laser-based payload show line-of-sight stabilisation improvements from $15.46\,\mathrm{dB}$ to $34.18\,\mathrm{dB}$. The results highlight the potential of data-driven uncertainty modelling and adaptive control for future spacecraft microvibration mitigation.

1. INTRODUCTION

1.1. Hybrid Microvibration Damping Platform (MIVIDA)

Future Earth observation, astronomy, and optical communication missions increasingly rely on instruments requiring sub-microradian pointing accuracy and exceptionally stable line-of-sight (LoS) performance. Achieving such levels of stability is challenging because spacecraft microvibrations generated by onboard equipment can propagate through the structure and induce disturbances at sensitive payload interfaces. Typical sources include reaction wheel assemblies, cryocoolers, propulsion systems, antenna pointing mechanisms, and solar-array drive mechanisms. As highlighted in several ESA studies, microvibration mitigation has become a critical system-level challenge for current and future high-performance spacecraft, requiring the combined consideration of disturbance generation, structural transmission paths, payload susceptibility, and active stabilisation strategies [1].

Historically, spacecraft microvibration mitigation has largely relied on passive isolation techniques. While these solutions provide robust broadband attenuation with limited complexity, increasingly stringent performance requirements are driving the development of active and hybrid active-passive isolation concepts capable of addressing low-frequency and narrowband disturbances. Recent European developments have explored configurable isolation architectures combining passive elements with active actuators and advanced control algorithms to achieve significantly improved disturbance rejection while maintaining acceptable mass, power, and reliability characteristics [2].

Within this context, CSEM has developed the hybrid microvibration damping platform (MIVIDA), a modular hybrid active-passive microvibration isolation platform dedicated to the experimental evaluation of advanced disturbance rejection concepts. The primary objective of the platform is to investigate the stabilisation of vibration-sensitive payloads exposed to multiple unknown time-varying perturbations. MIVIDA combines passive isolation elements with a set of proof-mass actuators (PMA) capable of generating forces and torques in all six degrees of freedom. A configurable payload interface enables the integration of different optical and inertial payloads, while high-sensitivity accelerometers located close to the payload provide the feedback measurements required for active disturbance rejection. Representative spacecraft disturbances are reproduced using an inertial excitation system acting as a controllable microvibration source. An illustration of the platform is shown in Figure 1.

The experimental investigations presented in this paper were performed at the Microvibration Characterisation Facility operated by CSEM in Neuchâtel, Switzerland [3]. The facility provides dedicated capabilities for both exported microvibration characterisation and susceptibility testing, allowing the experimental validation of advanced control methods under representative laboratory conditions.

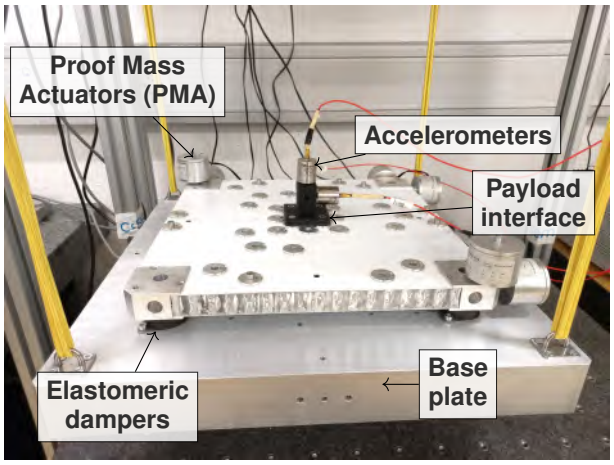


Figure 1. Hybrid microvibration damping platform MIVIDA developed at CSEM, Switzerland

1.2. Data-driven Robust Disturbance Rejection

Disturbance rejection is essential in control design, as external perturbations can degrade performance. When the disturbance model is known, the Internal Model Principle (IMP) enables adaptive rejection using observers. Alternatively, LPV models capture frequency variations via scheduling parameters [4]. A benchmark study [5] used an active suspension system to evaluate methods for the rejection of unknown, time-varying narrowband disturbances without direct measurement. These methods require accurate plant models, which are costly to identify.

Data-driven control is gaining traction due to improved computational power and sensors. It designs controllers directly from input-output data, avoiding modelling errors. Frequency domain methods such as loop shaping are widely used, and recent advances use convex optimisation for robust controller synthesis [6]. LPV extensions via gridding have been proposed [7], even if most methods only ensure local stability. More recently, data-driven robust control approaches have sought to reduce the conservatism associated with classical uncertainty descriptions derived from experimental measurements. In [8], uncertainty is identified directly from measured frequency response functions (FRFs) and represented using structured elliptical domains that capture the directional variability of the experimental data. By reformulating these uncertainty sets as Integral Quadratic Constraints (IQCs), robust stability constraints can be incorporated directly into frequency-domain convex optimisation problems. The resulting framework enables simultaneous optimisation of nominal performance and robustness while providing a less conservative representation of FRF variability than traditional disk-based uncertainty models.

IQC theory offers a framework for analysing systems

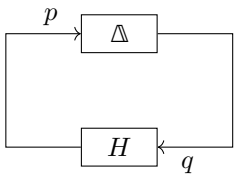


Figure 2. Basic feedback configuration

with uncertainties [9]. While well-developed in model-based contexts, its use for data-driven control design is emerging [10]. While well established in model-based robust control, its application to data-driven controller design remains an active research topic [10]. Recent developments demonstrate that experimentally identified uncertainty descriptions can be embedded directly into IQC-based synthesis procedures, thereby enabling robustness guarantees to be obtained without requiring an explicit parametric model of the plant [8].

An LPV controller synthesis approach is developed for the adaptive rejection of sinusoidal disturbances with varying harmonic frequencies, reducing computational complexity over existing approaches [11]. The LPV controller, designed using the frequency response function (FRF) of a linear time-invariant (LTI) multiple-input multiple-output (MIMO) system, stabilises the system for fast disturbance frequency variations. Global stability is achieved using IQCs to represent frequency variations. The LPV controller is computed by solving a convex optimisation problem in the frequency domain.

1.3. Paper Outline

The remainder of the paper is organised as follows: First, the IQC formalism, the basic problem statement and the data-driven control design algorithm for harmonic disturbance rejection and the data-driven robust control design framework are briefly reviewed (Section 2). Then, the results of the experimental validation campaign are presented in Section 3. An experiment is carried out to showcase the control robustness against mechanical system uncertainties. The benefits of using elliptical uncertainty domains are demonstrated by comparing the achieved performance with that obtained using conventional robust design approaches. In addition, the LoS stability of a laser-based payload is assessed. An accelerometer-based and a laser-based closed loop are implemented. The first closed loop simulates the hybrid platform in its classic use and the second closed loop corresponds to a simplified free space optic (FSO) stabilisation system.

2. PRELIMINARIES

2.1. Integral Quadratic Constraints

In the developments that follow, only discrete-time systems are considered. Two discrete-time signals p and

q are said to satisfy the IQC defined by a multiplier Π, if

$$\int_{\Omega} \begin{bmatrix} P(e^{j\omega}) \\ Q(e^{j\omega}) \end{bmatrix}^{*} \Pi(e^{j\omega}) \begin{bmatrix} P(e^{j\omega}) \\ Q(e^{j\omega}) \end{bmatrix} d\omega \geq 0 \qquad (1)$$

where $P(e^{j\omega})$ and $Q(e^{j\omega})$ are the Fourier transform of the signals p and q, respectively, and $\Omega := [-\pi/T_s, \pi/T_s)$ with the sampling time T_s [12]. From [9, Theorem 1], the feedback connection between $H \in \mathcal{RH}_\infty$ and a bounded causal operator $\mathbb{\Delta}$ (see Figure 2) is stable if,

1. the interconnection of H and $\tau\mathbb{\Delta}$ is well-posed for all $\tau \in [0, 1]$;
2. $\tau\mathbb{\Delta}$ satisfies the IQC defined by Π for all $\tau \in [0, 1]$;
3. The following inequality is satisfied:

$$\begin{bmatrix} H(e^{j\omega}) \\ I \end{bmatrix}^{*} \Pi(e^{j\omega}) \begin{bmatrix} H(e^{j\omega}) \\ I \end{bmatrix} \prec 0 \qquad \forall\omega \in \Omega \qquad (2)$$

Remark 1 *If the upper left corner of Π is positive semi-definite and the lower right corner is negative semi-definite, then using [9, Remark 2], $\tau\mathbb{\Delta}$ satisfies the IQC defined by Π for all $\tau \in [0, 1]$ if and only if $\mathbb{\Delta}$ satisfies the IQC.*

Numerous forms of multiplier matrices Π for different uncertainty types have been proposed in literature. For arbitrarily fast time-varying scalar uncertainties, i.e. $\mathbb{\Delta}(k) = \delta(k)I$, $|\delta(k)| \leq \eta, \forall k \in \mathbb{R}_+$, a stationary multiplier Π can be defined as [13]:

$$\Pi = \begin{pmatrix} \eta^2 D & E \\ E^T & -D \end{pmatrix}, \qquad (3)$$

where $D = D^T \succeq 0,\ E = -E^T$.

A system analysis step can be performed using (2) to find a multiplier matrix Π which satisfies the constraint. From (3), the upper bound η on $|\delta(k)|$ can be identified allowing to compute bounds on the uncertainty block $\mathbb{\Delta}(k)$. Similarly, the obtained IQC can be used as a control design constraint to guarantee robustness for a desired fixed upper bound η.

2.2. Basic Problem Statement

The system to be controlled is a multivariable linear time-invariant (LTI-MIMO) plant P_2 referred to as secondary path with n_u input channels and n_y output channels. The FRF matrix can be acquired from classical system identification experiments [14]. Given n_u sets of finite sampled input/output data which can be acquired from n_u open-loop identification experiments, the corresponding discrete-time FRF can be estimated using a persistently exciting input signal u:

$$P_2(e^{j\omega}) = \left[\sum_{k=0}^{M-1} \mathbb{Y}(k) e^{-j\omega T_s k}\right] \left[\sum_{k=0}^{M-1} \mathbb{U}(k) e^{-j\omega T_s k}\right]^{-1} \qquad (4)$$

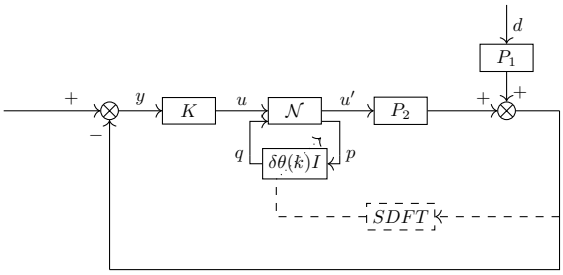


Figure 3. Control system architecture with LTI controller part

where M is the number of data points and each column of $\mathbb{U}(k)$ and $\mathbb{Y}(k)$ represents respectively the inputs and outputs at the time sample k at one experiment. It is assumed that $P_2(e^{j\omega})$ is bounded for all frequencies $\omega \in \Omega$. The estimation errors can be considered as model uncertainty and taken into account for the controller design, however, they are neglected to focus on the main subject of this paper. In addition, an LTI perturbation model $P_1(e^{j\omega})$ representative of the primary path can be used to model the propagation of an exogenous perturbation signal d to the measurement y (see Fig. 3). For the presented control method, the disturbance signal d is supposed to contain sinusoidal components with an unknown time-varying harmonic frequency $\rho(k)$. The variation of the frequency can be large and fast but occurs seldom. The control objective is to asymptotically reject this disturbance.

2.3. Data-driven LPV Control for Harmonic Disturbance Rejection

What follows is a summary of the work presented in [11]. Due to the time-varying nature of the disturbance frequency, P_2 shall be controlled by an LPV controller. We choose the LPV controller as the interconnection of an LTI controller $K(z)$ in series with a time-varying filter $N(z, \theta(k))$:

$$K_N(z, \theta(k)) = K(z)N(z, \theta(k)),$$

where $\theta(k) \in \Theta$ is the scheduling parameter. The architecture of the control system is presented schematically in Figure 3. A time-varying filter $N(z, \theta(k))$ for a fixed value of $\theta(k) = \theta_c$ ensures asymptotic performance for disturbance rejection. In accordance with the IMP, $N(z, \theta_c)$ is chosen as an approximation of the z-transform of a sinusoidal signal. Hence, in the steady-state case with θ_c constant, disturbance rejection is achieved based on the IMP. The scheduling parameter $\theta(k)$ is chosen such that $\theta(k) = -2\cos(T_s\rho(k))$ where $\rho(k)$ is the time-varying frequency of the sinusoidal disturbance. The scheduling parameter can be defined around a fixed frequency $\bar{\theta}$ as $\theta(k) = \bar{\theta} + \delta\theta(k)$ with $|\delta\theta(k)| \leq \eta$ such that $[\theta_{\min}, \theta_{\max}] = [\bar{\theta} - \eta, \bar{\theta} + \eta]$. A sliding discrete Fourier transform (SDFT) is used for the estimation of the unknown harmonic disturbance frequency $\rho(k)$. The objective is to guarantee the

closed-loop stability for fast variations of the estimated value. For a fixed stationary value of the scheduling parameter $\theta_c = \bar{\theta} + \delta\theta_c$, $N(z, \theta_c)$ can be defined as:

$$\begin{aligned} N(z,\theta_c) &= \frac{1}{1+\beta(\bar{\theta}+\delta\theta_c)z^{-1}+\beta^2 z^{-2}} \\ &= \frac{N(z,\bar{\theta})}{1+\beta z^{-1} N(z,\bar{\theta})\delta\theta_c}, \end{aligned} \tag{5}$$

where β is a scalar factor allowing to adjust the damping of the resonance frequency according to the desired attenuation performance. As shown in Equation (5), $N(z, \theta_c)$ can be represented as a feedback loop with $N(z, \bar{\theta})$ in the forward path and $\beta z^{-1}\delta\theta_c$ in the feedback. Then $\delta\theta_c$ can be pulled out as an uncertainty block in a lower fractional representation (LFR).

The time-invariant part of the controller is parameterised by $K(z) = Y(z)^{-1}X(z)$ and is computed by a convex optimisation problem to guarantee closed-loop stability for all variations in the scheduling parameter $\theta(k)$.

An LFR can be computed on the basis of an augmented plant mapping q and the control input u to p and y_2 the output of P_2. This augmented plant does not include the disturbance d and will be used exclusively to define a convex set of stabilising controllers without defining any performance objectives.

A stability condition for arbitrarily fast variation of the scheduling parameter is formulated using an IQC-based constraint. This constraint can be converted into a set of linear matrix inequalities (LMIs). These LMIs can be integrated into a feasibility problem allowing to calculate a stabilising controller $K(z)$ for a fixed value of η. A feasible but undesirable solution to this problem is the controller $K = 0$. To avoid this solution, a minimal steady-state gain $g_{\min}$ of K can be imposed.

Based on those constraints, an optimisation problem to maximise η can be defined. The objective is to compute a controller $K(z)$ which guarantees robust stability for all $\theta(k)$ satisfying $|\delta\theta(k)| \leq \eta$. The detailed development and the complete control design algorithm is presented in [11].

2.4. Data-driven Robust Control using Elliptical Uncertainty Domains

In [8], a data-driven robust control framework is proposed in which uncertainty is identified directly from a set of measured FRFs and incorporated into controller synthesis through IQCs. Rather than representing modelling uncertainty by frequency-dependent disk domains, the method computes a nominal frequency response model together with an element-wise elliptical uncertainty set that tightly encloses all available measurements. The nominal model and uncertainty ellipses are obtained by solving a convex optimisation problem that minimises the total uncertainty area while ensuring consistency with the measured FRFs. For each transfer function element, the uncertainty set is defined as

$$\|A_{kl}(\omega)\mathcal{C}(\Delta_{kl})\|_2 \leq 1, \tag{6}$$

where A_{kl} parameterises the ellipse and $\mathcal{C}(\cdot)$ separates the real and imaginary parts of the complex uncertainty. The resulting uncertainty description is generally less conservative than classical disk-based representations because it captures the anisotropic distribution of the measured FRF variations.

The central contribution of the work is the transformation of these elliptical uncertainty sets into an equivalent IQC representation. For each input-output pair, an IQC multiplier is derived directly from the ellipse parameters, yielding a dynamic multiplier of the form

$$\Pi_{kl}(j\omega) = \begin{bmatrix} 1 & 0 \\ 0 & -\bar{A}_{kl}^{*}(j\omega)\bar{A}_{kl}(j\omega) \end{bmatrix}. \tag{7}$$

The individual multipliers are then assembled into a structured block-diagonal IQC describing the complete MIMO uncertainty model. Using a split representation of the uncertainty block, the IQC condition is converted into a frequency-domain LMI that can be added directly to a convex data-driven controller synthesis problem. This enables simultaneous optimisation of nominal performance and robust stability with respect to all admissible FRF variations.

3. EXPERIMENTAL VALIDATION OF DATA-DRIVEN CONTROL DESIGN ALGORITHMS

3.1. Robust adaptive microvibration rejection

A controller for the MIVIDA platform was calculated by combining the methods introduced in Section 2.3 and Section 2.4 to obtain an LPV controller for adaptive disturbance rejection that is robust to screw torque uncertainties in the mechanical setup. The elliptical uncertainty set covering a multimodel identified from different screw torques applied, as presented in [8], is used for the control design. The controller is computed with the method presented in [11], and a robustness constraint in the form of [8, Eq. (21)] is added to the optimisation problem.

The closed-loop sensitivity function computed with the resulting controller for different values of θ is given in Figure 4. A value of $\delta\rho_{\max} = 7\,\mathrm{Hz}$ was achieved. This value is reduced compared to the case where no mechanical uncertainties are considered, for which a value of $\delta\rho_{\max} = 16\,\mathrm{Hz}$ was reported in [11, Section 4]. The reduction in admissible scheduling range can be attributed to the additional gain and phase uncertainty introduced by variations in the screw torque. In order to guarantee robust stability for all considered mechanical configurations, the controller must sacrifice disturbance rejection bandwidth and therefore exhibits a reduced robustness margin with respect to frequency variations.

The time-domain signal comparing open- and closed-

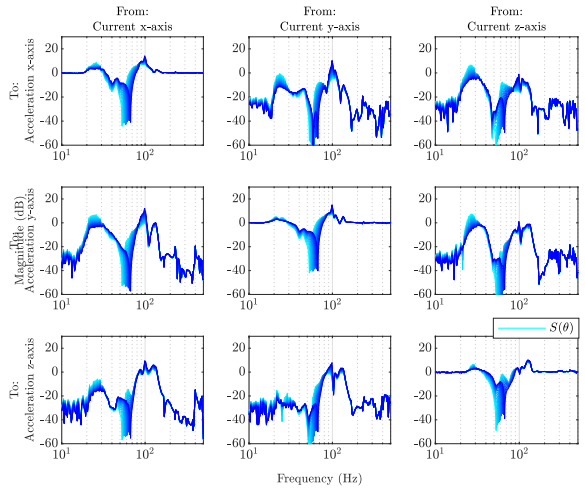


Figure 4. Closed-loop sensitivity function $S(\theta)$

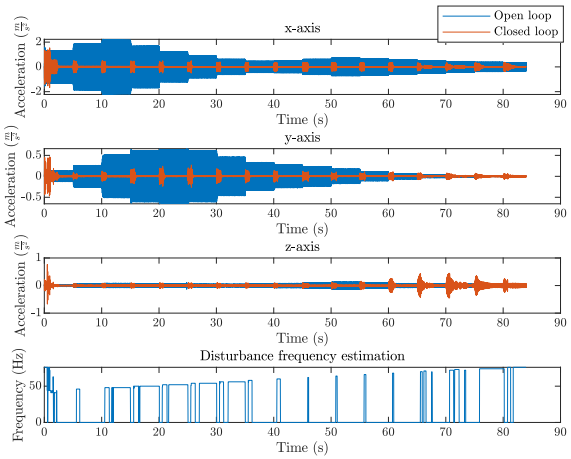


Figure 5. Comparison of open loop with closed loop disturbance rejection, the estimated perturbation frequency is shown below

loop operation is shown in Figure 5. The experiment was carried out up to a value of $\delta\rho_{\max} = 14\,\mathrm{Hz}$. A stable closed loop was experimentally observed for this value, demonstrating that the controller preserves stability beyond the nominal design range. However, the disturbance attenuation is no longer satisfactory for frequencies approaching $\rho(k) = \bar{\rho} \pm \delta\rho_{\max}$, as can be seen from the attenuation values reported in Section 3.1. This behaviour is expected since the controller operates closer to the extremal uncertainty conditions considered during synthesis, reducing the achievable rejection performance while maintaining robust stability.

To assess the quality of the obtained result, a second robust adaptive controller was computed using a classical disk uncertainty description. The attenuation performances achieved with this controller are given in parentheses in Section 3.1. The use of elliptical uncertainty domains leads to a performance increase of up to $19.74\,\mathrm{dB}$ compared with the controller designed using disk uncertainty domains. In the most favourable case, this corresponds to more than one order of magnitude reduction of the residual vibration amplitude. For some operating conditions, the disturbance is even amplified by up to $10.44\,\mathrm{dB}$ when using disk uncertainty domains, as no better-performing robust controller could be found for the associated uncertainty set. Such amplifications are significantly reduced when using elliptical uncertainty domains.

The superior performance obtained with elliptical uncertainty domains can be explained by the additional degree of freedom provided by the two independently tunable semi-axes in the Nyquist plane. In contrast to disk uncertainty domains, which enforce an isotropic uncertainty description through a single radius parameter, elliptical domains can more closely approximate the measured FRF variability, thereby reducing conservatism and improving closed-loop performance. The conservatism associated with disk uncertainty domains restricts the achievable closed-loop bandwidth and disturbance attenuation performance, whereas elliptical domains provide a substantially tighter uncertainty description. The experimental results demonstrate the effectiveness of the elliptical uncertainty representation for robust controller synthesis.

During the experimental campaign, no instability was observed for any of the mechanical configurations used to identify the uncertainty model. This confirms that the identified uncertainty set provides a suitable description of the plant variability and that the IQC constraint successfully guarantees robust stability for the considered mechanical conditions.

When comparing the results in Section 3.1 with the attenuation values obtained without considering robustness to mechanical uncertainties [11], it can be observed that robustness is achieved at the expense of a reduction in disturbance rejection performance. The trade-off between robustness and performance is a fundamental aspect of robust control design. Consequently, the choice of an uncertainty domain of appropriate size is critical to achieving a satisfactory balance between disturbance attenuation and robustness guarantees.

3.2. Line-of-Sight Stability Evaluation

An experimental evaluation of the line-of-sight (LoS) stability using a dedicated laser-based payload was performed [15]. The objective was to assess whether the data-driven LPV disturbance rejection approach could improve the pointing stability of a representative

Frequency $\rho(k)$	Axis	Attenuation Performance (dB)		
		Ellip.	Disk	Nom.
$\bar{\rho}$ 60 Hz	X	25.58	22.94	50.40
	Y	36.04	28.17	44.07
	Z	16.52	15.54	36.06
$\bar{\rho} - \delta\rho_{\max}$ 46 Hz	X	31.48	12.16	25.87
	Y	31.43	11.69	24.31
	Z	13.97	-10.44	15.30
$\bar{\rho} + \delta\rho_{\max}$ 74 Hz	X	19.12	15.35	38.38
	Y	0.82	-0.63	10.10
	Z	-3.75	-6.43	27.13

Table 1. Attenuation performance achieved at different values of $\rho(k)$. The proposed controller uses elliptical uncertainty domains. The disk-based controller is computed using classical disk uncertainty domains, while the nominal result corresponds to the controller reported in [11], where mechanical uncertainties are not considered.

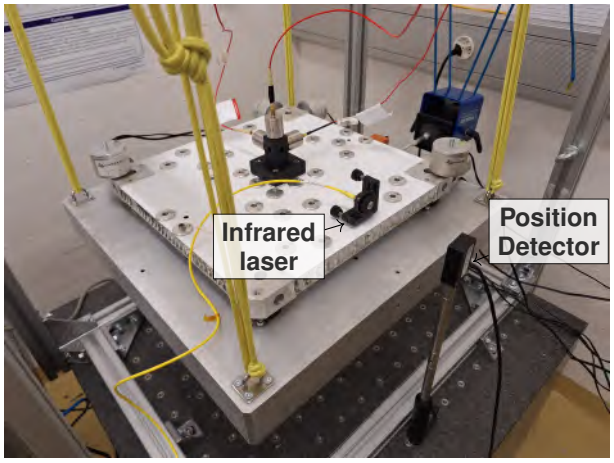


Figure 6. Hybrid microvibration isolation platform with laser-based payload

optical payload under harmonic disturbances.

The experimental setup consisted of an infrared laser mounted on the payload interface of the MIVIDA platform and a four-quadrant position detector fixed to the granite table. A picture of the setup is given in Figure 6. The detector measures the horizontal and vertical displacement of the laser spot through differential photodiode measurements, thereby providing a direct estimate of the beam motion. The arrangement was intended to emulate a spaceborne laser pointing application requiring high LoS stability. Two configurations were investigated, with the laser aligned successively along the platform x- and y-axes.

Since the addition of the laser payload modifies the mass and inertia properties of the platform, the dynamic behaviour of the system differs from that of the baseline MIVIDA configuration. Consequently, a new system identification experiment was conducted and a dedicated controller was synthesized using the data-driven LPV design method presented earlier in the paper. For this purpose, the frequency response function (FRF) of the modified system was identified using the proof-mass actuator command currents as inputs and the accelerometer signals as outputs. The resulting FRF served as the basis for the controller design.

The LoS performance was assessed by comparing open-loop and closed-loop measurements of the laser displacement while a harmonic disturbance was injected through the external shaker. The accelerometer-based controller was designed with a controller order of $n = 30$ and a nominal disturbance frequency of $\bar{\rho} = 60\,\mathrm{Hz}$. The synthesis procedure yielded a controller capable of maintaining stability for disturbance-frequency variations up to $\delta\rho_{\max} = 14\,\mathrm{Hz}$.

For the experimental validation, the disturbance frequency was varied over the interval 44–$74\,\mathrm{Hz}$, with increments of $2\,\mathrm{Hz}$ every five seconds. Comparison of the open-loop and closed-loop responses showed a clear reduction of the laser beam motion when the controller was activated. At the nominal frequency of $60\,\mathrm{Hz}$, attenuation values of approximately $15.5\,\mathrm{dB}$ were obtained for both measured tilt directions. At the lower frequency bound ($46\,\mathrm{Hz}$), attenuation remained above $11\,\mathrm{dB}$, whereas at the upper bound ($74\,\mathrm{Hz}$) the achieved attenuation decreased to approximately 2–$4\,\mathrm{dB}$. Overall, the results demonstrated that the data-driven LPV controller significantly improved the LoS stability of the laser payload over a broad range of harmonic disturbance frequencies, with the highest performance obtained near the design frequency.

4. CONCLUSION

The presented results demonstrate data-driven robust adaptive control for active microvibration mitigation under uncertain operating conditions. By exploiting elliptical uncertainty domains identified directly from experimental data, up to $19.74\,\mathrm{dB}$ higher disturbance attenuation can be obtained compared to conventional disk-based uncertainty descriptions. A testing campaign using a laser-based payload is performed that assesses the LoS stability of the laser. An accelerometer-based and a laser-based closed loop are implemented. Experimental results show that the attenuation performance can be increased from $15.46\,\mathrm{dB}$ to $34.18\,\mathrm{dB}$ for the nominal case when using the laser position measure in feedback.

The experimental results obtained on the MIVIDA platform demonstrate that data-driven uncertainty modelling enables improved disturbance attenuation while preserving robust stability in the presence of mechanical variations. The proposed approach provides a promising route towards robust adaptive microvibration mitigation for future spacecraft, as parameter variations arising from assembly tolerances, thermal ef-

fects, ageing, or payload replacement can be incorporated directly from experimental data without requiring a detailed parametric model. While the results highlight the fundamental trade-off between robustness and achievable disturbance rejection performance, they also demonstrate the potential of data-driven uncertainty descriptions for future high-performance vibration isolation systems.

REFERENCES

1. G. Smet and S. Patti, "A Mechanisms Perspective on Microvibration – Good Practices and Lessons Learned," in *Proceedings of the 44th Aerospace Mechanisms Symposium*, NASA Glenn Research Center, 2018.

2. A. Garcia, T. Gust, E. Basata, T. Gersting, M. Deka, S. Thiele, M. Salah, M. B. Koerner, T. Runte, and M. Gonzalez, "VIBES: Visionary Ingenuity Boosting European Spacecraft. Managing microvibrations for the future of spaceflight," *Archive of Mechanical Engineering*, pp. 183–197, Feb. 2023.

3. G. Borque Gallego, E. Klauser, and E. Onillon, "CSEM Micro-Vibration Characterisation Facility - Susceptibility to Received Accelerations," in *ESMATS 2023*, Warsaw, PL, Sep. 2023.

4. P. Ballesteros and C. Bohn, "Disturbance rejection through LPV gain-scheduling control with application to active noise cancellation," *IFAC Proceedings Volumes*, vol. 44, no. 1, pp. 7897–7902.

5. I. D. Landau, A. Castellanos Silva, T.-B. Airimitoaie, G. Buche, and M. Noe¨, "Benchmark on adaptive regulation—rejection of unknown/time-varying multiple narrow band disturbances," vol. 19, no. 4, pp. 237–252.

6. A. Karimi and C. Kammer, "A data-driven approach to robust control of multivariable systems by convex optimization," *Automatica*, vol. 85, pp. 227–233, Nov. 2017.

7. P. Schuchert and A. Karimi, "Frequency-domain data-driven position-dependent controller synthesis for cartesian robots," *IEEE Transactions on Control Systems Technology*, vol. 31, no. 4, pp. 1855–1866, 2023.

8. V. Gupta, Elias Klauser, and Alireza Karimi, "Data-driven IQC-Based Robust Control Design for Hybrid Micro-disturbance Isolation Platform," in *2023 62nd IEEE Conference on Decision and Control (CDC)*, Dec. 2023, pp. 6079–6085.

9. A. Megretski and A. Rantzer, "System analysis via integral quadratic constraints," *IEEE Transactions on Automatic Control*, vol. 42, no. 6, pp. 819–830, Jun. 1997.

10. T. Bloemers, T. Oomen, and R. Toth, "Frequency Response Data-Driven LPV Controller Synthesis for MIMO Systems," *IEEE Control Systems Letters*, vol. 6, pp. 2264–2269, 2022.

11. E. Klauser and A. Karimi, "Data-driven lpv control for harmonic disturbance rejection in a hybrid isolation platform," *IEEE Transactions on Control Systems Technology*, pp. 1–11, 2025.

12. J. Veenman, C. W. Scherer, and H. Köroğlu, "Robust stability and performance analysis based on integral quadratic constraints," *European Journal of Control*, vol. 31, pp. 1–32, Sep. 2016.

13. J. M. Fry, D. Abou Jaoude, and M. Farhood, "Robustness analysis of uncertain time-varying systems using integral quadratic constraints with time-varying multipliers," vol. 31, no. 3, pp. 733–758.

14. R. Pintelon and J. Schoukens, *System Identification: A Frequency Domain Approach*, 2nd ed. John Wiley & Sons, Ltd, 2012.

15. E. Klauser and A. Karimi, "Experimental Validation of Data-Driven Control Design Methods for Hybrid Microvibration Damping Platform," Lausanne, Switzerland, 2025, p. 8.

MVIS MICRO-VIBRATION ISOLATOR - OHB INDUSTRIAL APPLICATION

Alessandro Paci [(1)], Jonathan Senft [(1)], Nicola Riva [(1)], Harald Segelke [(1)], Antoine Pasquier [(1)], Christian Reeker [(1)], Valerio Illuminati [(1)], Jan Torben Runte [(1)], Celalettin Yumus [(1)], Quentin Bianco [(2)], Mohamed El Othmani [(2)], Lauren Mallet[(2)]

[(1)] OHB Systems AG, Universitätsallee 27-29, 28359, Bremen, Germany,
Email: {alessandro.paci; jonathan.senft, nicola.riva, harald.segelke, antoine.pasquier, christian.reeker, valerio.illuminati, torben.runte, celalettin.yumus}@ohb.de

[(2)] SMAC SAS, 66 Imp. Edouard Branly, 83130 La Garde, Toulon, France
Email: {quentin.bianco, mohamed.elothmani, lauren.mallet}@smac.fr

KEYWORDS

Micro-vibration, isolator

ABSTRACT

During spacecraft development, micro-vibrations induced by onboard mechanical and electrical equipment constitute a significant engineering challenge. Although typically of low amplitude, these disturbances can adversely affect the performance of sensitive subsystems during mission operations, particularly those requiring high pointing stability and measurement accuracy, such as star trackers, scientific payloads, and communication links (e.g. laser terminals). If not adequately controlled, micro-vibrations may jeopardize the achievement of mission objectives and, consequently, mission success.

Over the past year, OHB System AG, supported by SMAC SAS, has been developing an in-house micro-vibration isolation system (MVIS) for application in ongoing and future projects.

This paper presents OHB System experience in developing MVIS and qualifying for Space Flights.

1. INTRODUCTION

Micro-vibration excitations are typically generated by moving or rotating S/C equipment, such as:

- Reaction Wheels
- Gyros
- Cryocoolers
- Pumps and Compressors

Micro-vibrations are characterized by very low amplitude (from micrometres down to nanometres) and by a wide frequency range (from 1Hz to several kHz). Despite their low magnitude, these persistent disturbances can impair the stability and pointing accuracy of sensitive instruments and, if not adequately mitigated, can jeopardize the success of the mission.

To ensure compliance with spacecraft performance requirements, OHB System has developed a Micro Vibration Isolation System (MVIS) designed to mitigate the micro-vibration disturbances induced by reaction wheels (RWs).
The MVIS is designed for installation between the spacecraft (S/C) and the reaction wheel (RW), providing passive isolation of micro-vibration disturbances and thereby limiting their transmission to the spacecraft and its sensitive subsystems. A schematic is shown in Figure 1-1.

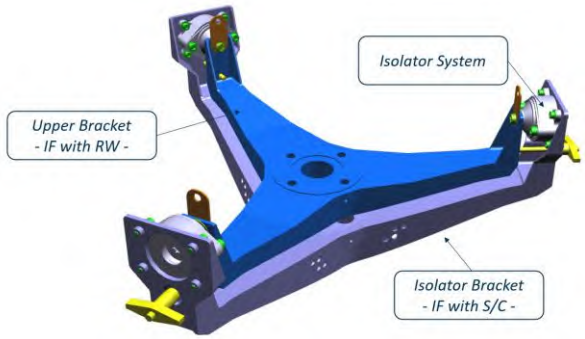


Figure 1-1 MVIS Schematic

The System is composed by three main parts:

- Upper Bracket (IF to RW)
- Isolator System
- Isolator Bracket (IF to S/C)

The core element of the MVIS is the isolator assembly, developed by SMAC SAS based on proven heritage from previous projects. The performance of the system and its ability to withstand the mechanical loads encountered during launch have been verified through a comprehensive qualification test campaign. The following chapters present an overview of the MVIS design, development, and qualification activities, with particular emphasis on its micro-vibration isolation performance and compliance with launch environment requirements:

Chapter 2 illustrates the main requirements which drove the MVIS development.

Chapter 3 provides a description of MVIS design with a focus on the isolator systems produced by SMAC SAS.

Chapter 4 describes the test campaigns performed to characterize the MVIS performances and to qualify it for space flight

Finally, Chapter 5 presents the future activities and applications of this system

2. REQUIREMENTS

MVIS has been designed to achieve two main objectives:

- Withstand launch environment loads
- Guarantee the requested micro-vibration isolation performances.

To meet both objectives, resonance frequency requirements were derived and subsequently used to guide the design of the MVIS isolator system. The first eigenfrequency of the MVIS must be low enough to ensure effective micro-vibration isolation, while remaining sufficiently high to prevent coupling with spacecraft structural modes and launcher excitations. Furthermore, the MVIS has been designed to withstand the specified launch load environments, including quasi-static loads, sine vibration, random vibration, and shock loads, thereby enabling its qualification for spaceflight applications.

3. MVIS ISOLATOR SYSTEM

The core part of MVIS is the isolator system.

The Original plan was to develop a single elastomer isolator system. However, such design could not meet stiffness requirement due to elastomer nonlinear behaviour. Elastomers stiffness is indeed sensitive to the intensity of the applied load, and this causes material:

- to react stiffer under the application of low intensity load
- to react softer under application of higher load.

Therefore, an elastomer which guarantees desired frequency under launch conditions, would react stiffer in orbit and, consequently, would jeopardize the micro vibration isolation performance. At the same time, an elastomer which guarantees the required stiffness in orbit, would react softer during launch, and, consequently, would risk dynamic coupling with launch main mode and damages due to high strain rate.

To find a working solution, SMAC SAS proposed a dual isolator concept composed by two elastomers with different stiffness.

- A **softer elastomer** guarantees a good micro-vibration isolation performance.

- A **stiffer elastomer** protects the softer elastomer from launch loads and prevents it to experience severe deformation rate which could compromise the “in-orbit” performance.

This design enables MVIS to meet both its main objectives and results in high nonlinear behaviour, which has been characterised through an extensive testing programme.

4. MVIS TEST CAMPAIGN

A test campaign has been performed to:

- characterize MVIS micro-vibration performance
- qualify MVIS to launch environments

The test campaign consisted in the following runs:

- Vibration under 0g
- Sine
- Random
- Shock

The Vibration under 0g aims to characterize the MVIS´ “in orbit” performances. Vibration was applied along the MVIS´ three directions X, Y and Z and test was performed keeping RW suspended to simulate a spacecraft operational condition (0g).

Sine, Random and Shock tests aim to verify the system´s capability to withstand launch environmental loads. Sine and Random Vibrations were performed in two different conditions:

- under Gravity
- under application of Launcher maximum QSL

Vibrations were performed along the MIVS´ X, Y and Z directions and, in order to replicate more closely a configuration expected during launch, a further vibration was performed with the MVIS oriented at 45° with respect to the vertical direction (see Figure 4-1).

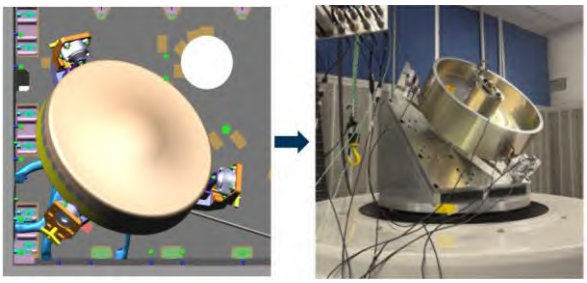


Figure 4-1 MVIS 45° orientation

Shock solicitations have been performed only under gravity condition instead, with load applied only along X, Y and Z. See Table 4-1

Table 4-1 MVIS Test Campaign overview

RUN	Test Condition			Test Directions			
	0g	Under Grav	Launch QSL	X	Y	Z	45°
micro-Vib	✓	✗	✗	✓	✓	✓	✗
SINE	✗	✓	✓	✓	✓	✓	✓
RND	✗	✓	✓	✓	✓	✓	✓
SHOCK	✗	✓	✗	✗	✗	✗	✗

Furthermore, all tests, except for shock, have been performed with MVIS equipped in two different ways:

- with a RW Dummy having same mass and inertia of the flight RW
- with RW Engineering Model (EM), to assess the impact of RW internal dynamics on MVIS performance.

Shock test has been performed only with MIVS equipped with RW Dummy instead (see Figure 4-2 and Table 4-2).

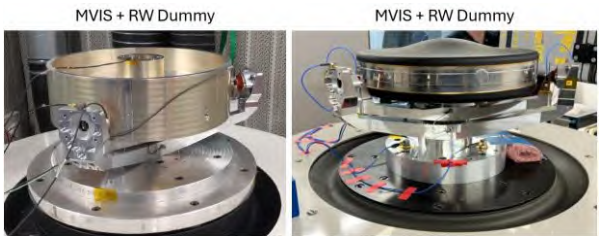


Figure 4-2 MVIS equipped with RW Dummy (Left) and RW EM (Left)

Table 4-2 MVIS Test Campaign – January 2026

RUN	Tested Item	
	MVIS + RW Dummy	MVIS + RW EM
micro-Vib	✓	✓
SINE	✓	✓
RND	✓	✓
SHOCK	✓	✗

Test Campaign results are detailed in the next subchapters.

4.1 VIBRATION UNDER 0G

Test consisted in applying a sine sweep of 0.05g from 10Hz to 1000Hz along MIVS´ X, Y and Z directions. Vibration has been applied at MVIS IF with S/C for the configuration equipped with RW Dummy (reverse micro-vibration). Vibration has been applied at RW IF (direct micro-vibration) for the configuration equipped with RW EM instead. In both the cases, RW was lifted to simulate an "in-orbit" configuration (0g). See Figure 4.1-1.

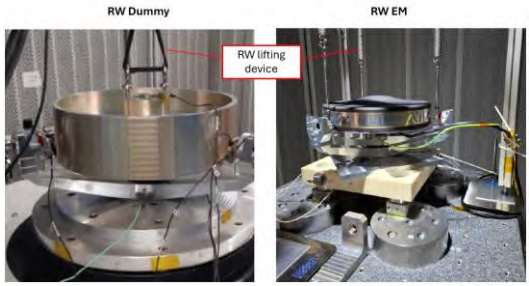


Figure 4.1-1 RW Dummy and RW EM lifted to simulate 0g configuration

The Frequency Response Functions (FRFs) measured during the reverse and direct micro vibration test are shown in the following pictures, See Figure 4.1-2 and Figure 4.1-3 respectively

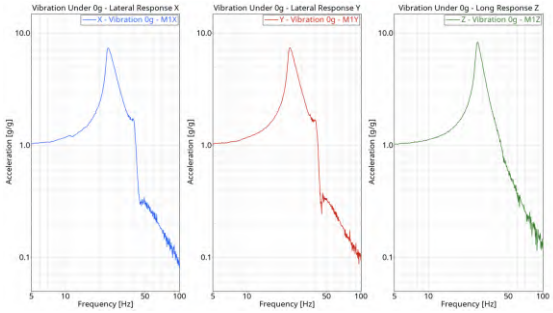


Figure 4.1-2 Vibration under 0g – RW Dummy, FRFs measured at MVIS IF

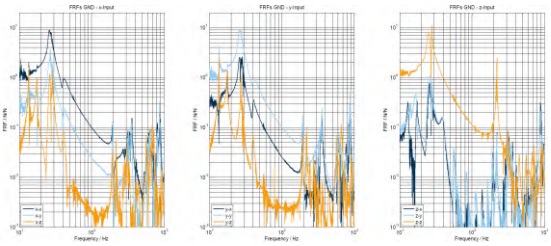


Figure 4.1-3 Vibration under 0g – RW EM, FRFs measured at MVIS IF

Results show how the FRFs measured in the two configurations are perfectly aligned, with only minor differences observed. This result demonstrates that RW dynamics do not affect the MVIS´ micro-vibration performance.

These Hard Mounted FRFs have been used to quantify the MVIS´ capability in attenuating the

disturbances injected from RW into the S/C. The results confirm the capability of MVIS to attenuate these disturbances to the specified micro-vibration isolation performances. Pictures below show a comparison between the RW disturbances transmitted into the S/C with and without the MVIS. (light and dark blue, respectively). See from Figure 4.1-4 to Figure 4.1-6

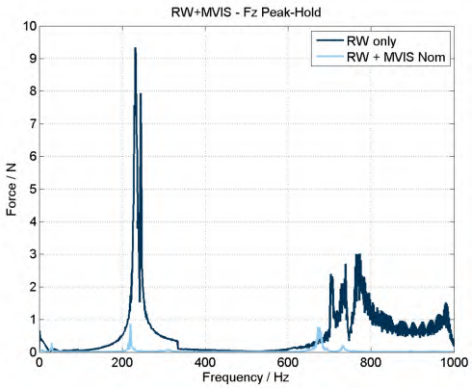


Figure 4.1-4 RW Axial Force transmitted to S/C attenuation

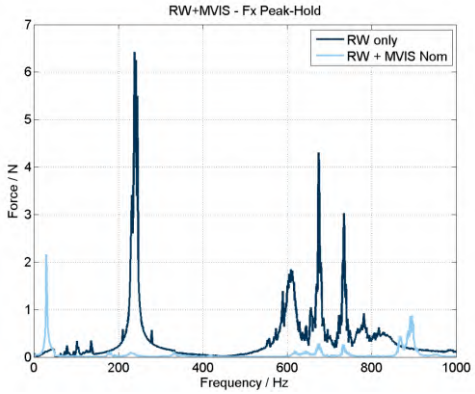


Figure 4.1-5 RW Lateral Force transmitted to S/C attenuation

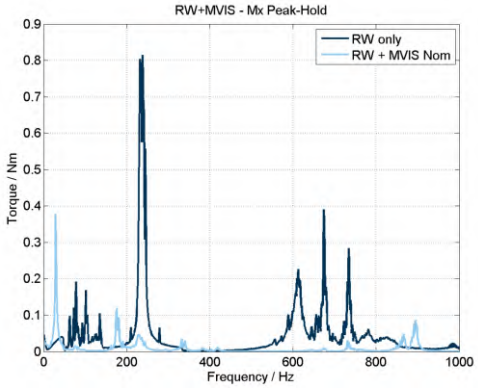


Figure 4.1-6 RW Bending moment transmitted to S/C attenuation

Results confirm the effectiveness of MVIS performance.

4.2 SINE TESTING

Sine vibration was performed by applying at MIVS Interface a Sine spectrum representative of the one expected during a S/C PFM vibration test. SINE Vibration was performed under two different conditions:

- under Gravity
- under Launcher (A6) maximum QSL (6.5g)

Vibration was performed along the MVIS´ X, Y and Z directions. Furthermore, an additional vibration was performed with MVIS oriented at 45° with respect to the vertical direction. For each direction, Low Level and Intermediate Levels were performed before Qualification:

1. LL – Low Level – Sine Sweep 0.05g
2. IL1 – Inter. Level I – Sine Sweep 1.0g
3. IL2 – Inter. Level II – Sine Sweep 2.0g
4. QL – Qual. Level – Primary Notched

This was done not only to adjust the need of potential notches, but also to characterize the system´s nonlinear behaviour under different load intensity.

MVIS successfully survived the application of Sine spectra both under gravity and under Launch QSL, demonstrating how the System can withstand SINE environment. Figure 4.2-1 shows MVIS response FRF under qualification load (RW Dummy under 1g) for longitudinal and lateral directions, where an evident nonlinear behaviour can be identified from the jump occurring in correspondence of the MVIS main eigenfrequency. This jump indicates a sudden change in the system dynamic behaviour, which is driven by the dual isolator system design.

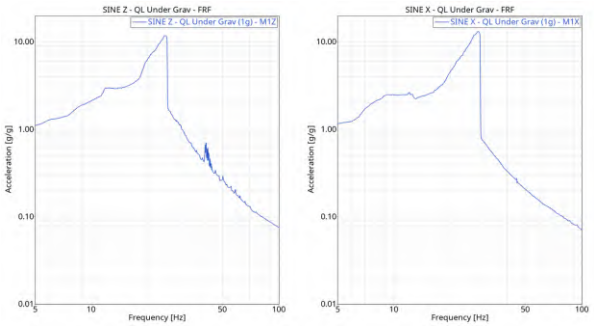


Figure 4.2-1 SINE Z and SINE X FRF – Qualification Load under 1g

The system nonlinear behaviour is strongly dependent on the intensity of the applied load. In Figure 4.2-2 and Figure 4.2-3, it can be seen the comparison of FRFs measured under the different inputs loads (LL, IL1, IL2 and QL) for longitudinal (Z) and lateral (X) directions. It can be observed how the system dynamic behaviour changes with the progressive increase of the input load, evolving from a more linear behaviour (a clean resonance

response) to a more non-linear behaviour characterized by a drastic change in the response.

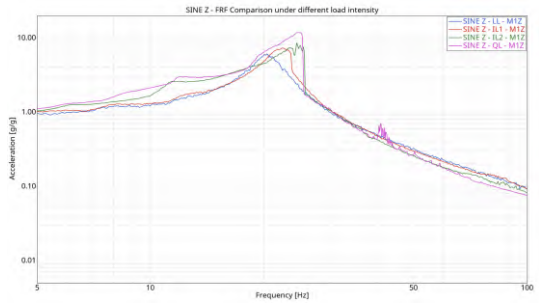


Figure 4.2-2 SINE Z – RW Response Z under 1g – Comparison LL, IL1, IL2 and QL

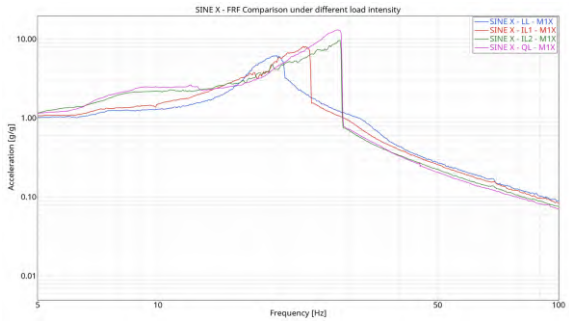


Figure 4.2-3 SINE X – RW Response X under 1g – Comparison LL, IL1, IL2 and QL

This nonlinearity is caused by the MVIS dual elastomer design: under low level inputs, MIVS response is mainly driven by the stiffness characteristic of the softer elastomer, while under the application of higher input loads, the contribution of stiffer elastomer becomes predominant.

The MVIS nonlinearity is also emphasized by the different response measured with vibration performed under gravity and under the application of Launcher QSL. A significant stiffening is indeed measured with vibrations performed in longitudinal direction (see *Figure 4.2-4*)

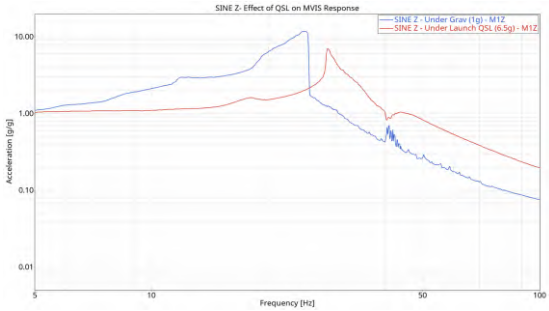


Figure 4.2-4 SINE Z – RW Response Z – Qual Spectrum – under 1g (blue) and under Launch QSL (red)

This occurs because under the application of Launcher QSL, the MIVS dynamic response is mainly driven by the stiffer elastomer, which causes a stiffening with respect to the condition under 1g. This effect is beneficial to avoid coupling with launch main mode. No stiffening is measured during vibration in lateral direction instead, see Figure 4.2-5.

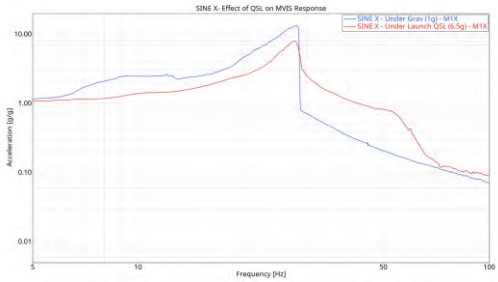


Figure 4.2-5 SINE X – RW Response X – Qual Spectrum – under 1g (blue) and under launch QSL (red)

Test Results show also that RW dynamics and the MVIS orientation do not play a significant role in the MVIS response. Figure 4.2-6 show the comparison between FRF measured at qualification level with RW Dummy and with RW EM. It can be seen how MVIS´ Sine response is not affected by RW Dynamics.

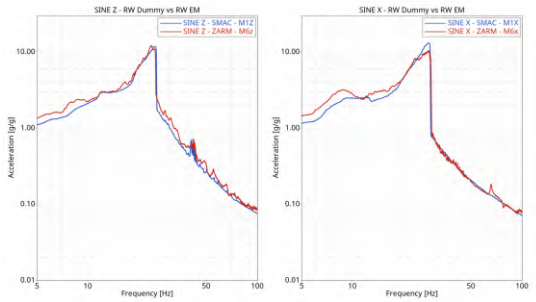


Figure 4.2-6 SINE Z and SINE X – Comparison between responses at RW Dummy (blue) RW EM (red)

Similarly, also the vibration performed with MVIS mounted at 45° shows a behaviour close to the one measured along X, Y and Z directions, which confirms that MVIS performances are independent by system orientation (see Figure 4.2-7).

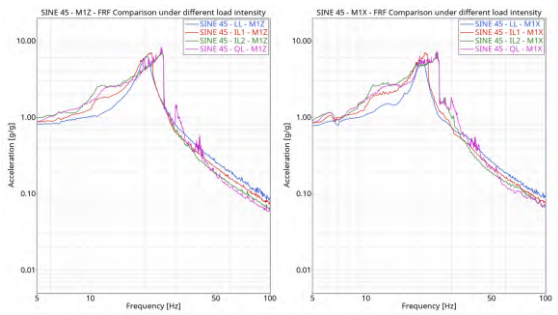


Figure 4.2-7 SINE 45° – RW Response Z and X under 1g – Comparison LL, IL1, IL2 and QL

4.3 RANDOM TESTING

Random vibration was performed by applying at MIVS Interface a Random spectrum which aims to cover the worst random environment expected during launch. Also in this case, Vibration was performed under two different conditions:

- under Gravity
- under Launcher (A6) maximum QSL (6.5g)

Vibration was performed along the MVIS X, Y and Z directions and with MVIS oriented at 45° with respect to the vertical direction. System successfully survived application of random load both under gravity and under Launch QSL, demonstrating how MVIS can withstand Random environment. Figure 4.3-1 shows MVIS Random response under qualification load (RW Dummy under 1g) for longitudinal and lateral directions, where significant response attenuation is observed after the MVIS 1st eigenfrequency.

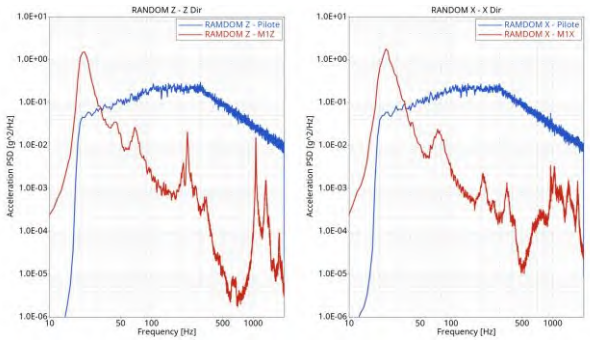


Figure 4.3-1 Random under 1g – Input and M1 Response for longitudinal (Z) and lateral (X) directions

The same effect has been measured with MVIS equipped with RW EM and with MVIS oriented at 45°, confirming that performance is independent by RW Dynamics and system orientation, see Figure 4.3-3 and *Figure 4.3-3*

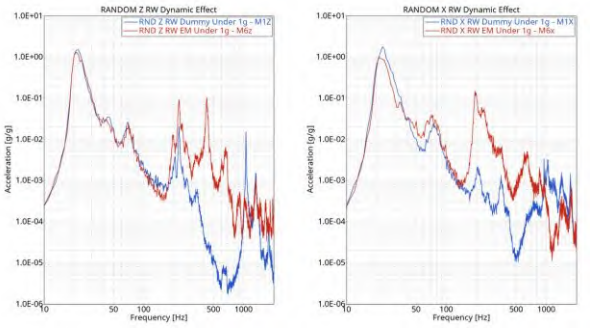


Figure 4.3-2 Random under 1g – M1 Response for longitudinal (Z) and lateral (X) directions. RW Dummy (blue), RW EM (red) – RW dynamic effect visible from 200Hz

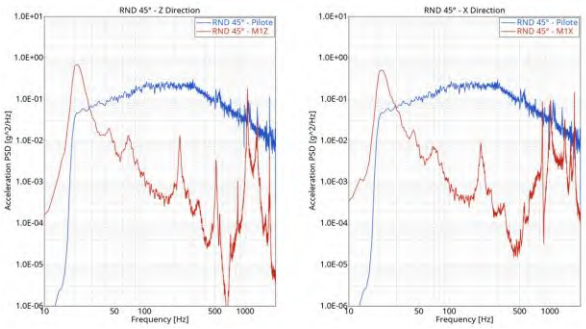


Figure 4.3-3 Random under 1g – Input and M1 Response for vibration with MVIS at 45°

Finally, results obtained under the application of Launcher QSL highlights the same nonlinear behaviour already observed during sine vibration, which consists in a system stiffening in correspondence of the main eigenfrequency. In Figure 4.3-4 the comparison of Random Response obtained under 1g (blue) and under Launch QSL (red) can be seen. A right shift of the system response in correspondence of the main eigenfrequency can be observed both for longitudinal and lateral directions.

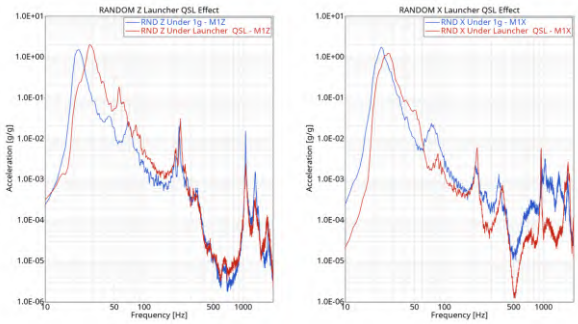


Figure 4.3-4 Random response under 1g (blue) and under Launcher QSL (red)

4.4 SHOCK TESTING

Shok test was performed applying at MIVS Interface a spectrum which aims to cover a worst-case environment expected during launch. Shock was performed along X, Y and Z directions repeating the test 3 times. Test results are shown pictures below from Figure 4.4-1 to Figure 4.4-3.

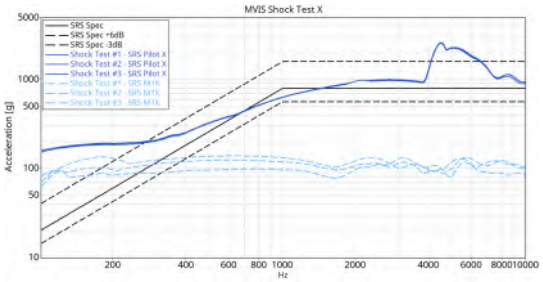


Figure 4.4-1 MVIS Shock Response X

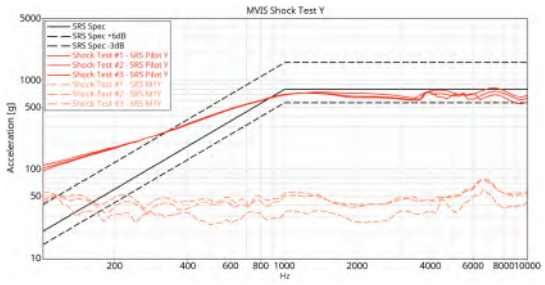


Figure 4.4-2 MVIS Shock Response Y

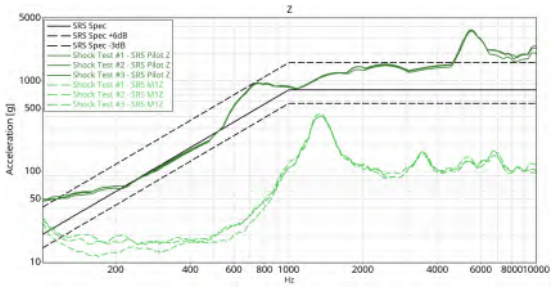


Figure 4.4-3 MVIS Shock Response Z

MVIS successfully survived the application of shock spectra and the exceedances with respect to tolerances are not deemed critical.

In fact, exceedances measured at lower frequency along X and Y directions are caused by test setup configuration. While for exceedances measured at higher frequency, the transmissibility function is always well below 1.0, which indicates a significant load attenuation on the shock transmitted to RW (see from Figure 4.4-4 to Figure 4.4-6).

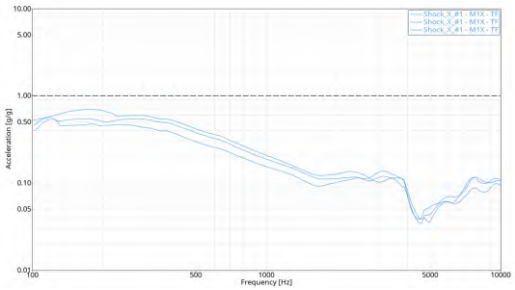


Figure 4.4-4 MVIS Shock Response X – Transfer Function

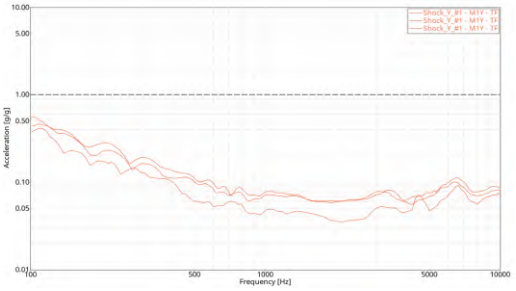


Figure 4.4-5 MVIS Shock Response Y – Transfer Function

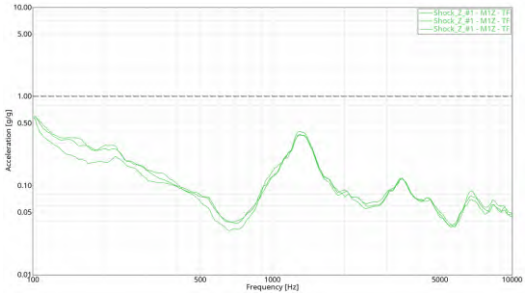


Figure 4.4-6 MVIS Shock Response Z – Transfer Function

5. NEXT STEPS AND FURHTER ACTIVITIES

Test campaign results demonstrated how MVIS is capable to guarantee excellent micro-vibration isolation performance while being at the same time able to withstand the severe loads expected during the launch.

After a deep and extensive review of test campaign results, ESA considered MVIS qualified to space flight. MVIS is now expected to be launched within FM3 satellite of CO2M mission, which OHB System is prime of.

In preparation of this event, an extensive FE-Model correlation activity is planned to be carried on at OHB System AG, which aims to reflect into an MVIS FE-Model the strong nonlinear behaviour measured during Test Campaign. Main objective is to develop a reliable mathematical model which can be used for detailed prediction at S/C level in preparation of the S/C launch. (CLA and micro-vibration analysis). See Figure 5-1

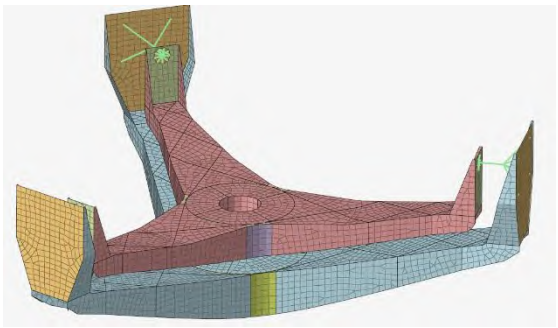


Figure 5-1 MVIS FE-Model

6. CONCLUSIONS

To protect a spacecraft from the micro-vibration environment generated by RW, over the past year a micro-vibration isolation system (MVIS) has been developed by OHB System AG in collaboration with SMAC SAS.

MVIS has been developed to guarantee the specified micro-vibration isolation performance and at the same time to survive launch load environment. To fulfil both objectives, a dual isolator system designed and developed by SMAC SAS has

been implemented in MVIS design introducing a high level of nonlinearity into the system behaviour.

The MVIS micro-vibration performance and its capability to withstand the severe loads coming from a launch environments have been demonstrated via an extensive test campaign. Test campaign results demonstrated how MVIS can fulfil all the requirements and helped to better understand the system strong nonlinear behaviour.

Results have been reviewed by ESA, which considered MVIS qualified for space flight and accepted MVIS to be installed and to be launched within FM3 satellite of CO2M mission, which OHB System is prime of. MVIS is also expected to be used for several other missions (ESA and national) which OHB System AG will be involved with.

Efforts will be invested in the next month by OHB System AG in deep correlation activity which aims to develop a reliable FE-Model to be integrated into the S/C mathematical model and to be used to run predictions in preparation of the S/C launch.

A COMPARISON OF AVAILABLE METHODOLOGIES FOR HARMONICS EXTRAPOLATION AND SUMMATION RULES IN MICRO-VIBRATION ANALYSIS

Salvatore De Lellis [(1)], Alexandru Vargalui [(1)]

[(1)] European Space Agency, ESTEC, Keplerlaan 1, Noordwijk (The Netherlands)
Email first author: Salvatore.DeLellis@esa.int

KEYWORDS

Micro-vibrations, harmonics, reaction wheels

ABSTRACT

Micro-vibrations generated on board the spacecraft can significantly degrade payload performance. As a mean of preliminary verification, micro-vibrations sources need to be characterised through (i) harmonics identification and (ii) response calculation at the location of interest through specific summation rules. In this paper the first point is addressed by comparing two methodologies for harmonics extraction on reaction wheels with and without resonance data. The paper shows that the classical approach based on Fourier transform over the entire frequency range provides better results than the envelope method which focuses on data extracted from reaction wheel resonance.
In addition, the paper compares different summation rules to account for the contribution of several Degrees of Freedom (DOFs) to obtain the response at sensitive locations. The comparison shows that widely adopted methodologies such as linear or root square summation provides a high degree of conservatism which need to be taken into account when performing preliminary analyses.

1. INTRODUCTION

1.1. Micro-vibration source characterization

When verifying the effects on performance of susceptible payload to micro-vibrations loads, one of the first step that needs to be addressed is the evaluation of all the contributing micro-vibration sources. These can be classified according to different criteria such as internal/external to the spacecraft or intermittent/continuous just to name a few, [1]. Research has shown [2-4] that, despite providing significant benefits in controlling the attitude of the spacecraft, reaction wheels are among the most severe sources in the micro-vibration budget. Their working principle, based on the momentum conservation through acceleration and deceleration of a flywheel, is also the source of unwanted micro-vibrations. These disturbances are coming, among others, from manufacturing defects on the inner mechanical parts used to guarantee the rotation of the flywheel (i.e. ball bearings, cage, inner and outer raceway), see *Figure 1-1*.

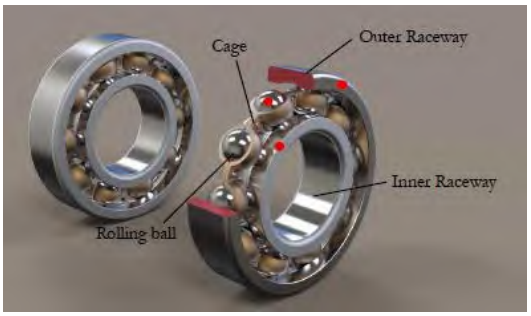


Figure 1-1 Ball bearing section view

These defects generate a repetitive response due to the wheel rotating at a certain speed which is converted to a specific frequency associated to the defect, known as harmonic disturbance. Mechanical non linearities strengthen harmonic content by creating multiples of the main harmonic frequency which appear as higher-order harmonics, *Figure 1-2*.
In addition, as any mechanical system, reaction wheels also exhibit structural resonances; they can be modelled as a rotation mechanism with one axial and two radial DOFs, leading to three fundamental resonances, [1]. Radial rocking mode (positive and negative) and radial translational mode are visible in *Figure 1-2* (black lines).
Reaction wheel harmonics can interact with the wheel resonances leading to large amplifications which might be a concern for sensitive payloads.
Some of these harmonics can be very well characterized using mathematical formulation. This is the case of the static and dynamic imbalance: the former due to an offset between centre of mass of the flywheel and axis of rotation of the shaft; the latter caused by misalignment of the flywheel principle axis and rotation axis, [5]. Although there have been attempts to characterise the ball-bearing harmonics numerically, [6,7], the most widely used approach relies on experimental methodologies for their identification.

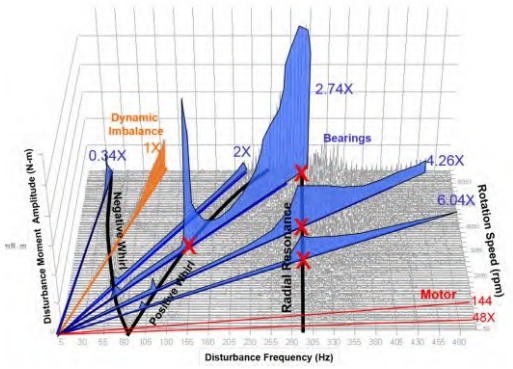


Figure 1-2 Reaction wheel waterfall plot, M_x, [8]

Harmonics identification methods can generally be split into two main categories, the former considering the whole data-set in the frequency regime, the latter considering only the data around the wheel resonance.

The first methodology checks for the presence of harmonics at different wheel speed and extracts information about the specific harmonic. This approach might or might not include data around the resonance, [9].

The second methodology is based on the envelope analysis using data in proximity of reaction wheel structural resonances. This method is usually adopted to detect faulty bearings [10], but can also be used to detect harmonics in healthy reaction wheels, with some limitations.

1.2. Degree-of-freedom summation rules

Once sources have been characterized, the influence of their disturbance signature is checked at the sensitive payload location through analysis. During this verification step, disturbances from different degrees of freedom are combined to obtain the final response of the sensitive payload. There are several methodologies that can be used for this step; the selection of the specific approach is usually dictated by available data, simplicity of application and heritage, [11]. Most summation rules discard the phase information between different DOFs, which might result in significant under or over estimation depending on the harmonics considered, [12].

2. REACTION WHEEL HARMONICS EXTRACTION

2.1. Fourier transformation based methods

This methodology is described in [13] and extended in [12]. It is based on reaction wheel disturbance data measured in steady state conditions from which harmonics are extracted looking at the Power Spectral Density (PSD) in different directions and cross-checked. The flowchart to retrieve harmonics is reported in Figure 2-1. More details on each of the steps are reported in the following section.

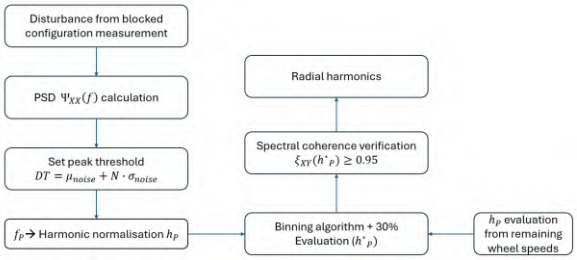


Figure 2-1 Reaction wheel harmonics identification

2.1.1. Disturbance from blocked configuration measurement

In this step, the data from the blocked configuration is gathered; this is generally retrieved from a Kistler table on which the reaction wheel is hard mounted. A set of force sensors is mounted between the wheel and the table while the wheel is spinning. Disturbances can be measured for all six DOFs.

2.1.2. Power Spectral Density Calculation

For the case under analysis, a specific direction is considered, in this case $F_x(t)$. The calculation is performed for a certain wheel speed. Welch method is used for this step.

2.1.3. Peak threshold definition

To remove peaks due to noise in the measurements, a threshold noise level is defined. This is expressed through Eq. 1:

$$DT = \mu_{noise} + N \cdot \sigma_{noise} \quad (1)$$

μ_{noise} and σ_{noise} represent the mean and standard deviation of the spike amplitudes and they are extrapolated from the histogram of the considered signal PSD. N is a user defined value and depends on the signal-to-noise ratio of the data, defined as noise isolation tolerance. This is an experimentally driven parameter and its usual value is 3, as shown in [13]. All the frequencies f_P which amplitude is above the noise threshold are considered as possible harmonics

2.1.4. Frequency normalization and binning algorithm

To confirm the subset of f_P representing harmonics, these frequencies are first normalized with respect to the rotational speed of the reaction wheel to obtain h_P and then verified against the remaining f_P from other wheel speeds. A binning procedure is then applied to verify the subset of harmonics which is present in at least 30% of the analysed wheel speeds.

2.1.5. Spectral coherence verification

Since harmonics are the consequence of an internal feature within the wheel, a correlation exists between PSDs of $F_X(t)$ and $F_Y(t)$ which can be quantified using the spectral coherence $\xi_{XY}(f)$. It is defined in Eq. 2:

$$\xi_{XY}(f) = \frac{\left|CPSD_{xy}(f)\right|^2}{\left|PSD_{xx}(f)\right| \cdot \left|PSD_{yy}(f)\right|} \quad (2)$$

where $CPSD_{xy}(f)$ is the Cross Power Spectral Density between signals $F_X(t)$ and $F_Y(t)$ while $PSD_{xx}(f)$ and $PSD_{yy}(f)$ are the Power Spectral Densities of signals $F_X(t)$ and $F_Y(t)$.
The spectral coherence ranges from 0 (uncorrelated signals) to 1 (fully dependant signals). In the harmonics extraction process the spectral coherence is checked and a threshold value of 0.98 is defined to identify reaction wheel harmonics.

2.2. Envelope approach

The envelope technique was introduced a few decades ago with the goal of identifying defect frequencies in bearings [10,14]. This approach relies on the reaction wheel data at resonance and is able to extract harmonics by modulating the structural resonance at the frequency of the defects. In fact, the harmonic frequency of the wheel acts as a carrier, while the wheel resonance as a modulator, *Figure 2-2*.

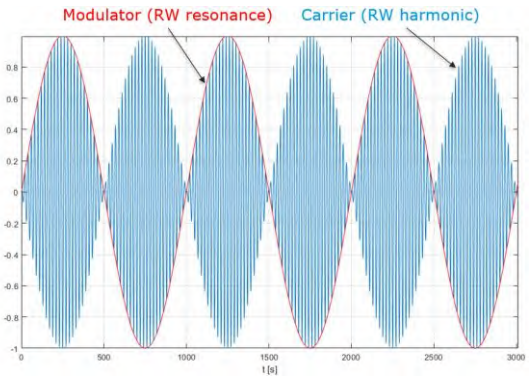


Figure 2-2 Modulator and carrier

Since the resonance acts as an amplitude modulator of the wheel harmonics, this enables to amplify the tiny vibrations coming from reaction wheel defects (i.e. harmonics).
The advantage of this approach with respect to the classical Fourier based transformation is the higher signal-to-noise ratio which is obtained from the data in proximity of the resonance of the wheel.
Historically, the envelope technique was developed as an analogue technique,[15], however a digital version of it has also been proposed, [16]. The main differences between the two methods are the flexibility provided by the digital version in selecting the band pass filters and using more modern tools such as the Hilbert transform.
The procedure for the envelope analysis is reported in Figure 2-3.

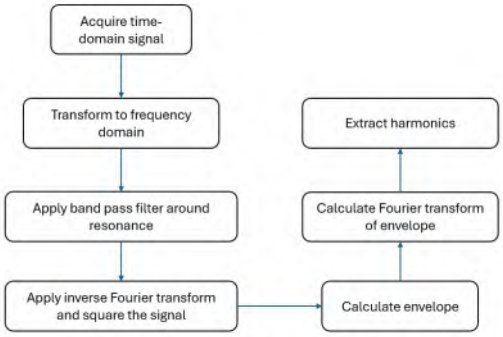


Figure 2-3 Envelope analysis for harmonics extraction

2.2.1. Acquire time-domain signal

This step is the same as section 2.1.1 where time domain disturbances of the wheel are acquired at different wheel speeds. Similarly to the Fourier transform method, disturbances are recorded in steady state configuration of the wheel.

2.2.2. Transform to frequency domain

The time domain disturbances are converted to frequency domain where reaction wheel structural resonances are visible.

2.2.3. Apply band pass filter around resonance

In this step a band pass filter is defined and applied around the reaction wheel resonance. If disturbance $F_x(t)$ is considered, the radial resonance will be the centre of the band pass filter. The width of the filter depends on the highest imperfection to capture; while the lower limit is dictated not to have known disturbances, such as imbalance, which might interfere with the bearing imperfections the method is trying to capture.

2.2.4. Apply inverse Fourier transform

Once the signal has been cleaned and shifted to zero, the inverse Fourier transform is applied.

2.2.5. Calculate envelope

It is then converted to an analytical signal using the Hilbert transform. This envelope contains the amplitude modulation caused by the repeated bearing impacts. Historically, the envelope technique has been used to detect ball bearings faults in reaction wheels, [10].
The main advantage of the Hilbert transform with respect to classical Fourier transform is that the latter assumes that the signal is made of summation of sinusoidal waves, while Hilbert analysis uses a signal of the form of a single but perturbed sine wave, [17]. Since the vibration signal represents exactly this case, it is accepted that the assumptions of the Hilbert transform are better suited than the Fourier analysis ones, [17].
The Hilbert transform of a signal *x(t)* is defined in Eq. 3, [17].

$$\mathcal{H}[x(t)] = \tilde{x}(t) = \frac{1}{\pi}\int_{-\infty}^{\infty}\frac{x(\tau)}{t-\tau}d\tau \qquad (3)$$

Assuming an original signal x(t) with positive and negative frequencies, the Hilbert transform of x(t) results in Eq. 4.

$$\tilde{x}(t) = e^{j\omega t - \pi/2} + e^{-j\omega t\pi/2} = -j(e^{j\omega t} - e^{-j\omega t}) \qquad (4)$$

From Eq.4 it can be noticed that the Hilbert transform does not change the amplitude of the signal *x(t)*, rather it shifts the signal phase by $\pm\pi/2$. The envelope is obtained as amplitude of its analytical signal $x_a(t)$ which is a complex signal made by the real part of *x(t)* and its Hilber transform $\tilde{x}(t)$ as imaginary part, [16].

2.2.6. Calculate Fourier transform and extract harmonics

Once the envelope is calculated, this is then converted to the frequency domain through Fourier transform. The resulting envelope spectrum contains the peaks which represent the harmonics.

3. SUMMATION RULES IN MICRO-VIBRATION ANALYSIS

Several methodologies are currently used in industry to sum the different DOFs when performing a microvibrations analysis. The most common ones are described hereafter.
For all the them, the micro-vibration response at the location of interest can be calculated as shown in Eq. (5).

$$\boldsymbol{\Psi}_{out}(f) = \boldsymbol{H}(f)\cdot\boldsymbol{\Psi}_{in}(f)\cdot\boldsymbol{H}^{H}(f) \qquad (5)$$

Where $\boldsymbol{H}(f)$ is the transfer function matrix from source to output; $\boldsymbol{\Psi}_{in}(f)$ is the disturbance input matrix and $\boldsymbol{H}^{H}(f)$ is the Hermitian of the transfer function matrix.

3.1. Full disturbance input matrix

This approach is often referred to as the benchmark case as it uses the complete disturbance input matrix. Such matrix is defined in Eq. (6).

$$\boldsymbol{\Psi}_{full}(f) = \begin{bmatrix} PSD_{xx}(f) & \dots & CPSD_{xMz}(f) \\ \vdots & \ddots & \vdots \\ CPSD_{Mzx}(f) & \dots & PSD_{MzMz}(f) \end{bmatrix} \qquad (6)$$

The full disturbance input matrix is fully populated at all the frequency steps of interest for the analysis. Depending on the configuration of the wheel some of these terms might be negligible (such as Mz). The peculiarity of this matrix is the presence of all the cross power spectral density terms (off-diagonal terms). These off-diagonal terms might be negligible for most of the frequencies; however, for those that represent harmonics, their magnitude will be significant with respect to the diagonal terms and they will have an influence on the final predicted response, [12]. With this approach the response in a specific direction includes the contributors from all the other DOFs.

3.2. Diagonal disturbance input matrix

In this case the disturbance input matrix is considered fully diagonal with no cross-power terms, as shown in Eq. (7).

$$\boldsymbol{\Psi}_{diag}(f) = \begin{bmatrix} PSD_{xx}(f) & \dots & 0 \\ \vdots & \ddots & \vdots \\ 0 & \dots & PSD_{MzMz}(f) \end{bmatrix} \qquad (7)$$

The cross power terms of the disturbance input matrix are completely omitted. Although this approximation is acceptable for several occurrences, it is still under or over estimating the contribution of the combined DOF when these become relevant, i.e. at some harmonics.

3.3. Quadratic summation

Following this approach the disturbance input matrix is further simplified. In fact, the response in the *i* direction is considered only in the corresponding diagonal term $\Psi_{diag\ i-i}(f)$, hence including only one disturbance input in the whole $\boldsymbol{\Psi}_{in}(f)$. As a consequence, the corresponding response in the direction of interest is calculated as a root sum square of the contributors $H_{ji}(f)\cdot\Psi_{ii}(f)$ as shown in Eq. (8).

$$\boldsymbol{\Psi}_{out-i}(f) = \sqrt{\sum_{j=1}^{6}[H_{ji}(f)\cdot\Psi_{ii}(f)]^2} \qquad (8)$$

Similarly to the diagonal disturbance input matrix it will be shown that this approach might lead to under/overestimation of response compared to the full disturbance input matrix.

4. APPLICATION AND RESULTS

The dataset used for the validation of the methodologies discussed above is obtained from a blocked configuration test using a Kistler table, Figure 4-1.

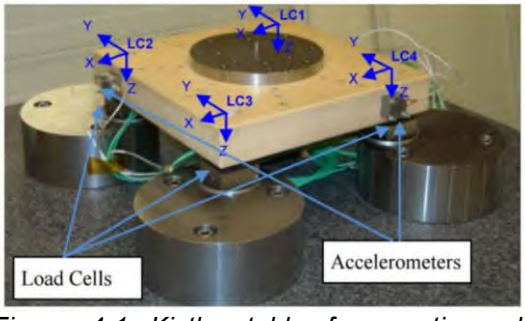


Figure 4-1 Kistler table for reaction wheel

disturbance measurement, [18].

The reaction wheel measured at steady state wheel speeds across a range from 155rpm to 5555rpm with 100rpm steps (note: values of wheel speeds and reaction wheel dependant info have been modified for confidentiality).

4.1. Harmonics extraction

Results for the extraction of reaction wheel harmonics are shown for the radial harmonics case, i.e. $F_x(t)$ and $F_y(t)$.

4.1.1. Results from Fourier based approach

Following the flowchart from Figure 2-1, the dataset is first converted to frequency domain using the Welch method. This method represents an improvement of the periodogram method as it enhances the variance properties of the result by introducing overlapping and windowing, leading to a smoother signal.
The results of the Welch method vary depending on the selected windowing strategy: in this case Hamming window is preferred to rectangular and Hann window. The main advantage of this window is the high ratio between the magnitude of central peaks vs sidelobes.
In addition, once the frequency signal has been obtained, a noise threshold is evaluated according to Eq.(1). Given the high sampling frequency for this measurement, i.e. 2560Hz, the parameter N_σ can be set to 3.

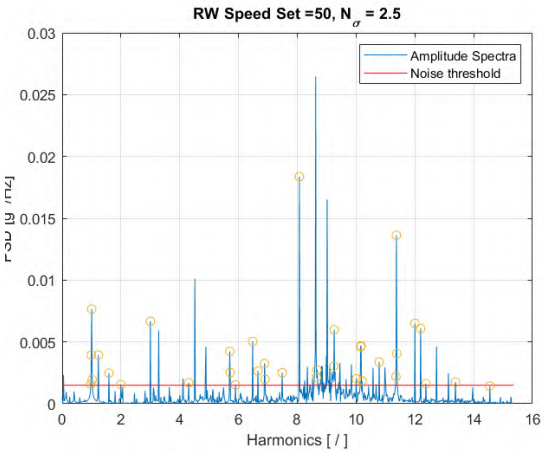


Figure 4-2 Harmonics identification at a specific wheel speed for $F_x(t)$, [19].

Figure 4-2 shows the harmonics extraction performed on one RW for $F_x(t)$ at a fixed wheel speed. The yellow circles represent the harmonics that respect the following conditions, as per flowchart from Figure 2-1:

- Amplitude above noise threshold
- Spectral coherence check ($\xi_{XY}(f) > 0.95$)

The full comprehensive list of extracted harmonics is reported in Table 4-1 where the following additional conditions are also included:

- Harmonic present in at least 30% of the wheel speed considered.
- Harmonics present on $F_y(t)$ disturbance too.

Table 4-1 Harmonics extraction with different extraction parameters

Harmonic	N_σ		
	2.5	**3**	**4**
1.0	X	X	X
1.2	X	X	
2.0	X	X	X
3.0	X	X	X
4.0	X	X	
4.3	X		
4.8	X	X	
4.9	X		
5.4	X	X	X
6.1	X	X	X
6.3	X		
6.9	X		
7.4	X	X	X
8.0	X		
8.6	X	X	X
9.25	X	X	X
10.0	X	X	X
10.2	X	X	X
10.8	X	X	X
11.0	X		
11.3	X	X	X

From Table 4-1 it can be noticed that the extracted harmonics are similar and some of them are excluded with a higher N_σ.

4.1.2. Results from Envelope approach

Similarly to the harmonics extraction based on Fourier approach, the same set of disturbances is used to calculate harmonics according to the procedure described in Section 4.1.1. The waterfall plot of the reaction wheel under investigation for $F_x(t)$ is reported in *Figure 4-3*.

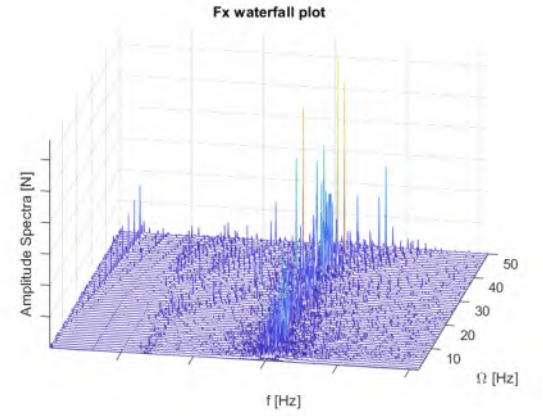


Figure 4-3 Waterfall plot for F_x distrubance

The extracted harmonics are reported in Table 4-2.

Table 4-2 Harmonics extraction using the envelope analysis

	Bandpass frequency	
Harmonic	$1000Hz$	$800Hz$
1.2	X	X
1.8	X	
1.9	X	
2.0	X	X
2.3	X	
2.5	X	
3.0	X	X
3.2	X	
3.4	X	X
3.8	X	X
4.0	X	X
4.3	X	X
4.8	X	X
4.9	X	
5.0	X	X
5.2	X	X
5.4	X	X
5.7	X	X
6.0	X	X
6.1	X	
6.3	X	X
6.9		

Results show that the harmonics extracted through the Fourier based approach are also visible in this case; however, the methodology is very sensitive to some parameters that needs tuning in the calculation, such as: bandwidth of the bandpass filter, identification of the central resonance frequency and filter type.
In the case under investigation, the bandpass frequency has been selected not to include the main harmonic as this is well known.

4.2. Summation rules

As explained in Section 3, there are several methodologies to sum different DOFs of the reaction wheel disturbance. In the current study, the structural model of a satellite platform is used for the evaluation of different methodologies to calculate responses. The details of the hardware are not fully disclosed for confidentiality; the satellite platform has a size of roughly 300kg and is used for Earth observation missions.

The performance of the different DOFs summation rules is assessed by looking at the response along *X* and *Y* directions. One reaction wheel is mounted on the structural platform and spinning at 4800rpm. The ratio η is introduced as a performance parameter and is defined as follows:

$$\eta(f) = \frac{\Psi_{DOF}(f)}{\Psi_{full}(f)} \qquad (9)$$

where $\Psi_{DOF}(f)$ is the response of the structure calculated at a specific harmonic using one of the methodologies described in Section 3; while $\Psi_{full}(f)$ is the response calculated using the full input matrix.

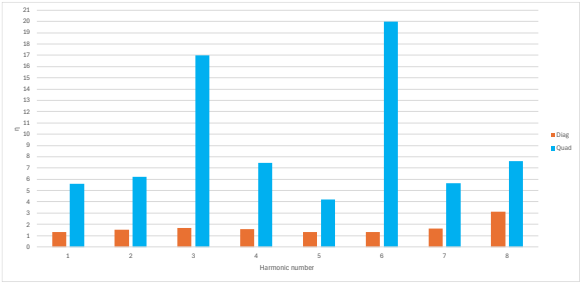


Figure 4-4 Comparison between different DOF summation rules in terms of response along X direction (note, diag: diagonal input matrix; quad: quadratic summation).

Results are reported in Figure 4-4 where the ratio of response using the two different methodologies (diagonal and quadratic) are compared with respect to the full input matrix case. It can be noticed that response in X direction depends on the methodology used and that the quadratic and diagonal approaches provide a more conservative estimation than the full one.

4.3. Results interpretation

4.3.1. Harmonics extraction

The results from the harmonics extraction confirm what is already available in the literature: the envelope approach finds its main application with respect to the identification of harmonics change due to faults in the reaction wheels, [17]. This methodology is more complex than the purely Fourier transform approach as it includes several parameters that need tuning before a correct extraction can be performed. In addition, it heavily relies on the data around reaction wheel resonance, which might not be correctly identified/available.
On the contrary the Fourier based approach has less parameters that need investigation, namely the noise threshold value for peak identification.

4.3.2. Summation rules and margin policy definition

Multiple methodologies have been presented for DOF summation. The results have shown different level of conservatism with respect to the benchmark methodology. This paper does not want to recommend a specific methodology, but simply highlight that a different level of conservatism is obtained depending on the selected one. As a consequence, also the margin policy should be adapted accordingly. When defining the margin policy for micro-vibrations, several uncertainty factors are included, as summarised below:

- Q factor: this is usually set to a minimum of 100 (except for possible isolators for which Q factor shall be discussed and agreed)
- Source frequency uncertainty: an uncertainty factor shall be applied on the frequency of the fundamental and its

harmonics (usually around 10%).

- Source amplitude uncertainty: an uncertainty factor shall be applied on the amplitude of the disturbance emitted by the wheel (fundamental and its harmonics). Such factor considers whether a wheel characterization has already been performed.
- Structure transfer function uncertainty: an uncertainty factor is applied on the transfer function from input to output locations all over the frequency range of interest.

Hence, different uncertainty factors are defined for microvibration analysis. From a source perspective, assuming the same information on sources is available and then applying the same amplitude uncertainty factor on the wheel disturbance obtained via full methodology or quadratic summation methodology (see Section 3) would not provide the same level of conservatism.

5. CONCLUSIONS

This paper investigates the characterization of micro-vibration sources, specifically reaction wheels. It compares two methodologies for harmonics extraction showing that the Fourier based approach provides easier implementation and clearer results. The envelope approach, on the contrary, can be a powerful tool especially when an in depth analysis of harmonic change is needed to investigate faulty bearings.

In addition, the topic of DOF summation for response calculation is addressed, comparing three different approaches to account for the contribution of exported disturbances along different DOFs. Results show that simplifying the PSD input matrix of the wheel might introduce a higher degree of conservatism. These findings should always be taken into consideration when defining the associated margin policy for microvibration characterization and analysis.

6. REFERENCES

1. ECSS-E-HB-32-26A. Spacecraft Mechanical Load Analysis Handbook (2013). European Space Agency, Noordwijk, The Netherlands, 2013.

2. Babuska, V., Beatty, SM., Deblonk, BJ. & Fausz, JL. (2004). A review of technology developments in flywheel attitude control and energy transmission, *IEEE Aerospace Conference Proceedings,* 4, Big Sky, Montana.

3. Fausz, J., Wilson, B., Hall, C., Richie, D., & Lappas V. (2009). Survey of technology developments in flywheel attitude control and energy storage systems, *Journal of guidance, control and dynamics,* 32(2).

4. Miller, S., Kirchman, P. & Sudey, J. Reaction wheel operational impacts on the goes-n jitter environment. (2007). *AIAA Guidance, Navigation and Control Conference and Exhibit,* Hilton Head, South Carolina.

5. Bialke, B. (1997). A compilation of reaction wheel induced spacecraft disturbances, *20th Annual AAS Guidance and Control Conference,* Breckenridge, Colorado.

6. Taniwaki, S., Kudo, M., Sato, M. & Okhami, Y. (2007). Analysis of retainer induced disturbances of reaction wheel. *Journal of System Design and Dynamics,* 1(2).

7. Harsha, SP. Nonlinear dynamic analysis of rolling element bearings due to cage run-out and number of balls. (2006). *Journal of Sound and Vibration,* 289 (1-2).

8. Bialke, B. Microvibration disturbance fundamentals for rotating mechanisms. (2011). *Advances in the Astronautical Sciences,* 141.

9. Neat, GW., Melody, JW. & Lurie, BJ. Vibration attenuation approach for spaceborne optical interferometers. (1998). *IEEE Transactions on control systems technology,* 6(6).

10. McFadden, PD. & Smith, JD. (1984). Vibration monitoring of rolling element bearings by the high-frequency resonance technique – a review. *Tribology international,* 17(1).

11. De Lellis, S., Stabile, A., Aglietti, G. & Richardson, G. (2018). A methodology for disturbance characterisation of families of mcirovibration sources, *European Conference on Spacecraft Structures, Materials & Environment (ECSSMET),* Noordwijk, The Netherlands.

12. De Lellis, S., Stabile, A., Aglietti, G. & Richardson, G. (2019). A semiempirical methodology to characterise a family of microvibration sources. *Journal of Sound and Vibration,* 1-18 (448).

13. Masterson, RA., Miller DW. & Grogan, RL. (2002). Development and validation of reaction wheel disturbance models: empirical model. *Journal of Sound and Vibration,* 249 (3).

14. Ho, D.& Randall, RB., (2000). Optimisation of Bearing Diagnostic Techniques using Simulated and Actual Bearing Fault Signals. *Mechanical Systems & Signal Processing.* 763-788 (14).

15. Randall RB. & Antoni, J. (2011). Rolling element bearing diagnostics. *Mechanical Systems & Signal Processing.* 485-520 (25).

16. Le, M.P. (2017). Micro-disturbances in reaction wheel. PhD Thesis. TU Eindhoven.

17. Feldman, M. (2010). Hilbert transform in vibration analysis. *Mechanical Systems & Signal Processing.* 735-802 (25).

18. Wagner, M., Airey, S., Piret, G. and Le., P., (2012). European Space Agency (ESA): New Reaction Wheel Characterisation Test Facility (RCF). *Advances in Astronautical Sciences,* 537-556 (144)

19. De Lellis, S., (2020). A methodology to account for dynamic variability in micro-vibration analysis of satellites. PhD Thesis. University of Surrey.

LAUNCH VIBROACOUSTIC PRESSURE DIFFERENTIAL ACROSS A THIN SPACE OPTICAL FILTER

Diagarajen Carpanen [(1)], James McKevitt [(1)], Duncan Rust [(1)], Patrick Curry [(1)], Sarah Matthews [(1)] , Berend Winter [(1)]

[(1)] Mullard Space Science Laboratory, University College London, Dorking RH5 6NT, UK
Email:d.carpanen@ucl.ac.uk

KEYWORDS

Diffuse sound field, FEM, vibroacoustic response of thin structures

ABSTRACT

The vibroacoustic environment during launch can generate dynamic loads that threaten sensitive spacecraft components. This study investigates the vibroacoustic response of the Short Wavelength (SW) camera of the JAXA SOLAR-C mission, focusing on an ultra-thin 150 nm aluminium filter supported by a nickel mesh. Because the filter is highly susceptible to dynamic loading, the pressure differential across it must remain below 1 Torr (133 Pa) to avoid damage.

To assess its performance without costly early-stage testing, numerical vibroacoustic models of both a preliminary telescope and a dummy test configuration were developed. Modal analyses and coupled structural-acoustic simulations were performed. Internal cavity pressures under launch acoustic excitation were computed and used to evaluate filter loading.

Predicted pressure differentials were 15.3 Pa-rms for the full telescope and 19.2 Pa-rms for the dummy configuration, both well below the allowable limit. The results demonstrate that the filter is expected to survive launch and validate the proposed modelling approach for delicate space optical systems.

1. INTRODUCTION

The launch acoustic environment is one of the most demanding mechanical environments experienced by spacecraft [1]. High sound pressure levels generated by the launch vehicle excite the spacecraft structure, producing structural vibration and internal acoustic pressure fluctuations throughout the payload. These dynamic loads are particularly challenging for lightweight optical components, where relatively small pressure differences across the filter can result in significant mechanical loading. Numerical vibroacoustic analysis therefore plays an important role during spacecraft development by supporting early design decisions and reducing technical risk before qualification testing [2].

The SOLAR-C mission, led by the Japan Aerospace Exploration Agency (JAXA), aims to investigate the physical processes governing the solar atmosphere using the Extreme Ultraviolet High-Throughput Spectroscopic Telescope (EUVST)[3]. EUVST will obtain high-resolution observations across multiple extreme ultraviolet wavelength bands to study plasma dynamics associated with coronal heating, magnetic reconnection and solar eruptions.

The Short-Wavelength (SW) camera, developed by the Mullard Space Science Laboratory (MSSL)[4], incorporates a thin optical filter [5] positioned immediately upstream of the detector to supress stray light [7]. During launch, acoustic excitation generates pressure fluctuations within the enclosed camera cavities, producing a pressure differential across the filter membrane. Since the filter manufacturer specifies a maximum allowable pressure differential, accurate prediction of the resulting pressure differential across the membrane is required during instrument development.

The work presented in this paper forms part of a preliminary design risk-reduction programme undertaken during the development of the SOLAR-C SW camera. At the time of the study, the telescope design was still evolving and complete structural models were not yet available. A coupled structural-acoustic finite element methodology was therefore developed to predict the pressure differential across the optical filter under representative launch acoustic environments. The study also supported the development of a representative dummy structural configuration for component-level acoustic qualification testing at MSSL.

2. SOLAR-C SW CAMERA AND OPTICAL FILTER

2.1. Short-Wavelength Camera

The Extreme Ultraviolet High-Throughput Spectroscopic Telescope (EUVST) separates the incoming solar radiation into short-wavelength (SW) and long-wavelength (LW) channels using a diffraction grating. The SW channel operates over the wavelength range of approximately 17–21 nm and is recorded by a dedicated focal plane

assembly developed at MSSL[4].

The SW camera employs back-illuminated charge-coupled device (CCD) detectors to provide the sensitivity required for high-resolution extreme ultraviolet observations. Although these detectors are highly efficient within the required EUV wavelength range, they also respond strongly to visible radiation. Suppression of visible light is therefore essential to prevent degradation of the scientific measurements. This is achieved through a combination of internal stray-light suppression features and an optical filter positioned at the entrance to the camera assembly (Fig. 1).

The filter is mounted within a dedicated plenum chamber located between the telescope optics and the focal plane. The surrounding structure incorporates internal baffling and venting paths that minimise stray light while allowing pressure equalisation during launch. The plenum chamber is specifically designed to reduce the loading acting on the optical filter during launch venting. Air enters and exits the chamber through relatively small vent openings into a substantially larger internal volume. The sudden expansion of the flow reduces the local air velocity and promotes pressure diffusion within the chamber, thereby reducing the transient pressure differential and the associated stresses acting on the filter membrane. Consequently, the geometry of the plenum chamber forms an important feature in the vibroacoustic assessment.

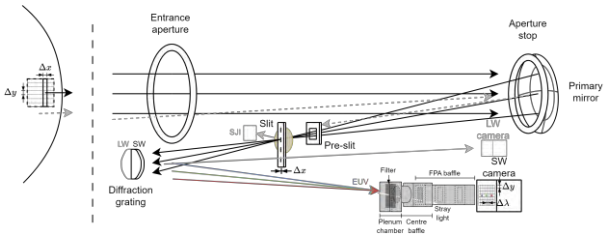


Figure 1: Schematic layout of the EUVST optical system showing the location of the SW camera and optical filter [6].

2.2. Optical Filter Assembly

The optical filter consists of a 150 nm aluminium membrane supported by a fine nickel mesh with 390 µm pitch and a 40 µm bar width (Fig. 2). The active filter area measures 43.35 × 47.5 mm. The aluminium layer provides high transmission within the required EUV wavelength range while effectively attenuating visible radiation. The nickel mesh provides the mechanical stiffness necessary for handling, integration and launch while maintaining a high optical open area (80%) and localising any tears.

Despite the supporting mesh, the filter remains one of the most mechanically sensitive components within the SW camera owing to its extremely thin aluminium membrane. Excessive loading during launch could damage the membrane and compromise the scientific performance of the instrument.

Most thin-film filters can only withstand a pressure differential of a few Torr [5], and so to ensure structural integrity during launch a pressure differential limit of 1 Torr (133 Pa) was adopted as the assessment criterion for this study. This limit was used throughout the numerical assessment.

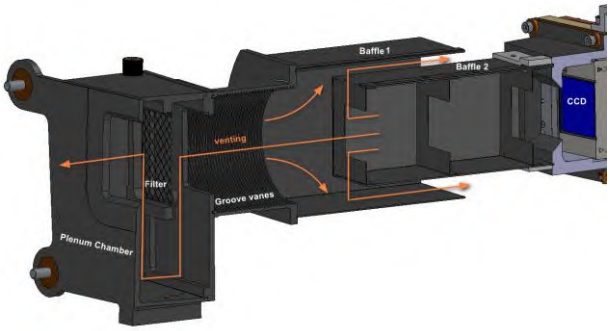


Figure 2: Cross sectional view of SW optical filter showing the filter aluminium membrane with supporting nickel mesh (not to scale) and mounting frame.

2.3. Assessment Strategy

The objective of the present work was to assess the acoustic pressure differential acting across the SW optical filter during launch and evaluate compliance with our allowable pressure limit.

At the time of the study, the SOLAR-C telescope design was still under development and representative qualification hardware was not yet available. Consequently, a coupled structural-acoustic numerical assessment was undertaken as part of an early design risk-reduction programme. In addition to predicting the pressure differential across the optical filter, the numerical models were used to develop a representative dummy structural configuration for a component-level acoustic qualification test to be conducted at the Mullard Space Science Laboratory (MSSL).

The numerical models and the coupled structural-acoustic analysis methodology are described in the following sections.

3. NUMERICAL MODELS

3.1. Overview

Two finite element models were developed to evaluate the vibroacoustic response of the SW optical filter during launch. The first represents the available telescope structural definition during the

preliminary design phase of the SOLAR-C programme, while the second is a simplified dummy configuration developed to support component-level acoustic qualification testing.

Both structural models were used to predict the acoustic pressure acting on either side of the optical filter under representative launch acoustic environments. The resulting pressure differential was subsequently compared with the allowable limit of 133 Pa.

Because the optical filter consists of an ultra-thin aluminium membrane supported by a fine nickel mesh, explicit representation of the detailed filter geometry within the global finite element models would be computationally expensive. An equivalent structural representation of the filter was therefore developed before constructing the two structural models. This equivalent model preserved the dynamic behaviour of the filter while allowing efficient incorporation into the coupled structural-acoustic analyses.

Both the numerical models and the corresponding dummy qualification hardware were deliberately simplified to reduce computational effort and manufacturing cost, respectively, while maintaining conservative predictions of the local vibroacoustic environment governing the pressure differential across the optical filter.

All structural finite element models were developed using MSC Apex 2025.1 and MSC Patran 2025.1 as pre-processors, with MSC Nastran 2025.1 used as the structural solver. The coupled structural-acoustic analyses were performed using Actran 2025.1.

3.2. Equivalent Orthotropic Filter Model

Direct representation of the optical filter within the global finite element model (FEM) would require approximately one million degrees of freedom owing to the explicit modelling of the nickel support mesh. Such a representation would result in a computationally expensive structural model, making the subsequent coupled structural-acoustic analyses impractical. An equivalent orthotropic shell representation of the filter was therefore developed to preserve the structural dynamic characteristics of the assembly while significantly reducing the model size.

A detailed FEM of the optical filter was first developed using shell elements to represent the 150 nm aluminium membrane and beam elements to represent the nickel support mesh (Fig. 3). A free-free normal modes analysis was performed to determine the natural frequencies of the filter assembly. An equivalent two-dimensional orthotropic shell model was subsequently generated using the same external geometry and equivalent boundary conditions. The orthotropic engineering constants were determined iteratively until the modal characteristics of the equivalent model provided an acceptable representation of those obtained from the detailed finite element model.

Table 1 compares the natural frequencies obtained from the detailed and equivalent finite element models. The equivalent orthotropic shell representation reproduces the dominant dynamic characteristics of the detailed model while reducing the number of structural degrees of freedom by several orders of magnitude. This reduction enables efficient incorporation of the optical filter within the coupled structural-acoustic models.

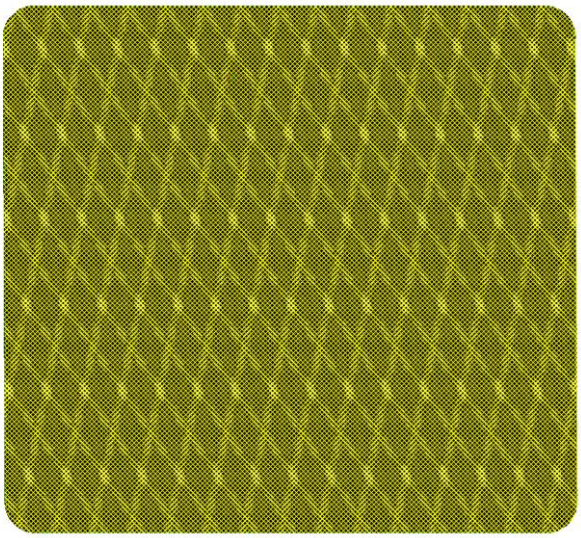


Figure 3: Detailed finite element representation of the optical filter showing the shell-element membrane and beam-element nickel support mesh.

Table 1: Comparison of natural frequencies between the detailed and equivalent filter models.

Full Filter Model	Equivalent 2D Orthotropic Model	% Difference
47.1	47.1	0.0
52.5	52.5	-0.1
67.4	67.4	0.0
109.4	109.4	0.0
114.9	114.8	-0.1
151.2	133.8	-11.6
181.7	168.7	-7.2
204.6	182.7	-10.7
208.6	200.7	-3.8
234.0	214.0	-8.6

3.3. Preliminary Telescope Structural Model

A finite element model representing the available telescope structural definition was developed using the engineering data released during the preliminary design phase of the SOLAR-C programme. The primary telescope structure was

idealised using shell elements representing carbon fibre reinforced polymer (CFRP) face sheets bonded to an aluminium honeycomb core. The SW camera assembly was modelled using a combination of shell and solid elements, with the equivalent two-dimensional orthotropic filter model incorporated into the structural assembly.

The anticipated launch mass of the complete telescope is approximately 500 kg. However, complete structural definitions for several telescope subsystems were not available at the time of the analysis. Consequently, the structural model represented approximately 80 kg of the total telescope mass. The telescope panels were modelled explicitly, while surrounding subsystems were represented by concentrated point masses located at their respective centres of gravity. The point masses were connected to the telescope structure using RBE2 rigid body elements, preserving the global mass distribution and inertial characteristics without introducing additional structural flexibility.

Although the model does not represent the complete flight telescope, it captures the primary structural load paths, local stiffness distribution and enclosed acoustic cavity geometry governing the vibroacoustic response of the SW camera. It was therefore considered suitable for predicting the local acoustic pressure environment surrounding the optical filter during the preliminary design phase.

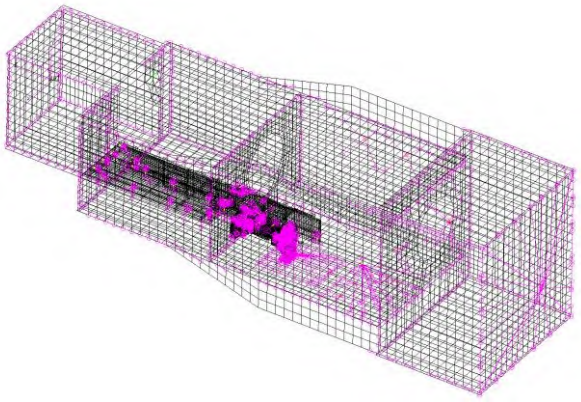


Figure 4: Preliminary telescope FEM model.

3.4. Dummy Qualification Model

A second finite element model was developed to provide a simplified structural representation of the SW camera for acoustic qualification testing. The dummy configuration retained the SW camera together with the surrounding structural components and enclosed acoustic cavities governing the pressure field acting on the optical filter.

The structure was constructed using aluminium face sheets bonded to an aluminium honeycomb core, providing a lightweight configuration that could be readily manufactured for testing. The model preserved the local structural interfaces, stiffness distribution and cavity geometry whilst significantly reducing the complexity of the global structural model.

The pressure differential predicted by the dummy model was subsequently compared with that obtained from the preliminary telescope model to assess the suitability of the simplified configuration for acoustic qualification.

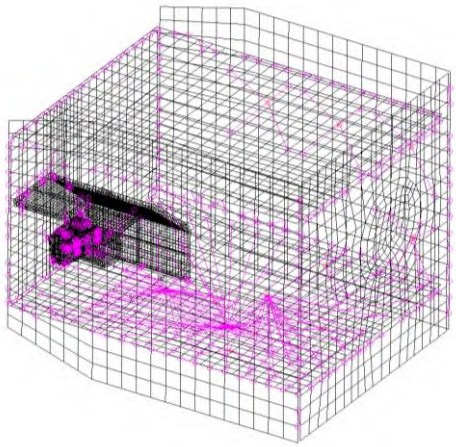


Figure 5: Dummy FEM.

3.5. Modal Analysis

Normal modes analyses of the preliminary telescope and dummy qualification models were performed in MSC Nastran 2025.1 to extract the structural eigenvalues and eigenvectors over the frequency range relevant to the launch acoustic environment. Figure 6 compares the first filter displacement mode, occurring at 92.3 Hz, for both structural models. The resulting modal basis was subsequently exported to Actran 2025.1 for the coupled structural-acoustic analyses.

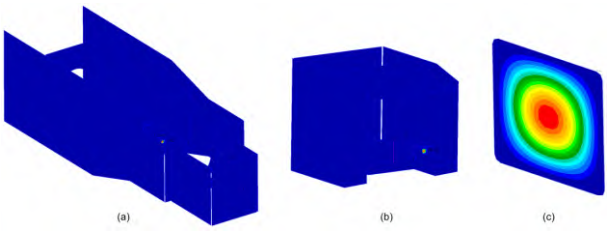


Figure 6: First displacement mode at 92.3 Hz of the optical filter for the (a) preliminary telescope model, (b) truncated qualification model, and (c) enlarged view of the filter mode shape.

4. VIBROACOUSTIC ANALYSIS

4.1. Coupled Structural–Acoustic Model

The vibroacoustic response of the telescope was predicted using a fully coupled structural–acoustic finite element approach implemented in Actran 2025.1. The structural modal basis obtained from the normal modes analyses described in Section 3 was imported together with finite element models representing both the external acoustic domain and the enclosed internal acoustic cavities.

The external acoustic domain was coupled to the telescope structure to simulate the transmission of the launch acoustic environment to the spacecraft. Simultaneously, the structural model was coupled to the enclosed internal acoustic cavities, allowing the interaction between the vibrating structure and the internal acoustic field to be represented over the frequency range of interest.

The coupled solution provided the structural response together with the acoustic pressure distribution within the internal cavities, from which the pressure differential across the optical filter was determined.

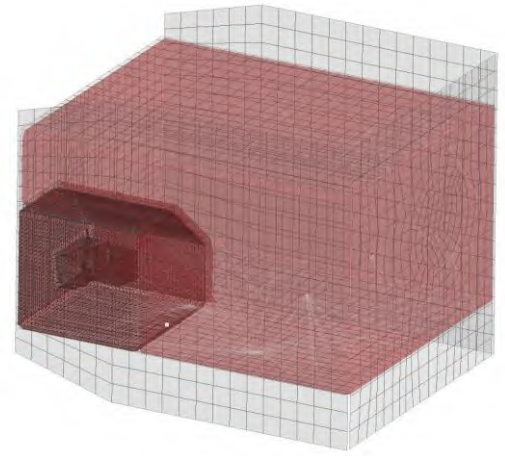


Figure 7: Coupled structural-acoustic finite element model showing the structural model and enclosed acoustic domains.

4.2. Launch Acoustic Loading

The coupled structural–acoustic analyses were performed using the qualification acoustic environments provided for the two candidate launch vehicle configurations considered during the preliminary design phase of the SOLAR-C mission. The qualification environments were defined by one-third octave band sound pressure levels over the launch frequency range. The corresponding acoustic spectra and overall sound pressure levels (OASPL) are summarised in Table 2.

Table 2: Overall Sound Pressure Level (OASPL) for each launch vehicle configuration.

Octave Band Centre Frequency [Hz]	Qualification Level 1 [dB]	Qualification Level 2 [dB]
31.5	120.2	127.0
63	126.7	133.0
125	131.7	138.0
250	135.5	142.0
500	129.7	140.0
1000	117.4	135.0
2000	110.6	130.0
4000	108.0	122.0
8000	105.0	118.0
OASPL	138.0	145.9

4.3. Pressure Differential Assessment

The acoustic pressures within the cavities immediately upstream and downstream of the optical filter were extracted from the coupled structural–acoustic analyses. The pressure differential across the filter was calculated from the difference between the two pressure responses over the analysis frequency range. The corresponding root-mean-square (RMS) pressure differential was subsequently evaluated for both structural configurations.

5. RESULTS

5.1. Pressure Differential Across the Optical Filter

Table 3 summarises the predicted RMS pressure differentials across the optical filter for the preliminary telescope and dummy qualification models under the two launch acoustic environments. The preliminary telescope model predicted RMS pressure differentials of 11.4 Pa and 15.3 Pa for Launch Configurations 1 and 2, respectively, while the dummy qualification model predicted 13.2 Pa and 19.2 Pa. A representative RMS sound pressure contour within the plenum chamber predicted by the coupled structural–acoustic analysis is shown in Fig. 8.

Table 3: Predicted RMS pressure differential across the optical filter.

Structural Model	Pressure Differential (Pa RMS) Launcher 1	Pressure Differential (Pa RMS) Launcher 2
Preliminary Telescope Model	11.4	15.3
Dummy qualification Model	13.2	19.2

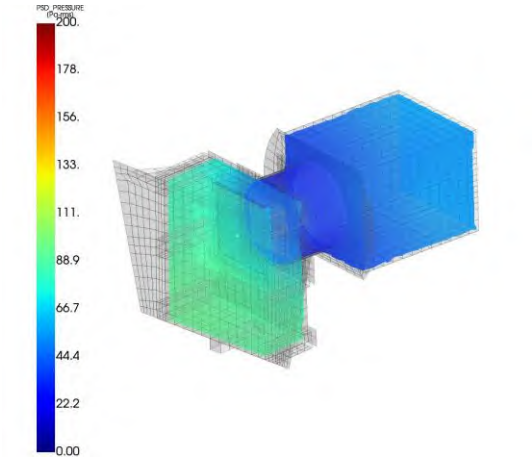


Figure 8: Representative sound pressure distribution (in Pa-rms) within the plenum chamber showing the predicted acoustic pressure field surrounding the optical filter.

5.2. Preliminary Acoustic Qualification Test

Following completion of the numerical assessment, the dummy qualification configuration was subjected to an acoustic qualification test using the applicable launch acoustic environment (Fig. 9). The objective of the test was to demonstrate the structural survivability of the optical filter under representative acoustic loading.

Post-test inspection confirmed that the optical filter remained intact with no visible damage or degradation. During the test, acoustic pressure measurements were acquired using a microphone positioned adjacent to the optical filter. These measurements represent the local acoustic pressure at a single location within the plenum chamber and do not provide a direct measurement of the pressure differential across the membrane. Consequently, direct quantitative comparison between the measured pressure and the predicted pressure differential was not possible. Accelerations were also measured throughout the test, with the highest response of 18 g-rms recorded at the plenum chamber during qualification test level 2.



Figure 9: Acoustic qualification test configuration for the dummy model.

6. DISCUSSION

The primary objective of this study was to evaluate the acoustic pressure differential acting across the SW optical filter during launch and assess compliance with our allowable pressure differential of 133 Pa (1 Torr). For both structural models and both launch acoustic environments, the predicted pressure differentials remained well below this limit, indicating that the pressure requirement is satisfied for the loading conditions considered.

A significant outcome of the study is that the dummy qualification model reproduced pressure differentials comparable to those predicted by the preliminary telescope model. Although the simplified configuration consistently produced slightly higher pressure differentials, the differences between the two models were small relative to our allowable limit. This indicates that the local vibroacoustic response of the optical filter is primarily governed by the surrounding camera structure and enclosed cavity geometry, supporting the use of the simplified configuration for component-level acoustic qualification testing.

The numerical models were developed during the preliminary design phase of the SOLAR-C programme using the engineering definition available at the time. Consequently, the structural model represented approximately 80 kg of the anticipated 500 kg telescope mass. As the telescope design matures and additional subsystem definitions become available, the global structural dynamics of the model are expected to evolve. The results presented in this paper should therefore be regarded as representative of the preliminary design rather than the final flight configuration.

The acoustic qualification test demonstrated that the optical filter successfully withstood the prescribed launch acoustic environment without visible damage. Although acoustic pressure measurements were obtained adjacent to the filter, they represent the pressure at a single location within the cavity and cannot be used to determine the pressure differential across the membrane. Consequently, the experimental measurements cannot directly validate the primary assessment parameter adopted in this study.

To the authors' knowledge, no published experimental data or validated numerical studies describing the structural failure behaviour of this specific 150 nm aluminium optical filter under launch vibroacoustic loading are currently available [2,5]. The previously published reasonable pressure differential limit [5] therefore provides the only available engineering criterion for assessing the numerical predictions.
The measured cavity pressures nevertheless provide valuable information for future model

refinement. Future work will focus on improving correlation between the predicted and measured cavity pressures, together with extending the experimental instrumentation to characterise the acoustic pressure field on both sides of the optical filter. This will enable more comprehensive validation of the coupled structural-acoustic model and increase confidence in the predicted pressure differential as the telescope design progresses

7. CONCLUSIONS

A coupled structural–acoustic finite element methodology has been developed to predict the acoustic pressure differential across the SOLAR-C SW optical filter during launch. An equivalent orthotropic shell representation of the filter enabled efficient incorporation of the membrane within the global vibroacoustic models while preserving its dynamic behaviour.

The predicted pressure differentials for both the preliminary telescope and dummy qualification models remained well below our allowable limit of 133 Pa (1 Torr) for the launch environments considered. Comparison of the two structural configurations showed that the simplified dummy model provides a representative approximation of the local vibroacoustic environment, supporting its use for component-level acoustic qualification testing.

An acoustic qualification test of the dummy configuration was successfully completed, with the optical filter surviving the prescribed loading. Future work will focus on correlating the numerical predictions with experimental cavity pressure measurements as the telescope design matures.

8. REFERENCES

1. Wijker, J. J. (2008). Spacecraft structures. Berlin, Heidelberg: *Springer* Berlin Heidelberg.
2. Rarata, Z., Dacko, A., Barciński, T., Polak, S., Musiał, J., Kubacki, S., ... & Baran, J. (2021). Vibro-acoustic response of spacecraft instrument subjected to diffuse sound field: Numerical simulations and experimental verification. *Applied Acoustics*, 184, 108338.
3. Shimizu, T., Imada, S., Kawate, T., Suematsu, Y., Hara, H., Tsuzuki, T., ... & Harra, L. (2020, December). The Solar-C (EUVST) mission: the latest status. *In Space Telescopes and Instrumentation 2020: Ultraviolet to Gamma Ray* (Vol. 11444, pp. 113-119). SPIE
4. McKevitt, J., Matthews, S., Brooks, D. H., Shimizu, T., Tei, A., Ugarte-Urra, I., ... & Harra, L. (2026). Pre-flare and active region plasma flows and structure seen by the short wavelength camera on SOLAR-C/EUVST. *Publications of the Astronomical Society of Japan,* psag078.
5. Powell, F. R. (1993, June). Care and feeding of soft x-ray and extreme ultraviolet filters. *In 24th Annual Boulder Damage Symposium Proceedings--Laser-Induced Damage in Optical Materials: 1992* (Vol. 1848, pp. 503-515). SPIE.
6. McKevitt, J., Rust, D., Winter, B., Walton, D., Matthews, S., Pyne, T., ... & Carpanen, D. (2026). Filter and baffle design for the short-wavelength camera on SOLAR-C EUVST. *Space Telescopes and Instrumentation 2026: Ultraviolet to Gamma Ray.*
7. Tsuzuki, T., Ishikawa, R., Katsukawa, Y., Kawabata, Y., Hara, H., Yasugaki, M., ... & Shimizu, T. (2026). High-fidelity stray-light analysis and control for the EUVST instrument on the SOLAR-C mission. *Space Telescopes and Instrumentation 2026: Ultraviolet to Gamma Ray.*

ECSSMET
Braunschweig Germany 2026

Production

DATA-DRIVEN PROCESS CONTROL FOR HIGH-TECH COMPOSITE MANUFACTURING

Silas Kirchhoff [1], Fabian Preller [1], Stefan Steeger [1]

[1] INVENT GmbH, Christian-Pommer-Str. 47, 38112 Braunschweig, Germany, silas.kirchhoff@invent-gmbh.de

KEYWORDS

Composites, Manufacturing Robustness, Statistical Process Design

ABSTRACT

Prototype-oriented space programs often require robust composite manufacturing with only a limited number of available test results, making data-intensive approaches to predict the process outcome, such as machine learning, difficult to apply. This paper presents a low-data methodology for data-supported process control in parameter-rich composite manufacturing. The approach combines physical process understanding, expert knowledge and statistical design of experiments to maximize the information gained from each specimen. In a first step, quality variables are defined, and the process is decomposed into meaningful subsystems. Influencing parameters are then classified as controllable factors, constant parameters or disturbances and ranked according to expected relevance using the Pareto principle. A screening design identifies dominant factors, which are subsequently quantified in a full factorial test set.
The methodology is demonstrated on wet filament winding, where it enables compact, explainable interpolation models for layer-thickness control and supports transferable, traceable decision-making in low-volume manufacturing.

1. INTRODUCTION

Modern lightweight designs rely on fibre-reinforced composites, because they combine high specific stiffness and strength with freedom in laminate design, allowing the material to be tailored to the application. However, this freedom also creates manufacturing complexity. Many process parameters interact, and their combined influence on dimensional quality can be difficult to quantify when only a few parts are manufactured. This is especially relevant for space programs, where development and qualification hardware is often produced in prototype quantities rather than in statistically rich serial production [1].

This work aims to bridge the gap between modern data-driven ambition and low-data industrial reality. Machine-learning-based methods can be valuable to predict a process output when hundreds or thousands of comparable process histories are available. In contrast, prototype composite hardware often provides only a small number of trials, limited opportunities for destructive inspection and strict cost and schedule constraints. In such a situation, process understanding becomes the substitute for data volume. The experiment must be designed so that every produced specimen generates maximum information.

The methodology is demonstrated on wet filament winding. For customized winding products, the typical industrial challenge is not the absence of automation, but the effort required to define robust process settings before manufacturing. Small deviations in layer thickness are particularly critical because they accumulate over many layers and can result in global dimensional deviations. Once a wet-wound laminate is cured, removing or adding individual layers is usually not acceptable. Fig. 1 illustrates this additive tolerance mechanism.

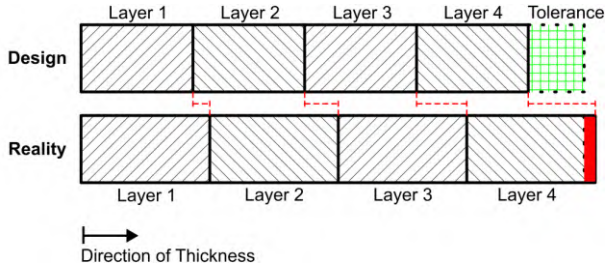


Figure 1: Additive tolerance mechanism for filament winding

Fig. 2 shows two exemplary wet-wound products. While more extensive trials are reasonable for smaller struts, it becomes very expensive for central tubes.

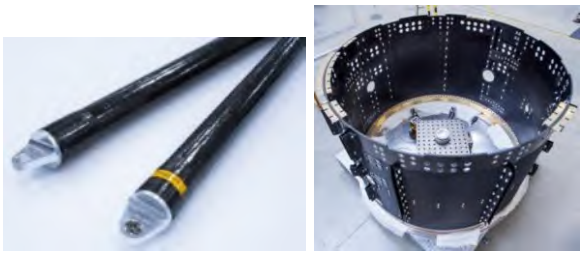


Figure 2: Exemplary wet-wound products: Left: Struts with integrated bushings Right: Central Tube for PLATO

The same methodological logic can be applied to

other parameter-rich composite processes where preliminary trials are expensive, and the allowable learning loop is short.

This paper first defines the methodological objective and positions the proposed approach within the constraints of low-data prototype manufacturing. It then introduces the individual methodological steps, from defining quality variables and decomposing the process to screening relevant factors and deriving an analytical model. The methodology is subsequently demonstrated using wet filament winding, including its experimental application, model generation and validation. Practical implementation and transferability to other composite manufacturing processes are then discussed. Finally, the risks and limitations of the approach are considered before the main findings and opportunities for further development are summarized.

2. METHODOLOGICAL OBJECTIVE

The objective of this paper is to establish a structured method that enables data-supported process control with the minimum necessary number of trials. The method should be usable by process experts without requiring extensive specialization in statistical design of experiments or machine learning. It therefore follows a hybrid logic: physical process understanding reduces the number of candidate variables, while Design of Experiments (DoE) provides the statistical discipline needed to quantify the remaining dominant effects.

Tab. 1 aligns the challenges in prototype manufacturing for space with the methodological response.

Table 1: Practical challenges for process control in prototype manufacturing and methodological response

Challenge in prototype space manufacturing	Methodological response
Very low number of comparable parts and limited historical data	Use process decomposition and expert knowledge before generating new data
High cost of sacrificial manufacturing trials	Apply screening DoE to identify dominant factors with a small number of variants
Many interacting process parameters	Separate parameters into factors, secondary variables and disturbances
Strict qualification and dimensional requirements	Monitor target and control variables simultaneously
Need for explainable engineering decisions	Use compact interpolation models instead of opaque black-box prediction

This objective differs from a purely data-driven black-box strategy [2], where predictions may be obtained without providing sufficient insight into the underlying physical relationships. The model is not expected to learn the entire manufacturing process from data alone. Instead, it formalizes existing process knowledge, tests the most relevant assumptions and translates the result into a practical engineering map for parameter selection.

3. METHOD OVERVIEW

The proposed method consists of five linked steps. First, target and control variables are defined. Second, the manufacturing process is decomposed into physically meaningful subsystems. Third, potential influencing parameters are collected and ranked according to expected effect, controllability and process limits. Fourth, a screening design identifies the dominant factors. Fifth, the dominant factors are quantified in a model that supports process planning and validation.

The analytical and experimental steps as well as their purpose and result are listed in Tab. 2 and further explained in the subsequent sections.

Table 2: Analytical and experimental steps

	Step	Purpose	Result
1	Define quality variables	Clarify what must be predicted and quality boundary conditions	Target response plus control variables
2	Decompose process	Structure the process into meaningful subsystems	Subsystems and parameter families
3	Rank parameters	Reduce dimensionality before trials	Candidate factors and secondary variables
4	Screen factors	Identify dominant effects efficiently	Shortlist of process levers
5	Quantify and validate	Generate usable process settings	Interpolation model and validation feedback

3.1. Quality variables

The expression quality variables describes the central target response as well as the control variables used to assess the overall quality of the product. The target response represents the characteristic to be predicted or deliberately adjusted through process control. Control variables define additional quality boundaries that must remain satisfied while the target response is optimized.

3.2. Process decomposition

The decomposition step is used to make a complex manufacturing process manageable before any experimental trials are planned. In this step, the complete process is divided into physically meaningful subsystems. This creates a structured overview of the process and helps to later distinguish between parameters that can be actively controlled, parameters that should be kept constant and disturbances that must be monitored. The method therefore prevents the experimental design from becoming a blind search through all possible machine settings.

The main benefit of decomposition is the reduction of complexity before data is generated. Especially in prototype manufacturing, where only a limited number of trials is possible, it is essential to avoid testing parameters without a plausible physical connection to the quality target. By breaking the process into subsystems, expert knowledge can be documented systematically and used to select only the most relevant factors for the subsequent screening experiment. This improves the information gained from each trial and reduces the risk of overlooking hidden process influences. In addition, the decomposition creates traceability, because every selected factor can be linked back to a specific part of the process and physical reasoning. As a result, the final model is not only data-driven, but also explainable and easier to transfer to similar composite manufacturing processes.

3.3. Parameter ranking

After the process has been decomposed into subsystems, the identified parameters are ranked according to their expected influence on the selected quality characteristic.

For this purpose, the parameters are first separated into three categories: actively controllable factors, parameters that should be kept constant during the trials, and disturbances that cannot be fully controlled but must be monitored. This classification is based on expert knowledge, existing manufacturing experience and, where available, results from pretrials. Actively controllable parameters are suitable candidates for the experimental design, while constant parameters are fixed to avoid unwanted variation in the results. Disturbances are documented so that unexpected deviations can later be interpreted correctly.

The ranking itself follows the idea of the Pareto principle, assuming that a small number of parameters is responsible for the major part of the quality variation [3]. Therefore, each parameter is assessed according to its expected physical relevance, its controllability and the practical feasibility of changing it within the manufacturing process. Parameters with a strong expected influence and good controllability receive the highest priority for the subsequent screening experiment. This step is essential in low-volume prototype manufacturing, because it prevents the experimental program from being overloaded with less relevant variables. The result is a focused list of candidate factors that allows the available trials to be used where the highest information gain can be expected.

3.4. Factor screening

The screening test is introduced because the process analysis identifies more potential influencing parameters than can be investigated quantitatively with the limited number of trials available in a prototype-oriented manufacturing environment. Often, the analyzed process contains a broad set of possible influences on the target response, but only a smaller number is expected to dominate the overall variation according to the Pareto principle. The purpose of the screening test is therefore not to build the final process model, but to separate the most relevant factors from parameters with minor or uncertain influence. For this reason, a reduced experimental design is acceptable, even if it does not fully resolve all interactions between parameters. The screening test acts as a decision gate: it identifies where further experimental effort is justified and prevents the final model from being overloaded with less relevant variables. The benefit is that the available trials are concentrated on the parameters with the highest expected contribution to product quality, which is essential when only a small number of manufacturing trials can be performed.

A set of seven variables is a reasonable size for the screening step because it is large enough to cover the most relevant parameter groups identified during the process decomposition and ranking, while still being small enough to be tested with manageable experimental effort. At the same time, a two-level screening design with seven factors can be performed with only eight variants [2], which is a practical compromise between information gain and manufacturing effort. Each factor is varied systematically, allowing the main effects to be compared and ranked, while the limited number of trials remains compatible with prototype production constraints.

The seven factors should include parameters from different parts of the process to ensure that the screening does not focus too narrowly on one subsystem but still reflects the broader process understanding developed beforehand.

3.5. Quantification for model derivation

After the screening step has reduced the parameter space to the most relevant factors, a second experimental step is used to quantify these factors in a more detailed and mathematically usable way. Methodologically, the objective of this test set is no longer only to rank parameters, but to describe their

influence on the selected quality characteristic with an analytical model. For this purpose, the most influential factors are investigated in a full factorial design, meaning that all possible combinations of the selected factor levels are tested. This ensures that the effect of each factor can be separated from the others and that interactions between factors can be identified.

The inclusion of two-factor interactions is important because process parameters rarely act completely independently. The effect of one factor may increase, decrease or even change direction depending on the setting of another factor. A full factorial test set allows these dependencies to be quantified instead of being hidden in the experimental scatter. As a result, the model does not only contain the individual main effects, but also terms that describe the combined influence of two parameters.

From a methodological standpoint, the resulting model can be written in the general form in equation (1), called the second-order polynomial response surface model [4]:

$$Y = c + \sum_{i=1}^{n} a_i x_i + \sum_{i=1}^{n} \sum_{j=1}^{n} a_{ij} x_i x_j \qquad (1)$$

Here, Y is the selected quality characteristic, n is the number of factors, x are the relevant factors identified during screening, c is the constant term, and the coefficients a describe the main effects as well as the two-factor interactions. The model is therefore still compact and explainable, but it captures more realistic process behavior than a model based only on isolated main effects.

The benefit of this step is that the experimental results are transformed into a usable process-control tool. Instead of only knowing which parameters are important, the engineer obtains a quantitative relationship between parameter settings and the expected process result. Within the tested process window, this model can be used to predict the outcome of a selected parameter combination or to identify suitable settings for a desired target value. This makes the method especially useful in low-data environments, because a limited number of structured trials is converted into an analytical and traceable basis for decision-making.

4. DEMONSTRATION CASE: WET WINDING

This chapter demonstrates the practical application of the proposed methodology using wet filament winding as a representative low-data composite manufacturing process. Wet winding is used as the demonstration case because it represents a highly parameterized composite manufacturing process in which product quality depends on the interaction of material, machine and part-specific settings.

The winding machine processes continuous fibre rovings that are supplied from spools and guided through the machine under controlled tension. Before deposition, the fibers are impregnated with resin in the laying head so that fibre and matrix are brought together during the manufacturing process itself. The impregnated roving is then deposited onto a rotating mandrel by coordinated movement of the mandrel and the laying head. During the deposition process, the rovings are transformed, stretched and spread by different sets of convex and concave rolls. After winding, the component is cured so that the resin solidifies and the final composite structure is formed. For the methodology presented in this paper, wet winding is not treated primarily as a machine-specific optimization problem, but as a representative use case for low-data process control in composite manufacturing. Its combination of many adjustable parameters, limited prototype quantities and strict dimensional requirements makes it well suited to demonstrate why structured process understanding is needed before data-efficient experiments can be planned.

The experimental program consisted of two winding series with eight variants each. The experiments used a carbon-fibre roving T700S 12K C 60E and an epoxy system consisting of Araldite LY 556, Araldur HY 906 and DY 070. The test bodies were cylindrical winding products manufactured with controlled secondary parameters.

4.1. Quality variables

The central target response is the single-layer thickness t_L, because total wall thickness can mask the influence of individual layers with different winding angles. Control variables are fibre angle, fibre volume fraction and laminate integrity, i.e. absence of delaminations and a pore content < 2.5 vol-% based on test standard used for comparable applications.

4.2. Process decomposition

For the wet winding demonstration, the process was divided into the subsystems Components, Fibre Guidance and Part. The component subsystem includes fibre, matrix and their uncured combination. The fibre-guidance subsystem covers the path from creel to laying point, including pretension, impregnation and laying-roll geometry. The part subsystem covers mandrel geometry, winding angle, auxiliary materials and curing.

4.3. Parameter ranking

In total, 26 potential influencing parameters were identified. Since not all of them are independently adjustable or relevant for short-run manufacturing, they were classified by expected influence and controllability. Seven were selected for the screening experiment according to their expected influence on the layer thickness:

- convex laying-roll radius $r_{V,knvx}$
- concave laying-roll radius $r_{V,knkv}$
- resin-gap thickness t_H
- fibre pretension F_V
- winding angle ϕ
- convex roll height h_{knvx}
- laydown temperature T.

4.4. Factor screening

The first series was a two-level fractional factorial screening design with seven factors and eight variants. It was selected to reduce experimental effort while still enabling a ranking of main effects.

The screening experiment showed that a limited number of controllable parameters explained the dominant part of the measured layer-thickness variation. Winding angle, fibre pretension and concave laying-roll radius were the largest contributors. The three strongest factors accounted for about 69% of the cumulative absolute effect, supporting the transition from broad screening to a focused quantitative model (s. Fig-3). The fibre volume fraction remained close to the nominal target, indicating that the thickness effects were not simply caused by uncontrolled resin dilution.

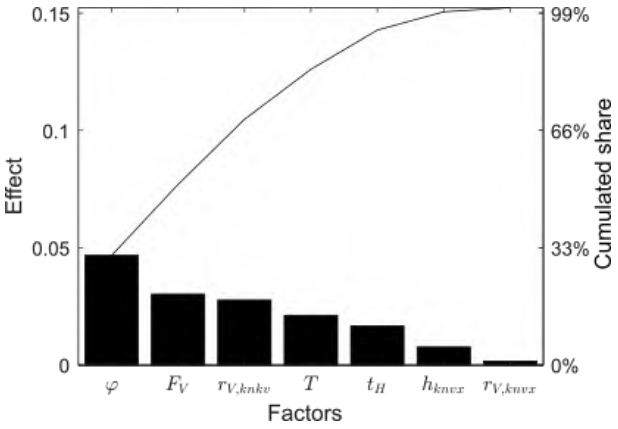


Figure 3: Separate and cumulative effects for tested factors

4.5. Quantification for Model Derivation

The follow-up quantitative experiment concentrated on the three strongest factors in a full factorial design: winding angle φ, fibre pretension F_V and concave laying-roll radius $r_{V,knkv}$.

Winding angle had the strongest measured effect on layer thickness. Fibre pretension and concave laying-roll radius were also relevant, and two-factor interactions are important for practical process control: selecting a single parameter in isolation is insufficient when the parameter effect depends on the selected winding angle and roller geometry.

The resulting interpolation model linked layer thickness to F_V, $r_{V,knkv}$ and ϕ including pairwise interactions. The weighted second order polynomial response is given in equation (2):

$$\begin{aligned} & t_L(F_V, R_{V,knkv}, \varphi) \\ & = 0.3386\ \text{mm} + 0.00202\ F_V \\ & + 0.000214\ r_{V,knkv} + 0.000093\ \varphi \\ & - 0.0001\ \mathrm{F_V r_{V,knkv}} - 0.000046\ F_V\ \varphi \\ & - 0.000002\ r_{V,knkv}\varphi \end{aligned} \qquad (2)$$

The numerical model is not intended for extrapolation outside the investigated process window. Its value is that it translates a small number of structured experiments into an explainable setting tool. A visual representation of the model is given in Fig. 4.

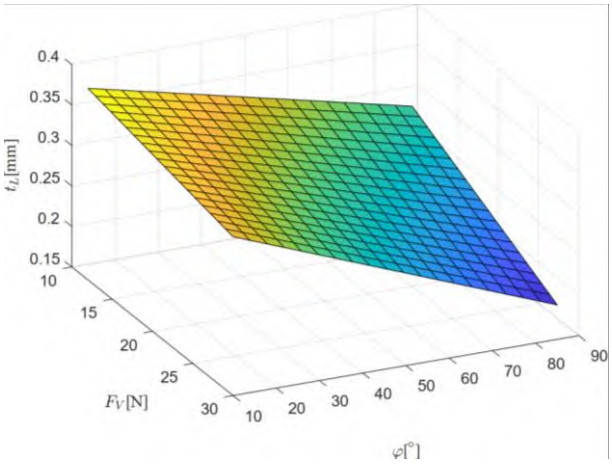


Figure 4: Layer thickness surface for one available concave roll

For a fixed winding angle, an engineer can select an available concave roll and determine the pretension needed to approach a target layer thickness. As an example, a target thickness of 0.3 mm at ±45° led to a required pretension of approximately 23.3 N for the suitable roll selection. This process is demonstrated in Fig. 5.

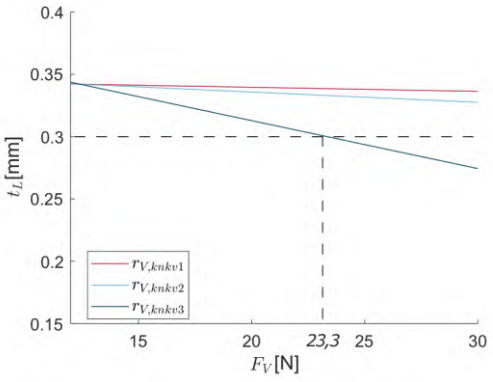


Figure 5: Calculation of target layer thickness of 0.3 mm for a given winding angle of ±45°

4.6. VALIDATION AND INTERPRETATION

During the validation step, the model was applied to an application-oriented tube with different layer angles and target thicknesses.

The results of the target response are given in Tab. 3.

Table 3: Validation configuration and test results

Layer	Angle	Thickness	
		Target	Real
1	±75°	0,30 mm	0,34 mm
2	±10°	0,75 mm	0,78 mm
3	±75°	0,40 mm	0,55 mm
4	±10°	0,75 mm	0,78 mm
5	±75°	0,30 mm	0,37 mm
6	±87°	0,75 mm	0,87 mm

The validation confirmed the usefulness of the workflow but also showed that the first model was not yet mature enough for unqualified production release. The component remained inside the reported global diameter tolerance of ± 0.5 mm in the application, but individual layer-thickness predictions deviated from target values, in some cases by up to 0.15 mm. This result should not be interpreted as a failure of the method. It is a typical outcome of a low-data first model: the experiment has reduced uncertainty and identified where further trials are most useful.

The validation feedback suggests that the linear model may need additional center points, quadratic terms or normalization for transfer to other roving types. It also highlights an important distinction between black-box prediction and methodology-driven learning. A black-box model with too little data may produce apparently precise but unreliable predictions. The presented method instead makes its assumptions visible: selected factors, process windows, interaction terms and validation deviations can all be inspected by process engineers.

5. PRACTICAL IMPLEMENTATION GUIDANCE

For application in a new program, the methodology should be started before the first manufacturing trial is released. The first workshop should define the quality response in measurable form and decide which quality characteristics are target variables and which are control variables. This distinction is important because a process setting that improves one response may create a hidden defect elsewhere. In the wet winding case, thickness was the target response, while fibre angle, fibre volume fraction and porosity were control variables. Other composite processes may use spring-in angle, void content, bondline thickness, surface waviness or residual moisture as equivalent responses.

The second implementation step is a structured process review with manufacturing engineers, design engineers, quality engineers and operators. The objective is to identify variables whose physical influence can be argued and whose limits can be stated. Each parameter should be documented with expected effect direction, qualitative effect strength, controllability, lower and upper process limits, measurement method and possible side effects. Parameters that cannot be controlled should not disappear from the analysis; they should be documented as disturbances and, where possible, randomized or kept constant during trials.

The third implementation step is selection of the smallest experiment that can answer the next engineering question. A screening design is appropriate when the dominant factors are unknown. A full factorial or response-surface extension becomes appropriate when the dominant factors have already been identified and a process-setting model is required. This staged logic prevents the team from spending valuable trials on high-resolution modelling of factors that later prove irrelevant. It also creates a clear decision gate after screening: either the dominant effects are sufficiently clear for quantification, or the process analysis must be revised before more material is consumed.

The final implementation step is model use with explicit validity limits. The model should be embedded in manufacturing planning as an engineering aid, not as an unrestricted automatic control law. The user should see the tested ranges, unavailable extrapolation zones, known process anomalies and validation errors. This makes the approach compatible with qualification work, because it documents why a setting was chosen and what evidence supports it.

6. TRANSFERABILITY TO OTHER COMPOSITE PROCESSES

Although the demonstrator is wet winding, the methodology is transferable to other composite manufacturing processes with many settings and low production quantities. Examples include resin transfer molding development, curing-cycle definition for new material systems, adhesive bonding process windows or automated tape placement parameter studies. The common requirement is that a capable process expert can decompose the process and rank parameters before experiments are executed.

At INVENT, the proposed methodology is currently applied to the CFRP machining process, aiming to reduce unwanted artefacts and local, micro-and macroscopic damage caused by the milling process.

7. RISKS AND LIMITATIONS

The reliability of the proposed methodology strongly depends on selecting the correct parameters for the screening experiment. Relevant influences that are overlooked during process decomposition or parameter ranking cannot be identified by the subsequent statistical evaluation and may instead appear as unexplained variation in the model. In addition, reduced screening designs may confound main effects with interactions, which can lead to incorrect rankings if strong interactions are present.

Expert knowledge and previous manufacturing experience should therefore be complemented by structured creativity and problem-solving techniques, such as brainstorming, cause-and-effect diagrams, process mapping or failure-mode analysis. Involving experts from manufacturing, design and quality assurance further reduces the risk of a one-sided parameter selection. Nevertheless, the resulting analytical model remains valid only for the materials investigated, factor ranges and process conditions. It should therefore be used as an explainable engineering aid within its validated process window, rather than as an unrestricted prediction model.

8. CONCLUSION AND OUTLOOK

A low-data, data-driven process-control methodology has been presented and demonstrated on composite wet winding. The central motivation is that modern machine-learning-based approaches often require more data than prototype-oriented space programs can realistically generate. Instead, the proposed method combines detailed process understanding, expert factor ranking, statistical screening, focused quantification and validation feedback. The case study for wet winding showed that winding angle, fibre pretension and concave laying-roll geometry dominate the investigated layer-thickness response, enabling a compact interpolation model for parameter selection.

The method supports a shift from experience-based trial-and-error loops to transparent, data-supported process planning with a minimum number of necessary trials. Future work should extend the model with additional data points for nonlinear terms to increase its accuracy. Additionally, transferability to other roving types, simultaneous multi-roving deposition and additional composite manufacturing processes should be tested. This aims to make engineering process knowledge structured with data, testable and useful for robust manufacturing in low-volume space applications.

9. REFERENCES

1. ECSS-E-ST-10-02C Rev.1 – Verification (2018), European Cooperation for Space Standardization.

2. Kleijnen, J. P. C. (2008). DESIGN OF EXPERIMENTS: OVERVIEW, in Mason, S. J. et al., *Proceedings of the 2008 Winter Simulation Conference*.

3. Kennet, R. S. (2021). Modern Industrial Statistics, 3rd ed., *Wiley*.

4. Montgomery, D. C. (2013). Design and Analysis of Experiments, 8th ed., *Wiley*.

SERIES PRODUCTION OF OPTICAL INSTRUMENT STRUCTURES FOR MEDIUMSIZED SATELLITES: CHALLENGES ARISING FROM DESIGNS NOT CONCEIVED FOR HIGH-RATE MANUFACTURING

Florian Kreißig[(1)], Martin Sauerbrey[(2)], Annabelle Sievert[(3)]

[(1)] INVENT GmbH, Christian-Pommer-Str. 47, 38112 Braunschweig, Germany, florian.kreissig@invent-gmbh.de
[(2)] INVENT GmbH, Christian-Pommer-Str. 47, 38112 Braunschweig, Germany, martin.sauerbrey@invent-gmbh.de
[(3)] INVENT GmbH, Christian-Pommer-Str. 47, 38112 Braunschweig, Germany, annabelle.sievert@invent-gmbh.de

KEYWORDS

Constellation, Earth Observation, Series Production, Optical Instruments, Instrument Structures, CFRP & Sandwich manufacturing

ABSTRACT

The demand for high-resolution optical imagery has grown substantially in recent years, driven by applications spanning reconnaissance, urban planning, agricultural monitoring, disaster response, and climate observation. This has greatly increased the demand for medium-sized Earth observation satellite constellations in low Earth orbit (LEO), with operators now routinely requiring 10 or more spacecraft per mission, transforming production requirements placed upon satellite manufacturers.
Optical instrument structures for such satellites must achieve extremely high geometrical stability across wide thermal ranges, whilst meeting stringent mass and cost requirements. The material system of choice is a sandwich construction with carbon fibre reinforced polymer (CFRP) face sheets, aluminium honeycomb, and titanium hard points.
This paper analyses manufacturing process improvements to transition an existing single-unit satellite design into series production and derives recommendations for future programmes where series producibility is a primary design requirement.

1 SATELLITE AND INSTRUMENT STRUCUTRE DESIGN

The satellite under consideration is a medium-sized Earth observation platform whose primary payload is an optical imaging instrument. A rendering of it is depicted in Fig. 1. The instrument structure is composed of three principal structural elements: a baseplate, an optical bench, and a cylindrical telescope tube. The baseplate provides the primary mechanical interface between the satellite bus and the instrument structure. Mounted upon the baseplate is the optical bench, upon which the primary mirror assembly is mounted. The secondary mirror is supported by the cylindrical telescope tube, which extends from the optical bench along the optical axis.
The baseplate and optical bench are realized as sandwich structures, comprising CFRP facesheets bonded to an aluminium honeycomb core. Load introduction and component interface locations are defined by titanium hard points and potted aluminium inserts integrated into the sandwich panels. The titanium hard points provide the direct mechanical interface for the bipod mounts of the primary mirror assembly, through which the mirror loads are introduced into the optical bench. The cylindrical telescope tube is likewise a sandwich construction with CFRP facesheets and an aluminium honeycomb core. The secondary mirror is mounted to the tube by means of additional sandwich structures, whilst monolithic CFRP stiffening elements are integrated on the exterior of the tube to ensure the required structural rigidity.



Figure 1: Computer generated rendering of the satellite [1]

The satellite was originally designed for a single-unit manufacturing approach, encompassing the production of a Structural and Thermal Model (STM), a Proto-Flight Model (PFM), and a single Flight Model (FM). Upon completion of this programme, the customer decided to deploy the satellite design within a constellation comprising a low two-digit number of units, to be manufactured within a two-year timeframe. This decision necessitated a systematic review of the existing manufacturing processes to identify improvements compatible with the required production rate.

The three structural elements, the baseplate, the optical bench, and the sandwich tube, that are discussed in this paper are the most critical with respect to manufacturing complexity. These components are both the most labour-intensive to produce and subject to the most stringent dimensional and thermo-mechanical requirements.

The manufacturing sequence for the sandwich panels begins with the layup and cure of the CFRP facesheets from unidirectional prepreg material. The cured facesheets, aluminium honeycomb core, and titanium hard points - all pre-machined to final contour - are subsequently assembled and bonded in a controlled bonding process. During this process, the titanium hard points are measured into position using an in-house coordinate measuring machine (CMM), ensuring the highest achievable positional accuracy, and providing early verification of interface locations prior to final cure. Once bonding is complete, the positions of all hard points are fixed; a misalignment detected after this stage would in most cases result in scrapping the assembly.

Following the bonding process, the panels receive holes for the insert potting in one machining step. The aluminium inserts are subsequently potted manually at varying heights above the facesheet surface to accommodate the differing interface requirements of the components to be mounted. The panels then undergo thermal cycling to achieve dimensional stabilisation. A post-machining operation follows the thermal cycling, during which the hard point interfaces and insert locations are milled to achieve the required planarity and positional tolerances, including the tight tolerances on locating pin holes. A finalisation process is then carried out, encompassing surface painting, installation of the electrical grounding network, proof load testing of all inserts, HELICOIL installation, visual inspection, cleaning, and part marking. Throughout all manufacturing steps, a rigorous measurement and inspection programme is conducted to verify dimensional compliance at each stage of production.

2 MANUFACTURING IMPROVEMENTS FOR SERIES PRODUCTION

The transition to series production required a structured analysis of the existing manufacturing processes. Three areas were identified as offering the most significant potential for improvement: the sandwich bonding process, the sandwich tube manufacturing, and the Product Assurance (PA) activities. The improvements implemented in each area are described in the following sections.

2.1 Sandwich Bonding of panels

The sandwich panel bonding process encompasses the bonding of the CFRP facesheets, the aluminium honeycomb core, and the titanium hard points into a panel assembly. In the single-unit manufacturing approach, each titanium hard point was individually adjusted to the local thickness of the honeycomb core in order to maintain the required bond line thickness. This process required the honeycomb core to be machined and measured first, after which the measurements were used as the basis for the subsequent machining of each individual hard point. This sequential dependency between the two machining operations consumed considerable time within the production flow. Furthermore, in the event of honeycomb damage requiring the replacement of the core, the associated hard points would in many cases also require replacement if their dimensions were not compatible with the substitute honeycomb. This dependency represented an unacceptable risk and source of delay in a series production context.

To decouple the titanium hard points from the honeycomb core, the height tolerance of the honeycomb was tightened and the permissible bond line thickness was increased. This modification allowed the machining of the honeycomb core and the machining of the hard points to be decoupled and therefore be performed in parallel, eliminating the sequential dependency and reducing the production time significantly. Hard points could furthermore be used interchangeably across panels. The continued compliance of the bond line with the required structural load introduction values was verified through a qualification campaign conducted at sub-component level, confirming that the increased bond line thickness did not compromise the mechanical performance of the interface.

The second improvement addressed the positioning of the titanium hard points during the bonding process. In the single-unit manufacturing approach, hard point positions were verified in real time using a handheld CMM arm operated by a skilled metrologist. Whilst this approach is cost and time effective for single-unit production, it is not scalable to series manufacturing, as it occupies a highly skilled operator for the duration of each bonding operation. A dedicated positioning jig was therefore designed and manufactured to locate the hard points accurately and repeatably without the need for real-time metrology. A minor design modification to several hard points was required to introduce pin hole features for positive location on the jig, as not all hard points in the original design incorporated such features. This design modification to the hard points reflects the limited possibility to change an

established satellite design in order to improve manufacturability, as any modification carries implications for the existing qualification status. The introduction of the jig released the skilled metrologist from the bonding process, making this resource available for other measurement tasks within the production flow. An improved hard point with the added pin holes is pictured in Fig. 2.

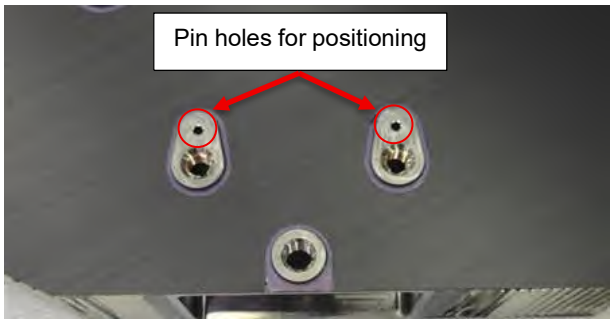


Figure 2: Hard point with added pin holes for positioning via jig

2.2 Sandwich Tube Manufacturing

The sandwich tube is one of the most labour-intensive components in the instrument structure. In the single-unit manufacturing approach, a single raw tube was manually laid up and cured in the autoclave, from which one finished tube was subsequently machined. For series production, the raw tube length was extended such that two finished tubes could be extracted from a single cured article. The additional time required for the layup of the extended raw tube is only marginally greater than that for the original length, with the primary additional effort arising from the increased difficulty of handling longer plies of prepreg material and honeycomb core. The principal benefit of this modification lies in the autoclave process: two finished tubes are produced from a single cure cycle, halving the time and costs per finished tube and eliminating one complete autoclave run for every two tubes produced compared to the original single-tube approach. In Fig. 3 the two raw tube sizes are depicted.

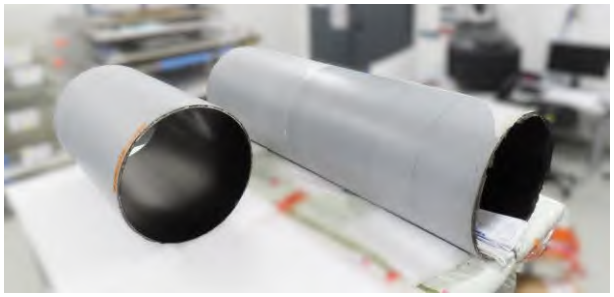


Figure 3: Comparison of short raw tube from the single-unit production to a long raw tube of the series production.

2.3 Product Assurance Activities

PA activities represent a significant time cost within the manufacturing process. The stringent quality requirements of the aerospace industry demand that every non-conformance (NC) identified during production is formally dispositioned before manufacturing can proceed. In the single-unit manufacturing approach, nearly each NC required a Non-conformance Review Board (NRB), a process involving considerable time in organisation, discussion, and formal documentation. Whilst this process is necessary to maintain the quality standards required for flight hardware, it was recognised that the majority of NCs encountered during the single-unit builds were of a minor and recurring nature. A significant proportion of these recurring NCs arise not from process failures but from requirements that are at the limit of what is achievable with the current design and available manufacturing technologies. These include tight positional and dimensional tolerances on interface features, as well as electrical requirements associated with the grounding network. Notably, such NCs are frequently dispositioned with a use-as-is conclusion, indicating that the deviated part is accepted without repair or rework. This outcome in itself suggests that the original requirement was set more stringently than the functional performance of the structure strictly necessitates and lends further support to the case for a rigorous tolerance reassessment in future programmes — a point that is discussed further in Sec. 4.2.

Upon completion of the single-unit production programme, the NC record was systematically reviewed and analysed. Minor and recurring NCs were identified, categorised, and documented in an internally designated Deviation and Repair Catalogue, agreed upon with the customer. Each entry in the catalogue defines the nature of the deviation, its classification, and an approved standard repair or acceptance disposition. For NCs that fall within the scope of the catalogue, the approved disposition may be applied directly by the manufacturing team and documented within the Major Inspection Point (MIP) Report, which is submitted to the customer. NCs of a major nature, or those falling outside the scope of the catalogue, continue to be processed through the standard NRB process. This approach significantly reduces the engineering response time associated with minor NCs, prevents interruptions to the manufacturing flow, and allows skilled engineering resources to focus on NCs of genuine technical significance.

3 RESULTS AND DISCUSSION

The manufacturing improvements implemented across the three identified areas yielded measurable benefits in production efficiency, schedule performance, and quality management, while maintaining the performance and precision established in the single unit production run. The

results for each improvement area are discussed in the following sections. A quantitative summary is provided in Tab. 1.

Table 1: Summary of Manufacturing Improvements for Series Production

Improvement Area	Key Benefit Achieved
Sandwich Bonding	
Hard point dimensional coupling	5% calendar time saved per panel; hard point procurement removed from critical path; scrap risk from honeycomb–hard point incompatibility eliminated.
Hard point procurement	Hard point unit cost reduced by an average of 65% (up to 80%)
Hard point positioning during bonding	13% in man-hours saved per panel bonding operation; operator-independent positioning repeatability achieved.
Sandwich Tube Manufacturing	
Raw tube batch size	Autoclave cost and time per finished tube reduced by 50%; net man-hour investment per finished tube reduced despite marginally longer layup.
Product assurance activities	
Non-conformance rate trend	Recurring NCR disposition time reduced by 99%; man-hours reduced by 85% per NCR.

3.1 Sandwich Bonding

The decoupling of the titanium hard point machining from the honeycomb core machining delivered a calendar time saving of approximately 5% per panel for both the optical bench and the baseplate. In the single-unit manufacturing approach, hard point procurement represented a recurring critical path item, adding four to five weeks to the production schedule of each unit. The dimensional decoupling was the technical enabler that made batch ordering of hard points possible, as the hard point dimensions were no longer dependent on the measured thickness of a specific honeycomb panel. During the single-unit production programme, one scrap event occurred across the six panels produced as a result of hard point and honeycomb incompatibility. The dimensional decoupling eliminates this risk entirely in the series production builds. Ordering the hard points for the entire constellation programme as a single batch from an external supplier removed procurement from the critical path and reduced the hard point unit cost by an average of 65%, with a maximum reduction of up to 80% compared to the unit costs achieved during single-unit production. It is noted that the decoupling of hard point dimensions from honeycomb thickness was a necessity for meeting the demanding production schedule from the customer, as without this modification the cumulative procurement delays alone would have rendered the required production rate unachievable.

The introduction of the dedicated positioning jig for hard point location during the bonding process reduced the man-hours required per panel bonding operation by 13% and releasing a skilled metrologist for deployment on other measurement tasks within the production flow. In addition, the jig ensures a repeatable and operator-independent positioning accuracy that is inherently more robust in a series production context than the real-time metrology approach employed in single-unit production.

3.2 Sandwich Tube Manufacturing

The extension of the raw tube to yield two finished tubes from a single cure cycle represents the most directly quantifiable improvement in the sandwich tube manufacturing process. The layup of the extended raw tube requires approximately 14% more man hours for the original short raw tube, while saving one complete autoclave cure cycle for every two finished tubes produced. As autoclave capacity is a constrained and costly resource, the reduction of one cure cycle per two finished tubes represents a significant saving in both machine time and operating cost per finished tube. The net result is that the man-hour investment per finished tube is reduced, the autoclave cost per finished tube is halved, and the throughput of the tube manufacturing process is doubled relative to the single-unit approach for the same number of cure cycles consumed. The length of a raw sandwich tube is restricted by the size of the available autoclave and the manual handling of the prepreg layers during layup.

3.3 Product Assurance Activities

The introduction of the Deviation and Repair Catalogue has delivered measurable improvements in the man-hour cost and production continuity associated with NC disposition. In the single-unit production programme, an average of 15 NCs were recorded per unit. Each NC required the convening of an NRB, consuming an average of two calendar weeks of elapsed time per disposition. The man-hour cost per disposition was approximately two hours for minor NCs and eight hours for major NCs. The Deviation and Repair Catalogue captures approximately 50% of the NCs encountered during production, corresponding to approximately seven to eight minor NCs per unit. For each NC dispositioned via the catalogue, the man-hour cost is reduced to between 15 minutes and one hour. It is noted that minor NCs, whilst requiring formal disposition, are in most cases not blocking the production flow and can be processed in parallel to ongoing manufacturing activities. The primary benefit of the catalogue for minor NCs therefore lies in the reduction of engineering man-hours rather than in a direct reduction of production elapsed time. Major NCs, by contrast, are frequently blocking to production and continue to be processed through the standard NRB process, where the two-

calendar-week disposition time represents a direct impact on the production schedule.
The NC rate has demonstrated a downward trend across the production series. Whilst the first series unit recorded an NC count comparable to the single-unit builds, attributable to the ramp-up phase and the introduction of new processes, the second series unit recorded ten NCs, representing a reduction of approximately 33% relative to the single-unit baseline. This trend is expected to continue with each subsequent unit as process familiarity increases and recurring NCs are progressively eliminated through process improvements.
The Deviation and Repair Catalogue is maintained as a living document, updated in formal agreement with the customer whenever new recurring NCs are identified and sufficiently understood to warrant a standard disposition. Findings from the first series unit have already been incorporated into an updated revision of the catalogue, expanding the scope of NCs eligible for standard disposition without NRB convening. This continuous update process ensures that the catalogue remains representative of the actual NC profile of the production programme and delivers increasing efficiency benefits as the series progresses.

3.4 Overall Production Time Improvements

The improvements described in Sections 3.1 to 3.3 represent the most significant individual contributions to production efficiency. However, a number of additional improvements have been implemented across the broader manufacturing programme that contribute to the overall reduction in production time.
Curing process optimisation has been applied where permitted by the applicable qualification baseline or supplier datasheet, shortening the adhesive curing cycle for selected bonding steps by 30%.
The post-machining operation, previously performed by an external supplier, has been brought fully in-house for the series production programme. The elimination of shipping time, combined with improved scheduling through direct access to in-house resources and the immediate availability of engineering support on the shop floor, has reduced the elapsed time for this operation by 60%.
The transition to series production has enabled the dedication of a fixed work area, including the necessary machines and equipment, exclusively to this programme. Critically, skilled workers are planned and allocated to this programme on a continuous basis, eliminating the productivity losses associated with frequent task switching between projects that characterised the single-unit production approach.
Batch-wise production has been extended beyond the sandwich tube to encompass a range of smaller components, including aluminium inserts, CFRP cleats and stiffening elements, and smaller sandwich components. Producing these in batches reduces setup time and improves process consistency across the production series.
The higher order volumes associated with a constellation programme have resulted in elevated priority status with external suppliers. This translates into shorter lead times and improved scheduling flexibility compared to the single-unit production context.
Finally, the manufacturing processes, work instructions, and documentation established during the single-unit production programme provide a validated baseline for the series production builds. The familiarity of the manufacturing team with the processes and documentation reduces the learning curve associated with each new unit and contributes to the downward trend in NC rate observed across the series.
Taken together, all implemented improvements have reduced the total production time for the optical bench and baseplate panels by 56% in calendar weeks relative to the single-unit production baseline. The sandwich tube manufacturing has achieved a comparable reduction of 58% in calendar weeks. These figures represent the combined effect of the process-specific improvements described in this paper and the broader programme-level measures outlined in this section and demonstrate that substantial efficiency gains are achievable even within the constraints of an existing satellite design not originally conceived for series production.

4 LIMITATIONS AND RECOMMENDATIONS FOR FUTURE PROGRAMMES

The improvements described in the preceding chapters demonstrate that a meaningful increase in production efficiency is achievable for satellite structures not originally conceived for series production. However, the scope of achievable improvement is fundamentally constrained by the existing design architecture. The following sections identify the principal limitations encountered and the design and process choices that would deliver significantly greater benefits in future programmes designed with series production as a primary requirement from programme outset.

4.1 Material Selection

The CFRP facesheets of the optical bench, baseplate, and sandwich tube are manufactured from a unidirectional prepreg material using a cyanate ester resin system. This material was selected for its low CTE, high resistance to micro-cracking under thermal cycling, low outgassing behaviour, and high toughness — all of which are critical for the dimensional stability requirements of an optical instrument structure. However, cyanate ester resin systems are significantly more

expensive than epoxy-based alternatives, impose more demanding cure cycle requirements, and are available from a more limited supplier base. Epoxy-based prepreg systems offer lower material cost, shorter and less energy-intensive cure cycles, and broader supplier availability. On the down side they exhibit higher moisture absorption and reduced resistance to micro-cracking, which may present unacceptable performance penalties for the dimensional stability requirements of optical instrument structures. Any transition to an alternative resin system would necessitate a full material and process qualification programme.

For any future programme, a detailed thermo-mechanical analysis driven by the actual performance requirements of the mission — rather than by conservative heritage material selection — should form the basis of the material specification. This analysis should be conducted in conjunction with a fibre-compatible structural concept, ensuring that the laminate architecture and resin system are selected on the basis of demonstrated mission requirements rather than as a precautionary performance margin. It is further noted that the significant decrease in cost-per-kilogram-to-orbit in recent years has reduced the primacy of minimum mass as a design driver. This shift creates an opportunity to reconsider mass-driven material and design choices that impose disproportionate manufacturing complexity and cost penalties in a series production context.

4.2 Tolerance Analysis

The dimensional tolerances applied to the structural components in the current design were established during the single-unit development programme, where conservative tolerance setting is common practice. Experience gained during the single unit production builds has demonstrated that a number of positional deviations, upon detailed engineering review, were found to be acceptable without any adverse effect on optical or structural performance. This retrospective finding suggests that a rigorous design-for-manufacturing tolerance analysis, conducted at programme outset, could identify tolerances that are more conservative than strictly necessary and relax them accordingly. A reduction in tolerance requirements, where analytically justified, directly enables simpler manufacturing processes, reduces the frequency of NCs, and lowers the skill level required for certain operations, all of which are significant benefits in a series production context. Even minor adjustments can yield significant benefits in manufacturing efficiency; for example, increasing a through hole diameter for an M6 bolt from 6.6 mm to 7.0 mm introduces negligible change to the structural analysis whilst meaningfully reducing the positional accuracy required during drilling and thus the associated manufacturing effort and NC risk.

This reassessment must however extend beyond dimensional tolerances alone. Requirements across all disciplines should be reviewed to determine whether they are strictly necessary at their current level of stringency or whether they can be relaxed without compromising the functional performance of the satellite. Mass tolerances on structural components, for example, are frequently set conservatively during early design phases when the overall mass budget carries significant margins; a review at programme outset for series production may reveal that these can be widened without impact on the mission. Electrical requirements within the grounding network represent a further area where the specified values are in some cases more stringent than the functional electrical performance of the satellite demands, as evidenced by the recurring use-as-is dispositions encountered during production. Documentation requirements equally warrant scrutiny; the scope and depth of manufacturing documentation specified for a single-unit programme may impose a disproportionate administrative burden in a series production context, where standardised and streamlined documentation processes would deliver significant time savings. A systematic review of all such requirements, conducted in collaboration with the customer at programme outset, represents one of the most impactful steps that can be taken to prepare an existing satellite design for series production.

4.3 Supply Chain Design

The current programme highlighted the risk of single-source dependencies for critical materials and processes. A flexible and multi-qualified supply chain is a significant enabler of series production efficiency, both in terms of procurement lead time and unit cost. The qualification of Surtec surface treatment, applied to aluminium inserts for corrosion protection and electrical conductivity, is supplier and material specific, meaning that any change of supplier necessitates a new qualification. Beyond surface treatments, a similarly flexible supply chain for other critical materials, including CFRP prepreg, structural adhesives, and paints, would provide comparable benefits. For each of these material classes, single-source dependencies expose the programme to procurement risk and limit the ability to leverage competitive pricing at the production volumes associated with constellation programmes.

4.4 Fibre Winding and Automated Fibre Placement

Fibre winding and Automated Fibre Placement (AFP) represent significant opportunities for reducing the manual labour content and process variability associated with CFRP face sheet and tube manufacturing. Both processes impose specific constraints on laminate design and part geometries that must be accommodated from the

outset, making retrofitting an existing design not feasible. INVENT GmbH currently operates a CFRP fibre winding machine, which is directly applicable to the cylindrical telescope tube. Winding enables a more optimised fibre orientation than is achievable through manual layup, improving the thermo-mechanical performance of the tube whilst reducing manual labour content. The process supports both prepreg winding, where pre-impregnated tows are wound onto a mandrel and subsequently cured, and wet fibre winding, where dry fibres are impregnated during the winding process. The cylindrical telescope tube in particular would benefit significantly from a design conceived from the outset for fibre winding, as its demanding geometry and laminate requirements necessitate labour-intensive manual manufacturing in the single-unit production context for which it was originally designed. Additionally it would enable a longer raw tube manufacturing, since the handling of the prepreg ply's is currently restricting the length of the raw tube manufacturing process.

4.5 Automated Insert Potting

The current insert potting process is entirely manual and represents one of the most labour-intensive and variability-prone operations in the panel manufacturing sequence. The insert potting process places high demands on the expertise of the operator, as insert height, orientation, and potting compound distribution are difficult to control consistently across a production series.

The introduction of an automated insert potting machine would address these limitations directly. Automated potting systems are capable of dispensing a precisely controlled volume of potting compound at a defined injection rate, eliminating the variability associated with manual injection. Automated height setting and positioning, integrated within the same system, would further reduce the operator dependency of the process. Beyond the reduction in man-hours, the primary benefit of automation in this context is the elimination of the risk of human error during a process whose outcomes are not fully verifiable until the post-machining stage, at which point a potting deficiency would most likely result in a scrapped panel.

In this context it is noted that INVENT GmbH is currently setting up a development program for automated insert potting technology, customized to the need of the space industry and will be able to offer this technology as part of its available manufacturing processes for future programmes.

4.6 Digitalisation of Manufacturing Processes

The digitalisation of manufacturing processes represents a significant opportunity for improving both production efficiency and quality assurance in a series production context. In the current manufacturing approach, the process documentation, measurement recording, and quality verification is performed manually, and documented on paper.

Adhesive mixing protocols represent an immediate candidate for digitalisation. Digital mixing protocols would not only provide operators with online access to the current and approved revision of the procedure, but would also enable real-time error checking during the mixing process, flagging deviations before a non-conforming batch is applied.

During the finalisation process, a large number of measured values – for example the electrical resistance measurements of the grounding network - are currently recorded manually by the operator. Digital recording of these values, with automated comparison against the specified requirement limits, would eliminate transcription errors, provide an immediate pass or fail indication, and generate a traceable digital record without additional administrative effort. This would deliver a direct benefit to PA activities, as the preparation of the MIP Report prior to part shipment currently requires the responsible engineer to manually retrieve and collate recorded values from printed manufacturing documentation.

Digital manufacturing documents would further enable a more detailed and structured description of each process step, with direct linking to adjacent work instructions and reference documents. This reduces ambiguity in the manufacturing process and supports the onboarding of less experienced operators. The real-time visibility of part status enabled by a digital manufacturing system would additionally improve production planning, as the current state of each part in the production flow can be monitored without physical inspection of the shop floor. Finally, design changes and document updates could be distributed and incorporated into the manufacturing documentation more rapidly and with greater control than is achievable with a paper-based system, reducing the risk of operators working to superseded instructions during a period of design evolution. INVENT GmbH has already established digital manufacturing documentation within its aviation division and is currently preparing to extend this capability across all divisions, drawing on the experience and lessons learned from the aviation implementation. A requirement for the adaptation to the space industry is the compliance to applicable ECSS and ISO standards. This positions the organisation to offer digital manufacturing documentation as a standard capability for future series production programmes in the space sector.

5 CONCLUSION

The work presented in this paper demonstrates that a structured optimisation of an existing satellite structural design for series production is both feasible and effective. The improvements implemented across the sandwich bonding process, the sandwich tube manufacturing, and the PA activities have delivered measurable reductions in production time, man-hour expenditure, and unit cost, whilst maintaining full compliance with the stringent dimensional stability and structural integrity requirements of an optical instrument structure. Additional programme-level measures — including curing process optimisation, in-house post-machining, dedicated resource allocation, batch-wise component production, and improved supplier priority — have contributed to an overall reduction in panel production time of 56% and tube production time of 58% in calendar weeks relative to the single-unit production baseline. Of the process-specific improvements presented, two emerge as the most broadly applicable: the introduction of dedicated process-specific jigs and tooling to reduce manual labour content and operator dependency, and the efficient utilisation of raw materials through batch-wise production strategies to minimise recurring process costs. These principles are not limited in their applicability to the processes discussed in this paper and should be among the first measures considered when adapting any existing satellite design for series production.

However, the scope of these improvements is inherently limited by the design decisions made during the original single-unit development programme. Material selections driven by performance margins rather than analytically justified mission requirements, tolerance schemes and requirements established without consideration of manufacturing process capability, process sequences optimised for craft manufacturing rather than repeatability, and structural geometries incompatible with automated manufacturing processes all represent constraints that cannot be fully overcome through process optimisation alone. The improvements achievable on an existing design are therefore incremental in nature, whereas the efficiency gains realised by a design conceived from the outset with Manufacturing, Assembly, Integration, and Testing (MAIT) in mind are of a fundamentally different order of magnitude.

It is therefore the conclusion of this paper that future satellite programmes intended for series production should establish design for MAIT as a primary programme requirement alongside the conventional performance, mass, and cost drivers. This implies that thermo-mechanical analyses should drive material selection rather than heritage conservatism, that tolerance schemes and requirements across all disciplines should be defined in conjunction with manufacturing process capability, that structural geometries should be assessed for compatibility with automated manufacturing processes such as AFP and fibre winding from the earliest design phases, and that verification and acceptance test philosophies should be tailored to the statistical nature of series production rather than the unit-by-unit paradigm of craft manufacturing. The digitalisation of manufacturing documentation, measurement recording, and quality verification represents a further significant lever for efficiency improvement in series production, delivering benefits in process control, PA efficiency, production planning, and configuration management. The reduced cost-per-kilogram-to-orbit offered by current launch vehicles further supports this shift, as the relaxation of minimum mass as an overriding design constraint creates additional degrees of freedom for design choices that prioritise manufacturability and repeatability.

The findings and recommendations presented in this paper are directly applicable beyond the optical instrument structures discussed herein. The underlying principles of design for series production, tolerance rationalisation, supply chain qualification, process automation, digitalisation, and systematic quality management, are transferable to other satellite subsystems and structural assemblies, and are expected to deliver comparable efficiency benefits wherever they are applied. As the demand for satellite constellations continues to grow, the ability to manufacture spacecraft structures efficiently and repeatably at scale will become an increasingly critical competency for the European space industry.

6 REFERENCES

1. Officina Stellare (04.09.2026). *Earth Observation – Platino 3 & 4*. https://www.officinastellare.com/wp-content/uploads/2024/08/leonardo_01-1318x1536.webp

MANUFACTURING THE PLATO OPTICAL BENCH: A LARGE, STABLE AND LIGHTWEIGHT STRUCTURE FOR 26 TELESCOPES

Lionel GURY [(1)], Stephan KRÜSI [(1)], Jascha SCHMIED [(2)]

[(1)] Beyond Gravity Schweiz AG, 8052 Zürich, Switzerland, stephan.kruesi@beyondgravity.com
[(2)] Bionic Composite Technologies AG, 9000 St. Gallen, Switzerland, jascha.schmied@biontec.ch

KEYWORDS

PLATO, satellite, structures, manufacturing, CFRP, integration, high-precision, alignment, stability, optical bench, exo-planets

ABSTRACT

The PLATO (PLAnetary Transits and Oscillations of stars) spacecraft is the next-generation exo-planet hunter in ESA's Cosmic Vision program.
The satellite has been developed by an industry consortium with OHB System as prime contractor and Beyond Gravity (formerly RUAG Space) and Thales Alenia Space as part of the Core Team. Beyond Gravity is responsible for the engineering and manufacturing of both the Optical Bench and Sun-shield (SSH) subsystems.
The ambitious goal of finding many Earth-sized exo-planets by performing long-term transit observations results in very challenging requirements on the Optical Bench, which is the 270 kg backbone of the Payload Module.

This paper focuses on the manufacturing, integration and verification of the Optical Bench Assembly (OBA), which has challenging requirements in terms of telescope co-alignment and in-orbit pointing stability.

1. INTRODUCTION

The PLATO Optical Bench Assembly (OBA) is the structural backbone carrying the payload of 26 cameras, as well as multi-layered insulation (MLI) and harness. The development of the cameras is led by a consortium of industry and academic partners from more than 13 European countries. The cameras are arranged in an array to redundantly cover a large field of view, offering different sensitivities over the field. The 26 cameras together will be the largest digital combined camera ever flown in space (1). The primary goal of the Optical Bench is to provide high pointing stability for the cameras over long observations (months to years), enabling the detection of Earth-sized exoplanets.

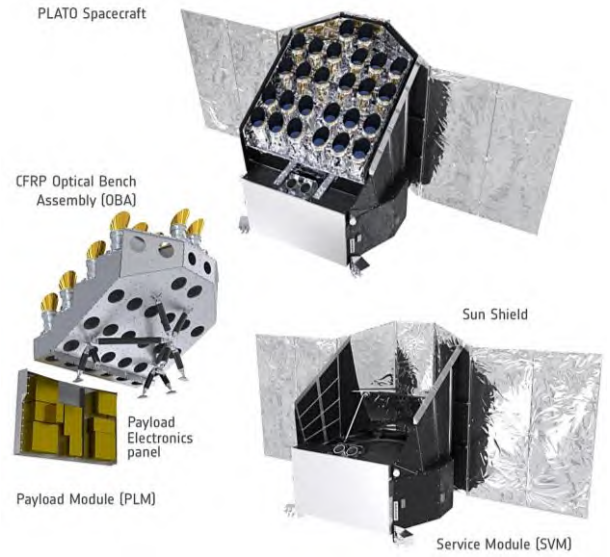


Figure 1: Overview of PLATO spacecraft subsystems (Image credit: ESA/ATG medialab (2))

The high pointing stability is achieved by the optimized design of the Optical Bench. The OBA structure is comprised primarily of carbon fiber reinforced plastic (CFRP) and titanium components. The "step" structure is made of sandwich panels with CFRP facesheets and aluminium honeycomb core and inserts (Figure 2). On this sandwich structure assembly, the camera support structures (CSS) are mounted which are also CFRP parts, manufactured using resin transfer moulding (RTM), with titanium interfaces to the cameras.

The truss structure (Figure 3), which provides interfaces for the Optical Bench to the Service Module (SVM), is composed of CFRP plates with titanium end fittings. The bi-flexible brackets and truss design achieve thermal decoupling from the service module and provide a quasi-isostatic boundary condition to the SVM.

The highly optimized OBA design minimizes the thermo-elastic distortions in the structure seen during the wide thermal range (-161°C to +90°C), as well as guaranteeing good accessibility for the cameras and a high stiffness to weight ratio.

Details of the engineering and mechanical testing of the PLATO OBA is discussed in (3).

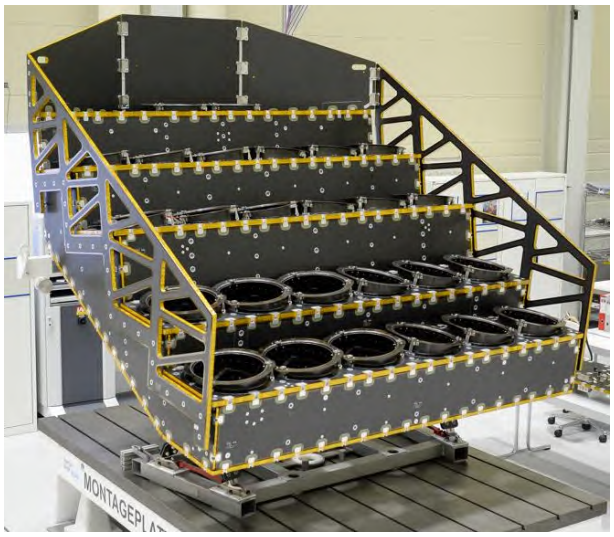


Figure 2: Optical Bench structure (without payload cameras, harness or MLI)



Figure 3: OBA (rear view) showing CFRP and titanium truss structure on integration stand

2. MATERIAL CHOICE

Carbon Fiber Reinforced Plastics have been used for space structures and are widely accepted as baseline material for space stable structures, mostly for their high specific stiffness, low thermal expansion. Cyanate Esters are used for their low moisture absorption properties (4).

Beyond Gravity has significant experience in the design and manufacturing of stable structures made from CFRP, such as the ExoMars Cassis telescope (5) (6) and PLANCK Telescope Support Structure and baffles which were designed and manufactured by Oerlikon Space, the predecessor of Beyond Gravity (7).

The choice of material and layup is driven by the requirement for high stability, in other words low coefficient of thermal expansion, low moisture absorption and low coefficient of moisture absorption. Ultimately, Toray M55J was chosen as a fiber which offers a good compromise and well characterised behaviour.

For the resin system a cyanate ester is chosen rather than epoxy due to lower moisture absorption.

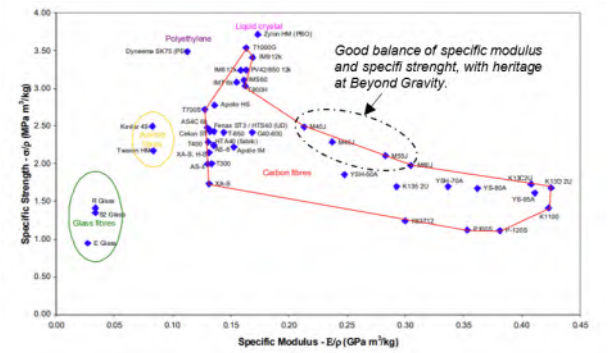


Figure 4: Specific tensile strength and specific tensile modulus for fibers, adapted from (8)

The layup chosen gives a quasi-isotropic behaviour and a near zero coefficient of thermal expansion.

Most of the structure consists of sandwich panels with CFRP facesheet and aluminium honeycomb, some of the key components are manufactured out of monolithic CFRP, those are the Camera support structures (CSS) directly interfacing with the instruments of PLATO, and the Truss structure.
Interfacing components, such as brackets are made out of titanium, chosen for low CTE. Radiators are made out of aluminium, a choice driven by the thermal properties required. Note that the radiators are mechanically decoupled from the structure by the provision of interfaces consisting of titanium blades.

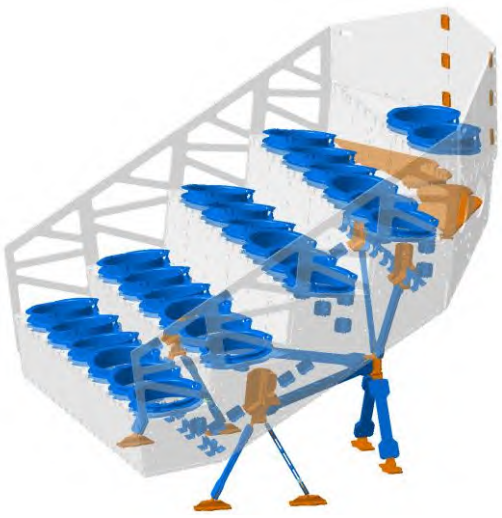


Figure 5: Monolithic CFRP parts shown in blue, CFRP sandwich shown in transparency and metallic in orange

3. MANUFACTURING OF THE CAMERA SUPPORT STRUCTURES

The camera support structures are the direct interface to the PLATO Instrument. The 26 cameras are arranged in 5 pointing groups. The goal was to find a common design, which could be adapted to each pointing direction.
Those components are particularly critical in terms of thermoelastic stability and mechanical loading, as each interface needed to survive a combination of 25 g axial and 15 g lateral acceleration.

The camera support structures consist of two concentric rings, inner L-shaped and outer C-shaped, which can be bonded on either side of the supporting panel. The concentric rings enable that a single CFRP blank can be machined and oriented in a way that it will fit any of the 5 pointing groups.

Beyond Gravity partnered with Bionic Composite Technologies AG (short Biontec) for the manufacturing of the camera support structures, a company experienced in the serial manufacturing of composite parts using Resin Transfer Moulding (RTM).
The RTM process of the CFRP part consists of using one main mould for both inner and outer rings. This main mould is modular and consists of a lower and an upper mould, complemented by seven metallic inlays for each ring of the camera support structure.

Dry CFRP preforms are manufactured with the Tailored Fiber Placement (TFP) process using an industrial embroidery machine. In this process a carbon fiber roving is positioned and oriented on a base substrate where it is fixed with thermoplastic stitching yarns. With this process the number of preforms is significantly reduced while the accuracy of the fiber orientation in all layers is predefined. The preforms are net-shape and can be manufactured with a varying number of layers and varying fiber angles within each layer.

The carbon fiber dry preforms are placed within the inlays, positioned in the mould, evacuated, infiltrated with resin, and then cured under controlled pressure and temperature conditions. This guarantees high dimensional accuracy and excellent repeatability.

For the PLATO camera support structure, a quasi-isotropic [0/60/-60]s layup was chosen, the carbon fiber is the Toray Torayca M40J. Variations of the stitching pattern were also studied and tested, in order to find the optimal parameters to maximize the performance.
Several resin systems were traded off, with respect to the compliance to the requirements such as outgassing, the suitability for the RTM process, and the availability. Lonza Primaset LECy Cyanate Ester was ultimately chosen.

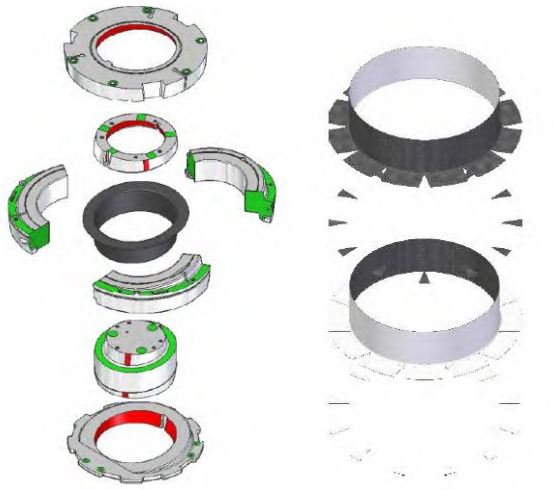


Figure 6: Camera support structure ring mould inlays (left) and preform (right)



Figure 7: CSS Inner Ring raw part (left) and CSS Outer Ring raw part (right)

4. STRUT DESIGN AND MANUFACTURING

Two design and manufacturing processes were investigated for the bipods: a “traditional” tubular strut, and an alternative design consisting of CFRP flat plates bolted together.
While the “traditional” tubular CFRP strut presents the advantage of having heritage, the alternative design consisting of plates is simpler to manufacture and integrate, thanks to no adhesive bonding, and easier to inspect by NDI Scan.



Figure 8: Two strut designs were evaluated

After qualifying both designs, the alternative “flat plate” design was adopted. A large, laminated plate

was manufactured, inspected and then machined into individual bipod components.

The individual bipod plates were match-drilled and bolted onto titanium end-fittings. The assembled strut design offered high axial stiffness while still being rotationally compliant, in order to accommodate thermo-elastic distortions of the PLATO Service Module below the Optical Bench.

5. MANUFACTURING OF THE PANELS

Manufacturing starts with the production of blank panels. The CFRP skins are adhesively bonded or co-cured to a shaped honeycomb core, then the panels are trimmed to the shape required to bond all the interfaces. Interfaces typically consist of a metallic insert providing the fitting for a bolted connection. One of the main challenges is obtaining a fitting matching the in-plane CTE of the CFRP, as well as the out-of-plane of the aluminium honeycomb core.

At this stage, the camera support structures are also bonded onto the panel. Rather than be fitted in their final shape and relying on a long tolerance chain, the camera interfaces come with additional material, which can then be post-machined away.



Figure 9: Precision machining of camera interfaces

During the post machining step, a single panel, equipped with 2 or 5 camera support structures (depending whether this is a panel for “fast” or “normal” cameras) is machined in a single step, such that all 6 or 18 camera interfaces on a single panel end up within a small tolerance. Measuring each camera IF relative to the reference fast camera IF, perpendicularity of less than 0.1 mm and angular tolerance of less than 5 arcmin were achieved.

The camera support structures within a panel are therefore all aligned well to each other. The next step is to assemble the 5 panels accommodating cameras support structures with high accuracy.

6. ASSEMBLY AND ALIGNMENT VERIFICATION

All interfaces and their reference point have been measured using a laser tracker before assembly. The as build model allowed to pre-align the camera plates by adding the required shim thickness where needed.

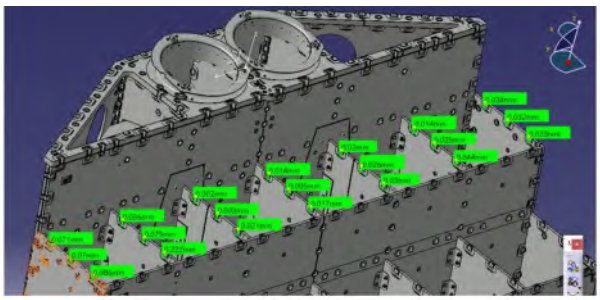


Figure 10: Shim calculation

After positioning each of the 5 camera plates onto the shimmed structure, the alignment is verified by laser tracker, once the required alignment is confirmed the camera plates were bolted down.
As for the final alignment verification since the main requirement is on the relative angular alignment of each of the cameras to the fast-Cam rather than a positioning requirement, a methodology was developed using high precision inclinometers.



Figure 11: Camera support structure interface pointing measurement

A dedicated plate to mount the inclinometer on the camera support structure was manufactured and calibrated. Each of the camera support structures were characterised in two axes with respect to the Fast Camera (the reference cam for observations).



Figure 12: Final assembly of the PLATO Optical Bench

7. INSPECTIONS AND VERIFICATIONS

Non-destructive inspection (NDI) was performed as part of the manufacturing process on all the CFRP components, with particular focus on the primary load path from the 26 telescopes down to the satellite interface.

Acceptance testing of the camera support structures (CSS) was done at sub-assembly level (camera plate and CSS), before final assembly onto the optical bench. Static loads were applied via a dummy camera, introducing acceptance loads into the 3 high-precision interfaces of each of the 26 camera support structures.
Acceptance testing of the CFRP and titanium truss structure (see Figure 3) was also performed in a similar fashion. Details on the mechanical testing are discussed in (3).

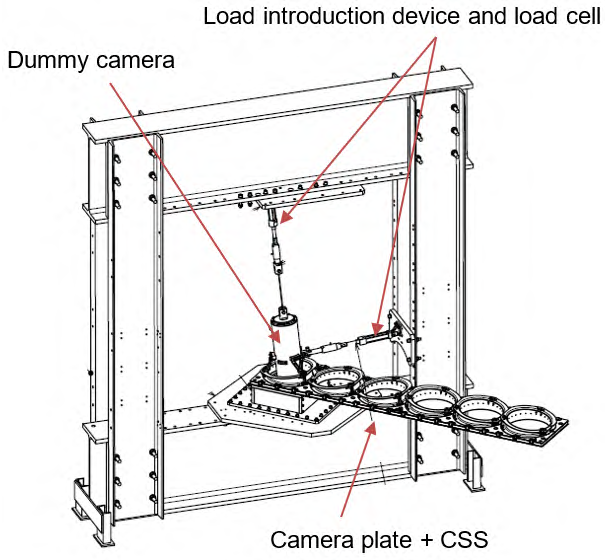


Figure 13: Acceptance testing of the camera IF

8. CONCLUSIONS

The PLATO Optical Bench Assembly demonstrates the successful manufacturing of a large, lightweight and dimensionally stable CFRP-based structure for a demanding multi-camera payload. The combination of CFRP sandwich panels, monolithic CFRP components and titanium interfaces provided a suitable compromise between stiffness, mass efficiency, thermo-elastic stability and manufacturability.
Several manufacturing routes were applied to address the different functional needs of the assembly. RTM was used for the camera support structures to achieve repeatable geometry and efficient serial production, while laminated CFRP plates were selected for the bipod components to simplify manufacturing and inspection. The panel manufacturing and post-machining approach enabled the camera interfaces to be generated with high relative accuracy at panel level, reducing the impact of tolerance build-up during final assembly.
The assembly sequence was supported by detailed metrology, as-built modelling and shimming, followed by final pointing verification using a dedicated inclinometer-based method. This approach allowed the relative alignment of the 26 camera interfaces to be controlled after integration, which is essential for the optical performance of the PLATO payload.
The inspection and verification activities performed throughout manufacturing, including non-destructive inspections and the subsequent acceptance test campaign, confirmed the suitability of the selected materials, processes and assembly concept for the flight hardware. The PFM Optical Bench was successfully manufactured and delivered in 2023, representing a major step towards the realization of the PLATO Payload Module.
Overall, the PLATO OBA manufacturing demonstrates that a highly integrated CFRP optical bench can be produced with the dimensional accuracy, repeatability and stability required for a next-generation exoplanet observation mission.

9. ABBREVIATIONS AND ACRONYMS

BG	Beyond Gravity
CFRP	Carbon Fiber Reinforced Plastic
CTE	Coefficient of Thermal Expansion
CSS	Camera Support Structure
IF	Interface
MLI	Multi-layered Insulation
NDI	Non-destructive Inspection
OBA	Optical Bench Assembly
PFM	Proto-flight Model
PLATO	PLAnetary Transits and Oscillations of stars
PLM	Payload Module
RTM	Resin Transfer Moulding
STM	Structural Thermal Model
TED	Thermo-Elastic Distortion
TFP	Tailored Fiber Placement

10. REFERENCES

1. **ESA.** ESA PLATO CCD. [Online] [Cited: 05 01 2023.] https://sci.esa.int/s/wV6y0Mw.
2. —. ESA PLATO Spacecraft. [Online] [Cited: 05 01 2023.] https://sci.esa.int/s/Aj6BrXA.
3. *PLATO OPTICAL BENCH MECHANICAL TEST CAMPAIGN.* **Stephan KRÜSI, Lionel GURY, Oliver NICOLAY, Daniele TETI, Arnoud KEEREMAN.** Toulouse : s.n., 2023. 17th ECSSMET.
4. *The Use of High Stiffness Material and Dimensionally Stable Materials in Spacecraft Applucations.* **David Bashford, David Eaton, Alain Pradier.** 1994. Workshowp on Advanced Materials for High Precision Detectors.
5. *The CaSSIS imaging system: optical performance overview.* **al., L. Gambicorti et.** 2016. Proceedings of SPIE.
6. *First light of Cassis: the stereo surface imaging system onboard the exomars TGO.* **L. Gambicorti, D. Piazza, A. Pommerol, V. Roloff, M. Gerber, R. Ziethe, M. R. El-Maarry, T. Weigel, M. Johnson, D. Vernani, E. Pelo, V. Da Deppo, G. Cremonese, I. Ficai Veltroni, N. Thomas.** 2017. SPIE.
7. *Planck pre-launch status: The optical system.* **Tauber, J. A., et al.** 2010. Astronomy and Astrophysics.
8. ***ECSS-E-HB-32-20 Part 1A – Structural materials handbook.* 2011.**

ECSSMET
Braunschweig Germany 2026

Shaker Test
Predicition & Testing

REASSESSING DYNAMIC MODEL PREDICTIONS THROUGH TESTING OF INVAP MODULAR ELECTRONIC UNITS

F. Teryda [(1)], N. Acuña [(1)]

[(1)] *INVAP S.A.U., San Carlos de Bariloche, Argentina. Email: fteryda@invap.com.ar, nacuna@invap.com.ar*

KEYWORDS

Modular Electronic Units, Modelling, Vibration, Testing, Correlation, Dynamics, Microslip.

ABSTRACT

Differences were identified when comparing the predicted FE (Finite Element) Model random vibration responses with the experimental results of vibration tests performed on the modular electronic units developed and qualified in-house at INVAP. In particular, the resonance frequency of the first vibration mode was underestimated. Moreover, the resonant frequency of the first mode was found to shift to lower frequencies for higher vibration test levels.

This paper studies the influence of multiple modeling assumptions that could have a considerable effect on the differences between the FE Model predictions and the dynamic test results. The analysis revealed that the interactions between modules had the biggest influence on the predicted dynamic response, challenging the previous understanding of how the structure of the unit works.

1. INTRODUCTION

INVAP develops and qualifies electronic boxes, such as PMU (Power Management Unit), PDU (Power Distribution Unit) and OBC (OnBoard Computer) subsystems that share the same modular architecture pictured in Fig. 1, configurable to attend specific mission requirements.

Pre-test structural analysis is performed to verify structural integrity of the units and assess compatibility of its components with the expected vibration environments.

This paper investigates the influence of multiple modeling assumptions that significantly affect the differences between the FE Model predictions and the dynamic test results.

An accurate representation of the structure's behavior presented a challenge across all modular units. This study focuses on the test and analysis of a 5 module variant of the PMU unit pictured in Fig. 2.

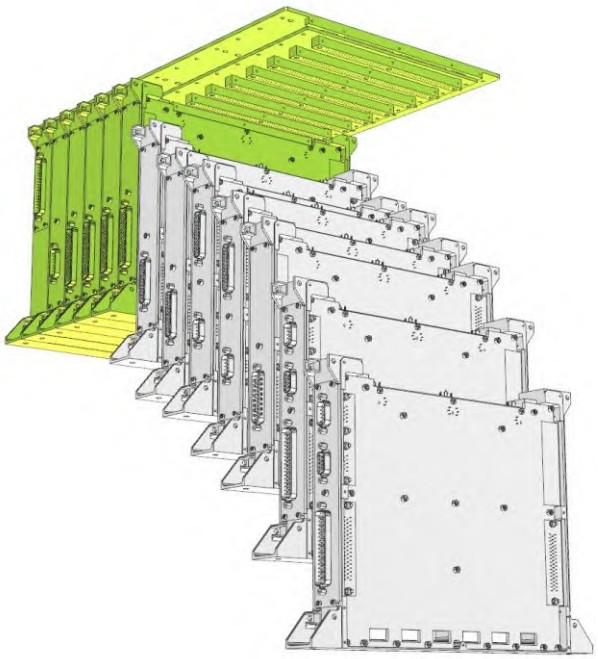


Figure 1 Modular philosophy of INVAP units.

The PMU unit is responsible for managing the electrical power generated by the solar panels and regulating the satellite's primary and secondary power buses to ensure stable voltage distribution. It monitors and controls the battery's state of charge through the main power bus voltage, while also enabling battery connection and disconnection when required. Additionally, the unit acquires telemetry from the satellite's subsystems and transmits it to the OBC via the CAN bus. Additionally, it provides the interface for battery charging and satellite power-up during ground testing.

The remainder of this paper is organized as follows. Section 2 details the original modelling strategy of the unit. Section 3 evaluates the effect of multiple modelling strategies on the response of the unit. Section 4 presents test results and compares them to the simulations. Section 5 explores non-linear behaviors identified during the tests. Finally, Section 6 presents the conclusions of this study and outlines directions for future work.

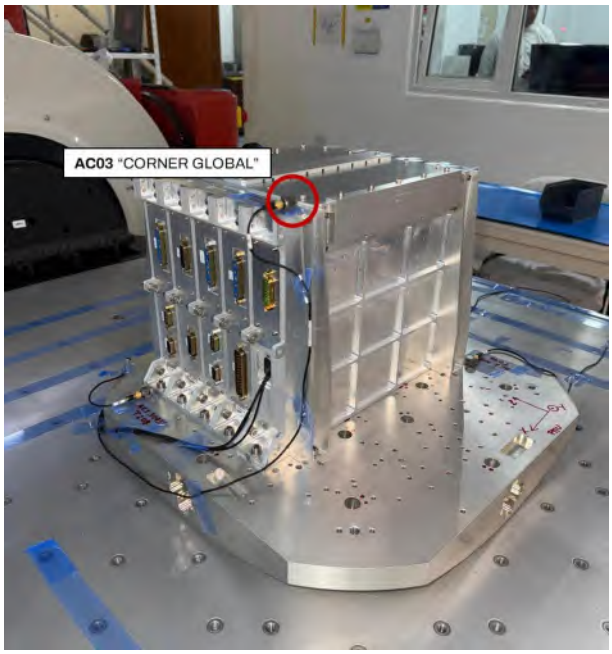


Figure 2: PMU Unit and instrumentation during vibration tests.

2. ORIGINAL FE MODELLING STRATEGY

The FE Model (Finite Element Model) of the unit is built using Siemens NX version 2312.

The 5 module variant of the PMU Unit weighs 17.05 kg and measures 276 x 347 x 250 mm.

The aluminium frames of the modules and aluminium side and top covers of the unit are meshed using CTETRA (10) elements. The aluminium connector covers are modelled using CQUADR 2D elements.

The PCBs (Printed Circuit Boards) are modelled with CQUADR 2D elements, using an orthotropic material with equivalent properties. Massive electronic components are represented with discrete 0D mass elements. The mass of the smaller electronic components is uniformly distributed over the surface of the PCBs.

Bolted joints are modelled using spring elements with stiffness $1 \times 10^9\,[N/m]$ and $1 \times 10^6\,[Nm/rad]$ for translations and rotations respectively. These are typical values for stiff joints based on INVAP previous experience. Neither bolt preloads nor friction are modelled in the FE Model. However they are considered in post-processing to assess the margin of safety of bolted joints. The only interaction between modules in the Original FE modelling strategy is through their bolted joints.

A typical damping ratio for the first mode of the unit was estimated from previous tests using the half power method [1], with a value of 3%. The same damping ratio is considered across the entire frequency bandwidth.

The boundary condition of the unit is modeled as a fixed rigid multi-node constraint connecting the interface points of the unit. Non dimensional spring elements are included in the interface to represent the stiffness of the interfaces.

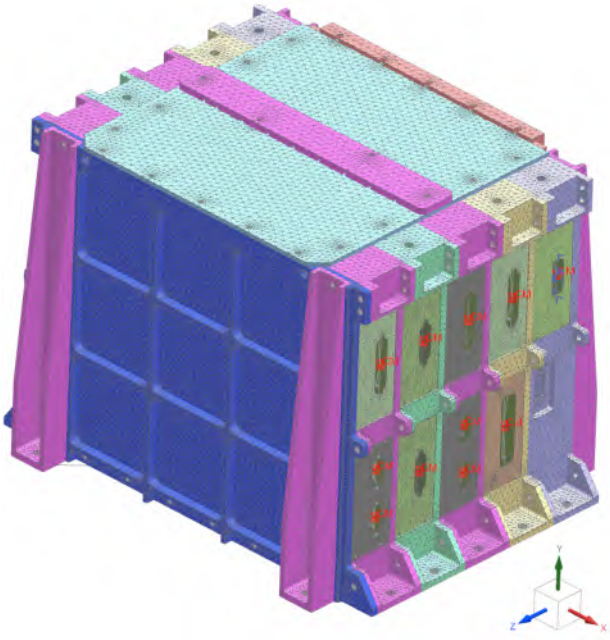


Figure 3: FE Model of the PMU unit.

A detailed mass breakdown of the components of the PMU was performed and total mass of the FE Model is adjusted to match the mass of the unit.

Under these modelling assumptions the FE Model simulations predict a resonance frequency of the first vibration mode at 174 Hz. The prediction is considerably lower than test results, where a resonance frequency of 225 Hz is found.

Since the total mass of the FE Model is adjusted to match the mass of the unit, the results suggest that the original modelling strategy does not accurately represent the stiffness of the unit, underestimating it.

3. PARAMETRIC STUDY ON MODELLING STRATEGIES

The effect of multiple variables in the resonance frequency of the first vibration mode is evaluated.

3.1. BOLTED JOINTS STIFFNESS

A verification is carried out by defining an unrealistically high value to the stiffness of bolted joints. Since the stiffness of the unit was underestimated with the original FE modelling strategy, the rigidity of bolted joints is increased by three orders of magnitude ($1 \times 10^{12}\,[N/m]$ N/m and $1 \times 10^9\,[Nm/rad]$ for translations and rotations respectively). Results are presented in Tab. 1.

The negligible sensitivity of the first-mode frequency to bolted-joint stiffness indicates that this parameter is not responsible for the discrepancy between FE Model predictions and test results.

Table 1: Bolted joint stiffness sensitivity test results

	Original	Stiff Joints	Frequency Change Δ%
1st mode Frequency	174 Hz	176 Hz	+1.1%

3.2. CONTACT BETWEEN MODULES

An analysis is performed considering surface-to-surface contact between the modules of the unit, allowing the components to move relative to one another without friction while preventing them from penetrating each other. The contact behavior is treated as nonlinear to establish the equilibrium configuration, but the modal analysis is still linear (prestressed modal analysis). Contact surfaces are presented in Fig. 4.

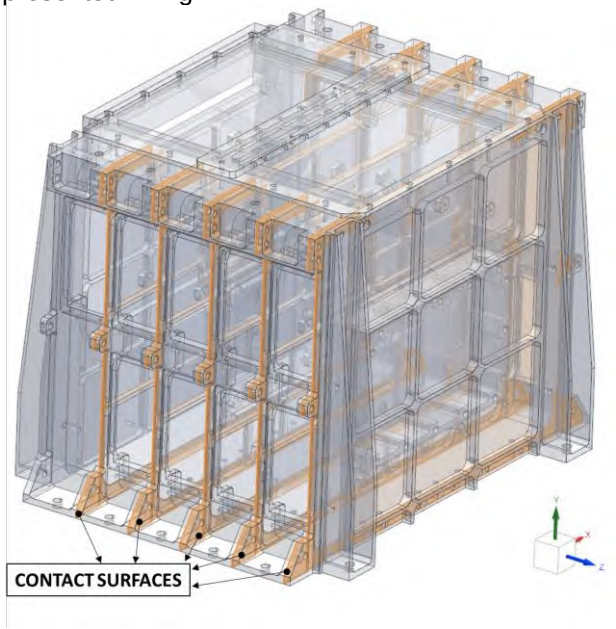


Figure 4: Contact surfaces between modules.

Table 2: Frictionless contact sensitivity test results

	Original	Contact Condition	Frequency Change Δ%
1st mode Frequency	174 Hz	178 Hz	+2.3%

As presented in Tab. 2, these results show that inter-module contact also fails to account for the observed frequency discrepancy.

3.3. GLUE CONDITION BETWEEN MODULES

An analysis is performed considering surface-to-surface glue condition between the modules of the unit. By considering a glue interaction, full compatibility of displacements between adjacent modules is enforced. Glued surfaces are the same as the contact surfaces presented in Fig. 4. Displacement results of the first vibration mode of the unit are presented in Fig. 5.

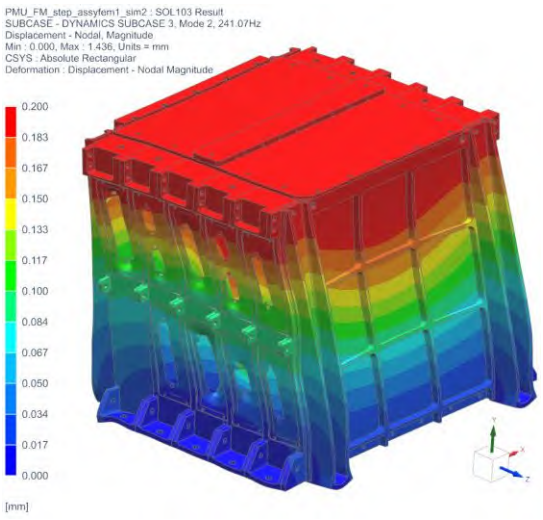


Figure 5: Displacement results of the first mode.

Table 3: Glue condition sensitivity test results

	Original	Glue Condition	Frequency Change Δ%
1st mode Frequency	174 Hz	240 Hz	+38%

As shown in Tab. 3, glue condition between modules has a considerable effect on the resonance frequency of the first vibration mode of the unit, and could explain the differences between the FE Model predictions and the dynamic test results.

4. TEST RESULTS

FE Model predicted transmissibilities and test results of the PMU unit are compared and presented in Fig. 6. It is important to note that test transmissibilities are extracted from low level (1grms) random (RD) vibration tests.

It is evident that model predictions derived from the glue condition between modules exhibit a significantly higher degree of precision than those produced by the original modelling strategy. Results are summarized in Tab. 4.

Table 4 FE modelling strategies compared with Test Results

	Original	Glue	1GRMS Test
Frequency	174 [Hz]	240 [Hz]	225 [Hz]
Frequency Relative Error %	-22.6%	+7.11%	-
Transmissibility	17.9	7.7	8.1
Transmissibility Relative Error %	+121%	-4.9%	-

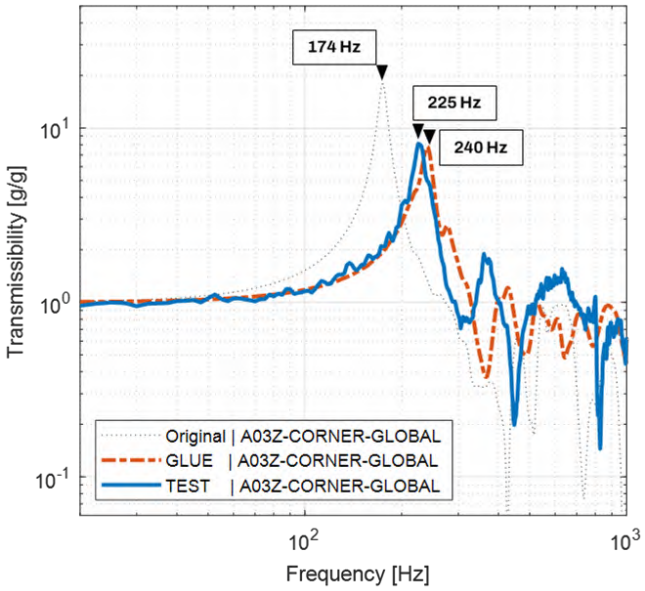


Figure 6: 1grms test results comparison with FE Model.

However, transmissibilities extracted from random tests were found to vary depending on test levels. Fig. 7 presents the difference found between low level random (1grms) and workmanship (6.7grms [1]) test transmissibilities. Resonance frequency of the first vibration mode of the unit shifted up to 7.8% with higher test levels.

Low level Sine Sweep tests (LLSS) are performed before and after random vibration tests to evaluate the structural integrity of the unit. As shown in Fig. 8, LLSS comparison before and after the tests do not present considerable frequency shifts or shape variations. The signature comparison verifies the structural integrity of the unit and confirms that the frequency shift found during random tests is not a consequence of physical degradation of the structure of the unit.

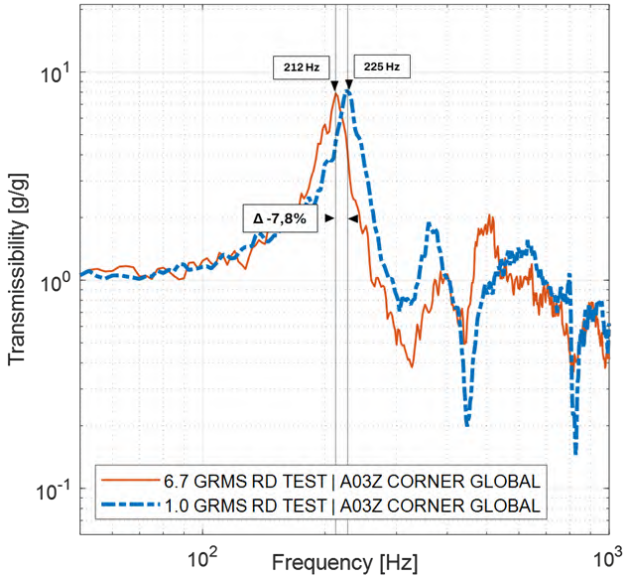


Figure 7 Transmissibilities on low level and workmanship random tests of the unit.

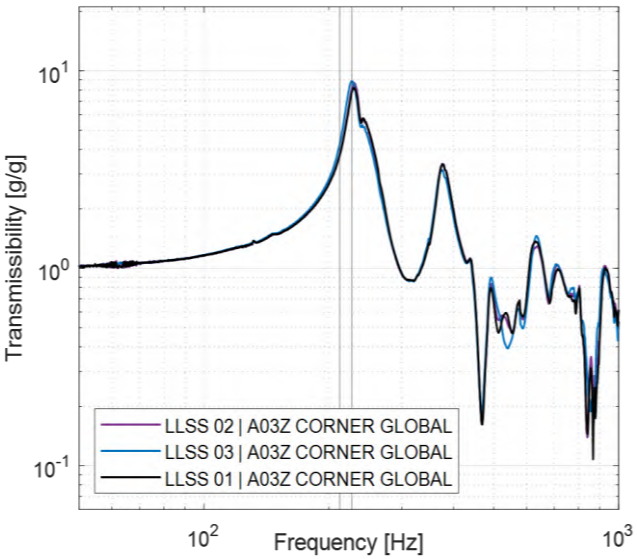


Figure 8 LLSS comparison during the test axis.

5. UNDERSTANDING TEST NON-LINEARITIES

5.1. RESONANT FREQUENCY SHIFT CAUSED BY DAMPING

Damping ratio is usually higher when the random vibration test levels are stronger. As a consequence, resonant frequency tends to shift. The damped natural frequency is always lower than the undamped natural frequency and, depending on the magnitude of the frequency shift, this phenomenon could be an explanation of the nonlinear behavior of the unit.

The formula for the damped natural frequency ω_d in a single-degree-of-freedom system is [2]:

$$\omega_d = \omega_n\sqrt{1-\zeta^2} \qquad (1)$$

In order to verify whether a higher damping ratio could be the explanation for the frequency shift, a sensitivity test was carried out. This involved defining an unrealistically high value of damping ratio (10%) for the first vibration mode of the unit (230 Hz).

$$\omega_d = 230\ Hz\sqrt{1-(0.1)^2} = 228.8\ Hz \qquad (2)$$

$$\Delta = -0.52\%$$

Under this unrealistic condition, damped natural frequency is only 0.52% lower than the undamped natural frequency. A nonlinear behavior of damping ratio with test levels does not explain the frequency shift measured during the random vibration tests of the unit.

5.2. MICROSLIP

In a bolted joint, the clamping force produced by the preload is not distributed uniformly across the contact surface. Some areas experience high

contact pressure, while other areas farther from the bolt experience low contact pressure.

When a tangential or cyclic load is applied, the behaviour of the interface depends on this pressure distribution. In areas of high normal pressure, friction is strong enough to prevent relative motion. However, in areas of low normal pressure, the available friction force is smaller than the applied tangential force, and these regions slip slightly relative to one another. This combination of stuck and slipping regions occurring at the same time on the same interface, while the joint as a whole stays fastened, is what defines microslip [3][4].

Cyclic loads may lead to microslip, which causes a significant contribution to structural damping and tends to decrease structural rigidity. This may explain the nonlinear behaviour of the unit.

5.3. PREVIOUS TEST EXPERIENCES

A similar nonlinear behavior was observed in another unit also built with a modular design philosophy. As shown in Fig. 9 and Fig. 10, resonant frequency decreases and damping ratio increases for higher test response levels. Low level signature comparison did not present considerable frequency shifts or shape variations.

The change of these parameters is gradual with test levels, there are no sudden variations. This behavior supports the microslip hypothesis, as low contact pressure regions are expected to slip gradually with test levels.

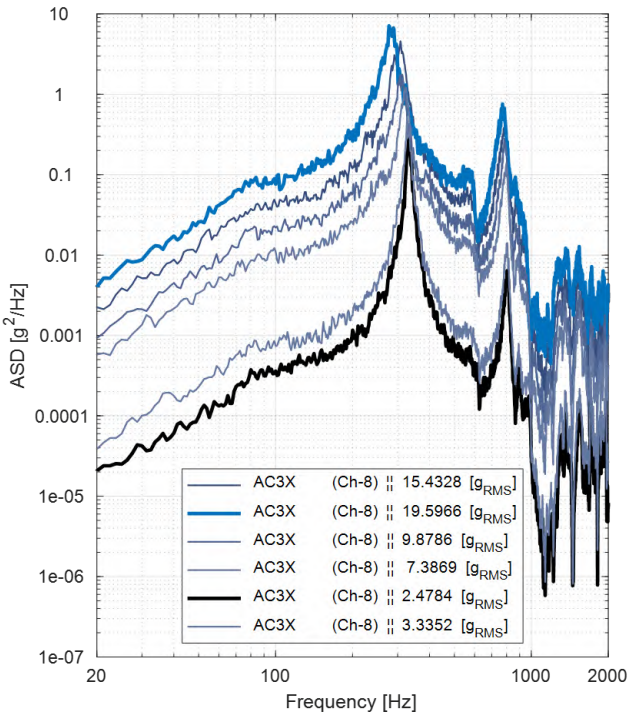


Figure 9 DIB Response across different test levels.

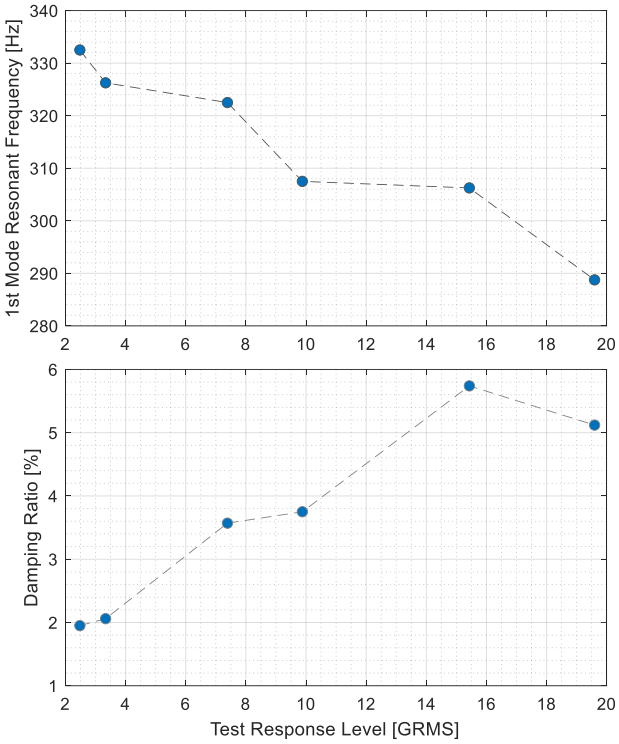


Figure 10 First mode of DIB: Damping Ratio and Frequency across different test levels.

6. CONCLUSIONS AND FUTURE WORK

6.1. CONCLUSIONS

The original modelling strategy of the PMU considered that the only interaction between modules was through their bolted joints. It did not accurately represent the stiffness of the unit, underestimating it.

Considering a frictionless contact condition between modules predicted a slightly higher frequency of the first mode of the unit, but it still was considerably lower than the test results.

The modelling strategy with glue condition between modules yielded much more precise predictions of the first mode, both in frequency and amplitude. By considering a glue type interaction, full compatibility of displacements between adjacent modules is enforced and a significantly improved correlation with the test data was achieved. This modelling approach yields the most accurate representation of the unit's response obtained in this study. The glue condition suggests that, at least for low vibration levels, there is no sliding between the modules.

However, during vibration tests it was found that the first mode of the unit shifted to lower frequencies when vibration levels were increased. The frequency shift found during random tests is not a consequence of physical degradation of the structure of the unit. A change in damping ratio and thus a variation in damped natural frequency could neither explain the magnitude of the shift.

The explanation for this phenomenon is that the frequency shift results from microslip at the joints between modules. Under these conditions, the interaction between adjacent modules behaves less like a glued interface and more like a frictionless contact.

6.2. FUTURE WORK

FE models of the unit are built to verify frequency requirements and to assess margins of safety of bolted joints, aluminium structures and PCBs. In addition, they are used to evaluate random responses of electronic components and compare them to their qualifications. Understanding the accuracy of our predictions is important to ensure the reliability of the units. This paper only studied the global response of the structure. Further work is needed to better understand the behavior of the PCBs. Variables such as board mechanical properties, interaction between boards and frames, and influence of electronic components on the stiffness of the PCBs are yet to be verified.

Moreover further work is needed to better understand the microslip behavior between modules. Useful further tests include:

- Higher level sine sweep tests with time history measurements to verify if there are discontinuities or sudden transitions in the signal. This test would also be useful to perform a mode shape map for different excitation levels. If the modal shape changes noticeably near the joints it reinforces the hypothesis of slippage occurring.

- Bolt torque variation test to determine if increasing the torque reduces or eliminates the dependence of frequency on test levels. This test would confirm whether the nonlinear behavior of the unit is a consequence of PCBs or any components of its interior.

- Microslip dissipates energy through friction, generating localized heating that might be measurable with an IR thermal camera. A localized temperature rise at the bolted interfaces would be direct physical evidence of active friction.

7. REFERENCES

1. Goddard Space Flight Center (2021). *General Environmental Verification Standard (GEVS) for GSFC Flight Programs and Projects*. GSFC-STD-7000B, NASA Goddard Space Flight Center, Greenbelt, MD, USA.

2. Rao, S.S. (2011). *Mechanical Vibrations*, Fifth Edition, Pearson Education, Upper Saddle River, NJ, USA.

3. Lenz, J. & Gaul, L. (1995). *The Influence of Microslip on the Dynamic Behavior of Bolted Joints.* In Proceedings of the 13th International Modal Analysis Conference (IMAC XIII), Nashville, TN, USA

4. Gaul, L. & Lenz, J. (1997). *Nonlinear Dynamics of Structures Assembled by Bolted Joints. Acta Mechanica* 125

EXPERIMENTAL VALIDATION OF A SEMI-DEFINED SD2DOF IMPEDANCE-BASED APPROACH FOR HORIZONTAL SATELLITE VIBRATION TESTING

Andrea Cambiaghi [(1)], Abdalla Reda [(2)]

[(1)] General Manager, Centrotecnica, Via F. Confalonieri, 23 - 20060 Masate (MI) - Italy, Email: a.cambiaghi@ctecnica.it

[(2)] Research and Development Department, Centrotecnica, Via F. Confalonieri, 23 - 20060 Masate (MI) - Italy, Email: a.reda@ctecnica.it

KEYWORDS

Vibration testing, Slip table rigidity, Finite Element Analysis correlation, Semi-defined Two-degree-of-freedom model, Facility mechanical impedance.

ABSTRACT

This study validates and extends a previously introduced semi-defined two-degree-of-freedom (SD2DOF) model for characterizing the influence of vibration test facilities on spacecraft qualification testing, focusing on the horizontal axis. Prior work showed that conventional Single-degree-of-freedom (SDOF) interpretations neglect key dynamic contributions from the test facility, and that the SD2DOF model offers a more accurate representation of the coupled satellite–facility system.

Experimental campaigns using slip table configurations with adjustable bearing arrangements enabled controlled tuning of the table's mechanical impedance, revealing systematic, repeatable shifts in resonance frequency and mode shape as a function of the imposed impedance. Accounting for slip table impedance within the SD2DOF model substantially improved experimental–numerical correlation compared to conventional rigid-constraint assumptions.

Results confirm that satellite compliance can be influenced by facility configuration alone, independent of satellite design. The study proposes mechanical impedance as a standard specification parameter for vibration facilities, improving finite element analysis (FEA) correlation and enabling more reliable, sustainable qualification testing.

1. INTRODUCTION

The dynamic interaction between a spacecraft and its vibration test facility has long been recognized as a potential source of discrepancy between FEA predictions and experimental test results. In a previous study [1], the authors introduced a SD2DOF model as an alternative to the conventional SDOF representation of the satellite – facility system. That work demonstrated, primarily through FEA and a first experimental validation on a resonant fixture, that neglecting the facility's mechanical impedance - its moving mass and stiffness - leads to systematic errors in predicted natural frequencies.

The present study extends and validates this approach for the horizontal axis, where satellites are mounted on a slip table guided in the direction of excitation. Unlike the vertical case, the horizontal configuration introduces an additional complexity: because the satellite's centre of gravity (COG) is offset from the slip table plane, horizontal excitation generates a pitch moment on the table, coupling the linear and rotational degrees of freedom of the facility. Prior work [2] identified the flexibility of the slip table as a significant contributor to the reduction of the fundamental lateral mode frequency, but a systematic experimental characterization of this effect - and of its correlation with the SD2DOF model - was still missing.

This work presents an experimental campaign conducted using slip table configurations with adjustable bearing arrangements, allowing controlled and repeatable tuning of the table's mechanical impedance.

Dummy payloads were tested across multiple impedance configurations to assess the resulting shifts in resonance frequency and in the actual vibration mode shape, and these results are correlated against FEA predictions using both the conventional rigid-constraint model and the SD2DOF impedance-based model.

The goal of this study is threefold: (1) to confirm experimentally that the SD2DOF model approach improves the correlation between FEA and test results in the horizontal axis; (2) to show that the mode shape discrepancy observed in conventional FEA is caused by the non-infinite rigidity of the slip table and launcher, not accounted for in standard boundary conditions; and (3) to propose mechanical impedance as a practical, standardizable parameter for facility specification and test preparation, ultimately contributing to more reliable and sustainable vibration qualification testing.

2. MATERIAL AND METHODS

2.1. Vibration system architecture

The complete horizontal vibration test system consists of several coupled substructures, each with its own mass, moment of inertia and stiffness properties, as shown in Fig.1. The shaker body mass houses the armature and driver bar mass, which generates the excitation force. The shaker as a whole is isolated from the floor and, in the frequency range of interest, can be considered in a free-free condition, consistent with the assumption already discussed for the vertical-axis case in [1].

The armature drives, through the driver bar, a slip table - characterized by its own mass and stiffness - which is connected to the combo frame mass through mechanical guides. The DUT is not mounted directly on the slip table but on an intermediate fixture, whose own stiffness further contributes to the dynamic chain between the excitation source and the DUT (here represented as a top box mass).

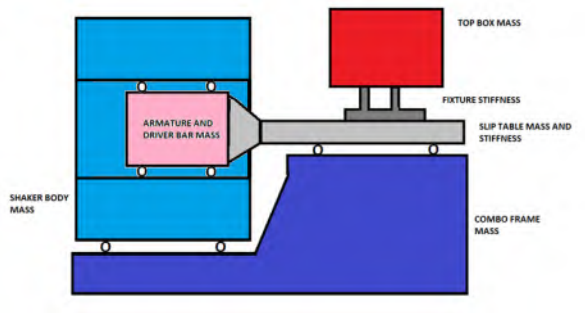


Figure 1: Vibration system architecture

This architecture shows that the DUT's dynamic response during a vibration test is not governed solely by its own structural properties, but by the combined behaviour of several coupled elements: DUT, fixture, slip table, driver bar and shaker armature are combined together in a new structure excited by a dynamic force. This new structure interacts with the shaker body, combo base frame s through bearings. Reducing this system to a single boundary condition - as done in a conventional rigidly-constrained FEM analysis - necessarily discards the dynamic contribution of all of these elements.

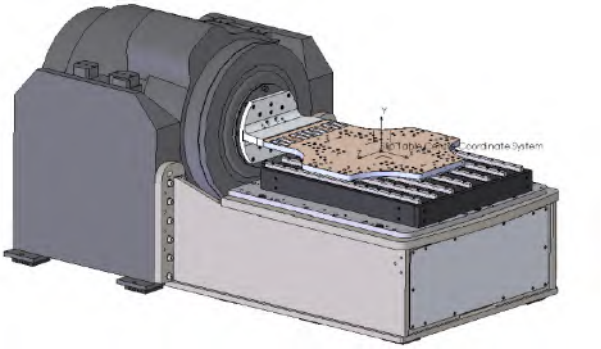


Figure 2: IMV A74 vibration system

To properly capture how these substructures influence the resonance frequency and mode shape measured on the DUT, their combined dynamic effect should be represented explicitly, rather than replaced by an idealized rigid or free boundary.

Rather than modelling every substructure of Fig.1 individually, this study adopts a reduced dynamic representation, lumping the facility's combined mass and stiffness contribution into two equivalent parameters - an equivalent inertia J_2 and an equivalent rotational stiffness k_β - consistent with the SD2DOF model developed in Section 3.

2.2. Test setup and instrumentation

The experimental campaign was conducted on a custom slip table, designed for the specific DUT configuration under study, mounted on an A74 electrodynamic shaker. As in the previous study [1], the shaker's control system regulates the excitation through a closed-loop vibration controller, modulating the drive signal to maintain a target acceleration at the control accelerometer position.

In this test campaign, the control accelerometer was located at the front point of the fixture (VTA vibration test adapter) - that is directly on the table surface, at the interface where the DUT is mounted - rather than on the DUT itself.

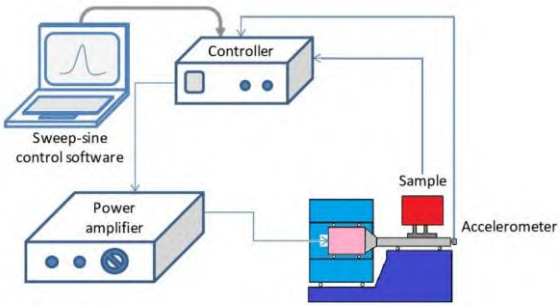


Figure 3: Closed-loop control system for constant excitation acceleration [3]

2.3. Device Under Test (DUT)

A dummy mass, representative of a satellite, was rigidly mounted on the slip table to simulate the DUT during testing. The dummy assembly consists of a cylindrical structure supporting a concentrated mass at its top, for a total mass of 300 kg. The centre of gravity (COG) is located at 600 mm above the slip table plane, and the DUT's moment of inertia about the mounting flange, $J_1 = 187\ kg\ m^2$, was calculated using the Computer-Aided Design (CAD) software.

The offset between the COG and the slip table plane is consistent with the pitch-coupling mechanism discussed in the previous vertical-axis study [1] and is expected to play a significant role in the horizontal-axis dynamic response.



Figure 4: Dummy mass on horizontal slip table

Two slip table bearing configurations were tested, allowing a controlled variation of the table's mechanical impedance without any modification to the dummy mass or its mounting interface. This enabled a direct experimental comparison of how facility impedance affects the measured resonance frequency and mode shape of the DUT.

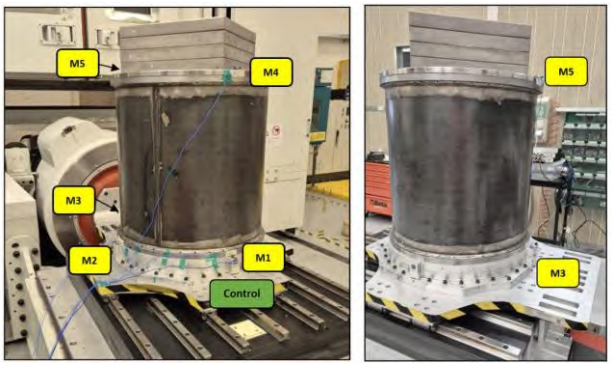


Figure 5: Accelerometers locations

The dynamic response was measured using five triaxial accelerometers: three positioned on the base of the dummy assembly (at the slip table interface) and two positioned on the upper part of the structure, near the concentrated mass. Acceleration was measured at all five locations during closed-loop sine sweep tests, with the vibration controller maintaining constant acceleration at the control position throughout the frequency sweep.

2.4. Slip Table Bearing configurations

To evaluate the influence of the slip table's rotational stiffness k_β on the DUT's measured resonance frequency, two bearing configurations were tested, differing in the number and arrangement of bearings supporting the slip table along the guides.

Configuration A: employs 16 bearings, arranged as in Fig.6.
Configuration B: employs 26 bearings, arranged as in Fig.7.

Both configurations use linear mechanical bearings, consistent with the assumption of a linear elastic guide stiffness, as opposed to hydrostatic bushing guides whose stiffness behaviour is markedly non-linear.

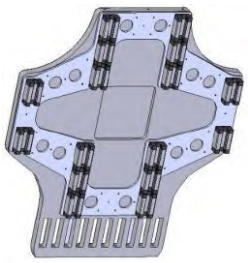
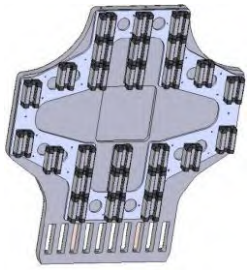
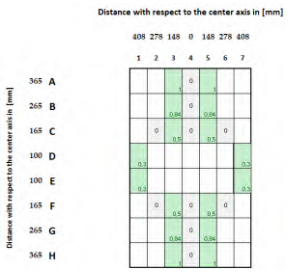
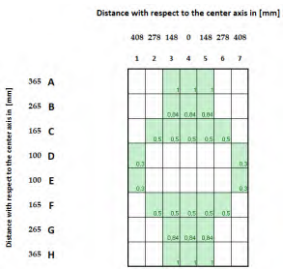
The equivalent rotational stiffness k_β of each configuration was estimated from the individual bearing stiffness and its geometric position along the table, following the same equivalent-elasticity approach described in [1].

For a set of n bearings, each with translational stiffness k_i located at a distance d_i from the table's rotation axis, the equivalent rotational stiffness is:

$$k_\beta = \sum_{i=1}^{n} k_i \, d_i^2 \qquad (1)$$

The increased number of bearings in Configuration B increases the equivalent rotational stiffness of the guidance system

Table 1: Configuration comparison

Configuration A	**Configuration B**
16 Bearings	26 Bearings
 *Figure 6: Configuration A 16 Bearings*	 *Figure 7: Configuration B 26 Bearings*
 *Figure 8: Bearings reaction force distribution A*	 *Figure 9: Bearings reaction force distribution B*

2.5. FEM model

The FEM correlation was performed as a free-free modal analysis of the complete simplified vibrating system, rather than a conventional fixed-base modal analysis. This choice is consistent with the free-free assumption already established for the shaker system in [1]: because the shaker is isolated

from the floor above the insulation frequency (about 10 Hz) and therefore, within the frequency range of interest, offers no reaction path to ground. The entire chain of coupled masses and stiffnesses - DUT, slip table, guide stiffness, and seismic base - should be analysed as an unconstrained, self-contained dynamic system.

The vibrating system was represented in a simplified finite element model, reducing the full facility architecture (shaker body, combo frame, eventual seismic mass) to a single equivalent inertia J_2, matching the moment of inertia estimated for the real facility structure. This inertia was connected to the slip table plate through modelling each individual bearing with the linear stiffness k_i.

The DUT - represented by the dummy described in Section 2.3 - was modelled and connected to the slip table through the fixing flange.

This simplified model directly reproduces the discrete SD2DOF schema of Section 3 (Fig.13): the DUT's own rotational stiffness k_α, the slip table node, the guide stiffness k_β, and the equivalent facility inertia J_2. A modal analysis was performed on this reduced model for both tested bearing configurations (Configuration A and Configuration B), providing the FEM-predicted natural frequencies.

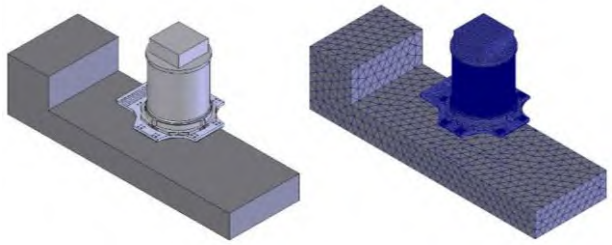


Figure 10: FEM model and Mesh

The analysis was repeated for both bearing configurations described in Section 2.4, by updating only the equivalent guide stiffness k_β in the model - while keeping the DUT properties (m_1, J_1) and the equivalent facility inertia J_2 unchanged - allowing a direct FEM-based verification of the frequency shift predicted analytically between Configuration A and Configuration B. This comparison - analytical prediction, FEM result, and experimental measurement, for each bearing configuration - is presented and discussed in Section 4.

3. THEORETICAL FRAMEWORK

Modelling assumption:

- J_1 *and* J_2 are the only rotational inertias.
- The slip table is treated as a massless rotational node. Its rotational inertia and stiffness can be included in the DUT similarly to the FEA model.
- k_α *and* k_β are linear torsional springs.
- Small-angle assumption.

3.1. Rotational SDOF model (rigid boundary)

As in the conventional FEM approach, the DUT is first modelled as a rigid body constrained at its mounting interface, with all translations and rotations fixed. Under horizontal base excitation, the relevant dynamic behaviour is governed by the DUT's own pitching stiffness: the satellite structure behaves as a rotational spring of stiffness k_α connecting its moment of inertia J_1 (about the mounting interface) to an infinitely rigid boundary.

The kinetic and potential energy of this system are:

$$T = \frac{1}{2} J_1 \dot{\theta}_1^2 \qquad (2)$$

$$V = \frac{1}{2} k_\alpha \theta_1^2 \qquad (3)$$

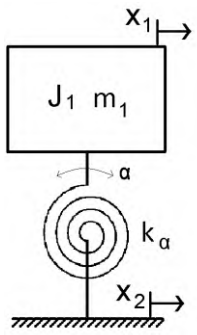
Applying Lagrange's equation:

$$\frac{d}{dt}\left(\frac{\partial T}{\partial \dot{\theta}_1}\right) - \frac{\partial T}{\partial \theta_1} + \frac{\partial V}{\partial \theta_1} = 0 \qquad (4)$$

Gives the equation of motion:

$$J_1 \ddot{\theta}_1 + k_\alpha \theta_1 = 0 \qquad (5)$$

Whose natural frequency is:



$$\omega_1 = \sqrt{\frac{k_\alpha}{J_1}} \qquad (6)$$

Figure 11: Rotational SDOF

3.2. Effect of finite facility inertia (finite J_2)

The next step introduces a facility of finite rotational inertia J_2. In this configuration, the slip table plate itself becomes free to rotate as a rigid body of inertia J_2, coupled to the DUT through the DUT's own bending stiffness k_α.

Let θ_1 and θ_2 be the absolute pitch rotations of the DUT and of the facility inertia J_2, respectively. Since the guides are rigid, θ_2 also represents the absolute rotation of the slip table, which is rigidly connected to the facility. The relative twist across the spring k_α is $(\theta_1 - \theta_2)$.

The energy functions of the system are:

$$T = \frac{1}{2} J_1 \dot{\theta}_1^2 + \frac{1}{2} J_2 \dot{\theta}_2^2 \qquad (7)$$

$$V = \frac{1}{2} k_\alpha (\theta_1 - \theta_2)^2 \qquad (8)$$

Applying Lagrange's equation to each coordinate gives the coupled equations of motion:

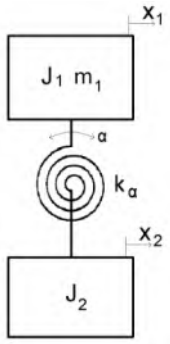
$$J_1 \ddot{\theta}_1 + k_\alpha (\theta_1 - \theta_2) = 0 \qquad (9)$$

$$J_2 \ddot{\theta}_2 - k_\alpha (\theta_1 - \theta_2) = 0 \qquad (10)$$

This is the classical free–free two-inertia torsional oscillator. As with any such system, one solution corresponds to a zero-frequency rigid-body mode ($\theta_1 = \theta_2$, both inertias rotating together with no spring deformation), while the second, non-trivial solution gives the elastic natural frequency:

$$\omega_n = \sqrt{k_\alpha \left(\frac{1}{J_1} + \frac{1}{J_2}\right)} = \sqrt{\frac{k_\alpha}{J_1}} \sqrt{1 + \frac{J_1}{J_2}} \qquad (11)$$

written in terms of the reference frequency ω_1 from Eq.(6):



$$\omega_n = \omega_1 \sqrt{1 + \frac{J_1}{J_2}} \qquad (12)$$

Figure 12: Finite facility inertia

3.3. Effect of finite guide stiffness (finite k_β)

The final step introduces the finite rotational stiffness k_β of the slip table guides, connecting the facility inertia J_2 to the slip table. As shown in Fig. 13, the table itself is now supported by two rotational springs in series: k_α representing the DUT's own bending stiffness, and k_β representing the rotational stiffness of the guides.

Let θ_1, φ, and θ_2 be the absolute pitch rotations of the DUT, the table node, and the equivalent facility inertia J_2, respectively. The relative rotations across the two springs are:

$$\alpha = \theta_1 - \varphi \ (\text{across } k_\alpha) \qquad (13)$$

$$\beta = \varphi - \theta_2 \ (\text{across } k_\beta) \qquad (14)$$

Because the table node carries no rotational inertia, φ does not contribute to the kinetic energy of the system:

$$T = \frac{1}{2} J_1 \dot{\theta}_1^2 + \frac{1}{2} J_2 \dot{\theta}_2^2 \qquad (15)$$

$$V = \frac{1}{2} k_\alpha (\theta_1 - \varphi)^2 + \frac{1}{2} k_\alpha (\varphi - \theta_2)^2 \qquad (16)$$

Applying Lagrange's equation to θ_1 and θ_2 gives:

$$J_1 \ddot{\theta}_1 + k_\alpha (\theta_1 - \varphi) = 0 \qquad (17)$$

$$J_2 \ddot{\theta}_2 - k_\beta (\varphi - \theta_2) = 0 \qquad (18)$$

Since φ carries no inertia, its own Lagrange equation $\left({}^{\partial T}/_{\partial \dot{\varphi}} = 0\right)$ degenerates into a static equilibrium condition rather than a dynamic one: the moment transmitted through the massless table node is continuous across the two springs at every instant.

$$k_\alpha(\theta_1 - \varphi) = k_\beta(\varphi - \theta_2) \qquad (19)$$

Solving Eq. (19) for φ:

$$\varphi = \frac{k_\alpha \theta_1 + k_\beta \theta_2}{k_\alpha + k_\beta} \qquad (20)$$

and substituting back into the twist expressions:

$$\theta_1 - \varphi = \frac{k_\beta (\theta_1 - \theta_2)}{k_\alpha + k_\beta} \qquad (21)$$

$$\varphi - \theta_2 = \frac{k_\alpha (\theta_1 - \theta_2)}{k_\alpha + k_\beta} \qquad (22)$$

Substituting into Eq. (17) and Eq. (18) eliminates the auxiliary coordinate φ, yielding the equations of motion of an equivalent free–free two-inertia torsional system connected by the equivalent series stiffness k_{eq}.

$$J_1 \ddot{\theta}_1 + k_{eq} (\theta_1 - \theta_2) = 0 \qquad (23)$$

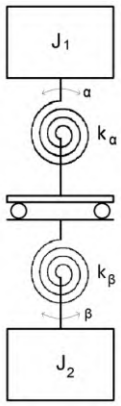
$$J_2 \ddot{\theta}_2 + k_{eq} (\theta_2 - \theta_1) = 0 \qquad (24)$$

$$k_{eq} = \frac{k_\alpha k_\beta}{k_\alpha + k_\beta} = \frac{k_\alpha}{1 + {}^{k_\alpha}/_{k_\beta}} \qquad (25)$$

As in Step 2, this system has one zero-frequency rigid-body mode and one non-zero elastic mode, whose frequency follows the same reduced-inertia formula, now with k_{eq} in place of k_α:

$$\omega_n = \sqrt{k_{eq} \left(\frac{1}{J_1} + \frac{1}{J_2}\right)} = \sqrt{\frac{k_\alpha}{J_1}} \sqrt{\frac{1 + {}^{J_1}/_{J_2}}{1 + {}^{k_\alpha}/_{k_\beta}}} \qquad (26)$$

Expressed in terms of the reference frequency ω_1:



$$\omega_n = \omega_1 \sqrt{\frac{1+\frac{J_1}{J_2}}{1+\frac{k_\alpha}{k_\beta}}} \quad (27)$$

Figure 13: SD2DOF in horizontal configuration

This is the complete SD2DOF natural frequency for the horizontal configuration, combining the effect of finite facility inertia (numerator, Step 2) and finite guide stiffness (denominator, this step). It reproduces exactly Eq. (11) of [1] by including the slip table rotational inertia and rotational stiffness in the DUT.

3.3.1. Physical interpretation

Eq. (27) separates two competing effects. The numerator term $\sqrt{(1+J_1/J_2)}$ is always ≥ 1 and tends to increase ω_n relative to the fixed-base reference ω_1: a facility of finite inertia participates in the motion, reducing the effective inertia the DUT rotates against.
The denominator term $\sqrt{(1+k_\alpha/k_\beta)}$ is always ≥ 1 and, conversely, tends to decrease ω_n.

4. RESULTS

4.1. Calculation and FEM results

The fixed-base natural frequency of the DUT, ω_1, was first computed via FEA, applying a rigid constraint at the mounting interface (Section 3.1 assumption):

$$\omega_1(\text{rigid base, FEA}) = 243\ [\text{Hz}]$$

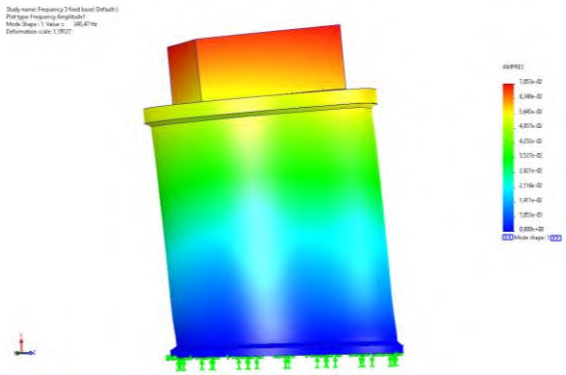


Figure 14: Fixed-base natural frequency ω_1

Since the moment of inertia about the fixing flange $J_1 = 187\ \text{kg m}^2$, of the DUT is directly available from the CAD software ,the DUT's equivalent rotational stiffness $\boldsymbol{k_\alpha}$ can be back-calculated by inverting Eq. (6):

$$k_\alpha = \omega_1^2 J_1 \quad (28)$$

$$k_\alpha = 4.36\text{x}10^8 \left[{}^{N\,m}/_{rad}\right]$$

The facility parameters are defined as follows: the equivalent inertia $\boldsymbol{J_2}$ of the seismic base is estimated using the CAD software, while the equivalent rotational stiffness $\boldsymbol{k_\beta}$ of each bearing configuration is computed from the corresponding bearing arrangement, as described in Section 2.4.

Table 2: Facility parameters

Parameter	Value
$\boldsymbol{J_2}$ [kg m^2]	15200
$\boldsymbol{k_\beta}$ [MN m/rad] -Configuration A	26.7
$\boldsymbol{k_\beta}$ [MN m/rad] -Configuration B	41.6

With k_α, J_1, J_2, and k_β determined for both tested configurations, the coupled SD2DOF natural frequency $\boldsymbol{\omega_n}$ was evaluated in two ways:

The first is analytical estimation, using the closed-form expression of Eq. (27):

Table 3: Analytical SD2DOF natural frequencies

Results	Value
$\boldsymbol{\omega_n}$ - Configuration A	58.8 Hz
$\boldsymbol{\omega_n}$ - Configuration B	72.3 Hz

The second is numerical: through the free-free modal analysis described in Section 2.5, which was performed for both bearing configurations, using the equivalent guide stiffness k_β reported in Table 2 as input to the FEM model. Consistent with the free-free boundary condition, the analysis returned a set of near-zero-frequency rigid-body modes, followed by the first non-zero elastic mode, identified as the coupled DUT–facility pitch resonance.

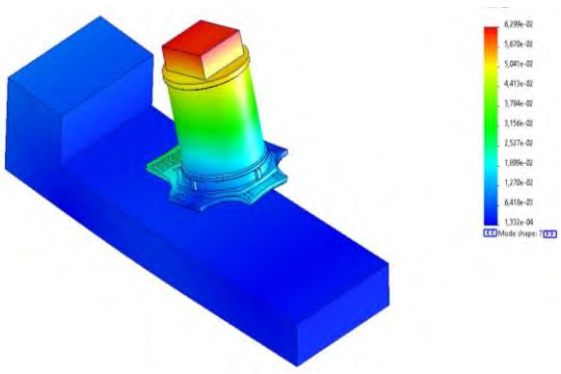


Figure 15: FEM natural frequency mode shape

Table 4: FEM natural frequencies results

Results	Value
ω_n - Configuration A	58.3 Hz
ω_n - Configuration B	70.7 Hz

the FEM mode shape confirms the DUT rotating about a node located near the slip table interface, consistent with the discrete SD2DOF schema of Fig.13.

4.2. Experimental Results - Configuration A vs Configuration B

The experimental sine sweep tests described in Section 2 were performed under closed-loop acceleration control, with the control accelerometer located at the fixture. The tests were repeated at three excitation levels (5, 10, and 20 m/s²) to verify the repeatability and consistency of the measured response across the tested amplitude range. Table 5 reports the measured resonance frequencies at the base of the DUT, from accelerometers M1 and M3, for both bearing configurations at each excitation level.

4.2.1. Measurements at accelerometer M1:

Fig.16-18 compare the frequency response profiles of Configuration A and Configuration B at accelerometer M1, located at the base of the fixture, at 5, 10, and 20 m/s² respectively, highlighting the shift in the pitch resonance peak between the two configurations.

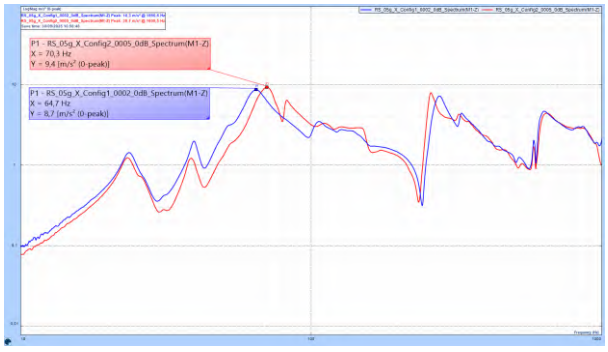


Figure 16: Acc. M1 - 5m/s²

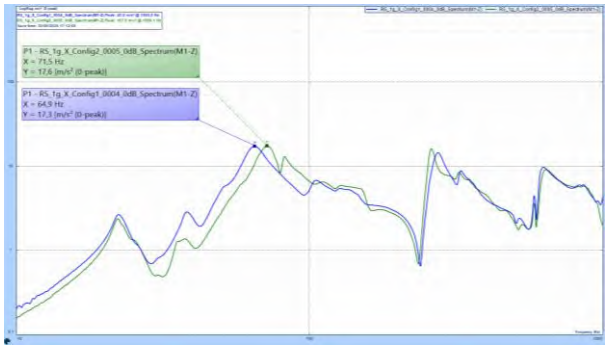


Figure 17: Acc. M1 - 10m/s²

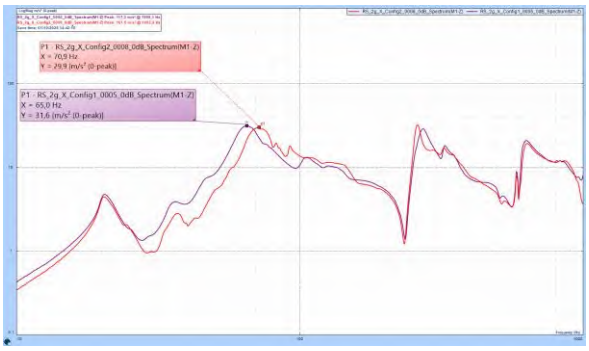


Figure 18: Acc. M1 - 20m/s²

4.2.2. Measurements at accelerometer M3:

Fig.19-21 compare the frequency response profiles of Configuration A and Configuration B at accelerometer M3, at 5, 10, and 20 m/s² respectively.

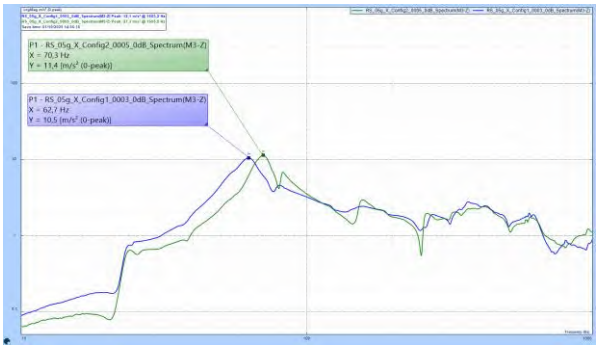


Figure 19: Acc. M3 - 5m/s²

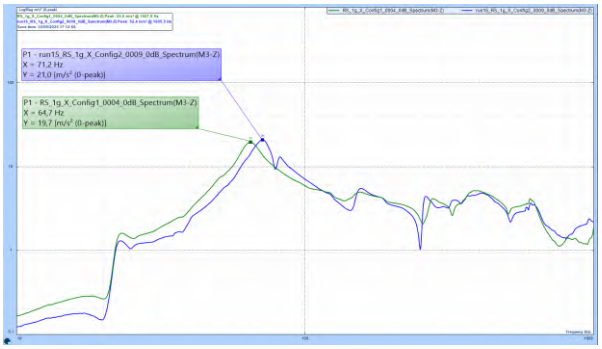


Figure 20: Acc. M3 - 10m/s²

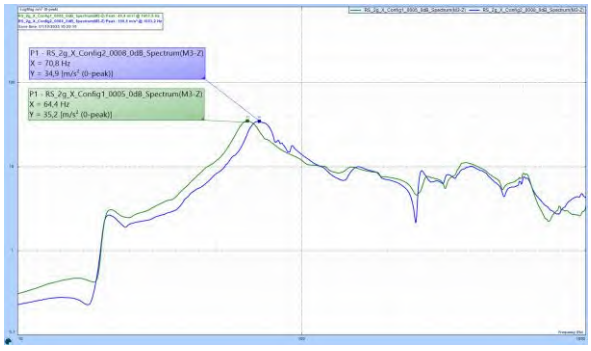


Figure 21: Acc. M3 - 20m/s²

Table 5: Experimental test results

Config.	Acc. [m/s²]	ω_n [Hz] Measured at M1	ω_n [Hz] Measured at M3
A	5	64.7	62.7
A	10	64.9	64.7
A	20	65.0	64.4
B	5	70.3	70.3
B	10	71.5	71.2
B	20	70.9	70.8

4.3. Discussion

The measured resonance frequencies show a shift between the two configurations consistent in direction with both the analytical prediction and the FEM results (Section 4.1).

Table 6: Summarized results

	Acc. m/s²	ω_n [Hz] SD2DOF	ω_n [Hz] FEM	ω_n [Hz] Measured at M1	ω_n [Hz] Measured at M3
A	5	58.8	58.3	64.7	62.7
	10			64.9	64.7
	20			65.0	64.9
B	5	72.3	70.7	70.3	70.3
	10			71.5	71.2
	20			70.9	70.8

It should be acknowledged that the lumped-parameter representation adopted in this study, reducing the entire facility to the two discrete parameters J_2 and k_β, is a deliberate simplification of the real vibration system. As such, it cannot represent the distributed mass and stiffness characteristics of the structure or fully capture its physical complexity. Consequently, while the model effectively describes the dominant dynamics governing the facility–DUT interaction, it is not intended to reproduce the complete dynamic behaviour of the actual system.

In reality, the dynamic chain between the DUT and the shaker includes additional flexible elements upstream of the slip table itself, such as the driver bar, shaker armature and armature guidance (Fig. 1, Section 2.1), each contributing its own inertia and stiffness to the excitation path. The FEM model used in this study does not explicitly represent these components, and their omission constitutes a simplification of the analysis, nevertheless it provides a faithful representation of the experimental response.

Despite these limitations, the results presented in Sections 4.1– 4.2 show that the lumped SD2DOF model is able to predict the experimentally observed resonance frequency shift between Configuration A and Configuration B with a significant accuracy.

This suggests that, for the present facility and DUT configuration, the dominant contribution to the observed frequency shift is governed by the slip table guide stiffness k_β and the equivalent facility inertia J_2.

Yet, even in its simplified form, the SD2DOF model represents a substantial step forward relative to the conventional rigid-base assumption, providing a practical, low-cost correlation tool without requiring a full structural model of the facility.

5. PROPOSAL FOR A MECHANICAL IMPEDANCE SPECIFICATION

5.1. Current practice and its limitations

Present-day launch vehicle interface documentation addresses spacecraft–launcher dynamic compatibility through a hierarchy of requirements with increasing levels of fidelity. At the preliminary design stage, launch providers typically impose simplified dynamic compatibility criteria, such as minimum spacecraft elastic natural frequencies in the lateral and axial directions and assumed damping ranges. These requirements are generally based on fixed-base modal analyses of the spacecraft and aim to prevent strong dynamic coupling between payload modes and the low-frequency structural modes of the launch vehicle.



Figure 22: Falcon 9 Example Mission Configuration using Rideshare Plates

Beyond these modal criteria, launch vehicle users' manuals provide standardized design environments, including quasi-static loads, sine vibration, random vibration, acoustic excitation, and shock response spectra. These environments represent conservative envelopes derived from launcher characterization, previous flight data, and dynamic analyses, allowing spacecraft designers to verify structural integrity and equipment qualification without requiring a complete representation of the launch vehicle dynamics.

For missions requiring higher fidelity, particularly for large or flexible spacecraft, coupled loads analysis (CLA) is performed by integrating the spacecraft and launch vehicle finite element models. CLA provides a more accurate prediction of interface

forces and dynamic responses by accounting for the interaction between the two structures. However, this approach requires detailed and often confidential launcher models, which may not be available during early design phases or for independent assessments.

Consequently, there remains a gap between simplified frequency-based compatibility criteria and full coupled dynamic analyses. Reduced-order models capable of capturing the dominant interaction mechanisms between coupled structures can provide an intermediate approach, enabling a more realistic assessment of dynamic compatibility while requiring significantly less information than a complete CLA.

5.2. Proposal for a Mechanical Impedance Specification

The results presented in Sections 4 demonstrate that the resonance frequency and mode shape of a DUT mounted on a slip table for horizontal vibration test are governed by two dominant facility-side lumped parameters: the equivalent interface rotational stiffness k_β and the moment of inertia J_2 of the structure to which the DUT is coupled. Unlike a full CLA model, these parameters provide a reduced-order representation of the boundary dynamics and can be obtained from a limited set of structural properties, such as adapter stiffness matrix and support inertia matrix, without requiring disclosure of the complete structural finite element model.

To illustrate the intended application of this approach, consider a satellite mounted on a representative payload adapter and evaluated against a minimum elastic fundamental frequency requirement, as commonly specified in launch vehicle interface control documentation. This requirement, typically verified through a fixed-base modal analysis of the spacecraft, defines the reference spacecraft frequency $\boldsymbol{\omega_1}$ used in Eq.(6).

The proposed impedance-based characterization introduces an intermediate level of information between the fixed-base modal requirement and a full coupled loads analysis, by describing the dynamic properties of the supporting structure through a small number of physically meaningful parameters.

5.3. Example for a Mechanical Impedance Specification

To illustrate the practical implementation of such a specification, consider the case of a satellite mounted on a launch vehicle payload adapter. The following Fig.23 is illustrative, notional values based on publicly available general dimensions and serves exclusively to illustrate the proposed methodology. It does not represent the actual geometry, structural properties, or mechanical impedance of any specific launch vehicle interface.

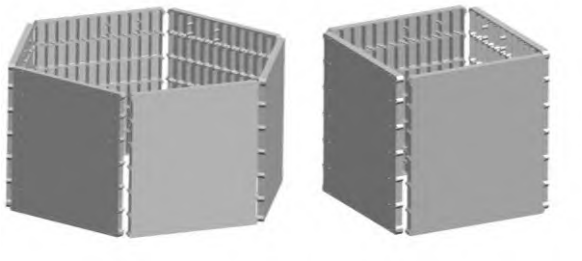


Figure 23: Mounting plate example [4]

5.3.1. Step 1: Interface rotational stiffness, k_β

For a bolted, ring-type payload adapter of diameter $D \approx 0.6096\ m$ (illustrative, comparable to a standard clamp band adapter), modelled as a circumferential array of n discrete axial stiffness elements (bolts/clamp band segments) of stiffness k_i, distributed at radius $r = \mathrm{D}/2$, the equivalent rotational stiffness about a diametral axis is:

$$k_\beta = \sum_{i=1}^{n} k_i\, r_i^2 \cos^2\theta_i \qquad (29)$$

For a notional case of n = 36 elements, each with axial stiffness $k_i \approx 5\mathrm{x}10^8 N/m$, uniformly distributed at $r \approx 0.3048\ m$:

$$k_{\beta,bolts} \approx \frac{n}{2} k_i r^2 \approx 18 \cdot (5\mathrm{x}10^8) \cdot (0.3048)^2 \approx 8.36\mathrm{x}10^8\ Nm/\mathrm{rad} \qquad (30)$$

This value represents the stiffness contribution of the clamp band/bolt ring alone. However, the adapter plate itself possesses finite bending stiffness, which acts as an additional compliance in series with the bolt ring, consistent with the spring-combination approach.

Treating the plate as an equivalent beam of width $b = 1200\ mm$, thickness $t = 50\ mm$, and elastic modulus $E = 70\ Gpa$, spanning the distance $L = 1000\ mm$ between the two bolted edges, and bending about the pitch axis under the differential load transmitted by the two edge fixing rows, its bending stiffness per unit rotation at the supports is governed by the flexural rigidity:

$$EI = E\frac{b\,t^3}{12} = (70 \cdot 10^9) \cdot \frac{1.2\mathrm{x}0.05^3}{12} = 8.8\mathrm{x}10^5\ N\ m^2 \qquad (31)$$

Modelling the plate as a beam simply supported at its two edges and subjected to a pure end moment, the equivalent rotational stiffness is:

$$k_{\beta,plate} = \frac{M}{\theta} = \frac{3EI}{L} = \frac{3 \cdot (8.8\mathrm{x}10^5)}{1.0} = 2.6\mathrm{x}10^6\ N\ m/\mathrm{rad} \qquad (32)$$

Since the bolt ring and the plate act as two rotational springs in series along the load path between the satellite interface and the launch vehicle body, the overall equivalent interface stiffness is:

$$k_\beta = \frac{k_{\beta,bolts}\, k_{\beta,plate}}{k_{\beta,bolts} + k_{\beta,plate}} = 2.6\text{x}10^6 N\, m/\text{rad} \quad (33)$$

Note that, because the plate is significantly less stiff than the bolt ring ($k_{\beta,plate} < k_{\beta,bolts}$), the equivalent stiffness k_β is dominated almost entirely by the plate's own bending behaviour - the bolt ring contributes only marginally to the overall interface compliance. This illustrates a general principle relevant to the proposed impedance specification: the least stiff element in the load path - not necessarily the most visible or easily characterized one (the bolted joint) - governs the overall interface impedance, and must therefore be identified and reported accordingly.

5.3.2. Step 2: Launch vehicle moment of inertia, J_2

The relevant inertia is that of the launch vehicle upper stage (or fairing/adapter interface structure) as seen from the payload interface, about the same axis. For an illustrative upper stage of mass ≈ 4,000 kg and radius of gyration ≈ 1.5 m about the relevant pitch axis:

$$J_2 \approx m_{stage}\rho_{gyr}^2 \approx 4000 \cdot (1.5)^2 \approx 9000\ kg\ m^2 \quad (34)$$

5.3.3. Step 3: Application to SD2DOF model

The above steps could be repeated to find all parameters for the interface stiffness and inertia matrix. The two values approximated above are sufficient to evaluate the behaviour of the satellite mounted on the slip table for the vibration tests.

Once these two values specified, Eq. (27) can be evaluated directly for any satellite of known J_1 and k_α, allowing the satellite's design team to predict, already at the design stage, how the vibration test facility will shift the satellite's fundamental frequency during vibration tests.

The use of a complete stiffness and inertia matrix could allow a more complete result to understand how the launch vehicle's mechanical impedance will shift the satellite's fundamental frequency relative to the conventional rigid-base assumption, without requiring a detailed, launcher-specific multibody model.

5.3.4. Practical implication

This example shows that a mechanical impedance specification does not require disclosing a full structural model of the facility or launch vehicle: it requires only a matrix of lumped parameters evaluated at the payload interface. The authors propose that these values to be included as standard entries in facility and launch vehicle interface control documents (ICDs), alongside the currently specified fundamental frequency, enabling direct use of the SD2DOF correlation method presented in this study without additional facility-specific modelling effort.

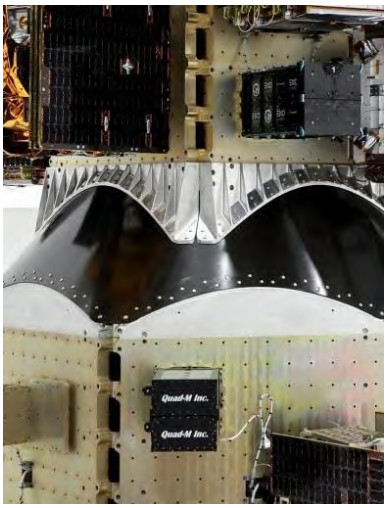


Figure 24: Interface structure example [4]

6. REFERENCES

1. A. Cambiaghi, A. Reda, "The influence of the vibration test facility in the resonance frequencies measured on a satellite structure, introducing facility mechanical impedance in FEA and facility characterisation" IAC-24-C2.IP.35.x83227, *75th International Astronautical Congress (IAC),* Milan, Italy, 14-18 October 2024.
2. R. K, "Influence of Slip Table of the Shaker System on the Experimentally Obtained Fundamental Lateral Mode Frequency of a Spacecraft" *Experimental Techniques*, vol. 48, p. 205–217, 2024.
3. H. Liu, L. Dhakar and C. Lee, “Ultra-broadband electromagnetic MEMS vibration energy harvesting” *Journal of Physics,* 2013.
4. Space Exploration Technologies Corp. (SpaceX), *Rideshare Payload User's Guide*, Version 8, Oct. 2022

Shock Response Prediction of a Spacecraft Structure Using Explicit Finite Element Analysis: Model Conversion, Damping Identification, and Test Correlation

Arun Prakash Ganapathy (1), Alexis Castel, Ph.D. (2), Simon Martin (3)

(1) Keysight Technologies, Amelia-Mary-Earhart-Straße 11a, 60459 Frankfurt, Germany,
Email: arun-prakash.ganapathy@keysight.com
(2) Keysight Technologies, 28350 Cabot Dr, Suite 100, Novi, MI 48377, USA,
Email: alexis.castel@keysight.com
(3) Keysight Technologies, 610 Wharfedale Road, Winnersh Triangle, Wokingham,
Email: simon.martin@keysight.com

KEYWORDS

spacecraft shock, explicit finite element analysis, modal hammer test, damping identification, contact friction, preload, shock response spectrum

ABSTRACT

Predicting shock propagation through complex spacecraft structures remains a significant challenge, largely due to the difficulty of accurately representing energy dissipation mechanisms at structural interfaces. This study investigates the application of explicit finite element analysis for simulating shock response in a representative spacecraft structure using the NASA ShockSat benchmark and available modal-hammer test data for correlation. A key focus of the work is the identification of valid damping parameters, including both material-level and interface-level dissipation, to improve agreement between simulation and measured acceleration histories and shock response spectra. Based on correlation results, critical joints where energy losses may significantly influence the response are modelled using contact formulations that account for friction and preload effects. Comparison between test measurements and simulation predictions is performed across multiple response locations to assess the accuracy and limitations of the approach. The study contributes practical guidelines for spacecraft shock simulation using explicit methods and highlights remaining challenges in achieving predictive capability for complex assembled structures.

1. INTRODUCTION

Spacecraft shock prediction is often controlled as much by joints, interfaces, fasteners and contact conditions as by the nominal stiffness and mass distribution of the primary structure. In assembled hardware, small relative motion at interfaces can dissipate vibration energy through friction, contact damping and local slip. These effects are difficult to represent with a single global damping value, yet they strongly influence acceleration time histories and shock response spectra (SRS).

The ShockSat work summarized here uses measured modal-hammer data to calibrate and transfer damping parameters in an explicit Virtual Performance Solution (VPS) finite element model. The project began with a damping-only model and later introduced a preload/contact/friction model intended to represent additional physical dissipation at structural interfaces. The main engineering question is whether damping identified in the simpler model remains appropriate once preload and contact/friction energy loss are active.

NASA ShockSat was created as an open benchmark for advancing shock prediction methods with public geometry, finite element models, instrumentation information and measured shock data [1]. The test article deliberately includes representative load paths: steel and aluminium plates, welded bulkheads, bolted joints, damped bulkheads, struts, cross members and a dish feature. That mix makes the benchmark useful for studying wave propagation through real interfaces rather than through an idealized plate.

Recent ShockSat studies support the use of explicit dynamics for this class of problem. Gorfain's ShockSat explicit-dynamics work applied measured hammer loads directly, processed test and simulation histories in the same way, and reported strong agreement in wave arrival timing, acceleration histories, SRS attenuation, and joint response [2]. That literature point is important for the present work: matching SRS alone is not enough if the model misses the time-domain propagation and ring-down behaviour that carry the physical evidence.

The wider pyroshock literature also explains why the correlation problem is difficult. Pyroshock environments are short-duration, high-amplitude, broad-frequency events, and traditional empirical attenuation or extrapolation approaches can have limited predictive value away from tested configurations [3]. Mechanical-impact shock systems are also widely used for controlled qualification and method verification because test parameters can be adjusted while preserving a repeatable structural input [5]. Frequency-response-function and hybrid FE-SEA methods have been proposed to improve wide-frequency spacecraft shock prediction [3,4]. The present study is narrower: it uses explicit transient analysis and measured modal decay to isolate how artificial damping should be interpreted when preload, contact, and friction are introduced.

2. SHOCKSAT DATA AND MODEL-WORKFLOW

2.1 Test article and naming convention

ShockSat is a metallic spacecraft-like structure with a roughly 1.5 ft square footprint and 5 ft height. Hammer tests use a measured point-force input at the lower structure, while accelerometers distributed through the article capture transmitted shock response [1,2].

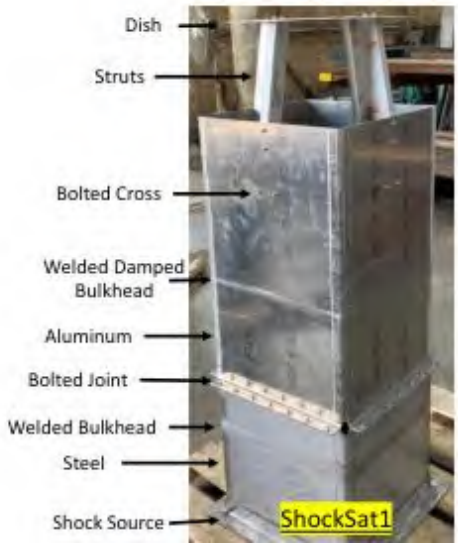


Figure 1: ShockSat test article and representative load-path features from the NASA overview material.

ShockSat test data labels encode both impact location and loading direction. In a label such as 990x or 990z, the digits denote the nominal impact coordinate near (9, 9, 0) in, while the final letter denotes the nominal hammer-input axis. Thus, 990x is the x-axis modal-hammer campaign at that corner region, and 990z is the z-axis campaign near the same corner region. Numbered records such as test001, test002 and test003 are repeated impacts within a campaign, each with its own measured hammer-force history and accelerometer responses.

2.2 Damping-only explicit FE model

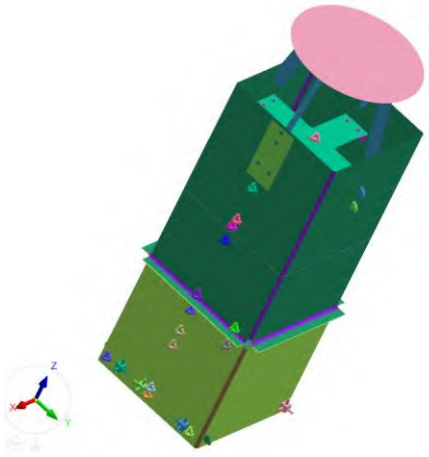


Figure 2: Damping-only ShockSat finite element model used for the modal-hammer correlation workflow.

The damping-only model is the baseline VPS explicit transient model used before introducing the preload/contact representation. The reusable workflow copies the VPS model into isolated run folders, patches run-local damping and load definitions, launches the transient solver, exports time-history accelerations from the result database, aligns FE and measured impacts, and generates objective scores, plots and per-channel damping metrics. Baseline/source decks are preserved; accepted parameters are applied to run-local copies until a deliberate model update is approved.

3. DAMPING IDENTIFICATION METHODOLOGY

3.1 Objective-Function Limitation

The first 990x optimization runs were useful because they proved that the automated correlation workflow could update damping parameters, execute the transient FE model, align the calculated response with the measured hammer test, and score the result. However, these runs also showed an important limitation of the original objective function. The objective combined the time-domain waveform error and the shock response spectrum (SRS) error with equal weighting. As a result, a parameter set could obtain a better numerical score without necessarily giving a more physically meaningful damping description.

Focused damping sweeps showed this clearly. The objective continued to improve as the low-frequency damping parameter approached the lower bound of the search range, even though the corresponding modal decay did not provide a robust physical interpretation. In other words, the optimizer could improve the mathematical match to selected waveform and SRS features while leaving the actual ring-down behaviour ambiguous. For this reason, the combined objective was retained as a useful validation metric, but it was not treated as the only authority for selecting the final damping parameters.

3.2 Modal-Decay-Based Damping Map

The damping-identification strategy was therefore shifted toward measured modal decay. This approach uses the observed rate at which the measured vibration response decays after the impact, rather than relying only on direct waveform or SRS agreement. In the VPS model, two artificial damping parameters are used to approximate the frequency-dependent damping behaviour:
LFDmp is the low-frequency artificial damping coefficient. Its contribution is largest at low modal frequencies and decreases as frequency increases.
HFDmp is the high-frequency artificial damping coefficient. Its contribution increases with frequency and therefore has a stronger influence on the high-frequency part of the shock response spectrum.
For each accepted measurement channel, dominant spectral peaks were identified and narrow-band response envelopes were extracted around those peaks. The decay envelope was then fitted with an exponential function:

$$A(t) = A_0 \exp(s^*t) \qquad (1)$$

where A(t) is the fitted modal response envelope, A_0 is the initial envelope amplitude, and s is the fitted exponential decay slope. For a decaying response, s is negative. The modal damping ratio at modal frequency f was then estimated from the fitted slope as:

$$\zeta(f) = -s \,/\, (2\pi f) \qquad (2)$$

The resulting measured damping ratios were then mapped onto the two-parameter VPS artificial damping approximation:

$$\zeta(f) = \mathrm{LFDmp} \,/\, (4\pi f) + (\mathrm{HFDmp} \cdot f) \,/\, 4000 \qquad (3)$$

In this expression, ζ(f) is the damping ratio assigned at frequency f. The LFDmp term is inversely proportional to frequency, so it controls the low-frequency part of the damping curve. The HFDmp term is proportional to frequency, so it controls the high-frequency part of the curve. Separating the two terms allowed the study to judge waveform agreement, SRS agreement, and late-time modal decay separately instead of collapsing all evidence into a single optimization score.

4. PRELOAD/CONTACT MODEL SETUP

4.1 Preload model architecture

The preload/contact model was used to check whether damping calibrated in the damping-only ShockSat model remains valid after preload, contact and friction are included. The damping-only model keeps the structural model simpler: it uses the calibrated artificial damping but does not include the clamped-interface load path.
The preload model adds that interface load path before the hammer impact. In the FE model, 44 preload body-force cards are applied. These preload forces ramp from zero to full value during the first 1 ms and are then held for the rest of the transient run. The reason for applying preload is to put the joint into its clamped operating state before the shock event. Preload closes the interface, creates normal contact pressure, and gives friction a realistic slip threshold. Without it, the contact interface can behave too loose at the start of the hammer event.
The MTOCO/constraint entries represent bolt-like kinematic connections around the fastener regions, while the Type 34 contact interfaces transfer load between mating parts, so after preload is established the model can dissipate energy through small interface slip/contact motion in addition to the calibrated artificial damping.

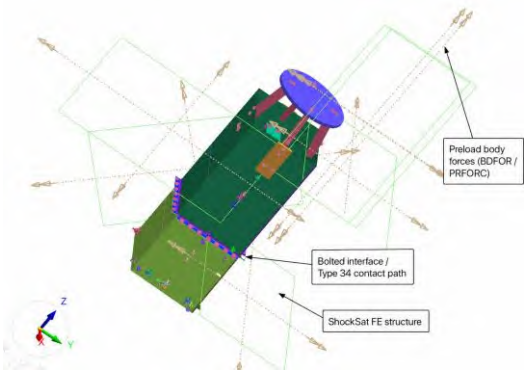
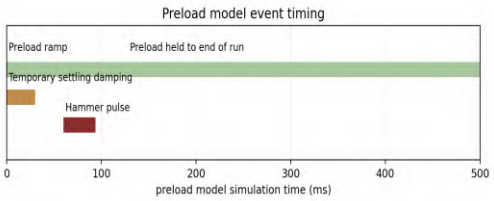


Figure 3: Detailed preload/contact ShockSat FE model. The labelled view identifies the BDFOR / PRFORC preload body-force directions and the bolted-interface Type 34 contact load path.

4.2 Damping and event timing

The shock-correlation damping remains the same calculated from the damping only model. LFDmp is the low-frequency artificial damping coefficient

applied through the damping card, while HFDmp is the high-frequency artificial damping coefficient used in the material/property damping definition.
A separate high damping value of 1000 is applied only up to 30 ms. This is a temporary numerical settling aid used after the preload ramp; it is not the damping value used to correlate the hammer shock response.
The preload event sequence is simple: preload ramps from 0 to 1ms, the model settles with the temporary high damping active until 30 ms, and the 990x hammer event begins at approximately 60 ms in the preload simulation.



For comparison, the damping-only and preload FE responses are placed on an impact-aligned time axis. The damping-only response starts from its hammer time of 0.0 ms, while the preload response is shifted by the approximate 60 ms hammer-start time. Both models are then compared over 0 to 440 ms after impact.

5. RESULTS

5.1 990z damping calibration results

The accepted damping basis comes from the corrected 990z multi-impact validation campaign. Here, 990z denotes the z-axis modal-hammer input at the nominal (9, 9, 0) corner region. A measured-only modal fit gave LFDmp = 19.832284 and HFDmp = 0.003110504; the rounded pair LFDmp = 20.0 and HFDmp = 0.00311 produced nearly the same fit error and was easier to apply consistently in run-local VPS decks.
Full 100 ms FE validation was performed across all six 990z impacts. At fixed LFDmp = 20, HFDmp = 0.00311 was selected over 0.00375 by SRS and all late-decay bands, while accepting a modest waveform tradeoff.

Table 1: 990z aggregate at LFDmp = 20. Lower values are better.

Metric	HFDmp=0.00311	HFDmp=0.00375
Waveform	1.184350	1.158393
SRS	0.500352	0.506186
Low decay	0.402588	0.404996
Mid decay	0.433415	0.444393
Broad decay	0.382180	0.392010

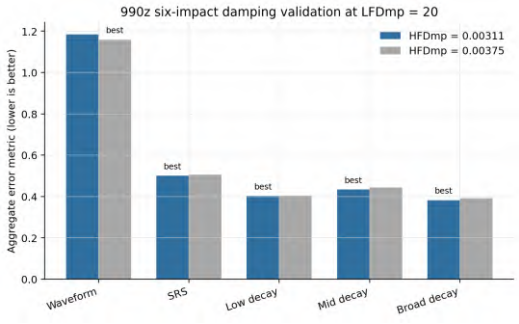


Figure 5: 990z damping validation summary. The accepted HFDmp = 0.00311 case improves SRS and all decay-band metrics relative to HFDmp = 0.00375, while accepting a small waveform tradeoff.

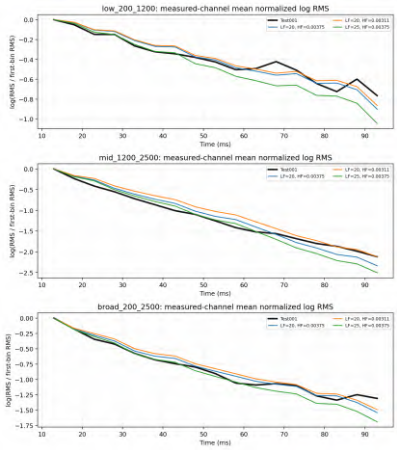


Figure 6: Mean modal-decay curves from the 990z damping validation, showing the decay evidence used to separate physical damping behaviour from waveform-only scoring.

The added damping-run figures make the calibration evidence explicit. Figure 5 shows why HFDmp = 0.00311 was accepted despite the slightly better waveform metric for HFDmp = 0.00375: the accepted value is better in SRS and in all three late-decay bands. Figure 6 shows the modal-decay behaviour that motivated treating decay as the primary physical damping target.

5.2 Representative damping-run waveform and SRS correlation

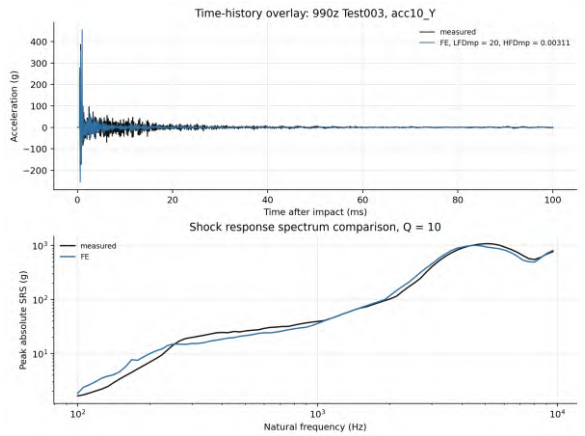


Figure 7: Representative 990z measured-vs-FE response for channel acc10_Y. The top panel shows impact-aligned acceleration history and the bottom panel shows the Q = 10 SRS comparison.

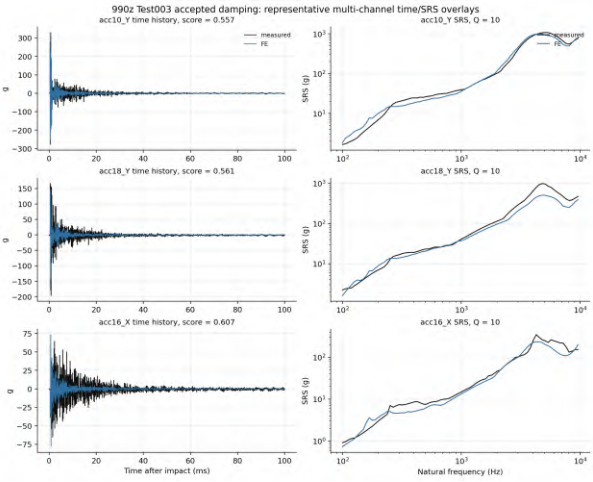


Figure 8: Additional 990z damping-only measured-vs-FE overlays for channels acc10_Y, acc18_Y and acc16_X. Each row pairs the impact-aligned time history with the corresponding Q = 10 SRS comparison.

Figures 7 gives a readable example for acc10_Y, while the Figure 8 adds acc18_Y and acc16_X to show that the accepted damping pair is not being judged from one favourable trace alone. Across these representative channels, the FE traces capture the initial high-amplitude response and ring-down timing with the closest agreement generally appearing in the high-frequency SRS region that is most relevant to shock qualification.

5.3 990x damping-only validation with accepted damping

The damping pair identified from the 990z campaign was applied directly to the independent 990x Test001 damping-only model. This transfer check asks whether damping calibrated from the z-axis hammer campaign remains reasonable for the x-axis hammer direction at the same nominal impact region.

The 990x validation used a 440 ms impact-aligned window. This longer window was chosen to match the later damping-only/preload comparison horizon: the preload simulation runs to 500 ms and its hammer event begins at approximately 60 ms, leaving 440 ms of post-impact response. Using the same 0 to 440 ms axis for the damping-only 990x case keeps the preload/contact comparison on a common basis and includes late ring-down behaviour beyond the initial shock pulse.

For each acceleration channel, a combined objective was calculated as the equally weighted average of the time-history and SRS mismatch scores. A second, more robust measure was calculated by excluding the worst-performing 15% of channels and averaging the remaining 86 channels i.e., Trimmed objective. Reporting both values shows the overall model performance while reducing the influence of a small number of locally poor channel correlations.

Table 2: 990x Test001 damping-only validation statistics using LFDmp = 20 and HFDmp = 0.00311.

Metric	990x damping-only value
Active channels	101
All-channel mean objective	0.9573
Trimmed objective	0.8942
Mean waveform score	1.2689
Mean SRS score	0.6457
Best channel score	0.7206
Worst channel score	1.5326

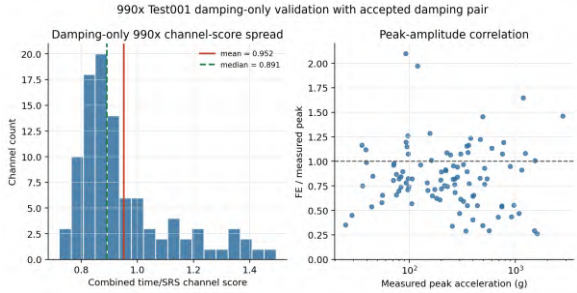


Figure 9: Damping-only 990x Test001 validation statistics using the accepted 990z damping pair, including channel-score spread and FE-to-measured peak-amplitude ratio.

The channel-score distribution and peak-ratio scatter in Figure 9 show that the transferred damping pair gives a reasonable broad response

but does not remove local channel variation. This is expected for a jointed shock structure because local sensor placement, nearby fasteners and path-dependent interface behaviour affect individual accelerometer responses.

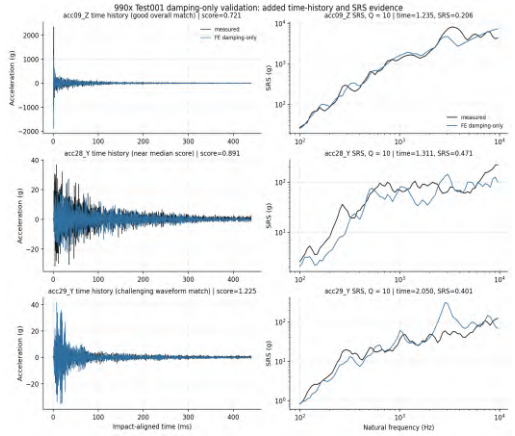


Figure 10: Representative 990x damping-only measured-vs-FE overlays using LFDmp = 20 and HFDmp = 0.00311. The selected channels show a good overall match, a near-median channel and a more challenging channel; each row pairs the 0 to 440 ms impact-aligned time history with the corresponding Q = 10 SRS comparison.

The Figure 10 traces show that the accepted damping pair gives a useful, but not perfect, 440 ms 990x correlation. For acc09_Z, the SRS shape follows the measured response well over most of the frequency range, although the first measured time-history peak is higher than the FE result. For the near-median acc28_Y channel, the FE response captures the general ring-down trend, but some measured low- and mid-frequency SRS content remains underpredicted. For acc29_Y, the comparison is more difficult: the FE time history is stronger during the early response and the SRS is overpredicted in part of the high-frequency band. Overall, the 440 ms plots support the transferred damping pair as a reasonable baseline for 990x, while also showing that the match is channel-dependent rather than uniformly tuned to every accelerometer.

5.4 Damping-only versus preload/contact transfer

The same accepted damping pair, LFDmp = 20 and HFDmp = 0.00311, was applied to both the damping-only and preload/contact models for 990x, test001. The damping-only model gives the lower overall objective, but the preload/contact model introduces stronger late-time attenuation through interface contact and friction.

Table 3: 990x measured-response comparison. Lower objective is better; lower late RMS and energy indicate stronger late-time attenuation.

Metric	Damping-only	Preload/contact
Overall objective	0.9573	0.9949
Trimmed objective	0.8942	0.9209
Median decay rate	**6.498 1/s**	**12.445 1/s**
Median late RMS	1.000	0.592
Median late energy	1.000	0.351

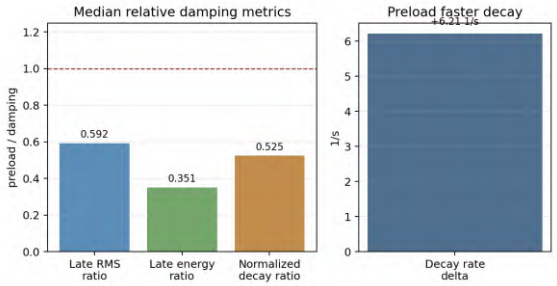


Figure 10: Summary metrics for the damping-only and preload/contact comparison.

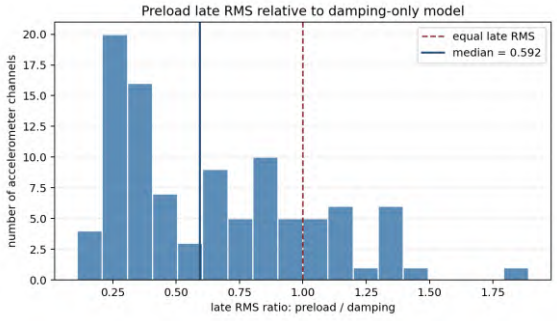


Figure 11: Distribution of late-time RMS ratios for preload response relative to the damping-only model.

The late-time comparison used a 100 to 440 ms ring-down window and the RMS value was calculated from the acceleration time history in the selected window, and the preload attenuation was reported as the preload RMS divided by the damping-only RMS:

$$\mathrm{RMS} = \sqrt{(\ \mathrm{mean}(\mathrm{a(t)\text{^}2})\ )} \qquad (4)$$

$$\text{late RMS ratio} = \mathrm{RMS}_{\mathrm{preload}} \ / \ \mathrm{RMS}_{\mathrm{damping}} \qquad (5)$$

79 of the 101 channels had lower preload late RMS than damping-only late RMS and lower preload late

acceleration energy, and all the channels had faster fitted preload decay rates. The median late RMS ratio was 0.592, or -4.55 dB, and the median late energy ratio was 0.351, corresponding to a 64.9 percent reduction in late acceleration energy.

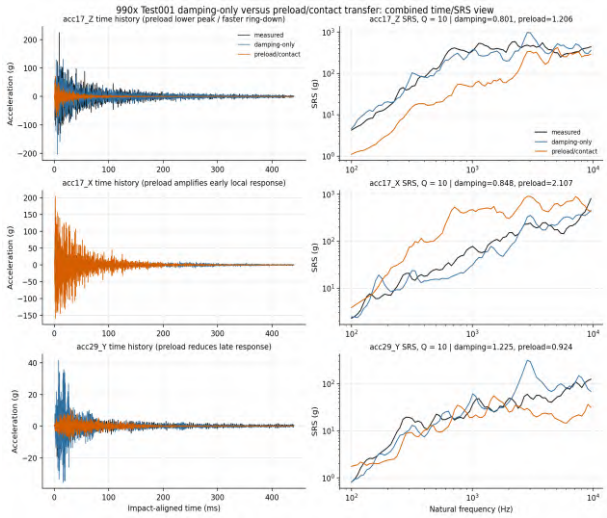


Figure 12: Additional 990x preload/contact correlation for channel acc29_Y. The paired time-history and SRS panels show a case where the preload/contact model reduces late-time response and high-frequency SRS relative to the damping-only run.

The combined plots show that preload/contact does not simply improve every channel objective. In some local channels, such as acc17_X, the preload model can increase the early response and worsen the direct waveform/SRS match. However, the broader late-time metrics support the main hypothesis: once the joint is preloaded, the contact interfaces carry normal pressure and friction can dissipate vibration energy through small relative slip and contact work. This added physical dissipation makes the preload/contact responses decay faster over the 100 to 440 ms window, which is why the preload model appears more damped even when the same artificial damping pair is used.

5.5 Preload-specific damping fit and corrected validation

Because the preload/contact model already adds dissipation, the damping-only artificial damping pair is not expected to be the final preload-model target. A preload-specific mode fit was therefore performed for 990x. The calculation extracted measured modal damping from the 440 ms test export, extracted effective modal damping from the preload run, estimated contact/friction excess damping relative to the current artificial damping curve, and fit the remaining desired artificial damping.

Table 4: Modal damping fits for 990x Test001. The preload-specific target removes estimated contact/friction damping before fitting the artificial damping curve.

Fit	LFDmp	HFDmp	Weighted RMSE
Measured-only 990x target	24.075544	0.002043	**0.0559 pp**
Preload-specific artificial target	19.123637	0.002432	**0.0554 pp**

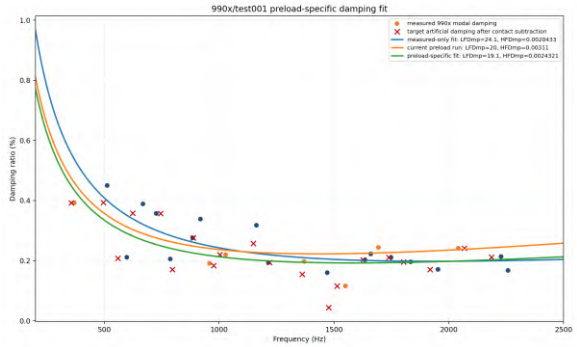


Figure 13: Preload-specific artificial damping fit for 990x after estimating the contact/friction contribution to Effective modal damping.

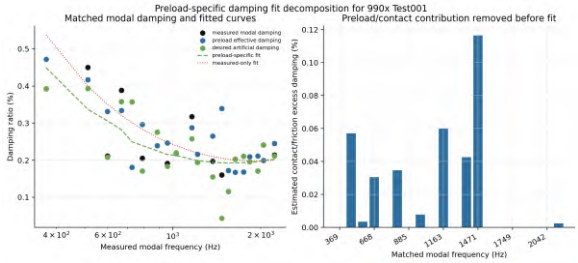


Figure 14: Matched-mode damping decomposition used for the preload-specific damping fit. The contact/friction contribution is removed before fitting the remaining artificial damping curve.

Figures 13 and 14 show the same idea in two views. Figure 13 compares the fitted damping curves. Figure 14 shows the mode-by-mode bookkeeping: the measured damping is treated as the total target, the preload/contact model is allowed to provide part of that damping through interface behaviour, and only the remaining part is assigned to the artificial VPS damping curve.

This explains why the preload-specific LFDmp is lower than the measured-only 990x value. LFDmp mainly controls the low-frequency part of the artificial damping curve. Once the bolted/contact interfaces are preloaded, they add real dissipation

through contact pressure, local slip and frictional work. Therefore the artificial low-frequency damping does not need to represent the full measured ring-down by itself, and the fitted LFDmp drops from 24.075544 to 19.123637.

The HFDmp trend needs a little more care. In the modal fit, HFDmp increases from 0.002043 to 0.002432 because the remaining artificial damping curve must still pass through the higher-frequency matched modal points after the low-frequency contact/friction contribution has been removed. HFDmp is the frequency-increasing term, so a small increase steepens the high-frequency end of the artificial damping curve.

The best completed preload validation case used LFDmp = 19.123637 and HFDmp = 0.00325, giving a mean objective of 0.993684 and a trimmed objective of 0.919707. This should be read as a validation result, not as the pure modal-fit target. The modal fit suggests the lower low-frequency artificial damping level, while the full transient waveform/SRS validation still benefits from a high-frequency term near, or slightly above, the accepted 990z level.

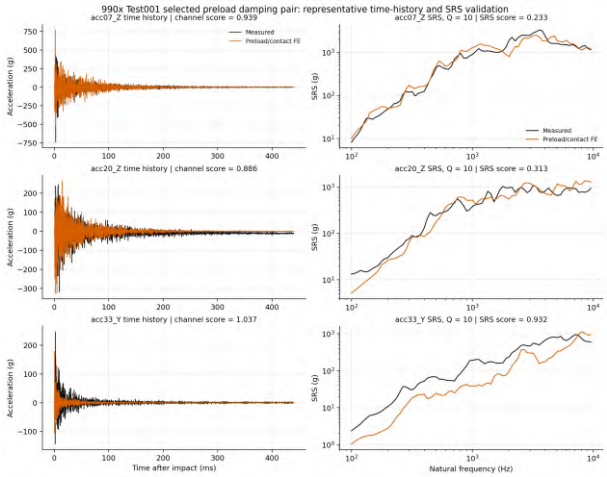


Figure 15: Impact-aligned time-history and Q = 10 SRS validation for representative 990x accelerometer channels using the selected preload damping pair, LFDmp = 19.123637 and HFDmp = 0.00325. Black denotes measurement and orange denotes the preload/contact simulation.

Figure 15 checks the selected damping pair directly against the measured acceleration histories and SRS curves over the 0 to 440 ms impact-aligned window. The acc07_Z and acc20_Z responses reproduce the measured peak levels closely and show good agreement over much of the SRS frequency range. The acc33_Y peak level is also captured, although the SRS comparison shows larger differences in some frequency bands.

These examples confirm that the selected pair gives a useful overall preload-model correlation, but not an exact match at every accelerometer. The remaining differences are channel dependent and are likely influenced by local structural and interface behaviour that cannot be corrected by changing only two global damping parameters.

In short, the lower LFDmp is physically consistent with preload/contact energy dissipation: part of the low-frequency ring-down is now handled by the interface rather than by artificial damping. The higher selected HFDmp is also reasonable because the high-frequency SRS response is judged by the full transient correlation, not only by the modal-decay fit. The final preload damping choice therefore separates two effects: reduced artificial damping where contact/friction already dissipates energy, and enough high-frequency damping to retain acceptable SRS control.

6. DISCUSSION

6.1 Damping and transfer interpretation

The main outcome of the damping study is that the final damping choice should not be based only on one combined waveform/SRS objective. The optimizer was useful for automating the workflow, but the damping values still needed a physical check. For this reason, measured modal decay was used as the main damping-identification evidence, while waveform and SRS agreement were used as validation checks.

The corrected 990z campaign supports LFDmp = 20 and HFDmp = 0.00311 as the accepted damping-only pair. When this pair was applied directly to 990x, the 440 ms comparison gave a reasonable baseline result, but the time-history and SRS plots show that the match is channel-dependent. Some channels follow the measured SRS trend well, while others still show local peak or high-frequency mismatch.

6.2 Preload/contact interpretation

The preload/contact model should not be judged only by whether it gives a lower overall objective than the damping-only model. In the current 990x case, the damping-only model remains the closer overall waveform/SRS match. However, the preload/contact model gives stronger late-time attenuation: the median late RMS ratio is 0.592 and the median late energy ratio is 0.351 relative to the damping-only response.

This supports the main preload hypothesis. After preload is applied, the contact interfaces carry

normal pressure, and friction can dissipate energy through small relative slip and contact work. The effect is not uniform across all accelerometers, but the late-time decay statistics show that the preload/contact model is adding physical dissipation that is not present in the damping-only model.

6.3 Preload-specific damping

Because the preload/contact model already adds dissipation, the artificial damping should be reduced where the interface is already doing part of the work. This is why the preload-specific fit gives a lower low-frequency damping target, LFDmp = 19.123637, instead of the measured-only 990x value of 24.075544.
The high-frequency damping term is more sensitive. The modal-fit target gives HFDmp = 0.002432, but the best completed transient validation used HFDmp = 0.00325. This is not a contradiction: the modal fit checks decay behaviour, while the full transient validation also has to maintain acceptable high-frequency SRS agreement.

7. CONCLUSIONS

The following conclusions are drawn from the updated damping-only, 990x transfer, and preload/contact validation results:

1. The damping-identification workflow is now physically grounded. The early combined waveform/SRS objective was useful for automation, but it was not sufficient as the only damping-selection criterion. The final approach therefore uses measured modal decay as the primary damping evidence, with waveform and SRS retained as validation checks.

2. The corrected 990z campaign defines the accepted damping-only basis. For the damping-only model, the corrected multi-impact 990z campaign supports LFDmp = 20 and HFDmp = 0.00311. This pair gives the preferred SRS and late-decay behaviour relative to the nearby HFDmp = 0.00375 case, while accepting only a small waveform tradeoff.

3. The accepted 990z damping pair transfers reasonably to 990x. Applying LFDmp = 20 and HFDmp = 0.00311 directly to the independent 990x damping-only model gives a mean objective of 0.9573 and a trimmed objective of 0.8942 over the 0.440 s impact-aligned window. The time-history and SRS plots show useful agreement with measurement, but the match is channel-dependent rather than uniformly good for every accelerometer.

4. The preload/contact model adds late-time physical dissipation. The preload/contact model does not improve every waveform/SRS objective, but it clearly changes the late response. In the 100 to 440 ms ring-down window, the median preload late RMS ratio is 0.592 and the median late energy ratio is 0.351 relative to the damping-only model. This supports the interpretation that preloaded contact interfaces and friction dissipate part of the vibration energy.

5. The preload-specific damping fit should be lower at low frequency. After estimating the contact/friction contribution, the remaining artificial damping target becomes LFDmp = 19.123637 and HFDmp = 0.002432. The reduction in LFDmp is expected because preload/contact/friction already supplies part of the low-frequency ring-down dissipation that the artificial damping term previously had to represent.

6. The high-frequency damping term remains governed by transient/SRS validation. Although the preload-specific modal fit gives HFDmp = 0.002432, the best completed corrected preload validation case used HFDmp = 0.00325 with LFDmp = 19.123637. This is reasonable because the modal fit checks decay behaviour, whereas the full transient validation also has to preserve high-frequency SRS agreement.

7. The current preload recommendation is case-specific. For 990x, the recommended completed preload/contact validation pair is LFDmp = 19.123637 and HFDmp = 0.00325, with mean objective 0.993684 and trimmed objective 0.919707. This should be treated as the current best validation result, not yet as a global ShockSat damping law.

8. Further validation is required before claiming broad transferability. The present evidence is strongest for the corrected 990z damping campaign and the 990x preload/contact transfer case. Repeated 990x impacts and at least one additional loading direction should be checked before generalising the preload-specific damping recommendation.

REFERENCES

1. NASA ShockSat team. ShockSat: A System to Provide Public Data for Advancing Shock Prediction, overview presentation, June 2022.

2. Gorfain, J. E. Insights Into the Shock Response of NASA ShockSat From Explicit Dynamics Finite Element Analysis, Quartus Engineering draft/presentation.
3. Wang, X.; Liu, W.; Ding, J.; Sun, Y.; Dang, Y. Pyroshock Response Prediction of Spacecraft Structure in Wide Frequency Domain Based on Acceleration FRF. Aerospace, 2022, 9, 54.
4. Wang, X.; Liu, W.; Li, X.; Sun, Y. The Shock Response Prediction of Spacecraft Structure Based on Hybrid FE-SEA Method. Applied Sciences, 2021, 11, 8490.
5. Kucukbayram, A. I. Analysis and Verification of a Pyroshock Test System, M.Sc. thesis, Middle East Technical University, 2021.

VIRTUAL SHAKER TESTING FOR TEST DE-RISKING: NOTCH PREDICTIONS ON A FULL-SCALE SPACECRAFT SETUP

Umberto Musella [(1)], Mattia Dal Borgo [(1)], Roland Pastorino [(1)], Silvia Vettori [(1)], Emilio Di Lorenzo [(1)], Bart Peeters [(1)], Vincenzo Di Pietro[(2)], Gawra Franceschini[(2)], Piersante Micciché[(2)]

[(1)] Siemens Digital Industries Software N.V., Interleuvenlaan 68, 3001 Leuven, Belgium, emails: umberto.musella@siemens.com, mattia.dal_borgo@siemens.com, roland.pastorino@siemens.com, emilio.dilorenzo@siemens.com, silvia.vettori@siemens.com, bart.peeters@siemens.com

[(2)] Thales Alenia Space Italia SPA, via Tiburtina 1210, 00131 Rome, Italy. Email: vincenzo.dipietro@thalesaleniaspace.com, gawra.franceschini@thalesaleniaspace.com, piersante.micciche@thalesaleniaspace.com

KEYWORDS

Spacecraft Testing, Vibration Control, Environmental Testing, Virtual Shaker Testing.

ABSTRACT

Vibration control tests are used to verify that a spacecraft and its sub-systems can withstand the specified launch vibration environment. Because these campaigns are executed under severe schedule constraints and involve high-value hardware, early, reliable and risk-free predictions of test responses are essential. A Digital Twin of the complete test set-up (spacecraft, shaker, and controller) can be used to replicate the physical campaign in a virtual environment for test de-risking. This approach - known in the dynamic environmental testing community as Virtual Shaker Testing (VST) - is particularly important when transient phenomena should be captured. One typical example is a sine control of a full spacecraft, where accurate simulation of primary and secondary notch behavior can support both notch definition and the optimal tuning of the controller parameters.

This paper proposes a new VST workflow that completely changes the traditional paradigm of Virtual Shaker Testing. Rather than building a simulation of the test, we propose a workflow that allows to test a simulation.

Test engineers first identify an onsite, executable Digital Twin (xDT) of the excited system and then use this stable model to generate high-fidelity VST predictions. The methodology is demonstrated on a full-scale industrial case study, where the proposed framework accurately predicts notch levels during a sine test of a spacecraft-representative mass model.

Finally, preliminary results indicates that the approach can be coupled with Frequency Based Substructuring to predict key test outcomes much earlier in the spacecraft development cycle.

1. INTRODUCTION AND OBJECTIVES

Environmental testing in spacecraft (S/C) engineering is critical to demonstrate and verify the global integrity of the designed structure, to screen the flight hardware for workmanship errors, and to validate mathematical models. In particular, vibration control (VibCo) testing is a mandatory part in the S/C development process to qualify the mechanical designed structure for launch as defined in several handbooks and standards by the National Aeronautics Space Agency (NASA) [1] and European Space Agency (ESA) [2].

During VibCo tests, dynamic coupling between the test specimen, the vibration testing facility, and the vibration controller can critically affect test outcomes [3,4], particularly in the presence of transient phenomena. The shaker (including amplifier), the Device Under Test (DUT), and any additional equipment such as fixtures and force measurement devices (FMDs) cannot be treated as independent systems; instead, the coupled dynamic ensemble must be accurately represented. To better assess control deviations and beating effects at structural resonances [5-8], Virtual Shaker Testing (VST) approaches have been developed to numerically simulate the entire closed-loop test environment [8-10].

Previous VST implementations have relied on detailed finite element models [7-8] or experimental data-driven approaches [9-12]. However, these often require deep simulation and testing expertise, which can generate challenges in translating information from one domain to the other. Moreover, they also require extensive data sharing among manufacturers, which can pose confidentiality challenges and impede industrial application. Despite its clear advantages, the widespread implementation of VST is often hindered by high computational costs and the lack of transparent, accessible mathematical models shared between spacecraft manufacturers and testing facilities.

2. REAL-TIME VIRTUAL SHAKER TESTING

To address these challenges and bridge the gap between test engineers and simulation specialists, this work presents a real-time VST framework where the physical twin (amplifier + shaker + DUT) is replaced by an executable digital twin (xDT) [13-

14], as illustrated in Figure 1.

There are three main actors in a real-time VST setup:

1. A vibration controller (e.g. Siemens Simcenter SCADAS and Testlab) for spacecraft qualification testing. This shall be the same system used during the physical shaker tests.
2. A real-time platform (e.g. Simcenter Testlab RT) connected to analogue input-output (I/O) modules via EtherCAT, where the virtual replica of the system can run in real-time.
3. A discrete state-space model of the coupled shaker-DUT system, exported as a Functional Mock-up Unit (FMU), capable of running in real-time with the required numerical stability.

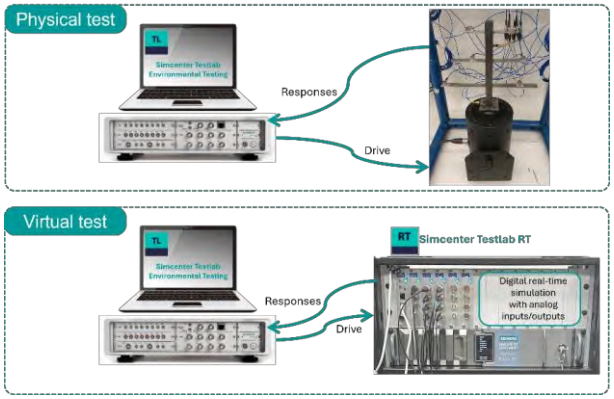


Figure 1 - Physical shaker test and real time Virtual Shaker Test

In the proposed approach, the vibration controller interfaces with the digital twin running on a real-time platform instead of the physical shaker facility and sensors. The output signal from the controller, which would normally drive the shaker amplifier, is then connected to the analogue input of the real-time platform. Similarly, the simulated sensor responses are fed back from the analogue output to the SCADAS input channels, in the same way a physical sensor is connected during the physical test. This approach enables the controller to drive a virtual replica of the test in real-time, accurately predicting transient responses and enabling optimization of control parameters.

There are two primary use-cases for the VST:

1. *Onsite derisking:* using stable experimental data driven model derived from System Identification to tune the controller settings and predict notches, including potential overshoots. This use-case requires the physical system in its final test configuration.
2. *Offsite derisking and test-informed design*: using hybrid or fully virtual multi-physics models to address test performances of a system early in the development cycle. The goal is still to allow test-engineers to run their vibration controller as they would do with the physical system.

This approach has been introduced and validated by Siemens and Thales Alenia Space Italy (TAS-I). Preliminary results were presented in previous works on small scale models the onsite derisking use-case, e.g. [15] and [16].

The idea of this paper is to demonstrate that the real-time VST can be used to predict sine control test results with a full-scale system. The data for the validation were provided by TAS-I.

3. REAL TIME VIRTUAL SHAKER TESTING PREDICTION FOR ONSITE DERISKING

The main goal of this work is to predict control, notch and measure responses of a sine control run performed on the LDS V994 shaker of TAS-I (Rome Tiburtina).

The different steps for the real time VST are reported in Figure 2 for the onsite derisking use-case.

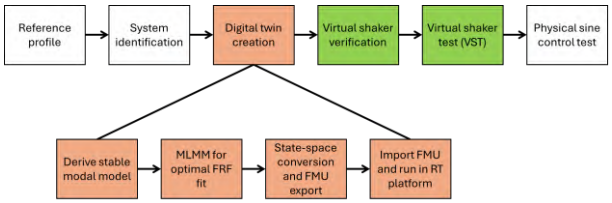


Figure 2 - Schematic of a sine control test workflow including the VST steps in orange and green.

TAS-I provided several runs performed for the characterization and the acceptance of their facility in longitudinal test configuration with a slip table. The runs and the System Identification data are here adopted to validate the onsite derisking use-case for the real-time VST.

In this exercise, the physical sine control tests were performed before the real-time VST predictions. This of course does not hinder the validation of the approach since the sine control settings could also be loaded to define the VST setup from the physical setup.

3.1. Physical Test setup

The physical test setup is shown in Figure 3. Figure 4 (top view) provides a visual representation of the location of the 4 pilots (P1, P2, P3 and P4). The excitation axis is the longitudinal axis X.



Figure 3 – LDS V994 shaker at Thales Alenia Space in Rome (via Tiburtina) and test setup adopted for the validation.

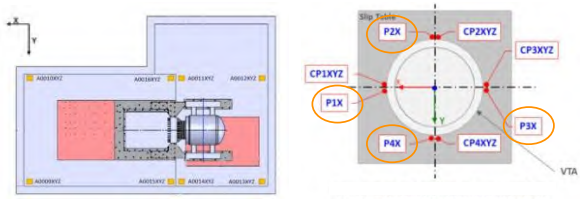


Figure 4 – Top view of the test setup. Slip table instrumented with 4 pilots (circled in orange).

The Device Under Test (DUT) is shown in Figure 3 and illustrated in Figure 5. It is an assembly of a conical structure and a cylindrical mass designed to replicate the mass and the modal properties of Sentinel-type spacecrafts.
The total mass of the device is 2390 Kg and its CoG is located at approximately 1.615 m from its base. The structure is axial-symmetric and attached to the shaker via a payload adapter.

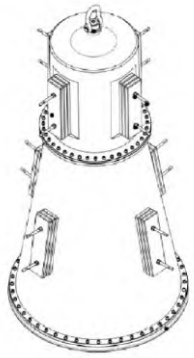


Figure 5 - Conical structure and a cylindrical mass designed to replicate the mass and the modal properties of Sentinel type spacecrafts.

The DUT was also instrumented with different accelerometers. The 4 locations illustrated in Figure 6 were identified as of interest by the experts of TAS-I. The sensors A10, A11 and A12 were connected on the cone in proximity of the attachment flanges. The sensor A14 is located on top of the cylindrical mass.

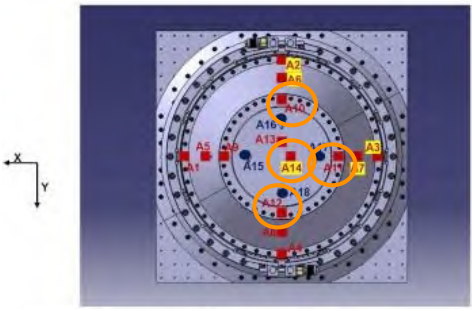


Figure 6 – instrumentation of the DUT (the sensors used for the validation are circled in orange).

As mentioned, different tests were recorded during the characterization, and the acceptance of the facility. Some of these runs were also replicated virtually. We will focus on a complete case of a longitudinal run with an activated notch to show the capability of the VST to also predict notch overshoots. The Sine Control setup for this run is illustrated in Figure 7. The main settings are also reported here below for completeness

- Sweep Mode: logarithmic
- Sweep Rate: 4 Oct/min
- Compression Factor = 4
- Control estimator: harmonic
- Control strategy: maximum

A flat 1.8 g notch profile was applied to the response channel A14:+X. The definition of the limit followed the application of an acceleration method that translates the interfaces force and moment to accelerations of the DUT. The notch profile is reported in Figure 8.

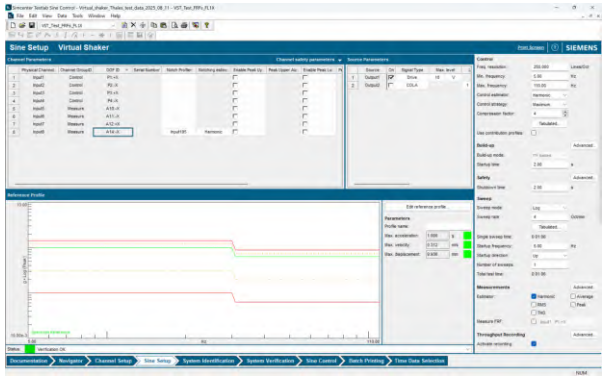


Figure 7 – Sine control setup

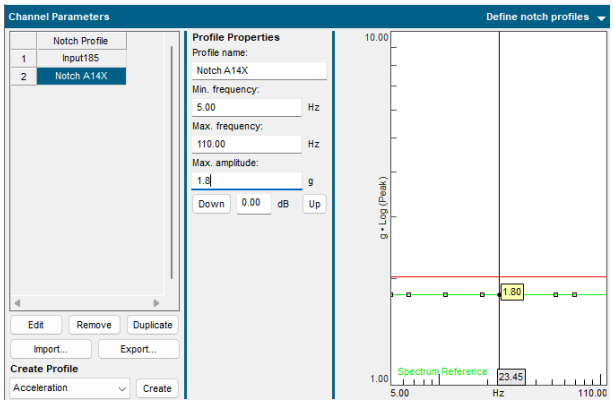


Figure 8 - Notch Profile applied on A14:+X

3.2. Virtual Shaker Test setup

Figure 9 shows the real-time VST system at the TAS-I facility in Rome Tiburtina.

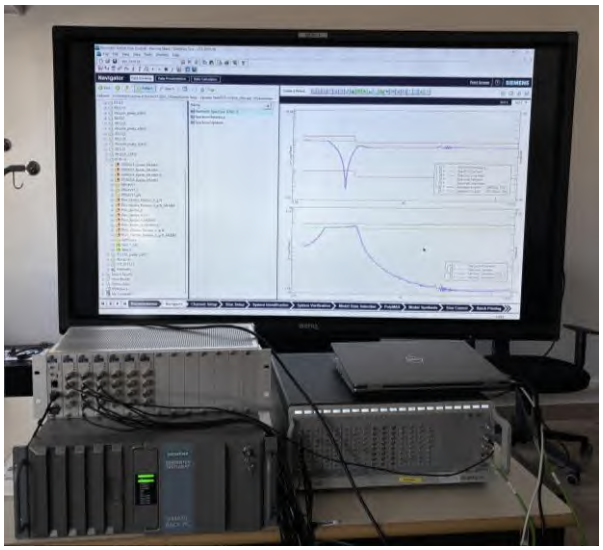


Figure 9 - Virtual Shaker Test setup in Thales Alenia Space Italy (Rome, via Tiburtina).

In this configuration, the vibration controller (Simcenter SCADAS and Testlab) is connected to the analog inputs and outputs slave devices that are connected via EtherCAT to the Simcenter Testlab RT Simatic IPC master device. Simcenter Testlab RT will execute a real time model derived from the physical test setup. When starting a test from Simcenter Testlab, the inputs and outputs of this model will be the drive voltage and the responses coming-from/going-to the Simcenter SCADAS.

3.3. Derivation of the executable digital twin

The main difference between the onsite and the offsite derisking use-cases is the origin of the model that is executed in real-time.

For the onsite derisking use-case, System FRFs obtained from a low-level System Identification runs (SI) can be used to derive the executable digital twin of the entire system under test as a state space model.

The algorithm developed in [9] and [10] can be used to derive a stable model directly from the System FRFs measured during System Identification.

- The Polymax algorithm is executed on the System FRF to synthetize a modal model. This step guarantees a stable system.
- The modal model obtained by Polymax is then modified into a maximum likelihood modal model (MLMM) [17]. This step is critical, because it optimizes the match between the System FRFs and the FRFs synthetized from the modal model and preserves its stability.
- The synthesized optimal stable model can then be converted to a discrete-time state-space model with a specified sampling frequency.

Figure 10 shows the results of applying this approach to the recorded SI data.

The results of the modal synthesis (green) and the derived state-space model (in blue) are shown in Figure 10 for the pilots, but comparable results can be obtained for the measure.

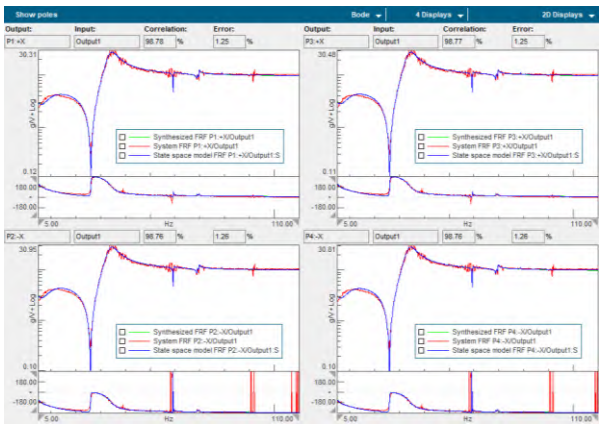


Figure 10 – State Space model (in blue) obtained from synthetized FRFs (green) fitting a stable modal model. In red measured FRF.

The state space model can then be exported as an fmu, uploaded in Simcenter Testlab RT (Figure 11) and executed in real time in the Siemens Simatic

IPC.

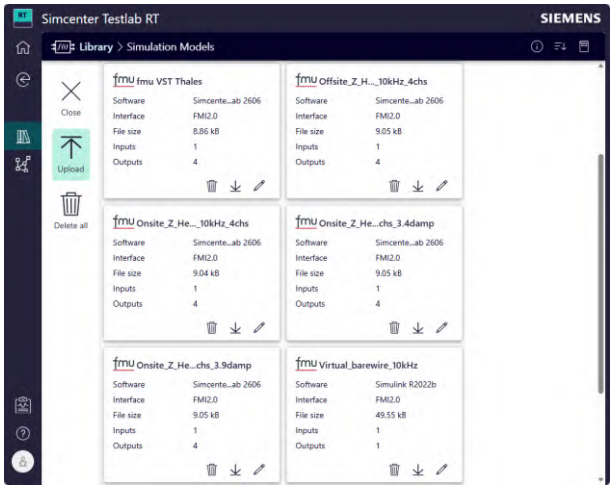


Figure 11 – the state space model can be uploaded and executed in real time in Simcenter Testlab RT

The setup can now be used to run tests virtually, optimize control settings and evaluate the effects on the test results, without exciting the spacecraft and adopting the same control hardware and software that are used during the physical tests.

3.4. Test Results

To validate the workflow, the settings of the virtual test described were loaded directly from the physical Sine Control run (see section 2.1). It is worth remembering that this is the inverse of what would be done during real test preparation, because the physical runs were chronologically executed earlier.

As a verification step of the VST setup, it is preferable to run a system identification on the virtual system. This is done to check that the test engineer has correctly defined the real-time settings, uploaded the right model and/or correctly mapped the sensors in the channel setup of the virtual test. These checks can be done by comparing the virtual System FRF from SI to the physical one. Figures 12 and 13 show the comparison between the System Identification results of the physical (magenta) and the virtual (blue) test. The figures show that the System FRF are matching accurately over the entire frequency range for the pilot and the measure channels.

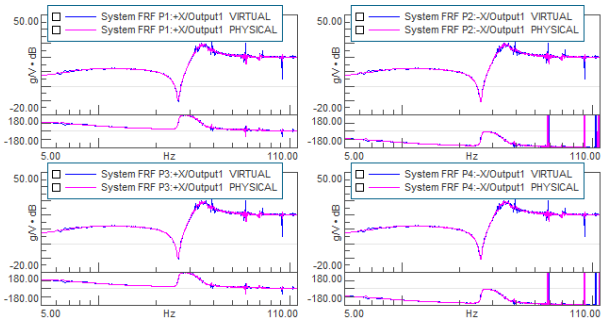


Figure 12 – Pilots system FRFs. Comparison between the SI on the physical (magenta) and virtual (blue) model.

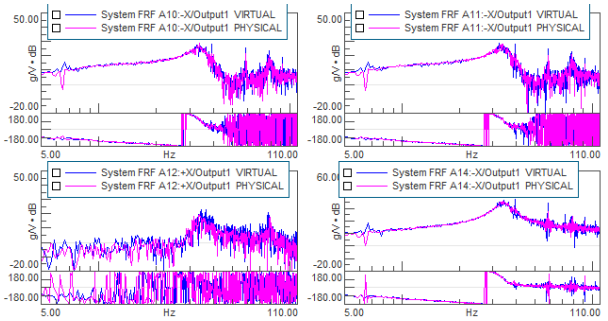


Figure 13 - Measure channels system FRFs. Comparison between the SI on the physical (magenta) and virtual (blue) model.

The comparison of the virtual (blue curves) versus the physical (magenta curves) sine control tests are finally shown in Figure 14, 15, 16 and 17. The results show that the VST can accurately predict the behavior of the physical test within the entire frequency range of interest. Transient phenomena that are characteristic of sine control runs, and that also depend on the control settings, are also well captured by the VST. Figure 17 shows for example how the proposed approach can capture notch overshoots. If needed, this overshoot could be mitigated with a local modification of the compression factor or ultimately a local negotiation on the sweep rate. Experimenting such changes would traditionally require at least a low-level sine test. The spacecraft will be subjected to the sine excitation, and the operators will be left with the uncertainty of what will happen at full level when sweeping through a local or global resonance and triggering a notch. The proposed VST approach provides the extra possibility of experimenting on a simulation model considering the transient nature of the test and the sensitivity to the control parameters.

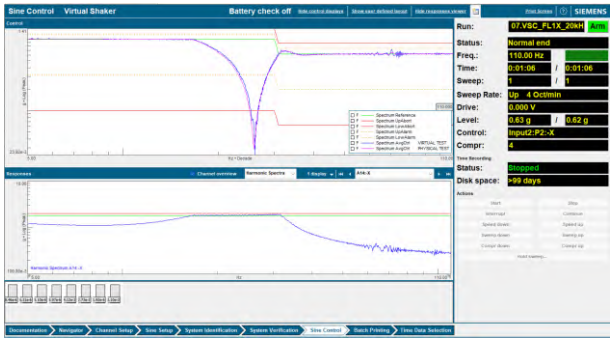


Figure 14 – VST online results. Physical Average control harmonic spectrum overlayed in the control display in magenta.

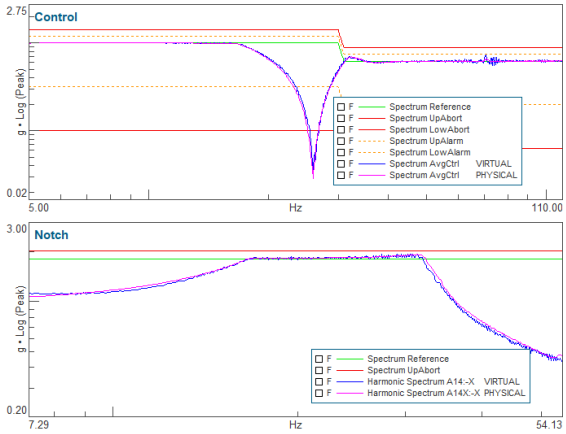


Figure 15 – Top: Average control harmonic spectrum. Bottom: harmonic spectrum of the notch channel A14:+X. VST results in blue, physical test results in magenta.

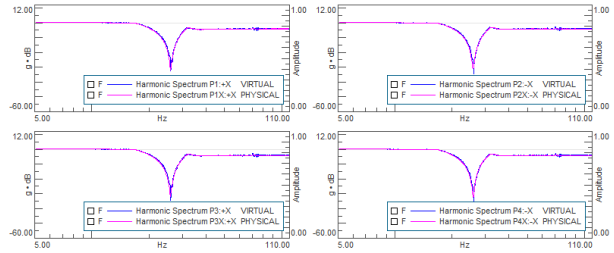


Figure 16 - Harmonic spectra of the individual pilots. VST results in blue, physical test results in magenta.

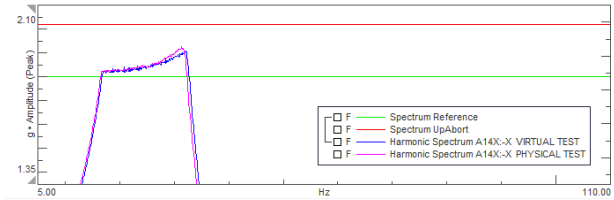


Figure 17 – Detail of a notch response overshoot (channel A14:+X).

4. HYBRID COUPLING FOR THE OFFSITE DE-RISKING USE-CASE

The present work focuses on a validation of the onsite derisking use-case. Validation of the off-site de-risking with the described full-scale setup is unfortunately still ongoing at the time of this publication.

Also in this case, the approach that is being developed tries to take a significant step forward compared with traditional methods. The idea is to perform off-site derisking adopting the real-time VST in combination with hybrid models, as shown in Figure 18**Error! Reference source not found.**.

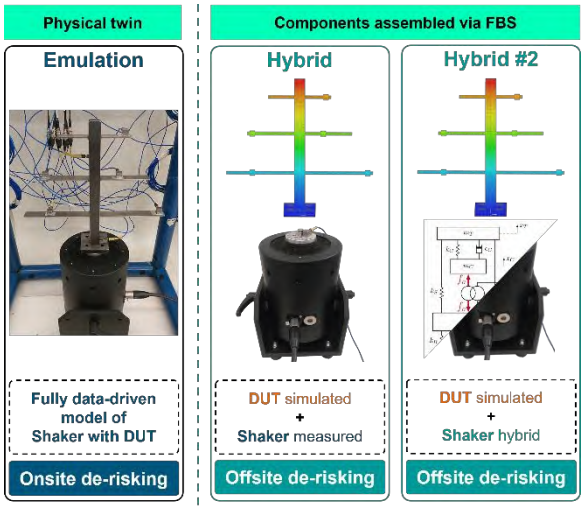


Figure 18 - Build a digital twin starting from a physical twin or a hybrid assembly of components.

Instead of requiring the physical assembly for system identification, the method developed combines:

- Experimental characterization of the shaker facility using multi-axis FRF measurements and Virtual Point Transformation (VPT) to extract complete 6-DoF dynamics.
- Numerical models of the head expander and DUT from Finite Element Analysis (FEA).
- Frequency-Based Substructuring (FBS) to couple these models in the frequency domain [18].

This approach offers several critical advantages:

- early-stage test predictions: virtual tests can be performed before the physical DUT is available, enabling test-informed design decisions during the spacecraft development process.
- Intellectual property preservation: only interface FRFs need to be shared between manufacturers and test facilities, not complete FE models, addressing confidentiality concerns.
- Ease of use and accessibility: the FBS-based workflow enables rapid assembly of FRFs from various sources without requiring deep expertise in both simulation and testing domains.
- Multi-DoF accuracy: the systematic application of VPT captures 6-DoF dynamics including rocking modes, essential for off-

centered or asymmetric spacecraft configurations that are common in practice.

The proposed method and the results on the small-scale setup shown in Figure 18 were recently published in [19] and are hereby reported for completeness.

The virtual tests for offsite derisking were performed on a hybrid system: experimentally measured shaker (force rating: 300 N) coupled with an FE model of a head expander and a DUT (a resonating structure with high COG).

Figure 19 presents the comparison of three scenarios for a centered DUT mounting.

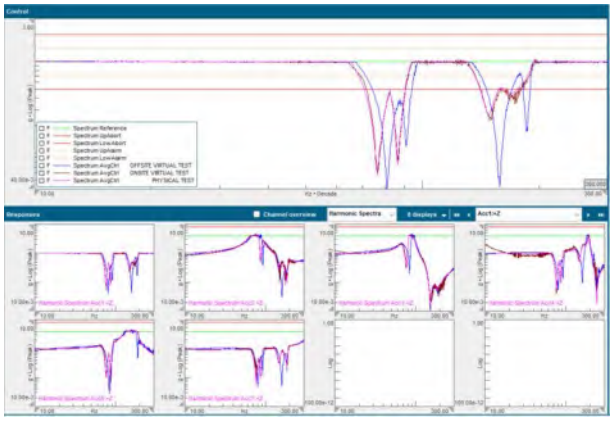


Figure 19 - Comparison of the Average control harmonic spectrum (top) and of notch channels (bottom). Offsite derisking (blue), onsite derisking (brown), and physical test (magenta).

The blue curve represents the harmonic spectrum of the control accelerometer (and the notching channels in the lower part of the picture) during the offsite de-risking virtual shaker test, performed with the hybrid coupled system. The brown curve, instead, shows the response of the virtual shaker test during the onsite derisking, hence using a fully experimental system identification of the physical twin to derive the FMU. The physical test is shown with the magenta curve, which confirms an excellent agreement when compared with the VST. The minor discrepancies are observed mainly for the offsite de-risking virtual test. Those can be attributed to the assumptions and approximations made in the FEM modelling of the DUT. As an example, the modal damping has been set to 1.5% for all modes, which is clearly not the case as the notch visible in Figure 19 shows that a higher damping is present. It is important to highlight that this exercise has been done without model updating of the FEM of the DUT in order to preserve the same scenario that test engineers will be confronted with in case of off-site de-risking, i.e. prediction potentially performed before the DUT is even built.

Figure 20 compares the harmonic spectrum of the control accelerometer for the virtual and the physical tests with an off-centered DUT configuration.

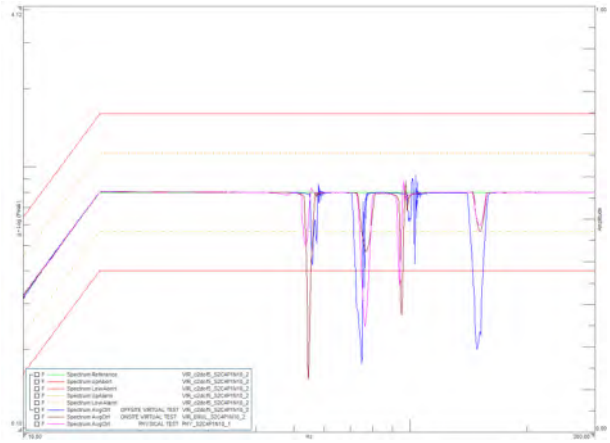


Figure 20 - Comparison of harmonic spectrum of control accelerometer. Offsite derisking (blue), onsite derisking (brown), and physical test (magenta) for the 3 scenarios with the off-centred DUT.

The blue curve represents the offsite VST, the brown curve shows the onsite VST and lastly the magenta curve reports the result of the physical test. This represents a more challenging test case where significant rocking modes are excited, and the cross-axis coupling is pronounced. The results demonstrate that the hybrid FBS approach successfully predicts the primary features of the dynamic behavior of the system even though some notches have significant discrepancy in terms of amplitude with respect to the onsite virtual shaker test and the physical test. Nevertheless, this approach allows to investigate such a complex scenario in advance of the physical test execution and can then be fine-tuned by running an onsite virtual shaker test prior to the physical test.

5. CONCLUSIONS

This work demonstrates on a full-scale system the application of a new real-time Virtual Shaker Testing workflow for onsite derisking. The physical system is replaced by an executable digital twin driven by the same vibration control hardware and software used during the physical test campaign. For the onsite de-risking case, a stable state-space model is derived from low-level System Identification FRFs.
Virtual sine-control runs accurately matched the physical tests in the control bandwidth in terms of average control, response at the individual pilots and notch behavior, including transient overshoots.

These results confirm that the proposed workflow can support test engineers in tuning the vibration controller and assessment the response at the notch channels before exposing a spacecraft to a sine excitation, particularly at full level.

Preliminary offsite de-risking results obtained on a small-scale system and based on hybrid coupling and Frequency Based Substructuring (FBS) indicate that early test predictions (before the complete physical system is available) are possible and can be accurate, considering the limited fidelity of early models. The proposed methodology for off-site derisking presents also several practical advantages derived from the fact that it combines via FBS an experimental characterization of the shaker facility using multi-axis FRF measurements and numerical models of the head expander and the DUT.

6. FUTURE WORK

It is the intention of the authors to apply the methodology described in [19] and section 4 to the full-scale setup described in section 3.

7. ACKNOWLEDGMENT

The authors would like to acknowledge the Agenzia Spaziale Italiana (ASI) for supporting this project as part of the Space Smart Factory initiative.

8. REFERENCES

1. NASA (2014). *Spacecraft Dynamic Environments Testing*. NASA-HDBK-7008, Office of the NASA Chief Engineer, NASA Technical Standards Program, National Aeronautics and Space Administration.
2. ECSS, *Space Engineering, Spacecraft Mechanical Loads Analysis Handbook*, ECSS-E-HB-32-26A, //ecss.nl/hbs/published-hbs-on-line/active-engineering-handbooks/, European Cooperation for Space Standardization (February 2013), Noordwijk, The Netherlands.
3. Appolloni, M. & Cozzani, A. (2007). Virtual testing simulation tool for the new quad head expander electrodynamic shaker. In *Proceedings of the 6th International Symposium on Environmental Testing for Space Programmes*, ESA-ESTEC, Noordwijk, The Netherlands.
4. Appolloni, M., Dacal, R. B., Cozzani, A., Knockaert, R. & Thoen, B. (2015). Multi-degree-of-freedom vibration platform with MIMO controller for future spacecraft testing: an application case for virtual shaker testing. In *Proceedings of the 29th Aerospace Testing Seminar*, Los Angeles, USA.
5. Bettacchioli, A. (2014). Simulation of satellite vibration test. In *Proceedings of the 13th European Conference on Spacecraft Structure, Materials and Environmental Testing*, Brunswick, Germany.
6. Bettacchioli, A. & Nali, P. (2015). Common issues in S/C sine vibration testing and a methodology to predict the sine test responses from very low-level run. In *Proceedings of the 29th Aerospace Testing Seminar*, Los Angeles, USA.
7. Nali, P. & Bettacchioli, A. (2014). Beating phenomena in spacecraft sine tests and an attempt to include the sine sweep rate effect in the test-prediction. In *Proceedings of the 13th European Conference on Spacecraft Structure, Materials and Environmental Testing*, Brunswick, Germany.
8. Nali, P., Augello, G., Bettacchioli, A., Landi, G. & Gnoffo, M. (2016). A virtual shaker testing experience: modeling, computational methodology and preliminary results. In *Proceedings of* the 14th European Conference on Spacecraft Structures, Materials and Environmental Testing, Toulouse, France.
9. Waimer, S., Manzato, S., Peeters, B., Carrella, A., Wagner, M. & Guillaume, P. (2018). Virtual Shaker Testing approach based on experimental data. In *Proceedings of the 31st Aerospace Testing Seminar*, Los Angeles, USA.
10. Waimer, S. (2018). *Advanced Environmental Dynamic Testing for Space Applications using Virtual and Physical Laboratories*. PhD thesis, Vrije Universiteit Brussel, Brussels, Belgium.
11. Remedia, M., Aglietti, G. S. & Kiley, A. (2015). Vibration testing: post-test correlation approach based on virtual testing. *In Proceedings of the 29th Aerospace Testing Seminar*, Los Angeles, USA.
12. Remedia, M., Aglietti, G. S., Appolloni, M., Cozzani, A. & Kiley, A. (2017). An enhanced methodology for spacecraft correlation activity using virtual testing tools. *Journal of Sound and Vibration*, 409, 180–200.
13. dos Santos, F. L. M., Pastorino, R., Peeters, B., Faria, C., Desmet, W., Góes, L. C. S. & Van Der Auweraer, H. (2016). Model based system testing: bringing testing and simulation close together. *In Structural Health Monitoring, Damage Detection & Mechatronics*, Volume 7: Proceedings of the 34th IMAC, A Conference and Exposition on Structural Dynamics 2016, pp. 91–97. Springer International Publishing.
14. Thielemans, L., Sputh, B. H. C., Pastorino, R., Desmet, W. & Swevers, J. (2024). Industrial application of residual power method as co-simulation performance indicator for e-motor hybrid-physical-virtual test setup. In *Proceedings of ISMA 2024*, Leuven, Belgium.
15. Dal Borgo, M., Musella, U., Thielemans, L.,

Vettori, S., Garcia de Miguel, A., Pastorino, R., Di Lorenzo, E. & Peeters, B. (2024). Real-time virtual shaker testing using an executable digital twin. In *Proc. ISMA 2024 – International Conference on Noise and Vibration Engineering*, pp. 684–693, Leuven, Belgium.

16. Dal Borgo, M., Musella, U., Thielemans, L., Vettori, S., Garcia de Miguel, A., Pastorino, R., Di Lorenzo, E. & Peeters, B. (2025). Virtual shaker testing: a real-time framework for predicting spacecraft vibration tests. In *Proc. 10th CEAS Aerospace Europe Conference and 28th AIDAA International Congress*, Turin, Italy.
17. El-Kafafy, M., Peeters, B., Geluk, T. & Guillaume, P. (2019). The MLMM modal parameter estimation method: a new feature to maximize modal model robustness. *Mechanical Systems and Signal Processing*, 120, 465–485.
18. Manzato, S., Risaliti, E., Napoli, C., Tamarozzi, T. & Peeters, B. (2015). A review of frequency-based substructuring methods and their applicability to engineering structures. In *Proc. Int. Conf. Structural Engineering Dynamics (ICEDyn)*, Lagos, Portugal.
19. Dal Borgo, M., Musella, U., Bentivoglio, F., Garcia de Miguel, A., Pastorino, R., Di Lorenzo, E. & Peeters, B. (2026). Real-time virtual shaker testing using hybrid coupling for shaker, head expander and device under test. To be included in the *Proceedings of the International Conference on Noise and Vibration Engineering*, Leuven, Belgium.

ECSSMET
Braunschweig Germany 2026

Shock testing

RELEVANT PARAMETERS FOR IMPROVED TRANSIENT SHOCK ANALYSIS AND TESTING OF A SATELLITE STRUCTURE

B. Brévart[1], D. Boban[2], S. Lemay[3]

[1] *Thales Alenia Space, 26, avenue J.-F. Champollion, BP 33787 - 31037 Toulouse Cedex 1, France*
bertrand.brevart@thalesaleniaspace.com
[2] *Thales Alenia Space, 5, allée des gabians, BP 99 - 06156 Cannes, France*
david.boban@thalesaleniaspace.com
[3] *CNES, 18, avenue Edouard Belin, 31401 Toulouse Cedex 9, France*
simon.lemay@cnes.fr

KEYWORDS

Shock test, simulation, transient acceleration, applied waveform, strain gage, ceramic materials, screw sliding

ABSTRACT

Shock events occurring in satellites are still a source of many concerns. Despite progress on the severity of the shock sources, with the use of Non-Explosive Actuators in release mechanisms for example, the multiplication of deployable appendages on smaller satellites brings shock sources closer to sensitive payload units and critical instruments. On the other hand, shock simulation remains difficult at system level in order to establish accurate specifications or to predict the response of a critical equipment. Not to talk of shock testing that often brings more questioning on the level of stress applied to the equipment w.r.t. system need. Because the SRS levels are getting lower, shock testing with a shaker is more often feasible, offering various options for the applied waveform.

In this context, this study first investigates analytically and experimentally the limit to rupture of various cantilevered beams with a reduced section. Both aluminium and ceramic materials are considered. The stress on the beams is monitored with strain gages. For a given SRS, various test methods are used, i.e. metal-metal impact on a ringing plate as well as shaker shock testing. The investigation shows the effect of the waveform on the stress level, with respect to the resonance frequency of the beam. Very good correlation of the simulations is obtained so that a parametric study yields more insight into the issue, and the effect of the applied waveform on the stress level is investigated.

Another part of the study is dedicated to sliding between screwed structural parts. An experimental setup allows fine measurement of the slippage with increasing shock levels. The effect of the shocks on the preload is measured. Pure sliding could not be achieved. A sliding threshold is identified but it is combined to a modification of the contact conditions.

These results give more confidence into the simulation of simple structures submitted to shock.

1. INTRODUCTION

Extensive work has been done on the shock environment over the past years. Most of the heritage and know-how on shock in Europe has been embedded in the ECSS Shock Handbook [1]. Yet the shock environment is still a source of many concerns.

One of them is the level of stress applied in test to the equipment w.r.t. system need, and the associated risk of excessive over-testing. This topic is largely addressed in [2].

Predicting a subsystem response under shock testing and quantifying the risk of damage is another remaining difficulty, even for structural assemblies like an optical instrument for example.

A new questioning concerns Non-Explosive Actuators (NEA). Fig. 1 shows the acceleration measured a few centimetres and one meter away from a solar array release mechanism using NEA. The acceleration near the source is low compared to a pyrotechnic shock but the time history is characterized by multiple shock events justified by the actuator kinematics. One meter farther, the acceleration has decreased of course and the time history appears as a single event whose duration reaches 100ms, far above pyrotechnic shock duration.

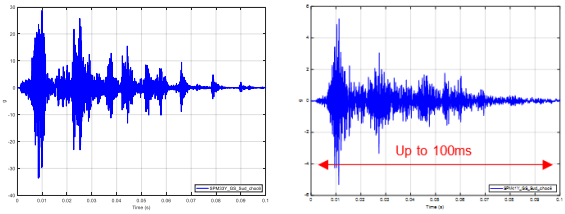


Figure 1: Acceleration measured during a Solar Array release using NEA, a few centimetres from the HRM (left) and 1m farther (right)

In this context, the present study had multiple objectives. The first one was to investigate experimentally the stress level in simple structural

parts (aluminium and ceramic material) up to rupture, using various test methods, i.e. metal-metal impact and shaker shock testing with various waveforms. The second was to consolidate shock simulation on these simple parts, comparing calculated stress level and strain gage response in particular. The last objective was to highlight screw sliding mechanisms in shock on a single screw assembly.

2. SHOCK TEST ON CANTILERED BEAMS

2.1. Preliminary investigation

A shaker shock testing has been applied to a ceramic cantilevered beam with a reduced section (Fig. 2). The test has been performed on a LDS V875-440 shaker (36 kN) and rupture was not achieved.

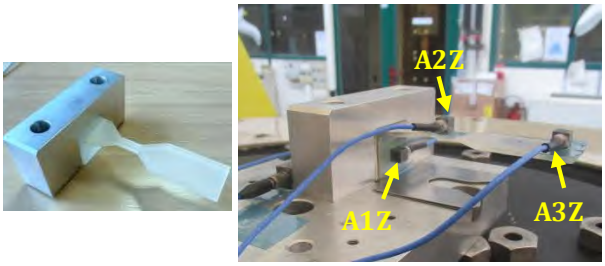


Figure 2: Zerodur ceramic beam, before instrumentation (left) and under shock testing (right)

The acceleration applied at the base of the beam is illustrated on Fig. 3 and the associated response of the beam is given on Fig. 4 in terms of Shock Response Spectrum (SRS). Shock duration of the excitation is around 40ms. The strain level in the reduced section has been measured with strain gages (Fig. 5).

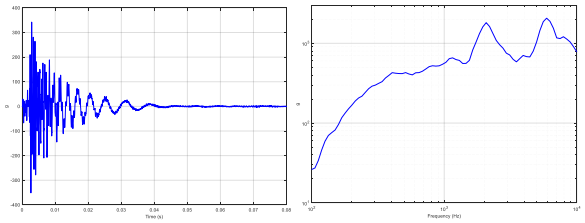


Figure 3: Time history (left) and SRS (right) of the acceleration A1Z applied at the base of the beam.

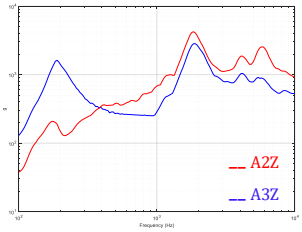


Figure 4: SRS (Q=10) of the accelerations in the middle (A2Z) and at the end of the beam (A3Z)

A Finite Element Model of the beam using 3D elements has been correlated to the sine survey response (Fig. 6). The resulting error on the first two resonance frequencies is lower than 2%.

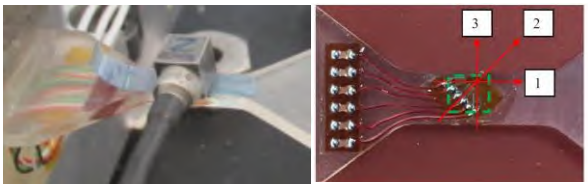


Figure 5: Strain gage on beam reduced section

The shock response to the above excitation has been simulated using modal transient analysis (Nastran SOL 112), with a modal base up to 10kHz, 2% damping and a time step of 10^{-5}s.

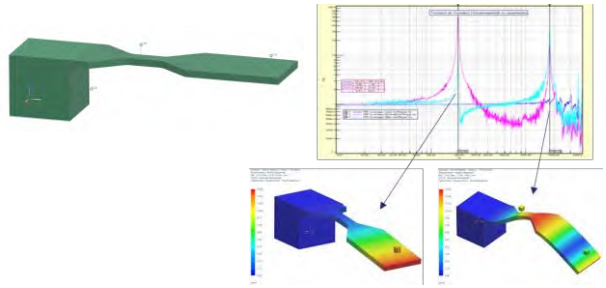


Figure 6: Beam FE model (left) and sine survey response with the associated mode shapes (right)

Very good correlation with the test results has been achieved. The beam acceleration is accurately predicted in the time domain and in terms of SRS (Fig. 7). Calculated stress in the reduced section has the expected waveform and measured peak value (141 MPa) is predicted with less than 5% error (Fig. 8).

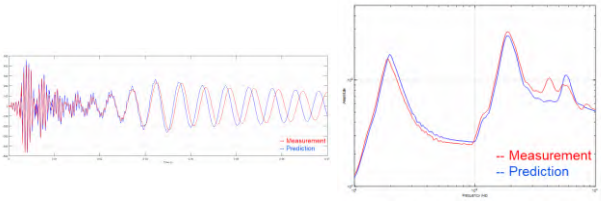


Figure 7: Measured and predicted beam end acceleration, time history (left) and SRS (right)

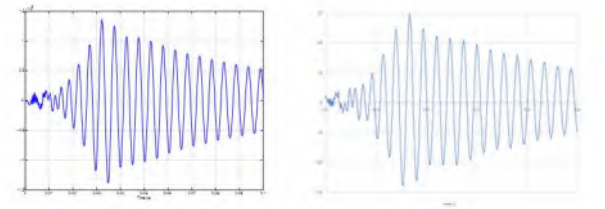


Figure 8: Measured (right) and predicted (left) longitudinal stress in reduced section

2.2. Sensitivity analysis of the simulation

Because the simulation is very reliable, a sensitivity analysis has been performed. Using *Vibrationdata* package on Matlab, various input accelerations with the same SRS (Fig. 9) have been created. To be precise, three waveforms with a different time duration, i.e. 40, 15 and 8ms, have been synthesized using a combination of damped sines (Fig. 10).

f	g level
100	20
200	200
400	400
10000	400

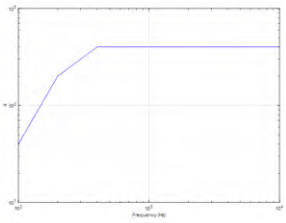


Figure 9: Input acceleration SRS level used in vibrationdata for waveform synthesis

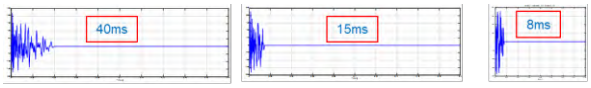


Figure 10: Acceleration synthesis using damped sines. 40, 15 and 8ms duration waveforms with the above SRS

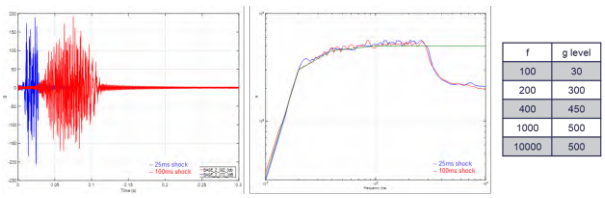
Applying these accelerations as input to the simulation, the stress level in the reduced section of the beam varies from 229 MPa with the 40 ms waveform to 141 MPa with the 8ms waveform. With the 15ms acceleration, the stress level is in between, at 163 MPa. The shock duration has thus a strong effect on the stress level (up to 40%) and on the beam response more generally.

Then, the stiffness of the beam has been increased by a factor 10 to move the first eigenfrequency from 200 to 620 Hz. The stress has been calculated with the 40 and 15ms base accelerations and the stress level is the same, near 400 MPa. Therefore, the dependence of the response to the shock duration is also a function of the specimen resonance frequency.

A new test campaign with similar parts has been prepared to consolidate these results.

2.3.New shaker shock tests

The objective was to reach yield or rupture on a maximum samples and, for this reason, all the tests have been performed on a more powerful shaker, i.e. UNHOLTZ-DICKIE T2000 (110 kN). Three types of beams have been prepared. Aluminium parts with two different stiffnesses, at 210 and 910 Hz respectively, and ceramic parts with a low stiffness (250 Hz). Two different shock durations, i.e. 25 and 100 ms, have been applied for a given SRS level. These accelerations have been synthesized using wavelets on Simcenter Testlab. Fig. 11 shows the resulting time histories for the nominal SRS profile (0 dB). Note that the shaker controlled frequency has been limited to 3000 Hz.



f	g level
100	30
200	300
400	450
1000	500
10000	500

Figure 11: Shock acceleration time histories (25 and 100ms) and associated SRS (0 dB reference)

The test sequence applied to ceramic parts (Fig. 12) has been an increasing level 1dB by 1dB from -12dB to +1 dB. Note that the strain has been measured in continuous as illustrated on Fig. 13.

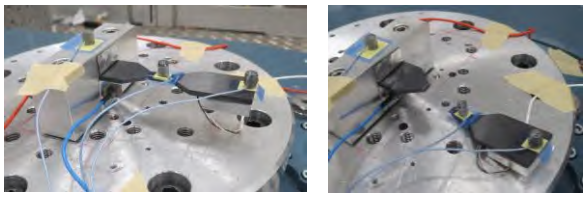


Figure 12: Ceramic part under shock testing (left) and after rupture (right)

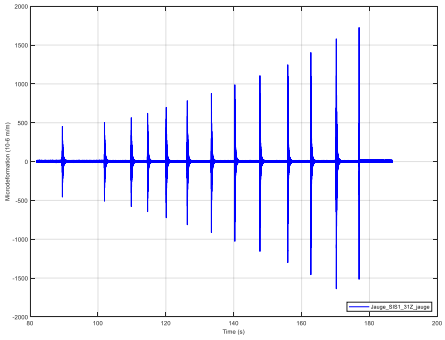


Figure 13: Strain measurement, shock test (-12 to 0 dB) on a ceramic part with 25ms accelerations

With the 25 ms shock, rupture has been achieved at 0 dB, when the stress level has reached 640 MPa at strain gage location. This level at strain gage location has been predicted with less than 1% error. The maximum stress resulting from the simulation (750 MPa) is not exactly at strain gage location but it points perfectly the observed rupture (Fig. 14).

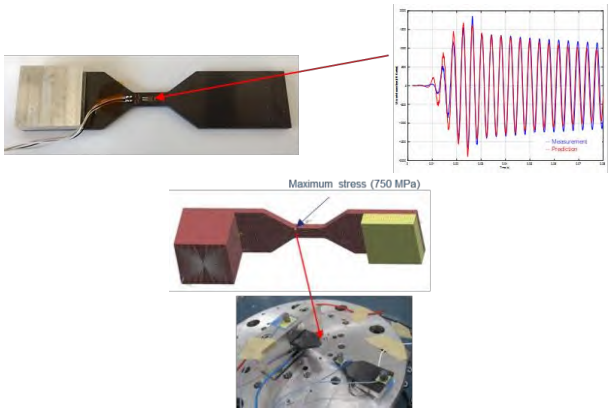


Figure 14: Measured and predicted strain at gage location (top) and maximum stress calculated at rupture location (bottom)

With the 100 ms acceleration, rupture has been reached on 2 samples at 0 and +1dB respectively, with a maximum stress measured at 570 and 660 MPa. Referring to the sensitivity analysis, this result is surprising as we obtained similar levels to rupture for the two shock durations. This result will be explained in Chapter 3.

Similar tests have been conducted on the rigid aluminium part (Fig. 15). At 0 dB, the beam end response is 50% larger with the 100 ms acceleration than with the 25 ms shock (Fig. 16).

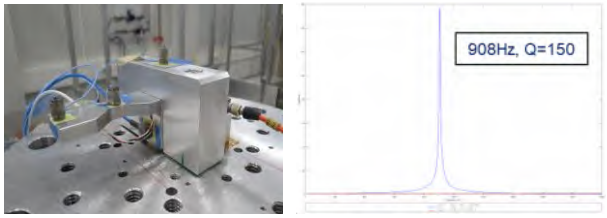


Figure 15: Rigid aluminium part under test (left) and low level sine response at beam end (right)

The stress level at 0 dB is 59 MPa with the 25 ms shock and it reaches 87 MPa with the 100 ms one (+3.4 dB). Additional tests have been performed at +6 dB (1000g SRS plateau). The stress level at +6 dB is 89 MPa with the 25 ms shock and it reaches 160 MPa with the 100 ms one (+5.1 dB). Thus, unlike the expectation from the sensitivity analysis, shock time duration has a strong effect on this part at 900 Hz. The explanation is given in Chapter 3.

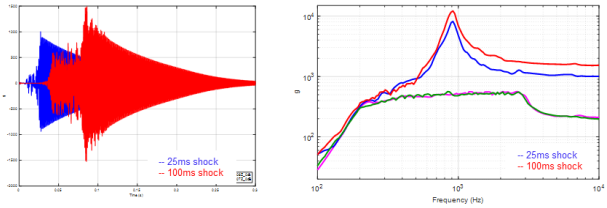


Figure 16: Rigid aluminium beam end response at 0 dB with 25 and 100 ms shock excitations, acceleration time history (left) and SRS (right)

The test sequence applied to the flexible aluminium part has been an increasing level 1dB by 1dB from -6dB to +6 dB. At 0 dB, the beam end response is similar with the two shock durations but the response is 10 to 12 dB larger at 1850 Hz with the 100 ms shock (Fig. 17). This will be justified later.

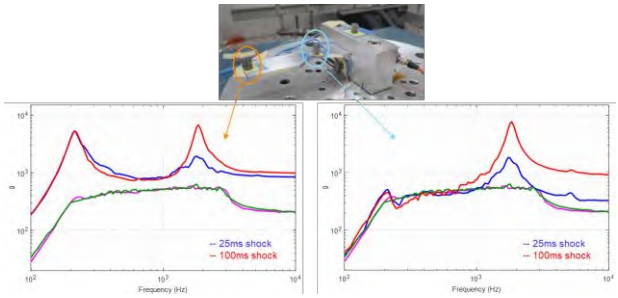


Figure 17: Flexible aluminium beam response (SRS) at 0 dB with 25 and 100 ms excitations

The achieved stress level with the 25 ms shock is:

- 197 MPa at 0dB
- 248 MPa at +2dB
- 374 MPa at +6dB

The achieved stress level with the 100 ms shock is:

- 188 MPa at 0dB
- 239 MPa at +2dB
- 373 MPa at +6dB

So, time duration has no effect on the stress level. This one is exclusively given by the low frequencies, so the result is consistent with the above beam end response.

The aluminium used for the parts is a 6061 T6, with a yield strength of 240 MPa and an ultimate strength of 270 MPa. A small yield can be observed when σ_y (0.2% residual strain) is reached with a low pass filter applied on the strain measurement (Fig. 18). Up to 410 MPa, well above σ_u, could be reached at +7dB with the 100 ms shock but no crack initiation could be observed on the beam. The ultimate strength of 270 MPa is a minimum guaranteed value, but it can be much higher for this specific part. After the shock, the residual strain is significant (46$\mu\varepsilon$), as illustrated on Fig. 18.

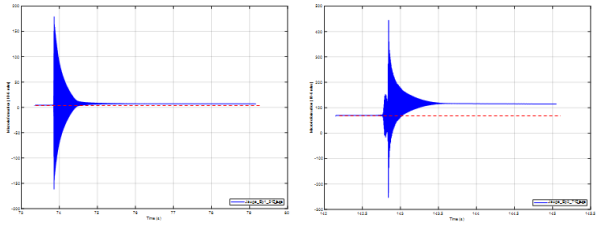


Figure 18: Low pass filtered (100 Hz) strain, after 25 ms shock at +2dB (left) and 100 ms shock at +7 dB (right)

2.4. Shock tests on a ringing plate

More shock tests have been conducted with the rigid and flexible aluminium parts on a ringing plate (metal-metal hammer impact). Fig. 19 shows the test setup along with the test vehicles.

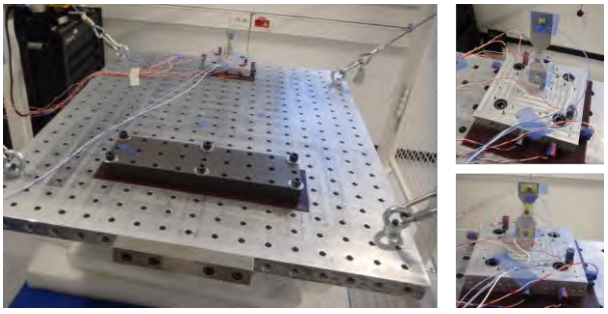


Figure 19: Ringing plate setup (metal-metal hammer impact)

Time duration of the applied acceleration at the base of the beams is around 10 to 15 ms (Fig. 20).

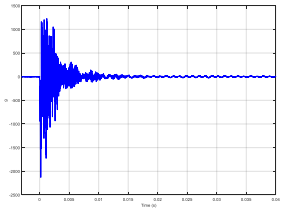


Figure 20: Acceleration waveform (metal-metal impact)

With the rigid beam, applying 1000g SRS level at 910 Hz (Fig. 21), the stress has been measured at 101 MPa. At the same level on the shaker, only the 25 ms shock duration gives similar result.

With the flexible beam, applying 300g SRS level at 210 Hz (Fig. 22), the stress has been measured at 150 MPa. At the same level on the shaker, the stress is 30% higher with both time durations. The explanation is given in next chapter.

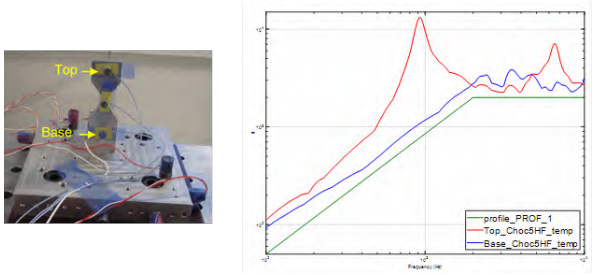


Figure 21: Rigid aluminium beam end response (metal-metal impact)

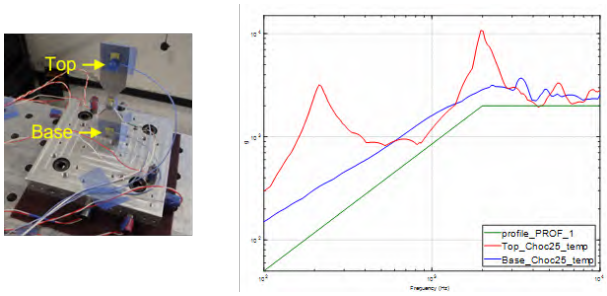


Figure 22: Flexible aluminium beam end response (metal-metal impact)

3. RATIONALE

The results obtained by test are not those expected from the sensitivity analysis. In fact, we obtain opposite results: the stress of the low frequency parts in test are not sensitive to the shock time duration but the rigid aluminum beam is.

All of this stands in the fact that the SRS (Q=10) which is used to control the applied levels, does not show the important information.

Indeed, the first ceramic beam (Zerodur) had a Q factor of 50 and the structural parts tested in the second campaign have a measured Q factor above 100. The other divergence point between the similarity analysis and the tests is the method used for the waveform synthesis. The first one (*Vibrationdata package*) used damped sine combinations when wavelet combinations were chosen in Testlab.

Fig. 23 shows the SRS of 15 and 100 ms waveforms obtained with damped sines and *vibrationdata*, calculated with a Q of 10 and a Q of 50.

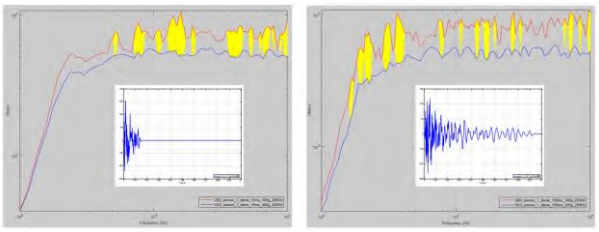


Figure 23: SRS (Q=10 and 50) of the acceleration waveforms obtained using damped sine synthesis. 15ms duration (left) and 100ms (right). Yellow zones indicate more than 3 dB difference.

Superposition of the two SRS with Q of 50 (Fig. 24) shows that the duration effect is mainly expected at low frequencies, i.e. below 400 Hz. And this is what was obtained by simulation.

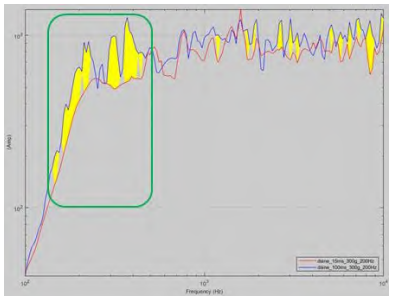


Figure 24: SRS (Q=50) of the shock acceleration waveforms (15 and 100 ms) obtained using damped sine synthesis. Yellow zones indicate more than 3 dB difference between curves.

Comparing the SRS of the two waveforms obtained with wavelets on Testlab with a Q of 100 (Fig. 25), it appears that the duration effect is mainly expected at high frequencies, i.e. higher than 250 Hz, and that is what was obtained by test.

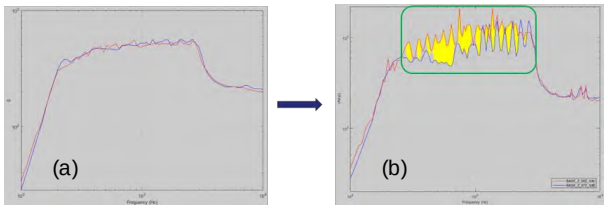


Figure 25: SRS with Q=10 (a) and Q=100 (b) of the shock acceleration waveforms (25 and 100 ms) obtained using wavelet synthesis.

For metal-metal impact, characterized by a high frequency content, moving from a Q of 10 to 100 (Fig. 26) does not modify the response level at low frequencies (below 1000 Hz). At 200 Hz, the SRS level thus remains at 300g. At this frequency with a representative Q factor, the SRS has reached 400g on the shaker with both time durations (Fig. 25b). This explains the additionnal 30% on the stress level. Without any effect of the Q factor on the SRS at low frequencies, metal-metal impact induces the lowest stress level in the part compared to other test methods.

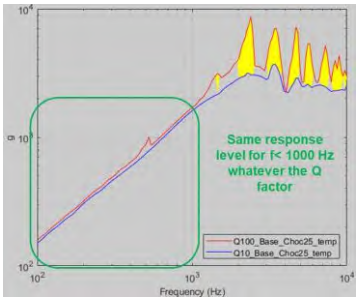


Figure 26: SRS (Q=10 and 50) of the shock acceleration illustrated on Fig.20, obtained by metal-metal impact.

4. SHOCK TEST ON A SCREW JOINT

The test setup is described on Fig. 27 and Fig. 28. A cylinder is fixed with one single screw on a baseplate with a rectified wedge. A 500gr cylinder has been used for shaker shock testing (Fig. 27)

and a 100gr cylinder has been used for metal-metal impact shock tests (Fig. 28) as higher peak accelerations could be reached. After each shock, sliding was measured precisely using micrometric slip gauges between the cylinder and the wedge (Fig. 28). In addition, during shaker shock testing, screw preload was measured in continuous using a small washer instrumented with strain gages. Only these tests are presented here but the results obtained with metal-metal impact do not modify the coming conclusions.

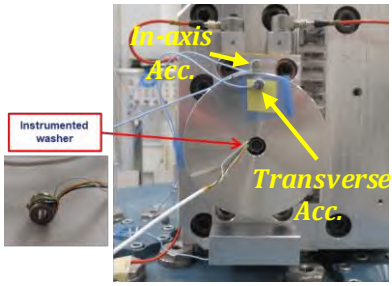


Figure 27: Screw assembly under shaker shock testing. Screw preload is monitored with a washer.

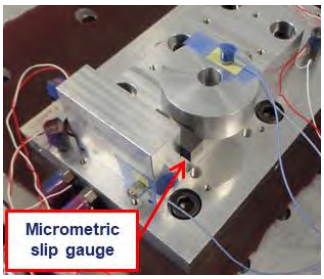


Figure 28: Screw assembly on the ringing plate (metal-metal impact), with a micrometric slip gauge

The screw is a M4 titanium screw lubricated with molykote. The installed preload was measured at 4420N applying a torque of 2.5N.m. Only the 25 ms shock was applied, with a level varying 1dB by 1dB from -25 to -5 dB of the nominal profile (Fig. 11).

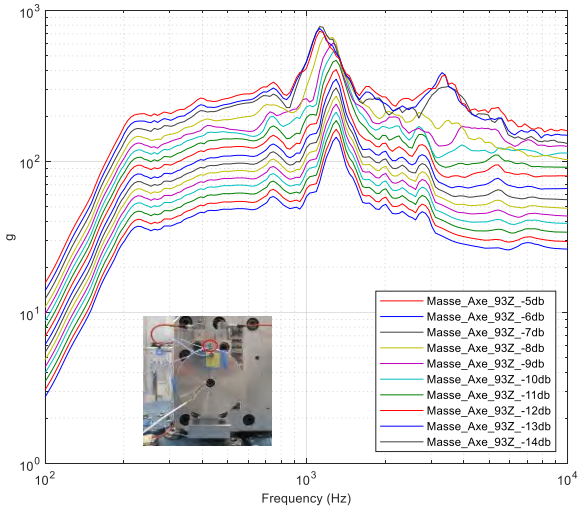


Figure 29: In-axis cylinder acceleration (SRS) for applied levels varying from -25 to -5 dB of the nominal SRS

Fig. 29 shows the SRS of the acceleration in the direction of excitation at all levels. A relatively smooth translation of the curve is noted up to -10dB.

A frequency shift of the cylinder mode (1300 Hz) is initiated at -9 dB. From -7 to -5 dB, the mode is at 1124 Hz and the level does not increase anymore. The corresponding shifts of the distance between the cylinder and the wedge are given in table 1.

Table 1: Relative distance cylinder/wedge w.r.t. initial for a given applied level

Level (dB)	Δd (µm)
-20	0
-19	0
-18	-2
-17	-2
-16	-3
-15	-3
-14	-3
-13	-3
-12	-3
-11	-4
-10	-7
-9	-14
-8	-10
-7	-20
-6	-51
-5	-73

Sliding is below 7 µm as long as the frequency does not shift, i.e. with an applied level below -10dB of the nominal profile. At -9 dB, the distance shift doubles and above -8 dB the shift exceeds 10 µm at each additional dB.

The question that is now raised is, when does sliding starts and what is the associated friction coefficient ? Note that Thales Alenia Space has long heritage with ultra-stable structures and uses a low friction coefficient to minimize micro-sliding (<1µm disp.). But the standard friction coefficient used for such assembly is around 0.2.

Fig. 30 shows the time history of the acceleration in the direction of excitation, for -9 and -8dB levels. The maximum absolute acceleration of the cylinder, i.e. 122g, is obtained at -9 dB, . Even though the level is raised, at -8 dB the peak absolute value is lower (100g) with obvious signs of slippage on the peak acceleration (circled in green).

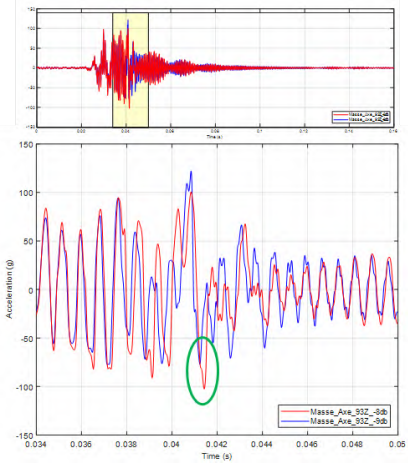


Figure 30: In-axis transient acceleration of the cylinder for the applied levels -9 and -8 dB. Overall time history (top) and zoom on yellow box (bottom)

Regarding the preload, it has been very stable during and after the shocks. Fig. 31 shows the preload during the highest shock level. After the 16 shock levels, it has only lost 0.6% w.r.t. the installed value.

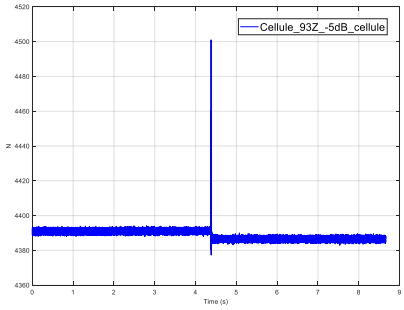


Figure 31: Screw tension measured with the instrumented washer as -5dB shock occurs

As there is only one mode in the frequency band, a friction coefficient of 0.14 is obtained considering the total mass of the cylinder and the acceleration of 122g. This value is slightly lower than expected.
With this test, a large moment is applied to the screw, resulting in a large transverse acceleration of the cylinder. Fig. 32 shows that the transient acceleration on the cylinder in both directions, i.e. in-axis and transverse, for levels between -13 and -11 dB. It appears that they raise proportionally.

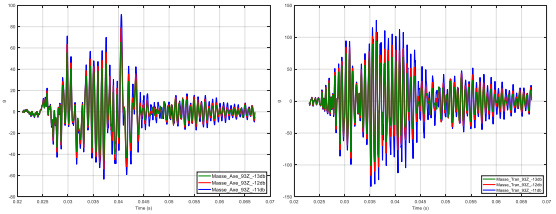


Figure 32: In-axis (left) and transverse (right) transient acceleration of the cylinder for the applied levels -13 to -8 dB

At -10 dB (Fig. 33), it appears that this proportionality is lost after the peak acceleration is reached on the direction of excitation, and it is lost even before on the transverse acceleration.

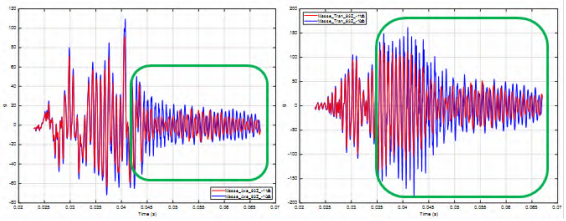


Figure 33: In-axis (left) and transverse (right) transient acceleration of the cylinder for the applied levels -11 and -10 dB

Analyzing the SRS of the transverse acceleration (Fig. 34), this non linearity is confirmed by the fact that a secondary mode of the cylinder is raising rapidly as the excitation level increases, around 5300 Hz.

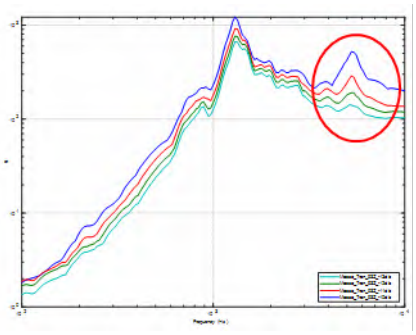


Figure 34: SRS of the cylinder transverse acceleration for the applied levels -13 to -10 dB

This phenomenon confirms that the contact is well altered from the -10 dB level.
Pure sliding could not be obtained with this single screw assembly that is not very representative of flight configurations. This means that the friction coefficient for pure sliding, i.e. without any contact modification, would have been higher than 0.14.

5. CONCLUSION

This study has demonstrated that for a given SRS calculated with a Q factor of 10, the waveform of the time history has a large influence on the resulting stress in the tested part. Compared to shaker shock testing, metal-metal impact will likely induce a lower stress level in structures with a Q factor above 10. It has been confirmed that shock simulation gives excellent results for acceleration and stress in simple parts (ceramic and aluminium), both for shaker shock excitation and metal-metal impact. Screw sliding has been observed both for shaker shock testing and metal-metal impact. It confirms that sliding is not linked to a loss of preload in the screw. Pure sliding could not be obtained with the chosen configuration to confirm that the friction coefficient used in static is the one to use in shock. Only a lower bound of the this value could be determined for an aluminium assembly and it does not contradict to use of the static friction coefficient.

6. REFERENCES

1. Mechanical Shock Design and Verification Handbook, ECSS-E-HB-32-25A, 14 July 2015.
2. Brévart, B. & Ait Zaid, S. (2014). Representative shock testing for satellite electronic units. Proceeding of the 13th European Conference on Spacecraft Structures, Materials and Environment Testing, Braunschweig, Germany.

SHOCK SUBSYSTEM QUALIFICATION TESTING: SECONDARY NOTCHING APPROACH

Martin Hofmann [(1)], Damien Abadie[(1)], Etienne Cavro[(1)], Maxime Perriquet[(1)] & Simon Lemay[(2)]

[(1)] Airbus Defence and Space, 31 Rue des Cosmonautes, 31000 Toulouse, France,
Email: martin.m.hofmann@airbus.com
[(2)] Centre National d'Etudes Spatiales (CNES), 18 Avenue Edouard Belin, 31400 Toulouse, France, Email: Simon.Lemay@cnes.fr

KEYWORDS

Shock, Test, Shaker, Notching, Qualification

ABSTRACT

Most of the satellites are exposed to significant launcher and appendages shock release which drives to specify and qualify the neighbouring units. The space industry is facing from time to time unit shock test failures coming from over specification, over test and rarely from a weak design.

This paper is addressing both the over specification and over testing topics through the comparison of a unit dummy internal response in both a satellite and a unit shock test configuration.

Demonstrating the ability of a subsystem to withstand the shock environment is typically performed through the following steps:

1) derivation of the expected shock environment at the unit interface;
2) realization of a shock test on a shock bench, vibrator aiming to reproduce the specified shock environment on a stiff setup.

Unfortunately, this methodology suffers from various approximations, resulting in high amplifications often not representative of flight conditions.

The methodology explored here aims at providing grounds to justify lowering the qualification levels (in specific frequency bands) by anticipating the amplifications that will be experienced in test but not in flight on a more flexible interface such as a satellite panel.This method is called shock secondary notching.

To do so, two batches of shock tests have been performed: First, a campaign aimed at exciting a dummy unit on a setup representative of a system test or flight conditions, with a flexible interface below the dummy and an excitation located a few interfaces away from the dummy itself. Then, a second campaign aimed at reproducing the shock observed on the first setup. But this time on a shaker with a stiff interface, allowing to test different ways of injecting the shock measured during the system test. The four methodologies investigated are:

- direct time history input
- time history synthesis from measured SRS
- time history synthesis from tailored SRS
- time history synthesis from tailored SRS + notching criteria on internal responses

The work presented in this paper highlights how much the "classical" approach can lead to significant overtesting of units, as well as proposing a way of avoiding those fictitious amplifications thanks to notching directly on the SRS. Of course, fine tuning time histories assumes the ability to perform the shock test on a shaker, which comes with some limitations in terms of size of tested units and achievable levels, which are discussed as well.

1. INTRODUCTION - OUTLINE

To address this issue, two test campaigns were conducted, aiming at quantifying the difference between a shock test on a flexible interface, representative of flight conditions and what happens during a shock qualification on a stiff interface.
The paper first presents the setup of the flexible / system shock test setup, and then the setup used to mimic a subsystem stiff-interface qualification campaign.
During the whole test campaign, a set of three dummies with increasing natural frequencies has been used. They are shown in the top left corner of Figure 2-1.

2. SYSTEM "FLEXIBLE" TEST (FLIGHT CONDITIONS)

2.1. Setup

The system test setup and its associated instrumentation is shown in Figure 2-1.

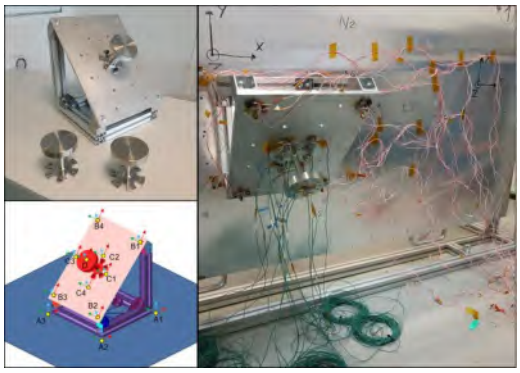


Figure 2-1 System test setup and associated instrumentation

The shocks were conducted on a shock bench which is made of a suspended aluminium plate (20 mm thick) on which a hammer delivers the shock in the out-of-plane direction. The dummies were mounted on a small support structure, made of tubular profiles on which a support plate (10 mm thick) was placed.
During this test campaign, two different anvils (alu & Teflon) were used, in order to generate different kinds of shocks.

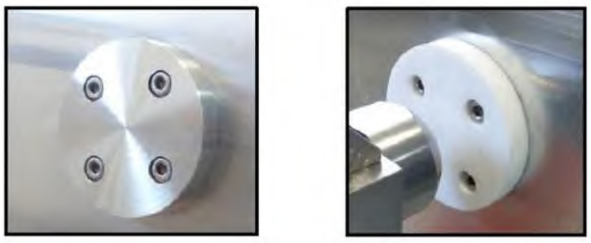


Figure 2-2 The two anvils used during the shock bench test campaign

2.2. Instrumentation

The primary instrumentation consisted of:

- 4 sensors around the dummy I/F (C1→C4 sensors)
- 1 sensor at the top of the dummy

3. SUBSYSTEM "STIFF" TEST (UNIT QUALIFICATION)

3.1. Setup & Instrumentation

For the subsystem test setup, the dummy was placed on an interface plate and directly bolted onto the shaker slip table.
Horizontal configuration have only been tested, as the dynamic of the dummy was not especially interesting axially.
The dummy was instrumented at its top (D sensor) and at its interfaces (C sensors).

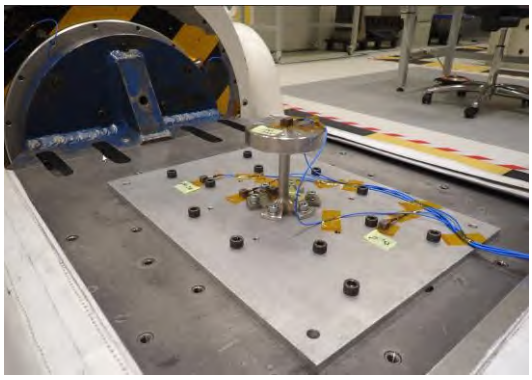


Figure 3-1 Setup of the subsystem level test

3.2. Four ways to derive shaker input levels

As there were 4 sensors at the base of the dummy, in each case, the chosen channel (when needed) was the one that exhibited the highest time history value.

The 4 identified methodologies were:

- direct time history input:
  *The **exact time history** measured on the shock bench is imposed at the basis of the dummy.*
- time history synthesis from **measured SRS**
  The SRS is computed, and then a time history is synthesised to match that exact SRS
- time history synthesis from **tailored SRS**
  The SRS is computed and then tailored, and then a time history is synthesised to match that exact SRS
- time history synthesis from **tailored SRS + notching** criteria on internal responses
  Same as above, but with an additional notching capability on the D sensor to limit internal amplifications.

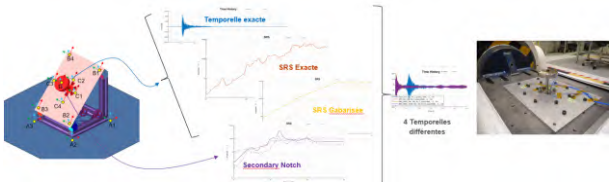


Figure 3-2 4 Ways to derive the shock input at shaker level

Whenever a time history had to be synthetized, a wavelet superposition was performed, based on the automatic algorithm available in TestLab. Time constraints were set on the generation of the time histories, based on the duration of the shock events observed on the shock bench.

3.3. Results – achievement of targets

Figure 3-3 & Figure 3-4 & Figure 3-5 show the accuracy with which the levels were achieved during the shaker test campaign.

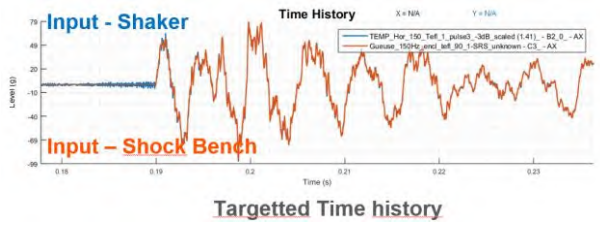


Figure 3-3 Achievement of levels – Exact time history

It is important to note that for this study, the amplitude of the shocks was not a concern, and it was hence allowed to lower by some dB (sometimes more than 10) the input level on the shaker, in order to:

1) Be compatible with shaker capacities
2) Allow better control of the shaker

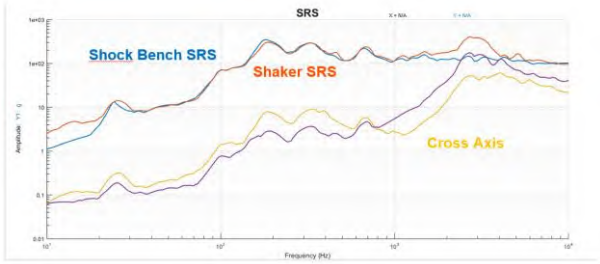


Figure 3-4 Achievement of levels – Exact SRS

In the context of unit qualification, such decreases of levels would of course not be possible. Shakers limitations are addressed with in §6.



Figure 3-5 Achievement of levels – tailored SRS

In some cases, achievement of the SRS targeted levels was not so easy, especially at low frequency (tendency to overshoot) and at high frequency, around 4000 Hz, where the antiresonance following a mode of the expander made the control of the input on the slip table rather complicated. Nevertheless, in the frequency bandwidth of interest (50-2000 Hz), the achievement was deemed very good.

4. OVERTESTING DURING SUBSYSTEM TEST

Then, once the results of both test campaigns were available, a comparison of the two campaigns reveals that there are some specificities to the stiff interface test setup, resulting in (very) conservative test results.

Amplifications at the top of the Dummy	150 Hz Dummy			
	Teflon		Alu	
	Peak SRS [g]	Overtest	Peak SRS [g]	Overtest
Shock Bench Test	712		396.3	
Shaker - Exact Time hist.	1072	51%	746.1	88%
Shaker - Exact SRS	1529	115%	1348	240%
Shaker - Spec. SRS	5863	724%	1842	365%
Shaker - Spec. SRS+Notch	2950	314%	1122	183%

Table 4-1 Overtesting associated with the various test configurations

As one can see, the levels reached on the shaker table significantly exceed those measured on the shock bench, with exceedance amplitude varying according to the shock input methodology.

Firstly, one can see that even imposing the exact time history is associated with an exceedance of 51% - 88% depending on the anvil considered. This is due to the fact that if the shaker imposes the same acceleration at all interfaces of the dummy, this is not true on the more flexible setup, where the interfaces are free to move relatively to each other, reducing amplifications at the top of the dummy. This exceedance is representative of the stiff interface test condition problematic, as previously discussed in [1].

Secondly, when going from the exact time history to the exact SRS, the levels are again multiplied by 1.5 leading to an overall overtest factor of 115%-240%. This is only due to the fact that time history synthesis based on a target SRS is not unique. This is representative of the issue there is in specifying a shock with an SRS only, as an SRS is not a precise description of a transient event. Current work is on-going to improve how shock time histories can be synthetized with less conservatism through better mathematical tools [3].

Then, the next step is due to the usual tailoring performed when measurements are available. Even if the tailoring performed was not extraordinarily conservative, the simple templating with straight lines above the measurement is associated with the most significant increase in levels, with an increase of level compared to the previous step between 1.5 and 4 times higher, leading to an overall overtest factor of 724% - 365% depending on the anvil considered.

Finally, the notching on the input SRS, described more in details in the next chapter, allows for a drastic reduction of the levels, by a factor ~2.

5. SECONDARY NOTCHING APPLIED TO SHOCK TESTS

As explained in the previous chapter, the time histories generated to match a given target SRS were performed in TestLab, by superposing Wavelets.
In the first place, the notches were computed

proportionally, so that the amplitudes of the wavelets corresponding to the frequencies exhibiting high amplifications would be reduced in order to reach the levels seen at the top of the dummy during the shock bench tests. This led to very light decrease of the SRS in the considered bandwidth. To push the concept to its limits, the values of the wavelets in the problematic bandwith were set to 0, which resulted in the SRS shown below.

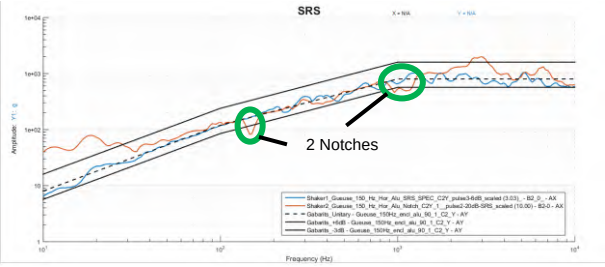


Figure 5-1 Comparison of notched / unnotched I/F SRS

As one can see, the notches are visible, but do not drastically reduce the SRS, contrarily to what notches can do on sine spectrums or random PSDs. The reason is that, at a given frequency coordinate on the X axis, the SRS is “polluted” by components coming from other frequencies, hence the non-0 value even if the matching wavelets were actually set to 0.

In terms of SRS compliance wrt. to classical test specifications (i.e. -3db / +6dB), the tuning performed here slightly deviates from the allowed corridor. In some cases (especially if there is a true hardware sensibility behind), this could be understandable and accepted by the one responsible for the specified levels, but in other cases less. In such cases, the magnitude of the notching could be adapted so that the SRS remains in the contractual boundaries, while ensuring minimal levels on critical modes of the specimen.

6. SHAKER SHOCK TESTS CONTROL AND LIMITATIONS

Under some conditions, shock tests on electrodynamic shakers are possible: shocks of simple shape or shocks specified in terms of SRS, this latter being experienced in the frame of this study.

In general, the feasibility of shocks on shaker specified through a SRS has to be studied on a case by case basis as several parameters are involved. This makes it quite difficult to define a generic maximum achievable SRS for a given shaker. Obviously, the compatibility with shaker capabilities has to be checked first.

The first known limitation of a shaker is in terms of maximum acceleration, velocity and displacement allowable. Classical electrodynamic shakers allow a maximum displacement of +/- 1 inch and a maximum velocity around 2 m/s. The maximum acceleration generally allowed by the coil technology lies around 200 g for frequencies lower than 1000 Hz and 300 g beyond. Some high-performance shakers (Unholtz Dickie brand) present enhanced capabilities with a maximum stroke of +/- 3 inches and a maximum peak acceleration of 600 g in shock configuration enabling to simulate higher SRS. This is due to the absence of glue between the coil turns, the coil being manufactured in one piece.

For a given test configuration, the maximum possible acceleration is related to the total mass in motion including the specimen mass but also the mass of the shaker table or expander (plus the mobile coil mass); this can be a significant limitation for tests which have to be performed on large shaker interfaces (for example, at ADS EVT the empty mobile mass of the 160kN shaker in lateral configuration is 360 kg).

Moreover, the interface flexibility (shaker table or expander) can generate difficulties to reach a specified SRS. Indeed, at high frequency modes of the shaker interface will come into play and between them some antiresonances which might be a real blocking point for the execution of the test as it will induce a significant demand in terms of drive input (voltage) beyond shaker and amplifier capacities.

Thus, during shock tests the drive measurement shall be considered with care and predicted from lower levels. Its conversion into a frequency spectrum enables to identify the frequency bands where a difficulty might occur and helps have the right interpretation and find possible solutions.

Figure 6-6 presents an example of Drive frequency spectrum highlighting the frequencies where significant Drive input is required to achieve the test.

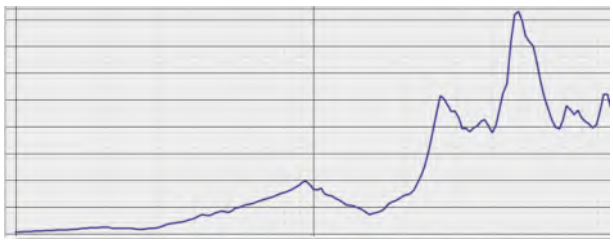


Figure 6-6 Drive input frequency spectrum

Predicting the next shock level from lower levels is also essential to verify the adequacy with shaker capabilities. However, this prediction is made on a linear assumption, which might not be fulfilled when getting close to the facility limits.

To achieve this kind of specification on shaker, a shock synthesis method needs to be used to build a time history. In the context of this study the method integrated in Siemens TestLab control system has been implemented and wavelet elementary waveforms have been considered associated to a

given maximum duration. The choice of wavelets has been guided by ADS EVT experience (most commonly used option) and duration has been defined by the duration of shocks generated on shock bench. The algorithm enables to define a time history which matches the specified SRS “at best” and produces a table describing the characteristics of each wavelet constituting the synthesized time history in terms of frequency, amplitude, delay and polarity. The resulting synthesized waveform generally does not perfectly match the specified SRS and wavelets can also be tuned individually to improve the result. This operation may reveal tricky as the interactions between all the wavelets cannot be anticipated and an iterative step by step approach must be considered, which may be time consuming.

In any case, this synthesis method is in general satisfying as it matches a given SRS within specified tolerances. The other advantage of the method is that it is also adapted to the case of notched SRS as described in the previous sections. An example of notched SRS and associated synthesized time history is displayed in Figure 6-7. Of course, it is difficult to match exactly the notched part of the SRS as only a limited number of discrete wavelets are available and interactions between them cannot be anticipated accurately. However, the feasibility of secondary notching on SRS has been demonstrated in principle.

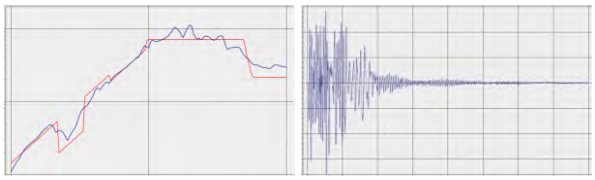


Figure 6-7 Drive Notched SRS and synthesis

7. CONCLUSIONS

The study concludes that the "classical" specification and qualification of units on a stiff interface leads to a significant over test compared to the real satellite shock environment.

This occurs due to various reasons:

- a stiff shaker setup forces all interface points to move in phase, whereas real-world flexible interfaces (such as satellite panels) allow for relative movement that naturally mitigates peak amplifications.
- The time synthesis from an SRS is not a deterministic task, and some choices might be better than others
- Applying margins on the SRS can seem inoffensive on classical log-log scales SRS plots, but templating of curves can have a strong impact.

The research quantifies these effect, showing that even using a direct time history may lead to a 90% exceedance, while moving to synthesized Shock Response Spectra (SRS) or using traditional "templating" may even lead to a 700% over test.

To avoid this, the paper proposes the use of SRS notching—adjusting the input spectrum to limit specific high-amplification frequencies—which can reduce overtest levels by a factor of approximately two. While SRS notching is more complex than notching sine or random vibrations due to frequency "pollution" from overlapping wavelets, it offers a way to align test levels more closely with actual flight conditions.
However, the authors note that fine-tuning time histories via shaker tests is not a universal solution, as these tests are subject to physical limitations regarding unit size and achievable acceleration levels; consequently, this methodology is more specifically adapted to components such as optical elements that are subject to relatively low shock levels.
Ultimately, while notching should be fine-tuned to remain within contractual compliance boundaries, it provides a useful tool for avoiding fictitious amplifications when the hardware and shaker capabilities allow.

The proposed shock secondary notch approach described in this paper should help to reduce significantly the number of unit shock test failures and even reduce the number of shock test requirements.

This approach requires a specific prediction capability of a unit shock internal response currently under study.

8. REFERENCES

1. Brevart, B. & Ait Zaid, S. (2014). Representative Mechanical Shock Testing for Satellite Electronic Units, *2014 ECSSMET Proceedings*, Braunschweig, Germany, p94.

2. Kolaini, A. & Pham, S. (2023). How to prevent Flight Hardware Failures During Shock Qualification Test, *2023 ECSSMET Proceedings*, Toulouse, France, p. 1282

3. Rodrigues, G., Caeiro, S., Kiryenko, S. & Laine, B., Prediction and Optimization of Shaker Shock Tests of Optical Unit, *2026 ECSSMET Proceedings (not yet published when this paper was written)*

SHOCK SPECIFICATION ENABLED BY ARTIFICIAL INTELLIGENCE TECHNIQUES

Maxime Perriquet [(1)], Lyès Badaoui[(2)] ,Deepak Sharma[(3)], Micha Knecht[(4)], Sebastian Thelemann[(5)], Goncalo Rodrigues[(6)], Benoit Laine[(6)]

[(1)] Airbus Defence & Space, Email: maxime.perriquet@airbus.com (France)
[(2)] Airbus Defence & Space, Email: lyes.badaoui@airbus.com (France)
[(3)] Airbus Defence & Space, Email: deepak.sharma@airbus.com (UK)
[(4)] Airbus Defence & Space, Email: micha.knecht@airbus.com (Germany)
[(5)] Airbus Defence & Space, Email: sebastian.thelemann@airbus.com (Germany)
[(6)] ESA, Email : goncalo.rodrigues@esa.int (Netherlands)
[(7)] ESA, Email : benoit.laine@esa.int (Netherlands)

KEYWORDS

Shock – Database – Artificial Intelligence – Specification

ABSTRACT

Traditionally, shock specifications have been based on conservative assumptions and simplified models, which can result in over-engineering or over qualification of spacecraft components. Moreover, the lack of a standardized approach for shock specification can lead to inconsistencies and errors in the specification, design and testing process.
In order to improve shock propagation prediction and specification, Airbus Defence & Space benefits from decades of shock testing on a large set of spacecrafts, resulting in vast amounts of data and metadata. By analysing these data, it is possible to identify the key parameters that affect shock propagation and response components.
The recent progress in data analysis and AI enables the reproduction of complex behaviours by efficiently learning from large databases. Multiple methodologies have surfaced, including statistical analyses, surrogate modelling, neural networks and data mining. The applications have been observed in a large number of technical domains, including the space industry.
The final goal of this study is to implement these surrogate models into a prototype software in the spirit of *VibroSpec* [2] for acoustics, allowing to perform shock predictions directly from the shock driving metadata.

1. ABREVIATIONS

Abreviation	Definition
S/C	Spacecraft
STM	Structural Model
SRS	Shock Response Spectrum
AI	Artificial intelligence
MEE	Maximum Expected Environment
FEM	Finite Elements Model
CoG	Center of Gravity
DMU	Digital Mock Up
PTF	(Shock) Pseudo Transfer Function
IP / OOP	In-Plane, Out-Of-Plane

2. INTRODUCTION

2.1. Context of the study

Over the years and the programs, many shock issues have been encountered on the developed spacecrafts. Most of the time, the shock specification combined to the difficulties to anticipate the shock environment have led to many delays and over costs. The necessity to elaborate new methods for shock specification became primordial. It is a direct continuation of the previous paper presented at ECSSMET 2023 in Toulouse called “Shock test database and statistical analysis tool” [3]. This new study is supported by a R&D activity under ESA contract. The goal of this project is to obtain a shock specification tool in the same spirit as *VibroSpec* [2] for acoustics.

2.2. Standard specification approach

Shocks are primarily derived from launch vehicle and release devices specifications. Usually, the SRS is provided and then it is necessary to derive the attenuation or possible amplification enabled by the structure itself. This is the most complex part.

2.2.1.Heritage

For recurrent platforms, shock tests have already been done. As a result, specifications are directly derived from those shock tests and used as specification for the future programs.

2.2.2.ECSS methods

For new platforms, the shock environment must be derived alternatively. The ECSS shock handbook preconisation for S/C structures is to use the called “Method D” which takes into account the shock source, the shock path characteristics provided by a series of structural segments and junctions plus some other measurement points characteristics (Out-of-plane, eventual equipment mass etc.). This method has the advantage to be easily applicable even in early stages, and is most of the time conservative.

2.2.3.Analysis

Analysis enabled by finite element models is possible. Application of analysis to several recent

programs have shown to be efficient for shocks sufficiently far away from the source location (so called “far field” shocks). The low frequency content is often well predicted by analysis when the shock source is sufficiently well known (transient signal).

2.3. Limits of standard specification approach

When method D is often too conservative, it also badly predicts the variability of attenuation variation with frequency, especially this method is unable to predict any eventual amplification of the shock that is often observed. Also, analysis fails to well predict the high frequency contents for two main reasons:

- The high non linearity of damping effects
- The difficulties raised to make sufficiently refined FE models to catch the smallest wavelengths.

2.4. Goal of the study

This study aims at proposing a heritage-based enabled by AI techniques to improve the specification process in early stages of platform development. The scope of the shock derivation will be restrained to the large S/C structures only. It is presented in three stages:

- Description of the database contents
- Outputs of data feature analysis
- Surrogate model generation and characterisation
- Way forwards.

The activities are performed in collaboration with data scientists in order to use state-of-the-art techniques in surrogate modelling.

3. DATABASE SPECIFICATION

This part aims at describing the data, metadata that have been chosen to be stored in this database and the methods to harvest it. The full specification of this database can be found in the reference document [4].

3.1. Satellite data

Satellite general information are stored in order to characterise the product with few parameters presented in Table 1.

Data name	***Description***
Program	Name of the program
Launcher	The launcher(s) of the program
Structure	The main architecture of the structure (hexagon, cube, central cylinder…)
Dimensions	The (X,Y,Z) spatial extension of the S/C
CoG Height	The height of the CoG of the specimen
Platform	The name of the platform family if applicable
Basic Axis	The longitudinal axis of the specimen
Panels Material	The main material used
Central Structure Material	The material of the central structure (if applicable)
Structural Model	Whether the structure tested is a STM or not.

Table 1 – Satellites metadata description

3.2. Shock test data

Data relative ton shock test source and conditions are described in Table 2.

Data name	***Description***
Mass	Mass of the specimen during test
Test	The test type name (Clamp band, pyro, low shock, Vesta…)
Tensioning	When applicable, the tension of the device (clamp band or other) in kN
Release Type	Whether the specimen is dropped or not after release
Excitation Direction	In-plane or out-of-plane, radial, axial type of shock
Source Closest Channels	The name of the measurement channels located at the shock input
Source subsystem	The subsystem where the shock is produced

Table 2 – Shock test metadata description

3.3. Measurement points description

A detailed description of the different measurement points that are acquired during the test is stored. The description of metadata stored is provided in Table 3.

Data name	***Description***
Measurement Point	The sensor name
Coordinates	The sensor coordinates (x,y,z) given in the S/C reference frame
Orientation matrix	The rotation matrix (3×3) from the sensor’s local frame to the S/C global axes
Axis	The degree of freedom label of the channels (X,Y,Z,U,V,W)
Excluded channels	A flag that identifies whether the X, Y or Z channel of the tri-axis must be excluded for any reason or not (i.e. in the case of bad quality data)
Frequency Mask	A frequency interval of validity of the SRS data
Out-of-Plane	The axis among those specified in “Axis” which corresponds to the out-of-plane
Time Data	The time series measured in test for this measurement point’s channels
SRS Data	The SRS obtained from Time data, computed with $Q = 10$
Zone	The location of the sensor in structure (top floor, shear walls, lateral walls…)
Sub assembly	The name of the sub system where sensor is located (Solar arrays, reflector, propulsion, instrument…)
Location	The location of the sensor on its panel (corner, edge, free edge…)

Apparent local mass	The total mass of the structure plus equipment located inside a sphere of influence, see **Error! Reference source not found.**.
Apparent local mass CoG	The vector between the measurement points and the CoG of the mass located in sphere of influence
Instrumentation status	The detailed diagnostics of the measurement quality (see 3.5)
Propagation	Load path full description, see 3.4.3.

Table 3 – Measurement points metadata description

3.4. Shock propagation data

Full description of the specimen with DMU would be too complicated to treat with a machine learning process with current state of the art of machine learning algorithms. It has been decided to provide only the load path information to the data analysis.

3.4.1. Definition of load path

There is no universal description of what is the load path. However, there is an important need of data harmonization for surrogate modelling to be effective. Intuitively, shock load path corresponds to the "trajectory of the shock". However strictly define this trajectory is tricky.

Mechanical waves are propagating within structure through flexural and in-plane waves. It is assumed that the "propagation path" between two points is the path where:

- the most of energy has transited through.
- the trajectory where the wave has propagated the fastest because energy is dissipating over time.

Flexural waves transport more energy than in-plane waves since the deformations are a lot higher in the out-of-plane direction. For those reasons, it is assumed as approximation that the propagation is defined as follow:

"Propagation path between two points is the minimal wave travel time trajectory of the flexural waves that propagated"

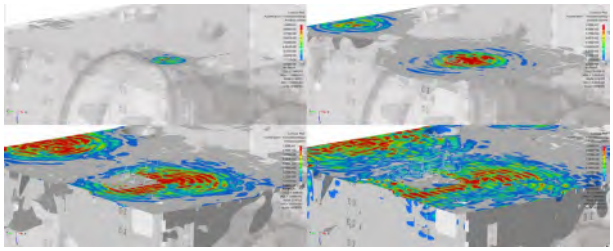


Figure 1 - Illustration of the concept of shock path with the wave propagation

3.4.2. Systematic derivation of load path

Based on this strict definition a load path derivation procedure from FE models, generally easily available in archives, have been established. The celerity of the flexural waves is computed automatically taking the hypothesis that frequency is 1kHz. Validity of this hypothesis will be assessed in 4.2.1. A sphere of influence (SOI) is defined as all the structural parts withing 1 wavelength around the sensor.

3.4.3. Load path data

Once the load path is determined as a series of nodes from source to measurement point, the mechanical description of the crossed parts must be derived. For that, a first step is automatic detection of junctions thanks to element patterns recognition, (for example Rigid + Spring + Rigid among other). Then, segments are built between those junctions and properties of structural parts in between are recovered from FEM with user intervention to specify the part type and the FEM property to use to recover the features from. Data recovered depend on the type of structure.

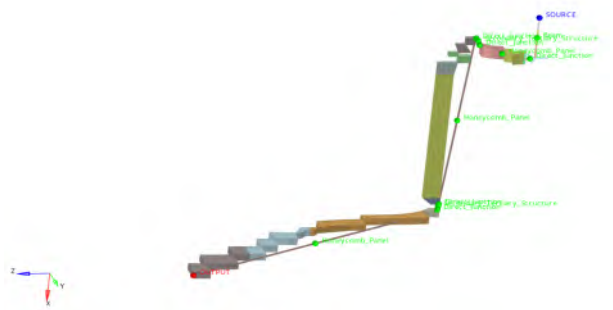


Figure 2 – Example of load path derived with the method

Metadata stored for each load path structural element is detailed in Table 4.

Data name	*Description*
Type	The type of structure
Vector	$(\delta x, \delta y, \delta z)$ vector of propagation of the shock in the medium
Material	Material used in the structure
Density	Density of the material: skin and core densities are dissociated for composite honeycombs
Elasticity modulus	The Young's modulus of the material: skin and core modulus are dissociated for composite honeycomb.
Cross Section	For beams: Area, Inertia
Thickness	For all plates: the thickness. Skin and core thicknesses are dissociated for composite honeycombs
Stiffener's size	For machined panels: the height of the stiffeners
Link Type	For junctions only: direct / indirect / damped
Number of plies	For composites: The number of plies in the composite (concerns the skin for honeycombs).
Part Type	For secondary and tertiary structures only: the type of structure (cleat, bracket etc.)

Table 4 – Load path element metadata description

3.5. Shock data quality

The data quality of the shock measurement is also assessed and recorded in database. The following criteria are assessed:

- Sensor dead
- Static and dynamic offsets
- Shock duration
- Piersol criterion (symmetry)
- SRS slope

4. DATABASE FEATURE ANALYSIS

In this part a feature analysis of data collected is provided. This means identify the correlation and driving parameters of the targeted observables. All the data displayed are done thanks to the post treatment tool *MecaLab.Shock* developed for the R&D.

4.1. Database contents

A database building phase has been led over several months. A database of more than 6000 shock responses (3 channels per measurement point) have been constituted.

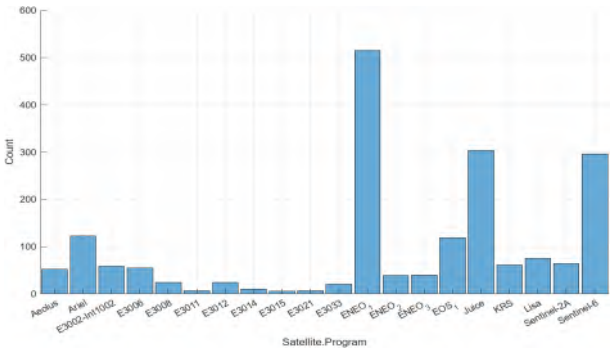


Figure 3 – Database measurements repartition per projects

Figure 4 displays the count of 3-axis measurements per projects. 20 different programs have been currently registered in database. Figure 4 shows the repartition of the measurements by shock type.

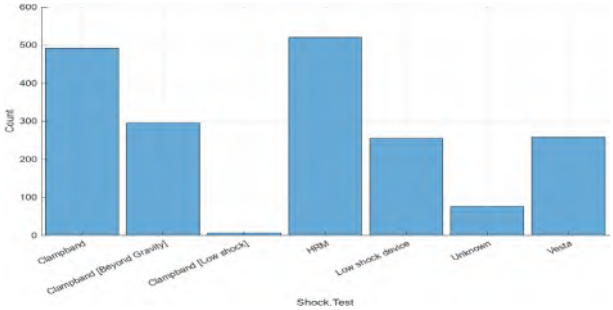


Figure 4 – Database measurements repartition per shock type

4.2. Wave travel time

In order to validate approach of wave travel time to compute propagation path, the wave travel time have been computed from database and correlated with the flexural waves approach.

4.2.1. Wave travel time method correlation

The hypothesis made in part 3.4.1 is that the shock is propagating from source to sensor through structure via flexural waves. To verify this hypothesis, the wave travel time have of each measurement point have been calculated.

In order to evaluate the wave travel time, first the time series are filtered with a bandpass filter [100Hz-100kHz] in order to remove low frequency parasite phenomena. Then, a moving standard deviation of the acceleration signals $\Gamma(t)$ is computed. Consider Γ_t the time series of duration dt centred around the study time t:

$$\Gamma_t = \left(\Gamma(t)\right)_{t_i} for\ t_i \in [t - \frac{dt}{2}, t + \frac{dt}{2}]$$

The interval time taken is of $dt = 1ms$. Then the moving variance is computed as follow:

$$\sigma(t) = \sqrt{\mu({X_t}^2) - \mu(X_t)^2}$$

This standard deviation is scaled with respect to the maximum value all time steps confound.

For each shock, the source standard deviation $\sigma_{IN}(t)$ is identified. For all channels measured during shock the intercorrelation of the $\sigma_{OUT}(t)$ with $\sigma_{IN}(t)$ is computed.

$$\Sigma(\tau) = xcorr(\sigma_{OUT}, \sigma_{IN})$$

The time delay of the first local maximum of $\Sigma(\tau)$ for $\tau > 0$ is the estimated shock wave arrival time step.

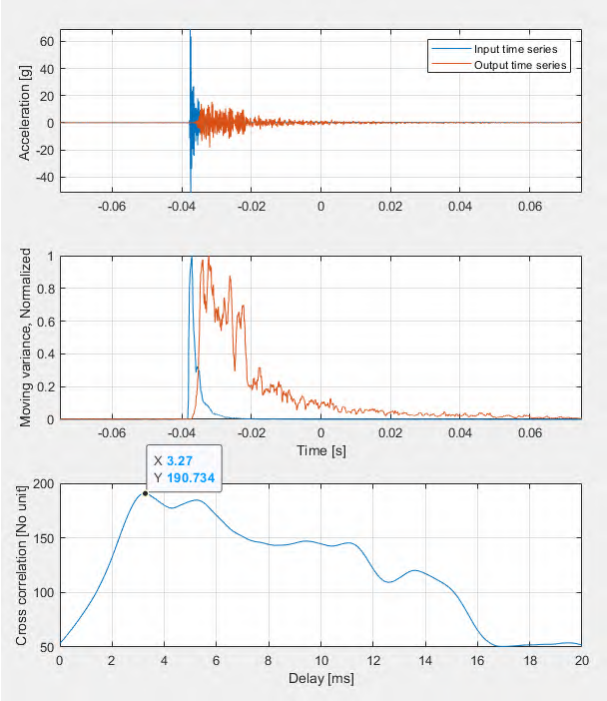


Figure 5 – Identification of the wave travel time with time series correlation analysis

The travel time computed is plotted with respect to the travel time estimated with the methodology presented earlier.

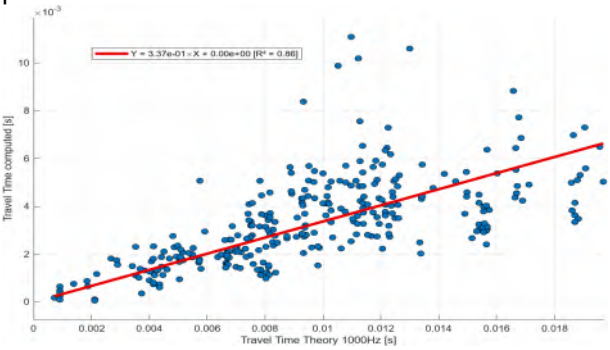


Figure 6 – Travel time computed for all channels with respect to the estimation [Y=0.34X, R²=0.86].

Figure 6 shows that correlation is good [R²=86%] between the travel time computed thanks to the flexural waves model and the measured travel time.

If only the mono-source shock events are taken, the correlation is even better. Indeed, the pluri-source shock events are generally not perfectly synchronised so estimation of shock travel time from measurement is more hazardous.

The regression curve equation is of $y = 0.33X$ so it seems that the wave time travel is in general around 3 times lower than expected. This corresponds to a frequency of waves of roughly 10 times higher. It means that our model would predict the travel time better if we take a frequency of computation of 10kHz.

The same computation is done filtering the signals between [500-1500] Hz. Then the moving variance time interval δt is set to 10ms in order to be able to catch the 1kHz wave variance with sufficient number of cycles. Results are shown on Figure 7.

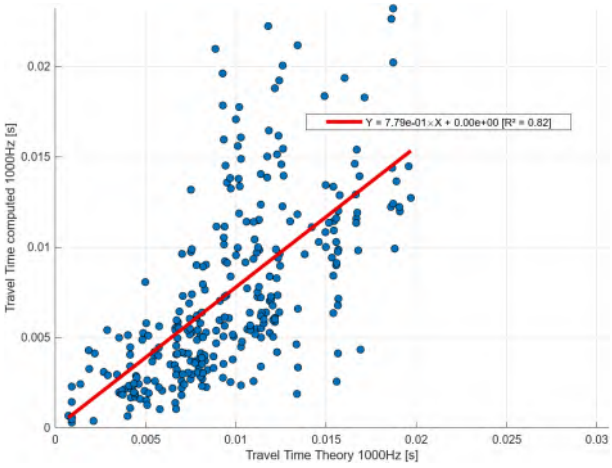


Figure 7 – Travel time computed for 1kHz waves with respect to the estimation [Y=0.78X, R²=0.82].

It shows a regression curve of now $y = 0.78x$, very close to $y = x$. It shows that when isolating the 1kHz waves, the estimated travel time is very close to measurement. This validates that the main waves are effectively flexural waves propagating through structure and that the model we elaborated for creation of database is coherent with observations.

4.2.2.Existence of In-plane waves

Now let's compute the travel time with in-plane waves and out-of-plane time series separately. The following graph shows a very impressive correlation between IP and OOP travel times. This means that the nature of waves generating in plane is the same as the out of plane. This argument allows to reinforce the hypothesis that in plane waves does not carry shock energy, and that the in-plane levels are only a consequence of OOP flexural waves that geometrically create IP level because of structure bending lever arm.

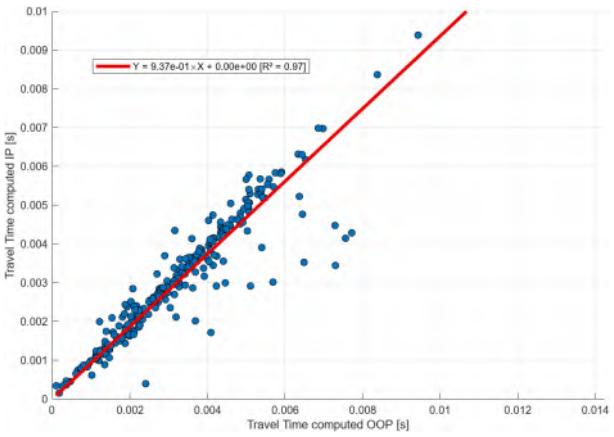


Figure 8 – Travel time computed with in plane and out-of-plane time series separately [Y=0.94X, R²=0.97].

4.3. Shock attenuation

The shock attenuation levels have been computed for all database and correlations with propagation path data have been assessed.

4.3.1. Shock response pseudo transfer function

The main observable that characterises the response of the structure to shocks is the Pseudo Transfer Function PTF. It is defined as follow:

$$PTF_{Q10} = 20\log_{10}\left(\frac{SRS_{Q10}^{OUT}}{SRS_{Q10}^{IN}}\right)$$

The input SRS_{Q10}^{IN} is defined with the max all channels of the measurement points representative of the input shock.
Level obtained at a given frequency of interest will be used in the next parts. To obtain a unique value at a frequency of interest f_0, a gaussian window w of size δf is used to reduce effect of noise:

$$w_{f_i} = e^{-\left(\frac{f_i - f_0}{\delta f}\right)^2}, \gamma_{f_0} = \frac{\sum_i w_{f_i} \times \gamma_{f_i}}{\sum_i w_{f_i}}$$

4.3.2. Expected environments

The expected environment is the statistical value that a random variable trial has a certain level of probability to not exceed. Often called A-Value B-Value. It is going to be called $P\alpha P\beta$ such as:

$$P(Y \leq P\alpha P\beta) = \alpha$$

And with β the confidence in this estimation. To compute that level, the "$n - DoF$ Student" probabilistic law is used.

4.3.3. Effect of distance

Here is analysed the effect of distance (not dissociated from the impact of junctions) on PTF with respect to frequency obtained with punctual shock sources HDRM-like on Figure 9.

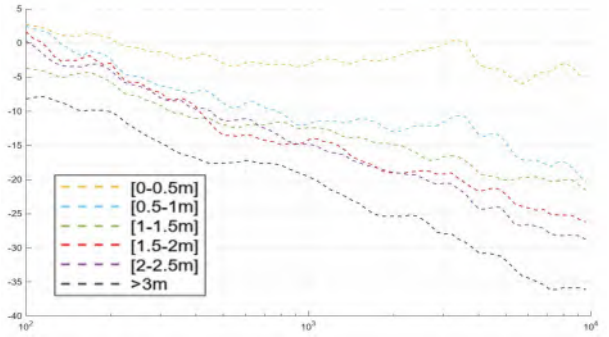


Figure 9 – PTF P90/90 with respect to distance from HRM

Figure 10 shows the same quantity for clamp band shock sources.

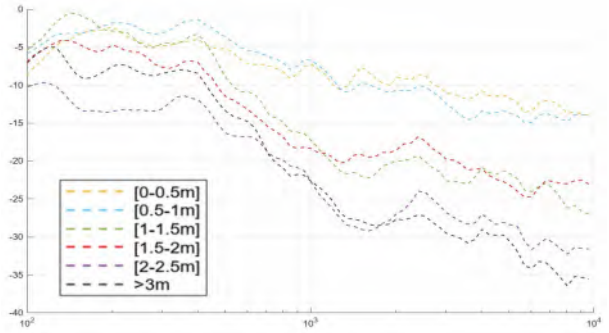


Figure 10 – PTF P90/90 with respect to distance from clamp band

The local HRM source decreases much more with distance in the first centimetres from source than with clamp band. The low frequency content is more present in clamp band environments. This indicates that the clamp band shock event excites more the spacecraft dynamics.

The Figure 11 shows the variation of PTF at 9000Hz for all shocks in database, coloured by program. Below 2 meters the variability by specimen is less important than above 2 meters. Some hidden variables must influence the variability for high distances.

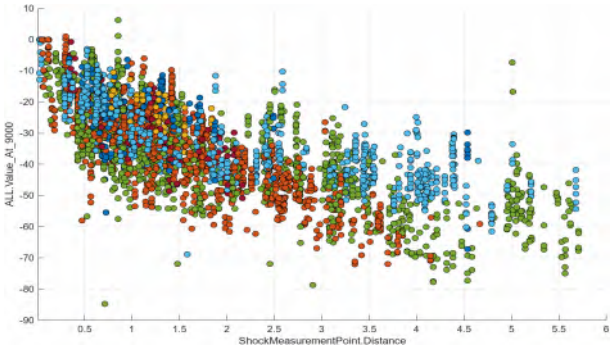


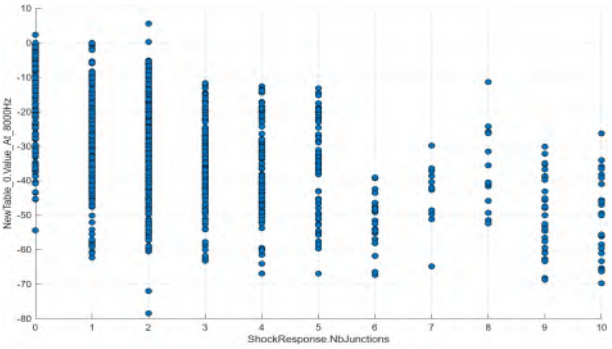
Figure 11 – Attenuation with distance at 9000Hz coloured by program, HRM + Clamp band

4.3.4. Effect of junctions

The data shows that a high correlation exists between the attenuation and the number of junctions. The junctions can be separated into two categories: the direct ones (contact) and indirect ones (by intermediate of a secondary part, two junctions). If we call the total number of junctions:

$$N_{junc} = 2N_{indirect} + N_{direct}$$

It is clear there is a strong correlation exists between the attenuation and the number of junctions.



4.3.5. Effect of direction of measurement In-plane or Out-of-plane

The effect of measuring in the plane or out of the plane on attenuation can also be assessed.

The Figure 12 shows the ratio between out-of-plane SRS and in plane for all measurements in database with respect to frequency. The average ratio is above 0 for all frequencies but the disparities tend to disappear at high frequency. The deviation is also lower at high frequencies.

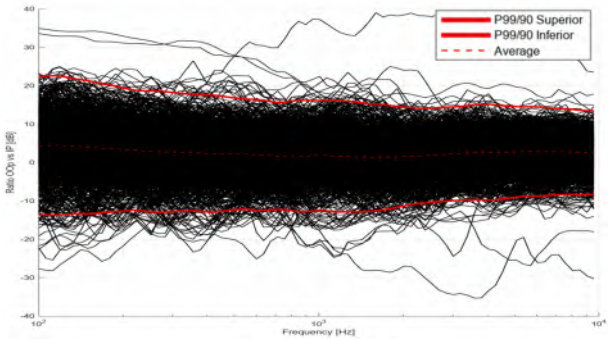


Figure 12 - Ratio SRS OOP vs. IP [dB]

If one frequency is isolated with gaussian average, The effects of sensor direction in-plane and out-of-plane can also be analysed for different shock source types can be assessed.

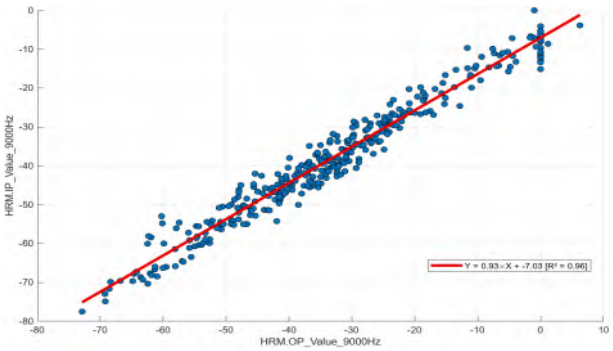


Figure 13 – PTF @9000Hz $[\delta f = 500Hz]$ for HRM sources OP versus IP

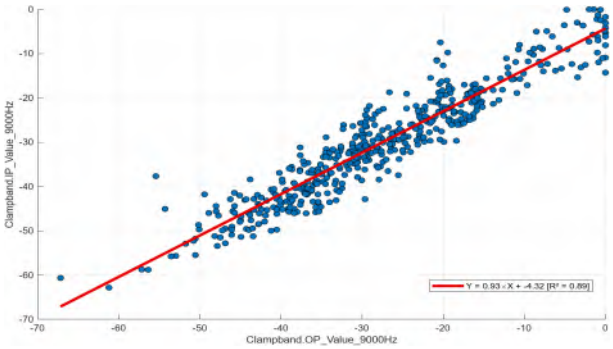


Figure 14 – PTF @9000Hz $[\delta f = 500Hz]$ for Clamp band sources OP versus IP

The difference of level between IP and OP directions is in average of $-7dB$ when the source is a HRM and $-4dB$ for clamp band source. The correlation is also less good for clamp band.

4.3.6. Effect of SOI mass

The mass contained inside the SOI of the measurement points has also an influence. This influence is shown on Figure 15. Even if the correlation is less important than other features identified before, a noisy correlation seems to exist and tends to decrease the shock levels when mass is higher.

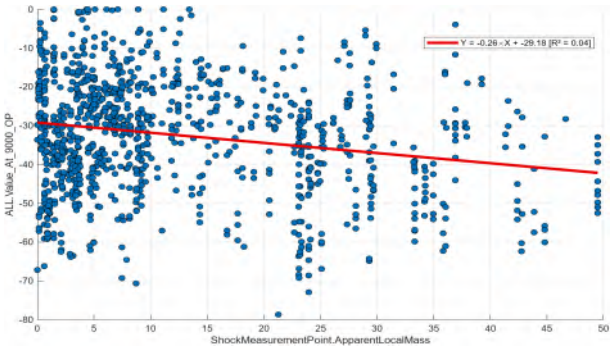


Figure 15 – Influence of SOI mass

5. SURROGATE MODELLING

5.1.1. Training sets

Database is post treated to extract features identified previously. This dataset is called “RES” dataset. The features are standardized so that all data has an average of 0 and a standard deviation of 1.

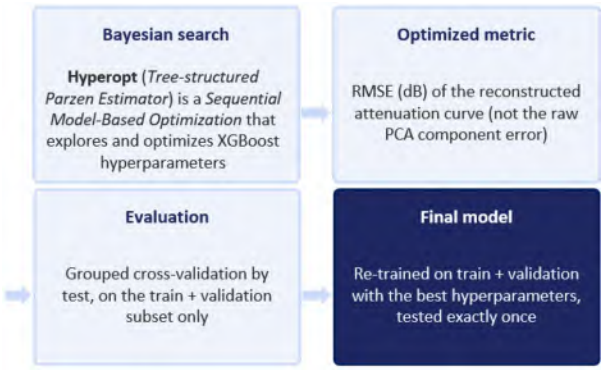


Figure 16 – Extraction of the “RES” dataset for training process

Attenuation curves are compressed thanks to a functional principal components analysis in order to reduce the dimensionality of the “RES” dataset from 80 dimensions to only 5 with a compression loss below <3%.

This dataset is split into:

- “TRAIN” [70%] dataset training process
- “VALIDATION” [15%] dataset for validation of the models
- “TEST” [15%] dataset for testing the final performances of the models.

5.1.2. Model’s algorithm

The algorithm chosen for training is the Gradient Boosting (XGBoost). This is a tree-based ensemble far more efficient than a deep neural network for limited amount of data. It is also better suited for natively handling a mix of numeric and categorical features. It captures non-linear interactions automatically. The model is trained

5.1.3. Model training pipeline

Two independent models are trained for inference of in-plane and out-of-plane levels.

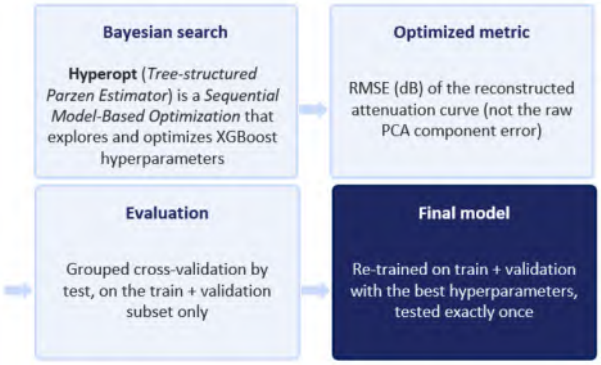


Figure 17 – Model training pipeline

5.1.4. Model performance

The model performance is evaluated compared to the naïve baseline predicting always the average of datasets. The Figure 18 shows the R^2 obtained for both models IP and OOP.

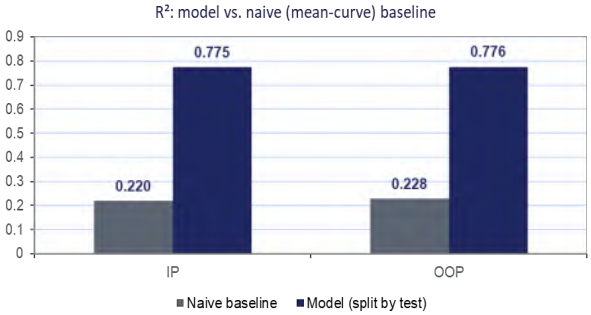


Figure 18 – Model performance compared to naïve baseline

The trained model clearly adds value over the naive baseline (R^2 × 3.5), reflecting real signal learned from the features. But the uncertainty band around any single number is wide given the size of the dataset.

5.1.5. Features importance

Figure 19 displays relative importance of input features categories in models’ decision process.

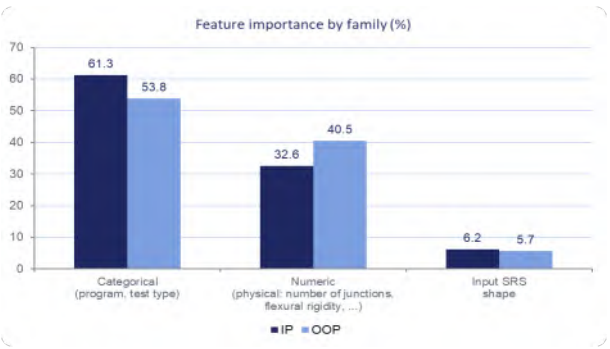


Figure 19 – Features importance in models’ decisions

Around 60% of the model's decision-making comes from categorical variables. Especially, 30% comes from program it belongs to. Consequence is that generalizing to a new program might be challenging. This issue is currently assessed and several mitigation policies are being studied to improve and anticipate this behavior.

6. CONCLUSIONS

This study is a direct continuation of the previous paper presented at ECSSMET 2023 in Toulouse called "Shock test database and statistical analysis tool" [3].

The database architecture have been improved for performance, collection process has been upgraded to increase efficiency and reduce the biases in propagation path determination.

The methodology proposed, based on the flexural waves celerity computation in structural parts have been validated by the correlation to the database.

Feature analysis showed that correlations are physically explained and consistent. A surrogate model has been trained to make it understand the feature correlations and produce predictions that fit to the datasets with a good accuracy.

7. WAY FORWARD

The surrogate model performances are really promising and allow to recover good prediction accuracy with monitored error levels.

However, some clues indicate that it is sensitive to the program where shock data has been measured. The capability to extrapolate to other programs must be measured and this will be the key point to study during incoming activities. For instance, quality of datasets will be investigated into details to identify potential outliers or instrumentation differences between programs that could bias the model.

This study is supported by a R&D activity under ESA contract. The goal of this project is to obtain a shock specification tool in the same spirit as *VibroSpec* [2] for acoustics. The model being trained and validated will be improved in the next months and will be implemented in the tool currently in development.

8. REFERENCES

[1] ECSS Secretariat ESA-ESTEC Requirements & Standards Division, Space engineering : Mechanical shock design and verification handbook, Noordwijk, The Netherlands, 2015.

[2] Kasper J., Derivation of Satellite Equipment Design and Test Specifications from Random Vibration Environments, ESA Contract No. 29502/06/NL/SFe, Title report "VibroSpec Methology & Tool" MTD.R &D.TN.2291, Issue1, 2010

[3] ECSSMET 2023, Shock test database and statistical analysis tool

[4] TN-ADST-1002185057, ADS01 - Shock Data and Metadata collection specification, ESA contract No. 4000148303/25/NL/RK

[5] Cormen, Thomas H.; Leiserson, Charles E.; Rivest, Ronald L.; Stein, Clifford (2001). "Section 24.3: Dijkstra's algorithm". Introduction to Algorithms (Second ed.). MIT Press and McGraw–Hill. pp. 595–601. ISBN 0-262-03293-7.

ENERGY-BASED SEVERITY METRICS FOR TRANSIENT SHOCK CHARACTERIZATION

Roberto Fagioli [1,2], Mattia Dal Borgo [3], Alberto García de Miguel [4], Umberto Musella [3], Emilio Di Lorenzo [5], Frank Naets [1,2]

[1] *Department of Mechanical Engineering, KU Leuven, Leuven, Belgium*
[2] *Flanders Make @KU Leuven, Belgium*
[3] *Siemens Industry Software NV, Leuven, Belgium*
[4] *Siemens Industry Software SL, Tres Cantos, Spain*
[5] *Siemens Industry Software S.r.l., Genova, Italy*

KEYWORDS

environmental testing, mechanical load severity comparison, shock response spectrum, shock characterization, shock synthesis

ABSTRACT

The design and execution of shock tests remain complex and time-consuming processes that rely heavily on iterative calibration and expert knowledge to meet strict qualification requirements. Achieving accurate reproduction of target conditions requires careful tuning of test parameters while balancing the risks of under- and over-testing, a task further complicated by the limitations of conventional metrics and by the non-unique relationship between target spectra and time histories. In current practice, shock characterization is carried out through the shock response spectrum, a metric that is coupled with time-based indicators such as T_e, representing the overall duration of the shock event, and T_E, denoting the duration of its strong phase, both outlined in the MIL-STD-810H (USA Military Standard for Environmental Testing). This work introduces a novel energy-based framework that complements existing metrics by enabling the characterization and comparison of transient load cases, while more directly capturing the physical mechanisms associated with both overstress and fatigue-type failure. The framework is further extended through the use of n^{th}-order moments, providing a refined description of the temporal features of transient events while also addressing the non-bijective nature of conventional spectral severity metrics. Finally, energetic metrics may serve as a unifying layer bridging traditional single-input-single-output approaches with more representative multi-degree-of-freedom testing scenarios, potentially accounting for the influence of cross-axis coupling on the overall severity of a multi-axial transient event. This potential is illustrated through a six-degree-of-freedom Coupled Loads Analysis case study representative of spacecraft launch loading. Combined with specific scalar quantities derived from the temporal moments, these metrics may also provide additional constraints for future shock synthesis methods, enabling the generation of time histories that better preserve both response, energetic and temporal characteristics. Overall, these developments may contribute to a more comprehensive and physically meaningful characterization, comparison, and synthesis of mechanical shock environments.

1. INTRODUCTION

1.1. Shocks and shock testing

A mechanical shock is a transient dynamic loading whose duration is short relative to the characteristic natural periods of the system being excited. Mechanical shocks can span different duration, amplitude, and frequency scales. Although high acceleration levels are associated with shock events, high acceleration is not an inherent requirement of their definition and should be regarded relative to the dynamic and load-carrying capabilities of the system. Despite their varying characteristics, all mechanical shock events involve the transfer of energy to a structure, i.e., they perform work on the system [1].

Shocks occur across a wide range of engineering fields, including civil, aerospace, and defense engineering. In civil engineering, earthquakes represent long-duration, low-frequency, and low-acceleration shock events, whereas pyrotechnic shocks encountered in aerospace applications are characterized by short durations (in the order of tens of ms), high-frequency content (up to 100 kHz), and acceleration levels that can reach several thousands of g. In the space sector, such shocks are generated during critical operational events such as the release of deployable appendages, booster separation, and fairing jettisoning [1].

The damaging effects of shocks fall into two main categories. The first is structural failure, which can take the form of yielding, cracking, rupture, or other modes of rapid system disassembly. Small components and subassemblies are particularly vulnerable to this type of damage due to their lower mass and structural margins. The second category is functional failure, most commonly manifesting as circuit breaker trips [1]. These potentially severe consequences make the study of shock environments essential for the accurate design and qualification of components and instruments.

Given the highly transient nature of shocks and their

extremely high-frequency content, numerical methods struggle to accurately capture their effects, particularly when wave-propagation phenomena, structural joints, damping, and local structural features need to be accurately represented. Finite Element Analysis can therefore provide valuable support during design and preliminary assessment, but experimental testing remains an integral part of the verification process [2]. In particular, shock testing forms part of the broader environmental testing practice used to demonstrate that hardware can withstand the mechanical environments encountered during its operational life and continue to function as intended. Depending on the verification objective, shock tests may reproduce a representative mission-specific environment or apply prescribed qualification levels, generally including appropriate margins, to demonstrate adequate robustness of the hardware. Common testing methods include drop tables, shaker-induced shocks, explosive-based pyroshock testing (Figure 1), and resonant plate testing (Figure 2), each offering different trade-offs in terms of accessibility, cost, and fidelity to the environment being reproduced, particularly with respect to achievable amplitude and frequency content [1]. Shaker-based testing provides a highly controllable and repeatable excitation, but current shaker technology is generally limited in its ability to simultaneously reproduce very high amplitudes and high-frequency content, especially for large devices under test, and typically excites only one axis at a time. High-performance shaker systems also require substantial initial investment, although their operating cost per test becomes comparatively low once the facility is available. Resonant plate testing offers a relatively inexpensive means of generating high-frequency responses, but accurately tuning the transmitted load to achieve the desired response at the device under test can be challenging. Explosive-based pyroshock testing provides the highest fidelity to real pyroshock environments, as the excitation mechanism closely resembles that encountered in service, but it involves significantly higher costs, more complex test preparation, and greater practical and safety constraints [1].



Figure 1: Explosive stage-separation test [1]

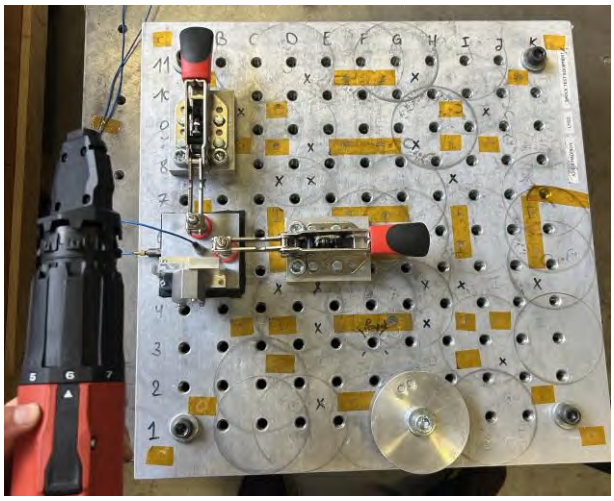


Figure 2: Resonant-plate testing setup at KUL

1.2. Load severity comparison & Shock Response Spectrum

To establish appropriate specifications for these shock testing methods, engineers require a framework to evaluate and compare the damage potential of different dynamic environments. This centres around the concept of *severity*, which is defined as the probability of failure under a given mechanical loading event [3]. Despite this intuitive qualitative definition, quantifying severity is not straightforward, since it depends on the metric used to characterize the loading event, meaning no univocal definition currently exists. Another key aspect of severity is that two dynamic environments, even if physically distinct in nature, are considered equivalent if they share the same severity metric curve [3]. Consequently, a qualification test is valid if its severity spectrum completely encompasses that of the real-world operational environment, ensuring the test subjects the component to an equal or greater level of damage in terms of failure risk.

To quantify severity for shock events, the Shock Response Spectrum (SRS) is the fundamental tool in shock analysis and characterization at the current state of the art. The SRS is computed by applying the shock's base acceleration input to a series of theoretical single-degree-of-freedom (SDOF) systems, each defined by an increasing natural frequency (f_n) and a fixed damping ratio (ζ). The maximum absolute acceleration response experienced by each SDOF oscillator is then mapped against frequency, resulting in the Maxi-Max Absolute Acceleration (MMAA) SRS, commonly referred to simply as the SRS. In such way, the SRS captures the maximum peak response of a transient signal across the frequency domain [4]. A visualization of this calculation is provided in Figure 3.

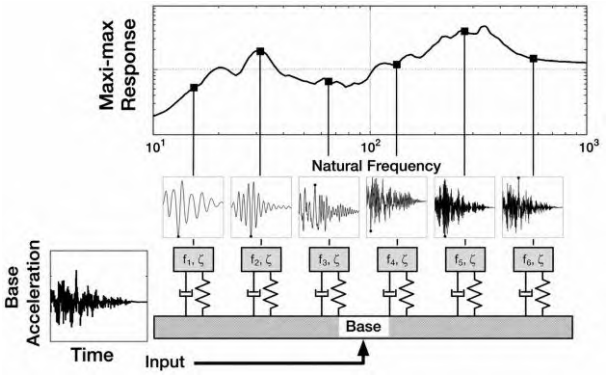


Figure 3: Shock response spectrum derived from a series of SDOF oscillators [1]

Alongside the MMAA SRS, the Pseudo-Velocity Shock Response Spectrum (PV-SRS) is commonly used to provide additional insight into the structural response. Pseudo-velocity is defined as:

$$PV = \omega_n x_{rel} \tag{1}$$

where ω_n is the natural angular frequency and x_{rel} is the relative displacement response of the SDOF oscillator. The PV-SRS is obtained from the peak pseudo-velocity response for every f_n and is particularly useful because of its relation to dynamic stress and relative displacement. The Fatigue Damage Spectrum (FDS), instead, incorporates material S-N curves to account for multi-cycle cumulative fatigue damage induced by operational loads [4].

In shock testing, the severity-based criterion introduced earlier is applied directly through comparison of the test and qualification SRS curves, as illustrated in Figure 4. The black curve represents the qualification level prescribed by space-industry standards (ECSS [5]) for the component under consideration, while the blue curves correspond to the SRS obtained during a pyroshock test. Since the measured test response exceeds the qualification curve by approximately 50%, the test environment is considered sufficiently severe and representative of the expected operational conditions. Consequently, if the component withstands the test without structural or functional failure, it can be considered qualified for the specified shock environment.

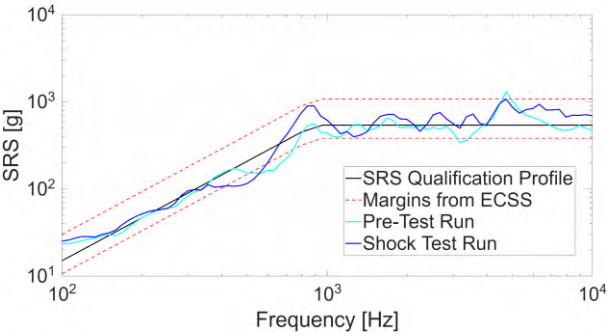


Figure 4: Pre-test and test SRS for a resonant plate shock test for a component

Beyond qualification testing, the SRS can also support the design of structures subjected to shock loading. By expressing the maximum response as a function of natural frequency, it helps to identify structural parameters that limit the response to acceptable levels. For example, when a structure can be approximated as an SDOF system, its natural frequency may be selected to lie within a region of the SRS associated with lower response amplitudes [1].

The SRS is widely used in shock data analysis because of its simplicity, intuitive physical interpretation, low computational cost [6], and ability to condense complex time histories containing thousands of samples into a compact spectrum that can be readily interpreted and compared. Its century-long use in shock specification and qualification has provided a well-established engineering framework for defining qualification curves and associated margins, making it a practical and reliable reference tool in the field [4].

These advantages, however, are accompanied by some inherent simplifications. Shock severity is inferred from the peak response of idealized SDOF oscillators, typically through acceleration or related kinematic quantities, whereas structural failure criteria are more directly associated with quantities such as stress, strain or yielding [7]. In particular, there is no general direct relationship between peak acceleration or velocity and peak strain [8], meaning that different excitation waveforms may generate similar peak responses while producing different strain states and therefore different damage potential. Furthermore, the dimensionality reduction that makes the SRS compact and convenient inevitably removes part of the temporal information contained in the original excitation [9]. As a result, substantially different time histories can produce identical or nearly identical SRS curves, making the SRS transformation non-bijective and preventing reconstruction of the original excitation from the spectrum alone. Finally, because the SRS is based on an array of independent linear SDOF oscillators, it does not explicitly capture the interactions occurring in real MDOF environments [10]. These considerations do not reduce the value of the SRS, but rather motivate the use of complementary descriptors aimed at reinforcing its characterization capabilities by providing additional information on aspects that the SRS does not directly retain.

2. ENERGY SPECTRA

The primary objective of this paper is to introduce a set of complementary metrics that reinforce the information provided by the widely used SRS, offering additional tools to evaluate the severity of a dynamic environment. To this end, energy response spectra are proposed. In the same fashion of the SRS, these are derived from solving the equation of motion of a base-excited SDOF system and

extracting interesting quantities to be presented as function of the natural frequency of the system.
The proposed metrics retain the same fundamental modelling assumptions as the SRS and therefore share its inherent limitations, including the non-uniqueness of the spectral representation and the inaccuracy in representing the failure probability of a real complex structure [1].
Their main advantage, however, lies in enriching this established framework rather than replacing it. By providing a simplified representation of how energy is distributed across the structural response, energy spectra provide additional information on the severity of the dynamic environment that may be more directly connected to physical damage mechanisms than peak acceleration alone [7]. Moreover, the energetic formulation naturally lends itself to extension beyond independent SDOF oscillators toward MDOF systems, as will be illustrated later in this work, providing a potential pathway for the characterization of multi-axial dynamic environments [8]. At the same time, the methodological continuity of the proposed approach with current SRS-based practice represents an important advantage, as it keeps the conceptual and procedural gap with the current state of the art small. This is particularly relevant in testing engineering, where qualification procedures are well established and the adoption of new methodologies is necessarily cautious. By complementing rather than overturning the existing framework, the proposed metrics may therefore offer a more realistic pathway toward practical implementation and eventual industry adoption.

2.1. Energy formulation in relative coordinates

The starting point is the common dynamic equation in relative coordinates for a SDOF system excited by an enforced-base motion, $\ddot{x}_g$. This formulation is adopted because, in practice, the equation of motion is first solved to obtain the system state variables, which are subsequently used to evaluate the individual energy terms [1]. The energies are therefore not solved for directly through the energy balance equation. The dynamic equation is:

$$m\,\ddot{x}_{rel}(t) + c\,\dot{x}_{rel}(t) + k\,x_{rel}(t) = -m\,\ddot{x}_g(t) \qquad (2)$$

Where $x_{rel} = x - x_g$, is the relative motion between the motion of the point mass, x, and the ground motion itself x_g, while *m*, *k* and *c* are respectively the mass, stiffness and damping of the system.
Equation 2 can be easily extended to a MDOF system by replacing the scalar mass, damping, and stiffness parameters with their corresponding matrices and the motion coordinates with vectors:

$$\boldsymbol{M}\,\ddot{\boldsymbol{x}}_{\boldsymbol{rel}}(t) + \boldsymbol{C}\,\dot{\boldsymbol{x}}_{\boldsymbol{rel}}(t) + \boldsymbol{K}\,\boldsymbol{x}_{\boldsymbol{rel}}(t) = -\boldsymbol{M}\,\ddot{\boldsymbol{x}}_{\boldsymbol{g}}(t) \qquad (3)$$

In the following equations, the time dependency will be neglected from now on to make the equations more compact. The dynamic equilibrium equation can be transformed into energetic equilibrium by multiplying it by the infinitesimal displacement of the relative coordinate and integrating for space [8]:

$$\int_{x_{rel}(-\infty)}^{x_{rel}(\infty)} \boldsymbol{dx_{rel}}^T\,\boldsymbol{M}\,\ddot{\boldsymbol{x}}_{\boldsymbol{rel}} + \int_{x_{rel}(-\infty)}^{x_{rel}(\infty)} \boldsymbol{dx_{rel}}^T\,\boldsymbol{C}\,\dot{\boldsymbol{x}}_{\boldsymbol{rel}} + \int_{x_{rel}(-\infty)}^{x_{rel}(\infty)} \boldsymbol{dx_{rel}}^T\,\boldsymbol{K}\,\boldsymbol{x}_{\boldsymbol{rel}} = -\int_{x_{rel}(-\infty)}^{x_{rel}(\infty)} \boldsymbol{dx_{rel}}^T\,\boldsymbol{M}\,\ddot{\boldsymbol{x}}_{\boldsymbol{g}} \qquad (4)$$

Then, the following algebraic identity, can be applied:

$$\dot{\boldsymbol{x}}_{\boldsymbol{rel}} = \frac{1}{dt}\cdot \boldsymbol{dx_{rel}} \;\rightarrow\; \boldsymbol{dx_{rel}} = \dot{\boldsymbol{x}}_{\boldsymbol{rel}}\cdot dt \qquad (5)$$

Thus, the integrals are rewritten in terms of the time differential dt:

$$\int_{-\infty}^{\infty} \dot{\boldsymbol{x}}_{\boldsymbol{rel}}^T\,\boldsymbol{M}\,\ddot{\boldsymbol{x}}_{\boldsymbol{rel}}\,dt + \int_{-\infty}^{\infty} \dot{\boldsymbol{x}}_{\boldsymbol{rel}}^T\,\boldsymbol{C}\,\dot{\boldsymbol{x}}_{\boldsymbol{rel}}\,dt + \int_{-\infty}^{\infty} \dot{\boldsymbol{x}}_{\boldsymbol{rel}}^T\,\boldsymbol{K}\,\boldsymbol{x}_{\boldsymbol{rel}}\,dt = -\int_{-\infty}^{\infty} \dot{\boldsymbol{x}}_{\boldsymbol{rel}}^T\,\boldsymbol{M}\,\ddot{\boldsymbol{x}}_{\boldsymbol{g}}\,dt \qquad (6)$$

By reformulating the equation of motion, a conservation of energy equation is obtained. From left to right, the terms represent the kinetic energy in relative coordinates, the energy dissipated by the system, and the absorbed energy. The right-hand side of the equation corresponds to the relative input energy, also referred to as the total energy [8]:

$$E_K^R + E_D + E_A = E_I^R \qquad (7)$$

Among all these energetic quantities, the relative input energy and absorbed energy are particularly useful for representing the damage potential of a shock environment. Similarly to the SRS, these quantities can be treated as frequency-based spectral metrics by extracting the maximum energy value for each natural frequency and plotting it as a function of frequency.

2.2. Absorbed Energy

Now, the focus will be on the absorbed energy:

$$E_A = \int_{-\infty}^{\infty} \dot{\boldsymbol{x}}_{\boldsymbol{rel}}^T\,\boldsymbol{K}\,\boldsymbol{x}_{\boldsymbol{rel}}\,dt \qquad (8)$$

The absorbed energy can be divided into strain-elastic energy, that is recoverable, and the non-recoverable energy lost to hysteresis [8], when the structure is excited beyond its yield limit:

$$E_A = E_{St} + E_{Hys} \quad (9)$$

In case of a viscously damped system, the Strain Energy (also known as Potential Energy) just equals the Absorbed Energy [1]. Figure 6 shows the time evolution of the strain energy (in black) caused by the shock presented in Figure 5, together with the corresponding kinetic energy expressed in relative coordinates (in magenta).

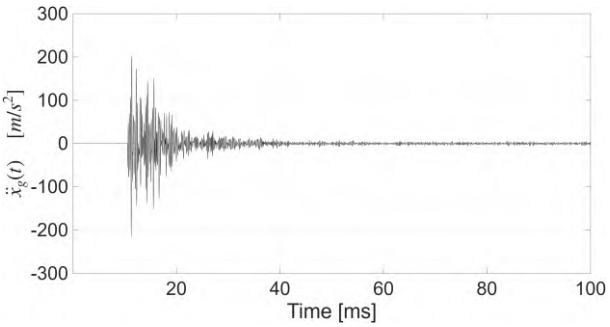


Figure 5: Shock signal time history

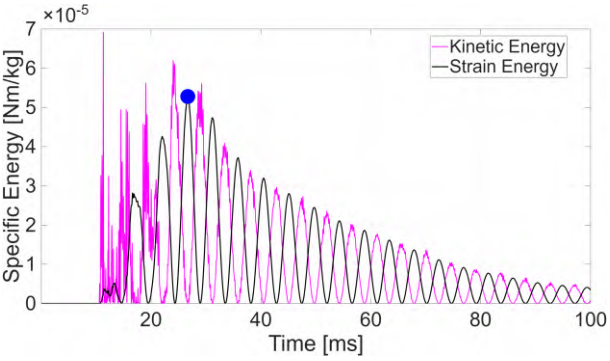


Figure 6: Strain energy and kinetic energy time evolution for a SDOF with f_n = 110 Hz

The blue point is the maximum of the strain energy and, in the same way as the acceleration response to compute the SRS, that value will be extracted and plotted as function to the frequency to create the Strain Energy Spectrum (SES). Figure 6 shows the out-of-phase oscillation between the strain energy and the relative kinetic energy after the initial transient has passed. The out-of-phase nature of the oscillation comes from the motion of the SDOF oscillator. When the displacement of the mass is greatest, the spring is stretched to its maximum but the velocity of the mass is zero [1]. These oscillations progressively decay as energy is dissipated by damping, continuing until the system returns to rest and both energy contributions tend toward zero [1].

For a SDOF linear system, $k = m\omega_n^2$. Therefore, the specific strain-elastic energy (E_{St}) can be written as:

$$\frac{E_{St}}{m} = \frac{1}{2}\frac{k}{m}x_{rel}^2 = \frac{1}{2}\omega_n^2 x_{rel}^2 = \frac{1}{2}PV^2 \quad (10)$$

A direct algebraic relationship exists between strain energy and pseudo-velocity. Consequently, this relationship also holds for their respective spectra:

$$SES = \frac{1}{2}PVS^2 \quad (11)$$

An example of this mathematical link can be visualized immediately, by plotting the SES and PV-SRS for the signal in Figure 7.

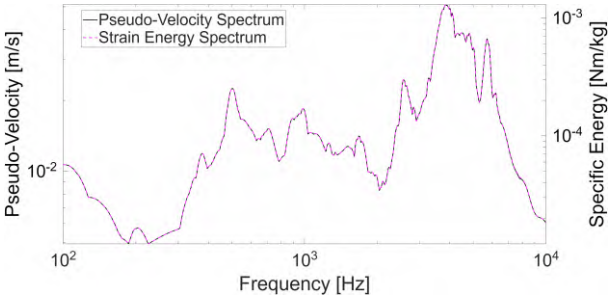


Figure 7: PV-SRS and SES comparison

The two graphs display identical geometric profiles, differing only in magnitude. Therefore, similarly to the PV-SRS, the SES can be used to assess the damage potential associated with overstress-type failure, while offering the additional advantage of being readily extendable to MDOF dynamic environments.

2.3. Relative Input Energy

The relative input energy, also referred to as total energy, is the total amount of energy that is inputted into a system by means of an acceleration load, namely the shock signal. Its definition is:

$$E_I^R = -\int_{-\infty}^{\infty} \dot{\boldsymbol{x}}_{\boldsymbol{rel}}{}^T \boldsymbol{M}\, \ddot{\boldsymbol{x}}_{\boldsymbol{g}}\, dt \quad (12)$$

Figure 8 shows the time evolution of the input energy (in black) and dissipated energy (in magenta) for the shock in Figure 5.

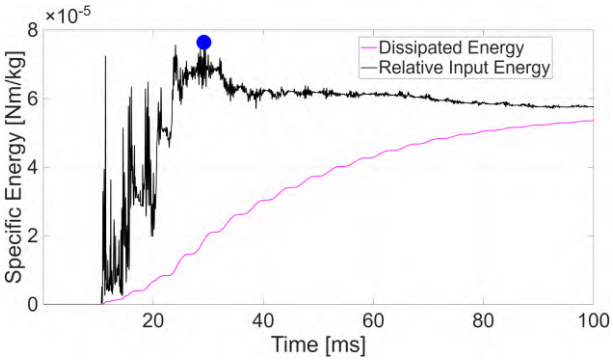


Figure 8: Relative input energy and dissipated energy time evolution for a SDOF with f_n = 110 Hz

Again, the blue point is the maximum of the energy and will be extracted to produce the Relative Input Energy Spectrum (RIES). The plot shows the input energy rising from zero to a nearly constant value at

the end of the shock pulse. The small residual fluctuations observed after the pulse are attributable to noise. The final magnitude of the input energy is approached by the monotonic dissipated energy [1]. The RIES is considered representative of damage mechanisms associated with a large amount of energy that is not dissipated by the structure, such as in the case of multiple shocks or longer dynamic events, including launch environments or earthquakes. In this respect, one of the main advantages of energy response spectra over the SRS is their cumulative nature, as total energy progressively accumulates throughout the response [1].

A first direct demonstration of this feature can be obtained by comparing the metrics associated with a single shock pulse (Figure 5) with those resulting from two identical shocks applied sequentially (Figure 9). For failure mechanisms influenced by cumulative loading, such as material fatigue or progressive damage [8], repeated exposure to the same damaging shock can result in greater severity than a single exposure. However, comparison of the corresponding SRS curves (Figure 10) shows practically identical results. Since the system fully returns to rest between the two pulses, each shock produces essentially the same maximum oscillator response, leaving the SRS unchanged. A similar behavior applies to the SES: as visible from the strain energy evolution in Figure 6.

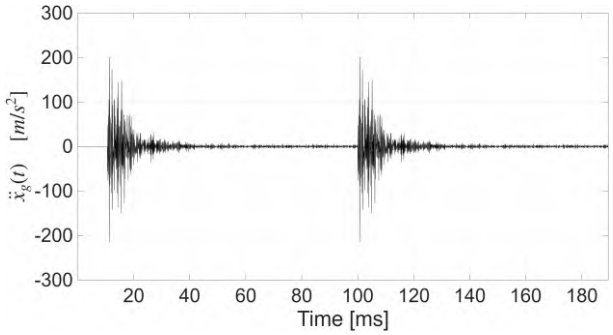


Figure 9: Shock signal repeated twice

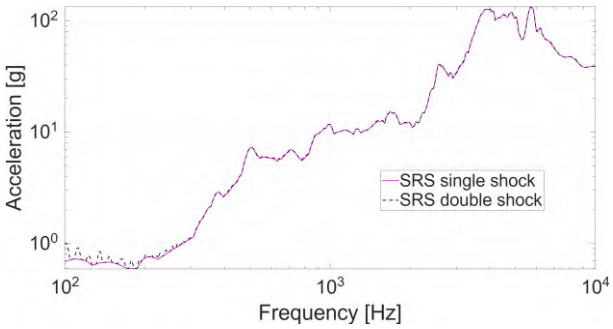


Figure 10: SRS (single vs double shock)

In contrast, the RIES accounts for the energy progressively transferred to the system and therefore clearly distinguishes between the single- and double-shock cases. This behavior is visible both in the time evolution of the relative input energy (Figure 11), where the second shock produces an additional increase in the accumulated energy, and in the corresponding RIES curves (Figure 12).

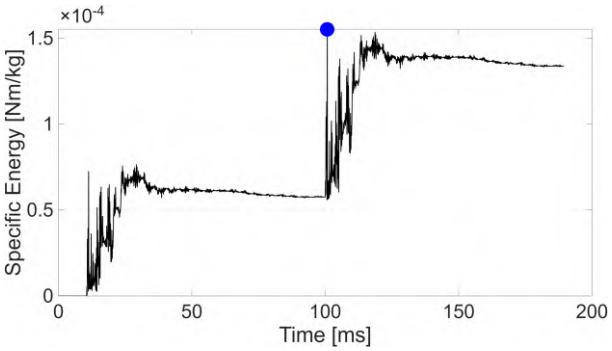


Figure 11: Double Shock Relative Input Energy time evolution for a SDOF with f_n = 110 Hz

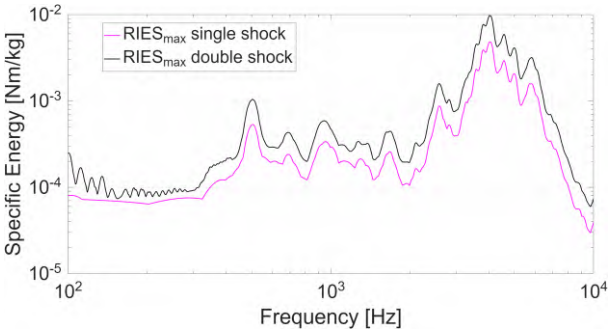


Figure 12: RIES (single vs double shock)

The same cumulative property can also be displayed by considering dynamic events of different durations. Figures 13 and 14 show a short and a long dynamic event, the second approximately 8 times longer than the first. Since the two time histories have similar peak acceleration levels, their SRS curves are also very similar, as shown in Figure 16.

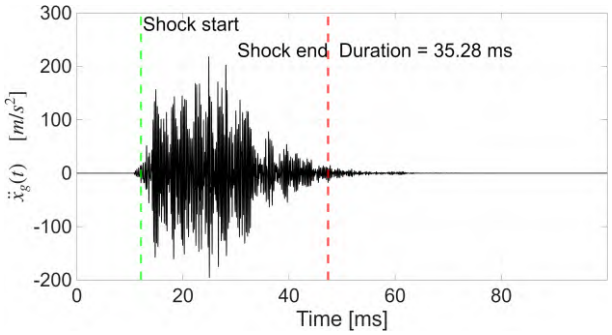


Figure 13: Short dynamic event (35.28ms)

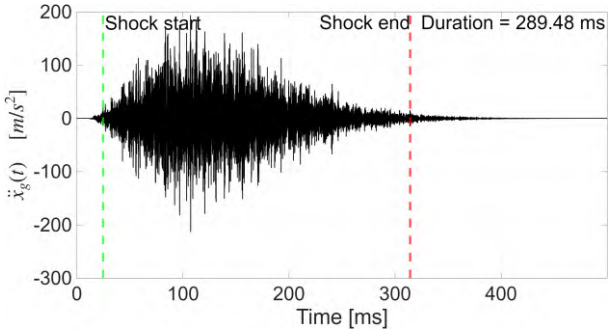


Figure 14: Long dynamic event (289.48ms)

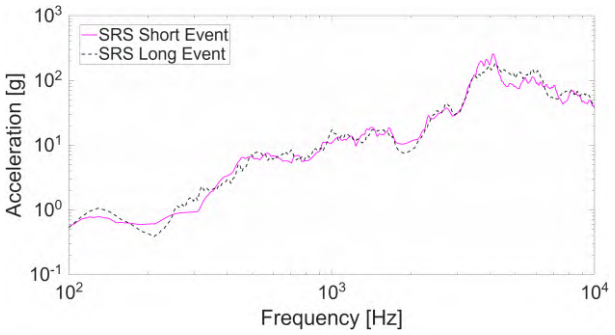


Figure 15: SRS (short vs long event)

The RIES comparison in Figure 16 instead clearly separates the two cases. The longer event transfers energy to the system over a substantially longer period, resulting in a larger accumulated relative input energy across much of the frequency range. This suggests that, by accounting for energy accumulation, the RIES may also provide some insight into the temporal development of the shock, distinguishing these events without explicit duration measures or the temporal metrics introduced in Section 3. A more detailed investigation of this aspect is left for future work.

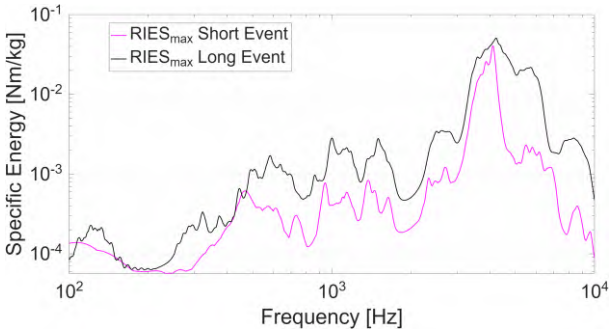


Figure 16: RIES (short vs long event)

To conclude, the proposed energy-based metrics provide complementary information related to two different damage mechanisms. The first concerns situations in which a structure is unable to dissipate all the energy introduced by the excitation. The RIES is able to describe this condition by accounting for the cumulative energy transferred to the structure over time. The SES, instead, is associated with overstress-type failure, occurring when the maximum strain energy exceeds the structural capacity. These concepts form the fundamental basis of energetic approaches to structural failure assessment [1].

3. TEMPORAL MOMENTS

3.1. Definition and physical meaning

Shocks cannot be fully characterized by frequency-based spectral metrics alone. As previously established, an infinite number of distinct time histories can share the same SRS or energy spectrum, meaning these metrics are inherently non-bijective. To complement them, temporal moments offer a way to describe the shape of shock time histories, providing additional information that spectral metrics alone cannot capture. Temporal moments are conceptually analogous to the moments of probability density functions used to characterize random signals, applying similar mathematical tools to describe the distribution of a shock's energy over time [11]. Rather than working directly with the time history, the squared time history is used in their definition, for two main reasons. First, squaring eliminates the issue of negative amplitudes, which would otherwise complicate interpretation. Second, working with the squared signal preserves useful mathematical relationships between the temporal moments and their counterparts in the frequency domain, allowing time-domain and frequency-domain descriptions of the shock to be connected in a consistent way [12]. The mathematical definition of temporal moments is given below:

$$m_i(a) = \int_{-\infty}^{\infty} (t-a)^i \, \ddot{x}_g{}^2 \, dt \qquad (13)$$

Where m_i is the temporal moment of i^{th}-order, about the time location a, of an input (ground) signal $\ddot{x}_g$. Although acceleration is used here for consistency with the nomenclature adopted in the previous section, the formulation is general and can be applied to any type of time-domain signal. From the first five temporal moments, from the 0th to the 4th order, several interesting scalar quantities can be derived to characterize shocks in terms of its shape.

- Energy: $E = m_0$
- Centroid: $\tau = {}^{m_1(0)}/_{m_0}$
- RMS Duration: $D = \sqrt[2]{{}^{m_2(\tau)}/_{E}}$
- Root Energy Amplitude: $REA = \sqrt[2]{{}^{E}/_{D}}$
- Skewness: $S_t = \sqrt[3]{{}^{m_3(\tau)}/_{E}} \rightarrow S_{norm} = {}^{S_t}/_{D}$
- Kurtosis: $K_t = \sqrt[4]{{}^{m_4(\tau)}/_{E}} \rightarrow K_{norm} = {}^{K_t}/_{D}$

It should be noted that the term “energy” used in the temporal-moment formulation differs from the mechanical energy quantities introduced in Section 2, as it refers to the signal’s energy defined by [11] as the integral of the squared signal’s time-history. It is therefore a signal-based mathematical quantity rather than a measure of energy physically transferred to, stored in, or dissipated by the mechanical system.
A clear visual representation, of τ, *D* and *REA* can be seen in Figure 17, where a synthetized acceleration signal is shown. The centroid, located at the energetic center of the shock, is in correspondence to the red vertical line. By adding and subtracting, the *D*, a time interval containing the

most significant portion of the shock is defined. Lastly, the *REA* indicates the measure of the energy amplitude of the signal [11].

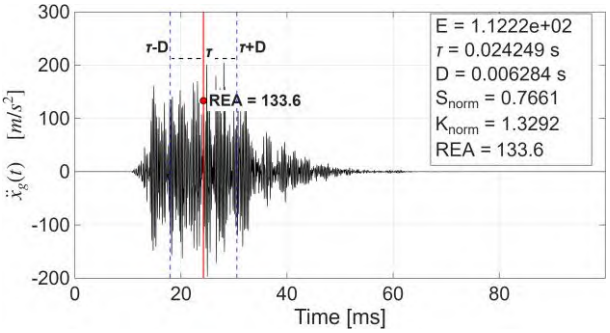


Figure 17: Visualization of the temporal moments

Skewness describes the asymmetry of the time history's shape about the centroid. Positive skewness indicates high amplitudes preceding the centroid followed by a long, low-amplitude tail; negative skewness indicates the reverse, a long low-amplitude tail before the centroid followed by high amplitudes. A symmetrical waveform has zero skewness. In practical terms, a large skewness magnitude corresponds to a short rise or fall time, which can influence system response, though this effect is not well characterized quantitatively [11].

Kurtosis measures a signal's impulsiveness relative to a Gaussian distribution, quantifying transient shock frequency in vibration analysis and condition monitoring [12]. While useful for detecting non-Gaussian peaks, its value depends on envelope shape: for unimodal envelopes with a single peak, moments beyond skewness add little insight. Kurtosis becomes far more relevant for multimodal envelopes, where it helps characterize the dispersion, spacing, and prominence of multiple distinct impact peaks across the time history [11].

These scalar quantities are illustrated for a Haversine signal (Figure 18), a distributed signal (Figure 19), and a localized signal (Figure 20). It is interesting to observe how *D* and *K* vary across the different cases, reflecting the temporal distribution, energy concentration and peakiness of the signal. Moreover, for the symmetric Haversine signal, the S is equal to zero, as expected.

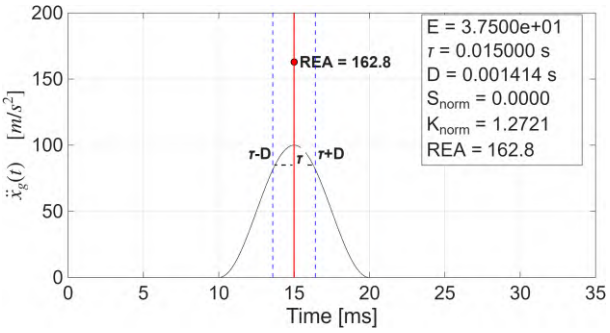


Figure 18: Temporal moments for a Haversine signal

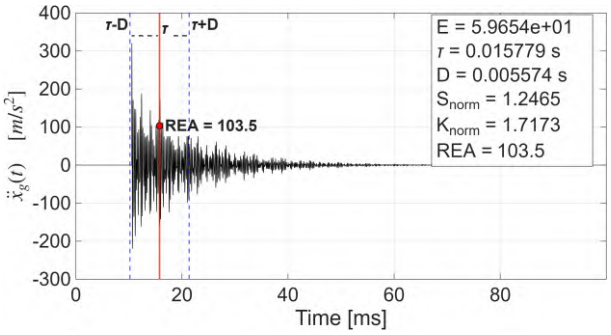


Figure 19: Temporal moments for signal synthesized with decayed sines

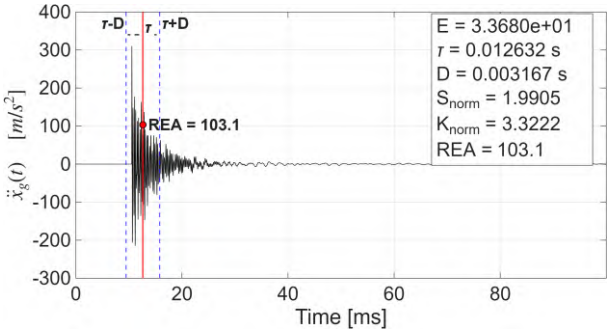


Figure 20: Temporal moments for a signal synthesized with Laplace functions

The mathematical definition of the temporal moments (Equation 13) uses an integral from −∞ to +∞, which might be problematic for realistic, noisy signals. In practice, this leads to greatly inconsistent values for signals that are otherwise identical but recorded over slightly different durations. Since it is common for recorded shocks to have slight different lengths, this sensitivity is undesirable: it means the computed temporal moments would depend on an arbitrary acquisition parameter (recording length), rather than depending only the underlying signal itself. Figure 21 shows the temporal moments on the signal in Figure 5 and Figure 22 shows the temporal moments on a longer version of the same shock. The inconsistency is easily noticeable by observing how dramatically the scalar quantities change in the plots. In the next subsection, a methodology is proposed to address this discrepancy by providing a more effective and reliable estimation of the duration of a shock signal.

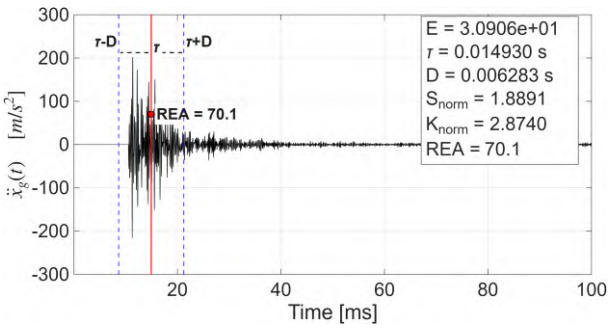


Figure 21: Temporal moments on a noisy shock

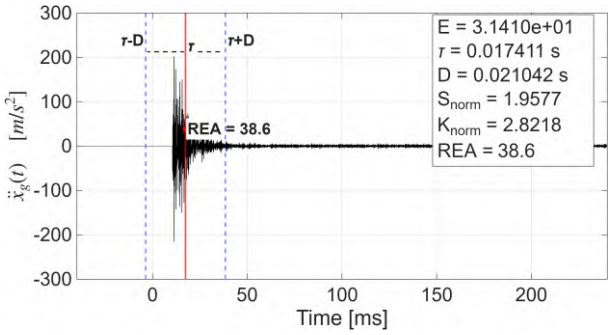


Figure 22: Temporal moments on a longer recording

3.2. Signal duration estimation via area method on 0th-order moment

Shock data analysis has long been constrained by the loss of temporal information, with pulse duration serving as the primary parameter used to characterize this dimension of a shock event. Defining pulse duration, however, remains a complex problem, since it requires identifying the point at which the shock response asymptotically decays to zero, a point frequently obscured within the signal's noise floor [9]. Existing standards attempt to resolve this ambiguity but generally rely on subjective judgment. MIL-STD-810H defines effective pulse duration according to the test engineer's perception [13], while the European Space Agency's guidance similarly depends on the assessment of an experienced analyst [5]. Even where standards specify quantitative parameters, such as total shock duration (T_e) and energy concentration duration (T_E, also referred to as the duration of the strong part of the shock), the resulting values remain highly dependent on the particular signal processing approach adopted, particularly for amplitude-based techniques.

To address these limitations, an alternative method based on the cumulative 0^{th}-order temporal moment of the shock signal (its energy evolution) was proposed in [9]. The method involves dividing the moment curve into geometric regions (Figure 23). A linear fit to the post-shock slope is used as a baseline, and three regions are defined: Region A (the area between the cumulative moment curve and the post-shock linear fit), Region B (the area under the cumulative moment curve), and Region C (the pre-shock area, which is excluded from final calculations). The point at which Region A reaches 99% of its value is the end of the signal, while the point at which Region A reaches 95% of its value is the end of the strong part of the shock. Region C is fairly easy to define by imposing a threshold that determines the start of the loading event. The results of this method on the shock in Figure 5 are shown in Figure 24.

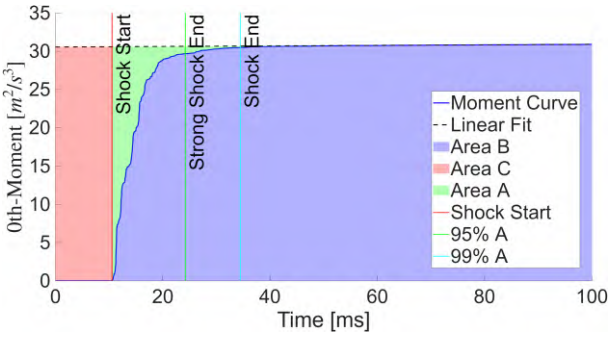


Figure 23: Area-method on 0^{th}-order moment

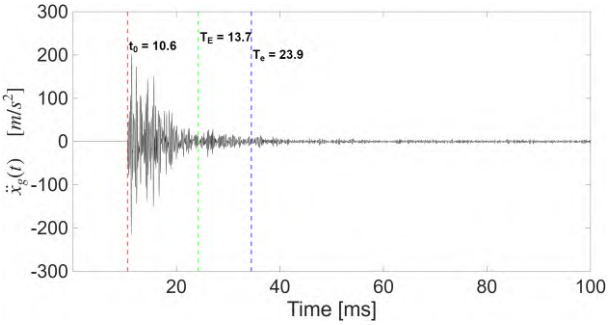


Figure 24: Shocks with T_e and T_E

The cumulative zeroth-order moment method produces markedly more stable and consistent pulse duration estimates than amplitude-based approaches, representing a substantial gain in robustness. This stability holds even under conditions that typically compromise conventional techniques: extraneous electrical spikes, elevated noise floors, and the filtering effects that often distort amplitude-based measurements have comparatively little effect on the cumulative moment curve [9].

The method also supports a more objective, analytical and reproducible assessment of shock events. Secondary impacts, for instance, are notoriously difficult for automated systems to interpret using amplitude criteria alone; under the cumulative moment approach, such events instead appear as a distinct change in slope, readily identified and analyzed. This characteristic reduces dependence on operator judgment and manual intervention, directly addressing the subjectivity noted in existing standards [9].

The previously defined quantities t_0 and T_e provide a consistent temporal interval for calculating the temporal moments and, consequently, the scalar metrics derived from them. The mathematical definition of temporal moments becomes:

$$m_i'(a) = \int_{t_0}^{T_e} (t-a)^i \, \ddot{x}_g{}^2 \, dt \qquad (14)$$

Where m_i' is the temporal moment with updated limits. The centroid is defined as $\tau = {}^{m_1(t_0)}/_{m_0}$.

The effects of this more robust method are visible on Figure 25 and 26, showing a significant

improvement with respect to the values of Figure 21 and 22.

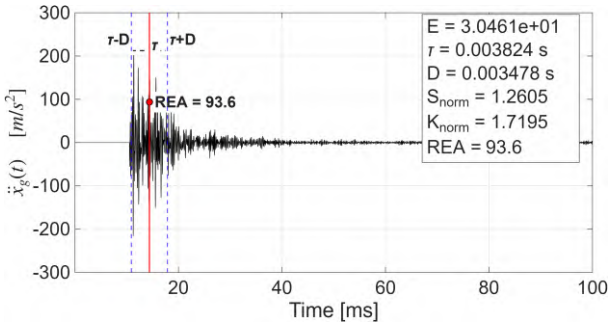


Figure 25: Improved temporal moments computation in a short signal

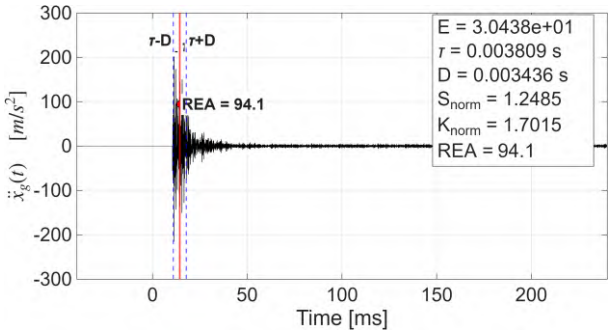


Figure 26: Improved temporal moments computation in a long signal

4. MULTIPLE DEGREES OF FREEDOM APPLICATION

This final section aims to demonstrate a potential application of the proposed energetic severity metrics, RIES and SES, in a MDOF context, where the limitations of the traditionally used SRS become particularly evident.

Consider a satellite structure mounted on the adaptor ring of the launcher vehicle. The loading condition applied to the spacecraft can contain multiple translational and rotational excitations acting simultaneously. Such loading conditions can also be reproduced experimentally using multi-axis shaker facilities, such as ESA's HYDRA [14], capable of applying simultaneous translational and rotational excitation in six-degrees-of-freedom (6DOF). Under these conditions, the SRS, PV-SRS and FDS are inherently limited, as they characterize only the response of an equivalent SDOF system subjected to excitation in the same direction. These metrics also cannot account for coupling effects between simultaneously excited degrees of freedom. Such interactions may be constructive or destructive, amplifying or attenuating the structural response, yet are neglected by classical SRS-based approaches. Consequently, SDOF-based metrics cannot adequately describe the complexity of a true MDOF environment. Therefore, there is a need for a metric capable of describing how a potentially 6DOF excitation influences the various structural modes of the system [10]. In this application, particular attention is given to the interaction between the longitudinal and lateral modes of a slender satellite structure, as these are expected to dominate the dynamic response [15].

To investigate this problem, a simplified MDOF model is developed. The model plays a role analogous to that of the classical SDOF oscillator used in SRS analysis, while additionally accounting for the effects of multi-axis base motion. Of particular importance is the offset between the center of mass (CoM) of the satellite and the shaker-table interface. For slender structures, the vertical displacement of the CoM relative to the base can generate significant lateral inertial forces and moments when subjected to multi-axis excitation, potentially resulting in a more severe dynamic environment than would be predicted by a purely longitudinal analysis. Figure 27 provides a schematic representation of the proposed system [15], while the corresponding coupled mass matrix to be employed in Equation 3 is presented in [16].

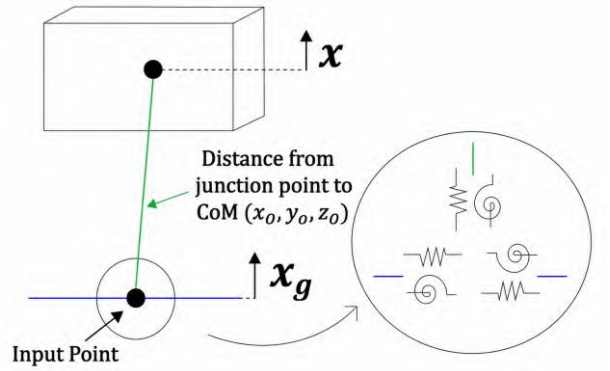


Figure 27: Spacecraft MDOF simplified system [15]

As can be observed, the mass matrix is formulated with respect to the base reference point, thereby naturally incorporating the inertial coupling effects introduced by the CoM offset. An additional assumption is that the structural stiffness is concentrated at the base interface. Consequently, the stiffness matrix is assumed to be diagonal [15], and stiffness coupling between different axes is considered negligible.

The proposed MDOF problem is defined by 6 time histories coming from a Coupled Load Analysis (CLA) for a Spacecraft characterized by 1st longitudinal mode at 75Hz, 1st lateral mode at 23Hz and 1st torsional mode at 55Hz (Figure 28) [16].

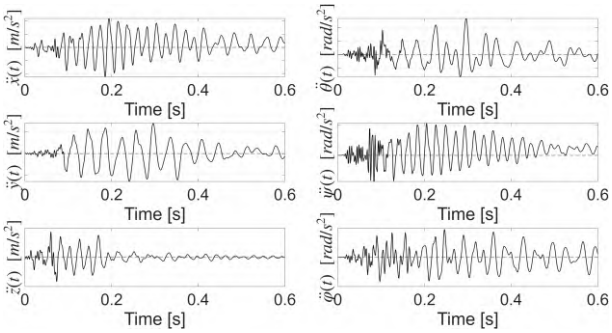


Figure 28: CLA 6DOF time histories [16]

To assess the severity of a MDOF system, the newly developed energetic metrics provide a valuable analytical tool [15]. The proposed approach evaluates the energy for all possible combinations of the system's longitudinal and lateral natural frequencies. These modes are typically the most influential for a satellite constrained to a launcher interface or a shaker table [15]. The resulting three-dimensional response surface maps are presented for the RIES (Figure 29) and the SES (Figure 30).

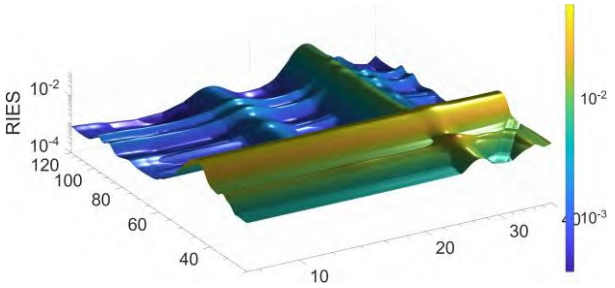


Figure 29: RIES for the 6DOF CLA

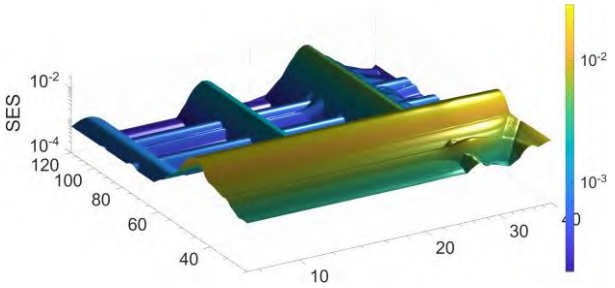


Figure 30: SES for the 6DOF CLA

An illustrative application of these 3D maps is presented in [14]. However, an in-depth discussion of MDOF energetic metrics lies beyond the scope of the present study and will be the subject of future work.

5. CONCLUSIONS AND FUTURE WORK

5.1. Conclusion

This paper provides a concise yet comprehensive review of established and emerging metrics for the characterization of mechanical shocks, covering both frequency-domain severity measures and time-domain descriptors. Starting from conventional metrics such as the SRS and the duration indicators (T_e) and (T_E), complementary energetic and temporal metrics were investigated to provide additional information on shock severity and time-history characteristics.

Among the energetic metrics, the Strain Energy Spectrum provides a physical interpretation associated with overstress-type failure, while the Relative Input Energy Spectrum captures the cumulative energy transferred to the system and is therefore better suited to describing cumulative damage effects that may not be distinguished by peak-response metrics such as the SRS. Their formulation also provides a natural extension toward MDOF environments, as illustrated through the 6DOF Coupled Loads Analysis case study.

Temporal moments complement these spectral metrics by providing a description of the shape and temporal characteristics of the shock time history. Through quantities such as the temporal centroid, root energy amplitude and skewness, they characterize how the signal energy is distributed over time. Through the zeroth-order moment area method, a more robust and analytical estimation of shock duration is established, thereby also enabling a more consistent computation of the temporal moments. In this way, temporal moments help address the non-bijective nature of frequency-based spectral metrics.

Overall, these metrics are intended to complement established SRS-based practice, providing a more comprehensive characterization of mechanical shock environments.

5.2. Future work

The present work sets the basis for several research lines that will focus on improving the current practice for shock testing. First, an important next step will be the experimental validation of the proposed energetic metrics through dedicated test campaigns, investigating their correlation with actual structural and functional damage and comparing their performance with established severity metrics.

Secondly, since SRS-based qualification curves follow well-established conventions, typically characterized by an ascending branch at low frequencies, a knee frequency, and a plateau at high frequencies, a natural next step is to investigate whether similar qualification curve standards can be developed for the newly introduced energetic metrics, enabling their adoption in industrial testing and qualification frameworks.

Finally, all the metrics developed could serve very well to establish shock synthesis algorithms capable of generating signals that match the energetic metrics and the temporal moments [17], greatly enhancing current algorithms that only match a target SRS. In this context, implementing artificial intelligence techniques could improve both the accuracy and computational speed of the shock synthesis process, while also enabling more straightforward adaptation of the method to MDOF time histories. Moreover, the shock synthesis algorithm itself could be used to generate the large and diverse datasets required to train and validate such AI-based approaches.

6. ACKNOWLEDGEMENTS

The authors gratefully acknowledge Vlaanderen Innoveren & Ondernemen (VLAIO) for funding MIMACOR (*MIcro and MAcro vibration measurement, modelling, mitigation and*

COmpensation supporting the space Revolution) under Project No. HBC.2025.0345.

7. REFERENCES

1. Sisemore, C. & Babuška, V. (2020). *The Science and Engineering of Mechanical Shock*, Springer Nature Switzerland AG, Cham, Switzerland.
2. García-Pérez, A., Sorribes-Palmer, F., Alonso, G. & Ravanbakhsh, A. (2018). Overview and application of FEM methods for shock analysis in space instruments. *Mechanics & Industry*, 19(4), 405. https://doi.org/10.1051/meca/2018029
3. Politecnico di Milano Lecture Notes (2022). *Analysis and Testing of Space Structures*. Lecture Notes, Politecnico di Milano, Milan, Italy.
4. Irvine, T. (2026). An Introduction to Shock & Vibration Response Spectra, enDAQ, Campbell, CA.
5. European Cooperation for Space Standardization. (2015). Space engineering: Mechanical shock design and verification handbook, ECSS-E-HB-32-25A, ESA Publications Division, European Space Agency, Noordwijk, The Netherlands, pp13-24.
6. Smallwood, D.O. (1981). An Improved Recursive Formula for Calculating Shock Response Spectra. Shock Vib. Bull. 51, 211-222.
7. Smallwood, D. & Edwards, T. (2008). Energy Methods for the Characterization and Simulation of Shock and Vibration. In Proc. Spacecraft and Launch Vehicle Dynamic Environments Workshop, Sandia National Laboratories, Albuquerque, NM.
8. Edwards, T.S. (2007). Using Work and Energy to Characterize Mechanical Shock. Sandia National Laboratories, SAND2007-0851J, Albuquerque, NM.
9. Sisemore, C. (2023). A Robust Method for Estimating the Transient Duration of Complex Shocks. *Proceedings of the 93rd Shock & Vibration Symposium*, Atlanta, Georgia.
10. Dal Borgo, M., de Miguel, A.G., Fagioli, R., Musella, U. & Di Lorenzo, E. (2025). Energy-Based Severity Metric for Multi-DOF Transient Testing. In *Proc. VIBFATIGUE 2025*, Siemens Industry Software, Leuven, Belgium.
11. Smallwood, D.O. (1994). Characterization and Simulation of Transient Vibrations Using Band Limited Temporal Moments. Shock and Vibration, 1(6), 507–527.
12. Cap, J.S. & Smallwood, D.O. (1997). A Methodology for Defining Shock Tests Based on Shock Response Spectra and Temporal Moments. In *Proc. 68th Shock and Vibration Symposium*, CONF-971164, SAND97-1480C, Sandia National Laboratories, Albuquerque, NM.
13. Department of Defense (2019). Environmental Engineering Considerations and Laboratory Tests, MIL-STD-810H, Department of Defense Test Method Standard, Washington, D.C.
14. European Space Agency (n.d.). HYDRA Multi-Axis Vibration Test Facility, ESA Space Engineering & Technology. Available at: https://www.esa.int/Enabling_Support/Space_Engineering_Technology/HYDRA_multi-axis_vibration_test_facility
15. Fagioli, R. (2025). New Severity Metrics for MDOF Environmental Transient Testing. Master's thesis, Politecnico di Milano, School of Industrial and Information Engineering, Milan, Italy.
16. Cavagna, F. (2024). A critical assessment on the mechanical load severity comparison, with focus on aerospace applications. Master's thesis, Politecnico di Milano, School of Industrial and Information Engineering, Milan, Italy.
17. Alexander, J.E. (2018). A New Method to Synthesize an SRS Compatible Base Acceleration with Energy and Temporal Moments to Improve MDOF System Response (First Part). *Sound and Vibration*, 52(12), 7–22.

IMPROVED SHOCK SPECIFICATION TOOL USING ARTIFICIAL INTELLIGENCE AND SPACECRAFT SURROGATE MODELS

B. Brévart, E. Glize, F. Ladagnous [(1)], R. Arena [(2)], G. Rodrigues, B. Laine [(3)]

[(1)] Thales Alenia Space, 26, avenue J.-F. Champollion, BP 33787 - 31037 Toulouse Cedex 1, France
bertrand.brevart@thalesaleniaspace.com
[(2)] Thales Alenia Space, 5, allée des gabians, BP 99 - 06156 Cannes, France
roberto.arena@thalesaleniaspace.com
[(3)] ESA/ESTEC, Keplerlaan 1, PO Box 299 NL - 2200 AG Noordwijk, The Netherlands
goncalo.rodrigues@esa.int

KEYWORDS

Shock, specification, artificial intelligence, data mining, machine learning, surrogate model, propagation, path

ABSTRACT

Shock events occurring in satellites are still a source of many concerns. Despite progress on the severity of the shock sources, accurate specifications are still difficult to establish. At early stages of a program, simulation is not appropriate to predict shock propagation and quantify the associated attenuations. Thus, to deal with a new spacecraft design, without a shock heritage, or to implement new shock sources, most engineers rely on MIL standards and ECSS rules to derive shock specifications for the sensitive equipment and instruments.

In this context, the present study initiated by ESA aims at creating a dedicated tool to specify the shock environment on spacecraft equipment and payloads, based on data mining of past test measurements and artificial intelligence.

The proposed approach is inspired from Method D of the ECSS Shock Handbook with all attenuation factors resulting from data mining. The propagation path between each source and the associated sensors is derived automatically from a 3D surrogate model of the satellite, including sensors and shock source locations. The strategy to build the surrogate models and calculate the propagation path is presented. The ambition for the application is to predict both in-plane and out-of-plane acceleration SRS at unit location. Predicted levels will be accompanied by confidence intervals.

To date, the database has been created. It covers 15 satellites and 270 shock events of all kinds. The surrogate models have been created and all propagation paths have been calculated. An automatic scheme has been used to identify input levels (in-plane and out-of-plane) as close as possible to the sources. The number of data available for mining exceeds 10000.

The machine learning phase has started and some preliminary results are presented.

1. INTRODUCTION

Extensive work has been done on the shock environment over the past years. Most of the heritage and know-how on shock in Europe has been embedded in the ECSS Shock Handbook [1]. Yet accurate specifications are still difficult to establish. Similarity-heritage-extrapolation, i.e. the creation of zones on similar design architectures to derive a Maximum Expected Environment (MEE) from the heritage data, is the best approach to derive shock specifications.

When heritage data is not available, the empirical methods existing in [1] have proved useful. But most often the result is awkward, with a remaining conservatism, because the rules are too simple, without much frequency dependence of the attenuation factors and without a distinction of the axes of excitation in particular.

The study initiated by ESA aims at creating a dedicated tool to specify the shock environment on spacecraft equipment and payloads, based on data mining of past test measurements and artificial intelligence. Such a tool already exists (Vibrospec [2]) to derive random specifications from the acoustic excitation profile. Similarly, the immense amount of available measurements from satellite shock tests and the corresponding design descriptions will be mined automatically and efficiently.

The objective of the future application is to predict the shock environment at a sensor location given the level at the source and the propagation path. Various learning strategies, and different algorithms used in Artificial Intelligence will be tested to reach the best overall performance. The quality of the results will be addressed by comparing predictions and measurements for various shock events on satellites out of the training dataset.

A database of shock tests has already been created in order to investigate propagation rules, and eventually derive shock specifications [3]. Filters were used to sort the data with the possibility to

compute MEE and perform linear or multi-linear regressions. A first limitation of this investigation is that only the overall distance is considered. The other one is in the derivation of the shock propagation path that is left at the appreciation of the mechanical engineer. Not only the variability of interpretation is a major source of dispersion for the predictions, but the link of the data with the design is lost after the above parameters have been extracted.

2. TECHNICAL SOLUTION OVERVIEW

The solution that is proposed is inspired from the ECSS method D [1] revisited with Artificial Intelligence.
The general idea behind Method D is that from a shock source to an output sensor, the shock will propagate through different structural elements such as panels, junctions, struts… The propagation should follow the stiffest path but no rule is proposed for its identification. Then, empirical attenuation rules are given for distance and junction attenuations, without any frequency dependence. Additional attenuation factors to account for heat pipe (HP) effect or equipment mass can be considered.

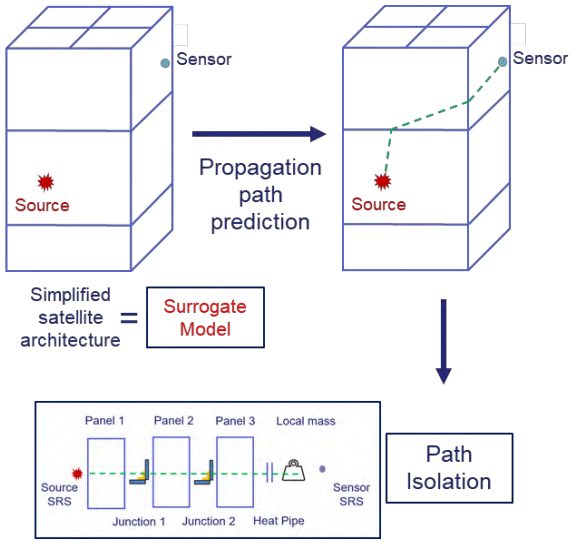


Figure 1: Automatic propagation path definition procedure

The proposed solution is trying to remedy all weak points of the current method D. First, the propagation path will be identified automatically from a simplified geometry (surrogate model) of the satellite (Fig. 1). Then, all attenuation factors, i.e. distance, junction, HP and mass effects, will be identified using Machine Learning at each frequency of the SRS. In-plane (IP) and out-of-plane (OOP) SRS levels will be predicted at the sensor location. Both predictions will be associated to a confidence interval.

3. S/C SURROGATE MODEL

The surrogate model (Fig. 2) is a geometry that has been created from a simplified finite element model (FEM) of the satellite. In this geometry, all the shock sources have been positioned, along with all the accelerometers that have been recorded during the shock events. Some part mechanical properties (infinite medium bending stiffness, surface density) and the junction type between the parts are also embedded in the model.

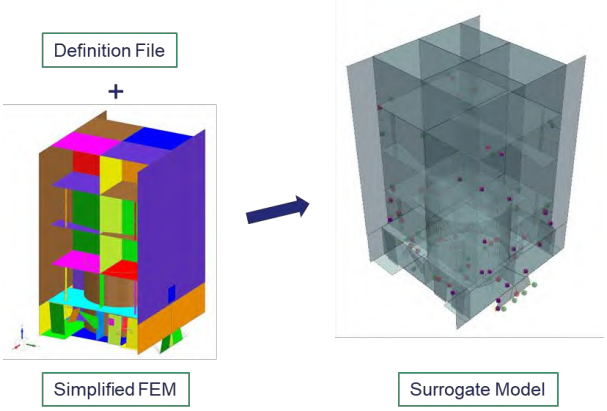


Figure 2: Surrogate Model creation procedure

The geometry, the sensor locations and the mechanical properties are imported from a simplified FEM. This has been created using the original satellite FEM through a an extreme simplification procedure, i.e. only one FE element has been used for each part. These NASTRAN elements are :

- CTRIA or CQUAD (and PSHELL property) for sandwich and ribbed panels
- CBEAM (and PBEAML property) for cylinders and cones
- RBE2 for beams and small solids

All the zones that are not expected to be on any propagation path have been removed. In the FEM, there is no link between the parts. A typical results is illustrated on Fig. 3.

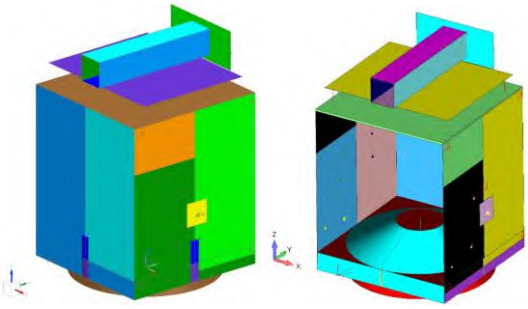


Figure 3: Simplified FEM of S/C 03

The rest of the information to be embedded in the surrogate model is indicated in a Definition File in Excel format. The first folder concerns the connectivity between the different parts. As illustrated on Fig. 4, for each part (one line), its type is recalled (Cylinder/Cone, Panel or Bar), followed by the list of connected parts and the type of

connection. Four types of connection have been considered to date. Types 1 to 3, named “Direct”, “Indirect”, and “Double indirect” are illustrated by examples on Fig. 4. A last junction (type 0) has been created. This junction allows to create more complex structures, a panel with a shape in L for example (Fig. 5). When calculating the propagation path, this junction will be considered like the others as possible crossing points but will not be counted as a junction in the end and of course it has no attenuation. This type has been largely used between bars as well, when a shock source for example is located on a tripod. The source is placed on a short bar connected to the tripod (3 other bars) by type 0 junctions. This way, the source is connected to the 3 bars at once.

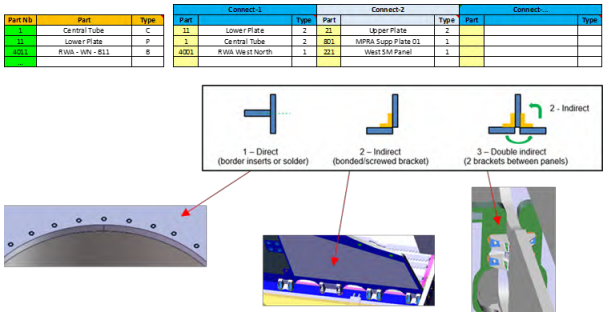


Figure 4: Connection folder illustration (top) and the corresponding junction types (1 to 3)

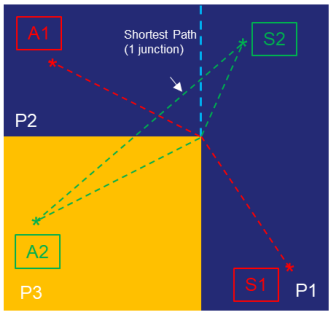


Figure 5: Junction type 0 (light blue dashed line) between 2 panels (P1 and P2)

The second folder of the definition file is named COCASSO (Fig. 6). It associates the sensor name to the grid ID. The part associated to the sensor and the local orientation of the measurement (IP or OOP) are indicated as well. The mass of the unit nearby is given when applicable and it is indicated whether the sensor is on heat pipe or not.

Accelerometers	PART Nb	GRID_ID	Inp / OoP	Local Mass	HP / No HP
NSM801X	201	1193410	InP	29.5	Yes
NSM802Y	201	1193410	OoP	29.5	Yes
NSM803Z	201	1193410	InP	29.5	Yes
NSM807X	201	1192331	InP	18.7	Yes
NSM808Y	201	1192331	OoP	18.7	Yes
NSM809Z	201	1192331	InP	18.7	Yes
NSM816X	201	1191490	InP	29.5	No
NSM817Y	201	1191490	OoP	29.5	No
NSM818Z	201	1191490	InP	29.5	No
SSM824X	211	1203337	InP	18.7	Yes
SSM825Y	211	1203337	OoP	18.7	Yes
SSM826Z	211	1203337	InP	18.7	Yes
SSM828X	211	1201542	InP	28.1	No
SSM829Y	211	1201542	OoP	28.1	No
SSM830Z	211	1201542	InP	28.1	No
SSM831X	211	1202204	InP	18.7	Yes
SSM832Y	211	1202204	OoP	18.7	Yes
SSM833Z	211	1202204	InP	18.7	Yes
...					

Figure 6: COCASSO folder illustration

The third and last folder, named SHOCKASSO (Fig. 7), list the shock events and the corresponding source locations (part number and grid ID).

Shock Event	Number	Type	GRID source	PART Nb
NSA	1	NEA6	1001	241
NSA	2	NEA6	1002	241
NSA	3	NEA6	1003	241
NSA	4	NEA6	1004	241
NSA	5	NEA6	1005	241
NSA	6	NEA6	1006	241
NSA	7	NEA6	1007	241
SSA	1	NEA6	1101	251
...				

Shock Type	ID
ClampBand	CB
VESTA	VESTA
Pyronut M10	PYR10
Pyronut M6	PYR6
Bolt Cutter	BC
NEA M6	NEA6
NEA M10	NEA10
Delatch Spring	DS
End Stop	ES

Figure 7: SHOCKASSO folder illustration

Fig. 8 illustrates the surrogate models of all the satellites, or satellite parts, in the database.

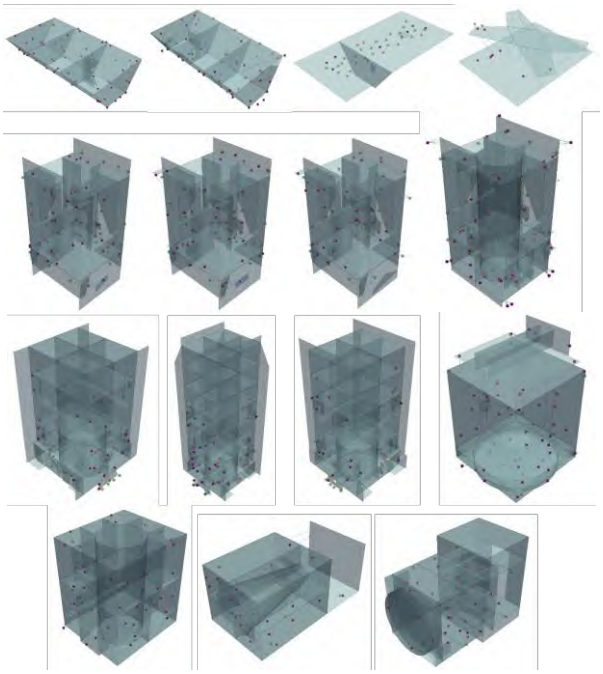


Figure 8: Surrogate models in the database

4. SHOCK EVENTS IN THE DATABASE

A specific attention has been paid to the choice of the shock events to record. It had to cover a large diversity of sources, i.e. S/C separations and internal satellite sources, with both pyrotechnic actuators and NEA. The existing types of shock event are listed below :

- S/C separation (Clampand release, VESTA)
- Solar Array release (pyrotechic actuator, NEA)
- Reflector release (pyrotechic actuator, NEA)
- Earth antenna reflector release
- ADPM separation (NEA)
- XPS Mechanisms (NEA)
- Mechanical shocks (spring antenna delach, end stops)

A total of 270 events has been recorded. Fig. 9 shows the events for each S/C in the database. In red are pointed the pyrotechnic events.

SAT ID	SA HRM	Refl. HRM	ADPM LLD	XPS Mech.	Clamp_B.	VESTA	Launch. Sep.	Spring Delatch / End Stop	Earth Ant. / Module
01	N + S 4 each								
02	N + S 6 each						4 Pyro shocks		
03								12 KA-Ant. 2 each	
04									Earth 2 Pyro shocks
05	N + S 8 Pyro shocks each	E + W 3 Pyro shocks each							
06	N + S 8 Pyro shocks each	E + W 3 Pyro shocks each							
07	N + S 8 Pyro shocks each								
08	N + S 8 Pyro shocks each	W_ULR 4 Pyro shocks			Yes				
09	N + S 7 each	E + W 4 + 3 HRMx2s	E + W 2 LLD each	N + S 4 each - EPPM	2 shocks				
10	South 7 shocks	West 4 HRMDs	West 2 LLD	N + S 2 each - ETHM				4 ETHM End Stop	
11	N + S 9 each	E + W 4 HRMx1s/2x each	E + W 1 LLD each	N + S 4 each - EPPM					
12	N + S 5 each				3 shocks				
13	N + S 6 each	1 Pyro shock			Yes				
14	6 shocks				2 shocks	2 shocks			
15	N + S 4 each				Yes	2 shocks			

Figure 9: Shock events recorded in the database

For each event, the time history and the SRS (Q=10, 12 pts/oct) of all valid measurements have been imported. The number of data exceeds 10000. The range of peak accelerations near the sources starts below 100g, up to several thousand gs. However, the database includes a lot of very low accelerations. As long as the shock event could be clearly identified (not only noise) and Piersol criterion on SRS was correct, the data has not been removed. The reason is, all these low accelerations are the result of all the attenuations factors we try to identify. No acceleration is a precious information in this context ! The application offers the possibility to filter out all the measurements that have 100% SRS values (80 points) below a certain threshold, 1g for example. Some sensibilities on the results will have to be performed in the future, knowing that the SRS threshold reduces simultaneously the noise and the number of data to mine.

5. PROPAGATION PATH IDENTIFICATION

5.1. Data parsing

The first step consists in reading Nastran bulk file of the simplified FEM to create the geometric representation of a satellite. Within this framework, a satellite may only be composed of the following elements:

- A segment defined by two three-dimensional points
- A triangle polygon defined by three three-dimensional points
- A quadratic polygon defined by four three-dimensional points
- A truncated cone defined by two three-dimensional points representing the centroids and two radii (if the radii are equal, the truncated cone is a cylinder)

The representation of the satellite contains the output sensors, the event source location and the list of connected elements with additional features.

5.2. Intersections between elements

For each couple of connected elements, the second step computes its geometric intersection. All cases are not taken into account. Considered connections are:

- Two segments
- A segment and a polygon (either triangle or quadratic)
- Two polygons (either triangle or quadratic)
- A polygon (either triangle or quadratic) and a truncated cone
- A segment and a truncated cone

Fig. 10 shows the various handled cases.

In addition, a specific case had to be considered. Some parallel parts have been connected. They can represent a stiffening panel (ADPM on Fig. 11) or an assembly baseplate for example. In this case, the junction is assumed on all the surface and the junction will generally be a type 1 (Direct). On Fig. 11, the sensor is on the small panel P3 at position B1. If the panel P3 is stiffer than the other (P2), then the path coming from P2 will jump on P3 at the periphery. In case P2 is stiffer, the path will continue up to B1 projection on P2 and then jump on P3.

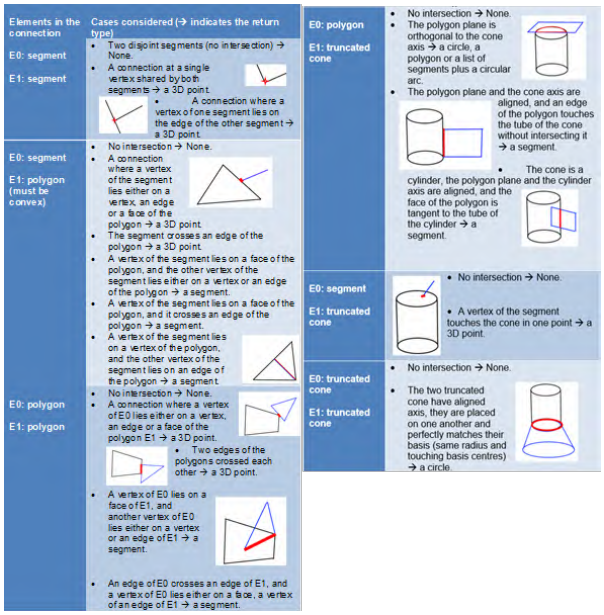


Figure 10: Handled intersection cases and returned geometry type

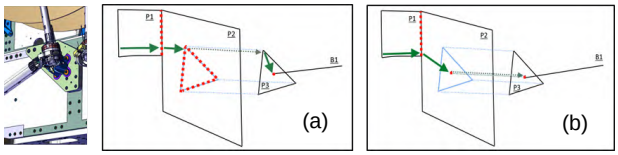


Figure 11: Illustrations of a junction between parallel panels. Sensor is at point B1 location. (a) P3 is stiffer than P2, (b) P2 is stiffer than P3.

5.3. Minimal-element path computation

ESA study bibliography has revealed that passing over junctions is the main driver of the attenuation, and not the distance.

Thus, as a first step, we compute the shortest path between the shock source and the target sensor in terms of minimal number of satellite elements

crossed. This abstraction aims at identifying all topologically minimal propagation routes, independently of their geometric length. To do so, the satellite geometry is transformed into a connection graph (Fig. 12), each node representing a part. Connections type 0 are weighted 0 in the graph, others are weighted 1.

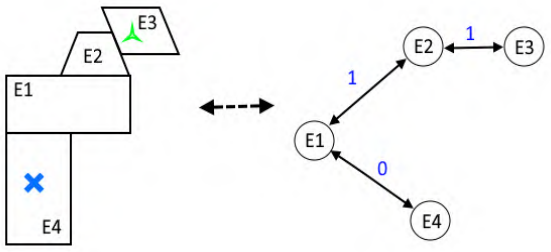


Figure 12: Example of a satellite geometry transformed into a connection graph

The shortest paths in the graph are computed using *Dijkstra's* algorithm. Note that in some satellite models, the number of components and interconnections is large, which can lead to a large number of possible paths with a minimal number of elements.

5.4. Stiffest propagation path

Each intersection between geometric elements is then discretized (Fig. 13). A spatial tolerance of one centimetre has been used. For each minimal-element path, a second connection graph is constructed to compute the physically stiffest propagation path of the shock. Nodes of this graph correspond to discretized points along the intersections of junctions between elements.

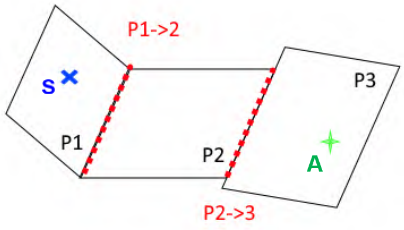


Figure 13: Example of a satellite geometry transformed into a connection graph

A weight is computed for each combination of intersection points (Eq. 1 is given for 2 intersection points as described on Fig. 13):

$$w_{i,j} = \frac{d(S, P^i_{1\to 2})}{k_1} + \frac{d(P^i_{1\to 2}, P^j_{2\to 3})}{k_2} + \frac{d(P^j_{2\to 3}, A)}{k_3} \qquad (1)$$

where d is the 3D distance between points in parenthesis and k_n denotes the bending stiffness of the element n.

The shortest path in this graph is computed using *Dijkstra's* algorithm, yielding the shortest physical propagation path for the considered minimal-element route. Among all minimal-element paths, the one with the smallest accumulated weight is selected as the stiffest shock propagation path.

Note that for clampband and VESTA shock events, a specific correction is applied to the source location. The initial impact point is shifted from the centre of the cylinder base to its boundary. This adjustment ensures a physically accurate initialization of the propagation path.

Fig. 14 illustrates some propagation paths for various shock events.

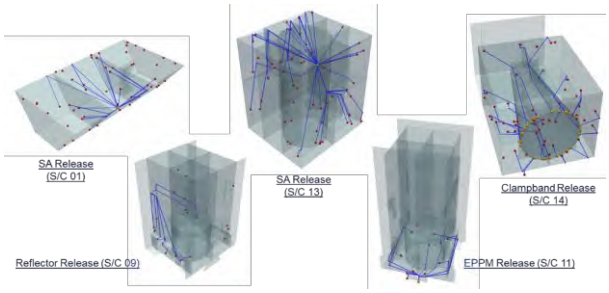


Figure 14: Propagation path illustrations for various shock events on different satellites

5.5. Identification path

Propagation paths are calculated considering the true position of the shock source. But, unlike clampband or VESTA release, several internal shock events, associated to appendage deployments, do not have a measurement very close to the source.

Thus, the ID path step consists in the identification of sensors (IP, OOP) to become the input levels for the Machine Learning phase. If a sensor is identified at a distance d from the source, a fictive source can be defined on the propagation path at the same distance (Fig. 15a). The hypothesis is that the shock is attenuated the same way in each direction from the source. If the closest sensor is on another panel, the same logic can apply, but related to the crossing point on the junction (Fig. 15b). Only panels directly connected to the source panel are considered.

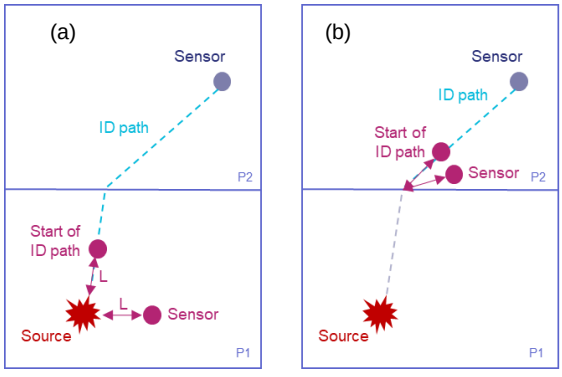


Figure 15: Computation principles of the identification paths. Input sensor located on the source panel (a) or on next panel on the path (b)

If both in-plane and out-of-plane sensors can be found on the same panel, two ID paths are created for the same output measurement (Fig. 16).

Twin data, i.e. two different outputs with the same input, will be created if we have two IP collocated

measurements (tri-axial accelerometer typically). Twin data must be eliminated. The solution when 2 in-plane sensors are collocated is to create a unique sensor with the SRS envelope of the 2 measurements.

Input Level	Path					Output SRS
IP SRS	Panel 1 (distance $s1_{IP}$)	Junction 1	Panel 2 (distance $s2$)	Heat Pipe	Local Mass	IP and/or OOP SRS
OOP SRS	Panel 1 (distance $s1_{OOP}$)	Junction 1	Panel 2 (distance $s2$)	Heat Pipe	Local Mass	IP and/or OOP SRS

Figure 16: ID path parameters (1 junction)

6. MACHINE LEARNING (AI)

This phase addresses the problem of shock propagation prediction between two sensors, namely an input sensor where an event-induced shock is measured and an output sensor where the resulting attenuated shock is observed. The objective is to obtain predictive models that estimate the shock level at the output sensor as a function of the input shock.
The available dataset consists of measured shock signals capturing the relationship between input and output sensors across a variety of configurations. A key assumption is that shock attenuation depends on the physical characteristics of the shortest propagation path between the two sensors. These characteristics include structural elements and local properties that influence how the shock wave is transmitted and dissipated.
Two different machine learning (ML) strategies illustrated on Fig. 17 will be investigated.

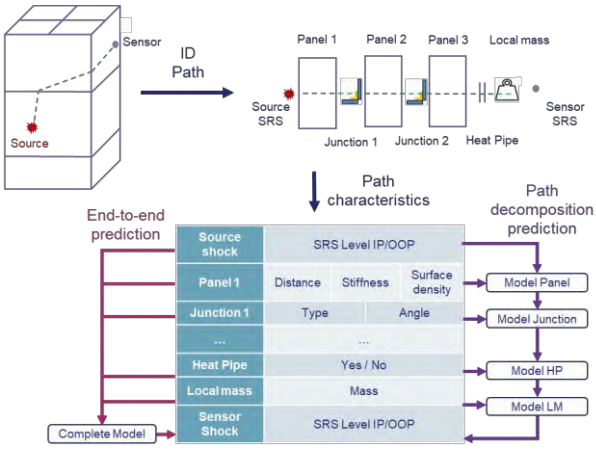


Figure 17: Machine Learning Strategies

The first option is to decompose the paths into multiple panels and junctions, and learn on the attenuation factors (panel, junction, local mass and HP effects) separately and iteratively. This methodology has the advantage of being easily understandable by humans, as every step can be analysed and corrected if needed. The main drawbacks are :

- It does not make use of the entire database for training, and thus loses learning capacity
- Prediction errors will accumulate over the propagation path. The prediction model on the panels will likely have some errors, but it will be used to train the next models on the local mass, heat pipe and junctions. Thus, the next models will be biased and might use slightly wrong training data.

To date, only this ML strategy has been initiated. Preliminary results for panel attenuation are given below.

The other option named end-to-end consists in training a prediction model giving a sequence of nodes that will impact the output. This training method will take as input the shock level at the source and the sequence of panels and junctions (knowing all their characteristics) and will output the sensor shock level. The performance of this method will be directly related to the size of the dataset.

6.1. Panel attenuation data

In order to study the distance attenuation on panels, only the following ID paths are selected (Fig. 18):

- No junction
- Small unit mass (below 5kg)
- Input and output sensors are both on heat pipe or not on heat pipe.
- Output sensor direction available for input sensor direction (IP -> IP, OOP-> OOP)

In addition to these filters, all sensors with 100% SRS values below 1g have been removed. Note also that frequency is an input parameter, so that each data point in the following sets corresponds to one single frequency.

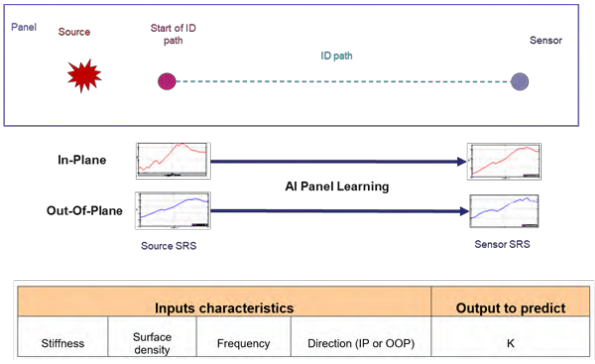


Figure 18: Path characteristics for the prediction model of the panel attenuation K

Fig. 19 shows the dataset distribution with distance. Most of the data corresponds to distances between 0.2 and 1.2m. Fig. 20 shows the distribution of attenuations. It is centred around -10dB but a relatively large number of data is above 0 dB. Some SRS amplifications are indeed possible but it seems the number of amplifications is too large and values as high as +20dB are unexpected.

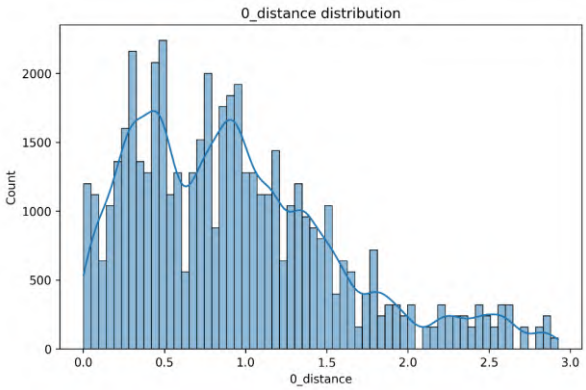


Figure 19: Data distribution with distance for panel attenuation prediction model

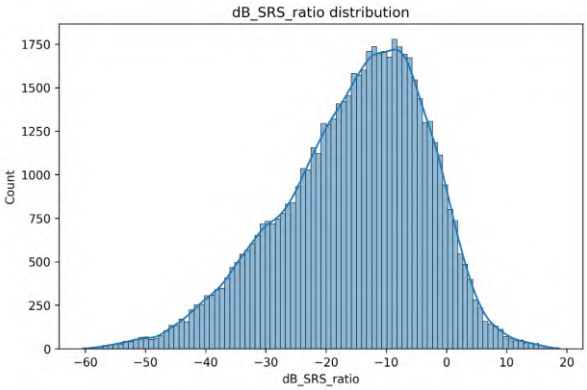


Figure 20: Panel attenuation distribution

Fig. 21 and 22 show the frequency distribution of the attenuations for various distances (colour dots), in plane and out-of-plane respectively. As expected, the attenuation increases with frequency for a given distance (IP, OOP). At high frequencies (>1000 Hz), the attenuations largely increase with distance, far above the point source attenuation rule in [1].
Some of the amplifications previously identified are obtained at high frequencies. This doubtful result is linked to very small distances between input and output sensors. In future investigations, the ID path strategy will be adjusted to eliminate this questionable data.

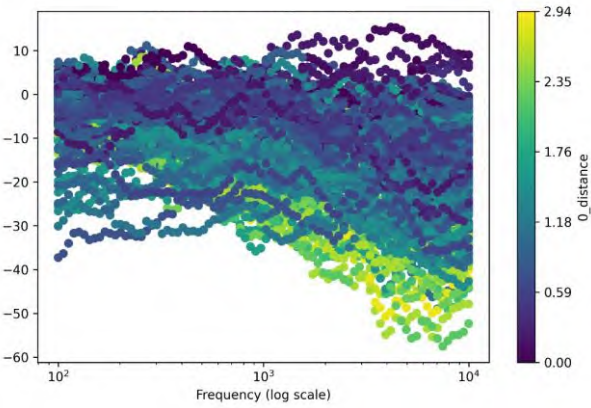


Figure 21: Frequency distribution of IP panel attenuation (dB) with distance (colour dots)

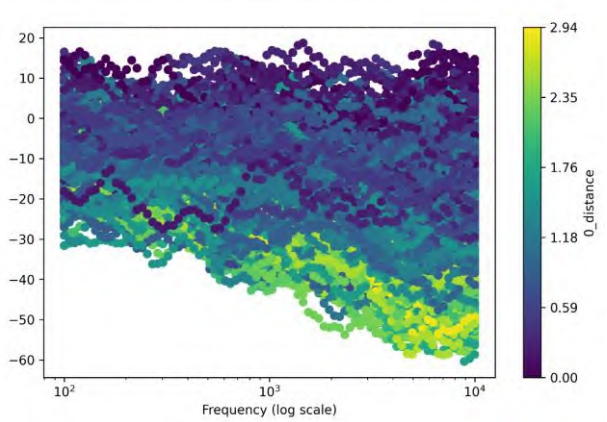


Figure 22: Frequency distribution of OOP panel attenuation (dB) with distance (colour dots)

These attenuation distributions are plotted w.r.t. stiffness on Fig. 23. It appears that the largest attenuations, at high frequencies, are mainly obtained with the lowest panel stiffnesses. This result is more visible in the OOP direction.

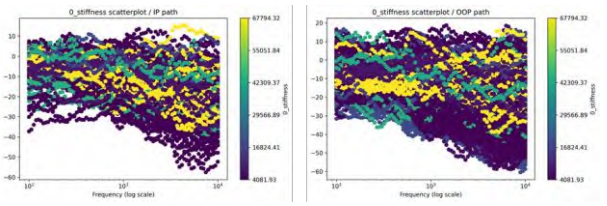


Figure 23: Frequency distribution of IP/OOP panel attenuation (dB) with stiffness (colour dots)

The attenuation distributions are plotted w.r.t. panel surface density on Fig. 24. With the highest attenuations coming from mid-range densities the attenuation (IP, OOP) does not seem much correlated to panel surface density.

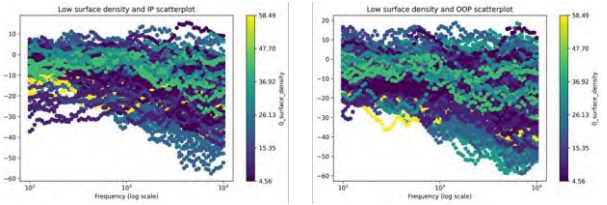


Figure 24: Frequency distribution of IP/OOP panel attenuation (dB) with surface density (colour dots)

6.2. Panel attenuation prediction model

Several regression models have been evaluated, among which Random Forest and LightGBM show the most promising performance.
Random Forest is an ensemble learning method based on aggregating multiple decision trees trained on bootstrapped subsets of the data. It reduces variance through averaging and is robust to noise and non-linear relationships. However, it may require larger computational resources and can be less efficient in capturing fine-grained patterns when compared to boosting methods.
LightGBM, on the other hand, is a gradient boosting framework that builds trees sequentially, each correcting the errors of the previous ones. It is

designed for efficiency and scalability. Compared to Random Forest, LightGBM often achieves higher accuracy and faster training times, particularly on large datasets, but may be more sensitive to hyperparameter tuning.
After optimizing hyperparameters using a grid search strategy, the models achieve a Root Mean Square Error (RMSE) of approximately 5 and a coefficient of determination (R^2) around 0.94. These metrics are computed by comparing the predicted shock level at the output sensor with the measured ground truth values, expressed in units of acceleration (G), as illustrated on Fig. 25.

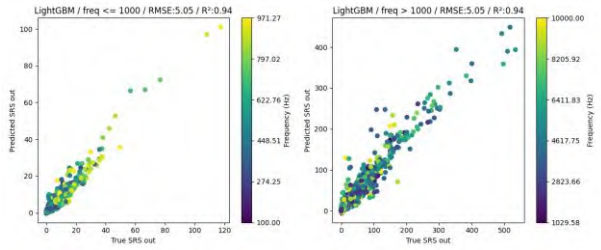


Figure 25: LightGBM panel attenuation estimator. Predicted and true SRS values comparison at low frequencies (left) and high frequencies (right).

An RMSE of 5 G indicates that, on average, the prediction error magnitude remains relatively small compared to typical shock levels observed in the dataset. The high R^2 value (94%) suggests that the model explains most of the variance in the output shock signal, reflecting strong predictive capability.
The presented diagrams compare predicted and actual values for low frequencies (< 1000 Hz) and high frequencies (> 1000 Hz). An ideal estimator would align perfectly with the identity line (y = x). In practice, the models exhibit a slight tendency to underestimate the output shock levels, particularly at high amplitudes. Despite this bias, the overall agreement between predictions and measurements remains strong, confirming the effectiveness of the proposed modelling approach.

7. CONCLUSION

A prototype tool to specify the shock environment for S/C equipment is under development. The solution that is proposed is inspired from the ECSS method D [1] revisited with Artificial Intelligence. To date, the database has been created. It includes more than 10000 measurements (time history and SRS) as well as satellite design features. All propagation paths have been identified automatically from a surrogate model of the satellites. The machine learning phase (AI) of the investigation has been initiated. The first approach consists in a path decomposition to learn on the attenuation factors separately and iteratively. Strong predictive capability of the panel attenuation model is obtained using LightGBM.

8. REFERENCES

1. Mechanical Shock Design and Verification Handbook, ECSS-E-HB-32-25A, 14 July 2015.
2. Kasper, J. (2010). Derivation of Satellite Equipment Design and Test Specifications from Random Vibration Environments, ESA Contract No. 29502/06/NL/SFe, Title report "VibroSpec Methology & Tool" MTD.R &D.TN.2291, Issue1.
3. Perriquet, M., Hofmann, M. & Le Moigne, J. (2023). Shock test database and statistical analysis tool. Proceeding of the 17th European Conference on Spacecraft Structures, Materials and Environment Testing, Toulouse, France.

PREDICTION AND OPTIMIZATION OF SHAKER SHOCK TESTS OF OPTICAL UNITS

Gonçalo Rodrigues[(1)], Sofia Caeiro[(1)], Stefan Kiryenko[(2)] and Benoit Laine[(3)]

European Space Agency, ESTEC, Keplerlaan 1, 2201 AZ Noordwijk, The Netherlands
[(1)] Structures Section, Mechanical Department, TEC Directorate
[(2)] NGGM Project, Directorate of Earth Observation Programs
[(3)] Mechanical Department, TEC Directorate

KEYWORDS

mechanical shock, optical units, shaker testing, shock response spectrum, modal participation factor, transient synthesis, transient analysis

ABSTRACT

Shock qualification of sensitive units using electrodynamic shakers offers significant advantages in controllability and test efficiency. However, acceleration transients having similar shock response spectra (SRS) can produce substantially different structural responses. This paper presents a response-based shock transient synthesis method that supplements conventional SRS compliance with prediction of the internal response of the test item. Multiple transients are generated using damped sinusoids and the resulting internal response is quantified by applying a computationally efficient modal transient formulation. Applying the method to an optical unit puts in evidence that different inputs compliant to the SRS specification can produce peak internal accelerations differing by more than a factor of three. The difference is explained by the spectral content of the synthesized transients relative to the critical modes of the unit and is largely masked by the conventional Q=10 SRS. The proposed approach enables shaker inputs to be selected according to relevant internal responses, reducing resonant over-testing during shock qualification.

1. INTRODUCTION

Optical instruments usually contain units whose alignment and dimensional stability are essential to mission performance. Typical examples include mirror, lens and filter assemblies, interferometers, optical mechanisms and focal-plane assemblies with detectors. Their elements must remain positioned, aligned and shaped with extreme accuracies throughout vibration, shock and thermal-vacuum verification. Even when a unit is located far from the principal spacecraft shock sources, shock verification of optical units remains relevant unless compatibility can be confidently demonstrated by analysis or by adequate environmental coverage [1, 2].

The shock response spectrum (SRS) is the standard descriptor used to specify and compare transient mechanical environments. It is widespread, but it is not a unique description of a transient. Different acceleration time histories can have similar SRS levels while differing substantially in duration, and spectral content and hence capability to excite structural modes. This awareness about non-uniqueness is especially important when synthesizing acceleration transients for reproduction on an electrodynamic shaker.

This paper addresses that problem by proposing a new method of synthetizing acceleration transients suited to be tested on shakers. The principal objective is not merely to generate a transient that lies inside an SRS tolerance band, but to choose a time history that generates an appropriate response in the test item. The approach combines damped-sine synthesis with a rapid modal transient calculation, and it is illustrated by applying it to an optical unit.

2. SHOCK VERIFICATION OF OPTICAL UNITS

2.1. Failure modes

Relevant failure modes of optical units extend beyond the fracture of glass or ceramic components and the failure of bonded joints. In fact, the functionality of optical units can also be compromised by permanent changes in the position, tilt, or shape of optical elements resulting from micro-slippage at bolted interfaces, uncontrolled release of assembly pre-stress, or local micro-yielding. For highly stable optical assemblies, the loss of alignment or degradation of optical surface figure typically occurs well before gross structural failure.

2.2. Shock bench and shaker testing

Spacecraft equipment is conventionally shock-tested using shock benches (ringing plates) or Hopkinson bars. The unit under test is mounted on these structures, which are then excited by an impact produced by a hammer, pneumatic device, or pyrotechnic device. As part of calibration, the impact intensity, the locations of the impact and specimen, the tooling plates, and the interface materials are iteratively adjusted until the levels measured by control accelerometers located in the vicinity of the unit comply with a shock specification expressed in terms of an SRS.

This calibration process can be a lengthy and laborious process, and achieving a close match to the prescribed SRS, typically defined by a series of slopes and plateaus, is particularly challenging. Respecting the standard lower test tolerance of −3 dB may consequently lead to significant over-testing in other frequency bands, which can be particularly detrimental to fragile units.

An electrodynamic shaker, on the other hand, operates in closed loop and can reproduce prescribed transient time histories with good accuracy. The process of generating a shock environment compliant with a prescribed SRS is therefore considerably smoother and faster than the calibration of an impact-based shock system. Furthermore, the same shaker used for the vibration testing of a unit can generally be reused for shock testing, making this approach particularly attractive from the programmatic perspective of a mechanical test campaign.

On the downside, the applicability of shaker-based shock testing is limited by the frequency range and acceleration capability of the shaker system. Most electrodynamic shakers used for vibration testing are effective only up to approximately 2–3 kHz, while the achievable SRS amplitudes are typically limited to a few hundred g. Although these limitations make shakers unsuitable for the generic qualification of, for example, electronic units subjected to severe high-frequency shock environments, they remain adequate for a broad range of optical units. Many optical-unit designs are mechanically sensitive primarily at lower frequencies and furthermore, the far-field shock environments experienced by instruments located far from the main spacecraft shock sources are generally characterised by lower frequencies and amplitudes.

An additional consideration is the mechanical impedance of the test interface. Shaker armatures, head expanders, and slip tables generally exhibit a substantially higher mechanical impedance than the corresponding spacecraft mounting structures, and usually also shock benches. This provides good spatial homogeneity of the imposed shock environment across the multiple mounting interfaces of the unit, which can be a curse in disguise. Homogeneity requirements become easier to fulfil but the loading of the unit interfaces occurs mostly in-phase resulting in a much higher excitation of the unit than with the less spatially coherent spacecraft mounting structure or shock bench.

The over-testing associated with the high mechanical impedance of shaker interface structures is also encountered during vibration testing and constitutes one of the motivations for applying notching to vibration test specifications. At the higher frequencies, characteristic of shock environments, this effect becomes more pronounced.

Consequently, a shaker can inject more energy into the structural resonances of the unit under test and may therefore produce stronger modal excitation than those that occur during flight or on a shock bench. This inherent tendency towards resonance over-testing must be carefully considered when shaker-based shock testing is applied to sensitive optical units.

2.3. Transient Shock Analyses

Prediction of shock environments is generally challenging due to their high-frequency content and the nonlinearities that may arise from contact, joint behaviour, local yielding, and other effects. Some particular scenarios, such as compact optical units, are nonetheless well suited. In these cases, the resonant response of a relatively small number of structural modes may dominate over stress-wave propagation effects, and the relevant dynamics can be accurately captured using finite element (FE) analyses. In this context, linear implicit transient methods have demonstrated their effectiveness in predicting the response of optical units during shock testing. Modal transient approaches, such as NASTRAN SOL 112, offer the additional advantages of shorter computational times and a convenient modal representation of damping.

The accuracy of these analyses can be improved by updating the model stiffness and damping following correlation with resonance-search sine sweeps or low-level shock tests. Further improvements can be obtained by using, as excitation inputs, actual acceleration measurements acquired in the vicinity of the unit interfaces and in multiple directions. When stresses, interface forces, or displacements are to be recovered, appropriate filtering of the measured acceleration signals is recommended to prevent low-frequency measurement noise and offsets from producing non-physical drift in these integrated response quantities.

Shaker shock tests can generally be predicted with greater accuracy. The high mechanical impedance of the shaker armature and test fixtures provides boundary conditions that more closely approximate an easier to simulate hard-mounted interface, while the generated excitations are highly predictable and repeatable. Consequently, meaningful analytical predictions can be obtained already prior to final calibration of the shaker to the prescribed transient time histories.

Transient analyses are also valuable for predicting tests performed on shock benches. In this case, the less well-defined boundary conditions at the unit mounting interfaces and the lower degree of control over the generated shock levels introduce additional

sources of uncertainty. These uncertainties can be reduced by explicitly including the shock-bench plate and associated test fixture in the FE model [3]. Once a well-correlated FE model and a detailed time-domain description of the shock environment are available, transient shock analyses can be used to verify and improve the unit design. Recovery of element stresses, interface forces, and other relevant response quantities enable the calculation of margins of safety (MoS) against failure mechanisms including fracture of glass and ceramic components, failure of bonded joints, local micro-yielding, and micro-slippage at bolted interfaces.

These analyses can also be used to demonstrate the suitability of electrodynamic shakers for the shock qualification of a particular unit. Since most available vibration shakers can apply a controlled transient input only up to approximately 2–3 kHz, it must be demonstrated that relevant failure modes of the unit are not driven by response at higher frequencies. This can be assessed by comparing the margins of safety obtained under a sufficiently broadband reference excitation with those obtained when the same excitation is low-pass filtered to represent the usable frequency range of the shaker. If the removal of the higher-frequency content does not significantly affect the governing margins of safety, the available shaker bandwidth can be considered adequate for the qualification of the unit

3. RESPONSE-BASED INPUT SYNTHESIS

3.1. Transient synthesis

Performing a shock test on an electrodynamic shaker requires the synthesis of an acceleration time history that satisfies the applicable test requirements. These requirements are typically specified in terms SRS calculated using a quality factor of (Q=10). The shaker is commanded to reproduce the synthesized time history using closed-loop control. Most electrodynamic shakers used for vibration testing can accurately reproduce such transients over a controlled frequency range extending to approximately 2–3 kHz.

Transient synthesis usually involves expressing the acceleration time history as a superposition of base functions. The parameters of these functions are then optimized to obtain an SRS that satisfies the specified target within tolerance limits [4,5].

Damped sinusoids constitute a suitable family of base functions. Their adjustable parameters include amplitude, frequency, damping ratio and starting time. These parameters provide direct insight into the frequency content and temporal decay of the synthesized signal, hence its potential to excite the resonances of the test item. Furthermore, the resulting transients have the appearance of a real shock signal.

In practice, a shaker command must also satisfy the velocity and displacement limitations of the test system, i.e. zero net velocity and displacement at the end of the transient. In general, a superposition of damped sinusoids does not necessarily satisfy these conditions, but this limitation can be overcome by performing a final reconstruction of the synthesized signal in terms of wavelets. Wavelets are a base of finite duration functions which exhibit zero net velocity and displacement and the final reconstruction step only introduces a very small error to the transient synthetized with damped sinusoids [6].

Experience from shock testing shows that different acceleration transients, with similar SRS levels, can produce substantially different modal responses in the test item. Synthesizing a transient solely on the basis of its agreement with the specified SRS is therefore insufficient. The capability of each candidate transient to excite the relevant structural modes must also be quantified. For compact units exhibiting a linear behaviour, this assessment can be performed using transient mechanical analysis.

In the approach proposed herein, the damped-sine shock input synthesis MATLAB routine available from Vibrationdata [7] is used to generate a large population of candidate transients. Instead of selecting only the candidate having the smallest SRS deviation from the specification, all candidates whose SRS remains above the specification minus 3 dB are retained in line with test acceptance criteria.

Each retained candidate is subsequently applied as the base excitation in a transient analysis of the unit. The final transient is selected by considering both compliance with the interface SRS requirement and the predicted internal response of the unit. The resulting synthesis procedure is illustrated in Fig. 1.

Because this process involves the evaluation of many candidate transients, an efficient method for calculating the response of the unit is essential.

3.2. Modal transient formulation

The equation of motion of a linear structure subjected to base excitation can be expressed in modal coordinates [8, 9, 10, 11] as :

$$\ddot{\eta}_i + 2\xi_i\omega_i\dot{\eta}_i + \omega_i^2\eta_i = -L_i\ddot{u}_B \qquad (1)$$

In this equation, ξ_i and ω_i are the damping ratio and circular natural frequency of mode i, respectively; $\ddot{u}_B$ is the imposed base acceleration at the base and η_i is the corresponding modal coordinate of the response.

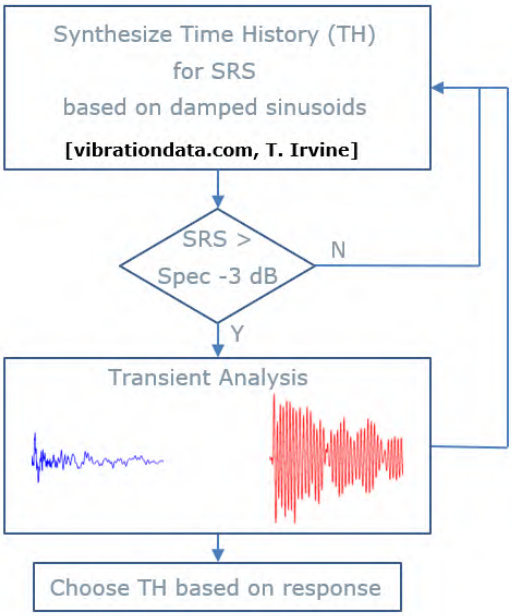


Figure 1: Response-based loop used to screen synthesized time histories.

The modal participation factor, L_i, represents the projection of a flexible mode shape on rigid-body modes through the mass matrix:

$$L_{ir} = \phi_i^T M \phi_r \qquad (2)$$

and it quantifies the responsiveness of each natural mode to base excitation in a given direction.

The required modal properties, i.e. the natural frequencies ω_i, mode shapes ϕ_i , and participation factors L_i, are standard outputs of a normal-modes FE analysis. For a prescribed base-acceleration time history, the modal coordinates can therefore be obtained by numerically integrating Eq. 1. The acceleration response at a selected degree of freedom is then recovered by combining the elastic response obtained through modal superposition together with the rigid-body acceleration imposed at the base:

$$\ddot{u} = \phi_i \ddot{\eta}_i + \phi_r \ddot{u}_B \qquad (3)$$

Equations 1 to 3 can be implemented in a short numerical script and do not require repeated solution of the complete physical finite-element model. Figure 2 demonstrates the accuracy of this formulation for a representative unit subjected to a step input. The response obtained by directly integrating modal equations of motion agrees closely with the modal-transient solution obtained using the physical FE model. Table 1 compares the associated computational times. We can see that the modal formulation reduces the calculation time by several orders of magnitude relative to NASTRAN runs with both the physical FE model and Craig–Bampton reduced model. Therefore, this computational efficiency makes the evaluation of a large population of synthesized transients practical.

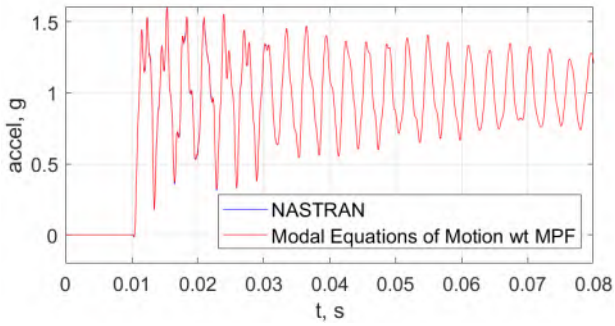


Figure 2: Agreement between the modal-participation implementation and the NASTRAN transient response for a verification input.

Table 1: Table caption

Method	Computation Time, s
Physical FE	84
Craig-Bampton	15.9
Modal Equations MPF	0.045

3.3. Modal effective transmissibility

By solving the modal equation of motion 1 in the frequency domain:

$$\eta_i(\omega) = \frac{-L_i \ddot{u}_B(\omega)}{\omega_i^2 + 2\xi_i \omega_i j\omega - \omega^2} \qquad (4)$$

and combining the flexible responses of all the retained modes and the rigid body motion, it is possible to express the transfer function between the base excitation and internal responses of locations and degrees-of-freedom of interest in the modal form:

$$\ddot{u}(\omega) = \left[1 + \sum_i^n \frac{\omega^2 \phi_i^T L_i}{\omega_i^2 + 2\xi_i \omega_i j\omega - \omega^2}\right] \ddot{u}_B(\omega) \qquad (5)$$

The contribution of each mode for the transmissibility consists of the frequency-dependent modal amplification factor and by the product between the mode-shape and the modal participation factor. This last term is called the Modal Effective Transmissibility:

$$T_i = \phi_i^T L_i \qquad (6)$$

and it quantifies how much a given mode contributes to the transmissibility of acceleration between the unit interface and a given location and degree-of-freedom of the unit.

A plot of the Modal Effective Transmissibility towards the critical degrees-of-freedom of a

particular unit expressed in terms of the respective natural frequencies puts in evidence the most critical frequencies of that unit under shock excitation. A large modal effective transmissibility identifies a mode that can dominate the respective internal shock response. and is therefore more useful for that purpose than effective mass alone. Figure 3 illustrates the Modal Effective Transmissibility of the unit on which the method will be applied in the following sections.

It is reminded that, in the same way as any linear modal transient analysis, this approach is only valid for predicting the excitation of the resonances of the unit to a shock input and is unable to capture the shock wave attenuation throughout the unit due to joints and direction changes throughout its propagation path.

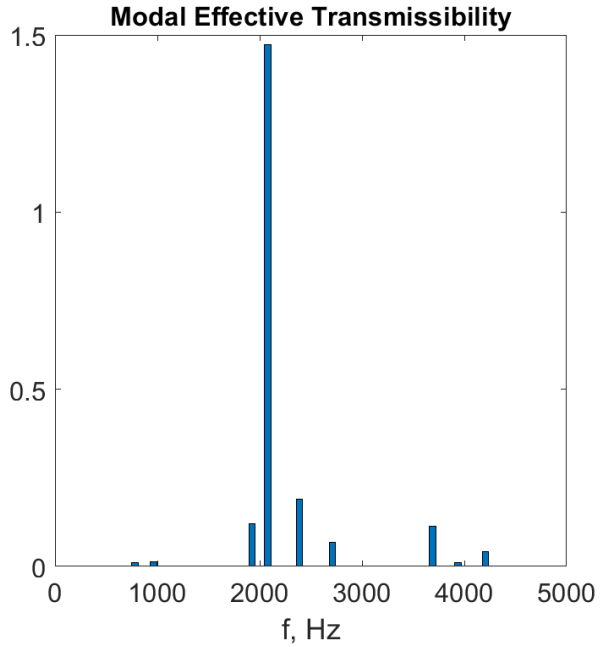


Figure 3: Modal effective transmissibility of the selected internal acceleration; the dominant mode is close to 2080 Hz.

4. APPLICATION TO AN OPTICAL UNIT

4.1. Inputs and Responses

The method described above was applied to an optical unit. A transient analysis was performed for each synthesized input whose SRS remained above the specification minus 3 dB and the acceleration response was recovered at its most critical location. For each analysed case, the maximum absolute peak acceleration at the selected location was retained. The scattering of the analysed peak responses is presented in Fig. 4.

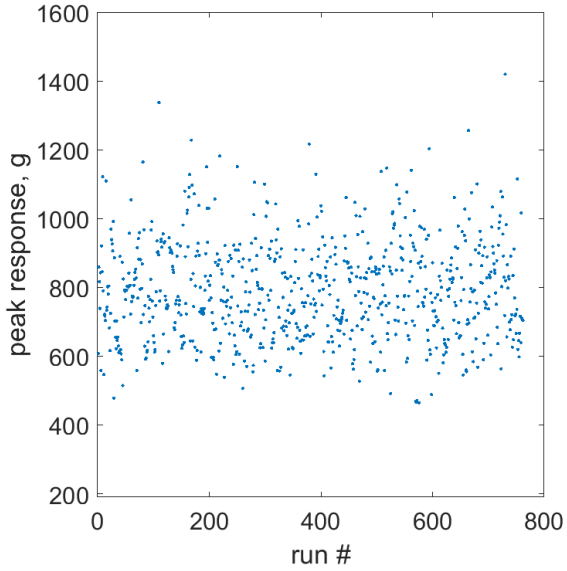


Figure 4: Peak internal acceleration for the retained synthesized inputs.

The results exhibit considerable dispersion, with the maximum and minimum responses differing by more than a factor of three. The input and response time histories associated with these two extreme cases are shown in Figs. 5 and 6, while their corresponding (Q=10) SRS curves are presented in Fig. 7. In both cases, the SRS follows the specification closely and remains well within the upper and lower test tolerance limits. Both inputs would therefore be considered acceptable for a qualification test based on the standard test SRS acceptance criterion.

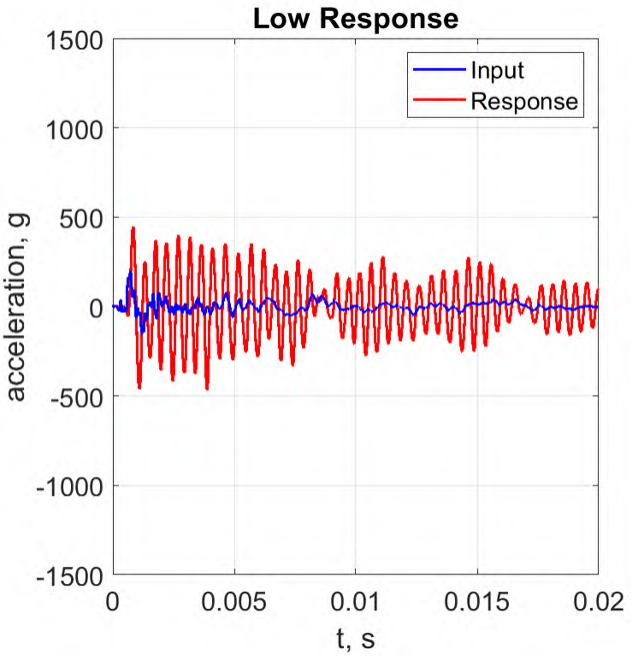


Figure 5: Input and internal response produced in the case of low - response transient.

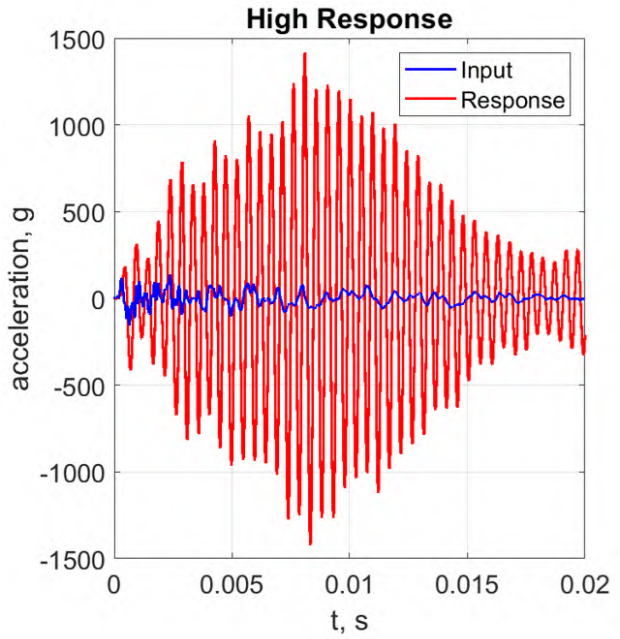


Figure 6: Input and internal response produced in the case of high - response transient.

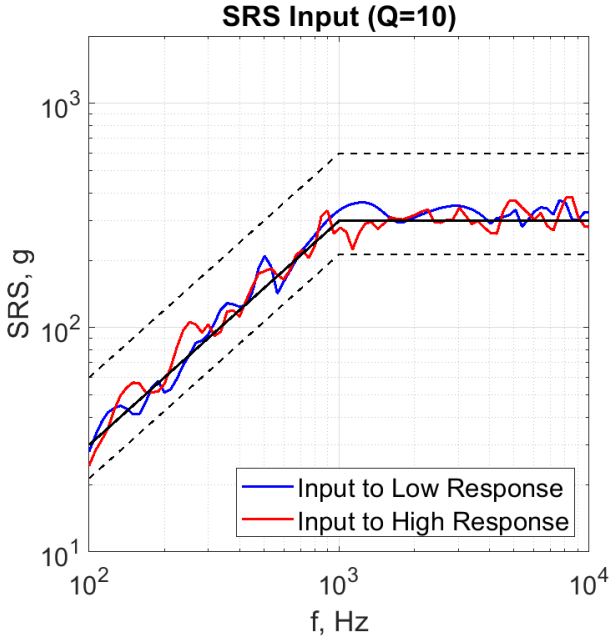


Figure 7: SRS (Q=10) of the low- and high-response inputs, including the test tolerances.

As can be observed, neither the input time histories nor their conventional (Q=10) SRS curves provide a clear indication of the large difference between the resulting internal responses they produce.

4.2. Input spectral content

The origin of this discrepancy becomes clearer when the spectral content of the inputs is examined in relation to the modal effective transmissibility of the unit. The normalized and scaled Fast Fourier Transform (FFT) of the inputs producing the two extreme responses are compared in Fig. 8. It is observed that around the frequency associated to the maximum modal effective transmissibility of the unit (2080 Hz), the Fourier amplitude of the low-response input almost vanishes, whereas the high-response input retains significant spectral content. The high-response transient therefore excites the critical mode much more effectively, explaining the substantial difference between the two internal responses.

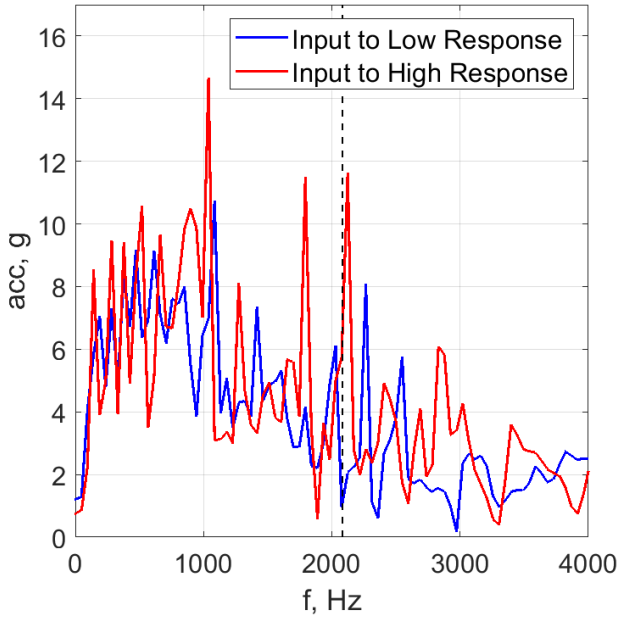


Figure 8: Fourier spectra of the low- and high-response candidate inputs.

4.3. Influence of the SRS quality factor

The difference in spectral content can also be identified using the SRS, but it is largely masked when the conventional value of Q=10 is employed. This damping broadens the frequency response of the virtual oscillators and reduces their frequency selectivity. When the SRS is recalculated using Q=100, the differences between the two input spectra near 2080 Hz become much more evident. Comparison of this higher-(Q) SRS with the modal effective transmissibility therefore makes it possible to anticipate which input will generate the larger internal response.

4.4. Limits of applicability

The proposed method is particularly effective for the shaker-shock testing of compact units with low modal density. Its effectiveness decreases for larger and more flexible structures, for which the higher modal density makes finite-element models more difficult to accurately correlate. The method also struggles when dealing with mechanisms containing moving parts and end stops or frictional joints. The associated nonlinearities can strongly affect the response and invalidate the assumptions underlying the linear modal formulation.

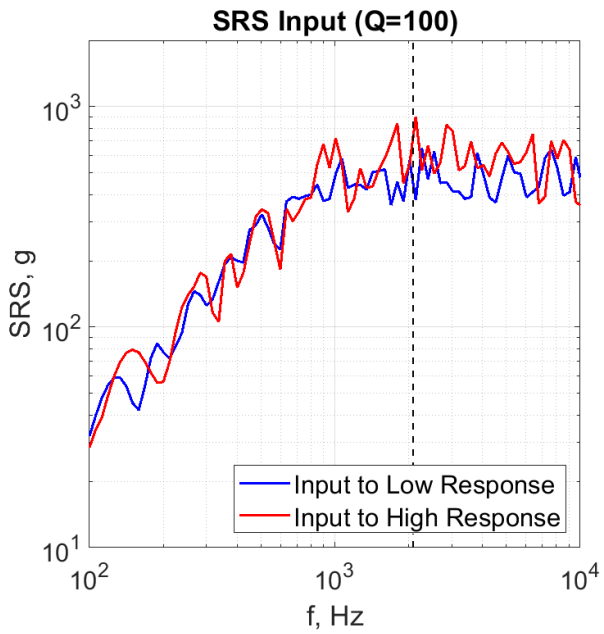


Figure 9: SRS (Q=100) of the same inputs; narrow-band differences are more visible.

5. CONCLUSIONS

Carrying out shock tests of spacecraft equipment using electrodynamic shakers offers several advantages over traditional shock benches. A shaker operates in closed loop and is commanded to follow a specified time history, which makes calibration simpler and faster. It can also simplify the equipment test campaign, since the shock test may be performed on the same shaker used for vibration testing. In addition, the input applied to the test item is more predictable and its shock response spectrum (SRS) can usually be matched very accurately to the specification.

However, shaker shock testing also has some disadvantages. The mechanical impedance of a shaker is much higher than that of a shock table or a typical spacecraft mounting structure. This produces a more spatially coherent excitation at the equipment interfaces and can excite the equipment resonances more strongly. As a result, shakers have a natural tendency to over-test equipment in shock. Shakers also have limitations in terms of operating frequency range and excitation amplitude. Nevertheless, they remain suitable for testing a broad range of units, in particular optical payload units, which are typically exposed to far-field shock environments with lower amplitudes and lower-frequency content.

Given this natural tendency to over-test, the use of shakers should be considered from the perspective of achieving target responses inside the unit rather than simply imposing specified levels at its interfaces. This would be similar to the use of notching during vibration testing.

This paper describes a method for synthesizing a transient input to be applied by a shaker during equipment shock testing. In addition to finding an optimal combination of bases functions that produces an SRS meeting the shock requirements, the proposed method includes an additional step in which the transient response of the unit is analysed. This makes it possible to recover internal responses at locations and degrees of freedom associated with critical failure modes. The transient analysis is performed using a simple time-marching numerical integration of the structural equations of motion written in modal form. This simplified approach shows negligible loss of accuracy compared with physical finite-element (FE) or Craig-Bampton reduced models of the same structure. On the plus side, it runs in a small fraction of the time, allowing several thousand responses to different transient inputs to be calculated in only a few minutes. If limits are defined for the internal responses of the unit, strict compliance with the specified interface SRS could potentially be relaxed in favour of response-limiting criteria.

In terms of future developments, the optimization strategy of the input can certainly be improved especially on what concerns inducing target responses at multiple locations of a unit. Moreover, achieving the desired internal responses requires sufficiently accurate models, whether FE models or other types. The ability to identify and update these models and then repeat the input optimization without removing the unit from the shaker would be very useful from a programmatic point of view. The possibility of recalibrating the shaker input while the unit remains mounted would also be an important advantage. These techniques still require development and consolidation.

Another issue that still needs to be addressed is how to derive suitable target internal responses when no results from spacecraft-level shock tests are available.

In addition, the results presented in this paper provide important lessons for shock verification in general, not only for tests performed using shakers. The first concerns the limitations of the standard practice of specifying the shock environment using an SRS with a mechanical amplification factor of (Q=10). Such an SRS can strongly mask the actual spectral content of the excitation. The shock environment applicable to each case should rather be described in terms of its spectral content and duration. As part of normal project activities, this should encourage engineers to challenge the shock specifications they receive, which are often too generic and include large margins.

It should also be highlighted the importance of predicting the response of sensitive units prior to any shock testing, regardless of the testing means.

This allows assessing both the likelihood of success and the suitability of the selected test method. Transient analyses can predict the modal responses of compact units with linear behaviour very accurately. The resulting mechanical quantities can then be used to calculate margins of safety for the critical failure modes, which must first be clearly understood. Knowing the input time histories applied during the test is a great advantage. This is easier when testing with shakers because the environment is more homogeneous and repeatable. However, the same approach can also be effective for shock-bench testing when it employs unit-input measurements taken from the actual test setup and in multiple directions.

Finally, the capability of a supporting structure to transmit mechanical energy to a mounted unit depends strongly on its mechanical impedance. Therefore, taking the internal side of the unit interface as the reference for assessing shock qualification would be very beneficial. This would minimise the ambiguities introduced by different flight and test mounting structures and is in fact already adopted when dealing with the thermal environment. Extending this principle to mechanical environments, and particularly to shock, therefore deserves further investigation..

6. ACKNOWLEDGMENTS

The authors would like to thank the colleagues from industry with whom they have shared the experience of numerous shock test campaigns and shock analyses, in particular Angelo Costantino from Redwire Space NV, Laura Feria from OIP NV, and Ron Nienkemper from OHB System AG.

Moreover, the fruitful discussions with the teams from Airbus Defence and Space and Thales Alenia Space, carrying out the ESA TDE activity on a data-driven shock specification tool, are hereby acknowledged.

The authors would also like to express their appreciation to Ralf Baumgartl and his team at IABG for their proactive approach in proposing the use of electrodynamic shakers for shock testing, for placing their extensive experience at the service of the many units tested together, and for their continuous efforts to improve shaker calibration and test performance.

7. REFERENCES

[1] European Cooperation for Space Standardization (2015). Mechanical Shock Design and Verification Handbook, ECSS-E-HB-32-25A, 14 July 2015.

[2] European Cooperation for Space Standardization (2022). Testing Guidelines, ECSS-E-HB-10-03A, 31 May 2022.

[3] Brévart, B. & Ait Zaid, S. (2014). Representative Mechanical Shock Testing for Satellite Electronic Units. In Proc. 13th ECSSMET, ESA SP-727, ESA-DLR, Braunschweig, Germany.

[4] Smallwood, D.O. & Nord, A.R. (1974). Matching Shock Spectra with Sums of Decaying Sinusoids Compensated for Shaker Velocity and Displacement Limitations. The Shock and Vibration Bulletin, 44(3), 43-56.

[5] Smallwood, D.O. (1975). Time History Synthesis for Shock Testing on Shakers. SAND75-5368, Sandia Laboratories, Albuquerque, USA.

[6] Irvine, T. (2023). An Introduction to Shock and Vibration Response Spectra, Revision B, Vibrationdata.

[7] Irvine, T. Vibrationdata — Shock & Vibration Analysis Software and Tutorials. Available at: www.vibrationdata.com

[8] Imbert, J.-F. (1995).
Analyse des Structures par Eléments Finis, 3ème édition, Cépaduès-Éditions, France.

[9] Clough, R.W. & Penzien, J. (2003). Dynamics of Structures, 2nd revised ed., Computers & Structures, Inc., Berkeley, CA.

[10] Chopra, A.K. (2020). Dynamics of Structures: Theory and Applications to Earthquake Engineering, 5th ed., Pearson Education Limited, Harlow, UK.

[11] Craig, R.R. & Kurdila, A.J. (2006). Fundamentals of Structural Dynamics, 2nd ed., John Wiley & Sons, Hoboken, USA.

ECSSMET
Braunschweig Germany 2026

Static load test
&
Test data evaluation

OPERATIONAL MODAL ANALYSIS – A ROBUST PROCESSING SCHEME TO EXTRACT DAMPING PROPERTIES FROM MEASURED TIMESERIES

R. Meitzner, S. Dumbre, and V. Ramanolla

ArianeGroup, Airbus-Allee 1, 28199 Bremen, Germany

ABSTRACT

Modern spacecraft consist of several components including main and secondary structures, tanks, engines, fluid control and electrical equipment. The mechanical justification of such components includes evaluation and analyses of dynamics behaviour.

Commonly the dynamics behaviour of components is evaluated based on **damped forced response calculations** using corresponding finite element models.

- **Forcing functions** are derived from spacecraft inherent excitation mechanisms (engines, aerodynamics, mechanisms, separation causing harmonic, random, acoustics, transient, shock excitation).
- **Damping assumptions** are typically taken from best practice heritage and available references based on dynamics tests.

To substantiate damping assumptions, operational and in-flight measurements can be analysed using **operational modal analysis** methods.

The possibility to extract and the quality of extracted damping properties depend on underlying measured timeseries (duration, transient or stable conditions, noise level, sensors).

This paper describes a **robust processing scheme to extract damping properties** from measured timeseries.

The following aspects are discussed.

- **Outline of proposed processing scheme.**
- **Processing of synthetically generated timeseries.**
- **Error estimation.**

The proposed processing scheme is based on various **computational methods**. Some insights into an available software implementation are provided.

Remarks about **error estimation** and **lessons learned** complete this paper.

1. PROCESSING SCHEME

Outline of proposed processing scheme.

Power spectra

The proposed processing scheme utilises Welch's method for power spectral density estimation to convert timeseries into power spectra.

Moving average

The parameters for Welch's method are selected based on expected frequency range and damping ratio range of interest. These parameters are chosen to ensure that low frequency eigenmodes are resolved with a sufficiently high frequency resolution. Since this parameter selection yields an excessively high frequency resolution for high frequencies, a frequency dependent moving average is applied to the power spectrum. The parameters for this moving average vary with frequency to reflect that the bandwidth of the eigenmodes is approximately proportional to their eigenfrequencies.

Eigenmode identification

The implemented automated eigenmode identification relies on the power spectrum smoothed by a frequency dependent moving average. Eigenmodes are then identified based on a peak search performed on the differentiated smoothed cumulative power spectrum. The plausibility of the detected eigenmodes is verified by comparing their identified bandwidth against the theoretical values for the expected damping ratio range at the respective eigenfrequencies.

Consequently, only isolated eigenmodes are detected, which inherently exhibit single-degree-of-freedom behavior. This constraint is introduced to ensure the robustness of the identification scheme.

Eigenmode fitting

The modal properties of the identified eigenmodes are extracted using a single-degree-of-freedom eigenmode fitter. Since the power spectra represent power spectral densities, the extracted modal properties are limited to real eigenfrequencies and damping ratios.

Error estimation

The expected error bounds of the estimated damping ratios are quantified using Monte-Carlo-simulations. These error bounds depend on the following parameters

- duration of timeseries
- samplingrate of timeseries
- expected eigenfrequency range
- expected damping ratio range
- eigenfrequencies of identified eigenmodes
- damping ratios of identified eigenmodes

The Monte-Carlo-simulation executes a sufficiently large number of damping ratio estimations for synthetic single-degree-of-freedom responses under varying random excitation with assumed damping ratios.

The error bounds are derived from statistical evaluations of assumed versus estimated damping ratios.

2. SYNTHETIC TIMESERIES

Processing of synthetically generated timeseries.

Synthetic timeseries are constructed by superimposing single-degree-of-freedom harmonic oscillator random responses. Damping ratios are 1% and 8% and the duration of timeseries is 112.5s.

Typical outputs of the **eigenmode identification** for different damping ratios are shown in Figure 1 and 3. With increasing frequency and damping ratio, the bandwidth of the eigenmodes widens and they begin to overlap, thereby limiting the capabilities of the eigenmode identification, see comparison of Figure 1 and 3.

Typical outputs of the **eigenmode fitting** for different damping ratios are shown in Figure 2 and 4. With increasing frequency and damping ratio, the underlying power spectra become more ill-defined, thereby limiting the accuracy of the eigenmode fitting, see comparison of Figure 2 and 4.

Typical outputs of the **error estimation** for different damping ratios are summarised in Table 1 and 2. For the assumed damping ratios of 1% and 8%, the errors of the estimated damping ratios are covered by the error bounds established by the Monte-Carlo-simulation. The error bounds are symmetric and are expected to encompass the actual errors in 99.46% of the cases.

A **synthetic timeseries** with a total duration of 3600s is constructed assuming a damping ratio of 3%. The estimated damping ratios for **sub-timeseries** with a duration of 450s are shown in Figure 5.

3. ERROR ESTIMATION

Error estimation.

Error bounds of the estimated damping ratios are quantified using Monte-Carlo-simulations. Damping ratios range from 1% to 8%, durations of timeseries range from 56.25s to 3600s and eigenfrequencies range from 10Hz to 350Hz.

Typical error bounds for different durations are shown in Figure 6 to 9. The error bounds are symmetric and are expected to encompass the actual errors in 99.46% of the cases.

To reduce error bounds, low frequency low damping ratio eigenmodes require longer timeseries. Conversely, the error bounds for high frequency eigenmodes are sufficiently small even for short timeseries.

4. CONCLUSION

This paper describes a **robust processing scheme to extract damping properties** from measured timeseries.

The accuracy of the estimated damping properties is quantified via **error estimation**.

The overall processing scheme yields **high confidence** in the reliability of both the estimated properties and their associated error bounds.

The **lessons learned** are

- With increasing frequency and damping ratio, the bandwidth of the eigenmodes widens and they begin to overlap, thereby limiting the capabilities of the eigenmode identification.
- With increasing frequency and damping ratio, the underlying power spectra become more ill-defined, thereby limiting the accuracy of the eigenmode fitting.
- To reduce error bounds, low frequency low damping ratio eigenmodes require longer timeseries.
- The error bounds for high frequency eigenmodes are sufficiently small even for short timeseries.

The **future activities** are as follows.

With increasing frequency and damping ratio, the bandwidth of the eigenmodes widens and they begin to overlap, thereby requiring advanced capabilities for robust

- **eigenmode identification**
- **eigenmode fitting**

of non-isolated eigenmodes.

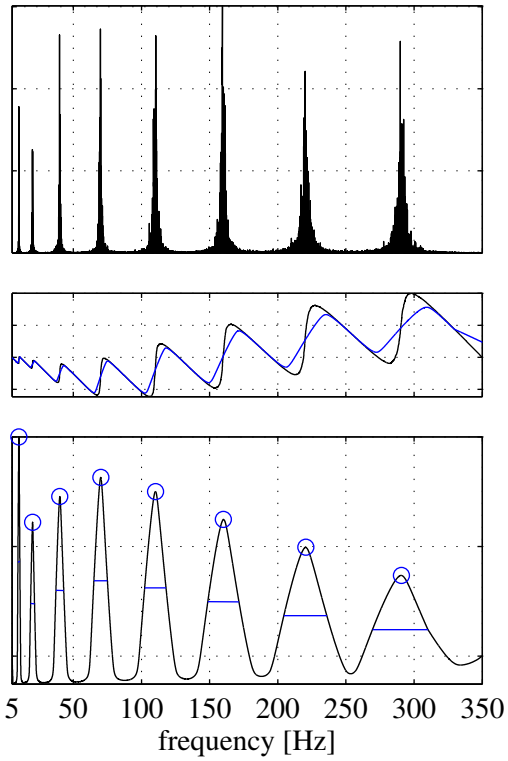


Figure 1: Eigenmode identification, timeseries, duration 112.5s, damping ratio 1%

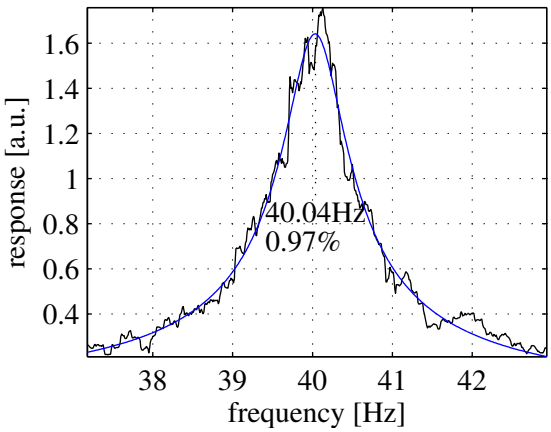


Figure 2: Eigenmode fitting, timeseries, duration 112.5s, damping ratio 1%

eigenfrequency	damping radio	error ref 1%	error bound
10.02	0.91	−8.92	61.11
20.01	0.86	−14.12	50.60
40.04	0.97	−2.60	41.30
69.95	0.91	−9.46	30.16
110.07	0.92	−7.85	23.50
159.98	1.01	0.49	20.50
220.07	1.00	0.05	16.84
290.19	0.96	−4.17	15.41
Hz	%	%	%

Table 1: Error estimation, timeseries, duration 112.5s, damping ratio 1%

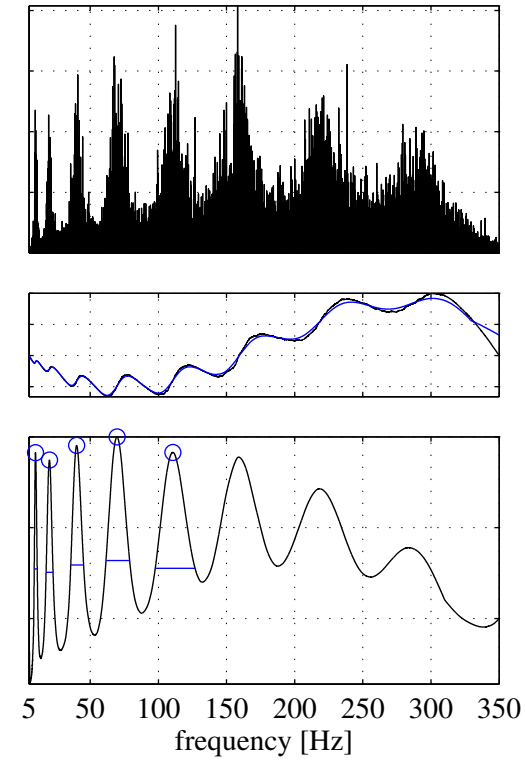


Figure 3: Eigenmode identification, timeseries, duration 112.5s, damping ratio 8%

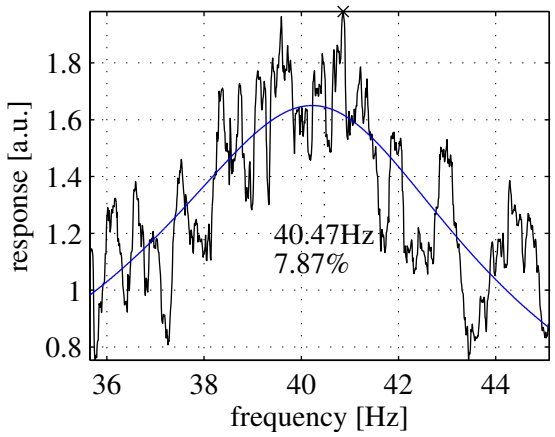


Figure 4: Eigenmode fitting, timeseries, duration 112.5s, damping ratio 8%

eigenfrequency	damping radio	error ref 8%	error bound
9.95	7.28	−9.05	53.26
20.27	9.00	12.47	41.19
40.47	7.87	−1.57	32.70
70.70	9.43	17.83	26.25
112.46	9.52	19.04	19.93
Hz	%	%	%

Table 2: Error estimation, timeseries, duration 112.5s, damping ratio 8%

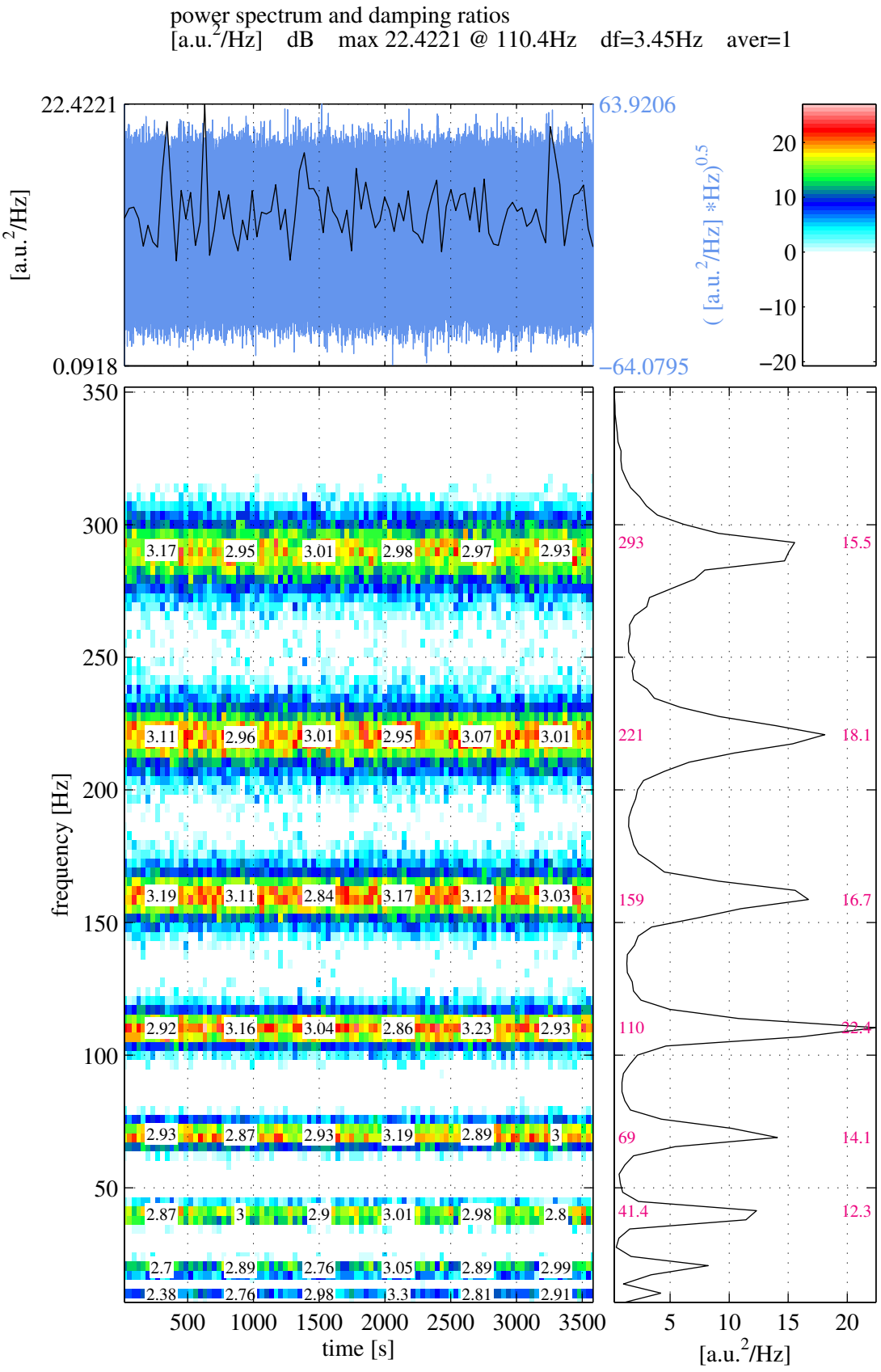


Figure 5: Eigenmode estimation, timeseries, duration 450s, derived from a synthetic timeseries with a total duration of 3600s, damping ratio 3%

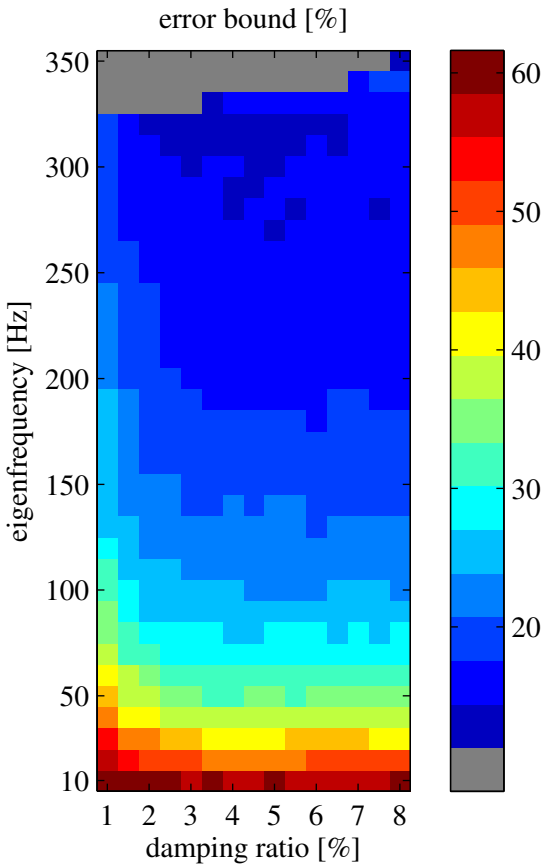


Figure 6: Error bounds, timeseries, duration 56.25

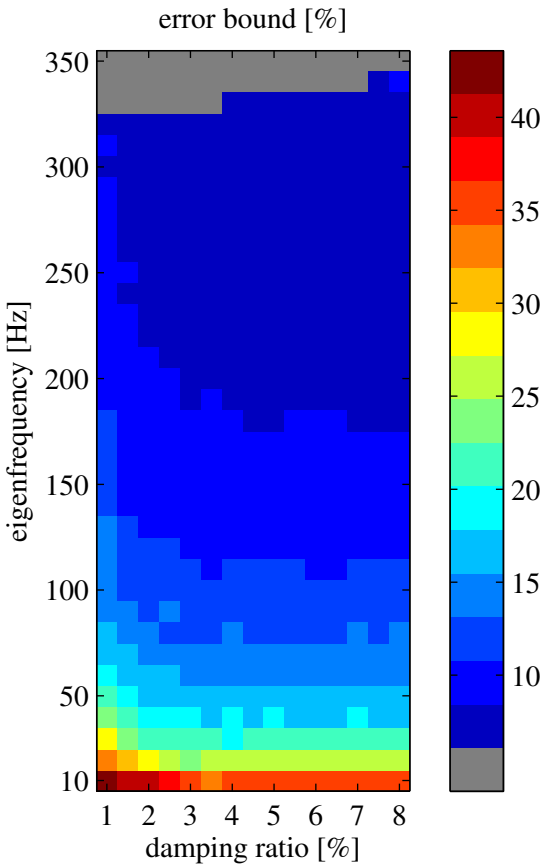


Figure 8: Error bounds, timeseries, duration 225.00

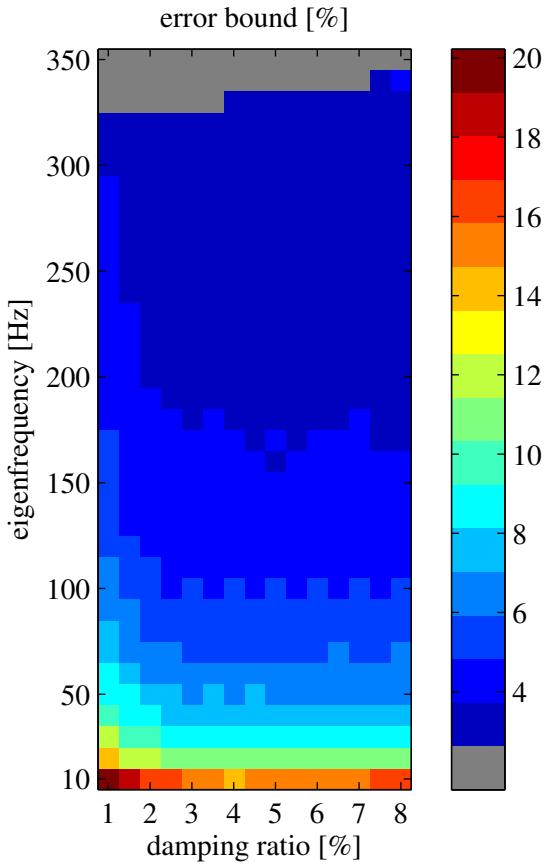


Figure 7: Error bounds, timeseries, duration 900.00

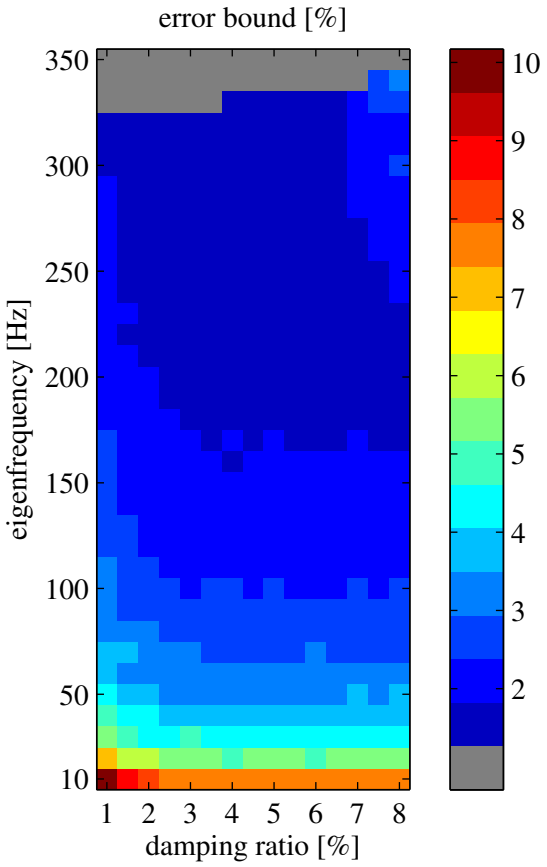


Figure 9: Error bounds, timeseries, duration 3600.00

STATIC QUALIFICATION TEST CAMPAIGN OF THE ROSE-L SATELLITE STRUCTURE SUBSYSTEM - INNOVATIVE APPROACHES AND RESULTS

Manuele Scipioni [(1)], David Krzikalla [(2)], Ivo Jebáček [(3)], Marek Horák [(4)]

[(1)] SAB Aerospace srl, via Marsala 15/C, 60121 Ancona (IT), mscipioni@sabaerospace.com
[(2)] SAB Aerospace sro, TechNest, Technická 23, 61600 Brno (CZ), dkrzikalla@sabaerospace.cz
[(3)] Vysoké učení technické v Brně - Fakulta strojního inženýrství, Technická 2896/2, 616 69 Brno (CZ), jebacek@fme.vutbr.cz
[(4)] Vysoké učení technické v Brně - Fakulta strojního inženýrství, Technická 2896/2, 616 69 Brno (CZ), horak@fme.vutbr.cz

KEYWORDS

satellite structures, static testing, test definition, test results

ABSTRACT

This paper presents the methodology, test setups and results of the static qualification campaign performed by SAB Aerospace on the structure subsystem of the ROSE-L satellite.

A major highlight was the development of an optimisation algorithm for verifying structural interfaces governed by a set of three forces and three moments. This enabled the execution of multi-axial load cases using a single linear actuator by optimizing its position, magnitude, and orientation. This approach significantly reduced the test setups complexity and the duration of the test campaign, with negligible impacts on the test accuracy.

The adequacy of all test setups was systematically validated by comparing FE simulations of the test configurations against the analysis on the satellite in its flight configuration.
The test campaign demonstrated excellent performance of the structure and a high degree of correlation between analytical predictions and empirical data, thereby validating the FE model ahead of system-level testing.

1. INTRODUCTION

As part of the European Space Agency's (ESA) Copernicus Space Segment Expansion program, the Radar Observing System for Europe in L-band (ROSE-L) is an Earth observation mission centred around a Synthetic Aperture Radar (SAR) instrument. The mission's operational objectives focus on monitoring geohazards, tracking land use, agriculture, and forestry, delivering high-resolution soil moisture telemetry, and observing Arctic and cryosphere dynamics.

Operating as a direct subcontractor to Thales Alenia Space Italia (TASI), SAB Aerospace, through the joint execution of its Italian and Czech subsidiaries, was responsible for the design, development, and verification of the satellite structure and thermal control subsystems.

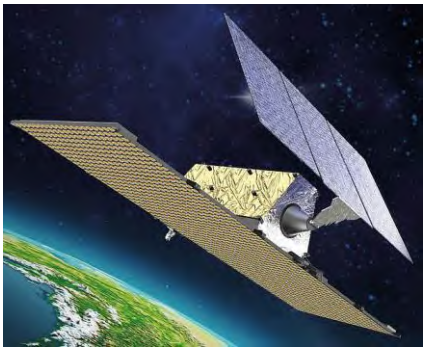


Figure 1: ROSE-L satellite in orbit (rendering)

The static qualification test campaign for the structure subsystem was successfully conducted in mid-2025. Physical testing was carried out inside SAB's dedicated ISO 8 cleanroom facility, specifically developed for satellite structural qualification within the Aircraft Testing Laboratory at the Brno University of Technology (BUT), Czech Republic.

1.1. ROSE-L description

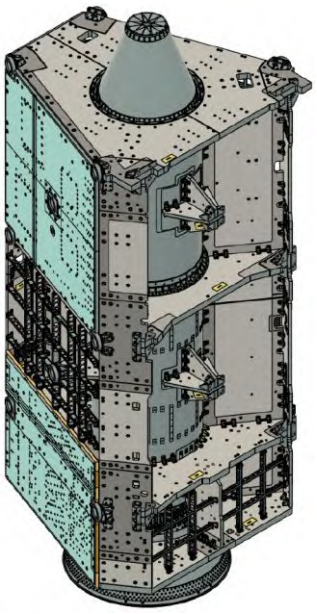


Figure 2: ROSE-L satellite structure subsystem

The ROSE-L satellite envelope measures approximately 4.8 m in height with a 1.8 m × 1.9 m cross-sectional footprint, operating under a maximum launch mass of 2350 kg. The structural subsystem accounts for a total mass of 468 kg and is partitioned into three functional tiers:

- Primary structure (135 kg): serves as the central backbone of the spacecraft, comprising a Carbon-Fiber Reinforced Polymer (CFRP) lower adapter cone interfacing with the launch vehicle, along with two stacked CFRP central cylinders that provide primary load-bearing attachment points for the surrounding structural components;
- Secondary structure (169 kg): supports the majority of the satellite's electronic equipment and units, consisting of sandwich panels constructed with CFRP skins and aluminium honeycomb cores, as well as radiator panels featuring aluminium skins and aluminium honeycomb cores.
- Tertiary structure (164 kg): provides localized interface fittings that route electronic units, equipment, and payload instruments to the primary and secondary structural assemblies.

Table 1: ROSE-L structure subsystem mass

	Mass [kg]
Primary structure	135
Secondary structure	169
Tertiary structure	164
Total structural mass	468

Additionally, the structure incorporates 24 critical interface regions distributed around its external perimeter to accommodate the Hold-Down and Release Mechanisms (HDRM) for both the Solar Array Wings (SAW) and the SAR antenna panels.

2. TEST DEFINITION

2.1. Test objectives

The primary objective of the static test campaign was to verify the structural strength and stiffness of the subsystem, demonstrating its capability to withstand peak launch loads while guaranteeing dynamic decoupling from the launch vehicle and ensuring an appropriate mechanical environment for payload assemblies and onboard equipment. Because a full dynamic qualification campaign, including sine vibration on a shaker and vibro-acoustic testing, was scheduled downstream at the system level, the qualification campaign for the structure subsystem was strictly limited to static loading scenarios.

2.2. Screening process

To minimize cost and schedule impact, a comprehensive screening process was executed in accordance to ECSS-E-ST-32-10C Rev.2 section 4.3.2. Under this standard, physical testing is mandatory for structural areas lacking a positive Margin of Safety (MoS) when incorporating additional "verification by analysis only" safety factors. This screening identified four primary load categories requiring empirical verification:

- Launcher’s quasi-static loads (L-QSL): uniform accelerations induced by the launch vehicle thrust;
- SAR/SAW appendage interface loads: local forces and moments transmitted through the 24 perimeter brackets, generated by the local dynamic behaviour of the SAR antenna panels and Solar Array Wings;
- Tank Holding Structure (THS) interface loads: forces and moments acting on the propellant tank interface brackets, driven by the local dynamic response of the tank assembly;
- Equipment and Units quasi-static loads (EQ-QSL): local acceleration loads acting on equipment mounting brackets, generated by the dynamic behaviour of individual units and their supporting structural panels.

Through this systematic screening, critical structural regions and specific load cases (LC) were formally identified for inclusion in the static test matrix.

2.3. Load cases definition

The screening process identified the necessity to empirically reproduce the following critical load cases within the qualification test campaign:

- Launcher’s QSL generating:
  - Maximum compression flux at the launch vehicle interface (LV I/F);
  - Maximum tension flux at the LV I/F;
  - Minimum MoS on each of the three Shear Panels (SP) and their associated I/Fs.
- SAR and SAW interface loads generating:
  - Minimum MoS across the 24 interface brackets and their associated I/Fs.
- Equipment and Units QSL generating:
  - Minimum MoS on the Ka-Band antenna (KBA) bracket interfaces.

Conversely, interface loads associated with the Tank Holding Structure (THS) did not induce critical stresses in the satellite structure and were additionally covered by coupon-level development tests executed by the primary structure manufacturer.

To optimise the qualification schedule and minimise structural fatigue by limiting load application cycles, structural design symmetries were leveraged wherever applicable. This approach was particularly effective in reducing the test matrix for the SAR and SAW interface regions. By combining the screening results with these design symmetries, testing only 7 of the 24 interface regions was technically justified, yielding significant cost and schedule benefits for the project.
The complete list of load cases designated for testing is detailed in Table 2 ÷ Table 4.

Table 2: L-QSL cases to be tested

Load case	Acceleration [g]		
	X	Y	Z
Max compression flux	-2.38	-1.06	-4.68
Max tension flux	2.38	1.06	0.65
Max stress on SP MY	0.00	-1.30	-7.80
Max stress on SP MXPY	-1.13	0.65	-7.80
Max stress on SP PXPY	1.13	0.65	-7.80

Table 3: SAR and SAW load cases to be tested

Load case	Force [N]			Moment [Nm]		
	X	Y	Z	X	Y	Z
PX-1	2377	4643	4452	183	-58	189
PX-2	2274	-3399	7503	-91	-98	-54
MX-4	-1732	3111	-6221	121	135	-76
MX-5	-1919	-5688	-4557	246	-56	-121
PY-1	-4120	4299	5639	-125	-318	271
PY-3	-1632	-287	2503	2	-306	-41
PY-4	2968	4773	-6789	149	481	154

Table 4: Equipment QSL cases to be tested

Load case	Acceleration [g]		
	X	Y	Z
KBA bracket I/Fs	0.00	20.00	20.00

2.4. Test setups definition

The definition of this test campaign required addressing two primary technical challenges:

1. L-QSL and EQ-QSL load cases: reconstructing stress and force distribution fields generated by global acceleration environments using only actuators applying loads at a finite number of discrete points.
2. SAR and SAW I/F forces and moments: recreating the stress and force distributions induced by a multi-axial load state, comprising three orthogonal forces and moments acting simultaneously at a single point, by means of a single linear actuator.

2.4.1. L-QSL load cases

To simulate these load cases, the methodology leveraged the satellite architecture, in which the SAR antenna and SAW are externally mounted via 24 interface brackets distributed across three structural sides. Because the combined mass of the SAR antenna, SAW, and equipment-bearing radiator panels constitutes the vast majority of the overall satellite mass, three large metallic load frames were constructed. Each frame was secured to 8 of the 24 interface brackets, closely representative of the stowed appendage launch configuration.
A dedicated linear actuator was interfaced with each frame at approximately the elevation of the global satellite Centre of Gravity (CoG). The spatial orientation of the actuators across all three coordinate axes, as well as their applied force magnitudes, was tuned to reproduce as closely as possible the stress and force distribution fields derived from launch configuration FE analyses under global acceleration loads.

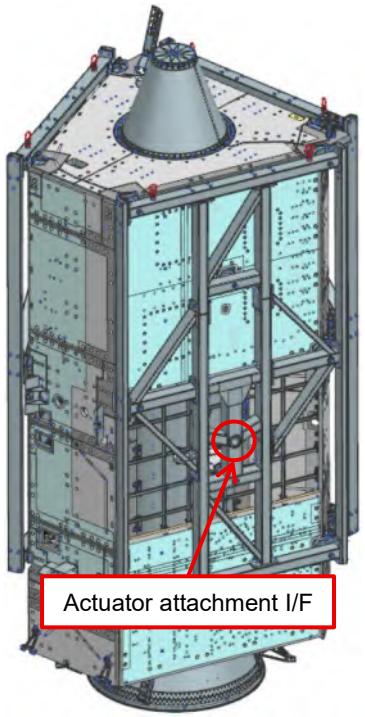


Figure 3: L-QSL test setup with metallic frames

The specified force components required for the three actuators to execute the load cases defined in Table 2 are detailed in Table 5 ÷ Table 9.

Table 5: L-QSL – Max compression flux test loads

Max compression flux			
Actuator	Force [N]		
	X	Y	Z
PX frame	-19386	-8634	-38121
MX frame	-19386	-8634	-38121
PY frame	-19386	-8634	-38121

Table 6: L-QSL – Max tension flux test loads

Max tension flux			
Actuator	Force [N]		
	X	Y	Z
PX frame	16783	12228	5195
MX frame	16783	12228	5195
PY frame	16783	12228	5195

Table 7: L-QSL – Max stress SP MY test loads

Max stress on SP MY			
Actuator	Force [N]		
	X	Y	Z
PX frame	2843	-1035	-60550
MX frame	-2843	-1035	-60550
PY frame	0	-6939	-24932

Table 8: L-QSL – Max stress SP MXPY test loads

Max stress on SP MXPY			
Actuator	Force [N]		
	X	Y	Z
PX frame	-6005	2186	-48139
MX frame	-3932	-1431	-48139
PY frame	0	3490	-41805

Table 9: L-QSL – Max stress SP PXPY test loads

Max stress on SP PXPY			
Actuator	Force [N]		
	X	Y	Z
PX frame	4079	-1484	-39575
MX frame	6203	2257	-39575
PY frame	0	3304	-39575

2.4.2. SAR and SAW interface forces and moments

The selection of a single-actuator loading strategy represented a significant operational optimization, drastically reducing test fixtures complexity and execution duration. However, applying six independent load components (three orthogonal forces and three moments) at a single interface point using a single linear force vector is a mathematically over-constrained problem.

To overcome this limitation, an optimization procedure was developed to determine the spatial position of the load introduction point. This approach ensured that the applied force vector and resulting interface moments matched reference specification values as closely as possible, prioritizing load components with the greatest impact on the structural Margin of Safety (MoS).

This optimization routine was executed iteratively for each SAR and SAW interface location through the following steps:

1. Sensitivity analysis: each of the six individual load components ($i \in \{F_X, F_Y, F_Z, M_X, M_Y, M_Z\}$) was applied independently to the nominal Finite Element (FE) model to extract component-specific Margins of Safety (MoS_i).
2. Weights derivation: weight coefficients w_i incorporated into the optimization algorithm were formulated inversely proportional to MoS_i, assigning higher priority to load components generating lower safety margins:

$$w_i = \frac{\frac{1}{MoS_i}}{\sum_j \frac{1}{MoS_j}} \qquad (1)$$

Where:

i: specific load component $F_x, F_y, F_z, M_x, M_y, M_z$

w_i: weight coefficient for load component i;

MoS_i: MoS for load component i;

3. Objective function minimization: the optimization algorithm was launched to minimize a normalized objective error function $f(P_x, P_y, P_z, F_x, F_y, F_z)$:

$$\begin{aligned} & f(P_x, P_y, P_z, F_x, F_y, F_z) \\ &= w_{F_x}\left(\frac{F_x - F_X}{F_X}\right)^2 + w_{F_y}\left(\frac{F_y - F_Y}{F_Y}\right)^2 \\ &+ w_{F_z}\left(\frac{F_z - F_Z}{F_Z}\right)^2 + w_{M_x}\left(\frac{M_x - M_X}{M_X}\right)^2 \\ &+ w_{M_y}\left(\frac{M_y - M_Y}{M_Y}\right)^2 + w_{M_z}\left(\frac{M_z - M_Z}{M_Z}\right)^2 \end{aligned} \qquad (2)$$

Where:

$w_{F_x}, w_{F_y}, w_{F_z}, w_{M_x}, w_{M_y}, w_{M_z}$: weight coefficients;

$F_X, F_Y, F_Z, M_X, M_Y, M_Z$: nominal reference force and moment targets specified in the project requirements;

P_x, P_y, P_z: spatial coordinates of the load application point;

F_x, F_y, F_z: actuator force vector components;

The induced interface moments are governed by static equilibrium equations:

$$M_x = P_y F_z - P_z F_y \qquad (3)$$

$$M_y = P_z F_x - P_x F_z \qquad (4)$$

$$M_z = P_x F_y - P_y F_x \qquad (5)$$

This procedure yielded the spatial coordinates defining the load application point (P_x, P_y, P_z) and the force vector components (F_x, F_y, F_z) governing actuator orientation and total load magnitude. These parameters are summarized in Table 10 ÷ Table 16. Interface moments enclosed in parentheses indicate values resulting directly from static moment arm equilibrium, rather than independently controlled test inputs.

Table 10: SAR and SAW – PX-1 test load

Load case	Force [N] / Mom [Nm]*			Coord [mm]		
	X	Y	Z	X	Y	Z
Ref	2377 183	4643 -58	4452 189	0	0	0
Test	2258 (71)	4413 (-166)	4228 (136)	100	136	115

Table 11: SAR and SAW – PX-2 test load

Load case	Force [N] / Mom [Nm]*			Coord [mm]		
	X	Y	Z	X	Y	Z
Ref	2274	-3399	7503	0	0	0
	-91	-98	-54			
Test	2331	-3484	7691	50	-64	119
	(-75)	(-106)	(-25)			

Table 12: SAR and SAW – MX-4 test load

Load case	Force [N] / Mom [Nm]*			Coord [mm]		
	X	Y	Z	X	Y	Z
Ref	-1732	3111	-6221	0	0	0
	121	135	-76			
Test	-1785	3204	-6408	53	-82	123
	(130)	(123)	(25)			

Table 13: SAR and SAW – MX-5 test load

Load case	Force [N] / Mom [Nm]*			Coord [mm]		
	X	Y	Z	X	Y	Z
Ref	-1919	-5688	-4557	0	0	0
	246	-56	-121			
Test	-1939	-5745	-4603	50	96	120
	(250)	(-3)	(-102)			

Table 14: SAR and SAW – PY-1 test load

Load case	Force [N] / Mom [Nm]*			Coord [mm]		
	X	Y	Z	X	Y	Z
Ref	-4120	4299	5639	0	0	0
	-125	-318	271			
Test	-4243	4428	5808	50	-16	-20
	(-3)	(-205)	(154)			

Table 15: SAR and SAW – PY-3 test load

Load case	Force [N] / Mom [Nm]*			Coord [mm]		
	X	Y	Z	X	Y	Z
Ref	-1632	-287	2503	0	0	0
	2	-306	-41			
Test	-1650	-290	2531	50	-8	60
	(-3)	(-226)	(-28)			

Table 16: SAR and SAW – PY-4 test load

Load case	Force [N] / Mom [Nm]*			Coord [mm]		
	X	Y	Z	X	Y	Z
Ref	2968	4773	-6789	0	0	0
	149	481	154			
Test	2894	4653	-6619	50	13	-29
	(47)	(248)	(195)			

Unavoidable deviations between the test load vectors and the nominal target forces and moments were systematically evaluated to confirm their acceptability. These discrepancies were verified to ensure that the required stress and force distribution fields were accurately reproduced without introducing unacceptably high local over-testing risks that could compromise structural integrity.
By applying these optimized parameters, test execution was significantly streamlined without compromising the campaign's validity or its capability to demonstrate structural qualification.

As a representative example, Figure 4 illustrates the CAD model of the test setup defined for the PX-1 SAR interface bracket.

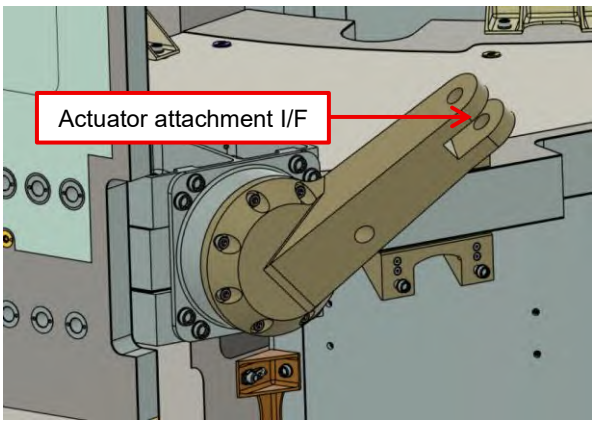


Figure 4: SAR load test setup – PX-1 I/F

2.4.3.Equipment and Units QSL

To recreate the stress and force distribution fields induced on the structure by the flight accelerations of the Ka-Band Antenna (KBA) and its associated bracket, a dedicated test jig was designed to interface the actuator directly at the Centre of Gravity (CoG) of the KBA-and-bracket subassembly. The applied force magnitude was calculated as the product of the subassembly's total mass and the applicable acceleration vector.
The force components specified for the actuators to reproduce the load cases defined in Table 4 are reported in Table 17.

Table 17: EQ-QSL – KBA I/F test loads

KBA I/F			
Actuator	Force [N]		
	X	Y	Z
KBA + bracket CoG	0	2870	2870

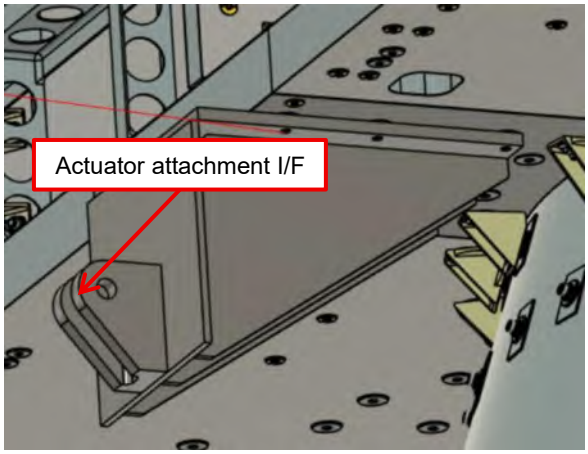


Figure 5: KBA I/F load test setup

2.5. Test setups validation

All test setups defined using the methodologies described in section 2.4 were validated against two primary evaluation criteria:

- Structural qualification fidelity: capability to qualify structural strength by accurately reproducing peak stress fields on critical components and peak force distributions across key interfaces;
- Structural safety assurance: ability to guarantee structural integrity and prevent unexpected damage, even in localized areas where mild over-testing was physically unavoidable.

To evaluate these criteria, dedicated Finite Element (FE) models were developed for every test configuration. These models incorporated the satellite Structural Model (SM) in its physical test state (i.e., devoid of payload and equipment units) along with high-fidelity representations of the test jigs, subjected to the nominal predicted actuator forces.

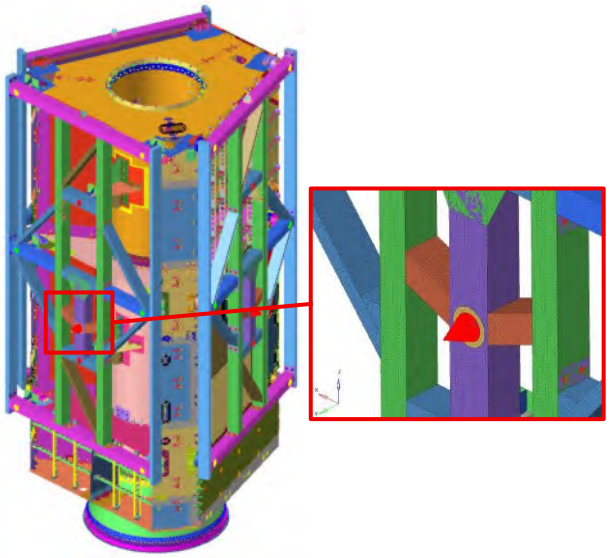


Figure 6: FE model for L-QSL test simulation

These setup-level models were analysed to derive detailed stress, strain, and interface force distributions across critical structural regions. The results were directly benchmarked against corresponding analytical outputs from the full satellite FE model evaluated under nominal flight launch loads.
Strong agreement between the setup-level and flight-configuration simulations confirmed that the proposed test setups were fully adequate for static qualification. For conciseness, some representative comparative contour plots and force vectors are illustrated in Figure 7 ÷ Figure 10.

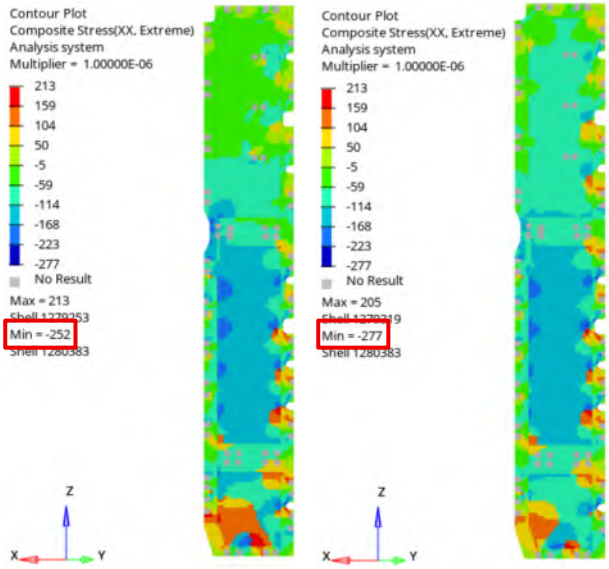


Figure 7: L-QSL, max stress on SP MXPY – Comparison between launch (left) and test (right)

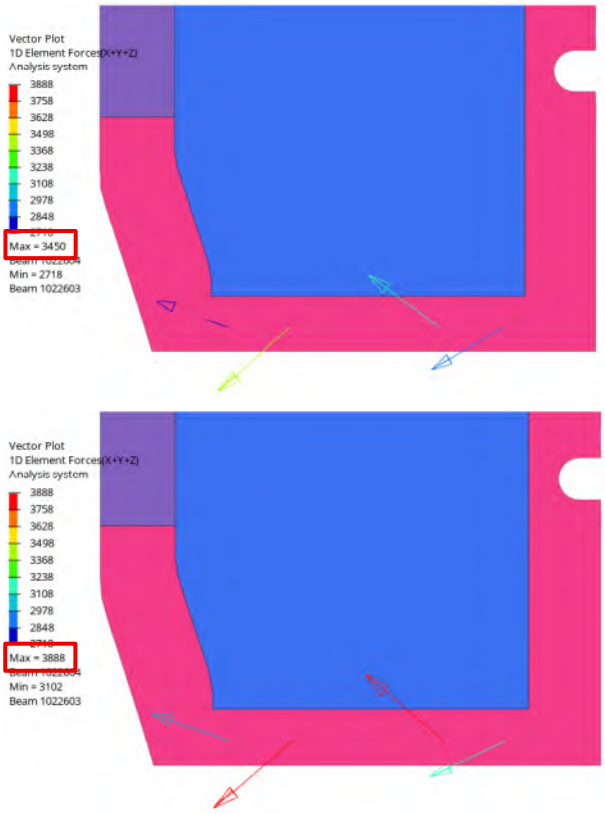


Figure 8: L-QSL, max force on SP MXPY I/Fs – Comparison between launch (top) and test (bot)

Furthermore, a comprehensive structural safety assessment of both the satellite structure and the test fixtures was performed to rule out any risk of premature failure or unrepresentative damage during test execution. Finally, these setup FE simulations served to establish baseline strain and displacement predictions, establishing quantitative metrics for real-time comparison against sensor telemetry during physical testing.

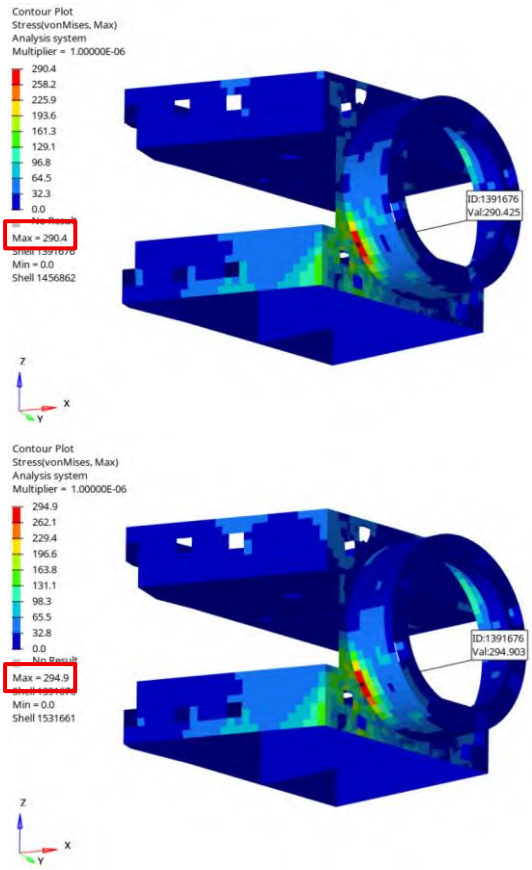


Figure 9: SAR loads, max stress on PX-1 bracket – Comparison between launch (top) and test (bot)

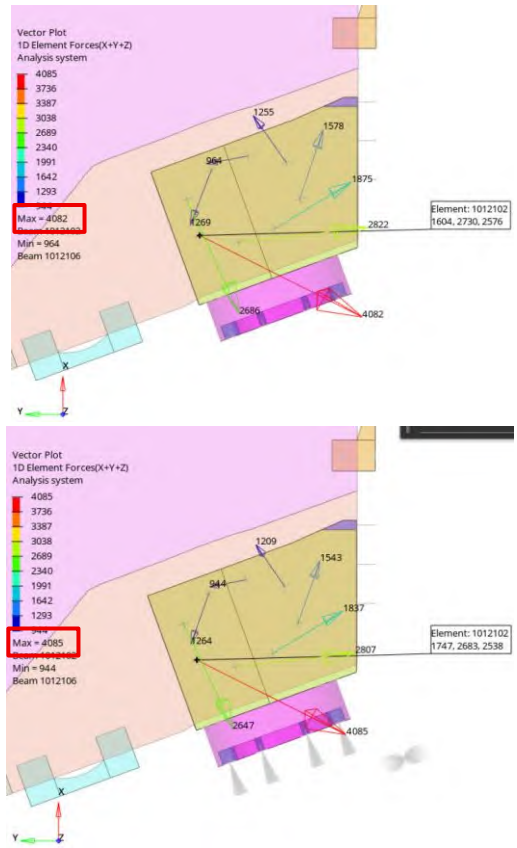


Figure 10: SAR loads, max force on MX-5 I/Fs – Comparison between launch (top) and test (bot)

3. TEST EXECUTION

3.1. Test facility

The qualification campaign was conducted in an ISO 8 facility developed by SAB Aerospace in collaboration with the Brno University of Technology (BUT), located within the Aircraft Testing Laboratory at the Faculty of Mechanical Engineering in Brno, Czech Republic.

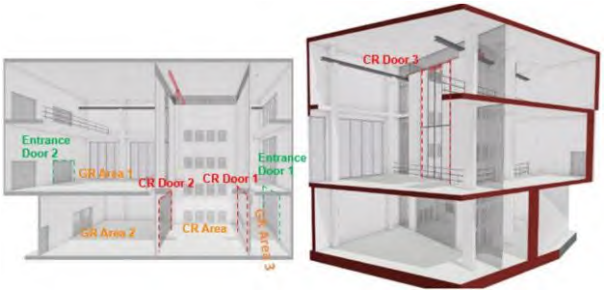


Figure 11: Test facility – clean room (CR) and grey (GR) areas

The facility comprises three distinct grey areas alongside a cleanroom enclosure equipped with an HVAC system for environmental control and a 5-tons portal crane capable of traversing between the cleanroom and Grey Area 1.

Table 18: Grey Areas dimensions

	Length [m]	Width [m]	Height [m]
GR Area 1	5	5	9
GR Area 2	5	5	4.5
GR Area 3	1.5	4	4.5

Table 19: Clean room dimensions

	Length [m]	Width [m]	Height [m]
Clean Room	7.6	6.5	13.2



Figure 12: Test facility – clean room

The cleanroom incorporates a reinforced steel grid floor that enables rigid ground anchoring of test equipment, a feature beneficial for integration operations and essential for high-load static testing.

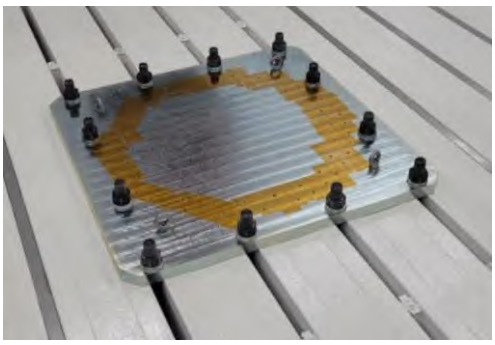


Figure 13: Test facility – grid floor

Standard steel reaction blocks of various dimensions, specifically engineered to interface with the facility's floor grid, served as structural mounting supports for the actuators.

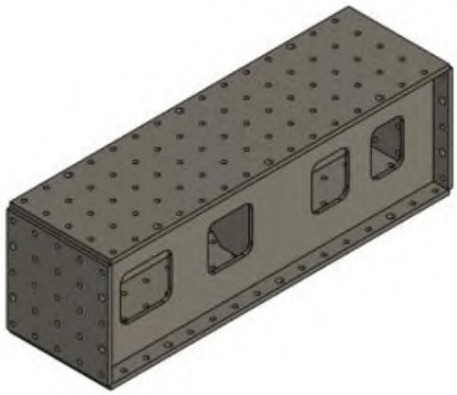


Figure 14: Standard steel blocks used as supports

Prior to testing, all physical setups were metrologically verified using a laser tracker to guarantee the precise spatial positioning of force introduction points and proper alignment of the actuators.

3.2. Test instrumentation

Real-time monitoring of the structure during load application was accomplished using three primary sensor categories:

- Load cells: installed in line with each linear actuator to continuously measure applied force vectors;
- Strain gauges (SG): distributed across structural components to capture local deformations;
- Linear Variable Differential Transformers (LVDTs): positioned at critical locations to record structural displacements.

3.2.1. Load cells

The following load cells were used during the test:

Table 20: Load cells list

Item name	Quantity
HBM U3 100kN	1
HBM U9C 50kN	1
HBM S9 50kN	1

3.2.2. Strain Gauges

The following SGs were used during the test:

Table 21: Strain gauges list

Item name	Channels	Quantity
Rosette 1-RY83-6/350	3	9
Rosette 1-RY91-6/120	3	42

The strain gauge network was conceptually partitioned into two functional categories based on their operational objectives:

- Monitoring SGs: applied in regions exhibiting high localized strains to monitor critical stress concentrations and rule out any risk of structural damage during test execution. Due to the steep strain gradients in these areas, sensor measurements were highly sensitive to minor installation positioning variations; consequently, these gauges were excluded from evaluating numerical model predictive accuracy.
- Correlation SGs: installed in regions characterized by uniform strain fields to capture the global response of the structure. The low strain gradient in these regions minimized measurement sensitivity to minor placement variations, rendering these sensors reliable metrics for validating Finite Element (FE) model predictions.

3.2.3. Linear Variable Differential Transformers

The following LVDTs were used during the test:

Table 22: LVDTs list

Item name	Channels	Quantity
HBM K-WA-L-010W-32K-K1-F1-2-2	1	3

Due to hardware availability constraints, displacement telemetry was measured using three LVDTs, arranged according to the following strategic placement rationale:

- Lateral displacement: one LVDT was aligned horizontally along the direction of the resultant lateral load vector, generated by the combined actuator forces, to measure global transverse displacement;
- Vertical displacement and bending response: two LVDTs were installed vertically on opposing sides of the structure to record vertical displacements, enabling the reconstruction of the overall structural bending behaviour.

3.3. Test article

Because this static qualification campaign introduced target loads directly through discrete actuators, physical testing was performed exclusively on the ROSE-L satellite structure subsystem. Consequently, representative dummy masses for payload instruments and equipment units were not required.

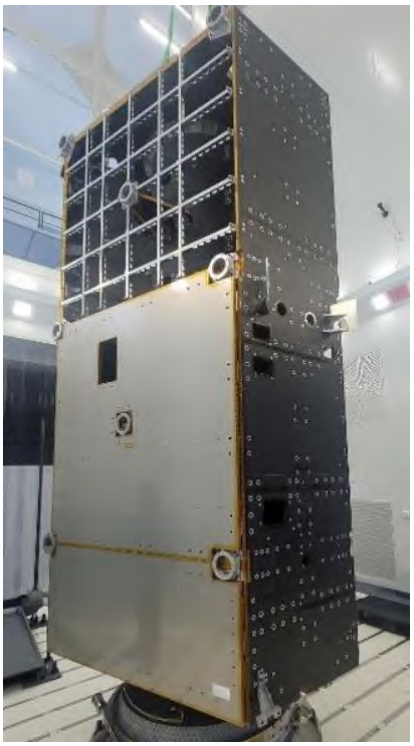


Figure 15: ROSE-L structure subsystem fully integrated before testing

3.4. Test results

To maintain a concise paper length, comprehensive empirical test results and finite element simulation comparisons are not reported for all load cases executed during the campaign. Instead, representative data are presented for the Launcher Quasi-Static Load (L-QSL) case inducing maximum compression flux at the Launch Vehicle Interface (LV I/F), as specified in Table 5.

Telemetry acquired from the instrumentation network described in section 3.2 was systematically evaluated against predefined success criteria, categorized into two operational tiers:

- Immediate success criteria: evaluated in real time following each incremental load step, including low and intermediate load levels, to authorize safe progression to subsequent load steps;
- Delayed success criteria: formally reviewed by the Test Review Board (TRB) post-test to confirm comprehensive structural qualification.

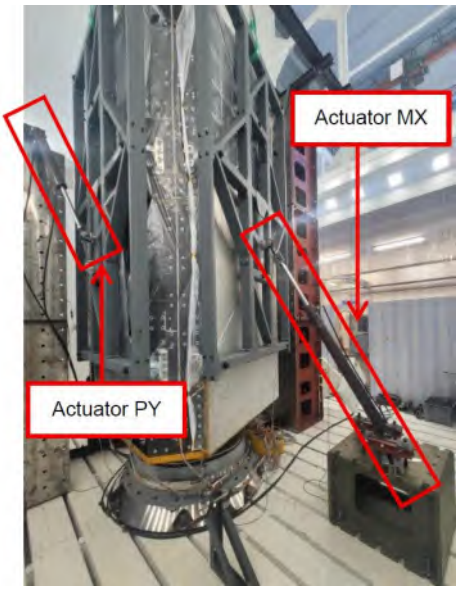


Figure 16: L-QSL, max compression flux test setup – detail of actuators placement (1)



Figure 17: L-QSL, max compression flux test setup – detail of actuators placement (2)

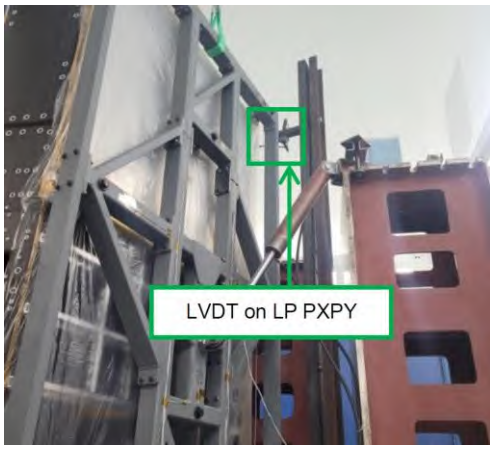


Figure 18: L-QSL, max compression flux test setup – detail of LVDTs placement (1)

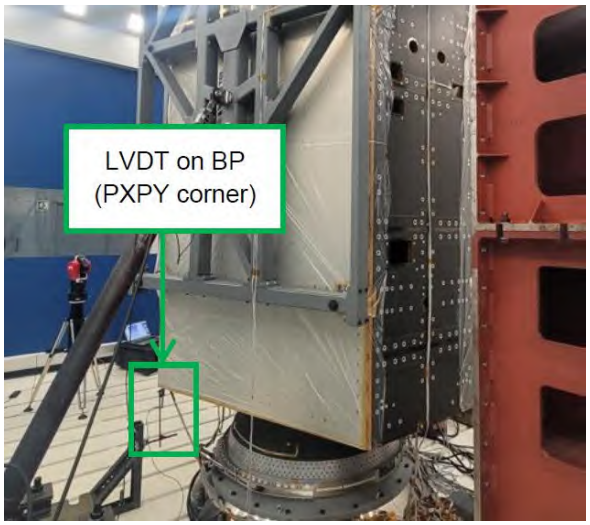


Figure 19: L-QSL, max compression flux test setup – detail of LVDTs placement (2)

3.4.1. Immediate success criteria

To authorize progression following each test run, the following immediate success criteria were systematically evaluated:

- Sensors' health and data integrity: sensors functioned correctly, exhibiting reliable sensitivity and ensuring complete data acquisition and storage across all telemetry channels;
- Load control tolerance and dwell time: peak applied force magnitudes were maintained within a tolerance window of -1.5% to +5% relative to specified nominal targets for a minimum dwell duration of 10 seconds;
- Structural integrity: the structure withstood load application without any evidence of structural degradation, debonding, or permanent deformation.

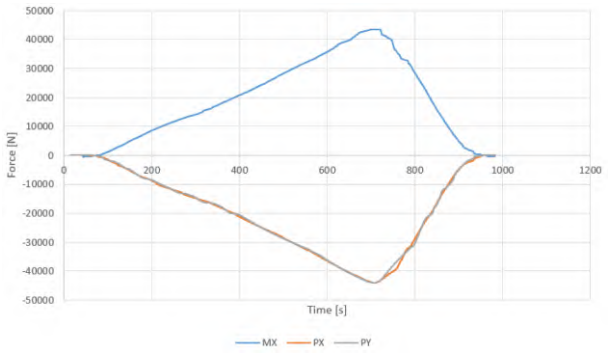


Figure 20: L-QSL max compression flux test – load time history

Structural integrity was verified by demonstrating purely linear elastic behaviour. This was achieved by checking that all strain (Figure 21) and displacement (Figure 23) measurements returned to zero upon complete unloading, confirming the absence of permanent deformation. Furthermore, constant slopes in both the force-displacement and force-strain curves across all test runs certified zero degradation in stiffness, proving that no structural damage occurred. Finally, telemetry confirmed that peak strain (Figure 22) and displacement (Figure 24) responses scaled strictly proportionally with load increments during progression from low-level to full-level test runs, validating linear structural behaviour across the entire applied load range.

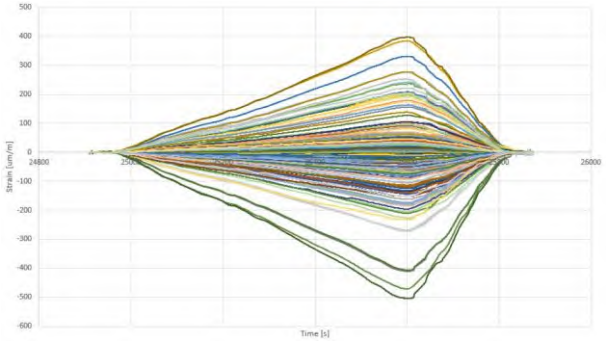


Figure 21: L-QSL max compression flux test – strain time history

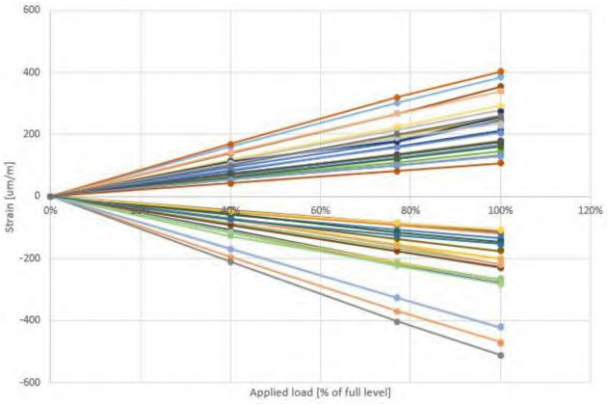


Figure 22: L-QSL max compression flux test – strain progression with load increment

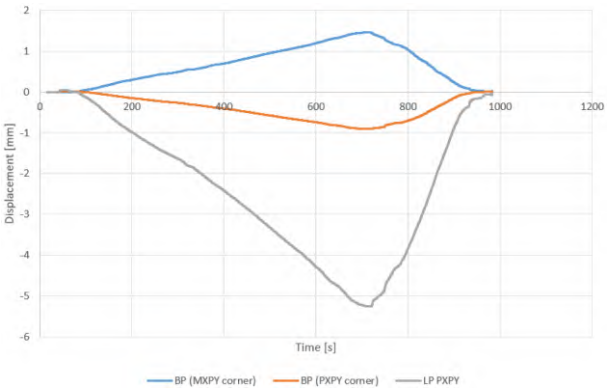


Figure 23: L-QSL max compression flux test – displacement time history

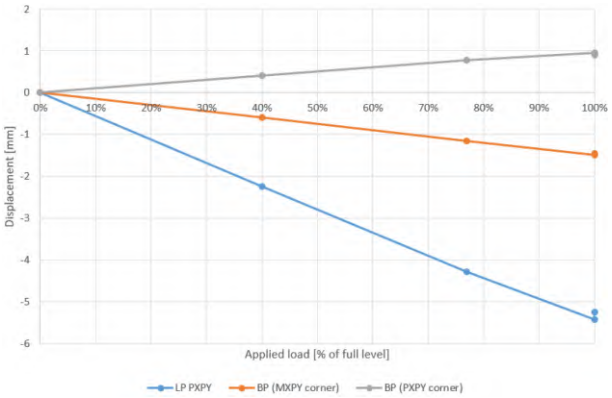


Figure 24: L-QSL max compression flux test – displacement progression with load increment

3.4.2. Delayed success criteria

To confirm structural qualification and validate the predictive capability of the Finite Element (FE) model against physical behaviour, the following delayed success criteria were applied:

- Displacement deviation threshold: Measured structural displacements not exceeding predicted values by more than 30%;
- Strain correlation threshold: Measured strains across all correlation strain gauges not exceeding predicted values by more than 30%;
- Interface alignment compliance: maintenance of critical interface geometries within specified design alignment tolerances post-test.

Table 23: L-QSL max compression flux test - correlation SGs

ID	Predictions [µm/m]		Test [µm/m]		Ratio	
	ε_1	ε_3	ε_1	ε_3	ε_1	ε_3
40_BP	137	-107	168	-118	1.23	1.10
81_SP	254	-264	278	-270	1.10	1.02
82_SP	173	-209	204	-218	1.18	1.04
86_SP	259	-306	253	-281	0.98	0.92
87_SP	121	-243	132	-229	1.09	0.94
91_SP	191	-234	174	-227	0.91	0.97
92_SP	187	-155	175	-173	0.94	1.12

As detailed in Table 23, empirical telemetry from all correlation strain gauges remained strictly within the +30% upper tolerance limit relative to analytical predictions, with the maximum observed exceedance reaching +23% at sensor ID 40_BP. Furthermore, the majority of correlation gauge channels demonstrated agreement within a ±10% threshold, confirming high predictive fidelity in global strain field modelling.

Table 24: L-QSL max compression flux test – peak displacements

LVDT	Predictions [mm]	Test [mm]	Ratio
LP PXPY	-5.47	-5.25	0.96
BP (MXPY corner)	-1.62	-1.46	0.90
BP (PXPY corner)	0.88	0.91	1.03

Displacement telemetry exhibited even higher correlation, as summarized in Table 24. All three LVDT sensors recorded displacements within a ±10% error band relative to predictions, with two sensors deviating by less than 5%. This close agreement confirms that the FE model accurately represents the global stiffness and deformation response of the structure under test loads.

Following campaign completion, the spatial coordinates of all 24 SAR antenna interface regions were metrologically re-checked using a laser tracker. All interface points remained fully compliant with requirement specifications, confirming zero permanent deformation or loss of alignment resulting from load application and ensuring that structural pointing accuracy will be preserved in the launch environment.

Although the correlation data detailed above correspond to one representative scenario out of the 13 total load cases executed during the ROSE-L structure subsystem static qualification campaign, strong agreement between analytical predictions and empirical telemetry was consistently demonstrated across all configurations. This high degree of correlation facilitated smooth transitions between test setups and supported rapid verification by the Test Review Board (TRB), which formally certified the qualification of the structure subsystem.
Downstream validation was subsequently achieved during system-level dynamic testing performed by the mission prime contractor, Thales Alenia Space Italia (TASI). Integrated with representative structural models and dummy masses simulating all remaining satellite subsystems, the identical structural model qualified via static testing by SAB Aerospace successfully survived sine vibration and vibro-acoustic testing. The structure satisfied all dynamic behaviour and decoupling objectives, confirming its structural integrity and performance under the launch vibration environment.

4. CONCLUSION

The static qualification test campaign for the ROSE-L satellite structure subsystem was successfully defined, executed, and completed at SAB Aerospace's cleanroom facility at the Brno University of Technology.
Significant effort was dedicated to developing strategies that minimised campaign complexity and execution duration without compromising qualification rigor. This was achieved by

systematically applying ECSS criteria for verification "by analysis only" and leveraging structural design symmetries.

A primary highlight of this campaign was the development and practical implementation of a single-actuator optimization algorithm. By solving for the optimal spatial coordinates, vector orientation, and force magnitude, 6-degree-of-freedom interface load states (3 forces and 3 moments) were accurately reproduced using a single linear actuator. This approach significantly simplified test fixture design, reduced setups complexity, and shortened execution schedules.

Prior to physical loading, dedicated setup-level Finite Element (FE) models confirmed that the proposed test configurations accurately reproduced the target stress fields and interface forces derived from nominal launch analyses.

During execution, live telemetry verified pure linear elastic behaviour with zero permanent deformation or stiffness degradation. Empirical data demonstrated high correlation with analytical predictions both for displacements and strain measured in multiple points around the structure.

The campaign concluded with formal certification by the Test Review Board (TRB), declaring the ROSE-L structure subsystem qualified. This qualification was further validated when the structural model subsequently underwent system-level sine vibration and vibro-acoustic testing at prime contractor Thales Alenia Space Italia (TASI), confirming excellent performance both in terms of strength and dynamic behaviour under the intense load environment it will encounter during launch.

ECSSMET
Braunschweig Germany 2026

Structural analysis & simulation

MESHLESS FEM APPROACH: CURRENT STATUS AND ROAD MAP - OHB INDUSTRIAL EXPERIENCE

Sarp Süloglu [(1)], Nicola Riva [(1)], Dominik Schlotz [(2)]

[(1)] OHB System AG, Universitätsallee 27-29, 28359 Bremen, Germany,
Email: {sarp.sueloglu; nicola.riva}@ohb.de
[(2)] Siemens AG, Werner-von-Siemens-Straße 1, 80333 München, Germany,
Email: dominik.schlotz@siemens.com

KEYWORDS

Structural engineering, structural analysis, finite element analysis, finite element method, external approximations method, Simcenter HyperWorks, Simcenter Hypermesh, Simcenter Simsolid

ABSTRACT

When it comes to commercial success, proposing shorter timelines, quicker deliveries, and securing project contracts, a research for cutting-edge finite element methods comes into prominence nowadays as well—a faster finite element analysis, especially during the satellite development phase that could be taken advantage of.

Therefore, a promising finite element analysis approach is put under the scope in this work—examining its benefits in a competitive environment where speed and reliability must be ensured, especially in the space industry. In contrast to conventional mesh-based FEA approach, the meshless FEA approach utilizes different mathematical foundation thus depends on less pre-processing, engineer workforce and input.

Various static and dynamic analyses are conducted with the goal of building a benchmark between the abovementioned approaches. To this end, a study was conducted at OHB, with the involvement of Altair Engineering (industrial simulation and CAE software company; currently acquired by Siemens).

1. INTRODUCTION

Static and dynamic structural analyses are based on the conventional, mesh-based finite element method in the industry for decades. However, building such accurate FEM model that complies with European space standards comes with a price: The time needed to accurately build those models (the system of equations) by an engineer, known as pre-processing, and the time consumed by the computer to solve those equations, also known as run-time.

This approach under the scope, so-called the successor, is a generalization and extension of the finite element method, i.e., External Approximations Method. This specially tailored generalization of FEM consists of arbitrary geometrical shapes as the “finite elements”. The shape functions (basis functions) approximating the field of interest in the “finite element” are independent of the “finite element” shape and selected from arbitrary class. This is achieved through the degrees of freedom are being the integrals over the corresponding geometrical entities—whereas the nodal values in mesh-based FEM—enabling the relaxation of continuity requirements [1].

Both the mesh-based and meshless approaches are based on the “weak formulation” of a Boundary Value Problem [2]. A generic variational equation (a weak form of Boundary Value Problem to derive numerical methods for solving it) which needs to be solved in certain Sobolev space V (functions that are smooth enough for a given problem, requiring the function and its derivatives up to a certain order to exist and have finite energy) is given in Eq. (1.1).

$$a(u,v) = f(v), \qquad \forall v \in V \tag{1.1}$$

The exact solution u is approximated by the function u_h which is represented by the linear combinations of shape functions P_i and degrees of freedom a_i as shown in Eq. (1.2) [1].

$$u_h = \sum a_i P_i \tag{1.2}$$

$$a(u_h, v_h) = f(v_h), \qquad \forall v_h \in X_h \tag{1.3}$$

$$[K]\{a\} = \{F\} \tag{1.4}$$

After the discretization of the variational equation, system of approximated solutions given by Eq. (1.3), where the v and v_h are arbitrary test functions and the X_h is the space of finite elements, yields a system of equation as shown in Eq. (1.4), where K is the stiffness matrix, a is the vector of degrees of freedom, and F is the load vector. The discretization of the variational equation is the same in both the mesh-based FEM and the meshless FEM: Stiffness matrices have the same properties of being symmetric, positively defined, and sparse [1] [2].

However, the difference is how the u_h is constructed and approximated. In mesh-based FEM, they are constructed in such way that they always belong to the Sobolev space (they are always in the Sobolev space) as shown in Eq. (1.5), and this is why such approach is called the internal approximations. In meshless FEM, u_h does not belong to the Sobolev space (they are always outside of the Sobolev space) as shown in Eq. (1.6), and this is why these approximations are called the external approximations [1] [2].

$$\begin{matrix} Mesh-based\ FEM \\ (internal\ approximations): u_h \in V \end{matrix} \quad (1.5)$$

$$\begin{matrix} Meshless\ FEM \\ (external\ approximations): u_h \notin V \end{matrix} \quad (1.6)$$

Hence, the fundamental difference is the approximate solutions u_h converge to the solution u from inside the Sobolev space in mesh-based FEM (e.g., Nastran, OptiStruct solvers), and from outside the Sobolev space in meshless FEM (e.g., SimSolid solver). In this way, the investigated meshless FEA solver SimSolid's external approximations framework eliminates the geometry-function coupling: Arbitrary shapes can be represented as the "finite element" such as a sub-volume or face of a part, a point or line cloud in a part in contrast to mesh-based FEA's quadrilaterals, tetrahedrons, and so on [1] [2]. After the shape functions of a "finite element" are found, the element stiffness matrices and load vectors are evaluated the same way in both the FEM approaches by integrating energy over the element volume and loads over the element boundary [2] [3]. The mathematical foundation of the meshless FEM is explained in [2].

This paper presents results and comparisons on a primitive cantilever beam model and a full-scale generic Low Earth Orbit satellite model. The primitive model is used for verification with the addition of an analytical lumped parameter model providing a reference solution, while mesh-based and meshless approaches are used to assess the accuracy of the computed eigenfrequencies—where the analytical spring-mass solution is regarded as a reduced-order benchmark of the continuous beam. Moreover, various static and dynamic analyses were conducted on the generic Low Earth Orbit satellite model for gaining insight on the usability of the meshless FEA in the industry.

2. LUMPED PARAMETER MODEL

The analytical lumped parameter model of the primitive model is developed while treating the mass of the beam as lumped elements and the stiffness of the beam as spring elements as shown in Fig. 1.

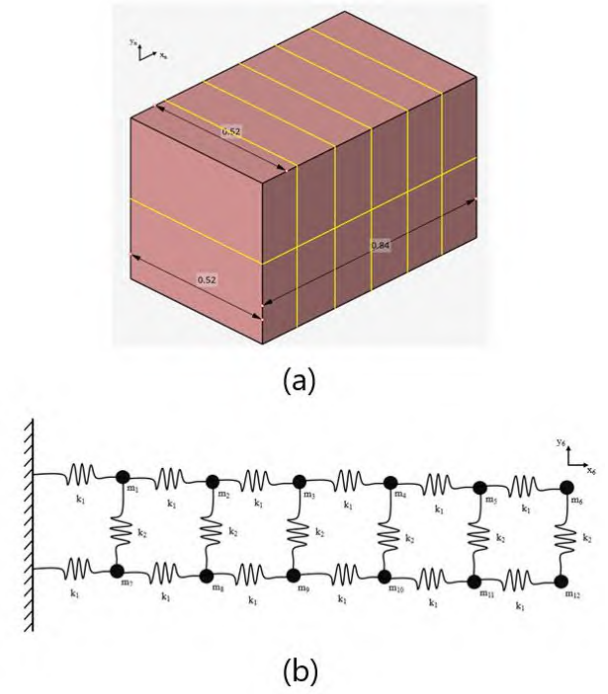


Figure 1: The primitive model (a) and its lumped parameter model (b)

While the lumped masses represent the mass of the sliced beam sections, the stiffness of the beam is represented by the spring coefficients in two directions between the lumped masses—that are calculated with the Eq. (2.1).

$$k = \frac{E * A}{L} \quad (2.1)$$

To eliminate the effect of insufficient degrees of freedoms in analytical solutions, the system is extended into multi degrees of freedom system in the direction of interest until the eigenfrequency does not change anymore as shown in Fig. 2.

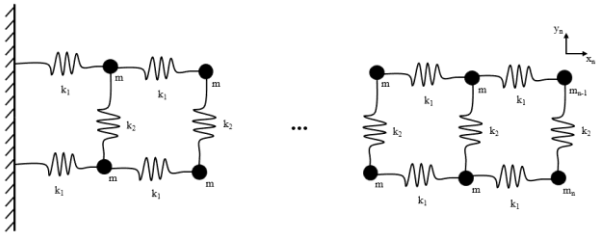


Figure 2: Two-dimensional MDoF spring-mass system

With the help of a MATLAB script, the eigenvalue problem of Eq. (2.2) and its convergence via the introduction of more DoF to the system is shown in Tab. 1.

$$det(\boldsymbol{K} - w^2\boldsymbol{M}) = 0 \quad (2.2)$$

Table 1: The convergence of MDoF systems

MDoF system layout	2x6	2x12	2x24	2x48	2x96	2x192
1st Natural Frequency [Hz]	1373	1430	1460	1476	1480	1480

The verification of the analytically calculated eigenvalue problem is done via an eigenvalue analysis with HyperWorks on the arbitrarily chosen 2x3 configuration. This spring-mass model is created with Single Point Constraint (SPC) representing the wall connections, CBUSH spring elements, and CMASS concentrated mass elements as shown in Fig. 3.

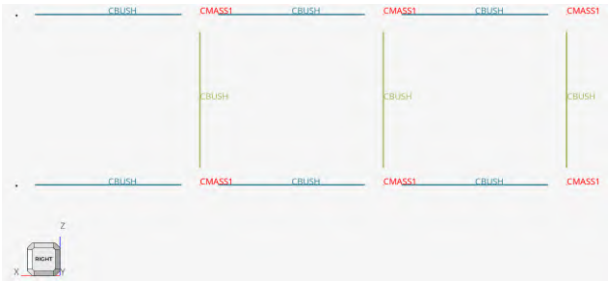


Figure 3: The representation of the 2x3 system in the FEA software

The analytical calculations and analysis results are shown in Tab. 2 with their corresponding mode shapes in Fig. 4. Therefore, it is demonstrated that the analytical results have been validated and are physically reasonable.

Table 2: Natural frequencies of the 2x3 system

	Natural Frequencies				
	FEA		Analytical Calculation		Difference [%]
Mode 1 (a):	1267	Hz	1267	Hz	0.0000
Mode 2 (b):	1267	Hz	1267	Hz	0.0000
Mode 3 (c):	3550	Hz	3551	Hz	0.0282
Mode 4 (d):	3550	Hz	3551	Hz	0.0282
Mode 5 (e):	5131	Hz	5131	Hz	0.0000
Mode 6 (f):	5131	Hz	5131	Hz	0.0000

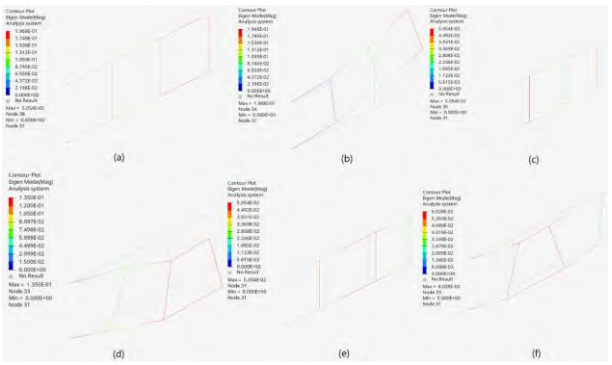


Figure 4: The mode shapes of the 2x3 system

In contrast to analytical calculations, the results of the primitive model shown in Fig. 1(a) acquired from two different softwares are presented in Tab. 3.

Table 3: Natural frequencies of the primitive model

	Mesh-based FEA (HyperWorks)	Meshless FEA (SimSolid)
1st Natural Frequency [Hz]	1524.8	1513.3
Difference [%]	0.76	

The comparison between the results presented in Tab. 1 and Tab. 3 are made and given in Tab. 4.

Table 4: Deviation of mesh-based and meshless models from analytical model

	Difference between the analytical calculation - FEA [%]					
MDoF system layout	2x6	2x12	2x24	2x48	2x96	2x192
Mesh-based FEA (HyperWorks)	10.4769	6.4167	4.3420	3.2525	2.9819	2.9819
Meshless FEA (SimSolid)	9.7218	5.6603	3.5852	2.4956	2.2250	2.2250

The drastic decrease in deviation with increasing DoF is eye catching, down to 2.98% compared to mesh-based FEA and 2.23% compared to meshless FEA.

3. FINITE ELEMENT ANALYSES

For the analyses based on mesh-based FEM, the solver used is OptiStruct v2024 (Altair-made solver that is built upon the foundation of Nastran) in combination with the pre-/post-processor HyperWorks v2024. On the other hand, for the meshless FEM, the solver used is SimSolid v2024 which embeds also the pre-/post-processor software as well.

3.1. Primitive Model

The primitive model was used to validate different solvers.

3.1.1. Modal (eigenfrequency)

The primitive model used in modal analysis is introduced in Fig. 5. The model is restrained via its narrow face so that it behaves as a cantilever beam.

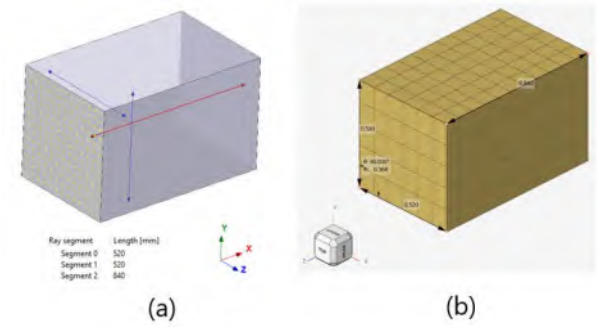


Figure 5: Primitive model used for modal analysis in meshless and mesh-based FEA

The eigenfrequency analysis of the primitive model is given below.

Mode	Frequency [Hz]	m-x [%]	m-y [%]	m-z [%]
1	490.30	61.28	0.00	0.00
Description	First lateral mode of the mesh-based primitive model			

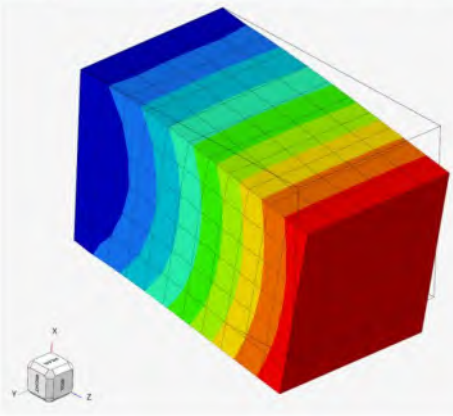


Figure 6: The primitive model 1st lateral mode in mesh-based FEA

Mode	Frequency [Hz]	m-x [%]	m-y [%]	m-z [%]
2	490.50	0.00	61.08	0.00
Description	Second lateral mode of the mesh-based primitive model			

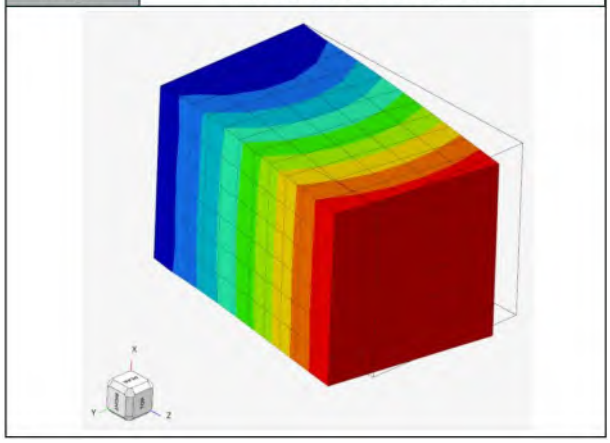


Figure 7: The primitive model 2nd lateral mode in mesh-based FEA

Mode	Frequency [Hz]	m-x [%]	m-y [%]	m-z [%]
4	1525.00	0.00	0.00	76.86
Description	First longitudinal mode of the mesh-based primitive model			

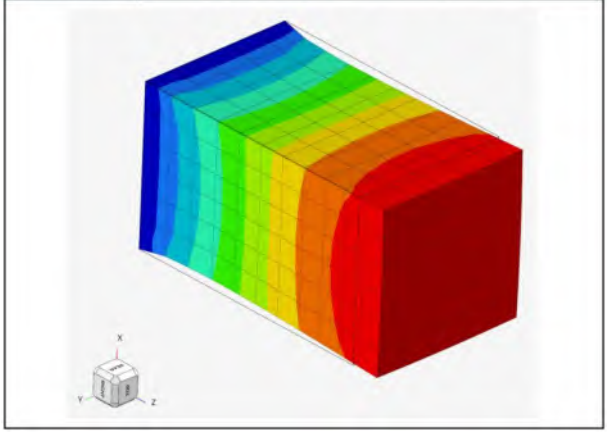


Figure 8: The primitive model 1st longitudinal mode in mesh-based FEA

Table 5: First ten modal effective masses of the primitive model with mesh-based FEA

		Modal Effective Mass [kg, kgm²]					
Mode	Frequency	X-TRANS	Y-TRANS	Z-TRANS	X-ROTAT	Y-ROTAT	Z-ROTAT
1	490.30	**391.00**	0.00	0.00	0.00	11.30	**39930.00**
2	490.50	0.00	**389.70**	0.00	11.48	0.00	**1845.00**
3	836.60	0.00	0.00	0.00	0.00	0.00	24.30
4	1525.00	0.00	0.00	**490.40**	**50080.00**	**2321.00**	0.00
5	1628.00	0.00	**145.40**	0.00	20.71	0.00	**688.20**
6	1630.00	**144.70**	0.00	0.00	0.00	20.71	**14770.00**
7	2483.00	0.00	0.00	0.00	0.00	0.00	2.66
8	3080.00	0.00	0.00	0.00	0.00	0.00	0.00
9	3230.00	0.00	26.76	0.00	3.53	0.00	**126.60**
10	3230.00	26.33	0.00	0.00	0.00	3.48	**2689.00**

Mode	Frequency [Hz]	m-x [%]	m-y [%]	m-z [%]
1	485.63	0.00	61.79	0.98
Description	First lateral mode of the meshless primitive model			

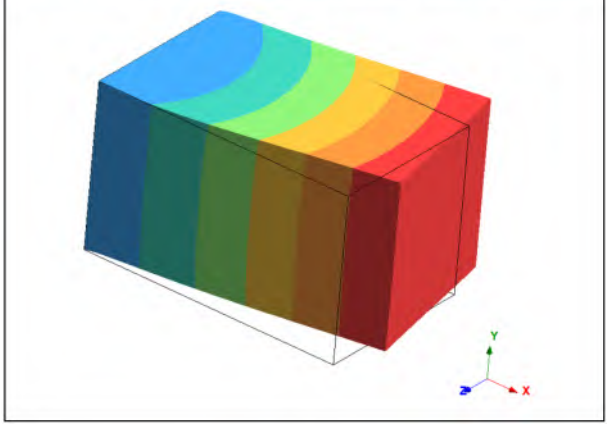


Figure 9: The primitive model 1st lateral mode in meshless FEA

Mode	Frequency [Hz]	m-x [%]	m-y [%]	m-z [%]
2	485.64	0.00	0.98	61.79
Description	Second lateral mode of the meshless primitive model			

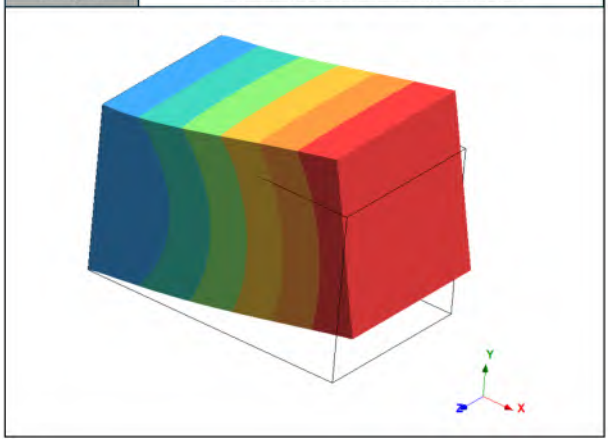


Figure 10: The primitive model 2nd lateral mode in meshless FEA

Mode	Frequency [Hz]	m-x [%]	m-y [%]	m-z [%]
4	1513.28	78.22	0.00	0.00
Description	First longitudinal mode of the meshless primitive model			

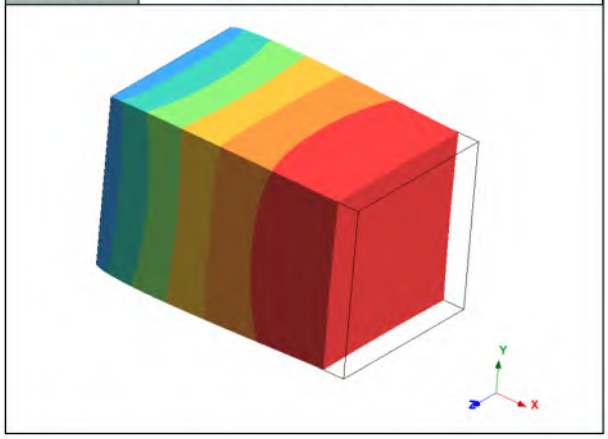


Figure 11: The primitive model 1st longitudinal mode in meshless FEA

Table 6: First ten modal effective masses of the primitive model with meshless FEA

		Modal Effective Mass [kg]		
Mode	Frequency	X-TRANS	Y-TRANS	Z-TRANS
1	485.63	0.00	**394.22**	6.25
2	485.64	0.00	6.25	**394.22**
3	847.40	0.00	0.00	0.00
4	1513.28	**499.04**	0.00	0.00
5	1631.08	0.00	**145.59**	0.06
6	1631.09	0.00	0.06	**145.59**
7	2533.37	0.00	0.00	0.00
8	3176.26	0.00	0.00	0.00
9	3255.84	0.00	26.09	0.06
10	3255.88	0.00	0.06	26.09

To sum up, as it is also presented in Tab. 7, modal analysis with both softwares conducted on the primitive model exhibits ~1% deviation. Therefore, it can be claimed that the mesh-based and meshless FEA behave the same for relatively basic models.

Table. 7: Percentage difference of the primitive model modal analyses

	Frequency [Hz]		
Mode	HyperWorks	SimSolid	Difference [%]
1	490.30	485.63	0.96
2	490.50	485.64	1.00
3	836.60	847.40	1.28
4	1525.00	1513.28	0.77
5	1628.00	1631.08	0.19
6	1630.00	1631.09	0.07
7	2483.00	2533.37	2.01
8	3080.00	3176.26	3.08
9	3230.00	3255.84	0.80
10	3230.00	3255.88	0.80

The difference in the effective mass reports from both the softwares is eye-catching: As it can be seen from the Tab. 5 and Tab. 6, the mesh-based FEA reports the modal effective mass in six DoF, whereas modal effective mass in only three DoF reported from the meshless FEA, SimSolid.

3.1.2. Dynamic response

The sine response analysis is conducted with 1 g excitation in longitudinal axis and the response at the shown locations in Fig. 12 are compared.

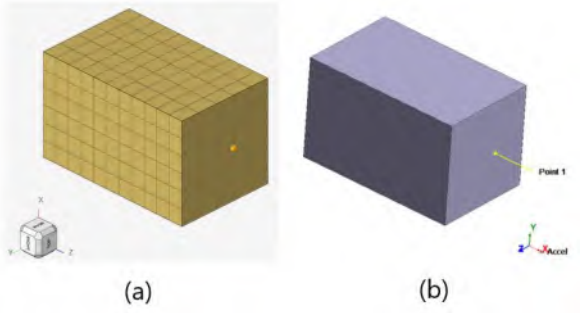


Figure 12: Primitive model in mesh-based and meshless FEA and the restitution nodes

Frequency response analysis results of the primitive model captured with both solvers and an arbitrarily chosen direction result is presented in Fig. 13. These results show that the dynamic response analyses from both softwares comply with each other and coincide for the primitive model.

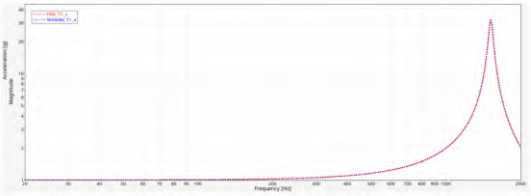


Figure 13: Frequency response analysis results of the mesh-based and meshless FEA on the primitive model

3.2. Generic Low Earth Orbit Satellite Model

3.2.1. Modal (eigenfrequency)

The generic Low Earth Orbit satellite models in different analysis environments are shown in Fig. 14 and Fig. 15.

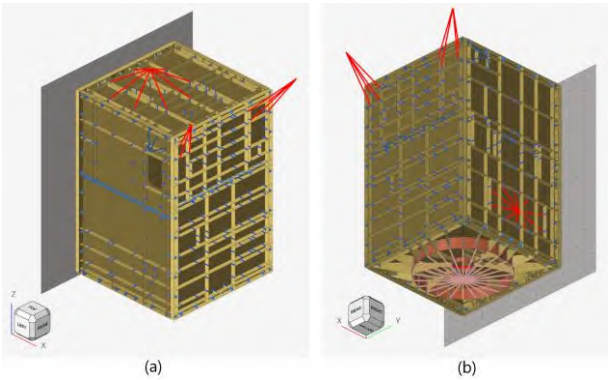


Figure 14: Mesh-based FEA model of the generic Low Earth Orbit satellite

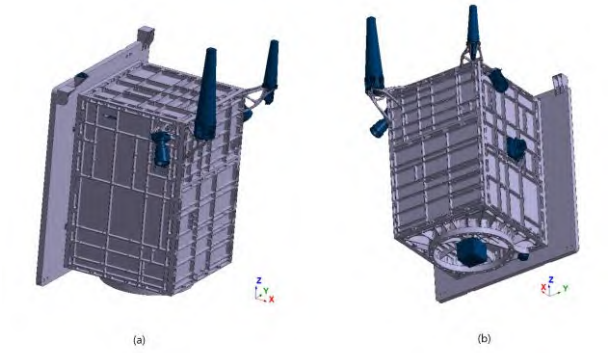


Figure 15: Meshless FEA (CAD) model of the generic Low Earth Orbit satellite

The eigenfrequency analysis of the generic Low Earth Orbit satellite model is given below.

Mode	Frequency [Hz]	m-x [%]	m-y [%]	m-z [%]
1	63.01	0.15	67.14	0.00
Description	First lateral S/C mode			

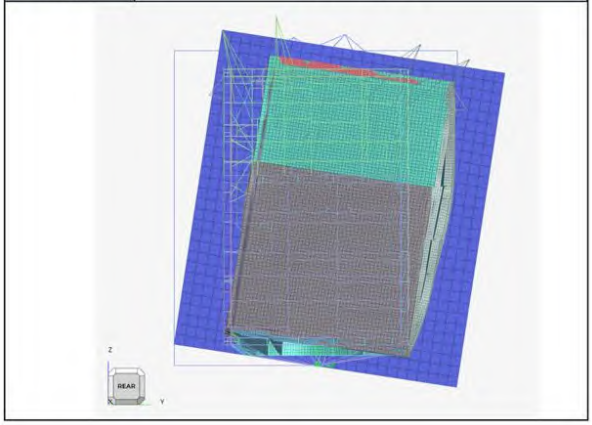


Figure 16: The generic Low Earth Orbit satellite 1st lateral mode in mesh-based FEA

Mode	Frequency [Hz]	m-x [%]	m-y [%]	m-z [%]
2	64.94	66.16	0.15	0.03
Description	Second lateral S/C mode			

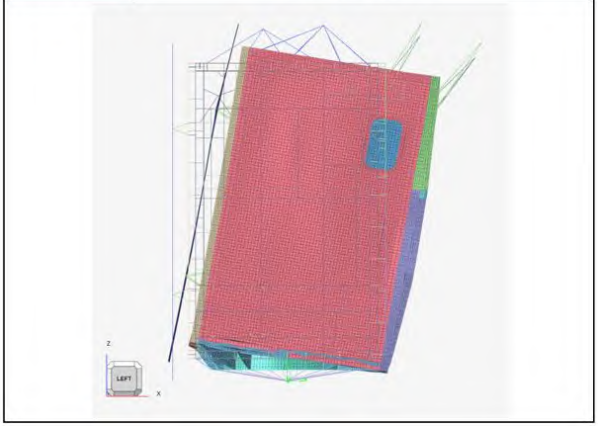


Figure 17: The generic Low Earth Orbit satellite 2nd lateral mode in mesh-based FEA

Mode	Frequency [Hz]	m-x [%]	m-y [%]	m-z [%]
5	137.60	0.10	0.00	9.85
Description	First longitudinal S/C mode			

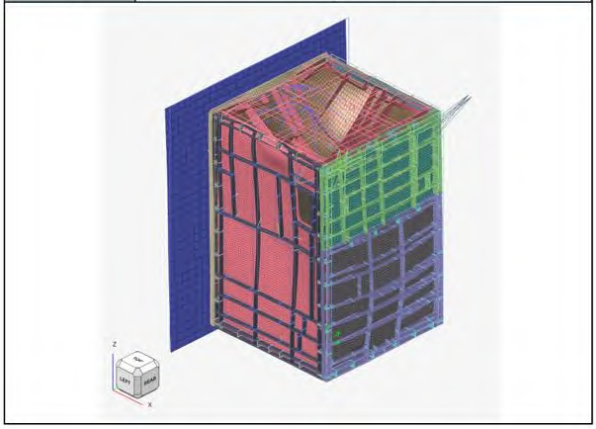


Figure 18: The generic Low Earth Orbit satellite 1st longitudinal mode in mesh-based FEA

Table 8: First ten modal effective masses of the generic Low Earth Orbit satellite in mesh-based FEA

		Modal Effective Mass [kg, kgm²]					
Mode	Frequency	X-TRANS	Y-TRANS	Z-TRANS	X-ROTAT	Y-ROTAT	Z-ROTAT
1	63.01	0.17	**71.10**	0.00	**33.39**	0.07	0.03
2	64.94	**70.06**	0.16	0.03	0.09	**34.00**	0.00
3	107.70	0.13	0.26	1.23	0.09	0.00	0.08
4	128.70	0.03	0.12	0.00	0.83	0.03	0.24
5	137.60	0.11	0.00	**10.43**	0.04	0.00	0.03
6	142.50	1.98	0.06	1.20	0.00	0.09	0.00
7	176.90	0.05	0.65	0.01	0.01	0.00	0.00
8	177.00	0.11	1.26	0.00	0.02	0.00	0.00
9	190.80	0.04	0.06	0.27	0.01	0.00	5.18
10	196.60	0.92	0.00	0.53	0.00	0.01	0.03

Mode	Frequency [Hz]	m-x [%]	m-y [%]	m-z [%]
1	68.20	0.06	62.76	0.00
Description	First lateral S/C mode			

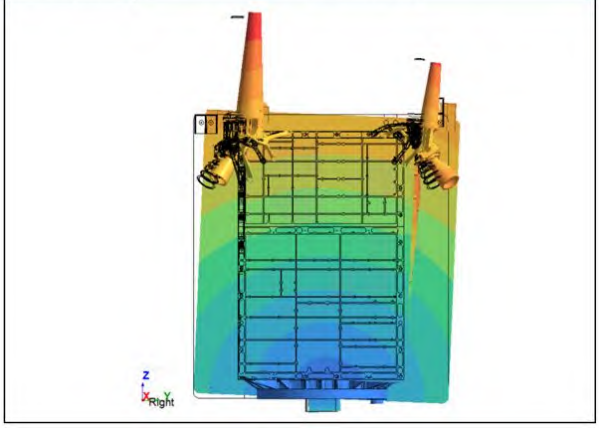


Figure 19: The generic Low Earth Orbit satellite 1st lateral mode in meshless FEA

Mode	Frequency [Hz]	m-x [%]	m-y [%]	m-z [%]
2	72.47	61.53	0.04	0.12
Description	Second lateral S/C mode			

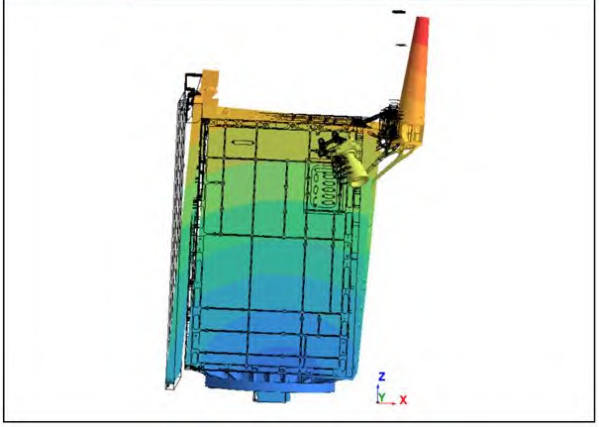


Figure 20: The generic Low Earth Orbit satellite 2nd lateral mode in meshless FEA

Mode	Frequency [Hz]	m-x [%]	m-y [%]	m-z [%]
6	143.29	0.04	0.67	4.62
Description	First longitudinal S/C mode			

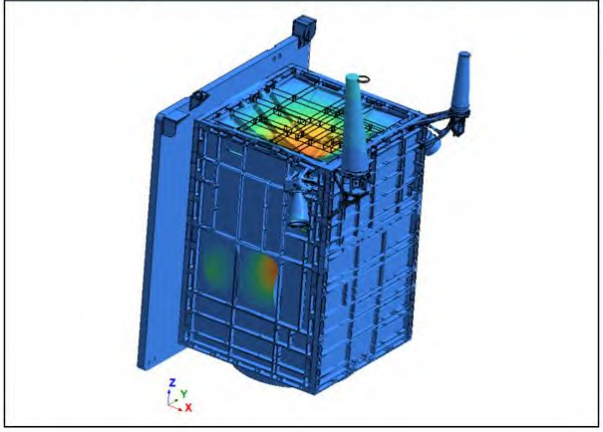


Figure 21: The generic Low Earth Orbit satellite 1st longitudinal mode in meshless FEA

Table 9: First ten modal effective masses of the generic Low Earth Orbit satellite in meshless FEA

		Modal Effective Mass [kg]		
Mode	Frequency	X-TRANS	Y-TRANS	Z-TRANS
1	68.20	0.06	**66.45**	0.00
2	72.47	**65.15**	0.04	0.12
3	111.27	0.03	0.21	0.70
4	129.21	0.02	0.00	0.00
5	139.24	0.00	0.13	0.54
6	143.29	0.04	0.71	**4.90**
7	147.75	0.00	0.02	2.24
8	162.37	0.05	1.61	0.00
9	170.44	0.11	0.15	0.09
10	171.37	0.03	0.01	0.23

The main lateral and longitudinal modes of the satellite are highlighted in Tab. 8 and Tab. 9.

Both softwares captured the first lateral mode at 1st eigenmode as shown in Fig. 16 and Fig. 19. From the same figures it reads, SimSolid provides it on more conservative side with 5.19 Hz while capturing 4.38% less mass participating to the mode. Similarly, both softwares captured the second lateral mode at 2nd eigenmode as shown in Fig. 17 and Fig. 20. SimSolid, again, provides it on more conservative side with 7.53 Hz while capturing 3.41% less mass participating to the mode. The first longitudinal modes are, however, occurred at different modes in HyperWorks and SimSolid (5th and 6th eigenmodes, respectively). Considering the same modes, a shift in mode number happened in SimSolid: Another different eigenmode is captured by SimSolid at the 5th mode, where the first longitudinal mode is seen in its mesh-based equivalent. SimSolid provides this natural frequency on more conservative side with 5.69 Hz while capturing 5.23% less mass participating to the mode.

3.2.2. Dynamic response

In SimSolid, in contrast to mesh-based FEA, instruments and payload do not have to be represented as concentrated masses. Instead, they can be set as so-called “rigid parts” with specific mass (visualized as dark blue) as shown in Fig. 22. Because SimSolid is developed specifically for evolving design and development phases, these rigid parts (as well as the concentrated masses representing the platform units) are recognized and copied with their properties to new design iteration. Moreover, SimSolid runs the FEA directly on the CAD model, therefore with the heritage taken over from the previous design iteration as well, pre-processing time is minimized.

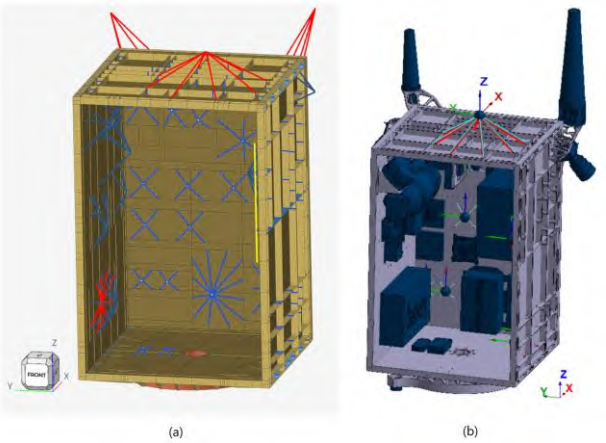


Figure 22: Platform equipment and payload representations in mesh-based and meshless FEA

The dynamic response analysis of the generic Low Earth Orbit satellite is conducted with 1g excitations in three dimensions. The chosen restitution points are shown in Fig. 23.

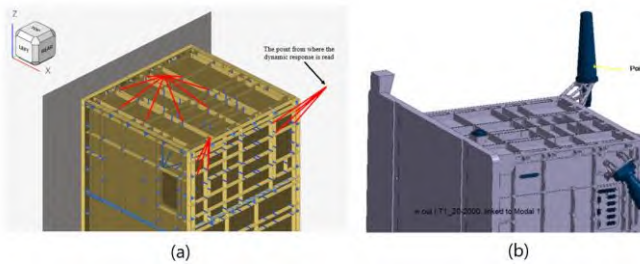


Figure 23: Response restitution points in mesh-based and meshless FEA

The dynamic response comparisons of the generic Low Earth Orbit satellite are given below; translational 1 (x-axis) excitation and responses in x, y, z axes are arbitrarily chosen to present.

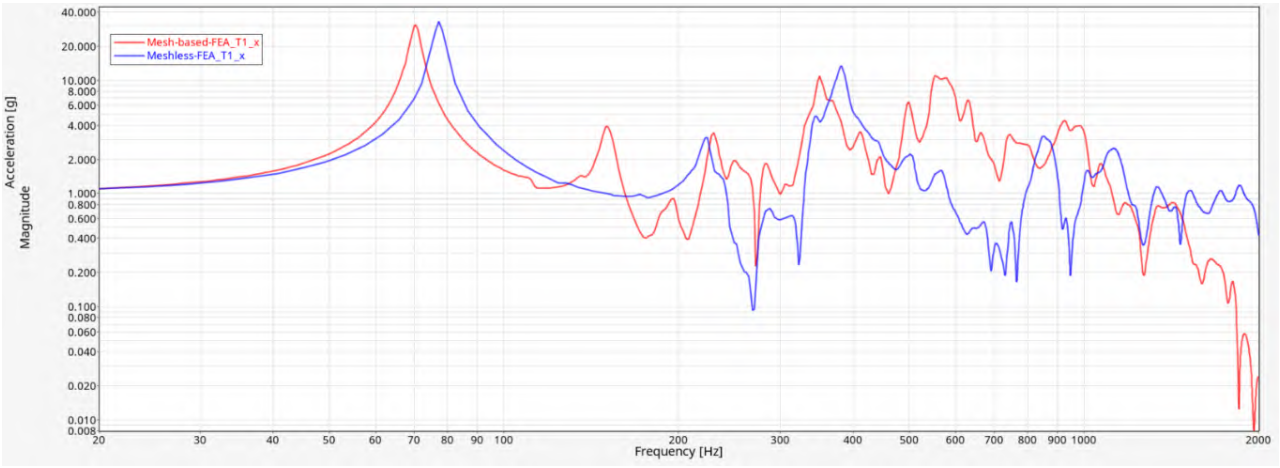


Figure 24: T1 excitation and x response frequency response analysis results of mesh-based FEA and meshless FEA on the generic Low Earth Orbit satellite

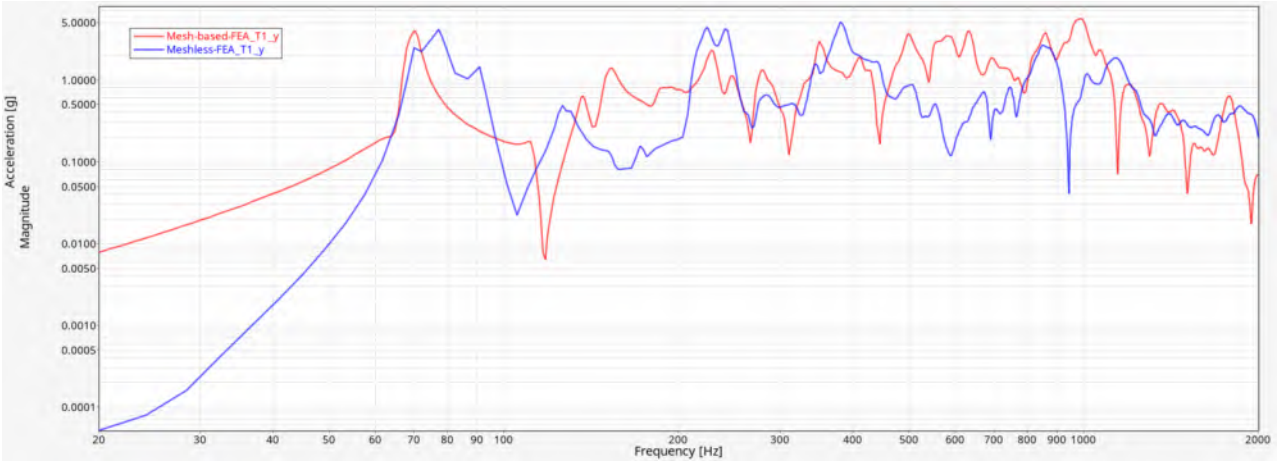


Figure 25: T1 excitation and y response frequency response analysis results of mesh-based FEA and meshless FEA on the generic Low Earth Orbit satellite

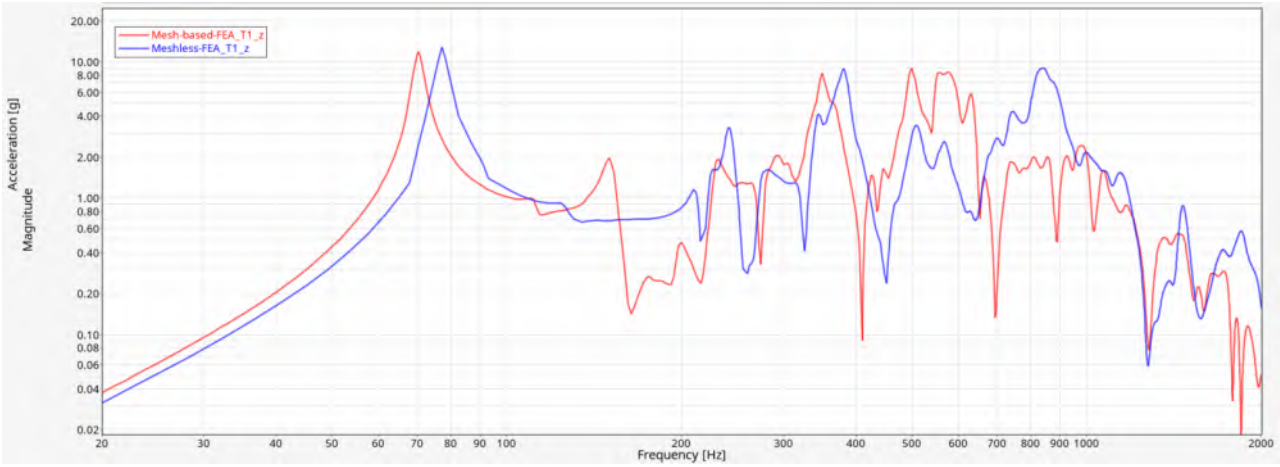


Figure 26: T1 excitation and z response frequency response analysis results of mesh-based FEA and meshless FEA on the generic Low Earth Orbit satellite

The Fig. 24, Fig. 25, and Fig. 26 clearly show the stiffer SimSolid model on the graphs with a conservative shift towards right-hand side. However, it can also be seen that the dampings of the models are the same as the acceleration peaks are the same. These lateral shifts in the graphs are thought to be (if not due to SimSolid's mathematical background) due to inherent deviations in how the boundary conditions and properties are assigned in two different softwares.

Regarding the frequency responses in all three axes, the first two bending modes provided by the meshless FEA seem trustable, compared to mesh-based FEA. However, the meshless FEA responses exhibit decoupling from their conventional FEA correspondence at high-frequency range and show random behaviour which deviates from the mesh-based FEA. The overall shift to a higher frequency due to increased stiffness of the model is thought to be because how the SimSolid models the contacts between the surfaces. However, local peaks of both softwares towards the higher frequencies (random domain) show inhomogeneous bias; which means the peak overlays are sometimes found far away from their opposing FEA correspondence and sometimes nearby in the vicinity. On the other hand, speaking exclusively for the y-axis responses, decoupling in the 20-60 Hz domain is eye catching: This is thought to be causing due to response in SimSolid cannot be read directly from the center of gravity of the part, but it must be a point on a surface as of now.

3.2.3. Quasi-static

To compare the mesh-based and meshless FEA's peak stress and distribution results, a combined quasi-static loading scenario is chosen. In this analysis, combined QSL of 10 g axial (z-axis) and 13.5 g lateral (x-axis) is applied to the system. The resultant stress distribution of the whole satellite is given below.

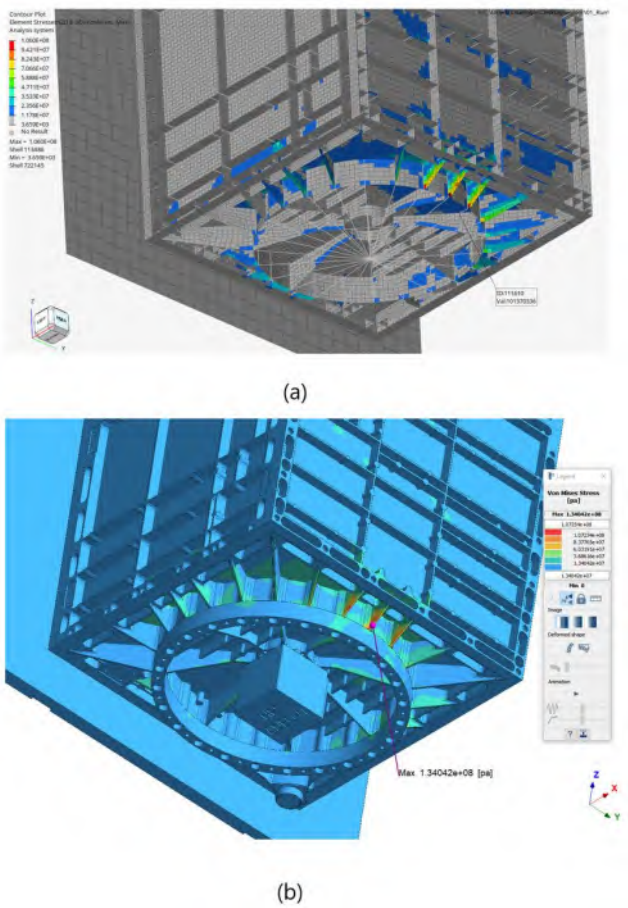


Figure 27: Stress distributions of the generic Low Earth Orbit satellite between mesh-based and meshless FEA

The quasi-static analysis results acquired from the OptiStruct and SimSolid are given in Fig. 27. The peak stresses are observed at the same locations on the models with 101.37 MPa and 134.04 MPa which corresponds to a higher stress of 28% in SimSolid. However, as it can be seen in the same figure, the stress behaviour is captured very similarly in both softwares.

From the QSL results of complex models it reads, the peak stress magnitudes gathered from SimSolid may be trusted depending on the project phase and the factors of safety decided along the project, moreover the stress distribution behaves as expected in solid panels and may be used to steer the development phase.

4. RESULTS AND EVALUATION

In conventional Finite Element Method strict requirements are imposed on element shapes, more specifically on the location of nodes, thus on shape functions that approximate the solutions within an element. The need to ensure sufficient smoothness of approximating functions at inter-element boundaries is the reason of limitations. As explained in earlier chapters, the geometry of finite elements for External Approximations only needs to have regular, sectionally smooth boundaries, and

thus, such elements can take arbitrary shapes [2]. Following this idea, the meshless “Finite Element” Method is invented and the solver utilizing its mathematical background, SimSolid, is developed.

SimSolid is found to be reliable and robust for relatively basic models’ analyses, e.g., panels, brackets, and so on. However, for complex models’ analyses, the results should be interpreted with caution. Nevertheless, SimSolid shows reliable and mature practice in some topics as well, e.g., first two bending modes. Despite its downsides, the meshless FEA shines in efficiency as the pre-processing time is minimized. Results gained from SimSolid may be used to steer the early development phases, however it is beneficial to take a decent time to conduct conventional mesh-based FEA for critical reviews.

It is found that SimSolid provides some benefits in the industry workflow. The overall time to get an analysis result is considerably less due to decreased pre-processing time. Moreover, thanks to SimSolid’s features particularly implemented for evolving designs and development phases, time spent on model preparation is ensured to be minimum. This enables project study phases (phase 0/A) to gain velocity with less resource costs. The opportunity to be able to iterate a design as per the meshless FEA results in a given timeframe is an advantage gained over the competitors working with conventional mesh-based FEA without a doubt.

On the other hand, SimSolid’s current status may not be applicable for taking decisions on the unit’s specification definition: The phase B1 is a preparation for the project implementation phases (called phase B2/C/D in the industry). Therefore, relying not only on SimSolid may be sensible in B2/C/D proposals. Moreover, avoiding SimSolid on test campaigns and reviews like preliminary design review (PDR) and critical design review (CDR) may be sensible; due to introduced and evaluated outcomes in above sections, it may be sensible not to accept Request for Deviation/Waiver(s) from SimSolid as of today.

5. CONCLUSION

A generic Low Earth Orbit satellite is chosen such that it is built of solid aluminium machined parts instead of traditional honeycomb sandwich panels with Aluminium/CFRP skins. Such demonstration satellite choice is particularly made due to current limitation of SimSolid: In contrast to mesh-based FEA, meshless FEA is not mature enough to consider CFRP plies, laminates, and honeycomb cores as of now. Moreover, in SimSolid, not all the instruments are represented as point masses at their CoG, because the software is capable of capturing the dynamic responses from the points on solid’s surfaces as of now. Therefore, in contrast to mesh-based FEA, the exact response in the instrument’s CoG cannot be read.

It was observed that the discrepancy is negligible on relatively basic models. However, on larger and more complex models, the percentage difference between the mesh-based and meshless FEA solvers are extending up to a couple of single digits. The meshless FEA seems a promising solution in the early stages of the satellite projects; it drastically reduces the pre-processing time while being able to provide decisive results and information to steer the project.

Finally, the boundaries of today’s SimSolid are reached, whether as in the software limitations or the accuracy its current state-of-the-art mathematical background can provide. The points where it lacks compared to industrywide renowned conventional mesh-based FEA are reported to the developer. In the light of the feedbacks and the meetings conducted throughout the work, development of the new implementations and improvements of the product is started, as anticipated by Siemens.

5.1. Outlook

The focus was on QSL, eigenfrequency, and sine response (up to high-frequency domain) analyses in this work. Besides investigating the improvements (that will be implemented to SimSolid in the future), domains that were not under scope may be researched and discrepancies may be determined in future works, e.g., thermo-elastic displacement analysis and random response analysis. Moreover, future works may expand the research on rotational modal effective mass capturing, accuracy of the random vibration environment (high-frequency domain in dynamic response analysis), and improved ply and laminate behaviours with orthotropic materials.

As of now, there is no SimSolid benchmark or comparison available online that incorporates such complex, large-scale satellite models. More data at hand could enable more comprehensive assessment of the result accuracy and precision. The discrepancies between the conventional mesh-based FEA and meshless FEA are demonstrated in this work. However, the real true solution is not known due to lack of real-world lab tests to compare. The laboratory and real-world test data (e.g., a shaker test) may be included with various demonstration models, and their deviations may be studied with future works.

As of today, inter-industrial data and model exchange is a problem with SimSolid “.ssp” project files. A SimSolid project file incorporating results inside, especially analysis solutions of a complex model, reaches around 10 gigabytes and more. It is not impossible to exchange such file, however the same job can be done, and it is being done, with

some megabytes of Nastran files. Developing a file and data exchange method or format by Siemens may be beneficial for the industry.

6. REFERENCES

[1] V. Apanovitch, “Theoretical Background of SimSolid by Victor Apanovitch,” 2023.

[2] V. Apanovitch, The Method of External Finite Element Approximations, 2021, p. 231.

[3] V. Apanovitch, “Altair SimSolid Technology Overview - White Paper,” Altair Engineering Inc., 2020.

DYNAMIC MODELLING OF FLUID-STRUCTURE INTERACTION IN THIN-WALLED LIQUID PROPULSION STAGES WITH THE REAL COUPLED MODES METHOD

Nelly MAUGIS [(1)], Sebastiaan FRANSEN [(2)]

[(1)] ESA, 2201 AZ Noordwijk, The Netherlands, Email: nelly.maugis@esa.int
[(2)] ESA, 2201 AZ Noordwijk, The Netherlands, Email: sebastiaan.fransen@esa.int

KEYWORDS

Fluid-structure interaction, liquid propellant tank, Finite Element Method, Real Coupled Modes method, superelement, damping, MSC Nastran

ABSTRACT

This paper presents a first validation and tuning of the RCM (Real Coupled Modes) method available in MSC Nastran for modelling FSI (fluid-structure interaction) in thin-walled liquid propulsion stages. The specificities of the finite element modelling are described, together with the methodology for performing free-free analyses, representative of launch load cases, and their validation. For liquid propellant applications, incompressibility is ensured through an MPC (Multi-Point Constraint) equation when required. As an initial validation, the RCM method is compared against the previous tool used at ESA (European Space Agency). Multiple benchmarks are investigated through dynamic response analyses to assess the method limitations and the influence of key parameters.

1. INTRODUCTION

The study presented in this paper – fully developed in [1] – focuses on the dynamic modelling of FSI in thin-walled liquid propulsion stages. For launchers using liquid propulsion, the propellant mass represents a significant fraction of the total mass; therefore, its coupling with the launcher structure must be considered to accurately predict the dynamic behaviour of the {launcher+spacecraft} assembly during CLA (Coupled Loads Analysis). Previously, the FABE (Fluid Analysis with Boundary Elements) software was used within ESA to model liquid propellant tanks for CLA of ARIANE-5 missions. As FABE is no longer supported, an alternative solution is required for future VEGA-E CLA activities. Since 2019, the RCM method available in MSC Nastran enables the modelling of FSI in thin-walled liquid-filled tanks.

2. FINITE ELEMENT MODELLING

FABE relied on the Boundary Element Method, generating fluid mass and stiffness matrices that were coupled to the structure at the fluid/structure interface in the FEM (finite element model). Unlike FABE, the RCM method uses FEM to model both the fluid and the structure.

2.1. The Model

2.1.1. Fluid Elements

The fluid is modelled using 3D solid elements, with each fluid node having a single pressure DOF (degree of freedom).

The fluid is automatically coupled to the structure at the fluid/structure boundary, with manual adjustments possible through the ACMODL parameter to fine-tune the coupling conditions. For efficiency and accuracy, the fluid boundary nodes should coincide with the structural nodes. If this is not possible, the fluid mesh should be coarser than the structure mesh to avoid inaccurate coupling.

2.1.2. Sloshing

For partially filled tanks subjected to gravity loads simulating the launcher steady-state longitudinal acceleration, sloshing effects can be considered. For incompressible fluids, sloshing of the FFS (free fluid surface) under gravity loads is the only wave effect. The FFS is modelled with negligible stiffness and zero mass. Since gravity loads affect the FFS stiffness, it is represented by scalar springs in the gravity direction, normal to the FFS.

The stiffness is defined at each FFS node i and derived from the potential energy E_i associated with a height variation Δh, as described in Eq. 1.

$$E_i = m \cdot g \cdot \Delta h = \rho \cdot A_i \cdot h \cdot g \cdot \frac{h}{2} = \rho \cdot A_i \cdot g \cdot \frac{h^2}{2} \qquad (1)$$

A_i is the area surrounding node i (depends on mesh size), ρ is the fluid density and g is the gravitational constant or the launcher steady-state longitudinal acceleration. Eq. 1 is illustrated in Fig. 1.

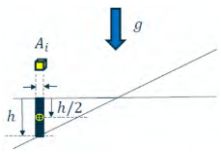


Figure 1: Potential energy Ei

Therefore, the gravity spring stiffness K_i is defined at each node i as in Eq. 2.

$$E_i = \frac{1}{2} \cdot K_i \cdot h^2 \Rightarrow K_i = A_i \cdot \rho \cdot g \qquad (2)$$

The springs connect the FFS to reference nodes linked to a reference frame. The definition of this reference frame is further investigated in Section 3.

2.1.3. Example

The FEM of a cubic tank is shown in Fig. 2. The structure (left) is modelled with shell elements and appropriate material properties, while the fluid (centre) is represented by solid elements with the corresponding fluid properties. The FFS (right) is modelled using shell elements with negligible stiffness and zero mass. At the tank/FFS interface, coincident nodes are created; the tank and FFS elements do not share the same nodes. Springs accounting for the longitudinal steady-state thrust are defined at each FFS node and provide the stiffness given by Eq. 2 in the direction normal to the FFS.

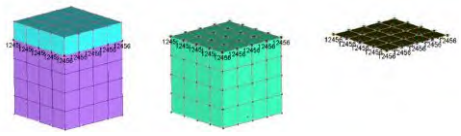


Figure 2: FEM example

2.2. The Real Coupled Modes Method

Before MSC Nastran 2019FP1, only uncoupled modal bases for the fluid and the structure could be computed, with each modal basis calculated independently. This approach does not provide satisfactory results for heavy fluids, such as liquids, as it neglects FSI. The RCM method accounts for FSI in the real modal basis.

Eq. 3, the governing equation of motion for the fluid-structure system, is derived from Euler's equation for an irrotational, inviscid fluid undergoing small-amplitude oscillations.

$$\begin{bmatrix} M_s & 0 \\ C & M_f \end{bmatrix} \begin{Bmatrix} \ddot{x} \\ \ddot{p} \end{Bmatrix} + \begin{bmatrix} K_s & -C^T \\ 0 & K_f \end{bmatrix} \begin{Bmatrix} x \\ p \end{Bmatrix} = \begin{Bmatrix} F \\ 0 \end{Bmatrix} \quad (3)$$

The DOFs are the structural displacements $\{x\}$ and the fluid pressures $\{p\}$. The coupling between the structure and the fluid is represented by the matrix $[C]$, which contains the fluid-structure interface conditions.

The mass and stiffness matrices in Eq. 3 are asymmetric because the mixed formulation combines kinematic $\{x\}$ and force $\{p\}$ quantities. To solve the problem in the real domain, the matrices must be symmetrized. The RCM method follows the strategy proposed by H. Wandinger in [2] to solve the fluid-structure eigenvalue problem using the Mobility-Flexibility or the Stiffness-Mass method.

The Mobility-Flexibility formulation symmetrizes the eigenvalue problem of Eq. 3. through the transformation described in Eq. 4.

$$\{X\} = [K_s]\{x\} \quad (4)$$

Substituting it into Eq. 3, neglecting the force $\{F\}$, and assuming harmonic solutions for $\{x\}$ and $\{p\}$ yields Eq. 5, a symmetric eigenvalue problem.

$$\omega^2 \begin{bmatrix} K_s^{-1} & 0 \\ 0 & M_f \end{bmatrix} \begin{Bmatrix} X \\ p \end{Bmatrix} + \begin{bmatrix} M_s^{-1} & -M_s^{-1}C^T \\ -CM_s^{-1} & K_f + CM_s^{-1}C^T \end{bmatrix} \begin{Bmatrix} X \\ p \end{Bmatrix} = \begin{Bmatrix} 0 \\ 0 \end{Bmatrix} \quad (5)$$

Eq. 5 is referred to as the Mobility-Flexibility formulation, as it involves the inverse mass matrix (mobility) and inverse stiffness matrix (flexibility).

The Stiffness-Mass formulation symmetrizes the eigenvalue problem of Eq. 3 through the transformation given in Eq. 6.

$$\{P\} = [M_f]\{p\} \quad (6)$$

Substituting it into Eq. 3, neglecting the force $\{F\}$, and assuming harmonic solutions for $\{x\}$ and $\{p\}$ yields Eq. 7, a symmetric eigenvalue problem.

$$\omega^2 \begin{bmatrix} M_s + C^T K_f^{-1} C & C^T K_f^{-1} \\ K_f^{-1} C & K_f^{-1} \end{bmatrix} \begin{Bmatrix} x \\ P \end{Bmatrix} + \begin{bmatrix} K_s & 0 \\ 0 & M_f^{-1} \end{bmatrix} \begin{Bmatrix} x \\ P \end{Bmatrix} = \begin{Bmatrix} 0 \\ 0 \end{Bmatrix} \quad (7)$$

Moreover, since MSC Nastran 2021.1, fluid-structure problems can be reduced using superelements. This approach relies on a modified CB (Craig-Bampton) formulation proposed by J. Wandinger in [3], enabling the use of standard procedures to solve the system equations.

By partitioning the displacement DOFs $\{x\}$ into J interface and I internal DOFs, and considering only an interface excitation $\{F_j\}$, Eq. 3 can be rewritten as Eq. 8.

$$\begin{bmatrix} M_{s_{jj}} & M_{s_{ji}} & 0 \\ M_{s_{ij}} & M_{s_{ii}} & 0 \\ C_j & C_i & M_f \end{bmatrix} \begin{Bmatrix} \ddot{x}_j \\ \ddot{x}_i \\ \ddot{p} \end{Bmatrix} + \begin{bmatrix} K_{s_{jj}} & K_{s_{ji}} & -C_j^T \\ K_{s_{ij}} & K_{s_{ii}} & -C_i^T \\ 0 & 0 & K_f \end{bmatrix} \begin{Bmatrix} x_j \\ x_i \\ p \end{Bmatrix} = \begin{Bmatrix} F_j \\ 0 \\ 0 \end{Bmatrix} \quad (8)$$

However, $[K_f]$ can be singular when constant-pressure modes $[\psi]$ exist in the fluid, as is the case for enclosed fluids in tanks with sloshing. For these modes, fluid motion cannot be captured through differential pressure effects, resulting in a non-unique solution. Therefore, constant-pressure modes must be separated.

Considering $[K_{f_{rr}}]$ as a regular submatrix of $[K_f]$ with maximum rank r, it is related to $[K_f]$ through the Boolean extraction matrix $[J]$, whose number of columns equals the rank of $[K_f]$, as shown in Eq. 9.

$$[K_{f_{rr}}] = [J]^T [K_f][J] \quad (9)$$

The pressure can be rewritten as Eq. 10 by considering a set of S constant-pressure modes $[\psi]$.

$$\{p\} = [J]\{p_r\} + [\psi]\{p_s\} \quad (10)$$

Applying Eq. 10 to the pressure formulation in Eq. 8 separates the constant-pressure modes, which are removed from the reduced model mode set, as discussed later. Additional algebra leads to a symmetric CB equation for the fluid-structure problem, enabling the use of standard procedures to solve the complete system equations.

2.3. Decoupled Equivalent Viscous Damping

Structural or modal damping is usually defined for frequency and transient response analyses. However, structural damping cannot be directly

applied to perform transient response analyses on a reduced model.

One possibility is to define an equivalent viscous damping independently for each mode p of the reduction subset: the decoupled equivalent viscous damping, as presented by X. Vaquer Araujo in [4] and [5]. However, this approach does not account for interface damping or modal coupling. Neglecting interface damping is acceptable when the interface is stiff and does not significantly contribute to the overall strain energy of the system.

At ESA, this definition has been demonstrated to be robust, reduce computational costs, and provide acceptable results, at least for models without fluid elements. However, for free-free coupled CB systems, the damping accuracy is affected. Indeed, the damping of each CB model is defined from the reduced set of P fixed-interface modes, and the damping coefficients must be projected onto the free-free system mode set. Since the free-free system modes differ from the fixed-interface modes of each model, errors are introduced in the damping coefficients. These errors can be compensated by tuning the forcing function levels (applied force or enforced motion) during CLA correlation with flight data. Alternatively, coupled system-level modal damping techniques can be used [4].

3. FREE-FREE CONDITION

The FFS nodes and the reference nodes connected to the gravity springs must be linked to the structure to follow the launcher rigid-body motion. This is achieved by connecting these nodes to a suitable reference frame describing the launcher rigid-body motion. Ideally, the launcher motion would be represented using its rigid body mass at the COG (center of gravity). However, this requires specific condensation techniques, such as the Hurty method described in [6], which are preferably avoided as they are not implemented in MSC Nastran. Nevertheless, such methods have been used in ESA CLA tools.

In this paper, following the approach described in [7], the first reference frame considered is the inertial frame, with the FFS grounded to Earth. Each DOF of the FFS and reference nodes is grounded through SPCs (Single-Point Constraints). Only the FFS DOFs in the gravity direction remain unconstrained, allowing sloshing displacements. However, this reference frame cannot represent the launcher rigid-body motion and is therefore unsuitable for lift-off-like analyses under free-free conditions.

A second reference frame enabling free-free analyses was introduced by S. Fransen in [8], based on a relative reference frame. The concept is to link the nodes to a reference point approximately following the tank rigid-body motion. Initially, a structural node at the tank bottom was considered as the reference point. However, this node is affected by structural deformation and cannot accurately represent rigid-body motion alone. The best compromise is to create a non-structural node rigidly linked to all tank interface nodes, as the interface is the stiffest region of the tank. As shown in Fig. 3, the rigid connection is achieved using an RBE3 (Rigid Body Element). The reference point motion corresponds to the average motion of the interface nodes. All DOFs of the FFS and reference nodes, except the FFS DOF in the gravity direction, are then rigidly connected to this reference point through RBE2s.

An example for the cubic tank is shown in Fig. 3. In this case, no physical interface exists, and the base is considered as the interface.

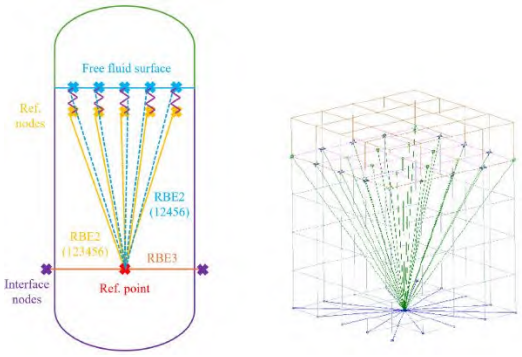


Figure 3: Free fluid surface reference frame

This reference frame definition for the FFS is adopted in this paper. But even a stiff interface remains subject to structural deformation, which affects the FFS motion. Thus, the interface must be sufficiently stiff to accurately represent the rigid-body motion through the reference point. If this cannot be achieved, an alternative method must be implemented, such as separating the motion into rigid and flexible contributions using ERD (explicit rigid DOFs), as described by S. Fransen, A. Kreis and M. Klein in [9]. However, this method requires further development for implementation in MSC Nastran and introduces high mathematical and numerical complexity. Hence, it is not considered in the present investigation.

4. INCOMPRESSIBILITY

Incompressibility should be ensured by defining a high bulk modulus in the fluid properties. To validate or refine the incompressibility assumption in MSC Nastran, an MPC enforcing incompressibility has been derived and is discussed in this section.

4.1. Multipoint Constraint Definition

Incompressibility is defined by maintaining a constant fluid volume. To achieve this, the approach described in [7] constrains the displacements of the nodes defining the fluid skin (tank and FFS nodes) to satisfy this condition. The resulting constraint between all relevant nodes ensures that the volume variation ΔV is null.

A MATLAB code has been developed to generate the MPC for a given FEM. The code reads the model and computes coefficients in the three directions for each fluid skin node. These coefficients depend on the number of plate elements connected to the node, their normal directions, and their areas. The incompressibility equation is given in Eq. 11, considering I as the set of fluid skin nodes and J_i as the set of elements connected to node i.

$$\Delta V = \sum_{i \in I} \sum_{j \in J_i} \Delta x_{n,i,j} A_{i,j} = 0 \qquad (11)$$

$\Delta x_{n,i,j}$ is the normal displacement of node i with respect to element j, and $A_{i,j}$ is the area of element j surrounding node i.

A detailed scheme is provided in Fig. 4. For example, for node #10 of the cubic tank, two coefficients are computed in the x and y directions. Element #1 connected to this node has x as its normal direction, and $A_{10,1}$, the area contribution surrounding node #10, corresponds to one fourth of the total element area A_1. Element #2 has $-y$ as its normal direction and the same area contribution, as all elements in this model are quadrilateral elements with identical dimensions. Similarly, elements #3 and #4 contribute to the x and $-y$ coefficients. For node #20 of the FFS, elements #5 to #8 contribute to the z-direction coefficient.

The normal direction of each fluid skin element is calculated from the cross product of two non-collinear vectors defined by the element nodes. The outward direction (± 1) is determined from the sign of the dot product between the cross-product vector and the vector connecting the tank centre non-structural node to an element node.

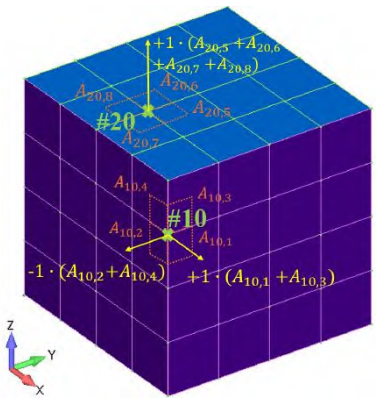


Figure 4: Incompressibility equation scheme

When writing the MPC equation, one DOF of one node has to be selected as the dependent DOF, as in Eq. 12 by considering node s as the slave DOF. The resulting incompressibility MPC is shown for the cubic tank in Fig. 5.

$$\sum_{j \in J_s} \Delta x_{n,s,j} A_{s,j} = \sum_{i \in I\{s\}} \sum_{j \in J_i} \Delta x_{n,i,j} A_{i,j} \qquad (12)$$

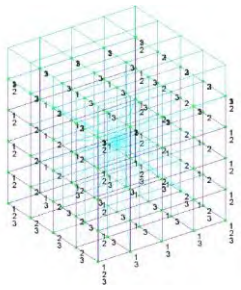


Figure 5: Incompressibility MPC for cubic tank

4.2. Constraint Validation

The effect of this MPC has been investigated for the cubic tank, considering different tank thicknesses and fluid properties. Normal modes analyses were performed to compare the results with and without the incompressibility MPC.

First, an additional MPC was created using a dummy non-structural node as the slave and all fluid skin nodes as masters, while retaining the same coefficients as the incompressibility MPC. In other words, Eq. 12 is re-implemented with the dummy non-structural node as slave $s$and a unit coefficient, resulting in Eq. 13.

$$\Delta x_s = \sum_{i \in I} \sum_{j \in J_i} \Delta x_{n,i,j} A_{i,j} \qquad (13)$$

By doing so, the global volume variation of the nodes of interest is represented by the 'displacement' Δx_s of the dummy node. This MPC provides a verification of the incompressibility MPC, as the dummy node 'displacement' should be zero if the incompressibility constraint is correctly implemented.

This verification was performed during normal modes analyses and resulted in zero volume variation for all modes, validating the implementation.

4.2.1. Cubic tank filled with water

The first model studied was the cubic tank presented in Fig. 2. The dimensions and properties of the tank and fluid are detailed in Tab. 1.

Table 1: Dimensions and properties

Dimensions of the tank	
Tank volume [m3]	0.2x0.2x0.25
Tank wall thickness [m]	0.001
Fluid volume [m3]	0.2x0.2x0.2
Fluid mass [kg]	8
Mesh dimensions	
CQUAD area [cm2]	25
CHEXA volume [cm3]	125
Aluminium properties	
Young modulus E [GPa]	70
Poisson ratio v [-]	0.3
Density ρs [kg/m3]	2700
Water properties	
Bulk modulus K [GPa]	2.1
Density ρf [kg/m3]	1000
Speed of sound C [m/s]	1449.14

The speed of sound is computed as in Eq. 14.

$$K = \rho_f C^2 \qquad (14)$$

It is recommended to use a large bulk modulus to model incompressible fluids with MSC Nastran, in particular, a value ensuring a wavelength of ten times the size of the structure is suggested. Since the following normal modes analysis will be performed up to $f = 100\ Hz$, the corresponding wavelength is $\lambda = \frac{C}{f} = 14.49\ m$.

This wavelength is more than ten times greater than the size of the structure (0.20m). Therefore, according to MSC Nastran, the fluid is considered incompressible. In this case, no compression waves would occur in the fluid for frequencies below $f = \frac{C}{10x0.2} = 725\ Hz$. The only wave type encountered is sloshing, due to gravity.

Normal modes analyses in free-free condition were conducted on the models both with and without the incompressibility MPC. The natural frequencies were compared and the MAC (modal assurance criterion) was computed to also compare the mode shapes of the two models, especially for the modes with a non-null volume variation for the model without the incompressibility MPC.

Fig. 6 shows the MAC. Except for the rigid-body modes and constant-pressure mode (first seven modes) that are different, the MAC is very close to one, the mode shapes are identical. The FSI modes are highlighted in the orange square, the preceding modes are sloshing modes. Two FSI modes with a MAC below one are highlighted in yellow. Indeed, the volume variation is not null for those two modes in the model without the incompressibility MPC. Nonetheless, the MAC coefficients are 0.91 and 0.89 and the errors in frequency are of the order of 0.001%, meaning that the normal modes are almost identical. The frequencies of the first – and main – sloshing modes and of the FSI modes highlighted in yellow in Fig. 6 are given in Tab. 2 while the corresponding mode shapes are displayed in Fig. 7. The mode shapes are shown for the model without the incompressibility MPC; those for the model with the MPC are very similar.

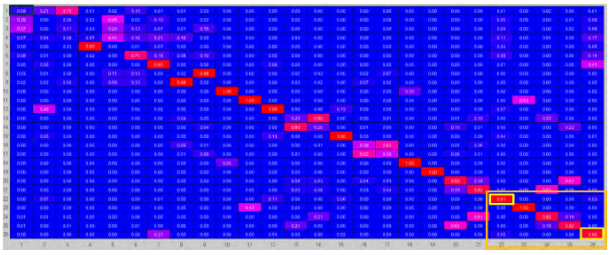
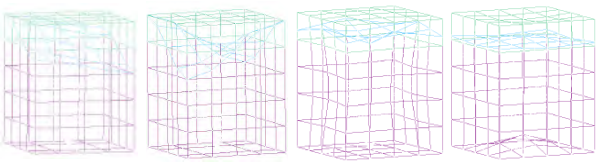


Figure 6: MAC matrix

Table 2: Natural frequencies

	Frequency [Hz]			
	Sloshing		FSI	
No MPC	2.646	3.023	35.216	90.463
MPC	2.646	3.023	35.217	90.463



Sloshing 2.65 Hz | Sloshing 3.02 Hz | FSI 35.22 Hz | FSI 90.46 Hz

Figure 7: Mode shapes

For this particular model with a frequency of interest up to 100Hz, the fluid can be considered incompressible and the MPC is not needed.

The same model has been further investigated, with only the panel thickness changed from 1mm to 0.5mm and 0.1mm. As a result, the FSI mode frequencies decrease, since the apparent stiffness of the structure is lower. Similarly, the MAC is close to 1 with errors in frequency of the order of 0.001%.

4.2.2. Cubic tank filled with low bulk modulus fluid

A final test was performed on the cubic tank, considering a fluid with a bulk modulus low enough to not respect the recommendation. The aluminium tank has a wall thickness of 1mm. Tab. 3 summarizes the properties of the artificial fluid. It is noted that the wavelength is not ten times greater than the size of the structure (0.20m), when frequencies up to 100Hz are considered.

Table 3: Low bulk modulus fluid properties

Bulk modulus K [GPa]	Density ρf [kg/m3]	Speed of sound C [m/s]	Wave-length λ [m]
0.0021	1000	45.83	0.46

Fig. 8 presents the MAC matrix up to 100 Hz. The MAC coefficients are close to one for every non-rigid body mode except the two FSI modes highlighted in yellow, that have a non-null volume variation and whose frequencies are given in Tab. 4. However, these two MAC coefficients are equal to 0.92 and 0.89, thus the mode shapes can be considered very similar. Nonetheless, a difference can be seen in the natural frequencies with a difference up to 1% for those two modes.

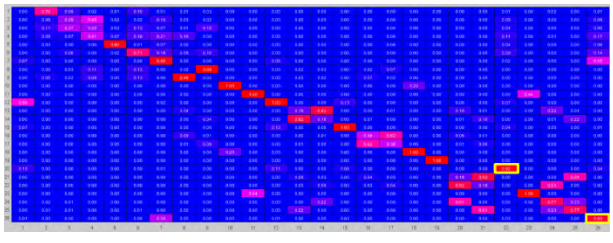


Figure 8: MAC matrix

Table 4: Natural frequencies

	Frequency [Hz]			
	Sloshing		FSI	
No MPC	2.646	3.023	34.907	87.701
MPC	2.646	3.023	34.654	86.897

4.2.3. Conclusions

A more extensive sensitivity analysis has been performed in [1]. Other examples were studied and frequency response analyses were performed to ensure that the results are not model dependent.

When the incompressibility condition suggested by MSC Nastran on the fluid is satisfied, the latter behaves as incompressible. Therefore, the incompressibility MPC is not required in these cases.

When the approximation for the fluid is not respected, it does not behave as incompressible – the natural frequencies start to diverge between the two models.

For each case studied in this paper, the condition will be checked and when verified the incompressibility MPC will not be used in order to save computational time.

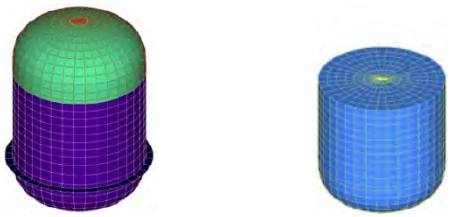
5. COMPARISON WITH FABE

Some examples from FABE are available. These include FEMs of the structure with the corresponding boundary fluid mass and stiffness matrices. To adapt these benchmarks to the RCM method, the boundary matrices that define the fluid are replaced by solid elements, the corresponding fluid properties and the FFS with the gravity stiffness are defined as described in Section 2.

By using the same meshes, these benchmarks can serve as a basis for a first validation of the RCM method and for performing a tuning of the FEM, especially of the FFS and the gravity stiffness definition. Normal modes analyses are carried out to this end.

5.1. Cylindrical Tank

A cylindrical tank with spherical ends as shown in Fig. 9 was available for comparison with FABE. The dimensions and properties of the tank and the fluid are detailed in Tab. 5.



Structure Fluid

Figure 9: Cylindrical tank

Table 5: Dimensions and properties

Dimensions of the tank	
Tank radius [m]	0.4375
Tank height [m]	1.33
Tank wall thickness [m]	0.003
Fluid mass [kg]	754.90
Mesh dimensions	
CQUAD/CTRIA min. area [cm2]	3.102
CQUAD/CTRIA max. area [cm2]	44.39
CHEXA/CPENTA min. vol. [cm3]	19.83
CHEXA/CPENTA max. vol. [cm3]	256.7
Aluminium properties	
Young modulus E [GPa]	70
Poisson ratio v [-]	0.3
Density ρs [kg/m3]	2700
Fluid properties	
Bulk modulus K [GPa]	2.1
Density ρf [kg/m3]	1448.28
Speed of sound C [m/s]	1204
Wavelength λ [m]	12.04

The normal modes analyses were performed with fixed-interface conditions, up to 100Hz, under the Earth's gravitational acceleration. Results are provided in Tab. 6. It is worth mentioning that a constant-pressure mode exists in the mode set of the model using the RCM method, but not in the one using the FABE method.

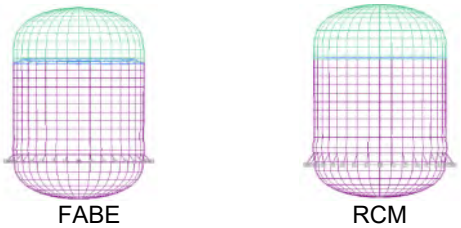
Table 6: Natural frequencies

	FABE	**RCM**
	Natural frequencies [Hz]	
Sloshing	1.03	1.03
	1.03	1.03
	1.33	1.36
	1.33	1.36
	1.48	1.57
	1.57	1.65
FSI	33.94	25.99
	45.83	45.13
	45.83	45.13
	73.79	74.70
	73.79	74.70
	74.72	76.46

The FSI modes are quite comparable between both models, with variations of less than 3%, except for the first mode, which exhibits a 30% variation.

When comparing this mode shape between the two models, they appear similar, with a main structural deformation occurring close to the interface. However, in Fig. 10, sloshing can be observed with the FABE model, whereas it does not appear for the RCM method model.

No further justification were found for the difference in frequency, and since it is the only structural mode with a non-negligible variation, overall the results for the FSI modes are considered consistent between both methods.



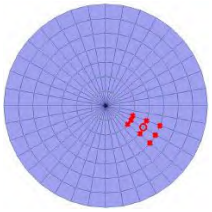
FABE RCM

Figure 10: FSI mode shape comparison

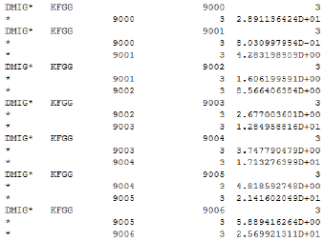
The sloshing modes at low frequency have similar frequencies between both methods, with variations of less than 5%. However, as the frequency increases, a divergence can be observed. For

instance the 50th sloshing frequency is 2.94Hz for the FABE model and 5.03Hz for the RCM method model.

To understand this divergence, the gravity stiffness definition of FABE has been studied: it is derived from the fluid's potential energy equation. The resulting values are in a DMIG file, partially displayed in Fig. 11. As it can be seen, some stiffness coupling between nodes is introduced. For instance, for node 9000 circled in red, coupled stiffness terms are considered with the surrounding nodes, represented with a red cross (nodes 9001, 9002, 9003, 9004, 9005, 9006, 9007 and 9008). This coupling does not exist in the gravity springs definition of the RCM method. However, the sum of all the stiffness terms for one node is equal to the stiffness introduced at one node with a gravity spring, showing consistency between the methods.



Gravity stiffness scheme



Gravity stiffness DMIG

Figure 11: FABE gravity stiffness definition

As a test, the gravity springs have been replaced by the gravity stiffness matrix from FABE in the RCM model. The comparison is presented in Tab. 7, only for the sloshing modes, as the FSI modes are not impacted by this modification. A divergence can still be observed but results are closer to FABE's one. It shows that the differences in the natural frequencies come partially from the gravity stiffness definition but also from the method itself.

However, the FABE gravity stiffness definition will not be used in this study, as it would require deriving the exact equations and developing a MATLAB code to create the DMIG given a FEM.

Finally, the FFS mesh was refined by factors of two and four, in an attempt to get closer to the results of the FABE model. Tab. 7 summarizes all the results. As the FFS mesh is refined, the divergence between the two methods decreases.

Overall, the two-time refined FFS provides the best results when compared to the FABE model. The divergence is notably reduced compared to the initial mesh and results are quite satisfactory, even when compared to the four-time refined mesh. The latter, requires more time to set up the model due to the non-automated creation of gravity springs and is more computationally costly. Moreover, like the model using the DMIG, it only improves the higher-order modes. These modes would solely induce a local behaviour – local waves on the FFS without shifting the fluid's COG – meaning no significant loads would be transmitted to the tank interface.

Table 7: Sloshing natural frequencies

FABE	RCM with DMIG	RCM	RCM x2 refined	RCM x4 refined
Natural frequencies [Hz]				
1.03	1.03	1.03	1.03	1.03
1.03	1.03	1.03	1.03	1.03
1.33	1.36	1.36	1.35	1.31
1.33	1.36	1.36	1.35	1.31
1.48	1.57	1.57	1.53	1.43
1.57	1.65	1.65	1.63	1.57
50th natural frequency [Hz]				
2.94	4.05	5.03	4.12	3.55

Hence, the results obtained with the RCM method are considered satisfactory for the sloshing modes too, with an improvement if the FFS is refined.

5.2. Conclusions

The results are consistent between the two methods for both sloshing and FSI modes. Regarding sloshing, variations become more apparent as the frequency increases. However, the high frequency sloshing behavior is not particularly relevant to the scope of this paper. Regarding FSI modes, the results are very similar with variations occurring for only few modes.

These comparisons provide an initial validation and final tuning of the RCM method. To further validate this approach, testing could be performed on flexible tanks, and flight data could be correlated to analysis. In literature, no data was found on tests performed with flexible tanks to assess the dynamic modelling of FSI problems.

6. DYNAMIC RESPONSE ANALYSES

6.1. First Example – Cubic Tank

After this first validation of the RCM method, some analyses of the dynamic response can be performed on a simple cubic tank model. Frequency and transient response analyses will be performed, both with the direct and modal methods. All these analyses will be carried out for the FEM and the SEM (superelement model). The objective is to compare the results between the direct and modal methods and between the FEM and SEM.

6.1.1. Superelement creation

The cubic tank is reduced to create a SEM. Node 1, at the base, has been selected as the interface, circled in red in Fig. 12. PLOTEL elements are used, as it can be seen in the figure. These elements serve as "dummy" elements for visualization purposes by connecting two nodes, but they do not contribute to the mass, stiffness or damping of the structure. They allow to plot the superelement's mode shapes or to retrieve the displacements and accelerations of internal nodes as the Output Transformation Matrix is applied to the boundary nodes of the PLOTELs.

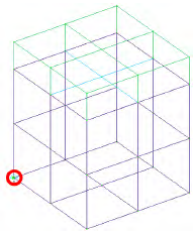


Figure 12: Cubic tank superelement

The condensation is performed up to 250Hz, as the subsequent analyses will be conducted up to 125Hz. Indeed, a rule of thumb for modal dynamic analysis is that the computed response is valid up to half the truncation frequency. Three residual vectors were computed during the reduction process, to account for the static contribution of the high-frequency truncated modes; they may also contribute to the MEM (modal effective mass).

The MEM has been computed for the selected subset of modes, residual vectors included. For the translational DOFs, 90% of the rigid mass is captured. For the rotational DOFs, 80% of the rigid mass is represented by the mode subset, and only 60% for the torsional DOF. Even when increasing the truncation frequency, reaching 90% of the rigid mass proves difficult, especially for the torsional DOF as these modes have a very high natural frequency. Since the tank is not subjected to torsional loading, the missing rigid mass is not a significant issue. The following analysis results will prove the consistency of this mode set.

It is worth mentioning that the MEM is computed via an in-house Python subroutine since MSC Nastran is not yet capable of computing it when solid fluid elements are included in the model.

Normal mode analyses in fixed-base condition are performed up to 125Hz to compare the modal basis of the FEM with that of the SEM. The natural frequencies are identical, as it can be seen in Tab. 8. The constant-pressure mode is removed from the mode set of the condensed model. The reasons are highlighted in [3] and have been discussed in Section 2.2.

In addition, normal modes analyses in free-free condition are performed up to 125Hz. Some natural frequencies are slightly different (1.5% for highest FSI frequency). These differences arise because for the SEM, the modes in free-free condition are approximated from the modes in fixed-interface condition.

Table 8: Natural frequencies comparison

	Fixed-base		Free-free	
	FEM	**SEM**	**FEM**	**SEM**
	Natural frequencies [Hz]			
Sloshing	2.21	2.21	2.58	2.58
	3.02	3.02	3.02	3.02
	5.06	5.06	5.06	5.06
FSI	21.58	21.58	35.20	35.21
	36.77	36.77	36.77	36.77
	55.05	55.05	66.91	67.33
	Highest error		90.80	92.18

6.1.2. Frequency response analyses

An applied force is implemented: a constant $F = 1\ N$ axial force from 1 to 1000Hz, and responses will be studied up to 125Hz, with $\Delta f = 1\ Hz$. This forcing function will act as a perturbation on the tank's steady-state. The steady-state vertical acceleration is assumed to be equal to the Earth gravitational acceleration.

The application of the load to the free-free tank model is depicted in Fig. 13. A residual structure is added. The force is applied to node #7777777, located at the center of the tank base. It is connected to node #6666666 – which is at the same location – through a stiff spring, in order to retrieve the applied force during the analyses. This latest node is rigidly connected to node #1, the interface node of the superelement, using an RBE2. Fig. 13 shows the FEM, the residual structure is the same for the SEM. During the analyses, different data are recovered. The applied force is recovered through the spring CBUSH #9999999 and axial accelerations are recovered at the internal node #178, on top of the tank, as highlighted in black.

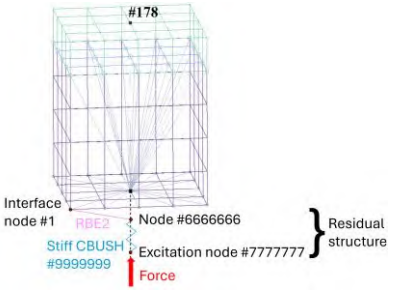
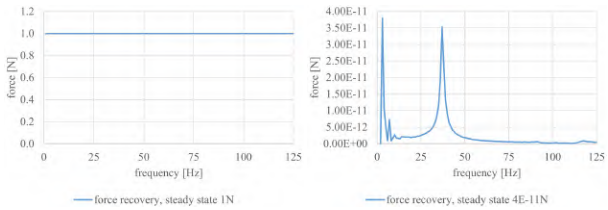
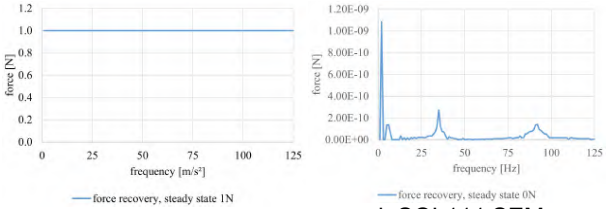


Figure 13: Forcing function application

SOL108 (direct frequency response) and SOL111 (modal frequency response) are performed for the FEM and the SEM. Results are shown in Fig. 14. The force is correctly recovered with the direct method, for the FEM and the SEM. When using the modal method, the force recovered is completely different from the applied one. No residual vectors were computed in the modal decomposition, leading to an incorrect force recovery. The absence of residual vector in the modal decomposition is due to the use of solid fluid elements, which are not yet fully supported by MSC Nastran. The same model has been considered without the solid fluid elements, in that case residual vectors were computed and the force was retrieved correctly.



a. SOL108 FEM b. SOL111 FEM



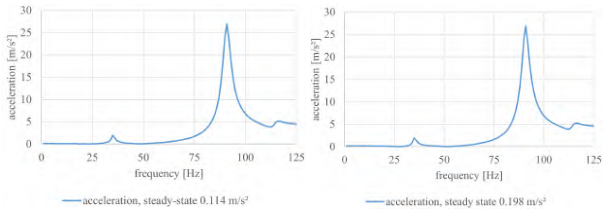
c. SOL108 SEM d. SOL111 SEM

Figure 14: Force recovery

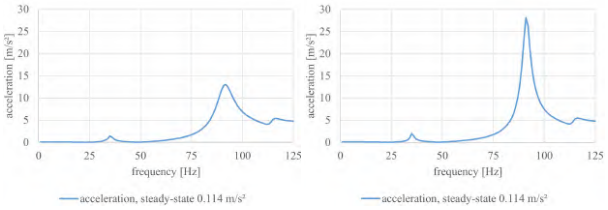
Different damping definitions are used. For the FEM SOL108, a structural damping of 4% is applied, corresponding to a common value for this type of structure. For the SOL111, a modal damping of 2% is applied to each mode to ensure equivalence with the structural damping coefficient. For the SEM SOL108, a decoupled equivalent viscous damping of 2% is defined for each modal coordinate.

The axial acceleration of node #178 at the top of the tank is recovered and shown in Fig. 15. For the FEM SOL111, the steady-state acceleration is incorrect (Fig. 15b). Considering an applied force $F = 1N$ and a tank mass $m = 8.756kg$, the acceleration at 0Hz should be $a = F/m = 0.114m/s^2$. However, the computed steady-state acceleration is $a = 0.198m/s^2$. This discrepancy results from the fluid elements: the constant-pressure mode of the fluid and the rigid-body modes of the structure are not correctly separated by MSC Nastran. The correct steady-state acceleration is recovered in the other analyses, as shown in Fig. 16, which compares all responses. It should be noted that SOL111 provides the correct steady-state solution for the SEM because the constant-pressure mode is removed from the reduced fluid mode set.

However, when using decoupled equivalent viscous damping, the acceleration is excessively damped (Fig. 15c). At 91Hz, the response reaches only 13m/s², compared to 27m/s² for the main peak in the other analyses. Sensitivity analyses presented in [1] indicate that this issue is mainly caused by the projection of the superelement damping matrix onto the free-free modes computed by component mode synthesis in SOL111.



a. SOL108 FEM b. SOL111 FEM



c. SOL108 SEM d. SOL111 SEM

Figure 15: Node #178 acceleration recovery

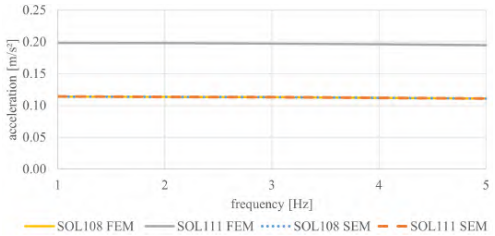


Figure 16: Steady-state acceleration comparison

6.1.3. Transient response analyses

The main axial mode of the cubic tank, identified at 91Hz through the frequency response analyses discussed in the previous section, is an axial FSI mode. The applied force F is defined to excite this mode and achieve a steady-state acceleration of 1g. This acceleration is used to define the gravity springs (Eq. 2). With a filled tank mass of $m = 8.756kg$, the required force is $F = ma = 85.89N$.

The analyses are performed over 0.20s with $\Delta t = 0.1$ms. The applied force spectrum is shown in Fig. 17 and applied as described in Section 6.1.2.

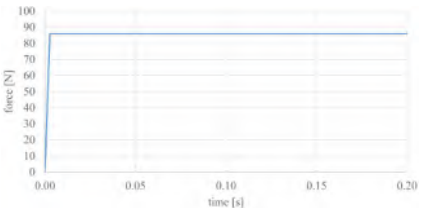


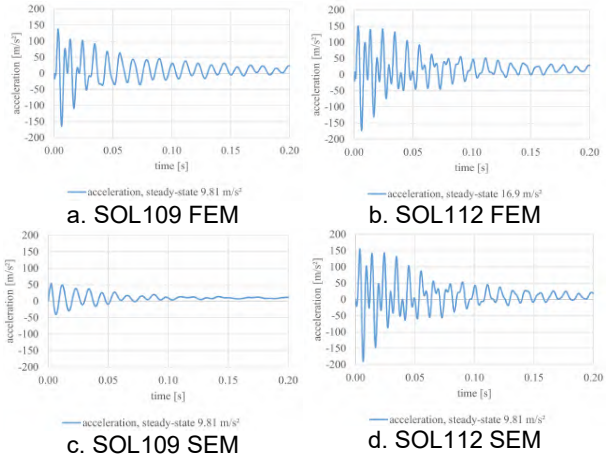
Figure 17: Applied force spectrum

SOL109 (direct transient response) and SOL112 (modal transient response) are performed for both the FEM and SEM. As in Section 6.1.2, the force is not correctly recovered using SOL112.

The same damping definitions as for the frequency response analyses are adopted, except for the FEM direct transient analyses. The complex structural damping used in frequency response analyses cannot be applied to transient analyses performed in the real time domain. Therefore, an equivalent viscous damping coefficient b, corresponding to $G = 4\%$, is defined at the main mode natural frequency (91Hz in this example). In MSC Nastran, this frequency is specified using PARAM,W3.

The axial acceleration of node #178 is recovered for all analyses and shown in Fig. 18. The same conclusions as for the frequency response analyses in Section 6.1.2 apply: the steady-state response is incorrect for the FEM SOL112 (Fig. 18b), and the

equivalent viscous damping leads to an overly damped acceleration spectrum.



a. SOL109 FEM b. SOL112 FEM

c. SOL109 SEM d. SOL112 SEM

Figure 18: Node #178 acceleration recovery

6.2. Second Example – Launcher Model

A more complex model representing the first stage of a launcher is studied. The model includes two liquid propellant tanks: one for liquid oxygen and one for liquid hydrogen. Frequency and transient response analyses are performed under fixed-interface and free-free conditions for different load cases. The objective is to perform analyses representative of a clamped static firing test and free-free lift-off conditions and compare the FEM and SEM responses.

Since the primary objective of these analyses is to compare the FEM and SEM, the incompressibility MPC is not included in the following results.

6.2.1. The model

The FEM section view is shown in Fig. 19. The nozzle is modelled in green, the LH2 tank in yellow, the LOX tank in dark blue, and the FFSs in light blue.

A SEM is generated from this FEM, including PLOTEL elements for data recovery and mode shape visualization. The interface is defined at node #1, rigidly connected to the upper nodes of the first stage through an RBE2. Internal loads are included in the SEM: axial and lateral thrust applied at the nozzle top, and lateral gust applied at the assembly COG. A longitudinal steady-state acceleration of 20 m/s² is considered for the gravity stiffness definition in all subsequent analyses and is representative of a lift-off acceleration after full thrust build-up.

The same damping definition as for the cubic tank is used for these analyses.

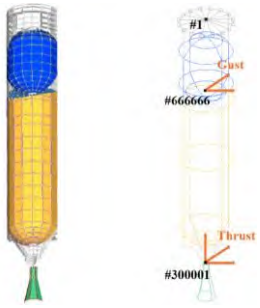


Figure 19: First stage models

For the lift-off-like analyses, a simplified spacecraft model is added on top of the first stage and connected at node #1. The spacecraft is designed to have one longitudinal z-direction natural frequency at 20Hz and two lateral x- and y-direction natural frequencies at 6Hz. These values are based on the ARIANE-6 satellite stiffness requirements.

The spacecraft model is presented in Fig. 20. It has a total mass of 3000kg, composed of a static mass $m_1 = 2000kg$ and a dynamic mass $m_2 = 1000kg$. The dynamic mass COG is located at a height $L = 1m$. The static mass is located at the spacecraft SEM interface node. To achieve the target natural frequencies, a 6-DOF spring is created using a CBUSH element between interface node #1 and coincident node #2. The longitudinal stiffness (DOF 3) and lateral stiffnesses (DOFs 4 and 5) are tuned to match the target frequencies.

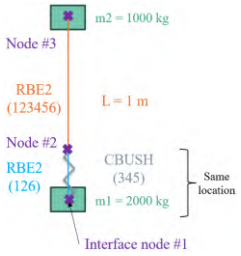


Figure 20: Spacecraft model

6.2.2. Static-firing-test-like analysis

Static-firing-test-like frequency response analyses are performed on the FEM and SEM of the first stage, with node #1 clamped to simulate a static firing test in which the booster/motor is fixed at one end by a concrete block to recover thrust data. Axial and lateral thrust perturbations are applied separately at node #300001. The forcing functions are defined as $F = 1N$ over the 1–100Hz frequency range, representing lateral thrust perturbations in x and y, and axial thrust perturbation in z.

Different nodes are selected for displacement and acceleration recovery. In the plots of this section, green curves represent interface and force application nodes, purple curves represent nodes on top of the spacecraft (when included) and at the bottom of the nozzle, orange curves represent FFS nodes, yellow curves represent LH2 tank nodes, and blue curves represent LOX tank nodes. A CBUSH element, created at the nozzle top to

connect it to the tanks, enables thrust force recovery.

Fig. 21 shows the x-displacement response for a lateral x-thrust perturbation. A peak occurs at low frequency, with the nozzle bottom exhibiting the highest displacement. This corresponds to the excitation of the main bending mode, as it can be seen with the mode shape. All displacement spectra are identical, and the FEM and SEM exhibit similar behaviour.

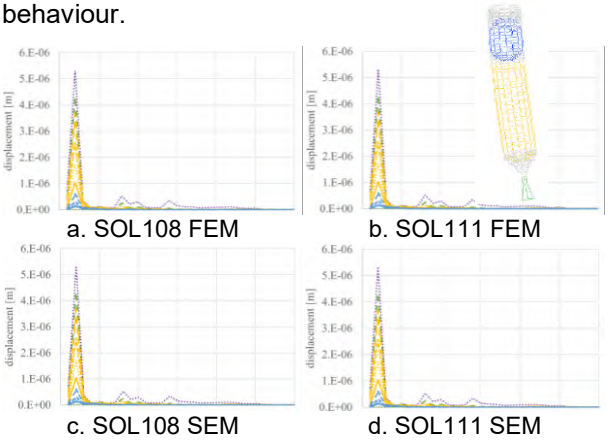


Figure 21: Displacement along x, lateral x thrust

Accelerations are also recovered, showing very similar responses for all methods, with only minor differences at high frequency, most likely due to the different damping definitions. The two other thrust perturbations lead to similar displacement and acceleration responses.

The thrust forces recovered through the CBUSH element are presented in Fig. 22. For the lateral thrust, the steady-state value of 1N is recovered. For the axial thrust, the correct value is obtained for all analyses except the FEM SOL111, as already discussed in Section 6.1.2. However, the force is correctly recovered for the SEM due to the inclusion of residual vectors.

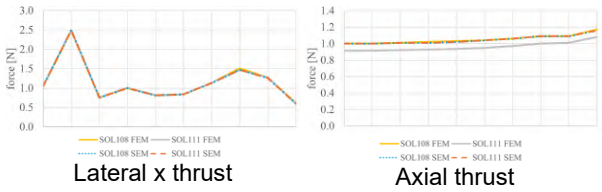


Figure 22: Thrust force

6.2.3. Lift-off-like frequency response analyses

Lift-off-like frequency response analyses are performed on the FEM and SEM of the assembly under free-free conditions. Axial thrust is applied at node #300001, while lateral gust loads in x and y are applied at node #666666, the assembly COG. The forcing functions are defined as $F = 1N$ over the 1–100Hz frequency range, with each perturbation treated separately. Node #666666 is rigidly linked to two rings of structural nodes through an RBE3 to distribute the gust load.

Fig. 23 shows the y-displacement response for a lateral y-gust perturbation. The large low-frequency displacements observed in all analyses correspond to rigid-body motion. The two peaks correspond to bending mode responses, as it can be seen with the mode shape. Overall, the spectra are very similar. Although the SEM responses are slightly overdamped when using decoupled equivalent viscous damping, the results are considered satisfactory. However, the FEM SOL111 displacement spectrum differs from the other analyses at low frequency, where rigid-body motion dominates. This drift is again caused by the interaction between structural rigid-body modes and fluid constant-pressure modes.

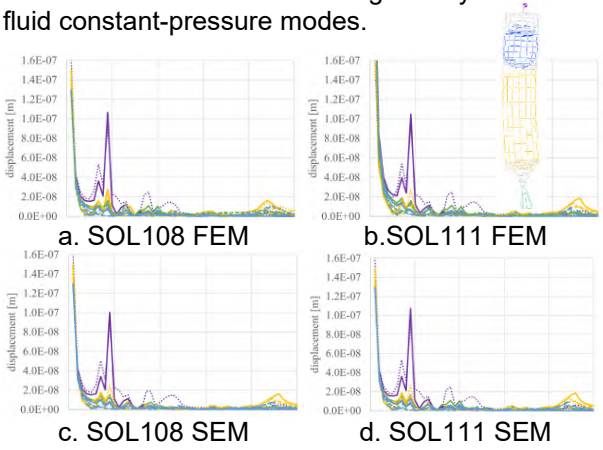


Figure 23: Displacement along y, lateral y gust

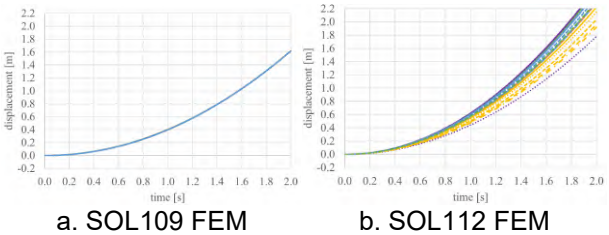
The lateral x gust and axial thrust load cases yielded similar results, as did the acceleration spectra. The same issue than for the cubic tank arose for the steady-state acceleration and force recovery with the SOL111 FEM.

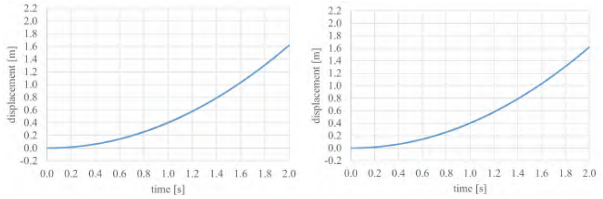
6.2.4. Lift-off-like transient response analyses

Lift-off-like analyses are performed in the time domain. Different axial thrust and lateral gust loads are defined, as in Section 6.1.3, to excite the main bending and axial modes.

The main displacement spectra for the lateral y gust are shown in Fig. 24. No major dynamic responses are visible due to the rigid-body motion occurring in the y-direction.

All analyses exhibit the same static displacement spectra and displacement values, except the SOL112 FEM, where non-physical drift is observed. A rigid-body rotation appears, with the displacement spectra of the two outermost nodes enclosing those of the other nodes. This drift was foreseen and explained in Section 6.2.3.





c. SOL109 SEM d. SOL112 SEM

Figure 24: Displacement along y, lateral y gust

6.2.5. Conclusions

For the static-firing-test-like frequency response analyses, the computed responses were very similar for all load cases. The FEM and SEM showed the same behaviour, with consistent results between modal and direct analyses and between damping definitions. In particular, the decoupled equivalent viscous damping provided accurate results under fixed-interface conditions.

For the lift-off-like frequency and transient response analyses, the responses were also very similar. The decoupled equivalent viscous damping introduced some overdamping under free-free conditions. However, the results remain sufficiently accurate.

Some issues were observed in the FEM SOL111 analyses. As no residual vectors were computed during the modal decomposition, the input force could not be correctly recovered. The same issue was observed for the SOL111 SEM of the cubic tank in Section 6.1. The reason why residual vectors are not always computed remains unclear.

The combination of rigid-body modes and constant-pressure modes leads to incorrect steady-state accelerations for the FEM SOL111 under free-free conditions. A non-physical drift was also observed in the low-frequency displacement responses of the frequency response analyses and in the transient response spectra.

This section confirms the results obtained for the cubic tank (and cylindrical tank in [1]) for more complex models and additional load cases.

7. CONCLUSIONS

First, an MPC equation enforcing incompressibility was derived and verified for cases where the condition required by MSC Nastran is not satisfied.

A first validation of the RCM method was performed by comparing the results with those obtained using FABE and by refining the modelling approach. Refinements were introduced in the FFS modelling, including the reference frame definition and mesh size, which are key parameters for the gravity stiffness definition.

Frequency and transient response analyses were performed on simple and complex models to compare FEM and SEM response spectra (displacement, acceleration, element forces) and evaluate different damping methods. Particular attention was given to the decoupled equivalent viscous damping method defined for the SEM, which is required for transient response analyses. Overall, consistent results were obtained between FEM and SEM models using different damping definitions for the considered benchmarks. The decoupled equivalent viscous damping method provided accurate results under fixed-interface conditions but introduced some overdamping under free-free conditions. Furthermore, issues were identified with modal approaches. Due to missing residual vectors during modal analyses, input forces could not always be correctly recovered, both for FEM and, in some cases, SEM models. For FEM models, the steady-state acceleration was incorrect due to the treatment of rigid-body and constant-pressure modes by MSC Nastran.

The next step is to include the incompressibility MPC in the first stage model and repeat the analyses. This MPC may be required since the incompressibility condition recommended by MSC Nastran is not satisfied for excitation frequencies above 20Hz in this model. In addition, the implementation of a coupled equivalent viscous damping matrix formulation is planned.

These analyses were performed with MSC Nastran 2023.3. Newer versions are now available, and preliminary testing has shown improvements in the RCM implementation, particularly regarding the issues observed with SOL111 and SOL112 analyses, namely the distinction between rigid-body and constant-pressure modes and the missing residual vector computation.

8. REFERENCES

1. N. Maugis (2024). Dynamic Modelling of Fluid-Structure Interaction in Thin-Walled Liquid Propulsion Stages with the Real Coupled Modes Method.
2. H. Wandinger (1988). Modal analysis of fluid-structure-systems by parallel subspace iteration, ECSSMET.
3. J. Wandinger (1996) A symmetric Craig-Bampton formulation for coupled fluid-structure systems, ECSSMET.
4. X. Vaquer Araujo (2011). Validation of Equivalent Viscous Damping Methodologies.
5. X. Vaquer Araujo, S. Fransen, S. Germès, N. Thiry (2012). Validation of equivalent viscous damping methodologies, CEAS Space Journal.
6. S. Fransen (2005). Methodologies for Launcher-Payload Coupled Dynamic Analysis.
7. S. Fransen, S. Caeiro, H. Fisher (2023). CLA Tool Preparation for VEGA-C/E - Progress, ESA internal report.
8. S. Fransen (2024). CLA Tool Preparation for VEGA-E - FSI, ESA internal report.
9. S. Fransen, A. Kreis, M. Klein (2005). Rigid body mode control of free-free launcher structural models in gravity fields, American Institute of Aeronautics and Astronautics.

LAUNCH VEHICLE ASCENT PHASE LOADING: COMPARING TRADITIONAL AND CFD-BASED APPROACHES

Alexis Castel (1), Arun Prakash Ganapathy (2)

(1) Keysight Technologies, 28350 Cabot Dr, Suite 100, Novi, MI 48377, USA,
Email: alexis.castel@keysight.com
(2) Keysight Technologies, Lyoner Str. 20, 60528 Frankfurt, Germany,
Email: arun-prakash.ganapathy@keysight.com

KEYWORDS

launch vehicle ascent, turbulent boundary layer, fluctuating surface pressure, wavenumber-frequency spectrum, hybrid FE-SEA, computational fluid dynamics

ABSTRACT

Launch vehicle ascent generates turbulent boundary layer (TBL) excitations that drive critical structural and acoustic responses. Three aero-vibroacoustic modelling approaches are compared on a common test case: the traditional Corcos TBL model with fitted decay coefficients, Fluctuating Surface Pressure (FSP) analysis applying computational fluid dynamics (CFD) wall-pressure histories with deterministic and random phase, and Generic Surface Pressure (GSP) characterisation using a wavenumber-frequency transformation applicable to both Finite Element and Statistical Energy Analysis subsystems. A Saturn V Spacecraft-Lunar Module Adapter is loaded by a transonic Mach 0.9 unsteady RANS simulation. Fitting the CFD field to a Corcos model retains only the energy the analytical form can represent, and under-predicts the enclosed cavity level by 14 dB overall and by 26 dB below 20 Hz. Applying the same field directly preserves both, which matters because at transonic conditions the convective and acoustic wavenumbers differ by a factor of only 1.6.

1. INTRODUCTION

Between lift-off and the end of the transonic regime, a launch vehicle is exposed to a fluctuating external pressure field that constitutes the dominant source of the payload vibro-acoustic environment. The field is generated by the attached turbulent boundary layer over the vehicle skin, and is locally reinforced by shock oscillation, flow separation and reattachment at geometric discontinuities such as adapter tapers, inter-stage flanges and protuberances. The resulting environment sets the qualification levels for the payload, the payload adapter, and the secondary structure inside the fairing.

The standard industrial practice is to describe this excitation with a semi-empirical cross-spectral model, most commonly the Corcos model [1], whose decay coefficients are obtained from wind tunnel measurements or from flight data on a comparable vehicle. The model is analytical, cheap to evaluate, and defined at every frequency, which makes it attractive for both deterministic and statistical solvers. Its central hypothesis, however, is that the wall pressure field is spatially homogeneous and that its entire energy is convected downstream at a single convection velocity.

Recent work has shown that this hypothesis is not universally satisfied on a real launch vehicle. Following Artemis I, NASA and Boeing conducted an extensive characterisation of the Space Launch System (SLS) ascent environment. Vortex shedding between the core stage and the solid rocket boosters produced a low-frequency excitation that the Corcos description could not reproduce, and comprehensive environment envelopes had to be derived instead from multiple trajectory cases using both random and deterministic fluctuating surface pressure representations. A dedicated validation study of the Corcos model against unsteady Pressure-Sensitive Paint (uPSP) measurements on the SLS [2] confirmed that the model hypotheses hold on smooth panels but break down where the pressure fluctuations are spatially non-uniform.

This motivates a systematic comparison of the alternatives. Two families of methods are available once a spatially resolved description of the wall pressure exists, either from CFD or from a high-density measurement technique such as uPSP:

- direct mapping of the pressure field onto the structural mesh, preserving its spatial variation and, optionally, its phase; and
- characterisation of the field in the wavenumber-frequency domain, producing a transferable source description that can excite both deterministic and statistical subsystems.

The second family has historically been restricted to SEA subsystems. Its recent extension to FE subsystems within VA One removes the frequency discontinuity that previously forced the analyst to change both the excitation description and the structural solver at the FE-SEA crossover.

The objective of this paper is to quantify what each modelling choice retains and what it discards. The three approaches are applied to a single test case — the Saturn V SLA loaded by a transonic URANS simulation — so that the differences observed in the response can be attributed to the excitation description alone. Section 2 describes the three approaches and their wavenumber content. Section 3 describes the CFD model, the load transfer and the vibro-acoustic model. Section 4 presents the responses and the wavenumber analysis of the CFD field. Section 5 discusses the engineering

consequences, including the deliberate use of a URANS simulation and what that implies for the interpretation of the results.

2. MODELLING APPROACHES

2.1. Approach 1: Traditional Corcos TBL

The Corcos model [1] describes the cross-spectral density of the wall pressure between two points separated by streamwise and cross-flow distances ξ_x and ξ_y as a single-point autospectrum multiplied by separable exponentially decaying coherence functions and a convective phase term:

$$S_{pp}(\xi_x, \xi_y, \omega) = \Phi_{pp}(\omega)\, e^{-c_x \left|\frac{\omega \xi_x}{U_c}\right|}\, e^{-c_y \left|\frac{\omega \xi_y}{U_c}\right|}\, e^{-i\frac{\omega \xi_x}{U_c}} \qquad (1)$$

where U_c is the convection velocity and c_x and c_y are the streamwise and cross-flow decay coefficients. For flow aligned with the x axis, representative values are $c_x = 0.10$ and $c_y = 0.72$.

Three parameters therefore define the whole spatial structure of the load, and a fourth function, $\Phi_{pp}(\omega)$, defines its level. The parameters are traditionally taken from wind tunnel measurements. Alternatively, and as done here, they can be identified from a CFD or measured pressure history through a fitting workflow that extracts the pressure spectrum, the convective wavenumber and the decay coefficients from the data.

Refinements of Eq. 1 exist. The models of Chase [4] and Efimtsov [5] modify the low-wavenumber content and the Reynolds number scaling respectively, and a comparative assessment of the common semi-empirical forms is given in [6]. All of them, however, retain the same underlying description of a homogeneous field convected at a single velocity, so the limitation examined in this paper applies to the family as a whole rather than to the Corcos form alone.

Equation 1 places all of the energy on a convective ridge in the wavenumber domain, centred on

$$k_c = \frac{\omega}{U_c}, \qquad k_0 = \frac{\omega}{c_0} \qquad (2)$$

where, in Eq. 2, k_c is the convective wavenumber and k_0 the acoustic wavenumber. Any energy in the physical field that does not lie on or near the convective ridge cannot be represented and is discarded by the fit. Consequently, acoustic content is removed to the extent that its wavenumber support remains distinct from the hydrodynamic convective ridge; where the two overlap within the available wavenumber resolution, the fit cannot provide a unique physical separation. The model is nevertheless defined analytically at all frequencies and can excite both FE and SEA subsystems, which is the principal reason for its continued use.

2.2. Approach 2: Fluctuating Surface Pressure (FSP)

The FSP approach maps the pressure time history $p(x,t)$ from the source mesh directly onto the structural mesh, without any intermediate analytical description. Two modes of application are available:

- **Deterministic**, in which the complex pressure spectrum including its phase is retained, so that the transient peak response and the correct relative phasing of spatially separated loads are preserved; and
- **Random**, in which a cross-spectral matrix is estimated from the time history using Welch averaging [11], and the response is obtained as a statistical envelope.

FSP retains all spatial variation present in the source data, including the local reinforcement near tapers and flanges that a homogeneous model cannot reproduce. The mapping between incompatible source and target meshes uses a consistent or conservative interpolation scheme designed to avoid aliasing of the pressure field when the structural mesh is coarser than the CFD mesh, which is normally the case.

The cost of this fidelity is that FSP requires a full spatially resolved dataset over the loaded surface, and that its accuracy is limited by the structural mesh. It is therefore best suited to the low-frequency modal regime, typically below a few hundred Hertz for a structure of this size.

2.3. Approach 3: Generic Surface Pressure (GSP)

The GSP approach performs a wavenumber-frequency transform of the same space-time pressure field,

$$\Phi(k_x, k_y, \omega) = \frac{1}{(2\pi)^2} \iint S_{pp}(\xi_x, \xi_y, \omega)\, e^{-i(k_x \xi_x + k_y \xi_y)}\, \mathrm{d}\xi_x\, \mathrm{d}\xi_y \qquad (3)$$

and stores the resulting wavenumber-frequency spectrum together with the pressure autospectrum as a reusable source definition. No analytical form is assumed: whatever the data contains is transformed, so the description automatically carries both

- **convective wavenumber components**, at $|k| \approx k_c$, which dominate the excitation of the structure through coincidence with the panel bending wavenumber, and
- **acoustic wavenumber components**, within the radiation circle $|k| \le k_0$, which dominate the transmission of energy through the panel in the mass-controlled regime.

Because the source is expressed in the wavenumber domain, it can be applied to any structure whose modal wavenumber content is known. It has therefore historically been applied to SEA subsystems, for which the response is obtained from the overlap between the source spectrum and the subsystem modal wavenumber filter. The capability has now been extended to FE subsystems, which is significant for two reasons. First, the same source dataset can drive the FE model at low frequency and the SEA model at high frequency, producing a continuous prediction across the crossover from a single characterisation. Second, the wavenumber content is filtered according to the FE mesh, which removes the "mesh too coarse" limitation encountered when a Corcos TBL load is applied directly to an FE model. Figs. 1 and 2 illustrate this on a simple flat panel

benchmark. A Corcos TBL load applied directly to the FE model triggers a mesh resolution warning and produces inaccurate results above approximately 1 kHz, because the FE mesh can no longer resolve the convective wavelength. The equivalent GSP source applied to the same FE model reproduces the TBL result across the whole band without degradation, since the wavenumber content is filtered consistently with the mesh rather than sampled by it.

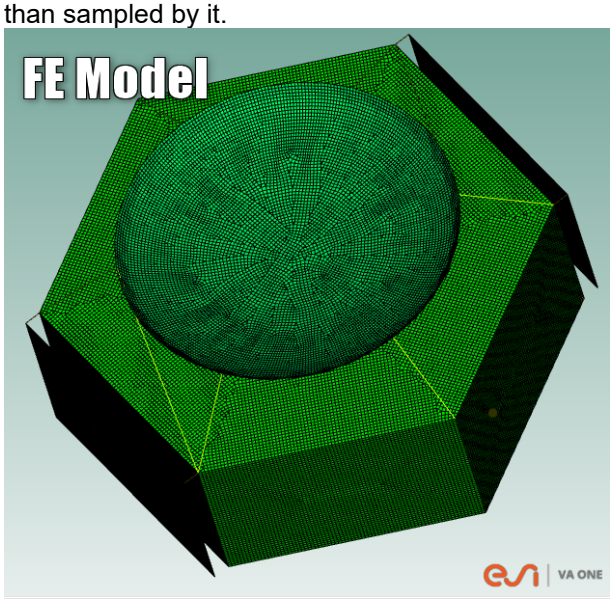


Figure 1: Flat panel benchmark model used to verify the GSP-on-FE implementation.

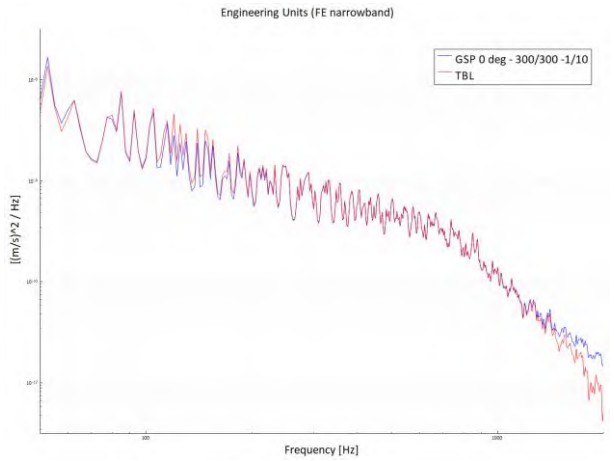


Figure 2: Narrowband velocity response of the flat panel benchmark, comparing a directly applied Corcos TBL load with the equivalent GSP source on the same FE mesh.

The price of the transform is the loss of phase: GSP describes the field statistically, through its cross-spectral content, and therefore cannot reproduce a deterministic transient peak. It also loses the local spatial detail of the source, since the transform is applied over a reference patch and the result is a homogeneous equivalent description.

2.4. Selection guidelines

Tab. 1 summarises the three approaches. The choice is not simply a matter of accuracy: each approach changes which physics is represented.

Table 1: Comparison of the three excitation modelling approaches

Approach	Applies to	Frequency range
TBL: fit Corcos parameters c_x, c_y, U_c to wind tunnel or CFD data	FE, SEA	Full (analytical)
FSP: map CFD $p(x,t)$ directly onto the structural mesh, deterministic or random	FE, BEM fluid	Low (modal regime)
GSP: wavenumber transform of CFD $p(x,t)$, giving a spectrum and a pressure autospectrum	SEA and FE	Low through high

As a practical guideline for an FE application: if the pressure distribution over the excited surface is known, whether from CFD, a boundary element solution or test, FSP gives the best accuracy because it retains local detail and phase. If the distribution is not known, or if an existing characterisation is to be re-used on a different structure, GSP provides a universal source description that transfers cleanly and does not suffer from mesh resolution limits.

3. TEST CASE: SATURN V SPACECRAFT-LUNAR MODULE ADAPTER

3.1. Vehicle and region of interest

The Saturn V was selected as a generic launch vehicle because its geometry and construction are extensively documented and publicly available, which allows the study to be published without restriction. The analysis focuses on the Spacecraft-Lunar Module Adapter, the tapered conical section that housed the Lunar Module between the S-IVB stage and the Service Module (Fig. 3). The SLA is a good candidate for an internal acoustics prediction: it is a closed conical shell enclosing a payload cavity, it presents two geometric discontinuities at its forward and aft interfaces, and its taper produces exactly the kind of non-equilibrium boundary layer for which the homogeneity hypothesis of Eq. 1 is questionable.

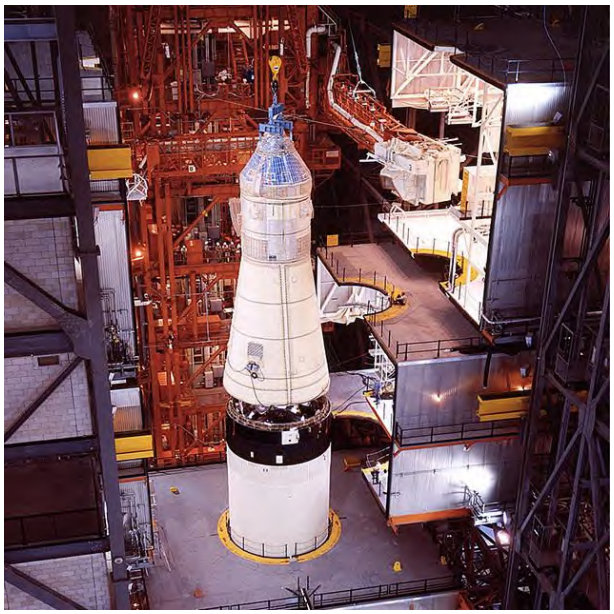


Figure 3: Saturn V launch vehicle showing the Spacecraft-Lunar Module Adapter between the S-IVB stage and the Service Module. Image credit: NASA.

3.2. CFD model

The external flow was computed with OpenFOAM v2112. A steady compressible RANS solution obtained with *rhoSimpleFoam* was used to establish the flow topology, and the production case was run as a compressible transient with *rhoPimpleFoam*. Turbulence was modelled with the *k-ω* SST model [7]. The main settings are listed in Tab. 2.

Table 2: CFD model settings

Parameter	Value
Solver	OpenFOAM v2112, *rhoPimpleFoam*
Turbulence model	*k-ω* SST (URANS)
Mach number	0.9 (transonic, compressible)
Atmosphere	16 000 ft standard
Freestream velocity	289.36 m/s
Static temperature	256.45 K
Static pressure	54 302 Pa
Density	0.736 kg/m³
Speed of sound	321.5 m/s
Dynamic pressure	30.8 kPa
Unit Reynolds number	1.3×10^7 m^{-1}
Mesh size	20.4×10^6 cells, 97 695 wall faces
Time stepping	Adaptive, CFL ≤ 0.25, $\Delta t_{max} = 10^{-5}$ s
Physical duration	0.5 s, of which 0.4 s usable
Pressure sampling	Δt = 0.2 ms on the vehicle wall patch
Output	Wall pressure time series in UNV format
HPC resources	128 MPI ranks, scotch decomposition

Figs. 4 and 5 show the velocity magnitude and static pressure fields in a longitudinal plane through the converged solution. The flow accelerates over the forward taper and separates locally at the interstage discontinuities, producing a strongly non-uniform mean pressure distribution over the adapter region.

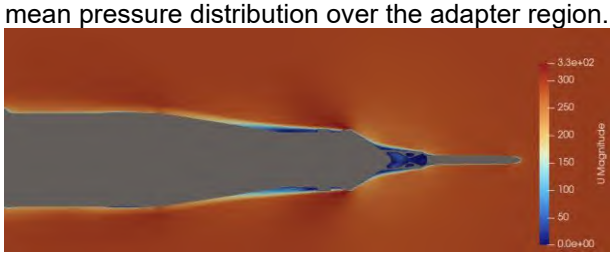


Figure 4: Velocity magnitude in a longitudinal plane, Mach 0.9.

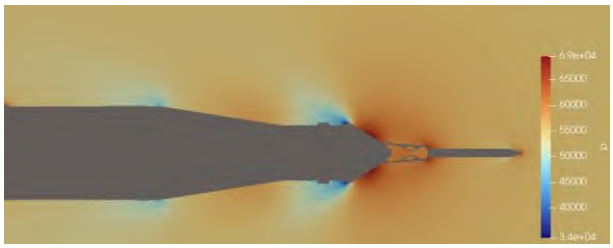


Figure 5: Pressure in a longitudinal plane, Mach 0.9.

3.3. Load extraction and transfer

Wall pressure was sampled on the vehicle wall patch every 0.2 ms, giving a sampling rate of 5 kHz and a Nyquist frequency of 2.5 kHz. The first 0.1 s of the transient was discarded as start-up, leaving 0.4 s of usable signal, which corresponds to 2000 samples and a frequency resolution of 2.5 Hz. The sampled surface was restricted to a band covering the adapter region, and the cell-centred OpenFOAM pressure was mapped onto the surface nodes by area-weighted averaging over the triangles sharing each node,

$$p_i = \frac{\sum_{c \in \mathcal{N}(i)} p_c A_c}{\sum_{c \in \mathcal{N}(i)} A_c} \qquad (4)$$

where, in Eq. 4, $\mathcal{N}(i)$ is the set of surface triangles containing node i. The nodal history was written as an ASCII universal file containing the node block, the element block, and one analysis dataset per time step, which is read directly by VA One.

The same dataset was then used three times: fitted to Eq. 1 to produce the Corcos parameters for Case 1, mapped directly onto the structural mesh for Case 2, and transformed with Eq. 3 to produce the wavenumber-frequency source for Case 3. This is what allows the comparison to isolate the effect of the excitation model.

Fig. 6 shows the overall root-mean-square level of the mapped pressure field on the adapter. The distribution is markedly non-uniform, spanning 108.8 to 150.1 dB over the loaded surface. Elevated levels appear as a streamwise band on the forward part of the cone and along the circumferential junction between the conical adapter and the cylindrical section, approximately 15 to 20 dB above the surrounding shell. This spatial structure is exactly what a homogeneous cross-spectral model is unable to represent.

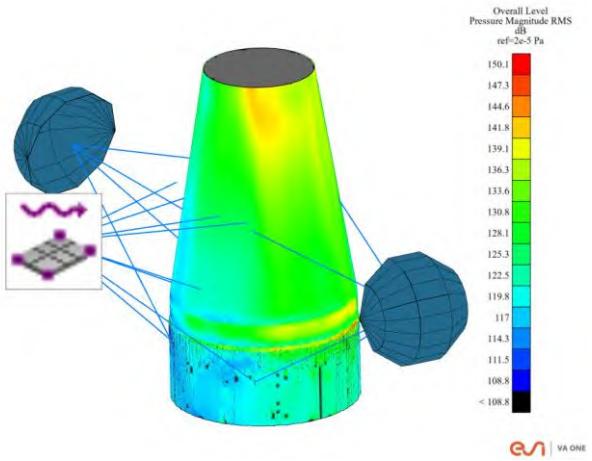


Figure 6: Overall RMS level of the CFD wall pressure mapped onto the adapter surface (dB ref 20 μPa).

3.4. Vibro-acoustic model

The vibro-acoustic model was built in VA One [10], which couples deterministic Finite Element subsystems to statistical subsystems using the hybrid FE-SEA formulation of Shorter and Langley [8]; the statistical subsystems themselves follow classical SEA [9]. Two representations of the same structure were created so that the full frequency range could be covered:

- an **FE model** of the adapter (Fig. 7), using equivalent generic material properties selected to be consistent with the documented construction: sandwich panels for the conical shell, a cork thermal protection layer, and a lumped mass representing the Lunar Module. The enclosed volume is modelled as an FE acoustic cavity generated by a shrinkwrap of the interior. The structural subsystems carry 3434 modes up to 300 Hz and the acoustic cavity 1588 modes up to 300 Hz, and the FE analysis is run from 5 to 250 Hz.
- an **SEA model** of the same adapter (Fig. 8), with the conical shell divided into circumferential and axial panel subsystems and the interior represented as an acoustic cavity subsystem, run from 200 to 2000 Hz.

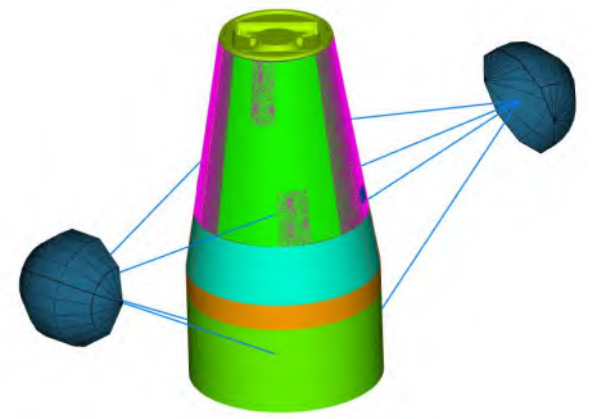


Figure 7: FE structural model of the adapter with the enclosed acoustic cavity.

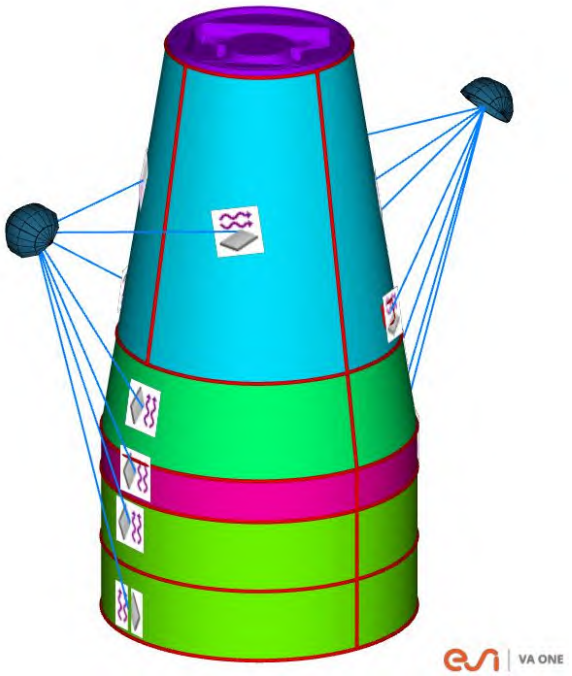


Figure 8: SEA model of the same adapter used above 200 Hz.

Two response quantities are reported: the space-averaged sound pressure level in the enclosed cavity, which is the quantity of interest for the payload environment, and the panel velocity response at forward and aft locations on the conical shell. Analytical treatments of sound transmission into a TBL-excited shell [3] show that the interior level is governed by the overlap between the excitation wavenumber content and the joint structural-acoustic modal content, which is the mechanism the present comparison probes numerically.

4. RESULTS

4.1. Case 1: fitted Corcos TBL loading

The CFD pressure history was processed to extract the pressure autospectrum, the convective wavenumber and the decay coefficients, and the resulting Corcos model was applied as a random load to the FE subsystems from 5 to 250 Hz and to the SEA subsystems from 200 to 2000 Hz. The two solutions are continuous across the crossover, confirming that the analytical source is consistently interpreted by both solvers.

This case is the reference against which the CFD-based approaches are compared, since it represents current practice: a CFD or wind tunnel dataset reduced to four parameters.

4.2. Case 2: FSP loading

The mapped CFD pressure was applied directly to the FE model in both deterministic and random mode. Only the FE regime is available for this case, as expected.

The difference between the two application modes is significant. In the random mode the response is 3 dB higher overall than in the deterministic mode,

and the difference is concentrated above 50 Hz, where the random application reaches 6 to 8 dB higher band levels. Below 20 Hz the two modes agree within 3 dB. The deterministic application preserves the particular relative phase contained in the sampled time history, so spatially separated contributions that are out of phase can cancel in the modal generalised force. The random application instead propagates the full cross-spectral description of the pressure field and combines the resulting mean-square modal contributions statistically. It therefore represents an ensemble of admissible phase relationships rather than one phase realisation and is more likely to excite a broader set of structural modes and propagation directions. In this engineering sense, the result behaves like a root-sum-square statistical envelope across phase contributions, although it should not be interpreted as a literal search for the single worst phase combination. The effect is expected to become more pronounced when several vortices shed simultaneously at low frequency, which is precisely the configuration reported on the SLS.

4.3. Case 3: GSP loading

The wavenumber transform of the same CFD field was applied as a general surface pressure to both the FE and the SEA representations. As in Case 1, the FE and SEA solutions join continuously at the crossover, which demonstrates the intended benefit of the extended capability: a single physics-based source dataset, derived from CFD without any analytical assumption, drives the whole frequency range.

4.4. Comparison of cavity levels

Fig. 9 compares the cavity sound pressure level obtained with all four load applications in the FE regime, and Fig. 10 compares the Corcos and GSP results in the SEA regime. Band-averaged levels are given in Tabs. 3 and 4.

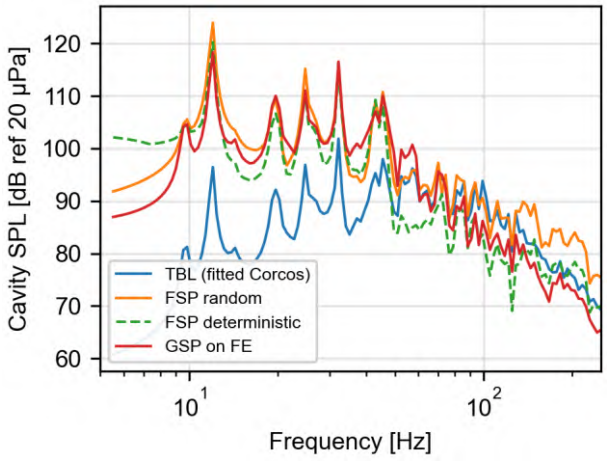


Figure 9: Cavity sound pressure level, FE regime (5-250 Hz), for the fitted Corcos TBL, FSP random, FSP deterministic and GSP loadings.

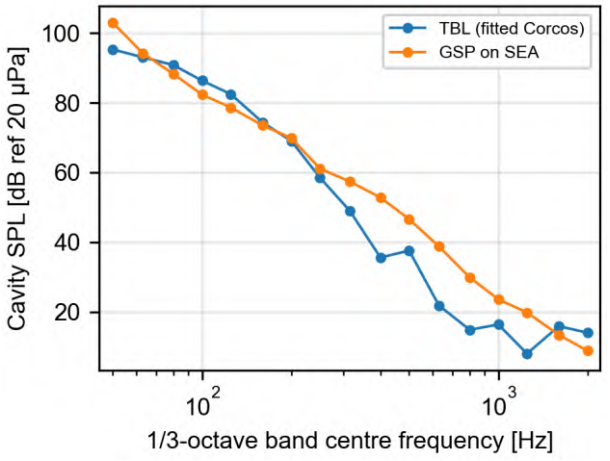


Figure 10: Cavity sound pressure level, SEA regime (1/3-octave bands, 50-2000 Hz), for the fitted Corcos TBL and GSP loadings.

Table 3: Band-averaged cavity sound pressure level, FE regime, dB ref 20 µPa

Band [Hz]	TBL (FE)	FSP random	FSP determ.	GSP (FE)
5-20	84.0	109.8	106.7	105.0
20-50	92.4	106.8	104.8	106.2
50-100	92.5	93.3	86.3	94.2
100-200	84.1	86.4	78.5	79.6
200-250	72.6	80.2	74.6	69.6
Overall 5-250	**110.6**	**127.7**	**124.9**	**124.5**

Table 4: Band-averaged cavity sound pressure level, SEA regime, dB ref 20 µPa

Band [Hz]	TBL (SEA)	GSP (SEA)
50-100	93.4	98.9
100-200	83.3	79.5
200-500	63.4	64.7
500-1000	33.0	42.6
1000-2000	14.6	19.5
Overall 50-2000	**98.6**	**103.7**

Three observations follow.

First, **the two CFD-based approaches agree with each other far better than either agrees with the fitted TBL model.** Over the FE range the FSP random and GSP overall levels differ by 3.2 dB, and their band levels agree within 5 dB up to 100 Hz. Both exceed the fitted TBL result by 14 to 17 dB overall.

Second, **the discrepancy is concentrated at low frequency.** Between 5 and 20 Hz the fitted TBL model is 21 to 26 dB below the CFD-based results, and between 20 and 50 Hz it is 12 to 14 dB below. Above 50 Hz the four predictions converge to within a few decibels. This is the signature of energy present in the CFD field that does not fit the convective form of Eq. 1: at low frequency the convective wavelength is long compared with the adapter, the resonant response is controlled by a small number of low-order modes, and the modal generalised force is dominated by the low-wavenumber content that the Corcos fit removes.

Third, **GSP is a good approximation of FSP.** GSP

loses the local spatial detail of the mapped field, which is why its band levels fall below the FSP result above 100 Hz, but it reproduces the overall level to within 3.2 dB while remaining applicable across the whole frequency range and to both solver types. The same ranking is observed for the panel velocity responses at the forward and aft locations on the conical shell, where the fitted TBL model again falls below both CFD-based random predictions.
The engineering consequence is direct: reducing a CFD dataset to Corcos parameters in a region of separated or non-equilibrium flow can lead to a **non-conservative** load prediction.

4.5. Wavenumber analysis of the CFD field

To understand why, the wavenumber-frequency spectrum of the CFD wall pressure was examined at individual frequencies. Fig. 11 shows the spectrum computed from a Corcos description at 2000 Hz for reference: the energy forms a single ridge centred on the convective wavenumber $k_c \approx$ 100 rad/m, elongated in k_y, exactly as Eq. 1 prescribes. This is the only structure a fitted TBL model can produce.

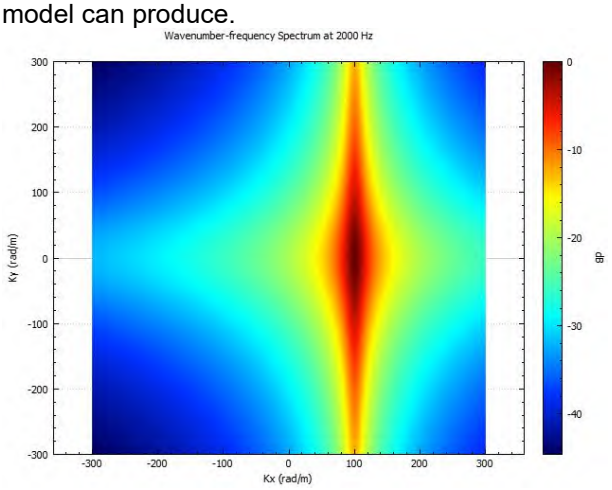


Figure 11: Wavenumber-frequency spectrum of a Corcos description at 2000 Hz, showing the single convective ridge.

Figs. 12 and 13 show the spectrum obtained from the CFD field at 50 Hz and at 120 Hz. The white circle marks the acoustic radiation circle $|k| = k_0$. At 50 Hz the energy is concentrated close to the origin and is elongated in the cross-flow direction, with both the convective and the acoustic content contained within a few rad/m of each other. At 120 Hz the distribution has two distinct features: a dominant peak inside the acoustic circle, and a weaker lobe at negative k_x around 8 rad/m. At this frequency the acoustic content is the stronger of the two.

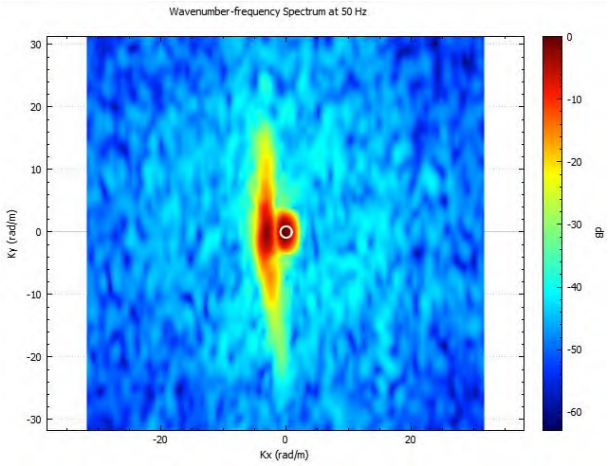


Figure 12: Wavenumber-frequency spectrum of the CFD wall pressure at 50 Hz. The white circle marks the acoustic wavenumber.

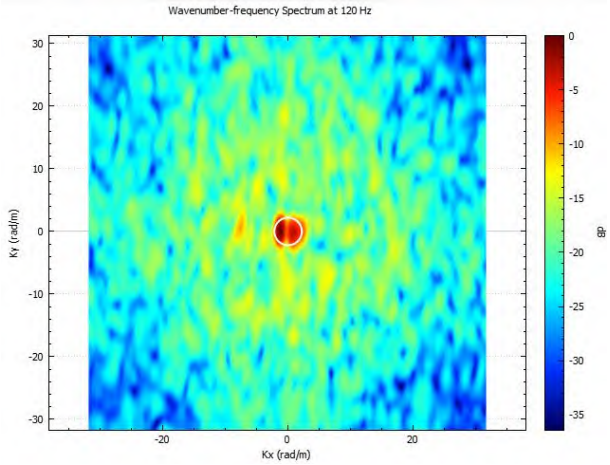


Figure 13: Wavenumber-frequency spectrum of the CFD wall pressure at 120 Hz, showing dominant energy inside the acoustic circle.

This is a consequence of the flow regime. The ratio of the convective to the acoustic wavenumber is

$$\frac{k_c}{k_0} = \frac{c_0}{U_c} = \frac{1}{\alpha M} \qquad (5)$$

where, in Eq. 5, M is the freestream Mach number and $\alpha = U_c/U_\infty \approx 0.7$. At $M = 0.9$ this gives $k_c/k_0 \approx 1.6$. In a low-speed application the two characteristic wavenumbers may be separated by an order of magnitude, whereas under the present transonic conditions they are much closer. The spectra in Figs. 12 and 13 nevertheless retain information outside the fitted convective ridge, including energy within the acoustic radiation circle. The distinction should therefore be interpreted from the full directional spectrum and its finite resolution, rather than from the ratio of wavenumber magnitudes alone. Within that limitation, assigning the complete field to a single convective ridge removes or misattributes the non-convective contribution represented in the CFD data.

5. DISCUSSION

5.1. On the use of a URANS simulation

The CFD simulation used here is an unsteady RANS calculation, not a scale-resolving one. In a

study of turbulent boundary layer excitation this is at first sight a serious limitation: an eddy-viscosity closure models the turbulent stresses rather than resolving them, so the wall pressure field contains only the unsteadiness that the mean-flow equations themselves produce — shock motion, separation and reattachment dynamics, and the large-scale unsteady loading of the geometric discontinuities — and not the broadband small-scale convective content of a resolved boundary layer. The resolved bandwidth is further limited by the surface mesh, which supports content up to roughly 1 kHz, well below the 2.5 kHz Nyquist frequency of the sampling.

For the specific question addressed in this paper, the URANS field provides a deliberate stress test of the load-reduction step. Because the resolved small-scale convective content is limited, the comparison emphasises the low-wavenumber, acoustic and large-scale unsteady contributions that are most vulnerable to removal by a convective-only fit. The 21 to 26 dB low-frequency deficit in Tab. 3 therefore quantifies what the fitted Corcos representation discards from this particular CFD field; it is not presented as a validation of the absolute launch environment or as proof that the same deficit applies to every ascent flow. A scale-resolving simulation would populate the convective ridge more fully and could reduce the difference between the methods, while any resolved content outside the fitted ridge would still be excluded by the reduction.

This leads to the central argument of the paper. Direct use of a CFD-derived load removes the additional uncertainty introduced by forcing the computed field into a prescribed analytical wavenumber form: the load is applied in a model-agnostic manner, carrying whatever acoustic and hydrodynamic content the simulation actually resolves. The structure then acts as the filter through the overlap between the source wavenumber spectrum and its own modal wavenumber content. This does not remove uncertainty in the CFD itself, which remains governed by the turbulence model, mesh, sampling duration and load-transfer procedure; it removes the separate doubt over which parts of that computed field survive an analytical fit. Fitting the data to Corcos instead imposes a convective wavenumber shape before the structure is given the opportunity to respond.

5.2. CFD-based loading changes the predicted physics

The results support a stronger statement than "CFD-based loading is more accurate". The three approaches do not converge on a common answer with different error bars; they represent different physics. The fitted TBL model represents a homogeneous convected field. FSP represents the actual spatial distribution of the load including its phase. GSP represents the actual wavenumber content of the load without its phase. Where the flow is smooth and attached the three descriptions are nearly equivalent, which is why the predictions agree above 50 Hz in this case. Where the flow separates or the geometry changes, they are not equivalent, and the choice determines the answer.

A practical corollary is that the GSP characterisation is transferable. Because it is a source description rather than a model of a particular structure, a random sound field that does not fit any standard analytical model can be established once — from CFD, from a rigid-model test, or from uPSP data — and then applied to a different structure. This is directly relevant to Direct Field Acoustic Testing, where the field generated in the test facility could be characterised on a rigid article with FSP or GSP and then applied as a load to the flight article model.

5.3. When to use what

FSP remains necessary where phase matters, where a deterministic peak response is required, and where the local environment must be resolved rather than averaged. GSP is preferable where a universal, transferable random load is required, where the excitation must be applied consistently to FE and SEA subsystems, and where the FE mesh would otherwise limit the applicability of a directly applied TBL load. The fitted TBL model remains appropriate for smooth, attached-flow regions and for rapid trade studies, provided the analyst is aware that its use in separated regions is likely to be non-conservative.

6. ONGOING WORK

The natural extension of this study is to repopulate the convective wavenumber range with a scale-resolving simulation and to repeat the comparison. Two configurations have been prepared for this purpose.

The first is a full 360-degree wall-modelled large eddy simulation on the existing 20.4 million cell mesh, using a WALE subgrid model initialised from the converged URANS solution. The second is a 90-degree rotational-cyclic sector using an improved delayed detached eddy simulation formulation, with the surface refinement on the adapter band increased to approximately 7.8 mm and ten near-wall layers, giving a ratio of boundary layer thickness to cell size of 20 to 26 and a resolved bandwidth of approximately 1 kHz. Rotational cyclic boundaries are used rather than symmetry planes so that turbulent structures convect through the sector boundary instead of being artificially correlated across it.

Both configurations are wall-modelled rather than wall-resolved, and neither has yet produced results suitable for quantitative comparison. Two limitations are already identified. The near-wall resolution corresponds to $y^+ \approx 140$, so the inner layer is modelled and the highest-wavenumber content will remain unresolved. The 90-degree sector restricts the circumferential content of the load to modes with $n = 0, 4, 8, \ldots$, so structural modes with other circumferential orders would receive no generalised

force; the intended mitigation is to assemble the load from four independent time windows of the same run, since the sector arc corresponds to 11 to 17 boundary layer thicknesses and is therefore much larger than the circumferential coherence length.
Comparison of the resulting responses against uPSP-derived environments, following the methodology of [2], is the intended validation route.

7. CONCLUSIONS

Three aero-vibroacoustic excitation modelling approaches were compared on a common test case, a Saturn V Spacecraft-Lunar Module Adapter loaded by a transonic URANS simulation at Mach 0.9, with all three loads derived from the same CFD dataset.

1. Reducing the CFD wall pressure field to fitted Corcos parameters under-predicted the enclosed cavity level by 14 dB overall over 5 to 250 Hz, and by 21 to 26 dB below 20 Hz, relative to the same field applied directly (Tab. 3). The deficit arises because the fit retains only the energy that lies on the convective ridge.
2. The two CFD-based approaches agree with each other to within 3.2 dB overall. FSP retains local spatial detail and phase; GSP loses both but reproduces the overall level closely while remaining applicable to both FE and SEA subsystems.
3. The extension of GSP to FE subsystems removes the frequency discontinuity in the workflow. A single CFD-derived source dataset drove a deterministic FE model from 5 to 250 Hz and a statistical SEA model from 200 to 2000 Hz with continuous results across the crossover, and the wavenumber filtering inherent to the method removes the mesh resolution limit that affects a directly applied TBL load on an FE mesh.
4. At transonic conditions the convective and acoustic wavenumbers are separated by a factor of only about 1.6. The wavenumber-frequency spectra of the CFD field show both contributions, with the acoustic content dominant at some frequencies. A model that places all energy on the convective ridge cannot represent this, which is a structural rather than a parametric limitation of the approach.
5. Applying CFD-derived loads in a model-agnostic manner, without fitting them to a prescribed cross-spectral form, preserves both the acoustic and the hydrodynamic content that the simulation contains and allows the structure to perform the wavenumber filtering. This is the recommended practice for regions of separated or non-equilibrium flow, where the use of a fitted TBL model is likely to be non-conservative.

8. REFERENCES

1. Corcos, G.M. (1964). The structure of the turbulent pressure field in boundary-layer flows. *J. Fluid Mech.* 18(3), 353-378.
2. Soranna, F., Heaney, P.S., Sekula, M.K., Piatak, D.J. & Ramey, J.M. (2022). Validation of the Corcos Model for the Space Launch System using Unsteady Pressure Sensitive Paint. In *AIAA AVIATION 2022 Forum*, Chicago, IL, USA.
3. Tang, Y.Y., Silcox, R.J. & Robinson, J.H. (1996). Modeling of Sound Transmission through Shell Structures with Turbulent Boundary Layer Excitation. NASA Langley Research Center, Hampton, VA, USA.
4. Chase, D.M. (1980). Modeling the wavevector-frequency spectrum of turbulent boundary layer wall pressure. *J. Sound Vib.* 70(1), 29-67.
5. Efimtsov, B. M. (1982). Characteristics of the field of turbulent wall pressure-fluctuations at large Reynolds-numbers. Soviet Physics Acoustics-USSR, 28(4), 289-292.
6. Hwang, Y. F., Bonness, W. K., & Hambric, S. A. (2009). Comparison of semi-empirical models for turbulent boundary layer wall pressure spectra. Journal of Sound and Vibration, 319(1-2), 199-217.
7. Menter, F.R. (1994). Two-equation eddy-viscosity turbulence models for engineering applications. *AIAA Journal* 32(8), 1598-1605.
8. Shorter, P.J. & Langley, R.S. (2005). Vibro-acoustic analysis of complex systems. *J. Sound Vib.* 288(3), 669-699.
9. Lyon, R.H. & DeJong, R.G. (1995). *Theory and Application of Statistical Energy Analysis*, 2nd ed., Butterworth-Heinemann, Boston, MA, USA.
10. Keysight Technologies (2026). *VA One User's Guide*.
11. Welch, P. (1967). The use of fast Fourier transform for the estimation of power spectra: A method based on time averaging over short, modified periodograms. *IEEE Transactions on Audio and Electroacoustics* 15(2), 70-73.

EVALUATION OF STRUCTURAL ANALYSIS FOR METUCUBE SATELLITE: LESSONS LEARNED

Elif Irmak Kaynar [(1)], İbrahim Doğa Ergin [(2)], Yasin Güngör [(3)], Assoc. Prof. Dr. Halil Ersin Söken [(4)], Asst. Prof. Dr. Görkem Eğemen Güloğlu [(5)]

[(1)] Middle East Technical University, METU Aerospace Engineering Department 06800 Çankaya Ankara/Turkey, Email: irmak.kaynar@metu.edu.tr
[(2)] Middle East Technical University, METU Aerospace Engineering Department 06800 Çankaya Ankara/Turkey, Email: doga.ergin@metu.edu.tr
[(3)] Middle East Technical University, METU Aerospace Engineering Department 06800 Çankaya Ankara/Turkey, Email: yasin.gungor@tubitak.gov.tr
[(4)] Middle East Technical University, METU Aerospace Engineering Department 06800 Çankaya Ankara/Turkey, Email: esoken@metu.edu.tr
[(5)] Middle East Technical University, METU Aerospace Engineering Department 06800 Çankaya Ankara/Turkey, Email: gguloglu@metu.edu.tr

KEYWORDS

CubeSat, structural optimization, finite element analysis, vibration.

ABSTRACT

This paper presents the structural verification and mass optimization of METUCube, a 3U Earth observation nanosatellite. To ensure survivability during severe launch environments, the primary structural skeleton was evaluated using static, modal, harmonic, and random vibration analyses. A comparative study between the unoptimized baseline framework and the final flight-ready configuration is conducted using ANSYS. The results demonstrate the efficiency of geometric modifications in reducing structural mass while maintaining critical dynamic stiffness and positive safety margins for mission qualification.

1. INTRODUCTION

The development of the Cube Satellite (CubeSat) standard has significantly lowered the barrier to entry for Low Earth Orbit (LEO) missions, enabling complex Earth observation and scientific payloads to be mounted within highly constrained form factors [1]. For a three-unit (3U) nanosatellite, the primary structural frame must securely accommodate embedded avionics and optical systems while strictly adhering to the volumetric and mass limitations dictated by standard deployer mechanisms [2]. Consequently, the structural skeleton must be engineered to provide maximum internal capacity and mass efficiency without compromising the critical dimensional stability required to survive the launch sequence [3].

During the launch phase, this primary structure is subjected to extreme mechanical loads including severe quasi-static accelerations, transient acoustic shocks, and broadband random vibrations [4]. To ensure mission success and prevent catastrophic structural failure, launch authorities require comprehensive environmental verification. Standards such as the NASA General Environmental Verification Standard (GEVS) and the European Cooperation for Space Standardization (ECSS) guidelines enforce that the fundamental natural frequency of the spacecraft remains sufficiently decoupled from low-frequency excitation modes of the launch vehicle [5, 6]. For small satellite structures, this typically requires achieving a first modal frequency well above 100 Hz, which is a target that demands highly optimized axial load paths and rigid transverse bulkheads [7].

Because empirical vibration testing of multiple physical prototypes is prohibitively expensive and time-consuming, Finite Element Analysis (FEA) is universally employed to predict and refine structural behavior during the preliminary design phases [8]. Recent advancements in satellite engineering emphasize the reduction of structural mass through iterative geometric pocketing and topological optimization of the primary chassis [9]. By strategically removing material from low-stress domains and relying on continuous longitudinal ribs to carry shear and axial loads, designers can significantly decrease the overall mass of the skeleton while preserving global torsional rigidity [10].

Building upon these structural optimization principles, this study details the mechanical development of METUCube, which is a 3U Earth observation nanosatellite designed by the Small Space Systems Laboratory (S3 Lab) at Middle East Technical University (METU). Intended for a 500-kilometer Sun-Synchronous Orbit (SSO) to monitor natural hazard progression, METUCube requires an exceptionally stable internal framework to support its precision optical payload. Rather than documenting the entire chronological design cycle, this paper presents a focused and comparative FEA study between the initial and unoptimized baseline

structural skeleton and the finalized flight-ready configuration. Through comprehensive static, modal, harmonic, and random vibration analyses, the efficiency of the applied lightweighting strategy is evaluated, demonstrating how severe dynamic launch constraints can be successfully satisfied within a highly restrictive mass budget.

2. METHODOLOGY

Prior to physical qualification, spacecraft shall obtain advanced computational validation to ensure structural survivability under severe launch vehicle environments. For the METUCube satellite, structural identification and verification were conducted utilizing FEA through ANSYS Mechanical 2024. The computational validation was structured around four essential aerospace analyses such as static structural, modal, harmonic response, and random vibration. Static analysis evaluates structural integrity against quasi-static launch accelerations, whereas modal analysis extracts the fundamental natural frequencies to ensure decoupling from launch vehicle resonances. Harmonic and random vibration analyses simulate the structural response and dynamic fatigue subjected to broadband vibroacoustic launch environments.

Because nanosatellite structural development is a highly iterative process, this study focuses on a comparative evaluation between the unoptimized baseline geometry and the final optimized flight configuration. Analyzing these two specific cases provides a consistent framework to quantify the mass reduction and structural performance enhancements achieved throughout the project, highlighting the key lessons learned from the design iterations.

2.1 Geometric Configurations and Design Evolution

Before establishing the finite element parameters, it is necessary to define the physical modifications that differentiate the baseline structural skeleton from the optimized flight configuration. The transition between these two iterations was driven by a combination of subsystem integration constraints and preliminary load path optimizations across the assembly. Isometric views for both of the designs are given in Fig. 1 and 2.

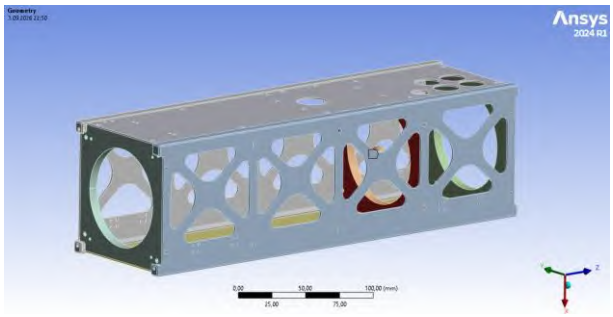


Figure 1: Geometry of initial baseline design

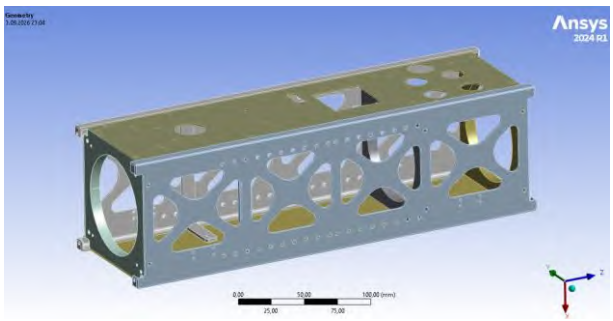


Figure 2: Geometry of final flight-ready design

To enhance the dynamic stability of the forward chassis, two supplementary rod-type supports were integrated directly above the middle bulkhead. This addition provides necessary longitudinal stiffening against lateral and axial vibrations experienced during the launch phase as illustrated in Fig. 3.

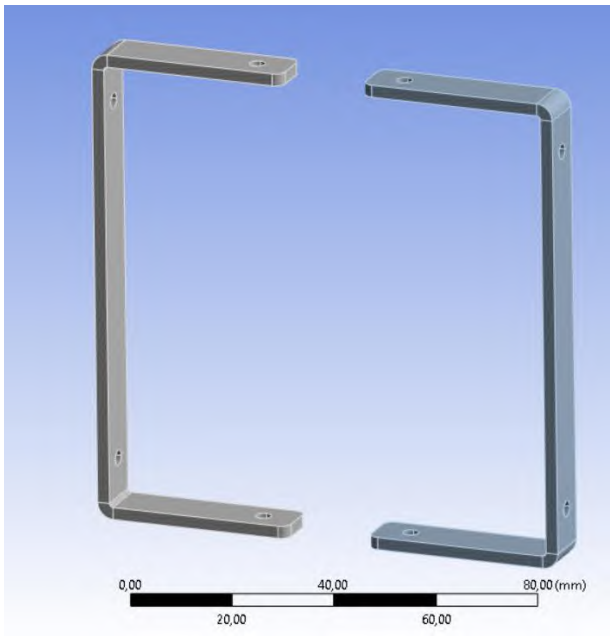


Figure 3: Supplementary rod-type supports

Furthermore, the top frame geometry was modified to include a dedicated square cutout to accommodate electronics significant for deployment. This precise structural vacancy was drilled to securely house the deployment printed circuit board (PCB), ensuring reliable mounting

without violating the external deployer envelope. The updated top frame configuration is detailed in Fig. 4.

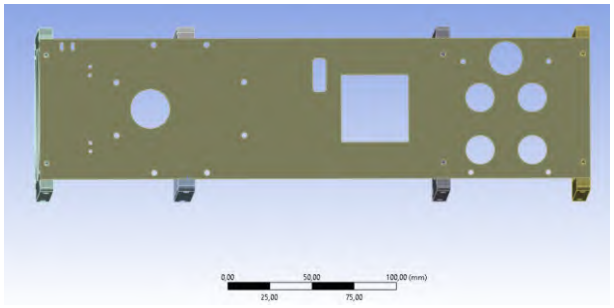


Figure 4: Updated top frame configuration

A critical aspect of the lightweighting strategy involved the topological reshaping of the structural vacancies along the side frames. The geometry of these machined cutouts was iteratively refined to alleviate localized stress concentrations and promote a more uniform load transfer across the primary structure. Fig. 5 displays the optimized geometry for right side frame of final design.

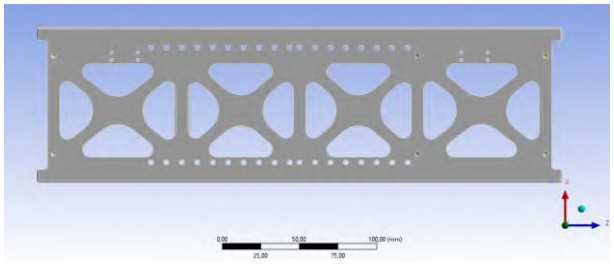


Figure 5: Right side frame of final flight-ready design

Finally, the internal architecture of the payload section was significantly altered through a spatial reconfiguration of the camera distribution. This redesign was implemented to improve volumetric efficiency and align the global center of gravity with the longitudinal axis, which minimizes eccentric loading during deployment and orbital maneuvers.

2.2 Material Definition

All primary structural components including external frames and internal bulkheads were defined as Aluminum 6061-T6. This space-grade alloy was selected for its high specific strength, exceptional machinability, and strict compliance with standard Picosatellite Orbital Deployer (POD) material requirements. The isotropic linear elastic properties utilized for the finite element analysis were obtained from standard aerospace material databases and imported directly into the ANSYS material library [11].

2.3 Mesh Discretization Strategy

Because the 3U skeletal framework is a highly complex assembly comprising interconnected frames and localized pocketing, a high-fidelity mesh discretization strategy was implemented. To balance computational efficiency with numerical accuracy, the global mesh utilized advanced sizing controls including high resolution, refined span angle centers, and slow element transitions. These specific controls were essential for accurately capturing the stiffness of structural components and preventing heavily skewed elements around complex fillets.

Furthermore, localized face and edge sizing tools were applied to regions prone to high stress concentrations such as fastener holes, modular cutouts, and asymmetric joint interfaces, where default meshing algorithms are typically inadequate. An orthogonal mesh quality threshold of 70% was strictly enforced across the assembly with particular emphasis on the critical external rail interfaces and primary load-bearing joints.

2.4 Boundary Conditions and Loading Scenarios

To accurately simulate the kinematic constraints of the satellite during the critical launch and deployment phases, geometric boundary conditions were defined to replicate the physical interfaces within the POD. Fixed supports were applied to the designated slider rail surfaces and kill switch contact points, restricting degrees of freedom to simulate the stowed launch configuration. The fixed boundary conditions applied to the final design version are shown in Fig. 6.

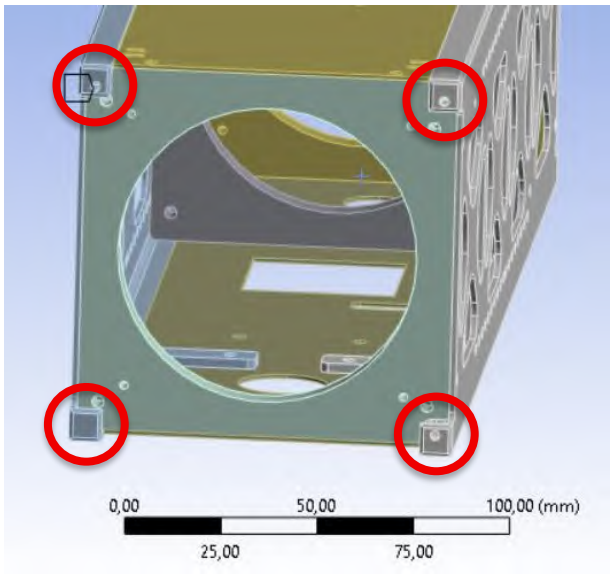


Figure 6: Fixed boundary conditions for structural analysis

The environmental loading profiles applied across all four FEA modules were explicitly derived from standard aerospace qualification guidelines such as

the NASA General Environmental Verification Standard (GEVS) and the European Cooperation for Space Standardization (ECSS) testing profiles [5, 6]. By applying these standardized quasi-static accelerations and Power Spectral Density (PSD) curves, identical loading boundary conditions were implemented on both the baseline and optimized models. The complete descriptions of loading scenarios corresponding to each specific structural analysis is detailed in Tab. 1.

Table 1: Descriptions of loading scenarios corresponding to each specific structural analysis

Type of Analysis	Type of Loading
Static Structural	Acceleration in all directions for tension with an amount of $60\ m/s^2$
Modal	No loading input required
Harmonic Response	Acceleration in all directions for tension with a frequency range between 20 to 2000 Hz and an amount of $20\ m/s^2$
Random Vibration	PSD Acceleration using 3σ for higher and realistic accuracy, $0.48\ (m/s^2)/Hz$ for 20 and 2000 Hz, and $2.4\ (m/s^2)/Hz$ for 50 and 800 Hz

2.5 Assembly Interfaces and Dynamic Properties

To optimize computational expense while maintaining high structural fidelity, specific modeling simplifications were implemented for the physical interfaces and internal subsystem masses. Simulating nonlinear frictional sliding and threaded bolt engagement across the entire 3U framework is computationally expensive for dynamic random vibration analyses. Therefore, all structural fastening interfaces were modeled utilizing standard **Bonded** contact formulations with default solver settings, ensuring a purely linear system response for efficient dynamic extraction.

The complex geometries of the internal electronics and optical payload components were excluded from the direct geometric mesh. Instead, their inertial contributions were embedded into the global mass matrix using **Point Masses** applied via remote attachments. Based on standard 3U mass estimations, a total of 1.0 kg point masses were assigned to represent the PC/104 avionics stack, and a 0.5 kg point mass was assigned to the payload block. Because the PC/104 section physically interfaces between the top and middle bulkheads in the structural Computer-Aided Design (CAD) model, the remote attachments were mounted directly between these components. A similar mounting strategy was employed for the payload unit with its representative point mass attached directly to the section between the middle and bottom bulkheads to accurately reflect its physical integration.

Finally, to prevent unconstrained resonant amplification during the harmonic and random vibration simulations, a constant global structural modal damping ratio of 2% was applied, representing the standard energy dissipation observed in bolted aluminum aerospace assemblies.

3. RESULTS AND DISCUSSION

The comprehensive results of the finite element analyses for both the initial baseline and the final optimized configurations are summarized in Tab. 2. This comparative overview details the maximum directional deformations, peak von Mises stresses including their respective geometric locations, the first six fundamental natural frequencies, and the calculated margins of safety across all four simulated aerospace load cases.

Table 2: Results of FEA for initial and final design versions

Analysis Module	Performance Metric	Initial Design	Final Design
Mass Properties	Total Framework Mass	748 grams	804 grams
Static Structural	Max Directional Deformation	0.056 mm on the bottom end surface of railroad which is near to where cameras are located	0.014 mm on the surface which does not have a kill switch hole but connected to the POD interface
	Max von Mises Stress	39.947 MPa on the surface which does not have a kill switch hole but connected to the POD interface	118.03 MPa on the top mounting hinge of left solar panel
	Margin of Safety (MoS)	+5.91	+1.34
Modal	First Natural	220,53	312.45 Hz

	Frequency	Hz	
	Second Natural Frequency	238,57 Hz	330.12 Hz
	Third Natural Frequency	387,39 Hz	485.60 Hz
	Fourth Natural Frequency	536,48 Hz	612.30 Hz
	Fifth Natural Frequency	608,38 Hz	680.15 Hz
	Sixth Natural Frequency	624,12 Hz	715.22 Hz
Harmonic Response	Peak Resonance Stress	170.09 MPa at 218 Hz on the kill switch surface near to the right-side frame	142.46 MPa at 312 Hz on the rod support interface
Random Vibration	Max 3σ von Mises Stress	195.30 MPa	165.28 MPa
	Max 3σ Deformation	0.18 mm	0.11 mm

4.1. Mass Properties and Static Structural Evaluation

The iterative development from the initial baseline to the final flight configuration prioritized dynamic stability and highly efficient load path continuity. As detailed in Tab. 2, the integration of the longitudinal rod supports and modified deployment brackets resulted in a moderate mass increase, bringing the total framework mass from 748 g to 804 g. Remarkably, this 7.5% mass addition yielded a massive improvement in global structural stiffness. Under the 60 m/s^2 quasi-static loading environment, the maximum directional deformation decreased by 75%, dropping from 0.056 mm in the initial chassis to just 0.014 mm in the final optimized design as shown in Fig. 7.

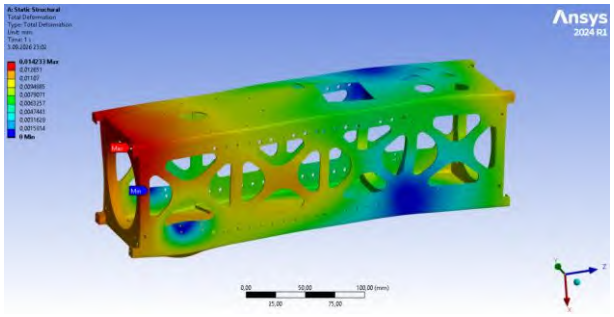


Figure 7: Total deformation under 60 m/s^2 loading for final design

While the global deformation improved significantly, the localized static stress profile exhibited an expected shift due to the new rigid constraints. The initial design recorded a highly distributed maximum von Mises stress of 39.947 MPa. In the final configuration, the integration of the deployment brackets and rod supports constricted the load paths, resulting in a peak stress of 118.03 MPa concentrated specifically at the hinge mounting holes on the primary top frame. Despite this localized spike at the fastener interfaces, the final structure maintains a robust Margin of Safety (MoS) of +1.34 against the 276 MPa yield strength of Aluminum 6061-T6, successfully satisfying static launch requirements with an excellent safety buffer.

4.2. Modal and Dynamic Response Analysis

The primary objective of the structural redesign was to optimally decouple resonant modes of METUCube from the low frequency vibroacoustic environment of the launch vehicle. The initial design exhibited a first fundamental natural frequency of 220.53 Hz, which comfortably cleared the 90 Hz aerospace requirement but indicated a relatively flexible longitudinal axis. By integrating the supplementary rod-type supports above the middle bulkhead, the structural stiffness-to-mass ratio was fundamentally optimized. This highly efficient physical stiffening successfully shifted the first natural frequency upward to 312.45 Hz, pushing dynamic response of the structure substantially further away from critical launch vehicle excitation zones.

This enhanced rigidity directly minimized structural fatigue during dynamic excitation. During the harmonic response analysis, the initial framework experienced a severe resonance amplification, generating a peak stress of 170.09 MPa at 218 Hz on the kill switch surface near to the right-side frame. Conversely, the finalized geometry overcame this resonant spike, reducing the peak harmonic stress to 142.46 MPa at 312 Hz near the new rod support interfaces. A parallel reduction was observed under standard broadband random vibration testing, where the maximum dynamic stress decreased from 195.30 MPa to 165.28 MPa, and maximum dynamic deformation was minimized to 0.11 mm. This ensures that internal optical payloads and avionics stacks are protected from critical mechanical binding or lens misalignment during ascent.

4.3. Intermediate Iterations and Design Trade-Offs

While this study isolates the unoptimized baseline and the final flight-ready geometry for direct comparison, the evolution of METUCube involved several undocumented intermediate steps. Early topological iterations heavily prioritized pure mass

reduction through aggressive wall thinning and maximum cutout dimensions on the side frames. However, computational evaluations of these middle steps revealed severe mechanical drawbacks such that fundamental frequencies dangerously approached the 100 Hz threshold, and lateral buckling occurred in the payload bay under simulated dynamic loading.

Consequently, the final engineering trade-off required abandoning pure lightweighting in favor of strategic stiffening. The primary advantage of the final 804-gram design is its exceptional rigidity-to-mass efficiency, achieving a 75% reduction in static deformation and a 38% reduction in dynamic deformation for a minor 56-gram penalty. The primary disadvantage of this approach is the introduction of highly localized stress concentrations at structural discontinuities, specifically the hinge mounting holes on the top frame. Because the global frame is now highly rigid, impact and vibrational loads are aggressively channeled into these smaller geometric features, requiring higher localized safety factors.

4.4. Lessons Learned in Computational Verification

A critical lesson learned during the design and verification cycle pertained to the severe influence of computational boundary conditions at deployable interfaces. During preliminary analyses, artificial stress singularities exceeding material yield limits were observed around the hinge mounting locations. It was subsequently determined that applying fixed boundary constraints to these hinge holes, meaning that mistakenly modeling them as joint points to the launch vehicle, prevented natural frame flexure under quasi-static acceleration. By restricting the fixed boundary conditions strictly to the external rails and kill switch surfaces that physically interface with the Picosatellite Orbital Deployer (POD), the localized singularities were eliminated. This adjustment underscored that high-fidelity aerospace FEA requires an exact mathematical translation of the physical deployment mechanism as over-constraining secondary mechanical interfaces will inevitably generate false-positive failure modes.

4. CONCLUSION

This study successfully verified the structural integrity and dynamic stability of the METUCube 3U nanosatellite framework under simulated severe launch environments. By conducting a comparative finite element analysis between the initial baseline and the finalized flight configuration, the research demonstrated that iterative geometric optimization must balance mass efficiency with targeted structural stiffening. While early design iterations favored pure mass reduction, the final engineering trade-off accepted a nominal 7.5% mass penalty to enhance global rigidity.

The integration of longitudinal rod supports yielded exceptional mechanical improvements. The optimized framework achieved a 75% reduction in static directional deformation and elevated the first fundamental natural frequency to 312.45 Hz, comfortably exceeding the 90 Hz aerospace testing mandate. Furthermore, this strategic stiffening takes control of critical resonance amplification, reducing the peak random vibration stress to 165.28 MPa and ensuring a robust static margin of safety against the yield limits of Aluminum 6061-T6.

Beyond validating the METUCube platform for its 500 km Sun-Synchronous Earth observation mission, this study highlights critical best practices for computational nanosatellite verification. The resolution of artificial stress singularities through the precise definition of deployer boundary conditions emphasizes the necessity of accurately modeling secondary mechanical interfaces rather than over-constraining the primary frame. Ultimately, the finalized 804-gram primary structure satisfies all volumetric, mass, and dynamic constraints dictated by standard Picosatellite Orbital Deployers, rendering the skeletal framework structurally qualified for physical manufacturing and subsequent environmental testing campaigns.

5. REFERENCES

1. A. Poghosyan and A. Golkar, "CubeSat evolution: Analyzing CubeSat capabilities for utility in science missions," *Progress in Aerospace Sciences*, vol. 88, pp. 59-83, 2017.
2. D. S. Ali and P. S. Ramprasad, "Design and Structural Analysis of Nano-satellite," *International Journal of Engineering Research & Technology*, vol. 10, no. 6, 2021.
3. A. K. M. et al., "Nano-satellite system-meshed model with modal analysis boundary conditions," *Journal of Aerospace Technology and Management*, 2020.
4. G. Veríssimo, G. Graça, M. Alves, and G. Miguéns, "Structural Analysis of LISAT-01 CubeSat," *LISAT Space Technical Reports*, 2024.
5. NASA Goddard Space Flight Center, "General Environmental Verification Standard (GEVS) for GSFC Flight Programs and Projects," NASA GSFC-STD-7000 Rev. A, Greenbelt, MD, USA, 2013.
6. European Cooperation for Space Standardization, "Space Engineering: Testing," ECSS-E-ST-10-03C, Noordwijk, The Netherlands, 2012.
7. L. Nguyen et al., "Structural Dynamics Analysis of 3-U CubeSat," *International Conference on Space Science and Communication*, 2019.
8. M. N. A. R. et al., "Structural Design and Verification of 3U Cubesat Structure using CFRTP/PEEK Material," *Journal of Physics: Conference Series*, 2023.
9. Z. Liu et al., "Topology Optimization of the

Bracket Structure in the Acquisition, Pointing, and Tracking System," *Aerospace*, vol. 11, no. 11, p. 939, 2024.
10. S. S. Kim et al., "Design and structural analysis of 3U CubeSat framework," *Journal of Aerospace Engineering*, vol. 31, no. 4, 2018.
11. MatWeb Material Property Data, "Aluminum 6061-T6; 6061-T651," MatWeb. https://www.matweb.com/search/datasheet.aspx?MatGUID=b8d536e0b9b54bd7b69e4124d8f1d20a

ECSSMET
Braunschweig Germany 2026

Structural dynamics

PREDICTING NONLINEAR VIBRATIONS OF THIN PLATES: THE COMET – I CASE STUDY

Davide Pederbelli [(1)], Alessandro Paci [(1)], Ivan Ngan [(2)], Harald Segelke [(1)], Nicola Riva [(1)], Ivan Gryaznov [(3)]

[(1)] OHB Systems AG, Universitätsallee 27-29, 28359, Bremen, Germany,
Email: davide.pederbelli@ohb.de; alessandro.paci@ohb.de; harald.segelke@ohb.de; nicola.riva@ohb.de

[(2)] ESA / ESTEC - European Space Agency, Keplerlaan 1, 2200 AG Noordwijk, The Netherlands,
Email: ivan.ngan@esa.int

[(3)] OHB Italy, Via Gallarate 150, 20151, Milano, Italy
Email: ivan.gryaznov@ohb-italia.it

KEYWORDS

Nonlinear vibrations, Transient analysis, Sinusoidal Vibrations, NASTRAN® DMAP

ABSTRACT

The Frequency Response Analysis (FRA) Sinusoidal test predictions for COMET-Interceptor revealed critical stress levels that could affect the Dust Shield development.
To ascertain the severity of the environmental non-conformity, the usual FRA approach has been bypassed in favour of test consistent excitations in the framework of linear and non-linear transient analyses over the project phases.
Transient analyses have been designed to accommodate all the physical and numerical details to reproduce the experimental scenario. A Finite Element model tuning along with the application of load-dependent input and fluid mass effects via NASTRAN® DMAP were carefully introduced for that purpose.
The use of such complex and computationally demanding procedure allowed an enhanced simulation of experimental conditions and ascertained stress level reduction passing from the FRA algorithms to the non-linear transient schemes. In such a way, the Dust Shield design robustness was confirmed in the framework of a component de-risking activity.

1. INTRODUCTION

A mandatory step to demonstrate compatibility with respect to the low-frequency launch environment is the Sinusoidal (sine) test. The conventional approach to simulate testing conditions relies on the linear Frequency Response Analysis (FRA), with modal superposition technique or direct ones. In the modal framework, each mode is damped with proper values (e.g., flat damping or skyline profiles) whereas, by using the direct procedure, the damping is introduced via the matrix assembly at physical matrix level [1].
Typically, there is an intrinsic mismatch between test reality and analyses conditions, either at spacecraft or component level. This is ascribable to boundary conditions mismatch, differences in the loading process and the absence control routines in standard computational environments [2].
From test perspectives, in the case of hardware components, or subassemblies, these mismatches can trigger structural non-linear responses (e.g. in mechanisms or large structures) and overloads with consequent overtesting due to high transmissibility.
From the analysis point of view, past studies and correlation activities suggested that is a good practice including additional contributions, such as the air-effect, within the Finite Element (FE) model to increase the model fidelity [3] with respect to test data.
Structural components, mainly composed by plate-like (or foils) geometries, have been extensively recognized as sensitive to loading levels and boundary conditions. These can easily express non-proportional responses (i.e., non-linear) ascribable to large vibrations problems and non-linear damping effects [4, 5].
In the specific case of the COMET-Interceptor´s Dust-Shield, these effects have been recognized as the main root cause of environmental non-conformity during preliminary analyses on the outer bumper layer. This occurrence enforced the need of a more detailed and representative predictions capable of demystifying the expectable test responses.
In this paper, a computationally demanding analysis cycle has been performed in the framework of a component´s de-risking activity. Thus, dedicated linear and non-linear transient analyses have been carefully designed in all the aspects, from the setup of the experimentally consistent loading process to the non-trivial fluid mass injection that have been approached via a specific NASTRAN® DMAP routine.
Numerical results demonstrated a completely different structural reality that was more in line with past heritage and experiences for similar structures.

This work is presented as follows: in *Section 2* a background on non-linear phenomena and non-linear analyses from the NASTRAN® perspective is provided. Then *Section 3* offers mission related information along which describes the technological problem that stimulated such detailed investigation. *Section 4* illustrates the effort toward linear and non-linear analysis setup and discusses the results.
Finally, *Section 5* wraps-up upon the conclusions of the study.

2. BACKGROUND ON NON-LINEARITIES AND ANALYSIS PROCEDURES

Structural non-linearities very often occur during testing scenarios of mechanical hardware. However, non-linear contributions are typically not accounted during hardware development for several reasons such as:

- the in-service structural behaviour is known beforehand to be linear or quasi-linear;
- the amount of non-linearity is limited to a localized area of the component that is negligible for the overall design or testing process;
- to orient the design though a non-linear philosophy requires in-depth knowledge that is not often available.

Nevertheless, there are specific items and applications whose correct in-service conditions are guaranteed only by introducing non-linear effects in the design and simulation loop as mechanical stoppers or joints [6].
In structural engineering, there are three main classes that express the possible non-linear sources such as:

- *Geometric*: problems of such nature invalidate the small displacement theory. It involves large displacement/rotations, large strain problems, post-buckling phenomena. In such case the root-cause is mainly attributed to kinematic and geometrical relations among model parts.
- *Material*: the stress-strain relation is neither no longer proportional nor guarantees the initial structural status after the load removal. Example of such models can include elastic-plastic behaviours, rate-dependent models, hyper elastic models.
- *Boundary conditions*: this class is mainly governed by alternated open-close gaps, impacts and contacts mechanics (e.g., stick-slip effects with or without lift-off), sudden removal of constraints.

In Finite Element Analyses several computational algorithms capable of solving non-linear processes (static or time-dependent) are available.
These require shifting and evolve the point of view during the analysis process to build and correct matrix forms that are no longer time invariant like in static linear analyses. In this regard, the Lagrangian approach describes the elemental deformation during the loading process. This approach can be classified in two well defined categories: the total Lagrangian method and the updated Lagrangian method [7].
These methods are illustrated shortly in the following.
Assuming Fig. 1 as the idealized evolution of a particle structure (or a point mass), the total Lagrangian approach assumes that the equilibrium is expressed on the original undeformed state as the reference one, whereas in the updated Lagrangian approach the current configuration acts as the reference state.

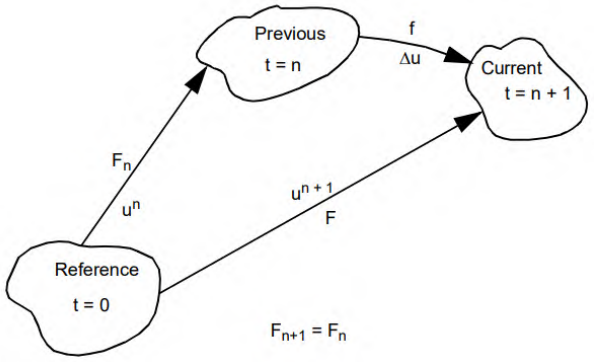


Figure 1: Assumed material motion

Mathematically, these two perspectives are associated and described by Eq.1 and Eq.2, respectively, for implicit time integration (damping is excluded from the formulation for simplicity).

In the case of total Lagrangian

$$\mathbf{M}^{t+\Delta t}\ddot{\mathbf{U}} + ({}_0^t\mathbf{K}_L + {}_0^t\mathbf{K}_{NL})\mathbf{U} = {}^{t+\Delta t}\mathbf{P} - {}_0^t\mathbf{F} \qquad (1)$$

Whereas for the updated Lagrangian

$$\mathbf{M}^{t+\Delta t}\ddot{\mathbf{U}} + ({}_t^t\mathbf{K}_L + {}_t^t\mathbf{K}_{NL})\mathbf{U} = {}^{t+\Delta t}\mathbf{P} - {}_t^t\mathbf{F} \qquad (2)$$

where

- $\mathbf{M}$ is the time-independent mass matrix
- ${}_0^t\mathbf{K}_L$ and ${}_t^t\mathbf{K}_L$ are the linear incremental stiffness matrices,
- ${}_0^t\mathbf{K}_{NL}$ and ${}_t^t\mathbf{K}_{NL}$ are the non-linear strain (geometric or initial stress) incremental stiffness matrices
- ${}^{t+\Delta t}\mathbf{P}$ is the vector of externally applied nodal point loads at $t + \Delta t$
- ${}_0^t\mathbf{F}$ and ${}_t^t\mathbf{F}$ vector of nodal point internal forces
- $\mathbf{U}$ is the vector of increments in nodal point displacements

Eq.1 and Eq.2 look similar at a first glance. However, the selection of a solution perspective

encapsulated within Eq.1 and Eq.2 implies the choice of the reference state for quantity estimation that will remain during the whole analysis process.

Analyses procedures are further complicated by the invalidity of classic linear modal superposition techniques [8] as the hypothesis of mode orthogonality is no longer valid

$$\phi_i{}^T \boldsymbol{M} \phi_j \neq 0 \qquad (3)$$

Eq.3 prohibits the application of the majority of computational algorithms that have been developed over the past decades and implemented in commercial Finite Element tools to speed-up and solve dynamic problems.
This implies that the analysis loop should rely on direct time integration with obvious computational efforts and increase of computational time.

In the complex numerical and scientific panorama that has been just briefly introduced, NASTRAN® offers some capability to solve such type of problems.

2.1. NASTRAN® and numerical schemes

Even though NASTRAN® is not a non-linear native software, it allows some capabilities for solving such problems [1, 9].
Two main analysis processes allow succeeding in direct transient non-linear computations namely the integration scheme and the incremental/iterative logic involved during the non-linear solution.

The most popular integration scheme, that is also embedded in NASTRAN®, is the Newmark-beta method reported in Eq. 4

$$\begin{aligned} \mathbf{U}^{n+1} &= \mathbf{U}^{n} + \Delta t \dot{\mathbf{U}}^{n} + \left(\frac{1}{2} - \beta\right)\Delta t^2 \ddot{\mathbf{U}}^{n} + \beta \Delta t^2 \ddot{\mathbf{U}}^{n+1} \\ \dot{\mathbf{U}}^{n+1} &= \dot{\mathbf{U}}^{n}(1-\gamma)\Delta t \ddot{\mathbf{U}}^{n} + \gamma \Delta t \ddot{\mathbf{U}}^{n+1} \end{aligned} \qquad (4)$$

Regardless from the selected Lagrangian method, and by assuming $\beta = 1/4$ and $\gamma = 1/2$, the equations of motion Eq.1 and Eq.2 can be rewritten as

$$\left.\frac{\partial \boldsymbol{R}(\mathrm{U}^{n+1})}{\partial \mathrm{U}^{n+1}}\right|_{\mathrm{U}^{n+1}} \Delta \mathrm{U}^{n+1} = -\mathbf{R}(\mathrm{U}^{n+1}) \qquad (6)$$

or, simply as

$$\mathbf{K}_{\mathbf{dyn}}^{\mathbf{t+1}} \Delta \mathrm{U}^{n+1} = -\mathbf{R}^{n+1} \qquad (5)$$

where

- $\mathbf{K}_{\mathbf{dyn}}^{\mathbf{t+1}} = \left(\frac{\mathbf{4}}{\mathbf{\Delta t^2 M}} + \frac{\mathbf{2}}{\mathbf{\Delta t C}} + \mathbf{K_L} + \mathbf{K_{NL}}\right)$ is the effective dynamic stiffness
- $-\mathbf{R}^{n+1} = \mathbf{P}^{n+1} - \mathbf{F}^{n} + \mathbf{M}\left(\ddot{\mathbf{U}}^{n} + \frac{4}{\Delta t}\dot{\mathbf{U}}^{n}\right) + \mathbf{C}\dot{\mathbf{U}}^{n}$ is the effective load vector (residual)

It is important to underline that in Eq.5 $\mathbf{K_{dyn}}$ also includes the effect of the tangent stiffness matrix ($\boldsymbol{K_T}$) the is the core non-linear part on the left-hand side member.

In such a way, a dynamic problem is first converted into a statically equivalent one, then it is solved through a root-finder method that minimize $\mathbf{R}^{n+1}$ every i[th] load incremental step. Among the root-finder methods, NASTRAN® works with Newton-Raphson and quasi-Newton methods for non-snap problems.
During the iterative process $\mathbf{K_{dyn}}$ is also typically revised and updated to guarantee an improved and an adaptive convergence.
Automatic and semi-automatic procedures can adjust either the integration time step to facilitate the calculation at those loading levels that are more iteration-demanding ($\Delta t = \lambda_1 \Delta t_0,\ \lambda_1 < 1$) and the injected load level per iteration step such as such as $P_j^{n+1} = \lambda_2 \mathrm{P}_{target}^{t+1}$ $(0 < \lambda_2 \leq 1)$.
The non-linear calculation is thus repeated for all the loading levels toward the analysis conclusion.

3. MISSION AND PRELIMINARY ANALYSES

3.1. The COMET-Interceptor mission

COMET-Interceptor (COMET-I) is an ESA F-class mission aiming at collecting valuable data about the origin of our solar system.
COMET-I will fly toward the Sun–Earth Lagrange point L2 at 1.5 million kilometres far from the Earth waiting for a pristine comet or interstellar object passing close by it.
The goal of the mission is achieved by a number of remote sensing and in-situ instruments accommodated on-board the main SC and two deployable probes. They will observe the target object from multiple angles and will collect information from close perspectives.
The COMET-I development is the expression of the combined effort between OHB-Italy and OHB System AG.

COMET-I is equipped with a Dust Shield that is mounted on top of the SC as illustrated in Fig. 2. Such component aims at protecting the SC, and the instruments within it, from dust and debris clouds that could irreversibly jeopardise the mission [10].
The Dust-Shield, which is based on a Whipple shield design for hypervelocity impact, consists of peculiar design aspects:

- an Outer Bumper of a 0.5 mm thin aluminium sheet,
- a Mid Bumper of a 1.3 mm Kevlar fabric layer, placed in between the outer bumper and the Top Deck,
- a Top Deck consisting of 20 mm sandwich panel that also serves as SC top panel.

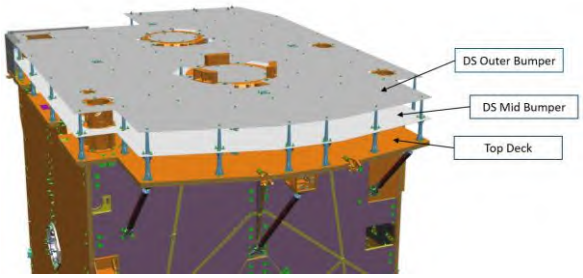


Figure 2: COMET-I Dust Shield Schematic

In specific, the Outer Bumper is a wide, thin aluminium sheet supported at specific locations by brackets and spacers. This design results into multiple suspended areas between the fixation points that are characterized by a low bending stiffness.

3.2. Environmental Sinusoidal analyses

To address the whole design, detailed mathematical models of the SC and the Dust Shield have been developed for combined and standalone environment analyses. The coupled FE model is depicted in Fig. 3. The SC model consists of 1.9 million of nodes (approx. 3 million of elements) whereas the Dust Shield one is 86 thousand nodes (approx. 85 thousand elements)

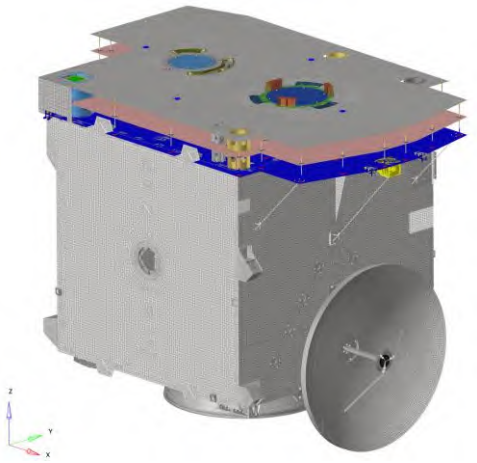


Figure 3: Dust Shield FE-Model on COMET-I Finite Element model

Finite Element FRA simulates the SC – Dust Shield coupled sine environment. Performing these analyses assumes modal superposition techniques along with the inclusion of air effects on the outer layer. Including air effects demonstrated improvement on the test – numerical correlation [3]. Indeed, it is an established procedure of OHB Systems AG structural department for similar components. Constant 2% modal damping along with qualification loads at the SC base have been injected.
The equivalent Von Mises (VM) stress has been used during the whole design and analysis process as a stress metric.

In this scenario, several areas of the Outer Bumper expressed negative/highly negative Margin of Safety (MoS) during longitudinal excitations induced by outer bumper local panel modes below 15 Hz that were associated to very low effective mass contributions.

Numerical results revealed stress peaks significantly above the material yield and ultimate strength (max VM≈900MPa) on the Outer Bumper, as depicted in Fig. 4.

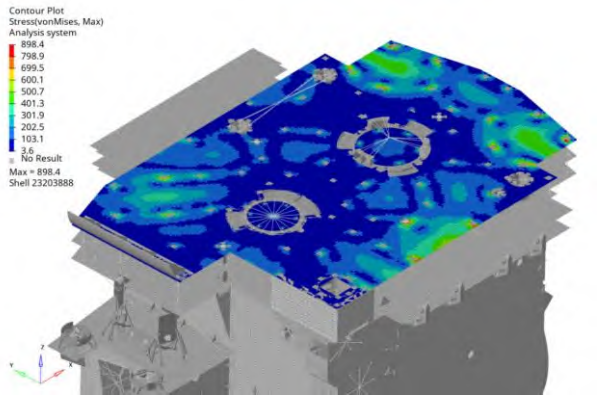


Figure 4: SINE Z - Max Von Mises stress across all the frequencies

For the sake of completeness, also the elemental component stresses have been object of analyses. Tab. 1 reports the elemental results for the most critical element observed during the harmonic analysis.

Table 1: SINE Z max stress peak – Von Mises and Components. Elemental example

	MPa
Von Mises	899
σ_{xx}	746
σ_{yy}	754
τ_{xy}	286

However, such peaks have been considered unrealistic as the associated displacement field predicted in that areas violate the *'small displacement hypothesis',* which is the baseline for standard linear analyses.
Numerically, during the FRA loop the stiffness of the outer bumper remains state-independent and referenced with respect to the undeformed initial configuration.
An example of the predicted displacement field is reported in Fig. 5.

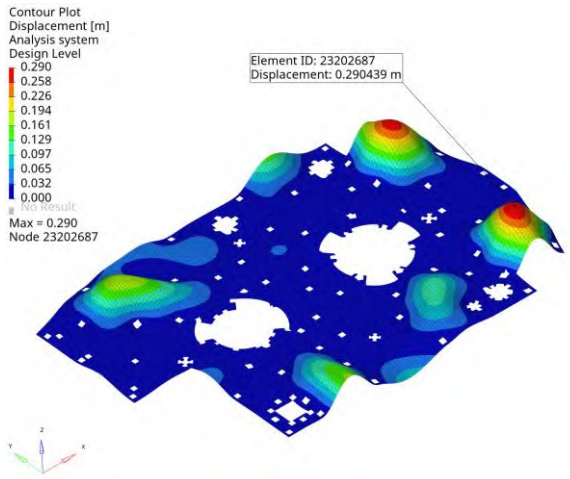


Figure 5: Maximum Displacement predicted at 11.5Hz – 0.29 m

This scenario forced a component de-risking activity to carefully investigate the real severity of the environmental non-conformity via dedicated non-linear transient analyses.

4. NON-LINEAR TRANSIENT ANALYSES

Non-linear procedures aim at increasing the analyses representation with respect to the real testing scenario. Trustworthy structural responses can be achieved by enhancing the computational detail going beyond the FRA limits.
For that purpose, a fine model and analysis tuning consisting of test-consistent transient inputs along with numerically compatible fluid effects have been carefully considered and setup.

4.1. Model and analysis tuning

Before delving into complex and challenging non-linear analysis, an intense activity of model and analysis tuning was performed.
Such activity was necessary to guarantee the correct model injection within the NASTRAN® non-linear solver (SOL129). Loading strategy and damping selection were also tuned and checked via intermediate linear transient procedures that are less time-consuming with respect to non-linear solvers.
This intermediate linear analysis loop has the unique goal of defining a representative model while spanning from the adopted representation in the framework of the FRA to the applicable one within non-linear computations.

For that purpose, the Dust Shield FE-Model has been analysed in Hard Mounted conditions, see Fig. 6. This configuration restricts the model validity up to 35 Hz (i.e., before the SC global modes in longitudinal direction) without affecting the local Dust shield dynamics.
The definition of the applicable damping was objects of an iterative manual process.
The standard 2% modal damping adopted in the FRA was substituted by a combination of structural damping values (i.e., NASTRAN® GE) along with the adoption of a global value (i.e., NASTRAN® PARAM, W4) [11] to specifically match the critical resonance that was leading high stresses. Modifying that global parameter allowed including different dynamic dissipation per analysis set.

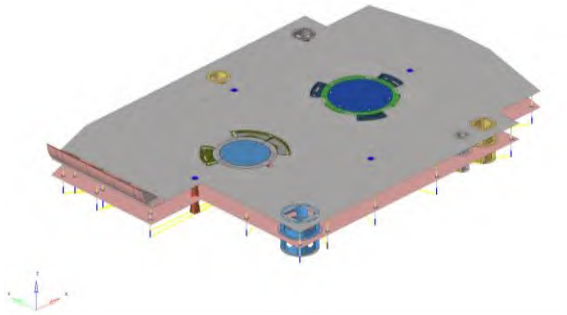


Figure 6: Dust Shield Stand Alone Finite Element Model

Moreover, the fluid card originally based on component mode superposition (i.e., structural modes and fluid modes) has been replaced by a discrete matrix. This matrix was ad-hoc prepared and generated via the NASTRAN® DMAP programming language. The DMAP routine pre-calculates the amount of fluid area spread over the panel surface and attributes a specific mass value to the FE nodes on the reference elemental surface. Such matrix has been supplied via standard Direct Matrix Input at Grid points during the analysis run.

The discrete fluid mass is mode independent thus resulting into a constat contribution over the time.
Within the assumption of the analyses, this inconsistency was under control via local damping modifications as described above.

Finally, a test consistent sinusoidal input profile was generated by assuming a sweep rate (R = 4 oct/min) within the [5 ÷ 100] Hz frequency interval and applied at the Dust Shield base via an enforced motion.
Time – based stress recovery is up to 30sec therefore covering the [5 ÷ 30] Hz frequency range.

Passing from FRA–based analyses to transient computations also requires redefining the stress criterion. If the standard VM is valid in the case of FRA, it should be adapted to account for negative stress values over time (compression components). The NASTRAN® fatigue guide [12] provides the valid solution for this circumstance as reported in Eq.7

$$\sigma_{SVM} = A \cdot \sqrt{\frac{(\sigma_{1-2})^2 + (\sigma_{2-3})^2 + (\sigma_{3-1})^2}{2}} \qquad (7)$$

where

- $\sigma_1, \sigma_2, \sigma_3$ are the principal stress components
- $\sigma_{i-j} = \sigma_i - \sigma_j$
- $A = \frac{\sigma_{amp}}{|\sigma_{amp}|}$ in which $\sigma_{amp} = \max(\sigma_1, \sigma_2, \sigma_3)$

Transient loads within the stress – frequency recovery interval were considered via a constant total input level of 1.65*g* (i.e., qualification and margins; g=9.81 m/s^2). Time integration adopts a time step of 2·10^{-3} sec.

Fig. 7 shows numerical results at the most severe location based on the FRA output whereas Fig. 8 reports a response involving multiple modal contribution over time during the same analysis run.
All the possible model – analysis combinations have been explored to increase and ascertain an adequate model confidence.
With respect to the reference solution that was fully based on modal superpositions and modal quantities (i.e., black curve), these combinations allowed:

- to explore the introduced damping model based on the GE and W4 strategy in the framework of the SPCD enforced motion and modal fluid application (i.e., red curve),
- to evolve the fluid representation by introducing the DMAP discrete fluid matrix (i.e., yellow curve),
- to shift the load injection via the Large Mass Method as further imposed by SOL129 (i.e., grey curve),
- to incorporate all the previous input within a direct dynamic solver that handle the full mass, damping and stiffness matrix within the time integration algorithms (i.e., green curve) [1].

Fig. 7 and Fig. 8 demonstrate comparable and repeatable results, with marginal mismatches at the resonance peak. This ensures the goodness of the model for non-linear analyses and its validity for the further steps.
Moreover, stress responses triggered by higher harmonics demonstrate reliable accuracy in replicating the baseline trends.
It should also be noted that a stress reduction is already well visible with respect to those in Tab. 1. Nevertheless, these outcomes are still affected by large displacements issues thus not valid toward final strength assessments.

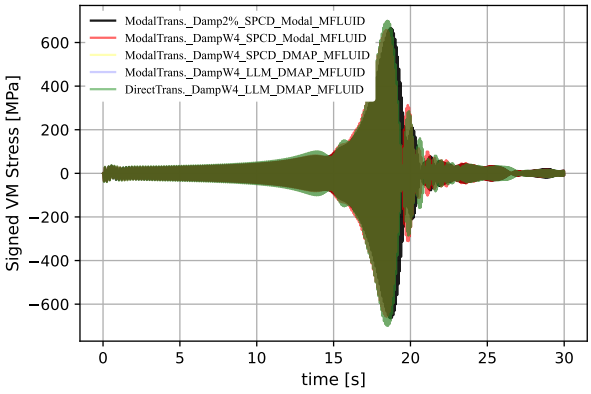


Figure 7: Signed Von Mises results for the most critical element

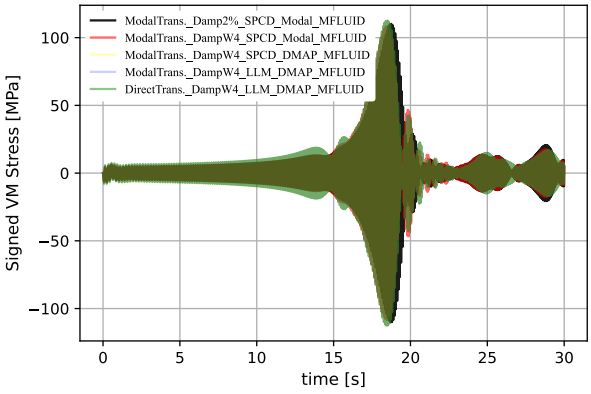


Figure 8: Signed Von Mises results with three modal contributions

4.2. Non-linear transient results

The model achieved in the previous section has been directly adopted for transient non-linear analysis where the non-linear source is ascribable to geometric contributions (i.e., large displacement problems).
Performing such calculation also required the definition of numerical tolerances for the convergence criterion and stiffness matrix update.

Tab. 2 summarizes the adopted tolerances that have been exploited within the framework of an Updated Lagrangian method.

Table 2: Non-linear analysis parameters

Analysis parameters	
Δt	2·10^{-3} sec
METHOD	ADAPT
KSTEP	2
MAXITER	50
CONV	UPW
EPSU	1·10^{-4}
EPSP	1·10^{-4}
EPSW	5·10^{-8}
MAXDIV	2
MAXQN	10
MAXLS	3
FSTRESS	NASTRAN Default
MAXBIS	9

ADJUST	NASTRAN Default
MSTEP	40
RB	NASTRAN Default
MAXR	NASTRAN Default
UTOL	NASTRAN Default
RTOLB	NASTRAN Default
MINITER	NASTRAN Default

To capture the non-linear behaviour, the load introduction followed a stepwise logic to simulate the real testing campaign.

For that reason, Low Level (LL), 1st Intermediate (IL1), 2nd Intermediate (IL2) and, finally, the Qualification Level (QL) loads have been progressively applied via separated analysis runs.
In specific, LL = 0.2*g*, IL1 = 0.8*g*, IL2 = 1.2*g*, QL = 1.65*g*.

This approach allowed tracking the non-linear trends of resonances, along with their magnitude, during the analysis evolution.

The detailed analysis of numerical results identified fully load-dependent non-linear behaviours for all the observed structural locations.
Among these, two main classes of dynamic trends clearly visible, namely:

- Hardening-like behaviours
- Load-step responses.

The first class, which an exemplary result of hardening-like is reported in Fig. 9, clearly demonstrates progressive resonant increments because of the additional stiffness quota as loads increase.
A sudden and jump-like response variation is already visible at LL despite of the short analysis interval. That elemental location, specifically subjected to precise loading levels and a loading frequency, absorbed the maximum amount of energy before redistributing it in the surrounding panel regions. This behaviour is typically associated to the sudden and instantaneous drop in the response.
Furthermore, the structural responses are no longer symmetric with respect to the stress amplitude axis because of the membrane effect that acts during the combined action of enforced motion and fluid effects.

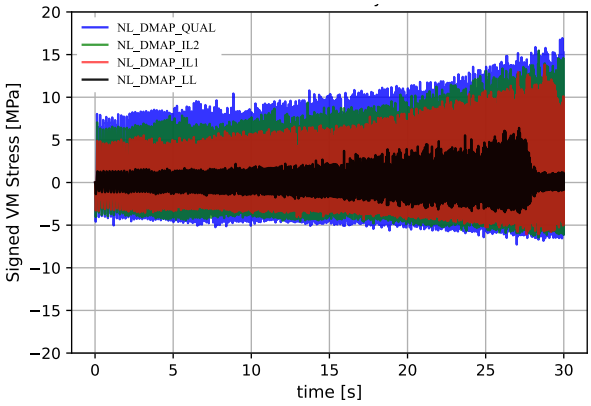


Figure 9: Hardening-like behaviours

The class ascribable to load and shape-dependent responses is captured by Fig. 10 where a clear and an evident evolution between the LL and higher levels can be observed. Specifically, the LL dynamics appears uncorrelated with respect to the other trends. This scenario could suggest a drastic change in the excitation state for the assessed element (and for those nearby it). This suggests as an unstable dynamic motion that progresses from an initial branch of solutions to another.

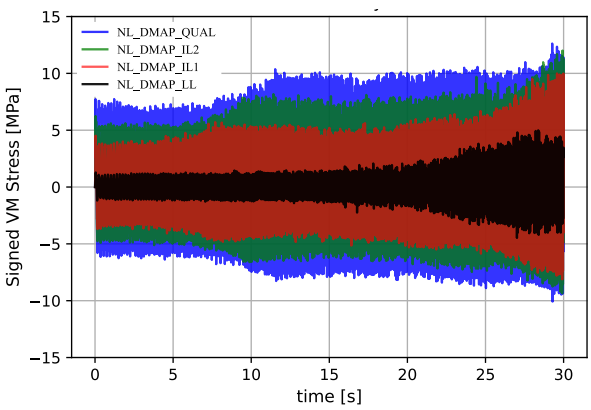


Figure 10: Load-step dependent responses

In general, these stress predictions revealed a completely different structural behaviours with respect to the linear ones (e.g., Figs. 7,8) that were adopted as a reference solution. Stress levels, that in the linear case exceeded the material proportional limit and caused negative MoS, find a more alleviated and mitigated stress environment.
An approximate reduction coefficient between linear FRA results and non-linear transient outcomes has been observed and spans between x30 – x60 depending on the specific panel recovery region.

From an analytical perspective, dynamic trends show an underling component of numerical noise which is mainly attributable to possible convergence issues during the incremental and iterative procedure. However, this component is limited for the majority of numerical outcomes and expectable due to the high complexity of the analysis framework that was setup.

5. CONCLUSIONS

This work explored and applied testing-consistent transient analyses to assist the Comet-Interceptor Dust Shield development over the project phases.
This approach bypasses the analysis-testing mismatch resulting from frequency response analysis that, in the case of the Dust Shield, leads to severe environmental stress incompliance.
A challenging and computationally demanding procedure, based on non-linear techniques, has been adopted in the framework of a component de-risk activity.
Performing such analysis loop required dedicate attentions to modelling and analysis setup before delving within the non-linear computations.
Transient non-linear analyses simulated large displacement vibrations of thin plates during sinusoidal environmental testing conditions where the fluid mass contribution was injected via NASTRAN DMAP® routines.
In such a way, a stress level reduction up to 60 times lower that in the pure linear domain has been observed.
This activity allowed increasing the experimental details thus safely de-risk the component design and the project activities.
Moreover, such analysis loop testifies adequate computational capabilities in simulating and predicting large displacement vibrations of thin plate in industrial scenarios of space projects.

6. REFERENCES

[1] MSC, NASTRAN Dynamic analysis user's guide v2022.2.

[2] D. Pederbelli, P. Nali und A. Calvi, „Euclid Spacecraft Sine Vibration Test Prediction Through the Virtual Shaker Testing Technique," *Journal of Spacecraft and Rockets,* 2023.

[3] V. Grosjean, R. Stelzer und F. Urbinati, „Vibration testing of solar array wings improving FEM correlation by considering air-effects," in *ECSSMET 2024, European Conference on Space Structures, Materials and Environmental Testing*, ESA-ESTEC, Noordwijk, The Netherlands, 2024.

[4] M. Amabili, „Nonlinear damping in large-amplitude vibrations: modelling and experiments," *Nonlinear Dynamics,* 2017.

[5] M. Amabili, „Theory and experiments for large-amplitude vibrations of rectangular plates with geometric imperfections," *Journal of Sound and VIbrations,* Nr. 291, pp. 539-656, 2006.

[6] J. P. Noel, S. Marchesiello und G. Kershen, „Subspace-based identification of a nonlinear spacecraft," *Mechanical Systems and Signal Processing,* Nr. 43, pp. 2017-236, 2014.

[7] K.-J. Bathe, Finite Element Procedures, Prentice Hall, 1996.

[8] A. H. Nayfeh und D. T. Mook, Nonlinear Oscillations, Wiley, 1995.

[9] MSC, Nastran 2022.4 Nonlinear SOL 400 User Guide.

[10] A. Mussita, A. C. Sanz, N. Riva, S. Hallström, V. Trickov and A. Robert, "Hyper-Velocity Impacts Modelling using SPH particles for the Comet-Interceptor Dust Shield," in *European Conference Spacecraft Structure Materials and Environmental Testing* , Toulose, 2023.

[11] MSC, NASTRAN Quick Reference guide v2022.1.

[12] MSC, Nastran 2022.4 Embedded Fatigue User Guide.

CHALLENGES AND COMPLEXITIES FOR LISA LV/SC COUPLED LOAD ANALYSIS

Davide Pederbelli, Gabriel Bianchi, Nicola Riva, Hugo Graça

OHB Systems AG, Universitätsallee 27-29, 28359, Bremen, Germany
Email: davide.pederbelli@ohb.de; gabriel.bianchi@ohb.de; nicola.riva@ohb.de; hugo.graca@ohb.de

KEYWORDS

Coupled Load Analysis, Damping, Transient Load Events, Craig – Bampton

ABSTRACT

The ultra-sensitive features of the payload instruments that are installed within the LISA Core Assembly (LCA) required ad-hoc mathematical models to inject the correct damping levels during the Launch Vehicle – Spacecraft Coupled Load Analysis (CLA) with Ariane 64.
For that reason, dedicated equivalent viscous damping models have been implemented in NASTRAN® format, via ad-hoc external routines, to convert the native damping scheme resulting from Craig – Bampton (CB) reductions. In such a way, analysis issues associated with the CLA transient load cases are easily overcome.
Structural responses at the LCA have been assessed in the harmonic and transient domain for the implemented dissipation models, thus assist the identification of the most representative description. As a result, the finalized CB model has been successfully communicated to Launch Authority by demonstrating the complete representativeness of the original behaviours that were based on full Finite Element Models.

1. INTRODUCTION

The Launch Vehicle – Spacecraft Coupled Load Analysis (LV – SC CLA) is the cornerstone analysis for all the space projects during the load analysis cycle. The CLA acts as a verification tool and, above all, is meant to derive mechanical loads, ascertain compatibility with the LV for all critical mission phases along with its flight mechanical environment, and, at last, justify notching requests.
In this process, the SC and the LV mathematical models are coupled together. Representative forcing functions that simulate the flight load cases are applied on the mechanical assembly in the framework of harmonic and transient analyses (e.g., wind gust, buffeting, thrust build-up,…) [1, 2].
The typical approach assumes that the SC prime contractor informs the Launch Authority about a representative model (typically in Craig – Bampton -CB- format) along with agreed Output Transformation Matrices (OTM), to perform and post-process CLA load cases.
In this framework, the main issue associated with the condensed damping matrix relies on the injected damping philosophy with respect to the analysis type for the assessed load cases. In specific, dynamic transient analyses pertains to the real-only values category. However, the use of structural damping description introduces components associated with complex values (i.e., real and imaginary) that provide not coherent outcomes with respect to the analysis logic.
Indeed, past studies have demonstrated the need of precise and corrected damping descriptions for the consistent treatment of the SC CLA model, at substructure or global level. Such damping descriptions are ascribable to Equivalent Structural Damping (ESD), the Inflated Damping Matrix (IDM) process as well as the Separation of Component Damping (SCD) [3, 4].
This issue has been also recognized as critical for the LISA LV – SC CLA because of the ultra-sensitive features of the payload instruments that are installed within the **L**ISA **C**ore **A**ssembly (LCA), as well as it's significant impact on the SC dynamic behaviour resulting from the large mass contribution.
For that purpose, ad-hoc viscous equivalent damping models aims at converting the native NASTRAN® structural damping scheme, that results from CB reductions, into an equivalent formulation valid and coherent for transient and harmonic analyses. In such a way, harmonic and transient load cases can be properly accounted when SC models are injected and coupled with those of the LV.
The implementation of such damping descriptions, along with the selection of the most representative damping candidate, leads to controlled and reduced risks associated with the dynamic behaviours of a complex and detailed payload assembly such the LISA LCA.
The work within this paper is organized as follows: *Section 2* introduces the LISA mission and motivates the efforts for the implementation of dedicated damping models. *Section 3* offers a concise mathematical background on CB models and the implemented damping models. *Section 4* illustrates the achievements and discusses the results of the analyses. Finally, *Section 5* wraps-up upon the conclusion of the study.

2. LISA MISSION AND EARLY WORKS TOWARDS THE COUPLED ANALYSES

The ***L***aser ***I***nterferometer ***S***pace ***A***ntenna (LISA) is an ESA Large Class Mission within the Cosmic Vision programme. The mission architecture consists of a constellation of three spacecrafts

placed at the vertexes of a near-equilateral triangle, with side length of about 2.5 million km and ~65 million km far from the Earth. LISA will investigate ripples of the spacetime by observing gravitational waves on-orbit within frequency band of 10^{-3} – 10^{2} Hz. The mission objectives will be accomplished via a sophisticated network of laser interferometers. The extreme low movements (10^{-9} – 10^{-12} m) of test masses, kept in a free-fall condition inside each spacecraft on-flight, will then detect gravitational waves.

The three spacecraft that compose the constellation will be inserted into orbit by a single launch of Ariane 64 that is planned for 2035. The launch configuration consists of a stacked setup, where each SC is placed one on top of the other.

Each SC carries a ~700 kg heavy payload, the Lisa Core Assembly (LCA), which contains ultra-sensitive instruments for detecting the gravitational waves.

The LCA installs a complex and ad-hoc designed Dissipation Isolation System (DIS) that is highlighted in Fig. 1. The DIS works as protection system against shock loads from clamp-band release during SC separations.

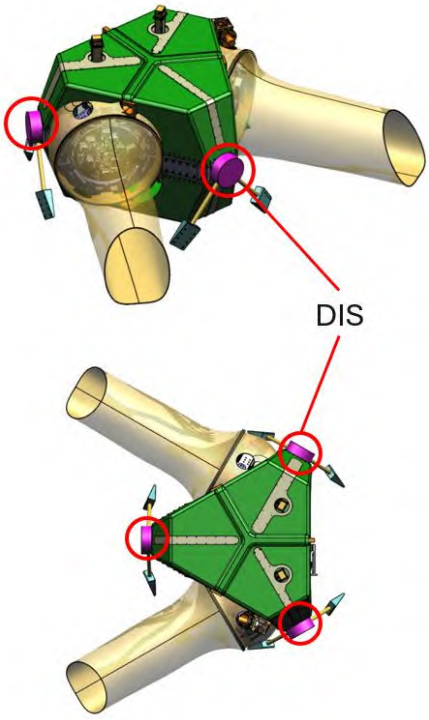


Figure 1: The LCA architecture

The DIS specific damping features along with the heavy mass of the overall payload have been recognized as the primal source of loads variation during the preparatory works of an early SC – LV CLA with Ariane 64.

Fig. 2 illustrates acceleration-equivalent loads at the LCA that result from sine domain assessments at 1g input across all the spectral lines. The main goal of such investigation aims at understanding and quantifying the DIS and the LCA damping sensitivity.

For that purpose, simple damping strategies were modelled to assess the amplification factor (Q-factor) effects associated to the baseline model that was originally developed for the CLA activity. These strategies assume a discrete variation of the Q-factor (i.e., Q=5, Q= 10 and Q→∞) along with a stiffer and damping-free behaviour expressed at the DIS components (black line). This last approach was specifically introduced to simplify, and numerically remove, damping uncertainties.

For the sake of completeness, numerical analyses adopt a 2% modal damping for all the cases via NASTRAN® inputs

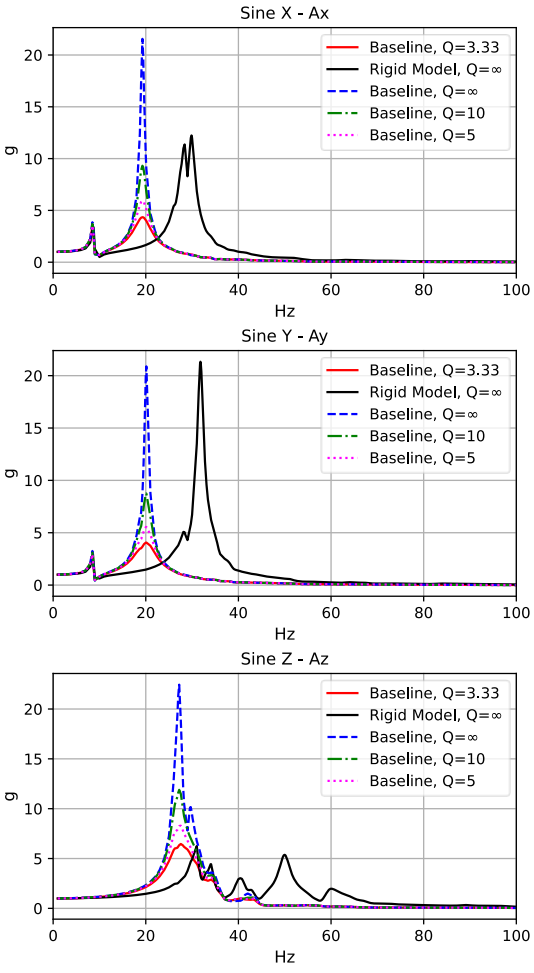


Figure 2: Low frequency environment assessment.

In essence, Fig. 2 ascertains the consequence of modelling schemes to address the CLA milestone to ensure the suitable level of conservativism, with respect to the design maturity, along with the adequate protection of the LCA.

The large amount of variation, either in frequency and amplitude, enforced the technical decision for a careful, and LISA-oriented, damping modelling toward the CB development, whose silhouette is depicted in Fig. 3.

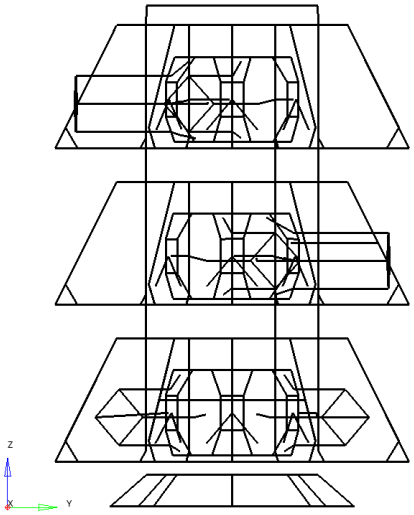


Figure 3: Reduced model for the LISA stack in launch configuration

In specific, injecting the correct and the model-representative damping contribution ensure the proper design conservativism without fictitiously altering the notching plan for the LCA because of an incorrect DIS modelling approach.
It should also be emphasized that the LCA is directly attached to the primary structure of LISA. Thus, a wrongly injected model within the CLA description could also severely impact the primary structure design with additional technical complexities

3. MATHEMATICAL FRAMEWORK

3.1. Background on Craig – Bampton models

Among the various reduction techniques that are available in the literature, the CB [5] environment is still the most widespread for communicating, exchanging and protecting structural representations during the project phases in industrial scenarios.
The CB framework assumes the existence of a transformation matrix $\boldsymbol{\Psi}$ which puts into relation the full model responses with a set of prescribed reduced motions. Eq.1 summarizes the CB nucleus:

$$\begin{Bmatrix} x_j \\ x_i \end{Bmatrix} = \underbrace{\begin{bmatrix} \boldsymbol{I}_{jj} & \boldsymbol{0}_{jp} \\ \boldsymbol{\phi}_{ij} & \boldsymbol{\varphi}_{ip} \end{bmatrix}}_{\boldsymbol{\Psi}} \begin{Bmatrix} x_j \\ q_p \end{Bmatrix} \qquad (1)$$

where, x_j is the interfaces DoFs set, x_i is the internal DoFs set, q_p is generalized coordinates set.
The $\boldsymbol{\phi}_{ij}$ is the *Constraint Mode* Matrix of unitary displacements that results from the problem presented in Eq. 2

$$\boldsymbol{\phi}_{ij} = -{K_{ii}}^{-1} K_{ij} \qquad (2)$$

where K_{ii}, K_{ij} are two partitions of the stiffness matrix associated to *i*, *j* sets.

The $\boldsymbol{\varphi}_{ip}$ is the p-subset of the *Fixed-interfaces Normal Modes* Matrix and is expressed by Eq. 3

$$[-\omega^2 M_{ii} + K_{ii}]\boldsymbol{\varphi}_{ii} = 0 \qquad (3)$$

The use of such $\boldsymbol{\Psi}$ matrix, in combination with mass-normalized fixed modes, allows writing the second-order mechanical damped problem. Structural and viscous contribution are assumed contributing to the condensed modes, as expressed by Eq. 4

$$\begin{bmatrix} \overline{M_{JJ}} & L_{jp} \\ L_{pj} & I_{pp} \end{bmatrix} \begin{Bmatrix} \ddot{x}_j \\ \ddot{q}_p \end{Bmatrix} + B_{CB} \begin{Bmatrix} \dot{x}_j \\ \dot{q}_p \end{Bmatrix} + \left(\begin{bmatrix} \overline{K_{JJ}} & 0_{jp} \\ 0_{pj} & \Lambda_{pp} \end{bmatrix} + iD_{CB} \right) \begin{Bmatrix} x_j \\ q_p \end{Bmatrix} = \begin{Bmatrix} F_j + \phi_{ij}^T F_i \\ \varphi_{ip}^T F_i \end{Bmatrix} + \begin{Bmatrix} R_{ij} \\ 0 \end{Bmatrix} \qquad (4)$$

where $\overline{M_{JJ}}$ and $\overline{K_{JJ}}$ are the statically reduced mass and stiffness matrix respectively, $L_{pj} = L_{jp}$ is the participation factor matrix, $\Lambda_{pp} = \Omega_{\mathrm{pp}}^2$ the generalized stiffness matrix.
In the case the full FE model includes viscous and structural damping properties, B_{CB} and D_{CB} have non-zero contributions. In a partitioned formulation

$$D_{CB},\ B_{CB} = \begin{bmatrix} D_{jj} & D_{jp} \\ D_{pj} & D_{pp} \end{bmatrix}, \begin{bmatrix} B_{jj} & B_{jp} \\ B_{pj} & B_{pp} \end{bmatrix} \qquad (5)$$

where,

$$\begin{aligned} D_{jj} &= K_{S_{jj}} + K_{S_{ij}}\phi_{ij} + {\phi_{ij}}^T K_{S_{ij}} + {\phi_{ij}}^T K_{S_{ii}} \\ D_{jp} &= K_{S_{ji}}\varphi_{ip} + {\phi_{ij}}^T K_{S_{ii}}\varphi_{ip} \\ D_{pp} &= {\varphi_{ip}}^T K_{S_{ii}}\varphi_{ip} \end{aligned} \qquad (6)$$

in which K_S is the structural damping matrix, and

$$\begin{aligned} B_{jj} &= B_{jj} + B_{ij}\phi_{ij} + {\phi_{ij}}^T B_{ij} + {\phi_{ij}}^T B_{ii}\phi_{} \\ B_{jp} &= B_{ji}\varphi_{ip} + {\phi_{ij}}^T B_{ii}\varphi_{ip} \\ B_{pp} &= {\varphi_{ip}}^T B_{ii}\varphi_{ip} \end{aligned} \qquad (7)$$

Once structural responses have been computed at substructure level, these are expanded towards the internal DoFs via the Displacement and Acceleration Transformation OTM (i.e., DTM, ATM) whose shapes depends on the recovery technique. In the case of the Mode Displacement Method, physical DoFs are back transformed though $\boldsymbol{\Psi}$ according to Eq.1. Conversely, If the Mode Acceleration Method is selected, the applicable OTMs must be adapted to account for the second order correction [6].

3.2. Damping Models

The general problem expressed by Eq. 4 remains valid as long as the model is linear and time invariant.
However, when dealing with structural dynamics

transient analysis [6] the choice of the correct damping scheme could highly affect the results with obvious design implications. The key issue relies on the nature of the physical problem itself along with analysis aspects. In specific, dynamic transient analyses pertains to the real-only values category whereas the structural damping D_{CB} introduces dissipation contributions acting on the system displacements via the imaginary unit "i". Thus, the D_{CB} presence introduces imaginary values (or phases) that cannot be managed for such types of analyses.
This mathematical issue imposes the dedicated treatment of the damping and thus the development of proper conversion strategies for passing from D_{CB} to B_{CB} without ambiguity, respecting the baseline results at full-model level. In such a way, the real-only values analysis type can be restored and performed within the computational environment.
For the sake of completeness, NASTRAN® has capabilities for superelement damping management (e.g., PARAM, SESDAMP). Nevertheless, due to the specific features of LISA along with the tight load levels to design the LCA and the sensitivity of instruments within it, ad-hoc damping models have been implemented. These models are inspired by previous works [7] which are currently part of the European Space Agency CLA Toolbox.
In the following Sections, the explored models have been reviewed in their main aspects by assuming the unique presence of D_{CB} as conversion target. D_{CB} is, in general, a full matrix (NASTRAN® K4) thus there is no visibility or a back-process to decompose such matrix in its constituents as in Eq.6.
For sake of completeness, the development of the CB model assumes including residual vector in the superelement generation run.

3.2.1. The Equivalent Viscous Damping Methodology (EqVD)

The EqVD method works via harmonic results defined at coupled modal components according to Eq.8

$$I_{pp}\ddot{q}_p + \Lambda_{pp} q_p + iD_{pp} q_p = \varphi_{ip}^T F_i = f_p \qquad (8)$$

By assuming a harmonic motion for q_p and f_p, the complex matrix transfer function can be defined as in Eq.9

$$H_{pp}(\Omega) = \left[-\Omega^2 I_{pp} + \Lambda_{pp} + iD_{pp}\right]^{-1} \qquad (9)$$

In such a way, calculating the transfer matrix in correspondence of the system natural frequency allows the derivation of the critical modal damping to be injected at component-mode level. In Eqs. 10-11 the mathematical derivation is illustrated

$$\zeta_p^{Eqv} = \frac{1}{2\omega_p^2 \left|H_{pp}(\omega_p)\right|} \qquad (10)$$

$$B_{CB} = \begin{bmatrix} 0_{jj} & 0_{jp} \\ 0 & \beta_{pp} \end{bmatrix} \qquad (11)$$

where

$$\beta_{pp} = diag\left(2\omega_p \zeta_p^{Eqv}\right) \qquad (12)$$

3.2.2. The System Structural Damping Craig – Bampton (SDCB) method

The SDCB method offers a first improvement of the D-EqVD method.

The model assumes the calculation of the CB eigenvalues and eigenvectors withing an external environment. Analytically,

$$\left[-\omega^2 M_{CB_{sys}} + K_{CB_{sys}}\right] \varphi_{sys} = 0 \qquad (13)$$

The system modes and the system natural frequencies are employed toward the Equivalent Viscous modal matrix as expressed in Eq. 14

$$C_{CB_{sys}} = \\ = diag\left(\varphi_{sys}^T D_{CB_{sys}} \varphi_{sys}\right) \cdot diag\left(\sqrt{\Lambda_{\text{sys}}^{-1}}\right) \qquad (14)$$

The back transformation of the previously introduced $C_{CB_{sys}}$ into the $B_{CB_{sys}}$ matrix relies on the following assumptions:

- $\varphi_{sys}^T M_{CB_{sys}} \varphi_{sys} = \varphi_{sys}^T \varphi_{sys} M_{CB_{sys}} = \\ = M_{CB_{sys}} \varphi_{sys}^T \varphi_{sys} = \mathbf{1}$
- The viscous damping is diagonal when projected on the system modal base (Basile Hypothesis)

Mathematically, the second assumption translates into Eq. 15

$$C_{CB_{sys}} = \varphi_{sys}^T B_{CB_{sys}} \varphi_{sys} = \begin{bmatrix} \mathbf{0}_{6x6} & & \\ & 2\omega_k \zeta_k & \\ & & \ddots \end{bmatrix} \qquad (15)$$

Finally, the viscous equivalent damping matrix is accomplished, and its analytical form is reported in in Eq. 16

$$B_{CB_{sys}} = M_{CB_{sys}} \varphi_{sys} C_{CB_{sys}} \varphi_{sys}^T M_{CB_{sys}}^T \qquad (16)$$

In such a way, the viscous equivalent matrix results from the CB eigenvectors projection on the $C_{CB_{sys}}$ matrix, properly pre/post-multiplied by the CB mass matrix.
It should also be emphasised that two modal truncations have been performed by such method. A first truncation is introduced by the initial CB reduction at system level. The second one limits the

modal contributions for the assembled and CB externally evaluated.

3.2.3. Enhanced System Structural Damping Craig – Bampton (E-SDCB) method

The SDCB in Section 3.3.2 assumes a fully diagonal and decoupled contribution within the $C_{CB_{sys}}$ matrix (Eq. 15) because of the Basile Hypothesis.

In this regard, the E-SDCB method offers a matrix enhancement by populating the off-diagonal contributions. The off-diagonal enrichment follows the model in Eq. 17

$$\left[C_{CB_{sys}}\right]_{mn} = \frac{\left[\varphi_{sys}^{T} D_{CB_{sys}} \varphi_{sys}\right]_{mn}}{\sqrt{\omega_n \omega_m}} \qquad (17)$$

where ω_n, ω_m derive from the CB assembly.
The associated $B_{CB_{sys}}$ is thus simply post assembled according to Eq. 16

3.2.4. The Structural Damping Modal Block (M-Block) method

The SDMB model exploits the direct conversion of the modal block in output from the structural damping matrix (D_{pp}). The mathematical conversion is obtained via normalizing the D_{pp} contribution with the circular natural frequencies such as

$$B_{CB} = \frac{D_{pp}}{\sqrt{\omega_i \omega_j}} \qquad (18)$$

where ω_i, ω_j are the contribution within generalized CB stiffness matrix. The application of such model implies the creation of a fully populated modal block as transmitter from D_{pp}. Furthermore, this model does not imply dissipation terms at the interfaces.

4. RESULTS AND DISCUSSION

4.1. The reference solution

The results provided from the application of such damping schemes have been assessed in frequency and time domain by using NASTRAN® and the full FE model.
The adopted reference model is assumed valid based on Q=10 as in Fig. 2. In such a way, an adequate level of model conservativism is introduced.

The frequency-based comparison has been simply computed via the 1*g* (*g*=9.81 m/s^2) refence solution along the three global translation directions. Conversely, the transient case adopts a single harmonic sine wave according to Eq. 19

$$\ddot{x}, \ddot{y}, \ddot{z} = \begin{cases} 0 & t < T^*_{x,y,z} \\ 1g \cdot \sin\left(\omega_{n_{LCA_{x,y,z}}} \cdot t\right) & t \in T^*_{x,y,z} \\ 0 & t > T^*_{x,y,z} \end{cases} \qquad (19)$$

where $\ddot{x}, \ddot{y}, \ddot{z}$ are the ground motions (i.e., translational accelerations) for each orthogonal directions, $\omega_{n_{LCA_{x,y,z}}}$ is the circular natural frequency at the LCA in the soft-mounted conditions (i.e., platform – LCA coupled) for each global mode direction and $T^*_{x,y,z}$ is the characteristic period associated with $\omega_{n_{LCA_{x,y,z}}}$.
Moreover, the transient reference adopted the conversion method reported in Eq. 20 and 21 to internally organize the Structural – to – Equivalent damping matrix (PARAM, WMODAL) [8] [9].

$$[\Lambda]^{-\frac{1}{2}} [\Phi^{\mathrm{T}}] (G[K^1_{dd}] + [K^4_{dd}]) [\Phi] [\Lambda]^{-\frac{1}{2}} \qquad (20)$$

$$[B_{dd}] = \\ = [B^1_{dd}] + [B^2_{dd}] + \frac{G}{W3}[K_{dd}] + \frac{1}{W4}[K^4_{dd}] \qquad (21)$$

where $[\Lambda]^{-\frac{1}{2}}$ is the diagonal matrix of constituted by $1/\sqrt{\omega_i}$ terms, $[\Phi]$ is the mode shapes matrix, G is a global damping coefficient, $[K^1_{dd}]$ and $[K^4_{dd}]$ are the global stiffness matrix and a structural damping attributed to NASTRAN® MAT entries, respectively, $[B_{dd}]$ is the damping matrix for transient analyses, $[B^1_{dd}]$ is the damping attribution to damping elements, and $[B^2_{dd}]$ is the direct input damping matrix. $W3$ and $W4$ are normalization terms defined as frequency of interest (rad/sec) for the conversion. In essence, Eq. 20 and Eq. 21 work in combination to extract the "best" value for $W3$ and $W4$.
In this work G=0, thus the research is restricted to W3 only.

Remark: the Launch Authority is considered NASTRAN® independent.
This procedure should be considered only to verify the CB model with respect to full FE results.

4.2. Numerical outcomes

The B_{CB} matrix from Eq. 11, Eq. 16 (SDCB, E-SDCB) and Eq. 18 has been numerically implemented within an external environment via simple and effective routines that convert the B_{CB} structure into NASTRAN® op4 formats compatible for Finite Element calculations.

Frequency solutions are sampled via an adaptive Δf whereas transient solutions adopt $\Delta T_{x,y,z} \leq \frac{1}{10 \cdot f_{n_{LCA_{x,y,z}}}}$ to avoid under-sampling problems.

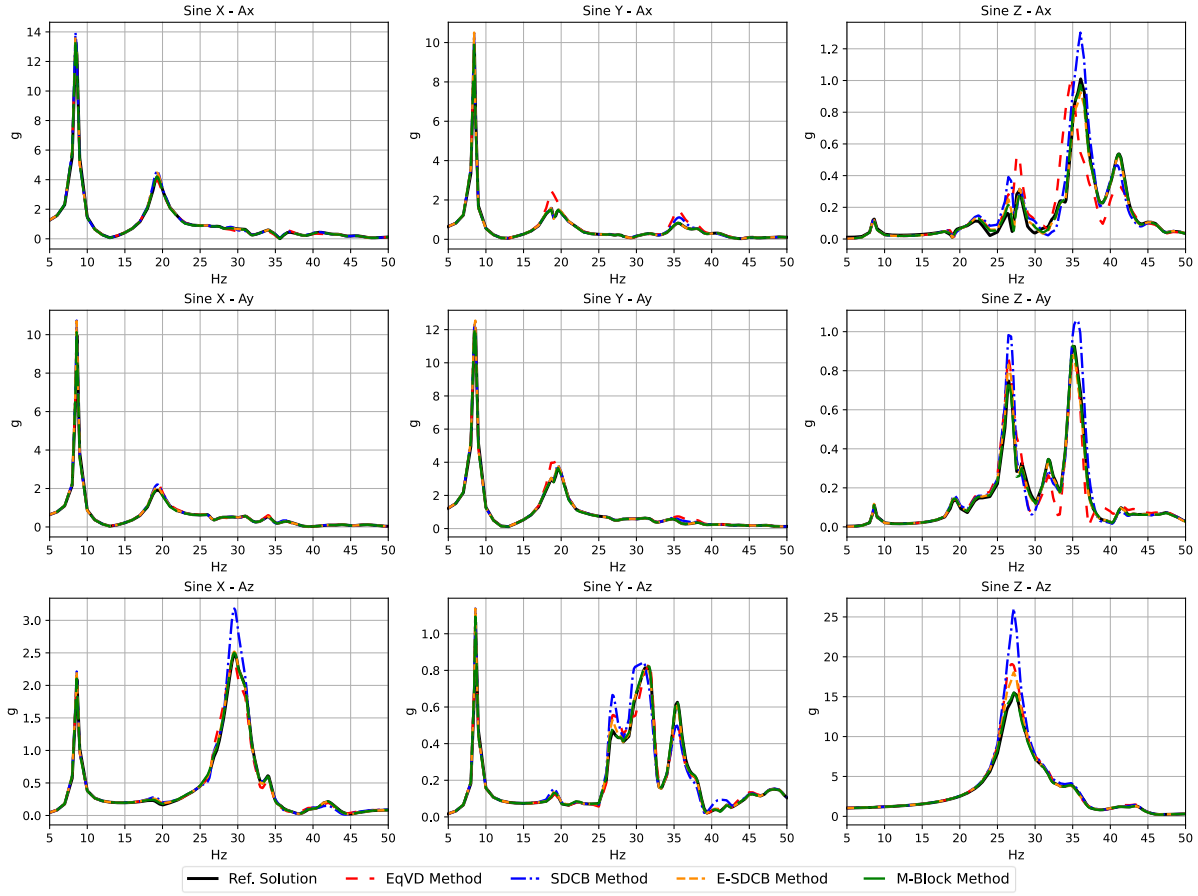


Figure 4: Sine outcomes at LISA SC2

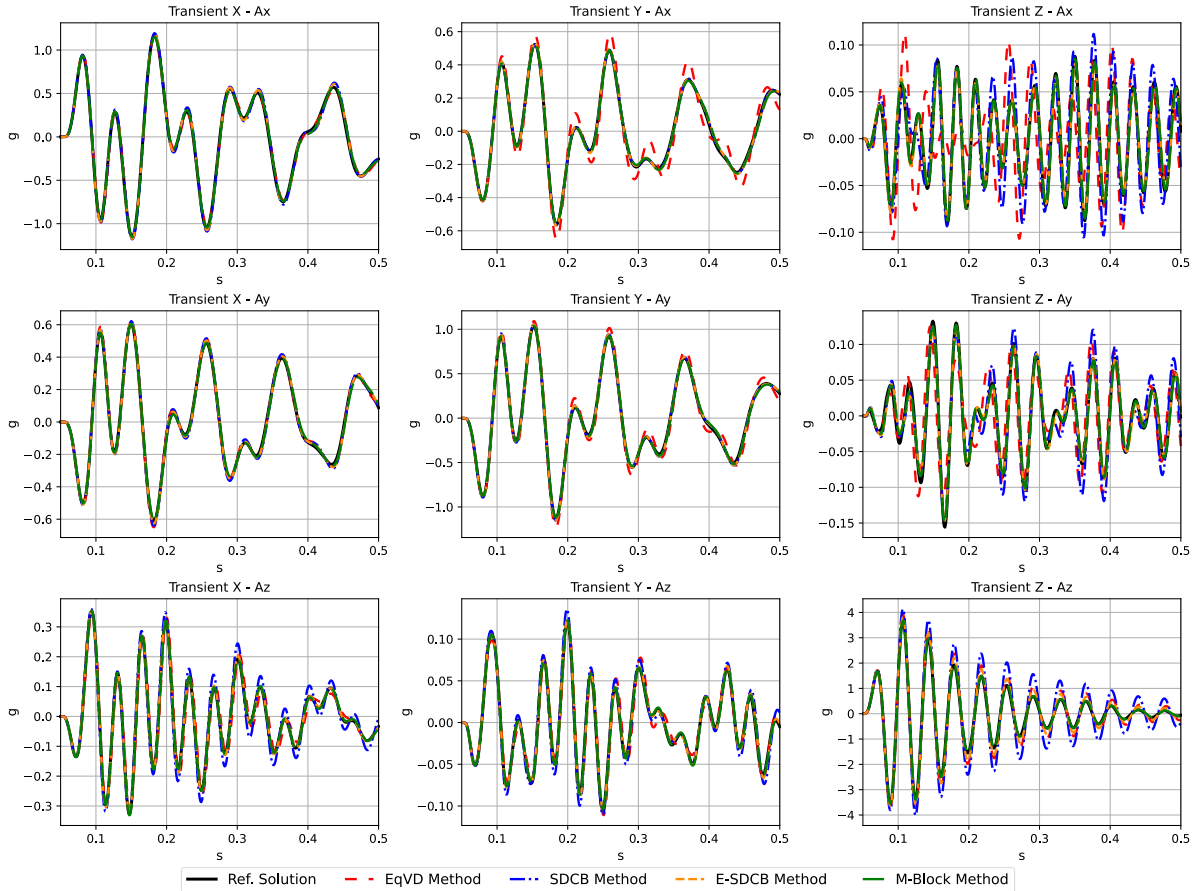


Figure 5: Transient outcomes at LISA SC2

Fig. 4 and Fig. 5 illustrate the model performances associated with the LISA LCA at SC 2 (i.e., the SC at the central stage of the Stack) for all the translational DoFs, namely three responses along the loading directions and six responses along the cross-axes.
In general, the in-plane outcomes, for Sine/Transient X, Y – Ax, Ay are well mapped by most of the models. There are marginal discrepancies in the frequency domain and amplified fluctuations in the time domain introduced by the EqVD Method (dashed red line) whose trend is anyhow globally acceptable.
Most likely, the in-plane responses are coherent because of the geometrical and mechanical boundary conditions, expressed the primary structure, which encapsulate the LCA.
The highest variation is foreseen along the out-of-plane axes namely Sine/Transient X, Y – Az. Along these DoFs the model choice plays the relevant role for the exact model derivation. It is worth noticing the Sine Z – Az behaviour, where the scatter amplitudes among models are ascribable up to ≈11*g*.
Similarly, Transient Z – Ax shows visible drift in the dynamic behaviours expressed by at least two models. In particular, the EqVD scheme highly underestimates time-dependent trends at ≈0.2s thus attests such description as the least precise for cross-axis predictions, whilst the SDCB scheme introduces amplified peaks but preserves the harmonic correspondences with respect to the original solution.
Finally, Transient Z – Az shows lower decays (i.e. longer time scales to extinguish the responses) for EqVD, SDCB, E-SDCB thus affecting the long-term dynamics.
Among all the explored models, the one capable of reproducing while minimizing the discrepancies with respect to the reference solution is the Structural Damping Modal Block (M-Block) method in green. Indeed, the M-Block method significantly improved, becoming almost indistinguishable from the reference solution.

According to the finding in Fig. 4 and Fig. 5, Tab. 1 summarizes the model's performances according to a qualitative scale Poor – Acceptable – Accurate – Excellent.
The attribution of such scale comes from pure curve comparison without any specific optimal metric.

Table 1: Sine and Transient model performances

	Sine	**Transient**
EqVD	Acceptable	Poor
SDCB	Poor	Acceptable
E-SDCB	Accurate	Accurate
M-Block	Excellent	Excellent

The final confirmation of such robust approach was also explored for DoFs not related to LCA components. The goal was ensuring that the additional internal responses, without specific attribution of structural damping, were well mapped and reproduced. For that purpose, Fig. 6 and Fig. 7 show an exemplary model trends that have been recursively found among the FE internal restitutions.

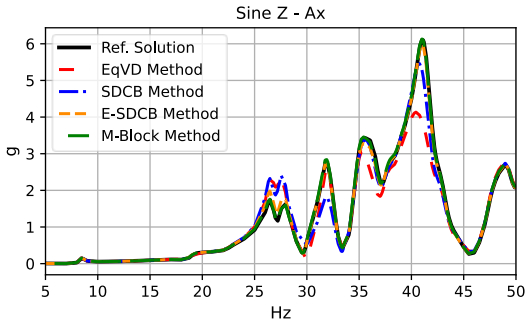


Figure 6: Sine outcomes at internal SC DoF

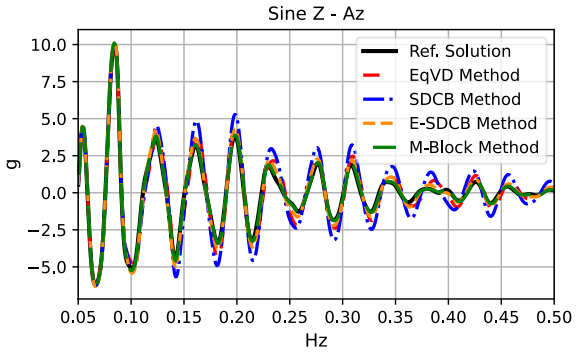


Figure 7: Transient outcomes at internal SC DoF

Fig. 6 and Fig. 7 demonstrate that the M-Block method also reproduces well the reference solution far from the structural damping area at the DIS LCA. Conversely, the other methods generate poor responses still in absence of structural damping quantities with similar patterns as illustrated in Fig. 4 and Fig. 5.
This further finding emphasizes the use of the M-Block scheme for developing reliable CB damping models. If a custom implementation should strictly rely on CB modes, the E-SDCB models demonstrates the best capabilities in preserving the underlying system dynamics because of the off-diagonal damping corrections.

5. CONCLUSIONS

This paper explored dedicated methods to convert the Craig – Bampton structural damping matrix into equivalent viscous representations.
The study has been performed in the view of the LISA Launch Vehicle – Spacecraft Coupled Load Analysis with Ariane 64 to transmit a reliable and representative numerical model.
These methods are ascribable to the Equivalent Viscous Damping Methodology (EqVD), the System Structural Damping Craig – Bampton (SDCB) method, the Enhanced System Structural Damping Craig – Bampton (E-SDCB) and the Structural Damping Modal Block (M-Block) method.

Such formulations have been assessed in frequency and time domain via simple and defined reference solutions.
Numerical outcomes ascertain the performances of such models and attribute the highest fidelity to the M-Block one which directly converts the Structural damping into an equivalent viscous representation. The M-Block model minimizes the numerical discrepancies introduced by the conversion procedure and results in the best candidate for reliable coupled analyses.

Acknowledgements
The authors are pleased to acknowledge Carlos Sanchez Herrera (ESA-ESTEC) for his support during the overall activity and Matthias Meschenmoser (OHB - Systems AG) for providing the detailed model of the Lisa Core Assembly.

6. REFERENCES

[1] ECSS-E-HB-32-26A, Spacecraft mechanical loads analysis handbook, Noordwijk, The Netherlands, 2013.

[2] NASA-STD-5002B, Load Analysis of spacecraft and payloads, 2026.

[3] J. Albus, W. Beuchel and S. Dieker, “A Consistent Approach of Damping Treatment in Coupled Dynamic Analysis and Test,” in *62nd International Astronautical Congress*, Cape Town, SA, 2011.

[4] A. Rittweger, S. Dieker, K. Abdoly and J. Albus, “Coupled Dynamic Load Analysis with Different Component Damping of the Substructures,” in *59th International Astronautical Congress*, Glasgow, UK, 2008.

[5] R. Craig and M. Bampton, “Coupling of SubStructures for Dynamic Analysis,” *AIAA Journal,* vol. 6, no. 7, pp. 1313-1319, 1968.

[6] A. Piersol and T. Paez, Harris's Shock and vibration handbook, Sixth Edition ed., McGraw Hill.

[7] X. V. Araujo, S. Fransen, S. Germès and N. Thiry, “Validation of equivalent viscous damping methodologies,” in *12th European Conference on Space Structures, Materials and Environmental Testing*, Noordwijk, The Netherlands, 2012.

[8] MSC, NASTRAN Quick Reference guide v2022.1.

[9] MSC, NASTRAN Dynamic analysis user's guide v2022.2.

ENHANCED DATA-BASED DYNAMIC CHARACTERIZATION OF PLATO SATELLITE THROUGH QUALIFICATION TESTING

Dario Anastasio [(1)], Davide Pederbelli [(2)], Stefano Marchesiello [(1)], Nicola Riva [(2)]

[(1)] Politecnico di Torino, Department of Mechanical and Aerospace Engineering, Corso Duca Degli Abruzzi 24, 10129, Torino, Italy.
Email: dario.anastasio@polito.it; stefano.marchesiello@polito.it

[(2)] OHB Systems AG, Universitätsallee 27-29, 28359, Bremen, Germany,
Email: davide.pederbelli@ohb.de; nicola.riva@ohb.de

KEYWORDS

spacecraft; vibration; nonlinear dynamics; experimental; qualification

ABSTRACT

The dynamic qualification of the ESA-PLATO (PLAnetary Transits and Oscillations of stars) Proto-Flight Model involved sine-sweep testing over multiple excitation levels and generated a large experimental dataset from several hundred measurement channels.
This work presents a data-driven methodology that combines conventional frequency-response functions with synchronized time-domain measurements to identify and characterize amplitude-dependent dynamic behavior. A Similarity Index is introduced to compare transmissibility functions acquired at different excitation levels and to automatically rank sensors and spacecraft modules according to their response evolution. The identified critical regions are subsequently investigated through time-frequency analysis and Fourier decomposition of the measured responses. The proposed workflow reveals resonance shifts, jump phenomena and significant changes in the harmonic content of selected structural regions. The results demonstrate that synchronized time-domain measurements provide valuable complementary information to conventional frequency-domain processing, enabling a more comprehensive interpretation of spacecraft qualification tests without requiring a priori numerical models.

1. INTRODUCTION

The dynamic qualification of spacecraft represents one of the most critical phases of the verification process, as it demonstrates the capability of the hardware to withstand the severe conditions experienced during launch. Among the various environmental tests, sine vibration testing is routinely employed to verify the structural integrity of the spacecraft and to identify possible dynamic anomalies over the operational frequency range [1, 2]. The interpretation and prediction of these tests have received considerable attention in recent years, particularly with the development of advanced numerical methodologies capable of reproducing the coupled spacecraft–shaker dynamics and the vibration control system [3].
The experimental results are traditionally evaluated through frequency-response functions (FRFs) or transmissibilities computed from the measured acceleration signals, allowing comparison with analytical models and verification of the spacecraft dynamic behavior. In this framework, the spacecraft is typically instrumented with many accelerometers and sensors distributed throughout the primary structure, payload assemblies and equipment interfaces. When multiple excitation directions and qualification levels are considered, the resulting dataset can easily reach a huge number of transmissibility functions. Although this wealth of information provides a comprehensive description of the spacecraft dynamics, it also makes the interpretation of the experimental results increasingly challenging. Detailed inspection of individual FRFs rapidly becomes impractical and the identification of the most critical structural regions often relies on the analyst's experience.
In addition, the standard post-processing adopted during qualification campaigns generally focuses on frequency-domain and linearized quantities, whereas the synchronized time histories used to compute the FRFs are often discarded after testing or only used for control purposes. Nevertheless, these signals contain valuable information that can reveal dynamic phenomena that are difficult to identify from frequency-domain representations alone, including harmonic generation, amplitude-dependent response evolution and transient phenomena associated with nonlinear structural behavior.
In contrast to linear structures, where the dynamic response is expected to scale proportionally with the excitation level and remain concentrated at the excitation frequency, nonlinear structural systems may exhibit much richer dynamic behavior. Typical manifestations include amplitude-dependent shifts of resonance frequencies, changes in effective

damping, jump phenomena associated with multiple stable response branches, and the generation of higher-order or fractional harmonic components [4, 5]. These effects are often localized in specific structural regions and may become apparent only above certain excitation levels, making their identification particularly challenging in large experimental datasets. Detecting and characterizing such phenomena is therefore of practical interest during experimental testing, as it provides additional insight into the dynamic behavior of the structure beyond the conventional comparison of frequency-response functions [6].

Beyond their scientific interest, these phenomena may also have practical implications during qualification testing. The appearance of pronounced amplitude-dependent behavior may require additional engineering assessments, refinement of vibration-control strategies or temporary interruption of the test. Early identification and localization of these behaviors can therefore contribute to reducing test risks, enabling a more predictable progression toward the final qualification level.

To address these challenges, this work presents a data-driven methodology developed within the collaboration between OHB System AG and the Dynamics of Mechanical Systems and Identification research group at Politecnico di Torino, for the analysis of the qualification campaign of the ESA-PLATO (PLAnetary Transits and Oscillations of stars) Proto-Flight Model. The proposed approach combines global frequency-domain indicators with targeted analyses of synchronized time-domain measurements. A similarity index is introduced to automatically compare transmissibility functions acquired at different excitation levels and to rank sensors and spacecraft modules according to the observed response evolution. The resulting ranking is then used to guide detailed investigations based on time-frequency representations and local Fourier decomposition of the measured responses.

The methodology is applied to the complete sine-vibration qualification dataset of the PLATO spacecraft. The results demonstrate that the proposed workflow effectively identifies the structural regions exhibiting the largest amplitude-dependent response variations and provides additional insight into the underlying dynamic mechanisms, enabling a more efficient interpretation of large experimental datasets acquired during spacecraft qualification testing.

2. TEST CAMPAIGN

The PLATO Proto-Flight Model (PFM) is composed of two main structural assemblies: the Payload Module (PLM) and the Service Module (SVM).

The Payload Module accommodates the complete scientific payload, including the cameras, the optical bench assembly, the supporting structures and the associated thermal-control hardware. The Service Module provides the mechanical interface with the launcher and hosts the subsystems required for spacecraft operation.

For the purposes of the present work, the measurement channels were grouped according to the main structural regions and equipment assemblies monitored during the qualification campaign. The considered groups include:

- Optical Bench Assembly (OBA);
- High Gain Antenna (HGA);
- Low Gain Antenna (LGA);
- Star Tracker (ST);
- Reaction Wheels (RW);
- Tanks (T);
- Sunshield and Solar Array (SSA);
- Platform Top Panel (PTP);
- Platform Radiator (PR);
- PLE Radiator (PLER);
- Orbital Control Thrusters (OCT);
- Reaction Control Thrusters (RCT);
- Fill and Drain Valves (FDV);
- Pressure Transducers (PT).

This grouping was used to aggregate the sensor-level indicators and to identify the spacecraft regions exhibiting the most significant dynamic response variations.

Figure 1 shows the spacecraft configuration together with the adopted global reference frame. The qualification tests were performed along the three principal spacecraft axes, referred to throughout the paper as x, y and z directions.

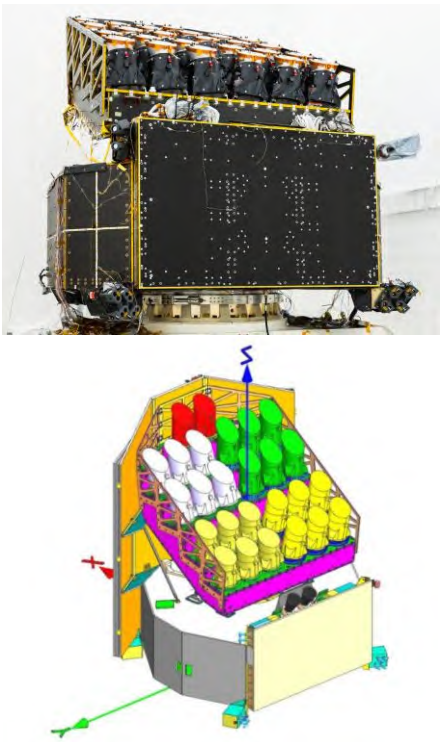


Figure 1. Photo and global reference frame. Photo credit: European Space Agency.

2.1. Test setup and instrumentation

The spacecraft was extensively instrumented with tri-axial accelerometers distributed throughout both the Payload Module and the Service Module. The

resulting instrumentation provided a high spatial resolution of the global and local dynamic response. Each accelerometer supplied three orthogonal acceleration measurements expressed either in the spacecraft global reference frame (x, y, z) or in local sensor reference frames (u, v, w), depending on the sensor location and installation requirements.
Vibration control was achieved using four pilot accelerometers located at the spacecraft interface.
The complete instrumentation comprised several hundred acquisition channels, resulting in a large experimental dataset for each excitation direction and excitation level.

2.2. Acquired dataset

For each excitation direction, measurements were acquired at four excitation levels:

1. a low-level reference condition (LL);
2. a first intermediate level (IL1);
3. a second intermediate level (IL2);
4. the final qualification level (QL).

The standard qualification test processing provided frequency spectra for all instrumented channels. In addition, synchronized time histories were retained for all acquisition channels, enabling further analyses beyond the conventional frequency-domain assessment.
Considering all excitation levels, test directions and instrumented channels, the resulting volume of data makes manual inspection of individual responses impractical and motivates the development of automated indicators capable of highlighting the most significant dynamic response variations.

3. DATA PROCESSING METHODOLOGY

Qualification testing of large satellites typically involves a relevant number of measurement channels, each recorded for multiple excitation levels and test directions.
The resulting dataset may therefore contain hundreds of frequency spectra and associated time histories thus making the in-situ detailed processing highly time consuming and not practical within the tight schedule of a test campaign.
While individual inspection of selected channels remains an essential step for the interpretation of specific phenomena, a systematic channel-by-channel analysis rapidly becomes impractical and strongly depends on the analyst's experience.
For this reason, the proposed methodology relies on a hierarchical approach.
First, a set of global indicators is computed for all measurement channels to automatically identify the sensors and structural regions exhibiting the most significant response variations across excitation levels. These indicators are then used to rank sensors and modules and to guide more detailed investigations based on frequency-domain, time-domain and harmonic analyses.
The workflow therefore combines two levels of analysis:

- a global screening stage, aimed at rapidly processing the complete dataset and identifying the most critical sensors and modules;
- a local stage, focused on a limited number of selected channels and based on detailed time-frequency and harmonic-content investigations.

This approach enables efficient exploitation of the large amount of experimental data available during qualification campaigns while preserving the possibility of investigating complex amplitude-dependent phenomena at sensor level.

3.1. Frequency response similarity index

For each excitation level, transmissibility functions were evaluated as the ratio between the complex spectra of the measured acceleration response at a given sensor and the reference acceleration at the shaker interface. For the general i^{th} sensor at excitation level k this reads:

$$T_{i,k}(f) = \frac{A_{i,k}(f)}{P_k(f)}, \qquad (1)$$

where $A_{i,k}(f)$ and $P_k(f)$ denote the complex Fourier spectra of the output acceleration and reference input acceleration, respectively. The reference input was obtained from the four control accelerometers by selecting, at each frequency, the pilot signal exhibiting the largest amplitude.
The low-level excitation condition was used as reference for all subsequent comparisons. Let $T_{i,1}(f)$ denote the transmissibility measured at the reference level for a given sensor i, and $T_{i,k}(f)$ the transmissibility measured at a different excitation level $k > 1$. A local normalized error was defined as

$$E_{i,k}(f) = \frac{\left|\,|T_{i,1}(f)| - |T_{i,k}(f)|\,\right|}{\left|\,|T_{i,1}(f)| + |T_{i,k}(f)|\,\right|}. \qquad (2)$$

A global indicator, referred to as Similarity Index (SI), was then computed by combining the RMS value of the local error $(E_{i,k}^{\text{RMS}})$ with the average value of its largest 5% samples $(E_{i,k}^{5\%})$. The former captures the overall evolution of the response, whereas the latter increases sensitivity to localized dynamic changes such as resonance shifts and jump phenomena. The resulting similarity index is defined as

$$SI_{i,k} = 1 - \left(\alpha E_{i,k}^{\text{RMS}} + (1-\alpha) E_{i,k}^{5\%}\right). \qquad (3)$$

The weighting factor α controls the relative importance of the two error terms. A value of $\alpha = 0.5$ corresponds to an equal weighting of the global and localized contributions, whereas larger values assign greater importance to the overall evolution of the transmissibility. In the present work, $\alpha = 0.7$ was selected empirically as a compromise between sensitivity to distributed response changes and localized phenomena. By construction, the SI approaches unity when the transmissibilities remain unchanged across excitation levels and decreases as the frequency response changes.

3.2. Sensors and modules ranking

The minimum SI observed across all excitation levels was adopted as a screening indicator for each measurement channel and denoted as $SI_i^{\min}$:

$$SI_i^{\min} = \min_k SI_{i,k}. \quad (4)$$

Sensors were then ranked according to this metric, allowing rapid identification of the regions exhibiting the strongest response evolution.

To facilitate interpretation at spacecraft level, sensors were grouped according to their associated subsystem or structural module. Module-level indicators were obtained by aggregating the SI values of the corresponding sensors, enabling identification of the spacecraft regions characterized by the largest amplitude-dependent response variations.

3.3. Time-frequency and harmonic analysis

The frequency-domain screening procedure was complemented by the analysis of time histories acquired during the qualification campaign. Unlike conventional post-processing approaches based solely on frequency-response functions, the availability of the raw time-domain signals enabled a more detailed investigation of the dynamic mechanisms responsible for the observed response variations.

The instantaneous excitation frequency was estimated from the average pilot signal and used to reconstruct the actual frequency evolution of the logarithmic sine sweep. This information allowed the measured responses to be represented as a function of the instantaneous excitation frequency rather than time, facilitating the interpretation of amplitude-dependent effects through time-frequency representations such as spectrograms.

To quantify the harmonic content of the measured responses, the output signals were locally decomposed into Fourier series synchronized with the instantaneous excitation frequency. For each frequency interval, the response of the i^{th} sensor at excitation level k, $a_{i,k}(t)$, was approximated as

$$a_{i,k}(t) = A_{i,k}^{(0)} + \sum_{h=1}^{H} A_{i,k}^{(h)} e^{ih\omega t}, \quad (5)$$

where $A_{i,k}^{(0)}$ is the mean value, $A_{i,k}^{(h)}$ is the complex Fourier coefficient associated with the h harmonic, H is the highest retained harmonic order and ω is the instantaneous angular frequency of the excitation. The Fourier coefficients were estimated through a least-squares fitting procedure applied over short time intervals containing a fixed number of excitation periods. The resulting coefficients provide a quantitative description of the evolution of the harmonic content throughout the sweep.

The transmissibility of the h harmonic content therefore reads:

$$T_{i,k}^{(h)} = \frac{A_{i,k}^{(h)}}{P_k^{(1)}}, \quad (6)$$

where $P_k^{(1)}$ denotes the complex Fourier coefficient of the fundamental harmonic of the reference input signal. By definition, $T_{i,k}^{(1)}$ corresponds to the conventional transmissibility, whereas $T_{i,k}^{(h)}$ for $h > 1$ quantifies the generation of higher-order harmonic components in the output response. This normalization removes the influence of the excitation amplitude, allowing harmonic contributions to be consistently compared throughout the sweep and across different excitation levels.

The combined use of the Similarity Index, time-frequency representations and local Fourier decomposition provides a comprehensive framework for the identification and interpretation of amplitude-dependent dynamic phenomena in large-scale spacecraft qualification datasets. The developed analysis environment was implemented as an interactive visualization tool, allowing rapid navigation of the complete dataset and direct access to detailed frequency- and time-domain analyses of individual sensors.

4. RESULTS

The first step of the analysis consisted of a global screening of the measured responses, enabling rapid identification of the spacecraft regions exhibiting the largest response variations with increasing excitation level.

Figure 2 shows the distribution of $SI_i^{\min}$ index with respect to the spectral median frequency for the excitation along the spacecraft y direction. Similar distributions were observed for the x and z excitation directions and are not reported here for conciseness. Each marker represents a tri-axial sensor (i) and is positioned according to its spectral median frequency and $SI_i^{\min}$ observed across all excitation levels. Sensors are grouped according to the module to which they belong, allowing a direct comparison of the dynamic behavior of the various spacecraft subsystems. Although a significant dispersion of the Similarity Index can be observed within individual subsystems, the figure already highlights that some structural regions are generally characterized by lower values than others.

The reference input spectra corresponding to the four excitation levels for the y-direction sine-sweep test are shown in Figure 3. The spectra exhibit an expected increase in excitation amplitude with increasing test level, together with several notches introduced by the vibration control strategy.

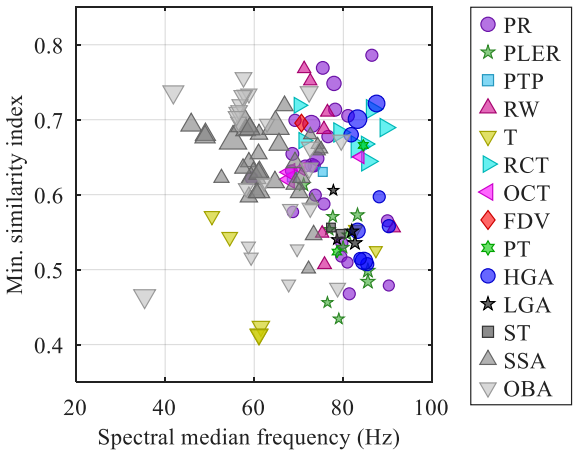


Figure 2. Sensor-level distribution of minimum SI and spectral median frequency (y-axis excitation).

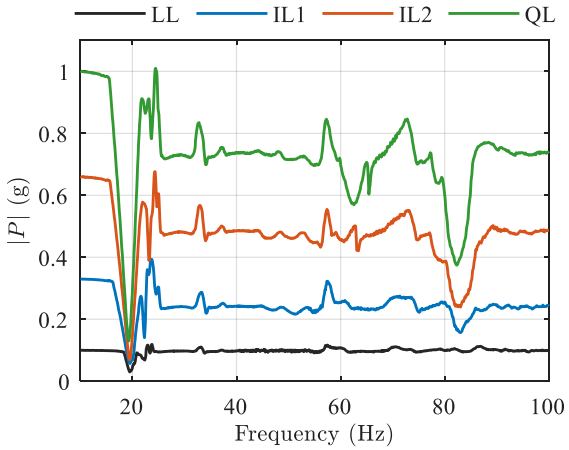


Figure 3. Input spectra for the four excitation levels (y-axis excitation).

A subsystem-level representation of the system response behavior can be obtained by aggregating the sensor indicators within each module. Figure 4 reports the 25th percentile of the $SI_i^{\min}$ values for each spacecraft module and excitation direction. This quantity corresponds to the Similarity Index below which 25% of the sensors of a given module are located and therefore provides a robust measure of the most critical portion of the sensor population without being dominated by isolated outliers.

Such representation reveals that the response evolution has significant differences among the various structural regions. Among all monitored subsystems, the Tank assembly consistently exhibits the lowest percentiles values in the three excitation directions. This indicates that a significant fraction of the sensors installed in this region experiences pronounced transmissibility variations when the excitation level is increased. Similar trends, although less pronounced, can be observed for the Star Tracker and PLE Radiator assemblies. Conversely, subsystems such as the Reaction Wheels, Fill & Drain Valves and Reaction Control Thrusters generally exhibit higher SI values, indicating a more stable dynamic response throughout the qualification campaign.

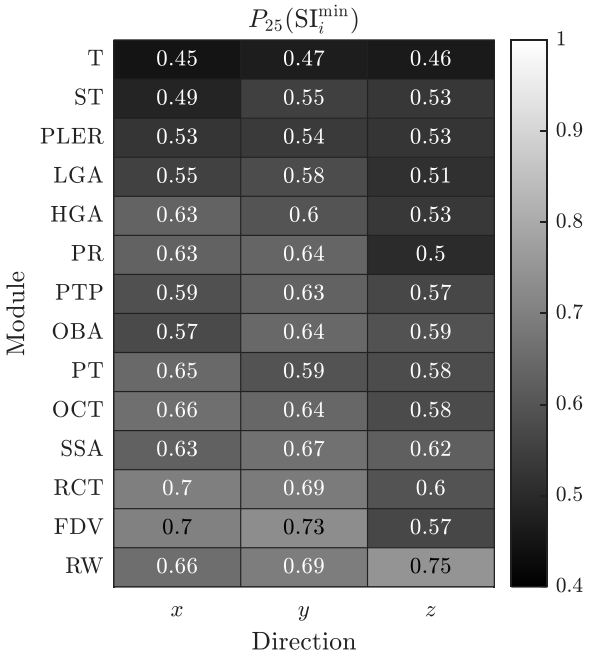


Figure 4. 25th percentile of the minimum SI for each module and excitation direction.

Based on these results, the Tank assembly was selected as the primary case study for further investigation. Figure 5 reports the transmissibility magnitude measured at a representative tri-axial sensor located on the Tank assembly during excitation along the spacecraft y-axis.

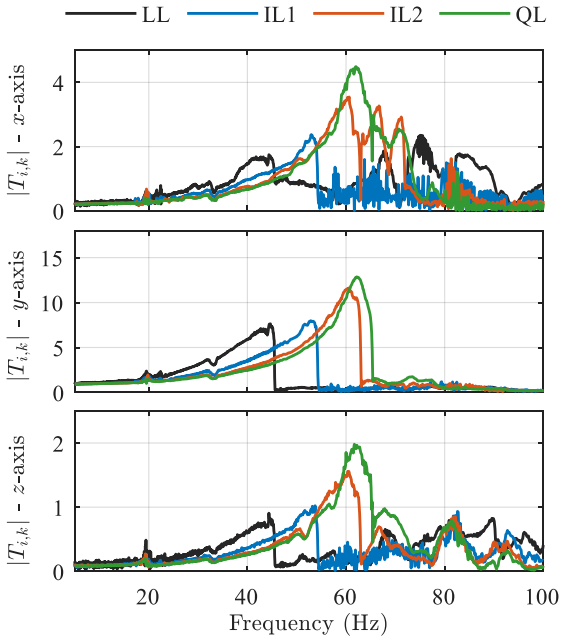


Figure 5. Transmissibility magnitude measured at a representative tri-axial sensor of the Tank assembly for the four excitation levels during y-direction excitation.

The comparison among the four excitation levels clearly illustrates the evolution of the measured

dynamic response as the excitation amplitude increases. Significant changes can be observed in both the resonance amplitudes and their frequency locations. Moreover, the response curves exhibit discontinuities, at all excitation levels. These discontinuities correspond to jump phenomena, which are typically associated with strongly amplitude-dependent and nonlinear dynamic behavior. The synchronized time histories associated with these measurements were further investigated to better understand the underlying dynamics.

Figure 6 reports the corresponding spectrograms for the same representative Tank sensor at the four excitation levels. The time-frequency representation provides additional insight into the response evolution observed in the transmissibility functions. Besides the fundamental excitation component, several higher-order harmonic contributions are clearly visible throughout the sweep. At the two lowest excitation levels (LL and IL1), the response also exhibits fractional spectral components, including half-order contributions. As the excitation level increases (IL2 and QL), these components become progressively less pronounced, while the response becomes increasingly dominated by integer super-harmonics of the excitation frequency. Moreover, additional spectral components appear around them, particularly in the frequency region where the transmissibility curves exhibit jump phenomena.

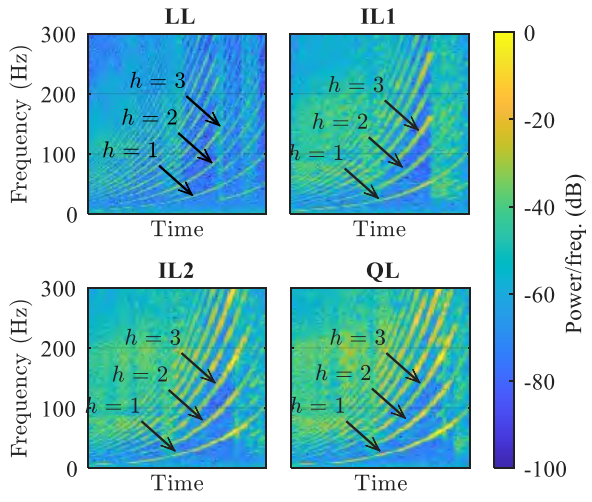


Figure 6. Spectrograms of the representative Tank sensor for the four excitation levels during y-direction excitation. The arrows indicate the excitation fundamental frequency ($h = 1$) and its second and third harmonics ($h = 2$ and $h = 3$).

For a linear system excited by a purely harmonic input, the response is expected to remain confined to the excitation frequency. The appearance of higher-order, fractional and sub-harmonic components therefore indicates that the measured response cannot be described by a linear dynamic model. From a physical standpoint, the generation of these additional frequency components corresponds to a redistribution of the vibration energy from the excitation frequency to other spectral components, potentially activating secondary resonances or other nonlinear dynamic mechanisms. Although the spectrograms alone do not allow the underlying source of the nonlinearity to be identified, they provide a powerful diagnostic tool for locating the frequency intervals and structural regions where further investigation should be focused.

In order to quantify the harmonic content observed in the spectrograms, the synchronized time histories were further processed through the local Fourier-series decomposition described in Section 3. Figure 7 reports the harmonic transmissibilities of the same representative Tank sensor for the four excitation levels. Only the integer harmonics of the excitation frequency are considered in the decomposition; therefore, the fractional spectral components highlighted in the spectrograms are not represented in the following analysis.

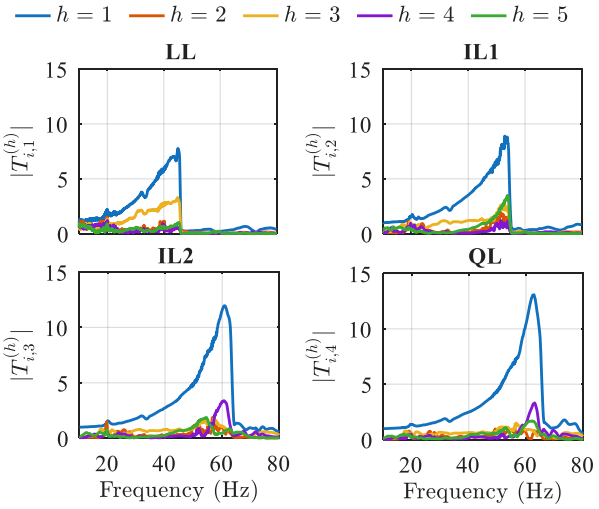


Figure 7. Magnitudes of the first five Fourier coefficients of the representative Tank sensor for the four excitation levels during y-direction excitation. The coefficients are plotted as a function of the instantaneous excitation frequency.

The local Fourier decomposition provides a quantitative description of the harmonic content throughout the sweep, enabling direct comparison of the contribution of each harmonic order at different excitation levels. The results confirm that significant higher-order harmonic components are present at all excitation levels. However, the response evolution cannot be interpreted as a simple increase of all harmonics with increasing excitation amplitude. Instead, both the relative amplitudes and the dominant harmonic orders evolve significantly with the excitation level and frequency. This observation indicates that the spectral signature of the response changes as different amplitude-dependent dynamic regimes are encountered during the sweep.

From a practical perspective, this analysis complements the spectrograms by identifying which

harmonic components dominate the response and where they occur along the frequency sweep. Combined with the Similarity Index, these quantities provide the analyst with objective indicators to identify the sensors and frequency regions that deserve further investigation.

In contrast with the Tank assembly, other spacecraft subsystems exhibit a considerably more regular response evolution. Figure 8 and Figure 9 report representative sensors belonging to PTP (25th percentile SI in y-direction of 0.63) and the OBA (25th percentile SI in y-direction of 0.68), respectively.

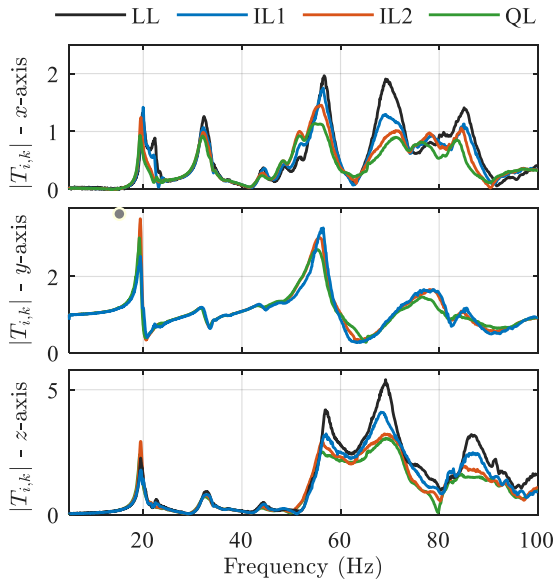


Figure 8. Transmissibility magnitude measured at a representative tri-axial sensor of the PTP assembly for the four excitation levels during y-direction excitation.

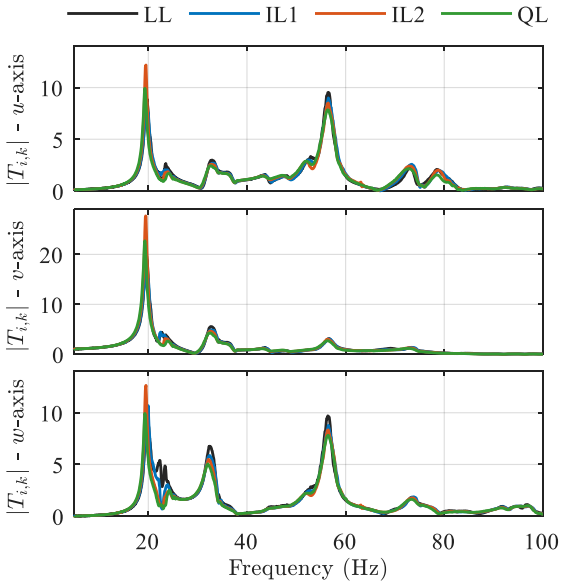


Figure 9. Transmissibility magnitude measured at a representative tri-axial sensor of the OBA assembly for the four excitation levels during y-direction excitation.

Although moderate changes in resonance amplitudes and slight frequency shifts can still be observed as the excitation level increases, the overall shape of the transmissibility functions remains essentially unchanged. In particular, no jump phenomena or abrupt response discontinuities are observed.

These examples illustrate the physical interpretation of relatively high Similarity Index values, confirming that the proposed screening procedure successfully discriminates between subsystems exhibiting pronounced amplitude-dependent behavior and those characterized by a comparatively stable dynamic response. Further confirmation of these observations is provided by the spectrograms of the selected OBA sensor, shown in Figure 10. In contrast to the Tank assembly (Figure 6), the response is largely dominated by the excitation fundamental frequency, while the higher-order harmonic components remain significantly weaker, typically 30–50 dB below the fundamental.

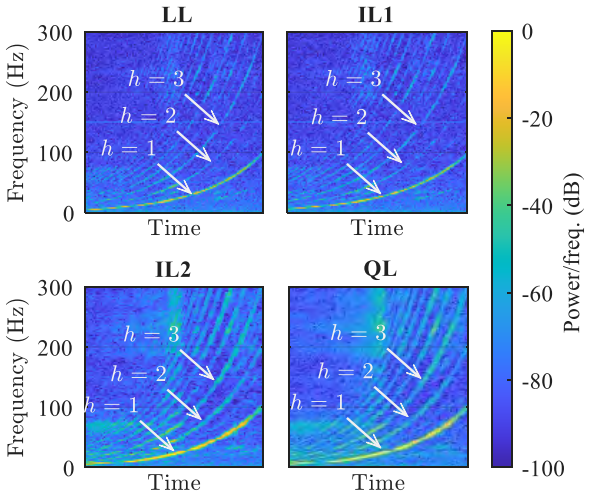


Figure 10. Spectrograms of the representative OBA sensor for the four excitation levels during Y-direction excitation. The arrows indicate the excitation fundamental frequency ($h = 1$) and its second and third harmonics ($h = 2$ and $h = 3$).

5. CONCLUSIONS

This work presented a data-driven methodology for the analysis of sine-vibration qualification tests on the ESA-PLATO Proto-Flight Model. The proposed workflow combines global frequency-domain indicators with targeted analyses of synchronized time-domain measurements.

A Similarity Index was introduced to compare transmissibility functions acquired at different excitation levels and to automatically rank sensors and spacecraft subsystems according to the observed response evolution. The resulting screening procedure proved effective in identifying the structural regions exhibiting the largest amplitude-dependent variations, considerably reducing the amount of data requiring detailed inspection.

The methodology was applied to the complete qualification dataset of the PLATO spacecraft. The subsystem-level analysis highlighted significant differences among the monitored structural regions, with the Tank assembly consistently exhibiting the lowest Similarity Index values across all excitation directions. Detailed investigation of representative sensors revealed pronounced amplitude-dependent response variations, including resonance shifts, jump phenomena and significant modifications of the harmonic signature of the measured response. Conversely, other spacecraft subsystems exhibited a much smoother evolution of the transmissibility functions, confirming the capability of the proposed Similarity Index to discriminate between markedly different dynamic behaviors.

The combined use of frequency-domain screening, time-frequency representations and local Fourier decomposition provides a practical framework for the investigation of complex spacecraft dynamics without requiring a priori numerical models. More importantly, the proposed methodology demonstrates that synchronized time-domain measurements, when available, represent a valuable complement to conventional frequency-domain processing and can significantly enhance the interpretation of spacecraft qualification tests. By exploiting information that is typically overlooked in standard post-processing, the proposed approach enables a more comprehensive characterization of amplitude-dependent dynamic phenomena and supports the identification of structural regions requiring further investigation during spacecraft qualification campaigns.

REFERENCES

1. ECSS (2013). ECSS-E-HB-32-26A: Spacecraft Mechanical Loads Analysis Handbook. ESA-ESTEC, Noordwijk, The Netherlands.
2. NASA (2019). NASA-STD-5002A: Load Analyses of Spacecraft and Payloads. National Aeronautics and Space Administration, Washington, D.C., USA.
3. Pederbelli, D., Nali, P., & Calvi, A. (2023). Euclid Spacecraft Sine Vibration Test Prediction Through the Virtual Shaker Testing Technique. *J. Spacecr. Rockets*. 60(5).
4. Strogatz, S.H. (2018). Nonlinear Dynamics and Chaos. *CRC Press,* Boca Raton, FL, USA
5. Worden, K., & Tomlinson, G.R. (2001). Nonlinearity in structural dynamics: detection, identification and modelling. *Institute of Physics Publishing*, Bristol, UK.
6. Anastasio, D., Marchesiello, S., Gatti, G., Gonçalves, P.J.P., Shaw, A.D., & Brennan, M.J. (2023). An investigation into model extrapolation and stability in the system identification of a nonlinear structure. *Nonlinear Dynamics*. 111(19).

MULTI-AXIS SHOCK SYNTHESIS FOR SPACECRAFT QUALIFICATION TESTING

Nicolas ROY [(1)], Etienne CAVRO [(2)], Simon LEMAY [(3)]

[(1)] Top Modal, 130 rue Galilée, 31670 Labège, FRANCE, Email: nicolas.roy@topmodal.fr
[(2)] Airbus Defence and Space, 2 rond point Pierre Guillaumat, 31029 Toulouse, FRANCE, Email: etienne.cavro@airbus.com
[(3)] CNES, 18 avenue Edouard Belin, 31401 Toulouse, FRANCE, Email: simon.lemay@cnes.fr

KEYWORDS

Shock Synthesis, Multi-axis, Coupled Analysis, Shock Response Spectrum, Effective Mass

ABSTRACT

Today, qualification of spacecraft structures in the low-frequency environment is performed using a single-axis slowly-varying sine sweep excitation. However, the majority of the launch events are short duration transients rather than steady-state harmonics. This produces excessive fatigue in the structure and requires the use of notching to avoid overtesting near the principal structural resonances.

Moreover, transient events comprise in general six components acting simultaneously on the spacecraft. For multi-axis test facilities, it is possible to reproduce these events sequentially, one after the other. However, methods to combine them into a single equivalent muti-axis transient are not available in current industrial practice.

This paper presents a method based on the shock response spectrum but adapted to the case of multi-axis excitation.

1. INTRODUCTION

The classical sine sweep test with notching is a practical and widely accepted way to qualify spacecraft structures. It ensures that the entire frequency band is covered without undertesting since the specified levels largely exceed the flight environment. However, within some critical frequency bands it is often necessary to introduce notching to avoid overtesting. Moreover, the use of notching must always be justified by the payload authority and can be a source of uncertainty and even contention during the test campaign.

To attenuate the risk of overtesting, the classical sine test could be replaced by a transient test. The main problem here is the elaboration of the specification which is much more involved than the classical sine sweep test.

Common practice makes use of the Shock Response Spectrum (SRS) originally conceived by Dr. Maurice Biot in 1932 during his Ph.D. studies at Caltech. The SRS provides the maximum response of a single degree of freedom (SDOF) system as a function of its natural frequency for a given damping ratio or Q factor. It has the advantage of representing transient severity and enveloping multiple transient events. From the SRS, transient excitations can be elaborated by the use of shock synthesis methods.

The main drawback of the SRS is the loss of information since it contains only the amplitudes thus making the transformation irreversible and non-unique. For example, a sine sweep lasting several minutes can be derived from the SRS of a one-second transient shock. Although both signals share the same SRS, they have different amplitudes and durations which is problematic. It is therefore important to add additional information or constraints such as the duration in order to produce more realistic transients, which might not necessarily be sufficient.

Previous studies on transient testing [1-4] funded in-part by the CNES have been carried out and led to a novel shock synthesis method that uses the ratio of two SRS with two different values of damping (Q factors) to produce a transient with more realistic durations.

In 2023, a workshop was organized by ESA/ESTEC on the topic of novel test methods for satellite testing as an alternative to fixed base sine tests [5]. Although there was a strong consensus that, in many cases, sine testing is not a representative environment, several topics still need to be addressed before transitioning to transient testing.

To help move forward with transient testing, an R&D study has been initiated this year by the CNES [6] with the goal of elaborating a shock synthesis method compatible with the following requirements which sine sweep testing cannot meet.

- Multi-axis transient events
- Different values of modal damping
- Simultaneous excitation of modes

The first phase of the study includes the theoretical development of the method along with numerical validation using a spacecraft finite element model (FEM) and results from coupled loads analysis

(CLA). The second and final phase of the study involves an experimental validation of the method using a simple structure on a 6-DOF test facility.

This paper presents the ongoing work of the first phase of the project. First, a description of the method is provided starting with classical (single-axis) shock synthesis using shock response spectrums (SRS). Next, the transition to multi-axis shock synthesis with the concept of modal SRS is detailed. In particular, it is shown how the method can accommodate one or several multi-axis events as input, and synthesize either an equivalent muti-axis or mono-axis event.

Finally, preliminary results using the MicroCarb satellite condensed FEM along with a set of multi-axis events from CLA are presented to illustrate the interest and capabilities of the method.

2. SINGLE-AXIS SHOCK SYNTHESIS

The topic of shock synthesis has been widely studied and in particular for reproducing input to a shaker table from a specified SRS. Vibration test facility tools include algorithms to perform this operation.

Most shock synthesis algorithms are based on the use of elementary waveforms each associated with a particular frequency. The goal is to determine the properties of each waveform such that the combined waveforms produce a transient whose SRS closely matches the reference SRS.

The most common waveforms used for shock synthesis include the damped sine, the compensated damped sine with zero residual displacement (ZERD) and the wavelet (or WAVSIN) function. Details on these waveforms can be found in [8].

In practice, the number of waveforms is defined at the start by specifying a number of waveforms per octave (typically between 12 and 24) along with the frequency range. The algorithms used to determine the optimal choice of the waveform parameters vary greatly depending on the type of waveform and the software used.

In the previous studies carried out for the CNES [1-4], shock synthesis was performed using a continuous function as opposed to the superposition of discrete waveforms. This function called the Fast Sine Sweep (FSS or SBR in French) is defined in Eq. 1 for the case of single-axis excitation

$$\ddot{u}_j(t) = A(t)\sin E(t) \qquad (1)$$

with $A(t)$ the amplitude function and $E(t)$ the phase function related to the sweep rate.

The optimization consists of determining $A(t)$ and $E(t)$ such that the corresponding SRS matches the reference SRS. A variant of the procedure allows matching the SRS for two different values of damping (Q factors) in order to obtain an excitation with more realistic duration.

Although the FSS has the ability to take into account the duration of the shock (information obtained from the use of two SRS), it has two drawbacks:

- A time consuming and complex optimization algorithm due to the use of continuous functions.
- A synthesized transient with sequential frequencies as opposed to more realistic superposed frequencies.

For these reasons, it was decided to set aside the FSS for shock synthesis in favor of a simpler and more standard method using discrete waveforms and in particular the wavelet.

A wavelet (sometimes referred to as the WAVSIN function) is a sine function modulated by another sine as illustrated in Fig. 1 and defined in Eq. 2.

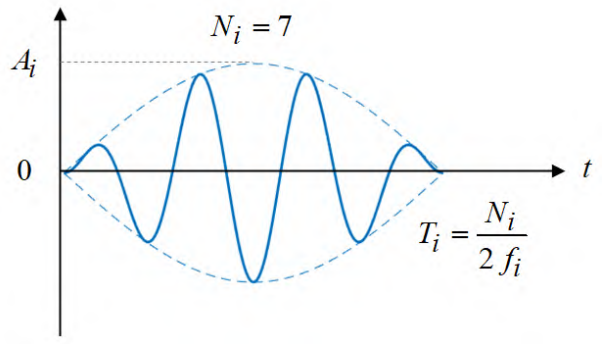


Figure 1: Wavelet Function

$$W_i(t) = A_i \sin\left(\frac{2\pi f_i}{N_i} t\right)\sin(2\pi f_i t) \qquad (2)$$

The three parameters defining the wavelet are 1) A_i the amplitude of the wavelet, 2) f_i the frequency of the wavelet in Hz, and 3) N_i the number of half-cycles composing the wavelet with $N_i = 3,5,7,\cdots$.

The duration of the wavelet T_i is governed by its frequency and the number of half-cycles as defined in Eq. 3.

$$T_i = \frac{N_i}{2 f_i} \qquad (3)$$

Moreover, all wavelets have zero final velocity and displacement ($t = T_i$) which is useful in terms of shaker table compatibility.

The procedure used in this study for single-axis shock synthesis is presented below. This procedure

is then adapted to the case of multi-axis shock synthesis discussed in the next chapter.

1) Select a reference SRS which can also be an envelope of several SRS coming from several events.
2) Specify a frequency range and a number of points per octave for the synthesis. This can correspond to the SRS resolution.
3) Specify the maximum time duration for the synthesis.
4) Select a value for *N* - the number of half-cycles to be used for all wavelets.
5) Create a wavelet for each frequency point with f_i the value of the frequency point, $N_i = N$ the number of half-cycles selected in step (4) and A_i the initial amplitudes with alternating signs.
6) Use optimization (Levenberg-Marquardt) to determine the final amplitudes A_i that minimize the error between the synthesized SRS and the reference SRS.

In the above procedure all wavelets start simultaneously at time zero (no offsets) and have the same number of half-cycles. The use of alternating signs in the amplitudes helps to limit amplitude buildup of the synthesized transient at startup. The number of half-cycles can be adjusted to better match the amplitudes and durations in the synthesized transient compared to the actual events.

3. MULTI-AXIS EQUATIONS OF MOTION

Consider the structure shown in Fig. 2 in test configuration with a rigid (statically determinate) junction *j* comprising 6 DOF (Tx, Ty, Tz, Rx, Ry, Rz) along with *i* internal DOF.

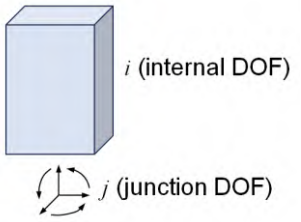


Figure 2: Structure with junction and internal DOF

The structure is excited by a multi-axis imposed base acceleration $\ddot{\mathbf{u}}_j(t)$ acting simultaneously on the 6 junction DOF.

The equation of motion for the generalized response of mode k with natural circular frequency ω_k and modal damping ratio ζ_k is expressed in Eq. 4

$$(\ddot{q}_k - \ddot{\bar{q}}_k) + 2\zeta_k\omega_k(\dot{q}_k - \dot{\bar{q}}_k) + \omega_k^2(q_k - \bar{q}_k) = -\ddot{\bar{q}}_k \quad (4)$$

where $\ddot{q}_k$ is the absolute generalized acceleration and $\ddot{\bar{q}}_k$ the imposed generalized acceleration given in Eq. 5

$$\ddot{\bar{q}}_k = \mathbf{L}_{kj}\,\ddot{\mathbf{u}}_j / m_k \quad (5)$$

with m_k the generalized mass of mode k (assumed to be the same for all modes) and $\mathbf{L}_{kj}$ the corresponding vector of 6 participation factors. The participation factors are directly related to the effective mass matrix $\tilde{\mathbf{M}}_{jj,k}$ as shown in Eq. 6.

$$\tilde{\mathbf{M}}_{jj,k} = \mathbf{L}_{jk}\,\mathbf{L}_{kj} / m_k \quad (6)$$

Using mode superposition, the physical responses at the junction and internal DOF may be derived as shown in Eqs. 7 and 8 for the interface reaction forces and internal accelerations

$$\mathbf{F}_j(t) = \sum_k \mathbf{L}_{jk}\,\ddot{q}_k(t) + \bar{\mathbf{M}}_{jj,res}\,\ddot{\mathbf{u}}_j(t) \quad (7)$$

$$\ddot{\mathbf{u}}_i(t) = \sum_k \mathbf{\Phi}_{ik}\,\ddot{q}_k(t) + \mathbf{T}_{ij,res}\,\ddot{\mathbf{u}}_j(t) \quad (8)$$

where $\mathbf{\Phi}_{ik}$ is the mode shape vector for mode *k*, $\bar{\mathbf{M}}_{jj,res}$ the residual mass and $\mathbf{T}_{ij,res}$ the residual transmissibility. The reader is referred to [7] for details concerning the modal approach and the concept of modal effective parameters.

4. MODAL SRS

4.1. Introduction

From Eq. 5 we see that the multi-axis physical accelerations are combined according to the participation factors $\mathbf{L}_{kj}$ to obtain a *single* generalized excitation for each mode thus leading to the modal SDOF equation of Eq. 4 which is analogous to the equation used for classical SRS calculations.

From Eq. 4 we can compute the SRS of the modal absolute acceleration $\ddot{q}_k$ for each mode using the generalized imposed acceleration $\ddot{\bar{q}}_k$ from Eq. 5.

This is the key point behind the proposed method for multi-axis shock synthesis. The single-axis SRS is replaced by a set of modal SRS with each mode being excited by a specific combination of the base excitations using the participation factors $\mathbf{L}_{kj}$.

It's interesting to note from Eq. 5 that in the case of a single-axis excitation the modal excitation $\ddot{\bar{q}}_k$ is the same for all modes (to within a scale factor L_{kj}) producing the same modal SRS differing only by the scale factor. In other words, the multi-axis modal SRS degenerate to the classical SRS for the case of single-axis excitation – assuming the same value of damping is used for all modes.

4.2. Selection of Modes

Although the participation factors allow us to combine the multi-axis transients, they pose a new problem in that we now have to handle many modal SRS instead of just one.

Dealing with a large number of modal SRS may appear troublesome. However, the intrinsic properties of the participation factors can be taken advantage of in order to significantly reduce the number of modal SRS required for the synthesis. These properties are discussed below.

4.2.1. Dominant Modes

For base excitation, only the modes with significant effective mass and inertia need to be considered. By simple examination of the participation factors and/or effective masses, a small number of dominant modes can be readily identified.

4.2.2. Rank of Participation Factors

By examination of the matrix of participation factors, it is straightforward to see that the rank of the matrix cannot exceed 6 (the number of junction DOF). In other words, there are at most 6 independent vectors of participation factors - the others being just a linear combination of the 6. Therefore, the choice of modes can be further limited to the 6 modes with the largest effective masses and inertias.

There is one important distinction that needs to be made here. The fact that the rank of $\mathbf{L}_{kj}$ cannot exceed 6 does *not* imply that the rank of the corresponding modal SRS does not exceed 6! This is because the SRS is a nonlinear transformation. Therefore, from a mathematical point of view the modal SRS are in general independent. However, from practical point of view, they display nearly the same degree of independence (rank) as the participation factors. Thus, the selection of modes based on the effective masses remains justified.

4.2.3. Coupling of Excitation Directions

From the participation factors (or effective masses) information concerning the coupling between the modes and the excitation directions (junction DOF) can be also obtained.

Consider a subset of excitation directions such as an axial direction (Tx) or a bending direction (Ty and Rz) along with the associated dominant modes. If the effective masses and inertias of these modes are negligible in all other excitation directions, then the given subset of excitation directions can be considered uncoupled from the other directions. This implies that the full multi-axis excitation can be replaced by an equivalent set of single-axis and/or reduced-size multi-axis excitations thus further reducing the number of modes.

For example, in the case of a symmetric beam clamped at the base, the effective masses will display perfect uncoupling between the axial direction [Tx], each of the bending directions [Ty, Rz] and [Tz, Ry], and the torsional direction [Rx]. Therefore, in this case, shock synthesis can be performed separately for each of these excitation subsets.

4.3. Modal Contributions

The synthesis strategy consists of generating a multi-axis transient with the same modal SRS as the envelope of the events' modal SRS.

Although it is important to match each modal SRS over all frequencies, the value at the natural frequency of the mode $f = f_k$ is the most critical value since the modal accelerations $\ddot{q}_k(t)$ in Eqs. 7 and 8 are evaluated at this frequency.

If the SRS from the enveloped events and the synthesis have the same value at the natural frequency of the mode, then the synthesized transients will have exactly the same *maximum* modal acceleration $\ddot{q}_k(t)$ as the enveloped events.

This, however, does not imply that the maximum *physical* responses will be the same! This is due to the superposition of the modal responses in Eqs. 7 and 8 and the fact the maxima do not necessarily occur at the same instant of time. Therefore, some discrepancies in the maximum response levels will occur due to the differences in the phase.

To better understand the influence of the phase on the maximum responses, we can approximate the maximum physical responses by a combination of the maximum modal response. Two types of combinations are of particular interest – the direct sum and the quadratic sum.

4.3.1. Direct Sum Estimation

The direct sum estimation for the physical responses is given in Eqs. 9 and 10 where the "+" superscript is the maximum value over time.

$$\mathbf{F}_j^+ \approx \sum_k \mathbf{L}_{jk}\, \ddot{q}_k^+ + \bar{\mathbf{M}}_{jj,res}\, \ddot{\mathbf{u}}_j^+ \qquad (9)$$

$$\ddot{\mathbf{u}}_j^+ \approx \sum_k \mathbf{\Phi}_{ik}\, \ddot{q}_k^+ + \mathbf{\Psi}_{ij,res}\, \ddot{\mathbf{u}}_j^+ \qquad (10)$$

The direct sum is highly conservative and often too severe since it assumes that all the maxima occur at the same instant. However, it does provide an upper limit to the physical responses which can be useful for comparison purposes and from a safety point of view

4.3.2. Quadratic Sum Estimation

The quadratic sum estimation is shown in Eqs. 11 and 12. The quadratic sum provides a more realistic

approximation though it can underestimate or overestimate the true maximum.

$$\mathbf{F}_j^+ \approx \sqrt{\sum_k (\mathbf{L}_{jk}\, \ddot{q}_k^+)^2 + (\bar{\mathbf{M}}_{jj,res}\, \ddot{\mathbf{u}}_j^+)^2} \qquad (11)$$

$$\ddot{\mathbf{u}}_j^+ \approx \sqrt{\sum_k (\mathbf{\Phi}_{ik}\, \ddot{q}_k^+)^2 + (\mathbf{\Psi}_{ij,res}\, \ddot{\mathbf{u}}_j^+)^2} \qquad (12)$$

By comparing the maximum response with the direct and quadratic approximations, we can evaluate how conservative (or not) the maximum value is.

5. MULTI-AXIS SHOCK SYNTHESIS

Using the modal SRS, a multi-axis shock synthesis procedure can be derived by adapting the single-axis shock synthesis procedure presented in chapter 2. The principal steps to the procedure are indicated in Fig. 3 and described in detail hereafter.

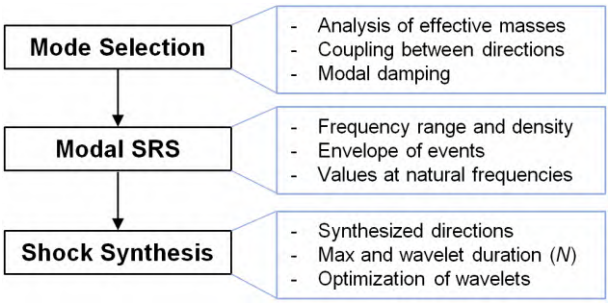


Figure 3: Steps for Multi-axis Shock Synthesis

5.1. Mode Selection

By evaluation of the effective masses the important (dominant) modes are identified. The degree of coupling between these modes and the excitation directions is used to determine if the synthesis can be decomposed into several uncoupled sets of excitation directions. For example, it may be possible to synthesize an axial excitation and a bending excitation separately. In the general case where the modes are coupled with all excitation directions then a single synthesis involving all 6 junction DOF is performed.

The participation factors and associated effective masses are obtained either through FEM simulation or extracted from test data (e.g. low-level sine sweep) using modal identification techniques.

In addition to the participation factors, the damping ratio (Q factor) are provided for each of the selected modes.

5.2. Modal SRS

The frequency range along with the number of points per octave (generally 12-24) are specified. The modal SRS for all events are computed for the selected modes and excitation directions. For each mode, the envelope of the SRS over all events is computed and retained as the modal SRS.

5.3. Shock Synthesis

The following inputs are required to initiate the shock synthesis.

- *Maximum duration for the synthesized transients*. This value is typically based on the duration of the events.
- *Excitation directions to be synthesized*. The synthesized excitation directions are usually the same as, or a subset of, the excitation directions used for the events. For example, an axial excitation will be synthesized with an axial transient. However, a bending excitation [Ty, Rz] can be synthesized using two directions [Ty, Rz] or using only a lateral excitation [Ty]. Similarly, a 6-axis excitation can be synthesized using just 3 translations [Tx, Ty, Tz]. The choice may depend on the capabilities of the test facility (single shaker vs 2-DOF, 3-DOF or 6-DOF systems).
- *Number of half-cycles (N) for wavelets*. This value is applied to all wavelets and in all directions. Typical values vary between 11 and 21. The number of half-cycles has an influence on the amplitude and duration of the synthesized transients and can therefore be used to better match these properties with those of the input events. For the low-frequency wavelets, the number of half-cycles may need to be reduced in order not to exceed the maximum duration of the synthesized transients.

Once the above inputs are provided, an initial set of wavelets is defined for each synthesized excitation direction with the following properties.

- Frequencies f_i the same as the SRS frequencies.
- Number of half-cycles N_i using value specified above (same for all wavelets).
- Initial amplitudes A_i with alternating signs.
- No offsets (all wavelets start simultaneously at time zero).

The last phase of the synthesis step is the determination of the final amplitudes of the wavelets. This is done using the Levenberg-Marquardt nonlinear optimization algorithm which minimizes the least squares distance between the modal SRS and the synthesized modal SRS obtained from the wavelets.

6. INDUSTRIAL EXAMPLE

6.1. Introduction

Preliminary results using the proposed multi-axis shock synthesis method were obtained by simulation using the Craig-Bampton condensed model of the MicroCarb satellite [9].

Three multi-axis events obtained through the coupled analysis (CLA) of the MicroCarb satellite and the Vega-C launcher were considered.

- Liftoff
- Z9 Ignition
- Z40 Ignition

Three synthesis cases summarized in Fig. 4 were studied to illustrate the different scenarios discussed in the preceding chapters.

Case	Modes	Exci Dir	Syn Dir
1	28 31	1	1
2	8 9	2 3 5 6	2 3
3	8 9 27 28 31	1 2 3 4 5 6	1 2 3 4 5 6

Figure 4: Cases for Shock Synthesis

The following parameters were used for all 3 cases:

- Duration 0.6 seconds (same as events)
- N = 17 half-cycles
- SRS from 10 to 200 Hz with 12 pts/oct

The following results are presented for all cases.

- Modal SRS
- Modal SRS at Natural Frequencies
- I/F Accelerations
- I/F Loads
- Internal Accelerations

The internal accelerations were computed at the MTBY_PX sensor location in the 3 translational directions.

6.2. MicroCarb Model

The FEM of the MicroCarb satellite is shown in Fig. 5.

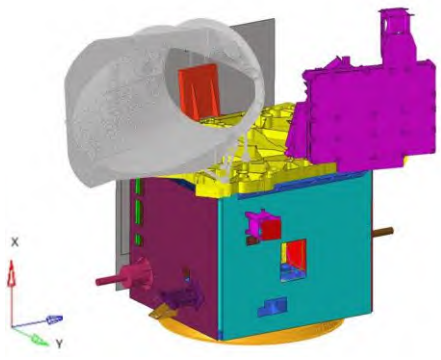


Figure 5: FEM View of MicroCarb Satellite

The model is condensed on a 6-DOF rigid junction with 38 modes up to 150 Hz. The effective masses and inertias are presented in Fig. 6. All values are expressed in SI units.

Mode (k)	Freq. (Hz)	Mxx	Myy	Mzz	Ixx	Iyy	Izz
1	2.39	0.0	0.4	0.1	0.0	0.0	0.3
2	2.39	0.0	0.1	0.4	0.0	0.3	0.0
3	2.39	0.4	0.0	0.0	0.0	0.0	0.0
4	2.65	0.1	0.2	0.1	0.0	0.1	0.2
5	2.65	0.1	0.1	0.2	0.0	0.2	0.1
6	2.65	0.3	0.0	0.1	0.0	0.0	0.0
7	14.94	0.0	0.0	0.0	0.0	0.0	0.0
8	**47.70**	**0.1**	**3.3**	**109.0**	**0.1**	**67.6**	**2.3**
9	**49.24**	**0.4**	**106.6**	**3.9**	**0.1**	**2.2**	**63.8**
10	58.58	0.0	0.4	0.0	0.0	0.0	0.0
11	59.02	0.0	0.0	0.1	0.1	0.0	0.0
12	59.78	0.8	0.0	0.1	0.0	0.0	0.0
13	59.84	0.1	0.1	0.0	0.0	0.0	0.0
14	60.82	0.1	1.7	0.0	0.0	0.0	1.3
15	76.68	0.1	0.0	0.0	0.0	0.0	0.0
16	77.68	1.0	0.3	1.6	0.0	0.1	0.0
17	87.62	3.3	0.0	0.0	0.0	0.0	0.0
18	87.84	0.0	0.0	0.0	0.0	0.0	0.0
19	88.51	1.2	0.0	0.0	0.0	0.0	0.0
20	88.58	0.0	0.6	0.0	0.1	0.0	0.0
21	91.11	2.5	0.3	0.1	0.1	0.1	0.0
22	91.67	2.9	0.3	2.8	0.0	0.1	0.0
23	92.28	0.0	0.6	0.1	0.0	0.0	0.0
24	92.52	0.1	0.0	0.1	0.0	0.0	0.0
25	92.55	0.0	0.0	0.0	0.0	0.0	0.0
26	101.12	0.2	1.7	0.0	0.0	0.0	0.6
27	**107.68**	**4.2**	**1.4**	**0.0**	**1.3**	**0.0**	**0.1**
28	**109.45**	**42.9**	**1.2**	**0.1**	**2.0**	**0.0**	**0.2**
29	116.47	7.6	0.3	1.7	0.0	0.1	0.0
30	119.99	0.0	0.0	0.0	0.0	0.0	0.0
31	**121.00**	**24.8**	**1.8**	**0.1**	**1.8**	**0.0**	**0.0**
32	125.27	4.6	0.0	0.4	0.1	0.1	0.0
33	127.74	4.5	5.2	0.8	0.0	0.0	0.2
34	130.93	0.3	0.6	0.0	0.0	0.0	0.0
35	131.06	0.0	0.2	0.1	0.0	0.0	0.0
36	135.17	0.1	1.7	3.3	0.2	0.1	0.0
37	138.32	0.0	4.1	2.6	0.0	0.0	0.1
38	147.45	0.0	0.0	0.0	0.2	0.0	0.0
	Sum	102.7	133.3	127.9	6.4	71.1	69.5
	Static	185.3	185.3	185.3	15.5	72.3	71.4
	Residual	82.6	52.0	57.4	9.1	1.2	1.9

Figure 6: Effective Masses

We can see that the dominant axial modes 28 and 31 are largely uncoupled from the other directions which justifies the synthesis Case 1 involving only the axial direction – even though there is some coupling with torsion [Rx].

Similarly, the bending modes 8 [Tz Ry] and 9 [Ty Rz] are also well uncoupled motivating Case 2.

The frequency-dependent modal damping values used for the modal SRS are presented in Fig. 7.

Freq (Hz)	All axes Q = 1/2ξ
5 – 48	25
48.1 – 50	16
50.1 – 60	3
60.1 – 80	30
80.1 – 89	3
89.1 – 92	15
92.1 – 93	3
93.1 – 108	15
108.1 - 110	10
110.1 – 120.5	15
120.6 – 125	10
125.1 – 150	25

Figure 7: Modal Damping

6.3. Case 1

This case represents a single-axis synthesis in the axial direction.

6.3.1. Modal SRS

The modal SRS for the two selected modes are plotted in Fig. 8 for each event. The synthesized modal SRS (dotted line) follows very closely the envelope of the modal SRS.

The circles on the SRS indicate the values at the natural frequency of the modes (109 and 121 Hz).

Note that the modal SRS of both modes are identical and differ only by a scale factor defined by the participation factors. This is result of selecting a single-axis excitation and selecting modes with the same modal damping (Q = 10). The same synthesis could therefore be obtained using only one of the two modes since no additional information is provided by the second mode.

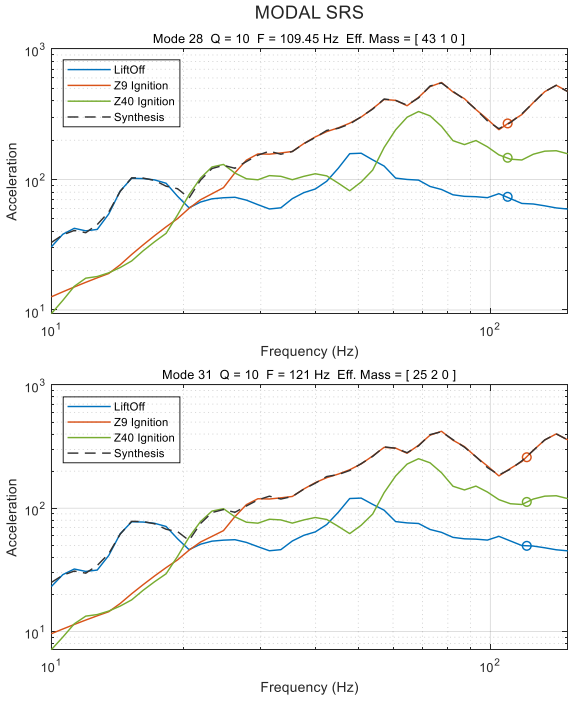


Figure 8: Case 1 Modal SRS

The modal SRS at the natural frequencies are plotted in Figure 9 showing good correlation for the dominant modes.

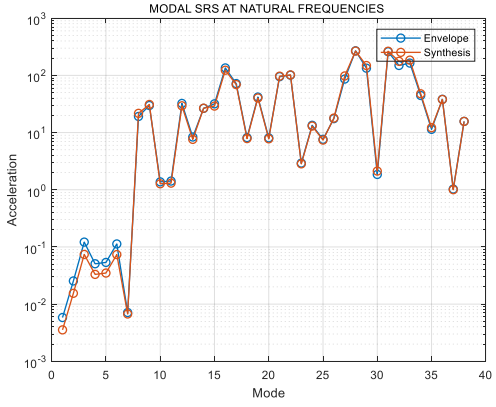


Figure 9: Case 1 Modal SRS at Nat. Freq.

6.3.2. I/F Accelerations

The I/F accelerations of the events limited to the axial direction are plotted in Fig. 10. The corresponding synthesized I/F acceleration is plotted in Fig. 11. We observe good agreement in terms of amplitude, duration and frequency content especially with the Z9 Ignition event which is the critical event near the axial modes.

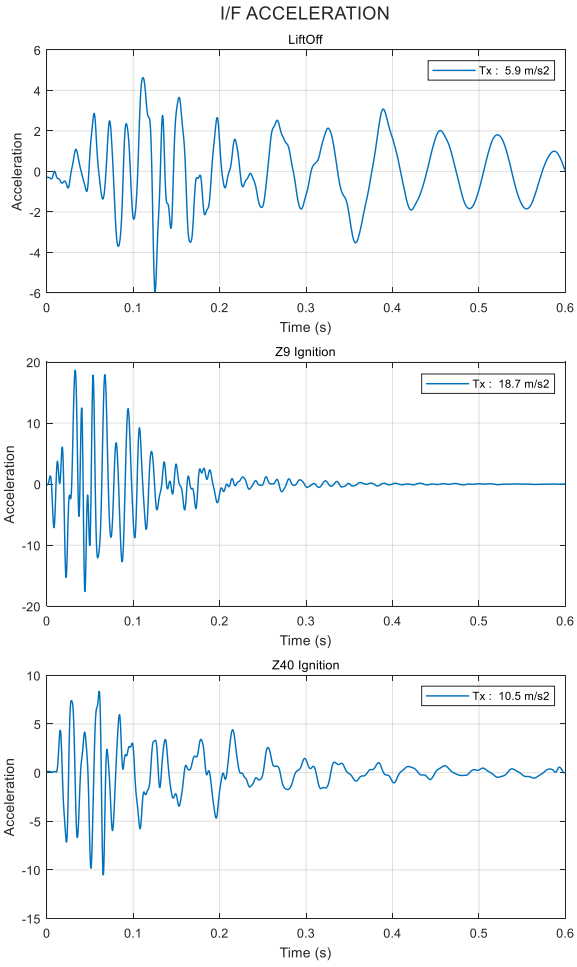


Figure 10: Case 1 I/F Accelerations

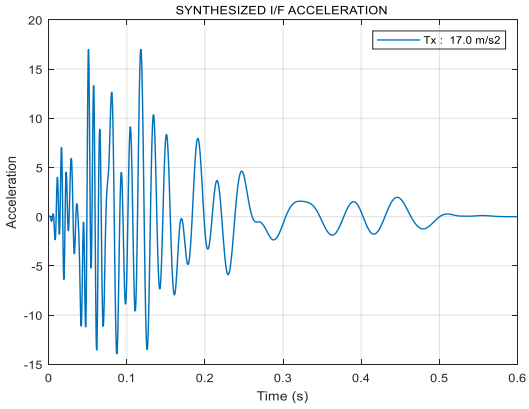


Figure 11: Case 1 Synthesized I/F Accelerations

6.3.3. I/F Loads

The I/F loads computed using Eq. 7 are plotted in Fig. 12 with the corresponding synthesized loads plotted in Fig. 13.

A comparison of the maximum interface loads is presented in Figure 14 including the direct sum and quadratic approximations. We see that the maximum axial force Fx found in the Z9 Ignition event is very close to the maximum force in the synthesized response (4644 N vs 4740 N).

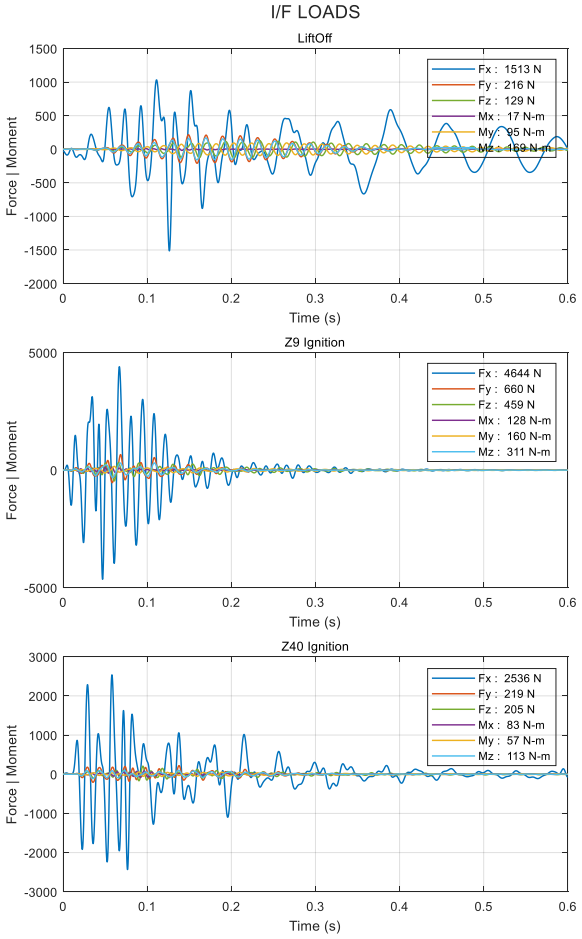


Figure 12: Case 1 I/F Loads

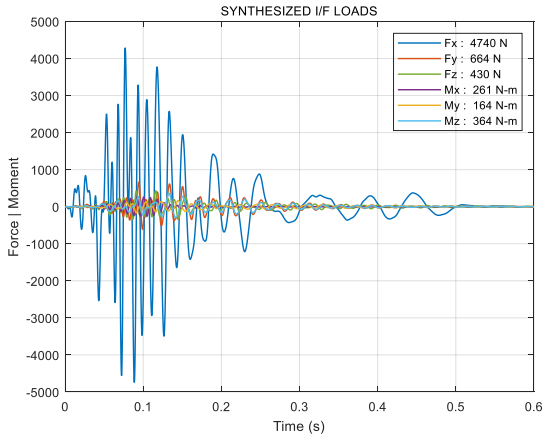


Figure 13: Case 1 Synthesized I/F Loads

Comp	Env	Syn	Error	Syn (DIR)	Syn (QUAD)
Fx (N)	4644	4740	2 %	6379	2652
Fy (N)	660	664	1 %	1996	712
Fz (N)	459	430	-6 %	1336	437
Mx (N-m)	128	261	103 %	1054	520
My (N-m)	160	164	3 %	446	194
Mz (N-m)	311	364	17 %	714	296

Figure 14: Case 1 Comparison of I/F Loads

6.3.4. Internal Accelerations

The internal accelerations at the MTBY_PX sensor location computed with Eq. 8 are shown in Fig. 15 along with the corresponding synthesized internal accelerations plotted in Fig. 16.

A comparison of the maximum internal accelerations is presented in Fig. 17. Again, we see good agreement between the maximum accelerations – especially in the Tx direction (31 m/s2 vs 35 m/s2).

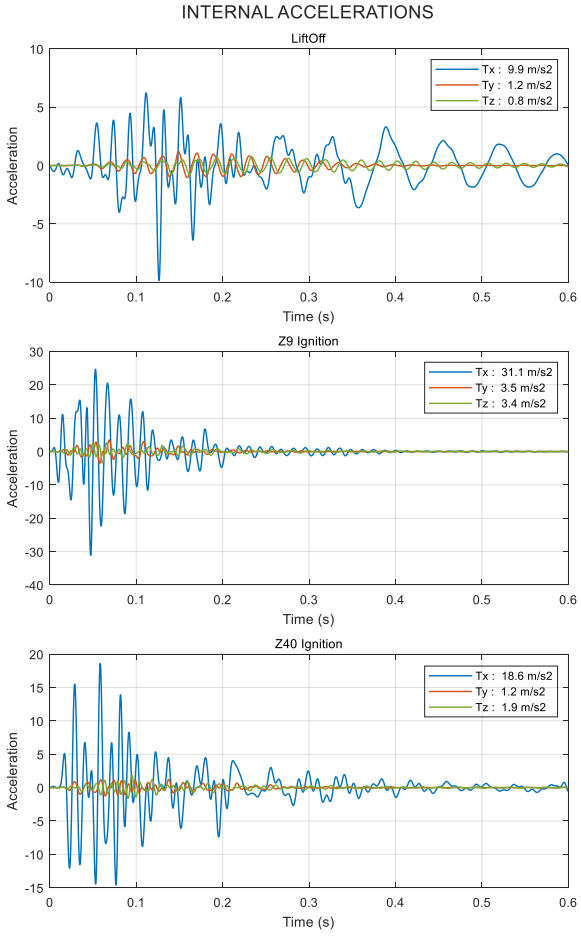


Figure 15: Case 1 Internal Accelerations

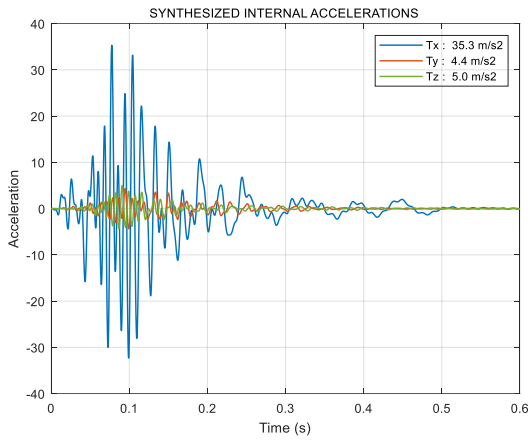


Figure 16: Case 1 Synthesized Internal Accel.

Comp	Env	Syn	Error	Syn (DIR)	Syn (QUAD)
Tx (m/s2)	31.1	35.3	13 %	61.7	25.4
Ty (m/s2)	3.5	4.4	26 %	16.9	6.8
Tz (m/s2)	3.4	5.0	47 %	13.3	4.2

Figure 17: Case 1 Comparison of Internal Accel.

6.4. Case 2

This case illustrates the use of excitations in both bending directions [Ty Tz Ry Rz] to synthesize an equivalent excitation using only the translational excitations [Ty Tz].

For this case the two main bending modes 8 and 9 are considered with their respective damping values Q = 25 and 16.

6.4.1. Modal SRS

The modal SRS for the two selected modes are plotted in Fig. 18 for each event. The synthesized modal SRS (dotted line) follows very closely the envelope of the modal SRS.

Note that the values of the modal SRS at the natural frequencies of the modes (indicated by the circles), are to the right of the principal peaks of the SRS. This indicates that the modes 8 and 9 respond rigidly or statically with respect to peaks with little dynamic amplification.

In this example the modal SRS are noticeably different since the participation factors are not at all the same and different values of damping are involved.

The modal SRS at the natural frequencies are plotted in Figure 19 again showing good correlation at the dominant modes.

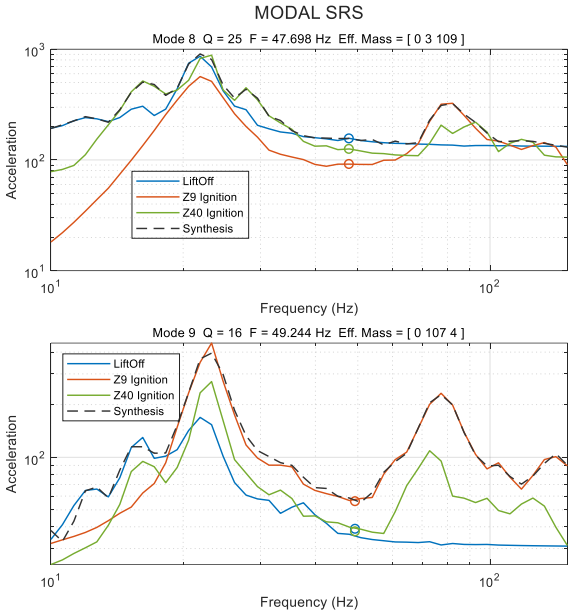


Figure 18: Case 2 Modal SRS

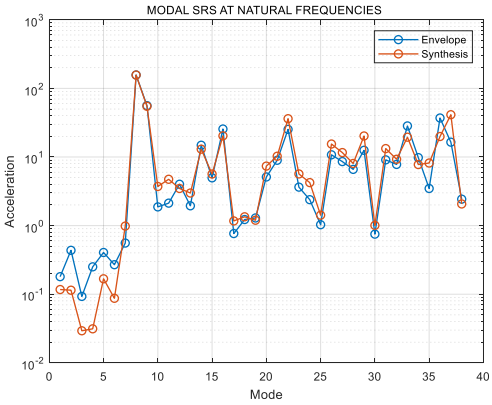


Figure 19: Case 2 Modal SRS at Nat. Freq.

6.4.2. I/F Accelerations

The I/F accelerations of the events limited to the bending directions are plotted in Fig. 20. The corresponding synthesized I/F accelerations are plotted in Fig. 21. We observe similar durations and frequency content between the two figures. However, the amplitudes in the synthesized accelerations are noticeably higher. This is due to fact that the synthesis involves only the translational accelerations, and that these synthesized translational accelerations must compensate for the rotational excitations as well.

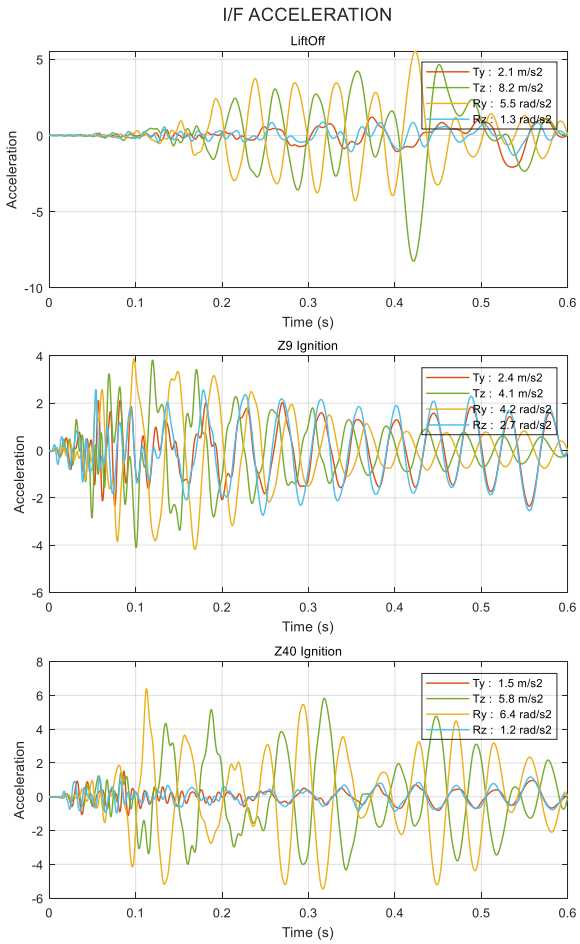


Figure 20: Case 2 I/F Accelerations

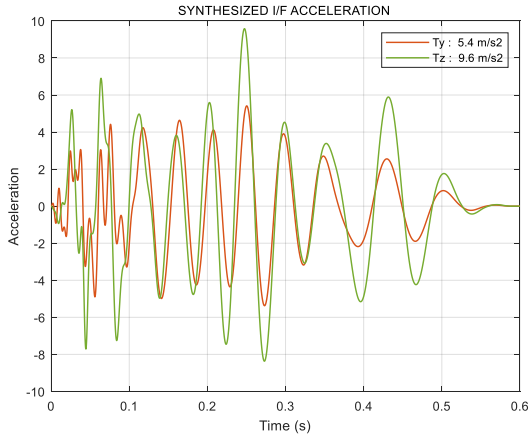


Figure 21: Case 2 Synthesized I/F Accelerations

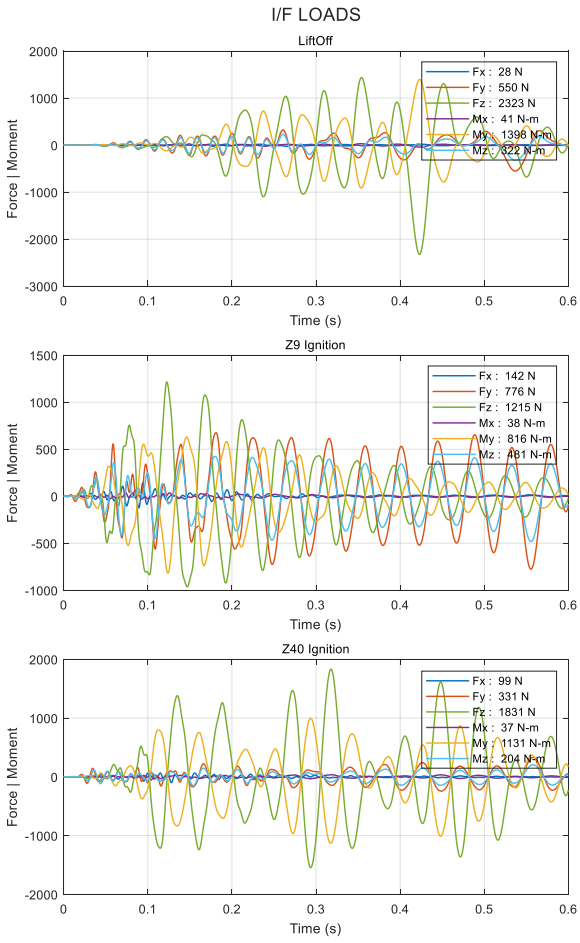


Figure 22: Case 2 I/F Loads

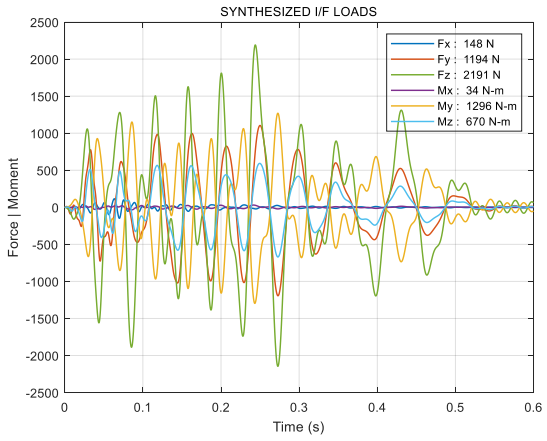


Figure 23: Case 2 Synthesized I/F Loads

6.4.3. I/F Loads

The I/F loads are plotted in Fig. 22 along with the corresponding synthesized loads in Fig. 23.

A comparison of the maximum interface loads is presented in Figure 24. The maximum force in the Y direction is over-estimated in the synthesis by 54 % whereas the maximum force in the Z direction is under-estimated by about 5 %.

Comp	Env	Syn	Error	Syn (DIR)	Syn (QUAD)
Fx (N)	142	148	4 %	466	137
Fy (N)	778	1194	54 %	1435	719
Fz (N)	2323	2191	-6 %	2561	1693
Mx (N-m)	41	34	-17 %	137	47
My (N-m)	1398	1296	-7 %	1391	1217
Mz (N-m)	481	364	40 %	785	519

Figure 24: Case 2 Comparison of I/F Loads

6.4.4. Internal Accelerations

The internal accelerations at the MTBY_PX sensor location are plotted in Fig. 25 with the corresponding synthesized internal accelerations in Fig. 26.

A comparison of the maximum internal accelerations is presented in Fig. 27. The Y direction synthesis overestimates the maximum acceleration by 37 % whereas the Z direction synthesis is very close to the maximum value of 12.9 m/s2.

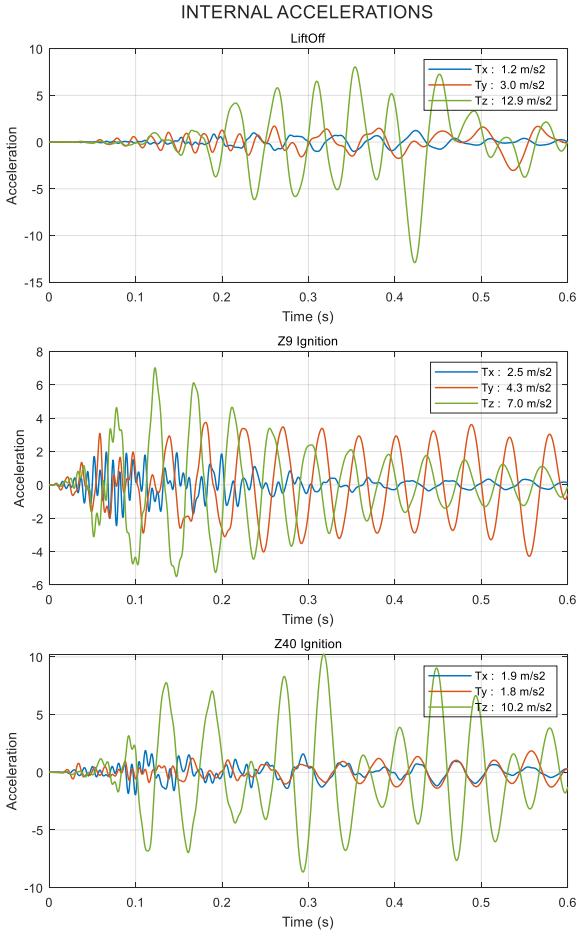


Figure 25: Case 2 Internal Accelerations

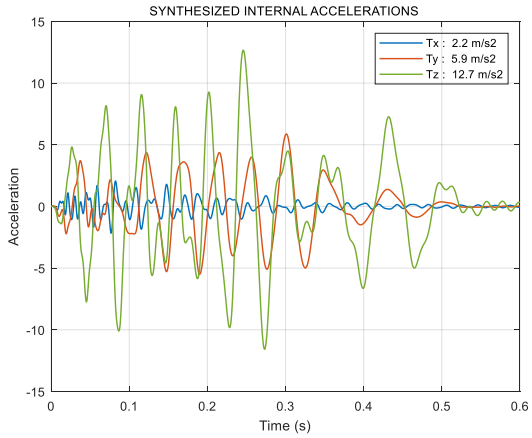


Figure 26: Case 2 Synthesized Internal Accel.

Comp	Env	Syn	Error	Syn (DIR)	Syn (QUAD)
Tx (m/s2)	2.5	2.2	-12 %	12.1	4.2
Ty (m/s2)	4.3	5.9	37 %	7.9	3.6
Tz (m/s2)	12.9	12.7	-2 %	14.4	9.2

Figure 27: Case 2 Comparison of Internal Accel.

6.5. Case 3

This final case illustrates the most general multi-axis synthesis where the 6-DOF events are used to synthesize a single 6-DOF excitation.

In other words, all 6 directions [Tx Ty Tz Rx Ry Rz] are selected for both the excitation and the synthesis.

For this case the dominant bending and axial modes are considered: 8, 9 27, 28 and 31. Damping for these modes varies between Q = 10 and 25.

6.5.1. Modal SRS

The modal SRS for the five selected modes are plotted in Fig. 28 for each event. The synthesized modal SRS (dotted line) follows closely the envelope of the modal SRS.

It is interesting to note the differences between the modal SRS. Here again the values of the modal SRS at the natural frequencies of the modes (circles), do not coincide with the peaks of the SRS.

The modal SRS at the natural frequencies are plotted in Figure 29 showing reasonably good correlation for the important modes.

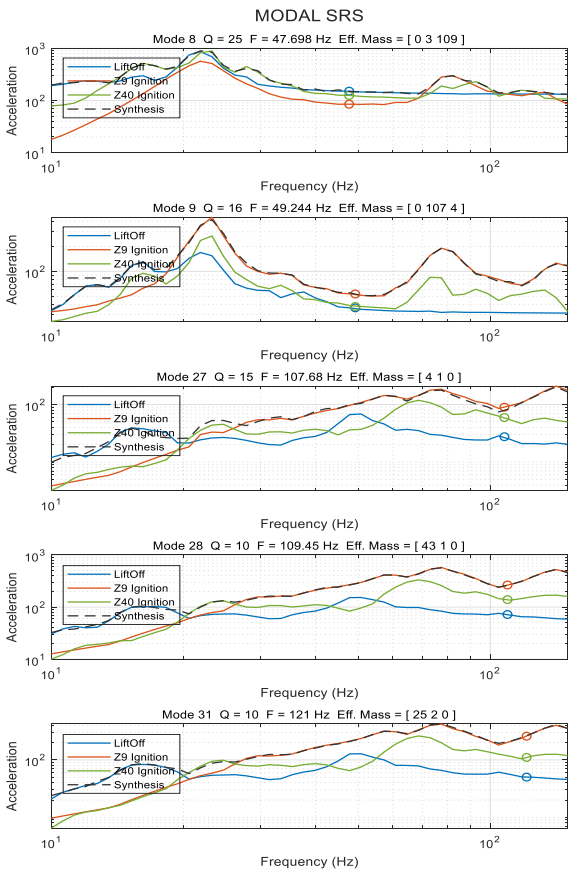


Figure 28: Case 3 Modal SRS

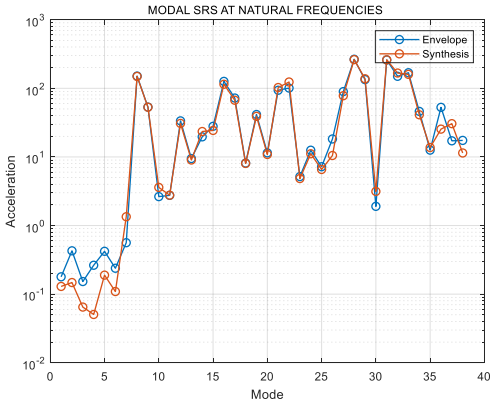


Figure 29: Case 3 Modal SRS at Nat. Freq.

6.5.2. I/F Accelerations

The I/F accelerations of the events in all six directions are plotted in Fig. 30 with the corresponding synthesized I/F accelerations plotted in Fig. 31.

The synthesized results are consistent with the physical accelerations in terms of maximum amplitudes, duration and frequency content including the rotations.

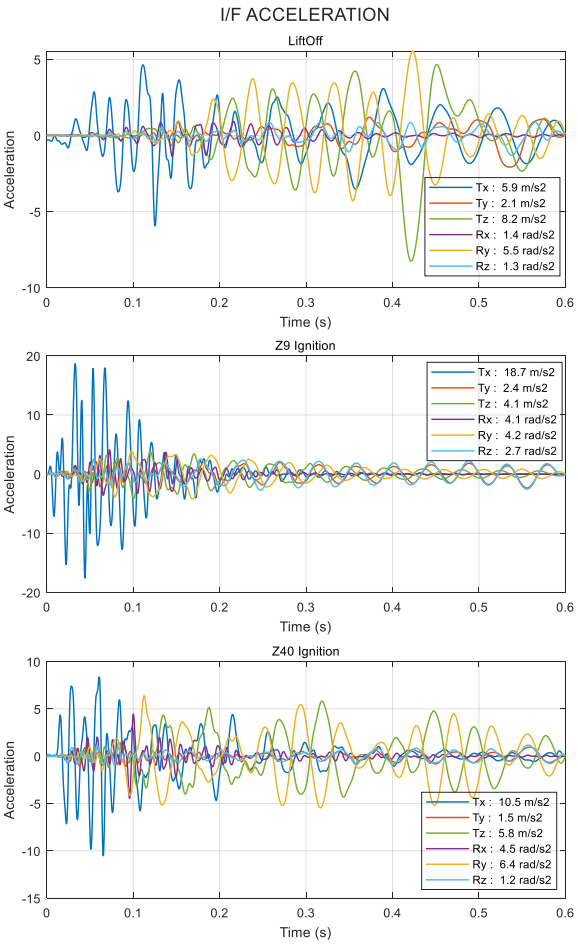


Figure 30: Case 3 I/F Accelerations

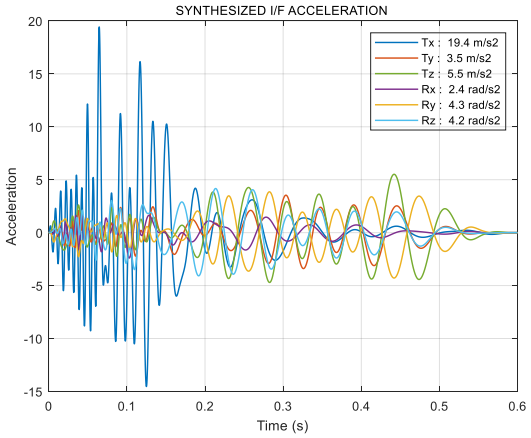


Figure 31: Case 3 Synthesized I/F Accelerations

6.5.3. I/F Loads

The I/F loads are plotted in Fig. 32 with the corresponding synthesized loads plotted in Fig. 33. The maximum interface loads are compared in Figure 34.

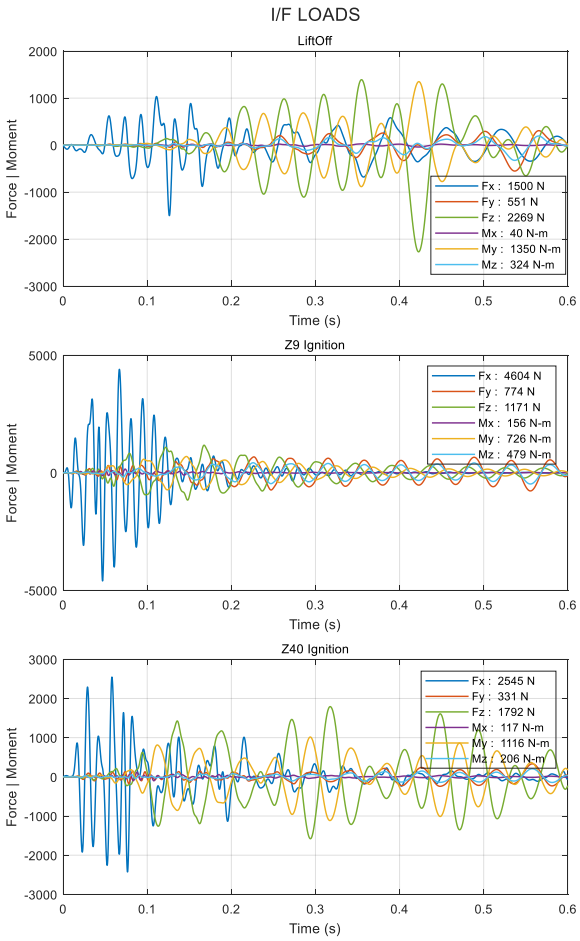


Figure 32: Case 3 I/F Loads

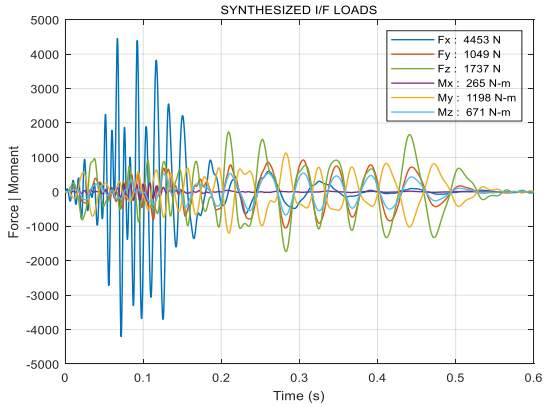


Figure 33: Case 3 Synthesized I/F Loads

Comp	Env	Syn	Error	Syn (DIR)	Syn (QUAD)
Fx (N)	4604	4453	-3 %	6095	2531
Fy (N)	774	1049	35 %	2504	844
Fz (N)	2269	1737	-23 %	2952	1551
Mx (N-m)	156	265	70 %	1030	484
My (N-m)	1350	1198	-11 %	1483	1145
Mz (N-m)	479	671	40 %	1033	479

Figure 34: Case 3 Comparison of I/F Loads

6.5.4. Internal Accelerations

The internal accelerations at the MTBY_PX sensor location are shown in Fig. 35. The corresponding synthesized internal accelerations are plotted in Fig. 36. A comparison of the maximum internal accelerations is presented in Fig. 37. Relative errors in this case are less than 27 %.

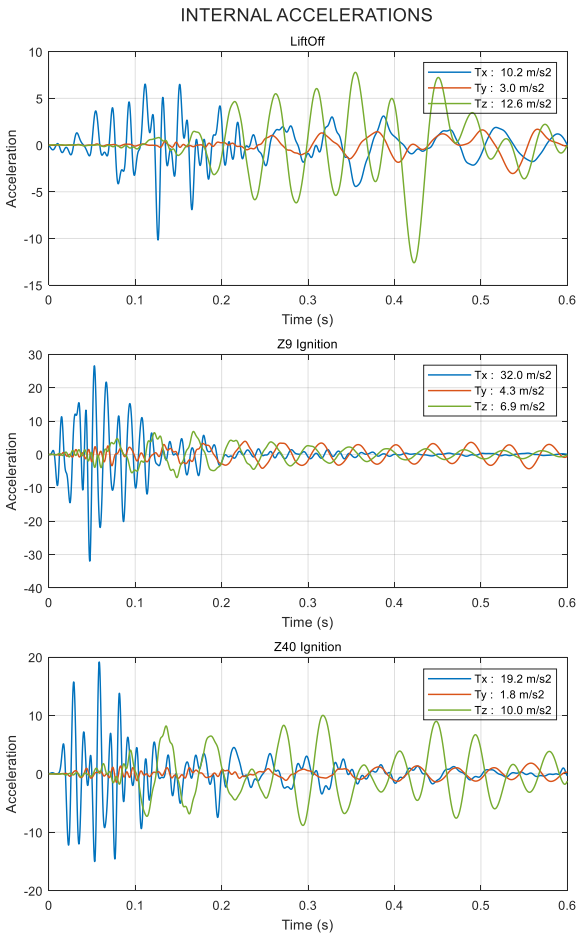


Figure 35: Case 3 Internal Accelerations

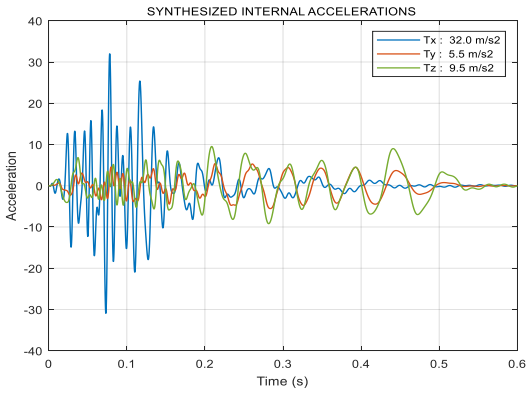


Figure 36: Case 3 Synthesized Internal Accel.

Comp	Env	Syn	Error	Syn (DIR)	Syn (QUAD)
Tx (m/s2)	32.0	32.0	0 %	60.0	23.1
Ty (m/s2)	4.3	5.5	27 %	18.9	6.8
Tz (m/s2)	12.6	9.5	-25 %	21.7	9.2

Figure 37: Case 3 Comparison of Internal Accel.

7. CONCLUSIONS

The paper presents the preliminary findings of a study whose primary objective is to extend shock synthesis to multi-axis excitations while maintaining the use of the shock response spectrum (SRS) as a metric of equivalence.

This has been achieved by the use of the modal participation factors whose role is to combine the multi-axis excitations into a single modal excitation compatible with the classical SRS.

Furthermore, the modal participation factors along with the related effective masses can be used to identify the dominant modes and determine the coupling between these modes and the different excitation directions.

In this way, multi-axis synthesis can be tailored to the capabilities of the test facility from 1-DOF to 6-DOF interfaces.

The method has been validated numerically using Vega-C flight events with a condensed finite element model of the MicroCarb satellite. The results are promising and demonstrate the feasibility of the method.

The advantages of the method include:

- Compatibility with the classical SRS
- Synthesis for 1 to 6 interface DOF
- Frequency dependent modal damping
- Use of wavelets for simultaneous excitation of modes and adjustable durations
- Efficient numerical algorithm

The following points are currently under study:

- Reduction of phase errors when combining modal contributions
- Taking into account harmonic and unspecified (default) events
- Implementation in the PRIMODAL software tool

The second phase of the study involves the experimental validation of the method using a simple structure on a 6-DOF test facility. This activity is planned for 2027.

8. REFERENCES

1. Girard, A., Dupuis P.E., Bugeat L.P., *Improved Shock Characterization*, European Conference on Spacecraft Structures, Braunschweig, Germany, 1998.
2. Girard, A., Cavro E., Dupuis P.E., *Transient testing from LV/SC coupled analysis by new shock synthesis*, European Conference on Spacecraft Structures, Materials and Environmental Testing, Toulouse, France, 2016.
3. Cavro E., Roy N. et al, *Fast Sine Sweep as an Alternative to Classical Sine Sweep for S/C Qualification*, European Conference on Spacecraft Structures, Materials and Environmental Testing, Noordwijk, The Netherlands, 2018.
4. CNES R&T RS19-TG2-130, *Environnement mécanique transitoire basses fréquences au lancement pour design et essais optimisés*, Airbus Defence and Space, Thales Alenia Space, Top Modal, 2020.
5. ESA Workshop, *Novel test methods for satellite vibration testing – alternatives to fixed base sine test?*, Noordwijk, The Netherlands, March 6 2023.
6. Cavro, E., Roy N., Lemay, S., *Synthèse de choc multiaxes pour la qualification satellite*, Journée des essais et de la simulation, ASTELAB, CETIM, Senlis, France, 1-2 Juillet 2026.
7. Girard, A., Roy N., *Structural Dynamics in Industry*, John Wiley & Sons, 2008.
8. Lalanne, C., *Mechanical Vibration and Shock Analysis - Mechanical Shock,* Volume 2, 3rd Edition, John Wiley & Sons, 2014.
9. https://cnes.fr/projets/microcarb

SHOCK PROPAGATION IN LAUNCHER AND SPACECRAFT STRUCTURES: NUMERICAL SIMULATIONS AND SOURCE CHARACTERIZATION

Rainer Stelzer [(1)], Francisco Marques Novo [(1)], Michele Bernasconi [(1)]

[(1)] Beyond Gravity Schweiz AG, The Circle 23, 8058 Zürich Flughafen, Switzerland, Email: rainer.stelzer@beyondgravity.com

KEYWORDS

Launcher structures, spacecraft structures, shock source characterisation; shock response; transient statistical energy analysis (TSEA), hybrid FE-TSEA approach

ABSTRACT

Shock response spectra (SRS) on space structures are still frequently estimated using analytic formulas. Although practical, these methods are generally conservative and may lead to unnecessarily high SRS levels, increasing the risk of over-design of instruments and subsystems.
To achieve more realistic and accurate shock predictions, advanced numerical simulations are essential. Classical finite element (FE) modelling of such shock events can provide detailed insights but typically requires substantial modelling effort and computational resources. More modern approaches, such as Transient Statistical Energy Analysis (TSEA) and hybrid FE-TSEA methods, provide computationally efficient solutions for shock analysis.
This paper investigates how these approaches can be applied to real separation-system shock problems and how the appropriate modelling strategy depends on the structural configuration and the available characterization of the shock source. The methodology is demonstrated for two case studies: a spacecraft subjected to shock from clamp band opening and a payload fairing subjected to pyrotechnic horizontal separation event.

1. INTRODUCTION

Launch vehicles, satellites, and their onboard equipment must withstand a wide range of extreme dynamic loads, including intense shock events. Such shock loads typically originate from highly energetic pyrotechnic or mechanical separation mechanisms such as the release of a PLF frangible joint or the opening of a clamp band used to separate a spacecraft from its launch vehicle. The severity of such shock events is commonly characterised using shock response spectra (SRS), which describe the maximum response of single-degree-of-freedom oscillators over a specified frequency range.
A classical way to estimate SRS at different locations within a structure is to use traditional analytic calculation methods, such as those described in [1]. In these methods, the shock source is represented by a SRS and the propagation of the shock through the structure is estimated based on parameters such as the distance from the source and the number and type of structural connections and junctions along the shock propagation path. As demonstrated for example in [2], these methods can provide rather conservative SRS predictions, particularly at low-to-medium frequencies. Although such conservatism is beneficial for establishing robust design envelopes, it can also result in unnecessary structural margins and over-design of spacecraft, payload-fairing components, and onboard equipment. Higher-fidelity numerical approaches are therefore desirable when a more realistic prediction of the shock environment is required.
Transient finite element (FE) analysis can provide detailed information on the structural response to shock events. One approach described in [3] is the modal transient FE analysis, in which a finite element model is excited by a time-history acceleration applied at the base and the structural response is calculated in modal coordinates using the structure's natural modes and modal damping. However, conventional transient FE modal analysis becomes increasingly computationally demanding at high frequencies, particularly for larger structures with high modal density. Statistical Energy Analysis (SEA) and hybrid FE-SEA approaches are therefore commonly used when a computationally efficient description of medium-to-high-frequency structural dynamics is required.
Several approaches have been developed to extend SEA-based methods to transient shock problems. In [4] SEA is combined with the Virtual Mode Synthesis and Simulation (VMSS). The classical SEA model is providing frequency-band-averaged frequency response functions (FRFs), modal densities, and damping characteristics. These SEA results are then used by VMSS to synthesize a set of "virtual modes" that approximate the high-frequency dynamic behaviour of the structure and VMSS then reconstructs the transient response and thus the SRS by solving modal equations based on the synthesized virtual modes and the force input. A similar idea of using traditional steady-state SEA energy transfer calculations in frequency domain for shock analysis and a method to reconstruct with it the resulting response over time can be found also in [5]. Both methods represent the shock source with a SRS as an energy constraint at the excited interface of the SEA model. In [6] such a SEA approach combined with a

time signal reconstruction method is applied only for high frequencies. The low-frequency response is calculated instead using a detailed FE model in time domain. The simulated time domain data for both frequency ranges is finally combined to one time domain response. Another way of combining FEA and SEA is presented in [7]. A hybrid FE-SEA model is built. Components with low modal density are modelled using FEA and components with high modal density are represented using SEA. Instead of representing the shock source with a SRS, a shock load force function in time domain is transformed from the time domain into the time–frequency domain using the Short-Time Fourier Transform (STFT). The responses are simulated still by a classical frequency domain simulation as in the methods described before. Finally, the calculated frequency responses are combined with the phase information of the original shock signal and transformed back into the time domain using inverse STFT (ISTFT). The SRS is calculated from the transient acceleration responses reconstructed in this way. To avoid transformations between time and frequency domain and to overcome the steady-state condition of the classical SEA, the most modern approach is the transient statistical energy analysis TSEA as described in [8]. In this paper a hybrid FEM/TSEA method is applied to a structure of a satellite. Some subsystems of the structure are treated as FE subsystems and others as (T)SEA subsystems and a time-frequency solver is used to simulate the shock response.

The objective of this paper is to demonstrate the application of pure TSEA and hybrid FEA/TSEA simulation methods for shock predictions in real space-industry applications and to identify the most suitable modelling approach depending on the structural configuration and on the available characterization of the shock source, focusing on two specific case studies, the shock generated by a clamp band and a pyrotechnic frangible joint separation system. Two different source representations are investigated. The structures are either excited directly by SRS or by a detailed description of a shock force that has the standard half-sine profile over time. For the latter, a detailed source characterisation is necessary. It combines small-scale testing of the separation mechanism with an optimisation-based excitation identification process that numerically reconstructs the measured response. All the simulations are performed using the commercial software WAVE6 from Dassault Systemes and the simulation results are compared to data from corresponding dedicated shock tests. Furthermore, for all the simulations the standard assumption of separated state is considered for structural parts on both sides of the separation system when starting the separation process (see for example [1]). That means that the shock simulations on each side of a separation system are independent from each other and can be performed separately.

2. CASE STUDY 1: CLAMP BAND RELEASE FROM PAYLOAD ADAPTER SYSTEM

During spacecraft development, the shock environment associated with separation from the payload adapter is often specified in the form of an SRS in the applicable user manual. Such an example SRS curve is shown in Figure 2-1 for a clamp band separation system connecting the payload to the payload adapter. To assess the shock environment experienced by sensitive spacecraft hardware, such as the structure shown in Figure 2-2, the corresponding SRS levels are predicted at specific locations, for example at instrument mounting locations. A first estimation can be performed using ECSS-E-HB-32-25A method C (see [1]). This approach generally leads to conservative SRS estimates, particularly at low-to-medium frequencies, as shown in Figure 2-3 by comparison with measured data.

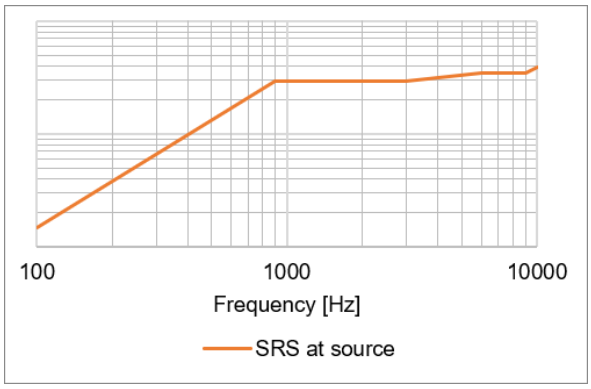


Figure 2-1: Defined source shock SRS for a clamp band release

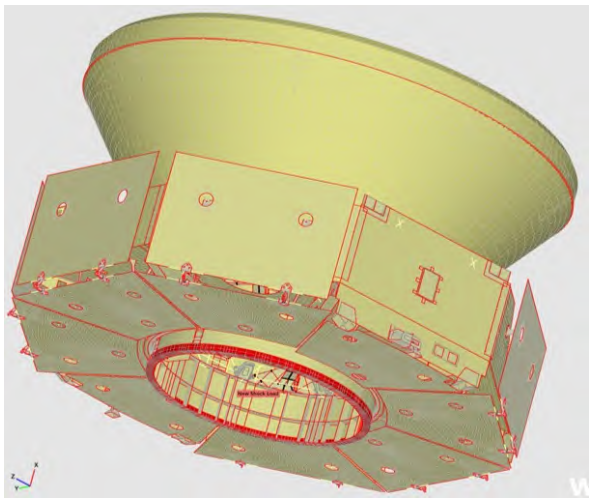
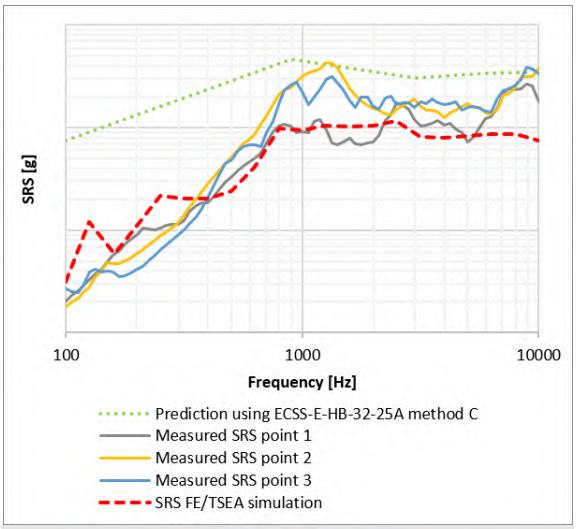


Figure 2-2: FE model of the spacecraft structure excited at the bottom by the shock-source SRS (bottom ring highlighted in red)

To avoid overengineered parts and instruments, more precise predictions are appreciated. For this reason, a shock simulation model is built that it is based on a standard structural FE model. All the panels and larger structural components are modelled as FE reverberant subsystems that are (T)SEA subsystems, for which the required SEA

parameters are derived from FE pre- simulations. Smaller structural components and discrete connections are retained as conventional FE subsystems. The big advantage of using a mixed FE/ FE reverberant approach is that a standard FE model used for other mechanical simulation can be directly taken over without modifications. Only the type of the different components is defined as reverberant or standard FE subsystems. In this way, all the detailed representations of the original FE model for the connections, that are using e.g. rigid body elements RBEs, spring and bar elements, are directly taken over for the shock model. This provides a significant advantage compared to classical SEA approach, as such discrete connection details cannot be represented explicitly in a conventional SEA model. The simulation model of the spacecraft is excited at the bottom ring subsystem with the SRS shown in Figure 2-2. The simulation is performed for the frequency range from 100 Hz to 10 kHz, being the range of interest considered in this particular study, using the time-frequency solver of WAVE6.



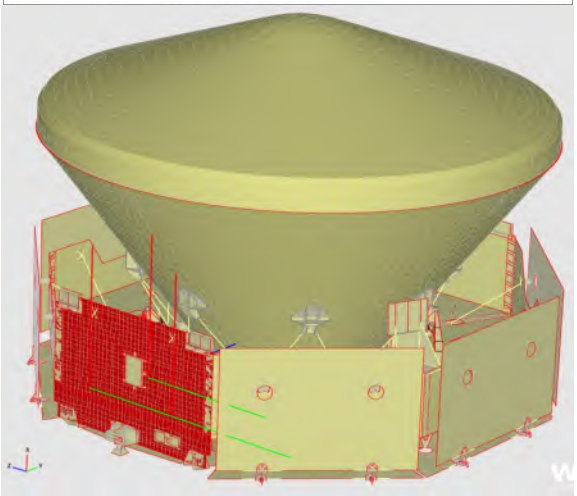
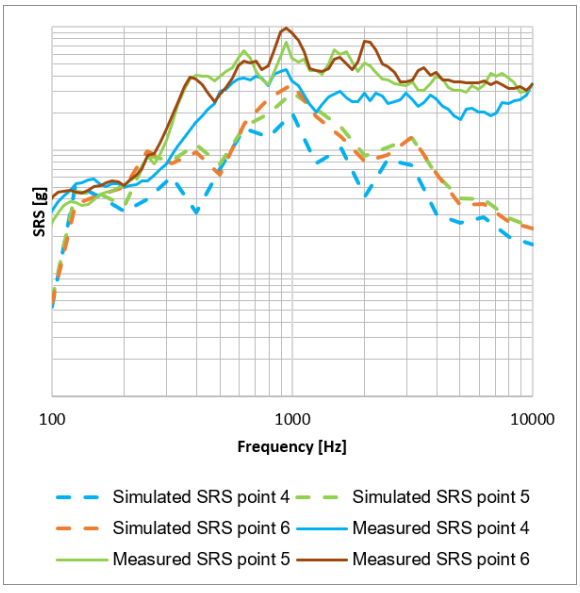


Figure 2-3: Simulated SRS for the first example panel (panels in red) of the spacecraft in comparison to the measured data

The average SRS simulated in this way is shown for an example panel of the spacecraft in Figure 2-3. As demonstrated the correlation between the simulation and the measurement is good considering how simple the shock source is represented with an approximate SRS curve. At higher frequencies, however, the simplified SRS representation of the shock source does not contain sufficient information to reproduce all individual resonant peaks associated with specific structural modes strongly excited by the clamp-band release. A more detailed source characterisation is therefore expected to improve the prediction in this frequency range. To achieve a good correlation, it is important to mention that the damping loss factor of the structure has to be defined carefully. For such a complex payload that contains of a lot of different parts like metallic beams and sandwich panels and where the shock is traveling rather complex and long ways, at least each type of part needs its unique damping loss factor instead of using one global damping loss factor for the whole spacecraft structure. Thus, for example for huge metallic rings and beams a damping loss factor of 0.1% is typically considered and 4% for sandwich panels. Another hurdle in shock simulations for complex structures is the representation of the high number of connecting components, like hinges or hold down release mechanisms. For most of the other mechanical simulations performed during the development phase of a payload, it is enough that their FE representations are working well at low frequencies. This can lead to the issue that the SRS simulation results are diverging more and more from the measured data with increasing frequency as shown on an example in Figure 2-4.



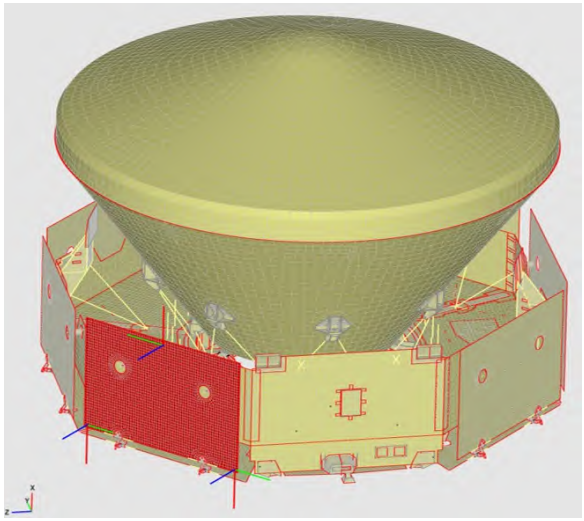


Figure 2-4: Simulated SRS for the second example panel (panels in red) of the spacecraft in comparison to the measured data

Overall, the simulation using a simplified SRS excitation significantly reduces the conservatism of the predicted shock environment, particularly in the low-to-medium frequency range. The calculation methods of the ECSS handbook [1] nevertheless remain valuable to obtain an initial estimate of the shock environment and to establish a conservative upper-bound assessment, particularly at high frequencies where the detailed simulation model may not capture all the relevant effects (see Figure 2-3).

3. CASE STUDY 2: PAYLOAD FAIRING HORIZONTAL SEPARATION

3.1. TSEA Modelling Approach

The first approach shown in this paper to estimate the shock levels generated by a horizontal separation system (HSS) of a PLF is based on a standard SEA model, as it is used for acoustic simulations (as shown for example in [9] and [10]), but using TSEA instead of the classical frequency domain SEA solver. The structure of the PLF is represented in the shock test and the simulation as a 14 m high cylindrical section of a PLF with a diameter of 5.4 m. The model is split into SEA panels, according to different lay-ups. Contrary to the spacecraft case of the previous chapter, such a PLF case is very suitable for using the SEA approach, as there are only a very few connecting components that can be well described with standard SEA connections. A SEA model is also very predestined for SRS-based excitation. Detailed localized sources like forces cannot be represented in SEA and would anyhow only be considered globally for a whole SEA subsystem. Thus, a SRS curve (see Figure 3-2) is used to represent the shock of the HSS release as it can be found sometimes in requirement documents for launchers.



Figure 3-1: Simulation model of the cylindrical section of a PLF that is excited at the bottom (area in red) with a shock source SRS related to a HSS release

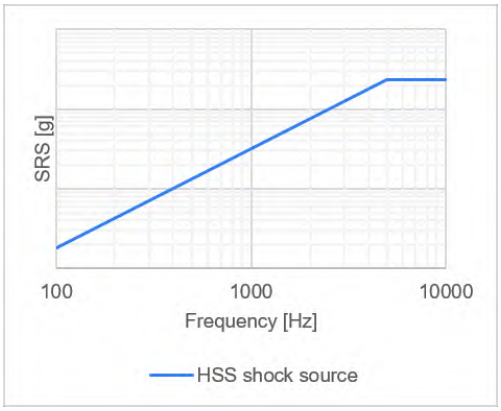


Figure 3-2: Defined source shock SRS for a HSS release

The SRS curves resulting from the TSEA model are shown in Figure 3-3 and Figure 3-4 in comparison to measured data. The SRS simulated for the region relatively close to the shock source (see Figure 3-3) is already much closer to the measured SRS data than the one predicted by analytic methods described for example in [1]. In a wide frequency range besides very high frequencies the analytic result is much more conservative than the SEA result. At frequencies above 4000 Hz the SEA result seems to overestimate more the SRS of this area. For an area quite far away from the shock source (see Figure 3-4) the simulated SRS is slightly underestimating the SRS at high frequencies, as some peaks that are appearing in the measured data are not visible. This is linked to the simplified representation of the shock source, as discussed in the following chapter. The same issue has been seen already in the payload separation case in the previous chapter. However, for areas in the far field of the shock source, the high-frequency trend of the SRS curve is captured very well by the TSEA results.

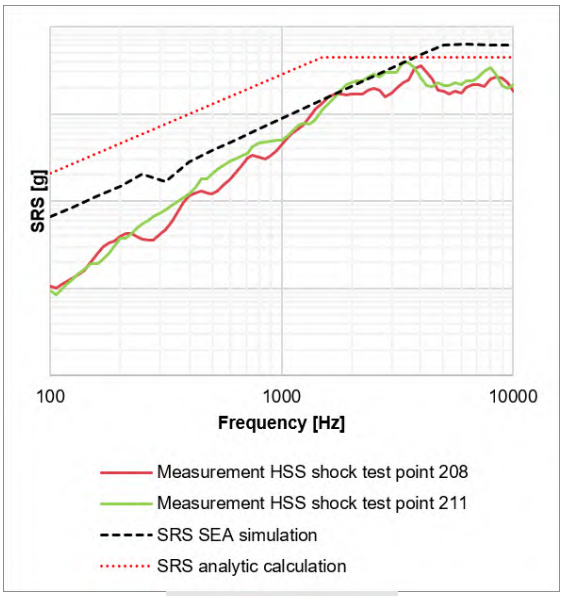




Figure 3-3: SRS simulated with SEA for the lower PLF area (area in blue) in comparison to measured data from a HSS shock test

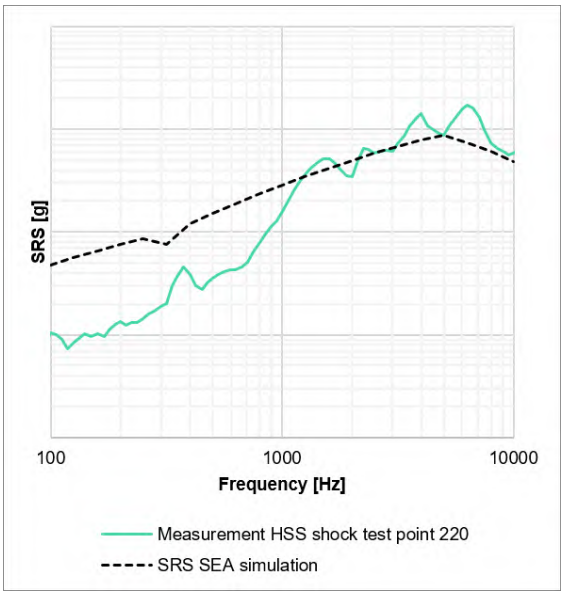




Figure 3-4: SRS simulated with SEA for an area in the mid of the PLF (area in orange) in comparison to measured data from a HSS shock test

3.2. FE/TSEA Modelling with Detailed Shock-Source Characterization

3.2.1. Shock-Source Characterisation using an Optimization Procedure

To get a more detailed representation of the excitation than the simple one with SRS (see previous chapters), a source characterisation of a frangible joint FJ - often used as an HSS separation system especially for large launch vehicles - can be performed by means of small-sample tests and a classical optimization procedure. First, several shock/ separation tests are performed on a small sample plate with the pyro-technical FJ (see Figure 3-5). An average RMS SRS for the plate is calculated from the SRS measured at several locations on the plate for these tests. Second, this test configuration is modelled using FE reverberant subsystems (see Figure 3-5). It is considered in the simulation that the FJ can be represented as point forces in axial in-plane direction at each node at the bottom of the plate, where the FJ is located. Furthermore, it is assumed that these forces F_s have a half-sine profile over time (see Figure 3-6) as widely used for shock simulations (see e.g. [1]).

$$F_s = A_F \sin\left(\frac{\pi\, t}{t_d}\right) \qquad (1)$$

The three unknown parameters for the forces are thus the amplitude A_F of the half-sine profile, the duration of this impulse t_d and the delay from one node to the other. To identify these three parameters a classical optimization procedure is set up. The average SRS is simulated for all the 1/3rd octave bands from 100 Hz to 10 kHz and the target of the optimization is to minimize the sum of the quadratic differences of the SRS for each frequency band between the measured average SRS and the simulated one.

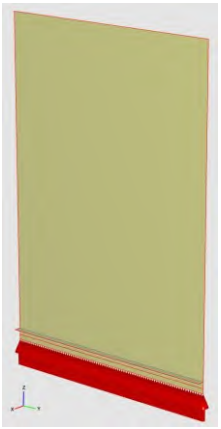


Figure 3-5: Simulation model of the small sample HSS shock test with shock forces in red at the bottom

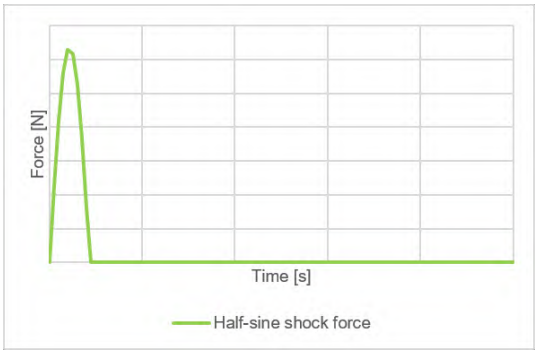


Figure 3-6: Example for a typical half-sine shock force impulse over time

To solve this optimisation problem, first an evolutionary optimization algorithm is used to investigate a wide range of possible solutions and second a gradient-based algorithm is used to refine the optimization result from the first optimization step. An example for a final SRS optimized in this way is shown in Figure 3-7. The simulation result matches very well with the measured average SRS. For a typical pyro-technical FJ separation system the duration of the half-sine force impulse is much below 1 ms and the delay is very low, as the propagation velocity of the pyro-technical separation is greater than 2000 km/h.

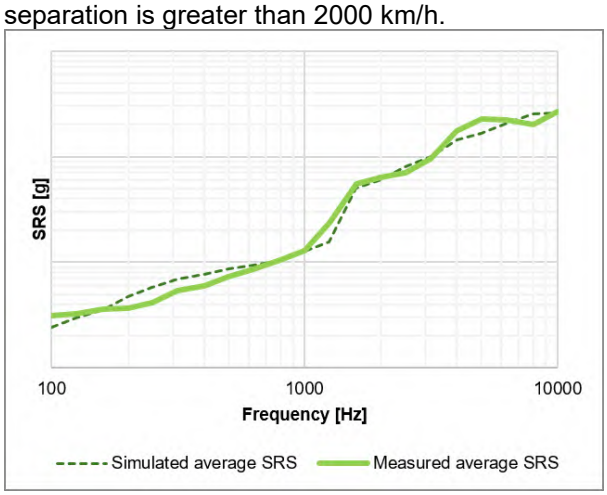


Figure 3-7: Measured average SRS of the plate in comparison to the final simulation result after optimization of the shock source parameters

3.2.2. FE/TSEA Shock Simulations

The shock source characterised by the procedure in the previous chapter is taken over for a second more detailed simulation model of the PLF under a HSS release as shock event. Due to the localized nature of the shock source defined in the previous chapter that is basically a force running around the lower PLF interface, this HSS shock model is only well suited for FE subsystems. Thus, a mixed FE/ FE reverberant approach (a variant of the TSEA approach) is applied as for the spacecraft in chapter 2. The excitation area, areas close to the sources and connecting elements (e.g. RBEs and spring elements) are modelled as FE subsystems, whereas the rest is modelled as FE-reverberant subsystems (see Figure 3-8). The areas of these FEA reverberant subsystems are the same as for the SEA panels representing the structure in the first simulation approach in chapter 3.1. The simulation results for the SRS are shown for the same two example areas as before in Figure 3-9 and Figure 3-10. As demonstrated in these figures, the results are matching now very well with the measured data. In particular, the SRS trend at low frequencies and the appearing resonances are much better captured by using the more detailed FE/TSEA simulation instead of the pure TSEA modelling approach.
Besides the final applied approach of modelling, the subsystems close to the source as FE subsystem and the others as FE-reverberant subsystems, it would in principle be possible to model all the 2D subsystems as FE reverberant subsystems (kind of SEA subsystems). This would however lead to results that are overestimating the SRS at high frequencies even at points in the far field of the shock source as demonstrated in Figure 3-11. Thus, it necessary to perform several simulation iterations with an increasing area close to source, for which FE subsystems are used, until the simulation results have converged against the final result.

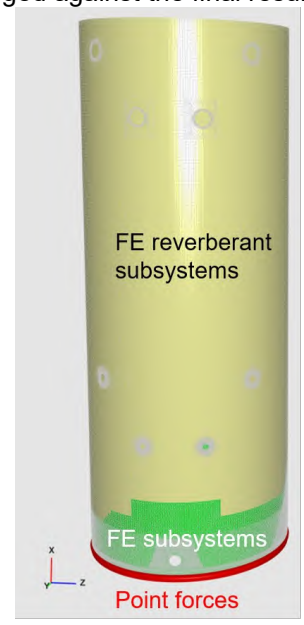


Figure 3-8: Simulation model of the PLF using FE and FE reverberant subsystems

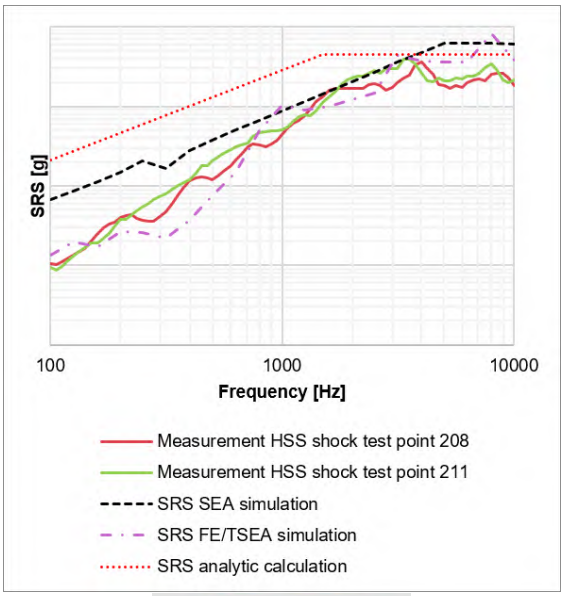




Figure 3-9: SRS simulated with FE/TSEA for the lower PLF area (area in blue) in comparison to measured data from a HSS shock test

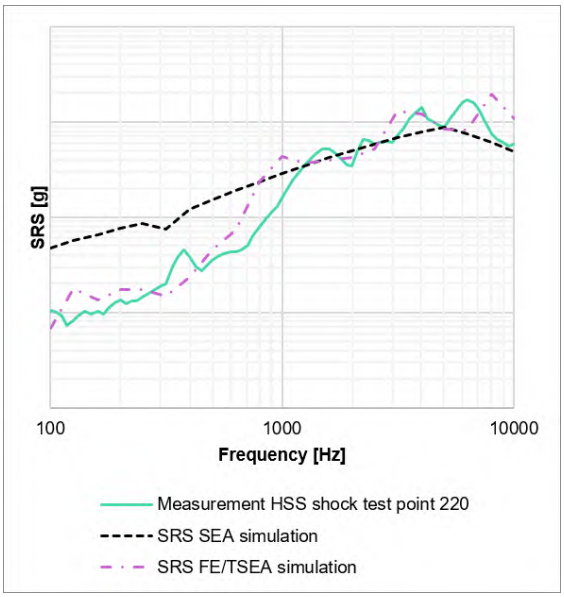




Figure 3-10: SRS simulated with FE/TSEA for an area in the mid of the PLF (area in orange) in comparison to measured data from a HSS shock test

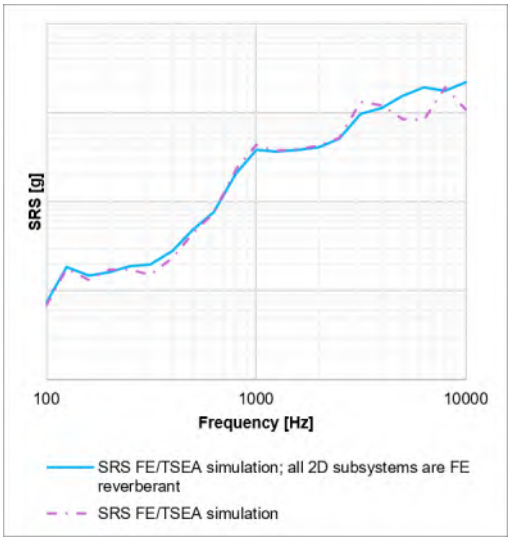


Figure 3-11: SRS simulated for an area in the mid of the PLF (see previous figure) in case that all 2D subsystems are FE reverberant subsystems

4. CONCLUSION

The presented case studies show that TSEA and hybrid FE/TSEA methods provide a practical route for shock prediction in launcher and spacecraft structures, as classical analytical SRS attenuation methods provide overly conservative predictions. For both the spacecraft clamp-band case and the PLF horizontal separation system case, the numerical simulations reduced the conservatism of the analytical predictions while retaining the main trends observed in the measured SRS. Even when the shock source is represented by a simple input Shock Response Spectrum (SRS), the predicted shock propagation and SRS levels show good agreement with the measurement data while remaining significantly less conservative than conventional analytic estimates.

Achieving highly accurate shock predictions, however, requires an appropriate representation of the excitation source, since the shock-generating mechanisms are not explicitly modelled in the numerical approaches presented in this work. To address this limitation, a dedicated source-characterisation methodology has been developed specifically for launch-vehicle separation systems as shown in chapter 3.2.1. The methodology combines small-scale testing of the separation mechanism with an optimisation-based excitation-identification process that numerically reconstructs the measured structural response. The resulting source models enable realistic predictions of the shock environment, facilitate objective comparisons between different separation technologies, and provide valuable insight into key physical characteristics — thereby supporting both the optimisation of existing systems and the development of future systems. Future work will focus on further refining the source characterisation, including a more detailed representation of the directional characteristics of the shock excitation, particularly the in-plane and out-of-plane components

In addition, accurate modelling of structural connections and interfaces, such as hinges and bolted joints, has been identified as essential for reliable shock propagation analyses. As demonstrated in this study, inadequate representation of these interfaces can lead to significant inaccuracies in the predicted shock transmission. Likewise, the damping loss factor plays a critical role in determining both shock attenuation and the reflection of waves throughout the structure. Together with improved source characterisation, accurate interface modelling and damping identification represent the principal areas for future development of high-fidelity shock simulation methodologies.

5. REFERENCES

[1] ESA-ESTEC, ECSS-e-HB-32-25a - Space Engineering - Mechanical Shock Design and Verification Handbook, Noordwijk, The Netherlands: ECSS Secretariat - Requirements & Standards Division, 2015.

[2] M. Perriquet, M. Hofmann and J. Le Moigne, “Shock test database and statistical analysis tool,” in *17th European Conference on Space Structures, Materials & Environmental Testing*, Toulouse, France, 2023.

[3] A. García-Pérez, F. Sorribes-Palmer, G. Alonso and A. Ravanbakhsh, “Overview and application of FEM methods for shock analysis in space instruments,” *Aerospace Science and Technology,* vol. 80, pp. 572-586, 2018.

[4] D.-O. Lee, J.-H. Han, H.-W. Jang, S.-H. Woo and K.-W. Kim, “Shock Response Prediction of a Low Altitude Earth Observation Satellite During Launch Vehicle Separation,” *International Journal of Aeronautical and Space Sciences,* vol. 11, no. 1, pp. 49-57, 2010.

[5] J. H. Hwang, “Pyrotechnic Shock Analysis Using Statistical Energy Analysis,” MIT Lincoln Laboratory, Lexington, USA, 2015.

[6] E. Bodin, B. Brévart, P. Wagstaff and G. Borello, “Pyrotechnic shock response predictions combining statistical energy analysis and local random phase reconstruction,” *J. Acoust. Soc. Am.,* vol. 112, no. 1, pp. 156-163, 2002.

[7] X. Wang, W. Liu, X. Li and Y. Sun, “The Shock Response Prediction of Spacecraft Structure Based on Hybrid FE-SEA Method,” *Applied Sciences,* vol. 11, 2021.

[8] N. Pascal, S. Lemay, F. Errico, F. Lachaud, M. Charlotte and A. Brugnoli, “Comparison of hybrid FEM/TSEA and explicit FEM numerical methods for mechanical shock modelling and test system dependence in shock source characterization,” in *European Conference on Space Structures, Materials & Environmental Testing*, Noordwijk, the Netherlands, 2024.

[9] R. Stelzer, G. Molinari, S. Freiburghaus and A. Sanchez Cebrian, “Optimization of fairing acoustic protections by means of measurements and CAE tools,” in *17th European Conference on Space Structures, Materials & Environmental Testing*, Toulouse, France, 2023.

[10] R. Stelzer, D. Tonon, J. Shields and G. Molinari, “Designing and optimizing fairing acoustic protections by means of CAE tools and measurements,” *Proc. Mtgs. Acoust.,* vol. 57, no. 1, 2025.

COMPLIANT STRUCTURE WITH INTEGRATED PASSIVE DAMPING

J.-L. Helfer [(1)], H. Saudan [(1)], L. Salamin [(1)], S. Hayoz [(1)], N. Blondiaux [(1)], M. Crenna [(1)], F. Cosandier [(2)]

[(1)] CSEM, Rue de l'Observatoire 58, 2002 Neuchâtel, Switzerland, Email: herve.saudan@csem.ch
[(2)] EPFL, STI IGM INSTANT-LAB, Rue de la Maladière 71b, 2002 Neuchâtel, Switzerland

KEYWORDS

compliant mechanisms, flexure blades, passive damping, additive manufacturing (LPBF)

ABSTRACT

Flexure-based compliant mechanisms offer high precision but suffer from high-quality factors, limiting their use in vibration environments. This work introduces a lattice sandwich flexure blade integrating a viscoelastic material to achieve passive damping while preserving frictionless guiding. The structure is manufactured by Laser Powder Bed Fusion and impregnated with a space-compatible silicone (MAPSIL® QS1123). Free oscillation tests show a reduction of the quality factor by close to 30x with a blade-to-blade variability below 20%. A finite element model using a Generalized Maxwell law predicts the behaviour with 10–15% accuracy. The results highlight a shear-driven damping mechanism and demonstrate potential for space and precision engineering applications, like flexure guiding, spring dampers or constrained layer damping.

1. INTRODUCTION

Compliant mechanisms guide parts through the elastic deformation of slender structures rather than through frictional or rolling contact between rigid components. This eliminates friction, wear, need for lubrication and backlash, which are significant advantages for high precision systems and space applications. Flexure blades are basic building blocks of compliant mechanisms and may be combined in many topologies to achieve linear or rotational motion guiding (Fig. 1), as well as motion transformation, or compliant interfaces (Fig. 2).

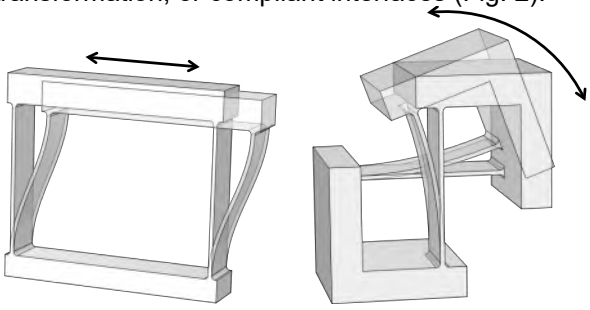


Figure 1: Examples of basic compliant mechanisms achieving linear and rotary guiding

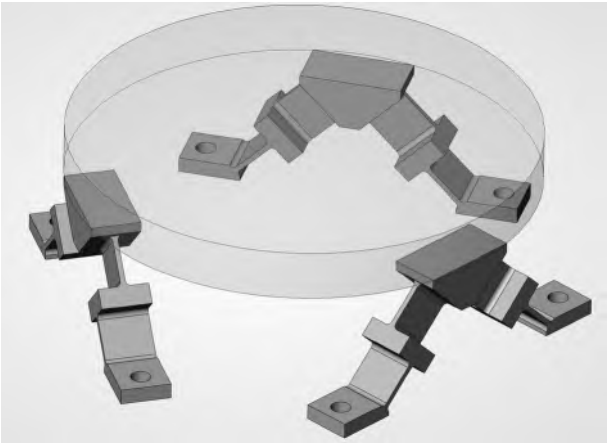


Figure 2: Example of an isostatic mount based on flexure elements

Examples of precision mechanisms for space applications using such flexure guiding can be found in [1], [2] and [3]. Such guiding mechanisms typically exhibit high quality factors (Q factors), which can make them challenging to qualify under random-vibration and shock loads during launch or to stabilize precision instruments in the presence of micro-vibrations during satellite operation. A damping solution that does not reintroduce mechanical friction is therefore needed.

Conventional damping solutions often rely on viscous fluids, which require careful sealing, as in automotive shock absorbers. Structural damping intrinsic to selected materials is better suited to the present application, as used in constrained-layer damping (CLD) [4] or passive hybrid mounts combining a spring and a damping material in parallel. This article presents an original approach for combining flexure blades with a structural damping material, preserving the benefits of compliant mechanisms while avoiding high Q factors. Position tuning of viscoelastic material in CLD exists [5], but the proposed design here reduces reliance on adhesion.

According to [6], potential applications may be divided into two main categories: protect sensitive systems from environmental vibrations or prevent vibrating systems from transmitting vibrations through their supports. The first category concerns for instance compliant scanner mechanisms, camera stabilization systems or other optical systems, in both terrestrial and space applications. For space applications, the second category notably includes cryocoolers and reaction wheels.

2. COMPONENT DESCRIPTION

The component investigated in this article is a flexure blade, consisting of a sandwich of two metal lattice blades between which a viscoelastic material is impregnated, as depicted in Fig. 3. The metal lattice blades are additively manufactured (AM) as a monolithic part, using Laser Powder Bed Fusion (LPBF), as explained in section 3.

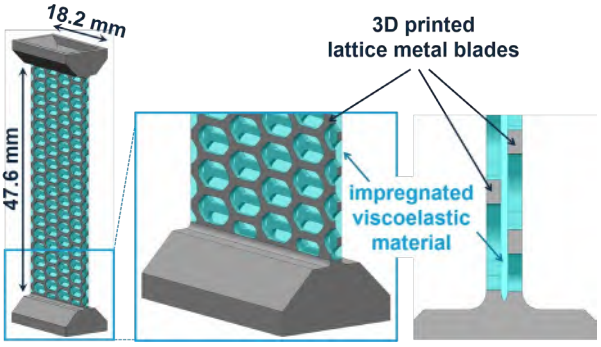


Figure 3: Schematic of the sandwich flexure blade. For thickness and gap, see Tab. 1.

The operating principle is based on a functional separation: the metal lattice blades provide guiding, while the induced deformation of the viscoelastic material generates damping. LPBF is one of the most widely used AM processes for metal parts and offers a clear advantage in its ability to produce highly complex monolithic parts without assembly, as seen for instance in [7]. In this context, lattices are used here for two reasons, as explained in the patent [8]:

- LPBF blades cannot have thicknesses as low as laminated blades, due to printing resolution. Larger thickness leads to high bending stiffness of LPBF blades (proportional to cube of thickness) which may be a drawback in many applications. Using lattices reduces the bending stiffness while maintaining a wall thickness compatible with LPBF.
- As will be further explained in section 5.3, the viscoelastic material is subjected to shear stress between the two metal blades. The adhesion to the metal blades is thus of high importance. The lattice geometry also improves mechanical interlocking and adhesion of the viscoelastic material to the metal blades.

The blades developed here may replace the conventional blades in all the examples shown in Fig. 1 and Fig. 2.

3. MANUFACTURING

The manufacturing process comprises two main steps, which are further detailed in the next sections:

- LPBF printing of the metal blades (monobloc)
- impregnation of the metal blades with viscoelastic material

3.1. LPBF printing

The manufacturing involves the following steps:

1. LPBF print in titanium
2. stress relief (thermal treatment)
3. removal of build plate
4. chemical surface treatment to clean the parts and reduce surface roughness

The printing is executed as shown in Fig. 4. Small bridges were added to maintain the gap between the two lattice blades during all processes. Those are removed after impregnation.

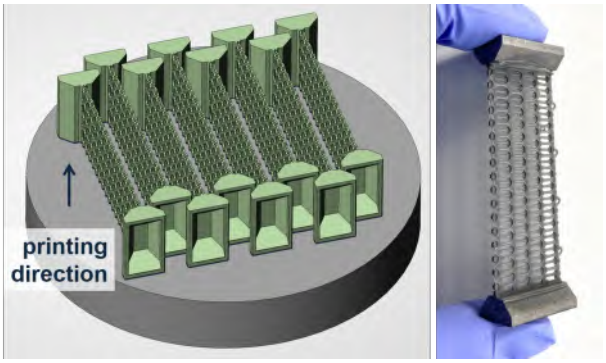


Figure 4: Build plate configuration and one sample after separation

A dedicated chemical surface treatment removed unfused powder particles from the flexures with a final overall smoother surface as illustrated in Fig. 5. Since this treatment removed several hundredths of a millimetre, the CAD geometry was compensated to account for this material removal. Dimensions were checked at this stage, as shown in Tab. 1, to be used as baseline for the simulations described in section 5.

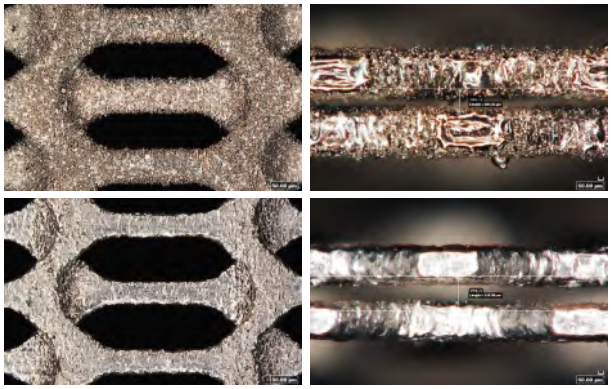


Figure 5: Details of blades before (top) and after (bottom) chemical surface treatment

	CAD ref.	After chem. Treat.	
		Mean	std dev
Thickness lattice blade 1	0.40	0.353	0.015
Gap between lattice blades	0.30	0.316	0.014
Thickness lattice blade 2	0.40	0.352	0.015

Table 1: Geometry check for 32 samples after

chemical surface treatment (dimensions in mm).

3.2. Impregnation

A viscoelastic material compatible with space applications (low outgassing, resistance to radiation) was chosen: MAPSIL® QS1123 [9]. Several iterations of the impregnation process were performed to address initial issues, including:

- leakage of uncured viscoelastic material
- adhesion to the jig
- bubble formation

Eventually, a jig was developed to better control the impregnation. Inspection of the blades after impregnation and curing showed some bubbles at the edges of the blades, as shown in Fig. 6, but no measurable difference in damping properties was observed between blades containing visible bubbles and blades without visible bubbles.

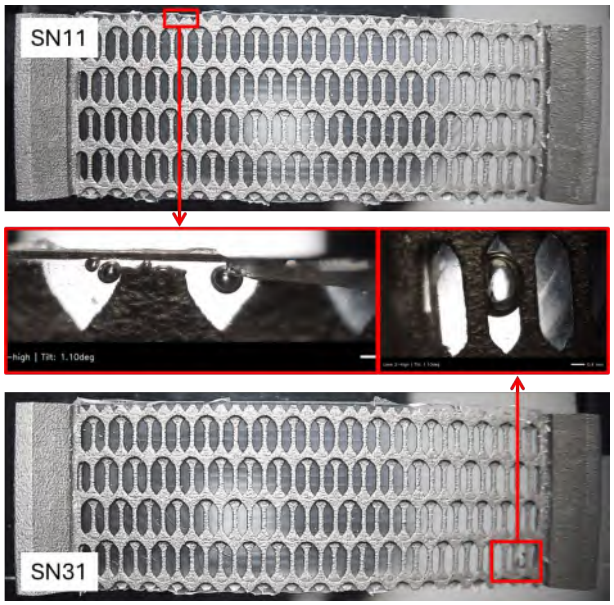


Figure 6: Last small defects (bubbles) observed after optimization of impregnation process

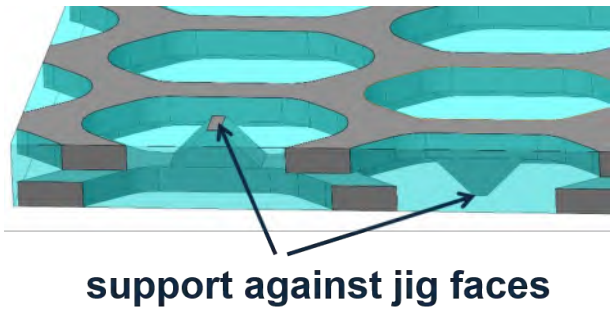


Figure 7: Possible improvement to ensure a well-defined gap during impregnation

Some deformation of the blades was also observed in some cases: on the side with no small bridges (build plate side, see Fig. 4), the gap had decreased after impregnation. A workaround to better control the gap could be to add small spikes to the design that would press on the jig faces to maintain the gap, as schematized in Fig. 7 and in the patent [8].

4. MEASUREMENTS

4.1. Test bench

Two measurement configurations were used throughout the project:

- single blade undergoing cantilever-type deformation
- parallelogram linear stage with two blades deforming in S-shape, as shown in Fig. 8

The compliant linear stage was initially chosen for its clean one-dimensional displacement, without rotation (easier for displacement sensing) and without low-frequency parasitic modes. Later, measurements were also performed directly on single blades, with one end clamped and the other end free. Single blade measurements were performed in two configurations: single blade without added mass, with bending eigenfrequency around 45 Hz, or single blade with added mass as shown in Fig. 8, to have an eigenfrequency near 15 Hz, compatible with the frequency range of DMA measurements described in section 4.5 (0.1 Hz to 30 Hz).

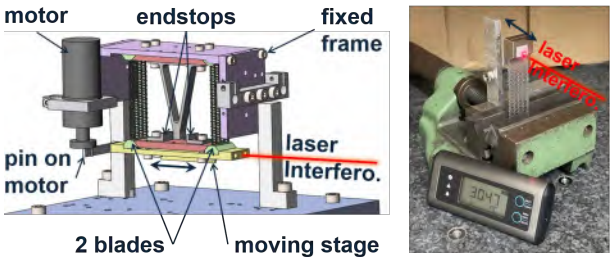


Figure 8: Schematic of the "compliant linear stage" setup (left) and "single blade" setup (right)

4.2. Free oscillation

In the free oscillation tests, the blades are bent with an initial displacement of order 4 mm and are then left free to oscillate. In the "compliant linear stage" case with two blades, the initial displacement is controlled by a slowly rotating motor with a pin (see Fig. 8), so that the initial conditions are highly reproducible. In the "single blade" case, the blade is moved by hand, and care has to be taken to avoid parasitic eigenfrequencies, like torsion. Velocity was measured using a Polytec laser interferometer. Damped oscillation signals are analysed as follows:

- Local minima and maxima of the oscillating signal are identified.
- Amplitude difference between one max and the next max (resp. one min and the next min) are computed, to get the amplitude loss per period ΔA_{maxs} (resp. ΔA_{mins}).
- Amplitude loss per period is plotted against amplitude (average amplitude A_{maxs} between the two maxs considered, resp. A_{mins} between the two mins considered).
- The times at which velocity vanishes are also identified and used to compute a

precise eigenfrequency at each period.

The analysis is schematized in Fig. 9. Note that the average amplitude computed here is independent of the 0 of the velocity (or displacement) scale, which avoids calibration offset problems.

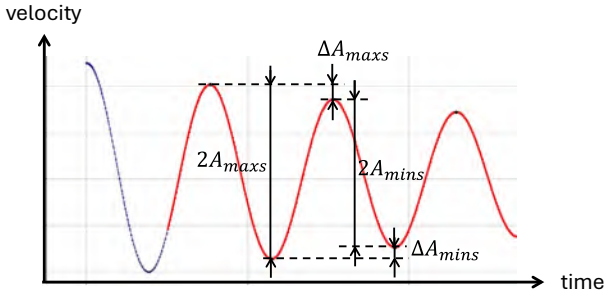
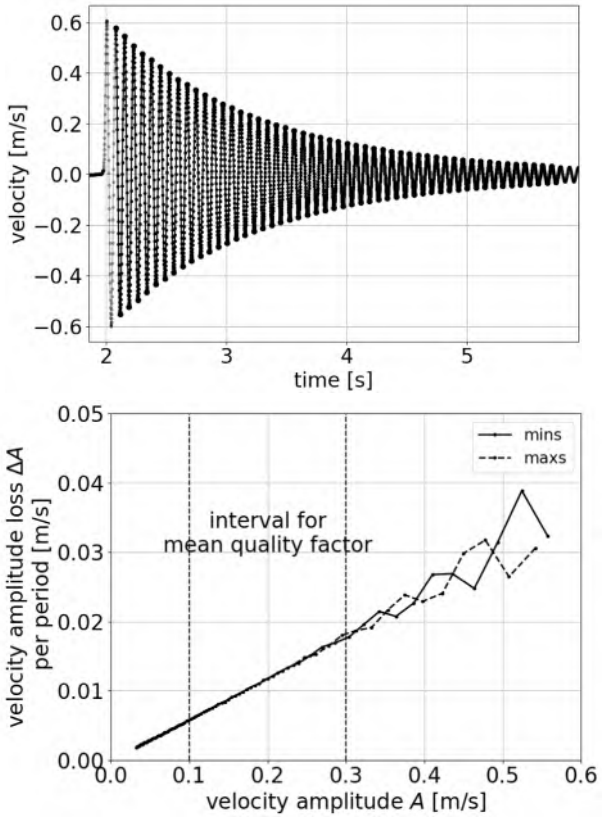


Figure 9: Schematic of the free oscillation analysis: amplitude loss per period ΔA_{maxs} and ΔA_{mins}, and average amplitude A_{maxs} and A_{mins}.

4.2.1. Single blade with added mass

An example of free oscillation measurement on a single blade with added mass is shown in Fig. 10.



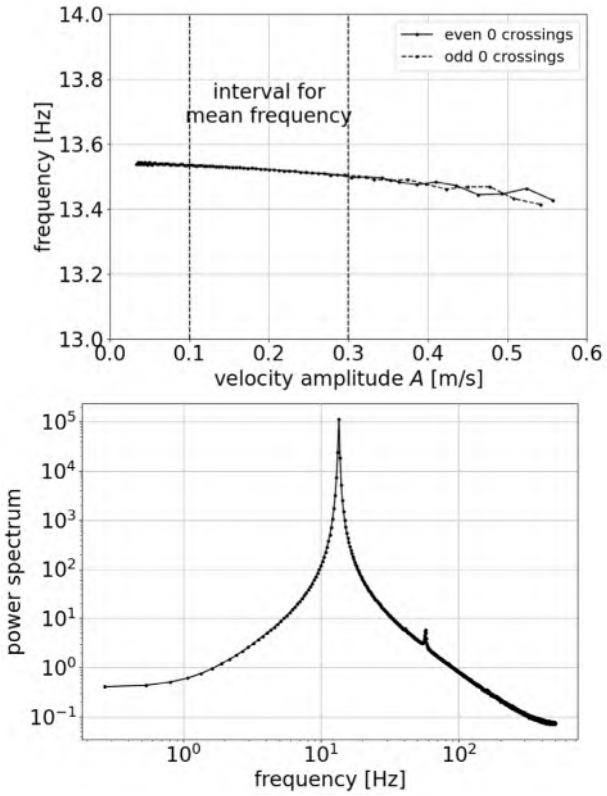


Figure 10: Example of free oscillation measurement on a single blade with added mass

Several interesting observations can be made from these plots:

- For an oscillator with viscous damping (fluid or structural), the amplitude loss per period should be linear with amplitude, which is the case here.
- The first few periods show more variability in the amplitude loss: this is due to initial excitation of a 2nd eigenmode, which is the torsion mode at ~ 57 Hz, as seen in the power spectrum. This mode is, however, damped much faster than the 1st mode, and thus a velocity amplitude interval of 0.1 m/s to 0.3 m/s is used to compute an average Q factor and average eigenfrequency, as sketched in the figures.
- The 1st eigenfrequency at ~ 13.5 Hz varies slightly with amplitude, by about 1%. This is due to some nonlinearity in the bending force of the blade, which was confirmed in the FEM simulations. This variation may seem small, but it has a significant effect on the shape of the resonance peak in the forced-oscillation measurements, as discussed in section 4.3.

Three blades were measured in this way with the added mass. Each blade was measured 5 times. The results are summarized in Fig. 11 and Tab. 2.

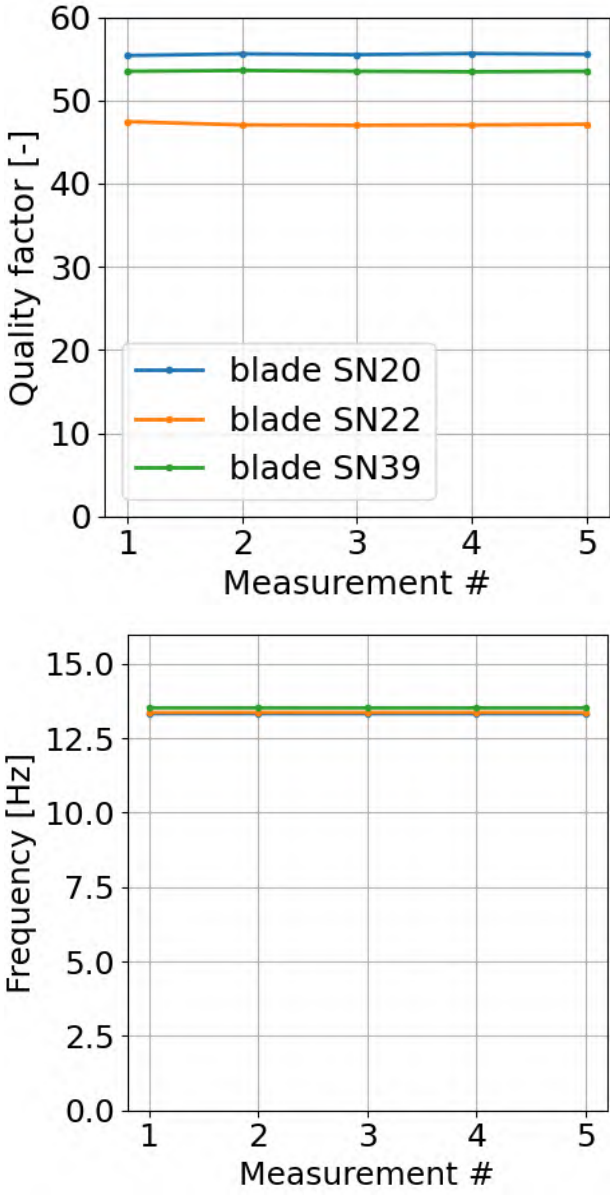


Figure 11: Free oscillation measurement of 3 single blades with added mass

Table 2: Free oscillation measurement of 3 single blades with added mass: for each blade, average over 5 measurements

Blade no	**SN20**	**SN22**	**SN39**	**Average**
Quality factor Q [-]	55.8	47.1	53.5	**52.1**
max Q diff. between 5 successive measures	0.2	0.4	0.2	**-**
Frequency [Hz]	13.33	13.37	13.52	**13.41**

4.2.2. Single blade without added mass

To check the blades for any damage during fatigue tests, free oscillation measurements as described above were also performed without added mass to allow a greater number of faster measurements and give an insight into the variation of the damping properties among blades: Q = 27.9 +/- 23% (2σ).

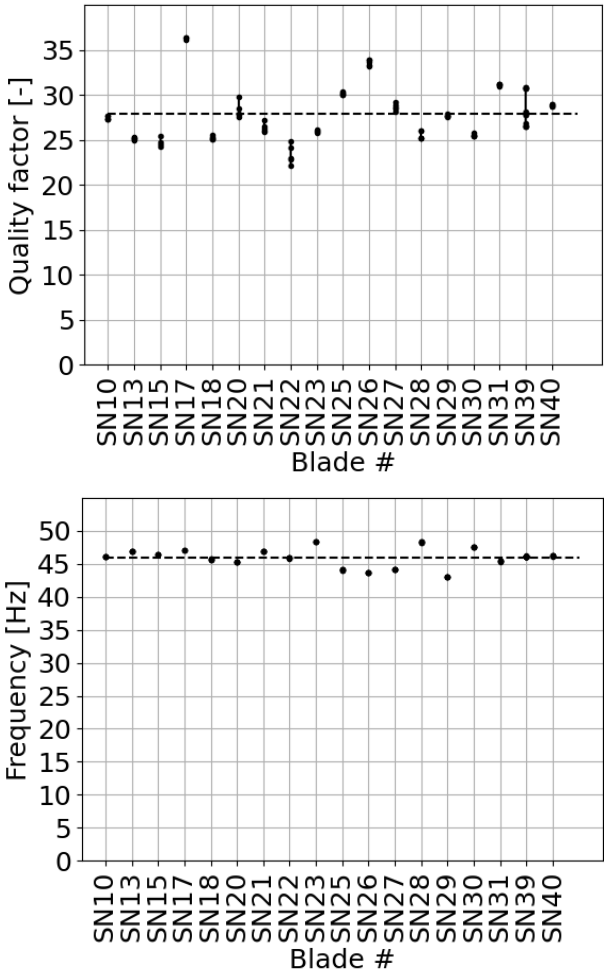


Figure 12: Overview of the single blade measurements without added mass

4.2.3. Two blades as linear stage

First measurements were performed with two blades mounted in parallel to form a linear stage, as shown in Fig. 8. However, the temperature during these first measurements was not characterized precisely, and small temperature differences as low as a few degrees were shown later to have a significant influence on the damping properties. Therefore, these measurements are not used to correlate with FEM simulations, but they are shown here because they have particularly low dispersion between the blades, as seen in Fig. 13.

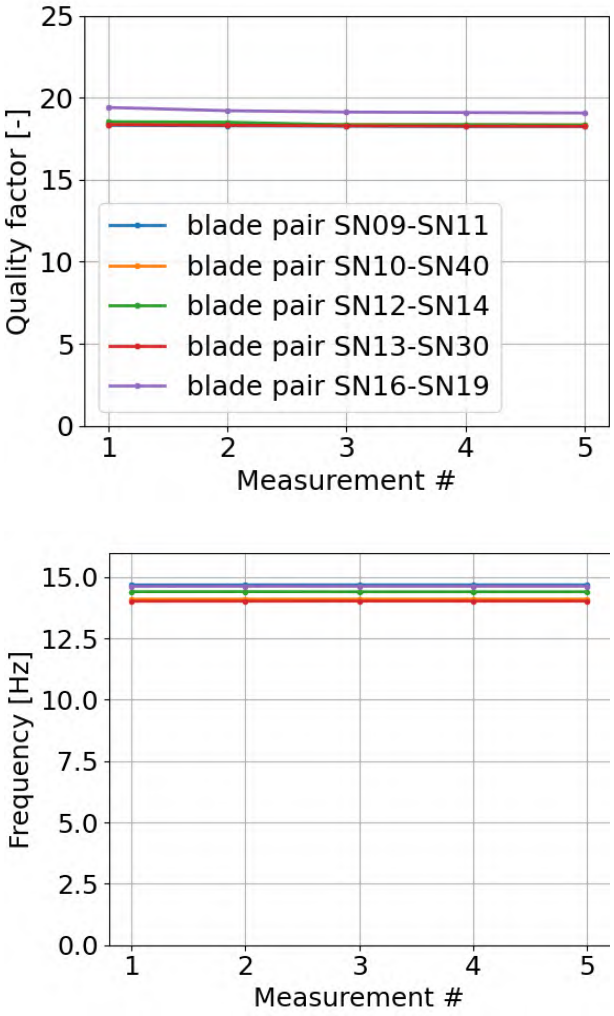


Figure 13: Free oscillation measurements of linear stage composed of two blades mounted in parallel

4.2.4. Choice of data for correlation

As discussed above, “two blades as linear stage” measurements have less dispersion between blade pairs, but temperature was not measured for these early measurements. Thus, “single blade with added mass” measurements shown in Tab. 2 will be used for the correlation with FEM simulation in section 5.

4.3. Forced oscillation

Forced oscillations were measured using a shaker[1] connected with decoupling rods to the fixed frame of the double blade linear stage shown in Fig. 8 (left), the fixed frame being now freely suspended by 3 threads so that it can follow the displacement imposed by the shaker. Fig. 14 shows the frequency response for a frequency sweep with amplitude 0.23 g. The 1st resonance peak is much wider than would be expected from the free oscillation measurements, as shown by the red dashed curve in Fig. 14 which represents the free oscillation values of 14.4 Hz, Q = 18.5 for SN12-SN14 (see Fig. 13). Even a fit of the measurement with a unique eigenfrequency does not accurately reproduce the top of the peak. One reason could be the slight frequency variation with amplitude, which widens the frequency range where resonance occurs. Thus, using forced oscillations to determine the Q factor does not seem reliable, therefore free oscillations were used.

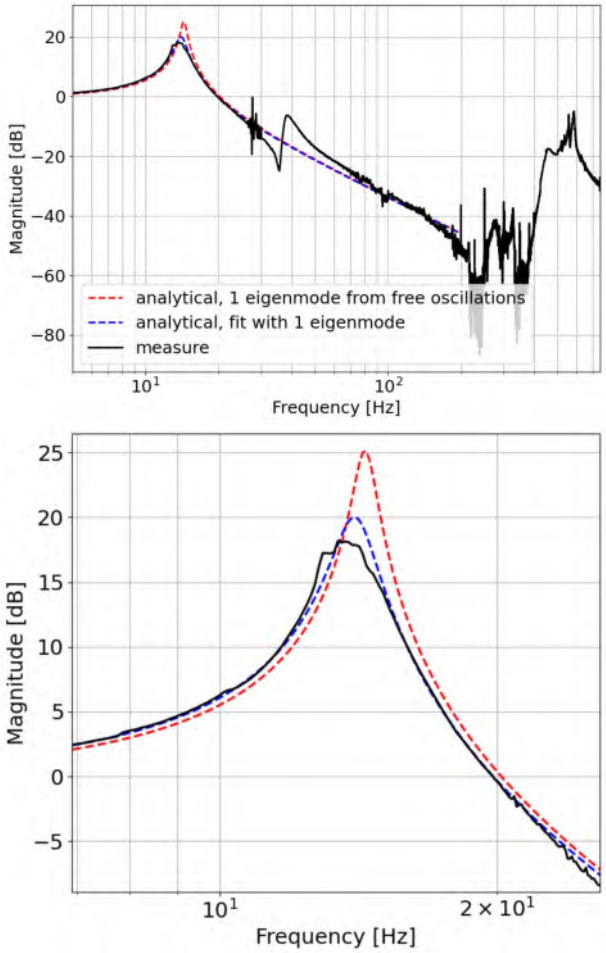


Figure 14: Frequency response of the linear stage formed by the pair of blades SN12-SN14

4.4. Fatigue

Single blades were tested on a fatigue test bench which imposes a ±4.1 mm displacement amplitude at the blade tip at a frequency of 20 Hz. The first

[1] LDS V406 from Ling Dynamic Systems.

tested blade survived 1.5 million cycles with only minor changes in damping properties (Q factor variation < 15%[2]) and no change of stiffness (eigenfrequency), as shown in Fig. 15. The eigenfrequency is extremely stable, with < 1% difference between all measurements. The Q factor shows two kinds of variation with number of cycles:

- a fast increase of Q factor at the very first cycles, of order 15%
- a slower drift of the Q factor, up to 10% after 1.5 million cycles

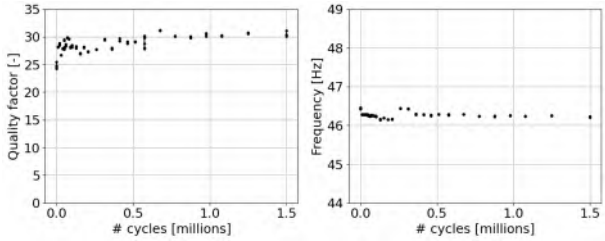


Figure 15: Fatigue results on single blade SN15.

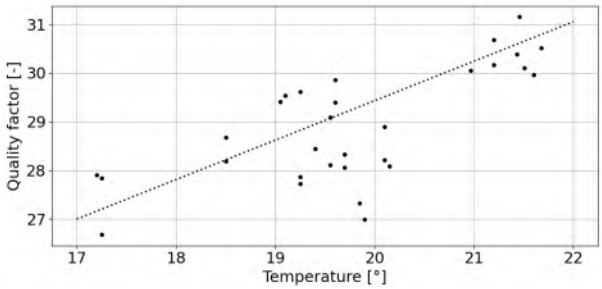


Figure 16: Q factor vs temperature correlation in the fatigue tests of Fig. 15. Dotted line corresponds to 3% Q factor variation per °C temperature change, as measured separately

Most of the drift is likely due to the seasonal temperature increase in the laboratory, which is not temperature controlled, see Fig. 16. A 2nd blade was tested up to 500'000 cycles with similar results. These results are promising, indicating that the damping properties remain stable over time.

4.5. DMA measurements

Dynamic Mechanical Analysis (DMA) measurements were performed at EPFL[3]. Rectangular samples of size 13 mm x 6 mm x 2 mm of the MAPSIL® QS1123 viscoelastic material were subjected to sinusoidal tensile displacement in the length direction with varying frequency, and the force necessary to deform the sample was measured. The phase shift between displacement and force allows the damping to be computed, expressed as a frequency-dependent complex elastic modulus. E' is the storage modulus, and E'' is the loss modulus, with the damping factor $\delta(\omega)$ expressed as :

$$E^*(\omega) = E'^{(\omega)} + iE''^{(\omega)} \qquad \tan\delta(\omega) = \frac{E''(\omega)}{E'(\omega)}$$

Fig. 17 shows an example of measurement.

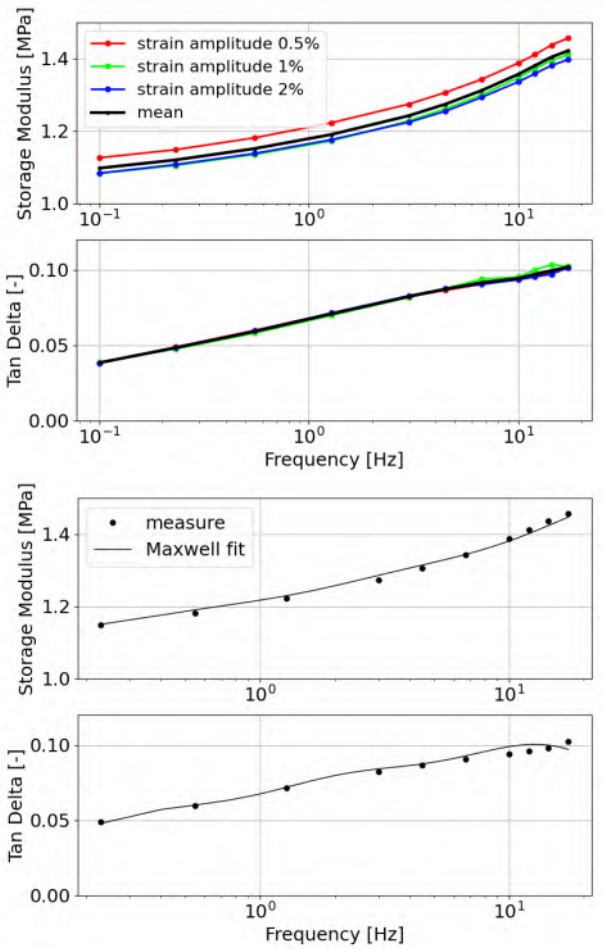


Figure 17: DMA measurement: on the upper graphs, results for 3 strains; on the lower graphs, Generalized Maxwell fit with 3 branches

The FEM tool used (COMSOL) did not allow to perform time-dependent simulations with a lookup table for viscoelastic properties. Thus, a Generalized Maxwell fit of the measurement data was performed, as commonly done to characterize viscoelastic properties. Three branches gave a good fit, as shown in Fig. 17 with parameters from Tab. 3 (EPFL lines). Note that storage modulus has slight variation with strain (Fig. 17), whereas tan delta does not seem to vary. This is further discussed in section 5.4.

First correlation with this material data gave poor correlation. A potential problem is that the DMA measurements were made under tensile loading, whereas viscoelastic material is primarily subjected to shear loading in the sandwich blade design, as explained in section 5.3. Thus, other material data were sought, with a comparison given in Tab. 4. It is observed that tan delta in shear is roughly 30% higher than in tension. The values from CNES database were thus finally used for the correlation with FEM, using the same Generalized Maxwell fitting procedure as explained above.

[2] once thermal effects are subtracted.

[3] EPFL, lpac.epfl.ch

Table 3: Generalized Maxwell fit of the DMA measurements.

Formulas	Param.	Source		branch j=1	branch j=2	branch j=3
$E^{'}(\omega) = E_o + \sum_j E_j \frac{(\tau_j \omega)^2}{1+(\tau_j \omega)^2}$	E_i [MPa]	EPFL	$E_o = 1.121$	$E_1 = 0.247$	$E_2 = 0.118$	$E_3 = 0.0852$
		CNES	$E_o = 0.453$	$E_1 = 0.139$	$E_2 = 0.0868$	
$E^{''}(\omega) = \sum_j E_j \frac{\tau_j \omega}{1+(\tau_j \omega)^2}$	τ_i [s]	EPFL		$\tau_1 = 0.00936$	$\tau_2 = 0.0688$	$\tau_3 = 0.493$
		CNES		$\tau_1 = 0.00450$	$\tau_2 = 0.0338$	

Table 4: Comparison of material mechanical properties from different sources, interpolated at 15 Hz.

Data source	EPFL measurements **@ 15 Hz, 20°C**	MAPSIL data @ 5 Hz, 20°C	CNES database **@ 15 Hz, 20°C**
Type of measure	tensile	tensile	shear
Shear storage modulus G' [MPa] @ 15 Hz	0.47 (*)	0.50 (*)	0.52
Tan delta @ 15 Hz	0.10	0.11	0.13

(*) *converted from tensile storage modulus E' using estimated Poisson ratio of 0.45.*

5. SIMULATIONS

5.1. FEM (COMSOL) model

As discussed in section 4.2.4, the "single blade with added mass" configuration is used for correlation between measurements and FEM simulation. The FEM model thus consists of a single blade, which is initially bent to 4 mm in a 1st quasistatic simulation step, and then left to oscillate freely in a 2nd time-dependent simulation step.
Since the two lattice blades are shifted (holes not aligned), it was not possible to use a sweep mesh across the whole volume. Second-order tetrahedral elements were thus used in the middle viscoelastic layer, imposing two elements along the thickness, as shown in Fig. 18.

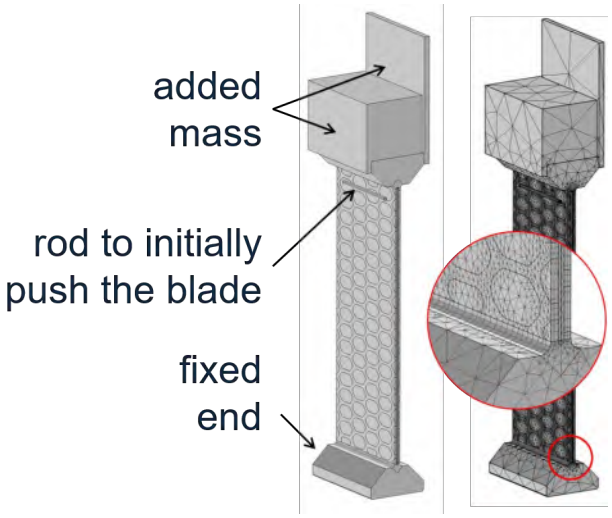


Figure 18: Left: FE model boundary conditions. Right: Overall view of the FE model mesh. With detailed view of the mesh

5.2. Correlation with measurements

The same analysis as for measurements (section 4.2) was performed on the time-dependent simulation results. Fig. 19 compares the FEM simulations to the measurements, with Q factor and frequency listed in Tab. 5. The agreement is within 15% for the Q factor and within 10% for the eigenfrequency.

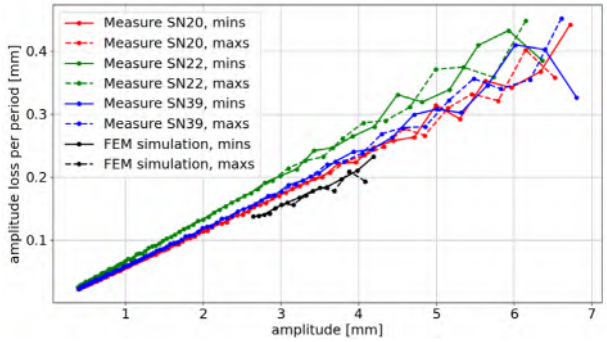


Figure 19: Correlation between measurements and FEM simulations

Table 5: Correlation between measurements and FEM simulations

	Measurement (average of 3 blades)	FEM simulations	Error (simulation relative to measurement)
Quality factor	52	60	+15%
Frequency	13.4 Hz	14.7 Hz	+10%

5.3. Understanding the viscoelastic behaviour

An advantage of the FEM model is its ability to provide detailed insight into the local behavior of the viscoelastic material. Several observations can be made:

- As expected in the clamp-free bending of a blade, the maximum Von Mises stress in the metal lattice blades is located near the clamping, as seen in Fig. 20
- More surprisingly, the max shear (and other) stress in the viscoelastic material is located near the middle of the length of the blade, as seen in Fig. 21. More precisely, the max shear is found at the overlapping regions of the two lattices.

This last observation may be explained by considering a simple model of plain (not lattice) sandwich blades, with the 3 cases shown in Fig. 22. To simplify the interpretation, the case of "two blades as linear stage" is chosen, which implies no rotation of the end of the sandwich blades (S-shape bending), but the explanation remains valid for the single blade case as well.

- If no middle layer is present (left of Fig. 22), the two blades deform in the same way, having slightly rotated cross sections at the same distance along the length.
- If the middle layer has the same elastic modulus as the outer layers (right of Fig. 22), the two blades behave as a single blade, with a unique cross section slightly rotated. There is no shear strain in the middle layer (cross section perpendicular to length).
- If the middle layer has an elastic modulus similar to silicone (here 1 MPa), 10^5 times more flexible than titanium (middle of Fig. 22), then the deformation of the two outer layers is close to "no middle layer", thus inducing a large shear strain in the middle layer.

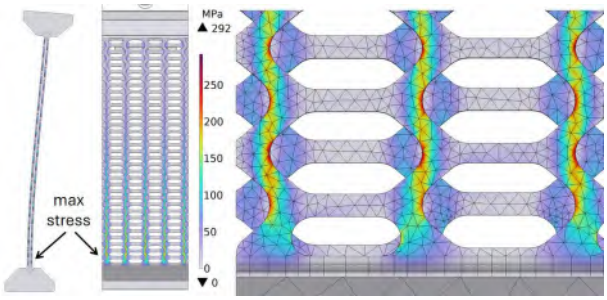


*Figure 20: Max. Von Mises stress in the **metal lattice blades** after 1st period (~ 4.3 mm displacement)*

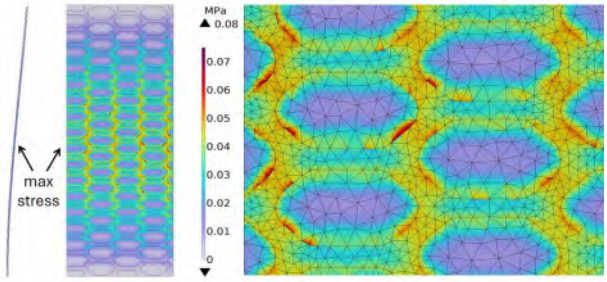


*Figure 21: Max. shear stress in the **viscoelastic material** after 1st period (~ 4.3 mm displacement)*

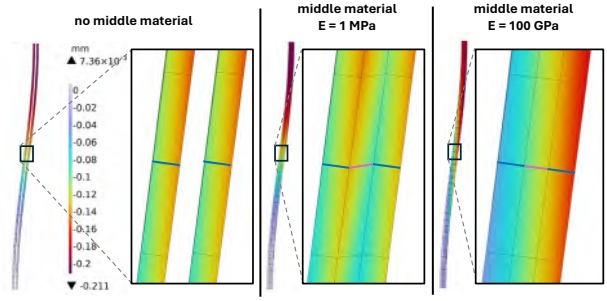


Figure 22: Understanding the shear strain in the viscoelastic layer with plain sandwich blades (no lattice): z displacement for 3 cases: left, no middle layer, middle, silicone layer, right inner layer identical to outer layers

In the real case, lattice blades are much less stiff in the length direction than plain blades, thus the shear strain in the viscoelastic layer is slightly smaller than the plain blades case: the viscoelastic layer is stiff enough in shear to deform the metal lattice blades in the length direction. This is also observed when computing the stiffness of the sandwich blade with lattices: 0.15 N/mm without viscoelastic material and 0.22 N/mm with viscoelastic material, corresponding to a 46% increase in stiffness, considering the elastic modulus 10^5 times smaller than titanium. Such a fine understanding of the behaviour of these lattice sandwich blades may help optimize the design to get desired damping and stiffness performance.

5.4. Influencing factors

The damping properties agreement between measurements and FEM simulation is good. However, to check if this agreement may be incidental or not, a list of factors influencing the Q factor was identified and their relative influence is discussed hereafter.

- **Geometrical dimensions:** as discussed in section 5.3, shear stress in the viscoelastic material (and thus damping) depends on the relative stiffness of the lattice blades and the viscoelastic middle layer. Thus, thickness variations of lattice blades or gap have a large influence on damping. This was verified by FEM simulations. To mitigate this error, the correlation was performed using blade thicknesses and gap measured on the final prototypes. However, since lattice cross sections are close to the resolution limit of AM, the edges are not sharp as in the FEM model, which could significantly change the stiffness of the metal lattices.
- **Viscoelastic material properties:** as discussed in section 4.5, measuring the damping properties in a stress state representative of the present application is important, since shear measurements give 30% larger damping than tensile measurements. Moreover, Generalized Maxwell fit is not always accurate at all frequencies. For free oscillations, it seems sufficient to check the quality of the fit near the eigenfrequency, but for forced oscillations with frequency sweep, more care should be taken. A slight strain dependence of the storage modulus is also observed, but no amplitude dependence of damping could be observed in the measurements.
- **Damping in metal:** some measurements without viscoelastic material were performed to estimate the damping in LPBF titanium, which could be higher than bulk titanium due to porosity defects for instance. Q factors were of the order of 800, thus about 30x higher than with viscoelastic material (at about 40 Hz without added mass). Damping in metal should thus be less than 4% of the total damping.
- **Air damping:** a foil was added at the end of the blade to artificially increase the possible air friction. No significant effect on the Q factor was measured (< 2%).
- **Temperature:** measurement from MAPSIL showed a significant variation of damping properties around room temperature. This was further confirmed by varying the temperature in the lab, leading to an estimation of 3% of Q factor variation per °C of temperature variation.
- **Adhesion:** adhesion of viscoelastic material to metal is considered perfect in the FEM simulation, whereas delamination may be present in practice. However, fatigue tests showed very little variation of damping in time,

suggesting that adhesion is likely adequate.

- **Ageing:** ageing of material properties, even without fatigue, has not been addressed in this work, but could be interesting to further investigate.
- **Mesh:** mesh of FEM model was rather coarse compared to feature dimensions, to keep simulation times reasonable (~ 1 day for the longest ones). However, tests with finer meshes did not show significant differences, perhaps because the stress gradient is almost linear in the thickness direction.

6. CONCLUSION AND OUTLOOK

Lattice sandwich blades with impregnated viscoelastic material demonstrated strong damping performance, reducing the Q factor by a factor of approximately 30. The damping properties were repeatable and stable, with limited blade-to-blade variability (< +/-23%) and across repeated measurements (< +/-10%). Fatigue tests are particularly promising, since only a small damping variation (< 15%) was observed after 1.5 million cycles on one sample. The FEM model showed good agreement with measurements (< 15% discrepancy), which should help optimize the present concept and support the development of other concepts, as discussed in next section.

Future work will consider the following topics:

- implement this technology in a use case
- better understand the potential of damping optimization supported by FEM simulations
- use small spikes as described in Fig. 7 to ensure well-defined gap between blades, which could help address more complex geometries
- further investigate fatigue behaviour on more samples, also addressing the risk of viscoelastic material ageing without any stress

7. ACKNOWLEDGEMENTS

This activity was supported through ESA OSIP funding (ESA Contract No. 4000143750).

8. REFERENCES

[1] A. Verhaeghe, G. Perruchoud, P. Schwab, M. Gumy and J. Rouvinet, "Lessons Learnt during the Development of a Compliant Focus Mechanism for the Exomars Rover Mission," in *ESMATS 2019*, Munich, Germany, 2019.

[2] P. Spanoudakis, P. Schwab, L. Kiener, G. Perruchoud, H. Saudan, M. Gumy and Y.-J. Regamey, "Corner Cube Mechanism (CCM) for MTG IRS: Qualification and Acceptance Test Campaign Results and Lessons Learned," in *ESMATS 2019*, Munich, Germany, 2019.

[3] P. Spanoudakis, L. Kiener, F. Cosandier, P. Schwab, D. Grivon, G. Psoni, D. Rellakis and N. Bencheikh, "Large Angle Flexure Pivot Development and Test Campaign Results," in *ESMATS 2021*, online only, 2021.

[4] B. M. Shafer, "An overview of constrained-layer damping theory and application," in *Proceedings of Meetings on Acoustics*, Montreal. Canada, 2013.

[5] M. Gröhlich, M. Böswald and J. Wallaschek, "Viscoelastic damping design – A novel approach for shape optimization of Constrained Layer Damping treatments at different ambient temperatures," 2022. Available online: https://elib.dlr.de/187991/1/Manuscript_Final_Version.pdf. [Accessed 2026].

[6] S. Hayoz, H. Saudan, J.-L. Helfer, L. Salamin and N. Blondiaux, "Damping of Flexure Blades based on Additive Manufacturing: Design for Space and Numerical Model Correlation," in *ESMATS 2025*, Lausanne, Switzerland, 2025.

[7] L. Kiener, H. Saudan, F. Cosandier, G. Perruchoud, P. Spanoudakis and J. Rouvinet, "Additive manufacturing: innovative concept of compliant mechanisms," in *EUSPEN*, Geneva, Switzerland, 2020.

[8] H. Saudan and F. Cosandier, "Method for Manufacturing a Damping Device, for Damping Vibrations and/or Absorbing Shocks". Patent EP4321339, 12 August 2022.

[9] O. Guillaumon, "Development of a new silicone adhesive for space use: MAPSIL QS1123," in *11th ISMSE International Symposium on Materials in a Space Environment*, Aix-en-Provence, France, 2009.

ECSSMET
Braunschweig Germany 2026

Structure design

ARGONAUT: THE MECHANICAL ARCHITECTURE OF THE PROPULSION SUBSYSTEM

Ettore Lamacchia [(1)], Prateek Garg [(2)], Ross Sample [(3)]

[(1)] Thales Alenia Space UK, Building 550, Bristol Business Park, Coldharbour Lane, BS16 1EJ, Bristol, UK. Email: ettore.lamacchia@thalesaleniaspace.com
[(2)] Thales Alenia Space UK, Building 550, Bristol Business Park, Coldharbour Lane, BS16 1EJ, Bristol, UK. Email: prateek.garg@thalesaleniaspace.com
[(3)] Thales Alenia Space UK, Building 550, Bristol Business Park, Coldharbour Lane, BS16 1EJ, Bristol, UK. Email: ross.sample@thalesaleniaspace.com

KEYWORDS

Argonaut LDE, Mechanical Architecture, Propulsion Subsystem.

ABSTRACT

The Argonaut space mission represents a major step forward in sustainable lunar exploration. Designed as a versatile lunar lander capable of delivering cargo, infrastructure and scientific payloads, Argonaut aims to support long-term robotic and human operations on the Moon's surface. This paper presents an overview of the Argonaut mission with particular focus on the mechanical architecture of the propulsion subsystem for the Lunar Descent Element (LDE), developed by Thales Alenia Space UK. The impact of the mission-specific profile and the resulting set of requirements on the design of the LDE is illustrated, including details of the qualification and delta qualification environmental test campaign performed for a number of units and equipment. By combining a robust propulsion design with a flexible mission architecture, the Argonaut lander provides a scalable platform capable of supporting a wide range of lunar exploration objectives and future sustained surface operations.

1. INTRODUCTION

The European Space Agency (ESA) Argonaut space mission represents a major step forward in sustainable lunar exploration and international space logistics and cooperation. Designed as a versatile lunar lander capable of delivering cargo, infrastructure and scientific payloads to the Moon's surface, Argonaut aims to support long-term robotic and human operations.

Thales Alenia Space in Italy (TASI) is the Prime Contractor and System Integrator of the mission. TASI lead a consortium of several entities, each one responsible for a specific subsystem [1]. The overall Argonaut System consists of two elements: the Lunar Descent Element (LDE) and the Passenger Module. In particular, the LDE incorporates transportation and landing capabilities, such propulsion, guidance and precise landing mechanisms [2]. This paper presents the mechanical architecture of the LDE propulsion subsystem, developed by Thales Alenia Space UK (TASUK). The propulsion subsystem plays a central role in enabling precise lunar descent, landing and surface delivery operations. It is designed to provide high reliability and controllability during critical mission phases, including trajectory corrections, powered descent and terminal landing. The mission-specific design requirements and payload size represent complex challenges, impacting a number of design aspects including equipment placement optimisation, tubing routing and system integrability. The unique characteristics of the mission require the incorporation from early phases of novel design for manufacturing constraints in order to enable smooth production and assembly phases, and the qualification of new methodologies and processes. Further to this, the mission poses additional thermo-mechanical challenges compared with more conventional programmes. Specifically, in addition to Launch loads, the mission profile prescribes a complex set of mechanical loads, such as Transfer Orbit loads, Lunar Orbit loads, Descend and Landing loads and Surface Operational loads, which often resulted in the re-assessment of already-qualified equipment in terms of thermo-mechanical environmental loads. Furthermore, as the spacecraft reaches the lunar sphere of influence, the lunar infrared flux can reach relatively high values at lunar noon on equatorial regions and drops to nearly zero in permanently shadow regions near the poles. Therefore, depending upon the orbit, the spacecraft can face radiative flux as high as twice the solar constant while orbiting equatorial regions and zero at the poles. The fast-changing thermal dynamics during the orbit requires robust thermal control of the spacecraft system. Thermo-mechanical solutions implemented within the LDE design are addressed in details in the remainder of this work.

This paper is structured as follows. Section 2 describes the overall architecture of the LDE propulsion subsystem, with details of the tubing routing, tanks accommodation and propulsion equipment. In Section 3 an overview of the tubing and tubing supports is presented, with details of welding processes and associated qualification

campaigns. Thermal control design is presented in Section 4. Section 5 concludes the paper.

2. ARGONAUT PROPULSION SUBSYSTEM

2.1. Mechanical Architecture

This section presents the architecture of the LDE propulsion subsystem as designed at the time of writing the paper. Further developments might still be envisaged as the maturity of the programme progresses. The propulsion subsystem for the Argonaut LDE presented in this work comprises two different solutions. A Main Engine (ME) system, powered by a combination of Mixed Oxides of Nitrogen (MON) and Monomethyl Hydrazine (MMH) and a Reaction Control System (RCS) [3]. The main engines require two dedicated ME tanks per fuel type. These are housed within a dedicated bay in four quadrants of the lander, as illustrated in Figure 1. With reference to Figure 2, the RCS requires four dedicated smaller Helium tanks, located at the centre of the lander and on a lateral bay (negative Y-axis). The propulsion architecture is further characterised by two additional subsystems, namely a pressurising gas line fed by the Helium tanks and a liquid system line serving both ME and RCS. With reference to Figure 3, the gas system is split between two lateral bays in the positive and negative X-axis, and it is accommodated over two shear panels dedicated to the associated propulsion system (ME-RCS).

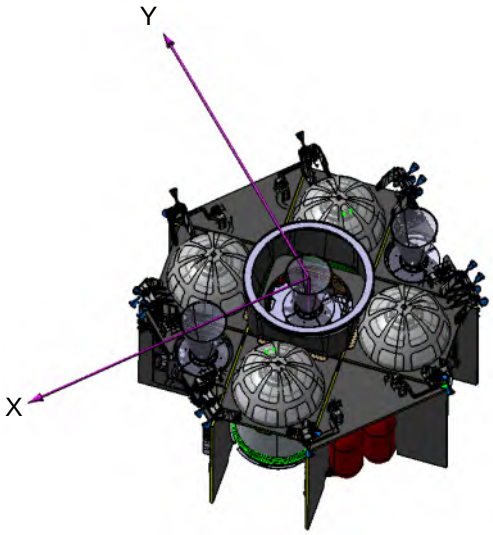


Figure 1: Bottom view of the LDE showing location of the Main Engine and the Main Engine Fuel Tanks (in gray).

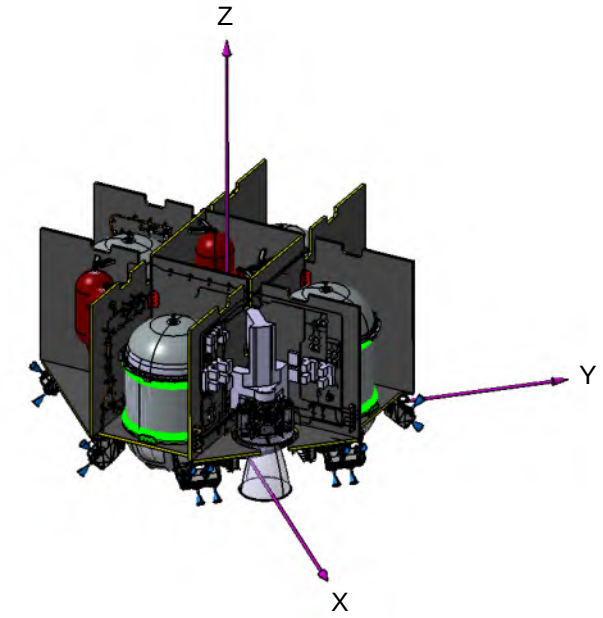
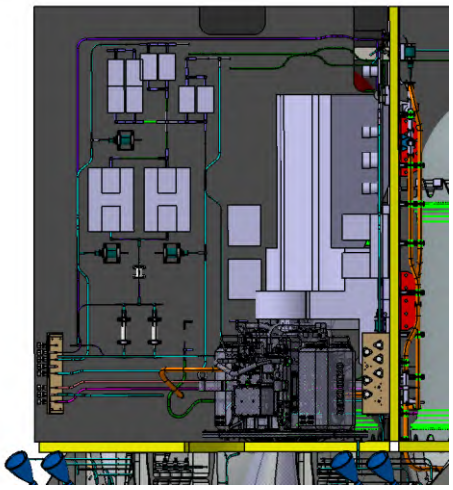
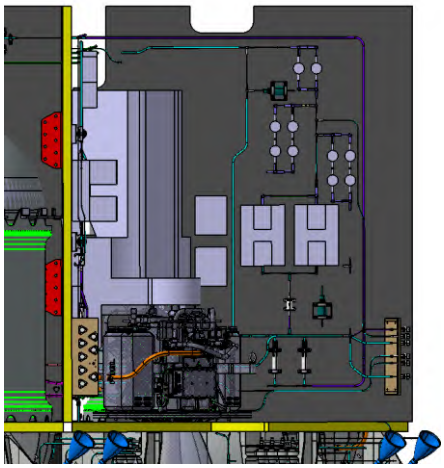


Figure 2: Top view of the LDE showing location of the helium Tanks (in red).



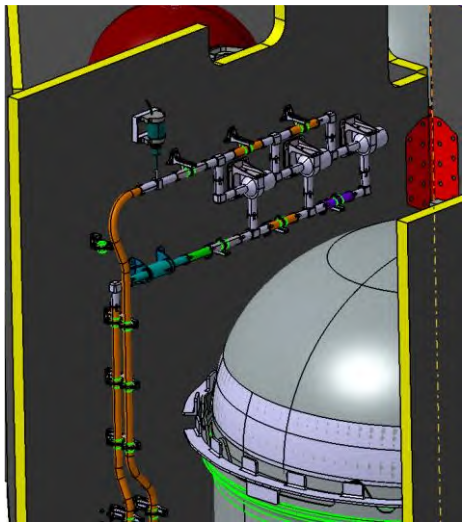
(a)



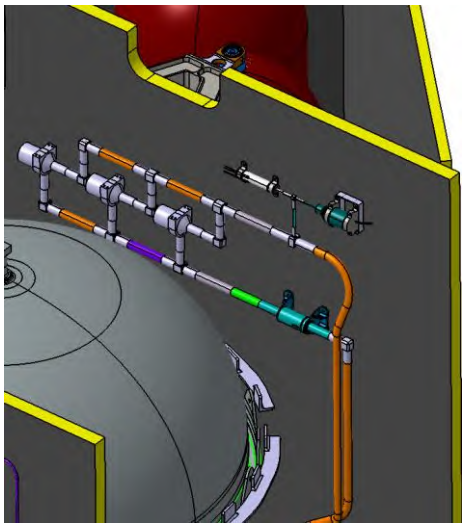
(b)

Figure 3: Pressurising gas system located on the ME shear panel (a) and on the RCS shear panel (b).

An illustration of the liquid system is reported in Figure 4. The liquid system comprises a number of Sub-System Isolation Valves (SSIV). An optimised



(a)



(b)

Figure 4: Sub-System Isolation Valves located on the ME shear panel (a) and on the RCS shear panel (b).

accommodation solution allows for tube routing and associated fuel tank to be placed on the same bank, allowing for easy integration in a relatively compact volume. Specifically, the ME fluid converges from the two tanks into a single manifold, where the highest mass flow rate is measured. Therefore, this manifold has increased diameter (1 inch) compared to the nominal fluid lines in order to reduce pressure drop. Conversely, the RCS does not require the flow to converge into a single manifold. Once the flow leaves the RCS SSIV, it enters a ½ inch tube section branching out into the lateral bays, through Thruster Isolation Valves (TIV) and into the RCTs. The TIVs are grouped in either four or eight sub-assemblies and accommodated on dedicated brackets. Similarly, the RCTs have dedicated Additive Manufactured (AM) brackets.

3. PROPULSION LINES

3.1. Tubing Characteristics and Welding Techniques

With reference to Table 1, the Argonaut LDE propulsion subsystem consists of a combination of High Pressure (HP) and Low Pressure (LP) TiAl2.5V tubing network. Due to the mission-specific requirements, a delta qualification for a number of tubing/fittings assemblies was necessary, with particular focus on welded joints de-risking activities through a trade-off between Autogenous Tungsten Inert Gas (TIG) and Root-Welding (T-ring) techniques. Specifically, Autogenous and T-ring welding approaches differ for the technique used to produce the weld interface. In Autogenous welding, the weld is formed entirely from the fusion of the parent tube material with no external filler metal being introduced into the weld pool. The T-ring technique uses the Gas Tungsten Arc Welding (GTAW/TIG) process with the controlled addition of compatible filler material to establish and maintain the required root weld profile. Both techniques utilise a non-consumable tungsten electrode and require precise control of the welding arc, shielding gas and heat input. For the mission-specific thin tubes, accurate joint preparation and process control are particularly important. The relatively thin wall makes the joint sensitive to excessive heat input, which may result in burn-through, excessive penetration, distortion or loss of tube geometry. Autogenous welding is especially dependent upon consistent tube dimensions, accurate alignment and close control of the root fit-up as there is no filler material available to compensate for variations in the joint gap. The amount of root penetration and reinforcement is therefore primarily determined by the joint geometry and welding parameters. Any significant variation in root gap may consequently produce corresponding variations in penetration and internal weld profile. The T-ring technique provides additional weld metal through controlled filler-wire addition. This allows the welder to have greater control over the amount of metal deposited at the root and it provides relatively larger flexibility in achieving the required root reinforcement and weld profile.

Table 1: Argonaut LDE Ti3Al2.5V Tubing and Manifold Specifications

Diameter [mm]-[inch]	Thickness [mm]	Operative Pressure [bar]
6.35-0.25	0.71	310
6.35-0.25	0.41	50
9.53-0.375	0.41	50
12.7-0.5	0.66	50
19.05-0.75	0.89	50
25.4-1.0	1.15	50

Further to this, the presence of filler material provides some tolerance to minor variations in joint fit-up, although accurate alignment and preparation remain essential. Excessive filler addition may result in an overly reinforced root, localised heat accumulation or an undesirable internal profile, whereas insufficient filler addition may result in inadequate root reinforcement or incomplete joint formation. An Autogenous weld can provide a smooth and uniform internal root when the tube ends are accurately prepared and the welding parameters are appropriately controlled. The absence of filler material also eliminates the need to manipulate filler wire within the relatively small weld pool, which may be advantageous when welding small-diameter/thin-walled tubing. However, the process places greater reliance on dimensional consistency and operator or equipment control. In comparison, T-ring welding offers greater control over the deposited weld metal but it requires accurate and consistent filler-wire feeding to prevent excessive reinforcement, lack of fusion or other weld discontinuities. TASUK heritage process indicates that the principal advantage of Autogenous welding is the capability to produce clean and controlled root without filler metal, provided that joint fit-up and welding parameters can be maintained consistently. On the other hand, it is clear that the principal advantage of the T-ring technique is the additional control provided by filler-metal deposition, which can facilitate the achievement of a specified root profile and provide greater tolerance to minor variations in joint geometry. From a process-control perspective, autogenous welding may be advantageous for highly repeatable production joints where tube dimensions, joint preparation and fit-up can be maintained within tightly controlled limits. It can provide a clean internal weld profile without the introduction of filler metal and may be particularly suitable where internal surface condition is an important requirement. T-ring welding may be preferable where the applicable specification requires filler metal, where a defined root reinforcement is necessary, or where the joint configuration requires additional deposited metal to achieve the specified weld geometry. The selection of either technique should therefore be based on the joint configuration, required weld profile, dimensional tolerances, internal surface requirements, production conditions and applicable engineering specification. The selected process should be demonstrated through an appropriate procedure qualification to establish that the resulting weld satisfies the required acceptance criteria. TASUK heritage approach is to associate to each weld within the network a number of acceptance criteria in order to assess acceptability of the final product. Typically, acceptance criteria specify a range of geometrical parameters of the final weld in terms of weld profile, i.e. internal and external radii and weld width, and in terms of number and dimensions of porosities and inclusions, verified either through external measurements or X-rays. The selection of the criteria is based on stress analysis of the nominal parts, with associated stress concentration factor function of the weld geometry. Structural allowables of each weld with respect to predictions are assessed via test campaigns which typically consist of material tests (Tensile tests) and vibration tests (Random vibration), followed by inspection via dye penetrant and X-rays, and final leak and pressure burst test. Illustrations of typical vibration and tensile test setups used for welded tubes coupons are reported in Figure 5 and Figure 6 for the sake of clarity.

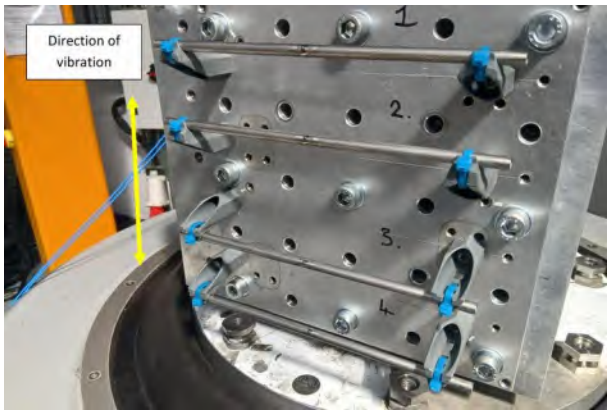


Figure 5: Typical setup of welded tubes for vibration tests. The picture shows 4 welded coupons, supported by flight-representative mountings.



Figure 6: Typical setup of welded tubes for tensile test.

4. THERMAL CONTROL OF THE PROPULSION SUBSYSTEM

Thermal control design of the LDE propulsion subsystem for the Argonaut mission is largely carried out using passive elements with active heaters. The thermal design is derived based on the requirements of the propellant feed system temperature and external environment. The propulsion system would encounter extreme thermal environment depending upon the phase of the mission. The thermal environment during each phase namely Launch and Early Orbit Phase (LEOP), Lunar Transfer Orbit (LTO), Low Lunar orbit (LLO), Near-Rectilinear Halo Orbit (NRHO) and during Descent and Landing phase would pose different challenges.

The lander would face colder environment during the LTO compared with the LLO due to the high infrared radiation from lunar surface and solar flux. Furthermore, during the descent and landing phase, the unprecedented attitude and varying velocity of the lander makes the thermal analysis and testing difficult and hence the thermal control more challenging.

The primary thermal control strategy is to protect the propellant feed system from running into possible thermal issues such as propellant freezing, vapor lock, and boiling and tank overpressure.

The propulsion system is isolated from external environment using Multi-Layer Insulation (MLI) blankets to prevent temperature swings throughout the mission. Propellant tank temperatures are controlled using MLI and appropriately sized heaters. Heaters and thermistors are used to ensure that equipment such as pressure regulators, flow control units and thrusters remain within specified temperature limits. Tubing heater ensures that there are no thermal gradients in the propellant across the feedlines.

The descent and landing phase puts the utmost stress on the propellant feed system, since it is required to perform a set of manoeuvres in a relatively short time.

The thermal control system keeps all the required equipment's within the specified temperature limits and thus it is important for flawless operation of the propulsion system.

5. CONCLUSION

In this paper, an overview of the mechanical architecture of the Argonaut LDE propulsion subsystem developed by Thales Alenia Space UK has been presented. The discussion highlights how the propulsion architecture supports the mission's critical phases, including trajectory corrections, powered descent and terminal landing, while meeting stringent requirements on reliability, controllability and integration.

The paper also describes the key mechanical and manufacturing drivers introduced by the mission-specific design requirements. In particular, the qualification and delta-qualification environmental test campaign applied to propulsion-related equipment and tubing/fittings demonstrates the need to de-risk design changes arising from implementation constraints and updated loads. The selection and justification of welding approaches for TiAl2.5V thin-walled tubing using an appropriate trade between autogenous TIG and T-ring techniques is addressed, together with the process qualification strategy and weld acceptance methodology.

Finally, the thermal control design approach for the propulsion subsystem is reviewed. By relying primarily on passive thermal isolation supported by appropriately sized heaters and sensing elements, the system is protected against potential propellant feed risks such as freezing, vapor lock and boiling, and tank overpressure across the mission thermal regimes.

Overall, the combination of a robust propulsion mechanical design, validated manufacturing and welding processes, and an appropriate thermal control strategy enables a scalable lunar lander platform capable of supporting a wide range of sustainable surface mission objectives.

6. REFERENCES

1. www.thalesaleniaspace.com/en/press-releases

2. Cifani G. et al., Argonaut: ESA's Versatile Lunar Lander Enabling Multiple Moon Missions. Proceedings of IAF, 2024.

3. Monello T. et al., Argonaut LDE Propulsion System Requirements and Design. Proceedings of SP, 2026.

STRUCTURAL DESIGN OF THE WIDE FIELD IMAGER FOR THE NEWATHENA X-RAY TELESCOPE

Jan Philipp Möller [(1)*], Valeria Antonelli [(2)*], Kirpal Nandra [(3)*], Daniel Pietschner [(4)*], Anirudh Mukund Saraf [(5)*], Rafael Strecker [(6)*]

**Max-Planck Institute for Extraterrestrial Physics, Giessenbachstrasse 1, 85748 Garching by Munich, Germany*
(1) E-Mail: jpmoeller@mpe.mpg.de, (2) E-Mail: vantonelli@mpe.mpg.de, (3) E-Mail: knandra@mpe.mpg.de ,
(4) E-Mail: pietschner@mpe.mpg.de, (5) E-Mail: amsaraf@mpe.mpg.de, (6) E-Mail: strecker@mpe.mpg.de,

KEYWORDS

NewATHENA, mechanical design, thermo-mechanical design, Wide Field Imager, WFI

ABSTRACT

After a two-year re-evaluation phase, the ATHENA (Advanced Telescope for High-ENergy Astrophysics) mission restarted as NewATHENA. The project is moving towards its second instrument system requirements review at the end of 2026, and with it, the implementation of the updated set of requirements. This paper presents the NewATHENA mechanical baseline design of the Wide Field Imager Main Assembly. It identifies the mechanical design drivers that serve as constraints in the design process and highlights the core mechanical design decisions made to accommodate them. After presenting the Wide Field Imagers' Main Assembly baseline design, an introduction to the current developments in the WFI is provided.

1. INTRODUCTION



Figure 1: Artist's impression of the NewATHENA X-ray observatory (©ESA) with approximate dimensions.

The NewATHENA X-ray observatory (Fig. 1) will be ESA's next flagship mission to explore the hot and energetic universe, following XMM-Newton and Chandra. Set to launch in 2039 aboard the Ariane 6-4, the NewATHENA telescope will feature a silicon pore optics mirror [1] with an approximate diameter of 2 m and a focal length of 12 m. With an angular resolution of 9 arcseconds half-energy width, a comparatively large field of view, and a large collecting area, NewATHENA will, among other topics, help to study active galactic nuclei, black hole accretion, neutron stars, and the formation of large-scale structures [2].

To conduct the necessary observations, NewATHENA will carry two instruments. The X-ray Integral Field Unit, X-IFU, and the Wide Field Imager, WFI. The X-IFU is designed to provide a spectral resolution of 4 eV at a 5 arcsecond resolution. The result is a complex but powerful instrument, with a small field of view and spatial resolution, but a high spectral resolution [3]. The WFI will provide high-spatial-resolution, high-time-resolution, and large field-of-view X-ray imaging capabilities. The objective of the WFI payload is to detect soft X-rays in the range from 0.2 keV up to 15 keV with a spectral resolution of less than 80 eV at 1 keV and less than 170 eV at 7 keV. Further, the WFI payload provides a field of view of 40 by 40 arcminutes, with a time resolution below 5 ms and, for bright individual objects, below 80 µs [4].

At the time of the writing of this paper, the competition for the awarding of the prime contract for the design of the spacecraft is still ongoing. Thus, one of the core challenges is accommodating both primes' designs from the WFI perspective and providing useful input to the competing prime contractors. The payload system requirements review (I-SRR) is scheduled for the end of 2026, with mission adoption expected in the second half of 2027.

1.1. WFI Configuration

The WFI payload (Fig. 2) comprises four major subsystems. The Camera Head (CH), the Primary Structure (PS) including the Baffle and Filter Wheel, a total of five Detector Electronic Units (DEUs), and two Instrument Control Units (ICUs). The PS top and bottom shells form the core mechanical structure of the WFI instrument, housing the Filter Wheel, holding the Baffle, and supporting the Camera Head. The PS assembled with the Camera Head is referred to as the Main Assembly (MA). The DEUs and ICSs are planned to be mounted on separate panels provided by the prime contractor. While the location of the ICUs is not restricted, the DEUs must be positioned in close proximity to the CH, as they will be electrically connected via flexible PCBs. The DEUs support detector operation, digitise photon detections, and convert them into an event list that is forwarded to the ICU. The ICU then forwards this data to the satellites' on-board

computers. Further, the ICU controls the WFI's global functions, such as internal temperature control of the Camera Head, Filter Wheel rotation, and positioning.

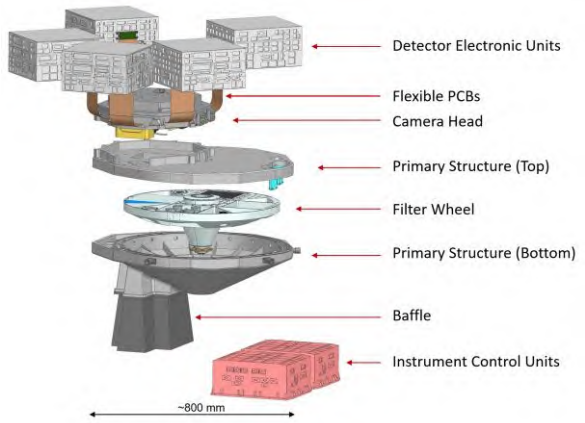


Figure 2: Exploded view of the WFI showing the Detector Electronic Units, the Camera Head, the Primary Structure, the Filter Wheel, and the Baffle.

2. PRIMARY STRUCTURE

The Primary Structure top and bottom form the core structure of the Main Assembly. It encapsulates the FW, supports the CH and the Baffle, and provides the primary mechanical interface to the payload compartment. Fig. 3 shows an exploded view of the PS's individual components and mechanical interfaces. The internal interfaces are marked in red, and the external interfaces are marked in light red. The internal design of the PS is driven by vibro-acoustic damping to protect the filters and the transfer of mechanical loads between the FW-PS and WFI-payload compartment mechanical interfaces.

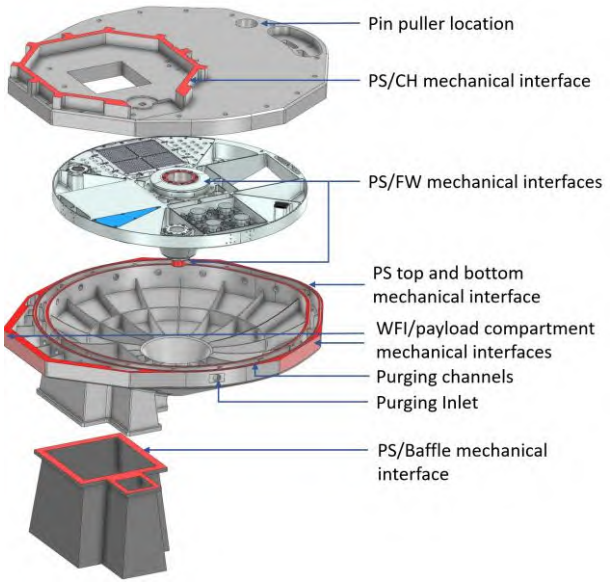


Figure 3: Exploded view of the PS top, FW, PS bottom, and Baffle.

2.1. Design of the PS top and bottom

The radial rib structures and the tangential stiffening structure are designed to fulfil these requirements, as shown in Fig. 3. In the bottom PS component, the top of the ribs follows the curved shape of the FW, with a minimal gap of 1 mm, sufficient to prevent contact between the surfaces, in accordance with the ECSS. This gap is kept as small as possible in order to reduce vibro-acoustic load propagation during launch. The ribs in the PS top are designed similarly. In the direct vicinity of the LDA filter, the rib heights are optimised to reduce vibro-acoustic loading on the filter. The current design is assumed to use AW-6061. With this assumption, the thicknesses of the ribs and skin of the PS top and bottom were set to 3 mm. Further optimisation of the PS top and bottom will be performed once the ongoing proton shielding analysis is complete. This analysis will identify locations where mass must be added to the PS, Baffle, and CH to sufficiently protect the detectors from proton radiation damage. The additional mass will determine which areas need additional stiffening to support it and where the structure can be thinned.

Fig. 3 also highlights one of the multiple purging inlets and the purging channels. A row of holes between the central volume of the PS and the purging channels has been designed to enable efficient purging of the Main Assembly during ground handling. The exact design is still being developed to establish an evenly distributed flow of dry air through the system, preventing contamination from entering or flushing it out. The protection of the filters from large differential pressures is again a driving factor, as is the provision of a sufficient flow rate to match the openings in the Main Assembly.

2.2. Design of the filter wheel

The filter wheel is being developed by the WFI consortium partners at CBK [5], the filters by the partners at the University of Palermo [8], and the calibration sources at MPE, based on eROSITA heritage [7]. With four positions for the LDA (open, closed, calibration, and LDA filter) and five for the FD (open, closed, calibration, thin filter, and thick filter), the FW accommodates a wide range of functional components. The Filter Wheel design must take the structural integrity of all into account. Further, the filter wheel needs to be balanced to reduce strain on the MGU. Since the functional components have different masses, additional mass must be added to the outer edge of the filter disc, where it is most effective in balancing the disc. This, in turn, influences the eigenmode frequencies, shapes, and mechanical loads on the functional components. To accomplish a light-weight design while providing a stiff interface for the functional components, it is made of high-strength aluminum AW-7075.

An overview of the Filter Wheel (FW) and its functional components is shown in Fig. 4. The central axle of the FW is made of the titanium alloy Ti6Al4V. It needs to have high strength to support the Primary Structure in the centre and the FW simultaneously. Further, it should have a high Youngs modulus to create a stiff support between the PS top and bottom components. The filter disk size is determined by the LDA filter size. To minimise the Filter Wheel diameter, the LDA filter frame has been optimised for size without compromising its integrity. The resulting FW has a diameter of about 620 mm.

Using a filter wheel design is especially advantageous for WFI. It allows the Motor Gear Unit (MGU), encompassing a static axle, a rotating axle, a stepper motor and the gear unit, to be placed at the centre of the filter wheel. In a trade study, WFI determined that other designs, such as a sliding mechanism, introduce greater complexity, reduce reliability, or increase mass. Further, the MGU shown above can be sealed well and has the lowest risk of molecular contamination escaping the inner cavity.

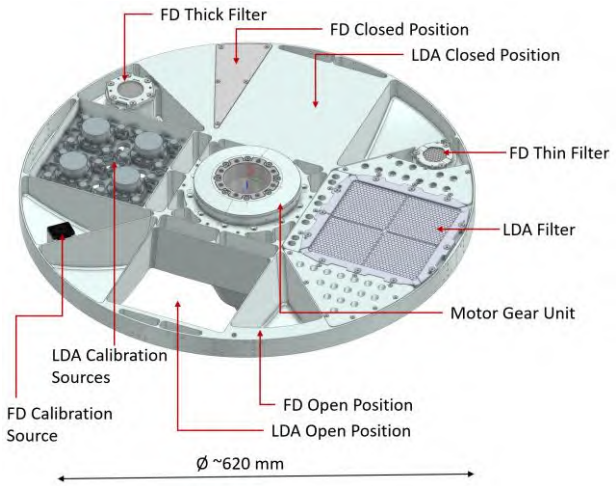


Figure 4: Depiction of the Filter Wheel and its components.

The large size of the filter disc is especially challenging for the LDA filter. With a 150 nm-thick filter membrane, it is delicate and should ideally have a very stiff, hard-mount-like interface to reduce bending loads. The LDA filter is currently being analysed against the new mechanical load environment derived from the NewATHENA mechanical loads for the Main Assembly.

A locking mechanism is baselined to hold the filter wheel in the closed position during launch until the start of operation. The selected mechanism, a pin-puller, is widely used in space applications and is highly reliable. This method is preferred to using the MGU's holding torque, which might damage the motor and gears.

3. CAMERA HEAD

To accomplish the scientific goals of WFI, the instrument will use four detectors arranged in a two-by-two grid, each with a sensitive area of about 7 cm by 7 cm. These are called the four Large Detectors (LDs), which are mounted on the Detector Array (DA) frame and their iso-static mounts (Fig. 5). This assembly is called the Large Detector Array (LDA), resulting in a sensitive area of 14 cm by 14 cm. For high-count-rate observations of especially bright objects or fast transient events, an additional detector with an active area of about 1 cm by 1 cm and a split readout is included in the CH. This detector, called the fast detector (FD), is shown in Fig. 6.

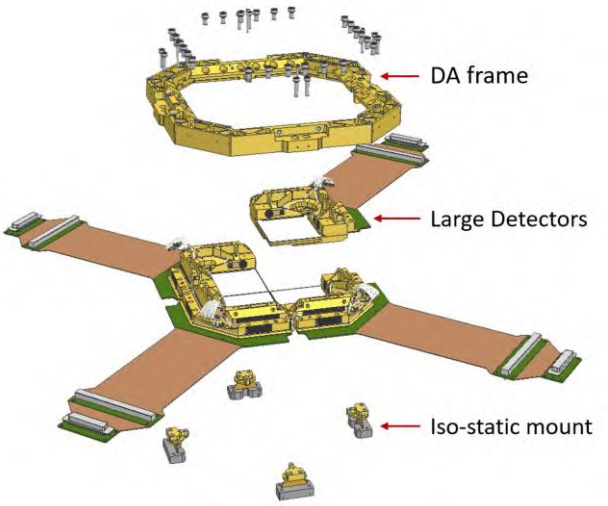


Figure 5: Exploded front-side view of the LDA showing the four LDs in a mosaic configuration, the DA frame that holds all four LDs, and the four iso-static mounts connecting the LDA to the rest of the Camera Head.

These five detectors use silicon-based depleted p-channel field-effect transistor (DEPFET) sensors [8]. To read out the DEPFET sensors, application-specific integrated circuits (ASICs) [9], together with additional discrete electronic components in the proximity of the detectors, form the front-end electronics (FEE).

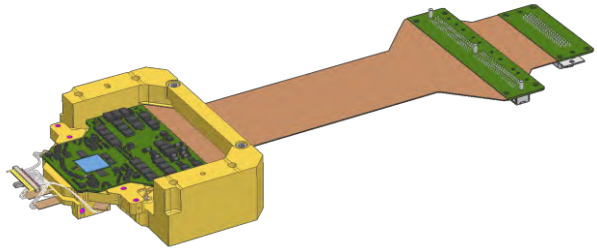


Figure 6: Backside view of the Fast Detector.

To cool the front-end electronics and the DEPFET sensors, two surfaces are provided on the top of the Camera Head as thermal interfaces. In Fig. 7, the thermal interfaces are depicted. The top surface of

the blue component provides the mounting area for the thermal hardware that cools the DEPFET detectors to -100°C. The top surface of the orange component serves as the mounting interface for the thermal hardware, cooling the front-end electronics to -30°C.

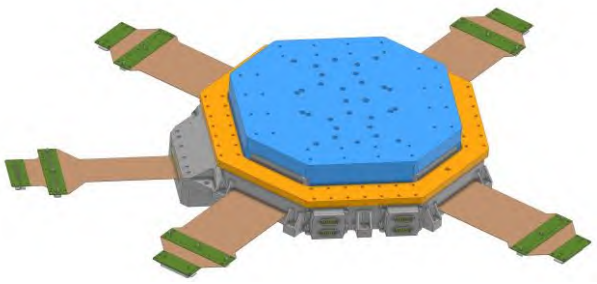


Figure 7: View of the thermal interfaces on the Camera Head for cooling the DEPFET sensors (blue) and the front-end electronics (orange).

The LDA, FD and thermal interfaces mounted to the Main Structure form the Camera Head. The illuminated side of the assembled CH is shown in Fig. 8 with the Camera Head Main Structure in grey, the Fast Detector on the left, and the Large Detector Array in the centre. The thermal interfaces, shown in Fig. 7, are on the backside. The front-end electronics, DEPFETs, and the Camera Head Enclosure are thermally isolated from each other. To accommodate the three temperature regimes of -30°C on the FEE, -100°C on the DEPFET, and approximately 10°C on the Main Structure, the components are thermally isolated from each other. A set of graphene thermal straps provides the thermal link between the DEPFETs, the FEE, and their respective thermal interfaces.

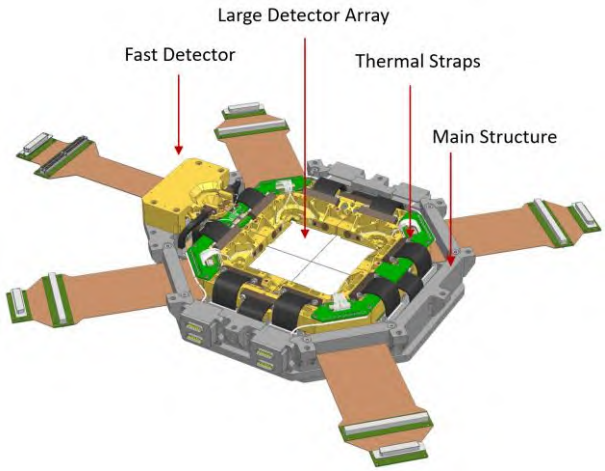


Figure 8: Depiction of the integrated Camera Head with the Large Detector Array and Fast Detector.

3.1. Matching coefficients of thermal expansion in the Camera Head

Next to the LDA and FD filters, the DEPFET sensors are another sensitive component. The Large Detector Array and Fast Detector material choices are largely driven by the coefficient of thermal expansion (CTE) of the DEPFET sensors. To match the CTE of Silicon (~2.6×10^{-6} 1/K), molybdenum (~4.7×10^{-6} 1/K) was chosen. It has good mechanical properties without stressing the DEPFET sensors under thermo-elastic loading. The major disadvantages of molybdenum are its high density, which results in a high system mass, and poor machinability. For heritage reasons, molybdenum was chosen in the baseline design.

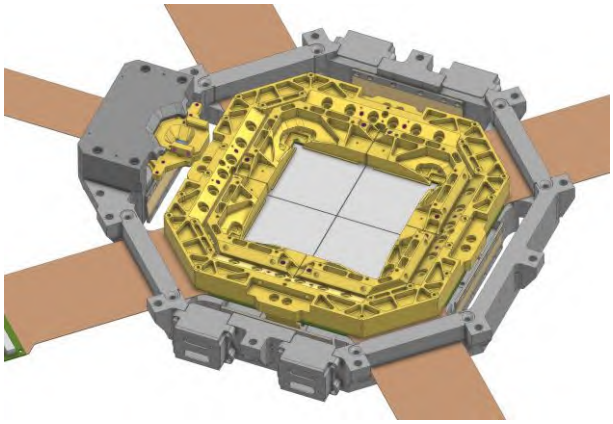


Figure 9: Depiction of the Camera Head, with components of aluminum in dark grey, of molybdenum in yellow, and of silicon in light grey.

Fig. 9 shows the molybdenum components in yellow. The use of molybdenum extends from the sensors to the thermo-elastic connection between the LDA and the Camera Head Main Structure, which is made with iso-static mounts, as shown in Fig. 5.

3.2. Structural accommodation of three temperature regimes in the Camera Head

A core challenge in the thermo-mechanical design of the WFI is accommodating three temperature regimes within the Camera Head. The Main Structure, assumed to be at about 10 °C; the FEE, which requires a temperature of -30 °C at the thermal interface; and the DEPFET, which requires temperatures as low as -100 °C at the thermal interface, need to be thermally isolated from one another while in close proximity, as depicted in Fig. 10 [10]. Using glass fibre-reinforced plastic (GFRP) tubes and blades from G10-CR, these regimes can be effectively isolated while supporting the heavy molybdenum components.

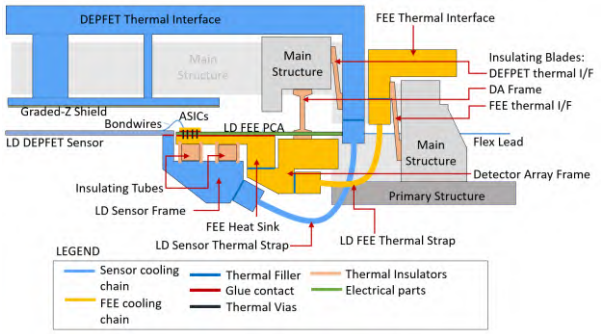


Figure 10: Schematic cross-section of the CH highlighting the three temperature regimes of the DEPFET (blue), the FEE (orange), and the Main Structure (light grey).

Utilising GFRP tubes as mechanical connectors between the LD Sensor Frame and the LD Heat Sink, as shown in the middle of Fig. 10, has proven effective. Using 7 G10-CR tubes with a free length of about 7 mm and a wall thickness of 1.5 mm per LD provides a good thermal insulation between the two temperature regimes while maintaining a high structural stiffness. This is especially important because the structure around the LD DEPFET sensor is supported by these tubes, providing the necessary structural stability for the bond wires that span the gap between the DEPFET and the ASICs to withstand launch [11].

3.3. Iso-static mounts of the Camera Head

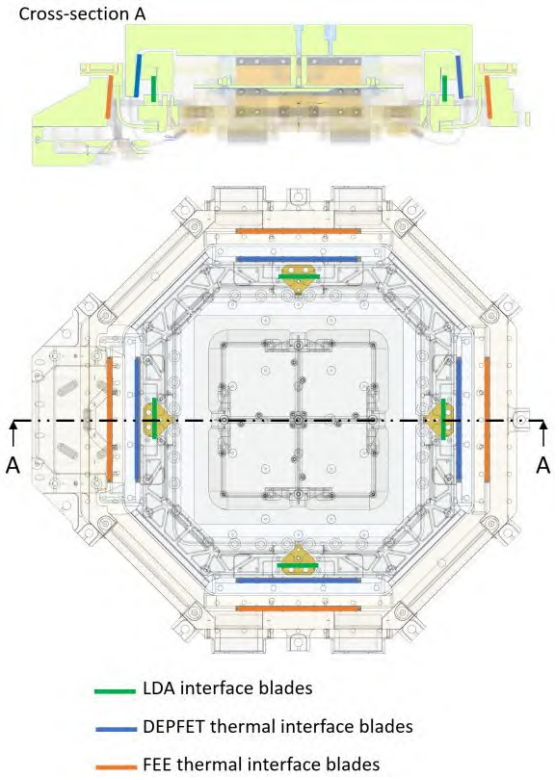


Figure 11: Transparent view of the camera head highlighting the placement of the GFRP blades supporting the LDA (green), the DEPFET thermal interface (blue), and the FEE thermal interface (orange).

The GFRP blades that connect the LDA, the DEPFET thermal interface, and the FEE thermal interface to the Proton Shield pose another challenge. Each component is connected to the Proton Shield using four G10-CR blades, offset by 90 degrees from one another. The arrangement of the 1 mm thick blades is shown in Fig. 11. This results in a thermo-elastic design that is well-suited to accommodate the thermal interfaces and LDA as they expand and contract relative to the centre of the focal plane. Further, it provides good internal thermo-elastic decoupling between the detectors and the thermal interfaces. However, when subjected to an external force acting in a specific direction, this arrangement of GFRP blades behaves very stiffly. Thus, an external force acting on the thermal interfaces can cause a misalignment of the entire WFI MA and, in turn, misalignment of the detectors. As a consequence, interface control requirements that limit external forces introduced by the payload compartment into the Camera Head have been established.

3.4. Thermal gradients within the Camera Head

Mechanically decoupling the CH thermal interfaces from the detectors and reducing thermal gradients between them are drivers of the thermal concept. This decoupling aims at mitigating the introduction of external forces into the LDA and FD detectors. The temperature at the respective thermal interfaces is driven by the maximum temperature of the DEPFET sensor active area and the temperature of the ASICs on the FEE. Raising the required thermal interface temperatures allows prime contractors to raise their radiators' operating temperatures. Since the heat-rejection capability of the radiators is approximately proportional to T^4, even slight temperature increases can either reduce the radiator area needed or increase the heat-rejection capability for the same radiator area.

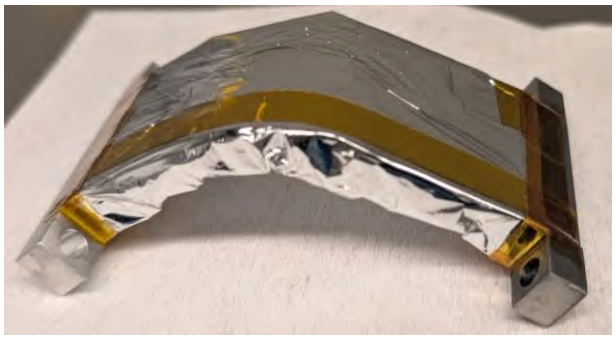


Figure 12: LD thermal strap modified with a fully sealed mylar wrapping and integrated Polyimide filter for venting.

To reduce the thermal gradient between the thermal interfaces and the internal components, the thermal straps, shown in Fig. 12, are layered graphene thermal straps. They are especially light, occupy only a small volume, and have very high thermal conductance. The displayed thermal strap has a

thermal conductance of ~1.4 W/K at 200 K, weighs ~70 g, and has a length of ~ 10 cm. As graphene thermal straps are a relatively new technology, and their compliance with the WFI requirements needs to be guaranteed, a thorough technology readiness assessment (TRA) has been conducted [12]. Within the TRA, the thermal straps had to be further developed to comply with the WFI particle-contamination requirements. Fully sealing the free length of the thermal straps with a thin Mylar foil and implementing a Polyimide filter with an 8 µm pore size for venting during the launch phase showed a significant reduction in particle contamination.

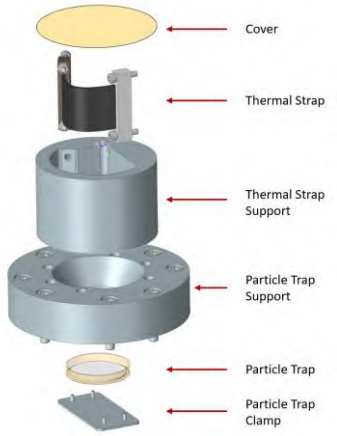


Figure 13: Exploded view of the LD thermal strap particle test set-up.

Comparing Fig. 14 with Fig. 15, the reduction in contamination is visible. For this test, the thermal straps were mounted in an enclosed structure (Fig. 13) equipped with a sticky particle trap measuring 47 mm in diameter (witness area: 17.35 cm²). On the shaker, the thermal straps were exposed to the derived qualification level launch loads. After the vibration test, the particle traps were evaluated using a microscope. For the evaluation shown in the following plots, it was assumed that every particle is electrically conductive, since the materials prone to shedding particles on the thermal straps are all electrically conductive.

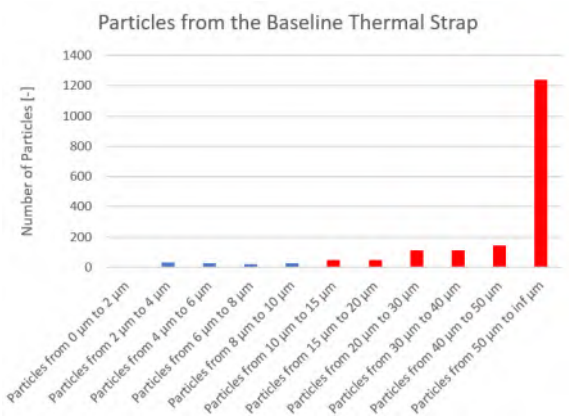


Figure 14: Particle count on the particle trap plotted over particle size for the unsealed baseline thermal strap, with non-compliant particles marked in red.

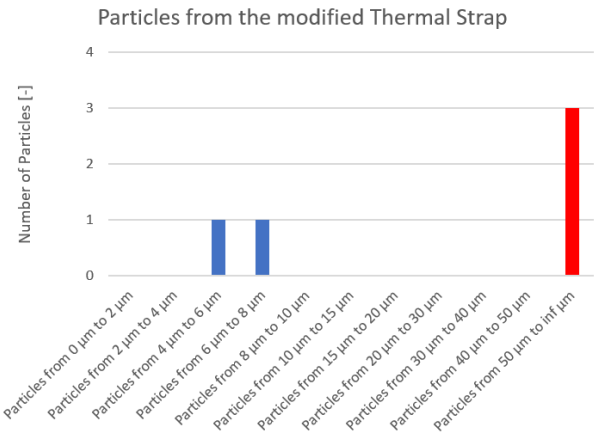


Figure 15: Particle count on the particle trap plotted over particle size for the modified thermal strap, with non-compliant particles marked in red.

Investigations into full compliance with the WFI contamination requirements, which prohibit electrically conductive particles ≥ 10 µm, are currently being finalised.

3.5. Straylight mitigation

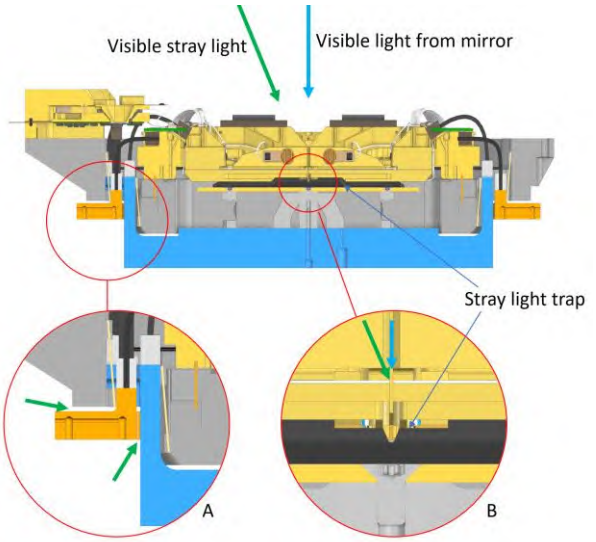


Figure 16: Cross-section view of the Camera Head, highlighting potential stray light paths to entering directly through the mirror (blue) or reflections or gaps in the payload compartment (green).

Small gaps in the camera head could allow visible stray light to reach the detectors. Two general ways for visible light to enter the detector area have been identified. One way is that it could be focused by, or shine through, potential gaps in the main mirror (highlighted in blue in Fig. 16). The second identified possibility is that reflections enter the system either through the optical path or through openings in the payload compartment (highlighted in green in Fig. 16). These light rays could then enter the Camera Head through small gaps in the CH, as shown in Fig. 16, detail A, or through the small gap between the four LDs, as shown in Fig. 16, detail B.

To reduce the detection of visible photons hitting the mirror-facing side of the detector, the detector is coated with aluminum on that side. The other side of the detector is uncoated and thus up to 40000 times more susceptible to unwanted visible photons interacting with it [13]. To ensure the payload's scientific performance, photons incident on the uncoated side of the detectors must be avoided.

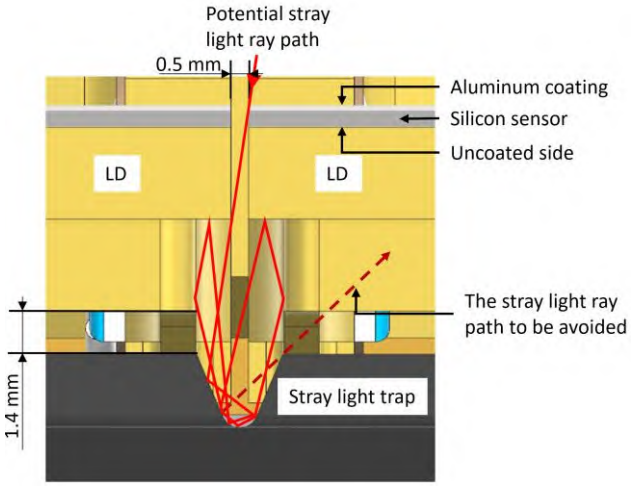


Figure 17: Functional concept of the stray light trap trying to avoid light following the dashed path.

In a first attempt at stray light mitigation, a stray light trap has been designed, with its intended functionality illustrated in Fig. 17. The concept uses a geometry that reflects a light ray until it is absorbed. The material is chosen based on its high absorption coefficient to maximise the likelihood of absorbing photons passing through the gap between the detectors. This design has not been verified yet and would still require gaps between the detectors and the stray light trap. Stray light entering through other openings remains an unresolved issue for this design.

4. CAMERA HEAD REDESIGN

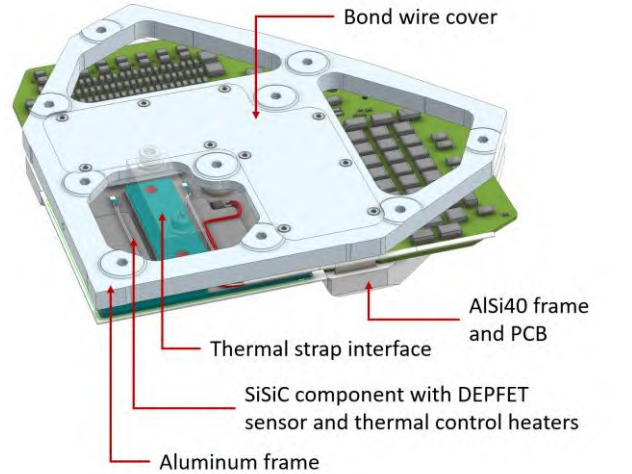


Figure 18: CAD depiction of a new LD design concept with a DEPFET sensor that is full-face glued to a SiSiC structure.

Building on lessons learned during the development of the baselined CH, an improved design is being developed. Drawing on experience from LD design, manufacturing, assembly, handling, and testing, a new design for the LD (Fig. 18) has been developed. Pending issues, such as stray light mitigation and proper accommodation of heaters for temperature fine control on the sensor, were incorporated.

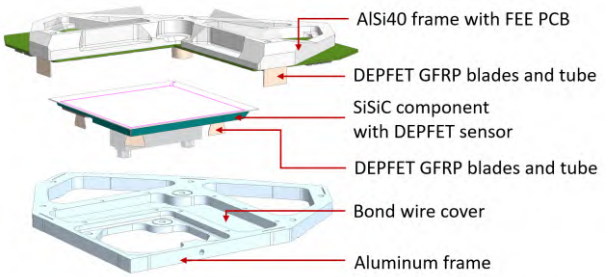


Figure 19: Exploded view of the new LD design, highlighting the individual components and the thermo-elastic GFRP mounting blades and tubes.

To match the CTE of the DEPFET sensor to its support structure, SiSiC is used instead of Molybdenum. The SiSiC part is glued to almost the entire face of the sensor. This provides a simpler support for the DEPFET sensor and achieves a more uniform temperature distribution across the sensor's active area. Further, it protects the backside of the sensor from stray light. This also creates space for a thermal strap interface directly at the sensor and for accommodating heaters to stabilise the temperature during observation. To match the CTE of the PCB and the PCB support structure, an AlSi40 alloy has been chosen to reduce thermo-elastic stresses. The DEPFET and PCB support structures are suspended individually from an aluminum frame using GFRP tubes and blades, visible in Fig. 19. The individual suspension of the components from the frame and the use of lighter materials reduce the mechanical load on each GFRP blade and tube, allowing them to be thinner. For example, the G10-CR blades supporting the detector are 0.3 mm thick, thereby improving thermal decoupling from the aluminum frame. The result is an LD that is approximately 60% lighter than the baseline design.

To assess the viability of the new design in the WFI context, a trade study was carried out. This included a qualification-level vibration test (Fig. 22), a thermal cycling test of the full-face glued DEPFET sensor, and a performance test of an existing functioning LD with a SiSiC plate glued to it. The vibration test, with the loads shown in Figs. 20 and 21, was successful and demonstrated the structural integrity of the new LD design and the delicate bond wires when exposed to launch loads.

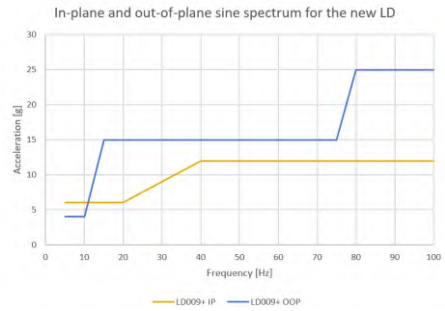


Figure 20: In-plane and out-of-plane qualification level sine spectra for the new LD design.

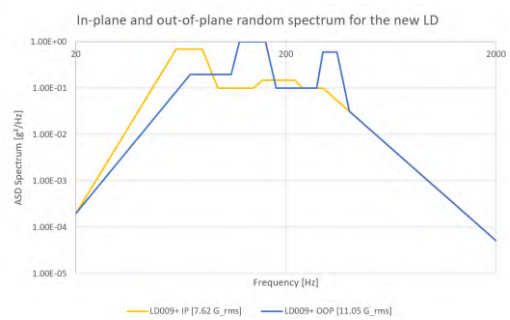


Figure 21: In-plane and out-of-plane qualification level random spectra for the new LD design.

The trade study showed that full-face glueing of the sensor is feasible, that detector performance is unaffected, and that the new design can withstand the estimated mechanical launch loads. Thus, WFI decided to further develop the new LD design. It allows for a lighter design, improved thermal architecture, better accommodation of thermal fine-control heaters, and a full-face glued design that eliminates the risk of stray light hitting the sensor's uncoated surface. Additionally, the full-face glued sensor reduces the thermal gradient across the active pixel area. Within the next year, WFI plans to conduct further tests and mature the new LD and CH design.

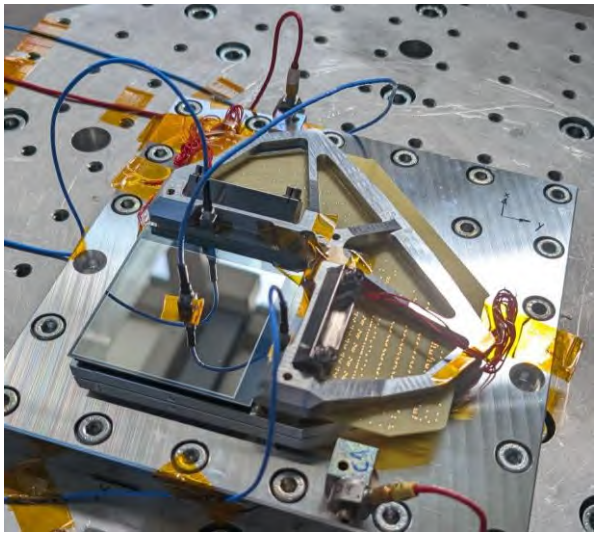


Figure 22: A structural prototype of the new LD design on the shaker for vibration testing.

5. CONCLUSION

To conclude, in the current phase of ATHENA's transition to NewATHENA, WFI has a good baseline mechanical and structural design. At the moment, the updated set of requirements needs to be implemented, and the existing component designs, especially the filters, need to be checked against them. The baseline design presented in this paper is continually updated as new information and analysis results become available, with the greatest impact on the mechanical and structural design of the Primary Structure expected to come from the ongoing proton-shielding analysis. The most recent improvement is the redesign of the Camera Head and detectors, reducing weight and complexity while improving its compliance with the WFI requirements. Within the next year, WFI expects to progress the new Camera Head design in time for its prototyping phase.

6. ACKNOWLEDGEMENTS

We are grateful to the whole NewATHENA WFI project team and all MPE colleagues, who contributed to the development, assembly, and testing. Further thanks go to the NewATHENA team at ESA for their support. The work was funded by the Max Planck Society and the German space agency DRL (FZK: 50 QR 2501).

7. REFERENCES

[1] Maximilien J. Collon, et al. "Silicon pore x-ray optics for the NewAthena telescope", Proc. SPIE 13093, *Space Telescopes and Instrumentation 2024: Ultraviolet to Gamma Ray*, 1309319 (21 Aug 2024); https://doi.org/10.1117/12.3019675Sdsd

[2] Kirpal Nandra et al., “The hot and energetic universe: A white paper presenting the science theme motivating the Athena+ mission,” (2013)

[3] Barret, Didier, et al. "The Athena X-ray Integral Field Unit: a consolidated design for the system requirement review of the preliminary definition phase." *Experimental Astronomy* 55.2 (2023): 373-426.Eraerds, Tanja, et al. "Enhanced simulations on the Athena/WFI payload background." *Space Telescopes and Instrumentation 2020: Ultraviolet to Gamma Ray*. Vol. 11444. SPIE, 2020.

[4] Meidinger, N. et al, "Development status of the wide field imager instrument for Athena", Proc. of SPIE, Vol. 11444 (2020)

[5] Polak, Szymon, et al. "Design and acoustic tests of the ATHENA WFI filter wheel assembly development model towards TRL5." Journal of Astronomical Telescopes, Payloads, and Systems 9.2 (2023): 024002-024002.

[6] Barbera, Marco, et al. "Athena WFI optical blocking filters development status towards the end of the payload phase-A."

[7] Michael J. Freyberg, et al. "Calibration of the eROSITA calibration source: design and trade-off analysis", Proc. SPIE 8443, Space Telescopes and Instrumentation 2012: Ultraviolet to Gamma Ray, 844351 (27 Sept 2012); https://doi.org/10.1117/12.927085
[8] Bähr, Alexander, et al. "Development of DEPFET active pixel sensors to improve the spectroscopic response for high time resolution applications." Space Telescopes and Instrumentation 2014: Ultraviolet to Gamma Ray. Vol. 9144. SPIE, 2014.
[9] Schweingruber, Anna-Katharina, et al. "The VERITAS 2.3 readout ASIC for the ATHENA Wide Field Imager." *Space Telescopes and Instrumentation 2024: Ultraviolet to Gamma Ray*. Vol. 13093. SPIE, 2024.
[10] Saraf, Anirudh Mukund, et al. "Thermal design and control of Athena Wide Field Imager (WFI) camera head." *Space Telescopes and Instrumentation 2024: Ultraviolet to Gamma Ray*. Vol. 13093. SPIE, 2024.
[11] Frank, Jintin, et al. "Structural analysis of Athena WFI Large Detector Array." Space Telescopes and Instrumentation 2020: Ultraviolet to Gamma Ray. Vol. 11444. SPIE, 2020.
[12] Möller, Jan Philipp, et al. "Technology readiness assessment of graphene thermal straps for the WFI payload." *Advances in Optical and Mechanical Technologies for Telescopes and Instrumentation VI*. Vol. 13100. SPIE, 2024.
[13] Behrens, Annika, et al. "Characterisation of the NewAthena WFI DEPFET detectors' on-chip optical blocking filter", Proc. SPIE 14146, Space Telescopes and Instrumentation 2026: Ultraviolet to Gamma Ray, 141462N (17 Aug 2026); https://doi.org/10.1117/12.3104479

TRIFILAR HELICOID ANTENNA DESIGN, PROTOTYPING AND TESTING

M. Longato[(1) *], **G. S. Aglietti**[(1)], **L. Marcaccioli**[(2)]

[(1)] *Space Institute, University of Auckland, Auckland,1010, New Zealand, Email: mattia.longato@auckland.ac.nz*
(2) RF Microtech Srl, Perugia, Italy, Email: marcaccioli@rfmicrotech.com

KEYWORDS

Deployable structures, helical antenna, damping mechanism

ABSTRACT

Deployable helical antennas are widely utilized in space systems operating in the VHF and UHF frequency ranges due to their ability to deliver high gain, broad bandwidth, and pronounced directivity with circular polarization, all while keeping manufacturing complexity relatively low. Usually, these deployable antennas consist of a main, foldable, non-conducting isolated structure which acts as the helicoid support for the main conducting wire element. This paper presents the design and prototyping processes used to develop a novel resettable trifilar helicoid deployable antenna. Three independent helix-shaped metallic wires fulfil a dual role: functioning both as the deployable support structure and as the primary radiating conductor within a single integrated system. The manufacturing process of the helix-shaped metallic wires is presented in this work, together with the corresponding numerical simulations. These are carried out to guarantee the required electrical performance and to achieve the desired deployed stiffness of the antenna, defined by a minimum natural frequency of vibration exceeding 1 Hz. Furthermore, various functional deployment tests of the antenna are performed and illustrated in this paper. In particular, the deployment accuracy tests need to meet the requirement of ±1 mm of maximum difference between real deployed structure and its nominal dimensions. Finally, these deployment tests are used to validate the functionality of the deployment damper and the incorporated resettable mechanism. On one hand, the damper is required to control the deployment velocity, reduce the final mechanical shock at the end of the stroke, and to ensure controlled deployment dynamics. On the other hand, the resettable mechanism enables easy stowage of the antenna, allowing repeated deployments during qualification and acceptance testing campaigns.

1. INTRODUCTION

The electromagnetic performance of a helical antenna is determined by key geometrical parameters such as helix diameter, pitch or turn spacing, and the number of turns. These parameters influence whether the antenna operates in normal mode or axial mode. In normal mode, which occurs when the helix dimensions are much smaller than the wavelength, the antenna radiates a linearly polarized wave in a direction perpendicular to the helix axis [1]. However, this configuration produces low gain and is therefore generally unsuitable for satellite communication applications. On the other hand, axial mode is achieved when the circumference of the helix approaches one wavelength, typically between 0.75λ and 1.33λ, and the pitch angle is between 12° and 15°. In axial mode, the antenna radiates circularly polarized waves along its longitudinal axis, with gain increasing as a function of the number of turns and total helix length [2].

Three types of antenna shapes are commonly used: the helix, conical horn and the Conical Log Spiral (CLS). Most of these systems are passively deployed, which does not use any active components to deploy in orbit. Different performance characteristics can be achieved from the different shapes as well as varying the conductor pitch, diameter and height of the helix and number of turns [3]. For example, a hyper-compact collapsible antenna which can fit in a 0.5U CubeSat volume has been constructed using a framework of fiberglass and thermoplastic pultruded tape strips. For stowing, the structure needs to be rolled up into a self-deploying ball without creating plastic deformation or damaging the structure [4]. This compact and lightweight design has a deployed to stowed ratio of 300:1 with an overall assembly weight of 300 g. An origami folding technique has been implemented in another example of packable and tuneable multi-radii helical antenna [5]. This antenna has two separate foldable sections with the conductor wire wound around the perimeter. The structure is divided into two independent sections with different radii and the capability to adjust the height independently. In contrast, a conical-shaped spiral antenna is made from an Astro quartz-epoxy shell with the conductor element wrapped around the main cone structure in a logarithmically progressive manner [6]. To collapse the antenna, the cone structure has

been divided into sections with hinges, such that it can be flattened and then folded for stowage. Concerning the helix type of antenna, other prototypes have the helicoid spiral acting as the main supporting structure and the conductor. This configuration has a stiff inner core with no electrical conductivity and a conductive coating applied on the surface with no mechanical stiffness [7]. Similarly, other prototypes use fabric membranes to increase the structural rigidity together with the main coil. In this case, the helicoid structure itself is manufactured to twice the extended length and compressed before slotting it into the fabric membrane, acting as a preloading mechanism increasing the stiffness of the antenna [8]. Similar passive helicoid antenna systems are already available in the market with possible customizations and operational range between 400 - 3000 MHz [9]. Other active antenna prototypes use stepper motors to control the deployment and adjust the final operating length of the helicoids [10]. Such systems ensure that the height and diameter are deployed correctly, however a more complex stowage technique is required. This deployment precision comes at the cost of a higher system mass, power consumption, mechanical complexity, and introduces various potential points of failure to consider in the antenna design.

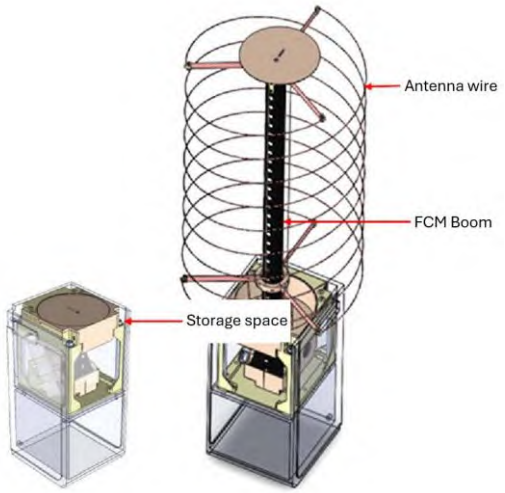


Figure 1: Deployable VHF/UHF helix antenna [10].

2. OBJECTIVES AND SCOPE

The purpose of this project is to develop an engineering model prototype of a passive deployable helicoid trifilar antenna. The design must comply with CubeSat dimensional constraints, with a height limit of the envelope of 20 mm. The antenna must be composed of three identical metal wires formed into helicoidal shapes and arranged at the base with a 120° phase offset. These three wires need to perform two functions: they act as the main deployable structure and as the electrical conductors.

The final antenna geometry must remain within the specified tolerances: the helicoid wire pitch, the final deployment height, outer diameter, concentricity and cylindricity of the perimetral antenna envelope must all remain within ±1 mm of their nominal values. In addition, the repeatability of the antenna deployment must be ensured, meaning that the specified tolerances are met in every deployment, regardless of how many times the antenna is stowed and deployed. Finally, the antenna deployment dynamics must be smooth and controlled, preventing any shock at the end of the travel.

The initial antenna design approach and electrical parameters are discussed in Section 3. The development of the first prototype is presented in Section 4, while Section 5 describes the helicoid forming process along with various bracing techniques supported by computational structural analysis. Finally, Section 7 reports the results of the deployment tests conducted to verify compliance with the requirements, including the accuracy and repeatability of the deployed antenna shape.

3. ELECTRICAL PERFORMANCE AND GEOMETRICAL DESIGN

The antenna's electrical performance, including gain and operating frequency band, dictates its geometrical configuration. Based on these requirements, parameters such as wire pitch, antenna height, and the outer diameter of the cylindrical envelope can be defined, within some range. The antenna is designed to operate in the UHF band between 0.86 GHz and 0.93 GHz, corresponding to IoT applications. In this design, the helix radius is set to 40 mm. With a pitch of nearly 70 mm a total length of 260 mm is reached in a few turns. These parameters are selected to approach axial-mode operation, ensuring suitable circular polarization and directive radiation characteristics.

The design of the deployable trifilar helix antenna is driven by the need to achieve circular polarization with stable radiation characteristics while remaining compatible with CubeSat volume constraints. In this configuration, three identical helicoidal conductors are symmetrically arranged around

the antenna axis with an angular separation of 120°, forming a tri-helix structure. This geometry enables the generation of circular polarization through the proper excitation of the three arms, typically with equal amplitude and a progressive phase shift of 120°, thereby producing a rotating electromagnetic field along the antenna axis.

The feeding network represents another critical aspect of the trifilar configuration. To ensure proper circular polarization, the three helices must be excited with precise phase relationships. This can be achieved using a three-way power divider combined with phase-shifting elements or through an integrated feeding structure at the antenna base. The design must ensure equal amplitude distribution and minimal phase error, as any deviation can significantly degrade the axial ratio and introduce polarization ellipticity.

Finally, the interaction between the electrical and mechanical design must be carefully considered. Variations in the deployed geometry such as deviations in helix diameter, pitch, or alignment can lead to performance degradation, particularly in terms of gain and axial ratio. Therefore, strict manufacturing tolerances and highly repeatable deployment behaviour are essential to ensure consistent antenna performance across multiple deployment cycles.

At this stage, the work is divided into two main phases. On one hand, the manufacturing of the three antenna helicoids is addressed; on the other hand, various bracing techniques are investigated and implemented to deploy the antenna and maintain the three metal wires in position.

4. HELICOID MANUFACTURING

The helicoid formation process is crucial, as it determines the antenna's overall geometry. First, the helicoid forming process must be repeatable, since the three wires need to have identical shapes.

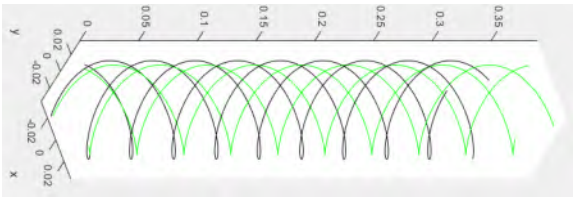


Figure 2: Free wire shape, no preload (green) and preloaded (black) wire shape of the antenna helicoids.

The implemented helicoid forming approach involves manufacturing a slightly longer helix with a smaller diameter, referred to as the construction / free wire shape helicoid (green in Figure 2). During the antenna assembly process, these helicoids are slightly compressed, allowing them to act as preloaded springs (black line in Figure 2). This ensures that the final antenna shape is achieved and maintained with a desired axial preloaded stiffness. Indeed, Figure 2 shows the theoretical free wire shape type of helicoids in green whereas the required antenna shape is illustrated with the black line.



Figure 3: Single helicoid compressed in stowed configuration.

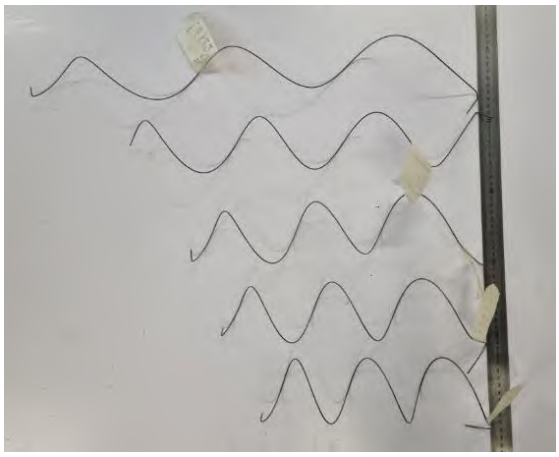


Figure 4: Various manufactured helicoidal wires.

A custom machine has been constructed in our laboratory, consisting of a rotating mandrel to which one end of the wire is firmly attached, while the other end is rigidly connected to a constant pulling force. With this setup, both the mandrel diameter and the angle of the pulling force can be finely adjusted within a specific range.

The mandrel diameter directly determines the antenna's outer diameter, whereas the pulling force angle mainly affects the wire pitch length and therefore the final length of the helicoid. Various diagrams were created experimentally to relate the mandrel diameter and the pulling force angle as a function of the selected steel wire diameter. As shown in Figure 4 several iterations of the helicoid forming process were necessary to achieve the desired final helix shape of the wire. The final goal is to create a metal conductive wire that can be stored at a

minimum height, as shown in Figure 3, and then redeployed a certain number of times to the original helicoid shape. The repeatability of the wire forming process is fundamental and crucial to ensure that all wires have the same curvature, helicoid pitch, and outer diameter.

5. ANTENNA STRUCTURE AND BRACING TECHNIQUE

Several alternative concepts for retaining the antenna structure were evaluated, including bistable rotary joints, bistable tape-spring joints, elastic detents, and tension springs. However, approaches relying on additional components were discarded, and it was decided to control the deployment and the antenna final shape through mechanical damping elements and structural bracing. Two similar bracing technique are investigated and shown in Figure 5 and in Figure 6. With these bracing configurations, the antenna height is divided into three sections of equal length. Each section includes a flexible triangular connecting element designed to maintain the nominal spacing between the helicoids. On one hand, the internal pyramid bracing technique shown in Figure 5 consists of three groups of concentric pyramidal wires which are arranged from each of the three central points and tighten at the antenna base.

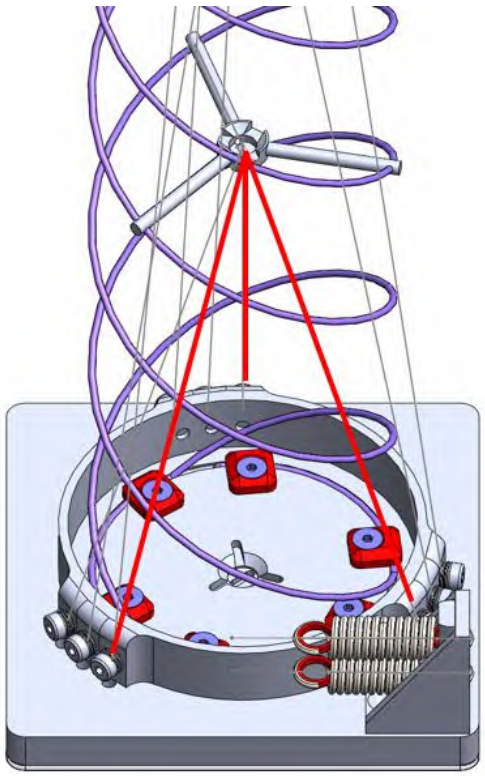


Figure 5: Internal pyramid bracing

This bracing configuration ensures that the central point of the three antenna sections remains at the correct height, centred and aligned with the vertical axis also ensuring the concentricity of the three helicoids. However, first- and second-order buckling modes of the antenna, resulting in “C” or “S” shaped deformations, cannot be entirely avoided. This wire-lashing technique uses nine wire strands arranged in three groups of different lengths that must be securely accommodated at the base during the antenna stowage process. This makes the procedure challenging and significantly increases the risk of the wires becoming tangled during deployment. In addition, due to the triangular pyramid configuration shown in Figure 5, the Dyneema lines must pass from the inner side of the antenna to the outer side in order to be anchored to the base with the widest possible footprint.

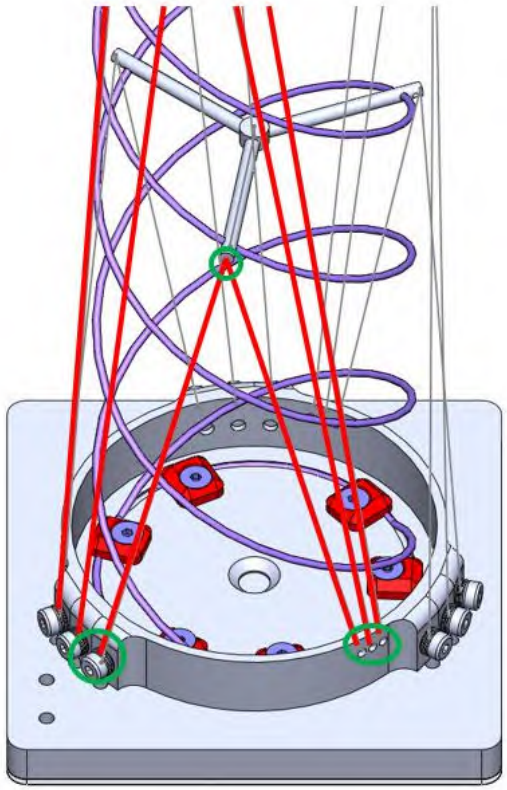


Figure 6: External pyramid bracing.

On the other hand, the external pyramid bracing technique is illustrated in Figure 6. With this approach, the antenna is also divided into three equal length sections. Each antenna section uses three pairs of wire strands arranged in a triangular configuration. These wires connect the three central stellar arms and the antenna base. A detailed bracing scheme is shown in Figure 6. With this configuration, the total number of wire strands increases to eighteen, which significantly raises the risk of tangling during deployment. However, the antenna

buckling previously occurring with the configuration shown in Figure 5 is no longer an issue. This is because the tilting of the central stellar sections can be now minimised by precisely adjusting the wire length of the triangles and by using the stellar elements as control points for the antenna height and concentricity.

Each of these bracing techniques presents various advantages and disadvantages. A common issue, however, is that the large number of long wires running along the antenna poses a significant challenge during the stowing process, as it requires meticulous arrangement at the antenna base. A major problem also arises during deployment, since the wires can repeatedly become entangled with each other and with other antenna components, such as the stellar spacer arms located at mid height and the base itself.

5.1. FINAL BRACING TECHNIQUE

For these reasons, a completely different type of bracing arrangement is required, and therefore a triangular wiring network applied along the antenna structure is investigated. As shown in Figure 7, the triangular net configuration connects two consecutive metal wires at three points, a, b, and c, forming the corresponding angles α, β and γ. To determine the optimal arrangement of the Dyneema bracing wires, a finite element (FE) analysis simulation is implemented in Ansys APDL.

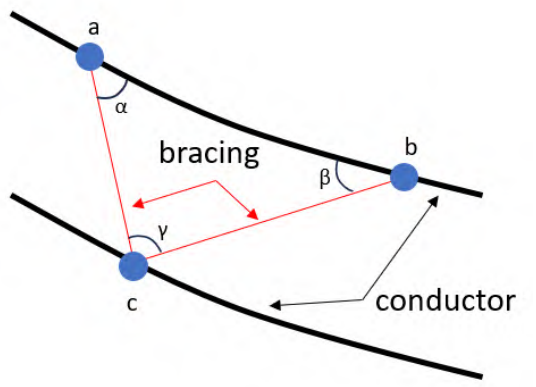


Figure 7: Triangular bracing net technique.

The simulation begins by importing the slightly longer formed helicoid wires, as manufactured from the description in Section 4. Various anchor points are then identified along the metal helicoid wires to create a triangular mesh as depicted with the blue points in Figure 7. A specific rigid displacement is then applied at each blue anchor point. This rigid displacement moves each blue anchor point of the three helicoids from the free / non-compressed configuration toward their final positions, creating the preloaded configuration by slightly compressing the helicoids. At this stage, a stress field is generated in the metal wires and consequently the direction of the resultant of the reaction forces acting on each of the preselected blue anchoring points indicates the orientation along which the Dyneema wire should be placed to brace the antenna.

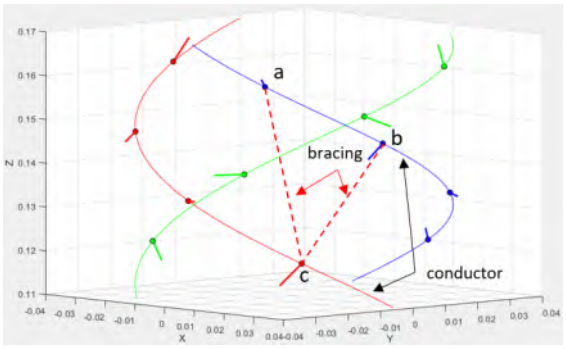


Figure 8: Antenna bracing pattern.

The three metal helicoid wires are schematically shown in red, blue and green in Figure 8. As a result of the simulation, the reaction forces that are acting on each anchoring point are illustrated with the respective colour. Therefore, the selected triangular bracing scheme is depicted with the dashed red line connecting the points a, b, and c.

The antenna bracing, in addition to ensuring the correct alignment between the wires, must also provide sufficient axial stiffness together with the applied preload in order to guarantee the minimum natural frequency of lateral oscillation in the deployed configuration. This requirement is very important to ensure that any oscillations of the deployed antenna do not interfere with the satellite attitude control system (ACS) during an orbital manoeuvre. In general, a safe requirement requires the natural frequency of a satellite appendage to be higher than 1 Hz, but this requirement can vary from application to application. Consequently, a pre-stressed modal analysis is performed to investigate the natural modes of the braced structure.

6. DYNAMIC MODEL OF THE ANTENNA CENTRIFUGAL FRICTION BRAKE

The aim of this centrifugal friction brake is to develop a passive mechanism that controls the deployment speed of the antenna without using an active motor or electronic control.

Table 1: Centrifugal break parameters.

Parameter	value	Units
n° of shoes (N)	2	
Shoe mass (m_s)	0.1	Kg
Housing radius ($r_{housing}$)	0.032	mm
Shoe radius (r_s)	0.03	mm
Return spring stiffness K_{return}	10	N/m
μ	0.4	
$c_{bearing}$	$1e^{-5}$	Nms

This idea uses the energy stored in the antenna spring to drive a rotating element through a wire. In Figure 9, the proposed centrifugal brake is schematised to passively control the antenna deployment speed.

The main objective of the model is therefore to describe the complete dynamic behaviour of the antenna, from the initial release of the spring to the end of deployment. In particular, the centrifugal brake should automatically increase its braking torque as the rotor speed increases and reduce the torque as the rotor slows down. This allows the mechanism to regulate its deployment speed while using only passive mechanical components.

As the antenna deploys, the blue wire accelerates the rotor underneath. At low rotational speeds, the centrifugal masses (shoes) remain close to the rotor and the brake produces little or no friction. As the rotor speed increases, the centrifugal force acting on the masses increases and causes them to move radially outward. Once the masses reach the static housing, a normal contact force is generated and the resulting friction torque between the shoes and the housing dissipates the excess mechanical energy stored in the springs.

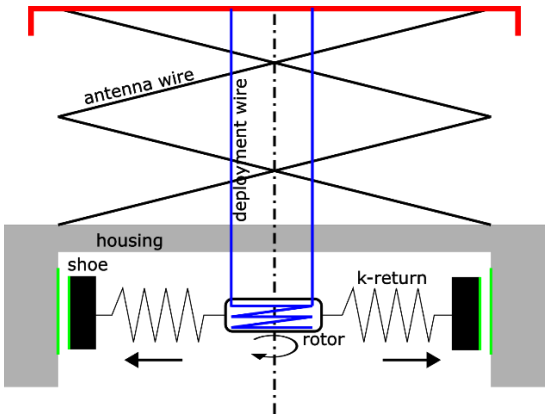


Figure 9: Antenna centrifugal brake.

This centrifugal brake converts part of the spring energy into frictional heat. The final objective is to obtain a controlled deployment of the antenna in which the spring reaches the required final position while the rotor speed is reduced to approximately zero. This ensures that no significant kinetic energy remains at the end of the deployment and thus the ultimate end-of-the-run antenna shock is minimised.

The complete dynamic behaviour therefore consists of three main stages. First, the spring releases its stored energy and accelerates the rotor. Second, the increasing rotor speed moves the centrifugal shoes
outward until they contact the belt. Third, the friction torque dissipates the rotor energy and reduces the speed. As the rotor slows, the centrifugal force decreases and the shoes move back inward. The spring can therefore continue its deployment while the brake regulates the rotor speed. The final condition is reached when the spring has completed its required travel and the remaining mechanical energy has been dissipated, giving a final rotor velocity close to zero. The spring constant is first obtained from the experimental force-height measurements illustrated in the following set of images.

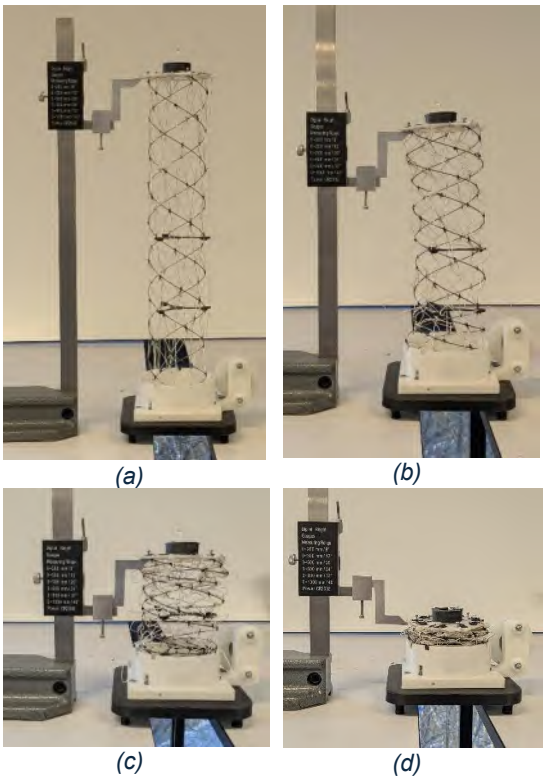


Figure 10: Antenna spring constant measurement: (a) fully deployed, (b) ¾ deployed, (c) 1/3 deployed, and (d) antenna stowed configuration.

As shown in Figure 10 the antenna measuring stiffness starts at an undeformed height of ≈410 mm and finishes at the fully compressed height of ≈50 mm. Therefore, the total spring elongation is ≈360 mm and it has been stored using roughly 1Kg of vertical pulling force. The resulting antenna stiffness measurements and the linear fit equation are shown in Figure 12 whereas the spring energy is then calculated and illustrated in Figure 12. This energy represents the total mechanical energy initially available to drive the rotor and the centrifugal brake.

Parameter	value	Units
n° of shoes (N)	2	
Shoe mass (m_s)	0.1	Kg
Housing radius ($r_{housing}$)	0.032	mm
Shoe radius (r_s)	0.03	mm
Return spring stiffness K_{return}	10	N/m
μ	0.4	
$c_{bearing}$	$1e^{-5}$	Nms

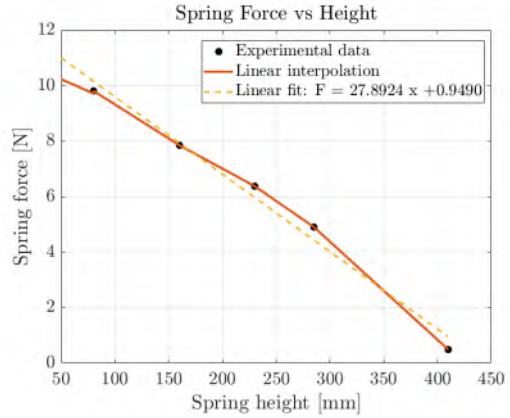


Figure 11: Antenna spring stiffness.

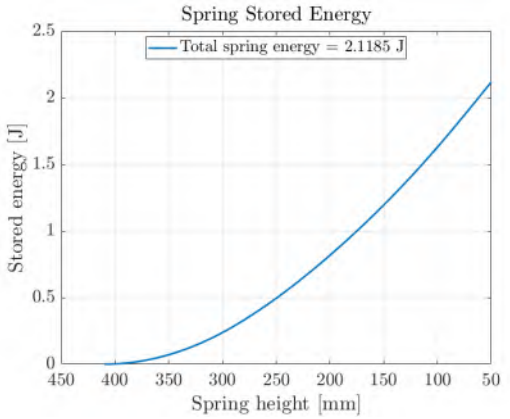


Figure 12: Mechanical spring energy.

The antenna vertical displacement is directly linked to the rotor brake motion underneath through the blue wire as shown in Figure 9. The deployment of the antenna generates a torque on the winding spool which is identified as the spring torque (T_s). If (r_w) is the winding radius of the blue wire, the antenna deployment speed is evaluated with Eq. (1).

$$\dot{x} = r_w \omega \quad (1)$$

where ω is the rotor angular velocity. The corresponding antenna deployment acceleration is therefore evaluated with Eq. (2).

$$\ddot{x} = r_w \dot{\omega} \quad (2)$$

The final antenna deployed height determines the blue wire length and therefore the maximum number of rotations of the centrifugal brake. Assuming no wire slip, the corresponding number of rotor revolutions performed during the antenna deployment are shown in Figure 13 whereas the rotating speed of the rotor is evaluated in Figure 14. These two figures show how the spring deployment is converted into rotational motion of the centrifugal brake.

With the current model parameters reported in , the antenna fully deploys in about 6s with almost 15 rotations of the brake's rotor as shown in Figure 13 by reaching the maximum spinning speed of 200rpm. This model assumes that the antenna stops at the final height of 410mm with a residual spring preload of 0.05Kg as shown in Figure 11. On the other hand the rotor is left free to spin and will slowly stop due to the bearing damping dissipative parameter ($c_{bearing}$).

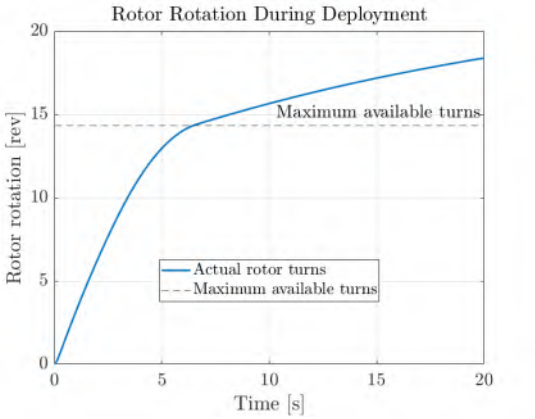


Figure 13: Rotor number of rotations.

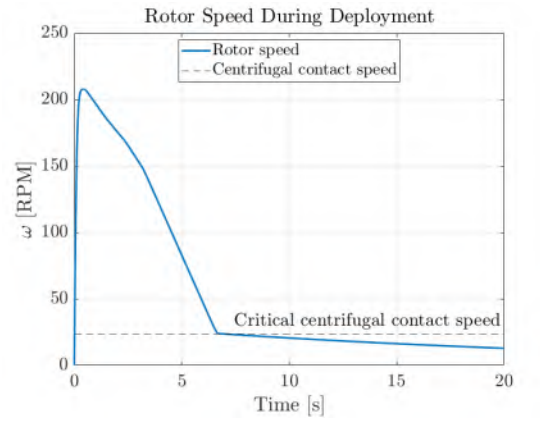


Figure 14: Rotational speed of the spool.

The rotor is connected to a set of centrifugal shoes. In the model, each shoe has mass (m_s) and radial position(r_s). The centrifugal force acting on each shoe is evaluated with Eq. (3).

$$F_c = m_s \omega^2 r_s \quad (3)$$

At low rotor speed, the return spring (k-return in Figure 9) keeps the shoes close to the rotor. As the rotor speed increases, the centrifugal force increases with the square of the angular velocity. The shoes therefore move outward. Once the shoe reaches the belt, a contact pressure is created and the respective friction generated produces a braking torque (T_b) from Eq. (4) that slows down the antenna deployment motion.

$$T_b = N\, F_c \mu\, r_{housing} \quad (4)$$

where (N) are the number of shoes and $r_{housing}$ is the radius of the static housing belt of the antenna centrifugal brake schematised in Figure 9. The deployment torque generated by the antenna deployment on the spinning rotor T_s is shown in Figure 15 together with the breaking torque T_b. Similarly, the breaking torque T_b is furthermore illustrated as a function o the rotor spinning speed in Figure 16

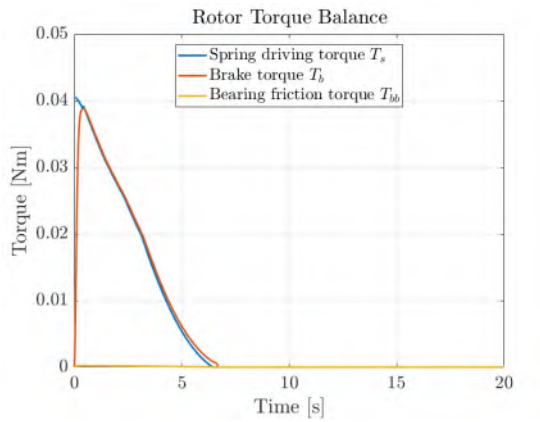


Figure 15: Centrifugal brake acting torque.

Figure 11 shows the centrifugal force acting on the shoes. Figure 9 shows how the braking torque changes with rotor speed.

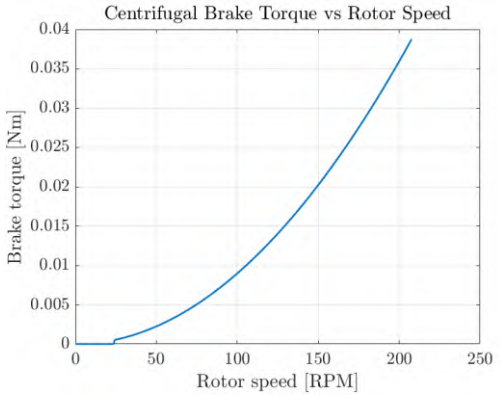


Figure 16: Breaking torque.

As the shoes contact the belt, the braking torque increases and the rotor begins to slow down. The friction brake converts the mechanical energy into heat. The instantaneous braking power is calculated from Eq. (5)

$$P_{break} = t_b \omega \quad (5)$$

whereas the total energy dissipated by the brake is calculated with Eq. (6) and illustrated in Figure 17.

$$E_b = \int_0^t T_b \omega \, dt \quad (6)$$

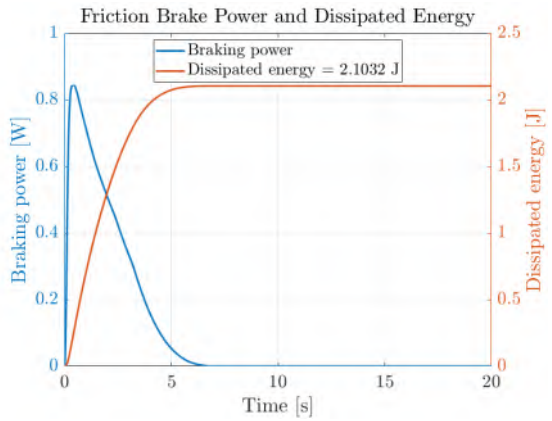


Figure 17: Breaking power, dissipated energy.

Finally, Figure 18 show the deployment velocity and acceleration directly as a function of the antenna height. At the end of deployment, the spring reaches its fully extended position at 410 mm. At this point, the spring has released almost all of its available energy however a small residual velocity and acceleration are left in the antenna. When the spring reaches its final position, the remaining motion must be stopped by a hard mechanical end stop. The end stop produces a short shock event. The

stopping distance determines the resulting deceleration, the shorter stopping distance the higher is the shock produced

To estimate this event, an equivalent 50 g of antenna moving mass is considered. The residual velocity from Figure 18 is used to calculate the kinetic energy that must be absorbed by the hard stop. The mechanical stop is assumed to provide a stopping distance of 0.500 mm. The resulting shock deceleration is approximately 0.160 m/s², corresponding to only 0.016 g. For the assumed 50 g of equivalent antenna moving mass at the tip, this produces a very small shock force of approximately 0.008 N. The estimated stopping time is approximately 79.1 ms. These values indicate that the final deployment stop produces a relatively low residual shock. Therefore, the final mechanical impact is not expected to be a significant contributor to the overall dynamic loads of the system and this centrifugal brake is a good solution for this antenna deployment.

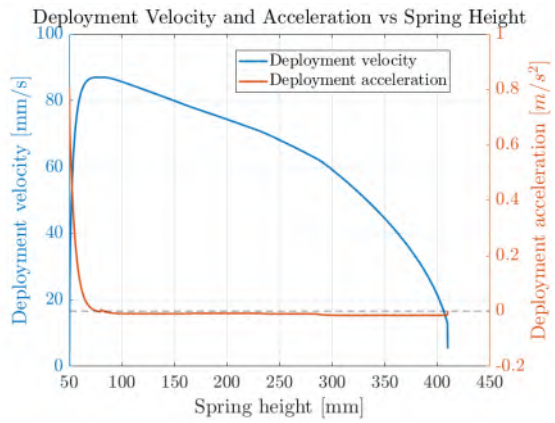


Figure 18: Deployment velocity & acceleration.

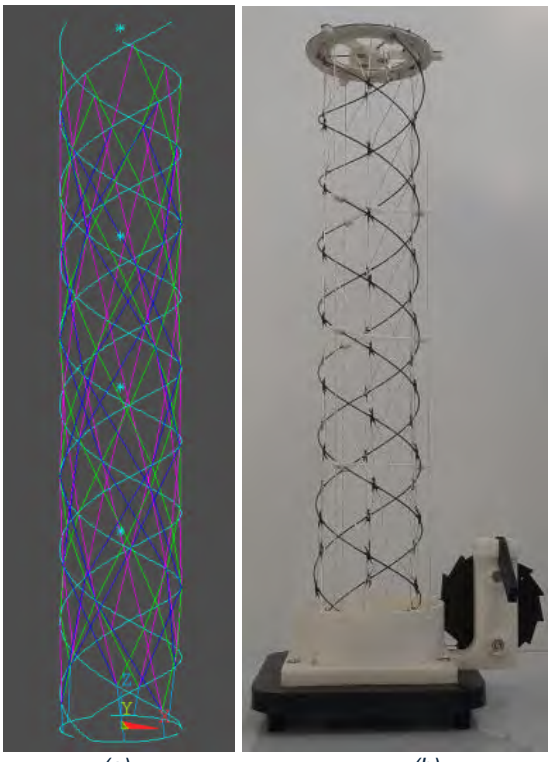
These plots are useful for evaluating the mechanical performance of the complete system because they show how the centrifugal brake needs to be designed to control the deployment speed of the antenna throughout the spring stroke. The model therefore links the experimental spring behaviour, wire kinematics, centrifugal shoe motion, friction torque, and energy dissipation in one dynamic simulation.

6.1. ANTENNA MODAL ANALYSIS

The final braced and axially preloaded configuration of the antenna structure, as investigated in Section 5.1, is imported to perform the prestressed modal analysis. The wire bracing pattern shown in Figure 7 and in Figure 7 is applied to the three helicoidal metal wires using spring elements connected to the group of specific selected nodes (anchor blue points in Figure 7).



Figure 19: Antenna prototype.



(a) *(b)*

Figure 20: Antena bracing structure. (a) finite element model (b) Physical antenna prototype.

Furthermore, four concentrated mass elements are introduced along the vertical central axis to represent the star-shaped spacing components.

The static structural analysis previously performed to establish the antenna axial preload (see Section 5.1) is now restarted. This additional step accounts for element stress redistribution and structural relaxation, as the preloaded antenna configuration is now held in place by the triangular bracing wire net.

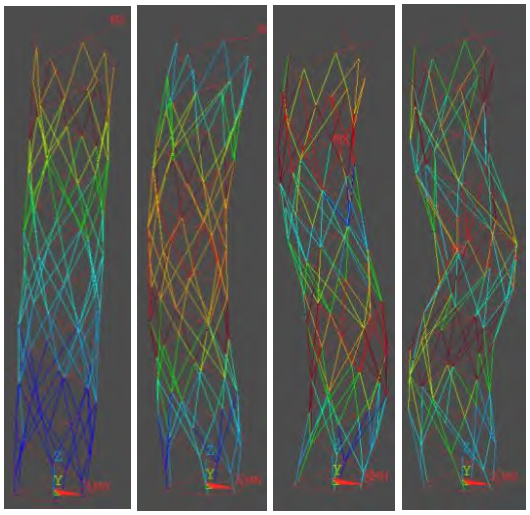


Figure 21: Antenna natural modes.

Finally, the prestress modal analysis is performed. The first set of the eigenmodes of the antenna are illustrated in Figure 21, while the respective eigenfrequencies are reported in Table 2.

Table 2: Antenna natural frequencies.

Natural mode	Frequency [Hz]
1st and 2nd	2.6
3rd and 4th	15
5th	22
6th	29

The first natural vibration mode of the antenna has also been measured on the prototype shown in Figure 20(b). An accelerometer is placed on the top section of the antenna while the input excitation is provided as shown by the red arrow in Figure 19. From the test results reported in Figure 22, the measured frequency between two antenna oscillations is 2.56Hz which is in good agreement with the simulation implemented in Figure 20(a).

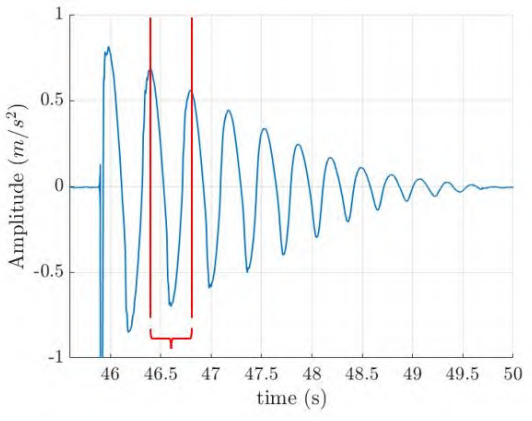


Figure 22: Antenna measurement of first natural mode.

7. DYNAMIC DEPLOYMENT TESTS

After several design iterations and structural simulations, the antenna is ultimately manufactured using the bracing pattern developed in Section 5. Moreover, the antenna base is designed and manufactured to support the lower interface of the helicoid wires and provide a structural frame for stowage. The base needs to be compatible with standard CubeSat integration requirements, featuring a footprint of 100 × 100 mm.

A central cylindrical cavity is incorporated to accommodate the three helicoid wires in their compressed configuration, along with the bracing wires, which are carefully folded toward the centre.
Furthermore, the upper interconnection element of the helicoidal wires also includes dedicated indentations and locking features to ensure secure engagement with the antenna base when stowed.

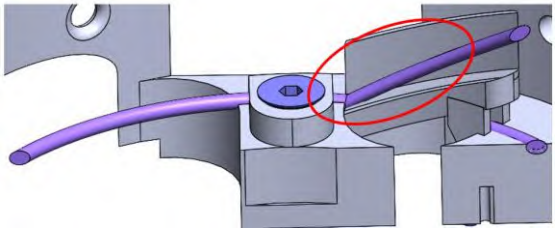


Figure 23: Design solution to minimise stress.

Figure 23 shows a section side of the antenna base element where the helicoidal wires are clamped and constrained. Figure 25 shows instead the stress distribution in the antenna base section when a vertical force is applied. This region at the base of the antenna represents the most critical area during the stowing process because it is the highest stress concentration zone. This is primarily due to the change in geometry of the helicoidal wires as they transition from a planar circular configuration to the helical shape of the antenna.

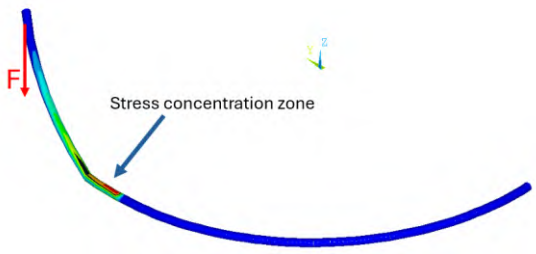
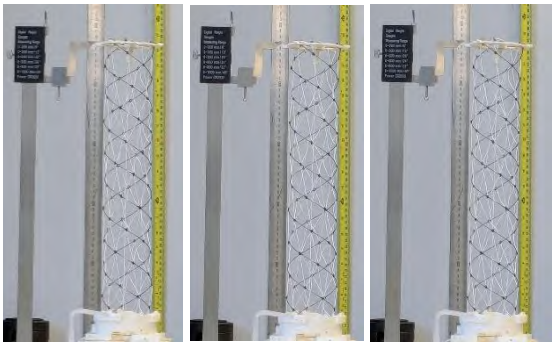


Figure 24: Stressed stowed part of the

antenna.

The stress analysis indicates that this transition region experiences significantly higher stress levels with respect to the rest of the structure. Since the helicoidal wires are manufactured from harmonic steel, it is important to maintain an adequate margin with respect to the material yield strength and avoid operating close to the elastic limit, particularly during the stowing process.

To reduce the stress concentration in this region, a ramp was introduced at the transition between the circular planar and the helicoidal shape, as shown in Figure 26. This curved ramp limits the maximum deflection of the wire during the folding stowage process and guarantees a smoother geometric transition by reducing the sudden change in wire curvature and consequently lowering the local stress concentration.



a *b* *c*

Figure 25: Antenna dynamic deployment tests.

At this stage, a large number of deployment tests are conducted to evaluate the dynamic behaviour of the system, particularly in terms of deployment velocity and end-of-stroke shock. These tests are also essential to assess the repeatability of the antenna deployment, ensuring that the structure consistently reaches the same deployed height, by maintaining the concentricity and cylindricity of the helicoid's perimeter within the specified geometric requirements with a tolerance of ±1 mm.

The implemented procedure consists of repeatedly stowing and deploying the antenna, capturing images from a fixed distance, and comparing them to evaluate deployment repeatability. As illustrated in Figure 25 , three examples of deployment tests are presented together with the measurement experimental setup which includes a set of graduated scale markings mounted on a white background to measure the antenna height. In addition, a digital height gauge is positioned laterally. Therefore, after each deployment test, the antenna height is accurately measured, and the structure is rotated through a full revolution about a fixed pivot point at the base to assess the concentricity at the top. The results are very encouraging since the antenna height consistently remains within the ±1 mm of height tolerance. The radial variation of the top concentricity remains within ±2 mm. These results show that the antenna can achieve an acceptable deployment accuracy and repeatability.

This performance was achieved through two main design solutions. First, the support implemented at the base of the antenna shown in Figure 23 prevents the wire from reaching its yield limit. This keeps the wire within its elastic range during deployment and stowing process. Second, the centrifugal brake implemented in Section 6 limits the shock amplitude at the end of the deployment and it also helps to control the antenna deployment speed.

8. CONCLUSIONS

This work aims to present the initial design and prototyping steps of the engineering model of a trifilar helicoid antenna. The requirements include the development of a single metal structure capable of acting both as the primary supporting structure and as the radiating elements of the antenna. In addition, the model must be cost-effective to manufacture, easy to assemble, and capable of ensuring repeatable deployments while maintaining the final deployed geometry within a tolerance of ±1 mm.

Following several design and simulation iterations, the antenna is manufactured, and a series of deployment tests are conducted to verify compliance with the project requirements. The deployment height accuracy is successfully achieved; however, the concentricity shows a slight deviation beyond the desired tolerance. Furthermore, it is observed that the end-of-stroke shock could be significant without the use of a damper. For this reason, the integration of the centrifugal break is essential to better control the deployment dynamics of the antenna deployment.

9. REFERENCES

1. C. A. Balanis, *Antenna Theory: Analysis and Design*. New York, NY, USA: Wiley, 1982.

2. G. Slade, *The Basics of Quadrifilar Helix Antennas*. Highfields, QLD, Australia: QSL.net Publishing, 2015.

3. J. Costantine, S. Pellegrino, and M. Sakovsky, “Rapid design of deployable antennas for CubeSats: A tool to help designers compare and select antenna topologies,” in *Proc. 31st Annual AIAA/USU Conf. Small Satellites*, Logan, UT, USA, Aug. 2017.

4. D. J. Ochoa, K. Hummer, and M. Ciffone, “Deployable helical antenna for nano-satellites,” in *Proceedings of the 28th Annual AIAA/USU Conference on Small Satellites*, Logan, UT, USA, Aug. 2014, pp. 1–7

5. C. L. Zekios, S. V. Georgakopoulos, and X. Liu, “Analysis of a packable and tunable origami multi-radii helical antenna,” in *Proc. IEEE Int. Symp. Antennas and Propagation and USNC-URSI Radio Science Meeting*, Atlanta, GA, USA, Jul. 2019.

6. G. Christodoulou, J. Costantine, G. Olson, I. Maqueda, S. Pellegrino, M. Sakovsky, and Y. Tawk, “UHF deployable helical antennas for CubeSats,” in *Proc. IEEE Antennas and Propagation Society Int. Symp. (APSURSI)*, Memphis, TN, USA, Jul. 2014.

7. J. Block, A. Bäger, T. D. J. Behrens, L.-C. Hauer, M. Schütze, R. Schütze, and T. Spröwitz, “A self-deploying and self-stabilizing helical antenna for small satellites,” in *Proc. 7th Eur. Conf. Antennas Propag. (EuCAP)*, Gothenburg, Sweden, Apr. 2013.

8. M. Sureda, M. Sobrino, O. Millán, A. Aguilella, A. Solanellas, M. Badia, J. F. Muñoz-Martín, L. Fernández, J. A. Ruiz-De-Azua, and A. Camps, “Design and testing of a helix antenna deployment system for a 1U CubeSat,” *IEEE Access*, vol. 9, pp. 66103–66114, 2021, doi: 10.1109/ACCESS.2021.3075660.

9. Helical Communication Technologies (HCT), “Helios deployable antenna,” 2016. https://www.cubesatshop.com/product/helios-deployable-antenna/

10. T. Huang, J. R. Reveles, Q. Harrington, V. Fraux, and V. Vinoth Gurusamy, “An innovative deployable VHF/UHF helical antenna for nanosatellites,” in *Proc. 13th Eur. Conf. Antennas Propag. (EuCAP)*, Krakow, Poland, Mar.–Apr. 2019.

ARIEL PRIMARY MIRROR MOUNTING RE-DESIGN

Umberto Barozzi [(1)], Giuseppe Maria Porcelluzzi [(1)], Simone Nordera [(1)], Alessandro Giachi [(1)], Andrea Paternoster [(1)], Federico Miceli [(1)], Francesca Dalla Nese [(2)], Lorenzo Maddii Fabiani[(1)], Davide Nuzzi [(1)], Lorenzo Barubiani [(1)], Matteo Pinna [(2)], Dervis Vernani [(4)], Angelo Olivieri[(5)], Delphine Maryse Jollet [(6)]

[(1)] Leonardo S.p.A., Via Delle Officine Galileo, 1, 50013 Campi Bisenzio FI, Italy, E-mail: umberto.barozzi@leonardo.com
[(2)] Experis S.r.l., Via Rossini, 6/8, 20122 Milano, Italy, Email: francesca.dallanese.ext@leonardo.com
[(3)] Okatim S.r.l., Corso Enrico Tazzoli 215, 12/b, 10137 Torino TO, Italy, Email: matteo.pinna.ext@leonardo.com
[(4)] Media Lario Srl, Via al Pascolo, 10, 23842 Bosisio Parini LC, Italy, Email: dervis.vernani@medialario.com
[(5)] ASI, Via del Politecnico, snc, 00133 Roma RM, Italy, Email: angelo.olivieri@asi.it
[(6)] ESA-ESTEC, Keplerlaan 1, 2201 AZ Noordwijk, The Netherlands, Email: delphine.jollet@esa.int

KEYWORDS

Architecture, Design, Aluminium, Large-size Mirrors, SFE, Bipods, Mounting

ABSTRACT

Mounting-induced deformations have a significant impact in the framework of the ARIEL mission, in which the Cassegrain telescope includes a large (1100 × 800 mm) elliptical primary mirror made of aluminium.
Lessons learned from the ARIEL TA (Telescope Assembly) SM and EM model, developed by the ARIEL Scientific team, showed that the aberrations introduced by the primary mirror (M1) mounting were not compatible with the mission science requirements.
In the context of getting appointed for the TA PFM design and verification, the industrial team in Leonardo (LDO) is proposing an alternative M1 mounting design, to minimise the corresponding deformation and at the same time improve the integration of the primary mirror in the assembly.
In this article, the new mounting concept and the iterations that have been performed to address mounting distortions and integration approach are outlined.

1. INTRODUCTION

In March 2018, ARIEL was selected as the fourth M mission of the European Space Agency (ESA) for the Cosmic Vision Program. It will observe transits of exoplanets around their star from L2 orbit. Exoplanets of particular scientific interest will be studied in depth, in order to determine their chemical and physical properties [1].
The optical payload that will scan the starry sky is an off-axis Cassegrain telescope that works in the Visible and Near-Infrared wavelength range (Figure 1) [2]. The incoming radiation is reflected over four aspheric mirrors (M1, M2, M3 and M4), directing the ray bundle into the optical bench, where detectors and sensors are placed. The entire structure and mirrors are made of aluminum EN AW 6061, in order to guarantee an approximately uniform volume contraction when reaching the operative temperature of around 50 K. A mechanism (M2M) behind secondary mirror (M2) allows the refocusing of the optical system by moving the M2 mirror at operative cryogenic temperatures.
The ARIEL payload is developed by a Consortium of multiple countries [3]. While RAL Space is the payload prime, an Italian and Spanish scientific consortium (INAF, CNR, UNIFI, UPM) is in charge of managing the Telescope Assembly (TA) SM (Structural Module) and EM (Engineering Model) models. In the SM and EM context, Leonardo is responsible for the MAIT (manufacturing, assembly, integration and testing) activities of TA. The manufacturing of the mirrors is in charge of MediaLario company.

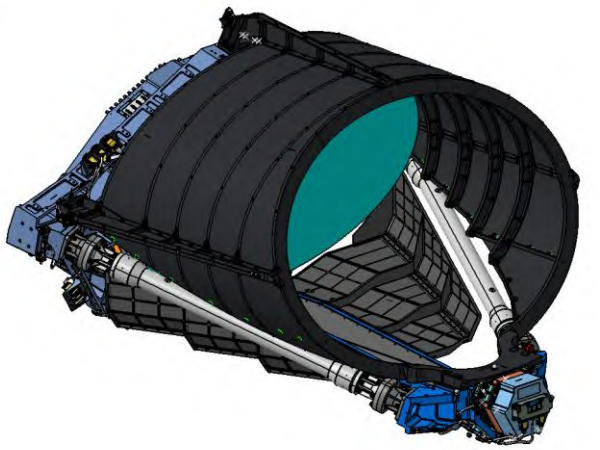


Figure 1: ARIEL Telescope EM - front view

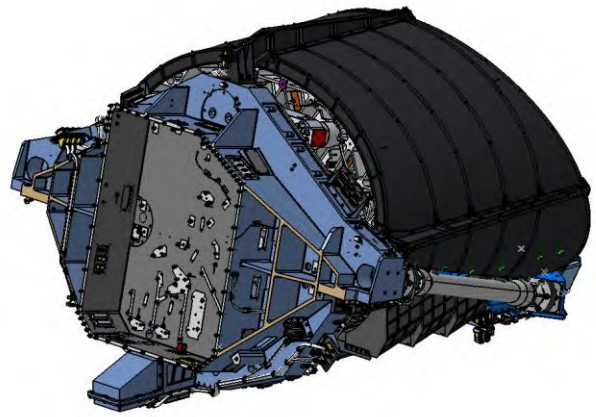


Figure 2: ARIEL Telescope EM - rear view

After the SM and EM development phase, Leonardo has been appointed as the industrial lead for TA PFM design and MAIT activities. In this transition phase, lessons learned by the scientific team on SM and EM models have been actively translated by Leonardo in modifications of the TA PFM design.
In particular, the design of SM and EM M1 mounting (Figure 3 and Figure 4), developed by the scientific consortium and driven by demanding stiffness requirements, consists of supports (flexure hinges) with stringent planarity requirements on M1 side and 3 spherical joints for isostatic mount on the optical bench. However, mounting deformations introduced on M1 SM and EM models have been deemed not compatible with mission performance requirements.

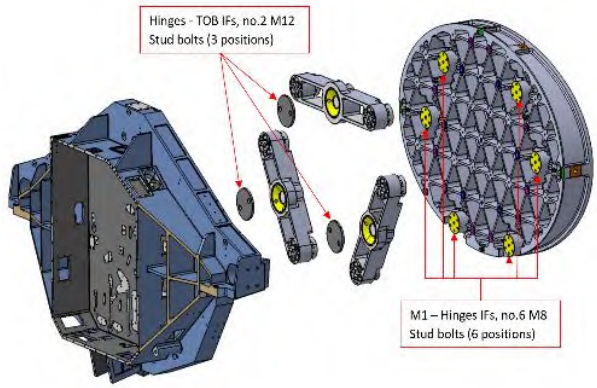


Figure 3: TA SM/EM M1 hinges mounting - back

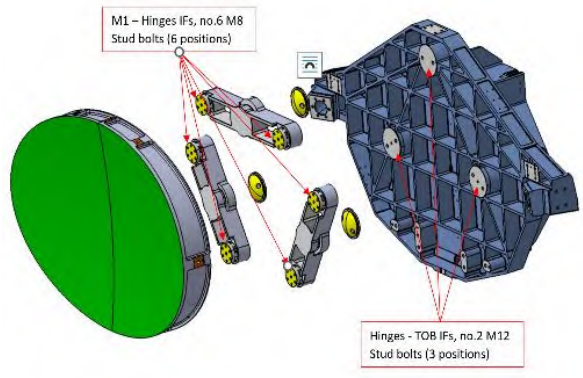


Figure 4: TA SM/EM hinges mounting - front

Therefore, for PFM design, Leonardo proposed a shift between a primary mirror (M1) mounting concept based on flexure hinges to a new one involving bipods. This conceptual change led to design modifications of the mating interfaces on both the primary mirror and the optical bench.

The performance of the new design has been verified by analysis at telescope level against TA mechanical loads, thermal environment and opto-mechanical performances, with the aim of increasing as much as possible the M1 mounting flexibility while also guaranteeing compliance to the TA environmental requirements. The analytical experience gathered on the TA SM mounting test [4] has been applied in the verification and optimisation of the bipods shape and interfaces.
The following paragraphs describe the new mounting concept and the analyses performed throughout its development.

2. PROPOSED CONCEPT AND OBJECTIVE

The target of the PFM design proposed by Leonardo has been to minimize the SFE deformation introduced on M1 mounting while at the same time guaranteeing structural resistance. The tradeoff led to the concept shown in Figure 5, which is a bipod mounting, with 3 interfaces on the mirror and 6 on the optical bench. Although this mounting concept is relatively traditional, the material, size and shape of the mirror are quite unconventional for a cryogenic space mission and required a thorough multidisciplinary study among optics, thermo-mechanics and AIT disciplines.

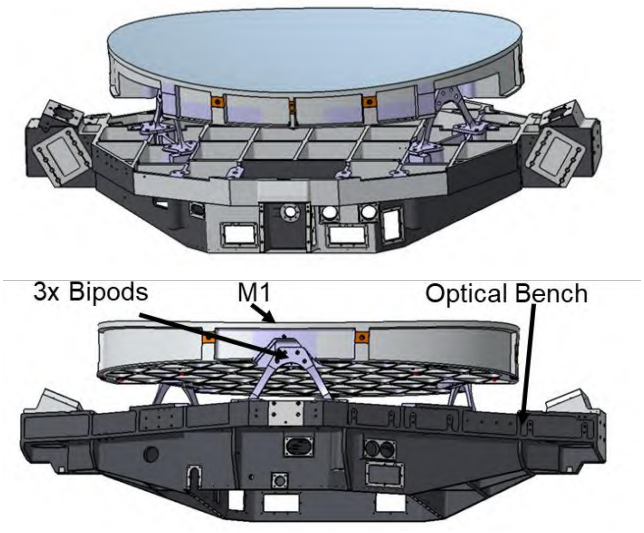


Figure 5: Leonardo PFM M1 mounting concept (bolts, nuts and washers removed)

Three bipods made of Al6061 (same material as the mirror) have been designed and their position on the optical bench has been optimised in order to achieve the best compromise between optical and mechanical performance. The main advantage in terms of optical performances is that the three bipod

interfaces on M1 side are now on the lateral sides of the mirror and the interface bolts tightening force acts exactly in the direction of flexibility of the bipod, minimising the SFE introduced on the primary mirror due to positioning errors. In addition, dedicated bolt elongation tools are used on the bipod-mirror interface, avoiding any torque application that may introduce additional SFE and guaranteeing a stable preload.
The bipod shape has been optimised via a dedicated trade-off study, acting on the geometrical parameters in Figure 6, until a satisfactory balance between flexibility and structural strength has been achieved. The final design of the bipod is shown in Figure 7.

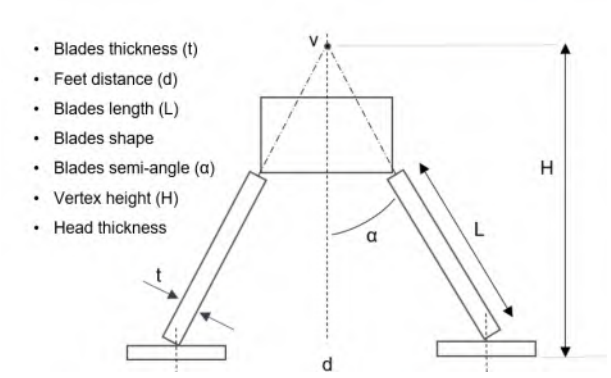


Figure 6: Parameters of the bipod tradeoff

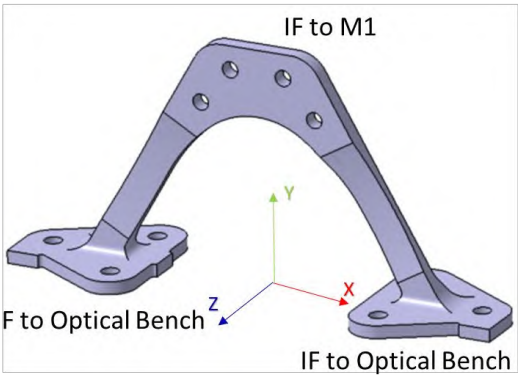


Figure 7: Bipod shape – final iteration

The effects of planarity tolerance at the bipod-optical bench interface on the bipod-M1 interface are significantly mitigated by their orthogonal relative positioning. The most significant effect on mirror SFE is introduced by tilts around X-axis on the bipod IF to M1 in Figure 7, which is mitigated by the blades flexibility. Apart from this offender, other tilts, non-planarity and positioning shifts can be compensated directly during bipods positioning, exploiting the clearance of the bipods through-holes either on M1 or optical bench side. An example is reported in Figure 8. A dedicated GSE has been envisaged to finely control the bipods positioning during integration, allowing fine compensation. A concurrent engineering between the mechanical and AIT teams has been carried out, to identify the compensation precision during mounting steps; these contributors have then been used as inputs in the opto-mechanical analyses of paragraph 4.

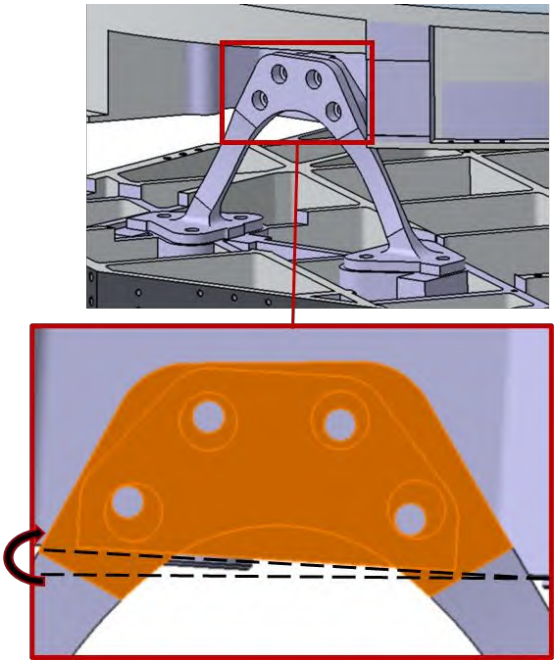


Figure 8: Example of tilt compensation prior to bolt tightening.

The concept modification also imposed different interfaces on the mirror and the optical bench, as shown in Figure 9 and Figure 10.
The new position of the mirror interface pads (at 120°) facilitates integration and improves the isostatic support of the mirror. The overall mass of the mirror has been kept approximately constant, while the rib height has been slightly increased to add stiffness to M1. In the previous design this modification was not possible due to the interface position on the back of the mirror.
Particular care has been taken on the M1 interface pads, which resemble a mushroom shape, with a central connection to the mirror and lateral threaded holes. The position of the interface holes is as far as possible from the central support, to decouple the optical surface from bolts tensioning and reduce the mounting SFE.

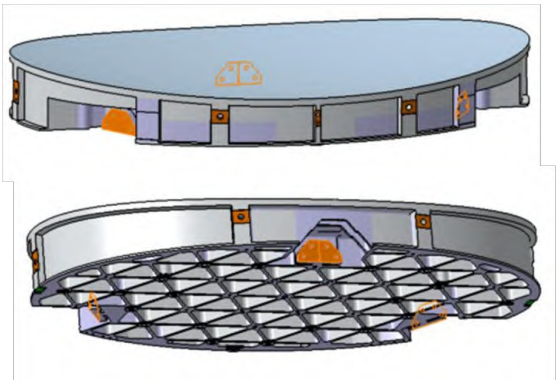


Figure 9: M1 interface concept

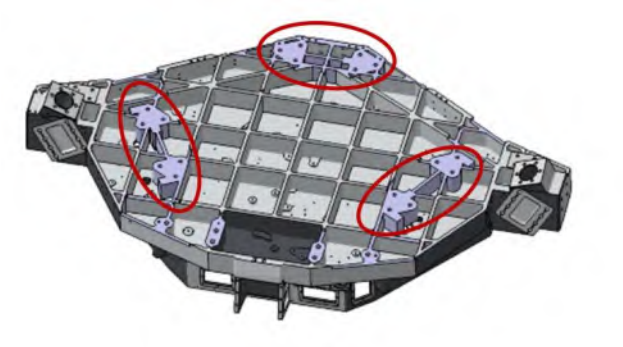


Figure 10: Optical Bench interface concept

Overall, the assembly mass has been reduced by around 12 kilograms between EM design and PFM design.

Item	EM mass [kg]	PFM mass [kg]
Optical Bench	85.3	83.5
M1	62.8	66.2
M1 supports	15.6	1.4
Total	163.7	151.1

Table 1: Mass comparison

3. THERMO-MECHANICAL ANALYSES

3.1. Structural Analyses

3.1.1. Modal Analysis

A modal analysis of the overall Telescope Assembly with new M1 mounting has been performed. Even if the proposed redesign affects the stiffness of the supports of a primary mirror weighing ~65kg, the modal behavior is very similar to the TA EM, especially for global modes. In the sine range, the modes affected by the modification are located in the 90-110 Hz frequency range.

Mode	Freq [Hz]	T1 (X)		T2 (Y)		T3 (Z)		R1 (@X)		R2 (@Y)		R3 (@Z)	
		Fraction	Sum	Fraction	Sum	Fraction	Sum	Fraction	Sum	Fraction	Sum	Fraction	Sum
1	37.01	0.11%	0.11%	74.20%	74.20%	0.02%	0.02%	56.30%	56.30%	0.12%	0.12%	7.60%	7.60%
2	38.79	47.40%	47.60%	0.19%	74.40%	8.21%	8.23%	0.16%	56.40%	49.10%	49.20%	0.09%	7.69%
3	60.45	44.90%	92.50%	0.00%	74.40%	17.90%	26.10%	0.00%	56.40%	18.30%	67.50%	0.00%	7.69%
4	80.07	0.00%	92.50%	11.80%	86.20%	0.02%	26.10%	26.50%	82.90%	0.01%	67.50%	9.79%	17.50%
5	84.68	0.93%	93.40%	0.00%	86.20%	61.30%	87.40%	0.00%	82.90%	11.50%	79.00%	0.00%	17.50%
6	97.00	0.54%	93.90%	0.00%	86.20%	0.06%	87.50%	0.00%	82.90%	7.59%	86.60%	0.00%	17.50%
7	99.52	0.02%	93.90%	2.36%	88.60%	0.01%	87.50%	0.46%	83.30%	0.02%	86.60%	3.86%	21.30%
8	107.68	0.03%	94.00%	0.04%	88.60%	0.01%	87.50%	0.80%	84.10%	0.01%	86.60%	22.90%	44.30%
9	112.83	0.01%	94.00%	0.00%	88.60%	0.38%	87.90%	0.00%	84.10%	0.57%	87.20%	0.05%	44.30%
10	116.70	0.00%	94.00%	0.11%	88.80%	0.00%	87.90%	0.50%	84.60%	0.00%	87.20%	2.61%	46.90%
11	119.31	0.02%	94.00%	0.00%	88.80%	0.01%	87.90%	0.00%	84.60%	0.02%	87.20%	0.00%	46.90%
12	124.25	0.01%	94.00%	1.99%	90.70%	0.01%	87.90%	7.40%	92.00%	0.00%	87.20%	0.00%	46.90%

Table 2: TA EM modal frequencies and effective masses

Mode	Freq [Hz]	T1 (X)		T2 (Y)		T3 (Z)		R1 (@X)		R2 (@Y)		R3 (@Z)	
		Fraction	Sum	Fraction	Sum	Fraction	Sum	Fraction	Sum	Fraction	Sum	Fraction	Sum
1	37.35	0.02%	0.02%	72.80%	72.80%	0.00%	0.00%	55.44%	55.44%	0.02%	0.02%	6.96%	6.96%
2	40.15	46.46%	46.48%	0.04%	72.84%	6.67%	6.67%	0.03%	55.47%	50.78%	50.81%	0.04%	7.01%
3	61.30	44.13%	90.61%	0.00%	72.84%	19.44%	26.12%	0.00%	55.47%	18.06%	68.87%	0.00%	7.01%
4	79.04	0.00%	90.61%	9.79%	82.63%	0.01%	26.13%	26.76%	82.23%	0.01%	68.87%	7.46%	14.47%
5	82.19	2.28%	92.88%	0.00%	82.63%	56.08%	82.22%	0.00%	82.23%	8.07%	76.94%	0.00%	14.47%
6	95.49	0.42%	93.30%	0.01%	82.64%	0.68%	82.89%	0.00%	82.23%	4.49%	81.43%	0.01%	14.49%
7	99.20	0.01%	93.31%	5.31%	87.94%	0.00%	82.90%	0.78%	83.02%	0.03%	81.46%	3.84%	18.32%
8	105.60	0.01%	93.32%	1.30%	89.25%	0.00%	82.90%	0.93%	83.95%	0.01%	81.46%	13.13%	31.45%
9	110.97	0.07%	93.39%	0.00%	89.25%	2.35%	85.25%	0.00%	83.95%	2.70%	84.16%	0.01%	31.46%
10	116.19	0.00%	93.39%	0.02%	89.27%	0.00%	85.25%	0.50%	84.45%	0.00%	84.16%	0.36%	31.82%
11	118.76	0.00%	93.39%	0.00%	89.27%	0.01%	85.26%	0.00%	84.45%	0.16%	84.32%	0.00%	31.82%
12	126.71	0.00%	93.39%	0.15%	89.42%	0.00%	85.26%	6.37%	90.82%	0.00%	84.32%	9.82%	41.64%

Table 3: TA PFM redesign modal frequencies and effective masses

The global modes of the TA PFM concept are reported in Figure 11 to Figure 13.
Table 4 compares the requirement with the natural frequencies obtained by analysis, including mass margin. All requirements are met.

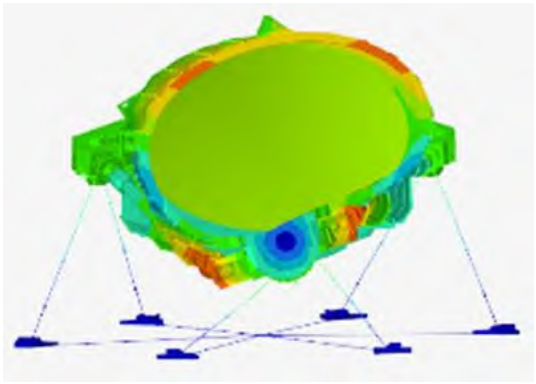


Figure 11: Mode 1 (lateral) - 37.4Hz

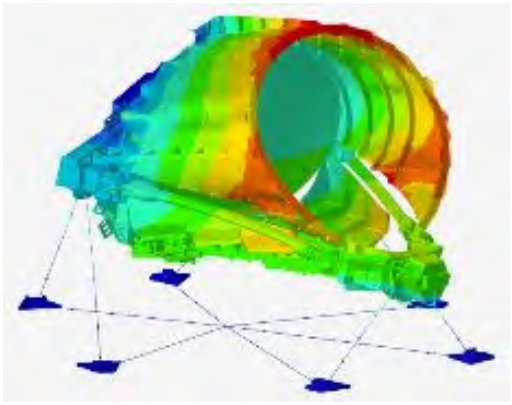


Figure 12: Mode 3 (first coupled mode) - 61.3 Hz

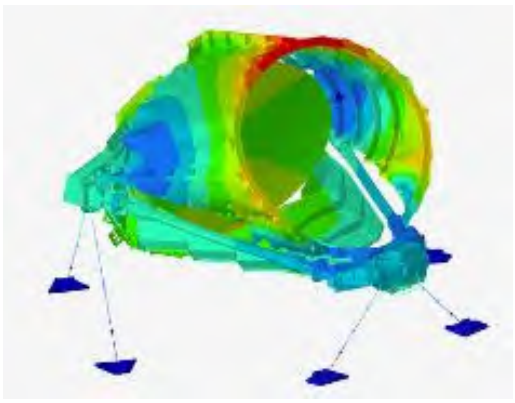


Figure 13: Mode 5 (first pure longitudinal)– 82.2 Hz

	Frequency [Hz]	Requirement [Hz]
First lateral mode (Y)	37.35	>25
First longitudinal mode (Z)	82.19	>42
First coupled mode (X-Z)	61.3	/

Table 4: TA PFM global modes vs. requirement

3.1.2. Sine Analysis

The dimensioning load case for the M1 bipods is the sine load condition. In addition to the maximum stress registered across the blades thickness, particular attention has been devoted to the sliding

margin of safety on the M1/bipods interface, which is critical between 95 and 110 Hz where the main M1 modes are acting.
The flat 3g sine specification of the ARIEL TA has been applied at the TA interface and notching of the new design has been evaluated. Figure 14 to Figure 16 include sine notching in the three direction load cases; in black the contribution from primary notching is displayed, while the green line that is visible only during Sine Y is the notch required to avoid average sliding of the M1-bipod interface. Feedback from the satellite SM test and from ESA sine analysis at satellite level confirmed that notches in the 100-110 Hz range are acceptable.

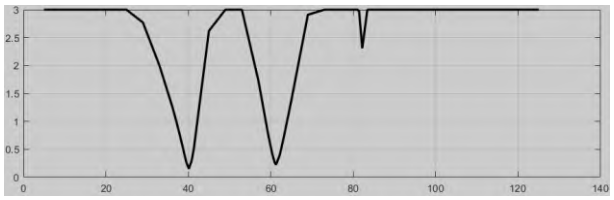


Figure 14: Notched profile on input load - Sine X

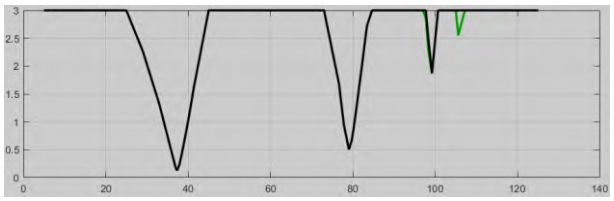


Figure 15: Notched profile on input load - Sine Y

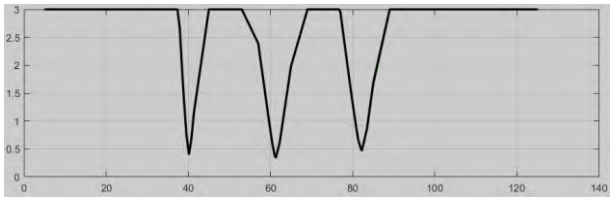


Figure 16: Notched profile on input load - Sine Z

These notched inputs have then been used to derive the M1 bipods margin of safety against yield and ultimate strength, including the appropriate safety factors (Kp=1.15, Km=1.2, FoSy=1.1, FoSu=1.25).
Margins of safety (MoS) are reported in Table 5, where it is possible to observe that the minimum margin of safety in Sine Z has been optimised close to zero, to grant maximum flexibility and minimise M1 mounting SFE. Bipods have been modelled with a detailed mesh and the peak stress has been considered conservatively for the MoS calculation.

Load (notched)	Bipod Max. Stress [MPa]	Frequency [Hz]	MoSy	MoSu
Sine X	148	81	0.69	0.68
Sine Y	171	98	0.47	0.45
Sine Z	232	85	0.08	0.07

Table 5: M1 bipods yield and ultimate MoS

3.2. Thermo-elastic Analysis

The selected bipod blades thickness significantly reduced the thermal conductance of the M1 supports with respect to the EM hinges. Consequently, a thermal analysis has been conducted to verify that no drawbacks had been introduced in thermal load cases due to the redesign.
The dimensioning thermal load case of the bipods is neither an operative nor a non-operative one, as the entire TA is passively cooled in L2 protected by radiative screens (V-grooves) and the temperatures reached at equilibrium are very similar across the whole TA. On the other hand, the worst thermal load case happens through the cooldown transient from 293K to 50K, during the orbit transfer to L2.
In particular, the time-window in which the maximum difference of temperature is expected is between 293K and 170K, when decontamination heaters on the mirror and optical bench are going to be turned on. As a first step, the time instant of maximum difference between average M1 and optical bench temperatures has been identified with a dedicated transient thermal analysis. Figure 17 shows that it is approximately after 13.5 hours after the start of the cooldown (maximum of purple line).

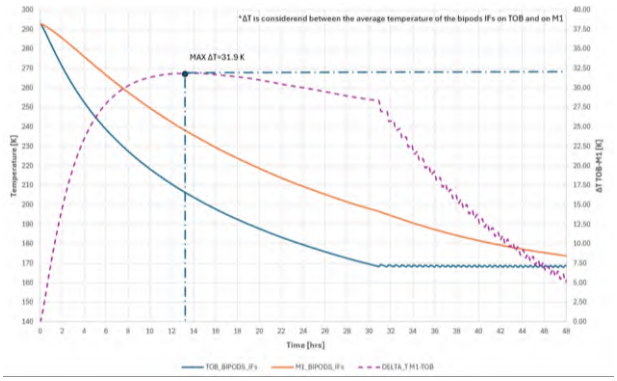


Figure 17: Cooldown analysis for maximum average temperature difference M1 – optical bench

The thermal map corresponding to the identified worst case, plotted in Figure 18 (overall TA) and Figure 19 (bipods detail), has then been applied to the structural FEM via conductive analysis (Figure 20).

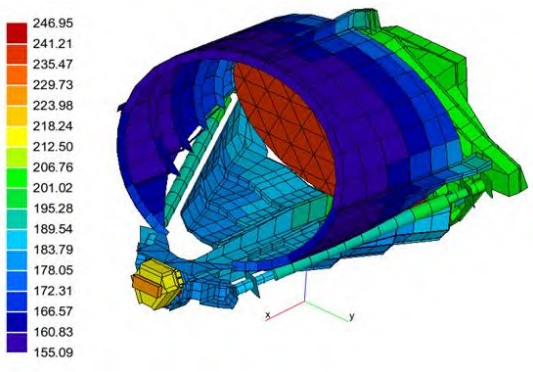


Figure 18: Bipods worst case thermal map – TA

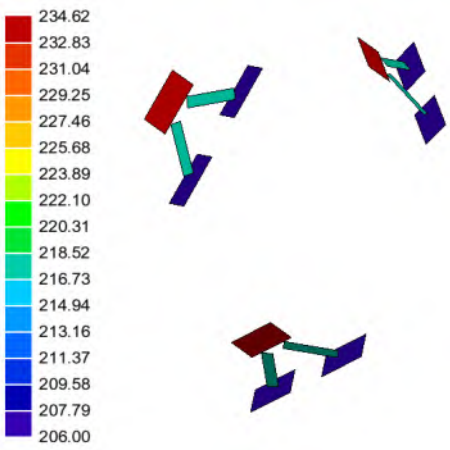


Figure 19: Bipods worst case thermal map - bipods

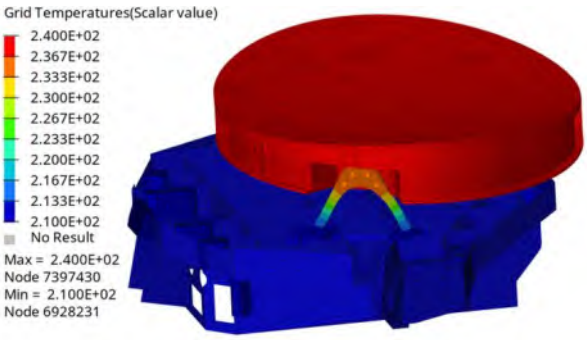


Figure 20: Worst thermal loadcase - temperature mapping on FEM

As a last step, a thermo-elastic analysis has been performed to derive both bipods maximum stress (Figure 21) and sliding margins of safety at their interface. The maximum Von Mises stress is 40MPa and the minimum sliding MoS is 184% (including margins), proving that even if the thermal conductance has been reduced the thermal load cases are not critical, especially in comparison with the sine environment.

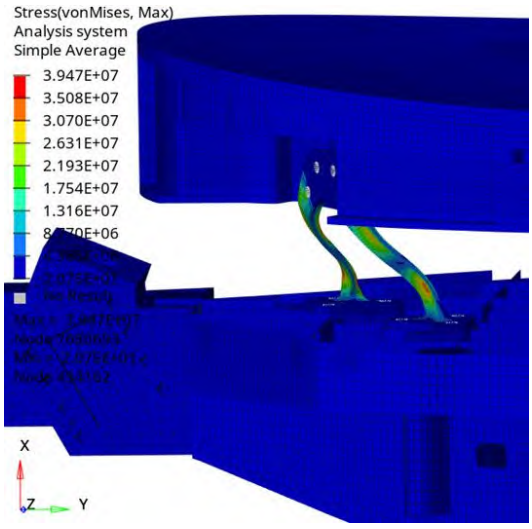


Figure 21: Maximum Von Mises stress during worst thermal load case

4. OPTO-MECHANICAL ANALYSES

4.1. Deformation under gravity

One of the main challenges of the ARIEL TA alignment is its deformation under gravity, which requires a substantial compensation from the secondary mirror in order to align it on ground. In particular, since M1 is an off-axis parabola, the secondary mirror (M2) compensates not only for power but also partially for additional Zernikes, for example astigmatism.
Two main drivers for M2 alignment on ground are:

1) The M1 gravity deformation
2) The rigid body motions of the mirrors

Figure 22 shows, on an enlarged scale, the deformation of the TA under gravity.

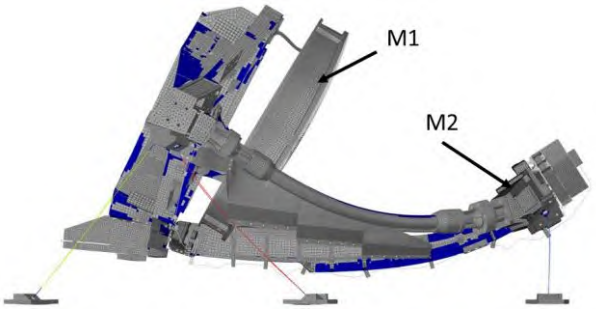


Figure 22: Telescope Assembly deformation under gravity - FE analysis

The M1 gravity deformation is significantly reduced between EM design and PFM redesign, as can be seen in Figure 23 and Figure 24.

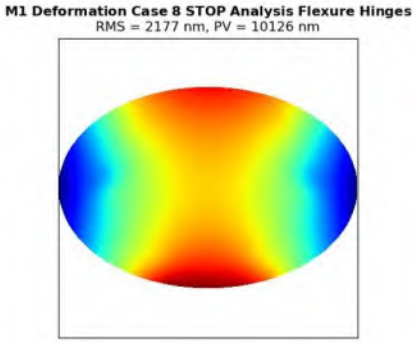


Figure 23: M1 gravity SFE with flexure hinges (EM) - power included

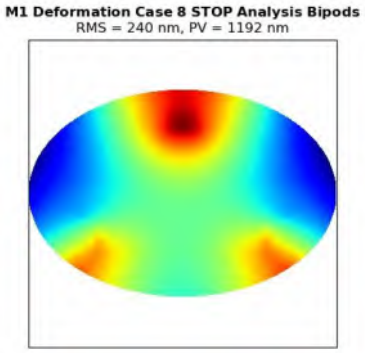


Figure 24: M1 gravity SFE with M1 bipods (PFM) - power included

Figure 23 and Figure 24 highlight the deformation prior to M2 compensation, i.e. the alignment starting point.
The M1 rigid body motions, instead, are slightly worse in the redesigned version (Table 6) due to the increase in mounting flexibility.

M1 rigid body motion	EM	PFM
Decenter x (µm)	-40.8	-39
Decenter y (µm)	-134.5	-128
Decenter z (µm)	-25.6	-42
Tilt x (arcsec)	3.4	16.4
Tilt y (arcsec)	-4.4	-4.6
Tilt z (arcsec)	-7.3	-7.6

Table 6: Comparison of M1 RBMs before and after implementation of M1 bipods

A dedicated TA optical analysis has then been performed to understand how the M2 compensators changed due to the redesign. Results are reported in Table 7, while the minimum reached telescope WFE (due to only gravity) after compensation is displayed in Figure 25 for the EM and Figure 26 for the PFM.

Compensators	EM	PFM
M2 Dec Z (µm)	276	39.5
M2 Dec X (µm)	25.3	14.1
M2 Dec Y (µm)	-749	-229

Table 7: Comparison of M2 alignment gravity compensators prior and after M1 bipods

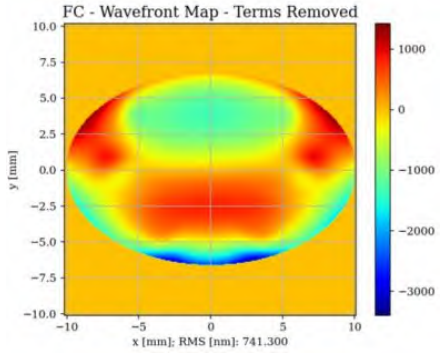


Figure 25: WFE after gravity compensation on TA EM – 741nm RMS

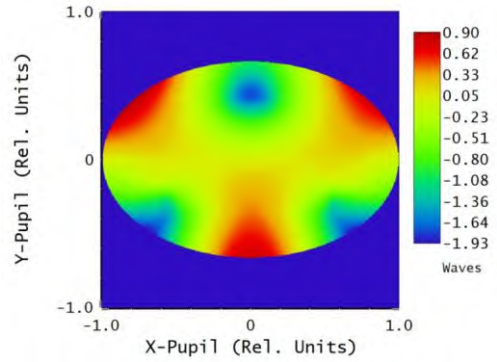


Figure 26: WFE after gravity compensation on TA PFM – 358nm rms

As a general remark, the redesign proved very effective in reducing the required compensation of the gravity distortion, mainly due to the strong reduction of the M1 deformation under gravity. The main cause lies in the more isostatic support of M1, which is connected to the bipods heads in the three locations which have been identified to minimise gravity deformation; at the same time the flexibility of the bipods absorbs the deformation due to the weight of the primary mirror.

4.2. Mounting analyses

The first step to evaluate the SFE introduced on the M1 mirror during bipod mounting is the definition of the offenders budget of the PFM redesign.
The first offender is the maximum tightening load that is transferred via bolt elongation tool. In terms of FE analysis, the SFE evaluation is deterministic and requires a single analysis. A detail of the FE tightening on one bipod is shown in Figure 27, while the resulting SFE on the primary mirror is in Figure 28, with power removed.

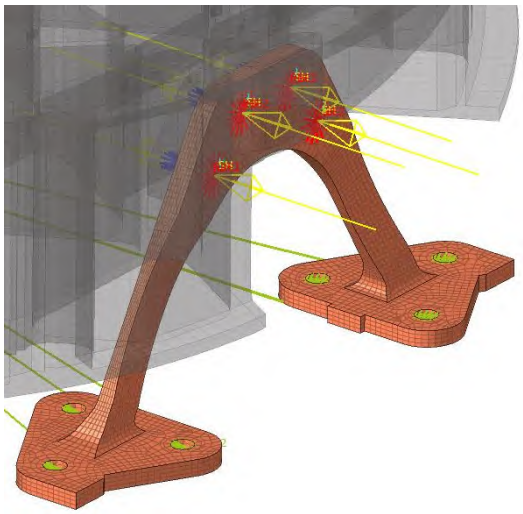


Figure 27: Detail of tightening analysis FEM

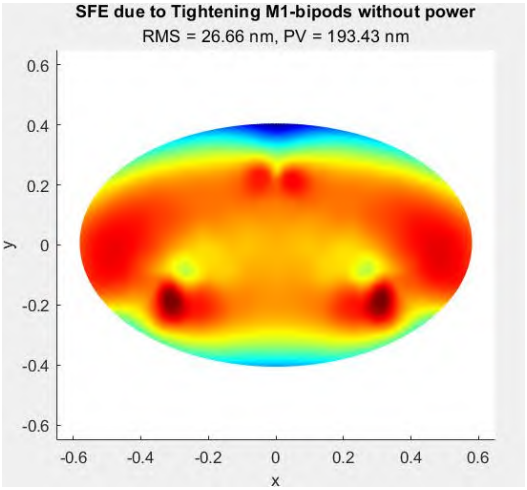


Figure 28: SFE due to M1-bipods tightening- power removed

In addition, the final mirror SFE depends also on the combination of as built finishing tolerances and positioning/measurement error of the bipods interfaces. In order to perform a worst-case assessment, a concurrent engineering has been conducted both with the TOB, M1 and bipods supplier for manufacturing tolerances and with AIT for positioning and measurement precision during M1 integration. Once the budget had been defined at M1-bipod interface (all offenders have been conservatively transferred to this interface), unitary load cases with imposed displacement at M1/bipod interface have been run (Figure 29). With reference to the frame in Figure 29, only unitary relative translation in Z and rotation in X and Y have been applied via MPCY Nastran cards; the other translations Y and Z and clocking rotation Z are compensated by the through holes at the optical bench interface.

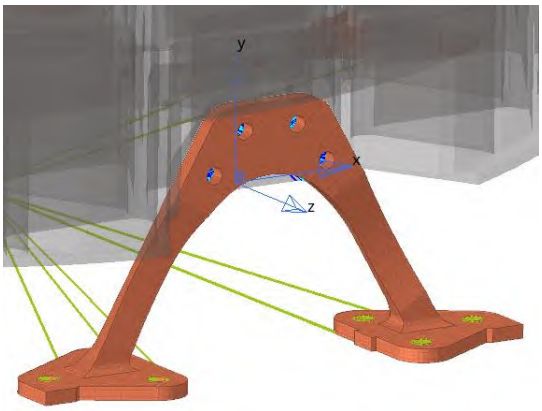


Figure 29: Reference frame for unitary imposed displacement (centered on M1-bipod IF)

Finally, a Monte Carlo analysis has been performed combining the unitary load cases and multiplying them by the calculated tolerance range between M1 and bipods.
The M1 SFE RMS has then been evaluated for the maps of all cases and the 95% confidence value has been calculated (Figure 30). Power has been removed via best-fit sphere approach.

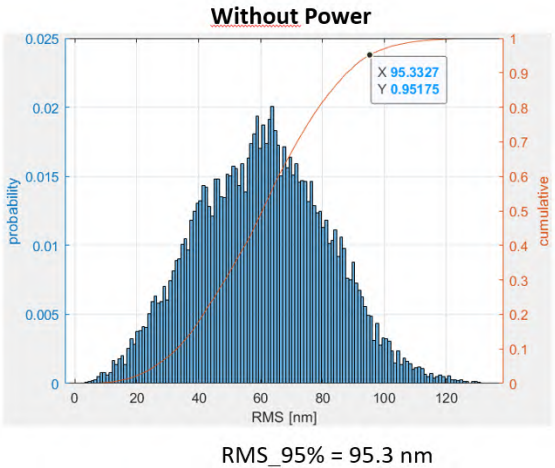


Figure 30: M1 SFE RMS due to tolerances and alignment errors – Monte Carlo analysis

The mirror SFE due to tightening has been conservatively summed to the Monte Carlo assessment and the final distribution of M1 SFE due to mounting has been identified.

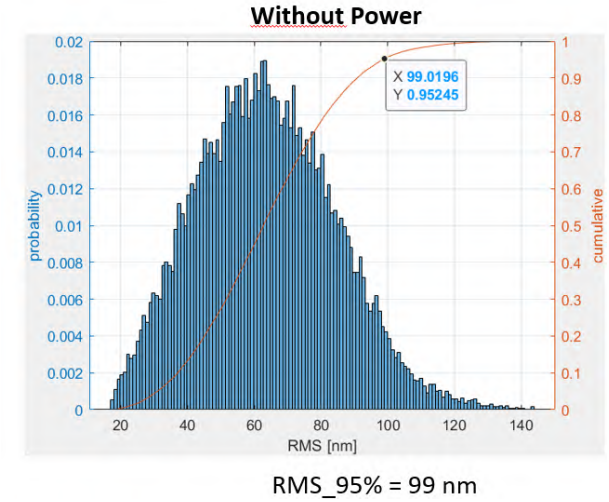


Figure 31: Overall M1 SFE RMS due to tightening, tolerances and alignment errors – Monte Carlo analysis

The final M1 mirror SFE RMS due to mounting is 99nm, which is in line with the requested performances and significantly reduced with respect to the corresponding deformation predicted and tested on SM and EM models.

5. CONCLUSION

The redesign of the primary mirror mounting of ARIEL conducted by LDO has been outlined.
The objective of the modification has been to achieve a performance of the Telescope Assembly in line with scientific requirements, while also simplifying the M1 AIT integration and alignment activities.
Due to the entity of the modification, not only performance analyses but also structural and thermal analyses have been performed, with the aim of acquiring a comprehensive view of the possible redesign impacts.
The modal analysis showed that main global modes are unaffected by the design change, while in the sine range only modes between 90 Hz and 110 Hz showed differences. Sine analysis with primary notch covered all structural needs apart from Sine Y, which required a slight secondary notch in the range 100-110 Hz. This notch has been assessed by ESA and deemed acceptable.
Dedicated thermo-elastic analyses have been performed to understand if the cooldown transient load case during transfer to L2 was critical, especially given the reduction in thickness of the M1 supports. The cooldown did not prove to be a dimensioning case, both in terms of stress on the M1 bipods and with respect to sliding margins of safety.
The impact of the M1 mounting redesign on TA

deformation under gravity has also been evaluated. The new design leverages the bipods flexibility to drastically reduce M1 SFE deformation under gravity, ultimately requiring a much smaller range of compensation on the secondary mirror for alignment on ground.
Finally, mounting analyses have been shown, implementing a Monte Carlo simulation for the assessment of a worst case M1 SFE rms (95% confidence). By analysis, the expected SFE has been substantially reduced with respect to the previous design.

6. ACKNOWLEDGEMENTS

The proposed redesign takes advantage of the lessons learned from the development plan outlined by the scientific team leading the TA SM and EM models. LDO thanks the University of Florence, the Universidad Politècnica de Madrid, INAF, CNR and the University of Rome for the precious feedback. It would not have been possible to proceed straightforwardly to a design improvement for PFM without these valuable inputs.

The activity has been performed under ASI contracts and with the support of Media Lario, in charge of the M1 mirror manufacturing.

7. REFERENCES

1. Salvignol, J., et al., “The Ariel Mission - A mission of the European Space Agency for the characterization of exoplanets”, Proceedings Volume 13092, Space Telescopes and Instrumentation 2024: Optical, Infrared, and Millimeter Wave; 130921A (2024) https://doi.org/10.1117/12.30163172.
2. Pace, E., et al., “The telescope assembly of the Ariel space mission”, Proc. SPIE 12180, Space Telescopes and Instrumentation 2022: Optical, Infrared, and Millimeter Wave, 1218011 (2022); https://doi.org/10.1117/12.2629432
3. Eccleston, P., Drummond, R., Caldwell, A., Bishop, G., Desjonqueres, L., Davidson, A., Tinetti, G., Fahmy, S., Puig, L., Salvignol, J., “Lessons in Cat Herding – methods used for managing a large international collaborative engineering project, the Ariel Mission Payload”, Proceedings Volume 13099, Modeling, Systems Engineering, and Project Management for Astronomy XI; 130990H (2024) https://doi.org/10.1117/12.3019819
4. S. Nordera, U. Barozzi, F. Miceli, et al. "Test and correlation of mounting effect on the surface form error of the ARIEL primary mirror", Proc. SPIE 13699, International Conference on Space Optics — ICSO 2024, 136995T (28 Jul 2025); https://doi.org/10.1117/12.3075148
5. Picchi, P, et al., “Aluminum based large telescopes: the ARIEL Mission case”, Proceedings Volume 13092, Space Telescopes and Instrumentation 2024: Optical, Infrared, and Millimeter Wave; 130924G (2024) https://doi.org/10.1117/12.3018855
6. D’Anca, F., et al., “Development, Manufacturing, and Testing of the Ariel’s Structural Model Prototype Flexure Hinges”, Proceedings Volume 13092, Space Telescopes and Instrumentation 2024: Optical, Infrared, and Millimeter Wave; 130924I (2024) https://doi.org/10.1117/12.3021633
7. Mahajan, V. N., “Optical imaging and aberrations – Part III – Wavefront analysis”, SPIE (2013)

A LANDER AND TRANSFER STAGE'S STRUCTURAL DESIGN CONCEPT STUDY FOR ASTEROID SAMPLE RETURN MISSIONS

Michael Lange [1], Jan Thimo Grundmann [2], Tra-Mi Ho [2], Eugen Ksenik [2], Olaf Mierheim [1]

[1] DLR Institute of Lightweight Systems, Lilienthalplatz 7, 38108 Braunschweig/GERMANY, Email: M.Lange@dlr.de
[2] DLR Institute of Space Systems, Robert-Hooke-Straße 7, 28359 Braunschweig/GERMANY

KEYWORDS

Asteroid Lander, Transfer Stage, Structures design, Apophis (99942), Sample Return

ABSTRACT

In the frame of 2029s near-Earth approach of asteroid Apophis (99942) a number of collaborative concurrent-engineering studies of the Max-Planck Institute for Solar System Research and DLR took place. Initially, a lander allowing a sample return was considered as a proposal to contribute to ESA's RAMSES mission study. In a second study, the lander and mission concept further evolved. Ultimately, it was decided to modify the concept again so that it became a mission to return asteroid samples, with the goal to submitting it under ESA's current M8 call for proposal. This paper introduces the several structural concepts studied, why and in which aspect they experienced conceptual changes.

1. INTRODUCTION

In the frame of 2029s near-Earth approach of asteroid Apophis (99942) a number of collaborative concurrent-engineering studies of the Max-Planck Institute for Solar System Research and DLR took place. Initially, a lander allowing a sample return was considered as a proposal to contribute to ESA's RAMSES mission study [1, 8]. It could have been accompanied by a smaller lander, derived from the MASCOT design [2, 9, 10] onboard the Hayabusa2, for in-situ investigations on Apophis. In a second study, the lander and mission concept further evolved into a stand-alone mission proposal and was temporarily aiming for ESA's mini-F call. Ultimately, it was decided to modify the concept again so that it became a mission to return asteroid samples, with the goal to submitting it under ESA's current M8 call for proposal. This paper introduces the several structural concepts studied, why and in which aspect they experienced conceptual changes.

The first concept 'APOSSUM (Piggy-back)', §2, studied for a potential Apophis sample return mission, was very briefly introduced in [3]. It is assembled from two main structures: one is the interface structure fitting a carrier S/C or a piggy-back launcher adapter, and the other a lander structure including a sampler and return capsule (cf. Fig. 1).

Moving from this first concept towards one that suits a variety of stand-alone missions (shared launch on the same vehicle as RAMSES, mini-F class, F-class), a dedicated transfer stage is added in the next design stage, §3. To save development costs, the transfer stage is based on the CALLISTO vehicle equipment bay [6]. Its design is similar to a conventional aluminium airframe with spars, ribs and an aluminium skin on the outside.

In a third step (dedicated M-class proposal [4, 7]), the target asteroid(s) changes, requiring an even larger lander structure and transfer stage to allow accommodating the required propulsion system adaptations (mostly larger fuel tanks). This third concept, introduced in §4, allows to reach and bring back samples form target asteroids further out.

The following paragraphs focus chronologically on one of the three development stages each.

2. APOSSUM (PIGGY-BACK)

APOSSUM (APOphiS SUrface Sampler), cf. Figure 1, is a small probe that was designed to launch on board of a larger carrier S/C or as piggy-back ride share option. The design described in the following is assumed to suit the RAMSES S/C as carrier, which is closely based on the HERA S/C structure [5].

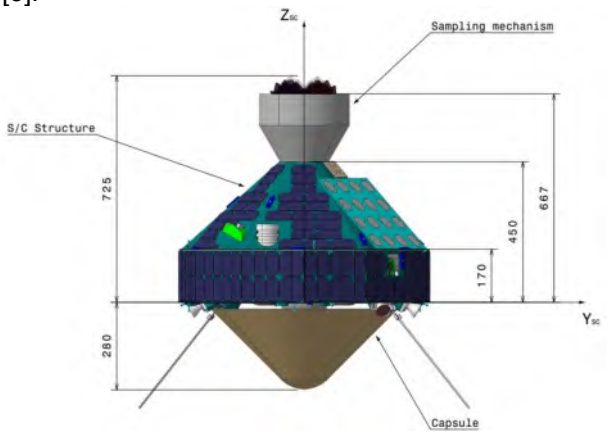


Figure 1: APOSSUM probe (w/o interface structure) for an Apophis mission.

In order to interface with the RASMES S/C (or any other one) a dedicated I/F (interface) structure is provided (Figure 2, blue part). However, it is also possible to directly body-mount APOSSUM via its three hold-down and release mechanisms (HDRM), which likely allows for a lighter system design, cf. [3]. The general advantage of a dedicated interface structure is its higher accommodation flexibility, the possibility to parallelize test and integration activities as well as the possibility to accommodate additional carry-on items on the interface structure. An APOSSUM-specific advantage of a dedicated I/F structure is that it allows to align the sampling mechanism together with the re-entry capsule opposite to each other in one axis, cf. Figure 1. Only with the I/F structure in place, it is possible to mount the whole assembly flat on a carrier S/C panel, cf. Figure 2. The decision leading to this stacked configuration, with the re-entry capsule and the sampler at two opposite ends, is based on three main aspects that are described in the following section: (1) sample transfer and storage, (2) re-entry capsule protection and (3) mass distribution.

2.1. APOSSUM configuration

(1) Due to the mission's nature, a reliable sample collection, its (contamination-free) storage and the safe transport back to Earth is the key aspect in the system design. For an unobstructed sample transport from the sampler into the capsule a straight and short path is favourable. Therefore, the sampling mechanism and the re-entry capsule are placed opposite to each other. A sampling tube connects both directly with each other. The tube runs thorough the cylindric APOSSUM bus compartment, which is located in between both, the capsule and the sampling mechanism. In the bus compartment, we find avionics, power units, further scientific payloads and so on.

(2) Another design driver for the stacked configuration is protection for the re-entry capsule's Ø700 mm heatshield. Design driver (1) inherently insures that during sampling the capsule is pointing away from the target and protect against debris. The stacked configuration with one distinct rotational axis also allows the capsule to be spin-stabilized before re-entry. At last, the heat shield shall be protected during transfer flight, too. This is partially connected to the third design driver.

(3) In order to protected the capsule during transfer flight, it is orientated with its heatshield towards the APOSSUM I/F structure and the carrier S/C. From structures point of view even more important is the mass distribution. In the presented configuration (cf. Figure 2) the re-entry capsule, which is the sub-system with the highest lumped mass, is placed as much as possible at the "bottom" of the APOSSUM stack. This brings the stack's centre of gravity (CoG) closer to the I/F structures baseplate and therefore also closer to the carrier S/C's panel. Thus, bending moments at the carrier S/C interface are reduced.

2.2. Structural details

This section discusses the structural design of APOSSUM and its interface structure in more detail. The APOSSUM interface structure (Figure 2) design is based on four CFRP honeycomb panels. One round Ø1100 mm base plate and three trapezoid plates to support APOSSUM. Those radially orientated trapezoid plates are placed in a 90° angle to the base plate and separated from each other by a 120° angle. Each tip of the trapezoids is again supported by two diagonal struts, pointing in circumferential direction and down towards the base plate. This provides a stiff support for the three HRDMs (outer light-blue dots) which fix the APOSSUM lander to the interface structure. In the center of the interface structure's base plate, we find a push-off mechanism that accelerates APPOSUM after HRDM release and allows a controlled separation. Next to the push-off mechanism, the base plate provides room for potential additional scientific payloads. The interface structure itself connects again at three points with the carrier S/C, e.g. RAMSES (black dots). Those three interface points are located in the same plane as the three trapezoids for direct axial load transfer.

The APOSSUM lander, also a CFRP sandwich structure, is sub-divided in two sections, a bus compartment and a lower (or sampler) compartment. The bus compartment is a Ø800 mm cylindric structure that features a circumferential load carrying cladding and three vertical shear panels. The separate rectangular cladding panels follow the cylindric bus shape, thus forming a dodecagon or a hexagon (as depicted in the sketch) when viewed from top. Solar cells cover the outside faces of the panels, and in order to allow access to the three behind bus compartment sections they are completely removable. The three shear panels, which separate the bus in the aforementioned sections, provide load transfer between the APOSSUM HDRMs and the re-entry capsule interface, also realized by three (smaller) HDRMs (inner light-blue dots). A triangular extension of the shear panels into the sampler compartment supports the sampling tube. At the end of the sampling tube the sampling mechanism is installed. From there another inner sample transport tube runs all the way to the capsule. The remaining room in the sampler compartment is used mostly for propellant tank accommodation (3x) and closed with cover panels. This results in a cone-shape appearance of the sampler compartment. Same as the cladding panels, the sampling compartment's cover panels have wherever possible and reasonable solar cells on their outside surface, too.

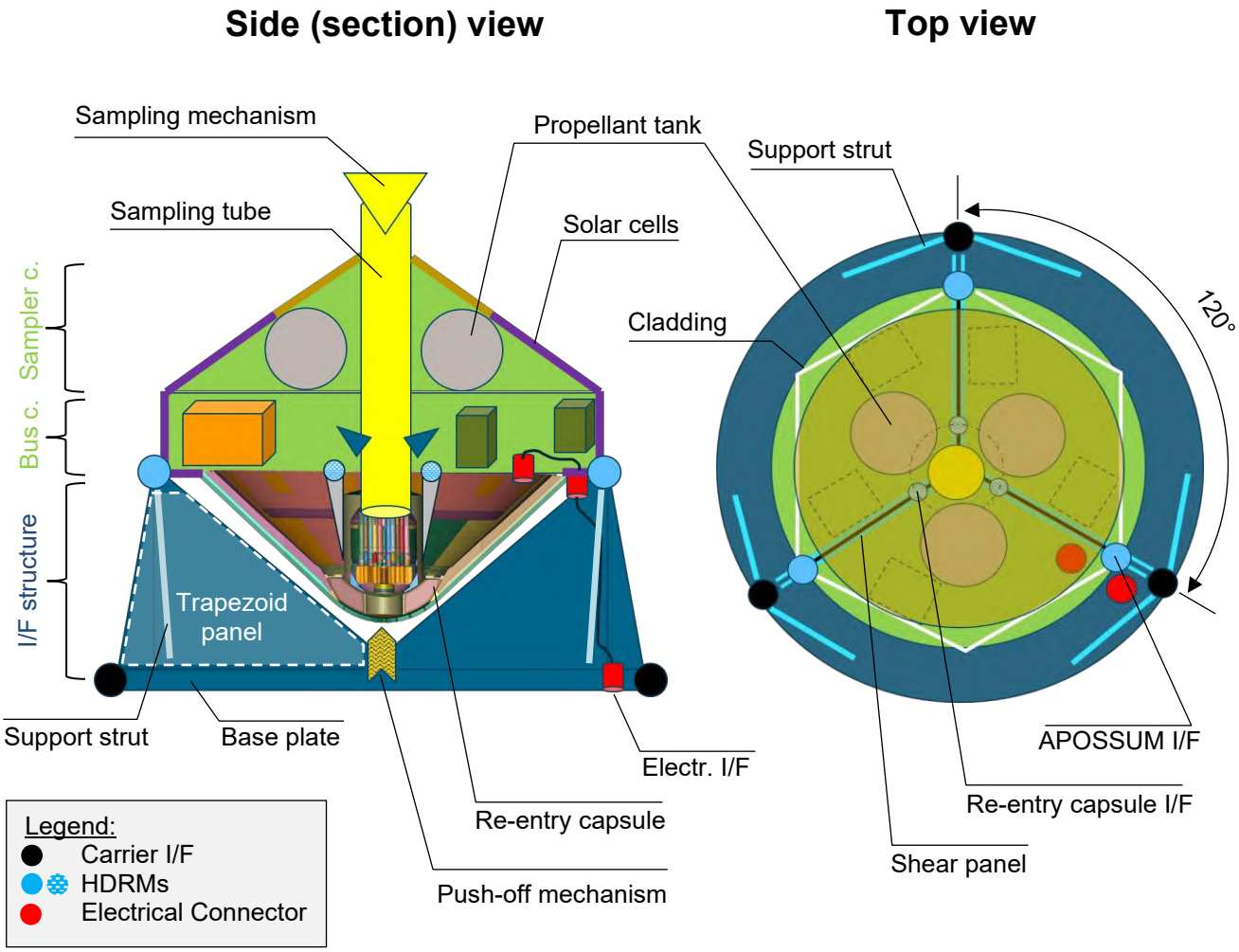


Figure 2: Section view (left) and top view (right) of the APOSSUM sample return probe with dedicated I/F (interface) structure to connect to a carrier spacecraft.

3. APOSSUM (MINI-F)

Providing a small transfer stage to APOSSUM leads to a high degree of autonomy. This is the focus of an APOSSUM configuration studied in the frame of ESA's mini-F-class call 2025. Hence, APOSSUM does not rely any longer to a carrier S/C, but is still relying to be co-launched (rideshare) in a transfer orbit with one of the various other planned missions aiming for Apophis [11, 12]. While maintaining the initial APOSSUM lander design, the major structural design work is on a newly designed transfer stage. It basically provides the required delta-v for the breaking manoeuvre at arrival and for landing/returning the APOSSUM S/C to Earth. Returning is "rather easy" due to the close Earth fly-by of Apophis.

Four different configurations were discussed for the transfer-stage's structural design:

A. "Bulky"
B. "Slender"
C. Framework + cone
D. Framework + framework

Those four variations are depicted in Figure 3.

The "bulky" or barrel shaped configuration (A) is a (stiffened) short aluminum cylinder housing three smaller propellant tanks (mid-blue) accommodated symmetrically around the central rotational axis. Mechanically, they are additionally supported by some mid-deck panel or structure. Even further below could be a helium (He) tank to pressurize the propellant tanks. A dedicated interface structure is no longer required. The interface to the APOSSUM lander is in configuration (A) realized as a body-mounted one with three HDRMs (blue dots) located at the upper circumference of the transfer stage (cf. Figure 2). At the same time the single push-off mechanism is 'devided' in three parts that are co-aligned with the HDRMs. This was already discussed during the first study in order to avoid anything in mechanical contact with the capsule's pressure-sensitive heat shield. The interface towards the launcher is a 610 mm (24") interface ring (black dots), corresponding to the ESPA Grande P/L adapter (PLA) standard.

In general, and this applies to all configurations presented in this paragraph, there is no significant change w.r.t the APOSSUM lander design described in the previous paragraph §2.

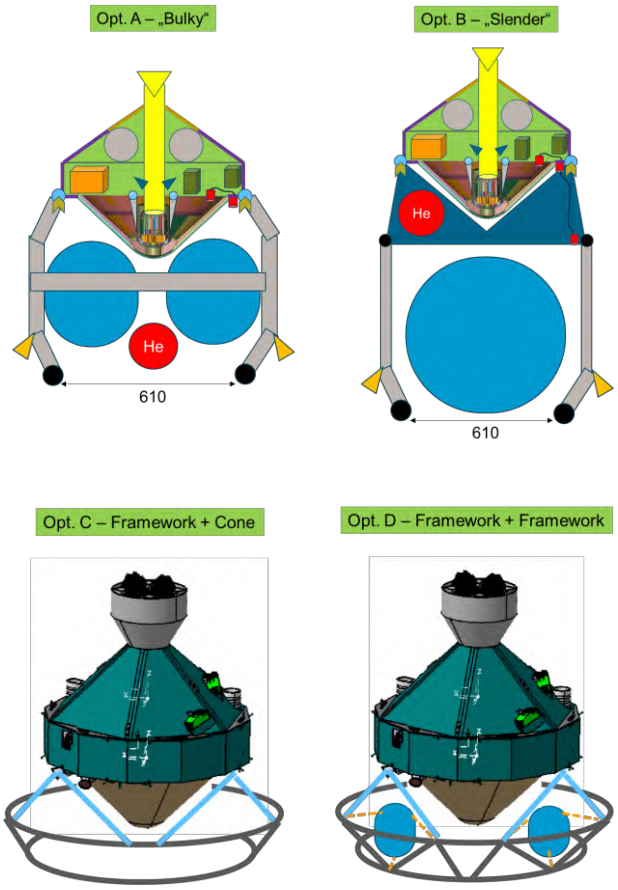


Figure 3: Four options for an APOSSUM (mini-F) transfer stage. (A) Body-mounted on cylinder configuration, (B) I/F structure on cylinder, (C) and (D) Bi-pod system on cone or framework.

The “slender” configuration (B) makes again use of the previously introduced APOSSUM interface structure (§1). In this case the additional He-tank is accommodated in a remaining free volume on the interface structure. The system of both, APOSSUM and interface adapter, is then directly bolted (at least) with its existing carrier I/F (cf. Figure 2) to a stiffened cylindric aluminum structure. More interface points might be reasonable. In this configuration the transfer stage houses only, but therefore larger spherical propellant tank (mid-blue). The interface towards the launcher is again a 610 mm (24”) ESPA Grande interface ring (black).

Option (C) and (D) are completely different. Both feature three bi-pod-like rods with an HDRM in their intersections each. The position is matching the APOSSUM lander interface location, which is similar to the configuration of the dedicated interface structure (§1). The lower end of the transfer stage could be a solid CFRP or metal cone (grey lines) for option (C) and a framework structure for option (D), respectively. Multiple propellant tanks could be accommodated for both options within the lower cone-shaped section as sketched exemplarily in option (D).

Even though the two latter options seemed to have a high potential for a quite lightweight design, they were descoped due to their estimated complexity. Option (A) is mainly discarded, because the three-tank configuration has only small flexibility to vary the propellant volume and system (mono- vs bi-propellent).

This leaves option (B) to be followed-up in more detail. Eventually, with back-up target asteroids requiring a larger propellent tank volume in the concept study further down, the tank is upgraded to the Arianegroup DT180 model. The resulting and final configuration is depicted in Figure 4. It still consists of three sections as introduced before: The APOSSUM lander, the central dedicated interface structure and the transfer stage.

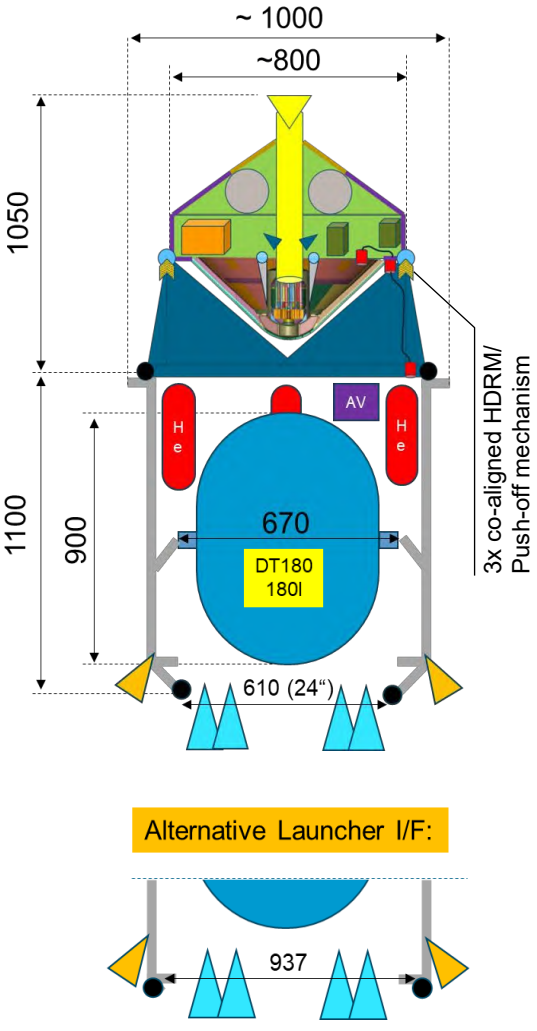


Figure 4: Final structural configuration of the APOSSUM lander incl. an own transfer stage for (mini)-F-class proposal.

The interface structure and the transfer stage section are still jointed via bolts to each. The push-off mechanism is realized as three distributed spring elements, which are co-aligned with the HDRMs that connect APOSSUM to the interface structure (as before). By increasing the propellant tank

volume, also more Helium for pressurization is required. The correspondingly larger tanks are accommodated now within the upper section of the transfer stage. Besides those, an avionics box for signal collection/distribution and local control is accommodated on the transfer stage. It distributes commands, send from APOSSUM to the propulsion module's units, and collects their housekeeping telemetry to bundle and forward it to APOSSUM for processing. Along with the larger tank, also the transfer stage structure's diameter is slightly increased. Coincidentally, the new diameter and length of the transfer structure are about the size of the CALLISTO vehicle equipment bay structure (Ø1100 mm, L=1300 mm) [6]. This vehicle equipment bay structure was designed, build and tested under DLR responsibility. Therefore, the design is already existing and a potential adaptation could be made available rather quickly to comply with the tight launch schedule to reach Apophis. As a side-effect, development costs could be reduced, too. Instead of the ESPA Grande PLA, this CALLISTIO vehicle equipment bay-based design potentially suits better the PLA 937 mm family.

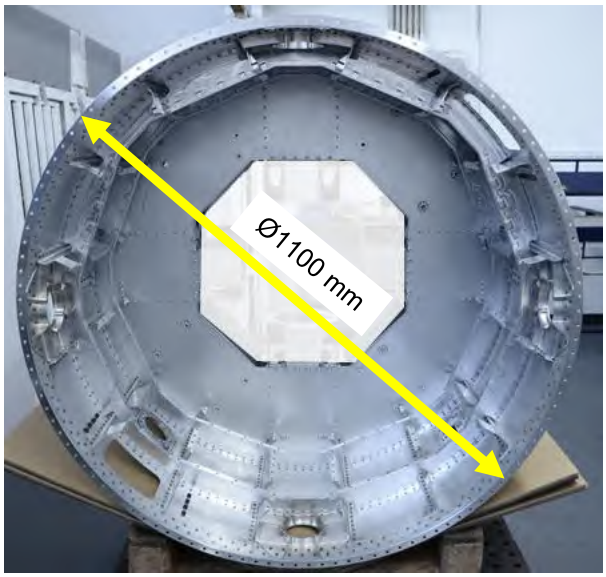


Figure 5. Structural model of the CALLISTO vehicle equipment bay structure.

4. PRIAMOS (M-CLASS)

The aim of the third study was to develop a mission concept that takes into account the high scientific and technical requirements of ESA's M8 call. An industrial partner joined this study. The mission scenario further evolved since the target object changed into D-type near-Earth asteroids (NEA) [4] meeting the anticipated launch period of the early 2040ies as required by ESA. Thus, the above introduced sample return lander, APOSSUM, was enlarged and experienced a redesign. However, the newly adapted spacecraft, PRIAMOS, still kept the transfer stage. In order to reach a reasonable number of D-type NEAs, notable changes in the system design are required. Further, to make the best possible use of the industrial partner's heritage, the redesign of the spacecraft resulted in a new configuration with units of partially higher mass, larger footprint and increased power demands. Consequently, the structure grew with the units and propellant tank volume (to reach a D-type NEA), too.

Figure 6 depicts the development of the PRIAMOS configuration, beginning from the earlier APOSSUM design (Figure 4). In a first iteration (Figure 6a) the transfer stage's propellant tank volume is increased significantly from 180 l to 769 l (Arianegroup OST 23/0). By slightly extending the length of the APOSSUM transfer stage design, this larger propellant tank system can be still accommodated in the previous design concept. Correspondingly, also the lander structure grew slightly in diameter.

After another iteration of orbit manoeuvre and delta-v calculations, it is found that the tank volume requires even further growth. Given that, the size of the CALLISTO vehicle equipment bay-based transfer stage structure is considered as no longer suitable "as is". Figure 6b indicates a slight grow in diameter, but a significant extension of 500 mm in length in order to accommodate a 1108 l propellant tank. An even bigger change, from configuration point of view, is the decision to discard in this course the dedicated interface structure. The required extension of the transfer stage provides sufficient room to (body-)mount the lander directly to the transfer stage structure. The lander's parallel growth in diameter, height and mass is mainly driven by the longer return flight propellant requirements and also by additional and partially exchanged sub-system units suggested by the industrial partner. At the same time the propellant tanks moved to the lower section of the bus compartment. The direct load transfer between PRIAMOS and the transfer stage might be realized by a clamp-band system (Ø1194 mm). At the upper circumference of the transfer stage (towards the lander) additional balconies are installed to support optical instruments for asteroid approach, remote characterization and observation after the lander is separated. Figure 6c depicts a variant on configuration Figure 6b, but with two tanks providing in sum an even larger tank volume. Form this "maximum system configuration" a flexible downgrade, depending on the target asteroid, is considered as possible. With the increased volume, the system mass and length grow as well. Similarly, the distance of the CoG w.r.t. separation plane grows and therefore requires a larger launcher adapter of Ø1194 mm type.

Eventually, the configuration submitted in the frame of the M8 call [7] differs again from the one in Figure 6c. As it is part of a proposal, it cannot be disclosed in full detail at present. The transfer stage remains a cylindric structure with similar dimensions and

same launcher adapter diameter, but is based on a structure already existing in the portfolio of the industry partner. It houses one large cylindrical propellant tank. Also, the accommodation of additional units on the transfer stage's cylinder surface is comparable to the one in Figure 6c, but with a different line of sight due to different modes of near asteroid operations. In contrast, the lander segment is quite different and no longer cylindrical, but box shaped and with deployable solar generators. The box is roughly 1500x1500x1500 mm³ in volume and features one central propellant tank. While the re-entry capsule is still mounted outside on one of the lander segment's panels, it was decided to alter the sampling mechanism configuration. It shall be noted that in context of the M8 proposal only the sampling unit incl. the re-entry capsule is referred to as APOSSUM (Asteroid Payload for Obtaining, Storing, and Sample return with Utility Module) and no longer the whole lander.

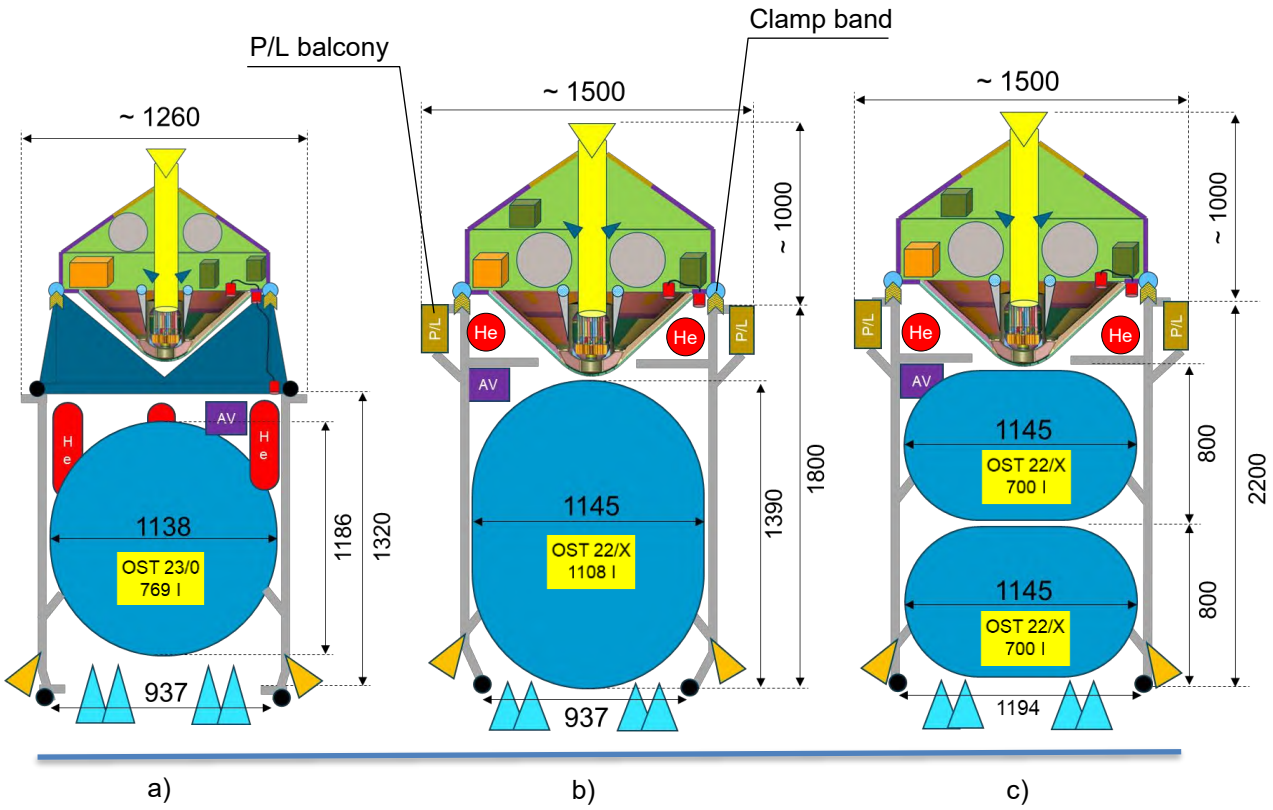


Figure 6: Three major evolution steps of the PRIAMOS configuration. The final configuration is not depicted.

5. SUMMARY

The goal of the present paper was to summarize the various studied structural concepts for an asteroid sample return mission. Initially planned for Apophis, ultimately the target asteroid became a NEA D-type one. With the target also the configuration and especially the dimension of the lander incl. a dedicated transfer stage grew. This becomes quite apparent when comparing the wet system mass of the different concepts.
Table 1 lists a rough mass estimation and distribution for structural mass and (wet) system mass. It should be noted that the numbers must not be compared 1:1 and are rather provided as an orientation.

With the dimension and mass growing, an initially planned dedicated interface structure got structurally as well as mass-wise inadequate.

*Table 1: Structure-related system mass distribution. *margin policy adjusted to suit the other listed designs, **incl. P/L adapter.*

	Mass [kg] Transfer Stage Structure	Mass [kg] Interface Structure	Mass [kg] Lander Structure	Mass [kg] System (wet)
APOSSUM (piggy-back)	n/a	6.1	8.4	105
APOSSUM (mini-F)	55	4.0	7.8	300
PRIAMOS (4c)	132	n/a	19.9	1149**
*PRIAMOS (M8)**	147.5	n/a	78.7	≈2600**

In consequence it is discarded for the PRIAMOS proposal. At the same time the transfer stage is significantly up-scaled with the required propellent and tank volume, respectively, for reaching the varying target objects. The lander itself grew moderately first. With a conceptual change, including amongst others a notably different sampler configuration, the structural mass increase in the very last iteration step was larger.

6. REFERENCES

1. Hilchenbach, Martin et al. (2024). Snatching a probe of a genuine near-earth asteroid: fast sample return opportunity in the frame of RAMSES mission scenario. In: Apophis T-5 Years Workshop, 22-23 April 2024, Noordwijk, Netherlands.
2. Ho, Tra-Mi et al. Scientifically strengthening an asteroid mission with small probes on RAMSES as use case (2024). In: 75th International Astronautical Congress (IAC), 14-18 October 2024, Milan, Italy.
3. Lange, Michael et al. A family concept for small body lander structures based on MASCOT. In: Proc. of European Conference on Spacecraft Structures, Materials and Environmental Testing 2024. 23-27 September 2024, Noordwijk, Netherlands
4. Marschall, Raphael; Kleine, Thorsten and the PRIAMOS team. ESA M8 Candidate PRIAMOS – A Sample Return Mission to a D-Type Near Earth Asteroid. 15th Asteroids Comets Meteors Conference (ACM 2026), 6-10 July 2026, Poznan, Polen.
5. Alessandro Paci, Baris Eroglu, Nicola Riva, Harald Segelke. HERA spacecraft´s lean PFM qualification approach - OHB-SE industrial experience. In: Proc. of European Conference on Spacecraft Structures, Materials and Environmental Testing 2024. 23-27 September 2024, Noordwijk, Netherlands
6. E. Dumont et al. CALLISTO Reusable rocket stage demonstrator: consolidating the design, 2024 IEEE Aerospace Conference, Big Sky, MT, USA, 2024, pp. 1-19.
7. Kleine, Thorsten and Marschall, Raphael. PRIAMOS – Primordial Asteroid Mission to understand the Origin of Solar system. Step-2 M8 mission proposal. Internal Communication.
8. Lazzarin, M. et al. (2025). The ESA RAMSES Mission: Rendezvous with the Asteroid Apophis during its Close Encounter with Earth in 2029. In: Proceedings of 76th International Astronautical Congress 2025 (IAC 2025), 2025-09-29 - 2025-10-03, Sydney, Australien.
9. Ho, Tra-Mi et al. (2025). BASTET – A MASCOT-style Nanolander Investigating the Subsurface of Apophis, Seismicity, and Tidal Forces during Earth Encounter. In: Apophis T-4 Years 2025 (LPI Contrib. No. 3083)
10. Ho, T.M. et al. (2017). MASCOT—the mobile asteroid surface scout onboard the Hayabusa2 mission. *Space Sci. Rev.* 208 (1–4), 339–374.
11. M. Pascual et al. Exploration of asteroid Apophis with the ExLabs Arachne spacecraft (2024). In: Apophis T-5 Years Workshop, 22-23 April 2024, Noordwijk, Netherlands.
12. S. Squyres, T. Randolph, and T. Sanford. blue origin's blue ring spacecraft enables detailed investigation of Apophis before, during, and after its earth encounter (2024). In: Apophis T-5 Years Workshop, 22-23 April 2024, Noordwijk, Netherlands.

PLANETARY PROTECTION PLATFORM RE-USE: OHB INDUSTRIAL EXPERIENCE

Matthias Sendecki [(1)], Angela Marco Mariscal [(1)], Alessandro Paci [(1)], Nicola Riva [(1)], Harald Segelke[(1)], Christian Vettore[(2)], Ivan Gryaznov[(2)]

[(1)] *OHB Systems AG, Universitätsallee 27-29, 28359, Bremen, Germany,*
Email: matthias.sendecki@ohb.de; angela.marco_mariscal@ohb.de; alessandro.paci@ohb.de; nicola.riva@ohb.de; harald.segelke@ohb.de

[(2)] *OHB Italia S.p.A, Via Gallarate 150, 20151 Milano, Italy,*
Email: christian.vettore@ohb-italia.it; ivan.gryaznov@ohb-italia.it

KEYWORDS

Reusability, qualification, structural concept, heritage, readiness

ABSTRACT

OHB has developed a family of three S/C within the framework of scientific and planetary defence missions led by ESA: Hera, Comet Interceptor, and RAMSES. All three share a common platform originally designed for Hera, characterized by a compact cubic shape with a primary structure based on a Central Tube. Hera was successfully launched in autumn 2024, while Comet Interceptor and RAMSES have completed their Critical Design Reviews (CDR) and are currently in the assembly phase, scheduled for launch in the coming years.

This common-platform approach enabled OHB to achieve substantial savings in development time and cost by leveraging the structural and programmatic heritage of Hera. This paper presents a comprehensive overview of all three S/C, describing the shared platform elements alongside mission-specific adaptations, and outlines potential future applications of this platform concept for upcoming planetary defence or scientific missions.

1. INTRODUCTION

The traditional approach of spacecraft structures design, verification and manufacturing relies on a stand-alone dedicated built-up logic, where each platform is designed for a specific mission. Typically, a lot of effort is spent in early phases to understand and meet the project goals via a dedicated platform configuration, and during implementation phases, as every component needs to be qualified against launch and in-orbit environments. This approach results in very cost and time expensive process needed to ensure a reliable product.

In this scenario, new space requests, along with shorter and more stringent schedules and budgets, are acting towards a change in this paradigm to meet these exigent needs. OHB System is working actively in implementing these modern development procedures to ensure shorter delivery times via a re-use approach of spacecraft platforms. In the case of the spacecraft structures, this re-use approach consists of taking one structural concept as a direct baseline and customize only the features that the specific mission requires. This approach not only shortens the development times, but also the qualification process can be shortened and simplified.

Among various examples, Hera's family is an outstanding case-study. After the successful launch of this mission in an already exigent timeframe, two other scientific and planetary defence missions have been developed based this structural concept: a compact, cubic structure made of sandwich panels based on a central tube (CT) primary structure. These two projects are Comet Interceptor and RAMSES.

The re-usability of this platform allowed both projects to compress the spacecraft development schedule in a way that would not have been possible under a conventional spacecraft development programme. The experience gained by OHB System in the development of these three spacecrafts opens the question of whether such a platform can be further standardized and maintained in a state of readiness for short-notice missions, and of the conditions required to make this possible. The successful implementation of such a concept would represent a major milestone in European spacecraft development, enabling a rapid-response capability for future Near-Earth Object (NEO) missions and demonstrating the feasibility of a partially serialized spacecraft platform approach within OHB System.

2. HERA'S STRUCTURAL CONCEPT AND VERIFICATION

Hera was launched in October 2024 to rendezvous with the Didymos binary asteroid system. Its structure is based on a cubic platform architecture centred around a central tube. This central tube is the primary load path between the launch vehicle interface and the propellant tank stack and represents the largest structural heritage item. At secondary structure level, Hera consists of six

external honeycomb panels and four shear webs that ensure the load transfer between the primary structure and sandwich panels. The tertiary structure assembly contains all the brackets required to accommodate, support and orient the different platform and payload units.

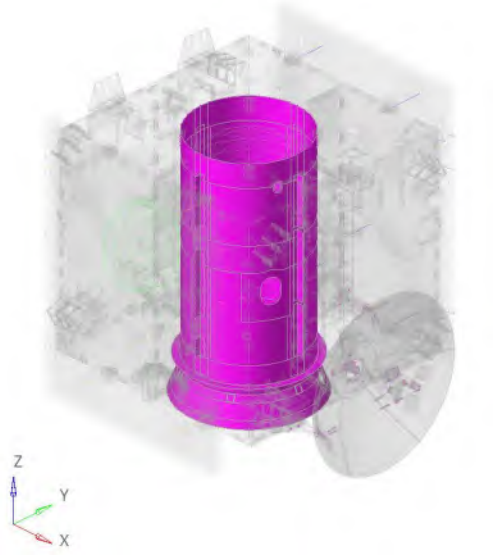


Figure 2-1 Hera's primary structure

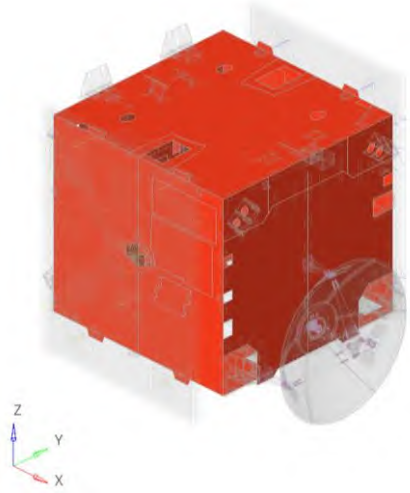


Figure 2-2 Hera's secondary structure

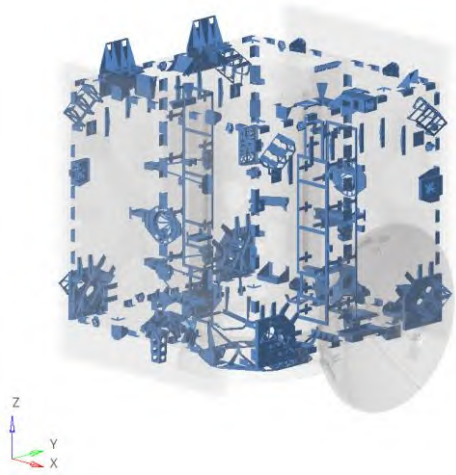


Figure 2-3 Hera's tertiary structure

The tight development schedule and available budget at the time established the first project of the family which was qualified following a lean and cost and schedule efficient approach. This approach consisted of a Proto-Flight Model (PFM) qualification and testing without an intermediate Structural Model (SM), where all the structural components are tested and successfully qualified at system level, while component level testing is only performed for the primary structure, which was verified under static load test (SLT). The secondary structure was only subjected to coupon level test to characterize the CFRP properties and the inserts' strength, while the tertiary structure development was carried out only via analysis instead. This lean verification approach can be seen in Table 2-1.

Table 2-1 Verification matrix for the Hera structural items

Verifiaction Method				
Structural Item	**Coupon Tests or Material Allowable Tests**	**Sub Assembly Level Tests**	**Structural Analysis**	**SC Level Environmental Tests**
Primary Structure				
Central Tube	✓	✓	✓	✓
Inserts	✓		✓	✓
Skins	✓		✓	✓
Honeycomb	✓		✓	✓
Shear Panel Cleats	✓		✓	✓
Fork Connection at CT		✓	✓	✓
Secondary Structure				
Structural Panels			✓	✓
Inserts	✓		✓	✓
CFRP Skins	✓		✓	✓
Al Skins			✓	✓
Honeycomb			✓	✓
Tertiary Structure				
Panel-Panel Cleats			✓	✓
Unit Brackets			✓	✓

3. RE-USE METHODOLOGY

Comet Interceptor and RAMSES are both based on a Hera re-used platform. They are currently in the assembly phase and are scheduled for launch in the coming years. Comet Interceptor is a scientific mission aimed at intercepting a pristine or interstellar comet and deploying two sub-probes to observe it from multiple viewpoints, whereas RAMSES is ESA's contribution, together with JAXA, to the investigation of asteroid Apophis during its close approach to Earth. Rather than following the traditional approach of developing a mission-specific spacecraft and performing a complete qualification programme, both projects were developed as evolutions of the already qualified Hera platform. The same compact cubic architecture based on a central tube primary structure was retained, while targeted modifications were implemented to address mission-specific requirements. These include the addition of a dust shield, a side-mounted balcony, and two deployable

sub-probes for Comet Interceptor, as well as the integration of larger protruding propellant tanks for RAMSES. Furthermore, Hera's lean structural qualification approach was adopted as the baseline and reduced when heritage and design similarity allowed, enabling significant savings in development effort and schedule.

The successful implementation of this approach is particularly noteworthy considering the differences between the three missions. As shown in Table 3-1, Hera, Comet-I, and RAMSES differ in several key aspects, including mission profile, launch vehicle, propellant capacity, and even industrial responsibilities for major structural elements. Nevertheless, the same fundamental platform concept could be retained and adapted to meet the specific requirements of each mission. This experience demonstrates the robustness and flexibility of the Hera's platform.

Table 3-1 Comparison of key programmatic parameters across the HERA-derived platform family

Parameter	HERA	COMET -I	RAMSES
Mission type	RDV	Flyby	RDV
Phase A–B2 duration	~2 years	1.5 years	0.9 years
Phase C KO – LRR	4 years	~5.5 years	3.5 years
Redundancy concept	Full redundant	Full redundant	Single string
S/C dry mass [kg]	603	747	510
S/C wet mass [kg]	1092	975	1244
PF dry mass [kg]	519.5	611.9	440
Propellant tank capacity	248 l biprop	198 l biprop	331 l biprop
Large-manoeuvre ΔV	~1200 m/s	~550 m/s	~1600 m/s
Launch vehicle	Falcon 9	Ariane 6	H3
Panel supplier	Invent	Invent	APCO
CT supplier	Beyond Gravity	MT Aerospace	Beyond Gravity

3.1. Comet Interceptor

COMET-I Primary, Secondary and Tertiary STR are based on HERA Platform. Regarding qualification strategy, the same lean approach that was used in Hera was adopted. Since the panel supplier was the same and there was enough heritage providing confidence to the structural properties, coupon level test of the secondary structure was not needed therefore reducing development time.

3.1.1. Central Tube

At primary structure level, the central tube (CT) is manufactured as a monolithic component by MTA, replacing the sandwich construction produced by Beyond Gravity Switzerland for Hera.

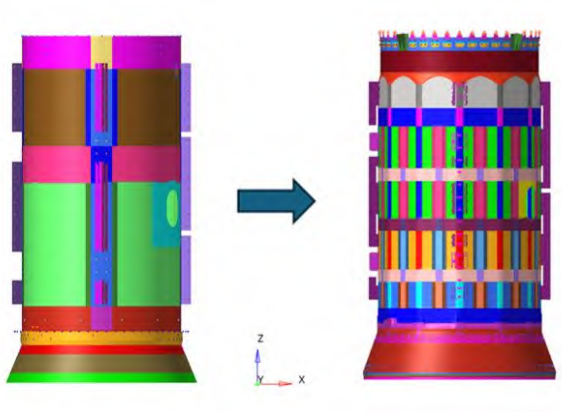


Figure 3-1 Comet-I Central Tube redesign with respect to Hera

Structural verification was performed under analysis and a Static Load Test (SLT) in the frame of the development of the CT for the Hera family, decoupled from the development of the Comet-I mission specific CT, which reduced significantly development time of the primary structure.

3.1.2. Coca Balcony

Coca balcony consists of an extension of the main structure in the -X direction. Coca Balcony aims to host the platform pointing instruments and some of the optical payloads (WAC Cameras and Coca Telescopes). Such instruments require a clean and unobstructed Field of View (FOW) which is guaranteed by moving these instruments outside the main Hera Platform perimeter. Coca Balcony is composed of sandwich panels with CFRP face skins, and it is supported by the main structure via shear webs, the radiator panel YN and struts.

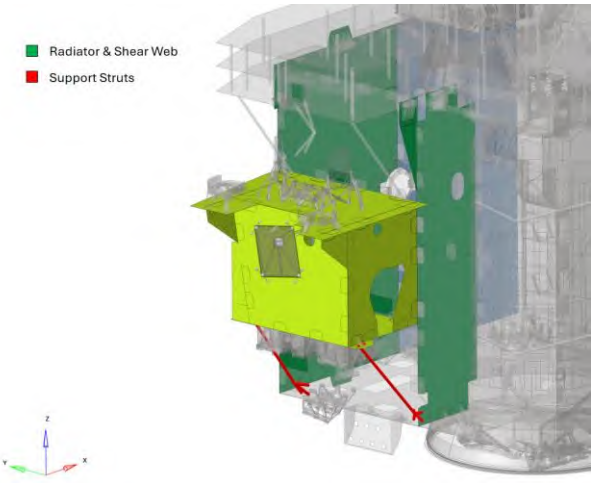


Figure 3-2 COMET-I COCA Balcony and supporting structures

COCA Balcony structural integrity has been verified mathematically under the application of the following launch load environments: Global Quasi-Static Loads (GQSL), sine and thermo-elastic. Furthermore, structural verification was performed also under Quasi Static Load (QSL) cases derived via sine analysis, which aim to add a further level of

confidence on the predicted margins of safety.

3.1.3. Dust Shield

Dust shield (DS) is a Comet-I subassembly added on the satellite upper section. Such component aims at protecting the SC, and the instruments within it, from dust and debris clouds that could irreversibly jeopardize the mission. The dust shield consists of peculiar design made of three main components, from the top to the bottom: an Outer Bumper of a 0.5 mm thin aluminum sheet, a Mid Bumper of a 1.3 mm Kevlar fabric layer, placed in between the outer bumper and the Top Deck, and a top deck consisting of 20 mm sandwich panel that also serves as SC top panel.

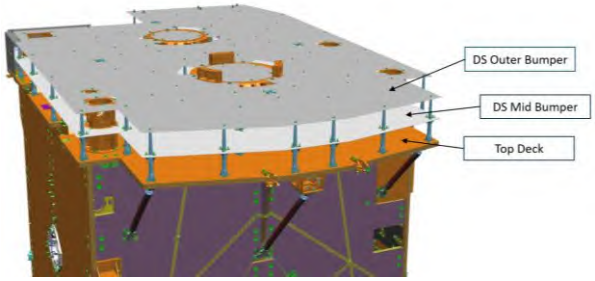


Figure 3-3 COMET-I Dust Shield

Outer and Mid bumpers are suspended over the Top Deck and supported via dedicated DS Standoffs and payload brackets. Furthermore, to protect from debris also HGA and the COCA Balcony, the dust shield is extended in + and – X direction outside the Hera Platform Perimeter. Such extensions are supported via dedicated struts.

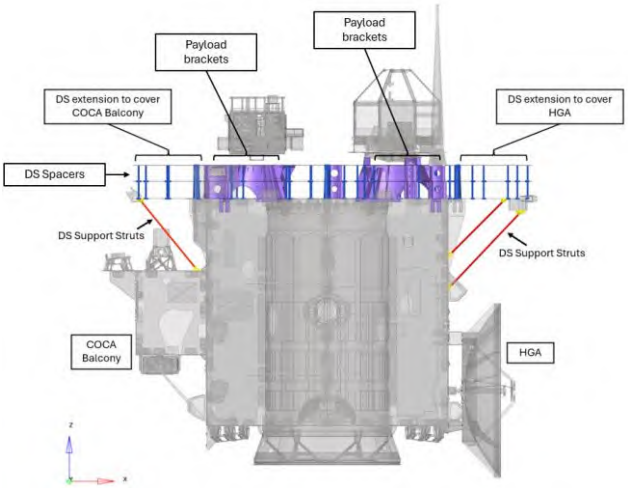


Figure 3-4 Dust Shield supporting structures and extensions

Dust shield integrity has been verified under the traditional Launch load environments: GQSL, sine, acoustic and thermo-elastic. Due to the peculiar design of this item, the traditional frequency response analysis was not sufficient to prove compliance with respect to sine environment. Therefore, a dedicated transient nonlinear analysis has been set up and performed [1].

Furthermore, also a dedicated Vibro-Acoustic test has been performed on a dust shield structural model, which consisted of a portion of the actual dust shield. This test aimed to verify the validity of the Dust Shield responses predicted during Vibro-acoustic analysis. Results showed a good correlation between measurement and predictions.

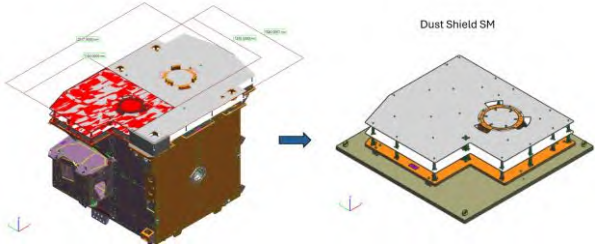


Figure 3-5 Dust shield structural model

3.2. RAMSES

RAMSES' structural concept takes as a direct baseline the structure developed for Hera. The main customizations done to the structure are mainly driven by the need of accommodating larger 331 l bipropellant tanks, compared to Hera's 248 l tanks, while preserving the external envelope and launcher interface.

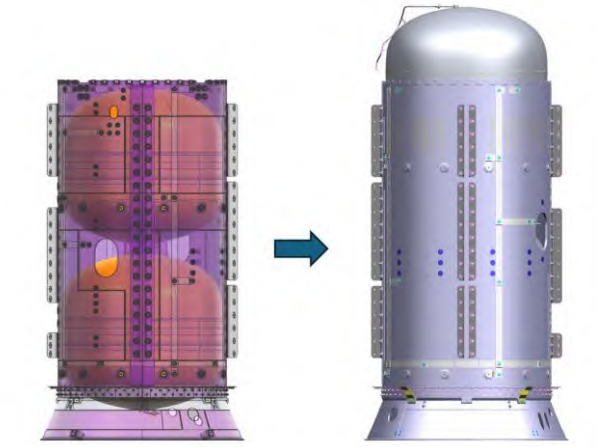


Figure 3-6 Comparison of Hera's and RAMSES's propellant tanks

These changes were primarily within the rebuilt central tube and the asteroid deck (AD).

3.2.1. Central Tube

The RAMSES Central Tube (CT) represents the most significant primary-structure modification with respect to the Hera heritage design. While preserving the overall architecture, load path philosophy, and launcher interface, the CT was redesigned to accommodate the increased propellant volume required by the RAMSES mission. The transition from Hera's 248 l bipropellant tanks to RAMSES's 331 l tanks necessitated a localized redesign of the primary structure while maintaining maximum commonality with the qualified Hera configuration.
The redesign was driven by the accommodation of the enlarged propellant tanks and resulted in three

principal modifications to the CT geometry:

- Adaptation of the MMH tank interface region through a revised composite ply lay-up.
- Relocation of the cylindrical cut-out in the positive Z-direction.
- Introduction of additional cone cut-outs to accommodate the modified propellant-line routing.

Despite these modifications, the global structural concept and load transfer mechanisms remained unchanged. The design therefore deliberately maximized the retention of heritage qualification evidence while limiting the scope of new verification activities. Figure 3-7 compares the Hera and RAMSES Central Tube configurations.

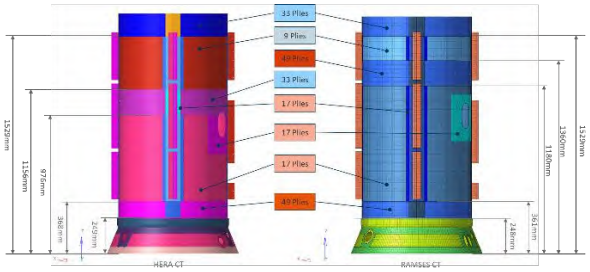


Figure 3-7 Comparison of CT design between HERA CT and RAMSES CT

Rather than repeating a full-scale structural qualification campaign, the RAMSES CT was verified through a delta-analysis approach, referenced against the correlated Hera Static Load Test (SLT) results. The assessment focused on demonstrating that the modified load paths and local structural changes remained bounded by the qualification evidence generated during the Hera programme. This approach was a key enabler for meeting the accelerated RAMSES development schedule while maintaining confidence in the structural integrity of the primary structure.

To support the re-use assessment, the load flux along the spacecraft height was compared against the load distribution measured during the Hera Central Tube SLT. An analytical equivalent cantilever-beam model was developed for the RAMSES configuration, considering the increased spacecraft mass and updated launch-load environment. The comparison confirmed a close correlation between the heritage qualification case and the RAMSES flight configuration, providing the technical basis for qualification by similarity. Figure 3-8 and Figure 3-9 illustrate the analytical model and the resulting load-flux comparison.

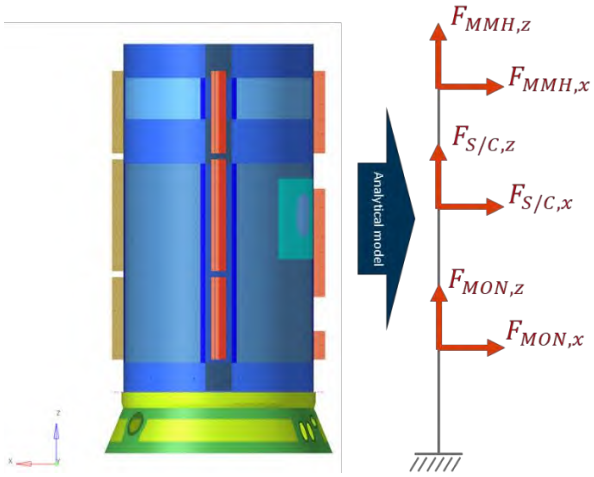


Figure 3-8 Analytical equivalent cantilever beam model

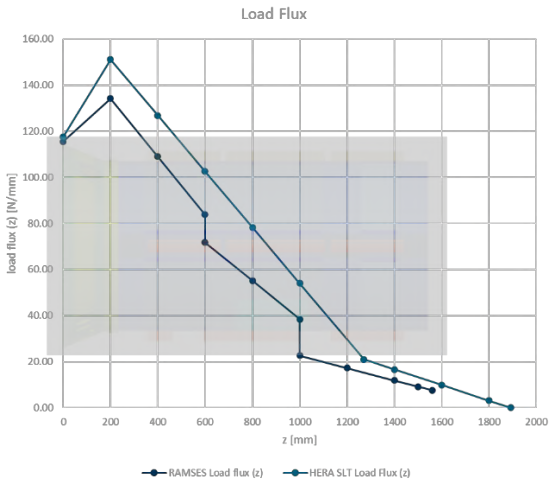


Figure 3-9 Comparison of load flux between HERA CT SLT and RAMSES

3.2.2. Asteroid deck and secondary structure lay-up

The asteroid deck (AD), which forms the upper deck of the RAMSES spacecraft structure, is a sandwich panel designed to accommodate most of the payload units. To accommodate the increased volume of the propellant tanks while maintaining maximum commonality with Hera's structural architecture and envelope, the RAMSES asteroid deck incorporates a large cut-out. This modification allows one of the propellant tanks to protrude through the panel.

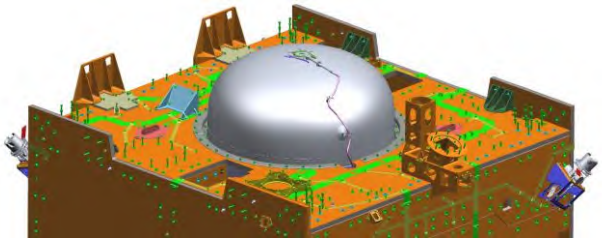


Figure 3-10 RAMSES Asteroid Deck cut out and protruding tank

Local panel reinforcements were introduced in all the secondary structure panels, based on lessons learned from Hera and the revised unit accommodation layout. In particular, the asteroid deck was strengthened through the introduction of structural doublers and high-density core regions around the central tube interface and at locations identified for future payload accommodation. As these design provisions were implemented before the final definition of the payload units, a conservative reinforcement approach was adopted.

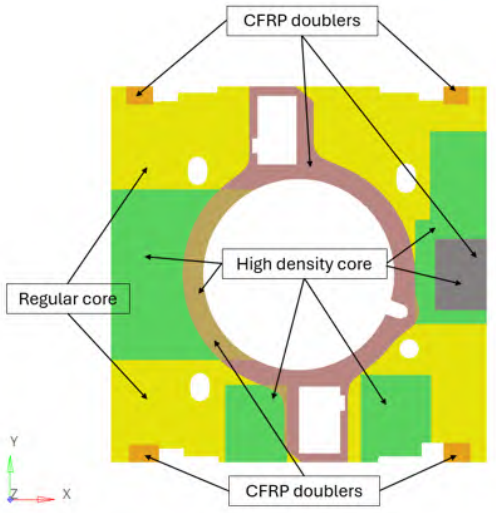


Figure 3-11 Asteroid deck internal lay-up

Even though the supplier of the secondary structure panels changed from Hera to RAMSES, the coupon level test was also not performed due to the existence of heritage from other OHB System projects with APCO. Therefore, material properties were already tested with sufficient confidence.

3.2.3. Interface ring between the AD and the CT

An interface ring is introduced in the RAMSES structure between the asteroid deck and the central tube to transfer loads from the top panel to the primary structure. The ring is manufactured from aluminium and features a Z-shaped cross-section. For manufacturing purposes, it is divided into three segments. This ring is not present in Hera, where the asteroid deck is connected directly to the central tube through edge inserts.

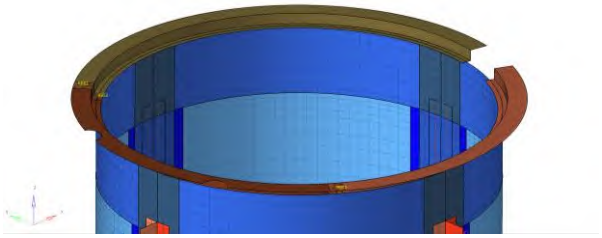


Figure 3-12 RAMSES Interface Ring between asteroid deck and central tube

Interface ring integrity has been verified under the traditional launch load environments as part of the normal work of the spacecraft structural verification.

4. RE-USE ASSESSMENT AND LESSONS-LEARNED

a. Checking re-use possibilities: Delta analyses and qualification by similarity

The reuse of Hera structural heritage relied on a systematic qualification-by-similarity assessment. For each inherited structural item, it was verified that the load environment remained within the qualified Hera envelope and that materials, manufacturing processes, and interfaces were unchanged. Where these conditions were not fully satisfied, delta analyses were conducted against the Hera correlated structural model to assess the impact of the modification. By limiting requalification activities to the affected areas, this approach preserved the maximum amount of qualification heritage and significantly contributed to the compressed development timeline.

b. Early decision making: Trades and consequences

The experience shows that trades made early, even before the payload complement was frozen, had an outsized influence on how much of the Hera heritage could ultimately be preserved. Decisions such as the tank size increase and the single-string architecture were taken deliberately early to protect schedule, at the cost of committing the Central Tube rebuild before all downstream requirements were known.

Conversely, RAMSES experienced late payload-accommodation changes driven by the finalization of the scientific payload complement, after completion of the structural design phase and internal lay-up of the asteroid deck. This resulted in the need for late delta qualification analyses under schedule pressure.

c. Lessons learned: Standardization of payload interfaces and top deck internal lay-up for real rapid response

During RAMSES development, the late definition of the scientific complement and its respective opportunity payloads led to negative margins on selected structural items. This experience directly motivates the development of a standardised platform architecture capable of accommodating any payload compliant with predefined specifications. In contrast to the RAMSES approach, which relied on local reinforcements introduced as payload requirements evolved, such a platform would incorporate a fully reinforced asteroid deck from the outset.

A second lesson learned concerns the definition of payload accommodation requirements. Even when the payload complement is not known from the outset, a realistic and comprehensive specification should be established early in the programme and imposed on payload developers, thereby freezing the platform interfaces. Such a specification should define a bounding payload mass, centre-of-gravity,

and inertia envelope, including appropriate margin reserves, together with a standard mechanical mounting pattern and associated keep-out zones. In addition, it should specify the bounding mechanical and thermal environments at the interface, as well as a pre-agreed verification approach defining which changes can be closed by analysis only and which require dedicated delta qualification activities.

d. Lessons learned: a missing toolset for rapid response

A recurring finding is that no dedicated, pre-qualified analysis toolset exists to rapidly assess whether a new mission's requirements remain within the Hera-platform structural envelope or to identify potential structural impacts early in the design process. Each re-use assessment required bespoke engineering judgement and manual delta-analysis set-up rather than a parametrized, fast-turnaround verification chain. For a genuine rapid-response capability, this toolset, ideally a pre-correlated, parametrized finite-element model of the platform with pre-approved analysis cases, would need to exist before the next call for a short-notice mission arrives.

5. OUTLOOK: STRUCTURAL READINESS FOR FUTURE SHORT-NOTICE NEO MISSIONS

Beyond RAMSES and Comet Interceptor, the underlying question for planetary defence and scientific missions' future development is how a Hera-like platform can be serialized and kept ready to respond with essentially no advance notice, and before the specific payload needed to characterize that object is known. From a structural standpoint, this reframes several of the re-use beforementioned lessons learned into standing engineering questions that should be answered once, in advance, rather than re-derived on every future short-notice mission:

- What is the bounding payload mass, centre-of-gravity and inertia envelope the platform can accommodate without triggering a Central Tube or primary structure redesign, and how much of it should be held as reserved margin rather than offered to the payload up front?
- Which mechanical, thermal and electrical interface standard (mounting pattern, keep-out zones, bounding environments) can be frozen today, so that any future payload developed against it is verifiable by analysis alone against a pre-qualified envelope?
- Which structural qualification evidence (Hera SLT, Hera Sine & Acoustic test, coupled loads) can be pre-packaged into a parametrized, re-usable verification toolset, so that a delta analysis for a new mission is a matter of days, not months?
- What minimum reserve of structural test capacity should be kept on standby, and for which items should physical re-test remain mandatory regardless of analysis results?
- What is the minimum necessary structures-department involvement at each phase of a rapid rebuild, and can a leaner, checklist-based sign-off process replace a full re-verification loop once the above points are in place?
- How should schedule margin be allocated structurally (e.g. late-integration brackets, de-coupled platform and payload build flows) so that a late payload selection — inevitable when the target and its required instrumentation are only defined after discovery — no longer produces late negative margins?

Answering these questions in advance, rather than under the schedule pressure of an active short-notice mission, is what would turn the Hera/Comet-Interceptor/RAMSES heritage from a successfully re-used bespoke platform into a genuine rapid-response asset.

6. CONCLUSIONS

The Hera structural re-use case demonstrates that a bottom-up, heritage-driven platform strategy can compress spacecraft development from Phase A/B2 kick-off to CDR to under a year, enabling rapid response for future Near-Earth Object (NEO) missions and demonstrating the feasibility of a partially serialised spacecraft platform approach within OHB System. It also shows the limits of ad-hoc re-use: without frozen interfaces, a parametrized analysis toolset, and standing test capacity, heritage preservation still requires late, schedule-critical delta analyses and case-by-case structures-department involvement.

At the same time, the Hera, Comet Interceptor, and RAMSES missions demonstrate the remarkable flexibility of the platform family. A common structural architecture was successfully adapted to three distinct mission profiles and qualified for three different launch vehicles, namely Falcon 9, Ariane 6, and H3. The platform robustness is further evidenced by the successful implementation of two different Central Tube designs and the qualification of secondary structures manufactured by two independent panel suppliers, while maintaining a high degree of structural heritage and commonality across the programme.

The lessons captured here, and the standing questions posed for future short-notice near-Earth-object missions, are intended to inform how OHB and ESA prepare the next generation of rapid-response planetary defence platforms.

7. REFERENCES

[1] D. Pederbelli, A. Paci, I. Ngan, H. Segelke, N. Riva and I. Gryaznov, "PREDICTING NONLINEAR VIBRATIONS OF THIN PLATES. THE COMET-I CASE STUDY," in *ECSSMET 2026, European Conference of Space Structures, Materials and Environmental Testing*, Braunschweig, 2026.

[2] L. Gury and V. Grosjean, "HERA CT Structure SLT Evaluation Report," beyond gravity, Zurich, 2023.

[3] A. Paci, B. Eroglu, N. Riva and H. Segelke, "HERA SPACECRAFT´S LEAN PFM QUALIFICATION APPROACH: OHB SYSTEM INDUSTRIAL EXPERIENCE," OHB-System AG, Bremen, 2024.

[4] P. Valero and V. Grosjean, "RAMSES Central Tube Analysis Report," beyond gravity, Zurich, 2025.

LANDING LEG SYSTEM DEVELOPMENT FOR REUSABLE LAUNCHERS

Tiziano Mascazzini [(1)], Anton Schneider [(2)], Josef Klevanski [(3)], Johannes Baumgarten[(4)]

[(1)] MT Aerospace AG, Franz-Josef-Strauß-Str. 5, 86153 Augsburg, Germany, Tiziano Mascazzini tiziano.mascazzini@mt-aerospace.de
[(2)] German Aerospace Center (DLR), Institute of Space Systems, Germany, Bremen, Anton Schneider, anton.schneider@dlr.de
[(3)] German Aerospace Center (DLR), Institute of Aerodynamics and Flow Technology, Germany, Cologne
[(4)] MT Aerospace AG, Franz-Josef-Strauß-Str. 5, 86153 Augsburg, Germany, Johannes Baumgarten johannes.baumgarten@mt-aerospace.de

KEYWORDS

reusable launch vehicle (RLV), landing leg, deployment dynamics, analysis, landing system, deployment test

ABSTRACT

Within the European reuSable strAtegic space Launcher Technologies & Operations (SALTO) project, a structural demonstrator for a landing leg of a reusable launch vehicle was developed.
The objective of this work, funded by European Space Agency ESA, through the Future Launchers Preparatory Programme (FLPP), is to further evolve this demonstrator into a robust system architecture to enhance the technology readiness level (TRL) of the landing system. Initially, relevant design boundary conditions are systematically derived based on mission and system requirements. A detailed load determination for the deployment is conducted, accounting for critical loading scenarios during deployment of the landing legs. The touch-down loading scenario is not investigated in this project.
The resulting load cases are transferred to the landing leg structure via Finite Element Method (FEM) simulations, enabling structural evaluation. Numerical analyses provide insight into stress and deformation states and allow identification of critical structural regions. Based on these simulation results, an experimental test campaign is defined to investigate the structural behaviour under representative loading conditions.
The key focus of this work is the analysis, integration, and structural as well as functional testing of the landing leg assembly at MT Aerospace AG (MTA) together with the pneumatically driven deployment subsystem supplied by the German Aerospace Center (DLR). This subsystem, developed as part of the CALLISTO project, is fundamental to the system functionality, as it enables the primary functions of the landing system. Experimental results are correlated with numerical models to validate model assumptions and, if necessary, refine the FEM model. This correlation improves model fidelity and establishes a reliable foundation for subsequent design iterations.
Additionally, DLR contributes to the assessment of deployment dynamics, a critical factor for mission success. The evaluation of the deployment system concept is carried out using a methodology, that establishes an aerodynamic database, defines the approach trajectory, and employs a validated deployment dynamics optimisation environment (DYNOS) – developed and validated within the CALLISTO project.
A use-case scenario based on the MTA landing leg and the Themis approach trajectory as well as an approximate approach trajectory from MAIA-Space is analysed to assess the landing leg's deployment dynamics, structural loads, and potential impacts on the launcher's guidance, navigation, and control systems during deployment. The integration of experimental validation with functional and structural simulation enables a robust feedback loop for design optimization, supporting the advancement of reusable launch vehicle technologies in Europe.

Certain information contained in this paper may be subject to export control restrictions under Regulation (EU) 2021/821 (EU Dual-Use Regulation), including Items 9E001 and/or 9E002. Any use, disclosure, transfer, or export of such information must be conducted in accordance with all applicable legal and regulatory requirements.

1. PROJECT OUTLINE

This paper is based on the ESA Project “Launcher Landing Leg Deployment System - L3DS” which enables the cooperation of MT Aerospace (MTA) with DLR (Bremen).
The main goal of this project is to apply and leverage existing know-how from all project partners to allow the definition, verification and validation of a deployment system for landing legs. The main contributions of the partners are as follows:

DLR :

- Deployment Simulator
- Deployment Sub-System Architecture
- Numeric Tool Chain

MTA:

- Design and Manufacturing of Full Scale Landing Leg
- Adaption of existing Test Facility
- Industrial Capability

Together, MTA and DLR aim at carrying out the following steps, to demonstrate the deployment of a full scale landing leg system for a D=3,5 m launcher. This includes the release, active deployment , locking and passivation of the landing legs in deployed configuration:

- Requirement definition for the deployment of landing legs in dense atmospheres.
- Derivation of the mechanical loads during the deployment phase using DYNOS and rigid body simulations.
- Derivation of design elements related to the deployment process
- Assessment of mechanical capabilities of the landing leg via FE-Analysis.
- Manufacturing, Procurement and Assembly of Breadboards and full-scale landing leg-
- Breadboard and full-scale tests.
- Verification of Requirements
- Validation of Simulation
- Assessment of Force and Shock levels at the launcher interface

2. DEPLOYMENT SUBSYSTEM

The previous project related to the landing leg prototype was deployed without any active elements, purely based on gravitational acceleration. The expected aerodynamic forces during a launcher landing sequence, are proven to intervene with the landing dynamics. To avoid any negative interactions between the launcher landing dynamics and deployment dynamics it is important to allow a controlled deployment. Using DLRs deployment Simulation, the landing trajectory and deployment sequence were simulated to quantify the and acting aerodynamic forces. They were then used to dimension the active deployment system, which was then retrofit to the existing landing leg system, with as little adaptions as possible.

The Deployment Subsystem integrates various equipment and actuators designed to extend the landing-leg primary strut. Included in the subsystem are a high-pressure storage vessel, an isolation valve, a pressure-relief valve, a fill-and-drain valve, a mechanical push-off mechanism, and electromechanical release mechanisms. The Deploy-command received from the launcher's onboard computer (OBC) is processed by a deployment controller to generate valve-opening signals, actuate the release mechanisms, and route key instrumentation data to the OBC. This architecture, adapted from CALLISTO’s Approach and Landing System, presents advantages such as limited interface management, adjustable pneumatic force, the mitigation of deployment asynchronicity, high reliability derived from the reliance on aerospace-grade commercial off-the-shelf (COTS) components, and reusability.
The electro-mechanical deployment chain involves the opening of the isolation valve, the firing of the Hold-Down and Release Mechanisms (HDRMs), and the utilisation of a push-off mechanism followed by pneumatic drive. The landing gear controller functions as an open-loop device comprising deployment logic, power distribution, HDRM driver, and valve driver modules. The HDRMs are COTS components selected based on the required hold-down force. A passive torsion spring is employed by the push-off mechanism to initiate leg rotation. Pneumatic equipment is connected by tubing, through which high-pressure gas is routed to the actuators. Owing to its inertness and high mass flow rate, gaseous helium is selected as the working gas. The high-pressure regime is serviced by the fill-and-drain valve for filling, flushing, and draining operations. Safe pressure levels are maintained by the pressure-relief valve. The working gas (helium) is stored in the pressure vessel, and the gas is routed to the actuators by the tubing. The primary functions of the pneumatic circuit are the storage, routing, and provision of working gas for landing-leg deployment. System pressure is monitored by the pressure transducer to detect leaks and ensure system integrity. The location of the described components is indicated in Figure 2-1.

Certain information contained in this paper may be subject to export control restrictions under Regulation (EU) 2021/821 (EU Dual-Use Regulation), including Items 9E001 and/or 9E002. Any use, disclosure, transfer, or export of such information must be conducted in accordance with all applicable legal and regulatory requirements.

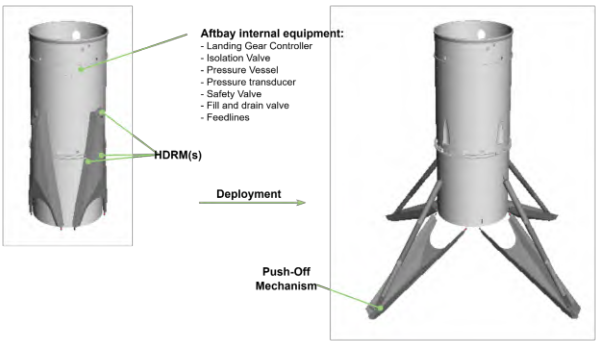


Figure 2-1: Deployment of the MTA inverse tri-pod landing leg. The deployment is the transient phase between stowed and deployed landing legs.

Note: the concept of the landing leg incl its mechanisms and structural design and manufacturing concept was already preliminary developed in several precursor programmes and thus are not object of change within the L3DS program.

3. DEPLOYMENT DYNAMICS

The deployment of landing legs in a dense atmosphere is characterised by a highly nonlinear interplay among aerodynamics, plume and leg structure interactions, vehicle dynamics, and the dynamic behaviour of the landing system, requiring high-fidelity numerical tools capable of predicting the leg's deployment dynamics in flight and on a test stand. CALLISTO's deployment dynamics have been studied in depth in [2]. Internal forces, torques, and dynamic states are provided by the deployment dynamic optimisation simulator (DYNOS), serving as input for the structural verification of the landing leg structure, alongside interface forces used for deriving and justifying system requirements. The top-level diagram is shown in Figure 3-1. Through its optimisation routine, a multi-criterion optimisation is performed by DYNOS to identify deployment parameters and operational regimes that satisfy the mission requirements and constraints of the vehicle. Complex landing leg deployment dynamics are predicted by this continuously improving numerical simulator, utilising an aerodynamic database (AEDB) that covers the influences of thrust level, the vehicle's attitude, the leg's opening angle, and Mach number, alongside the effects of plume and landing leg interactions. Furthermore, the deployment dynamics are influenced by the vehicle's dynamic state at approach, with external loads and the vehicle's orientation provided to the simulator by the aerodynamic database and approach trajectory. Based on the multi body governing equations, the deployment dynamics of all four legs are numerically calculated by the simulator, while internal loads are calculated within the push-off mechanism and pneumatic sub-models.

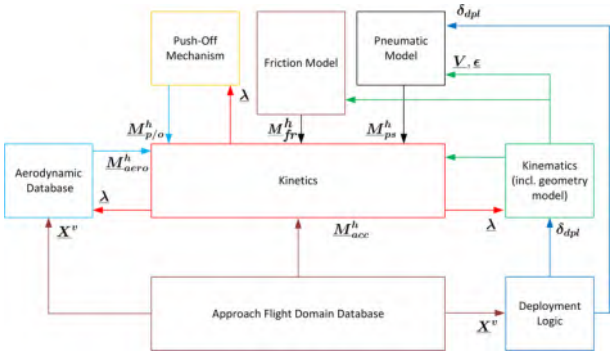


Figure 3-1: Block diagram of the DYNOS deployment dynamics simulator, with coloured blocks representing internal and external load models, and arrows indicating the data flow

3.1. Approach Flight

The final portion of the VTVL launcher trajectory prior to touchdown is represented by the approach flight, which concludes at the "arrival gate", where deployment is finalized and the functions of the landing system are enabled. The configuration for the reference approach trajectory is Themis T3 equipped with MTA landing legs, which is powered by three engines and is characterized by a dry mass of 25 tonnes. This approach trajectory is based on a one-dimensional simulation with variable thrust ranging from 100% to approximately 60%. In the approach strategy, the vehicle is aimed towards the desired trajectory with high thrust that is subsequently reduced to a mean value to maintain the course, thereby retaining thrust reserves to compensate for unwanted effects. For the landing leg deployment, the landing burn is considered the most influencing phase of the approach flight, as this event combines plume leg interaction and high non-gravitational acceleration with asymmetric aerodynamic load distribution.

3.2. Leg's Aerodynamic Database

The Aerodynamic Database (AEDB) of the landing legs focuses on the dynamic conditions of the legs during the approach phase, aiming to determine the influences of thrust level, angle of attack, angle of roll, leg opening angle, and Mach number on the aerodynamic forces acting on each individual leg. As analytical engineering methods cannot account for complex geometries and external influences such as the engine plume, multiple three-dimensional CFD simulations based on the Euler equations were performed using the DLR in-house TAU solver [1]. The engine plume was modelled as a two-gas mixture consisting on air and exhaust gas

Certain information contained in this paper may be subject to export control restrictions under Regulation (EU) 2021/821 (EU Dual-Use Regulation), including Items 9E001 and/or 9E002. Any use, disclosure, transfer, or export of such information must be conducted in accordance with all applicable legal and regulatory requirements.

without considering chemical reactions. The resulting aerodynamic data were processed into a multi-dimensional lookup table containing the aerodynamic hinge torque and force coefficients for each landing leg. Aerodynamic coefficients for flight parameters between AEDB grid points are interpolated linearly, whereas for flight parameter combinations outside the calculated parameter range, the nearest grid point is selected (i.e., no extrapolation is applied). The aerodynamic force and torque coefficients of a single leg with respect to the hinge frame are dependent upon the Mach number, angle of attack, angle of roll, opening angle, and thrust level. The calculated parameter range is defined as follows: the total angle of attack spans [80°, 90°, 100°, 110°, 120°, 130°, 140°, 150°, 160°, 165°, 170°, 175°, 180°]; the angle of roll is [0°, 45°]; and symmetry is assumed for the determination of other roll angles. The highly asymmetric flow-field around a generic VTVL launcher is shown in Figure 3-2.

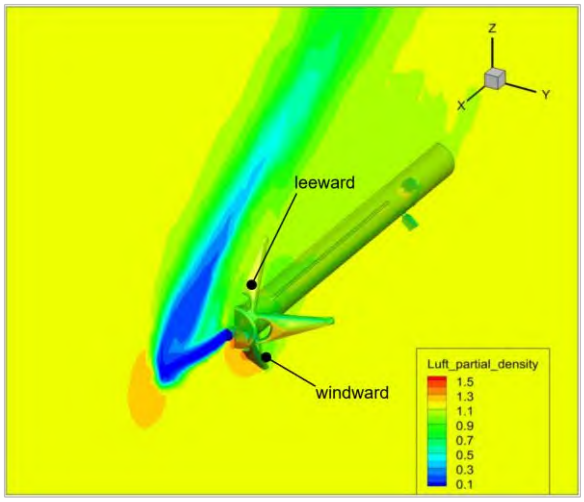


Figure 3-2: Flow field around a generic VTVL launcher at AoR of 0° One leg is oriented leeward and is therefore covered with plume. This reduces the aerodynamic forces, compared to the windward oriented leg.

3.3. Deployment Dynamics Analysis

The deployment of the landing legs is a mandatory function that enables the primary touchdown related functions of the landing gear. A pre-defined set of product parameters is required to ensure sufficient pneumatic energy is available, as the deployment initiation time point impacts the external environment and deployment dynamics. In this study, a set of deployment initiation time points is evaluated by conducting multiple simulations with various flight orientations. The pressure level is adjusted by an optimisation routine to achieve a successful deployment without violating deployment function-related requirements. The simulated parameter space covers scenarios of high interface forces and high induced disturbance torques and forces that challenges either the structural integrity of the aftbay or the GNC system performance. Furthermore, it is assumed that the parameter space in which the deployment can be conducted is unbounded, yet it must be reduced to a parameter set that is computationally manageable. The analysis focused on four different deployment initiation points to cover late (close to ground) as well as early deployments. Four analysed deployment initiation points spanning a broad range between early deployment #ID4 and late deployment #ID1. The corresponding vessel pressure range was set to 6 to 30 MPa, under the assumption that the upper boundary is common in the field of high-pressure equipment. The vehicle's attitude depends on the GNC control algorithms and other external influences. Three different angles of attack (0, 45, and 90 degrees) have been analysed to determine the effect of the vehicle's attitude on the deployment dynamics. Additionally, the reference approach trajectory is depicted in a height versus velocity diagram in Figure 3-3, with the deployment initiation time points marked accordingly.

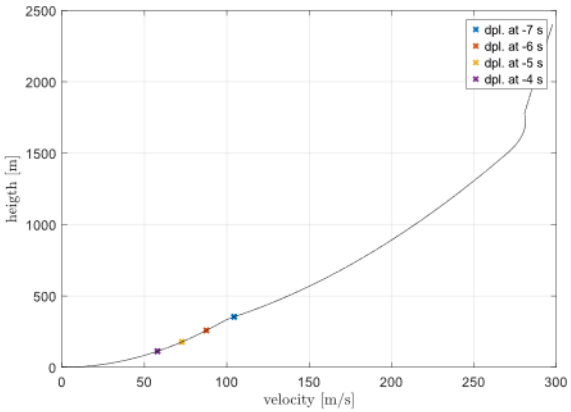


Figure 3-3: Exemplary trajectory for a Themis sized booster. The crosses indicate analysed deployment initiation time points

The opening angle vs. time plots are shown in Figure 3-4.

Certain information contained in this paper may be subject to export control restrictions under Regulation (EU) 2021/821 (EU Dual-Use Regulation), including Items 9E001 and/or 9E002. Any use, disclosure, transfer, or export of such information must be conducted in accordance with all applicable legal and regulatory requirements.

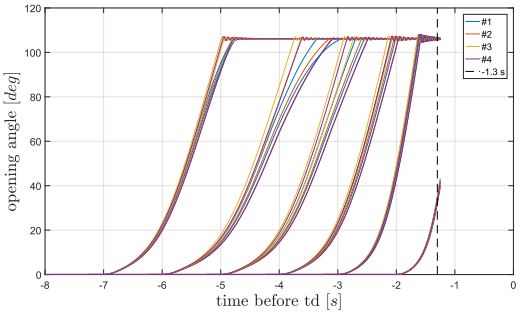


Figure 3-4:Opening angle vs. time. This plot shows the opening angle of the MTA landing leg for different deployment initiation time points. Deployment at -2 s does not finish prior to the arrival gate. #1 to #4 indicate the opening angle of the legs

The deployment simulation, assuming the reference trajectory, project constraints, and landing leg design described, shows that early deployment initiation generally leads to lower induced loads, while later deployment requires higher pneumatic force, increasing induced loads. Deployment initiated at -6 seconds results in the lowest interface loads due to a favourable balance between external load and internally generated forces. The total deployment duration tends to decrease from 4.25 seconds to 2.8 seconds with later initiation, which improves synchronicity between legs but requires a larger control capability to compensate for accumulated disturbance torques and forces. The deployment initiations from -7 to -4 seconds were used as baseline for interface and structural load requirement definition.

The slow case is represented by a leg deployment subjected to the maximum external aerodynamic load, representing the windward-oriented leg. The high-speed deployment test is used to simulate the leeward-oriented leg, which induces the highest interface loads and thereby determines the sizing of the landing leg and adjacent structures.
Beside proving the structural integrity and functional compatibility between the MTA landing leg and the DLR deployment subsystem, an objective is to acquire data for the validation process of the DYNOS simulator.

3.4. Slow - Case

The slow-deployment scenario is considered to be challenging for the deployment system because major part of the stored pneumatic energy must be converted into mechanical power. Initially, the energy required to deploy the landing legs successfully in flight is calculated. This required energy is then compared with the pneumatic energy stored in the deployment system. From these considerations, an equivalent counter-weight mass is derived, representing the energy required to deploy under worst-case lifted conditions.

The maximum energy required to unfold the legs W_{supply} is supplied by the pressure vessel, which stores helium gas at high pressure. The stored pneumatic energy must exceed the energy demand for unfolding the landing leg W_{demand}:

$$W_{supply} \geq s \cdot W_{demand} \quad (1)$$

Based on this assumption an equivalent counterweight mass is calculated as follows:

$$m_{equi} = \frac{W_{demand}}{g \cdot h} \quad (2)$$

The following figures show the resulting deployment dynamics of the single-leg test stand (see Figure 3-5) with the maximum counterweight of 710 kg and three different vessel pressures as a parameter. With the given test-stand configuration, the interface forces were reduced to the required specification during deployment under maximum counterweight.

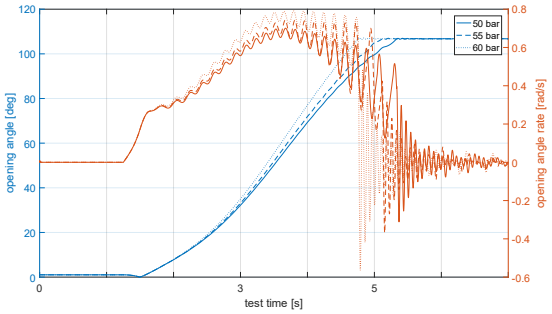


Figure 3-5: Deployment dynamics with maximum counterweight. As a parameter three different vessel pressure are shown. The oscillation in deployment velocity is caused by the elasticity of the counter weight rope.

3.5. Fast-Case

The second load case concerns the interface loads. It is assumed that the highest interface loads are generated at the event of latching, when the landing leg is abruptly stopped by the end-stops. The feasibility of the test set-up was assessed by conducting a sensitivity study with a single-leg deployment model in the DYNOS simulation tool, in which the counterweight mass and vessel pressure were varied. A counterweight of 300 kg produced feasible results, and varying the vessel pressure from 8.5 MPa to 5 MPa established whether the deployment velocity could be reduced so that the landing leg would not exceed its load-carrying capability. It is indicated by the results that the test set-up can modify the dynamics to achieve the

Certain information contained in this paper may be subject to export control restrictions under Regulation (EU) 2021/821 (EU Dual-Use Regulation), including Items 9E001 and/or 9E002. Any use, disclosure, transfer, or export of such information must be conducted in accordance with all applicable legal and regulatory requirements.

desired interface forces and/or deployment velocity. The deployment dynamics are shown in Figure 3-6

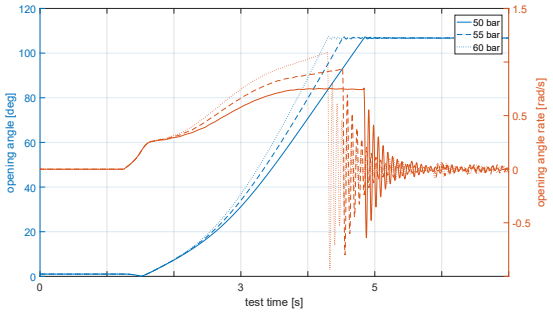


Figure 3-6: Deployment dynamics with max interface force. As a parameter three different vessel pressure are shown.

4. MECHANICAL JUSTIFICATION

This chapter represents an excerpt of the structural justification methodology applied to the landing leg assembly - with particular focus on the deployment test phase. Finite element analysis was conducted to demonstrate the structural integrity of the primary strut components under simulated flight loads, whereas additional connecting elements and secondary parts have been justified for test loads only. This differentiated approach enables the project to maintaining adequate safety margins while balancing project budget constraints.

The bare landing leg consisting of the primary and secondary strut was designed, produced and tested in a previous project. One of the main goals of this project was to re-use as much of the existing hardware as possible and adapt it to fit the deployment related components. Hence, a full redesign of the primary strut was not within project scope. Nonetheless, a major effort was made to optimise as much of the structure as possible to accommodate the design loads. The trade-off is described in the following chapters.

4.1. FE-Model

For the static design a FE models of the landing leg was developed. The secondary strut was taken from the previous project. Parts of the secondary strut were modelled using the Automatic Fiber Placement (AFP) programming data to make sure that all stacking and layup angles were properly represented in each element. This method allows a higher fidelity between the different digital models of the landing leg.
The primary strut was newly meshed within this project because the main adaptations related to the deployment system are done at the primary strut. CFAST Elements were used to represent the attachment fittings to the secondary strut, landing leg, fitting and touch pad. All joints in the primary strut are realised using RBE 2 elements.

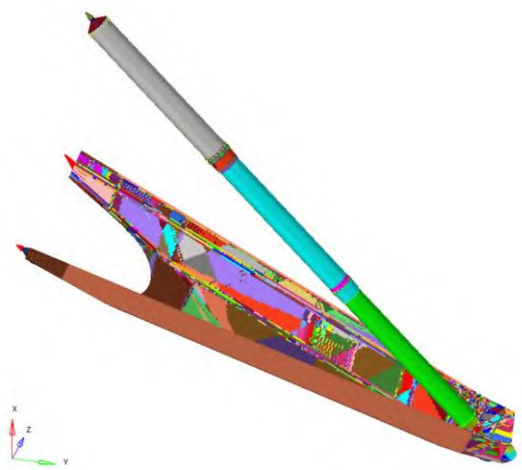


Figure 4-1 FE-Model of L3DS Landing Leg

Each component of the load bearing path is analysied either via analysical method or via FE analysis to ensure structural integrity during testing.

4.2. Dimensioning Loadcases and interface loads

The dimensioning load cases (DLC) were established through a multibody simulation conducted by DLR and described in the previous chapters. Building upon these findings and integrating key insights from the previous project, it is important to highlight that, according to the simulations, latching loads during the unfolding phase, driven by high velocities, are dimensioning.
Depending on the position of the leg with respect to the aerodynamic pressure, each leg has a different expected latching force during deployment. Leeward-facing legs deploy at higher speeds, thus leading to higher forces compared to windward facing legs which deploy slower due to the aerodynamic pressure acting on the aero-shield (secondary strut).
These latching loads are generated by the unfolding speed, which induces inertia forces as the mechanism locks. This phenomenon defines two critical load cases: the tension load case, which captures the immediate impact of inertia on the primary strut during the latching event, and the compression load case, which arises from structural flexibility causing a rebound effect following the latch engagement.
The application of these loads is achieved through

Certain information contained in this paper may be subject to export control restrictions under Regulation (EU) 2021/821 (EU Dual-Use Regulation), including Items 9E001 and/or 9E002. Any use, disclosure, transfer, or export of such information must be conducted in accordance with all applicable legal and regulatory requirements.

a linear acceleration field which depicts the inertia that arise when stopping a rotational motion.

4.3. Loads, Safety and Design Factors

The Loads which are considered in for the mechanical justification of the landing leg, for both flight loads and test loads are multiplied with safety and design factors to account for uncertainties in:

- Modelling, such as stiffness and dynamic uncertainties
- Project maturity and effect on load definition
- Local design discrepancies between CAD and FE-Modelling

Further Margins are multiplied to account for material related aspects such as yielding or rupture. Finally, an ultimate factor is applied.

4.4. Specific Load, Justification and evaluation

As mentioned in §4, the hardware of the landing leg was partially re-used from a previous project. This was done to remain within budgetary constraints but also to avoid redesigning a full-scale landing leg for a single sub-system. Instead, the CFRP tube dimensions were considered fixed, and the adjacent components were allowed to be as much adapted as much as possible, within the allowable design space, to fit the load requirements.

The following evaluations are based on the Limit Loads and the factors mentioned in § 4.3.



Figure 4-2 Max in-plane fiber stress Primary Strut, tension load case



Figure 4-3 Secondary Strut, min compressive fiber stress, tension ultimate test load case



Figure 4-4 Nut-300 stress at test ultimate load level

5. VALIDATION, VERIFICATION AND TESTING

To validate the results shown above, several full-scale deployment tests are planned. They shall verify the requirements to the deployment system, which are derived from the flight path, as described in §3 However, before carrying out the full-scale tests, several breadboard tests and low-risk deployment tests are planned.

5.1. Breadboard Tests

The main elements which allow a controlled deployment are the:

- Pressurization system
- Push-Off System
- Primary Strut (Pressure Cylinder)

Their main functions are interdependent and need to be verified independently before testing them as a complete system.

The Pressurization System together with the Push-off system and the hold-down and release mechanism need to be able to work within a specific sequence and time intervals. This shall be proven within the first set of breadboard tests related to the deployment system.

The second set of breadboards is related to the primary strut, which needs to withstand inner pressure, deploy under load and depressurize after successful deployment. These main functions as

Certain information contained in this paper may be subject to export control restrictions under Regulation (EU) 2021/821 (EU Dual-Use Regulation), including Items 9E001 and/or 9E002. Any use, disclosure, transfer, or export of such information must be conducted in accordance with all applicable legal and regulatory requirements.

well as force/displacement diagrams will be tested and fed back to the simulation tool, which will then provide more reliable simulation data for the full-scale deployment test.

5.2. Test Rig and Instrumentation

Full Scale deployment tests are carried out on a dedicated test rig, which is purposefully built to verify the requirements of the landing leg.
It Consists of the four main interface points of the landing leg as well as a counterweight system. This system is attached to the secondary strut of the landing leg and represents the aerodynamic pressure during deployment. By adapting the weight, the aerodynamic pressure of the windward and leeward leg can be emulated.



Figure 5-1 Test Rig with counterweight system.

To verify the requirements towards the launcher and validate the simulations, several the following measuremets will be carried out:

- Force measurement via Load cells on main interfaces to launcher.
- Acceleration monitors on main interfaces to launcher as well as on foot pad
- Strain gauges on primary strut
- Inertia measurement unit on foot pad
- Optical measurement system to measure the dynamic response of the landing leg during and after latching.

5.3. Full-Scale Deployment Test

The full-scale deployment Tests are designed to represent the worst-case scenarios for the involved systems. In this case, the windward facing leg represents the worst case for the deployment system as it must be able to generate enough energy to deploy the leg with high aerodynamic forces trying to act against it. The leeward facing leg on the other hand represents the worst case for the mechanical system as it deploys at the highest speed and thus induces the highest loads on both the landing leg and the launcher structure.

To test these scenarios the testing sequence shown below is designed to increase the necessary energy and reaction force and to avoid early failure.

1) Measurement Instrumentation Control, static application of forces
2) Low Kinetic Energy Drop test, without active deployment system.
3) Low Kinetic Energy deployment test, with active deployment system
4) High Pressure Deployment Test (representative for windward facing leg), described in § 3.4
5) High Speed deployment test (representative for leeward facing leg), described in § 3.5

6. OUTLOOK

Currently the primary strut is being assembled and preliminary breadboard tests are being carried out.



Figure 6-1 Partial Assembly of Primary Strut

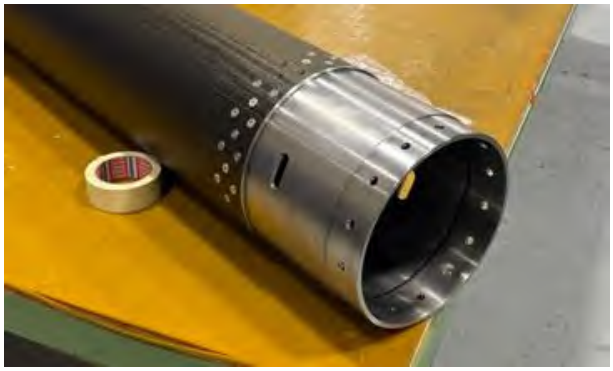


Figure 6-2 Close Up of CFRP- Metal Interface of Primary Strut

The aim of these preliminary tests is to verify the function of the primary strut, which consists of:

Certain information contained in this paper may be subject to export control restrictions under Regulation (EU) 2021/821 (EU Dual-Use Regulation), including Items 9E001 and/or 9E002. Any use, disclosure, transfer, or export of such information must be conducted in accordance with all applicable legal and regulatory requirements.

- sliding from a closed state to a deployed state
- locking at the deployed state
- withstand inner pressure
- passivate (release inner pressure after deployment)

Further, during these preliminary breadboard tests, the specific friction coefficients of the primary strut will be determined and fed back to the DYNOS Simulation. This increases the predictability of the full-scale tests described in §5.3.

The test data will allow a validation of the DYNOS Model, the Rigid Body Model and the Finite Element Model with respect to the MTA Landing Leg. Since the test object is a full-scale Landing Leg and the deployment scenarios are derived directly from realistic landing scenarios, the measured shock and force levels can be forwarded to launcher providers for reciprocal sizing efforts.

The test rig and necessary equipment including instrumentation is currently in the procurement and calibration process. According to current schedule, the final and full-scale tests will be carried out by the end of Q4 of 2026.

References:

→ Langer, S., Schwöppe, A., Kroll, N.: The DLR flow solver TAU—status and recent algorithmic developments. In: 52nd Aerospace Sciences Meeting (2014). https://elib.dlr.de/90979/

→ Schneider, A., Bertram, J., Schröder, S., Witte, L., Landing leg deployment dynamics simulation and excessive deployment test campaign of CALLISTO's Approach and Landing System. In: Proceedings of the International Astronautical Congress, IAC. Proceedings of the International Astronautical Congress, IAC, 2024, Milan, Italy, ISSN 0074-1795

→ Schneider, A., Desmariaux, J., Klevanski, J. et al. Deployment dynamics analysis of CALLISTO's approach and landing system. CEAS Space J 15, 343–356 (2023). https://doi.org/10.1007/s12567-021-00411-2

Certain information contained in this paper may be subject to export control restrictions under Regulation (EU) 2021/821 (EU Dual-Use Regulation), including Items 9E001 and/or 9E002. Any use, disclosure, transfer, or export of such information must be conducted in accordance with all applicable legal and regulatory requirements.

A SIMPLIFIED AND ROBUST APPROACH FOR PRELIMINARY TORQUE MARGIN SIZING OF LARGE AND DEPLOYABLE SPACE STRUCTURES

A. Colella [(1)], A. Fagotti [(1)], A. Nerattini [(1)], L. Palomba [(1)], F. Adamo [(1)], D. Scarozza [(1)], F. Gentile [(1)], D. Sannoner [(1)], M. Lanuti [(1)], M. Lapi [(1)], L. Scialanga [(1)], A. Adriani [(1)]

[(1)] Thales Alenia Space Italy, Via Saccomuro, 21-24, 00131, Roma (Italy), Email: antimo.colella@thalesaleniaspace.com , marco.lapi@thalesaleniaspace.com,

KEYWORDS

LDR, Space Large Deployable Reflectors, Mesh Reflectors, Multibody Dynamics Modelling, Space Structures, Space Mechanisms

ABSTRACT

In response to the growing demand for high-performance satellite antennas, Large Deployable Reflectors (LDRs) represent a highly promising solution for future space telecommunications and observation missions due to their reconfigurable architecture.

The purpose of this paper is to present a simplified multibody model of the deployable ring truss of a mesh reflector intended for space applications. The model is derived through a classical Lagrangian formulation, which allows to evaluate the torque margin in accordance with ECSS mechanisms standard (ECSS-E-ST-33-01C Rev.2), projecting the entire system equations of motion into a single degree of freedom state space.

To verify the reliability of the proposed formulation, the analytical results have been validated against those obtained from a commercial multibody simulation environment.

The results show that the simplified approach provides a computationally efficient and sufficiently accurate tool for preliminary torque-margin assessment of deployable space structures, thus representing a valuable support for early-stage design and system-level analyses of mesh reflector mechanisms, including optimization workflows.

1. INTRODUCTION

The new generation of space missions meant for telecommunications and Earth observation is characterized by the impellent need of higher operational electromagnetic gain (EIRP and G/T) in all frequencies and therefore larger antenna aperture diameters. The upper bound of the interval of feasible frequencies is generally linked to the reflector's surface accuracy, whereas the maximum aperture diameter is constrained by the typical available volume inside the fairing of current space transportation systems. Moreover, larger antennas result in higher masses that typically should be kept low to reduce the costs of the launch phase.

In the last thirty years, all these factors combined have paved the way for the development of Large Deployable Reflectors (*LDRs*) [1] consisting in parabolic antenna reflectors that are installed on the satellite in a stowed configuration to be later deployed in space. Depending on how this deployment is achieved, it is possible to divide the LDRs into different families: solid surface reflectors, inflatable reflectors, shell membrane reflectors, reconfigurable flexible shell reflectors and mesh reflectors [2]. Among them, mesh reflectors (Fig. 1) are the ones that have seen the largest use for several space applications ([3]) because of their advantageous combination of low mass, high surface accuracy and stowed-to-deployed ratio. At present, Astromesh design represents the state-of-the-art among the mesh reflectors [4]. These reflectors are generally characterized by a lightweight, articulated ring structure (the ring truss) actuated by mechanisms such as constant torque flat springs located at its junctions or cable and pulley systems driven by winches. Under the action of these actuators, the ring structure is forced to pass from a stowed configuration, which occupies little space inside the fairing of the launcher, to a fully deployed one, whose aperture diameter is often larger than 20 m. During this transition, the ring structure unfolds and drags a cable net which is attached to a reflective metallic membrane (i.e. the mesh) used for the reflection of the radio signal.

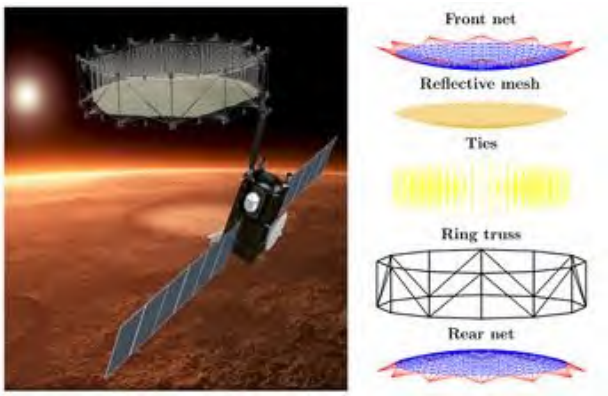


Figure 1: Rendering of a Large Deployable Reflector (left) in its deployed configuration and (right) an exploded view highlighting its main parts (courtesy of Thales Alenia Space Italy ®)

The net is composed of a front net and a rear net

that are interconnected to one another by means of tension ties.
In order to meet the designed performance in terms of stiffness of the whole assembly and stability of the reflective surface geometrical accuracy against external perturbations, the metallic surface has to be preloaded: this is typically achieved exploiting the last stage of the ring structure deployment motion. Therefore, before all the ring structure latches are engaged and the final deployed configuration is finally frozen, the actuators driving the deployment of the entire assembly shall guarantee to compensate the resistive action of the preloading tensile structure (net and mesh) as well as all the other passive torques due to hinges and latches friction, harness, synchronization gears (if any), etc. The robustness of the deployment shall be proven also against the variability of these resistive contributions with temperature. Moreover, for safer operations, the deployment velocity profile is often enforced as a design constraint. As a consequence, not only the actuators shall compensate passive forces and torques, but also surpass them with sufficient margin to successfully enforce the desired motion profile in the required time.
In space industry, such margin is also called Torque Margin or Motorization Factor and its sizing shall be performed according to specific rules specified in ECSS-E-ST-33-01C Rev.2 [5]. The standard generally prescribes that the minimum actuation torque in a space mechanism shall be:

$$T_{act} > T_{Min} = 2\,(1{,}1I + 1{,}2S + 1{,}5H_M + 3F_R + 3H_Y + 3H_A + 3H_D) + 1{,}25T_D + T_L \qquad (1)$$

With $\frac{T_{act}}{T_{Min}} - 1$ being the recalled Torque Margin whereas I is the inertial resistance to mechanism aperture due to an orbital load (e.g. the one induced by a spacecraft manoeuvre), S is the resistance produced by springs (if any), H_M is the torque due to magnetic effects, F_R is the internal friction of the mechanism, H_Y is the resistive contribution due to hysteresis, H_A is the one due to harness, H_D is the resistance due to adhesion of some components, T_D is the internal inertial load due to the enforcement of a prescribed law of motion and the T_L is the output external load that the mechanism shall be able to move. In a mechanism composed by only one hinge, the application of this rule is straightforward, but in a complex mechanical system like the one of a mesh reflector, a modelling strategy shall be found to correctly size the deployment actuators.
The purpose of this paper is to present a simplified and robust approach to compute the torque margin of the ring of a mesh reflector based on the Classical Lagrangian formulation of its equation of motion. The method is developed for a specific case study of ring geometrical design, but it can be generalized to any multibody system that can be reduced to a single degree of freedom through its internal kinematic constraints.
The remainder of this paper is organized as follows. Section 2 presents the case study and develops the mathematical model to compute the torque margin for a specific case of mesh reflector. Section 3 shows how to derive the torque margin exploiting the obtained equations from the previous section. Section 4 shows the comparison between the analytical results obtained with the proposed method and the ones derived from a commercial multibody software, thus validating the outcomes of the proposed approach. Section 5 gives an overview of the current experimental testing activities performed at Thales Alenia Space Italy on a mesh reflector demonstrator whose actuation mechanisms have been sized with the proposed workflow. Lastly, Section 6 summarizes the main conclusions of this work.

2. RING DYNAMIC EQUILIBRIUM

2.1. Ring Geometrical Design

This work adopts a specific case study as the geometrical design for the ring of a mesh reflector. The ring design is showed in Fig. 2 in its stowed configuration and in Fig. 3 in its deployed configuration. Basically, the ring is composed of 12 Synchronized Expandable Mechanisms (also known as *SEMs*) which are themselves composed by an upper and lower compass, two vertical pylons and a telescopic tube. Each SEM opens by means of a driving cable.

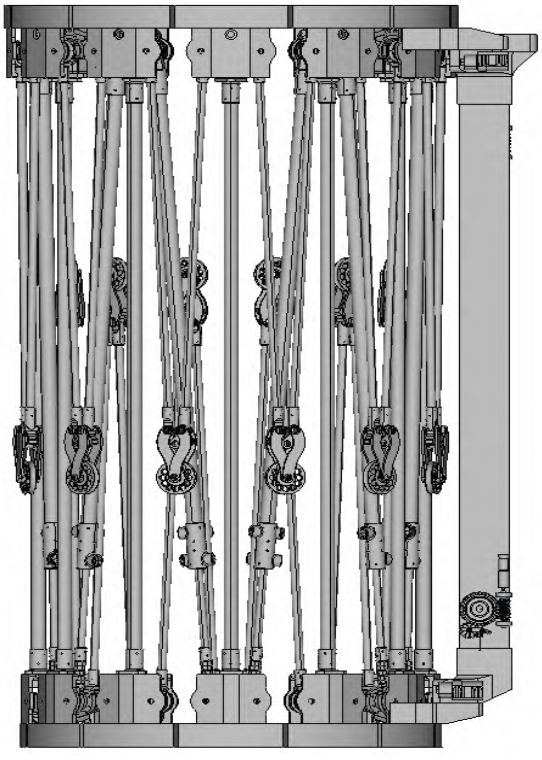


Figure 2: LDR assembly – Stowed Configuration

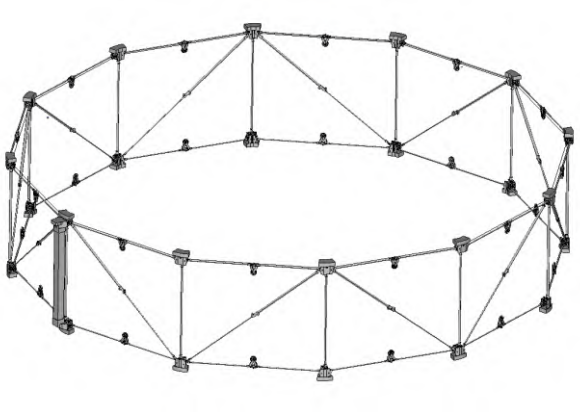


Figure 3: LDR assembly – Deployed Configuration

In Fig. 4, the SEM working opening sequence is shown for different aperture angles.

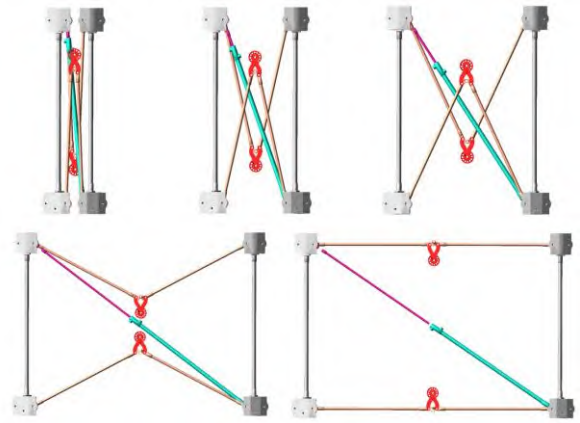


Figure 4: SEM working principle

2.2. Simplifying Assumptions

The main assumptions of the model are summarized hereafter:

- Symmetric catenaries
- Symmetric actuation between catenaries
- Synchronization between each SEM
- SEM bodies are considered as rigid

In Fig. 5, the main geometric variables of the model are defined.

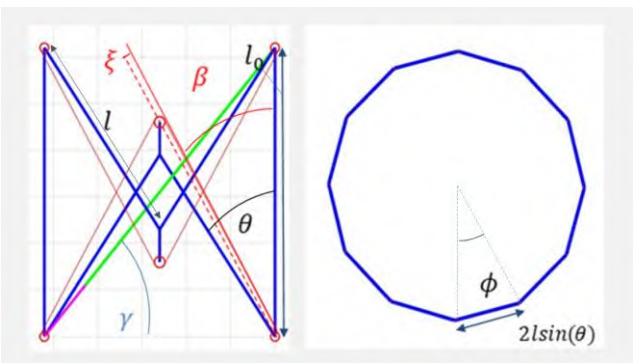


Figure 5: Definition of the geometric variables of the model

In particular:

- SEM aperture phase angle (single DoF of the entire multibody system): θ
- Pulley pins conjunction line:

$$\beta = \text{atan}\left(\frac{l\sin(\theta)}{d + l\cos(\theta)}\right) \qquad (2)$$

where l is the compass length and d is the pulley offset.

- Driving cable deviation due to pulley tangent condition:

$$\xi = \text{asin}\left(\frac{(D_2 - D_1)\cos(\beta)}{2(l\cos(\theta) + d)}\right) \qquad (3)$$

where D_1 and D_2 are the diameters of the compass and pylon pulleys.

- Telescopic pole phase angle:

$$\gamma = \text{atan}\left(\frac{l_0}{2l\sin(\theta)}\right) \qquad (4)$$

- Ring rotation angle for each SEM:

$$\Phi = \left(\frac{\pi(n-2)}{n}\right) \qquad (5)$$

where n is the number of SEMs of the ring.

2.3. Classical Lagrangian formulation of Equation of Motion

The torque margin standard computation can be applied also to the entire LDR ring if expressed in terms of its active, passive and inertial generalized torques. These can be derived by projecting the equations of motion of the entire multibody system in the 1DoF state space represented by the aperture angle of the 1st SEM, i.e. exercising the Classical Lagrangian formulation (*CLF*) of the dynamic equilibrium:

$$\frac{d}{dt}\left(\frac{\partial T^{RING}}{\partial \dot{\theta}}\right) - \frac{\partial T^{RING}}{\partial \theta} = Q_M - Q_P \qquad (6)$$

Or also:

$$Q_I = Q_M - Q_P \qquad (7)$$

where T^{RING} is the kinetic energy of the entire ring, Q_M is the generalized motor torque, Q_P is the summation of all generalized passive torques and Q_I is the total generalized inertial torque.

2.3.1.Active Generalized Torque

All the global velocities of the compass and pylon hinges for each k-SEM have been determined with respect to the local reference frame of the first SEM by Eqs. 8-10:

$$\overrightarrow{V_A^k} = \overrightarrow{V_F^k} + \underline{\underline{R}}_z\big((k-1)(\pi-\phi)\big)\overrightarrow{V_A^1} \qquad (8)$$

$$\overrightarrow{V_O^k} = \overrightarrow{V_F^k} + \underline{\underline{R}}_z\big((k-1)(\pi-\phi)\big)\overrightarrow{V_O^1} \qquad (9)$$

$$\overrightarrow{V_F^k} = \overrightarrow{V_A^{k-1}} \qquad (10)$$

where $\overrightarrow{V_A^1}$ is the velocity of the first SEM pylon hinge, $\overrightarrow{V_O^1}$ is the velocity of the first SEM compass hinge, $\overrightarrow{V_F^k}$ is the velocity of the k-SEM fixed pylon hinge and $\underline{\underline{R}}_z\big((k-1)(\pi-\phi)\big)$ is the space transformation matrix that rotates each SEM and hinge velocity according to the k-SEM.

On the other hand, the ring pulley reaction forces for each k-SEM have been evaluated with respect to the local reference frame of the first SEM by the Eq. 11:

$$\overrightarrow{F_i^k} = \big(\eta_{p0}\eta_{p1}\eta_{p2}\eta_{p3}\big)^{(k-1)}\underline{\underline{R}}_z\overrightarrow{F_i^1} \qquad (11)$$

Where $\overrightarrow{F_i^k}$ are the reaction forces acting on the pulleys of the first SEM and $\eta_{p0}, \eta_{p1}, \eta_{p2}, \eta_{p3}$ are the pulleys efficiencies.

As a first approximation, assuming a perfect adhesion of the cables on the pulleys, their efficiency can be estimated as per Eq. 12:

$$\eta = \frac{T_2}{T_1} = e^{-\frac{\mu_v d_b \Delta\theta}{D}} \qquad (12)$$

Where μ_v is the friction coefficient of the pulley, d_b is the pulley pin diameter, D is the pulley diameter and $\Delta\theta$ is the winding angle of the cable around the pulley.

Given the first SEM velocities and forces, one can retrieve iteratively the same quantities for all the SEMs exploiting the recursive geometry of the ring mechanism. These are recalled in Fig. 6:

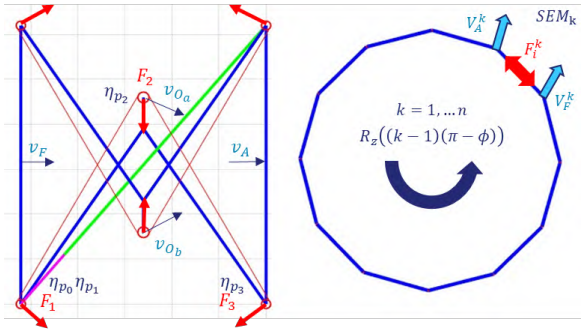


Figure 6: Definition of SEM forces and velocities

The first SEM velocities are derived as per Eq. 13:

$$\begin{aligned}\overrightarrow{V_F^1} &= [0;0;0]\\ \overrightarrow{V_{Oa}^1} &= \big[l\cos(\theta)\dot{\theta};0;-l\sin(\theta)\dot{\theta}\big]\\ \overrightarrow{V_{Ob}^1} &= \big[l\cos(\theta)\dot{\theta};0;l\sin(\theta)\dot{\theta}\big]\\ \overrightarrow{V_A^1} &= \big[2l\cos(\theta)\dot{\theta};0;0\big]\end{aligned} \qquad (13)$$

First SEM pulley's reaction forces are derived as per Eq. 14:

$$\begin{aligned}\overrightarrow{F_1} &= \begin{bmatrix}\eta_{p0}\eta_{p1}T\sin(\beta-\xi);\\ 0;\\ \eta_{p0}\eta_{p1}T\cos(\beta-\xi)-\eta_{p0}T\end{bmatrix}\\ \overrightarrow{F_2} &= \begin{bmatrix}-(1-\eta_{p2})\eta_{p0}\eta_{p1}T\sin(\beta-\xi);\\ 0;\\ -(1+\eta_{p2})\eta_{p0}\eta_{p1}T\cos(\beta-\xi)-\eta_{p0}T\end{bmatrix}\\ \overrightarrow{F_3} &= \begin{bmatrix}-\eta_{p2}\eta_{p0}\eta_{p1}T\sin(\beta-\xi);\\ 0;\\ -\eta_{p3}\eta_{p2}\eta_{p0}\eta_{p1}T+\eta_{p2}\eta_{p1}\eta_{p0}T\cos(\beta-\xi)\end{bmatrix}\end{aligned} \qquad (14)$$

By performing the scalar multiplication of the ring nodal velocities of the ring with the ring pulley reaction forces, it is possible to obtain the generalized motor torque through Eq. 15:

$$Q_M = \sum_{k=1}^{n}\frac{2\overrightarrow{F_1^k}\cdot\overrightarrow{V_F^k} + 2\overrightarrow{F_2^k}\cdot\overrightarrow{V_O^k} + 2\overrightarrow{F_3^k}\cdot\overrightarrow{V_A^k}}{\dot{\theta}} \qquad (15)$$

2.3.2.Passive Generalized Torques

The same approach is adopted to derive the generalized passive torques of the ring accounting all the resistive actions inside the multibody system (e.g. the hinges friction, synchronization gears efficiency, resistance due to latches friction, cables weight and interferences, harness resistance, etc.). The estimation of the passive torque contribution due to cable net and mesh tensioning is extremely delicate.

In [6], a method based on the definition of a potential elastic energy of the tensile network is proposed. The approach relies on the linearized force density method computed at each step of the unloading sequence to capture the transition from slack to tensioned state of the net cables. However, such approach does not take into account neither the geometric nor the constitutive non linearity typically observed for the cable net structures as well as the elastic contribution of the mesh.

In [7], a method based on a progressive and nonlinear unloading of a FEM model of a tensile network of cables and mesh is proposed to estimate

the unstressed configuration of the assembly (useful from a manufacturing standpoint).
The starting point of the unloading path is the design preloaded functional configuration, whose definition and sizing are obtained through a constrained optimization process based on the Force Density Method (*FDM*) described in [7] and [8].

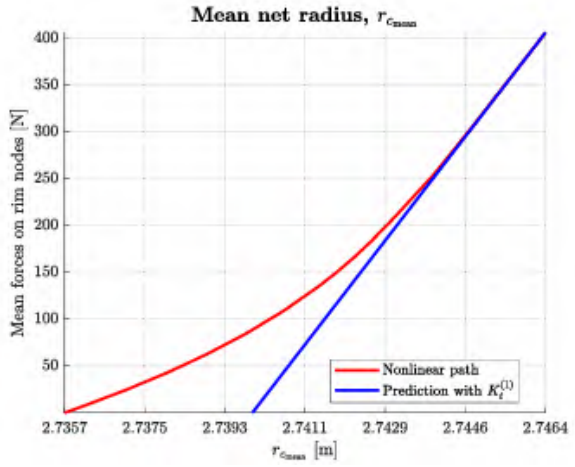


Figure 7: Reaction forces on LDR ring due to cable net tensioning ([7])

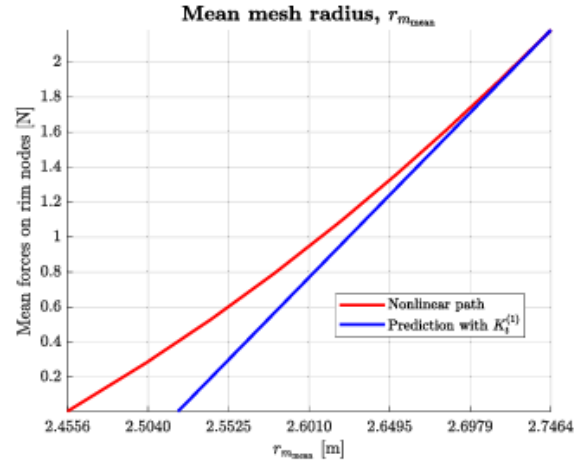


Figure 8: Reaction forces on LDR ring due to mesh tensioning ([7])

Fig. 7-8 show the effect of the geometrical nonlinearity in the prediction of the reaction forces due to the net and mesh tensioning against the LDR aperture state. In particular, given the higher flexibility of the mesh, one can notice that it activates way sooner than the cable net even if with a force contribution that is much lower at the end of the deployment.
Since

$$r = \frac{lsin(\theta)}{\sin\left(\frac{\phi}{2}\right)} = r(\theta) \qquad (16)$$

one can extrapolate the nonlinear function governing the resultant reaction forces at ring vertexes due to the cable net and mesh tensioning $\overrightarrow{T_L^k}(\theta)$ for each k-SEM and finally obtain:

$$Q_L = \sum_{k=1}^{n} \frac{2\overrightarrow{T_L^k} \cdot \overrightarrow{V_F^k}}{\dot{\theta}} \qquad (17)$$

to be included in the overall generalized passive torque Q_P computation.

2.3.3. Inertial Generalized Torques

In space applications, the deployment of mechanisms is typically controlled in order to follow a prescribed trajectory in a specified time, thus enforcing an acceleration profile to the deployment sequence. As recalled in Eq. 1, also this contribution shall be taken into account. In the formulation presented in this paper, it can be included in the inertial term Q_I of Eq. 7. Such inertial term is derived by the derivatives of the kinetic energy of the ring.
The velocities of the centre of mass of the two pylons of each SEM are basically $\overrightarrow{V_F^k}$ and $\overrightarrow{V_A^k}$. The velocities of the center of mass of the four compass tubes in the first SEM are reported in Eq. 18:

$$\begin{cases} \overrightarrow{V_{c1}^1} = \left[\frac{l}{2}cos(\theta)\dot{\theta}; 0; -\frac{l}{2}sin(\theta)\dot{\theta}\right] \\ \overrightarrow{V_{c2}^1} = \left[\frac{3}{2}lcos(\theta)\dot{\theta}; 0; -\frac{l}{2}sin(\theta)\dot{\theta}\right] \\ \overrightarrow{V_{c3}^1} = \left[\frac{l}{2}cos(\theta)\dot{\theta}; 0; \frac{l}{2}sin(\theta)\dot{\theta}\right] \\ \overrightarrow{V_{c4}^1} = \left[\frac{3}{2}lcos(\theta)\dot{\theta}; 0; \frac{l}{2}sin(\theta)\dot{\theta}\right] \end{cases} \qquad (18)$$

The velocities of the two sliding parts of the telescopic tubes of the first SEM can be derived as in Eq. 19:

$$\begin{cases} \overrightarrow{V_{g1}^1} = \left[\frac{l_1}{2}sin(\gamma)\dot{\gamma}; 0; -\frac{l_1}{2}cos(\gamma)\dot{\gamma}\right] \\ \overrightarrow{V_{g2}^1} = \overrightarrow{V_A^1} + \left[-\frac{l_1}{2}sin(\gamma)\dot{\gamma}; 0; \frac{l_1}{2}cos(\gamma)\dot{\gamma}\right] \end{cases} \qquad (19)$$

The velocity of the J-body for the k-SEM is defined as per Eq. 20:

$$\begin{aligned} &\overrightarrow{V_{cJ}^k} \\ &= \overrightarrow{V_F^I} \\ &+ \sum_{i=1}^{k-1} \underline{R_z}\left((i-1)(\pi-\varphi)\right)\overrightarrow{V_A^I} \\ &+ \underline{R_z}\left((i-1)(\pi-\varphi)\right)\overrightarrow{V_{CJ}^I} \end{aligned} \qquad (20)$$

Therefore, the total kinetic energy of the ring is given by summing the kinetic energy contribution of every J-body for each k-SEM:

$$
\begin{aligned}
&T^{RING} \\
&= \sum_{k=1}^{12} [\frac{1}{2}\, m\, \overrightarrow{V_{c1}^k} \cdot \overrightarrow{V_{c1}^k} \\
&+ \frac{1}{2} m \overrightarrow{V_{c2}^k} \cdot \overrightarrow{V_{c2}^k} + \frac{1}{2} m_0 \overrightarrow{V_{c3}^k} \cdot \overrightarrow{V_{c3}^k} \\
&+ \frac{1}{2} m_0 \overrightarrow{V_{c4}^k} \cdot \overrightarrow{V_{c4}^k} + \frac{1}{2} m \overrightarrow{V_{c5}^k} \cdot \overrightarrow{V_{c5}^k} \\
&+ \frac{1}{2} m \overrightarrow{V_{c6}^k} \cdot \overrightarrow{V_{c6}^k} + \frac{1}{2} m_1 \overrightarrow{V_{G1}^k} \cdot \overrightarrow{V_{G1}^k} \\
&+ \frac{1}{2} m_1 \overrightarrow{V_{G2}^k} \cdot \overrightarrow{V_{G2}^k}] + T_{rot}^C + T_{rot}^T
\end{aligned}
\tag{21}
$$

where m is the compass mass, m_0 is the pylon mass, m_1 is the telescopic tube mass, ${T^C}_{rot}$ is the rotational kinetic energy term of the compasses and ${T^T}_{rot}$ is the rotational kinetic energy term of the telescopic tubes.
In conclusion, the second order differential equations of motion of the ring are:

$$
\begin{aligned}
&l^2 \left\{ \left[f(\theta) + 12(1 + 8\, cos^2(\theta)) \right.\right. \\
&+ 4 + 2 \frac{m_1 l_1^2}{m l^2} F_T^1(\theta) \\
&+ 12 \frac{m_1 l_1^2}{m l^2} F_T^2(\theta) \\
&\left. + \frac{m_1 l_1^2}{m l^2} m F_T^3(\theta) \right] \ddot{\theta} \\
&+ \left[\frac{1}{2} \frac{\partial f}{\partial \theta}(\theta) - 48\, sin(2\theta) \right. \\
&+ \frac{m_1 l_1^2}{m l^2} \frac{\partial F_T^1}{\partial \theta}(\theta) + 6 \frac{m_1 l_1^2}{m l^2} \frac{\partial F_T^2}{\partial \theta}(\theta) \\
&\left. \left. + \frac{1}{2} \frac{m_1 l_1^2}{m l^2} \frac{\partial F_T^3}{\partial \theta}(\theta) \right] \dot{\theta}^2 \right\} \\
&= Q_M - Q_P
\end{aligned}
\tag{22}
$$

with:

$$
\begin{aligned}
&f(\theta) \\
&= \frac{1}{l^2} \left[(4 + 2p) \overrightarrow{V_A^{I^T}} \sum_k \underline{\underline{A}}_k \overrightarrow{V_A^I} \right. \\
&\left. + \overrightarrow{V_A^{I^T}} \sum_k \underline{\underline{B}}_k \overrightarrow{a^I} + \overrightarrow{a^{I^T}} \sum_k \underline{\underline{B}}_k \overrightarrow{V_A^I} \right]
\end{aligned}
\tag{23}
$$

Where

$$
\begin{aligned}
&p = \frac{m_0}{m} \\
&\overrightarrow{a^I} = \overrightarrow{V_{c1}^I} + \overrightarrow{V_{c2}^I} + p \left(\overrightarrow{V_{c3}^I} + \overrightarrow{V_{c4}^I} \right) + \overrightarrow{V_{c5}^I} + \overrightarrow{V_{c6}^I} \\
&= [(4 + 2p) l cos(\theta); 0; 0] \\
&\underline{\underline{A}}_k \\
&= \sum_{i=1}^{k-1} \underline{\underline{R}}_z \big((i-1)(\pi \\
&- \varphi) \big)^T \sum_{i=1}^{k-1} \underline{\underline{R}}_z \big((i-1)(\pi - \varphi) \big) \\
&\underline{\underline{B}}_k \\
&= \sum_{i=1}^{k-1} \underline{\underline{R}}_z \big((i-1)(\pi - \varphi) \big)^T \underline{\underline{R}}_z \big((i \\
&- 1)(\pi - \varphi) \big)
\end{aligned}
\tag{24}
$$

$$
F_T^1(\theta) = \frac{sin^2(2\theta)}{(2l\, sin(\theta) + l_0)^2} \tag{25}
$$

$$
\begin{aligned}
&F_T^2(\theta) \\
&= \left[\frac{l_1^2 l \sin^2(2\theta)}{2(l \sin(\theta) + l_0)^2} + 4l^2 \cos^2(\theta) \right. \\
&\left. - \frac{2 l^2 l_0 l_1 \sin(2\theta) \cos(\theta)}{(2l \sin(\theta) + l_0) \sqrt{4l^2 \sin^2(\theta) + l_0^2}} \right]
\end{aligned}
\tag{26}
$$

$$
\begin{aligned}
&F_T^3(\theta) \\
&= \overrightarrow{V_A^{I^T}} \sum_k \underline{\underline{A}}_k \overrightarrow{V_A^I} \\
&+ \overrightarrow{V_A^{I^T}} \sum_k \underline{\underline{B}}_k \left(\overrightarrow{V_{G1}^I} + \overrightarrow{V_{G2}^I} \right) + \left(\overrightarrow{V_{G1}^{I^T}} \right. \\
&\left. + \overrightarrow{V_{G2}^{I^T}} \right) \sum_k \underline{\underline{B}}_k \overrightarrow{V_A^{I^T}}
\end{aligned}
\tag{27}
$$

Q_I can be then estimated as the left-hand side of Eq. 22 assuming a prescribed acceleration and velocity profile of the ring deployment $\theta(t), \dot{\theta}(t), \ddot{\theta}(t)$.

3. TORQUE MARGIN DERIVATION

3.1.1. Torque Margin Rule Generalization

Applying Eq. 1 with the obtained generalized torques, one finds:

$$
Q_{MIN} = 2\big(3Q_f + 3Q_H\big) + 3Q_L + 1.25Q_I \tag{28}
$$

where Q_f is the friction loss, Q_H is the harness loss, Q_L is the output torque of the mechanism, which is assumed to be the net tensioning contribution, Q_I is the inertial contribution due to a specified acceleration profile and finally the expression of the torque margin is provided as:

$$
\frac{Q_M}{Q_{\text{MIN}}} - 1 > 0\% \tag{29}
$$

One should also note that, in Eq. 28, all the passive contributions and actuation losses are factorized according to ESA according to ESA standards.

3.1.2. Results at Nominal Temperature

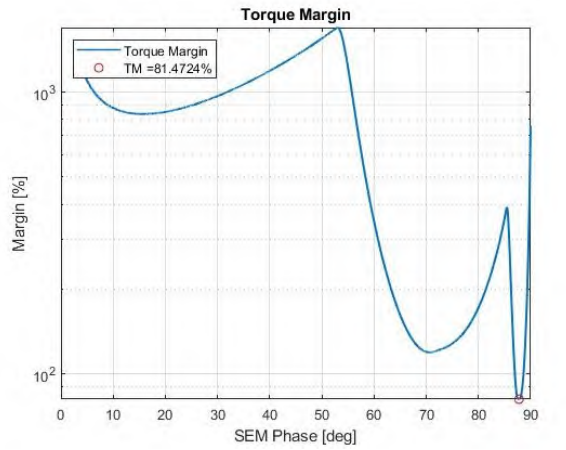


Figure 9: Torque Margin of the LDR ring as a function of the aperture angle

In Fig. 9, the torque margin for the present case study is shown as a function of the SEM aperture angle θ. Not surprisingly, the minimum value is reached during cable net tensioning. At the end of the deployment, the generalized torque contribution of the net action is nullified because equivalent component in the SEM plane is aligned with the compass tubes direction (this results in a zero-moment component). The residual resistance that the driving cable needs to compensate at the end of the deployment is only the hinge friction, which is high due to the pin compression under the net tension load. The drop of the Torque Margin starting from 55 degree of SEM aperture angle refers to the tensioning of the mesh that is extremely flexible and achieves its final tensioned state with great radial displacements of the ring vertexes.

3.1.3. Effects of Temperature

The torque margin is also affected by the operational temperature at which the deployment takes place in orbit.
Typically, thermal loads mostly affect the viscosity level in dampers and lubricants as well as the actuation capabilities of the motors under thermal load. In this case, several effects engaged by temperature have been taken into account:

- Variation of all the friction coefficients due to temperature
- Variation of the viscosity in pulley bearing lubrication (if any)
- Variation of the interference and reaction force (Hertzian theory) between jointed parts
- Thermal distortions in the driving cable and in the net cable system
- Variation of the motor output torque
- Variation of the strength limits of the driving cable and all the mechanical components of the ring (this may modify the design constraints assumed for torque margin computation)

The effects of different thermal environment on the minimum expected torque margin for the ring actuation is provided in Fig. 10.

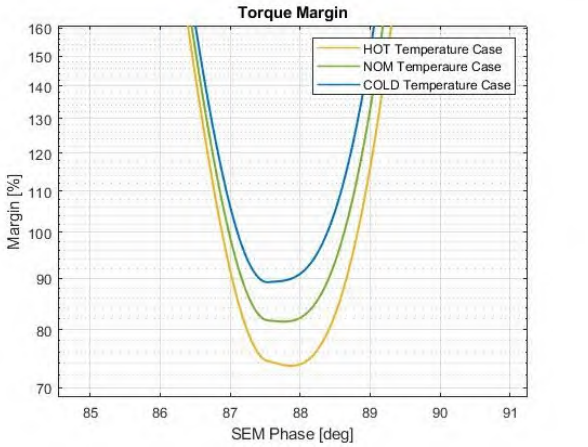


Figure 10: Effects of temperature on the minimum Torque Margin

4. RESULTS VALIDATION

To demonstrate the validity of the proposed approach, the reduced 1DoF multibody model based on the Classical Lagrangian formulation has been validated against the Adams commercial multibody dynamics software. Such model is used to demonstrate the suitability of actuators sizing, but also to verify the stability of the deployment sequence in presence of desynchronizations due to the flexibility of the ring. This is a typical verification process ([9]) that cannot be performed with the simplified 1DoF reduced order model adopted to size the actuation mechanism.

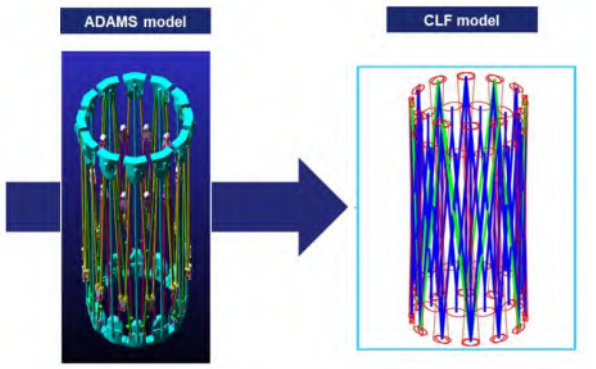


Figure 11: Comparison between the complete Adams Multibody Model of the LDR ring and the 1DoF reduced order model

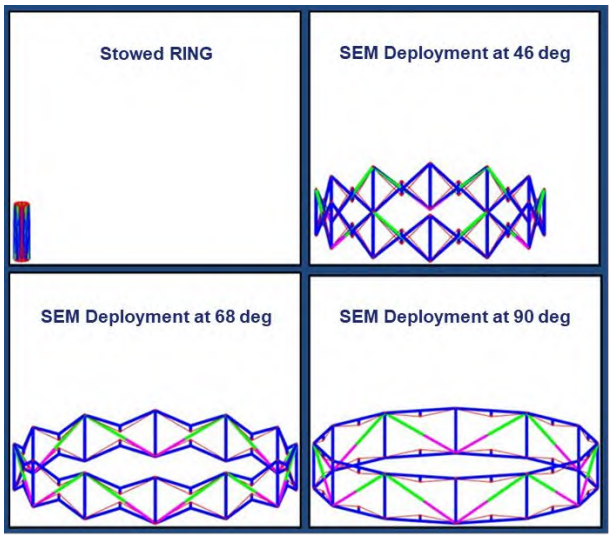


Figure 12: Deployment sequence of the LDR ring in the CLF reduced model

Fig. 11 displays the two models and Fig. 12-13 depict their respective deployment sequence at different SEM aperture angles.
Fig. 14 shows the comparison between the minimum driving cable tension needed for LDR deployment at different aperture steps derived with the two models, thus confirming the validity of the results obtained with the proposed CLF approach. As a remark, one can note that the effect of the mesh resistance has not been included in the models for results correlation, therefore only the peak of resistance due to the cable net tensioning alone is clearly visible in Fig. 14.

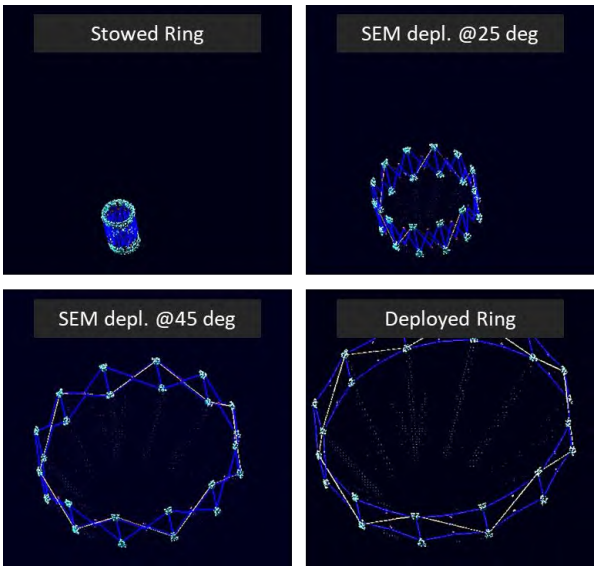


Figure 13: Deployment sequence of the LDR ring in the complete and flexible Adams Multibody model

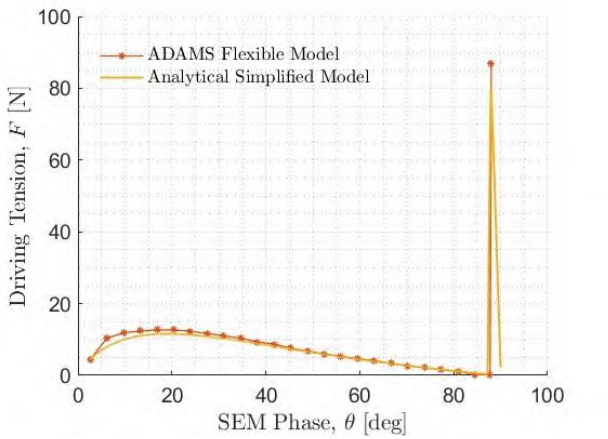


Figure 14: Correlation of the CLF model with complete Adams flexible multibody model

5. EXPERIMENTAL VALIDATION

In the frame of the program called International Mars Ice Mapper (Phase B) a complete LDR demonstrator has been designed, manufacture and tested. The MIM LDR is a 6 m diameter antenna working in L, X and ka frequency band (Fig. 15-16). The LDR has been subjected to an extensive test campaign (functional, vibration and thermal). One of the main tests was the successful full deployment of the antenna, that shown the correctness of the winch motors sizing with respect the overall torque margin (Fig. 17).

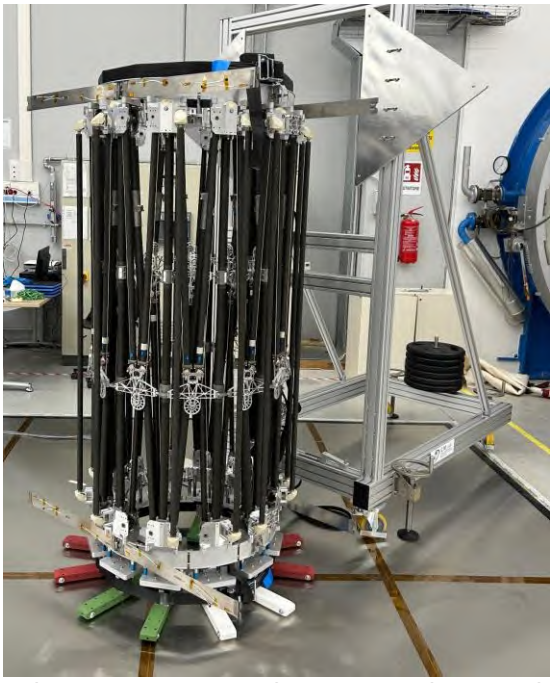


Figure 15: MIM LDR demonstrator in stowed configuration

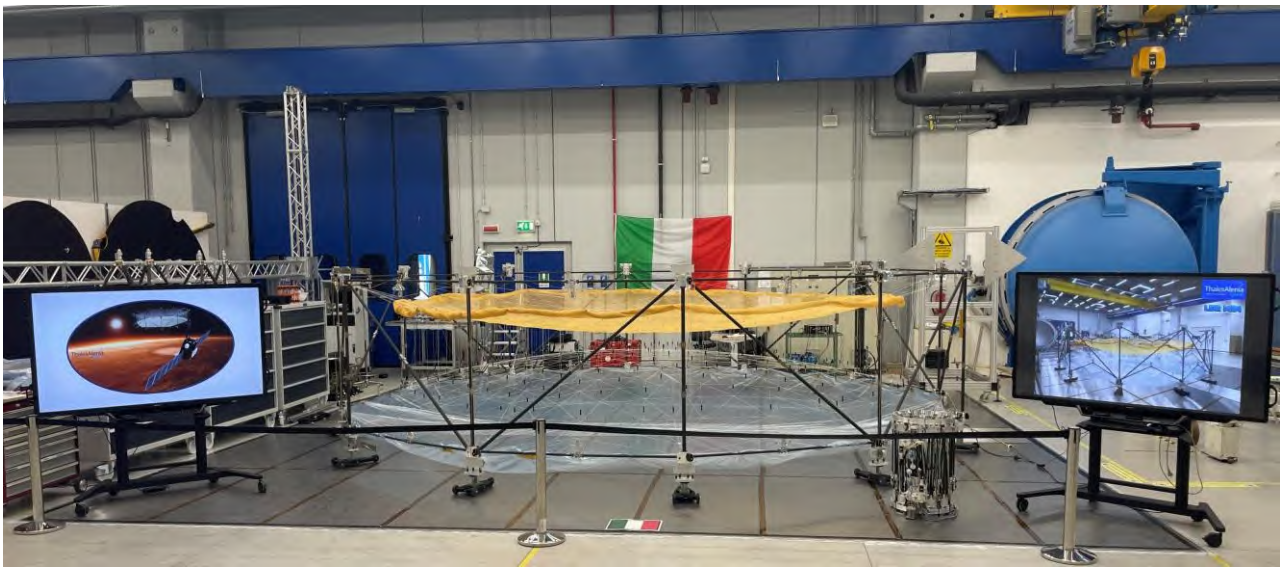


Figure 16: MIM LDR demonstrator in deployed configuration

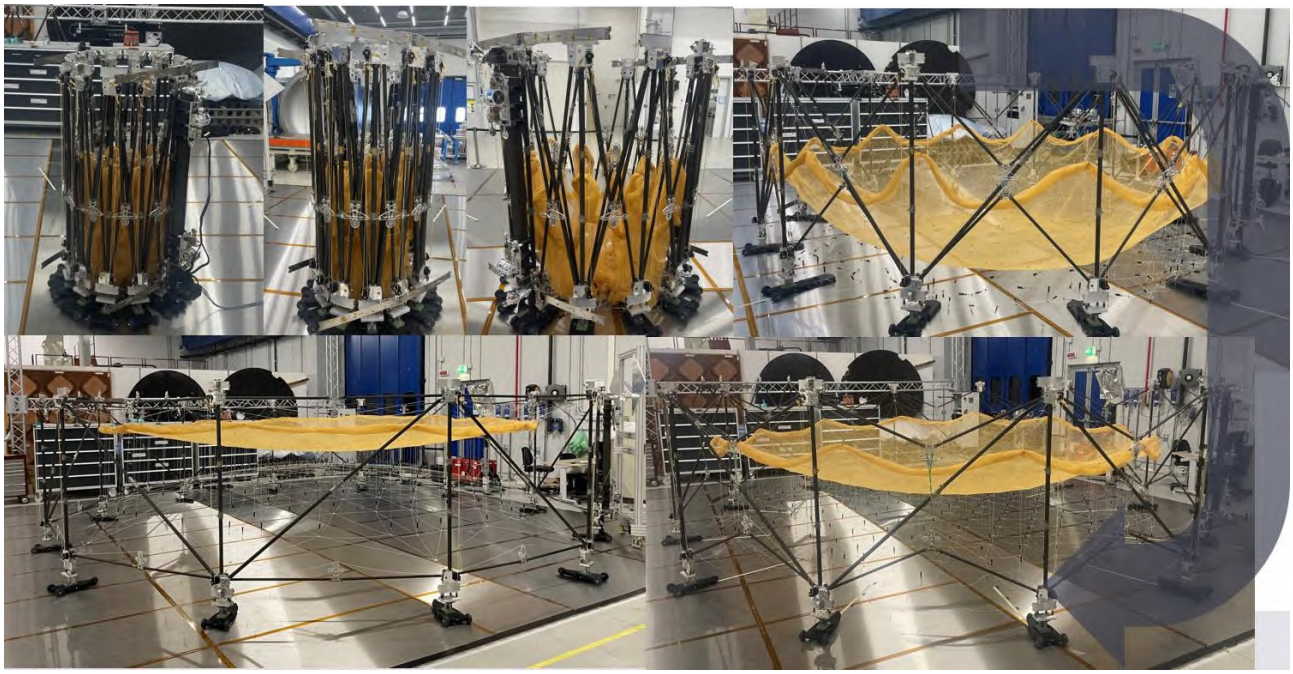


Figure 17: MIM LDR demonstrator deployment test

6. CONCLUSIONS

In conclusion, this paper has presented a simplified and physically consistent methodology for the evaluation of deployment torque margin of the ring mechanism of a mesh reflector in compliance with ESA/ECSS requirements. Starting from a classical Lagrangian formulation of the equations of motion, the proposed approach reduces the deployment dynamics of the ring to an equivalent single-degree-of-freedom representation. This reduction enables the direct and straightforward application of the torque margin verification rule prescribed by the ECSS standards, thus providing an efficient tool for the preliminary sizing and verification of deployment actuators.

The proposed methodology preserves the dominant active, passive and inertial contributions governing the deployment process while significantly reducing the complexity typically associated with high-fidelity multibody models. As a result, the torque margin assessment can be performed with limited computational effort and with a level of transparency that is particularly valuable during design iterations, system-level trade-off activities and multidisciplinary optimization analyses.

The validity of the approach has been assessed through a cross-correlation campaign with a detailed commercial multibody model, including flexible bodies. The comparison has shown a very good agreement in terms of deployment kinematics and required actuator torque, demonstrating that the simplified formulation is capable of capturing the relevant dynamic behaviour of the mechanism.

In addition, the first experimental evidence obtained

from a representative hardware setup is further confirming the soundness of the proposed approach and its capability to reproduce the observed deployment behaviour with satisfactory accuracy.
Overall, the presented method offers a practical framework for the early design phases of Large Deployable Reflectors (LDRs), where quick system analyses and motorization budget evaluations are essential for the selection of suitable deployment actuators.

7. REFERENCES

1. L. Puig, A. Barton, Rando N., “A review on Large Deployable structures for astrophysics missions”, *Acta Astronautica*, 67, 12-26, 2010.
2. Tibert G., “Deployable Tensegrity Structures for Space Applications”, PhD Thesis, Royal Institute of Technology, Department of Mechanics, Stockholm, 2002.
3. Focardi P., Brown P.R., Rahmat-Samii Y., “Deployable Mesh Reflector Antennas for Space Applications: RF Characterizations”, *Space Antenna Handbook*, eds W.A. Imbriale, S. Gao and L. Boccia, pp. 314-343, 2012.
4. Thomson M.W., “The Astromesh Deployable Reflector”, *Astro Aerospace*, CA, USA, 1999
5. ECSS Secretariat, ECSS-E-ST-33-01C Rev.2, ESA-ESTEC Requirements & Standards Division Noordwijk, The Netherlands, 2019.
6. Nie R., He B., Zhang L., “Deployment dynamics modeling and analysis for mesh reflector antennas considering the motion feasibility”, *Nonlinear Dynamics*, 549-564, 2018.
7. Argentesi F., Pasquali M., et al., “Geometrically nonlinear model of cable net and mesh for the manufacturing of large deployable mesh reflectors”, *Aerospace Science and Technology 178*, 2026
8. Labella G., Pasquali M., et al., “Optimizing the design of Large Deployable Mesh Reflectors in presence of Manufacturing Defects”, ECSSMET, 2024
9. Peng Y., Zhao Z., “Flexible Multibody Model and the Dynamics of the Deployment of Mesh Antennas”, *Journal of Guidance, Control and Dynamics,* March 2017.

STRUCTURAL ARCHITECTURE, MECHANISM DESIGN, AND INTEGRATION METHODOLOGY FOR METUCUBE SATELLITE

Elif Irmak Kaynar [(1)], İbrahim Doğa Ergin [(2)], Yasin Güngör [(3)], Assoc. Prof. Dr. Halil Ersin Söken [(4)], Asst. Prof. Dr. Görkem Eğemen Güloğlu [(5)]

[(1)] Middle East Technical University, METU Aerospace Engineering Department 06800 Çankaya Ankara/Turkey, Email: irmak.kaynar@metu.edu.tr
[(2)] Middle East Technical University, METU Aerospace Engineering Department 06800 Çankaya Ankara/Turkey, Email: doga.ergin@metu.edu.tr
[(3)] Middle East Technical University, METU Aerospace Engineering Department 06800 Çankaya Ankara/Turkey, Email: yasin.gungor@tubitak.gov.tr
[(4)] Middle East Technical University, METU Aerospace Engineering Department 06800 Çankaya Ankara/Turkey, Email: esoken@metu.edu.tr
[(5)] Middle East Technical University, METU Aerospace Engineering Department 06800 Çankaya Ankara/Turkey, Email: gguloglu@metu.edu.tr

KEYWORDS

CubeSat, deployment mechanism, integration, lightweight engineering, mechanical design.

ABSTRACT

This paper presents the structural architecture, mechanical optimization, and integration methodology for METUCube, a 3U Earth observation nanosatellite developed at Middle East Technical University (METU). To balance strict mass constraints with dynamic stiffness, the primary framework was subjected targeted mass reduction. Internally, a decoupled architecture isolates the optical payload from the PC/104 avionics stack, minimizing integration risks and enabling independent calibration. Additionally, monofilament burn-wire mechanisms ensure reliable mechanism deployment. The resulting modular platform achieves an optimal stiffness-to-mass ratio while complying with standard POD tolerances.

1. INTRODUCTION

The standardization of nanosatellites, most notably the CubeSat architecture, has fundamentally transformed access to Low Earth Orbit (LEO), evolving from compact educational demonstrators into sophisticated platforms capable of executing high-valued scientific research and operational Earth observation missions [6]. By constraining spacecraft geometries to standardized modular envelopes compatible with standard Picosatellite Orbital Deployers (PODs), CubeSats substantially reduce launch integration costs and development timelines [1, 3]. However, these rigid envelope constraints impose severe multidisciplinary design challenges on the primary structural platform. The mechanical framework must simultaneously provide a lightweight and high-stiffness skeleton to protect sensitive internal avionics and optical payloads while maintaining precise external rail tolerances to prevent damages during orbital ejection [1, 2]. Consequently, the primary structure represents a critical subsystem where mechanical robustness, volumetric efficiency, and assembly modularity must be carefully balanced.

During the launch phase, nanosatellite structures are subjected to severe static acceleration, shock, and broadband random vibration environments [4, 8]. To prevent mechanical amplification and structural failure, aerospace verification standards mandate that the first fundamental modal frequency of the primary structure remain sufficiently decoupled from the low-frequency acoustic and structural excitation thresholds of the launch vehicle [4, 5]. Applying established spacecraft systems engineering principles demonstrates that achieving modal frequencies above 100 Hz in 3U CubeSats requires optimized longitudinal load paths and rigid internal bulkheads [8]. Furthermore, dynamic response evaluations utilizing General Environmental Verification Standard (GEVS) and European Cooperation for Space Standardization (ECSS) profiles indicate that while global deformations in small spacecraft remain in the submicron regime under quasi-static loading, severe stress concentrations develop at rail interfaces, solar panel hinges, and fastener attachment points [4, 5].

To minimize structural mass while preserving required stiffness, recent CubeSat structural developments have increasingly moved away from uniform wall thicknesses toward geometric pocketing and computational topology optimization [7]. Traditional lightweighting methodologies rely on machining triangular or trapezoidal cutouts into outer panels while preserving continuous diagonal ribs to channel axial and shear loads across the frame [2]. Advancing upon parametric pocketing, density-based topology optimization methods are utilized to refine load transfer paths across

nanosatellite bulkheads and frames [7]. Optimizing material distribution along primary stress trajectories can reduce structural mass significantly while simultaneously increasing torsional rigidity and fundamental natural frequencies [7, 8]. Alongside designing lightweight components, the strategic development of fastener joints and standardized clamping preloads are essential implementations to simplify integration sequences and prevent joint relaxation under vibration loads without violating external POD clearance envelopes [9].

Beyond the static primary structure, small spacecraft missions frequently require deployable surface hardware such as solar panels and communication antennas to satisfy operational power and telemetry budgets. The deployment of these external mechanisms relies on low-shock hold-down and release mechanisms (HDRMs) that must remain securely stowed during launch and deploy reliably in orbital vacuum. Research by Thum et al. demonstrated that thermal burn-wire mechanisms using nylon monofilament loops provide a highly reliable, low-powered, and mechanically nonexplosive alternative to traditional pyrotechnic actuators, making them particularly suitable for CubeSat antenna and hinge release systems [10].

Within this context, this paper presents the structural design, optimization for lightweight design, and modular integration architecture of METUCube, which is a three-unit (3U) Earth observation CubeSat developed at the Small Space Systems Laboratory (S3 Lab) at METU. Designed to monitor the pre- and post-disaster phases of natural hazards such as wildfires and earthquakes from Sun Synchronous Orbit (SSO) at an altitude of 500 kilometers, the METUCube platform requires a robust structural framework capable of housing a multi-sensor optical payload alongside a standardized embedded avionics stack. This study details the methodology governing the lightweight primary structural assembly, evaluates its mechanical integrity and load path efficiency, and presents a decoupled internal integration strategy that isolates payload optical alignment from avionics bus maintenance.

2. METHODOLOGY

For nanosatellites such as CubeSats, highly efficient spatial integration and strict mass and volume optimization are critical considerations of structural design. Because the internal volume is severely restricted, the physical interfaces between subsystems must be engineered with high precision to ensure operational efficiency. The structural framework is governed by universal 3U CubeSat design specifications, which dictate that the satellite must securely fit within a standard POD during launch. Consequently, the primary structure is constrained to the standard 3U envelope of approximately 100 x 100 x 340.5 millimeters, excluding deployment mechanisms and allowable extension margins. To achieve optimal internal layout and structural integrity within these constraints, a design methodology with two major strategies was implemented for the METUCube structural architecture.

2.1 Structural Optimization and Fastener Standardization

The first design strategy focuses on the primary structural components including the exterior frames, bulkheads, hinges, deployment (kill) switches, and mechanical joints. The primary objective at this stage is to minimize mass while maximizing durability, ensuring the flight model can withstand severe launch loads and execute safe deployment. Weight reduction is achieved by systematically removing material from sections that does not bear any loading.

Furthermore, fasteners are strategically placed in high stress regions that require additional support. To sustain manufacturing and integration, the fastening system is highly standardized. Due to the high durability requirements and estimated launch loads, M3 bolts are utilized as the primary fasteners for assembling major spacecraft components. M3 represents the minimum bolt diameter necessary to safely withstand the maximum predicted stress concentrations relative to the scale of spacecraft. For smaller auxiliary mechanisms such as the deployment switches, M2 bolts are utilized. Consequently, the entire structural assembly is constrained to only two fastener types, significantly reducing integration complexity.

2.1 Modular Subsystem Integration Strategy

The second design strategy governs the internal settlement and the physical integration between the primary structure and the various electronic subsystems, which include Communication (COMM), Attitude Determination and Control (ADCS), On-Board Computer (OBC), Electrical Power System (EPS), and Payload.

To simplify the assembly process, the internal architecture is divided into two distinct modular blocks. The first block is strictly dedicated to the payload system. Regardless of the number of optical sensors or specific camera features, the payload components are mounted as a unified unit, directly interfaced with their dedicated printed circuit boards (PCBs). The second block comprises the remaining avionics and support subsystems, also referred as the spacecraft bus. This avionics stack is designed and assembled in strict accordance with the Personal Computer/104 (PC/104) embedded computing standard. Utilizing the PC/104 standard

allows the external structural framework to be modified or updated without disrupting the complex electronic interfaces of the internal stack. By isolating the payload and avionics into two independent blocks, the final integration sequence with the external structural frame is highly simplified, reducing the risk of component damage and facilitating the easiest possible assembly scenario. Furthermore, this separation establishes a modular platform by preserving the heritage-gaining avionics bus without modification. The novel payloads for subsequent missions can be integrated rapidly and seamlessly for this type of spacecraft integration.

3. RESULTS AND DISCUSSION

This section presents the final architectural outcomes derived from the methodology and details the geometric configurations of the primary exterior envelope, the internal load-bearing bulkheads, and the deployable surface mechanisms. Furthermore, it outlines the modular integration of the internal PC/104 avionics stack alongside the optical payload block. The structural mass budget and the system-based advantages of this decoupled architecture are evaluated to confirm compliance with standardized 3U CubeSat volumetric constraints and the specific operational requirements of the METUCube mission.

3.1 Primary Structural Assembly and Exterior Frames

Implementation of the design strategies resulted in the finalized geometries for all structural components, as well as the integrated spacecraft assembly. The complete primary structure without any bolts and joints, which includes four outer side frames, three internal bulkheads, two solar panel hinge assemblies with six interface brackets, and three kill switch mechanisms is illustrated in Fig. 1. As illustrated, the primary structural components have distinct colours for clarity as the four outer side frames are shown in blue, the three internal bulkheads in green, and the two deployable hinge assemblies with their corresponding interface brackets in pink. The mechanical kill switches are identified by black circles.

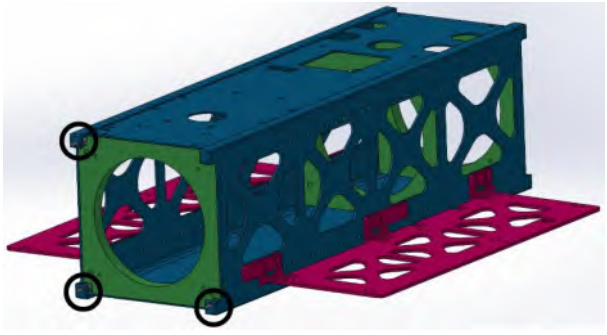


Figure 1: Primary structural components

The longitudinal structural envelope is defined by the left and right-side frames in Fig. 2 and Fig. 3, respectively, each measuring 100 × 340.5 × 8.5 mm including corner rails interfacing the external POD. To achieve mass reduction without compromising stiffness, smooth triangular cutouts were pocketed across both panels while preserving diagonal load-bearing ribs to optimize stress distribution. A standardized pattern of M3 mounting holes is distributed along the margins of both frames. These holes provide a modular interface, allowing internal additional support to be relocated along the longitudinal axis as integration requirements evolve if necessary. Additionally, dedicated recessed sections are integrated to accommodate kill switch spring compression with a configuration of one pocket on the left frame and two on the right frame.

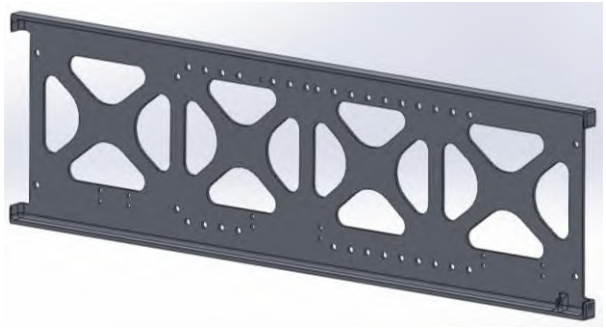


Figure 2: Left side frame of primary structure

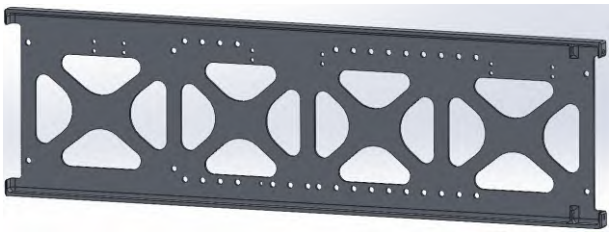


Figure 3: Right side frame of primary structure

The top frame given in Fig. 4 measuring 83 × 326.5 × 1 mm provides exterior interfaces and structural closure. There is a gap for the Sun Sensor positioned below the mounting interfaces for the middle bulkhead consisting of four 2.1 mm diameter through-holes and a central 7 mm diameter clear aperture. Adjacent to this section is a square cutout designed for Global Navigation Satellite System (GNSS) antenna integration. At the upper edge of the panel, four localized regions in Fig. 4 circled in red are machined to mount the microswitches for the deployment mechanisms.



Figure 4: Top frame of primary structure

The bottom frame given in Fig. 5 measuring 83 × 326.5 × 1 mm similarly features an upper interface for microswitch mounting. It includes an aperture section for the S-Band antenna, comprising eight 3.5 mm diameter mounting holes surrounding a 23.53 mm diameter central feed aperture highlighted in red. On the bottom part of the centerline, a 20 × 8 mm rectangular access cutout is provided for battery charging electronics, below which lies a 40 × 40 mm square cutout dedicated to the deployment interface PCB.

The bottom frame also defines the baseline layout for the payload block. The spacecraft accommodates four multispectral cameras positioned along the outer edges of the frame and a single thermal camera mounted centrally at the upper end. This geometric arrangement enables the star tracker to be mounted directly below the thermal camera, maximizing natural shading and shielding the optical sensor from direct solar irradiance.

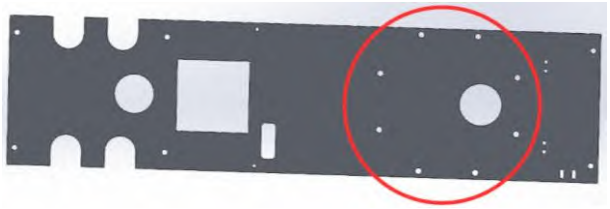


Figure 5: Bottom frame of primary structure

3.2. Internal Bulkheads and Load Distribution

Internal load transfer and structural rigidity are maintained by the top, middle, and bottom bulkheads shown in Fig. 6, 7, and 8. Measuring 97 × 96.2 × 8 mm, each bulkhead features a central 78 mm diameter aperture to facilitate internal harness routing and component clearance. Because their primary structural function is to tie the four exterior frames together and stabilize the primary skeleton, material is retained only where required for fastener engagement.

While the middle and bottom bulkheads share an identical geometry, the top bulkhead is geometrically distinct. The material is relieved from three of its corners to provide mechanical clearance for the kill switch assemblies mounted at the upper section of the spacecraft.

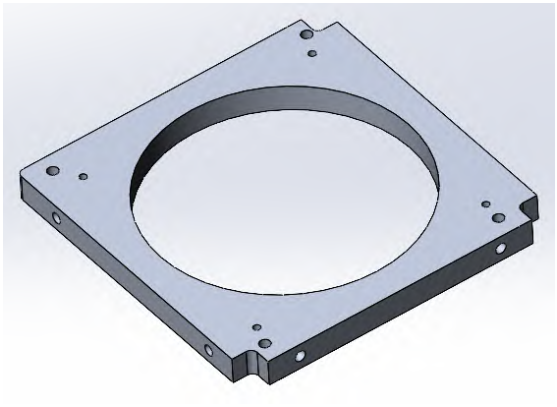


Figure 6: Top bulkhead of primary structure

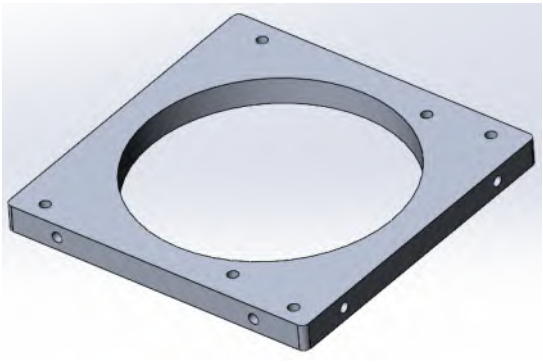


Figure 7: Middle bulkhead of primary structure

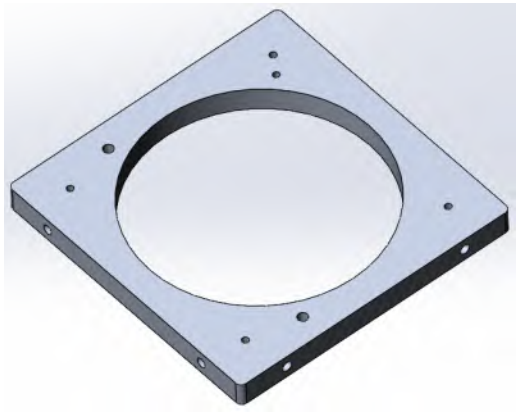


Figure 8: Bottom bulkhead of primary structure

3.3. Deployable Mechanisms and Surface Hardware

The deployable solar panel hinge assemblies and their corresponding mounting brackets are presented in Fig. 9. Each hinge panel measures 77 × 236.5 × 2 mm excluding brackets and interfaces with the primary structure via three mounting brackets positioned at the upper, middle, and lower sections. These brackets serve a dual purpose of securing the hinges to the primary structural frame and providing mechanical stabilization during post-deployment detumbling. Similar to the longitudinal frames, smooth triangular pockets are removed from the hinge plates while preserving diagonal load

paths for structural efficiency. Localized square reliefs circled in blue are machined into the panels to prevent fastener head interference during stowed configuration.

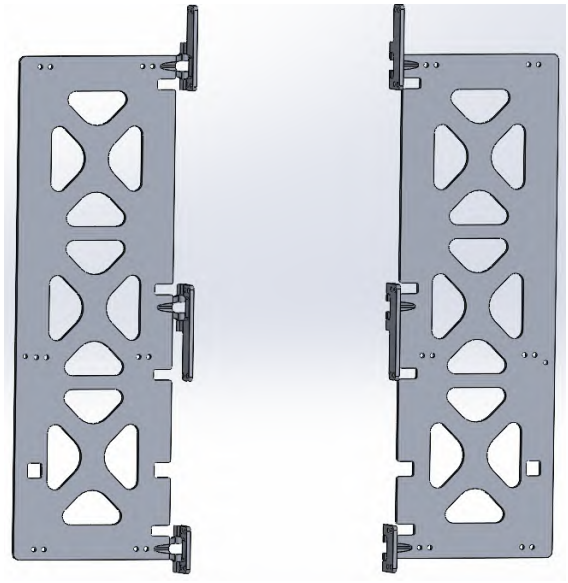


Figure 9: Deployable solar panel hinge assemblies and corresponding mounting brackets

Finally, the mechanical activation assembly is highlighted in Fig. 10, showing one of the three integrated kill switch mechanisms. Each assembly consists of a microswitch, an M2 male-female threaded standoff, a compression spring, and a 12 mm M2 fastener. The microswitches are secured to the top and bottom frames using two M2 bolt and nut sets. When the CubeSat is inserted into the POD, the walls of the deployer compress the spring-loaded standoff downwards against the switch. Upon orbital deployment, spring releases, mechanically activating the electrical systems of spacecraft.

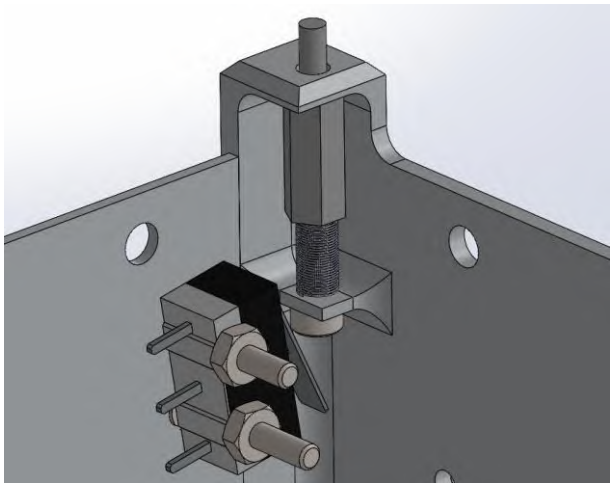


Figure 10: Kill switch mechanism for mechanical activation

To ensure high manufacturability and long-term durability, Aluminium 6061-T6 is utilized for the primary structural framework. The comprehensive mass budget of the structural body without bolts and joints is detailed in Tab. 1.

Table 1: Mass Budget of the Structural Body without Bolts and Joints

	Amount of Piece	Total Volume $[cm^3]$	Total Mass $[g]$
Left Side Frame	1	43.82	118.31
Right Side Frame	1	43.86	118.31
Top Frame	1	26.29	70.99
Bottom Frame	1	23.46	63.34
Top Bulkhead	1	34.49	93.13
Middle Bulkhead	1	35.52	95.89
Bottom Bulkhead	1	35.61	96.15
Deployable Solar Panel Hinges	2	28.37	76.59
Kill Switch Mechanisms (estimated)	3	Not Given	45.00

To quantify the efficiency of the lightweighting strategy, significant mass reductions were achieved across the primary components through the applied triangular pocketing. For instance, the original unoptimized mass of the two deployable solar panel hinge assemblies was 196.67 g. After the geometric optimization process, this number was reduced to 76.59 g, achieving an approximate 61% mass reduction. Similarly, the left and right-side frames were individually reduced from an initial solid mass of 183.87 g down to 118.31 each, representing a 35.6% mass saving per panel. Cumulatively, these specific optimizations removed over 250 grams of dead weight from the exterior envelope, directly expanding the available mass allocation for the multi sensor payload block and the high-capacity battery module.

3.4. Internal Stack Configuration and Subsystem Integration

Following the completion of the primary structural envelope, internal integration was executed by dividing avionics and scientific instruments into two distinct and decoupled assemblies of the payload block and the PC/104 avionics stack.

The integrated payload block is shown in Fig. 11. It comprises four multispectral cameras equipped with distinct spectral filters of gray, blue, red, and green, as well as one thermal camera, one star tracker, a custom aluminum mounting bracket, the dedicated payload processing card, and four M3 structural standoffs. The geometric layout of the payload block arranges the four multispectral cameras symmetrically on the outer flanks of the aluminum mounting bracket, while the thermal camera and star tracker occupy the central axis. The payload electronics card is mounted directly to the rear face of the bracket, minimizing harness lengths.

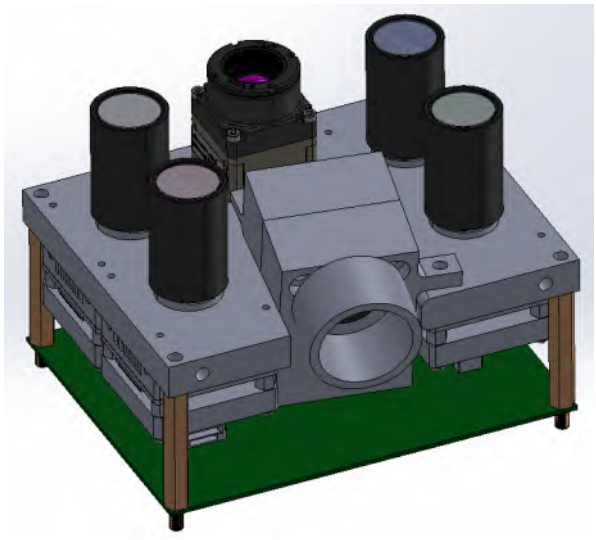


Figure 11: Integrated payload block

Prior to physical integration, a comprehensive electrical interconnection diagram, which is generated for mainly integration purposes, presented in Fig. 12 was established to map subsystem data and power routing. The architecture is designed around a centralized data and decentralized peripheral control strategy. OBC functions as the primary command and data handling node, establishing direct communication interfaces with all critical modules such as COMM board, ADCS, EPS, and the payload and deployment block. Power generation and distribution are strictly governed by EPS, which harvests energy from the solar panels and routes regulated power across the bus to all active subsystems. To ensure launch safety compliance, EPS is electrically interlocked with three mechanical kill switches that physically isolate the power supply while the satellite is in the deployer. To optimize processing loads, specific interconnections within the subsystems are managed locally. COMM board independently drives the S-Band and Ultra High Frequency (UHF) antennas, while the ADCS directly evaluates telemetry from its dedicated Sun Sensors, Star Tracker, and GNSS receiver. Finally, the multispectral and thermal cameras alongside the deployment electronics interface directly with the OBC for data transfer and EPS for power, demonstrating a highly decoupled and modular electrical architecture.

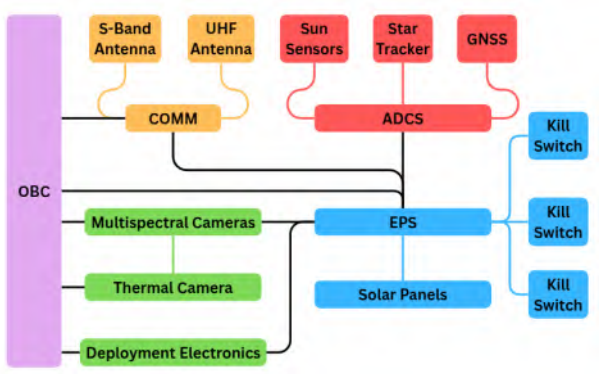


Figure 12: Electrical interconnection diagram

The PC/104 avionics stack is illustrated in Fig. 13. To optimize the center of gravity of spacecraft and ensure dynamic stability, the battery card representing the heaviest individual board is mounted directly above the middle bulkhead with the remaining EPS cards stacked sequentially above it. Because the payload block occupies the lower cavity beneath the PC/104 assembly, the S-Band antenna is mounted at the top of the satellite. To minimize RF trace losses, COMM card is positioned at the top of the PC/104 stack, directly adjacent to the S-Band feed. OBC is integrated immediately beneath COMM card followed by ADCS cards at the base of the stack. PC/104 mechanical standoffs are sized to match the electrical connector clearance heights. To minimize radiation damage and enhance structural rigidity, dedicated top and bottom aluminum shielding plates are mounted across one of EPS cards, one of ADCS cards, OBC and COMM cards. Four 25 mm continuous-thread tie rods (also known as studs) are utilized to clamp the stack and secure the entire PC/104 assembly to the primary structural frame. Utilizing continuous threaded rods provides a highly efficient fastening solution for complex and multi-board assemblies, eliminating the need to manufacture custom bolts for varying stack heights.

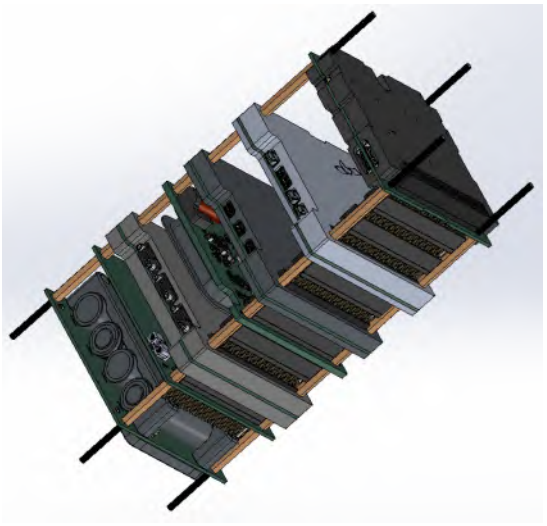


Figure 13: PC/104 avionics stack

Exterior integration is significantly less complex than internal assembly for METUCube satellite. Each side frame, the top and bottom bulkheads, and the deployable hinge surfaces are equipped with solar panels and exterior PCBs given in Fig. 14. On the bottom frame, two deployable UHF antennas are positioned above the S-Band antenna. The antenna deployment mechanism relies on a monofilament burn-wire retaining loop. The tips of the UHF antenna elements are drilled with 1.5 mm diameter holes, through which the monofilament is routed. The wire passes through 2 mm through holes on opposing side panels without invading the external POD interfacing corner rails circled red in Fig. 15. Upon orbital ejection, the deployment PCB operates a thermal cutter, which is also a resistor in this case, to cut the monofilament releasing the UHF antennas to assume their operational configuration. To accommodate these deployment routing holes without damaging active solar cells, the left solar panel layout is inverted. Finally, an auxiliary Sun Sensor is mounted directly to the bottom bulkhead as shown in Fig. 16.

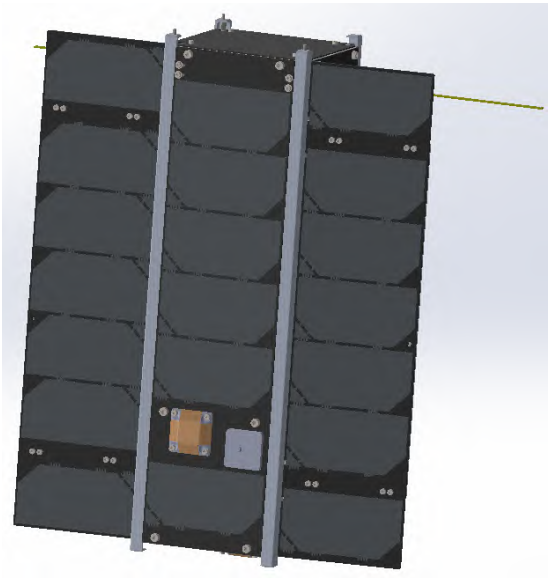


Figure 14: Exterior PCBs and solar panels

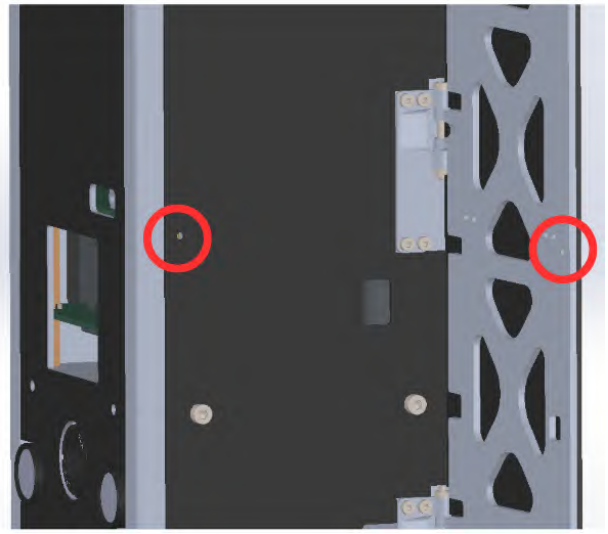


Figure 15: 2 mm through-holes on opposing side panels

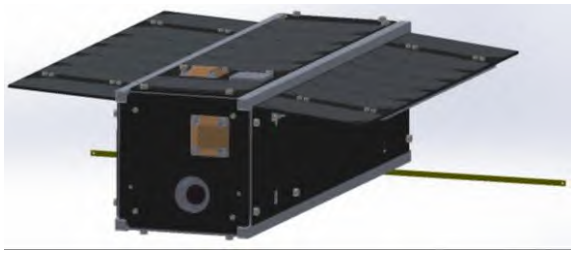


Figure 16: Mounting of Sun Sensor and Star Tracker to the bottom bulkhead

3.5. Architecture Synthesis

The results of structural design and integration demonstrate that the implemented methodology successfully balances mechanical robustness, volumetric efficiency, and assembly modularity. By utilizing topology-inspired triangular pocketing with preserved diagonal stiffeners across the longitudinal frames and hinge plates, the primary structure achieves a favorable stiffness-to-mass ratio. This configuration ensures that quasi-static and dynamic launch loads are distributed through the uninterrupted corner rails and diagonal struts, preventing stress concentrations around mounting apertures while maintaining total structural mass within the limitations.

From a systems engineering perspective, decoupling the internal architecture into independent PC/104 and payload blocks significantly minimizes assembly risk. In conventional CubeSat layouts, avionics and payload instruments are frequently interlinked within a single monolithic stack, requiring complete disassembly of the bus to service a single sensor. By isolating the optical payload block on a dedicated aluminum bracket below the middle bulkhead, optical alignment and sensor calibration can be performed independently of the main avionics stack.

Furthermore, the strategic placement of the heaviest component known as the battery module at the base of the PC/104 stack above the middle bulkhead lowers the center of mass of spacecraft, reducing potential errors during POD ejection and simplifying post-deployment attitude stabilization.

Finally, the thermal and optical layout of the bottom frame highlights an effective passive design trade-off. Mounting the star tracker directly beneath the satellite utilizes the structural advantage of spacecraft as a physical sunshade. This geometric shielding reduces the incidence of stray light and thermal radiation on the star tracker optics, enhancing attitude determination accuracy during sun-lit orbital phases without requiring additional mass for dedicated optical baffles. Similarly, routing the UHF burn-wire mechanism through dedicated clearances without violating POD rail tolerances confirms that the deployment of hardware complies with international CubeSat dispenser standards.

4. CONCLUSION

The structural and mechanical development of the METUCube platform demonstrates a highly effective approach to overcoming the volumetric and mass constraints inherent to the 3U CubeSat standard. By implementing a dual-strategy design methodology, the primary structural framework achieves optimal load distribution while successfully reducing the mass of critical exterior components such as the side frames and solar panel hinges by 35% to 61% through topology-inspired lightweighting. The decision to decouple the internal architecture into an independent PC/104 avionics stack and a dedicated optical payload block significantly enhances modularity, simplifies the integration sequence, and allows for isolated sensor calibration without disrupting the primary electronic bus. Furthermore, the integration of monofilament burn-wire mechanisms provides a low-power, reliable solution for deployable surface hardware, ensuring compliance with strict orbital deployment safety standards.

While the current structural iteration exhibits exceptional dynamic stiffness, preliminary load evaluations indicate opportunities for further refinement. Future work will focus on targeted structural reinforcements within the primary frame to elevate the safety margins under maximum quasi-static acceleration loads. Additionally, comprehensive environmental qualification campaigns including thermal vacuum (TVAC) and physical random vibration testing will be conducted. These physical tests will experimentally validate computational models and verify the ultimate flight compatibility of the METUCube structural assembly for its Earth observation mission.

5. REFERENCES

1. California Polytechnic State University, *CubeSat Design Specification (1U – 12U), Rev. 14.1*, San Luis Obispo, CA, 2022.
2. NASA Small Spacecraft Systems Virtual Institute, *State-of-the-Art of Small Spacecraft Technology: Structures, Materials, and Mechanisms*, NASA/TP-20240000000, 2024.
3. Puig-Suari, J., Turner, C., and Ahlgren, W., "Development of the Standard CubeSat Deployer and a Class of Picosatellites," *2001 IEEE Aerospace Conference*, Big Sky, MT, USA, 2001.
4. NASA Goddard Space Flight Center, *General Environmental Verification Standard (GEVS) for GSFC Flight Programs and Projects*, NASA/GSFC-STD-7000, 2013.
5. European Cooperation for Space Standardization, Space Engineering: Structural General Requirements, ECSS-E-ST-32C, ESA Requirements and Standards Division, 2008.
6. Woellert, K., et al., "CubeSats: Cost-effective science and technology platforms," *Acta Astronautica*, Vol. 69, No. 9-10, pp. 663–678, 2011.
7. Bendsøe, M. P., and Sigmund, O., *Topology Optimization: Theory, Methods, and Applications*, Springer Science & Business Media, 2003.
8. Fortescue, P., Swinerd, G., and Stark, J., *Spacecraft Systems Engineering*, 4th ed., Wiley, 2011.
9. Budynas, R. G., and Nisbett, J. K., *Shigley's Mechanical Engineering Design*, 10th ed., McGraw-Hill Education, 2014.
10. Thum, A., et al., "A Nichrome Burn Wire Release Mechanism for CubeSats," *41st Aerospace Mechanisms Symposium*, NASA/CP-2012-215882, pp. 479–488, 2012.

ECSSMET
Braunschweig Germany 2026

Structure engineering

SEMANTIC DATA EXCHANGE CAPABILITIES IN THE SPACE SUPPLY CHAIN TO REMOVE BARRIERS IN INTEROPERABILITY PROCESSES BY DEPLOYING OPEN STANDARDS (NASCENT)

Mona Chaure [(1)], Jens Tingstad [(2)]
[(1)] Jotne Connect AS, Norway, Email: mona.chaure@jotne.com
[(2)] Jotne Connect AS, Norway, Email: jens.fossan.tingstad@jotne.com

KEYWORDS
System Accommodation Requirements (SAR); Digital Mock-Up (DMU); AP242; AP209; STEP-TAS; NASTRAN; Thermal and Structural Analysis; Interoperability; Digital Engineering; Model-Based Engineering (MBE)

ABSTRACT
The increasing complexity of spacecraft development creates challenges in maintaining consistency, traceability, and interoperability across mechanical, structural, and thermal engineering activities. Engineering data is often distributed across discipline-specific tools and exchanged through documents, resulting in fragmented workflows and difficulties in demonstrating compliance with system requirements. To address these challenges, the NASCENT project developed a standards-based Digital Engineering Platform that integrates System Accommodation Requirements (SAR), Digital Mock-Up (DMU), structural and thermal analysis data, supplier information, and technical documentation within a unified engineering repository. The platform adopts a data-centric approach based on ISO 10303 (STEP) [1] standards, including AP242 [4], AP209 [3], and STEP-TAS [2], enabling interoperable management of engineering information across the spacecraft lifecycle. Validation was performed against a stakeholder-defined requirements baseline using representative accommodation, structural, and thermal engineering use cases. Results demonstrate improved traceability, multidisciplinary collaboration, supplier interoperability, and digital continuity, supporting the digitalization of spacecraft mechanical and thermal engineering processes through open standards.

1. INTRODUCTION

The development of modern spacecraft requires close collaboration between multiple engineering disciplines, including systems, mechanical, structural, thermal, manufacturing, and integration engineering. As spacecraft architecture becomes increasingly complex, maintaining consistency between requirements, design information, analyses, verification evidence, and supplier-provided data becomes increasingly challenging.

Many engineering processes remain dependent on discipline-specific tools and document-oriented information exchanges. While these approaches are well established, they often lead to duplicated effort, information silos, and limited traceability between engineering artefacts. These issues become particularly evident during accommodation verification activities, where stakeholders must demonstrate compliance with system requirements using information originating from multiple engineering domains.

This paper presents the results of the NASCENT project ("SemaNtic dAta exchange capabilities in the space Supply Chain to remove barriers in intEroperability processes by deploying opeN sTandards"), funded by the European Space Agency (ESA) under Contract No. 4000143890/23/NL/KML/cb – Engineering Digitalization within the ESA-STAR Technology Development Programme.

The project was led by Jotne Connect AS in collaboration with Airbus Defence and Space GmbH, which provided stakeholder input, representative use cases, engineering requirements, validation datasets, and assessment of the final demonstrator.

The primary objective was to develop and validate a standards-based Digital Engineering Platform capable of addressing identified interoperability and traceability challenges within spacecraft accommodation engineering. The platform was developed against a stakeholder-defined requirements baseline and validated through representative engineering use cases covering accommodation verification, structural analysis, thermal engineering, and supplier data exchange.

This paper presents the engineering challenges identified during the project, the requirements baseline used to guide development, the standards-based solution approach, the implemented capabilities, and the results obtained through stakeholder validation activities.

2. ENGINEERING CHALLENGES AND REQUIREMENTS

2.1. Engineering Challenges

The project began with an assessment of existing spacecraft accommodation engineering processes and the challenges associated with them.

2.1.1. Challenge1: Fragmented Accommodation Processes

System Accommodation Requirements (SAR) are frequently managed separately from design data and engineering analyses. As spacecraft configurations evolve, maintaining consistency between requirements and implementation becomes increasingly difficult.

2.1.2. Challenge 2: Limited Traceability

Verification evidence is often captured within reports and presentations that are disconnected from the design configuration used to demonstrate compliance. This limits end-to-end traceability across the development lifecycle.

2.1.3. Challenge 3: Isolated Engineering Analyses

Structural and thermal analyses are typically performed using specialized tools and reviewed independently from accommodation activities. This separation complicates multidisciplinary engineering reviews and reduces visibility across disciplines.

2.1.4. Challenge 4: Supplier Data Exchange

Spacecraft development involves extensive collaboration with suppliers. Engineering information exchanged across organisational boundaries often relies on different formats, tools, and data structures, increasing the effort required to achieve interoperability.

2.1.5. Challenge 5: Dependence on Proprietary Formats

Engineering data is frequently stored within proprietary software formats, limiting accessibility, reusability, and long-term preservation of information.

2.2. Requirements Baseline

Based on stakeholder input, project objectives, and identified engineering challenges, a requirements baseline was established as shown in Tab.1 below.

Table 1. Requirements Baseline

Requirement ID	Description
R1	Support digital management of SAR
R2	Enable DMU-based accommodation verification
R3	Integrate structural engineering models and results
R4	Integrate thermal engineering models and results
R5	Support supplier data exchange
R6	Use open standards-based representations
R7	Maintain traceability between requirements, design and verification evidence
R8	Support generation of customer-facing documentation

The requirements baseline formed the foundation for demonstrator development and subsequent validation activities.

3. SOLUTION APPROACH

3.1. Open Standards Strategy

To achieve interoperability across engineering domains, the project adopted a standards-based integration strategy founded on ISO (International Organization for Standardization) 10303 (STEP - Standard for the Exchange of Product Model Data) [1].
The selected standards included:

- AP242 (Application Protocol) for model-based 3D engineering information [4]
- AP209 for multidisciplinary analysis data [3]
- STEP-TAS (Thermal Analysis for Space) for thermal engineering information [2]

Together, these standards provide a common framework capable of representing geometry, product structures, simulation data, engineering properties, and associated metadata.

3.2. Data-Centric Integration

A key principle of the NASCENT approach is integration at the data-model level rather than through document exchange alone.
Within the platform, relationships are established between:

- System Accommodation Requirements
- Product structures
- CAD (Computer-Aided Design) geometry
- Structural analysis models
- Verification evidence
- Supplier information
- Documentation

This creates a digital thread capable of connecting engineering activities throughout the spacecraft development lifecycle.
The approach differs from traditional document-centric workflows by preserving semantic relationships between engineering artefacts and enabling direct navigation across engineering domains.

4. DEMONSTRATOR IMPLEMENTATION

4.1. Platform Architecture

The NASCENT Platform (conceptual architecture based on the selected technologies shown in Fig. 1 below) was implemented using the standards-based EDMopenSimDM (EDM - EXPRESS Data Manager; SimDM - Simulation Data Management) environment comprising repository, server, and

client components. The core architecture shown in Fig. 2 below illustrates the client, server, and database used to build the NASCENT platform.
The repository serves as the central source of engineering information and supports storage, management, visualization, sharing, and retrieval of artefacts originating from multiple engineering disciplines.

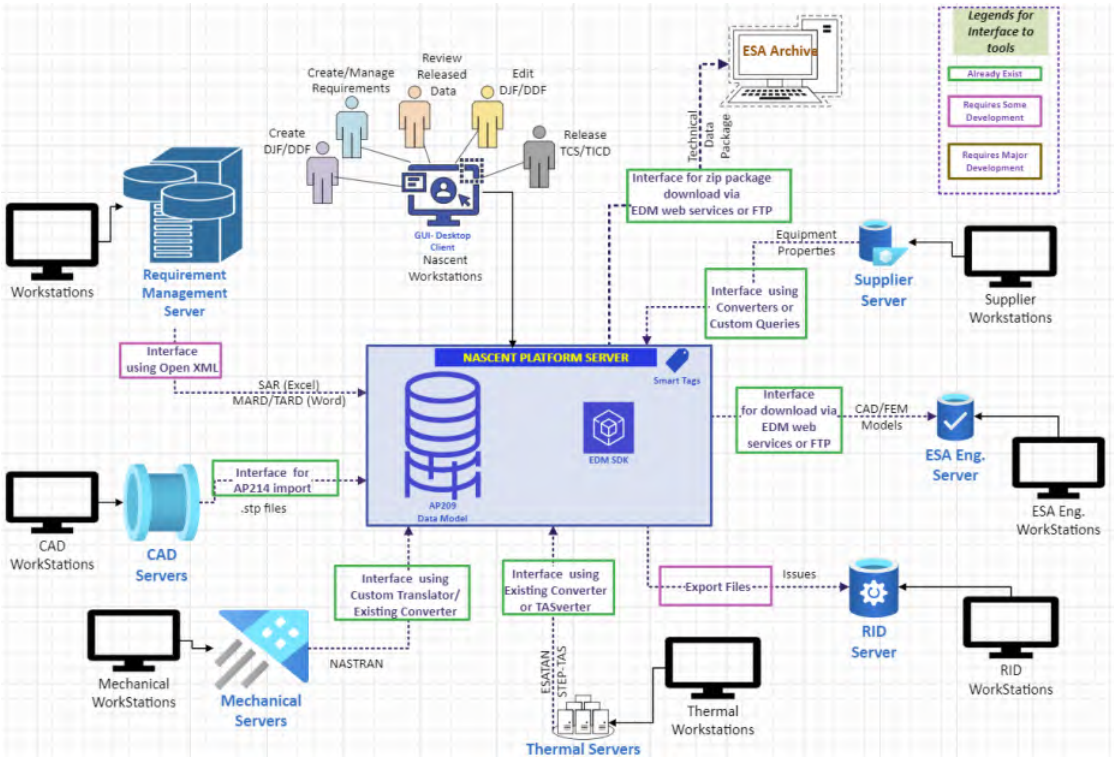


Figure 1: NASCENT Platform with selected technologies and data models

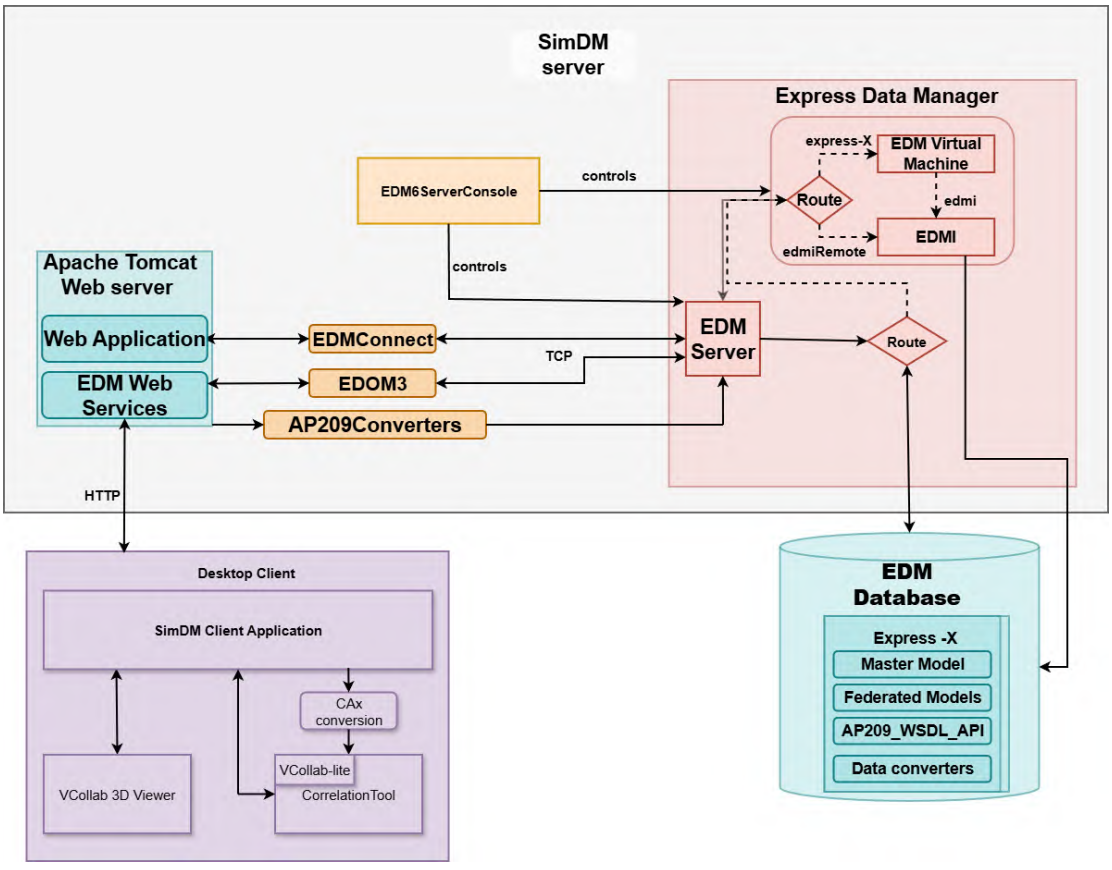


Figure 2: NASCENT Platform Core Architecture

4.2. Capabilities

4.2.1. Capability 1: Digital SAR Management

SAR were implemented as structured digital entities within the repository.
This capability enables stakeholders to:

- Define accommodation requirements
- Allocate requirements to spacecraft components
- Review requirement status
- Maintain traceability throughout design evolution

By treating requirements as managed engineering data rather than document content, stronger relationships can be maintained between requirements, design configurations, analyses, and verification evidence.

4.2.2. Capability 2: DMU-Based Verification

The platform integrates Digital Mock-Up capabilities to support accommodation verification activities.
Users can:

- Navigate spacecraft assemblies
- Inspect installation regions
- Review equipment interfaces
- Assess accommodation constraints

Verification activities can therefore be performed directly within a shared engineering environment, supporting collaborative reviews between systems, mechanical, thermal, and customer stakeholders.

4.2.3. Capability 3: Structural Analysis Integration

To support structural engineering workflows, NASTRAN analysis models are converted into ISO 10303 AP209 representations.
The developed conversion process preserves:

- Finite element meshes
- Material definitions
- Boundary conditions
- Analysis configurations
- Structural results

The resulting models can be visualized and reviewed alongside spacecraft geometry and accommodation requirements within the same environment.

4.2.4. Capability 4: Thermal Model Conversion and Visualization

Thermal engineering information is incorporated using STEP-TAS representations.
The implemented integration supports:

- Geometrical mathematical models
- Thermal node information
- Temperature distributions

Visualization is provided through a glTF (Graphics Library Transmission Format) - based rendering framework integrated directly within the platform environment.

4.2.5. Capability 5: Supplier Data Exchange

The platform supports controlled exchange of engineering information between customers and suppliers using open standards-based representations.

Supplier-provided data can be imported, reviewed, managed, and connected to the broader engineering context while maintaining consistency within the central repository.

4.2.6. Capability 6: Model-Based Documentation

To support generation of customer deliverables, the project introduced Information Panels (IP) as structured information containers.
Information Panels can combine:

- Requirements
- Engineering properties
- Analysis
- Textual content
- 3D viewpoints
- Linked engineering artefacts

This enables documentation to remain directly connected to the underlying engineering information, improving consistency, auditability, and review readiness.

5. VALIDATION THROUGH USE CASES

5.1. Validation Methodology

Validation was performed using a stakeholder-defined requirements baseline established at project initiation.

Demonstration scenarios as illustrated in Fig. 3 below were developed jointly with Airbus Defence and Space and used to assess whether the implemented capabilities addressed the identified engineering challenges.

The validation focused on interoperability, traceability, digital continuity, and usability across representative spacecraft engineering activities.

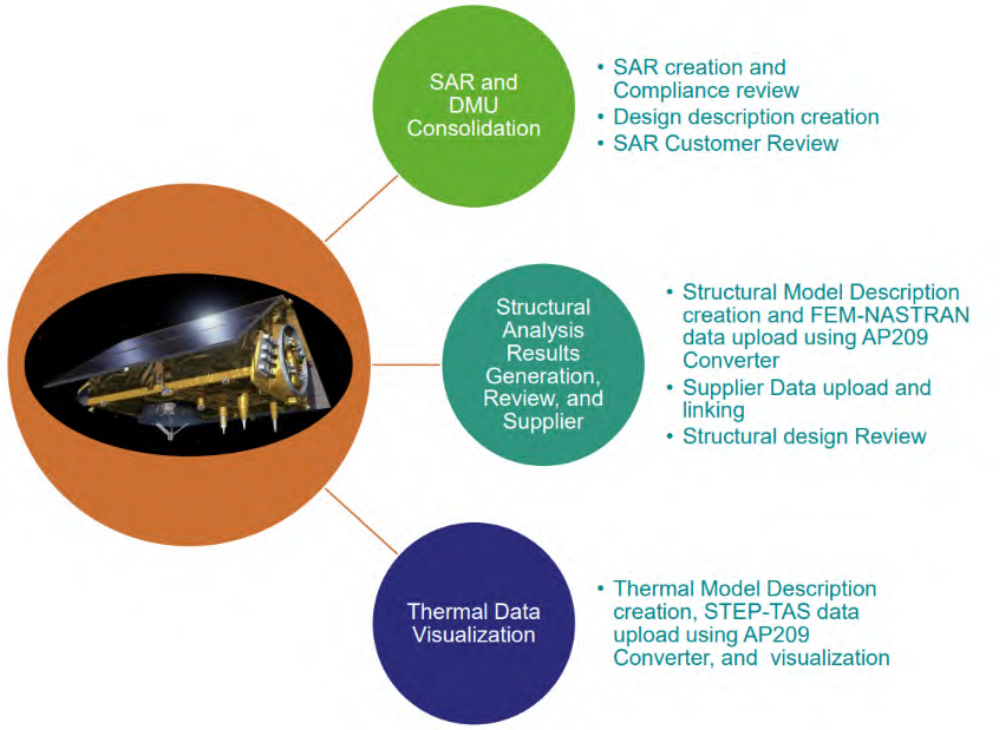


Figure 3: Validation Use Cases and Demonstration Scenarios [5]

5.2. Use Cases and Demonstrations

5.2.1. Use Case 1: SAR and DMU Integration

The first use case focused on digitalization of the spacecraft accommodation process.

Stakeholders demonstrated the creation, management, and review of System Accommodation Requirements (SAR) within the platform. Accommodation verification activities were then performed through interaction with the Digital Mock-Up environment.

Compliance evidence was generated directly from the model using:

- Annotated snapshots
- Geometric measurements
- Interface inspections
- Verification comments
- Linking the specific model or requirements

This established traceable relationships between requirements, spacecraft configurations, and verification evidence. The representative requirement dashboard along with its implementation state shown in Fig. 4 below.

Fig. 5 below shows features, benefits and meaning to the user consolidated as an Accommodation Management module which was demonstrated to validate the SAR and DMU integration scenarios

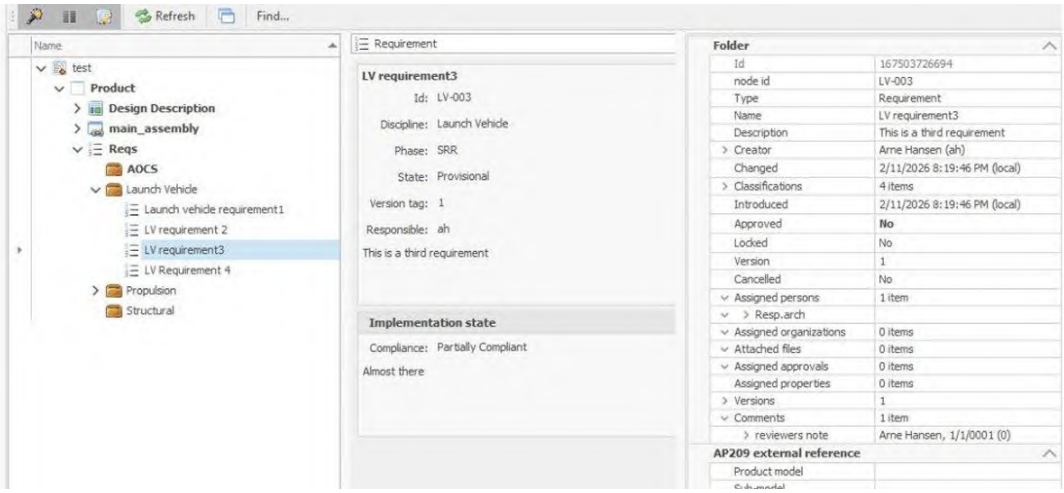


Figure 4: SAR Dashboard

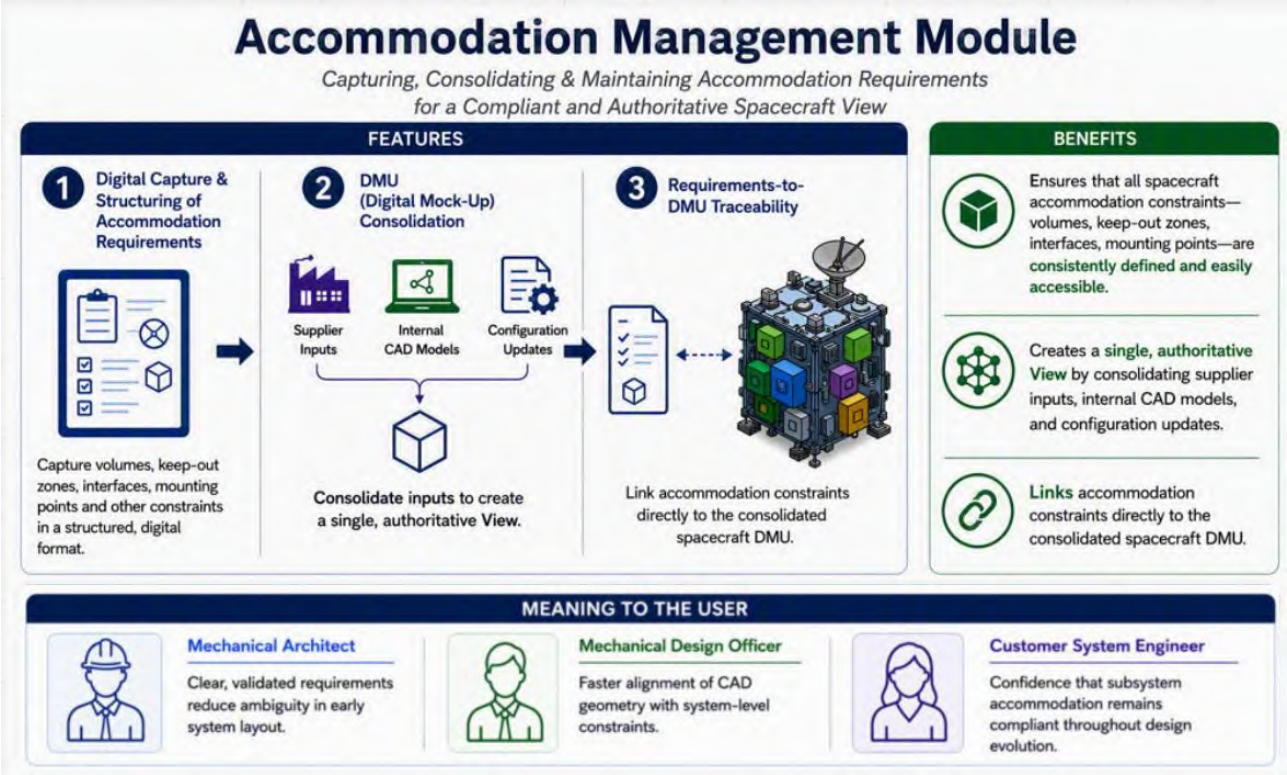


Figure 5: Spacecraft Accommodation Requirements Module

5.2.2. Use Case 2: Structural Analysis and Supplier Integration

The second use case focused on structural analysis integration and supplier interaction.

Structural models were converted from NASTRAN into AP209 representations (see Fig. 6) visualized within the platform environment.
Stakeholders reviewed:

- Structural meshes
- Material information

within the same environment used for accommodation verification.

Supplier exchange workflows were also demonstrated using standards-based representations. See Fig. 7 which highlights the developed features, benefits and meaning to the user under this use case.

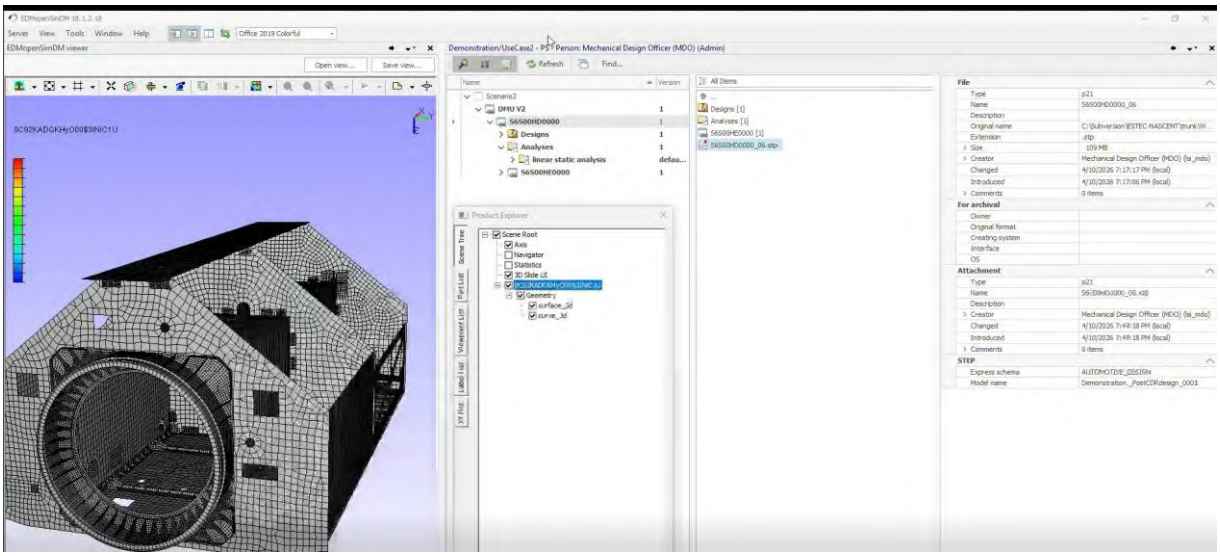


Figure 6: AP209 Structural Model converted from NASTRAN

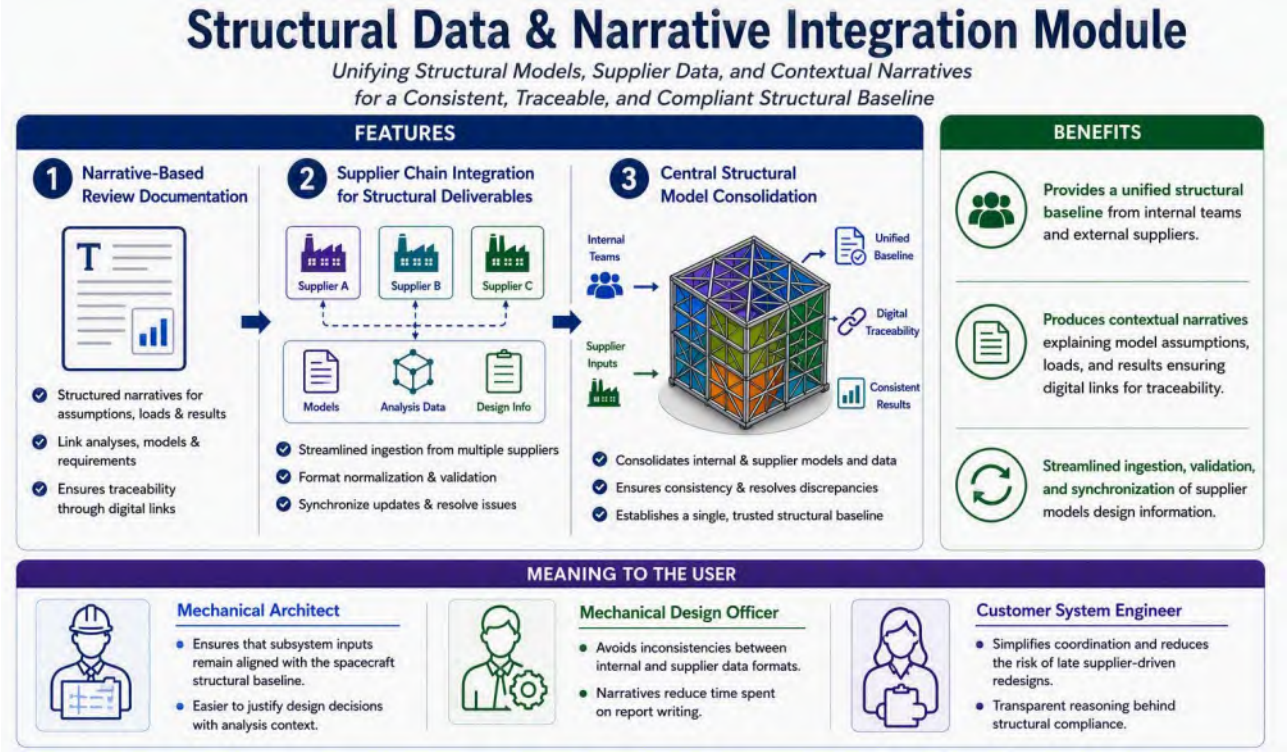


Figure 7: Structural Data and Supplier Area

5.2.3. Use Case 3: Thermal Data Visualization

The third use case focused on thermal engineering workflows.

STEP-TAS thermal information was imported into the repository and visualized (in glTF) through the integrated thermal environment, see Fig. 8 below. Users reviewed:

- Thermal node distributions
- Temperature information
- Material assignments
- Thermal properties

alongside spacecraft geometry.

The integrated environment improved visibility between thermal and mechanical engineering perspectives. The overall developed features, usage and benefits are depicted in Fig. 9 below.

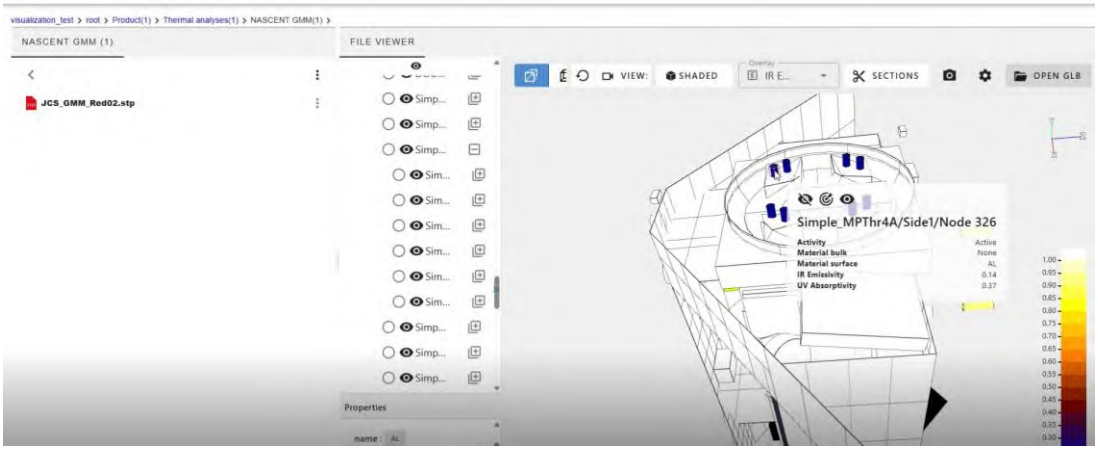


Figure 8: STEP-TAS Model Visualization

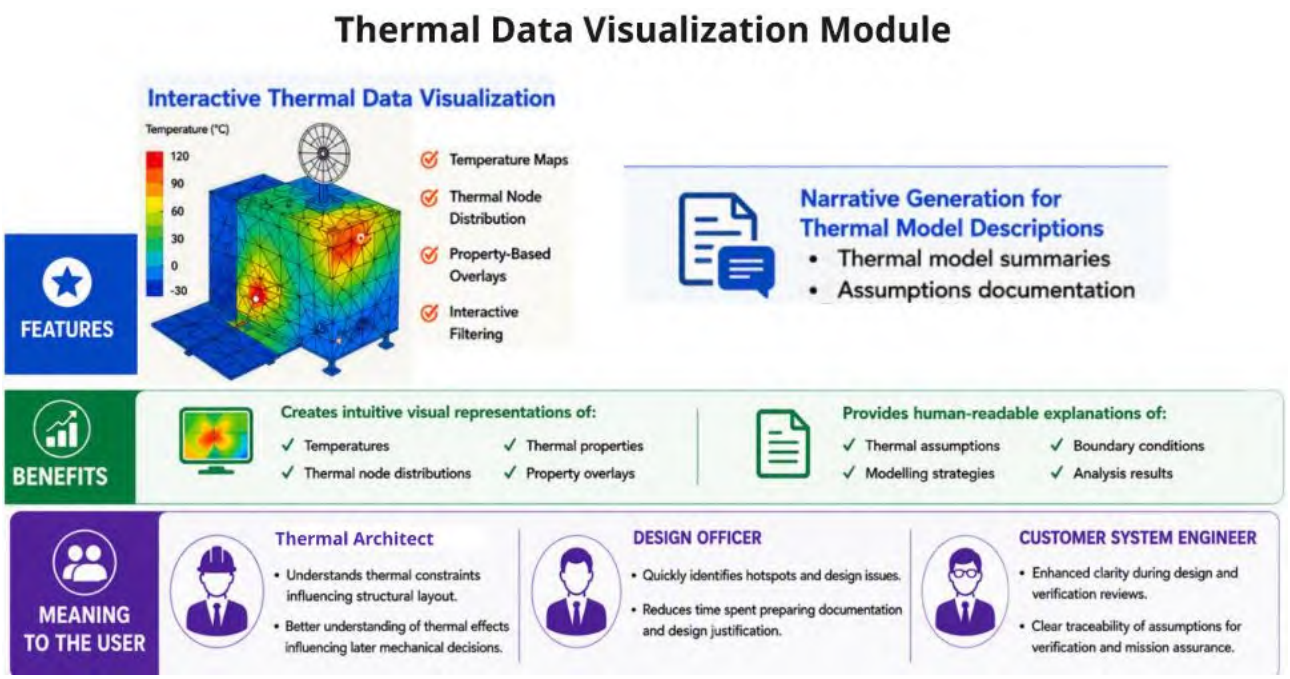


Figure 9: Thermal Data Visualization

6. VALIDATION RESULTS AND STAKEHOLDER FEEDBACK

Validation activities were conducted against the stakeholder - defined requirements baseline established at project initiation. Demonstrations involving accommodation engineering, structural analysis, thermal engineering, and supplier exchange scenarios confirmed that the implemented capabilities satisfied the major project requirements and addressed the interoperability and digital continuity challenges identified during the requirements phase.

The platform successfully demonstrated:

- Digital SAR management
- DMU-based accommodation verification
- Structural model integration using AP209
- Thermal model integration using STEP-TAS
- Supplier data exchange using open standards
- Model-based documentation
- Traceability between requirements, design, analyses, and verification evidence

Stakeholder observations collected during demonstration activities highlighted several benefits:

- Improved visibility of relationships between requirements and engineering data
- Easier navigation between design information and supporting evidence
- Better support for multidisciplinary engineering reviews
- Reduced dependence on document-centric workflows
- Improved interoperability across organisational boundaries

The demonstrations confirmed that standards-based representations can support practical digital engineering workflows while preserving information consistency throughout the review process.

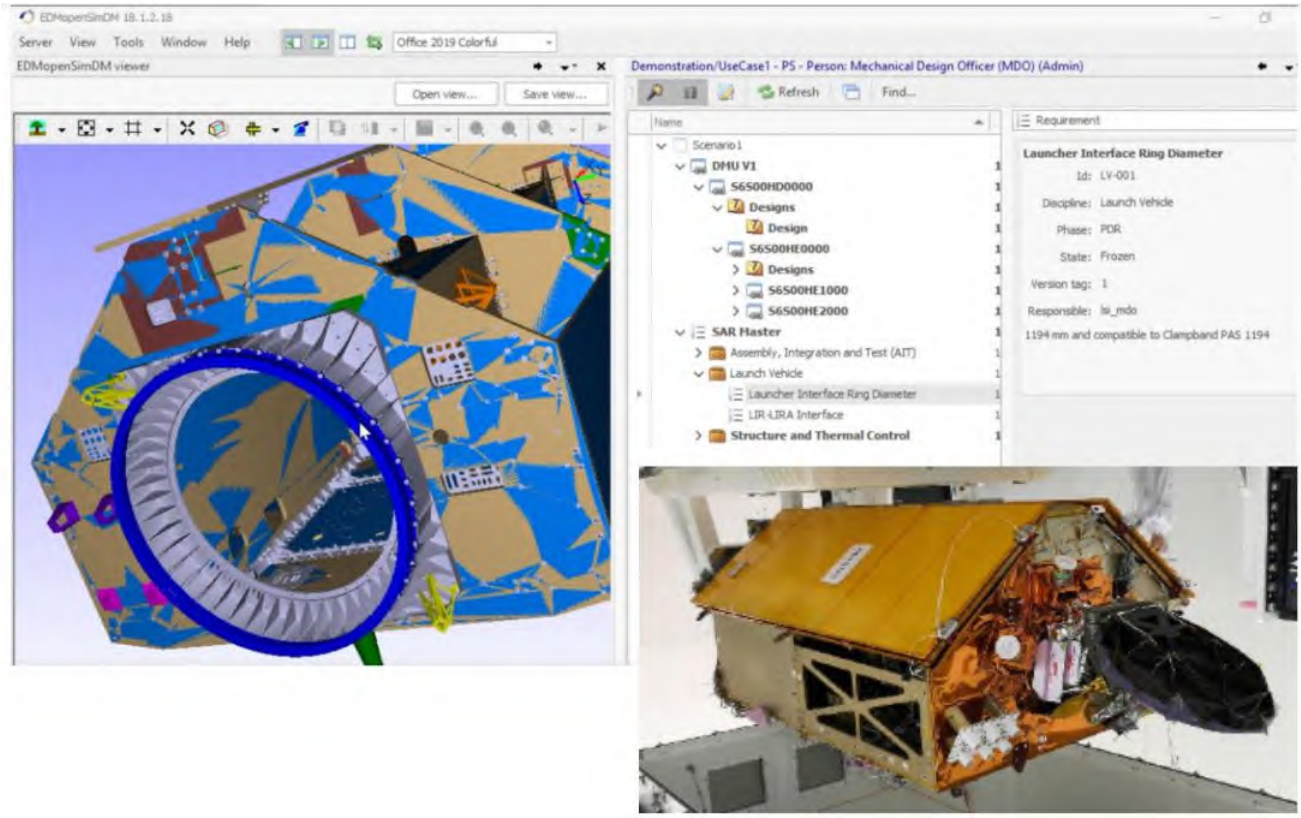


Figure 10: NASCENT Platform GUI with an example Sentinel-6 [5]

7. DISCUSSION

The project demonstrates that standards-based interoperability can be successfully applied to spacecraft accommodation, structural, and thermal engineering activities.

A key finding is that greater value can be achieved when integration is performed at the data-model level rather than through traditional document exchanges. By maintaining relationships between requirements, geometry, analyses, supplier information, and documentation, engineering artefacts remain connected throughout the development lifecycle.

The validation activities also demonstrated the importance of open standards for enabling supplier collaboration and reducing dependence on proprietary software ecosystems. The use of AP242, AP209, and STEP-TAS provided a common information foundation capable of supporting multiple engineering disciplines within a unified environment.

Several lessons were learned during development and validation. Maintaining semantic consistency during conversion of analysis data is essential to preserving engineering meaning across domains. Similarly, the quality and completeness of source data significantly influence the effectiveness of interoperability solutions.

The current demonstrator focused on selected accommodation, structural, and thermal engineering workflows. Future developments could expand support for additional engineering disciplines, increased automation of engineering data conversions, tighter integration with MBSE environments, and automated compliance assessment capabilities. Fig. 10 above shows NASCENT platform GUI (Graphical User Interface) with the representative DMU model of Sentinel-6 structure and related product structure breakdown along with SAR.

8. CONCLUSIONS

This paper presented the NASCENT Digital Engineering Platform, a standards-based solution developed to address interoperability and traceability challenges in spacecraft accommodation engineering.

Starting from an industry-derived requirements baseline, the project developed a software demonstrator capable of integrating System Accommodation Requirements, Digital Mock-Up data, structural analyses, thermal analyses, supplier information, and model-based documentation within a unified engineering repository.

Validation through representative use cases and stakeholder demonstrations confirmed that the developed capabilities address key challenges associated with fragmented engineering processes, disconnected analyses, supplier interoperability,

and document-centric review activities.
The results demonstrate that an open standard such as AP242, AP209, and STEP-TAS can provide a practical foundation for digitalizing mechanical and thermal engineering processes while maintaining traceability across the spacecraft design lifecycle.

The NASCENT Platform therefore represents an important step towards a more connected and interoperable approach to future spacecraft development, supporting improved collaboration, increased transparency, and more efficient engineering review processes.

9. REFERENCES

1. ISO 10303 – Industrial Automation Systems and Integration: Product Data Representation and Exchange (STEP).
2. ECSS-E-ST-31-04C – Thermal Analysis for Space Applications (STEP-TAS).
3. ISO 10303-209 – Multidisciplinary Analysis and Design.
4. ISO 10303-242 – Managed Model-Based 3D Engineering (AP242).
5. Sentinel-6 Mission images from the document https://www.eoportal.org/satellite-missions/copernicus-sentinel-6#payload-performances-of-sentinel-6

CALLISTO VEB STRUCTURES ENGINEERING – LESSONS LEARNED

Michael Lange [(1)], Etienne Dumont [(2)], Thilo Glaser [(1)], Sebastian Meyer [(1)], Olaf Mierheim [(1)]

[(1)] DLR Institute of Lightweight Systems, Lilienthalplatz 7, 38108 Braunschweig/GERMANY, Email: M.Lange@dlr.de

[(2)] DLR Institute of Space Systems, Robert-Hooke-Straße 7, 28359 Braunschweig/GERMANY

KEYWORDS

Lessons Learned, structures, CALLISTO VEB

ABSTRACT

CALLISTO (Cooperative Action Leading to Launcher Innovation in Stage Toss back Operations) is a re-usable launcher development conducted between DLR, CNES and JAXA. Its goal is to investigate and demonstrate technologies and operations for vertical take-off and landing launcher stages.

After completion of the vehicle equipment bay flight model structure's manufacturing and delivery, the present paper addresses lessons learned. The goal of the paper is to illustrate a number of factors – hard (engineering) and soft (human) ones – on the basis of actual examples experienced in CALLISTO, but also in other projects. It discusses what went well and what not so well, how we dealt with it in CALLISTO and proposes how to potentially deal with it in future.

1. THE CALLISTO PROJECT

CALLISTO (Cooperative Action Leading to Launcher Innovation in Stage Toss back Operations) is a re-usable launcher development conducted between DLR, CNES and JAXA [1]. Its goal is to investigate and demonstrate technologies and operations for vertical take-off and landing launcher stages. In this context the DLR Institute of Lightweight Systems is responsible for the developed, design and testing of the CALLISTO vehicle equipment bay (VEB) structure (cf. Figure 1). Its structural design is similar to a conventional aluminium airframe structure with spars, ribs and an aluminium skin on the outside. Additional secondary structures, designed as aluminium sandwich panels, are located within the VEB and support various payloads and instruments. Special to CALLISTO is the fact that the VEB does not only carry avionics such as on-board computer, power system, data system and telemetry and -command systems. It also accommodates two of the three flight control system of CALLISTO: the reaction control system (with H2O2 thruster and tank) and the deployable aerodynamic fin system (with electromechanical actuators) needed to steer the vehicle during the whole flight.

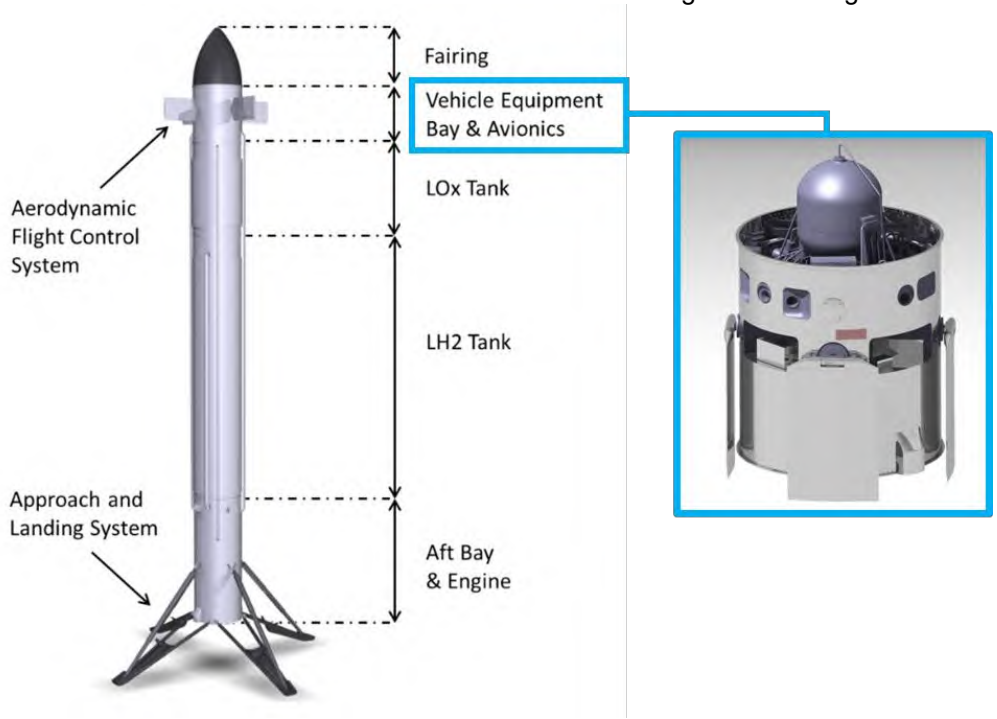


Figure 1: The CALLISTO launcher and a detail of the equipped vehicle equipment bay structure.

In April 2026, the VEB flight model manufacturing was completed and the structures delivered for thermal protection system application. Currently, the harness and sub-systems integration is ongoing.

2. PROJECT FACTORS

After completion of the VEB Flight Model structures (cf. Figure 2) manufacturing and its delivery, the present paper addresses lessons learned from the SM (structural model) and FM (Flight model) structure development as well as building and testing phase up until VEB FM hardware delivery.
It is important to mention that most of the noted points are to be understood as not limited to CALLISTO VEB only. They can apply widely to the CALLISTO project in general and to (m)any other S/C (structure) engineering project. Where we find that quite project-specific points are discussed, this is mentioned. Further the discussed points subdivide into two categories, which are characterized by ‘soft’ (human) project factors and “hard” (engineering) project factors.

Hard (engineering) factors relate to the actual engineering work. This could be testing and test preparation, test data acquisition (e.g. combination of optical and mechanical measuring systems), regulations in parts procurement processes et cetera. Also, how standards (e.g. ECSS) are applied and impacts prototype engineering is an important topic to discuss.

Soft (human) factors, for example, indicate different work culture, communication of technical and programmatic topics or technical meeting efficiency in a multi-entity environment. Those topics are typically not or not sufficiently addressed in mechanical engineering papers and courses, but play an immense and vital role. Everybody of us already came across them or at least some in one or the other way. Typically, they are “learned” by experience in day-to-day work.

The goal of the paper is to first illustrate a number of those different factors on the basis of sometimes actual examples experienced amongst others within the CALLISTO VEB SM/FM development and to discuss how they have impacted the structural engineering process. The perspective taken is in our case from an institutional point of view and in collaboration with SMEs. However, we believe that all factors can apply for almost every other project, too.

Regarding the order of mentioning, it does not imply any weighing, it only tries to group and connect topics to each other. The reader is encouraged to reflect from different perspectives and to compare with own experiences and observations; eventually the readers are encouraged to evaluate the importance on their own. Consequently, the reader will not find for each listed aspect a proposed ‘solution’.

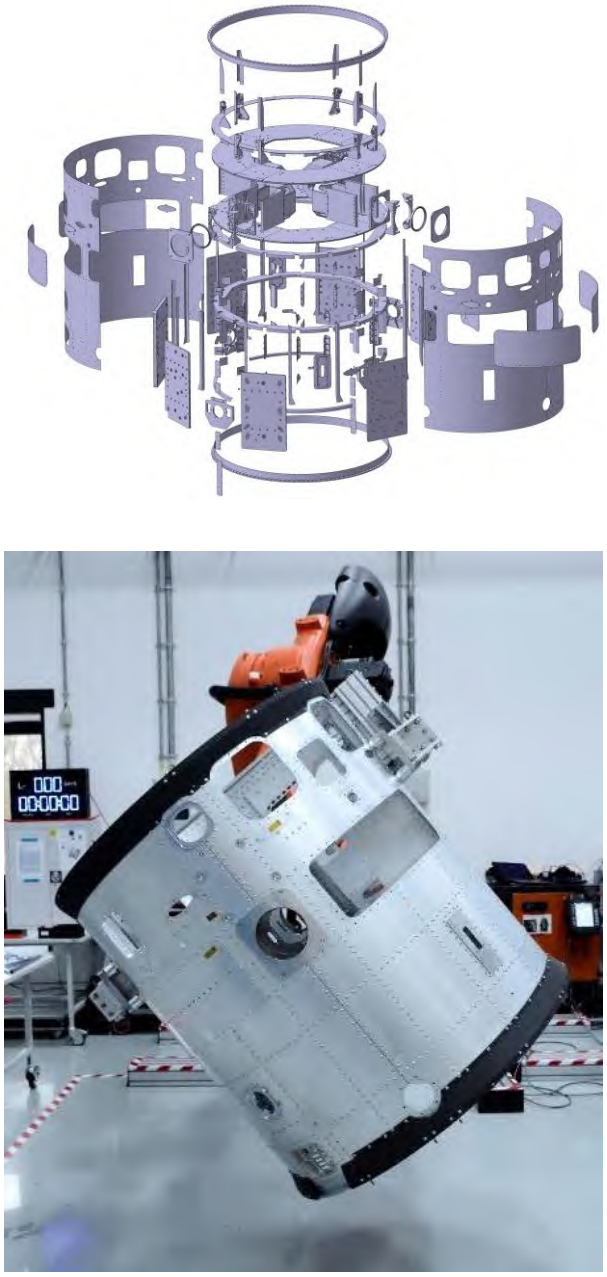


Figure 2: Exploded view of VEB structure (top); VEB flight structure during final outfitting and before shipment for thermal protection application (bottom).

2.1. Hard (engineering) factors

This paragraph focuses on technical aspects that we came across during the design, the engineering work and the procurement of CALLISTO VEB structure’s hardware. Partially, also the final design was influenced. That is the reason why they are listed as ‘hard’(ware) or engineering factors in the sense of how they influence the day-to-day engineering work and exchange:

- *ECSS factors of safety (FOS) & design factors (K) [2]*
  While FOS depend on the program, individual design factors *K* shall be transparently agreed upon in the beginning of the project. Further, loads (and load updates) shall be clearly and always indicated for every subsystem as limit loads and accompanied with a (requirement) justification. In this course it is also worth to evaluate on which level which factors are applied.

  Further, the current revision of [2] is from 2019, but the factors themselves were not updated with respect to the former revision. There is no debate on applying the factors as such, but since they were established, computational capabilities significantly improved and new computational methods are available. With that, also models can be refined easier where needed and provide higher confidence. Thus, factors such as K_{LD}, K_M and K_{DF} could be relaxed earlier in the project. To 'allow' relaxing the factors, e.g. K_M, a justification is to be provided. Here, ECSS notes that it can happen "based on relevant historical practice". Experience tells that such discussions, especially later in the project, can be difficult and lengthy, and still not leading to an agreement. A reason for this is that despite we agree on their need, the way how the factors are applied can differ from entity to entity. By implementing well-defined processes and responsibilities in the beginning of a project, those difficult situations can be navigated smoother and faster.

- *Test rig design*
  As a general rule (there are exceptions!) mass and stiffness govern. We do not want to test the test rig, but the test item. When significantly high loads are involved, it becomes difficult to guesstimate what is the load level in smaller parts when there are multiple of that kind. Therefore, also smaller test rig parts should be simulated and considered in the test prediction (instead for time reasons to replace them by 'dumb' RBEs, for example, and to follow up meticulously that not 'just any' material is used, if loads are critical. In consequence a static test was stopped for one day in order to replace a part that yielded. Luckily, the deformed part in the test rig got manufactured over weekend newly, thus test interruption was not too long and costly.

- *Multi-sensor suite*
  It is common practise to use a multiple-sensor suite, e.g. thermal and strain sensors or acceleration sensors and video. To combine static or quasi-static optical 3d measurement systems, such as ZEISS's *ARAMIS* [3], in large(r)-scale component or system tests in order to complement strain sensors is not everywhere common practice yet. Even though expensive, in terms of test costs and thorough data procession, the extra effort helped significantly to correlate FEM models and to identify unexpected, not obvious or otherwise not identifiable phenomena. Examples are, slippage, local yield, fine resolution of high stress gradients etc. Therefore, we now use such a system even in tests where such data is not actually 'needed' as long as everything runs well, but to have the data 'just in case'. When everything runs smoothly, the data is stored and its analysis is considered as only nice to have.

- *Shared responsibilities between entities*
  The sharing of responsibilities in a project is mostly done in a very early phase, well before real technical work is performed. Particular (i.e. politically driven) interests of the entities can play a role. At that time, it is often difficult to grasp what will be later technical challenges. In case of complex input/output interfaces between entities this can lead to relatively time-consuming exchanges and numerous iterations to reach a common understanding. This intensifies when engineering methods or the development philosophy of the entities differ. It is therefore very beneficial to avoid artificial sharing of tasks and responsibilities right in the beginning. Responsibilities must not overlap either and are always clearly defined on common grounds.

- *Interface management*
  Define a first set of the most important structural interfaces (borehole pattern + thread/hole size, envelope + add. Spaces/areas, mass) as soon as possible in a mechanical – and signed – ICD draft. If there is a CAD model available additionally, fine. But do not rely for too long on a CAD only. This has two effects: The written and signed ICD draft provides a certain degree of binding nature and the absence of any information points to potentially open points that require more exchange.

  Next to a mechanical interface definition, also a specification should be written based on requirements. Those, and this is key for well written requirements, have a clear justification and verification method. What was an issue in CALLSTIO, is the fact that

the wording specification conveyed a different meaning depending on the entity. On the one hand it was understood as a document of requirements to strictly comply with, on the other a suggestion of the ideal state and how to achieve it. This had significant impact on how entities worked with the document and caused at a rather late stage a significant gap in the interpretation and work to sort the situation. Eventually it was commonly solved, but time was time consuming. Therefore, be cautious about possibly differently used wordings and provide in documents as good style of writing always a purpose and scope. This is easy to achieve with very low effort and can avoid potentially difficult situations.

- *Hardware manufacturing*
  Typically, there are three options where to manufacture structural parts:
  1. Manufacturing on your own.
  2. Manufacturing by a 'traditional' contractor.
  3. Manufacturing by an 'on-demand' sub-contractor.

  Emphasises is here on the third option. There are more and more companies entering the market that provide on-demand manufacturing services. Compared to the "traditional" manufacturer they provide higher flexibility to influence from the customer side the cost-to-lead-time ratio. On the other hand, the manufacturing quality is not necessarily comparable to the traditional manufacturer and the feed-back loop before and during manufacturing of rather complicated parts is not necessarily offering the same flexibility and quality. Another point to take into account is repeatability of manufacturing parts in terms of process control. There are competitors who offer such services, but it is not the standard. Also, quality control was noted as not every competitor follows similar standards, sometime provided certificates were at least 'doubtful'. When there is the need for manufacturing quickly a prototype or rather simple parts for test setups etc., the on-demand services provide a considerable alternative.

- *Testing*
  Establish more of a "Test early and fail fast!" culture. Some of us may have come in tight schedule situations across statements that imply „if this test fails, the project is over". The result is that engineers could start working over duly to be on the safe side, optimising and simulating again and again, even though a product is already good. And exactly that can cause stretched schedules and actual delays as there is not enough room for failure (in test). In CALLISTO we tried to do this better than in previous projects. Having a structure model (or prototype) that could potentially take damage (not that this was our goal! and we didn't) allows to learn and gain confidence in the design. In case there was a damage, then you know early where to focus on. In another project we had such a situation that a prototype broke. We learned a lot from it, and the project continued.

  The opposite engineering approach was having a very sophisticated (potentially overengineered design) and at a rather late point in time validated simulation model. If at that point in time something goes wrong, this leaves you less time to react.

  Of course, a "test early and fail fast" approach is no call for lesser engineering effort. It is a call for a more agile mindset and to learn in smaller steps by intermediate tests where possible. Also, be clear about potential limitations of a test planned, if there are any. Limitations are not a flaw in your work, but will help to set common grounds and expectations of what can be achieved.

  Despite the call for (early) testing, it may still appear wiser to delay a test when preparation time is not sufficient instead of trying for whatever it takes to stay within schedule. In this case, have a plan B ready, especially for larger tests, and communicate the options with test facilities and project partners early.

- *Agile Working*
  We apply many agile concepts, not textbook-like, but to the extent that seems reasonable to us. May it be a weekly 30 minutes *Obeya* meeting, regularly interacting with contractors, stakeholders and re-aligning delivery and manufacturing schedules where required.

  For example, we postponed a formal manufacturing readiness review (and made it an assembly readiness review) by taking a well-defined 'risk'; detailed reviewable documentation was not ready in time and instead the most important content was defined and communicated in short presentations and regular meetings instead. The planned manufacturing was released in three steps instead (purchasing materials, manufacturing parts, assembly), and connected to newly defined "sub-milestones" (simulation A finalized, simulation B finalized, interfaces frozen). By doing so, at each step we had the option to

intervene, if required. Intervention was only 'required' in the last step, but eventually the delivery date was approx. five months earlier than without the above-described measure. However, that solution demanded a reasonable amount of trust, extra and sometimes bluntly open communication in the team and beyond, as well as a manufacturer that is flexible (i.e. agile) enough, too.

This last point directly connects to soft factors in the next section and could be listed there, too. The soft (human) factors build partially the pre-requisite for applying measures deviating from the classic engineering text books. Respecting and being aware of them, they help to navigate through the project, especially in difficult technical or management-related situations. Amongst us engineers they might sometimes fall shorter, but their relevance is high. Also, you do not "learn" those aspects during in engineering courses, but rather by experience in day-to-day work.

2.2. Soft (human) factors

- *Be predictable*
  … in your doing. This does not imply to share each and everything at any time, but it is helpful for your partner, especially in critical situations and decision makings, to have an idea of your potential acting. For example, it can be helpful to communicate openly different options and attributed consequences. Be clear about your red-line(s) and reasoning. This is no offence, but helpful.

- *(Technical) decision making*
  Technical questions shall be discussed and decided by the engineers/subsystem experts first and foremost. Work as much as possible 'bi-laterally' on engineering or specialist level to minimize unnecessary (micro-management) overhead. In first phases of projects when teams are not knowing each other, management is often involved in order to facilitate and streamline exchanges. This can however have negative effects, details that can be very important from an engineering point of view to establish a trust-based exchange and decision-making process between engineers are often very simplified at management level discussion. This can in the worst-case lead to mistrust, misunderstanding between technical teams and results in additional work that could have been avoided. Interestingly, it is noticed that the more intervention happens, the less the actually responsible may consider to be the responsible.

- *Know the team and yourself*
  Everyone will state: "Of course, I know our team" and hopefully everyone or at least the majority does. This aspect here is mentioned, because generally (and especially in time critical situations of which we unfortunately experienced a few) it is an important aspect which task is handled by whom. Ideally, a team features a whole bunch of characters (the finisher, the co-ordinator, the specialist, …) and tasks are ideally shared exactly by acknowledging those different individuals' strength [4]. There is no good or bad character, but there is a good and bad distribution of tasks in the team on the characters; surely an individual's 'role' may even change, over time or depending on the current project. Thus, the important part is to know and respect everyone's (including your own) capacity and strength in order to form the most successful team.

- *In-person meetings*
  Teleconferences do not replace (occasional) in-person meetings! Especially the pandemic proved that initially well-cooperating teams 'lost' the personal contact and cooperation became more difficult. Regular in-person meetings are very important to transport non-verbal communication, to have social interaction and to foster the team spirit. On such basis, trust in the other individuals' competences is higher and potential conflict in difficult situations with disagreement longer prevented, simply because there is potentially higher trust between individuals who 'know' each other.

- *Different work culture*
  Similar to the previous point, it is important to know your partner and how they work simply because of individual cultural aspects. Sometimes, a partner's 'behaviour' may seem strange, sometimes even offending, but it might be just the different culture, work culture, or usual role in projects. Similarly, the KPIs (key-performance indicator) that are ruling the different entities impact strongly the way of working and the aspects that each of the entities still try to pursue in a cooperation project.

- *E-Mails*
  Read e-mails, especially on critical topics, twice. When you receive them and when you answer them! Different mother-tongue can leads to mis-'interpretations' of what another individual actually! wants to convey.

Refrain from seemingly endless e-mail threads with comments over comments in various colours that go forth and back. You will lose track, overview and waste yours and others time. Instead, iterate on a shared workplace and for technical discussions, organize a dedicated meeting (in person) and document the outcome in minutes.

- *Holiday seasons (France / Germany / Japan)*
  Plan generously in summer season. It is known, especially in Germany and France, that from July until mid-September many people take vacation, which slows project speed down. Of course, this does not apply to the project members only, but also to contracted manufacturer, resulting in usually longer H/W lead times (typically +2…3 weeks) over this period. This must be considered in your schedule. For Japan, specifically the 'golden week' in spring and the 'silver week' in fall shall be mentioned here. In this period, almost everyone is off from work.

- *Unilateral decision*
  Sometimes unilateral decision is imposed by the circumstances and constraint of an entity. It is however seldom that this is happening without forewarning signs. Even if the other entity cannot influence the decision, it is very important to take it as much as possible in the boat and explain the background to increase acceptance and keep trust between the entities and personals.

  Similarly, sometimes technical decisions are (partially) driven by political-economic reasons and they can constrain the engineering team. Especially, if this imposes an engineering solution that is 'not ideal', it is due to the management to explain circumstances (to the engineering team) and to think of additional possibilities in case that constraints are tough to handle.

- *Do lessons learned / retrospective*
  In our day-to-day business we observe that a lesson learned or retrospective is not yet the set standard in projects. Actually, they should be part of project planning and considered like a 'deliverable'.

  In the Callisto VEB structures team, we did not perform a retrospective yet and already a few months after delivery, we realized that it took us already a while to realize what went well, what went not so well and what to bring forward into the next project. This is not only important to helps us grow, but also for the team's well-being and formation. In this sense, do note down from time to time and in the course of the running project your observations as 'input' for a retrospective. In some projects (not CALLISTO) we already sat together for an intermediate retrospective after SM-delivery. This was very helpful, as we were able to implement actions already for FM phase.

3. CONCLUSION

This paper listed a number of our lessons learned in the CALLISTO VEB development. Even though some of the listed factors may appear very trivial, and that is already part of the solution, it is a day-to-day challenge to make yourself aware of them. We found that many situations were experienced already before, but we were not necessarily aware of it before writing it down. In this sense, the preparation of the present paper is a significant part of our VEB structures team retrospective. Saying that, we want to encourage the reader to reflect on the mentioned aspects and to implement them were found useful.

4. ACKNOWLEDGMENT

This work has been performed in the frame of a project funded by the German Federal Ministry of Research, Technology and Space.

5. REFERENCES

1. Dumont, Etienne (2024). CALLISTO: Reusable rocket stage demonstrator: getting ready for implementation. Journal of Evolving Space Activities, 2024, Volume 2.
2. ECSS-E-ST-32-10C Rev.2 Corrigendum 1. Structural factors of safety for spaceflight hardware. 1 August 2019.
3. Link: https://www.zeiss.com/metrology/en/systems/optical-3d.html
4. Belbin, R. Meredith. *Team Roles At Work*. Butterworth Heinemann, Oxford 1993.

PREDICTION OF SHOCK INJECTION LEVELS USING NORMALIZED ENERGY REPRESENTATION OF THE SOURCE

Nathan PASCAL [(1)], **Simon LEMAY** [(2)], **Andrea BRUGNOLI** [(5)]
Frederic LACHAUD [(4)], **Miguel CHARLOTTE** [(4)]

(1) Centre National d'Etudes Spatiale (CNES), Centre Spatial de Toulouse (CST), 18 Avenue Edouard Belin, 31400, Toulouse, France, Institut Clément Ader (ICA), 3 Rue Caroline Aigle, 31400, Toulouse, France, ISAE-SUPAERO, 10 Av. Edouard Belin, 31400 Toulouse, nathan.pascal@cnes.fr
(2) Centre National d'Etudes Spatiale (CNES), Centre Spatial de Toulouse (CST), 18 Avenue Edouard Belin, 31400, Toulouse, France, simon.lemay@cnes.fr
(3) Institut Clément Ader (ICA), Université de Toulouse, CNRS UMR 5312, INSA, ISAE-SUPAERO, IMT Mines Albi, UPS, France frederic.lachaud@isae-supaero.fr ; miguel.charlotte@isae-supaero.fr andrea.brugnoli@isae-supaero.fr

KEYWORDS

Shock, Mechanical, SRS, Energy, Characterization, Normalization, Source

ABSTRACT

The mechanical shock levels induced by a source on a structure are inherently structure-dependent. Current prediction methods frequently rely on analogy and past experience. While experimental testing remains essential, it is subject to considerable uncertainties. The proposed methodology offers an approach to characterize a shock source as a Normalized Energy Spectral Density through a dedicated reference test. This shock source characterization can subsequently be applied to a structure of interest to predict the shock levels resulting from multiple injections of the characterized shock source. This methodology has several applications, which are: predicting shock source levels from specific shock sources; obtaining a more accurate estimate of the injection shock levels on a system for its preliminary design so that the sizing rules can subsequently be applied; comparing shock levels on a given system for different mechanisms; optimizing shock test means by predicting shock levels across configurations; or using the Normalized Energy Spectral Density as shock source modeling.

1. INTRODUCTION

The development of space systems must ensure reliable operations despite exposure to various environmental stresses. Mechanical shocks are one of them. The considered shocks arise from nominal system operations, excluding hypervelocity impacts such as space debris. They can originate from various sources, including launcher stage separations, spacecraft-launcher separations, or appendage deployments such as solar arrays or antennas, for example [1,2]. They may also result from collisions or drops during terrestrial transport of the system [3,4] or from system landings or splashdowns [2]. Furthermore, taking the example of multiple separation devices that all have the same purpose—locking, releasing, and separating [5]—each will have its own shock levels depending on the design and characteristics.

To maintain the integrity and performance of sensitive components—such as electronic boards and optical payloads—it is critical to accurately assess the system's resilience to anticipated flight shock events. Inadequate consideration may lead to performance degradation, underscoring the necessity of precise prediction and validation during the design phase. Currently, shock predictions are based on analogies with previous missions and empirical experience. However, the characterization of shock sources, the specifications of subsystems, and the qualification of components often depend on costly, risky, and poorly controlled tests. These tests introduce uncertainties, potentially resulting in under- or over-qualification due to inadequate representation of complex shock sources and their interactions with intricate structural systems.

The Shock Response Spectrum (SRS) [2,6–10] is commonly used to specify shock levels. For launcher-induced shocks, including separation events, launch service providers establish specifications at the launcher interface, with documented standards for vehicles such as Ariane 5 [2,11], Ariane 6 [12], Vega-C [13], Soyuz [2], and Falcon 9 [14], which are replicated in system-level tests. Besides, internal spacecraft shocks induced by appendage deployments, for example, require characterization through system-level or subsystem-level testing [2]. However, when testing subsystems or equipment, an accurate estimation of the interface shock levels is critical to ensure the representativeness of the test. Although methodologies for sinusoidal, random, and acoustic environments are well-established, mechanical shock prediction for space systems remains less mature, though progress is being made [2].

Numerical methods show promise, but require robust engineering methodologies to ensure accuracy for shock level prediction [15]. Among the numerical methods used for prediction in the field of mechanical shocks, the following can be cited: Finite Element Method (FEM), with explicit [16] or implicit [17] time-domain resolution, Statistical Energy Analysis (SEA) [18,19] and its hybridizations [20]. Other approaches, sometimes complementary to the previous methods, have been published, such as the work of Wang *et al.* [21] on Frequency Response Functions (FRF) or Zhao *et al.* [22]. However, current approaches in the field of mechanical shocks still rely on empirical sizing rules [9] and similarity methods based on previous projects [2].

Regarding the approaches presented previously, all require modeling of the shock source. Different methodologies exist for this modeling, but in all cases, one of the objectives of shock analyses is to determine the SRS levels at points of interest in structures, particularly at the source. This article presents a generalizable methodology for estimating shock levels at the shock source location. The proposed methodology is divided into two phases. Firstly, the Normlized Energy Representation of the source (NERS) approach aims at characterizing a shock source from an SRS, obtained experimentally on a reference specimen, in the form of a Normalized Energy Spectral Density (NESD). Subsequently, it can be transferred to another specimen to predict the expected shock levels when injecting one or more equivalent shock sources into the one characterized.

The article is organized as follows. First, Section 2 introduces the proposed methodology, presenting the overall process, without delving into specifics, and its potential applications. Then, Section 3 presents the various numerical tools used and the detailed methodology, including shock definitions and Shock Response Spectrum (SRS) specifications (Section 3.1); the computation of Energy Spectral Density from an experimentally obtained SRS (Section 3.2); the computation of the modal density weighted function by Kernel Density Estimation (KDE) methodology (Section 3.3); the Energy Spectral Density normalization (Section 3.4); and the overall process (Section 3.5).

Finally, having established the comprehensive set of computational tools, methodological conventions, and the overarching methodology, the article concludes with Section 4 by giving examples of the methodology applications, including ball drop tests with various masses and heights on different plates at multiple locations, as well as characterizations of different PyroShockGun (PSG) test configurations for injection shock level prediction on satellite structural models.

2. METHODOLOGY

In detail, the proposed methodology, illustrated in Figure 1, begins with step 0, obtaining a representative SRS of the injected shock levels from a characterized shock source on a reference specimen (see Section 3.1). Using this SRS and the total mass of the reference specimen, step 1 is the computation of an Energy Spectral Density (see Section 3.2).
Modal analysis enables the computation of a continuous frequency-based modal density function using Kernel Density Estimation (KDE) [23,24]. KDE is used, for example, in population density estimation and surface reconstruction from point clouds [25], but also for multimodality investigation [26] and density mode estimation [27]. Combined with modal weighting [28], the KDE is adapted for the proposed methodology in Section 3.3. This computation, step 2 of the methodology illustrated in Figure 1, results in a function that represents the number of modes per frequency band for a given impact location. This modal density weighted function is then used for step 3 to normalize spectral energy density, producing a Normalized Energy Spectral Density (NESD) for shock source characterization (see Section 3.4). The NESD can then be employed to estimate shock levels on a studied specimen by performing the inverse process (see Section 3.5).

For a studied specimen with multiple identical shock sources, the reverse processes of steps 2, 3, and 1 (denoted as steps 2', 3', and 1') can be applied to retrieve the SRS of the studied specimen. Modal analysis of the studied specimen combined with the NESD (scaled by the number of sources) enables the computation of injection Energy Spectral Density while applying energy conservation principles. Then the predictive SRS of injection levels can be recovered from the energy spectral density. When experimental data are available, numerical predictions can be compared with experimental results. The overall methodology is presented in Section 3.5.

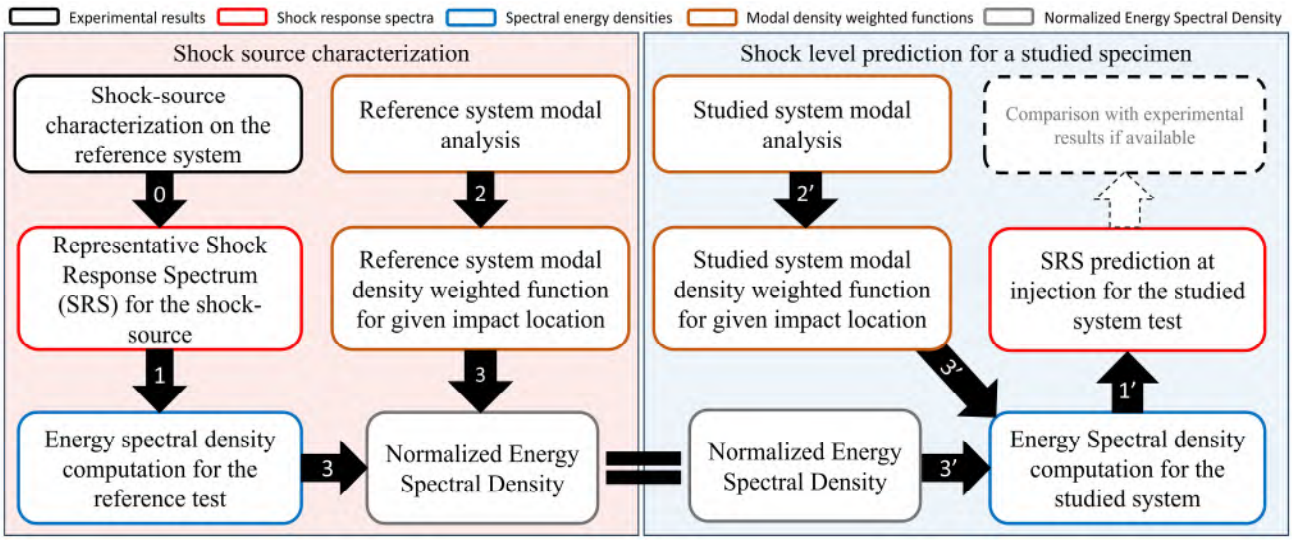


Figure 1 - Flowchart of the proposed methodology.

This methodology presents several applications in system development. In preliminary phases, it allows enhancing the precision of injection specifications for shock-sizing rules. One can characterize a shock source and estimate the shock levels expected on the studied specimen. This approach eliminates the need for a representative test, allowing appropriate injection level specifications to be defined during the early sizing phases with the estimation of injection shock levels. Additionally, for a studied specimen with multiple real shock-source variants (e.g., mechanisms, HDRMs), characterizing the sources and estimating the resulting shock levels on the structure enables efficient pre-selection of suitable shock-source designs without conducting tests on the structure itself. Furthermore, the normalized shock-energy representation, described by a Normalized Energy Spectral Density (NESD), can be used as a shock source model in simulation. The final example, and the examples given later, when considering various possible shock-test means or configurations for a specimen under study, characterizing the sources and estimating the shock levels on the structure allows for the pre-selection of the appropriate configuration of tests. This ensures that the required test specifications can be reproduced in advance.

At CNES, PyroShockguns (PSG) -- highly configurable shock generators that operate simultaneously -- are mounted directly on structures, including large spacecraft, to generate controlled mechanical shocks. The PSG operates by igniting a powder cartridge to propel an impactor, which strikes a damper at the end of the breech. The shock response exhibits significant variability based on the structural characteristics of the tested specimen, which complicates predictive modeling. This method would streamline the pre-determination of optimal parameters (damper materials, thicknesses, impactor travel distance, powder charge, number of shock sources) tailored to specific specimen requirements and specifications.

Ultimately, the proposed methodology can be applied to any shock source, in various domains. This generalization is feasible provided that the shock source can be characterized in another specimen, and that the modal density weighted function can be determined for the shock location in both the reference specimen and the specimen under study. The methodology maintains its assumptions across different applications as long as these fundamental conditions are satisfied.

The ensemble of tests conducted is performed for space applications and then are carried out under free-free boundary conditions. This is typically achieved by suspending the test specimen or placing it on foam supports. Experimental results obtained during experimental research at CNES have demonstrated that these boundary conditions effectively replicate the desired free-free conditions.

3. COMPUTATIONS TOOLS

3.1. Definition of a Shock and SRS Specification - Step 0

A mechanical shock, as defined in the ECSS handbooks [2,6], is a short-duration (50 µs–20 ms), high-frequency (100 Hz–100 kHz) transient load of significant amplitude with an exponentially decaying envelope. It generates tensile–compressive, bending, and shear waves, along with reflection, dissipation, and diffraction phenomena. The loading phase lasts 50 µs–20 ms, followed by a free-oscillation phase of up to 100 ms. While the time-domain signal provides useful information on peak amplitudes and event duration, it does not readily indicate the relative severity across the broad frequency content of a shock. Shock events typically contain short-duration high-frequency components and longer-lasting low-frequency structural responses. Frequency-domain analysis is therefore essential for accurately assessing shock severity and potential impact. For this reason, the Shock Response Spectrum (SRS) [9] is the widely adopted method for shock evaluation.

The SRS method [1] involves defining a set of single-degree-of-freedom (SDOF) systems, each characterized by its own natural frequency. The time-domain signal under study is applied as input to all of these SDOF systems. For each system, the absolute maximum temporal response is extracted and plotted against its natural frequency. In this case, acceleration time signals are used, and the process computes the absolute maximum temporal response of each SDOF with a given damping coefficient Q. This produces spectra that are easily comparable, unlike raw time-domain acceleration data. The SRS thus represents the shock severity across a studied frequency range. It is important to note that for a given time-domain signal, there is only one corresponding SRS. However, for a given SRS, there is an infinite number of time-domain signals that could produce it. Various SRS computation algorithms exist. While Kelly and Stricklin's method [7] is one example, the approach used in the present work follows Smallwood's method [8]. In the presented work, comparisons between numerical and experimental results will be accompanied by percentage values within the intervals of ±3, ±4, and ±6 dB from experimental results, as is customary in terms of shock tolerances [29] and a correlation coefficient, which ranges from 0 to 1, which is the covariance between the numerical and experimental SRS divided by the product of their standard deviations.

Step 0 in the presented methodology in Figure 1 requires that the SRS computed from the experimental accelerations during tests must represent the SRS of the accelerations measured closest to the shock source.

3.2. Frequency-Domain Energy Spectral Density Computation from an SRS – Step 1

The purpose of this section is to construct, from an SRS alone, an energy distribution as a function of frequency. To achieve this, an upper bound on the maximum energy for each frequency is conventionally computed. For every computation frequency, the bounded energy corresponds to that of a single-degree-of-freedom (SDOF) system whose natural frequency equals the computation frequency and that is subjected to an excitation so that the peak acceleration of the SDOF matches the SRS value at that same frequency.

If the SRS is computed for N_f single-degree-of-freedom systems with mass, stiffness, natural frequency, and maximum acceleration $\{m_k, k_k, f_k\}_{k=1,\dots,N_f}$, the excitation that enables an SDOF of frequency f_k to reach the value $SRS(f_k)$ is identified, and the associated maximum energy is computed—to conventionally express a maximum energy as a function of frequency— in (Eq. 1).

$$E_{max}(f_k) = \frac{1}{8\pi^2}\frac{m_k \times SRS^2(f_k)}{f_k^2} \qquad \textit{(Eq. 1)}$$

For a time-domain shock-acceleration signal examined with a sliding cumulative SRS, i.e., the Shock-Response Spectrum is recomputed at discrete time steps $t_i = i\Delta t$ on the signal segment that extends from the start $t = t_0$ to each t_i, it can be observed that initial high-frequency transients [2,6] produce early high-frequency SRS maxima. As modal behavior emerges, SRS maxima at lower frequencies are reached. This implies that the peak accelerations defined in the SRS do not occur simultaneously. Then, because of the non-simultaneous maxima, the effective mass for the mode associated to f_k can only be bound by total system mass denoted M_{tot} throughout the study. The bounded maximum energy is expressed as:

$$E_{sup}(f_k) = \frac{1}{8\pi^2}\frac{M_{tot} \times SRS^2(f_k)}{f_k^2} \qquad \textit{(Eq. 2)}$$

To express this in terms of spectral density, considering the frequency band $[b_{k-1}; b_k]$ around the central frequency f_k, the Energy Spectral Density is written as follows:

$$ESD_{sup}(f_k) = \frac{1}{8\pi^2}\frac{M_{tot} \times SRS^2(f_k)}{f_k^2\,(b_k - b_{k-1})} \qquad \textit{(Eq. 3)}$$

(Eq. 3) represents the step 1 of the methodology presented and illustrated in Figure 1. A frequency discretization example used for large frequency range events is generally expressed as a geometric distribution of central frequencies $\{f_1, \dots, f_{N_f}\}$ such as $f_{k+1} = rf_k \equiv f_1 r^k$ with $r = 2^\Gamma$, the b_k values are defined as $b_0 = \frac{f_1}{r^{1/2}}$ and $b_k = \sqrt{f_k f_{k+1}} \equiv f_k r^{1/2}$. In the presented work, $\Gamma = \frac{1}{24}$, which corresponds to a frequency discretization of $\frac{1}{24}$ octave. For illustration, Figure 2 shows the SRS and the corresponding computed energy for a 10.7 kg specimen across frequencies from 100 Hz to 10 kHz.

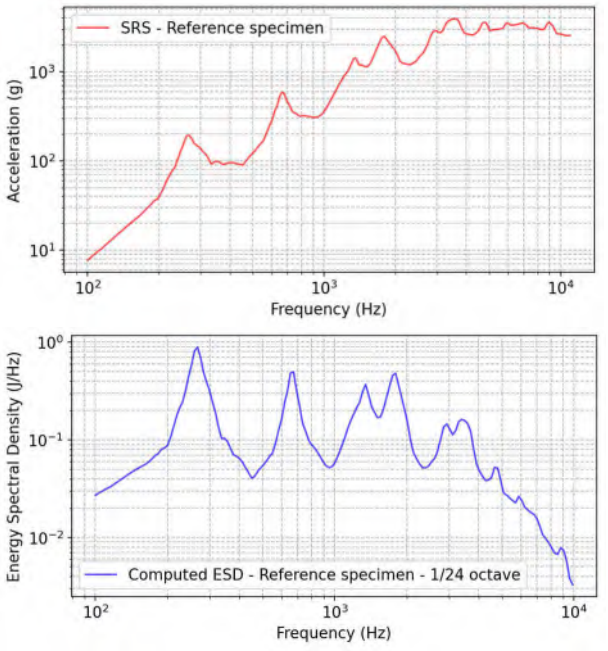


Figure 2 - A Shock Response Spectrum (SRS) and its associated maximum Energy Spectral Density for a frequency range of 100 Hz to 10 kHz, a 1/24 octave discretization $\Gamma = \frac{1}{24}$, and for a specimen with a total mass of 10.7 kg.

3.3. Computation of the Modal Density Weighted function – Step 2

The goal is to build a continuous frequency-dependent function representing the density of natural frequencies within a representative frequency range for a given impact zone and adapted for the normalization of the calculated energy spectral density. To quantify the distribution of natural frequencies in a structural system, we employ Kernel Density Estimation (KDE) [23], a non-parametric statistical method for estimating probability density functions.

At first, the kernel function is introduced and its relevance explained. Subsequently, the specific kernel function employed to adapt the modal density computation to the presented methodology is detailed. The last part provides a detailed explanation of the modal density computation, focusing on the modal weighting of the system's natural frequencies based on the modal amplitudes at the node located at the shock source, for a given direction.

Consider a system with N_{f_0} natural frequencies $\{f_{0_i}\}_{i=1,\dots,N_{f_0}}$, determined through modal analysis. Furthermore, consider again the set of $\{f_k = 2\pi\omega_k\}_{k=1,\dots,N_{f_k}}$ defining the frequency domain over which all quantities are evaluated. We propose a formulation for the weighted model density function $n(f_k)$ (the function is then normalized).

$$n_w(f_k) = \frac{1}{N_{f_0}}\sum K(f_{0,i}, f_k) * W_{n,}^{(d)} \qquad \textit{(Eq. 4)}$$

As explained previously, our suitable kernel function $K(f_{0,i}, f_k)$ must be chosen such that the shape factors around the peaks in the modal density weighted function are consistent with those of the spectral energy density. To achieve this, our strategy relies on the relationship between the potential energy of the spring and the imposed acceleration.
Considering a mass-spring-damper model and computing the relative energy through the spring's potential energy, one can define a function that expresses, in the Fourier domain, the ratio of this energy to the square of the mass's acceleration. Once normalized, this yields the following:

$$K(f_{0,i}, f_k) = \frac{1}{\pi Q} \frac{f_{0,i}^3}{(f_{0,i}^2 - {f_k}^2)^2 + (f_{0,i} f_k / Q)^2} \quad \textit{(Eq. 5)}$$

For the time being, $Q_i \equiv Q$ is taken as a constant—identical for every mode—to keep the methodology straightforward. Nevertheless, one could envisage a more general formulation in which a separate Q value is assigned to each individual natural mode.

Experimentally, the shock source will likely excite certain modes more than others. Consequently, in the experimental SRS of the system under study, only peaks at the likely-excited modes will appear. Therefore, the natural frequencies of the system for the computation of the modal density weighted function, determined through modal analysis, must be weighted so that modes likely to be excited, relative to the shock impact zone along the excitation axis, contribute more to the computation of the modal density weighted function than those that are not. This methodology particularly allows differentiation based on the injection zone of the shock source.

Regarding the literature on modal density computation methodologies, particularly mode weighting, several definitions of mode participation have been proposed. Some combine effective mass [30,31], while others rely on observability factors [31,32]. Other approaches use Frequency Response Functions (FRFs) [33], and some rely on experimental methods to directly estimate the modal density [34,35]. In this work, the effective mass is excluded because it is not directly applicable under free–free boundary conditions, as the effective mass is concentrated on rigid-body modes. Some methods, such as the Effective Interface Mass approach [36], do attempt to define an effective mass for free–free systems.
Experimental identification is also excluded, as the objective is to avoid physical testing of the specimen studied. The observability factor defined in the Primodal user's guide [37] is also not retained. This factor, normalized by the maximum mode shape displacement across all degrees of freedom at each frequency, only indicates whether a given degree of freedom dominates others for a particular natural frequency; it does not distinguish observability differences between modes. It should be noted that there are various methodologies for defining modal participation factors [28], including domain-specific mathematical formulations [38–40]. In the proposed approach, modal weighting is applied using a modal energy fraction. To weigh the modes in a multi-dimensional material system in space $\{X, Y, Z\}$, we limit our consideration to the discrete approximations of the material systems, based on the Finite Element Method (FEM). The latter allows for the computation of nodal displacements. The methodology presented introduces a modal participation factor $W_{n,i}^{(d)}$ within modal density weighted function computation, representing the fraction of modal energy associated with the displacement translation of the FEM discretization node n in the space axis direction $d \in \{X, Y, Z\}$ [28] such as:

$$W_{n,i}^{(d)} = \frac{\left|\phi_{ni}^{(d)}\right|^2}{\sum_{i=1}^{N} \left|\phi_{ni}^{(d)}\right|^2} \quad \textit{(Eq. 6)}$$

Here, $\phi_{ni}^{(d)}$ is the component of the mode shape vector for mode i at node n in direction (d), $\left|\phi_{ni}^{(d)}\right|$ is the absolute amplitude of this component and $W_{n,i}^{(d)}$ is the modal energy fraction. That last one is expressed between 0 and 1 such that when it is close to 1, the mode is highly likely to be excited by an impact at this location and in direction (d) and vice versa. The modal participation factor $W_{n,i}^{(d)}$ is defined with a normalization with respect to the sum of the squares of the magnitudes of all amplitudes rather than the maximum magnitude of amplitudes per mode to preserve comparison between modes [28].
The normalization of weighting factors is merely conventional. In any case, the modal density weighted function is normalized subsequently as follows:

$$n(f_k) = N_{f_0} \frac{n_w(f_k)}{\sum_{k=1}^{N_{f_k}} n_w(f_k)} \quad \textit{(Eq. 7)}$$

The (Eq. 7) with the kernel function of (Eq. 5) and the weighting of modes in (Eq. 6) represents the step 2 of the methodology presented and illustrated in Figure 1. Note that for the presented work, modal analyses were performed using NASTRAN software. An illustration of the modal density weighted function for plate 1, with characteristics presented in Table 1, is given in Figure 3.

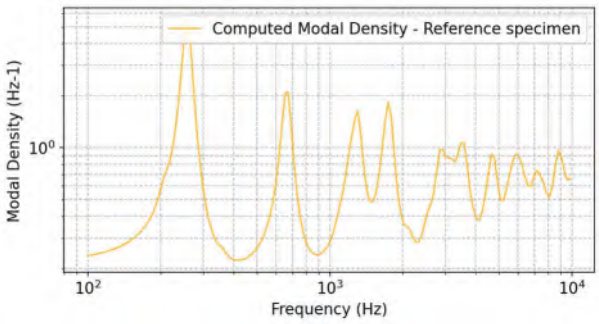


Figure 3 - Example of the modal density weighted function of plate 1 (see Table 1) for an impact at the center of the plate.

3.4. Energy Spectral Density Normalization - Step 3

In this section, we demonstrate the existence of a method to normalize energy in order to transfer this data from one system to another, thereby modeling a common source.
According to the works published by Cremer [41], or by Richard H. Lyon [42], and reused in works such as the thesis by Le Bot [43], the power input to a system, averaged over source location, excited by a noise excitation with a flat spectrum S_l over the band $\Delta\omega$, is expressed as follows:

$$\langle \Pi \rangle = \frac{\pi}{2} \frac{S_l \Delta\omega}{2\pi} \frac{n(\omega)}{M} \qquad \textit{(Eq. 8)}$$

Here, $n(\omega)$ is the modal density of the system and M its mass. In this manner, if we consider two systems 1 and 2 such that System 1 with mass M_1 and modal density $n_1(\omega)$ has undergone characterization of the impact source and received an average power $P_1(\omega)$ with spectrum $S_{l1}(\omega)$ over the interval $\Delta\omega$. System 2 with mass M_2 and modal density $n_2(\omega)$, must receive an average power $P_2(\omega)$ with spectrum $S_{l2}(\omega)$ over the interval $\Delta\omega$.
Then:

$$P_j = \frac{\pi}{2} \frac{S_{lj}(\omega)\Delta\omega}{2\pi} \frac{n_j(\omega)}{M_j} \ , \qquad j \in \{1,2\} \qquad \textit{(Eq. 9)}$$

By posing $P_{norm,j} = \frac{P_j(\omega) M_j}{n_j(\omega)}$, then if $S_{l1}(\omega) = S_{l2}(\omega)$, so $P_{norm,1} = P_{norm,2}$.
Through the energy-power relationship in the Laplace domain, and by dividing by the frequency band, we can then define a normalization by energy, in the form of a spectral energy density, such that The Normalized Energy Spectral Density (NESD) can be expressed as follows:

$$NESD = \frac{ESD(\omega) M_j}{n_j(\omega)}, \qquad \textit{(Eq. 10)}$$

respecting the same conclusions. This formulation of a normalized spectral energy density then allows us to transfer this data from one system to another by considering that the shock source is identical. The use of spectral energy density rather than energy allows us to disregard differences in the frequency discretization definition of the reference case data and the desired output data. The NESD is conventionally defined by analogy to the normalization process used for direct and reverberant energy fields in Statistical Energy Analysis (SEA), where energy densities are expressed in terms of modal density [2,44,45].

3.5. Shock source normalization and reverse process for prediction

The methodology illustrated in Figure 1 computes a normalized energy spectral density (NESD) from the SRS of a shock source on a reference system and the modal analysis of the complete configuration test (i.e. the reference system and the shock source). Reversing the process, using the NESD and a modal analysis of a target specimen subjected to identical shock sources, a representative SRS can be predicted. The computation steps will be described subsequently.

The analysis involves the following:

- a set of N_{f_k} frequencies $\left\{f_1, \dots, f_{N_{f_k}}\right\}$ as the discretization of the set of defined quantities.
- a Shock Response Spectrum (SRS) $SRS_{ref}(f_k)$ representative of the levels at the injection of a shock source on a reference specimen with a mass M_{ref}
- a studied specimen with a mass M_{study} and N_s shock source(s) identical to the shock source characterized.
- a single damping coefficient value $Q = \frac{1}{2\zeta}$ applied uniformly across the entire frequency range.

For reference specimen,

- a set of natural frequencies $\left\{f_{0_r,1}, \dots, f_{0_r,N_{f_{0_r}}}\right\}$ for the reference specimen.
- a modal density weighted function $n_{ref}(f_k)$ from (Eq. 7) with the proper mode weighting $W_r(f_{0_r,i})$. (Eq. 6) based on the contributions of the natural frequencies of the reference specimen to its behavior for the given shock source location.

Similarly, for the studied specimen,

- a set of natural frequencies $\left\{f_{0_s,1}, \dots, f_{0_s,N_{f_{0_s}}}\right\}$ for the reference specimen.
- a modal density weighted function $n_{study}(f_k)$ from (Eq. 7) with the proper mode weighting $W_s(f_{0_s,i})$. (Eq. 6) based on the contributions of the natural frequencies of the reference specimen to its behavior for the given shock source location.

The first part of the methodology, comprising steps 1–3, is dedicated to characterizing the shock source using the reference specimen of mass M_{ref}.
Following the approach described in Section 3.2, step 1 of the methodology presented in Figure 1 is the computation of the maximum Energy Spectral Density for the shock source on the reference specimen is expressed using

$$ESD_{ref}(f_k) = \frac{1}{8\pi^2} \frac{M_{ref} \times {SRS_{ref}}^2(f_k)}{f_k^2 \, (b_k - b_{k-1})}. \qquad \textit{(Eq. 11)}$$

Following the approach describes in Section 3.3, step 2 of the methodology is to compute $n_{ref}(f_k)$.
Following the approach described in Section 3.4, step 3 of the methodology is to compute the Normalized Energy Spectral Density (NESD) that can be expressed as follow:

$$NESD(f_k) = \frac{ESD_{ref}(f_k) M_{ref}}{n_{ref}(f_k)}, \qquad (Eq.\ 12)$$

The analysis now considers the specimen under study with mass M_{study}. This specimen is intended to receive N_s shock source(s) identical to the shock source characterized.
Following the approach described in Section 3.3, step 2' of the methodology is to compute $n_{study}(f_k)$.
Following the approach described in Section 3.4, step 3' of the methodology is to compute the Energy Spectral Density for the studied specimen using the NESD:

$$ESD_{study}(f_k) = \frac{NESD(f_k) n_{study}(f_k)}{M_{study}} N_s, \qquad (Eq.\ 13)$$

In practice, due to the methodology for computing the modal density weighted function, energy conservation is not necessarily maintained during the transfer. An energy conservation factor is introduced to enforce energy conservation:

$$k_{cons} = \frac{\sum_{k=1}^{N_{f_k}} ESD_{ref}(f_k)}{\sum_{k=1}^{N_{f_k}} ESD_{study}(f_k)} N_s \qquad (Eq.\ 14)$$

Thus, the conserved maximum energy spectral density can be expressed as:

$$ESD_{study,cons}(f_k) = ESD_{study}(f_k) k_{cons} \qquad (Eq.\ 15)$$

Consequently, following the approach described in Section 3.2, step 1' of the methodology is the computation of the predicted SRS for the injection of N_s shock sources into the specimen under study is given by:

$$SRS_{study}(f_k) = \sqrt{\frac{8\pi^2 f_k^2 (b_k - b_{k-1}) ESD_{study,cons}(f_k)}{M_{study}}}$$

(Eq. 16)

For example, from the SRS illustrated in Figure 2, the Energy Spectral Density has been computed and illustrated as well in Figure 2; then the weighted modal density function has been computed and illustrated in Figure 3; and finally, the NESD can be computed and illustrated in Figure 4.

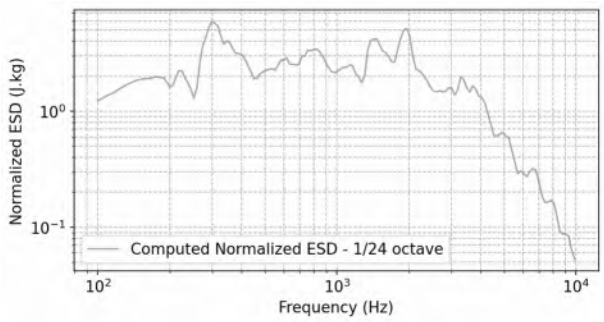


Figure 4 - Example of a NESD characterized for a 255g ball impact dropped at 15cm (frequency range 100 Hz to 10 kHz - 1/24 octave discretization).

4. APPLICATIONS

This section aims to apply the methodology to characterize a shock source on a reference system and to predict the injected shock level on a studied specimen. Plate and ball materials are detailed in Table 1, and specimens are illustrated in Figure 5 and Figure 6. Further complex specimens such as structural models of microsatellite are studied and illustrated in Figure 7.

Table 1: Material properties and experimentation mass characteristics for the ball impactor and the plate used in experimentation.

Material Name	Plate 1	Plate 2	Ball
Material	Al. 2618 T6	Aluminium	Stainless steel 304L
Density	2780 kg/m3	2854 kg/m3	7800 kg/m3
Young's Modulus	74.5 GPa	72.0 GPa	195 GPa
Poisson Coef.	0,3	0,3	0,3
Size (mm^3)	543.5×560 × 13	440×400 × 10	
Mass	10,7 kg	5 kg	67g to 535 g

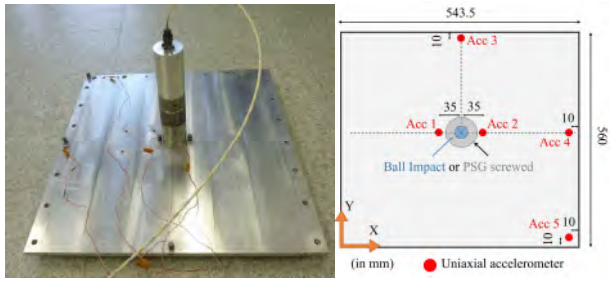


Figure 5 - On the left: Illustration of plate 1's instrumentation with the PyroshockGun shock source. On the right: scheme of the instrumentation of plate 1.

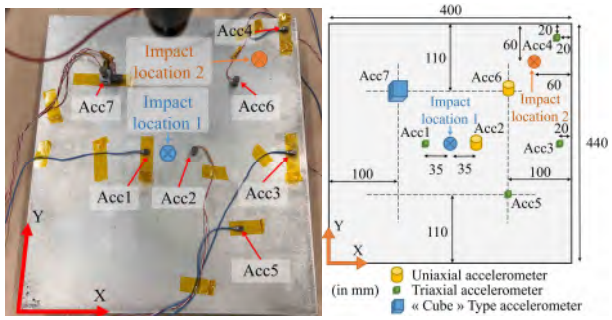


Figure 6 - On the left: Illustration of plate 2's instrumentation with the steel ball shock source, with two impact locations. On the right: scheme of the instrumentation of plate 2.

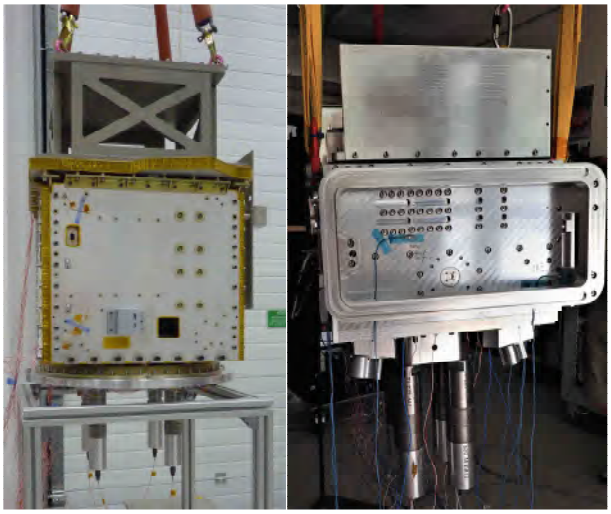


Figure 7 - On the left: Illustration of the MicroCarb Structural model with 4 PSG shock sources. On the right: Illustration of the Structural model of a microsatellite with 4 PSG shock sources.

4.1. Shock injection level prediction with NERS approach for ball drops on plates

In the following example, the same characterization is employed to predict two distinct shock levels applied at two different shock locations on the specimen under study.

- Figure 8: Characterization of a 255 g ball drop from 15 cm on Plate 1 providing the desired Normalized Energy Spectral Density (NESD).

- Figure 9: Use of the NESD from Figure 8 to predict shock injection level on Plate 2 for a **centered** drop.

- Figure 10: Use of the NESD from Figure 8 to predict shock injection level on Plate 2 for a **corner** drop.

Further examples can be presented using the characterization of a 255 g ball dropped from 60 cm and a 535 g ball dropped from 30 cm onto Plate 1. These data are then used to predict the corresponding shock-injection levels for centered drops on Plate 2. Figure 11 illustrates two points. First, the Normalized Energy Spectral Density (NESD) exhibits a higher-amplitude (more energetic) response than the NESD obtained with the 255-g ball released from a height of 15 cm. Second, the weighted modal-density function is identical to that shown in Figure 9, because both figures pertain to the same specimen and the same source location. Finally, through this methodology we consistently obtain results that are coherent between prediction and experimentation when looking at the SRS results.

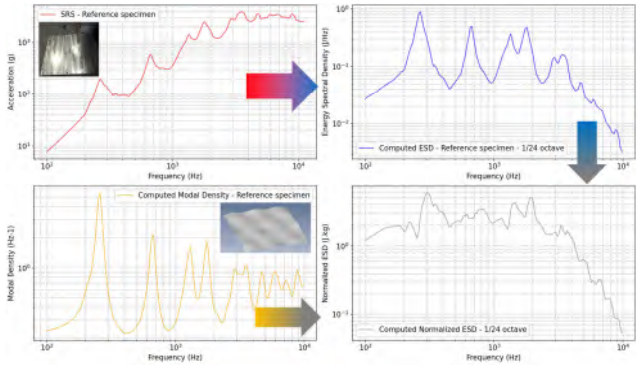


Figure 8 - 255 g ball drop from 15 cm on Plate 1 (center) – characterization.

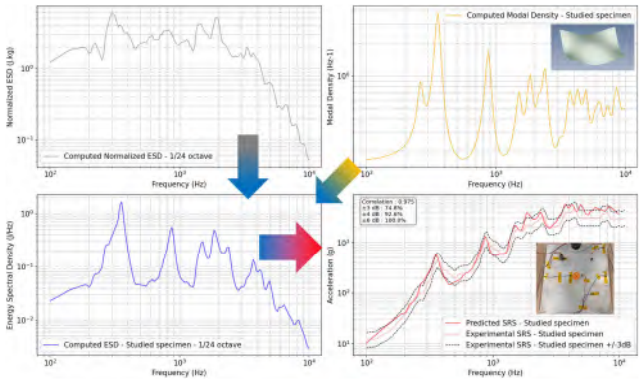


Figure 9 - Prediction for 255 g ball drop from 15 cm on Plate 2 (center) considering characterization illustrated in Figure 8.

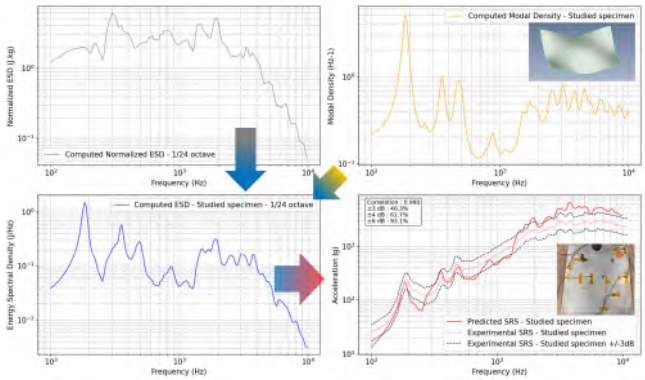


Figure 10 - Prediction for 255 g ball drop from 15 cm on Plate 2 (corner) considering characterization illustrated in Figure 8.

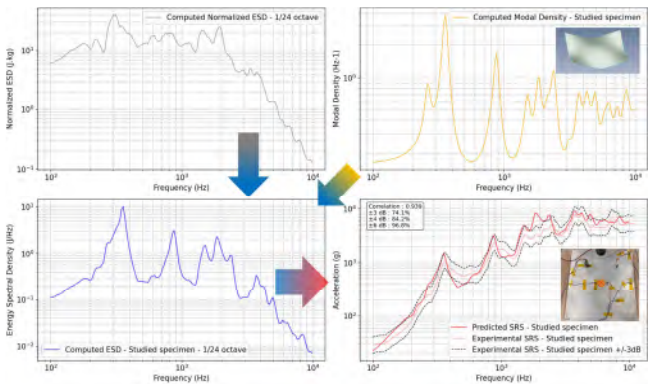


Figure 11 - Prediction for 535 g ball drop from 30 cm on Plate 2 (center) considering its (unillustrated) characterization.

4.2. Shock injection level prediction with NERS approach for concrete applications and operational outcomes

The subsequent examples present concrete engineering applications of the NERS approach. Several application contexts can be considered:

- **Enhanced precision of injection specifications for shock-sizing rules in preliminary analyses**: consider a studied specimen and an actual impact source. By characterizing the source and estimating the shock levels imparted to the structure, a representative test is no longer required; instead, appropriate level specifications can be defined for injection during the early sizing phases.
- **Pre-selection of the design for shock sources** (e.g., mechanisms, HDRMs, …): consider a studied specimen and several real shock-source variants. Characterizing the sources and estimating the resulting shock levels on the structure enables efficient identification of appropriate shock-source designs without conducting tests on the structure itself.
- **Pre-selection of the shock-test configuration**: consider a studied specimen and several possible shock-test setups. By characterizing the sources and estimating the shock levels on the structure, the appropriate configuration of shock sources can be identified in advance to reproduce the required test specifications.
- **Use of a normalized shock-energy representation for source simulation**: the characterization step and its description by a normalized spectral energy density enable the shock source to be represented in a simulation independently of the modeled structure.

In this section, examples of characterizations of the CNES shock test mean PyroShockGun are given for the purpose of determining the firing configurations needed to reproduce the prescribed SRS specifications on the satellite structural models studied. By first characterizing the PSG on a reference specimen, we were able to predict the SRS levels that would be injected into satellite models. These examples extend the validation to complex structures as for a full satellite structural model, thereby demonstrating the scalability and versatility of the proposed method for realistic applications.

4.2.1. ECY

For example, consider a satellite structural model that will be sent to a test campaign, illustrated on the right in Figure 7. The shock test means at CNES are primarily PSGs, whose configurations must be determined to reproduce the required test specifications. By conducting a characterization campaign of the PSG in various configurations on a reference structure—as shown in Figure 5—and having the modal analyses of both the reference tests and the SM, the methodology allows prediction of the injection levels that will be experienced in tests on the SM.

Consider the characterization performed for one “high-shock” configuration of the PSG. Using the experimental acceleration data from accelerometers 1 and 2 located near the source, and by computing a weighted modal-density function, a reference NESD is obtained for all subsequent predictions for this PSG configuration as illustrated in Figure 12.

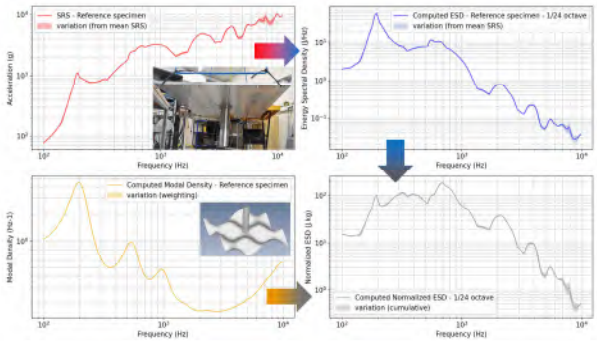


Figure 12 - ECPSG 2026: NERS approach for shock source characterization. Characterization of the PSG on the suspended EC1 plate.

Based on this characterization of the PSG in its firing configuration, the methodology can be used to predict shock levels for the structural model with the same firing configuration but potentially in different positions, as illustrated in Figure 13.

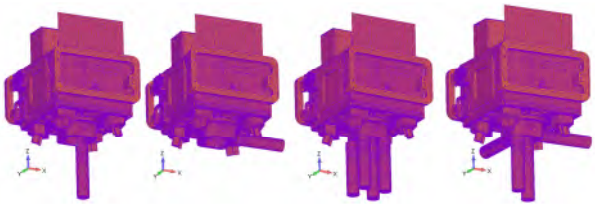


Figure 13 - Firing configurations for the ECY campaign.

Consequently, the use of the NERS approach is presented below for predicting shock levels on the structural model:

- for a PSG positioned along the Z-axis (out-of-plane), refer to Figure 14.
- for a PSG positioned along the X-axis (in-plane), refer to Figure 15.
- for four PSGs positioned along the Z-axis (out-of-plane), refer to Figure 16.
- for four PSGs with two on the Z-axis, one on X and one on Y, refer to Figure 17 focusing on the Y axis.

Further examples can be presented for the multi-axial shock test and with another PSG configuration.

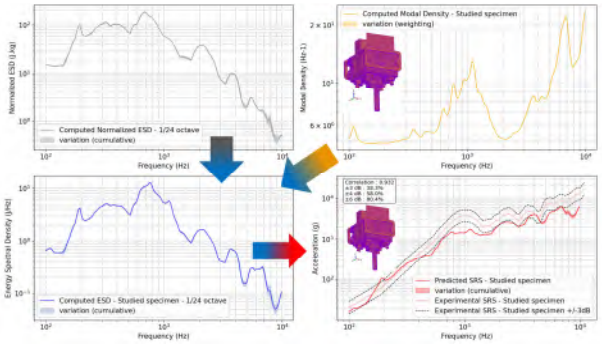


Figure 14 - ECY 2026: NERS approach for shock level prediction with one PSG in Z axis. Comparison between prediction and experimental results.

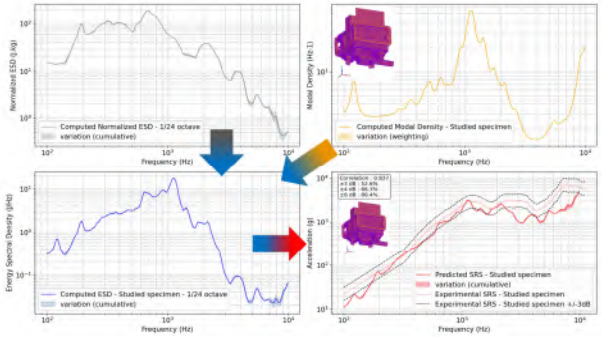


Figure 15 - ECY 2026: NERS approach for shock level prediction with one PSG in X axis. Comparison between prediction and experimental results.

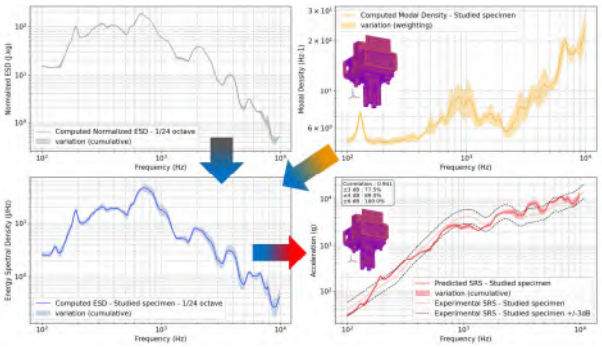


Figure 16 - ECY 2026: NERS approach for shock level prediction with four PSG in Z axis. Comparison between prediction and experimental results.

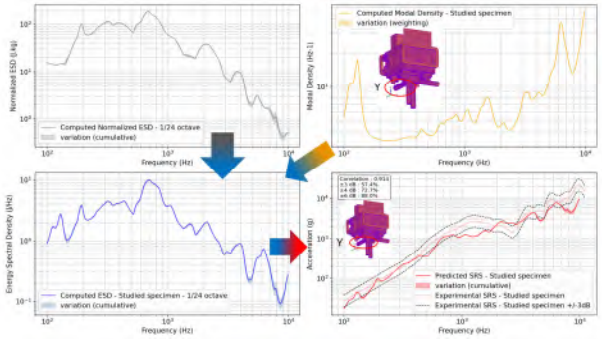


Figure 17 - ECY 2026: NERS approach for shock level prediction with four PSG in X,Y and Z axis, considering the Y axis. Comparison between prediction and experimental results.

4.2.2.EC MicroCarb SM

For example, consider the MicroCarb structural model that will be sent to a test campaign, illustrated on the left in Figure 7. The PSG configuration must be determined to reproduce the required test specifications. Considering 3 (unillustrated) characterizations of 3 different configurations of the PSG—as illustrated in Figure 5— categorized as “low shock”, “medium shock” and “high shock”, we obtain the shock source levels prediction in Figure 18,Figure 19 and Figure 20.

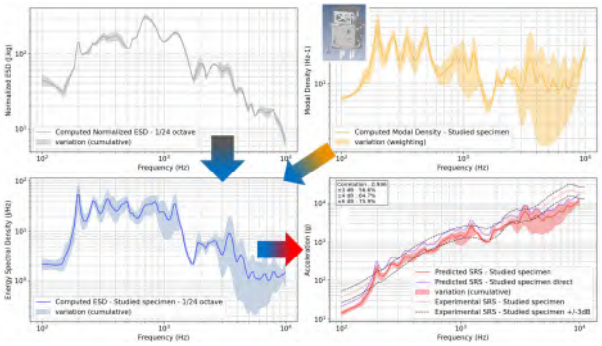


Figure 18 - ECSM 2020: NERS approach for shock level prediction with four PSG in Z axis in a “low-shock” configuration, considering the Z axis. Comparison between prediction and experimental results.

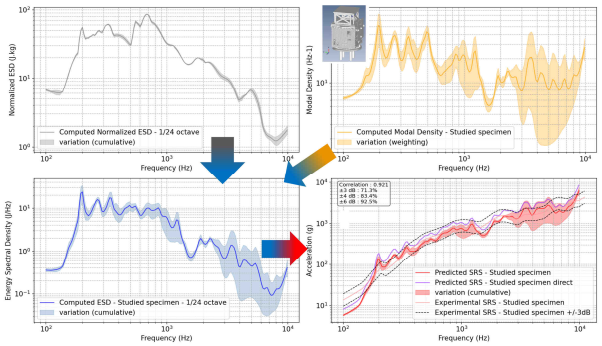


Figure 19 - ECSM 2020: NERS approach for shock level prediction with four PSG in Z axis in a “medium-shock” configuration, considering the Z axis. Comparison between prediction and experimental results.

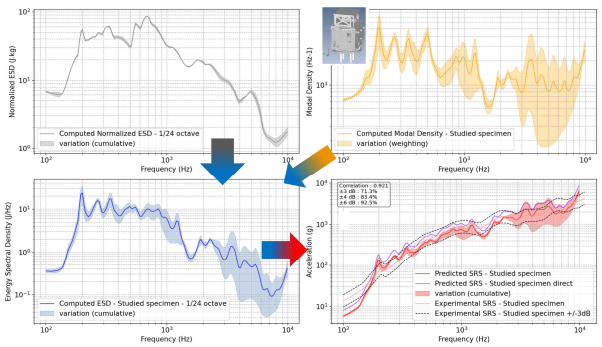


Figure 20 - ECSM 2020: NERS approach for shock level prediction with four PSG in Z axis in a “high-shock” configuration, considering the Z axis. Comparison between prediction and experimental results.

4.3. Empirical demonstration of the normalized shock source representation through the previous examples

The way to demonstrate the effectiveness of the methodology is to characterize the same shock source on different specimens, with distinct source locations and along various measurement axes. Experimental results show that the computed SRS depend entirely on the impacted structure and on the position of the source (unillustrated but demonstrated with the previous examples). In contrast, the figures presented below reveal a marked similarity among the Normalized Energy Spectral Densities (NESDs) obtained for these differing configurations.

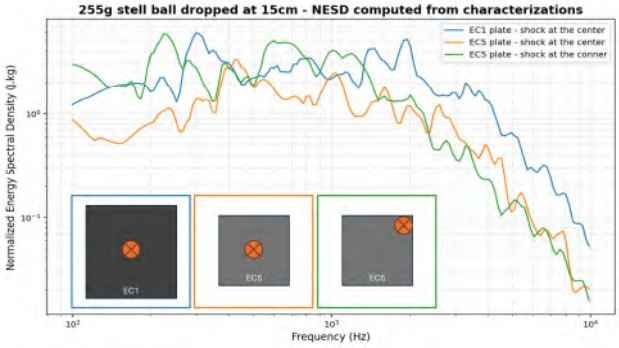


Figure 21 - Comparison of NESDs Characterized During the Ball-Drop-onto-Plate Campaign.

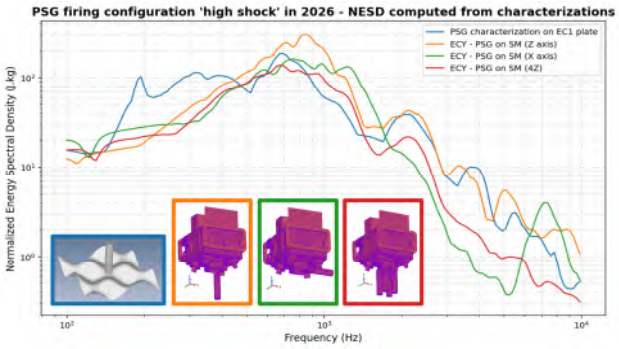


Figure 22 - Comparison of the NESDs characterized in the ECY campaign for a "high shock configuration".

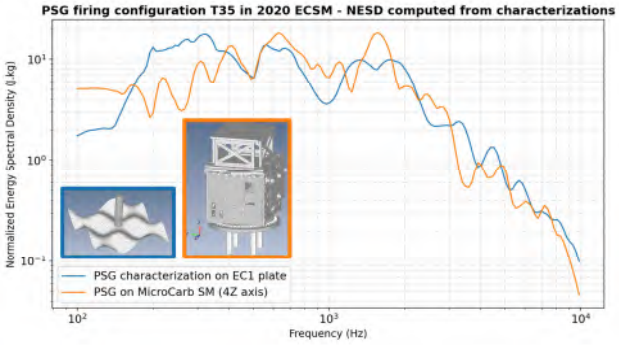


Figure 23 - Comparison of the NESDs characterized in the ECSM campaign for a "low shock configuration".

Several of the peak-like discrepancies can be traced to the simplifying assumption in the methodology of assigning a Q damping value to all natural modes. This uniform damping prevents a fitting normalization of the peaks observed in the experimental SRS, because those peaks are governed not only by the Q damping prescribed in the SRS formulation but also by the intrinsic damping of the structure itself.

5. CONCLUSIONS

In conclusion, this study introduces a novel methodology that **reliably represents a shock source through a normalized representation based on the Normalized Energy Spectral Density**, computed from a characterization test on a reference specimen. This NESD is then used for shock source levels prediction on a studied specimen subjected to the same shock sources as characterized. This approach not only achieves the objectives to **enhance the characterization of shock sources** and obtain **usable data for shock-source modeling in simulation** for example, but it also allows a **more accurate estimation of shock source level** for preliminary design sizing and application of ECSS rules, for example, and permits **prediction of injection shock levels**, **comparison and optimization for different configurations**, including **shock test means** by pre-defining optimal parameters tailored to a given specimen's specifications, **or mechanisms.**

The methodology highlighted several key aspects that prove to be essential to its effectiveness: using a representative computed SRS of the shock source levels from measurements in characterization, employing a kernel function specifically adapted to the methodology, defining modal weighting in the computation of the modal density weighted function, and the normalization of the energy spectral density by the weighted modal density function.

Finally, the versatility of this methodology lies in its ability to be applied across different domains as demonstrated with the given examples. This methodology represents a significant advancement in shock source modelling and in shock source level prediction, offering a more accurate, flexible, and efficient alternative to shock source level estimation and prediction for preliminary design phases or tests. Its implementation could streamline specimen development processes and improve the reliability of shock testing, ensuring better performance and safety in various engineering applications.

Improvements can be made in both determining and implementing distinct damping factors for each individual mode. Future work could also explore characterization based on alternative input data—such as a force—as a further avenue of investigation.

6. REFERENCES

[1] NASA, NASA Technical Handbook - Dynamic Environmental Criteria, NASA Engineering Standards, USA, 2001.

[2] ESA-ESTEC, ECSS-E-HB-32-25A - Space Engineering - Mechanical Shock Design and Verification Handbook, ECSS Secretariat - Requirements & Standards Division, Noordwijk, The Netherlands, 2015. https://ecss.nl.

[3] Department of defense test method standard, Environmental Engineering Considerations and Laboratory Tests - MIL-STD-810G, Department of defense test method standard, USA, 2008.

[4] Department of defense test method standard, Environmental Engineering Considerations and Laboratory Tests - MIL-STD-810H, Department of defense test method standard - USA, 2008.

[5] H. Yue, Y. Yang, Y. Lu, F. Yang, J. Wu, Q. Ruan, Z. Deng, Research progress of space non-pyrotechnic low-shock connection and separation technology (SNLT): A review, Chinese Journal of Aeronautics 35 (2022) 113–154. https://doi.org/10.1016/j.cja.2021.07.001.

[6] ESA-ESTEC, ECSS-E-HB-32-26A - Space Engineering - Spacecraft Mechanical Loads Analysis Handbook., ECSS Secretariat - Requirements & Standards Division, Noordwijk, The Netherlands, 2013. https://ecss.nl.

[7] J.N. Martin, A.J. Sinclair, W.A. Foster, On the Shock-Response-Spectrum Recursive Algorithm of Kelly and Richman, Shock and Vibration 19 (2012) 19–24. https://doi.org/10.1155/2012/824968.

[8] K. Ahlin, Shock Response Spectrum Calculation - An Improvement of the Smallwood Algorithm, Ingemansson technology, Stockholm, Norvège, n.d. http://www.vibrationdata.com/tutorials_alt/Ahlin_SRS.pdf.

[9] NASA, NASA Technical Standard - Pyroshock Test Criteria, NASA Engineering Standards, USA, 1999.

[10] V. Babuska, C. Sisemore, J. Booher, Energy Based Representations of Mechanical Shock for Failure Characterization, in: 57th AIAA/ASCE/AHS/ASC Structures, Structural Dynamics, and Materials Conference, American Institute of Aeronautics and Astronautics, San Diego, California, USA, 2016. https://doi.org/10.2514/6.2016-0473.

[11] Arianespace, Ariane 5 - User's Manual Issue 5 Revision 2, Arianespace, France, 2016.

[12] Arianespace, Ariane 6 - User's Manual Issue 2 Revision 0, Arianespace, France, 2021.

[13] E. Raynal, O. Daslandes, M. Hofmann, M. Perriquer, G. Zegre, A. SOLER, R. ARENA, J. D'AMICO, F. FAGOT, Vesta Test Exploitation, in: Proceedings, European Conference on Spacecraft Structures, Materials and Mechanical Testing, CNES, ADS & TAS, n.d. https://ecssmet2023.com/.

[14] SPACE X, FALCON User's Guide, Space Exploration Technologies Corp., USA, 2021. https://www.spacex.com/vehicles/falcon-9.

[15] N. Pascal, F. Lachaud, M. Charlotte, S. Lemay, A. Brugnoli, Shock Level Prediction in the Space Domain Using Explicit FEM on a Simplified Case Study, Results in Engineering (2026) 109932. https://doi.org/10.1016/j.rineng.2026.109932.

[16] J. Kim, J.-C. Yoon, B.-S. Kang, Finite element analysis and modeling of structure with bolted joints, Applied Mathematical Modelling 31 (2007) 895–911. https://doi.org/10.1016/j.apm.2006.03.020.

[17] J.S. Sun, K.H. Lee, H.P. Lee, Comparison of implicit and explicit finite element methods for dynamic problems, Journal of Materials Processing Technology 105 (2000) 110–118. https://doi.org/10.1016/S0924-0136(00)00580-X.

[18] J. Hwang, Pyrotechnic Shock Analysis Using Statistical Energy Analysis, in: 29th Aerospace Testing Seminar, Engineering Division MIT Lincoln Laboratory Lexington, MA, 2015. https://www.semanticscholar.org/paper/Pyrotechnic-Shock-Analysis-Using-Statistical-Energy-Hwang/1bc80854ea51d32ddd49bf0a1cb1f721abf0122e.

[19] S.-J. Lee, D.-H. Hwang, J.-H. Han, Development of Pyroshock Simulator for Shock Propagation Test, Shock and Vibration 2018 (2018) 9753793. https://doi.org/10.1155/2018/9753793.

[20] X. Wang, W. Liu, X. Li, Y. Sun, The Shock Response Prediction of Spacecraft Structure Based on Hybrid FE-SEA Method, Applied Sciences 11 (2021) 8490. https://doi.org/10.3390/app11188490.

[21] X. Wang, W. Liu, J. Ding, Y. Sun, Y. Dang, Pyroshock Response Prediction of Spacecraft Structure in Wide Frequency Domain Based on Acceleration FRF, Aerospace 9 (2022) 54. https://doi.org/10.3390/aerospace9020054.

[22] H. Zhao, J. Ding, W. Zhu, Y. Liu, Y. Sun, Shock Response Prediction of the Typical Structure in Spacecraft Based on the Hybrid Modeling Techniques, Aerospace Science and Technology 89 (2019) 460–467. https://doi.org/10.1016/j.ast.2019.04.018.

[23] S. Węglarczyk, Kernel density estimation and its application, ITM Web Conf. 23 (2018) 00037. https://doi.org/10.1051/itmconf/20182300037.

[24] T. Ledl, Kernel Density Estimation: Theory and Application in Discriminant Analysis, AJS 33 (2016) 267–279. https://doi.org/10.17713/ajs.v33i3.441.

[25] F. Zaman, Y.P. Wong, B.Y. Ng, Density-based Denoising of Point Cloud, (2016). https://doi.org/10.48550/ARXIV.1602.05312.

[26] B.W. Silverman, Using Kernel Density Estimates to Investigate Multimodality, Journal of the Royal Statistical Society Series B: Statistical Methodology 43 (1981) 97–99. https://doi.org/10.1111/j.2517-6161.1981.tb01155.x.

[27] P. Vieu, A note on density mode estimation, Statistics & Probability Letters 26 (1996) 297–307. https://doi.org/10.1016/0167-7152(95)00024-0.

[28] M. Guzman Nieto, M. S.A. Elsayed, D. Walch, Modal Participation Factors and theit Potential Applications in Aerospace: a Review, in: Proceedings of The Canadian Society for Mechanical Engineering International Congress 2018, CSME International Congress, Toronto, On, Canada, 2018.

[29] ESA-ESTEC, ECSS-E-ST-10-03C Rev.1 - Space Engineering - Testing, ECSS Secretariat - Requirements & Standards Division, Noordwijk, The Netherlands, 2022. https://ecss.nl.

[30] M. Aenlle, M. Juul, R. Brincker, Modal Mass and Length of Mode Shapes in Structural Dynamics, Shock and Vibration 2020 (2020) 1–16. https://doi.org/10.1155/2020/8648769.

[31] J.-S. Hwang, H. Kim, B.-H. Cho, Modal Parameters Estimation of Building Structures from Vibration Test Data Using Observability Measurement, Shock and Vibration 2015 (2015) 1–13. https://doi.org/10.1155/2015/627852.

[32] Z. Yilmaz, F.Y. Okur, M. Günaydin, A.C. Altunişik, Enhanced Modal Participation Ratio-Based Structural Damage Identification: A New Filtering Approach Using Modal Assurance Criteria, Buildings 13 (2023) 2467. https://doi.org/10.3390/buildings13102467.

[33] S. Hassani, F. Shadan, Using incomplete FRF measurements for damage detection of structures with closely-spaced eigenvalues, Measurement 188 (2022) 110388. https://doi.org/10.1016/j.measurement.2021.110388.

[34] K. Renji, S.J.K. Florence, S. Deshpande, An Experimental Investigation of Modal Densities of Composite Honeycomb Sandwich Cylindrical Shells, The International Journal of Acoustics and Vibration 25 (2020) 112–120. https://doi.org/10.20855/ijav.2020.25.11626.

[35] K. Ege, X. Boutillon, M. Rébillat, Vibroacoustics of the piano soundboard: (Non)linearity and modal properties in the low and mid-frequency ranges, Journal of Sound and Vibration 332 (2013) 1288–1305. https://doi.org/10.1016/j.jsv.2012.10.012.

[36] D.C. Kammer, J. Cessna, A. Kostuch, An Effective Mass Measure for Selecting Free-Free Target Modes, in: In Proceedings of the 23rd International Modal Analysis Conference, Quartus Engineering Inc, Orlando, Florida, 2005.

[37] N. Roy, PRIMODAL - User's Manual Version 3.0, (2018). https://primodal.com/.

[38] J.T. Chen, K.H. Chen, I.L. Chen, L.W. Liu, A new concept of modal participation factor for numerical instability in the dual BEM for exterior acoustics, Mechanics Research Communications 30 (2003) 161–174. https://doi.org/10.1016/S0093-6413(02)00351-8.

[39] P.F. Carlbom, Combining MBS with FEM for Rail Vehicle Dynamics Analysis, Multibody System Dynamics 6 (2001) 291–300. https://doi.org/10.1023/A:1012072405882.

[40] A.J. Salmonte, Considerations on the residual contribution in modal analysis, Earthq Engng Struct Dyn 10 (1982) 295–304. https://doi.org/10.1002/eqe.4290100210.

[41] L. Cremer, M. Heckl, B.A.T. Petersson, Structure-Borne Sound, Springer Berlin Heidelberg, Berlin, Heidelberg, 2005. https://doi.org/10.1007/b137728.

[42] R.H. Lyon, R.G. DeJong, Theory and Application of Statistical Energy Analysis, Elsevier Science, 1995.

[43] A. Le Bot, Foundation of Statistical Energy Analysis in Vibroacoustics, 1st ed., Oxford University PressOxford, 2015. https://doi.org/10.1093/acprof:oso/9780198729235.001.0001.

[44] B. Mace, Statistical energy analysis, energy distribution models and system modes, Journal of Sound and Vibration 264 (2003) 391–409. https://doi.org/10.1016/S0022-460X(02)01201-4.

[45] D.H. Hawes, R.S. Langley, T. Bultin, Y. Ishii, A hybrid Finite Element-Statistical Energy Analysis Method for Impulsive and Transient Loading, Journal of Sound and Vibration 459 (2019) 114849. https://doi.org/10.1016/j.jsv.2019.114849.

DESIGN PRINCIPLES OF A SPACECRAFT STRUCTURAL DIGITAL TWIN

Lydia Cabezudo Carrascal [(1)], Zahra Sharif-Khodaei [(2)], Samuel Gain [(3)], Haolin Li [(4)], Yuhang Pan [(5)], Carlos Juarez Porras [(6)], Javad Fatemi [(7)], Sofia Sinopoli [(8)]

[(1)] Airbus Defence and Space Ltd., Gunnels Wood Rd, Stevenage SG1 2AS (UK),

Email: lydia.cabezudo@airbus.com

[(2)] Imperial College London, Exhibition Rd, South Kensington, London SW7 2AZ (UK),

Email: z.sharif-khodaei@imperial.ac.uk

[(3)] Airbus Defence and Space Ltd., Gunnels Wood Rd, Stevenage SG1 2AS (UK),

Email: samuel.gain@airbus.com

[(4)] Imperial College London, Exhibition Rd, South Kensington, London SW7 2AZ (UK),

Email: haolin.li20@imperial.ac.uk

[(5)] Imperial College London, Exhibition Rd, South Kensington, London SW7 2AZ (UK),

Email: y.pan21@imperial.ac.uk

[(6)] Airbus Defence and Space Ltd., Gunnels Wood Rd, Stevenage SG1 2AS (UK),

Email: carlos.juarez@airbus.com

[(7)] Airbus Defence and Space Netherlands, Mendelweg 30, 2333 CS Leiden (Netherlands),

Email: javad.fatemi@airbus.com

[(8)] European Space Agency, Keplerlaan 1, 2201 AZ Noordwijk (Netherlands),

Email: sofia.sinopoli@esa.int

KEYWORDS

Digital Twin, Spacecraft, Structure, Health Monitoring, Machine Learning, Uncertainty Quantification, VVUQ

ABSTRACT

In space missions, in which physical inspection is rarely possible, the ability to remotely monitor structural performance and to predict, diagnose, and mitigate structural degradation can be critical for success.

A Structural Digital Twin (SDT) can provide these functionalities, but the transition to operational reality faces some significant challenges. The reliability and accuracy of the digital twin model is of paramount importance, as is the ability to transmit the right information for actionable insights over limited capacity data links, or the capability for autonomous decisions when the transmission over long distances does not allow quick communication with the twin. Overcoming these challenges requires following certain design principles during the SDT development.

1. INTRODUCTION AND STRATEGIC VIEW

The Digital Twin concept has gained significant traction in various industries due to its potential to enhance decision making, optimize processes and improve overall efficiency. The use of Digital Twins has evolved and expanded across different sectors, from medicine to aerospace, and they have been applied to many kinds of systems, from production processes, to buildings, vehicles or even the Earth itself. Moreover, the development of Structural Digital Twins (SDT) is fully aligned with the European Space Agency's (ESA) Technology 2040 vision, which highlights digitalization and AI-enabled technologies as fundamental enablers for future space missions. SDTs contribute to the transformation of traditional space engineering towards a more predictive, data-driven, and intelligent paradigm, strengthening Europe's competitiveness and strategic autonomy in the global space sector.

In the context of spacecraft structures, the Digital Twin refers to a digital representation of a physical structure in the form of a numerical model, which can be fed with data from the Structural Health Monitoring system (SHM) and other input information, to update the model with the actual conditions of use at any single moment and without performing the traditional full-system Finite Element Model (FEM) analysis each time; for the purpose of monitoring, diagnosing, and predicting the behaviour of the physical structure.

Consequently, in the case of an SDT, the physical

asset represented by the virtual twin is the structure subsystem and its behaviour under operating conditions; i.e., a certain load environment acting on the system. To provide actionable insights to the overall operation of the system, the SDT should be able to capture the mechanical responses of the physical asset under this load environment, and replicate its current state and the predicted variations during service.

An SDT, therefore, can monitor the current state of its connected physical structure from sensor input, and predict its response when the load environment changes. Moreover, it could potentially infer the state of the structure in areas not covered by physical sensors, detect anomalies should there be discrepancies between telemetry and predicted data (health monitoring), and project the evolution of the behaviour of the structure under future load conditions.

1.1. Use Cases

The use cases of an SDT cover all the life stages of a Spacecraft structure, from its initial design to the end of its service lifespan.

Concept design: Specially for recurring structures (e.g., Eurostar Neo platform) a working SDT of a previous, similar structure can provide crucial information for high-level design decisions and pre-sizing of platform and payload, allowing the optimisation of the design from very early in the development process.

Development: During this phase of a project, the design is still ongoing and test data is very limited. Collected data from digital twins of similar structures can be used to estimate the expected load environments based on real measured data, potentially relaxing some of the performance requirements and margins and avoiding over-design. Historical SDT data can also be used to conduct stochastic analysis as an integral part of sizing and development of the structure, ensuring robust designs that can cope with uncertainty in mechanical inputs and structural properties.

Verification: During this phase, the design is frozen and test campaigns are conducted to demonstrate that the spacecraft meets the specified requirements. An SDT can be used to monitor structural integrity and performance during the various phases of testing, capturing all the key mechanical parameters and their evolution during test; and also, to correlate the simulation predictions to measured data, providing test-corrected predictions. This can deliver an instant evaluation of the structural response against the qualification requirements, and detect possible anomalies as the test progresses, by comparing predicted and measured data in real time, reducing risk.

Operation: In the operational phase, the SDT offers a means to obtain information about the current and future state of the structure where it cannot be closely observed, which could potentially be mission-critical. In the case of sensitive optical instruments, for instance, the SDT can provide real time environmental data (thermoelastic, micro-vibration, …) to assess the stability and performance of the payload and inform decisions by the operator on ground.

Decommissioning: Space is a harsh environment, and structural performance can be degraded with time as materials age exposed to it, or it can be compromised due to other external, unpredictable factors such as space debris impact. An SDT can provide valuable information to estimate the useful lifespan of a structure with more accuracy, and potentially to extend it through predictive maintenance, if ageing factors can be detected and compensated.

1.2. Application Cases

The following application cases are examples of scenarios where an SDT could provide valuable inputs, but they are not exclusive of other potential applications.

Scientific and Telecommunications satellites normally carry equipment payloads that are sensitive to the mechanical performance of the structure, such as telescopes, navigation instruments, cameras, antennae, etc. These units can be damaged by vibrations transmitted by the structure during launch, or lose their pointing stability due to thermo-elastic deformations from temperature gradients, or micro-vibrations caused by mechanisms in the spacecraft, compromising the success of the mission.

An SDT can monitor these loads and the response of the structure and its instruments at critical locations, and detect potential damage or loss of performance due to exceedances in the mechanical environment, which might allow to take corrective measures in time to avoid these undesired effects.

An SDT can also provide crucial information about the mechanical performance of a **launcher structure**, the interaction between the launcher and its payload, and the generated loads during operation (quasi-static and dynamic, acoustic, shock, line loads, etc), which might affect both launcher integrity and payload survivability. Launchers such as Ariane 6 or Vega-C are also recurrent designs, so any SDT data of previous iterations of the structure can be used for Coupled Load Analysis (CLA), correlation and design optimisation.

In the particular case of **reusable structures**, such as Space Rider, an SDT can also enable preventive maintenance, indicating where and when the structure needs to be repaired or refurbished between missions to extend its usable lifespan, improve safety and optimize usage.

Lander structures such as the ones used in ExoMars and Rosetta present an additional set of structural challenges during the descent and landing phases. Manoeuvres like parachute deployment, thruster ignition and touchdown, or even the dust and particles blown from the landing surface by thruster plumes, can potentially cause damage and jeopardize the mission. In these cases, an SDT could help prevent or assess any caused damage, allowing mission control to take the appropriate decisions to minimize the problem.

Rover structures can also benefit from an SDT for health monitoring and preventive maintenance. For instance, monitoring acting loads and structural responses with changing terrain characteristics, speed of movement and environmental conditions, which would in turn allow to execute manoeuvres in a way that extends the rover's lifespan.

Deployable Spacecraft Structures like booms, antennae or mirrors such as the ones used in Juice, CIMR and JWST are dependent on adequate tolerances and free movement of their mechanisms for successful operation. Deformations in these structures can jam mechanisms and stop the structure's deployment, rendering the instrument useless or even causing mission failure. An SDT's monitoring capability could detect excessive deformations, and help in locating the cause and take corrective measures before even initiating the deployment sequence.

2. OVERALL DESIGN AND REQUIREMENTS OF A SPACECRAFT STRUCTURAL DIGITAL TWIN

Several aspects need to be considered in the design of an SDT with SHM capabilities:

- Inputs and Quantities of Interest (QoI),
- Operating conditions and data capture (sensors and data acquisition),
- System efficiency, communication links and bandwidth limitations,
- Type of model, model accuracy and data augmentation functions (e.g., data analysis and model evolution),
- Decision logic (e.g., healthy/unhealthy);
- Overall reliability

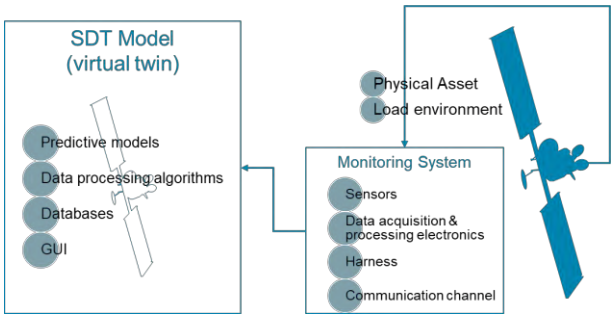


Figure 1: Components of a Spacecraft Structural Digital Twin

The Quantities of Interest (QoI) stem directly from the Application Case the twin is going to be used for. For most structural health monitoring applications, displacements, accelerations and/or strains are enough to understand the behaviour of the asset under typical conditions and to measure its performance. The selection of which QoI to monitor determines the type of data acquisition and processing that is going to be needed.

Regarding the type of model to be used, there are two general approaches. A Machine Learning model can be trained on sensor data only, which has the advantage of a simpler data chain with less error sources, but can only work as a “black box” of inputs and outputs, and can only provide information based on the sensors physically installed in the structure.

The second approach relies on the combination of physics-based simulation and sensor data. This type of hybrid digital twin is more complex to implement, but the distinct advantage is the amount of information that can be obtained from it. A simulation is based on the engineering knowledge about the structure’s physical properties and on the physical principles acting on it. This information can be included in the twin, opening the possibility of using real structural parameters, such as acting loads, geometry or material properties, as inputs to produce a QoI prediction. Furthermore, these predictions are not only limited to sensors physically installed in the structure, as the simulation is also able to provide an output where there is no sensor installed. The simulation can then be augmented with sensor data for calibration and correction of the prediction, providing a complete picture of the real behaviour of the structure. This is therefore the preferred approach if an understanding of the underlying reasons for the structure’s response is sought.

For complex structures under dynamic loads, as is the typical case in spacecraft, a precise characterisation of mass, stiffness and damping is necessary for an accurate and representative simulation, along with a validation of the modelling assumptions. This can be achieved through characterisation tests following a rigorous Validation, Verification and Uncertainty Quantification approach (VVUQ) (see §5).

The digital twin model should also be able to evolve based on the data captured by the sensors, correcting its predictions to adjust to the physical asset’s reality. For data-driven models, this could imply retraining the model as new data are fed into the system. In the case of simulation-driven hybrid models, it can be achieved through an Inverse Uncertainty Quantification (IUQ) loop, where the model’s inputs are inferred from the sensor measurements of the QoIs [1], and these values are used to obtain a new prediction from the simulation-

trained model. This could translate into a self-correlation capability, enabling the re-calibration of the SDT using data from its integrated sensors, particularly if independent data can be used to filter out concurrent solutions (see §6.3).

For structural dynamic responses, an added complication is the density of data captured by the sensors for an adequate monitorisation. Sampling rates of time series dynamic data need to be small enough to capture the signal's frequency range of interest without data loss, which is given by the Nyquist rate, $f_s > 2f_{max}$ [2]. As an example, if the frequency response of interest is in the range 0-750 Hz, at least 1500 samples per second need to be captured, more if anti-aliasing filter roll-off slopes or other factors are taken into account. This generates large datasets that, particularly for operational use cases, exceed the bandwidth of space communication links. Furthermore, the data link capacity to support the primary communication functions of the spacecraft cannot be compromised either. Thus, transmitting only the minimum information needed to reflect the structural state of the asset is essential to achieve a usable digital twin. This necessitates specialized architecture and capabilities in the spacecraft's on-board systems, such as initial data processing, feature extraction, and dimensionality reduction.

The indicators used to determine when the structure's behaviour lies within acceptable bounds are an important design aspect as well. Measurement deviation thresholds from nominal or predicted values can be defined based on structural requirements or similar criteria, depending on the particular needs of the structure. For dynamic responses, these thresholds can be defined around the modal characteristics of the structure, such as its natural frequencies, and modal / frequency response assurance criteria (e.g., MAC or FRAC), in line with established standards [3]. The applicability ranges of all integrated Machine Learning models shall be taken into account as well, in the definition of the acceptable ranges of the model's inputs.

The reliability and accuracy of the simulation are also critical for the SDT to be effective. To achieve enough understanding of the driving factors in the overall reliability of the system, and assess how it might affect its usability, a detailed analysis of error and uncertainty propagation is required along the whole data chain, from sensor measurements to the final comparison between the virtual and real assets, and through every step of the prediction path.

3. SOFTWARE ARCHITECTURE AND DATA LINKS

The type of software architecture to be used will determine the SDT System's effectiveness and how adaptable it is to future changes. Some crucial aspects to design for are:

Scalability: The twin should be robust against growth in complexity and size of the monitored physical system or systems. The data flows through the system should be managed efficiently, and the underlying software platform must scale up or down automatically. To achieve this, the system architecture must be modular, distributed, and event-driven.

Interoperability with different systems: It should be easy to interface with other systems, such as other digital twins (e.g., for thermoelastic applications where a thermal and a structural digital twin might need to interchange information), control systems (e.g., test control software), spacecraft platforms, etc. Modular architectures and standardised interfaces can provide this flexibility.

Real-Time Synchronisation: A digital twin must mirror its physical counterpart in real time. This means constantly receiving and processing data with minimal delay, a requirement known as low-latency digital coupling. In the case of an SDT, particularly one that is receiving data from orbit, and depending on the level of edge computing that has been implemented, this maximum latency interval is determined by the transfer rate of telemetry data.

Edge computing: Depending on the Application Case, a certain degree of edge computing might be required. As mentioned above, for in orbit applications and dynamic responses, the volume of time-series vibration data from sensor measurements is too big for a standard communications link, so the signal needs to be processed on board to reduce the amount of data transferred to ground; for instance, filtering noise, converting the time series signal to the frequency domain and extracting key magnitudes from the original high-density data. Other strategies like down-sampling or data compression can also be used to further reduce the size of the data packets. In the case of long-distance communications (e.g., extra planetary or deep space missions), lightweight machine learning and decision logic might also be needed on board to provide autonomous capabilities, as control from ground might be too slow or even impossible. On-board hardware architecture should be able to support these functions.

Data Analytics: The numerical and predictive models need to be seamlessly integrated in the data flow, ingesting inputs and providing outputs as required by the system.

Visualisation, post-processing and control: Visualisation and post-processing tools are crucial for the users to interact with the SDT and to extract insights from measurements and predictions. Healthy / unhealthy indicators need to be presented clearly and unequivocally, as well as alerts for

threshold breaches. It must also be possible for the user to control and configure the SDT flexibly for different scenarios as required.

Maintainability: The design of the SDT system must have a focus on software maintainability. Each modular component must be well sized, have appropriate code structure and be well documented. Logging should be implemented across all components such that a coherent picture of the data flow can be built after processing is completed. Standard frameworks and engineering approaches should be shared between the modular components where possible to reduce overall dependencies and complexity.

Cost-effectiveness: Whenever possible, the design of the SDT System should allow integration in current industrial processes with minimum intervention.

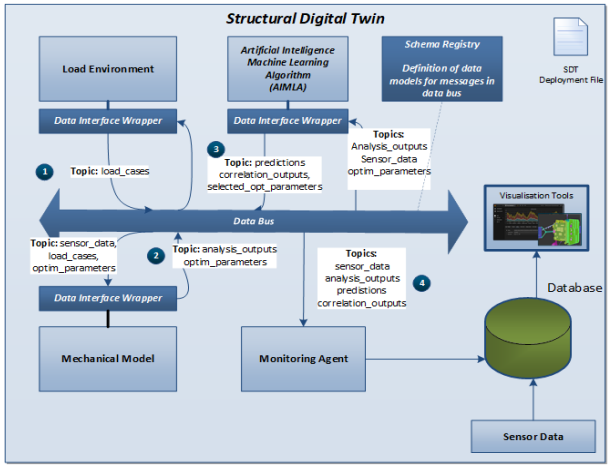


Figure 2: Example of SDT software architecture

4. MONITORING SYSTEM

To maintain a high-fidelity SDT of a spacecraft in orbit, the physical asset must be instrumented with a precise, real-time Monitoring System. The primary objective of this subsystem is to capture high-frequency dynamic responses, such as transient launch loads, pyrotechnic shocks, and low-amplitude micro-vibrations (1 Hz to 1 kHz), and feed this operational data back into the twin's predictive structural models. Implementing this closed-loop synchronization requires a paradigm shift from traditional, heavy telemetry systems toward distributed architectures and low mass sensing technologies.

4.1. Space-Qualified Data Acquisition Units (DAUs)

Traditional, centralized data handling topologies introduce large wiring harnesses that compromise spacecraft mass budgets and introduce electromagnetic interference (EMI). To satisfy the latency and high bandwidth demanded by an operational SDT, the DAU architecture must be designed around fully distributed processing core units.

De-centralized Signal Conditioning: Modern space-qualified DAUs utilize local, modular nodes situated in close physical proximity to the sensor clusters. Each input channel or localized cluster features integrated Digital Signal Processors (DSPs) or radiation-tolerant Field Programmable Gate Arrays (FPGAs). This allows the system to scale processing power linearly with instrument density

System-on-Chip (SoC) Integration: State-of-the-art DAUs leverage Radiation-Hardened-by-Design (RHBD) SoC and Radio-Frequency SoC (RFSoC) architectures. This type of integration minimizes analogic trace lines, reducing noise and latency. This delivers low noise floors capable of digitizing sub-micro-g accelerations at high sampling rates [4].

Wireless Subsystems: To bypass complex and heavy cable routing, modern platforms are shifting toward wireless internal telemetry nodes. Miniature, radiation-hardened wireless transceivers are placed on moving deployable structures (like solar arrays or reflector dishes) to broadcast dynamic response data directly to the central onboard data handling system [5].

Sensor Node Edge Intelligence: Advanced sensor nodes feature embedded micro-neural network accelerators. Instead of transmitting raw time-domain waveforms, the node computes Fast Fourier Transforms (FFTs) locally. [4].

4.2. In-Orbit Sensor Technologies

The sensing layer represents the nervous system of the Digital Twin. Capturing the full spectrum of structural dynamics requires a hybrid deployment of three mature, space-qualified sensor typologies:

Fiber Optic Sensing (FOS): Fiber Bragg Grating (FBG) sensors are rapidly replacing traditional strain gauges. A single, ultra-lightweight fibre optic strand can contain dozens of microscopic sensors etched into it. This allows the mapping of continuous, real-time dynamic responses and structural strains across large structures such as an entire telescope boom or solar array without adding heavy copper wiring. They are also immune to electromagnetic interference (EMI) [6].

Space-qualified IEPE Accelerometers: For wide-bandwidth shock and vibration capture (up to 10 kHz), Integrated Electronics Piezo-Electric (IEPE) sensors remain a cornerstone. These sensors maintain flat frequency responses across extreme cryogenic and high-thermal operational envelopes without encountering calibration drift, which make them able to feed the SDT with clear data during high-energy events like launcher separation.

High-Resolution Capacitive MEMS: Micro-Electro-Mechanical Systems (MEMS) have matured

to meet rigorous space qualification guidelines. Modern capacitive MEMS accelerometers achieve sub-micro-g resolutions while introducing negligible mass and power penalties. Their low profile allows them to be embedded directly inside instrument brackets --such as those housing optical payloads or sensitive cameras-- to provide localized micro-vibration data.

5. VVUQ AND SDT SYSTEM RELIABILITY

The hybrid model approach mentioned in §2 relies on a representative and accurate simulation as the first data source of the SDT. To achieve this level of credibility, a VVUQ process can be implemented following the steps described in [7].

In parallel, the reliability of the system as a whole also needs to be evaluated, with a detailed quantification of the accumulated error at the end of the data chain. Reliability is not treated as a single inherent property of the model. It is the degree to which a stated prediction can be relied upon for a *defined* use, within a *defined* operating domain, and with an explicitly understood consequence if the prediction is incorrect. This evaluation will provide the end user with a clear statement establishing the applicability and limits of the SDT System, as well as the accepted residual risk in the SDT outputs.

5.1. VVUQ Process

The Finite Element modelling assumptions are verified and uncertainties are quantified at each level of the assembly hierarchy, from single material properties through coupon and subsystem level (Figure 3), and these are incorporated into the final system-level analysis, which will be able to provide predictions with a high, and quantified, level of credibility. Additionally, the quantification of uncertainties will provide the range of normal variations expected from the structure's responses, and therefore a reference frame to detect if a given QoI is outside its normal operational range, which is very valuable information from an SHM point of view.

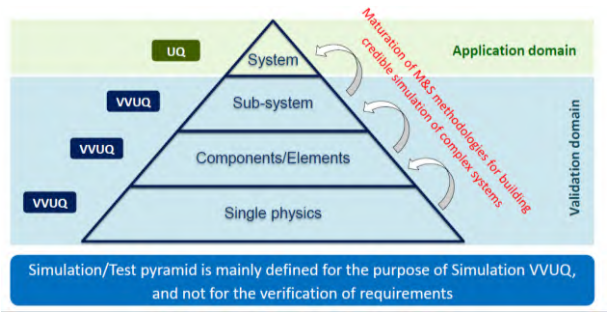


Figure 3: VVUQ pyramid

An initial sensitivity analysis of the whole structure, using a preliminary, not calibrated FEM, can provide an indication of the areas in the structure that have the greatest influence in the QoI and therefore need a detailed characterisation. This, along with engineering judgment, can guide the design of the coupon and subsystem tests (Figure 4) that need to be performed for VVUQ at every level of the pyramid.

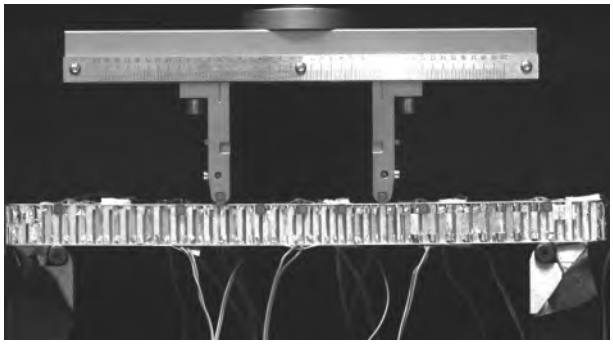


Figure 4: 4-point bending test of sandwich panel coupon

A dedicated FEM is created for each calibration test (Figure 5), and a VVUQ process is implemented using test and analysis data as follows:

1. Comprehensive listing of uncertainties and their expected ranges of variation and probability distributions.
2. Probabilistic sensitivity analysis, and random variables ranking/elimination.
3. Gathering of test data for all quantities of interest and measured probability distribution for each.
4. Verification of Finite Element Analysis (FEA) predictions against measured values of the quantities of interest (deterministic), therefore reducing model epistemic uncertainties and validating modelling assumptions.
5. Correlation of input variables to each individual test sequence and test specimen (experiment). A collection of correlated experiment simulations is obtained, each with its own correlated set of input variables.
6. Gathering of correlated data for all experiment simulations and generation of histograms/probability distributions for each input random variable and QoI.
7. Comparison with measured probability distributions for quantities of interest and validation of results.

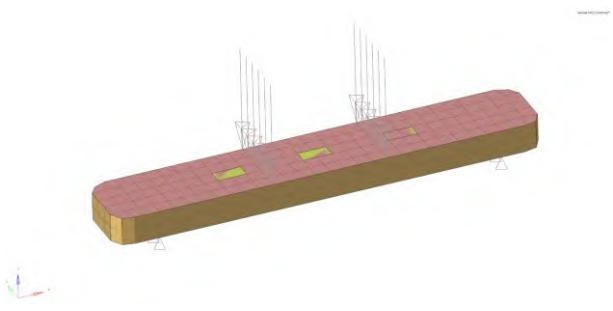


Figure 5: FEM representation of 4-point bending test of sandwich panel coupon

At the end of the process, the modelling assumptions are validated and probability distributions of both the QoI and the input parameters (modelling uncertainties) are obtained. These can be incorporated into the next level of the pyramid, and the process is then repeated. The final system FEM incorporates all the modelling assumptions validated through the lower levels, and the propagation of all the gathered uncertainties to the predicted QoI, through methods such as Monte Carlo, provides a nominal probabilistic baseline that accounts for both epistemic and aleatoric uncertainties.

5.2. SDT System Reliability

For an SDT, where uncertainty enters through sensing, data processing, physics-based modelling and machine-learning prediction, quantifying prediction reliability is essential to system performance and trustworthy decision-making. Reliability must therefore be assessed end-to-end for a defined use and operating domain, rather than treated as a single property of the numerical or machine-learning model. The uncertainty propagation chain is presented in Figure 6: physical structural response; sensor transduction; data acquisition and synchronisation; signal processing, compression and reconstruction; extraction of frequency-response functions or other quantities of interest; finite-element (FE) prediction; machine-learning surrogate prediction; comparison with measurements; and, finally, the health or acceptance decision.

Error sources enter at every stage. Measurement contributions include calibration, noise, drift, environmental sensitivity, sensor mounting, location and orientation, timing, digitisation and channel correlation. Processing introduces filter amplitude and phase distortion, windowing, spectral leakage, limited measurement duration and its effects on frequency resolution and compression or reconstruction error. The FE path adds uncertain material, geometry, joint, damping, load and boundary-condition parameters, together with discretisation, solver and residual model-form error. The surrogate adds approximation error, finite training-data coverage and sensitivity to out-of-domain inputs. These contributions are not generally independent: common calibration, environmental conditions, structural parameters and training data can correlate errors across sensors, frequencies and stages. Their importance is also application-dependent; a small local error may become significant near a resonance, modal node or decision threshold.

At the decision level, the propagated uncertainties should be expressed through the distribution of the decision margin, rather than applying a threshold only to the mean prediction: response, derived metric and decision margin. FE-to-reality discrepancy and surrogate-to-FE error are quantified separately, using independent physical validation data and held-out simulation cases, respectively. Reliability is therefore determined by how confidently the SDT distinguishes acceptable from anomalous behaviour within its validated operating domain. Any change to sensing, processing, FE assumptions, surrogate training or decision thresholds requires an impact assessment and proportionate revalidation.

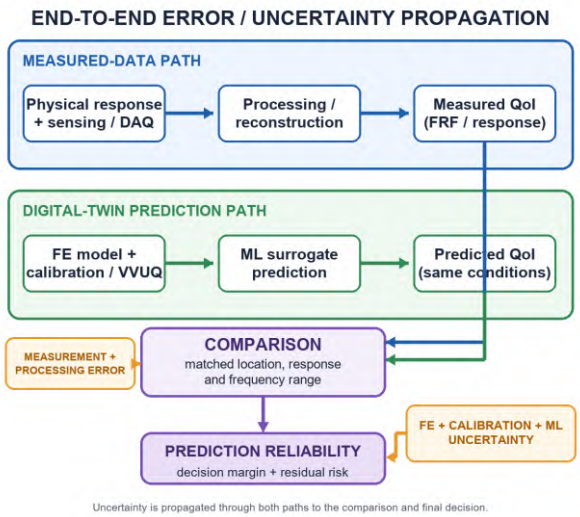


Figure 6: Simplified end-to-end error propagation through the measured-data and digital-twin prediction paths

The proposed end-to-end structure provides the traceability required for the SDT application: each credibility statement can be linked backwards from the decision to the metric, prediction, FE and ML evidence, processing transformation and physical measurement source that supports it

6. MACHINE LEARNING AND IUQ

Machine learning is used in the SDT to produce structural response predictions. In the case of a data-driven approach, the model learns the relationship between sensor readings and other operational parameters. For a simulation-driven approach, on the other hand, the machine learning model is used to replace repeated full-system FEM calculations once a representative simulation dataset is available. The machine learning model does not replace the physical description of the structure; instead, it learns the relationship established by the FEM between uncertain structural properties, spatial location and frequency-domain response. This hybrid arrangement retains the physical basis of the simulation while reducing the cost of repeated prediction, probabilistic analysis and calibration.

This section describes how different machine learning models can be combined to achieve a probabilistic prediction of structural dynamic responses, as well as self-correlation capabilities

through IUQ, based on the implementation of a simulation-driven approach that has been used in the Spacecraft Structural Digital Twin (SSDT) project, a collaboration between Airbus Defence and Space (ADS) and Imperial College London (ICL), sponsored by ESA as part of the General Support Technology Programme (GSTP).

6.1. Machine-Learning Forward Model

Separate forward models are used for the different load environments and response quantities because their response definitions and operating ranges are different. In each model, physically meaningful structural properties are provided directly as inputs, together with the spatial locations at which a prediction is required. This links the surrogate prediction to the parameterisation of the underlying FEM. During calibration, the trained network and its response definition remain fixed. Only the physical input parameters are updated within predefined admissible ranges. Calibration is therefore constrained to the FEM parameter space rather than applied as an unconstrained correction to the output. The end result is a surrogate model that can provide full-field responses in a wide range of combinations of different structural inputs, for different response types (e.g., strains and accelerations).

The implemented architecture follows a Deep Operator Network (DeepONet) arrangement. A branch network represents the structural parameters, a trunk network represents the requested coordinates, and a convolutional decoder reconstructs the frequency spectrum. The same compact model family is used across the different scenarios, with a separate trained model for each load environment and response definition.

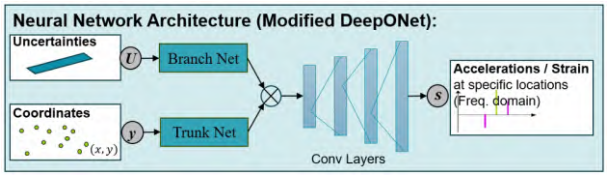


Figure 7: Implemented machine learning architecture

In the application example, training data were generated from FEM simulations covering the defined structural uncertainty range. Held-out validation confirmed reproduction of the resonance locations and response amplitudes across the supported parameter, coordinate and frequency domain. When an updated and validated FEM becomes available, the same workflow can be used to retrain or fine-tune the forward models.

6.2. Probabilistic Prediction

The deterministic models were extended to propagate uncertain structural inputs. A joint distribution is defined for the structural parameters, and parameter realisations are sampled and passed through the trained SDT model. The resulting ensemble provides a response distribution at every requested coordinate, response channel and frequency. It can be summarised using the mean, standard deviation and selected percentiles, producing probabilistic frequency-response functions at selected locations or probabilistic spatial response fields (Figure 8).

The probabilistic calculation uses the same interface and checkpoints as the deterministic prediction. Known dependencies between structural parameters are retained through joint sampling, and the samples are kept within the range represented by the FEM training data. The spread of the response ensemble represents propagated structural-input uncertainty. It is treated separately from the approximation error of the machine-learning model and from the sensor and modelling errors considered in the wider VVUQ assessment.

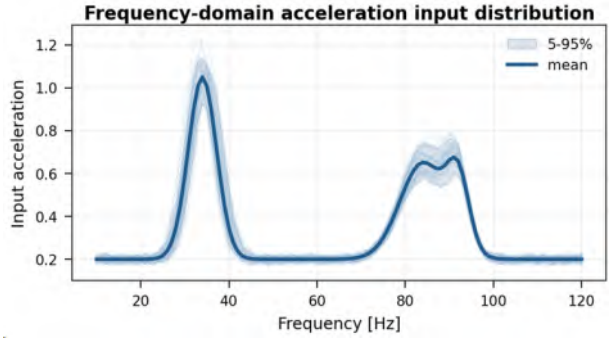


Figure 8: Probabilistic prediction

6.3. Inverse Uncertainty Quantification and Calibration

Inverse Uncertainty Quantification (IUQ) estimates uncertain structural parameters by minimising the discrepancy between predicted and measured or synthetic target responses. The forward surrogate reduces the computational cost by replacing repeated full-FEM evaluations during calibration. A controlled study with three sensitivity parameters demonstrated recovery of the imposed parameter changes under added response noise.

Physical parameter estimates are not necessarily identifiable from response data alone. Material, stiffness, damping, thickness and mass parameters can have correlated effects on the measured responses. Consequently, distinct parameter combinations may produce equivalent outputs, and output-level agreement does not establish unique parameter recovery. The calibrated vector is therefore interpreted as an effective parameter set for correcting the SDT response. Additional independent measurements, load cases or physical constraints are required for stronger parameter identification.

The implemented machine-learning and IUQ workflow therefore support two complementary SDT functions. Probabilistic forward prediction quantifies

how the structural uncertainty envelope affects the response, while calibration aligns the predicted output with measured behaviour. Both functions retain the same acceleration, strain and spatial-output definitions as the deterministic SDT model.

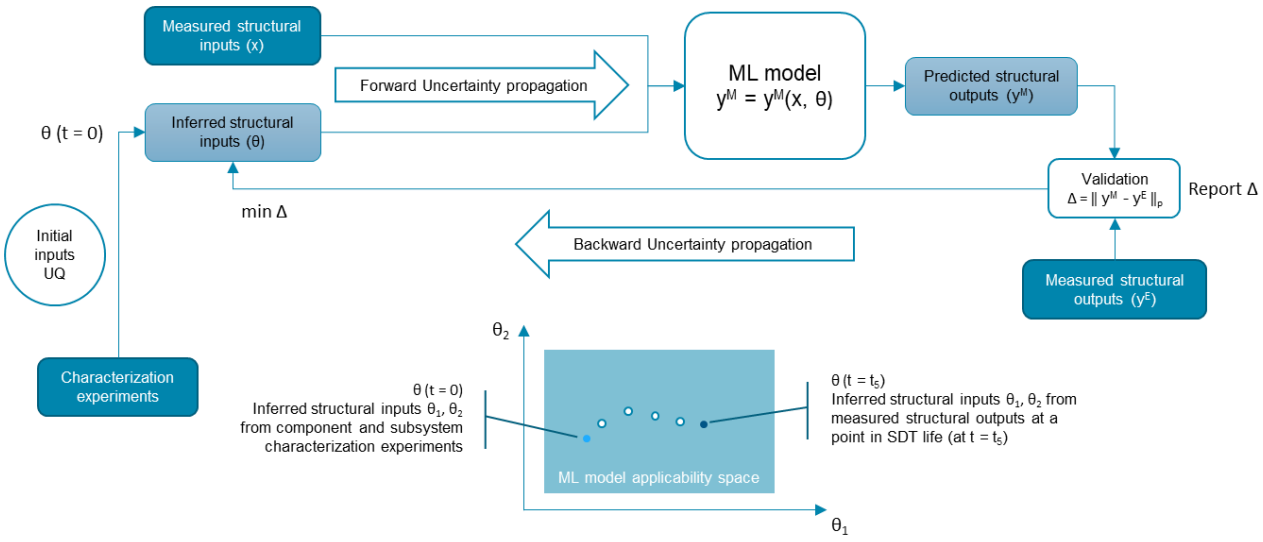


Figure 9: SDT data flow, uncertainty propagation and self-correlation logic. Dark blue boxes show measured data from sensors or experiments, light blue boxes represent calculated or predicted data.

7. SUMMARY

The design of a Structural Digital Twin (SDT) for Structural Health Monitoring applications must be approached as a holistic, lifecycle-long process. To achieve the credibility and reliability required for actionable engineering insights, the entire data chain must be considered. This spans continuous data acquisition from deployed sensors, robust and flexible software/hardware infrastructures, and automated anomaly detection to inform operational decisions.

Crucially, the system architecture must define explicit synchronization frequencies between the physical and virtual entities, account for latency and bandwidth limitations over ground-to-orbit data links, accommodate human-in-the-loop operational feedback, and adapt dynamically to the long-term, irreversible degradation of the changing asset.

The core predictive engine can be tailored based on the specific functionalities required. While data-driven approaches are simpler in terms of development and verification, integrating a physics-based simulation model provides a deeper mechanical understanding of structural behaviour. The added complexity of a simulation-driven twin, which necessitates a rigorous Verification, Validation, and Uncertainty Quantification (VVUQ) process, is greatly compensated by its utility. It delivers a quantified measure of prediction reliability, defines precise operational boundaries, and tracks structural evolution over time, rendering it a dependable tool for proactive lifecycle management.

8. REFERENCES

1. X. Wua, T. Kozlowski, H. Meidani and K. Shirvan, "*Inverse Uncertainty Quantification using the Modular Bayesian Approach based on Gaussian Process, Part 1: Theory*," 2018.

2. A. V. Oppenheim, R. W. Schafer and J. R. Buck, *Discrete-time Signal Processing*, Upper Saddle River, N.J.: Prentice Hall, 1999.

3. ESA-ESTEC, ECSS-E-ST-32-11C – *Modal survey assessment*, ECSS, 31 July 2008.

4. NASA, "*State-of-the-Art of Small Spacecraft Technology, 8.0 Small Spacecraft Avionics*," 2026. [Online]. Available: https://www.nasa.gov/smallsat-institute/sst-soa/small-spacecraft-avionics/.

5. A. G. Corporation, "*Customizable InterSystem Wireless Data/Energy Transfer (CUSTOS-WiT) System*," 2021. [Online]. Available: https://techport.nasa.gov/projects/102616.

6. T. Colicci, A. Noonan and A. Anilkuma, "*Structural Health Monitoring for Launch Vehicle Reusability Using Fiber Bragg Grating Written Optical Fiber*," AIAA, Orlando, FL, 2025.

7. G. Poort and J. Fatemi, *How to Build Credible Simulations for Development and Qualification of Composite Space Structures*, Airbus.

ECSSMET
Braunschweig Germany 2026

Stucture optimaziation

ECSS-COMPLIANT INSERT ANALYSIS AND OPTIMIZATION: AN AUTOMATED SOFTWARE APPROACH

Abdullah Emre Aksoy [1], Hasan Akçe [2], Atayıl Koyuncu [3]

[1] *Turkish Aerospace Industries, Ankara, Turkiye. Email: abdullahemre.aksoy2@tai.com.tr*
[2] *Turkish Aerospace Industries, Ankara, Turkiye. Email: hasan.akce@tai.com.tr*
[3] *Turkish Aerospace Industries, Ankara, Turkiye. Email: atayil.koyuncu@tai.com.tr*

KEYWORDS

Satellite Structural Analysis, Honeycomb Sandwich Panels, Inserts, Structural Optimization, Design Automation, Software Tool

ABSTRACT

Insert verification in satellite honeycomb sandwich panels is critical but highly repetitive: manual transfer between finite element solvers and spreadsheet calculations creates bottlenecks, human error and over-conservative insert selections. The presented framework establishes a fully digital pipeline from MSC/NX Nastran output to ECSS-E-HB-32-22A compliant Margin of Safety evaluation and deterministic insert optimization. Four isolated layers parse model and result files, map finite element nodes to physical inserts, envelope quasi-static, sinusoidal and thermo-elastic load cases, and evaluate the applicable analytical verifications; edge and group-interaction distances come from the mesh itself. The optimization module avoids stochastic methods incompatible with qualification traceability, operates in two user-selectable modes and, because capacity scales with insert size, removes installed mass wherever it removes unjustified margin. Overall, the framework enables rapid, traceable, and systematic insert verification and optimization, reducing manual engineering effort while supporting the identification of non-compliant and over-designed configurations.

1. INTRODUCTION

Structural verification of inserts in satellite honeycomb sandwich panels is among the most repetitive tasks in spacecraft structural analysis. After each MSC/NX Nastran solution, nodal forces must be extracted at hundreds of insert locations, transferred manually into spreadsheet-based calculation tools, and compared across load cases to identify the sizing condition; the entire sequence is then repeated at every design iteration. For a single equipment panel, this workflow can consume several days of engineering effort, devoted almost entirely to data handling rather than to engineering assessment.

The scale of the task is inherent to the design concept. Inserts bonded into honeycomb sandwich panels are the standard load-introduction elements of satellite structures, and a single satellite carries hundreds to thousands of them. Global finite element (FE) models idealize each insert as a single node or rigid element and therefore cannot resolve the local failure behaviour of the insert region; industry practice consequently verifies every insert analytically against the ECSS-E-HB-32-22A insert design handbook [1], within the structural verification framework of ECSS-E-ST-32-10C [2]. The analytical methods themselves are well established [3, 4]; the difficulty lies in applying them correctly and consistently at the scale of a complete spacecraft.

Beyond the effort it consumes, the manual process is error-prone in both directions. A transcription error or an overlooked load case can allow a non-compliant insert, one with a negative Margin of Safety (MoS), to remain undetected until late review or test stages. Conversely, the effort required to assess each location individually promotes uniform, conservative insert selections, leaving the majority of locations systematically over-designed with margins far above any rational target; MoS values of up to approximately 63 were observed on the industrial panel presented in Section 6. Both outcomes originate from the same limitation: the verification loop is too slow to be closed rigorously within project timescales.

This paper presents a software framework that removes this limitation by establishing a fully digital pipeline from raw MSC/NX Nastran files to a documented MoS for every insert on a panel, obtained in less than one minute. The framework parses model (.bdf) and result (.pch) files, correlates CBUSH element results with physical insert locations, maps the recovered CBUSH force components to the out-of-plane and in-plane loading directions defined for each insert type, and envelopes quasi-static, sinusoidal and thermo-elastic load cases. Edge and group-interaction distances are extracted automatically from the FE mesh, the analytical failure checks of ECSS-E-HB-32-22A are evaluated for every insert, and a deterministic MoS-driven optimization module re-selects or re-sizes each insert in one of two user-selectable modes: a scan of the insert catalogue, or analytical generation of a new insert geometry. Results are compiled into automated reports, including a colour-coded three-dimensional margin

visualization of the complete panel.

The main contributions of this paper are:

1. end-to-end automation of ECSS-E-HB-32-22A insert verification directly from native MSC/NX Nastran files, eliminating manual data transfer entirely;
2. automatic recovery of the geometric context required by each verification (local load frames, edge distances and group-interaction distances) from the FE model itself;
3. a deterministic MoS-driven optimization scheme that eliminates both negative margins and excessive over-design, converging the margins of a complete panel to a consistent, rational band;
4. an industrial demonstration on a 249-insert equipment panel of a geostationary (GEO) communication satellite, where the framework identified previously undetected negative-margin inserts and systematically reduced excessive design margins through deterministic optimization.

The remainder of the paper is organized as follows: Section 2 describes the software architecture and automated data pipeline, Section 3 the ECSS-based margin evaluation, Section 4 the optimization strategy, Section 5 verification and validation of the tool, and Section 6 the industrial application; Sections 7 and 8 close with lessons learned, limitations and conclusions.

2. SOFTWARE ARCHITECTURE AND AUTOMATED DATA PIPELINE

The framework is implemented in Python as a modular desktop application following object-oriented and Model–View–Controller design principles. Its purpose is to realize, without manual intervention, the complete chain from native MSC/NX Nastran files to a documented MoS for every insert on a panel. This section describes the architecture and the successive stages of the automated data pipeline; the end-to-end flow is summarized in Fig. 1.

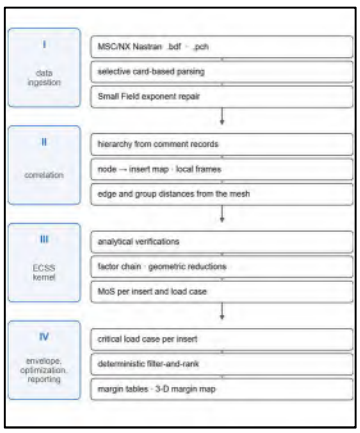


Figure 1: End-to-end data pipeline of the framework, from native MSC/NX Nastran input files to automated MoS reporting.

2.1 Layered architecture overview

The software is organized into four functionally isolated layers: (i) data ingestion, comprising input validation and the selective parsing of model and result files; (ii) CBUSH correlation and insert-specific load-component mapping, which links CBUSH element results to physical inserts and assigns the recovered force components to the corresponding out-of-plane and in-plane loading directions; (iii) the ECSS computational kernel, which evaluates the analytical failure checks of ECSS-E-HB-32-22A for every insert and load case; and (iv) envelope analysis, optimization and automated reporting. Each layer consumes only the validated output of its predecessor; a failure at any stage halts the process with corrective feedback before analytical processing begins.

A central data manager acts as the single source of truth: it holds the parsed model and result tables, the analysis parameters and the computed margins, and all interface modules read from and write to this synchronized state. The computational kernel is strictly isolated from the PyQt5-based graphical interface, so that it can be regression-tested against reference cases without any user interface present and the analytical methods can be exchanged without modification of the surrounding application. The supporting technology stack is summarized in Tab. 1.

Table 1: Technology stack of the framework.

Library	Role
Python	Core implementation language of all layers
PyQt5	Graphical interface with signal–slot event handling
NumPy / Pandas	Vectorized numerical processing and tabular filtering/merging of model and result data
PyVista / VTK	GPU-accelerated three-dimensional visualization of the panel model and colour-coded margins
Matplotlib / Plotly	Static publication-quality and interactive result plots
ReportLab	Automated generation of PDF reports in the corporate documentation format

2.2 Selective parsing of model and result files

Satellite-level finite element models comprise hundreds of thousands of nodes, and the corresponding files contain millions of text lines. Since insert verification requires only a small subset of card types, the ingestion layer performs a selective, card-based extraction. From the bulk data file (.bdf), only GRID, RBE2, CBUSH, CQUAD4/CTRIA3, CORD2R/CORD2C and $HMNAME cards are read; from the punch file (.pch), the force tables are extracted for all subcases, including the thermo-elastic ones.

Complete industrial models are thereby ingested within seconds. Fig. 2 shows the import stage, at which the model file and the result file of each load case are registered individually, together with the factor set later applied to that case.



Figure 2: Import interface. The model file and the result file of each load case are registered separately, and the qualification, model, project, local-design, thermal-degradation and factor-of-safety values are attached to each result file individually.

Beyond geometry and connectivity, the parser recovers engineering metadata from the $HMNAME component naming convention exported by the pre-processor: regular-expression matching of the component names links each insert component to its element set, its host panel and the associated local coordinate system, and forms the semantic basis of the correlation step described in Section 2.4.

A further robustness measure addresses the MSC/NX Nastran Small Field format, in which numerical values are constrained to fixed eight-character columns. To respect this width, the exponent character is dropped, so that a value such as -1.234E-5 is written as '-1.234-5'. Standard floating-point conversion fails on this representation, and silently discarding such entries would corrupt the recovered load set. The parser therefore applies a regular-expression correction layer that detects the anomalous pattern, reinserts the exponent character and converts the result to double precision.

2.3 Recovering the model hierarchy from the pre-processor comment records

A bulk data file describes grids and elements, but it does not state which insert belongs to which panel, nor which catalogue item each fastener element represents. In production models that information exists only in the comment records written by the pre-processor, and the framework reconstructs the entire analysis hierarchy from them.

Two record types carry it, and the reconstruction is summarized in Fig. 3. Named-component records associate a component identifier with a component name. Component-context records open a component block, so that every element card following such a record belongs to the component it names. Reading the file sequentially while tracking the currently open component therefore attributes each fastener element to its component without any geometric search. For each such element the framework retains the element identifier and its first grid, which is the point at which load is introduced into the panel and hence the location at which the insert is verified.

The component name is itself structured: it is a delimited string whose fields identify the item, and one field carries the insert type designation used to retrieve the allowables from the insert catalogue. Parsing that field replaces the manual assignment of an insert type to each location, which in the conventional workflow is transcribed by hand from the drawing.

The panel owning an insert is recovered from the same convention rather than from geometry. The name of the component owning a fastener element is reduced to a short key (its leading characters, with the single position that distinguishes a child item from its parent removed) and every component whose name begins with that key is collected as a related item. Within that set the shortest name is the panel itself, because the convention makes the panel name a prefix of the names of everything mounted on it. The result is a panel-to-insert classification covering the whole model, and it is what allows the geometric evaluations of Section 2.6 to be confined to a single panel: without it, an insert near a panel joint would be measured against a structure to which it is not attached.

Two further behaviours are driven by the same names. Components whose names contain analyst-specified substrings are excluded from the analysis, which is how non-structural or separately qualified items are kept out of the result set. And where the convention marks a location as a double insert (a single attachment introducing its load through two fastener elements), the recovered force components of the group are summed in absolute value rather than vectorially, so that opposing signs cannot cancel and understate the load. One catalogue category that shares the naming pattern but behaves as a single insert is explicitly exempted from this treatment.

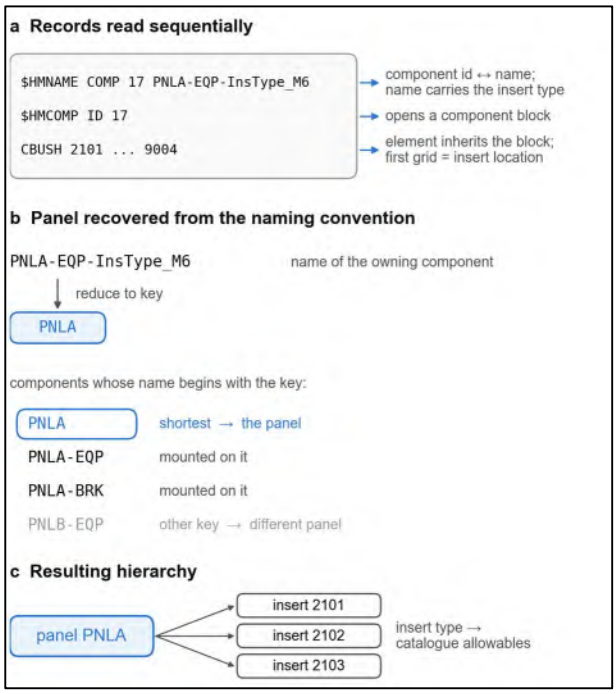


Figure 3: Recovery of the analysis hierarchy from the pre-processor comment records: sequential attribution of elements to components, derivation of the panel key from the component name, and the resulting panel-to-insert classification.

2.4 CBUSH correlation and insert-specific load-component mapping

The parsed model and result data are correlated directly through the CBUSH element identifiers. During BDF processing, each CBUSH element is associated with the component in which it is defined, and the corresponding component metadata are used to recover the insert type. The punch-file parser independently extracts the three force components reported for each CBUSH element and subcase. Since the CBUSH element identifier is retained in both the model and result data, the structural results can be assigned directly to the corresponding physical insert without an additional geometric or node-based search.

The orientation of each CBUSH element is already defined in the finite element model through its local directions. Therefore, the software does not perform an additional global-to-local transformation of the recovered force vector. Instead, the three local CBUSH force components are interpreted according to the physical loading directions of the associated insert type. For each insert type in the catalogue, the database specifies which of the CBUSH local directions 1, 2 and 3 corresponds to the out-of-plane direction and which two correspond to the first and second in-plane directions. The recovered force components are then reordered according to this assignment before being passed to the analytical verification. For example, for one insert type, CBUSH local directions 1, 2 and 3 may represent the out-of-plane, first in-plane and second in-plane loading directions, respectively. For another insert type, the out-of-plane load may instead be associated with local direction 3, while the in-plane loads are taken from local directions 1 and 2. The software applies this direction assignment automatically according to the selected insert type and handles all possible direction combinations consistently within the same mapping logic.

The separation between the recovered CBUSH force components and their physical interpretation is also used during insert-type changes. When the insert type assigned to a location is modified, the software first preserves the underlying three CBUSH force components and then remaps them according to the out-of-plane and in-plane direction definitions of the newly selected insert type. The corresponding catalogue allowables are updated at the same time, after which the Margin of Safety is recalculated. In this way, different insert configurations or orientations can be evaluated consistently while preserving the fundamental CBUSH force state recovered from the finite element solution.

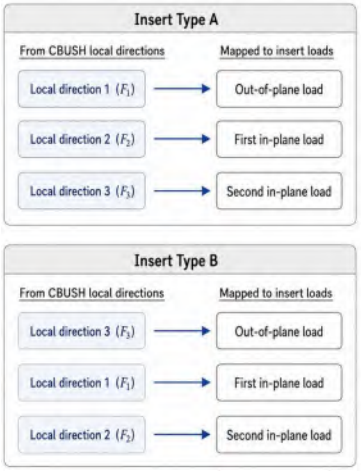


Figure 4: Insert-specific mapping of the three CBUSH local force components to the physical out-of-plane and two in-plane loading directions.

2.5 Load envelope analysis

Insert verification must consider the complete set of dimensioning load cases (quasi-static, sinusoidal excitations in the X, Y and Z directions, and thermo-elastic cases) which in a representative satellite project number in the hundreds. The framework evaluates the ECSS margin computation for every insert under every case and designates, per insert, the case yielding the minimum MoS as the critical load case. The result table is thereby condensed from hundreds of rows per insert to a single governing row, eliminating the manual cross-comparison of load cases.

An important consequence of enveloping over the full case set is that thermo-elastic conditions can govern over launch loads. In a representative example, an insert exhibits a margin of MoS = 0.45 in its governing launch case but MoS = 0.12 in the cold thermo-elastic case; the framework accordingly

reports the thermal case as critical, as shown in Fig. 5. A workflow restricted to mechanical launch cases would document a margin nearly four times larger than the true minimum.

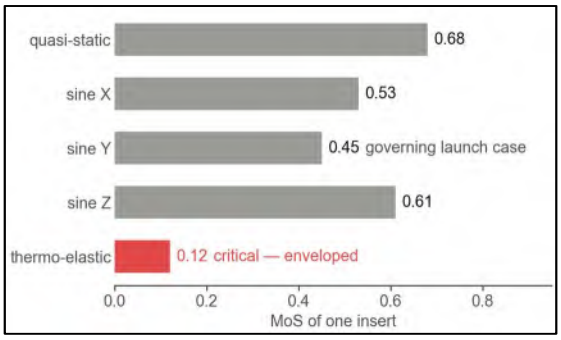


Figure 5: Load-case envelope of a single insert. The minimum margin over all cases defines the critical load case, here a thermo-elastic condition rather than a launch case. Representative values.

2.6 Automatic extraction of edge and group-interaction distances

The analytical failure checks of ECSS-E-HB-32-22A depend not only on loads but also on geometric context, in particular the distance of an insert to the nearest panel free edge and the distances to neighbouring inserts, which enter the edge-influence and group-interaction reduction factors introduced in Section 3. In current industrial practice these distances are measured manually in the pre-processor; the framework instead derives them from the finite element mesh topology, as illustrated in Fig. 6.

The edge distance is obtained from a purely topological property of the shell mesh that represents the panel skins. A grid in the interior of a meshed surface is shared by all the elements surrounding it, whereas a grid on a boundary is referenced by only a few. Counting, for every grid of the model, how many shell elements reference it and retaining those referenced by no more than two therefore identifies the boundary of the meshed surface in a single pass. This one criterion captures both the outer contour of the panel and the rim of every cut-out inside it, and requires no geometric interpretation of the model.

Applied directly, the criterion returns the wrong answer for the insert itself. An insert is modelled in a hole, the rim of that hole is a boundary, and the nearest boundary grid to any insert would therefore be its own hole, collapsing every edge distance to the insert radius. The framework consequently discards boundary grids lying closer to the insert than a fixed fraction of its diameter, which removes the insert's own rim while leaving genuine panel edges and neighbouring cut-outs in the candidate set. The search is further confined to the panel that owns the insert, using the classification of Section 2.3, so that an insert is never measured against the edge of an adjacent panel across a joint. The distances from the insert to all surviving boundary grids of its own panel are then evaluated as a single vectorized distance matrix and the minimum is retained. Where no boundary grid survives the filter, the location is treated as remote from any edge and no reduction is applied.

The group-interaction distance is obtained panel by panel from the same classification. For each panel the full pairwise distance matrix between its inserts is formed, self-distances are suppressed, and each row is ordered so that the nearest and the second-nearest insert are recovered together with their distances. Both are retained deliberately: the handbook treats the reduction caused by one adjacent insert differently from that caused by two, and the two contributions are combined rather than the nearest neighbour alone being used.

Both distances are then non-dimensionalized by the effective potting width, which the framework derives from the insert radius and the core cell size and which differs according to whether guaranteed-minimum or typical capacities are being computed and whether the core is perforated. Above the handbook thresholds, an edge distance of some five times the effective potting width, or a neighbour distance of some ten times, the corresponding factor is unity and no penalty applies; below them the handbook reduction relations are evaluated, with the group factor additionally floored so that a dense cluster cannot drive the capacity arbitrarily low. Edge and group factors are applied together to every allowable of the location, so that an insert which is both close to an edge and closely spaced accumulates both reductions. Insert categories qualified specifically for installation at a panel edge, whose catalogue allowables already reflect that condition, bypass the edge reduction. The complete evaluation runs for all inserts of a panel in a single pass, removing manual geometric measurement from the verification loop.

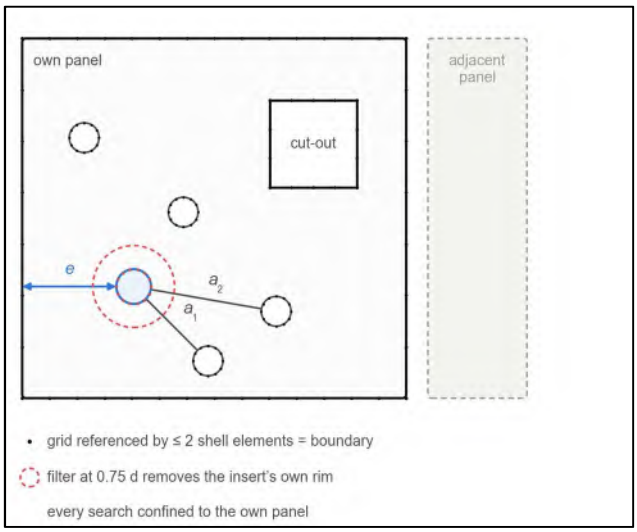


Figure 6: Automatic extraction of the critical edge distance by topological boundary detection and of the group-interaction distance by panel-confined neighbour search.

3. ECSS-BASED MARGIN OF SAFETY EVALUATION

For every insert and every load case delivered by the automated pipeline, the computational kernel evaluates the applicable insert strength verifications using the loads expressed in the local insert coordinate system. The allowable capacities are determined according to the ECSS-based analytical formulation and are subsequently modified by the applicable safety, uncertainty and geometric reduction factors. The Margin of Safety (MoS) is then evaluated for each load case, and the minimum value over the complete load-case set is retained as the governing margin of the insert.

3.1 Combined-load Margin of Safety formulation

Insert verification is generally governed by a combination of out-of-plane and in-plane loading rather than by a single load component. The framework therefore evaluates the Margin of Safety from the quadratic interaction of the normalized load components. To simplify the notation, the factors applied to the recovered insert loads are grouped as

$$\mathrm{K_L} = \mathrm{K_Q}\,\mathrm{K_p}\,\mathrm{K_m}\,\mathrm{K_{LD}}\,\mathrm{FOS_U} \tag{1}$$

For edge and border inserts, the interaction index is evaluated from the out-of-plane load P and the two orthogonal in-plane components Q1 and Q2:

$$I = \left(\frac{K_L P}{P_{\mathrm{allow}}}\right)^2 + \left(\frac{K_L Q_1}{Q_{1,\mathrm{allow}}}\right)^2 + \left(\frac{K_L Q_2}{Q_{2,\mathrm{allow}}}\right)^2 \tag{2}$$

where P denotes the out-of-plane insert load and Q1 and Q2 are the two in-plane load components in the local insert coordinate system. The corresponding Margin of Safety is

$$MoS = \frac{1}{\sqrt{I}} - 1 \tag{3}$$

Accordingly, MoS=0 defines the compliance boundary, while positive and negative values indicate compliant and non-compliant configurations, respectively. For protruding U-type inserts, for which a single in-plane resultant is considered, the interaction index reduces to

$$I = \left(\frac{K_L P}{P_{\mathrm{allow}}}\right)^2 + \left(\frac{K_L Q}{Q_{\mathrm{allow}}}\right)^2 \tag{4}$$

and the Margin of Safety is again obtained from Eq. (3). The allowable quantities in Eqs. (2) and (4) denote the capacities applicable to the insert configuration under consideration. Where required, these capacities include the edge-influence and group-interaction reductions described later in this section. The formulation is evaluated independently for every load case, and the lowest resulting MoS is retained as the governing value for the insert.

3.2 Safety, uncertainty and capacity corrections

The quantities entering the Margin of Safety calculation are modified by a set of project-specific safety parameters and ECSS-based capacity corrections. Since these quantities act at different stages of the verification, the computational kernel distinguishes between factors applied to the recovered insert loads and corrections introduced during the determination of the corresponding allowable capacities.

The load-side factors are represented by the combined factor K_L introduced in Section 3.1. Their values are supplied as analysis inputs and are applied consistently to the recovered local insert loads before normalization by the corresponding allowable capacities. This implementation allows project-specific factor sets to be used without modification of the analytical routines.

On the capacity side, the analytical formulation incorporates the corrections required to represent the local behaviour of the insert region. A model-correlation factor is applied where required to relate the analytical capacity to the test basis underlying the handbook. Effective core properties are used in the capacity calculations where the corresponding manufacturer values do not directly represent the behaviour observed in insert applications. Temperature-dependent degradation is likewise applied to the allowable capacities where required by the material definition and mission temperature range.

The principal safety parameters and capacity corrections implemented in the framework are summarized in Tab. 2. All quantities are maintained as configurable analysis inputs so that different project, material and capacity definitions can be evaluated using the same computational kernel.

Table 2: Safety parameters and capacity corrections used in the insert verification.

Quantity	Role	Value or treatment
Combined load factor, KL	Scales the recovered local insert loads before the interaction calculation	Project-defined factor set
Model correlation factor, RC	Correlates the analytical capacity with the underlying test basis	0.91 for guaranteed-minimum / 1.0 for typical; geometry-dependent for perforated aluminium cores
Thermal degradation factor	Reduces allowable capacities at mission temperature extremes	0.90–0.95, material and mission dependent

3.3 Capacity data and geometric reductions

The allowable capacities used in the Margin of Safety evaluation are obtained from the insert catalogue implemented within the framework.

Depending on the selected capacity basis, guaranteed-minimum or typical values are used consistently throughout the analysis.

The isolated-insert capacities are then corrected for the local geometric environment using the edge-influence and group-interaction factors defined in ECSS-E-HB-32-22A. The required edge and neighbouring-insert distances are extracted automatically from the finite element model as described in Section 2.6. When the corresponding handbook spacing criteria are exceeded, the reduction factor is unity; otherwise, the applicable reduction relation is evaluated.

The resulting isolated and reduced capacities, together with the corresponding edge and group factors, are presented to the analyst as illustrated in Fig. 7. These reduced capacities are subsequently used in the combined-load Margin of Safety calculation of Section 3.1.

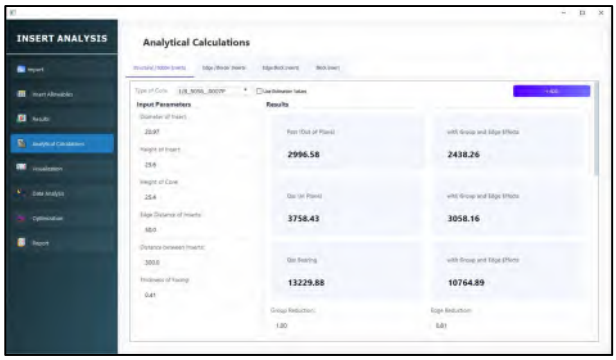


Figure 7: Analytical calculation interface. For a given insert and core the admissible loads are reported both as single-insert capacities and after the group and edge reduction factors, with the two reduction values displayed alongside the capacities they scale.

Every quantity entering a margin (recovered load, transformed load component, applied factor, catalogue allowable and geometric reduction) is retained and printed in the automated report. This traceability makes the deterministic optimization of Section 4 auditable: each re-sized insert is justified by the same documented chain that produced its margin.

4. DETERMINISTIC MOS-DRIVEN INSERT OPTIMIZATION

Because the evaluation of Section 3 resolves every insert of a panel within seconds, the configuration installed at each location becomes a tractable design variable rather than a fixed assumption assessed once. The objective of the optimization module is the correction of the margin population of the panel. Two deviations are treated as equally undesirable: negative and excessive margins. The module removes both, replacing non-compliant configurations and reducing unjustified margins to the least excess the analytical verification admits.

4.1 Design rationale: determinism for space qualification

Metaheuristic search methods and neural-network surrogates offer an alternative route to problems of this type; they were deliberately excluded. Space qualification requires reproducibility and auditability: identical inputs must yield identical outputs on every execution, and every proposed configuration must be traceable to the analytical verification that justifies it. A stochastic search satisfies neither condition, and a surrogate interposes a regression layer between the handbook method and the reported margin, so that the delivered configuration is no longer defensible by direct reference to ECSS-E-HB-32-22A. The module therefore implements an exhaustive, deterministic filter-and-rank search over an explicitly enumerated design space, in which every candidate is evaluated by the same computational kernel used for verification and the full candidate list, its margins and each elimination reason are exposed to the analyst.

4.2 Constraint set and objective

Constraints are enforced as hard filters rather than as penalty terms. A penalty formulation tolerates a small violation offset by a gain in the objective, which is admissible for a continuous engineering trade but not for a certification criterion: a negative margin is a binary reject condition and cannot be compensated. Candidates violating any constraint are therefore removed before the objective function is evaluated, and no penalty coefficients enter the formulation. Four constraint functions are applied, summarized in Tab. 3.

Table 3: Hard constraints applied to every candidate configuration.

Constraint	Description	Source
g1	Positive governing MoS under the critical load case, with the project factor set of Tab. 2	Analytical verifications of ECSS-E-HB-32-22A
g2	Geometric compatibility of insert height with the panel build-up, $h_{insert} \le h_{core} + 2 \cdot t_{face}$, reducing to equality for bobbin inserts	Panel definition
g3	Minimum edge distance, $e_{min} \ge 1.5 \cdot d_{insert}$; an installation screen applied in addition to, not instead of, the continuous edge-influence reduction of Section 3.3	Design rule adopted in the framework
g4	Admissibility of insert type and configuration at the location, such as a blind-type installation imposed by accessibility	Project design requirement

Let D denote the design space of admissible

configurations at a given insert location, and let S_valid⊆D denote the subset satisfying all constraints g1,…,g4. For a candidate configuration x, the governing Margin of Safety, MoS_gov(x), is defined as the minimum MoS over the load cases selected by the analyst for optimization. Since the feasibility condition g1 requires a non-negative governing margin, only compliant candidates are included in S_valid. The selected configuration is therefore

$$x^* = \arg\min\{ MoS_{\text{gov}}(x) \mid x \in S_{\text{valid}} \} \qquad (5)$$

Thus, among all feasible configurations, the optimization selects the candidate with the governing margin closest to the compliance boundary. Compliance is a binary admission criterion and is never traded against the ranking: a candidate with a single negative margin is discarded irrespective of how favourable its remaining margins are, while among the survivors the configuration closest to the compliance boundary is returned rather than the first compliant candidate encountered. Because the admissible capacity of an insert increases monotonically with its diameter, its height and the extent of its potting, the configuration retaining the least excess margin is also the one carrying the least insert and potting material. The mass of the installed hardware therefore follows the margin criterion instead of competing with it: it is reduced wherever unjustified margin is removed, and is never traded against compliance.

4.3 Catalogue mode and analytical generation mode

The module operates in two modes, catalogue mode and analytical generation mode, selected explicitly by the analyst for each insert location. In catalogue mode the candidate pool is drawn from the insert catalogue, pre-filtered by the constraint set, and each surviving entry is verified by the computational kernel. This mode preserves procurement standardization and reuses existing qualification evidence. In analytical generation mode a new insert geometry is synthesized through constrained iteration over diameter, height and potting extent, the potting radius being modelled from measurable parameters rather than from an uncertain cell-fill coefficient. This branch reaches configurations between the discrete catalogue steps and can close a margin deficit that no catalogue entry resolves without gross over-sizing. Where the analyst requires a direct comparison, both branches can additionally be executed together and their optima reported side by side.

The design space is enumerated explicitly rather than sampled. In the parameter-sweep branch each design variable is swept over a fixed discrete grid covering its manufacturable range (insert diameter in 0.5 mm steps, facing thickness in 0.1 mm steps, insert height in 0.5 mm steps, the outer and inner dimensions of edge configurations in 1 mm steps, and the core type over the qualified core list) so that every value the search can return is a producible one from the outset. For the variables whose capacity contribution is monotonic, the sweep is ordered by increasing value and terminated at the first compliant candidate: on an ascending grid the first value producing a positive margin is by construction the smallest sufficient one, so the early termination is not a heuristic shortcut but the exact answer to the criterion of Eq. (5). In the geometry-generation branch a bounded box is constructed around the installed geometry, each variable being varied within an analyst-defined interval and sampled at a chosen number of steps; the resulting combinations are enumerated exhaustively, with geometric admissibility enforced during enumeration so that inconsistent shapes (an inner dimension exceeding its outer counterpart, for instance) never reach the analytical evaluation.

A synthesized geometry is not adopted in its computed form. A theoretical continuous solution, for example a required diameter of 10.33 mm, is snapped to the nearest standard manufacturable dimension, and the margin is re-evaluated for the discretized geometry through the identical verification path. Only the re-verified result is reported, so that every proposed configuration is simultaneously producible and analytically justified. The decision flow of both branches and the re-verification loop are shown in Fig. 8.

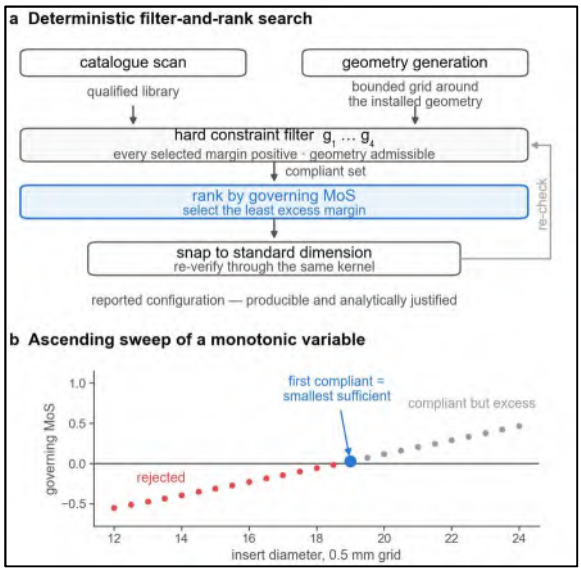


Figure 8: Deterministic optimization: hard constraint filtering of both candidate branches, ranking of the compliant set by governing MoS, and the ascending sweep of a monotonic variable in which the first compliant grid value is by construction the smallest sufficient one.

The module does not return a single global optimum. It reports the best compliant alternative obtainable by changing each design variable individually, so that the analyst is presented with the diameter change, the height change, the facing thickness change and the core substitution that

each resolve the location, together with the margin each achieves. This reflects how sizing decisions are actually taken in a programme, where the variables are not interchangeable in cost: substituting a core type affects panel manufacture, increasing an insert diameter affects procurement and the installation drawing, and increasing facing thickness affects the panel lay-up. The framework quantifies the alternatives and leaves the selection, which depends on programme constraints the analysis cannot see, with the engineer. The corresponding analyst interface is shown in Fig. 9.

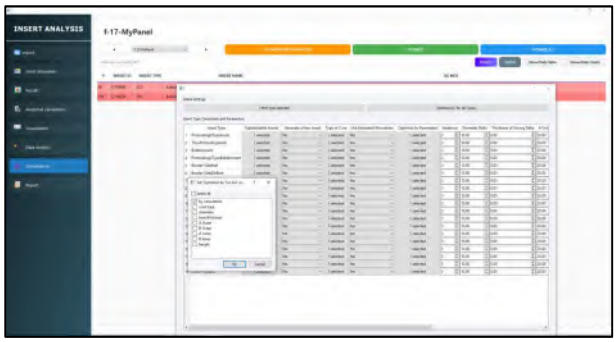


Figure 9: Optimization interface. The variables to be swept are enabled per insert type, together with the substitutable types, the bounded deltas, the number of iterations and the capacity level, so that one compliant alternative is returned for every variable the analyst allows to change.

Tab. 4 illustrates the resulting decision for a critical insert of a representative analysis scenario; the traceable elimination of each alternative shows that the selected candidate is neither the first compliant one found nor an arbitrarily conservative one.

Table 4: Candidate comparison for a critical insert of a representative analysis scenario, with the elimination reason of each rejected alternative.

Configuration	Governing MoS	Constraint status	Decision
Installed insert	−0.12	g1 violated	Non-compliant; replacement required
Candidate 1	−0.04	g1 violated	Eliminated: margin remains negative
Candidate 2	0.18	g1–g4 satisfied	Selected: least excess margin among compliant candidates
Candidate 3	0.46	g1–g4 satisfied	Eliminated: compliant but substantially oversized
Candidate 4	0.22	g2 violated	Eliminated: insert height incompatible with panel build-up

The same procedure is applied to every insert of the panel in a single execution: negative margins are corrected, unjustified margins are reduced to the least excess the verification admits, and the resulting margin population is documented candidate by candidate in the automated report.

5. VERIFICATION AND VALIDATION

The framework is qualified along the two axes distinguished by ECSS practice: verification, which establishes that the implemented equations are solved correctly, and validation, which establishes that those equations represent the physical behaviour of the insert region.

5.1 Code verification

Verification is performed by black-box unit testing of the computational kernel, which is exercised independently of the graphical interface through the data manager. Each module is driven with controlled inputs covering boundary values and every conditional branch of the ECSS formulation, and each output is compared against an independent hand calculation performed from ECSS-E-HB-32-22A. Every kernel module reproduces its reference results without deviation. The verified modules cover the correction of malformed exponent strings in MSC/NX Nastran bulk data, node and element extraction, load recovery from the punch file, edge and group-interaction distance extraction, allowable computation and margin evaluation; in each case the software result matches the independent hand calculation to all reported digits.

The chain is then verified end to end on a single insert taken from an industrial model. Insert CBUSH-21900001 is processed from bulk data parsing through CBUSH load recovery, insert-specific mapping of the recovered force components, application of the edge and group-interaction reduction factors, evaluation of the interaction index of Eq. (2), and calculation of the Margin of Safety using Eq. (3). Under its critical load case, the insert carries an out-of-plane force of 910 N and in-plane components of 1260 N and 640 N, against reduced allowables of 1708.95 N out of plane and 3097.76 N in plane, with the factor of safety applied in this project, 1.10. Evaluating Eqs. (2) and (3) with each load component normalized by its reduced allowable, hand calculation and software both return MoS = 0.296, with no deviation. The complete chain from file to reported margin is therefore traceable and reproducible by hand.

5.2 Validation against experimental data

Validation is carried out against static test data. The reference programme comprises a baseline configuration and five variants of aluminium honeycomb sandwich panels, each variant isolating the effect of a single parameter: insert diameter, core thickness, facesheet thickness, potting extent and load direction. The mean measured failure load

of each group is compared with the prediction of the uncorrected analytical model in Tab. 5.

Table 5: Correlation of the analytical model with experimental data, before and after correction. Deviation = (test/prediction ratio − correction factor) / (test/prediction ratio), i.e. the residual conservatism of the corrected prediction.

Group	Test configuration	Test/prediction	Deviation after correction
1	M6 through insert, 25.40 mm core, out of plane	1.49	12.7%
2	M8 insert, 25.40 mm core, out of plane	1.37	4.9%
3	M6 insert, 45.60 mm core, out of plane	1.34	3.3%
4	M6 insert, 0.30 mm facesheet, out of plane	1.54	15.8%
5	M6 partially potted insert, out of plane	1.30	0.0%
6	M6 insert, in-plane loading	2.49	3.5%

The uncorrected model is conservative in every group: measured capability exceeds prediction by factors of 1.30 to 1.54 under out-of-plane loading and by 2.49 under in-plane loading. Two physical mechanisms account for the difference. Out of plane, the potting compound penetrates the honeycomb cells and forms a mechanical interlock with the cell walls, mobilizing a larger effective load-introduction region than the analytical idealization assumes [3]. In plane, rotation of the insert engages the facesheet in local bearing, whereas the analytical formulation assumes pure shear transfer [4].

Load-direction-specific correction factors are derived from these data and made available as configurable inputs of the framework: 1.30 out of plane and 2.40 in plane. Both are taken at the conservative bound of the data set rather than at its mean, so that the corrected prediction remains at or below the measured capability in every group. Correction reduces the residual conservatism to below 16 %, and below 5 % in four of the six groups, converting the implementation into a semi-empirical predictor while preserving the conservative character required for certification. These factors were deliberately left disabled in the industrial application of Section 6, which is therefore reported on the unmodified handbook formulation and remains on the conservative side throughout.

6. INDUSTRIAL APPLICATION: GEO SATELLITE EQUIPMENT PANEL

The framework was applied to a complete equipment panel of a geostationary (GEO) communication satellite from an ongoing industrial programme. All modules were exercised in a single execution on a production model, so that the reported results correspond to the complete verification workflow.

6.1 Panel and load environment

The panel is a flat aluminium honeycomb sandwich structure of approximately 3000 × 1000 mm, with a 25 mm Al 5056 core and Al 7075-T6 facesheets, carrying six electronic units together with the structural attachments to the adjacent primary structure. Load introduction is realized through 249 inserts: 168 equipment-mounting inserts following the footprints of the units and 81 structural-attachment inserts along the panel boundaries and the interfaces with the neighbouring panels.

The panel was assessed under the launch load envelope comprising the quasi-static design cases and the sinusoidal excitations in X, Y and Z, all processed in a single run; the critical load case was determined independently for every insert by the envelope procedure of Section 2.5. The margins reported below were computed with the factor of safety applied in this project, 1.10, and with the unmodified handbook formulation; the optional correction factors of Section 5.2 were not enabled.

6.2 Baseline assessment

The as-designed configuration, produced by the conventional spreadsheet-based workflow, was evaluated without modification. The framework identified ten inserts with negative margins, the most severe at MoS = -0.10, at locations that the manual baseline had reported as compliant. The run summary produced for the panel is reproduced in Fig. 10, and the underlying per-insert table in Fig. 11. These locations lie close to panel free edges, where the edge-influence reduction lowers the admissible load appreciably. The reduction is prescribed by ECSS-E-HB-32-22A, but its systematic application requires the edge distance of every individual insert to be measured and carried into the calculation. In the baseline workflow of this panel the measurement was performed selectively rather than across the complete insert population, and the affected locations were consequently released with an apparent positive margin. Their detection is the principal outcome of the case study, since a non-compliant load-introduction point identified at a late review or test stage carries qualification and schedule consequences.

The same assessment revealed the opposite deviation at the other end of the population. Many locations exhibit margins far above any rational verification target, reaching MoS = 63.22. These follow from uniform insert selection: a single type,

sized for the most severely loaded attachment, is repeated across the panel irrespective of the local load level.

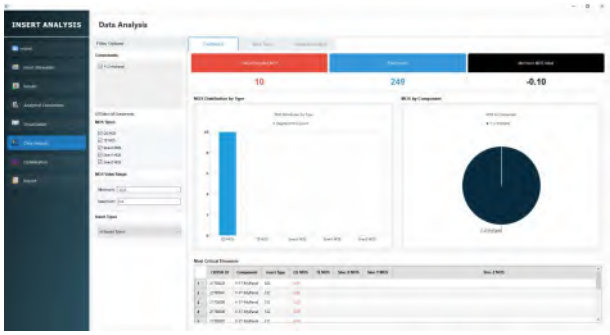


Figure 10: Run summary of the case study panel: 249 inserts assessed in a single execution, ten of them non-compliant, the most severe margin at −0.10, with the governing locations listed by identifier.

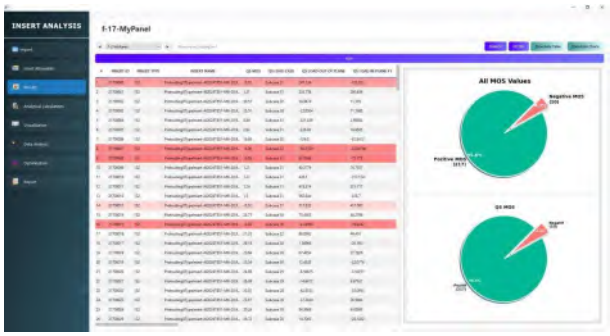


Figure 11: Results interface. Every insert is listed with its type, governing margin, critical load case and recovered local loads; non-compliant rows are flagged automatically and the margin population is summarized alongside the table.

6.3 Margin population after optimization

The deterministic optimization module of Section 4 was then applied to the complete insert population under the constraint set of Tab. 3 and the selection criterion of Eq. (5). Negative margins are eliminated and unjustified margins are reduced in the same pass, so that the margin distribution converges from the dispersed baseline range of -0.10 to 63.22 into a narrow compliant band; on this panel the optimized margins lie between 0 and approximately 0.05. This concentration is not an imposed target but the direct consequence of returning, at every location, the compliant configuration that retains the least excess margin. The two distributions are compared in Fig. 12.

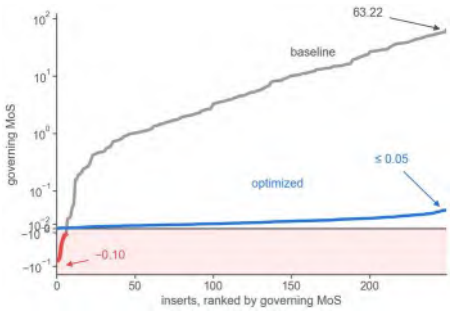


Figure 12: Governing Margin of Safety of the 249 inserts, ranked, before and after deterministic optimization.

Two contrasting locations illustrate the application of a single procedure to opposite conditions. At a structural attachment near a panel edge carrying a critical local load of approximately 5000 N, the installed insert is non-compliant; the module increases the insert diameter and the potting extent until the reduced admissible load restores a positive margin, while satisfying the geometric compatibility constraint on insert height. At a lightly loaded sensor attachment carrying approximately 150 N, the baseline margin lies far above any rational verification target; the module reduces the geometry to the smallest standard dimensions that still satisfy the constraint set, bringing the margin into the same band. The two locations are treated by identical logic and differ only in the local load recovered from the FE model.

6.4 Automated reporting and margin visualization

The run concludes with automated report generation: per-insert margin tables listing the recovered local loads, the critical load case, the applied reduction factors, the admissible loads and the resulting MoS, together with a configuration summary documenting the model files, load cases and factor settings. The same results are rendered as a colour-coded three-dimensional visualization of the margins on the panel model, in which non-compliant and over-designed regions are identifiable without inspection of the tabular output, as shown in Fig. 13.

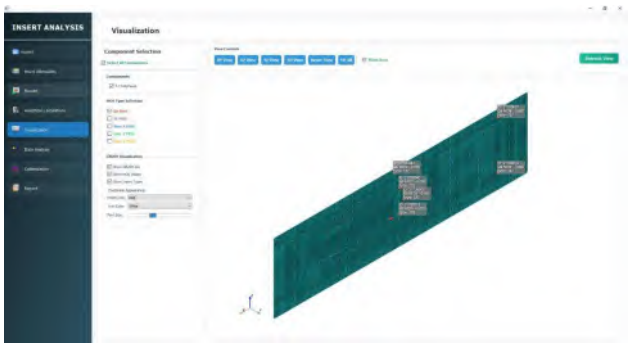


Figure 13: Visualization interface. Margins are mapped onto the panel model and non-compliant inserts are labelled with their identifier and margin, so that critical locations are identifiable without inspecting the tabular output.

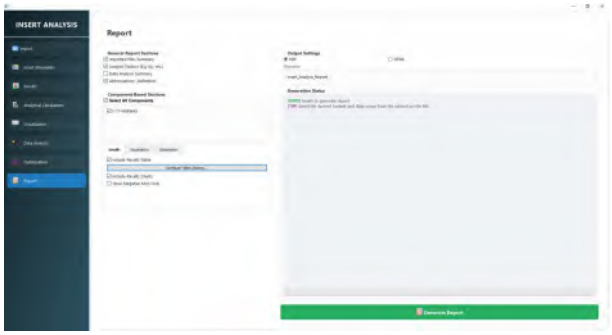


Figure 14: Report interface. The sections to be issued are selected (imported files, applied factors, per-component result tables and charts) and the document is generated in PDF or HTML without further post-processing.

7. LIMITATIONS

The framework addresses insert verification within an explicitly bounded scope. The analytical methods are those of ECSS-E-HB-32-22A and inherit their assumptions: linear elastic behaviour, quasi-static treatment of the enveloped load cases, and standard insert configurations installed in honeycomb sandwich panels. Fatigue, shock and progressive damage are outside the implemented scope, as are insert types not represented in the handbook formulation.

The results depend on the quality of the global finite element model that supplies them: an unrepresentative idealization of the panel or of the load introduction propagates directly into the reported margins. The framework verifies inserts, it does not validate the model that describes them.

Ingestion is currently bound to the MSC/NX Nastran bulk data and punch file formats. The correction factors of Section 5.2 are derived from a limited data set and require confirmation against a broader test population before they are applied in a qualification context. Finally, the exhaustive search of Section 4 scales with the size of the enumerated candidate pool, which is appropriate for the per-location sizing addressed here but does not extend to coupled sizing across multiple panels.

8. CONCLUSIONS AND FUTURE WORK

This paper has presented a software framework that automates the complete insert verification chain, from native MSC/NX Nastran model and result files to documented Margins of Safety and a deterministic re-sizing of every insert on a panel. It recovers the geometric context of each verification directly from the finite element mesh, envelopes the dimensioning load cases, evaluates the analytical verifications of ECSS-E-HB-32-22A and reports every quantity entering each margin.

Applied to a 249-insert equipment panel of a geostationary communication satellite, the framework substantially reduced the verification effort, identified inserts with negative margins that the manual baseline had released as compliant, and replaced a dispersed margin population with a consistent, documented one. Module-level verification against independent hand calculations showed no deviation, and comparison with test data confirmed that the implemented formulation remains conservative.

Full automation of insert verification within the ECSS framework is therefore attainable with deterministic, fully traceable methods. The benefit is not confined to engineering effort: an assessment repeatable at every model update turns the verification loop from a milestone activity into a continuous one, the margin criterion of Section 4.2 removes installed mass wherever it removes unjustified margin, and the defects reported here were detected precisely because every insert could be assessed individually.

Three extensions are foreseen. First, a solver-independent ingestion layer, decoupling the pipeline from a single result format. Second, confirmation and extension of the correction factors of Section 5.2 against a broader experimental population. Third, surrogate models to accelerate the candidate evaluation, subject to the traceability constraints discussed in Section 4.1.

9. REFERENCES

1. ECSS Secretariat (2011). Space Engineering: Insert Design Handbook, ECSS-E-HB-32-22A, ESA-ESTEC Requirements & Standards Division, Noordwijk, The Netherlands.
2. ECSS Secretariat (2009). Space Engineering: Structural Factors of Safety for Spaceflight Hardware, ECSS-E-ST-32-10C Rev.1, ESA-ESTEC Requirements & Standards Division, Noordwijk, The Netherlands.
3. Bunyawanichakul, P., Castanié, B. & Barrau, J.-J. (2005). Experimental and numerical analysis of inserts in sandwich structures. Applied Composite Materials, 12, 177-191.
4. Heimbs, S. & Pein, M. (2009). Failure behaviour of honeycomb sandwich corner joints and inserts. Composite Structures, 89(4), 575-588.

Visco-elastic vibration damper design using topology optimization

A Urbani [1,2], JS Petrulis [1,3], J Yang [2], A Delissen [1]

[1] TNO Optomechatronics, Stieltjesweg 1, Delft, the Netherlands, Email: arnoud.delissen@tno.nl
[2] TU Delft Mechanical Engineering, Mekelweg 2, Delft, the Netherlands
[3] TU Eindhoven Electrical Engineering, Groene Loper 19, Eindhoven, the Netherlands

KEYWORDS

vibration damping, micro-vibration, visco-elastic material, topology optimization

ABSTRACT

Visco-elastic materials are commonly used in vibration damping mounts due to its ability to dissipate energy. Recent advances in additive manufacturing enable the realization of complex geometries, creating new opportunities for the design of high-performance vibration dampers, balancing stiffness and damping. This paper investigates the application of topology optimization to the design of vibration dampers composed of a stiff material (*e.g.* aluminium) and a visco-elastic material (*e.g.* rubber). Unlike conventional constrained-layer damping concepts, the proposed approach allows both materials to be distributed freely throughout the design domain to maximize structural performance. The optimization framework supports objectives such as maximizing damping while maintaining minimum eigenfrequency requirements. Multiple vibration modes can be considered simultaneously, while the frequency-dependent behaviour of the visco-elastic material is explicitly accounted for. The resulting methodology provides a flexible framework for designing vibration dampers tailored to specific payload and performance requirements.

1. INTRODUCTION

Vibration damping and in extension, vibration isolation, is a useful concept to reduce launch loads or micro-vibrations on sensitive instruments, such as SmallCAT (Fig. 1) [1], which may otherwise damage the structure or harm its performance. Although active-type dampers have the potential for better damping properties, they also require continuous power, and usually come with additional mass, complexity, and failure modes [2]. Therefore, passive damping offers a simpler solution, while often still providing sufficient damping properties (depending on the materials used). In this work, passive damper design based on visco-elastic materials (*e.g.* rubbers) is considered.

In a damper design there is a clear balance between damping and stiffness, as the stiffness (together with the mass) determines the resonance *frequency* of the system, while the damping determines the *amplification* at resonance. One would ideally choose a very low resonance frequency with high damping for large attenuation of accelerations. In practice, however, this poses difficulties as large displacements will occur (due to low stiffness) and restrictions on minimum eigenfrequency are usually in place for payloads in space. Therefore, the goal would be to design vibration dampers with eigenfrequencies just high enough to meet requirements and with a high damping to avoid amplification at resonance.

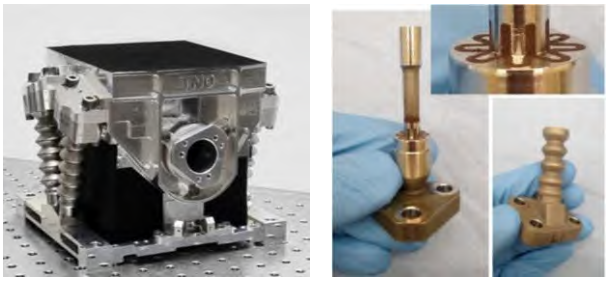


Figure 1: The SmallCAT instrument [1] launched on NorSat-TD in 2023 (left) and detailed images of the damped strut produced by AM [3] (right)

To realize a balance between damping and stiffness, two materials are used: a damping material (such as rubber), which has low stiffness and high damping, and a stiff material (such as a metal), which has low damping and high stiffness. One without the other would result in a structure too soft, or in one without sufficient damping. By combining these two materials in an effective way, virtually any stiffness and damping value can be obtained within the physical limitations of the chosen materials. Especially with stringent frequency and/or damping requirements for multiple modes, the design of a damper can be challenging.

With technology maturing for additive manufacturing (AM), the freedom to shape structural components is significantly increased, which has been applied successfully in passive vibration dampers [3] and is also demonstrated in orbit [1] (Fig. 1). Topology optimization provides a powerful tool to fully utilize the design freedom AM offers, as well as automating the design process for different payloads and/or requirements.

In this work, a general topology optimization framework is presented for the design of passive vibration dampers using a combination of two materials, focusing on its dynamic properties (eigenfrequencies and damping). In many cases there are additional considerations in material

choice, such as creep behaviour or thermal conductivity, which are considered out of scope for the current work. The frequency-dependent properties of the visco-elastic material are taken into account in the optimization framework for more accurate dynamic material properties. Additionally, an experimental validation of an optimized damper is presented.

This paper is organized as follows. First of all, in Section 2, the dynamic modelling is explained, starting from material properties and ending up with eigenmodes. This model is then used for an optimization framework as described in Section 3. Several optimized damper designs are provided in Section 4, as well the experimental validation of an optimized damper. Finally, conclusions are drawn in Section 5.

2. DYNAMIC MODEL

2.1. Visco-elastic material

For the analysis, it is important to account for the frequency-dependent material properties of visco-elastic materials, as large differences in value can be expected at different frequencies (Fig. 2). It is assumed the rubber material is near-incompressible and the damping mainly comes from shearing. To include damping, the complex shear modulus G^* is used [4], which consists of storage modulus G' and loss modulus G'' as

$$G^*(f) = G'(f) + iG''(f) \in \mathbb{C}. \qquad (1)$$

Note that the shear modulus is dependent on excitation frequency f (and temperature, which is assumed constant here). The amount of damping in the material is determined by the loss factor η, and the complex angle δ, of the shear modulus

$$\eta = \tan\delta = \frac{G''}{G'}. \qquad (2)$$

As the material is near-incompressible, a constant high bulk modulus $K \in \mathbb{R}$ is chosen, resulting in a Poisson's ratio close to 0.5. The frequency dependent material properties are typically measured with a dynamic mechanical thermal analysis (DMTA).

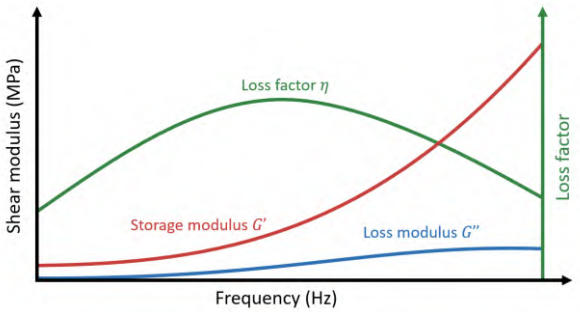


Figure 2: Illustration of frequency-dependent material properties of a visco-elastic material

2.2. Finite-element modelling

Finite-element analysis is used for the optimization, using the routines implemented in the pyMOTO framework [5]. The finite-element stiffness matrix is assembled based on the mixture of the two materials and their material properties, which makes the stiffness matrix frequency-dependent. With the stiffness matrix and n motion directions, Guyan reduction [6] is used to extract the effective stiffnesses in the different directions with respect to the input. This results in a smaller stiffness matrix $\boldsymbol{K} \in \mathbb{C}^{n\times n}$, which contains stiffness in $n = 3$ motion directions in 2D (two translations and a rotation) or $n = 6$ in 3D (three translations, three rotations) and is also frequency dependent.

The payload is modelled as a point mass (Fig. 3) connected to the n motion directions in mass matrix $\boldsymbol{M} \in \mathbb{R}^{n\times n}$, with given mass, centre of mass location, and inertia properties. In case the mass of the damper is not negligible compared to the payload mass, a correction can be added based on the Guyan reduction used for the stiffness matrix.

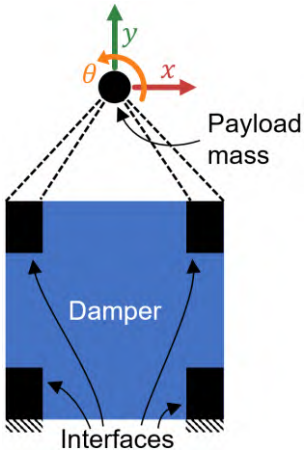


Figure 3: Schematic overview of the reduced degrees of freedom and connection to the payload

2.3. Modal analysis

Finally, the eigenmodes $\boldsymbol{\phi}_i$ and corresponding complex frequencies Ω_i are obtained from solving the non-linear eigenvalue problem in Eq. 3. This is done with a fixed-point iteration scheme, which converges when the change in frequency from iteration to iteration is sufficiently small.

$$\boldsymbol{K}(f_i)\boldsymbol{\phi}_i = \Omega_i^2 \boldsymbol{M}\boldsymbol{\phi}_i \text{ for } i \in \{1, \dots, n\} \qquad (3)$$

From the complex eigenfrequencies Ω_i, the actual oscillation frequency of the mode is the real part and the Q-factor of the mode is the ratio, calculated as.

$$f_i = \frac{\mathrm{Re}(\Omega_i)}{2\pi}, \text{ and } Q_i = \frac{\mathrm{Re}(\Omega_i)}{2\mathrm{Im}(\Omega_i)}. \qquad (4)$$

These values can be used as objective or constraints to perform an optimization on.

3. TOPOLOGY OPTIMIZATION FRAMEWORK

The damper, shown in Fig. 3 is discretized with a finite element mesh. At the bottom it is fixed to the interface of the platform, while the top is fixed to a payload. The goal is to perform optimization of the damper to meet the requirements. In this case the objective of the optimization is to maximize the damping (e.g. minimize the Q-factors), while requiring the eigenfrequencies to be between an upper and lower frequency bound (possibly different for each mode), which is mathematically described as

$$\begin{aligned} \min_{x} \quad & \sum_i Q_i^2 \\ \text{s.t.} \quad & f_{\text{low},i} \le f_i \le f_{\text{upp},i} \quad \text{for } i \in \{1, \dots, n\} \\ & 0 \le x_j \le 1 \quad \text{for } j \in \{1, \dots, N_{\text{el}}\} \end{aligned}$$

Each element j in de design domain has a design variable x_j, which characterizes the ratio in the element between two distinct materials (visco-elastic and stiff). If $x_j = 0$, the material is fully visco-elastic and completely of the stiff type when $x_j = 1$. Any x_j in between 0 and 1 represents a mixture of materials, where the material properties in each element are interpolated (using SIMP [7], Eqs. 5-6) between the properties (shear and bulk modulus) of the visco-elastic material $(G^*(f), K)$ from Eq. 1 and those of a stiff material (G_s, K_s).

$$G_j^*(f) = G^*(f)\left(1 - x_j^3\right) + G_s x_j^3 \qquad (5)$$

$$K_j = K\left(1 - x_j^3\right) + K_s x_j^3 \qquad (6)$$

The topology optimization is implemented in the pyMOTO optimization framework [5], which automatically calculates the design sensitivity information to perform the mathematical optimization using a gradient-based algorithm.

4. RESULTS

4.1. Numerical results

Several optimizations are performed with different requirements on the damper to demonstrate the effect and flexibility of the framework. In these examples, a payload of 2kg is used to design a damper of 100×100×10 mm. The materials used in the design are aluminium (Young's modulus of 68.9GPa and loss factor η=0.002) and a rubber material with frequency-dependent material properties (G'≈25MPa and η≈1.1 at 200Hz).

Case 1: Vertical damper

The first damper optimized is only minimized for a low damping in y-direction (vertical). The y-mode is required to be between 200 and 250Hz. On the other modes there are no requirements. The requirements are summarized in Table 1.

Table 1: Requirements for the vertical damper

Mode	x	y	θ
Lower frequency	-	200 Hz	-
Upper frequency	-	250 Hz	-
Minimize Q	-	Yes	-

The optimized design and eigenmodes are shown in Fig. 4, from which can be seen that the y-mode indeed satisfies the requirements in Table 1. In the design several channels containing rubber are created. Intermediate bodies embedded in rubber generate a shearing motion which results in damping.

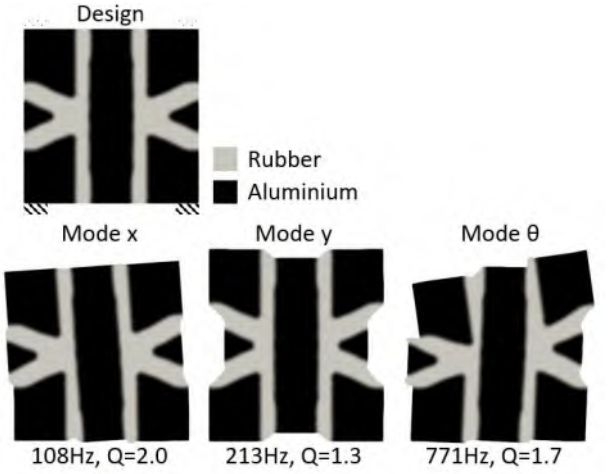


Figure 4: Design and modes of the vertical damper

Note that the damping in all modes is high, despite only the one in y-direction being maximized. This is a by-product of the optimization, since no requirements were set on the x- and θ-modes. Additionally, the mode in x-direction has a very low frequency.

Case 2: Vertical damper with additional frequency constraints

To ensure sufficiently high frequencies in the other modes than the y-mode compared to case 1, additional lower frequency constraints are introduced. The x- and θ-modes are now required to be above 500Hz, in addition to the same requirements as in case 1, as is summarized in Table 2.

Table 2: Summary of requirements for the vertical damper with additional frequency constraints

Mode	x	y	θ
Lower frequency	500 Hz	200 Hz	500 Hz
Upper frequency	-	250 Hz	-
Minimize Q	-	Yes	-

In Fig. 5 the resulting design and modes can be seen. Compared to case 1, the intermediate bodies on the left and right are still present to generate shear, but additional flexures on the top are created to add stiffness in the horizontal direction.

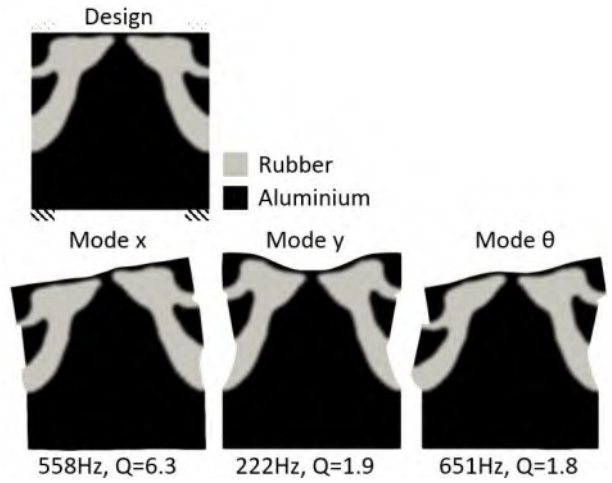


Figure 5: Design and modes of the vertical damper with additional frequency constraints

Due to the additional frequency constraints, the damping of all modes is worse than in case 1. Especially in the x-mode, additional stiffness is added at the cost of a Q-factor that is 3× higher, although still very low. Also note that the x- and θ-modes are very similar and both are a combination of horizontal translation and rotation.

Case 3: Horizontal damper with high support stiffness

In the third cases a damper is designed in horizontal direction, while having a high support stiffness in the y- and θ-directions. An overview of the requirements for this case can be found in Table 3.

Table 3: Requirements for the horizontal damper

Mode	x	y	θ
Lower frequency	200 Hz	1000 Hz	2000 Hz
Upper frequency	250 Hz	-	-
Minimize Q	Yes	-	-

The layout of the design (Fig. 6) is a parallel guiding flexure system to have low stiffness in x-direction, while being high in the other directions. On the middle beam of the two parallel guiding flexures, a protrusion is present generating shear with the intermediate bodies in between them.

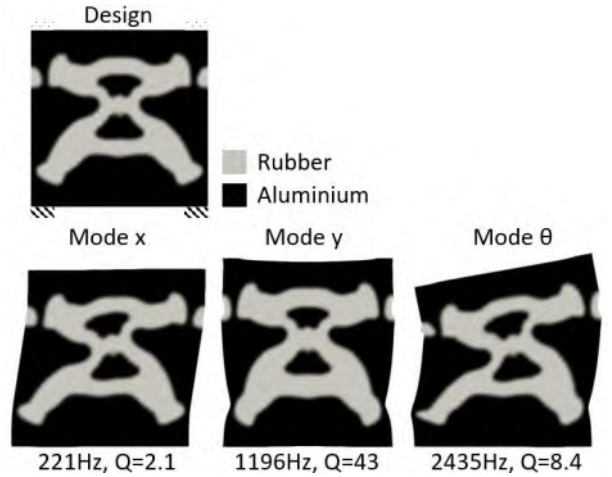


Figure 6: Results for the horizontal damper case

Again, all the modes satisfy the requirements in Table 3. Opposed to the previous two cases, the Q-factor in the non-optimized directions is much higher than that in the optimized direction (horizontal). Especially the Q-factor in y-mode is very high due to the high stiffness in that direction generating mostly strain in the aluminium parts.

Case 4: Unidirectional damper

The final case is a unidirectional damper optimized to have high damping in all modes. Additionally, the three modes should be between 200 and 250Hz (summarized in Table 4).

Table 4: Summary of requirements for the unidirectional damper

Mode	x	y	θ
Lower frequency	200 Hz		
Upper frequency	250 Hz		
Minimize Q	Yes		

In the resulting design (Fig. 7), the top attachments are surrounded by a layer rubber between an ‘A-shape` aluminium frame. The first two modes generate their damping locally in the thin layers of rubber close to the top interfaces, while the third mode utilizes more of the rubber material in the rest of the domain.

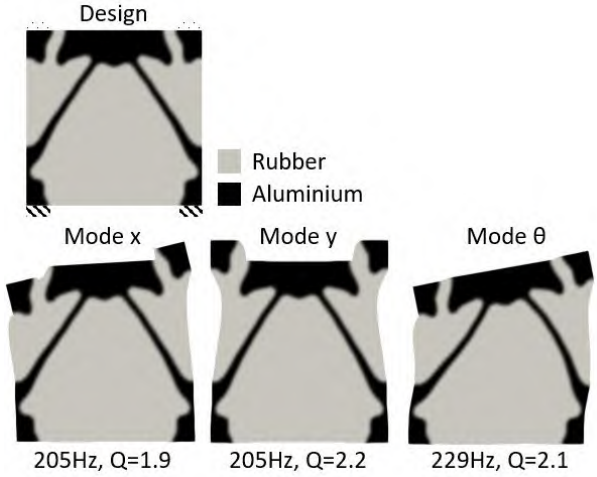


Figure 7: Optimized design and modes of the unidirectional damper

All modes satisfy the requirements in Table 4, while also having a low Q-factor around 2. Note that also here, the x- and θ-modes are very similar due to their frequencies being relatively close, resulting in a combination of x-displacement and rotation.

4.2. Experimental validation

Vibration tests were performed to verify the numerical results with a polymer 3D-printed vibration damper, using PLA as the stiff material (Young’s modulus of 2.6GPa and η=0.013) and TPU as the damping material (G’=51MPa and η=0.27 at 200Hz). The 2D damper designs are extruded sufficiently to avoid low frequency out-of-

plane modes. This is a cost effective way to validate the model and optimization results, allowing faster iterations as opposed to more performant materials which require more involved manufacturing steps (*e.g.* metal and vulcanized rubber). Due to the reduced stiffness of these polymer materials, the payload mass is also reduced to 300g, and the dimensions are 25×45×35 mm.

The test-setup used can be seen in Fig. 8. A sine-sweep from 10 to 2000Hz at an acceleration level around 1g is supplied by the shaker, while measuring accelerations with the pilot and output sensors.

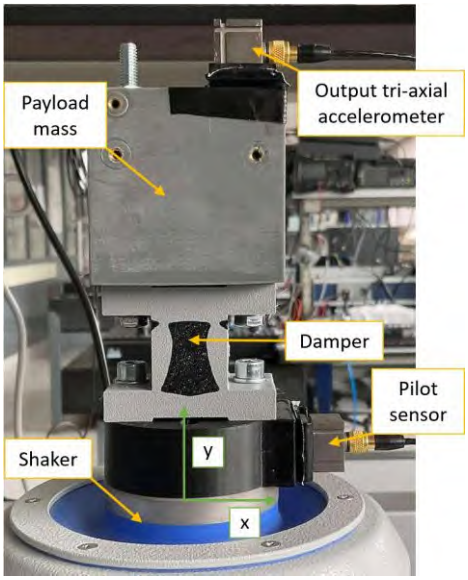


Figure 8: Overview of the vibration test-setup

The printed damper is optimized to have high damping in the θ -mode, while the frequencies for all modes are above 200Hz. From the measured accelerations, the transmissibilities can be calculated, as shown in Fig. 9. Additional FEM analysis were also performed in COMSOL, both in 2D and 3D. The optimized python result shows close correspondence with the FEM analyses in COMSOL, but there is a larger discrepancy compared to the measurements. The three modes considered during optimization are clearly recognizable. Note that some additional dynamic modes are present in the measured transmissibility, which may be caused by measurement setup dynamics, lack of input control, and/or out-of-plane modes. It is foreseen to redo the tests with better test equipment.

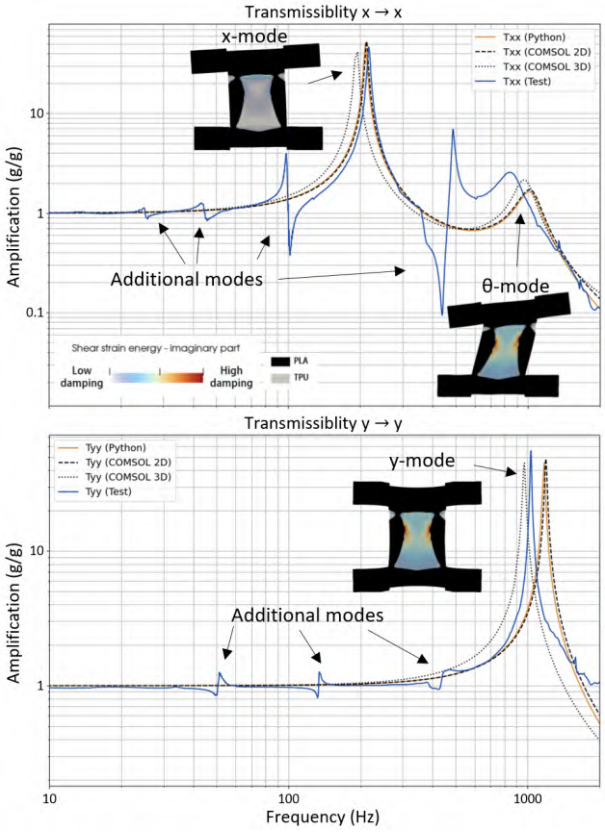


Figure 9: Transmissibility plots comparing FEM results with measured data in x and y directions. Additional modes from the measurement setup are indicated. The targeted rigid body modes are shown with insets.

The frequencies and Q-factors of the tests are compared with the FEM model in Table 5. Most frequencies are relatively close to the FEM model, although the x-mode (which was targeted to have low damping) is off by 20%. The Q-factor of the x-mode is tested even lower than in FEM, while the other modes (that are not optimized for low Q) have a high Q-factor as expected.

Table 5: Comparison of frequency and damping between the measurement and FEM

	Frequency		**Q-factor**	
	FEM	**Test**	**FEM**	**Test**
x-mode	210	217	39	38
x-mode	1022	840	5.2	4.0
y-mode	1171	1030	45	61
θ-mode	210	217	39	38

The differences in testing compared to FEM can be explained by an imperfect testing setup, lack of input control, temperature effects on material properties, anisotropy of the 3D-printed part, and more. Nonetheless, while being imperfect, the results do show the potential of using topology optimization to generate damper designs targeting frequency and Q-factors of specific modes.

5. CONCLUSION

In this paper we have explained and demonstrated a method to design vibration dampers with topology optimization using a distribution of stiff and damping material. It is shown that by changing the requirements of the damper, completely different concepts can be generated automatically.
Using filament polymers a 3D-printed damper is produced, demonstrating its manufacturability. The 3D printed damper is also tested with a shaker over a wide range of frequencies relevant for space instruments. This test shows the concept works as expected, even though the agreement between test and model is not perfect. Further tests and improved modelling are planned in the future to reduce this inaccuracy.
Further foreseen improvements are the usage of better materials than 3D printed polymers to perform a test, such as fluoro-rubber and aluminium. Additionally, the damper optimization framework can be extended by adding temperature-dependent material properties, thermal conductivity requirements, and stress limitations during vibration.

6. REFERENCES

[1] N. Doelman, G. Witvoet, D. de Bruijn, A. Bos, A. Delissen, D. Nguyen, L. Scheers, H. van Brug, R. Voorhoeve, K. Broekens, C.W. Korevaar, F. van Kempen, "Design and in-orbit performance of a 1U 1 Gbit/s optical communication terminal," *IEEE J. of Selected Topics in Quantum Electronics*, vol.32(1), 2026, doi: 10.1109/JSTQE.2026.3655556.
[2] H. Shi, M. Abubakar, X. Bai, Z. Luo, “Vibration isolation methods in spacecraft: A review of current techniques”, *Advances in Space Research*, vol.73(8), 2024, doi: 10.1016/j.asr.2024.01.020
[3] F. van Kempen, J. de Vreugd, G. Misiun, E. van Schreven, W. Crowcombe, O. van der Togt, A. Maaskant, M. Distelbrink, H. Pronk, J. Smets, R. Ska, “Damped support struts for optomechanical instruments enabled by additive manufacturing”, in *Proceedings of ECSSMET17*, 2023
[4] J. Ferry, *Viscoelastic properties of polymers*, Wiley & Sons, 1980
[5] A. Delissen, “pyMOTO – Modular topology optimization in Python”, *Zenodo*, 2026, doi: 10.5281/zenodo.8138859
[6] R. Guyan, “Reduction of stiffness and mass matrices”, *AIAA Journal*, vol.3(2), 1965, doi: 10.2514/3.2874
[7] M. Bendsøe and O. Sigmund, *Topology optimization: Theory, methods, and application*, Springer Berlin, Heidelberg, 2004, doi: 10.1007/978-3-662-05086-6

ECSSMET
Braunschweig Germany 2026

Sustainable Spacecraft Structures

EVOLUTION OF PERFORATION KINETIC ENERGY IN HYPERVELOCITY IMPACT ON WHIPPLE SHIELD BUMPERS

Christian PUILLET [(1)], Hélie REININGER [(1)]

[(1)] CNES, 18 avenue Édouard Belin, 31401 Toulouse Cedex 9, France, helie.reininger@cnes.fr

KEYWORDS

Orbital Debris, Hypervelocity impact (HVI), Ballistic Limit Equation (BLE), Smoothed Particle Hydrodynamics (SPH)

ABSTRACT

Widely used to design Whipple Shield structures, the Christiansen Ballistic Limit Equation (BLE) assumes that the projectile perforation-critical kinetic energy is constant in the hypervelocity regime. This hypothesis is known to be conservative, meaning the actual critical kinetic energy increases with projectile impact velocity. This article presents a study to quantify this increase, as part of the CNES Research and Technology program.

Thirteen aluminium projectiles with diameters in the range of 1.3 to 2.0 mm impacted a single design of Al 6061 Whipple Shield (0.8/25/0.8 mm) at velocities ranging from 7.1 to 9.3 km/s (kinetic energy ranging from 130 to 450 J). Six of these tests resulted in shield perforation. Assuming that the perforation critical diameter could be expressed as a product of the Christiansen BLE diameter and a power of the impact velocity, the possible value of this power coefficient was found to be likely around 0.2 (where 0.0 would indicate no increase in critical kinetic energy).

Independently, and based on test cases available in the Protection Manual of the Inter-Agency Space Debris Coordination Committee (IADC), hydrocode models were developed for a wide range of configurations, including aluminium Whipple Shields.

The models were used without tuning to numerically simulate the tested configuration using a fully automated procedure to compute and identify the perforation limit.
The difference between the test results and the numerically computed Ballistic Limit Curve is generally below 0.1 mm (100 µm) in terms of projectile diameter, to be compared with the model particle size of 40 µm. Additionally, the numerical model showed the same trend of increasing kinetic energy with impact velocity as experiments, without considering vaporisation of aluminium, thus allowing for possible further increases at higher velocities.

NOMENCLATURE

Notations	
Al	Aluminium
BLC	Ballistic Limit Curve
BLE	Ballistic Limit Equation
CNES	Centre National d'Études Spatiales (French Space Agency)
EOS	Equation of State
F	Fail (perforation)
GEO	Geostationary Orbit
HDF	Hierarchical Data Format
HVI	Hypervelocity impact
IADC	Inter-Agency Space Debris Coordination Committee
LGG	Light Gas Gun
MM	Micrometeoroids
OD	Orbital Debris
P	Pass (no perforation)
SPH	Smoothed Particle Hydrodynamics
SSO	Sun-Synchronous Orbit
α	Power coefficient
c	Critical (subscript)
d	Diameter (m, cm)
θ	Impact angle (°)
ρ	Density (kg/m3)
σ_1	Maximum principal stress (Pa)
σ_y	Yield stress (Pa)
V_h	Hypervelocity regime transition velocity (m/s, km/s)
W_c	Damage threshold (Pa)

1. INTRODUCTION

Because they are simple and efficient, Whipple shields are commonly used to protect vulnerable areas on satellites. They are also commonly designed using the Christiansen Ballistic Limit Equation [1]. (§ 3.1.2.1) This equation is divided into three regimes: (a) the ballistic regime, for impact velocities below typically 3 km/s, (b) the hypervelocity regime, for impact velocities typically above 7 km/s, and (c) the intermediate regime for intermediate velocities.
The hypervelocity regime equation was developed by extrapolation, assuming constant kinetic energy. This hypothesis is known to be conservative [2] (§4.2.1). The question then arises as to how significant this conservatism is, particularly in the context of the increasing threat of space debris and

limited resources for protecting vulnerable areas from impacts.

Previous studies [3,4] have shown that an increase in the perforation-critical kinetic energy with velocity can be expected.
We assume that the critical diameter can be expressed with a power law in the form given by Eq. (1), where α=0 gives the Christiansen BLE, and α>0 measures the increase in critical kinetic energy.

$$d_c = d_{c,Christiansen} \left(\frac{V}{V_h}\right)^{\alpha} \qquad (1)$$

As shown in Fig. 1 and Fig. 2 below, the value of α derived from [3] experiments would be around 0.5, whereas it would be around 0.2 from [4] experiments.

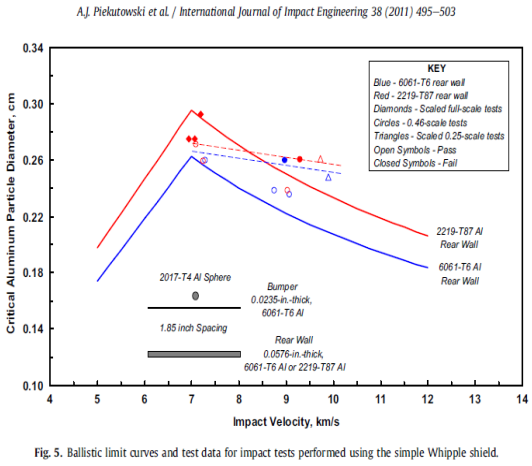


Figure 1: Tests results from [3]

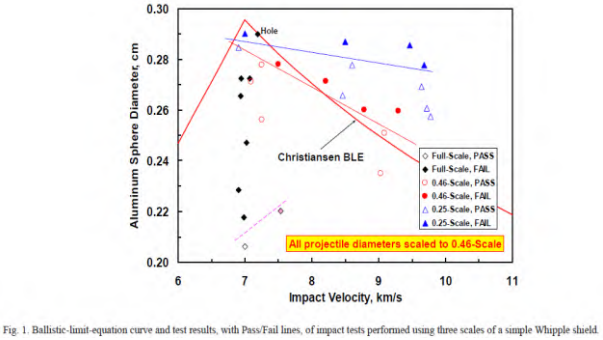


Figure 2: Test results from [4]

These studies were based on full-scale and sub-scale tests to address high velocities. The present study used a single design for all the tests performed at impact velocities ranging from 7.1 to 9.3 km/s.

The following points are presented in this paper:

- The experimental results (HVI tests)
- The analysis of the results, with some examples of consequences
- The development and validation of the SPH numerical model
- The numerical ballistic limit curve of the experiments and future possible developments

2. EXPERIMENTAL RESULTS

The design of the Whipple shield was based on the need to be able to perforate the shields with aluminium projectiles in the range of 1 to 2 mm in diameter with an impact velocity up to 10 km/s, in normal impacts ($\theta = 0°$). The Whipple shields eventually consisted of two Al 6061-T6 plates with 0.8 mm thickness and 25 mm spacing between them.

Thirteen HVI tests were performed by Thiot Ingénierie with the “Hermes” LGG, under a CNES Research and Technology contract. (Fig. 3)



Figure 3: Thiot Ingénierie LGG “Hermes” [1]

The projectiles were Al 2017-T4 spheres with diameters ranging from 1.3 to 2.0 mm and impact velocities ranging from 7.1 to 9.3 km/s (kinetic energy ranging from 130 to 450 J). Seven tests resulted in no perforation (“pass”) and six tests resulted in perforation (“fail”).



Figure 4: Test set-up, at Thiot Ingénierie [5]

Tab. 1 and Fig. 5 below summarise the impacts. Some tests that were deemed critical for the analysis of the results were duplicated. The uncertainty in velocity measurement ranges from 50 to 70 m/s. The uncertainty in kinetic energy ranges from 5 to 15 J. Unfortunately, no projectiles with diameters of 1.9 mm and 1.6 mm were available.

Table 1: Summary of results [5]

HE test	d (mm)	V (m/s)	KE (J)	P/F
1338	1.3	8993	126	P
1442	1.5	7392	130	P
1443	1.5	8587	176	P
1501	2.0	8786	437	F
1502	1.7	8856	272	P
1503	1.7	7525	197	P
1504	1.8	7085	207	F
1505	1.8	7780	250	P
1506	1.8	8681	311	F
1508	1.8	7124	209	F
1509	1.8	8229	279	F
1510	1.7	9292	300	F
1512	1.8	7832	253	P

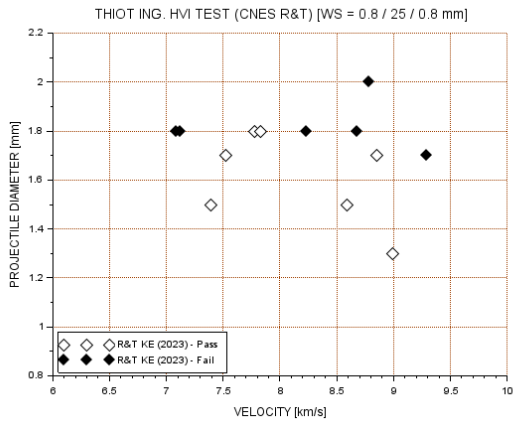
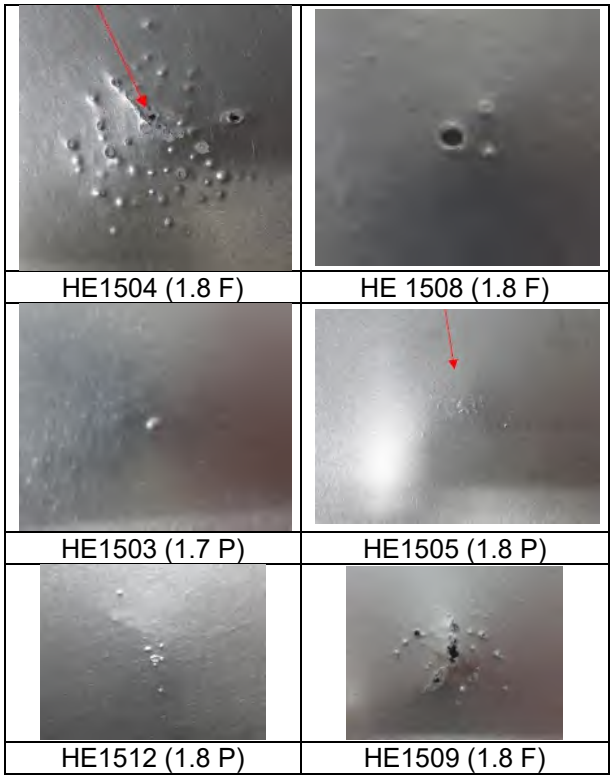


Figure 5: Plot of "Pass" and "Fail" status

Fig. 6 presents photographs of some of the rear plates (increasing velocity).



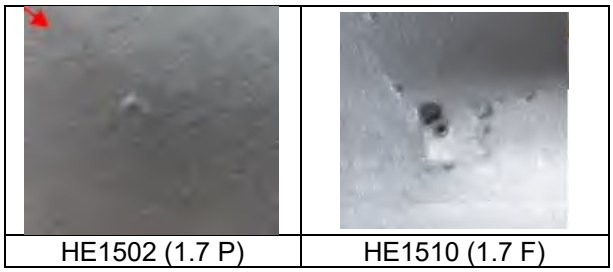


Figure 6: Rear plates [5]

3. ANALYSIS OF THE RESULTS & EXAMPLES

The purpose of the analysis part is to define the possible values of the power coefficient α, defined according to Eq. (1), and, if any, the possible related constraints

The critical diameter for velocities in the range of 7-9 km/s is 1.7 to 1.8 mm. This is slightly higher than initially anticipated from the aluminium alloy mechanical properties (hence the first tests with projectile diameters of 1.3 and 1.5 mm). To define the possible values of α, three parameters were then considered: 1) the power coefficient α, 2) the value of the shattering-to-hypervelocity regime velocity V_h, and 3) the yield limit of the bumper plates σ_y.
The following domains were considered: $0 \leq \alpha \leq 0.4$, $7.2 \leq V_h \leq 8.2$ km/s, and $92 \leq \sigma_y \leq 114$ ksi.

For each given value of V_h, (by steps of 0.1 km/s) the ballistic limit Eq. (1), with values of α and σ_y, was compared to the test results. The pair (α, σ_y) was valid if all the results were consistent with the test results (both "pass" and "fail"). It was verified that the domain boundaries were not valid. Specifically, no value of α above 0.34 was valid, no value of σ_y below 95 ksi or above 112 ksi was valid and no value of V_h below 7.4 km/s or above 8.0 km/s was valid. Thus, all the possible values were identified.

Fig. 7 plots the limits of the possible pair (α, σ_y) for velocities V_h.

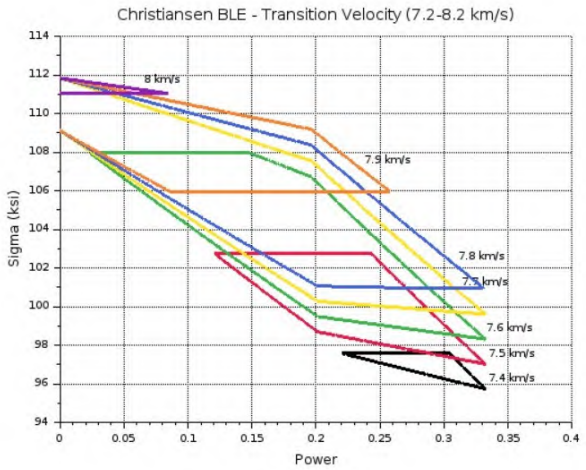


Figure 7: Limits of values for pairs (α, σ_y) The valid area is within the limits.

The largest parts of valid area sets $\alpha \approx 0.2$ and $V_h \approx 7.6$ km/s and σ_y in the range of 100-105 ksi (≈700 MPa). The value of the power coefficient α confirms results of [4], rather than those of [3].
It can be noted that the highest values of α are correlated with the lowest transition velocities.
Also, there is still a possibility of having $\alpha = 0$, for high velocities between 7.6 and 8 km/s and the highest values of σ_y, in the range of 109-112 ksi (≈760 MPa).

Fig. 8 and Fig. 9 below plot some BLEs with the three sets parameters provided in Tab. 2. All these BLEs are in the valid area and close to the limits.

Table 2: Examples of valid values

σ_y (ksi)	110	104	97
α	0.0	0.2	0.3
V_h (km/s)	7.9	7.6	7.4

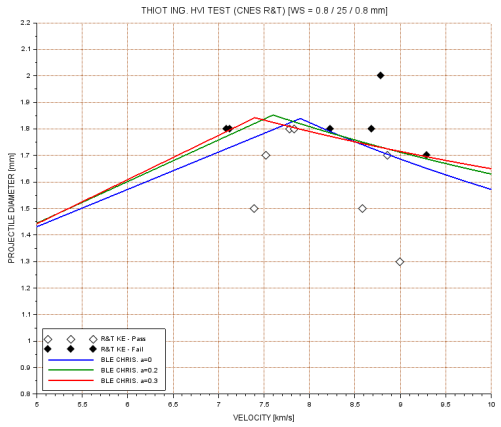


Figure 8: Critical diameters

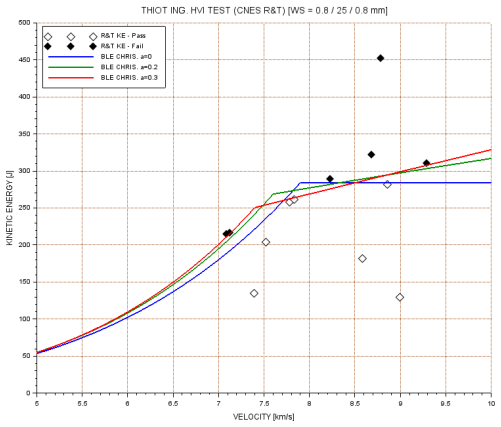


Figure 9: Critical kinetic energy

The consolidated values of α of 0.2 and 0.3 are used to compute the reduction of critical impacts for the tested Whipple Shield (0.8/25/0.8 mm) used as the velocity (ram) face in SSO (800 km, 98°, orbital debris) and GEO (micrometeoroids), in 2026.

Table 3: Reduction of critical impacts (from MASTER 8.3.2 [6])

Reduction (%)	$\alpha = 0.2$	$\alpha = 0.3$
SSO (OD)	13 %	18 %
GEO (MM)	58 %	69 %

The reduction is more significant for MM than for OD due to the relative impact normal velocities (14 km/s for OD vs. typically 22 km/s for MM).

So far, there is no evidence that the power coefficient can be extrapolated to velocities greater than the tested ones. However, the development of a numerical BLC presented in chapter 5 seems to indicate that there is room for further increase at higher velocities.

4. SPH MODELS BENCHMARK

Prior to the development of the BLC corresponding to the tests, chapter 4 presents the validation of Whipple Shield SPH models.

4..1 Models

SPH models of Whipple Shields with 2 or 3 walls were developed independently, using the ABSTRAO version 1.2 software tool [7]. Eight models with test results were used as test cases. They are all defined in the IADC Protection Manual [1]. Four models are defined in paragraph 5.2.1 “Definition of Benchmark Cases” and four models are defined in paragraph 4.3.4 “NASA JSC and CNES” as part of the “Hypervelocity Launchers and Calibration” activity.

The eight test cases are:

1. § 5.2.1.1 Whipple Shield (Al projectile)
2. § 5.2.1.2 Whipple Shield (Al projectile > 9 km/s)
3. § 5.2.1.3 Whipple Shield (Alumina projectile)
4. § 5.2.1.4 Whipple Shield (Nylon Projectile)
5. § 4.3.4 Test 1 (Whipple Shield)
6. § 4.3.4 Test 2 (Triple wall)
7. § 4.3.4 Test 3 (Triple wall)
8. § 4.3.4 Test 4 (Whipple Shield)

Detailed results are available in [8] and [9, 10].

4.2 Material properties

All aluminium parts and the nylon projectile use a Johnson-Cook constitutive model, a Mie-Grüneisen Equation of State and a Cockroft-Latham damage model. The alumina projectile uses a Johnson-Holmquist constitutive model.

The Al 6061 and Al 2219 Johnson-Cook models are taken from [8]. The nylon projectile Johnson-Cook model is taken from [11], quoted by [12]. The Alumina projectile Johnson-Holmquist model is taken from [13], quoted by [14].

The Cockroft-Latham damage model contains two damage parameters: one applies instantaneously Eq. (2), and one uses a time delay Eq. (3).

$$D = \frac{1}{W_c}\int_0^{\varepsilon_{eff}^P} max(0,\sigma_1)d\varepsilon_{eff}^P \qquad (2)$$

$$D = \frac{1}{t_s}\int_0^t (\bar{\sigma_1}/\sigma_s)^{\alpha_s}\, dt \qquad (3)$$

The instantaneous model was inhibited by defining a very large value of W_c.
For the time delay model, the spall properties are based on literature data for spall pressure, which were eventually slightly tuned to the tests results. The final values are not "strict" values but variations of more than 20% are likely to provide incorrect results.
The spall time was also defined based on test results, with a constant value of 30 ns for all the walls (bumpers and rear walls) and between 65 and 140 ns, increasing with impact velocity, for all the projectiles (except the alumina projectile which does not use a Cockroft-Latham damage model). These values are also not "strict" but a variation of more than 10% is likely to provide incorrect results.
It can be noted that the spall time of the nylon projectile fits well in the time series of the aluminium projectiles (see also Tab. 9 in paragraph 5). It has not been verified whether this was just by chance or not. Numerical simulations of experimental results of [15] could be used for such verification.

The material properties values are presented in Tab. 4 to Tab. 7 below.

Table 4: Johnson-Cook model properties

Parameter	Al 2017	Al 6061 T6	Al 2219 T87	Nylon
Johnson-Cook				
ρ (kg/m^3)	2785	2703	2810	1140
E (Pa)	72.4^{e}9	68.9^{e}9	73.1^{e}9	3.68^{e}9
ν	0.33	0.33	0.33	0.4
A (Pa)	270.68^{e}6	266.8^{e}6	274.9^{e}6	10.5^{e}6
B (Pa)	426^{e}6	126.8^{e}6	432.8^{e}6	32.5^{e}6
n	0.34	0.258	0.258	0.727
C	0.015	0.015	0.015	0.257
m	1.0	1.0	1.0	1.0
T_0 (K)	293.15	293.15	293.15	293.15
T_m (K)	914	800	800	541
$\dot{\varepsilon_0}$ (s^{-1})	1	1	1	1
C_p (J/kg/K)	880	896	864	1670

Table 5: Mie-Grüneisen EOS properties

Parameter	Al 2017	Al 6061 T6	Al 2219 T87	Nylon
Mie-Grüneisen				
S1	1.29	1.4	1.29	1.63
Γ	2.0	1.97	2.0	0.87
S2	0	0	0	0
S3	0	0	0	0
a	0	0	0	0
η_{min}	0.4	0.4	0.4	0.4
η_{max}	2.5	2.5	2.5	2.587

Table 6: Cockroft-Latham damage properties
(# refers to test-case number defined in 4.1 Models paragraph)

Parameter	Al 2017	Al 6061 T6	Al 2219 T87	Nylon
Cockroft-Latham				
W_c (Pa)	1^{e}15	1^{e}15	1^{e}15	1^{e}15
σ_s (Pa)	2.66^{e}9	3.1^{e}9	2.53^{e}9	2.77^{e}9
α_s	1	1	1	1
t_s (s) #1	8^e-8	3^e-8	3^e-8	
t_s (s) #2	14^e-8	3^e-8	3^e-8	
t_s (s) #3		3^e-8	3^e-8	7^e-8
t_s (s) #4		3^e-8	3^e-8	
t_s (s) #5,6,8	6.5e-8	3^e-8	3^e-8	
t_s (s) #7	7e-8	3^e-8	3^e-8	

Table 7: Johnson-Holmquist model properties

Parameter	Alumina
Johnson Holmquist	
ρ (kg/m^3)	3700
G (Pa)	90^{e}9
A	0.93
B	0.31
C	0
m	0.6
n	0.6
$\dot{\varepsilon_0}$(s^{-1})	1
T_0 (Pa)	0.2^{e}9
HEL (Pa)	2.8^{e}9
Phel (Pa)	1.46^{e}9
β	1
D1	0.005
D2	1
K1 (Pa)	131^{e}9
K2 (Pa)	0
K3 (Pa)	0

4.3 SPH particles sizes

The SPH particles sizes (in µm) and the number of particles (in millions) are presented in Tab. 8:

Table 8: SPH particles data
(projectile / bumper / plate 1 / plate 2)

Test	Sizes	Nr. particles
#1	35 / 70 / 90	10.9
#2	35 / 70 / 90	10.8
#3	35 / 35 / 70	19.4
#4	35 / 35 / 70	20.1
#5	150 / 150 / 300	8.6
#6	120 / 120 / 120 / 300	19.4
#7	150 / 150 / 150 / 300	23.0
#8	150 / 150 / 300	12.6

4.4 SPH simulations vs. tests results comparison

This comparison focuses on the final structural effects of the impacts. Time-dependent results, such as debris cloud shape and velocity field, are still to be compared.
Fig. 10 to Fig. 17 hereafter compare the simulation results with the test results for the eight test cases. Numerical simulations are very close to experimental results for all the test cases.

PARAVIEW software [16] was used to plot the results.
Note: all models are full models, i.e., the symmetry axes were not used to reduce the computation time.

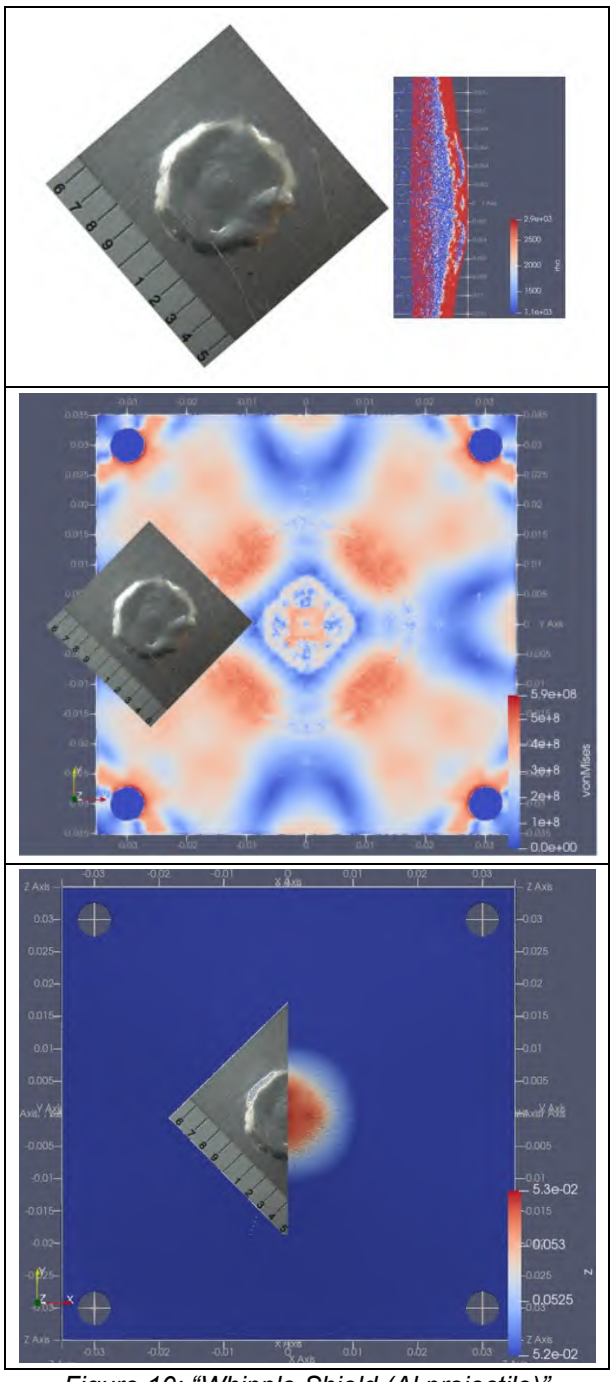


Figure 10: "Whipple Shield (Al projectile)" Rear wall back face

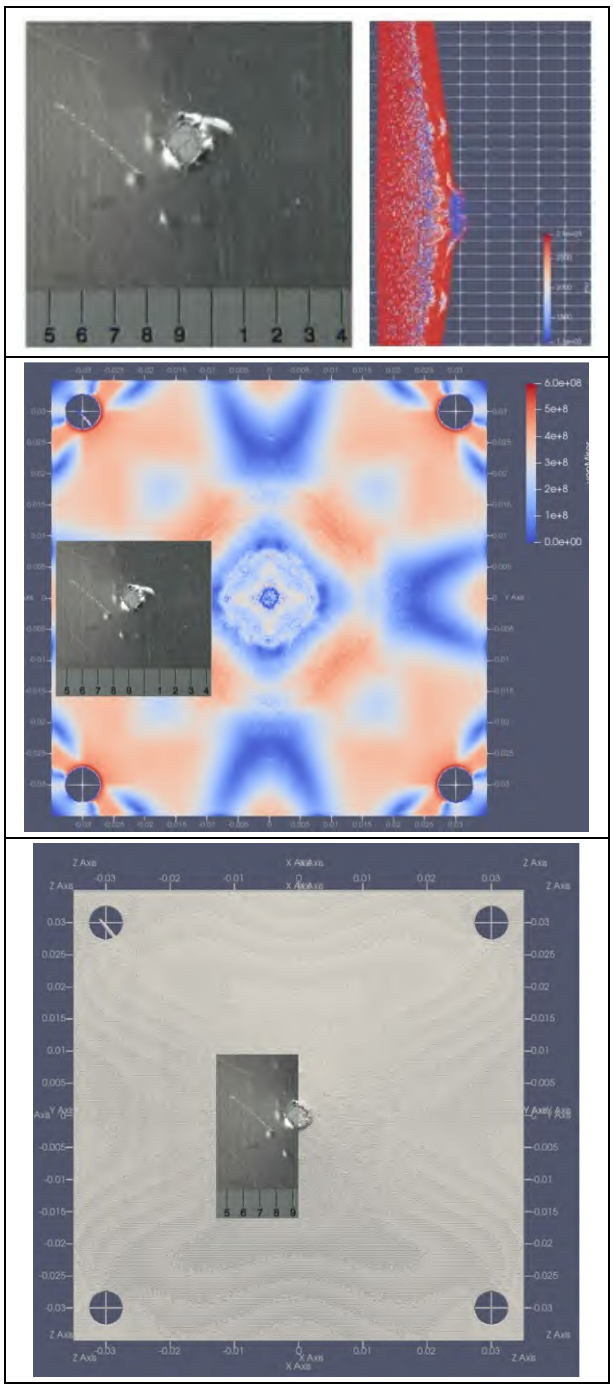


Figure 11: "Whipple Shield (Al projectile > 9 km/s)" Rear wall back face

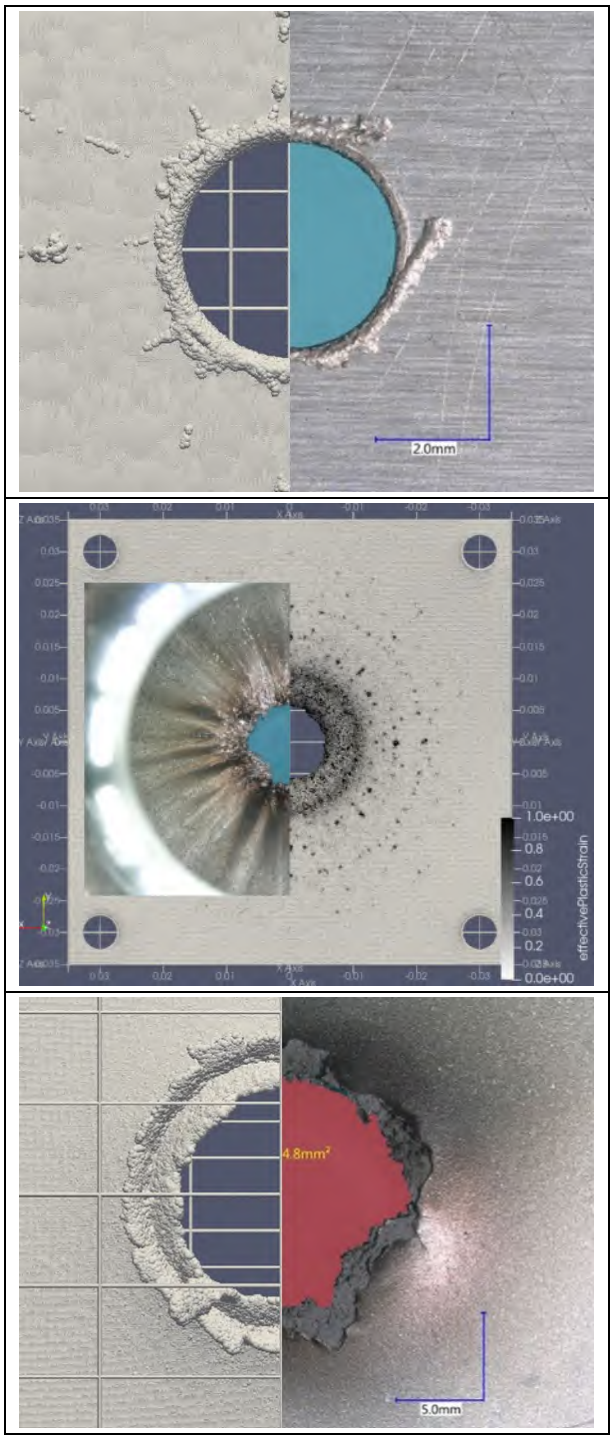


Figure 12: "Whipple Shield (Alumina projectile)" bumper front – rear wall (front) – rear wall (back)

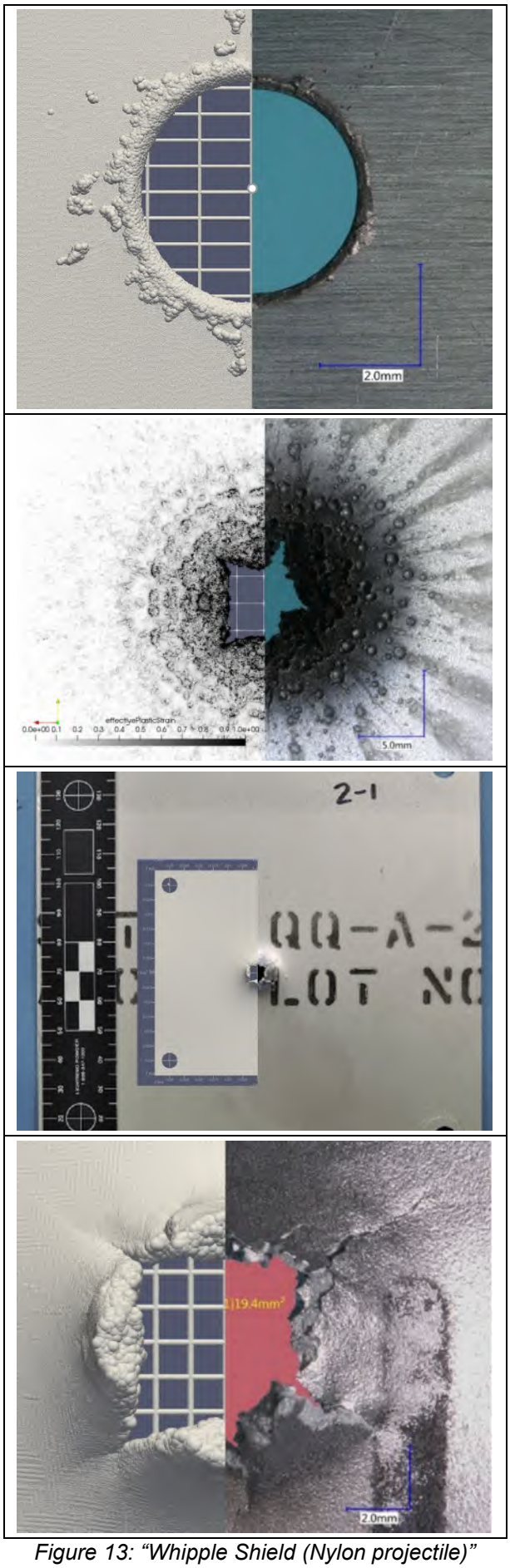


*Figure 13: "Whipple Shield (Nylon projectile)" bumper front – rear wall (front) – rear wall (back)*2*

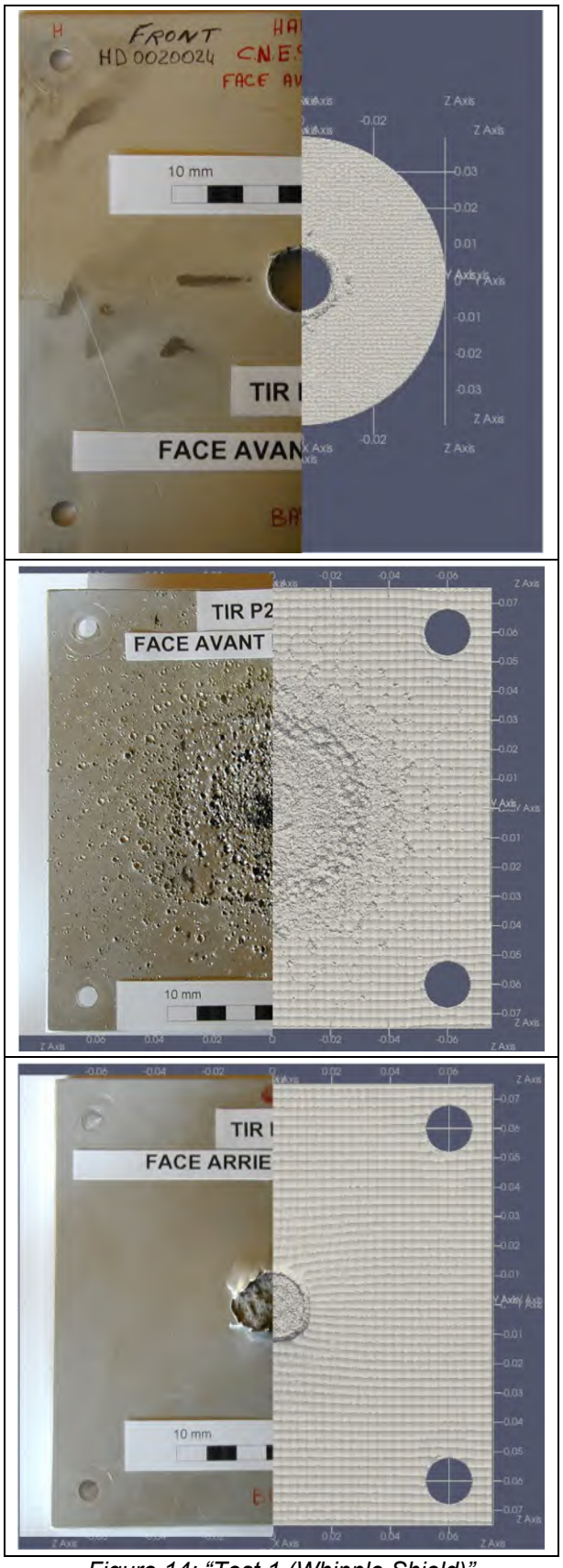


Figure 14: "Test 1 (Whipple Shield)"
bumper front – rear wall (front) – rear wall (back)

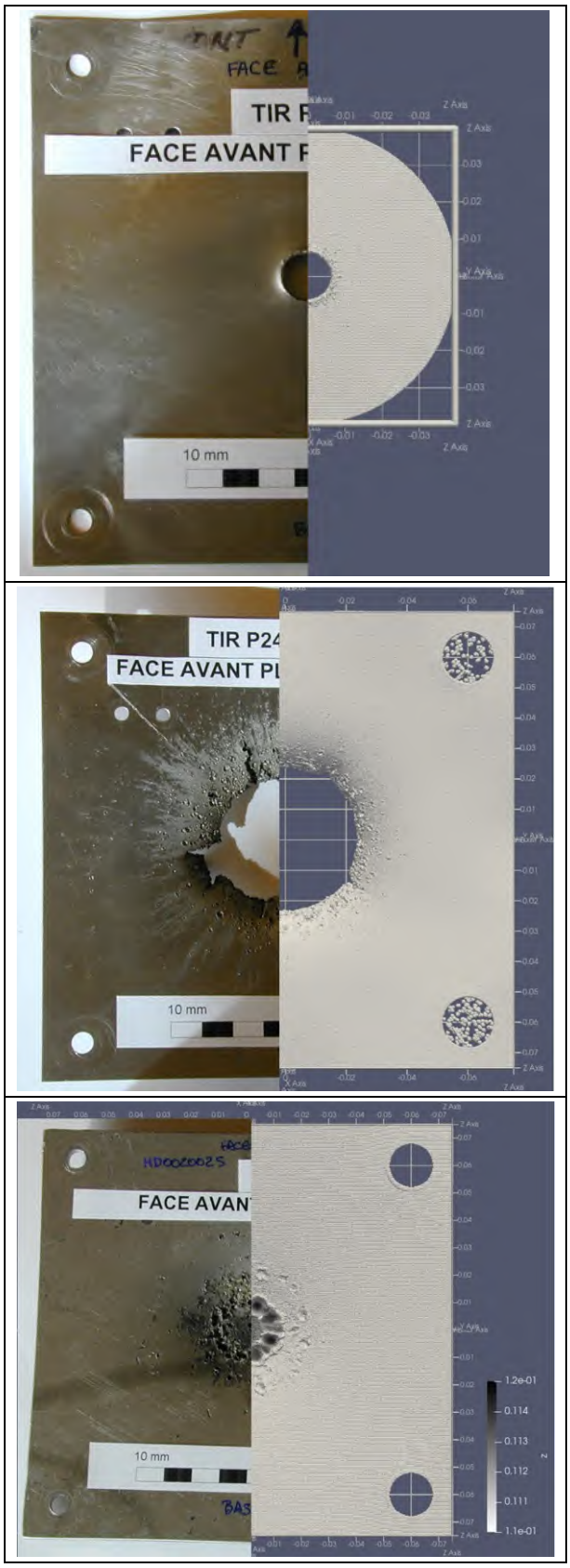


Figure 15: "Test 2 (Triple wall)"
bumpers #1 and #2 (front) – rear wall (front)

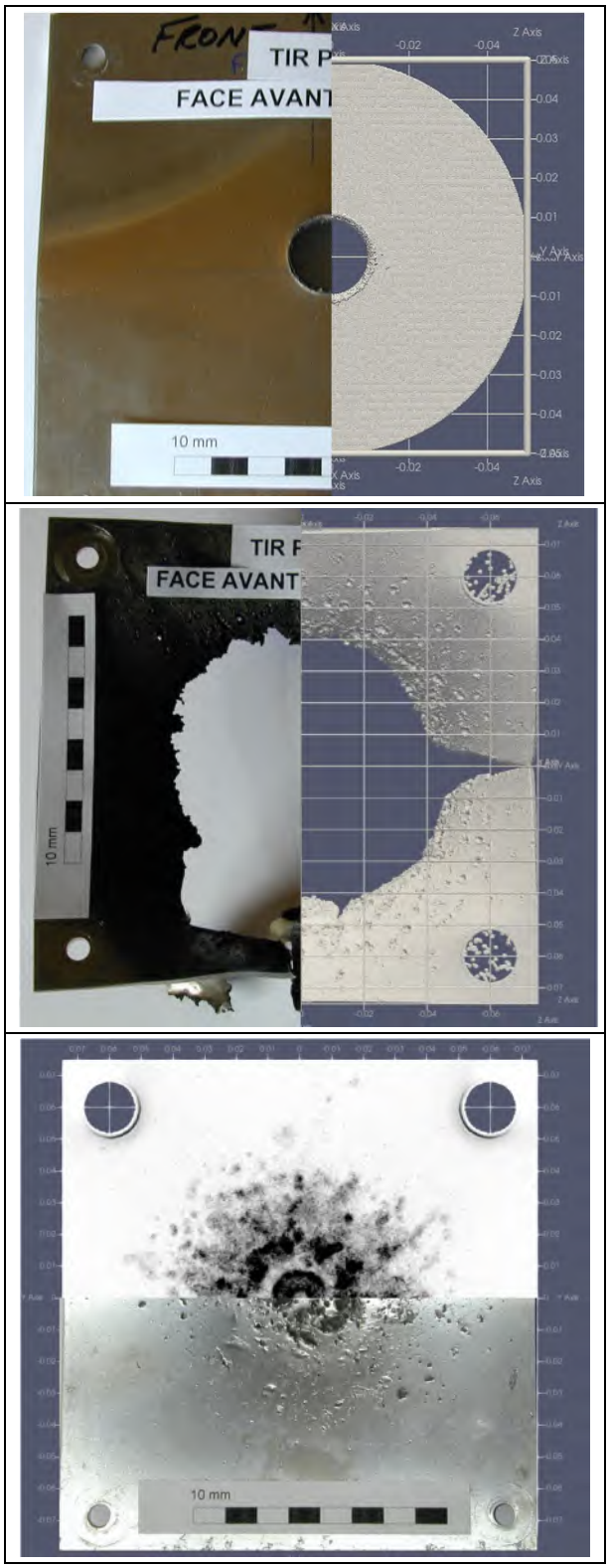


Figure 16: "Test 3 (Triple wall)"
bumpers #1 and #2 (front) – rear wall (front)

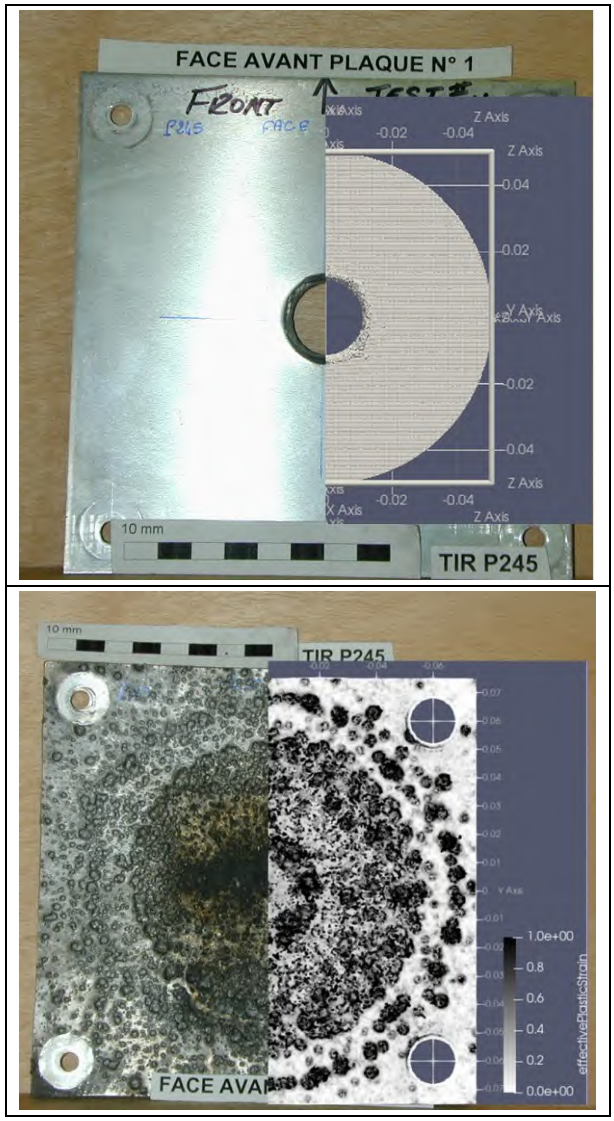


Figure 17: "Test 4 (Whipple Shield)"
bumper (front) – rear wall (front)

5. NUMERICAL BLE

The models presented in chapter 4 are conceived to be valid for a wide range of configurations. The tests presented in section 2 belong to this range of configurations. Therefore, the models were used to compute a ballistic limit curve for these tests, based on SPH simulations.

The parameters presented in chapter 4 were used 'as is', but the spall time had to be defined for impact velocities that were not tested against experimental results in chapter 4.
Tab. 9 below presents the list of spall times used in these simulations. Bold values are experimental cases from chapter 4. No experimental results from chapter 2 were used for the numerical simulations.

Table 9: Spall times

V (m/s)	t_s (ns)	Case #	V (m/s)	t_s (ns)	Case #
5500	65		7000	80	
5607	**65**	**6**	**7090**	**80**	**1**
5705	**65**	**5**	7500	80	
5738	**65**	**8**	8000	80	
5941	**70**	**7**	8500	100	
6000	70		9000	140	
6490*	**70**	**4**	**9290**	**140**	**2**
6500	70		9500	140	

*: nylon projectile

The identification of the result (i.e., perforation or non-perforation) is a fully automated process based on a dichotomy loop, controlled by a SCILAB [17] script, and an analysis of the impact geometry that reads ABSTRAO output files (in HDF5 format) and uses MATLAB's [18] alpha-shape function. The possibility to identify both attached spall and detached spall, in addition to perforation, was not used in this study.
The size of the SPH particles is 40 µm, which drives both the dichotomy convergence criterion and the alphaShape function parameters. The process also uses the fragment definitions included in ABSTRAO. To save computation time, the calculation is performed on a quarter model (total 70 hours, for 9 velocities, and typically 6 calculations per velocity for the dichotomy process)

Fig. 18 plots the computed critical diameter, and Fig. 19 plots the corresponding kinetic energy. The BLC based on Christiansen BLE with power coefficient α of 0.2 (from Tab. 2) is plotted for comparison.

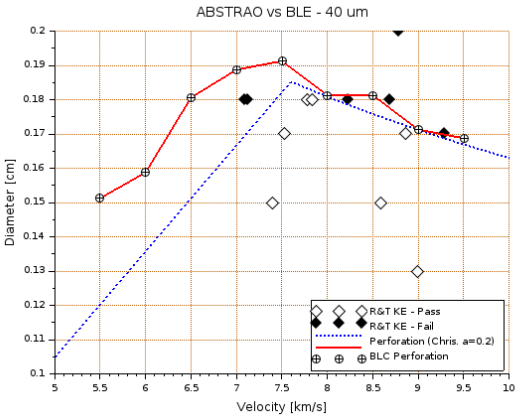


Figure 18: BLC for the tests: diameters

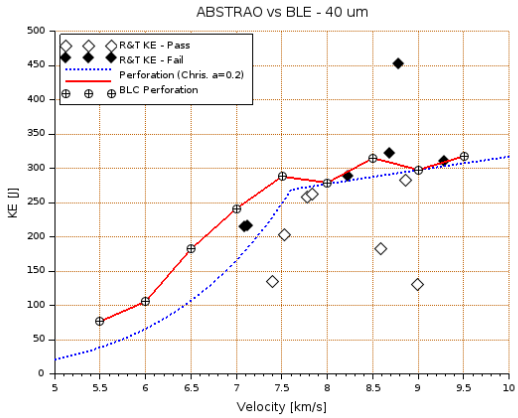


Figure 19: BLC for the tests: kinetic energy

The computed critical diameters are within the range of 0.1 mm (100 µm) of the test results, i.e., 5%.
It must be noted that, although this result seems accurate, an overestimation of 0.1 mm in critical diameter across the entire range of velocities results in an underestimation of 20 % of the OD impact flux for the SSO orbit presented in paragraph 3, and 70 % for the MM flux for the GEO case.

The most significant difference appears at 7 km/s (emphasised in the diameter plot as compared with the kinetic energy plot). This discrepancy was not fully investigated. There are still several possibilities for such a difference, including the tuning of the alpha shape parameters with respect to the SPH particle diameters. It must be noted that any modification will need to remain consistent with the test cases results and still allow a fully automated calculation.

This numerical BLC uses a Mie-Grüniesen EOS. For high-velocity impacts, typically above 9 km/s, the Tillotson EOS is often preferred because it includes a vapour phase transition. The ability of vapour to perforate a structure is much less than that of condensed matter (liquid and solid). Therefore, at high velocities it can be expected than part of the input kinetic energy will be lost for

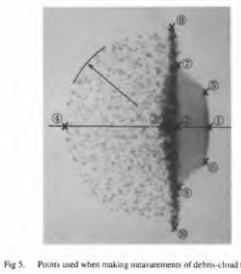
perforation because it is used for vaporisation. It is worth noting than this numerical BLC shows a trend of increasing kinetic energy at high velocities while it uses a Mie-Grüniesen EOS. Therefore, a higher increase of critical kinetic energy for perforation can be expected when an EOS adapted to high-velocity impacts is used for (future) numerical BLCs.

6. PRELIMINARY TRANSIENT RESULTS

The benchmark models used in section 4 were limited to steady-state (final) results. The verification of the SPH model with respect to transient results is in progress. The material models were first tested against test-cases from Piekutowski [19] [20]. This section presents one of the results.

The test-case is 4-1283, in which a 2017-T4 aluminium sphere of 9.53 mm diameter impacts a 0.97 mm thick 6061-T6 aluminium plate at 6.72 km/s. X-rays radiographs are available at times -3.1 µs, 7.3 µs and 20.4 µs (0 µs is the impact time). Lengths were measured at 20.4 µs, with origin at impact location. Velocity measurements are also available.
Tab. 10 presents the measured values and the associated locations on the generic debris cloud shape from [19] (lengths are converted from inches):

Table 10: Results from exp. 4-1283 at 20.4 µs

 Fig 5. Points used when making measurements of debris-cloud features.	V_1 = 6540 m/s d_1 = 133 mm d_2 = 127 mm d_3 = 123 mm d_4 = 88 mm $d_{5\text{-}6}$ = 20 mm $d_{7\text{-}8}$ = 31 mm $d_{9\text{-}10}$ = 68 mm

From Tab. 9, the spall time of the projectile is set to 70 ns. The other material properties are unchanged with respect to tables in section 4.

Fig. 20 presents the test X-rays radiographs, and Fig. 21 presents a cross section of the corresponding simulation results, with projectile in blue and bumper in red.

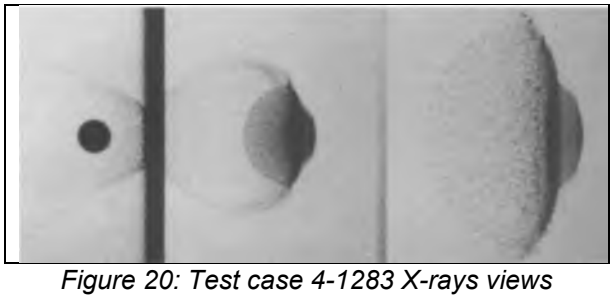


Figure 20: Test case 4-1283 X-rays views

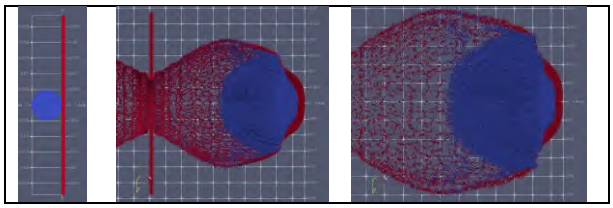


Figure 21: Simulation results of test case 4-1284

Fig. 22 superimposes the locations of point 1 (X), point 4 (+) and perpendicular distances on the simulation results at time 20.4 µs.

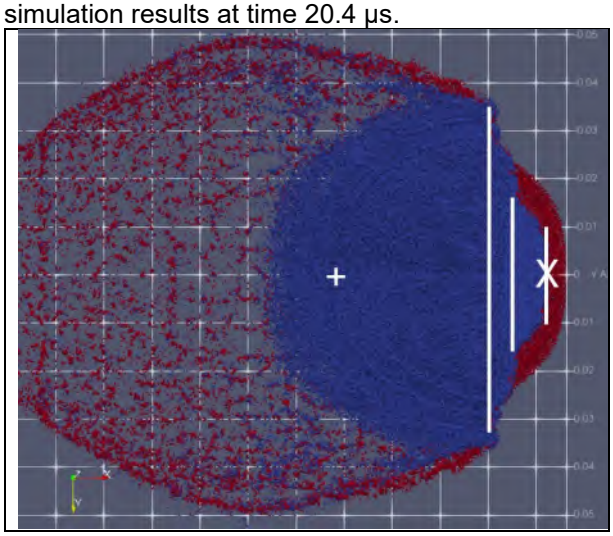


Figure 22: Test-simulation comparison

The simulation is quite accurate, provided that the remains of the bumper (red) in front of the projectile (blue) are not visible on the X-rays radiographs.

The densities of the SPH particles are close. Therefore, a simple count of the particles can represent the average density. Fig. 23 plots the number of SPH particles on 1mm*1mm squares along the impact axis in the Fig. 22 plane, integrated over the thickness of the cloud (perpendicular to the image plane). The distances d_1 to d_4 are also plotted.

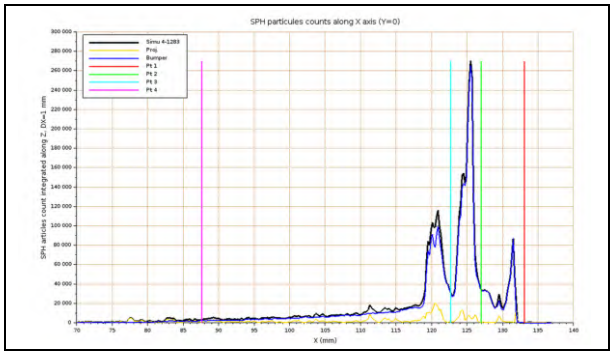


Figure 23: Apparent density

Fig. 23 shows the apparent density in front of the projectile is very low, thus likely not be captured by the X-rays radiograph.
The computed velocity at point 1 and time 20.4 µs is 6687 m/s, i.e. 2% above the measured velocity of 6540 m/s.

To illustrate the apparent density, Fig. 24 compares the front part of the cloud as seen from the outside, with two values of the opacity parameter of PARAVIEW post-processing software.

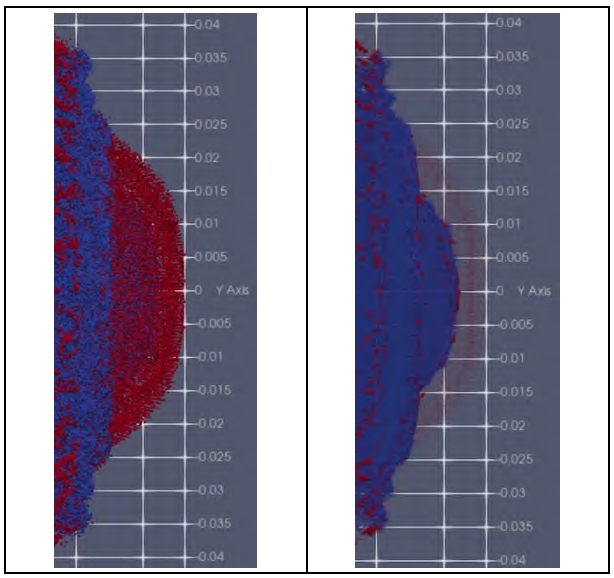


Figure 24. Opacity plots (left: 1; right: 0.05)

These first results provide confidence in the ability of these material properties to simulate accurately a wide range of impact conditions.

7. CONCLUSION

Widely used to design Whipple Shield structures, the Christiansen Ballistic Limit Equation (BLE) assumes that the projectile critical kinetic energy is constant in the hypervelocity regime. This paper presented a series of hypervelocity impact tests (in the range of 7 to 9 km/s) to measure this increase. A power law with a power coefficient around 0.2 was measured

In parallel, a hydrocode-based numerical ballistic limit curve for these tests was developed. Without tuning to these tests results, the curve's accuracy was around 0.1 mm for a critical diameter around 1.7-1.8 mm. In terms of critical kinetic energy increase in the hypervelocity regime, this ballistic limit curve shows the same trend as the test results. Because the vaporisation is not considered in the numerical models, one can expect higher increase of the critical kinetic energy for even higher velocities. This would allow reducing the computed risk of perforation of Whipple Shield structures with respect to the actual risk.

ACKNOWLEDGEMENT

This activity was funded under the CNES Research and Technology programme.

REFERENCES

1. *Protection Manual*, inter-Agency Space Debris Coordination Committee, IADC-04-03, Version 7.2 (2023)
2. E. Christiansen, *Handbook for Designing MMOD Protection*, NASA/TM–2009–214785 (2009)
3. A.J. Piekutowski et al., *Performance of Whipple shields at impact velocities above 9 km/s*, International Journal of Impact Engineering 38 (2011) 495 – 503
4. A.J. Piekutowski, K.L. Poormon, *Effects of Scale on the Performance of Whipple Shields for Impact Velocities Ranging from 7 to 10 km/s*, The 12th Hypervelocity Impact Symposium. Procedia Engineering 58 (2013) 642 – 652
5. *R&T Correction of ballistic equations*, Thiot Ingénierie Report TH-1198-R02A (in French), Dec. 2024
6. sdup.esoc.esa.int
7. www.abstrao.com
8. Miller, J.E., Davis, B.A., Deighton, K.D. and McCandless, R.J. *Rear Wall Perforation in Whipple Shields for Low- and High-Density Particles*. The 2nd International Orbital Debris Conference Proceedings, (2023)
9. V. Albouys, C. Loupias, *Calibration of the French CEG Hypervelocity launcher*, 3rd European Conference on Space Debris, 2001
10. J-M. Sibeaud, P.L. Héreil, V. Albouys. *Hypervelocity Impact on Spaced Target Structures: Experimental and Ouranos Simulation Achievements*. International Journal of Impact Engineering 29 (2003) 647-658
11. Jiana Yi et al., *Simulation Study on Expansive Jet Formation Characteristics of Polymer Liner*, Materials 2019, 12, 744
12. P.A. Trouche, *Simulation of hypervelocity impacts on spacecraft structures*, Internship report (in French), 2024
13. Anderson C.E., Johnson G.R., Holmquist T.J., *Ballistic experiments and computation of confined 99.5% Al2O3 ceramic tiles*, Proceedings of the 15th International Symposium on ballistics, Jerusalem, Israel, May 1995
14. D. Cronin, *Implementation and validation of the Johnson-Holmquist Ceramic Material model in LS-Dyna*, 4th Europeans LS-DYNA users Conference, 2003
15. K. Loft, M.C. Price, M.J. Cole, M.J. Butchell, *Impacts onto metal target at velocities greater than 1 km s-1: A new online resource for the hypervelocity impact community and an illustration of the geometric change of debris cloud impact patterns with impact velocity*, Int. J. Impact Eng., 56 (2013) 47-60
16. www.paraview.org
17. www.scilag.org
18. www.mathworks.com
19. A.J. Piekutowski. *Characteristics of debris clouds produced by hypervelocity impact of aluminum spheres with thin aluminum plates.* Int. J. Impact Eng., Vol. 14, pp. 573-586, 1993.
20. A.J. Piekutowski. *Formation of debris clouds produced by hypervelocity impact.* NASA 1996 CR-4707.

DEMISABLE KRYPTON TANK – FINAL PRESENTATION

Simone Hartl [(1)]

[(1)] *Peak Technology, Technologiepark Str. 6, 4615 Holzhausen (AUSTRIA), Email: simone.hartl@peaktechnology.at*

KEYWORDS

Design for demise, demisable COPV, re-entry

DISCLOSURE STATEMENT

This paper reports the final results of ESA Contract No. 4000143280/24/NL/GM/lf, “Demisable Krypton Tank”. The results of this activity were originally presented at the Space Propulsion Conference 2026, 21. May 2026 [1]. This paper has been prepared to fulfil the contractual Final Project Presentation requirement and presents the final data.

ABSTRACT

Uncontrolled atmospheric re-entry of orbital debris poses a growing risk to the population on ground, with an accepted casualty risk limit of 1 in 10,000. Type 3 COPVs (composite overwrapped pressure vessel), consisting of a metallic liner overwrapped with CFRP (carbon fiber reinforced polymers), are among the components least likely to demise during re-entry.

This paper reports the design of a demisable 1L Type 3 COPV, developed under an ESA ARTES-funded activity, using a modified CFRP overwrap intended to trigger earlier degradation during re-entry. Simulation and dedicated re-entry testing demonstrate a marked demisability improvement relative to a conventional tank design.

1. INTRODUCTION

An enormous number of objects in low Earth orbits re-enter the Earth's atmosphere uncontrolled due to friction drag and thus pose a danger to the population on ground. [2]

According to international safety guidelines, the on-ground casualty risk for a re-entering object must not be higher than 1 in 10000. The probability of an accident can be reduced by a controlled re-entry or by reducing the potential casualty area of the fragments, e.g. with a design for demise (D4D) approach. Due to the high cost of a controlled re-entry into an uninhabited area the latter option is usually preferred. [3]

Some of the most critical components regarding demisability are Type 3 COPVs (Composite Overwrapped Pressure Vessels) that are used to contain or pressurize propellants. [4] Type 3 COPVs consist of a thin metallic liner that is overwrapped with CFRP (Carbon Fiber Reinforced Polymers) by filament winding process. Fig. 1 shows an example of a Type 3 COPV.



Figure 1: Type 3 composite overwrapped pressure vessel

Due to this criticality aluminum is increasingly used instead of titanium for the internal metallic liner, enhancing demisability with the significantly lower melting point of aluminum. However, the main challenge is the degradation of the composite layer. [4]

This work presents the progress of the development of a demisable Type 3 COPV. The focus is on the CFRP overwrap since the carbon fibers, continuously overwrapping the liner, are preventing the COPV from full demise.

Previous activities addressed the development of a resin system as well as the modification of the CFRP to enable detachment from the COPV. The modification follows the patent from Peak Technology [5] by applying the CFRP (carbon fiber reinforced polymers) in a discontinuous way. A proof of concept of the developed demisable CFRP with tests in a plasma wind tunnel highlighted excellent demise behavior compared to standard CFRP material on coupon level.

The further activities presented in this paper aim to bring the developed technology to a component level comprising a FEM (Finite Element Method) based design of a 1L COPV and re-entry simulation thereof. For the re-entry simulation a material model is set up for the demisable CFRP.

2. DEVELOPMENT APPROACH

2.1. Baseline Overwrap Design

A baseline design of the overwrap is established with the standard CFRP material as starting point for first tests on component level and for later comparison with a demisable design.

The liner defines the COPV main geometrical characteristics volume and diameter. The size is selected in alignment with the maximum possible sample size for the plasma wind tunnel and covers the following characteristics:

- Material: aluminium
- Volume: 1 L
- Outer diameter: 90 mm
- Wall thickness: 1.3 mm

The material and shape of the liner, see Fig. 2, is representative to other Peak Technology COPVs and the wall thickness is selected to enable a stable sample manufacturing for later plasma wind tunnel tests, including sample instrumentation with thermocouples.

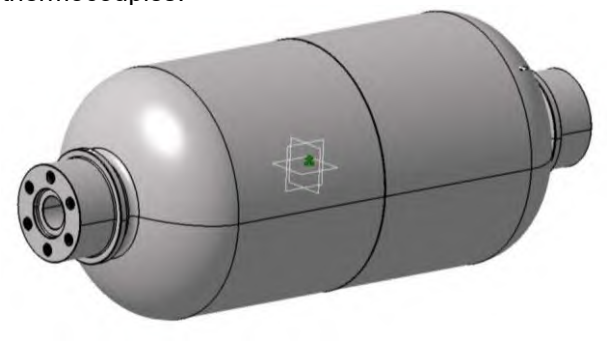


Figure 2: Liner for 1L COPV

The overwrap is designed with FEM analysis according to the following requirements:

- MEOP (Maximum Expected Operating Pressure): 310 bar
- Pressure safety factors: Proof 1.25xMEOP, Burst: 1.5xMEOP
- Demisability: boundary condition to have a minimum overwrap thickness

No further boundary conditions and requirements are considered at this development state but need to be considered for the future.

The material properties used are taken from an existing representative CFRP material.

2.2. Plasma Wind Tunnel Test Campaign

A plasma wind tunnel test campaign is performed on component level with samples with the baseline design and variations thereof to:

- Test demise behavior of demisable overwrap on a representative part
- Get initial results for the demise behavior of a COPV as a whole
- Collect data to build a material model for the re-entry simulation (see chapter 2.5)

The tests are conducted in the plasma wind tunnel “L2K” at the German Aerospace Center (DLR) in Cologne. In a plasma wind tunnel the strong aerothermal and mechanical loads that are typical for the re-entry of satellite components are simulated by generating a high enthalpy gas flow environment. [6]

The varying parameters for the test campaign are:

- **Heat flux**
  Representative low and high value: 300 kW/m², 600 kW/m² on the sample
- **CFRP thickness**
  CFRP thickness of baseline design and significantly higher CFRP thickness: 1.5 mm, 4.5 mm
- **Fiber length**
  Continuous fibers, short and long fiber length for comparison
- **CFRP material**
  Standard and demisable CFRP for comparison. Additionally, one sample is tested with the CFRP with the improved resin system but continuous fibers (improved CFRP) to show the effectiveness of the demisable CFRP.

The test matrix is given in Tab. 1.

Table 1: Test matrix plasma wind tunnel test campaign

No	CFRP [-]	Heat flux [kW/m²]	Fiber Length [mm]	Overwrap thickness [mm]
1	Demisable CFRP	300	Short	1.5
2	Demisable CFRP	600	Short	1.5
3	Demisable CFRP	300	Short	4.5
4	Demisable CFRP	300	Long	1.5
5	Improved CFRP	300	Conti-nous	1.5
6	Standard CFRP	300	Conti-nous	1.5

Thermocouples are implemented in different areas and depths in the samples that measure the temperature during the test to generate data for the material model for the re-entry simulation (see chapter 2.5).

Additionally, the surface temperature of the samples is measured with a spectral pyrometer, a two-color pyrometer and an infrared camera.

2.3. Mechanical Testing

For the following design of the demisable overwrap the mechanical properties of the material are required.

Since extensive material characterization was not possible within the scope of the project, only longitudinal tensile properties are evaluated.

The stiffness of the demisable CFRP material is considered comparable to standard CFRP material based on preliminary tests conducted within a previous activity.

The tensile strength of the demisable CFRP is derived by applying a knock-down factor that is calculated by comparing the strain at break of the demisable and standard CFRP.

To measure the strain at break a tailored test method is developed that is more representative to the manufacturing method and loading of a COPV than according to common test standards.

As shown in Fig. 3, CFRP rings, supported by steel rings for uniform load transfer, are pressed onto a steel cone to continuously strain them radially until rupture. The reason for measuring the strain at break instead of directly deriving the tensile strength is the friction between steel cone and steel ring, even though it is lubricated, possibly influencing the measured forces.

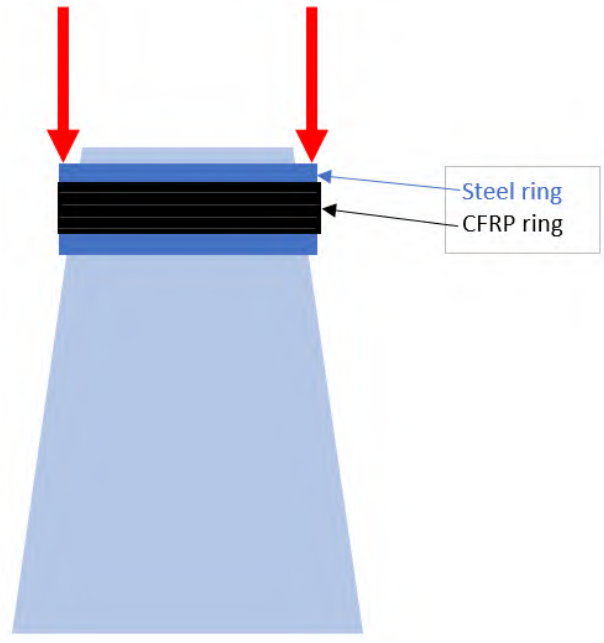


Figure 3: Tensile test set up

The CFRP rings have a width of 20 mm, inner diameter of 100 mm and wall thickness of 0.75 mm and are manufactured with the same method as the COPV samples for the plasma wind tunnel, which is filament winding. The layup is unidirectional with the fiber direction in the circumference to generate a longitudinal tensile load case.
To measure the radial strain of the CFRP rings, one linear strain gauge is applied on each sample. The test speed is set at 20 mm/min.

The test is conducted for the demisable CFRP and standard CFRP, five samples are tested each.

2.4. Demisable Overwrap Design

The baseline overwrap design is updated with the mechanical properties of the demisable CFRP.

All other requirements, including liner geometry, remain unchanged.

2.5. Re-entry Simulation

For the re-entry simulation a material model is required that represents the demise behavior of the developed demisable CFRP material.

The modelling is performed by Belstead Research. Main part of the input for the material model is the data from previous plasma wind tunnel tests with the same material. Physical and thermos-physical properties are taken from literature or testing, if available. For the liner an existing generic material model for aluminium is used.

To verify the developed material model at that stage, test predictions are done for the plasma wind tunnel test campaign by performing re-entry simulations based on the defined test plan. With data from this test campaign the model can be improved.

A re-entry simulation is performed for the 1L COPV with the demisable overwrap design. For the simulation a deterministic analysis is performed with the destructive re-entry tool SAMj, complemented with a probabilistic analysis to produce demisability maps using SAMj in conjunction with the tool PADRE.

As starting condition, the COPV is released from a fictional parent vehicle at a randomly selected altitude from 70 km to 100 km and on a randomly selected inclination. Altogether 2000 simulations are run, allowing to generate a comprehensive map of the demise behavior of the COPV.

Furthermore, a proxy model is established for the software DRAMA which is the standard re-entry simulation tool from ESA.

3. RESULTS

3.1. Baseline Overwrap Design

The output of the performed FEM analysis is a layup of the standard CFRP for the defined liner. The layup has a thickness of 1.88 mm in the cylindrical part and a model of the COPV with the baseline

overwrap design is shown in Fig. 4.



Figure 4: 1L COPV with baseline overwrap design

For the burst pressure load case, being the driving load case, the Margin of Safety (MoS) for the overwrap is 0.45.

This design serves as baseline for plasma wind tunnel testing of the demisable layup and re-entry simulation.

3.2. Plasma Wind Tunnel Test Campaign

The test campaign demonstrates the significant impact of the demisable CFRP overwrap on the demisability of the tested COPV as well as the improvement compared to standard CFRP overwrap.

For the sample with the demisable CFRP and the lower heat flux (test 1) the liner was initially revealed after ~50 s and fully exposed after ~65 s. Whereas for the same sample and the higher heat flux (test 2) the liner was initially revealed after ~30 s and fully exposed after ~50 s.

For the sample with the higher thickness (test 3) the test lasted longer with ~120 s until the liner was revealed and ~140 s until the liner was fully exposed.

Since the test with the sample with the longer fiber length (test 4) is comparable to the test with the shorter fiber length, the fiber length has no influence on the demise behavior within the tested range. This conclusion is only applicable up to a certain threshold which is not known.

A sample after the test, representative for test 1-4 is shown in Fig. 5.



Figure 5: Sample test 1 after plasma wind tunnel test

For the sample with continuous fibers (test 5), the resin is degraded. However, the continuous carbon fibers cannot detach from the liner except for the outermost layer. The test stopped after ~180 s after the liner is fully melted and the sample slipping from the clamping. The residual of the sample is shown in Fig. 6.



Figure 6: Sample test 5 after plasma wind tunnel test

The test with the sample with the standard CFRP (test 6) is stopped after ~180 s, since no significant degradation is observed, see Fig. 7. The liner is not fully melted after the same test time as for test 5, due to the compact CFRP material isolating the liner compared to the loose fiber structure.



Figure 7: Sample test 6 after plasma wind tunnel test

This test campaign highlights the enhanced demisability of the developed demisable CFRP material, hereby also proven on component level.

3.3. Mechanical Testing

The test results are given in Tab. 2. Since two samples failed during testing, four valid tests are conducted per material.

Table 2: Test results strain at break

Material	Strain at Break (Mean) [%]	Strain at Break (Standard deviation) [%]	No
Standard CFRP	1.20	0.03	4
Demisable CFRP	1.03 (-14%)	0.06	4

A sample (standard CFRP) after testing with is shown in Fig. 8.



Figure 8: Standard CFRP sample after testing

The strain at break of the demisable CFRP is ~14% lower than of the standard CFRP. This reduction is applied to the longitudinal tensile strength of the standard CFRP as a knock-down factor of 0.86 to calculate the longitudinal tensile strength of the demisable CFRP.

This initial test of the demisable CFRP gives a good indication for the mechanical performance, however, further extensive testing is required for the future.

3.4. Demisable Overwrap Design

To define the demisable overwrap design, the previous FEM analysis is repeated with the calculated longitudinal tensile strength of the demisable CFRP.

The outcome is a new layup with a thickness of 2.82 mm.

A comparison of the overwrap design for the standard and demisable 1L COPVs is in Tab. 3.

Table 3: Comparison of standard and demisable overwrap design

	Overwrap thickness [mm]	Margin of safety (burst pressure load case) [-]
Baseline overwrap design	1.88	0.45
Demisable overwrap design	2.82 (+50%)	0.17

Since the fibers of the demisable CFRP are discontinuous, the resulting increase of the overwrap thickness is as expected. For COPVs with a bigger volume, the relative increase might be smaller and should be evaluated in the future.

3.5. Re-entry Simulation

The material model of the demisable CFRP is established with the data from the plasma wind tunnel tests as final input and the re-entry simulation of the 1L COPV performed accordingly.

The simulations suggest that the COPV can demise during re-entry if it is released at a sufficiently high altitude. Considering the median of all runs, the COPV is demisable until a release altitude of 84 km, as shown in Fig. 9. Below a release altitude of 77 km, the COPV is predicted to always have some part reaching the ground.

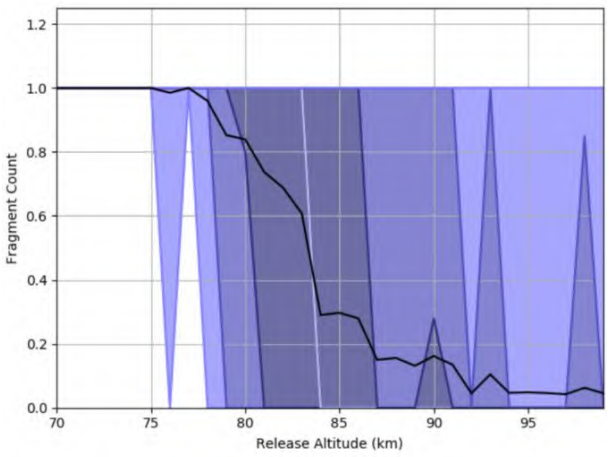


Figure 9: 1L COPV fragment number probability map

The key for Fig. 9, also applicable for Fig. 10 to Fig. 14, is shown in Fig. 10.

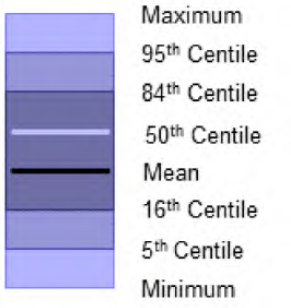


Figure 10: Key for re-entry simulation probability maps

Due to the small part size of the 1L COPV, the casualty area is small even for the cases where the COPV survives, with a maximum of 0.52 m², as shown in Fig. 11.

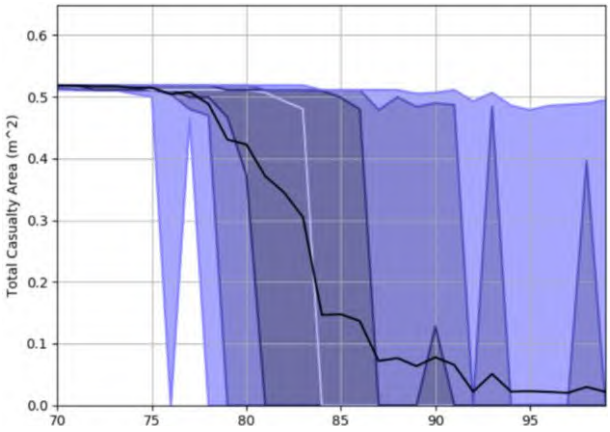


Figure 11: 1L COPV casualty area probability map

The landed mass probability indicates a landed mass below half of the original tank mass of ~600 g in essentially all cases, with the average landed mass being below 50 g for release altitudes above 85 km, see Fig. 12.

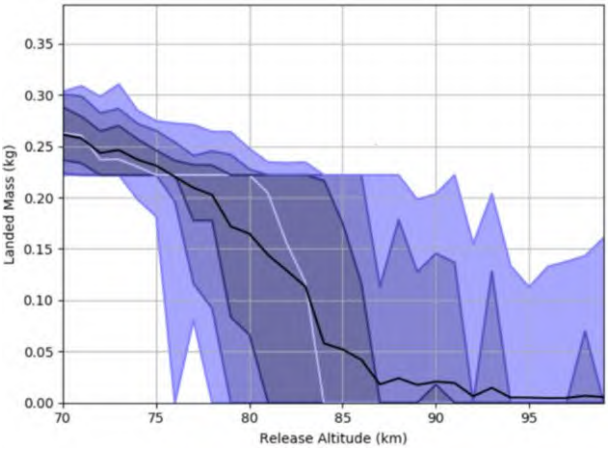


Figure 12: 1L COPV landed mass probability map

For a direct comparison of the demisable and standard CFRP, a simulation is performed additionally with the 1L COPV with an already existing standard CFRP material model. According to the simulation the 1L COPV with the standard CFRP there is no case where the CFRP is demising (see Fig. 13) which is in alignment with the test in the plasma wind tunnel.

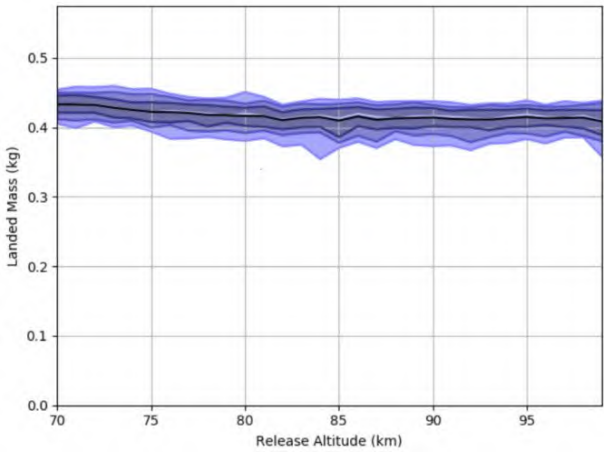


Figure 13: 1L COPV with standard CFRP landed mass probability map

Approximately 25 % of the mass is still degrading for all cases, however, this corresponds to the mass of the bosses and some decomposition of the resin system. This extremely low recession rate of the standard CFRP material and consistent behavior over all release altitudes is a typical behavior of a Type 3 COPV with a standard CFRP overwrap.

The results demonstrate the extremely low demisability of standard CFRP materials and highlight the excellent demise performance of the demisable CFRP developed by Peak Technology.

To make the material model usable for the ESA re-entry tool DRAMA a proxy model is created. Since for SAMj a higher range of material properties is used as input, the proxy model for DRAMA is modified until the results are matching.

For comparison, the landed mass probability map created with the proxy model is shown in Fig. 14.

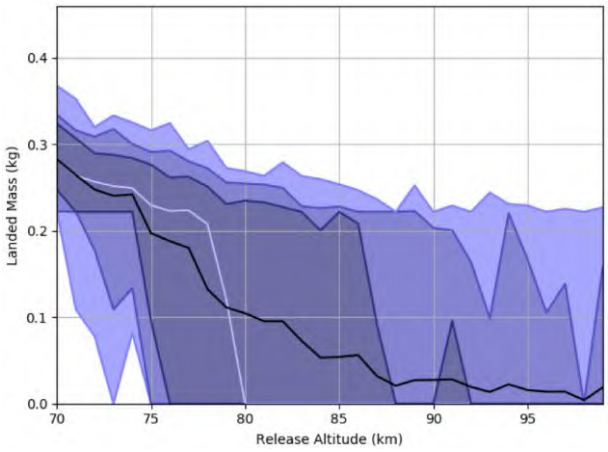


Figure 14: 1L COPV proxy model landed mass probability map

Even though the demisability of the 1L tank is slightly overpredicted, it provides a good first estimate of the demisability of a given tank design using the demisable CFRP material given that the key material physics is missing in the DRAMA model.

4. CONCLUSION & OUTLOOK

This study demonstrates the feasibility of a demisable Type 3 COPV through a modified CFRP overwrap with discontinuous fibers. Plasma wind tunnel tests confirm a significantly enhanced degradation behavior compared to standard CFRP, enabling early liner exposure under representative re-entry conditions. The demisable CFRP material shows a reduction in tensile performance and therefore increased overwrap thickness to meet the technical requirements.

Re-entry simulations, supported by a material model that was set up based on plasma wind tunnel test data, indicate a high demisability potential of the 1L COPV and a substantial reduction in landed mass and casualty area compared to conventional designs.

Future work will focus on upscaling the developed technology to industrial relevant COPV sizes and further material characterization of the demisable CFRP as well as mechanical testing with full scale COPVs with the demisable CFRP.

5. REFERENCES

1. Hartl, S. (2026). DESIGN FOR DEMISE DEVELOPMENT FOR HIGH PRESSURE PROPELLANT TANKS. In *10th 3AF International Space Propulsion Conference 2026*. Bari.
2. Torres-Herrador, F., Eschenbacher, A., Blondeau, J., Magin, T. E., & Van Geem, K. M. (2022). Study of the degradation of epoxy resins used in spacecraft components by thermogravimetry and fast pyrolysis. *Journal of Analytical and Applied Pyrolysis*, *161*. https://doi.org/10.1016/j.jaap.2021.105397
3. Kärräng, P., Lips, T., & Soares, T. (2019). Demisability of critical spacecraft components during atmospheric re-entry. *Journal of Space Safety Engineering*, *6*(3), 181–187. https://doi.org/10.1016/j.jsse.2019.08.003
4. Parigini, C., Riley, D., Fuentes, I. P., Meyer, J.-C., Leyland, P., Hannema, G., … Lips, T. (2016). " DESIGN FOR DEMISE " TECHNIQUES TO REDUCE RE-ENTRY CASUALTY RISK. In *66 th International Astronautical Congress*. Jerusalem. https://doi.org/10.13140/RG.2.1.1897.1281
5. Umwicklung aus einem Faserverbundkunststoff für einen Raumfahrtbehältermantel. (2022, October 15). Austria.
6. Beck, J., Caiazzo, A., Gülhan, A., Innocenti, L., Schleutker, T., & Soares, T. (2019). Plasma Wind Tunnel Demisability Testing of Spacecraft Equipment. In *International Orbital Debris Conference*.

INTEGRATING DEMISABILITY AND ATMOSPHERIC IMPACT INTO SUSTAINABLE SPACECRAFT MATERIAL SELECTION

Benjamin Krolitzki [(1)], Amelie Katzke [(1)], Manuela Perthold [(2)], Joachim Strittmatter [(2)], Frank Best [(2)], Christian Nied [(2)], Lazar Bošković [(2)]

(1) CarboSpaceTech GmbH (CST), Seelbachstraße 9, 88090 Immenstaad, Germany, Email: benjamin.krolitzki@carbospacetech.com

(2) HTWG Konstanz, Alfred-Wachtel-Straße 8, 78462 Konstanz, Germany

KEYWORDS

Sustainable spacecraft design; Design for Demise; CFRP sandwich structures; atmospheric reentry residues; life cycle assessment methodology; environmental impact of space activities

ABSTRACT

Design for Demise (D4D) and debris mitigation guidelines reduce ground casualty risk by ensuring spacecraft structures ablate fully during atmospheric reentry, but thereby increase the fraction of mass converted into high-altitude gaseous and particulate residues. This environmental trade-off is not yet reflected in material selection or life cycle assessment (LCA) practice, even as mass launched into orbit grows exponentially. Aluminium oxide reentry products already show measurable atmospheric effects; carbon fibre reinforced polymer (CFRP) sandwich structures, an increasingly used lightweight alternative, may shift rather than remove this risk, since their combustion residues remain largely uncharacterised. This paper presents a combined industry-academia methodology contribution: controlled laboratory oxidation and pyrolysis of a generic, flight-representative CFRP sandwich panel and candidate core materials, coupled with aerosol, particle and residue analytics, informing a proposed cradle-to-grave life cycle inventory (LCI) and impact assessment framework, extended by a dedicated deorbit and atmospheric release module, as a methodological basis for future, industry-relevant material selection.

1. INTRODUCTION

The number of active satellites in Earth orbit continues to grow at an unprecedented rate, driven primarily by large communication constellations. In 2024 alone, 2,695 satellites were launched into orbit, adding an estimated 2,172 t of material [1]. Agency projections anticipate on the order of 100,000 active satellites in orbit by 2030 [2], although estimates vary.

To limit the long-term accumulation of orbital debris, international guidelines such as the Inter-Agency Space Debris Coordination Committee (IADC) 25-year post-mission disposal rule [3] and the United Nations Committee on the Peaceful Uses of Outer Space COPUOS long-term sustainability guidelines [4] are increasingly translated into requirements, notably ISO 24113 [5]. A central strategy to comply with these requirements is D4D: spacecraft structures are deliberately engineered to fully disintegrate during atmospheric reentry, reducing the risk that debris fragments reach the ground [6, 7]. According to ESA's 2025 Space Environment Report, controlled reentries of rocket bodies outnumbered uncontrolled ones for the first time in 2024, a practice that increased from around 10% to over 65% over the last decade [7].

D4D is effective at reducing ground casualty risk, but it does so by converting spacecraft mass into gaseous and particulate residues at high altitude instead. The environmental relevance of these residues is not yet systematically addressed: material selection for spacecraft structures is governed by mechanical performance, flight heritage, processability and qualification status, while LCA practice for space systems typically ends at launch and does not yet include a dedicated reentry or atmospheric release module [8].

Aluminium is the dominant structural material in current satellites and is already known to produce climate-relevant reentry residues: aluminium oxide (Al_2O_3) particles have been identified in stratospheric aerosol samples [9] and are associated with ozone-depleting heterogeneous chemistry [10, 11], changes to the stratospheric radiative balance [10], and act as condensation nuclei potentially affecting cloud formation [14]. CFRP sandwich structures offer a lightweight, mass-efficient alternative to aluminium and are already used at scale, for example in satellite solar generator substrates. However, their thermal decomposition mechanism during reentry differs fundamentally from that of metals: instead of oxidation to a stable oxide, CFRP resin systems undergo pyrolysis and combustion, processes known from industrial-scale composite recycling to release carbon monoxide, hydrogen cyanide, and respirable fibre fragments [12], none of which have been characterised under reentry-relevant conditions. Replacing aluminium with CFRP may therefore shift the environmental burden rather than remove it, unless the resulting residues are characterised and included in material selection. Beyond substituting one material for another, structural design choices such as core geometry –

for example, folded-core concepts as an alternative to conventional honeycomb – further broaden the space of options to be evaluated.

2. STATE OF THE ART

2.1. Atmospheric relevance of reentry residues

Recent literature provides an increasingly detailed picture of the atmospheric relevance of reentry residues, almost exclusively for metallic, and predominantly aluminium-based, materials. Al_2O_3 particles are estimated to persist in the stratosphere for up to two years [10] and are already present in around 10% of stratospheric aerosol particles analysed to date [9]. Beyond ozone depletion and radiative effects, reentry has been proposed as one of several possible, but not unequivocally confirmed, sources of carbonaceous particles observed in the polar stratosphere [13], and simulation studies using modal aerosol models indicate potential effects on atmospheric circulation and precipitation patterns, although experimental validation of these effects remains limited [9, 14]. Ongoing observation campaigns, such as the 2024 Cluster-Salsa reentry observation campaign [15] and NASA's DebriSat programme, together with dedicated laboratory ablation facilities such as the MASI rig [16], are actively extending this evidence base, but remain focused on metallic constituents.

2.2. Facilities and tools for material demise characterisation

The ESA ESTIMATE database [17] provides a systematic, agency-maintained repository of material demisability parameters, informed substantially by plasma wind tunnel testing, but is presently centred on established, predominantly metallic materials rather than resin-based composites. Plasma wind tunnel facilities, notably the High Enthalpy Flow Diagnostics Group (HEFDiG) at the University of Stuttgart [18] and the Scirocco and Ghibli tunnels operated by CIRA [19], realistically reproduce the aerothermal flow conditions of reentry and are used extensively to assess structural survivability and heat shield performance. However, they are not primarily designed to provide an independently controllable oxidation chemistry comparable to laboratory combustion or pyrolysis experiments – and are not primarily configured for the collection and chemical analysis of residues.

Bonvoisin et al. [20] tested a CFRP sample (EX-1515 cyanate ester resin with Torayca M55J carbon fibres) in a plasma wind tunnel and characterised the resulting mechanical property changes, but did not analyse chemical or particulate residues. Greene et al. [21], validating NASA's Object Reentry Survival Analysis Tool (ORSAT) for GFRP and CFRP components, found that these composites survived substantially longer than the model predicted and were not fully destroyed even at 6,000 K with added oxygen; the residue characterisation planned for the second phase of that study has not yet been published.

2.3. Life cycle assessment approaches for spacecraft

Space-specific LCA practice is evolving but remains structurally limited with respect to reentry. ESA's LCA handbook for space systems [8] includes composite materials for the first time and notes that toxic gases can be released during the manufacture of glass-fibre composites. A dedicated annex reviews the state of the art of atmospheric impact from launches and reentry and recommends its inclusion in future LCA studies, but explicitly does not yet require it. Koffler et al. [22] combined the Environmental Footprint 3.1 method with a dedicated Space Debris Indicator (SDI) to evaluate end-of-life scenarios for satellites, covering solar panel glass and silicon, aluminium structures, and energy storage systems, but did not address CFRP-metal sandwich systems or extend the system boundary to full cradle-to-grave. EcoDeltaV's Assessment and Comparison Tool (ACT) provides prospective, system-level LCA covering both launch and reentry emissions, adapting the Launch and Re-entry Emission Assessment Tools (LEAT/REAT) originally developed at the University of Stuttgart [23], and has been applied to the upper stages of Ariane 6, Falcon 9 and Long March 2D. However, its emission estimates are derived from chemical equilibrium modelling rather than measurement, use simplified geometry and generic literature material data, and focus on metallic residues; according to its developers, without measurement data this represents only a first approach [23], and chemical characterisation at the level of individual composite material systems is described as not presently possible.

3. RESEARCH GAP AND OBJECTIVES

The reviewed state of the art shows a consistent pattern across three complementary aspects of the problem.

Gap A – Reentry residue characterisation: quantitative understanding of reentry residues and their atmospheric relevance is well developed for aluminium but essentially absent for CFRP resin systems, despite their growing structural use.

Gap B – Integrated LCA: no published LCA framework combines terrestrial manufacturing impacts, mass-dependent launch effects and reentry emissions within a single, cradle-to-grave system boundary for composite spacecraft structures.

Gap C – Material alternatives: even where alternative, potentially lower-impact core materials for sandwich structures exist in principle (e.g. folded-core concepts offering greater material freedom than conventional honeycomb manufacturing), no methodological basis exists to relate their reentry residues to the aluminium

honeycomb baseline.
Addressing these gaps, the work presented here pursues the following objectives: (i) to experimentally characterise the gaseous and particulate residues released during controlled, defined-atmosphere oxidation and pyrolysis of a representative CFRP sandwich panel and at least one alternative core material; (ii) to derive material- and process-specific emission factors suitable as primary input data for LCA; and (iii) to propose a cradle-to-grave LCI and impact assessment framework, extended by a dedicated deorbit and atmospheric release inventory module, that structures how terrestrial, launch and reentry-related environmental effects can be consistently related, exploring pathways for decision support that could inform, at a later application stage, industry-relevant material selection. Table 1 summarises how the presented approach relates to the reviewed tools and facilities.

Table 1: Positioning of this work relative to existing tools and facilities

Approach	***Relation to this work***
ESA ESTIMATE [17]	Established / metallic focus; could receive CFRP factors as future input
Plasma wind tunnels, HEFDiG [18] / CIRA [19]	Complementary flow realism; no defined O_2 chemistry
EcoDeltaV / ACT, LEAT+REAT [23]	Model-based, metallic focus; this work supplies measured CFRP factors
This work	Measured gas/particle/ash residues, feeding a proposed LCA framework

4. METHODOLOGY

4.1. Reference component and material alternatives

The reference component is a generic CFRP-aluminium honeycomb sandwich panel, representative in production process, material selection and documentation of the type commonly used as a solar generator substrate in flight hardware, selected because it reflects established industry practice rather than a laboratory specimen, and because aluminium honeycomb represents the established baseline for which reentry effects are comparatively well characterised. As a candidate alternative, folded core structures are evaluated: unlike conventional honeycomb, which is constrained to available fibre and resin systems when bought off the shelf, folded cores are produced by defined sequential folding of flat sheet or laminate material, in principle permitting a substantially broader range of constituent materials. Folded core prototypes of this type, including first concepts for load-introducing inserts compatible with the open folded-core cross-section, have previously been manually folded and vacuum-formed, while commercially available aluminium- and aramid-folded cores have undergone basic processability-trials within a previous research project. Folded cores are included in this work as a concrete, industry-relevant test case for illustrating whether a broadened material spectrum also represents a net environmental benefit once reentry residues are taken into account, rather than merely shifting the burden to an uncharacterised material system.

4.2. Experimental approach

Reentry-relevant thermal decomposition is approximated using a modified hardening furnace (up to 1,200°C) rather than a plasma wind tunnel. This substitutes aerodynamic and flow realism – a strength of plasma wind tunnels – for a defined, controllable combustion atmosphere established via a vacuum pump and dedicated gas supply lines, which plasma wind tunnels do not provide. The furnace is instrumented for combined gas- and solid-phase residue analysis (Table 2).

Table 2: Experimental measurement chain

Stage / instrument	***Measured quantity / range***
Furnace atmosphere control	Temperature up to 1,200°C; vacuum + defined gas dosing
Aerosol spectrometer	Airborne particle size / concentration, 200 nm–40 µm, direct gas sampling
Filter + SEM/EDX	Elemental / chemical composition of particulates and ash
Laser diffraction	Ash particle size distribution, 2–500 nm
IR cameras with filters	Gas-phase composition, wavelength-resolved

Together, these methods yield material-specific emission factors, expressed as mass of residue per unit mass of starting material, for both gaseous species and particulates, across the reference aluminium-honeycomb system and the folded core alternative.

4.3. Life cycle assessment framework

The generated emission factors feed a proposed LCI and impact assessment approach, structured cradle-to-grave in line with the general framework of ISO 14040 / 14044 [24, 25]. Rather than a certified, comparative life cycle assessment of specific products, this work develops the underlying methodology: the functional unit and system boundary are defined to enable consistent characterisation of material / resin systems under identical conditions; the LCI is organised into modular process blocks (Table 3); and impact assessment is carried out for the terrestrial and atmospheric impact categories addressed in this work, applying established characterisation methods per category. A central methodological question addressed here is how these structurally different, not directly commensurable impact

categories – terrestrial CO_2-equivalent footprint versus atmospheric effects such as ozone depletion and radiative forcing from reentry residues – can be related to each other; rather than establishing a validated weighting or normalisation scheme, this work explores pathways for decision support for industrial users. For the deorbit module, project-generated primary emission factors are combined with established LCI background data; the currently sparse data situation in this domain, and its implications for data quality requirements, is treated as a further methodological question, with remaining uncertainties made explicit through scenario and sensitivity analysis.

Table 3: LCA system boundary modules

Module	***Content***
Raw material	Fibre, resin, core material (LCI databases)
Manufacturing / integration	Panel lay-up, curing, assembly (representative production data)
Launch	Mass-dependent launch emissions (literature)
Use phase	In-orbit operation (out of primary scope)
Deorbit / atmospheric release	Reentry residues (this work + LCI background data)

5. WORK PLAN AND EXPECTED OUTCOMES

The work is structured into five work packages over a 24-month period: (WP1) test methodology development based on a systematic literature-based classification of degradation products and candidate materials; (WP2) design, construction and validation of the experimental test rig, identified as the critical path, since all subsequent experimental work depends on a calibrated and validated setup; (WP3) experimental campaigns on the reference and alternative material systems; (WP4) data analysis and development of predictive decomposition models; and (WP5) derivation of methodological recommendations for material and design evaluation, publication of results, and presentation to standardisation bodies.

Expected outcomes include: an emission factor dataset characterising a generic CFRP-aluminium-honeycomb sandwich system and a CFRP-foldcore alternative under defined reentry-relevant conditions, illustrating rather than certifying material-level differences; a life cycle inventory and impact assessment framework, including an explicit deorbit module and explored pathways for decision support across terrestrial and atmospheric impact categories, applicable beyond the two material systems investigated here; and a basis for future collaboration with existing system-level tools such as ESA ESTIMATE and EcoDeltaV/ACT, which could incorporate the resulting composite-specific emission factors as improved input data.

6. CONCLUSION

D4D reduces ground casualty risk by design, but the resulting increase in high-altitude material release is not yet matched by a comparable increase in understanding of its environmental consequences, particularly for the growing share of composite spacecraft structures. This paper has outlined an industry-academia methodology contribution that combines controlled, defined-atmosphere laboratory oxidation and pyrolysis of a generic, flight-representative CFRP sandwich panel and a candidate alternative core material with dedicated gas- and particle-phase residue analytics, feeding a proposed cradle-to-grave LCI and impact assessment framework extended by a dedicated deorbit module. The approach is deliberately positioned as complementary to existing plasma wind tunnel facilities and system-level LCA tools rather than as a substitute for them, and is intended to generate the primary, composite-specific emission data and methodological basis that these tools currently lack.

7. ACKNOWLEDGEMENT

The work presented in this paper forms part of the project ‘SpaceBURP’, submitted as a joint proposal by CarboSpaceTech GmbH and HTWG Konstanz for funding by the Deutsche Bundesstiftung Umwelt (DBU); at the time of writing, the funding decision is still pending.

8. REFERENCES

1. Satellite Industry Association (2025). *28th Annual State of the Satellite Industry Report.* www.sia.org.
2. ESA (n.d.). Around 100,000 satellites are expected to be in orbit by 2030. https://www.esa.int/ESA_Multimedia/Images/2025/04/Around_100_000_satellites_are_expected_to_be_in_orbit_by_2030
3. Inter-Agency Space Debris Coordination Committee (IADC) (2021). *Space Debris Mitigation Guidelines, Rev. 4.* https://www.iadc-home.org/documents_public/view/id/318
4. UNOOSA, Committee on the Peaceful Uses of Outer Space (COPUOS). *Guidelines for the Long-term Sustainability of Outer Space Activities.* https://www.unoosa.org/oosa/en/ourwork/topics/long-term-sustainability-of-outer-space-activities.html
5. ISO 24113. *Space systems – Space debris mitigation requirements.* International Organization for Standardization / DIN Media.
6. ESA (n.d.). Design for Demise: Bringing spacecraft down safely and efficiently. https://www.esa.int/Enabling_Support/Preparing_for_the_Future/Discovery_and_Preparation/Design_for_demise_bringing_spacecraft_down_safely_and_efficiently
7. ESA (2025). ESA's Annual Space Environment Report (Issue 9). https://www.sdo.esoc.esa.int/environment_report/Space_Environment_Report_latest.pdf

8. ESA (2025). Life Cycle Assessment (LCA) Guidelines for Space Systems (ESSB-HB-U-005, Issue 2 Rev 0). Issued 19 December 2025.
9. Murphy, D.M. et al. (2023). Metals from spacecraft reentry in stratospheric aerosol particles. *Proceedings of the National Academy of Sciences*, 120(43), e2313374120.
10. Jain, A.K. (2023). *On the atmospheric saliency of space debris reentries: Estimating distribution, lifetime and radiative forcing of reentry-ablated alumina.* Massachusetts Institute of Technology.
11. Maloney, C.M., Portmann, R.W., Ross, M.N. & Rosenlof, K.H. (2025). Investigating the potential atmospheric accumulation and radiative impact of the coming increase in satellite reentry frequency. *Journal of Geophysical Research: Atmospheres*, 130, e2024JD042442.
12. Stockschläder, J. et al. (2019). Carbonfaserhaltige Abfälle in der thermischen Abfallbehandlung – Zwischenergebnisse aus praktischen Untersuchungen im industriellen Maßstab. *Energie aus Abfall*, 333-356. TK Verlag, ISBN 978-3-944310-45-9.
13. Schütze, K. et al. (2017). Sub-micrometer refractory carbonaceous particles in the polar stratosphere. *Atmospheric Chemistry and Physics*, 17, 12475-12493.
14. Schulz, L. et al. (2026). Space waste: An update of the anthropogenic matter injection into Earth's atmosphere. *Advances in Space Research*, 77, 9589-9616.
https://doi.org/10.1016/j.asr.2026.03.026
15. Mueller, C. et al. (2025). First results from the Salsa airborne re-entry observation campaign. *Proc. 9th European Conference on Space Debris*, Bonn, April 2025, ESA Space Debris Office.
16. Bones, D.L., Gómez Martín, J.C., Empson, C.J., Carrillo Sánchez, J.D., James, A.D., Conroy, T.P. & Plane, J.M.C. (2016). A novel instrument to measure differential ablation of meteorite samples and proxies: The Meteoric Ablation Simulator (MASI). *Rev. Sci. Instrum.*, 87, 094504. DOI: 10.1063/1.4962751.
17. ESA. ESTIMATE material demisability database. https://estimate.sdo.esoc.esa.int/
18. HEFDiG – High Enthalpy Flow Diagnostics Group, Institute of Space Systems, University of Stuttgart. https://www.irs.uni-stuttgart.de/forschung/raumtransporttechnologie/diagnostik_hochenthalperstroemungen/
19. CIRA – Centro Italiano Ricerche Aerospaziali, Plasma Wind Tunnel Complex. https://www.cira.it/en/infrastructures/plasma-wind-tunnel-complex/ See also: Borrelli, R. & Martucci, A. Scirocco Plasma Wind Tunnel: Synergy between Numerical and Experimental Activities for Tests on Aerospace Structures; Marini, M. et al. (2007). Test Design Methodologies for Flight Relevant Plasma Wind Tunnel Experiments. West-East High Speed Flow Field Conference, Moscow; Di Benedetto, S. et al. Plasma Wind Tunnel Test Design Methodologies for Re-entry Vehicle Components. EUCASS.
20. Bonvoisin, B. et al. (2023). Demisability of space materials. *CEAS Space Journal*, 15, 213-235.
21. Greene, B.R. et al. (2019). Demisability of GFRP and CFRP components of reentering orbital debris: Phase I test results. *IAASS Conference*, El Segundo, CA.
22. Koffler, J. et al. (2025). Evaluating end-of-life scenarios for satellites using life cycle assessment. *11th European Conference for Aeronautics and Space Sciences (EUCASS)*. DOI: 10.13009/EUCASS2025-203.
23. Fischer, J.-S. & Fasoulas, S. (2024). LEAT & REAT – Development of a tool for the assessment of launch and re-entry emissions of space transportation systems and their environmental impact. *ESA Clean Space Days 2024*, Noordwijk, 9 October 2024. See also EcoDeltaV, https://ecodeltav.com/
24. DIN EN ISO 14040:2021-02. *Environmental management – Life cycle assessment – Principles and framework.* DIN Media.
25. DIN EN ISO 14044:2021-02. *Environmental management – Life cycle assessment – Requirements and guidelines.* DIN Media.

Development of a Cost-Efficient Fused Filament Fabrication-Printable Thermoplastic for Structural and Non-Structural Low Earth Orbit Applications

Lisa Wolf [1], Ugo Lafont [2], Holger Ruckdäschel [3], Philipp Häfner[4]

[1] University of Bayreuth, Universitätsstraße 30, 95447 Bayreuth, Germany, Email: l.wolf1@gmx.de
[2] European Space Agency, ESTEC Keplerlaan 1, PO Box 299, Netherlands Email: ugo.lafont@esa.int
[3] University of Bayreuth, Universitätsstraße 30, 95447 Bayreuth, Email: ruckdaeschel@uni-bayreuth.de
[4]Ansbach University of Applied Sciences, Residenzstraße 8, 91522 Ansbach, Email: philipp.haefner@hs-ansbach.de

KEYWORDS

UV, gamma irradiation, outgassing, thermoplastic, additive manufacturing, Fused Filament Fabrication (FFF)-printing, CubeSat, Shaker testing

ABSTRACT

Additive manufacturing is becoming increasingly important for the production of cost-effective, lightweight, and geometrically complex components for both structural and non-structural space applications. At present, however, most flight-qualified components are still manufactured from metallic materials because of their superior mechanical strength and stiffness. Nevertheless, thermoplastics processable by Fused Filament Fabrication (FFF) are attracting increasing interest in the space sector due to their lower manufacturing costs, broader accessibility, and inherent recyclability. Current research and industrial activities predominantly focus on FFF-printable high-performance materials such as polyether ether ketone (PEEK), polyether ketone ketone (PEKK), and polyetherimide (PEI). Although these polymers have demonstrated suitability for space applications, they are associated with high material costs and demanding processing requirements. Consequently, the development of low-cost, readily processable materials capable of withstanding the space environment represents a highly attractive alternative.

The objective of this work is to develop and evaluate a novel FFF-printable material that combines cost-efficiency, ease of processing on commercially available desktop printers, and resistance to the environmental conditions encountered in Low Earth Orbit (LEO). To assess its suitability for space applications, established environmental testing procedures and characterization methods were employed, including outgassing investigations as well as vacuum ultraviolet (VUV) and gamma irradiation exposure. The developed material was characterized before and after environmental exposure with respect to its mechanical performance, using tensile testing, and its thermo-optical properties. The obtained results provide insight into the material's potential for lightweight and cost-effective space applications.

1. INTRODUCTION

High performance thermoplastic material, such as PEEK, PEKK and PEI are increasingly applied for non-structural applications such as sensor boxes and mounts. Nowadays, they are able to compete with thermoset materials in non-structural applications. However, the usage of thermoplastics in structural applications is still limited to a few thermoplastics, due to the sparce knowledge of the material behaviour, such as outgassing, erosion, mechanical strength etc. under space conditions. So far, only selective smaller secondary structure applications were manufactured using thermoplastics, [1]. Processing was mainly performed by conventional, time consuming and expensive methods such as autoclave consolidation and/or milling compression-moulded semi-finished compounds [2], [3].

Additive manufactured thermoplastics for structural and non-structural parts is only recently emerging for spaceflight applications [4]. In this context, mainly Selective Laser Sintering (SLS) is used for smaller structural parts such as picosat launch systems from alba obital [5]. Fused Filament Fabrication (FFF) based methods are currently used for prototyping and in-situ space manufacturing of smaller tools for ISS, and not for structural applications in space [4], [6]. Here, only small parts, mainly based on PEEK compounds, are produced, due to ductility and toughness of PEEK. However, material costs, the printability and reproducibility limit applications [7].

These limitations highlight the need for cost-effective, readily printable, and reproducible FFF materials. Despite the increasing relevance of thermoplastics in space applications, reservations remain regarding the use of newly developed FFF-printed thermoplastics in structural and non-structural flight components, particularly with

respect to their reliability after exposure to the space environment.

Therefore, this study addresses the following research question: Can a cost-effective FFF-printable thermoplastic provide the environmental stability and reliability required for structural and non-structural applications in Low Earth Orbit (LEO)?

2. FFF-PRINTED PARTS FOR LOW EARTH ORBIT APPLICATIONS

2.1. Material development

For the material formulation, a literature review was conducted to identify the most relevant environmental factors in LEO and to select a suitable base polymer and potential fillers using a simple target weighting method that can withstand LEO conditions. The base polymer and the fillers were then compounded via a micro compounder (Xplore MC15) and then injection-moulded into tensile probes after ISO 527-1 1A (thickness 2 mm).

The following formulations were produced:

- Raw Polymer (Raw)
- Polymer + Filler 1 (F1)
- Polymer + Filler 2 (F2)
- Polymer + Filler 1 + Filler 2 (F1+F2)

To investigate if the material can reach a tensile strength of at least 50 MPa and to find the best formulation, the injection-moulded probes were tensile tested on a Zwick & Roell ProLine machine. The best mixture was then compounded on a twin-screw extruder, pelletized and finally extruded on a single screw extruder to obtain filaments. The raw material was also extruded to filaments. Both filaments were used to print tensile probes according to ISO 527-1 1A (2 mm thickness).

For printing the optimal printing parameters, i.e. nozzle temperature, bed temperature and printing speed, regarding warping, layer adhesion and dimensional stability were chosen via the Taguchi-Method. X-Y-Z Cubes were printed at different parameters and the dimension, warpage was measured via 3D-Scanning, the layer adhesion was tested by pressing the Cube with a defined force and a visual inspection of the breaking damage. Numbers from 1-10 (10 best result) were given to each parameter. Out of these parameter sets the best parameter were chosen.

The material was then prepared as described in Section 2.2.2 for further testing under LEO-relevant environmental conditions, as outlined in Section 2.2.

2.2. Material testing for LEO

2.2.1. Material testing standards

To evaluate the potential behavior of the material in the LEO environment, the following standards were applied:

- Outgassing after ECSS-Q-ST-70-02
- Thermal vacuum cycling (TVAC) after ECSS-Q-ST-70-04C15
- UV and particle testing after ECSS-Q-ST-70-06

In addition, the material was characterized before and after UV exposure, thermal-vacuum cycling (TVAC), and particle irradiation using the following methods:

- Thermo-optical properties after ECSS-Q-ST-70-09C 31.
- Tensile testing

The shaker test was performed according to the guidelines specified in the CubeSat Handbook provided by SpaceX. The test setup and applied vibration loads were selected to evaluate the structural integrity of the CubeSat assembly under representative launch-induced mechanical conditions.

2.2.2. FFF printing material qualification

Outgassing tests were conducted on both printed and injection-moulded materials in the unirradiated state, as described in Section 2.2.1.

The printed specimens described in Section 2.1 were subsequently subjected to tensile testing. Selected printed and injection-moulded specimens were gamma-irradiated using a Co-60 source at Helmholtz-Zentrum Berlin for 13 h and 54 min at a dose rate of 3.6 krad/h and at room temperature (24 °C ± 6 °C). This corresponds to Level F (50 krad/500 Gy) and to the standard dose-rate range according to Window 1 (3.6 to 36 krad/h, equivalent to 36 to 360 Gy/h) as specified in ESCC 22900.
The irradiated printed specimens were subsequently tensile tested using the ZwickRoell testing machine.

Some of the printed non-irradiated, printed γ-irradiated and injection-moulded non-irradiated and injection-moulded γ-irradiated tensile probes were then subjected to TVAC for 25 circles from -100 °C to +120 °C with (± 5 °C). The heating rate was 3 K per minute and a dwell time at 125 °C (± 2 °C) (baseplate temperature) for 30 minutes. The cooling rate was 3 K per minute with 110 °C (± 2 °C) and a dwell time of 35 minutes (baseplate temperature). The vacuum was in the range of 10^{-6} to 10^{-5} mbar.

Furthermore, samples of the following materials were subjected to VUV irradiation:

- printed F1+F2 γ-irradiated
- printed F1+F2 non irradiated
- injection-moulded F1+F2 y-irradiated

material were VUV irradiated in Vacuum at 10^{-6} mbar with 3,65 solar constants for 350 hours, resulting in 1260 equivalent sun hours (ESH) and with 3,65 solar constants for 137 hours resulting in 500 ESH.

Spectral reflectance (see figure 4) of the samples was measured with the help of Cary 5000 UV-Vis-NIR spectrometer over a wavelength range of 300 – 2500 nm.

2.3. Applications in LEO

Although a material can be developed and optimized based on LEO environmental requirements, its evaluation has limited relevance without a defined application scenario.

Therefore, the developed material was considered for use as a CubeSat frame structure in a Low Earth Orbit mission. Because the material is intended for structural applications, its mechanical integrity and resistance to launch-induced vibrations must also be validated. Accordingly, the CubeSat structure was subjected to shaker testing to assess its structural performance under representative launch conditions.

Shaker testing was performed in accordance with the SpaceX CubeSat Handbook, which specifies random vibration testing. Low-level sine sweeps were conducted before and after the vibration test as described in the handbook. In addition, the CubeSat frame was 3D scanned before and after the shaker test, and the resulting scans were compared to identify geometric deviations. The frame was also optically inspected and documented photographically.

3. RESULTS

Tensile Testing

The tensile strength of the best-performing filled formulation remained close to that of the neat polymer, despite the incorporation of fillers (Table 1), indicating effective filler-matrix adhesion. However, filler addition also increased the brittleness of the material. Formulations containing only F1 or F2 exhibited slightly lower performance than the combined F1+F2 formulation, suggesting improved compatibility or synergistic effects when both fillers were used. The neat polymer, the F1+F2 formulation, and the F2-containing formulation exceeded the required tensile strength of 50 MPa, whereas the F1-containing formulation remained below this threshold. After TVAC treatment, the injection-moulded materials generally exhibited increased brittleness compared with the untreated specimens, as reflected by reduced elongation at break. Compared with the unfilled material, the filled material showed a reduction in tensile strength after TVAC treatment. By contrast, TVAC treatment of the injection-moulded neat polymer led to increased stiffness, reflected by a higher Young's modulus, and, in the gamma-irradiated material, a slight increase in tensile strength. The underlying mechanisms require further investigation.

Table 1: Medium tensile test values of Injection Moulded Formulations and preparations

Material	Young's modulus [MPa]	Tensile strength [MPa]	Elongation at breake [%]
IM Raw	1220 (σ=288)	65,6 (σ=7,7)	8 (σ=0)
IM Raw TVAC	2546 (σ=34)	64 (σ=11,6)	4,7 (σ=1,2)
IM Raw y-TVAC	2444 (σ=77)	71,2 (σ=3,5)	4,6 (σ=1,2)
IM F1+F2	3310 (σ=657)	61,9 (σ=2,9)	6 (σ=0,5)
IM F1+F2 y-TVAC	2953 (σ=12)	51,2 (σ=3,7)	3 (σ=0,3)
IM F1	3330 (σ=727)	59 (σ=2,9)	6 (σ=0,5)
IM F2	2790 (σ=138)	42,6 (σ=6,8)	4 (σ=0,9)

As expected, the tensile strength of the FFF-printed specimens was reduced to less than half of the corresponding injection-moulded values. Compared with the printed neat polymer, the filled best-performing formulation showed improved printability and consequently higher tensile strength (Table 2), while also exhibiting slightly higher stiffness.

Gamma irradiation further reduced the tensile strength of the printed filled formulation to an average value of 22 MPa. However, the irradiated material displayed slightly higher flexibility than the non-irradiated filled material, similar to the behavior observed for the printed neat polymer.

After TVAC treatment, all printed materials showed increased brittleness, similar to the injection-moulded specimens, resulting in reduced elongation at break. An increase in Young's modulus was observed for the printed neat polymer, indicating material stiffening after TVAC exposure. The filled printed material exhibited a reduction in Young's modulus, consistent with the behavior observed for the injection-moulded filled material. However, when the filled material was first gamma-irradiated and subsequently subjected to TVAC, the reductions in stiffness, ductility, and tensile strength were less pronounced than in the non-irradiated TVAC-treated material. An increase in tensile

strength was observed for the gamma-irradiated and TVAC-treated material. The reduced tensile strength of the printed TVAC-treated material may also be related to printing variability, since these specimens were not manufactured in the same batch as the other printed specimens.

Table 2: Medium tensile test values of FFF-printed Formulations and preparations

Material	Young's modulus [MPa]	Tensile strength [MPa]	Elongation at breake [%]
Print Raw	925 (σ=84)	31,5 (σ=5,0)	6,3 (σ=2,0)
Print Raw γ-TVAC	1689 (σ=173)	26,4 (σ=2,6)	2,1 (σ=0,2)
Print F1+F2	4228 (σ=373)	37,2 (σ=7,4)	3,8 (σ=0,9)
Print F1+F2 γ	1332 (σ=128)	22,1 (σ=1,3)	5,6 (σ=1,6)
Print F1+F2 γ-TVAC	1633 (σ=306)	34,6 (σ=9,1)	3,4 (σ=0,3)
Print F1+F2 TVAC	1377 (σ=159)	25,3 (σ=4,3)	2,6 (σ=0,5)

The increase in Young's modulus while maintaining tensile strength observed for the unfilled TVAC-treated materials, irrespective of the manufacturing process, suggests physical ageing and/or post-crystallisation induced by the TVAC treatment. However, further investigations are required to confirm the underlying mechanisms.

A slight increase in tensile strength after γ-irradiation and TVAC was observed for the injection-moulded neat material and the printed filled material. This behaviour may indicate delayed crosslinking through recombination of residual radicals and/or thermally induced annealing or post-crystallisation, resulting in improved load transfer within the material. This interpretation is supported by the initial reduction in both tensile strength and Young's modulus observed for the printed filled material after γ-irradiation alone. Nevertheless, additional characterisation, such as differential scanning calorimetry (DSC) and dynamic mechanical analysis (DMA), is required to verify these assumptions.

In contrast, the Young's modulus of the filled materials generally decreased after TVAC treatment and γ-irradiation compared with the untreated reference. This indicates that any beneficial changes within the polymer matrix were insufficient to compensate for the reduced reinforcing efficiency of the fillers. A possible explanation is degradation of the filler–matrix interface during TVAC exposure, leading to impaired stress transfer between the matrix and the reinforcing particles. However, this hypothesis likewise requires further experimental validation

Outgassing

The outgassing test of the FFF-printed optimum F1+F2 formulation fulfilled the requirements specified in ECSS-Q-ST-70-02C. In contrast, the injection-moulded F1+F2 formulation slightly exceeded the specified limits (see Table 3).

Regarding the total mass loss (TML), the injection-moulded specimens exhibited lower values compared with the printed material. However, the recovered mass loss (RML) was higher for the injection-moulded samples. This behaviour indicates differences in moisture storage and desorption mechanisms between the two manufacturing approaches. Water within polymer-based materials can be present as molecularly dissolved moisture within the polymer matrix or accumulated within porous regions. The desorption kinetics are therefore influenced by diffusion pathways, material morphology, and the accessible surface area.

The higher porosity of the FFF-printed parts (see Figure 1) may result in increased moisture uptake due to additional storage sites, while simultaneously facilitating moisture release during the outgassing procedure through increased surface accessibility and shorter diffusion pathways. Consequently, a larger fraction of the absorbed moisture may be removed within the initial test period, resulting in a lower RML compared with the injection-moulded material. In contrast, the denser structure and the presence of an injection-moulding skin may limit moisture transport and slow down both desorption and subsequent moisture exchange with the environment.

Additional measurements of the injection-moulded material after 72 h under the controlled recovery conditions specified in ECSS-Q-ST-70-02C support this interpretation. Compared with the measurement directly after 24 h of vacuum exposure, the specimens exhibited a slight weight increase, indicating moisture reabsorption from the environment. The slower moisture uptake compared with the FFF-printed material may be attributed to the denser morphology and the presence of an injection-moulding skin, which reduce the accessible surface area and limit diffusion pathways.

For both manufacturing approaches, the collected volatile condensable material (CVCM) remained well below the ECSS-Q-ST-70-02C limit, indicating negligible condensation of volatile species (see Tables 3 and 4).

3Table : Outgassing Test Results injection-moulded F1+F2

		TML [%]	CVCM [%]	RML [%]
Injection Moulded Material		1.340	0.02	1.025
		1.487	0.02	1.117
		1.353	0.02	1.036
	Average	**1.39**	**0.02**	**1.06**
	SD	**0.08**	**0.00**	**0.05**
	Uncertainties k=2	0.06	0.05	0.06

4Table : Outgassing Test Results 3D-printed F1+F2

		TML [%]	CVCM [%]	RML [%]
3D Printed		2.086	0.00	0.731
		2.062	0.00	0.718
		2.100	0.03	0.746
	Average	**2.08**	**0.01**	**0.73**
	SD	**0.02**	**0.04**	**0.01**
	Uncertainties k=2	0.06	0.05	0.06

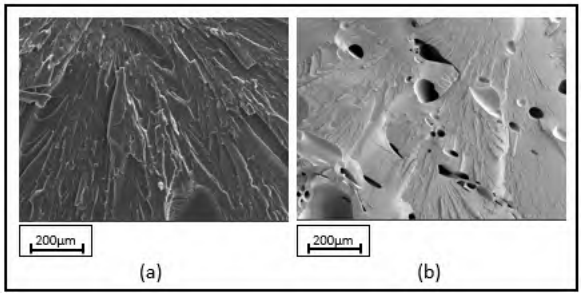


Figure 1: Structure Injection Moulded Material raw (a) and FFF-printed raw (b)

Furthermore, FTIR analysis of the collector plates after the outgassing tests (see Figures 2 and 3) revealed no significant traces of additional volatile compounds. This suggests that the majority of the released mass can be attributed to moisture rather than to low-molecular-weight degradation products or processing-related volatiles.

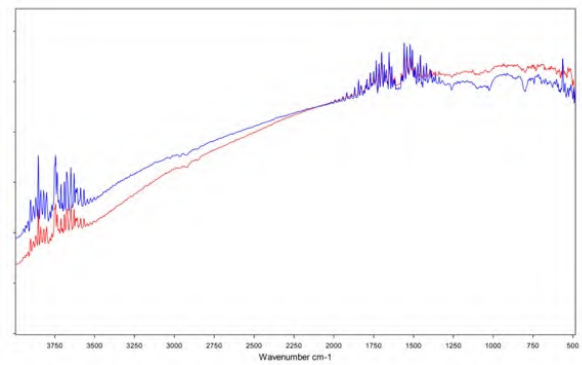


Figure 2: FTIR of the outgassed CVCM according to AD2 (based in RD2) Injection Moulded F1+F2

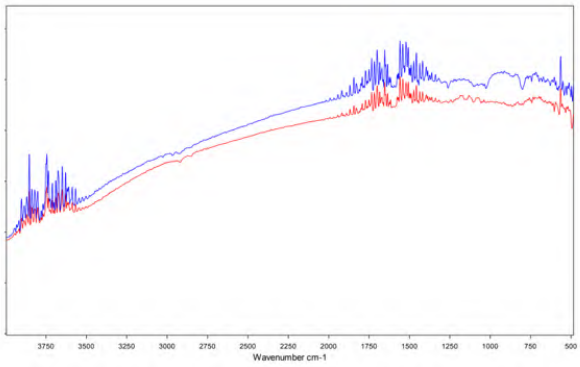


Figure 3: FTIR of the outgassed CVCM according to AD2 (based in RD2) 3D-Printed F1+F2

Thermo-Optical Properties

Irrespective of the manufacturing route, the neat polymer exhibited high solar absorptance values in the range of approximately α = 0.74-0.82, as well as high thermal emissivity values of ε = 0.91-0.93. Due to the opacity of the neat material, these values should be interpreted with caution. In contrast, injection-moulded and FFF-printed F1+F2 specimens exhibited favorable thermo-optical properties irrespective of gamma irradiation, with α = 0.26 for the printed specimens, both irradiated and non-irradiated, and α = 0.33 for the injection-moulded specimens. Thermal emissivity remained high, with ε = 0.89-0.91. The α / ε ratio of the F1+F2-filled materials was approximately 0.3-0.4, which is favorable for passive thermal-control applications. The best overall performance was observed for the non-irradiated printed F1+F2 specimens and the gamma-irradiated printed F1+F2 specimens, which combined low solar absorptance with high thermal emissivity. In addition, F1+F2-containing specimens showed increased reflectance in the near-infrared range (1.5-2.0 um), with values of approximately 0.44-0.47, whereas the neat pressed materials remained below 0.07 in the same spectral range. However, due to the opacity of the neat pressed material, these values are not fully conclusive. Reflectance in the thermal infrared range (5-21 um) remained relatively low for all samples. Gamma-irradiated specimens showed no significant changes compared with the non-irradiated material, indicating good environmental stability. Only negligible differences were observed. Furthermore, vertically and horizontally oriented printed F1+F2 specimens showed nearly identical optical properties, suggesting that the investigated printing orientation of 45° had no significant influence on the thermo-optical properties of the material system.

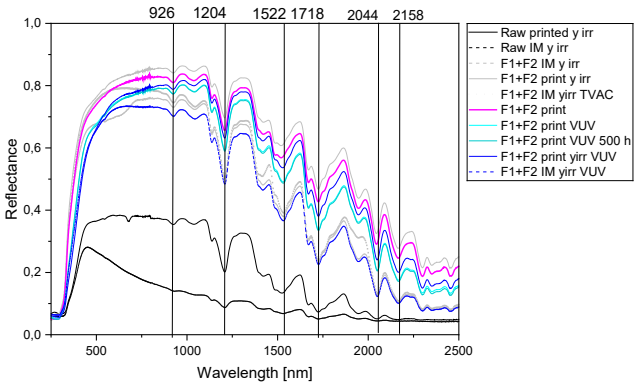


Figure 4: Spectral reflectance (300 - 2500 nm) of printed and injection-moulded, filled and unfilled, samples before and after space environmental exposure

The untreated neat material showed substantially lower reflectance than the filled materials, which can be attributed to its opacity. In contrast, all filled materials exhibited higher reflectance, particularly in the visible and near-infrared regions. This indicates that the addition of fillers may have a beneficial effect on the optical performance of the material.

Injection-moulded specimens exposed to TVAC, gamma irradiation, and VUV irradiation exhibited similar behavior in the wavelength range from 750 to 2500 nm, suggesting that these treatments had only a minor influence on reflectance. The injection-moulded specimens showed slightly lower reflectance than the printed specimens. Although this difference was small, it may be attributed to differences in surface morphology, leading to variations in light scattering.

The printed VUV-irradiated material exhibited similar reflectance curves irrespective of irradiation duration, indicating that prolonged VUV exposure did not substantially alter the material within the investigated parameter range. Gamma irradiation, with or without additional VUV exposure, tended to result in higher reflectance than VUV treatment alone or the untreated reference state. This suggests that gamma irradiation may induce slight surface or chemical modifications affecting optical response, whereas VUV irradiation may promote photo-induced degradation. The exact mechanisms remain unresolved and require further investigation.

Shaker Testing

The evaluation of the CubeSat structure before and after the shaker test was performed using visual inspection and 3D scanning to assess potential damage, deformation, or dimensional changes induced by the applied mechanical loads (see figure 5). No visible differences or signs of damage were observed after the vibration test. Furthermore, the positions and orientations of all screws within the CubeSat structure remained unchanged, as confirmed by the applied markings. The markings were still aligned after the test, indicating that no relative movement or loosening of the screw connections occurred. Additionally, the screws used for mounting the CubeSat structure within the shaker fixture showed no signs of rotation or loosening during the test.

The 3D scan comparison further confirmed the mechanical stability of the structure, with all measured dimensional deviations remaining within the defined tolerance range (green area) and below 0.1 mm. These results demonstrate that the applied vibration loads did not induce measurable deformation or compromise the structural integrity of the CubeSat assembly

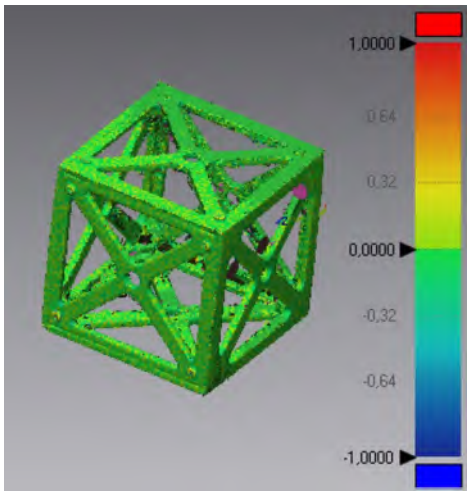


Figure 5: Dimensional deviation analysis of the CubeSat structure before and after the shaker test obtained by 3D scanning.

4. CONCLUSION

The developed material shows promising potential for use in small structural components. Tensile testing demonstrated that filler addition, gamma irradiation, TVAC treatment, and the manufacturing route significantly influence material flexibility and tensile strength. The combination of fillers F1+F2 suggests improved compatibility and resulted in enhanced tensile properties. The filled printed material also exhibited improved printability, which irradiation reduced the tensile strength of the printed specimens but also reduced brittleness. TVAC treatment generally increased brittleness irrespective of the manufacturing route. In the neat materials, Young's modulus increased after TVAC treatment, whereas filled materials showed a decrease, suggesting changes in filler-matrix adhesion and/or crystallinity. Indications of delayed crosslinking and/or crystallinity changes after TVAC exposure were observed, although further research is required to confirm these mechanisms. Overall, both gamma irradiation and TVAC treatment contributed to aging of the polymer.
The outgassing investigations demonstrated that the FFF-printed material fulfilled the ESA-

recommended requirements for space applications. The observed differences in moisture recovery behaviour depending on the manufacturing process highlight the importance of considering material morphology and moisture transport mechanisms in future outgassing evaluations.

Regarding the thermo-optical properties, the filled material exhibited promising characteristics independent of the manufacturing approach. The combination of low solar absorptance and high thermal emittance indicates a high potential for efficient thermal management by reducing solar heat input while promoting heat dissipation.

Comparable results were obtained by UV-Vis-NIR spectroscopy using the Cary 5000, where the filled specimens exhibited increased reflectance over the investigated wavelength range. This behaviour is beneficial for thermal control applications, as enhanced reflectance reduces the absorption of incident solar radiation and can therefore contribute to lower component temperatures.

Only negligible changes in reflectance were observed after TVAC exposure, indicating good environmental stability of the investigated materials under combined vacuum and thermal cycling conditions. In contrast, VUV irradiation resulted in a slight reduction in reflectance, suggesting photo-induced surface modifications or degradation processes. However, the limited difference between 500 ESH and 1260 ESH of VUV exposure indicates that the material retains its favourable reflective properties even after prolonged irradiation, demonstrating its potential for long-term application in space environments.

The comparison of the CubeSat structure before and after the shaker test using 3D scanning revealed no visible damage or measurable dimensional changes. This indicates that the mechanical loads applied during the vibration test did not negatively affect the structural integrity of the CubeSat structure.

Overall, the material shows promising potential for use in CubeSat structures or smaller components located in shielded environments. Nevertheless, VUV- and gamma-irradiation induced degradation should be considered when assessing the lifetime and application limits of the material.

5. REFERENCES

[1] U. Lafont, E. Laurent, E. Amorim, and C. Semprimoschnig, ‘Future of Thermoplastics in Space’. n.d.

[2] N. Shetty, S. M. Shahabaz, S. S. Sharma, and S. Divakara Shetty, ‘A review on finite element method for machining of composite materials’, *Composite Structures*, vol. 176, pp. 790–802, Sep. 2017, doi: 10.1016/j.compstruct.2017.06.012.

[3] E. T. M. Krämer, J. N. Swamy, T. J. Asijee, and S. Wijskamp, ‘Advances in out-of-autoclave consolidation of thermoplastic composites’, in *Int SAMPE Tech Conf*, Soc. for the Advancement of Material and Process Engineering, 2023. doi: 10.33599/nasampe/s.23.0320.

[4] S. K. Georgantzinos *et al.*, ‘A Comprehensive Review of Additive Manufacturing for Space Applications: Materials, Advances, Challenges, and Future Directions’, *Adv. Eng. Mater.*, vol. 27, no. 22, 2025, doi: 10.1002/adem.202501082.

[5] 3Druck.com, ‘Mit 3D-Druck hergestellte System zur Freisetzung von Mikrosatelliten’, 3Druck.com - The Independent AM Magazine. Accessed: May 11, 2026. [Online]. Available: https://3druck.com/case-studies/3d-druck-mikrosatelliten-21108391/

[6] D. Thomas, ‘Improving the Reliability of Satellite Components Using Finite Element Analysis and 3D Printing as a Vital Tool for Modern Space Missions’, *J Fail. Anal. and Preven.*, vol. 25, no. 2, pp. 552–554, Apr. 2025, doi: 10.1007/s11668-025-02145-3.

[7] A. El Magri, S. Vanaei, and S. Vaudreuil, ‘An overview on the influence of process parameters through the characteristic of 3D-printed PEEK and PEI parts’, *High Perform Polym*, vol. 33, no. 8, pp. 862–880, 2021, doi: 10.1177/09540083211009961.

ECSSMET
Braunschweig Germany 2026

Test Predicition & Testing

QUASI-STATIC FREQUENCY RESPONSE ANALYSIS FOR SIMULATION OF NONLINEAR TRANSFER FUNCTIONS

Tom Tankink [1], Dario Di Maio [1]

[1] *University of Twente, Drienerlolaan 5, 7522 NB Enschede, The Netherlands, d.dimaio@utwente.nl*

KEYWORDS

Forced vibrations, system assembly, nonlinearity, Nonlinear Frequency Response Surface

ABSTRACT

This paper presents a novel analysis framework for calculating nonlinear frequency response functions using the Quasi-Static Frequency Response method. The motivation for developing this technique is to help structural engineers estimate resonance peak amplification and natural frequency deviations using a nonlinear static stress model. During an early design phase, engineers want to know whether a specific material selection or geometrical shape can withstand both static and dynamic loads. This is typically challenging when a system is vibrated at high amplitude (operational levels), as the response becomes nonlinear and, due to the computational cost, is often not calculated. Therefore, design optimisation might lack an important piece of information when decisions must be taken. *The scientific challenge is to derive hysteresis curves using displacement shape functions, in this case mode shapes, to calculate amplitude-dependent stiffness and damping. Once the nonlinear dynamic parameters are calculated, the Nonlinear Frequency Response Surface can be simulated.* This surface is the solution space for all the nonlinear FRFs defined within the ODS's displacement range. At this point, the engineer can observe hysteresis behaviour in the frequency domain and thus assess variations in the natural frequency and the resonant peak response. The new analysis framework will be illustrated using a simple double-cantilever beam with one end fitted with a leaf spring. A nonlinear FE model is generated to determine the hysteresis curve using mode shapes from the linear modal analysis. The comparison between the nonlinear experimental and the nonlinear simulated FRFs is presented and discussed. This procedure avoids performing nonlinear modal analysis on experimental FRFs, as overlaying them indicates how well the nonlinear static stress model fits. Once the comparison is achieved, the engineer can decide which design optimisation to pursue and whether additional QSFR and NFRS are required for calibration.

1. INTRODUCTION

In the space industry, vibration qualification tests serve an essential purpose: to evaluate the behaviour of a structure under conditions it would typically experience during launch. However, the current approach of performing qualification tests on fully assembled systems and subsystems has its limitations. By the time dynamic behaviour is tested, it may be too late to make required design changes, which can result in costly redesigns and delays. Thus, it is crucial to develop a more proactive approach to assessing the vibration response of systems earlier in the design and manufacturing process.

While modelling individual components in a system can be relatively straightforward, accurately modelling their assembly, particularly the connections between components, is complicated by the nonlinear transfer behaviour at the joints [1]. As such, predictive modelling of the forced vibrations of assembled structures has been challenging for many years [2,3]. This can be achieved by reducing the computational effort required to solve the dynamic response of nonlinear systems, either by using lumped-parameter joint models, such as the Iwan model [4,5], or by assuming a polynomial function. These are phenomenological rather than fundamental models describing the physics, and thus still require expert knowledge or calibration using test data. On the other hand, more efficient solution methods have been developed for obtaining the forced vibration behaviour of nonlinear systems (compared to, e.g., direct time integration), such as the harmonic balance method [6], continuation-based methods [7], and quasi-static approaches [8,9,10]. Yet predicting the nonlinear dynamic behaviour of assembled structures remains a challenge (in an industrial context).

Research on predicting nonlinear eigenfrequencies is extensive, and some tools are available to identify nonlinear dynamic behaviour. A common limitation is that the mathematical basis and understanding of nonlinear dynamics required to apply these techniques are well beyond the reach of most structural engineers. These techniques are developed to achieve very high accuracy, but this comes at the cost of practical applicability. In many engineering applications, such intensive methods become too time-consuming to apply in practice, particularly when designing less demanding structures in which nonlinear dynamics still play a significant role. As a result, (structural) engineers often return to linear analysis despite knowing it will not capture the nonlinear behaviour. Hence, an engineer cannot assess whether the design system will support a dynamic load and whether a different design choice could mitigate or improve potential load-path weaknesses. This motivates the need for a faster, more accessible approach to give (structural) engineers a first insight into the

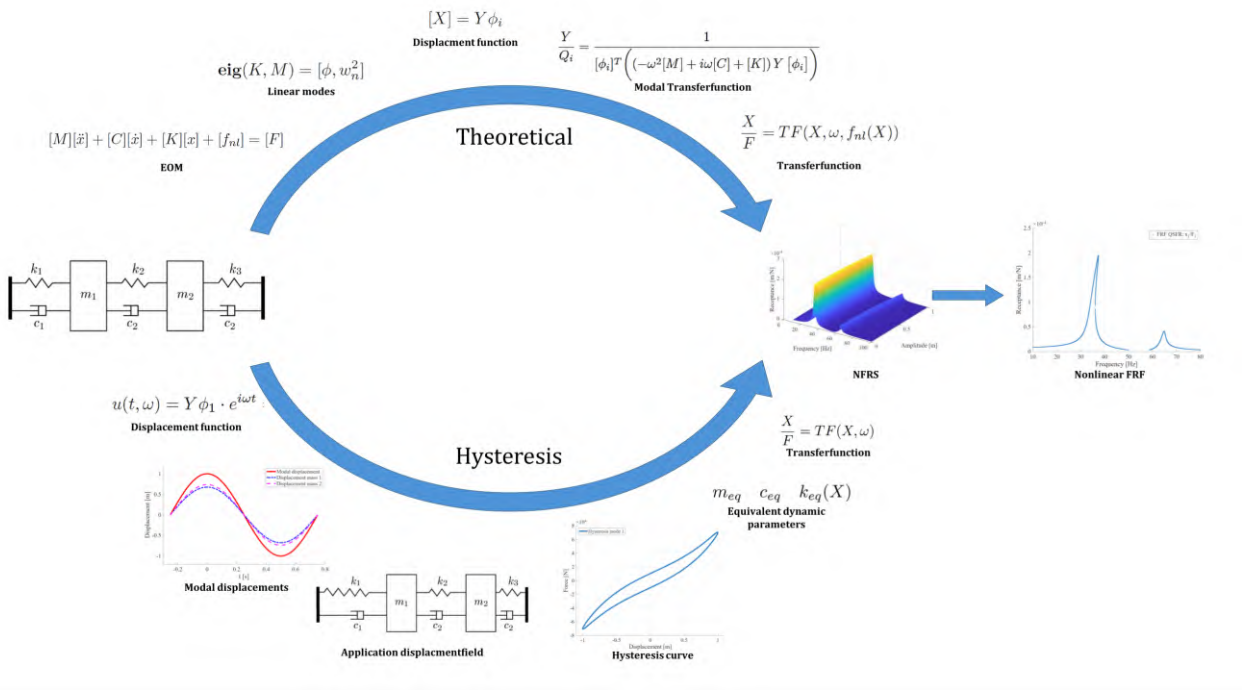


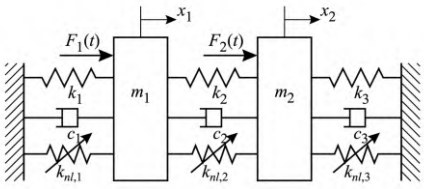
Figure 2.1: The flowdiagram of the QSFR framework for a 2-DOF system

nonlinear dynamic behaviour. *The goal of this work is to derive a new framework that enables prediction of the nonlinear behaviour of a dynamic system, with a focus on a fast, applicable, and understandable solution. The ambition is to anticipate dynamic calculations. This will be based on the analysis of hysteresis curves. From a hysteresis curve, the equivalent dynamical parameters are derived.* The interpretation of these parameters could enable engineers to anticipate nonlinear dynamic responses and make structural changes before the critical design review.

This brief context will help the reader understand that one of the main shortcomings is the simulation and characterisation of nonlinear vibration responses. Although academia has developed several simulation and testing techniques for characterising and comparing nonlinear vibrations over the past years, industry has integrated only a tiny fraction of that knowledge [11]. The main reason is the lack of implementation of the proposed methods into industrial standards, which still relies on the
Measurement of Frequency Response Functions (FRFs). These measurement are used to characterise the dynamics of structures. Engineers find FRFs very useful because they relate the response at any point on the structure to the input force applied elsewhere. This allows an engineer to evaluate an appropriate response to design requirements. For this reason, the Quasi-Static Frequency Response (QSFR) is a first-order approximation method for simulating nonlinear FRFs from a static nonlinear stress model, often available during the design phase.

2. THEORETICAL FORMULATIONS OF THE NONLINEAR FREQUENCY RESPONSE SURFACE FROM THE QUASI-STATIC FREQUENCY RESPONSE FRAMEWORK

This section will explain the theoretical formulation of the quasi-static frequency response framework. Figure 2.1 shows the schematic of the formulation for a two-degree-of-freedom system. The diagram describes the procedure for going from a static nonlinear stress model to the calculation of a nonlinear frequency response function. The procedure does not involve any nonlinear dynamic calculations at the outset. It solely requires a linear modal analysis to derive the mode shapes and a static nonlinear stress model of a possibly used nonlinear material (or in this case, the cubic springs).



The linear mode shapes are used as displacement functions for calculating hysteresis curves. Therefore, a nonlinear static stress model can be deformed according to the modal displacement loading pattern to derive amplitude-dependent hysteresis curves. The mode shape is treated as a unique shape function that can be scaled to produce large displacements in the nonlinear static model, in this case a two-DOF nonlinear system.

The idea is to exploit that type of model to simulate hysteresis curves. When the nonlinearity is amplitude-dependent, the hysteresis nonlinearity depends on the deflection generated by the mode shape. This means that, for each amplitude, equivalent dynamic parameters such

as mass, damping and stiffness can be calculated from the hysteresis. Hence, a Nonlinear Frequency Response Surface, which is a waterfall of quasi-linear FRFs, can be simulated from these amplitude-dependent hysteresis curves. Finally, a nonlinear FRF can be extracted from the NFRS for any given excitation force.

The graphics in Figure 2.1 show an upper and lower branch. The upper branch is the theoretical formulation derived from the algebra of a two-DOF nonlinear system, while the lower branch shows the same process but derived from nonlinear hysteresis curves.

The simulation process generates modal FRFs because the analysis framework is based on mode shapes. Therefore, an additional transformation is required to convert the modal FRF into a physical FRF, which is typically measured in the laboratory. This latter process is not explained in this manuscript. Moreover, the analysis framework assumes that the mode shapes are not amplitude-dependent, which is valid for well-separated modes. The example in Figure 2.1 is based on geometrical nonlinearity, where the damping is assumed linear. However, the proof-of-concept validation case shows that the method works with both stiffness and damping amplitude-dependent behaviour. For a structural engineer, the benefit of the proposed analysis framework is the ability to observe the amplification of the response at resonance, starting from a static nonlinear model. This means that an engineer can assess whether the design criteria will meet the allowable peak stress, both static and dynamic, and evaluate what should be changed if these allowable limits are not met. Clearly, it is a first-order approximation of the amplification of the response, but it is quite inexpensive compared to other costly dynamic computations.

The next section will focus on the case study, which is a double cantilever beam presenting a stiffness and damping nonlinearity.

3. CASE STUDY: DOUBLE CANTILEVER BEAM WITH NONLINEARITY

This section presents a case study of a double cantilever beam with two different cross-sections, introducing geometric nonlinearity at one of the cantilever ends. The beam is modelled by the finite element method to simulate nonlinear FRFs using the QSFR analysis framework. The linear and nonlinear FRFs are compared with the experimental results to demonstrate that the first-order approximation provides useful insights for a structural engineer in the early design phase.

3.1. FE model and QSFR implementation

The model is based on the setup presented in [13]. This setup consists of a square beam (10 mm × 10 mm) with a thin plate of thickness 0.5 mm attached to one end. Both the square beam and the thin plate are clamped at their ends. The required material dimensions were not available at the UT, and therefore two different sizes were selected. The square beam was replaced by a rectangular beam. The 0.5 mm-thick plate was replaced by a 1 mm-thick plate. The lengths of the two beams remain the same, that is, 700 mm, and the thin lamina is 40 mm. The mesh consists of 7 nodes, which are connected using BEAM188 elements. The first five elements have the geometrical and material properties of Beam 1. The sixth element has the properties of the thin plate. The node numbering generated by ANSYS can be seen in Figure 3.2. Standard mild steel properties were used to model the material behaviour of the large cross-section, while the lamina material behaviour was characterised by experiments to extract the nonlinear stress-strain relationship.

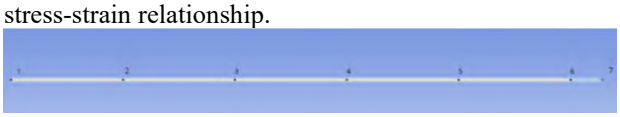
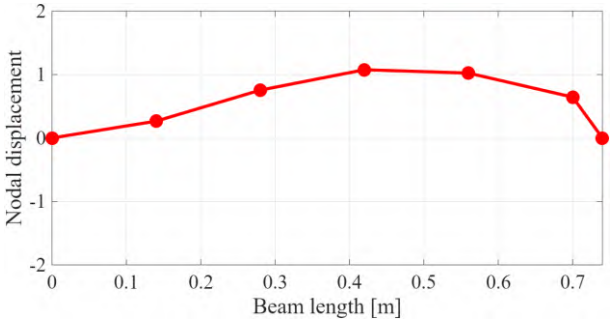
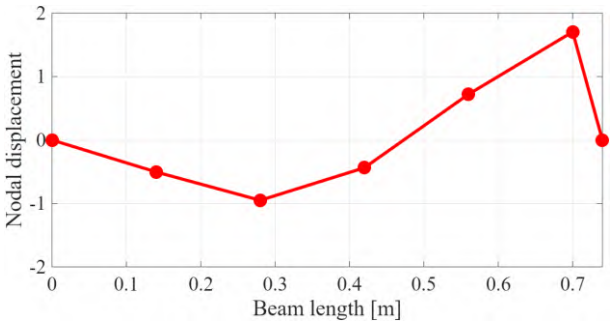


Figure 3.2: FE model of the beam

The first step is to perform a linear modal analysis to extract the mode shapes, which will be used as displacement loading functions for the QSFR analysis. The first two mass-normalised mode shapes were calculated at 53.37 Hz and 129.63 Hz.



a) Mode 1

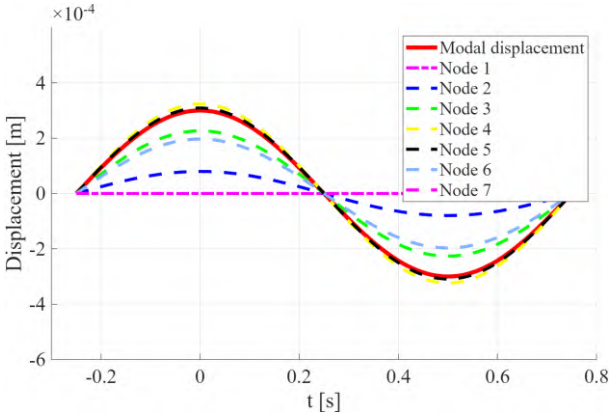


b) Mode 2

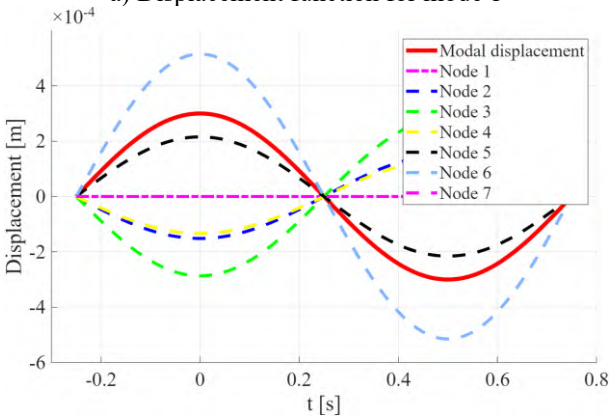
Figure 3.3: Mode shapes of the beam

Once the mode shapes are available, the QSFR analysis can be planned. Quasi-static means that each node of the FE model will be displaced according to a modal displacement. In simple terms, this involves performing quasi-static loading tests in which the applied displacements will statically deform the beam to match a selected mode shape. It is also critical to impose fully reversed loading, as naturally occurs under vibration. By applying a quasi-static deflection at a very low rate, the main nodal force contributions will come from stiffness and damping; the inertia force is assumed negligible for this case study. However, both inertia and damping can be rate-dependent, so such an assumption must be considered carefully. The mode shapes are thus converted into fully reversed displacement functions, sinusoids at 1 cycle/sec. Figure 3.4 (a) and (b) show the quasi-static fully reversed displacement functions

applied to each node of the FE model visible in Figure 3.5.



a) Displacement function for mode 1



b) Displacement function for mode 2

Figure 3.4: Displacement functions.

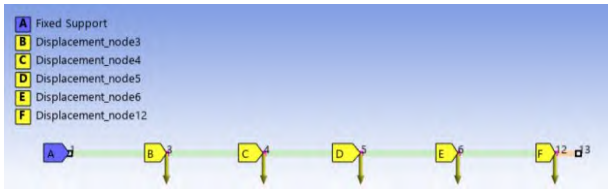


Figure 3.5: FEM and node displacement.

Once the displacement loads are applied to the nodes of the beam model, a nonlinear static simulation is performed. The resulting nonlinear nodal forces are exported and converted to the modal domain to create the displacement dependent modal hysteresis. Figure 3.6 shows the modal hysteresis for mode 1. The simulation of the hysteresis is the key calculation for extracting the equivalent damping and stiffness values to model the transfer function. Since the hysteresis is amplitude-dependent because of the intrinsic nonlinearity caused by the thin lamina, the transfer function will also be amplitude-dependent. This evaluation creates FRF's for the amplitude- and frequency range of interest, *it is thus possible to derive all relevant possible outcomes within the frequency and amplitude range of interest.*
This process is called Quasi-Static Frequency Response. The waterfall of the equivalent linear FRFs, from low to high amplitude deflection applied, will generate the Nonlinear Frequency Response Surface [12], which will allow evaluation of a nonlinear FRF, as measured in the laboratory. Figure 3.7 shows the NFRS which is a waterfall of linear FRFs calculated for each value of the nonlinear stiffness and damping.

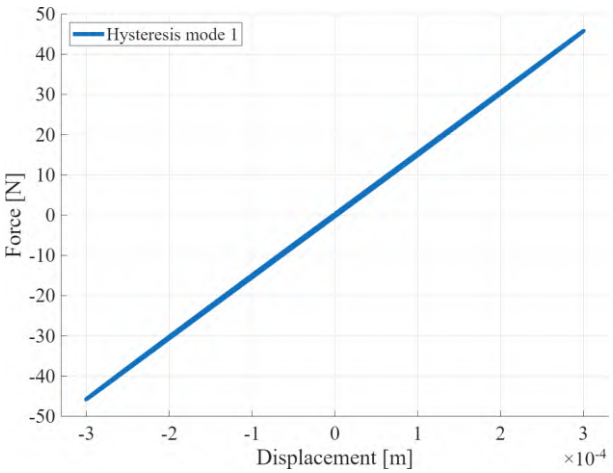
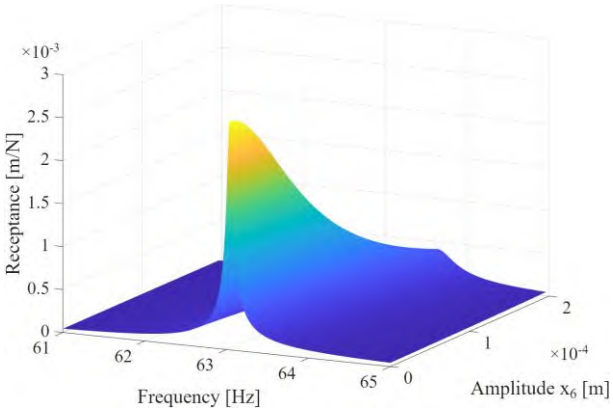
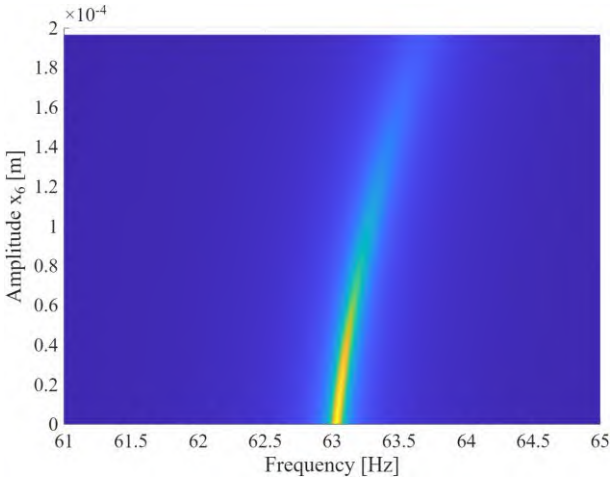


Figure 3.6: Nonlinear hysteresis of mode 1.



a) 3D perspective of the NFRS



b) Top-view of the NFRS

Figure 3.7: NFRS of mode 1.

Initially, the material damping was set to a constant value, but during the experiment it was observed that the damping exhibited amplitude dependence, which had to be included in the simulation of the FRFs. The FE model had access to the nonlinear stiffness but not to the damping nonlinearity, so the hysteresis showed dependence on stiffness but not on damping. The

damping nonlinearity was caused by the bolt connections at either end of the beam; those boundary conditions were not modelled for simplicity. The final step is to evaluate linear and nonlinear FRFs, which can then be compared with the experimental results. Figure 3.8 shows an example of those FRFs, already corrected for the nonlinear damping observed in the measurements. It is worth noting that an engineer can already gain insight into the effects of nonlinear stiffness in the frequency domain, that is, how much frequency deviation a dynamic system will experience under certain input loads.

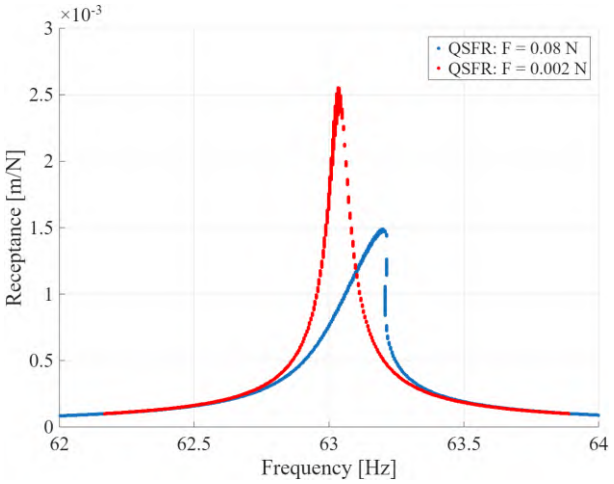


Figure 3.8: Linear and nonlinear FRFs of mode 1 created with the QSFR.

The final step is to compare the simulated and experimental FRFs. This section will not describe the experiments in detail because of the extensive trial and error the authors underwent during the measurements. In brief, the double cantilever beam exhibited higher damping at the constrained ends due to the bolted joints and poor welding between the main beam and the lamina. Moreover, the shaker test proved very challenging because of mass loading and added damping, both of which masked the true nonlinear dynamic behaviour. Therefore, a tap test with a modal hammer was performed to avoid these issues. The frequency response showed some damping nonlinearity caused by the jointed ends of the beam, as well as stiffness nonlinearity effects on the FRFs. Figure 3.9 shows the simulated linear FRF using the QSFR method and the linear synthesis of the FRF obtained from the experimental modal analysis. For this case, the QSFR and NFRS were scaled accordingly. Figure 3.10 a) shows the experimental FRFs, the linear one derived from the modal synthesis, and the nonlinear one. Figure 3.10 b) shows the linear and nonlinear FRFs obtained from the QSFR and NFRS methods. Both nonlinear FRF's show to behave in the same type of way compared to their linear counterpart. However the overlay is not carried out for the nonlinear FRFs. The reason is that the QSFR is based on steady-state analysis, whereas the experiment is achieved by impact excitation. Under linear vibrations, both steady-state and impact-derived FRFs are the same, but under nonlinear vibrations, that equivalence must be proven, and it is not done in this research.

As a final remark, the simplicity of the QSFR, which is based on a nonlinear static model, is notable. Therefore, a structural engineer might know little or nothing about dynamics but still use a tool that provides fundamental insights into design, such as the allowable peak amplitude under resonant conditions.

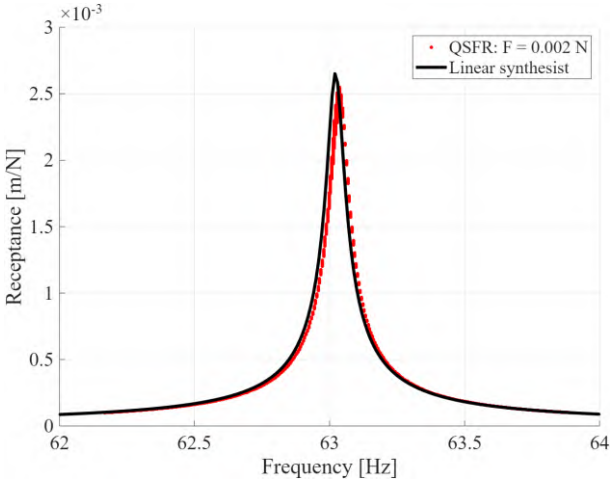
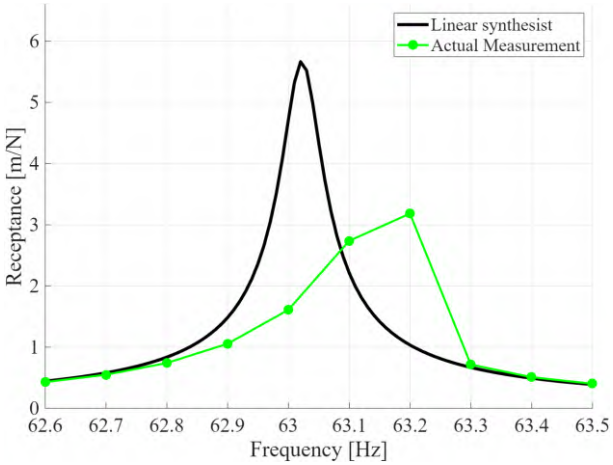
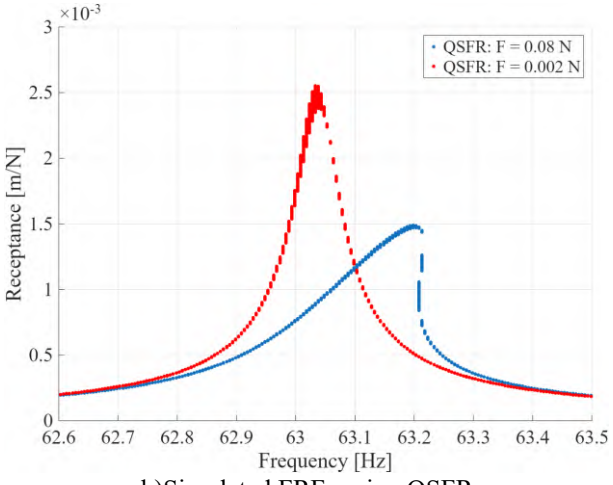


Figure 3.9: Linear FRFs of mode 1.



a) Experimental FRFs



b)Simulated FRFs using QSFR

Figure 3.10: Comparison between experimental and simulated FRFs.

4. CONCLUSIONS

This short paper introduces a new analysis framework to aid structural engineers in gaining insights into the amplification of the response at resonance. The main objective of the authors of this manuscript is to leverage the nonlinear static model, which is achieved during the early phases of a design project. That is the phase when structural modifications are still possible without altering or compromising the original design. Therefore, the nonlinear static model is loaded with shape functions, as the modal displacements. This process is called QSFR, and it aims to derive the hysteresis nonlinear curves, which are the source of the equivalent dynamic parameters. This process is demonstrated using a double cantilever beam, the static nonlinear model of which allows us to prove the underlying idea of QSFR. The comparison with the experimental results shows that the proposed approach meets the initial objectives of the authors, and it shows that the QSFR and NFRS are simple and effective first-order simulation techniques which can improve the design workflow.

5. REFERENCES

[1] Gaul, L., Lenz, J. (1997). Nonlinear Dynamics of Structures Assembled by Bolted Joints. *Acta Mechanica* 125, 169–181.

[2] Segalman, D.J. (2006). Modelling Joint Friction in Structural Dynamics. *Struct. Control Health Monit*. 13(1), 430-453.

[3] Brake, M.R.W. (2018). The Mechanics of Jointed Structures: Recent Research and Open Challenges for Developing Predictive Models for Structural Dynamics, *Springer International Publishing*.

[4] Iwan, W. D. (1966). A Distributed-element Model for Hysteresis and its Steady-state Dynamic Response. *Journal of Applied Mechanics*, 33(4), 893–900.

[5] Segalman, D. J. (2005). A Four-Parameter Iwan Model for Lap-Type Joints, *ASME J. Appl. Mech.*, 72(5), 752–760.

[6] Nakhla, M.S., Vlach, J. (1976). A Piecewise Harmonic Balance Technique for Determination of Periodic Response of Nonlinear Systems. *IEEE Transactions on Circuits and Systems*, 23(2):85–91.

[7] Renson, L., Kerschen, G., Cochelin, B. (2016). Numerical Computation of Nonlinear Normal Modes in Mechanical Engineering. *Journal of Sound and Vibration*, 364, 177–206.

[8] Festjens, H., Chevallier, G., Dion, J. L. (2013). A numerical tool for the design of assembled structures under dynamic loads. *International Journal of Mechanical Sciences*, 75, 170–177.

[9] Allen, M. S., Lacayo, R. M., Brake, M. R. (2016). Quasi-static Modal Analysis based on Implicit Condensation for Structures with Nonlinear Joints. *In: International conference on noise and vibration engineering, Leuven, Belgium*.

[10] M. S. Allen, J. Schoneman, W. Scott, and J. Sills, (2020) "Application of quasi-static modal analysis to an orion multi-purpose crew vehicle test," NASA Johnson Space Center, Tech. Rep. SAND2020-13841C,

[11] Carrella A., Ewins D.J. (2011). Identifying and Quantifying Structural Nonlinearities in Engineering Applications from Measured Frequency Response Functions. *Mech. Syst. Signal Process*. 25(3), 1011–27.

[12] Di Maio, D., 2024. A novel analysis method for calculating nonlinear Frequency Response Functions. arXiv preprint arXiv:2404.01972.

[13] M. Peeters, G. Kerschen, and J.-C. Golinval, "Modal testing of nonlinear vibrating structures based on nonlinear normal modes: Experimental demonstration," Mechanical Systems and Signal Processing, vol. 25, no. 4, pp. 1227–1247, 2011. DOI: 10.1016/j.ymssp.2010.11.006.

Vibroacoustic Prediction of the Internal Acoustic Environment in a Launch Vehicle Payload Fairing

Mara S. Escartí-Guillem [1,2], Pepe Nieto Mocholí[1], José Antonio Temprado Cano[1]

[1] COMET Aerospace, PARQUE TECNOLOGICO, Ronda Auguste y Louis Lumière, 23, Nave 7, 46980 Paterna, Valencia (Spain), email: mara.escarti@comet-aerospace.com, pepe.nieto@comet-aerospace.com, jose.temprado@comet-aerospace.com

[2] Instituto Universitario de Matemática Pura y Aplicada, Universitat Politècnica de València, Camino de Vera, s/n, 46022 València, Spain, email: maesgui2@doctor.upv.es

KEYWORDS

Vibroacoustic analysis, Payload fairing, Launch vehicle acoustics

ABSTRACT

Launch vehicles are subjected to severe acoustic loads during lift-off, which generate a critical vibroacoustic environment for the payload. Accurate prediction of the internal acoustic field is therefore essential for payload qualification and acoustic mitigation design. This work presents a numerical vibroacoustic analysis of a launch vehicle fairing using MSC Actran. Two configurations are analysed: the bare fairing and the fairing equipped with acoustic blankets, allowing the influence of the acoustic treatment to be quantified. The resulting spatial and spectral distributions of the internal sound pressure levels are used to characterize the payload acoustic environment and identify critical frequency ranges.

1. INTRODUCTION

Launch vehicles are exposed to severe acoustic loads during lift-off. The interaction of the exhaust plume with the atmosphere and the launch pad generates an intense acoustic field that acts on the vehicle and can be transmitted into the payload compartment. These loads can affect both the launcher structure and sensitive payload components, making the prediction of the vibroacoustic environment an important part of spacecraft design and verification [1,2]. The acoustic environment generated during lift-off and the influence of the launch pad configuration have also been extensively studied through numerical simulations and scaled experiments [3].

The payload fairing provides some attenuation of the external acoustic field, but part of the acoustic energy is transmitted through the structure. The vibration of the fairing then excites the enclosed air volume, resulting in a coupled structural-acoustic problem. Acoustic blankets are commonly installed on the inner surface of the fairing to reduce the internal sound pressure levels [4,5]. They provide a passive solution with a relatively low mass impact, an important aspect in launch vehicle applications where additional mass is strongly constrained. However, their performance is frequency dependent and becomes limited at low frequencies [4]. Different solutions have therefore been investigated to improve low-frequency attenuation, including tuned vibration absorbers and Helmholtz resonators [5], as well as locally resonant acoustic systems specifically designed for launcher fairings [6].

Different numerical approaches can be used to predict the vibroacoustic response of a payload fairing. FEM is well suited to the low-frequency range, where the structural and acoustic modes can be explicitly represented. At higher frequencies, the increasing modal density makes a deterministic solution increasingly expensive, and SEA or hybrid FEM-SEA approaches are commonly used. Pirk and Souto [7], for example, combined FEM/FEM, hybrid FEM/SEA and SEA models to cover the low-, mid- and high-frequency response of a launcher fairing. Hybrid FE-SEA approaches have also been used to evaluate the effect of acoustic blankets and resonators on the internal acoustic environment [8].

In this work, the complete frequency range from 31.5 Hz to 2 kHz is analysed using a FEM-based approach. The aim is to investigate the feasibility of using a single deterministic model over the complete frequency range while retaining the spatial information provided by the finite element solution. This choice results in a large numerical problem: the original structural modal basis contains 22,557 modes up to 2.4 kHz. A modal reduction strategy is therefore required before performing the coupled vibroacoustic analysis.

The model consists of a detailed finite element representation of the fairing coupled to the internal acoustic cavity. Two configurations are considered: the bare fairing and the fairing with acoustic blankets covering 75% of its internal surface. The comparison between both configurations is used to characterize the acoustic transmission through the fairing and, in particular, to quantify the noise reduction provided by the acoustic blankets over the frequency range considered. The analysis also allows the frequency ranges where the treatment is most effective, as well as those where its performance is more limited, to be identified.

2. METHODOLOGY

A coupled structural-acoustic finite element model was developed to predict the sound pressure levels inside the payload fairing. The model includes three main components: the fairing structure, the internal acoustic cavity and the acoustic treatment. The payload volume was also included in the acoustic domain and modelled as a rigid obstacle. The analysis was performed over the frequency range from 31.5 Hz to 2 kHz.

2.1. Structural model

A detailed finite element model of the fairing was used to represent its structural dynamic response. The structural modal basis was calculated in MSC Nastran and subsequently imported into MSC Actran for the coupled vibroacoustic analysis. A global structural damping ratio was considered.

The structural mesh was defined according to the bending wavelength of the different materials. A minimum of six elements per bending wavelength at the maximum frequency of interest was considered.

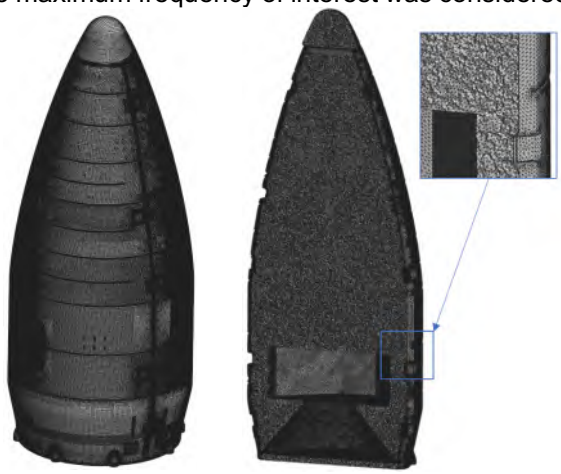


Figure 1: On the left, FE mesh of the structural fairing model. On the right, 3D acoustic mesh.

The original structural modal basis contained 22,557 modes up to 2.4 kHz. The upper frequency was extended by 20% with respect to the maximum analysis frequency to account for the contribution of modes above the frequency range of interest. Due to the size of the modal basis, its direct use in the coupled analysis would result in a high computational cost. A modal filtering procedure was therefore introduced to reduce the number of modes while retaining those considered most relevant for the structural response.

The reduction was performed in two steps. First, modes were selected according to their effective modal mass in the three translational directions. A second criterion was then introduced to maintain an adequate representation throughout the frequency range. For this purpose, the spectrum was divided into frequency bands and, within each band, the modes with the highest modal mass contribution in each direction were retained. This procedure reduces the size of the modal basis while avoiding the loss of frequency regions in which the individual modal contributions may be relatively small. Table 1 shows the percentage of effective mass displaced in the three directions of translation for each band in thirds of octave.

Table 1: Summary of modal basis filtering in third octaves.

	Accumulated mass relative to each bandwith in 1/3 oct		
Frequency (Hz)	T1	T2	T3
20	100.0%	100.0%	100.0%
25	100.0%	100.0%	100.0%
31.5	100.0%	100.0%	100.0%
40	100.0%	100.0%	100.0%
50	99.3%	95.8%	97.6%
63	98.9%	97.4%	96.3%
80	89.2%	83.2%	81.2%
100	90.3%	86.1%	85.4%
125	93.9%	82.3%	83.2%
160	84.4%	86.7%	83.9%
200	71.7%	74.7%	72.0%
250	71.9%	72.1%	71.7%
315	61.5%	60.0%	61.1%
400	61.6%	62.5%	61.6%
500	61.2%	60.0%	60.8%
630	36.8%	35.7%	36.2%
800	30.6%	32.0%	31.4%
1000	25.1%	27.5%	26.7%
1250	21.6%	21.8%	20.7%
1600	21.7%	20.4%	21.3%
2000	15.2%	16.4%	15.2%
2500	15.1%	16.7%	16.6%

Due to the large number of structural modes, the use of the complete modal basis over the full frequency range resulted in a very high computational cost. The reduced modal basis was therefore used for the complete analysis up to 2 kHz. To assess the influence of this reduction on the predicted acoustic response, an additional calculation was performed using the complete structural modal basis up to 480 Hz.

2.2. Acoustic model and excitation

The air volume enclosed by the fairing was represented using three-dimensional acoustic finite elements. The acoustic mesh was defined considering at least eight elements per wavelength at the maximum analysis frequency. The resulting maximum element size was approximately 21.4 mm. The volume corresponding to the satellite and the payload adapter has been removed from the mesh, simulating its effect as a rigid obstacle, which allows for a more accurate assessment of the acoustic field distribution around the payload. Details of the 3D acoustic mesh can be seen in Figure 2.

The external acoustic excitation was defined according to SMC-S-016 and applied directly to the

external surface of the fairing as a diffuse acoustic field. The diffuse field was generated using a spherical distribution of incident acoustic waves, discretized into 10 parallel planes and 30 samples. This approach provides a spatially distributed excitation over the fairing surface rather than considering a single direction of incidence.

2.3. Acoustic blankets

Two configurations were analysed to quantify the contribution of the acoustic treatment. The first configuration corresponds to the bare fairing and provides the reference response associated with the structural transmission alone. In the second configuration, acoustic blankets were applied over 75% of the internal fairing surface.

The blankets were introduced in the vibroacoustic model through an impedance boundary condition applied to the structural surface. The boundary condition specifies the absorption coefficient of the acoustic blanket shown in Figure 2.

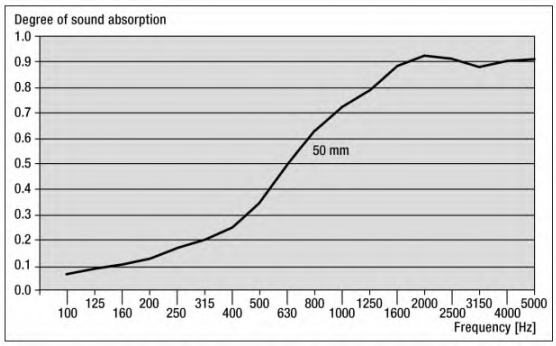


Figure 2: Absorption coefficient of acoustic blankets.

3. RESULTS

The internal acoustic response was first evaluated for the bare fairing to characterize the attenuation provided by the structure itself. The results were then compared with those obtained after including acoustic blankets over 75% of the internal fairing surface. The analysis was performed both for the volumetric average sound pressure level inside the fairing and for the acoustic pressure acting on the payload surface.

3.1. Internal acoustic field

The acoustic response inside the fairing was first evaluated in terms of the volumetric average sound pressure level. Figure 3 compares the external acoustic excitation applied to the fairing with the internal response for the bare fairing and for the configuration with 75% acoustic blanket coverage.

Table 2: Attenuation between the external acoustic excitation and the volumetric average SPL inside the fairing, integrated into octave bands.

	Bare fairing	75% of acoustic blankets	
Freq [Hz]	**Attenuation [dB]**	**Attenuation [dB]**	**ΔAt [dB]**
31.5	13.37	13.82	0.45
63	7.61	8.33	0.72
125	3.30	9.05	5.76
250	6.84	12.77	5.93
500	6.62	19.75	13.13
1000	11.83	35.31	23.48
2000	10.90	43.71	32.81
OASPL	5.80	11.10	5.30

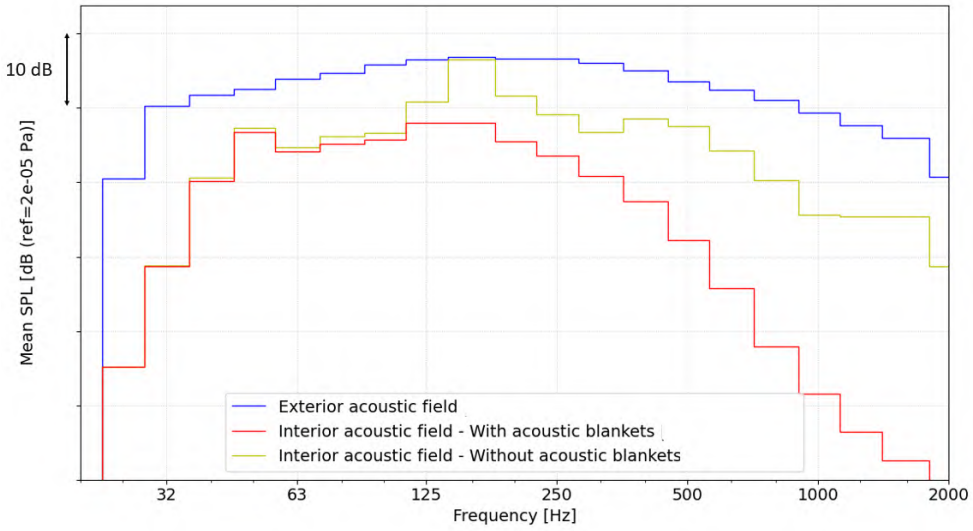


Figure 3: Volumetric average of sound pressure level (SPL) integrated in 1/3 octave for the external acoustic field (blue), the internal acoustic field applying acoustic blankets at 75% (red) and the acoustic field without applying acoustic blankets (yellow).

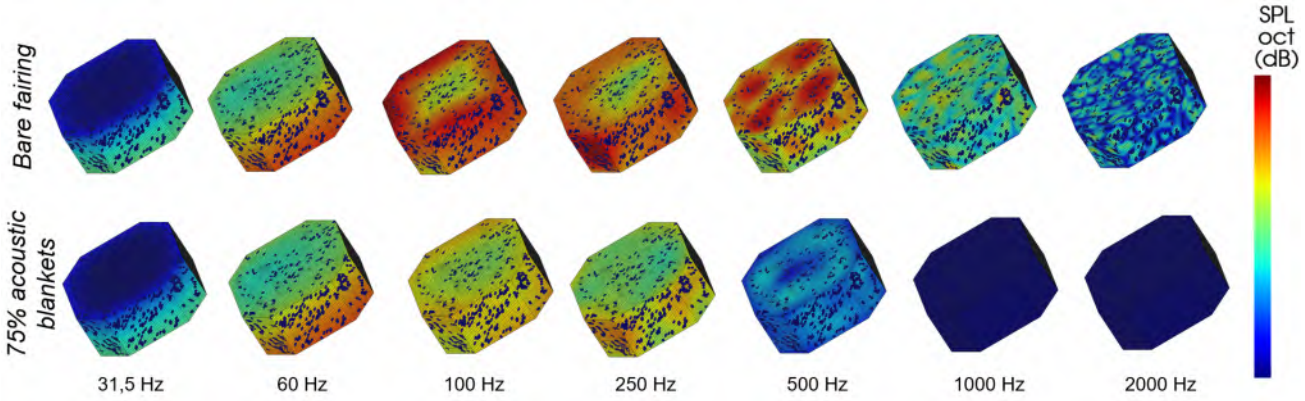


Figure 4: Sound pressure level (SPL) contours on the payload surface. The upper row is the bare fairing and the lower row belongs to the case with 75% of acoustic blankets. The SPL values have been eliminated due to confidentiality.

The corresponding attenuation values, integrated into octave bands, are summarized in Table 2. The additional attenuation provided by the acoustic blankets, ΔAt, is defined as the difference between the attenuation obtained with and without acoustic blankets, and so it represents the net contribution of the acoustic treatment to the reduction of the internal sound pressure level.

The addition of acoustic blankets reduces the internal sound pressure levels over most of the frequency range. Their effect is small in the two lowest frequency bands, with additional attenuations of only 0.45 and 0.72 dB at 31.5 and 63 Hz, respectively. From 125 Hz onwards, their contribution progressively increases, providing an additional attenuation of 5.76 dB at 125 Hz, 13.13 dB at 500 Hz and more than 20 dB above 1 kHz. This frequency-dependent behaviour is consistent with the expected performance of porous acoustic treatments, whose effectiveness increases as frequency increases [4].

These results show that for the configuration considered, the acoustic treatment provides an additional 5.30 dB reduction in OASPL inside the fairing.

3.2. Acoustic environment on the payload surface

In addition to the volumetric average, the acoustic pressure acting directly on the payload surface was evaluated. This quantity provides a more local description of the acoustic environment and allows regions of higher acoustic pressure to be identified.

Figure 4 shows the SPL distribution over the payload surface at selected frequencies for the bare fairing and the configuration with 75% acoustic blanket coverage. Table 3 presents the attenuation between the external acoustic excitation and the average SPL on the payload surface, integrated into octave bands.

Table 3: Attenuation between the external acoustic excitation and the maximum SPL on the payload surface, integrated into octave bands.

	Bare fairing	75% of acoustic blankets	
Freq [Hz]	**Attenuation [dB]**	**Attenuation [dB]**	**ΔAt [dB]**
31.5	12.95	13.21	0.26
63	0.07	0.82	0.75
125	-4.69	3.40	8.08
250	-1.52	2.40	3.92
500	-4.71	11.03	15.73
1000	-2.01	21.66	23.67
2000	-3.74	30.88	34.62
OASPL	-3.00	3.52	6.53

For the bare fairing, the attenuation calculated on the payload surface is strongly frequency dependent. At 31.5 Hz, the fairing provides an attenuation of 12.95 dB, whereas at 63 Hz the attenuation is almost negligible. From 125 Hz onwards, negative attenuation values are obtained, indicating that the average SPL on the payload surface is higher than the applied external acoustic level at these frequencies. This behaviour is associated with the coupled structural-acoustic response of the fairing and the internal cavity, which can produce local amplification of the acoustic field. The resulting OASPL attenuation on the payload surface is −3.00 dB.

The addition of the acoustic blankets significantly reduces the pressure levels acting on the payload, although their contribution is again strongly dependent on frequency. At 31.5 and 63 Hz, the additional attenuation is limited to 0.26 and 0.75 dB, respectively. From 125 Hz onwards, the effect becomes more significant, with additional attenuations of 8.08 dB at 125 Hz, 15.73 dB at 500 Hz and more than 20 dB above 1 kHz. As a result,

the OASPL attenuation increases from −3.00 dB for the bare fairing to 3.52 dB with the acoustic treatment, corresponding to an overall contribution of 6.53 dB from the acoustic blankets.

The spatial distributions in Figure 4 provide further information that cannot be obtained from the averaged values alone. At low and intermediate frequencies, the acoustic field is clearly non-uniform, with regions of higher SPL concentrated mainly around the upper part of the payload. The blankets reduce these local pressure levels, with the effect becoming particularly evident from 500 Hz onwards. At 1 and 2 kHz, the pressure levels over most of the payload surface are substantially reduced compared with the bare configuration.

These results confirm the frequency-dependent behaviour already observed for the volumetric average response. The acoustic blankets provide limited additional attenuation at the lowest frequencies but become increasingly effective as frequency increases. The surface results also show the importance of considering the spatial distribution of the acoustic field when characterizing the payload environment, since local pressure levels can differ significantly from the volumetric average response.

3.3. Influence of the modal basis reduction

The influence of the modal reduction was evaluated by comparing the internal acoustic response obtained with the reduced modal basis against a calculation including the complete structural modal basis up to 480 Hz. Figure 5 shows the volumetric average SPL obtained with both approaches, while Table 4 summarizes the SPL differences at selected frequencies together with the fraction of modal mass retained by the reduced basis.

The reduced modal basis reproduces the general spectral trend of the complete solution over the analysed frequency range. However, a systematic underestimation of the internal SPL is observed. The contribution of the modes removed during the filtering process is therefore not negligible for the coupled vibroacoustic response, even when their individual effective modal mass is relatively small.

At low frequencies, both modal bases provide similar results. Below 100 Hz, the SPL difference remains below 1 dB, except at 100 Hz, where it increases to 1.33 dB. In this frequency range, the retained modal mass is generally above 80% in the three translational directions. At 125 and 160 Hz, the difference remains below 1.5 dB.

Table 4. Attenuation between the external acoustic excitation and the maximum SPL on the payload surface, integrated into octave bands.

Freq [Hz]	Absolute variation [dB]	Percentage of modal mass fraction [%]		
		T1	T2	T3
31.5	0.83	100.0%	100.0%	100.0%
40.0	-0.42	100.0%	100.0%	100.0%
50.0	-0.57	99.3%	95.8%	97.6%
63.0	0.56	98.9%	97.4%	96.3%
80.0	0.59	89.2%	83.2%	81.2%
100.0	1.33	90.3%	86.1%	85.4%
125.0	1.49	93.9%	82.3%	83.2%
160.0	1.47	84.4%	86.7%	83.9%
200.0	2.43	71.7%	74.7%	72.0%
250.0	3.79	71.9%	72.1%	71.7%
315.0	4.33	61.5%	60.0%	61.1%
400.0	5.32	61.6%	62.5%	61.6%

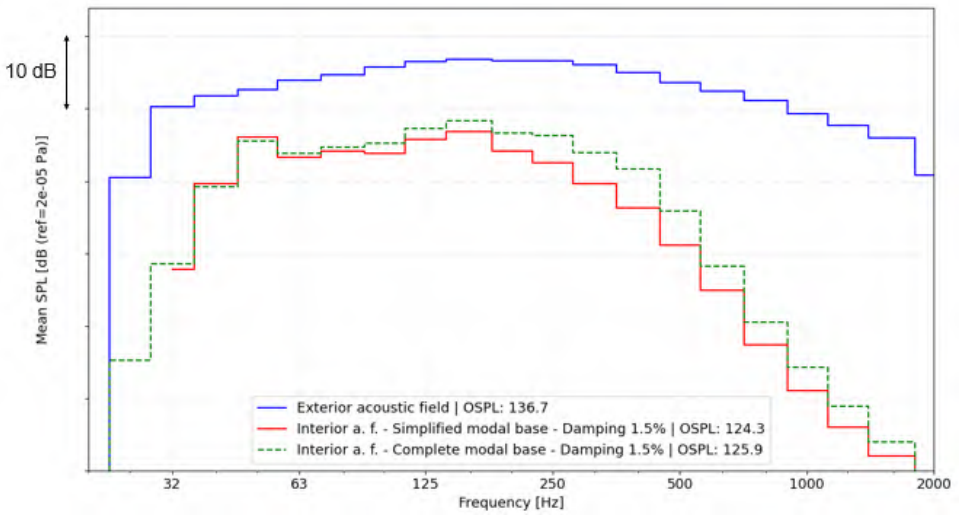


Figure 5: Volumetric average of sound pressure level (SPL) integrated in 1/3 octave for the external acoustic field (blue), the internal acoustic field applying acoustic blankets at 75%considering the simplified modal base (red) and the complete modal base up to 480 kHz (green).

As frequency increases, the effect of the modal reduction becomes more significant. The SPL difference increases to 2.43 dB at 200 Hz, 3.79 dB at 250 Hz, 4.33 dB at 315 Hz and 5.32 dB at 400 Hz. Over the same frequency range, the fraction of retained modal mass progressively decreases, reaching approximately 60–62% at 315–400 Hz. A clear relationship is observed between the fraction of retained modal mass and the difference between the reduced and complete solutions. When the retained modal mass decreases below approximately 70%, differences above 4 dB are observed. In contrast, retaining more than 80% of the modal mass generally limits the SPL difference to less than 2 dB, while differences below 1 dB are obtained when more than 95% of the modal mass is retained.

Despite the increasing discrepancy at higher frequencies, the comparison provides useful information for defining future modal reduction strategies. For the present model, retaining more than approximately 80% of the modal mass generally results in SPL differences below 2 dB, while retaining more than 95% reduces the difference to below 1 dB. These values could be used as preliminary criteria to select the level of modal reduction according to the accuracy required and the available computational resources. Moreover, when a more aggressive modal reduction is required, the observed deviation could be used to estimate the uncertainty associated with the predicted internal SPL, provided that the reduced model is first characterized against the complete solution over a representative frequency range.

4. CONCLUSIONS

A deterministic FEM-based vibroacoustic model was used to characterize the acoustic transmission through a launcher fairing and to evaluate the performance of acoustic blankets covering 75% of its internal surface. The results show a strongly frequency-dependent response, with local amplification on the payload surface at several frequencies due to the coupled structural-acoustic behaviour of the fairing and the internal cavity.

The acoustic blankets significantly improve the internal acoustic environment, particularly at mid and high frequencies, while their effect remains limited at the lowest frequencies. The treatment provides an additional OASPL attenuation of 5.30 dB for the volumetric average and 6.53 dB on the payload surface. Above 1 kHz, the additional attenuation exceeds 20 dB. These results indicate that acoustic blankets are effective for controlling a significant part of the spectrum, although complementary solutions may be required when further attenuation at low frequencies is needed.

The modal basis assessment showed that the reduced model reproduces the general response of the complete solution, although the discrepancy increases as the retained modal mass decreases. For the present model, retaining more than approximately 80% of the modal mass generally limits the SPL difference to less than 2 dB, while differences below 1 dB are obtained when more than 95% is retained. These results provide a practical criterion for balancing computational cost and accuracy in future analyses.

The increasing discrepancy also suggests that effective modal mass alone may not fully represent the relevance of a structural mode to the internal acoustic response. Future modal reduction strategies could therefore include structural-acoustic coupling criteria in addition to effective modal mass. At higher frequencies, where maintaining a sufficiently complete modal basis becomes increasingly expensive, hybrid FEM–SEA approaches may also provide a more efficient alternative.

5. REFERENCES

1. NASA (2026). NASA-STD-7001C: Payload Vibroacoustic Test Criteria. National Aeronautics and Space Administration, Washington, DC, USA.
2. European Cooperation for Space Standardization (2013). ECSS-E-HB-32-26A: Spacecraft Mechanical Loads Analysis Handbook. ESA Requirements and Standards Division, Noordwijk, The Netherlands.
3. Tsutsumi, S., Ishii, T., Ui, K., Tokudome, S. & Wada, K. (2015). Study on Acoustic Prediction and Reduction of Epsilon Launch Vehicle at Liftoff. J. Spacecr. Rockets 52(2), 350-361.
4. Lane, S.A., Johnson, M., Fuller, C. & Charpentier, A. (2006). Active Control of Payload Fairing Noise. J. Sound Vib. 290, 794-819.
5. Howard, C.Q., Hansen, C.H. & Zander, A. (2005). Vibro-Acoustic Noise Control Treatments for Payload Bays of Launch Vehicles: Discrete to Fuzzy Solutions. Appl. Acoust. 66(11), 1235-1261.
6. Chimeno-Manguán, M., Simon Hidalgo, F., Barriuso Feijoo, P., Escartí-Guillem, M.S., Nieto, P., Groby, J.-P., Leng, J. & Romero-García, V. (2024). Design of a Locally Resonant System to Reduce Noise Inside the Payload Fairing of a Launcher During the Lift-Off. Aerosp. Sci. Technol. 155, 109592.
7. Pirk, R. & Souto, C.d'A. (2015). Deterministic, Hybrid and Statistical Vibro-Acoustic Models – a Methodology to Determine the VLS Payload Fairing Acoustic Behavior. J. Aerosp. Technol. Manag. 7(1).
8. Choi, I., Park, S. & Lee, S. (2020). A Study on In-Flight Acoustic Load Reduction in Launch Vehicle Fairing by FE-SEA Hybrid Method. J. Acoust. Soc. Korea 39(4), 351-363.

ECSSMET
Braunschweig Germany 2026

Thermal testing

DEVELOPMENT AND VALIDATION OF A THERMAL CONTROL SYSTEM FOR THE LARGE SPACE TEST CHAMBER LOADING TROLLEY

Jack Pleasant

(1) RAL Space, Oxford, United Kingdom, jack.pleasant@stfc.ac.uk

KEYWORDS

Thermal Vacuum Testing, Thermal modelling, Thermal Control System

1. NOMENCLATURE

LSTC – Large Space Test Chamber
IUT – Item Under Test
GFRP – Glass Fibre Reinforced Polymer
TCS – Thermal Control System
NSTF – National Satellite Test Facility
TCU – Thermal Conditioning Units
TTA – Thermal Test Adapter
LT – Loading Trolley
MLI – Multi Layer Insulation
TMM - Thermal Mathematical Model

2. ABSTRACT

A Thermal Control System has been developed for the 6 Tonne Large Space Test Chamber Loading Trolley housed at RAL Space. The loading trolley is a novel piece of equipment designed to suspend the Item Under Test (IUT) in the chamber. Although the design of the trolley intrinsically minimises the conductive heat flow path to the IUT through the use of an insulating GFRP spacer at the interface, thermal regulation of the loading trolley is required to further conductively decouple it from the IUT. A Thermal Control System (TCS) has been developed for the loading trolley to maintain steady state temperatures during Thermal Vacuum Testing. A computational modelling approach was adopted for test heater sizing, resulting in an installed capacity of 9KW heater power (including redundancy). A mixture of closed and open-loop control is used to regulate the output of 600W DC power supplies, with 52 T-type thermocouples instrumented for detailed temperature distribution measurement. Thermal vacuum balance test cases were carried out to assess heater performance and for thermal model correlation purposes. This paper outlines the Thermal Control System design process including the thermal modelling approach, practical aspects of thermal instrumentation, and thermal vacuum test results used for verification of the thermal model.

3. FACILITY DESCRIPTION

3.1. Large Space Test Chamber

The Large Space Test Chamber (LSTC) is a test facility located in the National Satellite Test Facility (NSTF) – the latest addition to the suite of space environment testing facilities offered at RAL Space. The LSTC is a 7m diameter x 12m length horizontally loaded thermal vacuum test chamber, with shroud temperature regulation capability of 95K to 400K. The thermal shroud is comprised of 10 black painted thermal zones, each controlled by an individual Thermal Conditioning Unit (TCU). The shroud is fed with gaseous nitrogen, the temperature of which is controlled using liquid nitrogen and a heater element and circulated using a blower unit.

The chamber rails are of stainless-steel construction and are capable of supporting a load of 20T. The 12 rail legs penetrate through the vessel and are fixed to the building foundations. The vessel is capable of achieving pressures of $<1e^{-5}$ mbar, depending on the IUT and temperature profiles.

3.2. LSTC Loading Trolley

The LSTC Loading Trolley is a critical piece of MGSE used to suspend the IUT in a cantilever configuration during Thermal Vacuum Testing. This is a common approach for TVAC testing, which minimises conductive coupling of the IUT and the test chamber, providing a more representative space-like environment for testing and characterisation.

The Loading Trolley can be manipulated using the Integration Stand, allowing a transformation from horizontal (adapter plate facing up) to vertical (adapter plate facing forward) configurations, to facilitate the loading and mechanical fastening of the IUT to the trolley before transitioning into the chamber. The general specifications of the Loading Trolley are summarised below:

Table 1 - Loading Trolley specification

Mass	6772 Kg
Bulk material	Stainless Steel
Payload capacity	6000 Kg @ 3.8m from adapter
Compatible Temp Range	93k to 400k
Adjustments	5° fine pitch/roll

A key requirement of the test campaign for which this loading trolley was initially designed was to limit the heat transfer between the IUT Thermal Test Adapter (TTA) and the LT adapter to 50W for -20°c ≤ T_{TTA} ≤ 50°c. This is important in order to most accurately represent flight conditions, where the environmental heat fluxes are purely radiative. The Loading Trolley was designed with a Glass Fibre Reinforced Polymer 'washer' at the interface, Figure 1. GFRP composites have thermal conductivity values in the range of 0.25 – 0.4 W/mK, providing excellent resistance to the heat flow path. The LT Washer thickness is 42mm, therefore the heat flow across the washer can be derived from Fourier's law:

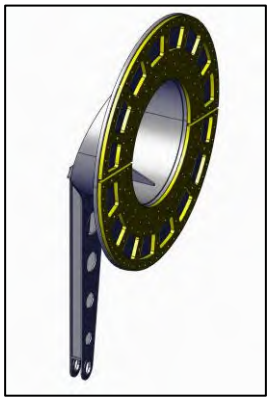


Figure 1 - LSTC Rolling Frame and Washer

$$Q = \frac{kA}{l}\Delta T \qquad \textit{Equation 1}$$

The resultant heat flow per unit temperature is ~ 11W/K. Therefore, to limit the heat flow to <50W, the temperature difference across the boundary must be kept < 4.5K (ignoring radiative heat transfer effects). This introduces the need for a thermal control system, to regulate and monitor the Loading Trolley temperature during the TVAC test, to ensure the heat transfer requirement is satisfied.

4. THERMAL CONTROL SYSTEM

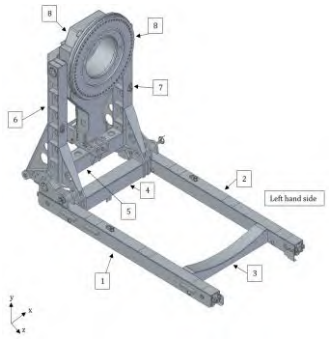


Figure 2 - Loading Trolley Thermal Zones

The Loading Trolley Thermal Control System (TCS) is comprised of resistive heaters, temperature sensors, power supplies and Multi-Layer Insulation (MLI). Owing to the large size and mass of the loading trolley structure, the system is subdivided into nine independently controlled thermal zones (Figure 2).

Under steady-state conditions, the thermal control system must satisfy the energy balance of the loading trolley:

$$Q_{rad_LT\text{-}SHROUD} + Q_{cond_LT\text{-}LSTC} + Q_{rad_LT\text{-}IUT} + Q_{gen_TCS} = Q_{cond_LT\text{-}IUT}$$

Where $Q_{cond_LT\text{-}IUT} \leq 50$ W Equation 2

in order to satisfy the maximum allowable conductive heat transfer requirement between the loading trolley and the IUT.

During test phases in which the shroud temperature is lower than that of the loading trolley and IUT, the radiative heat exchange with the shroud and conductive heat transfer to the chamber act as significant heat sinks to the Loading Trolley. Depending on the thermal mass and exposed surface area of the IUT, its transient thermal response may differ from that of the loading trolley. Consequently, a compensating heat input, $Q_{gen,TCS}$, is required to regulate the loading trolley temperature and minimise conductive heat transfer across the loading trolley-to-IUT interface.

Furthermore, sufficient thermometry is required to be installed on the Loading Trolley for monitoring and control purposes.

4.1. Thermal Model

To determine the required heater power capacity and distribution, a thermal model of the Large Space Test Chamber and Loading Trolley was developed using ESATAN-TMS. The software was selected due to its extensive heritage within the European space industry and its proven capability for coupled conductive and radiative thermal analysis of spacecraft and ground support equipment. The model was used to assess worst-case thermal environments, predict temperature distributions throughout the loading trolley structure, and support optimisation of the thermal control system design.

4.1.1. Shroud Thermal Zones

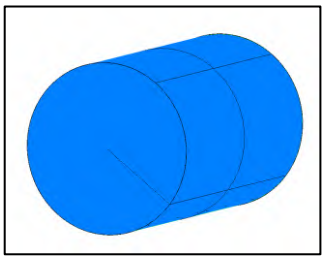


Figure 3 - Shroud thermal zones geometrical model

For modelling purposes, the chamber vessel was omitted from the thermal mathematical model (TMM), as heat transfer between the vessel and shroud does not significantly influence the thermal behaviour of the loading trolley. The Thermal Conditioning Units which control the shroud temperature are capable of providing < 1K temperature uniformity for heat loads < 50KW. Therefore, only the ten actively controlled thermal shroud zones were included in the test environment representation.

The shroud assembly was modelled as a cylindrical enclosure comprising of 8 body thermal zones and two end zones representing the chamber door and rear closure, as shown in Figure 3. In reality, the shroud zones are comprised of several panels – this

is simplified for the thermal model.

The external surfaces of the shroud zones were defined as inactive boundaries, whilst the internal surfaces were modelled as radiative surfaces. Conductive coupling between adjacent shroud zones was neglected, as the objective of the model was to characterise the thermal environment experienced by the loading trolley rather than the thermal behaviour of the shroud system itself.

The thermo-optical properties of the active shroud surfaces were assigned using manufacturer data for Aeroglaze Z306 black paint, which was applied to the chamber shroud interior surfaces. For the purposes of this analysis, the absorptivity and emissivity values were assumed to be independent of temperature.

4.1.2.Internal Rails

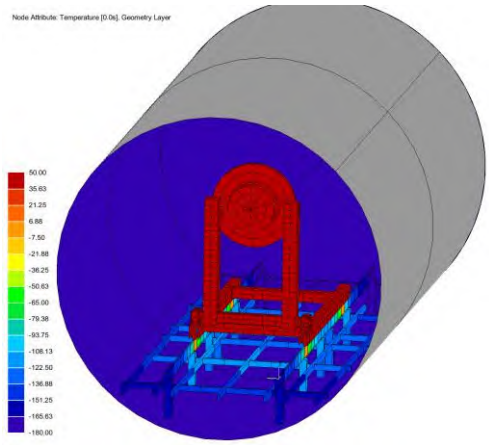


Figure 4 - Nodal temperature plot of steady state simulation with T_{LT}=50°c and T_{SHROUD} = -180°c

The chamber internal rails were included within the thermal model due to the conductive link between the LT wheels and the rails, and the radiative 'shadowing' effect between the trolley and certain shroud zones. The contact conductance between the wheels and the rails was estimated based on empirical data of contact areas and thermal contact conductance data for stainless steel based on the estimated contact pressure. Hetrzian contact theory (Hertz, 1882) was used to estimate the contact area, which is estimated to be ~18mm^2 per wheel assembly. Based on the weight of the loading trolley, the average contact pressure was calculated to be ~ 890MPa. From this, a thermal contact conductance of 0.32W/K per wheel assembly was assumed, and were modelled as contact zones.

The rail structure was modelled using the material properties of stainless steel 304L, with temperature-dependent thermal properties obtained from literature sources (Harvey, 1982). The thermo-optical properties were selected from published data corresponding to an unpolished stainless-steel surface finish (Kumar, 2025). These properties were applied to all radiating surfaces of the rail assembly.

A geometrical representation of the chamber rail model geometry is shown in Figure 5 .

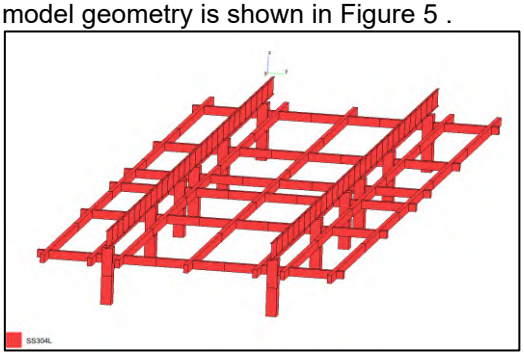


Figure 5 - Geometrical model of LSTC Internal Rails

Individual rail components were linked using fused conductive contacts. This assumption was considered appropriate as the majority of the rail structure is fabricated using welded joints, resulting in low thermal contact resistance values.

Finally, the conductive path between the rail legs and the foundation is omitted from the thermal model for simplicity.

4.1.3.Loading Trolley

The loading trolley is divided into 9 thermal zones, illustrate in Figure 6. The zones are described in Table 2.

Table 2 - LT Thermal Zone location

Zone 1	Longitudinal Beam RHS
Zone 2	Longitudinal Beam LHS
Zone 3	Lateral Beam Far
Zone 4	Lateral Beam Close
Zone 5	Horizontal Brace
Zone 6	Vertical Brace RHS
Zone 7	Vertical Brace LHS
Zone 8	Adapter Ring Structure
Zone 9	Adapter Interface

The loading trolley mechanical and thermo-optical properties were set to those of Stainless Steel 304L and 2205. The Loading Trolley structure is largely divided into two sections, the horizontal 'base' and the vertical 'frame'. The two pivot about each other along the tilting axis. Aside from the moveable components, the majority of the Loading Trolley frame components are welded, and as such fused contacts were assumed for all conductive couplings. Therefore, thermal contact resistances between the moveable components are assumed to be zero in the analyses. The Permaglass adaptor washer was modelled using appropriate bulk and thermo-optical properties.

4.1.4.Item Under Test

The IUT was represented in the thermal model by a fixed temperature boundary condition, reflecting the

temperature of the TTA. In this approach, the temperature distribution of the IUT is not modelled. A non-geometrical node was used to represent the TTA, and a conductor representing the thermal contact conductance between the TTA and LT adapter was assigned. The value was estimated using the contact area and bolting torque values. The initial estimate was $G_{c,I}$ = 257 W/K. Experimentally obtained data from thermal balance cases was used to tune this parameter to provide the most accurate representation.

4.2. Heater Power Sizing

Achieving a completely uniform temperature distribution across the Loading Trolley was not the objective of the thermal control system. The control system ideology is to provide coarse thermal control of Zones 1-8, and precise control at Zone 9, where the IUT interfaces with the Loading Trolley. Without temperature control in Zones 1-8, the temperature at the interface would be unstable due to heat transfer with the wider Loading Trolley structure.

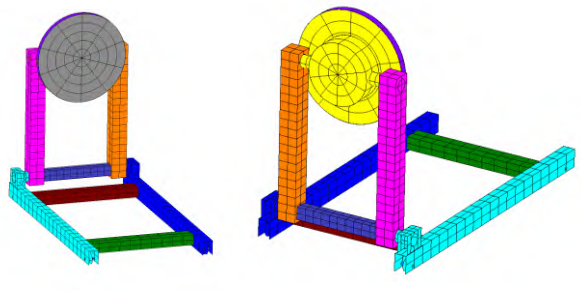


Figure 6 - Loading Trolley Zones Graphic

First, the total heater power required to maintain the loading trolley temperature during max. power condition of T_{LT}=50°c (maximum temperature of the TTA) and T_{SHROUD} = -180°c (lower limit of the LSTC) was determined using the results of a steady state simulation. The results nodal temperature plot is shown in Figure 4.

The total heat flux between the shroud and loading trolley in this steady state case was determined to be ~ 7.3KW. This is the total heat input that the thermal control system must compensate for.

Due to simplifications and assumptions applied to the thermal model, a safety factor of ~25% was applied when determining the total installed heater power. Since there is no benefit to be had by optimizing the heater capacity (i.e. no total mass restrictions), an over-engineering approach was taken to ensure sufficient heating power.

4.3. Multi-Layer Insulation Modelling

The maximum power requirement was determined without the use of MLI covering the Loading Trolley structure. It was decided MLI blankets would be used to cover all exposed surfaces of the structure for two reasons. The first was to limit the radiative heat transfer between the IUT and the Loading Trolley, and the second was to limit the radiative heat losses from the Loading Trolley to the shroud. An additional advantage was the improvement in temperature uniformity of the Loading Trolley.

To obtain an approximation of the Loading Trolley's heat loss to the shroud when using MLI, a new radiative and thermal case were run in ESATAN with the optical properties of the Loading Trolley structure set to those of the outer surface of the MLI to be used (Beyond Gravity COOLCAT 2 NW, aluminized polyester). The updated heat exchange with the shroud reduced to ~ 2.4KW. Although the method used to model the MLI is simplistic, it was believed to provide a good enough estimation for the purpose of the thermal model.

Nevertheless, it was decided that the initial estimate of 9KW primary heater power was to be used for the loading trolley thermal control system to account for the simplifications in the thermal model.

4.4. Heater Placement

In order to determine the most effective heater placement for the loading trolley, steady state simulations were conducted with a cold shroud configuration, and heat load boundary conditions applied to groups of nodes representing heaters. The distribution of heaters was adjusted until the uniformity of the temperature distribution was acceptable. This process was done qualitatively – no specific criteria was used when adjusting the heater distribution. Once the heater distribution had been finalised, the heater output boundary conditions were adjusted between 100w and 500w per zone, to see the effect on the overall temperature uniformity of the Loading Trolley. This analysis was conducted under no-MLI conditions (i.e. with SS thermo-optical properties for the loading trolley surface.) The results are depicted in Figure 7.

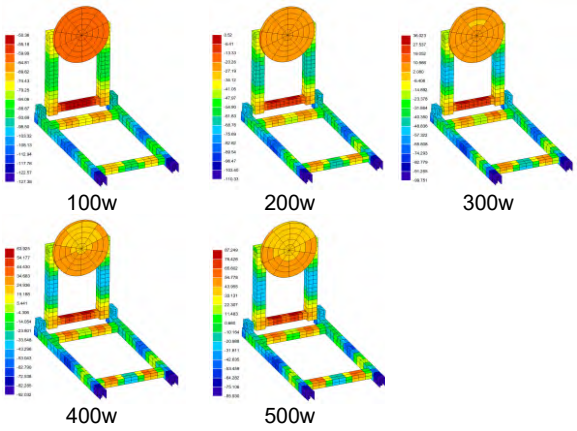


Figure 7 - Nodal Temperature Plot of Loading Trolley at 5 different power configurations

It can be seen that 500w heater power per zone is sufficient to maintain ~50°c on Zone 9 (IUT interface). Zones 3, 4 and 5 are seen to exhibit the highest temperatures, due to the relative size of the structural components. There is a large temperature difference across certain zones, with a gradient of >100°c visible on certain thermal zones. The gradients are due to the lack of MLI, the relatively low thermal conductivity of Stainless Steel, and the large surface area of the loading trolley structure. It was anticipated that the experimentally observed temperature uniformity would be much greater.

4.5. Thermal instrumentation

4.5.1. Heaters

The heater type chosen was Clayborn Lab 28 series heat tape. This type of heater has a long heritage in the space sector and uses acrylic adhesive which has low outgassing properties. It was also chosen for its versatility since it can be folded to conform to various surfaces. Additionally, the conductors can be configured in different ways to obtain different resistance levels for the same length of heat tape.

The heaters were laid in a 'snaking' pattern (Figure 8), which facilitated the best distribution for a given length. The tape was applied directly to the surface of the loading trolley and secured with aluminium foil tape. Care was taken to fully conform the heaters to the loading trolley surface, ensuring good contact and heat dissipation.



Figure 8 - Zone 1 heat tape placement

The 3 wiring configurations available for the Clayborn heat tape are depicted in the figure below. The configurations correspond to 1.7, 28 and 7 Ω/ft respectively.
Configuration 3 was chosen as it corresponded to the most appropriate length heater for the required power.
Using the Clayborn heat tape meant that the heaters could be cut to a specific length very easily, allowing the total power to configured

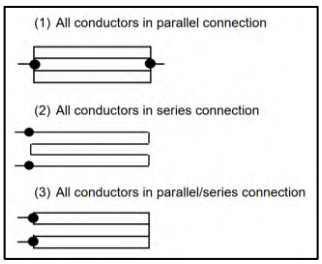


Figure 9 - Clayborn heat tape wiring configurations

4.5.2. Power Supply Units

The LSTC was designed with 140 power supply units (PSUs) for use by the facility and the customer hardware. The PSUs have a 0-60v output voltage and rated maximum output current of 12.5A, with a resultant maximum power output of 750W

Once of the restrictions applied to the LT TCS was to minimise the PSU usage in order to free up availability for customer hardware. Consequently, it was decided that 2 PSUs were to be used per thermal zone (1 primary and 1 redundant), with a total of 18 being used for the Thermal Control System.

4.5.3. Thermometry

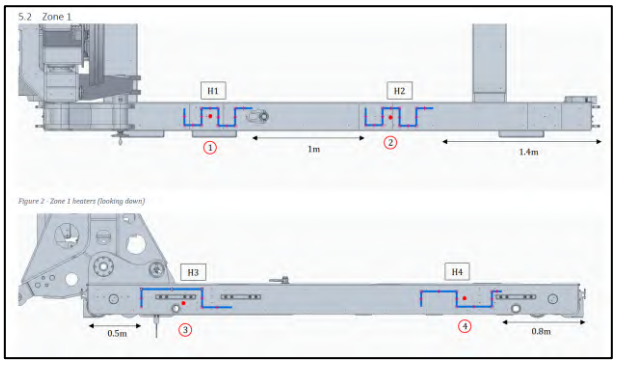


Figure 10 - Zone 1 heater and thermocouple mapping

T-type thermocouples were used to monitor the temperature of the Loading Trolley. 6 thermocouples were placed per zone for Z1-8, and a further 4 thermocouples were placed on Z9 (IUT interface). The thermocouples were distributed to provide representative measurements of both local heater influence and bulk structural temperatures. Placement was focused on areas expected to experience the largest thermal gradients, including heater locations, structural junctions, and extremities of the primary beams.

To ensure good thermal contact, thermocouple junctions were attached directly to the stainless-steel structure using aluminium foil tape. Care was taken to minimise conduction through the thermocouple wires by securing leads to the structure at multiple locations and routing

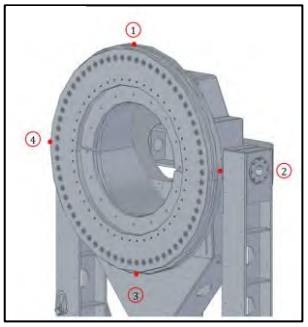


Figure 11 - Zone 9 thermocouple locations

them along local isothermal surfaces where practical. This approach reduced measurement errors caused by parasitic heat transfer. Great care also had to be taken to account for the movement of the loading trolley during rotation.

4.5.4. MLI

The loading trolley structure was covered with Beyond Gravity Coolcat 2 NW multi-layer insulation. The blanket design was tailored to maximise coverage of the primary structural members whilst maintaining access to mechanical interfaces, lifting features, adjustment mechanisms and thermal instrumentation. The MLI was also designed to be removable through the use of Velcro fasteners, for Loading Trolley maintenance purposes.

4.6. Control System Architecture

The thermal control infrastructure is separated into independent monitoring and control systems. Temperature acquisition is performed through VTI EX1048A thermocouple acquisition modules connected to the chamber thermocouple patch panel. The chamber has 1000 T-type thermocouple channels available to use. Measurement data is logged and visualised using the facility Orchestrator data acquisition server. In parallel, a subset of 96 thermocouple channels is routed directly to the Omron Programmable Logic Controller (PLC), which forms the core of the thermal control system. The PLC monitors temperature feedback and controls the 18 TDK-Lambda GENH60-12.5 programmable power supplies supplying heater power to the loading trolley. Operator interaction with the control system was provided through the Experimental Physics and Industrial Control System (EPICS) graphical user interface, which serves as the primary front-end for system monitoring, configuration and commanding.

Since the PLC only has the hardware capability for 96 control thermocouples (which are also shared with customer use) the number of LT zones available for closed loop control was restricted. As such, only Zone 9 was chosen to be controlled in closed-loop configuration. The TCS uses the 4 available TCs placed on the zone to control the heater power using the average temperature. PID parameters are tuneable manually and using an auto-tune function. The rest of the Loading Trolley thermocouples are logged and viewed in the Orchestrator server system, and the power control for these zones relies on manual operator adjustments of the voltage setpoints. This is justifiable since the precise control of these zones is not crucial.

A schematic of the control system and thermometry DAQ systems is displayed in Figure 12.

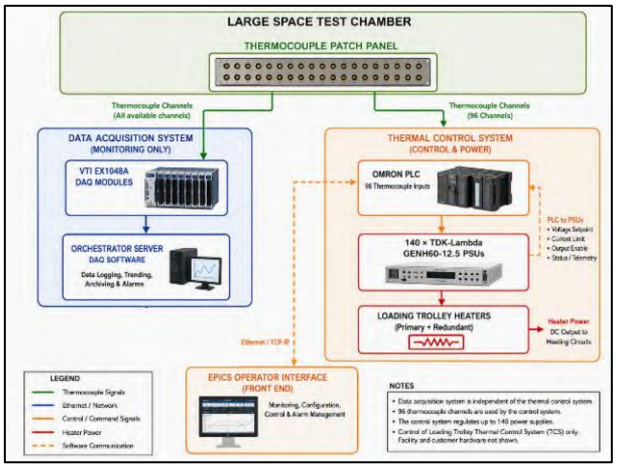


Figure 12 - LSTC Thermal Control System and Data Acquisition system schematic

4.7. Thermal Vacuum Validation Testing Results

4.7.1. Test Objectives

Thermal vacuum balance (TBAL) tests were conducted to verify the performance of the loading trolley thermal control system and to generate data for thermal model correlation. The test data was obtained during an operational TVAC test, and as such an IUT TTA with temperature regulation was mounted to the LT adapter.

The principal objectives of the TVAC test were:

1. Demonstrate the functionality of the heater system under representative vacuum conditions.
2. Validate thermocouple installation and measurement repeatability.
3. Characterise thermal gradients throughout the structure.
4. Verify that adequate control authority existed at the adapter interface.
5. Correlate the ESATAN-TMS thermal model against measured data.

4.7.2. Transitional performance: 173k to 100k

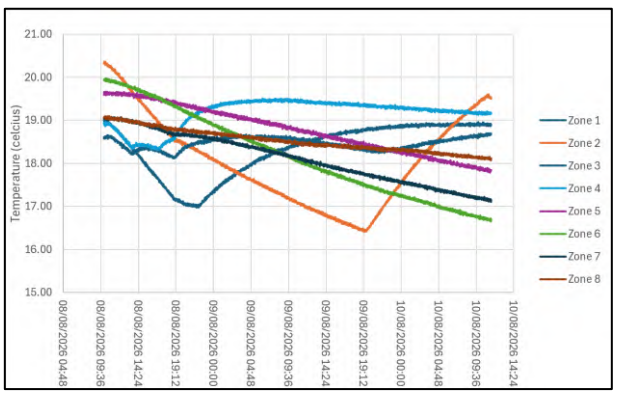


Figure 13 - Loading Trolley Average temperature (excl. Z9) – transitional 173k to 100k

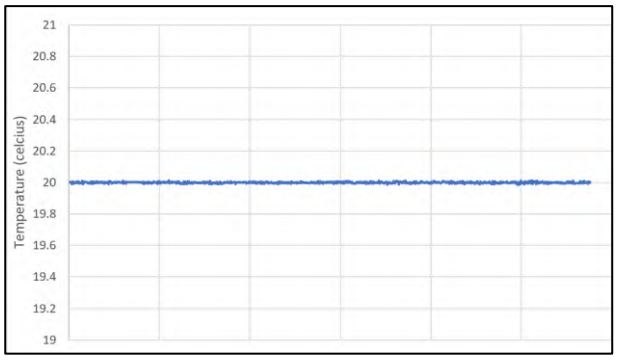


Figure 14 - Z9 average temperature (transitional 173k to 100k)

The transitional performance of the TCS is first assessed during a transition from two dwells, 173k to 100k. The LT Z1-Z8 average temperatures are displayed in Figure 13. Since these zones rely on manual intervention by the operator, clear setpoint changes can be observed on the plot. Nevertheless, the Zones were maintained within the required tolerance of 20 ± 5 °c. Ideally, closed loop temperature control would be implemented to all zones in order to improve the transient temperature response of the loading trolley during transitions. However, as previously mentioned, only the Z9 temperature is critical for the test requirement.

The Zone 9 average temperature during the transition is displayed in Figure 14. Since Zone 9 heaters are configured using PID control on the PSUs, the average temperature is kept very close to the setpoint of 20°c throughout the duration of the transition. This proves that Z9 exhibits very good temperature control, even during a strenuous transitional period, and the capability of the TCS.

4.7.3. Thermal Balance (Shroud at 103k)

The first TBAL case conducted was with the shroud at 103k. Figure 15 displays the zonal average temperatures over a period of hours while the shroud is maintained at 103k. The temperature stability can be seen to be very good. All the zones have been maintained within the defined tolerance range of 20°c ± 5°c.

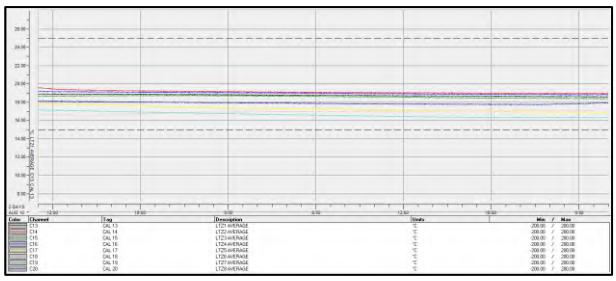


Figure 15 - LT Zone averages (shroud at 103k)

The power setpoints of each loading trolley zone are displayed in Table 3, alongside the setpoints predicted by the thermal model at these conditions.

The model predictions were obtained using proportional control thermostatic power boundary conditions applied to the heater zone groups. The experimental setpoints were extracted from the last hour before the setpoint change. The first conclusion is that the actual power required is consistently significantly lower than the predicted model requirement for most zones. The results identify the inadequacy of the modelling approach taken for the MLI. A recommended work package is to update the model using MLI features now available within recent versions of ESATAN-TMS.

Table 3 - TBAL @ 103k shroud / TTA @ 278k - heater power vs model predictions

Zone	Heater power output (W)	Thermal model prediction (W)
Zone 1	143.2	201.6
Zone 2	132.1	198.4
Zone 3	108.2	142.9
Zone 4	119.0	137.8
Zone 5	25.5	36.1
Zone 6	102.3	185.1
Zone 7	66.3	185.1
Zone 8	60.7	105.5
Zone 9	143 (average)	100.4

4.7.4. Thermal Balance (Shroud at 193k)

A second thermal balance case was conducted at 193k setpoint. Figure 16 displays the Loading Trolley zonal average temperatures for Z1-8 for the duration of the dwell. Again, the TCS is capable of maintaining the desired setpoint across all zones.

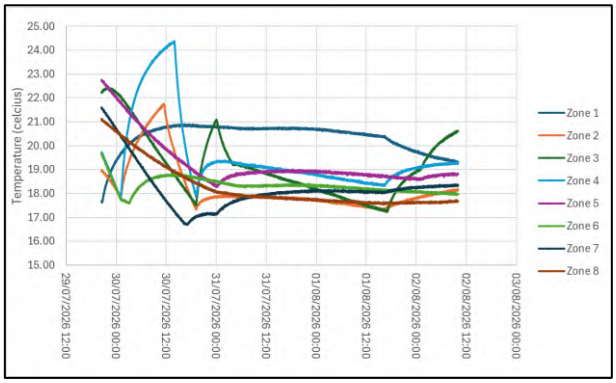


Figure 16 - Loading Trolley Average temperature (excl. Z9) – 193k

Table 4 displays the as-set heater power outputs for the TBAL, at the final hour of the dwell, as well as the predicted heater setpoints from the thermal model. Again, the thermal model over-predicts the power output significantly, up to 160% increase in some cases. Some zones are well represented by the thermal model.

Table 4 - TBAL @ 193k shroud / TTA @ 278k - heater power vs model predictions

Zone	Heater power output (W)	Thermal model prediction (W)
Zone 1	106.4	166.3
Zone 2	97.4	163.6
Zone 3	76.6	115.8
Zone 4	96.7	113.6
Zone 5	19.4	28.6
Zone 6	70.4	140.3
Zone 7	54.0	140.3
Zone 8	28.2	87.2
Zone 9	34.9 (average)	74.1

4.7.5.Zonal Thermal Gradients

The maximum thermal gradients across each thermal zone are listed in Table 5. These were taken at the 103K TBAL, where the gradients were expected to be largest.

Table 5 - Zonal Temperature Gradients @ 103K

Zone	Maximum temperature (°c)	Minimum temperature (°c)	Max gradient (°c)
Zone 1	29.4	5.7	23.7
Zone 2	29.2	11.05	18.15
Zone 3	19.9	16.3	3.6
Zone 4	22.2	14.0	8.2
Zone 5	18.3	14.3	4
Zone 6	29.2	8.5	20.7
Zone 7	22.9	8.6	14.3
Zone 8	26.8	11.5	15.3
Zone 9	20.6	19.6	1

There is a clear correlation between zones which have complete MLI coverage and lower temperature gradients. Zones which could not have implemented full MLI coverage due to restrictions in movement (Z1,2,6,7,8) experienced larger zonal temperature gradients. This is expected due to the radiative heat exchange between the exposed surfaces and the shroud. This supports the need to improve the MLI coverage on these zones, by increasing the overall coverage whilst maintaining the freedom of movement.

5. DISCUSSION

The first finding is that the thermal model significantly over-predicts the power setpoint of the heaters required to maintain the Loading Trolley zones at the temperature setpoint during TBAL cases. The likely explanation for this is the inadequacy of the approach used to model the MLI in the thermal model, which used a more simplistic method of simulating outer layer thermo-optical properties. To combat this, a more thorough approach will be used for MLI modelling in the updated model. Additionally, it is possible the TBAL durations were not sufficient to determine the final steady state temperature and subsequent power outputs for the heaters, and a higher power setpoint may have been required if the TBAL was extended. Unfortunately, it was not possible to alter the test profile in this case due to the nature of the testing approach. Further testing is to be conducted including only the Loading Trolley, to more accurately assess the prediction of the thermal model.

The temperature gradients observed across each zone were quite large, especially on zones which were not fully covered with MLI due to movement considerations. It is felt with sufficient re-work of the MLI, the gradients can be minimised. However, this is not the primary focus of the TCS which is to maintain a temperature setpoint at the Zone 9 interface.

The Zone 9 temperature control was very good at maintaining the required setpoint for the duration of the test. The temperature was kept within ±1°c of the setpoint at all times. The power output varied during the test according to temperature of the IUT TTA and environment temperature as expected.

6. FUTURE WORK

The principal area for future work is the conducting of a dedicated thermal balance test for correlation of the thermal model. Although some trends and vague correlations were made using the TVAC test results, complete correlation was not possible.

The thermal control system has successfully demonstrated its ability to regulate the temperature of the Large Space Test Chamber loading trolley and minimise conductive heat transfer between the loading trolley and the IUT. Nevertheless, several opportunities for further development have been identified.

The current control philosophy utilises a combination of open-loop control for the primary structural zones and closed-loop control at the adapter interface. Future developments may include implementation of fully closed-loop control across all thermal zones. Such an approach could further improve temperature uniformity, reduce operator intervention and automatically compensate for varying thermal environments encountered during different test campaigns.

Further investigation into the thermal performance of the MLI is also recommended. The current thermal model represents the MLI using equivalent thermo-optical properties applied to external surfaces. Development of a more detailed MLI representation may improve prediction accuracy, particularly for transient thermal analyses and local temperature gradients.

7. CONCLUSION

Generally, the results of the TBAL test demonstrate that sufficient heater power was installed on the Loading Trolley to maintain it at the required setpoint during the coldest environmental temperatures achievable by the shroud and the closed loop temperature control of Zone 9 was found to be very good. These were the two most important objectives of the TCS. The thermal model consistently over-predicted the power required for each zone at both TBAL setpoints. This is attributed to inadequate MLI modelling, and the inability to maintain steady state conditions during the thermal vacuum testing due to testing constraints. Further testing will allow a more thorough correlation of the thermal model.

8. BIBLIOGRAPHY

Harvey, P. D. (1982). *Engineering Properties of Steels.* Metals Park: American Society for Metals.

Hertz, H. (1882). On the contact of elastic solids. *Journal für die reine und angewandte Mathematik* , 156–171.

Kumar, U. (2025). *EFFECT OF SURFACE TREATMENTS ON THE THERMAL EMISSIVITY OF SS304L.*

TCS PERFORMANCE OF THE NEW THERMAL VACUUM FACILITY AT IABG'S COMPETENCE CENTRE OPTICS

Daniel Winter [1], Bastian Söllner [2], Stefan Zirngibl [3], Daniel Döring [4], Matthias Friemel [5]

[1] *IABG Space Test Centre, Einsteinstr. 20, 85521 Ottobrunn, Germany, Email: WinterD@iabg.de*
[2] *IABG Space Test Centre, Einsteinstr. 20, 85521 Ottobrunn, Germany, Email: Soellner@iabg.de*
[3] *IABG Space Test Centre, Einsteinstr. 20, 85521 Ottobrunn, Germany, Email: Zirngibl@iabg.de*
[4] *IABG Space Test Centre, Einsteinstr. 20, 85521 Ottobrunn, Germany, Email: Doering@iabg.de*
[5] *IABG Space Test Centre, Einsteinstr. 20, 85521 Ottobrunn, Germany, Email: FriemelM@iabg.de*

KEYWORDS

Test Facilities, Thermal Control Systems (TCS), Optical Ground Support Equipment (OGSE), Temperature Stability & Uniformity

ABSTRACT

IABG has developed, built and commissioned a new large Thermal Vacuum Facility (TVA), which serves as the heart of its Competence Centre Optics (CCO). As a second core element of the CCO, IABG has also procured Optical Ground Support Equipment (OGSE) consisting of vacuum compatible high precision flat mirror assemblies, reference coordinate system and alignment and measurements systems, which can be made available to customers for dedicated test campaigns. Together, TVA and OGSE enable IABG and its space clients to carry out large-scale performance testing, characterization, and precise calibration of current and next-generation optical space systems in a thermal vacuum and microvibration low-grade environment, pushing the boundaries of what is technically feasible.

To meet the stringent stability requirements that have to be fulfilled to enable IABG's OGSE to be used for alignment and calibration of optical components and systems, the TVA features a high-performance thermal control system (TCS) ensuring excellent temperature uniformity and stability. For the first time, IABG has taken over the role as manufacturer for the TVA, engaging in the construction and verification well ahead of its traditional responsibility as facility operator. This dual role enabled IABG to tailor the facility design – especially of the TCS – utilizing decades of expertise in thermal vacuum testing.

The TCS comprises 10 independently controlled shroud segments, each designed to operate in a temperature range from -173°C to +120°C using gaseous nitrogen, with the option to reach below -188°C in liquid nitrogen mode. Each segment is supplied by a dedicated Thermal Conditioning Unit (TCU), with one spare unit available for redundancy. Additionally, four auxiliary TCUs can independently support customized test setups within the chamber, such as optical calibration targets, thermal or albedo plates, in both gaseous and liquid nitrogen modes. Two further liquid nitrogen loops inside the chamber and an additional one outside the TVA are available for cold targets, cold traps, or heat sinks.

At the current stage, IABG has successfully qualified the TVA for operation in the range of -163°C to +61°C, with an upgrade to the full design range already being in progress. The facility, including OGSE and surrounding ISO class 5 clean room infrastructure, has been certified already according to the ECSS quality standard for space test centres ECSS-Q-ST-20-07C.

This presentation outlines the architecture and key characteristics of the TVA's thermal control system, including temperature range, uniformity, and stability. It also highlights the actual thermal performance achieved during the commissioning phase and demonstrates the system's readiness for demanding optical space system testing

1. INTRODUCTION

Future optical payloads require increasingly stringent thermo-elastic stability during calibration and optical performance and verification tests. Conventional thermal vacuum facilities are often optimized for thermal balance or thermal cycling tests rather than precision optical measurements.

To address this gap, IABG has built a new set of facilities, the Competence Centre Optics (CCO), including its new thermal vacuum chamber (TVA).

A key design driver for the TVA was therefore the achievement of exceptional thermal stability and uniformity.

The core of CCO is optical ground support equipment (OGSE) that allows the characterization of different optical payloads. The CCO is providing an ISO class 8 test hall with a dedicated thermal-vacuum facility equipped with optical benches and ISO class 5 cleanrooms for test preparation, as well as the OGSE needed for test execution in ambient and vacuum conditions. For detailed information regarding the OGSE refer to [1].

Derived from the design of instrument or spacecraft tests and the necessary boundary conditions of the OGSE, the new TVA has been specified, built and commissioned by IABG.The new chamber has already demonstrated its performance and reliability in several customer tests.

2. OVERVIEW OF THE TVA FACILITY

The essential feature of the TVA is an optical bench assembly mounted on an independent foundation with mechanical decoupling from both the TVA (vessel, thermal shrouds, pumping systems, etc.) as well as the CCO building. Since the facility fulfils the VC-E microvibration criterion, it is considered a high-performance microvibration environment suitable for instruments with sub-micrometer precision. For reference, VC-E allows maximum one-third-octave RMS vibration velocities of 3.125 µm/s, which is 16 times lower than a VC-A laboratory and roughly two orders of magnitude lower than an ordinary office environment [2].

The vacuum system reaches a pressure of <1e-5 mbar. The inner usable diameter of the cylindrical shrouds is 5 m. The chamber can be split to provide both a long (14 m) and a short (7 m) configuration so it can be adapted to different test setups: Long with all OGSE accommodated inside the vacuum, short with OGSE under ambient, ISO class 5 clean room conditions (looking inside through corresponding windows). In the default long configuration the vessel is divided into a north and a south test volume by a pair of separation shrouds (one facing the north vessel, the other one facing south). The separation shrouds have a central opening with a diameter of 1.75 m, which can be closed or opened by the shutter door segments. The shutter door segments are actively temperature controlled and are thermally coupled to the corresponding shutter shroud.

All shroud segments and visible parts inside the test volume are painted black with Aeroglaze Z306 and have an $\varepsilon_H \geq 0.90$ and $\alpha_S = 0.95$. The rear side of the shrouds is electropolished.

The TVA is accessible from the north (dedicated for customer preparation activities) north and south (mainly foreseen for IABG activities, mostly regarding the OGSE) from two ISO class 5 clean rooms. The TVA and all relevant parts and components are designed and chosen for being ISO class 5 compatible, which is crucial for the high cleanliness standards of optical equipment. The circumference of the cylindrical vessel is accessible from outside of the chamber via an ISO class 8 clean room and provides easy access for feedthrough flanges and accommodation for Electrical Ground Support Equipment (EGSE) with less stringent cleanliness requirements. For further information refer to [3].



Figure 1:TVA in longitudinal cut



Figure 2: TVA in long configuration with optical bench and independent foundation

3. OGSE OVERVIEW

The Optical Ground Support Equipment (OGSE) available at IABG is fully vacuum compatible and can be integrated in the TVA together with the customer instruments in order to remove the influence of air turbulence and optical windows on the quality of the measurements.

At the moment, the OGSE consists of the following components:

- a high precision flat mirror assembly (FMA) with a silver coated Zerodur mirror, usable mirror diameter of 1.45 m and a surface flatness error (SFE) of 10.8 nm RMS on a positioning system that allows azimuth and elevation movements of ±2° with sub-arcsec accuracy. A second flat mirror with aluminium coating and larger travel range (±5°) will be available soon.
- a reference coordinate system (RefCOS) fabricated from Zerodur that is acting as absolute reference and alignment monitoring system for the OGSE and the customer instruments. For this purpose, the coordinate system is equipped with a high precision autocollimator with sub-arcsec accuracy and several optical reference mirrors which are all manufactured from the same batch of Zerodur to assure maximum stability of the optical references throughout the test campaign.
- two high resolution autocollimators and four differential interferometer setups that can

be positioned on the optical benches to monitor the angular alignment, or to track the movement of OGSE or customer instruments in the test setup with sub-arcsec accuracy.

A typical setup with all components installed on the optical bench can be seen in the following Figure 3 and Figure 4



Figure 3: OGSE setup consisting of (left to right side) FMA and RefCOS



Figure 4: Rear view of the setup including the HRA (monitoring the alignment and movement of the FMA) and two differential interferometer setups targeting the RefCOS to monitor thermally induced defromations of the optical bench

Additional OGSE that will extend the test capabilities of the CCO will be available in the near future, i.e.:

- two off-axis collimator mirror assemblies (CMA) with aluminium and silver coated Zerodur mirrors, a usable diameter of 1.5 m and positioning systems for azimuth and elevation movements of ±5° with sub-arcsec accuracy.
- two calibration source assemblies (CSA) providing different light sources, targets and wave front measurement systems for the characterisation and calibration of customer instruments. These CSAs can be used with the CMAs or independently.

While all OGSE systems have been designed for maximum thermal stability in their operational temperature window of +21°C (±3) and measures have been taken to reduce the impact of temperature changes and thermal gradients on the performance and stability of the components, temperature changes and thermal gradients still affect the optical performance and due to the size of the components especially the alignment of the components in the setup.

Taking into consideration that – while in a separate volume of the TVA – the OGSE is in the TVA also during thermal balance tests and thermal cycling of the customer instrument and has to deal with the impact of temperature settings and thermal gradients from the customer side during optical performance testing, the quality of the thermal environment provided by the TVA is one of the key factors to achieve and maintain the optical performance and stabilities of the OGSE throughout a test campaign.

To achieve and maintain the optimum optical performance and alignment of the optical components of the OGSE the TVA has to be able to fulfil the following thermal requirements of the OGSE throughout all phases of the test campaign and in consequence over a duration of several weeks:

- $T_{Set,OGSE}$ = +21°C (±0.5)
- $T_{max,TVC}$-Shroud = +23°C
- $T_{min,TVC}$-Shroud = +19°C
- $T_{Slope,max} \leq$ 1.0 K/min
- $T_{Gradient,max} \leq$ 0.5 K (FMA mirror)
- $T_{Gradient,max} \leq$ 1.0 K (OGSE mech. parts)
- $T_{Gradient,max} \leq$ 1 K (all other components)

4. THERMAL CONTROL SYSTEM (TCS) DESCRIPTION

4.1. Thermal shroud system

To meet the stability requirements of the optical components, the TVA must provide very good uniformity and excellent stability of the shroud temperatures. Each of the two vessel parts consists of five individual controllable thermal circuits: cylinder segment west, cylinder segment east, separation shroud and chamber door. An optional rectangular shroud can be installed to cover the optical bench. Hence, in total ten thermal circuits can be used, see Figure 5. Nitrogen gas (GN2) or liquid nitrogen (LN2) is circulated in closed loops. Each thermal circuit is operated by an individual thermal conditioning unit (TCU). One redundant TCU is available and can be operated on any other thermal circuit if necessary.

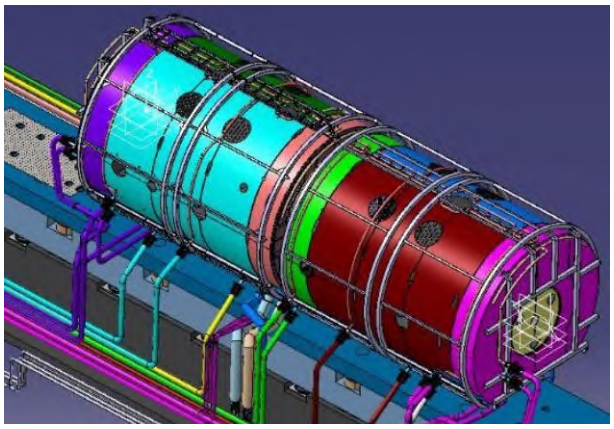


Figure 5: Thermal system, colored for each individual circuit

The maximum temperature change rate of each circuit is 1 K/min.

In principle every circuit can be operated at any individual temperature needed. The maximum allowed delta between two circuits is limited to 218 K though (i.e. delta between liquid nitrogen level in test volume north and room temperature in test volume south). If needed, a higher temperature difference is possible, however at the cost of lower uniformity on each of the segments.

4.2. Open Loop circuits

Furthermore, there are four additional temperature controllable gaseous nitrogen loops (“Open Loops”) available which can be used for active temperature control of test-specific components (e.g. thermal plates, calibration sources) inside the test volume. All Open Loops can also be supplied by LN2, in case low temperatures are needed.

4.3. LN2 circuits

The Open Loop system is complemented by two additional LN2 circuits inside the TVA, and one LN2 circuit outside the TVA, each capable of providing independent LN2 supply and exhaust to test-specific consumers (e.g. customer provided cold black bodies), whenever needed. The block diagram is shown in Figure 7.

4.4. LN2 supply/ GN2 exhaust system

A LN2 supply system distributes the liquid nitrogen to all individual TCUs and other consumers such as cryo panels or additional Open Loop circuits and LN2 circuits. It includes three external LN2 tanks and two redundant liquid nitrogen pumps and a phase separator. The phase separator recovers the liquid nitrogen from the LN2 return lines of all circuits to the LN2 supply system, while only the exhaust gaseous nitrogen from the TCUs and other return lines is finally depleted into the chimney. This way it is possible to minimise the LN2 consumption of the facility and to operate it in a cost-effective manner.

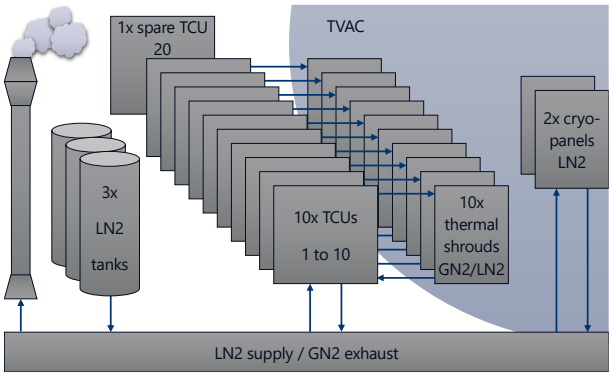


Figure 6: Block diagram of thermal system and LN2 supply / GN2 exhaust

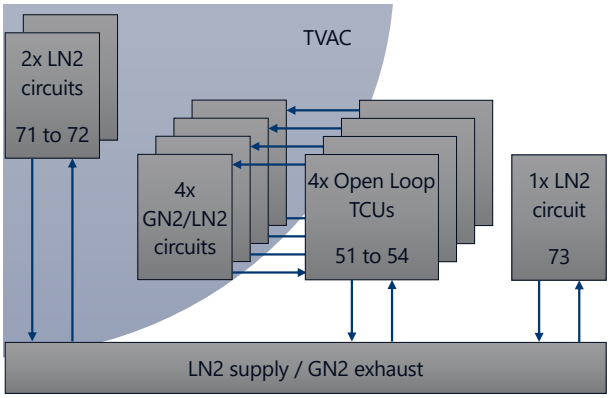


Figure 7: Block diagram of “Open Loop” circuits and additional LN2 circuits for test-specific setups

5. VERIFICATION OF TCS PERFORMANCE

5.1. Temperature range

The performance of the new thermal vacuum facility has been verified in a series of commissioning runs which led to final acceptance in December 2024. In spring 2025 the OGSE was set up inside the south test volume to characterise the performance of both the OGSE and the TVA in a typical scenario for customer tests.

For each of the ten TCUs shroud segments, the temperature range from -163°C to +61°C was successfully verified. As the temperature reference for this range, the average temperature per shroud segment was used, since this is the most relevant parameter for customer tests.

The open loop circuits have been qualified in the temperature range from -163°C to +65°C. Since the open loop circuits can be used to supply any kind of thermal plate inside the chamber, the achievable temperature on the thermal plate depends heavily on the test setup (plate mass, heat load, hose lengths, parasitic heat fluxes etc.). For that reason, the temperature reference point for the open loop circuits was selected to be at the nitrogen inlet feedthrough to the chamber, rather than at the thermal plate itself.

In an exemplary test setup using thermal plates with adjustable electrical heat loads, it was shown that

the temperature delta between flange inlet (reference temperature) and thermal plate average temperature (relevant for customer) may reach up to 20 K for a non-optimized test setup (e.g. poor conductive decoupling of the plate from the environment and using long connection hoses of up to 17 m inside vacuum). Minimizing this offset is considered in the design for test-specific setups by IABG.
The facility's qualified temperature range was in line with the needs of the first customer test campaigns in the new facility, which have been successfully concluded in 2025 and 2026.
In order to achieve the full design range on the thermal shrouds (-175°C to +120°C in gaseous mode, <-188°C in LN2 mode), a modification of the facility is already ongoing.
Analogue to the chamber shrouds, also the open loop circuits will be upgraded to cover the full design temperature range (-175°C to +120°C in gaseous mode, <-188°C in LN2 mode) after the ongoing modification. In addition, the two additional LN2 circuits inside the TVA, and the one LN2 circuit outside the TVA will be qualified for nominal use in customer tests. In November 2025 the CCO, including TVA and OGSE, has been successfully certified according to ECSS quality standard for space test centres ECSS-Q-ST-20-07C [4]. Therefore, the modification will be performed fully in line with ECSS processes.

5.2. Temperature homogeneity

The TVA is designed to achieve a thermal homogeneity after a stabilization phase over the entire test volume of <4 K at a moderate thermal load inside the test volume (originated from the specimen) of 1 kW maximum. A thermal homogeneity of <8 K can be reached at 10 kW thermal load.
In several test runs, the homogeneity was demonstrated to stay well below the <4K requirement.
At +18°C, the most relevant temperature set point for stable operation of the OGSE, all shrouds even stay within <1.5 K of homogeneity, as shown in Figure 8. Homogeneity is evaluated for each shroud segment individually and is defined as the difference between the hottest sensor and the coldest sensor on the shroud segment.

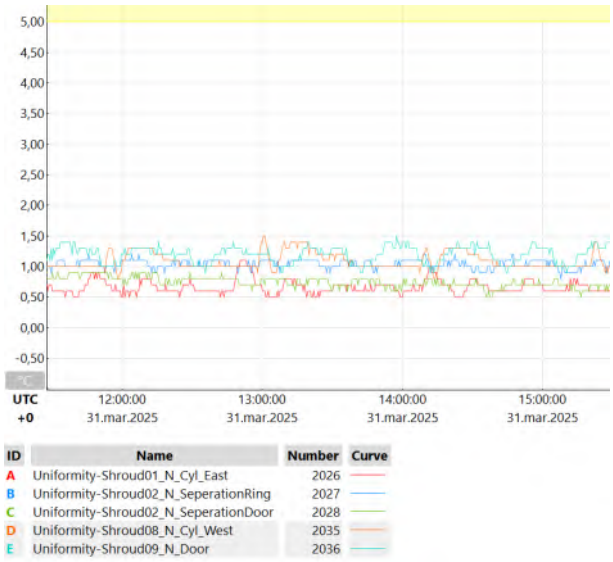


Figure 8: Temperature homogeneity of individual shroud segments at +18°C (requirement of <5K highlighted in yellow)

One special case is the separation shroud, which consists of two components: the separation shroud ring, i.e. the circular main part of the separation shroud, with a circular aperture in the centre; and the separation shroud door, which opens or closes the aperture and is also actively temperature controlled. Since ring and door are connected to the same TCU, there may be an offset between them, which is typically <1.5 K in the moderate temperature range between +52°C and -30°C.
While all shrouds within one test volume (either test volume North or South) are usually kept at the same temperature, it is possible to set individual shroud segments to different temperatures. However, this comes with a penalty in the achievable homogeneity, as shown in Table 1.

Table 1: Thermal homogeneity for different temperature setpoints on individual shrouds in test volume North

Separation shroud (North)	All other shrouds (North)	Resulting homogeneity (North)
+52°C	+52°C	<4 K
+18°C	+18°C	<1.5 K
-40°C (ring: -43°C door: -39.8°C)	+18°C	<7 K (<8 K on separation shroud ring) (<14 K on separation shroud door)
-80°C (ring: -80°C door: -75.7°C)	+18°C	<8 K (<10 K on separation shroud ring) (<20 K on separation shroud door)
-100°C (ring: -103°C door: -97°C)	+18°C	<10 K (<14 K on separation shroud ring) (<25 K on separation shroud door)

It is worth noting that with the separation door closed, the shroud temperatures in test volume South remain completely un-affected by the temperature changes in test volume North. Even the separation shroud door on the South side remains with a homogeneity of better than <2 K, while it is only a few centimetres from the nearly 100 K colder separation shroud door North (in the case -80°C/+18°C).

5.3. Temperature stability

In general, the thermal shrouds achieve a thermal stability of <1.5 K within the full qualified temperature range. In practice, after the control parameters have been optimized during numerous internal test runs, the thermal shrouds now regularly achieve a thermal stability of < 0.5 K during stable phases.
Figure 9 shows the stability of the individual shroud segments after setting the shroud temperatures to +18°C. Temperature stability is defined as the difference between the highest and lowest temperature of the shroud average temperature, evaluated over a time period of the previous 30 minutes.

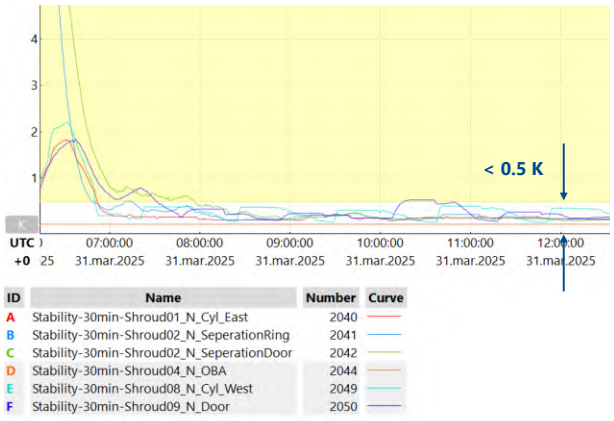


Figure 9: Temperature stability of individual shroud segments at +18°C

The stability is driven by periodic refilling of the cold gas generator (CGG). The CGG uses a liquid nitrogen reservoir and acts similar to a heat exchanger to provide cold nitrogen gas for the precise control of shroud temperature. Whenever the CGG is refilled with LN2, the pressure changes, which leads to periodic temperature fluctuations in the nitrogen gas supplying the shrouds. The same effect can be observed in the Open Loop circuits, which are supplied by an CGG. However, due to sufficiently long pipes and large thermal inertia of the shrouds (or thermal pates in the case of the Open Loops), the resulting fluctuation on the shrouds/thermal plates are barely visible and maintain within the <0.5 K stability requirement.

If an even better stability is desired, e.g. during critical optical measurements, a “maximum stability mode” is available, which suppresses the refilling of the TCU’s CGG and therefore improves thermal stability to values between 0.25 K and 0.5 K for the duration of up to several hours.

In order to evaluate the thermal performance with respect to the requirements of the OGSE, Figure 10 shows the temperature profile on the chamber shrouds for a time period of 7 days. The shrouds in the South of the chamber, where the OGSE is located, were kept at a setpoint of 21°C over the whole period, while the shrouds in the North side have executed a thermal cycling profile. In this specific profile, the separation shroud on the North side has been commanded to temperatures which were very different from the remaining shrouds in the same vessel North (down to -100°C on the separation shroud vs. +18°C on the other shroud segments). The shutter door, connecting vessels North and South was closed during cycling to insulate the vessel South, and therefore the OGSE, from these harsh environmental temperatures.



Figure 10: Average temperature of thermal shroud segments

The impact of those temperature cycles on the RefCos is visualized in Figure 11, which shows the individual temperature sensors on the RefCos over the same period of 7 days. As written in chapter 3, the requirements for the RefCos state that all sensors shall remain within a temperature band of +21°C (±0.5).

Even with the large temperature gradients imposed on the North vessel, the thermal control of the facility is able to maintain the OGSE in its required temperature band, as shown by the example of the RefCos. The RefCos temperature is sensitive only to fluctuations in the shroud temperatures in the South vessel, as can be seen in the final hours of the plot, where RefCos temperature predominantly follows the average of the shrouds in vessel South. However, temperature changes on the separation shroud North, or any other North shrouds, hardly

show on the RefCos, as long as the shutter door is closed. The uniformity of all RefCos sensors is well below <0.3K during thermal balance and <0.5K during thermal cycling.

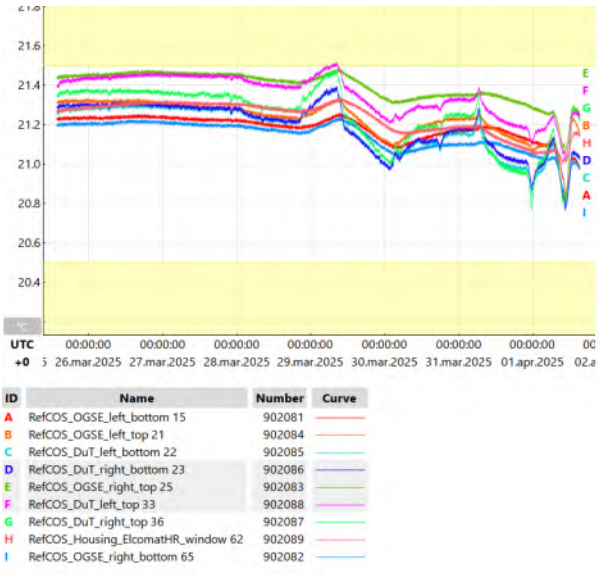


Figure 11: Temperatures of RefCos sensors with required band of 21°C (±0.5) highlighted

6. CONCLUSION

The Thermal Control System of the new TVA at IABG's Competence Centre Optics has successfully demonstrated in numerous internal test runs, as well as in customer test campaigns that it achieves all requirements in terms of temperature range, thermal homogeneity and thermal stability, in order to fulfil the highly demanding needs of OGSE. The commissioning campaign demonstrated operation of the shrouds in the temperature range from -163°C to +61°C on the thermal shrouds and from -163°C to +65°C and on the Open Loop circuits. It was demonstrated that the facility achieves a shroud homogeneity better than 1.5 K at the OGSE operating temperature of +18°C. A temperature stability of +-0.5K of the shrouds was demonstrated during steady state operation. The TVA's thermal control system has shown that it maintains the OGSE within its required temperature range of +21°C (±0.5) for extended periods of several days, even for large temperature gradients between vessel north and vessel south.
These results show that the TVA provides the thermal environment required for high-precision optical verification and calibration activities. Ongoing delta-qualification will extend operation to the full design range of -175°C to +120°C in GN2 mode, and below -188°C in LN2 mode.

7. REFERENCES

1. Friemel, M., Stangner, T. & Brachmann, J. (2023). Finalizing the implementation of IABG's Competence Center Optics. ECSSMET 2023.
2. Verein Deutscher Ingenieure (VDI) (2013). VDI 2038 Part 2. VDI, Düsseldorf, Germany.
3. Söllner, B., Schindler, R., Zirngibl, S., Döring, D., (2023). Finalizing the implementation of IABG's Competence Center Optics: A new thermal-vacuum chamber to house state of the art optical qualification tests. ECSSMET 2023
4. ECSS-Q-ST-20-07C - Quality and safety assurance for space test centres (2014). European Cooperation for Space Standardization, Noordwijk, The Netherlands.

SUN SIMULATOR MIRROR ALIGNMENT USING LASER RADAR

Angelina Jerjomina [(1)], Steven Sablerolle [(1)]

[(1)] European Space Agency (ESA), Keplerlaan 1, 2200AG Noordwijk, the Netherlands, Emails:
angelina.jerjomina@esa.int
steven.sablerolle@esa.int

KEYWORDS

Laser radar, automation, optical alignment, mirror adjustment, methodology development, Sun simulator, Large Space Simulator

ABSTRACT

The Large Space Simulator is a thermal-vacuum (TVAC) test facility for large spacecraft, capable of operating at pressures down to 5×10^{-7} mbar, at cryogenic temperatures below 100 K, and with high-flux solar radiation. The Sun Simulator comprises a 7 m collimation mirror composed of 121 segments with a 30 m radius of curvature, producing a 6 m diameter collimated beam with irradiance up to 2400 W/m². A reconfiguration in 2010 enabled a convergent, conical beam profile achieving much higher irradiance levels up to 11000 W/m², using a complex methodology based on an alignment with one theodolite and two laser trackers. In 2025, laser-radar technology was investigated to simplify operations and improve the angular measurement accuracy. This paper presents the development and validation of an automated laser-radar-based mirror alignment procedure, comparison with optical ray-tracing model, and corrective realignment to the nominal mirror configuration, demonstrating improved efficiency and alignment precision.

1. INTRODUCTION

Pre-launch spacecraft testing is essential to ensure mission success and protect major scientific and financial investments. Operating in extreme and non-serviceable environments, spacecraft must be thoroughly verified on the ground to identify potential design flaws and failure modes. Rigorous environmental, mechanical and electrical testing is therefore critical to reduce the risk and ensure the reliable mission performance. The European Space Research and Technology Centre (ESTEC) in Noordwijk is the principal technical establishment of European Space Agency (ESA), providing the engineering and verification capabilities for the development of space missions. It hosts extensive test facilities for thermal-vacuum, vibration, acoustic, antenna, and electromagnetic compatibility testing, as well as specialised laboratories for materials, optics, laser technologies, and metrology.

Within this testing infrastructure, thermal vacuum testing plays a central role in verifying spacecraft performance under space-equivalent conditions. For the fully completed spacecraft, these activities are primarily conducted in the Large Space Simulator (LSS), one of the largest TVAC facilities worldwide. The LSS enables qualification and acceptance testing of a complete spacecraft by creating the combined effects of high vacuum, solar irradiation, and deep-space cold conditions. The LSS is equipped with a Sun simulator (SUSI), which employs a collimation mirror composed of 109 hexagonal and 12 half-hexagonal mirror segments. The alignment of each collimation mirror segment is critical to achieve the required sun irradiance homogeneity. Originally configured to provide a uniform beam with irradiance levels up to 2400 W/m², the system was reconfigured in 2010 to generate a convergent beam, enabling irradiance levels of up to 11 000 W/m² at the LSS mid-plane.

At first, the mirror alignment relied on an intensity-based optimisation approach using imaging of a target screen inside the chamber, achieving the required beam power and diameter but resulting in notable irradiance non-uniformities, particularly at high concentration levels. After this, a second mirror-segment alignment procedure combined optical measurements with a ray-tracing model. A theodolite equipped with a laser is directed toward the centre of each segment, and the reflected beam is projected onto a screen located at the centre of the LSS vacuum chamber. The theodolite position is measured using a laser tracker and imported into the optical model, which computes the expected reflection point on the screen for the targeted solar configuration. This reference position is then projected onto the screen using a second laser tracker, and the mirror segment is mechanically adjusted until the reflected and reference spots coincide. Due to its labour-intensive and time-consuming nature, this method motivated the evaluation of laser-radar technology to simplify operations and improve alignment accuracy.

This paper presents the development of an automated laser-radar-based measurement and adjustment methodology for SUSI mirror segments. The study addresses the determination of the achievable measurement accuracy, the validation of all mirror segments in the LSS against the nominal

configuration defined in the optical ray-tracing model, and the corrective adjustment of outlier segments to restore compliance with the nominal configuration using this newly developed alignment procedure.

Laser radar has been widely studied for large-scale dimensional metrology, demonstrating sub-100 µm accuracy over tens of metres and suitability for high-precision, large-volume measurements (Estler et al., 2002; Summers et al., 2004). Its application has expanded to industrial inspection and alignment of freeform, reflective, and specular surfaces (Peggs et al., 2009; Muralikrishnan et al., 2015), as well as the coarse alignment and validation of segmented mirror systems in optical and astronomical contexts (Smith et al., 2012; Schwier et al., 2016). Comparative studies further highlight the advantages of laser radar over laser trackers in terms of automation potential and reduced operational complexity for complex alignment tasks (Schmitt et al., 2018). However, the end-to-end alignment and validation of high-flux sun-simulator mirror systems in spacecraft thermal-vacuum facilities remains sparsely addressed. This work addresses this gap through a laser-radar-based alignment and validation methodology applied to the SUSI mirror system of the ESTEC Large Space Simulator.

2. METHODOLOGY

This chapter describes the methodology that was developed for the mirror system measurement and alignment using laser radar functionality. The extensive study and investigation of the laser radar capabilities was performed in the period of 2024 and early 2025. Based on the results of the study the most optimal methodology for the mirror surface measurement was determined and implemented in current study, described in the following paragraphs.

The validation campaign was divided into two phases. Phase 1 involved laboratory testing of a single hexagonal mirror segment to assess the performance and measurement capabilities of the laser radar. Phase 2 was carried out within the LSS to validate the proposed methodology on the complete SUSI mirror assembly of 109 hexagonal mirror segments.

2.1. Apparatus

This paragraph describes instrumentation, test items and environmental conditions of all the performed tests.

2.1.1. Instrumentation

Laser radar is a non-contact large-volume metrology instrument that determines three-dimensional coordinates by combining angular measurements with absolute distance measurements obtained from a laser beam. Unlike conventional laser trackers, it can automatically acquire surface points without the need for retro-reflective targets, making it particularly suitable for the measurement of complex and difficult-to-access geometries. This capability enables efficient and highly automated inspection and alignment of large structures, including reflective surfaces and optical systems.

Tab. 1 lists the measurement equipment and software used in both phases of testing. The table is also presenting the maximum permissible errors (MPE) of the instrumentation and versions of the software.

Table 1: Instrumentation and software

Instrumentation / Software	**MPE/Version**
APDIS Nikon MV430E	20 µm + 5 µm/m (range) 13.6 µm/m (angular)
Leica AT960	15 µm + 6 µm/m
Spatial Analyzer Ultimate	2023.2.0926.6.(x64)

Spatial Analyzer (SA) software was used throughout all the measurement phases including the data postprocessing. The measurement plan (MP) functionality of the SA was used to automatise measurement processes of the laser radar.

2.1.2. Test items

Each hexagon-shaped segment is a non-flat mirror, with the edge length ~ 378 mm and the radius of curvature 30 m. When all the 109 mirror segments are aligned in the LSS to the configuration of 2400 W/m² they form part of the 30 m – radius sphere.

2.1.3. Environmental conditions

Both phases of testing were performed under following environmental conditions: cleanroom cleanliness class 8 (ISO 14644-1) or 100 000 (FED STD 209E); temperature range 20°C < T < 22°C; relative humidity range 40% < R.H. < 60%.

2.2. Laser-radar-based alignment methodology

The mirror segment measurement consists of 3 main steps that are described in paragraphs 2.2.1. – 2.2.3.

2.2.1. Manual measurement of the mirror corners

The MP is created in such a way that the program asks user to measure manually 3 predefined corners using the surface point measurement functionality of the laser radar. The pointing is performed through the camera view, and it does not require high precision (typically the measurement point should stay within 1 cm from the real corner, with the maximum tested error ca 2 cm). Further, the MP is calculating the approximate location of the

other 3 corners of the hexagon-shaped mirror.

2.2.2. Automated measurement of the mirror edges

This automated step is required to determine more precise locations of the mirror segment corners compared to the manual measurement. The MP is creating the vector group (VG) with the number of vectors defined by the user, perpendicular to the theoretical edge defined from the approximate corner points. During the laboratory testing the segment was measured with 13, 7, 5 and 3 points per edge using the edge search function of the laser radar. Then the MP is fitting a best-fit line through the measured points. The last part of the MP is intersecting each two neighbouring edge lines to create a precise corner point of the mirror segment. Due to the spherical shape of the mirror surface the edge measurement function is very sensitive to the full continuity of the edge measurement; for example, if points are skipped, the best fit line will have a wrong orientation which will influence the mirror segment direction. To remove the influence of the in-plane error component the MP continues with step 3 described in the next paragraph.

2.2.3.Automated measurement of the mirror surface.

To determine the direction of the mirror segment a symmetric star pattern is used. First the MP is calculating the centre point of the mirror segment using the corner points from the edge search measurement. The best-fit plane is created using the same corner points. The star pattern is created using the centre point of the mirror. The star pattern consists of 108 points placed in symmetrical, circular pattern around the mirror centre point (Fig. 1). The laser radar is measuring the star pattern using the surface point measurement profile. By fitting the plane through all the measured surface points, it is possible to determine the direction of the mirror segment with high precision.

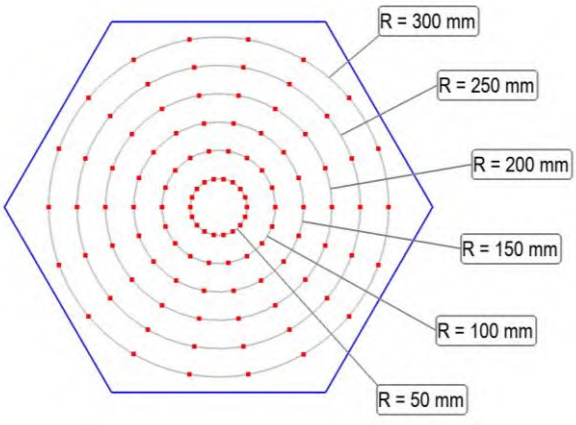


Figure 1: Star pattern measurement – blue hexagon shows the shape of the mirror segment; red dots show the concentric star pattern for the measurement.

2.3. Laboratory testing

The laboratory measurements were performed to determine the possible error sources of the mirror measurements, compare the accuracy of the laser radar to the laser tracker and test the measurement methodology before moving into the LSS.

Using the measurement methodology described above, several tests were performed to determine the precision and accuracy of the parameters described in following paragraphs 2.3.1. – 2.3.4. For all the tests the laser radar was positioned ca 7.3 m in front of the mirror segment, to simulate the actual distance in the LSS.

2.3.1.Star pattern concentricity influence on the mirror segment direction

Due to the mirror curvature the concentricity of the star pattern is very important. If the measured pattern is non-concentric then the fitted plane determining the mirror direction would be wrong. Fig. 2 explains the influence of the star pattern concentricity on the best-fit plane through the measured star pattern points on mirror surface.

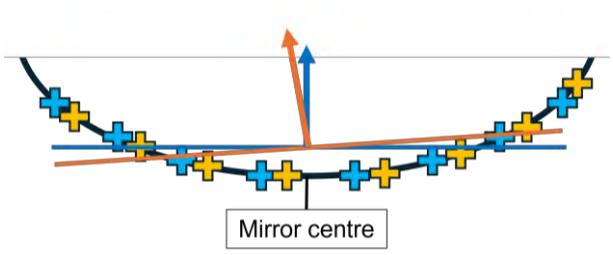


Figure 2: Star pattern concentricity influence on the determination of the mirror direction. Black curve represents the mirror side view; blue crosses are representing the concentric measurement of the star pattern; yellow crosses are representing the non-concentric measurement of the star pattern; blue line is representing the best-fit plane with its normal through the concentric measurement points; orange line is representing the best fit plane with it's normal through non-concentric measurement points.

To determine the quantitative influence of the star pattern concentricity, 5 measurement cases were conducted (Fig. 3). In first case the pattern was centred with the mirror segment. In cases 2 and 3 the pattern was shifted along the vertical axis by ±10 mm. In cases 4 and 5 the pattern was shifted along the vertical axis by ±20 mm. After all the measurements were performed it was possible to compare the angular components and determine the maximum possible non-concentricity of the star pattern in order to still reach good quality of the measured plane.

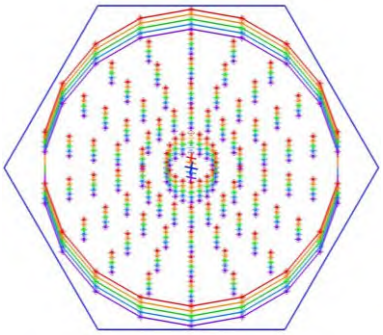


Figure 3: Star pattern shift along vertical axis. Green – concentric star pattern; Orange – shifted +10 mm; Red – shifted +20 mm; Blue – shifted -10 mm; Purple – shifted -20 mm.

2.3.2. Manual pointing precision influence on the mirror segment centre location determination

To test how much influence the manual pointing has on the determination of the centre of the mirror segment, following tests were conducted: the pointing was performed in 3 different ways. First, the pointing was done through the camera view, with the maximum zoom in on the corner (Fig. 4a). The red circle of the target in the camera view was positioned in the way that it touches 2 edges of the mirror segment. Once 3 corners of the mirror segment were measured following this "precise" pointing strategy, the mirror segment centre point was determined using measurement methodology described in paragraph 2.2. "Precise" pointing measurement was repeated 5 times.

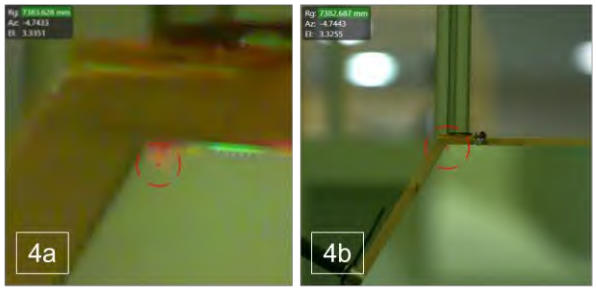


Figure 4: Precise (a) and unprecise (b) pointing using the laser radar camera view

Secondly, to test "unprecise" pointing a similar strategy was used, but instead of zooming in on the corner and pointing manually in the repeatable way, the unprecised pointing was performed visualy close to the mirror corner (Fig. 4b). The centre point was calculated again using the real corners of the mirror segment that were determined with the edge measurement – 3 points per edge.

As last "worst case" scenario the pointing was performed with a large mispointing around 3 cm from the corner. The centre of the segment was calculated again as described previously.

As a result 3 sets of measurements were obtained:

- 5 measurements using "precise" pointing
- 5 measurements using "unprecise" pointing
- 1 measurement using "worst case" pointing

The determined coordinates of the centre point in all the measurement configurations were then compared, to see how big is the difference between precise and unprecise pointing and how much it influences the calculation of the mirror segment direction.

2.3.3. Edge measurement precision depending on the number of points measured on edge

For this test the mirror segment was measured with the laser radar repeatedly with the different number of points measured on edge. This was done to investigate what could be the compromise between the least possible measurement time and acceptable precision. The manual pointing of the corners was performed only once. Following the VGs with 13, 7, 5 and 3 vectors per edge were created. The measurement continued with the automatic part of the edge search functionality. Once all the measurements were finished it was possible to create the real mirror corner points and the centres of the mirror segment. After that, the star pattern measurement was performed and the mirror direction determined by the best-fit planes. The angular components of the planes were then compared within all cases.

2.3.4. The accuracy of the star pattern measurement with different angle of incidence

To see the limitations of the laser radar the test with different angles of incident of the mirror segment was conducted. The mirror segment was placed on the rotation table. Three retro-reflective 0.5-inch targets were glued onto the edges of the mirror segment (Fig. 5). The 0.5-inch targets were used for the measurements with the laser tracker, to determine the relative accuracy of the laser radar.

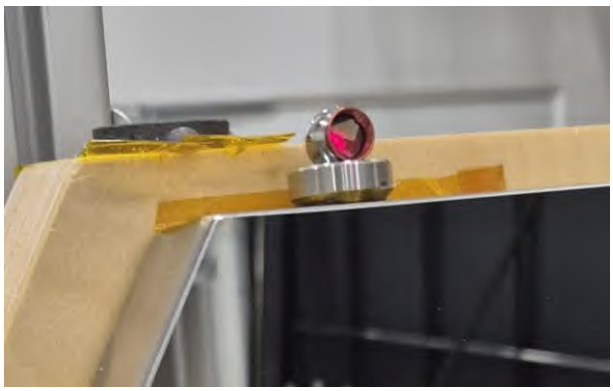


Figure 5: 0.5-inch retro-reflective target glued to the edge of the mirror segment

For this test all the steps described in paragraph 2.2. were performed consecutively. First, the mirror

segment was positioned with 0° angle of incidence towards the laser radar, and the measurement sequence was performed. Following, the mirror was rotated using the rotation table into positions of 10°, 20°, 30°, 40° and 50°. For each position the full measurement sequence with the laser radar was performed, as well as the measurement with the laser tracker. All the edge measurements with the laser radar were performed using 3 points per edge and the star pattern. As a result, 5 best-fit planes measured with the laser radar were compared to 5 best-fit planes measured with the laser tracker.

2.4. Large Space Simulator testing

The LSS is a very complicated environment for creating the proper setup. To reach the optimal position for the laser radar, e.g. to be positioned exactly in the middle of the 7-m mirror structure and approximately 7 m away from the segments, it was necessary to build the supporting platform (Fig. 6).



Figure 6: Laser radar platform inside the LSS

The laser radar was positioned on top of the tripod, in front of and at the height of the centre segment of the SUSI. The reference points with the reference system of the LSS were positioned around the laser radar (Fig. 7) and measured beforehand with the laser tracker. The laser tracker was referenced to the LSS reference system using stable, predefined points outside of the chamber. Following, five temporary points LSS_REF-01-05 inside the chamber were measured using the laser tracker. Then, the same points were measured with the laser radar, and the best-fit transformation was used to locate the instrument within LSS reference system. Additional 2 points LSS_REF-06 and 07 were then measured by laser radar to improve the geometry of the reference system inside the vacuum chamber. The same reference points were then used to verify the position and stability of the laser radar within the day and every new day of the measurement process.

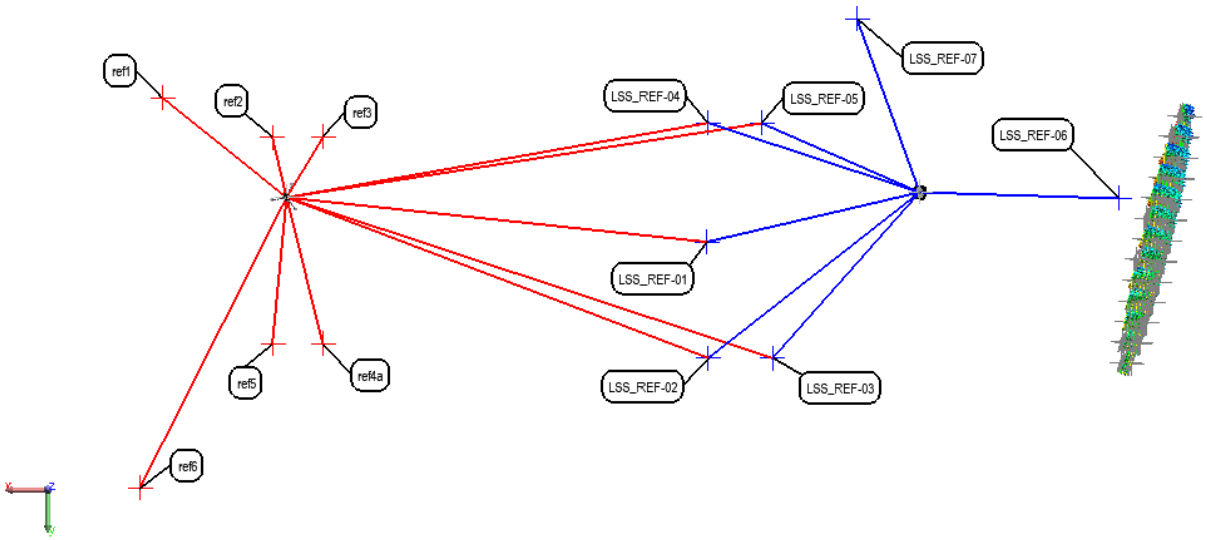


Figure 7: The top view of the reference system inside the LSS. Red lines represent the reference points measured from outside of the vacuum chamber using the laser tracker and 0.5-inch retro-reflective targets. Blue lines represent the reference points measured from inside the vacuum chamber using the laser radar and 0.5-inch tooling balls. Green ellipse represents the SUSI.

As the first step, all the mirror segments were measured with the laser radar using the manual pointing methodology described in the paragraph 2.2.1. Once all the approximate corners were determined, it was possible to run the MP with edge measurement (described in paragraph 2.2.2.) automatically overnight. The VG was created with 3 points per edge. Once all the edge measurements were finished and the real corner points determined, it was possible to proceed with the star pattern measurement described in paragraph 2.2.3. This measurement was performed in fully automatic way without operator supervision. Then, the best-fit planes of all the segments were created and compared to CAD nominal planes, which were imported from the ray-tracing model using the common LSS reference system. By comparison of each CAD plane and best-fit plane of the measured segment, the best-fit planes were colorised using following colour scale:

- 0 … 20 arcsec difference to CAD – **green**
- 21 … 30 arcsec difference to CAD – **yellow**
- 31 … 40 arcsec difference to CAD – **orange**
- 41 … arcsec difference to CAD – **red**

The goal was to adjust all the red and orange segments into range of green / yellow. Each hexagon-shaped mirror segment has three adjustment screws on the back, the location of the screws within the segments is known and identical. By pointing to the location of each screw the laser radar was measuring the surface point on the mirror front surface. Knowing the initial location of the screws and the directional deviation of the best-fit plane from CAD plane, the depth deviation at each screw location was calculated.

The adjustment procedure required the second operator behind the mirror. First operator was measuring one of the screws in real time, while the second operator was adjusting the same screw. Using the MP, it was possible to measure and calculate the deviation from the target point. Once first screw was adjusted, the procedure was repeated with 2nd and 3rd screw. In theory, the mirror segment is designed in such a way that while touching one of the screws, the other two should not move. However, in practice it was discovered, that about 25% of the segments were not behaving as designed and while touching one of the screws the second or even both other's screws were moving with it. In that case the adjustment was performed in smaller steps with more than one iteration.

Once the mirror segment was adjusted to the best possible target values, typically within ±0.020 mm from the target point, the verification measurement of the segment was performed using the same star pattern as before the adjustment. If the adjusted segment best-fit plane did not reach the green / yellow range compared to CAD, the adjustment and verification procedure were repeated until the segment was within the satisfactory range.

3. RESULTS

3.1. Laboratory testing

This paragraph describes all the results obtained during the testing in the metrology laboratory.

3.1.1. Star pattern concentricity influence on the mirror segment direction

Tab. 2 and Fig. 8 are showing the star pattern concentricity influence on the mirror segment direction determination. Tab. 2 column "Rx from Y [deg]" represents the change of the elevation of the mirror segment in degrees, if the star pattern is non-concentric / misaligned along the vertical axis. "dRx [arcsec]" column is showing the deviation from the

concentric best-fit plane to all shifted best-fit planes in arc seconds. Fig. 8 is showing that the star pattern shift of 10 mm causes approximately 70 arc seconds of angular error of the best-fit plane.

Table 2: Star pattern concentricity influence

Star pattern position along vertical axis	Rx from Y [deg]	dRx [arcsec]
+20 mm	90.0382	-138
+10 mm	90.0190	-68
0 mm	0.0000	0
-10 mm	89.9803	71
-20 mm	89.9611	140

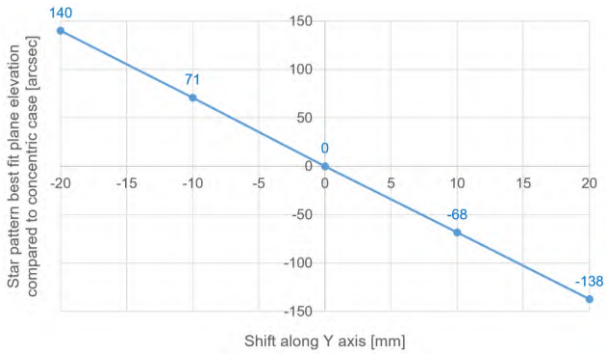


Figure 8: Star pattern concentricity influence on the mirror best-fit measured plane direction

3.1.2. Manual pointing precision influence on the mirror segment centre location determination

Fig. 9 represents the graphs of manual pointing precision using different pointing methodologies. The graph consists of three different parts, representing three different corners where the manual pointing was performed. Corner 1 is the top-left corner of the mirror segment; Corner 2 – top-right; Corner 3 – bottom-right. The green marker shows the location of the measured corner using the methodology described in paragraph 2.2.2. with 3 points per edge. Blue markers are showing the measurements performed with the precise manual pointing (e.g. Fig. 4a); yellow markers – unprecise manual pointing (e.g. Fig. 4b); red marker – worst case manual pointing.

Corner 1 and 3 of Fig. 9 are showing similar pattern of the manual pointing distribution close to the real corner, while corner 2 “Worst-case” red marker is dispositioned purposely by approximately 3 cm, to simulate the real worst-case scenario with a bigger shift of the mirror segment centre point. After the manual pointing and following steps of the measurement process described in the paragraph 2.2. were performed, the mirror segment centre location of each manual pointing case was determined.

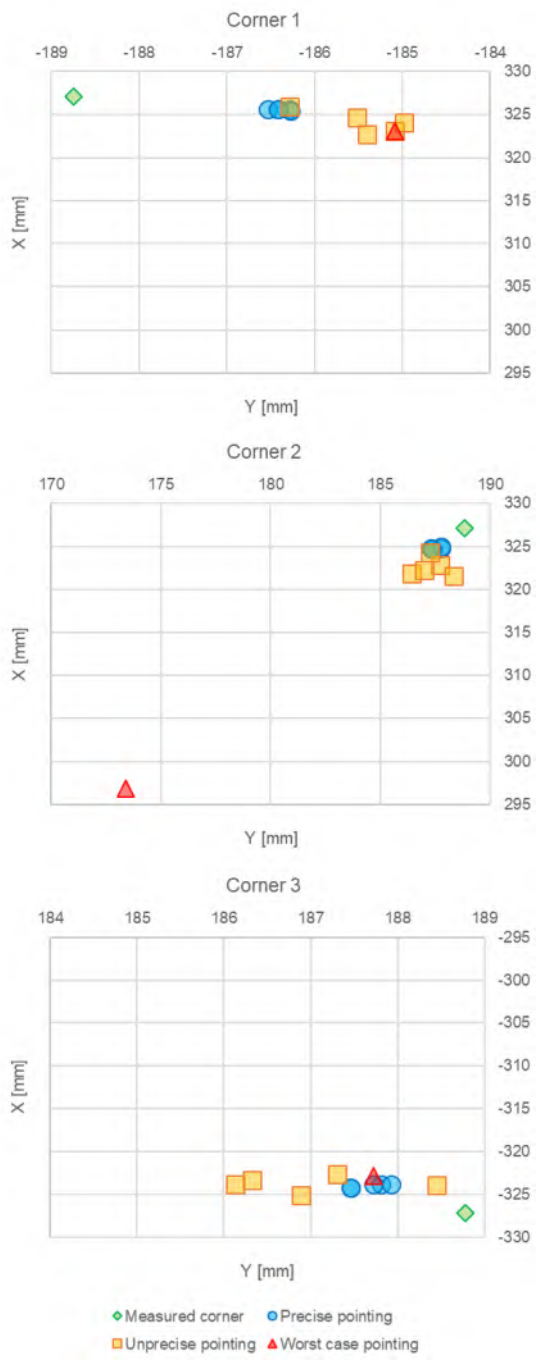


Figure 9: Manual pointing precision

The lateral coordinates of the centre points are presented in Tab. 3. For the manual precise and unprecise pointing the centre point coordinates are showing similar values, with the maximum deviation close to 0.2 mm. The worst-case centre coordinates deviation is close to 3 mm. In practice it means that for both, precise and unprecise pointing, the star pattern for the last step of the measurement might be concentric typically within 0.2 mm, which can be correlated with the results obtained in the paragraph 3.1.1. and transformed into angular error of around 1.4 arc seconds. The worst-case manual pointing is introducing the angular error of around 21 arc seconds.

Table 3: Mirror centre coordinates determined from manual pointing with different precision

Manual pointing method	X [mm]	Y [mm]
Precise 1	0.000	0.000
Precise 2	-0.106	-0.042
Precise 3	-0.173	-0.010
Precise 4	-0.100	-0.039
Precise 5	-0.136	-0.097
Unprecise 1	-0.189	-0.006
Unprecise 2	0.057	-0.021
Unprecise 3	-0.083	-0.022
Unprecise 4	-0.140	-0.072
Unprecise 5	-0.059	-0.087
Worst case	-0.355	2.968

3.1.3. Edge measurement precision depending on the number of points measured on edge

Tab. 4 contains the directional information of the best-fit planes created through the mirror segment corner points determined with the edge search function with different measurement density. Column "Rx from Y [deg]" represents the azimuth component of the mirror segment best fit plane; "Ry from Z [deg]" – elevation component; "dMagR [arcsec]" – magnitude of deviation.

Table 4: Influence on the mirror segment direction determination using different edge measurement density

Measurement method	Rx from Y [deg]	Ry from Z [deg]	dMagR [arcsec]
Edge search 13 pts	90.0000	0.0000	
Edge search 7 pts	89.9998	-0.0011	4
Edge search 5 pts	89.9993	-0.0016	6
Edge search 3 pts	89.9992	-0.0014	6

Tab. 5 contains the directional information of the best-fit planes created through the mirror segment star pattern measurements that were based on the previously measured edge search function with different density. Column "dMagR [arcsec]" represents the magnitude of deviation of the best fit planes with the star pattern measurements compared to the best fit plane through mirror corner points of the edge measurement density with 13 points per edge.

Table 5: Influence on the mirror segment direction determination using different edge measurement density in combination with star pattern measurement

Measurement method	Rx from Y [deg]	Ry from Z [deg]	dMagR [arcsec]
Star based on Edge search 13 pts	89.9987	-0.0008	5
Star based on Edge search 7 pts	89.9991	-0.0006	4
Star based on Edge search 5 pts	89.9987	-0.0008	5
Star based on Edge search 3 pts	89.9988	-0.0005	5

All the best fit planes presented in the Tab. 4 and 5 have very similar directional results, with the biggest deviation of 6 arc seconds. This concludes that the edge measurement functionality in combination with the star pattern measurement works equally good with the high density and low-density edge measurement profile. In that case lower density of the edge measurement can be used to reduce the total measurement time for the SUSI measurements.

3.1.4. The accuracy of the star pattern measurement with different angle of incidence

Tab. 6 represents the results of the accuracy verification of the laser radar with increasing angle of incidence. "Mirror POS" column indicates what was the nominal angle of incidence between mirror surface normal and laser radar pointing direction. Angular deviation is the delta between laser radar and laser tracker. Based on the results represented in the table below it appears that the laser radar can determine the mirror segment direction with up to 50 degrees angle of incidence with the maximum deviation of 12 arcsec compared to the laser tracker measurement. The angular range used during this test is larger than intended setup inside the LSS and is therefore sufficient for the developed methodology.

Table 6: Laser radar star pattern measurement accuracy compared to the laser tracker with increasing angle of incidence

Mirror POS [deg]	Angular deviation LR to LT [deg]	[arcsec]
0	0.0000	0
10	-0.0016	-6
20	-0.0006	-2
30	0.0011	4
40	0.0004	1
50	0.0034	12

3.2. Large Space Simulator testing

This paragraph describes all the results obtained during the measurement and alignment inside the LSS.

Fig. 10 shows 2 iterations of adjustment procedure. The colour scale is as follows:

- 0 … 20 arcsec difference to CAD – **green**
- 21 … 30 arcsec difference to CAD – **yellow**
- 31 … 40 arcsec difference to CAD – **orange**
- 41 … arcsec difference to CAD – **red**

Fig. 10a represents the initial measurement of all the mirror segments. According to the measurement results, only 39% of the segments were within 0…30 arc seconds difference to CAD range. Once the deviations to CAD were determined, the adjustment procedure for all the segments outside of this range was implemented. Fig. 10b shows the result of the

first adjustment. The percentage of the aligned segments better than 30 arcseconds increased after the first adjustment to 85%. The segments that were still misaligned were adjusted again. Fig 10c shows the result of the second and final adjustment.

The results after the final alignment are following:

- 0 … 20 arcsec difference to CAD - **57.8%**
- 21 … 30 arcsec difference to CAD - **37.6%**
- 31 … 40 arcsec difference to CAD - **3.7%**
- 41 … 50 arcsec difference to CAD - **0.9%**

The five segments that are still out of the yellow range are among the group of segments that do not behave as designed during the adjustment procedure. While adjusting one of the screws all the other screws are moving at the same time influencing the mirror direction in an unpredictable way. It is possible to adjust the segments within 30 arc seconds difference to CAD, but considering timeframe it was decided not to do so. Additionally, the influence of those segments to the final homogeneity of the full reflection of the light should be assessed but in theory will not have a big impact.

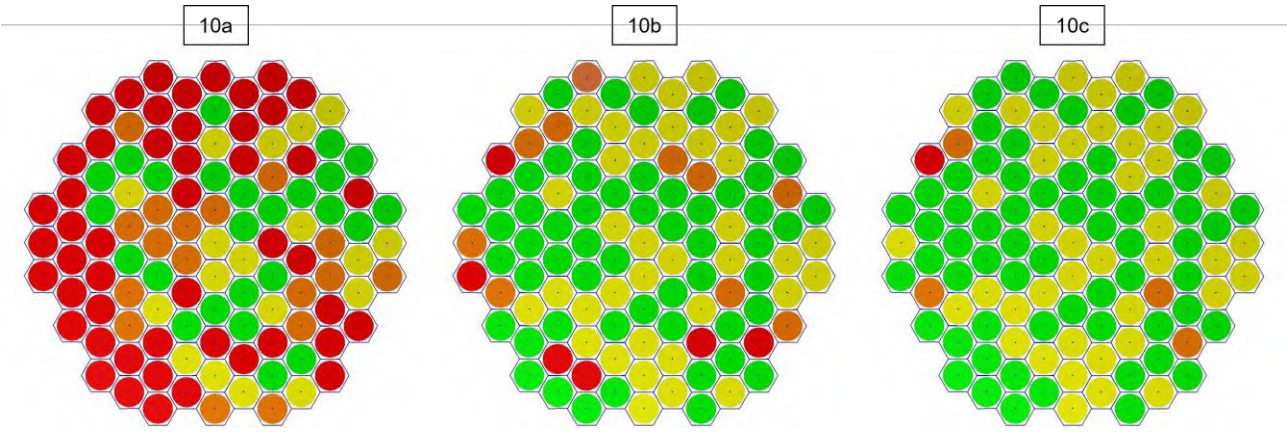


Figure 10: SUSI mirror alignment in initial configuration (a), after first adjustment (b) and after final adjustment (c).

Fig. 11 shows the alignment of the SUSI mirror compared to the CAD nominal planes of the ray-tracing model. Fig. 11a represents the initial configuration before any adjustment of the mirror segments. The colour scale on the figure is ±0.070 mm, that corresponds to approximately 50 arc seconds of deviation to CAD. It is noticeable that the left and top part of SUSI shows bigger misalignment of the segments than middle and right part. It can be explained by the previous alignment activity when the laser radar was tested inside the vacuum chamber during the period of July 2024 and January 2025. During that period the extensive investigation of the laser radar capabilities was conducted including alignment activities of all the segments.

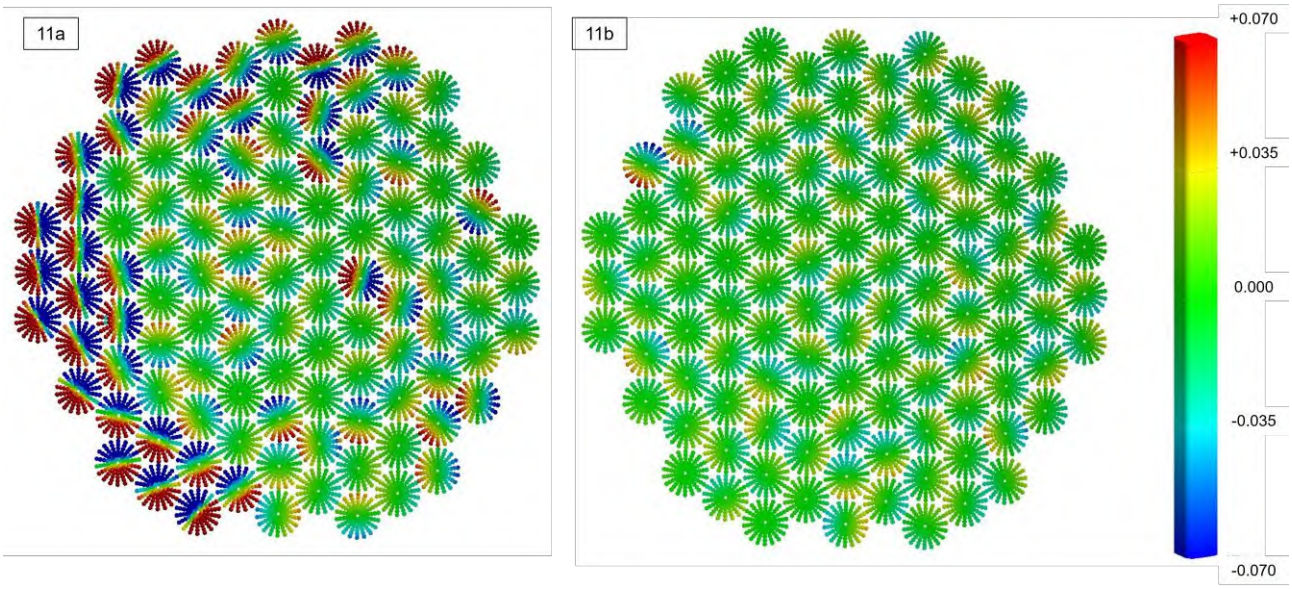


Figure 11: SUSI mirror alignment in initial configuration (a) and final configuration (b) compared to CAD reference.

The alignment pattern presented on Fig. 11a includes two different error sources:
1) During the measurements in previous testing campaigns the location for the laser radar was not optimised yet, it was not possible to place the instrument in the middle of the chamber. Therefore, the alignment activities were performed from two different stations. The middle and the right part of the SUSI was aligned using the instrument positioned more on the right side of the chamber. The left part was not reachable from that station, due to the increasing angle of incidence. The location of the instrument using the best-fit functionality on the temporary reference points introduced additional alignment errors.
2) During the previous investigation it was not possible to install the laser radar at the optimal height in order to reach the top segments. The angle of incidence was getting again too steep. Therefore, the top segments of SUSI were not adjusted using the laser radar in previous campaigns.

Fig. 11b represents the final alignment of all the segments using the methodology described in the paragraph 2.2. All the segments of final configuration are aligned towards the CAD nominal with a maximum deviation of 0.071 mm, which corresponds to 50 arc seconds misalignment. However, the majority of the segments (95%) are aligned towards the deviation to CAD nominal within 0.044 mm, which corresponds to 30 arc seconds misalignment.

4. DISCUSSION

The laboratory and Large Space Simulator tests demonstrate that laser radar can be used to determine and correct the angular orientation of the SUSI mirror segments with a high degree of automation.

Accurate positioning of the star pattern was identified as the most critical factor. The 10 mm of the introduced offset has an influence on the angular error of approximately 70 arcsec. However, the automated edge measurement limited the centre-position deviation to approximately 0.2 mm, corresponding to an estimated angular contribution of only 1.4 arcsec. Even the deliberately introduced worst-case manual pointing error resulted in an estimated angular contribution of approximately 21 arcsec. These results indicate that the initial corner pointing does not need to be highly precise, provided that the corners are subsequently refined through automated edge measurement and the resulting centre point is used to position the star pattern.

Furthermore, reducing the edge measurement density from 13 to 3 points per edge resulted in a maximum directional difference of 6 arcsec, supporting the use of the faster, lower-density measurement strategy. The comparison with the laser tracker also showed stable performance up to the maximum tested incidence angle of 50°, with a maximum relative deviation of 12 arcsec.

Application of the procedure inside the LSS confirmed that the methodology could be transferred to the complete SUSI mirror system from one single laser radar station. Initially, only 39% of the segments were aligned within 30 arcsec of the nominal CAD orientation. This increased to 85% after the first adjustment and 95.4% after the final alignment. The improvement across the adjustment iterations demonstrates that the measured plane deviations can be converted into practical correction values at the adjustment-screw locations and used to guide real-time mechanical alignment.

The remaining deviations were mainly associated with the mechanical behaviour of the adjustment system. For approximately 25% of the segments, adjusting one screw also caused movement at the other screw locations, requiring smaller corrections and additional iterations. Five segments remained outside the 30 arcsec target range, although all were within 50 arcsec of deviation. This indicates that the remaining alignment deviations were not necessarily limited by the laser radar measurement capability, but also by the repeatability and predictability of the mechanical adjustment mechanism and by the number of adjustment iterations that could be completed within the available campaign period.

Overall, the methodology provides a more automated and traceable alternative to the previous alignment approach. It enables direct comparison with the ray-tracing model and creates a consistent digital measurement record for all segments. However, this study evaluated geometrical alignment only. Future work will assess the effect of the residual deviations on irradiance homogeneity, develop a complete measurement uncertainty budget and further investigate the mechanical coupling between the adjustment screws.

5. CONCLUSION

An automated laser-radar-based methodology was developed and validated for measuring and aligning the 109 hexagon shaped mirror segments of the Large Space Simulator. The procedure combines automated edge detection with a symmetric surface measurement pattern, enabling the orientation of each mirror segment to be determined and compared directly with the nominal planes of the optical ray-tracing model.

Laboratory testing demonstrated that reliable measurements can be achieved using three edge points per side, while the laser-radar results

remained stable over the tested incidence-angle range up to 50°. The tests also confirmed that accurate determination of the mirror centre is essential for positioning the surface measurement pattern and minimising angular errors.

The methodology was successfully applied to the complete SUSI mirror alignment. The proportion of segments aligned within 30 arcsec of the nominal orientation increased from 39% in the initial configuration to 95.4% after two adjustment iterations. All segments were ultimately aligned within approximately 50 arcsec of deviation. The remaining deviations were primarily associated with unpredictable coupling between the mechanical adjustment screws rather than with the laser-radar measurement procedure.

Overall, the developed methodology provides a more automated, traceable and efficient alternative to the previous alignment approach. It enables direct geometrical comparison with the optical model, supports real-time mirror adjustment and creates a consistent digital record of the complete mirror configuration. Future work should assess the influence of the residual alignment deviations on irradiance homogeneity and further investigate the mechanical behaviour of the segment adjustment system.

6. ACKNOWLEDGEMENTS

The authors would like to thank the European Test Services (ETS) personnel involved in the campaign for their support during the operations within the Large Space Simulator and the adjustment of the SUSI mirror segments. Special thanks are extended to Sara Caliari for the design and assembly of the laser-radar platform used during the measurements. The authors also gratefully acknowledge the support of the Engineering Services Section personnel for their assistance with the setup activities, logistics and the technical expertise required throughout the campaign.

7. REFERENCES

1. Summers et al., *Precision Engineering* (2004). Demonstrated laser radar for large-scale dimensional metrology with sub-100 µm range accuracy over tens of metres.
2. Peggs et al., *CIRP Annals* (2009). Reviewed industrial laser radar applications, including freeform and reflective surfaces.
3. Muralikrishnan et al., *Journal of Manufacturing Systems* (2015). Discussed metrology strategies for specular surfaces using laser-based systems.
4. Smith et al., *Applied Optics* (2012). Laser-based measurement of segmented telescope mirrors for coarse alignment.
5. Schwier et al., *Optical Engineering* (2016). Use of laser radar for alignment validation of large reflective structures.
6. Estler et al., *CIRP Annals* (2002). Comparison of large-scale metrology systems.
7. Schmitt et al., *Measurement* (2018). Laser radar vs. laser trackers for complex alignment tasks.

AUTOMATED THERMAL CYCLING TESTS WITH RADIATIVE TRANSFER UNDER HIGH VACUUM ENVIRONMENT

Rémi LAMANDE , Yann BOUETARD , Paul-Eric DUPUIS

Airbus Defence & Space 2, rond-point Pierre Guillaumat, 31000 Toulouse, France.
remi.lamande@airbus.com, yann.bouetard@airbus.com, paul-eric.dupuis@airbus.com,

KEYWORDS

Thermal Regulation. Thermal Vacuum Test. Predictive Command. Radiative Thermal Exchange.

ABSTRACT

The thermal vacuum test is a costly phase in a spacecraft development. It remains necessary to qualify thermal design development and innovations. To keep efficiency and stay competitive, Airbus Defence & Space in Toulouse developed a control system in order to increase the automation of its test facilities operation.
The first key development is a software interface to program and manage automatically thermal cycling progress as required by test specifications: control of temperature set points, dwells duration, transient speeds without overshoots.
Standard regulation loop may be used to manage conductive or convective heat transfers as they have a linear behaviour on the whole working temperature range.

But if there are some radiative heat transfers exchanged between the test specimen and the test facility, up to now, these cycles had to be performed manually thanks to operator's monitoring (specimen temperature) and settings (test facility temperature set points).

So, a dedicated algorithm running a new regulation loop based on a predictive command has been developed.
This innovative regulation loop offers the possibility to perform new types of thermal cycling tests, under vacuum environment, in a full automated mode.

1. GENERAL SPECIFICATIONS

1.1. Introduction

In the framework of its Thermal Vacuum facility modernisation, AIRBUS Defence & Space developed different types of thermal regulations to answer to various customer test specifications.

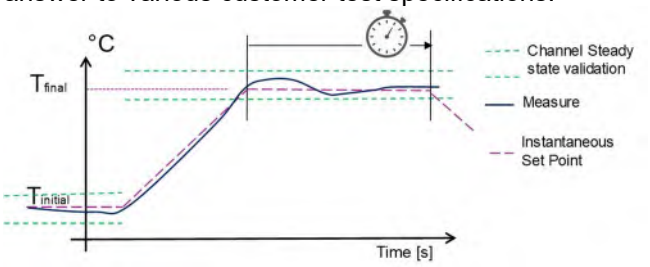


Figure 1: Thermal Vacuum test specifications

If the specified regulation temperature is based on a fluid or shroud surface temperature, conductive or convective heat transfers happen: they have a linear behaviour in function of the delta temperature:

- $\Phi_{conductive} = K_{Conductive} \times (T_1 - T_2)$
- $\Phi_{convective} = K_{Convective} \times (T_1 - T_2)$

Standard common regulation loops can manage these types of heat transfers. As an example, they are deployed and used to control regulation directly on shrouds temperature surface or in fluidic lines of Thermal Control Unit.

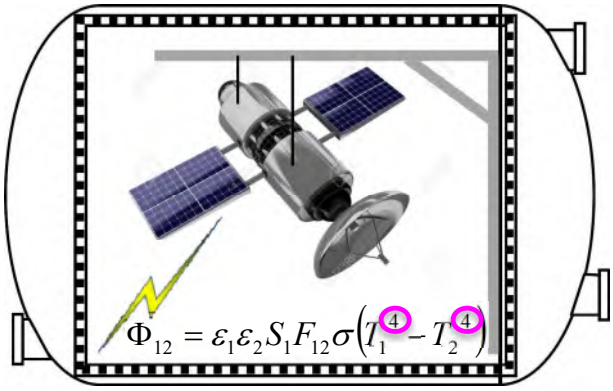


Figure 2: Radiation in a Thermal Vacuum Facility

But these regulations are not effective and cannot be used if the specified regulation temperature is on specimen surface and radiative heat transfers are involved. The non-linearity at the power 4 of the delta temperature creates a very variable behaviour on the working temperature range:

- $\Phi_{radiative} = K_{radiative} \times (T_1^4 - T_2^4)$

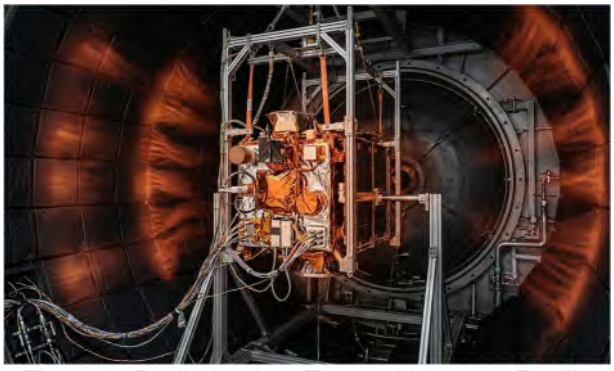


Figure 3: Radiation in a Thermal Vacuum Facility

To test antennas or radiators in a Thermal Vacuum test facility, a common specification is to perform

various temperature transitions and steady states at specific temperature levels with all sensors in a channel of +/- 1.5 °C. These sensors are located on the test specimen surface. Due to radiation's non-linearity, test operator is obliged to monitor the test item sensors, to evaluate their behaviour and to control in real time the TCU by adjusting in consequence the shroud surface set points.

The development described in this article aims to automate this operation. The new regulation loop shall be able to control the TCU and adjusts automatically the shroud temperature to reach the specified temperatures at specimen level, while minimizing overshoots.

1.2. Technical specifications

The thermal regulation shall permit to control automatically the heating and cooling actuators of the Thermal Control Unit on the basis of temperature sensor exposed to radiation of Thermal Vacuum shrouds.
This regulation loop shall be adaptable and reliable for very different types of test specimen. They may differ in terms of absorptivity and thermal inertia.
It shall be adapted to Thermal Control Unit features:

→ Working temperature range from -170°C to +150°C.

→ Transient speed up to 120 °C/hr.

It shall limit temperature overshoots to 2°C, specifically when reaching a steady state or during test specimen heating.

1.3. Development requirements

Before any deployment in the test facility, the regulation loop shall be tested and evaluated through a simulator in order to mitigate TV facility downtime.
The regulation loop shall be an open software code without any additional licence costs.
It shall be easily adaptable to various Programmable Logical Controller manufacturer brands like SCHNEIDER or SIEMENS.
The regulation loop computing shall be integrated in S/W object to ease its deployment and maintenance in other TV facility PLC.

1.4. Operational & Maintenance requirements

The Graphical User Interface of this regulation loop shall be adapted and integrated in existing AD&S TV supervision views.
Depending on the test item features and involved heat exchanges, the test operator shall be able to select the appropriate regulation loop with adequate parameters values.

1.5. Project requirements

The development of the project shall follow standard project milestones like Kick Off, Preliminary & Critical Design Review, S/W development phase and several acceptance tests:

- An acceptance test platform shall permit to validate the S/W development thanks to simulation.
- A Site Acceptance Test shall permit to validate the regulation loop in the TVC facility with various representative test specimens.

2. PREDICTIVE LAW STUDY & MODELLING

2.1. Thermal Vacuum Facility

The goal of the Thermal Vacuum test is to permit to simulate the environmental space conditions. For this, the Device Under Test is placed in a volume where a high vacuum is created and exposed to radiation of thermal shrouds.

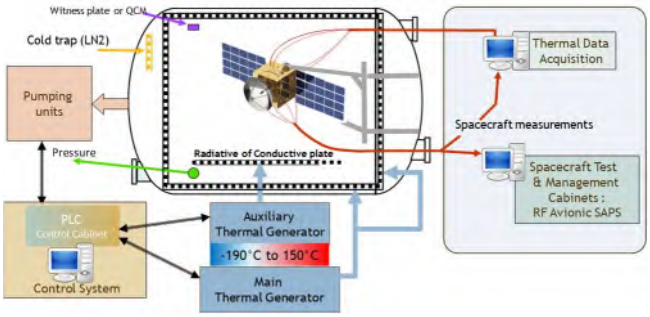


Figure 4: Thermal Vacuum Facility

The thermal control system we have developed offers a new regulation mode based on specimen measurement (movable sensors glued on specimen surface).

Intermediate sensors and regulation loops based on fluid temperature measurement or shroud surface measurement are used.

The main objective of this study is the development of a user-friendly regulation integrated in the control system.

It is dedicated to tests which require a temperature control on the specimen surface (TRP), where the primary thermal exchange is by radiation with thermal shrouds under vacuum.

This regulation allows to perform automatic temperature cycling tests for a large range of test specimens on the full temperature range of the test facility.

Test specimens may be very different in terms of mass, thermal conductivity and absorptivity. As an example, the behaviour is widely different between an antenna made of 15 kg of black carbon and a radiator made of 120 kg of shiny aluminium alloy.

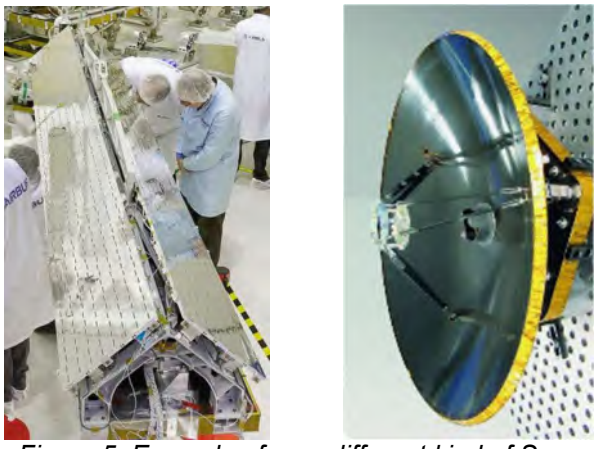


Figure 5: Example of very different kind of Space Antennas

Temperature of fluid (gaseous nitrogen or GN2) produced by thermal generator (TCU) may vary on the range from -170°C to 150°C.

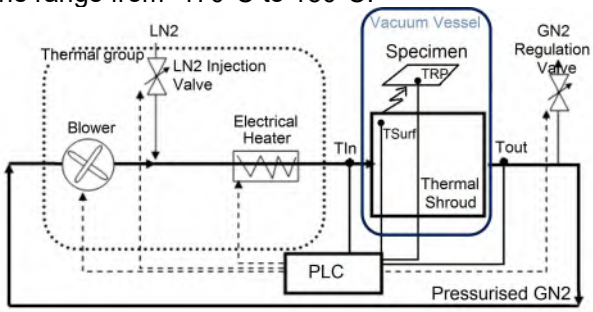


Figure 6: Thermal System

Table 1 hereafter gives an order of magnitude permitting to understand the difficulty encountered with radiation through an example of thermal exchanges between TV shrouds ($\varepsilon_{TRP} = 0.85$) and a test specimen ($\varepsilon_{SUR} = 0.6$)

Table 1: Order of magnitude of radiative exchange

Radiative Flux	$\Delta(T_{SUR} - T_{TRP})$	T_{SUR}	T_{TRP}
135 W/m²	-160°C	-170°C	-10°C
-790 W/m²	160°C	+150°C	-10°C

These results illustrate that for the same temperature gradient (ΔT = 160°C), between specimen and shroud surfaces, there is almost a factor 6 on involved exchanged thermal powers. Variation rate of thermal exchange is definitively not linear.

2.2. Physical approach

The temperature of the specimen (T_{TRP}) may be linked to the shroud surface temperature (T_{SUR}) thanks to Stefan-Boltzmann radiation law:

$$\emptyset = C.\frac{dT_{TRP}(t)}{dt} = \varepsilon_{SUR}.\varepsilon_{TRP}.S_{SUR}.F_{SUR\to TRP}.\sigma.\left({T_{SUR}}^4 - {T_{TRP}}^4\right) \quad (1)$$

This physical modelling brings difficulties in terms of:

→ Solving this type differential equation,

→ Evaluating the coefficients $(\varepsilon_1.\varepsilon_2.S_1.F_{1\to 2})$ for various tests and specimens.

That is the reason why a different approach was chosen: the transfer function, modelling radiative exchanges, is considered as a kind of "black box" driven by an easier known exponential mathematical equation, which still remains to be defined.

2.3. "Black box" modelling approach

Very different dummy specimens are integrated in the TV chamber:

→ A black carbon plate,

→ A grey aluminium honeycomb,

→ A thick aluminium plate,

→ A massive stainless-steel flange,

→ A black aluminium honeycomb,

→ A black / shiny stainless-steel shroud

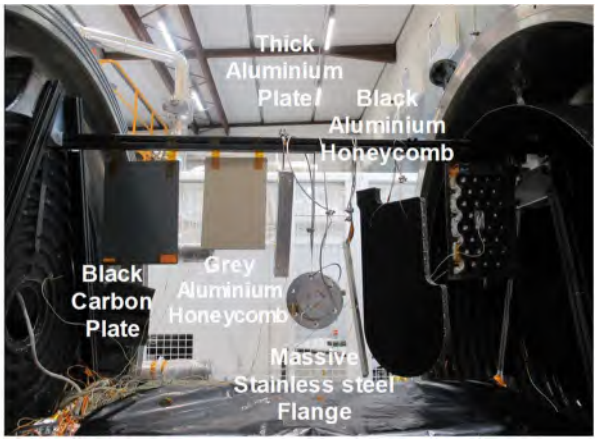


Figure 7: Various test specimens used for identification

Plenty of steps (20°C to 40°C) of cooling and heating were performed thanks to thermal system on its working temperature range [-170°C ; +150°C].

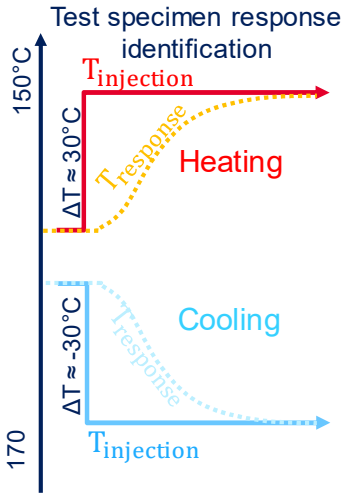


Figure 8: Heating & Cooling for identification

3 levels of temperature were recorded in function of the time following the TCU injection of cooling and heating temperature:

→ The fluid (GN2) temperature: T_{FLD}.
→ The shroud surface temperature: T_{SUR}.
→ The specimen temperature: T_{TRP}.

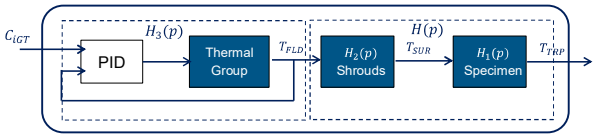


Figure 9: View of thermal system transfer functions

The analysis of the response and the transfer functions has shown that it may be modelized thanks to an exponential mathematical formula, a first-order model.

$$H(p) = \frac{\Delta T_{TRP}(p)}{\Delta C_{iGT}(p)} = K.\frac{e^{-R.p}}{1+\tau.p} \qquad (2)$$

K: gain, τ : time constant, R : delay.

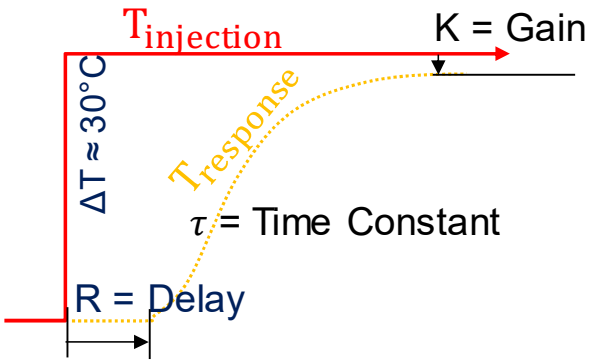


Figure 10: K, τ, R parameters of 1st order model

2.4. Identification and process modelling

The regulation architecture is defined as follow:

- the existing regulation loops for the fluid and shroud surface temperatures are kept.
- The new regulation loop based on specimen temperature T_{TRP} will command in cascade the thermal group set point C_{iGT}.

Each run of cooling and heating with test specimen responses were analysed.

K value represents the difference of stabilised temperatures between the fluid and the specimen. K is equal to 1 at ambient temperature. K varies as heat losses are increasing at maximum and minimum temperatures.
A 1st order polynomial is issued to compute the K gain value in function of the temperature [in Kelvin]. The K gain variations are between 0.8 (Tmax or Tmin) and 1 (Tamb).

τ and R values are evaluated thanks to MATLAB scripts. For each recorded run (heating or cooling), this script permits to define the convergence level and a value assumption of the τ and R values for defined temperatures.

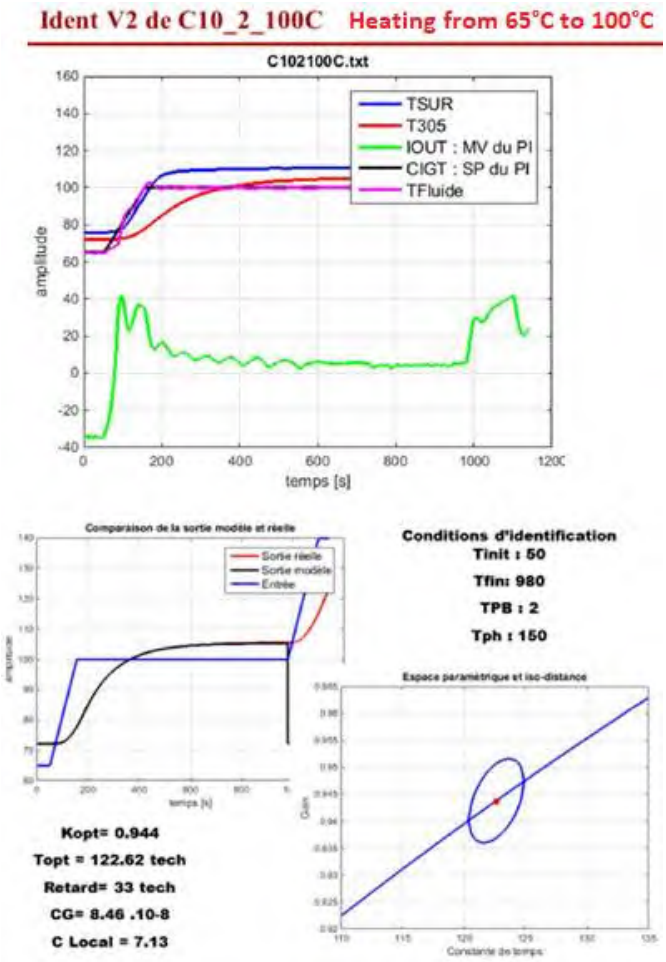


Figure 11: MATLAB script analysis & results

All spots of τ and R values are interpolated to established continuous mathematical functions $\tau(T)$ and $R(T)$.

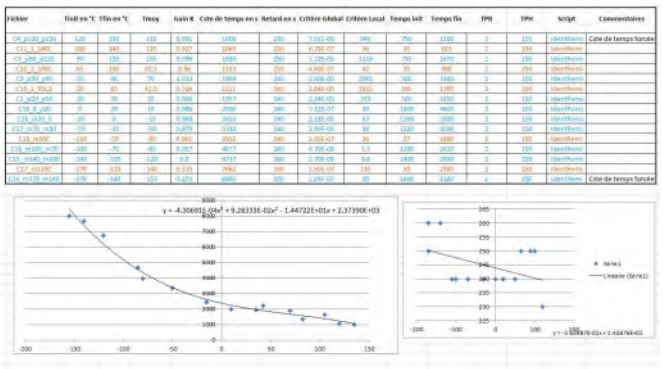


Figure 12: τ Time constant & R delay identification

The analysis of identification results has shown that the R delay is not function of the test specimen features and its evolution is negligeable with respect

to a working temperature change.

R value is constant, it is set up at a value of around 120 sec.

What shall be highligted is that the most sensible parameter is the time constant τ.

Its value is highly changing, following an exponential shape, depending on:

- The test specimen features: aborptivity, thermal conductivity, mass,
- The working test temperatures.

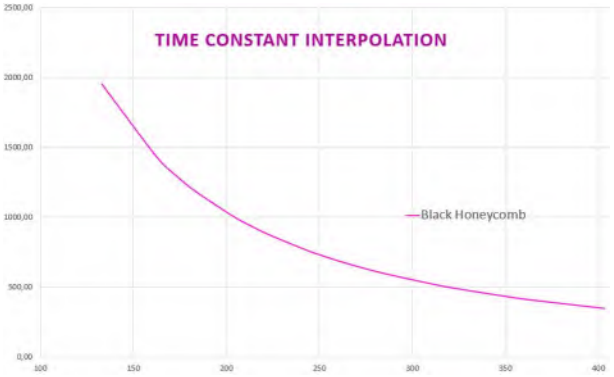


Figure 13: Time constant interpolation of black honeycomb

As an example for a black aluminium honeycomb wall, the time constant (pink curve) is passing from 400 sec to 2000 sec on the temperature range.

This represents a factor 5 between Tmin and Tmax.

It appears to be flat when it is compared to the time constant interpolated for the grey aluminium plate or the stainless flange. It is a matter of scale as they can rise up to 120000 sec; factor 60 in comparison with the 2000 sec of the black aluminium honeycomb wall.

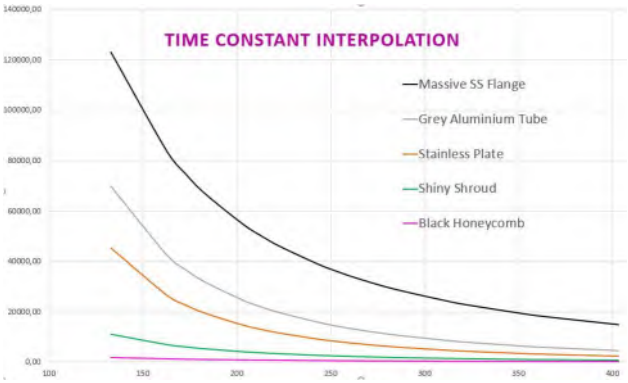


Figure 14: Time constant interpolation per specimen

Depending on the working temperatures and particularly the test specimen features (absorptivity, thermal conductivity, mass), the time is highly different in terms of order of magnitude.

2.5. Predictive command modelling

Thanks to the process identification, by knowing the future, a predictive law based on first order model is then established and computed in MATLAB script for simulation.

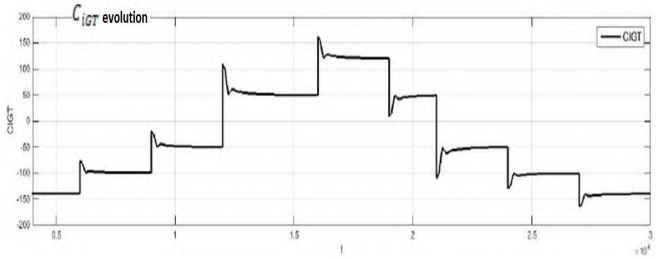


Figure 15: C_{iGT} instantaneous set point command

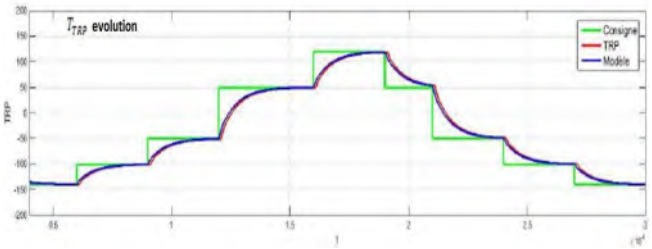


Figure 16: T_{TRP} Specimen temperature response

To give robustness and increase or boost the command, a performance coefficient C_{perf} is computed based on response time in closed loop.

Figures 15 and 16 show the modelling of several steps of heating and cooling on working temperature range of thermal system.
For one specimen temperature set point (green curve on figure 16), figure 15 shows the output of predictive command value as the instantaneous command C_{iGT} (black curve) created to manage the TCU temperatures (fluid and shroud surfaces).

Figure 16 displays the response curve of specimen temperature (red & blue curves) linked to command value C_{iGT}. This prediction is obtained thanks to process modelling.

As the study and MATLAB modelling are successful, this milestone has been validated. It is allowed to pass to next step: programming and deployment of this command in the test facility PLC.

3. PREDICTIVE COMMAND VALIDATION

3.1. Integration in TV Control System

The predictive command is replicated and computed in an object to be deployed in the SCHNEIDER PLC program managing the thermal Groups (or also called TCU) of the TV facility.

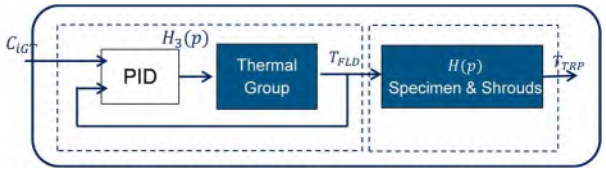


Figure 17: PLC thermal system transfer functions

As it is a literal code, this could be also written in a SIEMENS PLC program.

The supervision is also upgraded to integrate the dedicated views linked to the new predictive command regulation loop.

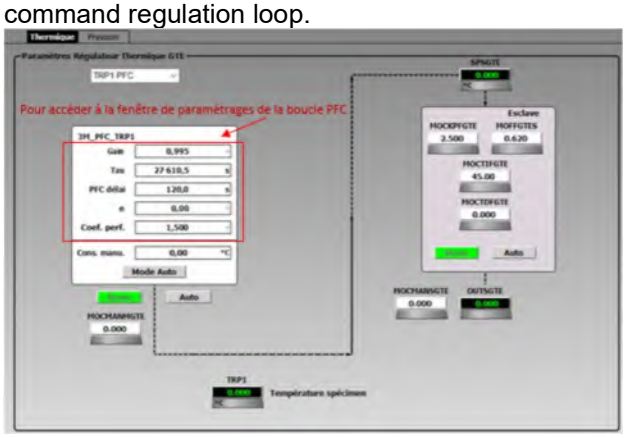


Figure 18: TRP regulation supervision view

These new views shall permit to ease operator's setting and monitoring of parameters: K, τ , R, C_{perf} of predictive command.

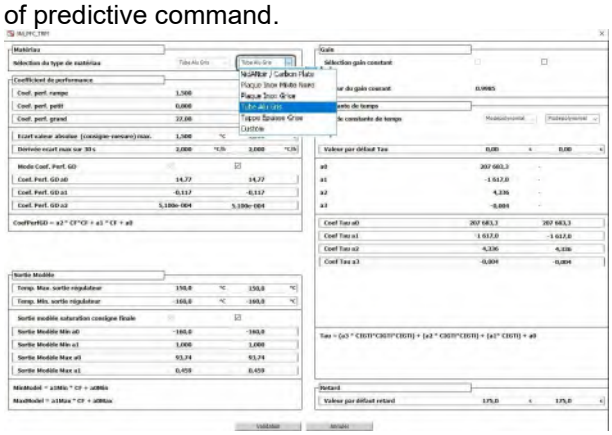


Figure 19: Predictive command parameters view

Depending on test specimen, the test operator may choose, in a samples list, specimen features as similar as possible to the real one.
The proposed specimen features are:

- Black carbon plate: Low inertia with a good absorptivity.
- Black stainless-steel plate: medium inertia with a good absorptivity.
- Grey stainless-steel plate: medium inertia with a poor absorptivity.
- Grey aluminium tube: big inertia with a poor absorptivity.
- Grey massive stainless-steel flange: very big inertia with a poor absorptivity.

Once the material is selected, all associated parameters are defined to compute the time response τ.

The Gain K and Delay R are more linked to the thermal group itself with no influence coming from test specimen features.

So a new regulation solution is proposed in the Graphical User Interface of our Thermal Vacuum control system: a radiative regulation may be chosen by the operator in case of temperature sensors (TRP) located directly on test specimen surface implying a radiative exchange.

Graphical User Interface allows the operator to select a large quantity of Thermocouples T types (up to 45 depending on the TVAC) and define the calculation to be performed. The test may be conducted on the average, the minimum or maximum value of this batch of sensors declared as TRP.

3.2. Predictive command acceptance

Dummy specimens are integrated in the TV vessel for acceptance tests.
It is chosen not to hang them but to use the standard integration system used in the 3M3, different to the one used during the identification.

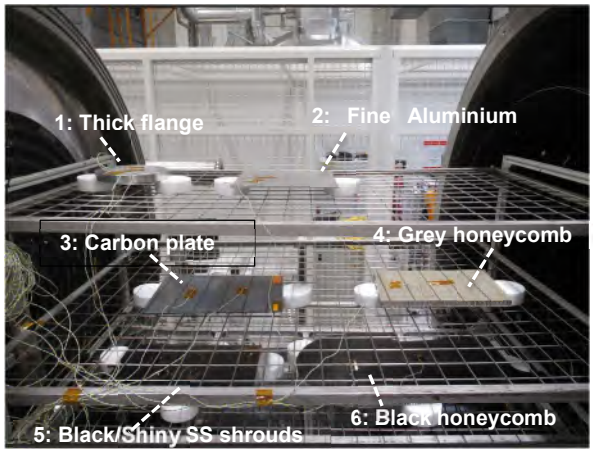


Figure 20: Acceptance test configuration

This permits to trial the efficiency and robustness of the predictive command to configuration variations.

Also, six following materials are selected with an objective to vary the absorptivity factor, the thermal conductivity and inertia:

→ 1: Thick grey aluminium flange
→ 2: Grey aluminium plate
→ 3: Dark carbon plate.
→ 4: Grey aluminium honeycomb structure.
→ 5: Black/shiny stainless-steel shrouds.
→ 6: Black aluminium honeycomb structure.

For all test specimens, thermal cycling was programmed in advance and played to run and execute all transitions automatically, from one set point to the next one.
The curve in blue is the shroud temperature, the other curve (green ,red) is the specimen response.

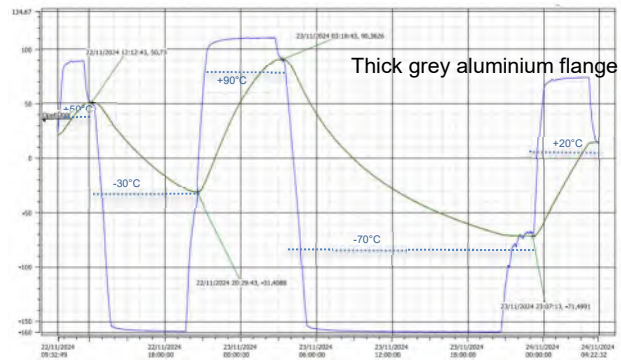


Figure 21: Specimen 1 thermal cycling results

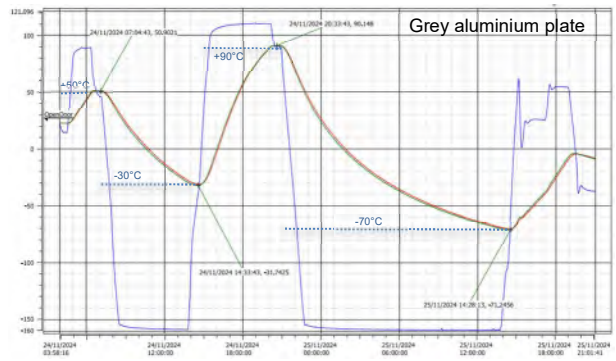


Figure 22: Specimen 2 thermal cycling results

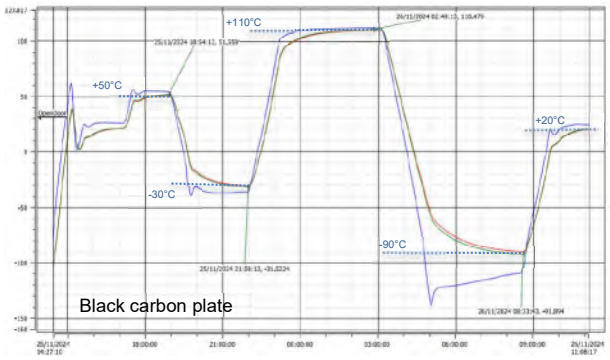


Figure 23: Specimen 3 thermal cycling results

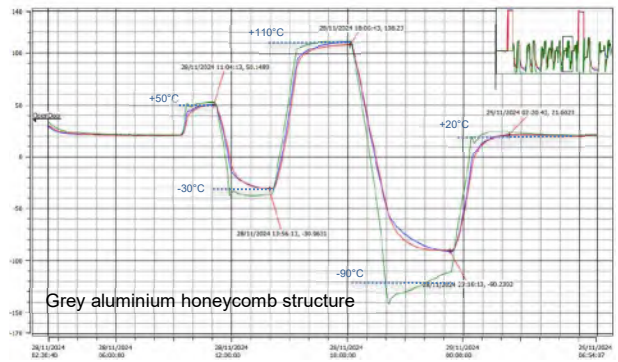


Figure 24: Specimen 4 thermal cycling results

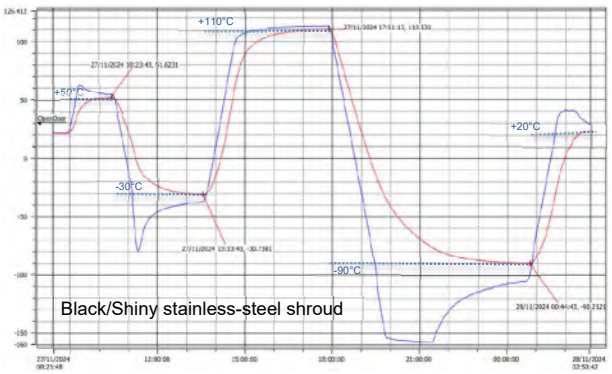


Figure 25: Specimen 5 thermal cycling results

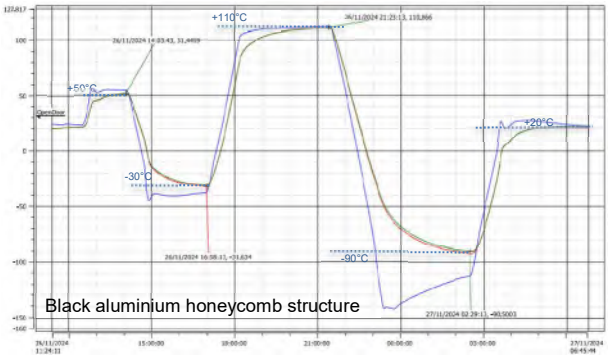


Figure 26: Specimen 6 thermal cycling results

It shall be notice that from one specimen to the other, it is not the same behaviour in terms of order of magnitude.

As an example, we may highlight and compare the grey thick flanges (specimen 1) and the dark carbon plate (specimen 3):

- The specimen 3 cooling from +90°C to -70°C (ΔT=160°C) takes 8.5 hours in comparison to the 20 hours for the cooling of specimen 1 from +110°C to -90°C (ΔT=200°C).
- The lowest shroud temperature to cool down specimen 3 at -90°C is -130°C in comparison to the lowest for specimen 1 which is -160°C during 15 hours to get -70°C.

In 2021, with the first predictive command developments, we were not able to succeed correctly to regulate with acceptable overshoots when the test sample had a significant mass and a low absorptivity.

As shown in this document, the predictive command functioning based on new samples identification is now successful for the complete batch of test specimens despite their differences in terms of thermal inertia, conductivity and absorptivity.

The predictive command is showing a large scale of adaptation in terms of temperatures and duration to

heat up or cool down very different specimens in terms of thermal features.

3.3. Predictive command improvements

Initially the predictive command is foreseen to manage passive specimens.
An improvement of the predictive command has been programmed and deployed to manage an active specimen delivering a random perturbation like a thermal power injection.
For this, the script deployed in PLC program has been upgraded:
During steady state, the performance coefficient is computed differently to increase the speed of command response in case of detection of an unexpected temperature rise corresponding to a thermal power injection.

4. PREDICTIVE COMMAND COMMISSIONING

The predictive command is now deployed in the control system of two AD&S thermal vacuum test facilities; the 3M3 and the SIMDIA (27M3 of usable volume).

Since 2021, AIRBUS DS is testing reflectors in the SIMDIA thanks to these predictive regulation loops.



Figure 27: Preparation of reflectors test in SIMDIA

In SIMDIA up to 45 thermocouples may be fixed on reflector surface. They are declared in control system as specimen temperature.

Automatic thermal cycles are programmed in advance in the facility supervision. It is possible to run the test automatically on the TRP; the maximum value, the minimum value, or the average depending on operator selection.
The thermal cycling is run and driven automatically.

The criterion for test success is that each TC shall be in a channel of 3°C around the set points. This is controlled by the machine and the steady state duration is counted automatically by SIMDIA control system.

Thanks to the last developments performed in the 3M3, it will be possible to upgrade the SIMDIA predictive command in order to be able to pass specimen like the MetOp-SG Scatterometer, a big antenna made of 120 kg of grey aluminium alloy.

This improvement will be performed once SIMDIA Thermal Group is refurbished, which is scheduled in 2027.



Figure 28: AIT of MetOp-SG-B Scatterometer antenna

5. ABBREVIATIONS AND ACRONYMS

3M3:	AD&S Space Simulator
AD&S:	AIRBUS DEFENCE & SPACE SAS
AIT:	Assembly Integration Test
Amb:	Ambient
CS:	Control System
DUT:	Device Under Test
ΔT:	Temperature gradient or difference
ε:	Emissivity
F12:	View Factor between Surface 1 & 2
$\Phi_{conductive}$:	Conductive Thermal Flux
$\Phi_{convective}$:	Convective Thermal Flux
$\Phi_{radiative}$:	Radiative Thermal Flux
GN2:	Gaseous Nitrogen
K:	Gain of predictive command
$K_{conductive}$:	Thermal Conductive Constant
$K_{convective}$:	Thermal Convective Constant
$K_{radiative}$:	Thermal Radiative Constant
LN2:	Liquid Nitrogen
PLC:	Programmable Logical Controller
R:	Delay of predictive command
Si or SUR:	Surface i
SIMDIA :	AD&S Space Simulator (27 m3)
S/C:	Space Craft
T :	Temperature
Tamb:	Ambient Temperature
TC:	Thermocouple
TCU:	Thermal Control Unit
Tmax / Tmin:	Maximum / minimum Temperature
TRP:	Test Reference Point
TV:	Thermal Vacuum
τ:	Time constant predictive command
S/W:	Software
sec:	Second
°C:	Degree Celsius

DEVELOPMENT OF A FULL-RANGE TEMPERATURE CALIBRATOR FOR SENSORS TO BE USED IN THERMAL-VACUUM TESTING FOR SPACE QUALIFICATION

Andreas Fleck (1), Christoph Werner (2), Daniel Döring (3)

(1) IABG mbH, Einsteinstraße 20, 85521 Ottobrunn, Germany; fleck@iabg.de
(2) IABG mbH, Einsteinstraße 20, 85521 Ottobrunn, Germany; wernerc@iabg.de
(3) IABG mbH, Einsteinstraße 20, 85521 Ottobrunn, Germany; doering@iabg.de

KEYWORDS

Thermal-Vacuum Testing, Thermocouple, Calibration

ABSTRACT

Surface temperature sensors are used extensively in space qualification tests for regulation and monitoring purposes. The most popular sensor type for practical and cost reasons is still the stick-on thermocouple type T (copper/constantan).
These sensors are typically delivered with a temperature calibration certificate according to DIN EN 60584-2, which is acceptable regarding the sensor uncertainty (± 0.5°C for class 1), but the data is only valid for temperatures above -40°C.
However, as the thermocouples are being used for full range in thermal-vacuum testing (approx. -190°C … +160°C), there is the need of performing an additional in-house calibration for low temperatures using a liquid nitrogen bath for the -196°C temperature point and a commercial temperature chamber for -75°C to +160°C with extrapolation over the gap.
To improve the calibration process (e.g. closing the gap between liquid nitrogen bath and minimum oven temperature, unifying the calibration to only one calibration device, and implementing a process automation), a calibration system has been developed and manufactured in cooperation with an external company.
This paper presents the technical design, performance and first application experience of the new system.

1. INTRODUCTION

IABG's Space Test Centre in Ottobrunn is dedicated to performing space qualification tests for all kinds of hardware, from small subsystems to full satellite system tests. Latter mentioned tests require the largest and most complex of IABG's thermal vacuum chambers, the "Weltraumsimulations-anlage" (Space Simulation Facility), WSA, that allows the highest complexity of tests:

- General high vacuum and temperature-controlled shrouds (90 to 385 K)
- 1000 or more temperature measurement channels for customer data acquisition
- above-average sensor cable length of up to 30 meters (length within the test object, sufficient slack to enable the movement of the motion simulator, distance to the feedthroughs of the vacuum chamber.)

Measuring a temperature with thermocouples comprises a lot of variables that need to be considered and therefore known. The influences on temperature deviations or errors are huge:

- sensor calibration
- implementation in data acquisition software
- sensor cable
- extension cables
- cable connectors
- data scanner
- cold junction

In this paper, the focus will be on the measurement chain of the test-ready manufactured stick-on thermocouples, which consists of the sensor itself, the thermocouple extension cable as well as Sub-D crimping contacts.

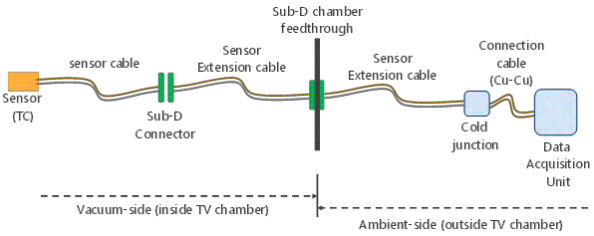


Figure 1: Thermocouple measurement chain in thermal valcuum tests.

2. THERMOCOUPLE SENSOR CALIBRATION FOR THERMAL TESTING

Stick-on thermocouples are for single-use purposes. Depending on the test article, up to 1.000 sensors are being installed for a single thermal vacuum test. Since at IABG premises, many thermal vacuum tests are being performed, there is a need for a vast amount of these single-use sensors. Therefore, the sensors are being ordered in distinct batches. Every order needs to be prepared and inspected carefully to ensure that all requirements are being met.

Before applying the stick-on thermocouples to test objects, a thermocouple extension cable as well as crimping contacts need to be connected to the sensor.
It is well known that thermocouples of different

batches deliver different measurement results. As internal investigations show, this effect is already detectable when using different extension cable batches; this influence on the measurement results can be significant, especially in cold temperatures. A comparison of two calibration processes (Fig. 2) shows that using a different extension cable batch ID, the standard deviation within one batch can exceed the allowable value to maintain ECSS requirements [1].
The calibration curves in Fig. 3 show that the deviation from the DIN curve is not by default linear.

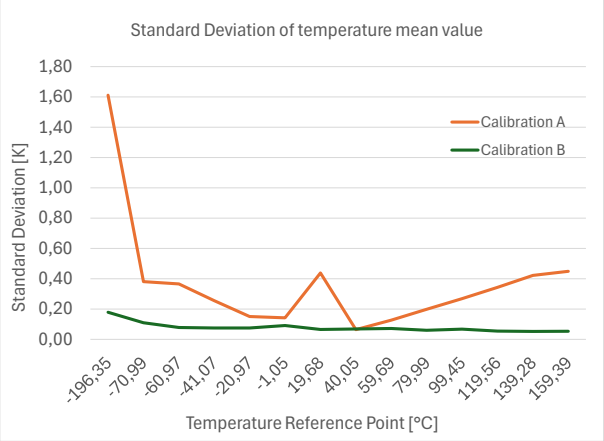


Figure 2: Example for standard deviation of thermocouple calibrations.

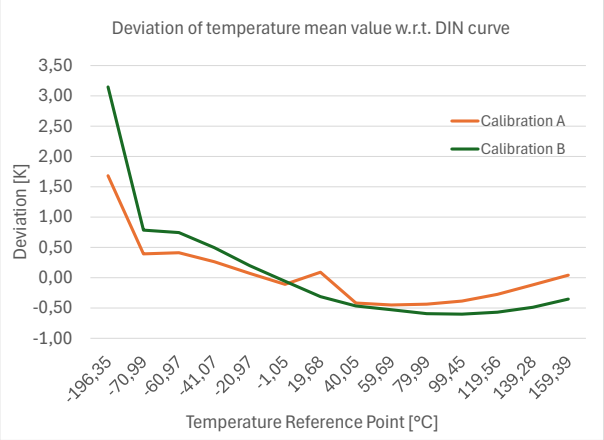


Figure 3: Example for temperature deviation w.r.t. DIN curve of thermocouple calibrations.

Therefore, the sensors and cables need to be out of one manufacturing charge, and the manufacturing process of the test-ready sensor must be of identical quality for the entire batch.
Given the fact of utilizing single-use sensors, the calibration process must be limited to a pre-defined number of sensors (depending on the number of sensors ordered). This is done by choosing sensors from the beginning and the end of the manufacturing process, as well as random samples.

3. REQUIREMENTS FOR A FULL-RANGE TEMPERATURE CALIBRATOR

The following core requirements must be met:

- Main use is the calibration of stick-on thermocouples
- Simultaneous calibration of multiple temperature sensors
- Movable
- Definition of the temperature reference points by the user
- Up to 10 temperature reference points within one calibration process
- Possibility of an end-to-end calibration
- Representable temperature range from -196°C (77K, LN2) to +160°C (433K)

4. TECHNICAL CONCEPT

The full range temperature calibrator is designed to either offer the possibility to calibrate thermocouple samples for an entire batch, or to perform an end-to-end calibration to exclude the measurement errors of the measurement chain.
The calibrator can be seen as a cryogenic storage dewar with vacuum insulation between the outer walls and an internal LN2 reservoir located at the bottom. Two main temperature-controlled and regulated housings ensure a high accuracy calibration of thermocouples – the cold junction reference point and the sensor reference point. Through a metallic thermal connector, being partially submerged in LN2, the LN2 temperature reaches the sensor. The exact temperature is being PID controlled.
On top, a 3.5" TFT capacitive touch display allows to set calibration parameters (which can also be set via control software on the computer). Sub-D feedthroughs allow to connect the reference sensors to the TFT display and the thermocouple sensors to the data acquisition unit.

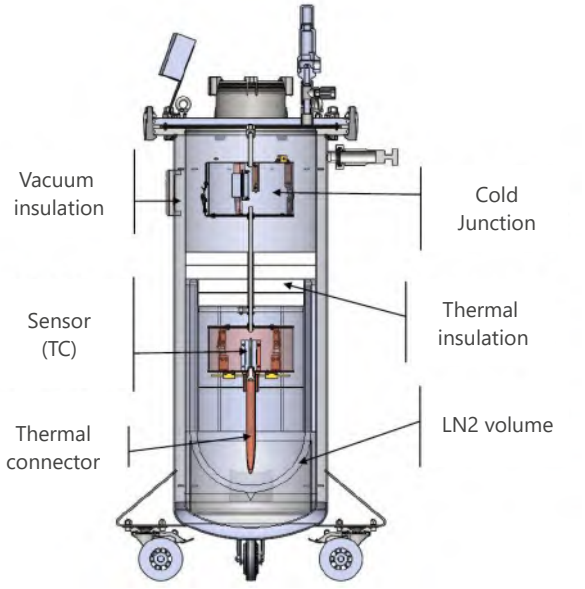


Figure 4: Technical concept of the full-range temperature calibrator.

It is possible to set up to 10 temperatures for one calibration process. In addition, the option to only use the highest and lowest temperatures while choosing a calibration process featuring equidistant temperature reference points is given.
Also, dwell times as well as allowable temperature gradients can be set as parameters on the controller.
If working with another software, the data can be collected via USB (MODBUS-RTU protocol).
After initiating, the process is being performed fully automated.

The two following pictures show the parameters on the TFT display of the controller. In Fig. 5, the reference sensor temperatures T01 to T06, the PID heater power, the dwell time t_d as well as the allowable temperature gradient TG can be seen. In Fig. 6, the temperature reference points are displayed and can be adjusted as required.

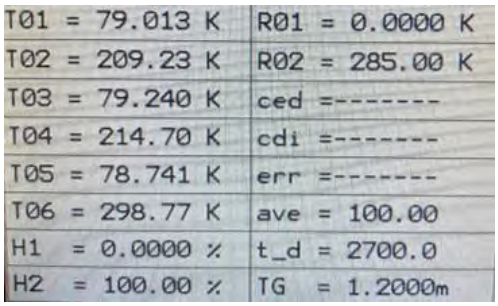


Figure 5: Page 1 of the TFT fisplay with control parameters.

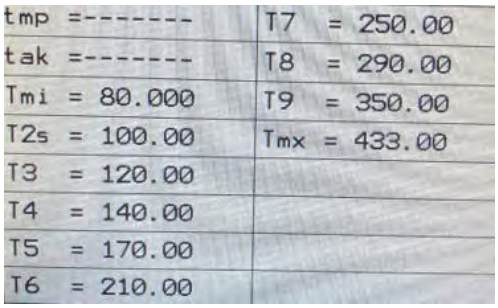


Figure 6: Page 2 of the TFT fisplay with control parameters.

4.1. Configuration A: sensor calibration

The initial goal was to substitute the existing calibration chain with closing the gap between LN2 temperature and -75°C. The final design is shown in Fig. 7.

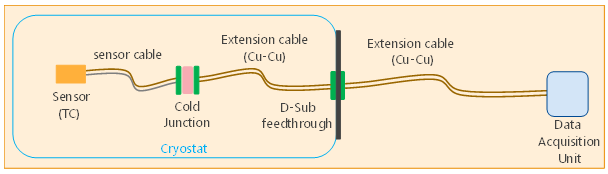


Figure 7: Configuration A: Sensor calibration.

The calibration measurement chain only uses a thermocouple cable from sensor to the connection point on the cold junction. The remainder of the measurement chain consists of regular Cu-Cu signal cables.

4.2. Configuration B: end-to-end calibration

The temperature calibrator also allows to perform an end-to-end calibration of the entire measurement chain including the thermocouple sensors being used for testing (Fig. 8). This allows to minimize the measurement error at room temperature while gaining low measurement uncertainties.
It is to mention that the calibration can only be done at approximate room temperatures. The influence of temperature on the various components needs to be considered when defining and calculating the measurement uncertainty of the measurement chain being used.
Also, it is of importance to acknowledge that disconnecting the cables might influence the measurement values and thus the accuracy. The awareness of the contributing factors is crucial for a high-quality temperature measurement process.

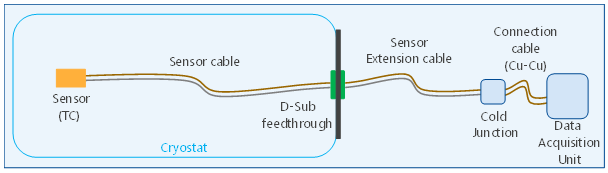


Figure 8: Configuration B: End-to-end calibration.

5. QUALIFICATION AND VERIFICATION

5.1. Calibration process

The qualification has been made by measuring 18 thermocouple sensors inside of the calibrator during a calibration process. The results can be seen in Fig. 9.

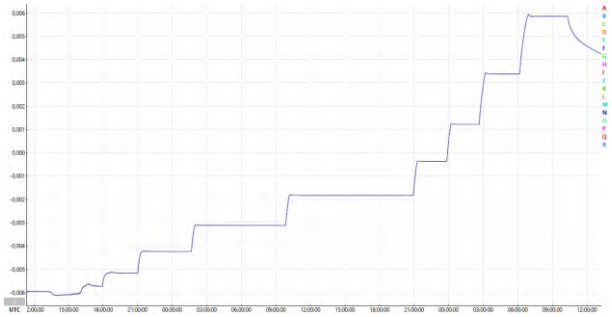


Figure 9: Calibration measurement results.

It is visible that the durations of the individual temperature reference points is varying. As the dwell time is equal for each temperature reference point, the different durations result from insufficient stability of the measured temperatures; before the dwell time is started the temperature stability criteria need to be satisfied.

Zooming in on one specific temperature reference point (Fig.10), it displays the importance of knowing on which time stamp the respective dwell time start has been reached. This can currently be seen in the controller software, where the stability channel is being set to “1” when the dwell time interval is active.

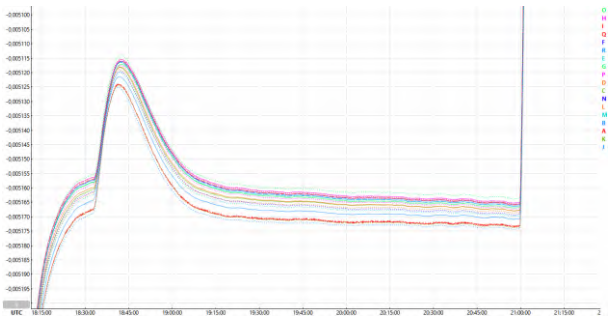


Figure 10: Dwell time measurement results.

5.2. Measurement uncertainty contributors

Besides the thermal homogeneity of the cold junction, the presence of isothermal conditions in between the sensors to be calibrated is of high importance.
For the calibration, a so-called “transition sleeve”, similar to the one used in a block calibrator, is being utilized. For the design of this transition sleeve, the temperature distribution has been simulated and evaluated.
The evaluation showed that the most crucial parameters are:

- Thermal connectivity of the sensors to the transition sleeve
- Thermal connectivity of the thermocouple sensor cable (Guarding)
- Length of the sensor cable

While the thermal connectivity of the sensors and the cables are already optimized in this case, the thermal homogeneity is highly sensible for temperature influences contributed by the sensor cables. When choosing a sufficient cable length inside the homogeneous reference points, the influence can be minimized. In Tab. 1, the simulation shows a maximum temperature difference of all 18 calibrated sensors of 0.034K with a 3m sensor length inside the temperature-controlled volume (“Sensor box” as well as Cold Junction).

Table 1: Temperature inhomogeneity on sensors.

Target Temperature [°C]	TCs (Tmin) [°C]	TCs (Tavg) [°C]	TCs (Tmax) [°C]	Maxdif TCs [K]
22	22	22	22	0.000
-196	-195.855	-195.838	-195.821	0.034
-75	-74.947	-74.939	-74.931	0.016
0	-0.033	-0.031	-0.029	0.004
65	64.967	64.970	64.974	0.007
165	164.896	164.906	164.917	0.022
22	22.032	22.033	22.033	0.001

6. WAY FORWARD

It is not yet possible to receive all data in one single software. This currently only allows to measure voltage on the thermocouples with one acquisition software and temperature on the reference sensors with the other software. As an additional step, the data needs to be merged with the correct time stamps using a suitable software such as Excel to be able to evaluate the temperature results of the thermocouple sensors.
By using only one software, it allows to analyse, print and compare the data immediately, also by using the extra stability channel for the indication of the dwell time status.
Therefore, the next step will be to implement the temperature calibrator into the data acquisition software STAMP.
Furthermore, this will allow to perform comparison measurement with the calibration process of IABG’s DAkkS accredited laboratory using the same measurement chain and calibration devices.

Moreover, another future idea is to have a fully automated calibration process that delivers a calibration certificate with the relevant data to the user. In order to reach this goal, many variables and therefore a lot of effort must be considered, which is why this goal is currently proposed for the future.

7. CONCLUSIONS

The performed tests and gathered test data show that the core requirements of the full range calibrator have been met.
The relevant calibration results can currently only be used and gathered with minor difficulty.
To process the calibration data in a more convenient way, it is advisable to gather all data in one acquisition program such as STAMP.
Also, the comparison measurement with a DAkkS accredited laboratory ensures that the data is plausible and within expected values.

8. REFERENCES

[1] ECSS-E-ST-10-03C Rev.1, Space engineering – Testing, ESA Requirements and Standards Section, 31 May 2022, p.35

ECSSMET
Braunschweig Germany 2026

Thermoelastic

COMPOSITE METERING STRUCTURE OPTIMIZATION FOR HIGH RESOLUTION ELECTRO-OPTIC SPACEBORNE CAMERAS

Nehir Atasay Orulluoğlu [1*,2], M. Uğur Dilberoğlu [1], Erdem Acar [3], Murat Altın [4], Alpaslan Atmanlı [2] Özgür Karcı [1], Sibel Velioğlu [1]

[1]Turkish Aerospace Industry, Ankara, Türkiye
[2]National Defence University, Ankara, Türkiye
[3]TOBB University of Economics and Technology, Ankara, Türkiye
[4]Gazi University, Ankara, Türkiye, Ankara, Türkiye
** Email: nehir.atasay@tai.com.tr*

KEYWORDS

Metering structure, optimization, electro-optic camera, optical alignment, stability, despace.

ABSTRACT

Composite metering structures used in Cassegrain telescope systems require high dimensional stability under thermal and environmental loads. In such systems, minimizing axial deformation (despace) between optical components is critical for diffraction-limited optical performance. This study presents a Genetic Algorithm (GA)-based optimization framework for a composite cylindrical metering structure subjected to thermal and moisture-induced effects. The optimization considers laminate thickness, ply orientations, and stacking sequence while satisfying structural and dynamic constraints including natural frequency, failure index (FI), and axial deformation limitations. Initially, the GA framework was validated against Finite Element Method (FEM)-based optimization results. Subsequently, the search space was expanded to investigate lighter laminate configurations with reduced ply count. Finally, moisture expansion effects were incorporated into the optimization framework through equivalent Coefficient of Moisture Expansion (CME) evaluation based on Classical Lamination Theory (CLT). Results demonstrate that the proposed framework improves environmental dimensional stability while satisfying structural and dynamic design constraints.

1. INTRODUCTION

In high-precision optical systems, maintaining the relative positioning of the primary and secondary mirrors is critical for diffraction-limited optical performance. One of the key parameters governing this performance is the axial distance between the mirrors, commonly referred to as despace. Even small variations in this distance can introduce optical aberrations and degrade imaging performance [1].

In the Cassegrain electro-optical camera considered in this study, the Primary Mirror (M1) and Secondary Mirror (M2) are arranged along a common optical axis. Owing to the highly symmetric opto-mechanical configuration, decenter, tip, and tilt effects are inherently minimized. Consequently, axial displacement between M1 and M2 (despace) becomes the dominant contributor to optical performance degradation and is therefore selected as the primary design driver in this study.

Metering structures used to maintain optical alignment have been implemented in various forms, including metering shells, truss structures, optical benches, and integrated CFRP configurations [2–4]. This axial stability is primarily governed by the metering structure, which connects optical components and defines their relative positioning. CFRP is particularly attractive for high-stability space optical structures because of its high specific stiffness and tailorable thermal expansion characteristics [2–5]. However, composite materials are sensitive to environmental effects such as temperature and moisture.

Thermal expansion (CTE) and moisture expansion (CME) directly influence the dimensional stability of the metering structure, leading to undesired axial displacement. Moisture absorption and desorption can produce measurable dimensional changes in CFRP metering structures, making hygroscopic stability relevant in addition to thermal stability [5]. Therefore, minimizing both CTE- and CME-induced deformations is essential for ensuring optical stability.

This requirement naturally leads to a multi-objective optimization problem, where laminate configuration must be designed to simultaneously satisfy mechanical and environmental constraints. While conventional Finite Element Method (FEM)-based optimization tools enable the optimization of laminate configurations with respect to CTE, they do not allow the inclusion of CME effects within the same optimization framework, which limits their applicability for fully representative environmental conditions. This limitation necessitates the development of a dedicated optimization methodology capable of simultaneously addressing CTE, CME, and structural performance

requirements.
To better illustrate the opto-mechanical configuration and the origin of despace deformation, a simplified representation of the electro-optical camera structure is presented in Figure 1. A simplified 2D sketch illustrating the basic dimensions and main structural elements is provided. Accordingly, the Primary Mirror (M1) and Secondary Mirror (M2) lie on the same optical axis (i.e., z-axis in Figure 1), where the despace between them must be maintained within a defined stringent tolerance. Both reflective optics are made up of a low-CTE-glass. A Carbon Fiber Reinforced Polymer (CFRP) composite Sandwich Panel accommodate the overall opto-mechanical structure, to which M1 is attached to and positioned via M1. The secondary mirror is located at the end of a Composite Metering Tube with the help of an aluminum Spider and M2 Holder.

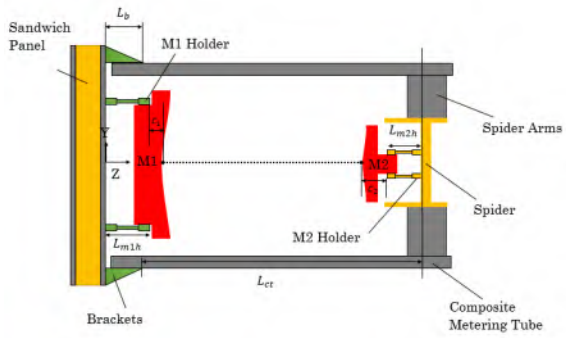


Figure 1: A simplified 2D sketch of the metering structure of the electro-optic camera

2. PROBLEM DEFINITION

The primary objective of this study is to minimize axial deformation (despace) between the two mirrors connected by a composite metering structure.
The axial displacement is driven by:

- Thermal expansion stability (CTE-induced deformation)
- Moisture expansion stability (CME-induced deformation)

In addition to minimizing these effects, the structure must satisfy the following constraints:

- Structural integrity: failure index (FI < 1)
- Dynamic requirement: First natural frequency ($f_1(x) \geq f_{min}$)
- Manufacturability and laminate feasibility

The optimization constraints are formulated using the first natural frequency $f_1(x)$, failure index $FI(x)$, thermal-induced axial displacement $\delta_{th}(x)$, and moisture-induced axial displacement $\delta_{cme}(x)$, where x represents the candidate laminate configuration. The corresponding allowable limits are 140 Hz for the first natural frequency, 1 for the failure index, 3 µm for thermal-induced axial displacement, and 5 µm for moisture-induced axial displacement. Thus, the optimization problem can be formulated as:

- Objective: min N_{ply}
- Constraints:

$$g_1(x) = 1 - \left(\frac{f_1(x)}{140}\right) \leq 0 \quad (1)$$

$$g_2(x) = FI(x) - 1 \leq 0 \quad (2)$$

$$g_3(x) = \frac{|\delta_{th}(x)|}{3} - 1 \leq 0 \quad (3)$$

$$g_4(x) = \frac{|\delta_{cme}(x)|}{5} - 1 \leq 0 \quad (4)$$

- Fitness Function:

$$F_{fitness} = N_{ply} + \sum_{i=1}^{4} \lambda_i \ max(0, g_i(x))^2 \quad (5)$$

3. CONVENTIONAL FEM-BASED OPTIMIZATION

Conventional FEM-based optimization tools (e.g., Hypermesh with Optistruct Solver) are employed to obtain an initial optimized laminate configuration for the composite metering structure. The optimization process is carried out using a multi-stage strategy consisting of:

- Free-size optimization
- Size optimization
- Shuffle optimization

Within this framework, the laminate design is defined by the following design variables:

- Ply orientations & stacking sequence
- Number of plies

Accordingly, the laminate design space is defined based on the initial stacking sequence, and the optimization process is limited to the predefined set of ply the orientations available within this baseline configuration. The optimization is therefore performed within a constrained laminate design space rather than a fully unrestricted orientation

search.
The optimization is performed under the following constraints:

- FI ≤ 1
- $f_1 \geq f_{min}$
- $\delta_{th} \leq \delta_{max}$

The objective of the optimization is defined as:

- Minimization of the total number of plies

This objective is selected to reduce overall structural mass, which is directly related to manufacturing cost and system-level efficiency.
Geometric parameters such as tube length and diameter are kept fixed throughout the optimization process and are defined based on system-level design requirements. Despite its effectiveness, this optimization framework does not include CME effects. Therefore, one of the environmental constraints defined in Section 2 is not considered in the FEM-based optimization. As a result, the obtained laminate configurations are optimized only with respect to thermal and mechanical performance, lacking full representation of environmental influences.

3.1. Initial laminate design

An initial laminate configuration is defined to establish a baseline design for the composite metering structure prior to optimization.
The selected stacking sequence is given as:

$$[(0)_3/45/90/-45]_s$$

This laminate is chosen as a symmetric and balanced configuration, ensuring stable mechanical behavior and eliminating bending–twisting and extension–shear coupling effects [6].
The laminate consists of 12 plies, each having a uniform thickness of 0.101 mm, resulting in a total laminate thickness of 1.212 mm. The selection of this initial stacking sequence is based on well-established composite design guidelines [7]. In particular:

- 0° plies primarily carry axial loads and contribute to stiffness and buckling resistance
- ±45° plies provide shear and torsional stiffness
- 90° plies improve transverse stability and dimensional resistance

Furthermore, the laminate satisfies recommended orientation distributions commonly adopted in composite design practices [8], where:

- 0° plies dominate axial stiffness
- ±45° plies ensure shear load transfer
- 90° plies enhance dimensional stability

In addition, symmetry and balance conditions are enforced to:

- Prevent bending–twisting coupling under thermal and mechanical loads
- Avoid torsional deformation under in-plane loading conditions

This initial configuration provides a mechanically stable and manufacturable baseline, serving as a reference for subsequent optimization studies.
This baseline laminate is also consistent with conventional aerospace composite design practices [7]. This baseline configuration is subsequently used as the starting point for the FEM-based optimization process and serves as a reference for evaluating the performance of the proposed Genetic Algorithm (GA)-based optimization framework.

3.2. FEM-based optimization procedure

The FEM-based optimization procedure described in Section 3 is performed using Optistruct, following the multi-stage strategy consisting of free-size, size, and shuffle optimization.
The FEM model of the composite tube is shown in the Figure 2. The composite tube is modeled in 2D with the plies explicitly defined layer by layer. Based on the baseline laminate configuration described in Section 3.1, the design space is restricted to ply orientations of 0°, 90°, +45°, and −45° during the optimization process. Since the primary focus is the composite tube itself, the M2 assembly is located at concentrated mass (CONMASS). Boundary conditions are applied at the regions where the composite tube interfaces with the sandwich panel.
The schematic representation of the ply orientation modelling used in the FEM framework is presented in Figure 3. To meet the optimization requirements, free-size, size, and shuffle optimization will be carried out sequentially. In this framework, the result of each optimization step serves as the input for the subsequent one.
In the free-size stage, the laminate thickness distribution and orientation usage are determined locally throughout the structure. The size optimization stage subsequently refines the laminate configuration while satisfying manufacturability constraints. Finally, shuffle optimization rearranges the stacking sequence of

the laminate without altering the overall ply content.

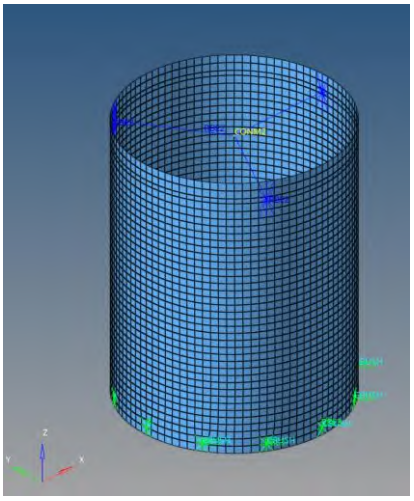


Figure 2: FEM of the composite metering structure

Free-size optimization locally optimizes the ply thickness, ply number, and orientation. Size optimization also deals with the ply thickness, ply number, and orientation subject to manufacturing constraints. Finally, shuffle optimization only alters the stacking sequence of the orientations. The details of the optimization process are summarized in Table 1.

The evolution of the laminate configuration throughout the free-size and size optimization stages is illustrated in Figure 4. The figure demonstrates how the laminate distribution becomes progressively refined and simplified during the optimization process.

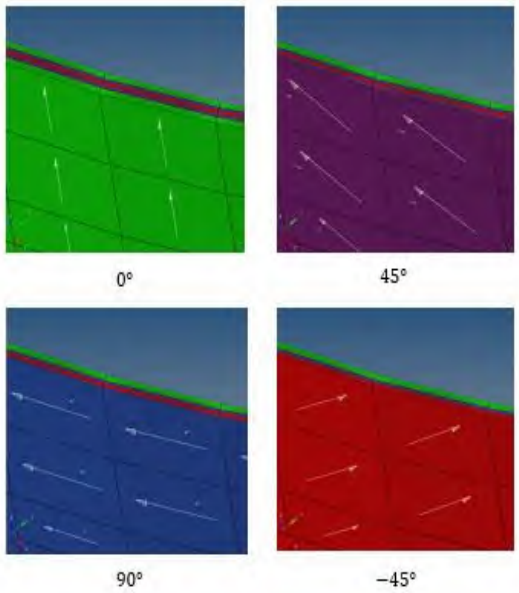
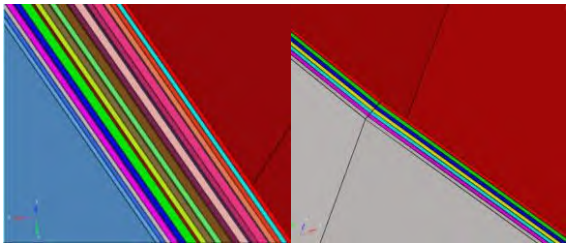


Figure 3: Composite tube ply orientations with respect to the reference coordinate system, where the 0° ply orientation is defined along the x-axis and the z-axis corresponds to the optical axis.

Table 1: Overview of the three-stage composite optimization process

Optimization Phase	***Objective***	***Requirements & Constraints***	***Design Variables***	***Output (to next phase)***
Stage I: Free-Size	Establish conceptual thickness orientation and distribution across laminate	**Static:** Withstand 30 g quasi-static launch loads, FI < 1 **Modal:** f_1 > 140 Hz	Super-ply thickness contributions	Thickness distribution & laminate bundles ➔ Size
Stage II: Size	Optimize ply/bundle thicknesses for manufacturability while meeting performance targets	**Static:** Withstand 30 g quasi-static launch loads, FI < 1 **Modal:** f_1 > 140 Hz **Thermal:** Operating range T_{ref} = 20℃, ΔT= ±1℃ Displacement δ_{th}< 3 μm.	Ply/bundle thicknesses & counts	Final ply counts & bundle thicknesses ➔ Shuffle
Stage III: Shuffle	Determine final stacking sequence ensuring performance	**Static:** Withstand 30 g quasi-static launch loads, FI < 1 **Modal:** f_1 > 140 Hz **Thermal:** Operating range T_{ref} = 20℃, ΔT= ±1℃ Displacement δ_{th}< 3 μm.	Ply stacking sequence	Production-ready final stacking sequence



(a) (b)

Figure 4: Variation of the lay-up of the composite tube: (a) free size optimization output, (b) size optimization output

In the final stage, shuffle optimization keeps the number and thickness of the plies constant and achieves the most suitable lay-up only altering their sequence. Iteration process of the shuffle optimization is shown in Figure 5.

Iteration 0	Iteration 1	Iteration 2	Iteration 3	Iteration 4
3101	4101	4101	5101	5101
4101	6101	5101	8101	8101
5101	5101	8101	4101	4101
6101	8101	9101	9101	9101
7101	9101	3101	3101	3101
8101	7101	6101	6101	6101
9101	3101	7101	7101	7101

Legend
90.0 degrees
45.0 degrees
0.0 degrees
-45.0 degrees

Figure 5: Shuffle optimization iteration process Numerical values represent Ply IDs, while colors indicate ply orientations.

3.3. FEM-based optimization results

The optimization results and the variation of design parameters across each optimization steps are presented in Tab. 2 and Tab. 3.
The resulting optimized stacking sequence is obtained as:

$$[90\ 90\ 45\ 45\ 0\ -45\ -45]$$

Table 2: Variation of design parameters across each optimization steps

Opt. Step	*# of Plies*	*Mass (kg)*	*# of Iteration*	*Axial CTE (1/℃)*
Initial Design	12	1.327	-	α_1= -0.466E-06
Free - Size	48	0.858	12	α_1= -0.042E-06
Size	7	0.862	3	α_1= -0.879E-06
Shuffle	7	0.862	4	α_1= -0.835E-06

Table 3: Comparison of the optimization results of the composite tube

Opt.	*First Natural Frequency (Hz)*	*Failure Index*	*Displacement at Z (μm)*
Free-Size	138.7	0.013	-
Size	141.9	0.015	-0.879
Shuffle	141.9	0.015	-0.835

The optimized laminate achieves the desired thermal and mechanical performance while minimizing the total number of plies, thereby reducing structural mass.
These results serve as a reference solution for subsequent validation and comparison with the proposed GA-based optimization framework. The obtained FEM-based solution does not include CME effects, which will be addressed in the following section.

4. GA-BASED OPTIMIZATION APPROACH

To overcome the limitations of FEM-based optimization, a GA-based optimization framework is developed.
GA is a population-based optimization method inspired by the principles of natural selection and evolution [9]. Unlike gradient-based optimization methods, GA does not require gradient information and is well suited to discrete design spaces involving variables such as ply orientations and stacking sequences [9]. Therefore, to overcome the limitations of the FEM-based optimization approach described in Section 3, a GA-based framework is developed to explore laminate configurations while incorporating thermal, moisture, structural, and dynamic requirements.
In this approach:

- Each individual represents a laminate stacking sequence
- The selected orientation set is established based on conventional aerospace composite design practices and manufacturability considerations, as described in Section 3.1.
- The fitness function provides a quantitative measure of each candidate laminate configuration and guides the GA toward the optimal solution. In this study, it evaluates laminate feasibility based on structural, thermal, moisture, and dynamic performance criteria.
- Constraint violations are handled using penalty functions incorporated into the fitness evaluation process.

- FI < 1 (Tsai-Wu criterion)
- $f_1(x) \geq f_{min}$
- Thermal deformation (via equivalent CTE)
- Moisture deformation (via equivalent CME)

- The objective of the optimization is defined as:
  - min N_{ply}

This framework enables simultaneous consideration of thermal, moisture, structural, and dynamic performance requirements within a unified optimization process.
The developed GA framework is first validated against the FEM-based optimization results presented in Section 3. Subsequently, the optimization space is expanded to investigate improved laminate configurations and finally extended to include CME effects.

4.1. Modelling assumptions and problem formulation

In order to develop the GA-based optimization framework, several modeling assumptions are adopted to represent the structural, thermal, and moisture behavior of the composite metering structure.

4.1.1. Classical Lamination Theory Assumptions

In order to evaluate the thermo-mechanical behaviour of the composite metering structure during the optimization process, Classical Lamination Theory (CLT) is employed. The CLT framework enables the calculation of equivalent laminate stiffness, thermal deformation, moisture-induced deformation, and structural response based on ply-level material properties and stacking sequence configuration.

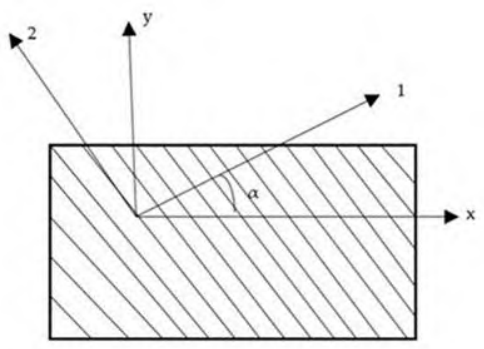


Figure 6: Local (1–2) and global (x–y) coordinate systems for an arbitrarily oriented ply [6]

As illustrated in Figure 6, each lamina is defined by a local material coordinate system (1−2) oriented with respect to the global laminate coordinate system (x−y) through the fiber angle α. Therefore, ply stiffness and strain quantities are transformed into the global coordinate system prior to the laminate-level calculations.
Local stiffness matrix (1-2) defines as where E_1 and E_2 are the longitudinal and transverse Young's moduli, respectively; ν_{12} and ν_{21} are the major and minor Poisson's ratios; and G_{12} is the in-plane shear modulus. Q_{11}, Q_{22}, Q_{12}, and Q_{66} are the corresponding components of the reduced stiffness matrix. For an orthotropic lamina expressed in its principal material coordinate system (1–2), the coupling terms Q_{16} and Q_{26} are zero.

$$[Q] = \begin{bmatrix} Q_{11} & Q_{12} & Q_{16} \\ Q_{12} & Q_{22} & Q_{26} \\ Q_{16} & Q_{26} & Q_{66} \end{bmatrix} \tag{6}$$

$$Q_{11} = \frac{E_1}{1 - \nu_{12}\nu_{21}}, \qquad Q_{22} = \frac{E_2}{1 - \nu_{12}\nu_{21}},$$
$$Q_{12} = \frac{\nu_{12}E_2}{1 - \nu_{12}\nu_{21}}, \quad Q_{66} = G_{12} \tag{7}$$

Local Thermal and Moisture-Induced Strains (1–2) are defined as

$$\varepsilon_{12}^T = \begin{bmatrix} \alpha_1 \\ \alpha_2 \\ 0 \end{bmatrix} \Delta T, \qquad \varepsilon_{12}^M = \begin{bmatrix} \beta_1 \\ \beta_2 \\ 0 \end{bmatrix} \Delta M \tag{8}$$

where α_1 and α_2 are the coefficients of thermal expansion in the longitudinal and transverse material directions, respectively; β_1 and β_2 are the corresponding coefficients of moisture expansion; and ΔT and ΔM denote the changes in temperature and moisture concentration, respectively. $\boldsymbol{\varepsilon}_{12}^T$ and $\boldsymbol{\varepsilon}_{12}^M$ represent the thermal- and moisture-induced strain vectors in the local material coordinate system (1–2), respectively.
Transformation into the Global Coordinate System (x–y):

$$[\bar{Q}] = [T_\sigma]^{-1}[Q][T_\varepsilon]^{-T} \tag{9}$$

$$\varepsilon_{xy}^T = [T_\varepsilon]^{-1}\varepsilon_{12}^T \tag{10}$$

$$\varepsilon_{xy}^M = [T_\varepsilon]^{-1}\varepsilon_{12}^M \tag{11}$$

where $[\bar{Q}]$ is the transformed reduced stiffness matrix in the global coordinate system (x-y), $[Q]$ is the reduced stiffness matrix in the local material coordinate system (1-2), and $[T_\sigma]$ and $[T_\varepsilon]$ are the stress and strain transformation matrices, respectively. The vectors $\boldsymbol{\varepsilon}_{xy}^T$ and $\boldsymbol{\varepsilon}_{xy}^M$ represent the

thermal- and moisture-induced strains transformed into the global coordinate system, respectively.
Each composite ply is modelled as an orthotropic lamina under plane stress assumptions. The local constitutive matrix [Q] is obtained from the engineering constants of the composite material. Thermal and moisture-induced strains are introduced through the coefficients of CTE and CME, respectively. Since each ply may have a different fiber orientation, local stiffness and strain quantities are transformed into the global laminate coordinate system.

$$\begin{bmatrix}\{N\}\\ \{M\}\end{bmatrix} = \begin{bmatrix}[A] & [B]\\ [B] & [D]\end{bmatrix}\begin{bmatrix}\{\varepsilon_0\}\\ \{K\}\end{bmatrix} - \begin{Bmatrix}\{N^T\}\\ \{M^T\}\end{Bmatrix} - \begin{Bmatrix}\{N^M\}\\ \{M^M\}\end{Bmatrix} \quad (12)$$

$$\{N\} = \begin{Bmatrix}N_x\\ N_y\\ N_{xy}\end{Bmatrix}, \qquad \{M\} = \begin{Bmatrix}M_x\\ M_y\\ M_{xy}\end{Bmatrix} \quad (13)$$

$$N^T = \sum_{k=1}^{N} \bar{Q}_{ij}^{(k)} \varepsilon^T (z_k - z_{k-1}),$$

$$M^T = \sum_{k=1}^{N} \bar{Q}_{ij}^{(k)} \varepsilon^T \frac{\left(z_k^2 - z_{k-1}^2\right)}{2} \quad (14)$$

In addition to the moisture-induced in-plane force resultant, the corresponding moisture-induced moment resultant is obtained by integrating the hygroscopic stresses through the laminate thickness as

$$N^M = \sum_{k=1}^{N} \bar{Q}_{ij}^{(k)} \varepsilon^M (z_k - z_{k-1}),$$

$$M^M = \sum_{k=1}^{N} \bar{Q}_{ij}^{(k)} \varepsilon^M \frac{\left(z_k^2 - z_{k-1}^2\right)}{2} \quad (15)$$

where N is the total number of plies, z_k and z_{k-1} denote the through-thickness coordinates of the upper and lower surfaces of the k-th ply, respectively, and $\bar{Q}_{ij}^{(k)}$ represents the transformed reduced stiffness components of the k-th ply.
The laminate extensional, coupling, and bending stiffness matrices are subsequently obtained by integrating the transformed ply stiffnesses through the laminate thickness as

$$A_{ij} = \sum_{k=1}^{N} \bar{Q}_{ij}^{(k)} \left(z_k - z_{k_{-1}}\right) \quad (16)$$

$$B_{ij} = \frac{1}{2}\sum_{k=1}^{N} \bar{Q}_{ij}^{(k)} \left(z_k^2 - z_{k_{-1}}^2\right) \quad (17)$$

$$D_{ij} = \frac{1}{3}\sum_{k=1}^{N} \bar{Q}_{ij}^{(k)} \left(z_k^3 - z_{k_{-1}}^3\right) \quad (18)$$

where A_{ij}, B_{ij}, and D_{ij}denote the extensional, bending–extension coupling, and bending stiffness components of the laminate, respectively.
Using the resulting A, B, and Dmatrices, the laminate equilibrium equations are formulated by relating the mid-plane strains and curvatures to the thermal- and moisture-induced force and moment resultants as

$$A\varepsilon_0 + B\kappa = N_T + N_M \quad (19)$$

$$\mathrm{B}\varepsilon_0 + D\kappa = M_T + M_M \quad (20)$$

where ε_0 and κ represent the mid-plane strain and curvature vectors, respectively. while $N_T$and $N_M$denote the thermal- and moisture-induced force resultants, and M_T and M_M denote the corresponding moment resultants.
After transformation of the ply properties into the global coordinate system, laminate-level stiffness matrices are assembled through thickness integration. The extensional [A], coupling [B], and bending [D] matrices are computed according to CLT. In addition, thermal and moisture-induced force and moment resultants are calculated to evaluate environmentally induced deformation behaviour.
For symmetric laminates, the coupling matrix [B] becomes negligible, eliminating bending-extension coupling effects and improving dimensional stability.

4.1.2. Thermal & moisture modelling

In order to evaluate environmentally induced deformation of the composite metering structure, equivalent laminate thermal and moisture expansion coefficients are calculated using the CLT framework. Thermal and moisture-induced force and moment resultants are first obtained for the laminate, and the corresponding mid-plane strain vector is determined through the laminate constitutive equations.

$$\alpha_{eq} = \frac{\varepsilon_0^T}{\Delta T} \quad (21)$$

$$\beta_{eq} = \frac{\varepsilon_0^M}{\Delta M} \quad (22)$$

Here, α_{eq} and β_{eq} denote the equivalent laminate coefficients of CTE and CME, respectively. The obtained coefficients represent the effective thermo-hygroscopic behavior of the laminate in the global coordinate system.
After determining the equivalent laminate expansion coefficients, the corresponding axial deformation of the composite metering tube is calculated under thermal and moisture loading conditions.

$$\Delta L_{thermal,z} = L_{\mathrm{x}} \cdot \alpha_{eq} \cdot \Delta T \tag{23}$$

$$\Delta L_{moisture,z} = L_{\mathrm{x}} \cdot \beta_{eq} \cdot \Delta \mathrm{M} \tag{24}$$

where L_{x} denotes the initial length of the composite metering tube, ΔT is the temperature variation, and ΔM represents the moisture concentration change, the resulting axial deformation directly corresponds to the despace variation between the optical elements and therefore constitutes one of the primary optimization metrics within the proposed framework.

4.1.3. First natural frequency estimation approach

Since direct finite element modal analysis for every laminate configuration would significantly increase the computational cost of the optimization process, a frequency estimation framework was developed based on a pre-generated FEM database.
In this approach, a Python-based automation script was implemented in HyperMesh/OptiStruct to generate a large number of random laminate stacking sequences and automatically extract their first natural frequencies. The laminate configurations were generated using the angle pool [0°,±30°,±45°,±60°,90°], while the number of plies was randomly selected between 6 and 24.
For each laminate configuration, the Python script automatically modified the PCOMP definitions in the FEM model, executed the OptiStruct modal analysis, and stored the obtained first natural frequency values in a frequency database.
Each database entry contains the laminate stacking sequence together with the corresponding first natural frequency value obtained from FEM analysis.
During the optimization process, the first natural frequency of a candidate laminate was estimated using a nearest-neighbour-based interpolation approach.
Each candidate laminate j is characterized by its number of plies $N_{ply}^{(j)}$, ply-orientation vector $\theta^{(j)}$, laminate family $family^{(j)}$, and corresponding first natural frequency $f_1^{(j)}$.
The laminate sequence was compared with the existing database entries, and the closest laminate configurations were identified based on stacking-sequence similarity.
If multiple neighbouring configurations were available, the estimated frequency value was obtained using inverse-distance weighted interpolation.

$$\Delta\theta_i^{(j)} = \theta_i^{in} - \theta_i^{(j)} \tag{25}$$

$$\delta_i^{(j)} = \min\left(\left|\Delta\theta_i^{(j)}\right|, 180 - \left|\Delta\theta_i^{(j)}\right|\right) \tag{26}$$

$$d^{(j)} = \sqrt{\frac{1}{N_{ply}} \sum_{i=1}^{N_{ply}} {\delta_i^{(j)}}^2} \tag{27}$$

where $\Delta\theta_i^{(j)}$ is the angular difference between the i-th ply of the candidate laminate and the j-th database laminate, $\delta_i^{(j)}$ is the corresponding minimum angular difference accounting for orientation periodicity, and $d^{(j)}$ denotes the normalized stacking-sequence distance.
The two closest database configurations are then selected based on $d^{(j)}$, with their frequency–distance pairs denoted by $\left(f_1^{(1)}, d^{(1)}\right)$ and $\left(f_1^{(2)}, d^{(2)}\right)$.

$$\omega_i = \frac{1}{(\, d^{(i)} + \varepsilon)^2} \tag{28}$$

$$f_1^{est} = \frac{\omega_1 f_1^{(1)} + \omega_2 f_1^{(2)}}{\omega_1 + \omega_2} \tag{29}$$

where ω_i is the inverse-distance weighting factor of the i-th neighboring configuration, $\varepsilon = 1 \times 10^{-6}$ is a small regularization parameter introduced to avoid division by zero, and f_1^{est} is the estimated first natural frequency of the candidate laminate.
The estimated first natural frequency values were subsequently used to calculate the equivalent root rotational stiffness K_θ for each laminate configuration [10].
The obtained K_θ values were then incorporated into the load and FI calculations through the rotational boundary correction parameter η.

$$EI\frac{d^4w(x)}{dx^4} - \rho A_\omega^2 w(x) = 0 \tag{30}$$

$$w^4(x) - \beta^4 W(x) = 0 \tag{31}$$

$$\beta^4 = \frac{\rho A \omega^2}{EI} \tag{32}$$

where $w(x)$ is the transverse displacement of the equivalent beam, E is the effective Young's modulus, I is the second moment of area, ρ is the material density, A is the cross-sectional area, ω is the angular natural frequency, and β is the corresponding frequency parameter.
In this manner, the dynamic characteristics of the laminate indirectly influenced the structural load distribution and failure assessment process.
Using the estimated natural frequency, the equivalent root rotational stiffness is obtained as

$$K_\theta = E_{eff} I \beta L \frac{sinh(\beta L)\, cos(\beta L) - cosh(\beta L)\, sin(\beta L)}{-L[cosh(\beta L)\, cos(\beta L) + 1]} \quad (33)$$

where K_θ denotes the equivalent root rotational stiffness and E_{eff} is the effective axial modulus of the laminate; the remaining parameters are defined above.

4.1.4. Failure Index Evaluation

In order to evaluate the structural integrity of the laminate during the optimization process, the Tsai–Wu failure criterion is adopted. This criterion enables the combined assessment of normal and shear stress components within an orthotropic composite lamina under multi-axial loading conditions.

$$F_1\sigma_1 + F_2\sigma_2 + F_{11}\sigma_1^2 + F_{22}\sigma_2^2 + F_{66}\tau_{12}^2 + 2F_{12}\sigma_1\sigma_2 = FI \quad (34)$$

$$F_1 = \frac{1}{X_t} - \frac{1}{X_c}, F_2 = \frac{1}{Y_t} - \frac{1}{Y_c}, F_{11} = \frac{1}{X_t X_c}$$

$$F_{22} = \frac{1}{Y_t Y_c}, F_{12} = -\frac{1}{2}\sqrt{F_{11}F_{22}}, F_{66} = \frac{1}{s_{12}^2} \quad (35)$$

where σ_1, σ_2, and τ_{12} represent the in-plane stresses in the material coordinate system; X_t, X_c, Y_t, Y_c, and S_{12} denote the tensile, compressive, and shear strengths of the lamina; and F_1, F_2, F_{11}, F_{22}, F_{12}, and F_{66} are the corresponding Tsai–Wu strength coefficients. The resulting FI is used as a structural constraint throughout the optimization process. Laminates satisfying FI<1 are considered structurally safe, whereas values exceeding unity indicate failure initiation.
The stress state used in the failure assessment is obtained from the quasi-static launch loading condition described in the 4.1.4.1.

4.1.4.1. Quasi-static load case definition

In order to evaluate the failure behavior of the composite metering tube, a quasi-static launch load of 30 g is considered. The load is evaluated in two representative directions: axial loading along the tube axis and lateral loading producing lateral-direction response. Due to the cylindrical coordinate definition adopted in the analytical formulation, the axial z-direction in the FEM model corresponds to the x-direction in the MATLAB implementation, while the FEM x-direction corresponds to the circumferential y-direction in the analytical model.
The applied acceleration is defined as:

$$\text{a} = 30 \text{ x } 9.81 = 294.3 \text{ m}/s^2 \quad (36)$$

The mass per unit length of the composite tube is calculated as:

$$m' = A_{sec}\, \rho \quad (37)$$

where A_{sec} is the cross-sectional area of the composite tube and $\rho$is the CFRP material density. For the axial load case, the total axial force is calculated by considering both the distributed tube mass and the concentrated tip mass:

$$F_z = (m' L_x + m_{tip})\text{a} \quad (38)$$

where L_x is the tube length and m_{tip} is the concentrated tip mass representing the secondary-mirror assembly. Although this load acts along the global Z-axis in the FEM, it is represented as the axial laminate direction in the CLT formulation. Therefore, the membrane force resultant is defined as [11]:

$$N_x = \int_{-h/2}^{+h/2} \sigma_x(z)\, dz = \frac{F_z}{2\pi r} \quad (39)$$

$$N_x = \frac{F_z}{2\pi r}, N_y = 0, N_{xy} = 0 \quad (40)$$

where r denotes the mean radius of the composite tube. In addition to the axial membrane load, the concentrated tip mass induces an additional bending effect on the composite tube. Accordingly, the corresponding bending moment resultant is defined as:

$$M_y = \int_{-h/2}^{+h/2} \sigma_y(z) z\, dz = \eta_z \frac{F_z h}{\pi r} \quad (41)$$

$$\eta_z = \frac{K_\theta}{K_\theta + \frac{EI_y}{L_x}} \quad (42)$$

$$\mathrm{M_x} = 0\,, \mathrm{M_{xy}} = 0 \quad (43)$$

where I_y is the second moment of area about the corresponding bending axis the rotational boundary correction parameter η_z was determined using the equivalent rotational stiffness K_θ derived from the frequency estimation approach presented in Section 4.1.3.

For the lateral loading case, the transverse acceleration acting on the cylindrical structure generates circumferential stress resultants. The corresponding membrane force resultant is approximated as:

$$N_y = \int_{-h/2}^{+h/2} \sigma_y(z)\, dz = \rho a r^2 \quad (44)$$

$$N_y = \rho a r^2\,, \qquad N_{xy} = 0\,, N_x = 0 \quad (45)$$

where $\sigma_y(z)$ represents the through-thickness distribution of the circumferential stress. The bending moment resultant is calculated as:

$$M_x = \int_{-h/2}^{+h/2} \sigma_x(z) z\, dz = \eta_{xy}\, N_x h \quad (46)$$

$$\eta_{xy} = \frac{K_\theta}{K_\theta + \frac{EI_x}{L_x}} \quad (47)$$

$$M_x = \eta_{xy} N_x h\,, M_y = 0\,, M_{xy} = 0 \quad (48)$$

where h is the laminate thickness, I_x is the second moment of area about the corresponding bending axis, and η_{xy} is the rotational boundary correction factor associated with the lateral loading condition.

4.2. Validation of GA model using FEM results

To verify the accuracy of the developed GA-based optimization framework, the FEM-based optimization problem defined in Section 3, which does not account for moisture-related effects, was replicated using GA-based model.

Using HyperMesh OptiStruct, the optimization process applied to the baseline laminate configuration $[(0)_3\ 45\ 90\ -45]_s$ resulted in the laminate $[90\ 90\ 45\ 45\ 0 - 45 - 45]$.

Subsequently, the proposed GA framework produced the laminate configuration as

$$[-45\ 0\ 90\ 90\ 45\ -45\ 45].$$

The obtained laminate sequence represents a shuffled variation of the FEM-based solution while preserving similar thermo-mechanical behavior and stiffness characteristics.

The GA model was executed under the same constraints used in the FEM-based optimization procedure, including frequency, FI, and equivalent CTE limitations.

The laminate configurations obtained from the GA framework showed close agreement with the FEM-based optimization in terms of frequency response, FI, stiffness behavior, and equivalent thermal expansion characteristics.

The close agreement between FEM and GA results validates the reliability of the proposed optimization framework and demonstrates that the developed GA model can successfully reproduce FEM-based optimization trends.

4.3. GA-based optimization for improved performance

Following the validation study, the GA framework was further utilized to explore laminate configurations beyond the design space considered in the FEM-based optimization. In the FEM-based optimization, the allowable ply orientations were restricted to the predefined angle set of [0°, ±45°, 90°]. Therefore, the laminate configurations containing additional ply orientations could not be explored.

To investigate whether improved solutions could be obtained using a reduced ply count and an expanded orientation search space, the developed GA framework was employed by extending the angle pool from [0°, ±45°, 90°] to [0°, ±30°, ±45°, ±60°, 90°].

The expanded search space enabled the GA-based optimization to identify a 6-ply laminate satisfying the frequency, FI, and equivalent CTE constraints. The resulting stacking sequence was determined as [45 60 -45 -60 -45 45], achieving the required structural and thermo-mechanical performance with a reduced ply count compared to the FEM-based solution.

4.4. Inclusion of moisture expansion (CME)

As defined in the optimization problem presented in Section 2, both thermal- and moisture-induced axial deformations were considered as independent design constraints.

While the previous optimization stages focused on equivalent thermal expansion behaviour, moisture-induced expansion effects may also produce significant dimensional changes in composite

laminates under environmental exposure conditions.

To incorporate this effect, equivalent moisture expansion coefficients β_{eq} ,were evaluated using CLT, following a procedure analogous to that used for the equivalent laminate CTE calculation. The resulting moisture-induced axial deformation constraint was then incorporated into the GA-based optimization together with the previously defined frequency, FI, and thermal deformation constraints. The final optimization stage therefore considers both thermal and moisture expansion effects within a unified framework, allowing the laminate configuration to be optimized with respect to thermos-mechanical and hygroscopic dimensional stability simultaneously. The resulting laminate configuration, $[0\ 60\ 90 - 60]_s$, satisfied the frequency, FI, thermal deformation, and moisture-induced deformation constraints.

5. RESULTS AND DISCUSSION

Table 4 presents the baseline laminate, the FEM-based optimization result obtained using OptiStruct, the validated GA solution, and the reduced-ply laminate configuration obtained through the expanded GA search space.

The FEM-based optimization reduced the laminate ply count from 12 to 7 while satisfying the structural and thermal constraints. However, although the obtained laminate configuration provided acceptable equivalent CTE behavior, the equivalent CME values increased significantly compared to the baseline laminate.

Using the same optimization constraints, the developed GA framework successfully reproduced a shuffled variation of the FEM-based laminate configuration, validating the accuracy and reliability of the proposed optimization methodology.

Subsequently, the design space was expanded by introducing additional ply orientation candidates within the GA framework. This enabled the optimization process to explore laminate configurations beyond the orientation combinations defined in the original FEM-based optimization.

As a result, a 6-ply laminate configuration was identified while still satisfying the frequency, FI, and thermal deformation constraints. This demonstrated that comparable thermo-mechanical performance could be achieved with a reduced laminate thickness and lower structural mass.

In the final optimization stage, moisture expansion effects were incorporated into the GA framework through equivalent CME constraints. The resulting laminate configuration achieved balanced thermal and moisture expansion behavior while satisfying all structural and dynamic requirements simultaneously.

These results demonstrate that optimization strategies considering only thermal expansion behavior may lead to unfavorable moisture-induced deformation characteristics. Therefore, simultaneous consideration of both CTE and CME effects is critical for lightweight composite metering structures operating under environmental exposure conditions.

Table 4: Laminate configurations and equivalent CTE&CME values throughout the optimization process

	# of Plies	***Lay-up***	***Equivalent CTE (1/℃)***	***Equivalent CME (1/%M)***
Initial Lay-up	12	$[(0)_3\ 45\ 90\ -45]_s$	α_1= -4.66E-07 α_2 = 1.62E-06	β_1 = -2.39E-05 β_2 = -5.93E-05
Lay-up After Optistruct Optimization	7	[90 90 45 45 0 -45 -45]	α_1= 5.02E-06 α_2 = 5.60E-06	β_1= -2.23E-04 β_2 = -1.03E-03
Lay-up After Expanded GA Optimization	6	[45 60 -45 -60 -45 45]	α_1= 3.55E-06 α_2 = -1.71E-06	β_1= -1.48E-04 β_2 = -1.89E-04
Lay-up After GA Optimization with CME	8	$[0\ 60\ 90 - 60]_s$	α_1= 1.20E-06 α_2= -3.38E-07	β_1= -9.78E-07 β_2 = -6.77E-05

6. CONCLUSION

This study presented a GA-based optimization framework for composite metering structures used in thermo-mechanically sensitive optical systems.
Initially, the developed GA framework was validated against FEM-based optimization results obtained using HyperMesh/OptiStruct. The proposed methodology successfully reproduced the FEM optimization trends and generated laminate configurations with comparable structural and thermo-mechanical performance.
Subsequently, the optimization search space was expanded by introducing additional ply orientation candidates, allowing the GA framework to identify lighter laminate configurations while maintaining the required structural and dynamic constraints.
In the final stage, moisture expansion effects were incorporated into the optimization framework through equivalent CME evaluation based on CLT. In contrast to the FEM-based optimization considered in this study, the proposed GA-based methodology enabled simultaneous consideration of:

- CTE
- CME
- Structural performance (FI)
- Dynamic behavior (first natural frequency)

The obtained results demonstrated that laminate configurations optimized only for thermal expansion behavior may exhibit unfavorable moisture-induced deformation characteristics. Therefore, the simultaneous consideration of CTE and CME effects is important for achieving stable and reliable composite metering structures under environmental exposure conditions.
Overall, the proposed GA-based framework provided an effective multi-physics optimization methodology capable of reducing despace deformation while satisfying structural and dynamic design constraints.

7. REFERENCES

1. Yoon, J. S., Kim, H. I., Han, J. H. & Kim, H. B., Effect of Dimensional Stability of Composites on Optical Performances of Space Telescopes, Journal of Aerospace Engineering, 27(1), 2014.
2. Design, Fabrication, and Test of a Graphite/Epoxy Metering Shell (GEMS), NASA-CR-143870, 1975.
3. Space Telescope Optical Telescope Assembly Structural Materials Characterization, 1982.
4. Stability metering method for high-resolution space telescope with large F-number based on combination optimization, Optik, 277, 170693, 2023.
5. High-fidelity simulation model for moisture-induced deformation of CFRP structure considering anisotropic nonlinear moisture absorption-desorption characteristics, Composites Part B, 2023
6. A. K. Kaw, Mechanics of Composite Materials, 2nd ed., Boca Raton, FL, USA: CRC Press, 2006.
7. MIL-HDBK-17, Composite Materials HandBook-Part A: Guidelines for Characterization of Structural Materials
8. MIL-HDBK-17-3F, Composite Materials Handbook, Vol. 3
9. Goldberg, D. E. (1989). Genetic Algorithms in Search, Optimization, and Machine Learning. Addison-Wesley
10. S. S. Rao, Mechanical Vibrations, 6th ed.,Upper Saddle River, NJ, USA: Pearson Education.
11. Timoshenko, S. & Woinowsky-Krieger, S., Theory of Plates and Shells-Nasa SP-8007, Buckling of Thin-Walled Circular Cylinders

AEOLUS-2 PLH THERMO-ELASTIC ANALYSIS AND TEMPERATURE MAPPING FOR PRELIMINARY DESIGN REVIEW

Guglielmo Landi [1,2], Simon Appel [3], Miriam Zazza [1], Lorenzo Ammannati [4], Ludovica Cavallucci [5], Alessandro D'Ottavi [6], Francesco Coppola [6], Paolo Bravetti[3], Elena Checa Cortes [3], Maria Lopez Alvarez[3], Sofia Sinopoli[3], Dorothee Darsonval[7], Mathieu Ballester [7], Frederic Chaumeil [7], Sylvain Arnaud [7], Vincent Pecastaing [7]

[1] Leonardo S.p.a., Space Division, Via delle Officine Galileo, 1, Campi Bisenzio, FI, 50013, Italy,
Email: guglielmo.landi@leonardo.com, miriam.zazza@leonardo.com
[2] International PhD Programme, UNESCO Chair "Environment, Resources and Sustainable Development", Università degli Studi di Napoli "Parthenope", Napoli, NA, 80143, Italy,
Email: guglielmo.landi@phds.uniparthenope.it
[3] European Space Agency, Keplerlaan 1, 2200 AG Noordwijk, The Netherlands,
Email: simon.appel@esa.int, paolo.bravetti@airbus.com, elena.checa@esa.int, maria.lopezalvarez@esa.int, sofia.sinopoli@esa.int
[4] Alten Italia S.p.a., Via Raffaello Lambruschini 33, Firenze, FI, 50134, Italy,
Email: lorenzo.ammannati@alten.it
[5] Akkodis Italy S.r.l., Via Umberto Forti, 6, Montacchiello, PI, 56121, Italy,
Email: ludovica.cavallucci@akkodis.com
[6] Leonardo S.p.a., Space Division, Via Industria, 4, Pomezia, RM, 00071, Italy,
Email: alessandro.dottavi@leonardo.com, alessandro.dottavi@leonardo.com
[7] Airbus Defense&Space, rue des Cosmonautes, 31, Toulouse, 31402, France,
Email: dorothee.darsonval@airbus.com, mathieu.ballester@airbus.com, frederic.chaumeil@airbus.com, mathieu.ballester@airbus.com, vincent.pecastaing@airbus.com

KEYWORDS

TEV, LIDAR, Thermoelastic, PAT, Mapping

ABSTRACT

The Aeolus-2 PLH demands unprecedented structural stability to ensure the pointing accuracy and optical performance required for Doppler Wind LIDAR (DWL) mission. This paper summarizes the thermo-elastic verification (TEV) done for the Power Laser Head (PLH) Preliminary Design Review (PDR).

The analysis focuses on the critical interaction between thermal gradients and structural deformations, which are primary drivers for performance degradation in orbit. The proposed methodology strictly follows the European Guidelines for Thermo-Elastic Verification (STM-285) [1], adopting a multi-disciplinary approach that integrates thermal, structural and optical domains.

A central element of this work is the implementation of an advanced Temperature Mapping process. To ensure physical consistency and energy balance between the Geometrical/Thermal Mathematical Model (GMM/TMM) and the Structural Finite Element Model (FEM), the Prescribed Average Temperature (PAT) method is employed. This method has been selected for its superior ability to handle high temperature gradients and its consistency across non-conformal meshes, minimizing the numerical noise typically associated with geometric interpolation or point-to-point mapping. Once the temperature field has been established, the structural analysis is carried out to evaluate the coupled thermo-mechanical response of the PLH across all mission phases, including ground verification, launch environments and in-orbit operation.

The assessment focuses on controlling thermoelastic distortions that may impact optical alignment, cavity stability and pointing accuracy, while also addressing the effects of differential thermal expansion among dissimilar materials such as optical mounts and structural supports. As a high-precision optical subsystem with stringent stability requirements, the PLH is inherently sensitive to temperature gradients. The analysis results confirm that the current PLH design meets the stability requirements consistent with the PDR design phase. The thermo-mechanical workflow provides a rigorous analytical baseline for subsequent design maturation, ensuring that the instrument can meet the mission's scientific performance requirements with the necessary levels of structural robustness, optical stability and operational reliability.

A significant milestone of this work is the implementation of the pySinas temperature mapping process, representing the first application of the new ESA STM-285 Iss.2 guidelines within a major institutional space program.

1. AEOLUS-2 MISSION OVERVIEW

Aeolus-2 is the future European operational Doppler Wind Lidar mission jointly developed by ESA and EUMETSAT as the successor to the highly successful Aeolus and EarthCARE missions.
The mission aims to provide continuous global observations of atmospheric wind profiles, supporting numerical weather prediction, climate monitoring and atmospheric research. The mission marks the transition from a technology-demonstration approach towards a long-term operational wind observing capability within the global meteorological infrastructure [2].

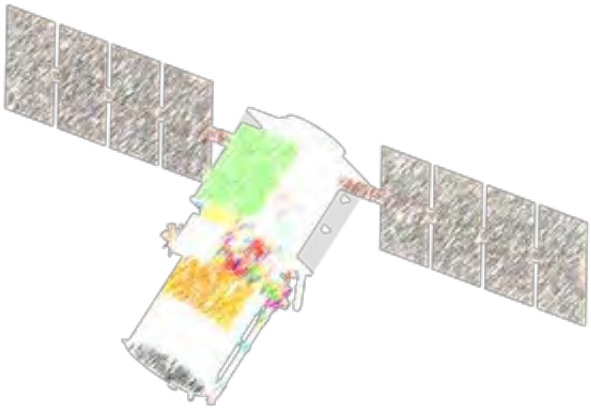


Figure 1-1: Blurred Aeolus-2 satellite layout.

1.1. Mission Heritage

The mission heritage originates from Aeolus, launched in 2018, which demonstrated for the first time the feasibility of measuring global wind profiles from space using the ALADIN (Atmospheric Laser Doppler Instrument) Doppler Wind Lidar. Although initially conceived as a technology demonstrator, Aeolus exceeded expectations and its measurements were successfully assimilated into operational weather prediction models, significantly improving forecast accuracy and filling critical data gaps over oceans and remote regions. [3]

Figure 1-2: Aeolus mission logo.

The development of Aeolus also generated a substantial technological legacy in the field of spaceborne ultraviolet lidar systems. This heritage was subsequently exploited by the EarthCARE mission through the development of the ATLID (Atmospheric Lidar) instrument, which further matured key laser, optical and opto-mechanical technologies required for high-performance atmospheric sounding from space [4].

Figure 1-3: EartCARE mission logo.

The experience accumulated through ALADIN and ATLID constitutes the technological foundation upon which the Aeolus-2 Doppler Wind Lidar instrument is being developed.

1.2. Power Laser Head Unit

The Aeolus-2 payload consists of a next-generation Doppler Wind Lidar (DWL) operating in the ultraviolet spectral range. The instrument employs a bi-static architecture combining a high-energy laser transmitter, beam steering and expansion optics, a large-aperture receiving telescope and dedicated Rayleigh and Mie spectrometers for molecular and aerosol wind retrieval. Compared to its predecessor, the instrument is designed to provide improved measurement accuracy, enhanced robustness, increased reliability and higher operational availability throughout the mission lifetime [2].
A key element of the DWL instrument is the Power Laser Head (PLH), developed by Leonardo Space Division, which generates the high-energy ultraviolet laser pulses required for atmospheric backscatter measurements. The PLH represents one of the most critical subsystems of the instrument, combining demanding optical, mechanical, thermal and electronic requirements within a highly integrated assembly.



Figure 1-4: AE2 PLH render.

The subsystem directly benefits from the technological heritage gained during the development of the laser systems for both ALADIN

and ATLID, while introducing significant performance enhancements required to meet the operational objectives of Aeolus-2 [5].
Given the stringent stability requirements imposed by Doppler wind measurements, the thermo-elastic behaviour of the PLH is a key design driver. Thermally induced deformations can affect optical alignment, pointing stability and laser performance, making thermo-elastic verification a fundamental activity from the earliest project phases. Consequently, the PLH Preliminary Design Review represented an important milestone for demonstrating compliance with optical stability requirements and for validating the thermo-elastic verification methodologies implemented within the development programme.

2. USE OF PYSINAS

The complexity and performance requirements of the PLH unit demand robust and traceable thermoelastic verification methodologies from the earliest project phases. While hardware testing remains a cornerstone of the ECSS verification approach, its application during preliminary design stages is inherently limited by hardware availability, cost and schedule constraints. Consequently, simulation-based engineering plays a key role in supporting design verification through the assessment of thermo-mechanical behaviour under representative operational and environmental conditions. High-fidelity modelling enables efficient evaluation of thermoelastic performance, facilitates design iterations and contributes to the reduction of technical risk prior to qualification testing.
In this context, pySinas enables seamless transitions between thermal and structural models, which are typically developed using different software tools and data structures that do not readily communicate with each other. This capability ensures effective integration within existing engineering toolchains and supports a consistent transfer of thermal loads for thermoelastic analyses. Furthermore, dedicated thermoelastic test campaigns are generally resource-intensive, requiring specialized facilities, extensive instrumentation and significant preparation time. As a result, their execution is often incompatible with the development schedules and rapid design iterations required during the early phases of a space project, further reinforcing the importance of predictive simulation-based verification approaches.

2.1. Thermo-elastic Testing Considerations

Thermo-elastic testing is mentioned within the ECSS-E-HB-32-26A [6] and described in STM-285 Iss.2 as an important element of the thermo-elastic verification process, providing experimental evidence for model validation and verification of thermoelastic performance under representative thermal environments. The guideline describes a comprehensive testing framework, including dedicated model validation activities, controlled thermal boundary conditions and advanced measurement techniques such as strain gauges, Fibre Bragg Gratings, laser trackers, photogrammetry, Digital Image Correlation, interferometry and wavefront sensing systems.
However, despite their recognized value within the verification process, thermo-elastic tests remain challenging to implement in the development of modern space products. Dedicated test campaigns typically require specialized facilities, sophisticated metrology equipment, extensive preparation efforts and significant engineering resources. Consequently, they often entail substantial costs and long execution times, making their application difficult to reconcile with the increasingly constrained development schedules and rapid design iterations characteristic of current space programmes. For this reason, thermo-elastic testing is nowadays generally reserved for selected critical activities, while high-fidelity simulation and model-based verification approaches play an increasingly important role throughout the design and verification process.

3. THERMO-ELASTIC VERIFICATION FLOW

The Thermo-Elastic Verification workflow is structured into four main phases:

1. Identification;
2. Modelling;
3. Analysis;
4. Final Compliance Verification.

The process combines thermal, structural and performance analyses within a single workflow, enabling the prediction and verification of thermoelastic effects throughout the project lifecycle.

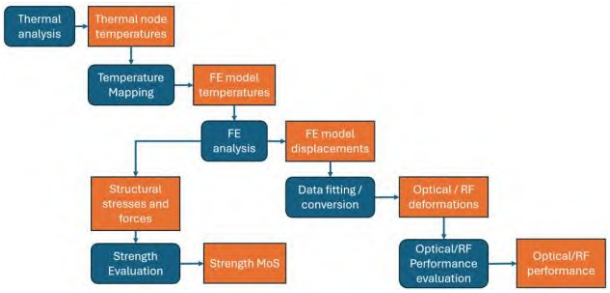


Figure 3-1: Overview of all the analysis and data conversion steps involved in the TEV process.

3.1. Identification Phase

The identification phase aims at defining the thermoelastic phenomena that can affect system performance. Starting from mission and instrument requirements, the performance parameters have to be identified to be monitored, such as relative displacements, rotations, line-of-sight variations, surface form errors, or thermo-mechanical loads. For each performance parameter, the underlying

deformation mechanisms are identified. These mechanisms originate from the interaction between temperature distributions, material thermal expansion properties and the structural constraint conditions. The outcome of this phase is a clear understanding of which thermoelastic effects must be represented by the analysis models and subsequently verified during the development process.

3.1.1.PLH performance parameters

Two types of thermoelastic performances are relevant for the PLH structural verification: strength and optical performance.
For the verification of the strength performance, stress distributions in all components and interface loads between the optical bench and its attached equipment were needed to be computed and evaluated in terms of margins of safety against the material allowable. For the optical performance analysis, displacements and rotations of the optical elements' centres were derived with the structural model and then post-processed by the Optical Geometrical Model (OGM) to assess the PLH Line of Sight stability (LoS) stability performance under thermoelastic loads. The OGM is not described in detail in this paper, as it falls outside the scope of the thermoelastic activities presented herein. A comprehensive description of the optical modelling approach and its implementation would deserve dedicated treatment in a separate publication.

3.2.Modelling Phase

Once the critical deformation mechanisms have been identified, dedicated thermal and structural models are developed.

3.2.1.Thermal Model

The thermal model, typically based on a TMM/GMM approach [7], must accurately represent the thermal behaviour of the hardware, including local and global temperature gradients relevant to thermoelastic performance. In essence the thermal model must be able to produce temperature fields that can excite the deformation mechanisms that were identified to be relevant for the performances. A detailed description of the PLH Thermal Model is provided in the section §4.

3.2.2.Structural Model

The structural model is developed such allowing the temperature fields to excite the identified deformation mechanisms and predict the resulting displacements, rotations and stresses. The FEM [8] must provide an adequate representation of stiffness distributions, interfaces and boundary conditions.
A detailed description of the PLH Structural Model is provided in the sections §5.

3.3.Analysis Phase

The space-unit development often generates thousands of thermal environments, making a full thermoelastic assessment of every temperature field impractical. For this reason, the TEV process includes a dedicated screening activity aimed at identifying the thermal conditions producing the most severe structural deformations, optical misalignments, pointing errors or thermo-mechanical stresses. As regards the AE2 PLH optical stability, the following loading conditions were selected:

- For LT optical stability, the hot and cold operative worst case scenario, in terms of thermal excursion, was considered.
- For MT optical stability, the effects of temperature variations at the PLH conductive interfaces schematized in Figure 3-2 were evaluated.

Non-operative hot and cold conditions were also analysed for thermo-mechanical stress verification.

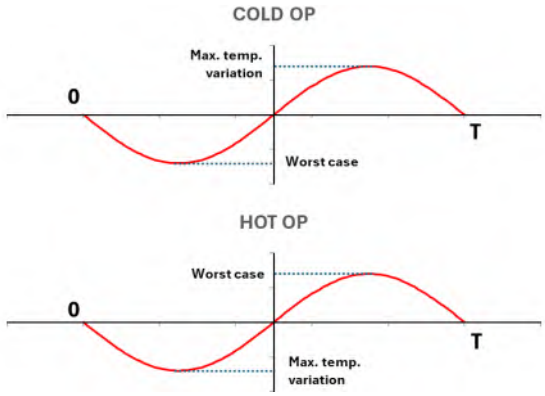


Figure 3-2: Cold/Hot operating temperature variation.

To reduce computational effort, the guidelines recommend the use of accelerated techniques such as Thermo-Elastic Transfer Matrices (TETMs), Performance Transfer Matrices and similarity criteria for displacement fields. These methods allow a rapid ranking of candidate cases and the identification of the worst thermoelastic scenarios with limited execution time.
In this paper, the transient MT COLD OP environment is taken into account and results are obtained using both pySinas and TEV.

3.4.Final Compliance Verification

After worst-cases selection, the models are used for the formal verification of thermoelastic requirements. The final assessment includes the evaluation of structural margins, performance budgets and modelling uncertainties, together with the generation of the required verification documentation. The resulting evidence provides full traceability from the thermal environment definition to the demonstration of compliance with system performance requirements.

4. PLH THERMAL MODEL DESCRIPTION

The thermal model of the AE2 PLH was derived by updating and refining the one developed during the AFO design phase. AFO is the Aeolus Follow-On, namely the pre-development phase of Aeolus-2. For contractual reasons, LDO, that was contract responsible, assigned the thermal modelling activities to ADS, which developed the thermal models in Thermica-Systema software. Once the Aeolus-2 contract was launched and LDO began developing the models internally for the PDR, these were subsequently converted into ESATAN-TMS 2024 software, where new items were added or improved in the details, for example the presence of heaters commanded by a PID logic.

The sub-components for which the temperature field variations were assessed to have a negligible impact on structural deformation were represented using one or a limited number of nodes. Components identified as having a significant influence on the overall deformation mechanisms were modelled with a refined representation using multiple nodes. Example of such components are the optical bench, where geometry may induce temperature variations, or the parallelepiped crystals and laser diodes, where material properties or high-power dissipation are the driving factors. This approach provides an accurate temperature distribution, which is also essential for thermo-elastic evaluation.

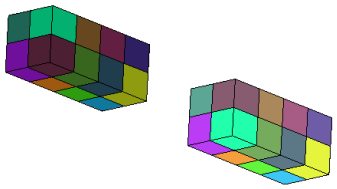


Figure 4-1: Parallelepiped crystals GMM.

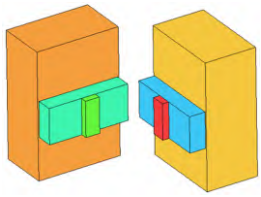


Figure 4-2: Laser diods GMM.

A total of 2201 nodes defines the AE2 PLH thermal model. The Figure 4-3 respectively shows the inside upper and lower view of the AE2 PLH GMM.

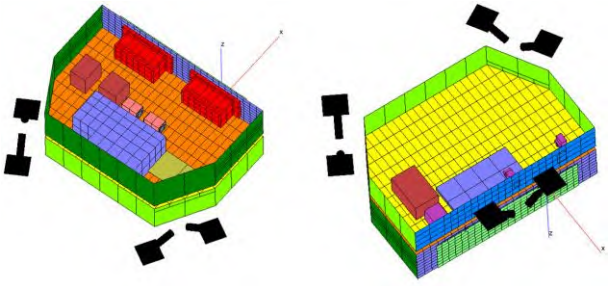


Figure 4-3: PLH GMM internal views.

5. PLH STRUCTURAL MODEL

The Finite Element Model of the PLH was developed with a level of detail sufficient to ensure a reasonable accuracy in the prediction of the dynamic and thermos-elastic response. All subcomponents were modelled in detail to account for the different materials and geometries used in each part, allowing an accurate evaluation of the deformations and then the LoS deviation. The FE Model was primarily built using CHEXA8 and CPENTA6 solid elements, as well as CQUAD4 and CTRIA3 shell elements, since this modelling approach ensures higher numerical accuracy, more stable stiffness characteristics and better mesh quality control compared with tetrahedral elements. A total of 1320855 nodes defines the AE2 PLH FE Model. The Figure 5-1 and Figure 5-2 show the inside upper and lower view of the AE2 PLH structural model compared with the CAD one.

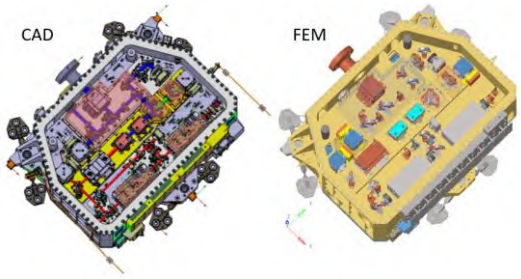


Figure 5-1: CAD vs FE Model of upper PLH view.

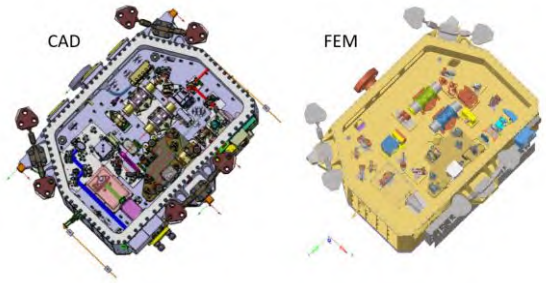


Figure 5-2: CAD vs FE Model of bottom PLH view.

Rigid RBE2 elements were employed, together with CBUSH elements, to represent the bolted connections and to extract the interface forces.

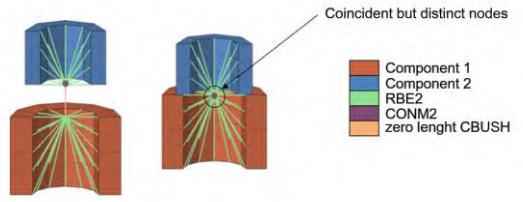


Figure 5-3: FE bolted connection schematization.

This modelling approach is commonly adopted in the spaceborne domain and is effective for dynamic analysis; however, thermal map generation requires specific adaptations and the creation of what is typically referred to as a conductive model. RBE2

and CBUSH elements do not transmit heat, meaning that the FE structural model, although directly usable for thermo-elastic analyses, cannot be used for thermal diffusion. In particular, the temperature fields obtained from the thermal model, which features a much coarser nodal discretization than the FEM, cannot be directly mapped onto a structural mesh built with rigid and CBUSH spring elements. The implementations proposed by LDO to the thermoelastic support on several pySinas commands simplify this process, with the goal of managing the transfer of thermal maps from the thermal model to the structural one directly through the structural FEM alone. This avoids the need to generate a second model, the conductive one.
For the AE2 PLH performance assessment, the restitution requires extracting the displacements and rotations of the optical components. This was accomplished by employing RBE3 elements. The dependent node of the RBE3, defined in a local reference system, represents the optical component without altering the stiffness of the underlying structure. An example of this modelling approach is shown in Figure 5-4 below.

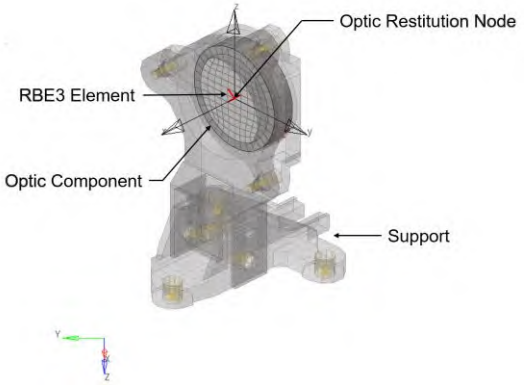


Figure 5-4: Example of RBE3 and local reference system for LoS dispacements/rotations recovery.

6. TEMPERATURE MAPPING

As a matter of fact, the thermoelastic analyses have always been subjected to a high level of uncertainty, basically due to the difficulty in transferring ESATAN temperatures to FEM. The difficulty is caused by two principal aspects:

- Software for thermal analyses such as ESATAN are based on thermal lumped parameters method, while the structural model is based on the finite element method;
- The level of detail is extremely different between FEM and thermal model.

The level of accuracy given by classic temperature mapping procedures are not acceptable for PLH, which needs an extremely precise and stable optical alignment to meet its optical performance.
For this reason, the PAT based temperature mapping process has been used through pySinas for the thermoelastic verification.

6.1. pySinas temperatures mapping step-by-step procedure

A scheme of the temperatures mapping step-by-step procedure used to generate the PLH temperature maps in operative and not operative conditions is reported hereafter.

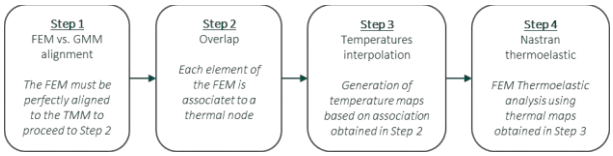


Figure 6-1: Step-by-step procedure for thermo-elastic evaluations using pySinas.

A brief description and results are also provided in the following sections.

6.1.1. FEM vs. TMM alignment

First step of the procedure is the FEM and GMM alignment, that is essential to obtain a good temperature mapping. To simplify this step, pySinas provides the *'steptas_to_patran'* routine which allows to convert the GMM in *.ses* format, compatible with Patran. In this way, FEM and GMM can be viewed into the same software (see Figure 6-2) for an easier alignment check of the two models. A check of the differences between the two models can be also performed.

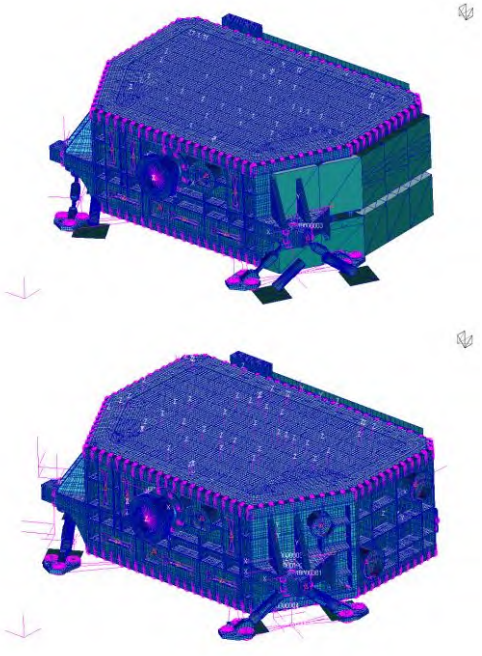


Figure 6-2: FEM and GMM visive check before (top) and after (bottom) alignment.

As showed in figure, the two models were not perfectly aligned and the following translations were necessary:

- FEM to TLP Y alignment: -0.0456 m
- FEM to TLP Z alignment: -0.0215 m

This operation does not require physically moving the two models; it can be performed directly in file *ovlsettings.json* by using the task *'fem_to_tlp_alignment'*, resulting in a significant time saving.

```
"fem_to_tlp_alignment": {
    "A": [ 0.0, -0.0456, -0.0215 ],
    "B": [ 0.0, -0.0456, 0.9785 ],
    "C": [ 1.0, -0.0456, -0.0215 ]
},
```

Figure 6-3: Example using task 'fem_to_tlp_alignment'.

6.1.2. Overlap

Next step is the overlap between thermal nodes and structural elements. The implemented method is the minimum distance one and determines for each element the closest thermal node. This step can be handled by pySinas *'overlap'* routine with an extremely time-saving especially for large size models as per AE2 PLH. Some "groups" of thermal nodes and FEM elements were defined, together with the max_distance parameter, which specifies the maximum distance for FEM elements association.
The AE2 PLH groups definition is reported in Figure 6-4 for the internal components while in Figure 6-5 for the PLH Optical Bench faces.

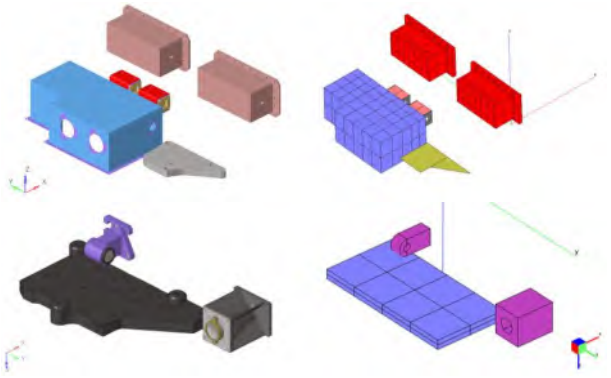


Figure 6-4: Example of internal components with maximum distance tolerances of 0.01 m.

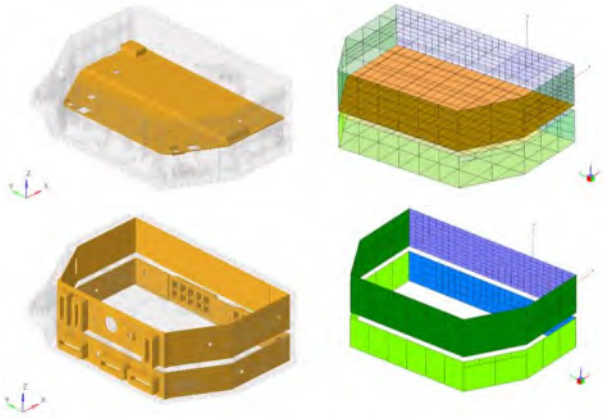


Figure 6-5: Example of PLH Optical Bench faces with maximum distance tolerances of 0.03 m.

The overlap routine provided a perfect FEM to GMM matching on almost all the groups. Just for the smallest and most detailed subassemblies a manual association was necessary. In this context, LDO developed routines to manage and organise the various groups directly within Altair preprocessing software, HyperMesh, ensuring proper graphical handling when the automatic assignment process fails to correctly overlap entities due to the required level of detail. A couple of examples are shown below, referring to parallelepiped crystals (see Figure 4-1 and Figure 6-6) and to the laser diode (see Figure 4-2 and Figure 6-7), both of which require a high degree of accuracy to meet performance requirements.

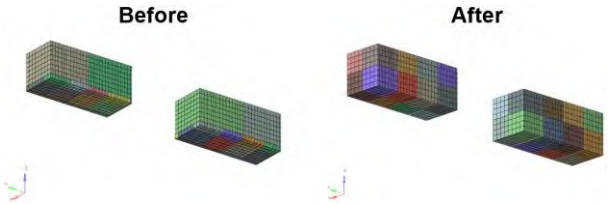


Figure 6-6: Example of groups adjusment for parallelepiped crystals.

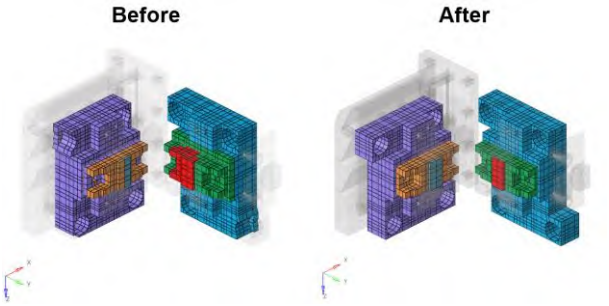


Figure 6-7: Example of groups adjusment for LDs.

By using the task *'overlap_colour_coding'* that assigns different colours to the different sets of elements corresponding to a thermal node, a quick visual check of the overlap relations can be obtained. Currently the colour coding visualisation is only supported on Patran, but LDO developed an internal routine to manage it in HyperMesh. The result for the AE2 PLH overlap is reported in the following figures.

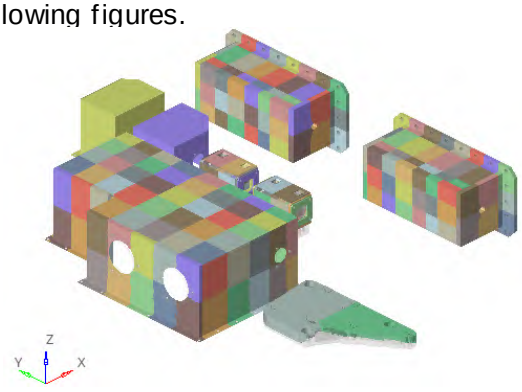


Figure 6-8: PLH internal Upper side components overlap_colour_coding.

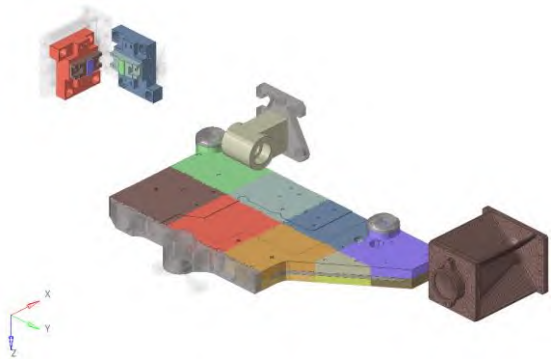


Figure 6-9: PLH internal Lower side components overlap_colour_coding.

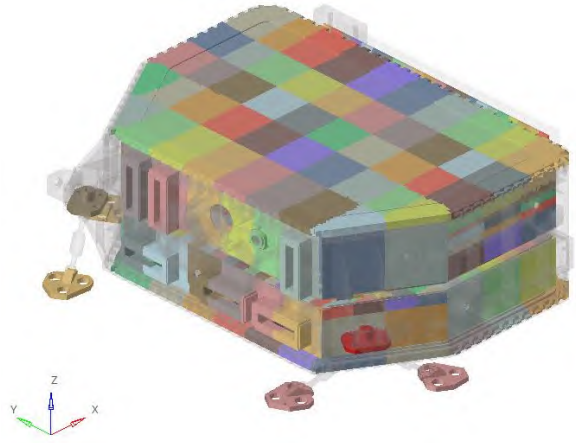


Figure 6-10: PLH external faces overlap_colour_coding.

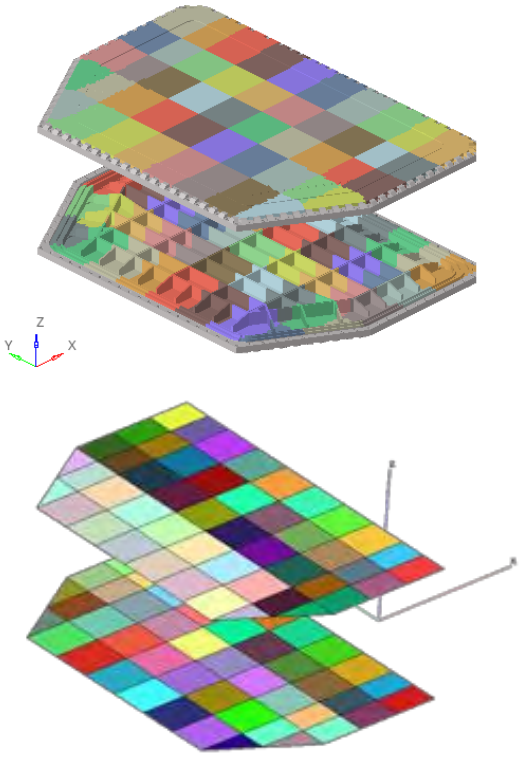


Figure 6-11: PLH covers 'overlap_colour_coding' compared with ESATAN model.

6.1.3. Temperature mapping

Last step is the temperature mapping, handled by the task *'allinone'* pySinas task. The code uses the so-called Prescribed Average Temperature (PAT) method [9] to transfer the ESATAN temperatures to an FE model. The result is an extremely precise temperature map like that showed in figures below. These results are then used as thermoelastic load cases.

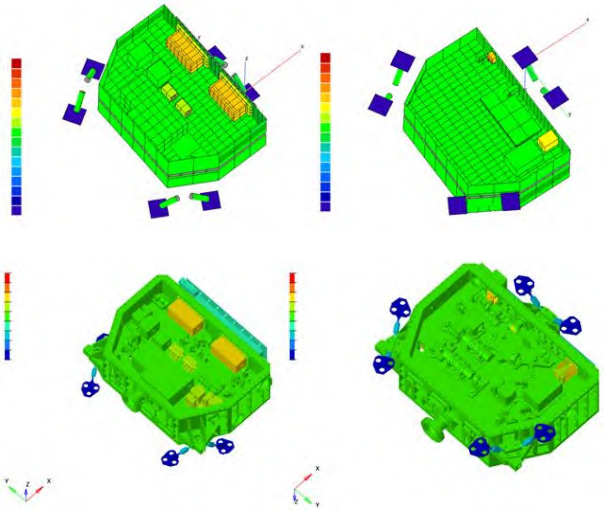


Figure 6-12: AE2 PLH cold case themal map comparison between thermal and structural model.

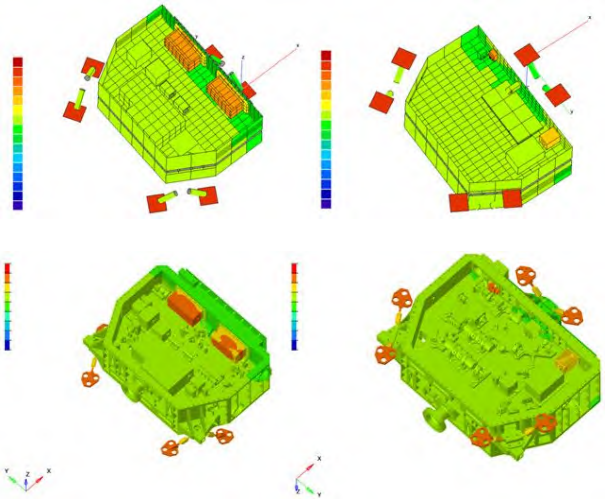


Figure 6-13: AE2 PLH hot case themal map comparison between thermal and structural model.

6.2.Thermo-Elastic Analysis

Subsequently the thermoelastic analyses have been performed using the temperature map previously obtained as the target temperature starting from a fixed initial temperature for the entire model. Stress distributions and interface loads have been obtained for the strength analysis whereas displacements and rotations of the optical elements' centres were derived for the performance analysis.

7. TEV

The performance evaluations are usually extremely time-consuming for the large number of potentially relevant cases and the large amount of data to be analysed. Purpose of the TEV tool is to implement an automated and extremely time-saving procedure that allow users to process a great amount of data with small computational costs. This procedure is based on Thermo-Elastic Transfer Matrix (TETM) evaluation for FEM reduction. The TEV thermoelastic step-by-step procedure is schematized hereafter.

As showed in the following scheme, the first two steps are in common with pySinas. The other two steps are briefly described in the following sections

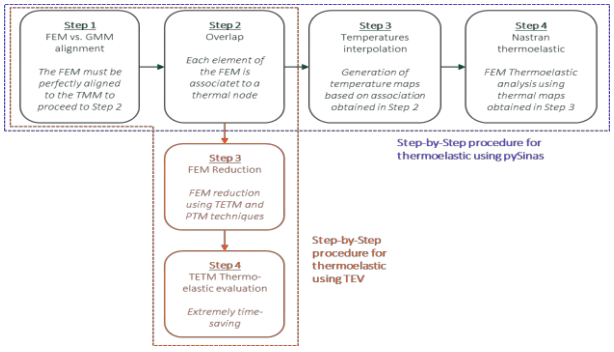


Figure 7-1: Step-by-step procedure for thermo-elastic evaluations using TEV.

7.1. Temperature Mapping Reduction

To improve the computational efficiency the thermal mapping reduction methodology can be used. First, the Temperature Transfer Matrix (TTM) must be generated using the *ttm_gen* routine. This rectangular matrix is defined according to the following formula:

$$\{T_s\} = [M_T]\{T_t\}$$

Where $\{T_s\}$ is the vector of the mapped temperature field on the structural FE model, $[M_T]$ is the TTM matrix and $\{T_t\}$ is the vector of the thermal model temperature field.

Then, the Thermo-Elastic Transfer Matrix (TETM) is generated by evaluating each thermal node's contribution to thermoelastic deformation. The TETM is defined by the following formula:

$$\{u\} = [M_{TE}]\{\Delta T_t\}$$

Where $\{u\}$ is the FE displacements vector, the $[M_{TE}]$ is the TETM where the columns are the thermo-elastic responses due to a unit temperature increase of a thermal node and $\{\Delta T_t\}$ the vector of the thermal model temperature field. This procedure might take some hours, but the result is a reduced thermoelastic model that gives a direct link between thermal model and thermos-elastic responses. This allows users to process thousands of load-cases in a bunch of minutes, leading to extremely precise performance evaluations.

7.2. TETM thermoelastic evaluations

Once the TETM is obtained, the ESATAN TTM results can be used to evaluate the TE response on the chosen recovery nodes. The AE2 PLH variational cold case, showed in Figure 3-2, has been analysed and some results are reported below.

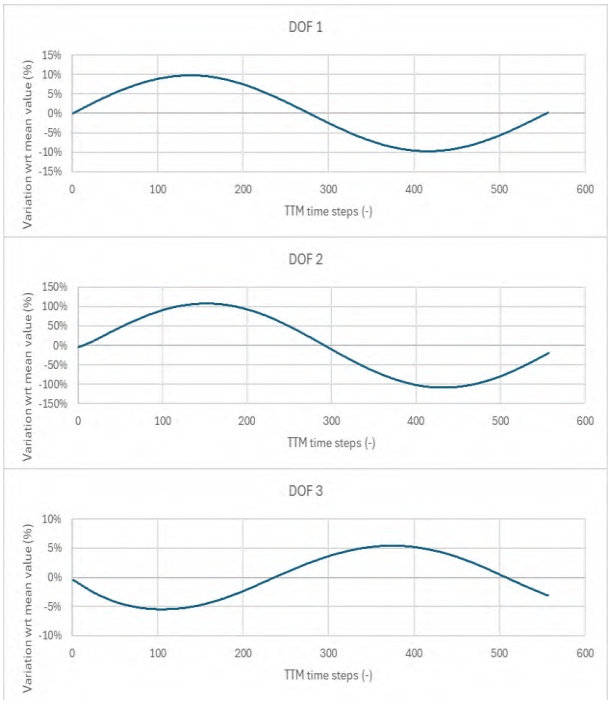


Figure 7-2: Variation of translational DoFs under COLD OP temperature variation.

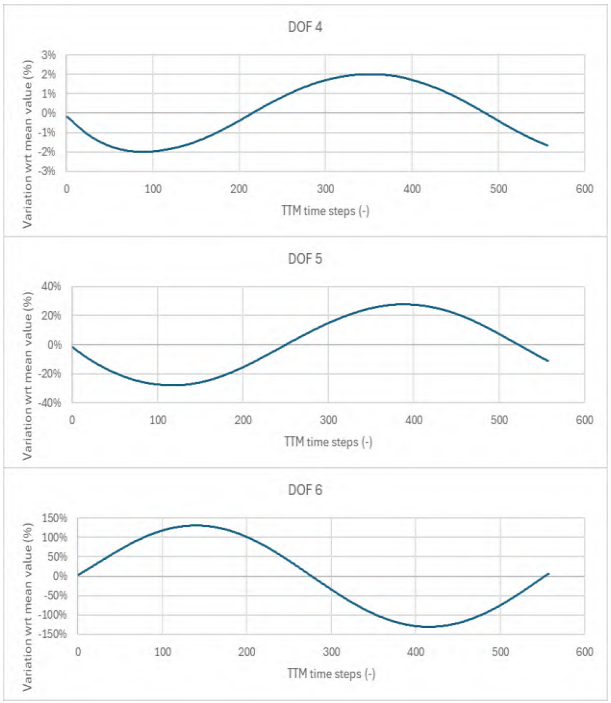


Figure 7-3: Variation of rotational DoFs under COLD OP temperature variation.

The contribution of different groups of thermal nodes can be also extrapolated. An example is provided in the next page.

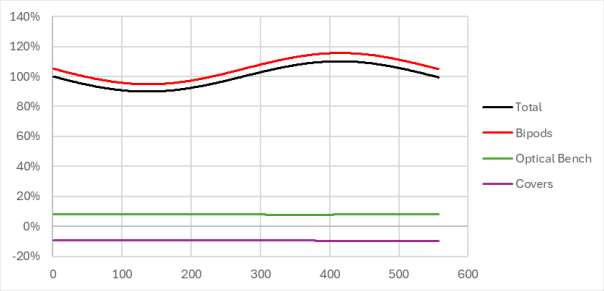


Figure 7-4: Bipods, OB and Covers contribution to the total deformation.

In this case, the main contribution to the total displacement (black line) is given by the bipods' deformation.

8. CONCLUSION

The thermo-elastic assessment performed for the Aeolus-2 Power Laser Head during the Preliminary Design Review phase demonstrated the applicability of a PAT-based temperature mapping approach implemented through pySinas. The methodology enabled a consistent transfer of thermal results from the GMM/TMM to the structural FEM, reducing numerical inaccuracies commonly associated with manual mapping techniques and improving the reliability of the predicted thermo-mechanical response.

To optimise the workflow, the LDO team developed several routines to refine the definition of groups and facilitate overlapping in cases where the *'max_distance'* parameter could not correctly assign group membership due to the required level of detail. LDO also provided comments and suggestions to streamline the use of the '*allinone*' task for the thermal-mapping, aiming to rely on a single FEM model and avoid the need to generate a dedicated conductive model.

Once the adequacy of the pySinas implemented thermal-mapping method was confirmed, the assessment moved to the systematic identification and ranking of thermo-elastic worst cases. In this phase, the TEV tool greatly facilitated the process by using optical displacements and rotations, parameters directly affecting the Line-of-Sight, as key indicators for determining the performance of an opto-mechanical payload.

This work represents an important milestone in the maturation of thermo-elastic verification processes for space applications. It demonstrates the feasibility of implementing advanced temperature-mapping techniques within an institutional and industrial development programme [10]. Furthermore, it represents a preview of the upcoming publication of the STM-285 European Guidelines for Thermo-Elastic Verification, Issue 2, which will provide a clear and rigorous framework for temperature modelling and mapping, as well as for the verification logic applied to thermoelastic verification.

9. NEXT STEPS

The next step towards a more efficient process is the implementation of an automated multidisciplinary workflow driven by a dedicated orchestration layer. In this context, HyperStudy, an Altair suite software, now integrated into Siemens, has been identified as a potential candidate to act as the workflow orchestrator, ensuring the seamless execution and data exchange between the thermal, structural and optical domains, typically originating from different software environments.

The envisioned workflow starts with the thermal mapping activity performed through pySinas, which transfers the temperature field from the thermal model to the structural Finite Element Model. The mapped temperatures are then used to automatically generate and execute the NASTRAN thermo-elastic analysis for the selected TEV case, producing the displacement and rotation outputs required for downstream performance assessments. Subsequently, these results are converted into a format compatible with Zemax, where the thermo-elastic displacements and rotations of the optical elements are applied to the optical model. Zemax then evaluates the resulting optical performance and the Line-of-Sight variation induced by the thermo-mechanical distortions of the payload.

By automating the execution chain from thermal mapping to optical performance assessment, the orchestrator would guarantee consistency, traceability and repeatability across all analysed cases while significantly reducing manual effort. Furthermore, such a framework would provide a solid foundation for future sensitivity analyses, design optimization activities and large-scale thermo-elastic verification campaigns.

10. ACKNOWLEDGEMENT

The authors would like to emphasise the contribution of the LDO team in developing a robust laser transmitter that will support climate monitoring and atmospheric science by enhancing weather-prediction capabilities in the next Aeolus-2 mission.

In addition, the LDO team's expertise in modelling, preprocessing and thermoelastic data preparation was essential to this work.

Appreciation is extended to the ADS team for their system-wide coordination and continuous technical support, as well as to ESA for their constructive reviews and for fostering harmonised practices within the thermoelastic domain.

The authors also wish to thank the thermoelastic community, together with the various working groups, for the shared experience and exchange of best practices that significantly shaped the methodology adopted for the thermoelastic verification of the AE2 PLH in the PDR phase.

11. ABBREVIATIONS AND ACRONYMS

ADS	Airbus Defense and Space
AFO	Aeolus Follow-On
AE2	Aeolus-2
ALADIN	Atmospheric Laser Doppler Instrument
ATLID	ATmospheric LIDar
CBUSH	Generalized Spring-and-Damper Connection
CHEXA	Six-Sided Solid Element Connection
CPENTA	Five-Sided Solid Element Connection
CQUAD4	Quadrilateral Plate Element Connection
CTRIA3	Triangular Plate Element Connection
DWL	Doppler Wind LIDAR
EarthCARE	Earth Clouds, Aerosols and Radiation Explorer
ESA	European Space Agency
ESATAN	ESA Thermal ANalysis
EUMETSAT	EUropean organisation for the exploitation of METeorological SATellites
FEM	Finite Element Model
GMM	Geometrical Mathematical Model
LD	Laser Diode
LDO	Leonardo S.p.a.
LIDAR	LIght Detection And Ranging
LoS	Line of Sight
NASTRAN	NASA STRuctural ANalysis
OGM	Opto-Geometrical Model
PAT	Prescribed Average Temperature
PDR	Preliminary Design Review
PLH	Power Laser Head
pySinas	Pyton based SINAS (SINDA and ASKA)
RBE2	Rigid Body Element, Form 2
RBE3	Interpolation Constraint Element
STM	Scientific and Technical Memoranda
TETM	Thermo-Elastic Transfer Matrix
TEV	Thermo-Elastic Verification
TLP	Thermal Lumped Parameter
TMM	Thermal Mathematical Model
TMS	Thermal Modelling Suite

12. REFERENCES

1. STM-285 European Guidelines for Thermo-Elastic Verification https://esamultimedia.esa.int/multimedia/publications/STM-285/STM-285.pdf
2. Berceau, P., Albano, C., Ballester, M., Belhadj, T., Bellouard, R., Bon, D., et al., “Aeolus-2 instrument: the new Doppler wind LIDAR", Proceedings of SPIE, Vol. 13699, https://doi.org/10.1117/12.3072768
3. Reitebuch, O. et al., “Challenges and achievements of ESA’s Aeolus mission”, Proceedings of SPIE, Vol. 13699, https://doi.org/10.1117/12.3072760
4. Hélière, A., Gelsthorpe, R., Le Hors, L., et al., "ATLID, the atmospheric lidar on board the Earthcare Satellite”, Proceedings of SPIE, Vol. 10564, https://doi.org/10.1117/12.2309095
5. Hélière, A., Wernham, D., Mason G., et al., “AEOLUS-2 mission pre-development status" Proceedings of SPIE, Vol. 11858, https://doi.org/10.1117/12.2599797
6. ECSS-E-HB-32-26A: Spacecraft mechanical loads analysis handbook (19 February 2013) ECSS-E-HB-32-26A: Spacecraft mechanical loads analysis handbook (19 February 2013) | European Cooperation for Space Standardization
7. ECSS-E-ST-31C: Thermal control (15 November 2008) ECSS-E-ST-31C – Thermal control (15 November 2008) | European Cooperation for Space Standardization
8. ECSS-E-ST-32-03C: Space engineering Structural finite element models (31 July 2018) ECSS-E-ST-32-03C – Structural finite element models (31 July 2008) | European Cooperation for Space Standardization
9. Appel S., Wijker J., “Simulation of Thermoelastic Behaviour of Spacecraft” Springer International Publishing (2022), https://doi.org/10.1007/978-3-030-78999-2_8
10. Landi, G., Appel, S., “Industrial Application of pysinas to Transit Temperatures from Thermal to Structural Model” ECSSMET 2024

A Sensitivity-Driven Thermoelastic Methodology for Robust Assessment of Payload Distortions in Satellite Structures

Gabriele Muto [(1)], Alexander Ihle [(2)], Daniele Cardinali [(1)], Pietro Nali [(1)], Rocco Raffaele Trento [(1)], Amedeo Giancarlo Tenore [(1)]

(1) Thales Alenia Space Italia, 00131 Rome, Italy, Email: gabriele.muto@thalesaleniaspace.com
(2) European Space Agency, 2200 AG Noordwijk, The Netherlands, Email: alexander.Ihle@esa.int

KEYWORDS

thermoelastic analysis, thermal sensitivity, temperature gradients, CTE variability, structural distortions, satellite payload

ABSTRACT

This paper presents a thermoelastic analysis methodology to support the design and analysis of satellite structures, aiming to reduce distortions that may degrade payload performance while accounting for model and material uncertainties. The approach has been implemented within the framework of the European Union's and European Space Agency - ESA's Copernicus Radar Observing System for Europe at L-band (ROSE-L mission), focusing on the identification of key drivers of thermoelastic distortions. The proposed methodology introduces the early-stage integration of uncertainties associated with temperature mapping and material coefficients of thermal expansion (CTE), enabling a more robust structural design process. This represents a shift from traditional deterministic approaches toward a sensitivity-driven framework supporting design trade-offs and material selection, and allowing the assessment of the robustness of the predicted distortions with respect to thermal and material variability. The thermoelastic mapping procedure applied to the ROSE-L finite element model is based on temperature fields derived from ESATAN thermal analyses, which are mapped onto the structural mesh through a HyperMesh-based geometrical interpolation process. A dedicated sensitivity analysis is then performed, focusing on two main parameters:

- scaling of temperature distributions to simulate variations in thermal gradients;
- dispersion of material CTE properties.

The resulting distortions, evaluated at payload level (SAR antenna), are used as quantitative indicators to assess the influence of thermal uncertainties and the robustness of the structural response. The methodology enables the identification of the most critical contributors to thermoelastic deformation[4,6,8] and supports the definition of design margins consistent with mission requirements.
The proposed approach provides a practical and scalable tool for preliminary and early detailed design phases, enhancing the capability to control thermoelastic distortions under realistic operational conditions and increasing confidence in payload performance through a more robust characterization of uncertainty effects.

1. INTRODUCTION

In satellite platform design, in-orbit thermoelastic deformations can critically affect payload performance by inducing misalignments, optical aberrations, and pointing errors [1,2]. Therefore, integrating detailed thermoelastic distortion assessments during the initial design phases is essential to mitigate risks and optimize system robustness. Early-stage evaluation not only informs material selection and mechanical architecture but also guides design strategies aimed at minimizing thermoelastic-induced distortion and ensuring operational stability under varying thermal environments.
The primary drivers of thermoelastic deformation include the spatial temperature distribution and the coefficient of thermal expansion (CTE) of the structural materials[5,7,9]. Thermo-mechanical coupling necessitates accurate thermal modeling to capture transient thermal gradients and steady-state conditions that influence structural behavior. Temperature boundary conditions, typically sourced from high-fidelity thermal simulations such as ESATAN, enable precise loading input for finite element thermoelastic analyses [3,10]. These analyses reveal how thermal gradients translate into distortions affecting critical interfaces and payload alignment.
Given the inherent uncertainties in thermal loading due to orbital dynamics, varying solar flux, Earth infrared radiation, and internal heat dissipation, it is imperative to perform robust thermal sensitivity studies. These studies assess the impact of temperature variations and gradient fluctuations on structural deformation, thus fostering design resilience.
Furthermore, material property variability particularly in composite structures where manufacturing-induced heterogeneity leads to CTE anisotropy and dispersion—plays a significant role in thermoelastic response. Sensitivity analyses

focused on CTE not only characterize the range of possible distortions but also support material qualification and acceptance criteria when experimental data is limited or unavailable.
Integrating multidisciplinary optimization that couples thermal, structural, and optical performance analyses early in the design cycle enables more comprehensive mitigation strategies. This holistic approach ultimately enhances the satellite platform's ability to maintain payload alignment and ensures mission success despite the demanding in-orbit thermal environment.

2. THERMOELASTIC AND DISTORSIONS MATHEMATICAL FORMULATION

This work presents a thermoelastic modelling and pointing-evaluation workflow consistent with a discrete finite element (FE) formulation and suitable for satellite payload alignment assessment. Starting from the fundamental thermoelastic constitutive relations in a FE setting, the strain state is expressed as the superposition of an elastic stress contribution and a thermal expansion contribution, i.e.,

$$\{\varepsilon\} = [\ D\ ]^{-1}\{\sigma\} + \{\alpha\}\,\Delta T \qquad (1)$$

Where ε denotes the strain vector, D the elastic stiffness matrix, σ the stress vector, α the CTE vector and ΔT temperature difference wrt the reference.
The subsequent strain/displacement field is obtained by solving the full FE thermoelastic problem under thermal loads using Nastran, yielding the complete deformation response of the structural model.
To evaluate the pointing error from FE analysis, a method has been defined which allows to directly obtaining the overall distortion information on the SAR Antenna.
The method consists in defining a SAR Antenna IF central node in which retrieve directly the output rotation.
This node is defined in the geometric center of the eight brackets, and then a RBE3 element is defined connecting this central node (dependent node) to all the eight brackets central nodes (independent nodes).
The Nastran RBE3 elements formulation for the rotation vector u can be expressed by the following formula:

$$u_{dep}^{i} = \frac{\sum_{j=1}^{n} W_j u_j^i}{N} \qquad (2)$$

Where:

- u_{dep}^{i} is the i^{th} rotational component (4,5,6) of the dependent node (defined central node of the antenna).
- W_j is the weighting factor associated to the j^{th} payload interface.
- u_j^i is the i^{th} rotational component of the j^{th} indipendent node (one reference node for each interface bracket).
- N is the number of interfaces
- i index going from 4 to 6.
- j index going from 1 to N.

Regarding the RBE3 defined:

- The DOF specified when defining the RBE3 are the Nastran rotation DOF for each bracket central node (components 4,5,6).
- The weighting factors specified when defining the RBE3 are 1.0 for each brackets central node.

This modeling allows the estimation of the average equivalent interface motion, obtained by weighted kinematic interpolation of RBE3 element, with which is possible to obtain directly the global distortion of the payload (components 4,5,6 of the SAR central node).

The distortion angles are defined as follows:

α: Roll (Rotation around X Axis)
β: Pitch (Rotation around Z Axis)
γ: Yaw (Rotation around Y Axis)

The advantage of this method is that the Roll, Pitch and Yaw angles are directly outputted form Nastran analysis and does not need any post process activity: in fact the distortion angles obtained are evaluated wrt the undeformed (no thermal loads applied) configuration, which is taken as reference.

3. FE MODELING, THERMAL MAPPING AND PARAMETERS DEFINITION

To perform these analysis campaign classical commercial softwares for mechanical analysis such as MSC Nastran and Hypermesh has been used.
The satellite platform FE Model has been integrated with the static reduced model of the SAR antenna in deployed configuration to have a proper boundary condition on the SAR brackets, which are the main output for TED analysis.
Being a reduced model no thermal maps have been created for SAR but the use of this model is crucial to properly represent the stiffnesses of the interface between the antenna and the S/C Brackets; a graphic representation of this model is reported in Figure 3.1.

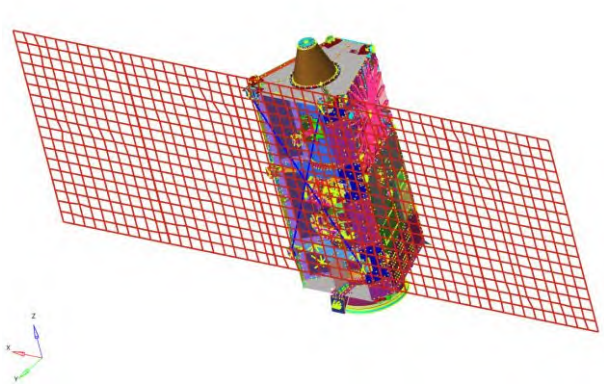


Figure 3.1 ROSE-L Deployed FE Model

The analysis was performed in two different stages

- Hypermesh: the Hypermesh interpolation capability has been used to generate the thermal maps on the nodes of the structure. Starting from the temperature and the geometric coordinate of the Esatan thermal nodes. The linear interpolation tool present in Hypermesh has been used.
  The Hypermesh interpolation process gives very accurate thermal mapping on the platform FE Model, an example of the accuracy is reported in the Figure 3.2 and 3.3

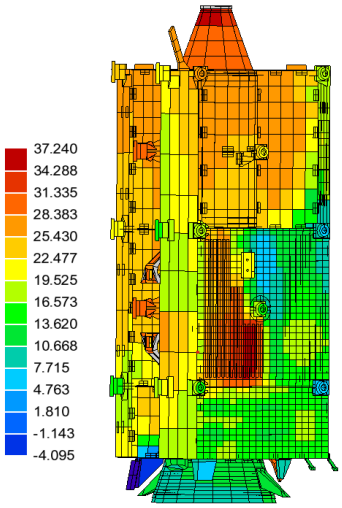


Figure 3.2 Esatan Reference Case Results

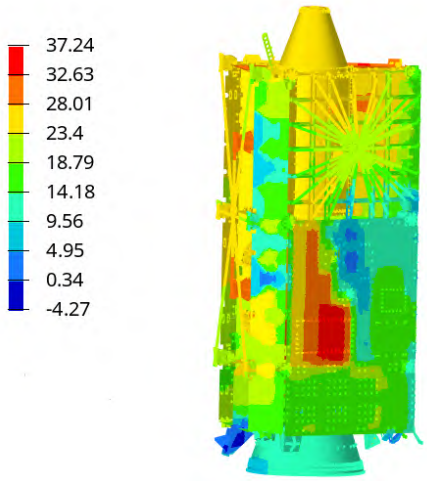


Figure 3.3 Hypermesh interpolation Reference Results

- Nastran: the TEMP card obtained from Hypermesh interpolation has been used as thermal loading condition for TED.
  Nastran SOL 101 static analysis has been performed. PARAM,INREL,-2 has been used for inertia relief that allow to run unconstrained static analysis to match orbital condition.
  Reduced static model of SAR in deployed configuration has been included in Nastran input file.
  For each thermal case the full orbit has been considered, so a thermal map for each instant taken into account has been created.

4. SENSITIVITY ANALYSIS RESULTS

For ROSE-L TED Analysis campaign a reference thermal case has been considered, which was the one giving as output the worst distortion on the antenna.
Two different sensitivity analysis has been performed:

- Thermal gradients variation.
- Carbon fiber CTE variation.

From this analysis the result in terms of angular distortion of the SAR antenna are compared to understand the effect of this parameters variation and the range of variation of the output distortion.
The distortion are evaluated considering the whole orbit, in particular 12 time instants equally distributed between 0 s and 5940 s.

4.1. THERMAL MAP SENSITIVITY ANALYSIS

Starting from the baseline thermal mapping (temperature distribution obtained directly by ESATAN thermal analysis), new temperature distributions are obtained using the Hypermesh capability to scale the nodal temperatures.
Two different cases have been analysed:

- Case1: + 10%
- Case2: – 10%.

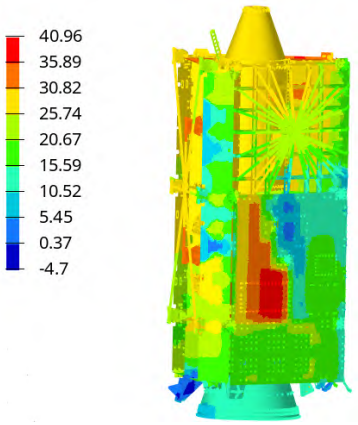


Figure 4.1 Reference Case T+10%

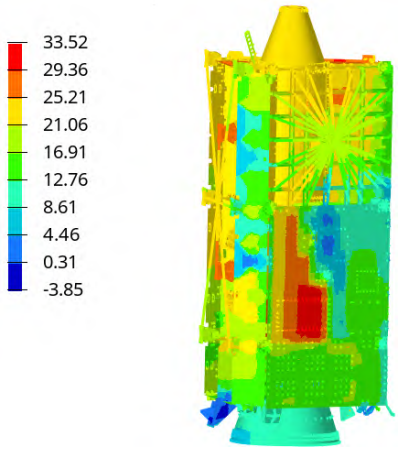


Figure 4.2 Reference Case T-10%

In this way the thermal gradients distribution on the structure is increased and decreased and from the results it is possible to evaluate the relative effect on the overall distortion.
The graphs below show the trend of the distortion during the entire orbit considering the gradient variation described previously.

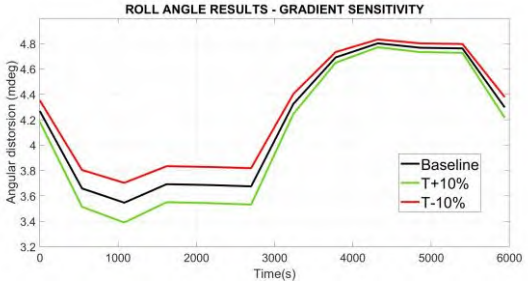


Figure 4.3 Roll angle variation during orbit (Gradient Sensitivity)

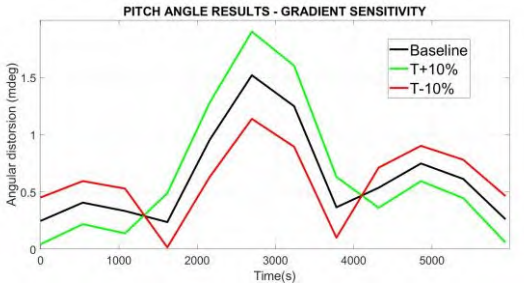


Figure 4.4 Pitch angle variation during orbit (Gradient Sensitivity)

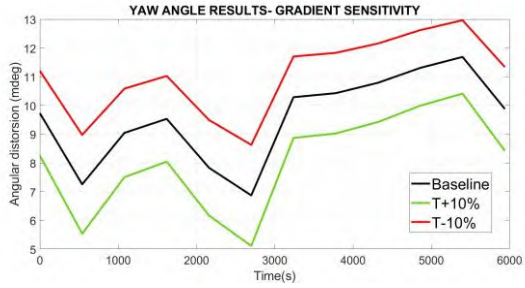


Figure 4.3 Yaw angle variation during orbit (Gradient Sensitivity)

The output of the sensitivity analysis of the thermal gradients shows a low impact on the Roll distortion angle during the entire orbit.
A higher influence on Pitch and Yaw is evaluated and a general linear trend variation is observed for all the time instants considered.
In Table 1 are reported the maximum variation of distortion angles wrt the baseline case in both +10% and -10% sensitivity analysis.

	Max α variation wrt baseline(%)	**Max β variation wrt baseline(%)**	**Max γ variation wrt baseline(%)**
T+10%	4.4%	93.3%	23.7%
T-10%	4.4%	93.3%	23.7%

Table 1 Gradient Sensitivity: Distortion angles maximum variation wrt baseline case

4.2. CTE SENSITIVITY ANALSYSIS

The second sensitivity analysis performed considered two main cases of carbon fiber materials CTE variation.
The material used for ROSE-L primary and secondary Structure is:

Material	**Reference CTE ($\frac{1}{K}$)**
M55J - EX1515 UD	3.68e-05

- Case 1: Doubled CTE
- Case 2: Halved CTE

This selected cases represent a parametric analysis to investigate the CTE variation effect.
For this analysis the thermal map considered on the

structure is the baseline (no gradients variation), in this way it possible to evaluate just the CTE effects on distortion.
The results are reported in the graphs below

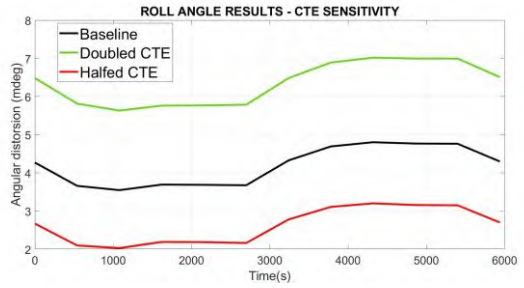


Figure 4.6 Roll angle variation during orbit (CTE Sensitivity)

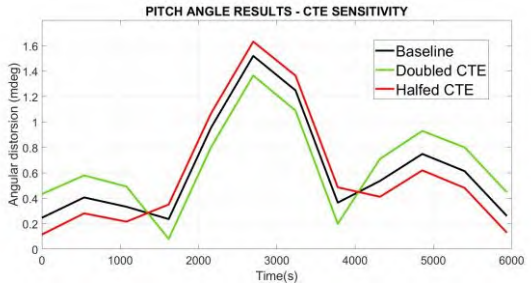


Figure 4.7 Pitch angle variation during orbit (CTE Sensitivity)

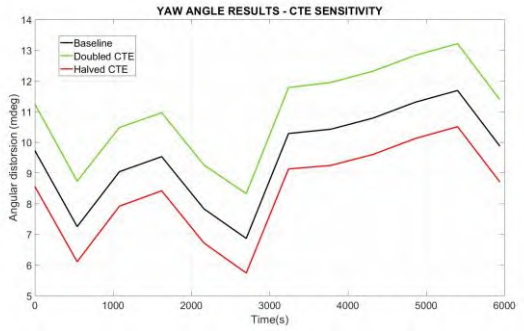


Figure 4.4 Yaw angle variation during orbit (CTE Sensitivity)

This second sensitivity analysis, in contrast wrt what has been evaluated from the previous one, a higher effect on the Roll is observed:
this means that due to the platform configuration a dispersion on the carbon fiber CTE has a stronger influence mostly in the rotation around X axis.
Similar behaviour is found for Pitch and Yaw angle: so the effect of thermal gradients and CTE are comparable in terms of overall rotation around Y and Z axis.
In Table 2 are reported the maximum variation of distortion angles wrt the baseline case in both +10% and -10% sensitivity analysis.

	Max α variation wrt baseline(%)	Max β variation wrt baseline(%)	Max γ variation wrt baseline(%)
Doubled	42.8%	75.4%	21.3%
Halved	58.8%	53.4%	16.4%

Table 2 CTE Sensitivity:CTE: Distortion angles maximum variation wrt baseline case

5. CONCLUSION

This article presents a practical methodology for conducting thermoelastic sensitivity analyses relevant to satellite platform structural design. The mathematical and physical foundations underlying structural thermoelastic modeling and the subsequent derivation of pointing errors have been reviewed, with emphasis on how modeling assumptions propagate to payload performance metrics.
The capabilities of commonly used aerospace tools for each stage of the workflow have been discussed, including thermal analysis (e.g., ESATAN), structural modeling and solution workflows (e.g., Nastran), and pre-processing/meshing environments (e.g., HyperMesh). The integration of these tools enables a consistent process from thermal loading definition to structural deformation prediction and pointing evaluation.
The sensitivity study is primarily focused on the dominant contributors to thermoelastic deformation, namely the thermal gradient distribution (i.e., the spatial temperature field used to drive the thermoelastic load cases) and the material coefficient of thermal expansion (CTE). By perturbing these inputs, the analysis quantifies how uncertainties in thermal boundary conditions and in material thermo-physical properties translate into uncertainties in platform distortion and, consequently, in instrument distortion.
Performing this type of analysis at early design stages provides actionable guidance on where effort should be concentrated to reduce risk. In particular, it supports informed decisions regarding material selection and structural design choices when CTE characterization (e.g., for composite components) is limited or not yet available. From an antenna and payload performance perspective, the results can also be used to identify the most critical distortion directions and to define whether alignment/compensation strategies should be applied at the payload level, the platform level, or through iterative co-design of both subsystems.
Overall, thermoelastic sensitivity analysis offers a structured approach to assess—early in the project—the impact of uncertainties in thermoelastic distortion inputs on payload pointing performance, improving design robustness and supporting more efficient trade-offs between structure, materials, and optical/electrical alignment requirements.

6. ACKNOWLEDGEMENTS

This work has been developed within the framework of the European Union and the European Space Agency (ESA) Copernicus programme, in the context of the ROSE-L (Radar Observing System for Europe at L-band) mission.

7. REFERENCES

1. ECSS (2013). Spacecraft Mechanical Loads Analysis Handbook, ECSS-E-HB-32-26A, ESAESTEC, February.
2. ESA pointing error engineering handbook
3. ECSS-E-HB-31-03A-Thermal-Analysis
4. Thermoelasticity' P.Heinz
5. Mechanics of Composite Materials R.M. Christensen
6. D.W. Nicholson, Finite Element Analysis Thermomechanics of Solids (CRC Press, Boca Rton, 2003)
7. Robert M. Jones Mechanics of Composite Materials – Second Edition
8. The Linear Theory of Elasticity and Thermoelasticity Donald E. Carlson
9. Design and analysis of composite strucutres with application to aerospace structures – Christos Kassapogloul
10. Meseguer J, Perez-Grande I, Sanz-Andres A (2012) Spacecraft thermal control. Elsevier, Amsterdam

THERMAL DESIGN AND SIMULATION OF THE HIGH-RESOLUTION SPACEBORNE ELECTRO-OPTIC CAMERA FOR THERMO-ELASTIC STABILITY

Süleyman Şahin [(1)], Fatma Nur Gökyürek [(1)], Mecid Uğur Dilberoğlu [(1)], Sibel Velioğlu [(1)], Özgür Karcı [(1)]

[(1)] Payload Engineering Directorate, Turkish Aerospace Industries, Inc., Fethiye District, Havacılık Avenue No:17, 06980 Kahramankazan, Ankara, Turkey, Email: suleyman.sahin2@tai.com.tr, fatmanur.gokyurek@tai.com.tr, mecidugur.dilberoglu@tai.com.tr, sibel.velioglu@tai.com.tr, ozgur.karci@tai.com.tr

KEYWORDS

Thermo-elastic, thermal design, earth-observation telescope, carbon fibre reinforced polymer

1. INTRODUCTION

Earth-observation electro-optic telescopes (EOTs) are required to maintain optical and dimensional stability under the severe and cyclic thermal conditions encountered in orbit. Variations in temperature can induce thermo-elastic deformation due to the coefficient of thermal expansion (CTE) of structural and optical components. Such deformations may alter the position, alignment, and surface figure of mirrors and lenses, as well as the position of the focal plane array (FPA), thereby affecting the imaging performance of the system [REFERENCES]. Consequently, achieving thermo-elastic stability relies directly on an optimized thermal design that suppresses both spatial temperature gradients and temporal fluctuations across critical structural components.

Thermal management consequently constitutes a critical aspect of the opto-mechanical design of high-resolution Earth-observation EOTs. In addition to the external thermal environment, localized heat dissipation from internal components may introduce temperature gradients and thermal interactions between adjacent components. Maintaining a stable and spatially uniform temperature therefore requires an integrated thermal-management strategy combining passive and active thermal-control measures. Passive thermal-control measures can moderate the effects of the external thermal environment and control heat transfer through the spacecraft interface and internal payload interfaces, while active thermal control can regulate the temperature of thermally sensitive components in response to residual temperature variations. For example, the ASTERIA optical payload was thermally isolated from the spacecraft bus to reduce temperature transients, while a controlled conductive path was provided from the imager to the telescope baffle and heaters were used for active temperature regulation [REFERENCES]. Such an architecture demonstrates the use of controlled conductive and radiative heat-transfer paths to maintain thermal stability of an optical payload.

Building on established thermal-control principles reported in the literature, the thermal design of the electro-optic camera in the present study adopts an integrated thermal-management strategy combining passive and active thermal-control measures to satisfy a temperature requirement of 20±1 °C. Multiple thermally decoupled zones are implemented to manage heat transfer within the camera, while finite element method (FEM) thermal analysis is used iteratively to characterize thermal behaviour, identify critical thermal paths, and determine suitable locations for heaters and thermistors. The resulting thermal architecture is evaluated in terms of temperature stability, temperature gradients, and heater power consumption, with the objective of satisfying the thermal requirements while minimizing thermo-elastic effects.

2. THERMAL DESIGN REQUIREMENTS AND CONSTRAINTS

Thermal design of the EOT is driven by temperature stability, temperature gradients, and allocated power budget. The governing requirements are established to constrain thermo-elastic deformations of opto-mechanical structure, thereby ensuring required imaging quality.

2.1. Temperature Stability

The primary requirement of thermal design is to maintain opto-mechanical structure of EOT within a temperature range of 20±1 °C -a constraint governed by the environmental conditions of the integration facility- under operational conditions detailed in Section 3.4. This requirement applies specifically to structures directly related to positioning of optical elements, such as optical bench, metering structure, and spider arms.

2.2. Temperature Gradients

Temperature gradients across individual structural elements serve as a governing design constraint. Spatial temperature differentials induce non-uniform thermal expansion, which directly drives thermo-elastic distortion. Accordingly, the thermal control subsystem is optimized to mitigate intra-component temperature gradients while sustaining the target operational temperature. Specifically, thermal variations across structures governing the positioning of optical elements are constrained within a margin of 2 °C.

2.3. Power Budget

The thermal control subsystem is subject to an allocated power limit of 50 W peak and 30 W average consumption. These spacecraft-level constraints serve as primary design drivers, requiring the thermal architecture to satisfy the specified temperature stability and gradient criteria while strictly adhering to the allocated power budget.

Table 1:Summary of Thermal Design Requirements

Constraint	Design Requirement
Operational Temperature	20 ± 1 °C
Intra-Component Gradient	≤ 2 °C
Power Consumption	≤ 50 W (Peak) ≤ 30 W (Average)

3. THERMAL CONTROL

The thermal control strategy relies on the configuration of the opto-mechanical structure and its interaction with the space environment and satellite platform. The telescope comprises structural and optical assemblies, alongside internal opto-electronic components. Together with external boundary conditions from space, internal heat sources and interfaces dictate conductive and radiative heat-transfer paths, establishing the foundation for the thermal-control design.

The applied strategy integrates passive and active techniques to satisfy the temperature stability, temperature-gradient, and power constraints defined in Section 2. Passive measures limit the influence of environmental thermal fluctuations, retain thermal energy within the system, and suppress parasitic heat exchange, whereas active control delivers localized regulation via heaters and thermistors. Furthermore, these measures are partitioned into thermally decoupled zones to minimize cross-coupling and enable independent temperature control of critical regions. Subsequent sections detail the opto-mechanical structure, the implementation of passive and active control methods, and the application of the zoning strategy.

3.1. Opto-Mechanical Structure

The opto-mechanical structure of the EOT provides the conductive paths through which heat is transferred between the optical, structural, and electronic components. Figure 1 presents a simplified representation of the EOT to illustrate the principal assemblies and their relative arrangement. The configuration comprises structural elements, optical components, and the FPA that contribute to the system's thermal behaviour. The structural elements mainly consist of low CTE carbon fibre reinforced polymer (CFRP), Al 7050, and Ti-6Al-4V, in addition to Zerodur optical components. The structural interfaces between these elements are of particular importance to the subsequent thermal-control design, as they govern the conductive heat-transfer paths within the telescope.

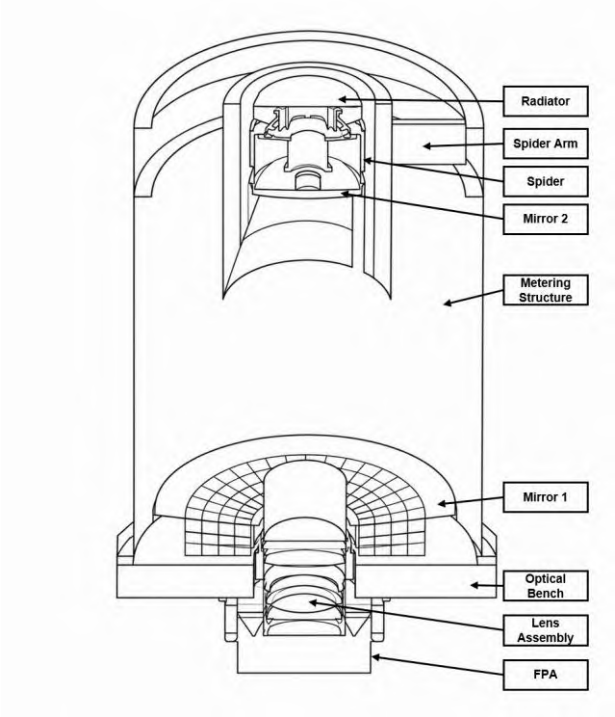


Figure 1: EOT Opto-mechanical Structure

3.2. Thermal Control Strategy

The EOT employs an integrated passive and active thermal-control methodology based on dividing the opto-mechanical structure into 12 thermally de-coupled zones. Each zone -except for three thermal control zones on metering structure- is designed to be both conductively and radiatively insulated from the adjacent zones, thereby limiting thermal cross-coupling within the structure. Following the definition of the thermal zones, each zone is further insulated from the external environment and the satellite platform enclosure to reduce the influence of external thermal fluctuations and parasitic heat exchange. The insulation contributes to maintaining a more stable thermal condition within each zone, reducing temperature gradients within the structural components, and decreasing the effect of heat load generated within FPA during imaging over EOT structure.

Passive thermal control is implemented through insulation at structural interfaces using titanium washers, multi-layer insulation (MLI) blankets, and surface coatings, while active control is provided by heaters and thermistors. The combined application of the measures is intended to maintain the required temperature range and minimise the power required for active temperature regulation.

3.3. Passive Thermal Control

Passive thermal control is implemented to reduce parasitic heat transfer within the EOT and between

the thermal zones and their surroundings. Conductive thermal insulation is achieved primarily via low-thermal-conductivity materials and thermal insulation at structural interfaces. The main purpose of the interface materials is to increase the thermal contact resistance at structural interfaces, thereby reducing conductive heat transfer between adjacent thermal zones. Titanium washers are employed at selected interfaces where additional reduction of conductive heat transfer is required.

Radiative heat transfer is controlled using MLI (which has effective emissivity of 0.03) and surface coatings. Two different MLI configurations are employed in the EOT according to the requirements of the respective surfaces. MLI with a black polyimide outermost layer is used on the space side of the metering structure and on the spider arms, where stray-light suppression is required. MLI with a vapour-deposited aluminium (VDA) outermost layer is used on the satellite side of the metering structure, the optical bench, and the FPA assembly, where atomic oxygen exposure is not a concern.

Although low-infrared-emittance coatings can provide effective radiative thermal control, high-infrared-emittance black paint is used on selected surfaces in the EOT to satisfy stray-light requirements. For radiator surfaces, a high-infrared-emittance second surface mirror (SSM) is employed to enhance radiative heat rejection to the space environment. The combined application of these passive measures reduces thermal coupling between zones and environmental thermal disturbances, thereby supporting temperature stability and reducing the demand for active thermal control.

3.4. Active Thermal Control

Active thermal control is implemented to regulate the temperature of the 12 thermal control zones (TCZs) and compensate for variations in the thermal environment and internal heat loads. Each TCZ is equipped with one or more heater–thermistor couples, with their quantity and placement optimised based on the thermal characteristics and requirements of optical and structural components within the respective zone. The heaters supply the necessary thermal input, whereas the thermistors provide temperature feedback for closed-loop regulation. Operating on an on–off control principle, the system samples thermistor readings at 10-second intervals to monitor the thermal state of each TCZ and command the heaters accordingly. Combined with a control hysteresis band of ± 0.3 °C below the target thresholds, the 10-second sampling rate provides effective and stable temperature regulation within the targeted 20±1 °C window without triggering rapid switching oscillations.

Table 2 summarises the TCZs, detailing their physical locations, the number of heater–thermistor couples, and the allocated heater power for each zone. This configuration ensures independent temperature control across all regions while maintaining overall power consumption within the allocated budget.

Table 2: TCZ Configuration

TCZ	Location	Heater – Thermistor Couples	Allocated Power (W)
TCZ-1	Metering Structure Mirror 2 Side	9	13.5
TCZ-2	Metering Structure Middle Section	3	6.0
TCZ-3	Metering Structure Mirror 1 Side	3	6.0
TCZ-4	Optical Bench	3	4.5
TCZ-5	Spider Arm 1	1	1.0
TCZ-6	Spider Arm 2	1	1.0
TCZ-7	Spider Arm 3	1	1.0
TCZ-8	Spider	3	3.0
TCZ-9	Flexure 1	1	1.0
TCZ-10	Flexure 2	1	1.0
TCZ-11	Flexure 3	1	1.0
TCZ-12	Radiator	1	5.0
Total	-	28	44.0

4. THERMAL ANALYSIS AND DESIGN OPTIMISATION

The thermal design of the EOT was developed through an iterative FEM-based analysis and optimisation process. The analysis was used to characterise the thermal behaviour of the system, evaluate the effects of relevant thermal parameters, and guide the refinement of the thermal-control configuration. The overall analysis strategy is presented in Figure 2, and the individual stages are described in the following sections.

4.1. Finite Element Model and Boundary Conditions

The thermal behaviour of the EOT was evaluated using a three-dimensional FE model, in which the opto-mechanical structure and relevant thermal interfaces were discretised using two-dimensional shell elements. Thermal properties were assumed to be constant over the analysed temperature range, consistent with the expected operating temperature near 20 °C. The model incorporates conductive and radiative heat-transfer mechanisms, internal heat loads, and the relevant thermal boundary conditions. The FE model and boundary conditions used for the analysis are described in the following subsections.

4.1.1.Finite Element Model

The thermal analysis was performed using Simcenter 3D Space System Thermal (SST) with the Thermal/Flow Solver. The opto-mechanical structure was discretised using two-dimensional shell elements, while the relevant thermal interfaces

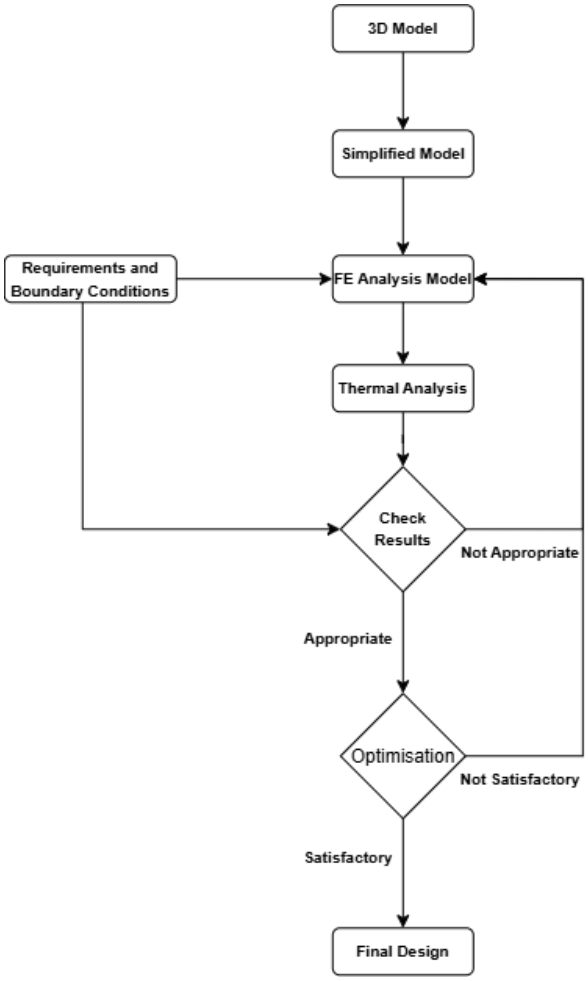


Figure 2: Overall Analysis Strategy

were represented through conductive connections. Radiative heat transfer was modelled using separate radiative enclosures, with view factors calculated using the software-integrated Monte Carlo ray-tracing method. The material properties, thermo-optical properties, and heat-transfer coefficients used in the model are presented separately in Table 3.

Table 3: Material Properties

Material	Density (kg m^{-3})	Specific Heat (J kg^{-1} K^{-1})	Conductivity (W m^{-1} K^{-1})
Al 7050	2823	900	190.00 [REFERENCES]
Ti-6Al-4V	4430	538	7.30 [REFERENCES]
CFRP	1850	880	120.00 [REFERENCES]
Zerodur	2530	800	1.46 [REFERENCES]

Table 4: Thermo-Optical Properties [REFERENCES]

Surface	IR ε	UV α BOL	UV α EOL
SSM	0.80	0.10	0.14
VDA	0.05	-	-
Black Polyimide	0.87	0.90	0.95
Zerodur	0.90	0.25	0.25
Mirror Coating	0.05	0.15	0.20
CFRP	0.85	0.90	0.95

Table 5: Heat Transfer Coefficients

Contact Type	Heat Transfer Coefficient (W m^{-2} K^{-1})
Aluminium - Aluminium	300
Aluminium - Titanium	20
Glue	1000

4.1.2.Analysis Cases

The thermal analysis considers two operational cases, referred to as the hot and cold cases, which represent the extremes of the thermal environment. The cases incorporate environmental conditions and internal heat dissipation to drive the thermal control design in accordance with the predefined temperature limits of the EOT. The cold case is used to size the required heating capability to maintain the EOT between its temperature control range, while the hot case evaluates passive cooling and thermal control performance to limit maximum temperatures. Heat dissipation is included in the hot case to account for operational thermal inputs and provide a conservative basis for control, whereas no internal heat dissipation is considered in the cold case to represent the minimum thermal input condition. The main parameters defining the hot and cold cases are summarised in Table 6.

Table 6: Hot and Cold Case Parameters [9]

Parameter	Cold Case	Hot Case
Date	21st of June	21st of December
Solar Flux	1323 W m^{-2}	1414 W m^{-2}
Earth Albedo	0.20	0.35
Earth IR	216 W m^{-2}	258 W m^{-2}
FPA Heat Dissipation	-	20 W for 240 s Per Orbit Period

4.1.3.Thermal Boundary Conditions

The EOT exchanges heat with the spacecraft through both radiative and conductive interfaces. Radiative heat transfer to the spacecraft is represented through VDA coated MLI, while conductive heat transfer occurs through the telescope mounting structure. Radiative exchange with the space environment is also considered for the externally exposed surfaces. Separate thermal

boundary conditions are defined for the hot and cold cases. The spacecraft and space environment are represented by constant-temperature boundaries, with temperatures assigned for each operational case. These boundary temperature values for the hot and cold cases are summarised in Table 7.

Table 7: Boundary Temperatures

Boundary	Temperature (°C)	
	Cold Case	Hot Case
Mounting Interface	15.00	25.00
Space Craft	-15.00	25.00
Near Space	-269.15	-269.15

4.2. Sensitivity Analysis

The sensitivity of the thermal analysis model was investigated to assess the influence of numerical modelling parameters on the calculated thermal response of the EOT. The study focused on mesh density and the radiative computation settings, with the objective of ensuring that the selected analysis model provides sufficiently stable results for the subsequent thermal design optimisation. Mesh independence and radiative computation sensitivity were evaluated separately, as described in the following subsections.

4.2.1. Mesh Independence Study

A mesh independence study was performed to assess the influence of mesh density on the calculated thermal response of the EOT. Element sizing and the level of model detail were iteratively adjusted while maintaining a reasonable solution time. The grid refinement process commenced with an initial mesh of 9153 elements (10697 nodes) and was systematically refined up to 24699 elements (26387 nodes). The iterative assessment was concluded when further mesh refinement produced a maximum temperature variation of less than 0.05 °C across critical optical components, confirming numerical convergence. Based on this iterative assessment, a configuration providing stable thermal results with reasonable computational cost was selected for the subsequent analyses and thermal design optimisation.

4.2.2. Radiative Computation Sensitivity

Radiative heat-transfer calculations were performed using the Monte Carlo ray-tracing method integrated within the SST software. The calculations commenced with an initial ray density of 1000 rays per element and were progressively scaled up to 3000 rays per element. At each step, the sum of the view factors for each radiating element was evaluated against the theoretical target of unity. The ray count was raised until the view-factor sum for each element approached 1 within a 20% margin. Following the achievement of this criterion, the ray density was further incremented to assess the stability of the radiative solution. Radiative heat fluxes, radiative couplings, heater duty cycles, and EOT temperatures were closely monitored. Convergence was achieved when further increases produced radiative flux variations of less than 0.1 W m^{-2}, and the optimized ray density (3150 rays per element) was adopted for all subsequent analyses and thermal design optimisation.

4.3. Thermal Design Optimization

The thermal design optimisation was performed by evaluating three alternative thermal-control configurations for the EOT. The options were developed by varying the MLI coverage on the EOT and FPA to balance radiative heat exchange with space and conductive heat transfer to the spacecraft. The first configuration uses no MLI on the space-facing surfaces of the EOT, while the FPA is fully covered with MLI. The second configuration also omits MLI from the EOT's space-facing surfaces but intentionally leaves one surface of the FPA open to provide a heat-discharge path to the spacecraft. The third configuration employs MLI on the EOT space-facing surfaces while similarly leaving one FPA surface open to facilitate heat discharge. Following analysis and comparison, the third configuration was selected as the final thermal-control architecture based on its suitability for satisfying the predefined temperature requirements. Following the selection of the third configuration, the heater dimensions and locations, as well as the thermistor locations, were further optimised to achieve a more uniform temperature distribution and a more balanced heater duty-cycle distribution.

4.3.1. Configuration 1

The first thermal-control configuration was defined without MLI on the space-facing surfaces of the EOT, while the FPA was fully covered with MLI, as illustrated in Figure 3. Leaving the EOT surfaces directly exposed to space increased radiative heat loss from the EOT, resulting in a higher heater power requirement which exceeds 50 W peak and 30 W of average power consumption requirements in the cold case. Meanwhile, the full MLI coverage of the FPA restricted the available heat-transfer path for the internally generated heat toward the spacecraft. Consequently, the heat dissipated within the FPA was retained within the telescope, causing the EOT temperature to exceed the predefined temperature control range of 20±1 °C in the hot case. This configuration therefore could not satisfy the temperature requirements and was not selected for the final thermal-control architecture.

4.3.2. Configuration 2

The second thermal-control configuration retained the absence of MLI on the space-facing surfaces of the EOT, while one surface of the FPA was intentionally left open to provide a heat-discharge path to the spacecraft, as illustrated in Figure 4. The exposed EOT surfaces continued to increase

radiative heat loss to space, resulting in a higher heater power consumption which exceeds 50 W peak and 30 W of average power consumption requirements in the cold case. In contrast to the first configuration, the open FPA surface provided a radiative path for the internally generated heat to be transferred toward the spacecraft, reducing heat retention within the telescope during the hot case.

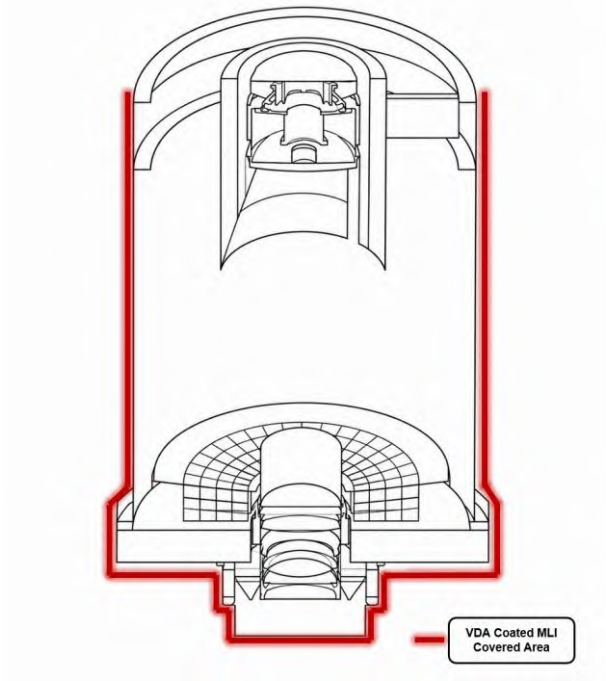


Figure 3: Illustration of Configuration 1

However, the absence of MLI on the space-facing surfaces of the EOT structure reduced its passive thermal protection during the launch and early orbit phase (LEOP), when the exposed structural surfaces could experience temperatures below the survival limit during cooling conditions or above the survival limit under direct solar flux, causing increased vulnerability of the EOT during LEOP and introducing an additional design constraint. Although the configuration improved the heat-dissipation capability compared with the first configuration, these limitations made it less suitable as the final thermal-control architecture.

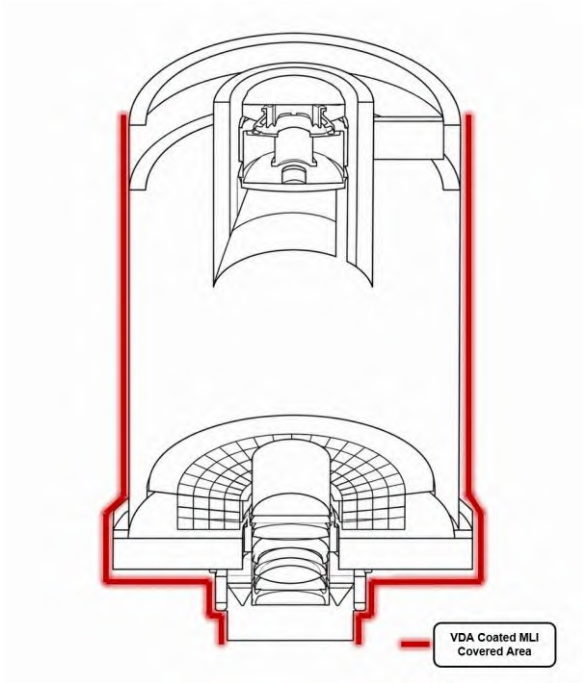


Figure 4: Illustration of Configuration 2

4.3.3.Configuration 3

The third thermal-control configuration employs MLI on the space-facing surfaces of the EOT, while one surface of the FPA is intentionally left open to provide a radiative heat-discharge path to the spacecraft, as illustrated in Figure 5. The MLI coverage of the EOT space-facing surfaces reduces radiative heat loss to space and consequently lowers the heater power requirement in the cold case. At the same time, the intentionally open FPA surface provides a radiative path for the internally generated heat to be transferred toward the spacecraft, improving heat dissipation during the hot case. The MLI coverage also provides passive thermal protection for the EOT structure during LEOP, reducing the thermal impact of excessive cooling and direct solar flux. This configuration therefore provides a more balanced thermal-control strategy by combining reduced heat loss in the cold case with an effective heat-discharge path in the hot case. Based on the analysis results, this configuration was selected as the final thermal-control architecture for subsequent optimisation of the heater dimensions and locations and thermistor locations.

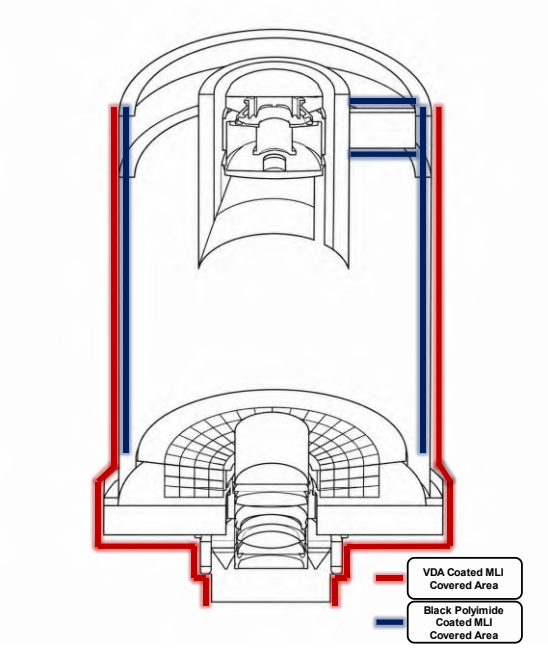


Figure 5: Illustration of Configuration 3

4.4. Thermal Analysis Results

The final thermal-control design, including the optimized heater and thermistor configurations, was evaluated under the defined hot- and cold-case conditions. The FE analysis results were assessed in terms of temperature stability and spatial uniformity within the TCZs, as well as the overall thermal behaviour of the telescope structure. Table 8 summarizes the minimum and maximum temperatures and temperature gradients obtained for each TCZ at the selected time increments for both the cold and hot cases. Table 9 presents the corresponding heater duty cycles, peak power, and average power for each TCZ. Together, the results provide a quantitative assessment of the thermal performance of the final design and the heater power required to maintain the prescribed temperature range.

The results indicate that the temperature requirements are satisfied for the TCZs subject to the general 20±1 °C requirement, except for TCZ 7, where the maximum temperature exceeds the upper limit by approximately 0.1 °C. Given the small magnitude of the deviation and the temperature gradient remaining below 2 °C, a design trade-off assessment indicated that additional thermal modifications for TCZ 7 would introduce unnecessary design complexity without providing meaningful thermal gain. Consequently, the thermal condition of TCZ 7 was deemed acceptable. Therefore, the slight temperature exceedance in TCZ 7 does not compromise the overall thermal performance of the system.

TCZ 12 is intentionally excluded from the general 20±1 °C temperature requirement. Although its temperature range falls outside the general requirement, the obtained thermal condition is considered satisfactory for the overall thermal design.

The corresponding temperature distributions for the cold and hot cases are presented in Figure 6 and Figure 7, respectively, illustrating the spatial temperature gradients and overall thermal distribution across the telescope structure.

Table 8: Temperature and Temperature Gradient Data at TCZs

Zone	Cold Case			Hot Case		
	Min Temp (°C)	Max Temp (°C)	Temp Gradient (°C)	Min Temp (°C)	Max Temp (°C)	Temp Gradient (°C)
TCZ 1	19.22	20.09	0.87	19.18	20.13	0.95
TCZ 2	19.71	20.01	0.31	19.80	20.27	0.47
TCZ 3	19.81	19.94	0.14	19.66	20.08	0.42
TCZ 4	19.84	20.06	0.21	19.66	20.07	0.41
TCZ 5	20.21	20.99	0.78	20.01	20.32	0.30
TCZ 6	20.20	20.88	0.68	20.12	20.69	0.57
TCZ 7	20.21	21.10	0.90	19.86	20.60	0.75
TCZ 8	19.98	20.31	0.32	19.00	19.34	0.35
TCZ 9	19.50	20.00	0.50	19.49	20.00	0.51
TCZ 10	19.50	20.00	0.50	19.49	20.00	0.51
TCZ 11	19.50	20.00	0.50	19.49	20.00	0.51
TCZ 12	15.84	15.92	0.08	16.15	16.35	0.20

Table 9: Heater Duty Cycles and Average Power Consumptions

Zone	Heater Power (W)	Cold Case		Hot Case	
		Duty Cycle (%)	Average Power (W)	Duty Cycle (%)	Average Power (W)
TCZ 1	13.5	67	9.0	41	5.5
TCZ 2	6.0	40	2.4	33	2.0
TCZ 3	6.0	44	2.6	35	2.1
TCZ 4	4.5	57	2.6	40	1.8
TCZ 5	1.0	45	0.5	42	0.4
TCZ 6	1.0	46	0.5	44	0.4

TCZ 7	1.0	45	0.5	42	0.4
TCZ 8	3.0	62	1.9	52	1.6
TCZ 9	1.0	42	0.4	41	0.4
TCZ 10	1.0	42	0.4	41	0.4
TCZ 11	1.0	42	0.4	41	0.4
TCZ 12	5.0	47	2.4	39	2.0
Total	44.0	-	23.5	-	17.4

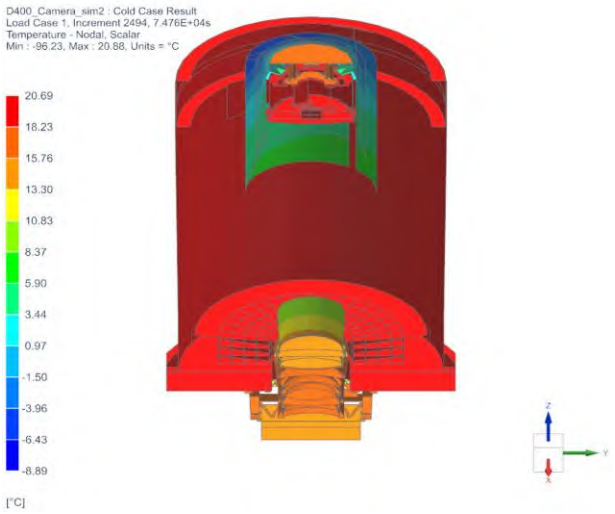


Figure 6: Cold Case Temperature Distribution

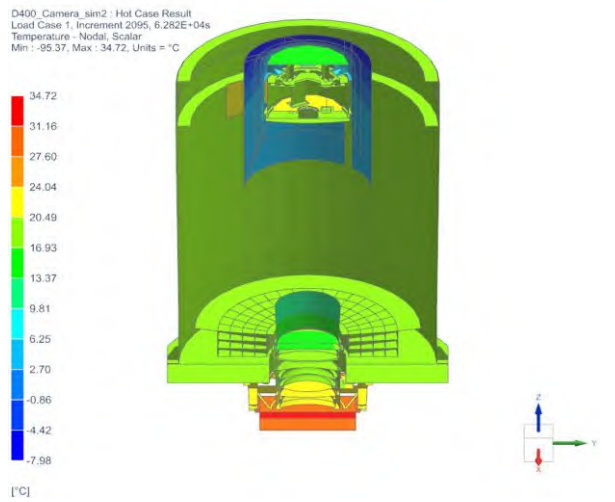


Figure 7: Hot Case Temperature Distribution

5. CONCLUSION

The developed thermal-control design successfully maintained the EOT within the prescribed 20±1 °C temperature range under the defined hot- and cold-case conditions. The combined application of passive thermal control, thermal decoupling, and active heater control provided adequate temperature stability and limited thermal gradients across the thermally sensitive zones. The optimized heater and thermistor configuration further enabled effective temperature regulation while maintaining reasonable heater duty cycles. The results demonstrate that the final thermal architecture provides a suitable thermal-control solution for the EOT, successfully satisfying the thermal control requirements necessary to achieve the thermo-elastic stability. As part of future work, thermal balance and thermal vacuum (TVAC) tests will be conducted to validate the numerical predictions and refine the thermal model through test-analysis correlation.

6. REFERENCES

1. Spitzer, L. & Boley, B. A. (1967). Thermal Deformations in a Satellite Telescope Mirror. *J. Opt. Soc. Am. 57(7)*, 901-913.
2. Cho, M., Corredor, A., Pootrakul, S., Vogiatzis, K. & Angeli, G. (2008). Thermal Performance Prediction of the TMT Optics. *Proc. SPIE*.
3. Yoo, J., Han, J. Y., Kim, H. K., Choi, S., Lee, W. K. & Kim, D. (2025). Thermal Design Analysis of Low Earth Orbit Optical Telescope ROKITS. *Int. J. Aeronaut. Space Sci. 26*, 834-846.
4. Knapp, M., Seager, S., Demory, B.-O. et al. (2020). Demonstrating High-Precision Photometry with a CubeSat: ASTERIA Observations of 55 Cancri e. *Astron. J. 160(1),* 23
5. NASA (2006). Aluminum 7050 Material Properties. NASA Technical Reports Server
6. NASA (2024). Space Nuclear Propulsion Material Property Handbook. NASA Technical Reports Server.
7. Mitsubishi Chemical Corporation (2022). Carbon Fiber Tow (Continuous Fiber): K13C2U Carbon Fiber Properties. Mitsubishi Chemical Corporation.
8. SCHOTT AG (2024). ZERODUR® Technical Properties. SCHOTT AG.
9. Gilmore, D. G. (2002). *Spacecraft Thermal Control Handbook Volume I: Fundamental Technologies 2nd ed.* El Segundo; Reston, CA, VA, United States of America: El Segundo; American Institute of Aeronautics.

ECSSMET
Braunschweig Germany 2026

Vibration testing

Decoupling Spacecraft Dynamics from Shaker Table Interactions for Fixed-Base Modal Characterization

F. Cavagna[1], G. Kosova[2], E. Di Lorenzo[2], L. Dozio[1]

[1] *Politecnico di Milano, Department of Aerospace Science and Technology, Via La Masa, 34, 20156, Milano, Italy, email: fabio.cavagna@polimi.it*

[2] *Siemens Digital Industries Software, Interleuvenlaan 68, 3001, Leuven, Belgium, email: giancarlo.kosova@siemens.com*

KEYWORDS

Modal analysis, shaker table testing, dynamic decoupling

ABSTRACT

Part of the environmental qualification of spacecraft is carried out on shaker tables, and it would be convenient to also perform the modal survey in the same configuration to save time and cost. However, when the test article is massive, its dynamics couple with those of the fixture. This work exploits the use of a multi-degree-of-freedom fixture-to-structure transmissibility that shares the poles of the fixed-base Frequency Response Function (FRF) matrix of the structure. The approach is validated on a Finite Element (FE) model of a satellite mounted on a flexible shaker table. The results show that the transmissibility extracts fixed-base frequencies and mode shapes accurately.

1. INTRODUCTION

During their operational lifespan, spacecraft structures are subjected to severe loading conditions. To ensure resilience against these conditions, environmental testing is performed during the development phase to qualify the design of the spacecraft. These tests confirm the ability of the structure to withstand the operational environments, and they are typically carried out using a shaker table to replicate the loads with the prescribed margins. Modal surveys, on the other hand, are usually not performed together with the environmental qualification, both because of the complexity of conducting them on a large and massive structure, and to avoid directly vibrating the spacecraft. It would therefore be convenient to perform this type of test with the spacecraft already mounted on the shaker table, in order to save time and costs.

The goal of the modal survey is to obtain the fixed-base dynamic characteristics of the spacecraft, namely its natural frequencies, mode shapes, and damping ratios. These quantities are usually retrieved by performing a low-level sine sweep or a broadband random excitation; however, when the item under test has a significant mass, a dynamic coupling with the shaker table may arise, so that the measured dynamics no longer correspond to those of the fixed-base structure. Experimentally measuring the fixed-base dynamic characteristics of the spacecraft brings two main advantages. The first is to obtain a more accurate estimate of its natural frequencies, in order to comply with the launch vehicle user manual requirements and to compute the Craig-Bampton reduced model used to couple the spacecraft with the launch vehicle. The second is the possibility of updating a Finite Element (FE) model, which is then employed to perform qualification test predictions.

The extraction of fixed-base modal parameters from a structure mounted on a dynamically active fixture has received considerable attention over the last decades. The key quantity behind these techniques is a corrected fixed-base Frequency Response Function (FRF) of the structure. In the literature, this FRF can be computed through two approaches. The first is based on the partial inversion of the measured system (structure and fixture) FRF matrix [1, 2]. The second exploits the accelerations measured at the interface (or on the fixture) as references, together with the forces on the structure, when computing the FRFs: since the mode shapes associated with the resulting FRFs are those of the reference degrees of freedom (DOFs) held fixed, the FRF is directly obtained without the need to measure the driving point on the fixture [2–4]. A key element common to both approaches is the use of a small set of shapes that adequately describe the motion of the fixture in the frequency range of interest.

These methodologies have been successfully applied to several space test campaigns. Winkel et al. [5] extracted the fixed-base modal parameters of the Orion European Service Module Structural Test Article while it was mounted on the multi-axis shaker table of the NASA Glenn Research Center Mechanical Vibration Facility. Measured constraint shapes of the table, obtained through the Singular Value Decomposition (SVD) of the table accelerations, were used as virtual references when computing the FRFs, allowing the fixed-base modes of the article to be identified without a dedicated fixed-base modal survey and providing considerable cost and schedule savings [6]. Napolitano et al. [7] combined direct field acoustic excitation with con-

ventional base excitation to perform a modal survey in an acoustic qualification test configuration: the acoustic sources excite the acoustically sensitive modes, while the base inputs excite the high-effective-mass modes, and the fixed-base correction technique removes the effect of the uncertain boundary condition introduced by the transportation cart. Finally, Kerrian et al. [8] applied the fixed-base correction method to a free-free modal survey to extract the target flight modes of the structure, showing the flexibility of using interface accelerations as references also for boundary conditions other than a fixed base.

This paper exploits the use of a fixture-to-structure transmissibility, which differs from the standard direct transmissibility employed in environmental testing and can be used for the extraction of the fixed-base modal parameters of the spacecraft. It is shown that this transmissibility can be obtained through the two methodologies available in the literature: a partial inversion of the FRFs of the coupled system (structure and fixture), or the use of the table accelerations as references to compute the transmissibility directly, the latter having the advantage that the driving point does not need to be measured. In both cases, the fixed-base natural frequencies, mode shapes, and damping ratios can then be extracted from the transmissibility using standard curve-fitting procedures.

The remainder of the paper is organized as follows. Section 2 presents the theoretical background of the decoupling methodologies. Additionally, the reduction of the number of DOFs through constraint shapes is discussed within the same section. The methodologies are then validated on a numerical test case in Section 3, consisting of the FE model of a satellite mounted on a flexible shaker table through a rigid adapter. Two case studies are presented to demonstrate the effectiveness of both approaches for extracting fixed-base natural frequencies and mode shapes. In Section 4, a discussion of the results is provided, highlighting the key advantages of using the transmissibility. Finally, concluding remarks and main outcomes are summarized in Section 5.

2. THEORETICAL BACKGROUND

Let us consider a structure S (for example, a spacecraft) mounted on a flexible fixture F (for example, a shaker table). The dynamics of the structure S are coupled with those of the fixture F, preventing direct extraction of fixed-base modal parameters. The measured dynamics of the coupled system can be represented by the following equation:

$$\mathbf{a} = \mathbf{H}\mathbf{f} \tag{1}$$

Here, **a** is the vector of measured accelerations, **f** is the vector of applied forces, and **H** is the FRF matrix of the coupled system. Equation 1 can be expanded as follows:

$$\begin{bmatrix}\mathbf{a}_S\\ \mathbf{a}_F\end{bmatrix} = \begin{bmatrix}\mathbf{H}_{SS} & \mathbf{H}_{SF}\\ \mathbf{H}_{FS} & \mathbf{H}_{FF}\end{bmatrix}\begin{bmatrix}\mathbf{f}_S\\ \mathbf{f}_F\end{bmatrix} \tag{2}$$

where subscripts S and F denote the structure and fixture, respectively. It is assumed, without loss of generality, that the applied forces and the measured accelerations are collocated.

The goal is to decouple the dynamics of the structure S from those of the fixture F in order to obtain the fixed-base modal parameters of S. If the forces were applied only on the structure S, and the accelerations were measured only on the structure S, the measured FRF matrix would be $\mathbf{H}_{SS}$, which does not represent the fixed-base FRF matrix of the structure S, $\mathbf{H}_{SS}^{FB}$, since the accelerations on the fixture F are not zero. It is possible to express $\mathbf{a}_S$ as a function of $\mathbf{f}_S$ and $\mathbf{a}_F$ by rearranging the second row of the expanded equation:

$$\mathbf{f}_F = -\mathbf{H}_{FF}^{-1}\mathbf{H}_{FS}\mathbf{f}_S + \mathbf{H}_{FF}^{-1}\mathbf{a}_F \tag{3}$$

and substituting it into the first row, yielding:

$$\mathbf{a}_S = \left[\mathbf{H}_{SS} - \mathbf{H}_{SF}\mathbf{H}_{FF}^{-1}\mathbf{H}_{FS}\right]\mathbf{f}_S + \left[\mathbf{H}_{SF}\mathbf{H}_{FF}^{-1}\right]\mathbf{a}_F \tag{4}$$

By constraining the accelerations on the fixture F to be zero ($\mathbf{a}_F = 0$), the fixed-base FRF matrix of the structure S is obtained as:

$$\mathbf{H}_{SS}^{FB} = \mathbf{H}_{SS} - \mathbf{H}_{SF}\mathbf{H}_{FF}^{-1}\mathbf{H}_{FS} \tag{5}$$

where $(\cdot)^{FB}$ stands for fixed-base. Therefore, once the full FRF matrix of the coupled system is measured, it is possible to extract the fixed-base FRF matrix of the structure S by applying Eq. 5. The fixed-base modal parameters of the structure S can then be extracted from $\mathbf{H}_{SS}^{FB}$ using standard modal analysis techniques. Note that, to obtain the full FRF matrix of the coupled system, it is necessary to apply forces on both the structure S and the fixture F. In a real experimental setup, one does not want to apply forces to the structure in order to avoid damaging it, and only the FRF columns associated with the forces on the fixture are measured. In this case, one can still perform the matrix inversion of $\mathbf{H}_{FF}$ and obtain the second term of Eq. 4, which can be defined as the transmissibility between the fixture and

the structure when the forces applied to the structure are zero:

$$\mathbf{T}_{SF}^{f_S=0} = \mathbf{H}_{SF}\mathbf{H}_{FF}^{-1} \tag{6}$$

where $(\cdot)^{f_S=0}$ indicates that the forces applied to the structure S are zero. The transmissibility is demonstrated to have the same poles as the fixed-base FRF matrix of the structure S, $\mathbf{H}_{SS}^{FB}$, and can be used to extract the fixed-base modal parameters of the structure S without applying forces on it [9]. Eqs. 5 and 6 can be substituted into Eq. 4 to obtain the following expression:

$$\mathbf{a}_S = \begin{bmatrix}\mathbf{H}_{SS}^{FB} & \mathbf{T}_{SF}^{f_S=0}\end{bmatrix}\begin{bmatrix}\mathbf{f}_S \\ \mathbf{a}_F\end{bmatrix} \tag{7}$$

Note that the matrix in Eq. 7 can be computed using the forces on the structure and the accelerations on the fixture as references, together, and the accelerations on the structure as outputs using a Multiple-Input Multiple-Output (MIMO) H1 estimator. The matrix can then be partitioned over the S DOFs or F DOFs to obtain the fixed-base FRF matrix of the structure S and the transmissibility between the fixture and the structure when the forces applied to the structure are zero. This approach does not require the measure of the forces on the fixture (they still need to be applied, but they do not need to be measured), which can be an advantage in a real experimental setup where the fixture is not instrumented with force transducers. It is also important to note that, while $\mathbf{H}_{SS}^{FB}$ cannot be experimentally measured (since it requires the accelerations on the fixture to be zero), $\mathbf{T}_{SF}^{f_S=0}$ can be experimentally measured by not applying the forces on the structure and measuring the accelerations on the fixture $\mathbf{a}_F^{f_S=0}$ and on the structure $\mathbf{a}_S^{f_S=0}$ and computing the transmissibility using a MIMO H1 estimator as:

$$\mathbf{T}_{SF}^{f_S=0} = \mathbf{S}_{a_S a_F}^{f_S=0}\left(\mathbf{S}_{a_F a_F}^{f_S=0}\right)^{-1} \tag{8}$$

where $\mathbf{S}_{a_S a_F}^{f_S=0}$ is the cross-spectral density matrix between the accelerations on the structure and the fixture, and $\mathbf{S}_{a_F a_F}^{f_S=0}$ is the auto-spectral density matrix of the accelerations on the fixture, both computed when no forces are applied to the structure.

2.1. DOFs reduction

When computing the fixed-base FRF matrix of the structure (or the transmissibility), a matrix inversion has to be performed. In the partial inversion of the system FRF matrix (Eqs. 5 and 6), the matrix to be inverted is $\mathbf{H}_{FF}$, while in the direct calculation the matrix to be inverted is the auto-spectral density matrix of the references ($\mathbf{f}_S$ and $\mathbf{a}_F$, or $\mathbf{a}_F^{f_S=0}$). These matrices are often ill-conditioned since the accelerations on the fixture are often highly correlated, especially at resonances. This can lead to numerical issues when performing the matrix inversion, resulting in inaccurate estimates of the fixed-base FRF matrix or transmissibility. To mitigate this issue, it is possible to reduce the number of DOFs of the fixture by approximating the measured accelerations as a linear combination of constraint shapes as:

$$\mathbf{a}_F \approx \mathbf{R}\mathbf{q} \tag{9}$$

where $\mathbf{R}$ is a matrix containing the constraint shapes and $\mathbf{q}$ is the vector of generalized coordinates which is computed as:

$$\mathbf{q} \approx \mathbf{R}^{\dagger}\mathbf{a}_F \tag{10}$$

The matrix $\mathbf{R}$ must be chosen so that it captures the main dynamics of the fixture, while reducing the number of DOFs. The constraint shapes can be defined a priori based on the knowledge of the fixture dynamics, or they can be extracted from the measured experimental data. In this paper, the constraint shape matrix is defined using a Principal Component Analysis (PCA). The PCA is performed on the measured accelerations on the fixture, and the constraint shapes are defined as the first n principal components, where n is chosen to capture a sufficient amount of variance in the data. The reduced number of DOFs can then be used to compute the fixed-base FRF matrix or transmissibility, improving the numerical stability of the matrix inversion. In order to apply the PCA, the measured accelerations on the fixture are arranged in a matrix $\mathbf{a}_F$ of size $n_{a_F} \times n_t$, where n_{a_F} is the number of DOFs of the fixture and n_t is the number of time samples. The PCA is performed computing the SVD on the covariance matrix of $\mathbf{a}_F$ as:

$$[\mathbf{U}, \mathbf{\Sigma}, \mathbf{V}] = \text{svd}\left(\mathbf{C}_{a_F, a_F}\right) \tag{11}$$

The constraint shapes are then defined as the first n columns of $\mathbf{U}$, corresponding to the largest n singular values:

$$\mathbf{R} = \mathbf{U}^{(1:n)} \tag{12}$$

Once the constraint shapes are defined, Eq. 9 can be substituted into Eq. 2 to obtain the following expression:

$$\begin{bmatrix}\mathbf{a}_S \\ \mathbf{q}\end{bmatrix} = \begin{bmatrix}\mathbf{H}_{SS} & \mathbf{H}_{SF} \\ \mathbf{R}^{\dagger}\mathbf{H}_{FS} & \mathbf{R}^{\dagger}\mathbf{H}_{FF}\end{bmatrix}\begin{bmatrix}\mathbf{f}_S \\ \mathbf{f}_F\end{bmatrix} \tag{13}$$

Eq. 7 can then be rewritten as:

$$\mathbf{a}_S = \begin{bmatrix} \mathbf{H}_{SS}^{FB} & \mathbf{T}_{Sq}^{f_S=0} \end{bmatrix} \begin{bmatrix} \mathbf{f}_S \\ \mathbf{q} \end{bmatrix} \tag{14}$$

where

$$\mathbf{H}_{SS}^{FB} = \mathbf{H}_{SS} - \mathbf{H}_{SF}\mathbf{H}_{qF}^{\dagger}\mathbf{H}_{qS} \tag{15}$$

$$\mathbf{T}_{Sq}^{f_S=0} = \mathbf{H}_{SF}\mathbf{H}_{qF}^{\dagger} \tag{16}$$

with $\mathbf{H}_{qF} = \mathbf{R}^{\dagger}\mathbf{H}_{FF}$ and $\mathbf{H}_{qS} = \mathbf{R}^{\dagger}\mathbf{H}_{FS}$.

It is important to note that the fixed-base FRF matrix of the structure is no longer obtained by mathematically constraining the physical fixture accelerations to be zero, but by constraining the generalized coordinates to be zero. The generalized coordinates are the coefficients of the constraint shapes; therefore, setting a generalized coordinate equal to 0 signifies that the fixture motion is constrained along that shape direction.

3. FEM NUMERICAL TEST CASE

An FE model is created to illustrate the application of the methodologies. The model is built using Simcenter 3D and consists of an axisymmetric satellite (named DAMIS (Decoupling Analysis for Modal Identification Satellite)) mounted on a flexible shaker table through a rigid adapter. The connections between the satellite and the adapter, and between the adapter and the shaker table, are modeled as rigid connections through RBE2 elements; while the shaker table is connected to ground through a set of springs, one for each direction, to simulate three pseudo-rigid suspension modes. The satellite is modeled so that its first natural frequencies, associated with the bending and longitudinal modes, have realistic values. The shaker table is modeled so that its first three suspension modes are in the frequency range of interest so that the dynamics of the satellite and the shaker table are coupled. The FE model of the system is depicted in Fig. 1.

The goal of the analysis is to decouple the dynamics of the satellite from the shaker table. To do so, the mass and stiffness matrices of the system are exported into MATLAB and a modal truncation is applied to reduce the number of DOFs of the system. Before simulating the system, a modal analysis is performed to compute the natural frequencies and mode shapes of the system. The eigenpairs are compared with those obtained by performing a modal analysis of the FE model of the satellite, with its base clamped to represent a fixed-base condition. The natural frequencies of the coupled system, f_{S+F}, and of the fixed-base satellite, f_S, are listed in Tab. 1.



Figure 1: FE model of the coupled satellite-shaker system used for the numerical test case.

Table 1: Comparison between coupled-system and fixed-base natural frequencies.

Mode	f_{S+F} [Hz]	Note	f_S [Hz]	Note
1	4.68	B-X-1	18.67	B-X-1
2	5.70	B-Y-1	18.67	B-Y-1
3	20.63	L-Z-1	54.59	T-Z-1
4	21.66	B-Y-1	58.98	L-Z-1
5	21.75	B-X-1	67.34	B-X-2
6	54.52	T-Z-1	67.34	B-Y-2
7	71.52	B-X-2		
8	71.54	B-Y-2		
9	71.84	L-Z-1		

Note: Label format in the Note columns is {B: Bending, L: Longitudinal, T: Torsional}-{axis}-{order}. For example, B-X-2 indicates the second bending mode around the X axis.

The first pair of bending modes (B-X-1 and B-Y-1) and the first longitudinal mode of the satellite (L-Z-1) are coupled with the first three suspension modes of the shaker table. In particular, the first bending mode of the satellite (B-X-1) is coupled with the first suspension mode of the shaker table (translation in Y), while the second bending mode of the satellite (B-Y-1) is coupled with the second suspension mode of the shaker table (translation in X). The longitudinal mode of the satellite (L-Z-1) is coupled with the third suspension mode of the shaker table (translation in Z). The second couple of bending modes is also slightly coupled with the shaker table. The torsional mode of the satellite is not coupled with any mode of the shaker table; this is expected since the rotational stiffness of the table is very high. The resulting effect of the coupling is a split of the first pair of bending modes and the first longitudinal mode of the satellite into two modes each, with a frequency shift. One of these two modes has a frequency lower than the original fixed-base mode of the satellite; the other mode, instead, has a higher frequency. This effect can also be seen in the Modal Assurance Criterion (MAC) matrix, computed between the fixed-

base mode shapes of DAMIS and the mode shapes of the coupled system, partitioned over the DOFs of the satellite. The MAC matrix is shown in Fig. 2.

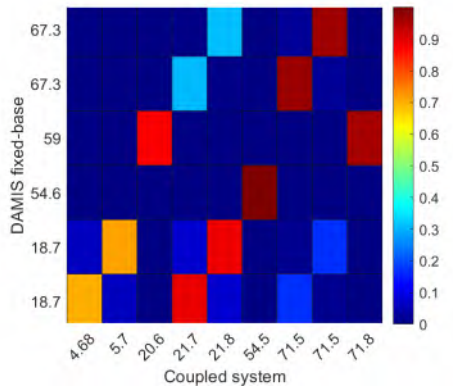


Figure 2: Modal Assurance Criterion (MAC) matrix between the fixed-base mode shapes of the satellite and the mode shapes of the coupled system, partitioned over the DOFs of the satellite.

From the MAC matrix, it is possible to notice that, for the three coupled modes, the MAC values are lower than 1, indicating that the mode shapes of the coupled system are different from those of the fixed-base satellite. The torsional mode of the satellite, instead, has a MAC value equal to 1, indicating that the mode shape is not affected by the coupling with the shaker table. When looking at the rows associated with the first pair of bending modes and the first longitudinal mode of the satellite, it is possible to notice that the MAC values are split between two modes of the coupled system, indicating that the original mode shape of the satellite is now represented by two different mode shapes of the coupled system. Of these two modes, the one at lower frequency is most likely the suspension mode of the shaker table, affected by the coupling with the satellite, while the one at higher frequency is most likely the original mode of the satellite, affected by the coupling with the shaker table.

3.1. Case studies

Two case studies are considered:

- Case A: the system is excited only on the shaker table and $\mathbf{T}_{SF}^{f_S=0}$ is computed;
- Case B: the system is excited both on the shaker table and on the satellite and $\mathbf{H}_{SS}^{FB}$ is computed.

where the DOFs of the structure are denoted by S, the DOFs of the shaker table are denoted by F, while a set of DOFs of the adapter is included in F in order to obtain the constraint shapes, and another set of DOFs of the adapter is included in S in order to visualize whether the fixture has residual motion while displaying the fixed-base modes. For both case studies, a state-space representation of the system is built. The system is excited with a set of uncorrelated periodic-random signals (leakage-free) generated with n_r realizations, n_p periods per realization, n_{fft} samples per period, and sampling frequency f_s. Only the final steady-state periods are averaged. Simulation parameters are listed in Tab. 2. The forces represent the excitation of the system through a set of modal shakers or through an impact hammer. The accelerations are measured at a set of points on the satellite and on the shaker table. The locations represent the position of the accelerometers used in a real test. The coupled FRFs of the system are computed from the measured accelerations and the applied forces, and a partial matrix inversion is performed to decouple the dynamics of the satellite from the shaker table.

Table 2: Simulation parameters.

Parameter	Symbol	Value
Sampling frequency	f_s	1500 Hz
FFT block length (period)	n_{fft}	32768
Number of realizations	n_r	40
Number of periods	n_p	6

3.2. Case A: decoupling with excitation on the shaker table only

Three uncorrelated forces are applied on the shaker table, one for each direction. As the number of independent deformations of the shaker table in the frequency range of interest is three, the minimum number of forces that has to be applied to the system in order to decouple the dynamics of the satellite from the shaker table is three. In addition, four points at the corners of the table and twelve points on the adapter are selected to measure the accelerations of the fixture, while other points on the satellite and on the adapter are selected in order to obtain clear mode shapes. The measured accelerations are used to compute the coupled FRFs of the system, $\mathbf{H}_{SF}$ and $\mathbf{H}_{FF}$. The Complex Mode Indicator Function (CMIF) of $\mathbf{H}_{SF}$ is computed and shown in Fig. 3.

The peaks of the CMIF are associated with the natural frequencies of the coupled system. Therefore, it is clear that $\mathbf{H}_{SF}$ contains the dynamics of both the satellite and the shaker table and cannot be used for modal extraction to characterize the dynamics of the satellite alone. Before performing the correction, the

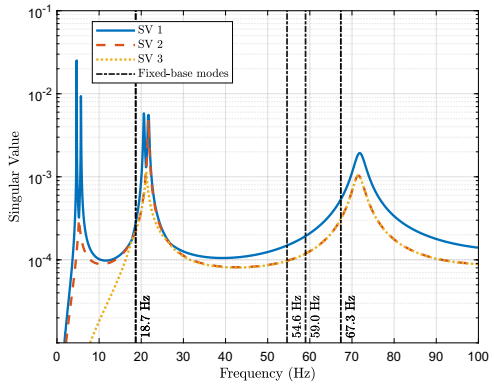
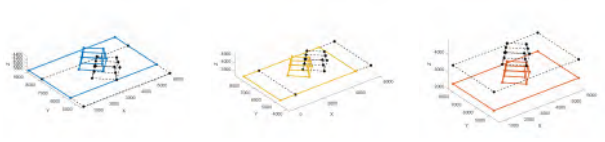


Figure 3: CMIF of $\mathbf{H}_{SF}$.

constraint shapes can be identified using the procedure described in Section 2.1. In particular, PCA is performed on the measured accelerations of the fixture, $\mathbf{a}_F$, to identify the number of independent deformations of the fixture in the frequency range of interest. As expected, the three constraint shapes are the three suspension modes of the shaker table. The constraint shapes are shown in Fig. 4. The first constraint shape is associated with the first suspension mode of the shaker table, which is a translation in Y; the second constraint shape is associated with the second suspension mode of the shaker table, which is a translation in X; and the third constraint shape is associated with the third suspension mode of the shaker table, which is a translation in Z.



(a) Mode 1 (Y translation) *(b) Mode 2 (X translation)* *(c) Mode 3 (Z translation)*

Figure 4: Constraint shapes of the shaker table identified via PCA of the fixture accelerations.

Once the constraint shapes are identified, Eq. 16 is used to compute the transmissibility matrix $\mathbf{T}_{Sq}^{f_S=0}$. The CMIF of $\mathbf{T}_{Sq}^{f_S=0}$ is computed and shown in Fig. 5. The peaks of the CMIF are associated with the fixed-base natural frequencies of the satellite. From the CMIF, one can observe that the first singular value peaks at the first fixed-base natural frequency of the satellite, and that the second singular value peaks at the same frequency; this indicates that two modes are present at this frequency, which are the first pair of bending modes of the satellite. Then, a single mode is present at around the third fixed-base natural frequency of the satellite, which is the first longitudinal mode; once again, the first and second singular values peak at the same frequency at the fourth fixed-base natural frequency of the satellite, indicating that the second pair of bending modes of the satellite is present at this frequency. The first singular vector associated with the first three peaks of the CMIF is the mode shape of the satellite associated with the respective peak. The mode shapes associated with the first pair of bending modes around X and the first longitudinal mode are shown in Fig. 6. From the plot of the mode shapes, it is possible to notice that the adapter motion is effectively removed, and that the mode shapes of the satellite are correctly extracted. The first bending mode around Y is not shown since it is very similar to the first bending mode around X, but rotated by 90°. The same applies to the second pair of bending modes around X and Y.

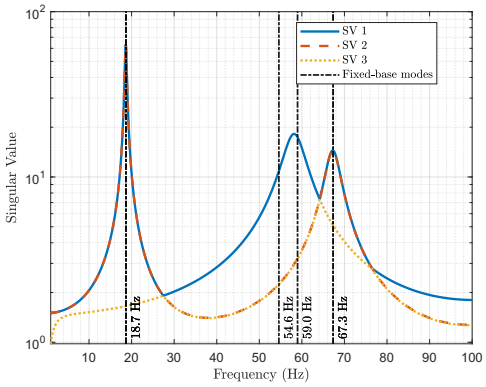
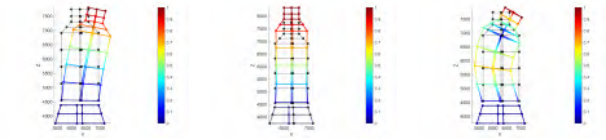


Figure 5: CMIF of $\mathbf{T}_{Sq}^{f_S=0}$.



(a) B-X-1 *(b) L-Z-1* *(c) B-X-2*

Figure 6: Mode shapes extracted from the first three peaks of the CMIF of $\mathbf{T}_{Sq}^{f_S=0}$.

It is interesting to study whether the direct transmissibility computed from one measured acceleration on the shaker table, representative of a control accelerometer in a real test, to the accelerations on the structure, is equivalent to the transmissibility matrix $\mathbf{T}_{Sq}^{f_S=0}$ in terms of peaks and mode shapes. To do so, the direct transmissibility is computed from one reference accelerometer on the shaker table in the Y direction to the accelerations on the satellite measured in the Y direction. The magnitude sum of the direct transmissibilities is computed and

compared against the magnitude sum of the column of the transmissibility matrix $\mathbf{T}_{SF}^{f_S=0}$ associated with the same reference accelerometer used in computing the direct transmissibilities. The comparison is shown in Fig. 7.

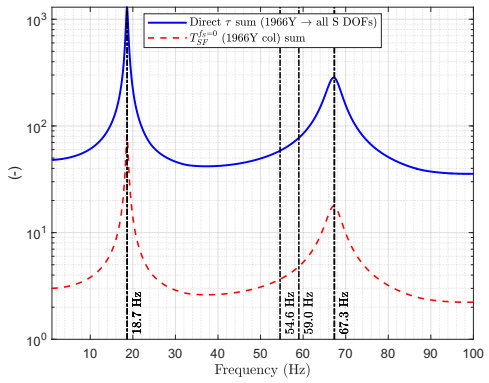


Figure 7: Comparison between the magnitude sum of direct transmissibilities and the magnitude sum of a column of the transmissibility matrix $\mathbf{T}_{Sq}^{f_S=0}$.

In this case, the peaks of the direct transmissibility and of the transmissibility matrix $\mathbf{T}_{Sq}^{f_S=0}$ are in good agreement, indicating that the direct transmissibility can be used to extract the mode shapes of the satellite. However, this is not always the case. In fact, if a mode of the satellite is coupled with two or more modes of the shaker table simultaneously, the direct transmissibility may not be able to extract the mode shape of the satellite correctly. In this scenario, the transmissibility matrix $\mathbf{T}_{Sq}^{f_S=0}$ should be used instead. In a strict sense, the direct transmissibility is a transmissibility only if a single force is applied [10]. The difference in magnitude between the direct transmissibility and the transmissibility in Fig. 7 can be understood by considering the definition of the two quantities. The direct transmissibility is nothing more than the FRF obtained by imposing an acceleration on the reference DOF (typically a control accelerometer), measuring the response on the structure, and computing the ratio. When the acceleration is imposed on the reference DOF, the other DOFs on the fixture are free to move. Instead, a term in the transmissibility matrix $\mathbf{T}_{SF}^{f_S=0}$, say T_{ij}, represents the response at DOF i due to a unit acceleration imposed at DOF j while all other DOFs on the fixture are constrained. This motion, however, is physically impossible since the fixture is designed to have pseudo-rigid modes only; hence, the motion of the reference DOF j is spread among the other DOFs on the fixture, leading to a difference in magnitude between the direct transmissibility and the transmissibility matrix. In the case at hand, there are 16 fixture DOFs in the Y direction (4 on the shaker table and 12 on the adapter) and the magnitude of the transmissibility in Fig. 7 is the magnitude of the direct transmissibility divided by 16.

3.3. Case B: decoupling with excitation on both the shaker table and DAMIS

In this case study, the system is excited both on the shaker table and on the satellite. In addition to the forces applied to the shaker table in the previous case study, an additional set of uncorrelated forces is applied to the satellite. With both $\mathbf{f}_F$ and $\mathbf{f}_S$ applied to the system, the full FRF matrix $\mathbf{H}$ can be computed and Eq. 15 can be used to compute the fixed-base FRF matrix $\mathbf{H}_{SS}^{FB}$. Note that the constraint shapes of the shaker table and adapter are the same as those identified in Case A. Before applying the procedure, it is interesting to analyze the CMIF of $\mathbf{H}_{FF}$, as $\mathbf{H}_{SF}$ was analyzed in the previous case study. The CMIF of $\mathbf{H}_{FF}$ is shown in Fig. 8.

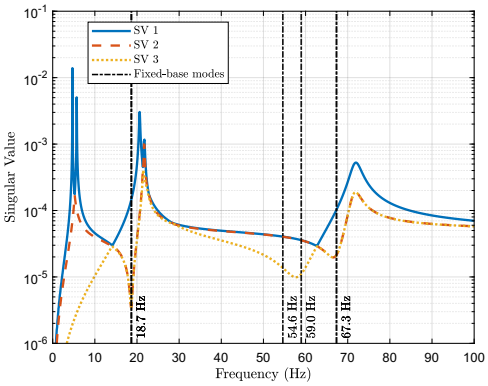


Figure 8: CMIF of $\mathbf{H}_{FF}$.

The peaks of the CMIF are associated with the natural frequencies of the coupled system, as was the case for $\mathbf{H}_{SF}$. However, here, some antiresonances are present in the curve associated with the lowest singular value. The frequencies of the antiresonances are associated with the fixed-base natural frequencies of the satellite. This is logical since $\mathbf{H}_{FF}$ is the FRF matrix that is going to be inverted in order to obtain $\mathbf{T}_{SF}^{f_S=0}$ and $\mathbf{H}_{SS}^{FB}$, and the antiresonances become the resonances of these two matrices. Therefore, $\mathbf{H}_{FF}$ could be used to check whether the fixed-base natural frequencies will be present in the transmissibility matrix $\mathbf{T}_{SF}^{f_S=0}$ and in the fixed-base FRF matrix $\mathbf{H}_{SS}^{FB}$, before performing the correction. The CMIF of $\mathbf{H}_{SS}^{FB}$ is shown in Fig. 9. The peaks of the CMIF are associated with the fixed-base natural frequencies of the satellite. As for the CMIF of $\mathbf{T}_{Sq}^{f_S=0}$, both pairs of bending modes and the first longitudinal mode of the satellite are present. Note

that, now, the peak associated with the first torsional mode of the satellite is also present. This is due to the fact that the torsional mode is not coupled with any mode of the shaker table, and therefore it is not excited when only the shaker table is excited. This mode appears in the CMIF of $\mathbf{H}_{SS}^{FB}$ since the satellite is excited directly and the mode is present in $\mathbf{H}_{SS}$. The mode shape associated with the first torsional mode of the satellite is shown in Fig. 10.

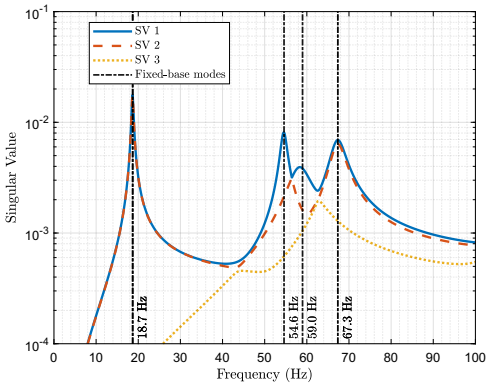


Figure 9: CMIF of $\mathbf{H}_{SS}^{FB}$.

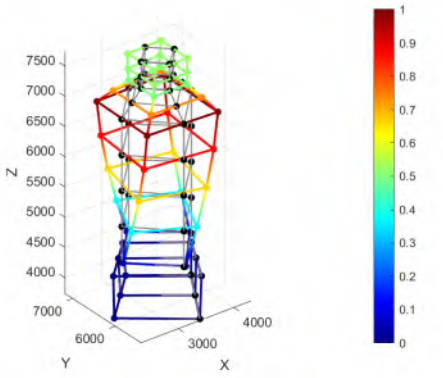


Figure 10: First torsional mode shape of the satellite extracted from $\mathbf{H}_{SS}^{FB}$.

3.4. Results

Tab. 3 compares the fixed-base natural frequencies of the satellite, f_S, with those obtained from the CMIF of $\mathbf{T}_{Sq}^{f_S=0}$ in Case A, f_S^A. The agreement between the fixed-base and extracted frequencies is generally very good, especially for the two pairs of bending modes; the longitudinal mode, instead, has a relative error that remains below 1.5%. The torsional mode is listed for completeness but marked with "/" since it is not excited in Case A and therefore cannot be extracted. Fig. 11 shows the MAC matrix between the fixed-base mode shapes and the extracted mode shapes for Case A. The correlation is strong along the diagonal, indicating a good match between the fixed-base and extracted mode shapes. The only mismatch is associated with the bending modes around the Y axis; however, the MAC is still higher than 90%.

Table 3: Comparison between fixed-base natural frequencies and those extracted from $\mathbf{T}_{Sq}^{f_S=0}$ (Case A).

Mode	Note	f_S [Hz]	f_S^A [Hz]	Error [%]
1	B-X-1	18.67	18.66	-0.08
2	B-Y-1	18.67	18.66	-0.08
3	T-Z-1	54.59	/	/
4	L-Z-1	58.98	58.17	-1.38
5	B-X-2	67.34	67.24	-0.15
6	B-Y-2	67.34	67.24	-0.15

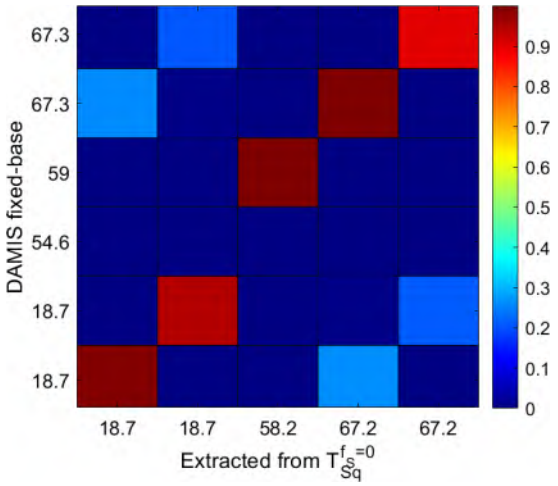


Figure 11: MAC matrix between the fixed-base mode shapes of the satellite and the mode shapes extracted from $\mathbf{T}_{Sq}^{f_S=0}$ (Case A, f_S^A).

Tab. 4 compares the fixed-base natural frequencies of the satellite, f_S, with those extracted from the CMIF of $\mathbf{H}_{SS}^{FB}$ in Case B, f_S^B. Again, there is generally good agreement between the fixed-base and extracted frequencies, with relative errors remaining below 1.5% for all modes. Fig. 12 shows the MAC matrix between the fixed-base mode shapes and the extracted mode shapes for Case B and confirms a strong correlation along the diagonal, indicating a good match between the fixed-base and extracted mode shapes.

4. DISCUSSION

Both $\mathbf{T}_{SF}^{f_S=0}$ and $\mathbf{H}_{SS}^{FB}$ provide accurate estimates of the fixed-base natural frequencies and mode shapes of the satellite, as demonstrated by the comparisons

Table 4: Comparison between fixed-base natural frequencies and those extracted from $\mathbf{H}_{SS}^{FB}$ (Case B).

Mode	Note	f_S [Hz]	f_S^B [Hz]	Error [%]
1	B-X-1	18.67	18.66	-0.08
2	B-Y-1	18.67	18.66	-0.08
3	T-Z-1	54.59	54.55	-0.08
4	L-Z-1	58.98	58.35	-1.07
5	B-X-2	67.34	67.38	0.06
6	B-Y-2	67.34	67.38	0.06

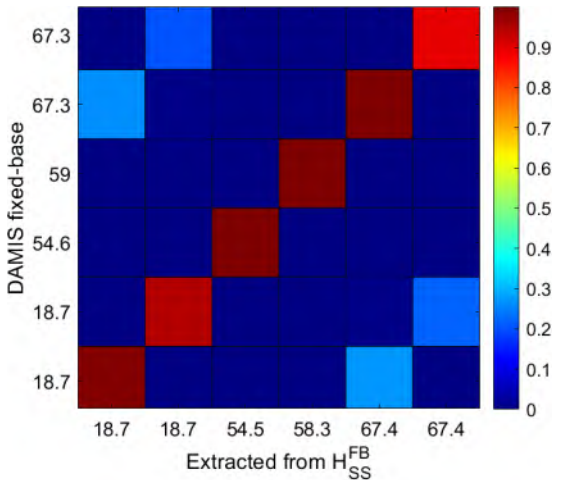


Figure 12: MAC matrix between the fixed-base mode shapes of the satellite and the mode shapes extracted from $\mathbf{H}_{SS}^{FB}$ (Case B).

in Tabs. 3 and 4 and the MAC matrices in Figs. 11 and 12. The main difference in the results is that $\mathbf{T}_{SF}^{f_S=0}$, in this case, cannot be used to extract the torsional mode of the satellite; however, the torsional mode of a satellite is usually not of interest since it is not expected to couple significantly with the launch vehicle. The advantage of using $\mathbf{T}_{SF}^{f_S=0}$ to extract fixed-base modes is that it does not require applying forces directly to the structure, which is usually not desired in practical testing scenarios, in order to avoid potential damage or undesired excitation of sensitive components. The magnitude of the forces on the fixture should be large enough to excite the desired modes of the structure so that they can be extracted after the decoupling procedure. In the present work, the validation focuses on the fixed-base natural frequencies and mode shapes; the estimation of the fixed-base damping ratios, although enabled by the shared-pole property of the transmissibility, is left to future work.

5. CONCLUSION

The use of the fixture-to-structure transmissibility has been exploited for extracting the fixed-base modal parameters of a spacecraft tested on a flexible shaker table.

The methodology was validated on the FE model of the DAMIS satellite mounted on a flexible shaker table, whose suspension modes were tuned to couple with the bending and longitudinal modes of the satellite. Two case studies confirmed that both $\mathbf{T}_{SF}^{f_S=0}$, computed with excitation on the fixture only, and $\mathbf{H}_{SS}^{FB}$, computed with excitation on both the fixture and the structure, recover the fixed-base natural frequencies and mode shapes, with relative frequency errors below 1.5% and high MAC values.

The main outcomes are twofold. First, the transmissibility $\mathbf{T}_{SF}^{f_S=0}$, and not only $\mathbf{H}_{SS}^{FB}$ as reported in previous publications, can be used to extract the fixed-base characteristics, with the practical advantage that no forces need to be applied directly to the structure. Second, $\mathbf{T}_{SF}^{f_S=0}$ is the appropriate quantity to use when several excitations act on the fixture and multiple fixture modes couple with the modes of the structure; although in the present example the direct transmissibility yields equivalent results owing to the simplicity of the test case, this equivalence does not hold in general.

ACKNOWLEDGMENTS

This work has been funded by the European Union – Next Generation EU, Missione 4 Componente 1, CUP D43C24001610008, PNRR DM 630/24 – Ciclo 40 – Innovazione.

Finanziato dall'Unione europea – Next Generation EU, Missione 4 Componente 1, CUP D43C24001610008, PNRR DM 630/24 – Ciclo 40 – Innovazione.

6. REFERENCES

[1] Randy L. Mayes and L. D. Bridgers. Extracting fixed base modal models from vibration tests on flexible tables. In *Proceedings of the 27th International Modal Analysis Conference (IMAC-XXVII)*, page 67, Orlando, FL, 2009.

[2] Kevin L. Napolitano. Fixing degrees of freedom of an aluminum beam by using accelerometers as references. In *Topics in Modal Analysis & Testing, Volume 8*, pages 53–60, 2020.

[3] Kevin L. Napolitano and Nathanael C. Yoder. Fixed base frf using boundary measurements as references: Analytical derivation. In *Topics in Modal Analysis I, Volume 5*, pages 299–308, 2012.

[4] Nathanael C. Yoder and Kevin L. Napolitano. Fixed base frf using boundary measurements as references: Experimental results. In *Topics in Modal Analysis I, Volume 5*, pages 309–317, 2012.

[5] James P. Winkel, James C. Akers, Vicente J. Suárez, Lucas D. Staab, and Kevin L. Napolitano. Modal survey of the mpcv orion european service module structural test article using a multi-axis shake table. In *Topics in Modal Analysis & Testing, Volume 9*, pages 347–358, 2019.

[6] Lucas D. Staab, James P. Winkel, Vicente J. Suárez, Trevor M. Jones, and Kevin L. Napolitano. Fixed base modal testing using the nasa grc mechanical vibration facility. In *Sensors and Instrumentation, Volume 5*, pages 143–161, 2016.

[7] K. Napolitano, M. Yang, D. Schick, and D. Kimpton. Modal survey testing using combined acoustic and conventional excitation techniques. In *IMAC XLIV*, 2026.

[8] Peter A. Kerrian, Kevin Napolitano, James Winkel, and Theodore J. Bartkowicz. Application of the fixed base correction method to extract flight modes from free-free modal survey data. In *Proceedings of the 34th Aerospace Testing Seminar*, Los Angeles, CA, 2025.

[9] F. Cavagna, G. Kosova, E. Di Lorenzo, and L. Dozio. Methodologies for fixed-base modal analysis derived from shaker table testing. In *International Conference on Noise and Vibration Engineering (ISMA)*, Leuven, Belgium, 2026.

[10] Nuno M.M. Maia, A.P.V. Urgueira, and R.A.B. Almeida. An overview of the transmissibility concept and its application to structural damage detection. In *Topics in Modal Analysis I, Volume 5*, pages 137–151, 2025.

Phase-Locked Loop-Based Vibration Testing: A Versatile Framework for Advanced Structural Testing

François Winand [1,2], **Gaetan Kerschen** [1], **Christophe Collette** [1,2], **Bruno Bernay** [3], **Nicolas Coudou** [4], **Francesco Mancini** [4], **Hugues Libotte** [5]

[1] *University of Liège, Allée de la Découverte 13, Bâtiment B52/3, 4000 Liège, Belgium, Email: francois.winand@uliege.be*
[2] *Université Libre de Bruxelles, Avenue Franklin Roosevelt 50, CP 177, 1050 Bruxelles, Belgium*

[3] *SONACA, SA, 6041 Gosselies, Belgium*

[4] *Von Karman Institute for Fluid Dynamics, 1640 Rhode-St-Genèse, Belgium*

[5] *Altéris Technologies, 4845 Jalhay, Belgium*

KEYWORDS

Phase-locked loop; Resonance tracking; Nonlinear Vibrations; Backbone;

ABSTRACT

Phase-locked loops (PLLs) are emerging as a powerful tool for vibration testing of mechanical and aerospace structures. By enforcing a prescribed phase relationship between excitation and response, PLLs continuously adapt the excitation frequency to maintain resonance, providing an automated and robust approach to resonance tracking.
PLLs are especially valuable when resonance conditions vary — either with vibration amplitude in nonlinear systems, or over time as structural properties evolve. In this contribution, the practical relevance of PLL-based testing is demonstrated through two applications on representative industrial structures. First, PLLs are applied to the characterization of nonlinear behavior in large-scale aircraft components, enabling the identification of backbone curves and the exploration of dynamical regimes that are unstable under open-loop excitation. Second, PLL-based frequency tracking is used to monitor natural frequency variations during ice accretion, opening perspectives for structural health monitoring and de-icing applications.
Overall, this work highlights PLLs as a versatile and practically relevant technique for nonlinear characterization and structural monitoring in aerospace testing.

1. INTRODUCTION

Modal identification and analysis are fundamental to experimental vibration testing. Under the assumption of linear behavior, mature and well-validated methods are available and widely used in industry. Linear dynamics offers two key conveniences: modal properties, natural frequencies, damping ratios, and mode shapes, are essentially invariant to vibration amplitude, and the superposition principle allows complex structural responses to be decomposed and reconstructed from individual modes. These properties underpin the model building and validation workflows used across the aerospace industry, where ground vibration testing has become a standard and mandatory step in the development of aircraft, spacecraft, and launch vehicles. [1-3]

Modern aerospace structures increasingly exhibit nonlinear dynamic behavior [4]. Driven by the adoption of lightweight composite materials and high-performance design, structures are more flexible and more susceptible to nonlinear effects: friction and clearance at joints and assembly interfaces, or from large deflections arising from material or geometric properties. In practice, these nonlinearities manifest as amplitude-dependent resonance frequencies, jump phenomena between coexisting vibration states, rich harmonic content, and nonlinear modal interactions. Taken together, they significantly complicate dynamic characterization: modal properties are no longer amplitude-invariant, superposition no longer holds, and standard linear testing procedures can yield incomplete or misleading results.

Within this context, phase-locked loops (PLLs) provide a now well-established solution for nonlinear vibration testing. The method belongs to the broader field of experimental continuation, which leverages feedback control to systematically explore the nonlinear dynamic behavior of structures [5]. The underlying principle is straightforward: the phase lag between the excitation force and the structural response is measured in real time, and a PI controller adjusts

the excitation frequency to maintain that phase lag at a prescribed value. This allows the full nonlinear frequency response to be traced including branches that are naturally unstable under open-loop swept-sine excitation, thereby eliminating the hysteresis and jump phenomena that classical sine sweeps cannot avoid (Fig.1). The method also naturally lends itself to backbone curve identification, continuously tracking the locus of resonance peaks as the excitation level is increased. Beyond nonlinear systems, the method naturally accommodates for tracking resonances of structures whose natural frequencies evolve over time, for example during ice formation on aeronautical surfaces or during fatigue testing as damages accumulate and cause the natural frequencies to drift. For these situations, a fixed-frequency excitation would progressively drift off resonance, whereas a PLL continuously adapts and maintains lock throughout the test.

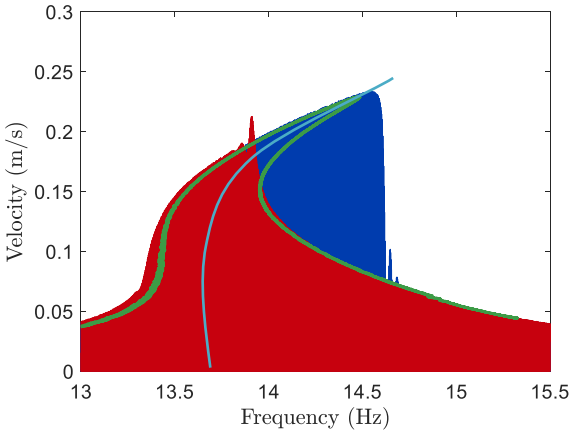


Figure 1: Example of a nonlinear frequency response. Blue and red curves show measurements obtained with classical up and down sine sweeps, respectively, illustrating the hysteresis and jump phenomena inherent to open-loop testing. The green curve is the full nonlinear frequency response measured using a phase-locked loop, including the unstable branch inaccessible to swept-sine excitation. The light blue curve represents the backbone curve, tracing the locus of resonance peaks with increasing vibration amplitude.

In this contribution, PLL-based testing is demonstrated through applications on representative industrial structures. Section 2 first presents the method. Section 3 then addresses nonlinear characterization of a large-scale aircraft component, and natural frequency tracking during ice accretion. Conclusions are drawn in Section 5.

2. PHASE-LOCKED LOOP TESTING

Over the last decades, phase-locked loops have emerged as a robust model-free technique for tracking resonance and measuring nonlinear responses. Initially introduced for MEMS fatigue testing [6], they have since then successfully been applied to a wide range of systems, from academic benchmark structures such as slender beams or plates to full scale engineering structures such as a turbine blade [7-11].

A typical PLL architecture is displayed in Fig. 2. The system connects an exciter — shaker or base excitation — to the structure under test, and associates three main building blocks: a phase detector, a numerically controlled signal generator, and a PI controller. Several options are available to compute the phase online and common approaches synchronous demodulation or adaptive filtering [12,13]. In this contribution, adaptive filtering is chosen as it performs an online Fourier decomposition of the measured signals, which is particularly useful when the structural response contains multiple harmonics.

Compared to classical modal testing, the excitation frequency is now continuously adjusted by the PI controller according to

$$\omega(t) = \omega_0 + K_p\left(\Phi_{ref} - \Phi(t)\right) + K_i \int \left(\Phi_{ref} - \Phi(\tau)\right) d\tau \ . \qquad (1)$$

Since the controller will adjust the frequency until Φ reaches Φ_{ref}, accurate online phase estimation is crucial to testing efficiency.

Using adaptive filtering, the measured response $x(t)$ (and similarly excitation $f(t)$) is reconstructed using a truncated Fourier series of N_h harmonics:

$$\hat{x}(t) = a_0 + \sum_{k=1}^{N_h}[a_k \sin(k\omega t) + b_k \cos(k\omega t)] \ . \qquad (2)$$

The Fourier coefficients are updated according to a least-mean-squares adaptation law:

$$\begin{aligned} \dot{a}_k &= 2\omega_{lp}\big(x(t) - \hat{x}(t)\big)\sin(k\omega t) \\ \dot{b}_k &= 2\omega_{lp}\big(x(t) - \hat{x}(t)\big)\cos(k\omega t) \end{aligned} \qquad (3)$$

where ω_{lp} is a user-defined cutoff frequency that controls the speed of coefficient estimation. The response and excitation phases, denoted by Φ_x and Φ_f, respectively, are extracted from the first-harmonic Fourier coefficients. The instantaneous phase lag is then computed as

$$\begin{aligned} \Phi_x &= atan2(b_{1,x}, a_{1,x}) \\ \Phi_x &= atan2(b_{1,x}, a_{1,x}) \\ \Phi &= \Phi_x - \Phi_f. \end{aligned} \qquad (4)$$

To measure the nonlinear frequency response, the reference phase is slowly swept across its full range while the controller adapts the excitation frequency accordingly. Throughout this test, the forcing level is kept constant. Each point of the resulting frequency response curve (green curve in Fig. 1) corresponds to a specific phase value, including branches that are naturally unstable under open-loop excitation.

In typical situations, resonance corresponds to a phase $-\frac{\pi}{2}$, as in linear systems. By keeping the system locked at this condition and by progressively increasing the forcing level (for example by increasing the supplied voltage U in Fig. 2), the backbone curve (light blue curve in Fig. 1) can be traced. This quantity provides a compact characterization of the nonlinear structure, directly

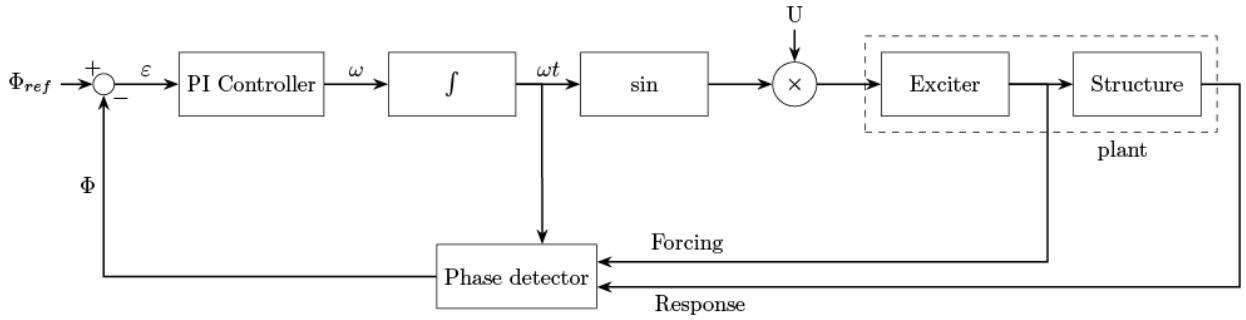


Figure 2: Typical PLL implementation

giving the amplitude-dependent resonance frequency. From the backbone curve, key quantities such as a nonlinear damping ratio and its evolution with vibration amplitude can also be extracted.

Practical implementation requires tuning of the PI gains and the adaptive filter cutoff frequency ω_{lp}. This step is critical to ensuring efficient and reliable testing: poorly tuned parameters can lead to slow convergence or loss of lock, significantly impacting test quality. Recently, systematic tuning rules and procedure have been proposed, enabling robust and repeatable testing without extensive trial-and-error calibration. A detailed discussion of these guidelines is beyond the scope of this work, and the interested reader is referred to [7,14] for further details.

3. APPLICATIONS AND RESULTS

In this section, the practical relevance of PLL-based testing is demonstrated on two industrial test cases. First, the nonlinear dynamic behavior of an F16 aircraft component is characterized using PLL testing. Second, resonance tracking during ice accretion on an aeronautical structure is illustrated, showcasing the ability of the method to follow time-varying natural frequencies in real time.

3.1. Nonlinear vibration testing of an F-16 aircraft

The following results and graphs were first reported in [15] and are reproduced here to illustrate the capabilities of PLL-based nonlinear vibration testing on an industrial-scale structure.

The test was conducted during a ground vibration testing (GVT) campaign organized by Siemens in September 2023 at the Air Force Campus Saffraanberg in Sint-Truiden, Belgium. The test article was a decommissioned F-16 aircraft, positioned on the ground with slightly flattened tires to approximate free boundary conditions (Fig. 3). Two dummy missiles were mounted on their respective wing tip launchers, which are recognized as potential sources of nonlinearity due to friction and clearance at the wing-to-payload interfaces.

Two electromagnetic shakers were positioned beneath the right and left wings near the wing tips. For the PLL-based nonlinear modal analysis, only the shaker under the right wing was used, providing single-point harmonic excitation in the vertical direction with a maximum force of approximately 200 N. A total of 60 accelerometers were distributed across the airframe, yielding 108 measured degrees of freedom. The sensor network and control scheme are illustrated in Fig. 4.

The impedance head mounted on the stinger provided simultaneous collocated measurement of the excitation force and structural acceleration at the driving point. These two signals were fed to a dSPACE MicroLabBox real-time controller operating at a sampling frequency of 10 kHz, with the control algorithm implemented in Matlab/Simulink. The phase lag was estimated online using adaptive filtering with a cutoff frequency of $\omega_{lp} = 5$Hz, and the excitation frequency was continuously adjusted by the PI controller to maintain the prescribed phase condition.



Figure 3: Set-up of the F-16 testing.

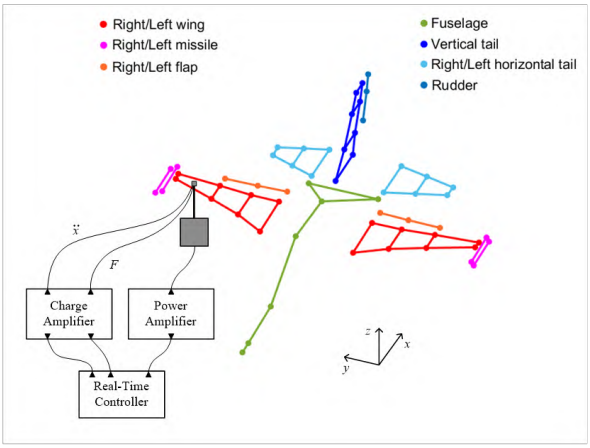


Figure 4: Sensor network and control architecture.

The second wing torsion mode, exhibiting a symmetric wing deflection at a linear natural frequency of 7.66 Hz, was selected for nonlinear modal analysis. The backbone curve was obtained by slowly sweeping the input voltage up and down at a rate of 0.005 V/s while the PLL maintained a fixed phase lag of 1 rad, which is the value corresponding to amplitude resonance for this mode. It is worth noting that amplitude resonance does not occur at phase quadrature ($\pi/2$ rad) here due to the influence of closely spaced modes, but the PLL readily accommodates this by simply targeting the appropriate reference phase. Fig. 5 presents the identified backbone curve alongside several nonlinear frequency response curves (NFRCs) obtained by stepped sine testing at forcing levels of F= 5, 18, 32, 40 and 48 N. The backbone closely tracks the peaks of the NFRCs across all forcing levels, confirming an effective identification. Each NFRC required approximately 2 minutes to acquire, while a single PLL backbone test was completed in around 4 minutes, providing equivalent nonlinear modal information in a single run rather than one test per forcing level and significantly reducing overall test duration.

The backbone curve reveals a clear softening behavior, with the resonance frequency decreasing from 7.66 Hz down to approximately 7.4 Hz as the vibration amplitude increases, which is typical of frictional systems. A discontinuity is further observed around 7.56 Hz, attributed to the onset of contact at the left wing tip missile launcher interface. Another useful output of backbone testing is the nonlinear damping ratio [10]. Using a power balance approach, it can be extracted at each amplitude level as

$$\xi_{NL} = \frac{P_1}{\omega_{NL}^3 a^2} \qquad (5)$$

where $P_1 = 0.5 F_1 V_1 \cos\Phi$is the active power provided by the excitation at the fundamental harmonic, F_1 and V_1 are the force and velocity magnitudes, and $\omega_{NL}$and $a$are the nonlinear modal frequency and amplitude extracted from the backbone. Fig. 6 shows the evolution of the damping ratio along the backbone curve: it approximately doubles with increasing vibration amplitude, which is again typical of frictional systems where energy dissipation grows with the relative sliding velocity at the interface.

Overall, these results demonstrate the practical relevance of PLL-based testing for full-scale industrial structures. Compared to classical stepped sine testing, the PLL provides equivalent nonlinear modal information in a single run, significantly reducing test duration. Beyond efficiency, the backbone curve provides direct physical insight: the softening behavior and discontinuity observed here identified friction and contact at the missile launcher interface as the source of nonlinearity, which is directly actionable for design improvement. Quantitatively, a 2% shift in resonance frequency was observed between low and high vibration amplitudes and the nonlinear damping ratio was found to double. This is non-negligible and particularly useful, for example for model validation, aeroelastic calculations, or fatigue life prediction. Further results from this campaign, including the analysis of additional modes and superharmonic resonances, are available in the original publication [15].

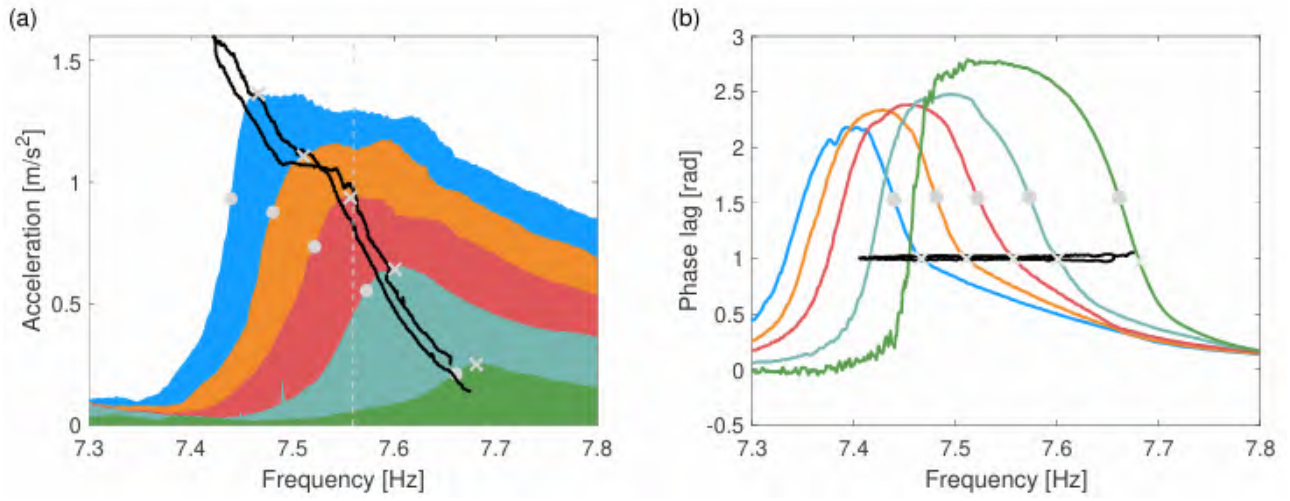


Figure 5: Backbone curves (black) of the second wing torsion mode identified by PLL and colored NFRCs: (a) Amplitude and (b) phase.

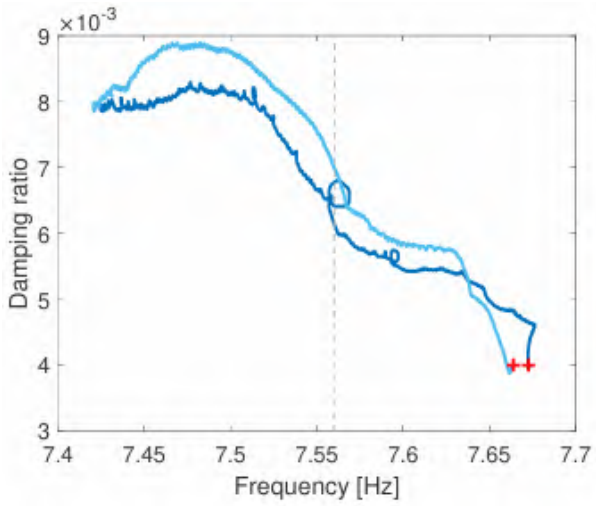


Figure 6: Nonlinear damping ratio extracted from the backbone. Red crosses indicates the linear case.

3.2. Natural frequency tracking during ice accretion

Ice accretion on aeronautical surfaces is a well-known safety concern, affecting both the aerodynamic performance and the structural integrity of aircraft. As ice accumulates, it modifies the mass and stiffness distribution of the structure, causing its natural frequencies to shift over time. This second application demonstrates that a PLL can track these frequency shifts in real time, maintaining resonance continuously throughout the icing process. Beyond structural monitoring, this capability is directly relevant to vibration-based de-icing: by always keeping the structure excited at resonance, the mechanical stress at the ice-substrate interface is maximized, ensuring optimal energy transfer for ice shedding regardless of how much ice has accumulated.

The experiment was conducted at the von Karman Institute (VKI) in Brussels as a proof-of-concept investigation, along with the companies Sonaca. The test article was a plate instrumented with two piezoelectric patches used as actuators for structural excitation and two piezoelectric sensors for response monitoring, under free-free boundary conditions (Fig. 7). The PLL was implemented on a dSPACE MicroLabBox operating at a sampling frequency of 20 kHz. Prior to the icing test, initial frequency sweeps were performed to identify the natural modes of the clean structure and select a suitable target mode for PLL tracking. A mode at approximately 1880 Hz was selected, as it exhibited a well-defined phase evolution in its vicinity, a necessary condition for reliable PLL operation. The sample was then placed inside the VKI freezer (Fig. 8) and water was sprayed onto the surface to simulate an icing event, while the PLL maintained continuous structural excitation at resonance throughout the deposition process.

For the PLL implementation, the phase lag between the drive signal and the response of sensor S_2 was used as the feedback signal, with a target phase of $-\pi/2$ corresponding to phase quadrature at the 1800 Hz mode. Controller gains were set to ensure fast phase control and precise tracking performance during the transient icing phase where the natural frequency evolves continuously over a short duration.

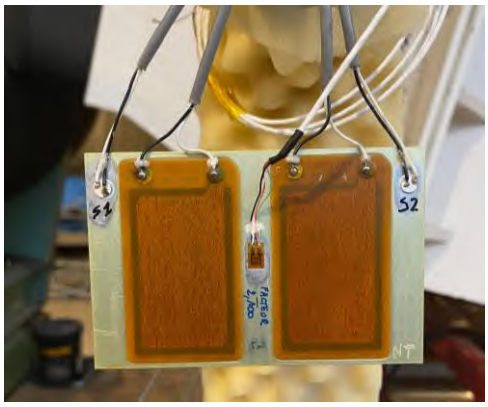


Figure 7: Sample plate actuated with piezoelectric patches, featuring sensors S_1 and S_2.



Figure 8: Experimental setup inside the VKI freezer after ice deposition.

The tracking performance of the PLL during the icing process is illustrated in Fig. 9. Starting from a stable resonance at approximately 1880 Hz, ice deposition was initiated and maintained for approximately 20 seconds by spraying water onto the surface of the plate. As ice accumulated, the natural frequency shifted continuously downward, and the PLL automatically adjusted the excitation frequency to follow it, maintaining phase quadrature throughout. By the end of the deposition process, the resonance frequency had decreased to approximately 1660 Hz, representing a shift of over 220 Hz. The effectiveness of the tracking is evidenced by the phase signal, which remained locked near $-\pi/2$ without significant deviation throughout the entire process. Furthermore, no loss of lock was observed despite the transient mechanical disturbances induced by the water spray, confirming the robustness of the PLL under realistic perturbations.

These results constitute a successful proof-of-concept for PLL-based resonance tracking during active ice accumulation. From a structural monitoring perspective, the continuous frequency measurement provides a real-time indicator of ice accumulation, offering a basis for load estimation or trigger-based de-icing systems. Looking further ahead, these results open direct perspectives for active vibration-based de-icing: by maintaining resonance throughout the icing process, the mechanical stress at the ice-substrate interface is always maximized regardless of the accumulated ice mass, ensuring optimal energy transfer for ice shedding. A dedicated de-icing campaign with higher excitation power would be a natural and promising next step to validate this concept on a representative aeronautical structure.

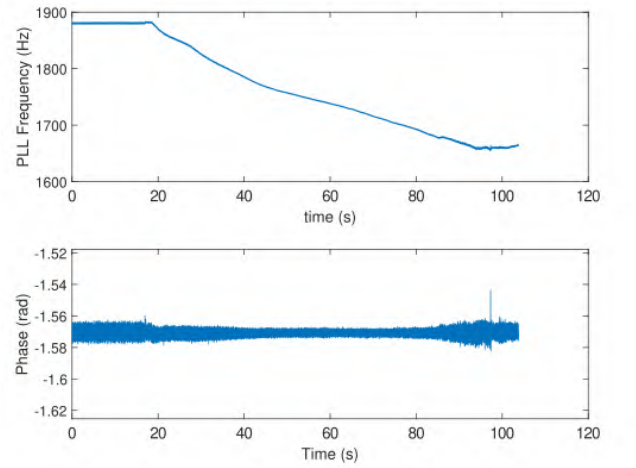


Figure 9: Resonance tracking during icing. Frequency shifts from 1880 Hz to 1660 Hz while maintaining phase quadrature.

4. CONCLUSION

This paper demonstrated the practical relevance of phase-locked loop testing through two applications on representative industrial structures. On a full-scale F-16 aircraft, PLL-based testing successfully characterized the nonlinear dynamic behavior of wing modes, identifying backbone curves, amplitude-dependent damping ratios, and the physical source of nonlinearity at the missile launcher interfaces. On an aeronautical plate subjected to active ice deposition, the PLL continuously tracked a frequency shift of over 220 Hz in real time, maintaining resonance throughout the process and opening direct perspectives for structural health monitoring and vibration-based de-icing.

Taken together, these results illustrate that PLL-based testing is no longer solely an academic tool. Its ability to handle both nonlinear structures and time-varying systems, combined with the availability of systematic implementation guidelines, makes it a mature and versatile technique ready for deployment in industrial testing campaigns. Beyond the applications demonstrated here, the ability of the PLL to maintain continuous resonance excitation over extended periods also makes it a natural candidate for fatigue testing, where sustained high-amplitude excitation at resonance is required. Future work will focus on extending these applications to other large-scale aerospace structures, further establishing PLL testing as a

standard complement to conventional ground vibration testing procedures.

5. REFERENCES

[1] Göge, D., Böswald, M., Füllekrug, U. & Lubrina, P. (2007). Ground Vibration Testing of Large Aircraft — State-of-the-Art and Future Perspectives. In *Proc. 25th International Modal Analysis Conference*, Orlando, FL.

[2] Kerschen, G., Peeters, M., Golinval, J.-C. & Stéphan, C. (2013). Nonlinear Modal Analysis of a Full-Scale Aircraft. *Journal of Aircraft*, 50(5), 1409–1419.

[3] Akers, J., Winkel, J., Chin, A., Parks, R., Chandler, D., Stasiunas, E. & Allen, M. (2024). Operational Modal Analysis of the Artemis I Dynamic Rollout Test and Wet Dress Rehearsal. In Proc. *International Modal Analysis Conference* (IMAC) XLII, pp. 91–112.

[4] Noël, J.-P. & Kerschen, G. (2017). Nonlinear System Identification in Structural Dynamics: 10 More Years of Progress. *Mechanical Systems and Signal Processing*, 83, 2–35.

[5] Raze, G., Abeloos, G. & Kerschen, G. (2025). Experimental Continuation in Nonlinear Dynamics: Recent Advances and Future Challenges. *Nonlinear Dynamics*, 113.

[6] Sun, X., Horowitz, R. & Komvopoulos, K. (2002). Stability and Resolution Analysis of a Phase-Locked Loop Natural Frequency Tracking System for MEMS Fatigue Testing. *Journal of Dynamic Systems, Measurement, and Control*, 124, 599–605.

[7] Denis, V., Jossic, M., Giraud-Audine, C. et al. (2018). Identification of Nonlinear Modes using Phase-Locked-Loop Experimental Continuation and Normal Form. *Mechanical Systems and Signal Processing*, 106, 430–452.

[8] Abeloos, G. (2022). Control-Based Methods for the Identification of Nonlinear Structures. *PhD Thesis*, Université de Liège, Liège, Belgium.

[9] Schwarz, S., Kohlmann, L., Hartung, A. et al. (2020). Validation of a Turbine Blade Component Test with Frictional Contacts by Phase-Locked-Loop and Force-Controlled Measurements. *Journal of Engineering for Gas Turbines and Power*, 142(5), 051011.

[10] Scheel, M., Peter, S., Leine, R.I. et al. (2018). A Phase Resonance Approach for Modal Testing of Structures with Nonlinear Dissipation. *Journal of Sound and Vibration*, 435, 56–73.

[11] Zhou, T. & Kerschen, G. (2024). Identification of Secondary Resonances of Nonlinear Systems using Phase-Locked Loop Testing. *Journal of Sound and Vibration*, 590, 118549.

[12] Haykin, S.S. (2014). *Adaptive Filter Theory*, 5th ed. Pearson, Upper Saddle River, NJ.

[13] Abeloos, G., Raze, G. & Kerschen, G. (2023). Stepped and Swept Control-Based Continuation using Adaptive Filtering. *Nonlinear Dynamics*, 111, 14841–14856.

[14] Hippold, P., Scheel, M., Renson, L. et al. (2024). Robust and Fast Backbone Tracking via Phase-Locked Loops. *Mechanical Systems and Signal Processing*, 220, 111670.

[15] Zhou, T., Raze, G., Kosova, G. et al. (2025). Experimental Nonlinear Modal Analysis of an F-16 Aircraft using Phase-Locked Loop Control. *Journal of Aircraft*. DOI: 10.2514/1.C038195.

ECSSMET
Braunschweig Germany 2026